Talanta 132 (2015) 1–7

Contents lists available at ScienceDirect

Talanta

journal homepage: www.elsevier.com/locate/talanta

Comparison of capillary electrophoresis–mass spectrometry and hydrophilic interaction chromatography–mass spectrometry for anionic metabolic profiling of urine

Miranda G.M. Kok [a,b,*], Govert W. Somsen [a,c], Gerhardus J. de Jong [a,b]

[a] Biomolecular Analysis, Department of Pharmaceutical Sciences, Utrecht University, P.O. Box 80082, 3508 TB Utrecht, The Netherlands
[b] Research group Analysis Techniques in Life Sciences, Avans Hogeschool, P.O. Box 90116, 4800 RA Breda, The Netherlands
[c] AIMSS Division of BioAnalytical Chemistry, Department of Chemistry and Pharmaceutical Sciences, VU University, De Boelelaan 1083, 1081 HV Amsterdam, The Netherlands

ARTICLE INFO

Article history:
Received 20 March 2014
Received in revised form
13 August 2014
Accepted 18 August 2014
Available online 27 August 2014

Keywords:
Hydrophilic interaction chromatography
Capillary electrophoresis
Mass spectrometry
Anionic metabolic profiling
Urine

ABSTRACT

In order to assess the utility of a recently developed capillary electrophoresis–mass spectrometry (CE–MS) method for the study of anionic metabolites in urine, a comparison was made with hydrophilic interaction chromatography–MS (HILIC–MS) using negative electrospray ionization. After optimization of the HILIC conditions, a gradient employing 10 mM ammonium acetate (pH 6.8) in acetonitrile–water (5 min 90% acetonitrile followed by 90%–50% acetonitrile in 10 min) was selected, providing baseline separation of five representative anionic test metabolites. Relative standard deviations (RSDs) for HILIC retention times and peak areas were below 0.2% and 7.7%, respectively, and detection limits were in the range 0.04–2.21 μM. Metabolites in rat urine could also be analysed in a reproducible way with retention time and peak area RSDs below 0.6% and 13.6%, respectively. The CE–MS and HILIC–MS methods were compared in terms of reproducibility, sensitivity, selectivity and coverage of the anionic urinary metabolome. In general, peak area RSDs were similar whereas HILIC–MS yielded better retention-time repeatability and up to 80 times lower detection limits (expressed in injected concentration) for test metabolites as compared to CE–MS. Rat urine analysis by HILIC–MS provided detection of 1360 molecular features compared to 347 molecular features revealed with CE–MS. Of these, a number of 144 molecular features were found with both HILIC–MS and CE–MS, which showed on average 10 times higher peak areas in HILIC–MS. The HILIC retention and CE migration times of the common features were clearly not correlated. The HILIC and CE behavior of the test metabolites and 16 putatively identified common features were evaluated involving their physicochemical properties, indicating a markedly different separation selectivity, and thus significant degree of orthogonality of HILIC and CE.
© 2014 Elsevier B.V. All rights reserved.

1. Introduction

Elucidation and understanding of biochemical pathways require accurate and specific determination of metabolite levels in biofluids and tissues. Metabolites may exhibit very diverse physicochemical properties and can be present in a wide range of concentrations [1]. Capillary electrophoresis (CE) coupled to mass spectrometry (MS) is particularly suitable for the direct profiling of highly polar and charged metabolites as predominantly present in urine. CE can provide efficient separation of metabolites based on their charge-to-size ratios without the need for analyte derivatization [2]. Recently, we have developed a CE–MS method for the profiling of anionic metabolites applying triethylamine in the background electrolyte (BGE) and sheath liquid [3]. This new method provided significantly higher signal intensities as compared to other CE–MS methods in negative ionization mode. Urine samples from antibiotic-treated rats and control rats could be distinguished, and potential biomarkers were revealed [4]. Having this new method available, the question arises to what extent CE–MS can provide complementary information on the anionic metabolome with respect to more common liquid chromatographic (LC) techniques for metabolic profiling.

LC–MS can provide information on the quantity of low-abundant metabolites without the need for analyte derivatization. Common reversed-phase (RP) LC, however, is less suited for the analysis of highly polar compounds, and for small charged

Abbreviations: BGE, background electrolyte; CE:, capillary electrophoresis; ESI:, electrospray ionization; GC:, gas chromatography; HILIC:, hydrophilic interaction chromatography; LC, liquid chromatography; LOD, limit of detection; MS, mass spectrometry; RP:, reversed-phase; RSD, relative standard deviation; TOF, time-of-flight

* Corresponding author.Tel.: +31302537307; fax: +31302536655.
E-mail address: M.G.M.Kok@uu.nl (M.G.M. Kok).

http://dx.doi.org/10.1016/j.talanta.2014.08.047
0039-9140/© 2014 Elsevier B.V. All rights reserved.

compounds, ion-pairing agents are frequently used to increase their retention [5]. Unfortunately, ion-pairing agents can cause substantial ionization suppression of compounds in MS and source contamination. Hydrophilic interaction chromatography (HILIC) allows profiling of polar compounds, providing complementary information to RPLC, as has been demonstrated by numerous metabolomics studies [6–19]. HILIC utilizes a highly organic mobile phase (often acetonitrile) containing water in combination with a polar stationary phase. Analyte separation is based on partitioning between the mobile phase and a layer of adsorbed water molecules on the stationary phase as well as electrostatic interactions with polar groups on the stationary phase [20–22]. Hence, in order to appreciate the utility of CE–MS for profiling of anionic metabolites, comparison with HILIC–MS seems indicated.

So far, only a few studies have been conducted in which both CE–MS and HILIC–MS were used for comparative and comprehensive profiling [17,23–26]. Sugimoto *et al.* applied HILIC–MS and CE–MS to analyse edamame and Japanese sake [23,24]. However, as HILIC–MS was used to profile sugars only, no conclusions could be drawn on the complementarity of HILIC–MS and CE–MS for untargeted metabolite profiling. Büscher and colleagues extensively compared CE, LC and gas chromatography (GC) methodologies, all in combination with MS [25]. Metabolites were analysed with GC–MS after two different derivatization procedures. Ion-pair RPLC and HILIC were used as LC separation modes and two CE–MS methods were employed for the analysis of cationic and anionic metabolites. A mixture of 91 test metabolites representing central carbon and energy metabolism was used for comparison. Of these test metabolites, 33 compounds could be detected by all three platforms. CE and LC showed the greatest overlap in metabolite coverage (26 compounds) and each analytical technique was capable to measure two compounds which could not be detected with the two other methodologies. The CE–MS, LC–MS and GC–MS methodologies were considered in general, that is, GC, HILIC, ion-pair RPLC and cationic and anionic CE methods were not individually compared. Moreover, the evaluation of the complementarity of the techniques for metabolic profiling was limited since it was based on a confined number of test metabolites in standard solutions [25]. Ibáñez and coworkers studied the effect of dietary polyphenols on the proliferation of colon cancer cells with CE–MS, HILIC–MS and RPLC–MS [26]. Saric *et al.* used the same techniques to analyse the metabolome of the *Fasciola hepatica* worm [17]. In both studies, a small part of the detected metabolite features was identified. There was no or a limited overlap of identified metabolites detected by CE–MS, HILIC–MS and RPLC–MS, indicating the potential complementarity of the analytical techniques [17,26]. It should be noted, however, that Ibáñez *et al.* as well as Saric *et al.* employed positive electrospray ionization (ESI) for HILIC–MS and/or CE–MS, and thus could only compare the methodologies based on detected cationogenic compounds. Still, a significant number of urinary metabolites is acidic and can only be detected using negative ESI. Therefore, in order to achieve comprehensive profiling and to evaluate the complementarity of HILIC–MS and CE–MS, particular attention should also be paid to anionic metabolites.

In the present study, we compared a previously optimized CE–MS method with HILIC–MS for anionic metabolic profiling of urine samples. We first optimized a HILIC–MS method by carrying out infusion experiments to determine and evaluate the effect of different HILIC mobile phase compositions on the signal intensities of representative anionic test metabolites. An efficient gradient HILIC–MS method applying an acetonitrile–water mobile phase containing ammonium acetate was developed and the performance was assessed in terms of sensitivity, linearity and repeatabilities of peak area and retention time. Furthermore, HILIC–MS was applied to urine analysis and the number of detected molecular features of urine components was determined. Outcomes were extensively compared with results obtained with the earlier developed CE–MS method for anionic urinary profiling [3,4]. Numbers of common and unique urinary molecular features were considered and MS responses of common features were compared. Moreover, differences in separation selectivity of CE–MS and HILIC–MS were assessed by comparing migration and retention times of test metabolites as well as putatively identified common features.

2. Materials and methods

2.1. Chemicals

Acetic acid, ammonium formate, ammonium hydroxide (25% solution), acetonitrile, formic acid, methanol, glutaric acid, hippuric acid, DL-pyroglutamic acid and uridine were obtained from Fluka (Steinheim, Germany). Sodium hydroxide and L-proline were purchased from Sigma Aldrich (Steinheim, Germany). Triethylamine was from Fisher Scientific (Loughborough, UK), piperidine was from Alfa Aesar (Karlsruhe, Germany) and ammonium acetate was supplied by Merck (Darmstadt, Germany). Water was deionized and purified with a Milli-Q purification system (Millipore, Bedford, USA) prior to use.

2.2. Test mixture and rat urine sample

Stock solutions (50 mM) of the metabolites glutaric acid, hippuric acid, proline, pyroglutamic acid and uridine were prepared in deionized water. Stock solutions of the metabolites were mixed and diluted to obtain a test mixture in which each metabolite was present at the appropriate concentration (0.25–80 μM). Test metabolite mixtures were prepared in water–acetonitrile (1:4, v/v) and water for HILIC–MS and CE–MS analyses, respectively.

A mixture of aliquots of rat urine samples provided by AstraZeneca (Department of Drug Metabolism and Pharmacokinetics, Macclesfield, UK) [27] was prepared and stored at −80 °C. Prior to analysis, the urine sample was thawed. For HILIC–MS, urine was diluted with acetonitrile in a proportion of 1:4 (v/v) and centrifuged at 10,000 rcf for 10 min in order to attain proper metabolite peak shapes (see Section 3.1). When analysed with CE–MS, dilution of urine with BGE in a proportion of 1:1 (v/v) was sufficient to achieve good CE performance [3,4].

2.3. HILIC–MS

All samples were analysed on an LC system (Shimadzu, Kyoto, Japan) coupled online via an electrospray interface to a time-of-flight (TOF) mass spectrometer (micrOTOF, Bruker Daltonics, Bremen, Germany) using a Waters XBridge™ Amide column (3.5 μm, 3.0 × 100 mm).

In the optimized HILIC–MS method, the test metabolite mixture and urine sample (5 μL; approximately 1.5% of column volume) were injected and analysed under gradient elution with mixing solvent A (10 mM ammonium acetate in water–acetonitrile (1:1, v/v)) and solvent B (10 mM ammonium acetate in water–acetonitrile (1:9, v/v)) in varying ratios at an overall flow rate of 0.5 mL/min. The gradient scheme was as follows: 0.0–5.0 min, 100% B; 5.0–15.0 min, from 100% B to 100% A; 15.0–20.0 min, 100% A; 20.1–30.0 min, 100% B. Column temperature was 45 °C during separation.

Optimal signal intensities for test metabolites were obtained using the following interface conditions: dry gas temperature, 180 °C; dry gas flow, 4 L/min, nebulizer pressure, 50 psi; ESI voltage, 2 kV. Data were acquired in negative ionization mode in the mass range *m/z* 50–800 with a repetition rate of 1 Hz.

Recorded mass spectra were internally calibrated using sodium acetate clusters which were detected within every run.

2.4. CE–MS

The CE–MS experiments were performed and described before [3,4]. Briefly, CE–MS was carried out on a Beckman P/ACE MDQ instrument (Beckman Coulter, Fullerton, USA) coupled to a micrOTOF mass spectrometer using a sheath-liquid electrospray interface from Agilent Technologies (Waldbronn, Germany). A BGE of 25 mM triethylamine (pH 11.7) and a sheath liquid of 5 mM triethylamine in water–methanol (1:1, v/v) were used. Fused-silica capillaries (Polymicro Technologies, Phoenix, USA) had a total length of 100 cm and an internal diameter of 50 μm. Hydrodynamic injections were performed using a pressure of 0.5 psi for 30 s (16 nL; approximately 0.8% of capillary volume). The separation voltage was 30 kV and the capillary temperature was set at 20 °C. The sheath liquid was delivered with a flow rate of 5 μL/min by a 10 mL gas-tight syringe of Hamilton (Reno, USA) using a syringe pump (KD Scientific, Holliston, USA). The following optimized CE–MS interface conditions were applied: dry gas temperature, 180 °C; dry gas flow, 4 L/min; nebulizer pressure, 10 psi; ESI voltage, 4 kV. The negative ionization mode was used and data were acquired in the mass range 50–800 *m/z* with a rate of 1 Hz. Sodium formate clusters were used for internal calibration.

2.5. Data analysis

Data were processed using the DataAnalysis software of Bruker Daltonics. Using the 'Find Molecular Features' function of this software, the number of molecular features obtained during urine analysis was determined. A molecular feature was defined as the unique combination of an *m/z* value and retention time (HILIC–MS) or migration time (CE–MS), present in ten consecutive MS spectra with a signal-to-noise ratio of at least three. Peak areas and peak heights of metabolites were assessed using extracted-ion chromatograms (HILIC–MS) or electropherograms (CE–MS).

3. Results and discussion

3.1. HILIC–MS method

For the optimization of the HILIC–MS method for anionic metabolic profiling, the composition of the mobile phase was studied. Ammonium acetate, sometimes in combination with acetic or formic acid, is often used as mobile phase additive in HILIC–MS for urinary metabolic profiling studies [28]. In a previous CE–MS study, we found triethylamine and piperidine to be more favourable salts with respect to attainable signal intensities for anionic metabolites [3]. Infusion experiments were performed to study the influence of several mobile phase additives on signal intensities of the test metabolites glutaric acid, hippuric acid, proline, pyroglutamic acid and uridine. These metabolites represent the diverse compound classes present in urine. The metabolites (100 μM each) were dissolved in acetonitrile–water (1:1, v/v) with and without 10 mM ammonium acetate, 10 mM ammonium formate, 0.1% formic acid, 0.1% triethylamine or 0.1% piperidine. Using ammonium formate and formic acid, test metabolite signals were lower as obtained with ammonium acetate. With triethylamine, the signal intensities of the tested metabolites were on average 6.5 times higher compared to ammonium acetate. Similar results were obtained using piperidine with 6.3 times higher signals. However, the use of triethylamine and piperidine as mobile phase additives in HILIC–MS resulted in reduced retention times (too fast elution) and broad and asymmetric peaks. Overall this led to reduced plate numbers and poor metabolite resolution. Furthermore, proline and pyroglutamic acid could not be detected. Therefore, ammonium acetate was selected and the influence of its concentration (0–10 mM) in a mobile phase of acetonitrile–water was further evaluated. The separation, peak shapes and signal intensities of the five test metabolites obtained with HILIC–MS were taken into consideration. A concentration of 10 mM ammonium acetate in the eluent yielded more symmetric and narrow peaks as compared to 0 and 5 mM ammonium acetate. This was especially apparent for the compounds uridine and hippuric acid of which the peak widths were about 40% smaller at 10 mM ammonium acetate. Furthermore, only at 10 mM ammonium acetate, baseline separation of proline and pyroglutamic acid was achieved. Still, the increase of ammonium acetate concentration from 0 to 10 mM resulted in up to 59% lower signal intensities, except for proline which showed a remarkable signal increase of 67%. Adjusting the pH of the mobile phase to 9.0 with ammonium hydroxide did not affect the separation of the test metabolites, but decreased their signal intensities up to 60% as compared to pH 6.8 (not adjusted) due to ion suppression.

The acetonitrile–water gradient of the mobile phase containing 10 mM ammonium acetate (pH 6.8) was optimized to obtain a large separation window without deteriorating the peak shape and detection limits (LODs) of metabolites. A high percentage of acetonitrile in the mobile phase at the start of the analysis is desirable in order to maximize the separation of metabolites. Therefore, the start of the gradient was set at 90% acetonitrile and held at 90% for 5 min to enhance the separation of metabolites eluting in the beginning of the chromatogram. Then, the percentage acetonitrile was gradually decreased to 50% and different slopes of the gradient were tested to maximize peak separation and minimize the peak widths. A gradient of 4% acetonitrile per min appeared to be optimum by providing the best resolution of metabolite peaks within a relatively short analysis time. The mobile phase was held at 50% acetonitrile for another 5 min in order to elute all compounds from the column. Thereafter, the percentage acetonitrile in the mobile phase was switched back to 90% and hold for 10 min to allow reequilibration of the HILIC–MS system.

Because of the high percentage of acetonitrile at the start of the gradient, the sample injection solvent had to contain a large amount of acetonitrile to prevent peak splitting and to achieve narrow and symmetric peaks. The maximum allowable acetonitrile percentage in the sample is, however, limited by the solubility of polar and charged compounds. More than 80% acetonitrile in the sample solvent resulted in precipitation of metabolites. Moreover, dilution of the sample with acetonitrile will reduce the concentration sensitivity. Using a sample injection volume of 5 μL containing 80% acetonitrile in combination with a gradient starting at 90% acetonitrile resulted in narrow and symmetric peaks. Injection volumes of 7.5 μL and larger, or a gradient starting at 95% acetonitrile, gave deformed and splitted peaks.

The optimized HILIC-MS method comprised gradient elution employing 10 mM ammonium acetate (pH 6.8) in acetonitrile–water, an injection solvent containing 80% acetonitrile and an injection volume of 5 μL.

3.2. Comparison of CE–MS and HILIC–MS

3.2.1. Reproducibility, sensitivity and metabolite coverage

Using the optimized HILIC–MS method, the test metabolites were baseline separated with retention times ranging from 3.1 to 13.5 min (Fig. 1). The retention times were highly reproducible for all metabolites with relative standard deviations (RSDs) below 0.2%. Also peak area repeatability was acceptable with RSD values below 8% for ten consecutive measurements (Table 1). Mixtures of

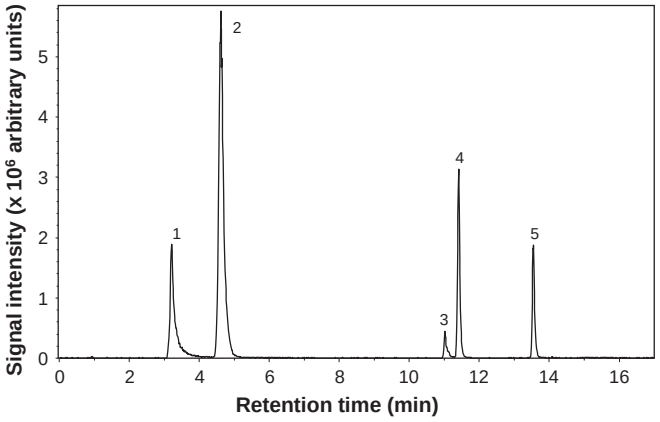


Fig. 1. Multiple extracted-ion chromatogram obtained during HILIC–MS of a test metabolite mixture (50 μM each). Metabolites: 1. uridine (*m/z* 243.06); 2. hippuric acid (*m/z* 178.05); 3. proline (*m/z* 114.06); 4. pyroglutamic acid (*m/z* 128.04); 5. glutaric acid (*m/z* 131.04). Gradient elution with (a) 10 mM ammonium acetate in water–acetonitrile (1:1, v/v) and (b) 10 mM ammonium acetate in water–acetonitrile (1:9, v/v): 0–5 min, 100% b; 5–15 min, from 100% b to 100% a; 15–20 min, 100% a. See Section 2 for other experimental conditions.

Table 1
Retention/migration time and peak area repeatability (RSD (%), n = 10) for five test metabolites analysed using HILIC–MS and CE–MS.

Compound	Retention/migration time		Peak area	
	HILIC–MS	*CE–MS*	*HILIC–MS*	*CE–MS*
Glutaric acid	0.03	0.33	7.70	10.83
Hippuric acid	0.13	0.38	5.26	6.57
Proline	0.03	0.34	2.42	6.08
Pyroglutamic acid	0.04	0.42	6.14	7.25
Uridine	0.16	0.36	4.56	3.97

the five test metabolites in the concentration range 0.25–80 μM were analysed to determine the linearity of the method. For all compounds, a good linearity was observed with coefficients of determination (R^2) above 0.99. LODs (signal-to-noise ratio of 3) for the test metabolites were in the range 0.04–2.21 μM (Table 2).

The anionic test metabolites have previously been analysed with an optimized CE–MS method employing a triethylamine-containing BGE and sheath liquid [3]. In CE–MS, all metabolites were baseline separated with migration times from 7.0 to 17.5 min. RSDs for elution/migration time of the test compounds were lower with HILIC–MS, but repeatability for peak areas was similar for most metabolites (Table 1). Using CE–MS, detection limits for the five test metabolites ranged from 0.92 to 9.08 μM [3]. Thus, the LODs obtained with HILIC–MS were up to 80 times lower for these compounds (Table 2). Most likely, this can be explained by the larger sample injection volume employed in HILIC (5 μL) as compared to CE (16 nL). The injection volumes relative to capillary and column volume are approximately 0.8% and 1.5%, respectively. Notably, the sensitivity difference is not as severe as supposed from the difference in injection volume (factor 300) only. Furthermore, the ionization efficiencies of the test metabolites may be relatively higher under the applied CE–MS conditions. The observed difference in signal-to-noise ratios between HILIC–MS and CE–MS was not the same in magnitude for each test metabolite. Noise levels varied extensively throughout the HILIC chromatograms and CE electropherograms. Furthermore, ionization conditions in HILIC–MS vary due to the gradient elution leading to different ionization efficiencies.

In order to examine the applicability of the optimized HILIC–MS and CE–MS method for the analysis of biological samples, a rat urine sample was repetitively analysed. Notably, in CE–MS urine samples were diluted with BGE in a proportion of 1:1 (v/v), whereas for HILIC–MS a dilution of 1:4 (v/v) with acetonitrile was required for proper HILIC separation. Based on the analysis of rat urine, the CE–MS and the HILIC–MS method were compared in terms of number of observed molecular features, analyte elution/migration order and repeatability. The base-peak chromatograms and electropherograms obtained with the optimum HILIC–MS and CE–MS method showed large numbers of peaks, which were widely spread over the elution/migration time window (Figs. 2A and C). Overall, the absolute signal intensities were higher with HILIC–MS. HILIC–MS provided almost four times more molecular features than CE–MS (1360 vs. 347 features). Five molecular features, which were detected with both systems (same *m/z* value) and which were spread over the elution/migration window (Figs. 2B and 2D), were selected to assess repeatability. Ten consecutive measurements of the urine sample showed that the elution time repeatabilities of these urine metabolites were better for HILIC–MS (0.17-0.55%) with respect to CE–MS (5.93–11.8%), whereas peak area repeatabilities were similar (Table 3). As demonstrated before [4], CE–MS migration time repeatability for the rat urine components could be reduced to $< 0.4\%$ by applying a proper alignment procedure.

Table 2
Limits of detection (μM) for five test metabolites applying HILIC–MS and CE–MS.

Compound	HILIC–MS	CE–MS[a]	Factor difference
Glutaric acid	0.75	9.08	12.1
Hippuric acid	0.05	0.92	18.4
Proline	2.21	3.99	1.8
Pyroglutamic acid	0.04	3.21	80.3
Uridine	0.06	1.61	26.8

Test metabolites were dissolved in acetonitrile-water (4:1, v/v) and water using HILIC–MS and CE–MS, respectively

[a] Previously reported by Kok *et al.* [3].

Taken all molecular features into account, proportionately more molecular features with *m/z* values below 200 were detected with CE–MS, whereas the relative number of features with *m/z* values above 400 was higher in HILIC–MS (Fig. 3). To compare the two analytical methodologies more extensively, molecular features which were detected with both CE–MS and HILIC–MS (common molecular features) were determined. Molecular features were considered to be common if the difference of the respective *m/z* values was less than 10 mDa. An *m/z* value only detected with one of the two methods was regarded as a unique molecular feature for the respective method. Based on these criteria, HILIC–MS and CE–MS revealed 1216 and 203 unique features, respectively, and 144 common molecular features were found with *m/z* values ranging from 108 to 503 of which most had *m/z* values below 300. There were 28 isobaric compounds among the 144 common molecular features. These features could not be assigned unambiguously based on mass only and were therefore dismissed during further evaluation. The ratios of peak areas and peak heights of the remaining 116 common molecular features were calculated to compare the signal intensities obtained with HILIC–MS and CE–MS (Fig. 4). The ratios of peak area and height ranged from 0.20–63.9 and 0.59–130.5, and were on average 10.1 and 16.3, respectively. For 11 compounds, peak abundances in CE–MS were even higher than obtained with HILIC–MS. The large variance in intensity ratio between HILIC–MS and CE–MS might be caused by varying degrees of ionization suppression. As the separation principles of HILIC and CE are so manifestly different, the co-migration of urinary compounds and thus ionization conditions may vary strongly along the elution/migration window.

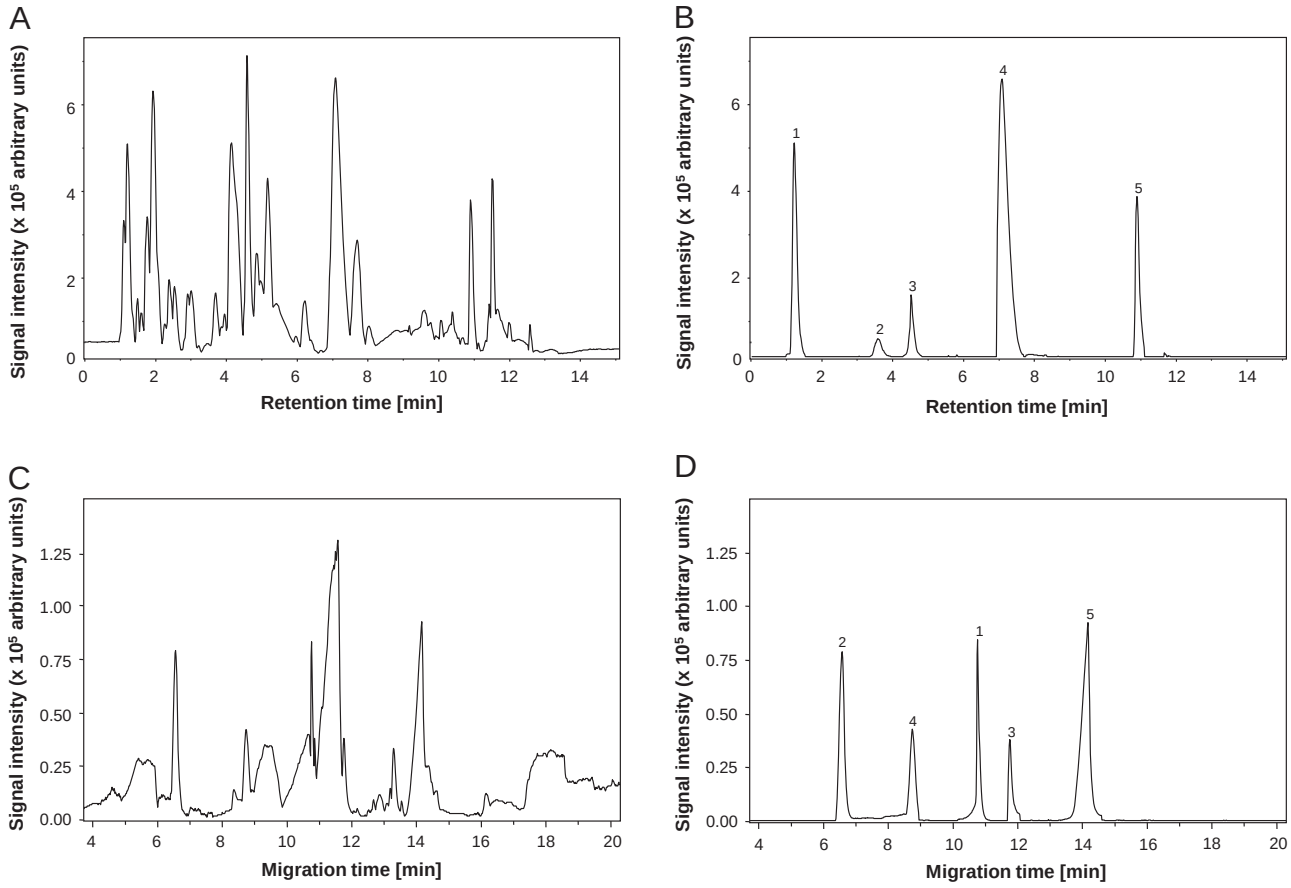


Fig. 2. Base-peak and multiple extracted-ion chromatograms and electropherograms obtained when analysing a rat urine sample by HILIC–MS (A, B) and CE–MS (C, D). Peaks: 1. *m/z* 212.00; 2. *m/z* 112.05; 3. *m/z* 124.99; 4. *m/z* 243.06; 5. *m/z* 167.02. HILIC–MS conditions: gradient elution with (a) 10 mM ammonium acetate in water–acetonitrile (1:1, v/v) and (b) 10 mM ammonium acetate in water–acetonitrile (1:9, v/v): 0–5 min, 100% b; 5–15 min, from 100% b to 100% a; 15–20 min, 100% a. CE–MS conditions: BGE, 25 mM triethylamine (pH 11.7); sheath liquid, 5 mM triethylamine in water–methanol (1:1, v/v). See Section 2 for other experimental conditions.

Table 3
Retention/migration time and peak area repeatability (RSD (%), n=10) for five metabolites in rat urine detected with HILIC–MS and CE–MS.

m/z value	Retention/migration time		Peak area	
	HILIC–MS	*CE–MS*[a]	*HILIC–MS*	*CE–MS*[a]
212.00	0.17	10.8	7.89	13.3
112.05	0.29	5.93	11.6	8.58
124.99	0.55	10.8	13.6	13.2
243.06	0.39	8.09	10.5	13.5
167.02	0.23	11.8	7.68	7.85

[a] Previously reported by Kok *et al.* [4].

3.2.2. Separation selectivity

In order to appreciate the observed differences in selectivity between CE–MS and HILIC–MS, the elution and migration behavior of the test metabolites and common features in rat urine were evaluated, involving – when possible – the molecular structure of the compounds. The observed elution order of the test metabolites in HILIC roughly follows compound polarity (Fig. 1). Uridine is the only test metabolite that is uncharged at the applied pH of 6.8, which may explain its fast elution. The aromatic ring of hippuric acid reduces its overall polarity leading to modest retention in HILIC. Proline and pyroglutamic acid have a rather polar structure providing significant retention. The dicarboxylic glutaric acid is highly polar and strongly retained in HILIC. In CE–MS, proline migrated first, followed by successively uridine, hippuric acid, pyroglutamic acid and glutaric acid [3], exhibiting a different order than observed during HILIC–MS. The CE migration order largely follows the overall negative charge of the compounds at pH 11.7. The amino group of proline is partly protonated, whereas glutaric acid is doubly charged at pH 11.7.

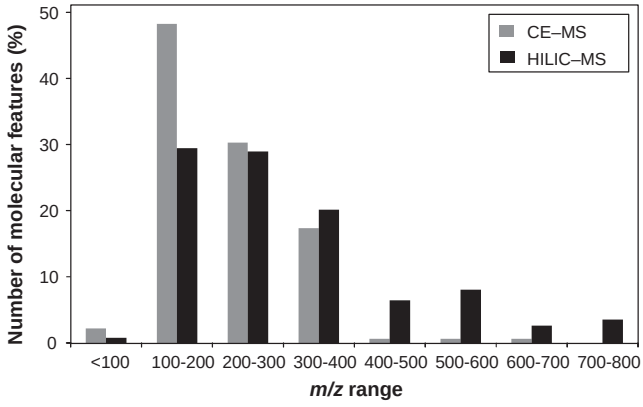


Fig. 3. Distribution of *m/z* values of molecular features detected during CE–MS and HILIC–MS of a rat urine sample. The relative number of features (%) in the various *m/z* ranges is depicted taking the total number of molecular features detected with the respective analytical method as 100%.

The distinctive separation selectivity of CE and HILIC was strongly underlined by plotting the CE–MS migration times and the HILIC–MS retention times of the 116 common features observed during the analysis of rat urine (Fig. 5). Compounds are

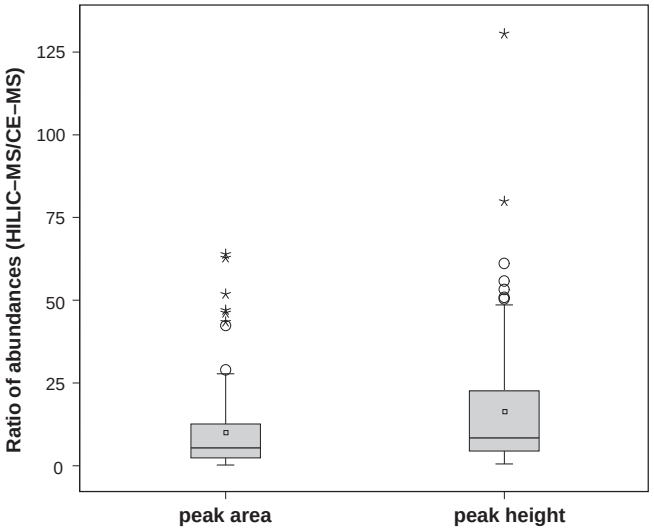


Fig. 4. Box plot of the ratio of peak areas and peak heights of 116 common molecular features in a rat urine sample detected with both HILIC–MS and CE–MS. The 25th percentile, median and 75th percentile are represented by the boxes. The whiskers indicate the 5th and 95th percentile and the squares represent the average ratio of the peak areas and peak heights, respectively. Circles indicate ratios higher than 95% of the observed ratios and asterisks symbolize outliers.

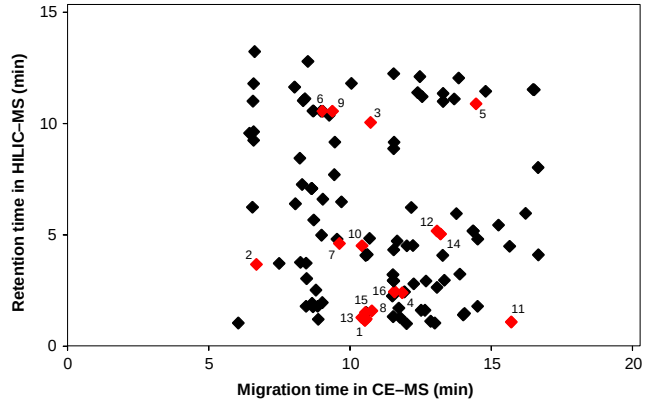


Fig. 5. Relation between migration times and retention times of common molecular features obtained during CE–MS and HILIC–MS of a rat urine sample. The red diamonds with numbers represent metabolites which were putatively identified based on accurate mass. The identities together with the corresponding numbers are given in Table 4.

scattered over the entire plot, indicating a clear lack of correlation between CE migration and HILIC retention. To explore the observed differences in separation selectivity of CE and HILIC in more molecular detail, the *m/z* values of the common features were searched against metabolomics databases [29–31]. This way, 16 molecular features could be assigned based on accurate mass. These features included typical urinary compounds, such as allantoin, glucuronic acid, hippuric acid, indoxyl sulfate, phenol and uric acid (Table 4 and red diamonds in Fig. 5). As can be expected, all identified compounds, except creatinine, have an acidic group allowing their negative ionization.

The CE and HILIC migration and retention data of the identified metabolites in Table 4 confirm the different selectivity of the methods. For example, the sulfonic acids cresol sulfate, benzenediol sulfate, methoxycatechol sulfate and indoxyl sulfate were hardly retained and not separated in HILIC–MS, whereas in CE–MS these compounds showed considerable migration times. Moreover, benzenediol sulfate could be separated from the other sulfonic acids in CE, most probably because it carries relatively more negative charge due to deprotonation of its phenol group. In

Table 4
Retention (RT) and migration times (MT) of putatively identified urinary metabolites detected with both HILIC–MS and CE–MS.

#	*m/z* Value	RT ($_{min}$) HILIC–MS	MT ($_{min}$) CE–MS	Putative identity
1	93.03	1.14	10.67	Phenol
2	112.05	3.59	6.51	Creatinine
3	124.01	10.05	10.73	Taurine
4	157.09	2.39	11.86	Allantoin
5	167.02	10.89	14.47	Uric acid
6	168.08	10.55	8.99	Methylhistidine
7	178.05	4.61	9.64	Hippuric acid
8	187.01	1.48	10.78	Cresol sulfate
9	187.07	10.55	9.38	Glycylhydroxyproline
10	188.03	4.50	10.43	Kynurenic acid
11	188.99	1.08	15.72	Benzenediol sulfate
12	193.05	5.17	13.09	Glucuronic acid
13	203.00	1.20	10.67	Methoxycatechol sulfate
14	204.03	5.03	13.21	Xanthurenic acid
15	212.00	1.23	10.70	Indoxyl sulfate
16	276.14	2.43	11.58	Methionine–lysine

contrast, taurine, also comprising a sulfonic acid group, could only be separated from the other sulfonic acids in HILIC. In CE–MS, uric acid (diprotic) and its oxidation product allantoin (monoprotic) were separated based on their charge-to-size ratios. For these compounds, a large difference in retention times was observed in HILIC–MS, although the molecular structures of allantoin and uric acid are highly similar. Another example is the separation of compounds having a carboxylic group. Methylhistidine, hippuric acid, glycylhydroxyproline, kynurenic acid, glucuronic acid, xanthurenic acid and methionine–lysine had retention times between 2.43 and 10.55 min, and migration times ranged from 8.99 to 13.21 min. The elution order of these metabolites in the CE system differed completely from their elution order in HILIC. Furthermore, despite the apparent larger separation window in the optimized HILIC method, methylhistidine and glycylhydroxyproline coeluted, whereas separation of these compounds was achieved in CE.

4. Concluding remarks

In order to assess the added value of CE–MS for anionic metabolic profiling of urine, a previously developed CE–MS method was compared to an optimized HILIC–MS method using ammonium acetate as mobile phase additive. In general, higher signal intensities were obtained with HILIC–MS compared to CE–MS. This is mainly due to the considerably larger injection volume applied in HILIC–MS. Still, the average difference in analyte response between CE–MS and HILIC–MS is much less than estimated from injection volume only, indicating overall higher absolute sensitivity in CE–MS. Notably, CE–MS can be particularly useful when volume-limited samples have to be analysed. The separation selectivities of CE–MS and HILIC–MS appeared to be considerably different, as demonstrated by the low correlation between CE migration and HILIC retention of urinary metabolites. The unique detection of 203 and 1216 molecular features in rat urine by CE–MS and HILIC-MS, respectively, further demonstrated the different selectivity of the methods. Hence, although HILIC–MS revealed significantly more molecular features than CE–MS, there is a clear added value for CE–MS. In metabolomics studies, CE–MS could aid in finding discriminatory compounds (e.g. potential biomarkers) and help to elucidate metabolic pathways.

References

[1] N.L. Kuehnbaum, P. Britz-Mckibbin, Chem. Rev. 113 (2013) 2437–2468.
[2] R. Ramautar, G.W. Somsen, G.J. de Jong, Electrophoresis 34 (2013) 86–98.

[3] M.G.M. Kok, G.J. de Jong, G.W. Somsen, Electrophoresis 32 (2011) 3016–3024.
[4] M.G.M. Kok, M.M.A. Ruijken, J.R. Swann, I.D. Wilson, G.W. Somsen, G.J. de Jong, Anal. Bioanal. Chem 405 (2013) 2585–2594.
[5] L. Coulier, R. Bas, S. Jespersen, E. Verheij, M.J. van der Werf, T. Hankemeier, Anal. Chem. 78 (2006) 6573–6582.
[6] X. Cai, L. Zou, J. Dong, L. Zhao, Y. Wang, Q. Xu, X. Xue, X. Zhang, X. Liang, Anal. Chim. Acta 650 (2009) 10–15.
[7] J. Chen, W. Wang, S. Lv, P. Yin, X. Zhao, X. Lu, F. Zhang, G. Xu, Anal. Chim. Acta 650 (2009) 3–9.
[8] Y. Chen, W. Bicker, J. Wu, M.Y. Xie, W. Lindner, J. Chromatogr. A. 1217 (2010) 1255–1265.
[9] H.G. Gika, G.A. Theodoridis, I.D. Wilson, J. Sep. Sci. 31 (2008) 1598–1608.
[10] Z. Huang, L. Lin, Y. Gao, Y. Chen, X. Yan, J. Xing, W. Hang, Mol. Cell. Proteomics 10 (2011) (M111.007922).
[11] H. Idborg, L. Zamani, P.O. Edlund, I. Schuppe-Koistinen, S.P. Jacobsson, Life. Sci. 828 (2005) 9–13.
[12] L. Lin, Z. Huang, Y. Gao, X. Yan, J. Xing, W. Hang, J. Proteome Res 10 (2011) 1396–1405.
[13] R. Mohamed, E. Varesio, G. Ivosev, L. Burton, R. Bonner, G. Hopfgartner, Anal. Chem. 81 (2009) 7677–7694.
[14] B. Preinerstorfer, S. Schiesel, M. Lämmerhofer, W. Lindner, J. Chromatogr. A 1217 (2010) 312–328.
[15] M. Storme R. T'kindt, D. Deforce, J. Van Bocxlaer, J. Sep. Sci. 31 (2008) 1609–1614.
[16] P. Yin, D. Wan, C. Zhao, J. Chen, X. Zhao, W. Wang, X. Lu, S. Yang, J. Gu, G. Xu, Mol. Biosyst. 5 (2009) 868–876.
[17] J. Saric, E.J. Want, U. Duthaler, M. Lewis, J. Keiser, J.P. Shockcor, G.A. Ross, J.K. Nicholson, E. Holmes, M.F.M. Tavares, Anal. Chem. 84 (2012) 6963–6972.
[18] J. Chen, L. Zhou, X. Zhang, X. Lu, R. Cao, C. Xu, G. Xu, Electrophoresis 33 (2012) 3361–3369.
[19] G. Tan, Z. Lou, W. Liao, X. Dong, Z. Zhu, W. Li, Y. Chai, Mol. BioSyst. 8 (2012) 548–556.
[20] K. Spagou, H. Tsoukali, N. Raikos, H. Gika, I.D. Wilson, G. Theodoridis, J. Sep. Sci. 33 (2010) 716–727.
[21] M.R. Gama, R.G. da Costa Silva, C.H. Collins, C.B.G. Bottoli, TrAC - Trends Anal. Chem 37 (2012) 48–60.
[22] A.J. Alpert, J. Chromatogr. 499 (1990) 177–196.
[23] M. Sugimoto, M. Kaneko, H. Onuma, Y. Sakaguchi, M. Mori, S. Abe, T. Soga, M. Tomita, J. Agric. Food Chem. 60 (2012) 2586–2593.
[24] M. Sugimoto, H. Goto, K. Otomo, M. Ito, H. Onuma, A. Suzuki, M. Sugawara, S. Abe, M. Tomita, T. Soga, J. Agric. Food Chem. 58 (2010) 8418–8425.
[25] J.M. Buscher, D. Czernik, J.C. Ewald, U. Sauer, N. Zamboni, Anal. Chem. 81 (2009) 2135–2143.
[26] C. Ibáñez, C. Simó, V. García-Cañas, A. Gómez-Martínez, J.A. Ferragut, A. Cifuentes, Electrophoresis 33 (2012) 2328–2336.
[27] J.R. Swann, K.M. Tuohy, P. Lindfors, D.T. Brown, G.R. Gibson, I.D. Wilson, J. Sidaway, J.K. Nicholson, E. Holmes, J. Proteome Res 10 (2011) 3590–3603.
[28] S. Cubbon, C. Antonio, J. Wilson, J. Thomas-Oates, Mass Spectrom. Rev. 29 (2010) 671–684.
[29] D.S. Wishart, C. Knox, A.C. Guo, R. Eisner, N. Young, B. Gautam, D.D. Hau, N. Psychogios, E. Dong, S. Bouatra, R. Mandal, I. Sinelnikov, J. Xia, L. Jia, J.A. Cruz, E. Lim, C.A. Sobsey, S. Shrivastava, P. Huang, P. Liu, L. Fang, J. Peng, R. Fradette, D. Cheng, D. Tzur, M. Clements, A. Lewis, A. de souza, A. Zuniga, M. Dawe, Y. Xiong, D. Clive, R. Greiner, A. Nazyrova, R. Shaykhutdinov, L. Li, H.J. Vogel, I. Forsythei, Nucleic Acids Res. 37 (2009) D603–D610.
[30] C.A. Smith, G. O'Maille, E.J. Want, C. Qin, S.A. Trauger, T.R. Brandon, D.E. Custodio, R. Abagyan, G. Siuzdak, Ther. Drug Monit. 27 (2005) 747–751.
[31] H. Horai, M. Arita, S. Kanaya, Y. Nihei, T. Ikeda, K. Suwa, Y. Ojima, K. Tanaka, S. Tanaka, K. Aoshima, Y. Oda, Y. Kakazu, M. Kusano, T. Tohge, F. Matsuda, Y. Sawada, M.Y. Hirai, H. Nakanishi, K. Ikeda, N. Akimoto, T. Maoka, H. Takahashi, T. Ara, N. Sakurai, H. Suzuki, D. Shibata, S. Neumann, T. Iida, K. Tanaka, K. Funatsu, F. Matsuura, T. Soga, R. Taguchi, K. Saito, T. Nishioka, J. Mass Spectrom 45 (2010) 703–714.

Talanta 132 (2015) 8–14

Contents lists available at ScienceDirect

Talanta

journal homepage: www.elsevier.com/locate/talanta

Rapid and high-precision measurement of sulfur isotope and sulfur concentration in sediment pore water by multi-collector inductively coupled plasma mass spectrometry

Xiao-Peng Bian [a], Tao Yang [a,b,*], An-Jun Lin [a], Shao-Yong Jiang [a,c,d]

[a] State Key Laboratory for Mineral Deposits Research, Nanjing University, Nanjing 210093, PR China
[b] Collaborative Innovation Center of South China Sea Studies, Nanjing University, Nanjing 210093, PR China
[c] State Key Laboratory of Geological Processes and Mineral Resources, China University of Geosciences, Wuhan 430074, PR China
[d] Faculty of Earth Resources and Collaborative Innovation Center for Scarce and Strategic Mineral Resources, China University of Geosciences, Wuhan 430074, PR China

ARTICLE INFO

Article history:
Received 24 May 2014
Received in revised form
6 August 2014
Accepted 7 August 2014
Available online 27 August 2014

Keywords:
MC–ICP–MS
Sulfur isotope
Sulfur concentration
Concentration effect

ABSTRACT

We have developed a technique for the rapid, precise and accurate determination of sulfur isotopes ($\delta^{34}S$) by MC–ICP–MS applicable to a range of sulfur-bearing solutions of different sulfur content. The 10 ppm Alfa-S solution (ammonium sulfate solution, working standard of the lab of the authors) was used to bracket other Alfa-S solutions of different concentrations and the measured $\delta^{34}S_{V-CDT}$ values of Alfa-S solutions deviate from the reference value to varying degrees (concentration effect). The stability of concentration effect has been verified and a correction curve has been constructed based on Alfa-S solutions to correct measured $\delta^{34}S_{V-CDT}$ values. The curve has been applied to AS solutions (dissolved ammonium sulfate from the lab of the authors) and pore water samples successfully, validating the reliability of our analytical method. This method also enables us to measure the sulfur concentration simultaneously when analyzing the sulfur isotope composition. There is a strong linear correlation ($R^2 > 0.999$) between the sulfur concentrations and the intensity ratios of samples and the standard. We have constructed a regression curve based on Alfa-S solutions and this curve has been successfully used to determine sulfur concentrations of AS solutions and pore water samples. The analytical technique presented here enable rapid, precise and accurate S isotope measurement for a wide range of sulfur-bearing solutions – in particular for pore water samples with complex matrix and varying sulfur concentrations. Also, simultaneous measurement of sulfur concentrations is available.

© 2014 Elsevier B.V. All rights reserved.

1. Introduction

Sulfur is a relatively active chemical element and it occurs in various oxidation states, such as sulfate, elemental sulfur and metal sulfides. Various biological and geochemical processes result in variations in sulfur oxidation states and impart sulfur isotope fractionations. Therefore, sulfur isotopes have diverse applications in geological science and variations in sulfur isotopic compositions act as useful tracers of the sources and cycling of sulfur species in biological and geochemical processes [1–4].

Sulfur isotope ratio measurements are conventionally performed by gas source isotope ratio mass spectrometry (GS-IRMS) in which S is measured as SO_2 or SF_6 [1,5–7]. Compared with SO_2, SF_6 is preferable for high-precision sulfur isotope analysis because it has no spectral interferences from oxygen species [7] while the corrections for the oxygen isotopic contributions are necessary when using SO_2 as the analyte [8]. For GS-IRMS, however, the sample preparation method is complex. In the case of water samples (e.g., pore water), the sulfate is precipitated as $BaSO_4$ first and then reduced to hydrogen sulfide, and then converted to metal sulfide (Ag_2S) for combustion to generate SO_2. Furthermore, the complicated and time-consuming sample preparation methods may lead to additional sulfur isotopic fractionation or contamination from the reagents employed. Moreover, different $\delta^{34}S$ values for the same material are obtained depending on which species (SO_2 or SF_6) is introduced into the GS-IRMS [9]. Continuous flow isotope ratio mass spectrometry (CF-IRMS) has been widely used for sulfur isotope analysis in which sulfur is introduced as SO_2 [10–12]. The generation and purification procedures for the SO_2 gas source are automated and rapid sulfur isotope analyses (< 15 min per sample) are realized. However, poor reproducibility of oxygen isotope variations in SO_2 results in calculated $\delta^{34}S$ values in error by up to 1–3‰ [13].

* Corresponding author at: State Key Laboratory for Mineral Deposits Research, Nanjing University, Nanjing 210093, PR China.
E-mail address: yangtao@nju.edu.cn (T. Yang).

http://dx.doi.org/10.1016/j.talanta.2014.08.053
0039-9140/© 2014 Elsevier B.V. All rights reserved.

There are other alternative methods for sulfur isotope analysis such as multiple-collector thermal ionization mass spectrometry (MC–TIMS) and secondary ion mass spectrometry (SIMS). For MC–TIMS, S is measured as AsS^+ at masses 107 and 109 and a very small sample mass (<2 μg S) is needed [14,15]. However, the sample preparation method is also complex and time-consuming. The ion microprobe (SIMS) enables in situ measurement of S isotopes at high spatial resolution (8–25 μm). However, it is subject to shortcomings including spectral interference and matrix effects and is not suitable for water samples.

Multiple-collector inductively coupled plasma mass spectrometry (MC–ICP–MS) has been widely applied to sulfur isotope ratio measurement [16–18]. Compared with single-collector ICP–MS, whose precision is limited because data are acquired sequentially and variability of plasma conditions are not accounted for, multi-collector ICP–MS enables precise measurement of isotope ratios with instrumental precision between 0.1% and $<0.005\%$ [19] due to its ability to measure multiple isotopes simultaneously. Another advantage of MC–ICP–MS is its compatibility with diverse sample introduction schemes, enabling both bulk solution analysis and in situ laser-ablation analysis.

When applying MC–ICP–MS to measure the $\delta^{34}S$ values of sulfur-containing solutions, isobaric interferences and matrix effects have strong influences on the accuracy and the precision of $\delta^{34}S$ values. Isobaric interferences from oxygen species can be removed by using the medium-to-high mass resolution and the interference-free plateau is chosen to detect sulfur isotopes [20,21]. Conventionally, prior chemical purification is necessary to avoid matrix effects. For water samples, the ion exchange purification step is necessary which is complex, multistep and time-consuming. Moreover, quantitative recovery of sulfur is essential to avoid potential isotope fractionation [20].

Another method to correct matrix effects has been developed by using matrix-matched standards to bracket the samples such that they can be analyzed without chemical purification [21], which provides a method that significantly simplifies the analysis procedure. However, the sulfur concentrations of sample solutions need to be known in advance to prepare the corresponding standards, which is not always available. Furthermore, if the sulfur concentrations vary in a large range, for each sample the corresponding standard is needed to be prepared, which impairs the convenience of this method. Also, in this case, because the standard-sample bracketing (SSB) method is applied and different samples cannot share the same working standard, the corresponding working standard of each sample needs to be measured twice (before and after the sample) and the number of standards to be measured is almost twice as many as that of samples.

In this study, we did research on concentration effect, that is to say, we used the same standard to bracket sulfur-bearing solutions that have the same matrices as the standard while different sulfur concentrations from that. We have investigated how the concentration difference between samples and standards influence the measured $\delta^{34}S$ values and made an attempt to utilize the correction curve we constructed to correct the pore water samples and the results are satisfactory.

Sulfur concentrations of sediment pore water samples are variable and usually decrease with depth [22–24] and thus conventionally for each sample the corresponding standard is needed to be prepared. And in pore water research, it is quite common that dozens of samples need to be analyzed. Consequently, as discussed above, a large number of standards need to be measured. However, with the help of our technique, only one working standard needs to be prepared and can be shared by different samples, thus reducing the standard preparation time greatly. Moreover, because the same working standard is used to bracket different samples, the number of standards to be measured will be reduced significantly. Furthermore, the matrix-matched standard also enables samples to be measured directly without prior chemical purification. Therefore, the new analytical protocol is more rapid than other ones and our research will simplify the analysis procedure significantly and bring much convenience to the pore water research. Besides, not only is this technique applicable to pore water samples but also to other geological samples that vary in sulfur concentration. And we believe that this method provides an idea which could be transferred to other isotopic analysis and will arouse a lot of interest and concerns from other researchers.

2. Analytical methods

2.1. Preparation of standards and samples

The water used for dilutions and rinses was prepared using a Milli-Q system (Millipore, Billerica, MA, USA) operated at 18.2 MΩ cm. High-purity nitric acid (HNO_3) was prepared by sub-boiling distillation. All bottles and vials used for sample preparation and storage were cleaned for at least 24 h in 10% HNO_3 and rinsed three times with 18.2 MΩ cm Milli-Q water. All standard and sample solutions were prepared in a clean lab for analysis as matrix-matched solutions stabilized in 2% (w/w) HNO_3.

Four sediment pore water samples (DH-5, DH-12, DH-18, and DH-25) from the South China Sea were volumetrically diluted 100 times for sulfur isotopic determination. The $\delta^{34}S$ values of standard solutions (Alfa-S and AS) were first measured using the CF-IRMS method on a MAT 253 isotope ratio mass spectrometer (ThermoFisher, Bremen, Germany) at the Institute of Mineral Resources, Chinese Academy of Geological Sciences, Beijing, China (Table 1). Matrices of modern seawater are mainly composed of Cl^- (~19,344 ppm), Na^+ (~10,773 ppm) and sulfur (~907 ppm). Sediment pore water below the seafloor has almost the same matrices as seawater while the sulfur concentrations vary with depth. The water samples were volumetrically diluted 100 times and about 193 ppm Cl^-, 108 ppm Na^+ and 9.1 ppm sulfur can be estimated. Therefore, the matrix-matched working standard (discussed below) should contain 200 ppm Cl^- (added as NaCl) and 10 ppm sulfur.

Two standard solutions (Alfa-S and AS) were prepared as in-house standards. The Alfa-S solution was made by diluting an Alfa Aesar Specpure^{TM} 1000 μg mL^{-1} S stock (Alfa Aesar, Johnson Matthey Co., Ward Hill, MA, USA), and the AS solution by dissolving solid ammonium sulfate provided by the laboratory of the authors. We prepared a series of Alfa-S and AS solutions which contained different concentrations of sulfur to investigate the concentration effect during the MC–ICP–MS measurement. Specifically, the Alfa-S solutions contained 1 ppm, 3 ppm, 5 ppm, 7 ppm, 9 ppm, 10 ppm, 11 ppm, 15 ppm, and 20 ppm S respectively, and the AS solutions contained 2 ppm, 4 ppm, 5 ppm, 8 ppm and 15 ppm S respectively. In addition, all standard solutions were matrix-matched (contain 200 ppm Cl^-) to eliminate mass bias arising from matrix effects during the measurement of sediment pore water [21]. In this study, all the Alfa-S and AS solutions mentioned were matrix-matched.

2.2. Instrumentation and apparatus

The isotopic measurements were performed using a Neptune Plus MC–ICP–MS (ThermoFisher, Bremen, Germany) at the State Key Laboratory for Mineral Deposits Research, Nanjing University, Nanjing, China. The Neptune Plus is a double-focusing magnetic sector instrument with variable dispersion (17%) ion optics. It is equipped with one fixed central Faraday cup and eight motorized Faraday cups that locate on both sides of the center cup. Typical

Table 1
Reference values of Alfa-S and AS[a].

Sample ID	Sample type	$\delta^{34}S_{V-CDT}$(‰)[b]	$\delta^{34}S_{V-CDT}$(‰)[c]
Alfa-S	Ammonium sulfate solution, working standard	–	1.90 ± 0.17
AS	Ammonium sulfate, sample from the lab of the authors	6.78 ± 0.07	6.67 ± 0.22

[a] Published data from Lin et al. [21].
[b] Data measured on MC–ICP–MS using SSB method with pure (with no matrices) Alfa-S as working standard (11 replicates), State Key Laboratory for Mineral Deposits Research, Nanjing University, Nanjing, China.
[c] Data measured on a MAT 253 isotope ratio mass spectrometer, Institute of Mineral Resources, Chinese Academy of Geological Sciences, Beijing, China; errors are given at 2σ.

Table 2
Operating conditions and data acquisition parameters for the MC–ICP–MS for sulfur isotopic measurements.

Mass spectrometer setup	
MC–ICP–MS	Thermo Electron NEPTUNE plus
Cooling gas flow rate	~15 L min^{-1}, Argon
Auxiliary gas flow rate	~1.30 L min^{-1}, Argon
Sample gas flow rate	~1.006 L min^{-1}, Argon
Extraction lens	~2000 V
Interface cones	Ni cones
Analyzer pressure	~10^{-9} Torr
RF forward power	~1162 W
RF reflect power	~4 W
Data acquisition parameters	
Mass resolution mode	Medium resolution ($m/\Delta m \approx 3000$)
Acquisition mode	Static
Detection system	Faraday cups
Cup configuration	^{32}S (C), ^{33}S (H2), ^{34}S (H3)
Wash-out time	2–3 min

operating parameters are summarized in Table 2. The solutions were aspirated using argon as the nebulizer gas.

2.3. Isotope measurement and data acquisition

Isotope ratio measurements are performed in medium-to-high mass resolution mode to remove the isobaric interferences resulting from oxygen species. Medium mass resolution ($m/\Delta m \sim 3000$) can separate the peaks of $^{16}O_2^+$ from $^{32}S^+$ efficiently [21]. Elemental sulfur species are lighter than molecular interferences from $^{16,17,18}O_2$, so isotopes of sulfur are determined on the interference-free plateau at lower mass to remove interferences from O_2^+ [20].

Standard-sample bracketing (SSB) was used to determine the δ^{34}S values of Alfa-S and AS solutions of different concentrations and pore water samples [25–27]. Specifically, for each sample, the standards were analyzed immediately before and after the sample analysis. And the true S isotope ratio is calculated by interpolating the mass bias of an unknown sample between the biases inferred from two neighboring standard analyses. In this study, the 10 ppm Alfa-S solution was used as standard whereas other Alfa-S and AS solutions were viewed as 'samples'. All the data for the sulfur isotope composition are reported as δ^{34}S values related to the Vienna-Cañon Diablo Troilite (V-CDT) scale [28] (Eq. 1):

$$\delta^{34}S_{V-CDT} = \left[\frac{\left(\frac{^{34}S}{^{32}S}\right)_{Samp}}{\left(\frac{^{34}S}{^{32}S}\right)_{V-CDT}} - 1\right] \times 1000 \quad (1)$$

In this research, we used the 10 ppm Alfa-S solution as the in-house working standard and δ^{34}S data for samples (including Alfa-S and AS solutions of different concentrations) are calculated according to the following equation:

$$\delta^{34}S_{V-CDTSamp} = \left[\frac{2 \times \left(\frac{^{34}S}{^{32}S}\right)_{Samp}}{\left(\frac{^{34}S}{^{32}S}\right)_{Alfa-1} + \left(\frac{^{34}S}{^{32}S}\right)_{Alfa-2}} - 1\right] \times 1000 + 1.90 \quad (2)$$

where $\left(\frac{^{34}S}{^{32}S}\right)_{Alfa-1}$ and $\left(\frac{^{34}S}{^{32}S}\right)_{Alfa-2}$ are sulfur isotope ratios of two neighboring working standards (10 ppm Alfa-S) of a sample. Constant value 1.90 is δ^{34}S value of working standard solution Alfa-S on the scale of V-CDT (measured on Thermo MAT 253 isotope ratio mass spectrometer).

Raw mass spectrometry data were reduced using the software Iolite [29]. The Data Reduction Scheme (DRS) file for sulfur isotope analysis was written by the authors. The $\delta^{34}S_{V-CDT}$ values of samples were calculated according to Eq. (2). Interpolation of the standards was achieved by choosing Iolite's 'Automatic' spline type option and the background signals (~3 mV ^{32}S intensity) were removed by on-peak zero subtraction. Errors given in Section 3 are standard errors (2σ) calculated by Iolite.

2.4. Instrument mass bias and matrix effects

In this study, we applied the standard-sample bracketing (SSB) method to correct instrumental mass discrimination. The matrix-matched 10 ppm Alfa-S solution was used as the bracketing standard and other matrix-matched Alfa-S and AS solutions were used as samples.

Instrumental mass bias within ICP–MS arising from so-called 'space-charge' and 'ion-diffusion' effects on the transmission of ionized particles [30–32] is sensitive to matrix composition (matrix effects) [33,34]. In this study, the sediment pore water samples used were prepared without chemical purification, so the matrix-matched Alfa-S solution was used to bracket water samples to correct matrix effects [21].

3. Results and discussion

3.1. Concentration effect of sulfur

In order to explore concentration effect, we prepared a set of Alfa-S solutions (matrix-matched) of different concentrations. The 10 ppm one was used as the standard and the SSB technique was applied to get the $\delta^{34}S_{V-CDT}$ values of other Alfa-S solutions. These solutions have identical isotopic composition and the difference between them is that they have different sulfur concentrations. However, as shown in Table 3 and Fig. 1, the measured $\delta^{34}S_{V-CDT}$ values of Alfa-S solutions of different concentrations all deviate from the reference value (1.90 ± 0.17‰). It shows that when the concentrations of samples are lower than that of the standard, the measured $\delta^{34}S_{V-CDT}$ values are smaller than the reference value

Table 3
Measured $\delta^{34}S_{V-CDT}$ values of Alfa-S solutions of different concentrations.

Sample ID	Sulfur concentration (ppm)	$2I_{sample}/(I_{std\ 1}+I_{std\ 2})$[a]	$(I_{std\ 1}+I_{std\ 2})/2I_{sample}$[b]	$\delta^{34}S_{V-CDT}$(‰)[c]	$\Delta\delta^{34}S_{V-CDT}$(‰)[d]
1 ppm Alfa-S	1	0.1007 ± 0.0007	9.9400 ± 0.0670	−23.65 ± 0.44	−25.55 ± 0.44
3 ppm Alfa-S	3	0.2906 ± 0.0021	3.4420 ± 0.0250	−4.47 ± 0.31	−6.37 ± 0.31
5 ppm Alfa-S	5	0.4822 ± 0.0028	2.0740 ± 0.0120	−1.09 ± 0.27	−2.99 ± 0.27
7 ppm Alfa-S	7	0.6660 ± 0.0051	1.5020 ± 0.0120	0.92 ± 0.27	−0.98 ± 0.27
9 ppm Alfa-S	9	0.9106 ± 0.0040	1.0983 ± 0.0048	1.53 ± 0.22	−0.37 ± 0.22
11 ppm Alfa-S	11	1.0419 ± 0.0085	0.9604 ± 0.0078	2.20 ± 0.22	0.30 ± 0.22
15 ppm Alfa-S	15	1.4130 ± 0.0210	0.7080 ± 0.0100	2.80 ± 0.36	0.90 ± 0.36
20 ppm Alfa-S	20	1.9890 ± 0.0160	0.5023 ± 0.0042	3.23 ± 0.27	1.33 ± 0.27

[a] The ^{32}S intensity ratios of samples and the standard. I_{sample} is the ^{32}S intensity of the sample and $I_{std\ 1}$ and $I_{std\ 2}$ are the ^{32}S intensities of the neighboring standards.
[b] The ^{32}S intensity ratios of the standard and samples. I_{sample}, $I_{std\ 1}$ and $I_{std\ 2}$ have the same meanings as above.
[c] The measured $\delta^{34}S_{V-CDT}$ values of Alfa-S solutions of different concentrations by MC–ICP–MS.
[d] The deviation values of measured $\delta^{34}S_{V-CDT}$ values from the reference value (1.90‰), i.e. $\Delta\delta^{34}S_{V-CDT} = \delta^{34}S_{V-CDT(measured)} - \delta^{34}S_{V-CDT(referencevalue)}$.

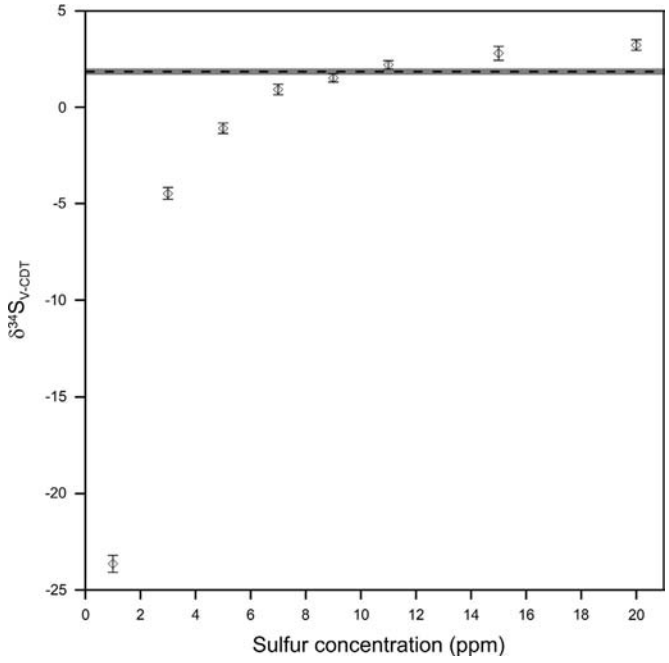


Fig. 1. The measured $\delta^{34}S_{V-CDT}$ values of Alfa-S solutions of different concentrations. All the measured values of Alfa-S solutions deviate from the reference value (gray bar) to different degrees according to their concentrations.

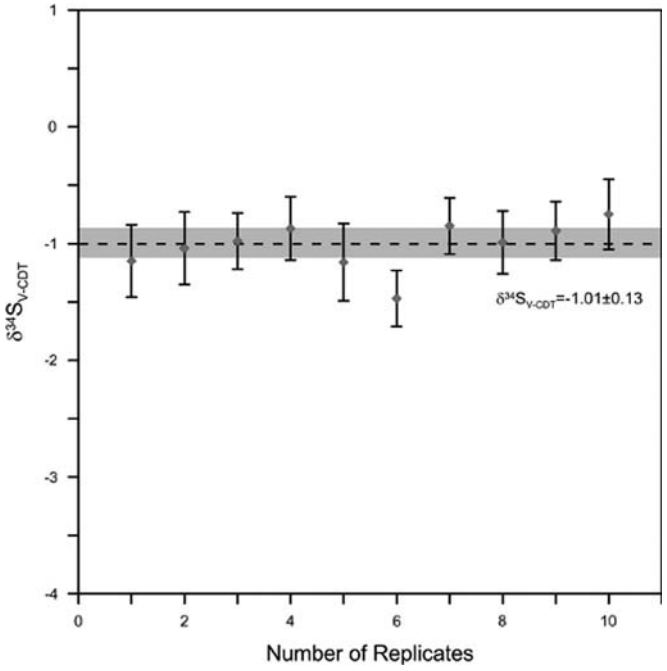


Fig. 2. Long-term reproducibility of S-isotope for 5 ppm Alfa-S solution over multiple, independent analytical sessions. Data are shown relative to the V-CDT scale. The estimated external uncertainty is ± 0.13‰ based on 10 replicates.

while when the concentrations of samples are higher than that of standard, the measured values are larger than the reference value. Besides, the difference between the reference value and the measured $\delta^{34}S_{V-CDT}$ values has relationships with the concentration difference of the standard and samples. The larger the concentration difference is, the more the measured $\delta^{34}S_{V-CDT}$ value deviates from the reference value. Because the difference between measured $\delta^{34}S_{V-CDT}$ values and the reference value is relatively large (the largest difference is −25.55‰), it is necessary to correct the measured values and the qualitative description above is not enough. In this study, the concentration range (1–20 ppm) is large enough for pore water research because in practice, pore water samples are volumetrically diluted 100 times and the sulfur concentrations of diluted water samples are usually lower than 10 ppm. For other geological samples that vary in sulfur concentration, the final sulfur-bearing solutions can be diluted to this concentration range. And we believe that this concentration range is sufficient for most samples because the maximum concentration (20 ppm) is 20 times as high as the minimum concentration (1 ppm).

Before we find out how to correct the measured values, we need to investigate the stability of concentration effect, i.e. whether the concentration effect varies with time during one experiment under the same instrumental operating conditions. Also, we want to replace sulfur concentrations with ^{32}S signal intensities because in practice sulfur concentrations of samples are usually unknown while ^{32}S intensities can be measured during the isotopic determination. These two questions are discussed in Section 3.2 and Section 3.3.

3.2. The stability of concentration effect

We used the 10 ppm Alfa-S solution as the working (in-house) standard to measure the 5 ppm Alfa-S solution over multiple, independent analytical sessions (Fig. 2) to test the stability of concentration effect. As shown in Fig. 2, we estimate an external precision of ± 0.13‰ (2σ) within 10 replicates. And the $\delta^{34}S_{V-CDT}$ value of the 5 ppm Alfa-S solution is stable within analytical uncertainty, which indicates that the concentration effect does not vary with time, thus we have verified the stability of concentration

effect. The external precision given here also describes the long-term stability and the precision of MC–ICP–MS method.

3.3. Sulfur concentration determination

Before we introduce the correction method, we introduce the sulfur concentration determination method first because here we present the relationships between sulfur concentrations and ^{32}S signal intensities and we replace S concentrations with ^{32}S intensity ratios in Section 3.4. So that in practice, it is not necessary to know sulfur concentrations of samples in advance to utilize the correction curve we constructed (discussed in Section 3.4).

During the exploration of concentration effect, we get the relationships between concentrations and intensities (Fig. 3). Alfa-S solutions of different concentrations were used to determine the concentration–intensity relationship (Table 3). We used $2I_{sample}/(I_{std\ 1}+I_{std\ 2})$ as the *X*-axis, where I_{sample} is the ^{32}S intensity of the sample and $I_{std\ 1}$ and $I_{std\ 2}$ are the ^{32}S intensities of the neighboring standards, and sulfur concentration as the *Y*-axis. We used the intensity ratio instead of absolute intensity value of ^{32}S as the *X*-axis to eliminate the instrumental intensity drift, which is similar to the SSB method.

As shown in Fig. 3, we constructed a regression curve which is based on best-fit linear function (through origin) to represent the relationships. The correlation coefficient is 0.9993, which indicates that concentrations and intensity ratios have a strong linear correlation.

We applied the constructed curve to AS solutions of different concentrations to test the validity of it (Table 4). We calculated the concentrations of AS solutions according to their intensity ratios and compared the results with the known concentrations. It shows that the calculated concentrations are consistent with the known ones (within 0.3 ppm) and thus indicates that the curve is also applicable to AS solutions.

Because our pore water samples were analyzed without chemical purification, there was no loss of sulfur content. We applied the regression curve to pore water samples (Table 4). The results are quite satisfactory: all the calculated sulfur concentrations of pore water samples are consistent with their concentrations measured by ion chromatography (within 0.1 ppm), which indicates that this technique can determine the sulfur concentration of pore water samples. Therefore, we can measure the sulfur concentration simultaneously when analyzing the sulfur isotope compositions.

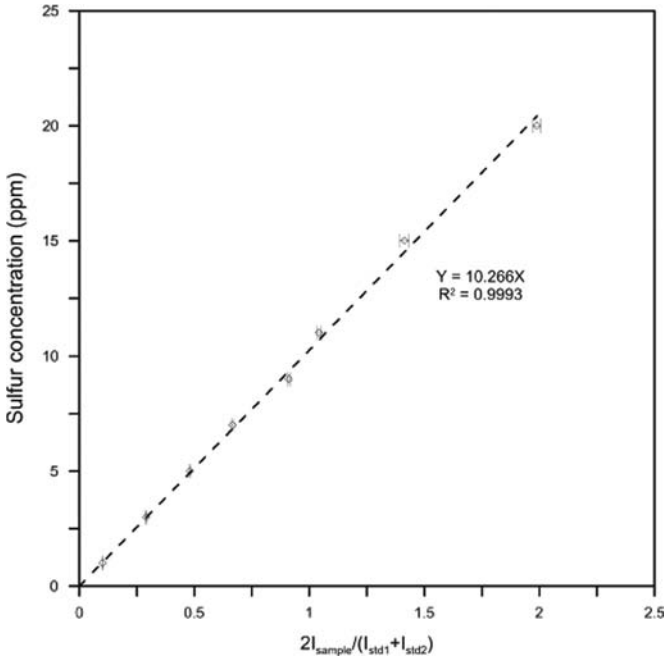


Fig. 3. The linear relationships between sulfur concentrations and intensity ratios. $Y=10.266X$, ($R^2=0.9993$), where *Y* is sulfur concentration (ppm) and *X* is $2I_{sample}/(I_{std\ 1}+I_{std\ 2})$.

3.4. Concentration effect correction

3.4.1. The construction of correction curve

In the previous discussion, we have verified the stability of concentration effect and the feasibility of replacing S concentrations with ^{32}S intensity ratios. Our following work is to correct the measured $\delta^{34}S$ values. During the exploration of concentration effect (Section 3.1), we found that the difference between measured $\delta^{34}S$ values and the reference value has relationships with the concentration ratios of the standard and samples. The larger $(I_{std\ 1}+I_{std\ 2})/2I_{sample}$ is, the smaller $\Delta\delta^{34}S_{V-CDT}$ is (Table 3). Here we use $(I_{std\ 1}+I_{std\ 2})/2I_{sample}$ to represent the concentration ratios of

Table 4
Calculated sulfur concentrations of AS solutions and pore water samples.

Sample ID	$2I_{sample}/(I_{std\ 1}+I_{std\ 2})$	Calculated sulfur concentration (ppm)	Sulfur concentration (ppm)
2 ppm AS	0.207	2.120	2.00
4 ppm AS	0.397	4.077	4.00
5 ppm AS	0.497	5.098	5.00
8 ppm AS	0.806	8.272	8.00
15 ppm AS	1.479	15.183	15.00
DH-5	0.186	1.913	1.82[a]
DH-12	0.475	4.871	4.78[a]
DH-18	0.261	2.679	2.59[a]
DH-25	0.353	3.619	3.72[a]

[a] Data measured by Ion chromatography, State Key Laboratory for Mineral Deposits Research, Nanjing University, Nanjing, China.

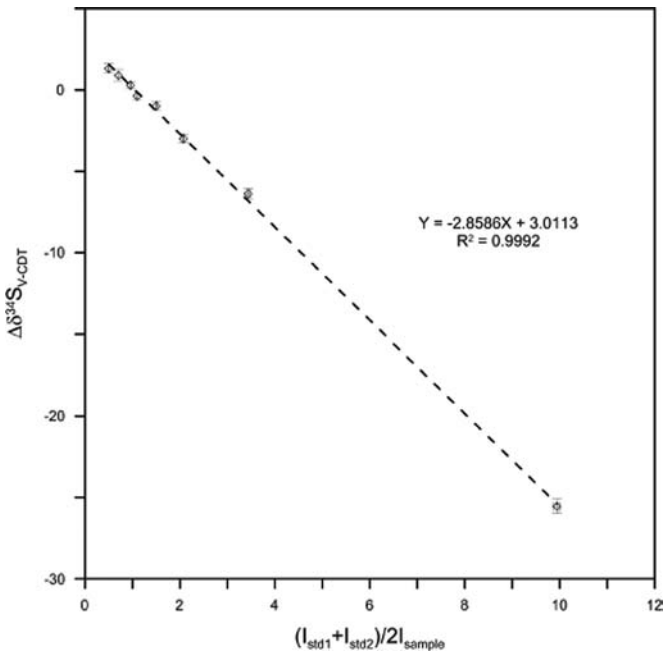


Fig. 4. The scatter plot of $(I_{std\ 1}+I_{std\ 2})/2I_{sample}$ and $\Delta\delta^{34}S_{V-CDT}$. The dash line is the linear regression curve that represents the relationships between $(I_{std\ 1}+I_{std\ 2})/2I_{sample}$ and $\Delta\delta^{34}S_{V-CDT}$. $Y=-2.8586X+3.0113$, ($R^2=0.9992$), where *Y* is $\Delta\delta^{34}S_{V-CDT}$, i.e. the difference between measured $\delta^{34}S_{V-CDT}$ values and the reference value and *X* is $(I_{std\ 1}+I_{std\ 2})/2I_{sample}$, i.e. the concentration ratios of the standard and samples.

the standard and samples, where $I_{std\ 1}$, $I_{std\ 2}$ and I_{sample} have the same meanings as in Section 3.3. Also, we define $\Delta\delta^{34}S_{V-CDT}$ as the difference between measured $\delta^{34}S_{V-CDT}$ values and the reference value ($\Delta\delta^{34}S_{V-CDT}=\delta^{34}S_{V-CDT(measured)}-\delta^{34}S_{V-CDT(referencevalue)}$).

We used $(I_{std\ 1}+I_{std\ 2})/2I_{sample}$ as the *X*-axis and $\Delta\delta^{34}S_{V-CDT}$ as the *Y*-axis to draw the scatter plot (Fig. 4). It seems that they have a linear correlation, so we constructed a regression curve based on best-fit linear function to represent the relationships. The correlation coefficient is 0.9992, which indicates that they have a strong linear correlation. Also, the function of this regression curve is $Y=-2.8586X+3.0113$, where Y is $\Delta\delta^{34}S_{V-CDT}$ and X is $(I_{std\ 1}+I_{std\ 2})/2I_{sample}$. When X is 1 (the standard and the sample have same sulfur concentration), the calculated Y is 0.1527, which is very close to the theoretical value (0, i.e. the measured value is same as the reference value). Therefore, the regression curve is very satisfactory.

This linear regression curve seems to provide a method of correcting the measured $\delta^{34}S_{V-CDT}$ values. We used the AS solutions of different concentrations to investigate whether this curve could be used to correct other standard solutions. SSB method was used to get the $\delta^{34}S_{V-CDT}$ values of AS solutions and the 10 ppm Alfa-S solution was used as the standard. As shown in Fig. 5 and Table 5, all the measured $\delta^{34}S_{V-CDT}$ values of AS solutions also deviate from the reference value ($-6.78\ \pm0.07$‰).

We used the correction curve to calculate the $\Delta\delta^{34}S_{V-CDT}$ values of AS solutions and the corrected $\delta^{34}S_{V-CDT}$ values of AS solutions are calculated by subtracting the $\Delta\delta^{34}S_{V-CDT}$ values from the measured $\delta^{34}S_{V-CDT}$ values. As shown in Fig. 5 and Table 5, the results are quite satisfactory. All the corrected $\delta^{34}S_{V-CDT}$ values of AS solutions are consistent with the reference value when considering the errors, which strongly indicates that the correction curve is applicable to AS solutions.

3.4.2. *Applications to pore water samples*

We have constructed a correction curve based on Alfa-S solutions of different concentrations and verified its applicability to AS solutions. Our following work is to investigate whether this correction curve is also applicable to water samples. We used the 10 ppm Alfa-S solution as the standard to bracket water samples, and the results are shown in Table 5. The standard solution has been matrix matched to remove matrix effects, but its sulfur

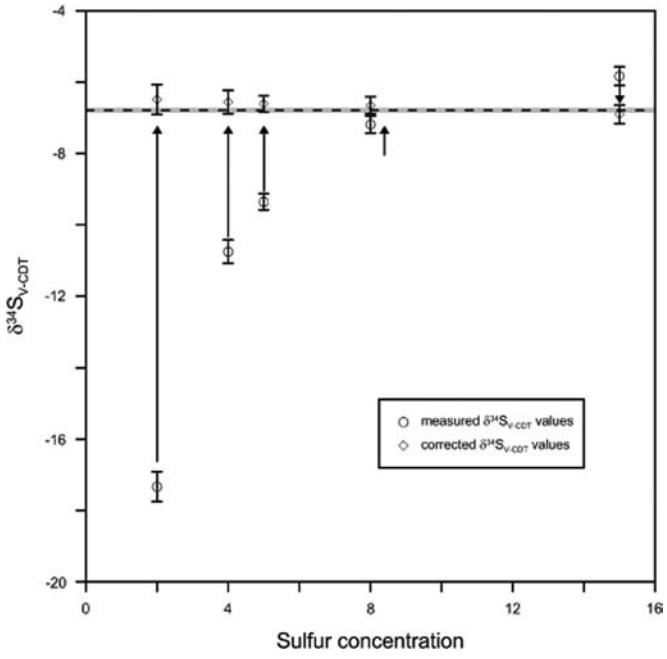


Fig. 5. The measured and corrected $\delta^{34}S_{V-CDT}$ values of AS solution. All the measured values (circle) of AS solutions deviate from the reference value (gray bar). And all the corrected values (diamond) are consistent with the reference value when considering the errors.

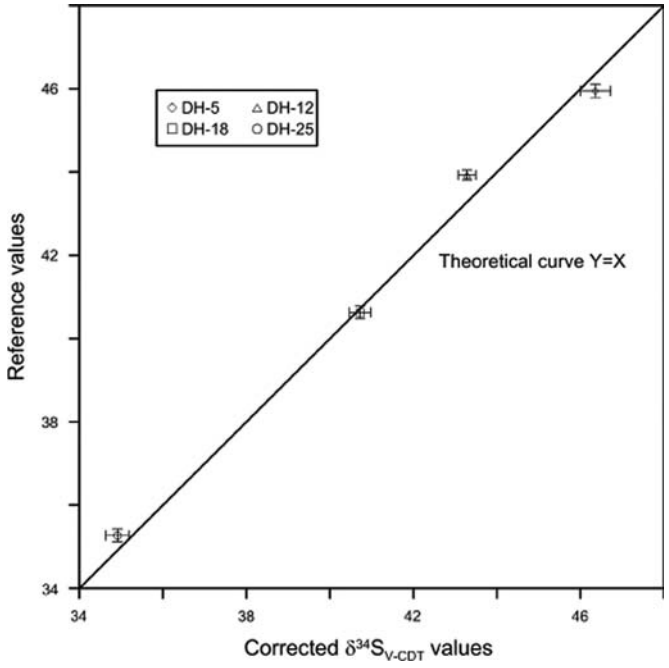


Fig. 6. The scatter plot of corrected and reference $\delta^{34}S_{V-CDT}$ values of pore water samples. The solid line is the theoretical curve ($Y=X$, where Y is reference values and X is corrected $\delta^{34}S_{V-CDT}$ values of pore water samples) that means corrected values are consistent with reference values. DH-12 point is very close to the theoretical curve and other points fall on the curve when considering the errors.

Table 5
Corrected $\delta^{34}S_{V-CDT}$ values of AS solutions and pore water samples.

Sample ID	$(I_{std\ 1}+I_{std\ 2})/2I_{sample}$	$\delta^{34}S_{V-CDT(measured)}$ (‰)[a]	$\Delta\delta^{34}S_{V-CDT}$(‰)	$\delta^{34}S_{V-CDT(corrected)}$ (‰)[b]	Reference values (‰)
2 ppm AS	4.846	−17.33 ±0.42	−10.841	−6.49 ±0.42	−6.78 ±0.07
4 ppm AS	2.519	−10.75 ±0.33	−4.190	−6.56 ±0.33	−6.78 ±0.07
5 ppm AS	2.015	−9.36 ±0.23	−2.749	−6.61 ±0.23	−6.78 ±0.07
8 ppm AS	1.242	−7.19 ±0.24	−0.539	−6.65 ±0.24	−6.78 ±0.07
15 ppm AS	0.677	−5.83 ±0.26	1.077	−6.91 ±0.26	−6.78 ±0.07
DH-5	5.370	34.02 ±0.36	−12.339	46.36 ±0.36	45.95 ±0.16
DH-12	2.108	40.27 ±0.21	−3.014	43.28 ±0.21	43.93 ±0.12
DH-18	3.832	32.78 ±0.25	−7.943	40.72 ±0.25	40.63 ±0.15
DH-25	2.839	29.81 ±0.28	−5.104	34.91 ±0.28	35.27 ±0.15

[a] The measured $\delta^{34}S_{V-CDT}$ values of AS solutions and pore water samples by MC–ICP–MS.
[b] The corrected $\delta^{34}S_{V-CDT}$ values of AS solutions and pore water samples, $\delta^{34}S_{V-CDT(corrected)}=\delta^{34}S_{V-CDT(measured)}-\Delta\delta^{34}S_{V-CDT}$.

concentration is different from that of the water samples, so the measured values also deviate from the 'true' values.

By strict matrix-matched, we can get the convincing $\delta^{34}S_{V-CDT}$ values of water samples [21]. We prepared four other matrix-matched Alfa-S solutions, which contain the same concentrations of sulfur as the pore water samples respectively, to bracket the pore water samples and the results (convincing values) are shown in Table 5. We used the correction curve to calculate the $\Delta\delta^{34}S_{V-CDT}$ values of pore water samples and then got the corrected $\delta^{34}S_{V-CDT}$ values of them.

When comparing the corrected $\delta^{34}S_{V-CDT}$ values of pore water samples with their reference values, we drew a scatter plot (Fig. 6). We used corrected $\delta^{34}S_{V-CDT}$ values as the *X*-axis and reference values as the *Y*-axis. As shown in Fig. 6, the points of DH-5, DH-18 and DH-25 all fall on the theoretical curve ($Y = X$) when considering the errors and the DH-12 point is very close to the theoretical curve. These results indicate that the corrected $\delta^{34}S_{V-CDT}$ values of pore water samples are consistent with their reference values and the correction curve can be used to correct pore water samples.

With the help of matrix match and the correction curve we constructed, we have developed a new analytical technique for sulfur isotope measurement which is rapid, precise and accurate.

4. Conclusions

We have developed a technique for the rapid, precise and accurate determination of S isotopes ($\delta^{34}S$) by MC–ICP–MS applicable to a range of sulfur-bearing solutions of different sulfur content. The major isobaric interferences from molecular $^{16}O_2^+$ on sulfur masses are removed in the medium resolution mode ($m/\Delta m \approx 3000$). Standard-sample bracketing (SSB) method is used to correct the instrument mass bias and matrix-matched standard solutions are used to eliminate the mass bias arising from the matrix effects. We have investigated the concentration effect and it shows that the measured $\delta^{34}S_{V-CDT}$ values of Alfa-S solutions of different concentrations deviate from the reference value to varying degrees. We have verified the stability of concentration effect and constructed a correction curve to correct measured $\delta^{34}S_{V-CDT}$ values. When applying the curve to correct AS solutions of different concentrations, the results are very satisfactory. We use the same method to correct the pore water samples and the corrected $\delta^{34}S_{V-CDT}$ values of them are consistent with the reference values, which validates the reliability of our analytical method.

This method also enables us to measure the sulfur concentration simultaneously when analyzing the sulfur isotope composition. There is a strong linear correlation between the sulfur concentrations and the intensity ratios. We have constructed a regression curve based on Alfa-S solutions and this curve is also applicable to AS solutions and pore water samples.

The analytical technique presented here enable rapid, precise and accurate S isotope measurement for a wide range of sulfur-bearing solutions – in particular for pore water samples with complex matrix and varying sulfur concentrations. Another advantage of this method is we can measure the sulfur concentrations simultaneously because the samples are analyzed without chemical purification, which will simplify the analysis procedure significantly.

Acknowledgments

The authors thank three anonymous reviewers for their valuable comments. This study was supported by the National 973 Project (Grant no. 2013CB835000) and the National Natural Science Foundation of China (Grant nos. 41230102 and 40903002) and a National Key Scientific Project organized by the China Geological Survey (Grant no. GZH201200305-06-04).

References

[1] H. Thode, J. Monster, H. Dunford, Geochim. Cosmochim. Acta 25 (1961) 159–174.
[2] M. Goldhaber, I. Kaplan, in: E. Goldberg (Ed.), The Sea, Wiley, New York, 1974, pp. 569–655.
[3] H. Ohmoto, R. Rye, in: H. Barnes (Ed.), Geochemistry of Hydrothermal Ore Deposits, John Wiley and Sons, New York, 1979, pp. 509–567.
[4] D. Canfield, Rev. Miner. Geochem. 43 (2001) 607–636.
[5] P. Fritz, R. Drimmie, V. Nowicki, Anal. Chem. 46 (1974) 164–166.
[6] B.W. Robinson, M. Kusakabe, Anal. Chem. 47 (1975) 1179–1181.
[7] C. Rees, Geochim. Cosmochim. Acta 42 (1978) 383–389.
[8] M. Coleman, Handbook of Stable Isotope Analytical Techniques, vol. I, Elsevier, Amsterdam, 2004.
[9] H. Qi, T.B. Coplen, Chem. Geol. 199 (2003) 183–187.
[10] A. Giesemann, H.-J. Jäger, A. Norman, H. Krouse, W. Brand, Anal. Chem. 66 (1994) 2816–2819.
[11] N. Grassineau, D. Mattey, D. Lowry, Anal. Chem. 73 (2001) 220–225.
[12] S. Studley, E. Ripley, E. Elswick, M. Dorais, J. Fong, D. Finkelstein, L. Pratt, Chem. Geol. 192 (2002) 141–148.
[13] B. Fry, S.R. Silva, C. Kendall, R.K. Anderson, Rapid Commun. Mass Spectrom. 16 (2002) 854–858.
[14] P. Paulsen, W. Kelly, Anal. Chem. 56 (1984) 708–713.
[15] W.R. Kelly, P.J. Paulsen, K.E. Murphy, R.D. Vocke Jr., L.-T. Chen, Anal. Chem. 66 (1994) 2505–2513.
[16] R. Clough, P. Evans, T. Catterick, E.H. Evans, Anal. Chem. 78 (2006) 6126–6132.
[17] P.R. Mason, J. Košler, J.C. de Hoog, P.J. Sylvester, S. Meffan-Main, J. Anal. At. Spectrom. 21 (2006) 177–186.
[18] R. Santamaria-Fernandez, R. Hearn, J.-C. Wolff, J. Anal. At. Spectrom. 23 (2008) 1294–1299.
[19] G. Nowell, D. Pearson, C. Ottley, J. Schwieters, D. Dowall, in: G. Holland, S. Tanner (Eds.), Plasma Source Mass Spectrometry: Applications and Emerging Technologies, Royal Society of Chemistry, London, 2003.
[20] P.R. Craddock, O.J. Rouxel, L.A. Ball, W. Bach, Chem. Geol. 253 (2008) 102–113.
[21] A.-J. Lin, T. Yang, S.-Y. Jiang, Rapid Commun. Mass Spectrom. 28 (2014) 750–756.
[22] J.T. Westrich, R.A. Berner, Limnol. Oceanogr. 29 (1984) 236–249.
[23] D.E. Canfield, Am. J. Sci. 291 (1991) 177–188.
[24] W.S. Borowski, C.K. Paull, W. Ussler, Geology 24 (1996) 655–658.
[25] N. Belshaw, P. Freedman, R. Onions, M. Frank, Y. Guo, Int. J. Mass Spectrom. 181 (1998) 51–58.
[26] X. Zhu, Y. Guo, R. Williams, R. Onions, A. Matthews, N. Belshaw, G. Canters, E. De Waal, U. Weser, B. Burgess, et al., Earth Planet. Sci. Lett. 200 (2002) 47–62.
[27] F. Albarède, B. Beard, Rev. Mineral. Geochem. 55 (2004) 113–152.
[28] H. Krouse, T. Coplen, Pure Appl. Chem. 69 (1997) 293–295.
[29] C. Paton, J. Hellstrom, B. Paul, J. Woodhead, J. Hergt, J. Anal. At. Spectrom. 26 (2011) 2508–2518.
[30] S.D. Tanner, Spectrochim. Acta Part B: At. Spectrosc. 47 (1992) 809–823.
[31] F. Vanhaecke, R. Dams, C. Vandecasteele, J. Anal. At. Spectrom. 8 (1993) 433–438.
[32] C.N. Maréchal, P. Télouk, F. Albarède, Chem. Geol. 156 (1999) 251–273.
[33] A. Galy, C. Pomiès, J.A. Day, O.S. Pokrovsky, J. Schott, J. Anal. At. Spectrom. 18 (2003) 115–119.
[34] A.J. Pietruszka, R.J. Walker, P.A. Candela, Chem. Geol. 225 (2006) 121–136.

Talanta 132 (2015) 15–22

Contents lists available at ScienceDirect

Talanta

journal homepage: www.elsevier.com/locate/talanta

Development of a MSFIA sample treatment system as front end of GC–MS for atenolol and propranolol determination in human plasma

María del Rosario Brunetto [a,*], Sabrina Clavijo [a], Yelitza Delgado [a], Wendy Orozco [a], Máximo Gallignani [a], Carlos Ayala [a], Víctor Cerdà [b]

[a] Molecular Spectroscopy Laboratory, Department of Chemistry, Faculty of Sciences, Los Andes University, La Hechicera, Mérida 5101, Venezuela
[b] Laboratory of Environmental Analytical Chemistry-LQA2, University of the Balearic Islands, Cra. Valldemossa km 7.5, 07122 Palma de Mallorca, Spain

ARTICLE INFO

Article history:
Received 23 June 2014
Received in revised form
20 August 2014
Accepted 21 August 2014
Available online 30 August 2014

Keywords:
Gas chromatography–Mass spectrometry (GC–MS)
Multisyringe flow injection analysis (MSFIA)
Solid-phase extraction (SPE)
Microwave assisted derivatisation
Human plasma
Atenolol
Propranolol

ABSTRACT

An on-line solid-phase extraction (SPE) method coupled to gas chromatography–mass spectrometry (GC–MS) has been developed for the determination of atenolol (ATN) and propranolol (PRO) in human plasma. The hyphenation of SPE with multisyringe flow injection analysis (MSFIA) allows the simultaneous GC–MS determination of ATN and PRO with high selectivity and sensitivity. On-line preconcentration and derivatisation of the analytes were carried out by means of using restricted access materials (RAM) and microwave (MW) assisted derivatisation reactions with N-methyl-N-(trimethylsilyl) trifluoroacetamide (MSTFA)+1% trimethylchlorosilane (TMCS). Multivariate optimization was applied to optimize experimental conditions. The whole procedure comprising sample pretreatment and analyte determination took about 15 min. However, the overlap of the automatic sample treatment with the GC separation increased the frequency to 7 samples h^{-1}. The validated method was successfully applied to direct ATN and PRO determination in human plasma.

© 2014 Elsevier B.V. All rights reserved.

1. Introduction

Beta-blockers (BB), also called beta-adrenergic antagonists, constitute one of the most frequently prescribed drugs to treat heart rhythm disorders, angina pectoris, hypertension, tachycardia or acute myocardial infarction [1,2]. Atenolol and propranolol have been considered a first-line treatment for hypertension [1]. Due to its wide therapeutic range, these drugs require periodic monitoring for adjusting the corresponding dose [3]. For this purpose, sensitive and accurate analytical methodologies for quantification of these compounds in biological fluids are required.

Several methods have been described for the determination of ATN and PRO in human plasma using different techniques such as: immunoassays [4], spectrofluorimetry [5,6], electrochemistry [7] and liquid chromatography (LC) with photodiode array (UV), fluorescence detection (FLD) [8–11] and mass spectrometry (LC–MS) [12–15]. The latter have proved to be selective and sensitive methods for the simultaneous determination of BB in biological fluids. However, LC–MS is not as common as GC–MS in routine laboratories.

Gas chromatography with mass spectrometry detection (GC–MS) is an alternative to LC–MS systems that has also been used for the determination of ATN and PRO in different matrices, with successful results [16–19], providing extra technical advantages, such as good separation, high sensitivity, robustness, and the availability of large spectrum libraries for accurate analyte identification.

The very low concentration of ATN and PRO in biological samples and the complexity of these matrices make necessary a sample preparation step. Selective extraction of analytes from complex matrices is recognized as a very difficult task because these contain a large variety of compounds that may difficult the analysis, leading to a lengthy purification processes. Most of the drugs bind to proteins for circulation in the body. Therefore, for the quantitative determination of ATN and PRO, a deproteinizing process should be carried out, which not only releases the analytes of interest and increases the selectivity in the subsequent steps of sample treatment, but also prevents the appearance of unknown peaks in the chromatogram that can be generated due to contamination.

In this sense, generally determination of BB in biological samples requires conventional sample preparation procedures

* Corresponding author. Tel.: +58 274 2715415; fax: +58 274 2714223.
E-mail address: brunetto@ula.ve (M.d.R. Brunetto).

http://dx.doi.org/10.1016/j.talanta.2014.08.056
0039-9140/© 2014 Elsevier B.V. All rights reserved.

prior to injection, such as: liquid–liquid extraction (LLE) and solid-phase extraction (SPE) [16–21], being latter the most used, since time consuming procedures, errors and the risk of low recoveries can be significantly reduced [16–19].

During the last years, special SPE supports have been developed to allow direct injection of plasma samples into on-line SPE liquid chromatography systems. These sorbents called restricted access materials (RAMs) [20,21], combine size exclusion of proteins without destructive accumulation, and other macromolecular matrix components with the simultaneous enrichment of low-molecular analytes, which can be retained and extracted selectively [22,23]. Low-molecular-mass analytes are retained by conventional retention mechanisms such as hydrophobic, ionic or affinity interactions at the inner surface of the sorbent particles. The access of proteins is prevented by a physical diffusion barrier or a chemical barrier. In the majority of the applications described in the literature, RAMs are used in on-line coupled-column SPE–LC systems. These systems require highly sophisticated apparatuses, high operating cost and expensive instrumentation (column switching system, programs equipment and two pumps). In the search of more affordable approaches, other methods exploiting flow-techniques (FT) with on-line column switching schemes have been described [24].

FT-based methods allow well-defined and precisely metered reagent and sample volumes handling, along with miniaturization and automation of SPE based sample processing, and its possible hyphenation with a plethora of instrumental techniques [25,26]. Multisyringe flow injection analysis (MSFIA) has played a major role in SPE automation, providing rapid procedures with low solvent/sample consumption and generation of waste [25]. Potentialities of this technique have been previously discussed in the literature [26].

It is well known that GC analysis is restricted to volatile compounds, so that, polar analytes such as BB, require a derivatisation reaction to achieve the most adequate conditions for GC separation and MS detection. Different derivatising reagents have been used with this purpose [16,27], including MSTFA, which through a silylation reaction produces volatile and thermally stable trimethylsilated (TMS) derivatives [17–19,28]. Reported standard conditions for these reactions are mainly represented by the use of temperatures between 30 and 60 °C with thermal heating and reaction times between 10 and 60 min [16,17,28]. In order to decrease derivatisation time, we propose employing microwave radiation (MW) instead of direct thermal heating [29], exploiting the advantages of MSFIA for coupling auxiliary microwave energy devices, allowing the automation of this step in the sample treatment.

Therefore, the objective of the present work was the development of a MSFIA-SPE-MW procedure coupled to GC–MS as an alternative to existing methods, for determination of ATN and PRO in human plasma samples. Main advantages of the developed method are simplicity, high automation degree and inexpensiveness, simplifying the hyphenation of plasma sample treatment with GC–MS.

2. Materials and methods

2.1. Reagents and standards

Reagents used were of analytical grade and solvents were of HPLC grade. Acetonitrile and methanol were supplied by JT Baker (Phillipsburg, NJ, USA). The derivatising reagent N-Methyl-N-trimethylsilyltrifluoroacetamide (MSTFA)+1% trimethylchlorosilane (TMCS), and USP atenolol were supplied by Sigma Chemical Co. (St. Louis, MO, USA). USP propranolol (available in the market as Propranolol Hydrochloride) was kindly provided by Inversiones Dayamar CA (Venezuela). Double deionized and distilled water was obtained with a Milli-Q water purification system (Millipore, Bedford, MA, USA).

Stock solutions of ATN and PRO (1000 mg L^{-1}) were prepared in acetonitrile and stored in amber bottles under refrigeration at 4 °C until use. Working solutions at different concentrations were prepared daily by dilution in acetonitrile and/or water:acetonitrile 98:2 v/v.

2.2. Plasma sample preparation

For the optimization and validation of the method, a pool of 30 mL of human plasma from healthy adult volunteers was used. All volunteer patients signed an informed consent to participate in the study.

Blood samples (10 mL) were drawn from a forearm vein into vacutainer® blood collection tubes with EDTA (as K_2EDTA). Subsequently, samples were centrifuged at 4800 rpm for 10 min. Finally, the plasma was isolated and kept frozen at −20 °C until analysis.

At the time of analysis, plasma samples were diluted 1:2 (v/v) in water/acetonitrile 98:2 v/v and centrifuged at 12000 rpm for 5 min. The supernatant was separated and filtered through 0.22 μm polyvinylidene difluoride (PVDF) syringe filters (Millipore). A volume of 0.200 mL of filtrate was then ready to be injected into the extraction precolumn for analysis. Samples were analysed within two days after being collected.

2.3. GC–MS system

Derivatised samples were analysed using a Varian 3800 Gas Chromatograph equipped with a Varian 8200 autosampler and Saturn 2000 ion trap mass spectrometer (IT-MS) detector (Varian, CA, USA). Data acquisition and analysis were performed using standard software supplied by the manufacturer (Varian Saturn 2000). Samples were injected under splitless mode and the injector temperature was set initially at 120 °C held for 2 min and then ramped at 200 °C min^{-1} up to 325 °C and held for 5 min. This temperature programme allowed the injection of at least 9 μL of sample into the GC inlet liner at a temperature below the boiling point of the solvent.

The analyte separation was achieved on a fused silica capillary column AV-5-MS (Varian-MS, 30 m length, 0.25 mm i.d. with 0.25 mm film thickness) with an oven temperature set at 120 °C during 3 min and then programmed to reach 290 °C at 35 °C min^{-1} and held 5 min. Helium was used as carrier gas at a flow rate of 1.0 mL/min.

The MS detector was operated in electron impact ionization mode at 70 eV and the temperatures of the ion trap, manifold and transfer line were set at 230, 40 and 280 °C respectively. Ions monitored, in SIM mode, were m/z 72, 188, 294 and 395 for ATN-diTMS and 72, 115 and 332 for PRO-TMS.

2.4. SPE-MSFIA-MW system

The MSFIA manifold devised for SPE and MW assisted derivatisation is shown in Fig. 1. The system is constituted by a multisyringe automatic burette (MicroBU Crison, Barcelona, Spain), equipped with four high-precision bidirectional syringes (S1–S4) (Hamilton, Bonaduz, Switzerland). Each syringe has a three-way commutation valve at the head (V1-V4) (N-Research, Caldwell, NJ, USA) which helps reducing reagent consumption. In the proposed system, only three syringes were used: S1 (10 mL), S2 (10 mL) and S3 (5 mL). Depending on the position of the solenoid valves, the fluids contained in the syringes were loaded (pickup) or dispensed to the flow network (ON) or to their reservoirs (OFF). Additionally

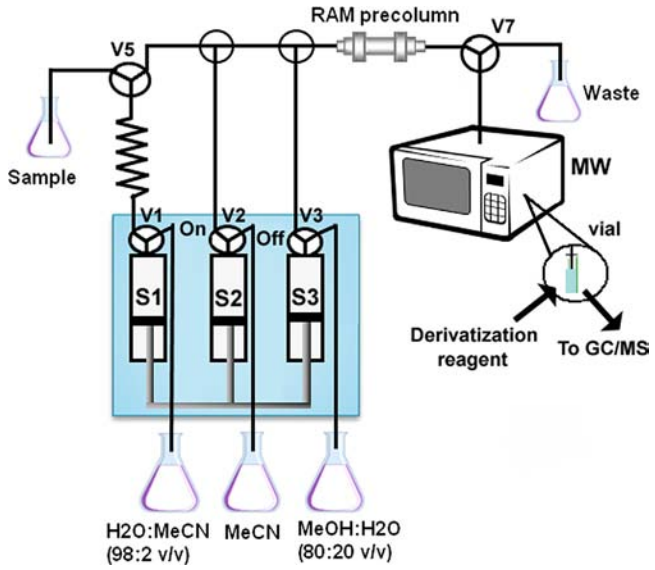


Fig. 1. Schematic illustration of the SPE-MSFIA-MW system. MeCN: acetonitrile, MW: microwave, GC/MS: gas chromatograph/mass spectrometer, S (1–3): syringes, V (1–7): valves, RAM: restricted access material.

two extra commutation valves (V5 and V7) (Takasago Electric, Nagoya, Japan) were connected to and controlled through the burette.

The automatic control of the flow system via PC was made through an RS232C interface [25]. The manifold was constructed with PTFE tubing of 0.8 mm i.d. and T connectors which were made from polytetrafluoroethylene, resisting organic solvents better than typical methacrylate connectors. The plasma sample treatment was performed in a LiChrospher RP-18 ADS precolumn with 25 mm × 4 mm i.d., 25 μm particle diameter (Merck, Darmstadt, Germany), which can be directly connected to the flow system without generating high back-pressure. To control the conditions of the derivatisation reaction a domestic microwave-oven (LG Intelowave, MS-0745 V with a nominal power of 750 W) was incorporated in the MSFIA system as shown in Fig. 1. The microwave oven used in the proposed system was modified by adding a cooling condenser to pass the PTFE tube to the vial. Before and after the modification, microwave power was calibrated. No significant loses of energy were denoted and the nominal power of the microwave (750 w) remained constant. System control was performed using the Autoanalysis 5.0 software package (Sciware Systems, Bunyola, Spain) [25].

2.5. MSFIA-SPE-MW procedure

The automated protocol of the developed MSFIA-SPE-MW is described in Table S1 of supplementary information and summarized as follows:

System initialization. With all valves in OFF position, syringes were filled from their respective reservoirs at a flow rate of 5.0 mL min^{-1}. S1 contained the extraction mobile-phase (water: acetonitrile 98:2 v/v), S2 the elution mobile-phase (acetonitrile) and S3 the mobile-phase for precolumn conditioning (methanol: water 80:20 v/v).

Conditioning step. ADS precolumn was conditioned with 5 mL of the mixture methanol:water (80:20 v/v) supplied by S3. Next, S1 dispensed a volume of 0.8 mL of H_2O:MeCN (98:2 v/v) through the precolumn to remove residual methanol which could be present in the dead volume, after the conditioning step.

Sample loading. S1 was connected to V5 in position OFF for sample loading into the 0.200 mL loop. The same syringe (S1) but with valve V5 in ON position, introduced the sample into the ADS precolumn to isolate the analytes from matrix constituents.

Clean-up. After analytes retention, the precolumn was rinsed with 2 mL of H_2O:MeCN (98:2 v/v) with the aim to remove the non-retained plasma matrix compounds, and therefore, to prevent interferences in the subsequent derivatisation reaction.

Elution. Firstly, S2 with the valve V7 in OFF position dispensed acetonitrile to the precolumn to remove any water present in the dead volume of the precolumn that could interfere during the derivatisation reaction. Thereafter, S2, with the valve V7 in ON position supplied the organic solvent to elute the analytes from the precolumn into the vial. Afterwards the derivatising reagent (MSTFA + 1% TMCS) was added to the vial and sealed. The vial was located in the microwave oven where derivatisation was carried out. Then, the determination of ATN and PRO was performed by GC–MS. The operational sequence was repeated three times for each sample. The entire procedure, i.e. SPE and derivatisation of the analytes, was done in 7.70 min.

2.6. Optimisation strategy

An on line procedure based on SPE with assisted microwave derivatisation was proposed. In this context, the analytical cycle involved four main steps: (1) loading the sample onto the precolumn and removing the proteinaceous ballast material, (2) washing the column and removing the more polar interfering substances, (3) elution of the analytes and (4) microwave assisted derivatisation.

The composition and volume of the extraction and elution phases were optimized using the MSFIA system with UV and fluorescence (FL) detection. Standard solutions of ATN and PRO (0.5 μg mL^{-1}) were used for all the experiments. On the one hand, SPE parameters were optimized using the OVAT method (one variable at time) aiming to extract the analytes with an effective removal of the proteinaceous matrix and other interfering components of the sample and to attain an efficient elution (quantitation) of the analytes.

On the other hand, factors corresponding to microwave assisted sylilation reaction with MSTFA + 1% TMCS were optimized using a factorial experimental design for screening the variables and a central composite design (CCD) to investigate the interactions among the principal affecting variables, and to obtain the critical values corresponding to the most favourable conditions, respectively. The experimental matrix design and data analysis were carried out by the software package STATISTICA 6.0 (Statsoft Inc. Tulsa, USA). Peak areas of ATN and PRO derivatives, as well as total peak area (average of ATN and PRO derivatives) were used as response variables in all multivariate experiments.

3. Results and discussion

3.1. Optimisation

3.1.1. MSFIA-SPE-MW system

The priority of our study was to optimise the composition of all the mobile phases (washing and elution) in order to obtain the maximum recovery in the shortest analysis time.

The washing mobile phase was proposed for propelling of the sample to the precolumn and proteins removal. The content of organic solvent is limited to avoid proteins denaturation and system clogging. However, addition of a small amount of organic solvent is recommended to achieve the release of the drug from the binding sites of plasma proteins enhancing the selectivity and sample clean up. In this sense acetonitrile:water (2:98 v/v) was employed as washing mobile phase with satisfactory results.

Flow rates in MSFIA are limited by back-pressure of the RAM column, and the viscosity of the plasma that restricted the use of high flow rates without increasing the back-pressure in the column during the elution process. This technique allows a maximum pressure of about 2.5 MPa [24]. For this reason, a flow rate of 0.6 mL min^{-1} was proposed for this step to prevent overloading of the syringe pump and to provide enough contact time between the analytes and the sorbent. The removal of the proteinaceous ballast was monitored by direct connection of the ADS precolumn to the diode array UV detector set at 254 nm and the fluorescence detector at $\lambda_{ex}=230$ nm, $\lambda_{em}=310$ nm.

For this purpose, 0.200 mL of a blank plasma sample and a plasma sample spiked with ATN and PRO were injected into the ADS precolumn. Quantitative recoveries of ATN and PRO were obtained with a washing time of 3 min. Recoveries were calculated by comparing the peak areas of each compound after extraction with those obtained by direct injection of the same amount of analyte in aqueous solution.

These results showed that this washing mobile phase provided a good reproducibility and selectivity in the subsequent derivatisation step. Moreover, the endogenous components from the plasma were completely removed from the precolumn while the analytes remained retained. Thus, this washing mobile phase was used for further analysis.

Once the clean up step was accomplished, it was necessary to optimise the composition of the eluting mobile phase to achieve convenient conditions for elution and derivatisation reaction. Acetonitrile provided best results, because of its stronger elution power, allowing analytes peak compression. Also this solvent has an acceptable dielectric constant ($\varepsilon'=37$) which gives a good sensitivity to microwave radiation [30–32]. Therefore, analytes were eluted from the ADS precolumn at a flow-rate of 0.6 mL min^{-1} during 0.8 min.

MSFIA is generally characterized by short analysis times and high sample throughput. However, in the proposed MSFIA-SPE-MW system, the analytical procedure is quite complex comprising sample pretreatment and derivatisation what leads to reduced sample throughput. Moreover, the flow rates used with this technique are limited by back-pressure of the RAM column especially when loading the viscous proteinaceous sample.

Different flow-rates of sample introduction within 0.4–0.8 mL min^{-1} were studied. 0.6 mL min^{-1} was chosen as an optimal value. Higher flow rates could cause back-pressure, worsening the repeatability of the signal.

Sample volumes were also tested in the range from 0.050 to 0.500 mL. Higher values of peak area of analytes were obtained by increasing sample volume. However, values above 0.500 mL affected RSD of the analysis measurements. In order to achieve a high sensitivity with a low relative standard deviation a volume of 0.200 mL was selected as a reasonable compromise.

3.1.2. Microwave assisted derivatisation

ATN and PRO, given their polarity, are not stable and decompose at high temperatures. For this reason, they were derivatised before GC–MS analysis using a silylation reaction. In this case, N-methyl-N-(trimethylsilyl) trifluoroacetamide (MSTFA) was used for this purpose, which is one of the most widely used for the identification and quantification of BB in biological samples [17,18,28]. MSTFA is an effective trimethylsilyl donor that replaces labile hydrogens atoms with this group on polar compounds such as ATN and PRO. Secondary amine (–NH) and hydroxy (–OH) groups present in the molecular structures of ATN and PRO, are converted to the corresponding (–N-TMS) and (–O-TMS) groups [27].

Previous studies describe derivatisation procedures prior to GC–MS analysis of ATN and PRO which are time-consuming, e.g. with conventional heating process. In our case, to shorten the sample preparation time, we used microwave radiation to supply high acceleration rates to the derivatisation reaction [29,30–33].

When microwave assisted derivatisation is employed, reaction solvent, microwave power and reaction time are important parameters that must be controlled. In contrast with conventional heating, the amount of heat transferred to the reaction mixture depends on the dielectric properties of the molecules [31,32]. Since polar molecules have a permanent dipole moment, they can absorb the microwave energy and convert it into heat. Methanol and acetonitrile have a high polarity, being very suitable for absorbing electromagnetic energy [31,32,34]. However, methanol has an hydroxyl group susceptible to be derivatised, therefore acetonitrile was selected.

To investigate the yield of the derivatisation reaction with microwave energy, a comparison using conventional heating was made. Two calibration curves were graphed by spiking 6 blanks of plasma with ATN and PRO at different concentration levels (0.006–2000 μg mL^{-1}). For assisted microwave derivatisation a reaction time of 90 s and a power of irradiation of 30% (250 W) were used, while for the conventional heating the conditions were 10 min at 30 °C. The equations of both calibration curves are showed in Supplementary Information (Fig. S2). As can be seen coefficients of correlation were higher than 99% in both cases. Results showed that, there were not significant differences between microwave heating and the classical method. Being both methods suitable for ATN and PRO determination.

After choosing the derivatisation reagent and the solvent, the remaining conditions were optimised using a multivariate design. These procedures provide relevant knowledge on the effect of variables within the entire selected experimental domain, and the variance of the estimate of the response in every point of the domain is better than that obtained by univariate methods [34]. Full factorial designs are the most popular first order designs owing to their simplicity and relatively low cost. They are very useful for preliminary studies or in initial optimisation steps. Full factorial designs at two levels are mainly used for screening, that is, to determine the influence of a number of effects on a response, and to discard those that are not significant [34].

Based on preliminary experiments, at least three factors might affect the experimental response (total peak area) in the present work: microwave irradiation power, reaction time and molar relation between the analyte and the sylilation reagent. Three levels were selected and a 2^3 factorial design with twelve experiments was carried out to optimise the analytical conditions that affect the analytes response signals (Table 1). The analysis of variance (ANOVA) results were evaluated to determine the significant effects (see supporting information Table S3). Normalized results of the experimental design were evaluated at a 5% of significance and analyzed by standardized Pareto chart (Fig. 2). The vertical line on the plot judges statistically significant effects, i.e. the bar extracting beyond the line corresponds to the effects that are statistically significant at the 95% confidence level [35]. Furthermore, the positive or negative sign also provides information about the effect of the variables upon the response signal.

Table 1
Factor codes, low, medium and high in 2^3 factorial design.

Factors	Levels		
	Low (−1)	Medium (0)	High (+1)
Reaction time (s)	20	55	90
Microwave irradiation power (%)	20	55	90
Molar relation (analyte:MSTFA) (v/v)	1:1	1:2	1:3

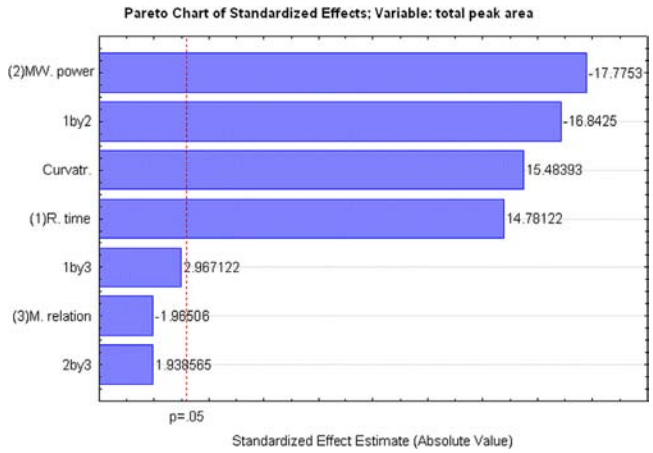


Fig. 2. Standarized main pareto chart for 2^3 factorial design. Vertical line in the chart defines 95% of confidence level.

According to Fig. 2, microwave power was the most significant factor having a negative effect on the peak area in this study. Reaction time has a positive significant effect, while molar relation showed a negative but non-significant effect on the peak area (taking into account the dilution effect). Molar relation was not a significant factor for the studied BB. For this reason, a 1:1 molar relation analyte: MSTFA volume was chosen as an adequate compromise between reactive amount and derivatisation yield.

In the next step, a central composite design (CCD) including quadratic terms was applied to optimise the two significant factors (microwave power and reaction time) according to the screening results (supplementary information Table S4).

In the central composite design levels varied from 20% to 90% for irradiation power and between 20 and 90 s for reaction time. The centre point was executed eight times resulting in a total of 16 experiments, which were made in random order.

The ANOVA table and the pareto chart (supplementary information Table S5 and Fig. S6, respectively) show that microwave irradiation power has the largest influence on the peak area and a negative effect upon the reaction yield. Results showed that at higher values of microwave irradiation power and reaction time the derivatisation efficiency increases up to 70%. However, microwave irradiation power higher than 70% had a negative effect on the reaction, because the effect called "bumping" occurred. Bumping is a sudden heating inhomogeneous in time, with high-energy radiation. This is due to physicochemical properties of acetonitrile, which has a large dielectric constant ($\varepsilon = 37.1$) and a boiling temperature close to 80 °C, thus, an abrupt behaviour can occur while irradiation power rises [36].

On the other hand, the reaction time has a significant positive effect upon the peak area. Nevertheless, its interaction with microwave irradiation power, produces a significant negative effect in the peak area of both analytes (see Fig. S6).

Response surface mapping was an effective way to find the optimum conditions. The design fitting a full quadratic model is provided below:

$$\text{Peak area} = 101499.087 + 3957.610x - 16.675x^2 + 4266.878y - 34.757y^2 - 19.894xy$$

where, y represents the microwave irradiation power and x the reaction time of the model obtained by multiple regression.

The regression models obtained were used to calculate the response surface for each variable separately. The response surface plot for the peak areas (Fig. 3) shows a curvature that demonstrates a significant interaction between microwave irradiation power and reaction time, indicating that higher reaction time values and lower microwave power are optimal for the extraction process.

According to the overall results of the optimisation study, the following experimental conditions were chosen: microwave irradiation power 20% (140 w) and a reaction time of 90 s (Fig. S7 of supplementary material). Fig. 4 shows the chromatogram of spiked plasma solution (0.5 μg mL^{-1} ATN and PRO) analyzed under the most favourable conditions described above.

3.2. Method validation

The validation of the proposed method was carried out by establishing linearity, intra- and inter-day precision, accuracy, selectivity and sensitivity parameters according to International Conference on Harmonization (ICH) guidelines [37]. Regression equations, correlation of determination (r^2), linear dynamic ranges (LDRs), limits of detection and quantitation (LODs and LOQs) were calculated under optimal conditions and are summarized in Table 2.

3.2.1. Linearity

Calibration curves of the analytes were obtained for standard ATN and PRO solutions prepared in MeCN and for spiked plasma samples. Each calibration set included seven data points and each point was run at least three times. Table 2 shows the regression equations of the peak areas of ATN and PRO as a function of concentration. As can be seen, the calibration curves were linear over the concentration range studied, indicating no significant deviation from linearity ($r^2 > 0.9982$) for all cases. Matrix effects were determined by comparing the slopes of the calibration curves obtained with the standard solutions and spiked plasma. A paired Student t-test indicated that the slopes of the calibration (using standard solutions) and the addition standard graphs were not statistically different ($P < 0.05$). Hence, the standard calibration technique with standard solutions could be used for the determination of ATN and PRO in plasma samples.

3.2.2. Precision and recovery

Precision of the proposed procedure was characterised by the repeatability, which was calculated for 5 consecutive measurements at three concentration levels 0.05, 0.25 and 0.75 μg mL^{-1} of ATN and PRO in spiked plasma samples. The precision expressed as

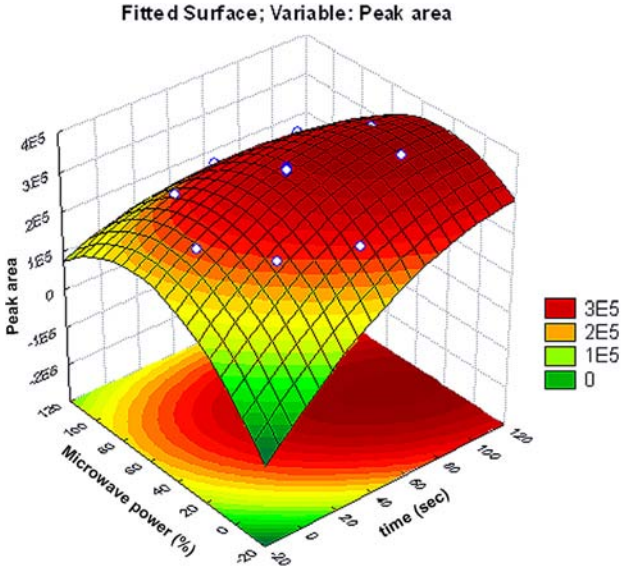


Fig. 3. Surface response using central composite design obtained by plotting microwave irradiation power vs. reaction time.

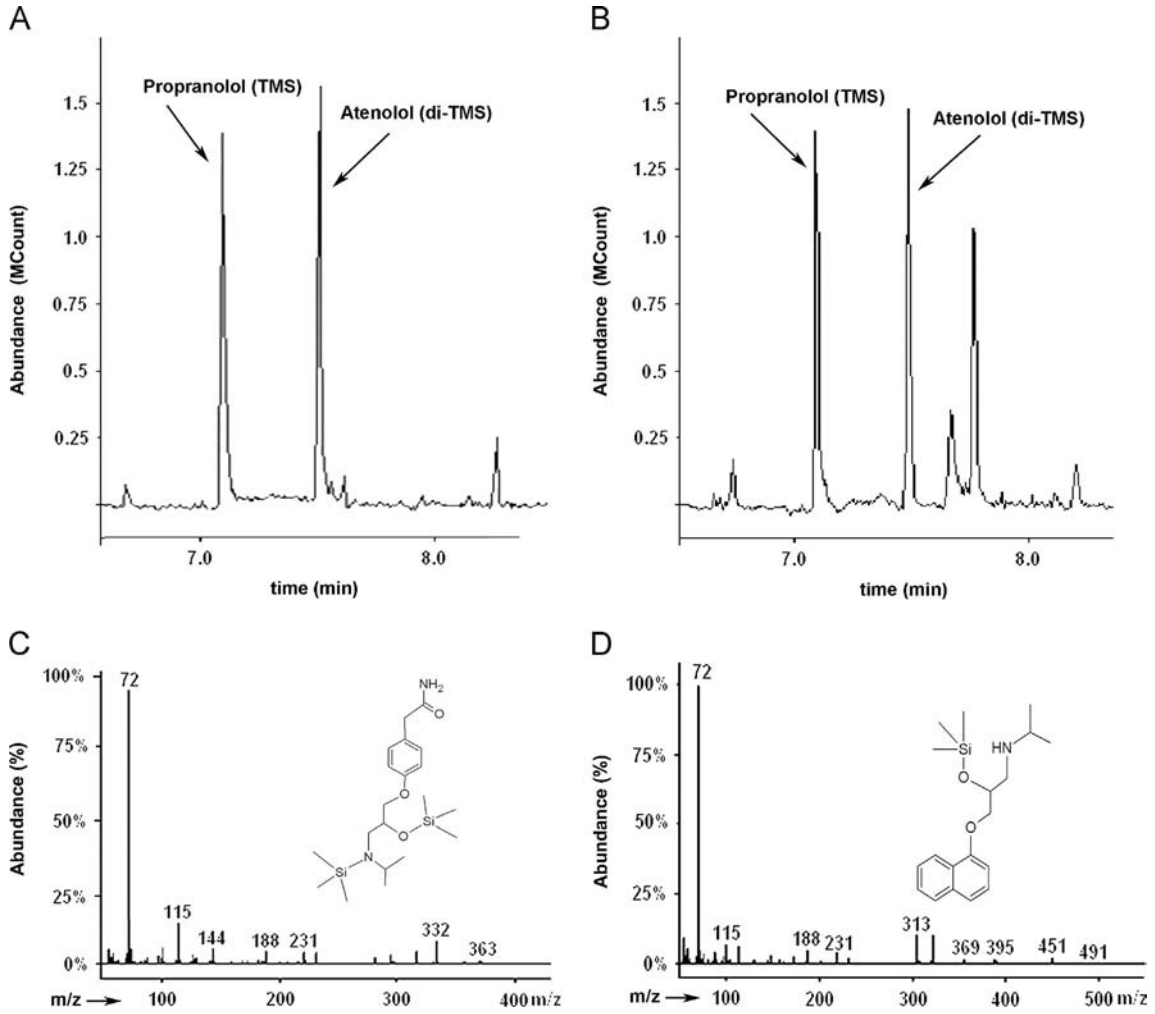


Fig. 4. Chromatograms obtained under optimised conditions of the method for (A) standard solution spiked with 0.5 μg mL^{-1} of ATN and PRO and (B) human plasma spiked at the same concentration. (C) and (D) mass spectra of ATN and PRO TMS derivatives, respectively.

Table 2
Analytical figures of merit of the developed SPE-MSFIA-MW/GC–MS system for ATN and PRO analysis.

Analytical parameter	ATN[a]	ATN[b]	PRO[a]	PRO[b]
Dynamic range (μg mL^{-1})	0.006–1.000	0.006–1.000	0.006–1.000	0.006–1.000
Slope ± RSD (n=5)	800765(±851)	808197(±832)	753838(±993)	749078(±311)
Intercept ± RSD (n=5)	+2160 (±45)	+2798 (±46)	+1262 (±55)	+1990 (±32)
r^2 (n=5)	0.9990	0.9989	0.9982	0.9995
LOQ (μg mL^{-1})	0.006	0.006	0.006	0.006
LOD (μg mL^{-1})	0.002	0.002	0.002	0.002
RSD intraday (%) (n=5)	2.72[c]	2.76[c]	2.60[c]	1.51[c]
	2.11[d]	0.58[d]	2.12[d]	0.83[d]
	2.85[e]	2.90[e]	0.48[e]	2.86[e]
RSD inter day (%) (n=5)	0.25[c]	1.27[c]	1.59[c]	1.24[c]
	2.61[d]	2.11[d]	2.70[d]	2.18[d]
	3.85[e]	3.49[e]	3.92[e]	2.58[e]
Recovery (%)		95.2[c]		99.0[c]
		102.0[d]		106.4[d]
		104.4[e]		103.7[e]

[a] Standard solution.
[b] Spiked plasma; concentration level.
[c] 0.75 μg mL^{-1}.
[d] 0.5 μg mL^{-1}.
[e] 0.25 μg mL^{-1}.

coefficient variation (CV) was $<3.85\%$ for all tested concentrations. The inter-day-assay precision was also determined on five different days. The CV did not exceed 3.0% demonstrating the good stability and repeatability of the developed pretreatment system.

The recovery was calculated at three concentration levels 0.05, 0.25 and 0.75 μg mL^{-1} by comparison of responses of ATN and PRO from spiked plasma samples with those found by injection of standard solutions at the same concentrations.

The mean absolute recovery was between 90.25% and 106.32% for both analytes, and the extraction efficiency was constant over the range mentioned above. These values demonstrated that the RAM column could be used repeatedly in the MSFIA system without loss of extraction efficiency.

3.2.3. Selectivity

The selectivity criterion demonstrated that the proposed method is not affected by the presence of interferences. The method selectivity was determined by checking the chromatograms obtained from blank plasma samples and plasma spiked with ATN and PRO (0.5 $\mu g\ mL^{-1}$). Each sample was tested for interferences and no endogenous compounds were encountered. The retention time of ATN-di-TMS and PRO-TMS were 7.10 and 7.50 min, respectively.

3.2.4. Sensitivity

Sensitivity was determined by the limits of detection (LOD) and limits of quantitation (LOQ). The LOD and LOQ defined as the lowest concentration with a signal to noise ratio of at least 3:1 and 10:1, respectively. The lowest concentration that can be quantified with acceptable accuracy and precision was 0.006 $\mu g\ mL^{-1}$ for ATN and PRO, respectively. Furthermore, the limits of detection for both analytes were of 0.002 $\mu g\ mL^{-1}$. As can be seen, the method has sufficient sensitivity for real drug level monitoring of ATN and PRO in human plasma. The values of the analytical parameters reported in Table 2 are comparable with those obtained by other reported methods [8,10,12–14,18] making our approach competitive in terms of reproducibility and sensitivity. Table 3 presents a comparison of the developed MSFIA-SPE-MW/GC–MS results for on-line sample treatment and determination of ATN and PRO in human plasma with other methods (off line) found in the literature. The present method has comparable LODs, repeatability and extraction time. Also, it provides the possibility of overlapping the microwave-assisted derivatisation step, with the clean up, preconcentration, chromatographic separation and reconditioning of the RAM column, increasing the overall sample throughput (one sample every 7 min). This is a compelling reason to select the present method, with advantages of being faster, simpler, and more environmentally friendly since smaller volumes of organic solvents are used,

3.3. Application to plasma samples

The effectiveness of the proposed method was examined by analyzing plasma samples of 6 hypertensive volunteers, i.e. patients receiving ATN or PRO treatment. The plasma samples were supplied by the Department of Cardiology of the Hospital of the University of Los Andes (HULA). The criteria for inclusion in the study were: being over 18 and treated for hypertension with 50 mg ATN or 80 mg PRO. All blood samples were taken in the range between 2 and 4 h after dosing. For analysis, samples were prepared according to the proposed procedure and were measured at least three times. Table 4 shows the results of each sample analysed with the present method.

The mean concentrations found were $0.107 \pm 0.030\ \mu g\ mL^{-1}$ for ATN and $0.155 \pm 0.040\ \mu g\ mL^{-1}$ for PRO, respectively. These values were consistent with those reported in the literature in pharmacokinetic studies [10,13,18,38] indicating that the method is suitable for routine monitoring of the considered drugs. Additionally, plasma samples were also analysed by another validated method previously developed in our laboratory [39]. There was a good correlation between concentrations determined by both methods (r^2 correlation graph 0.9885 see Fig. S-8). The proposed method presents improved or similar analytical characteristics concerning the application range and limits of detection. Indeed, considering the organic solvent consumed and the effluent produced in the sample preparation step, the proposed MSFIA-SPE system is "greener", with lower values for both of them. In comparison with other automatic strategies proposed for the same analytes but not based on SPE hyphenated schemes, the present method is undoubtedly more suitable for screening purposes, attaining also a higher determination frequency (see Table 3.).

4. Conclusions

A semi-automated analytical method was developed and successfully applied to human plasma samples for the determination of ATN and PRO by GC–MS. The methodology includes an automatic SPE-MSFIA-MW procedure for extraction and derivatisation of analytes avoiding manual sample preparation. Microwave heating yielded excellent results regarding recovery and sensitivity of analytes, and also increasing the sample preparation throughput. The minimum manipulation of plasma samples

Table 4
Results obtained applying the developed SPE-MSFIA-MW system coupled to GC/MS to real plasma samples.

Sample	Analyte	Dosage (mg)	Concentration found ($\mu g\ mL^{-1}$)
1	Atenolol	100	0.250 ± 0.002
2	Atenolol	100	0.302 ± 0.003
3	Atenolol	100	0.498 ± 0.006
4	Propranolol	80	0.155 ± 0.007
5	Propranolol[a]	40	0.102 ± 0.006
6	Propranolol[a]	40	0.092 ± 0.007

[a] Day and night dosages.

Table 3
Comparison of different off-line methods for ATN and PRO determination in human plasma with the proposed in-syringe-SPE-MSFIA-MW/GC–MS system.

Analyte	Method	Sample preparation time (min)[a]	Recovery (%)	LOD–LOQ ($\mu g\ mL^{-1}$)	Ref.
ATN–PRO	LLE/LC-UV	30	ATN: 100 PRO: 50.0	6.0–25	[8]
PRO	SPE/LC–MS	10	98	0.05 - 0.20	[9]
ATN	LLE/LC-FLD	20	98	6.0 - 25	[10]
ATN–PRO	SPME[b]/LC–MS	100	77	LOD: 3800	[11]
ATN	SPE/LC–MS	10	98	1.0	[12]
ATN	SPE/LC–MS	10	90	LOQ: 10	[14]
ATN	LLE/GC–MS	20	90	5.0–15	[18]
ATN–PRO	SPE/LC-FLD	6	98	ATN: 15–6.0 PRO: 8–3	[39]
ATN–PRO	SPE-MSFIA-MW/GC–MS	7	ATN: 100 PRO: 103	2.0–6.0	Present method

[a] Previous procedures to sample extraction not included.
[b] SPME: Solid Phase Microextraction.

improved the precision, shortened the analysis time and lowered costs per analysis, compared to conventional "off-line" methods. This method has been successfully applied to several plasma samples from drug users with a sampling throughput of 7 samples h^{-1}, achieving the overlapping of the microwave-assisted derivatisation step, with the clean up, preconcentration chromatographic separation and reconditioning of the RAM column, increasing its usefulness for routine analysis. In addition, results were in good agreement with those obtained by a previously validated LC-FLD method conferring robustness to the proposed methodology. Thus, this method is proposed as an attractive alternative to perform pharmacokinetic studies in determination of ATN and PRO for clinical use. Further research will be focused in total automation of the entire analytical setup by hyphenation of the sample treatment with GC–MS injection, which would represent a significant improvement in sample manipulation and analysis throughput.

Acknowledgements

The authors are very grateful to FONACIT of Venezuela for financial Project G-2005000641. S. Clavijo is very grateful with Esther Giménez for its invaluable collaboration in blood sample taking.

Appendix A. Supporting information

Supplementary data associated with this article can be found in the online version at http://dx.doi.org/10.1016/j.talanta.2014.08.056.

References

[1] M. Velasco, B. Romero, M. Betancourt, Archivos Venezolanos de Farmacología y Terapéutica (AVFT) 21 (2002) 139–147.
[2] J. Flórez, Farmacología Humana, third ed., Masson, Barcelona, España, 1998.
[3] F. Quevedo, Diagnóstico 43 (2004) 94–96.
[4] R. Ventura, G. González, M.T. Smeyers, R. de la Torre, J. Segura, J. Anal. Toxicol. 22 (1998) 127–134.
[5] L.C. Silva, M.G. Trevisan, R.J. Poppi, M.M. Sena, Anal. Chim. Acta 595 (2007) 282–288.
[6] T.P. Ruiz, C. Martinez-Lozano, V. Tomas, J. Carpena, Talanta 45 (1998) 969–976.
[7] R.N. Goyal, V.K. Gupta, M. Oyama, N. Bachheti, Electrochem. Commun. 8 (2006) 65–70.
[8] M. Delamoye, C. Duverneuil, F. Paraire, P. de Mazancourt, J.C. Alvarez, Forensic Sci. Int. 141 (2004) 23–31.
[9] M.H. Iha, A.S. Martinez, P.S. Bonato, J. Chromatogr. B 767 (2002) 1–9.
[10] L.R. Pires de Abreu, S.A. Calafatti de Castro, J. Pedrazzoli Jr., J. Am. Assoc. Pharm. Sci. 5 (2003) 1–7.
[11] X. Hu, J. Pan, Y. Hu, G. Li, J. Chromatogr. A 1216 (2009) 190–197.
[12] L. Dong, J. Huang, Chromatographia 64 (2006) 583–586.
[13] P. Partani, Y. Modhave, S. Gurule, A. Khuroo, T. Monif, J. Pharmaceut. Biomed. 50 (2009) 966–976.
[14] W. Li, Y. Li, D.T. Francisco, W. Naidong, Biomed. Chromatogr. 19 (2005) 385–393.
[15] R.D. Johnson, R.J. Lewis, Forensic Sci. Int. 156 (2006) 106–117.
[16] M.J. Paik, D.T. Nguyen, K.R. Kim, Chromatographia 64 (2006) 673–679.
[17] M.J. Paik, J. Lee, K.R. Kim, Anal. Chim. Acta 601 (2007) 230–233.
[18] B. Yilmaz, S. Arslan, Chromatographia 70 (2009) 1399–1404.
[19] B. Yilmaz, S. Arslan, J. Chromatogr. Sci. 49 (2011) 365–369.
[20] S. Souverain, S. Rudaz, J.L Veuthey, J. Chromatogr. B 801 (2004) 141–156.
[21] C. Mišl'anová, M. Hutta, J. Chromatogr. B 765 (2001) 167–177.
[22] K. Boos, A. Rudolphi, S. Vielhaver, S. Walford, D. Lubda, F. Eisenbiess, J. Anal. Chem. 352 (1995) 684–690.
[23] K. Boos, C. Grimm, Trends Anal. Chem. 10 (1990) 175–180.
[24] D. Šatínský, H.S. Serralheiro, P. Solich, A.N. Araújo, M.C.B.S.M. Montenegro, Anal. Chim. Acta 600 (2007) 122–128.
[25] A. Cerdà, V. Cerdà, An Introduction to Flow Analysis, first ed., Sciware, S.L., Palma de Mallorca, España. 2009.
[26] M. Miró, V. Cerdà, J.M. Estela, Trends Anal. Chem. 21 (2002) 199–210.
[27] M. Caban, P. Stepnowski, M. Kwiatkowski, N. Migowska, J. Kumirska, J. Chromatogr. A 1218 (2011) 8110–8122.
[28] E. Pujos, C. Cren-Olivé, O. Paisse, M.M. Flament-Waton, M.F. Grenier-Loustalot, J. Chromatogr. B 877 (2009) 4007–4014.
[29] L. Chen, D. Song, Y. Tian, L. Ding, A. Yu, H. Zhang, Trends Anal. Chem. 27 (2008) 151–159.
[30] K. Madej, Trends Anal. Chem. 28 (2009) 436–446.
[31] J.M. Halket, V.G. Zaikin, Eur. J. Mass Spectrom. 9 (2003) 1 (Review).
[32] K. Blau, Handbook of Derivatives for Chromatography, Second ed., Wiley Interscience, 1998.
[33] J.L. Luque-García, M.D. Luque de Castro, Trends Anal. Chem. 22 (2003) 90–98.
[34] L. Amendola, F. Molaioni, F. Botré, J. Pharmaceu. Biomed. 23 (2000) 211–221.
[35] C.R.T. Tarley, G. Silveira, W.N.L. Santos, G.D. Matos, E.G.P. Silva, M.A. Bezerra, M. Miró, S.L.C. Ferreira, Microchem. J. 92 (2009) 58–67.
[36] D. Montgomery, Diseño y Análisis de Experimentos, second ed., Limusa – Willey, México, 2005.
[37] International Conference of Harmonization (ICH) Q2B: Validation of Analytical Procedures Methodology. US FDA Federal Register, 62 (1997) pp. 27463–27467.
[38] A. Khuroo, S. Mishra, O. Singh, S. Saxena, T. Monif, Chromatographia 68 (2008) 721–729.
[39] M.R. Brunetto, S. Clavijo, Y. Delgado, W. Orozco, C. Ayala, M. Gallignani, L. Calderón, Revfarm 53 (2011) 28–37.

Talanta 132 (2015) 23–28

Contents lists available at ScienceDirect

Talanta

journal homepage: www.elsevier.com/locate/talanta

Non-chromatographic speciation of chromium at sub-ppb levels using cloud point extraction in the presence of unmodified silver nanoparticles

Ignacio López-García, Yesica Vicente-Martínez, Manuel Hernández-Córdoba *

Department of Analytical Chemistry, Faculty of Chemistry, Regional Campus of International Excellence "Campus Mare Nostrum" University of Murcia, E-30100 Murcia, Spain

ARTICLE INFO

Article history:
Received 2 July 2014
Received in revised form
8 August 2014
Accepted 12 August 2014
Available online 21 August 2014

Keywords:
Chromium
Speciation
Cloud point extraction
Silver nanoparticles
Water
Beer
Wine
ETAAS

ABSTRACT

The cloud point extraction (CPE) of silver nanoparticles (AgNPs) by Triton X-114 allows chromium (III) ions to be transferred to the surfactant-rich phase, where they can be measured by electrothermal atomic absorption spectrometry. Using 20 mL sample and 50 μL Triton X-114 (30% w/v), the enrichment factor was 1150, and calibration graphs were obtained in the 5–100 ng L^{-1} chromium range in the presence of 5 μg L^{-1} AgNPs. Speciation of trivalent and hexavalent chromium was achieved by carrying out two CPE experiments, one of them in the presence of ethylenediaminetetraacetate. While in the first experiment, in absence of the complexing agent, the concentration of total chromium was obtained, the analytical signal measured in the presence of this chemical allowed the chromium (VI) concentration to be measured, being that of chromium (III) calculated by difference. The reliability of the procedure was verified by using three standard reference materials before applying to water, beer and wine samples.
© 2014 Elsevier B.V. All rights reserved.

1. Introduction

In the environment chromium is present in two oxidation states, Cr(III) and Cr (VI), which have different physiological effects [1,2]. Due to the high toxicity of the hexavalent form, several countries have established severe restrictions concerning the presence of this metal in waters and, since both the authorized concentrations and those usually found in these samples are very low, at the μg L^{-1} level [3,4], the need exists for sensitive, easy-to-carry out analytical procedures to facilitate routine control in the laboratory. The very low concentration involved means that inductively coupled plasma mass spectrometry (ICP-MS) should be a suitable analytical technique for the purpose. However, the difficulty of dealing with such low concentrations is increased by the need to speciate both forms of the metal due to the above mentioned toxicity, the result of which is that a liquid chromatographic (LC) step is often included in the analytical procedure [5]. The LC–ICP-MS combination allows the determination to be carried out but is not always easily available at the laboratory. Consequently, interest has increased in recent years to develop other approaches involving instrumentation that is commonly present in the laboratory and which may be underused.

The analytical procedures for the speciation of chromium at low concentrations have been reviewed by several authors [4,6–9] and the recent literature shows an increasing use of miniaturized preconcentration techniques to achieve an improvement in sensitivity with minimal handling of the sample. As a result, a diversity of non-chromatographic alternative choices to LC–ICP-MS has been proposed. Leaving aside a number of liquid–liquid microextraction systems [10–16], sometimes involving ionic liquids or hollow fibers [17–19], followed by the use of an atomic or even molecular technique for the final measurement, cloud point extraction (CPE) would seem to be a promising method. CPE is based on the observation that solutions of non-ionic surfactants may form micelles and become turbid when heated above the cloud point temperature, giving rise to two fractions that can be separated by centrifugation. The surfactant-rich phase (coacervate) concentrates the analyte, as occurs with classical liquid–liquid extraction, but with no need for an organic solvent [20]. CPE followed by measurement of the chromium in the coacervate by means of an atomic technique has already been used for chromium determination and speciation [21–26]. A complexing agent is usually incorporated in the sample solution to facilitate the transfer of the metal to the surfactant-rich phase. Most authors

* Corresponding author. Tel.: +34 868 887406; fax: +34 868 887682.
E-mail address: hcordoba@um.es (M. Hernández-Córdoba).

http://dx.doi.org/10.1016/j.talanta.2014.08.036
0039-9140/© 2014 Elsevier B.V. All rights reserved.

have proposed electrothermal atomic absorption spectrometry (ETAAS) for the final measurement since, in addition to its high sensitivity, this analytical technique is selective and only requires a low volume of sample to be injected into the electrothermal atomizer.

During a study recently carried out in our laboratory on the CPE of silver nanoparticles (AgNPs) [27], it was observed that chromium species were also coextracted into the coacervate despite the absence of an auxiliary complexing agent. The AgNPs were used as obtained, with no modification by functionalization or physico-chemical treatment, so that they apparently acted directly as efficient carriers, transferring ultratraces of chromium to the coacervate. The direct interaction of chromium species with AgNPs has already been reported and represents the basis for sensitive molecular spectrophotometric and fluorimetric procedures [28–30] for determination in aqueous solutions but, to the best of our knowledge, there are no previous reports describing the analytical benefit that can be obtained by using the above mentioned co-extractant effect. Taking into account both the characteristics of CPE and ETAAS, a sensitive procedure for the speciation of extremely low chromium concentrations seemed feasible, and the results of the research into such a possibility are described in this manuscript.

2. Experimental

2.1. Instrumentation

All the measurements were carried out with a model 600 atomic absorption spectrometer (Perkin-Elmer, Shelton, USA) equipped with a transversely heated graphite atomizer and a Zeeman-effect background correction device. Pyrolytic graphite platforms inserted into pyrolytically coated tubes were obtained from the same manufacturer. Argon flowing at 250 mL min^{-1} was used as inert gas. Measurements were carried out using a chromium hollow cathode lamp (Perkin-Elmer) as the radiation source. Integrated absorbance was exclusively used as the analytical signal. The instrumental parameters are summarized in Table 1.

Once the procedure had been optimized, the autosampler provided with the instrument was not used. Instead, the aliquots were introduced into the atomizer by manual injection using a chromatographic-type syringe provided with a polytetrafluoroethylene tube in its tip to avoid physical contact between the plunger of the syringe and the solutions.

A 50 W ultrasound bath (ATU, Valencia, Spain) with temperature control was also used.

Table 1
Instrumental parameters for chromium determination.

Parameter			
Lamp current, mA	30 (HCL)		
Wavelength, nm	357.9		
Bandwidth, nm	0.7		
Atomizer type	Pyrolytic tube with L'Vov platform		
Injected volume, μL	10		
Chemical modifier	Pd(II) 2000 μg mL^{-1} (20 μL)		
Background correction	Zeeman		
Furnace heating program			
Step	Temperature, °C	Ramp, s	Hold, s
1: Dry	110	10	30
2: Dry	300	5	30
2: Ash	900	10	20
3: Atomize[a],[b]	2300	0	5
4: Clean	2450	1	5
Sequence			
Step A: Pipet the modifier and run step 1			
Step B: Pipet sample or standard and run the entire program			

[a] Internal argon flow stopped;
[b] Reading step.

2.2. Reagents and samples

All the solutions were prepared with pure water (18 MΩ cm resistivity) obtained with a Milli-Q system (Millipore, Bedford, MA, USA). The glassware and plasticware (polypropylene) was washed with 1% (v/v) concentrated nitric acid solution, and then rinsed with water before use.

The chromium (III) and (VI) stock standard solutions (1000 μg mL^{-1}) were prepared from $Cr(NO_3)_3 \cdot 9H_2O$ and $K_2Cr_2O_7$ (Fluka, Buchs SG, Switzerland), respectively, in water, and diluted daily to obtain appropriate working solutions. Triton X-114, sodium tetrahydroborate ($NaBH_4$) and silver nitrate ($AgNO_3$) were obtained from Fluka. Concentrated nitric acid (65%), disodium ethylenediaminetetraacetate (EDTA) and the rest of the chemicals used were obtained from Merck (Darmstadt, Germany).

Tap water was collected from the mains supply of the University of Murcia and analyzed both directly and after passing through a domestic water purifier system. Wine, beer and bottled water samples were purchased in a supermarket. The seawater samples were obtained from near the shore, close to a harbor in south-eastern Spain. These later samples were filtered and maintained in plastic containers at 4 °C until they were analyzed (less than 48 h) by the general procedure.

In addition, three standard reference materials, namely NIST 1640a (trace elements in natural water), NASS-6 (seawater reference material for trace metals) and SPS-SW2 Batch 125 (reference material for measurement of elements in surface waters) with a certified content of total chromium were obtained from the National Institute of Standards and Technology, National Research Council Canada and Spectrapure Standards, respectively.

2.3. Preparation of silver nanoparticles (AgNPs)

The silver nanoparticles (AgNPs) were prepared according to the scientific literature [28]. For this purpose, 100 mL of 0.1 mM silver nitrate solution were placed in a flat-bottomed flask and, while the solution was vigorously stirred, 0.012 g of solid $NaBH_4$ were incorporated, maintaining the stirring for 10 min. The mixture was aged overnight in the dark. The AgNPs suspension thus prepared was stable for several days at room temperature.

2.4. General procedure

The sample solution (20 mL) containing chromium in the 5–100 ng L^{-1} range was placed in a centrifuge tube and 0.2 mL of a 1 mol L^{-1} nitric acid solution was incorporated to bring the pH close to 2, before heating to 60 °C. Next, 10 μL of a 0.1 mM AgNPs suspension and 50 μL of a 30% w/v Triton X-114 solution were added. The tube was gently shaken for a few seconds and then maintained at 60 °C for 10 min. The turbid mixture obtained was centrifuged at 4000 rpm for 5 min and a 10 μL aliquot of the recovered surfactant-rich solution was injected into the electrothermal atomizer. The heating program given in Table 1 was run, and the analytical signal due to total chromium was obtained.

For speciation, the experiment was repeated but incorporating 0.4 mL of a 0.3 mol L^{-1} EDTA solution immediately before adding the AgNPs suspension, while the rest of the procedure was the same. The analytical signal obtained corresponded to Cr(VI) which permitted Cr(III) concentration to be calculated by difference.

Calibration was carried out using Cr(III) and Cr(VI) standard solutions treated in the same way.

The wine samples were first diluted to ensure that the ethanol concentration was below 5% (v/v). In the case of beer samples, the same dilution step was carried out when necessary and the samples sonicated for 30 min for degasification.

3. Results and discussion

The literature reports [28–30] that AgNPs treated with citric or ascorbic acid interact with Cr(III), leading to a red-shift change in color from yellow to purple. The chromium (III) ions bind to the citrate or ascorbate covering the AgNPs, giving rise to a change in the aggregation of the solid particles and hence to a change in the color. The effect is also observed when hexavalent chromium is used, since this species is reduced by ascorbate or by the excess of reductant present in the dispersion of AgNPs, and is the basis for sensitive colorimetric and fluorimetric procedures for determining chromium. This spectral change is noticeable when AgNPs concentration is at the mg L^{-1} level. By our part it was observed that there is also an interaction between chromium ions and AgNPs in the absence of citrate and ascorbate, when using extremely low concentrations of the solid particles at the μg L^{-1} level. In such conditions, the dispersion is colorless and apparently not altered by the presence of chromium traces. However, when Triton X-114 is incorporated above the critical micellar concentration (0.2 mM) and the mixture is heated to provoke CPE, the AgNPs are extracted into the coacervate, a fact which is already known, but chromium ions are also transferred to the surfactant-rich phase, which has not been described before. The extraction of both AgNPs and chromium ions is practically complete. The transfer effect, that occurs for both Cr(III) and Cr(VI) does not occur in the absence of AgNPs and is the basis for the determination of the extremely low amounts of chromium studied here.

3.1. Optimization of the CPE

A number of experiments were carried out in which small amounts of AgNPs (in the 1–50 μg L^{-1}) range were first incorporated in solutions containing Cr (III) and Cr(VI) and then CPE was carried out with Triton X-114. The effect of the experimental conditions was studied for each of the chemicals involved.

In order to obtain a high enrichment factor, 20 mL of aqueous sample were used. The amount of Triton X-114 affects the final volume of the coacervate recovered. Thus, for 150 μL of 30% Triton X-114, the volume recovered was approximately 60 μL. To attain maximum sensitivity, most of the experiments were finally carried out using 50 μL of the surfactant solution, which permitted the recovery of approximately 18 μL of coacervate. The optimal temperature for the CPE was found to be 60 °C maintained for 10 min. The optimal pH was studied experimentally and found to be in the 1.5–2.5 range for both Cr(III) and Cr(VI). Consequently, the incorporation of a small volume of nitric acid to the water samples to achieve a pH close to 2 is recommended. A monochloroacetic/monochloroacetate buffer solution provides the same result but the direct adjustment of the pH proved suitable and was used in the rest of the experiments.

The results obtained when the effect of the AgNPs concentration was studied for both Cr(VI) and Cr(III) are shown in Fig. 1. As can be seen in the graphs, chromium species were not extracted in the absence of AgNPs but, when present, even in a small concentration, the analytical signals obtained in the coacervates were maximal and constant. It should be noted that the AgNPs solutions contain an excess of reductant (sodium tetrahydroborate) due to the way in which they are prepared. This means that Cr(VI) is reduced and then interacts with the solid particles, meaning that the response is not dependent on the oxidation degree of the chromium. A 5 μg L^{-1} AgNPs concentration was found to be sufficient to completely transfer the chromium species to the coacervate for the whole range of analyte concentrations studied.

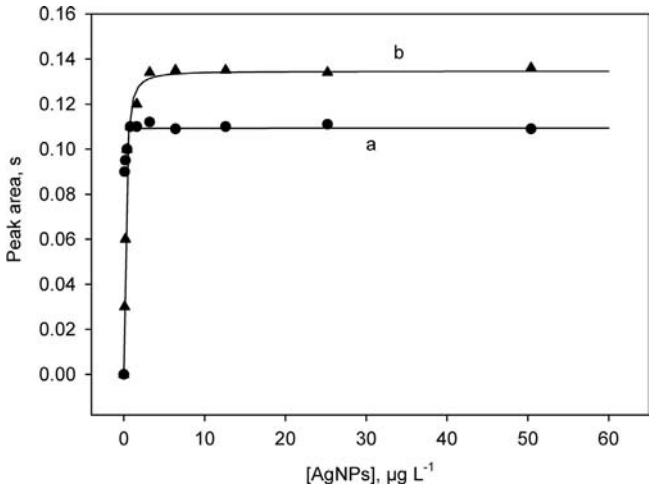


Fig. 1. Effect of the AgNPs concentration on the chromium signal obtained from the surfactant-rich phase. Lines a and b correspond to sample solutions containing 14 ng L^{-1} Cr(III) and 17 ng L^{-1} Cr(VI), respectively.

3.2. Optimization of ETAAS measurement

When the coacervates were injected into the electrothermal atomizer, the characteristic mass of chromium was higher than expected, probably as a consequence of the formation of chromium carbide due to the high amount of organic matter. To overcome this deleterious effect without diluting the coacervate (which would result in a decrease of the enrichment factor), a chemical modifier was tried. Some reports suggest the use of complexing agents [11,31,32], coating the atomizer with iridium [33] or the addition of a palladium salt [34]. The last was considered to be the most suitable way to increase sensitivity. A number of ashing–atomizing graphs were obtained in the usual way and it was verified that the incorporation of 20 μL of a 2000 μg mL^{-1} palladium solution together with the use of 1000 and 2300 °C as the calcination and atomization temperatures, respectively, resulted in well-defined chromium atomization profiles with a low characteristic mass (6 pg) and a low background, which was easily corrected by the Zeeman device. To avoid practical problems derived from the difference in the physicochemical properties of the coacervate and the modifier solution, the latter was first injected into the atomizer and the drying stage of the heating program was run. Next, the aliquot of coacervate was injected by means of a chromatographic syringe, and the entire program was run.

3.3. Chromium speciation

Since the chromium species transferred to the surfactant-rich phase with the aid of AgNPs is the trivalent form, speciation is possible. For this purpose, advantage can be taken of the relatively slow kinetics of Cr(III) complexation by the ethylenediaminetraacetate (EDTA) anion compared with the kinetics of the retention of this species on AgNPs. As can be seen in Fig. 2, the presence of a low EDTA concentration prevented Cr(III) from being transferred to the surfactant-rich phase. However, when the experiments were made using hexavalent instead of trivalent chromium, the

analyte was extracted in an extension that depended on the concentration of both AgNPs and the complexing agent. Since the experiments were carried out by first incorporating the EDTA solution in the sample solution and then the AgNPs suspension, a reasonable explanation for the observed behavior is that the retention of Cr(III) by the AgNPs is much faster than its complexation with EDTA. According to this hypothesis, the Cr(III) resulting from the reduction of Cr(VI) in the presence of EDTA is not complexed but rapidly and strongly retained on the solid particles. Only when the complexing agent concentration is high enough there is competition for Cr(III) with the nanoparticles and the signal decreases. If the AgNPs concentration increases, more EDTA is required for the competition effect to be observed. A 6 mmol L^{-1} EDTA and 5 μg L^{-1} AgNPs concentration were found to be suitable for the low concentrations of chromium involved in the experiments.

The reliability of the speciation scheme was checked by applying it to solutions prepared at three Cr(VI)/Cr(III) ratios. The results shown in Table 2 demonstrate that speciation at these low analyte concentrations is feasible.

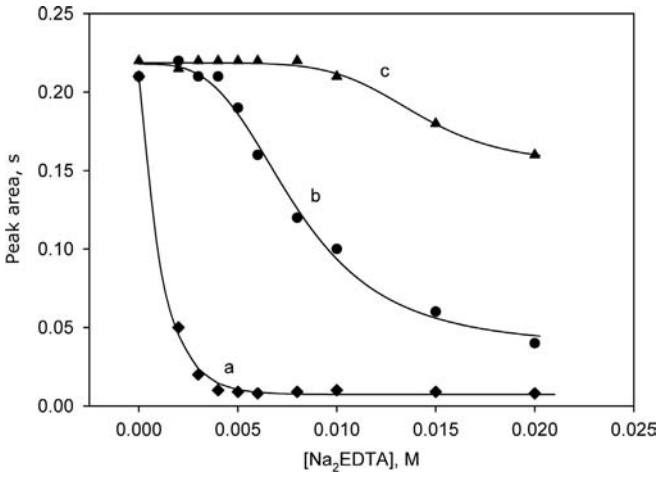


Fig. 2. Effect of the EDTA concentration on the chromium signal obtained from the surfactant-rich phase. Line a corresponds to a sample solution containing 50 ng L^{-1} Cr(III) in the presence of 5 μg L^{-1} AgNPs. Lines b and c, a 27 ng L^{-1} Cr(VI) solution in the presence of 0.5 and 5 μg L^{-1} AgNPs, respectively.

Table 2
Results (mean ± s, $n=5$) for the determination of Cr(VI) and Cr(III) in aqueous solutions.

Cr(VI)/Cr(III) ratio	Cr(VI), ng L^{-1}			Cr(III), ng L^{-1}		
	Added	Found	Recovery, %	Added	Found	Recovery, %
0.1	8	8 ± 1	101	80	81 ± 3	101
1	50	51 ± 2	102	50	51 ± 3	103
10	80	79 ± 3	99	8	8 ± 2	94

3.4. Analytical figures of merit: analysis of real samples

Using the optimized conditions, a linear relationship between the analytical signal and the chromium concentration in the sample was verified in the 5–100 ng L^{-1} range, with a detection limit (calculated on the basis of three times the standard deviation of y-residuals from the calibration graph) of 2 ng L^{-1}. The repeatability of the measurements was studied for three concentrations, namely 10, 20 and 50 ng L^{-1} and the relative standard deviations for 5 consecutive experiments in each case were 4.3, 3.8, and 3.8, respectively. The enrichment factor (EF) was calculated using the ratio between the slopes of a calibration line obtained from aqueous solutions submitted to the CPE procedure and the slope of a calibration line obtained with solutions that were not extracted. This experimental EF was found to be 1150.

Due to the characteristics inherent to ETAAS, selectivity was excellent. This foreseeable feature was verified by incorporating several foreign ions (Mg(II), Ca(II), Ba(II), Zn(II), Pb(II), Hg(II), Co(II), Ni(II), Cd(II), As(III), Al(III), Fe(III), Sb(III), As(V), sulfate and phosphate) up to a foreign ion:chromium ratio of 10,000 with no deleterious effect on the analytical signal. Only in the case of an AgNPs concentration of 0.5 μg L^{-1} was there a decrease in the analytical signal caused by Co (II), Ni(II) and Cd(II) when present in ion:chromium molar ratios exceeding 1000. This deleterious effect was attributed to the competition of these ions with chromium for the active sites of the solid particles, and disappeared when the recommended AgNPs concentration (5 μg L^{-1}) was used. Table 3 shows a summary of the main characteristics of the optimized procedure and of other comparable procedures based on CPE and ETAAS.

The procedure was checked by applying it to several real samples, namely water, beer and wine samples. The very low concentrations involved make it difficult to check the reliability of the results by direct comparison with those obtained using other approaches, and so three water samples with certified chromium contents were first used for this purpose. It should be noted that, due to the extreme sensitivity of the procedure here studied, these samples had to be diluted before being analyzed. The results obtained for these certified reference materials as well as for another six water samples of different origins are shown in Table 4, together with the results found by applying the standard additions method. When wine and beer samples were analyzed the presence of ethanol was seen to affect the CPE process. Additional experiments demonstrated that this

Table 3
Characteristic performance data of some procedures using CPE and ETAAS for chromium determination.

Analyte	Sample	Chelating agent	Surfactant	Enrichment factor	LOD, ng/L	Ref.
Cr(III), Cr(VI)	Human serum	PAN	Triton X-114	83.5	20	[35]
Cr(III), Cr(VI)	Water	Cupferron	Triton X-114	20	0.98 pg	[22]
Cr(III), Cr(VI)	Water	Br-PF	Triton X-100	50	10	[23]
Cr(III), Cr(VI)	Water	DPC	Triton X-114+SDS	92	1	[34]
Cr(VI)	Water	APDC	Triton X-114	200	3	[33]
Cr(III)+Cr(VI)	Vegetal leaf	5-Br-PADAP	Triton X-114	26.2	23	[36]
Cr(III), Cr(VI)	Water	PMBP	Triton X-114	42	21	[31]
Cr(III)	Water	8-Ox	Triton X-100	50	23	[32]
Cr(III), Cr(VI)	Water, wine and beer	AgNPs	Triton X-114	1150	2	This work

PMBP: 1-phenyl-3-methyl-4-benzoylpyrazol-5-one; PAN: 1-(2-pyridylazo)-2-naphtol; 5-Br-PADAP: 2-(5-bromo-2-pyridylazo)-5-(diethylamino)-phenol; 8-Ox: 8-hydroxyquinoline; APDC: ammonium pyrrolidine dithiocarbamate; DPC: 1,5 diphenyl carbazide; SDS: sodium dodecyl sulfate; Br-PF: dibromophenylfluorone.

Table 4
Determination of Cr(III) and Cr(VI) in water samples.

Sample	Cr(III)[a], ng L^{-1}			Cr(VI) [a], ng L^{-1}		
	Added	Found	Recovery, %	Added	Found	Recovery, %
TW[b]	0	6 ± 2	–	0	< 2	–
	20	27 ± 2	105	20	21 ± 2	105
	50	56 ± 3	100	50	49 ± 3	98
TW+ORS[c]	0	39 ± 2	–	0	20	–
	20	60 ± 4	105	20	40 ± 4	100
	50	88 ± 4	98	50	68 ± 4	96
BMW[d] 1	0	10 ± 3	–	0	< 2	–
	20	29 ± 4	95	20	21 ± 4	105
	50	61 ± 4	102	50	49 ± 4	98
BMCW[e] 1	0	13 ± 2	–	0	18 ± 2	–
	20	32 ± 2	95	20	37 ± 2	95
	50	64 ± 4	102	50	69 ± 4	102
SW[f] 1	0	18 ± 2	–	0	23 ± 2	–
	20	37 ± 2	95	20	42 ± 2	95
	50	69 ± 3	102	50	74 ± 3	102
SW[f] 2	0	15 ± 2	–	0	18 ± 2	–
	20	36 ± 3	105	20	39 ± 3	105
	50	64 ± 3	98	50	67 ± 3	98
SRM 1640a[g]	0	14 ± 3	–	0	26 ± 4	–
	20	33 ± 4	95	20	45 ± 4	95
	50	65 ± 4	102	50	75 ± 4	98
NAAS-6[h]	0	36 ± 3	–	0	22 ± 2	–
	20	55 ± 4	95	20	43 ± 4	105
	50	87 ± 4	102	50	73 ± 4	102
SPS-SW2[i]	0	8 ± 2	–	0	3 ± 1	–
	20	27 ± 3	95	20	22 ± 3	95
	50	59 ± 3	102	50	52 ± 3	98

[a] Mean value ± standard deviation (n=3);
[b] TW: tap water;
[c] TW+ORS: tap water with reverse osmosis system;
[d] BMW: bottled mineral water;
[e] BMCW: bottled mineral carbonated water;
[f] SW: sea water;
[g] Total chromium after 1:1000 dilution, certified value: 40.22 ± 0.28 μg kg^{-1}, ;
[h] Total chromium after 1:2 dilution, certified value: 118 ± 8 ng L^{-1};
[i] total chromium after 1:1000 dilution, certified value: 10.0 ± 0.05 μg L^{-1}.

Table 5
Determination of Cr(III) and Cr(VI) in wine samples.

Sample	Cr(III)[a], ng L^{-1}			Cr(VI) [a], ng L^{-1}		
	Added	Found	Recovery, %	Added	Found	Recovery, %
Red wine (DO[b] 1)	0	17 ± 2	–	0	57 ± 3	–
	50	67 ± 3	100	50	108 ± 4	102
Red wine (DO 2)	0	26 ± 2	–	0	61 ± 3	–
	50	75 ± 4	98	50	110 ± 4	98
Red wine (DO 3)	0	23 ± 2	–	0	73 ± 4	–
	50	72 ± 4	98	50	124 ± 4	102
Red wine (DO 4)	0	18 ± 2	–	0	40 ± 2	–
	50	70 ± 3	104	50	88 ± 4	96
Red wine (DO 5)	0	10 ± 2	–	0	135 ± 4	–
	50	59 ± 3	98	50	183 ± 5	96
Red wine (DO 6)	0	11 ± 2	–	0	61 ± 3	–
	50	62 ± 3	102	50	110 ± 4	98
White wine (DO1)	0	21 ± 3	–	0	56 ± 3	–
	50	70 ± 4	98	50	107 ± 4	102
White wine (DO2)	0	14 ± 2	–	0	51 ± 3	–
	50	65 ± 4	102	50	103 ± 4	104

[a] Mean value ± standard deviation (n=3);
[b] DO: designation of origin.

Table 6
Determination of Cr(III) and Cr(VI) in beer samples.

Sample	Cr(III)[a], ng L^{-1}			Cr(VI) [a], ng L^{-1}		
	Added	Found	Recovery, %	Added	Found	Recovery, %
Beer 1 (bottle)	0	37 ± 2	–	0	< 2	–
	50	86 ± 3	98	50	49 ± 2	98
Beer 2 (bottle, without alcohol)	0	48 ± 3	–	0	58 ± 3	–
	50	99 ± 4	102	50	109 ± 4	102
Beer 3 (canned)	0	< 2	–	0	24 ± 2	–
	50	52 ± 3	104	50	72 ± 4	96
Beer 4 (canned, without alcohol)	0	< 2	–	0	104 ± 4	–
	50	52 ± 3	104	50	156 ± 4	104

[a] Mean value ± standard deviation (n=3).

deleterious effect only appears for ethanol concentrations above 6% v/v, approximately. Taking advantage of the sensitivity of the procedure, this inconvenience can be easily overcome by dilution. Thus, wine and beer samples were diluted four and two times, respectively. In the case of beer, sonication for 20 min was used to degas the samples before analysis. The final results for wine and beer samples are given in Tables 5 and 6, respectively, together with its additional verification by means of the standard additions method.

4. Conclusion

Silver nanoparticles (AgNPs), even at the μg L^{-1} level, when submitted to CPE, interact with Cr(III) and completely transfer this species to the coacervate, where the metal can be measured by ETAAS. Due to the high sensitivity of ETAAS and the preconcentration factor inherent to CPE, a large enrichment factor for chromium is achieved, and extremely low amounts can be measured. Speciation is possible if ethylenediaminetetraacetate is used as an auxiliary reagent. The chemical reagents, as well as the instrumentation, are easily available so that the combination AgNPs–CPE–ETAAS appears to be a suitable alternative choice to LC–ICP-MS for the speciation of low amounts of chromium.

Acknowledgments

The authors are grateful to the Spanish MEC (Project CTQ 2012-34722/BQU) and to Comunidad Autónoma de la Región de Murcia (CARM, Fundación Séneca, Project 11796/PI/09) for financial support. YVM acknowledges a fellowship of MEC.

References

[1] K.R. Di Bona, S. Love, N.R. Rhodes, D. McAdory, S.H. Sinha, N. Kern, J. Kent, J. Strickland, A. Wilson, J. Beaird, J. Ramage, J.F. Rasco, J.B. Vincent, J. Biol. Inorg. Chem. 16 (2011) 381–390.
[2] M. Costa, C.B. Klein, Crit. Rev. Toxicol. 36 (2006) 155–163.
[3] C.J. Seidel, C.J. Corwin, J. Am. Water Works Assoc. 105 (2013) 37–38.
[4] R. Rakhunde, L. Deshpande, H.D. Juneja, Crit. Rev. Environ. Sci. Technol. 42 (2012) 776–810.
[5] H. Hagendorfer, W. Goessler, Talanta 76 (2008) 656–661.
[6] K. Pyrzynska, Int. J. Environ. Anal. Chem. 92 (2012) 1298–1311.
[7] X. Zhao, N. Song, W. Zhou, Q. Jia, Cent. Eur. J. Chem. 10 (2012) 927–937.
[8] C.D. Pereira, J.G. Techy, E.M. Ganzarolli, S.P. Quinaia, J. Environ. Monit. 14 (2012) 1559–1564.
[9] J. Namiesnik, A. Rabajczyk, Crit. Rev. Environ. Sci. Technol. 42 (2012) 327–377.
[10] M.M. López Guerrero, E. Vereda Alonso, J.M. Cano Pavon, M.T. Siles Cordero, A. García de Torres, J. Anal. At. Spectrom. 27 (2012) 682–688.
[11] A.S. Amin, M.A. Kassem, Spectrochim. Acta A 96 (2012) 541–547.

[12] R.A. Gil, S. Cerutti, J.A. Gasquez, R.A. Olsina, L.D. Martinez, Talanta 68 (2006) 1065–1070.
[13] H. Abdolmohammad-Zadeh, G.H. Sadeghi, Talanta 94 (2012) 201–208.
[14] S.M. Yousefi, F. Shemirani, J. Hazard. Mater. 254 (2013) 134–140.
[15] M. Alexovic, I.S. Balogh, J. Skrlikova, V. Andruch, Anal. Methods 4 (2012) 1410–1414.
[16] I. López-García, M. Briceño, Y. Vicente-Martínez, M. Hernández-Córdoba, Talanta 115 (2013) 166–171.
[17] C.J. Zeng, Y. Lin, N. Zhou, J.T. Zheng, W. Zhang, J. Hazard. Mater. 237 (2012) 365–370.
[18] S. Sadeghi, A.Z. Moghaddam, Talanta 99 (2012) 758–766.
[19] I. López-Garcia, Y. Vicente-Martinez, M. Hernández-Córdoba, J. Anal. At. Spectrom. 27 (2012) 874–880.
[20] A. Ballesteros-Gómez, M.D. Sicilia, S. Rubio, Anal. Chim. Acta 677 (2010) 108–130.
[21] M. Sun, Q.H. Wu, J. Pharm. Biomed. Anal. 60 (2012) 14–18.
[22] L. Machackova, M. Zemberyova, Anal. Methods 4 (2012) 4042–4048.
[23] X. Zhu, B. Hu, Z. Jiang, M. Li, Water Res. 39 (2005) 589–595.
[24] H.I. Ulusoy, R. Gurkan, O. Yilmaz, M. Akcay, J. Anal. Chem. 67 (2012) 131–139.
[25] M. Hashemi, S.M. Daryanavard, Spectrochim. Acta A 92 (2012) 189–193.
[26] P. Liang, H.B. Sang, J. Hazard. Mater. 154 (2008) 1115–1119.
[27] I. López-García, Y. Vicente-Martinez, M. Hernández-Córdoba, Spectrochim. Acta B 101 (2014) 93–97. http://dx.doi.org/10.1016/j.sab.2014.07.017.
[28] X.Y. Wu, Y.B. Xu, Y.J. Dong, X. Jiang, N.N. Zhu, Anal. Methods 5 (2013) 560–565.
[29] A. Ravindran, M. Elavarasi, T.C. Prathna, A.M. Raichur, N. Chandrasekaran, A. Mukherjee, Sensor Actuart. B – Chem. 166–167 (2012) 365–371.
[30] M. Elavarasi, M.L. Paul, A. Rajeshwari, N. Chandrasekaran, A.B. Mandal, A. Mukherjee, Anal. Methods 4 (2012) 3407–3412.
[31] P. Liang, H. Sang, J. Hazard. Mater. 154 (2008) 1115–1119.
[32] X.S. Zhu, Z.C. Jiang, B. Hu, M.F. Li, Chinese J. Anal. Chem. 31 (2003) 1312–1316.
[33] N.N. Meeravali, M.A. Reddy, S.J. Kumar, Anal. Sci. 23 (2007) 351–356.
[34] M. Ezoddin, F. Shemirani, R. Khani, Desalination 262 (2010) 183–187.
[35] M. Sun, Q. Wu, J. Pharm. Biomed. Anal. 60 (2012) 14–18.
[36] M.A. Bezerra, A.R.A. Nogueira, S.G. Lemos, S.L.C. Ferreira, Int. J. Environ. Anal. Chem. 88 (2008) 131–140.

Talanta 132 (2015) 29–36

Contents lists available at ScienceDirect

Talanta

journal homepage: www.elsevier.com/locate/talanta

Rapid determination of canagliflozin in rat plasma by UHPLC–MS/MS using negative ionization mode to avoid adduct-ions formation

Muzaffar Iqbal [a,b,*], Essam Ezzeldin [b], Khalid A. Al-Rashood [a], Yousif A. Asiri [c], Naser L. Rezk [d]

[a] Department of Pharmaceutical Chemistry, College of Pharmacy, King Saud University, Riyadh 11451, Saudi Arabia
[b] Bioavailability Laboratory, College of Pharmacy, King Saud University, Riyadh 11451, Saudi Arabia
[c] Department of Clinical Pharmacy, College of Pharmacy, King Saud University, Riyadh 11451, Saudi Arabia
[d] Department of Medical Laboratory Sciences, College of Applied Health Sciences, Taibah University, Madina, KSA & Andor Labs, Durham, NC, USA

ARTICLE INFO

Article history:
Received 19 May 2014
Received in revised form
13 August 2014
Accepted 14 August 2014
Available online 23 August 2014

Keywords:
Canagliflozin
UHPLC–MS/MS
Adduct ions
Pharmacokinetics
Rat plasma

ABSTRACT

Canagliflozin is the first sodium–glucose co-transporter-2 inhibitor, approved by the US Food and Drug Administration for the treatment of type 2 diabetes mellitus. In this study, a sensitive UHPLC–MS/MS assay for rapid determination of canagliflozin in rat plasma was developed and validated for the first time. Chromatographic separation of canagliflozin and zafirlukast (IS) was carried out on Acquity BEH C18 column (100 × 2.1 mm, i.d. 1.7 μm) using acetonitrile–water (80:20, v/v) as mobile phase at a flow rate of 0.3 mL min^{-1}. Canagliflozin and IS were extracted from plasma by protein precipitation method using acetonitrile. The mass spectrometric detection was performed using electrospray ionization source in negative mode to avoid canagliflozin adduct ions formation. Multiple reaction monitoring were used for quantitation of precursor to product ion at *m/z* 443.16 > 364.96 for canagliflozin and *m/z* 574.11 > 462.07 for IS, respectively. The assay was fully validated in terms of selectivity, linearity, accuracy, precision, recovery, matrix effects and stability. The validated method was successfully applied to the characterization of oral pharmacokinetic profiles of canagliflozin in rats. The mean maximum plasma concentration of canagliflozin of 1616.79 ng mL^{-1} was achieved in 1.5 h after oral administration of 20 mg kg^{-1} in rats.

© 2014 Elsevier B.V. All rights reserved.

1. Introduction

Sodium–glucose co-transporter-2 (SGLT-2) inhibitors have emerged as a novel class of oral anti-diabetic agents [1]. Canagliflozin is the first orally active SGLT-2 inhibitor, approved by both US Food and Drug Administration (March, 2013) and European Medicines Agency (November, 2013) for the treatment of type 2 diabetes in adult patients [2–4]. It is a specific SGLT2 inhibitor and exhibits approximately 200-fold higher selectivity for SGLT2 over SGLT1[5]. Canagliflozin inhibits reabsorption of filtered glucose from the lumen of the proximal tubules of the kidney, thereby leading to lowered renal threshold for glucose (RTG) and increased urinary glucose excretion [2,5,6].

Absorption of canagliflozin is rapid with peak plasma concentrations (C_{max}) achieved within 1–2 h following oral administration. After multiple dose administration, steady state levels were attained in 4–5 days [2,6,7]. Absolute oral bioavailability of canagliflozin is 65%, and it is highly bound to plasma protein (99%), mainly albumin [8]. Following single dose oral administration, the terminal half-life was in the range of 10.6–13.1 h with a large volume of distribution of 119 L [6,9]. It is mainly metabolized by glucuronidation via uridine diphosphate glucuronosyltransferase 1A9 (UGT1A9) and uridine diphosphate glucuronosyltransferase B4 (UGT2B4) into two inactive metabolites (M1 and M7). About 33% of metabolites are eliminated in the urine and approximately 42% are excreted in the feces [2,10].

Being a novel oral antidiabetic agent, a sensitive and robust bioanalytical assay is required for the determination of canagliflozin in plasma samples to support pharmacokinetic, therapeutic drug monitoring and drug interaction studies. Previous literature published on pharmacokinetic characterization of canagliflozin only described the summary of the bioanalytical assay for the determination of canagliflozin [10]. In spite of its global approval, to our knowledge there is no published method exist for canagliflozin quantification in biological matrices.

* Corresponding author at: Department of Pharmaceutical Chemistry, College of Pharmacy, King Saud University, Riyadh 11451, PO Box No. 2457, Saudi Arabia. Tel: +966 1469 7565, Mobile: +966 53 566 7290; fax: +966 1467 6220.
E-mail addresses: muziqbal@gmail.com, muziqbal@ksu.edu.sa (M. Iqbal).

http://dx.doi.org/10.1016/j.talanta.2014.08.041
0039-9140/© 2014 Elsevier B.V. All rights reserved.

Amongst the available analytical techniques, UHPLC–MS/MS has gained attention as both chromatographic separation and assay selectivity have been significantly improved using this technology. The use of Aquity BEH column in UPLC increases the separation efficiency by reducing the retention time and solvent consumption during chromatographic separation [11–14]. The present work is aimed at developing a sensitive, robust and specific UHPLC–MS/MS method, which can facilitates the rapid determination of canagliflozin in plasma samples.

2. Materials and methods

2.1. Chemicals and reagents

Canagliflozin (purity > 99%) was purchased from Beijing Mesochem Technology Co. Ltd. (Beijing, China). Zafirlukast was used as an internal standard (IS, purity > 98%) from AstraZeneca Pharmaceutical Wilmington, UK. HPLC grade methanol and acetonitrile were obtained from Fisher Scientific UK Limited, Leicestershire UK, whereas ammonium acetate of analytical grade was obtained from Qualikems Fine Chem. Pvt. Ltd. Vadodara, India. All aqueous solutions used in this study were obtained from Milli-QR Gradient A10R (Millipore, Moscheim Cedex, France) having pore size 0.22 μm. Blank plasma was prepared in laboratory from drug free healthy rats which were obtained from the Animal Care and Use Centre, College of Pharmacy, King Saud University, Riyadh, Saudi Arabia.

2.2. Stock solution preparation

Stock solutions (500 μg mL^{-1}) of canagliflozin and IS were prepared by dissolving accurately weighed amount of their respective standards in methanol. Two stock solutions for canagliflozin were prepared from two separate weightings. One solution was used for calibration curve samples while other for quality control samples (QCs). All solutions were stored in refrigerator at 4 °C.

2.3. Calibration standards, quality control and internal standard (IS) preparation

Stock solutions of canagliflozin and IS were further diluted with acetonitrile–water (50:50, v/v) to prepare the working solutions of calibration standards, quality control and IS. Nine concentration levels of the plasma calibration standards were prepared by spiking working standard solutions into rat blank plasma to obtain final concentration levels of 3.76, 10.7, 30.7, 76.8, 192, 640, 1600, 4000 and 6666 ng mL^{-1}. Similarly four QCs, at 4.31, 12.3, 320 and 5333 ng mL^{-1} was also prepared by spiking in the blank plasma and treated as LOQ QC, LQC, MQC and HQC, respectively. All calibration standards and QC concentrations were prepared by serial dilution of stock solutions using Microsoft excel version 2010. Both plasma standards and QC samples were kept at −80 °C until used during validation and/or samples analysis. The IS working solution (1000 ng mL^{-1}) for routine use was prepared by diluting the IS stock solution in acetonitrile–water (50:50, v/v) and stored in refrigerator at 4 °C.

2.4. Chromatographic separation and MS/MS conditions

The ACQUITY™ UPLC system coupled to triple–quadruple tandem mass spectrometer (Micromass® Quattro micro™ Waters Corp., Milford, MA, USA) was used in this study. The UHPLC system consisted of quaternary solvent manager, a binary pump, degasser, autosampler with an injection loop of 10 μL and a column heater–cooler. The chromatographic separation was achieved on Acquity BEH™ C_{18} column (100 × 2.1 mm, i.d., 1.7 μm, Waters, USA) maintained at 40 °C temperature. An isocratic flow, comprising of acetonitrile:10 mM ammonium acetate (80:20, v/v) as mobile phase was used at a flow rate of 0.3 mL min^{-1}. Canagliflozin and IS were eluted within one min with a total run time of 1.5 min only. The injection volume was 10 μL in partial loop mode and the temperature of the autosampler was kept at 15 °C.

Both canagliflozin and IS were detected by triple–quadruple tandem mass spectrometric detection with an electrospray ionization (ESI) interface running in negative ionization mode. The multiple reaction monitoring (MRM) transitions of m/z 443.16 > 364.96 for canagliflozin and m/z 574.11 > 462.07 for IS were used with dwell time 0.106 s. Nitrogen was employed as a desolvating gas at a flow rate of 600 L h^{-1}. The desolvation line temperature was 350 °C whereas source temperature was 150 °C. The collision gas (argon) flow was 0.1 mL min^{-1} and capillary voltage was set at 4.0 kV. The compound specific parameters like cone voltage and collision energy were set at 40 V and 16 eV for canagliflozin and 66 V and 32 eV for IS, respectively. The Mass Lynx software (Version 4.1, SCN 714) was used to control the UPLC–MS/MS system, and data was collected and processed using Target Lynx™ program.

2.5. Sample preparation

Plasma samples (calibration standards, QCs and unknown samples) stored at −80 °C were thawed at room temperature and vortexed for 30 s before sample preparation. In a fresh 1.5 mL centrifuge tube, 200 μL aliquot of plasma (blank, calibration standards, QCs and unknown samples) was added followed by 15 μL of IS (1000 ng mL^{-1}). The samples were vortexed for 30 s and were deproteinized by adding 385 μL of acetonitrile and again gently vortexed for one min. The samples were centrifuged for 10 min at 11,000g at 4 °C. After centrifugation, supernatant was transferred to a fresh tube and evaporated to dryness. The residues were reconstituted in 200 μL of mobile phase out of which 10 μL was injected into UHPLC–MS/MS for analysis.

2.6. Method validation

Method validation was performed following guidelines set by the US FDA and EMEA [15,16]. A full validation was performed in rat plasma in terms of selectivity, linearity of response, accuracy and precision, recovery, matrix effects, carry over effects and stability of analyte in various conditions.

2.6.1. Selectivity

Method selectivity was determined in rat plasma to rule out any interferences from endogenous matrix compounds with analyte and/or IS. Six different lots of blank plasma which was obtained from different rat along with plasma sample spiked with canagliflozin at LLOQ level (3.76 ng mL^{-1}) and IS at 100 ng mL^{-1} level were processed by the proposed extraction method and analyzed. The response of co-eluting interferences was evaluated by comparing the chromatograms of blank plasma with the spiked plasma with analyte and IS.

2.6.2. Calibration curve and assay linearity

Calibration curves in triplicate were prepared in spiked rat plasma samples at 9 different concentration levels in the range of 3.76–6666 ng mL^{-1}. The linearity of each calibration curve was evaluated by plotting the peak area ratios of analyte to IS versus the concentration of analyte and determined by weighted least squares linear regression method of $1/X^2$. The suitability of calibration curve was assessed by measuring the accuracy and precision value at each concentration level, which must be ≤ 15%. The lowest concentration of analyte in calibration curve was recognized as LLOQ, having a signal-to-noise ratio of ≥ 5

compared with blank sample and acceptable accuracy and precision of $\leq 20\%$.

2.6.3. Precision and accuracy

Precision and accuracy were determined in rat plasma at four different QC concentrations (LOQ QC, LQC, MQC and HQC). The intraday precision and accuracy were determined in replicate ($n=6$) on same day, while the inter-day precision and accuracy were determined in replicate ($n=18$) over three consecutive days. The deviation in mean value of precision was limited to $<20\%$ for the lowest QC samples and 15% for the other QC samples and accuracy was limited to be within $\pm 20\%$ for the lowest QC samples and $\pm 15\%$ for the other QC samples.

2.6.4. Recovery and matrix effects

The recovery and matrix effects in rat plasma were investigated at three QC levels (LQC, MQC and HQC). The recovery of canagliflozin from rat plasma was determined by comparing peak response ratio of plasma spiked with analyte prior to extraction (A) with those spiked with analyte after the extraction (B) i.e., the ratio A/B × 100 is defined as a percentage recovery. The absolute matrix effect (expressed as matrix factor) was determined by dividing the response of post-extraction spiked sample (B) to the analyte in to reconstitution solution (C) in the same concentration (B/C × 100). Same procedure was followed for IS (100 ng mL^{-1}) to assess recovery and matrix effects. Deviation in canagliflozin and IS response of a maximum of 15% was considered acceptable as recommended in EMEA bioanalytical guidelines [16].

2.6.5. Carry-over effects

For a robust method, it is important to eliminate any possible carry-over effect and to ensure long term performance of the method. The carry-over effects of canagliflozin in respect to autosampler contamination in rat plasma were investigated by injecting a double blank plasma extract samples after a ULOQ extract sample in triplicate. The carry-over effects were calculated by comparing the percentage peak area of double blank plasma to the area of the LLOQ sample. Same procedure was followed for IS also. The peak area response for blank plasma extract was limited to $\leq 20\%$ of the peak area of the LLOQ and $\leq 5\%$ of the IS to rule out any carry-over effect.

2.6.6. Stability

The stability experiments for canagliflozin were performed in rat plasma by analyzing six replicates of QC samples (LQC and HQC) under different conditions. All stability parameters were evaluated against freshly prepared calibration curve. Short-term stability of canagliflozin was assessed by processing and analyzing QC plasma samples after 12 h storage at room temperature. Freeze–thaw stability was determined after freezing the spiked QC samples at -80 °C and thawing at 25 °C three times. Auto-sampler stability was determined by keeping the reconstituted QC samples for about 48 h in the auto-sampler at 15 °C before analysis. Long-term stability of canagliflozin was determined by analyzing the spiked QC plasma samples which were stored at -80 °C for 30 days. The stock solutions and working solutions of canagliflozin and the IS were also evaluated for their stability at room temperature for 12 h and at refrigerator temperature (below 10 °C) for 15 days. The canagliflozin samples were considered stable if the deviation from the mean calculated concentration of quality control samples were found to be within the limits of accuracy ($\pm 15\%$) and precision ($\leq 15\%$).

2.7. Application to pharmacokinetic study in rats

This newly developed assay was applied to a canagliflozin pharmacokinetic study in male Wistar Albino rats weighing 220–230 g ($n=6$). Animal experiments were conducted in accordance with the guidelines of the Experimental Animal Care and Use Committee of College of Pharmacy, King Saud University Riyadh, KSA. After overnight fasting, all rats received canagliflozin (20 mg kg^{-1} oral, dissolved in HPMC) and blood samples (approximately 0.5 mL) were collected from the retro-orbital plexus into heparinized tubes at different time intervals (0, 0.5, 1, 1.5, 2, 2.5, 3, 4, 6, 8 and 20 h). Plasma samples were harvested by centrifuging the blood at 4500*g* for 8 min and frozen at -80 ± 2 °C until analysis. The pharmacokinetic parameters such as C_{max}, T_{max}, area under curve (AUC), half-life ($T½$), mean residence time (MRT) and elimination rate constant (K_{el}) were calculated using WinNonlin software (Pharsight Co., Mountain View, CA, USA).

3. Results and discussion

3.1. Optimization of mass spectroscopy condition

Initially 400 ng mL^{-1} solution of canagliflozin was directly infused using ESI sources in positive ion modes. Results of precursor ion spectra gave sodium $[M+Na]^+$ and ammonium $[M+NH4]^+$ adduct of canagliflozin at *m/z* 467 and 462 as strong signal instead of protonated molecule (which is commonly observed with neutral compound) during full scan mass analysis (Fig. 1). In previous reported studies, ammonium adducts ions in ESI positive mode (MRM transition of *m/z* 462.1 > 267.0) was adopted for canagliflozin determination and identification [10,17]. Due to possibility of contamination of alkali metal ions

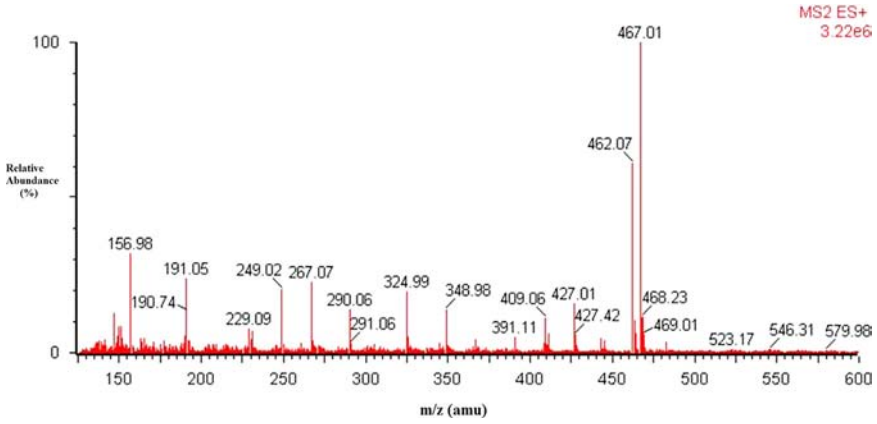


Fig. 1. Precursor ion spectra in positive ionisation mode which produced ammonium $[M+NH4]^+$ and sodium $[M+Na]^+$adduct of canagliflozin.

from other sources e.g. laboratory glassware and biological matrices and for selective and robust performance of assay, it is recommended to avoid adduct ions formation in LCMS/MS analysis [18]. Furthermore, presence of competitive metal adducts ions, may also reduce the sensitivity of the target analyte detection and assay performance. In order to avoid this competitive adduct ions formation, ESI in negative mode was chosen as an alternative source for ionization instead of positive mode. ESI^- produced a single abundant product ion peak at m/z 443 which consequently produced one major stable product ion at m/z 365. Using negative ionization conditions, we have successfully achieved sensitive detection and completely avoided the adduct ions formation of canagliflozin. Zafirlukast (IS) which also produced most abundant precursor ions in negative mode at m/z 574 and its fragment ions at m/z 462 was used as internal standard. Thus MRM detection was carried out by monitoring of precursor to product ion at m/z 443.16 > 364.96 for canagliflozin and m/z 574.11 > 462.07 for IS.

UPLC–MS/MS operation parameters, such as capillary and cone voltage, desolvation temperature, ESI source temperature and flow rate of desolvation gas and cone gas were further tuned to achieve optimum intensity of negative molecular ions $(M–H)^-$ of canagliflozin and IS. Canagliflozin produced predominant singly charged precursor $(M–H)^-$ ion when cone voltage was set at 40 V and dominant product ion (m/z 364.96) when collision energy was set at 16 eV. Similarly for IS, the optimized cone voltage was set at 66 V for precursor $(M–H)^-$ ion (m/z 574.11) and collision energy 32 eV for dominant product ion (m/z 462.07). Precursor ion and product ion spectra $(M–H)^-$ of canagliflozin and IS after infusion of 400 ng mL^{-1} solution in acetonitrile are shown in Fig. 2 and Fig. 3, respectively.

3.2. Optimization of chromatographic conditions

The chromatographic condition was optimized to achieve efficient separation of analyte and IS with good resolution, symmetric peak shape, minimum interferences with high signal response and shorter run time. Initially acetonitrile as organic modifier along with three aqueous phase (A) 0.1% formic acid (B) simple water (C) 10 mM ammonium acetate and (D) 10 mM ammonium acetate with 0.1% formic acid were tried in different ratios as isocratic mobile phase. Although the separation of analyte and IS were achieved with all combinations when the ratio of acetonitrile and aqueous phase was kept at 80:20. However, the highest ionisation response of both analyte and IS was achieved with acetonitrile and aqueous phase (B) i.e. simple water. The presence of formic acid or buffers in mobile phase may lead to adduct ions formation which results in suppression of responses. With respect to column, the Acquity BEH^{TM} C_{18} column of 100 × 2.1 mm and 50 × 2.1 mm diameter having the same particle size (i.d. of 1.7 μm) were tested. Best peak resolution was obtained with 100 × 2.1 mm diameter and was used for this assay with column oven temperature of 40 °C. Zafirlukast was selected as the IS, because it was separated sufficiently from analyte, had sensitivity in ESI negative mode and almost similar extraction recovery to the analyte. Both analyte and IS were eluted within 1 min with a total run time of 1.5 min which was sufficient for high throughput determination of canagliflozin. The representative total ion chromatography (TIC) of both canagliflozin and IS are presented in Fig. 4.

3.3. Sample extraction optimization

The purpose of sample extraction optimization is mainly to achieve high extraction recovery and low matrix effects in order to improve sensitivity and reliability of LC-MS/MS analysis. Strategy usually includes all possible common sample extraction options including solid phase extraction, liquid extraction and protein precipitation. With the emergence of UHPLC technology combined with high sensitive tandem mass spectroscopy, it is possible to quantify analytes at a low concentration without having a high extraction recovery, provided that the recovery remains constant over time and concentration [19]. With time-saving advantage and simplicity, the protein precipitation method was chosen as

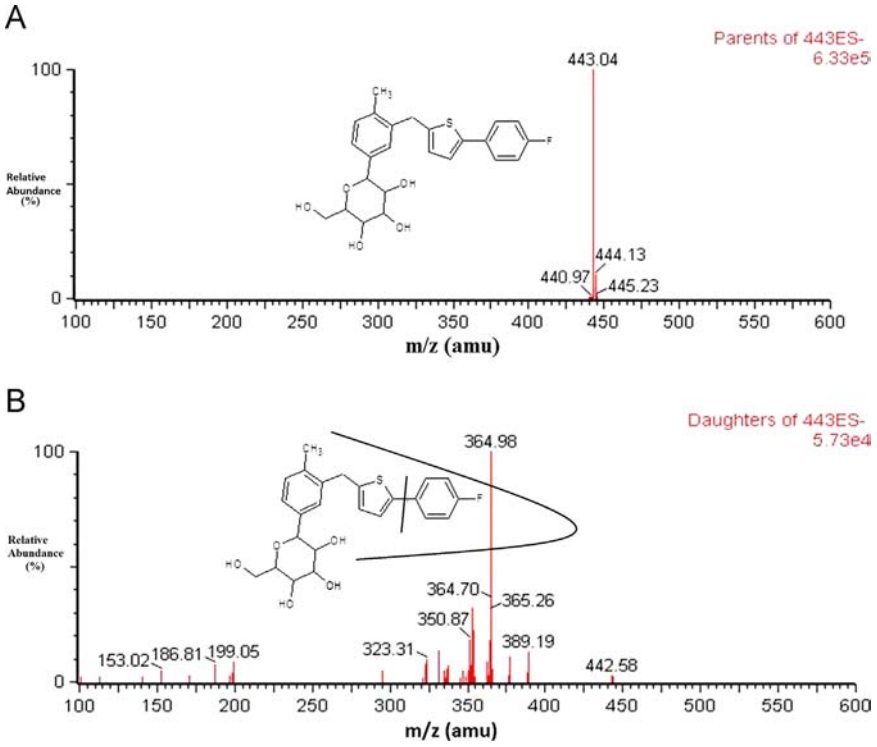


Fig. 2. Precursor ion (A) and product ion (B) spectra of canagliflozin.

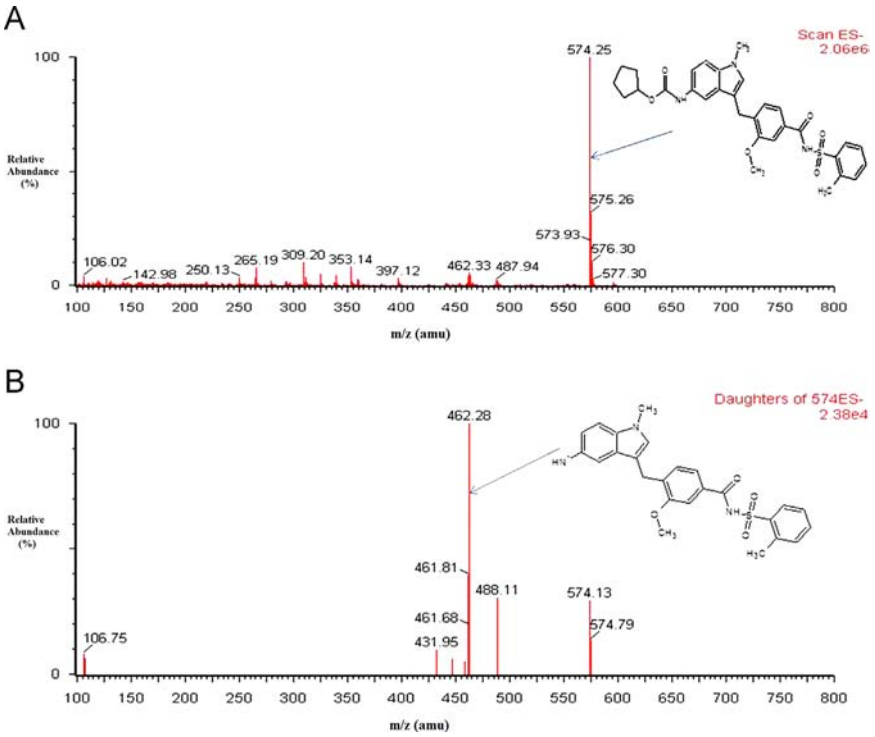


Fig. 3. Precursor ion (A) and product ion (B) spectra of IS.

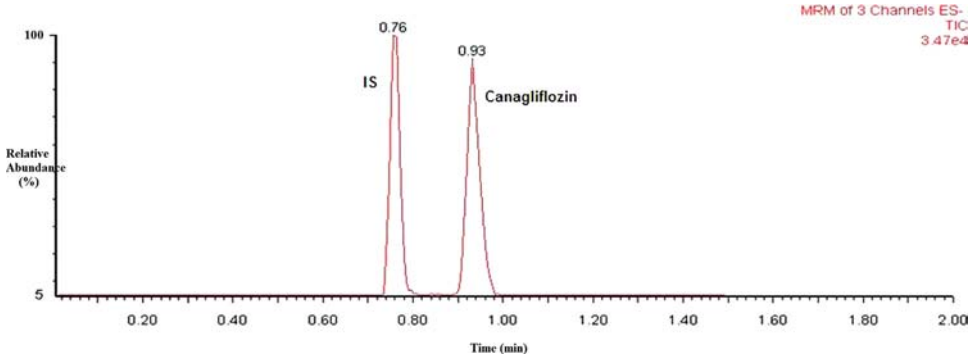


Fig. 4. TIC of canagliflozin and IS in mixed standard solution.

a generic extraction method. Initially we used both acetonitrile and methanol for protein precipitation. The result with methanol was not satisfactory as it resulted in high matrix effects, poor separation and low recovery of analytes compared to acetonitrile. Acetonitrile produced better results and was further optimized by evaporation of solvent under the stream of nitrogen and reconstituted in mobile phase to achieve high sensitivity and low ion suppression effects. The low ion suppression effects produced after sample drying and reconstitution in mobile phase might be due to more clean samples and compatibility of reconstitution solution (mobile phase) with eluting solvent.

3.4. Method validation

3.4.1. Selectivity

In this study, no significant interfering peaks ($\geq$ 20% in comparison to the spiked LLOQ and $\geq$ 5% in comparison to IS) in blank plasma (obtained from different rats) were observed at the corresponding elution time of canagliflozin and IS under the present optimal chromatographic conditions. This indicates that the present assay is selective for the test compound and suitable for quantification. Typical MRM chromatogram of canagliflozin and IS for blank plasma (showing no significant interference at the elution time of canagliflozin and IS) are shown in Fig. 5A.

3.4.2. Linearity and lower limit of quantification

The calibration curves were obtained by plotting the peak area ratios of canagliflozin to IS versus the nominal concentration of canagliflozin. The best linear fit with lowest total bias was achieved using $1/X^2$ weighing factor and adopted for method validation. Calibration curve showed good linearity in the range of 3.75–6666 ng mL^{-1} in plasma samples with the coefficient of correlation (R^2) of $\geq$ 0.997 during validation. The lowest point on the standard curve was 3.75 ng mL^{-1} and was accepted as LLOQ for this assay. Notably the present LLOQ is slightly lower than the previous reported HPLC–MS/MS method where $NH4^+$ adduct was used for canagliflozin quantification in ESI positive mode. Representative MRM chromatograms of canagliflozin and IS in spiked plasma at LLOQ level and 1 h after administration of canagliflozin in rat are shown in Fig. 5B and C, respectively.

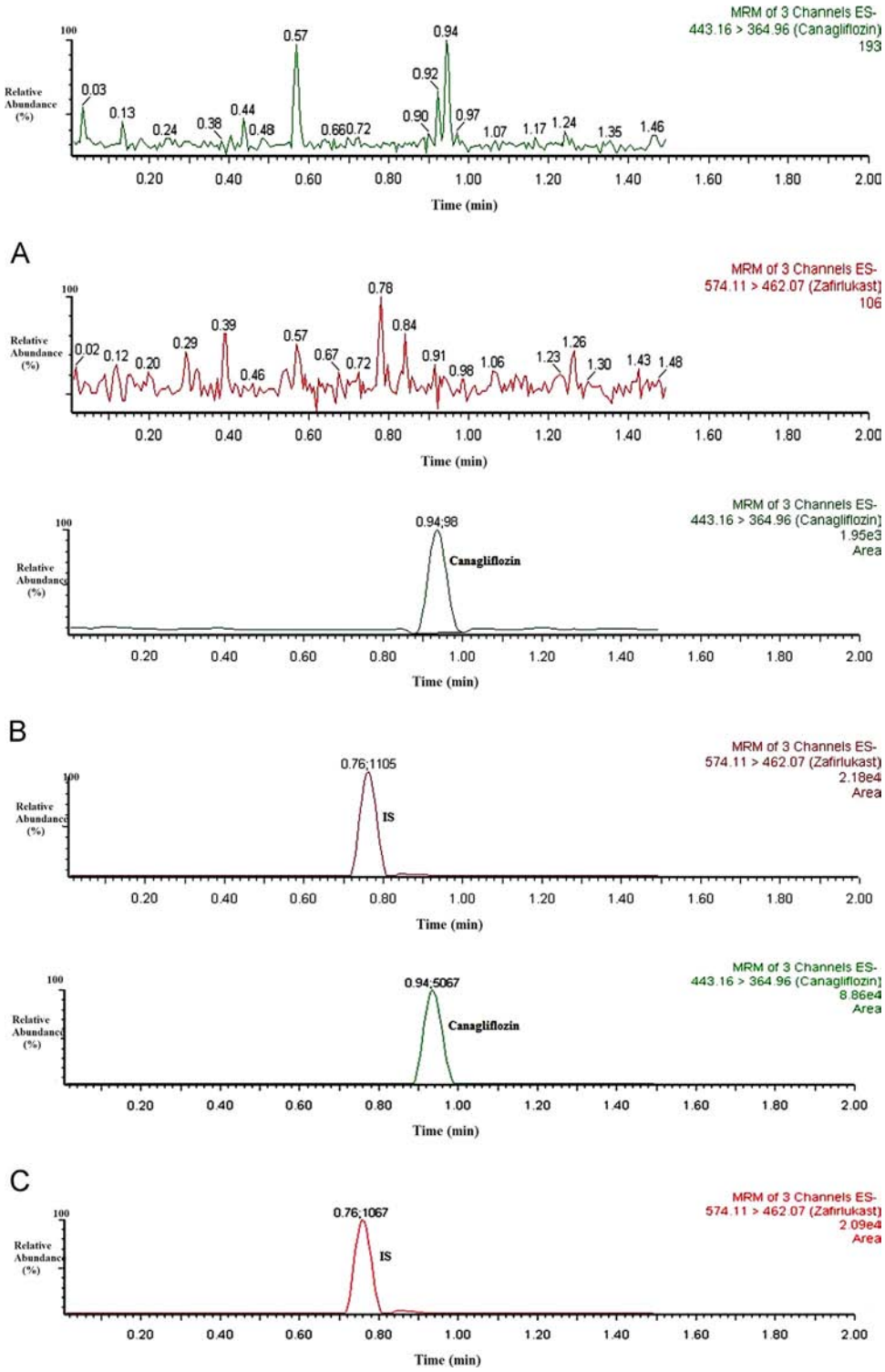


Fig. 5. Typical chromatograms of canagliflozin and IS in blank plasma (A); spiked plasma at LLOQ level (B) and 1 h after administration of canagliflozin (20 mg kg^{-1}, p.o.) in rat (C).

3.4.3. *Precision and accuracy*

The data for intra- and inter-day precision and accuracy of canagliflozin at four different QC levels in rat plasma are summarized in Table 1. The results demonstrated that the variation in intra-day and inter-day precision was ≤ 9.4 and ≤ 8.5, respectively. Similarly, the intra-day and inter-day accuracy ranged from 91.4 to 108.9 and 93.5 to 106.8, respectively. The results showed that the assay met the desired level of acceptance criteria and hence was considered accurate and precise for the analysis of canagliflozin in plasma sample and in other biological fluids.

3.4.4. *Recovery and matrix effects*

The extraction recovery and matrix effects for canagliflozin at three different QC levels (12.3, 320 and 5333 ng mL^{-1}) and IS (100 ng mL^{-1}) are presented in Table 2. The mean recovery of

Table 1
Intra-day and inter-day precision and accuracy values of canagliflozin in rat plasma.

Nominal conc. ($ng\ mL^{-1}$)	Run	Measured conc ($ng\ mL^{-1} \pm SD$)	Precision (CV, %)	Accuracy (recovery, %)
Intraday variation (6 replicate at each concentration)				
4.31	1	4.69 ± 0.44	9.3	108.9
	2	4.50 ± 0.34	7.5	104.3
	3	4.61 ± 0.43	9.4	107.0
12.3	1	11.9 ± 0.53	4.5	96.9
	2	12.3 ± 0.14	1.1	100.3
	3	12.0 ± 0.48	4.0	97.8
320	1	338.3 ± 26.8	7.9	105.7
	2	328.7 ± 9.07	2.8	102.7
	3	323.5 ± 15.2	4.7	101.1
5333	1	5078 ± 282.3	5.6	95.2
	2	4999 ± 372.1	7.8	93.7
	3	4873 ± 327.4	6.7	91.4
Inter-day variation (18 replicates at each concentration)				
4.31		4.60 ± 0.39	8.5	106.8
12.3		12.1 ± 0.44	3.6	98.3
320		330.2 ± 18.5	5.6	103.2
5333		4983.7 ± 321.4	6.4	93.5

Table 2
Extraction recovery and matrix effect of canagliflozin (three QC samples) and IS in rat plasma ($n=6$).

Compound	Nominal concentration ($ng\ mL^{-1}$)	Extraction recovery		Matrix effects	
		%Mean ± %SD	CV%	%Mean ± %SD	CV%
Canagliflozin	12.3	82.7 ± 3.0	3.6	96.3 ± 1.9	2.0
	320	77.9 ± 5.6	7.2	93.7 ± 3.2	3.4
	5333	74.4 ± 4.1	5.6	91.5 ± 2.9	3.2
	Mean	78.3 ± 4.1	5.3	93.8 ± 2.4	2.6
IS	100	75.6 ± 4.3	5.6	92.5 ± 3.6	4.0

Table 3
Stability data of canagliflozin in rat plasma ($n=6$).

Stability	Nominal concentration ($ng\ mL^{-1}$) ($n=6$)	Mean ± SD	Precision (%CV)	Accuracy (%)
Bench top (6 h)	12.3	11.9 ± 0.53	4.5	96.8
	5333	5528 ± 121	3.5	103.8
Freeze thaw (3 cycle)	12.3	11.9 ± 0.76	6.4	96.5
	5333	5535 ± 193	8.3	89.3
In Injector (48 h)	12.3	13.3 ± 1.10	8.2	108.4
	5333	5730 ± 154	2.7	107.5
30 days at −80 °C	12.3	11.15 ± 0.56	5.0	90.6
	5333	4989 ± 231	4.6	93.6

canagliflozin was found to be 78.3% with a CV of 5.3% only. The recovery for IS was 75.6%. This result indicates that the recovery of canagliflozin by protein precipitation was in the acceptable range, consistent and concentration independent.

No significant matrix effects for canagliflozin were observed, suggesting that the ion suppression or ion enhancement due to plasma is negligible for this assay. The mean absolute matrix effect value was only 93.8% with CV of 2.6% for the three different concentrations.

3.4.5. Carry-over effects

No significant eluting peaks (peak area ≥20% for LLOQ and ≥5% for IS) were observed in the chromatograms of blank plasma samples injected after highest concentration level of calibration curve. Therefore, the carryover effects were negligible for this assay. A flush solvent of 80:20 v/v acetonitrile:water was used for the injection needle washing after every 10–15 unknown samples and is recommended for future application of this assay.

Table 4
Pharmacokinetic parameters of canagliflozin in male rats after administration of single dose (20 mg kg p. o.).

Pharmacokinetic parameters	Unit	Values (mean ± SEM)
C_{max}	$ng\ mL^{-1}$	1,616.79 ± 565.94
T_{max}	h	1.5
AUC_{0-20}	$ng\ h\ mL^{-1}$	14,721.36 ± 3,383.72
AUC_{0-inf}	$ng\ h\ mL^{-1}$	26,426.36 ± 7,287.83
$T^{1/2}$	h	21.34 ± 9.63
MRT	h	30.13 ± 14.06
K_{el}	h^{-1}	0.04 ± 0.02

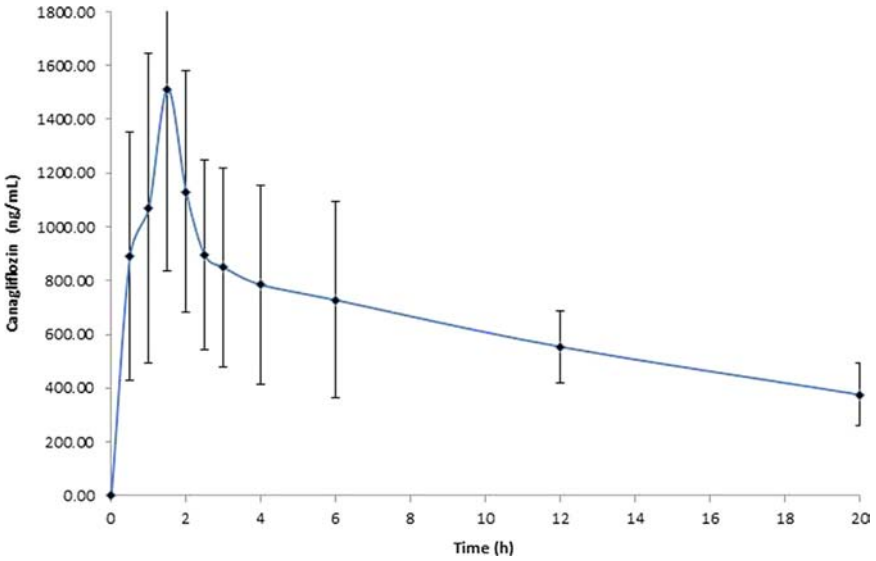


Fig. 6. Mean ± SE plasma concentration–time curves of canagliflozin after a single dose administration of 20 mg kg^{-1} p.o. in rats.

3.4.6. *Stability*

The canagliflozin stability (freeze–thaw, autosampler, short-term and long-term) results in rat plasma are summarized in Table 3. The results demonstrated that canagliflozin spiked in rat plasma was stable during three cycle of freeze–thaw, 48 h in autosampler after post preparation, at least 12 h at room temperature, and up to 30 days at around −80 °C. The stock solutions and working standard of canagliflozin and IS were also found to be stable for 15 days at refrigerator temperature (below 10 °C). Thus, there is no indication of canagliflozin instability in biological samples which can affect the method performance.

3.5. *Pharmacokinetic study in rats*

The validated UPLC–MS/MS assay was successfully applied to pharmacokinetic characterization of canagliflozin in healthy rats following oral administration of 20 mg kg^{-1}. The main pharmacokinetic parameters are summarized in Table 4. As shown, canagliflozin was found to be rapidly absorbed but slowly eliminated ($T_{,}^{1/2}$ 21.3 h) in rats. The corresponding mean peak plasma concentration of 1616.79 ng mL^{-1} was achieved after 1.5 h. The mean $AUC_{0-20\ h}$ was 14,721.36 ng mL h^{-1} with MRT of 30.13 h. The mean plasma concentration versus time profile of canagliflozin in rats is shown in Fig. 6.

4. Conclusion

In this study, we have developed and validated UPLC–MS/MS assay for the accurate quantification of canagliflozin in rat plasma. The assay is simple, rapid and sensitive over a wide calibration range (3.76–6666 ng mL^{-1}). The assay simplicity and short run time (only 1.5 min) enables high-throughput analysis of canagliflozin in a wide variety of clinical and experimental settings. The validated assay was successfully applied to a pharmacokinetic characterization of canagliflozin in rats.

Acknowledgements

The authors are thankful to Deanship of Scientific Research and Research Center, College of Pharmacy, King Saud University for their funding and support.

References

[1] J. Cuypers, C. Mathieu, K. Benhalima, Acta Clin. Belg. 68 (4) (2013) 287–293.
[2] S. Elkinson, L.J. Scott, Drugs 73 (9) (2013) 979–988.
[3] U.S. FDA Approves Canagliflozin (TA-7284) for the Treatment of Adult Patients with Type 2 Diabetes, 2013, Janssen Pharmaceuticals, Inc.: USA.
[4] INVOKANA™ (Canagliflozin) Approved In The European Union For Treatment Of Adults With Type 2 Diabetes, 2013, Janssen-Cilag International NV: Belgium.
[5] C.J. Bailey, Trends Pharmacol. Sci. 32 (2) (2011) 63–71.
[6] InvokanaTM (Canagliflozin) Tablets, US Prescribing Information 2013.
[7] S. AJ, Clin. Pharmacokinet. (2014).
[8] Y. Toderika, N. Ferguson, Cardiol. Rev. 22 (2) (2014) 97–104.
[9] S. Sarnoski-Brocavich, O. Hilas, Pharm. Ther. 38 (11) (2013) 656–666.
[10] D. Devineni, et al., J. Clin. Pharmacol. 53 (6) (2013) 601–610.
[11] A. Kumar, et al., Acta Pol. Pharm. 69 (3) (2012) 371–380.
[12] F. Li, et al., Rapid Commun. Mass Spectrom. 22 (4) (2008) 486–494.
[13] L. Novakova, L. Matysova, P. Solich, Talanta 68 (3) (2006) 908–918.
[14] G. Liu, et al., Anal. Chem. 81 (22) (2009) 9225–9232.
[15] Guidance for Industry on Bioanalytical Method Validation, Center for Drug Evaluation and Research (CDER), (Ed.), 2001, US Food and Drug Administration: Rockville, MD.
[16] Guideline on Bioanalytical Method Validation, 2011, European Medicines Agency.
[17] R.N. Mamidi, et al., Drug Metab. Dispos. 42 (5) (2014) 903–916.
[18] H. Hirabayashi, et al., J. Chromatogr. B 879 (32) (2011) 3837–3844.
[19] N. Zheng, et al., J. Pharm. Biomed. Anal. 83 (2013) 237–248.

Talanta 132 (2015) 37–43

Contents lists available at ScienceDirect

Talanta

journal homepage: www.elsevier.com/locate/talanta

A Sensitive capacitive immunosensor for direct detection of human heart fatty acid-binding protein (h-FABP)

Carmen-Marinela Mihailescu [a,*], Dana Stan [b], Rodica Iosub [c], Carmen Moldovan [c], Mihaela Savin [d]

[a] Department of Physical Chemistry, Faculty of Chemistry, University of Bucharest, Bd. Regina Elisabeta, No. 4-12, Bucharest, Romania
[b] DDS Diagnostic, Gh. Sincai Street no. 9A, 040312 Bucharest, Romania
[c] National Institute for R&D in Microtechnologies (IMT), 126A Erou Iancu Nicolae, 077190 Bucharest, Romania
[d] Telemedica, Str. Ion Calin, No. 13, Bucharest, Romania

ARTICLE INFO

Article history:
Received 16 May 2014
Received in revised form
20 August 2014
Accepted 28 August 2014
Available online 6 September 2014

Keywords:
Self-assembled monolayer
Cardiac marker
Acute myocardial infarction
Capacitive immunosensor
h-FABP

ABSTRACT

The fabrication of a capacitive interdigitated immunosensor (CID) based on a mixed self-assembled monolayer (mSAM) film for the direct detection of heart fatty-acid binding protein (h-FABP) without any labeling is described. The capacitance changes of mSAMs vs. homogenous ordered self-assembled monolayers (hSAMs) on gold work electrodes/covalently bonded antibodies/buffered medium are utilized for monitoring the specific antibody–antigen interaction. Capacitance measurements in the absence and presence of Faradaic currents were performed. The electrochemical properties of mixed monolayers were compared with those of a pure monolayer of 11-mercaptoundecanoic acid (MUA) self-assembled on gold surfaces. Taking into account the stability of the studied monolayers during the electrochemical experiments with the Faradaic process, the best SAM functionalization method was used for developing a sensitive capacitive immunosensor with a non-Faradaic process for direct immune detection of human h-FABP. Under the optimized conditions, the proposed mixed self-assembled monolayer ($mSAM_1$) on gold electrode exhibited good insulating properties such as a capacitive behavior when detecting h-FABP from human serum in the range of 98 pg ml^{-1}–100 ng ml^{-1}, with a detection limit of 0.836 ng ml^{-1} comparative with a homogenous self-assembled monolayer (hSAM).
© 2014 Elsevier B.V. All rights reserved.

1. Introduction

Biochemical markers have an excellent sensitivity for the diagnosis of acute myocardial infarction (AMI), the world's main cause of morbidity and mortality (according to WHO's report for 2008).

Heart-type FABP (h-FABP) was first shown to be released from injured myocardium in 1988 [1]. Afterwards, several studies have investigated its application as a biochemical marker of myocardial damage, following the finding that h-FABP is the earliest available and probably most sensitive marker for injured myocardium [2,3]. The possibility of an early and quick diagnosis is extremely important in establishing the guiding therapy in order to save patients' lives. Likewise, the use of protein markers of low molecular weight leads to an earlier detection time [4,5]. In this context, h-FABP (15 kDa), a small protein that becomes elevated in concentration shortly after an AMI onset, appears to be an ideal target as a biomarker.

In the last 20 years, the development of various biosensors has been the objective of a large volume of research in both academic and industry enviroments, in order to develop alternative methods to the ELISA-based immunoassay [6–10]. Although used for many applications in medical diagnostics, ELISA methods are time consuming and involve relatively expensive equipment.

In the case of AMI, speed, specificity and sensitivity of the biochemical markers quantification are key factors in its diagnosis and treatment. Developing a simple, sensitive, regenerable capacitance-based immunosensor is of considerable interest because the capacitive measurement is a simple, rapid and inexpensive method based on the change in the capacitance electrode–electrolyte interface [11–15]. To the best of our knowledge, there are no reports of an interdigitated electrode immunosensors that use capacitive detection of the h-FABP cardiac biomarker.

When constructing a capacitive biosensor, the electrode surface is usually covered with an additional insulating layer to reduce Faradaic currents and the biorecognition element is immobilized on top of this layer [16]. Capacitance measurements in the absence of Faradaic currents also allow for the investigation of the influence of the electrical field on the biological recognition event by applying different direct current (dc) working potentials, and

* Corresponding author. Tel.: +40 724503682; fax: +40 214104009.
E-mail addresses: carmen_mihailescu1234@yahoo.com (C.-M. Mihailescu), mihaelasvn@yahoo.com (M. Savin).

http://dx.doi.org/10.1016/j.talanta.2014.08.067
0039-9140/© 2014 Elsevier B.V. All rights reserved.

have the advantage that no additional reagent is required for non-Faradaic impedance spectroscopy, rendering non-Faradaic schemes somewhat more amenable to point of care (POC) applications.

Two types of capacitive measurements can be performed: (1) using a single modified working electrode as a sensor, and (2) between and/or on the electrodes (in-plane arrangement of the interdigitated electrodes, or IDEs). The principle of the capacitance transducer is based on the theory of the electrical double-layer [17]. A metal electrode modified with a recognition biolayer can be described as a capacitor when placed in an electrolyte solution. The total capacitance is represented by the equivalent capacitance (C_e) and is built from several components. In this case, the first is the capacitance of the monolayer, C_{SAM}. The second is the capacitance of the protein layer and any part from the Stern layer, C_{pl}. The third is the capacitance of the diffuse layer, C_{dl}. The total value of the capacitance can be described by the following equation [18]:

$$1/C_e = 1/C_{SAM} + 1/C_{psl} + 1/C_{dl} \quad (1)$$

In the case of capacitive immunosensors, an electrode is coated with an antibody, which represents the biorecognition element and has a stable capacitance. When the analyte binds to the specific antibody on the electrode, it causes a change in the total capacitance. The use of the second type of capacitive immunosensors, IDEs, can provide a larger sensor surface for the immunoreaction. The capacitance between the IDEs can be described by the Helmholtz model by Eq. (2) [19]

$$C = \frac{A \times \varepsilon \times \varepsilon_0}{d} \quad (2)$$

where ε is the dielectric constant of the medium between the plates, ε_0 is the permittivity of free space, A is the area of the electrodes and d is the distance between the two electrodes.

For a biosensor based on a capacitive transducer, the immobilization of the recognition element is of vital importance for the ability to detect the binding event. The homogenous ordered self-assembled monolayers (hSAMs) ensure well-controlled surface structure and offer many advantages as far as the performance of the sensor, but they may lead to steric hindrance and disorder of the bulky terminal groups. In our prior study we have demonstrated distinguishable modification when the electron transfer resistance (R_{CT}) was recorded on mSAMs vs. hSAMs using a Faradaic process [20]. Also, the most widely used parameter for the characterization of SAM electrochemical properties is capacitance. The capacitance of a defect-free SAM is 20–100 times lower than that of bare gold, owing to the very low dielectric constant of the alkyl monolayer [21,22]. Prolonged incubation of the gold substrate in the thiol solution is necessary to prepare a stable SAM with a good capacitive behavior.

In the current work we have designed and fabricated a new capacitive immunosensor for h-FABP detection, without Faradaic process, by using self-assembled monolayers, which we have heterogeneously integrated onto the microelectrode microfluidic platform. Also, by using the Faradaic process we have carried out a comparative test of stability in terms of capacity changes between long-chain alkanethiols (11-mercaptoundecanoic acid, MUA) that formed a homogeneous adsorbed monolayer on the gold electrode, and a mixture of long chains and short chains adsorbed on the gold electrodes.

Under the optimized conditions, the proposed mSAMs on gold electrode exhibited good insulating properties such as a capacitive behavior to h-FABP from human serum in the ranges of 98 pg ml^{-1}–100 ng ml^{-1} with a detection limit of 0.830 ng ml^{-1} compared with hSAMs. Also, the results of these studies could be the starting point to developing multiplexed POC with panels of biomarker tests.

2. Experimental details

2.1. Materials

Monoclonal mouse anti-human h-FABP antibody and human antigen h-FABP were purchased from HyTest (Finland). A human serum assayed chemistry control, Lyphochek, was obtained from Bio-Rad Laboratories (USA). All other chemicals were purchased from Sigma-Aldrich (Germany).

2.2. Gold interdigitated electrodes (GID) preparation

The silicon sensor has gold interdigitated microelectrodes (GID), patterned by photolithography on silicon substrate. The fabrication summary steps are:

- p (100) type silicon wavers with 3 in. (76.2 mm) diameter and resistivity $\rho = 16$ W cm,
- oxidation layer (SiO_2) with 800 nm thickness;
- Ti/Au layer deposition with 15 nm/200 nm, deposition and patterning of a passivation layer phosphosilicate glass (PSG 4%) with the help of a mask for a lift-off process leaving open the electrodes' active area and the pads. The sensor chip has a 6 mm^2 × 12 mm^2 area and the IDE has a 1 μm width with a 10 μm gap. As a result, each gold interdigitated array contains 16 gold interdigitated fingers.

2.3. Gold surface preparation for electrochemical impedance spectroscopy (EIS) methods

The surfaces were a 3-inch silicon wafer p-type (100) with thickness of 350 μm and 16 Ω cm resistivity. On the oxide (thickness 800 nm) was deposited a metal layer sandwich consisting of 15 nm Ti produced by evaporation in high vacuum and a 200 nm Au layer deposited by the evaporation method. The working area is 0.9 cm^2.

2.4. Formation of the self-assembled monolayers

The gold interdigitated microelectrodes were cleaned sequentially in methanol, acetone and isopropanol for 10 min each. This was followed by a quick 2 min dip in piranha solution (H_2SO_4 70%, H_2O_2 30%, 3:1 v/v), then rinsed with deionized water. We repeated the procedure twice and finally dried them under a nitrogen flow.

Before placing the biosensor in the flow cell, the electrodes were treated and the hSAM and mSAMs were formed, following these procedures: for the hSAM, the GID electrode area was immediately immersed in an ethanol solution of 5 mM MUA; for the first mixed self-assembled monolayer ($mSAM_1$) other GID electrodes were immersed in 10 mM mixed solution consisting of MUA and MPOH in a 7:3 M ratio in absolute ethanol; for the second mixed monolayer ($mSAM_2$) the GID electrodes were immersed in 10 mM mixed solution of MUA: MPOH in a 1:9 M ratio. Different times were allowed for interaction between the alkanethiols and the GID electrodes: 1 min, 10 min, 30 min and 24 h.

The gold surfaces used for electrochemical characterization of the monolayers were similarly functionalized to form mSAMs and hSAM. Also, different times were allowed for the interaction between the alkanethiols and the gold surfaces: 1 min, 10 min, 30 min and 24 h. The capacitance EIS measurements were performed immediately after each incubation time.

Fig. S1 (Supplementary material) schematically illustrates (a) the gold interdigitated (GID) clean electrode, (b) $mSAM_1$/gold electrode fabrication, (c) $mSAM_2$/gold electrode fabrication and (d) hSAM/gold electrode fabrication. All fabricated electrodes were characterized using EIS.

2.5. SAMs characterization

The EIS was performed using the conventional three-electrode system with Ag/AgCl as a reference electrode, platinum as the counter electrode, and gold surface as the working electrode. The EIS measurement was carried out at equilibrium potential (open circuit potential generated between electrodes dipped in electrolyte), without external biasing in the frequency range of 100 mHz–100 kHz, with 10 mV amplitude using VoltaLab PGZ 100 Potentiostat/Galvanostat (Germany). The EIS and cyclic voltammetry (CV) measurements were performed using a cell with PBS solution (pH=7.4) containing a mixture of 5 mM $Fe(CN)_6^{4-}$ and 5 mM $Fe(CN)_6^{3-}$. For the intensity/V measurement, the potential was swiped from −50 mV to 900 mV with a rate of 100 mV/s.

2.6. Integrated microfluidic platform for detection of h-FABP

Scheme 1 depicts the block diagram of the microfluidic platform with GID integration. The legend explains all the components of the microfluidic platform. The immunosensor has a total area of $6\ mm^2 \times 12\ mm^2$ with the interdigitated gold electrode having a thickness of 10 μm; the active area is connected using pads (gold) to the capacitance read with AGILENT 4263B RCR.

2.6.1. Activation with EDC/NHS

The GID areas functionalized with SAM were immersed into a solution with NHS (20 mM) and EDC (100 mM) in PBS (pH=7.4) for 1 h to activate the terminal carboxylic groups to NHS esters. The modified electrodes were then rinsed with PBS and used immediately for antibody attachment.

2.6.2. Antibody immobilization

The hSAMs and mSAMs activated GID electrodes were incubated with 100 μl of 8 μg ml^{-1} anti-h-FABP antibody in PBS, which was pulled by a micropump system for 1 h at room temperature, then rinsed in PBS. After antibody covalent immobilization, the surfaces were blocked with a solution of 1% BSA in PBS for 1 h at room temperature, to avoid unspecific interaction, and then rinsed with PBS. The GID can be stored in the refrigerator until use for antigen h-FABP detection.

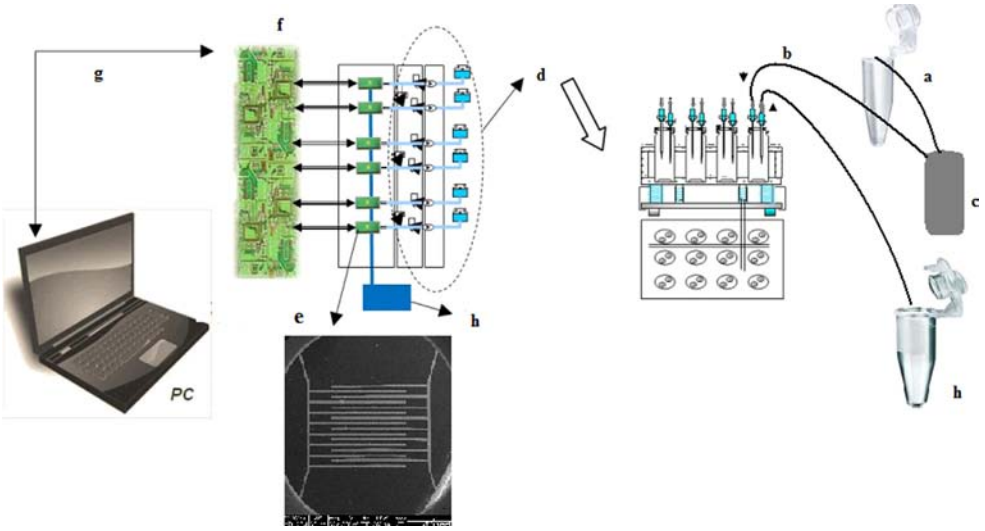
2.6.3. Antigen detection

For antigen detection, the GID electrodes immobilized with anti-hFABP antibodies were used to detect different antigen concentrations in the range 98 pg ml^{-1} to 100 ng ml^{-1} in PBS buffer. After the suction of the antigen solution and before recording of the capacitance, the signal was stabilized by washing with 5 ml PBS buffer, this being the base line. Two biofunctionalized immunosensors of $mSAM_1$ and hSAM were introduced in the microfluidic system as shown in Scheme 1e. After reading the blank signals (in PBS), the first step of the serial dilution was performed, namely 50 μl of antigen solution was suctioned on each electrode with the aid of micropumps, which are represented in Scheme 1c. A constant frequency of 1 kHz with an amplitude of 100 mV was applied. The capacitances for both electrodes were measured in real time for 30 min, at room temperature, until a constant value was attained. The same procedure was applied for each concentration of antigen in PBS. The specificity of the modified GID electrodes was determined by the antigen concentrations that have been spiked in BioRad human control serum. Then, the other new modified electrodes ($mSAM_1$ and hSAM) were introduced in the microfluidic system and the serial dilutions of the antigen were made in PBS: control serum (1:1). The same procedure as described above was performed.

2.7. Immunosensor non-Faradaic measurements

The potentiostatic-step method was chosen to be used as a transduction element for our immunosensor because the system at low frequency and low voltage could be described as a simple RC model [13,23]. An Agilent LCR Meter is connected through LabView interfaces for data acquisition, data analysis and presentation in real time.

All biochemical reactions between the h-FABP antigen added on the GID electrodes areas, and the antibodies the latter has been functionalized with, were transferred in capacitance changes that were measured in real time with AGILENT 4263B LCR meter, stored on the computer and interpreted. The measurement was



Scheme 1. The block diagram of the platform: (a) container with the biological sample or washing solution; (b) transport capillary samples/washing solutions; (c) peristaltic micropumps; (d) microvalve system, canals and reservoirs; (e) immunosensor with active area represented by gold interdigitated electrodes; (f) unit for electronic measurement signal amplification Agilent; (g) PC for data recording; and (h) exhaust system for biological sample/washing liquid.

carried out by applying a constant frequency of 1 kHz with an amplitude of 100 mV.

3. Results and discussion

3.1. SAMs characterization

Fig. S1 shows the different functionalization strategies tested to form three monolayers: $mSAM_1$, $mSAM_2$ and hSAM.

EIS with Faradaic process was used to characterize the insulating properties and to determine the capacitive behavior of the gold electrode at each stage of functionalization.

Although it has been demonstrated that long chain SAMs are much less easily damaged, thin layers are preferred for developing an immunosensor with direct detection of a small amount of protein because of the larger relative changes in capacitance caused by immune reactions [24]. mSAMs allow control of the density of the reactive species, to increase its accessibility and to bring chemical inertness to the underlying surface. Therefore, in order to control the accessibility of the carboxyl groups on the electrode surface, we used molar ratios with either MUA or MPOH excess in absolute ethanol ($mSAM_1$, 7:3 MUA: MPOH, and $mSAM_2$, 1:9 MUA: MPOH). For comparing the results we also used the homogeneous MUA layer on the electrode (hSAM). The functionalization of the gold surfaces was characterized using two electrochemical techniques: CV and EIS with Faradic and non-Faradic measurements.

3.1.1. Cyclic voltammetry measurements

Fig. 1(a–c) shows the cyclic voltammograms of the modified gold electrode for different immobilization periods of time (1 min, 10 min, 30 min and 24 h) in solutions of hSAM, $mSAM_1$ and $mSAM_2$, respectively. For all bare gold electrodes modified with monolayers, a decrease in the current is produced compared to that obtained at the non-modified electrodes. This is due to the blocking properties of the monolayers. The decrease of the anodic and cathodic currents in the first few minutes is more rapid for hSAM compared to $mSAM_1$ and $mSAM_2$. The $mSAM_2$ presents pinholes on the monolayer through which the redox probe can penetrate onto the surface, which explains why the ΔE_p value is smaller than that for hSAM and $mSAM_1$, even after a long time of incubation (>20 h). These pinholes are caused by the low percentage of MUA compared to MPOH that promotes the transfer of the negative redox ions $Fe(CN)_6^{3-/4-}$ to the electrode surface, thus decreasing the blocking properties of the $mSAM_2$ monolayer. Because the $mSAM_1$ monolayer shows the highest difference in the responses of bare gold vs. modified electrode, it was chosen for further development of the immunosensor.

According to the voltammetric behavior, the blocking reaction occurred more rapidly for hSAMs compared to mSAMs. The efficiency of the formation of SAMs for different immobilization times is more precisely described by the EIS results.

3.1.2. Electrochemical impedance spectroscopy measurements

In order to characterize the stability of the monolayers onto gold, the insulating properties and the capacitive behavior of the gold surfaces for each stage of functionalization with hSAM, mSAM1 and $mSAM_2$ have been investigated by EIS experiments with a Faradaic process.

The results can be interpreted using the equivalent circuit presented in the inset of Fig. 2 that includes the solution resistance (R_s), double layer capacitance (C_{dl}) and electron transfer resistance (R_{CT}) [17,22]. The Auto.R1R2C Fitting method is used to fit the

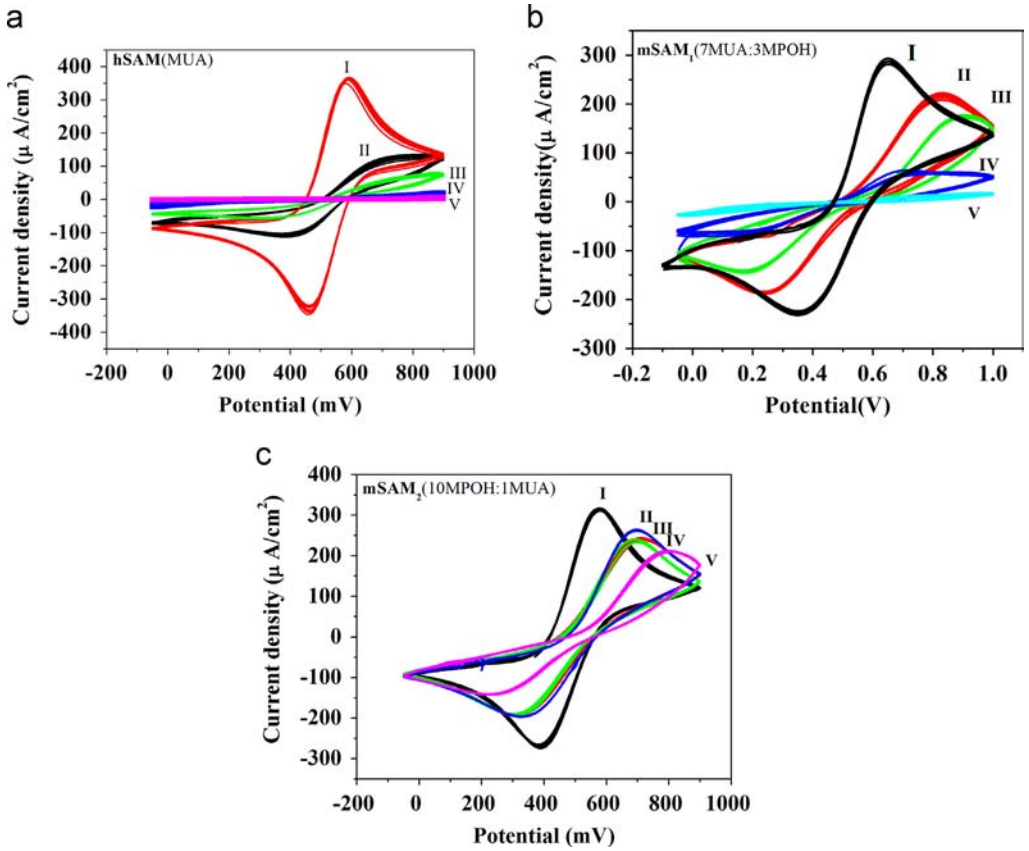


Fig. 1. Cyclic voltammograms of (a) hSAM, (b) $mSAM_1$ and (c) $mSAM_2$ on (I) bare gold and at different interaction times: (II) 1 min, (III) 10 min, (IV) 30 min and (V) 24 h. The electrolyte is PBS solution (pH=7.4) containing $Fe(CN)_6^{3-/4-}$ as a redox couple and the scan rate is 100 mV/s.

curve to a circle while running the sequence and the Bode Plot is used for monitoring the phase angle and capacitance after various incubation times of gold surfaces with thiol solutions for further formation of $mSAM_1$, $mSAM_2$ and hSAM. It is well known that the insulating properties in a high ionic strength solution are low and therefore the capacitance greatly increases and the stability of the monolayer decreases [13,25]. So, to keep a stable capacitance, a low ionic strength of 10 mM PBS was used. Also, it is known that SAM is viewed as a pure capacitor and is deemed defect-free when the phase angle (φ) is $\geq 88^\circ$ (for practical purposes), and to be a leaky capacitor when the φ value is $< 87^\circ$ over 1 kHz–50 Hz range [23,26].

As shown in Fig. 2, the phase angle (the Bode phase plots) for all SAMs formed after adsorption during 24 h increases with time and $mSAM_1$ and hSAM become capacitors. Regarding the adsorption kinetics of the hSAM layer, we monitored the capacitance values after incubation of the gold surfaces in MUA solution. The adsorption is fast after only 1 min of immersion and the capacity begins to decrease. After 10 min the capacitance decreases by 83% compared to the capacitance of bare gold (from 20.54 $\mu F\,cm^{-2}$ to 3.53 $\mu F\,cm^{-2}$). From 10 to 30 min, the capacitance slightly decreases (from 3.53 $\mu F\,cm^{-2}$ to 2.12 $\mu F\,cm^{-2}$). After 24 h of incubation, the capacitance for hSAM becomes 1.28 $\mu F\,cm^{-2}$, which indicates a 94% decrease compared to bare gold. A minimum 24 h incubation in thiol solutions is necessary to achieve $\varphi_{1\ Hz} \geq 88^\circ$ for hSAM. Similarly, a decrease in the capacitance and adsorption time has been observed for $mSAM_1$. After 24 h of incubation, it achieves the maximum phase angle of 88.66° for $mSAM_1$. Compared to hSAM, the capacitance for $mSAM_1$ decreases in the same way, but after 24 h of immersion it is slightly higher (1.616 $\mu F\,cm^{-2}$).

By comparison, capacitance in the first few minutes of immersion shows a slight instability for $mSAM_2$, mostly due to the lower percentage of MUA in the mixed solution. After 1 min, the capacity decreases significantly by 56%. However, after 10 min, there is a noticeable increase in capacity—by 33% compared to that at 1 min—probably due to the high percentage of MPOH compared to MUA that leads to the formation of pinholes in the structure of the monolayer. Only after 24 h does the capacity stabilize at a value lower than that of bare gold. It can be seen from Fig. 2 that the phase angle values of these SAMs follow the order hSAM > $mSAM_1$ > $mSAM_2$. Regarding the phase angle, there is a completely different behaviors for $mSAM_2$ because it does not achieve capacitive behavior even after 24 h of immersion. This probably happens because of the many defect sites that favor the leakage current, thus confirming that the blocking effect of $mSAM_2$ is low (also demonstrated by CV) and that the well-ordered structure is not obtained. Therefore, our results are in agreement with the observation made by Whitesides' group that the blocking effect of SAMs increases with the MUA percentage in the mixture [27].

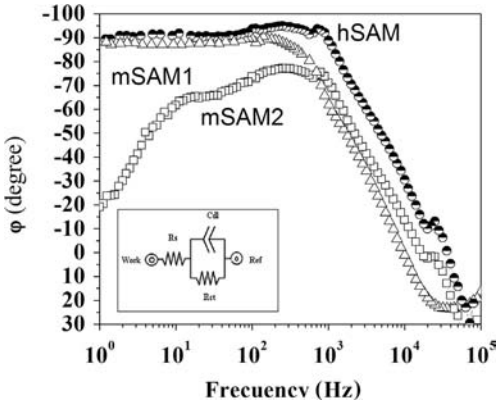


Fig. 2. Bode phase plots (φ vs. frequency) for $mSAM_1$, $mSAM_2$ and hSAM after 24 h immersion time in the PBS solution (pH=7.4). The inset figure is the equivalent electrical circuit with solution resistance (R_s), double layer capacitance (C_{dl}) and electron transfer resistance (R_{CT}).

3.2. Immunosensor non-Faradaic detection of h-FABP with microfluidic platform

The capacitance changes between the initial baseline in PBS and the measured capacitance values at specific concentrations of h-FABP (in PBS or human serum) immobilized onto functionalized GID electrode areas with antibody were used as the sensing signal. The experiments can be described as a simple RC model, as shown in the inset A of Fig. 3a and b, where R_s is the resistance at the electrode surface and C the total capacitance, according to Eq. (1).

To avoid the effect of the high conductivity of the working solution, the immunoassay binding event was performed in pH 7.4 at 10 mM PBS. The principle of our method is as follows: the binding of the h-FABP antigen to the $mSAM_1$/anti-h-FABP antibody/BSA surface and hSAM surface/anti-h-FABP antibody/BSA produces an increase in layers, and thus of the total capacitance for each surface according to the Eq. (1). The incubation time for

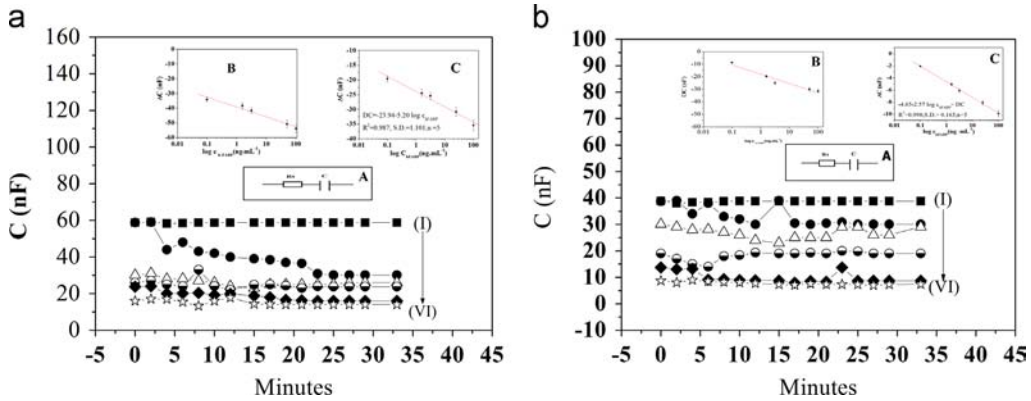


Fig. 3. The capacitance responses of (a) mSA1/EDC/NHS/anti-h-FABP/BSA GID electrode and (b) hSAM/EDC/NHS/anti-h-FABP/BSA GID electrode after suction of 100 μL of buffer or of h-FABP solutions of different concentrations onto electrodes' surfaces: (I) 0 pg ml^{-1}, (II) 98 pg ml^{-1}, (III) 1.56 ng ml^{-1}, (IV) 3.125 ng ml^{-1}, (V) 50 ng ml^{-1}, (VI) 100 ng ml^{-1}. The inset figures B are the linearity curves for the capacitance measurements with different h-FABP concentrations in PBS for (a) $mSAM_1$/EDC/NHS/anti-h-FABP/BSA GID electrode and respectively for (b) hSAM/EDC/NHS/anti-h-FABP/BSA GID electrode; the inset figures C are the linearity curves for the capacitance measurements with different h-FABP concentrations in PBS:human serum for (a) $mSAM_1$/EDC/NHS/anti-h-FABP/BSA GID electrode and respectively (b) hSAM/EDC/NHS/anti-h-FABP/BSA GID electrode; the inset figure A is the RC model circuit with solution resistance (Rs) at the electrode surface and C is the total capacitance of the electrode layers; each capacitance measurement was run in triplicate and represented with error bars.

Table 1
The curve parameters of hSAM/EDC/NHS/anti-h-FABP/BSA GID electrode vs. $mSAM_1$/EDC/NHS/anti-h-FABP/BSA GID electrode after different hFABP concentrations in PBS.

Curve parameters	hSAM/EDC/NHS/anti-h-FABP/BSA GID electrode	$mSAM_1$/EDC/NHS/anti-h-FABP/BSA GID electrode
Linear equation	DC (nF) = −17.98 − 7.40 log $C_{h\text{-}FABP}$	DC (nF) = −39.27 − 6.71 log $C_{h\text{-}FABP}$
Correlation coefficient	R^2 = 0.975	R^2 = 0.981
Detection limit	968 pg ml^{-1}	836 pg ml^{-1}

immunoassay after each addition of h-FABP was 30 min. After immunoreaction, the capacitance decreases with incubation time and becomes constant after 30 min, indicating that saturation has begun. For each added concentration the capacitance change was monitored for 30 min. As is shown in Fig. 3a, the fabricated immunosensor is sufficiently sensitive to exhibit a change in signal for $mSAM_1$. The thickness of the layers is a very important characteristic of a capacitive sensor. It should be as thin as possible, so that the capacitive response due to the antigen − antibody interaction increases in size comparable with the recognition layer. In the case of hSAM, as shown in Fig. 3b, the decrease of the functionalized electrode capacity is obtained in a range of capacitance values lower than that for the $mSAM_1$ functionalized electrode. So, although long-chain SAMs are much less easily damaged, thin sensing layers are preferred for directly detecting small amounts of protein. For our mixed monolayer $mSAM_1$ with short and long chains, a larger change in relative capacitance comparative with hSAM was obtained. Under the optimization of experimental conditions, for the GID electrode $mSAM_1$/h-FABP antibody and hSAM/h-FABP antibody, both blocked with BSA, it was found that the capacitance changes (ΔC) were proportional with the logarithm of h-FABP concentration in the range of 98 pg ml^{-1}–100 ng ml^{-1} in PBS buffer, as can be seen in Fig. 3a (inset B) and respectively Fig. 3b (inset B). The regression equation, correlation coefficient and sensitivity for both gold electrode surfaces are presented in Table 1. The limit of detection for $mSAM_1$ and hSAM was found to be approximately 3× the standard deviation of the baseline samples (with PBS) and, combined with the good linear response, yielded the values 0.836 ng ml^{-1} for $mSAM_1$ and 0.968 ng ml^{-1} for hSAM.

3.2.1. Selectivity of the immunosensor

The selectivity of the immunosensor refers to the effect of possible interferences with the determination of the h-FABP in samples. For this, both biofunctionalized $mSAM_1$ and hSAM GID electrodes were introduced in the microfluidic system, and were exposed and incubated with BioRad control serum spiked with five concentrations of h-FABP: 98 pg ml^{-1}, 1.56 ng ml^{-1}, 3.125 ng ml^{-1}, 25 ng ml^{-1} and 100 ng ml^{-1}. The regression equation and the correlation coefficient for both gold electrode surfaces are presented in Fig. 3a (inset C) and b (inset C). As can be seen, the capacitance changes for $mSAM_1$ were evidently on a larger range than for hSAMs. It is probably that the high density and homogeneity of the hSAMs is a non-essential feature for the efficiency of our future capacitive sensor. The steric hindrance that can occur after the interaction between the h-FABP antigens with antibodies can lead to its removal from hSAM. It is evident that the interaction between anti-h-FABP and h-FABP was strong in the case of the mSAM/anti-h-FABP compared with hSAM/anti-h-FABP when the serum samples were used. The steric hindrance was higher for homogenous SAMs and therefore this decreased the capacity of the anti-h-FABP antibody to bind the h-FABP antigen in human serum.

The relative standard deviations (R.S.D) of the intra- and inter-assay for the immunosensor chip fabricated with $mSAM_1$ in order to detect h-FABP antigen in the linear detection range were 8% (n=5) for intra-assay and 12.1% (n=3) for inter-assay.

Table 2
The recovery of the prepared mSAM1/EDC/NHS/anti-hFABP/BSA GID capacitive immunosensor for h-FABP detection.

Sample no.	Added h-FABP (ng ml^{-1})	DC (nF)	Recovery (%)	R.S.D (%)
1	100	−55	102	1.03
2	50	−49.95	98.4	0.83
3	12.5	−45.91	95.82	2
4	1.56	−38.94	101	0.52

3.2.2. Recovery test of hFABP assay

Four samples with different hFABP concentrations were performed. All the experiments were carried out three times. As seen in Table 2, the average recovery was 99.3% with a relative standard derivation (R.S.D) of 0.52–2%.

3.2.3. Regeneration of immunosensor

Antigens were released from the GID electrode surfaces after suction of 50 μl of glycine: HCl (pH 2.5) for 3 min only, as the acid solutions may disturb the SAMs layers. After this, the electrode surfaces were incubated with h-FABP protein to verify the capacitance response and no noticeable change in capacitance response to the same amount of h-FABP in PBS was observed after quick acidic washing.

4. Conclusions

An integrated microfluidic platform with GID electrodes for direct detection of h-FABP is described. The $mSAM_1$ are suitable for fabrication of a label-free capacitive immunosensor. The capacitive immunosensor prepared with $mSAM_1$ can provide a low detection limit compared with a homogenous SAMs, due to a higher starting capacitive signal than that obtained when using a mixed SAM with short and long chains. The percentage of the long chain was optimized, and for the presented methods it has been demonstrated that the blocking effect of the SAM, and therefore the capacitive behavior, increased with the percentage of MUA in the mixture. The low percentage of MUA is not essential for this type of electrode, probably because the signal of the capacitance response will become unstable, as for the case of $mSAM_2$. Also, the 100% figure of MUA in the mixture decreased the efficiency of the future immunosensor due to the steric hindrance that can occur after interaction between antigens with antibodies. The low detection limit of the presented immunosensor, the good specificity of the assay for h-FABP detection, and the cheaper and faster capacitive measurements method were demonstrated for GID electrodes functionalized with $mSAM_1$. Also, this platform could provide a faster and cheaper system without susceptibility of antibodies for cross-reaction when using a multiplexed test with other important cardiac markers.

Acknowledgments

The authors would like to thank the National Project PN-II-PT-PCCA-2011-3.2-0649 (IMUNOPLAT) for the financial support. We are also grateful to Dr. Iulia Matei for the critical reading and for her support.

Appendix A. Supporting information

Supplementary data associated with this article can be found in the online version at http://dx.doi.org/10.1016/j.talanta.2014.08.067.

References

[1] J.F.C. Glatz, M. Van Bilsen, R.J.A. Paulussen, J.H. Veerkamp, G.J. Van der Vusse, R.S. Reneman., Biochim. Biophys. Acta 961 (1988) 148–152.
[2] R.H. Christenson, H.M.E. Azzazy, Clin. Chem. 44 (1998) 1855.
[3] B. McDonnel, S. Heary, P. Leonard, R. O'Kennedy, Clin. Biochem. 42 (2009) 549–561.
[4] F. Ghani, A.H.B. Wu, L. Graff, C. Petry, Clin. Chem. 46 (2000) 718–719.
[5] K. Kurz, E. Giannitsis, M. Becker, G. Hess, D. Zdunek, H.A. Katus, Clin. Res. Cardiol. 100 (2011) 209–215.
[6] A. Quershi, Y. Gurbuz, W.P. Kang, J.L. Davidson, Biosens. Bioelectron. 25 (2009) 877–882.
[7] C. Berggren, B. Bjarnason, G. Johansson, Biosens. Bioelectron. 13 (1998) 1061–1068.
[8] O. Pänke, T. Balkenhohl, J. Kafka, D. Schäfer, F. Lisdat, Adv. Biochem. Eng. Biotechnol. 109 (2008) 195–237.
[9] C. Berggren, B. Bjarnason, G. Johansson, Electroanalysis 13 (2001) 173–180.
[10] C. Berggren, G. Johansson, Anal. Chem. 18 (1997) 3651–3657.
[11] D. Jiang, J. Tang, B. Liu, P. Yang, Z. Shen, J. Kong, Biosens. Bioelectron. 18 (2003) 1183–1191.
[12] D. Li, Y. Feng, L. Zhou, Z. Ye, J. Wang, Y. Ying, C. Ruan, R. Wang, L. Yanbin, Anal. Chim. Acta 687 (2011) 89–96.
[13] M. Billah, H.C.W. Hays, P.A. Millner, Microchim. Acta 160 (2008) 447–454.
[14] J.S. Daniels, N. Pourmand, Electroanalysis 19 (2007) 1239–1257.
[15] R.P. Janek, R. Fawcett, A. Ulman, J. Phys. Chem. 101 (1997) 8550–8558.
[16] A.J. Bard, L.R. Faulker (Eds.), Electrochemical Methods – Fundamentals and Applications, Wiley, New York, 1980.
[17] S.J. Ding, B.W. Chang, C.C. Wu, M.F. Lai, H.C. Chang, Electrochim. Acta 18 (2005) 3660–3666.
[18] L. Yang, R. Bashir, Biotechnol. Adv. 26 (2008) 135–150.
[19] L. Yang, Talanta 74 (2008) 1621–1629.
[20] D. Stan, C.M. Mihailescu, R. Iosub, C. Moldovan, M. Savin, Thin Solid Films 526 (2012) 143–149.
[21] M.D. Porter, T.B. Bright, D.L. Allara, C.E.D. Chidsey, J. Am. Chem. Soc. 109 (1987) 3559–3568.
[22] E. Katz, I. Willner, Electroanalysis 15 (2003) 913.
[23] Z. Zou, J. Kai, M.J. Rust, J. Han, C.H. Ahn, Sens. Actuators A 136 (2007) 518–526.
[24] S.J. Ding, B.W. Chang, C.C. Wu, M.F. Lai, H.C. Chang, Anal. Chim. Acta 554 (2005) 43–51.
[25] S. Campuzano, M. Pedrero, C. Montemayor, E. Fatas, J.M. Pingarron, J. Electroanal. Chem. 586 (2006) 112–121.
[26] H.C.W. Hays, P.A. Millner, M.I. Prodromidis, Sens. Actuators B 114 (2006) 1064–1070.
[27] C.D. Bain, G.M. Whitesides, J. Am. Chem. Soc. 111 (1989) 7164–7175.

Talanta 132 (2015) 44–51

Contents lists available at ScienceDirect

Talanta

journal homepage: www.elsevier.com/locate/talanta

Ultrasensitive detection of target analyte-induced aggregation of gold nanoparticles using laser-induced nanoparticle Rayleigh scattering

Jia-Hui Lin [a], Wei-Lung Tseng [a,b,c,*]

[a] Department of Chemistry, National Sun Yat-sen University, 70, Lien-hai Road, Kaohsiung 804, Taiwan
[b] School of Pharmacy, College of Pharmacy, Kaohsiung Medical University, Taiwan
[c] National Sun Yat-sen University and Center for Nanoscience & Nanotechnology, Taiwan

ARTICLE INFO

Article history:
Received 18 June 2014
Received in revised form
19 August 2014
Accepted 20 August 2014
Available online 27 August 2014

Keywords:
Laser-induced Rayleigh scattering
Gold nanoparticles
Smart phone
Sensor

ABSTRACT

Detection of salt- and analyte-induced aggregation of gold nanoparticles (AuNPs) mostly relies on costly and bulky analytical instruments. To response this drawback, a portable, miniaturized, sensitive, and cost-effective detection technique is urgently required for rapid field detection and monitoring of target analyte *via* the use of AuNP-based sensor. This study combined a miniaturized spectrometer with a 532-nm laser to develop a laser-induced Rayleigh scattering technique, allowing the sensitive and selective detection of Rayleigh scattering from the aggregated AuNPs. Three AuNP-based sensing systems, including salt-, thiol- and metal ion-induced aggregation of the AuNPs, were performed to examine the sensitivity of laser-induced Rayleigh scattering technique. Salt-, thiol-, and metal ion-promoted NP aggregation were exemplified by the use of aptamer-adsorbed, fluorosurfactant-stabilized, and gallic acid-capped AuNPs for probing K^+, *S*-adenosylhomocysteine hydrolase-induced hydrolysis of *S*-adenosylhomocysteine, and Pb^{2+}, in sequence. Compared to the reported methods for monitoring the aggregated AuNPs, the proposed system provided distinct advantages of sensitivity. Laser-induced Rayleigh scattering technique was improved to be convenient, cheap, and portable by replacing a diode laser and a miniaturized spectrometer with a laser pointer and a smart-phone. Using this smart-phone-based detection platform, we can determine whether or not the Pb^{2+} concentration exceed the maximum allowable level of Pb^{2+} in drinking water.

© 2014 Elsevier B.V. All rights reserved.

1. Introduction

Numerous nanomaterials, including magnetic nanoparticles (NPs), metal NPs, quantum dots and carbon-based nanomaterials, have served as signal transducers in a number of reported biosensors because they exhibit high surface area-to-volume ratio, strong signal intensities, and tunable surface chemistry [1–3]. Gold nanoparticles (AuNPs) provide several physical and chemical advantages, making them one of the most popular materials for the fabrication of chemical and biological sensors. First, a number of chemical approaches have been available for a one-pot synthesis of highly stable AuNPs [4]. Second, they possess surface Plasmon resonance (SPR), Rayleigh scattering, electric conductance, redox behavior, and enzyme-mimetic activity [4–8]. Third, they offer extremely large ensemble surface areas with tunable modification options [9]. Fourth, these properties of AuNPs can be readily tuned by varying their size, shape, and the surrounding chemical environment [4]. With these advantages, the binding event between the recognition element and the analyte can cause the change in physicochemical properties of transducer AuNPs, such as the intensity and wavelength of SPR [10], the magnitude of conductivity [11], and the behavior of redox reaction [6]. These changes in turn can produce a detectable response signal for detecting a variety of analyte, such as heavy metal ions, anions, small molecules, proteins, and nucleic acids [4,8,10,12,13].

Because the optical properties of SPR of the AuNPs are strongly dependent on interparticle separation distances and particle size, the current gold standard for detecting the analyte-induced aggregation and growth of the AuNPs is to measure the wavelength and intensity of SPR, respectively. For example, the analyte-stimulated aggregation of the AuNPs drives interparticle surface plasmon coupling, causing a red-shift in the SPR peak [14]. Moreover, the H_2O_2- and dopamine-mediated enlargement of the AuNPs produced an increase in the intensity of SPR peak [15,16]. However, most of these sensors exhibit moderate sensitivity with detection limits for target analyte in the micromolar range. The plasmon scattering intensity of a single 60-nm diameter AuNPs resembles the fluorescence intensity of 10^5 fluorescein molecules. The strong scattering light of the AuNPs arises from the collective oscillation of conducting electrons. Thus, to improve the

* Corresponding author at: Department of Chemistry, National Sun Yat-sen University, 70, Lien-hai Road, Kaohsiung 804, Taiwan. Fax: +11 886 7 3684046.
E-mail address: tsengwl@mail.nsysu.edu.tw (W.-L. Tseng).

http://dx.doi.org/10.1016/j.talanta.2014.08.055
0039-9140/© 2014 Elsevier B.V. All rights reserved.

sensitivity of AuNP-based colorimetric assays, numerous sensors are established based on the measurement of size-induced change in the maximum peak and intensity of a resonant Raleigh scattering [17]. For example, as compared to the dispersed AuNPs, the analyte-triggered aggregation of the AuNPs can scatter electromagnetic radiation strongly; this change can be monitored using dark-field light scattering [18], dynamic light scattering [19], hyper-Rayleigh scattering [20], and resonance Rayleigh scattering techniques [21]. Dark-field light scattering technique can observe the scattering light of the AuNPs at the single-particle level, but such technique are limited to the detection of relatively large particles (>40 nm) and the quantification of target analyte. Additionally, dynamic light scattering, hyper-Rayleigh scattering, and resonance Rayleigh scattering techniques are rather costly, time-consuming procedure, sophisticated, and non-portable.

Herein, we reported a highly sensitive light-scattering technique for sensing K^+, *S*-adenosylhomocysteine hydrolase (SAHH) activity, and Pb^{2+} based on the fact that salt- thiol-, and metal ion-induced aggregation of the AuNPs greatly enhances light scattering, respectively. The measurement of light scattering is easy to perform using a miniaturized spectrometer as a scattering detector and a 532-nm laser as an excitation light. The integrated scattering spectrum was obtained by placing the detector at right angle to the excitation beam. The proposed method can provide more than 10-fold improvement in limit of detection (LOD) compared to colorimetric assay.

2. Experimental

2.1. Chemicals

S-adenosylhomocysteine (SAH), SAHH (rabbit erythrocytes; 50,000 units/L; MW 240,000), homocysteine (HCys), bovine serum albumin (BSA, from bovine serum), human serum albumin (HSA, from human serum), trypsin (from porcine pancreas), lysozyme (from human milk), thrombin (from bovine plasma), myoglobin (from equine heart), cytochrome c (from bovine heart), hemoglobin (from bovine blood), fluorosurfactant (FSN), trisodium citrate, $HAuCl_4$, gallic acid, NaH_2PO_4, Na_2HPO_4, NaCl, $NaClO_4$, $MgCl_2$, $FeCl_3$, NH_4HCO_3, $Cd(ClO_4)_2$, NaOH, $Pb(NO_3)_2$, and $HgCl_2$ were obtained from Sigma-Aldrich (St. Louis, MO). $FeCl_2$, $CuCl_2$, $SrCl_2$, LiCl, KCl, $CoCl_2$, $NiCl_2$, $CaCl_2$, $MnCl_2$, $BaCl_2$, $ZnCl_2$ were obtained from Acros Organics (Geel, Belgium). The molecular formula of FSN is $F(CF_2CF_2)_{3-8}CH_2CH_2O(CH_2CH_2O)_xH$. Gold nanoparticles (15, 30, 50 nm) were purchased from Ted Pella Inc. (Redding, California). DNA sample (K^+ aptamer, 5′-GGG TTA GGG TTA GGG TTA GGG-3′) was synthesized from GenScript Corporation (Taipei, Taiwan). Isotonic phosphate-buffered saline ($1\times$ PBS; pH 7.4) was prepared by dissolving $Na_2HPO_4{\cdot}2H_2O$ (22.05 g), $NaH_2PO_4{\cdot}H_2O$ (2.07 g), and NaCl (4.5 g) in H_2O (1.0 L). Water used in all of the experiments was doubly distilled and purified by a Milli-Q system (Millipore, Milford, MA, USA).

2.2. Synthesis of 4 nm-sized AuNPs

The preparation of AuNPs was conducted by adding $NaBH_4$ (0.1 M, 1.5 mL) to a solution (50 mL) containing 250 μM $HAuCl_4$ and 250 μM trisodium citrate under vigorous stirring. The image of transmission electron microscopy (Tecnai 20 G2 S-Twin, Philips/FEI, Hillsboro, Oregon) demonstrated the size of the as-prepared AuNPs (Fig. S1, Supplementary information).

2.3. Apparatus

A diode-pumped solid state continuous laser (Labguide Co., Ltd) with a wavelength of 532 nm was used as an excitation light source when its output power was 5 mW. A miniaturized QE65000 Scientific-grade Spectrometer (Ocean Optics, Inc.) was used for collecting the scattering of the AuNPs. An Ocean Optics CUV-ALL-UV four-way cuvette holder (Ocean Optics, Inc.) equipped with fiber-optic couplings at each of four quartz *f*/2 collimating lenses was incorporated to a 1000 μm illumination fiber and a 1000 μm read fiber. An illumination fiber brings the excitation beam to a cuvette, while a read fiber transports the scattering signal back to Ocean Optics QE65000 spectrometer. The scattering spectrum was recorded using Ocean optics SpectraSuite spectroscopy software with 100 ms integration time. To reduce the cost of instrumentation and toward more portable system, a battery-operated green laser point (532 nm) and a smart-phone (Samsung, Galaxy SIII) were used in place of a diode-pumped solid state continuous laser and a Ocean Optics QE65000 spectrometer, respectively.

2.4. Sensing of potassium ion

Citrate-capped AuNPs (15 nm; 1.5 nM, 10 mL) were modified with K^+ aptamer (100 μM, 100 μL) for 2 h at ambient temperature. Metal ions (4–5000 μM) reacted with aptamer-modified AuNPs (0.75 nM) for 5 min at ambient temperature. The resulting solutions were incubated with $0.1\times$ PBS solution for 5 min at ambient temperature. The scattering spectra were collected using the proposed detection system.

2.5. Sensing of SAHH activity

Citrate-capped AuNPs (15 nm; 2.5 nM, 60 mL) were modified with FSN (10% w/v, 240 μL). FSN-stabilized AuNPs were stored at 4 °C until further use. Proteins (0–100 units/L, 100 μL) reacted with SAH (100 μM, 100 μL) in 50 mM phosphate buffer (pH 7.2) at 37 °C for 20 min. We incubated the resulting solutions (200 μL) with a solution (800 μL) containing FSN-AuNPs (0.1 nM) and phosphate buffer (100 mM, pH 5) for 10 min and recorded their scattering spectra.

2.6. Sensing of lead ion

The pH of $HAuCl_4$ was adjusted to 11.1 by adding 100 μL of 0.5 M NaOH. A solution of gallic acid was heated to 50 °C. Subsequently, gallic acid (0.1 mL, 38.8 mM) was added slowly to $HAuCl_4$ (10 mL, 1 mM) under vigorous stirring at ambient temperature for 6 h. The particle size of the formed AuNPs was 9 ± 1 nm. To estimate the concentration of gallic acid-capped AuNPs, we assumed that the reduction from gold(III) to gold atoms was 100% complete. According to this hypothesis, the concentration of gallic acid-capped AuNPs was calculated to be 40 nM. Metal ions (1–40 nM) were incubated with a solution containing gallic acid-capped AuNPs (0.63 nM), $NaClO_4$ (1 mM) and formic acid buffer (pH 4.5, 20 mM) for 20 min at ambient temperature. The scattering spectra were collected using the proposed detection system.

3. Result and discussion

3.1. Sensing of K^+ by salt-induced NP aggregation

Because the scattering cross section of a single AuNPs is proportional to the sixth power of its diameter [22], we initially investigated the effect of different-sized AuNPs (4, 15, 30, and 50 nm) on their light-scattering intensity in deionized water and $0.5\times$ PBS solution under irradiation with a 532-nm diode laser. The concentrations of different-sized AuNPs were all adjusted to 10^8 particles mL^{-1}. Note that the AuNPs are dispersed in deionized water, whereas they aggregated to large-sized particles in $0.5\times$ PBS. Salt-induced aggregation of the

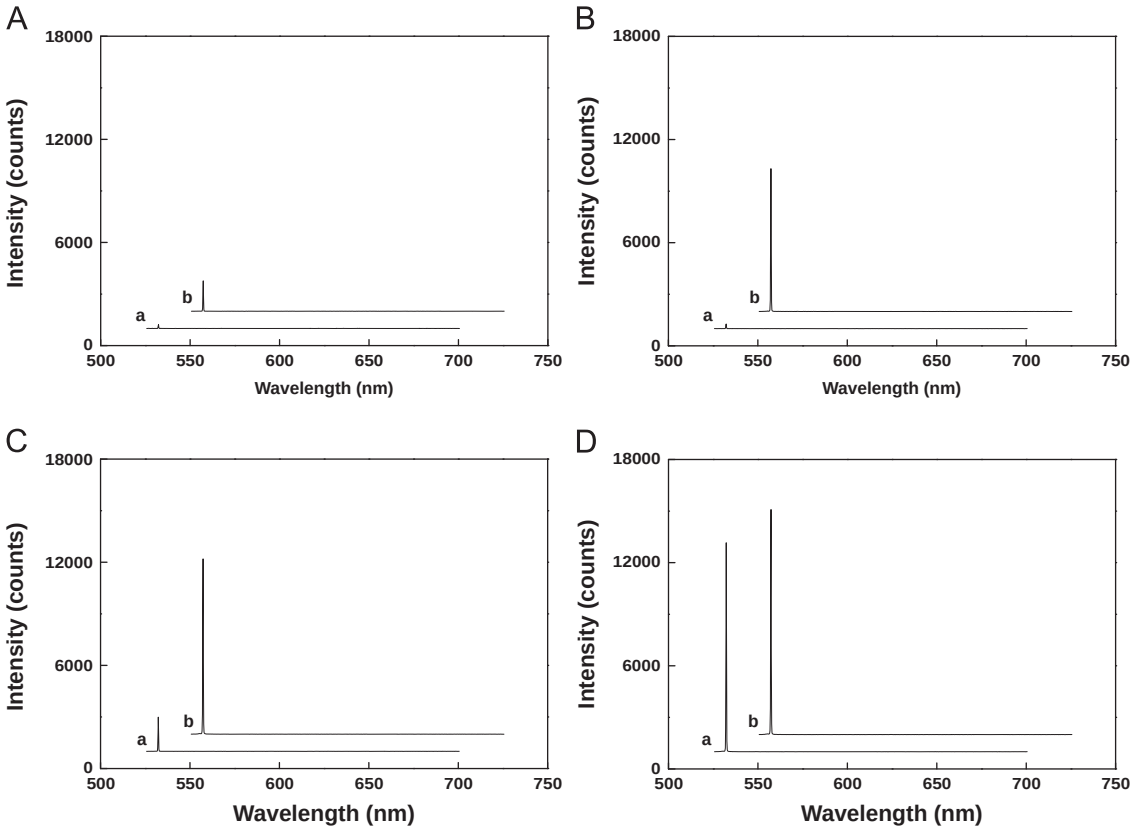


Fig. 1. Scattering spectra of (A) 4 nm, (B) 15 nm, (C) 30 nm, (D) 50 nm-sized AuNPs in the (a) absence and (b) presence of 0.5 × PBS. The concentration of the AuNPs was fixed at 10^8 particles mL^{-1}.

AuNPs is attributed to the fact that salt efficiently screens the surface charges of individual AuNP [23]. Fig. 1 shows a comparison of difference in light-scattering intensity between the dispersed and aggregated AuNPs. Expectably, the light-scattering intensity of the dispersed AuNPs tremendously increased with increasing their particle size, which is in agreement with Mie or Rayleigh scattering theory. Following the addition of 0.5 × PBS to 4, 15, 30, and 50 nm of the dispersed AuNPs, we observed a 8-, 30-, 5-, and 1-fold increase in the light-scattering intensity at 532 nm, respectively. For larger particles (30 and 50 nm), the light-scattering intensity at 532 nm was very strong even in the absence of salt, thus failing to measure the presence of the aggregated AuNPs. For smaller particles (4 nm), the aggregated AuNPs were too small to exhibit strong light-scattering intensity. We suggest that 15 nm AuNPs were more suitable for salt-induced aggregation of AuNP probes, owing to low background scattering from the dispersed AuNPs and an enormous increase in light-scattering intensity from the aggregated AuNPs.

Previous studies demonstrated that salt-induced aggregation of citrate-capped AuNPs was implemented for selective and sensitive detection of K^+, thrombin, and adenosine triphosphate [24–26]. This was exemplified with the use of aptamer-modified AuNPs for detecting K^+ (Fig. 2A). Citrate-capped AuNPs interacting with aptamer are dispersed well under high-ionic-strength conditions. The presence of K^+ induces the formation of K^+ – aptamer complexes, enabling aptamer to be removed from the NP surface [24,27–34]. Because of the removal of aptamer from the NP surface, salt-induced aggregation of the AuNPs occurs and causes an enhancement in light-scattering intensity. Because the enhancement of the light-scattering intensity mainly arose from the degree of the NP aggregation, the effect of salt concentration on the stability of aptamer-modified AuNPs was explored in the next study. Fig. S2 Supplementary information shows that aptamer-modified AuNPs remained dispersed when the concentration of PBS varied from 0–0.2 × PBS. Thus, in 0.1 × PBS, the scattering intensity of aptamer-modified AuNPs was measured before and after the addition of K^+. As the concentration of K^+ increased at fixed concentrations of citrate-capped AuNPs and aptamer, the scattering intensity of aptamer-capped AuNPs was progressively enhanced (Fig. 2B). The linear relationship (R^2 = 0.9965) of the light-scattering intensity at 532 nm *versus* the K^+ concentration was from 4–5000 μM (inset in Fig. 2B). Because 0.1 × PBS contains 17 mM Na^+ ions, we suggest that this system is capable of selectively detecting 4 μM K^+ in the presence of a 21,000-fold excess of Na^+ ions. This system enabled the detection of K^+ with limit of detection (LOD) corresponding to 1 μM, which is much lower than the LOD values obtained from aptamer-based colorimetric, electrochemical, and fluorescent sensors probes [24,27–34] (Table 1). Although dynamic light scattering, hyper-Rayleigh scattering, and resonance Rayleigh scattering techniques can be also utilized for observing salt-induced NP aggregation, the developed system consisting of miniaturized QE65000 spectrometer and diode laser can be portable and is interfaced to a personal computer via USB port. We next evaluated the specificity of the aptamer-based probe by monitoring the light-scattering intensity in the presence of other cation ions. Fig. 2C shows that only K^+ ions induced a remarkable change in light-scattering intensity because other cations were unable to remove aptamer from the NP surface. The combination of laser-induced Rayleigh scattering technique and aptamer-based sensor therefore provided high sensitivity and selectivity for K^+ ions.

3.2. *Sensing of SAHH activity by homocysteine-mediated NP aggregation*

Numerous previous studies reported that aminothiol triggered the aggregation of nonionic FSN-stabilized AuNPs through interparticle H-bonds and electrostatic attraction between adsorbed aminothiol molecules [35]. The successful monitoring of salt-induced NP aggregation suggests that laser-induced Rayleigh scattering technique may be

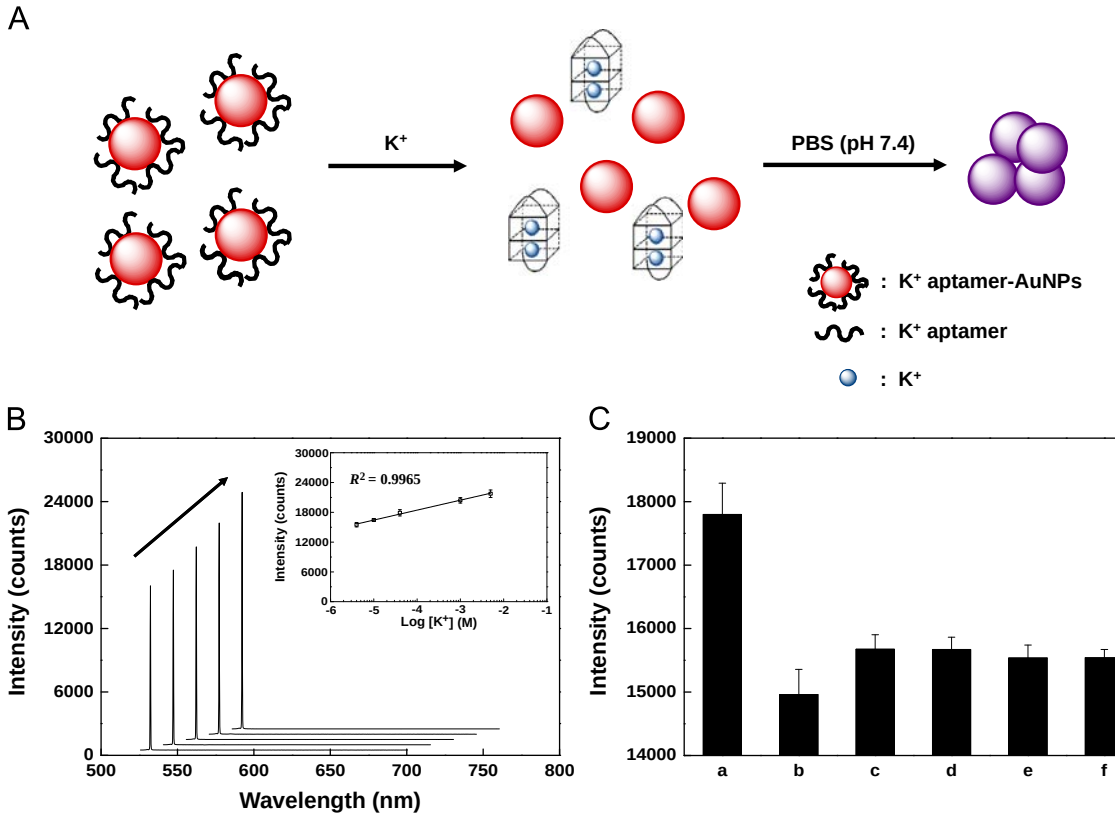


Fig. 2. (A) Illustration of the mechanism of aptamer-modified AuNPs for sensing K^+ *via* salt-induced NP aggregation. (B) Scattering spectra obtained from the addition of aptamer-modified AuNPs and 4–5000 μM K^+ to 0.1 × PBS (pH 7.4). The arrows indicate the signal changes with increase in K^+ concentration (4, 10, 40, 1000, 5000 μM). (C) Scattering intensity at 532 nm obtained from the addition of a mixture of aptamer-modified AuNPs and analyte to 0.1 × PBS (pH 7.4). Analyte: (a) 10 μM K^+, (b) 5 mM Li^+, (c) 5 mM Na^+, (d) 5 mM Mg^{2+}, (e) 5 mM Ca^{2+}, and (f) 5 mM NH_4^+. Metal ions were incubated with aptamer-modified AuNPs (0.75 nM) for 5 min at ambient temperature. The resulting solutions were mixed with 0.1 × PBS solution for 5 min at ambient temperature.

Table 1
Comparison of other AuNP-based sensors for the determination of K^+.

Sensing system[a]	detection	MDC[b]	LOD[c]	Reference
aptamer-modified AuNPs	Colorimetry	1 mM	N.A.	[24]
Nicking endonuclease-assisted AuNPs sensor	Colorimetry	0.1 mM	N.A.	[27]
G-quadruplex DNA-based electric switch	Electrochemical detection	N.A.	N.A.	[28]
aptamer/pyrene-labeled molecular beacon	Fluorescence	0.6 mM	0.4 mM	[29]
G-quadruplex/crystal violet complexes	Fluorescence	0.1 mM	N.A.	[30]
Pyrene-labeled G-quadruplex DNA sensor	Fluorescence	0.5 mM	N.A.	[31]
G-quadruplex DNA fluorescent sensor	Fluorescence	2 mM	N.A.	[32]
aptamer-based DNA/CCPs	Fluorescence	2 mM	N.A.	[33]
G-quadruplex DNA-based electric switch	Electrochemical detection	0.1 mM	N.A.	[34]
aptamer-modified AuNPs	Light scattering	4 μM	1 μM	This study

[a] CCPs: cationic conjugated polymers.
[b] LDC: minimum detectable concentration.
[c] N. A.: not available.

implemented to follow aminothiol-induced NP aggregation. In the presence of homocysteine, FSN-stabilized AuNPs with size of 15 nm provided relatively large difference in light-scattering intensity between the dispersed AuNPs and aggregated AuNPs as compared to 4, 30, and 50 nm-sized AuNPs (Fig. S2, Supplementary information). Thus, we proposed that this system was utilized to detect the activity of SAHH. Fig. 3A illustrates that SAHH catalyzes the hydrolysis of SAH to produce homocysteine and adenosine [30,36]. The produced homocysteine, at low pH condition, triggers the aggregation of FSN-stabilized AuNPs, leading to strong light-scattering under the excitation at 532 nm. As the concentration of SAHH increased at a fixed concentration of SAH, the light-scattering intensity at 532 nm of FSN-stabilized AuNPs was gradually enhanced (Fig. 3B). By plotting the light-scattering intensity at 532 nm against the SAHH concentration, a linear range (R^2=0.9962) for quantification of SAHH was observed from 15–50 units/L^{-1}. The LOD of SAHH was determined to be 3 units L^{-1} (approximately 0.2 nM). Our proposed system provided the greatest sensitivity toward SAHH activity among other reported methods, including AuNP-based colorimetric assay [36], UV–vis absorption [37], Ellman's reagent [36], and luciferase-based assay [38] (Table 2). Additionally, the combination of FSN-stabilized AuNPs and laser-induced Rayleigh scattering technique has great potential for sensing SAHH activity in red blood cells [39]. Other proteins were examined to determine the selectivity of our analytical system toward SAHH. Fig. 3C shows that SAHH caused a dramatic change in the light-scattering intensity, whereas the remaining proteins exhibited a negligible effect under an identical condition. According the abovementioned results, we suggest that our analytical system is

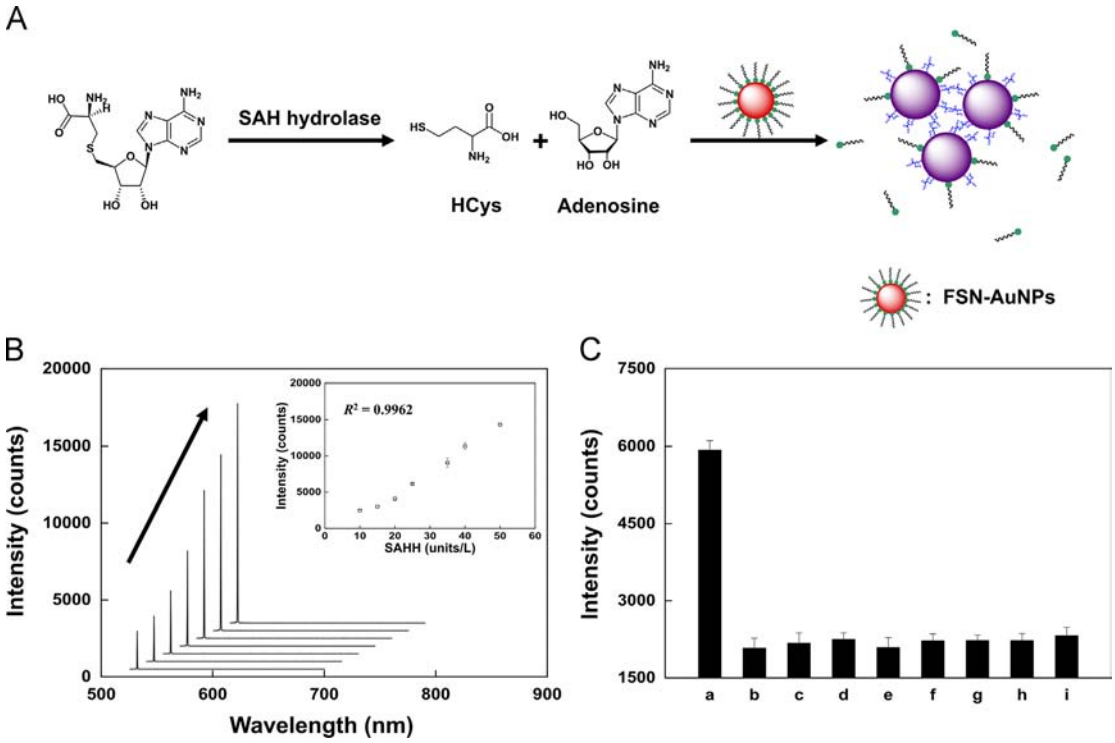


Fig. 3. (A) Illustration of the mechanism of FSN-stabilized AuNPs for sensing SAHH activity *via* thiol-induced NP aggregation. (B) Scattering spectra of FSN-stabilized AuNPs obtained after the addition of a mixture of 50 μM SAH and 10–50 units/L SAHH. The arrows indicate the signal changes with increase in SAHH concentration (10, 15, 20, 25, 35, 40, and 50 units/L). (C) Scattering intensity at 532 nm obtained from the addition of FSN-stabilized AuNPs to a mixture of 1.5 nM protein and 50 μM SAH. Protein: (a) SAHH, (b) trypsin, (c) thrombin, (d) lysozyme, (e) myoglobin, (f) cytochrome c, (g) hemoglobin, (h) Human serum albumin, and (i) bovine serum albumin. (B, C) Proteins reacted with SAH in 50 mM phosphate buffer (pH 7.2) at 37 °C for 20 min. The resulting solutions were incubated with a solution containing FSN-AuNPs (0.1 nM) and phosphate buffer (100 mM, pH 5) for 10 min at ambient temperature.

Table 2
Comparison of other methods for the determination of SAHH.

Sensing system	Detection	MDC[a]	LOD[b]	Reference
FSN-stabilized AuNPs	colorimetry	9 nM	6 nM	[36]
Ellman's reagent	Absorption	2 nM.	N.A.	[36]
Luciferase-based assay	fluorescence	2 nM	N.A.	[39]
FSN-stabilized AuNPs	light scattering	0.9 nM	0.2 nM	This study

[a] MDC: minimum detectable concentration.
[b] N. A.: not available.

well suited to monitor thiol product-related enzyme reactions, such as glutathione reductase-catalyzed cleavage of glutathione disulfide [40], homocysteine thiolactonase-induced hydrolysis of homocysteine thiolactone [41], and acetylcholinesterase-triggered hydrolysis of acetylthiocholine [42].

3.3. Sensing of Pb^{2+} by interparticle crosslinking aggregation

Because the threat of heavy-metal pollution in environmental water is still an important issue for public health, laser-induced Rayleigh scattering technique was used to detect the conditions in which metal ions act as a bridge to link ligand-modified AuNPs together. Intensive researches revealed that AuNP-based colorimetric sensors were simple, selective, and sensitive to detect heavy metal ions in environmental waters [10,12]. This was exemplified by the use of gallic acid-capped AuNPs for probing Pb^{2+} in an aqueous solution [43–45]. Fig. 4A illustrates that Pb^{2+}-stimulated aggregation of gallic acid-capped AuNPs results from multivalent coordination between Pb^{2+} and phenolic hydroxyl groups of gallic acid [43–45]. As shown in Fig. 4B, the light-scattering intensity at 532 nm of gallic acid-capped AuNPs incrementally increased with increasing the concentration of Pb^{2+}. The calibration curve for quantifying Pb^{2+} was obtained by plotting the light-scattering intensity at 532 nm *versus* the concentrations of Pb^{2+} over the range from 1–40 nM (inset in Fig. 4B). The LOD of Pb^{2+} was estimated to be 0.3 nM, which is superior to the LOD values measured from AuNP-based colorimetric sensors [7,43–45], nanoparticle – DNAzyme-based colorimetric probes [46–49], AuNP-based hyper-Rayleigh scattering sensor [50], and AuNP-based dynamic light scattering sensor [51] (Table 3). Additionally, the LOD of the proposed method is much lower than the maximum level (15 μg L^{-1}–72 nM) of lead in drinking water permitted by the United State Environmental Protection Agency. Fig. 4C depicts that only addition of Pb^{2+} to a solution of gallic acid-capped AuNPs caused a dramatic change in the light-scattering intensity at 532 nm, signifying that our analytical system exhibited excellent selectivity toward Pb^{2+} over other metal ions. We suggest that the combination of laser-induced Rayleigh scattering technique and AuNP-based metal ion sensor could be used to probe other metal ions by modified specific ligand onto the surface of the AuNPs.

3.4. Smart-phone-based heavy metal ions reader

To further reduce the cost of instrumentation and toward more portable system, a laser pointer (< 20 mW) and a smart-phone were substituted for a diode laser and a miniaturized spectrometer, respectively (Fig. 5A). Fig. 5B shows a representative smart-phone-captured image of solutions of gallic acid-capped AuNPs in the absence and presence of 72 nM Pb^{2+}, *i.e.*, the safety level recommended by U. S. EPA, in drinking water. The illumination intensity of the laser pointer was sufficient to pass through the sample and control cuvettes, forming two readable signals in two image frames. To determine whether the contamination of Pb^{2+} in drinking water, the acquired scattering images (164 × 5 pixels) of these cuvettes were converted to pixel intensity (0–256 counts)

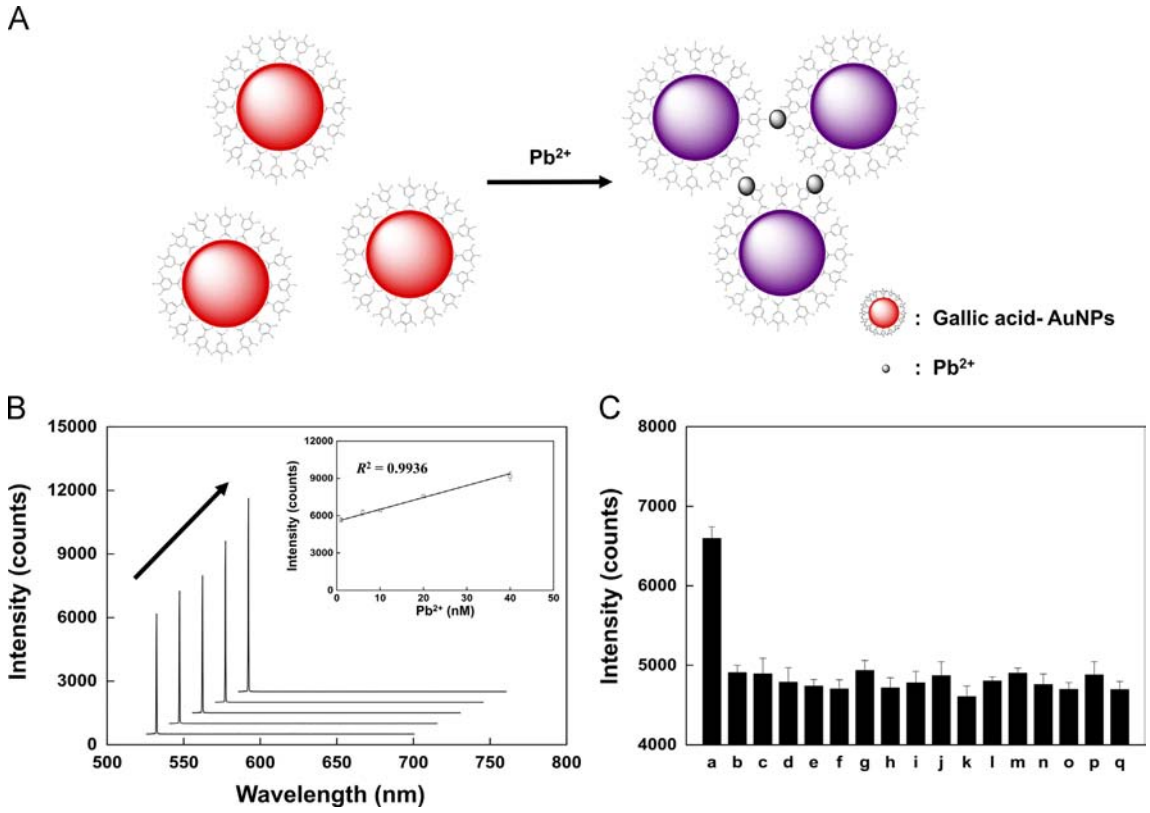


Fig. 4. (A) Illustration of the mechanism of gallic acid-capped AuNPs for sensing Pb^{2+} *via* the coordination between gallic acid and Pb^{2+}. (B) Scattering spectra of gallic acid-capped AuNPs in the presence of increasing Pb^{2+} concentration. The arrows indicate the signal changes with increase in Pb^{2+} concentration (1, 6, 10, 20, and 40 nM). (C) Scattering intensity at 532 nm obtained from the addition of metal ion to a solution of gallic acid-capped AuNPs. Metal ion: (a) Pb^{2+}, (b) Li^{+}, (c) Na+, (d) K+, (e) Mg^{2+}, (f) Ca^{2+}, (g) Sr^{2+}, (h) Ba^{2+}, (i) Fe^{2+}, (j) Fe^{3+}, (k) Co^{2+}, (l) Ni^{2+}, (m) Cu^{2+}, (n) Zn^{2+}, (o) Mn^{2+}, (p) Hg^{2+}, (q) Cd^{2+}. The concentration of Pb^{2+} is 10 nM, while the concentration of other metal ion is 1 μM. (B, C) Metal ions were incubated with a solution containing gallic acid-capped AuNPs (0.63 nM), $NaClO_4$ (1 mM) and formic acid buffer (pH 4.5, 20 mM) for 20 min at ambient temperature.

Table 3
Compared of other methods for the determination of Pb^{2+}.

Sensing system	Detection[a]	MDC[b]	LOD[b]	Reference
Glutathione-capped AuNPs	Colorimetry	0.1 μM	100 nM	[7]
Gallic acid-capped AuNPs	Colorimetry	10 nM	N.A.	[43]
Gallic acid-capped AuNPs	Colorimetry	15 μM	N.A.	[44]
Gallic acid-capped AuNPs	Colorimetry	50 nM	25 nM.	[45]
DNAzyme, DNA-capped AuNPs	Colorimetry	0.4 μM	N.A.	[46]
DNAzyme, citrate-capped AuNPs	Colorimetry	N.A.	500 nM	[47]
DNAzyme-AuNPs dipstick test	Colorimetry	N.A.	0.5 μM	[48]
Crown ether-modified AuNPs	Colorimetry	0.25 μM	N.A.	[49]
11-mercaptoundecanoic acid-modified AuNPs	HRS	N.A.	25 μM	[50]
GSH-AuNPs	DLS	50 ppt	N.A.	[51]
Gallic acid-capped AuNPs	Light scattering	1 nM	0.3 nM	This study

[a] HRS: Hyper-Reyleigh scattering; DLS: dynamic light scattering.
[b] N.A.: not available.

via Image J (Fig. 5C). The intensity ratio of the sample to the control cuvette was calculated by the following equation:

$$\text{Ratio} = (I_1/A_1)/(I_0/A_0)$$

I_1 and I_0 are the integrated pixel intensities of the selected images in the sample and control cuvettes, respectively, while A_1 and A_0 are the area of the selected images in the sample and control cuvette. The intensity ratio of the sample to the control cuvette was computed to be 1.5, which corresponds to the maximum allowable level of Pb^{2+} in drinking water. In other words, if the intensity ratio of the sample to the control cuvette is higher than 1.5, samples of drinking water will contain above 72 nM Pb^{2+}. Thus, the combination of a laser point, a smart-phone, and a AuNP-based probe was suited to monitor the maximum allowable levels of Pb^{2+} in drinking water defined by the U. S. EPA.

4. Conclusion

We have reported a miniaturized, sensitive, and cost-effective platform for monitoring the change in light scattering from three AuNP-based sensing systems, including salt-, thiol-, and metal ions-induced

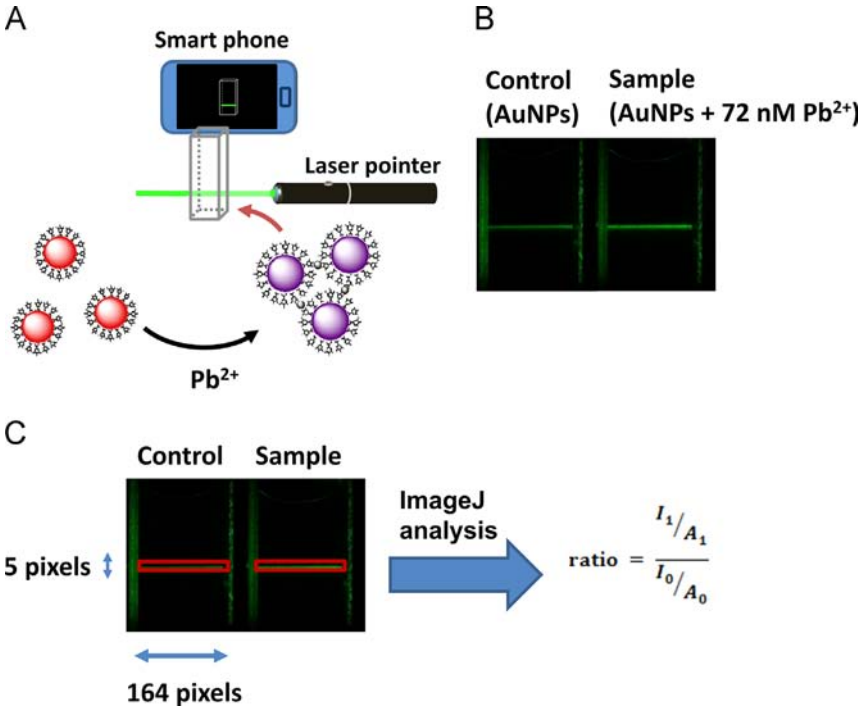


Fig. 5. (A) Schematic illustration of the portable device for the determination of Pb^{2+} in drinking water. (B) Photo images captured on the smart-phone under laser illumination. The left cuvette contained a mixture of gallic acid-capped AuNPs (0.63 nM), $NaClO_4$ (10 mM), formic acid buffer (pH 4.5, 20 mM), and drinking water, while the right cuvette contained the above mentioned mixtures in the presence of 72 nM Pb^{2+}. (C) Flow of image-processing steps to compute normalized pixel intensity. Conversion of selected image to integrated pixel intensity by ImageJ. The integrated pixel intensity was normalized by dividing it by the sum of pixel areas.

aggregation of the AuNPs. Salt-induced aggregation is exemplified by the use of aptamer-modified AuNPs for sensing K^+ in a high-ionic-strength solution. Laser-induced Rayleigh scattering technique coupled to aptamer-based sensor provided high sensitivity (LOD = 1 μM) and selectivity (21,000-fold) for K^+ ions. Thiol-triggered aggregation of the AuNPs is exemplified by the use of FSN-stabilized AuNPs for probing homocysteine, which is generated from SAHH-induced hydrolysis of SAH. The proposed detection system combined with FSN-stabilized AuNPs was highly responsive and selective for the SAHH/SAH system. Metal ion-promoted assembly of the AuNPs is exemplified by the detection of Pb^{2+} with gallic acid-capped AuNPs. By combining laser-induced Rayleigh scattering technique with gallic acid-capped AuNPs, the LOD of Pb^{2+} was down to 0.3 nM. Also, a sensitive, portable cost-effective smart-phone-based Pb^{2+} sensor platform was developed by replacing a diode laser and a miniaturized spectrometer with a laser pointer and a smart-phone. Previous studies reported that Cr^{3+} and Hg^{2+} triggered the aggregation of 5-thiol-(2-nitrobenzoic acid)- and 3-mercaptopropionate acid-capped AuNPs [8,52]. In the opinion of the authors, the smart-phone-based detection system combined with 5-thiol-(2-nitrobenzoic acid)- and 3-mercaptopropionate acid-capped AuNPs could be implemented for sensing Cr^{3+} and Hg^{2+} in an aqueous solution, respectively.

Acknowledgment

We would like to thank Ministry of Science and Technology 100-2628-M-110-001-MY 4) for the financial support of this study.

Appendix A. Supporting information

Supplementary data associated with this article can be found in the online version at http://dx.doi.org/10.1016/j.talanta.2014.08.055.

References

[1] J.S. Beveridge, J.R. Stephens, M.E. Williams, Annu. Rev. Anal. Chem. 4 (2011) 251.
[2] D. Jariwala, V.K. Sangwan, L.J. Lauhon, T.J. Marks, M.C. Hersam, Chem. Soc. Rev. 42 (2013) 2824.
[3] I.L. Medintz, H.T. Uyeda, E.R. Goldman, H. Mattoussi, Nat. Mater. 4 (2005) 435.
[4] M.C. Daniel, D. Astruc, Chem. Rev. 104 (2004) 293.
[5] K.L. Kelly, E. Coronado, L.L. Zhao, G.C. Schatz, J. Phys. Chem. B 107 (2002) 668.
[6] W.J. Luo, C.F. Zhu, S. Su, D. Li, Y. He, Q. Huang, C.H. Fan, ACS Nano 4 (2010) 7451.
[7] F. Chai, C.A. Wang, T.T. Wang, L. Li, Z.M. Su, ACS Appl. Mater. Int. 2 (2010) 1466.
[8] C.J. Yu, W.L. Tseng, Langmuir 24 (2008) 12717.
[9] E. Katz, I. Willner, Angew. Chem. Int. Ed. 43 (2004) 6042.
[10] G. Aragay, J. Pons, A. Merkoci, Chem. Rev. 111 (2011) 3433.
[11] S.J. Park, T.A. Taton, C.A. Mirkin, Science 295 (2002) 1503.
[12] D. Liu, Z. Wang, X. Jiang, Nanoscale 3 (2011) 1421.
[13] E. Hutter, D. Maysinger, Trends Pharmacol. Sci. 34 (2013) 497.
[14] D. Vilela, M.C. Gonzalez, A. Escarpa, Anal. Chim. Acta 751 (2012) 24.
[15] M. Zayats, R. Baron, I. Popov, I. Willner, Nano Lett. 5 (2005) 21.
[16] R. Baron, M. Zayats, I. Willner, Anal. Chem. 77 (2005) 1566.
[17] Y. Li, C. Jing, L. Zhang, Y.T. Long, Chem. Soc. Rev. 41 (2012) 632.
[18] T. Bu, T. Zako, M. Fujita, M. Maeda, Chem. Commun. 49 (2013) 7531.
[19] X. Liu, Q. Dai, L. Austin, J. Coutts, G. Knowles, J. Zou, H. Chen, Q. Huo, J. Am. Chem. Soc. 130 (2008) 2780.
[20] G.K. Darbha, A.K. Singh, U.S. Rai, E. Yu, H. Yu, P. Chandra Ray, J. Am. Chem. Soc. 130 (2008) 8038.
[21] B.A. Du, Z.P. Li, C.H. Liu, Angew. Chem. Int. Ed. 45 (2006) 8022.
[22] M.A. van Dijk, A.L. Tchebotareva, M. Orrit, M. Lippitz, S. Berciaud, D. Lasne, L. Cognet, B. Lounis, Phys. Chem. Chem. Phys. 8 (2006) 3486.
[23] W. Zhao, M.A. Brook, Y.F. Li, Chembiochem 9 (2008) 2363.
[24] L. Wang, X. Liu, X. Hu, S. Song, C. Fan, Chem. Commun. (2006) 3780.
[25] H. Wei, B. Li, J. Li, E. Wang, S. Dong, Chem. Commun. (2007) 3735.
[26] J. Wang, L. Wang, X. Liu, Z. Liang, S. Song, W. Li, G. Li, C. Fan, Adv. Mater. 19 (2007) 3943.
[27] X. Zhu, J. Zhao, Y. Wu, Z. Shen, G. Li, Anal. Chem. 83 (2011) 4085.
[28] Z.S. Wu, C.R. Chen, G.L. Shen, R.Q. Yu, Biomaterials 29 (2008) 2689.
[29] C. Shi, H. Gu, C. Ma, Anal. Biochem. 400 (2010) 99.
[30] D.M. Kong, J.H. Guo, W. Yang, Y.E. Ma, H.X. Shen, Biosens. Bioelectron. 25 (2009) 88.
[31] S. Nagatoishi, T. Nojima, B. Juskowiak, S. Takenaka, Angew. Chem. Int. Ed. 44 (2005) 5067.
[32] S. Nagatoishi, T. Nojima, E. Galezowska, A. Gluszynska, B. Juskowiak, S. Takenaka, Anal. Chim. Acta 581 (2007) 125.
[33] F. He, Y. Tang, S. Wang, Y. Li, D. Zhu, J. Am. Chem. Soc. 127 (2005) 12343.

[34] A.E. Radi, C.K. O'Sullivan, Chem. Commun. (2006) 3432.
[35] Lim II, W. Ip, E. Crew, P.N. Njoki, D. Mott, C.J. Zhong, Y. Pan, S. Zhou, Langmuir 23 (2007) 826.
[36] J.H. Lin, C.W. Chang, Z.H. Wu, W.L. Tseng, Anal. Chem. 82 (2010) 8775.
[37] J.L. Palmer, R.H. Abeles, J. Biol. Chem. 254 (1979) 1217.
[38] E.S. Burgos, S.A. Gulab, M.B. Cassera, V.L. Schramm, Anal. Chem. 84 (2012) 3593.
[39] F. Carlucci, A. Tabucchi, A. Aiuti, F. Rosi, F. Floccari, R. Pagani, E. Marinello, Clin. Chem. 49 (2003) 1830.
[40] P. Monostori, G. Wittmann, E. Karg, S. Turi, J. Chromatogr. B 877 (2009) 3331.
[41] J. Perla-Kajan, H. Jakubowski, Amino Acids 43 (2012) 1405.
[42] Y. Miao, N. He, J.J. Zhu, Chem. Rev. 110 (2010) 5216.
[43] K.W. Huang, C.J. Yu, W.L. Tseng, Biosens. Bioelectron. 25 (2010) 984.
[44] K. Yoosaf, B.I. Ipe, C.H. Suresh, K.G. Thomas, J. Phys. Chem. C 111 (2007) 12839.
[45] N. Ding, Q. Cao, H. Zhao, Y. Yang, L. Zeng, Y. He, K. Xiang, G. Wang, Sensors 10 (2010) 11144.
[46] J. Liu, Y. Lu, J. Am. Chem. Soc. 126 (2004) 12298.
[47] H. Wei, B. Li, J. Li, S. Dong, E. Wang, Nanotechnology 19 (2008) 095501.
[48] D. Mazumdar, J. Liu, G. Lu, J. Zhou, Y. Lu, Chem. Commun. 46 (2010) 1416.
[49] S.Y. Lin, S.H. Wu, C.H. Chen, Angew. Chem. Int. Ed. 45 (2006) 4948.
[50] Y. Kim, R.C. Johnson, J.T. Hupp, Nano Lett. 1 (2001) 165.
[51] L. Beqa, A.K. Singh, S.A. Khan, D. Senapati, S.R. Arumugam, P.C. Ray, ACS Appl. Mater. Interfaces 3 (2011) 668.
[52] Y.J. Lai, W.L. Tseng, Analyst 136 (2011) 2712.

Talanta 132 (2015) 52–58

Contents lists available at ScienceDirect

Talanta

journal homepage: www.elsevier.com/locate/talanta

Novel strategy for online monitoring of the degradation kinetics of propantheline bromide via a calixarene-based ion-selective electrode

Mohamed K. Abd El-Rahman, Hala E. Zaazaa, Norhan Badr ElDin *, Azza A. Moustafa

Analytical Chemistry Department, Faculty of Pharmacy, Cairo University, Kasr-El Aini Street, Cairo 11562, Egypt

ARTICLE INFO

Article history:
Received 13 June 2014
Received in revised form
29 August 2014
Accepted 30 August 2014
Available online 6 September 2014

Keywords:
Propantheline bromide
On-line monitoring
Degradation kinetics
Calixarene
Ion-selective electrode
Activation energy

ABSTRACT

Propantheline bromide (PB) is a hydrolysable anti-cholinergic drug. A novel strategy for the online monitoring of PB degradation kinetics catalysed by hydroxyl ions is presented. This is achieved by the incorporation of an on-site PB-selective electrode constructed using as an ionophore. This sensor was used to track the hydrolysis of PB by continuous measurement of the decrease in the produced emf over time. The use of this new technique provides real-time observation and yields a continuous profile of the hydrolysis behaviour of PB under various pH conditions as well as the temperature dependency of each reaction. Moreover, a great advantage of this proposed on-line system is its higher accuracy for rate constant estimation relative to other off-line methods. This kinetic data analysis permitted the determination of the hydrolysis activation energy and prediction of the drug shelf life. The estimated activation energy from Arrhenius plot was 20.77 kcal mol^{-1}.

© 2014 Elsevier B.V. All rights reserved.

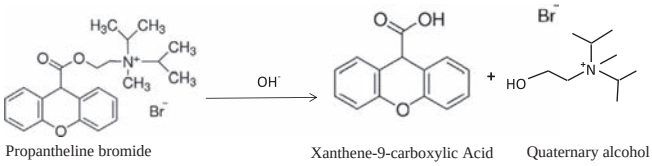
1. Introduction

In modern analytical laboratories, kinetic studies and accelerated stability experiments are the most important tools for solving problems encountered in quality control and for predicting both the optimum storage conditions and the expiry dates of pharmaceutical products. For the continuous monitoring of degradation kinetics, potentiometric sensors offer many attractions and considerable advantages. However, although the last 15 years have seen very rapid developments in the design of a wide range of electrode types selective towards a vast number of ions with varying degrees of selectivity [1,2], relatively little attention has been paid to the novel use of such electrodes. For tracking the concentration of easily hydrolysable drugs, it is sufficient to immerse the ion-selective electrode (ISE) in the degradation medium together with a suitable reference electrode and record the continuous decrease in emf due to the gradual decrease in the drug ion concentration. This permits real-time observation and yields a continuous profile for the hydrolysis behaviour of the drug under various pH conditions and the temperature dependency of each reaction. The presently used offline techniques, UV spectroscopy and HPLC–UV, yield discontinuous profiles and suffer from numerous problems, such as requiring multiple sample withdrawals, several sample preparation steps, expensive instrumentation and long monitoring time [3]. Meanwhile, an ISE must satisfy a set of general requirements common to all detection systems for monitoring a degradation process, i.e., sufficient sensitivity and stability, low background noise, low drift, rapid response time and sufficient selectivity for the drug over the product of the degradation reaction. Although the literature concerning the chemical stability of hydrolysable substances in drug preparations as analysed by offline chromatographic and spectrometric techniques is extensive [4–8], only a few cases have been reported for online monitoring techniques [9,10]. To the best of our knowledge, no wide systematic study of on-line drug degradation kinetics using on-line potentiometric sensors has been published in the literature. Only some papers have reported on similar topics, such as the in situ study of the dissolution of formulations of pharmaceutically active drugs [11] and electrochemical sensors for environment monitoring [12].

The present study was undertaken to further explore how potentiometry can be used for the reliable online monitoring of the degradation kinetics of easily hydrolysable ionisable/ionic drugs. Propantheline bromide (PB) was selected as a model based on its ester linkage and quaternary ammonium group, which endow it with the character of a strong cationic electrolyte. In this work, an ISE for PB was fabricated using a PVC membrane doped with 4-tert-butylcalix [8] arene as an ionophore. The ISE was used to detect PB, and the figures of merit were calculated and then used to detect PB in the presence of its alkaline degradation products, xanthene-9-carboxylic acid(XA) and diisopropyl(2-hydroxyethyl)methylammonium bromide (quaternary alcohol) (Scheme 1). Finally, the ISE was used to study the kinetics of the PB degradation in alkaline medium and calculate the hydrolysis rate constant and the hydrolysis

* Corresponding author.
E-mail address: norhan.ibrahim@pharma.cu.edu.eg (N. Badr ElDin).

http://dx.doi.org/10.1016/j.talanta.2014.08.068
0039-9140/© 2014 Elsevier B.V. All rights reserved.



Scheme 1. Alkaline degradation of propantheline bromide [18].

activation energy. One advantage of this technique is that more data points can be monitored than when using the off-line methods. Thus, all constants found for the kinetics of PB hydrolysis will be more accurate because they will be based on a larger number of data points.

2. Experimental

2.1. Chemicals and reagents

Propantheline bromide (PB), sodium tetraphenyl borate (NaTPB), and 4-*tert*-butylcalix [8] arene (*t*-Bu-CX8) were purchased from Sigma-Aldrich (Steinheim, Germany). Polyvinyl chloride (PVC) and 2-nitrophenyl octyl ether (NPOE) were obtained from Fluka Chemie GmbH (St. Louis, MO, USA), and tetrahydrofuran (THF) was obtained from BDH (Poole, England). Probanthin® tablets (15 mg/tablet) were purchased from Sigma Pharmaceuticals (New Zealand). Britton–Robinson buffer (BRB) (pH 2–12) was prepared by mixing different volumes of 0.04 mol L^{-1} acetic acid, 0.04 mol L^{-1} phosphoric acid, 0.04 mol L^{-1} boric acid and 0.2 mol L^{-1} sodium hydroxide.

2.2. Fabrication of membrane sensors

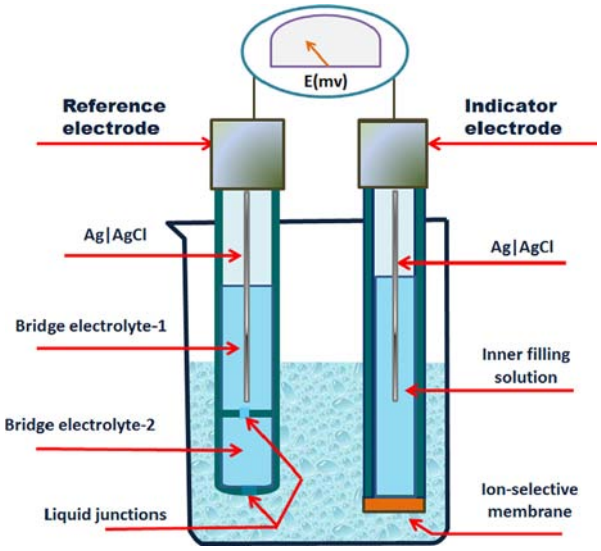
The PVC membranes were prepared in two separate 5-cm Petri dishes by mixing PVC (33.50%), NPOE (66.34%) and NaTPB (0.16%, 5.0 mmol kg^{-1}) to prepare sensor 1 and PVC (33.50%), NPOE (65.05%), NaTPB (0.16%, 5.0 mmol kg^{-1}) and *t*-Bu-CX8 (1.29%, 10.0 mmol kg^{-1}) to prepare sensor 2. The membrane components (600 mg in total) were dissolved in THF (6.0 mL), and the Petri dishes were covered with filter paper and left to stand overnight at room temperature to allow solvent evaporation, leaving a homogeneous, flexible and transparent membrane. Master membranes of 0.1 mm in thickness were obtained. From each master membrane, a disk (approximately 8 mm in diameter) was cut using a cork borer and pasted using THF to an interchangeable PVC tip that was clipped to the end of an electrode glass body. The electrodes were then filled with an internal solution of equal volumes of 10^{-4} mol L^{-1} PB and 10^{-4} mol L^{-1} KCl. Ag/AgCl wire (1-mm diameter) was used as an internal reference electrode. The sensors were conditioned by soaking in 10^{-4} mol L^{-1} aqueous PB solution for 24 h and stored in the same solution when not in use. The electrode produced in this way is shown in Scheme 2.

2.3. Potentiometric measurements

Potentiometric measurements were carried out using an Ag/AgCl double-junction-type external reference electrode (Thermo Scientific Orion 900200, MA, USA; 3.0 M KCl saturated with AgCl as an inner filling solution and 10% KNO_3 as a bridge electrolyte) and Jenway digital ion analyser (model 3330; Essex, UK). A Jenway pH glass electrode (Essex, UK) was used for pH adjustments.

2.3.1. Sensors calibration

The conditioned sensors were calibrated by separately transferring 50-mL aliquots of solutions (10^{-7} –10^{-2} mol L^{-1}) of PB into a series of 100-mL beakers. The membrane sensors, in conjunction



Scheme 2. Potentiometric cell assembly with a conventional, liquid inner contact ion selective membrane electrode as indicator electrode and a double junction reference electrode.

with the Ag/AgCl reference electrode, were immersed in the above test solutions and allowed to equilibrate under stirring. The potential difference (emf) between the membrane sensor (indicator electrode) and the reference electrode was recorded after stabilising to ±1 mV, and the emf was plotted as a function of the logarithm of PB concentration for a BRB solution of pH 7.0.

2.3.2. Potentiometric determination of PB in pharmaceutical preparation

Ten tablets were ground to a powder. A quantity of the powder equivalent to 112.09 mg of PB was transferred to a 25-mL volumetric flask, which was then filled to the mark with BRB of pH 7. The concentration of this solution was 10^{-3} mol L^{-1}. The potentiometric measurements were performed using the proposed sensor in conjunction with the Ag/AgCl reference electrode, and the potential readings were compared to the calibration plots.

2.3.3. Effect of pH on electrode response

The effect of pH on the response of the investigated electrodes was studied using 10^{-3} and 10^{-4} mol L^{-1} solutions of PB in BRB with pH ranging from 2.0 to 12.0.

2.3.4. Preparation of degradation product

A degraded sample of PB was prepared by adding 5 mL of NaOH (0.1 mol L^{-1}) to 10 mL of drug solution (10^{-2} mol L^{-1}) and refluxing for 10 min. The resulting solution was tested for complete degradation by HPLC using a mobile phase of 40:60 acetonitrile:0.05 mol L^{-1} phosphate buffer (pH 2.5), as reported previously [13]. The degraded solution was neutralised, transferred quantitatively into a 100-mL volumetric flask and brought to volume with deionised water.

2.3.5. Kinetic studies

2.3.5.1. Reaction order. A volume of 45.0 mL of BRB of pH 9.5 was placed into a 100-mL beaker on a hotplate thermostated at 25 °C. The PB-selective electrode and the reference electrode were immersed, and the data acquisition was started. Once the potential is stabilised, an appropriate volume (5 mL of 10 mmol L^{-1}) of the PB working solutions was added. The emf values for the solution [initial concentration C_o=448.4 μg mL^{-1} (10^{-3} mol L^{-1})] were measured continuously. The concentration of PB was calculated from the

corresponding regression equation using a calibration graph for PB in BRB solution of pH 9.5. The log % of remaining concentration against time was constructed for different pH buffers. The rate constants and the corresponding half-lives ($t_{1/2}$) were calculated.

2.3.5.2. Effect of buffer pH on reaction rate. A 5-mL volume of a 10 mM standard solution of PB was added into each of three 100-mL beakers, which contained 45.0 mL of BRB solution of pH 9.5, 10.0 and 10.5 thermostatically controlled at 25 °C. The emf values were monitored continuously as described above. The log % of the remaining concentration was plotted against time for different pH buffers. The rate constants and corresponding half-lives ($t_{1/2}$) were calculated.

2.3.5.3. Effect of temperature on reaction rate. A volume of 45.0 mL of pH 9.5 BRB was placed into a 100-mL beaker. This solution was heated thermostatically at 25 °C, 30 °C and 35 °C. The emf was monitored continuously as described above. The log % of the remaining concentration was plotted against time for different temperatures. Furthermore, an Arrhenius plot was constructed for the temperature effect on hydrolysis rate.

3. Results and discussion

Pharmaceutical product quality is of vital importance for patient safety. The presence of impurities may influence the efficacy and safety of pharmaceuticals. Impurities and potential degradation products can cause changes in the chemical, pharmacological and toxicological properties of drugs and thereby have a significant impact on product quality and safety [14].

This paper is positioned at the promising junction of two areas of recent and increasing interest: chemical kinetics and electroanalysis. To the best of our best knowledge, no ISE for the on-line monitoring of the degradation kinetics of drug hydrolysis has been reported so far. Thus, PB-selective sensors were fabricated in the hope that they may be used as a model system for on-line monitoring. Subsequently, the same procedure could be extended to other hydrolysable organic compounds without significant modification. This should provide a viable platform for the on-site monitoring of hydrolysis processes using ISEs.

3.1. ISE characteristics using t-Bu-CX8 as a sensing ionophore

The response of ionophore-based potentiometric sensors is usually governed by the molecular recognition between the analyte (guest) and the host molecule. Different macrocyclic ionophores have been proposed for use with organic drug guest molecules, such as crown ethers, calixarenes, cyclodextrins (CDs) and porphyrins.

The most important property of calixarenes (nano-baskets) is their ability to form supramolecular (inclusion) complexes with many appropriately sized organic ions and molecules, where the driving forces for this complexation are directed hydrogen bonding and cation–π-interactions (electrostatic attraction between the positive charge of the guest and the electron-rich faces of the aromatic rings of the phenol units) [15,16]. In the present work, the ionophore 4-*tert*-butylcalix [8] arene (*t*-Bu-CX8) was chosen because it possesses outstanding complexation properties toward quaternary ammonium ions [17].

The positive PB ion prefers the prevalent donation sites (OH groups) and large cavity size (11.7 Å) of calixarene structure. Fig. 1 shows the calibration curves for sensors 1 and 2. In the absence of the ionophore, i.e., in the case of sensor 1, the lowest slope and the highest selectivity coefficient values are found. A higher selectivity coefficient value corresponds to a more extensive attack of the electrode membrane by interfering cations. On the other hand, the *t*-Bu-CX8-based sensor 2 shows the best Nernstian slope (59.4 mV/decade) and selectivity coefficient values (discussed below). The host–guest complex is stabilised via the strong interaction between the cationic PB and the eight H-bonding sites of *t*-Bu-CX8. Moreover, calix [8] arene has a large internal cavity size (11.7 Å), which allows the drug to fit well in the calixarene cavity and bond strongly to the calixarene donation sites.

The electrochemical performance characteristics of the proposed sensors were systematically evaluated according to IUPAC standards [18]. Table 1 shows the results obtained over a period of one month for two different assemblies of each sensor. Typical calibration plots are shown in Fig. 1. The slopes of the calibration plots are 55.1 and 59.4 mV/concentration decade for sensors 1 and 2, respectively. Deviation from the ideal Nernstian slope (60 mV) is due to the response of the electrodes to the activity of the drug cation rather than its concentration.

The sensors displayed constant potential readings for day-to-day measurements, and the calibration slopes did not change by more than ±2 mV/decade over a period of 25 and 30 days for sensors 1 and 2, respectively. The detection limits of the two sensors were estimated according to the IUPAC definition. Table 1 shows that sensor 2 can detect PB in very dilute solutions down to 1×10^{-7} mol L^{-1}. This finding agrees with the idea that PB is

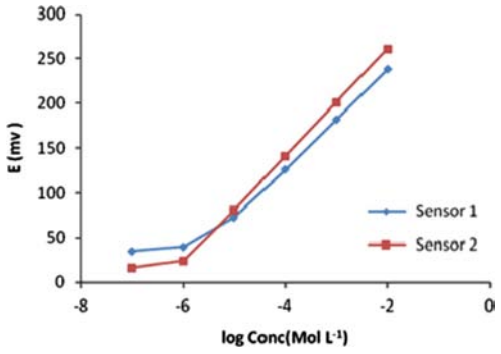


Fig. 1. Profile of the potential in mV versus log concentrations of PB in mol L^{-1} obtained with sensors 1 and 2.

Table 1
Electrochemical response characteristics of the two investigated PB sensors.

Parameter	Sensor 1	Sensor 2
Slope (mV/decade)[a]	55.1	59.4
Intercept *t* (mV)	347.6	379.2
LOD (mol L^{-1}) [b]	5×10^{-7}	1×10^{-7}
Response time (s)	10	6
Working pH range	3–7	3–7
Concentration range (mol L^{-1})	1×10^{-2}–5×10^{-6}	1×10^{-2} –1×10^{-6}
Stability(days)	25	30
Correlation coefficient	0.9997	0.9999
Repeatability [c]	1.230	1.012
Intermediate precision[d]	1.468	1.249
Ruggedness[e]	99.23	99.30
Accuracy ± S.D.	99.75 ± 0.590	100.14 ± 0.482

[a] Average of five determinations.
[b] Limit of detection measured by interception of the extrapolated arms of Fig. 1.
[c] The intra-day (n=3) RSD % of concentrations 1×10^{-3} mol L^{-1}, 1×10^{-4} mol $L^{-1}$and 1×10^{-5} mol L^{-1} PB.
[d] The inter-day (n=3) RSD % of concentrations 1×10^{-3} mol L^{-1}, 1×10^{-4} mol $L^{-1}$and 1×10^{-5} mol L^{-1} PB.
[e] Average recovery per cent of determining 10^{-3} and 10^{-4} mol L^{-1} PB for the studied electrodes using Jenway 3510 digital ion analyser instead of the 3330 model.

typically accommodated and bonded by the large cavity size and prevalent H-bonding sites of the *t*-Bu-CX8 ionophore.

3.2. Effect of pH and temperature

The optimal experimental conditions for quantitative measurements with the ion-selective electrodes were investigated. A pH value within the range of 3–7 is found to be best from the perspective of sensor function and the chemical form of the test solution of PB. Fig. 2 shows the potential-pH profile for 10^{-3} and 10^{-4} mol L^{-1} drug solutions. The slight change in potential readings at pH values below the previously mentioned range is attributed to the interference of hydronium ions, while the potential readings decrease gradually at pH values higher than the given ranges, which can be attributed to the degradation of the drug molecules.

The results suggest that the electrodes exhibit a slight increase in potential with increasing temperature in the range of 25–35 °C. However, the calibration plots obtained at different temperatures are parallel, and the limit of detection, slope and response time do not vary significantly with temperature, indicating a reasonable thermal stability of the PVC membranes up to 35 °C.

3.3. Dynamic response time

The dynamic response time is an important factor for analytical applications of ion-selective electrodes. In this study, the practical response time was recorded by increasing the PB concentration by up to 10-fold. The required time for the sensors to reach values within ± 1 mV of the final equilibrium potential was 10 and 6 s for sensors 1 and 2, respectively. The time traces of the calibration curve of the ISE for pH 7.0 BRB are presented in Fig. 3.

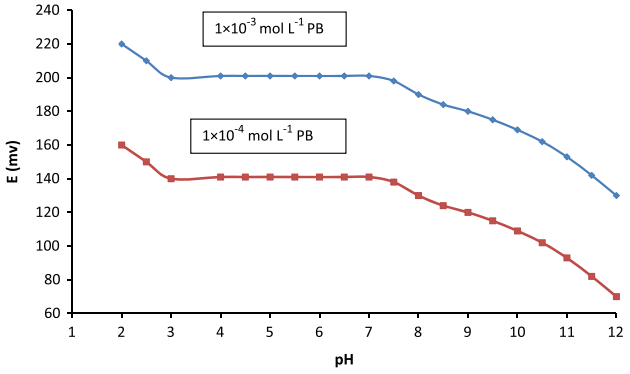


Fig. 2. Effect of pH on the performance of sensor 2.

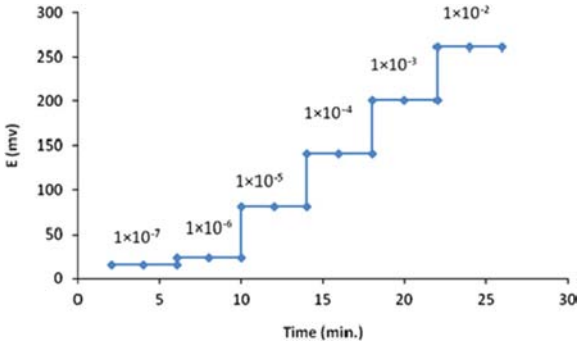


Fig. 3. Time traces of the response of sensor 2 towards PB.

3.4. Sensor selectivity

The selectivity of the fabricated ISE sensor was investigated in the presence of structurally related organic quaternary ammonium ions and in the presence of XA and the quaternary alcohol, the hydrolytic product of PB [19]. Fig. 4 shows the calibration curves for pyridostigmine bromide (PYD), neostigmine bromide (NEO) and rivastigmine hydrogen tartrate (RIV). It is obvious that near-Nernstian slopes and thus unbiased selectivity coefficients were obtained, as shown in Table 2. This can be attributed to the fact that these ions are easily ion-exchanged into the membrane. It is worth noting that an ammonium quaternary ion was expected to be bound by *t*-Bu-CX8. An explanation for the higher selectivity of the ISE towards PB could be its higher lipophilicity compared to other organic ions. The

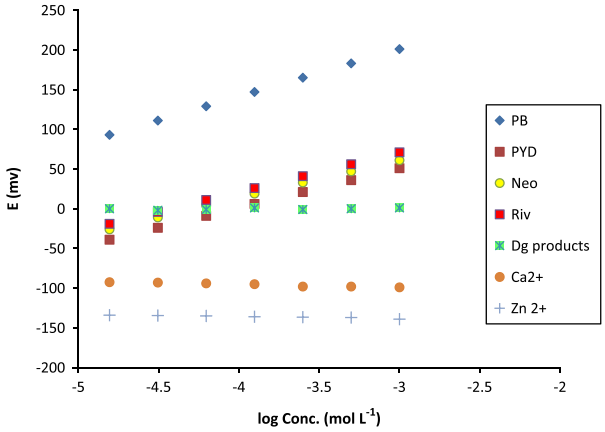


Fig. 4. Calibration curves obtained for PB, PYD, Neo, Riv, Dg. Products, Ca^{2+} and Zn^{2+} for sensor 2.

Table 2
Logarithmic selectivity coefficients, Log $K^{pot}_{PB,I}$, for Sensor 2 using the separate solutions method (SSM). [17].

Interferent	Log $K^{pot}_{PB,I}$ [a]
Pyridostigmine	−2.50
Neostigmine	−2.34
Rivastigmine	−2.17

[a] Each value is the average of three determinations. Calibration curves were obtained by successive dilution and Nernstian response was confirmed in the concentration range where selectivity was measured.

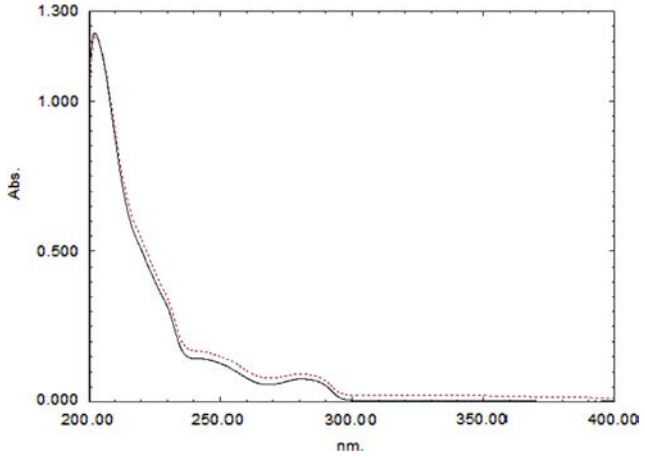


Fig. 5. Zero order spectra of 14 μg mL^{-1} of PB (—) and14 μg mL^{-1} XA (———).

inorganic ions exhibited an obvious non-Nernstian response, and to avoid biased values, no selectivity coefficients were determined. This can be attributed to the difficulty of the ion exchange of these inorganic ions into the lipophilic membrane. The XA shows a marked non-Nernstian response due to the absence of an electroactive group. This facilitates the development of a PB ISE for studying the kinetics degradation process. Reviewing other analytical methods, this may be considered a challenging analytical task. UV-spectrophotometry was unable to provide insight into the degradation process due to the complete overlap (superimposition) of the absorption spectra of XA and PB, as shown in Fig. 5. Moreover, PB was reported to be hydrolysed by adsorption into silica, catalysing the rate of ester decomposition [19] and thereby hindering the monitoring by TLC densitometry.

3.5. Potentiometric determination of PB in pharmaceutical formulation

The proposed sensor was successfully employed to assay PB in bulk powder and pharmaceutical formulation (Pro-Banthine® tablets). The results clearly indicated satisfactory agreement between the PB contents in different samples determined by the developed sensor and the official method (Table 3). The time

Table 3
Determination of PB in pharmaceutical formulation using sensor 2 and the official USP method.

Pharmaceutical formulation	Recovery (%) ± S.D. [a]	
	Sensor 2	Official method [b]
Probanthin ® tablets (15 mg/tablet)	100.48 ± 0.846	99.54 ± 1.256
t-test [c]	1.449 (2.306)	
F [c]	1.484 (6.39)	

[a] Average of five determinations.
[b] Non-aqueous titration was done using crystal violet as indicator and perchloric acid as titrant.
[c] The values in parentheses are the corresponding theoretical values for *t* and *F* at *P*=0.05.

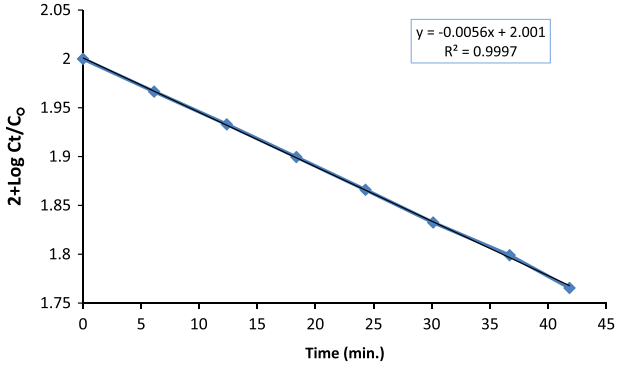


Fig. 6. First order plot of the hydrolysis of PB (1×10^{-3} mol L^{-1}) with a BRB of pH 10 at temp 25 °C.

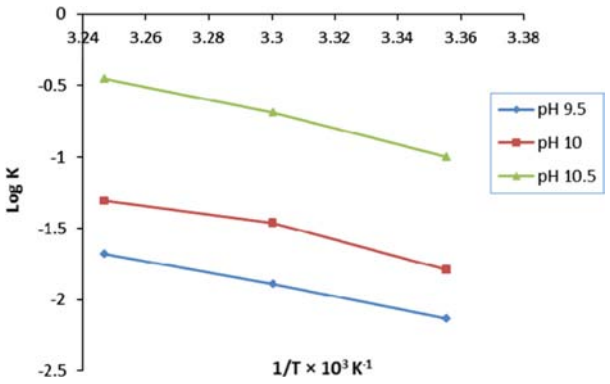


Fig. 8. Arrhenius plot for the hydrolysis of PB (1×10^{-3} mol L^{-1}) with BRB of pH 9.5, 10.0, 10.5.

Table 4
Kinetic data of PB alkaline degradation.

pH of buffer	Temperature (°C)	*K* (min^{-1})	$T_{1/2}$ (min)	$T_{90\%}$ (min)
9.5	25	0.007	94.035	13.976
	30	0.013	53.734	7.986
	35	0.021	33.067	4.915
10	25	0.016	42.972	6.387
	30	0.034	20.195	3.002
	35	0.049	14.061	2.090
10.5	25	0.101	6.870	1.021
	30	0.195	3.561	0.529
	35	0.357	1.943	0.289

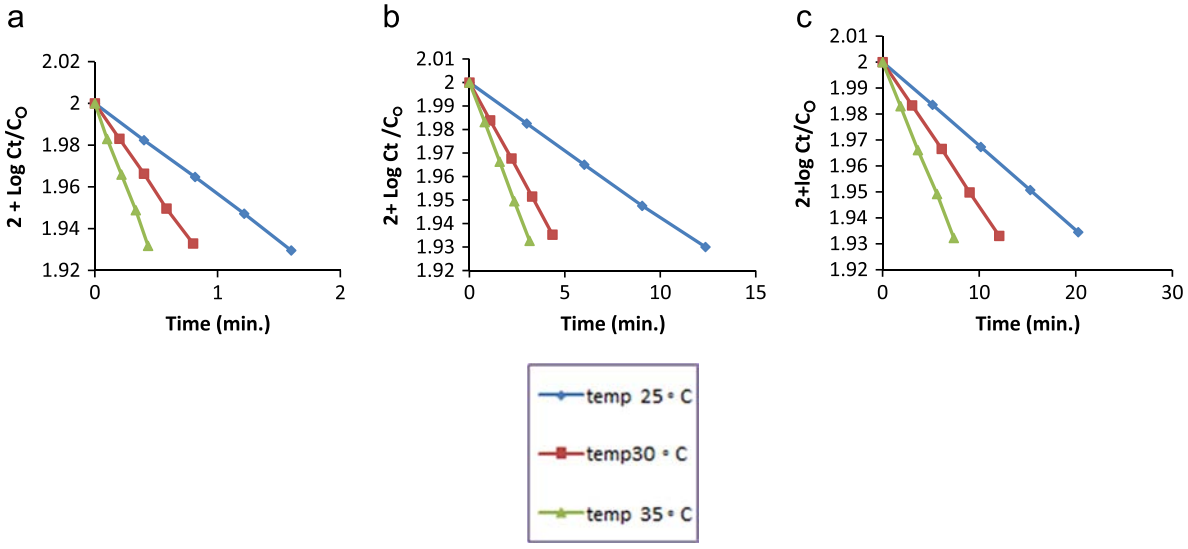


Fig. 7. First order plot of the hydrolysis of PB (1×10^{-3} mol L^{-1}) with BRB of pH (a) 10.5, (b) 10.0 and (c) 9.5 at different temperatures.

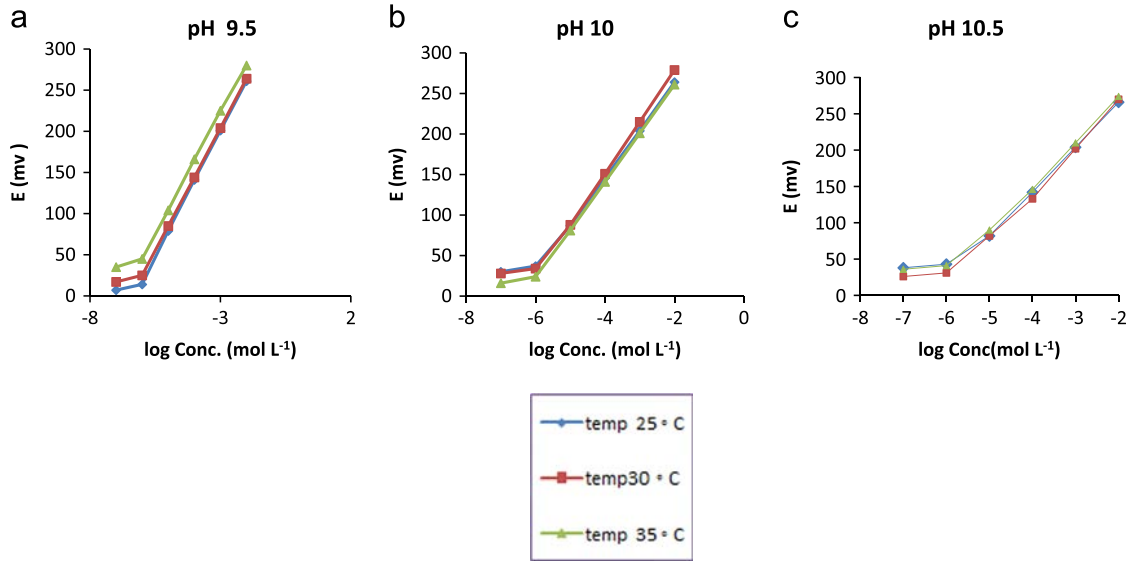


Fig. 9. Profile of the potential in mV versus log concentration of PB (a) at pH 9.5 (b) at pH 10.0 and (c) at pH 10.5 at different temperatures.

required for sample analysis was shorter (less than 1 min) than that of the British pharmacopeial (BP) official method (approximately 30 min) [20]. Moreover, the proposed sensor does not require preliminary drug extraction, as described in the BP method.

3.6. Degradation kinetics

Initial experiments were performed for the offline monitoring of the degradation of PB using ISE by placing a fixed concentration in BRB (pH 10.0) and then withdrawing aliquots at 30-s intervals. The aliquots were neutralised to pH 7 and completed to a definite volume, and then the emf was recorded. Such a kinetic study was tedious, produced a discontinuous nonlinear profile and hindered an accurate estimation of the rate constants.

The incorporation of ISE for on-site monitoring of the concentration of the target ion (drug) has the advantage of enabling real-time observation of the hydrolysis behaviour. The analytical throughput is controlled by the performance of the specific electrode, which mainly depends on the sensitivity and response time of the electrode used. Experimentally, the linear relationship between the log % of the remaining concentration against time indicated first-order degradation, as shown in Fig. 6. However, as the hydrolysis was performed in a large excess of BRB (pH 10), it follows a pseudo-first-order reaction rate, which is the term used when two reactants are involved in the reaction but one of them is in such a large excess (BRB) that any change in its concentration is negligible compared with the change in the concentration of the other reactant (drug).

Different parameters that affect the rate of the reaction were studied. The temperature dependence of PB degradation was studied by conducting the reaction at different temperatures using BRB of different pH, as shown in Fig. 7. At each temperature, the rate constant and $t_{1/2}$ were calculated. Next, the log of the rate constant was plotted against the reciprocal of the temperature in Kelvin (Arrhenius plot, Fig. 8) to demonstrate the effect of temperature on the rate constant. It was concluded that as the temperature increased, the rate of hydrolysis increased with a decrease in $t_{1/2}$ (Table 4). In addition, the energy of activation was determined by calculating the rate constant from the following equation [21]:

$$\log \frac{k_2}{k_1} = \frac{E_a}{2.303\,R}\left(\frac{T_2 - T_1}{T_1\,T_2}\right)$$

where "E_a" is the activation energy, "T_1" and "T_2" are the two temperatures in Kelvin, "R" is the gas constant, and "k_1" and "k_2" are the rate constants at the two temperatures used.

The calculated "E_a" was found to be 20.77 kcal mol^{-1}, which was consistent with the reported values of the hydrolysable esters, confirming the instability in alkaline medium[22].

Another factor that affects the rate of the reaction is the pH of the buffer solution. Therefore, BRB solutions of different pH were used to study the hydrolysis reaction. The rate of hydrolysis increased with increasing pH of BRB. It should be noted that the calibration curves at these higher pH values show no statistically significant difference in the corresponding Nernstian slope, as shown in Fig. 9. This is attributed to the instantaneous response time of the sensor, which facilitates the recording of the emf at higher pH before the start of the hydrolysis process.

Overall, we can conclude that extensive decomposition of PB was observed in aqueous alkaline solution. Consequently, appropriate protection is recommended during storage, and it is advisable to avoid alkaline conditions during analytical assays of PB.

4. Conclusion

The development of a new method was motivated by not only the search for better performance but also a problem in the actual application. To this end, a novel approach for further exploring the potential of ISE technique in online monitoring and real-time observation of the PB degradation was presented here. It should be emphasised that this study used as a model system for the degradation of PB only to evaluate the feasibility and benefits of the on-line coupling of a highly selective ISE system to a system of alkaline degradation, which can be extended to other degradation processes. The monitoring analyses are usually performed off-line and sometimes several days after the hydrolysis was performed and therefore do not reflect the actual values obtained. In the proposed system, quite reliable results are obtained using a selective, robust and easily constructed sensor, which provided

a low-cost, fast method for the real-time monitoring of the alkaline degradation of PB.

Appendix A. Supporting information

Supplementary data associated with this article can be found in the online version at http://dx.doi.org/10.1016/j.talanta.2014.08.068.

References

[1] E. Bakker, P. Bühlmann, E. Pretsch, Chem. Rev. 97 (1997) 3083–3132.
[2] E. Bakker, E. Pretsch, P. Bühlmann, Anal. Chem. 72 (2000) 1127–1133.
[3] C. Wu, X. Xu, C. Feng, Y. Shi, W. Liu, X. Zhu, J. Zhang, J. Pharm. Biomed. Anal. 98 (2014) 356–363.
[4] S. Singh, B. Singh, R. Bahuguna, L. Wadhwa, R. Saxena, J. Pharm. Biomed. Anal. 41 (2006) 1037–1040.
[5] I.A. Darwish, M.A. Sultan, H.A. Al-Arfaj, Talanta 78 (2009) 1383–1388.
[6] M. Suleiman, H. Muti, M. Abdel-Hamid, M. Hassan, Y. El-Sayed, N. Najib, Anal. Lett. 22 (1989) 1499–1512.
[7] H.E. Abdellatef, J. Pharm. Biomed. Anal. 29 (2002) 835–842.
[8] J.O. Fubara, R.E. Notari, J. Pharm. Sci. 87 (1998) 1572–1576.
[9] Q. de Oliveira, M. Calora, A.A. Tanaka, M.R. de Vasconce los Lanza, M. Del PilarTaboada Sotomayor, Electroanalysis 23 (2011) 2616–2621.
[10] F. Walsh, D. Gabe, J. Appl. Electrochem. 11 (1981) 117–127.
[11] H. Bohets, K. Vanhoutte, R. De Maesschalck, P. Cockaerts, B. Vissers, L.J. Nagels, Anal. Chim. Acta 581 (2007) 181–191.
[12] G. Hanrahan, D.G. Patil, J. Wang, J. Environ. Monit. 6 (2004) 657–664.
[13] B. Charles, P. Ravenscroft, J. Pharm. Sci. 72 (1983) 96–98.
[14] H.H. Tønnesen, Int. J. Pharm. 225 (2001) 1–14.
[15] J.L. Atwood, A. Szumna, J. Supramol. Chem. 2 (2002) 479–482.
[16] J. Hong, J. Song, S. Ham, Tetrahedron Lett. 48 (2007) 1327–1330.
[17] A. Späth, B. König, Beilstein J. Org. Chem. 6 (2010) 32.
[18] Y. Umezawa, P. Buhlmann, K. Umezawa, K. Tohda, S. Amemiya, Pure Appl. Chem. 72 (2000) 1851–2082.
[19] R. Daniels, H. Rupprecht, Pharm. Res. 2 (1985) 170–175.
[20] British Pharmacopoeia, Medicines and Healthcare Products Regulatory Agency, Volume III, Stationary Office, London (2010) 3041.
[21] A. Martin, J. Swarbrick, A. Cammarata, Physical Pharmacy, Third ed., Lea and Febiger, Philadelphia, USA, 1983.
[22] T. Suzuki, Y. Tanimura, Yakugaku zasshi 90 (1970) 762–770.

Talanta 132 (2015) 59–64

Contents lists available at ScienceDirect

Talanta

journal homepage: www.elsevier.com/locate/talanta

A novel magneto-DNA duplex probe for bacterial DNA detection based on exonuclease III-aided cycling amplification

Yan Zeng [a,b], Yi Wan [a], Dun Zhang [a,*], Peng Qi [a,b]

[a] Key Laboratory of Marine Environmental Corrosion and Bio-fouling, Institute of Oceanology, Chinese Academy of Sciences, 7 Nanhai Road, Qingdao 266071, China

[b] University of the Chinese Academy of Science, 19 (Jia) Yuquan Road, Beijing 100039, China

ARTICLE INFO

Article history:
Received 23 June 2014
Received in revised form
18 August 2014
Accepted 20 August 2014
Available online 27 August 2014

Keywords:
Magneto-DNA duplex probe
Magnetic microparticle
Exonuclease III
Bacterial DNA detection

ABSTRACT

A novel magneto-DNA duplex probe for bacterial DNA detection based on exonuclease III (Exo-III) aided cycling amplification has been developed. This magneto-DNA duplex probe contains a partly hybrid fluorophore-modified capture probe and a fluorophore-modified signal probe with magnetic microparticle as carrier. In the presence of a perfectly matched target bacterial DNA, blunt 3′-terminus of the capture probe is formed, activating the Exo-III aided cycling amplification. Thus, Exo-III catalyzes the stepwise removal of mononucleotides from this terminus, releasing both fluorophore-modified signal probe, fluorescent dyes of the capture probe and target DNA. The released target DNA then starts a new cycle, while released fluorescent fragments are recovered with magnetic separation for fluorescence signal collection. This system exhibited sensitive detection of bacterial DNA, with a detection limit of 14 pM because of the unique cleavage function of Exo-III, high fluorescence intensity, and separating function of magneto-DNA duplex probes. Besides this sensitivity, this strategy exhibited excellent selectivity with mismatched bacterial DNA targets and other bacterial species targets and good applicability in real seawater samples, hence, this strategy could be potentially used for qualitative and quantitative analysis of bacteria.

© 2014 Elsevier B.V. All rights reserved.

1. Introduction

The analysis of bacterial DNA, which is a commonly used genetic marker, is important in the molecular diagnosis of infectious diseases, rapid classification, and phenotyping of bacterial species [1–3]. Most diagnostic approaches related to 16S ribosomal RNA (16S rRNA) segment are based on polymerase chain reaction (PCR) [4,5]. However, some drawbacks, such as critical experiment conditions and complex operation [6], made it become a significant bottleneck in molecular diagnosis. There is therefore a need of detecting method of bacterial DNA segment in a more rapid, convenient and easily operated manner, which could also be used for bacteria and cell analysis.

A nuclease-assisted biosensor capable of amplified detection of single-stranded DNA is of great demand in nucleic acids, molecule detection, and gene diagnosis [7,8]. Various signal amplification strategies based on nuclease, including FokI enzyme [9], polymerase, and nicking endonuclease [10,11] have been developed. Compared with other nucleases, exonuclease III (Exo-III) does not require a specific recognition site, and is effective on the blunt or recessed 3′-terminus substrates of double-stranded DNA [12,13]. Moreover, Exo-III can provide a diverse platform for amplified DNA detection [14].

Most Exo-III aided signal amplification methods reported were carrier-mobilized strategies, including the use of nanoparticles [15], quantum dots [16], single-walled carbon nanotube [17] and graphene oxide [18]. However, most of them, such as quantum dots, or gold nanoparticles, suffer severe background interference from absorption, scattering, especially in complex biological media, and their detection capability would be greatly diminished. So, some advanced carriers need to be developed. Magnetic microparticles (MMPs) [19,20], which can be easily separated and are biocompatible and stable, were rarely reported in this field. In comparison with the above material, some advantages can be shown. First, most biological samples exhibit virtually no magnetic background, so the above background problem would be circumvented. Second, MMPs show fast binding kinetics with single-stranded DNA with larger surface area and high flexibility in homogeneous solution with easy separation. He and his coworkers recently designed an approach using Exo-III coded MMP probes that can simultaneously detect two kinds of DNA [21]. However, the fluorescence signal decreased correspondingly as the two different DNA strands co-assembled at MMPs. Lu and her coworkers fabricated a large diameter microsphere with high density of DNA probes to

* Corresponding author. Tel./fax: +86 532 82898960.
E-mail address: zhangdun@qdio.ac.cn (D. Zhang).

http://dx.doi.org/10.1016/j.talanta.2014.08.054
0039-9140/© 2014 Elsevier B.V. All rights reserved.

increase the sensitivity of the analytical technique [14]. However, the sensitivity of analytical technique with a fixed diameter microsphere remains a challenging issue [22], as the coverage of single DNA strands on MMPs possibly reach saturation.

Based above, we presents a novel perspective for bacterial DNA detection based on fixed-diameter MMPs. Coupled with Exo-III aided cycling amplification, the magneto-DNA duplex probe was introduced to enhance sensitivity. The reaction mechanism of this strategy is based on the following: first, the construction of magneto-DNA duplex probes composed of two fluorophore-modified DNA probes easily captures target DNA and enhances final fluorescence signal. Second, fluorescent dyes and fluorophore-modified signal probes are recovered because of easy separation of MMPs. Third, Exo-III provides a unique cleavage function for amplifying reaction. To the best of our knowledge, our strategy for the first time reported novel perspective of magneto-DNA duplex probe to improve detection sensitivity based on fixed-diameter MMPs. Further more, this strategy offers the merits of high sensitivity, excellent selectivity, and easy operation.

2. Material and methods

2.1. Chemicals and instruments

All of the oligonucleotides were custom synthesized and high-performance liquid chromatography (HPLC) purified by Sangon Biotechnology Co., Ltd. (Shanghai, China). The library of oligonucleotide sequences used in this study is shown in Table S1. The stock solution of DNA were dispersed in TE buffer (10 mM Tris–HCl, 1 mM Ethylene diamine tetraacetic Acid/EDTA, pH 8.0), and diluted to different concentrations with the same TE buffer when needed. Streptavidin-modified MMPs (1.0 μm, 10 mg/mL) were purchased from HuiEr Nanotechnology Co., Ltd. (Henan, China). Exo-III was ordered from Sangon Biotechnology Co., Ltd. (Shanghai, China), and Tris (hydroxymethyl) aminomethane hydrochloride (Tris) was purchased from Sinopharm Chemical Reagent Co., Ltd. (Shanghai, China). Seawater was collected from Huiquan Bay of Qingdao (zone approximately 120° 15′ to 120° 25′ N, 36° 00′ to 36° 06′ E, 10 m to 20 m deep), and then filtered with cellulose acetate ultra-filtration membrane (4 μm). Cellulose acetate ultra filtration membrane was purchased from Bioscience Biotechnology Co., Ltd. (Shanghai, China). All chemicals and solutions used throughout this study were dissolved or diluted with ultrapure water.

An 8-well magnetic rack was ordered from Sangon Biotechnology Co., Ltd. (Shanghai, China), and a KYC-1102C air constant temperature table was purchased from Jiangnan instrument factory (Ningbo, China). The fluorescence spectra data were recorded from F-4500 Fluorescence spectrophotometer (Hitachi High-technologies Corporation, Tokyo, Japan). A laser scanning confocal microscope image analysis system (MRC-1024, Carl Zeiss AG, Germany) and a DYCZ-24DN mini double vertical electrophoresis apparatus (Liuyi instrument factory, Beijing, China) were also used. The ultrapure water was produced by Storage & Distribution system (Millipore Corporation, USA).

2.2. Determining capture probe coverage on MMPs

A 100 μL fluorescence and biotinylated capture probe (500 nM) was mixed with varying amount of MMPs (0, 1, 3, 5, 7, 10, 15, and 20 μL). The supernatant was obtained with magnetic separation after 30 min of incubation at room temperature. Fluorescence signal was recovered with Hitachi F-4500 fluorescence spectrophotometer (excitation wavelength = 494 nm).

2.3. Magneto-DNA duplex probe preparation

Streptavidin-modified MMPs (10 μL) was washed five times with 1 mL of washing buffer (10 mM Tris–HCl, 1 mM EDTA, 2 M NaCl, pH 7.5). The ultimate magnetic absorptions were resuspended in 1 mL binding buffer (10 mM Tris–HCl, 1 mM EDTA, 2 M NaCl, pH 7.5). The streptavidin-modified MMPs suspension were mixed with 100 μL–500 nM biotin-modified capture probes (S1) and 100 μL of 500 nM signal probes (S2). The mixture was incubated at 25 °C for 120 min with gentle shaking. The weekly bound capture probes were removed after repeated magnetic separation and cleaning. The rest of the absorption was resuspended in 1 mL reaction buffer (20 mM Tris–HCl, 5 mM $MgCl_2$, pH 8.0) and stored at 4 °C for further use.

2.4. Fluorescence microscopy imaging of the magneto-DNA duplex probe

Streptavidin-modified MMPs and fluorescence probe-conjugated MMPs (10 μL) were added onto a glass slide, and a cover slip was glued onto the glass slide using nail polish. The sample was then imaged using a confocal laser scanning fluorescence microscope.

2.5. Gel electrophoresis

Polyacrylamide gel electrophoresis (PAGE) was performed by using an unmodified capture probe, unmodified signal probe, and target DNA with the same sequence, as described in Table S1. The polyacrylamide gel was prepared with 30% (w/v) acrylamide solution, 10% (w/v) ammonium persulfate, 50 × Tris–acetate–EDTA (10 mM Tris, 5 M acetic acid and 0.625 M EDTA, pH 8.5, TAE), tetramethylethylenediamine with 1 × TAE buffer. Then, 10 μL of sample was mixed with 2 μL of loading buffer. The mixtures were run through PAGE at 170 V for 5 min and then 110 V for 60 min. The gel was stained with 0.5 μg/mL of anthodium bromide for 20 min, and a picture was taken using a digital camera under UV illumination.

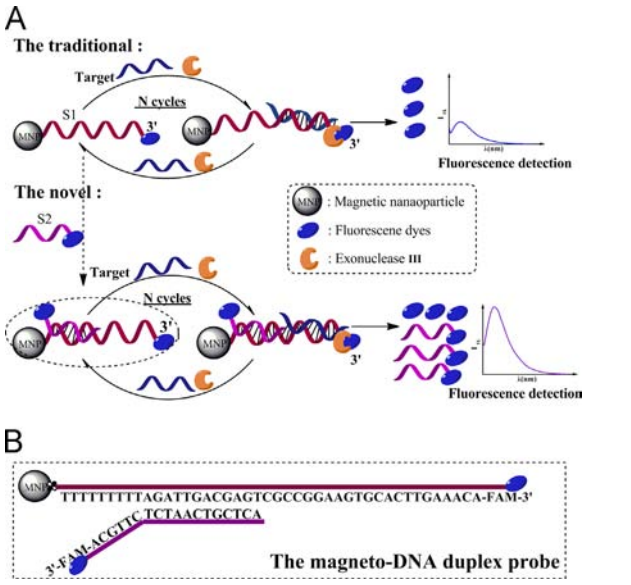
2.6. Procedure for bacterial DNA detection

The detection of bacterial DNA based on Exo-III cycling amplification reaction was performed by mixing 10 μL magneto-DNA duplex probe, 10 μL of different concentrations of the target DNA, 4 μL of 10 × reaction buffer and 75 units of Exo-III to a final volume of 40 μL, followed by incubation at 37 °C for 90 min. The MMPs were then removed by magnetic separation, and the fluorescence signals of the supernatant were measured with synchronous scanning fluorescence spectrometry. Fluorescence was measured with 494 nm as the excitation wavelength, and the fluorescence emission spectra range was recorded from 500 nm to 650 nm. Excitation and emission slits were both set as 5 nm. Each experiment was repeated at least thrice to test reproducibility.

3. Results and discussion

3.1. Design and validation of the assay

We presented a novel magneto-DNA duplex probe for bacterial DNA detection. The magneto-DNA duplex probe was constructed as follows: fluorophore-modified capture probe (S1) was assembled on the streptavidin-modified MMPs, with optimized amount ratio of MMPs and S1 during the experiment. With the addition of fluorophore-modified signal probe (S2), S1 would hybridized with S2, leaving a 24-nt single-stranded DNA segment overhanging at its 3′-terminus (B part of Scheme 1). It should be noted that S2 only hybridizes partly with S1, leaving 5 nt single-stranded DNA segments overhanging at its 3′-terminus to resist the cleavage by Exo-III (Supplementary section S1.1.) because the resistance degree of Exo-III on single-stranded DNA at the 3′-protruding terminus is dependent on the length of the extension, with extensions 4 nt or longer being



Scheme 1. (A) Schematic of traditional Exo-III aided cycling amplification for DNA detection (top) and the novel Exo-III aided cycling amplification for DNA detection based on magneto-DNA duplex probe (bottom); (B) the base sequence diagram of the magneto-DNA duplex probe.

essentially resistant to cleavage [12]. The target DNA would partly hybridize with the overhanging single-stranded DNA segments of S1 to form a double-stranded structure with its 5 nt single-stranded DNA segments overhanging at the 3′-terminus to resist cleavage by Exo-III. Thus, only blunt 3′-terminus of S1 becomes an active site, which would stimulate the activity of Exo-III. Exo-III catalyzes the stepwise removal of mononucleotides from the 3′-hydroxyl termini of duplex DNA, liberating the fluorescent dyes of the capture probe and releasing signal probe S2. With the hydrolyzation of mononucleotides from the 3′-terminus, the target DNA is released and binds again to the single-stranded DNA segments of S1, which catalyzes a new cleavage cycle. After numerous cycling reactions, a certain amount of the S1′ s fluorescent dyes and the fluorophore-modified signal probe S2 were released into the supernatant. Released fluorescent fragments are recovered by applying a magnetic field to remove MMPs. The fluorescence signals of the supernatant are recorded with fluorescence spectrophotometer.

A small fragment of characteristic DNA sequences from the genome of each species was prepared to detect the bacterial DNA segment. *Desulfobacter curbatus* DNA was selected as the target DNA [23].

We studied the feasibility of this strategy. Fig. 1A shows that fluorescence intensity was weak in the absence of target DNA, this result can be attributed to the overhanging single-stranded DNA segments at the 3′-terminus to resist Exo-III cleavage and excellent separating ability of MMPs. On the other hand, in the presence of target DNA, the overhanging single-stranded DNA segments at the 3′-terminus of S1 would hydride with target DNA to form active site, activating the Exo-III aided cycling amplification. The fluorescence signals of the supernatant were observed with a $552 \pm 15\%$ signal increase, however, the corresponding signal gain of the traditional method was only $221\% \pm 7\%$ at the target concentration of 0.15 nM. The reaction buffer exhibited low fluorescence signals. Overall, this novel magneto-DNA duplex probe-aided method was feasible and more sensitive than the traditional one. The assay was further verified by PAGE test as shown in Fig. 1B. Compared with lane 1 (the blank), lane 2 (traditional method) and lane 3 (novel method) exhibited a bright band at 4 bp, indicating that the hydrolyzed segments produced by the Exo-III-aided cycling amplification shifted rapidly to the bottom. In contrast with the traditional one, the novel one showed an evident band of signal probe, indicating that the probe was released and can be captured for signal enhancement.

We further performed fluorescence imaging of the novel magneto-DNA duplex probe (Fig. 1C). The streptavidin-modified MMPs exhibited no fluorescence signal in the absence of capture probes and signal probes. Once the fluorescence-conjugated probes were introduced, a fluorescence image brighter (c) than the traditional one (b) was captured, indicating the successful building of the magneto-DNA duplex probe.

3.2. Determining capture probe coverage on MMPs

The capture probe coverage on MMPs was optimized. As shown in Fig. 2, a high fluorescence signal was observed at first. With more MMPs being added, more DNA was removed and a lower fluorescence signal was observed until 10 μL of MMPs was added, indicating that 10 μL of MMPs (10 mg/mL) can take 100 μL of FAM and biotinylated capture probe (500 nM) at most. The average number of capture probe on each MMP was estimated as 1.49×10^6 (Supplementary section S1.2). This result indicated that the capture probe coverage on fixed-diameter MMPs possibly reached saturation, hence, we designed the novel duplex probe to enhance fluorescence intensity.

3.3. Optimization of assay conditions

The activity of Exo-III is critical to the whole cycling amplification reaction under certain temperatures. This optimization experiment was performed by detecting 0.15 nM target DNA at 4, 25, 37, and 45 °C, and the blank was carried out without any target DNA. Fig. S2 (see Supplementary section S1.3) shows the experimental results that indicate the signals increased with temperature from 4 °C to 37 °C, which means the Exo-III activity enhanced and the relative fluorescence signal between target and the blank increased. When the temperature increased, the sample and the blank fluorescence signals decreased simultaneously, and the relative fluorescence signal narrowed. This phenomenon can be attributed to the high temperature that decreases the activity of Exo-III and the capture probe cannot be digested. Therefore, 37 °C was considered the optimum incubation temperature.

The fluorescence signal was measured by detecting 0.15 nM target DNA with 0, 25, 50, 75, and 100 units of Exo-III to investigate the influence of the amount of Exo-III used throughout this assay on target DNA detection. The blank sample was treated in the same concentration of Exo-III without target DNA. Fig. S3 (see Supplementary section S1.3) shows that the maximum interval of fluorescence between the target DNA and the blank sample was obtained at 75 units of Exo-III. Thus, 75 units of Exo-III were used in the following assay.

The incubation time was optimized for the performance of Exo-III-aided reaction upon analyzing the target DNA at a concentration of 0.15 nM. Fig. S4 (see Supplementary section S1.3) shows that the fluorescence signal gradually increased and reached the maximum value at 90 min. The signal intensity stabilized after 90 min. The incubation of 90 min was considered the optimized time of the whole reaction.

3.4. Analytical performance

Under optimal conditions, the relationship between the change of fluorescence intensity and the concentration of target DNA was investigated. Fig. 3 shows the fluorescence spectrum in the presence of different target DNA ranging from 40 pM to 800 pM and the related linear relationship. The relative signal intensity exhibited a

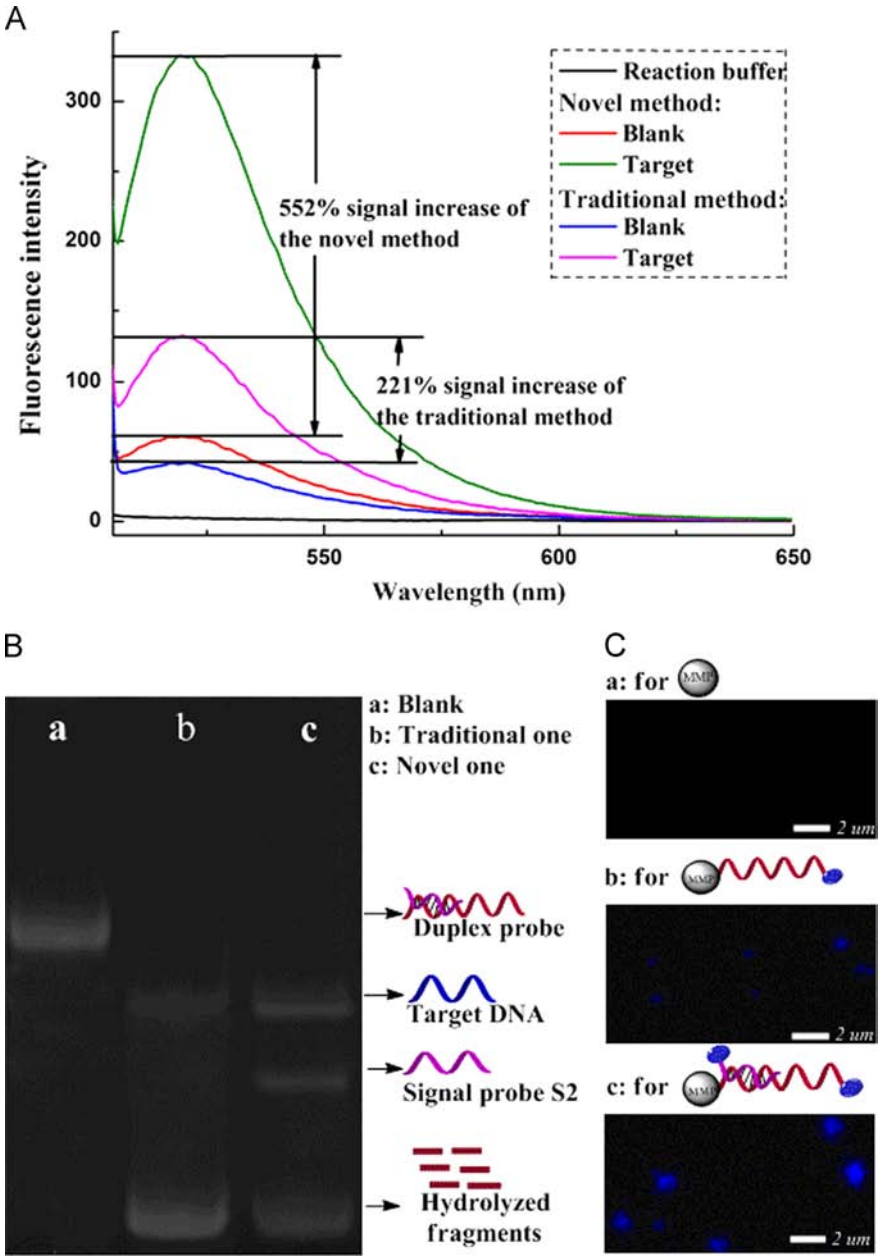


Fig. 1. (A) Fluorescence spectra and (B) polyacrylamide gel electrophoresis of (c) the novel cycling amplification reaction; (b) the traditional cycling amplification, and (a) blank with a target DNA of 0.15 nM. Experiment conditions: 75 U Exo-III, 37 °C with 90 min incubation; and (C) fluorescence imaging of (a) streptavidin-modified MMPs, (b) the single DNA probe (10 μM) modified MMPs, and (c) the magneto-DNA duplex probe-modified MMPs with 10 μM capture probe and 10 μM signal probe.

linear relationship with the concentration of target DNA in the range of 40–150 pM, and the regression equation can be represented as $Y=2.357X-73.00$ ($R^2=0.9985$, where Y is the relative fluorescence intensity and X is the concentration of the target DNA, The relative fluorescence intensity was calculated by $FL-FL_0$, where FL and FL_0 are the fluorescence intensities in the presence and in the absence of target DNA, respectively). The detection limit was determined to be 14 pM based on a linear fitting and the noise level of 3σ (where σ is the standard deviation of a lank solution, $n=12$), which was comparable to the reported Exo-III aided cycling amplification method (see Supplementary Table S3). Obviously, the introduction of magneto-DNA duplex probe presents a novel perspective of improving sensitivity based on fixed diameter MMPs. The sensitivity of this proposed method could be improved with more signal probes (S2) conjugated with capture probes (S1), as all signal probes would be released into the supernatant when Exo-III is activated. As a result, the sensitivity and flexibility of this strategy greatly improved.

3.5. Selectivity of the assay

The selectivity of an assay is another critical factor besides detection sensitivity. The selectivity of this magneto-DNA duplex probe-based strategy was evaluated in this assay with perfectly matched, single-base mismatched, three-base mismatched, and completely mismatched target DNA sequences at a concentration of 0.15 nM. Fig. 4A shows that the fluorescence signal decreased with the increase of mismatched base counts, and the completely mismatched sequence showed the same fluorescence signal with the control sample. Therefore, this proposed strategy is highly capable of differentiating perfectly matched and mismatched DNA targets. Control DNA targets of *Desulfobulbus propionicus*, *Desulfobacterium autotrophicum*, and *Desulfosarcina variabilis* were also employed to replace the same concentration of *D. curbatus* (0.15 nM) under the same experimental conditions for the *Magneto-DNA duplex probe* assay [23]. The results established the specificity of this method that could be

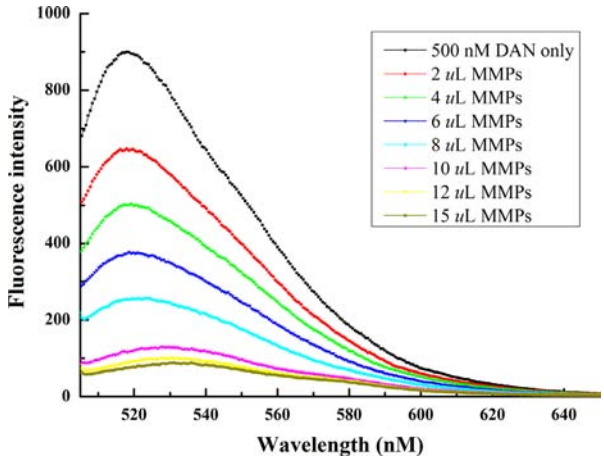


Fig. 2. Fluorescence spectra of the supernatant after incubating varying amounts of streptavidin-coated magnetic microparticles with biotinylated and FAM-labeled DNA;100 μL FAM and biotinylated capture probe (500 nM) was mixed with varying amounts of MMPs (0, 1, 3, 5, 7, 10, 15, and 20 μL).

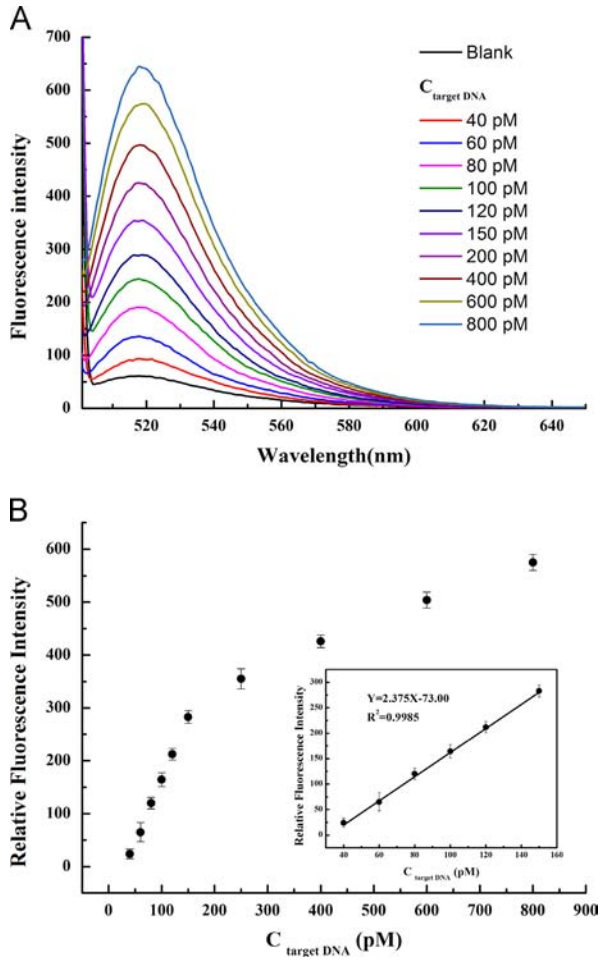


Fig. 3. (A) Fluorescence spectra of Exo-III aided cycling amplification reaction based on magneto-DNA duplex probes with different concentrations of target DNA from 40 pM to 800 pM and blank; (B) the corresponding calibration curve of the relative fluorescence intensity (emission wavelength is 517 nm) with different concentrations of target DNA. Error bars are the standard deviation of three repetitive measurements.

attributed to the specific hybridization of target DNA and the excellent digestion property of Exo-III. Thus, the proposed magneto-DNA duplex probe strategy exhibits high selectivity between target DNA, mismatched DNA targets, and good specificity in bacterial DNA target.

3.6. Strategy application in different fluids

Spike and recovery experiments were performed to further investigate the application of this technique in a complex environment. The bacteria used in this experiment are all marine corrosive microbes,

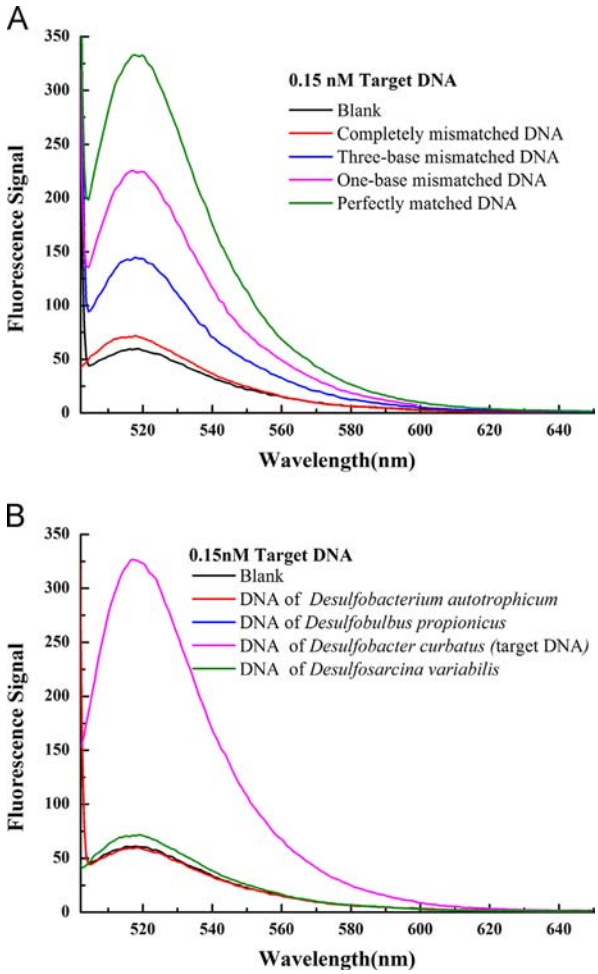


Fig. 4. Fluorescence spectra yielded by Exo-III aided cycling amplification reaction based on magneto-DNA duplex probes with mismatched target DNA (A) and DNA segments of *Desulfobulbus propionicus*, *Desulfobacterium autotrophicum*, and *Desulfosarcina variabilis* (B).

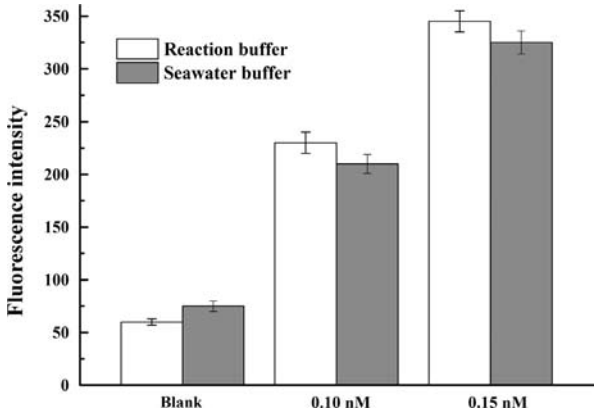


Fig. 5. Comparison of fluorescence spectra yielded by Exo-III aided cycling amplification reaction based on magneto-DNA duplex probes with different concentrations of target DNA (0 nM, 0.10 nM, and 0.15 nM) in reaction buffer and seawater sample. Error bars are the standard deviation of three repetitive measurements.

and 10% of seawater sample (see Supplementary section 1.4) was selected as the reaction buffer, spiked with 0, 0.10, and 0.15 nM of target DNA. As shown from Fig. 5, the seawater sample and reaction buffer with same concentration of target DNA did not exhibit obvious fluorescence difference. The ultimate concentration of target DNA was determined by using calibration method, and the recovery rate was calculated at $97 \pm 5\%$, which reflects good application of the proposed strategy in different fluids.

4. Conclusion

We proposed a novel perspective of the magneto-DNA duplex probe-based strategy for bacterial DNA detection based on Exo-III-aided cycling amplification. This approach is simple, fast, and easy to operate, resulting in good separating ability of MMPs and excellent fluorescence intensity of DNA duplex probes. With the unique cleavage function of Exo-III, this approach exhibits excellent sensitivity with a detection limit as low as 14 pM, high specificity to well discriminate a one-base difference in DNA sequences, and favorable application in real seawater samples. The new perspective of magneto-DNA duplex probe can be potentially applied in bacterial detection and cell analysis.

Acknowledgments

This study was supported by the National Natural Science Foundation of China (Grant No. 41306072), the Shandong Provincial Natural Science Foundation, China (Grant No. BS 2013HZ005), and the Science & Technology Basic Research Program of Qingdao (Grant No. 13-1-4–181-jch).

Appendix A. Supporting information

Supplementary data associated with this article can be found in the online version at http://dx.doi.org/10.1016/j.talanta.2014.08.054.

References

[1] Y.G. Li, Y.T.H. Cu, D. Luo, Nat. Biotechnol. 23 (2005) 885–889.
[2] H.J. Chung, C.M. Castro, H. Im, H. Lee, R. Weissleder, Nat. Nanotechnol. 8 (2013) 369–375.
[3] K. Rijal, X. Bao, C.S. Chow, Chem. Commun. 50 (2014) 3918–3920.
[4] N.J. Loman, C. Constantinidou, J.Z-M. Chan, M. Halachev, M. Sergeant, C.W. Penn, E.R. Robinson, M.J. Pallen, Nat. Rev. Microbiol. 10 (2012) 599–606.
[5] C. Pohlmann, I. Dieser, M. Sperinzl, Analyst 139 (2014) 1063–1071.
[6] E.A. Ottesen, J.W. Hong, S.R. Quake, J.R. Leadbetter, Science 314 (2006) 1464–1467.
[7] C.F. Chen, J.J. Zhao, J.H. Jiang, R.Q. Yu, Talanta 101 (2012) 357–361.
[8] A.H. Zheng, M. Luo, D.S. Xiang, X. Xiang, X.H. Ji, Z.K. He, Talanta 114 (2013) 49–53.
[9] P.D. Hsu, F. Zhang, ACS Chem. Neurosci. 3 (2012) 603–610.
[10] A.R. Connolly, M. Trau, Angew. Chem. 49 (2010) 2720–2723.
[11] C. Russell, K. Welch, J. Jarvius, Y.X. Cai, R. Brucas, F. Nikolajeff, P. Sevedlindh, M. Nillson, ACS Nano 8 (2014) 1147–1153.
[12] S. Henikoff, Gene 28 (1984) 351–359.
[13] C.C. Richardson, I.R. Lehman, A. Kornberg, J. Biol. Chem. 239 (1964) 251–258.
[14] J. Lu, I.T. Paulsen, D.Y. Jin, Anal. Chem. 85 (2013) 8240–8245.
[15] Q. Fan, J. Zhao, H. Li, L. Zhu, G.X. Li, Biosens. Bioelectron. 33 (2012) 211–215.
[16] R. Freeman, X.Q. Liu, I. Willer, Nano Lett. 11 (2011) 4456–4461.
[17] G.F. Wang, G. Xu, Y.H. Zhu, X.J. Zhang, Chem. Commun. 50 (2014) 747–750.
[18] L. Peng, Z. Zhu, Y. Chen, D. Han, W.H. Tan, Biosens. Bioelectron. 35 (2012) 475–478.
[19] Y. Wan, D. Zhang, B.R. Hou, Biosens. Bioelectron. 25 (2010) 1847–1850.
[20] Y. Wan, Y. Sun, P. Qi, P. Wang, D. Zhang, Biosens. Bioelectron. 55 (2014) 289–293.
[21] M. Luo, X. Xiang, D.S. Xiang, S. Yang, X.H. Ji, Z.K. He, Chem. Commun. 48 (2012) 7416–7418.
[22] P-J.J. Huang, J.W. Liu, Anal. Chem. 82 (2010) 4020–4026.
[23] K. Daly, R.J. Sharp, A.J. Mccarthy, Microbiology 146 (2000) 1693–1705.

Talanta 132 (2015) 65–71

Contents lists available at ScienceDirect

Talanta

journal homepage: www.elsevier.com/locate/talanta

A luminol electrochemiluminescence aptasensor based on glucose oxidase modified gold nanoparticles for measurement of platelet-derived growth factor BB

Jing-Jing Zhang [a], Jun-Tao Cao [a], Gui-Fang Shi [a], Ke-Jing Huang [a], Yan-Ming Liu [a,*], Shu-Wei Ren [b]

[a] College of Chemistry and Chemical Engineering, Xinyang Normal University, Xinyang 464000, PR China
[b] Xinyang Central Hospital, Xinyang 464000, PR China

ARTICLE INFO

Article history:
Received 13 July 2014
Received in revised form
19 August 2014
Accepted 21 August 2014
Available online 30 August 2014

Keywords:
Electrochemiluminescence
Aptasensor
PDGF-BB
Glucose oxidase (GOD)
Luminol

ABSTRACT

A sandwich-type luminol electrochemiluminescence (ECL) aptasensor for highly sensitive and selective detection of platelet-derived growth factor BB (PDGF-BB) is fabricated. For this proposed ECL aptasensor, a multilayered AuNPs-electrochemically reduced graphene (AuNPs-EG) nanocomposite film was formed on the GCE surface as the base of the aptasensor through a co-electrodeposition method. The AuNPs-EG composites possess high conductivity to promote the electron transfer at the electrode interface and good biocompatibility and large surface area to capture large amounts of primary aptamer (Apt1), thus amplifying the detection response. Moreover, glucose oxidase (GOD) functionalized AuNPs labeled secondary aptamer (GOD–Apt2–AuNPs) was designed as the signal probe for the sandwiched aptasensor. Enhanced sensitivity was obtained by in situ generation of H_2O_2 from reaction between GOD and glucose and the excellent catalytic behavior of AuNPs to the ECL of the luminol–H_2O_2 system. Under the optimal conditions, the as-prepared ECL aptasensor exhibited excellent analytical property for the detection of PDGF-BB in the range from 1.0×10^{-13} to 5.0×10^{-10} mol L^{-1} with a detection limit of 1.7×10^{-14} mol L^{-1} ($S/N=3$). The application of the present protocol was demonstrated by analyzing PDGF-BB in human serum and human urine samples with the recoveries from 85.0% to 110%.

© 2014 Elsevier B.V. All rights reserved.

1. Introduction

Diabetic nephropathy (DN) is a major chronic microvascular complication of diabetes mellitus (DM), which is an important cause of increased morbidity and mortality in patients with DM [1]. Strong evidence suggests that several growth factors may contribute to the initiation and progressive fibrosis of DN.

Platelet derived growth factor (PDGF), one of the critical growth factors found in human platelets, has increased in importance due to its role in the regulation of cell growth and division [2]. It is composed of two disulfide-linked polypeptide chains, designated A and B, occurs in three isoforms: PDGF-BB, PDGF-AB and PDGF-AA [3]. Among these isoforms, PDGF-BB is known to be directly implicated in the cell transformation process and in tumor growth and progression [4]. Moreover, PDGF-BB is considered as a good predictor for early deterioration of renal function in DN [5]. Thus, precise and sensitive evaluation of PDGF-BB in biological samples will be substantial for disease diagnosis.

Detection of PDGF-BB has been attempted including the traditional antibody based radioisotropic method and ELISA [6,7]. However, the antibody used in these methods is temperature-sensitive, irreversibly denatured, and has a limited shelf life. These drawbacks limit the applications of the antibody-based assay. Aptamer is a specific DNA or RNA strand obtained from random-sequence nucleic acid libraries by SELEX (systematic evolution of ligands by exponential enrichment) technology [8]. They have been widely used as recognition elements for biochemical analysis due to their advantages of simpler synthesis, easier storage, lower cost and higher specificity [9]. Several aptasensors have been developed for detecting PDGF-BB based on electrochemistry (EC) [10], fluorescence [11,12], colorimetric colorimetry [13], chemiluminescence (CL) [14], and electrochemiluminescence (ECL) [15]. Among all the aptasensors, ECL-based methods have attracted intensive and extensive research interests, as they integrate the advantages of EC detection and chemiluminescent techniques, such as high sensitivity, low background, cost-effectiveness and high specificity [16]. Zhu et al. [17] reported an aptamer-based bio bar code immunomagnetic separation and ECL detection of PDGF-BB. [$Ru(bpy)_3^{2+}$] (TBR)-Au bio bar code-labeled aptamer was used as an ECL nanoprobe in the method. Recently, our group [15]

* Corresponding author. Tel./fax: +86 376 6392889.
E-mail address: liuym9518@sina.com (Y.-M. Liu).

http://dx.doi.org/10.1016/j.talanta.2014.08.058
0039-9140/© 2014 Elsevier B.V. All rights reserved.

developed an ECL aptasensor featuring MoS_2–AuNPs composites as a matrix and aptamer modified CdSe–ZnS quantum dots as a signal probe for PDGF-BB detection.

Luminol, one of the most widely used efficient ECL luminophores, has some excellent inherent properties such as inexpensive, nontoxic and high light-emission yield [18,19], and luminol-based ECL studies have caught scientists' eyes in biochemical analysis. To achieve a sensitive detection for biochemical samples, many efforts have been devoted to amplifying the ECL signal of luminol. Generally, dissolved oxygen and hydrogen peroxide are used as a coreactant for the luminol ECL reaction to enhance the ECL intensity [20–22]. Nanoparticles with the merits of good biocompatibility, large surface area, excellent electrocatalytic activity and conductivity, could act as a versatile role for biochemical analysis, such as a good matrix for electrode modification or biological labels decorated with enzyme, aptamer or protein [23–26]. Moreover, some of the nanoparticles could catalyze H_2O_2 to generate a great amount of reactive oxygen species which could greatly accelerate the oxidization of luminol, leading to an amplified ECL signal. Cao et al. [27] developed an ECL immunosensor for ultrasensitive detection of carcinoembryonic antigen with a detection limit of 0.03 pg mL^{-1} using Pd and Pt nanoparticles decorated reduced graphene oxide (Pd&PtNPs@rGO) and glucose oxidase (GOD) labeled secondary antibody as the trace label. The sensitivity was enhanced by in situ generation of hydrogen peroxide with GOD and the catalysis of Pd&PtNPs to the ECL reaction of the luminol–H_2O_2 system. The synergetic effects of enzyme and nanopartciles for amplifying the luminol ECL signal in immunoassay provide an ingenious idea for the construction of aptasensors.

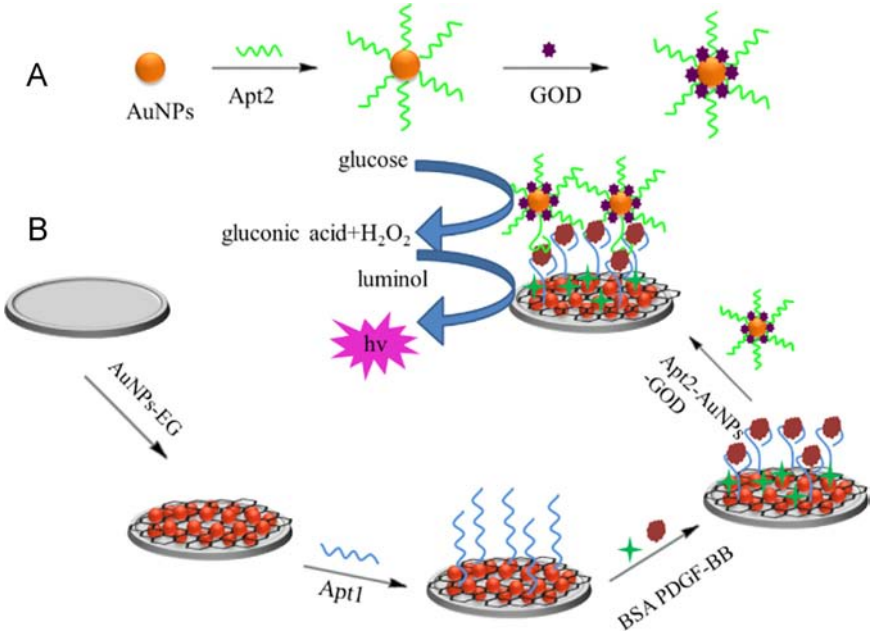
Herein, we developed a novel sandwich-type luminol ECL aptasensor for PDGF-BB detection using GOD decorated Au nanoparticles as labels. In this protocol, AuNPs-electrochemically reduced graphene (AuNPs-EG) composites were firstly electrodeposited on the glassy carbon electrode (GCE) as an aptasensor platform which could amplify the ECL signal of the luminol–H_2O_2 system for its fascinating conductivity and served as carrier to immobilize primary aptamers (Apt1) through chemical absorption between AuNPs and –NH_2 of aptamers [28,29]. Then, secondary aptamers (Apt2) and GOD decorated AuNPs were designed as the signal probe for the sandwiched aptasensor. The proposed ECL aptasensor exhibited a sensitive and stable response for the detection of PDGF-BB and achieved a wider linear range and lower detection limit. The proposed ECL aptasensor was applied to the detection of PDGF-BB in human serum samples and human urine samples.

2. Experimental

2.1. Reagents and apparatus

Human platelet-derived growth factor-BB (PDGF-BB) was purchased from Peprotech (USA). The aptamers for PDGF-BB (Apt1: 5′-NH_2-$(CH_2)_6$-TTT TTT TTT TCA GGC TAC GGC ACG TAG AGC ATC ACC ATG ATC CTG-3′, Apt2: 5′-SH-$(CH_2)_6$-TTT TTT TTT TCA GGC TAC GGC ACG TAG AGC ATC ACC ATG ATC CTG-3′), glucose oxidase (GOD) and 10 mmol L^{-1} phosphate buffer saline (PBS, pH 7.4) were purchased from Sangon Biological Co., Ltd. (Shanghai, China). The aptamer and protein solutions were prepared with 10 mmol L^{-1} pH 7.4 PBS, containing 137 mmol L^{-1} NaCl, 2.7 mmol L^{-1} KCl, and 1 mmol L^{-1} $MgCl_2$ and were stored at 4 °C until being used. Hydrogen tetra chloroaurate (III) trihydrate ($HAuCl_4 \cdot 3H_2O$) was obtained from Alfa Aesar (A Johnson Matthey Company, Ward Hill, MA), luminol from Sigma-Aldrich (St. Louis, MO, USA) and bovine serum albumin (BSA) from Siobio Biotechnology Inc. (Shanghai, China). All reagents were of analytical reagent grade and used without further purification. Ultrapure water was used throughout the experiments.

ECL emission was monitored with a model BPCL ultraweak luminescence analyzer (Institute of Biophysics, Chinese Academy of Science, Beijing, China). Cyclic voltammetry (CV) and electrochemical impedance spectroscopy (EIS) measurements were carried out with a RST 5200 electrochemical workstation (Zhengzhou Shiruisi Technology Co., Ltd.). A conventional three-electrode system was used with a GCE (Φ=3 mm) as the working electrode, an Ag/AgCl (sat. KCl) as the reference electrode and a platinum electrode as the counter electrode. The morphologies of the samples were recorded on a Hitachi S-4800 scanning electron microscope (SEM) and a Tecnai G2 F20 transmission electron microscope (TEM).



Scheme 1. The procedure of the ECL aptasensor preparation.

2.2. Preparation of GOD–Apt2–AuNPs bioconjugates

AuNPs were prepared according to the previously described procedure [30]. The concentration of the AuNPs was calculated to be about 1.4×10^{-9} mol L^{-1}. The GOD–Apt2–AuNPs bioconjugates was prepared according to the literature reported previously [31,32]. 4 μL 10% (v/v) Tween 80 was firstly added into 1 mL AuNPs, and then the mixture was incubated for 30 min at 25 °C under gentle stirring. Subsequently, 50 μL of GOD (1 mg mL^{-1}) and 50 μL of Apt2 (5 μmol L^{-1}) were added into the as-mixture. After incubation at 25 °C under shaking for 4 h and keeping overnight at 4 °C, the resulted solution was isolated by centrifugation at 10,000 rpm for 15 min to remove the unconjugated aptamer and GOD. The GOD–Apt2–AuNPs hybrid nanoprobes were obtained by re-dispersing the conjugates in pH 7.4 0.1 mol L^{-1} PBS containing 0.05% (v/v) Tween 80 and 0.1% BSA and stored at 4 °C.

2.3. Assembly of sandwich-type ECL aptasensor

Scheme 1B shows the strategy for constructing the ECL aptasensor. First of all, the GCE was carefully polished by 1.0, 0.3, and 0.05 mm alumina powder respectively to a mirror finish and then sonicated in ethanol and ultrapure water in turn. A multilayered AuNPs-EG composite film was formed on the GCE surface through a co-electrodeposition method in a dispersion containing 1.0 mg mL^{-1} graphene oxide (GO) and 100 mmol L^{-1} $HAuCl_4$, while applying scan potential between −1.5 and 0.6 V and scan rate at 25 mV s^{-1} as previously demonstrated by Zhu et al. [31]. After deposition, the electrode was rinsed with H_2O. Then, 6 μL of 0.1 μmol L^{-1} capture Apt1 of PDGF-BB was applied to the AuNPs-EG modified electrode and incubated overnight at room temperature according to the literature [10]. After incubation, the Apt1/AuNPs-EG/GCE was rinsed with PBS (pH 7.4) carefully, immersed in 1% BSA solutions for 30 min at 37 °C to block the nonspecific binding sites. Followed by washing thoroughly with PBS, the modified GCE was incubated in PDGF-BB solution for 1 h at 37 °C (abbreviated as PDGF-BB/BSA/Apt1/AuNPs-EG/GCE). At last, as a sandwich format, the resultant electrode was immersed in the GOD–Apt2–AuNPs solution. Thus the proposed aptasensor was constructed successfully.

2.4. Measurement procedure

The aptasensors incubated with different PDGF-BB concentrations were placed in an ECL detector cell containing 3 mL PBS with 1.0×10^{-4} mol L^{-1} luminol and an appropriate concentration of glucose to record the change of ECL signals. ECL signals were obtained by CV scans with potential varying from −0.2 to 0.8 V and scan rate at 100 mV s^{-1}. The CV and ECL curves were recorded simultaneously.

2.5. Preparation of real-world samples

Human blood samples and human urine samples were from volunteers in Xinyang Central Hospital (Xinyang, China). The complete ethical approval has been obtained, and all the female volunteers gave written informed consent. The study was approved by the Institutional Review Board of Xinyang Central Hospital. The fresh blood samples were centrifuged immediately at 1000 rpm for 15 min to obtain serum. These serum samples were

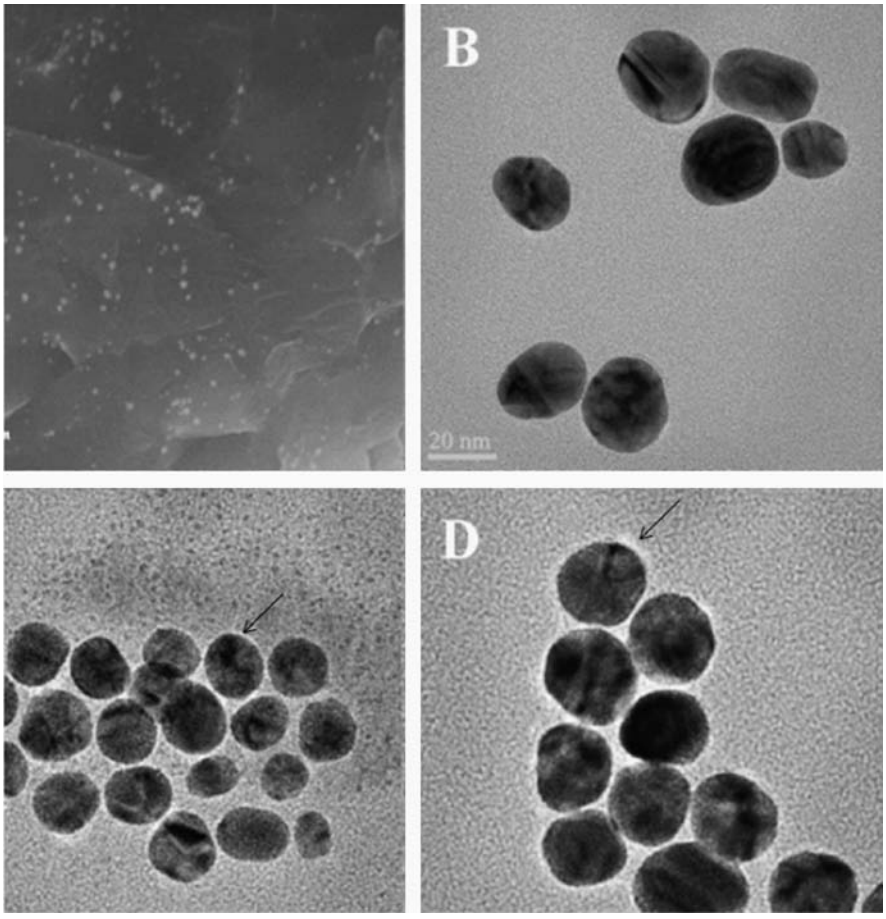


Fig. 1. SEM image of AuNPs-EG nanocomposite (A) and TEM images of bare AuNPs (B), AuNPs-aptamer (C), and GOD–Apt2–AuNPs (D).

stored at −20 °C before use. Urine samples were detected without pretreatment.

3. Results and discussion

3.1. Characterization of the AuNPs-EG nanocomposite, AuNPs, AuNPs–aptamer, and GOD–Apt2–AuNPs

Fig. 1 shows the SEM image of AuNPs-EG nanocomposite and TEM images of bare AuNPs (B); AuNPs–aptamer (C) and GOD–Apt2–AuNPs (D). Fig. 1A reveals that AuNPs (with an average diameter of ~18 nm) of AuNPs-EG nanocomposite were uniformly distributed between the graphene sheets. As for the bare AuNPs to prepare the GOD–Apt2–AuNPs nanoprobe, the average diameter was about 20 nm (Fig. 1B). As seen in Fig. 1C and D, AuNPs-aptamer and GOD–aptamer–AuNPs were surrounded by a transparent ring compared to the bare AuNPs images.

3.2. The characterization of ECL aptasensor

3.2.1. Electrochemical characterization

The stepwise ECL aptasensor assembly process was monitored by CV measurements. Fig. 2A presents the CV curves of the modified electrodes at different stages in the presence of a 5 mmol L^{-1} $K_3[Fe(CN)_6]/K_4[Fe(CN)_6]$ (1:1) mixture containing 0.1 mol L^{-1} KCl. It can be seen that the bare GCE produced relatively low CV intensity (curve a). Compared with the electrode only electrodeposited with AuNPs (curve b), the peak current of the electrode co-electrodeposited with AuNPs-EG nanocomposites further increased (curve c), which suggested the AuNPs-EG nanocomposites film significantly increased the surface area and electro-conductivity of the electrode interface and thus facilitated the interfacial electron transfer process. After Apt1 functionalization (curve d), the peak current significantly decreased due to the fact that aptamer severely blocked the electron transfer tunnel and reduced effective area of electron transfer. It demonstrated that Apt1 has been immobilized successfully. When the aptasensor was blocked with BSA (curve e) and incubated with PDGF-BB (0.1 nmol L^{-1}) (curve f), the CV responses were declined in succession for the hindrance of BSA and aptamer–PDGF-BB complex. Finally, the attachment of the hybrid nanoprobes onto the PDGF-BB surfaces further decreased the peak current (curve g) owing to the barrier effect of the conjugates against the electron communication between $[Fe(CN)_6]^{3-/4-}$ and the electrode surface.

As an effective method to investigate the interface properties of modified electrodes, EIS was also carried out to study the stepwise assembly of the aptasensor. The semicircle diameter which equals the electron-transfer resistance, reflects the restricted diffusion of the redox probe through the multilayer system related directly to film permeability. As can be seen from Fig. 2B, the results of EIS are consistent with the CV characterization.

3.2.2. ECL characterization

In the case of the luminol–H_2O_2 system, ROSs such as superoxide anion ($O_2^{\bullet -}$) and hydroxyl radical ($OH^{\bullet}$) reacts with luminol to produce excited 3-aminophthalate dianion and then emit lights [33]. According to the literatures [34], the probable mechanism is shown as follows: (LH^- is the deprotonated luminol and Ap^{2-*} is 3-aminophthalate)

$$LH^- - e^- \rightarrow LH^{\bullet} \rightarrow L^{-\bullet} + H^+ \quad (1)$$

$$\text{Glucose} + O_2 \xrightarrow{\text{GOD}} \text{Gluconic acid} + H_2O_2 \quad (2)$$

$$H_2O_2 + L^{-\bullet} \xrightarrow{\text{AuNPs}} Ap^{2-*} + \text{products} \quad (3)$$

$$Ap^{2-*} \rightarrow Ap^{2-} + h\nu \quad (4)$$

The fabrication process of the ECL aptasensor was characterized by ECL in 0.1 mol L^{-1} PBS contain 1.0×10^{-4} mol L^{-1} luminol and 10 mmol L^{-1} glucose solution. As shown in Fig. 3, the bare GCE produced low ECL intensity (curve a). After electrodepositing of AuNPs, a sharp increase of the ECL intensity was observed (curve b). Such improvement reflects that AuNPs can catalyze ECL of luminol. The ECL intensity further improved at AuNPs-EG/GCE

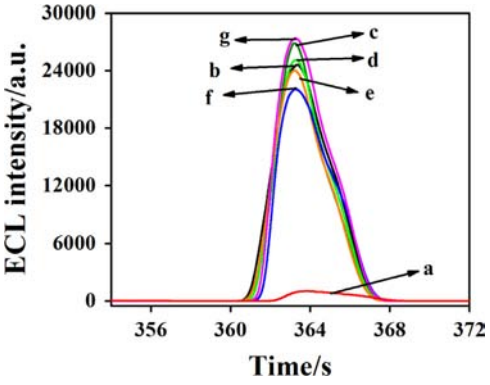


Fig. 3. ECL profiles of the stepwise modification. Bare GCE (a); AuNPs/GCE (b); AuNPs-EG/GCE (c); Apt1/AuNPs-EG/GCE (d); BSA/Apt1/AuNPs-EG/GCE (e); PDGF-BB/BSA/Apt1/AuNPs-EG/GCE (f); GOD–Apt2–AuNPs/PDGF-BB/BSA/Apt1/AuNPs-EG/GCE (g).

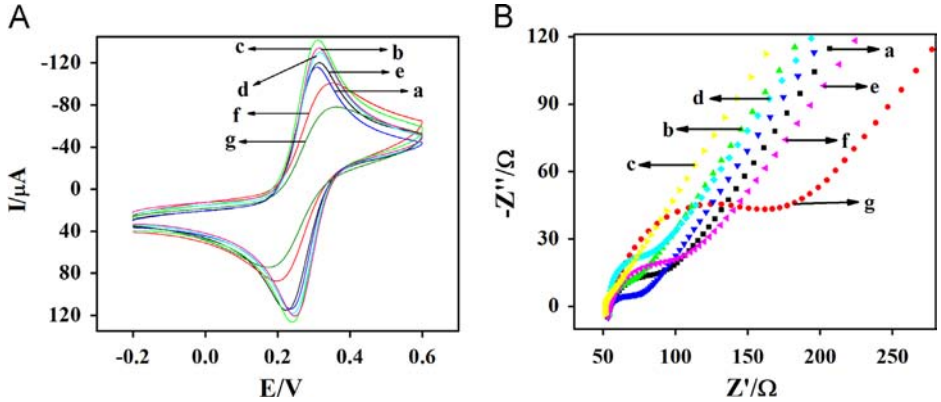


Fig. 2. CVs (A) and EISs (B) of electrodes at different stages in 5.0 mmol L^{-1} $K_3[Fe(CN)_6]/K_4[Fe(CN)_6]$ (1:1) containing 0.1 mol L^{-1} KCL. Bare GCE (a); AuNPs/GCE (b); AuNPs-EG/GCE (c); Apt1/AuNPs-EG/GCE (d); BSA/Apt1/AuNPs-EG/GCE (e); PDGF-BB/BSA/Apt1/AuNPs-EG/GCE (f); GOD–Apt2–AuNPs/PDGF-BB/BSA/Apt1/AuNPs-EG/GCE (g). $c_{PDGF-BB}$: 0.1 nmol L^{-1}.

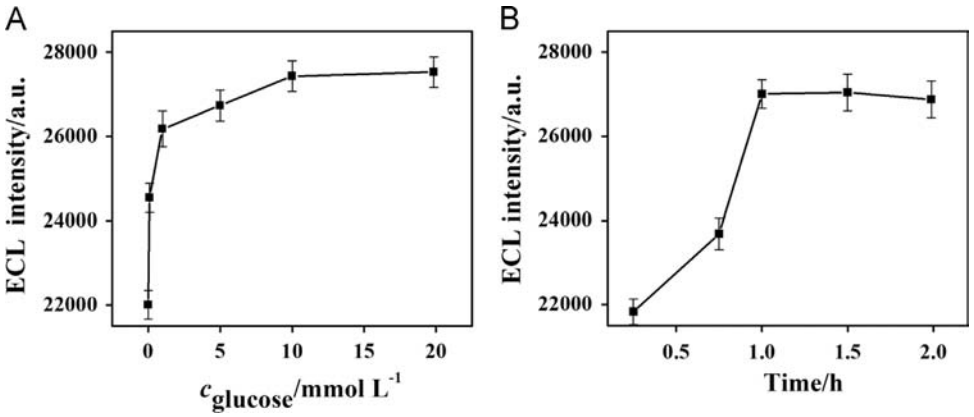


Fig. 4. Effect of the glucose concentration (A) and incubation time (B) on ECL response. Working solution: 0.1 mol L^{-1} pH 7.4 PBS containing 1.0×10^{-4} mol L^{-1} luminol and different concentrations of glucose, scan rate: 100 mV s^{-1}, scan range: −0.2–0.8 V.

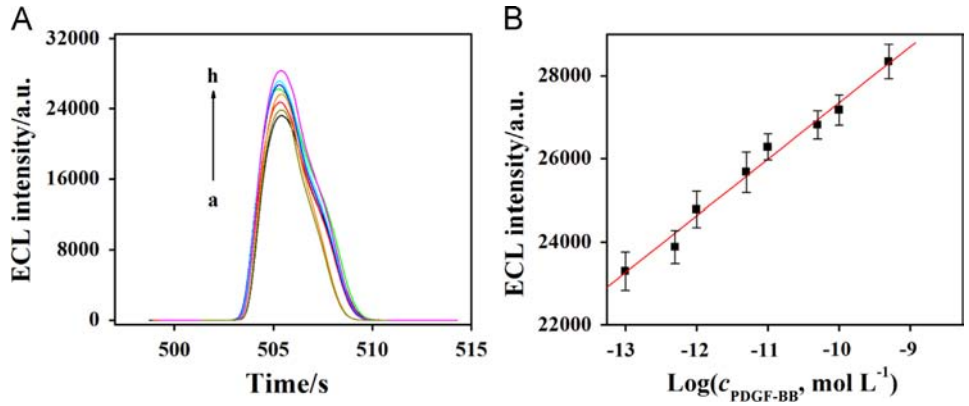


Fig. 5. ECL intensity–time curves of the aptasensor with different concentrations of PDGF-BB (A). The calibration plot against the corresponding log $c_{PDGF-BB}$ (B). Other conditions are as in Fig. 4.

(curve c), which is attributed to the AuNPs-EG nanocomposite films increased the surface area and electrical conductivity and facilitated the reduction of O_2 to generate $O_2^{\bullet -}$ in the solution dissolved with trace oxygen thus increase the ECL intensity. Then the ECL intensity dropped with the immobilization of Apt1 (curve d), blocking with BSA (curve e) and incubating with PDGF-BB (curve f) because of the formation of less conductive layers, which slowed down the electron transfer speed significantly and led to the decrease of ECL signal. However, when the GOD–Apt2–AuNPs bioconjugates were immobilized onto the modified electrode surface, an obvious enhancement of the ECL signal (curve g) appeared. The enhanced signal could be ascribed to the in situ generated H_2O_2 from reaction of GOD with glucose and the excellent catalytic behavior of AuNPs to the ECL emission of the luminol–H_2O_2 system.

3.3. Optimization of experimental conditions

The glucose concentration is an important factor for the ECL intensity. Fig. 4A displays the influence of the glucose concentration. With the increase of the glucose concentration, the ECL signal increased and then reached a plateau in 10 mmol L^{-1}. Hence, 10 mmol L^{-1} was selected. The effect of the incubation time of aptamer with PDGF-BB on the ECL signal was also investigated (Fig. 4B). The ECL emission was found to gradually increase with the increase of time and reach a constant value at 1 h. Therefore, 1 h was chosen.

3.4. Performance of the proposed ECL aptasensor

Fig. 5 depicts ECL signals of the aptasensor in response to PDGF-BB of varying concentrations under the optimal conditions. The calibration plot reveals that the ECL intensity of the aptasensor increases linearly with the logarithm of PDGF-BB concentration in the range of 1.0×10^{-13}–5.0×10^{-10} mol L^{-1}. The linear regression equation is I=40,959.0+1361.1 log$c$ with a correlation coefficient of R=0.9931. The detection limit was calculated to be 1.7×10^{-14} mol L^{-1} (S/N=3). Furthermore, the comparison of the proposed method with previous reports was listed in Table 1. Compared with other methods, the proposed ECL aptasensor exhibits high sensitivity and a wide linear range.

3.5. Specificity, reproducibility, and stability of the ECL aptasensor

Specificity is an important criterion for ECL aptasensor. To investigate the specificity of the aptasensor, some proteins such as human serum albumin (HSA), human immunoglobulin G (hIgG) and thrombin were used as the interferences to evaluate the specificity of the ECL aptasensor. The concentrations of the interfering substances were 0.6 mmol L^{-1}, 50 μmol L^{-1}, and 1.0 nmol L^{-1} respectively and the results are illustrated in Fig. 6A. In the absence of target protein, no apparent change of the ECL intensity was observed compared with that of the testing blank solution. Furthermore, the ECL signals of the mixture samples containing 0.01 nmol L^{-1} PDGF-BB, 0.6 mmol L^{-1} HSA, 50 μmol L^{-1} hIgG, and 1.0 nmol L^{-1} thrombin presented neglectable changes compared with that of the determination of 0.01 nmol L^{-1} PDGF-BB only. These results clearly indicated that the as-constructed sensor had an excellent sensing specificity

Table 1
Comparison of different methods for PDGF-BB detection.

Analytical methods	Linear range (nmol L^{-1})	Detection limit (nmol L^{-1})	References
Sandwich-type colorimetric aptasensor	10–100	6	[13]
Sandwich-type ECL aptasensor	0.00001–0.1	0.0000011	[15]
Fluorescence aptasensor	1–50	0.37	[35]
Chemiluminescence aptasensor	0.0001–1.0	0.0001	[14]
Sandwich-type electrochemical aptasensor	0.01–35	0.008	[10]
ECL aptasensor	0.001–10	0.001	[17]
Sandwich-type ECL aptasensor	0.0001–0.5	0.000017	This work

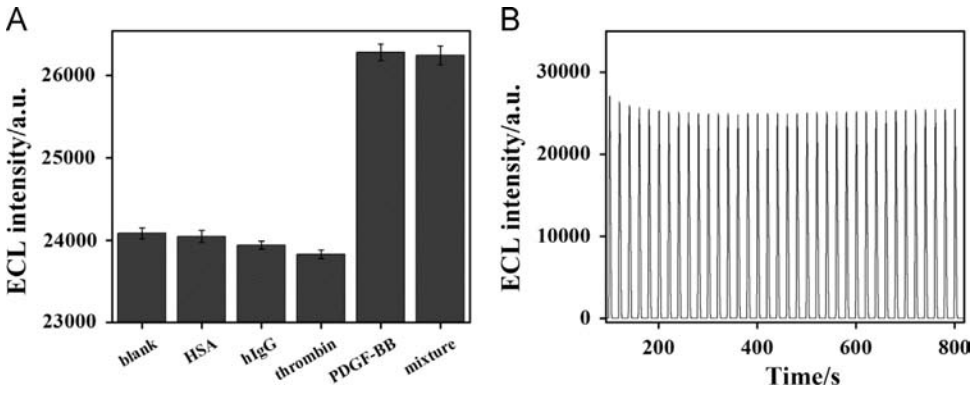


Fig. 6. The specificity of the ECL aptasensor towards different targets (A). c_{HSA}: 0.6 mmol L^{-1}, c_{hIgG}: 50 μmol L^{-1}, $c_{thrombin}$: 1.0 nmol L^{-1}, $c_{PDGF-BB}$: 0.01 nmol L^{-1}. The stability of the ECL aptasensor under consecutive cyclic potential scans for 36 cycles (B). $c_{PDGF-BB}$: 1.0 pmol L^{-1}.

Table 2
Analytical results of human serum and urine samples ($n=3$).

Type of samples	No. of samples	PDGF-BB in patients (pmol L^{-1})	RSDs (%, $n=3$)	No. of samples	PDGF-BB in healthy people (pmol L^{-1})	RSDs (%, $n=3$)
Human serum	1	6.31	3.2	7	0.14	3.6
	2	6.76	4.1	8	–	–
	3	5.0	5.2	9	–	–
Human urine	4	46.2	4.9	10	0.43	3.4
	5	52.8	3.7	11	0.31	2.9
	6	11.5	5.3	12	0.12	5.7

-: not detected

Table 3
Recovery of PDGF-BB in human serum and urine samples.

Samples	Found	Added	Total found	Recovery
	(pmol L^{-1})	(pmol L^{-1})	(pmol L^{-1})	(%)
Human serum	5.0	1.0	5.9	90.0
		10.0	15.2	102
		100.0	94.7	89.7
Human urine	52.8	1.0	53.9	110
		10.0	61.3	85.0
		100.0	143.9	91.1

and was feasible for the determination of PDGF-BB in complex samples.

The reproducibility of the aptasensor was investigated. The inter-assay precision of the aptasensor was evaluated with the application of five electrodes. The relative standard deviation (RSD) is less than 5.0%. The stability of the ECL aptasensor was also recorded and the results are presented in Fig. 6B. Under consecutive cyclic potential scans for 36 cycles, the RSD for the change of the ECL signal is less than 1.0%, manifesting that the sensor had good stability.

3.6. Analytical application

It has been reported that PDGF might play a very important role in the initiation and progression of DN [1]. Determination of PDGF-BB in human body fluid could be used for early diagnosis of diabetic renal dysfunction. To demonstrate the applicability of the proposed method, the contents of PDGF-BB in human urine and human serum samples collected from DN patients and healthy people at Xinyang Central Hospital (Xinyang, China) were determined and the results are listed in Table 2. The results show that the value of DN in six patients (5.0–6.76 pmol L^{-1} for human serum, 11.5–52.8 pmol L^{-1} for human urine) is much higher than that in six healthy persons (0.14 pmol L^{-1} for human serum, ;0.12–0.43 pmol L^{-1} for human urine). The recovery of the aptasensor was also estimated by standard addition method (Table 3). Three different concentrations of PDGF-BB (1.0, 10, and 100 pmol L^{-1}) were added into human serum and urine samples with recoveries from 89.7–102% for human serum sample and 85.0–110% for human urine sample, respectively.

4. Conclusions

The work reported here develops a novel sandwich-type luminol ECL aptasensor for PDGF-BB detection based on in situ generated H_2O_2 as coreactant with GOD anchored AuNPs labeling. The high sensitivity and wide linear range obtained should be taken into account for the following reasons: (1) the hierarchical assembly of AuNPs-EG composite films and aptamer functionalization on the GCE surface provide not only a highly conductive and biocompatible electrode interface for ECL sensing but also an analog of extracellular matrix for the specific target recognition and adhesion; (2) AuNPs acted as an versatile platform not only to provide biocompatible surface area for the immobilization of abundant GOD and Apt2, but also to catalyze the ECL reaction of the luminol–H_2O_2 system; (3) amplified ECL of luminol response was obtained by in situ production of H_2O_2 with GOD as coreactant and the catalysis of AuNPs. The applicability of the aptasensor was successfully demonstrated in the determination of PDGF-BB in human serum and human urine samples. With high sensitivity, good selectivity and stability, the as-proposed ECL aptasensor provided great potential in biochemical analysis.

Acknowledgment

This work was supported by the National Natural Science Foundation of China (Grant 21375114, U1304214), the Project of Science and Technology Development of Henan Province (142300410197) and the Foundation of Henan Educational Committee (14A150013).

References

[1] Q.Y. Wang, Q.H. Guan, F.Q. Chen, Diabetes Res. Clin. Pract. 85 (2009) 166–170.
[2] N. Kohler, A. Lipton, Exp. Cell Res. 87 (1974) 297–301.
[3] H.Q. Zhang, X.F. Li, X.C. Le, Anal. Chem. 81 (2009) 7795–7800.
[4] X.H. Yang, S. Sun, P. Liu, K.M. Wang, Q. Wang, J.B. Liu, J. Huang, L.L. He, Chin. Chem. Lett. 25 (2014) 9–14.
[5] G.F. Pierce, J.E. Tarpley, J. Tseng, J. Bready, D. Chang, W.C. Kenney, R. Rudolph, M.C. Robson, J.V. Berg, P. Reid, J. Clin. Investig. 96 (1995) 1336–1350.
[6] X. Fang, Z. Cao, T. Beck, W. Tan, Anal. Chem. 73 (2001) 5752–5757.
[7] C. Huang, Y. Huang, Z. Cao, W. Tan, H. Chang, Anal. Chem. 77 (2005) 5735–5741.
[8] X.Y. Wang, A. Gao, C.C. Lu, X.W. He, X.B. Yin, Biosens. Bioelectron. 48 (2013) 120–125.
[9] Y.H. Wang, L. Bao, Z.H. Liu, D.W. Pang, Anal. Chem. 83 (2011) 8130–8137.
[10] L.J. Bai, R. Yuan, Y.Q. Chai, Y. Zhuo, Y.L. Yuan, Y. Wang, Biomaterials 33 (2012) 1090–1096.
[11] X. Jin, J.J. Zhao, L.L. Zhang, Y. Huang, S.L. Zhao, RSC Adv. 4 (2014) 6850–6853.
[12] J.F. Liang, R. Wei, S. He, Y.K. Liu, L. Guo, L.D. Li, Analyst 138 (2013) 1726–1732.
[13] C.C. Chang, S.C. Wei, T.H. Wu, C.H. Lee, C.W. Lin, Biosens. Bioelectron. 42 (2013) 119–123.
[14] Y.H. Sun, S. Cai, C.W. Lau, J.H. Zhu, J.Z. Lu, Proced. Eng. 25 (2011) 1565–1568.
[15] Y.M. Liu, M. Zhou, Y.Y. Liu, G.F. Shi, J.J. Zhang, J.T. Cao, K.J. Huang, Y.H. Chen, RSC Adv. 4 (2014) 22888–22893.
[16] X.B. Yin, Y.Y. Xin, Y. Zhao, Anal. Chem. 81 (2009) 9299–9305.
[17] D.B. Zhu, X.M. Zhou, D. Xing, Anal. Chim. Acta 725 (2012) 39–43.
[18] W. Qin, Z.J. Zhang, H.J. Liu, Anal. Chem. 70 (1998) 3579–3584.
[19] K.C. Lin, S.M. Chen, J. Electroanal. Chem. 589 (2006) 52–59.
[20] H. Dai, Y.W. Chi, X.P. Wu, Y.M. Wang, M.D. Wei, G.N. Chen, Biosens. Bioelectron. 25 (2010) 1414–1419.
[21] X. Cai, J.L. Yan, H.H. Chu, M.S. Wu, Y.F. Tu, Sens. Actuators B: Chem. 143 (2010) 655–659.
[22] Z.Y. Lin, J.H. Chen, G.N. Chen, Electrochim. Acta 53 (2008) 2396–2401.
[23] Y.M. Liu, M. Zhou, Y.Y. Liu, K.J. Huang, J.T. Cao, J.J. Zhang, G.F. Shi, Y.H. Chen, Anal. Methods 6 (2014) 4152–4157.
[24] Y.M. Liu, J.J. Zhang, G.F. Shi, M. Zhou, Y.Y. Liu, K.J. Huang, Y.H. Chen, Electrochim. Acta 129 (2014) 222–228.
[25] B. Kavosi, R. Hallaj, H. Teymourian, A. Salimi, Biosens. Bioelectron. 59 (2014) 389–396.
[26] B. Rezaei, M.K. Boroujeni, Ali A. Ensafi, Electrochim. Acta 123 (2014) 332–339.
[27] Y.L. Cao, R. Yuan, Y.Q. Chai, H.J. Liu, Y.H. Liao, Y. Zhuo, Talanta 113 (2013) 106–112.
[28] B. Ipe, K. Yoosaf, K.G. Thomas, J. Am. Chem. Soc. 128 (2006) 1907–1913.
[29] N.R. Jana, J.Y. Ying, Adv. Mater 20 (2008) 430–434.
[30] G. Frens, Nat. Phys. Sci. 241 (1973) 20–22.
[31] T.T. Zheng, T.T. Tan, Q.F. Zhang, J.J. Fu, J.J. Wu, K. Zhang, J.J. Zhu, H. Wang, Nanoscale 5 (2013) 10360–10368.
[32] Y.M. Liu, Y.Y. Liu, M. Zhou, K.J. Huang, J.T. Cao, H. Wang, Y.H. Chen, J. Chromatogr. A 1340 (2014) 128–133.
[33] S.F. Li, X.M. Zhang, W.X. Du, Y.H. Ni, X.W. Wei, J. Phys. Chem. C 113 (2009) 1046–1051.
[34] X.J. Jiang, Y.Q. Chai, H.J. Wang, R. Yuan, Biosens. Bioelectron. 54 (2014) 20–26.
[35] J.J. Liu, X.R. Song, Y.W. Wang, A.X. Zheng, G.N. Chen, H.H. Yang, Anal. Chim. Acta 749 (2012) 70–74.

Talanta 132 (2015) 72–76

Contents lists available at ScienceDirect

Talanta

journal homepage: www.elsevier.com/locate/talanta

A fluorescence turn-on detection of copper(II) based on the template-dependent click ligation of oligonucleotides

Fangyuan Wang [a,b], Yongxin Li [a], Wenying Li [a,b], Jian Chen [a], Qingfeng Zhang [a,b], Sohail Anjum Shahzad [a,c], Cong Yu [a,b,*]

[a] State Key Laboratory of Electroanalytical Chemistry, Changchun Institute of Applied Chemistry, Chinese Academy of Sciences, Changchun 130022, PR China
[b] University of Chinese Academy of Sciences, Beijing 100049, PR China
[c] Department of Chemistry, COMSATS Institute of Information Technology, Abbottabad 22060, Pakistan

ARTICLE INFO

Article history:
Received 13 June 2014
Received in revised form
22 August 2014
Accepted 27 August 2014
Available online 6 September 2014

Keywords:
Copper
Click chemistry
Fluorescence
Molecular beacon

ABSTRACT

In this work, a fluorescence turn-on method for copper(II) detection is reported. A molecular beacon (MB) was designed as a template. Cu^{2+} was reduced to Cu^{+} in the presence of a reductant (ascorbic acid). Two short single-stranded oligonucleotides one was labeled with a 5′-alkyne and the other with 3′-azide group, proceeded a template-dependent chemical ligation through the Cu(I)-catalyzed azide-alkyne cycloaddition. The newly generated click-ligated long chain oligonucleotide, which was complementary to the MB, opened the MB hairpin structure and resulted in a turn on fluorescence. The increase in fluorescence intensity is directly proportional to the amount of Cu^{2+} added to the assay solution. The present assay is quite sensitive and allows the detection of 2 nM Cu^{2+}. The described assay also exhibits high selectivity over other metal ions.

© 2014 Elsevier B.V. All rights reserved.

1. Introduction

Copper is one of the most abundant transition metals in the human body and is essential for human health [1]. Copper plays important biological roles as enzyme cofactors and as structural components of proteins [1–3]. The lack of copper in the human body may cause copper deficiency diseases, such as coeliac disease and anaemia [4]. However, high concentration of copper is also harmful to the human body, which may cause gastrointestinal disturbance [5], liver or kidney damage [6,7], and various neurological diseases, such as Alzheimer's disease and Parkinson's disease [8,9]. In recent years, continuous release of copper(II) into environmental water has been witnessed due to its extensive use in industry [5]. Therefore, selective and sensitive detection of copper(II) is of great importance.

Great efforts have been made for the development of techniques for selective copper(II) sensing. They include absorption spectrometry [10], atomic absorption spectrometry [11], inductively coupled plasma atomic emission spectroscopy [12], inductively coupled plasma mass spectrometry [13], and various electrochemical [14,15], colorimetric [16–19], and fluorescent methods [20–23]. Fluorescent methods have attracted more and more attentions because of their high sensitivity, simple operation, good reproducibility, and low-cost. Although a number of fluorescent sensors for copper(II) detection have been reported, simple, sensitive and selective methods without the use of harmful substances are still highly demanded.

The Cu(I)-catalyzed azide-alkyne cycloaddition (CuAAC) reaction reported by Sharpless [24] has emerged as one of the most prominent click chemistry reactions. And it has been used as a versatile, highly efficient and selective chemical tool in many fields [25,26]. It also possesses characters of high-speed and simplicity under mild conditions which earned its name "click reaction" [27]. A trace amount of Cu(I) could catalyze the Huisgen 1,3-dipolar cycloaddition reaction between an alkyne and an azide to form a 1,2,3-triazole [25], and the overall percentage of conversion is related to the amount of Cu(I) added to the reaction mixture. Based on the reduction reaction of Cu(II) to Cu(I) in the presence of a reductant, a number of methods for copper(II) sensing were proposed [28–34]. Recently, a few copper(II) sensors based on template-dependent oligonucleotide ligation were developed [35–39]. It has been shown that the CuAAC driven click reaction enables the ligation of oligonucleotides without any biological enzymes and it shows good biocompatibility [40–44]. However, these methods require the use of additional signaling unit, such as gold nanoparticles, graphene or organic dye, thus the reaction could not be monitored in a real-time fashion, and some used fluorescent turn-off sensing strategy which may increase the possibility of false positive signals [36–39].

Molecular beacon (MB) was originally designed for the sensing of oligonucleotides, nucleic acid point mutations, RNA targets in vivo, and for monitoring PCR reactions in real time [45].

* Corresponding author at: State Key Laboratory of Electroanalytical Chemistry, Changchun Institute of Applied Chemistry, Chinese Academy of Sciences, Changchun 130022, PR China. Fax: +86 -431 85262710.
E-mail address: congyu@ciac.ac.cn (C. Yu).

http://dx.doi.org/10.1016/j.talanta.2014.08.064
0039-9140/© 2014 Elsevier B.V. All rights reserved.

The method shows high sensitivity and selectivity. Since its first report, MB has also been used for the development of a number of novel fluorescence turn-on assays for the sensing of nucleic acid binding protein, gene expression in living cells, enzyme activity, and many aptamer targeted proteins and small biomolecules, etc [46–51].

Herein, we describe a novel fluorescence turn-on strategy for copper(II) detection based on the template-dependent click ligation (Scheme 1). In the present method, a rationally designed MB (Oligo-MB) was adopted as a template. Two short oligonucleotides (Oligo-A and Oligo-B) labeled with a 5′-alkyne and a 3′-azide groups, respectively, were used. Oligo-A and Oligo-B could hybridize to the complementary sequences of the Oligo-MB, which brought the azide and the alkyne functional groups closer to each other. In the presence of Cu^{2+} and ascorbic acid, Cu^{2+} was reduced to Cu^{+}, and the two short oligonucleotides were ligated by the formation of a triazole linkage. The Cu(I) catalyzed click reaction between the azide and the alkyne functional groups resulted in the connection of Oligo-A and Oligo-B. The newly formed long chain oligonucleotide (Oligo-A-B) opened the Oligo-MB hairpin structure and turn on fluorescence was therefore observed. The increase in intensity could be directly related to the amount of Cu(II) added to the assay solution. Our Cu^{2+} detection method is sensitive, selective, simple, and inexpensive.

2. Experimental section

2.1. Materials

The oligonucleotides (Oligo-A, Oligo-B and Oligo-MB) and L-ascorbic acid were obtained from Sangon Biotechnology Co., Ltd. (Shanghai, China). Cupric sulfate pentahydrate ($CuSO_4 \cdot 5H_2O$) were purchased from Sinopharm Chemical Reagent Co., Ltd. (Beijing, China). All other chemicals were of analytical reagent grade and used without further purification. The ultra pure water used in all experiments was obtained with a Milli-Q system (Millipore, MA, USA).

2.2. Instrumentation

Fluorescence measurements were performed using a Fluoromax-4 spectrofluorometer (Horiba Jobin Yvon Inc., USA). Sample solutions were excited at 480 nm and the fluorescence emission spectra were recorded with slits for excitation and emission both of 5 nm. The quantification of nucleic acids was carried out via UV–vis absorption recorded on a Cary 50 Bio Spectrophotometer (Varian Inc., CA, USA). A PB-10 pH meter (Sartorius Scientific Instrument Co., Ltd. Beijing) was used to adjust the pH value of all buffer solutions.

2.3. Assay procedures

Oligonucleotide stock solutions were prepared with Tris–HCl buffer (20 mM, pH 7.4) and stored at 4 °C. Prior to the addition of different concentrations of Cu^{2+} at room temperature, the oligonucleotides and ascorbic acid were mixed and stored at 4 °C for 10 min. The assay solutions were incubated at 25 °C for an appropriate period of time before the fluorescence measurement. The final concentrations of Oligo-A, Oligo-B and Oligo-MB were 30 nM, 30 nM and 10 nM, respectively.

2.4. Lake water sample analysis

Lake water samples were acquired from the South Lake of Changchun, Jilin province, China. The samples were first centrifuged at 12,000 rpm for 10 min and filtered through a nitrocellulose filter (0.45 μm) to get rid of the insoluble materials. 100 μL lake water sample was added into the assay solution for the quantitative analysis (final sample volume: 400 μL). Known quantities of Cu^{2+} were added to the assay solutions and their recoveries were determined. The experiments were repeated three times and the average recovery values were obtained.

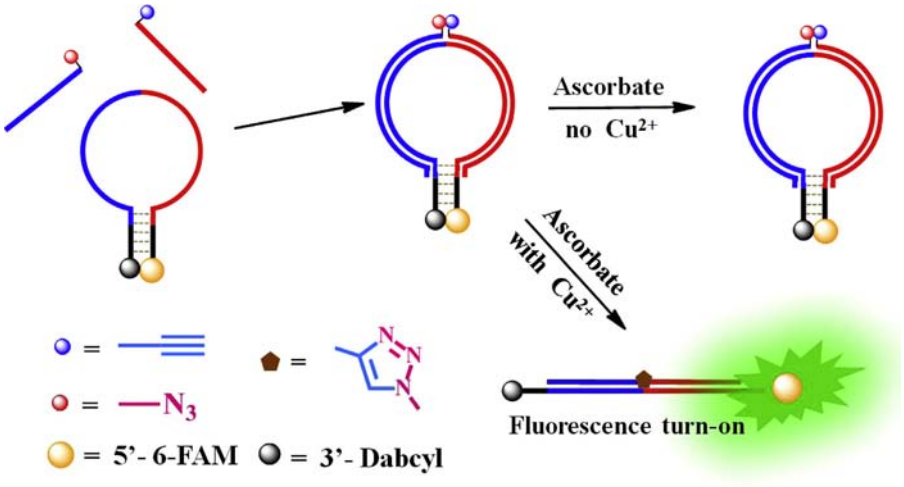
3. Results and discussion

3.1. The assay strategy

The sequences of the oligonucleotides for Cu^{2+} detection were carefully selected (Table 1). Oligo-MB with a fluorophore and a quencher at its termini was selected as a template. It was designed to be a stable hairpin structure at an ambient temperature. When Oligo-MB was in its hairpin state, the fluorophore and the quencher interacted with each other and the fluorescence of the

Table 1
The oligonucleotides employed in the current investigation.

	Oligonucleotide sequence (5′→3′)
Oligo-A	alkyne-GAA ACT GAT AG
Oligo-B	CTA AAT TCC AA-azide
Oligo-MB	FAM-TCG CTA TCA GTT TCT TGG AAT TTA GCG A-Dabcyl
Oligo-A-B	CTA AAT TCC AA-ligated-G AAA CTG ATA G



Scheme 1. Schematic representation of the copper(II) sensing strategy.

fluorophore was quenched [45]. Oligo-A and Oligo-B (each of 11 nt long) were complementary to Oligo-MB and could bind to Oligo-MB. Since they were relatively short oligonucleotides, their binding could not open the MB hairpin structure. However, their binding allowed to bring azide and alkyne groups labeled on Oligo-A and Oligo-B, respectively, more closer to each other, which effectively increased the local molarity of the reaction groups. The close proximity of Oligo-A and Oilgo-B and subsequently increase in local molarity enhanced the rate of click reaction. The newly formed longer Oligo-A-B through efficient click reaction could easily open the Oligo-MB hairpin structure and a turn on fluorescence was observed.

3.2. Feasibility of the assay

The melting temperature of Oligo-A and Oligo-B was approximately 23–24 °C. Oligo-MB has a melting temperature of 43 °C (Fig. 1). When the oligonucleotides were mixed and incubated for 120 min, the fluorescence intensity of the assay mixture did not increase. The results suggest that Oligo-A and Oligo-B could not open the Oligo-MB hairpin structure. However, when 50 nM Cu^{2+} was introduced, Cu^{2+} was reduced to Cu^{+}. Click reaction-assisted formation of Oligo-A-B stimulated the unfolding of Oligo-MB and subsequent gradual increase in the fluorescence intensity was observed with the prolonged reaction time, and the fluorescence intensity reached a plateau after about 120 min of reaction (Fig. 2). The results clearly demonstrate that our strategy for Cu^{2+} sensing is valid.

3.3. Optimization of assay conditions

To achieve the best sensing performance, important experimental conditions were optimized. In order to investigate the temperature effect on assay solution, we used various temperatures to probe the sensing performance as shown in Fig. 3. There was a rapid increase in the emission intensity as the solution temperature raised from 10 °C to 25 °C. It seems that the ligation efficiency increased at a higher temperature. However, if the assay temperature was higher than 30 °C, considerable amounts of Oligo-A and Oligo-B would dissociate from Oligo-MB which resulted in decreased ligation efficiency. Therefore, 25 °C was chosen as the reaction temperature in the following experiments. The concentration of ascorbic acid added to the assay solution was also optimized. We have experimented various concentrations of ascorbic acid as shown in Fig. 4. It was found that 500 μM ascorbic acid gave the best sensing performance. The assay buffer pH was selected at 7.4 since it was reported that at acidic pH values, the Cu^{+} catalytic activity may be reduced because of the disproportion reaction [36,39].

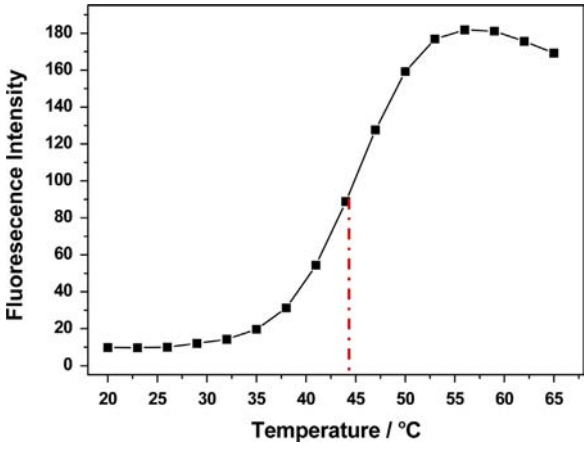


Fig. 1. Melting temperature determination of Oligo-MB in 20 mM Tris–HCl (pH 7.4). The solution was equilibrated for 5 min prior to the fluorescence measurement. Data points were taken at 3 °C intervals. Fluorescence intensity changes were recorded at 514 nm.

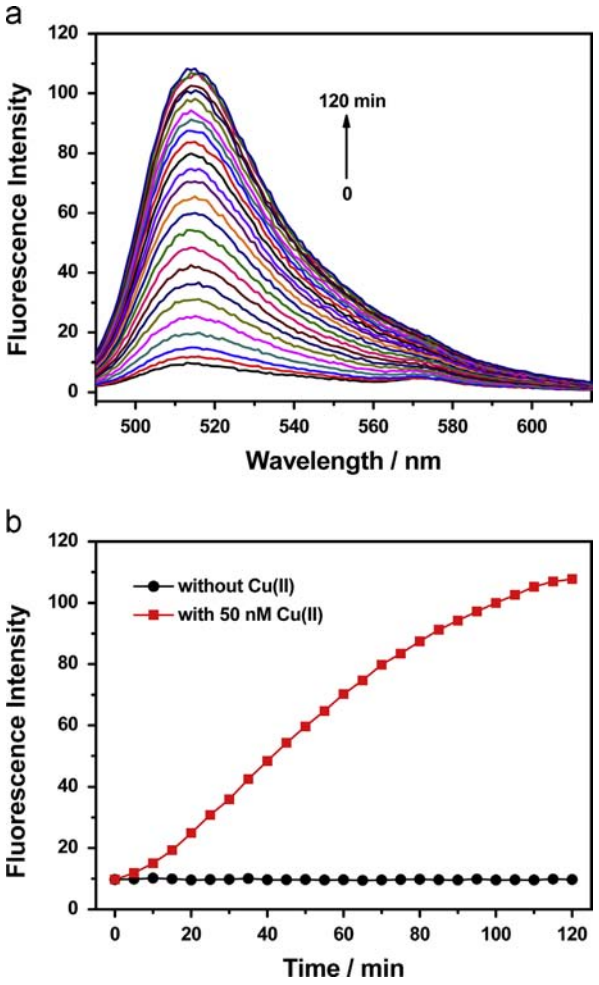


Fig. 2. (a) Oligo-MB emission spectral changes with reaction time; (b) changes in fluorescence intensity with reaction time with (red) and without (black) the addition of Cu^{2+}. The concentrations of ascorbic acid and Cu^{2+} were 500 μM and 50 nM, respectively. Buffer: 20 mM Tris–HCl (pH 7.4). The emission intensity was recorded at 514 nm at 25 °C. (For interpretation of the references to color in this figure legend, the reader is referred to the web version of this article.)

3.4. Sensitivity of the assay

Under the optimized conditions, we tested the sensitivity of the assay by adding different concentrations of Cu^{2+}. Fig. 5 shows gradual increase in the fluorescence intensity with the increasing concentration of Cu^{2+} from 0 nM to 50 nM, and the fluorescence intensity reached a plateau at about 50 nM Cu^{2+}. The linear detection range is 2–40 nM, and the linear calibration curve is: $I=2.73C+9.77$ (I and C refer to the fluorescence intensity and the concentration of Cu^{2+} in nM, respectively). The method is highly sensitive, 2 nM Cu^{2+} could be easily detected [16–23,35–39], which is much lower than the maximum allowed level of Cu^{2+} (20 μM, 1.3 ppm) in drinking water defined by the United States Environmental Protection Agency.

3.5. Selectivity of the assay

To evaluate the selectivity of the assay, other common metal ions including Ba^{2+}, Mg^{2+}, Ni^{2+}, Co^{2+}, Fe^{2+}, Cd^{2+}, Ca^{2+}, Zn^{2+},

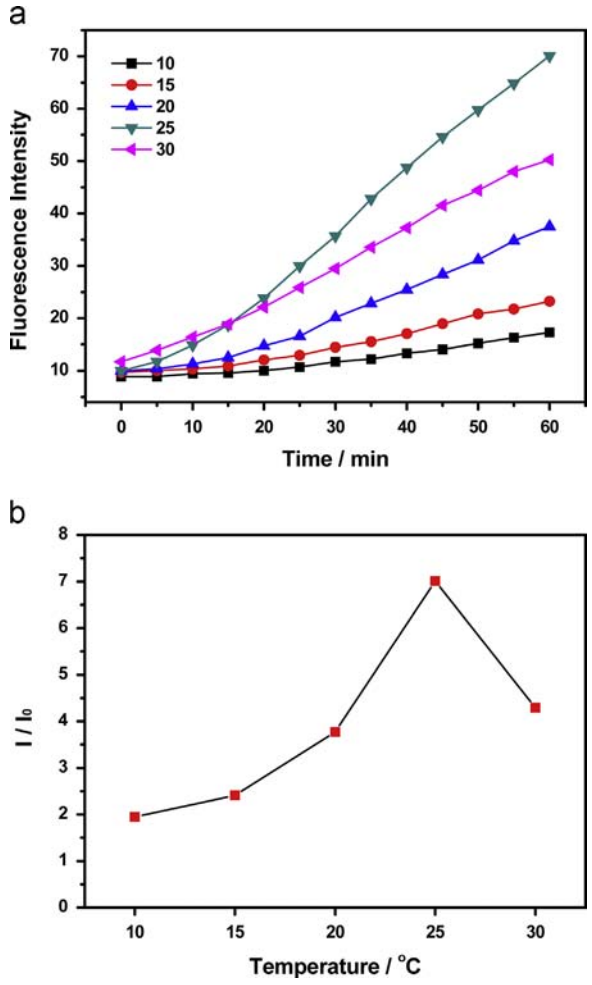


Fig. 3. (a) Fluorescence intensity changes with reaction time at different reaction temperatures. (b) Enhancement of fluorescence intensity after 60 min of reaction at different temperatures. The concentrations of ascorbic acid and Cu^{2+} were 500 μM and 50 nM, respectively. Buffer: 20 mM Tris–HCl (pH 7.4). Emission intensity was recorded at 514 nm.

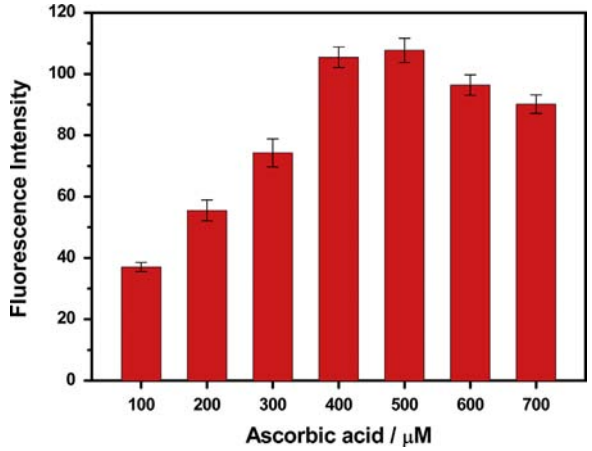


Fig. 4. Effect of the concentration of ascorbic acid on the performance of the assay. All the solutions were incubated with 50 nM Cu^{2+} at 25 °C for 120 min in 20 mM Tris–HCl (pH 7.4). The experiments were repeated three times and the average intensity values were given.

Mn^{2+}, Hg^{2+}, Pb^{2+}, Li^{+}, Na^{+}, K^{+}, and Ag^{+} were tested. As shown in Fig. 6, the results indicate that the proposed method is highly selective for Cu^{2+}. None of these metal ions interfered with the assay, even at much higher concentrations (50 μM).

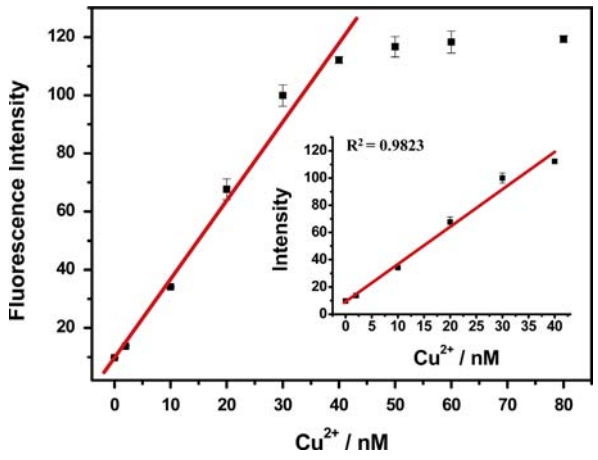


Fig. 5. Changes in emission intensity with Cu^{2+} concentration (0, 2 nM, 10 nM, 20 nM, 30 nM, 40 nM, 50 nM, 60 nM, 80 nM). The solutions were incubated at 25 °C for 120 min in 20 mM Tris–HCl (pH 7.4). The concentration of ascorbic acid was 500 μM. The experiments were repeated three times and the average intensity values were given.

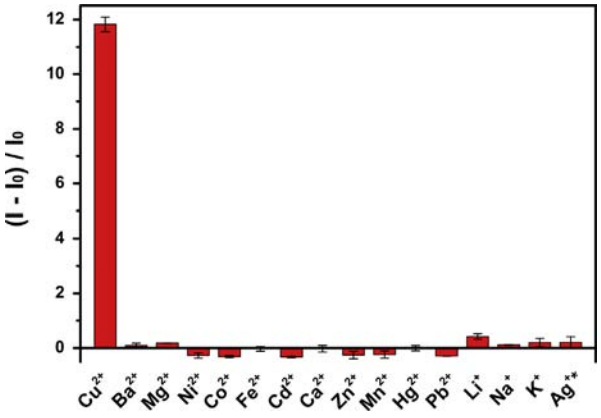


Fig. 6. Selectivity of the assay. The concentration of Cu^{2+} was 50 nM and the concentrations of the other metal ions (Ba^{2+}, Mg^{2+}, Ni^{2+}, Co^{2+}, Fe^{2+}, Cd^{2+}, Ca^{2+}, Zn^{2+}, Mn^{2+}, Hg^{2+}, Pb^{2+}, Li^{+}, Na^{+}, K^{+}, Ag^{+}) were 50 μM each. The experiments were repeated three times and the average intensity values were given. *Ag^{+} formed precipitate with Cl^{-} which was removed by centrifugation prior to analysis. If the precipitate was not removed, it caused slight interference with the assay.

Table 2
Copper(II) recovery in lake water samples.

Samples	Added (nM)	Found (nM)	Recovery (%)	RSD[a] (%, $n=3$)
1	20.0	20.6 ± 0.6	103.0	2.9
2	40.0	39.5 ± 0.9	98.8	2.3

[a] RSD: relative standard deviation.

3.6. Cu^{2+} assay in environmental water samples

To demonstrate the potential practical application of the assay for real sample analysis, lake water samples were tested. The water samples were acquired from the South Lake of Changchun (Jilin province). The samples were first centrifuged at 12,000 rpm for 10 min and filtered through a nitrocellulose filter (0.45 μm) to get rid of the insoluble materials. Recovery experiments were carried out. Different concentrations of Cu^{2+} (20 nM, 40 nM) were added to the assay solutions, and satisfactory recovery values were obtained. The results clearly show that our method could be used for the detection of Cu^{2+} in complex sample mixtures (Table 2).

4. Conclusions

In conclusion, a copper(II) ion sensing method with high selectivity and sensitivity has been developed. The concentration of Cu^{2+} in an aqueous buffer solution could be determined by the molecular beacon fluorescence recovery assay. 2 nM Cu^{2+} could be easily detected, and a linear response range of 2–40 nM Cu^{2+} was obtained. The fluorescent turn-on Cu^{2+} sensing strategy would reduce the possibility of false positive caused by the turn-off mode. And it could also be used for the analysis of environmental water samples. The method is simple, sensitive and selective, and it could potentially be used for the analysis of real biological samples because of the good biocompatibility and low toxicity.

Acknowledgments

This work was supported by the National Natural Science Foundation of China (21275139), the National Basic Research Program of China (973 Program, Grant 2011CB911002), and the Open Project of the State Key Laboratory of Supramolecular Structure and Materials (Grant No. SKLSSM201415).

References

[1] E.L. Que, D.W. Domaille, C.J. Chang, Chem. Rev. 108 (2008) 1517–1549.
[2] B.-E. Kim, T. Nevitt, D.J. Thiele, Nat. Chem. Biol. 4 (2008) 176–185.
[3] A.K. Boal, A.C. Rosenzweig, Chem. Rev. 109 (2009) 4760–4779.
[4] M. Bonham, J.M. O'Connor, B.M. Hannigan, J.J. Strain, Br. J. Nutr. 87 (2002) 393–403.
[5] P.G. Georgopoulos, A. Roy, M.J. Yonone-Lioy, R.E. Opiekun, P.J. Lioy, J. Toxicol. Environ. Health Part B 4 (2001) 341–394.
[6] S.H. Hahn, M.S. Tanner, D.M. Danke, W.A. Gahl, Biochem. Mol. Med. 54 (1995) 142–145.
[7] B.P. Zietz, J.D. de Vergara, H. Dunkelberg, Environ. Res. 92 (2003) 129–138.
[8] D.R. Brown, H. Kozlowski, Dalton Trans. 13 (2004) 1907–1917.
[9] K.J. Barnham, A.I. Bush, Curr. Opin. Chem. Biol. 12 (2008) 222–228.
[10] M.R. Callahan, J.B. Rose, R.H. Byrne, Talanta 58 (2002) 891–898.
[11] J.R. Chen, K.C. Teo, Anal. Chim. Acta 450 (2001) 215–222.
[12] O. Abollino, M. Aceto, M.C. Bruzzoniti, E. Mentasti, C. Sarzanini, Anal. Chim. Acta 375 (1998) 299–306.
[13] A.T. Townsend, K.A. Miller, S. McLean, S. Aldous, J. Anal. At. Spectrom. 13 (1998) 1213–1219.
[14] W. Yantasee, K. Hongsirikarn, C.L. Warner, D. Choi, T. Sangvanich, M.B. Toloczko, M.G. Warner, G.E. Fryxell, R.S. Addleman, C. Timchalk, Analyst 133 (2008) 348–355.
[15] S.Y. Qiu, L.D. Xie, S. Gao, Q.D. Liu, Z.Y. Lin, B. Qiu, G.N. Chen, Anal. Chim. Acta 707 (2011) 57–61.
[16] Z.Y. Yao, B.H. Huang, X.P. Hu, L. Zhang, D.P. Li, M. Guo, X.H. Zhang, H. Yuan, H.-C. Wu, Analyst 138 (2013) 1649–1652.
[17] Q.L. Xu, K.M. Lee, F. Wang, J. Yoon, J. Mater. Chem. 21 (2011) 15214–15217.
[18] C.-H. Lu, Y.-W. Wang, S.-L. Ye, G.-N. Chen, H.-H. Yang, NPG Asia Mater 4 (2012) 1884–4057.
[19] X.R He, H.B. Liu, Y.L. Li, S. Wang, Y.J. Li, N. Wang, J.C. Xiao, X.H. Xu, D.B. Zhu, Adv. Mater. 17 (2005) 2811–2815.
[20] J.H. Huang, Q.B. Zheng, J.-K. Kim, Z.G. Li, Biosens. Bioelectron. 43 (2013) 379–383.
[21] J.W. Liu, Y Lu, J. Am. Chem. Soc. 129 (2007) 9838–9839.
[22] H.X. Qin, J.T. Ren, J.H. Wang, E.K. Wang, Chem. Commun. 46 (2010) 7385–7387.
[23] A.W. Zhu, Q. Qu, X.L. Shao, B. Kong, Y. Tian, Angew. Chem. Int. Ed. 51 (2012) 7185–7189.
[24] H.C. Kolb, M.G. Finn, K.B. Sharpless, Angew. Chem. Int. Ed. 40 (2001) 2004–2021.
[25] M. Meldal, C.W. Tornøe, Chem. Rev. 108 (2008) 2952–3015.
[26] F. Amblard, J.H. Cho, R.F. Schinazi, Chem. Rev. 109 (2009) 4207–4220.
[27] T. Efthymiou, W. Gong, J.-P. Desaulniers, Molecules 17 (2012) 12665–12703.
[28] Y. Zhou, S.X. Wang, K. Zhang, X.Y. Jiang, Angew. Chem. Int. Ed. 47 (2008) 7454–7456.
[29] C. Hua, W.H. Zhang, S.R.M. De Almeida, S. Ciampi, D. Gloria, G.Z. Liu, J.B. Harper, J.J. Gooding, Analyst 137 (2012) 82–86.
[30] S. Park, H.-J. Kim, Tetrahedron Lett. 53 (2012) 4473–4475.
[31] Z.Y. Lin, S. Gao, J. Lin, W.L. Lin, S.Y. Qiu, L.H. Guo, B. Qiu, G.N. Chen, Anal. Methods—UK 4 (2012) 612–615.
[32] A. Lee, J. Chin, O.K. Park, H. Chung, J.W. Kim, S.-Y. Yoon, K. Park, Chem. Commun. 49 (2013) 5969–5971.
[33] J. Su, J. Xu, Y. Chen, Y. Xiang, R. Yuan, Y.Q. Chai, Biosens. Bioelectron. 45 (2013) 219–222.
[34] T. Sanji, M. Nakamura, M. Tanaka, Tetrahedron Lett. 52 (2011) 3283–3286.
[35] X.Y. Xu, W.L. Daniel, W. Wei, C.A. Mirkin, Small 6 (2010) 623–626.
[36] Q.P. Shen, W.H. Li, S.Y. Tang, Y.F. Hu, Z. Nie, Y. Huang, S.Z. Yao, Biosens. Bioelectron. 41 (2013) 663–668.
[37] L.F. Zhou, Q.P. Shen, P. Zhao, B.B. Xiang, Z. Nie, Y. Huang, S.Z. Yao, Methods 64 (2013) 299–304.
[38] Q.P. Shen, S.Y. Tang, W.H. Li, Z. Nie, Z.L. Liu, Y. Huang, S.Z. Yao, Chem. Commun. 48 (2012) 281–283.
[39] Q.P. Shen, L.F. Zhou, Y.J. Yuan, Y. Huang, B.B. Xiang, C.Y. Chen, Z. Nie, S.Z Yao, Biosens. Bioelectron. 55 (2014) 187–194.
[40] A.H. El-Sagheer, T. Brown, Chem. Soc. Rev. 39 (2010) 1388–1405.
[41] H.B. Sun, X.H. Peng, Bioconjugate Chem 24 (2013) 1226–1234.
[42] R. Kumar, A. El-Sagheer, J. Tumpane, P. Lincoln, L.M. Wilhelmsson, T. Brown, J. Am. Chem. Soc. 129 (2007) 6859–6864.
[43] D.S. del Amo, W. Wang, H. Jiang, C. Besanceney, A.C. Yan, M. Levy, Y. Liu, F.L. Marlow, P. Wu, J. Am. Chem. Soc. 132 (2010) 16893–16899.
[44] A.H. El-Sagheer, T. Brown, Chem. Sci 5 (2014) 253–259.
[45] S. Tyagi, F.R. Kramer, Nat. Biotechnol. 14 (1996) 303–308.
[46] K.M. Wang, Z.W. Tang, C.Y.J. Yang, Y.M. Kim, X.H. Fang, W. Li, Y.R. Wu, C.D. Medley, Z.H. Cao, J. Li, P. Colon, H. Lin, W.H. Tan, Angew. Chem. Int. Ed. 48 (2009) 856–870.
[47] Z.W. Tang, P. Liu, C.B. Ma, X.H. Yang, K.M. Wang, W.H. Tan, X.Y. Lv, Anal. Chem. 83 (2011) 2505–2510.
[48] Z.W. Tang, K.M. Wang, W.H. Tan, C.B. Ma, J. Li, L.F. Liu, Q.P. Guo, X.X. Meng, Nucleic Acids Res. 33 (2005) e97.
[49] F. Chen, Y.X. Zhao, L. Qi, C.H. Fan, Biosens. Bioelectron 47 (2013) 218–224.
[50] Y. Cheng, J.P. Lei, Y.L. Chen, H.X. Ju, Biosens. Bioelectron. 51 (2014) 431–436.
[51] A.A. Goulko, F. Li, X.C. Le, TrAC, Trends Anal. Chem 28 (2009) 878–892.

Talanta 132 (2015) 77–86

Contents lists available at ScienceDirect

Talanta

journal homepage: www.elsevier.com/locate/talanta

Rapid analysis of trace organic compounds in water by automated online solid-phase extraction coupled to liquid chromatography–tandem mass spectrometry

Tarun Anumol, Shane A. Snyder*

Department of Chemical & Environmental Engineering, University of Arizona, 1133 E James E Rogers Way, Harshbarger 108, Tucson, AZ 85721-0011, USA

ARTICLE INFO

Article history:
Received 17 April 2014
Received in revised form
2 August 2014
Accepted 5 August 2014
Available online 27 August 2014

Keywords:
Automated online extraction
Pharmaceuticals
Personal-care products
Tandem mass spectrometry
Water
LC–MS/MS

ABSTRACT

A fully automated online solid-phase extraction (SPE) with directly coupled liquid chromatography–tandem mass spectrometry (LC–MS/MS) method for analysis of 34 trace organic compounds in diverse water matrices has been developed. The current method offers several advantages over traditional offline SPE methods including low sample volume (1.7 mL), decreased solvent use, higher throughput, and increased reproducibility. The method uses simultaneous positive and negative ESI for analysis of all compounds in one injection, which reduces cycle time (extraction+analysis) to <15 min. Method optimization included testing different online SPE cartridges, mobile phase compositions, and flow rates. The method detection limits (MDLs) ranged from 0.1 to 13.1 ng/L with 80% of the compounds having an MDL <5 ng/L. Matrix spike recoveries in three different water qualities were evaluated and ranged from 61.2% to145.1% with 95% of the recoveries ranging between 70–130%. As part of the method validation studies, linearity (0.9911–0.9998), intra-day variability (1.0–10.4%), inter-day variability (1.0–11.9%), and matrix effects were also assessed. The use of 26 isotopically-labeled standards increased the reliability of the method while retention time locking and use of two transitions for most compounds increased the specificity. The applicability of the method was tested on samples across treatment points from two wastewater plants, a septic tank, surface water and groundwater.

© 2014 Elsevier B.V. All rights reserved.

1. Introduction

The extensive utilization of organic compounds in modern society combined with increasing demands for water resources have resulted in widespread contamination of water resources. Many of these compounds have anthropogenic sources and are being produced in greater quantities than ever before around the globe [1,2]. These compounds including pharmaceuticals, personal-care products, pesticides, hormones and industrial contaminants, and are collectively termed as trace organic compounds (TOrCs). Several studies have shown that conventional water treatment processes generally are not effective in removal of TOrCs thus leading to their release into the environment with potential for contamination of drinking water sources [3,4]. While the adverse effects associated with exposure to individual compounds from drinking water is not expected to pose significant risk to public health [5], the long term exposure to mixtures of TOrCs and potential for synergistic effects is largely unknown [6–8]. Due to the vast number of TOrCs detected in water, regulatory actions to determine acceptable levels of all detected TOrCs is not feasible despite studies documenting adverse effects to the environment and wildlife [9–11]. Thus, it is prudent to monitor indicator TOrCs in water while sufficient toxicological data can be collected and studies on any potential mixture effects performed.

Currently, methods utilizing liquid chromatography–tandem mass spectrometry (LC–MS/MS) are considered the gold standard for sensitive analysis of multiple TOrCs in water [12–14]. However, to achieve requisite detection limits of low ng/L for many TOrCs, time consuming sample preparation steps are often required before LC–MS/MS analysis. The sample preparation step generally involves extraction and concentration of the target analytes with commensurate elimination of many interferences in the original matrix. Traditional off-line solid-phase extraction (SPE) and liquid–liquid extraction (LLE) are the most commonly used concentration and clean-up steps for analysis of TOrCs in environmental matrices [12,15,16]. These two techniques require a relatively large sample volume, are extremely time consuming, laborious, and require considerable amounts of organic solvents to perform. Further, these methods can potentially decrease the reproducibility and accuracy of analysis due to multiple sample manipulations that are required [17]. Considering the high degree of temporal [18] and geographical [19] variability, high-throughput time-sensitive analytical screening

* Corresponding author. Tel.: +1 520 621 2573.
E-mail address: snyders2@email.arizona.edu (S.A. Snyder).

http://dx.doi.org/10.1016/j.talanta.2014.08.011
0039-9140/© 2014 Elsevier B.V. All rights reserved.

methods would greatly advance the resolution of environmental monitoring. Also, considering the variability of methods currently used for TOrC analyses [20], the reproducibility and accuracy of the data must be enhanced by introducing automation into the entire analytical procedure.

The online SPE process offers several advantages over the offline techniques including reduction in sample preparation and thus increase in productivity [21]. Further, online SPE minimizes operator contact which reduces the possibility of contamination while also eliminating a solvent evaporation step that can result in loss of target analytes [22]. The introduction of the entire mass of analyte to the detector allows injection of much lower sample volumes while increasing the sensitivity of analysis [23]. Automation of the entire process (extraction+analysis) also improves the reproducibility of the method. In addition, online SPE cartridges can be reused as they are amenable to backwashing and have been shown to perform well even after treating several hundred water samples [24].

Over the last few years, several manufacturers have developed fully automated online SPE systems coupled to LC–MS/MS which has allowed for integration of sample clean-up, extraction and analysis. Consequently the use of online SPE methods in bioanalytical [25,26] and environmental [21,27] applications has increased. However, most of these methods have focused on analysis of specific classes of TOrC such as pharmaceuticals [28–30], hormones [24,31] or pesticides [32] only. Other methods still require multiple injections for analysis of all analytes [33], large sample volumes [34], require derivitization [35], or are not completely automated which may reduce the reproducibility and/or increase time of analysis.

The focus of this study was to develop a single method for rapid analysis of 34 indicator compounds comprising several classes of TOrCs in different water matrices with a fully automated online SPE coupled to LC–MS/MS. The objectives were to (i) use low sample volume (<2 mL), (ii) employ minimal sample preparation and automate the extraction step to reduce variability, (iii) perform simultaneous analysis of TOrCs both in electrospray (ESI) positive and negative mode with one injection, (iv) rapid cycle (extraction+analysis) time (<20 min) for high throughput analysis of samples, (v) achieve desired sensitivity of low ng/L detection limits for all analytes, and (vi) provide 'cleaner' and 'greener' methods for analysis of TOrCs in aqueous matrices compared to conventionally used offline pre-concentration techniques.

2. Experimental

2.1. Chemicals and reagents

All analytical standards used during the study were at least $>97\%$ purity and every effort was made to use standards of the highest purity commercially available. All native standards were purchased from Sigma-Aldrich (St. Louis, MO) except DEET and triclosan from Alfa Aesar (Ward Hill, MA) and meprobamate from Cerilliant (Round Rock, TX). Labeled surrogate standards were purchased from Cambridge Isotope Laboratories (Andover, MA) except $^{13}C_2$-PFHxA, $^{13}C_4$-PFOA and $^{13}C_4$-PFOS from Wellington Laboratories (Ontario, Canada); primidone-d_5, meprobamate-d_3, triclocarban-$^{13}C_6$ and $^{13}C_6$-diclofenac from Toronto Research Chemicals (Ontario, Canada); and gemfibrozil-d_6, benzophenone-d_{10}, benzotriazole-d_4, and diphenhydramine-d_5 from C/D/N Isotopes (Quebec, Canada). All solvents used were of purity suitable for LC–MS analysis. Methanol, isopropyl alcohol (IPA), and acetic acid were obtained from Fisher Scientific (Pittsburgh, PA), while acetonitrile (ACN) and HPLC grade water were purchased from Burdick and Jackson (Muskegon, MI). Detailed information about all target analytes and isotopes used in this study are shown in Table 1.

2.2. Selection of target list

The selection of TOrCs analyzed in this study was based on data presented in previous literature that rely on occurrence data, detection frequency, toxicological relevance, availability of robust analytical methods and ability to pose as 'indicators' of water quality [36–38]. Additionally, emerging classes of TOrCs like perfluorinated compounds and glucocorticoid steroids were also represented in our target list to show that the method can be used for their detection. The aim was to select a diverse list of compounds in terms of physical, chemical properties while representing traditionally monitored and frequently detected TOrCs along with newer classes of interest.

2.3. Sample collection and preparation

During this study, grab samples were collected from two wastewater treatment plants, a surface water, groundwater, and septic tank from various locations across the USA. All samples were collected in 20 mL amber glass vials dosed with 1 g/L of sodium azide as a preservative and stored in ice before transport to the laboratory. The samples were stored in a refrigerator at 4 °C on arrival at the lab. Five-ml of sample was then aliquoted into a 6-ml glass vial before being spiked with a mixture of all isotopically-labeled surrogates to achieve a final concentration of 100–200 ng/L in the sample depending on the type of analyte and sample matrix. All samples were doped with the surrogate standards within 72 h of collection to account for losses due to storage and degradation of analytes. The samples were then filtered using a 0.2 μm Captiva polyethylene styrene (PES) filter from Agilent Technologies (Santa Clara, CA) prior to analysis. All samples were analyzed within two weeks of collection.

2.4. Online SPE configuration

Automated pre-concentration of all samples was performed using an Agilent flexible cube (FlexCube) module coupled to a large volume autosampler (900 μL) with a programmable multi-draw capacity. In this method, 1.7 mL of sample was injected into the sample loop using two 850 μL autosampler injections. A schematic of the different valve positions on the online SPE system is shown in Supplementary materials (Fig. S1). The FlexCube online SPE unit consists of a built in single piston pump with four solvent lines and a 10-port switching valve that houses two online SPE cartridges for simultaneous loading of one cartridge while the other is being eluted or backwashed. Initially, the switching valve on the FlexCube was set to the LOAD position (position 1) during which the sample was loaded onto the SPE cartridge with 95/5 (v/v) water/ACN mixture containing 0.1% acetic acid (line A) from the FlexCube pump. During this time, the aqueous waste and matrix not retained on the SPE cartridge was allowed to go to waste. After loading was complete, the valve switched to the ELUTE position which resulted in the binary pump back-flushing SPE cartridge 1 to allow a gradient elution of the target analytes onto the analytical column. At the same time, SPE cartridge 2 was being cleaned with a strong solvent mix of 1:1:1 (v/v/v) isopropyl alcohol, methanol and ACN (line B) by the FlexCube pump to remove any retained target analytes or matrix from causing blank contamination and interferences in subsequent runs. A few minutes before the end of the run, the solvent channel on the FlexCube pump was switched back to its original line (line A) to allow SPE cartridge 2 to equilibrate and prepare it for the next sample.

Table 1
Class and use of TOrCs selected in this study with isotopes used for quantification.

Compound	Use	Category	Isotope[a]
Atenolol	β-Blocker	Pharmaceutical	Atenolol-d_7
Carbamazepine	Anti-seizure	Pharmaceutical	Carbamazepine-d_{10}
Clofibric acid	Lipid regulator metabolite	Pharmaceutical	Bisphenol A-$^{13}C_{12}$
Diclofenac	Anti-arthritic	Pharmaceutical	Diclofenac-$^{13}C_6$
Diphenhydramine	Antiarrhythmic	Pharmaceutical	Diphenylhydramine-d_5
Diltiazem	Anti-histamine	Pharmaceutical	Diltiazem-d_3
Fluoxetine	Anti-depressant	Pharmaceutical	Fluoxetine-d_5
Gemfibrozil	Anti-cholesterol	Pharmaceutical	Gemfibrozil-d_6
Hydrochlorothiazide	Antihypertensive	Pharmaceutical	Benzotriazole-d_4
Ibuprofen	Analgesic	Pharmaceutical	Ibuprofen-d_3
Meprobamate	Anti-anxiety	Pharmaceutical	Meprobamate-d_7
Naproxen	Analgesic	Pharmaceutical	Naproxen-$^{13}C_1d_3$
Primidone	Anticonvulsant	Pharmaceutical	Primidone-d_5
Propranolol	β-Blocker	Pharmaceutical	Atenolol-d_7
Sulfamethoxazole	Antibiotic	Pharmaceutical	Sulfamethoxazole-d_6
Trimethoprim	Antibiotic	Pharmaceutical	Trimethoprim-d_3
Benzophenone	UV blocker	Personal care product	Benzophenone-d_{10}
Caffeine	Stimulant	Personal care product	Caffeine-$^{13}C_3$
N,N-Diethyl-m-toluamide (DEET)	Insect repellant	Personal care product	DEET-d_6
Propylparaben	Preservative in cosmetics	Personal care product	Propylparaben-d_4
Tris (2-chloroethyl) phosphate (TCEP)	Flame retardant	Personal care product	TCEP-d_{12}
Tris (2-chloropropyl) phosphate (TCPP)	Flame retardant	Personal care product	TCEP-d_{12}
Triclocarban	Antibiotic	Personal care product	Triclocarban-$^{13}C_6$
Triclosan	Anti-microbial	Personal care product	Triclosan-$^{13}C_{12}$
Benzotriazole	Corrosion inhibitor	Industrial compound	Benzotriazole-d_4
Bisphenol A	Plasticizer	Industrial compound	Bisphenol A-$^{13}C_{12}$
Perfluoro hexanoic acid (PFHxA)	Fluorosurfactant	Industrial compound	PFHxA-$^{13}C_2$
Perfluoro octanoic acid (PFOA)	Fluorosurfactant	Industrial compound	PFOA-$^{13}C_4$
Perfluoro octane sulfonate (PFOS)	Fluorosurfactant	Industrial compound	PFOS-$^{13}C_4$
Hydrocortisone	Anti-inflammatory glucocorticoid	Hormone	Carbamazepine-d_{10}
Norgestrel	Hormonal contraceptive	Hormone	Primidone-d_5
Testosterone	Androgen	Hormone	Carbamazepine-d_{10}
Atrazine	Herbicide	Pesticide	Atrazine-d_3
Simazine	Herbicide	Pesticide	Atrazine-d_3

[a] Used for quantification.

2.5. Liquid chromatography

An Agilent 1290 UHPLC binary pump was used to perform liquid chromatography for all analyses. Polypropylene solvent lines with metal frits were used to minimize potential system contamination of perfluorinated materials. An Agilent Poroshell 120 EC C-18 (2.1 mm × 50 mm, 2.7 μm) column was used for chromatographic separation of all analytes. The column was maintained at 30 °C throughout the run. A dual eluent mobile phase comprising of water with 0.1% acetic acid (A) and ACN with 0.1% acetic acid (B) at 350 μL/min was used for separation. For the first 4 min, the gradient was held at 5% B while the sample was loaded onto the online SPE cartridge and the binary pump was conditioning cartridge 2. At 4 min, the switching valve turned to the ELUTE position (position 2) and solvent B was linearly increased to 100% at 11 min. This gradient was held till 12 min before returning to the initial condition at 12.5 min. A post-time of 2 min was added to allow the column to re-equilibrate before the next analysis. This resulted in a total cycle time (extraction + analysis) of 14.5 min per sample.

2.6. Mass spectrometry

Mass spectrometry was performed on an Agilent 6460 triple quadrupole mass spectrometer. The optimization of the mass spectrometer was divided into two: (i) compound-specific optimization and (ii) source-dependent optimization. Details of the optimization process have been published previously [14]. The optimized compound parameters and retention times (RT) are shown in Supplementary material (Table S1) while source-dependent parameters for both ESI positive and negative modes (run simultaneously) are shown in Table S2.

The mass spectrometer was run in dynamic multiple reaction monitoring (DMRM) mode with a delta RT of 0.7 min for each compound. Fast polarity switching with the dielectric capillary allowed for simultaneous analysis in ESI positive and negative in the same run. Two transitions: a quantifier (most-abundant product) and qualifier were used for most of the compounds to increase specificity of the method. Data acquisition and analysis was performed using Agilent MassHunter software (version Rev B.06.00). Isotope dilution was used for quantification of all analytes [39]. In cases where the identical isotopic standard was not available, a closely-related isotope was used as a replacement (Table 1). RT locking and product ion ratio monitoring reduced the possibility of false positives in the method.

3. Results and discussion

3.1. Solid phase extraction cartridge selection

The selection of the online SPE cartridge is critical to the success of the entire analysis. Presently, the availability of different online SPE cartridges is significantly lower than conventional offline cartridges. Three online SPE cartridges from Agilent and an experimental cartridge packed in the lab were tested for their suitability to extract the target analytes from aqueous samples. PLRP-s (styrene-polydivinylbenzene, 2.1 mm × 12.5 mm, 15–20 μm), ZORBAX SB-AQ (reversed-phase alkyl group bonded to high-purity porous silica microsphere, 2.1 mm × 12.5 mm, 5 μm), ZORBAX Phenyl-hexyl (dimethylphenylhexylsilane, 2.1 mm × 12.5 mm, 5 μm) from Agilent and Carbon-X (experimental phase with activated charcoal, 2.1 mm × 12.5 mm 5 μm) were evaluated. To

assess which of these cartridges was most appropriate for extraction of target analytes, the absolute recoveries were calculated by comparing the peak areas obtained in online SPE mode and direct injection mode with the same amount of analyte in ultrapure water in five replicate injections. Fig. 1 shows the range of absolute recoveries obtained for the 32 target analytes tested with each cartridge (propranolol and hydrochlorothiazide were not tested). An absolute recovery between 70–130% was considered as acceptable and used as the criteria for cartridge selection. The PLRP-s cartridge had 26 analytes in this range and good reproducibility (RSD < 10%) for all but three analytes (bisphenol A, propylparaben and TCEP) so was the most suitable choice. The SB-AQ cartridge performed similarly but had slightly less reproducibility while extraction efficiency of some compounds with –NH group was lower than the PLRP-s. The Carbon-X cartridge had poor extraction recoveries (< 50%) for several of the analytes and it was later discovered that many of the target analytes were very strongly bound onto the cartridge and not entirely eluted. This was confirmed by passing 100% ACN through the Carbon-X cartridge at the end of the five replicates and monitoring the spectrum. Further, several analytes (like meprobamate, atrazine and carbamazepine) had very high extraction recoveries (> 150%) and large %RSDs probably due to carryover from one injection to the next for the Carbon-X. It should be noted that low absolute recoveries for some compounds are automatically corrected as both the calibration standards and samples are processed in exactly the same manner and go through the entire analytical process (extraction + analysis) in an automated online SPE setup. However, it is always desirable to get the maximum recoveries for best sensitivity but with a highly diverse analyte list trade-offs are inevitable. With this in mind, the PLRP-s cartridge was selected for all further analyses. The complete dataset of absolute recoveries for all four online SPE cartridges is provided in the supplementary material (Table S3).

3.2. Washing mobile phase composition and volume

The presence of organic substances in the matrix can cause severe matrix suppression especially in complex water matrices such as wastewater [40]. Hence a wash step is often needed after the sample has been loaded onto the online SPE cartridge. The wash mobile phase composition in the FlexCube pump was tested at three different ACN concentrations (0%, 5% and 10%) in water with 0.1% acetic acid. An aqueous mobile phase of 5% ACN with 0.1% acetic acid was finally used as it provided the best recoveries with high reproducibility. The 10% ACN mobile phase resulted in significant loss of the early-eluting polar compounds while the 0% ACN phase had lower recoveries for the apolar compounds. Similarly, the wash volume is another important parameter for optimization as too small a volume may not eliminate the interferences in the matrix while too large a volume can cause the target analytes to be washed off the cartridge. Six different wash volumes (2, 2.5, 3, 3.5, 4, and 5 mL) were tested with the loading flowrate maintained at 1 mL/min. Fig. 2 provides the range of absolute recoveries of all target analytes with the different wash volumes. It was found that a 4 mL wash volume provided best recoveries for most of the target analytes. The 2 mL load volume had poor recoveries for all compounds tested possibly due to the fact that there was not enough washing time to elute the target analytes off the cartridge. The 5 mL load volume had very low recoveries for the polar compounds that were likely washed out of the cartridge into waste before the switching valve sent the sample onto the analytical column. The supplementary material (Table S4) contains information of specific recoveries of each analyte with all six loading volumes.

3.3. Loading flowrate

In online SPE analysis, the autosampler injects the sample into the large-volume loop which is then carried onto the cartridge by the loading mobile phase solvent from the FlexCube pump. A high flowrate may result in less adsorption of target analytes onto the cartridge while a slow flowrate increases time of analysis and also provides competing matrix elements time to attach onto the cartridge. In this study, three different loading flowrates were tested by comparing the peak areas of each analyte with direct chromatographic injection. This analysis was run in multiple-reaction monitoring (MRM) mode where RTs were not locked due to the fact that different flowrates with same loading volume

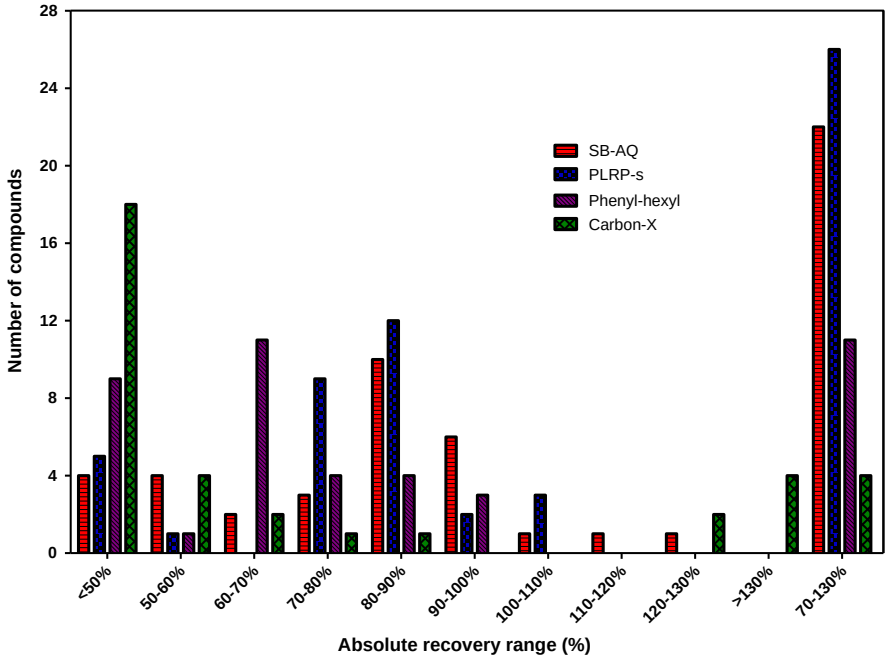


Fig. 1. Range of absolute recoveries for target analytes with four different online SPE cartridges.

caused the target analyte RT to shift. The absolute recoveries of all target analytes for the three different loading flowrates in order of increasing RT is illustrated in Fig. 3. It was found that the 1 mL/min flowrate provided best recoveries for the target analytes compared to the other flowrates. After all replicates for the condition were run, a set of blanks were injected to look for carryover. No carryover was found in the 1 mL/min samples indicating that the strong solvent mix was successful in washing any remaining analytes of the cartridge. The 1.5 mL/min flowrate had higher recoveries for the late-eluting analytes but some recoveries were extremely high with low reproducibility possibly due to carryover from previous injections. However, since 1 mL/min provided better results the potential carryover for the 1.5 mL/min flowrate was not investigated further.

3.4. Limit of detection (LOD) and method detection limit (MDL)

The instrument limit of detection (LOD) was based on an analyte signal to noise ratio (SNR) greater than three. A set of standards at 0.1, 0.2, 0.5, 1.0, 2.5, 5.0, 10 and 20 ng/L were analyzed to determine the LOD. The method detection limit (MDL) was calculated based on previous literature [41] by injecting eight

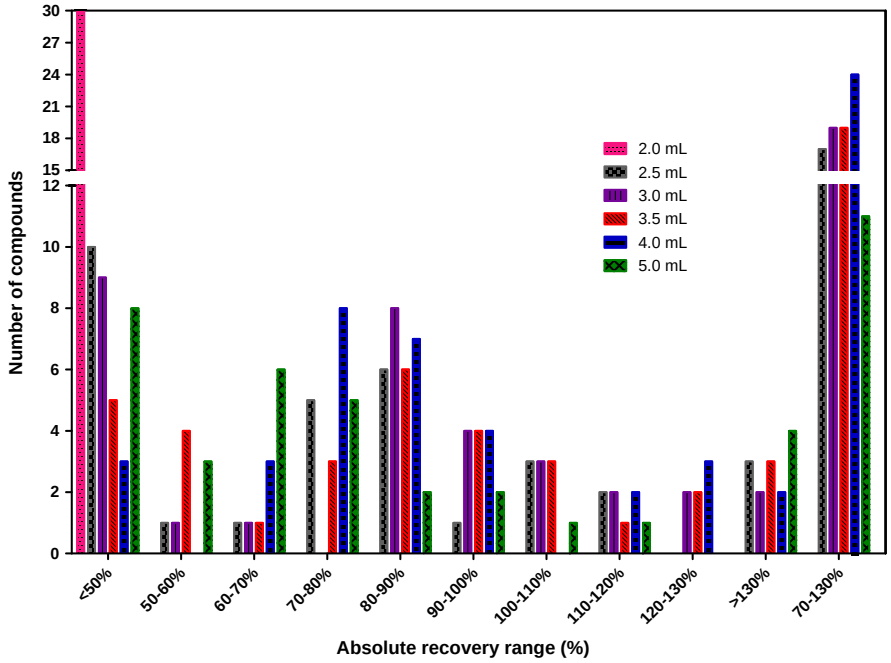


Fig. 2. Range of absolute recoveries for target analytes with different loading volumes.

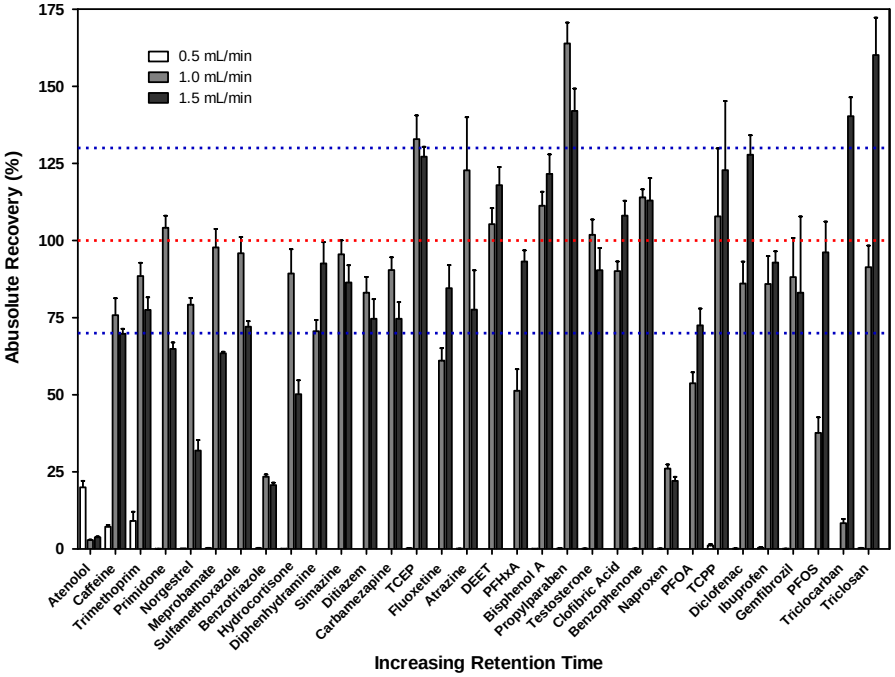


Fig. 3. Absolute recoveries of target analytes with three loading flowrates.

samples fortified with isotopically-labeled surrogate standards and target analytes at 2–5 times the LOD. The standard deviation of the eight replicates was multiplied by the student's *t*-test value for $n-1$ degrees of freedom at 99% confidence levels to determine the MDL of each target analyte. The calculated MDL for most analytes was <5 ng/L with only four compounds (benzophenone, benzotriazole, bisphenol A, and norgestrel) being >10 ng/L. The MDLs in this study (Table 2) were comparable and in most cases lower than previously published literature while using lower sample volumes of 1.7 mL [33,42]. A further advantage of using low sample volume was that the mass of isotopically-labeled standard added to each sample was much lower when compared to other published methods. The cost of isotopically-labeled IS standards can be prohibitively expensive often resulting in having to select a few IS to represent many compounds. With addition of lower masses of IS per sample, analysis costs are significantly lowered.

The method reporting limits (MRL) were determined individually for each sample as each water quality has different matrix effects on each analyte. When analyzing several different samples, it is not practically feasible to determine the MRL for each water quality. Hence, this method has been used to provide a realistic MRL for each sample while avoiding time-consuming MRL studies for each specific water quality. The details of this process have been described earlier [14]. Briefly, to calculate the MRL, the lowest calibration standard (usually at or close to MDL) was divided by isotope standard recovery (calculated by comparing peak area in ultrapure water) in that matrix to give the true MRL for each analyte in a sample. For analytes where matrix enhancement (IS recovery $>100\%$) was encountered, the isotope recovery was assumed to be 100% so not to get artificially low MRLs. For samples, where dilution was performed, the MRLs were suitably adjusted taking this into account. This method provides a realistic MRL for each sample without having to perform MRL studies on each water matrix.

Table 2
LODs, MDLs and practical MRLs in ultrapure water for all target analytes.

Analyte	LOD (ng/L)	MDL (ng/L)
Atenolol	1	2.5
Atrazine	0.2	0.3
Benzophenone	5	11.3
Benzotriazole	10	10.8
Bisphenol A	10	13.1
Caffeine	0.2	0.5
Carbamazepine	0.1[a]	0.1
Clofibric acid	0.2	0.7
DEET	0.1	0.3
Diclofenac	2	2.8
Diphenhydramine	0.5	0.9
Ditiazem	0.1	0.2
Fluoxetine	1	3
Gemfibrozil	0.2	0.5
Hydracortisone	5	9.3
Hydrochlorothiazide	0.2	0.4
Ibuprofen	0.5	1.9
Meprobamate	0.2	0.4
Naproxen	1	2.5
Norgestrel	10	11.6
PFHxA	1	3.6
PFOA	0.5	3
PFOS	5	6.1
Primidone	0.5	2
Propranolol	1	1.2
Propylparaben	1	1.4
Simazine	0.2	0.4
Sulfamethoxazole	0.2	0.5
TCEP	1	2.1
TCPP	5	9
Testosterone	2.5	4.4
Triclocarban	0.5	1.1
Triclosan	1	2.6
Trimethoprim	0.1[a]	0.1

[a] Assumed as the lowest calibration standard (SNR $\gg 3$ at this concentration).

3.5. Matrix spike recoveries

Three different water matrices (ultrapure water, surface water and wasterwater effluent) were tested to evaluate the suitability of the method for analyte spike recoveries. Five replicate samples of ultrapure water and surface water (SW) were spiked with all target analytes at two levels (30 ng/L and 100 ng/L) while a wastewater effluent ($5\times$ diluted) was spiked at 100 ng/L. A summary of the recoveries for each analyte is shown in Table 3. In ultrapure water, recoveries were acceptable (70–130%) for all target analytes except norgestrel (61.2%) and fluoxetine (132.6%) in the low spike of 30 ng/L. The %RSD for both spiking levels in ultrapure water was $<10\%$ for more than 90% of the target analytes with most compounds having an RSD $<5\%$. In SW, recoveries varied from 69.2–137.1% for the 30 ng/L spike and 68.4–136.3% in the 100 ng/L spike with only two compounds outside the acceptable range in both spikes. The reproducibility for all compounds in SW was good as RSDs were $<12\%$ in both spike levels. All target analytes recoveries were within the acceptable range for the wastewater effluent (WWE) spike with the exception of PFOS (145.1%) while RSDs were less than 10% for all compounds but hydrocortisone (13.1%). The data shown is for the isotope corrected recoveries while absolute recoveries were lower as seen in earlier sections.

3.6. Matrix effect assessment

Matrix effects can pose severe challenges for low level quantification of analytes using ESI-LC–MS/MS [43]. Generally caused by interferences of co-eluting constituents in the matrix, they can result in loss of sensitivity and reproducibility. In this study, the matrix effect was calculated using 26 isotopically labeled standards in the analytical method. The isotopically labeled standards were spiked at 100 ng/L into three different matrices (surface water, wastewater effluent, 1:5 diluted wastewater effluent) and the matrix effect was calculated by comparing the peak area obtained in the matrix with peak area obtained in an ultrapure water sample according to Eq. (1).

$$\text{Matrix effect } (\%) = \frac{(PA_S - PA_M) \times 100}{PA_S} \quad (1)$$

where PA_s is the peak area in the standard (ultrapure water) and PA_M is the peak area obtained in the matrix. A positive value of matrix effect indicates signal suppression while a negative value indicates signal enhancement. Five replicate samples were analyzed in each matrix and of the standard in ultrapure water. The matrix effects for each analyte in the three different water qualities are represented in Fig. 4. The results indicate that while all the analytes were affected by suppression or enhancement in the three water qualities, the magnitude of effect was vastly different. For example, diltiazem-d_3 had $<10\%$ matrix effect in the three different water qualities whereas meprobamate-d_3 experienced much stronger suppression in all three water qualities (73.7%, 92.1% and 47.9% in SW, WWE and 1:5 WWE, respectively). Generally, the effects were greater in more complex matrices with the average matrix effect in the WWE (53%), being higher than SW (38%) and 1:5 diluted WWE (19%). The results from this study are in agreement with other studies and show the propensity of ESI methods to matrix effects. Hence, the authors strongly recommend the use of isotopically labeled surrogate standards for quantification in aqueous samples. For analytes where an isotopically labeled standard is not available, assigning an

Table 3
Compound matrix recoveries in three different water matrices.

Compound	Ultrapure water				Surface water				Wastewater effluent (1:5 dilution)	
	30 ng/L ($n=5$)		100 ng/L ($n=5$)		30 ng/L ($n=5$)		100 ng/L ($n=5$)		100 ng/L ($n=5$)	
	Recovery (%)	RSD (%)	Recovery (%)	RSD (%)	Recovery (%)	RSD (%)	Recovery (%)	RSD (%)	Recovery (%)	RSD (%)
Atenolol	102.2	1.2	110.8	4.5	115.8	2.4	90.9	5.8	86	3.4
Atrazine	88.9	3.3	98.8	1.2	103	0.2	97.4	2.6	94.7	1.9
Benzophenone	98.9	4.8	128.9	2.7	93.8	1.8	111.6	8.6	120.4	7
Benzotriazole	108.6	1.9	114.7	9.7	81.5	8.8	98	7.1	75.2	7.4
Bisphenol A	127.9	3.1	101.9	6.7	101.8	3.6	88.6	10.3	76.2	5.4
Caffeine	88.8	3	96.1	2.9	118.5	0.9	100.4	4.9	99.7	3.5
Carbamazepine	96.6	0.9	101.3	0.9	105.8	0.3	99.3	3.3	95.3	0.9
Clofibric acid	85.5	4.2	93.9	1.5	117.5	1.2	118	4.6	115.3	1.9
DEET	95.1	0.8	100.1	1.3	109.9	2.3	128.2	3.1	111.2	1.1
Diclofenac	81	1.8	78.1	3	106.2	2.2	99.1	1.9	111.1	2.8
Diphenhydramine	88.1	0.3	93.2	0.8	123.9	0.2	94.4	0.8	95.9	6.1
Ditiazem	81.1	0.7	87.4	2	118.7	0.3	102.2	1.4	104.9	1.8
Fluoxetine	132.6	2.4	128.3	4.2	92.4	1.5	68.4	4.5	112.7	3.5
Gemfibrozil	83.8	3.1	92.6	2.1	96.7	0.8	92.9	3.2	73.7	2.2
Hydrochlorothiazide	90.1	4.1	93.2	3.2	90.4	4.2	96.3	3.3	86.2	4.7
Hydrocortisone	98.1	9.7	86.5	10.3	137.1	11.5	95.7	3.8	97.6	13.1
Ibuprofen	90.7	5.8	91	3.8	103	1.6	91.8	1.6	89.8	3.5
Meprobamate	86.7	1.5	98.2	1.1	105.1	1.6	96.9	2.9	105.2	1.6
Naproxen	86.3	5.5	94.8	2.5	104.7	1.5	98.2	3.8	99.9	3.1
Norgestrel	61.2	4.9	91.7	1.6	119.5	2.5	101.4	5.4	75.1	6.8
PFHxA	91.6	5.3	93	3	69.2	8.3	91.3	3.4	88.3	2.4
PFOA	100.4	5.4	107.3	4.2	88.1	1	124.6	0.8	85.5	2.6
PFOS	121.2	7.3	128.6	4	125.6	0.3	136.3	0.8	145.1	1.8
Primidone	85.8	9.1	92.3	4.7	79.2	3.8	98.6	5.2	91.6	5.8
Propranolol	84.0	6.1	89.2	3.9	80.3	4.4	86.8	4.1	83.1	5.6
Propylparaben	86.2	2.2	91.2	3.3	116.1	1.8	108.3	9.6	100	5.3
Simazine	96.6	7	104.3	2.7	127.7	1.6	117.6	2.7	103.3	5.7
Sulfamethoxazole	80.9	4.2	90.5	2.1	119.7	2	101.5	4.1	102.1	5.9
TCEP	102.2	3.3	73.7	12	NA	NA	103.1	4.1	90.1	7.2
TCPP	119.7	4.9	109.4	3.1	113.7	1.6	111.8	3.9	88.3	5
Testosterone	103	10.3	116	5.4	123.4	2.3	117.5	6.1	91.8	9.9
Triclocarban	121.6	11.3	78.8	5.3	104.7	1.9	80.4	3.5	102.8	1.4
Triclosan	91.5	10.4	102.6	4.4	114.9	2.3	105.9	3.8	91.3	3.1
Trimethoprim	75.1	1.1	83.5	1	90	3.6	75.7	11.2	74.8	5.9

NA: not analyzed.

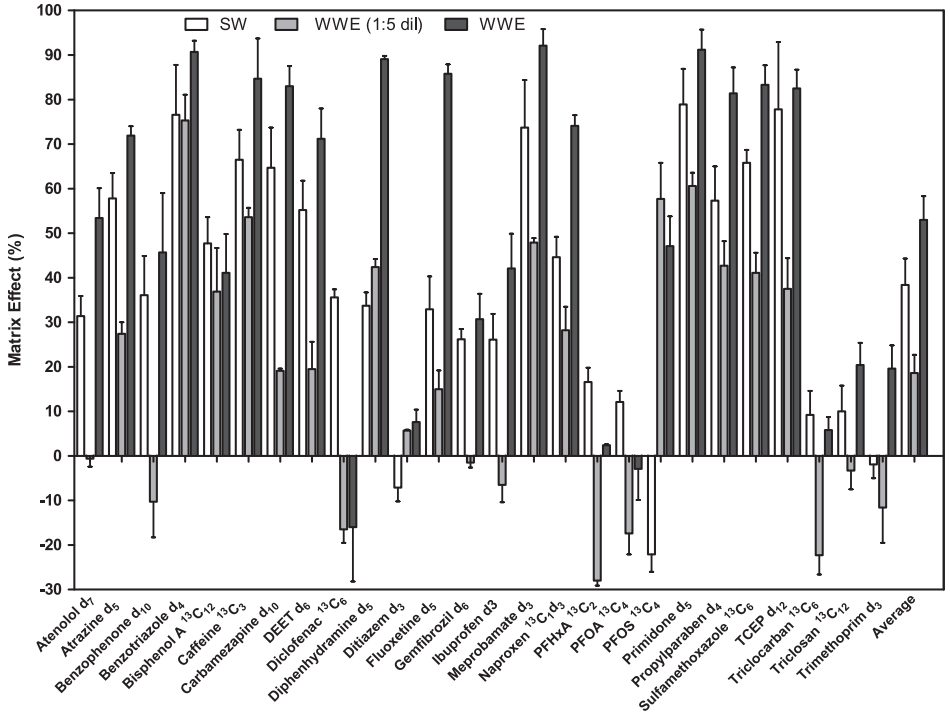


Fig. 4. Matrix effect (%) of isotopically labeled standards in different water qualities.

appropriate one is critical as matrix effects are different for every analyte in each matrix and depend on chemical structure, retention time and nature of ionization [16,44].

3.7. Blanks, linearity and precision

The analysis of compounds at trace levels in any matrix is always susceptible to contamination. The use of automated extraction and analysis techniques reduces the possibility of contamination due to sample handling and human error. In this study, blanks with and without isotopically labeled standards were analyzed to check for the presence of target analytes. Except for DEET, none of the target analytes were detected in blanks. Only a small trace of DEET was detected similar to that reported previously [14]. Subsequently, the MDL and MRL for DEET were adjusted to minimize the possibility of false positives. Special precautions were taken to avoid contamination of prefluorinanted compounds including replacing all Teflon lines in the instrument with PEEK or stainless steel, use of metal solvent liner frits in the mobile phase bottles and use of a Poroshell EC 120 C-18 (2.1×30 mm^2, 2.7 μm) trapping column after the mixer of the pump to avoid potential contamination from solvents. Finally, a series of blanks ($n=5$) were analyzed for all the target analytes and all values were below the MDL. For analysis of real water samples, true blanks, method blanks and matrix spikes were run frequently to monitor contamination, instrument carry-over and robustness of the method.

The linearity of the calibration curves for each analyte was verified by preparing seven standards from the MDL to 100 ng/L (six points if the MDL > 10 ng/L) fortified with isotopically-labeled standards. The correlation coefficient (R^2) for all analytes was > 0.99 with 24 compounds (71%) having an $R^2 > 0.995$. The precision of the analytical method was verified using the intra-day and inter-day reproducibility (Table S7). Intra-day reproducibility calculated as % RSD was evaluated by analyzing four replicate injections of a 50 ng/L standard injected over the same day approximately three hours apart. The intra-day variability ranged from 1 to 10.4% with all the analytes except fluoxetine within 10%. The inter-day variability (% RSD) was determined by analyzing a 50 ng/L standard, prepared fresh everyday over four consecutive days and was < 10% for all compounds except atenolol with a range of 1–11.9%.

3.8. Analysis of water samples

The optimized method was used to determine the concentration of the 34 TOrCs in different environmental waters. Two conventional wastewater treatment plants (WWTP) were sampled at different treatment points to study treatment efficacy. WWTP 1 serves a largely urban population and has a capacity of 70 million gallons per day (MGD). It employs flocculation/sedimentation as primary treatment followed by an activated sludge process (sludge retention time ~4 days) as a secondary treatment and disinfection with free chlorine. WWTP 2 has a capacity of 2 MGD and serves a much smaller population (~17,000 people) with > 70% of the residents over 65 years in age. The first step in treatment of raw sewage is bar screens for grit removal followed by a biological oxidation ditch treatment (primary effluent), the mixed liquor is then sent to secondary clarifiers (secondary effluent) after which the water is disinfected with chlorine as hypochlorite before discharge (final effluent).

All pharmaceuticals analyzed were detected in the influent of both WWTPs with the anti-inflammatory drug Naproxen (avg. conc.:61,000 ng/L) and pain reliever Ibuprofen (35,000 ng/L) detected at highest concentrations. The metabolite clofibric acid however was not detected in both plants. Generally, most pharmaceuticals were present at > 1000 ng/L in the influent possibly indicating significant loading from humans as both plants served a domestic population. Similarly, all personal-care products analyzed were detected in the influent of the two WWTPs. Caffeine was the highest detected TOrC in the influent with an average concentration of 74,500 ng/L while none of the hormones tested were detected. No pesticides or perfluoroalkyl substances tested in this study was detected in the two plants. This could be due to the highly domestic nature of the wastewater indicating a lack of industrial and agricultural contribution to the waste.

The removal of TOrCs in wastewater depends on a number of factors including type of treatment process used, characteristics of the plant (like sludge retention time, pH and temperature) and physicochemical properties of the compound like biodegradability, sorption capacity, and water solubility [45,46]. The pharmaceuticals atenolol, trimethoprim, carbamazepine and sulfamethoxazole have low sorption coefficients and had poor removal after primary treatment in WWTP 1[47]. However these compounds with the exception of carbamazepine are well removed by biological processes as shown in the data (secondary effluent in WWTP 1 and primary effluent in WWTP 2) and corroborated by previous studies [48,49]. Similarly, caffeine has been shown to be easily biodegraded in activated sludge processes and this was evinced here as well with concentrations > 50,000 ng/L reduced to < 5 ng/L after biological treatment in both plants [50]. Moderate to high removals were seen for personal-care products like benzophenone and DEET in the primary and secondary treatments which is in agreement with previously published literature [51,52]. Finally, disinfection by chlorine can also oxidize some TOrCs leading to additional removal. Antimicrobial agents triclosan and triclocarban are extremely well removed by chlorine while flame retardants (TCEP and TCPP) have been shown to be resistant to most oxidants used in water treatment [4] and this was seen in the results as well. While several factors at each individual plant dictate the removals of these TOrCs, it can be seen that conventional treatment processes are not effective in complete attenuation of these compounds.

Analysis of a surface water revealed the presence of seven pharmaceuticals (carbamazepine, diltiazem, meprobamate, naproxen, primidone, sulfamethoxazole, and trimethoprim) ranging from 1.4 to 18 ng/L (Table 4). Five personal-care products (Benzophenone, caffeine, DEET, triclocarban and TCEP) were detected, with the UV-screen benzophenone (47 ng/L) being the highest detected TOrC in the SW. Both pesticides (atrazine and simazine) analyzed were present at < 5 ng/L. PFOA was detected at 27 ng/L in the SW while the other two PFCs analyzed were absent.

The groundwater (GW) sample collected from Tucson, AZ had the pharmaceutical-metabolite clofibric acid (22 ng/L) and insect-repellant DEET (5.4 ng/L) present at low concentrations while all other TOrCs analyzed were < MRLs. A grab sample collected from a septic tank showed the presence of all the personal-care products tested at concentrations > 100 ng/L. Caffeine (19,000 ng/L) was the TOrC detected at highest concentration with benzophenone (1600 ng/L) and triclocarban (1400 ng/L) also present at > 1000 ng/L in this sample. Only two pharmaceuticals (diphenhydramine and primidone) were present in this sample while all the hormones, pesticides and industrial compounds analyzed were not detected. The occurrence for all waters tested is presented in Table 4.

The presence of several trace-organic contaminants in surface and ground waters indicates that release of these compounds into the environment can enter water supplies and hence it would be prudent to monitor these chemicals while relevant toxicological studies are performed to evaluate health risk from water exposures.

4. Conclusions

A method utilizing fully automated online SPE coupled to LC–MS/MS with simultaneous positive and negative ESI for

Table 4
Concentration of analytes (ng/L) in different water matrices.

Compounds	WWTP 1				WWTP 2				SW	Septic tank	GW
	Influent	1° Effluent	2° Effluent	Final effluent	Influent	1° Effluent	2° Effluent	Final effluent			
Pharmaceuticals											
Atenolol	4000	3400	510	620	14,000	600	1000	590	< 3.5	< 19	< 2.5
Carbamazepine	1300	1400	350	340	300	320	300	300	< 0.7	< 1.9	< 0.2
Clofibric acid	< 40	< 37	< 5.1	< 4.8	< 18	< 16	< 12	< 2.8	< 1.2	< 21	< 1.1
Diclofenac	1400	1200	1300	680	9000	9300	7800	1800	< 4.9	< 76	< 6.3
Diltiazem	280	260	130	59	320	110	80	60	< 0.2	< 5.0	< 4.8
Diphenhydramine	4900	3800	820	670	25,000	1500	1100	340	< 1.4	710	< 1.1
Fluoxetine	60	< 24	< 17	< 11	92	74	19	< 16	< 4.4	< 73	< 3.5
Gemfibrozil	5200	5000	120	49	6800	200	190	21	< 0.7	< 2.8	< 0.7
Hydrochlorothiazide	3800	3100	540	360	7400	5100	5300	5100	< 0.6	< 23	< 0.6
Ibuprofen	33,000	32,000	27	45	35,000	64	63	53	< 2.4	< 21	< 1.9
Meprobamate	980	970	790	820	460	160	180	180	< 1.4	< 36	< 0.9
Naproxen	46,000	44,000	< 39	< 41	76,000	80	64	59	1.4	< 57	< 5.4
Primidone	350	360	300	53	2900	840	840	730	18	310	< 3.6
Propranolol	19	< 14	< 6.9	< 1.6	460	110	120	11	< 1.3	< 31	< 1.3
Sulfamethoxazole	3200	3200	1500	820	2600	2700	1500	470	4.5	< 35	< 0.6
Trimethoprim	1800	1900	320	250	2000	150	110	19	4.3	< 2.5	< 0.1
Personal-care products											
Benzophenone	2200	620	420	200	2500	300	190	94	47	1600	< 14
Caffeine	64,000	44,000	< 4	< 3	85,000	40	< 4	< 3	4.4	19,000	< 0.8
DEET	800	340	80	120	1100	21	29	48	4.9	760	5.4
Propylparaben	530	320	< 30	< 25	540	230	< 27	< 22	< 3.0	490	< 2.0
Triclocarban	540	520	100	< 14	6800	200	190	21	19	1400	< 1.1
Triclosan	2000	1800	81	28	3000	750	26	< 13	< 2.8	770	< 3.0
TCEP	5000	4900	4200	4000	810	370	210	190	19	370	< 3.9
TCPP	6600	5100	4900	4100	850	640	450	440	< 25	190	< 16
Industrial compounds											
Benzotriazole	1800	2300	1600	850	5600	2700	1700	1500	< 54	< 100	< 11
Bisphenol A	190	< 120	< 89	< 67	< 160	< 150	< 73	< 48	< 24	< 190	< 39
PFHxA	< 38	< 18	< 4.6	< 3.9	< 36	< 19	< 4.8	< 4.0	< 4.3	< 21	< 3.6
PFOS	< 60	< 52	< 13	< 10	< 66	< 57	< 19	< 11	< 3.4	< 51	< 6.1
PFOA	< 22	< 15	9	< 5	< 32	< 37	< 13	< 6	27	< 44	< 3.1
Hormones											
Hydrocortisone	< 102	< 64	< 51	< 21	< 85	< 75	< 57	< 23	< 28	< 31	< 10
Norgestrel	< 86	< 79	< 23	< 21	NA	NA	NA	NA	< 17	< 46	< 12
Testosterone	< 150	< 140	< 32	< 29	NA	NA	NA	NA	< 12	< 41	< 11
Pesticides											
Atrazine	< 8.3	< 6.4	< 1.5	< 1.4	< 5.2	< 4.1	< 4.6	< 1.0	2.1	< 1.5	< 0.3
Simazine	< 9.6	< 10	< 1.9	< 2.1	< 5.9	< 5.4	< 6.1	< 1.2	4.1	< 1.1	< 0.4

NA: not analyzed.

analysis of 34 diverse trace organic contaminants including pharmaceuticals, personal-care products, hormones, pesticides, and industrial compounds in water has been developed. The method presented provides rapid screening and low-level quantification of analytes without sacrificing sensitivity, with MDLs ranging from 0.1 to 13.1 ng/L. Further, a method to determine the MRL of each sample using isotope recovery data without having to perform time-consuming MRLs in each matrix tested is described. A low sample volume (1.7 mL) coupled with a cycle time of < 15 min allows for high-throughput analysis. Critically, the use of fast polarity switching allowed for analysis of all 34 TOrCs in both ESI positive and negative mode with just one injection resulting in large time savings that is unique compared to other published OSPE methods. This fully automated online extraction coupled to LC–MS/MS method provides significant time, labor and solvent savings compared to previously published methods while also increasing the reproducibility of analysis. Results indicate that optimization of the type of online SPE cartridge, washing mobile phase composition, washing volume and flowrate are critical to obtain best sensitivity for analysis. The method has been validated with analysis of TOrCs across several different environmental water matrices.

Acknowledgments

The authors would like to thank Dr. Sheher Mohsin from Agilent Technologies for assistance in setup and technical expertise. We also acknowledge Dr. Sonia Dagnino at the University of Arizona for help in reviewing this manuscript.

Appendix A. Supporting information

Supplementary data associated with this article can be found in the online version at http://dx.doi.org/10.1016/j.talanta.2014.08.011.

References

[1] E. Barral, G. Cohen, Ann. Pharm. Fr. 56 (1998) 277–281.
[2] T.G. Hinton, K. Aizawa, Multiple Stressors: A Challenge for the Future 200757–69.
[3] M.J. Benotti, R.A. Trenholm, B.J. Vanderford, J.C. Holady, B.D. Stanford S.A. Snyder, Environ. Sci. Technol. 43 (2009) 597–603.
[4] P. Westerhoff, Yoon Yeomin, Shane Snyder, Eric Wert, Environ. Sci. Technol. 39 (2005) 6649–6663.
[5] G.M. Bruce, R.C. Pleus, S.A. Snyder, Environ. Sci. Technol. 44 (2010) 5619–5626.

[6] C.G. Daughton, in: H. Kris (Ed.), International Encyclopedia of Public Health, Academic Press, Oxford, 2008, pp. 66–102.
[7] K.A. Strauch, Am. Assoc. Occup. Health Nurses J. 59 (2011) 525–532.
[8] B.I. Escher, C. van Daele, M. Dutt, J.Y.M. Tang, R. Altenburger, Environ. Sci. Technol. 47 (2013) 7002–7011.
[9] P.J. Novak, W.A. Arnold, V.S. Blazer, R.U. Halden, R.D. Klaper, D.W. Kolpin, D. Kriebel, N.G. Love, D. Martinovic-Weigelt, H.B. Patisaul, S.A. Snyder, F.S. vom Saal, A.V. Weisbrod, D.L. Swackhamer, Environ. Sci. Technol. 45 (2011) 3829–3830.
[10] F.S. vom Saal, C. Hughes, Environ. Health Perspect. 113 (2005) 926–933.
[11] J.P. Sumpter, S. Jobling, Environ. Toxicol. Chem. 32 (2013) 249–251.
[12] C. Zwiener, F.H. Frimmel, Anal. Bioanal. Chem. 378 (2004) 862–874.
[13] I. Ferrer, J.A. Zweigenbaum, E.M. Thurman, J. Chromatogr. A 1217 (2010) 5674–5686.
[14] T. Anumol, S. Merel, B. Clarke, S. Snyder, Chem. Cent. J. 7 (2013) 104.
[15] D.W. Kolpin, E.T. Furlong, M.T. Meyer, E.M. Thurman, S.D. Zaugg, L.B. Barber H.T. Buxton, Environ. Sci. Technol. 36 (2002) 1202–1211.
[16] B.J. Vanderford, R.A. Pearson, D.J. Rexing, S.A. Snyder, Anal. Chem. 75 (2003) 6265–6274.
[17] G.E. Batley, Mar. Pollut. Bull. 39 (1999) 23–31.
[18] E.D. Nelson, H. Do, R.S. Lewis, S.A. Carr, Environ. Sci. Technol. 45 (2011) 1228–1234.
[19] S.A. Snyder, M.J. Benotti, Water Sci. Technol. 61 (2010) 145–154.
[20] B.J. Vanderford, J.E. Drewes, A. Eaton, Y.C. Guo, A. Haghani, C. Hoppe-Jones, M. P. Schluesener, S.A. Snyder, T. Ternes, C.J. Wood, Anal. Chem. 86 (2013) 774–782.
[21] R.A. Trenholm, B.J. Vanderford, S.A. Snyder, Talanta 79 (2009) 1425–1432.
[22] L. Chen, H. Wang, Q. Zeng, Y. Xu, L. Sun, H. Xu, L. Ding, J. Chromatogr. Sci. 47 (2009) 614–623.
[23] I. Liska, J. Chromatogr. A 655 (1993) 163–176.
[24] L. Viglino, K. Aboulfadl, M. Prevost, S. Sauve, Talanta 76 (2008) 1088–1096.
[25] M. Rogeberg, H. Malerod, H. Roberg-Larsen, C. Aass, S.R. Wilson, On-line solid phase extraction-liquid chromatography, with emphasis on modern bioanalysis and miniaturized systems, J. Pharm. Biomed. Anal. (2014) 120–129.
[26] Z. Kuklenyik, A.M. Calafat, J.R. Barr, J.L. Pirkle, J. Sep. Sci. 34 (2011) 3606–3618.
[27] R. Lopez-Serna, S. Perez, A. Ginebreda, M. Petrovic, D. Barcelo, Talanta 83 (2010) 410–424.
[28] M. Tagiri-Endo, S. Suzuki, T. Nakamura, T. Hatakeyama, K. Kawamukai, Anal. Bioanal. Chem. 393 (2009) 1367–1375.
[29] M.J. Garcia-Galan, T. Garrido, J. Fraile, A. Ginebreda, M.S. Diaz-Cruz, D. Barcelo, Anal. Bioanal. Chem. 399 (2011) 795–806.
[30] V.R. Panditi, S.R. Batchu, P.R. Gardinali, Anal. Bioanal. Chem. 405 (2013) 5953–5964.
[31] F. Guo, Q. Liu, G.-B. Qu, S.-J. Song, J.-T. Sun, J.-B. Shi, G.-B. Jiang, J. Chromatogr. A 1281 (2013) 9–18.
[32] C. Jansson, J. Kreuger, J. AOAC Int. 93 (2010) 1732–1747.
[33] C.T. Wang, P.R. Gardinali, J. Mass Spectrom. 47 (2012) 1255–1268.
[34] S. Rodriguez-Mozaz, M.J.L. de Alda, D. Barcelo, Anal. Chem. 76 (2004) 6998–7006.
[35] A. Salvador, C. Moretton, A. Piram, R. Faure, J. Chromatogr. A 1145 (2007) 102–109.
[36] P. Anderson, N. Denslow, J.E. Drewes, A. Olivieri, D. Schlenk, S. Snyder 2010.
[37] E.R.V. Dickenson, S.A. Snyder, D.L. Sedlak, J.E. Drewes, Water Res. 45 (2011) 1199–1212.
[38] H.D. Zhou, Q.J. Zhang, X.L. Wang, Q.Q. Zhang, L.X. Ma, Y. Zhan, Environ. Sci. Pollut. Res. 21 (2014) 7113–7129.
[39] B.J. Vanderford, S.A. Snyder, Environ. Sci. Technol. 40 (2006) 7312–7320.
[40] T. Benijts, R. Dams, W. Lambert, A.De Leenheer, J. Chromatogr. A 1029 (2004) 153–159.
[41] J.A. Glaser, D.L. Foerst, G.D. McKee, S.A. Quave, W.L. Budde, Environ. Sci. Technol. 15 (1981) 1426–1435.
[42] S. Huntscha, H.P. Singer, C.S. McArdell, C.E. Frank, J. Hollender, J. Chromatogr. A 1268 (2012) 74–83.
[43] P.J. Taylor, Clin. Biochem. 38 (2005) 328–334.
[44] R. Bonfiglio, R.C. King, T.V. Olah, K. Merkle, Rapid Commun. Mass Spectrom. 13 (1999) 1175–1185.
[45] M. Gros, M. Petrovic, A. Ginebreda, D. Barcelo, Environ. Int. 36 (2010) 15–26.
[46] C.I. Kosma, D.A. Lambropoulou, T.A. Albanis, Sci. Total Environ. 466–467 (2014) 421–438.
[47] L. Yu, G. Fink, T. Wintgens, T. Melin, T.A. Ternes, Water Res. 43 (2009) 951–960.
[48] N. Kreuzinger, M. Clara, B. Strenn, H. Kroiss, Water Sci. Technol. 50 (2004) 149–156.
[49] N. Vieno, T. Tuhkanen, L. Kronberg, Water Res. 41 (2007) 1001–1012.
[50] P. Gao, Y. Ding, H. Li, I. Xagoraraki, Chemosphere 88 (2012) 17–24.
[51] A. Wick, O. Marincas, Z. Moldovan, T.A. Ternes, Water Res. 45 (2011) 3638–3652.
[52] Q. Sui, J. Huang, S.B. Deng, W.W. Chen, G. Yu, Environ. Sci. Technol. 45 (2011) 3341–3348.

Talanta 132 (2015) 87–95

Contents lists available at ScienceDirect

Talanta

journal homepage: www.elsevier.com/locate/talanta

Review

Increasing energy efficiency and sensitivity with simple sensor platforms

J.L. Gole [a,b,*]

[a] School of Physics, Georgia Institute of Technology, Atlanta, GA 30332, USA
[b] School of Mechanical Engineering, Georgia Institute of Technology, Atlanta, GA 30332, USA

ARTICLE INFO

Article history:
Received 14 July 2014
Received in revised form
11 August 2014
Accepted 12 August 2014
Available online 21 August 2014

Keywords:
Sensors
Metal-oxide
Deposited directing nanostructures
IHSAB principle

ABSTRACT

We outline and review an approach to the construction of conductometric sensors that demonstrate considerably higher sensitivities than traditional metal oxide sensors. Simple sensor platforms do not require film-based technology, operate at room temperature, and can be obtained without the use of time consuming self-assembly processes. A combined nanopore coated micro-porous array is deposited with nanostructure directing acidic metal oxide island sites which vary in their Lewis acidity, decorate the micropores, and control an electron transduction process. The interaction of analytes with these island sites varies in a predictable manner and can be modified through in-situ functionalization of their Lewis acidity. The micropores allow rapid Fickian diffusion of analytes to the active nanostructured island sites whose reversible interaction with the analyte dominates the sensor response. We require only that the island sites be deposited at sufficiently low concentration so as not to interact electronically with each other. Highly accurate repeat placement of the depositions is not required. The nanoporous walls of the microarray act as a phase match for the deposition of a diversity of nanostructures that are selected for deposition from a variety of easily obtained solution-based sources as the forgiving deposition process requires a minimum of energy consumption and time. Comparisons to a variety of metal oxide systems are considered. Observed sensitivities and the sensor system reversibility can be predicted from the recently developing IHSAB model.

© 2014 Elsevier B.V. All rights reserved.

Contents

1. Introduction . . . 87
2. The interface . . . 89
3. Discussion . . . 89
4. Power consumption . . . 90
5. Inverse Hard/Soft Acid/Base concept . . . 93
6. Conclusion . . . 94
Acknowledgment . . . 95
References . . . 95

1. Introduction

Regulations for the detection, monitoring, and transformation of environmental constituents are increasing at a significant rate so sensor interfaces must be sensitive to low level exposures and have fast response times [1]. With concerns about the impact of gases on health and environmental concerns increasing, the reliable detection of several gases over a range of temperatures including, for example, NO_x associated with air pollution, combustion, and respiratory disease [2,3] is critical. NO is the primary monitor of an asthmatic attack and can also provide rapidly accessed noninvasive disease [4] detection. NH_3, which plays an especially important role in urban environments [5,6], is also produced albeit at much lower levels, during an asthma attack.

* Correspondence address: School of Physics, Georgia Institute of Technology, Atlanta, GA 30332, USA.

http://dx.doi.org/10.1016/j.talanta.2014.08.038
0039-9140/© 2014 Elsevier B.V. All rights reserved.

SO_x as well as NO_x play an important role in automotive and industrial exhaust, acid rain, photochemical smog, and corrosion [3]. Fuel combustion products contain toxic and odorless CO. PH_3 is an extremely toxic gas used for fumigation in agriculture and is a byproduct in the production of methamphetamines [7,8]. Historically, advances in gas sensor technology used to monitor these exemplary gases have been driven by sensitivity, selectivity, stability, response time, and durability.

There are a wide variety of gas detection devices which include infrared spectroscopic, mass sensitive, and solid-state sensors. Here, we consider solid-state devices which detect analytes by measuring an electrical property of the detection interface and from this measurement we can evaluate an interacting gas. These conductometric gas sensors can be made to consist of a sensitive interface layer decorated by nanostructure island sites. The nanostructure decorated interfaces that can be easily constructed, do not demand complex self-assembly, are much easier to implement and reproduce than film depositions, and require far fewer starting materials. These attributes suggest enhanced energy efficiency both in the transduction mechanism and in the simplicity of a design involving minimal manufacturing time.

The most common type of solid state sensor is the metal oxide sensor. These sensors [9,10] use the metal oxides of tungsten (WO_3), nickel (NiO), copper (Cu_xO), aluminum (Al_2O_3), titanium (TiO_2), tin (SnO_x), and zirconium (ZrO_2). Of the methods used to prepare these oxides, those that are most commonly cited in the literature require the use of thin films (< 1 μm). However, in some cases thick films are used, doped with noble metals or various nanoshapes designed to effect grain boundaries [10–17]. These metal oxide sensors must be heated to elevated temperatures that range from 100 to 600 °C [10,18–20] and, in many cases for the effective monitoring of a given analyte, must be precisely controlled.

The required temperature control of typical metal oxide sensors and the necessity to generate the sensing interface from film technology are two key problems that can be overcome with the technology that we outline in this monograph. We describe a conductometric gas sensor that can be made to consist of an easily designed sensitive hybrid nano/microporous interface transformed through the introduction of select nanostructures. Although the current interface is designed from porous silicon, the distinct approach that we employ can be extended to any extrinsic semiconductor onto which the hybrid nanopore coated microporous structure can be generated. This hybrid structure facilitates rapid Fickian [21,22] diffusion into a microporous framework whose nanoporous wall covering serves to provide a phase match for the selectively deposited nanostructures. In contrast to both

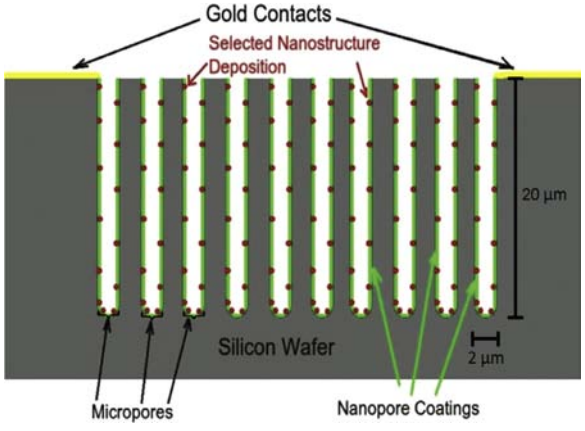


Fig. 1. Schematic representation of PS sensor system [22]. Reprinted from J.L. Gole, S. Ozdemir, Nanostructure directed physisorption vs. chemisorption at semiconductor interfaces: the inverse of the hard–soft acid–base (HSAB) concept, Chem. Phys. Chem. 11, Copyright © 2010 WILEY-VCH Verlag GmbH & Co. KGaA, Weinheim [29].

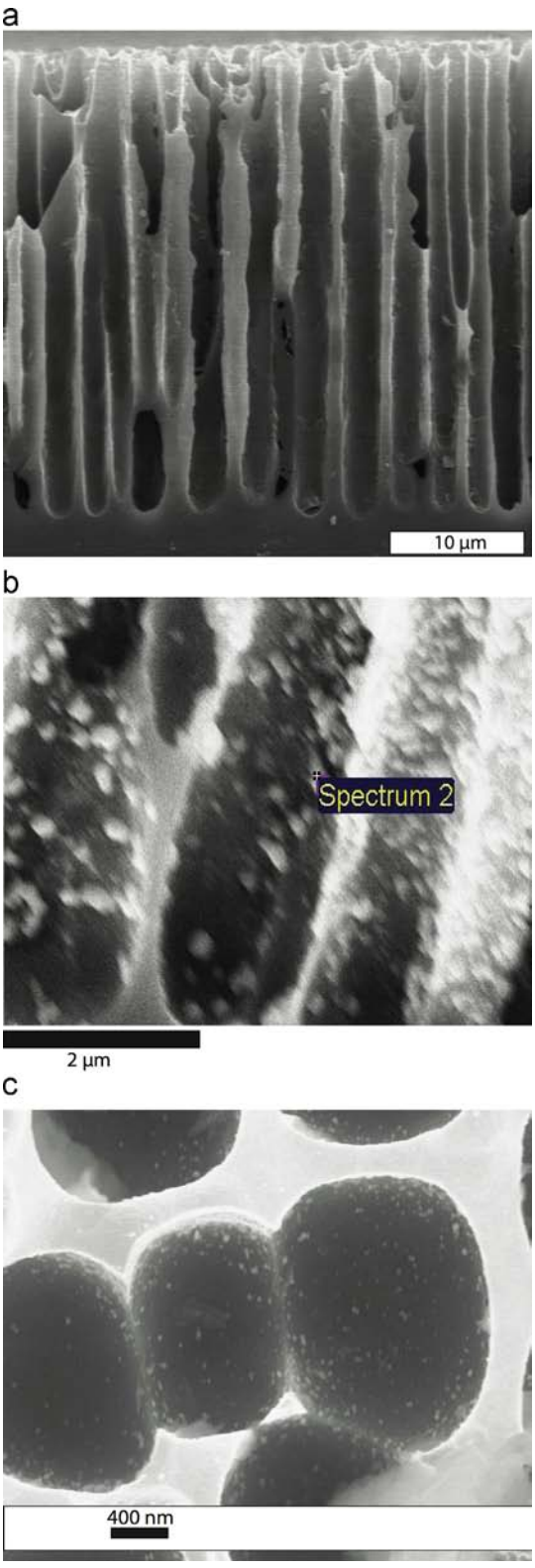


Fig. 2. a) Close-up side view of *p*-type porous hybrid porous silicon (PS) film. [scale bar corresponds to 10 μm.] b) Nanoparticle tin-oxide coating on PS micropores. c) 10–30 nm Au_xO nanostructure. Reprinted from Chem. Phys. Chem., 11, 2573–2581, Copyright (2010), with permission from Elsevier [29]. Reprinted from J.L. Gole, S. Ozdemir, Nanostructure directed physisorption vs. chemisorption at semiconductor interfaces: the inverse of the hard–soft acid–base (HSAB) concept, ChemPhysChem, 11, Copyright © 2010 WILEY-VCH Verlag GmbH & Co. KGaA, Weinheim [29].

thin and thick films, which may respond in minutes [23] due to slow diffusion, the current structure, with which analyte interaction is diffusion dominated, allows a response in less than 2 s [22].

2. The interface

The basic semiconductor interface is illustrated in Fig. 1 [22]. This structure is produced by a hybrid etch procedure used to create the desired interfacial porous silicon support structure. The nanopore covered microporous structure of the interface has been created specifically to facilitate efficient gaseous diffusion [21,22] to the highly active nanostructure modified nanoporous coating. The active nanostructures can be chosen from a continuously expanding selection of metal oxides including, for example [21,22], MgO, TiO_2, SnO_x, NiO, Cu_xO, and Au_xO ($x \gg 1$), decreasing in the Lewis acidity of the metal sites. The surface-attached nanoparticles possess unique size dependent and electronic structure properties that form a basis for changing the sensitivity for exposure to specific analyte gases. This exposure alters the conductivity of the porous silicon attached to the gold contacts shown in Fig. 1. When operated in the electron transduction mode, the transfer of electrons to an *n*-type PS interface, as would occur with a basic analyte, increases the majority charge carriers which are electrons, decreases the conductometric resistance and increases conductance. The removal of electrons, as would occur with an acidic analyte, decreases the majority charge carrier concentration and the conductance and increases resistance. The opposite behavior will be observed for a *p*-type semiconductor interface.

The sensors we describe are fabricated from *n*-type and *p*-type silicon wafers as multiple sensors are created from a single wafer using an insulating and etch-resistant mask layer with an array of 2 mm × 5 mm windows. An insulating etch-resistant layer is created by depositing 200 nm of SiC by plasma-enhanced chemical vapor deposition (PECVD) and windows are removed from the SiC layer by reactive ion etching (RIE) where photoresist guides the RIE etching pattern. The revealed silicon is then electrochemically etched in a single cell configuration to produce a nanopore coated microporous interface. The PS morphology can be adjusted by adjusting etch parameters including time of etch and current density. The details of the micro-fabrication processes are straightforward and are described elsewhere [22,24,25].

3. Discussion

The nanostructure-decorated configuration depicted in Fig. 1 has several properties that are superior to traditional metal oxide thin film designs. First, the nanostructures are readily deposited to the microporous interface from a variety of solution-based sources (ex: electroless metal, sol–gel generated nanostructures, soluble metal chlorides) [22], which require no heating. Second, once deposited, the nanostructures can be readily functionalized, in-situ, predictably changing their interaction with a given analyte. This is exemplified as we convert the metal oxides to oxynitrides [24,26] or as we functionalize the nanostructured metal oxides with S–$H_z(CH_x)_y$ ($z=0,1$) groups [27,28]. The important consideration is that the nanostructured sites are easily modified.

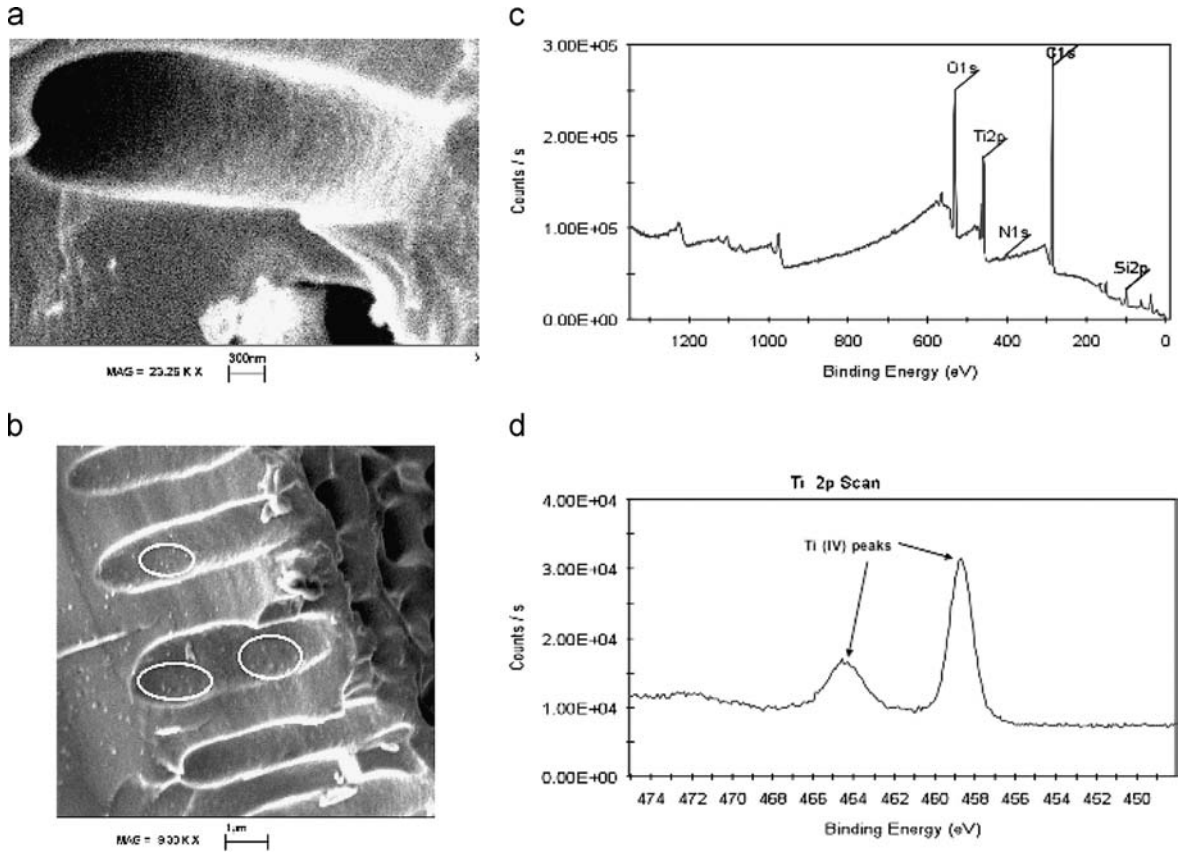


Fig. 3. (a) SEM image of undecorated *n*-type PS pore structure. The pore is approximately 1 μm in diameter and 4 μm in length. (b) SEM image of porous silicon structure deposited with TiO_2. Some of the TiO_2 nanostructures (10–20 nm) are encircled in white. (c) XPS spectrum for the decorated porous structure showing the overall XPS spectrum including background peaks and (d) close-up of Ti 2p XPS region. Those nanostructures can be subsequently nitridated to form $TiO_{2-x}N_x$ [30]. Reprinted from W. Laminack, J.L. Gole, Light enhanced electron transduction and amplified sensing at a nanostructure modified semiconductor interface, Advanced Functional Materials, 23 Copyright © 2013 WILEY-VCH Verlag GmbH & Co. KGaA, Weinheim [30].

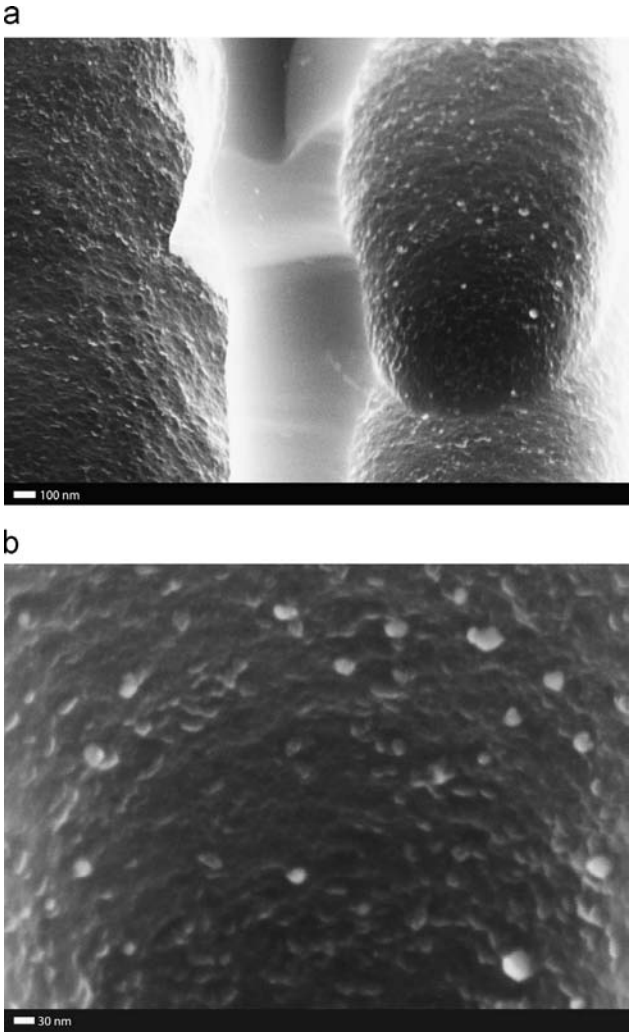


Fig. 4. (a) SEM image of thiol treated TiO_2 decorated porous silicon at 87.36 KX magnification. (b) SEM image of thiol treated TiO_2 decorated porous silicon at 274.17 KX magnification. The lighter images in the micrographs correspond to sulfur-based moiety functionalized titanium oxide [28]. Reprinted from W. Laminack, C. Baker, J.L. Gole, Sulfur–$H_z(CH_x)_y$ ($z=0,1$) functionalized metal oxide nanostructure decorated interfaces: evidence of lewis base and brönsted acid sites—influence on chemical sensing, Chemistry of Materials Submitted [28].

We provide examples of this ready deposition in Figs. 2–4. Note that the deposition does not require time consuming and costly self-assembly or the application of costly and time-intensive lithographic assembly. The nanostructured island sites once deposited to the interface are sustained on that interface in the size range 10–30 nm with no evidence for sintering. We require only that the concentration of the nanostructures be maintained at a level so as to avoid cross talk between these structures which will degrade the conductometric response of the interface.

In other words, there is an optimum deposition concentration for each nanostructure deposition. However, the deposition process requires no additional control and does not demand that the nanostructured islands be placed precisely at the same points in the micropores. This simplicity of design follows a process that is much more energy efficient than is thin or thick film design. With this form of interface preparation, we provide ready reproducibility, a factor that is not easily obtained in film preparation.

Counter to traditional metal oxide systems dispersed metal oxides on PS do not operate at high temperature. Therefore, they are more energy efficient and respond more rapidly due to their dispersed nature. Our room temperature operative design adds considerable flexibility not possible in a singly or multiply "coated" metal oxide interface. As metal oxide sensors need to operate at elevated temperatures, a power consuming heating element must be provided with the sensor housing. In several applications it is necessary to tightly control the temperature of the sensor element. This is intimately tied to the correct identification of the gas of interest. Distinguishing one gas from another requires that the heating element and sensor be well separated (channel) from the remaining electronics. This means that this configuration can be greatly affected by an impinging combustion or flue gas, rendering difficult the correct identification of gaseous species in the flow. In contrast, the PS sensor configuration depicted in Fig. 1 consumes less power as it does not require the complexity of a system separated sensor/heater configuration. However, again in contrast to traditional metal oxide systems, the PS sensor depicted in Fig. 1 can be extended in a heat sunk configuration to probe elevated temperature environments. This suggests that it might be used to monitor high temperature flue gas flows [22]. Figs. 5–8 provide an indication of the conductometric responses observed for several nanostructure directed systems.

The sensitivity obtained for the conductometric responses in Figs. 5–8 not only is greater than that for a typical metal oxide deposition but also compares very favorably with other modes of detection. X-ray Photoelectron (XPS) spectra taken for the nitridated and sulfur functionalized PS interfaces are sensitive to 0.1%. The typical time frame for the depositions used to obtain the conductometric data in Figs. 7 and 8 is 15–30 s. To obtain the XPS data we use deposition times which are at least 5 min. This corresponds approximately to an order of magnitude increase in concentration to generate signals in the 0.1% range. This indicates the significant sensitivity of the conductometric sensor responses. The magnitudes of the observed reversible interactions are described by the developing IHSAB model.

4. Power consumption

We have examined the *IV* response associated with the porous silicon sensor substrates, testing for linearity and bias. Fig. 9 shows the *IV* curves obtained for the operating sensor of Fig. 1. Here, we demonstrate forward and reverse scans for recently produced sensors which feature linearity over the entire testing range as well as no bias. Based on the linear *IV* curve, the continuous power consumption is between 25 and 60 μW/s over the range 1–1.5 V. We compare this result to the results of Ahlers et al. [32] (Fig. 10). The *IV* curves in Fig. 9 in concert with the analysis of Ahlers et al. [32] (Fig. 10) demonstrate that the nanostructure directed sensor systems require considerably less power for operation than do thick or thin film sensors. Mueller et al. [33] following Ahlers et al. [32] have recently discussed a MEMS toolkit for metal oxide based sensing systems. Using silicon micromachining technologies they have developed metal oxide gas sensor elements with very small heat consumption. The power of a single micromachined sensor element is found to be an order of magnitude less (Fig. 10) than that of thick film devices. In their Table 1, these authors quote heating powers, and necessary overhead heating requirements which sum to 1–1.5 W for a Thick-film sensor (column 1 Fig. 10) and 0.4–0.6 W (0.8 W including sensor) for a micromachined sensor array. The required power for the nanostructure directed PS systems we have considered is virtually in the noise level of Fig. 10. For this reason they are not shown in Fig. 10. We emphasize that the described system competes quite favorably with those micro-machined sensor systems whose construction may be more costly and time consuming.

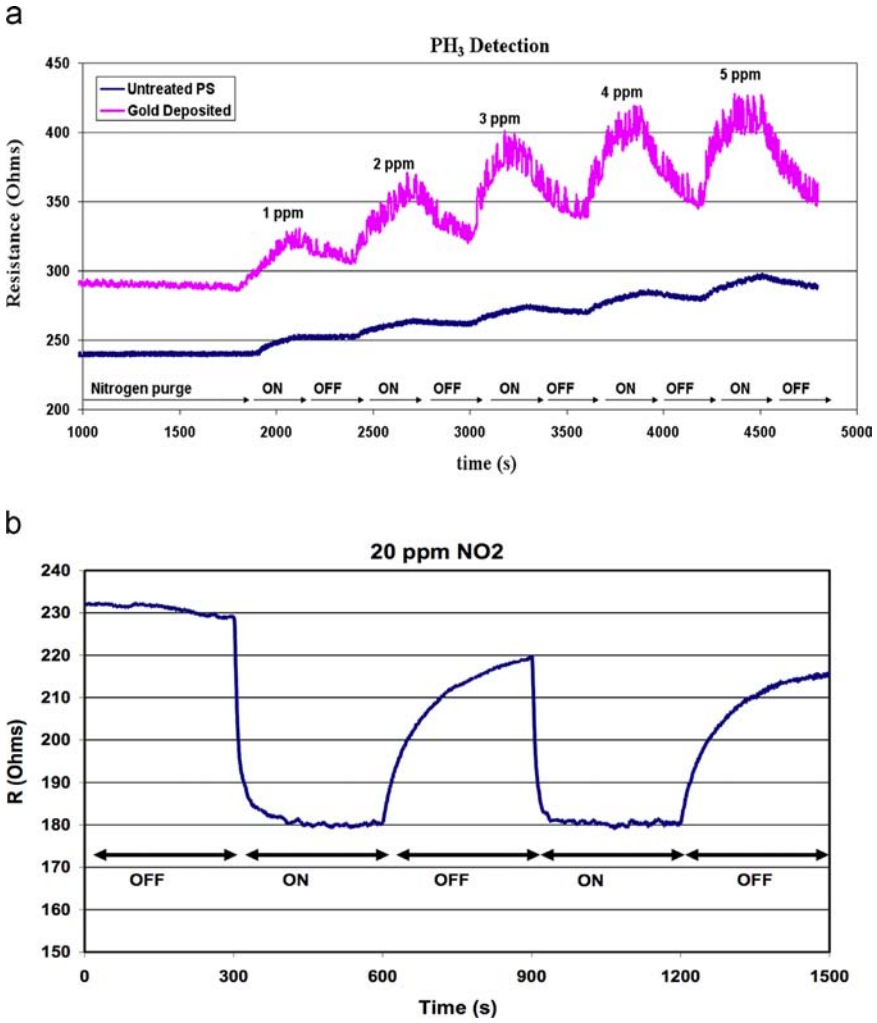


Fig. 5. (a) Improved response of a basic analyte, PH_3, to a *p*-type PS sensor with an electroless Au_xO coating. Here, 1, 2, 3, 4, and 5 ppm of PH_3 are pulsed onto the sensor surface every 300 s. A *p*-type sensor is used as the gold clustered oxide deposition enhances the response of the un-treated porous silicon interface by a factor of five. Reprinted from Chem. Phys. Chem., 11, Copyright (2010), with permission from Elsevier [29]. Reprinted from J.L. Gole, S. Ozdemir, Nanostructure directed physisorption vs. chemisorption at semiconductor interfaces: the inverse of the hard–soft acid–base (HSAB) concept, Chem. Phys. Chem. 11, Copyright © 2010 WILEY-VCH Verlag GmbH & Co. KGaA, Weinheim [29]. (b) Response of an acidic analyte, NO_2, to a *p*-type PS sensor. Conductivity increases upon exposure to the moderate acid. The return to baseline is not complete at this concentration as NO_2 sticks to the surface in this open experimental configuration [31]. Reprinted with permission from S. Ozdemir, T. Osburn, J.L. Gole, Nanostructure modified gas sensor detection matrix for NO transient conversion of NO to NO_2, Journal of the Electrochemical Society. 158 (2011) J201–J207 [31].

It is appropriate that we compare the outlined nanostructure directed interface with other metal oxide-based systems. While it is possible to create an exhaustive list of these sensor systems, this information can be obtained from several reviews in the literature [34]. Because SnO_2 and ZnO have been workhorses of the metal oxide sensor community we summarize a number of recent applications to the detection of several of the analytes that we have indicated in Section 1. Table 1 provides data on the detection of H_2S, SO_2, NO_2, CO, and NH_3. CO and NH_3 have also recently been detected using CuO thick films and nanowires. These results provide a comparative but by no means exhaustive list. For these analytes, concentrations at the sub-ppm level can be routinely measured at *room temperature* using the configuration of Fig. 1 (LEL (Lower Exposure Limit)=0.94 ppm for H_2S [35], 0.84 ppm for SO_2 [35], <0.5 ppm for NO_2 [36], 1 ppm for CO [37], <0.5 ppm for NH_3 [38] with low ppb range readily accessible [38], and <0.5 ppm for PH_3 [38–40] (amenable to extension to the ppb range)). The LEL's that we quote here correspond to the lowest measured concentration directly accessible to our measurements, in the linear regime of response, with no extrapolation. Thus the quoted LEL's are all upper bounds. Table 1 demonstrates that virtually all metal oxide systems operate at elevated temperatures. Further, processes that create thick film sensor elements, while sensitive, display significant response times, which can be on the order of minutes [23] (vs. seconds).

The data in Table 1 relate primarily to film based configurations where grain boundaries can pose complications. The data in the latter part of the table correspond to single crystalline nanowires or nanobelts, whose study can reveal important information concerning the reaction between target analytes and metal oxide surfaces free of grain boundaries. Nanowire and nanobelt diameters are on the order of several nanometers, comparable to the Debye length. This provides a much larger sensitivity than the corresponding thin film or bulk counterparts and several of these studies suggest the possibility of sensitivities in the ppb range. On a somewhat larger scale, Liao et al. [50] in detecting H_2S (100 ppm) found that thin nanorods have a much better sensing performance than thick nanorods. In extrapolation, researchers generally use the Langmuir absorption isotherm to fit the sensitivity–concentration curves of single nanowires whereas the power law, $S=a+bc^{\rho}$, is used to fit the concentration–sensitivity curves of film-based sensors [51]. It is to be noted that the sensitivities of single nanowire gas sensors are invariably less than nanowire film

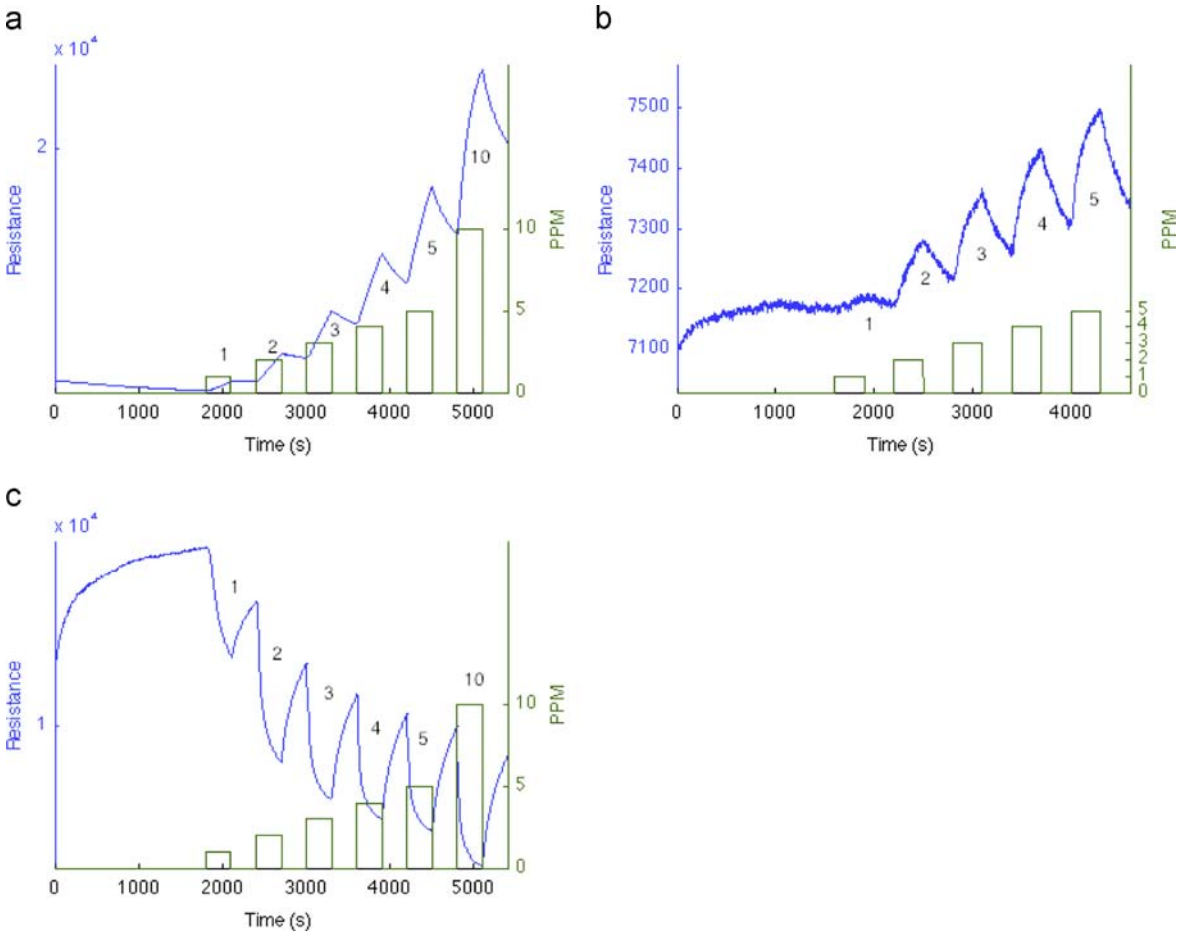


Fig. 6. Resistance response of *n*-type porous silicon sensors to 1–5 ppm and 10 ppm of (a) NO_2, (b) NO and (c) NH_3 [22,25]. NO_2 acts as a moderate acid, NO as a weak acid (resistance increase), and NH_3 as a strong base (conductance increase). Compare the results for NH_3 to those for PH_3 (Fig. 5(a)). Reprinted with permission from J.L. Gole, E. C. Goude, and W. Laminack, ChemPhysChem 13 (2012) 549–561 [25].

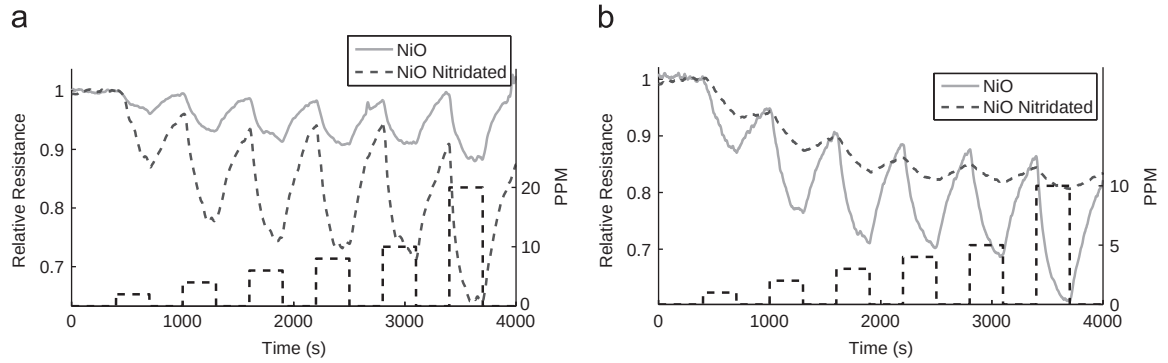


Fig. 7. Response to NH_3 (a) and NO (b) of a NiO treated PS interface before (solid gray) and after (dotted gray) a nitridation of the surface for 15 s with triethylamine. The boxes (black dashes) denote the analyte concentration from 1 to 10 ppm over the time of analyte gas exposure to the sensors. A rapid response is observed at each concentration. For NH_3, nitridation produces an increase in the interface response as monitored as an increase in conductance (decrease in resistance); however, for NO the nitridation decreases the interface response [26]. These responses are explained by the IHSAB concept. Reprinted by permission from W. Laminack, J.L. Gole, Direct in situ nitridation of nanostructured metal oxide deposited semiconductor interfaces: tuning the response of reversibly interacting sensor sites, ChemPhysChem, Copyright © 2014 WILEY-VCH Verlag GmbH & Co. KGaA, Weinheim [26]

gas sensors. For most of the elevated temperature studies in Table 1, there are difficulties in assessing whether an optimum temperature has been explored. Further, researchers studying 1D nanostructures, in general, may not follow a unified limit of detection when claiming the detection limit of their gas sensor reaches some ppb or ppm level [52].

Four of the last six entries in Table 1 suggest the possibility of extension to the ppb level of detection using nanowire or nanorod configurations. These studies show future promise but are somewhat difficult to gauge. For example, while it has been suggested [52] that Hernández-Ramírez et al. [57] can monitor CO concentrations of 100 ppb, these authors indicate only that they can measure concentrations less than 5 ppm. This is a very comprehensive study, which shows the promise for CO measurements both in dry air and at enhanced humidity levels. The results obtained by Zhao and Zhu [55] for NH_3 are impressive; however, it should be apparent that 5 nm nano-wire bundles are not easily

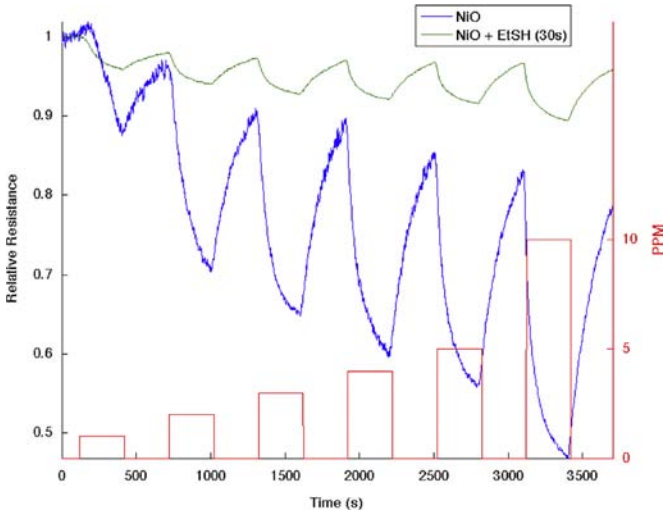


Fig. 8. (a) Response of ethanethiol treated nickel oxide nanostructure deposited porous silicon (PS) interface to NH_3 (a) exposure for 30 s and (b) exposure only to nickel oxide. The treated interface is more acidic than the Ni_xO treated PS acidic sites after a 30 s exposure. The boxes denote the analyte concentration from 1 to 10 ppm from the beginning of the gas introduction to the end. A rapid response is observed at each concentration [28]. These responses are explained by the IHSAB concept. Reprinted with permission from W. Laminack, C. Baker, J.L. Gole, Sulfur–$H_z(CH_x)_y$ ($z=0,1$) functionalized metal oxide nanostructure decorated interfaces: evidence of lewis base and brönsted acid sites—influence on chemical sensing, Chemistry of Materials. Submitted [28].

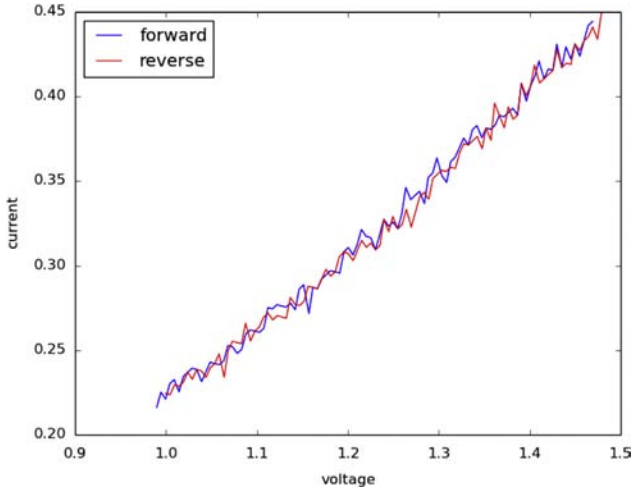


Fig. 9. *IV* curves for continuous sensor response.

prepared. The coupling of nanowires to a MEMS microhotplate again offers impressive results [56], but, however, this is again a difficult device to fabricate. Perhaps the most impressive result in Table 1 is the nanowire–nanogenerator self-powered gas sensor of Xue et al. It is clear that nanostructure bundles and nanorods can play a role of increasing importance in sensor applications.

5. Inverse Hard/Soft Acid/Base concept

By depositing metal oxide nanostructure islands to the PS interface, shown schematically in Fig. 1, the response of the sensor can be enhanced or diminished [25]. The Inverse Hard/Soft Acid/Base (IHSAB) model explains this phenomenon by linking chemical

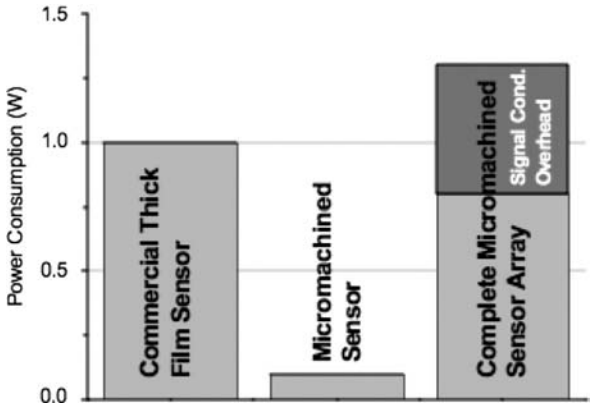


Fig. 10. A comparison of power consumptions. A full-fledged micro-machined sensor array with heater driver requires as much power as a single commercial thick film device. Additional power for signal conditioning electronics for a micro-machined sensor *array* is also indicated (from Ahlers et al. [32]). Reprinted by permission from S. Ahlers, P. Kreisl, G. Müller, A low-power metal-oxide based gas sensing system, 203rd ECS meeting, paper 2873, April 28, 2003, The Electrochemical Society [32].

selectivity and the balance of electron transduction and chemisorption [22,24–26] with the sensor response mechanisms. The IHSAB model predicts the interaction of acidic, basic, and amphoteric gas analytes with the nanostructure treated PS sensor interfaces. Table 2 provides an outline of the Hard/Soft identification of acids and bases. A hard acid will form a strong ionic bond with a hard base and a soft acid will form a strong covalent bond with a soft base. For the purposes of chemical sensing, we wish to minimize this bond formation [59–61]. The IHSAB model directs the fabrication of a nanostructure-treated PS gas sensor that behaves to stimulate an electron transduction physisorption-dominated mode as an inorganic gas analyte interacts with a decorated interface. Electron transduction dominates chemisorption, through the interaction of a hard acid and soft base or soft acid and hard base. There are different ways to control the size of the interaction of those molecules that are to be sensed with variably doped metal oxide nanostructure deposited sensing interfaces. However, the dominant factor is the HOMO–LUMO energy increment. If the donor orbital energy (highest occupied molecular orbital, HOMO) is not well matched with the acceptor (lowest unoccupied molecular orbital, LUMO), then the interaction will be weak. As the HOMO (donor)–LUMO (acceptor) energy gap decreases, there can be more charge transfer between the molecule (analyte) and the created interface, leading to a stronger Lewis acid–base interaction. Conversely, the greater the HOMO–LUMO energy gap, the greater the orbital mismatch, enhancing the electron transduction mode. The IHSAB principle is in large part based on controlling the size of the Lewis acid–base bond dissociation energy.

The estimated positions of deposited nanostructures and gas analytes on the IHSAB scale are shown in Fig. 11 relative to PS. As dictated by the scale and following the IHSAB model of interactions, PS deposited with Au_xO nanostructures will produce the largest response to NH_3 and PS deposited with TiO_2 will produce the largest response to CO. Within the IHSAB framework, metal/metal oxide nanostructure depositions can be selected for the PS sensor interface to create a predictable range of sensitivities for various gases [22,24–26]. The relative responses which we have observed to select *n*-type and for *p*-type systems thus allow the construction of the "Materials Positioning Table" for the acids and bases within the IHSAB concept. The analyte response data forms the basis for the development of this materials positioning diagram based largely on the interaction of the acidic metal oxides ranging from TiO_2 to Au_xO ($x \gg 1$) and the bases NH_3 to CO.

Table 1
Lower Exposure Limit of various gas sensor materials and methods.

Gas	Gas Concentration Lower Exposure Limit (LEL)	Response sensitivity	Operating temperature	Material	Method	Author
H_2S	1 ppm	5900[a]	200 °C	Ag (8 nm)-doped SnO_2	DC magnetron sputtering (SnO_2); Ag film coating	Jin et al. [41]
H_2S	3 ppm; 1 ppm LEL	40%[b]; unreported	74 °C	Ag-doped SnO_2	Polymeric sol–gel	Gong et al. [42]
H_2S	2.5 ppm	~85%[b]	400 °C	SnO_2	Spray pyrolysis	Griessler et al. [43]
H_2S	0.5 ppm	~1.4[a]	300 °C	SnO_2	Flame spray pyrolysis (FSP) (nanopowders); spin coating (sensor)	Liewhiran et al. [44]
H_2S	10 ppm	~1.45[a]	300 °C	CuO	Heating in open-air high purity copper foils (nanowires)	Shao et al. [45]
H_2S	1 ppm	~5[c]	25 °C	PS untreated	Nanopore covered μ-pores	Lewis et al. [35]
SO_2	50 ppm	~40%[b]	300 °C	SnO_2	Spray pyrolysis	Griessler et al. [43]
SO_2	20 ppm	~3.8[a]	300 °C	SnO_2	FSP (nanopowders) spin coating (sensor)	Liewhiran et al. [44]
SO_2	5 ppm	~45%[b]	350 °C	0.15 wt% V_2O_5/SnO_2	Simultaneous precipitation technique (nanopowder); painting (sensor)	Das et al. [46]
SO_2	1 ppm	~5[c]	25 °C	PS untreated	Nanopore covered μ-pores	Lewis et al. [35]
CO	50 ppm	8[a]	350 °C	0.2 wt% Pt/SnO_2	FSP (nanopowders); thermophoresis (sensor)	Mädler et al. [47]
CO	500 ppm	N/A[d]	200–400 °C	SnO_2	FSP (nanopowders); drop coating (sensor)	Sahm et al. [48]
CO	10 ppm	N/A	150 °C	CuO	Soft chemistry (nanospheres); thick film screen printing (sensor)	Hübner et al. [49]
CO	1 ppm	~3[c]	25 °C	PS, SnO_2 treated	Sn electroless solution	DeBoer et al. [37]
NO_2	5000 ppb	20[a]	220 °C	SnO_2	FSP (nanopowders); drop coating	Sahm et al. [48]
NO_2	< 500 ppb	~10[c]	25 °C	PS, TiO_2 treated	TiO_2 nanoparticle solution doped nanopore covered μ-pores	Laminack et al. [36]
NH_3	100 ppm	3.1[a]	200 °C	CuO	Heating in open-air high purity copper foils (nanowires)	Shao et al. [45]
NH_3	< 500 ppb	~50[c]	25 °C	PS, Au_xO treated	Au electroless solution	Ozdemir et al. [38]
PH_3	< 500 ppb	~10[c]	25 °C	PS, Au_xO treated	Au electroless solution	Ozdemir et al. [38,39] Laminack et al. [40]
H_2S	50 ppb	N/A	25–200 °C	ZnO	Nanorods	Wang et al. [53]
H_2S	1 ppm	N/A	RT[e]	In_2O_3	Nanowires 2–3 min response	Zeng et al. [54]
NH_3	10 ppb	(N/A)	RT	$W_{18}O_{49}$	Ultrathin (5 nm) nanowire bundles	Zhao et al. [55]
NH_3	100 ppb	N/A	300 °C	SnO_2	Coupling SnO_2 nanowire to MEMS microhotplate	Meier et al. [56]
CO	100 ppb (quote < 5 ppm)	N/A	300 °C	SnO_2	Single nanowire	Hernández-Ramírez et al. [57]
H_2S	100 ppm	N/A	RT	ZnO	ZnO nanowire nanogenerator-possible self-powered gas sensor	Xue et al. [58]

[a] Sensitivity $=((R_{air}-R_{gas})/R_{air})\times 100\%$.
[b] Sensitivity $=R_{gas}/R_{air}$.
[c] from $\Delta=\frac{\Delta R(\text{deposited})/R_0(\text{deposited})}{\Delta R(\text{untreated})/R_0(\text{untreated})}$.
[d] N/A = Not Available.
[e] RT = room temperature.

Table 2
Sampling of Hard/Soft Acid/Base designation of various materials [22,29].

	Hard	Borderline	Soft
Acids	H^+, Li^+, Na^+, K^+ Be^{2+}, Mg^{2+}, Ca^{2+} Cr^{2+}, Cr^{3+}, Al^{3+} SO_3, BF_3, Sn^{4+}, Ti^{4+}	Fe^{2+}, Co^{2+}, Ni^{2+} Cu^{2+}, Zn^{2+}, Pb^{2+} SO_2, BBr_3, Sn^{2+} NO_2	Cu^+, Au^+, Ag^+, Tl^+, Hg Pd^{2+}, Cd^{2+}, Pt^{2+}, Hg^{2+} BH_3
Bases	F^-, OH^-, H_2O, NH_3 CO_3^{2-}, NO_3^-, O_2	NO_2^-, SO_3^{2-}, Br^- N_3^-, N_2, H_2S C_6H_5N, SCN	H^-, R^-, CN^-, CO, I SCN^-, R_3P, C_6H_5 R_2S

6. Conclusion

The data that we have summarized indicate a novel mode to create metal oxide sensors with significant ease that facilitates the development of reversible conductometric sensor systems. These are energy efficient forgiving systems. We deposit metal oxide

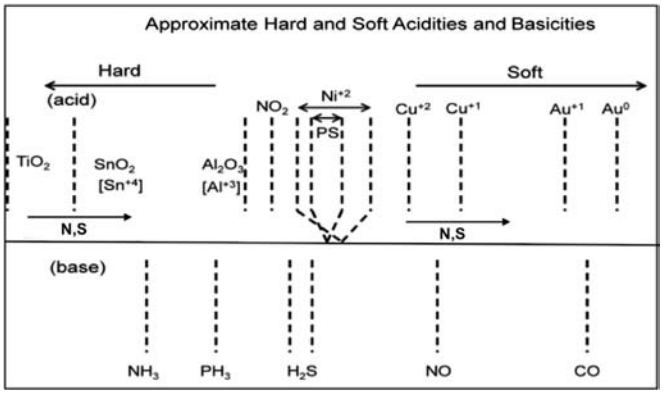


Fig. 11. IHSAB scale and estimated hard and soft acidities and basicities based on resistance changes relative to a *p*- and *n*-type PS interface [24]. Reprinted by permission from W. Laminack, J.L. Gole, Nanostructure-directed chemical sensing: the IHSAB principle and the effect of nitrogen and sulfur functionalization on metal oxide decorated interface response, Nanomaterials. 3 (2013) 469–485 [24].

sites with sufficient control so that thin (or thick) films are no longer required. The process enhances diffusion time and facilitates the ease and repeatability of construction. Rapidly responding, reversible, *room temperature* sensors have been created and evaluated for the detection of various inorganic gas analytes at low ppm concentrations. Counter to traditional metal oxide systems the dispersed metal oxides on PS operate at room temperature and can be heat sunk to operate at elevated temperatures. Therefore, they are more energy efficient as they respond more rapidly due to their dispersed nature. These sensors can be constructed using easily accessible solution based sources. This suggests that their scalability is eminently possible and multiple sensor configurations have already been constructed. Within the framework dictated by the IHSAB model, select metal oxide nanostructures have been deposited to the PS interface, to create an array of sensitivities to a variety of gas analytes. This array has been extended by the in-situ nitridation of metal oxide islands deposited to the PS interface, allowing greater flexibility for tuning the sensor response. The observed response behavior is explained largely by the developing IHSAB concept.

Acknowledgment

I acknowledge helpful discussions with Caitlin Baker.

References

[1] G. Korotcenkov, B. Cho, Crit. Rev. Solid State Mater. Sci. 35 (2010) 1–37.
[2] C. Eranna, B. Joshi, D. Runthala, R. Gupta, Crit. Rev. Solid State Mater. Sci. 29 (2004) 111–188.
[3] S. Ozdemir, J. Gole, Curr. Opin. Solid State Mater. Sci. 11 (2007) 92–100.
[4] M.R. Zeidler, E.C. Kleerup, D.P. Tashkin, Curr. Opin. Pulm. Med. 10 (2004) 31–36.
[5] G. Teague, private communication.
[6] M. Gomzi, Atmos. Environ. 33 (1999) 4081–4086.
[7] B. Berck, J. Agric. Food Chem. 16 (1968) 419–425.
[8] J.L. Burgess, J. Burgess, J. Toxicol. Clin. Toxicol. 39 (2001) 165–168.
[9] N. Barsan, M. Schweizer-Berberich, W. Göpel, Fresenius J. Anal. Chem. 365 (1999) 287–304.
[10] E. Comini, Anal. Chim. Acta 568 (2006) 28–40.
[11] L.J. LeGorea, R.J. Lada, S.C. Moulzolfa, J.F. Vetelinoa, B.G. Fredericka, E.A. Kenike, Thin Solid Films 406 (2002) 79–86.
[12] S. Rani, S.C. Roy, M. Bhatnagar, Sens. Actuators B: Chem. 122 (2007) 204–210.
[13] I. Jiménez, J. Arbiol, G. Dezanneau, A. Cornet, J.R. Morante, Sens. Actuators B: Chem. 93 (2003) 475–485.
[14] S.C. Moulzolf, S. Ding, R.J. Lad, Sens. Actuators B: Chem. 77 (2001) 375–382.
[15] M. Ponce, C. Aldao, M. Castro, J. Eur. Ceram. Soc. 23 (2003) 2105–2111.
[16] A. Rothschild, Y. Komem, J. Appl. Phys. 95 (2004) 6374–6380.
[17] D.H. Yoon, G.M. Choi, Sens. Actuators B: Chem. 45 (1997) 251–257.
[18] S.R. Morrison, Sens. Actuators 12 (1987) 425–440.
[19] J. Watson, Sens. Rev. 14 (1994) 20–23.
[20] N. Yamazoe, K. Shimanoe, D.K. Aswal, S.K. Gupta, Overview of Gas Sensor Technology, Nova Science Publishers Inc., New York, 2007.
[21] P.A. Kottke, A.G. Federov, J.L. Gole, in: M. Schlesinger (Ed.), Modern Aspects of Electrochemistry, 43, Springer, New York, 2009, pp. 139–168.
[22] J.L. Gole,W. Laminack in: G. Korotcenkov (Ed.) Chemical Sensors: Simulation and Modeling, Volume 3—Solid State Sensors, Momentum Press, New York, pp. 87–136.
[23] I. Schechter, M. Ben-Chorin, A. Kux, Anal. Chem. 67 (1995) 3727.
[24] W. Laminack, J.L. Gole, Nanomaterials 3 (2013) 469–485.
[25] J.L. Gole, E.C. Goude, W. Laminack, Chem. Phys. Chem. 13 (2012) 549–561.
[26] W. Laminack, J.L. Gole, Chem. Phys. Chem. 15 (2014) 2473–2484. http://dx.doi.org/10.1002/cphc.201402108.
[27] J.L. Gole, W. Laminack, Beilstein J. Nanotechnol. 4 (2013) 20–31.
[28] W. Laminack, C. Baker, J.L. Gole, Chemistry of Materials, (submitted).
[29] J.L. Gole, S. Ozdemir, Chem. Phys. Chem. 11 (2010) 2573–2581.
[30] W. Laminack, J.L. Gole, Adv. Funct. Mater. 23 (2013) 5916–5924. http://dx.doi.org/10.1002/adfm.201301250.
[31] S. Ozdemir, T. Osburn, J.L. Gole, J. Electrochem. Soc. 158 (2011) J201–J207.
[32] S. Ahlers, P. Kreisl, G. Müller, A low-power metal-oxide based gas sensing system, in: Proceedings of the 203rd ECS Meeting, paper 2873, April 28, 2003.
[33] G. Mueller, A. Friedberger, P. Kreisl, S. Ahlers, O. Schulz, T. Becker, Thin Solid Films 436 (2003) 34–45.
[34] C. Wang, L. Yin, L. Zhang, D. Xiang, R. Gao, Sensors 10 (2010) 2088–2106; N. Bârsan, U. Weimar, J. Phys.: Condens. Matter 15 (2003) R813. http://dx.doi.org/10.1088/0953-8984/15/20/201; J. Huang, Q. Wan, Sensors 9 (2009) 9903–9924 (doi:10.3390/s91209903); G. Korotcenkov, Mater. Sci. Eng. B 139 (2007) 1–23; G.W. Ho, Sci. Adv. Mater. 3 (2011) 150–168.
[35] S. Lewis, J.L. Gole, to be published.
[36] W. Laminack, N. Pouse, J.L. Gole, ECS J. Solid State Sci. Technol. 1 (2012) Q25–Q34. http://dx.doi.org/10.1149/2.002202jss.
[37] J.L. Gole, S.C. Lewis, J.R. DeBoer, P.J. Hesketh, Sens. Actuators B 110 (2005) 54–65.
[38] S. Ozdemir, J.L. Gole, ECS Trans. 16 (2008) 379–387.
[39] S. Ozdemir, J.L. Gole, Sens. Actuators B 151 (2010) 274–280.
[40] W. Laminack, J.L. Gole, IEEE Sens. 14 (2014) 2731–2738. http://dx.doi.org/10.1109/JSEN.2014.2316117.
[41] C. Jin, T. Yamazaki, K. Ito, T. Kikuta, N. Nakatani, Vacuum 80 (2006) 723–725.
[42] J. Gong, Q. Chen, M. Lian, N. Liu, R. Stevenson, F. Adami, Sens. Actuators B: Chem. 114 (2006) 32–39.
[43] C. Griessler, E. Brunet, T. Maier, S. Steinhauer, A. Köck, T. Jordi, F. Schrank, M. Schrems, Microelectron. Eng. 88 (2011) 1779–1781.
[44] C. Liewhiran, N. Tamaekong, A. Wisitsora-at, S. Phanichphant, Eng. J. 16 (2012) 123–134.
[45] F. Shao, F. Hernándes-Ramírez, J.D. Prades, C. Fábrega, T. Andreu, J.R. Morante, Appl. Surf. Sci. 311 (2014) 177–181.
[46] S. Das, S. Chakraborty, O. Parkash, D. Kumar, S. Bandyopadhyay, et al., Talanta 75 (2008) 385–389.
[47] L. Mädler, A. Roessler, S.E. Pratsinis, T. Sahm, A. Gurlo, et al., Sens. Actuators B: Chem. 114 (2006) 283–295.
[48] T. Sahm, L. Mädler, A. Gurlo, N. Barsan, S.E. Pratsinis, U. Weimar, Sens. Actuators B: Chem. 98 (2–3) (2004) 148–153.
[49] M. Hübner, C.E. Simion, A. Tomescu-Stanoiu, S. Pokhrel, N. Bârsan, U. Weimar, Sens. Actuators B: Chem. 153 (2011) 347–353.
[50] L. Liao, H.B. Lu, J.C. Li, H. He, D.F. Wang, D.J. Fu, C.J. Liu, Phys. Chem. C 111 (2007) 1900–1903.
[51] D. Zhang, Z. Liu, C. Li, T. Tang, X. Liu, S. Han, B. Lei, C. Zhou, Nano Lett. 4 (2004) 1919–1924.
[52] J. Huang, Q. Wan, Sensors 9 (2009) 9903–9924. http://dx.doi.org/10.3390/s91209903.
[53] C. Wang, X. Chu, M. Wu, Sens. Actuators B: Chem. 113 (2006) 320–323.
[54] Z. Zeng, K. Wang, Z. Zhang, J. Chen, W. Zhou, Nanotechnology 20 (2009) 045503.
[55] Y.M. Zhao, Y.Q. Zhu, Sens. Actuators B: Chem. 137 (2009) 27–31.
[56] D.C. Meier, S. Semancik, B. Button, E. Strelcov, A. Kolmakov, Appl. Phys. Lett. 91 (2007) 063118.
[57] F. Hernández-Ramírez, A. Tarancón, O. Casals, J. Arbiol, A. Romano-Rodríguez, J.R. Morante, Sens. Actuators B: Chem. 121 (2007) 3–17.
[58] X. Xue, Y. Nie, B. He, L. Xing, Y. Zhang, Z.L. Wang, Nanotechnology 24 (2013) 225501.
[59] R.G. Pearson, Coord. Chem. Rev. 100 (1990) 403–425.
[60] R.G. Parr, R.G. Pearson, J. Am. Chem. Soc. 105 (1983) 7512–7516.
[61] R.G. Parr, W. Yang, Density Functional Theory of Atoms and Molecules, Oxford University Press, New York, 1989.

Talanta 132 (2015) 96–105

Contents lists available at ScienceDirect

Talanta

journal homepage: www.elsevier.com/locate/talanta

Photometric flow injection determination of phosphate on a PDMS microchip using an optical detection system assembled with an organic light emitting diode and an organic photodiode

Rong Liu [a], Ryoichi Ishimatsu [a], Masayuki Yahiro [b,c], Chihaya Adachi [a,c], Koji Nakano [a], Toshihiko Imato [a,*]

[a] Department of Applied Chemistry, Graduate School of Engineering, Kyushu University, 744 Motooka, Nishi-ku, Fukuoka 819-0395, Japan
[b] Institute of System, Information Technology and Nanotechnology, 2-1-22 Momochihama, Swawara-ku, Fukuoka 819-0395, Japan
[c] Center for Organic Photonics and Electronics Research (OPERA), Kyushu University, 744 Motooka, Nishi-ku, Fukuoka 819-0395, Japan

ARTICLE INFO

Article history:
Received 30 May 2014
Received in revised form
20 August 2014
Accepted 21 August 2014
Available online 30 August 2014

Keywords:
Organic light emitting diode
Organic photodiode
Microfluidic
Photometry of phosphate

ABSTRACT

A compact photometric detector was constructed from an organic light emitting diode (OLED) based on a europium complex, europium(diben-zoylmethanato)$_3$(bathophenanthroline) (Eu(DBM)$_3$bath), as the light source and an organic photodiode (OPD) fabricated from a hetero-junction of two layers of copper phthalocyanine (CuPc)/fullerene (C_{60}) as the photo-detector on a microchip prepared from poly (dimethylsiloxan) (PDMS) and was applied to the determination of phosphate. The OLED and the OPD were fabricated by a vapor deposition method on an indium tin oxide (ITO) coated glass substrate with the following layered structure; Glass (0.7 mm)/ITO (110 nm)/4,4′-bis[N-(1-naphthyl)-N-phenyl amino]-biphenyl (α-NPD) (30 nm)/4,4′-di(N-carbazolyl)biphenyl (CBP): Eu^{3+} (8 wt%, 30 nm)/bathocuproine (BCP) (30 nm)/aluminum tris(8-hydroxyquinoline) (Alq_3) (25 nm)/magnesium and silver (MgAg) (100 nm)/Ag (10 nm) and Glass (0.7 mm)/ITO (110 nm)/CuPc (35 nm)/C_{60} (50 nm)/BCP (10 nm)/Ag (50 nm), respectively. The OLED based on the europium complex emitted a sharp light at the wavelength of 612 nm with a full width at half maximum (FWHM) of 8 nm. The performance of the photometric detector assembled was evaluated based on measurements of the absorbance of different concentrations of malachite green (MG) solutions for a batch system with 1 cm long path length. The molar absorptive coefficient of the MG solution, calculated from the photocurrent of the OPD, was in good agreement with the value reported in the literature. A microchip with two inlets and one outlet U-shaped channel was prepared by a conventional photolithograph method. The OLED and the OPD were configured so as to face each other through the PDMS microchip in parallel in order to align the light axis of the OLED and the OPD with the flow cell (optical path length of 5 mm), which was located at the end of outlet. For the determination of phosphate, an ion-association reaction between MG and a molybdenum-phosphate complex was utilized and a good linear relationship between the concentration and absorbance was observed in the concentration range 0–0.2 ppm, with a detection limit ($S/N=3$) of 0.02 ppm. The assembled photometric detector was also applied to the determination of phosphate by the flow injection of river water samples using the reagent solution containing MG and molybdenum ammonium in sulfuric acid. A good recovery (97–99%) for the river water samples, which had been spiked with the standard 0.08 ppm, with an RSD of ca 5% ($n=5$) was obtained using the constructed system.

© 2014 Elsevier B.V. All rights reserved.

1. Introduction

Phosphates, which are founds in bones, proteins, and which participate in energy production, are very important for the health of all living organisms. However, phosphate together with nitrogen compounds such as nitrate and nitrite also participate in eutrophication in aquatic environments, which can result in the production of algal blooms. Therefore, the determination of trace levels of phosphate has become a very important issue. A photometric flow injection analysis (FIA) system was proposed for the determination of phosphate, based on various methods, including a yellow vanadomolybdate method [1], a molybdenum blue method [2] and a malachite green method [3,4].

Attempts to downsize analytical systems by integrating separation, reaction, mixing and detection onto a single microchip, a so-called miniaturized total analysis system (μ-TAS) and a lab-on-a

* Corresponding author. Tel./fax: +81 92 802 2889.
E-mail address: imato@cstf.kyushu-u.ac.jp (T. Imato).

http://dx.doi.org/10.1016/j.talanta.2014.08.057
0039-9140/© 2014 Elsevier B.V. All rights reserved.

chip (LOC) system have been of great interest in terms of making further progress in analytical chemistry and has attracted the interest of researchers from interdisciplinary fields [5,6]. The technique has many advantages such as rapid analysis, high portability, reduction in separation time, and negligible consumption of reagents due to its micrometer sized flow channels. The systems have been applied to numerous fields, including environmental monitoring, food safety and clinical diagnosis.

Numerous types of detectors for the μ-TAS and the LOC system, such as optical detectors, electrochemical detectors have been developed. The functional integration of a light source and a photo-detector within a microchip is the key issue for successfully assembling a micro-fluidic system [7,8]. There have been many reports dealing with the fabrication of optical detectors onto the μ-TAS and LOC systems, including inorganic light emitting diodes (LEDs) [9–14] as the light source and a silicon photodiode [15] as a photo-detector. For example, Yang et al. [12] reported on the development of a simple detection system based on light emitting diode induced fluorescence for microscale electrophoresis on a microfluidic platform. Under optimal conditions, a very high sensitivity to fluorescein and fluorescein thiocyanate (FITC) with a detection limit of 0.09 fmol and 0.18 fmol, respectively was achieved for a limited sample volume of 0.37 nL. This device has been successfully employed for the separation and detection of penicillamine enantiomers by derivatization with FITC. Recently a new light source and a new type of photo-detector based on organic materials, a so called organic light emitting diode (OLED) [16–20] and an organic photodiode (OPD) [21–23] have been utilized as an optical system for use in conjunction with the μ-TAS and LOC systems. Yao et al. [17] fabricated an optical system using a green OLED for the fluorescence detection of rhodamine 6 G and alexa 532. In this case they used a thin film interference filter to reduce the effect of the excitation light on the detection of fluorescence, as a result detection limits of 1.4 fmol and 35 fmol for alexa and rhodamine, respectively, were obtained for an injection volume of 0.7 nL. The results proved that OLEDs are promising light sources for use in microfluidic fluorescence detection systems which have a small size and are easy to integrate. Hofmann et al. [24] demonstrated the performance of an OPD based on CuPc/C_{60} for the monitoring of a peroxyoxalate based chemiluminescence reaction on a microfluidic device. A detection limit for peroxyoxalate of 1 mM was obtained with a good reproducibility of the photocurrent of the OPD below 1.5% ($n=3$) as the RSD.

However, only a very few attempts have been reported regarding assembling an optical system in which an OLED is combined with an OPD [25,26]. Banerjee et al. [25] reported on a method for the sensitive detection for rhodamine 6 G and fluorescein by the combined use of an OLED based on Alq_3 with an OPD based CuPc/C_{60}. The novel idea for this device involved the use of a pair of cross-polarization filters, which effectively eliminates the effect of the excitation light on the OPD detector. As a result they achieved a detection limit of 10 nM for the both fluorescent reagents. Pais et al. [26] reported a highly sensitive and disposable LOC for measuring fluorescence signals from rhodamine 6 G and fluorescein by combining an OLED based on a N,N-bis(1-naphthyl)-N,N-diphenyl-1, 1-biphenyl-4,4-diamine (NPB)/Alq_3 thin-film as the light source with an OPD based on a CuPc/C_{60} thin-film as the photo-detector. A limit of detection of 100 nM was reported for rhodamine 6 G, and 10 μM for fluorescein. These studies suggest that an integrated microfluidic device, with an OLED as the light source and an OPD as the detector, could be fabricated to produce a compact and economical LOC device for point-of-care diagnostics and on-site analysis. However, to date most of the above studies have been primarily limited to fluorescence detection, with no applications to analytically important needs.

In the present paper, we report on the fabrication of a highly sensitive photometric system for the determination of phosphate on a microchip via the use of a combination of an OLED and an OPD. One of the advantages of the proposed photometric detector for the microchip is the fact that the shape of the OLED and the OPD was flat, thus making it suitable for assembling on a flat shaped microchip. In this work, we used a new type of Eu^{3+} rare earth complex as an emission material for the OLED. Because the emission spectra of the OLED based on this complex is very sharp, with a FWHM of less than 10 nm, this OLED is suitable for the selective absorption of a reagent (MG) for phosphate. This is the first report of the use of a Eu^{3+} rare earth complex based OLED in a photometric detection system constructed by integrating with an OPD as a photo-detector. In this study, the performance of the photometric detector comprised of an OLED combined with the OPD was examined by the detection of MG solutions and the photometric detector was successfully applied to the determination of phosphate on a microfluidic platform.

2. Experimental

2.1. Materials and reagents

For the fabrication of the OLED, α-NPD, CBP, Eu(DBM)$_3$bath, BCP and Alq_3 were obtained from Tokyo Kasei Co., Ltd., (Tokyo, Japan) and were used without further purification. An ITO deposited glass plate (thickness of the ITO layer, 110 nm) was purchased from Sanyo Vacuum Industries Co., Ltd. (Osaka, Japan) and was cut at a size of 25 mm × 25 mm (including patterns of 7 stripes of 2 mm width and 23 mm length).

For the fabrication of the OPD, CuPc, obtained from Tokyo Kasei Co., Ltd., (Tokyo, Japan), was purified by three sublimations and was used as a p-type semiconductive material. C_{60}, 99.95% pure, was obtained from Material Technologies Research Ltd., (OH, USA) and was used as received as an n-type semiconductive material.

All solutions were prepared from analytical grade chemicals. Deionised water was purified by means of a Direct-Q™ water purification system and was used for preparing all solutions used in this study.

2.2. Preparation of solutions

To evaluate the performance of the OLED and OPD assembled on the PDMS microchip, MG (Wako Chemical Co., Ltd., Osaka, Japan) was utilized for absorbance detection. A 100 μM MG solution was used as a stock solution and stored in the dark at 4 °C. Working solutions were prepared by diluting the MG solution to various concentration before analysis.

To determine the absorbance of phosphate, a MG–molybdate reagent consisting of 2.2×10^{-4} M MG, 0.11 M $(NH_4)_6Mo_7O_{24}$, 1.3 M H_2SO_4 and 25% methanol was prepared as follows; a 7 mL aliquot of concentrated sulfuric acid (H_2SO_4, 98%, Wako Chemical Co., Ltd., Osaka, Japan) was slowly added to approximately 40 mL of deionised water in a beaker. The solution was allowed to cool to room temperature and 1.94 g of ammonium molybdate ($(NH_4)_6Mo_7O_{24}\cdot4H_2O$, 99%, Wako Chemical Co., Ltd., Osaka, Japan) and 0.0092 g of MG were then dissolved into the sulfuric acid solution. Finally this mixed solution was transferred to a 100 mL-volumetric flask and 25 mL methanol (Wako Chemical Co., Ltd., Osaka, Japan) was added to the flask and the solution made up to 100 mL with deionized water. The resulting solution was stored in the dark at 4 °C.

A 100 ppm phosphate stock solution was prepared at weekly intervals by dissolving potassium dihydrogenphosphate (KH_2PO_4, Wako Chemical Co., Ltd., Osaka, Japan) in deionized water. Standard solutions of phosphate were prepared daily by dilution of the stock solution.

2.3. Preparation of organic light emitting diode (OLED)

The OLED was fabricated by multilayer thermal deposition, as follows. A 25 mm × 25 mm glass substrate pre-coated with a 110 nm thick ITO layer (sheet resistance ≈30 Ω/square) of 7 stripes was degreased with solvents (acetone, isopropyl alcohol and deionized water) and cleaned in a UV–ozone chamber (Nippon Laser & Electronics Lab., NL-UV253) before being loaded into the deposition system. First, a 25 mm × 25 mm shadow mask with 12 mm × 16 mm opening was placed on the ITO deposited glass substrate. A 30 nm thickness of a α-NPD film layer was prepared by deposition onto the glass substrate, as a hole-transport layer (HTL) at deposition rates of 1 nm s^{-1}. Next, a 30 nm thick layer of CBP co-doped with $Eu(DBM)_3$bath was deposited onto the α-NPD film layer, as an emission layer (EML) at deposition rates of 0.08 nm s^{-1} for $Eu(DBM)_3$bath and 0.92 nm s^{-1} for CBP, respectively. As a result, the weight percentage of the Eu^{3+} complex in the EML was 8 wt%. A 30 nm thick layer of BCP was then deposited onto the EML as a hole-blocking layer (HBL), and a 25 nm thick layer of Alq_3 was deposited on the HBL as an electron-transport layer (ETL) at deposition rates of 0.8 nm s^{-1} and 1 nm s^{-1}, respectively. The resulting mask was replaced with another mask with an opening area of 2 mm × 19 mm for the preparation of a metal cathode. In order to prepare a metal cathode consisting of a MgAg (the ratio of Mg and Ag was 10:1) layer with a thickness of 100 nm, Mg and Ag were deposited onto the Alq_3 layer at deposition rates of 3 nm s^{-1} and 0.3 nm s^{-1}, respectively. A 10 nm thick Ag layer was deposited onto the MgAg layer. Finally, the resulting OLED was encapsulated by placing a cover glass with a UV cured epoxy seal at the perimeter, followed by irradiation with UV light in a nitrogen-filled glove box (KK-011 AS-Extra, ALS Technology, Kanagawa, Japan) to protect the OLED from humidity. The schematic of the OLED and a photograph are shown in Fig. 1(a) and (b), respectively.

2.4. Preparation of organic thin film photodiode (OPD)

Fabrication procedures for the present OPD were essentially the same as that for the OLED described in the previous section, as well as previously reported [27]. Briefly, a CuPc layer, a C_{60} layer and a BCP layer were prepared on the ITO deposited slide glass by a vapor deposition method. The thickness of the CuPc layer, the C_{60} layer and the BCP layer were 50 nm, 40 nm and 10 nm, respectively, and were controlled by adjusting the time and deposition rate (0.3 nm s^{-1}, under ca 5×10^{-4} Pa). Finally the organic layers of the resulting OPD were sealed by a cover glass with a UV-cured layer in a glove box, similar to the OLED encapsulation process. The structure of the OPD is the same as that of the OLED as shown in Fig. 1(a) and a photograph of the OPD is shown in Fig. 1(c).

2.5. Design and preparation of PDMS microchip

The microchip composed of polydimethylsiloxane (PDMS) with a U-turn shaped type microchannel (two inlets and one outlet) was prepared on the PDMS coated glass substrate using conventional soft lithography techniques [28]. The mask shown in Fig. 2 (a) was designed and printed onto a transparency sheet. The width, depth and the total length of the U-turn shaped channel to the outlet was 1.5 mm, 80 μm and 33.4 cm, respectively. The preparation procedures were as follows. To fabricate a mold for the PDMS microchip, 2 mL of SU-8 was spun onto the glass substrate (500 rpm for 10 s and then 2000 rpm for 30 s) using a spin coater (1H-DX, Mikasa Co., Ltd., Tokyo, Japan) and the resulting substrate was then heated on a hot plate (ND-1, As One, Osaka, Japan) at 65 °C for 3 min and then at 95 °C for 9 min. The mask was placed on the SU-8 coated substrate and the resulting mask was irradiated with a UV light for 60 s in an exposure box (BOX-W9B, Sunhayato, Tokyo, Japan). The resulting substrate was again heated at 65 °C for 2 min and then at 95 °C for 7 min on a hot plate. The substrate was immersed in a SU-8 Developer solution for about 10 min and washed with isopropyl alcohol and then baked at 150 °C for 5 min on a hot plate. To fabricate a flow cell for absorbance detection at the end of the outlet, an iron rod with a 2 mm∅ diameter and a length of 5 mm was placed at the position of the outlet of the mold. A 30 g aliquot of the pre-polymer of PDMS was mixed with 0.3 g of a cross-linking agent at a 10:1 ratio and the resulting mixture was then degassed in a vacuum for about 30 min. The resulting mixture was poured onto the mold with the perimeter surrounded by scotch tape and was heated at 75 °C for about 2.5 h. The PDMS mold and the iron rod were then detached from the PDMS with a microchannel and a glass substrate (0.7 mm × 70 mm × 50 mm), the surface of which was coated with a thin PDMS film formed by spin-coating at a rotation speed of 1000 rpm for 60 s. The PDMS with a microchannel and the glass substrate with the PDMS thin film were placed in a plasma generator (BD-20AC, Electro-Technic Products Inc., IL, USA) and irradiated with the plasma for 45 s. The resulting PDMS microchip and the glass substrate with the thin PDMS film were immediately attached and heated at 120 °C for 4 h in an oven to complete the adhesion process. Finally PEEK tubes (0.75 mm i.d.,

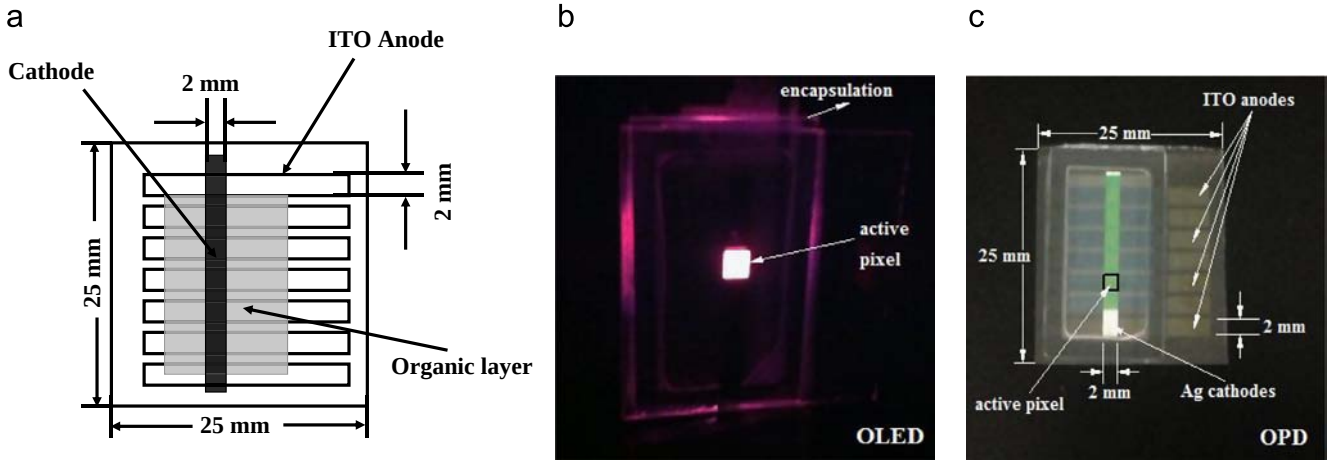


Fig. 1. (a) Schematic illustration of the structure an organic light emitting diode (OLED) and an organic photodiode (OPD) and photographs of (b) the OLED and (c) the OPD.

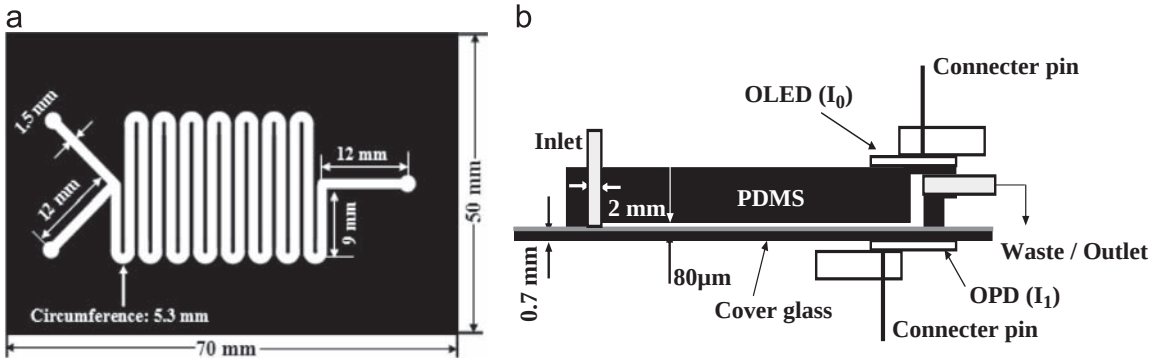


Fig. 2. (a) The top view of a microchip made by poly(dimethylsiloxane) (PDMS) with a U-turn shaped type microchannel and (b) the side view of the PDMS microchip equipped with a photometric detector assembled with an organic photodiode (OPD) and an organic light emitting diode (OLED). The length of the light pass of the flow cell is 5 mm.

1/16 in., o.d. 40 mm long) were mounted at the inlets and the outlet of the microchip with a silane-modified urethane resin adhesive (Epoclear, Konishi Co., Japan).

2.6. Characterizations of the present OLED and OPD and the experimental setup

The photoluminescence (PL) spectrum of the Eu^{3+} complex coated on a glass substrate was recorded using a spectrofluorometer (FP-6500, Jasco, Japan) at room temperature. The electroluminescence (EL) spectrum of the OLED was recorded using a multi-channel spectrometer (UBS2000, Ocean Optics). The current density (*J*)–voltage (*V*)–brightness (*B*) characteristics and external quantum efficiency (EQE) of the OLED were measured in ambient air with a semiconductor parameter analyzer (E5273A, Agilent) and an optical power meter (1930C, Newport).

The fabricated OPD was placed on a solar illumination stage and current-voltage curves (*JV* curves) in the dark and under simulated AM 1.5 solar illumination (Otento-Sun II, KP type, Bunkokeik, Japan) with a Xe-lamp (Model XCS-150A, Jasco, Japan) were obtained using a source meter (R6423, Advantest, Japan). The incident photo-to-current conversion efficiency (IPCE) was calculated from the photocurrent of the OPD, which was measured using the source meter under irradiation with monochromatic light, generated by a Xe lump source (SK-U1152X, Ushio Inc., Japan) and a monochrometer (SM-10P, Bunkokeiki, Japan) in the wavelength range from 400 nm to 800 nm at intervals of 10 nm. The incident light power of the monochromatic light was calibrated by using a Si photodiode (BS-520, Bunkokeiki, Japan) for calculating the conversion efficiency of the OPD.

In order to evaluate the performance of the photometric detector combined the OPD with the OLED, both of them were placed in the flow cell on the PDMS microchip, as described in the experimental section. The applied voltage to the OLED was changed from 5 V to 15 V and the photocurrents of the OPD were then measured for about 2 h while water was flowing through the microchannel of the PDMS microchip.

The schematic flow diagram for the photometric determination of phosphate using the optical detector assembled with the OPD and the OLED on the PDMS microchip is shown in Fig. 3. The OPD was directly placed on the PDMS microchip in order to adjust its detection area to the flow cell position in parallel to the PDMS microchip. The OLED was placed underneath the PDMS microchip in order to adjust its emission area to the flow cell to provide incident light for photometry. The photocurrent from the OPD for light transmitted through the flow cell was measured by a picoammeter (6485, Keithley Instruments, Inc., OH, USA). A DC voltage–current source meter (6146, DC Instruments, Inc., Japan) was used to supply current to the OLED. The intensity of the light

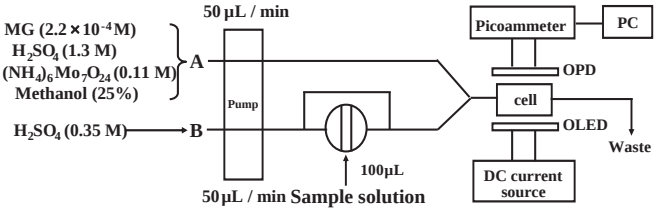


Fig. 3. Schematic flow diagram for the photometric flow injection determination of phosphate by the malachite green method (the flow cell is shown in Fig. 2, MG: malachite green).

emitted from the OLED was controlled by adjusting the applied voltage of the source meter.

2.7. Procedures for the determination of phosphate in a flow system

The flow system, shown in Fig. 3, consisted of two syringe pumps (NE-1002X, New Era Pump Systems Inc., NY, USA), one injector (9725, Rheodyne, CA, USA), the prepared PDMS microchip, the fabricated OLED and OPD, the DC voltage–current source and a picoammeter. Two black-color mask sheets with a pin hole of 2 mm in diameter were placed on the both side of a detection area of the flow cell on the PDMS microchip, and then the active pixel area of the OLED and the OPD were placed to adjust with the pin holes. The black mask sheets prevent the stray light from the OLED to the OPD. A MG–molybdate reagent solution containing 0.11 M ammonium molybdate, 2.2×10^{-4} M MG, and 1.3 M sulfuric acid was pumped using syringe pump 1 at a flow rate of 50 μL/min, and a 0.35 M sulfuric acid solution, used as a carrier solution, was pumped using syringe pump 2 at the same flow rate as the MG reagent solution. Sample solutions of phosphate at the different concentrations (0.04–0.2 ppm) were injected into the carrier stream from a sample injector with a 100 μL loop. The transmitted light from the OLED was detected by the OPD as a photocurrent in a peak-shaped signal.

3. Results and discussion

3.1. Fundamental performance of OLED and OPD

3.1.1. PL and EL characteristics of OLED

The current density (*J*)–voltage (*V*)–brightness (*B*) characteristics and the external quantum efficiency (EQE) of the OLED are described in the supplemental information together with Figs. S1 and S2. Fig. 4 shows the PL spectrum of a $Eu(DBM)_3$bath film coated on a glass substrate and the EL spectrum of an OLED, with a layered structure: ITO (110 nm)/α-NPD (30 nm)/CBP:Eu^{3+} (8 wt%

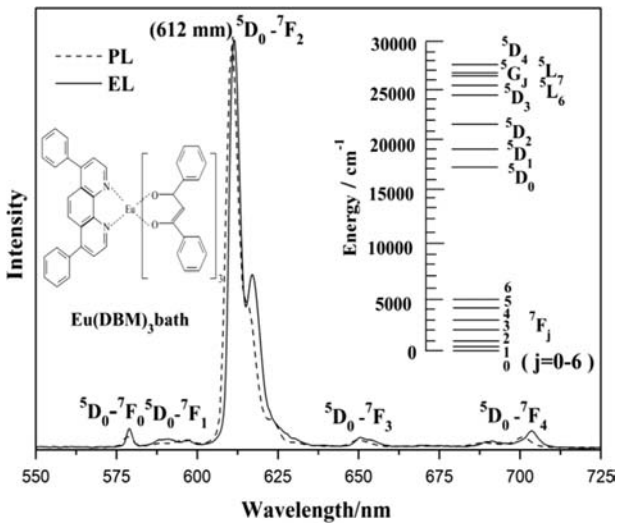


Fig. 4. PL spectrum of a Eu(DBM)$_3$bath film (thickness: ca 100 nm) coated on a glass substrate and the EL spectrum of an OLED based on a Eu(DBM)$_3$bath. Inset: molecular structure of Eu(DBM)$_3$bath and the partial energy level diagram of the free Eu^{3+} ion. The excitation wavelength of the PL is 254 nm. The structure of the OLED: ITO (110 nm)/α-NPD (30 nm)/CBP:Eu^{3+} (8 wt% Eu(DBM)$_3$bath doped in a CBP layer, 30 nm)/BCP (30 nm)/Alq_3 (25 nm)/MgAg (100 nm)/Ag (10 nm). The current density applied to the OLED is 1 mA/cm^2.

Eu(DBM)$_3$bath doped in a CBP layer, 30 nm)/BCP (30 nm)/Alq_3 (25 nm)/MgAg (100 nm)/Ag (10 nm). The EL spectrum of the OLED remained unchanged with the change in applied current density at 10 mA/cm^2 and 100 mA/cm^2. The inset shows the molecular structure of the Eu (DBM)$_3$bath complex and the energy level of free Eu^{3+} ions [29]. The Eu (DBM)$_3$bath was found to have excellent electron-transport properties in an earlier study [30–32]. From Fig. 4, the EL spectrum of the present OLED is almost the same as the PL spectrum of the europium complex, which is used as the emitting material of the OLED. This observation is common for many OLED emission spectra. The emission peaks are assigned based on the transition between energy levels shown in the figures. The main and strong emission was observed at 612 nm, which is a $^5D_0$–$^7F_1$ transition. The emission light of the OLED was red, as shown in Fig. 1(b). The Commission Internationale de L'Eclairage (CIE) coordinates of the EL of the Eu (DBM)$_3$bath-based device were calculated from the EL spectrum data to be $x=0.672$ and $y=0.335$, which are very close to the values of the National Television Standards Committee (NTSC) standard red of (0.67, 0.33) and the Phase Alternating Line (PAL) standard red of (0.64, 0.33). The only difference between the PL spectrum and the EL spectrum is that the PL spectrum at around at 612 nm is split into two peaks, at 612 nm and 616 nm in the EL spectrum. This phenomenon has been previously reported in the literature [33,34] and can be explained by the fact that the local symmetry of the crystal-field (CF) around the Eu^{3+} ion causes peak splitting. Namely, the observed split peaks are due to transitions to the $^7F_2$ multiplet, which is attributed to the CF acting on the Eu^{3+} ion in the complex. When a potential is applied to the OLED devices, the peak splitting becomes more prominent than the PL spectrum with the movement of electrons. The FWHM at 612 nm is 8 nm and the total peak width, including the split peak, is about 15 nm for the baseline of the spectrum.

3.1.2. *Incident photon to current conversion efficiency of OPD*

The current–voltage curves (*JV* curves) in the dark and under simulated AM 1.5 solar illumination of the OPD are described in the supplemental information together with Fig. S3. The incident photon-to-current conversion efficiency (IPCE) of the fabricated OPD is shown in Fig. S4, where a power of a standard light source was initially calibrated using the Si photodiode. As shown in Fig. S4, the maximum values of more than 25% of *IPCE* were achieved using the developed OPD at around 450 nm, which is due to the absorbance band of the C_{60} used for an accepter layer. Double peaks of the IPCE are observed at around 620 nm and 700 nm, which are due to the absorbance bands of the CuPc complex used as a donor layer. This IPCE spectrum indicates that the photosensitivity of the OPD to light in the wavelength range of around 600 nm to 700 nm is quite good. The latter conditions correspond to an absorbance spectrum of MG ($\lambda_{abs}=617$ nm) and the ion association complex of phosophomolybdate with MG ($\lambda_{abs}=640$ nm) (as shown in Fig. 6). The IPCE for the OPD is known to be governed by several factors. Since the diffusion length of the exiton is in the order of several nanometers, the charge carrier generated at the p-n junction interface is thought to affect the IPCE. Therefore the efficiency of absorbance of the organic layers of the OPD contributes to the IPCE. The data was shown in Fig. S4 suggests that the photocurrent mainly arises from C_{60} and CuPc. To study the effect of the thickness of the C_{60} and CuPc, we compared the fabricated OPD to a similar OPD reported in the literature [27]. A maximum IPCE of about 23% was obtained between 400 and 500 nm, which is lower than that obtained for the present OPD, which can be attributed to the thickness of the fabricated C_{60} layer, which was thicker (40 nm) than that reported in the literature (35 nm).

3.1.3. *Evaluation of light intensity of OLED as a light source and the photosensitivity of OPD as a photodetector*

The performance of the OPD as a phtodetector for the present work was evaluated by measuring the photocurrent when the light with the different powers from a conventional LED (maximum wavelength 630 nm) was irradiated to the OPD. The power of the light from the LED was determined preliminary by using a power meter (1918-C, Newport Co., CA, USA) by changing the applied current to the LED (0.01–0.1 mA) and the distance between the LED and the power meter or the LED (2–10 cm). As shown in Fig. 5(a), there was a linear relationship between the photocurrent of the OPD and the power of the light irradiated to the OPD.

The performance of the OLED as a light source for the present work was also evaluated by measuring the power of the emitted light from the OLED by the power meter at the constant distance between the power meter and the OLED. As a result, the relationship between the power of the OLED and the applied current to the OLED shown in Fig. 5(b) was obtained.

3.1.4. *Optimization of applied voltage to the OLED for detecting its light with the OPD*

When the OLED and the OPD were assembled into the flow cell, as shown in Fig. 6(a) as a photometric detector and water was then allowed to flow into the flow cell, the photocurrent of the OPD was monitored for about 10–50 min under the conditions where a constant voltage (5–15 V) was applied to the OLED. As shown in Fig. 6(b), when 5 V was applied to the OLED, no photocurrent in the OPD was observed. This observation is reasonable judging from the *J–V–B* characteristics of the OLED showed in Fig. S1, because of the turn on voltage of the OLED is 5.5 V. When the applied voltage was increased from 5 V to 15 V at ca 25 min intervals, the photocurrent of the OPD increased and a linear relationship between applied voltage and photocurrent was observed. However, when the applied voltage was as high as 15 V, the photocurrent gradually declined, reaching more than 85% of the initial photocurrent after about 25 min. This observation may be mainly due to the working current between the metal

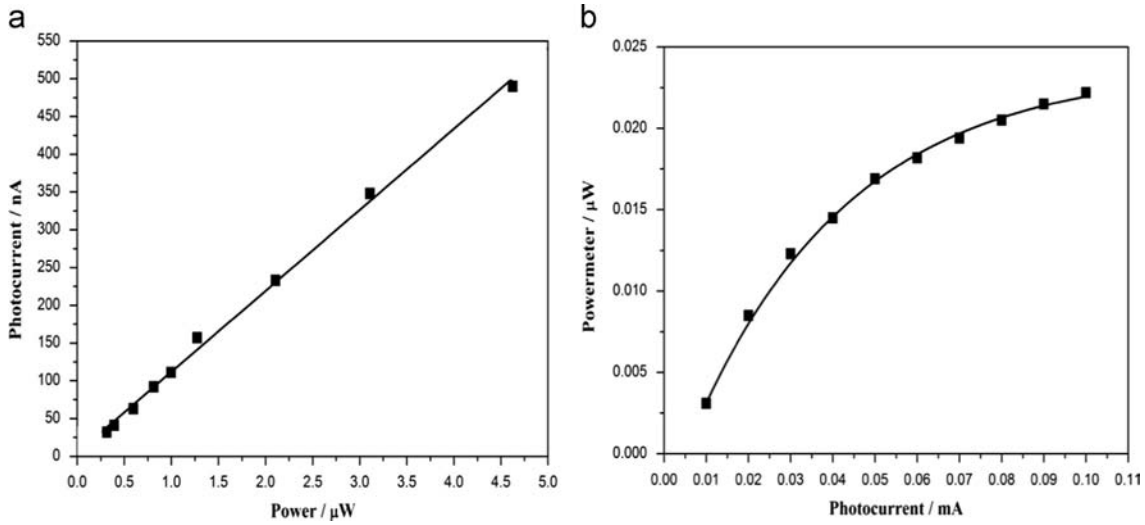


Fig. 5. (a) Relationship between the photocurrent of the present OPD and LED power measured by a power meter based on a silicon diode. The LED used for the light source has peak maxima of 630 nm (red). (b) Relationship between the given current of the present OLED and the power measured by a power meter based on a silicon diode.

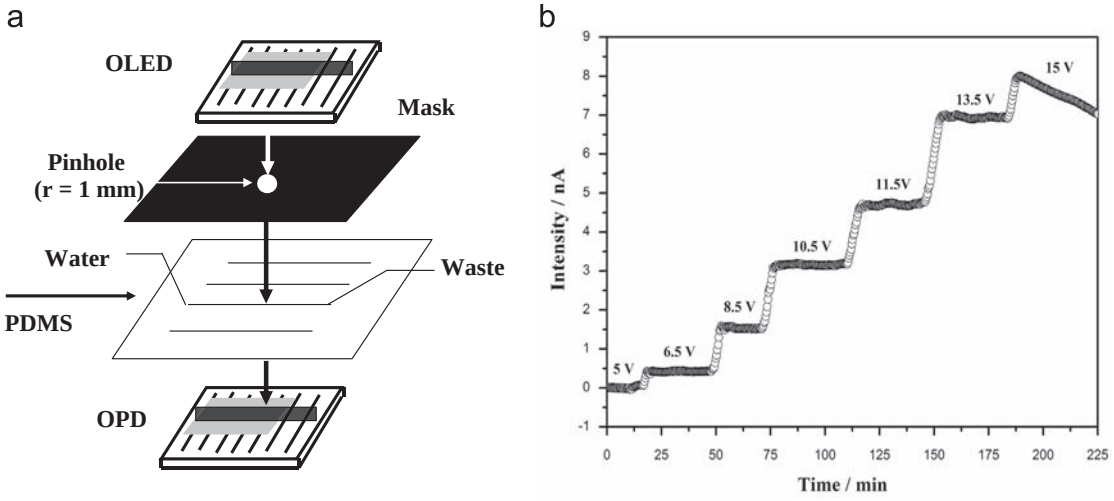


Fig. 6. (a) Experimental set up for evaluating the performance of a photometric detector assembled with the OPD and the OLED on a microchip and (b) the time-course of the photocurrent of the OPD for the emission light from the OLED at different applied voltages. The applied voltage to the OLED was increased from 5 V to 15 V every ca. 25 min. (Flow rate of water: 50 μL/min, the width, length and depth of the microchannel of the PDMS microchip are 3 mm, 5 cm, and 1 mm, respectively.)

cathode and the ITO anode of the OLED exceeding rated upper limit and excessive Joule heat generation would then lead to irreversible damage, as reported in the literature [24]. Indeed the OLED used in this experiment was no longer usable after this experiment. From Fig. 6(b), the applied voltages between 10 and 12 V appear to be the optimal operation voltage for the present OLED, because, if the applied voltage is too high, the OLED device can easily be broken, contrarily if the applied voltage is too low, the brightness of the light source is insufficient for photometric detection. An applied voltage of 10 V was used as the power supply for the OLED in the following experiments.

3.2. Performance of the OLED and the OPD for detecting MG absorbance

Fig. 7(a) and (b) shows the emission spectrum of the present OLED and the absorption spectrum of the MG solution, respectively. These spectra indicate that the maximum emission wavelength λ_{max} (612 nm) of the OLED is located almost the same wavelength of the maximum absorbance of the MG solution (615 nm). Prior to utilizing the OLED and the OPD as a photometric detector for the measurement of phosphate on a microchip, the photometric detector assembled with the OLED and the OPD was evaluated for detecting the absorbance of different concentrations of the MG solutions by a batch system using a quartz cell (1 cm path length). In this case, the OLED and the OPD were arranged in parallel through the quartz cell filled with the MG solutions. 10 V was applied to the OLED and the photocurrents of the OPD were measured using a picoammeter. As shown in Fig. 8(a). A 2.5 mL aliquot of the MG solution (0–8 μM) was placed in a quartz cell, the OLED and the OPD were facing each other, to permit the light axis through the quartz cell to be adjusted appropriately. In this case water was added to the quartz cell as a reference for the absorbance calculation. The time-course of the photocurrent of the OPD for different concentrations of MG solutions are shown in Fig. 8(b). The response of the OPD was rapid when a voltage of 10V was applied to the OLED. The fluctuation of the photocurrent was $\pm$0.02 nA for 2 min. The absorbance of the MG solution was

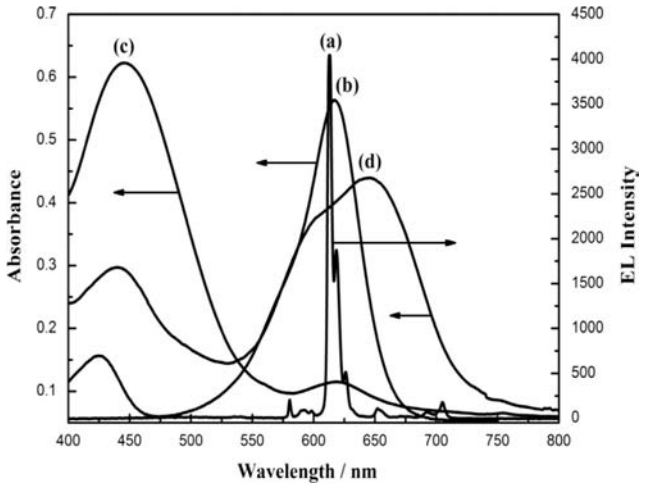


Fig. 7. (a) Emission spectrum (λ_{max}=612 nm) from the OLED, (b) absorption spectrum (λ_{max}=615 nm) of a 5 μM MG solution, (c) absorption spectrum of a 25% methanol water mixture containing 2.2×10^{-4} M MG solution and 0.11 M ammonium molybdate (λ_{max}=450 nm, abbreviated as MG reagent solution) and (d) absorption spectrum of a 25% methanol water mixture containing 2.2×10^{-4} M MG solution and 0.11 M ammonium molybdate and 0.14 ppm phosphate (λ_{max}= 640 nm).

calculated from the photocurrent of the OPD using the following equation based on the Lambert–Beer's law.

$$A\ (\text{absorbance}) = -\log\frac{I_1}{I_0} \quad (1)$$

where I_1=photocurrent for the MG solutions, I_0=photocurrent for water. A good linear relationship between absorbance and the concentration of the MG solutions was obtained with a correlation coefficient of 0.9977, as shown in Fig. 8(c). The molar absorptivitiy coefficient of the MG solution calculated from the calibration line in Fig. 8(b) is $9.78\times10^4\ M^{-1}\ cm^{-1}$, which is in good agreement with the reported value, $9.25\times10^4\ M^{-1}\ cm^{-1}$ [35]. This result indicates that the combination of the OPD and the OLED can function as a good photometric detector for the sensitive detection of MG solutions.

3.3. Phosphate determination on a microchip by using the photometric detector assembled with the OLED and the OPD

3.3.1. Suitability of OPD and OLED for the malachite green method for the determination of phosphate

The spectrophotometric determination of phosphate based on the molybdenum yellow method, in which phosphate reacts with ammonium molybdate to form a molybdenum phosphate complex, is well known. In order to enhance the sensitivity of this method, Motomizu et al. proposed a sensitive method (malachite green method) by taking advantage of an ion association reaction of MG with molybdenum phosphate [36] and their proposed method has been applied to flow injection analysis [37–39]. Namely the following reaction was used after the formation of molybdenum phosphate in an acidic medium at low pH.

$$H_3PMo_{12}O_{40}(\text{Yellowcolor}) + HMG^{2+}(\text{Yellowcolor},\ \lambda_{max} = 446\ \text{nm}) \rightarrow (MG^{+})(H_2PMo_{12}O_{40}^{-})(\text{Greencolor},\ \lambda_{max} = 640\ \text{nm}) + 2H^{+} \quad (2)$$

To stabilize the ion associate in the aqueous solution, methanol is added to the reaction solution. Another advantage of the method based on the formation of the ion associate with MG is that the color-forming reaction is fast and no heating is needed, as shown in Fig. 7(c) and (d) shows absorption spectra of the MG

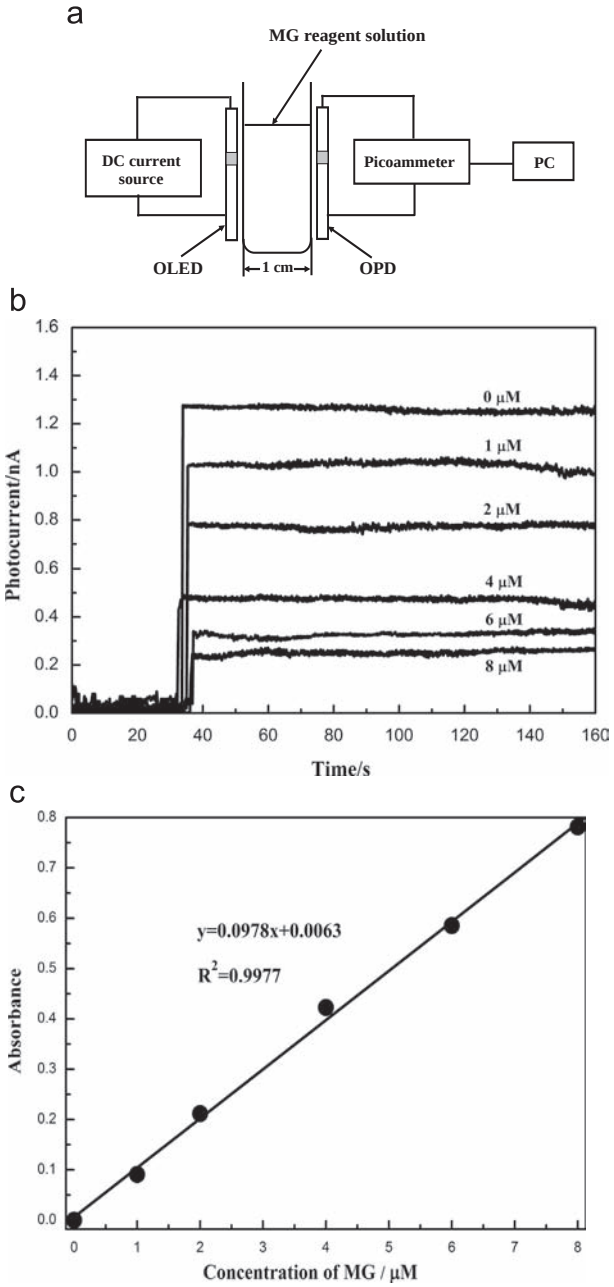


Fig. 8. (a) Experiment setup for measurements of the absorbance of a malachite green (MG) solution in a batch system, (b) the time-course of the photocurrent of the OPD for MG solutions at different concentrations during irradiation of the light from the OLED (applied voltage is 10 V) and (c) calibration plot for the MG solutions. The absorbance of the MG solutions was calculated from the photocurrent as a reference of the photocurrent observed for water.

reagent solution (a mixture of the MG solution and molybdenum ammonium) and a solution of the ion associate of MG with molybdenum phosphate, respectively. This indicates that after phosphate is added to the MG reagent solution, the maximum wavelength of the MG reagent observed at 450 nm is shifted to the maximum absorbance wavelength at 640 nm. The absorbance spectrum of the ion associate of the MG–molybdenum phosphate (in the range ca. 600–650 nm) is efficiently overlapped with the emission spectrum of the OLED. As shown in Fig. S3, the OPD shows sensitivity to the emission light of the OLED (λ_{max}= 612 nm) because the OPD has a broadband photo response from 600 to 700 nm. This means that the photometric detector

combined with the OLED and the OPD is suitable for the determination of phosphate based on the malachite green method.

3.3.2. Optimization of flow conditions and determination of phosphate

A flow system for the determination of phosphate shown in Fig. 3 was constructed according to the report by Motomizu et al. [36]. The concentration of the reagents of MG–molybdate and the carrier solution of hydrogen sulfate are adopted from the report. In order to optimize the flow condition, the flow rate was changed from 20 to 200 μL/min and the sample volume was changed from 20 to 150 μL. The results are shown in Fig. 9. As a result, the flow rates of the reagent solution and the carrier solution and the sample volume were selected as 50 μL/min and 100 μL, respectively, as shown in Fig. 3. Fig. 10(a) shows the photocurrent peak signals from the OPD for three injections of the same sample concentration. In this case, a voltage of 10 V was applied to the OLED. As shown in Fig. 10(a), the reproducibility of the peak height for the three injections is in the acceptable range. The noise level of the photocurrent of the OPD for the baseline signal was

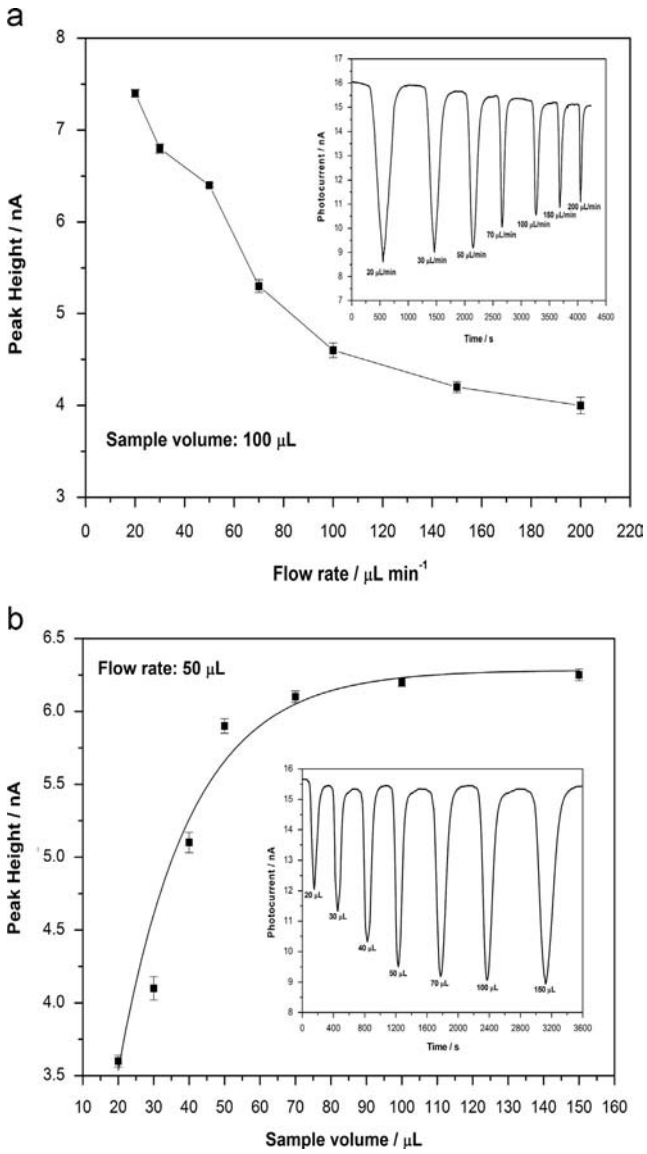


Fig. 9. (a) Effect of the flow rate on the peak height and (b) effect of sample volume on the peak height. The concentration of sample is 0.20 ppm. The corresponding peaks based on absorbance are shown in the inset.

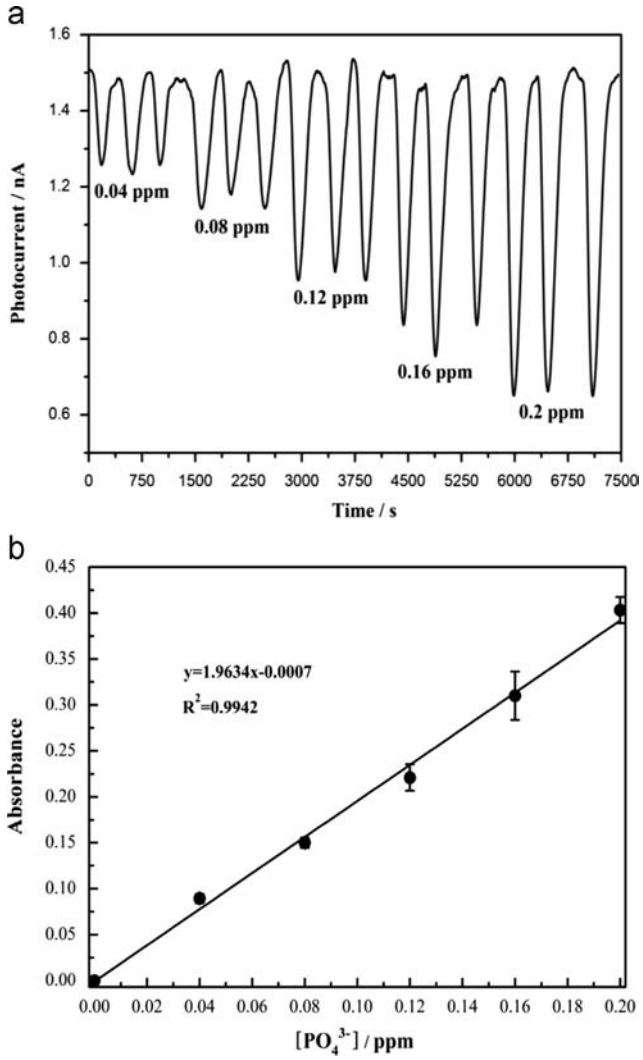


Fig. 10. (a) The output photocurrent signals of the OPD for different concentrations of phosphate solutions by the flow injection system, (b) the calibration line calculated from (a). The error bars represent the standard deviations for three times measurements. The applied voltage to the OLED was 10 V. The other flow conditions are the same as shown in Fig. 3.

± 0.015 nA. The sampling rate of this method was ca 10 h^{-1}. According to Eq. (1) and Fig. 10(b), the absorbance calculated from the photocurrent signal is plotted against the concentration of phosphate, as shown in Fig. 10(b). A good linear relationship between the absorbance and the phosphate concentration was observed, with a correlation factor of 0.9942. The lower detection limit defined as $S/N=3$ is ca. 0.02 ppm for phosphate using the present method. The comparison of the lower detection limit of our method with the other relevant method is shown in Table S1.

3.4. Application of the present method to river water samples

In order to apply the developed analytical system for determining phosphate levels in actual water samples, we collected samples of water from a river in Fukuoka city at distances of 300 m, 2100 m and 3000 m from the seashore. After obtaining the samples, they were filtrated through a membrane filter with the pore size of 0.45 μm and stored in a refrigerator at 4 °C. 22.5 mL aliquots of these samples were spiked by adding 2.5 mL of the 0.8 ppm standard phosphate solution, and the recoveries of phosphate added to the sample were measured by the procedure described in section of 2.7. In this case, the FIA system shown in

Table 1
Application of the photometric detector to the determination of phosphate in river water samples.

Sample	Added (ppm)	Found (ppm)	R.S.D, % (n=5)	Recovery, % (n=5)
River water 1	0.00	0.00	–	–
	0.080	0.076	4.0	99.3
River water 2	0.00	0.00	–	–
	0.080	0.076	4.7	98.4
River water 3	0.00	0.00	–	–
	0.080	0.075	3.9	97.5

Fig. 3 was applied to the determination of phosphate levels in river water samples. When we attempted to measure the concentration of phosphate in the river water samples in a preliminary experiment, we were unfortunately not able to detect phosphate, we spiked the river water sample with the standard phosphate solution at 0.08 ppm. Recovery tests were then carried out for the spiked samples using the FIA system and the results are listed in Table 1. Recoveries of 97–99% were obtained for the river water samples. The good recovery of the present method comes from the high selectivity of the reaction of molybdate with phosphate, which is used as the methods of the molybdenum blue and molybdenum yellow [40,41]. This indicates that the performance of the photometric detector assembled with the OPD and the OLED is similar to that for a conventional photometric detector.

4. Conclusions

In this work, we report on the development of a photometric detector assembled with an OLED and an OPD for the photometric flow injection determination of phosphate based on the malachite green method on a microchip. The performance of the photometric detector was evaluated by measuring the molar absorptivity of a MG solution and the result was in good accordance with the reported value. Under the optimized flow conditions for the determination of phosphate, a linear calibration line between the peak height based on an absorbance unit and the concentration of phosphate was observed in the range 0–0.2 ppm with the regression coefficient of 0.9942 and the detection limit of 0.02 ppm was obtained. In addition, we successful applied the present flow system with the photometric detector to the determination of phosphate in river water samples. The present photometric detector was assembled on a microchip because the shape of the OLED and the OPD was flat, thus making it suitable for insertion on a flat shaped microchip. In order to fabricate an OLED as a suitable light source for the malachite green method, a rare earth complex, $Eu(DBM)_3$bath, doped CBP was used as the emitting layer, since it provides a narrow emission spectrum (FWHM is ca. 10 nm). This type of light source is very suitable for the selective determination of analytes, because it is not necessary to use a grating, a monochromater or a band pass filter for the separation of a wavelength from the broadband light source. Especially for case of a fluorometric determination, such a type of sharp a light source has an advantage for the selective excitation of an analyte. We are currently attempting to fabricate an optical sensing system combining a sharp emission green OLED based on another type of rare earth complex with the OPD on a microchip for fluorescence detection. One of drawbacks of the OLED is a limited life time due to oxygen and humidity and fluctuation of the light intensity for long-life and stable light source for the photometric system. In the future it will be possible to fabricate optical devices such as the OPD and the OLED directly on a microchip by improving and enhancing the life time and stability.

Acknowledgments

This research was supported in part by the Japan Society for the Promotion of Science (JSPS) through its “Funding Program for World-Leading Innovative R&D on Science and Technology (FIRST Program)” and by JSPS KAKENHI Grant no. 25620117.

Appendix A. Supplementary information

Supplementary data associated with this article can be found in the online version at http://dx.doi.org/10.1016/j.talanta.2014.08.057.

References

[1] M. Bowden, D. Diamond, Sens. Actuators B: Chem. 90 (2003) 170–174.
[2] P.J. Worsfold, L.J. Gimbert, U. Mankasingh, O.N. Omaka, G. Hanrahan, P.C. F. C. Gardolinski, P.M. Haygarth, B.L. Turner, M.J. Keith-Roach, I.D. Mckelvie, Talanta 66 (2005) 273–293.
[3] K.L. Linge, C.E. Oldham, Anal. Chem. Acta 450 (2001) 247–252.
[4] T. Uemura, T. Ogusu, M. Takeuchi, H. Tanaka, Anal. Sci. 26 (2010) 797–801.
[5] H. Nakajima, Y. Okuma, K. Morioka, M. Miyake, A. Hemmi, T. Tobita, M. Yahiro, D. Yokoyama, C. Adachi, N. Soh, K. Nakano, S.H. Xue, H.L. Zeng, K. Uchiyama, T. Imato, J. Sep. Sci. 34 (2011) 2906–2912.
[6] J.W. Choi, D.K. Kang, H. Park, A.J. deMello, S.I. Chang, Anal. Chem. 84 (2012) 3849–3854.
[7] S. Götz, U. Karst, Anal. Bioanal. Chem. 387 (2007) 183–192.
[8] B. Kuswandi, G. Nuriman, J. Huskens, W. Verboom, Anal. Chim. Acta 601 (2007) 141–155.
[9] K. Miyaki, Y. Guo, T. Shimosaka, T. Nakagama, H. Nakajima, K. Uchiyama, Anal. Bioanal. Chem. 382 (2005) 810–816.
[10] G.E. Collins, Q. Lu, N. Pereira, P. Wu, Talanta 72 (2007) 301–304.
[11] D. Xiao, L. Yan, H.Y. Yuan, S.L. Zhao, X.P. Yang, M.M.F. Choi, Electrophoresis 30 (2009) 189–202.
[12] F. Yang, X.C. Li, W. Zhang, J.B. Pan, Z.G. Chen, Talanta 84 (2011) 1099–1106.
[13] G. Ryu, J.S. Huang, O. Hofmann, C.A. Walshe, J.Y.Y. Sze, G.D. McClean, A. Mosley, S.J. Rattle, J.C. deMello, A.J. deMello, D.D.C. Bradley, Lab Chip 11 (2011) 1664–1670.
[14] S.H. Xue, K. Uchiyama, H.F. Li, J. Environ. Sci. 24 (2012) 564–570.
[15] Y.H. Kuo, C.J. Wu, F.T. Kuo, J.Y. Yen, Y.Y. Chen, Microelectron. Eng. 103 (2013) 137–143.
[16] O. Hofmann, X.H. Wang, J.C. DeMello, D.D.C. Bradley, A.J. deMello, Lab Chip 5 (2005) 863–868.
[17] B. Yao, G.A. Luo, L.D. Wang, Y.D. Gao, G.T. Lei, K.N. Ren, L.X. Chen, Y.M. Wang, Y. Hu, Y. Qiu, Lab Chip 5 (2005) 1041–1047.
[18] B. Yao, H.H. Yang, Q.L. Liang, G.A. Luo, L.D. Wang, K.N. Ren, Y.D. Gao, Y.M. Wang, Y. Qiu, Anal. Chem. 78 (2006) 5845–5850.
[19] K.N. Ren, Q.L. Liang, B. Yao, G.A. Luo, L.D. Wang, Y.D. Gao, Y.M. Wang, Y. Qiu, Lab Chip 7 (2007) 1574–1580.
[20] C. Merfort, K. Seibel, K. Watty, M. Böhm, Microelectron. Eng. 87 (2010) 712–714.
[21] B.H. Tanaka, T. Yasuda, K. Fujita, T. Tsutsui, Adv. Mater. 18 (2006) 2230–2233.
[22] X.H. Wang, M. Amatatongchai, D. Nacapricha, O. Hofmann, J.C. deMello, D.D. C. Bradley, A.J. deMello, Sens. Actuators B 140 (2009) 643–648.
[23] T. Mayr, T. Abel, E. Kraker, S. Köstler, A. Haase, C. Konrad, M. Tscherner, B. Lamprecht, Proc. Eng. 5 (2010) 1005–1008.
[24] O. Hofmann, P. Miller, P. Sullivan, T.S. Jones, J.C. deMello, D.D.C. Bradley, A.J. deMello, Sens. Actuators B 106 (2005) 878–884.
[25] A. Banerjee, A. Pais, I. Papautsky, D. Klotzkin, IEEE Sens. J. 8 (2008) 621–627.
[26] A. Pais, A. Banerjee, D. Klotzkin, I. Papautsky, Lab Chip 8 (2008) 794–800.
[27] M. Miyake, H. Nakajima, A. Hemmi, M. Yahiro, C. Adachi, N. Soh, R. Ishimatsu, K. Nakano, K. Uchiyama, T. Imato, Talanta 96 (2012) 132–139.
[28] D. Onoshima, J. Wang, M. Aki, K. Arinaga, N. Kaji, M. Tokeshi, S. Fujita, N. Yokoyama, Y. Baba, Anal. Methods 4 (2012) 4368–4372.
[29] V. Lavín, U.R. Rodríguez-Mendoza, I.R. Martín, V.D. Rodríguez, J. Non-Cryst. Solids 319 (2003) 200–216.
[30] C.J. Liang, D. Zhao, Z.R. Hong, D.X. Zhao, X.Y. Liu, Appl. Phys. Lett. 76 (2000) 67–69.
[31] P.P. Sun, J. Duan, H. Shih, C.H. Cheng, Appl. Phys. Lett. 81 (2002) 792–794.
[32] G. Law, K. Wong, H. Tam, K. Cheah, W. Wong, Inorg. Chem. 48 (2009) 10492–10494.
[33] T. Oyamada, Y. Kawamura, T. Koyama, H. Sasabe, C. Adachi, Adv. Mater. 16 (2004) 1082–1086.
[34] M. Sun, H. Xin, K.Z. Wang, Y.A. Zhang, L.P. Jin, C.H. Huang, Chem. Commum. 5 (2003) 702–703.

[35] J. Lux, E.J. Peña, F. Bolze, M. Heinlein, J.F. Nicoud, ChemBioChem 13 (2012) 1206–1213.
[36] S. Motomizu, Z.H. Li, Talanta 66 (2005) 332–340.
[37] T. Uemura, T. Ogusu, M. Takeuchi, H. Tanaka, Anal. Sci. 26 (2010) 797–801.
[38] J. Feng, Y. Chen, J. Pu, X.L. Yang, C. Zhang, S. Zhu, Y.S. Zhao, Y.H. Yuan, H.H. Yuan, F. Liao, Anal. Biochem. 409 (2011) 144–149.
[39] E. D'Angelo, J. Crutchfield, M. Vandiviere, J. Environ. Qual. 30 (2001) 2206–2209.
[40] S. Motomizu, Y. Saio, K. Toei, Proceedings of the 18th Semi-Annual Meeting of the Japanese Association for Flow Injection Analysis, Abstract FI-25, Tokyo, 1993.
[41] L.S. Clesceri, A.E. Greenberg, A.D. Eaton, Standard Methods for the Examination of Water and Wastewater, 20th ed., APHA-AWWA-WEF, 1998, pp. 4–151.

Talanta 132 (2015) 106–111

Contents lists available at ScienceDirect

Talanta

journal homepage: www.elsevier.com/locate/talanta

Dielectric barrier discharge micro-plasma emission source for the determination of lead in water samples by tungsten coil electro-thermal vaporization

Hongtao Zheng [a,b], Jingzhi Ma [a,b], Zhenli Zhu [a,*], Zhiyong Tang [b], Shenghong Hu [a,c]

[a] State Key Laboratory of Biogeology and Environmental Geology, China University of Geosciences, Wuhan 430074, China
[b] Faculty of Material Science and Chemistry, China University of Geosciences, Wuhan 430074, China
[c] Faculty of Earth Sciences, China University of Geosciences, Wuhan 430074, China

ARTICLE INFO

Article history:
Received 18 June 2014
Received in revised form
26 August 2014
Accepted 31 August 2014
Available online 6 September 2014

Keywords:
Tungsten coil
Electro-thermal vaporization
Dielectric barrier discharge
Atomic emission spectrometry
Lead

ABSTRACT

In this study, a fast and simple approach to directly determinate lead in water samples by a low power dielectric barrier discharge (DBD) excitation source was developed using tungsten coil electro-thermal vaporization (WC ETV) for liquid microsample introduction. A 20 μL sample was dropped onto the WC, and then the sample went through the drying, pyrolysis, subsequently the analyte was vaporized and swept directly into the dielectric barrier discharge micro-plasma for emission, and the whole process took only 3 min. The effects of operating parameters such as plasma gas flow rate, plasma input voltage, pyrolysis current, vaporization current and interferences from concomitant elements were investigated. Under the optimal conditions, the limit of detection (LODs, 3σ) was calculated to be 7.7 μg L^{-1}. Repeatability, expressed as the relative standard deviation of the spectral peak height, was 4.6% ($n=11$) for 0.1 mg L^{-1} lead standard solution. The proposed method was successfully applied to the determinations of Pb in water samples.

© 2014 Elsevier B.V. All rights reserved.

1. Introduction

The contamination of lead in water has become a problem of global concern [1]. Of all the heavy metals, Pb(II) is important to consider in terms of food chain contamination because of its toxicity [2,3]. Pb(II) ions causes both acute and chronic poisoning, exhibits adverse effects on the kidney, liver, heart, vascular and immune system. Moreover, Pb(II) exposure causes chromosome aberration, skin allergy, cancer and birth defects [4,5]. Hence, there is a great demand to develop a simple and reliable method for the determination of the level of lead in water on-site.

In this perspective a number of methods have been developed for the determination of Pb(II) the well-known high-performance spectrometric instruments, such as atomic absorption spectrometry (AAS) [6], atomic fluorescence spectrometry (AFS) [7], inductively coupled plasma atomic emission spectrometry (ICP-AES) [8] and inductively coupled plasma mass spectrometry (ICP–MS) [9] can perform fast, sensitive, and accurate lead determinations. However, these methods are generally performed at laboratories, requiring complicated equipment (e.g., high power, large inert or special gases, high vacuum). These disadvantages limit their applications primarily to laboratory settings, and prohibit their use for rapid analyses under field conditions. Therefore, it is of much significance to develop compact and low-cost instruments [10], for in situ monitoring of Pb contamination in water.

In recent years micro-plasmas [11–15], embedded in portable analytical instrumentation, such as corona discharge, glow discharge, capacitively coupled plasma, and dielectric barrier discharge (DBD) [16] received increased attention for the development of portable instruments for elemental analysis because of their small size, low power consumption, cost effectiveness, and reduced inert gas requirement. The unique advantages of DBD include simple construction, low temperature and power consumption, and atmospheric operation [14]. However, direct introduction of liquid sample into the DBD micro-plasma for analytical atomic spectrometry can be a problem for its lowered excitation capability or can even extinguish it. Tombrink et al. [17] first introduced direct liquid analysis by using a capillary DBD, and Zhu et al. [18] developed a liquid-film DBD (LFDBD). In their studies, they solved the liquid sampling problem to some extent. Nevertheless, residual or concomitant moisture and matrix from liquid sample introduction still restrict the analytical performance of DBD micro-plasma for AES. The vapor generation (cold vapor and hydride generation) was mostly employed in DBD-AES for the sample introduction since it improves the sample introduction efficiency and reduces the introduction of water. However, only a limited number of elements is applicable to

* Corresponding author.
E-mail addresses: zhuzl03@gmail.com, zlzhu@cug.edu.cn (Z. Zhu).

http://dx.doi.org/10.1016/j.talanta.2014.08.070
0039-9140/© 2014 Elsevier B.V. All rights reserved.

CVG and the reported research mainly focused on mercury, arsenic and some nonmetals [11,15,19].

As well known, electro-thermal vaporization (ETV) has long been considered as an excellent sample introduction technique for analytical atomic spectrometry. It offers several advantages, including improved sample introduction efficiency, efficient separation matrix, requirement of small amounts of sample, and the capability to perform direct analysis of slurries and solids [20–27]. Most works on ETV employ graphite furnaces as electro-thermal vaporizers [22,24,26–28]. However, it requires heavy power supplies and water cooling systems, so they are seldom used in portable instrumentation [29]. A simpler and less expensive alternative is to use tungsten coil, which can be extracted from commercially available stage light bulbs. Because of their low mass and the specific heat of tungsten, tungsten coils (WC) present a faster heating–cooling regimen, which requires no complex bulky chillers. In addition, a simple low power source is enough to efficiently vaporize samples. Another advantage of WC vaporizers when compared to graphite furnaces is that carbon species are not formed from atomizer surface vaporization, which minimizes the formation of carbides [30,31]. In the past studies, tungsten coil has been widely used as atomizers in atomic absorption and atomic fluorescence spectrometry [32,33]. Meanwhile, it has also been employed as electro-thermal vaporizers in atomic emission [10,34,35], as for inductively coupled plasma [21,36] and microplasma [37–39]. For years, to the best of our knowledge, there are no reports on the hyphenation of ETV with DBD microplasma emission source. Until more recently, Hou et al. [40] firstly coupled W-coil ETV with DBD-AES and applied it to the determination of Hg, Zn, and Cd.

In the present study, the feasibility of coupling W-coil ETV with DBD-AES for directly Pb determination was demonstrated. A tungsten coil extracted from commercially available stage light bulb was used to vaporize samples without any previous sample treatment. The analyte vaporized from the tungsten coil ETV was transported to the DBD source for excitation, and then the lead could be measured by atomic emission spectrometry. Several experimental parameters were optimized, and analytical figures of merit were evaluated. Both the WC ETV device and DBD system are simple, easily fabricated, and low cost of operation, it provided a possibility to design a portable, miniature, and mobile AES instrument, especially for field analysis of Pb with low-power supply.

2. Experimental

2.1. Instrumentation

The W-coil ETV–DBD-AES system consisted of an ETV generation unit for sample introduction and a DBD atomic emission system for Pb excitation. For ETV unit, the tungsten filament extracted from a commercially available halogen display lamp

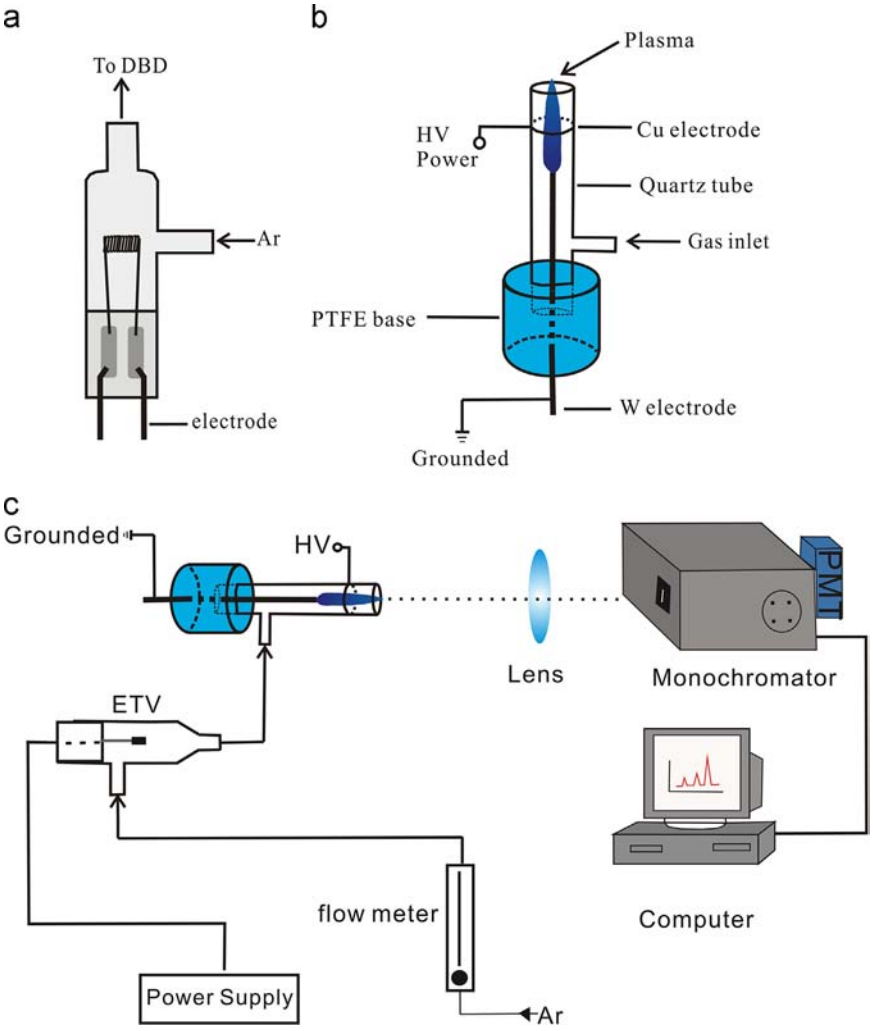


Fig. 1. The schematic diagram of the equipment. Vaporizer (a) and the DBD setup (b) and the whole instrument (c).

(G6.35, 24V, 300W, MINGAN, Jiangsu. China) was used as the vaporizer. The filament was coiled in ten turns when viewing from the side, the turns were 3 mm high and together they occupy a width of 6 mm. The glass envelope was carefully installed two branch pipes, argon gas flowed from lateral branch pipe (23 mm × 3 mm i.d., 5 mm o.d.) and swept the analyte into DBD plasma from the top of branch pipe (14 mm × 5 mm i.d., 7 mm o.d.) Fig. 1a provided the schematic diagram of the vaporizer. A commercial computer controlled DC power supply (ATTEN PPS3205T-3S., Shenzhen. China) was used as a programmable power supply for the W-coil ETV. A 15 cm polytetrafluoroethylene (PTFE) tube (1.2 mm i.d.) connected the ETV cell to the DBD instrument and served as the interface between the ETV cell and DBD instrument.

As the center unit of the entire system, the homemade cylindrical DBD emission source mainly consisted of a quartz tube, a tungsten rod electrode and a copper coil electrode. The 65 mm long quartz tube (3 mm inner diameter, 5 mm outer diameter) was mounted on a PTFE base. A tungsten rod (1 mm diameter) centered at the axis of quartz tube acted as the grounded electrode. Another copper coil electrode (HV) was wrapped tightly outside the quartz tube, 15 mm away from the top of the tube. The distance between the tip of the tungsten electrode and the copper coil electrode was about 5 mm. Fig. 1b provides the schematic diagram of the DBD setup. When an ac high voltage was applied to the electrodes, discharge plasma was self-ignited upon the tip of the tungsten rod, even appeared outside the quartz tube. The ac high voltage was provided by a CTP-2000 K discharge power supply (Suman Elec-tronics Co., Ltd., Nanjing, China). The input voltage for the discharge power supply was controlled by a TDGC2-1 voltage regulator (CHINT Electrics Co., Ltd., China). The discharge gas and sample flowed into the quartz tube through the sample introduction port at the bottom. Vaporized lead originating from electro-thermal evaporation was excited in the plasma. The emission signal was measured along the axial direction through the center of the quartz tube. The discharge was imaged 2.5:1 with a fused-silica lens (focal length = 100 mm) to the entrance slit of a monochromator (Zolix Instruments, Omni-λ5008, focal length = 500 mm) with a 1200 grooves mm^{-1} holographic grating. The monochromator is supplied with slits of 14 mm height, whose width could be adjusted from 10 μm to 3 mm. A PMTH-S1-CR131A photomultiplier tube was used as the detector.

The whole schematic diagram of the W-coil ETV–DBD plasma AES instrument was showed in Fig. 1c and the optimized operating parameters were given in Table 1. Inductively coupled plasma mass spectrometry (PerkinElmer Instrument., ELAN DRC-e., America.) was used to determine the groundwater samples to validate our results. The operating parameters of ICP–MS were also listed in Table 1.

2.2. Reagents and samples

The stock standard solution of lead (1000 mg L^{-1}) was purchased from National Analysis Center for Iron and Steel (Beijing, China). Working solutions were prepared by serial dilution of the stock solutions and stabilized in 0.5% HNO_3. Single-element standard solutions of Ba^{2+}, Ca^{2+}, Cd^{2+}, Co^{2+}, Cr^{3+}, Cu^{2+}, Fe^{3+}, K^{+}, Mg^{2+}, Mn^{2+}, Na^{+} and Zn^{2+} were used to assess the interferences from individual metals present at concentrations of 50 mg L^{-1} and 20 mg L^{-1} in solutions of 0.1 mg L^{-1} lead. All chemicals were analytical or even higher grade. Argon with a purity of 99.999% was used. Ultrapure water (18.2 MΩ cm^{-1}, resistivity) was obtained from a water purification system (9000502, Labconco water props, USA) and used for preparation of all solutions.

To obtain reliable analytical results, two reference solutions of water (GSB 07-1183-2000 and GBW (E) 080399) were used to check accuracy of the proposed method. Five groundwater samples (pH = 7.12–7.26) were acidified to a final HNO_3 concentration of 0.5%. In order to make the samples more homogeneous, 5 min ultrasonic vibration was used.

2.3. Experimental procedure

A 20-μL of a sample solution containing lead was deposited directly onto the W-coil with an Eppendorf Research Pipette. As the ETV program shown in Table 2, the tungsten coil was then heated to remove the solvent. As the liquid dried, the resistance of the W-coil increased, so progressively smaller currents were used to gradually dry the sample in order to avoid the loss of analytes. After the dry step, 5 s of pyrolysis step at 2.7 A was employed to eliminate the sample matrix, then 20-s cooling interval (0 current) for allowing the W-coil return to room temperature. This ensured that the high temperature heating step was most reproducible. During the cooling time, the catheter was connected with the DBD from the top of branch pipe of ETV, and then ignites the DBD plasma. The high temperature step was achieved 6.0 A applied for 3 s to vaporize the analyte. The vaporized lead was transported into the DBD plasma through the PTFE tubing by the Ar carrier gas stream. During this step, the transient emission signal was recorded, and the peak height was measured. A 20-s cooling step was employed at the end, to ensure that the W-coil was ready for the next injection of sample. The optimized experimental conditions are summarized in Table 2. Some of the optimum operating conditions given in Table 2 will be discussed below.

3. Results and discussion

3.1. Optimization of experimental conditions

In order to introduce vaporized lead into DBD efficiently, the interface between DBD and W-coil should be as short as possible. However, we found that the high voltage of the DBD would disturb the ETV if the W-coil was placed too close to the DBD. Thus, 15 cm length of connection tube was adopted after optimization. The effect of monochromator slit widths on the measurement of Pb emission was investigated. Because the 0.4 mm slit width gave the greatest signal-to-background intensity ratios (SBR), it was

Table 1
The optimized operating parameters of WC–ETV–DBD-AES and ICP–MS.

W Coil–ETV–DBD-AES		ICP–MS	
Negative high voltage of PMT (V)	850	Mass (Pb)	208
Integration time of PMT (ms)	50	RF power (W)	1100
Slit width of monochromator (mm)	0.4	Plasma gas flow rate (L min^{-1})	15
Wavelength (nm)	368.3	Auxiliary gas flow rate (L min^{-1})	1.2
Input voltage (V)	23	Carrier gas flow rate (L min^{-1})	1.2
Input current (A)	1.25	Dwell time (ms)	50
Working gas and flow rate (L min^{-1})	Argon and 0.6	Internal standard element	In

Table 2
The operating condition of tungsten coils electro-thermal vaporization cycles.

Step	WC	
	Current (A)	Time (s)
1	2.6	35
2	2.4	45
3	2.2	20
4	2.7	5
5	0	20
6	6.0	3
7	0	20

selected in the whole experiments. Subsequently, several important parameters such as the flow rate of the Ar carrier gas, input voltage, pyrolysis current and vaporization current were evaluated by a univariate approach.

3.1.1. Effect of Ar carrier gas flow rate

In this system, the working gas plays three important roles: protecting tungsten filament from oxidation, transporting the vaporized analyte from the W-coil ETV to the DBD plasma and supporting the discharge. Low argon flow rate may lead to analyte loss during the transportation, while high argon flow rate results in short residence time of atoms in the DBD thus short time for excitation and measurements. In our study, Pb transient atomic emission signal (at 368.3 nm) generally presented asymmetric, irreproducible, and sometimes double-peaked, at an argon flow rate below 400 mL min^{-1}. The intensity of atomic emission for Pb increased sharply when argon flow rate increased from 400 mL min^{-1} to 600 mL min^{-1} and then began to decrease. Hence, an argon flow rate of 600 mL min^{-1} was selected for Pb.

3.1.2. Effect of input voltage of DBD

A voltage regulator was applied to control the input voltage for the discharge power supply. The impacts of the input voltage on the response signal intensity was studied. It was observed that when the voltage got 23 V the net Pb emission peak height signals was almost unchanged and signal to background ratio obtained the maximum. Finally 23 V was employed as the optimum input voltage in the subsequent studies.

3.1.3. Effect of pyrolysis current

In a typical heating program for the electro-thermal vaporization, a first drying step and a subsequent pyrolysis step were commonly used for removing the solvent and matrix from the sample, ideally without any analyte loss. As well known, higher current may cause serve analyte loss due to higher temperature, while lower current could not eliminate the solvent and matrix thoroughly. The effect of pyrolysis current was evaluated from 2.5 A to 2.9 A, and the result was shown in Fig. 2. The maximum intensity was obtained at 2.7 A, thus pyrolysis current of 2.7 A was selected in the subsequent study.

3.1.4. Effect of vaporization current

The vaporization current, responding to the temperature of the W-coil, was an essential factor for the vaporization. Analyte on the W-coil was released during the vaporization step, so the vaporization current significantly influenced the sample introduction efficiency. The effect of vaporization current from 4.5 A to 7.0 A on the DBD-AES responses of Pb were summarized in Fig. 3. No measurable signal from Pb was observed when current was less than 4.0 A, which because no analyte was released from the W-coil for the low temperature. The maximum responses were obtained

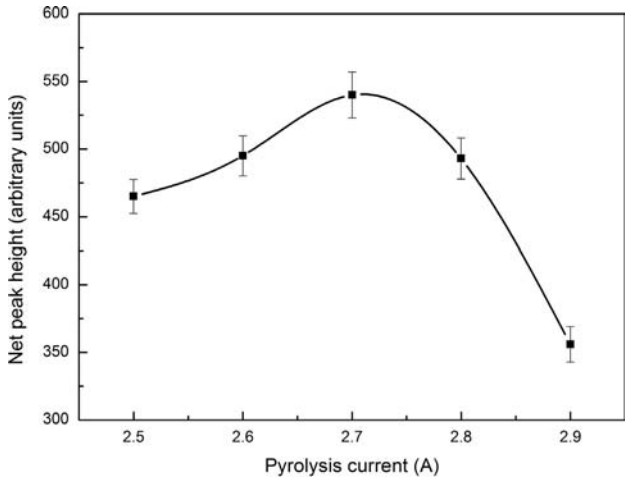


Fig. 2. Effect of the pyrolysis current (n=3). Experimental details: sampling volume, 20 μL; Pb concentration, 0.2 mg L^{-1}.

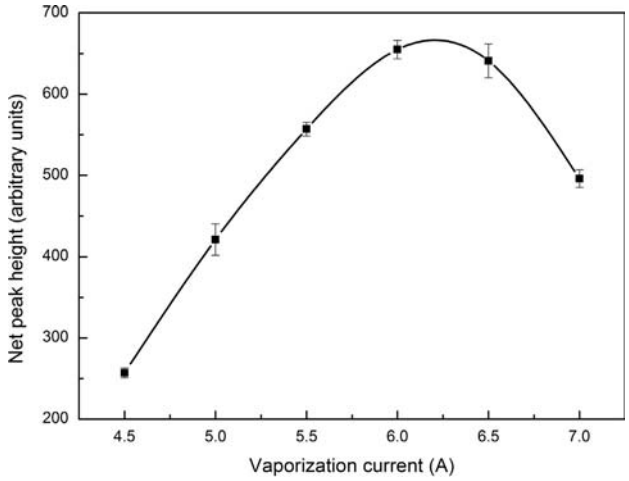


Fig. 3. Effect of the vaporization current (n=3). Experimental details: sampling volume, 20 μL; Pb concentration, 0.2 mg L^{-1}.

at 6 A. Therefore, 6 A was selected as the vaporization current for detection of Pb.

3.2. Interference study

In a ETV process, several metal ions may be simultaneously evaporated to their metallic states or colloidal forms, which covered the analyte to cause serious interferences [33]. To evaluate the analytical applicability of the proposed technique, the interferences caused by a series of metal elements including Ba^{2+}, Ca^{2+}, Cd^{2+}, Co^{2+}, Cr^{3+}, Cu^{2+}, Fe^{3+}, K^{+}, Mg^{2+}, Mn^{2+}, Na^{+} and Zn^{2+} in determining 0.1 mg L^{-1} lead were examined using WC–ETV–DBD-AES method and the results were summarized in Table 3. It is clear that there is no significant interference from these studied ions at concentrations of 20 mg L^{-1} or 50 mg L^{-1}. However, depression effects were observed for Na^{+}, Zn^{2+} or Cd^{2+} at concentrations of 200 mg L^{-1}. The interference mechanism is at present unclear. It indicated that the proposed method could be used for determination of trace lead in water sample almost free of interference from the complex matrix.

3.3. Analytical figures of merit

Under the optimized operating conditions, analytical working graphs were obtained for lead at 368.3 nm by ETV–DBD-AES. The

linearity of the calibration curve was examined by detecting of a series of standard solutions with concentrations ranging from 25 μg L^{-1} to 500 μg L^{-1}, which provided linear correlation coefficients (R) 0.9989 (Fig. 4). The limits of determination (LODs), calculated using the definition $3\sigma/S$ (σ is the standard deviation of 11 measurements of the blank and S is the slope of the calibration curve), was calculated to be 7.7 μg L^{-1}. Since only 20 μL sample volume was injected, the absolute LODs (equivalent to the absolute mass of the analyte) was 154 pg. The relative standard deviation of the spectral peak height was 4.6% ($n=11$) for 0.1 mg L^{-1} lead standard solution. All these results indicated that our proposed method has good sensitivity and repeatability and it could be used for the direct measurement of Pb in water samples.

Table 3
Recovery of Pb in the presence of metal ion interferences (Pb concentration: 0.1 mg L^{-1}, $n=3$).

Element	[M]/[Pb^{2+}]*	Recovery (%)	[M]/[Pb^{2+}]*	Recovery (%)
K^{+}	500	97.4 ± 3.3	2000	94.7 ± 2.0
Ca^{2+}	500	100.5 ± 6.2	2000	98.8 ± 5.4
Na^{+}	500	99.4 ± 5.3	2000	79.8 ± 7.4
Mg^{2+}	500	102.8 ± 3.5	2000	96.4 ± 2.3
Ba^{2+}	200	98.1 ± 4.4	2000	103.7 ± 4.9
Cd^{2+}	200	100.7 ± 7.6	2000	90.3 ± 3.7
Co^{2+}	200	98.4 ± 3.8	2000	96.3 ± 5.3
Cr^{3+}	200	97.3 ± 7.8	2000	97.8 ± 4.6
Cu^{2+}	200	105.5 ± 3.7	2000	99.2 ± 1.6
Fe^{3+}	200	103.6 ± 3.4	2000	96.2 ± 2.8
Mn^{2+}	200	102.8 ± 6.1	2000	99.4 ± 4.1
Zn^{2+}	200	94.8 ± 2.9	2000	88.2 ± 4.8

3.4. Real sample analysis

To validate the accuracy of the proposed method for water sample analysis, two reference solutions of water (GSB 07-1183-2000 and GBW (E) 080399) were analyzed with analytical results listed in Table 4. The t-test showed that there was no significant difference between the analytical results obtained by the proposed method and the certified value at the confidence level of 95%. Moreover, the proposed method was applied to the analysis of five groundwater samples. We also compared the results with those of the same samples determined from ICP–MS. According to the F-test, the F-statistics values of five sets of data are less than 10.00, and when the confidence level in 95%, $F=19.00$. Therefore, there was no significant difference between the analytical results obtained by the proposed method and ICP–MS at the confidence level of 95%. All the results indicated that our proposed method can be used for the determination of water sample.

4. Conclusion

A sensitive, simple and cost-effective method for determination of lead in water samples was developed. The proposed cylindrical DBD plasma could be readily coupled to tungsten coil electrothermal vaporization and the plasma source could excite lead

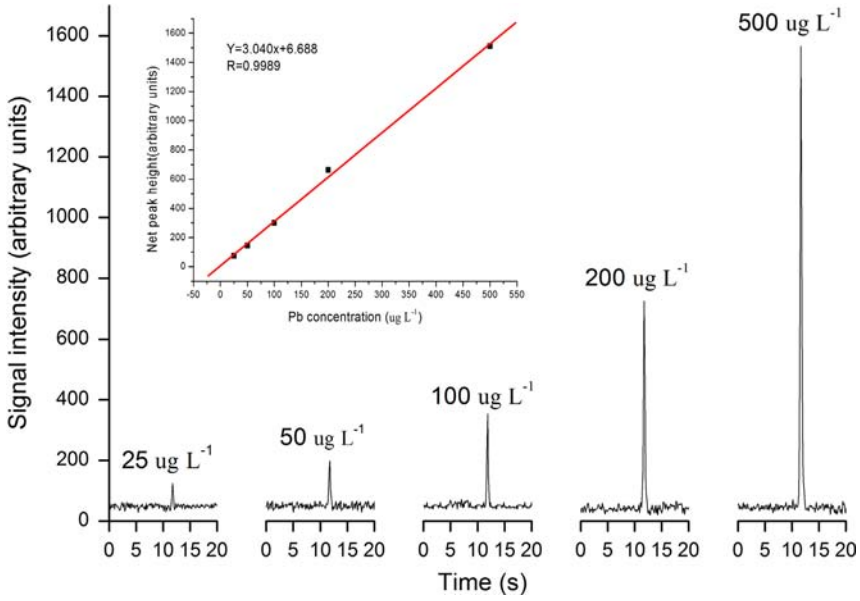


Fig. 4. Typical recoding of Pb emission signals obtained with standard solutions having Pb concentrations between 25 μg L^{-1} and 500 μg L^{-1}. The inset shows the calibration curve with peak height as the analytical parameter.

Table 4
Analytical results of for the determination of lead ($n=3$) in real samples.

Sample	Certified	This work	Found by ICP–MS
GSB 07-1183-2000	0.378 ± 0.017 mg L^{-1}	0.370 ± 0.018 mg L^{-1}	–
GBW (E) 080399	5.000 ± 0.100 mg L^{-1}	5.064 ± 0.106 mg L^{-1}	–
Sample1	–	46.6 ± 2.0 ng mL^{-1}	42.5 ± 0.7 ng mL^{-1}
Sample 2	–	102.3 ± 2.3 ng mL^{-1}	108.3 ± 2.2 ng mL^{-1}
Sample 3	–	133.4 ± 6.1 ng mL^{-1}	144.6 ± 2.5 ng mL^{-1}
Sample 4	–	145.4 ± 4.0 ng mL^{-1}	134.3 ± 2.0 ng mL^{-1}
Sample 5	–	215.6 ± 6.8 ng mL^{-1}	228.1 ± 3.9 ng mL^{-1}

effectively. It offers several important advantages over other analytical method: low power consumption (< 30 W), small size, requirement of small amounts of sample (merely 20 μL), low cost of operation, and ease of fabrication. With all these merits, it provides a possibility to design a portable, miniature, and mobile AES instrument, especially for field analysis of elements with low-power supply. Moreover, ETV–DBD-AES system can be used to determine other elements simultaneously. In the future work, further improvement in the sensitivity and application for other type environmental samples would be of great interest to extend its use in field analytical chemistry.

Acknowledgments

This work was supported by Fundamental Research Funds for the Central Universities, China University of Geosciences (Wuhan) (CUG120117, CUG120502), and Foundation of Geological Survey of China: Trace elements detection in polymetallic deposit with novel techniques of separation and enrichment (no. 12120113014300).

References

[1] P. Wongsasuluk, S. Chotpantarat, W. Siriwong, M. Robson, Environ. Geochem. Health 1 (2014) 169–182.
[2] W.J. Mok, S. Senoo, T. Itoh, Y. Tsukamasa, K. Kawasaki, M. Ando, Food Chem. 4 (2012) 1326–1332.
[3] M. Tufekci, V.N. Bulut, H. Elvan, D. Ozdes, M. Soylak, C. Duran, Environ. Monit. Assess. 2 (2013) 1107–1115.
[4] S. Abbasi, K. Khodarahmiyan, F. Abbasi, Food Chem. 1 (2011) 254–257.
[5] Y. Shih, J. Zen, A.S. Kumar, Y. Lee, H. Huang, Bull. Chem. Soc. Jpn. 2 (2004) 311–312.
[6] P. Hashemi, H. Hassanvand, H. Naeimi, A.R. Ghiasvand, Microchim. Acta 2 (2005) 147–151.
[7] K. Huang, H. Xia, M. Li, Y. Gao, C. Zheng, X. Hou, Anal. Methods 12 (2012) 4058–4062.
[8] A. Massadeh, A. Gharibeh, K. Omari, I. Al-Momani, A. Alomari, H. Tumah, W. Hayajneh, Biol. Trace Elem. Res. 1 (2010) 1–11.
[9] E.Z.B. Skrzydlewska, M. Balcerzak, F. Vanhaecke, Anal. Chim. Acta 2 (2003) 191–202.
[10] J. Gu, S.R. Oliveira, G.L. Donati, J.A. Gomes Neto, B.T. Jones, Anal. Chem. 7 (2011) 2526–2531.
[11] Z. Zhu, H. He, D. He, H. Zheng, C. Zhang, S. Hu, Talanta (2014) 234–239.
[12] H. He, Z. Zhu, H. Zheng, Q. Xiao, L. Jin, S. Hu, Microchem. J. (2012) 7–11.
[13] C. Meyer, S.M U Ller, E.L. Gurevich, J. Franzke, Analyst 12 (2011) 2427–2440.
[14] J. Hu, W. Li, C. Zheng, X. Hou, Appl. Spectrosc. Rev. 5 (2011) 368–387.
[15] Z. Zhu, G.C. Chan, S.J. Ray, X. Zhang, G.M. Hieftje, Anal. Chem. 22 (2008) 8622–8627.
[16] M. Miclea, J. Franzke, Plasma Chem. Plasma Process. 2 (2007) 205–224.
[17] S. Tombrink, S. Mueller, R. Heming, A. Michels, P. Lampen, J. Franzke, Anal. Bioanal. Chem. 7 (2010) 2917–2922.
[18] Q. He, Z. Zhu, S. Hu, H. Zheng, L. Jin, Anal. Chem. 9 (2012) 4179–4184.
[19] M. Puanngam, S. Ohira, F. Unob, J. Wang, P.K. Dasgupta, Talanta 3 (2010) 1109–1115.
[20] X. Mao, J. Liu, Y. Huang, L. Feng, L. Zhang, X. Tang, J. Zhou, Y. Qian, M. Wang, J. Agric. Food Chem. 4 (2013) 848–853.
[21] A. Matsumoto, S. Osaki, T. Kobata, B. Hashimoto, H. Uchihara, T. Nakahara, Microchem. J. 1 (2010) 85–89.
[22] Y. Tseng, C. Liu, S. Jiang, Anal. Chim. Acta 2 (2007) 173–178.
[23] Y. Li, B. Hu, Z. Jiang, Anal. Chim. Acta 2 (2006) 207–214.
[24] G. Xiang, Z. Jiang, M. He, B. Hu, Spectrochim. Acta, Part B 9 (2005) 1342–1348.
[25] T.D. Saint'Pierre, L.U.C.F. Dias, D. Pozebon, R.Q. Auc, E Lio, A.J. Curtius, B. Welz, Spectrochim. Acta, Part B 12 (2002) 1991–2001.
[26] I. Gelaude, R. Dams, M. Resano, F. Vanhaecke, L. Moens, Anal. Chem. 15 (2002) 3833–3842.
[27] R.E. Sturgeon, J.W. Lam, J. Anal. At. Spectrom. 5 (1999) 785–791.
[28] N.H. Bings, Z. Stef, A Nka, J. Anal. At. Spectrom. 9 (2003) 1088–1096.
[29] J.A. Rust, J.A.N O Brega, C.P. Calloway Jr, B.T. Jones, Spectrochim. Acta, Part B 2 (2006) 225–229.
[30] G.L. Donati, R.S. Amais, J.A.N O Brega, J. Anal. At. Spectrom. 2 (2013) 280–287.
[31] P. Wu, Y. Zhang, R. Liu, Y. Lv, X. Hou, Talanta 5 (2009) 1778–1782.
[32] M. Williams, E.H. Piepmeier, Anal. Chem. 7 (1972) 1342–1344.
[33] X. Jiang, P. Wu, D. Deng, Y. Gao, X. Hou, C. Zheng, J. Anal. At. Spectrom. 10 (2012) 1780–1786.
[34] L.N. Santos, G.L. Donati, C.P. Calloway, B.T. Jones, J.A.N O Brega, J. Anal. At. Spectrom. 12 (2012) 2082–2087.
[35] X. Hou, K.E. Levine, A. Salido, B.T. Jones, M. Ezer, S. Elwood, J.B. Simeonsson, Anal. Sci. 1 (2001) 175–180.
[36] H.R. Badiei, C. Liu, V. Karanassios, Microchem. J. (2013) 131–136.
[37] Q. Jin, H. Zhang, W. Yang, Q. Jin, Y. Shi, Talanta 9 (1997) 1605–1614.
[38] V. Karanassios, K. Johnson, A.T. Smith, Anal. Bioanal. Chem. 8 (2007) 1595–1604.
[39] S. Weagant, V. Karanassios, Anal. Bioanal. Chem. 3 (2009) 577–589.
[40] X. Jiang, Y. Chen, C. Zheng, X. Hou, Anal. Chem. 11 (2014) 5220–5224.

Talanta 132 (2015) 112–117

Contents lists available at ScienceDirect

Talanta

journal homepage: www.elsevier.com/locate/talanta

Aptamer-functionalized localized surface plasmon resonance sensor for the multiplexed detection of different bacterial species

Seung Min Yoo, Do-Kyun Kim, Sang Yup Lee*

Department of Chemical and Biomolecular Engineering (BK21 plus program), KAIST, Daejeon 305-701, Korea

ARTICLE INFO

Article history:
Received 21 May 2014
Received in revised form
1 September 2014
Accepted 2 September 2014
Available online 9 September 2014

Keywords:
Aptamer
Bacterial cell detection
Localized surface plasmon resonance sensor
Label free

ABSTRACT

A localized surface plasmon resonance (LSPR)-based sensor with an immobilized aptamer ligand was developed and used for the label-free and accurate detection of bacteria through observing the changes in the peak extinction intensity. The ability of this biosensor to recognize pathogenic bacteria was analyzed and conditions were optimized with different probe concentrations, incubation time for aptamer immobilization, and incubation time for cell binding. A single LSPR-based sensor was used to successfully detect and identify three different bacterial species as proof-of-concept experiments; in all cases, the sensor showed a detection limit of 30 cfu per assay. Furthermore, the sensor system could clearly identify various target bacterial species in a multiplexed mode with high specificities on a single chip. The label-free bacteria sensor developed by combining LSPR and aptamers will be useful for diagnosing various infectious diseases through a single convenient assay.

© 2014 Elsevier B.V. All rights reserved.

1. Introduction

Bacteria, which are part of a very large group of single-celled organisms, exist in all human habitats. Some of these bacteria are causative agents of various infectious diseases and can often cause death if not treated properly, in particular in immnuo-compromised patients. Pathogenic bacteria can infect humans, animals, and plants through the intake of food, water, and air, while can be transferred through the contact with infected surface or liquid. Thus, the rapid and accurate detection of pathogenic bacteria is of great importance in all areas related to health and safety, including clinics, food industries, environment, and defense. This has prompted the need for accurate assay systems for detecting bacteria, which could facilitate the use of early antibiotic interventions to treat infectious diseases associated.

Molecular diagnostic methods, which typically rely on the detection of nucleic acids (DNA or RNA) from clinical and environmental samples, can effectively detect bacteria with high sensitivity and specificity. In particular, polymerase chain reaction (PCR)-based assays have been demonstrated successful for the detection of small numbers of bacterial cells present in some samples [1,2]. However, these assays are time-consuming and require preparation of the target DNA, limiting their widespread use as diagnostic platforms. Thus, there has been an urgent need for new strategies for the rapid and simple detection of bacterial species with high sensitivity and specificity. Recently, various platforms for the direct detection of bacterial cells have been developed through the use of different sensing approaches, including the assessment of electrical signals [3,4], electrochemical sensing [5–8], surface-enhanced Raman scattering (SERS) [9–11], fluorescence signals [12,13], localized surface plasmon resonance (LSPR) [14], and optical sensing [15,16].

Among these sensing strategies, LSPR is considered a promising method for label-free and sensitive detection of biomolecules, as it displays an intensity change and/or a shift of the single sharp spectral extinction peak when an unmodified analyte binds to a local dielectric surface [17–20]. Another exciting technique that can be used for sensing cells is the employment of nucleic acid ligands known as aptamers. Compared with the antibodies that have traditionally been used for cell sensing, aptamers have the benefits of high affinity and specificity, long-term stability, easy synthesis and modification, low cost, and a wide spectrum of target analytes that can be designed [21]. These distinctive advantages of aptamers can potentially employ for the efficient detection of pathogenic bacteria.

Interestingly, however, despite such superb sensing capabilities of LSPR-based strategies and advantages of aptamer ligands, there has been no report, to our knowledge, on the use of LSPR-based bacterial cell sensor that employs aptamer ligands.

Here, we describe the label-free and accurate detection of bacteria using an aptamer-immobilized LSPR-based sensor. In this system, a multispot gold-capped nanoparticle array (MG-NPA) chip is composed of a dielectric layer comprising a thin gold (Au) layer on silica (Si) nanoparticles (NPs)-absorbed glass slide.

* Corresponding author. Tel.: +82 42 350 3930; fax: +82 42 350 8800.
E-mail addresses: leesy@kaist.ac.kr, mbelmbel99@gmail.com (S.Y. Lee).

http://dx.doi.org/10.1016/j.talanta.2014.09.003
0039-9140/© 2014 Elsevier B.V. All rights reserved.

Using this sensor system, we successfully detected and identified three different bacterial species in a multiplexed mode. Combination of LSPR sensing platform with aptamer provides unique advantages. First, the well-defined MG-NPA structure used in this study results in sensitive and reproducible LSPR peaks [22–24]. Second, functionalization of specific aptamer ligands on the MG-NPA structure surface allows the simple and rapid detection of bacterial species without the need for any modification or the purification process of the test samples. Third, the use of multiple spots with different aptamers on a single chip allows us to simultaneously identify different bacterial species in a single assay. Therefore, the aptamer-immobilized LSPR-based sensor system developed in this study will be useful for convenient, rapid and accurate identification of bacterial species, including pathogenic bacteria, by simple assay.

2. Experimental

2.1. Materials

All chemicals were purchased from Sigma-Aldrich Co. Glass slides were purchased from Matsunami Glass Ind., Ltd, Japan. Si NPs were purchased from Polysciences Inc. NAP-5 column was purchase from GE healthcare Co. Reference bacteria were obtained from the Korean Collection for Type Cultures (KCTC; Korea) and the American Type Culture Collection (ATCC; USA), and cultured according to the provided instructions (Table S1 in Supporting information). Oligonucleotides were synthesized at Genotech (Korea). The sequences of the bacterial species-specific aptamers are as follows: *Lactobacillus acidophilus*-specific aptamer (Lac-apt), 5′-AGCAGCACAGAGGTCAGATGTAGCCCTTCAACATAGTAATATCTCT-GCATTCTGTGTGCCTATGCGTGCTACCGTGAA-$(CH_2)_3$-SH-3′ [25]; *Salmonella typhimurium*-specific aptamer (Sty-apt), 5′-TATGGCGG-CGTCACCCGACGGGGACTTGACATTATGACAG-$(CH_2)_3$-SH-3′ [26]; and *Pseudomonas aeruginosa*-specific aptamer (Pae-apt), 5′-CCCCCGTTG-CTTTCGCTTTTCCTTTCGCTTTTGTTCGTTTCGTCCCTGCTTCCTTTCTTG-$(CH_2)_3$-SH-3′ [27].

2.2. Preparation of the LSPR-based sensor

Glass slide (76 mm × 26 mm × 1 mm^3) was treated by ultrasonication for 10 min in acetone, ethanol, and ultrapure deionized (DI) water and then deposited subsequently with chromium (5 nm in height) and gold (40 nm in height) by using an E-beam evaporator (MHS 1800; MooHan Vacuum Co., Korea) at a base pressure of 4×10^{-6} Torr (1st Au layer deposition process on a glass slide, see Fig. 1a). For forming multiple spots on a single chip, a multi-spot (3 nm in diameter) silicon-rubber mask was attached to the surface of the Au-deposited glass slide. The slide with the mask was then treated with 1 mM 4,4′-dithiobutyric acid (DDA) for 1 h, and then incubated with Si NPs (100 nm in diameter) activated by 1% (v/v) 3-aminopropyltriethoxy silane (γ-APTES) and 400 mM 1-ethyl-3-(3-dimethylaminopropyl) carbodiimide (EDC) for 1 h (Silica nanoparticle deposition process, see Fig. 1a). The Si NP-modified slide was then rinsed thoroughly with DI water to remove the excess surface modified nanoparticles, and subsequently dried at room temperature (RT). Finally, a top Au layer (30 nm in height) was deposited onto the Si NP-modified substrate using the E-beam evaporator (2nd Au layer deposition process, see Fig. 1a).

2.3. Functionalization of the sensor surface using aptamers

The thiolated aptamers were treated with 1 M dithiothreitol (DTT) and purified using NAP-5 column. The sensor surface was exposed to 10 μM aptamer in phosphate buffered saline (PBS) at RT for 4 h under humidified condition, and then washed with 0.1% (w/v) sodium dodecyl sulfate (SDS) for 5 min, rinsed with DI water, and dried under a nitrogen stream.

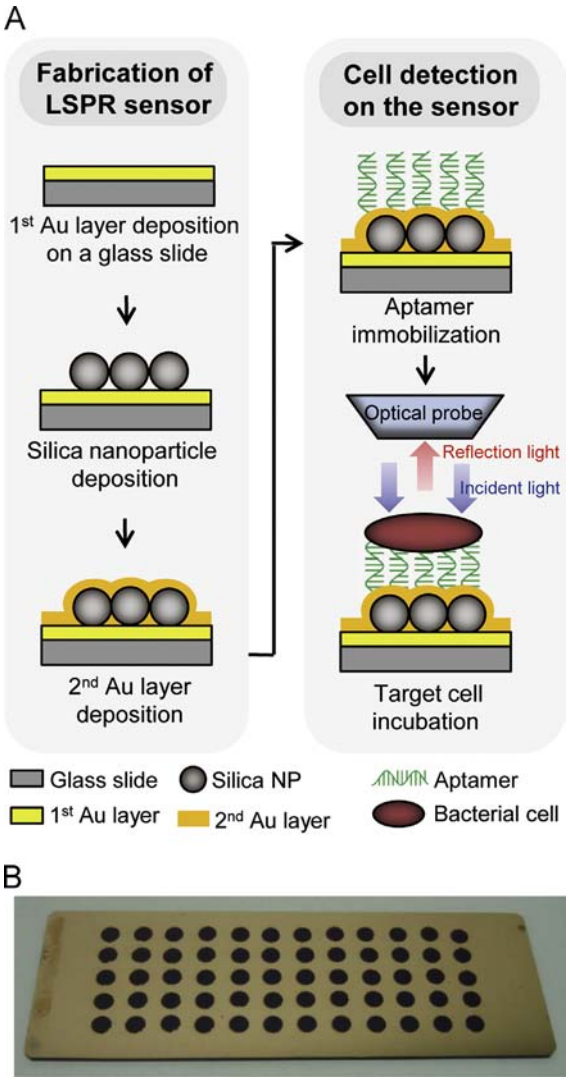


Fig. 1. Aptamer-immobilized LSPR sensor system. (a) Schematic representing the detection of bacterial cells using the aptamer-functionalized LSPR-based sensor; (b) multispot gold-capped nanoparticle array (MG-NPA) chip. Each spot (diameter of 3 mm) on chip consists of Si NPs with dielectric structure formed by the deposition of Au layer.

2.4. Detection of bacterial species

The samples with different bacterial species were dropped and incubated on different spots of the aptamer-functionalized sensor chip at RT for 1 h under humidified condition to prevent the evaporation of the samples. The slide was washed with PBS for 5 min and dried under the nitrogen stream. The LSPR spectra from the chip were measured at ambient conditions.

2.5. Instrumentation

The optical measurement system used to assess the LSPR spectra consisted of a light source (wavelength range, 360–2000 nm), spectrophotometer (wavelength range, 200–1100 nm) and an optical fiber probe bundle (fiber core diameter, 300 m; wavelength range, 250–900 nm) as a spectroscopy system, purchased

from Ocean Optics (USA). The optical properties of the LSPR sensor were assessed across a wavelength range of 400 to 750 nm, using the optical measurement system at RT. Scanning microscopic images of particles and cells were obtained using Hitachi SEM (S-4800; Hitachi, Japan).

3. Results and discussion

A schematic representation of bacterial species detection using the LSPR-based sensor is shown in Fig. 1a. First, the MG-NPA chip was fabricated by stepwise deposition of Au and Si NPs on a glass

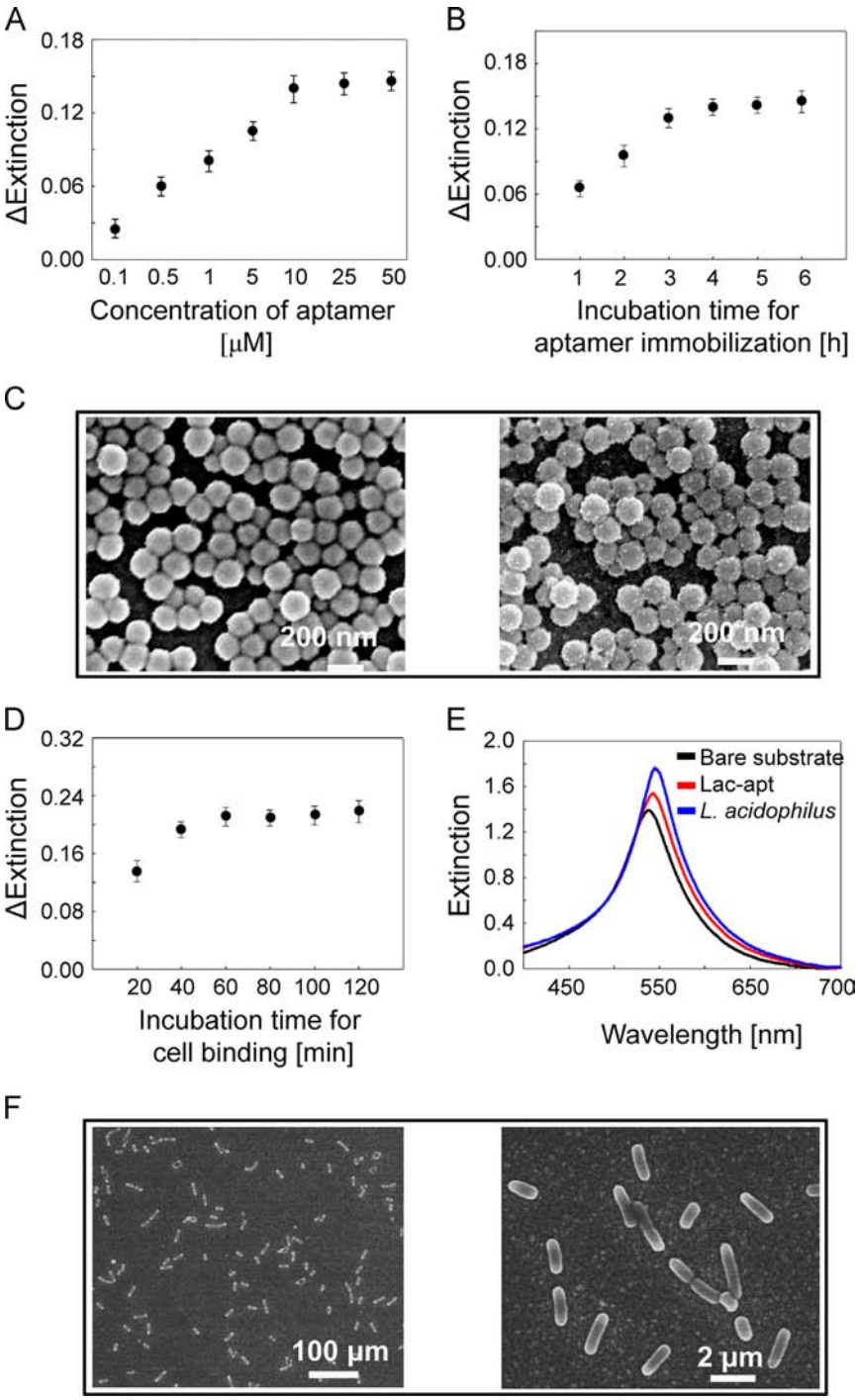


Fig. 2. Optimal conditions for cell sensing using the aptamer-immobilized LSPR-based sensor system. (a) Effect of aptamer concentration on LSPR optical properties. MG-NPA chips were incubated with different concentrations of the *Lactobacillus acidophilus*-specific aptamer (Lac-apt; 0.1, 0.5, 1, 5, 10, 25, and 50 μM); (b) effect of aptamer incubation time on LSPR optical properties. Aptamers (10 μM) were incubated with the chip for various times (1, 2, 3, 4, 5, and 6 h); (c) scanning electron microscope (SEM) images obtained (left panel) before and (right panel) after the immobilized aptamer on a chip was bound with its complementary DNA-attached Au NPs (see Supporting Information for a detailed method); (d) effect of cell incubation time on LSPR optical properties. *L. acidophilus* (10^9 cfu mL^{-1}) was incubated with the aptamer-immobilized chip for various times (20, 40, 60, 80, 100, and 120 min); (e) LSPR spectrum profiles obtained from the aptamer-immobilized chip after binding of the target cells; and (f) SEM images of bound cells (10^9 cfu mL^{-1} of *L. acidophilus*) on a chip.

substrate (see Section 2 and Fig. 1b). The dielectric structure of the chip yields a sharp and simple LSPR peak and shows sensitive responses upon binding of biomolecules [22–24]. The stepwise deposition of well-arranged Si NPs on the substrate produces a stable and reproducible LSPR peaks [22–24]. Next, the chip was functionalized with an aptamer, to enable subsequent binding reactions with the corresponding bacterial species. Aptamer-functionalized surface does not require any pre-treatment of test samples, allowing the simple and rapid detection of bacterial cells. Upon incubation of the chip with a sample, the presence of the target bacterial cells in the sample could be determined by observing a change in the LSPR peak. The LSPR-sensing process can be generally visualized by observing a red shift in the wavelength and/or a change in the extinction intensity of the peak. Unlike other noble metal structures, MG-NPA chip exhibits a clearer change in the peak extinction intensity compared to the wavelength shift upon binding of the target biomolecule [22–24].

To determine the optimal assay condition, the aptamer concentrations and incubation times were varied for aptamer immobilization and for cell-aptamer interaction on chips. First, the effect of varying conditions on aptamer immobilization on chips was investigated by using an aptamer specific to *L. acidophilus*. As shown in Fig. 2, the LSPR peak intensity was changed by varying the aptamer concentration (50, 25, 10, 5, 1, 0.5, and 0.1 μM) and incubation time (1, 2, 3, 4, 5, and 6 h). The change in LSPR peak intensity was maximized and saturated upon incubation of the chip with 10 μM aptamer for 4 h, indicating that the maximum binding of aptamer on the sensor surface was achieved under these conditions (Fig. 2a and b). In order to confirm the aptamer-binding capacity of the chip, the chip was sequentially treated with aptamer (Lac-apt) and its complementary DNA-attached Au NPs, and subjected to scanning electron microscope (SEM) analysis (see Fig. 2c and Supporting information). The Au NPs (~10 nm) were found to be densely and evenly bound on the Au chip surface. The number of aptamers on the spot of the chip was calculated following the method reported previously (see Supporting information) [28]. These data demonstrate that the chip was successfully functionalized with the utilized aptamer.

Next, the incubation time for cell-aptamer binding was optimized. The chip treated with 10 μM aptamer for 4 h was incubated with *L. acidophilus* (10^9 cfu mL^{-1}) for different times (20, 40, 60, 80, 100, and 120 min). As seen for the aptamer-bound chip, the cell–aptamer interaction on the chip also induced a change in the peak extinction intensity (Fig. 2d and e), which increased with the incubation time up to 1 h and became saturated thereafter (Fig. 2d). Cells captured by the aptamer-functionalized chip were also confirmed by SEM analysis (Fig. 2f). The bacterial cells went through the fixation process with 2.5% glutaraldehyde during the preparation of SEM specimen (see Supporting information). The fixation process can effectively maintain cell morphology [29]. Fig. 2 shows that an aptamer concentration of 10 μM per assay, an aptamer incubation time of 4 h, and cell binding time of 1 h are optimal. Thus, all subsequent experiments were performed under this condition.

As a proof-of-concept multiplex detection of bacterial species, the sensitivity and specificity of the assay were determined using three different bacteria, *L. acidophilus, S. typhimurium,* and *P. aeruginosa*, under the optimal condition determined above. *S. typhimurium* is a representative food-borne pathogen; together with *Escherichia coli* O157:H7, they cause an estimated 76 million illnesses and nearly 5000 deaths annually in the US [26]. *P. aeruginosa* is among the pathogens that cause nosocomial infections with increasing threat, and thus significantly increases the mortality risk of inpatients [27]. The detection limit of the assay was determined by changing the number of target bacterial cells per volume (cell concentration hereafter) over a range of 10^9–10^1 cfu mL^{-1} (upper panels of Fig. 3). The extinction intensity showed a logarithmic increase with respect to cell concentration over a range of 10^9–10^4 cfu mL^{-1} (lower panels of Fig. 3). The SEM images confirmed that the changes in LSPR peak intensities reflected the concentrations of bacterial cells bound to the chip surface (Fig. S1 in Supporting information). Interestingly, the slopes of these plots displayed subtle variations, indicating that the binding affinities between the different aptamers and their target cells were slightly different. The K_d values previously reported for these aptamers were 13 ± 3 nM for the *L. acidophilus*-specific

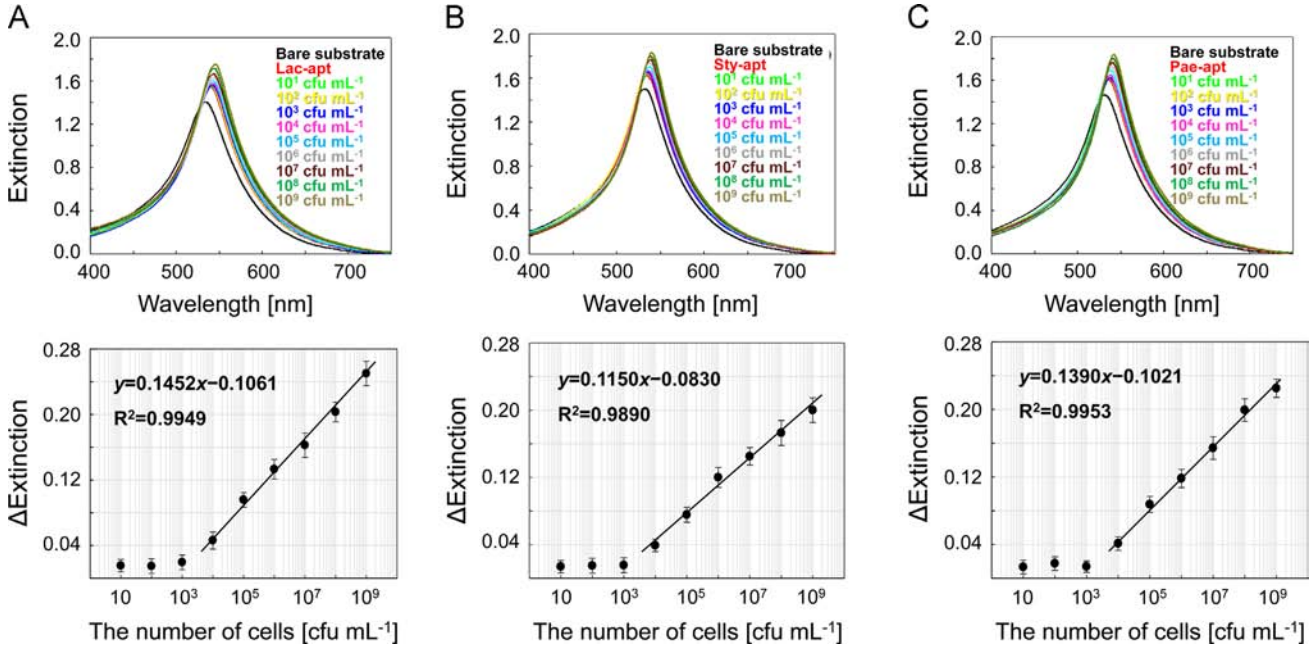


Fig. 3. The detection limits of the LSPR-based cell sensor. The detection limit was determined by observing the increases in LSPR peak intensities in response to different cell concentrations (10^1–10^9 cfu mL^{-1}) of (a) *L. acidophilus*, (b) *S. typhimurium*, and (c) *P. aeruginosa*. The upper panels show the LSPR spectrum profiles. The lower panels show the plots of the changes in LSPR signal intensity versus the target cell concentration. The data was obtained from three measurements, and the error bars represent standard deviations. Lac-apt, *L. acidophilus*-specific aptamer; Sty-apt, *S. typhimurium*-specific aptamer; Pae-apt, *P. aeruginosa*-specific aptamer.

aptamer [25] and 17.27 ± 5 nM for the *P. aeruginosa* specific aptamer [27]. Thus, our results suggest that the LSPR sensor enables the quantitative detection of bacterial cells. Considering the assay volume (3 μl), this sensing system can detect 30 colony forming unit (cfu) of bacteria in an assay. This detection limit is comparable to or slightly higher than other sensing methods including electrical signals [3,4], electrochemical sensing [5,7,8], SERS [11] and optical sensing [15,16] which showed the detection limit of 10^1–3×10^4 cfu mL^{-1}. It should be noted that very small amount of sample volume (3 μl) was used in our study, as compared to other sensors, which generally require samples ranging from tens to hundreds of microliters. Thus, the use of a larger assay volume with, for example, a microfluidic flow cell could allow more efficient detection of bacteria. The detection limit of our assay could also be improved by employing the aptamer with higher affinity and specificity. The detection limit of the aptamer-LSPR sensor system developed here is quite impressive when compared with those of other optical sensors [8–13,16].

In order to determine assay selectivity which is important for multiplexed detection, the multispot LSPR chip was functionalized with three different species-specific aptamers (Lac-apt, Sty-apt, and Pae-apt) and cross-checked whether each corresponding bacterial species were bound specifically to their corresponding aptamers. As shown in Fig. 4, the highest LSPR peak intensities were observed with proper binding between each aptamer and its specific target bacterium. As negative controls, cell-free PBS solution and *E. coli* were used; these did not trigger any significant change in LSPR peak intensity. Thus, these results indicate that the aptamer-functionalized LSPR-based sensor could clearly identify various target bacterial species in a multiplexed mode with high specificities on a single chip.

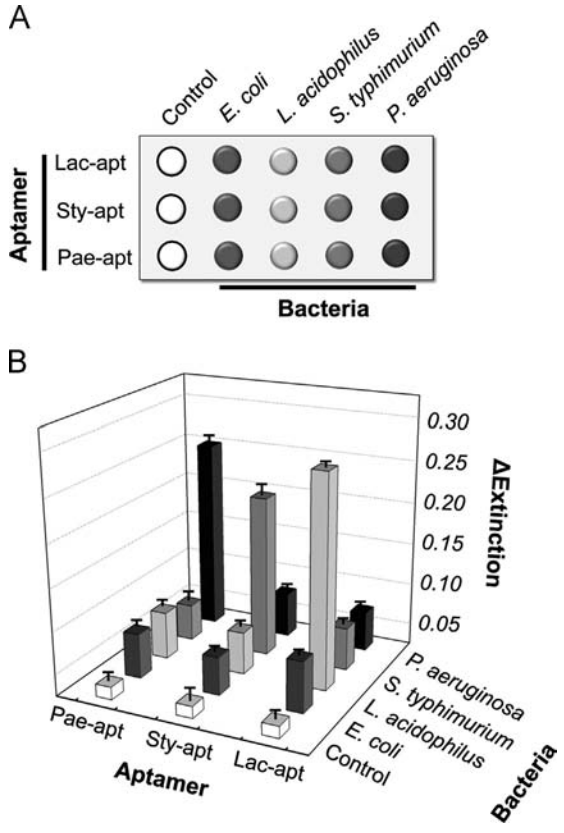


Fig. 4. Selective binding of bacterial cells to the aptamers immobilized on the LSPR sensor. (a) Design of the MG-NPA chip developed for the selectivity assay. Each species-specific aptamer was immobilized on each spot of chips and subsequently 10^9 cfu mL^{-1} of different bacterial cells were applied to spots; (b) a change in the extinction intensity of the peak at each spot could be used to assess the stringency of affinity. Cell-free PBS solution and *E. coli* were applied to chips as negative controls. The data were obtained from three independent measurements, and the error bars represent standard deviations.

In order to be useful in practice, a pathogen-diagnosing assay should be simple, sensitive, fast, and high-throughput. To date, aptamer-based assays for bacterial detection have employed electrical and optical sensors. These approaches have achieved high sensitivities, but are not amenable to high throughput detection in a single assay [3,4,7]. In contrast, the aptamer-immobilized LSRP sensing assay developed here is rapid, simple, and most importantly, capable of simultaneously identifying different bacterial species in a single assay by employing various specific aptamers. Although relatively few aptamers have been developed for clinically important pathogenic bacteria, the future availability of aptamers will allow multiplex detection of many different bacterial species in a single assay, thereby increasing the potential usefulness of this assay in a wide range of fields, including pathogen diagnostics. Furthermore, although the LSPR signals reported herein were measured using a large home-made instrument, portable instruments with LSPR-based sensors can be employed, enabling the facile and mobile detection of pathogenic bacteria in point-of-care diagnostics.

4. Conclusions

In summary, we developed an easy-to-build, aptamer-immobilized LSPR-based sensor for the simple, rapid, sensitive, specific, and multiplex sensing of bacterial species. Using this sensor system, three different bacteria could be detected with high sensitivity and specificity as a proof-of-concept demonstration. It is thus expected that the use of an LSPR-based sensor coupled with bacterial species-specific aptamers will enable efficient diagnostics of different bacterial species including pathogenic bacteria.

Acknowledgments

This work was supported by the Bio-Synergy Research Project (grant no. 2012M3A9C4048759) of the Ministry of Science, ICT and Future Planning through the National Research Foundation of Korea. S.M.Y. and D.-K.K contributed equally to this work.

Appendix. Supporting information

Supplementary data associated with this article can be found in the online version at http://dx.doi.org/10.1016/j.talanta.2014.09.003.

References

[1] R.P. Peters, M.A. van Agtmael, S. Gierveld, S.A. Danner, A.B. Groeneveld, C. M. Vandenbroucke-Grauls, P.H. Savelkoul, J. Clin. Microbiol. 45 (2007) 3641–3646.
[2] P. Tissari, A. Zumla, E. Tarkka, S. Mero, L. Savolainen, M. Vaara, A. Aittakorpi, S. Laakso, M. Lindfors, H. Piiparinen, M. Mäki, C. Carder, J. Huggett, V. Gant, Lancet 375 (2010) 224–230.
[3] H.M. So, D.W. Park, E.K. Jeon, Y.H. Kim, B.S. Kim, C.K. Lee, S.Y. Choi, S.C. Kim, H. Chang, J.O. Lee, Small 4 (2008) 197–201.
[4] M.S. Mannoor, S. Zhang, A.J. Linkb, M.C. McAlpine, Proc. Natl. Acad. Sci. USA 107 (2010) 19207–19212.
[5] Z.T. La Belle, M. Shah, J. Reed, V. Nandakumar, T.L. Alford, J.W. Wilson, C. A. Nickerson, L. Joshi, Electroanalysis 21 (2009) 2267–2271.
[6] G.A. Zelada- Guillén, J. Riu, A. Düzgün, F.X. Rius, Angew. Chem. Int. Ed. 48 (2009) 7334–7337.
[7] R. de la Rica, C. Pejoux, C. Fernandez-Sanchez, A. Baldi, H. Matsui, Small 6 (2010) 1092–1095.
[8] A. Shabani, C.A. Marquette, R. Mandeville, M.F. Lawrence, Talanta 116 (2013) 1047–1053.
[9] S. Patel, W.R. Premasiri, D.T. Moir, L.D.J. Ziegler, Raman Spectrosc. 39 (2008) 1660–1672.

[10] W.R. Premasiri, D.T. Moir, M.S. Klempner, N. Krieger, G. Jones, L.D. Ziegler, J. Phys. Chem. B 109 (2005) 312–320.
[11] S.P. Ravindranath, Y. Wang, J. Irudayaraj, Sen. Actuators B 152 (2011) 183–190.
[12] H.-J. Lee, B.C. Kim, K.-W. Kim, Y.K. Kim, J. Kim, M.-K. Oh, Biosens. Bioelectron. 24 (2009) 3550–3555.
[13] Y. Wana, Y. Suna, P. Qia, P. Wanga, D. Zhanga, Biosens. Bioelectron. 55 (2013) 289–293.
[14] L. Fua, B. Parkc, Y. Zhaoa, Sens. Actuators B 141 (2009) 276–283.
[15] C. Wang, J. Irudayaraj, Small 4 (2008) 2204–2208.
[16] G. Wandermur, D. Rodrigues, R. Allil, V. Queiroz, R. Peixoto, M. Werneck, M. Miguel, Biosens. Bioelectron. 54 (2014) 661–666.
[17] J.N. Anker, W.P. Hall, O. Lyandres, N.C. Shah, J. Zhao, R.P. Van Duyne, Nat. Mater. 7 (2008) 442–453.
[18] K.M. Mayer, S. Lee, H. Liao, B.C. Rostro, A. Fuentes, P.T. Scully, C.L. Nehl, J. H. Hafner, ACS Nano 2 (2008) 687–692.
[19] H. Li, W. Qiang, M. Vuki, D. Xu, H.-Y. Chen, Anal. Chem. 83 (2011) 8945–8952.
[20] L. Xie, X. Yan, Y. Du, Biosens. Bioelectron. 53 (2014) 58–64.
[21] K. Sefah, D. Shangguan, X. Xiong, M.B.O′ Donoghue, W. Tan, Nat. Protoc. 5 (2010) 1169–1185.
[22] T. Endo, K. Kerman, N. Nagatani, H.M. Hiepa, D.-K. Kim, Y. Yonezawa, K. Nakano, E. Tamiya, Anal. Chem. 78 (2006) 6465–6475.
[23] T. Endo, S. Yamamura, K. Kerman, E. Tamiya, Anal. Chim. Acta 614 (2008) 182–189.
[24] S.Y. Yoo, D.-K. Kim, T.J. Park, E.K. Kim, E. Tamiya, S.Y. Lee, Anal. Chem. 82 (2010) 1349–1357.
[25] L. Hamula, H. Zhang, L.L. Guan, X.F. Li, X.C. Le, Anal. Chem. 80 (2008) 7812–7819.
[26] R. Joshi, H. Janagama, H.P. Dwivedi, T.M. Senthil Kumar, J. Jaykus, L.A. Schefers, S. Sreevatsan, Mol. Cell. Probes 23 (2009) 20–128.
[27] Y. Wang, Y.L. Zeng, X.Y. Yang, W.B. Li, X.P. Lan, Eur. J. Clin. Microbiol. Infect. Dis. 30 (2011) 273–278.
[28] T. Stakenborg, S. Peeters, G. Reekmans, W. Laureyn, H. Jans, G. Borghs, H. J. Imberechts, Nanopart. Res. 10 (2008) 143–152.
[29] Y. Chao, T. Zhang, Appl. Microbiol. Biotechnol. 92 (2011) 381–392.

Talanta 132 (2015) 118–125

Contents lists available at ScienceDirect

Talanta

journal homepage: www.elsevier.com/locate/talanta

Preparation of mesoporous ZrO_2-coated magnetic microsphere and its application in the multi-residue analysis of pesticides and PCBs in fish by GC–MS/MS

Xi-Tian Peng [a,b], Li Jiang [b], Yan Gong [a], Xi-Zhou Hu [a], Li-Jun Peng [a], Yu-Qi Feng [b,*]

[a] Institute of Agricultural Quality Standards and Testing Technology Research, Hubei Academy of Agricultural Science, Wuhan 430064, China
[b] Key Laboratory of Analytical Chemistry for Biology and Medicine (Ministry of Education), Department of Chemistry, Wuhan University, Wuhan 430072, China

ARTICLE INFO

Article history:
Received 16 June 2014
Received in revised form
26 August 2014
Accepted 31 August 2014
Available online 8 September 2014

Keywords:
Pesticides
Polychlorinated biphenyls
ZrO_2
Magnetic materials
QuEChERS
Fish

ABSTRACT

A novel mesoporous ZrO_2 immobilized magnetic Fe_3O_4 microsphere (m-ZrO_2@Fe_3O_4) was successfully synthesized and characterized by transmission electron microscope (TEM), X-ray diffractometer (XRD), nitrogen adsorption measurement (NAM), energy-dispersive X-ray analysis (EDX), vibrating sample magnetometer (VSM). Then the resultant m-ZrO_2@Fe_3O_4 and an n-octadecylphosphonic acid modified magnetic microsphere (Fe_3O_4-OPA) were employed as clean-up co-adsorbents of QuEChERS (Quick, Easy, Cheap, Effective, Rugged, Safe) method for the analysis of 42 pesticides and 7 polychlorinated biphenyls (PCBs) in fish samples. Lipid co-extractives such as fatty acids in QuEChERS extracts could be efficiently removed through the Lewis acid–Lewis base interaction between m-ZrO_2@Fe_3O_4 and carboxylic groups, while some other apolar interferents could be adsorbed through hydrophobic interaction by Fe_3O_4-OPA. Meanwhile, the magnetic property of adsorbents endows the clean-up procedure with manipulative convenience. Several parameters affecting the clean-up performance were investigated. Under the optimal conditions, the modified QuEChERS method combined with gas chromatography–tandem mass spectrometry (GC–MS/MS) for the multi-class, multi-residue analysis of pesticides and PCBs in fish samples was validated according to linearity, recovery and precision. Good linearities were obtained for all analytes with R^2 larger than 0.9903. Limits of detection (LODs) were found to be in the range of 0.02–4.40 ng/g. The method recoveries of all analytes spiked at three concentration levels in blank fish samples were from 69.8% to 117.1%, with the intra-day and inter-day relative standard deviations (RSDs) less than 13.4% and 16.5%, respectively.

© 2014 Elsevier B.V. All rights reserved.

1. Introduction

As an important source of proteins, minerals, vitamins and unsaturated essential fatty acids, fish have been considered to be an irreplaceable consumption component of a balanced human diet and their consumption has increased over worldwide [1,2]. However, fish can also significantly contribute to dietary exposure to various contaminants [1], such as pesticides and polychlorinated biphenyls (PCBs). Pesticides are widely used in agricultural and farming production all over the world to control a wide range of pests and diseases [3]. However, the unreasonable and excessive use of those substances present a concern in humanment health [4]. Polychlorinated biphenyls (PCBs) and some organochlorine pesticides, which are semivolatile, highly toxic, chemically stable, and persistent, have been identified as persistent organic pollutants (POPs) by the Stockholm Convention [5,6]. Those hazardous chemicals can be accumulated and amplified through the food chain, particularly in animal fat tissue [7]. Therefore, in order to decrease dietary exposure to pesticides and PCBs from fish, it is favorable to develop simple, efficient and sensitive method for the monitoring of their concentration level in fish.

Generally, the contaminants in fish are in low concentration and simultaneously accompanied by a large number of interferences, especially some lipid coextractives, which adversely affect the extraction efficiency and instrument performance [8,9]. Therefore, sample pretreatment techniques are highly required to remove those lipid coextractives prior to chromatography and/or mass spectrometry analysis. Conventional methods for analysis of pesticides and PCBs in fatty matrices such as fish always involve with Soxhlet extraction [10], pressurized liquid extraction (PLE)

* Corresponding author. Tel./fax: +86 27 68755595.
E-mail address: yqfeng@whu.edu.cn (Y.-Q. Feng).

http://dx.doi.org/10.1016/j.talanta.2014.08.069
0039-9140/© 2014 Elsevier B.V. All rights reserved.

Table 1
The retention time and MS parameters of the target pesticides and PCBs for quantification and confirmation.

Pesticides and PCBs	Retention time (min)	Quantication ion (m/z)	CE1	Confirmation ion (m/z)	CE2
alpha-HCH	15.359	218.9 > 182.90	8	218.90 > 144.90	20
Dimethoate	15.596	125.00 > 79.00	8	125.00 > 47.00	14
beta-HCH	15.927	218.90 > 182.90	8	218.90 > 144.90	20
gamma-HCH	16.055	218.90 > 182.90	8	218.90 > 144.90	20
Quintozene	16.152	294.80 > 236.80	16	294.80 > 264.80	12
Pyrimethanil	16.266	198.10 > 183.10	14	198.10 > 158.10	18
Diazinon	16.271	304.10 > 179.10	10	304.10 > 162.10	8
delta-HCH	16.548	218.90 > 182.90	10	218.90 > 144.90	20
PCB28	17.184	256.00 > 186.00	26	256.00 > 221.00	10
Vinclozolin	17.287	285.00 > 212.00	12	285.00 > 178.00	14
Parathion-methyl	17.316	263.00 > 109.00	14	263.00 > 136.00	8
Fenitrothion	17.855	277.00 > 260.00	6	277.00 > 109.10	14
PCB52	17.868	292.00 > 220.00	25	292.00 > 257.00	20
Malathion	18.013	173.10 > 99.00	14	173.10 > 127.00	6
Chlorpyrifos	18.263	313.90 > 257.90	14	313.90 > 285.90	8
Parathion	18.286	291.10 > 109.00	14	291.10 > 137.00	6
Dicofol	18.328	208.10 > 181.00	10	208.10 > 127.00	14
Triadimefon	18.363	250.00 > 139.00	14	250.00 > 215.00	8
Isocarbophos	18.411	289.10 > 136.00	14	289.10 > 113.00	6
Isofenphos-methyl	18.761	199.00 > 121.00	14	241.10 > 121.10	22
Fipronil	19.049	366.90 > 212.90	30	366.90 > 254.90	22
Phenthoate	19.139	273.90 > 125.00	20	273.90 > 246.00	6
Procymidone	19.275	283.00 > 96.00	10	283.00 > 255.00	12
PCB101	19.582	326.00 > 256.00	30	326.00 > 291.00	20
alpha-Endosulfan	19.736	338.90 > 160.00	18	338.90 > 266.90	8
Profenofos	20.025	336.90 > 266.90	14	336.90 > 308.90	6
p,p′-DDE	20.123	246.00 > 176.00	30	246.00 > 211.00	22
PCB 118	20.787	326.00 > 256.00	25	326.00 > 291.00	15
p,p′-DDD	20.927	235.00 > 165.00	24	235.00 > 199.00	14
o,p′-DDT	21.004	235.00 > 165.00	24	235.00 > 199.00	14
PCB 153	21.198	360.00 > 290.00	25	360.00 > 325.00	15
Triazophos	21.206	257.00 > 162.00	8	257.00 > 134.00	22
p,p′-DDT	21.631	235.00 > 165.00	25	235.00 > 199.00	15
PCB 138	21.731	360.00 > 290.00	25	360.00 > 325.00	15
Iprodione	22.319	314.00 > 245.00	12	314.00 > 56.00	22
Bifenthrin	22.488	181.10 > 166.10	12	181.10 > 153.10	8
Phosmet	22.549	160.00 > 133.00	14	160.00 > 77.00	24
Fenpropathrin	22.64	265.10 > 210.10	12	265.10 > 172.10	14
PCB180	22.961	394.00 > 324.00	25	394.00 > 359.00	15
Phosalone	23.234	182.00 > 111.00	14	182.00 > 138.00	8
Cyhalothrin-1	23.281	197.00 > 161.00	8	197.00 > 141.00	12
Cyhalothrin-2	23.477	197.00 > 161.00	8	197.00 > 141.00	12
Pyridaben	24.434	147.10 > 117.10	22	147.10 > 132.10	14
Cyfluthrin-1	24.830	226.10 > 206.10	14	226.10 > 199.10	6
Cyfluthrin-2	24.911	226.10 > 206.10	14	226.10 > 199.10	6
Cyfluthrin-3,4	25.033	226.10 > 206.10	14	226.10 > 199.10	6
Cypermethrin-1	25.158	181.10 > 152.10	22	181.10 > 127.10	22
Cypermethrin-2	25.249	181.10 > 152.10	22	181.10 > 127.10	22
Cypermethrin-3	25.364	181.10 > 152.10	22	181.10 > 127.10	22
Flucythrinate-1	25.362	199.10 > 157.10	10	199.10 > 107.10	22
Cypermethrin-4	25.564	181.10 > 152.10	22	181.10 > 127.10	22
Flucythrinate-2	25.563	199.10 > 157.10	10	199.10 > 107.10	22
Fenvalerate-1	26.223	419.10 > 225.10	6	419.10 > 167.10	12
Fluvalinate-1	26.405	250.10 > 55.00	20	250.10 > 200.00	20
Fluvalinate-2	26.468	250.10 > 55.00	20	250.10 > 200.00	20
Fenvalerate-2	26.472	419.10 > 225.10	6	419.10 > 167.10	12
Difenoconazole-1	26.806	323.00 > 265.00	14	323.00 > 202.00	28
Deltamethrin-1	26.919	252.90 > 93.00	20	252.90 > 171.90	8
Difenoconazole-2	26.900	323.00 > 265.00	14	323.00 > 202.00	28
Deltamethrin-2	27.216	252.90 > 93.00	20	252.90 > 171.90	8

[11,12], microwave assisted extraction (MAE) [13,14], followed by elimination of co-extracts using gel permeation chromatography (GPC) or solid-phase extraction (SPE) with different sorbents. Nevertheless, those methods usually need tedious extraction steps and use a great amount of organic solvent, which makes the whole analysis process time-consuming, labor-intensive and environmentally-unfriendly. Therefore, development of new sample pretreatment methods for determination of pesticides and PCBs in fish would be necessary.

The QuEChERS (quick, easy, cheap, effective, rugged and safe) method, which was originally developed by Anastassiades et al. for pesticide residue analysis in fruit and vegetables [15], has recently been applied to the analysis of various environmental contaminants in fish and shrimp [1,5,7,16–18], and other food [19,20]. In conventional QuEChERS methods, adsorbents are separated from the acetonitrile extract by centrifugation, which takes extra time and is not conducive to the high-throughput detection of a large number of samples [21]. Magnetic solid phase extraction (MSPE) is a novel sample preparation technique, in which the magnetic materials are first dispersed in a sample solution to adsorb target analytes or matrix components, and then the powdery magnetic materials can be easily and rapidly isolated from the solution with the help of an external magnetic field [22]. Recently, our group proposed a modified QuEChERS method by using magnetic graphitized carbon black and primary secondary amine as adsorbents for the analysis of pesticide residues in vegetables [21]. To the best of our knowledge, there were no available literatures using magnetic adsorbents in QuEChERS method for the simultaneous analysis of pesticides and PCBs in fish.

Zirconium dioxide (ZrO_2) has an amphoteric characteristic and its surface has amount of Lewis acid sites, which make it a good adsorbent of Lewis bases such as fatty acids. It has been reported that Lewis acid–Lewis base interaction and electrostatic interaction contributed to the adsorption of fatty acids on the surface of ZrO_2 [23]. Recently, a commercial sorbent composed of C_{18} and silica coated with ZrO_2 was used to remove matrix components for the analysis of hazardous substances in fish [5], bovine muscle [24], avocado and almonds [9,25], and edible oils [26]. Their results indicated that the matrix components such as fatty acids and glycerides could be efficiently removed from sample extracts by this ZrO_2 composite.

Although the appropriate sample preparation methods can remove most of the sample matrix components, the selection of chromatographic separation and detection methods for the qualitative and quantitative analysis of target analytes is of equal importance, especially for those complex food matrices accompanied with a low residue level of target analytes. Gas chromatography (GC) combined with various detectors was frequently used to inspect pesticides and PCBs in fish samples. In order to meet the growing number of test items and increasingly strict limits, the application of gas chromatography–tandem mass spectrometry (GC–MS/MS) for the simultaneous detection of multi-component has become popular due to its higher sensitivity and higher specificity [1,5,27,28]. In the present study, a novel mesoporous ZrO_2 immobilized magnetic Fe_3O_4 microspheres (m-ZrO_2@Fe_3O_4) and an n-octadecylphosphonic acid modified magnetic microspheres (Fe_3O_4-OPA) were prepared and employed as co-adsorbents of QuEChERS method for the analysis of 42 pesticides and 7 PCBs in fish. The mesoporous structure gave m-ZrO_2@Fe_3O_4 with a high surface area and high adsorption capacity, which was very significant to remove abundant coextractives in QuEChERS extract. At the same time, the magnetic property of adsorbents endows the clean-up procedure with manipulative convenience compared to traditional dispersed solid phase extraction (dSPE) in QuEChERS method. Based on this modified QuEChERS method using the magnetic m-ZrO_2@Fe_3O_4 and Fe_3O_4-OPA as co-adsorbents, a rapid, simple, efficient and sensitive GC–MS/MS method for the monitoring of 42 pesticides and 7 PCBs in fish samples was developed.

2. Experimental

2.1. Reagents and materials

Individual standard solution (1000 μg/mL) of 42 high purity pesticides and a mixture standard solution (10 μg/mL) of 7 PCBs

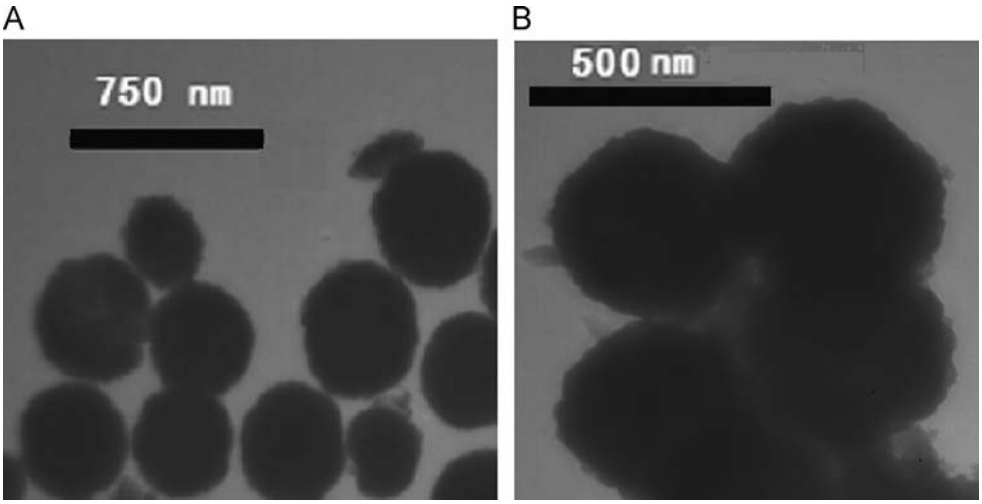


Fig. 1. TEM images of Fe_3O_4 (A) and m-ZrO_2@Fe_3O_4 (B).

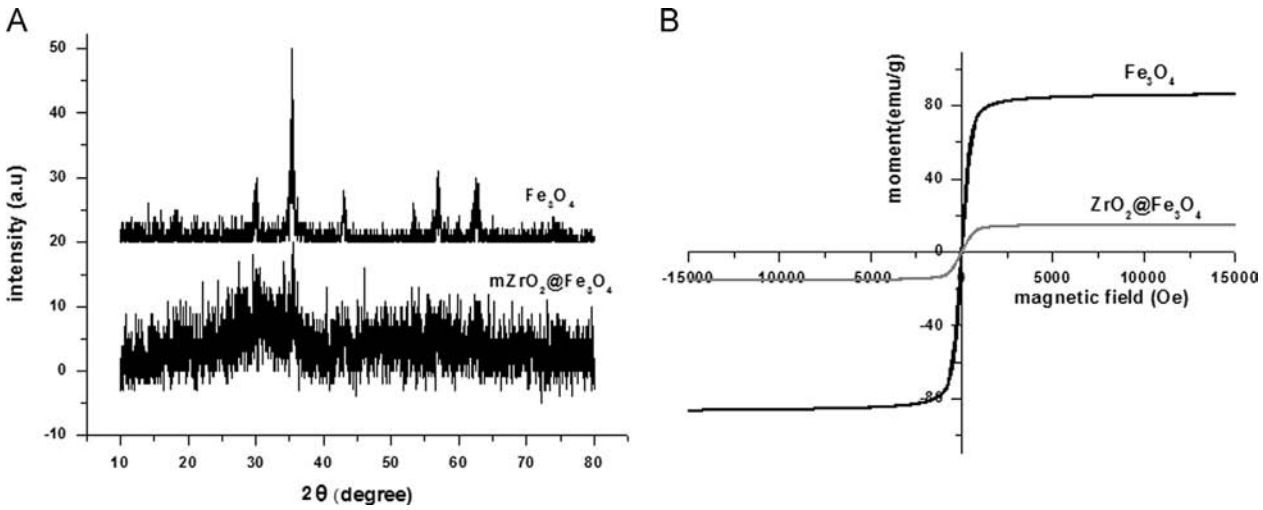


Fig. 2. (A) XRD patterns of Fe_3O_4 and m-ZrO_2@Fe_3O_4; (B) magnetization curves of Fe_3O_4 and m-ZrO_2@Fe_3O_4.

were purchased from Agro-Environmental Protection Institute, Ministry of Agriculture (Tianjin, China) and Anpel Scientific Instrument Co., Ltd. (Shanghai, China), respectively. The standard stock solution of a mixture 42 pesticides and 7 PCBs was made up to 2 μg/mL with acetone and stored at −18 °C. The working standard solutions were prepared daily.

Sodium chloride (NaCl), anhydrous magnesium sulfate ($MgSO_4$), iron (III) chloride hexahydrate ($FeCl_3 \cdot 6H_2O$), anhydrous sodium acetate (NaAc), polyethylene glycol 10000 (PEG 10000), ethylene glycol, ethanol (EtOH), ammonium hydroxide (NH_4OH), tetrahydrofuran (THF), and zirconyl chloride octahydrate ($ZrOCl_2 \cdot 8H_2O$) were all of analytical reagent grade and supplied by Shanghai General Chemical Reagent Factory (Shanghai, China). n-Octadecylphosphonic acid was purchased from TCI (Shanghai, China). Acetonitrile (ACN), methanol (MeOH) and acetone of HPLC-grade were obtained from Tedia (Ohio, USA).

2.2. Equipments and analytical conditions

GC–MS/MS analysis was performed using a Shimadzu GCMS-TQ8030 equipped with an AOC-20i autosampler (Kyoto, Japan). Data acquisition and analysis were performed using software from GCMS Solution (Shimadzu, Kyoto, Japan). The separation was . achieved on a fused silica capillary column (Rtx–5MS, 30 m × 0.25 mm i.d., film thickness 0.25 μm) (Restek, Pennsylvania, USA). The oven temperature was programmed at 40 °C for 4.0 min, increased to 125 °C at a rate of 25 °C min^{-1}, and then increased to 300 °C at a rate of 10 °C min^{-1} and held for 6.0 min. The solvent cut time was 7 min. The injection volume was 1.0 μL and splitless injection mode was used. The splitless time was 1.0 min. Helium (purity 99.999%) was used as the carrier gas at a flow rate of 1.0 mL min^{-1}. Argon (purity 99.999%) was used as a collision cell gas. The injection port, ion source and interface temperatures were set at 250, 230 and 250 °C, respectively. The QqQ mass spectrometer was operated in selected reaction monitoring mode detecting two transitions per analyte, which are listed together with the particular collision energies in Table 1.

2.3. Preparation of m-ZrO_2@Fe_3O_4 and Fe_3O_4-OPA magnetic microspheres

The magnetite microspheres were prepared through solvothermal reaction [29], which are described as follows: $FeCl_3 \cdot 6H_2O$ (5.4 g) was dissolved in ethylene glycol (160 mL) under magnetic

stirring for 0.5 h. Then NaAc (14.4 g) and polyethylene glycol (4.0 g) were added to the solution. After stirring for another 0.5 h, the resultant solution was transfered into a 200 mL Teflon lined stainless-steel autoclave. The autoclave was sealed and heated at 200 °C for 24 h, and then cooled to room temperature. The magnetic microspheres were collected with the help of magnet, followed by washing with ethanol and deionized water for 4 times. The product was dried in vacuum at 60 °Cfor 8 h.

Mesoporous ZrO_2 was directly coated onto the surface of magnetic Fe_3O_4 by the hydrolysis of $ZrOCl_2$ and using CTAB as the mesoporous template reagent according to a previous report with minor modification [30]. Fe_3O_4 microspheres (0.5 g) were dispersed in a solution containing 1.5 g CTAB, 400 mL deionized water, 7.5 mL concentrated NH_4OH solution (28%) and 300 mL ethanol. The mixture was stirred continuously for 30 min to form a homogenized dispersion. To the above dispersed solution, an aqueous solution of $ZrOCl_2$ (3.1 g dissolved in the minimum volume of water) was added drop-wise and then the reaction mixture was stirred for 6 h. Then the product was collected by a hand-held magnet and washed repeatedly with ethanol and deionized water. The obtained particles were redispersed in 250 mL of acetone and refluxed at 80 °C for 60 h. The resultant particles were then washed with deionized water, separated through magnetic decantation and dried in vacuum at 60 °C for 12 h. At last, the obtained m-ZrO_2@Fe_3O_4 was further calcined at 300 °C for 6 h to age.

The Fe_3O_4-OPA was prepared according to the previously described method [31]. OPA (1.0 g) was dissolved in 50 mL THF, then bare Fe_3O_4 (5.0 g) was added into the solution. The mixture was refluxed at 80 °C for 12 h. The final product was magnetically

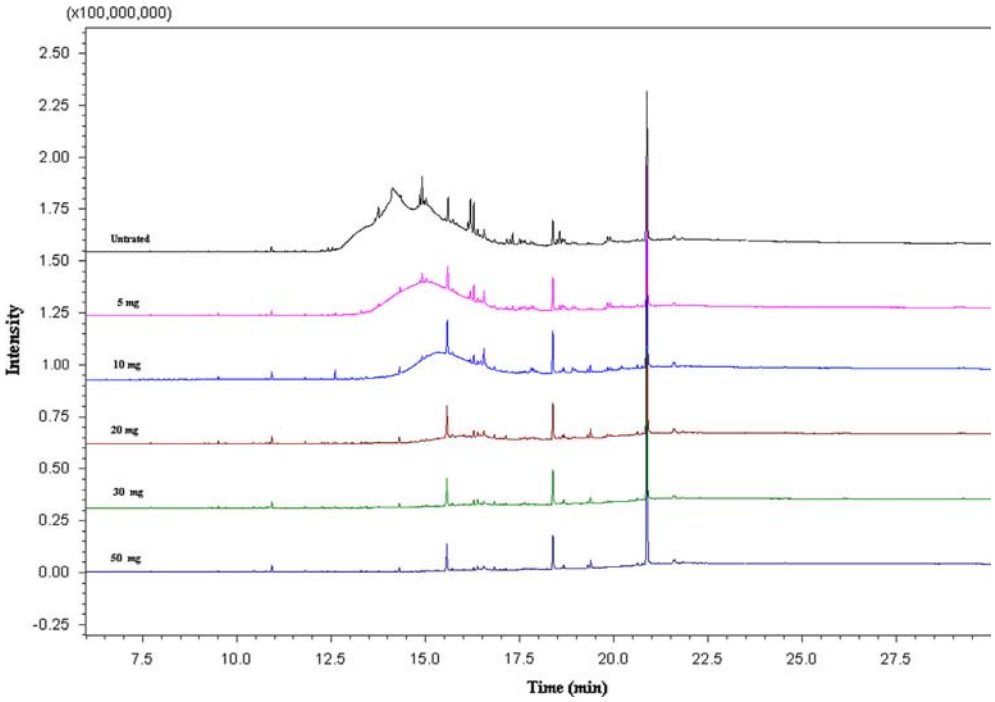


Fig. 3. Effect of the amount of m-ZrO_2@Fe_3O_4 on the clean-up performance.

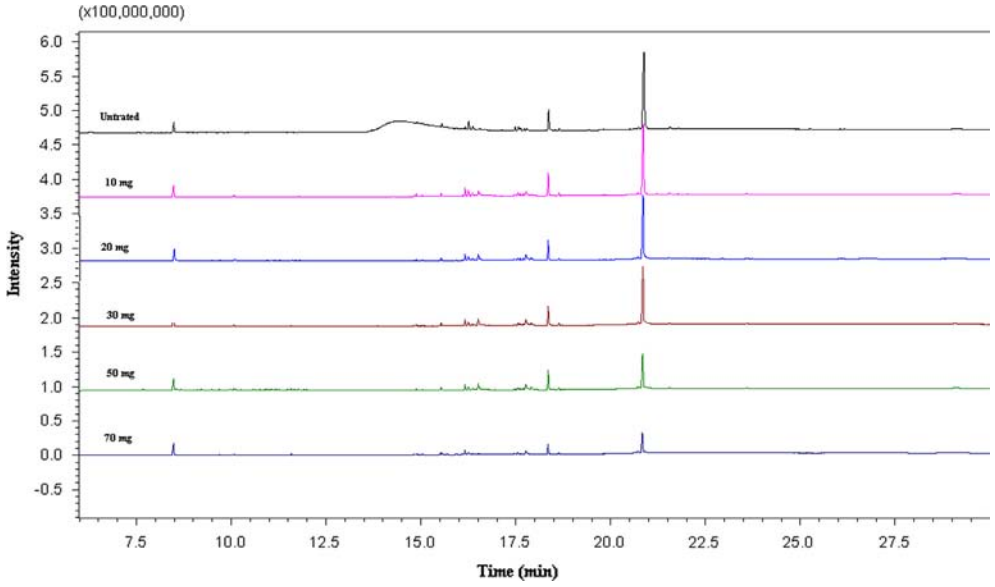


Fig. 4. Effect of the amount of Fe_3O_4-OPA on the clean-up performance.

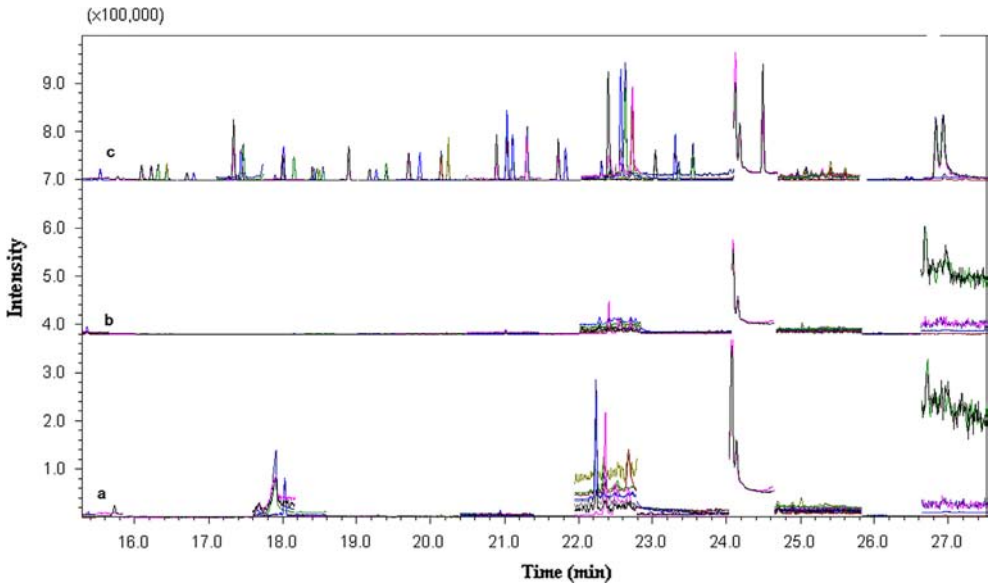


Fig. 5. Typical chromatograms of blank fish extract without clean-up (a) and after clean-up (b), and a blank fish extract after clean-up and spiked with 10 ng/mL analytes (c).

collected and washed by water/ethanol/acetone/n-hexane successively and repeatedly, followed by drying at 60 °C for 6 h.

2.4. Characterization

The morphology of the particles was observed with a transmission electron microscope (TEM) (JEOL, Kyoto, Japan). The crystal structure of the materials was determined with a Bruker SMART APEX II X-ray diffractometer (XRD, Billerica, German) using Cu Kα radiation and rotating anode operated at 40 KV and 30 mA. The species of iron and zirconium was determined with a Shimadzu EDX-720 energy-dispersive X-ray analyzer (EDX, Kyoto, Japan) by using Mg-Ka radiation as the excitation source. Magnetization curves were determined with a PPMS-9 vibrating sample magnetometer (Quantum Design, San Diego, CA, USA). Nitrogen adsorption measurement was measured at 77 K on a JW-BK surface area and pore size analyzer (JWGB Sci. & Tech., Beijing, China). The composites were activated under vacuum and heated to 423 K for 6 h to remove any physically adsorbed substances before analysis. The specific surface area was calculated according to the BET (Brunauer–Emmett–Teller) equation at P/P_0 between 0.05 and 0.3. The pore volume and pore diameter were evaluated from the desorption branch of isotherm based on BJH (Barrett–Joyner–Halenda) model.

2.5. Sample preparation

The homogenized fish sample (10.0 g) was weighed into a 50 mL centrifugal tube. The samples was mixed with 10 mL ACN. Subsquently, the mixture was vortxed by hand for 1 min. Then 1.0 g NaCl and 4.0 g anhydrous $MgSO_4$ was added and shaken vigorously for 30 s. After centrifugation (7000 rpm, 8 min), the extract was transferred to an eppendorf vial (15 mL) containing 1.0 g of anhydrous $MgSO_4$. The vial was shaken by hand followed by standing for 1 min, and the supernatant was collected for the subsequent steps.

The clean-up procedure was performed by MSPE using m-ZrO_2@Fe_3O_4 and Fe_3O_4-OPA as co-adsorbents. 1 mL Supernatant was added into a 2 mL centrifugal tube containing a certain amount of magnetic adsorbents (m-ZrO_2@Fe_3O_4 and Fe_3O_4-OPA), then the mixture was shaken vigorously for 0.5 min. The supernatant was transfered into another tube with the aid of an external magnet, and was evaporated to dryness under a mild nitrogen stream at room temperature. The residue was dissolved in 1 mL acetone for GC–MS/MS analysis.

For recovery experiments, the known variable amounts of analytes were firstly spiked for 15 min in fish samples before sample preparation, and the following steps were the same as described above.

3. Results and discussion

3.1. Characterization of materials

The morphology and size of the prepared magnetic particles were characterized by TEM (Fig. 1). Obviously, bare Fe_3O_4 and m-ZrO_2@Fe_3O_4 were nearly monodispersed and sphere-like, with a diameter of 250–400 nm. The thickness of ZrO_2 coating layer was about 30 nm. Although there is slight aggregation or adhesion on the magnetic microspheres after the coating with ZrO_2, the overall morphology still maintains a distributed uniform state to some extent.

To further confirm that the m-ZrO_2@Fe_3O_4 microspheres are prepared successfully, EDX spectroscopy was applied to analyze the microspheres obtained, as shown in Supporting information Fig. S1. The results indicated the presence of Fe, Zr and O elements. Furthermore, a relative low level of Fe content obtained by EDX spectroscopy analysis further indicated that the surface of the Fe_3O_4 microspheres was successfully coated by ZrO_2.

Bare Fe_3O_4 and m-ZrO_2@ Fe_3O_4 were characterized by N_2 adsorption/desorption. It can be found that the surface area and pore volume of bare Fe_3O_4 are merely 17 m^2/g and 0.039 cm^3/g, respectively. The two parameters of m-ZrO_2@ Fe_3O_4 reach up to 221 m^2/g and 0.493 cm^3/g. Furthermore, the m-ZrO_2@ Fe_3O_4 yielded typical IV adsorption isotherm and H1 hysteresis loop, which are characteristic of a mesoporous material. Those results indicated that the mesoporous structure has formed on m-ZrO_2@Fe_3O_4. The highly porous ZrO_2 shell should be beneficial to enhance adsorption capacity of magnetic sorbent and speed up mass transfer to shorten equilibrium time.

Structural characterization of bare Fe_3O_4 and m-ZrO_2@ Fe_3O_4 has been carried out by wide angle XRD, as shown in Fig. 2A. For bare Fe_3O_4, the well defined crystal structure is evidenced by the corresponding peaks with 2θ at 30.1°, 35.3°, 43.1°, 53.5°, 57.0°, and 62.7° in the X-ray diffractogram, which are identified as the spinel phase of Fe_3O_4. After coating with ZrO_2, the diffraction peaks characteristic of magnetite nearly disappeared while a broad peak

Table 2
Linear range, determination coefficients (R^2), limit of detection (LOD) and limit of quantification (LOQ) of the target pesticides and PCBs in fish samples.

Pesticides and PCBs	Linear range (ng/g)	R^2	LOD (ng/g)	LOQ (ng/g)
alpha-HCH	1–500	0.9999	0.09	0.30
Dimethoate	5–500	0.9984	0.58	1.93
beta-HCH	1–500	0.9986	0.18	0.59
gamma-HCH	1–500	0.9998	0.14	0.46
Quintozene	1–500	0.9996	0.28	0.92
Pyrimethanil	1–500	0.9998	0.19	0.64
Diazinon	1–500	0.9989	0.14	0.48
delta-HCH	1–500	0.9998	0.18	0.59
PCB28	1–500	0.9999	0.02	0.06
Vinclozolin	1–500	0.9999	0.24	0.80
Parathion-methyl	1–500	0.9944	0.13	0.45
Fenitrothion	1–500	0.9924	0.14	0.47
PCB52	1–500	0.9999	0.04	0.14
Malathion	1–500	0.9984	0.04	0.14
Chlorpyrifos	1–500	0.9992	0.10	0.32
Parathion	1–500	0.9903	0.10	0.32
Dicofol	1–500	0.9996	0.22	0.75
Triadimefon	1–500	0.9997	0.06	0.20
Isocarbophos	5–500	0.999	0.84	2.81
Isofenphos-methyl	1–500	0.9988	0.02	0.07
Fipronil	1–500	0.9961	0.11	0.38
Phenthoate	1–500	0.9991	0.19	0.62
Procymidone	1–500	0.9999	0.24	0.80
PCB101	5–500	0.9999	0.06	0.20
alpha-Endosulfan	20–500	0.9999	4.40	14.66
Profenofos	5–500	0.9981	0.51	1.69
p,p′-DDE	1–500	0.9999	0.05	0.15
PCB 118	1–500	0.9999	0.04	0.12
p,p′-DDD	1–500	0.9998	0.06	0.20
o,p′-DDT	1–500	0.9978	0.09	0.31
PCB 153	1–500	0.9999	0.02	0.08
Triazophos	1–500	0.9975	0.09	0.29
p,p′-DDT	1–500	0.9957	0.16	0.54
PCB 138	1–500	0.9997	0.04	0.13
Iprodione	5–500	0.9989	0.75	2.49
Bifenthrin	1–500	0.9999	0.16	0.52
Phosmet	1–500	0.9981	0.10	0.32
Fenpropathrin	1–500	0.9996	0.27	0.90
PCB180	5–500	0.9999	0.06	0.20
Phosalone	1–500	0.9977	0.08	0.26
Cyhalothrin	5–500	0.9979	0.98	3.27
Pyridaben	1–500	0.9985	0.07	0.23
Cyfluthrin	10–500	0.9978	0.52	1.72
Cypermethrin	10–500	0.9962	3.18	10.62
Flucythrinate	5–500	0.9975	1.45	4.84
Fenvalerate	1–500	0.9975	0.18	0.61
Fluvalinate	5–500	0.9964	1.31	4.36
Difenoconazole	1–500	0.9984	0.11	0.36
Deltamethrin	5–500	0.9967	0.83	2.77

Table 3
Average recoveries and RSDs of 42 pesticides and 7 PCBs spiked in fish at three different concentration levels via GC–MS/MS analysis ($n=4$).

Pesticides and PCBs	10 ng/g Spiked level		50 ng/g Spiked level		100 ng/g Spiked level	
	Recovery (%)	RSD (%)	Recovery (%)	RSD (%)	Recovery (%)	RSD (%)
alpha-HCH	82.8	2.8	84.9	4.7	84.7	3.3
Dimethoate	112.3	4.1	100.2	1.1	98.8	3.7
beta-HCH	87.3	6.3	86.4	3.9	86.4	4.2
gamma-HCH	83.6	6.3	86.0	4.5	85.1	4.3
Quintozene	83.3	4.8	79.5	3.8	76.8	2.9
Pyrimethanil	74.5	3.1	84.6	3.0	81.1	2.0
Diazinon	91.8	4.7	92.1	4.4	89.6	4.1
delta-HCH	101.1	1.7	94.2	4.1	92.9	4.9
PCB28	114.0	1.4	84.3	1.1	91.6	1.5
Vinclozolin	86.0	6.8	87.9	6.6	91.6	4.5
Parathion-methyl	105.2	4.5	99.2	4.7	94.5	5.3
Fenitrothion	106.9	5.5	104.5	2.0	99.2	5.2
PCB52	115.7	1.0	86.2	4.9	94.0	4.6
Malathion	93.2	5.9	94.0	2.3	95.5	3.0
Chlorpyrifos	86.7	5.8	87.1	2.1	93.0	4.1
Parathion	108.7	9.7	102.3	3.6	102.7	5.9
Dicofol	83.0	6.5	86.6	3.5	91.9	5.1
Triadimefon	74.7	10.0	78.2	3.8	85.1	3.3
Isocarbophos	107.0	5.0	95.9	2.8	98.3	5.8
Isofenphos-methyl	94.4	4.1	92.6	2.2	92.4	5.5
Fipronil	104.4	4.1	98.8	3.8	96.1	6.3
Phenthoate	104.1	5.7	92.9	3.2	92.4	6.9
Procymidone	81.4	10.4	87.2	3.1	89.1	5.8
PCB101	103.3	5.5	77.5	6.6	88.3	6.7
alpha-Endosulfan	71.9	8.7	81.2	4.5	80.1	3.3
Profenofos	82.5	3.7	80.8	3.1	80.2	3.1
p,p′-DDE	79.4	8.4	71.8	3.8	69.8	4.2
PCB 118	96.0	2.7	71.1	4.7	81.1	5.4
p,p′-DDD	86.0	9.0	83.8	4.6	81.6	3.5
o,p′-DDT	72.6	5.3	73.3	6.4	70.4	2.8
PCB 153	92.4	2.9	72.8	2.0	78.0	7.0
Triazophos	100.2	6.4	94.3	5.5	90.2	1.9
p,p′-DDT	83.2	4.0	79.7	8.5	73.6	4.6
PCB 138	94.2	0.9	74.4	0.8	80.9	6.0
Iprodione	103.2	9.5	95.1	4.2	89.8	1.0
Bifenthrin	76.1	1.7	83.3	0.8	81.6	1.6
Phosmet	112.6	5.4	112.7	2.2	97.3	2.5
Fenpropathrin	86.4	4.3	89.8	2.7	86.8	3.0
PCB180	82.6	1.0	81.2	2.3	78.5	0.6
Phosalone	107.6	4.6	98.1	4.1	89.2	3.3
Cyhalothrin	93.6	3.2	93.6	9.2	82.4	4.4
Pyridaben	105.6	4.0	102.9	11.7	89.1	6.0
Cyfluthrin	98.8	12.5	95.6	13.8	92.2	11.6
Cypermethrin	103.3	12.0	101.2	7.4	88.7	4.7
Flucythrinate	102.9	7.0	102.8	7.7	94.1	6.1
Fenvalerate	112.3	5.6	100.5	8.4	87.4	4.6
Fluvalinate	117.1	8.6	112.4	10.3	88.6	5.8
Difenoconazole	98.8	8.8	93.5	4.6	87.5	3.7
Deltamethrin	109.5	9.4	100.1	7.6	92.0	7.1

around 30° was visible, which was likely due to the formation of amorphous ZrO_2 on the surface of Fe_3O_4.

The magnetic properties of bare Fe_3O_4 and m-ZrO_2@Fe_3O_4 were investigated by a vibrating sample magnetometer. As shown in Fig. 2B, both curves had no magnetic hysteresis loops, indicating that the as-prepared magnetic materials were super paramagnetic. Furthermore, the saturation magnetization (Ms) of m-ZrO_2@Fe_3O_4 (17.5 emu/g) is obviously lower than that of bare Fe_3O_4 (86.3 emu/g), implying the existence of a significant amount of ZrO_2 on the surface of Fe_3O_4. Because of the relatively high saturation magnetization values, the magnetic m-ZrO_2@Fe_3O_4 and Fe_3O_4-OPA could be rapidly and efficiently separated from the sample solution by an external magnet (as shown in Fig. S2 of Supporting information).

3.2. Optimization of sample pretreatment

To remove matrix components and obtain satisfactory recoveries of target analytes, several parameters including the adsorption time, the amounts of m-ZrO_2@Fe_3O_4 and Fe_3O_4-OPA were optimized in detail.

3.2.1. Optimization of the amount of m-ZrO_2@Fe_3O_4

The surface of m-ZrO_2@Fe_3O_4 has an amount of Lewis acid sites, which could adsorb Lewis bases such as fatty acids in QuEChERS extract of fish samples. The experiment was performed using 1.0 mL of the blank fish extract that was placed into a 2 mL Eppendorf vial containing a certain amount of m-ZrO_2@Fe_3O_4. After clean-up, the samples were analyzed by GC–MS in full scan mode, as shown in Fig. 3. The wide spectrum bands in chromatograms were indentified as fatty acids. With the increase

Table 4
Comparison of method performance and the time with the previous method for detection of pesticides and PCBs in fish samples.

Technique	Determination method	Analytes and LODs	Recoveries (%)	RSD (%)	Time required (min)[a]	Ref.
Traditional QuEChERS method	GC–MS/MS	14 PCBs: 0.1–0.5 μg/kg 18 pesticides: 0.5–5 μg/kg	72-119	< 20	> 5	[5]
	GC–MS	9 OCPs: 0.3–4.5 μg/kg	90-105	< 15	> 8	[16]
	GC-ECD	6 Pyrethroids: 8–14 μg/kg	81.1-108.0	< 4	> 8	[17]
	GC–MS/MS	16 OCPs: n.a[b] 18 PCBs: n.a	70-120	< 20	> 10	[1]
MSPD	GC–MS	7 Pesticides: n.a	57-107	< 26	> 15	[3]
ASE + GPC + SPE	GC-FPD	17 OPPs: 0.6–9.0 μg/kg	64.5-98.6	< 15	> 60	[11]
Proposed QuEChERS method	GC–MS/MS	7 PCBs: 0.02–0.06 μg/kg 45 Pesticides: 0.02–4.40 μg/kg	69.8-117.1	< 17	< 3	This work

[a] Time required referred to the time of clean-up process for pesticides and PCBs detection in fish samples, and was approximately estimated according to the literatures above.
[b] n.a, Not available.

in the amount of m-ZrO_2@Fe_3O_4, this wide peak gradually disappeared. 30 mg of m-ZrO_2@Fe_3O_4 was enough to remove those fatty acids.

3.2.2. Optimization of the amount of Fe_3O_4-OPA

Fe_3O_4-OPA with an octadecyl chain could remove some apolar matrix components. 30 mg m-ZrO_2@Fe_3O_4 and different amounts of Fe_3O_4-OPA (i.e. 10, 20, 30, 50, 70 mg) was used as co-adsorbents for clean-up in QuEChERS method. As shown in Fig. 4, the peak at 20.89 min in chromatograms was indentified as hydrophobic cholesterol. The peak intensity of cholesterol and other apolar matrix components gradually decreased with the increase in the amount of Fe_3O_4-OPA. Further increase of the amount of Fe_3O_4-OPA was problematic because some analytes may also be adsorbed by Fe_3O_4-OPA. Therefore, 70 mg of Fe_3O_4-OPA was selected to remove those matrix components.

3.2.3. Optimization of the adsorption time

The optimization of the adsorption time was performed under the optimal amounts of m-ZrO_2@Fe_3O_4 and Fe_3O_4-OPA. The adsorption time was conducted by increasing the vortex time from 0.5 to 3 min. The result indicated that the adsorption time had no significant influence on the clean-up efficiency. This phenomenon might be attributed to a thin porous layer of m-ZrO_2 on the surface of Fe_3O_4, which was favorable for the mass transfer of analytes. Therefore, 0.5 min of the vortex time was selected.

3.2.4. Reusability of m-ZrO_2@Fe_3O_4 and Fe_3O_4-OPA

The reusability of m-ZrO2@Fe_3O_4 and Fe_3O_4-OPA was also investigated to access the feasibility of the method for routine analysis. The magnetic materials were repeatedly subjected to perform MSPE of the fish QuEChERS solution. No obvious change in clean-up performance was found after five repetitive applications of the magnetic materials that were sequentially washsed with 1 mL MeOH/$NH_3 \cdot H_2O$ (v/v, 97/3) and 1 mL ACN. Therefore, the presented method is expected to be effective in practical applications.

Under the optimal conditions, typical chromatograms of blank fish extract without clean-up (a) and after clean-up (b), and blank fish extract after clean-up and spiked with 10 ng/mL analytes (c) were shown in Fig. 5. It can be seen that the as-prepared magnetic materials have good clean-up performance and only few interferences from the chromatogram of the clean-up sample are observed.

3.3. Validation of the method

3.3.1. Calibration curves, detection limits, limits of quantification

Matrix effects in the form of signal enhancement were always observed in GC–MS/MS, leading to unacceptable high recoveries [32]. Therefore, matrix-matched standards are necessary to correct for matrix effect for quantification analysis in the GC–MS/MS. In this study, matrix-matched calibration solutions spiking in blank fish extracts at seven concentration levels from 1 to 500 ng/mL were prepared to avoid the matrix effects. The calibration curves were established by plotting the peak areas of the analytes versus the concentrations of pesticides and PCBs. Limits of detection (LODs) and limits of quantifications (LOQs) were calculated as the concentrations corresponding to a signal of 3 and 10 times the standard deviation of the baseline noise, respectively. As listed in Table 2, all analytes showed good linearity with satisfactory squared regression coefficients (R^2) greater than 0.9903. The LODs and LOQs for these analytes were found to be in the range of 0.02–4.40 ng/g, and 0.08–14.66 ng/g, respectively.

3.3.2. Accuracy and precision

To assay the accuracy of the method, recoveries were investigated in spiked fish samples at three concentration levels of 10.0, 50.0 and 100.0 ng/mL. The recoveries were determined by comparing the calculated amounts of pesticides and PCBs in the samples (using calibration curves) with the spiking amounts. The precision of the method was assessed by determining the intra- and inter-day relative standard deviations (RSDs) at three concentration levels. As listed in Table 3, the method recoveries were in the range of 69.8% to 117.1% with RSDs less than 13.8%. Meanwhile, the intra-day and inter-day RSDs were below 13.4% and 16.5%, respectively.

3.3.3. Comparison with the previous methods

The comparison of method performance and clean-up time of our developed method with the previous methods are studied. As illustrated in Table 4, our proposed method took less clean-up time, had satisfactory precisions and recoveries, and showed better sensitivity than the previous method. The experimental and comparative results well indicated that our proposed method may be used to effectively monitor pesticides and PCBs in fish matrices.

3.3.4. Application of the proposed method for determination of pesticides and PCBs in fish

The proposed GC–MS/MS method was applied to the trace analysis of pesticides and PCBs in four kinds of fish samples (silver carp, bighead carp, mandarin fish, snakehead) from different

sources in Wuhan. No analytes were detectable in those samples. The recoveries for 42 pesticides and 7 PCBs spiked at 50 ng/g in those five fish samples were in the range of 80.8–116.7%, with RSDs less than 17.5%, indicating the good reliability and applicability of the proposed method for the analysis of pesticides and PCBs in different kinds of fish samples.

4. Conclusions

In this work, a mesoporous ZrO_2 immobilized magnetic Fe_3O_4 microspheres (m-ZrO_2@Fe_3O_4) and an n-octadecylphosphonic acid modified mesoporous magnetic particles (Fe_3O_4-OPA) were used as co-adsorbents of QuEChERS method for the analysis of 42 pesticides and 7 PCBs in fish samples, followed by separation and detection with GC–MS/MS. Compared to traditional QuEChERS method in which phase separation must be achieved by centrifugation, the modified QuEChERS method using magnetic adsorbents endows the clean-up procedure with manipulative convenience through applying an external magnetic field. Lipid coextractives such as fatty acids could be efficiently removed thorough the Lewis acid–Lewis base interaction between m-ZrO_2@Fe_3O_4 and carboxylic groups, while some other apolar coextractives such as cholesterol could be adsorbed through hydrophobic interaction by Fe_3O_4-OPA. The amounts of m-ZrO_2@Fe_3O_4 and Fe_3O_4-OPA, the adsorption time were optimized in detail to remove the matrix interferences as much as possible and obtain high recoveries of target analytes. Under the optimized conditions, the modified QuEChERS method combined with GC–MS/MS was applied to analyze pesticides and PCBs in real samples. Recoveries of 49 analytes spiked in three concentration levels were between 69.8% and 117.1% with RSDs less than 16.5%, indicating good reliability of the proposed methods.

Acknowledgments

This work was supported by the National Natural Science Foundation of China (91017013, 91217309), the Fundamental Research Funds for the Central Universities (2042014kf0262), and the Youth Fund for Hubei Academy of Agricultural Science (2013NKYJJ18).

Appendix A. Supporting information

Supplementary data associated with this article can be found in the online version at http://dx.doi.org/10.1016/j.talanta.2014.08.069.

References

[1] K. Kalachova, J. Pulkrabova, T. Cajka, L. Drabova, M. Stupak, J. Hajslova, Anal. Bioanal. Chem. 405 (2013) 7803–7815.
[2] M.J. Ramalhosa, P. Paiga, S. Morais, C. Delerue-Matos, M.B. Oliveira, J. Sep. Sci. 32 (2009) 3529–3538.
[3] S.S. Caldas, C.M. Bolzan, E.J. de Menezes, A.L.V. Escarrone, C.D.G. Martins, A. Bianchini, E.G. Primel, Talanta 112 (2013) 63–68.
[4] V. Andreu, Y. Pico, Anal. Bioanal. Chem. 404 (2012) 2659–2681.
[5] Y. Sapozhnikova, S.J. Lehotay, Anal. Chim. Acta 758 (2013) 80–92.
[6] A.R. Fontana, A. Camargo, L.D. Martinez, J.C. Altamirano, J. Chromatogr. A 1218 (2011) 2490–2496.
[7] H.R. Norli, A. Christiansen, E. Deribe, J. Chromatogr. A 1218 (2011) 7234–7241.
[8] N. Chamkasem, L.W. Ollis, T. Harmon, S. Lee, G. Mercer, J. Agric. Food Chem. 61 (2013) 2315–2329.
[9] L. Rajski, A. Lozano, A. Ucles, C. Ferrer, A.R. Fernandez-Alba, J. Chromatogr. A 1304 (2013) 109–120.
[10] P. Manirakiza, A. Covaci, L. Nizigiymana, G. Ntakimazi, P. Schepens, Environ. Pollut. 117 (2002) 447–455.
[11] Y. Wang, S.B. Liu, C.M. Xie, H.X. Zhang, W.H. Lu, J. Anal. Chem. 39 (2011) 67–71.
[12] Z.L. Shen, D. Yuan, H. Zhang, M. Hu, J.H. Zhu, X.Q. Zhang, Q.D. Su, J. Chin. Chem. Soc. 58 (2011) 494–502.
[13] A.M. Wilkowska, M. Biziuk, J. AOAC Int. 93 (2010) 1987–1994.
[14] T. Otake, Y. Aoyagi, M. Numata, T. Yarita, J. AOAC Int. 91 (2008) 1124–1129.
[15] M. Anastassiades, S.J. Lehotay, D. Stajnbaher, F.J. Schenck, J. AOAC Int. 86 (2003) 412–431.
[16] N. Omar, J. Bakar, K. Muhammad, Food Control 34 (2013) 318–322.
[17] F.Y. Jia, W.W. Wang, J. Wang, J.A. Yin, Y.M. Liu, Z.B. Liu, Anal. Methods 4 (2012) 449–453.
[18] A. Lazartigues, L. Wiest, R. Baudot, M. Thomas, C. Feidt, C. Cren-Olive, Anal. Bioanal. Chem. 400 (2011) 2185–2193.
[19] A.Y. Sirhan, G.H. Tan, A. Al-Shunnaq, L. Abdulra'uf, R.C.S. Wong, J. Liquid Chromatogr. Relat. Technol. 37 (2014) 321–342.
[20] D. Moreno-Gonzalez, J.F. Huertas-Perez, A.M. Garcia-Campana, L. Gamiz-Gracia, Talanta 128 (2014) 299–304.
[21] H.B. Zheng, Q. Zhao, J.Z. Mo, Y.Q. Huang, Y.B. Luo, Q.W. Yu, Y.Q. Feng, J. Chromatogr. A 1300 (2013) 127–133.
[22] X.S. Li, G.T. Zhu, Y.B. Luo, B.F. Yuan, Y.Q. Feng, Trac-Trends Anal. Chem. 45 (2013) 233–247.
[23] P.J. Thistlethwaite, M.L. Gee, D. Wilson, Langmuir 12 (1996) 6487–6491.
[24] L. Geis-Asteggiante, S.J. Lehotay, A.R. Lightfield, T. Dutko, C. Ng, L. Bluhm, J. Chromatogr. A 1258 (2012) 43–54.
[25] A. Lozano, L. Rajski, S. Ucles, N. Belmonte-Valles, M. Mezcua, A.R. Fernandez-Alba, Talanta 118 (2014) 68–83.
[26] D. Moreno-González, J.F. Huertas-Pérez, A.M. García-Campaña, L. Gámiz-Gracia, Talanta 128 (2014) 299–304.
[27] F. Hernandez, M.I. Cervera, T. Portoles, J. Beltran, M.E. Pitarch, Anal. Methods 5 (2013) 5875–5894.
[28] K. Kalachova, T. Cajka, C. Sandy, J. Hajslova, J. Pulkrabova, Talanta 105 (2013) 109–116.
[29] G.T. Zhu, X.S. Li, Q. Gao, N.W. Zhao, B.F. Yuan, Y.Q. Feng, J. Chromatogr. A 1224 (2012) 11–18.
[30] A. Sarkar, S.K. Biswas, P. Pramanik, J. Mater. Chem. 20 (2010) 4417–4424.
[31] J. Ding, Q.A. Gao, D. Luo, Z.G. Shi, Y.Q. Feng, J. Chromatogr. A 1217 (2010) 7351–7358.
[32] D. Lu, Y. Yang, X. Luo, C. Sun, Anal. Methods 5 (2013) 1721–1732.

Talanta 132 (2015) 126–131

Contents lists available at ScienceDirect

Talanta

journal homepage: www.elsevier.com/locate/talanta

Quantum-DoT submicrobead-based immunochromatographic assay for quantitative and sensitive detection of zearalenone

Hong Duan [a], Xuelan Chen [b], Wei Xu [a], Jinhua Fu [c], Yonghua Xiong [a,*], Andrew Wang [d]

[a] State Key Laboratory of Food Science and Technology, Nanchang University, Nanchang 330047, China
[b] Key Laboratory of Functional Small Organic Molecule (Ministry of Education), Jiangxi Normal University, Nanchang 330022, China
[c] Jiangxi Institute of Veterinary Drug and Feedstuff Control, Nanchang 330047, China
[d] Ocean NanoTech, LLC., San Diego, CA 92126, USA

ARTICLE INFO

Article history:
Received 24 July 2014
Received in revised form
28 August 2014
Accepted 31 August 2014
Available online 6 September 2014

Keywords:
Quantum dot submicrobeads
Immunochromatographic assay
Zearalenone
Quantitative detection

ABSTRACT

Mycotoxin pollutants are commonly related to cereal products and cause fatal threats in food safety, and therefore require simple and sensitive detection. In this work, quantum-dot (QD) submicrobeads (QBs) were synthesized by encapsulating CdSe/ZnS QDs using the microemulsion technique. The resultant QBs, with approximately 2800 times brighter luminescence than the corresponding QDs, were explored as novel fluorescent probes in the immunochromatographic assay (ICA) for sensitive and quantitative detection of zearalenone (ZEN) in corns. Various parameters that influenced the sensitivity and stability of QB-based ICA (QB–ICA) were investigated and optimized. The optimal QB–ICA exhibits good dynamic linear detection for ZEN over the range of 0.125 ng/mL to 10 ng/mL with a median inhibitory concentration of 1.01 ± 0.09 ng/mL ($n=3$). The detection limits for ZEN in a standard solution and real corn sample (dilution ratio of 1:30) are 0.0625 ng/mL and 3.6 μg/kg, respectively, which is much better than that of a previously reported gold nanoparticle-based ICA method. Forty-six natural corn samples are assayed using both QB–ICA and enzyme-linked immunosorbent assay. The two methods show a highly significant correlation ($R^2=0.92$). Nine ZEN-contaminated samples were further confirmed with liquid chromatography–tandem mass spectrometry (LC–MS/MS), and the QB–ICA results also exhibited good agreement with LC–MS/MS method. In brief, this work demonstrates that QB–ICA is capable of rapid, sensitive screening of toxins in food analysis, and shows great promise for point-of-care testing of other analytes.

© 2014 Elsevier B.V. All rights reserved.

1. Introduction

Zearalenone (ZEN) is an estrogenic and carcinogenic mycotoxin produced by some *Fusarium* species, which can be found in corn, wheat, and cereal products. ZEN commonly remains in the food chain in the form of original molecules, and produces severe damage on the reproductive system of humans and animals [1]. Many countries have established regulations governing levels of ZEN in agricultural products. To minimize the risk to humans and animals, several analytical methods have been developed for the detection of ZEN in food samples, including gas chromatography (GC) [2], high-performance liquid chromatography (HPLC) [3,4], liquid chromatography-tandem mass spectrometry (LC-MS/MS) [5], as well as some immunochemical methods, such as enzyme-linked immunosorbent assay (ELISA) [6,7], fluorescence polarization immunoassay (FPIA) [8], and use of other immunobiosensors [9,10]. However, these methods are unsuitable for on-site routine screening because they require professional laboratory conditions, skilled operators, expensive instruments, and time-consuming sample pretreatments.

Recently, use of gold nanoparticle-based immunochromatographic assay (AuNP–ICA) has been recommended for ZEN qualitative and quantitative detection because of its rapidity, ease of use, and suitability for on-site analysis [11]. For example, Shim et al. and Li et al. reported AuNPs–ICA for qualitative determination of ZEN with visual detection limits (vLOD) at 2.5 ng/mL and 1.0 ng/mL, respectively [12,13]. Wang et al. also used AuNP-ICA for rapid simultaneous quantification of ZEN and Fumonisin B_1 (FB_1), in which the LODs for ZEN in a standard solution and real corn sample (dilution ratio of 1:60) were 0.35 ng/mL and 21 μg/kg, respectively [14]. Compared with fluorescent nanoparticle probes, traditional AuNP–ICA is always limited by its relatively low sensitivity. Quantum dots (QDs) are ideal fluorescent labels and have been widely used for improving the detection sensitivity of ICA due to their incomparable optical properties, such as broad UV excitation with narrow fluorescent emission spectra, large molar extinction coefficient, and high quantum yield

* Correspondence to: State Key Laboratory of Food Science and Technology, Nanchang University, 235 Nanjing East Road, Nanchang 330047, PR China.
Tel.: +86 791 8818 2405; fax: +86 791 8833 3708.
E-mail address: yhxiongchen@163.com (Y. Xiong).

http://dx.doi.org/10.1016/j.talanta.2014.08.076
0039-9140/© 2014 Elsevier B.V. All rights reserved.

[15]. A few research groups have reported QD-based ICA methods (QD–ICA) for rapid detection of protein biomarkers and other small molecule compounds, and achieved high sensitivity [16,17]. Quantum-dot submicrobeads (QBs), in which numerous QDs are embedded in a polymer matrix, exhibit advantages in improving the sensitivity of immunoassay due to their stronger fluorescence intensity than the corresponding single QD. Zhang et al. used QBs as luminescent amplification probes and developed a dot-blot sandwich immunoassay for ultrasensitive detection of hepatitis B-virus surface antigen with a LOD at 0.078 ng/mL [18]. Li et al. also reported a QB-based sandwich ICA for quantitative and sensitive detection of prostate-specific antigen, in which the LOD achieved about 12-fold enhancement compared with QDs as probes [19]. However, the use of QBs as fluorescent probes for competitive ICA sensors has not been reported.

In the present study, highly luminescent QBs with carboxyl groups were introduced as ICA signal-amplification probes for sensitive and quantitative determination of ZEN in corns. A portable strip reader was used to record the fluorescent intensity of the test (FI_T) and control (FI_C) lines. The FI_T/FI_C ratio was adjusted to offset the interference from the inherent heterogeneity of the test strips according to our previous work [20]. Various parameters that influence the sensitivity and reproducibility of QB–ICA were systematically optimized. The performance of QB-ICA, including its LOD, median inhibitory concentration (IC_{50}), specificity, accuracy and precision, was evaluated. Moreover, the practicality and reliability of the proposed quantitative strip were compared with a commercial ELISA kit and were further confirmed by LC-MS/MS.

2. Materials and methods

2.1. Reagents and apparatus

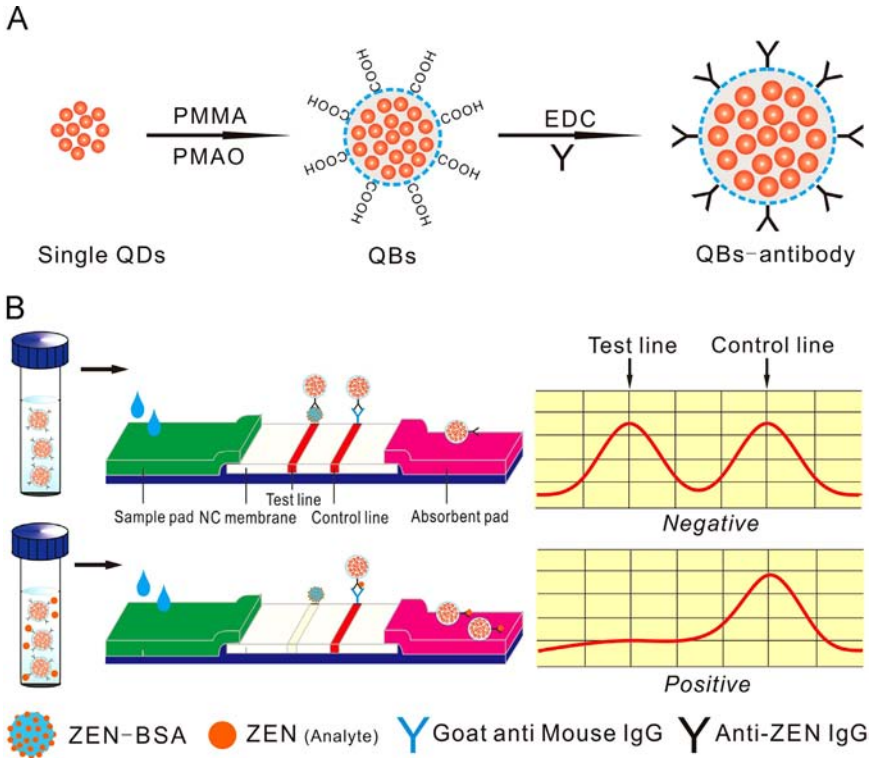
ZEN, N-(3-dimethylaminopropyl)-N′-ethylcarbodiimide hydrochloride (EDC · HCl), bovine serum albumin (BSA), and N-hydroxysuccinimide (NHS) were purchased from Sigma-Aldrich Chemical (St. Louis, MO, USA). Donkey anti-mouse IgG antibodies were purchased from Beijing Zhongshan Biotechnology Inc. (Beijing, China). ZEN–BSA conjugates (mole ratio of 8:1) and anti-ZEN monoclonal antibodies (anti-ZEN mAbs) were prepared in our laboratory. The sample pad, nitrocellulose (NC) membrane, and absorbent pad were purchased from Schleicher and Schuell GmbH (Dassel, Germany). The ELISA kit was provided by Shanxi Defcred Biotech Co., Ltd (Shanxi, China). All other reagents were of analytical grade and purchased from Sinopharm Chemical Corp. (Shanghai, China).

Forty-six natural corn samples were collected from the grain procurement agencies in Shandong Province, China. All samples were ground and well mixed prior to use. The sample extraction was as follows: 5.0 g of the pulverized sample was extracted with 25 mL methanol–water mixture (6:4, v/v) for 20 min with vigorous shaking. After centrifuging at 5000 *g* for 10 min, the supernatant solutions were diluted six-fold with 0.01 M phosphate buffer saline (pH 5.0, PBS) for further use.

The BioDot XYZ platform, combined with a motion controller, BioJet Quanti3000 k dispenser, and AirJet Quanti3000 k dispenser for solution dispensing, was supplied by BioDot (Irvine, CA). The automatic programmable cutter was purchased from Shanghai Jinbiao Biotechnology Co., Ltd. (Shanghai, China). The portable fluorescent strip reader was obtained from Huguo Science Instrument Co., Ltd. (Shanghai, China). The water used for all the experiments was purified by Elix-3 and Milli-QA apparatus (Molsheim, France).

2.2. Preparation and characterization of QBs

As shown in Schematic 1A, the quantum-dot submicrobeads (QBs) were synthesized as previously reported with some modifications [21]. Briefly, CdSe/ZnS QDs with a maximum emission wavelength at 623 nm in $CHCl_3$ (1 mL; 20 mg/mL) were mixed with 1 mL $CHCl_3$ containing polymethyl methacrylate (60 mg/mL) and poly (maleic anhydride-alt-1-octadecene) (40 mg/mL). An



Schematic 1. (A) Schematic illustration of the quantum-dot submicrobead formation. (B) Schematic illustration of the QB-ICA method for quantitative detection of ZEN.

emulsion was obtained with sodium dodecyl sulfate (3 mg/mL; 5 mL) in water, using an ultrasonic homogenizer for 2 min. The nonpolar solvent ($CHCl_3$) was then evaporated using a rotary evaporator. The resulting water-soluble QBs were purified by centrifugation (6500 *g*, 10 min) and washed three times with pure water.

Fluorescence intensity of the resultant QBs was monitored using a Hitachi F-4500 fluorescence spectrophotometer (Tokyo, Japan). The average size and morphology of the spMNBs were determined using a high-resolution transmission electron microscope (JEOL JEM 2100, Tokyo, Japan).

2.3. Preparation and characterization of anti-ZEN mAb-labeled QBs

The unpurified ascitic fluid containing anti-ZEN mAbs was used to directly conjugate with QBs as previously reported with some modifications [22]. Briefly, 5 μg EDC, 0.6 mg QBs, and 300 μL of unpurified anti-ZEN ascitic fluid (0.3 mg/mL) were added to 1.8 mL of 0.01 M PB buffer (pH 6.0). After reacting at room temperature for 1 h under magnetic stirring, the mixtures were centrifuged at 13 500 *g* for 10 min. The QBs and anti-ZEN mAb conjugates (QB-mAbs) were resuspended with 2.0 mL of PBS (0.01 M, pH 7.4) containing 2% fructose, 1% polyethylene glycol (PEG 20000), 5% sucrose, 1% BSA, and 0.4% Tween-20. The resuspension solution was stored at 4 °C for further use. Dynamic light scattering (DLS) analysis of the free QBs and QB-mAbs probe was performed using a particle size analyzer (Malvern Instruments Ltd., Worcestershire, UK) to confirm the immobilization of anti-AFB_1 mAbs on the QB surface.

2.4. Preparation of QB-ICA sensor

The QB-ICA sensor was made of three parts: sample pad, nitrocellulose (NC) membrane, and absorbent pad. The ZEN–BSA conjugates (0.8 mg/mL) and goat anti-mouse IgG (1.0 mg/mL) were spotted onto NC membranes as the test (T) and control (C) lines, respectively, and then dried at 37 °C for 12 h. The sample pads were treated with 20 mmol/L sodium borate buffer (pH 8.0) containing 1.0% (w/v) BSA, 0.1% (w/v) NaN_3, and 0.25% Tween-20. The distance between the T and C lines was about 5 mm. After drying at 60 °C for 2 h, the sample pad, NC membrane, and absorption pad were attached to a plastic backing plate, and then cut into 4-mm-wide strips and packaged in a plastic casing for subsequent storage in a drying cylinder at room temperature.

2.5. Immunoassay procedure

As presented in Schematic 1B, the QB-mAbs probe and sample solution were pre-mixed at room temperature for 1.0 min, and then added onto the sample pad. With the aid of the capillarity of the absorbent pad, the QB-mAbs and ZEN immunocomplex formed migrate across the NC membrane and react with the goat anti-mouse IgG while excess QB-mAbs is captured by the ZEN–BSA, which results in a fluorescent band on the control and test lines, respectively. The more ZEN in the sample extracts, the lower the fluorescence intensity appears on the test line.

2.6. Assay validation

The accuracy and precision of QB–ICA were evaluated by analyzing the recovery and variation coefficients of the intra- and inter-assays [23]. The intra-assays were estimated by one batch of test strips for five replicates, while the inter-assays were analyzed once every day for three sequential days. The QB–ICA specificity was evaluated by analyzing the cross-reaction rate (Cr%) with five other common mycotoxins, including citrinin (CIT), ochratoxin A (OTA), deoxynivalenol (DON), FB_1, and aflatoxin B_1 (AFB_1). Cr% was calculated according to the following equation: $Cr\% = [(IC_{50\ ZEN})/(IC_{50\ analog})] \times 100\%$ [24]. The practicality of the QB–ICA sensor was compared with a commercial ELISA kit by analyzing 46 natural corn samples. To evaluate the method reliability, nine ZEN-contaminated samples were further confirmed with LC-MS/MS system (Agilent Corporation, MA, USA), which composed of a triple-quadrupole instrument (Agilent 6410) and an LC system (Agilent 1200 series). The sample cleaning up and LC–MS/MS operation were performed according to local standard GB/T 22286-2008 (Sichuan, China) with some modifications. Briefly, 5 g of ZEN-contaminated sample was extracted with acetonitrile: water (90:10, v/v) for 20 min on a horizontal shaker. After centrifugation at 8000 *g* for 10 min, 1 mL of supernatant and 9 mL of ultrapure water were mixed, and then passed through an immune affinity column which purchased from Beijing Rapid Bioscience Co., Ltd. (Beijing, China). The purified solution was filtered through a 0.22 μm cellulose membrane for the LC–MS/MS analysis. The LC system conditions for ZEN detection were as follows: the column was Agilent Zorbax Eclipse XDB-C18 (100 mm × 2.1 mm, 2.4 μm), which was maintained at 35 °C for chromatographic separation. The flow rate of the mobile phase was 0.30 mL/min and the injection volume of sample solution was 5 μL. The mobile phase consisted of solvent A (ammonium acetate, 10 mM) and solvent B (methanol). The chromatographic separation was performed as a gradient elution as follows: 0 to 6.0 min (80% A, 20% B), 6.0 to 6.1 min (15% A, 85% B), 6.1 to 8.1 min (5% A, 95% B), 8.1 to 12.0 min (80% A, 20% B). Ionization was achieved using electrospray ionization in anion mode with a spray voltage of −3500 V. The MS/MS acquisition was performed in multiple-reaction monitoring mode. The temperature and flow velocity for the desolvation gas (high-purity nitrogen, 99.99%) were 350 °C and 13 L/min, respectively. The monitoring ion pairs were chosen as ZEN m/z 317.1/175.2 (quantitation ion) and 317.1/131.2 (qualitative ions).

3. Results and discussion

3.1. Characterization of QBs and QBs-mAbs conjugates

The highly luminescent QBs were obtained by encapsulation of organic-soluble CdSe/ZnS QDs according a microemulsion method. To evaluate the fluorescent enhancement of the resultant QBs, fluorescence intensities of water-soluble CdSe/ZnS QDs with a maximum emission wavelength at 623 nm and the resultant QBs were monitored. As shown in Fig. 1A, the fluorescence intensity of QBs at concentration of 3.5×10^{-3} nM (dissolved in ultrapure water) was the same as that of water-soluble CdSe/ZnS QDs at 10 nM (dissolved in ultrapure water). Hence for the same numbers of QB and QD particles, the luminescence intensity of QBs was 2857 times higher than that of QDs according to the ratio of their concentrations under the same fluorescence intensity [$Con._{QD}/Con._{QB} = (10\ nmol/L)/(3.5 \times 10^{-3}\ nmol/L) = 2857$]. High-resolution transmission electron microscope (HRTEM) images (Fig. 1B) show that the QBs have relatively uniform size distribution with an average diameter of 247 nm, while Fig. 1B (inset) further indicates that numerous dark QDs are tightly embedded in the polymer matrix. Fig. 1C confirms a macroscopic metal lattice structure of CdSe/ZnS QDs. DLS analysis shows that the hydrodynamic diameter of the free QBs is about 255 nm, whereas that of the QBs-mAbs increases to about 295 nm. The results confirm that the anti-ZEN mAbs was successfully coupled on the surface of the QBs.

3.2. Optimization of the QB-based ICA and detection conditions

The QBs-mAbs probe was obtained by coupling the amino group of anti-ZEN mAbs with the carboxyl group of the QBs using

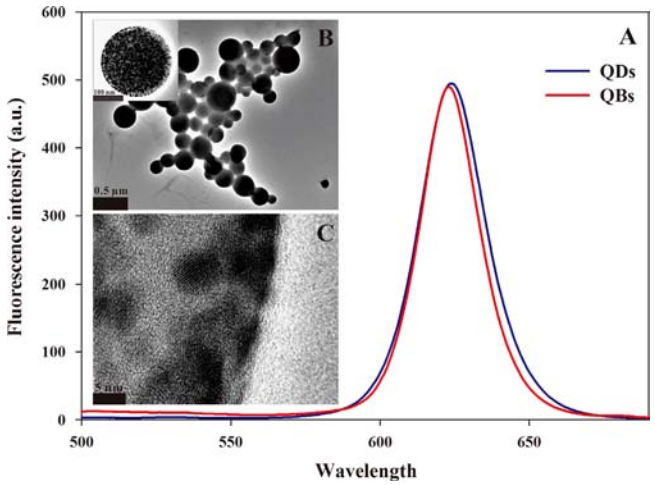


Fig. 1. Characterization of QBs. (A) The fluorescence intensities of water-soluble CdSe/ZnS QDs and the resultant QBs. The concentrations of QDs and QBs were 10 nM and 3.5×10^{-3} nM, respectively. (B) High-resolution transmission electron microscope image of the quantum-dot submicrobeads. Inset: image of individual quantum-dot submicrobeads at high magnification. (C) Part of the individual quantum-dot submicrobead image at high magnification.

an active ester method. The unpurified anti-ZEN ascites were used to label QBs directly to reduce the QB nonspecific bond with the NC membrane and the ZEN–BSA on the test line, because the mass of miscellaneous proteins in the ascites blocked the excess carboxyl groups of the QBs when the anti-ZEN mAbs bound on the surface of the QBs. To achieve the best sensitivity and high FI signals on both lines, a similar checkerboard titration was performed with a series of ZEN–BSA concentrations on the test line for various different contents of the QB-mAbs probe. The FI signals on both lines were recorded at 30 min. The means of FI on both lines were based on three duplicate measurements with the blank corn extract solution. The competitive inhibition rates are obtained by $(1-B_x/B_0) \times 100\%$, where B_0 and B_x represent FI_T/FI_C of the negative sample and a ZEN-spiked corn extract solution (1.0 ng/mL), respectively. As shown in Table 1, the optimal combinations were as follows: 0.8 mg/mL ZEN–BSA on the test line and 1 μL of QB-mAbs (60 μg/mL) pre-mixed with 69 μL sample solution. Under the optimal combination, the means of the FI_T and FI_C signals on both lines were 748 ± 18 and 539 ± 20, respectively. The competitive inhibition rate for the 1 ng/mL spiked sample was 59.9 ± 0.7% ($n=3$).

In a conventional strip, the labeled probes are irregularly sprayed on the conjugated pad which can hardly be standardized and easily lead to certain variability of FIs on both lines between the different strips [25,26]. In the present study, the conjugated pad was integrated with sample pad, and the QB-mAbs probe was introduced to pre-incubate with the ZEN standard (or sample) solution for 1 min to improve the quantitative reproducibility of QB-ICA sensor (Schematic 1B). The immunological dynamic analysis was used to optimize the detection conditions that influence the stability and sensitivity of ICA, including the interpretation time, the pH value, and methanol content in the sample solution. The immunological dynamic curve for QB-ICA was obtained as described in our previous work [20]. Briefly, 1 min after the solution was added onto the sample pad, the strip was inserted into a portable fluorescent reader. The FI_T, FI_C, and FI_T/FI_C ratio were recorded every 1 min for 30 min. The kinetic curves representing the interaction between the QB–mAbs probe and antigens (on NC membrane) are described by plotting the values of FI_T, FI_C, and FI_T/FI_C against running time. As shown in Fig. 2A, FI signals on both lines continue to increase sharply in the initial 25 min, and then kept gently increasing for the succeeding 30 min observation time. However, the FI_T/FI_C ratio quickly stabilized after 10 min. Thus, the interpretation time for ZEN quantitative analysis was set at 10 min for all succeeding studies.

The effect of pH value on the sensitivity of the strip was evaluated by running a series of solutions with pH values in the range of 5.0 to 9.0. The results in Fig. 2B indicate that the FI_T/FI_C value of the negative sample significantly decreased from 1.54 ± 0.10 to 0.60 ± 0.08 as the pH increased from 5.0 to 9.0. The competitive inhibition rate for the 1.0 ng/mL ZEN-spiked sample reached a maximum of 63% ± 6% in the pH 5.0 solution. These results indicate that weak acidic conditions (pH 5.0) improve the sensitivity of QB-ICA by promoting anti-ZEN mAbs and ZEN-BSA recognition.

The effect of methanol concentration on the sensitivity of QB-ICA was also investigated. The results, shown in Fig. 2C, indicate that the inhibition of QB-ICA continuously declined from 62.5% ± 4% to 32.8% ± 6% as the methanol concentration increased from 0 to 15%, and then remained relatively stable from 32.8 ± 6% to 34.4 ± 1% as the methanol content increased further to 25%. Due to the hydrophobicity of the ZEN molecule, the methanol content in the buffer was set at 10%.

Considering the above results, the optimized experimental conditions of QB-ICA for ZEN quantitative analysis are recommended as follows: the corn extract containing 60% methanol was diluted six-fold with 0.01 M PBS (pH 5.0); 69 μL of the diluted solution and 1 μL of QB-mAbs probe (60 μg/mL) were pre-mixed at room temperature for 1.0 min and then added onto the sample pad; after 10 min, the strip was scanned by a portable fluorescent reader for ZEN quantitative analysis.

3.3. Assay validation

Under optimal experimental conditions, a standard curve for the QB-ICA method was constructed by plotting the ratio of B_X/B_0 against the logarithm of ZEN concentrations. The standard solutions were prepared by spiking a ZEN stock solution (1.0 μg/mL) with a blank corn sample extract to final concentrations of 0, 0.0625, 0.125, 0.35, 0.75, 2.0, 5.0, 7.5, 10, 15, and 20 ng/mL, respectively. The results, shown in Fig. 2D, indicate that the method exhibits a wide dynamic linear range of 0.125 ng/mL to 10 ng/mL with a median inhibitory concentration (IC_{50}) of 1.0 ng/mL ($n=3$). The regression equation of the standard curve was $y=-0.160\ln(x)+0.504$ with a reliable correlation coefficient ($R^2=0.994$).

The LOD of the QB-ICA method was calculated at 10% inhibitory concentration to be 0.0625 ng/mL, which is 5.6 times higher than that of the previously reported AuNPs–ICA quantitative method. The LOD for a real corn sample was 3.6 μg/kg, according to the mean determined concentration of 20 randomly negative corn samples plus three-fold standard deviation [27,28], and then multiplied by the dilution factor of 30. The intra-assay recovery rates for ZEN-spiked concentrations of 0.5, 1.0, and 2.0 ng/mL were 108.0 ± 3.0%, 97.0 ± 1.5%, and 89.5 ± 1.7%, and those for the inter-assay were 106.0 ± 1.9%, 95.0 ± 3.5%, and 93.5 ± 4.4%, respectively (Table 2). The above results indicate that the precision and accuracy of the QB–ICA method are acceptable for ZEN quantitative detection. The QB-ICA specificity exhibits negligible cross-reactivity with other five common mycotoxins: CIT, OTA, DON, FB_1, and AFB_1.

To verify the practicability of the QB–ICA sensor, 46 real corn samples were analyzed using both QB–ICA and a commercial ELISA kit. The results indicate that the two methods have a good agreement ($R^2=0.92$, Fig. 3A). Nine random corn samples, found to be ZEN-contaminated using QB-ICA, were further analyzed by LC–MS/MS to confirm the reliability of QB-ICA. The results from

Table 1
Optimization of the concentrations of QB-mAbs probe and ZEN-BSA using a checkerboard titration.

No.	The concentration of ZEN-BSA (mg/mL)	The volume of QB-mAbs (μL)	The FI of test lines[a]	The FI of control lines[a]	FI_T/FI_C	The inhibitionrate (%)[b]
1	0.8	2.0	1049 ± 33	839 ± 4	1.25 ± 0.03	35.41 ± 1.66
2	0.8	1.5	844 ± 16	627 ± 5	1.35 ± 0.02	44.54 ± 1.60
3[c]	0.8	1.0	748 ± 18	539 ± 20	1.39 ± 0.02	59.90 ± 0.70
4	0.6	2.0	906 ± 14	933 ± 24	0.97 ± 0.01	28.45 ± 2.80
5	0.6	1.5	726 ± 6	708 ± 3	1.02 ± 0.01	37.86 ± 2.17
6	0.6	1.0	480 ± 21	407 ± 20	1.2 ± 0.01	52.85 ± 2.96
7	0.4	2.0	669 ± 28	1029 ± 31	0.65 ± 0.04	33.38 ± 4.57
8	0.4	1.5	532 ± 44	757 ± 45	0.70 ± 0.07	42.03 ± 0.22
9	0.4	1.0	328 ± 15	533 ± 27	0.6 ± 0.04	30.41 ± 5.96

[a] The means of the FI_T and FI_C values are based on three duplicate measurements with the negative corn extract solution.
[b] The inhibition rates are obtained from the 1 ng/mL ZEN-spiked sample.
[c] The optimal parameters of QB–ICA.

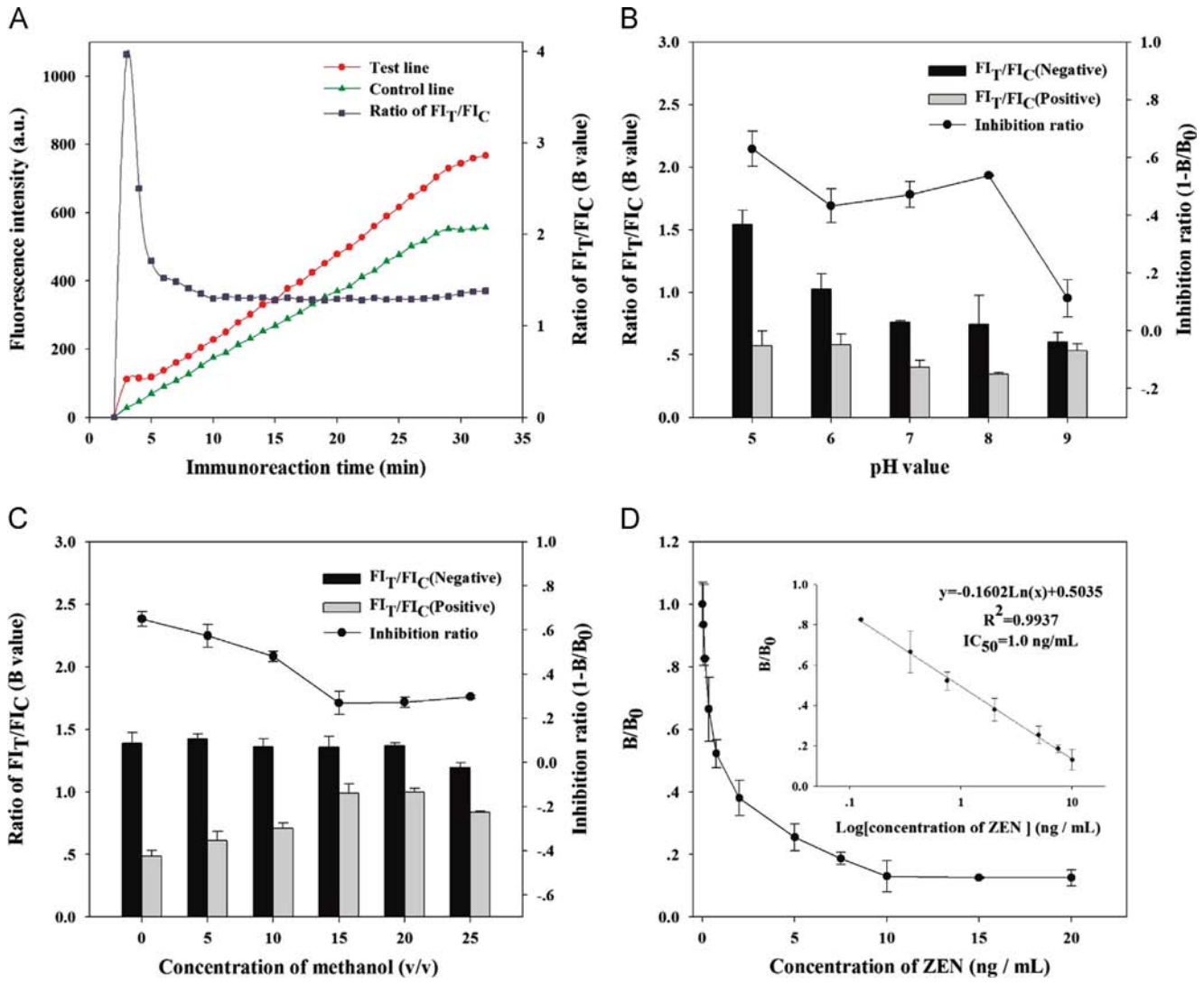


Fig. 2. Optimization detection conditions of the QB-ICA. (A) Immunoreaction dynamics of FI_T, FI_C, and FI_T/FI_C ratios. (B) The effects of pH on the FI_T/FI_C and inhibition ratios. (C) The effects of methanol concentration on the FI_T/FI_C and inhibition ratios. (D) Calibration curves for ZEN using mouse anti-ZEN mAbs-labeled QBs.

QB-ICA sensor also shows a highly significant correlation with LC-MS/MS method (R^2 = 0.96, Fig. 3B).

4. Conclusions

In summary, highly luminescent QBs have been employed to provide a competitive ICA system for rapid (10 min) and quantitative detection of ZEN in corn samples, in which the QBs have more than 2800 times brighter luminescence than the corresponding CdSe/ZnS QDs. The optimal QB-ICA exhibits a detection limit of 0.0625 ng/mL for ZEN, which is 5.6 times higher than that of a previously reported AuNPs-ICA quantitative method. Moreover, QB-ICA shows acceptable precision and accuracy, and has a highly significant correlation to the conventional ELISA and LC–MS/MS methods. On account of its significant advantages in luminescent signal amplification, the

Table 2
Precision and accuracy of QB-based ICA in ZEN-spiked samples.

Spiked ZEN (ng/mL)	Intra-assay		Inter-assay[a]	
	Recovery (%)[b]	CV (%)	Recovery (%)[b]	CV (%)
0.5	108.0	3.0	106.0	1.9
1.0	97.0	1.5	95.0	3.5
2.0	89.5	1.7	93.5	4.4

[a] Assay was completed every 1 days for 3 days continuously.
[b] Recovery was obtained from five replicates at each spiked concentration.

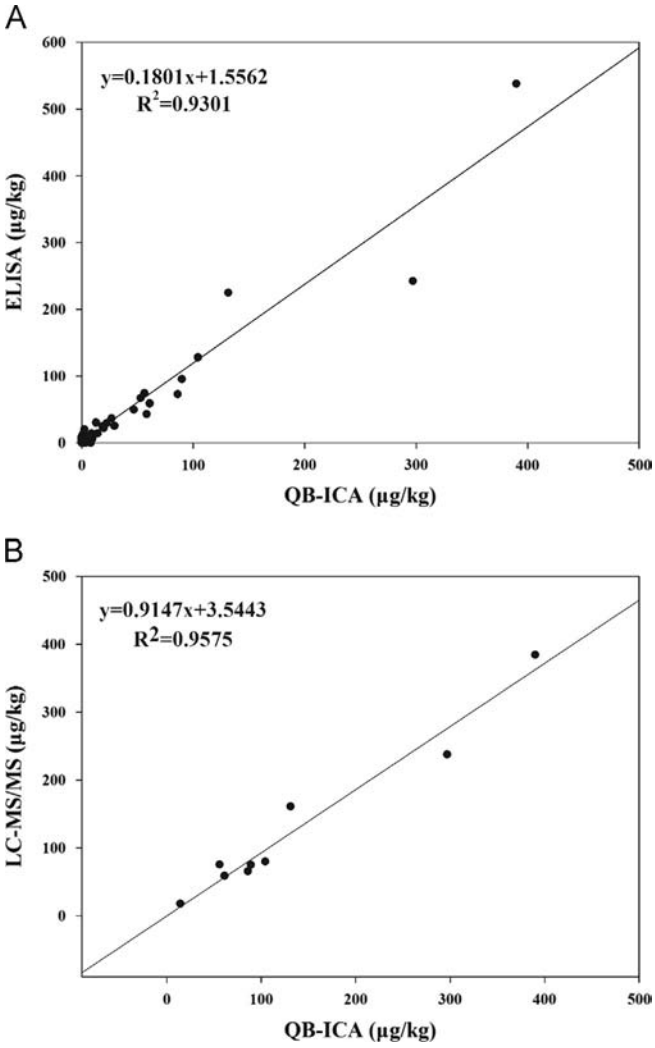


Fig. 3. Methodology comparison. (A) Methodology comparison between the QB-ICA and ELISA methods ($n=46$). (B) Methodology comparison between the QB-ICA and LC-MS/MS methods ($n=9$).

proposed QB-ICA method offers great potential for rapid and sensitive analysis of various contaminants in food safety monitoring.

Acknowledgments

This work was supported by a grant from the National Basic Research Program of China (2013CB127804), "Twelfth Five-Year Plan" for National Science and Technology Support Program (2013BAD19B02), the National Natural Science Foundation of China (Grant No. 31160323), the Training Plan for the Main Subject of Academic Leaders of Jiangxi Province (20142BCB22004), and National Institute of Health of United State (1R43AI092962).

References

[1] A. Zinedine, J.M. Soriano, J.C. Molto, J. Mane, Food Chem. Toxicol. 45 (2007) 1–18.
[2] V.G. Amelin, N.M. Karaseva, A.V. Tretyakov, J. Anal. Chem 68 (2013) 61–67.
[3] Y.L. Wang, T.J. Chai, G.J. Lu, Environ. Res. 107 (2008) 139–144.
[4] E.O. Bennekom, L. Brouwer, E.H.M. Laurant, H. Hooijerink, M.W.F. Nielen, Anal. Chim. Acta. 473 (2002) 151–160.
[5] E. Perez-Torrado, J. Blesa, J.C. Molto, Food Control 21 (2010) 399–402.
[6] Y.H. Huang, Y. Xu, Q.H. He, Food Agric. Immunol. 25 (2014) 186–199.
[7] A. Kuzdralinski, E. Solarska, M. Muszynska, Food Control 29 (2013) 22–24.
[8] A.P. Bondarenko, S.A. Eremin, J. Anal. Chem 67 (2012) 790–794.
[9] E. Schneider, E. Usleber, E. Martbaur, R. Dietrich, G. Terplan, Food Addit. Contam. 12 (1995) 387–393.
[10] J.L. Urraca, J.L. Benito-Pen, C. Perez-Conde, M.C. Moreno-Bondi, J. Agric. Food Chem. 53 (2005) 3338–3344.
[11] A.Y. Kolosova, S. De Saeger, L. Sibanda, R. Verheijen, C.V. Peteghem, Anal. Bioanal. Chem. 2389 (2007) 2103–2107.
[12] X. Li, P.W. Li, Q. Zhang, Biosens. Bioelectron. 49 (2013) 426–432.
[13] W.B. Shim, K.Y. Kim, K.Y. Chung, J. Agric. Food Chem. 57 (2009) 4035–4041.
[14] Y.K. Wang, Y.X. Yan, W.H. Ji, H.A. Wang, J. Agric. Food Chem. 61 (2013) 5031–5036.
[15] X. Michalet, F.F. Pinaud, L.A. Bentolila, Science 307 (2005) 538–544.
[16] Q. Yang, X. Gong, T. Song, J. Yang, S. Zhu, Y. Li, Biosens. Bioelectron. 30 (2011) 145–150.
[17] Z. Zou, D. Du, J. Wang, J. Smith, C. Timchalk, Y. Li, Y. Lin, Anal. Chem 82 (2010) 5125–5133.
[18] P.F. Zhang, Q. Li, J. Chen, H. Yan, W. Ma, Theranostics 4 (2014) 307–315.
[19] X. Li, W.B. Li, Q.H. Yang, X.Q. Gong, W.S. Guo, C.H. Dong, J.Q. Liu, L.X. Xuan, J. Chang, Mater. Interfaces (2014), http://dx.doi.org/10.1021/am5012782.
[20] X.L. Huang, X.L. Aguilar, H.M. Li, W.H. Lai, H. Wei, H.Y. Xu, Y.H. Xiong, Anal. Chem. 85 (2013) 5120–5128.
[21] R. Xie, U. Kolb, J. Li, T. Basché, A. Mews, J. Am. Chem. Soc. 127 (2005) 7480–7488.
[22] R.K. Mendes, R.F. Carvalhal, D.R. Stach-Machado, L.T. Kubota, Biosens. Bioelectron. 24 (2009) 2483–2487.
[23] W. Xu, X.L. Chen, X.L. Huang, Y.H. Xiong, Talanta 114 (2013) 160–166.
[24] H.M. Li, W.H. Lai, H.Y. Xu, B. Xu, W. Luo, H. Wei, S.X. Wang, Y.H. Xiong, Chinese J. Anal. Chem. 39 (2011) 1647–1652.
[25] V. Gubala, L.F. Harris, A.J. Ricco, M.X. Tan, D.E. Williams, Anal. Chem. 84 (2011) 487–515.
[26] L. Anfossi, M. Calderara, C. Baggiani, C. Giovannoli, E. Arletti, G. Giraudi, Anal. Chim. Acta 682 (2010) 104–109.
[27] S.W. Oh, Y.M. Kim, H.J. Kim, H.J. Kim, J.S. Cho, E.Y. Choi, Clin. Chim. Atca 406 (2009) 18–22.
[28] J. Pleadin, J. Vulić, J. Perši, N. Vahčić, Meat Sci 86 (2010) (2010) 733–737.

Talanta 132 (2015) 132–136

Contents lists available at ScienceDirect

Talanta

journal homepage: www.elsevier.com/locate/talanta

Ultra-hydrophobic ionic liquid 1-hexyl-3-methylimidazolium tris(pentafluoroethyl)trifluorophosphate supported hollow-fiber membrane liquid–liquid–liquid microextraction of chlorophenols

Dandan Ge [a,b], Hian Kee Lee [a,*]

[a] Department of Chemistry, National University of Singapore, 3 Science Drive 3, Singapore 117543, Singapore
[b] Department of Chemical Science & Technology, Kunming University, Kunming 650214, PR China

ARTICLE INFO

Article history:
Received 26 June 2014
Received in revised form
28 August 2014
Accepted 28 August 2014
Available online 10 September 2014

Keywords:
Ionic liquid
Hollow fiber liquid–liquid–liquid microextraction
Environmental samples
Liquid chromatography
Chlorophenols

ABSTRACT

An ultra-hydrophobic ionic liquid, 1-hexyl-3-methylimidazolium tris(pentafluoroethyl)trifluorophosphate ([HMIM][FAP]) was immobilized in the pores of a polypropylene hollow fiber for liquid–liquid–liquid microextraction (HF-LLLME) of chlorophenols (CPs) (4-chloro-3-methylphenol, 2,4-dichlorophenol and 2,4,6-trichlorophenol). The analytes were first extracted from 10 ml of water sample into the ionic liquid membrane, and then were extracted back into 5 μl of sodium hydroxide aqueous solution in the hollow fiber channel. After extraction, the acceptor solution was directly injected into a high-performance liquid chromatographic system for analysis. Extraction parameters such as extraction time, salt concentration in the sample, the pH of the sample and acceptor phase, and stirring rate during extraction were investigated. The relative standard deviations of the analytes varied from 4 to 6%. Limits of detection of <0.5 ng/ml were obtained for the three analytes. The squared regression coefficients relating to the calibration curve were ≥ 0.9941. The proposed method was applied to the analysis of CPs in canal water.

© 2014 Elsevier B.V. All rights reserved.

1. Introduction

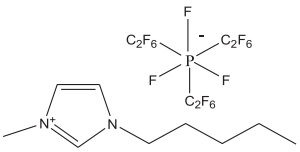
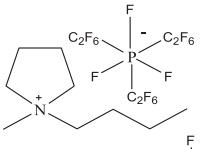
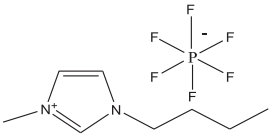
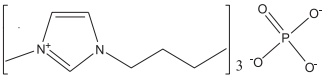
Sample preparation is a critical step in analytical chemistry, particularly in environmental analysis. In general, liquid–liquid extraction (LLE) [1,2] is one of the most widely used pretreatment procedures. However, it is labor-intensive and time-consuming. In addition, it generally requires a large amount of potentially toxic and high-purity solvents. Over the past 2 decades, miniaturized, microscale sample preparation techniques have been developed as alternatives to LLE, such as liquid-phase microextraction (LPME) [3,6–10] and solid-phase microextraction (SPME) [4,5]. Jeannot and Cantwell developed a liquid-based extraction procedure based on a microdrop of solvent suspended at the tip of a Teflon rod [3]. They referred to the method as solvent microextraction. Later, the same authors [6] and He and Lee [7] developed an approach whereby the organic drop was supported at the tip of a micro-syringe needle. Different types of LPME, as this microscale liquid-based extraction mode is now generally known, have been investigated, such as continuous flow microextraction [8], static LPME [7] (later referred to as single-drop microextraction (SDME)), dynamic LPME [9] and headspace LPME [10]. The technique has been demonstrated to be a simple, fast, and cost-effective sample pretreatment method [11]. However, the instability of the solvent microdrop, problematic application to complex aqueous samples, relative low precision (when conducted manually), and sensitivity were often encountered [12]. In order to overcome these disadvantages, hollow fiber protected LPME was introduced. One mode of HF-LPME is HF-LLLME [12–14] which is a simple technique in which analytes are extracted into an organic phase from an aqueous donor phase, and subsequently extracted back into an aqueous acceptor phase. For this method, a hollow fiber is used to support the organic phase (held within the wall pores) and acceptor phase (confined within the channel of the membrane). Since the final phase is aqueous, it can be introduced into a reversed-phase high-performance liquid chromatographic (HPLC) system without further treatment. For HF-LLLME, the selection of the organic phase is a critical step to obtain efficient extraction. It should be immiscible with water, relatively less volatile, and be compatible with the hollow fiber. 1-Octanol [13], toluene [15], and undecane [16] are commonly used solvents in HF-LLLME. Since these are volatile organic chemicals, they pose potential risks to users.

Room temperature ionic liquids (ILs) are composed of organic cations and various anions. ILs have some significant advantages over organic solvents, such as low volatility, high thermal stability and the ability to interact with a variety of organic and inorganic

* Corresponding author. Tel.: +65 6516 2995; fax: +65 6779 1691.
E-mail address: chmleehk@nus.edu.sg (H.K. Lee).

http://dx.doi.org/10.1016/j.talanta.2014.08.074
0039-9140/© 2014 Elsevier B.V. All rights reserved.

Table 1
Structures and Physical properties of studied ILs at 20 °C.

Ionic liquid	Structure	Density (g/cm^3)	Viscosity (cP)	Surface tension (mN/m)
[HMIM][FAP]		1.557	119	33.2
[BMPL][FAP]		1.589	292	35
[BMIM][PF_6]		1.36	312	43.21
[BMIM][PO_4]		–	–	–

compounds [17]. Furthermore, they are considered as environmentally friendlier solvents, and thus serve as alternatives to conventional organic solvents. Since IL was used by Liu et al. in LPME [18], their application has become widespread in the extraction field [19,20]. ILs containing the hexafluorophosphate (PF_6^-) anion have been applied as supporting liquid for HF-LLLME. For example, 1-butyl-3-methylimidazolium hexafluorophosphate ([BMIM][PF_6]) was used in this manner for the extraction of aliphatic and aromatic hydrocarbons [21]. 1-Octyl-3-methylimidazolium hexafluorophosphate ([OMIM][PF_6]) was employed for the extraction of chlorophenols (CPs) [22] and sulfonamides [23]. However, Swatloski et al. reported that these ILs are hydrolytically unstable [24]. It has been found that after 5 min of SDME via direct immersion using [BMIM][PF_6], 50% of the microdrop volume was lost [25]. [OMIM][PF_6] is more hydrophobic; however, it was found that this IL also partially dissolved in aqueous solution after 30 min [18,26]. Recently, ILs containing tris(perfluoroalkyl)trifluorophosphateanion (FAP^-) have been shown to have excellent hydrolytic, thermal and electrochemical stability. The water uptake of these ILs are more than 10 times less than that of ILs with the PF_6^- [27]. Cong et al. have applied FAP-based ILs as SDME extraction solvents [25]. In our previous studies, 1-hexyl-3-methylimidazolium tris(pentafluoroethyl)trifluorophosphate ([HMIM][FAP]) was successfully used as extraction solvent in HF-LPME [28] and dispersive liquid–liquid microextraction [29,30] of analytes from aqueous samples.

CPs were used as the analytes in the present work. LPME methods, including ultrasound-headspace LPME [31], dispersive liquid–liquid microextraction (DLLME) [32], single drop LPME [33] and HF-LPME [34] have been applied to extract CPs from environmental water samples. [OMIM][PF_6] as the impregnated IL in the hollow fiber wall pores for HF-LLLME [22] and [BMIM][PF_6] based three-phase liquid–liquid–liquid solvent bar microextraction [35] of CPs from environmental water samples have been reported. In this work, we investigated the FAP-based IL, [HMIM][FAP], as the wall pore-impregnated solvent in HF-LLLME. The influence of HF-LLLME parameters such as extraction time, pH of the donor sample and acceptor phase, stirring rate during extraction, and salt concentration in the sample were optimized and the proposed method, with HPLC, were applied to determine CPs in canal water samples.

2. Experimental

2.1. Chemicals and materials

HPLC grade methanol was purchased from Tedia (Fairfield, OH, USA) and acetone was supplied by Merck (Darmstadt, Germany). 4-Chloro-3-methylphenol (p*K*a 9.6), 2,4-dichlorophenol (p*K*a 7.8), and 2,4,6-trichlorophenol (p*K*a 6.2) were supplied by Aldrich (Milwaukee, WI, USA), Ultrapure water was produced on a Milli-Q water purification system (Millipore, Milford, MA, USA). Sodium chloride was obtained from GCE (Chula Vista, CA, USA). [HMIM][FAP] and 1-butyl-1-methylpyrrolidinium tris(pentafluoroethyl) trifluorophosphate [BMPL][FAP] were purchased from Merck. 1-Butyl-3-methylimidazolium phosphate ([BMIM][PO_4]) and [BMIM][PF_6] were bought from Strem Chemicals (Newburyport, MA, USA). The structures and physical properties of the ILs investigated in this study are shown in Table 1. Sodium hydroxide and sodium dihydrogen phosphate were purchased from Merck and orthophosphoric acid (85% purity) was supplied by Carlo Erba (Milan, Italy).

Individual stock solutions of the pure CPs were prepared in methanol at 1 mg/ml concentrations and stored at 4 °C. Working aqueous solutions containing all three CPs at different concentrations were prepared daily. The concentrations of the analytes in the working solutions for the optimization experiments, were 1 μg/ml. Real water samples were collected from a canal in Singapore, and stored at 4 °C until ready for extraction.

Accurel Q3/2 polypropylene hollow fiber membrane with an inner diameter of 600 μm, wall thickness of 200 μm, and wall pore size of 0.2 μm, was obtained from Membrana (Wuppertal, Germany).

2.2. Instrumentation

HPLC analysis was carried out on a Waters (Milford, MA, USA) instrument with a Rheodyne (Cotati, CA, USA) 77251 injector equipped with a 20 μl sample loop, a Degasys DG-2410 degasser, a Waters 1525 μ binary pump and a Waters 2487 dual λ absorbance detector. The detection wavelength was set at 240 nm. Data was collected and processed by Empower version 5.0 (Waters) data analysis software.

Chromatographic separation was conducted on a Metaphase KR100-5-C18 (Bioscience, Kuala Lumpur, Malaysia) column (250 × 4.6 mm i.d.; packed with 5 μm particles) The mobile phase used consisted of 70% methanol and 0.01 M sodium dihydrogen phosphate solution, acidified to pH 2.5 with orthophosphoric acid, and delivered at a flow rate of 0.5 ml/min.

2.3. HF-LLLME procedure

Prior to extraction, a hollow fiber tubing was cut manually into a length of 2.5 cm and one end was heat sealed, before being cleaned with acetone under ultrasonication, and air dried. A 10 ml aliquot of sample solution was added to a 15 ml sample vial with a 15 mm × 6 mm magnetic stirring bar. The vial was placed on a MR3001K magnetic stirrer plate (Heidolph, Kelheim, Germany). Five microliters of the acceptor phase solution was introduced into the clean and dry hollow fiber using a 25-μl microsyringe with a flat needle tip. The fiber was then immersed in [HMIM][FAP] for 5 s for impregnation of its wall pores. The IL impregnated fiber, together with the needle, were placed in the sample solution. The magnetic stirrer was switched on to start the extraction. After extraction for a prescribed time, the hollow fiber assembly was removed from the sample solution. The extract was withdrawn into the microsyringe, and injected directly into the HPLC system for analysis. The used hollow fiber was discarded and a fresh one was used for the next extraction.

3. Results and discussion

3.1. Selection of IL

The type of solvent immobilized in the pores of the hollow fiber is an essential consideration for HF-LLLME. In general, the solvent selected should be compatible with the polypropylene fiber so as to be able to easily fill its wall pores. The immiscibility with the water sample and the acceptor phase should also be seriously considered as it acts as a suitable medium between the two phases. Furthermore, reasonably higher solubility of the analytes in the organic phase than in the water sample is necessary, as is the higher solubility of analytes in the acceptor phase than in the organic phase. The following ILs, i.e. [BMIM][PO_4], [BMIM][PF_6], [HMIM][FAP] and [BMPL][FAP] were investigated. All were easily immobilized in the pores of the hollow fiber by immersion into them for 5 s. Fig. 1 shows the extraction efficiencies for the three selected analytes using the 4 ILs during 20 min of extraction. The results clearly showed that higher extraction efficiency was achieved by [HMIM][FAP]. [HMIM][FAP], most probably by virtue of its high hydrophobicity and the presence of the imidazolium group (allowing π–π interactions between [HMIM][FAP] and the CPs), has greater affinity for the analytes compared with [BMPL]

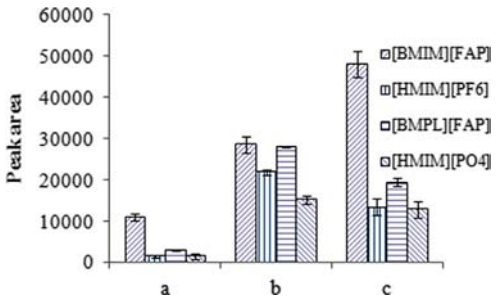


Fig. 1. Effect of different ILs on HF-LLLME efficiency. Spiked concentrations in water, 1 μl/ml for individual analytes; pH of sample solution, 2.5; pH of acceptor solution, 13; stirring rate, 500 rpm, extraction time, 20 min; (a) 4-chloro-3-methylphenol, (b) 2,4-dichlorophenol, and (c) 2,4,6-trichlorophenol.

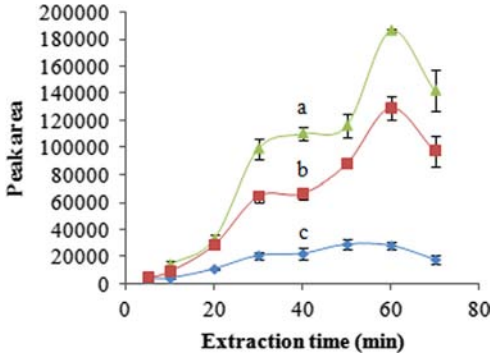


Fig. 2. Effect of extraction time on HF-LLLME efficiency. Spiked concentrations in water, 1 μl/ml for individual analytes; pH of sample solution, 2.5; pH of acceptor solution, 13; stirring rate, 500 rpm; (a) 2,4,6-trichlorophenol, (b) 2,4-dichlorophenol, and (c) 4-chloro-3-methylphenol.

[FAP]. The high viscosity of [BMIM][PF_6] may make it difficult for analytes to diffuse into the IL, thus leading to lower extraction efficiency. [BMIM][PO_4] provided the lowest extraction efficiency for the CPs. The reason may be due to the anions (PO_4^-) imparting less hydrophobic character causing small amounts of the IL to dissolve in the aqueous sample after 20 min extraction [18,26]. Thus, of the four ILs considered, [HMIM][FAP] was the only suitable solvent for the present work.

3.2. Effect of extraction time

HF-LLLME is an equilibrium-based process rather than an exhaustive extraction procedure. The extraction efficiency depends on the partition between the sample phase and the solvent phase, and further, between the solvent phase and the acceptor phase. A series of extraction times was investigated by considering a water sample containing 1 μg/ml of each analyte, at 500 rpm stirring speed. It can be seen from Fig. 2 that all analytes reached equilibrium after 60 min extraction. The reason for comparatively longer extraction times (in comparison to classical HF-LLLME using organic solvents and aqueous solutions) was that the relatively high viscosity of [HMIM][FAP] inhibited the mass transfer rate between the sample and the acceptor phase. Nevertheless, provided additional time (60 min) was allowed for, extraction efficiency was not compromised.

3.3. Effect of the acidity of donor phase and the alkalinity of the acceptor phase

The acidity of the sample phase and alkalinity of the acceptor phase are of great importance for HF-LLLME. As is known, CPs are weak acids. The pH of the sample solution should be lower than the p*K*a's of the CPs so as to suppress their ionization CPs so that they exist in their neutral states. In the present work, the pH of the sample solution was adjusted by adding different amounts of 30% orthophosphoric acid. The extraction efficiency showed no significant change across a pH range of between 1 and 4. Thus, a pH value of 2.5 was sufficient to maintain the neutrality of the CPs. Based on the extraction principles of HF-LLLME, the pH of the acceptor phase should trap the analytes to prevent them from being extracted back into the IL. Increasing the pH in the acceptor phase hastens the ionization of the analytes (via an acid–base reaction). As Fig. 3 shows, the peak areas of all the analytes increased with increase of the pH from 11 to 13. Relatively higher extraction efficiency was achieved at a pH of 13. However, at a pH of 14, the peak areas decreased. The reason for this observation is that the acceptor phase would be sufficiently alkaline to ionize the analytes when the pH of the acceptor phase at a value of 13.

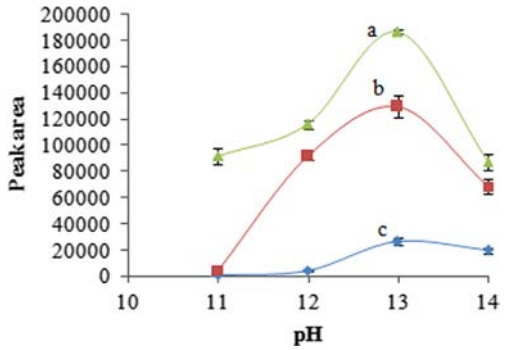


Fig. 3. Effect of pH of acceptor phase on HF-LLLME efficiency. Spiked concentrations in water, 1 μl/ml for individual analytes; pH of sample solution, 2.5; extraction time, 60 min; stirring rate, 500 rpm; (a) 2,4,6-trichlorophenol, (b) 2,4-dichlorophenol, and (c) is 4-chloro-3-methylphenol.

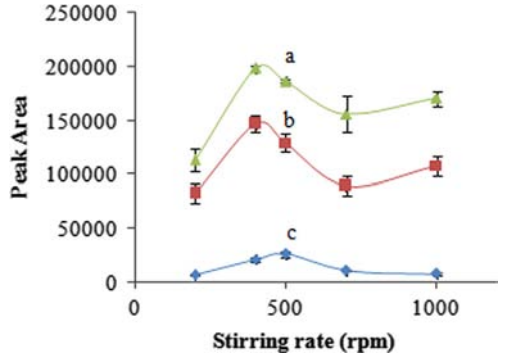


Fig. 4. Effect of stirring rate on HF-LLLME efficiency. Spiked concentrations in water, 1 μl/ml for individual analytes; pH of acceptor solution, 13; pH of sample solution, 2.5; extraction time, 60 min; (a) 2,4,6-trichlorophenol, (b) 2,4-dichlorophenol, and (c) 4-chloro-3-methylphenol.

However, at a pH of 14, the buffer capacity of the phosphate in the mobile phase was not high enough to neutralize the ionized CPs in the NaOH acceptor solution, and a proportion of the analytes was still ionized after injection into the HPLC system. Thus this led to the lower peak areas observed [22].

3.4. Effect of stirring rate

Agitation of the sample solution to mix it well, is one way to accelerate the mass transfer of the analytes from the sample, through the IL membrane and to the acceptor phase. In this study, different sample solution stirring rates were investigated. As seen from Fig. 4, peak areas increased with increasing stirring rates up to 400 rpm. However, at >400 rpm, peak areas decreased. It was observed that at >400 rpm the formation of air bubbles attached to the surface of the hollow fiber occurred, thus inhibiting the extraction across the wall pores by reducing the contact surface area between the hollow fiber and the sample. Thus higher stirring rates >400 rpm were detrimental to the extraction process. Therefore, 400 rpm was chosen for the subsequent experiments.

3.5. Effect of salt addition

In general, organic analyte solubility in aqueous solutions decreases with increasing salt concentration. Addition of salt to a sample solution can potentially increase analyte recovery in the most of the microextraction procedures through such a salting-out effect. The variation in salt (sodium chloride) concentration (5 to 40 mg/ml) on HF-LLLME was investigated. As Fig. 5 shows extraction efficiency improved with increasing salt concentration to a

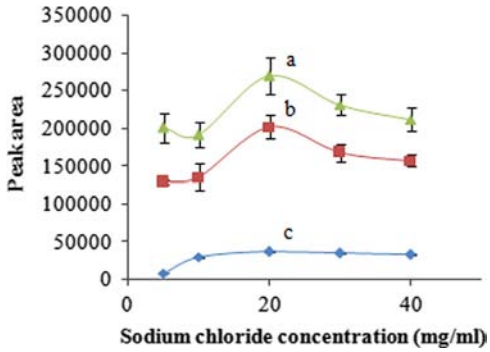


Fig. 5. Effect of salt concentration on HF-LLLME efficiency. Spiked concentrations in water 1 μl/ml for individual analytes; pH of acceptor solution, 13; pH of sample solution, 2.5; extraction time, 60 min; stirring rate, 400 rpm;(a) 2,4,6-trichlorophenol, (b) 2,4-dichlorophenol, and (c) 4-chloro-3-methylphenol.

Table 2
Quantitative results of HF-LLLME.

Analyte	RSD% ($n=6$)	Linear range (ng/ml)	r^2	LOD (ng/ml)
4-Chloro-3-methylphenol	4.3	10–500	0.9941	0.5
2,4-Dichlorophenol	4.6	5–1000	0.9994	0.3
2,4,6-Trichlorophenol	5.7	5–1000	0.9991	0.3

maximum value of 20 mg/ml of sodium chloride. Beyond 20 mg/ml, lower peak areas were observed. There was conceivably a threshold of optimum salt concentration for the most favorable extraction; beyond this value, the increase in viscosity due to higher salt concentration began to impede the mass transfer process.

3.6. Method validation

Under the optimum extraction conditions, linearity, repeatability and limits of detection (LODs) were investigated using spiked ultrapure water samples. The results are shown in Table 2. The linearity of calibration curves was studied for analytes at a concentration range between 5 and 1000 ng/ml (except for 4-chloro-3-methylphenol, between 10 and 500 ng/ml). All analytes showed good linearity with squared regression coefficients of between 0.9941 and 0.9994. The LODs were calculated based on a signal to noise ratio of 3, and ranged between 0.3 and 0.5 ng/ml. The repeatability of the chromatographic peak areas was studied for six replicate experiments using the optimum extraction conditions. The relative standard deviations (RSDs) were from 4 to 6%. The obtained results were comparable or better than those reported in previous microextraction studies, in which [OMIM][PF_6] was used as the impregnated IL in the hollow fiber wall pores for HF-LLLME [22], and [BMIM][PF_6] was employed in IL-based three-phase liquid–liquid–liquid solvent bar microextraction [35], of CPs from environmental water samples.

3.7. Canal water analysis

The proposed method was applied to the determination of CPs in canal water samples. There were no target analytes detected in the original samples, indicating that either the CPs were below the LODs of the present procedure, or the water was free of these contaminants. Nevertheless, in order to evaluate matrix effects, the samples were spiked at 50 and 500 ng/ml of the analytes. The spiked samples were extracted without pretreatment (i.e. unfiltered). For all sample solution at different concentrations, three

Table 3
Relative recoveries and precision of HF-LLLME of canal water spiked with CPs at different concentrations (50 ng/ml and 500 ng/ml).

Analyte	50 ng/ml		500 ng/ml	
	Relative recovery (%)	RSD (%)	Relative recovery (%)	RSD (%)
4-Chloro-3-chlorophenol	80	2.9	93	3.8
2,4-Dichlorophenol	102	4.5	97	6.1
2,4,6-Trichlorophenol	99	4.0	101	4.2

replicate extractions were conducted. The relative recoveries (Table 3), defined as the ratio of peak areas of the spiked real water extracts to spiked ultrapure water extracts, showed that these values varied between 80 and 102%, and RSDs were from 3 to 6%. These results showed that the matrix had little effect on HF-LLLME, due to the protection afforded by the hollow fiber. This indicates the present method is suitable for application to real world environmental waters.

4. Conclusion

In the present study, a new IL, FAP-based IL, [HMIM][FAP] was for the first time applied to HF-LLLME. In comparison with commonly used ILs containing PF_6^- and PO_4^-, [HMIM][FAP] is more hydrophobic, making it suitable for the HF-LLLME of CPs from aqueous samples. The proposed technique showed very effective sample clean-up and high sensitivity, with LODs of between 0.3 and 0.5 ng/ml levels, and satisfactory repeatability (RSDs lower than 6%). In addition, matrix effects did not pose significant problems, with relative recoveries of $>80\%$. It is likely that with its ultra-hydrophobility and compatibility with polypropylene hollow fiber membrane, [HMIM][FAP] has the potential to be applied to the HF-LLLME of trace levels of other acidic or basic analytes.

Acknowledgements

The authors are grateful for the financial support (Grant no. R-143-000-438-272) of this work by the Singapore National Research Foundation under its Environmental & Water Technologies Strategic Research Programme administered by the Environment & Water Industry Programme Office (EWI) of the Public Utilities Board, Singapore, and the National University of Singapore.

References

[1] M. Czaplicka, T. Manko, J. Wypych, Chem. Anal. 50 (2005) 887.
[2] E. Manoli, C. Samara, Trends Anal. Chem 18 (1999) 417.
[3] M.A. Jeannot, F.F. Cantwell, Anal. Chem. 68 (1996) 2236.
[4] C.L. Arthur, J. Pawliszyn, Anal. Chem. 62 (1990) 2145.
[5] F.S. Mirnaghi, Y. Chen, L.M. Sidisky, J. Pawliszyn, Anal. Chem. 83 (2011) 6018.
[6] M.A. Jeannot, F.F. Cantwell, Anal. Chem. 69 (1997) 235.
[7] Y. He, H.K. Lee, Anal. Chem. 69 (1997) 4634.
[8] W. Liu, H.K. Lee, Anal. Chem. 72 (2000) 4462.
[9] J. Lee, H.K. Lee, Anal. Chem. 83 (2011) 6861.
[10] G. Shen., H.K. Lee, Anal. Chem. 75 (2003) 98.
[11] L. Zhao, L. Zhu, H.K. Lee, J. Chromatogr. A 963 (2002) 239.
[12] S. Pedersen-Bjergaard, K.E. Rasmussen, Anal. Chem. 71 (1999) 2650.
[13] J. Wu, H.K. Lee, J. Chromatogr. A 1092 (2005) 182.
[14] S. Pedersen-Bjergaard, K.E. Rasmussen, Trends Anal. Chem 23 (2004) 1.
[15] E. Psillakis, N. Kalogerakis, Trends Anal. Chem 22 (2003) 565.
[16] N. Fontanals, T. Barri, S. Bergström, J. Jönsson, J. Chromatogr. A 1133 (2006) 41.
[17] C. Chiappe, D. Pieraccini, J. Phys. Org. Chem. 18 (2005) 275.
[18] J.-F. Liu, G.-B. Jiang, Y.-G. Chi, Y.-Q. Cai, Q.-X. Zhou, J.-T. Hu, Anal. Chem. 75 (2003) 5870.
[19] M. Cruz-Vera, R. Lucena, S. Cardenas, M. Valcarcel, J. Chromatogr. A 1202 (2008) 1.
[20] J.-F. Liu, Y.-G. Chi, G.-B. Jiang, Y.-Q.C. Tai, J.-F. Peng, J.-T. Hu, J. Chromatogr. A 1026 (2004) 143.
[21] C. Basheer, A.A. Alnedhary, B.S.M. Rao, R. Balasubramanian, H.K. Lee, J. Chromatogr. A 1210 (2008) 19.
[22] J.-F. Peng, J.-F. Liu, X.-L. Hu, G.-B. Jiang, J. Chromatogr. A 1139 (2007) 165.
[23] Y. Tao, J.-F. Liu, X.-L. Hu, H.-C. Li, T. Wang, G.-B. Jiang, J. Chromatogr. A 1216 (2009) 6259.
[24] R.P. Swatloski., J.D. Rolbrey, R.D. Rogers, Green Chem. 5 (2003) 361.
[25] C. Yao, W.R. Pitner, J.L. Anderson, Anal. Chem. 81 (2009) 5054.
[26] J.F. Liu, Y.G. Chi, G.B. Jiang, J. Sep. Sci. 28 (2005) 87.
[27] N.V. Ignat'ev, U W-Biermann, A. Kucheryna, G. Bissky, H. Willner, J. Fluorine Chem. 126 (2005) 1150.
[28] D. Ge, H.K. Lee, J. Chromatogr. A 1229 (2012) 1.
[29] D. Ge, H.K. Lee, J. Chromatogr. A 1251 (2012) 27.
[30] D. Ge, H.K. Lee, J. Chromatogr. A 1317 (2013) 217.
[31] H. Xu, Y. Liao, J. Yao, J. Chromatogr. A 1167 (2007) 1.
[32] N. Fattahi, S. Samadi, Y. Assadi, M.R.M. Hosseini, J. Chromatogr. A 1169 (2007) 63.
[33] X. Wang, L. Luo, G. Ouyang, L. Lin, N.F.Y. Tam, C. Lan, T. Luan, J. Chromatogr. A 1216 (2009) 6267.
[34] J.-F. Peng, J.-F. Liu, X.-L. Hu, G.-B. Jiang, J. Chromatogr. A 1139 (2007) 165.
[35] L. Guo, H.K. Lee, J. Chromatogr. A 1218 (2011) 4299.

Talanta 132 (2015) 137–145

Contents lists available at ScienceDirect

Talanta

journal homepage: www.elsevier.com/locate/talanta

Click N-benzyl iminodiacetic acid: Novel silica-based tridentate zwitterionic stationary phase for hydrophilic interaction liquid chromatography

Wei Yin [a], Huihui Chai [a], Renhua Liu [a], Changhu Chu [a,*], John A. Palasota [b], Xiaohui Cai [b]

[a] School of Pharmacy, Shanghai Key Laboratory of New Drug Design, East China University of Science and Technology, 130 Meilong Road, Shanghai 200237, P. R. China

[b] Department of Chemistry and Physics, University of St. Thomas, Houston, TX 77006, USA

ARTICLE INFO

Article history:
Received 12 July 2014
Received in revised form
25 August 2014
Accepted 31 August 2014
Available online 6 September 2014

Keywords:
N-benzyl imino diacetic acid
Hydrophilic interaction chromatography
Zwitterionic
Stationary phase

ABSTRACT

Iminodiacetic acid (IDA) is dicarboxylic acid amine, which may produce stronger interaction with polar or charged compounds than bidentate α,β-amino acid. In this article, a novel type of tridentate zwitterionic HILIC stationary phase was prepared by covalently bonding N-benzyl IDA on silica gel *via* copper(*I*) catalyzed Huisgen azide-alkyne 1,3-dipolar cycloaddition (CuAAC). The structure of this stationary phase and all related intermediates was confirmed by NMR, FT-IR, MS spectrum and elemental analysis. The new stationary phase showed good HILIC characteristics and high column efficiency (the theoretical plate number is up to 44000 plates m^{-1} in the case of guanosine) in the application of separation of polar compounds, including organic acids, organic bases, as well as highly polar and hydrophilic compounds, such as cephalosporins and carbapenems. Most of them displayed good peak shape and selectivity.

© 2014 Elsevier B.V. All rights reserved.

1. Introduction

Hydrophilic interaction liquid chromatography (HILIC) has been developed as a powerful separation technique for highly polar compounds that do not bind to reverse phase (RP) stationary phases. Owing to many specific advantages over conventional normal phase liquid chromatography (NP-LC) and reverse phase liquid chromatography (RP-LC), applications of HILIC on separation and analysis of highly polar and hydrophilic compounds have greatly increased [1–9]. For example, in proteomics, it has been applied in multidimensional peptide separation [10,11], analysis of posttranslational modifications (PTMs) such as glycosylation, N-acetylation and phosphorylation [12], as well as enrichment of low-abundance compounds in biological samples [13,14]. Highly polar zwitterionic HILIC stationary phases possess polar groups bearing both positive and negative charges, which may produce both hydrophilic and weak electrostatic interactions with polar and charged compounds easily. Mobile phase with lower content aqueous buffer can be used in LC for efficient separation and analysis, which results in a lower head pressure, thereby allowing for higher flow rates. Furthermore, the higher organic content makes it conveniently coupled to mass spectrometry (MS), and the high organic content in mobile phase can increase the MS sensitivity as well [15,16]. Up to now, a series of the zwitterionic HILIC stationary phases has been prepared by covalently bonded polar groups with both positive and negative charges on the surface of polymers, silica gel or other support materials, and most of them are zwitterionic phosphorylcholine and betaine type [17–20]. Only a few of α, β-amino acid type of zwitterionic stationary phases have been reported, which display good HILIC properties [21,22]. On the other hand, as a typical reaction of click chemistry, Cu(I) catalyzed Huisgen azide-alkyne 1,3-dipolar cycloaddition (CuAAC) reaction was widely applied in variant fields [23], such as bioconjugation [24–26], material sciences [27–29], organic synthesis [30–32] and drug discovery [33,34], and it has been regarded as a powerful strategy. So far, several covalently bonded stationary phases have been prepared by CuAAC [35–40], and all of them showed good chromatographic properties when they are applied in liquid chromatography. In previous work, we have developed click-lysine as a zwitterionic stationary phase for HILIC purpose, which could be applied not only in the separation and analysis of hydrophilic organic compounds under HILIC mode, but also separation and analysis of inorganic ions under ion chromatography(IC) mode [41,42]. Iminodiacetic acid (IDA) is a dicarboxylic acid amine, which

* Corresponding author at: East China University of Science and Technology, Shanghai, China. Tel./fax: +86 21 6425 0627.
E-mail address: chuch@ecust.edu.cn (C. Chu).

http://dx.doi.org/10.1016/j.talanta.2014.08.077
0039-9140/© 2014 Elsevier B.V. All rights reserved.

can act as a tridentate ligand. Chelex 100 resin, which is a styrene-divinylbenzene copolymer containing IDA groups, has been utilized in ion exchange columns, DNA extraction in preparation for polymerase chain reaction (PCR), trace metal removal, metal analysis, as well as in water testing in environmental and agricultural laboratories [43–45]. All of these applications are attributed to the strong interactions between IDA and polar or charged compounds, and these interactions should be stronger than the bidentate ligand such as α, β-amino acid. Herein, we designed and prepared the covalently bonded N-benzyl IDA to silica beads to form a new kind of stationary phase, which may display much different chromatographic properties. Applications in separation polar or charge compounds are expected.

2. Experimental

2.1. Apparatus and chromatographic conditions

FT-IR measurements were performed on a Nicolet 5SXC (USA). ^{1}H NMR was carried out on a Bruker 400 (Germany). Elemental analysis was measured on an elemental Vario EL III (Germany); high-resolution mass spectra (HRMS) were performed using Waters GCT Premier.

An Shimadazu LC-20AT HPLC system consisting of a binary pump, a degasser, an auto sampler, an automatic thermostatic column compartment, and a UV detector were used to perform the chromatographic experiments. Click N-benzyl IDA column (5 μm, 150 × 4.6 mm, i.d., homemade). HPLC acetonitrile and water were used as mobile phase, and ammonium formate buffer solutions (concentration from 10 mM to 40 mM) with pH ranging from 3.4 to 6.0 (adjusted by adding formic acid) were used as buffer.

2.2. Chemicals and reagents

Spherical silica (5 μm partical size; 10 nm pore size; 300 m^2 g^{-1} surface area) was purchased from Fuji Silysia Chemical Ltd. (Japan). HPLC grade acetonitrile and formic acid were from Sigma (USA) and Tedia (USA), respectively. Milli-Q ultrapure water was used throughout the HPLC experiment. Imino diacetic acid, 4-nitrobenzyl chloride, imidazole, sodium azide, acetylchloride, $CuSO_4$.5 H_2O, ammonium formate and sodium ascorbate were all domestic reagent (National Medicine Corporation Chemical Reagent Ltd., Shanghai, China) and used without further purification. 3-isocyanatopropyl-triethoxysilane and propargylamine (National Medicine Corporation Chemical Reagent Ltd., Shanghai, China) were purified by distillation before use. The solvent N-dimethyl formamide, methanol and ethanol (Ninfeng Chemical Reagent Ltd., Shanghai, China) were used as received. The test solutes used for HILIC evaluation were commercially available test compounds such as sulfadiazine, uracil, adenosine, uridine, inosine, adenine, guanosine, sorbic acid, orotic acid, 4-aminobenzoic acid, 4-hydroxybenzoic acid, 3,4-dihydroxybenzoic acid, caffeine, theobromine, theophylline, diprophyllin, quercetin from Aladdin Reagent Ltd., Shanghai, China, and cemandil sodium, ceftezole sodium, cefodizime, cephalosporins diltiazem, cefotiam hydrochloride, ceftazidime sodium, cefepime hydrochloride, cephradine, biapenem, doripenem, and meropenem from Zhejiang Hisoar Pharm. & Chem. Co., Ltd., Taizhou, China). Test solutes were filtered with a 0.45 mm membrane filter (organic membrane, BJ225-PT, Shanghai Jiapeng Science and Technology Ltd., Shanghai).

2.3. Sample preparation

The model compounds (sulfadiazine, uracil, adenosine, uridine, inosine, adenine and guanosine) were used for the performance and retention mechanism evaluation of click N-benzyl IDA column. The test compounds (uracil, uridine, guanosine, 3,4-dihydroxybenzoic acid, orotic acid and diprophylline) were used for the

Table 1
Elemental analysis of alkyne-silica and click N-Benzyl IDA stationary phases.

Stationary phase	C%	N%	Surface coverage (μmol m^{-2})
Alkyne-silica	9.76	2.81	4.43
Click N-Benzyliminodiacetic acid	12.66	4.20	2.23

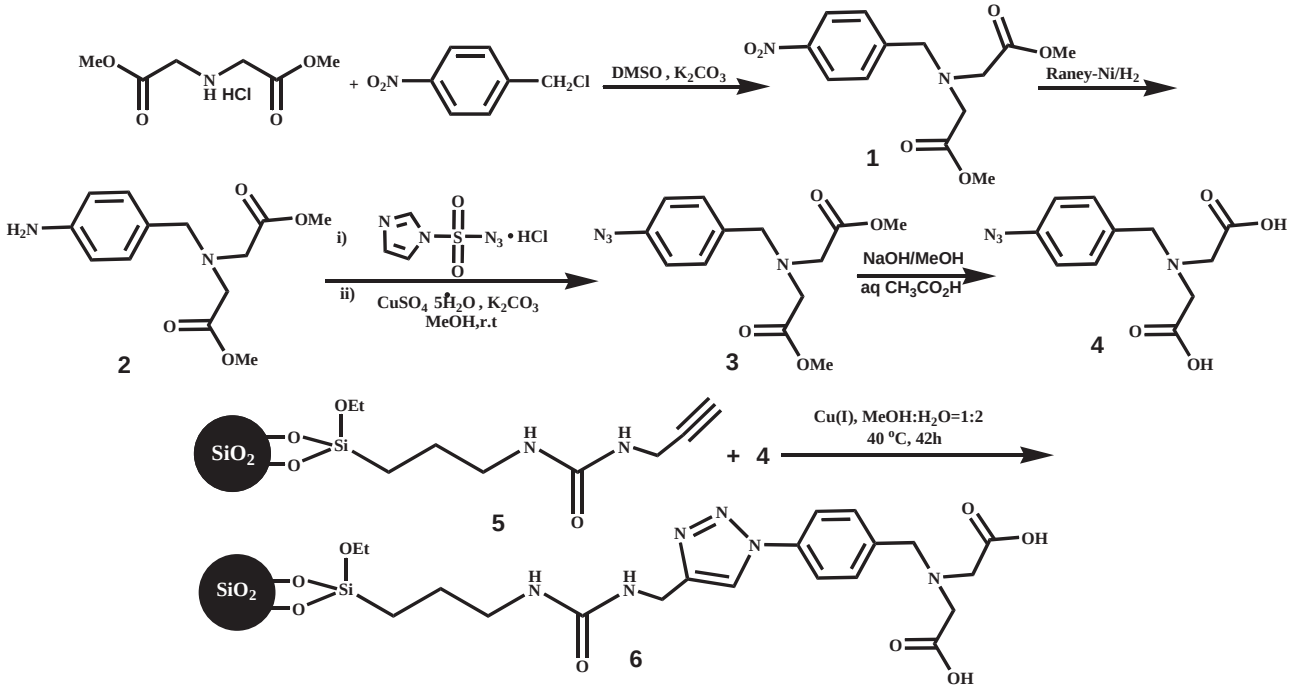


Fig. 1. The preparation of click N-benzyl IDA.

investigation of retention behavior. The probe organic acids and alkaloids (sorbic acid, 4-aminobenzoic acid, 4-hydroxybenzoic acid, 3,4-dihydroxybenzoic acid, caffeine, theobromine, theophylline, diprophyllin and quercetin) were dissolved in ACN/H_2O (4:1, v/v) for chromatography test. The solutions of cephalosporins (cemandil sodium, ceftezole sodium, cefodizime, cephalosporins diltiazem, cefotiam hydrochloride, ceftazidime sodium, cefepime hydrochloride and cephradine) and carbapenems (biapenem, doripenem and meropenem) were all prepared by dissolving them in ACN/H_2O(1:2), followed by storage in a refrigerator for analysis and preparation of mixed samples.

2.4. Preparation of click N-benzyl IDA stationary phase and column packing

Hydrochloride catalyzed esterification of IDA in methanol afforded dimethyl imino diacetate, subsequent condensation with 4-nitrobenzyl chloride gave dimethyl N-4-nitrobenzyl imino

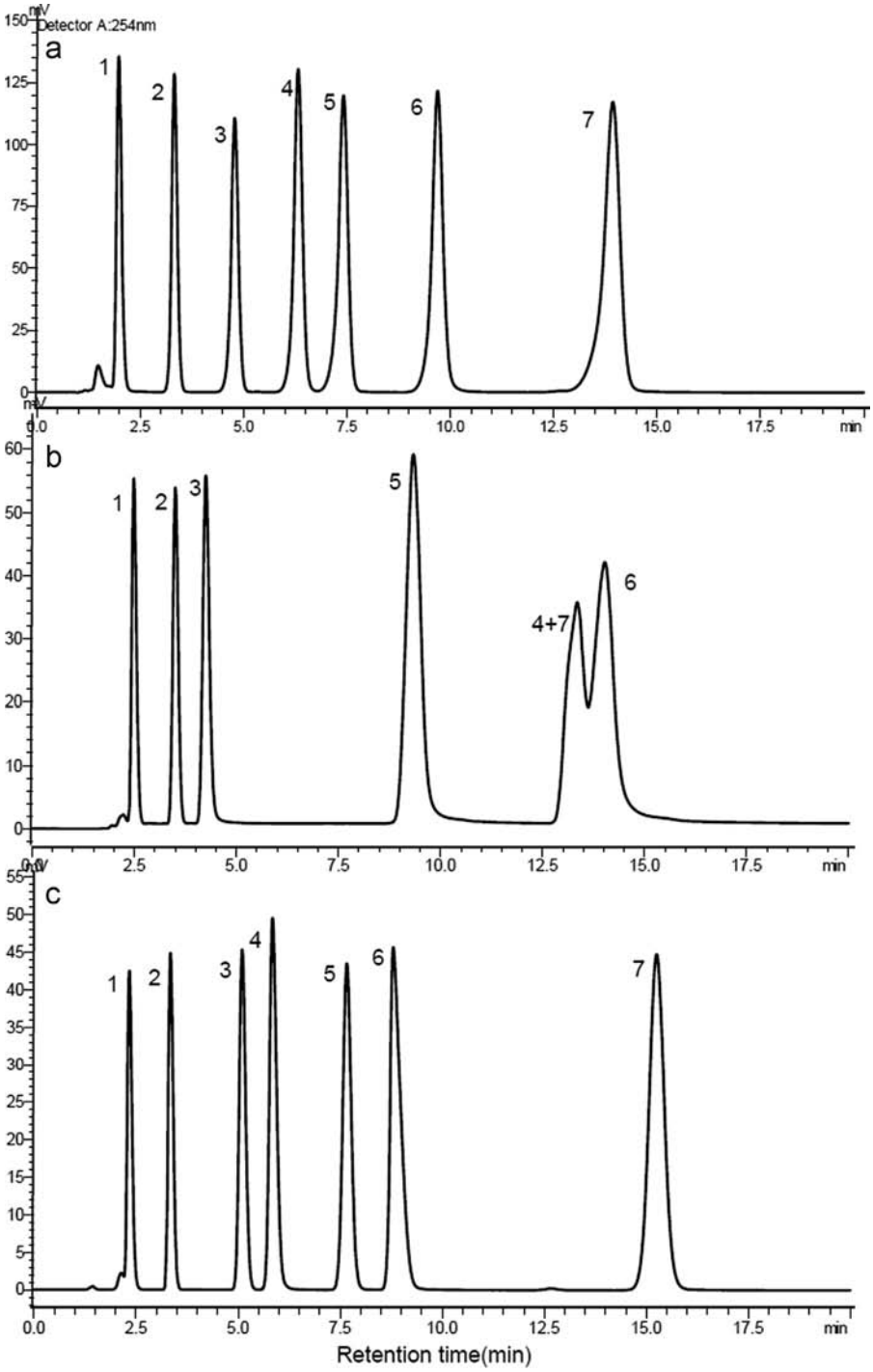


Fig. 2. Separation of nucleosides and bases on Click N-Benzyl IDA ((a) 5 μm, 150 mm × 4.6 mm i.d.), conditions: flow rate 1 mL min^{-1}; 35 °C; mobile phase: acetonitrile: water (80:20, v/v); UV: 254 nm. Peak identification: (1) sulfadiazine, (2) uracil, (3) uridine, (4) adenosine, (5) inosine, (6) adenine, (7) guanosine. Atlantis HILIC-silica ((b) 5 μm, 150 mm × 4.6 mm i.d.), conditions: flow rate 1 mL min^{-1}; 35 °C; mobile phase: ACN/50 mM ammonium formate (95/5, v/v), pH=4.6; UV: 254 nm. and ZIC-HILIC ((c) 5 μm, 150 mm × 4.6 mm i.d.), conditions: flow rate 1 mL min^{-1}; 35 °C; mobile phase: acetonitrile:water (90:10, v/v); UV: 254 nm.

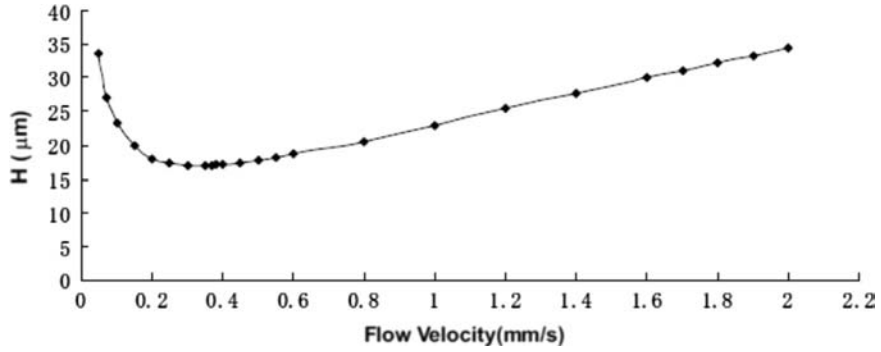


Fig. 3. Van Deemter plot for inosine on Click N-Benzyliminodiacetic acid (5 μm, 150 mm × 4.6 mm i.d.), conditions: column temperature, 30 °C; mobile phase: acetonitrile: water (80:20, v/v); UV: 254 nm.

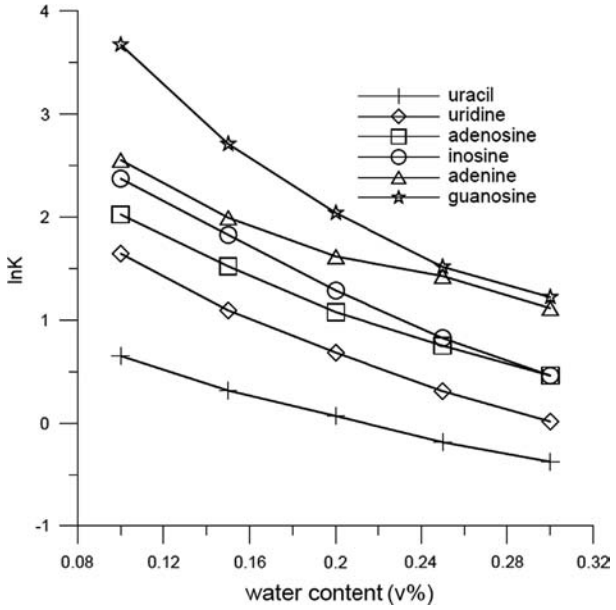


Fig. 4. The natural logarithmic plots of retention factors k versus water content ψ in mobile phase. Chromatographic conditions: flow rate 1 mL min^{-1}; 35 °C; mobile phase: acetonitrile/water(v/v) and water changed from 10 to 30% (v); UV: 254 nm. Model sample: uracil, uridine, adenosine, inosine, adenine and guanosine.

Table 2
Retention time ($_{min}$) of nucleosides and bases at different water content[a].

Compounds	Retention time ($_{min}$) at different water content (v %)							
	90%	80%	70%	60%	40%	30%	20%	10%
Sulfadiazine	2.81	2.34	2.15	2.00	1.87	1.82	1.98	2.40
Uracil	2.38	2.26	2.21	2.22	2.42	2.71	3.32	4.68
Uridine	2.26	2.17	2.15	2.21	2.63	3.23	4.78	9.91
Adenosine	5.10	3.59	3.11	2.96	3.54	4.15	6.32	13.74
Inosine	2.54	2.33	2.29	2.37	3.08	4.15	7.41	18.79
Adenine	15.79	9.24	7.10	6.94	6.89	6.50	9.69	22.20
Guanosine	3.80	3.11	2.93	3.04	4.35	7.06	13.93	64.55

[a] Mobile phase: Column temperature: 35 °C. Flow rate: 1.0 mL min^{-1}. UV detection: 254 nm, t_0 = 1.6 min.

diacetate **1**. The nitro group was reduced by Raney nickel catalyzed hydrogenation to get corresponding free amine **2**. The free amino group in **2** was transferred by an inexpensive and shelf stable diazotransfer reagent (imidazole-1-sulfonyl azide hydrochloride) to obtain dimethyl N-4-azido benzyl imino diacetate **3** [46]. Finally, hydrolyses of **3** achieved the key intermediate N-4-azidobenzyl IDA **4**. On the other hand, the terminal alkyne-silica

Table 3
Retention time ($_{min}$) of model compounds at different buffer pH values[a].

Compounds	Retention time($_{min}$) at different buffer pH values		
	3.4	4.6	6.0
Guanosine	13.90	14.28	14.34
Uracil	3.31	3.33	3.33
Uridine	4.80	4.62	4.91
3,4-dihydroxybenzoic acid	3.28	3.50	3.48
Orotic acid	2.81	2.47	2.41
Diprophylline	2.98	2.97	2.97

[a] Mobile phase: ACN/10 mM ammonium formate (80/20, v/v). Column temperature: 35 °C. Flow rate: 1.0 mL min^{-1}. UV detection: 254 nm, t_0 = 1.6 min.

Table 4
Retention time of model compounds at different ammonium formate concentrations[a].

Compounds	Retention time($_{min.}$) at different ammoniumformate concentrations		
	10 mM	20 mM	40 mM
Guanosine	13.90	14.05	14.11
Uracil	3.31	3.33	3.35
Uridine	4.80	4.84	4.88
3,4-dihydroxybenzoic acid	3.28	3.35	3.41
Orotic acid	2.81	3.51	4.50
Diprophylline	2.98	3.00	2.99

[a] Mobile phase: ACN/ammonium formate, pH = 3.4, (80/20, v/v) for model compounds. Column temperature: 35 °C. Flow rate: 1.0 mLmin^{-1}. UV detection: 254 nm, t_0 = 1.6 min.

beads **5** were prepared by condensation of 3-isocyanatopropyl triethoxysilane with propargylamine in anhydrous DMF, and then directly polymerized with silica beads [35–37]. The click reaction between terminal alkyne-silica beads **5** and N-4-azidobenzyl IDA **4** via CuACC afforded the new stationary phase click N-benzyl IDA **6** (Fig. 1).

The click N-benzyl IDA stationary phase thus prepared was slurry-packed into stainless-steel columns (150 mm × 4.6 mm i.d.) with MeOH as slurry and propulsion solvents for the study of chromatographic behavior.

3. Results and discussion

3.1. Characterization of click N-benzyl IDA

The terminal alkyne-silica and click N-benzyl IDA stationary phase were characterized by FT-IR and elemental analysis. All

datum, including the increase of carbon content, the weakness of νCH on alkyne-silica at 2928 cm^{-1} and the enhancement of νC=O at 1650 cm^{-1} on click N-benzyl IDA stationary phase after "click" step, demonstrated that N-benzyl IDA was bonded to alkyne silica successfully. The results of elemental analysis and the surface concentration are shown in Table 1. The surface concentration (calculated from nitrogen content) of alkynyl group on alkyne-silica was 4.43 μmol m^{-2}, and the surface concentration of click N-benzyl IDA (calculated from the nitrogen content) was 2.23 μmol m^{-2}.

3.2. Chromatographic evaluation under HILIC model

After the click N-benzyl IDA column was prepared, the performance evaluation was carried out by using nucleosides and bases as probe compounds. As show in Fig. 2, seven nucleosides and bases were well separated with acetonitrile/water (80/20, v/v) as mobile phase. This new type of stationary phase showed great separation ability and selectivity, the mixed model compounds could be separated clearly in an appropriate time without using any buffer, and very good peak shapes are displayed. In addition,

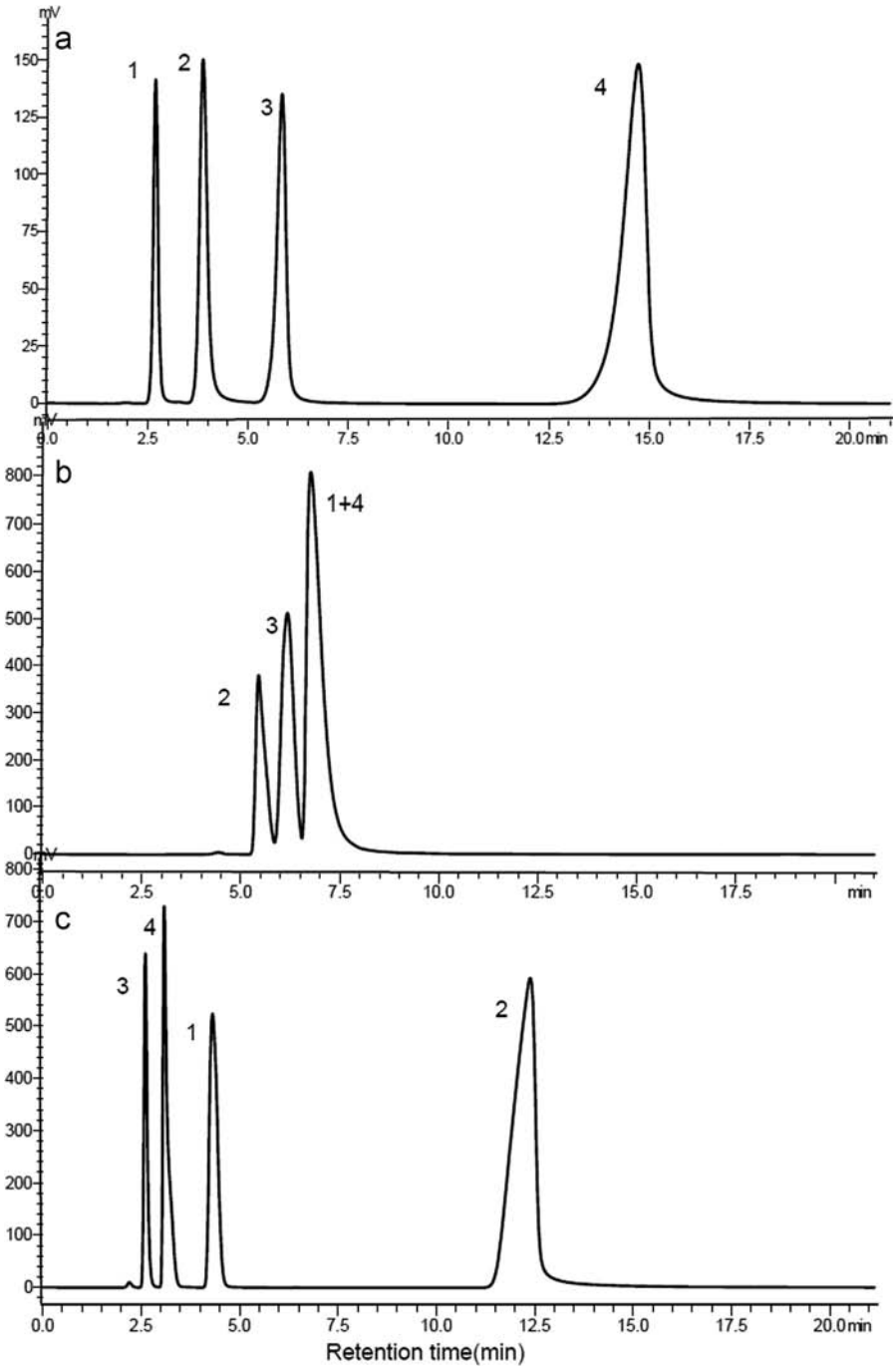


Fig. 5. The separation of four organic acids on Click N-Benzyl IDA ((a) 5 μm, 150 mm × 4.6 mm i.d.), Chromatography conditions: 95% ACN/5% H_2O (v/v), the column temperature: 35°C. Flow rate: 1 mL min^{-1}. Wavelength: 254 nm. Sample: the mixed acids. Injection volume: 5 μL. Peak identification: (1) sorbic acid, (2) 4-aminobenzoic acid, (3) 4-hydroxybenzoic acid, (4) 3,4-dihydroxybenzoic acid. Atlantis HILIC-silica ((b) 5 μm, 150 mm × 4.6 mm i.d.), chromatography conditions: flow rate 0.5 mL min^{-1}; 35 °C; mobile phase: ACN/50 mM ammonium formate (95/5, v/v), pH=3.2; UV: 254 nm. and ZIC-HILIC ((c) 5 μm, 150 mm × 4.6 mm i.d.), chromatography conditions: flow rate 1 mL min^{-1}; 35°C; mobile phase: ACN/10 mM ammonium formate (95/5, v/v), pH=3.2; UV: 254 nm.

the symmetry factors of these compounds are quite good with appropriate retention. In the case of guanosine, the peak symmetry factor is 1.07, retention factor is 7.71, and the theoretical plate number was about 44000 plates m^{-1} calculated according to the USP method. Compared with commercial HILIC (atlantis, Waters) and ZIC-HILIC (Merck), the hydrophilic characteristics were obviously enhanced. Under optimized chromatographic conditions, Click N-benzyl IDA displayed similar separation ability and chromatographic behavior to ZIC-HILIC, while Atantis column could not separate these analytes well, and it displayed different retention behavior from Click N-benzyl IDA. Furthermore, based on the polarity of mobile phase in this separation procedure, Click N-benzyl IDA should possess the strongest retention ability among the three stationary phases, which should be a good advantage for separation more broad range of polar compounds. The Van Deemter plot [47] for inosine on click N-benzyl IDA showed the optimal linear velocity was around 0.35 mm/s [Fig. 3].

Next, the chromatographic behavior of click N-benzyl IDA was studied by investigating the relationship between retention factors and the water content by using nucleosides and bases as probes, and the acetonitrile in combined with water was used as eluent (water content ranges from 10 to 30%, v). The natural logarithmic of retention factors (lnk) was plotted versus the water content (ψ) in the mobile phase. As shown in Fig. 4, Click N-benzyl IDA exhibited typical HILIC characteristics, and the retention time became shorter with the water content increase. The nonlinear relationship between lnk and ψ (Fig. 4) showed that there existed not only one pure partitioning mechanism but other interactions, such as hydrogen bonding, dipole–dipole interaction, ion exchange, chelation and electrostatic interactions. Good liner

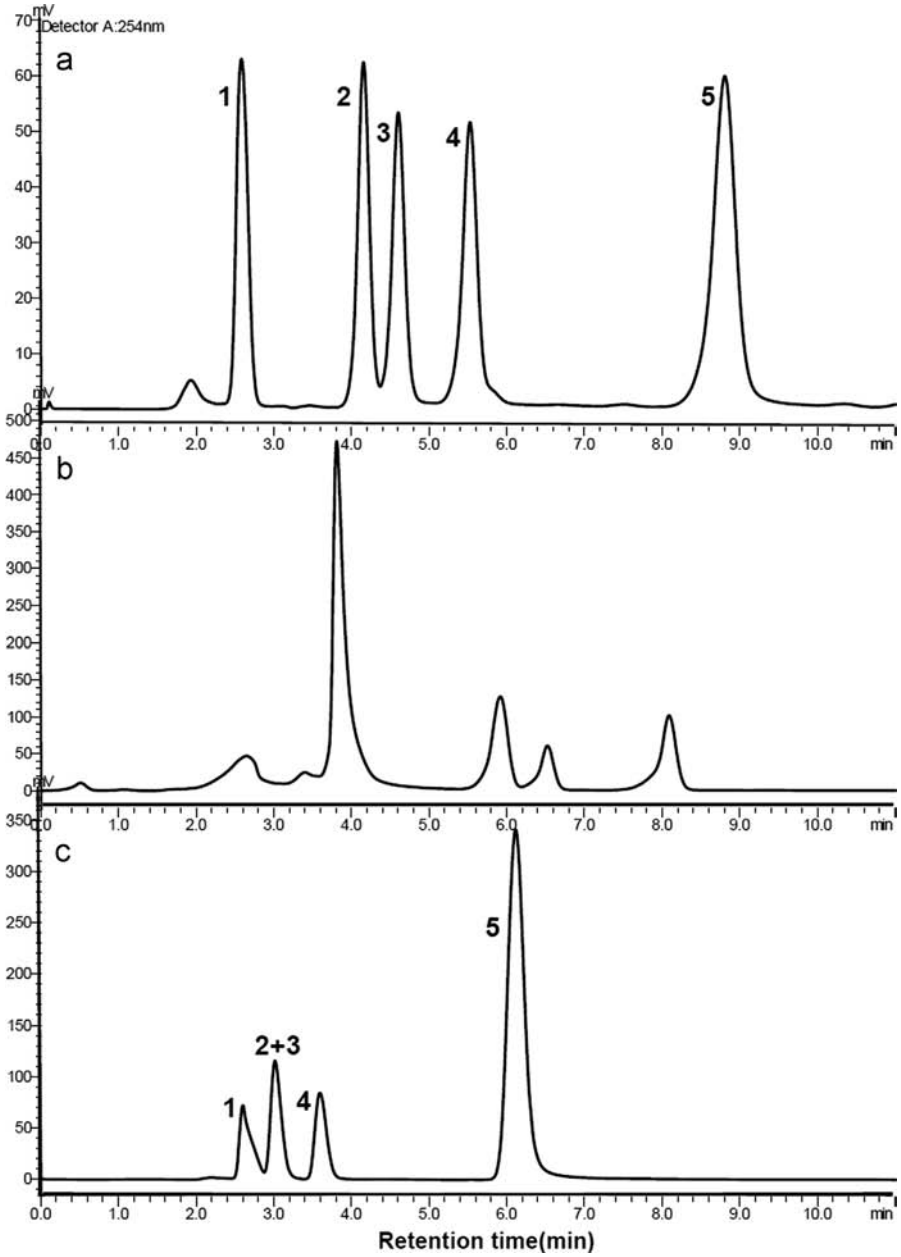


Fig. 6. The separation of five organic bases on Click N-Benzyl IDA ((a) 5 μm, 150 mm × 4.6 mm i.d.), Atlantis HILIC-silica ((b) 5 μm, 150 mm × 4.6 mm i.d.) and ZIC-HILIC ((c) 5 μm, 150 mm × 4.6 mm i.d.). Chromatography conditions: 95% ACN/5% H_2O (v/v), the column temperature: 35 °C. Flow rate: 1 mL min^{-1}. Wavelength: 254 nm. Sample: the mixed bases. Injection volume: 5 μL. Peak identification: (1) caffeine, (2) theobromine, (3) theophylline, (4) diprophyllin, (5) quercetin.

relationship between lnk and lnψ was also observed, and the correlation coefficient R of these nucleosides and bases (sulfadiazine, uracil, uridine, adenosine, inosine, adenine and guanosine) are −0.9967, −0.9976, −0.9989, −0.9988, −0.9956, −0.9975 and −0.9989, respectively. The results further demonstrated that the retention behaviors of these test compounds on click N-benzyl IDA were majorly consistent with the HILIC characteristics and controlled by several interactions. However, when the water content was further increased, some analytes (such as sulfadiazine, adenosine and adenine) displayed obvious mixed-mode chromatographic characteristics. The others also showed such characteristics, though it is not so obvious (Table 2).

The major functional groups of IDA are an amino diacetic acid, its pK_a value was 1.873 and its pK_b value is 12.124. Though the introduction of benzyl group and covalently bonding on silica gel may change its pK value little, its zwitterionic and HILIC property could be kept. Thus, the pH value and salt concentration may affect the retention of many analytes. We then investigated the retention of a wide range compounds (organic acids, nucleosides and bases as well as organic base) on click N-benzyl IDA under different pH values and salt concentrations. First, 10 mM ammonium formate buffer solutions with pH ranging from 3.4 to 6.0 (adjusted by adding formic acid) were used to investigate the retention behaviors of click N-benzyl IDA under different pH values. As shown in Table 3, with the pH value of the eluent increasing (pH from 3.4–6.0), the retention time of guanosine was increased, while the retention time of orotic acid was decreased. At this range of pH value, no obvious effect on their retention was observed for the separation of acids. These facts can be explained that the zwitterionic tridentate IDA containing both carboxylic acid and amine groups may produce several different interactions with different analyte structures, more detailed retention mechanism was not clear yet.

Under HILIC model, the salt concentration usually has obvious effect on retention, so the relationship between salt concentration and retention was investigated by varying ammonium formate concentration from 10 to 40 mM (pH 3.4) in the mobile phase of acetonitrile/water (80/20, v/v). As shown in Table 4, there is little change on the retention time of nucleosides and bases except orotic acid, this may be attributed the fact that most of these analytes were not charged in the mobile phase, thus the electrostatic effect was not applicable to nucleosides and bases. The

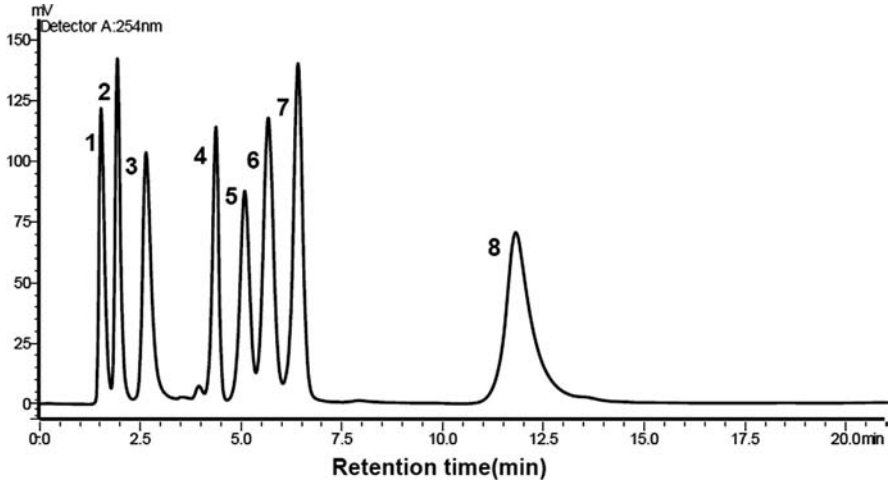


Fig. 7. Separation of eight cephalosporins on Click N-Benzyliminodiacetic acid (5 μm, 150 mm × 4.6 mm i.d.), conditions: mobile phase: ACN/10 mM ammonium formate (80/20, v/v). The column temperature: 35 °C. Flow rate: 1 mL min^{-1}. Inject volume, 3 μL. Wavelength: 254 nm. Peak identification: (1) cemandil sodium, (2) ceftezole sodium, (3) cefodizime, (4) cephalosporins diltiazem, (5) cefotiam hydrochloride, (6) ceftazidime sodium, (7) cefepime hydrochloride, (8) cephradine.

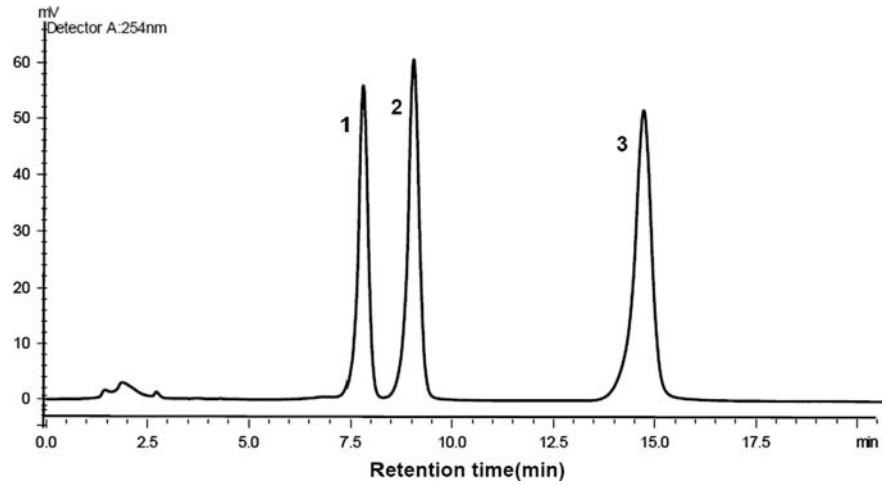


Fig. 8. Separation of three carbapenems on Click N-Benzyliminodiacetic acid (5 μm, 150 mm × 4.6 mm i.d.), conditions: mobile phase: ACN/10 mM ammonium formate (75/25, v/v), pH=4.5. The column temperature: 35 °C. Flow rate: 1 mL min^{-1}. Inject volume, 3 μL. Wavelength: 254 nm. Peak identification: (1) biapenem, (2) meropenem, (3) doripenem.

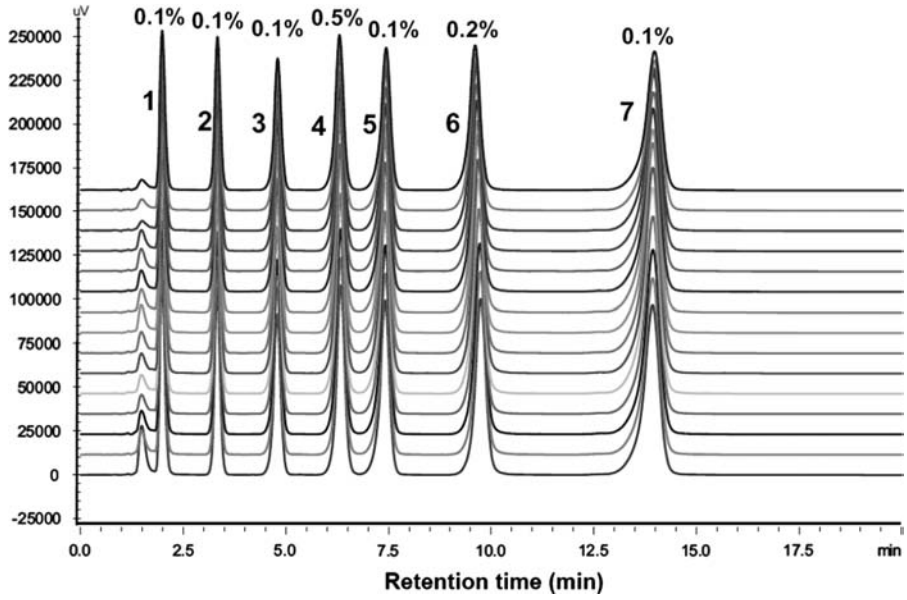


Fig. 9. Retention stability of seven nucleosides and bases on Click N-Benzyliminodiacetic acid by continuously injecting 15 times the mixed nucleosides and bases. Mobile phase: acetonitrile/H_2O (80/20, v/v). The column temperature: 35 °C. Flow rate: 1 mL min^{-1}. Inject volume, 1 μL. Wavelength: 254 nm. Peak identification: (1) sulfadiazine, (2) uracil, (3) uridine, (4) adenosine, (5) inosine, (6) adenine, (7) guanosine.

retention time of most of these analytes become longer with the increase of salt concentration, which is consistent with the HILIC chromatographic properties.

3.3. Application in separating of organic acids and organic bases

In order to broaden the applications of click N-benzyl IDA, it was then applied to the separation of organic acids and organic bases by using ACN:water (95:5, v-v) as mobile phase. The moderate-polar compounds, four organic acids (Fig. 5) and five organic bases (Fig. 6) were well separated with good peak shapes and good efficiency, and without using any other eluent additives. Usually, in order to obtain better peak shape and separation performance, especially for separation acids or bases, eluent additives such as acids, bases or buffers are used either in C18 or HILIC stationary phases. Under optimized conditions, ZIC-HILIC displayed similar separation ability to organic acids, while analytes elution order was different from Click N-benzyl IDA, which may be attributed to their different retention mechanisms. However, both atlantis and ZIC-HILIC could not separate these base analytes well, even many efforts on optimization of mobile phase were made.

3.4. Application in separating of cephalosporins and carbapenems

Cephalosporins and carbapenems are important antibiotics in pharmacology. Analysis requirements related to cephalosporins and carbapenems are very important for the pharmaceutical industry, thus HPLC and HPLC-MS techniques are powerful analysis tools for testing shelf stability, antibiotic resistance, detecting impurities and so on. When Click N-benzyl IDA was applied in the separation and analysis of cephalosporins and carbapenems, it displayed good retention and separation selectivity. As shown in Figs. 7 and 8 (see supporting information), the cephalosporins and carbapenems were efficiently separated with good peak shapes and appropriate retention time.

3.5. The stability of click N-benzyl IDA

Chemical stability is an important parameter for stationary phases. A mixture of nucleoside and base (sulfadiazine, uracil, uridine, adenosine, inosine, adenine and guanosine) was utilized to investigate the stability of click N-benzyl IDA through 15 continuous injections (Fig. 9, see supporting information). The relative standard deviations (RSDs) of the most nucleosides and bases were all at 0.1%, except adenosine and adenine were 0.2% and 0.5%, respectively. This result demonstrated a good stability of click N-benzyl IDA. In addition, the column was used for over one year without any deterioration, which further showed that the stationary phase can be widely and reliably used as separating material.

4. Conclusion

A zwitterionic tridentate click N-benzyl IDA column was prepared *via* click chemistry. This method showed high efficiency for bonding functionalized zwitterionic groups. Click N-benzyl IDA displayed good HILIC properties in the separation of hydrophilic nucleosides and bases. The chromatographic mechanism showed that this type stationary may possess several retention mechanisms, such as partition mechanism, hydrogen bonding interaction, chelate and electrostatic interaction mechanisms. The effect of pH and salt concentration on retention were investigated in order to understand its chromatographic properties. Under isocratic elution conditions, this new type of tridentated zwitterionic stationary phase could be used to efficient separate a wide range of compounds, from moderate to highly polar compounds. Furthermore, this type of stationary demonstrated good stability. Additional studies concerning the development of click N-benzyl IDA for the separation and detection of pharmaceuticals are underway.

Acknowledgments

We acknowledge the financial support from the National Natural Science Foundation of China (No. 21172072, No. 21372081) and the Shanghai Natural Science Foundation (No.11ZR1408500)

Appendix A. Supporting information

Supplementary data associated with this article can be found in the online version at http://dx.doi.org/10.1016/j.talanta.2014.08.077.

References

[1] P.G. Wang, W. He, Hydrophilic Interaction Liquid Chromatography (HILIC) and Advanced Applications, CRC press, 2011.
[2] T. Ikegami, K. Tomomatsu, H. Takubo, K. Horie, N. Tanaka, J. Chromatogr. A 1184 (2008) 474.
[3] B. Buszewski, S. Noga, Anal. Bioanal. Chem. 402 (2012) 231.
[4] Y. Mechref, M.V. Novotny, Chem. Rev. 102 (2002) 321.
[5] M. Wuhrer, A.R. de Boer, A.M. Deelder, Mass Spectrom. Rev. 28 (2009) 192.
[6] M.J. Omaetxebarria, P. Hgglund, F. Elortza, N.M. Hooper, J.M. Arizmendi, O.N. Jensen, Anal. Chem. 78 (2006) 3335.
[7] T.A. Blake, T.L. Williams, J.L. Pirkle, J.R. Barr, Anal. Chem. 81 (2009) 3109.
[8] J. Nawarak, S. Phutrakul, S. Chen, J. Proteome Res. 3 (2004) 383.
[9] W. Jian, R.W. Edom, Y. Xu, N. Weng, J. Sep. Sci. 33 (2010) 681.
[10] S. Di Palma, M.L. Hennrich, A.J. Heck, S. Mohammed, J. Proteomics 75 (2012) 3791.
[11] S. Di Palma, R. Raijmakers, A.J. Heck, S. Mohammed, Anal. Chem. 83 (2011) 8352.
[12] P.J. Boersema, S. Mohammed, A.J.R. Heck, Anal. Bioanal. Chem. 391 (2008) 151.
[13] S. Mysling, G. Palmisano, P. Højrup, M. Thaysen-Andersen, Anal. Chem. 82 (2010) 5598.
[14] L. Yu, X. Li, Z. Guo, X. Zhang, X. Liang, Chem. Eur. J 15 (2009) 12618.
[15] L. Novakova, T. Gottvald, H. Vlckova, F. Trejtnar, J. Mandíková, P. Solich, J. Chromatogr. A 1259 (2012) 237.
[16] M.J. Omaetxebarria, P. Ha1gglund, F. Elortza, N.M. Hooper, J.M. Arizmendi, O. N. Jensen, Anal. Chem. 78 (2006) 3335.
[17] M. Mori, W. Hu, K. Hasebe, S. Tanaka, K. Tanaka, Anal. Bioanal. Chem. 374 (2002) 75.
[18] W. Jiang, G. Fischer, Y. Girmay, K. Irgum, J. Chromatogr. A 1127 (2006) 82.
[19] J. Charlwood, H. Birrell, E.S.P. Bouvier, J. Langridge, P. Camilleri, Anal. Chem. 72 (2000) 1469.
[20] S. Di Palma, P.J. Boersema, A.J.R. Heck, S. Mohammed, Anal. Chem. 83 (2011) 3440.
[21] A. Shen, Z. Guo, X. Cai, X. Xue, X. Liang, J. Chromatogr. A 1228 (2012) 175.
[22] A. Shen, Z. Guo, L. Yu, L. Cao, X. Liang, Chem. Commun. 47 (2011) 4550.
[23] J.E. Moses, A.D. Moorhouse, Chem. Soc. Rev. 36 (2007) 1249.
[24] C. Uttamapinant, A. Tangpeerachaikul, S. Grecian, S. Clarke, U. Singh, P. Slade, K.R. Gee, A.Y. Ting, Angew. Chem. Int. Ed. 51 (2012) 1.
[25] A. Samanta, A. Krause, A. Jaschke, Chem. Commun. 50 (2014) 1313.
[26] S.K. Mamidyala, M.G. Finn, Chem. Soc. Rev. 39 (2010) 1252.
[27] F. Santoyo-Gonzalez, F. Hernandez-Mateo, Chem. Soc. Rev. 38 (2009) 3449.
[28] W.H. Binder, R. Sachsenhofer, Macromol. Rapid Commun. 28 (2007) 15.
[29] Z. Guo, A. Lei, Y. Zhang, Q. Xu, X. Xue, F. Zhang, X. Liang, Chem. Commun. (2007) 2491.
[30] V.V. Rostovtsev, L.G. Green, V.V. Fokin, K.B. Sharpless, Angew. Chem. Int. Ed 41 (2002)2596 and there in 41 (2002).
[31] S. Wallyn, M. Lammens, R.K. O'Reilly, F.D.U. Prez, J. Polym., Sci. Pol. Chem 49 (2011) 2878.
[32] A. Qin, J.W.Y. Lam, B. Tang, Chem. Soc. Rev. 39 (2010) 2522.
[33] C.J. Monceaux, C. Hirata-Fukae, P.C.-H. Lam, M.M. Totrov, Y. Matsuoka, P.R. Carlier, Bioorg. Med. Chem. Lett. 21 (2011) 3992.
[34] C.D. Hein, X. Liu, D. Wang, Pharm. Res. 25 (2008) 2216.
[35] C. Chu, R. Liu, Chem. Soc. Rev. 40 (2011) 2177.
[36] M. Xue, H. Huang, Y. Ke, C. Chu, Y. Jin, X. Liang, J. Chromatogr. A 1216 (2009) 8623.
[37] H. Huang, Y. Jin, M. Xue, L. Yu, Q. Fu, Y. Ke, C. Chu, X. Liang, Chem. Commun. (2009) 6973.
[38] H. Huang, H. Guo, M. Xue, Y. Liu, J. Yang, X. Liang, C. Chu, Talanta 85 (2011) 1642.
[39] Y. Liu, Q. Du, B. Yang, F. Zhang, C. Chu, X. Liang, Analyst 137 (2012) 1624.
[40] L. Moni, A. Ciogli, I. D'Acquarica, A. Dondoni, F. Gasparrini, A. Marra, Chem. Eur. J 16 (2010) 5712.
[41] H. Guo, R. Liu, J. Yang, B. Yang, X. Liang, C. Chu, J. Chromatogr. A 1223 (2012) 47.
[42] H. Guo, C. Chu, Y. Li, B. Yang, X. Liang, Analyst 136 (2011) 5302.
[43] S. Currivan, P. Jandera, Chromatography 1 (2014) 24.
[44] E. Gillespie1, D. Connolly1, P.N. Nesterenko, B. Paull1, J. Sep. Sci. 32 (2009) 2659.
[45] P.N. Nesterenko, P. Jones, J. Chromatogr. A 770 (1997) 129.
[46] E.D. Goddard-Borger, R.V. Stick, Org. Lett. 9 (2007) 3797.
[47] T. Ikegami, K. Tomomatsu, H. Takubo, K. Horie, N. Tanaka, J. Chromatogr. A 1184 (2008) 474.

Talanta 132 (2015) 146–149

Contents lists available at ScienceDirect

Talanta

journal homepage: www.elsevier.com/locate/talanta

Short communication

Enhanced electrochemiluminescence sensing platform using nitrogen-doped graphene as a novel two-dimensional mat of silver nanoparticles

Xiaojiao Du, Ding Jiang, Qian Liu, Jing Qian, Hanping Mao, Kun Wang*

Key Laboratory of Modern Agriculture Equipment and Technology, School of Chemistry and Chemical Engineering, Jiangsu University, Zhenjiang 212013, PR China

ARTICLE INFO

Article history:
Received 27 June 2014
Received in revised form
20 August 2014
Accepted 27 August 2014
Available online 6 September 2014

Keywords:
Nitrogen-doped graphene
Ag nanoparticle
Enhanced electrochemiluminescence
Pentachlorophenol detection

ABSTRACT

This communication clearly highlights the importance and necessity for a comparison investigation between nitrogen-doped graphene (N–G) and graphene as a two-dimensional mat of metal nanoparticles (NPs). We presented Ag NPs as a model of metal NPs for fabricating Ag/N–G and Ag/graphene nanocomposites, respectively. Compared with Ag/graphene nanocomposites, the Ag/N–G nanocomposites could facilitate the electrochemical redox process of $S_2O_8^{2-}$, and showed improved electrochemiluminescence (ECL) performances including increasing ~2.25-fold ECL intensity and decreasing ~330 mV onset potential of $S_2O_8^{2-}$, respectively. Further, the as-prepared pentachlorophenol ECL sensor based on Ag/N–G nanocomposites showed a wider linear range and lower detection limit than those of the Ag/graphene nanocomposites. This study could be potentially useful for understanding the role of N–G in electrochemistry, and opening a new aspect for exploring and developing potential application of N–G based materials in electrocatalysis and sensing fields.

© 2014 Elsevier B.V. All rights reserved.

1. Introduction

Nitrogen-doped graphene (N–G), a novel kind of graphene derivatives, has received considerable interests due to its advantages superior to graphene including much larger functional surface area, higher ratio of surface active groups to volume, and higher electrical conductivity [1]. In particular, as a new desirable two-dimensional mat, N–G possesses more chemically active sites for further anchoring metals [2,3] metallic oxides [4–6] and other metallic compounds [7]. For example, Liang et al. [5] fabricated SnO_2/N–G nanocomposite as a high-performance electrode material for Li-ion batteries, which showed higher capacity than SnO_2. Yang and coworkers [6] found that the ultrathin MnO_2/N–G nanocomposite displayed enhanced electrochemical capacitive performances than MnO_2. Yang et al. [2] reported that the Au/N–G nanocomposite facilitated robust immobilization of antibodies, promoted electron transfer and exhibited excellent electrochemical activity, and the proposed immunosensor displayed excellent analytical performance for metalloproteinase-2 detection. Further, our recent study [3] proved that compared with pure Cu NPs, the Cu/N–G nanocomposite showed enhanced electrocatalytic activity to glucose oxidation, and the presented sensor showed excellent performances for glucose detection including wide linear range, low detection limit, high sensitivity and fast response time. All these results indicated that just like graphene, N–G could be used as a two-dimensional mat to fabricated N–G-based materials, which showed improved electrochemical performances. However, the comparison investigation between N–G and graphene as the two-dimensional mat in the electrochemical research has rarely been reported which is of great theoretic and applicable value.

Electrochemiluminescence (ECL) has gradually become an important and powerful analytical tool in many fields, such as environmental pollutant determination, pharmaceutical analysis and immunoassay owing to its distinct advantages of simplicity, rapidity, sensitivity, controllability and low background [8–10]. Among the different ECL types that have been classified, the kind of cathodic ECL reaction systems involving peroxydisulfate ($S_2O_8^{2-}$) plays an important role [11,12]. Although the ECL of $S_2O_8^{2-}$ solution is quite simple and cheap, its ECL application in sensing was still scarce due to the relatively weak ECL intensity. Therefore, it is very urgent to explore more effective methods to improve the ECL of $S_2O_8^{2-}$ and further develop the ECL applications of $S_2O_8^{2-}$ solution.

In this communication, Ag NPs as a model of metal NPs for fabricating Ag/N–G and Ag/graphene nanocomposites were presented, and the ECL performance between Ag/N–G and Ag/graphene in $K_2S_2O_8$ solution was compared. Using pentachlorophenol

* Corresponding author. Tel.: +86 511 88791800; fax: +86 511 88791708.
E-mail address: wangkun@ujs.edu.cn (K. Wang).

http://dx.doi.org/10.1016/j.talanta.2014.08.065
0039-9140/© 2014 Elsevier B.V. All rights reserved.

(PCP) as an analyte model, Ag/N–G-based ECL sensor exhibited a wider linear range and lower detection limit than that of Ag/graphene, which could broaden the application of N–G-based material in the electrocatalytic and sensing fields.

2. Experimental

2.1. Chemicals and reagents

Graphite was purchased from Qingdao Tianhe Graphite Co., Ltd. PCP was purchased from Sigama Aldrich. $AgNO_3$, $K_2S_2O_8$ and glycine were purchased from Sinopharm Chemical Reagent Co., Ltd. Graphene oxide (GO) was prepared using modified Hummers method from graphite powders [13]. 0.1 M phosphate buffered solution (PBS, pH 7.0) was prepared by mixing stock standard solutions of NaH_2PO_4 and Na_2HPO_4. All the PBS solutions were air-saturated and doubly distilled water (18.2 MΩ; Millpore Co.) was used in all experiments and to prepare all buffers.

2.2. Apparatus

The morphologies were performed via transmission electron microscopy (TEM, Hitach H800, Japan). X-ray diffraction (XRD) was acquired on an X'Pert X-ray diffraction spectrometer (Philips, USA). X-ray photoelectron spectroscopy (XPS) was performed on a Thermo VG Scientific ESCALAB 250 spectrometer with a Mg *K*α radiator. The ECL emission was detected using a model MPI-A electro-chemiluminescence analyzer (Xi'an Remex Analysis Instrument Co. Ltd. Xi'an, China) with 800 V photomultiplier tube voltage. The conventional three-electrode system was employed with a modified glassy carbon electrode (GCE) as the working electrode, an Ag/AgCl (saturated KCl) as reference electrode and a Pt wire as the counter electrode.

2.3. Preparation of samples

Ag/N–G was prepared according to the literature with some modifications [14]. Briefly, 5 mL solution containing 10 mg GO, 30 mg glycine and 15 mg $AgNO_3$ was sonicated for 2 h, and then the resulting mixture was poured into an alumina crucible which was gradually increased from room temperature to 500 °C under argon atmosphere and maintained for 2 h. Ag/graphene was prepared using the same method without adding glycine. Similarly, N–G was prepared without adding silver nitrate, and graphene was prepared using the same treatment without adding silver nitrate and glycine.

2.4. Preparation of the modified electrodes

6 μL of 2 mg mL^{-1} Ag/N–G suspension was spread evenly onto the cleaned GCE surface and allowed to dry in ambient air for 24 h. For comparison, N–G/GCE, graphene/GCE and Ag/graphene/GCE were also prepared using a similar procedure.

3. Results and discussion

3.1. Characterization of the samples

The typical TEM images and the size-distribution histogram of Ag/N–G and Ag/graphene samples (Fig. 1A–C) show that Ag NPs ranging from 30 to 60 nm are evenly distributed on graphene and N–G sheet, respectively. Moreover, in both cases, particles appeared spherical, well dispersed and well-separated. And XRD

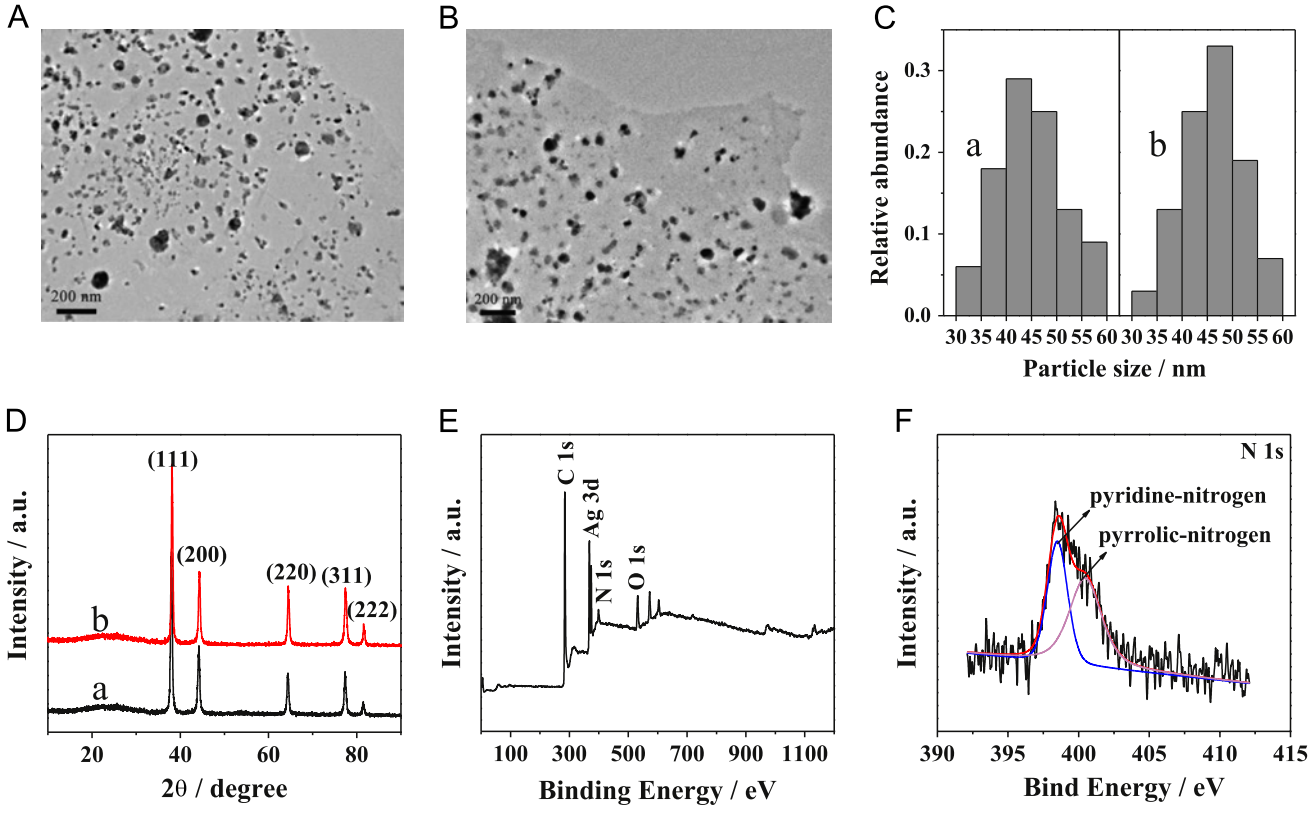


Fig. 1. TEM image of (A) Ag/N–G and (B) Ag/graphene. (C) The histogram of particle size distribution for Ag/N–G (a) and Ag-graphene (b). (D) XRD patterns of Ag/graphene (a) and Ag/N–G (b). (E) XPS spectra of Ag/N–G. (F) The high-resolution N 1s spectrum of Ag/N–G.

analysis (Fig. 1D) shows that Ag/N–G and Ag/graphene exhibited no obvious differences from the structure, which displayed obvious peaks corresponding to (1 1 1), (2 0 0), (2 2 0), (3 1 1) and (2 2 2) of metallic Ag [14,15]. Further, the full range XPS analysis (Fig. 1E) of Ag/N–G sample clearly illustrated the presence of nitrogen in the nanocomposite, which confirmed the successful doping of nitrogen atoms into the graphene networks. In addition, it can be seen that pyridinic and pyrrolic nitrogen species are formed in Ag/N–G (Fig. 1F). Pyridine N bonds with two C atoms at the edges or defects of graphene and contribute one *p* electron to the π system, while pyrrolic N refers to N atoms that contribute two *p* electrons to the π system.

3.2. Electrochemical and ECL behaviors of samples

Fig. 2A displays the ECL–time curves of the as-fabricated electrodes in the presence or absence of 0.1 M $K_2S_2O_8$. Compared with bare GCE (curve *a*), graphene/GCE (curve *b*) and N–G/GCE (curve *c*) in the presence of 0.1 M $K_2S_2O_8$, the ECL emissions of both Ag/graphene/GCE (curve *d*) and Ag/N–G/GCE (curve *e*) were enhanced obviously, and it should be highlighted that the ECL intensity from Ag/N–G/GCE is about 2.25-fold higher than that observed from Ag/graphene/GCE. On the other hand, no ECL emission was observed on either Ag/graphene/GCE (curve *f*) or Ag/N–G/GCE (curve *g*) in blank PBS solution. All these results above indicated that the ECL emission was produced from $K_2S_2O_8$ solution, which is similar to previous reports [16,17]. The possible ECL mechanisms are described as follows: the dissolved oxygen was reduced to $OOH^{\bullet}$ upon the potential scan with an initial negative direction, meanwhile $S_2O_8^{2-}$ was reduced to the strong oxidant $SO_4^{\bullet-}$, which could react with $OOH^{\bullet}$ to produce light-emitting species $^1(O_2)_2^*$.

To gain a better understanding of Ag/N–G enhancing the ECL signal of the peroxydisulfate solution, ECL–potential curves and cyclic voltammograms of Ag/N–G and Ag/graphene have been investigated in Fig. 2B. It can be seen that the ECL onset potential of the Ag/N–G/GCE (−0.41 V) was ~330 mV more positive than that of Ag/graphene/GCE (−0.74 V), which indicated that N–G could decrease the potential barriers of the ECL reaction obviously. Moreover, the reduction peak potential of $K_2S_2O_8$ at Ag/N–G/GCE was more positive for ~270 mV and exhibited higher reduction peak current of $K_2S_2O_8$ than Ag/graphene/GCE (inset of Fig. 2B). All these results suggested that N–G could be used as a excellent two-dimensional mat to anchor Ag NPs for accelerating the electron-transfer processes and improving the electrocatalytic activity, which could be attributed to the introduction of nitrogen in graphene. According to previous studies, the pyridinic nitrogen in N–G can provide a pair of electrons for conjugation with the π-conjugated rings which can introduce electron donor properties to graphene and improve the electrochemical performances of N–G; the pyrrolic nitrogen has higher charge mobility in N–G due to better electron-donor characteristics and enhanced carbon catalytic activity in electron-transfer reactions [3,6].

3.3. Analytical application of cathodic ECL emission of Ag/N–G/GCE and Ag/graphene/GCE

In order to compare the analytical application of cathodic ECL emission of Ag/N–G/GCE and Ag/graphene/GCE, the developed sensors were applied in the detection of PCP, which has been widely used in agriculture and industry and may cause the acute toxicities of organisms, endocrine disruptor and potentially carcinogenesis [18].

Fig. 3A and B presented the effect of various concentration of PCP on the cathodic ECL intensity of $K_2S_2O_8$ solution on Ag/N–G and Ag/graphene modified electrodes, and the ECL intensity decreased linearly with the increase of PCP concentration. Furthermore, the Ag/N–G/GCE displayed a wider linear range (0.1 pg mL^{-1}–110.1 μg mL^{-1}) and lower detection limit (0.03 pg mL^{-1}) than that of Ag/graphene/GCE (linear range: 10.0 pg mL^{-1}–11.1 μg mL^{-1}, detection limit: 3.3 pg mL^{-1}). These results might be ascribed to the introduction of nitrogen in graphene which enlarge the ECL signal for sensitive detection.

The detection of PCP has been reported based on its quenching effect on the ECL of carbon quantum dots resulting from an electron-transfer process [18,19]. Thus, the ECL quenching mechanism of PCP here might be attributed to electron transfer annihilation of $SO_4^{\bullet-}$. When PCP was added, it could would be adsorbed on the N–G surface and be oxidized resulting in a decrease in ECL.

The reproducibility of the sensor based on Ag/N–G was examined by measuring the ECL intensity responses upon 1 ng mL^{-1} PCP in 0.1 M PBS containing 0.1 M $K_2S_2O_8$. In a series of five electrodes prepared in the same way, a relative standard deviation (RSD) of 5.1% was obtained, indicating the reliability of this method. While 5 measurements for a single electrode were made upon the addition of 1 ng mL^{-1} PCP with RSD of 3.6%, demonstrating excellent reproducibility.

Furthermore, the selectivity of the ECL sensor was investigated using 2,6-dichlor-ophenol (2,6-DCP), 2,4,6-trichlorophenol (2,4,6-TCP) as the interferents. The $\Delta I/I_0$ (where I_0 is the initial intensity,

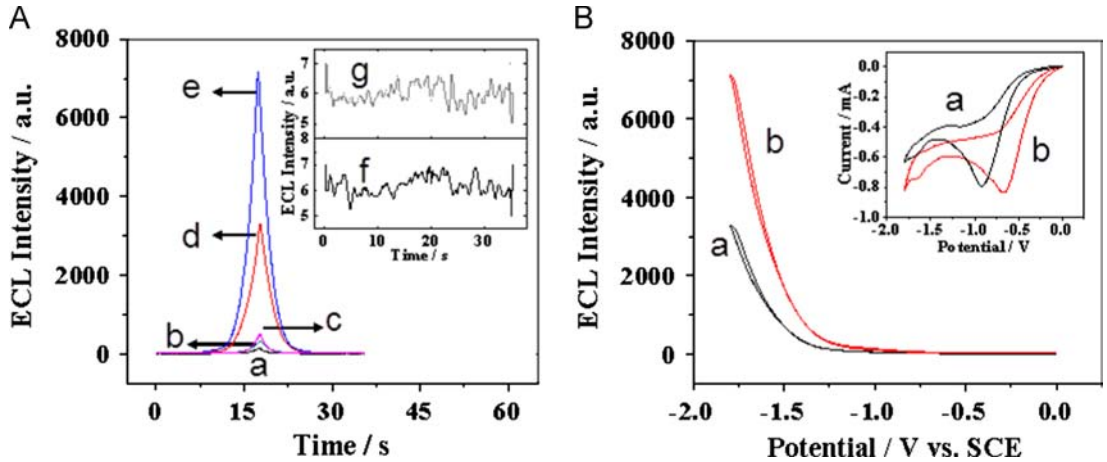


Fig. 2. (A) ECL–time curves of bare GCE (*a*), GS/GCE (*b*), N–G/GCE (*c*), Ag/graphene/GCE (*d*) and Ag/N–G/GCE (*e*) in the presence of 0.1 M $K_2S_2O_8$ in 0.1 M PBS. Inset: the ECL–time curves of Ag/graphene/GCE (*f*) and Ag/N–G/GCE (*g*) in 0.1 M PBS. (B) ECL–potential curves of Ag/graphene/GCE (*a*) and Ag/N–G/GCE (*b*) in 0.1 M PBS containing 0.1 M $K_2S_2O_8$. Inset: the corresponding cyclic voltammograms of them.

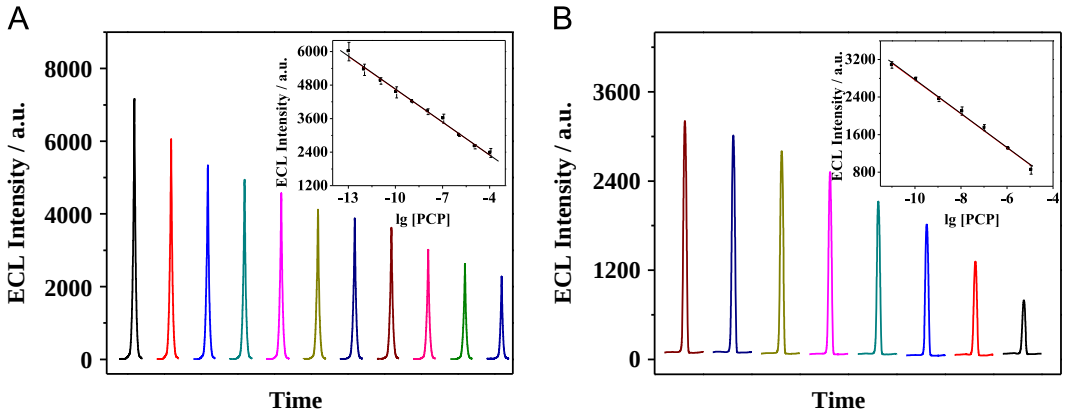


Fig. 3. ECL–time curves of (A) Ag/N–G/GCE and (B) Ag/graphene/GCE in 0.1 M PBS with different concentrations of PCP. Inset: the corresponding calibration curve for PCP determination.

and ΔI is the interferent induced decrease in ECL intensity) to 1.0 ng mL^{-1} of these compounds were 4.49% (2,6-DCP), and 3.53% (2,4,6-TCP), whereas the $\Delta I/I_0$ to 1.0 ng mL^{-1} of PCP was 37.27%. Comparing the ECL inhibition ratio of these compounds with those of PCP, the ECL sensor showed a relatively high selectivity to PCP. In addition, some common ions (cations and anions), such as Na^+, K^+, Mg^{2+}, Cl^-, NO_3^-, also showed little effect on the ECL emission of Ag/N–G and thus did not interfere with the PCP detection.

4. Conclusions

In summary, a comparison of the electrochemical and ECL behavior based on graphene and N–G as substrates to anchor Ag NPs was achieved in peroxydisulfate solution. Compared with Ag/graphene, Ag/N–G showed improved electrocatalytic activity and enhanced ECL intensity in $K_2S_2O_8$ system. The enhancement could be attributed to the introduction of nitrogen in graphene, which in favor of the reduction of $S_2O_8^{2-}$, leading to generation of more quantity of excited states. The present work would be potentially useful for understanding the role of N–G in electrochemistry, and broaden the application of N–G-based materials in the electrocatalytic and sensing fields.

Acknowledgments

The present work was supported by the National Natural Science Foundation of China (nos. 21175061 and 21375050), Key Laboratory of Modern Agriculture Equipment and Technology (No. NZ201109), and a Project Funded by the Priority Academic Program Development of Jiangsu Higher Education Institutions (no. PAPD-2014-37).

References

[1] H.B. Wang, T. Maiyalagan, X. Wang, ACS Catal 2 (2012) 781.
[2] G.H. Yang, L.L. Li, R.K. Rana, J.J. Zhu, Carbon 61 (2013) 357.
[3] D. Jiang, Q. Liu, K. Wang, J. Qian, X.Y. Dong, Z.T. Yang, X.J. Du, B.J. Qiu, Biosens. Bioelectron. 54 (2014) 273.
[4] D.D. Cai, D.D. Li, S.Q. Wang, X.F. Zhu, W.S. Yang, S.Q. Zhang, H.H. Wang, J. Alloys Compd 561 (2013) 54.
[5] J.F. Liang, Z. Cai, Y. Tian, L.D. Li, J.X. Geng, L. Guo, ACS Appl. Mater. Interfaces 5 (2013) 12148.
[6] S.H. Yang, X.F. Song, P. Zhang, L. Gao, ACS Appl. Mater. Interfaces 5 (2013) 3317.
[7] B.T. Liu, L.L. Tian, Y.H. Wang, ACS Appl. Mater. Interfaces 5 (2013) 8414.
[8] W.J. Miao, Chem. Rev. 108 (2004) 2506.
[9] H.Y. Wang, F.Q. Zhang, Z.A. Tan, Q.F. Chen, L. Wang, Electrochem. Commun. 12 (2010) 650.
[10] K. Zeng, M.L. Guo, Y.J. Zhang, M. Qing, A.F. Liu, Z. Nie, Y. Huang, Y.L. Pan, S. Z. Yao, Electrochem. Commun. 13 (2011) 1353.
[11] H. Niu, R. Yuan, Y.Q. Chai, L. Mao, Y.L. Yuan, Y. Zhuo, S.R. Yuan, X. Yang, Biosens. Bioelectron. 26 (2011) 3175.
[12] H.J. Wang, R. Yuan, Y.Q. Chai, H. Niu, Y.L. Cao, H.J. Liu, Biosens. Bioelectron. 37 (2012) 6.
[13] S. Gilje, S. Han, M.S. Wang, K.L. Wang, R.B Kaner, Nano Lett. 7 (2007) 3394.
[14] S. Mayavan, J.B. Sim, S.M. Choi, Carbon 50 (2012) 5148.
[15] X.Z. Tang, X.F. Li, Z.W. Cao, J.L. Yang, H. Wang, X. Pu, Z.Z. Y, Carbon 59 (2013) 93.
[16] H. Niu, R. Yuan, Y.Q. Chai, L. Mao, Y.L. Yuan, Y. Zhuo, S.R. Yuan, X. Yang, Biosens. Bioelectron. 26 (2011) 3175.
[17] H.J. Wang, R. Yuan, Y.Q. Chai, H. Niu, Y.L. Cao, H.J. Liu, Biosens. Bioelectron. 37 (2012) 6.
[18] S.L. Yang, J.S. Liang, S.L. Luo, C.B. Liu, Y.H. Tang, Anal. Chem. 85 (2013) 7720.
[19] J.Z. Li, N.Y. Wang, T.T. Tran, T, C.A. Huang, L. Chen, L.J. Yuan, L.P. Zhou, R. Shen, Q.Y. Cai, Analyst 138 (2013) 2038.

Talanta 132 (2015) 150–154

Contents lists available at ScienceDirect

Talanta

journal homepage: www.elsevier.com/locate/talanta

A simple and sensitive impedimetric aptasensor for the detection of tumor markers based on gold nanoparticles signal amplification

Xi Liu [a], Yun Qin [a], Chunyan Deng [a,b,*], Juan Xiang [a,*], Yuanjian Li [b]

[a] College of Chemistry and Chemical Engineering, Central South University, Changsha 410083, PR China
[b] Pharmacology Section, Department of Pharmacology, School of Pharmaceutical Sciences, Central South University, Changsha 410083, PR China

ARTICLE INFO

Article history:
Received 19 June 2014
Received in revised form
27 August 2014
Accepted 31 August 2014
Available online 7 September 2014

Keywords:
Impedimetric aptasensor
Signal amplification
Gold nanoparticles
Mucin 1

ABSTRACT

A simple and sensitive electrochemical impedimetric aptasensor based on gold nanoparticles (AuNPs) signal amplification was developed for the ultrasensitive detection of tumor markers (mucin 1 protein, MUC1 as a model). The designed cDNA, which is partly complementary with the aptamer of MUC1 was immobilized on the gold electrode. The detection of MUC1 could be carried out by virtue of switching structures of aptamers from DNA/DNA duplex to DNA/target complex. The change of the interfacial feature of the electrode was characterized by electrochemical impedance analysis (EIS) with the redox probe $[Fe(CN)_6]^{3-/4-}$. The quantitative detection of MUC1 protein was obtained from the changes of electron-transfer resistance (ΔR_{et}). Moreover, as the signal enhancer, the aptamer-modified AuNPs (Apt@AuNPs) conjugates was introduced on the electrode by the hybridization of cDNA with aptamer. As expected, the detection sensitivity for MUC1 was greatly improved, which may be due to the specific binding of MUC1 onto the surface of the Apt@AuNPs modified electrode. This proposed simple aptasensor has a low detection limit of 0.1 nM, and also exhibits several advantages of high sensitivity and good selectivity. This present work may provide a general model for the detection of tumor marker based on impedimetric aptasensor.

© 2014 Elsevier B.V. All rights reserved.

1. Introduction

Tumor marker is a substance abnormally expressed in malignancy and benign tumor compared with normal tissues. The content of tumor marker represents the current state of the tumor. The detection of tumor marker is significant for clinical diagnosis and judging those diseases related to tumor. For breast cancer, since human mucin-1 (MUC1) has been found highly over-expressed in breast cancer, it becomes one of the most common tumor markers to diagnose the breast tumor [1]. Therefore, enhancing the detection level of MUC1 plays an important role in the diagnosis of breast cancer.

Aptamers are nucleic acid ligands (DNA or RNA) which are artificially synthesized and selected in vitro through SELEX (systematic evolution of ligands by exponential enrichment) [2,3]. They have high specificity and affinity to various target molecules that includes peptides [4], dopamine [5], adenosine and ATP [6], metal ions [7], as well as proteins, such as growth factors [8] and thrombin [9]. In addition, the immunogenicity and toxicity of aptamers are proved much lower compared with antibodies when they used in biological environment or as a part of therapeutic and diagnostic agents [10], so aptamer has been widely used as a sensing element for developing biosensor. In recent years, aptamers have been screened for targeting and measuring some tumor markers, which have great value in evaluating the progress of cancer, monitoring the therapeutic response and predicting the recurrence [11].

MUC1 aptamers are of great importance in the assessment of breast cancer [12,13]. Up to now, limited researches have been conducted to directly detect the concentration of MUC1. Pang's group designed a fluorescent aptasensor utilizing graphene oxide (GO) to quench the fluorescence of single-stranded dye-labeled MUC1 aptamer, when MUC1 added, the quenched fluorescence was recovered significantly [14]. Yu's group constructed a hairpin DNA aptamers on gold and labeled with methylene blue (MB) for electrochemical measurements [15]. They also reported a method of quantitative detection of MUC1 by labeling a 3-component DNA hybridization system with quantum dot (QD)-based fluorescence readout [16]. Wei et al. performed a method based on electrochemiluminescence (ECL) resonance energy transfer (ERET) to detect MUC1 protein and MCF-7 cancer cells [17]. Among these studies, the electrochemical methods are more remarkable in the

* Corresponding authors at: College of Chemistry and Chemical Engineering, Central South University, Changsha 410083, PR China. Tel.: +86 731 88876490; fax: +86 731 88879616.
E-mail addresses: dengchunyan@csu.edu.cn (C. Deng), xiangj@csu.edu.cn (J. Xiang).

http://dx.doi.org/10.1016/j.talanta.2014.08.072
0039-9140/© 2014 Elsevier B.V. All rights reserved.

development of aptasensors due to their fast response, high sensitivity, low cost and the result can be obtained at real-time.

As an effective electrochemical method, electrochemical impedance spectroscopy (EIS) can measure the response (current and its phase) of an electrochemical system to an applied oscillating potential as a function of the frequency [18–21]. The immobilization of biomaterials, including enzymes, antigens/antibodies or DNA on electrodes alters the capacitance and interfacial electron transfer resistance of the conductive electrodes. On account of its sensitivity with the changes of interfacial properties, this method has been extensively used to study the electrochemical changes induced by protein binding reactions resulting in interfacial electron transfer kinetics between the redox probe and the electrode changes notably when the binding procedure taking place [22,23]. Therefore, EIS can be used to monitor the different stages of each fabrication step for the biosensor, and the detection of identification process when an immobilized molecule interacts with analytes. Besides, in consequence of the advantages of EIS, for instance, high sensitivity, simplicity and requiring no external modification of the biomolecules, it is an ideal technology for label-free detection.

In the present work, a sensitive and label-free impedimetric aptamer-based electrochemical biosensor for the tumor marker of breast cancer (MUC1 as the model) was simply fabricated. A cDNA was used as the linker DNA, which was designed to be complementary with the MUC1 aptamer. Moreover, aptamer functionalized gold nanoparticles (Apt@AuNPs) were used as the signal amplifier and to capture the target molecule MUC1. The introduction of gold nanoparticles is favorable for amplifying electrochemical signals and the resulted electrochemical aptasensor shows high sensitivity, MUC1 can be specifically detected at a concentration down to 0.1 nM. This proposed aptasensor for tumor maker has some advantages of simplicity, high sensitivity, acceptable selectivity, good reproducibility and stability. Therefore, this work would lay a potential foundation for clinical application of the early breast cancer diagnosis, and it is also significant for the development of the electrochemical aptasensor for sensing other tumor markers.

2. Experimental

2.1. Materials and chemicals

$HAuCl_4 \cdot 3H_2O$ was from Sigma (St. Louis, MO). 6-Mercaptohexanol (MCH), Tris-(hydroxymethyl) aminomethane (Tris), Trisodium citrate was purchased from Bio Basic Inc. NaCl, $MgCl_2 \cdot 6H_2O$ were obtained from Amresco. All other reagents are of analytical purity and used as received. All samples and buffer solutions were prepared using ultrapure water obtained from a Milli-Q water purification system (Simplicity 185, Millipore Corp., Billerica, MA).

DNA1 (thiolated MUC1 aptamer, 5′–HS-$(CH_2)_6$-GCA GTT GAT C**CT TTG GAT A**CC CTG G-3′) and cDNA (5′-HS-$(CH_2)_6$-TTT TT**T ATC CAA AG**A-3′) were manufactured by Sangon Biological Engineering Technology & Services Co., Ltd. (Shanghai, China). DNA1 is a 25-base sequence that is MUC1 aptamer, as well as complementary sequence (bold part) to cDNA.

Thiolated MUC1 aptamer was diluted to 10 μM in 34 mM Tris–HCl buffer (pH 7.4, 233 mM NaCl, 8.5 mM KCl, 1.7 mM $MgCl_2$, 1.7 mM $CaCl_2$) for use. The obtained solution was stored at 4 °C before use. MUC1 (from the N terminus to the C terminus: APDTRPAPG) was purchased from Shanghai Apeptide Co., Ltd. The peptides were suspended in 10 mM phosphate buffer solution (PBS, pH 7.4) to obtain different concentrations for the subsequent experiment.

2.2. Preparation of AuNPs and DNA1-modified AuNPs (apt@AuNPs)

AuNPs with the diameter of about 13 nm were prepared by the reduction of $HAuCl_4$ in citrate solution according to reports in the literatures [24,25]. Briefly, 100 mL 0.01% (w/v) $HAuCl_4$ aqueous solution was heated and stirred vigorously with reflux, 2 mL 2% (w/v) trisodium citrate was added rapidly when $HAuCl_4$ aqueous solution became boiled. Color variation was obviously observed and then it was refluxed for an additional 15 min. The solution color turned to wine red, indicating the formation of AuNPs. The solution was cooled to room temperature with continuous stirring. The diameter of AuNPs was determined by UV–vis spectra with an characteristic absorption peak at 520 nm [24,26].

The DNA1-modified AuNPs (Apt@AuNPs) were prepared according to the procedures reported in literatures [27,28]. Briefly, a solution of AuNPs (1 mL) was mixed with the thiolated DNA1 (1 OD) overnight and then slowly brought to 0.05 M NaCl by adding concentrated NaCl solution (3 M), 10 mM phosphate buffer (pH 7.0). Then, after standing for 6–8 h, the concentration of NaCl was brought to 0.1 M and the solution was allowed to age for another 6–8 h. To remove the excess free aptamers, the conjugates were purified by centrifuging for 30 min at 14,000 rpm. The red precipitate was washed, centrifuged, and dispersed in 1.5 mL of 34 mM Tris–HCl buffer solution containing 233 mM NaCl, 8.5 mM KCl, 1.7 mM $MgCl_2$, 1.7 mM $CaCl_2$ (pH 7.4). A characteristic absorption of the Apt@AuNPs conjugates was at 523 nm, which indicates the MUC1 aptamers have been successfully attached onto Au nanoparticles, according to reports in the literature [24].

2.3. Preparation of the modified electrode

Before modification, the bare gold electrode (2 mm in diameter) was polished sequentially with 0.3 μm and 0.05 μm alumina slurry followed by ultrasonic cleaning in ethanol and ultrapure water. Subsequently, the gold electrode was cleaned in piranha solution (v/v 3:1 H_2SO_4/H_2O_2) (Caution: piranha solution reacts violently with many organic materials and should be handled with great care), followed by treatment with nitric acid. Afterward, the gold electrode was washed thoroughly with ultrapure water and dried under nitrogen gas. For modification of the electrode, 10 μL of cDNA (10 μM) was dropped onto the cleaned electrode and incubating for 16 h to form the self-assembled monolayer. After modification, the gold electrodes were incubated in 1 mM 6-mercaptohexanol (MCH) solution for 1 h to block the unmodified region of the gold surface. Then a 10 μL droplet of Apt@AuNPs conjugates solution was covered onto the Au/cDNA/MCH electrode and kept for 2 h to obtain the Au/cDNA/MCH/Apt@AuNPs electrode. For comparison, the Au/cDNA/MCH/Apt electrode was also fabricated by dipping 10 μL of thiolated MUC1 aptamer (Apt) solution onto the Au/cDNA/MCH electrode and incubating for 2 h. After each step, the electrode was rinsed thoroughly with ultrapure water and dried under highly pure nitrogen stream prior to electrochemical characterization. For each step of immobilization, the electrochemical impedance measurements were performed in the presence of equimolar $[Fe(CN)_6]^{3-/4-}$ as redox probe.

2.4. Apparatus and electrochemical measurements

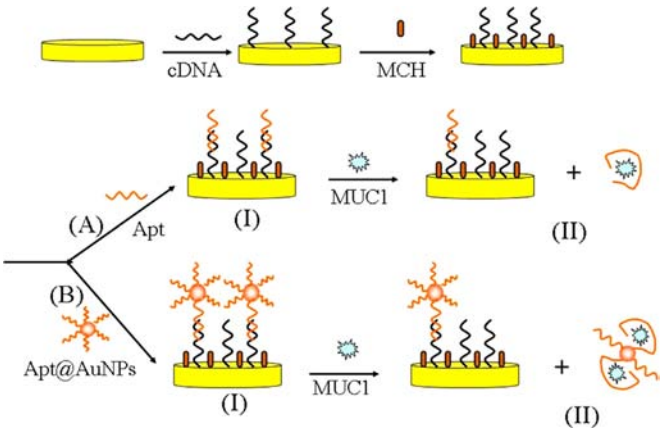
Electrochemical impedance spectroscopy (EIS) measurements were performed on a CHI650D electrochemical workstation. A conventional three-electrode system was used with bare gold electrode as the working electrode, a platinum wire as counter electrode and a saturated calomel electrode (SCE) as reference electrode. All the potentials in this paper were in respect to SCE. All experiments were carried out at laboratory temperature.

For the detection of MUC1, the modified gold electrodes were immersed in the MUC1 solution (10 mM phosphate buffer solution, pH 7.4) with various concentrations and kept for 2 h, followed by a 5 min washing to remove Apt@AuNPs@MUC1 and nonspecific bound of MUC1. The impedance spectra were obtained in a frequency range from 100 mHz to 100 kHz and the amplitude of 5 mV in 5 mM $[Fe(CN)_6]^{3-/4-}$ solution containing 0.1 M KCl. The impedance spectra were plotted in the form of Nyquist plots.

3. Results and discussion

3.1. Design strategy of the aptasensor

An electrochemical sensing platform for highly sensitive detection of tumor marker (MUC1 as a model) was proposed. The assay protocol of the electrochemical aptasensor was depicted schematically in Scheme 1. The surface of the gold electrode was first modified with the thiolated cDNA and MCH via the self-assembly. The bold part of the MUC1 aptamer hybridized to the bold part of cDNA. The sensing interface was ready for the detection of MUC1. For Scheme 1A, when MUC1 introduced, the MUC1 aptamer-contained DNA1 preferred to form the aptamer-MUC1 complex, which resulted in the dehybridization and the MUC1-aptamer released into the solution (Scheme 1A-II). In this case, it was expected that the EIS of the DNA-modified electrode would decrease. On the other hand, in order to improve the sensitivity of the sensing interface, Apt@AuNPs was employed to hybridize with the MUC1 aptamer, as shown in Scheme 1B. Since Apt@AuNPs can bind more MUC1 molecules, and folding into a well-defined three-dimensional structure, which would lead to the Apt@AuNPs/MUC1 complex of huge weight falling off from the electrode (Scheme 1B-II). This may result in an obvious EIS signal change of the modified electrode, and offering a significant amplification for the detection of MUC1. The design is to fabricate an aptamer based biosensor by relying on the structure-switching properties of aptamers binding to their target molecules, which is applicable for the fabrication of other aptasensor.



Scheme 1. Schematic representation of the electrochemical aptasensor for the detection of MUC1.

3.2. EIS characterization of the modified electrode

On the basis of the charge transfer kinetics of the $[Fe(CN)_6]^{3-/4-}$ redox probe, faradaic impedance spectra with an $[Fe(CN)_6]^{3-/4-}$ redox probe were modeled using the equivalent circuit approach of Radi et al. [22], as shown in the inset of Fig. 1. The circuit includes the commonly existing electrolyte resistance (R_s) and Warburg impedance (Z_w) resulting from the diffusion of ions from the bulk of the electrolyte to the interface, double-layer capacitance (C_d), and the electron-transfer resistance (R_{et}). Among them, Ret can directly and sensitively respond to changes of the electrode interface [29,30]. Whereas a linear section characteristic at the lower frequency is attributable to a diffusion-limited process, a squeezed semicircle portion observed at higher frequencies corresponds to the electron-transfer limited process.

Electrochemical impedance spectroscopy (EIS) has been employed to characterize the modified electrode. Fig. 1 displays the EIS results of the (a) bare Au, (b) Au/cDNA, (c) Au/cDNA/MCH, (d) Au/DNA/MCH/Apt@AuNPs and (e) Au/cDNA/MCH/Apt electrodes in the presence of the equimolar $[Fe(CN)_6]^{3-/4-}$ redox probe, respectively. In the Nyquist plots of impedance spectra, a linear section at the lower frequencies is attributable to a diffusion-limited process, and a squeezed semicircle portion observed at higher frequencies would correspond to the electron-transfer limited process. The increase of the diameter of the semicircle reflects the increase of the interfacial charge-transfer resistance (R_{et}) [31]. It is noted that the bare gold electrode shows a very small semicircle domain

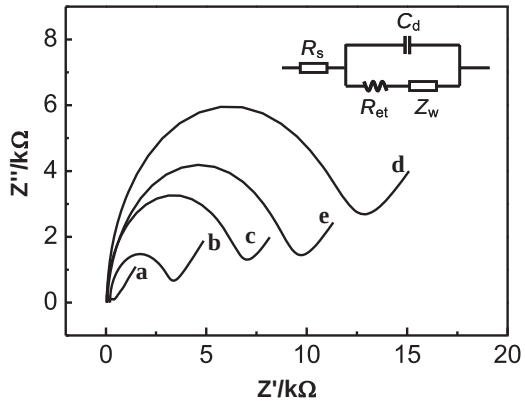


Fig. 1. Electrochemical impedance spectra of (a) the bare Au electrode, (b) the Au/cDNA electrode, (c) the Au/cDNA/MCH electrode, (d) the Au/cDNA/MCH/Apt@AuNPs electrode, (e) the Au/cDNA/MCH/Apt electrode in aqueous solution containing 0.1 M KCl and 5 mM $[Fe(CN)_6]^{3-/4-}$ (1:1) as the redox probe. The impedance spectra were obtained at the frequency range from 100 mHz to 100 kHz with a DC potential of +0.224 V. The amplitude was 5 mV.

(R_{et}=200 Ω, curve a in Fig. 1), indicating a very fast electron transfer process of $[Fe(CN)_6]^{3-/4-}$ [29]. The self-assembly of a negatively charged cDNA on the Au electrode surface effectively repels the $[Fe(CN)_6]^{3-/4-}$ anions and thus leads to an enhanced electron-transfer resistance (R_{et}=3540 Ω, curve b in Fig. 1), which demonstrates that thiolated cDNA has been self-assembled successfully on the electrode. It is also found that the assembly of MCH on the cDNA-modified electrode leads to a significant increase of R_{et} to 6890 Ω (curve c in Fig. 1). After hybridization with Apt@AuNPs, the value of R_{et} increases significantly to 12,690 Ω (curve d in Fig. 1). Compared to the Au/DNA/MCH/Apt@AuNPs electrode, the changes of electron-transfer resistance of the Au/DNA/MCH/DNA1 electrode modified without AuNPs is only varied from 6890 Ω to 8280 Ω (curve e in Fig. 1). This may be attributed to the bulky effect of Apt@AuNPs that hinders the electron-transfer on the surface of the electrode. Besides, the Apt@AuNPs bioconjugates will introduce more aptamers on the electrode, considering the property of the aptamer, it is not only nonconductive, but also the negatively charged phosphate backbone of aptamer repelling $[Fe(CN)_6]^{3-/4-}$ anions from the electrode surface [32], which would lead to an obvious change of R_{et}. Therefore, it is expected that the application of DNA-functionalized AuNPs can further enhance the sensitivity of the present sensing strategy.

3.3. Signal amplification of AuNPs for sensing MUC1

In order to prove the signal amplification of AuNPs in the electrochemical aptasensor for sensing tumor biomarker, we investigated the changes of the electron-transfer resistance (ΔR_{et}) of the two modified electrode, (a) Au/cDNA/MCH/DNA1 electrode and (b) Au/cDNA/MCH/Apt@AuNPs electrode in the equimolar $[Fe(CN)_6]^{3-/4-}$ solution after incubation with 10 nM MUC1 for 2 h. As shown in Fig. 2, the ΔR_{et} of the Au/cDNA/MCH/Apt@AuNPs electrode (ΔR_{et}=4960 Ω in Fig. 2b) is about 7 times higher than that of the Au/cDNA/MCH/Apt electrode (ΔR_{et}=690 Ω in Fig. 2a). This demonstrates that for sensing the MUC1, the Au/cDNA/MCH/Apt@AuNPs electrode exhibits much stronger impedance signal than the Au/cDNA/MCH/Apt. This can be ascribed to that more aptamers introduced by Apt@AuNPs can bind more MUC1, forming huge molecular weight of Apt@AuNPs/MUC1. Once the Apt@AuNPs/MUC1 falls down from the electrode can lead to much more obvious decrease of ΔR_{et}. Therefore, it is believed that the introduction of Apt@AuNPs is effective to improve the sensitivity of the aptasensor.

3.4. The EIS detection of MUC1

In this work, different concentrations of the target protein, MUC1, was detected by the EIS method using the Au/cDNA/MCH/Apt@AuNPs electrode. The electrochemical measurements were conducted after the Au/cDNA/MCH/Apt@AuNPs electrode was treated with (a) 0 nM, (b) 0.5 nM, (c) 1 nM and (d) 5 nM MUC1 for 2 h respectively, the corresponding results are shown in Fig. 3. It can be observed from Fig. 3 that the R_{et} values of the modified electrode decrease with the increase of the concentration of MUC1.

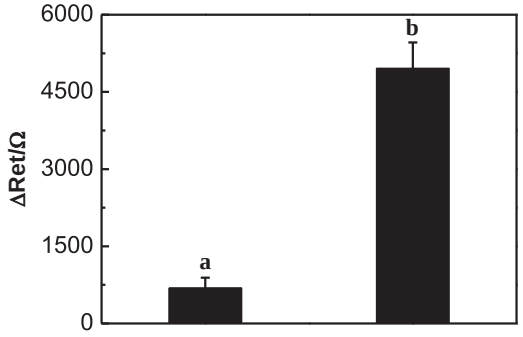


Fig. 2. The changes of the electron-transfer resistance (ΔR_{et}) of (a) the Au/cDNA/MCH/Apt electrode, (b) the Au/cDNA/MCH/Apt@AuNPs electrode after incubation with 10 nM MUC1 for 2 h.

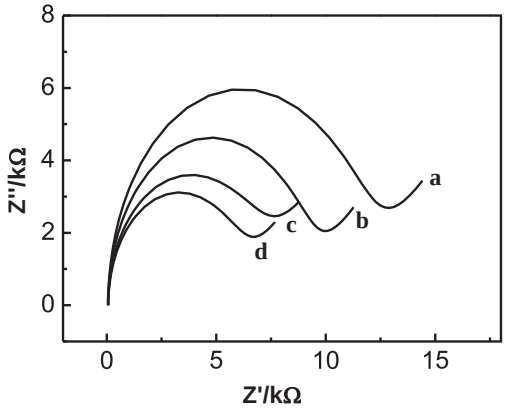


Fig. 3. Electrochemical impedance spectra of the Au/cDNA/MCH/Apt-AuNPs electrode after incubation with (a) 0 nM, (b) 0.5 nM, (c)1 nM, (d) 5 nM MUC1 for 2 h.

This is due to that more MUC1 protein was introduced on the modified electrode, and more Apt@AuNPs/MUC1 bioconjugates with high molecular weight would be formed. When the modified electrode was rinsed thoroughly with ultrapure water, the formed bioconjugates would fall down from the surface of the modified electrode because of the gravity, leading to a marked decrease of R_{et}. Therefore, it can be elucidated that the designed electrochemical aptasensor is feasible and effective for the sensitive detection of tumor biomarkers (MUC1 as a model).

Herein, the detection sensitivity of the present aptasensor was further investigated according to the above procedure. Fig. 4 represents the impedance response of the sensing platform to different concentrations of MUC1. As illustrated in Fig. 4, a series of MUC1 solutions from 0.1 nM to 50 nM were investigated, it can be seen that the ΔR_{et} values of the Au/cDNA/MCH/Apt@AuNPs electrode increase obviously with the increase of MUC1 concentration from 0.1 nM to 10 nM, and the ΔR_{et} values no longer increase significantly as the concentration increases from 10 nM to higher concentrations. Meanwhile, as the insert of Fig. 4 displayed, there is a linear relationship between ΔR_{et} and the concentration of MUC1 ranging from 0.5 nM to 10 nM, and the regression equation was ΔR_{et} (Ω)=0.8128+0.3884 c_{MUC1} (nM) (r=0.9658). This demonstrates that the designed aptasensor possesses the high detection sensitivity with a linear range, and MUC1 can be detectable at a concentration as low as 0.1 nM, which is much lower than that of some existing electrochemical aptasensor for MUC1. For example, Zhao et al. reported a "signal-on" electrochemical aptasensor for determination of two tumor markers with the detection of MUC1 is 20 nM [33]. Hu et al. developed a electrochemical aptamer biosensor based on HO-functionalized AuNPs amplification coupled with enzyme-linkage reactions with a detection limit of 2.2 nM [34]. Meanwhile, the detection limit of this label-free impedimetric aptasensor is also much simpler and more sensitive than the sensor based on other methods,for example, a detection limit of 250 nM was obtained by using quantum dot-labeling fluorescence method [16] or by using aptamer–antibody sandwich enzyme immunoassay [35].

3.5. Selectivity, reproducibility and accuracy

From the practical point, a biosensor should be not only sensitive but also specific. In order to evaluate the selectivity of the aptasensor, control experiments were performed using different proteins, including carcinoembryonic antigen (CEA) and tumor necrosis factor-α (TNF-α) to replace MUC1. The Au/cDNA/MCH/Apt@AuNPs modified electrode was incubated with 1 μM CEA, 1 μM TNF-α and 0.01 μM MUC1 for 2 h, respectively. As shown in

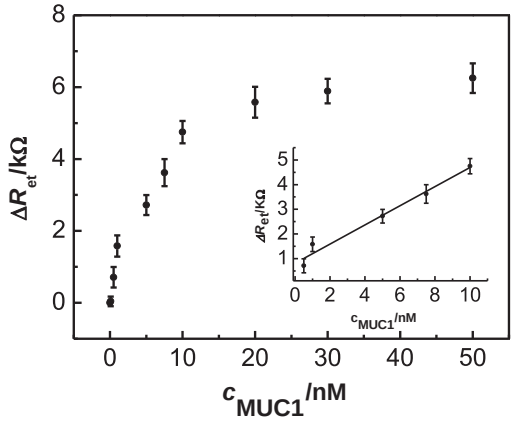


Fig. 4. The calibration curve corresponding to the detection of MUC1 based on the changes of electron-transfer resistance (ΔR_{et}) at the Au/cDNA/MCH/Apt@AuNPs electrode. The inset shows the linear curve of the aptasensor for MUC1.

Fig. 5, it is noted that incubation of the Au/cDNA/MCH/Apt@AuNPs electrode with TNF-α (Fig. 5b) or CEA (Fig. 5c) does not produce significant changes of ΔR_{et} response as compared to the case of MUC1 (Fig. 5a). These results demonstrate that the developed aptasensor has a sufficient specificity to its target molecule, MUC1.

The reproducibility of the aptasensor was also investigated at the MUC1 concentration of 10 nM. Every five freshly prepared modified electrodes have been used for the detection of 10 nM MUC1. All electrodes exhibited similar electrochemical response and the relative standard deviation is 4.1% for MUC1 detection. In addition, the reproducibility of measurements for the same electrode was investigated at the MUC1 concentration of 10 nM, and the relative standard deviation for six times is 4.6%. This demonstrates the aptasensor for MUC1 detection is highly reproducible.

The long-term stability of the sensing interface is further studied since it is an important issue for the practical implementation of MUC1 detection. The modified electrode, which was stored in Tris–HCl at 4 °C for 10 days, could still be used for the measurement of MUC1 without significant change of R_{et}. This implies that the proposed aptasensor has a sufficient stability for detection of MUC1.

Additionally, the accuracy of the impedimetric aptasensor has been evaluated by the standard addition method. A series of samples were prepared by adding MUC1 of different concentrations to human blood serum (obtained from Cancer Hospital of Hunan Province, China). The analytical results for MUC 1 are shown in Table 1. From Table 1, it can be seen that the recovery and relative standard deviation values are acceptable. This implies that the impedimetric aptasensor has a good accuracy, which also indicates a promising feature for the analytical application in complex biological samples.

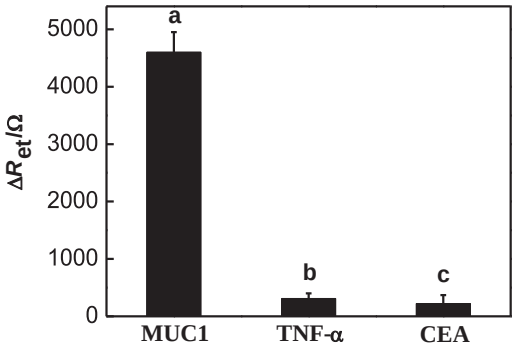


Fig. 5. The changes of the electron-transfer resistance (ΔR_{et}) of the Au/cDNA/MCH/Apt@AuNPs electrode after incubation with (a) 0.01 μM MUC1, (b) 1 μM TNF-α, and (c) 1 μM CEA for 2 h. The R_{et} of the Au/cDNA/MCH/Apt@AuNPs electrode was considered as the background.

Table 1
Determination of MUC1 added in human blood serum ($n=5$) with the proposed aptasensor[a].

Serum samples	Concentration of *MUC1* added (nM)	Concentration obtained with aptasensor (nM)	RSD (%)[b]	Recovery (%)
1	0.65	0.59	3.7	90.8
2	2.80	2.58	4.1	92.1
3	7.50	6.86	4.5	91.5
4	10.5	9.56	5.2	90.2

[a] Impedance measurements were carried out within the range of 100 kHz–100 mHz at the formal potential of the $[Fe(CN)_6]^{3-/4-}$ (1:1). The amplitude of the alternate voltage was 5 mV.

[b] RSD is relative standard deviation.

4. Conclusion

In this paper, a simple electrochemical impedimetric aptasensor for the detection of MUC1 protein has been developed based on AuNPs signal amplification. EIS method has been demonstrated to be a sensitive way to monitor the changes on the surface of the electrode during the process of building the aptasensor. With this aptasensor, MUC1 can be detected at a concentration down to 0.1 nM. The electrochemical aptasensor possesses good selectivity, reproducibility and stability. Besides, taking advantage of EIS technology, this label-free aptasensor is not only convenient for building and detection, it is also satisfying the fast speed and good detection limit. By changing aptamers of different target molecules, this method can be used to detect many kinds of tumor markers, so it may have potential prospect for other studies.

Acknowledgment

Partial support of this work by the National Nature Science Foundation of China (21273288, 20773165, 21005090, 13JJ3004), the Fundamental Research Funds for the Central Universities (2011JQ1004) and the China Postdoctoral Science Foundation (2012M510136, 2013T60774) is acknowledged.

References

[1] J.-S. Chu, K.-J. Chang, Cancer Lett. 142 (1999) 121–127.
[2] A.D. Ellington, J.W. Szostak, Nature 346 (1990) 818–822.
[3] C. Tuerk, L. Gold, Science 249 (1990) 505–510.
[4] D. Nieuwlandt, M. Wecker, L. Gold, Biochemistry 34 (1995) 5651–5659.
[5] C. Manironi, A. Di Nardo, P. Fruscoloni, G. Tocchini-Valentini, Biochemistry 36 (1997) 9726–9734.
[6] D.E. Huizenga, J.W. Szostak, Biochemistry 34 (1995) 656–665.
[7] D. Tan, Y. He, X. Xing, Y. Zhao, H. Tang, D. Pang, Talanta 113 (2013) 26–30.
[8] C.-C. Huang, Y.-F. Huang, Z. Cao, W. Tan, H.-T. Chang, Anal. Chem. 77 (2005) 5735–5741.
[9] X. Zhang, R. Hu, N. Shao, Talanta 107 (2013) 140–145.
[10] E.N. Brody, L. Gold, Rev. Mol. Biotechnol. 74 (2000) 5–13.
[11] Y.-A. Shieh, S.-J. Yang, M.-F. Wei, M.-J. Shieh, ACS Nano 4 (2010) 1433–1442.
[12] J.J. Rahn, L. Dabbagh, M. Pasdar, J.C. Hugh, Cancer 91 (2001) 1973–1982.
[13] P. Mukhopadhyay, S. Chakraborty, M.P. Ponnusamy, I. Lakshmanan, M. Jain, S.K. Batra, BBA-REV Cancer 1815 (2011) 224–240.
[14] Y. He, Y. Lin, H. Tang, D. Pang, Nanoscale 4 (2012) 2054–2059.
[15] F. Ma, C. Ho, A.K. Cheng, H.-Z. Yu, Electrochim. Acta 110 (2013) 139–145.
[16] A.K. Cheng, H. Su, Y.A. Wang, H.-Z. Yu, Anal. Chem. 81 (2009) 6130–6139.
[17] W. Wei, D. Li, X. Pan, S. Liu, Analyst 137 (2012) 2101–2106.
[18] J.T. La Belle, J.Q. Gerlach, S. Svarovsky, L. Joshi, Anal. Chem. 79 (2007) 6959–6964.
[19] E. Katz, I. Willner, Electroanalysis 15 (2003) 913–947.
[20] C. Ocaña, E. Arcay, M. del Valle, Sens. Actuators B—Chem. 191 (2014) 860–865.
[21] Z. Lin, H. Huang, Y. Xu, X. Gao, B. Qiu, X. Chen, G. Chen, Talanta 103 (2013) 371–374.
[22] A.-E. Radi, J.L. Acero Sánchez, E. Baldrich, C.K. O'Sullivan, Anal. Chem. 77 (2005) 6320–6323.
[23] A. HuilingáLoo, H. LingáPoh, Nanoscale 4 (2012) 921–925.
[24] J.J. Storhoff, R. Elghanian, R.C. Mucic, C.A. Mirkin, R.L. Letsinger, J. Am. Chem. Soc. 120 (1998) 1959–1964.
[25] C.-C. Huang, S.-H. Chiu, Y.-F. Huang, H.-T. Chang, Anal. Chem. 79 (2007) 4798–4804.
[26] K.C. Grabar, R.G. Freeman, M.B. Hommer, M.J. Natan, Anal. Chem. 67 (1995) 735–743.
[27] S.O. Obare, R.E. Hollowell, C.J. Murphy, Langmuir 18 (2002) 10407–10410.
[28] J.J. Storhoff, R. Elghanian, C.A. Mirkin, R.L. Letsinger, Langmuir 18 (2002) 6666–6670.
[29] D. Xu, D. Xu, X. Yu, Z. Liu, W. He, Z. Ma, Anal. Chem. 77 (2005) 5107–5113.
[30] C.-Z. Li, Y. Liu, J.H. Luong, Anal. Chem. 77 (2005) 478–485.
[31] D. Aurbach, M.D. Levi, E. Levi, H. Teller, B. Markovsky, G. Salitra, U. Heider, L. Heider, Electrochem. Soc. 145 (1998) 3024–3034.
[32] J.A. Hansen, J. Wang, A.-N. Kawde, Y. Xiang, K.V. Gothelf, G. Collins, J. Am. Chem. Soc. 128 (2006) 2228–2229.
[33] J. Zhao, X. He, B. Bo, X. Liu, Y. Yin, G. Li, Biosens. Bioelectron. 34 (2012) 249–252.
[34] R. Hu, W. Wen, Q. Wang, H. Xiong, X. Zhang, H. Gu, S. Wang, Biosens. Bioelectron. 53 (2014) 384–389.
[35] C. Ferreira, K. Papamichael, G. Guilbault, T. Schwarzacher, J. Gariepy, S. Missailidis, Anal. Bioanal. Chem. 390 (2008) 1039–1050.

Talanta 132 (2015) 155–161

Contents lists available at ScienceDirect

Talanta

journal homepage: www.elsevier.com/locate/talanta

Molecularly imprinted polymer grafted graphene for simultaneous electrochemical sensing of 4, 4-methylene diphenylamine and aniline by differential pulse voltammetry

Ningning Chen [a], Li Chen [b], Yuxiao Cheng [b], Kai Zhao [a], Xiaohong Wu [b], Yuezhong Xian [a,*]

[a] Department of Chemistry, East China Normal University, 500 Dongchuan Road, Shanghai 200241, China
[b] Shanghai Entry-Exit Inspection and Quarantine Bureau, Shanghai 200135, China

ARTICLE INFO

Article history:
Received 22 May 2014
Received in revised form
29 August 2014
Accepted 3 September 2014
Available online 16 September 2014

Keywords:
Molecular imprinting polymers
Graphene
Aromatic amines
Electrochemical sensor

ABSTRACT

A sensitive and selective electrochemical sensor based on molecular imprinting polymers grafted graphene (MIPs-G) was developed for simultaneous measurement of 4, 4-methylene diphenylamine (MDA) and aniline by differential pulse voltammetry (DPV). MIPs-G was synthesized via free radical polymerization reaction using MDA and 4-vinyl pyridine as template molecule and functional monomer respectively. The obtained nanocomposites were characterized by transmission electron microscope, scanning electron microscope, Fourier transform infrared spectrometry, Raman spectroscopy and thermal gravimetric analysis. After removal template molecules, MIPs-G was used as electrode material for aromatic amines measurements. Due to the high binding affinity towards MDA and the π-π interaction with aniline, the MIPs-G based electrochemical sensor can be used for simultaneous detection of MDA and aniline by DPV. Under the optimized condition, the oxidation potentials for MDA and aniline were observed at 0.62 and 0.72 V, respectively. Moreover, MIPs-G modified glassy carbon electrode shows linear response towards MDA and aniline simultaneously over the range of 1.0 to 15 μM. The MIPs-G based electrochemical sensor has been applied for simultaneous measurement of MDA and aniline in plastic tableware.

© 2014 Elsevier B.V. All rights reserved.

1. Introduction

Since the concept of molecular imprinting was first realized by Dickey in 1949 [1], molecular imprinting technology has become a well-established approach to generate molecular recognition materials (molecularly imprinted polymers (MIPs)) with tailor-made selective recognition sites [2]. Due to high specificity, low cost, ease of preparation, thermal and chemical stability, MIPs have attracted considerable interest in a variety of fields, such as chromatographic separations [3], biomimetic sensors [4], solid-phase extraction [5], drug delivery [6], and catalysis [7] etc. MIPs have artificial antibody-like recognition ability because they bear cavities that are complementary in size, shape, and chemical functions to a target molecule. However, traditional MIPs suffer from some drawbacks such as high diffusion barrier, low-rate mass transfer, low binding capacity and poor site accessibility because of their high cross-linking nature [8]. In recent years, to overcome these drawbacks, a surface imprinting technique on nanomaterials has been developed to enable the recognition sites at the surface or in the proximity of the surface [9]. It has been proved that the nanostructured MIPs own the advantages of favorable selectivity and fast association/dissociation kinetics. For example, the nanostructured materials with a large surface area and high porosity, such as nanoparticles [10,11], nanowires [12], nanotubes [13,14], nanofibers [15,16], are excellent candidates for MIPs by surface imprinting.

Recently, graphene has attracted tremendous attention since it is mechanically exfoliated and observed by Novoselov and coworkers in 2004 [17]. Its unique thermal, electronic, mechanical properties and high specific surface area endow graphene with various applications in scientific and technological fields [18]. Moreover, as the thinnest nanomaterial ever discovered, graphene shows great promise as a versatile platform for MIPs with excellent performances, such as the high binding capacity, fast binding kinetics, good accessibility to the target species, low mass-transfer resistance, and easy removal of template molecules, etc. It is because that the atomic-thick structure of graphene could make most of template molecules situate at the surface [19]. Numerous methods have been made to synthesize graphene-based MIPs (MIPs-G), including atom transfer radical polymerization [20], reversible addition fragmentation chain transfer polymerization [19], free radical polymerization (FRP) [21] and electrochemical polymerization [22]. Due to its applicable to almost all of vinyl monomers with simple operation, FRP shows obvious

* Corresponding author. Tel./Fax: +86 21 54340046.
E-mail address: yzxian@chem.ecnu.edu.cn (Y. Xian).

http://dx.doi.org/10.1016/j.talanta.2014.09.008
0039-9140/© 2014 Elsevier B.V. All rights reserved.

advantages in synthesis MIPs-G [23]. The applications of MIPs-G in adsorption [24], optosensing [25] and electrochemical recognition [26–30] were reported.

Aromatic amines are a class of toxic substances and represent one of the most important classes of environmental pollutants. In addition, aromatic amines have been widely used as raw materials in the manufacture of plastic tableware. Major types of aromatic amines in the plastic tableware are 4, 4-methylene diphenylamine (MDA) and aniline [31]. MDA and aniline have been identified as potential carcinogen by International Agency for Research on Cancer, and are limited to ppb levels in natural waters [32]. Therefore, it demands reliable, sensitive and repaid analytical methods for the measurement of MDA and aniline. Gas chromatography, liquid chromatography and capillary electrophoresis were reported to separate and detect aromatic amines [33–35]. These methods have the advantage of high-efficient separation, however, complicated procedure (for instance, chemical derivation) and expensive instruments are required. In view of time consuming and easy operation, there are growing needs to seek some other sensitive and rapid methods. Electrochemical method has emerged as fast and efficient tool for the analysis of aromatic amines [36,37]. However, as a disadvantage, this method has poor selectivity because of the similar structure of MDA and aniline. In this work, we describe a new strategy for simultaneous detection of MDA and aniline using MIPs-G as electrode material and the procedure is illustrated in scheme 1. MDA was used as the template and adsorbed on the surface of graphene through the π-π interaction [38], and 4-vinyl pyridine (4-VP) could pre-polymerize with template molecules via hydrogen bonds and van der Waals interaction [39]. After the thermal decomposition of 2, 2'-azobis (2-methylpropionitrile) (AIBN), free radicals would occur and the polymerizations begin to form MIPs-G nanocomposites. After removal of template molecules (MDA) through linear sweeping voltammetry, MIPs-G was used as electrode materials for simultaneous detection of MDA and aniline. MDA is binding preferentially at imprinting cavities and is oxidized electrochemically due to the high affinity and fast kinetics to uptake the template molecules. As for aniline, it is adsorbed on graphene via π-π stacking and then electrochemically oxidized. Due to the difference on surrounding environment, the electrochemical responses of MDA and aniline at MIPs-G modified electrode can be discriminated easily.

2. Materials and methods

2.1. Reagents

Graphene (physical reduction, Nanjing XFNano Chemicals, China), MDA (99.5%, Shanghai J&K Chemicals, China). Ethylene glycol dimethacrylate (EGDMA) and 4-VP were purchased from Aldrich and were distilled under reduced pressure to remove inhibitors. AIBN (99%) was purchased from Aladdin Chemicals (Shanghai, China). Other chemicals were purchased from Sinopharm Chemical Reagent Company. Phosphate buffer solution (PBS) was prepared with KH_2PO_4 and Na_2HPO_4. The solutions of MDA and aniline (1.0 mmol L^{-1}) were made by ethanol.

2.2. Apparatus

The surface morphological images were characterized by transmission electron microscope (TEM, TECNIG20, 200 KV) and scanning electron microscope (SEM, HITACHI S-4800). Fourier transform infrared (FTIR) spectra were performed on a NEXLIS FTIR (Nicolet, USA). Raman measurements were carried out using a confocal microprobe Raman system (LabRam II, Dilor, France). Thermal gravimetric analysis (TGA) was conducted on a SDTA851 TGA analyzer (Mettler Toledo, Switzerland) with temperature ranging from room temperature to 700 °C at a heating rate of 10 °C min^{-1} in the nitrogen flow.

Electrochemical measurements were conducted with a computer-controlled Autolab (TYPE III, Netherlands) electrochemical workstation at room temperature. A glassy carbon electrode (GCE, d = 3 mm) or modified-GCE was used as working electrode, with a platinum wire as auxiliary electrode and a saturated calomel reference electrode (SCE).

The official method based on liquid chromatography was performed on Aglint 1200 with a diode array detection (DAD) system. The DAD monitoring wavelength was set at 240 nm. An Eclipse Plus C18 column (4.6 × 250 mm, 5 μm) was used for separation and the injection volume was 10 μL. The stationary phase was a mixture of water and acetonitrile (9:1, v/v) at a flow rate of 1.0 mL min^{-1}.

2.3. Synthesis of MIPs-G

MDA molecules were used as the template and the synthesis route of MIPs-G was described as follows. Firstly, 20 mg graphene were dispersed in 20 mL mixed solution of trichloromethane and acetonitrile (v/v, 1:3). Then, 0.2 mmol MDA was added into the solution and mixed by ultrasonic for about 30 minutes until MDA was homogeneously dispersed. After that, 0.8 mmol 4-VP, 4.0 mmol EGDMA, and 30 mg AIBN were added and the resultant mixture was stirred at 60 °C for about 24 hours under the nitrogen protection. The resulting products were collected through centrifugation and washed thoroughly with methanol. Finally, the materials were dried under vacuum at 55 °C for 12 hours. As controlled samples, non-imprinted polymers (NIPs-G) were also synthesized by the same protocol of MIPs-G but in the absence of MDA.



Scheme 1. The synthesis route for MIPs-G via FRP and the electrochemical sensing of MDA and aniline.

2.4. Electrochemical measurements

1 mg MIPs-G (or NIPs-G, graphene) were added into 1 mL of 0.1 mol L^{-1} HAc with 0.5% chitosan under ultrasonication for one hour. Prior to use, the GCE was polished with 0.5 μm alumina powder and dried at room temperature. Then, 5 μL MIPs-G (1 mg mL^{-1}) were dropped on the surface of GCE and dried under IR lamp. The templates were removed by linear sweeping until no electrochemical signal of MDA was observed. After extracting the templates, the electrode was used to detect target molecules using differential pulse voltammetry (DPV) in 10 mL PBS containing different amount of MDA and aniline.

2.5. Sample treatment

As for plastic samples, white spoon, black spoon and black spatula were selected for market. Based on GB/T 5009.156-2003, the volume of soak solution was about 6 mL dm^{-2} based on the fixed contact area. 3% acetic acid was chosen as soak solution and the sample was soaked in it for two hours at 100 °C. After that, the extracting solution was adjusted to pH=9.0 with sodium hydroxide. Envi Chrom P solid-phase extraction column was used to enrich aromatic amine according to the literature [31].

3. Results and discussions

3.1. Characterization of MIPs-G

The morphology of graphene and MIPs-G was characterized by SEM and TEM, respectively. As shown in Fig. 1(a-d), the feature structure of graphene with some folds and wrinkles could be observed in all of the images, and these wrinkles are important for preventing aggregation of graphene and maintaining high surface area [40]. As for MIPs-G (Fig. 1(c) and (d)), some granular substances were grafted on the surface of graphene, indicating the formation of MIPs through FRP.

Fig. 2(A) shows the FTIR spectra of graphene, MIPs-G and MIPs. As shown in Fig. 2A(a), the absorbance at 1641 cm^{-1} was assigned to C=C stretch vibration of graphene, while the absorbance at 1103 cm^{-1} was attributed to C-O-C stretch, indicating the existing of oxygen-rich groups [41]. Fig. 2A(b) presents the characteristic vibration of MIPs. The bands at 1637, 1458 and 1390 cm^{-1} were assigned to C=N, C=C, and C-N stretching vibration, respectively, which indicated the existence of vinyl pyridine [42]. The peaks at 1731 and 1156 cm^{-1} were characteristics of the C=O and C-O stretching vibration of EGDMA. The characteristic peaks of MIPs were also appeared in the sample of MIPs-G (Fig. 2A(c)) with little blue shift to 1726, 1636, 1452 and 1252 cm^{-1}. It is probably due to the interaction between graphene and MIPs. Owing to the weak vibration, the absorption for graphene is hardly observed in Fig. 2A(c).

The Raman spectrum of graphene in Fig. 2B(a) exhibits a D-band at 1350 cm^{-1} due to the breathing mode of κ-point phonons of A1g symmetry, while the G-band at 1608 cm^{-1} is corresponding to the E2g phonon of the sp2 hybridization carbons in the 2-D lattice [43]. It can be seen that the similar peaks of D-band (1365 cm^{-1}) and G-band (1621 cm^{-1}) were also appeared in Fig. 2B(b), but the intensities were reduced obviously, probably due to the lower content of graphene in the composite [44]. The intensity of D and G expresses the sp2/sp3 carbon ratio, a measure of the extent of disorder present within the materials [45]. The i_D/i_G ratios of graphene and MIPs-G are 1.81 and 1.56, respectively, reflecting the decrease in disorder after polymerization. In addition, the G-band of MIPs-G shows a little blue shift, which provides an evidence for the strong interaction and charge transfer between graphene and MIPs [19].

The TGA curves of MIPs and MIPs-G are shown in Fig. 3. For MIPs (Fig. 3(a)), it appeared a gradual weight loss below 300 °C, which was likely due to the decomposition of labile oxygen functional groups [44]. The weight loss increased obviously from 300 °C to 430 °C and remained stable about 450 °C with about 89% total weight loss, which might be corresponding to the degradation of carbon skeleton for MIPs [44]. The TGA curve of MIPS-G shows a similar weight loss from 300 to 400 °C with about 84% weight loss. As graphene is relatively

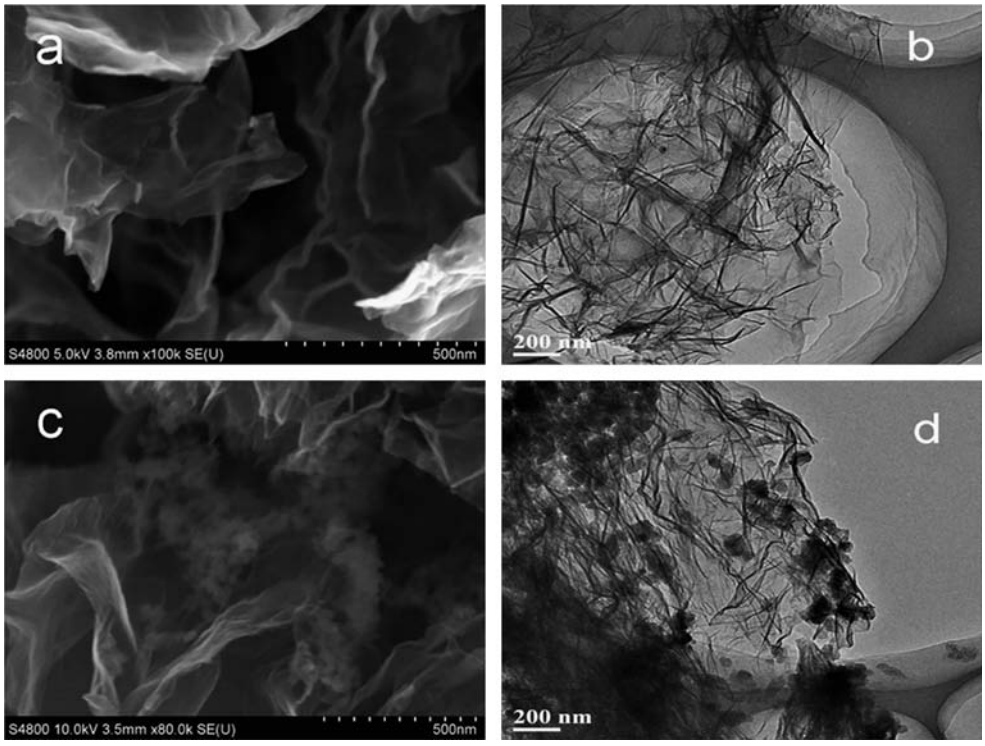


Fig. 1. SEM and TEM images of graphene (a, b) and MIPs-G (c, d) respectively.

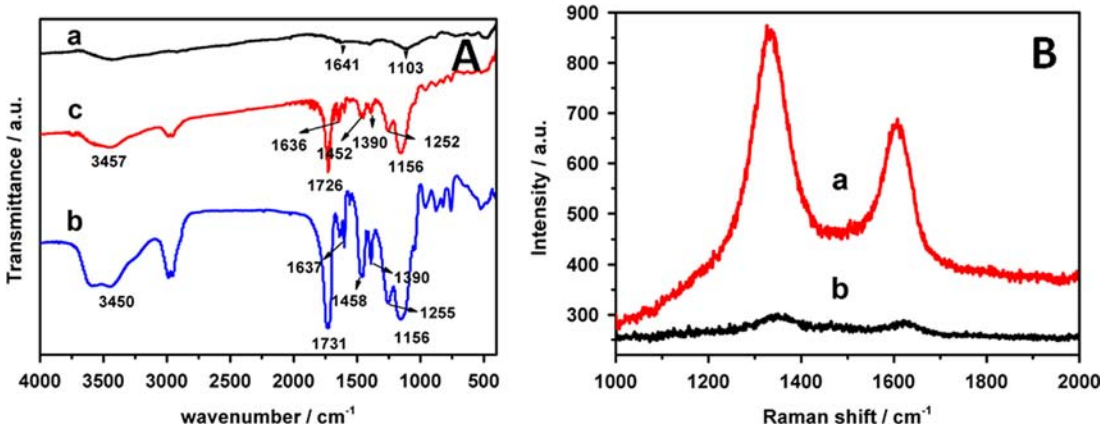


Fig. 2. (A). FTIR spectra of graphene (a), MIPs (b) and MIPs-G (c). **(B).** Raman spectra of graphene (a) and MIP-G (b).

thermal stable below 700 °C under nitrogen [46], the difference on weight loss between MIPs and MIPs-G was likely assigned to the existence of graphene. Based on the above results, the weight content of MIPs grafted on the surface of graphene was up to almost 95%.

3.2. Electrochemical characteristics of MIPs-G modified electrode

EIS is an effective method for exploring the features of the modified electrode [47]. The impedance measurement was performed in 5 mM $[Fe(CN)_6]^{3-/4-}$ with 0.1 mol L^{-1}KCl over the frequency ranged from 0.1 to 10^4 Hz at the formal potential of 0.18 V. The Rct for bare GCE (Fig. 4A(a)) is about 56 Ω, while the EIS for graphene modified electrode (Fig. 4A(b)) is almost straight due to the excellent electron-transfer ability. As for MIPs-G modified electrode (Fig. 4A(c)), the Rct is about 20 Ω, which is larger than that of graphene modified electrode because of the poor conductivity of MIPs.

The electrochemical behavior of MIPs-G modified electrode was also studied by cyclic voltammetry in 5 mM $K_3[Fe(CN)_6]$ solution. As shown in Fig. 4B, the oxidation and reduction peak currents increased with the scan rate over the ranging from 30 to 300 mV s^{-1}. A liner correlation of I_{pa} or I_{pc} versus $v^{1/2}$ is observed in the insert plot of Fig. 4B, indicating the electrochemical reaction is diffusion controlled.

3.2.1. Electrochemical behaviors of MDA and aniline

Graphene has been widely used as electrode materials because it has many advantageous properties like good conductivity, wide potential window, good electrocatalytic activity, easy modification, large specific surface areas and the capability of being mass-produced from bulk graphite [48]. The electrochemical behaviors of MDA and aniline at graphene modified GCE were investigated (Fig. 5). As shown in Fig. 5(a), MDA is electrochemically oxidized at 0.50 V and reduced at 0.11 V. As for aniline (Fig. 5b), an oxidation peak at 0.52 V and a reduction peak at 0.11 V are observed. It can be seen that the electrochemical responses of MDA and aniline at graphene modified electrode occur at almost the same redox potentials because of the similar chemical structure. Hence, MDA and aniline can't be detected at graphene modified electrode.

Fig. 6 demonstrates the DPV responses of MDA and aniline at MIPs-G modified electrode. As shown in Fig. 6(a) and (b), the oxidation potential for MDA and aniline is observed at 0.62 and 0.72 V, respectively. Fig. 6(c) shows the electrochemical responses of mixture of MDA and aniline (1:1) at MIPs-G modified electrode. It can be seen that two oxidation peaks at 0.62 and 0.72 V appear simultaneously, indicating the electrochemical oxidation of MDA and

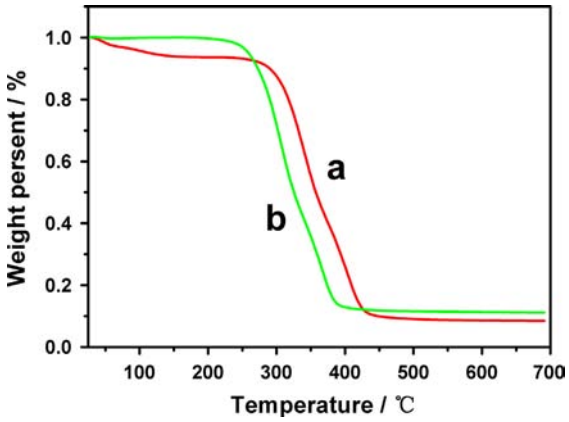


Fig. 3. TGA curves of MIPs (a) and MIPs-G (b) at a heating rate of 10 °C min^{-1} from room temperature to 700 °C under a nitrogen flow.

aniline, respectively. It shows that MDA and aniline can be differentiated at MIPs-G modified electrode. It can be explained that MDA and aniline can be simultaneously adsorbed on the surface of graphene because of the π-π interaction [49], therefore, the electrochemical behaviors of MDA and aniline at graphene modified electrode cannot be discriminated due to the similar chemical structure. As for MIPs-G, we assume that MIPs presenting on the surface of the graphene have special binding capability for template molecules, thus, MDA can be adsorbed preferentially by the imprinting sites due to the selective recognition. In addition, aniline is adsorbed on the surface of graphene which is not occupied by MIPs through π-π interaction. Due to the difference on surrounding environment, the electrochemical behaviors of MDA and aniline can be discriminated at the MIPs-G modified electrode. Furthermore, the cross-talk experiment between aniline and MDA was further investigated (shown in Fig. 6(d) and (e)). While the concentration of aniline is fixed (5 μM), the oxidation current varies linearly with the concentration of MDA over the range from 1.0 to 15 μM (R^2=0.9923) (Fig. 6(d)). On the other hand, the peak current is also linear with the concentration of aniline while the concentration of MDA is fixed (5 μM) (Fig. 6(e)). In addition, the oxidation peak current of MDA is almost the same with the change of the concentration of aniline, which might originate from the special binding capacity of MIPs-G for MDA. Moreover, the electrochemical behaviors of MDA and aniline at NIPs-G modified electrode were also studied (Fig. 6(f)). In a mixture with equal amount of MDA and aniline, only one obvious oxidation peak at 0.72 V can be observed, indicating the two aromatic amines can't be measured simultaneously due to the lack of recognition sites on the surface of NIPs-G. It is further confirmed

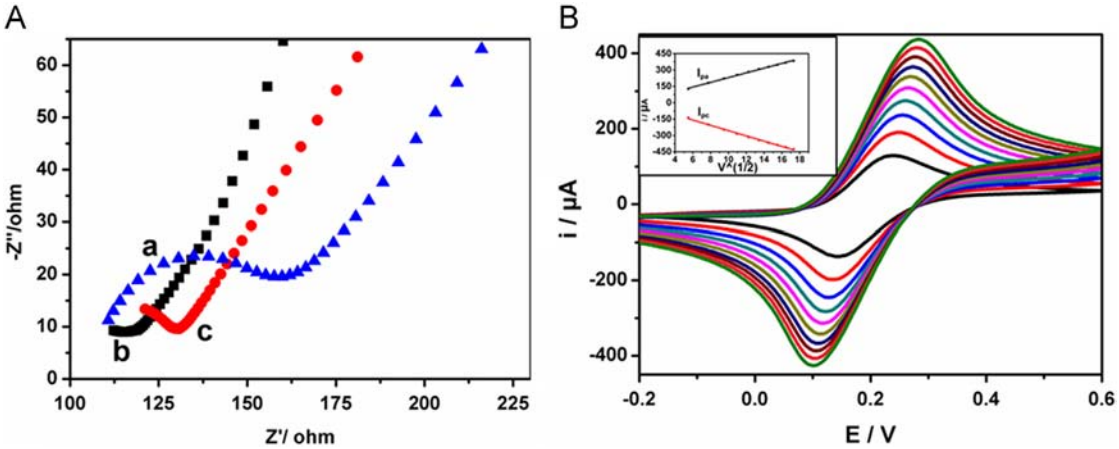


Fig. 4. (A). Electrochemical impedance spectra recorded in 5.0 mM $K_3[Fe(CN)_6]$ containing 0.1 M KCl at bare GCE (a), graphene modified GCE (b) and MIPs-G modified electrode (c). **(B).** Cyclic voltammograms of MIPs-G modified GCE in 5.0 mM K_3 $[Fe(CN)_6]$ with scan rate increasing from 30 to 300 mV s^{-1}, and the insert is the peak currents versus $v^{1/2}$.

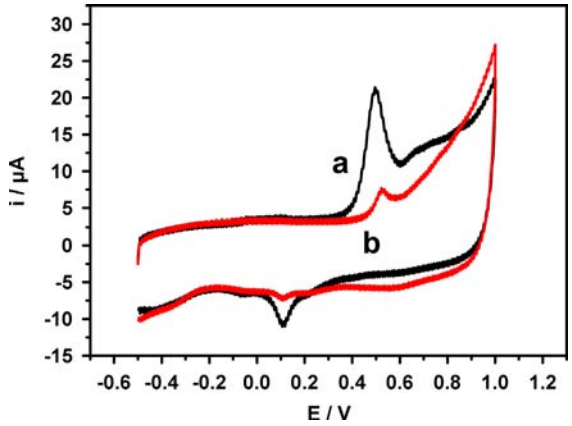


Fig. 5. Cyclic voltammograms of graphene modified electrode in PBS (pH=7.0) containing 10 μM MDA (a) and aniline (b) with scan rate of 100 mV s^{-1}.

that MIPs-G has a special binding capacity for the template molecules and can be used to detect MDA and aniline simultaneously.

3.3. Optimization of electrochemical conditions

The effect of experiment condition on the electrochemical response of MDA at MIPs-G modified electrode were further investigated (data not shown). The oxidation peak current gradually increased with an increasing pH from 4.0 to 7.0 and then decreased from 7.0 to 10.0. Thus, the experiment was performed at pH 7.0. Meanwhile, the oxidation potential shifts negatively and linearly with the increasing of the pH. The relationship between the potential and pH obeys the equation as follows, $E_{pa}(V)$= 0.78361–0.02625 pH. The potential negatively shifts 26.25 mV per pH unit, indicating one proton per two electrons involved in the electrochemical reaction [50]. The amount of the MIPs-G on the electrode surface also plays an important role for detecting MDA and aniline. In this work, the concentration of MIPs-G was fixed as 1.0 mg mL^{-1} and the amount of modifier on the electrode was controlled by change the dropped volume of modifier. As a consequence, the electrochemical response of MDA reaches maximum while the volume of modifier is 5 μL. Hence, 5 μL of MIPs-G (1.0 mg mL^{-1}) was chosen as the optimized amount of modifier. The accumulation time is also an important parameter that might affect the electrochemical response. In this work, MIPs-G modified electrode was dipped in the solution for a certain time to accumulate MDA and aniline before electrochemical detection, and the optimized accumulation time is 60 s. Under these conditions, the determination of MDA and aniline at different concentrations was performed. The DPV response was linear to the concentration of MDA and aniline over the range of 1.0 to 15 μM, and the linear equation was $I_{pa}(\mu A)=0.0352c(\mu M)-0.0113$ ($R^2=0.9962$) for MDA and $I_{pa}(\mu A)=0.0162c(\mu M)+0.0123$ ($R^2=0.9962$) for aniline, respectively.

3.4. Repeatability, stability and selectivity of MIPs-G electrode

Under the optimal conditions mentioned above, MDA and aniline solution were measured successively for five times with the same electrode. The relative standard deviation (RSD) of the peak current for MDA and aniline was 2.89% and 2.57%, respectively. The reproducibility of the imprinted sensor was investigated by measurement 2.0 μM MDA and aniline in PBS using three MIPs-G modified electrodes which were prepared under the same procedure. The RSD for MDA and aniline is about 4.18% and 6.80%, indicating a good sensor-to-sensor reproducibility. While the electrode was not used, it was stored in refrigerator in 4 °C. After one month, the electrochemical sensor was used to simultaneously measure MDA and aniline and about 92.0% of the initial peak current was obtained. It suggests that the imprinted electrochemical sensor exhibits satisfactory stability.

As for the selectivity of the sensor, some aromatic amines (such as phenylenediamine, hexamine, naphthylamine and 4-acetylene aniline) were selected to test the anti-interference ability of the MIPs-G modified electrode. The concentration of these substrates was the same as that of MDA. The results show that no electrochemical signal is observed for o-phenylendiamine and hexamine. It indicates o-phenylendiamine and hexamine could not affect the detection. As for naphthylamine and 4-acetylene aniline, the oxidation peak was located at 0.54 and 0.73 V, respectively. However, naphthylamine has no influence on the performance of the electrochemical sensor because the oxidation potential can be differentiated clearly. The oxidation peak of the 4-acetylene aniline is very close to that of aniline, indicating the potential interference. However, the major types of aromatic amines in plastic tableware were MDA and aniline [31], other aromatic amines was not found. It demonstrates that MIPs-G modified electrochemical sensor can be used for aromatic amines detecting in plastic tableware samples.

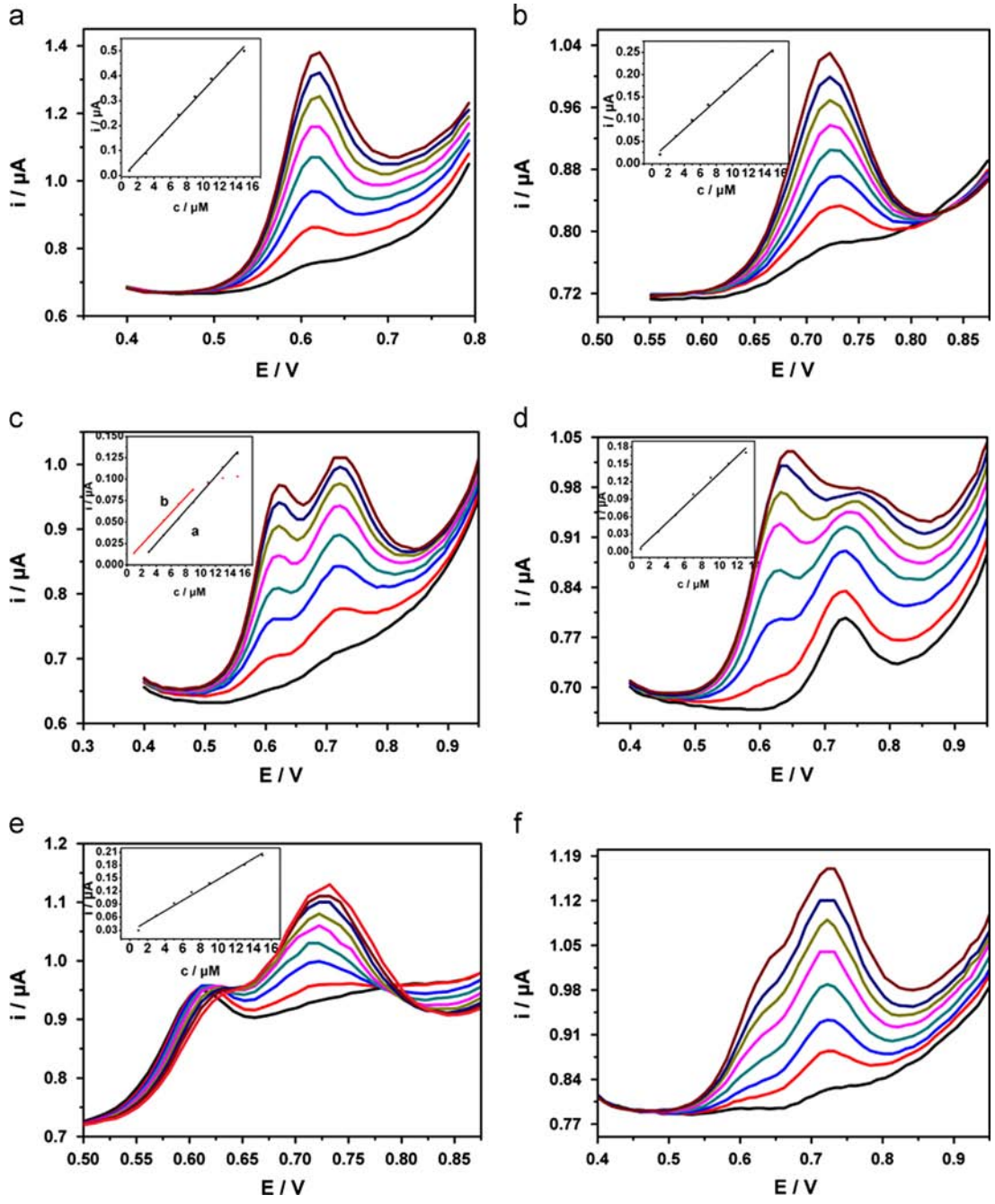


Fig. 6. DPV responses of MIPs-G modified electrode in PBS containing MDA (a), aniline (b), MDA and aniline (1:1) (c), fixed aniline (5 μM) with different concentration of MDA (d) and fixed MDA (5 μM) with different concentration of aniline (e). (f) DPV responses of NIPs-G modified electrode in PBS with MDA and aniline (1:1). The concentration of MDA and aniline varied from 1–15 μM. The inserts are the linear plots between the peak current and the concentration of analyte.

3.5. Sample analysis

In order to evaluate the practical application of MIPs-G modified electrode, MDA and aniline in white spoon (sample 1), black spatula (sample 2) and black spoon (sample 3) were measured. For the electrochemical measurements, 1 mL samples were diluted to 10 mL with PBS (pH7.0). However, no MDA and aniline were detected in all samples. Therefore, standard addition method was further used to evaluate the potential application MIPs-G modified electrode in sample analysis. A known amount of MDA and aniline were added into the solutions and the recovery was obtained (shown in Table 1). The recovery was ranging from 93.5% to 106%, indicating the electrochemical sensor can be applied for detecting MDA and aniline simultaneously in real samples. Meanwhile, the samples were measured by HPLC and the results were very close to these of MIPs-G modified electrochemical sensor (shown in Table 1). The consistency between electrochemical sensor and the official method confirms the imprinted electrode could be used in practice.

4. Conclusions

In this work, a sensitive and selective electrochemical sensor based on MIPs-G was developed for simultaneous measurement MDA and aniline. Owing to the unique conductivity and large surface area, graphene provides an excellent platform for the

Table 1
Determination of MDA and aniline in white spoon (sample 1), black spatula (sample 2) and black spoon (sample 3) by MIPs-G modified electrode and HPLC.

Samples ($n=3$)	Added (μM)		Found by sensor (μM)		Recovery (%)		Found by HPLC (μM)	
	MDA	aniline	MDA	aniline	MDA	aniline	MDA	aniline
1	0.00	0.00	–	–	–	–	–	–
	1.00	1.00	0.99	0.96	99.2	96.0	1.02	1.04
	2.00	2.00	2.06	2.02	103	101	1.91	1.95
	3.00	3.00	3.12	2.90	104	96.6	2.92	2.86
2	0.00	0.00	–	–	–	–	–	–
	1.00	1.00	1.02	0.94	102	93.6	1.09	1.03
	2.00	2.00	2.12	2.02	106	101	2.01	1.93
	3.00	3.00	3.07	2.84	102	94.7	2.97	3.05
3	0.00	0.00	–	–	–	–	–	–
	1.00	1.00	0.99	0.95	98.6	94.5	1.05	1.07
	2.00	2.00	2.09	1.87	104	93.5	2.03	2.01
	3.00	3.00	2.97	2.83	99.1	94.3	3.07	3.09

development of MIPs-G based electrochemical sensing system. The MIPs-G modified electrode displays linear response towards MDA and aniline over the range of 1.0 to 15 μmol L^{-1}. Furthermore, the MIPs-G based sensor was used to determine MDA and aniline simultaneously in plastic food packing samples, and the acceptable recovery implied its feasibility for practical application.

Acknowledgments

This work was supported by the National Natural Science Foundation of China (No. 21175046), General Administration of Quality Supervision, Inspection and Quarantine of China (Nos. 2011IK041, 2012IK048 and 2013IK017) and Open Foundation of Shanghai Key Laboratory of Green Chemistry and Chemical Process.

References

[1] F. Dickey, Proc. Natl. Acad. Sci. USA 35 (1949) 227–229.
[2] L. Chen, S. Xu, J. Li, Chem. Soc. Rev. 40 (2011) 2922–2942.
[3] S. Ambrosini, M. Serra, S. Shinde, B. Sellergren, E. De Lorenzi, J. Chromatogr. A 1218 (2011) 6961–6969.
[4] C. Malitesta, I. Losito, P.G. Zambonin, Anal. Chem. 71 (1999) 1366–1370.
[5] E. Turiel, J.L. Tadeo, A. Martin-Esteban, Anal. Chem. 79 (2007) 3099–3104.
[6] A. Bossi, F. Bonini, A.P.F. Turner, S.A. Piletsky, Biosens. Bioelectron. 22 (2007) 1131–1137.
[7] J. Orozco, A. Cortés, G. Cheng, S. Sattayasamitsathit, W. Gao, X. Feng, Y. Shen, J. Wang, J. Am. Chem. Soc. 135 (2013) 5336–5339.
[8] L.I. Andersson, J. Chromatogr. B 745 (2000) 3–13.
[9] P.S. Sharma, M. Dabrowski, F. D'Souza, W. Kutner, Trac-Trends Anal. Chem 51 (2013) 146–157.
[10] P. Cakir, A. Cutivet, M. Resmini, B.T.S. Bui, K. Haupt, Adv. Mater. 25 (2013) 1048–1051.
[11] A.B. Descalzo, C. Somoza, M.C. Moreno-Bondi, G. Orellana, Anal. Chem. 85 (2013) 5316–5320.
[12] H.H. Yang, S.Q. Zhang, F. Tan, Z.X. Zhuang, X.R. Wang, J. Am. Chem. Soc. 127 (2005) 1378–1379.
[13] D. Cai, L. Ren, H. Zhao, C. Xu, L. Zhang, Y. Yu, H. Wang, Y. Lan, M.F. Roberts, J.H. Chuang, M.J. Naughton, Z. Ren, T.C. Chiles, Nat. Nanotech 5 (2010) 597–601.
[14] H.J. Wang, W.H. Zhou, X.F. Yin, Z.X. Zhuang, H.H. Yang, X.R. Wang, J. Am. Chem. Soc. 128 (2006) 15954–15955.
[15] I.S. Chronakis, B. Milosevic, A. Frenot, L. Yes, Macromolecules 39 (2006) 357–361.
[16] Y. Li, M. Hong, Q. Miaomiao, Z. Bin, Z. Lin, G. Cai, J. Chen, Mater. Chem. B 1 (2013) 1044–1051.
[17] K.S. Novoselov, A.K. Geim, S.V. Morozov, D. Jiang, Y. Zhang, S.V. Dubonos, I.V. Grigorieva, A.A. Firsov, Science 306 (2004) 666–669.
[18] D. Abergel, V. Apalkov, J. Berashevich, K. Ziegler, T. Chakraborty, Adv. Phys 59 (2010) 261–482.
[19] Y. Li, X. Li, C. Dong, J. Qi, X. Han, Carbon 48 (2010) 3427–3433.
[20] L. Chang, S. Wu, S. Chen, X. Li, J. Mater. Sci. 46 (2011) 2024–2029.
[21] Y. Mao, Y. Bao, S. Gan, F. Li, L. Niu, Biosens. Bioelectron. 28 (2011) 291–297.
[22] X. Xing, S. Liu, J. Yu, W. Lian, J. Huang, Biosens. Bioelectron. 31 (2012) 277–283.
[23] L. Kan, Z. Xu, C. Gao, Macromolecules 44 (2010) 444–452.
[24] F. Duan, C. Chen, G. Wang, Y. Yang, X. Liu, Y. Qin, RSC Adv 4 (2014) 1469–1475.
[25] Y. Zhou, Z.B. Qu, Y. Zeng, T. Zhou, G. Shi, Biosens. Bioelectron. 52 (2014) 317–323.
[26] H. Lian, Z. Sun, X. Sun, B. Liu, Anal. Lett. 45 (2012) 2717–2727.
[27] X. Wang, J. Dong, H. Ming, S. Ai, Analyst 138 (2013) 1219–1225.
[28] P. Qi, Y. Wan, D. Zhang, Biosens. Bioelectron. 39 (2013) 282–288.
[29] M. Cui, S. Liu, W. Lian, J. Li, W. Xu, J. Huang, Analyst 138 (2013) 5949–5955.
[30] H.J. Chen, Z.H. Zhang, R. Cai, X.Q. Kong, X. Chen, Y.N. Liu, S.Z. Yao, Analyst 138 (2013) 2769–2776.
[31] L. Sun, Z. Chen, X. Chu, Food Mechinery 22 (2006) 121–126.
[32] Z.F. Chen, X.H. Liu, L. Sun, Packag. Eng. 3 (2010) 013.
[33] T.M. Lizier, M.V. Boldrin Zanoni, Molecules 17 (2012) 7961–7979.
[34] M.L. Di Gioia, A. Leggio, A. Le Pera, A. Liguori, A. Napoli, F. Perri, C. Siciliano, J. Chromatogr. A 1066 (2005) 143–148.
[35] A. Asthana, D. Bose, A. Durgbanshi, S. Sanghi, W.T. Kok, J. Chromatogr. A 895 (2000) 197–203.
[36] M. Van Dyck, B. Rollmann, C. De Meester, J. Chromatogr. A 697 (1995) 377–382.
[37] D. Shin, D.A. Tryk, A. Fujishima, A. Muck, G. Chen, J. Wang, Electrophoresis 25 (2004) 3017–3023.
[38] K.P. Loh, Q. Bao, P.K. Ang, J. Yang, J. Mater. Chem. 20 (2010) 2277–2289.
[39] J. Bastide, J.-P. Cambon, F. Breton, S. Piletsky, R. Rouillon, Anal. Chim. Acta 542 (2005) 97–103.
[40] H.C. Schniepp, J.L. Li, M.J. McAllister, H. Sai, M. Herrera-Alonso, D.H. Adamson, R.K. Prud'homme, R. Car, D.A. Saville, I.A. Aksay, J. Phys. Chem. B 110 (2006) 8535–8539.
[41] Y. Si, E.T. Samulski, Nano Lett. 8 (2008) 1679–1682.
[42] W. Chi, H. Shi, W. Shi, Y. Guo, T. Guo, J. Hazard. Mater. 227 (2012) 243–249.
[43] Y. Guo, Y. Han, S. Shuang, C. Dong, J. Mater. Chem. 22 (2012) 13166–13173.
[44] Y. Zeng, Y. Zhou, L. Kong, T. Zhou, G. Shi, Biosens. Bioelectron. 45 (2013) 25–33.
[45] M. Fang, K. Wang, H. Lu, Y. Yang, S. Nutt, J. Mater. Chem. 19 (2009) 7098–7105.
[46] S. Stankovich, D.A. Dikin, R.D. Piner, K.A. Kohlhaas, A. Kleinhammes, Y. Jia, Y. Wu, S.T. Nguyen, R.S. Ruoff, Carbon 45 (2007) 1558–1565.
[47] A.S. Bondarenko, I.E. Stephens, H.A. Hansen, F.J. Pérez-Alonso, V. Tripkovic, T.P. Johansson, J. Rossmeisl, J.K. Nørskov, I. Chorkendorff, Langmuir 27 (2011) 2058–2066.
[48] X. Huang, Z. Zeng, Z. Fan, J. Liu, H. Zhang, Adv. Mater. 24 (2012) 5979–6004.
[49] G. Zhao, L. Jiang, Y. He, J. Li, H. Dong, X. Wang, W. Hu, Adv. Mater. 23 (2011) 3959–3963.
[50] H. Fan, Y. Li, D. Wu, H. Ma, K. Mao, D. Fan, B. Du, H. Li, Q. Wei, Anal. Chim. Acta 711 (2012) 24–28.

Talanta 132 (2015) 162–174

Contents lists available at ScienceDirect

Talanta

journal homepage: www.elsevier.com/locate/talanta

Review

Applications of electrochemical immunosensors for early clinical diagnostics

Elif Burcu Bahadır [a], Mustafa Kemal Sezgintürk [b,*]

[a] Namık Kemal University, Scientific and Technological Research Center, Tekirdağ, Turkiye
[b] Namık Kemal University, Faculty of Science, Chemistry Department, Biochemistry Division, Tekirdağ, Turkiye

ARTICLE INFO

Article history:
Received 4 July 2014
Received in revised form
18 August 2014
Accepted 27 August 2014
Available online 6 September 2014

Keywords:
Biosensor
Cancer biomarkers
Immunosensor
Electrochemical biosensors
Early diagnosis

ABSTRACT

Cancer and cardiovascular diseases are the major threats to global health. Hence, there is a growing demand for a range of portable, rapid and low cost biosensing devices for the detection of these diseases. Electrochemical immunosensors are simple, rapid, reliable and inexpensive devices and they have sensitive detection limits to monitor both levels of the biomarkers in normal and patient serum. Due to the specific binding of antibody to its corresponding antigen, immunosensors based on antibody–antigen interaction are one of the most widely used analytical techniques in the quantitative detection of these diseases. The changed levels of markers in patients are associated with diseases. In this article the biosensors and biomarkers, which were commonly used in terms of monitoring the diagnosis and treatment of cancer and cardiac diseases, are reviewed. In addition, the developed biosensors are compared in terms of precision, reproducibility, regeneration, stability and specificity.

© 2014 Elsevier B.V. All rights reserved.

Contents

1. Introduction . . . 162
2. Electrochemical immunosensors . . . 163
3. Tumor and cardiac markers . . . 164
   3.1. Tumor markers . . . 164
   3.2. Cardiac markers . . . 170
4. Future outlook . . . 172
5. Conclusion . . . 172
Acknowledgment . . . 172
References . . . 173

1. Introduction

The pioneering study of Clark and Lyons, more than four decades ago, shed light on some analytical researchers in designing of biosensors, which perform as economical and fast tools for clinical, chemical, environmental and pharmaceutical studies. Because of its simple use and portability in relatively complex samples, biosensors offer a potential alternative to advanced bioanalytical systems [1].

A biosensor is composed of two components, a bioreceptor and a transducer. First part, the bioreceptor is a biomolecule that recognizes the target analyte, and second part the transducer converts the recognition event into a measurable signal [2]. Immunosensors are antibody–antigen based affinity biosensors, in which the detection of antigen as a target analyte is a result of the specific binding of the antigen to particular region of an antibody on the electrode surface [3]. Also, in electrochemical immunosensors antibody acts as a bioreceptor and antigen acts as a target analyte and transducer can be able to quantify the antigen concentration by using amperometric, potentiometric, impedimetric or conductometric signals. Fig. 1 shows a schematic presentation of an electrochemical immunosensor.

In recent years, optical and electrochemical detection methods have been used in early clinical diagnosis. Optical detection transduction method is less sensitive when coupled with radioimmunoassay, has short half-life of radioactive agents, concern of health hazards, and has disposal problems. On the other hand, electrochemical

* Corresponding author. Tel.: +90 282 250 26 05.
E-mail addresses: msezginturk@hotmail.com, msezginturk@nku.edu.tr (M. Kemal Sezgintürk).

http://dx.doi.org/10.1016/j.talanta.2014.08.063
0039-9140/© 2014 Elsevier B.V. All rights reserved.

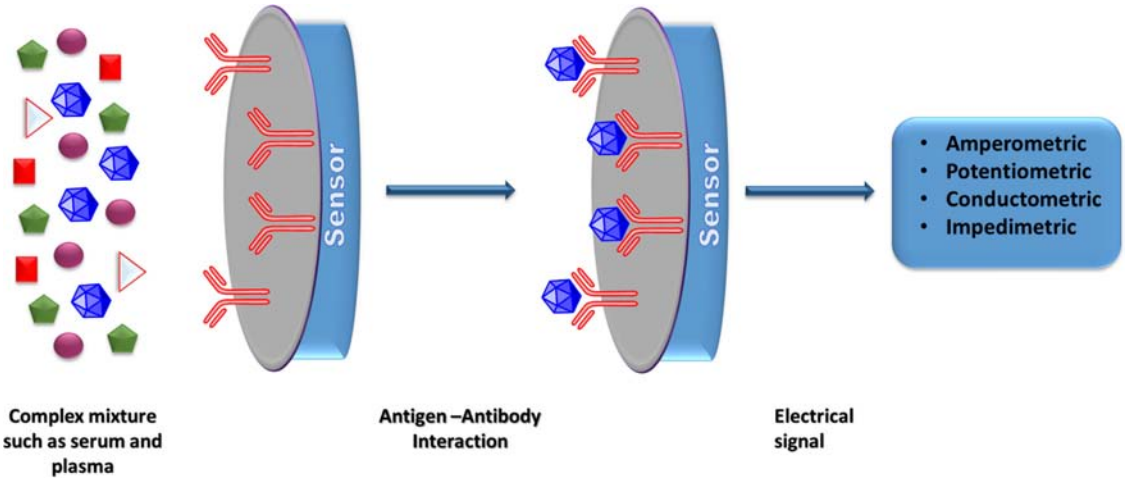


Fig. 1. Schematic representation of electrochemical immunosensor.

detection method shows no similar problems and electrochemical immunoassays and immunosensors enable fast, simple, and economical detection [4].

Electrochemical immunosensors are used as care devices since they are portable, simple, easy to use, cost effective and disposable in most cases [5,6]. Compared with traditional immunoassay methods, electrochemical immunosensors are specific, simple and convenient, and can offer multitarget analyses and miniaturization. They can perform in situ, real-time, automation detection [7].

Specificity for any given biomarker is often achieved by use of antibodies. The specific binding of an antibody to its target antigen in a complex mixture such as serum and plasma provides the detection and quantification of diseases at levels as low as picograms (pg) [8]. Also, this is another advantage of immunosensors.

In this study the biosensors and biomarkers, which were commonly used in terms of monitoring the diagnosis and treatment of cancer and cardiac diseases, are reviewed. And also, it focuses on recent development for tumor markers and cardiac markers testing and monitoring in clinical diagnosis. However, a wide range of researches have been published in this area. This review is limited to recent publication within the past nine years. Most reviews have been organized around only tumor or cardiac biomarkers and their diagnosis of biosensors. Herein we present different biomarkers used in several publications of electrochemical immunosensors for tumor and cardiac diseases and highlighted the major clinically relevant parameters, such as their detection limit/range and designing of bioassay. Moreover, in this review, we emphasize on the opportunities for further improvement in tumor and cardiac diseases diagnostic and treatment monitoring.

2. Electrochemical immunosensors

An antibody based biosensor was applied for the first time in the 1950s, leading the possibility of immune-diagnosis [4]. These types of biosensors have high specificity and low limit of detection due to their extreme antibody affinity to their antigen. Antibodies are proteins produced by the immune system. However, antigens can be a variety of different molecules, from protein to DNA, lipids, etc [6].

In developing immunosensors, the immobilization of antibody is an important step because antibody acts as the recognition element for antibody–antigen reaction. The performance of the detection and antigen binding capacity can be increased by a proper antibody surface. Thus the choice of the antibody immobilization method is very important in the design of an immunosensor. Several methods including physical [9–10] and chemical adsorption have been used for the preparation of oriented antibody molecular layers on the surface of the transducer. Self-assembly (SAM) technique has been used as chemical adsorption method for immobilization of antibody [11–13]. In this technique, a self-assembly monolayer is fixed on the surface through chemical bonds. Then the antibody is covalently attached to the monolayer by using cross-linkers.

Transducer types used in immunosensors are electrochemical (amperometric, potentiometric, conductometric, capacitative), optical (fluorescence, luminescence, refractive index), piezoelectric or calorimetric. The electrochemical immunosensors rely on the measurements of currents and/or voltage to detect binding between antibody and antigen.

In potentiometric measurements, the potential difference between a working and a reference electrode is determined by a voltammeter when there is no significant current flowing through them. The potential difference is measured due to the oxidation and reduction of the species in sample solution. The transducer may be an ion selective electrode (ISE) based on thin film or selective membranes as recognition elements. Analytical information is obtained when the ISE convert the biorecognition process into a potential signal.

In amperometric measurements, a current occurs as a result of electrochemical oxidation or reduction of an electroactive species. This type of measurement is taken by maintaining a constant amplitude voltage at working electrode (gold, platinum, and carbon) related to reference electrode, under a fixed potential, current pass through sample [8].

In impedimetric measurements, when biorecognition elements occur at the modified surfaces, the interfacial properties change. Thus impedimetric immunosensors can be used to determine quantitative parameters of electrochemical properties. Electrochemical reactions, known as electron transfers at the electrode surface, involve electrolyte resistance, adsorption of electroactive species, charge transfer at the electrode surface, and mass transfer from the bulk solution to the electrode surface. Each reaction process represented by an electric circuit consists of resistance, capacitors, or constant phase elements combined in parallel or in series. The most favorite model of electric circuit for a simple electrochemical reaction is the Randles–Ershler electric equivalent circuit model, consisting of electrolyte resistance (R_s), charge-transfer resistance (R_{ct}) at the electrode/electrolyte interface, double-layer capacitance (C_{dl}), and mass transfer resistance (R_{mt}), also Warburg impedance (W) [2,14].

In conductometric measurements, there is a relationship between a biorecognition event and conductance. While a reaction, a change in the ionic species concentration leads to change

the solution's electrical conductivity or current flow. A conductometric biosensor consists of two metal electrodes (usually platinum or silver) separated by a certain distance. An ohmmeter (or multimeter) is used to measure the change in conductance between the metal electrodes [15].

3. Tumor and cardiac markers

The National Cancer Institute (NCI) defines a biomarker as "a biological molecule found in blood, other body fluids, or tissues that is a sign of a normal or abnormal process or of a condition or disease. A biomarker may be used to see how well the body responds to a treatment for a disease or condition". Biomarkers can derive from various molecular origins, including DNA (i.e., specific mutation, translocation, amplification, and loss of heterozygosis), RNA, or protein (i.e., hormone, antibody, oncogene, or tumor suppressor) [16]. Different diseases are known to produce or alter the levels of different biomarkers. Therefore, sensitive and rapid diagnosis methods are very important for their detection. Tumor biomarkers are potentially one of the most valuable tools for early cancer detection, accurate pretreatment staging, determining the response of cancer to chemotherapy treatment, and monitoring disease progression. Also in tumor process, changed levels of tumor markers in patients are associated with certain tumor [17]. In addition, the early and quick diagnosis of cardiovascular disease is important not only for patient survival but also saving cost and a lot of time. Discussion of some of the major tumor and cardiac markers and developed for immunosensors for these diseases are presented below.

3.1. Tumor markers

Cancer is defined as abnormal and uncontrolled cell growth due to an accumulation of specific genetic and epigenetic defects and it is one of the main causes of mortality worldwide. Many factors including exposure to carcinogenic chemicals, radiation, genetic and environmental factors cause cancer [16]. There are more than 200 distinct diseases associated with cancer affecting different parts of the body and so clinical test of cancer is very complex [5]. In clinical analysis sensitive, precise, and accurate assays for the determination of tumor markers with low concentration level in complex biological samples are necessary for effective early diagnosis and treatment of cancer [18–20].

In the absence of a tumor, the tumor marker is of low level. Even a small tumor forms, levels of some markers rise. Thus the limits of detection (LODs) are important for early screening of a small tumor [7]. Methods and strategies based on biochemistry, immunology and molecular biology have been developed and used for the determination of tumor markers in human serum. Immunoassay techniques, which show highly specific molecular recognition, are frequently used methods in clinical quantitative detection of tumor markers. Radioimmunoassay, enzyme-linked immunosorbent assay (ELISA), fluoroimmunoassay, chemiluminescent immunoassay, and electrochemiluminescent immunoassays are present among these techniques. Beside the sensitivity, precision and selectivity advantages, there are several disadvantages of these techniques. For instance they have radiation hazards, high cost, require qualified personnel and sophisticated instrumentation and they are also time consuming. Moreover, existing diagnostic tests (e.g., microtiter-plate ELISAs) are not sensitive enough for screening cancer at an early stage and can only detect proteins at levels corresponding to advanced stages of disease [7,21]. Compared with conventional immunoassay methods, electrochemical immunosensor offer several advantages, such as high sensitivity, fast analysis, simple pretreatment, small analyte volume, simple instrumentation, and minimal manipulation and therefore they are largely used [17,22].

Biomarkers can be presented intracellular or extracellular. Intracellular markers need to be collected and enriched if their concentration is very low [5]. In Table 1, the most common biomarkers is listed and in Table 2, the thresholds of some basic tumor markers in human serum are listed [7,23].

Carcinoembriyonic antigen (CEA) is a cell surface glycoprotein with a molecular weight of about 200 kDa [24,25] used as a biomarker for clinical diagnosis of colon tumors, breast tumors, ovarian carcinoma [25–27], gastric, pancreatic, lung carcinomas [18,25,26]. Therefore, CEA is a broad spectrum multi-tumor marker for clinical diagnosis [18]. The level of CEA for a non-smoker adult is < 2.5 ng/mL and for a smoker < 5.0 ng/mL [26,28]. A rising CEA level indicates progression or recurrence of the cancer [26,28,29,30].

Prostate-specific antigen (PSA) is one of the first tumor biomarkers for screening and diagnosing prostate cancer [16,31]. PSA is a 32–33 kDa single-chain glycoprotein [31]. A very low amount of this substance reaches the bloodstream forming free PSA (fPSA) and PSA complexed to a-1-antichymotrypsin (PSA-ACT). Total PSA (tPSA) is the sum of f-PSA and PSA-ACT complex in serum. tPSA level, in healthy males, is usually less than 4 ng/mL and increases in serum during prostate cancer [32].

Tumor marker, α-1-fetoprotein (AFP) is an oncofetal glycoprotein [33,34,35,36] with a single-chain alpha globulin containing

Table 2
The thresholds of basic tumor markers in human serum [5,7].

Tumor markers	Thresholds	Tumor markers	Thresholds
NSE	12.5 mg/L	CEA	3 μg/L
PSA	4 μg/L	CA125	35 kU/L
GST	3.2 U/L	CA153	25 kU/L
ALP	0	CA27-29	36.4 kU/L
CT	100 ng/L	CA549	11 kU/L
SCCA	1.5 μg/L	CA19-9	37 kU/L
Ferritin	250 μg/L	CA50	14–20 kU/L
hCG	5.0 IU/L	CA242	20 kU/L
AFP	10 μg/L	CA72-4	6 kU/L

Table 1
Common biomarkers utilized for cancer detection [16].

Type of cancer	Biomarker
Breast	BRCA1, BRCA2, CA 15-3, CA 125, CA27.29, CEA, NY-BR-1, ING-1, HER2/NEU, ER/PR
Colon	CEA, EGF, p53
Esophageal	SCC
Liver	AFP, CEA
Lung	CEA, CA 19-9, SCC, NSE, NY-ESO-1
Melanoma	Tyrosinase, NY-ESO-1
Ovarian	CA 125, HCG, p53, CEA, CA 549, CASA, CA 19-9, CA 15-3, MCA, MOV-1, TAG72
Prostate	PSA

590 aminoacids and 3.4% carbohydrate and has molecular weight of approximately 70 kDa [34]. In the blood of healthy adults, AFP presents less than 20 ng/mL [35]. The concentration increases in response to hepatocellular carcinoma [33,34,37,38], teroblastoma [34,37,38] and especially liver carcinoma.

Carbohydrate antigen 19-9 (CA 19-9) is a vital carbohydrate tumor marker [39,40]. It is commonly used for many malignancies, such as colorectal, gastrointestinal, hepatic carcinomas and pancreatic and biliary cancer [39].

Myeloctomatosis oncogene (c-Myc) oncoprotein, a product of c-Myc proto-oncogene, regulates the transcription of genes involved in normal cell growth, differentiation, and apoptosis [41]. The level of c-Myc oncoprotein increases when human cancers including breast cancer, lung cancer, melanoma and lymphoblastic leukemia develop [42].

Cancer antigen 125 (CA125) is a membrane mucin-like glycoprotein greater than 200 kDa, and has been used for monitoring the epithelial ovarian tumors [43,44].

Neuron specific enolase (NSE), a widely used biomarker for small-cell lung cancer, neuroblastoma, and neuroendocrine cancers, increases up to 1 μg/mL in serum of serious cancer patients [45,46].

Epidermal growth factor receptor (EGFR, ErbB-1; HER1 in humans) is a cell trans-membrane glycoprotein located at the cell surface. EGFR is useful in many tumors of epithelial origin, such as non-small cell lung cancer (NSCLC), breast, head and neck, gastric, colorectal, esophageal, prostate, bladder, renal, pancreatic, and ovarian cancers [47].

Cancer antigen 15-3, as a breast-associated mucin, and it is used as a biomarker for breast carcinoma patients with distant metastases [44,48,49].

Murine double minute 2 (MDM2) is a proto-oncogene, which can be amplified and over-expressed in a wide range of neoplasm tumors, such as sarcomas, lymphomas, breast cancers, lung cancers, and testicular germ cell tumors, 10% of glioblastomas and astrocytomas, and 40% of oral squamous cell carcinomas [50].

Squamous cell carcinoma antigen (SCCA), which is subfraction of the tumor antigen TA-4, is a tumor marker of cervical cancer. It is also associated with other types of cancer with epithelial or endodermal origins, including lung cancer, head and neck cancer, melanomas, and hepatocellular carcinoma. Squamous cell carcinoma antigen (SCC-Ag) is a glycoprotein with isoforms ranging from 45 to 55 kDa. The serum level of SCC-Ag is increased when the tumor size gets bigger or the disease reoccurs [51].

Human chorionic gonadotrophin (hCG) is an important diagnostic marker of pregnancy and one of the most important carbohydrate tumor markers. It is increased when abnormal placental invasion and placental immaturity occurs [52,53].

Human epididymis-specific protein 4 (HE4) is a new ovarian biomarker, originally predicted to be a protease inhibitor involved in sperm maturation. When HE4 over expresses in ovarian neoplastic tissue its level rises in the serum of patients with ovarian cancer. HE4 is not only expressed in the early stages of the disease, but is also an early indicator of disease recurrence [54].

HER-3 is a type of transmembrane growth factor receptor, which can activate intracellular signaling pathways in response to extracellular signals. Because of HER-3 being an incomplete receptor functionally, it is a dependent protein. Studies show that tumor progression in breast, ovarian, and pancreatic cancers, gastric carcinoma, malignant melanoma and metastases, and head and neck squamous cell carcinoma are linked to over expression of HER-3 [55].

VEGF is an important regulator of angiogenesis and vascular permeability, and is a powerful mitogen for endothelial cells. In breast cancer, VEGF is used as a marker of unfavorable prognosis. However, angiogenesis is essential for growth and tumor progression. It has been observed that patients with metastasis have higher levels of serum VEGF [12].

The developed immunosensors for cancer diagnosis in literature are summarized in Table 3.

Limbut et al. [56] developed an immunosensor for AFP detection. They used self-assembled thiourea monolayer (SATUM), self-assembled thioctic monolayer (SATAM) and 3-mercaptopropionic acid (SAMPAM) for covalent coupling of anti-AFP. They reported that all systems have given the same linear range with nearly the same sensitivity and detection limits. They obtained that all the systems had good stability, could be regenerated and reused up to 48 times with good reproducibility. On the other hand thiourea, which is cheaper than thioctic acid and 3-mercaptopropionic acid, is certainly a good alternative to be applied for the immobilization of antibodies on gold surfaces [56].

Precision, reproducibility, regeneration, stability, and specificity are the important parameters in terms of monitoring the quality of a newly developed biosensor.

The precision of the electrochemical immunosensor was evaluated by calculating the intra- and inter-assay variation coefficients (CVs). The CVs of intra- and inter-assay were similar; therefore precision and reproducibility of the immunosensors were acceptable. Zhong et al. [22] developed an electrochemical immunosensor for CEA detection. They calculated the CVs of intra- and inter-assays. The intra-assay precision of the analytical method was evaluated by analyzing four concentration levels five times per run. The CVs of intra-assay were 5.7, 4.9, 4.1 and 6.5% at 0.1, 10, 100 and 300 ng/mL CEA, respectively. Similarly, the CVs of the inter-assay were 5.3, 7.8, 6.7 and 6.1% at 0.1, 10, 100 and 300 ng/mL CEA, respectively. Another method for reproducibility of the immunosensor is calculating of relative standard deviation (RSD) in different electrodes for each concentration of antigen [22]. Yu et al. [82] and Han et al. [95] developed an electrochemical immunosensor for CEA detection. For all these immunosensors, the reproducibility of the response was examined by analysis of the same concentration of CEA (20 ng/mL) using independent determinations. The immunosensors have acceptable reproducibility with a relative standard deviation of 0.45 and 2.45% (less than 5.0%), respectively.

Yang et al. [111] and Li et al. [100] developed an electrochemical immunosensor for PSA detection. To evaluate the reproducibility of the immunosensors, they prepared a series of five electrodes for the detection of 1 ng/mL PSA and the relative standard deviation (RSD) of their measurements for five electrodes were 7.9 and 6.7%, respectively.

Regeneration is a key factor in their application and development of immunosensors; therefore many immunoanalysts are interested in reusing of immunosensors. Even though the antibody–antigen linkage can be broken under drastic conditions (e.g., in alkaline or acidic solutions or with chaotropic agents), the immobilized immunoreagents could also suffer from the functional damage or even be released from the immunosorbents [43,60]. Tang et al. [43] regenerated the immunosensor by dipping into versatile solution consisting of glycine–HCl (0.2 mol/L, pH 3.6) and NaCl (0.25 mol/L) for 5 min and then rinsing with a phosphate buffer solution of pH 7.0. Because of effectively dissociating the antigen–antibody complex and peeling the captured antigens off the immunosensors, they preferred glycine. Additionally, NaCl provides properly high ion-strength to partition of antibodies and antigens easily. After treatment with glycine solution and NaCl, anti-CA125 is still bound on the film surface and therefore again ready for antigen–antibody reaction. And they reported that no remarkable decrease was observed in current response after five measurements [43]. Zhuo et al. [93] rinsed immunosensor with 0.05 M NaOH and then used 0.05 M HCl, 4 M urea, 0.2 M glycine–hydrochloric acid (Gly–HCl) buffer solution to break bond between CEA and anti-CEA and the regenerated immunosensors were used to detect the same concentration. After first seven times regeneration by urea solution kept 95.97% of the original amperometric responses, first

Table 3
The developed immunosensors for cancer diagnosis in literature.

Biomarker	Immobilization strategies	Assay principle	Linear range	Limit of Detection	Reference
Alpha- fetoprotein (AFP)	Au/3-MPA/EDC/NHS/anti-AFP/1-dodecanethiol/AFP Au/thioctic acid/EDC/NHS/anti-AFP/1-dodecanethiol/AFP Au/thiourea/glutaraldehyde (glu)/anti-AFP/ethanolamine/1-dodecanethiol/AFP	Capacitive	0.001–100 μg/l	10 ng/L	[56]
AFP	SPCE/chitosan (Chi)/HRP-labeled anti-AFP/AFP	Amperometric	0–150 ng/mL	0.74 ng/mL	[57]
Carcinoembriyonic antigen (CEA)	GCE/MWCNTs-Chi/AuNPs/anti-CEA/BSA/CEA	Differential pulse voltammetry	0.3–20 ng/mL	0.01 ng/mL	[17]
CEA	SPCE/Chi/colloidal Au/CEA/HRP-labeled anti-CEA	Amperometric	0.5–25 ng/mL	0.22 ng/mL	[58]
CA 19-9 Carcinoma antigen (CA 125)	Graphite electrode/cellulose acetate (CA)/CA 19-9+CA 125+thionine/HRP-labeled antibodies	Differential pulse voltammetry	0–144 U/mL 0–150 U/mL	0.2 U/mL 0.4 U/mL	[59]
PSA	GCE/MWCNTs/ionic liquid/chitosan nanocomposite (MWCNTs/IL/Chi)/AuNPs-incorporated polyamidoamine dendrimer (AuNPs-PAMAM)/phtaloyl chloride (Ph)/anti-PSA+thionine/PSA/HRP-labeled anti-PSA	DPV impedimetric	0.05–80 ng/mL 5–25 ng/mL	0.001 ng/mL 0.5 ng/mL	[60]
CEA	ITO/polydopamine (PDA)/mesoporous silica nanoparticles (MSNs)-Ab1 (anti-CEA)/BSA/CEA/HRP-Ab2-AuNPs	Amperometric	10^{-2}–40 ng/mL	1.7 10^{-3} ng/mL	[61]
CEA	Au/o-aminophenol/glutathione (GSH) monolayer modified AuNPs/EDC/NHS/anti-CEA/CEA	Impedimetric	0.5–20 ng/mL	0.1 ng/mL	[62]
CEA	ITO/reduced graphene oxide (rGO)/Thi/AuNps/anti-CEA/BSA/CEA	SWV	0.01–300 ng/mL	0.065 pg/mL	[63]
AFP	ITO/rGO/Prussian blue (PB)/AuNPs/anti-CEA/BSA/CEA			0.885 pg/mL	
CEA	ITO/polyvinyl alcohol (PVA)/ferrocene carboxylic acid encapsulated mesoporous silica (FCA-MPS)/anti-CEA/BSA/CEA	DPV	0–45 ng/mL	0.2 ng/mL	[64]
AFP	ITO/PVA/HRP-MPS/anti-AFP/BSA/AFP		1–90 ng/mL	0.5 ng/mL	
PSA	Glass fiber pad/anti-PSA-Quantum Dots (QD) (ZnS and CdSe)conjugates/nitrocellulose membrane with second anti-PSA/BSA/PSA	SWV	0.05–4 ng/mL	0.02 ng/mL	[65]
PSA	Au nanowire (Au NW)/anti-PSA doped polypyrole/BSA/PSA	DPV	10 fg/mL–10 ng/mL	0.3 pg/mL	[66]
CA 125	GCE/Chi-poly(diallydimethylammonium chloride) (PDDA)-Prussian blue (PB)/AuNPs/anti CA125/BSA/CA 125	DPV	2–100 U/mL	0.71 U/mL	[67]
AFP	Pt/gelatin/AgNPs/anti-AFP/glu/AFP	Potentiometric	2–197 μg/L	0.8 μg/L	[37]
CEA	Au/4-aminothiophenol (4ATp)/nano Au/monoclonal anti-CEA/BSA/CEA/HRP/anti-CEA/AuNPs/Thi-4Atp@AuNPs	Amperometric	2 pg/mL–40 ng/mL	0.7 pg/mL	[18]
PSA	Au/cys/glu/capture anti-PSA/BSA/PSA/functionalized SiNPs (with anti-PSA and alkaline phosphatase (ALP)/glycine containing AgNO3 and ascorbic acid-2-phosphate	Amperometric	1–35 ng/mL	0.76 ng/mL	[31]
CEA	GCE/AuNPs decorated thionine/infite coordination polymer (AgNPs/Thi/ICP)/anti-CEA/BSA/CEA	Amperometric	50- fg/mL–100 ng/mL	0.5 fg/mL	[68]
CEA	GCE/[Ag-AgO2]/SiO2/BSA/nano-Au/anti-CEA/BSA/CEA	Amperometric	0.5–160 ng/mL	0.14 ng/mL	[24]
AFP	Au/1,1′-bis-(2-phosphoethyl)-4,4′-bipyridinium dibromide-titanium dioxide nanoparticle)/AuNPs/anti-AFP/BSA/AFP	Amperometric	1.25–200 ng/mL	0.6 ng/mL	[33]
CEA	GCE/AuNPs-Thi-graphene oxide/anti-CEA/BSA/CEA	Amperometric	10–500 pg/mL	4 pg/mL	[69]
AFP	GCE/sulfhydryl viologen-AuNPs (SV-AuNPs)/anti-AFP/BSA/AFP	Amperometric	0.25–200 ng/mL	0.23 ng/mL	[70]
AFP	GCE/Gold nanowires (AuNWs)/ZnO nanorods (NRs)/Chi/anti-AFP/glycin-HRP-labeled AFP	Amperometric	0.5–160 ng/mL	0.1 ng/mL	[34]
CEA	Au/thiourea/anti-CEA/ethanolamine/CEA	Capacitance	0.01–10 ng/mL	10 pg/mL	[25]
AFP	GCE/nano-Au film/MWCNT-PDDA/DNA/Thi/nano-Au/anti-AFP/BSA/AFP	Amperometric	0.01–200 ng/mL	0.04 ng/mL	[35]
CEA	GCE/nano-Au film/Chi/nano-Au/anti-CEA /BSA/CEA	Amperometric	0.2–120 ng/mL	0.06 ng/mL	[71]
CA 19-9	3 DOMM Au electrode/Au-SiO2@Fe3O4 nanospheres/streptavidin/biotinylated-Ab1/BSA/CA 19-9/HRP-Ab2/Au@SB-15(Santa Barbara Amorphous 15)	Amperometric	0.05–15.65 U/mL	0.01 U/mL	[21]

Table 3 (*continued*)

Biomarker	Immobilization strategies	Assay principle	Linear range	Limit of Detection	Reference
AFP	GCE/Chi-TiO2-Gr films/AuNPs/anti-AFP/BSA/AFP	Amperometric	0.1–300 ng/mL	0.03 ng/mL	[72]
CEA	GCE/negatively charged polysulfonilic acid (PSAA)/toluene blue (TB)/nano-Au/anti-CEA/HRP/CEA	Amperometric	0.5–120 ng/mL	0.2 ng/mL	[73]
CEA	GCE/negative charged PDDA-wrapped CNTs (PDCNTs)/negative charged poly (sodium-*p*-styrene-sulfonate) (PSS)/gold nanoclusters/anti-CEA/BSA/CEA	Amperometric	0.1–160 ng/mL	0.06 ng/mL	[74]
CA 125	GCE/carbon nanofiber (CNF)/EDC/NHS/CEA antigen/HRP labeled anti-CEA/CEA	Amperometric	2–75 U/mL	1.8 U/mL	[75]
AFP	Carbon ionic liquid electrode (CILE)/amino functionalized graphene sheets (GR-NH2)/AuNPs/anti-AFP/BSA/AFP	Amperometric	1–250 ng/	0.1 ng/mL	[76]
c-Myc	Au/cys/glu/primary c-Myc antibody (C_{ab})/6-mercapto-1-hexanol (MCH)/ethylenediamine/target c-Myc oncoprotein (C_{ag})/AuNP labeled c-Myc antibodies (AuNPs-C_{ab})	Impedimetric	43 pM–43 nM	1.5 pM	[42]
CEA	Au/1,6-hexanedithiol (HDTS)/AuNPs/Staphylococcal protein (SPA)/anti-CEA/BSA/CEA	Impedimetric	1 pg/mL–100 ng/mL	0.1 pg/mL	[10]
CA 19-9	GCE/Chi-MWCNTs/GOD/Fe3O4@SiO2-Au@mSiO2/anti-CA 19-9/CA 19-9	CV	0.01–1.11 U/mL	0.004 U/mL	[39]
		DPV	11.11–476.11 U/mL		
CEA	GCE/PB/AuNPs/anti-CEA/CEA/horseradish peroxidase conjugated anti-CEA anti-CEA antigen (HRP-anti-CEA)/NCAuPt	Amperometric	0.01–200 ng/mL	0.11 pg/mL	[77]
CA 125	Gold rod electrode/11-mercaptoundecanoic acid/1-dodeccanethiol etholic acid/anti-CA 125/CA 125	Capacitive	0.05–40 U/mL	0.05 U/mL	[78]
CEA	SPE/polyethyleneimine wrapped multiwalled carbon nanotube (MWCNT-PEI)/anti-CEA/ethanolamine+BSA/CEA/anti-CEA tagged ferrocene carboxylic acid encapsulated liposomes	Voltammetric	5.10^{-12}–5.10^{-7} g/mL	5.10^{-12} g/mL	[79]
CEA	SPCEs/CNTs-Chi/AuNPs/anti-CEA(Ab1)/BSA/CEA/SiO2 nanosphere+GOD+anti-CEA(Ab2)	Amperometric	5 pg/mL–2 ng/mL	3.2 pg/mL	[80]
	SPCEs/CNTs-Chi/AuNPs/anti-AFP (Ab1)/BSA/AFP/SiO2 nanosphere+GOD+anti-AFP(Ab2)	Amperometric	5 pg/mL–1 ng/mL	4.0 pg/mL	
CEA	GCE/thionine functionalized CNTs(Thi-CNTs/AuNPs/anti-CEA(Ab_1)/BSA/CEA/HRP labeled signal antibody-AuNPs-PAN@CNT nanocomposite (HRP-Ab_2-AuNPs-PAN@CNT)	Amperometric	0.02–80 ng/mL	0.008 ng/mL	[81]
CEA	GCE/nano-Au/nickel hexacyanoferrates nanoparticles (NiHCFNPs)/nano-Au/anti-CEA/BSA/CEA	Amperometric	0.5–160 ng/mL	0.1 ng/mL	[28]
CEA	Carbon ionic liquid electrode (CILE)/rGO/poly(L-Arg)film/AuNPs/anti-CEA/BSA/CEA	Amperometric	0.5–200 ng/mL	0.03 ng/mL	[82]
CA 125	GCE/Au-CA 125/cellulose acetate (CA)/HRP-labelled CA 125 antibody/CEA	Amperometric	0–30 U/mL	1.73 U/mL	[83]
CEA	GCE/sulfonated graphene sheets(HSO_3-GS)/Thi/Chi-PdCu/anti-CEA/BSA/CEA	Amperometric	0.01–12 ng/mL	4.86 pg/mL	[27]
CEA	GCE/gold nanoparticle-graphite composite (Au-GN)/HRP labelled anti-CEA antibody (HRP-anti CEA)/CEA	Amperometric	0.1–80 ng/mL	0.04 ng/mL	[26]
CA 125	CPE/AuNPs-Thi mixture/anti CA-125/BSA /CA 125	Amperometric	10–30 U/mL	1.8 U/mL	[43]
CEA	Nano Fe_3O_4 modified CPE/(3-mercaptopropyl)trimethoxysilane (MPTS)/nanogold/CEA/BSA/HRP labeled anti-CEA	Amperometric	1–55 ng/mL	0.13 ng/mL	[84]
CEA	ITO/hyper branched polyester(HPDMPA-COOH)/EDC/NHS/Ab_1/BSA/CEA/HRP labeled antibody conjugated AuNPs (HRP-Ab_2-AuNPs)	Amperometric	0.1–80 ng/mL	2.36 pg/mL	[85]
CEA	GCE/$(AuNPs\text{-}AgNPs)_n$/Thi/AuNPs/anti-CEA/BSA/CEA	Amperometric	10 pg/mL–100 ng/mL	3 pg/mL	[19]
AFP	Pt disk electrode/poly(3,4-ethylenedioxythiophene)(PEDOT)/AuNPs/Azure I/ZnSe QDs/anti AFP/HRP/AFP	Amperometric	5.10^{-5}–250 ng/mL	1.1 fg/mL	[38]
CEA	Magnetic carbon paste electrode (MCPE)/magnetic beads (MB)/o-phenylene diamine (PPD)/AgNPs/anti-CEA/BSA/CEA	Amperometric	0.01–40 ng/mL	0.001 ng/mL	[86]
Neuron specific enolase (NSE)	GCE/SWCNT/EDC/NHS/NSE/BSA/anti-NSE primary antibody/alkaline phosphatase conjugated secondary antibody labeled gold nanoparticle (AP-anti IgG-AuNPs)/α-naphthyl phosphate (α-NP)	Amperometric	0.1 ng/mL–2 μg/mL	0.033 ng/mL	[46]
CEA	GCE/Au-TiO_2/anti-CEA/BSA/HRP-Ab_2 labeled Pt hallow nanospheres (HRP-Ab_2-HPtNPs)/CEA	Amperometric	0.02–120 ng/mL	12 pg/mL	[30]
PSA		Amperometric	–	–	[87]

Table 3 (*continued*)

Biomarker	Immobilization strategies	Assay principle	Linear range	Limit of Detection	Reference
	Au/4-(2-(4-acetylthio)phenyl)ethynyl) benzoic acid (APBA)/EDC/NHS/PAMAM/ Ab1(monoclonal antibody)/PSA/polyclonal antibody labeled biotin (Ab_2)/ alkaline phosphatase-labeled avidin				
CEA+AFP	GCE/Chi-AuNPs/capture anti-CEA ($Ab_{1,1}$) +capture anti-AFP ($Ab_{1,2}$)/BSA/ CEA+AFP/biofunctional carboxyl graphene nanosheets –toluidine blue-$Ab_{2,1}$(CGs-TB- $Ab_{2,1}$)+ CGs-TB-$Ab_{2,2}$	Amperometric	5–60 ng/mL	0.01 ng/mL–0.05 ng/mL	[88]
Tumor necrosis factor α (TNF-α)	GCE/hydrogel+chitosan/AuNPs/primary anti-TNF-α antibody/TNF-α/ALP and Ab_2 modified polystrene sphere (PS-ALP-Ab_2)	Amperometric	1 pg/mL–10 ng/mL	0.5 pg/mL	[89]
Carbohydrate antigen15-3 (CA 15-3)	GCE/N-doped graphene-anti CA 15-3/BSA /CA 15-3	Amperometric	0.1–20 U/mL	0.012 U/mL	[90]
Epidermal growth receptor (EGFR)	Au/AuNPs/Cys (1,4-phenylenediisothiocyanate) (PDITC)/protein G/ ethanolamine/anti EGFR/EGFR	Impedimetric	1 pg/mL–1 μg/mL	0.34 pg/mL	[47]
CA 125	GCE/MWCNT-Nafion/tris (2,2′-bipyridyl) cobalt Co $(bpy)_3^{+3}$/AuNPs/anti-CA 125/ BSA/CA 125	Amperometric	1–150 U/mL	0.36 U/mL	[91]
CEA	Au/cys/*p*-phthaloyl chloride/thionine/HRP-labeled anti-CEA/CEA	Amperometric	0.6–200 ng/mL	0.2 ng/mL	[92]
AFP	GCE/MWCNts/Au-PtNPs/anti-AFP/HRP/AFP	Amperometric	0.5–200 ng/mL	0.17 ng/mL	[20]
CEA	Au/cys/AuNPs/SiO2/thionine nanocomposite/AuNPs/anti-CEA/CEA	Amperometric	1–100 ng/mL	0.34 ng/mL	[93]
CA 15-3	Au/amino functionalized Fc-COOH-doped SiNPs/glu/anti CA 15-3/BSA/CA 15-3	Amperometric	2–240 U/mL	0.64 U/mL	[48]
CEA	GCE/AuNPs/Chitosan nanocomposite/Ab_1/BSA/CEA/Ab_2-AuNPs/DNA/methylene blue (MB)	Amperometric	0.1–2 pg/mL	0.05 pg/mL	[94]
CEA	GCE/TiO_2 doped chitosan-branched ferrocene complex film (CS-Fc-TiO2)/gold nanoparticles-graphene (Au-Gra) nanohybrid/anti-CEA/BSA/CEA	Amperometric	0.01–80 ng/Ml	3.4 pg/mL	[95]
PSA	GCE/MWCNTs-ionic liquid (ILs)-thionine (IL/MWCNTs/Thi)/anti-PSA/PSA/HRP-labeled PSA	Amperometric	0.2–40 ng/mL	20 pg/mL	[96]
AFP	GCE/AuNPs/graphene nanosheet nanocomposite (Au-Gra)/anti-AFP (Ab_1)/BSA/ AFP/SWCNTs-bienzyme (HRP+ GOD)-Ab_2	Impedimetric	0.001–60 ng/mL	0.33 pg/mL	[97]
CEA	GCE/1,4-phenylenediamine(H_2N-Ph-NH_2)/AuNPs/anti-CEA/BSA/CEA	Amperometric	10 pg/mL–100 ng/mL	3 fg/mL	[98]
AFP	GCE/SBA-15/1-naphthyl phosphate (1-NP)/alkaline phosphatase (ALP)-labeled antibody antibody/ionic chitosan hybrid (IL-Chi)/AFP	Amperometric	1–150 ng/mL	0.8 ng/mL	[99]
CA 19-9	Graphite electrode (GE)/titania sol-gel/CA 19-9/HRP labeled CA 19-9 antibody	Amperometric	3–20 U/mL	2.68 U/mL	[40]
PSA	GCE/MWCNTs/anti-PSA(Ab_1)/PSA/anti-tPSA IgG-HRP conjugate	Amperometric	0.08–0.5 μg/L	0.03 μg/L	[32]
CA 15-3	GCE/functionalized Ab_1 loaded graphene (GS-Ab_1) ionic liquid (IL)/BSA/CA 15-3/ Ab_2-f-TiO_2-Cd+2 nanocomposite	Amperometric	0.02–60 U/mL	0.008 U/mL	[5]
PSA	GCE/graphene sheet (GS)-cobalt hexacyanoferrate nanoparticles (CoNP)-1-pyrene butanoic acid, succinimidyl ester (PBSE) composite film/anti-PSA/BSA/ PSA	Amperometric	0.02–2 ng/mL	0.01 ng/mL	[100]
PSA	GCE/silver hybridized mesoporous silica nanoparticles (Ag@MSNs)/glu/anti-PSA/ BSA/PSA	Amperometric	0.05–50 ng/mL	15 pg/mL	[101]
AFP	GCE/Pd nanoplates/anti-AFP/BSA/AFP	Amperometric	0.01–75 ng/mL	4 pg/mL	[36]
Murine double minute 2 (MDM2)	Polycrystalline Au/cys/PDITC/MDM2 antibody/ethanolamine/MDM2	Impedimetric	1 pg/mL–1 μg/mL	0.29 pg/mL	[50]
CEA	GCE/platinum-thionine-graphene nanocomposite (PTGOs)/anti-CEA/BSA/HRP-PtNW-CEA bioconjugates	Amperometric	0.01–60 ng/mL	5 pg/mL	[102]
CEA	GCE/o-aminobenzoic acid (o-ABA)/EDC/NHS/anti-CEA (Ab_1)/ethanolamine/CEA/ BSA/SWCNT-$(PDDA/ALP)_4$-PDDA-poly(sodium 4-styrenesulfonate) (PSS)-Ab_2	Amperometric	0.1–1000 pg/mL	0.04 pg/mL	[103]
CEA	GE/magnetic beads coated capture antibodies (MBs-Ab_1)/CEA/Ab_2-AuNPs-HRP	Amperometric	5–60 ng/mL	5 ng/mL	[1]
CEA	GCE/PB/Fe_3O_4-Chi suspension/AuNPs/HRP labeled anti-CEA/CEA	Amperometric	0.1–220 ng/mL	10 pg/mL	[104]
CEA	GCE/PB/AuNPs/anti-CEA/BSA/HRP conjugated anti-CEA secondary antibody attached on nanogold enwrapped graphene nanolabels (HRP-anti-CEA-NGGN)	Amperometric	0.05–350 ng/mL	0.01 ng/mL	[22]
CEA	GCE/graphene film/Chi/glu/Ab_1/blocking solution/CEA/Ab_2 functionalized AuNPs mesoporous carbon foam (Ab_2/Au/MCF)	Amperometric	0.05 pg/mL–1 ng/mL	0.024 pg/mL	[105]
AFP	GCE/AuNPs/2-aminoethanethiol (AET)/PAMAM/EDC/NHS/capture anti-AFP (Ab_1)/BSA/AFP/HRP conjugated Ab_2	Voltammetric	5–500 ng/mL	3 ng/mL	[106]
CA 125	Screen printed graphite electrode (SPGE)/AuNPs/11-mercaptoundecanoic acid (MUA)/EDC/NHS/MCH/anti-CA 125/rabbit IgG(rIgG)/CA 125	Impedimetric	0–100 U/mL	6.7 U/mL	[107]
CA 15-3		Chronoamperoetry			[49]

Table 3 (*continued*)

Biomarker	Immobilization strategies	Assay principle	Linear range	Limit of Detection	Reference
	GCE/capture anti CA 15-3 (Ab_1) immobilized graphene sheet(GS-Ab_1)/BSA/CA 15-3/nanoporous PtFe alloys labeled Ab_2 (NP-PtFe-Ab_2)		0.002–40 U/mL	3.10^{4-} U/mL	
NSE	GCE/AuNPs/nickel hexacyanoferrate nanoparticles (NiHCFNPs)/Au-Gra/anti-NSE/BSA/NSE	Amperometric	0.001–100 ng/mL	0.3 pg/mL	[45]
PSA	Au/11-mercapto-1-undecanol (MU)/MUA+ 3-aminophenylboronic acid (APBA)/HRP-labeled anti-PSA/BSA/PSA	Amperometric	2–120 ng/mL	1.1 ng/mL	[108]
AFP	GCE/AuNPs and CNT doped chitosan (AuNPs/CNT/Chi) film/AFP/BSA/ALP labeled antibody	Amperometric	1–55 ng/mL	0.6 ng/mL	[109]
CEA	GCE/PB-graphene hybrid nanosheets (PBGPs) doped chitosan (CS-PBGP)/AuNPs/anti-CEA/BSA/CEA/anti-CEA-gold-silver hallow nanospheres (AuAgHSs)–GOD	Amperometric	0.005–50 ng/mL	1 pg/mL	[110]
PSA	Electrode/GS/1-pyrenebutanoic acid, succinimidyl ester (PBSE)/Ab1/BSA/PSA/QD functionalized GS-Ab2	Amperometric	0.005–10 ng/mL	3 pg/mL	[111]
AFP	GCE/GS/mesoporous silica (MPS) with trimethylchlorosilane (TMCS)/CNTs/anti-AFP/AFP	Amperometric	0.1–100 ng/mL	0.06 ng/mL	[112]
AFP	GCE/GS-Thi composite film/glu/anti-AFP (Ab1)/BSA/AFP/PB modified hydroxyapatite loaded with HRP and secondary anti-AFP antibody (PB@HAP-HRP-Ab2)	Amperometric	0.02–8 ng/mL	9 pg/mL	[113]
PSA	GCE/GO-Ab1/BSA/PSA/ferrocene (Fc) incorporated polystyrene spheres (Ps-Fc)-chitosan-Ab2	Amperometric	0.01–20 ng/mL	1 pg/mL	[114]
AFP	GCE/Au-Chi/anti-AFP/BSA/AFP/HRP conjugated anti AFP-silver nanowire-graphene hybrid nanomaterials (HRP-anti-AFP-AuNW-GPs)	Amperometric	0.05–400 ng/mL	5 pg/mL	[115]
Squamous cell carcinoma antigen (SCCA),	GCE/reduced graphene oxide-tetraethylene pentamine (rGO-TEPA)/Ab1/BSA/SCCA/Au@mesoporous carbon CMK-3-Ab2	Amperometric	0.03–20 ng/mL	0.01 ng/mL	[116]
CEA			0.05–20 ng/mL	0.013 ng/mL	
PSA	GCE/polyethyleneimine functionalized 3,4,9,10-perylenetetracarboxylic acid (PEI-PTCA)/AuNPs/Ab_1/BSA/PSA/biotinylated ALP/streptavidin (SA)/anti-PSA/Ab2/Au modified nickel hexacyano ferrates (Au@NiNPs)/onion like graphene sheets (O-GS)	Amperometric	0.01–50 ng/mL	3.4 pg/mL	[117]
fPSA	GCE/PEI-PTCA/AuNPs/Ab1/BSA/fPSA/bio-ALP/SA/anti-fPSA/Au modified prussian blue nanoparticles	Amperometric	0.02–10 ng/mL	6.7 pg/mL	
CEA	GCE/MWCNTs/EDC/NHS/Ab1/CEA/GOD-Aushell@GOD nanospheres	Amperometric	0.02–5 ng/mL	6.7 pg/mL	[118]
CEA	Au/Nafion-cysteine composite membrane/AuNPs/anti-CEA/BSA/CEA	Amperometric	0.01–100 ng/mL	3.3 pg/mL	[119]
Mucin-16 (MUC-16)	SPE/gold nanoelectrode ensemble (GNEE)/2-mercaptopropionic acid/2-mercaptoethanol/sulfo-NHS/EDC/anti-MUC-16/ethanolamine+BSA/MUC-16	Amperometric	0.001–300 U/mL	5.10^{4-} U/mL	[120]
CEA	GCE/three dimensional macro porous gold nanoparticles-graphene composites (3D-AuNPs/GN)/Ab1/BSA/CEA/HRP labeled anti-CEA (HRP-Ab2)/Thi/nanoporous silver (NPs)	Amperometric	0.001–10 ng/mL	0.35 pg/mL	[121]
SCCA	GCE/nitrogen doped graphene sheets (N-GS) in chitosan/glu/Ab1/BSA/SCCA/Pt-FeO4-Ab2	Amperometric	0.05–18 ng/mL	15.3 pg/mL	[51]
Human chorionic gonadotropin (hCG)	GCE/GS/acid treated MWCNTs/Au/Ab1/BSA/hCG/HRP-Ab2/Au/Thi/MCM-41	Amperometric	0.005–500 mIU/mL	0.0026 mIU/mL	[53]
Human epididymis-specific protein-4 (HE4)	ITO/chitosan-titanium carbide (TiC)/AuNPS/anti-HE4/BSA/HE4/biotin labeled HE4	Amperometric	3–300 pM	0.06 pM	[54]
CEA	GE/GS/EDC/NHS/Ab1/BSA/CEA/mesoporous platinum nanoparticles labeled antibody (M-PtNP-Ab2)	Amperometric	0.02–20	7 ng/mL	[122]
CA 125			0.05–20	0.002 U/mL	
CA 153			0.008–24	0.001 U/mL	
Apurinic/apyrimidinic endonıuclease-1/redox factor-1 (APE-1)	GCE/ethylenediamine/protein A(PA)/EDC/NHS/Ab1/BSA/APE-1/biotinylated ALP/nanochain modified streptavidin/Ab2/nickel hexacyanoferrates nanoparticle-decorated Au nanochains (Ni-AuNCs)	Amperometric	0.1–100 pg/mL	3.9 fg/mL	[123]
Vascular endothelial growth factor (VEGF)	Au/3-mercaptopropionic acid (3-MPA)/EDC/NHS/VEGF-R1/BSA/VEGF	Impedimetric	10–70 pg/mL	10 pg/mL	[12]
HER-3	Carbon nanotubes modified screen printed electrode/EDC/NHS/anti-HER-3/BSA/HER-3	Impedimetric	2–14 fg/mL	2 fg/mL	[124]
HER-3	ITO/APTES/glu/anti-HER-3/BSA/HER-3	Impedimetric	40–200 fg/mL	40 fg/mL	[55]
HER-3	Au/4-aminothiophenol/glu/anti-HER3/BSA /HER3	Impedimetric	0.4–2.4 pg/mL	0.28 pg/mL	[125]
HER-3	Au/hexandithiol(HDT)/AuNPs/Cys/glu/anti-HER-3/BSA/HER-3	Impedimetric	0.2–1.4 pg/mL	0.2 pg/mL	[126]

four times regeneration by Gly–HCl solution kept 96.21%, first three times regeneration by HCl solution kept 95.97%, first two times regeneration by NaOH solution kept 95.97%. Thus they chose urea solution as a suitable reagent for recycling the immunosensors [93].

Specificity is vital point of using biological molecules as recognition elements to develop immunosensors. To evaluate the specificity of the electrochemical immunosensor, control experiments are performed by adding other possible interferents. Yang et al. [30] studied specificity of immunosensor in the solution with 20 ng/mL CEA and with interference substance such as, α-1-fetoprotein (20 ng/mL), hepatitis B surface antigen (20 ng/mL), human chorionic gonadotropin (20 mIU/mL), carcinoma antigen 125 (20 ng/mL), prostate specific antigen (20 ng/mL), immunoglobulin G (20 ng/mL) and BSA (100 ng/mL). The ratios of current responses with CEA to the interfering substance were 5.69, 5.64, 5.74, 5.67, 5.75, 5.73 and 5.71, respectively [30]. Another specificity study was performed by Ravalli et al. [107] and they evaluated the experiment by using electrochemical impedance spectroscopy. And they observed that relative change in impedance originated from the specific monoclonal anti CA125 antibody and CA125 interactions, not from the inferences. So anti CA125 showed a good selectivity when compared with CA 125 [107].

Usually long time stability of the immunosensors was studied on a 30-day period. Feng et al. [81] measured the stability of the immunosensor by testing the response value. The response value of the immunosensor at 5 days, 10 days, 15 days, 20 days and 30 days maintained 98.8, 97.7, 95.9, 93.7, 90.9% of its initial response (C_{CEA} = 10 ng/mL), indicating the immunosensor had good stability. According to them, the Thi-CNTs sensing platform prevents the leak of hydrophilic thionine from the electrode, but also avoid the addition of mediator to the solution which may affect the activity of the antibody [81].

Liu et al. [38] developed an immunosensor for AFP detection. Its current response maintained about 96.2% of the original value after the storage periods of 40 days. They reported that the good stability of the immunosensor depended on two factors: the first one was the microenvironment of the layer-by-layer assembly film; the second was the polymer PEDOT, which offered a stable substrate for the immobilization of molecules [38].

3.2. Cardiac markers

Cardiovascular disease (CVD) is a kind of disease that affects heart and blood vessels. Many factors such as genetic, gender, age, high blood pressure and cholesterol, diabetes, obesity and overweight, smoking and stress cause CVD. It develops when a plaque builds up in the walls of the arteries. This plaque narrows the arteries and makes it difficult for blood to flow through and causes a heart attack or stroke [127,128].

Cardiovascular disease (CVD) leads to human death and World Health Organization (WHO) estimated that 17.3 million (30%) of all global deaths in 2008 were linked with CVD, 7.3 million of which were heart disease and 6.2 million were stroke [129]. Over 80% of the world's deaths from CVDs occur in low- and middle-income countries [127]. The number of people, who die from CVDs, mainly from heart disease and stroke, will increase to 23.3 million by 2030 [127,130].

The current diagnostic methods routinely used for CVD are electrocardiography (ECG), chest X-ray, echocardiography, cardiac catheterization, CT heart scan and blood tests [131]. For successful prognosis of the disease, early and quick diagnosis is vital for patients. The diagnosis of CVD has been based on the WHO criteria, whereby patients must meet at least two of three conditions: characteristic chest pain, diagnostic electrocardiogram (ECG) changes, and elevation of the biochemical markers in their blood samples. Although ECG is an important management tool for guiding therapy, it might not be always useful in every case because some patients might have normal electrocardiograms. Therefore, measurement of cardiac markers is critical in assisting the diagnosis of CVD [128].

There are several important characteristics of a biomarker including (a) high clinical sensitivity and specificity, (b) quick release of biomarker in the blood enabling early diagnosis, (c) capability to remain elevated for longer time in the blood, and (d) ability to be assayed quantitatively. For the accurate disease diagnosis, different types of biomarkers should be analyzed simultaneously because it is difficult to select a specific marker for the diagnosis of CVD [127].

Clinically used cardiac markers are summarized in Table 4 [127].

Myoglobin is a non-enzymatic cardiac protein and is the earliest marker of the acute myocardial infarction (AMI). As a cardiac biomarker, myoglobin is used together with troponin to help diagnosis of heart attack. Because of its small size of 17.8 kDa, it is released into plasma in major amount within 3 h of the onset of AMI and the plasma concentrations usually return to normal within 24 h. Normal serum myoglobin levels range from 30 to 90 ng/mL. After 1 h of the onset of myocardial infarction, serum myoglobin level can raise to 200 ng/mL or even higher. During a peak hour myoglobin level can raise to 900 ng/mL [132].

Human cardiac troponins (cTnT and cTnI) is known 'gold standard' because of their specificity and sensitivity to serological diagnosis and prognosis of acute myocardial infarction and acute coronary syndrome (ACS) [133,134]. cTnI has not been identified outside of the myocardium, but, cTnT is expressed in skeletal

Table 4
Clinically cardiac markers.

Cardiac Biomarker	Type of cardiovascular diseases	Cut-off levels
Troponin I (cTnI)	Detection of acute myocardial infarction (AMI)	0.01–0.1 ng/mL
Troponin T (cTnT)	Detection of AMI	0.05–0.1 ng/mL
Myoglobin	Early detection of AMI	70–200 ng/mL
C-reactive protein (CRP)	Early detection of inflammation/cardiac risk factor	$< 10^3$ ng/mL low risk 1–3 × 10^3 ng/mL intermediate risk > 3–15 × 10^3 ng/mL high risk
Creatine kinase MB subform (CK-MB)	Early detection of AMI	10 ng/mL
B-type natriuretic peptide (BNP)	Acute coronary syndromes/diagnosis of heart failure/ventricular overload	
N-terminal pro-B-type natriuretic peptide (NT-proBNP)	Acute coronary syndromes/diagnosis of heart failure/ventricular overload	0.25–2 ng/mL
Myeloperoxidase (MPO)	Detection of inflammation	> 350 ng/mL stratification risk
Heart fatty acid binding protein (11-FABP)	Myocardial necrosis	≥ 6 ng/mL stratification risk
TNF-α	Inflammation/cardiac risk factor	< 0.0036 ng/mL low risk ≤ 0.0036 ng/mL high risk
Interlukin-6 (IL-6)	Inflammation/cardiac risk factor	Low < 0.0013 ng/mL Mid 0.00138–0.002 ng/mL High > 0.002 ng/mL
Fibrinogen		Low < 3.58 × 10^6 ng/mL Mid 3.58–4.20 × 10^6 ng/mL

muscle to a smaller extent. Especially, the cTnT levels increase 2–4 h after the acute myocardial infarction symptoms and could be evaluated up to 14 days after the acute episode of myocardial damage [133]. cTnI starts to rise rapidly in the blood stream within 3–4 h after onset of acute myocardial infarction and remains to rise up to 4–10 days. The level of cTnI in normal patients levels of cTnI are around 10 ng/mL, but the cTnI concentration of AMI in patients goes up to 112 ng/mL (range 20–550 ng/mL) at 18 h.

C-reactive protein (CRP) is one of the plasma proteins known as acute-phase proteins, an indicator of a viral and bacterial infection, however low concentrations of CRP may also predict the risk of heart attack and stroke. CRP levels can rapidly increase up to 1000-fold over normal trace amounts with bacterial infection, trauma, surgery and other inflammatory events and decrease to normal within 12–14 days. The CRP level is typically less than 2 mg/L for healthy individuals. If CRP is higher than 3 mg/l, a person is at high risk of developing a cardiovascular disease [135].

Myeloperoxidase (MPO) is an abundant mammalian phagocyte hemoprotein which caused suddenly cardiac death. In acute coronary syndrome patients (ACS), MPO serum levels predict an increased risk for subsequent cardiovascular events [136].

P-selection, known as CD62P is a granule membrane protein 140 (GMP-140), and platelet activation dependent granule activation protein (PADGEM), was first discovered in endothelial cells in 1989 as platelet activation marker and categorized as one member of the cell adhesion molecules (CAM) family [137].

Soluble lectin-like oxidized low density lipoprotein receptor (sLOX-1) is an extracellular domain of lectin like oxidized

Table 5
The developed immunosensors for cardiovascular disease diagnosis in literature.

Biomarker	Immobilization strategies	Assay principle	Linear range	Limit of detection	Reference
Human cardiac troponin (cTnT)	NH_2-CNT-SPEs/polyethylene terephtalate (PET)/NHS-EDC-anti-cTnT/glycine/cTnT	Amperometric	0.0025–0.5 ng/mL	0.0035 ng/mL	[139]
cTnT	Au/polyethyleneimine (PEI)/carboxylated CNTs (COOH-CNT)/anti-cTnT/glycine/cTnT	Amperometric	0.1–10 ng/mL	0.033 ng/mL	[140]
CRP	Au/nanocrystalline diamond film (NCD)/mercaptopropionic acid (MPA)/EDC/NHS/anti-CRP/ethanolamine/CRP	Capacitance	25–800 ng/mL	-	[135]
cTnT	GCE/*o*-aminobenzoic acid (poly-*o*-ABA)/EDC/NHS/anti-cTnT/ethanolamine/cTnT	Amperometric	0.05–5 ng/mL	0.016 ng/mL	[141]
Myeloperoxidase (MPO)	GCE/*N*,*N*-dimethylformamide (DMF)-MWCNTs/1-ethyl-3-methylimidazolium tetrafluoroborate (EMIMBF4)/chitosan-cerium oxide (CeO2)/anti-MPO/BSA/MPO	Amperometric	5–300 ng/mL	0.2 ng/mL	[136]
P-selection	SPCE/CNT/gold nanobone /GNB)/3,4-ethylenedioxythiophene (EDOT)/EDC/NHS/anti-P-selection/BSA/P-selection/α-P-selection Ab-tagged liposome containing K4Fe(CN)6	Amperometric	10^{-13}–10^{-5} g/mL	0.85 pg/mL	[137]
Myoglobin	Au/4-aminothiophenol(4-ATP)/sulfosuccinimidyl 4-(*N*-maleimidomethyl) cyclohexane-1-carboxylate(sulfo-SMCC)/half-antibody fragment/myoglobin	Impedimetric	10^{-14}–10^{-7} M	10–14 M	[142]
cTnT	SPE/polyethylene terephtalate (PTE)/anti-cTnT/biotin/glutaraldehyde (glu)/streptavidin microsphere/glycine/cTnT/HRP- conjugated anti-cTnT	Amperometric	0.1–10 ng/mL	0.2 ng/mL	[133]
Cardiac troponin I (cTnI)	İnterdigitated array (IDA) chip/poly(dimethylsiloxane) (PDMS)/NHS/BSA/anti-cTnI/protein G/cTnI/alkaline phosphatase (AP)-labeled anti-CTnI/enzyme substrate (PaPP)	Amperometric	0.2 ng/mL–10 μg/mL	148 pg/mL	[143]
cTnI	PDMS-GNP composite/anti-cTnI and anti-CRP (Ab1)/BSA/CdTe and ZnSe quantum dots-anti-cTnI and anti-CRP (Ab2)	Amperometric	0.01–50 μg/l	5 amol	[144]
Myoglobin (Mb)	Au/11-mercaptoundecanoic acid (MUA)+3-mercaptopropionic acid (MPA)/NHS-EDC/anti-Mb/BSA/Mb	Impedimetric	10–650 ng/mL	5.2 ng/mL	[132]
Mb	Graphite electrode/didodecyldimethylammonium bromide (DDAB)-Au/EDC/NHS/anti-human myoglobin (anti-HMB)/glycine/Mb	SWV	10–1780 ng/mL	10 ng/mL	[145]
hFABP	Au/MUA+3-mercaptopropanol (MPOH)/EDC/NHS/anti-hFABP/BSA/hFABP	Impedimetric	98 pg/mL–100 ng/mL	117 pg/mL	[146]
cTnI	SPE/AuNPs/anti-cTnI/BSA/cTnI	Capacitance	0.2–12.5 ng/mL	0.2 ng/mL	[147]
Mb	Crystal (E)-1-decyl-4-(4-decyloxyphenyl) diazenyl)pyridinium bromide (Br-Py) coated GCE)/polyethyleneimine-cp Coated gold nanoparticles film/anti-Mb/glycine/Mb	Amperometric	9.96–72.8 ng/mL	6.29 ng/mL	[148]
Soluble lectin-like oxidized low-density lipoprotein receptor I (SLOX-1) cTnI	Au/6-mercaptohexadecanoic acid/biotin-caproyl-DPPE/neutravidin/biyotinylated anti-SLOX or anti-cTnI/SLOX-1 or cTnI	Impedimetric	10^{-13}–10^{-7} M	10^{-13} M	[134]
Mb	Au-SPE/Myoglobin solution/(Mb imprinted) M1 film/proteinase K/poly(*o*-aminophenol) (PAP)/Myoglobin	Impedimetric Amperometric	0.5–53.5 μg/mL	1.5 μg/mL 0.8 μg/mL	[149]
Mb	ITO glass/APTES/AuNPs/MUA-MPA/antiMb/BSA/Mb	Impedimetric	0.01–1.65 μg/mL	1.4 ng/mL	[150]
CRP	Au-SPE/carboxylic-modified magnetic beads (HOOC-MBs)/EDC/sulfo-NHS/ethanolamine /biotinylated anti-CRP/streptavidin HRP (strp-HRP)/CRP	Amperometric	0.07–1000 ng/mL	0.021 ng/mL	[151]

low-density lipoprotein receptor-1 and releases as a soluble form. sLOX-1 is a useful marker for early diagnosis of acute coronary syndrome (ACS) [138] (Table 5).

Ko et al. [143] developed an immunosensor for cTnI detection. The detection limit from the calibration curve was calculated as 148 pg/mL. First, the proper orientation of antibodies by protein G that binds the Fc portion of the antibodies might lead to an effective recognition of the analyte. If the antibodies are randomly immobilized on the surface of the PDMS channel, the amount of immunoreaction between antibodies and antigens may be reduced because the Fab portion of antibodies may not sufficiently orient toward the target antigens. Therefore, the immobilization of the antibodies was performed through the interaction between Fc portion of the antibodies and protein G. Second, the best packing density of antibodies increased the sensitivity of their device by avoiding low numbers of antibodies immobilized onto the channel surface and steric hindrance. Third, avoiding the electrode fouling also contributed to the low limit of detection of this device [143].

Mattos et al. [141] developed an *o*-aminobenzoic acid film-based immunosensor for CTnT detection. It showed good performance in terms of operational stability, measuring it 100 times every 2 min. The relative standard deviation was approximately 3% [141].

Mattos et al. [141] and Lu et al. [136] kept the immunosensors they developed in the refrigerator at 4 °C and one found to be 91,6% of initial response after 18 days and the other 90% after 20 days.

Ávila et al. [151] used magnetic beads (MBs) for amperometric immunosensor development. MBs have demonstrated to be a useful tool to improve their sensitivity, reduce time of analysis of complex samples without pre-enrichment or purification steps. Au-SPEs and carboxylic-modified magnetic beads (HOOC-MBs) were used for the first time. Biotinylated anti-CRP reacted with streptavidin HRP (strp-HRP). The electrochemical detection of the enzymatic reaction product was measured disposable Au/SPE using 3,3′,5,5′-tetramethylbenzidine (TMB) as the electron transfer mediator and H_2O_2 as the enzyme substrate. They evaluated the selectivity of the magnetoimmunosensor toward various non-target compounds at their concentrations of 5 mg/mL BSA, 500 ng/mL D-dimer and 4000 g/mL heparin and two other non-target cardiac proteins of 7.5 ng/mL of amino-terminal pro-B-type natri-uretic peptide (NT-proBNP) and 500 ng/mL of cardiac troponin T (cTnT). The tests were performed either in the absence or in the presence of the potential interfering compounds by comparing with the magnetoimmunosensor for 500 ng/mL CRP. The presence of BSA, D-dimer and heparin did not interfere significantly in the CRP determination. Moreover, the target cardiac protein can be accurately determined in the presence of other two cardiac proteins (cTnT and NT-proBNP) at a concentration much higher than that normally found in these biological samples. A great selectivity achieved by using two specific antibodies in the design of the sandwich magnetoimmunosensor [151].

4. Future outlook

The antibodies for construction of immunochemical biosensors–immunosensors have been extensively used more than 35 years. Immunosensors are miniaturized analytical devices which selectively detect analytes and provide a concentration as a result of signal. In this review, attention is focused on the electrochemical immunosensors for tumor and cardiac biomarkers in clinical diagnosis.

In literature, the developed immunosensors were evaluated for the analysis of clinical serum samples and received a good corre lation with the enzyme linked immunosorbent assay (ELISA) [17,18,31,34,35,37,67,68,70]. Huang et al. [17] developed an immunosensor for CEA determination. They compared the results obtained from five human serum samples with the purposed method and ELISA. They reported that a good correlation between the results obtained by the proposed immunosensor and ELISA [17].

Kavosi et al. [60] evaluated the feasibility of their immunosensor for real sample analysis by using standard addition methods. They observed no significant difference results of two methods [60].

Zhang et al. [21] compared their biosensor response with the commercialized electrochemiluminescent method. They found no significant difference [21].

The electrochemical immunosensor can be miniaturized to a small pocket size device which makes them applicable for home use or the doctor's surgery as point of care (POC). For example, glucose biosensor is the most widely used an electrochemical biosensor which is based on a screen-printed amperometric disposable electrode. This type of biosensor has been widely used throughout the World for glucose testing in the home diagnosis. The recognition element of prostate cancer is anti-PSA antibody. The developed immunosensor for PSA offers an attractive possibility to screen prostate cancer in real time and on site. Also, electrochemical immunosensors offer a great selectivity and sensitivity for early clinical analysis. However, moving technology to commercial products may require more time and investments.

5. Conclusion

Biosensors, especially immunosensors, are of great value for use in clinical testing, because they are based on antigen–antibody reactions which are highly sensitive and specific. Moreover, they have vital role in measuring specific compounds in biol;ogical matrices, such as blood and plasma. Electrochemical immunosensors are simple, rapid, reliable and inexpensive devices. Thus they can be used in clinical diagnosis with confidence.

In this review, recent researches on biomarkers used for detecting cancer and cardiovascular diseases are summarized. Carcinoembriyonic antigen(CEA), prostate-specific antigen (PSA), α-1-fetoprotein (AFP), carbohydrate antigen 19-9 (CA 19-9), myeloctomatosis oncogene (c-Myc), cancer antigen 125 (CA125), neuron specific enolase (NSE), epidermal growth factor receptor (EGFR), cancer antigen 15-3, murine double minute 2 (MDM2), Squamous cell carcinoma antigen (SCCA), human chorionic gonadotrophin (hCG), human epididymis-specific protein 4 (HE4), HER-3, vascular endothelial growth factor (VEGF) are commonly used biomarkers in cancer diagnosis and Human cardiac troponins (cTnT and cTnI), myoglobin, C-reactive protein (CRP), myeloperoxidase (MPO), P-selection, soluble lectin-like oxidized low density lipoprotein receptor (sLOX-1) are commonly used cardiovascular disease biomarkers.

In developing immunosensors, the immobilization of antibody is an important step because antibody acts as the recognition element for antibody–antigen reaction. The performance of the detection of antigen binding capacity can be increased with a proper antibody surface. Thus the choice of the antibody immobilization method is very important in the design of an immunosensor. Several methods including physical and chemical adsorption have been used for the preparation of oriented antibody molecular layers on the surface of the transducer. The sensitivity of biomarkers is important for early diagnosis of diseases. Furthermore, the coupling of electrodes with nanostructured materials such as silicon nanowires, gold nanop;articles, carbon nanotubes, magnetic particles, quantum dots offer multiplexing capability for simultaneous measurements of biomarkers.

Acknowledgment

The support from TÜBİTAK (The Scientific and Technological Research Council of Turkey, Project number: 113 Z 678) is greatly acknowledged.

References

[1] B. Jin, P. Wang, H. Mao, B. Hu, H. Zhang, Z. Cheng, Z. Wu, X. Bian, C. Jia, F. Jing, Q. Jin, J. Zhao, Biosens. Bioelectron. 55 (2014) 464–469.
[2] A. Sassolas, L.J. Blum, B.D. Leca-Bouvier, Biotechnol. Adv. 30 (2012) 489–571.
[3] Q. Xu, J.J. Davis., Electroanalysis 26 (2014) 1249–1258.
[4] V. Perumal, U. Hashim, J. Appl. Biomed. 12 (2014) 1–15.
[5] I.E. Tothill, Semin. Cell Dev. Biol. 20 (2009) 55–62.
[6] M. Diaz-Gonzalez, X. Munoz-Berbel, C. Jimenez-Jorquera, A. Baldi, C. Fernandez-Sanchez, Electroanalysis 26 (2014) 1154–1170.
[7] J. Wu, Z. Fu, F. Yan, H. Ju, TrAC, Trends Anal. Chem. 26 (2007) 679–688.
[8] R.K. Iles, H. Kallichurn, J. Bioeng. Biomed. Sci. 2 (2012) 1–5.
[9] B. Rezaei, N. Majidi, H. Rahmani, T. Khayamian, Biosens. Bioelectron. 26 (2011) 2130–2134.
[10] J. Zhou, L. Du, L. Zou, Y. Zou, N. Hu, P. Wang, Sens. Actuators, B 197 (2014) 220–227.
[11] T. Yang, S. Wang, H. Jin, W. Bao, S. Huang, J. Wang, Sens. Actuators, B 178 (2013) 310–315.
[12] M.K. Sezgintürk, Biosens. Bioelectron. 26 (2011) 4032–4039.
[13] D.E. Souto, J.V. Silva, H.R. Martins, A.B. Reis, R. Luz, L.T. Kubota, Biosens. Bioelectron. 46 (2013) 22–29.
[14] X. Yuan, C. Song, H. Wang, J. Zhang, Electrochemical Impedance Spectroscopy in PEM Fuel Cells Fundamentals and Applications, Springer-Verlag, London, USA, 2010.
[15] A.C. Mongra, A. Kaur, R.K. Bansal, Int. J. Eng. Res. Appl. 2 (2012) 743–749.
[16] B. Bohunicky, S.A. Mousa, Nanotechnol. Sci. Appl. 4 (2011) 1–10.
[17] K. Huang, D. Niu, W. Xie, W. Wang, Anal. Chim. Acta 659 (2010) 102–108.
[18] W. Jiang, R. Yuan, Y. Chai, L. Mao, H. Su, Biosens. Bioelectron. 26 (2011) 2786–2790.
[19] X. Sun, Z. Ma, Anal. Chim. Acta 780 (2013) 95–100.
[20] Y. Li, R. Yuan, Y. Chai, Z. Song, Electrochim. Acta 56 (2011) 6715–6721.
[21] Q. Zhang, X. Chen, Y. Tang, L. Ge, B. Guo, C. Yao, Anal. Chim. Acta 815 (2014) 42–50.
[22] Z. Zhong, W. Wu, D. Wang, D. Wang, J. Shan, Y. Qing, Z. Zhang, Biosens. Bioelectron. 25 (2010) 2379–2383.
[23] J Wu, Z Zhang, Z Fu, H. Ju, Biosens. Bioelectron. 23 (2007) 114–120.
[24] Y. Yuan, R. Yuan, Y. Chai, Y. Zhuo, L. Mao, S. Yuan, J. Electroanal. Chem. 643 (2010) 15–19.
[25] W. Limbut, P. Kanatharana, B. Mattiasson, P. Asawatreratanakul, P. Thavarungkul, Anal. Chim. Acta 561 (2006) 55–61.
[26] L. Zhu, L. Xu, N. Jia, B. Huang, L. Tan, S. Yang, S. Yao, Talanta 116 (2013) 809–815.
[27] Y. Cai, H. Li, Y. Li, Y. Zhao, H. Ma, B. Zhu, C. Xu, Q. Wei, D. Wu, B. Du, Biosens. Bioelectron. 36 (2012) 6–11.
[28] Y. Yuan, R. Yuan, Y. Chai, Y. Zhuo, X. Miao, J. Electroanal. Chem. 626 (2009) 6–13.
[29] K. Matsuoka, S. Sumitomo, N. Nakashima, D. Nakajima, N. Misaki, Eur. J. Cardiothorac. Surg. 32 (2007) 435.
[30] H. Yang, R. Yuan, Y. Chai, L. Mao, H. Su, W. Jiang, M. Liang, Biochem. Eng. J. 56 (2011) 116–124.
[31] B. Qu, X. Chu, G. Shen, R. Yu, Talanta 76 (2008) 785–790.
[32] N.V. Panini, G.A. Messina, E. Salinas, H. Fern´andez, J. Raba, Biosens. Bioelectron. 23 (2008) 1145–1151.
[33] W. Liang, R. Yuan, Y. Chai, Y. Li, Y. Zhuo, Electrochim. Acta 53 (2008) 2302–2308.
[34] X. Lu, H. Bai, P. He, Y. Cha, G. Yang, L. Tan, Y. Yang, Anal. Chim. Acta 615 (2008) 158–164.
[35] X. Ran, R. Yuan, Y. Chai, C. Hong, X. Qian, Colloids Surf. B 79 (2010) 421–426.
[36] H. Wang, H. Li, Y. Zhang, Q. Wei, H. Ma, D. Wu, Y. Li, Y. Zhang, B. Du, Biosens. Bioelectron. 53 (2014) 305–309.
[37] Z. Qiang, R. Yuan, Y. Chai, N. Wang, Y. Zhuo, Y. Zhang, X. Li, Electrochim. Acta 51 (2006) 3763–3768.
[38] K. Liu, J. Zhang, Q. Liu, H. Huang, Electrochim. Acta 114 (2013) 448–454.
[39] F. Hu, S. Chen, R. Yuan, Sens. Actuators, B 176 (2013) 713–722.
[40] D. Du, F. Yan, S. Liu, H. Ju, J. Immunol. Methods 283 (2003) 67–75.
[41] I.J. McEwan, K. Dahlman-Wright, J.e Ford, A.P.H. Wright, Biochemistry 35 (1996) 9584–9593.
[42] J. He, Y. Tian, Z. Cao, W. Zou, X. Sun, Sens. Actuators, B 181 (2013) 835–841.
[43] D. Tang, R. Yuan, Y. Chai, Anal. Chim. Acta 564 (2006) 158–165.
[44] I. Diaconu, C. Cristea, V. Hârceagă, G. Marrazza, I. Berindan-Neagoe, R. Săndulescu, Clin. Chim. Acta 425 (2013) 128–138.
[45] J. Han, Y. Zhuo, Y. Chai, Y. Yuan, R. Yuan, Biosens. Bioelectron. 31 (2012) 399–405.
[46] S. Yu, X. Cao, M. Yu, Microchem. J. 103 (2012) 125–130.
[47] R. Elshafey, A.C. Tavares, M. Siaj, M. Zourob, Biosens. Bioelectron. 50 (2013) 143–149.
[48] C. Hong, R. Yuan, Y. Chai, Y. Zhuo, Anal. Chim. Acta 633 (2009) 244–249.
[49] Y. Li, C. Xu, H. Li, H. Wang, D. Wu, H. Ma, Y. Cai, B. Du, Q. Wei, Biosens. Bioelectron. 56 (2014) 295–299.
[50] R. Elshafey, C. Tlili, A. Abulrob, A.C. Tavares, M. Zourob, Biosens. Bioelectron. 39 (2013) 220–225.
[51] D. Wu, H. Fan, Y. Li, Y. Zhang, H. Liang, Q. Wei, Biosens. Bioelectron. 46 (2013) 91–96.
[52] K. Handschuh, J. Guibourdenche, V. Tsatsaris, M. Guesnon, I. Laurendeau, D. Evain-Brion, T. Fournier, Endocrinology 148 (2007) 5011–5019.
[53] J. Lu, S. Liu, S. Ge, M. Yan, J. Yu, X. Hu, Biosens. Bioelectron. 33 (2012) 29–35.
[54] L. Lu, B. Liu, Z. Zhao, C. Ma, P. Luo, C. Liu, G. Xie, Biosens. Bioelectron. 33 (2012) 216–221.
[55] M.Ç. Canbaz, M.K. Sezgintürk, Anal. Biochem. 446 (2014) 9–18.
[56] W. Limbut, P. Kanatharana, B. Mattiasson, P. Asawatreratanakul, P. Thavarungkul, Biosens. Bioelectron. 22 (2006) 233–240.
[57] H. Yu, F. Yan, Z. Dai, H. Ju, Anal. Biochem. 331 (2004) 98–105.
[58] J. Wu, J. Tang, Z. Dai, F. Yan, H. Ju, N.E. Murr, Biosens. Bioelectron. 22 (2006) 102–108.
[59] J. Wu, Z. Zhang, Z. Fu, H. Ju., Biosens. Bioelectron. 23 (2007) 114–120.
[60] B. Kavosi, A. Salimi, R. Hallaj, K. Amani, Biosens. Bioelectron. 52 (2014) 20–28.
[61] X. Wang, J. Miao, Q. Xia, K. Yang, X. Huang, W. Zhao, J. Shen, Electrochim. Acta 112 (2013) 473–479.
[62] H. Tang, J. Chen, L. Nie, Y. Kuang, S. Yao, Biosens. Bioelectron. 22 (2007) 1061–1067.
[63] X. Jia, Z. Liu, N. Liu, Z. Man, Biosens. Bioelectron. 53 (2014) 160–166.
[64] J. Lin, Z. Wei, C. Mao, Biosens. Bioelectron. 29 (2011) 40–45.
[65] Y. Lin, J. Wang, G. Liu, H. Wu, C.M. Wai, Y. Lin, Biosens. Bioelectron. 23 (2008) 1659–1665.
[66] J. Moon, Y.H. Kim, Y. Cho, Biosens. Bioelectron. 57 (2014) 157–161.
[67] S. Chen, R. Yuan, Y. Chai, Y. Xu, L. Min, N. Li, Sens. Actuators, B 135 (2008) 236–244.
[68] W. Lu, X. Cao, L. Tao, J. Ge, J. Dong, W. Qian, Biosens. Bioelectron. 57 (2014) 219–225.
[69] F. Kong, M. Xu, J. Xu, H. Chen, Talanta 85 (2011) 2620–2625.
[70] W. Liang, W. Yi, S. Li, R. Yuan, A. Chen, S. Chen, G. Xiang, C. Hu, Clin. Biochem. 42 (2009) 1524–1530.
[71] X. He, R. Yuan, Y. Chai, Y. Shi, J. Biochem. Biophys. Methods 70 (2008) 823–829.
[72] K. Huang, J. Li, Y. Wu, Y. Liu, Bioelectrochemistry 90 (2013) 18–23.
[73] X. Li, R. Yuan, Y. Chai, L. Zhang, Y. Zhuo, Y. Zhang, J. Biotechnol. 123 (2006) 356–366.
[74] X. Gao, Y. Zhang, H. Chen, Z. Chen, X. Lin, Anal. Biochem. 414 (2011) 70–76.
[75] L. Wu, F. Yan, H. Ju, J. Immunol. Methods 322 (2007) 12–19.
[76] K. Huang, D. Niu, J. Sun, J. Zhu, J. Electroanal. Chem. 656 (2011) 72–77.
[77] X. Cao, N. Wang, S. Ji, L. Guo, K. Li, Biosens. Bioelectron. 39 (2013) 226–230.
[78] S. Suwansa-ard, P. Kanatharana, P. Asawatreratanakul, B. Wongkittisuksa, C. Limsakul, P. Thavarungkul, Biosens. Bioelectron. 24 (2009) 3436–3441.
[79] S. Viswanathan, C. Rani, A.V. Anand, J.A. Ho, Biosens. Bioelectron. 24 (2009) 1984–1989.
[80] G. Lai, J. Wu, C. Leng, H. Ju, F. Yan, Biosens. Bioelectron. 26 (2011) 3782–3787.
[81] D. Feng, L. Li, X. Fang, X. Han, Y. Zhang, Electrochim. Acta 127 (2014) 334–341.
[82] T. Yu, W. Cheng, Q. Li, C. Luo, L. Yan, D. Zhang, Y. Yin, S. Ding, H. Ju, Talanta 93 (2012) 433–438.
[83] L. Wu, J. Chen, D. Du, H. Ju, Electrochim. Acta 51 (2006) 1208–1214.
[84] D. Tang, B. Xia, Microchim. Acta 163 (2008) 41–48.
[85] J. Miao, X. Wang, L. Lu, P. Zhu, C. Mao, H. Zhao, Y. Song, J. Shen, Biosens. Bioelectron. 58 (2014) 9–16.
[86] H. Chen, D. Tang, B. Zhang, B. Liu, Y. Cui, G. Chen, Talanta 91 (2012) 95–102.
[87] M. Namgung, S. Jung, C.M. Chung, S. Oh, Ultramicroscopy 109 (2009) 907–910.
[88] X. Chen, X. Jia, J. Han, J. Ma, Z. Man, Biosens. Bioelectron. 50 (2013) 356–361.
[89] Y. Hou, T. Li, H. Huang, H. Quan, X. Miao, M. Yang, Sens. Actuators, B 182 (2013) 605–609.
[90] H. Li, J. He, S. Li, A.P.F. Turner, Biosens. Bioelectron. 43 (2013) 25–29.
[91] S. Chen, R. Yuan, Y. Chai, L. Min, W. Li, Y. Xu, Electrochim. Acta 54 (2009) 7242–7247.
[92] Z. Dai, J. Chen, F. Yan, H. Ju, Cancer Detect. Prev. 29 (2005) 233–240.
[93] Y. Zhuo, R. Yu, R. Yuan, Y. Chai, C. Hong, J. Electroanal. Chem. 628 (2009) 90–96.
[94] F. Kong, X. Zhu, M. Xu, J. Xu, H. Chen, Electrochim. Acta 56 (2011) 9386–9390.
[95] J. Han, Y. Zhuo, Y. Chai, L. Mao, Y. Yuan, R. Yuan, Talanta 85 (2011) 130–135.
[96] A. Salimi, B. Kavosi, F. Fathi, R. Hallaj, Biosens. Bioelectron. 42 (2013) 439–446.
[97] F. Yang, J. Han, Y. Zhuo, Z. Yang, Y. Chai, R. Yuan, Biosens. Bioelectron. 55 (2014) 360–365.
[98] X. Sun, Z. Ma, Biosens. Bioelectron. 35 (2012) 470–474.
[99] J. Lin, C. He, S. Zhang, Anal. Chim. Acta 643 (2009) 90–94.
[100] T. Li, M. Yang, H. Li, J. Electroanal. Chem. 655 (2011) 50–55.
[101] H. Wang, Y. Zhang, H. Yu, D Wu, H. Ma, H. Li, B. Du, Q. Wei, Anal. Biochem. 434 (2013) 123–127.
[102] B. Su, D. Tang, J. Tang, Y. Cui, G. Chen, Biosens. Bioelectron. 30 (2011) 229–234.
[103] Y. Xiang, Y. Zhang, B. Jiang, Y. Chai, R. Yuan, Sens. Actuators, B 155 (2011) 317–322.
[104] H. Chen, J. Tang, B. Su, G. Chen, J. Huang, D. Tang, Anal. Chim. Acta 678 (2010) 169–175.
[105] D. Lin, J. Wu, H. Ju, F. Yan, Biosens. Bioelectron. 52 (2014) 153–158.
[106] M. Giannetto, L. Mori, G. Mori, M. Careri, A. Mangia, Sens. Actuators, B 159 (2011) 185–192.
[107] A Ravalli, G. Pilon dos Santos, M. Ferroni, G. Faglia, H. Yamanaka, G. Marrazza, Sens. Actuators, B 179 (2013) 194–200.
[108] S. Liu, X. Zhang, Y. Wu, Y. Tu, L. He, Clin. Chim. Acta 395 (2008) 51–56.
[109] J. Lin, C. He, L. Zhang, S. Zhang, Anal. Biochem. 384 (2009) 130–135.

[110] J. Tang, D. Tang, Q. Li, B. Su, B. Qiu, G. Chen, Anal. Chim. Acta 697 (2011) 16–22.
[111] M. Yang, A. Javadi, S. Gong, Sens. Actuators, B 155 (2011) 357–360.
[112] J. Lin, Z. Wei, H. Zhang, M. Shao, Biosens. Bioelectron. 41 (2013) 342–347.
[113] Y. Dai, Y. Cai, Y. Zhao, D. Wu, B. Liu, R. Li, M. Yang, Q. Wei, B. Du, H. Li, Biosens. Bioelectron. 28 (2011) 112–116.
[114] L. Ding, J. You, R. Kong, F. Qu, Anal. Chim. Acta 793 (2013) 19–25.
[115] J. Tang, D. Tang, B. Su, Q. Li, B. Qiu, G. Chen, Electrochim. Acta 56 (2011) 8168–8175.
[116] D. Wu, A. Guo, Z. Guo, L. Xie, Q. Wei, B. Du, Biosens. Bioelectron. 54 (2014) 634–639.
[117] J. Han, Y. Zhuo, Y. Chai, R. Yuan, W. Zhang, Q. Zhu, Anal. Chim. Acta 746 (2012) 70–76.
[118] Z. Song, R. Yuan, Y. Chai, W. Jiang, H. Su, X. Che, X. Ran, Biosens. Bioelectron. 26 (2011) 2776–2780.
[119] Y. Liao, R. Yuan, Y. Chai, Y. Zhuo, X. Yang, Anal. Biochem. 402 (2010) 47–53.
[120] S. Viswanathan, C. Rani, C. Delerue-Matos, Anal. Chim. Acta 726 (2012) 79–84.
[121] G. Sun, J. Lu, S. Ge, X. Song, J. Yu, M. Yan, J. Huang, Anal. Chim. Acta 775 (2013) 85–92.
[122] Z. Cui, D. Wu, Y. Zhang, H. Ma, H. Li, B. Du, Q Wei, H. Ju, Anal. Chim. Acta 807 (2014) 44–50.
[123] J. Han, Y. Zhuo, Y. Chai, Y. Xiang, R. Yuan, Y. Yuan, N. Liao, Biosens. Bioelectron. 41 (2013) 116–122.
[124] E. Asav, M.K. Sezgintürk, Int. J. Biol. Macromol. 66 (2014) 273–280.
[125] M.N. Sonuç, M.K. Sezgintürk, Talanta 120 (2014) 355–361.
[126] M.Ç. Canbaz, Ç.S. Şimşek, M.K. Sezgintürk, Anal. Chim. Acta 814 (2014) 31–38.
[127] World Health Organization, Global Status Report on Noncommunicable Diseases 2010, World Health Organization, Geneva, 2011.
[128] A. Qureshi, Y. Gurbuz, J.H. Niazi, Sens. Actuators, B 171– (172) (2012) 62–76.
[129] World Health Organization, Global atlas on Cardiovascular Disease Prevention and Control, World Health Organization, Geneva, 2011.
[130] C.D. Mathers, D. Loncar, PLoS Med. 3 (2006) 442.
[131] A. Kakoti, P. Goswami, Biosens. Bioelectron. 43 (2013) 400–411.
[132] R.V. Sharma, V.K. Tanwar, S.K. Mishra, A.M. Biradar, Thin Solid Films 519 (2010) 1167–1170.
[133] B.V.M. Silva, I.T. Cavalcanti, A.B. Mattos, P Moura, M.D.P.T. Sotomayor, R. F. Dutra, Biosens. Bioelectron. 26 (2010) 1062–1067.
[134] M.M. Billah, H.C.W. Hays, C.S. Hodges, S. Ponnambalam, R. Vohra, P.A. Millner, Sens. Actuators, B 173 (2012) 361–366.
[135] A. Quershi, K.S. Saravan, Y. Gurbuz, M. Howell, W.P. Kang, J.L. Davidson, Procedia Chem. 1 (2009) 1079–1082.
[136] L. Lu, B. Liu, C. Liu, G. Xie, Bull. Korean Chem. Soc 31 (11) (2010).
[137] J.A. Ho, A.F. Jou, L. Wu, S. Hsu, Methods 56 (2012) 223–229.
[138] A. Pirillo, A.L. Catapano, Dis. Markers 35 (2013) 413–418.
[139] B.V.M Silva, I.T. Cavalcanti, M.M.S. Silva, R.F. Dutra, Talanta 117 (2013) 431–437.
[140] S.L.R. Gomes-Filho, A.C.M.S. Dias, M.M.S. Silva, B.V.M. Silva, R.F. Dutra, Microchem. J. 109 (2013) 10–15.
[141] A.B. Mattos, T.A. Freitas, L.T. Kubota, R.F. Dutra, Biochem. Eng. J. 71 (2013) 97–104.
[142] M.M. Billah, C.S. Hodges, H.C.W. Hays, P.A. Millner, Bioelectrochemistry 80 (2010) 49–54.
[143] S. Ko, B. Kim, S. Jo, S.Y. Oh, J. Park, Biosens. Bioelectron. 23 (2007) 51–59.
[144] F. Zhou, M. Lu, W. Wang, Z. Bian, J. Zhang, J. Zhu, Clin. Chem. 56 (2010) 1701–1707.
[145] E. Suprun, T. Bulko, A. Lisitsa, O. Gnedenko, A. Ivanov, V. Shumyantseva, A. Archakov, Biosens. Bioelectron. 25 (2010) 1694–1698.
[146] D. Stan, C. Mihailescu, R. Iosub, C. Moldovan, M. Savin, I. Baciu, Thin Solid Films 526 (2012) 143–149.
[147] V. Bhalla, S. Carrara, P. Sharma, Y. Nangia, C.R. Suri, Sens. Actuators, B 161 (2012) 761–768.
[148] E. Zapp, E. Westphal, H. Gallardo, B. Souza, I.C. Vieira, Biosens. Bioelectron. http://dx.doi.org/10.1016/j.bios.2014.03.026.
[149] F.T.C. Moreira, S. Sharma, R.A.F. Dutra, J.P.C. Noronha, A.E.G. Cass, M.F. Sales, Sens. Actuators, B 196 (2014) 123–132.
[150] Rajesh V. Sharma, S.K. Mishra, A.M. Biradar, Mater. Chem. Phys. 132 (2012) 22–28.
[151] B.E. Ávila, V. Escamilla-Gómez, S. Campuzano, M. Pedrero, J.P. Salvador, M. P. Marco, J.M. Pingarrón, Sens. Actuators, B 188 (2013) 212–220.

Talanta 132 (2015) 175–181

Contents lists available at ScienceDirect

Talanta

journal homepage: www.elsevier.com/locate/talanta

Dealing with heterogeneous classification problem in the framework of multi-instance learning

Zhaozhou Lin [a], Shuaiyun Jia [a], Gan Luo [a], Xingxing Dai [a], Bing Xu [a], Zhisheng Wu [a], Xinyuan Shi [a,b,*], Yanjiang Qiao [a,b,*]

[a] College of Chinese Medicine, Beijing University of Chinese Medicine, Beijing 100102, China
[b] Research Center of TCM-information Engineering, State Administration of Traditional Chinese Medicine of the People's Republic of China, Beijing 100102, China

ARTICLE INFO

Article history:
Received 21 April 2014
Received in revised form
28 August 2014
Accepted 3 September 2014
Available online 16 September 2014

Keywords:
Heterogeneous spectra
Multi-instance learning (MIL)
Error-Correcting Output Codes (ECOC)
Maximum count least square support vector machine (maxc-LS-SVM)
Geographical origins

ABSTRACT

To deal with heterogeneous classification problem efficiently, each heterogeneous object was represented by a set of measurements obtained on different part of it, and the heterogeneous classification problem was reformulated in the framework of multi-instance learning (MIL). Based on a variant of count-based MIL assumption, a maximum count least squares support vector machine (maxc-LS-SVM) learning algorithm was developed. The algorithm was tested on a set of toy datasets. It was found that maxc-LS-SVM inherits all the sound characters of both LS-SVM and MIL framework. A comparison study between the proposed approach and the other two MIL approaches (i.e., mi-SVM and MI-SVM) was performed on a real wolfberry fruit spectral dataset. The results demonstrate that by formulating the heterogeneous classification problem as a MIL one, the heterogeneous classification problem can be solved by the proposed maxc-LS-SVM algorithm effectively.

© 2014 Elsevier B.V. All rights reserved.

1. Introduction

The application of near infrared spectroscopy (NIR) to perform classification has been spread across the analysis of food, agricultural, petroleum, and pharmaceutical products [1–3]. However, spectra obtained on heterogeneous objects, such as corn and pharmaceutical tablet, are often of high variance. Applying common classification methods on these spectra will result in weak conclusion. This is one typical category of heterogeneous classification problem. However, the heterogeneous classification problem has not yet been solved thoroughly [4].

The key on solving heterogeneous classification problem is to represent each heterogeneous object efficiently. In the literatures, pre-treatment is the most successfully and widely used techniques for solving the heterogeneous classification problem. One builds certain measurement protocol to improve the representativeness of measurements. Spectra measured by using integrating sphere [5–10], rotating the sample during spectra collection, or grinding the samples [11–14] are of this type. Significantly better results were observed while the measurement was taken by a patented measurement method [15]. However, when the spectra are needed to be collected in-situ, none of the above methods are applicable. Hwang et al. [16] developed a fast and non-destructive analytical method to identify geographical origins of rice samples via transmission spectral collected through packed grains. But the variation of packing thickness will prevent the measurement from yielding reproducible spectra.

Instead of receiving a set of measurements, each for a sample, an object can be represented by a set of measurements (instances). Therefore, the heterogeneous classification problem can be solved by formulating it as a multi-instance learning one. Instead of receiving labeled instances as in traditional supervised learning, the MIL learner receives a set of labeled bags. The majority of MIL studies are concerned with binary classification problems [17]. Most of these studies assume that a bag is labeled positive if there is at least one instance in it being positive. Otherwise, a bag is labeled negative if all the instances in it are negative.

Based on the classical MIL assumption, numerous MIL methods have been proposed in the literatures, and most of them have been reviewed in earlier studies [17–19]. These algorithms use mainly the information of one instance from each positive bag. However, there is commonly more than one instance in any positive bags and much of the information contained in these instances is lost.

The MIL assumption is first used to solve the problem of *musk* drug activity prediction problem [20]. From then on, many problems have been formulated as MIL problem, such as image categorization, object detection, and human active recognition

* Corresponding authors at: College of Chinese Medicine, Beijing University of Chinese Medicine, Beijing 100102, China. Tel.: +86 10 84738621; fax: +86 84738661.
E-mail addresses: xyshi@126.com (X. Shi), yjqiao@263.net (Y. Qiao).

http://dx.doi.org/10.1016/j.talanta.2014.09.007
0039-9140/© 2014 Elsevier B.V. All rights reserved.

[18,21,22]. Although all early work in MIL assumes a specific concept class known to be appropriate for a drug activity prediction like domain, the classical MIL assumption is not guaranteed to hold in other domains. Recently, a significant amount of researches in MIL are concerned with cases where the classical view of MIL problem is relaxed, and alternative assumptions are considered instead [17]. Although not all these works clearly state what particular assumption is used and how it relates to other assumptions, the use of alternative assumptions has been clarified by reviewing the studies in this area.

In this work, a variant of count-based binary MIL assumption was adopted. It assumes that a bag is labeled positive if the product of the positive posteriors of instances, weighted by the bag prior, is larger than that of the negative ones. Otherwise, a bag is labeled negative. Base on this assumption, the maxc-LS-SVM algorithm was proposed to deal with the heterogeneous classification problem. For multi-class cases, the original classification problem was decomposed in the framework of Error-Correcting Output Codes (ECOC) by one-versus-one design [23]. The maxc-LS-SVM algorithm was modified correspondingly and its performance was compared with mi-SVM and MI-SVM [24] algorithm. The results of applying these approaches on toy datasets and a real herbal dataset clearly showed the advantage of maxc-LS-SVM algorithm.

2. Theory and algorithm

2.1. Least squares-support vector machine (LS-SVM)

This study will briefly focus on the basic concepts of LS-SVM because the theory of LS-SVM has been described extensively in the literatures [25,26]. LS-SVM encompasses similar advantages as SVM, but additionally, it requires solving only a set of linear equations, which is much easier and computationally very simple. The objective function defined in LS-SVM is [27]

$$\min_{\omega,b,e} J_P(\omega,e)=\tfrac{1}{2}\omega^T\omega+\gamma\tfrac{1}{2}\sum_{i=1}^{N}e_i^2$$
$$\text{subject to(s.t.)}: y_i[\omega^T\varphi(x_i)+b]=1-e_i,\quad i=1,\ldots,N \tag{1}$$

where w denotes the normal vector to the classification hyperplane, γ is the hyperparameter tuning the amount of regularization versus the sum squared error, e is the error variable, and $\varphi(x)$is the nonlinear map from original space to the high (and possibly infinite) dimensional space.

To solve the optimization problem efficiently, a Lagrange function is constructed and translated into its dual form

$$L(\omega,b,e;\alpha)=J_P(\omega,e)-\sum_{i=1}^{N}\alpha_i\{y_i[\omega^T\varphi(x_i)+b]-1+e_i\} \tag{2}$$

where α_i values are the Lagrange multipliers.

The conditions for optimality are

$$\begin{cases}\frac{\partial L}{\partial\omega}=0\rightarrow\omega=\sum_{i=1}^{N}\alpha_i y_i\varphi(x_i)\\ \frac{\partial L}{\partial b}=0\rightarrow\sum_{i=1}^{N}\alpha_i y_i\\ \frac{\partial L}{\partial e_i}=0\rightarrow\alpha_i=\gamma e_i,\qquad i=1,\ldots,N\\ \frac{\partial L}{\partial\alpha_i}=0\rightarrow y_i[\omega^T\varphi(x_i)+b]-1+e_i=0,\quad i=1,\ldots,N\end{cases} \tag{3}$$

From the conditions for optimality, it can be concluded that no α_i values will be exactly equal to zero, meaning that the advantages of automatic sparseness are lost. However, the model can be trained much more efficiently after constructing the Lagrangian by solving the linear Karush–Kuhn–Tucker (KKT) system, since it yields a linear system instead of a quadratic programming problem

$$\begin{bmatrix}0 & 1_N^T\\ 1_N & \boldsymbol{\Omega}+\gamma^{-1}I_N\end{bmatrix}\begin{bmatrix}b\\ a\end{bmatrix}=\begin{bmatrix}0\\ \boldsymbol{y}\end{bmatrix} \tag{4}$$

where $\boldsymbol{y}$ is a vector containing the reference values, $\boldsymbol{1}_N$ is a $[N\times 1]$ vector of ones and $\mathbf{I}$ is an $[N\times N]$ identify matrix. $\boldsymbol{\Omega}$ is the kernal matrix defined by $\boldsymbol{\Omega}_{ij}=\varphi(x_i)^T\varphi(x_j)=\mathbf{K}(x_i,x_j)$.

The classifier in the dual space takes the form

$$y(x)=sign\left[\sum_{i=1}^{N}\alpha_i y_i K(x,x_i)+b\right] \tag{5}$$

2.2. Maximum margin formulation of MIL

In traditional supervised learning framework, an object is represented by one single instance, i.e. measurement vector, and associated with a class label. The goal is to induce a classifier to label instances. While, MIL groups instances into bags and each bag is attached with a class label. More formally, an object is represented by a bag $\boldsymbol{B}=\{\boldsymbol{x}_1,\boldsymbol{x}_2,\ldots,\boldsymbol{x}_p\}$, which contains a set of D-dimensional instances. Each bag is associated with a label $\boldsymbol{Y}$.

Both mi-SVM and MI-SVM approaches [24] are modified and extended from Support Vector Machines (SVMs). The mi-SVM approach explicitly treats the instance labels as unobserved integer variables subjected to constrain defined by the (positive) bag labels. A generalized soft-margin SVM is defined as follows in primal form

$$\min_{\{y_i\}}\min_{w,b,\xi}\tfrac{1}{2}\|w\|^2+C\sum_i\xi_i$$
$$\text{s.t. }\forall i:\ y_i(\langle w,x_i\rangle+b)\geq 1-\xi_i,\xi_i\geq 0,y_i\in\{-1,1\} \tag{6}$$

where ξ is a non-negative slack variable, C is the hyperparameter tuning the amount of the degree of misclassification versus the sum squared error, y_i is the label of instance.

The mi-SVM formulation leads to a mixed integer programming problem. One has to maximize a soft-margin criterion jointly over possible label assignments and hyperplane. While, the MI-SVM approach extends the notion of margin to bag and maximizing the bag margin directly. The bag margin with respect to a hyperplane is defined by

$$\gamma_I\equiv Y_I\max_{i\in I}(\langle w,x_i\rangle+b) \tag{7}$$

Incorporating the above bag margin, an MIL version of the soft-margin classifier is defined by

$$\min_{w,b,\xi}\tfrac{1}{2}\|w\|^2+C\sum_I\xi_I$$
$$\text{s.t. }\forall I:\ Y_I\max_{i\in I}(\langle w,x_i\rangle+b)\geq 1-\xi_I,\xi_I\geq 0 \tag{8}$$

Unfolding the max operation by introducing inequality constraint per instance for the negative bags, or by introducing a selector variable $s(I)\in I$ which denotes the positive instance selected for the positive bags, one can obtain the following equivalent formulation

$$\min_s\min_{w,b,\xi}\tfrac{1}{2}\|w\|^2+C\sum_I\xi_I$$
$$\text{s.t.}\quad \begin{array}{l}\forall I:\ Y_I=-1\wedge-\langle w,x_i\rangle-b\geq 1-\xi_I,\forall i\in I,\\ \text{or}Y_I=1\wedge-\langle w,x_{s(I)}\rangle-b\geq 1-\xi_I,\xi_I\geq 0.\end{array} \tag{9}$$

MI-SVM can also be cast as mixed-integer program. One has to find both the optimal selectors and hyperplane.

A heuristic optimization scheme has been proposed to solve the mixed-integer programs by alternating the following two steps (i) for a given integer variables, solve the associated Quadratic Programming (QP) and find the optimal discriminant function,

(ii) for a given discriminant function, update the label of each instance in mi-SVM or the single selector variable in MI-SVM.

2.3. Multi-class classification

The above three algorithms are originally designed to perform binary classification. Although binary LS-SVM can be easily extended to deal with multi-class problems, it is usually more preferable to build a classifier distinguishing only two classes rather than to consider more than two classes in a model. In this study, the original multi-class problem was decomposed into easier to solve binary classifications by using a common strategy "one-versus-one" in the framework of ECOC, which is a simple but powerful framework to deal with the multi-class classification problem based on the embedding of binary classifiers [23].

The "one-versus-one" decomposition scheme divides an m class problem into $M=m(m-1)/2$ binary problems. Each problem is faced by a binary LS-SVM classifier, which is responsible for distinguishing between a pair of classes. The learning phase of the classifiers is done using a subset of samples, which contains any two classes of them, whereas samples with different class labels are simply ignored.

In prediction phase, a sample is presented to each of the binary classifiers. The output of a classifier, $r_{ij} \in \{0, 1\}$, denotes the output of the ith sample on the jth binary classifier. These outputs are represented by a vector $\mathbf{r}_i$

$$\mathbf{r}_i = [r_{i1}, r_{i2}, \cdots, r_{ij}, \cdots, r_{iM}], j = 1, \cdots, M \tag{10}$$

The predicted class can be obtained by Hamming decoding strategies as follows [23]:

$$Class = \min_{c=1,\ldots,m} \sum_{j=1}^{M} (1 - sign(r_{ij}, y_{cj}))/2 \tag{11}$$

where y_c is a codeword corresponding to class c.

The classification of individual instances was performed by using binary classification algorithm.

2.4. Maximum count LS-SVM

For a binary classifier, let $\mathbf{Y} \in \{-1,1\}$. It is assumed that a bag is labeled positive if more than half of the instances in the bag are drawn from positive sets. Specifically, the sum rule is used to decide the label of the bag

Classify $\mathbf{B}=\{\boldsymbol{x}_1, \boldsymbol{x}_2, \ldots, \boldsymbol{x}_p\}$ as positive, i.e. $\mathbf{Y}_i=1, j=1, 2, \ldots, p$ if

$$\sum_{j=1}^{p} \frac{y_{ij}+1}{2} \geq \sum_{j=1}^{p} \frac{1-y_{ij}}{2} \tag{12}$$

or negative, i.e. $\mathbf{Y}_i=-1, j=1, 2, \ldots, p$ if

$$\sum_{j=1}^{p} \frac{y_{ij}+1}{2} < \sum_{j=1}^{p} \frac{1-y_{ij}}{2} \tag{13}$$

where N is the number of bags, p denotes the number of instances in each bag.

For multi-class cases, let $Y \in \{1, 2, 3, \ldots, m\}$. Every instance of one object is presented to each of the basic *ovo*-LS-SVM classifiers. The classification result of one instance is represented by a vector $\boldsymbol{c}_j$ with element c_{kj} taken from {0, 1}. The value 1 means the instance is assigned to class k, while 0 not. These outputs are then combined into a score matrix $\mathbf{C}$:

$$\mathbf{C} = \begin{pmatrix} c_{11} & c_{12} & \cdots & c_{1m} \\ c_{21} & c_{22} & \cdots & c_{2m} \\ \vdots & & & \vdots \\ c_{p1} & c_{p2} & \cdots & c_{pm} \end{pmatrix} \tag{14}$$

From the score matrix, bags can be directly classified with the following determination function:

$$\mathbf{Y}_i = \arg \max_{k=1,\ldots,m} \sum_{j=1}^{p} c_{kj} \tag{15}$$

$i=1, 2, \ldots, N, j=1, 2, \ldots, p, k=1, 2, \ldots, m$. Tie break arbitrarily.

where m denotes the number of categories. The above equation is also fit to binary cases.

The main steps of maxc-LS-SVM can be summarized as follows:

Training data formalization: assign the bag label to its instances and use all instances for training.

Basic classifier training: estimate parameters of the basic classifiers.

Individual instance classification: classify each instance using the basic classifiers.

Bag classification: classify an object or bag B according to Eq. (15).

2.5. Performance indicator

For binary classification problem, there are a large number of well-known statistical metrics such as accuracy, precision, sensitivity, specificity, AUC, Cohen's kappa, etc. However, most of these performance indicators cannot be directly used for multi-class cases. In this work, only the metrics whose successful application on multi-class problems had been proved experimentally were adopted.

Accuracy rate, also known as classification rate, is the proportion of correctly classified instances in the population.

Cohen's kappa [28] is an alternative measure to accuracy rate, compensating for random hits. It evaluates the degree of agreement in classification over which would be expected by chance. Based on an m-class confusion matrix, the Cohen's kappa can be computed as follows:

$$kappa = \frac{N \sum_{i=1}^{m} h_{ii} - \sum_{i=1}^{m} T_{ri} T_{ci}}{N^2 - \sum_{i=1}^{m} T_{ri} T_{ci}} \tag{16}$$

where h_{ii} is the number of true positives for each class, N is the number of bags, m is the number of labels, T_{ri} is the rows' total counts and T_{ci} is the columns' total counts.

The theoretical range of Cohen's kappa statistic is from -1 (total disagreement) through 0 (random classification) to 1 (perfect agreement), which seems difficult to compare kappa with accuracy (0–1). Actually, most classifiers do at least the same as random guessing on most real-world datasets, so their kappa values score higher than zero by definition. It is generally assumed that a kappa score lying between 0.8 and 1 indicates that the corresponding classifier is almost in perfect agreement with the actual pattern.

The bootstrap cross-validation method (BCV) [29], which is a bootstrap smoothing version of cross-validation, was used to estimate the generalization error of each classification algorithm because it has less variation and bias. The bootstrap datasets are drawn with replacement for some large B between 50 and 200. For each dataset, an internal cross-validation error estimator was obtained with a predetermined classification rule. After B times

repeat, the averaged error estimation was calculated over all bootstrap bag sets.

3. Experimental

3.1. Toy data

The toy data has three classes (A, B and C). For each bag of one specific class, ρ percent of its instances were sampled from the Gaussian located at either (0, 0), (4, 1), or (1, 4), the rest were sampled from the Gaussian located at (2, 2). Every bag contains 30 instances. To be comparable with common NIR classifications, 50 bags were generated for each class. A sketch map of the two-way datasets with $\rho \in \{0.2, 0.4, 0.6, 0.8\}$ is shown in Fig. 1.

The toy data was used to simulate the heterogeneous classification problem. The feasibility of formulizing the heterogeneous classification problem as a multi-instance learning problem and the influence of bag size on the proposed maxc-LS-SVM algorithm were investigated on the toy data.

3.2. Herbal geographical origins data

Generally, the quality of *wolfberry fruit* varies with geographical origin, which makes its medical efficacy diverse. Therefore, it is necessary to distinguish accurately the geographical origins of *wolfberry fruit* to assure a traditional Chinese prescription effective. The *wolfberry fruit* dataset consists of samples collected from Inner Mongolia, Ningxia, and Qinghai provinces of China. For each sample, ten spectra (i.e. instances) were measured respectively on ten different parts of the *wolfberry fruit* surface. A sketch map of the ten instances is shown in Fig. 2(a).

Each instance was measured by using a portable Near-infrared Spectrophotometer (Ocean quest 256-2.5) equipped with an InGaAs detector and diffuse reflection optical fiber probe. The spectrum covering the range of 870–2530 nm at distinguishability of 9.5 nm was recorded. All the raw spectra were transferred into logarithm mode because they were initially recorded in reflectance mode. Totally, 29, 45, and 45 bags were formed for each geographical origin, respectively. An overlap plot of the transformed spectra is shown in Fig. 2(b).

The *wolfberry fruit* data was used to further illustrate the feasibility of formulizing the heterogeneous classification problem as a multi-instance learning one. A comparison study between the proposed maxc-LS-SVM and the mi-SVM, MI-SVM algorithm were also performed on the *wolfberry fruit* data.

3.3. Single instance pseudo dataset

In traditional learning framework, each object is represented by a single labeled instance. Thus, one instance from each bag was drawn randomly to form the pseudo dataset. Each instance was labeled with its bag's label.

3.4. Software and algorithms

All calculations were performed on a personal computer i7 880 processor with 6GB RAM under the Win7 Professional operating system using Matlab 7.9 (Mathworks, Inc., Natick, MA). The

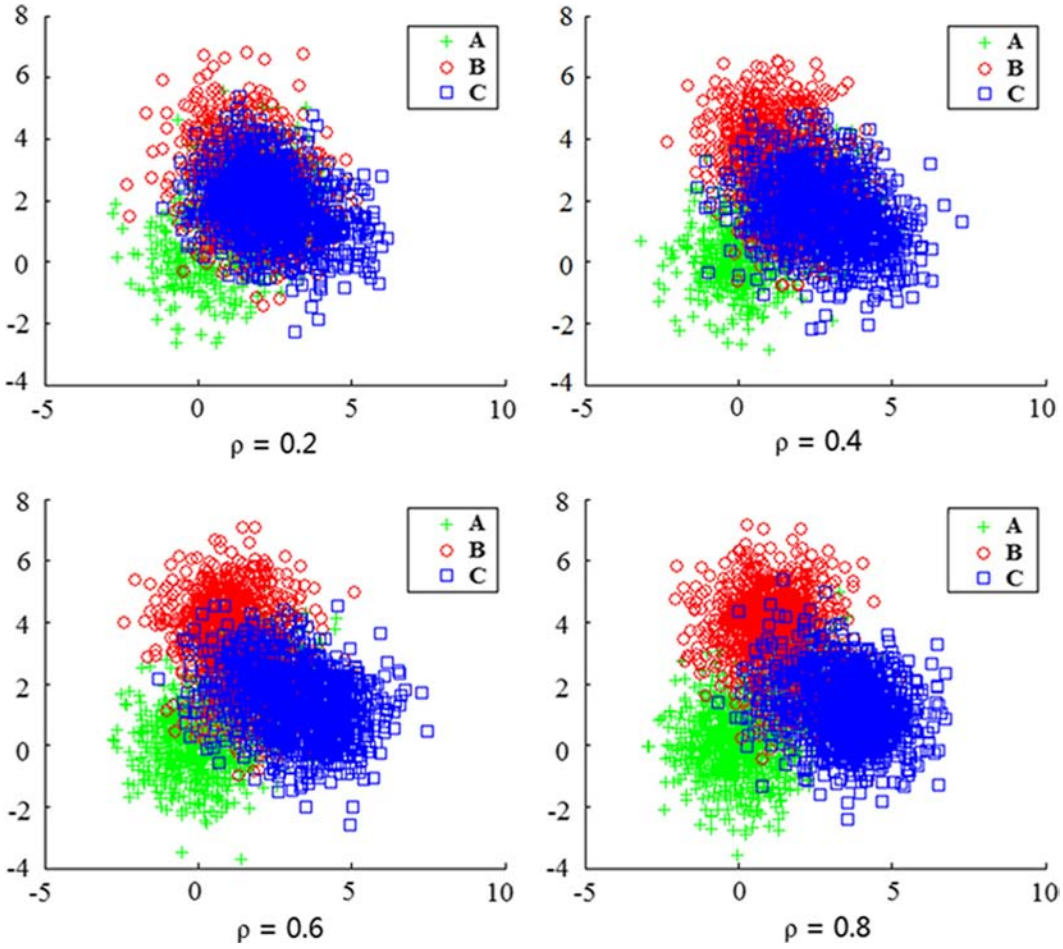


Fig. 1. The two way toy data with ρ=0.2, 0.4, 0.6, and 0.8, respectively.

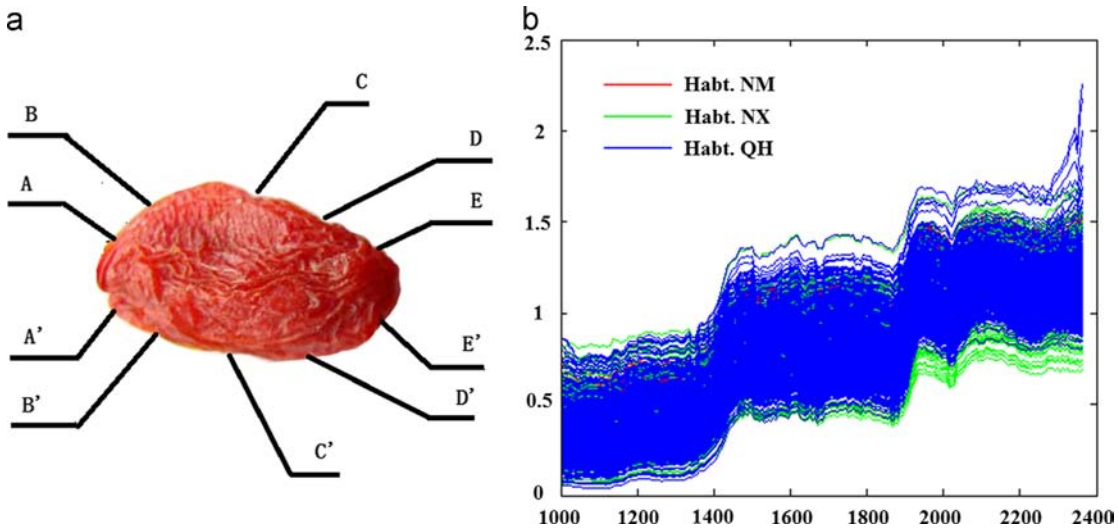


Fig. 2. (a) A sketch map of the locations of the ten instances for each wolfberry fruit sample; (b) an overlap plot of the transformed spectra. Habt. NM means the samples were original sampled from Inner Mongolia, similar, Habt. NX stands for Ningxia and Habt. QH denotes Qinghai.

maxc-LS-SVM algorithm was modification of function in the LS-SVMlab v1.8 [30]. The implementation of the MI-SVM and mi-SVM algorithm was based on a MIL toolbox publicly available at http://www.cs.cmu.edu/~juny/MILL/.

4. Results and discussion

A grid search method guided by 10-fold cross-validation was adopted to optimize the hyperparameters of MI-SVM and mi-SVM. Each pair (C, γ) in the cross-product of C ranging from 2^{-15} to 2^{3} and γ ranging from 2^{-5} to 2^{15} at the increment of 2 in the exponent was used to train every dichotomous classifier. Meanwhile, the optimal hyperparameters of LS-SVM were determined by coupled simulated annealing (CSA) algorithm and simplex algorithm.

4.1. The toy data

To be consistent with traditional classification method, one single-instance pseudo dataset was drawn for every bag datasets. The Cohen's kappa and accuracy were calculated by the BCV procedure on the single-instance pseudo dataset. However, the randomizations in producing the toy bag sets and in drawing the single-instance pseudo datasets present variability in the prediction metrics. Therefore, each of the four toy datasets was regenerated 100 times respectively to present a stable evaluation on the applicability of traditional classification method in heterogeneous classification problem.

With respect to $\rho=0.2$, the *Mann–Whitney U* test did not reject the equivalence between the linear and RBF (radial basis function) kernel using accuracy with the significance level of $\alpha=0.01$ (Table 1). However, opposite results were obtained on the comparison study between the linear and RBF kernel in term of Cohen's kappa. In addition, from the decision boundary illustrated in Fig. 3, it was observed that the decision boundary of RBF kernel was more efficient to separate one class from another, but was too complex and specific. Meanwhile, the decision boundary of linear kernel separate linearly the pseudo samples well. This means that the *ovo*-LS-SVM model built with RBF kernel overfit the classification problem. Thus, liner kernel is used in maxc-LS-SVM model to prevent possible over-fitting.

The results of applying maxc-LS-SVM on the simulated heterogeneous classification data were shown in Figs. 4 and 5. From the results on the toy data with $\rho=0.2$, it was found that the prediction ability of the model built using maxc-LS-SVM improved quite a lot, when it was compared with the model constructed using the base *ovo*-LS-SVM classifier (Fig. 4(a) and (b)). By varying the bag size from 5 to 30 at the increment of 5, the classification accuracy increased gradually. These results indicate that a powerful decision function can be constructed even the data is too weak to build a usable base classifier. The results presented in Fig. 5 support this opinion.

Table 1
A comparison between the learning effectiveness of linear kernel and RBF kernel LS-SVM on the toy datasets ($\alpha=0.01$).

ρ	Accuracy		*p*-Value	Kappa		*p*-Value
	Linear	*RBF*		*Linear*	*RBF*	
0.2	0.4355	0.4253	0.0405	0.1453	0.1813	**0.0000**
0.4	0.5753	0.5655	0.0439	0.3516	0.3357	0.0264
0.6	0.6703	0.6708	0.9318	0.4921	0.4906	0.7947
0.8	0.7981	0.7961	0.7851	0.6832	0.6816	0.8632

Regarding $\rho=0.4$, 0.6 and 0.8, the statistical analysis does not reject the null hypothesis that the base classifiers with linear and RBF kernel perform equally (Table 1) in terms of both kappa and accuracy. Further examination on the decision boundaries of RBF kernel reveal that each pair of classes can be separated linearly in the raw space (Figs. S1–S3 in the supplementary material). Considering the computational burden, linear kernel is preferred and used for further investigation.

The results presented in Fig. 4(a) clearly shows that the effect of random success on the accuracy matric decrease with the increase of ρ. In addition, a base LS-SVM classifier which performs better than random guessing can be obtained, even most of the instances from the toy data with ρ equal to 0.2 were shared by three classes (Fig. 5(a)). From the results summarized in Figs. 4 and 5, it can also be observed that all the classifiers built using maxc-LS-SVM perform significantly better than their corresponding base classifiers on the toy datasets ($\rho=0.4$, 0.6, 0.8, respectively). This means maxc-LS-SVM inherits the sound characters of LS-SVM. With the bag size varying from 5 to 30 at the increment of 5, the prediction accuracy gradually improved and even approached perfect agreement. Therefore, it can be concluded that by formulating the heterogeneous classification problem into a multiple instance

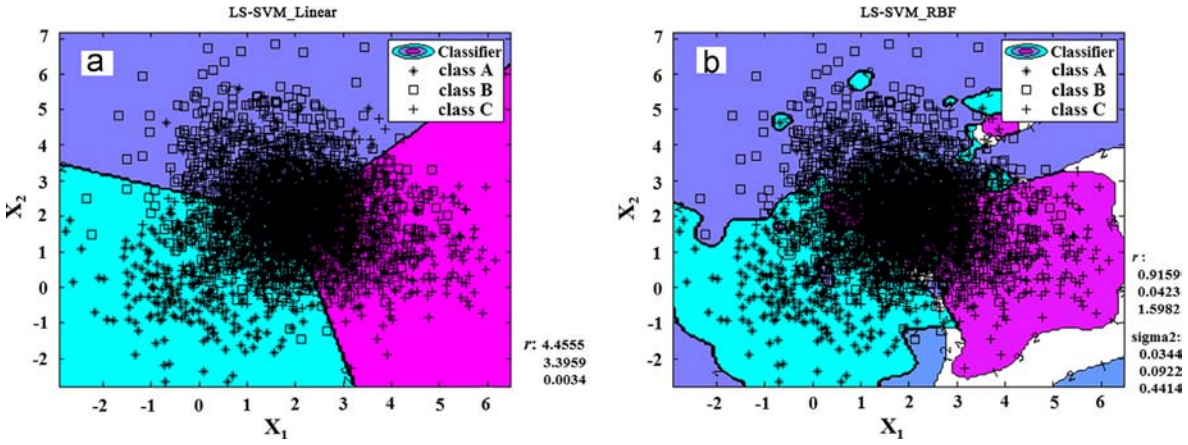


Fig. 3. The LS-SVM decision boundaries of linear kernel and RBF kernel on the toy data with ρ equal to 0.2.

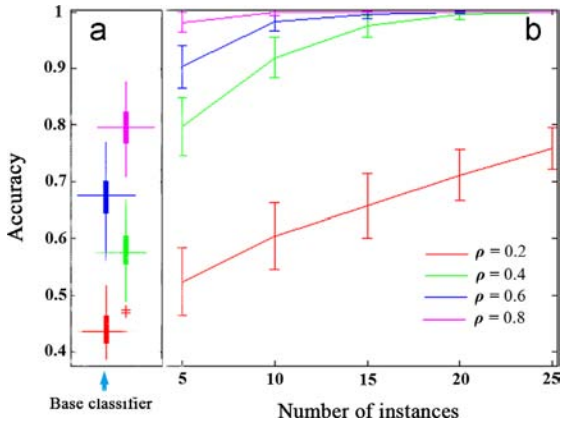


Fig. 4. The classification accuracy results of applying maxc-LS-SVM algorithm on the four toy datasets with the number of instances ranging from 5 to 25 at the increments of 5.

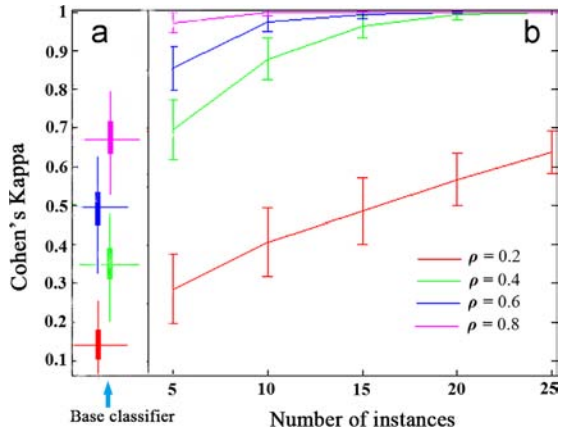


Fig. 5. A summary of the Cohen's kappa results of applying maxc-LS-SVM algorithm on the toy datasets with the number of instances ranging from 5 to 25 at the increments of 5.

learning one, the heterogeneous classification problem can be solved effectively.

4.2. The wolfberry fruit data

The results of applying *ovo*-LS-SVM method on the bootstrap pseudo data sets were listed in Table 2. It can be observed that the prediction accuracy of linear kernel *ovo*-LS-SVM was larger than that of the RBF kernel. That means linear kernel is more acceptable than RBF kernel in classifying the geographical origin of wolfberry fruits. From the results obtained on the toy data, it is concluded that the prediction ability of maxc-LS-SVM will be improved if more instances are included in a bag. So all instances measured on one wolfberry fruit were used to investigate the prediction performance of MIL algorithms. Besides, with bag size fixed, the comparisons among MIL algorithms become more objective.

Table 2
A summary of the prediction performance of the base classification method LS-SVM and the three multi-instance learning methods i.e. mi-SVM, MI-SVM, maxc-LS-SVM on the wolfberry fruit data.

	Accuracy		**Kappa**	
	Liner	*RBF*	*Linear*	*RBF*
LS-SVM	0.9276	0.7868	0.8870	0.6667
mi-SVM	0.5929	0.5371	0.4427	0.3741
MI-SVM	0.8205	0.7414	0.7106	0.5934
maxc-LS-SVM	0.9898	0.9754	0.9840	0.9616

The comparison results between maxc-LS-SVM and the other two MIL algorithms were tabulated in Table 2. For mi-SVM algorithm, neither linear nor RBF kernel could produce classifier comparable to LS-SVM algorithm in terms of both classification accuracy and kappa. There are two factors contributing to this phenomenon, one is the MIL assumption and the other is the relationship between bag and its instances. Since mi-SVM is a present based MIL algorithm, MI-SVM is first brought into comparison.

MI-SVM algorithm extends the notion of a margin from individual patterns to sets of patterns. And its prediction performance improved quite a lot when it was compared with mi-SVM algorithm. But the classification accuracy and kappa of MI-SVM algorithm were all still worse than that of LS-SVM algorithm. That means considering all instances in a bag as a whole is benefit for constructing a powerful classifier. However, adopting the whole learning strategy along is not enough to solve the heterogeneous classification problem thoroughly.

The maxc-LS-SVM algorithm, whose MIL assumption is different from that of mi-SVM and MI-SVM, performed much better than the base classifier in terms of classification accuracy for both linear and RBF kernel. And the kappa of liner kernel maxc-LS-SVM reached as high as 0.9840, which indicates that random success take a limited impact on the prediction results. Compared with the results obtained using mi-SVM and MI-SVM algorithm, it can be concluded that maxc-LS-SVM algorithm is more powerful in classifying the geographical origin of wolfberry fruit.

All the results demonstrate that by forming the heterogeneous classification problem into a multiple instance learning one, the heterogeneous classification problem can be solved effectively. The power of mi-SVM and MI-SVM has been demonstrated experimentally in image classification, which is a well-studied topic in the field of computer vision. But heterogeneous classification is a rather different application; the present-based MIL assumption is no longer applicable.

Additionally, it may be argued that it is unnecessary to complicate the heterogeneous classification problem, since the accuracy of base classifier using one instance for a object is already larger than 0.90. But it is still need to build a more powerful decision rule, because the wolfberry fruit is used as tonic Chinese herbal medicine, and distinguishing explicitly the geographical origin of wolfberry fruit is necessary to keep the prescription effect. Moreover, the kappa of linear kernel *ovo*-LS-SVM is only 0.8870, a more credible classifier should be constructed.

5. Conclusions

In this study, the heterogeneous classification problem was formulated as a multi-instance learning one. Based on a variant of count-based MIL assumption, the maxc-LS-SVM algorithm was developed to deal with multi-instance learning problem. The proposed algorithm inherits all the sound characters of both the base classifier and MIL framework. By incorporating the maximum count MIL assumption into the process of constructing a suitable learning algorithm, maxc-LS-SVM make full use of the information of each instance in the positive (or class specific) bags. A real wolfberry fruit spectral dataset, which contains 119 objects from geographical origins, was used in this experiment. In multi-class classification, the proposed method presented the optimal classification accuracy and kappa compared with the other two MIL methods (i.e., mi-SVM and MI-SVM). More importantly, it was concluded that the maximum count based MIL assumption was more applicable in the heterogeneous classification domain. While being potentially promising, the maxc-LS-SVM approach needs to be further evaluated with other heterogeneous classification applications. This is currently being pursued.

Acknowledgments

The authors would like to thank the anonymous reviewers for their kind and insightful comments. Financial supports from the Innovation Group Projects of Beijing University of Chinese Medicine (no. 2011-CXTD-11) and the National Natural Science Foundation of China (no. 81303218) are gratefully acknowledged. The computation was partly supported by CHEMCLOUDECOMPUTING (Beijing University of Chemical Technology, Beijing, China).

Appendix A. Supplementary materials

Supplementary data associated with this article can be found in the online version at http://dx.doi.org/10.1016/j.talanta.2014.09.007.

References

[1] S. Naik, V.V. Goud, P.K. Rout, K. Jacobson, A.K. Dalai, Renew. Energy 35 (2010) 1624–1631.
[2] T. De Beer, A. Burggraeve, M. Fonteyne, L. Saerens, J.P. Remon, C. Vervaet, Int. J. Pharm. 417 (2011) 32–47.
[3] L.J. Xie, X.Q. Ye, D.H. Liu, Y.B. Ying, Food Res. Int. 44 (2011) 2198–2204.
[4] L. Esteve Agelet, C.R. Hurburgh Jr., Talanta 121 (2014) 288–299.
[5] E. Ziémons, J. Mantanus, P. Lebrun, E. Rozet, B. Evrard, P. Hubert, J. Pharm. Biomed. Anal. 53 (2010) 510–516.
[6] O.Y. Rodionova, A.L. Pomerantsev, Trends Anal. Chem. 29 (2010) 795–803.
[7] J. Märk, M. Andre, M. Karner, C.W. Huck, Eur. J. Pharm. Biopharm. 76 (2010) 320–327.
[8] J. Mantanus, E. Ziémons, P. Lebrun, E. Rozet, R. Klinkenberg, B. Streel, B. Evrard, P. Hubert, Talanta 80 (2010) 1750–1757.
[9] B. Wang, G. Liu, Y. Dou, L. Liang, H. Zhang, Y. Ren, J. Pharm. Biomed. Anal. 50 (2009) 158–163.
[10] S. Tripathi, H.N. Mishra, Food Control 20 (2009) 840–846.
[11] J. Moros, J.J. Laserna, Anal. Chem. 83 (2011) 6275–6285.
[12] M. Blanco, A. Peguero, Trends Anal. Chem. 29 (2010) 1127–1136.
[13] C.-O. Chan, C.-C. Chu, D.K.-W. Mok, F.-T. Chau, Anal. Chim. Acta 592 (2007) 121–131.
[14] S. Wold, H. Antti, F. Lindgren, J. Öhman, Chemom. Intell. Lab Syst. 44 (1998) 175–185.
[15] J. Janni, B.A. Weinstock, L. Hagen, S. Wright, Appl. Spectrosc. 62 (2008) 423–426.
[16] J. Hwang, S. Kang, K. Lee, H. Chung, Talanta 101 (2012) 488–494.
[17] J. Foulds, E. Frank, Knowl. Eng. Rev. 25 (2010) 1–25.
[18] Y. Li, D.M.J. Tax, R.P.W. Duin, M. Loog, Pattern Recognit. 46 (2013) 865–874.
[19] Z.-H. Zhou, J. Comput. Sci. Technol. 21 (2006) 800–809.
[20] T.G. Dietterich, R.H. Lathrop, T. Lozano-Pérez, Artif. Intell. 89 (1997) 31–71.
[21] Y. Shi, Y. Gao, R. Wang, Y. Zhang, D. Wang, Artif. Intell. 38 (2013) 16–28.
[22] Z. Liang, Z. Bo, G. Yang, Fifth International Conference on Fuzzy Systems and Knowledge Discovery, FSKD 2008, pp. 487–492.
[23] S. Escalera, O. Pujol, P. Radeva, J. Mach. Learn. Res. 11 (2010) 661–664.
[24] S. Andrews, I. Tsochantaridis, T. Hofmann, Adv. Neural Inf. Process Syst. 15 (2002) 561–568.
[25] F. Chauchard, J. Svensson, J. Axelsson, S. Andersson-Engels, S. Roussel, Chemom. Intell. Lab Syst. 91 (2008) 34–42.
[26] S. Ren, L. Gao, Analyst 136 (2011) 1252–1261.
[27] J.A. Suykens, T. Van Gestel, J. De Brabanter, B. De Moor, J. Vandewalle, J. Suykens, T. Van Gestel, Least Squares Support Vector Machines, World Scientific Publishing, Singapore, 2002.
[28] M. Galar, A. Fernández, E. Barrenechea, H. Bustince, F. Herrera, Pattern Recognit. 44 (2011) 1761–1776.
[29] W.J. Fu, R.J. Carroll, S. Wang, Bioinformatics 21 (2005) 1979–1986.
[30] ⟨http://www.esat.kuleuven.be/sista/lssvmlab/⟩.

Talanta 132 (2015) 182–190

Contents lists available at ScienceDirect

Talanta

journal homepage: www.elsevier.com/locate/talanta

Search prefilters to assist in library searching of infrared spectra of automotive clear coats

Barry K. Lavine [a,*], Ayuba Fasasi [a], Nikhil Mirjankar [a], Collin White [a], Mark Sandercock [b]

[a] Department of Chemistry, Oklahoma State University, Stillwater, OK 74078, United States
[b] Royal Canadian Mounted Police Forensic Laboratory, 15707-118th Avenue, Edmonton, AB, Canada T5V 1B7

ARTICLE INFO

Article history:
Received 26 May 2014
Received in revised form
24 August 2014
Accepted 25 August 2014
Available online 3 September 2014

Keywords:
Search prefilters
Infrared library searching
Automotive paints
Forensic analysis
Pattern recognition analysis
Genetic algorithms
Wavelets
Feature selection
Automotive clear coats

ABSTRACT

Clear coat searches of the infrared (IR) spectral library of the paint data query (PDQ) forensic database often generate an unusable number of hits that span multiple manufacturers, assembly plants, and years. To improve the accuracy of the hit list, pattern recognition methods have been used to develop search prefilters (i.e., principal component models) that differentiate between similar but non-identical IR spectra of clear coats on the basis of manufacturer (e.g., General Motors, Ford, Chrysler) or assembly plant. A two step procedure to develop these search prefilters was employed. First, the discrete wavelet transform was used to decompose each IR spectrum into wavelet coefficients to enhance subtle but significant features in the spectral data. Second, a genetic algorithm for IR spectral pattern recognition was employed to identify wavelet coefficients characteristic of the manufacturer or assembly plant of the vehicle. Even in challenging trials where the paint samples evaluated were all from the same manufacturer (General Motors) within a limited production year range (2000–2006), the respective assembly plant of the vehicle was correctly identified. Search prefilters to identify assembly plants were successfully validated using 10 blind samples provided by the Royal Canadian Mounted Police (RCMP) as part of a study to populate PDQ to current production years, whereas the search prefilter to discriminate among automobile manufacturers was successfully validated using IR spectra obtained directly from the PDQ database.

© 2014 Elsevier B.V. All rights reserved.

1. Introduction

Automotive paint systems consist of multiple layers of paint: a top coat consisting of a clear coat and a color coat layer which in turn is over one or more undercoats [1,2]. With the exception of the clear coat, each layer contains pigments and fillers. Paint data query (PDQ) is a forensic database of the physical attributes (color and layer sequence) and the chemical composition (filler, general binder and extended pigment composition) of each layer of the original manufacturer's paint system [3,4]. Digital libraries containing infrared (IR) spectra for each of these layers accompany the physical and chemical data. If the original manufacturer's paint system is present in a paint chip recovered from the scene of a crime, PDQ can assist in identifying the manufacturer and model of the vehicle provided that at least the color coat or one of the undercoat layers (primer, or e-coat) is present in the paint sample.

PDQ contains the physical and chemical data of each paint layer as well as search and retrieval software to generate a hit list. Searches of PDQ require the user to translate the composition of each layer of the unknown paint chip into specific text codes based on their IR spectra. A search query is then constructed based on the color, chemical composition and its layer sequence. In the case of an unknown sample consisting of only the clear coat, the text based portion of PDQ produces an unusable number of hits that span multiple manufacturers, models and years because modern clear coats in PDQ are designated as having only one of two possible formulations: acrylic melamine styrene or acrylic melamine styrene polyurethane. (For modern automotive paint systems, the clear coat is all too often the only layer of paint left at the crime scene.) Furthermore, there are no inorganic fillers or color with which to visually discriminate the paint sample except for the rare tinted clear coat. Pattern recognition methods applied directly to the IR spectra of clear coats through the development of search prefilters hold the potential for more specific searches.

In this study, library search prefilters were developed from IR spectra in the PDQ database using a two step procedure to determine the assembly plant and model of an automobile from a clear coat paint smear. The first step involves preprocessing the IR spectra using wavelets [5,6] to enhance subtle but significant features in the spectral data. In the second step, wavelet coefficients characteristic of the assembly plant of the automobile are identified using a genetic algorithm (GA) for pattern recognition

* Corresponding author. Tel.: +1 405 744 5945; fax: +1 405 744 6007.
E-mail address: bklab@chem.okstate.edu (B.K. Lavine).

http://dx.doi.org/10.1016/j.talanta.2014.08.061
0039-9140/© 2014 Elsevier B.V. All rights reserved.

analysis and feature selection [7–10]. Previously published studies of IR search prefilters developed using this two step procedure [11–16] were limited to an individual class of compounds (e.g., carboxylic acids) or the modeling problems addressed were simpler because smaller training sets were used. This study is unique since both the manufacturer (General Motors, Ford, or Chrysler) and the assembly plant of the vehicle could be simultaneously ascertained from an IR spectrum of a clear coat paint sample using library search prefilters. All search prefilters (vehicle manufacturer and automotive assembly plant) developed in this study were successfully validated. Even in challenging trials where the samples evaluated were all the same manufacturer (General Motors) within a limited production year range 2000–2006, the respective assembly plant could be correctly identified. For the GM search prefilters, successful validation was demonstrated using 10 blind samples provided by the Royal Canadian Mounted Police (RCMP). Search prefilters developed for automotive manufacturer were successfully validated using IR spectra of clear coats obtained from the PDQ database.

The proposed search prefilters can simplify IR library searching of the PDQ database. Improving the discrimination capability between IR spectra in the PDQ database using this two step procedure also allows for comparison of all automotive clear coats in the database, reducing the dependence of the search on text based fields, resulting in improved ease of use and fewer errors by eliminating IR spectra in the PDQ library from the search that are not related to the unknown.

2. Materials and methods

IR spectra of 1314 clear coat paint samples applied to the metal surfaces of automobiles and trucks assembled at 21 General Motors (GM), 18 Chrysler, and 13 Ford assembly plants within the limited production year range of 2000–2006 were measured on four different spectrometers: two Thermo-Nicolet 6700s FTIR spectrometers, one BioRad 40A and one BioRad 60 FTIR spectrometer. All four spectrometers were equipped with DTGS detectors and all paint samples were collected in transmission mode using high pressure diamond anvil cells. For the two BioRad instruments, Harrick 4x beam condensers were used, whereas a Harrick 6x beam condenser was used in each Thermo-Nicolet 6700s instrument.

IR spectra of clear coats from plastic and fiberglass substrates were not used in the development of the search prefilters since automotive paint is often applied to these substrates at the plant that manufactures these components, not at the plant where the automotive vehicle containing these components is assembled. Table 1 lists the 21 g automotive assembly plants used in this study.

Data preprocessing was crucial to ensure a successful analysis of the data. In this study, data preprocessing consisted of aligning the IR spectra along the wavelength axis, application of the discrete wavelet transform to resolve overlapping spectral bands, and feature selection to identify informative wavelet coefficients using a genetic algorithm. Each step is described in detail below.

2.1. Spectral alignment

IR spectra of the clear coats were not properly aligned along their x or y-axes because the spectra were collected on four different spectrometers. There were differences in the alignment of the optical systems as these spectrometers were from different vendors and were manufactured in different years. Differentiating assembly plants within a plant group required finding small differences in similar IR spectra; hence, spectral alignment was crucial.

Sample preparation and placement can also affect wavelength alignment and the measured absorbance. If the aperture of the sample cell is small enough to become the limiting aperture of the spectrometer, any shift in the position of the sample from the center of the beam causes a shift in wavenumber and instrument line shape function. Under circumstances where the sample itself is not the limiting aperture, small wavenumber shifts may be observed if the sample is not positioned at a fixed angle from the IR beam. The beam may be refracted at an angle that displaces the image on the detector as the beam traverses the sample. As a result, the pathlength of the beam would be changed through the interferometer, altering the relationship of the interferogram to the He–Ne laser, resulting in small wavenumber shifts. For samples titled with respect to the laser beam, the pathlength within the sample changes, which may alter the measured absorbance.

The first step in this study was to align all spectra (along the wavelength axis) using OMNIC. For the measured absorbance to be very nearly equal to the true absorbance, the interferograms were multiplied by the Norton-Beer medium apodization function before application of the Fourier transform [17]. Although all spectra were measured at a nominal 4 cm^{-1} resolution, variations in the apparent frequency of the helium neon laser used and the alignment of the optical systems of the four instruments resulted in differences in the number of points in each spectrum for the same wavenumber range and their alignment along the wavenumber axis. The number of points collected per spectrum using the two Thermo-Nicolet instruments varied from 1878 points to 1958 points, whereas all spectra from the two BioRad instruments were represented by 1944 points. For a particular sample measured on all four instruments, spectral subtraction of the wavenumber axis for each measurement yielded a nonzero response at each wavelength when spectra from different spectrometers were compared. To remedy these two problems, each spectrum was normalized to the helium neon laser frequency of 15,798.0 cm^{-1}. An instrumental line shape function representative of the Thermo Nicolet instruments and developed in OMNIC was applied to the Bio-Rad spectra to ensure that all measurements made by the Bio-Rad instruments were comparable to spectra collected by the two Thermo-Nicolet instruments. The laser frequency value was set to that measured at the aperture setting to make peak positions independent of aperture setting. This ensured wavelength alignment along the x-axis for all clear coat paint spectra. After this preprocessing, each spectrum consisted of 1869 points for the entire mid-IR range of 400 cm^{-1} to 4000 cm^{-1}.

Variations in the spacing of the data points by the BioRad and Thermo-Nicolet instruments in the spectral range investigated is due to differences in the software used by the respective instrument manufacturers. It is well known among practitioners in IR spectroscopy that even if two spectrometers are off by only a quarter-point, pattern recognition methods that utilize the covariance matrix will perform poorly. Although the differences between the instruments were large enough to require alignment, these differences could not be detected visually. To authenticate wavelength alignment along the x-axis for all clear coat paint spectra of GM automobiles between the years 2000–2006, IR spectra of the same clear coat samples collected on both the BioRad and Thermo Nicolet instruments were subtracted before and after performing the alignment procedure. The subtraction yielded a nonzero response at each wavelength before the alignment procedure was implemented but zero at each point after alignment.

2.2. Wavelets

The fingerprint region of each spectrum (600 cm^{-1} to 1500 cm^{-1}), which is comprised of 468 points, was normalized to unit length and subject to wavelet analysis using the MATLAB

Table 1
GM plants used to develop the prefilters for spectral library searching.

Plant ID	Plant	Make	Line
1	Arlington	Cadillac, Chevrolet, GMC	Suburban, Yukon, Escalade, Tahoe
3	Bowling Green	Cadillac, Chevrolet	Corvette, XLR
4	Doraville	Pontiac	Venture, Silhouette, Montana, Uplander, Terraza
5	Fairfax	Chevrolet, Oldsmobile, Pontiac	Grand AM, Malibu, Intrigue
6	Flint	Chevrolet, GMC	Silverado, Sierra
8	Fort Wayne	Chevrolet, GMC	Silverado, Sierra
9	Fremont	GMC	Vibe, Tacoma Cobalt, Grand Prix
10	Hamtramck	Buick, Cadillac, Pontiac	Bonneville, Deville, Lucerne, LeSabre, Seville, Eldorado
12	Janesville	GMC	Tahoe, Suburban, Yukon
14	Lansing	Pontiac	STS
16	Linden	Chevrolet, GMC	Blazer, Jimmy, S10
17	Lordstown	Pontiac	Sunfire, Cavalier, Cobalt, Pursuit
18	Moraine	Chevrolet, GMC, Saab	Jimmy, Envoy, 9S7, Blazer, Trailblazer, Sonoma
20	Oklahoma City	Chevrolet, GMC	Malibu, Trailblazer, Envoy, Equipe, XUV
21	Orion	Pontiac, Buick	Bonneville, PG6,LeSabre, Aurora, Park Avenue
22	Oshawa	GMC, Pontiac	Allure, Regal
23	Pontiac	Chevrolet, GMC	Silverado, Sierra, Silhouette
24	Ramos	Buick, Chevrolet, Pontiac	Cavalier, Sunfire, Rendezvous, Aztek, Hummer HR
25	Shreveport	Chevrolet, GMC	S10, Cologne, Sonata
26	Silao	Chevrolet, GMC, Saab	Avalanche, Suburban, Yukon XL
27	Spring Hill	Starlet	SSL,ION,SC1,SC2,SL1,VUE

Wavelet toolbox 3.0.4 (MathWorks, Natick, MA). Outside of the fingerprint region, each IR spectrum consisted of only C–H stretching bands present in all clear coat paint spectra and noise (2100 cm^{-1} to 2500 cm^{-1}) due to the uncompensated absorption of IR radiation by the diamond anvil cell. Applying the discrete wavelet transform [18] to the fingerprint region, the 1314 IR spectra that served as the training set for the development of search prefilters for the PDQ database were decomposed into wavelet coefficients representing both the high and low frequency components of the signal. In this study, the Symlet6 mother wavelet at the 8th level of decomposition, i.e., 8Sym6, was used to denoise and to resolve overlapping spectral responses in the fingerprint region of each IR spectrum. Preprocessing of the IR spectra by wavelets produced 1080 wavelet coefficients for each IR spectrum.

2.3. Genetic algorithm for variable selection

Wavelet coefficients that contain information about the manufacturer or the assembly plant of the automotive vehicle were identified by a genetic algorithm (GA) for pattern recognition analysis. The pattern recognition GA identifies a set of wavelet coefficients that optimizes the separation of the classes in a plot of the two or three largest principal components of the aligned and wavelet transformed data. Because principal components maximize variance, the bulk of the information encoded by the selected coefficients is about the classification problem of interest. Spurious or chance classification, which often occurs when using other variable selection methods [19–21], is mitigated using principal components to assess the information content of the various wavelet coefficient subsets identified by the pattern recognition GA.

The principal component (PC) plot functions as an embedded information filter. A good PC plot can only be generated by coefficients whose variance or information content is primarily about class membership differences. Hence, the principal component analysis routine incorporated into the fitness function of the pattern recognition GA limits the search to these types of feature sets, thereby significantly reducing the size of the search space. In addition, the pattern recognition GA focuses on those classes and/or samples that are difficult to classify as the pattern recognition GA trains by boosting the relative importance (i.e., weights) of those classes and/or samples (i.e., vehicles). Samples that consistently classify correctly are not as heavily weighted as samples that are difficult to classify. Over time, the pattern GA is able to learn its optimal parameters in a manner similar to a neural network. The pattern recognition GA integrates aspects of artificial intelligence and evolutionary computations to yield a “smart” one-pass procedure for variable selection and classification. Further details about the operation of the pattern recognition GA can be found elsewhere [22,23].

3. Results and discussion

A hierarchical classification scheme was used to develop search prefilters for GM assembly plants, where the 21 g assembly plants were divided into five major plant groups based on a visual analysis of the extended fingerprint region (2000–600 cm^{-1}) of the clear coats. These five plants groups correspond to the two labels used by PDQ for modern automotive clear coats: acrylic melamine styrene and acrylic melamine styrene polyurethane. For Plant Groups 2 and 5, the carbonyl band corresponds to a doublet (see Fig. 1) indicative of acrylic melamine styrene polyurethane. The appearance of the doublet is due to the fact that there are two chemical sources for the carbonyl: acrylate and urethane. For Plant Groups 1, 3, and 4, the carbonyl band corresponds to a singlet (see Fig. 1) indicative of acrylic melamine styrene because only acrylate possesses a carbonyl. The fact that acrylic melamine styrene polyurethane can be divided into two distinct groups based on visual analysis of the fingerprint region of the IR spectra of GM automotive clear coats indicates that differences exist within this formulation in the relative amounts of styrene and urethane and it is reflected in the fingerprint region of the IR spectra of these clear coats. By the same token, differences in the fingerprint region of the clear coats for plant groups 1, 3, and 4 are based on changes in the relative amounts of the chemical components that define the acrylic melamine styrene formulation. The validity of the plant group concept to construct search prefilters has been demonstrated through extensive validation in previously published studies involving hundreds of samples [14,15]. The spectral analysis described in this paper utilizes this same approach in the identification of the blind paint samples provided by the RCMP. The delineation of the IR spectra, first by plant group, is based on

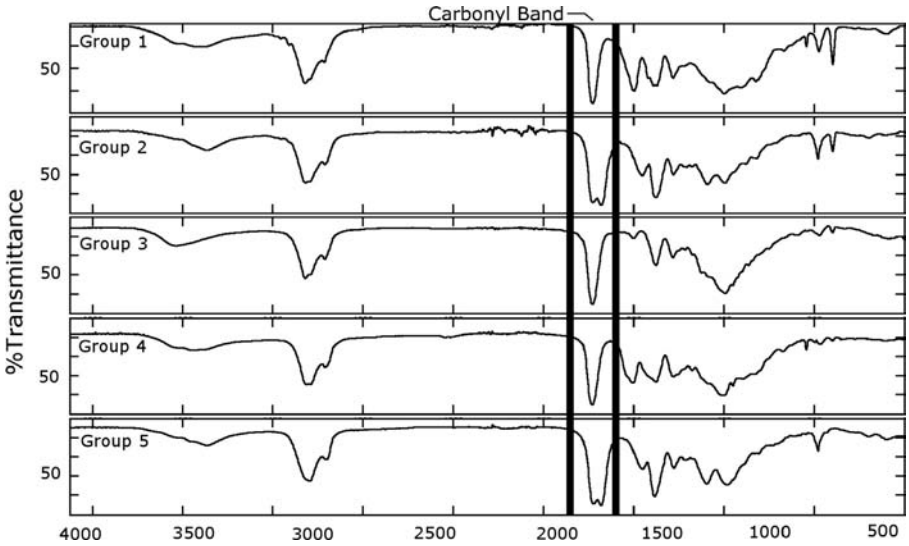


Fig. 1. IR spectra of clear coats from the PDQ library that are representative of the five GM plant groups. Carbonyl band in each IR spectra is denoted.

Table 2
Assembly plants comprising each plant group.

Plant group	Plant ID number	Assembly plant
1	1, 4, 5, 8, 14, 18, 23	Arlington, Doraville, Fairfax, Fort Wayne, Lansing, Moraine, Pontiac
2	3, 10, 21	Bowling Green, Hamtramck, Orion, Wilmington
3	6, 9, 16, 17, 20, 22, 25	Flint, Fremont, Linden, Lordstown, Oklahoma City, Oshawa, Shreveport
4	12	Janesville
5	24, 26, 27	Ramos Arizpe, Silao, Spring Hill, St. Therese

the paint chemistry of automotive clear coats and is necessary due to the large number of assembly plants (i.e., classes) in this study and the similarity of the IR spectra within each plant group.

An unknown is first assigned to a plant group using a single search prefilter and then a second search prefilter is used to identify the specific assembly plant or assembly plants within the plant group to which membership of the unknown is assigned. The assembly plants comprising each plant group are listed in Table 2. Several previously published studies on the use of the pattern recognition GA to develop IR search prefilters from wavelet transformed spectral data have demonstrated both the efficacy of this methodology and the low probability of overfitting the data using the pattern recognition GA for variable selection [11–16].

The first step in this study was to apply PCA [24] to the wavelet transformed IR spectra. Prior to PCA, each wavelet coefficient was autoscaled [25] to ensure that it had a mean of zero and a standard deviation of one. Autoscaling removes inadvertent weighting of the wavelet coefficients that otherwise would occur due to differences in magnitude among the coefficients. This ensures that each wavelet coefficient has an equal weight in the pattern recognition analysis of the data.

The 464 IR spectra that served as the training set for the development of the search prefilters for the PDQ database are summarized in Table 3. Fig. 2 shows a PC plot of the two largest principal components of the 464 wavelet transformed IR spectra and the 1080 wavelet coefficients representing each IR spectrum. Each paint sample is represented as a point in the PC map of the data (T-1=Plant Group 1, T-2=Plant Group 2, T-3=Plant Group 3, T-4=Plant Group 4, and T-5=Plant Group 5). The overlap of the clear coats from each plant group in the map of the data is evident.

The pattern recognition GA was used to identify wavelet coefficients characteristic of plant group. Informative coefficients were identified by sampling key feature subsets, scoring their PC plots, and tracking those plant groups and/or IR spectra that were most difficult to classify. The boosting routine used this information to steer the population to an optimal solution. After 200 generations, the pattern recognition GA identified 14 wavelet coefficients whose PC plot (see Fig. 3) showed clustering of the IR spectra on the basis of plant group.

To assess the predictive ability of the 14 wavelet coefficients identified by the pattern recognition GA, a validation set of 10 blind samples was used. The blind samples were not part of the PDQ database nor were they part of the training set used to develop the search prefilters. These samples were obtained by the RCMP as part of a project to populate PDQ to current production years.

IR spectra from the validation set were projected directly onto the PC map developed from the 464 IR spectra of the training set and 14 wavelet coefficients identified by the pattern recognition GA. Fig. 4 shows the projection of the blind samples onto the PC map of the training set data. Nine of the 10 blind samples are located in a region of the map occupied by samples from the same plant group.

Fig. 5 shows an IR spectrum of the misclassified blind sample (Sample #8) compared to an IR spectrum of a clear coat paint sample of the same make, model, year, and assembly plant from the PDQ database. The dissimilarity between these two IR spectra is evident. Both the blind sample and the library sample were measured on a Thermo-Nicolet 6700s FTIR spectrometer. To ensure that measured absorbances were nearly equal to the true absorbance values, the interferograms were multiplied by the Norton-Beer medium apodization function before application of the Fourier transform [17].

Fig. 6 shows the best hit from the PDQ database for blind sample #8 using the library search algorithm in OMNIC (Thermo Nicolet Corporation). Of all the modes available for the library search in OMNIC (correlation, absolute derivative, square derivative, absolute difference and square difference), correlation gave the most useful results in terms of the number of hits and the hit quality index. Consequently, the correlation mode was applied in library searching for all blind samples. Restricting the search to the fingerprint region gave the same results as using the entire mid-IR region after eliminating noise present in the clear coat paint spectra caused by the diamond transmission cell. The hit obtained from the PDQ database is a clear coat on a plastic bumper. In many

Table 3
Training set for plant group search prefilter.

Group	Number of training set samples
1	164
2	54
3	141
4	21
5	84
Total	464

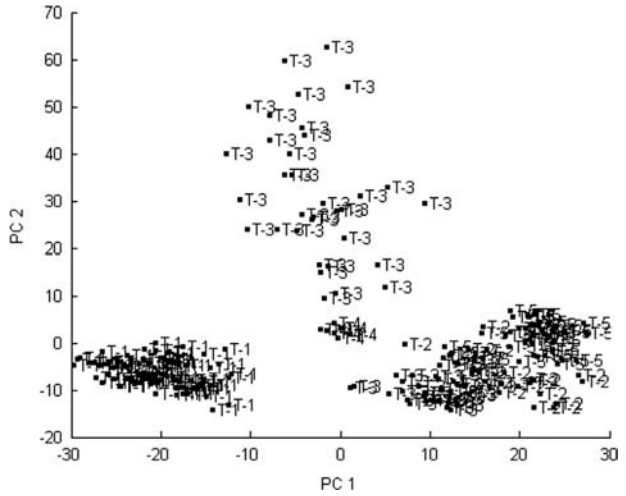


Fig. 2. PC plot of the two largest principal components of the 464 IR spectra and the 1080 wavelet coefficients comprising the training set. Each paint sample is represented as a point in the PC plot of the data (T-1=Plant Group 1, T-2=Plant Group 2, T-3=Plant Group 3, T-4=Plant Group 4, and T-5=Plant Group 5).

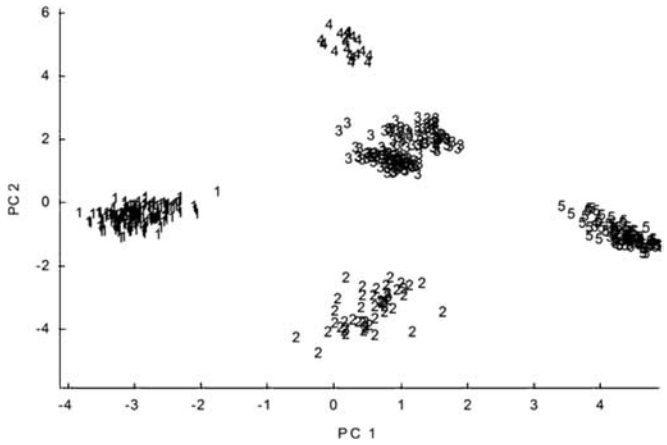


Fig. 3. PC plot of the two largest principal components of the 464 IR spectra of the training set and the 14 wavelet coefficients identified by the pattern recognition GA. Each paint sample is represented as a point in the PC plot of the data (1=Plant Group 1, 2=Plant Group 2, 3=Plant Group 3, 4=Plant Group 4, and 5=Plant Group 5).

cases, a clear coat is applied to plastic automotive components in the plant that manufactures the automotive component, not in the plant where the vehicle is assembled. (For metallic automotive components, the paint system for the component is applied to the substrate in the same plant where the vehicle is assembled.) Furthermore, bumpers and other plastic automotive components are replaceable and may not have the original automotive paint system of the vehicle. For these reasons, the training set used in this study is limited to automotive paint from metallic automotive components.

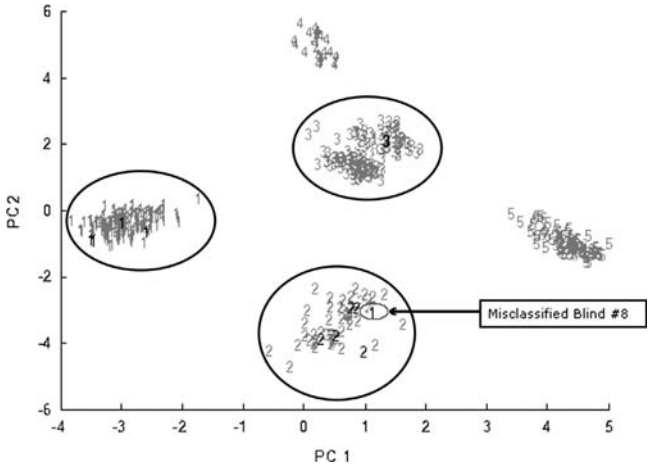


Fig. 4. Projection of the blind samples (in black) onto the PC map of the training set data (gray) for Plant Group. 9 of the 10 projected IR spectra are located in a region of the map occupied by spectra possessing the same class label. (1=Plant Group 1, 2=Plant Group 2, 3=Plant Group 3, 4=Plant Group 4, and 5=Plant Group 5.).

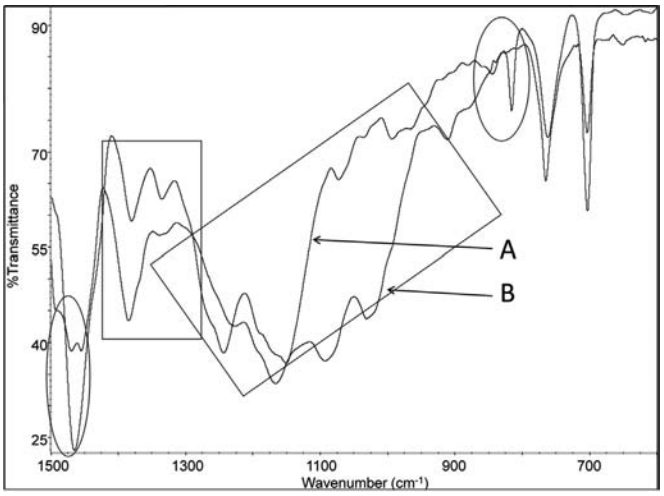


Fig. 5. An IR spectrum of (a) the misclassified blind sample (Sample #8) compared to (b) an IR spectrum of a clear coat paint sample of the same model, year and assembly plant from the PDQ database.

The next step in this study was to develop search prefilters to identify the IR spectra of the blind clear coat paint samples by assembly plant. For each plant group, a search prefilter was developed to discriminate the IR spectra by assembly plant within a plant group. Fig. 7 shows a plot of the two largest principal components of the 33 wavelet coefficients identified by the pattern recognition GA for the assembly plants comprising the first plant group (see Table 2). Each IR spectrum is represented as a point in the PC plot of the data. Plant 18 (Moraine OH) represented by the symbol T-18 in the PC plot is well separated from the other 6 assembly plants represented by the symbol T-1 in the plot. The IR spectra from the other 6 assembly plants (Arlington TX, Doraville GA, Fairfax KS, Fort Wayne IN, Lansing MI, and Pontiac MI) are superimposable, which prevented further discrimination by assembly plant of these clear coats. However, automobiles from these 6 assembly plants in the PC plot could be discriminated by production year. Furthermore, projecting the blind samples assigned to Plant Group 1 onto the PC map showed that each projected sample (P-18 for Moraine OH and P-1 for the other 6 assembly plants) lies in a region of the map with paint samples

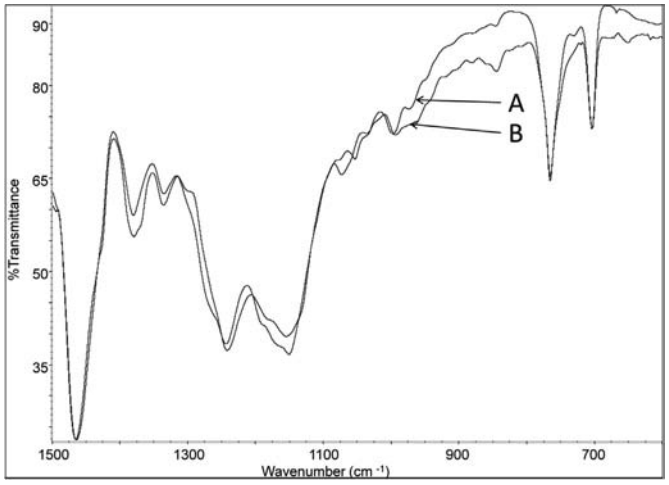


Fig. 6. An IR spectrum of (a) the misclassified blind sample and (b) the first hit from the PDQ database using OMNIC.

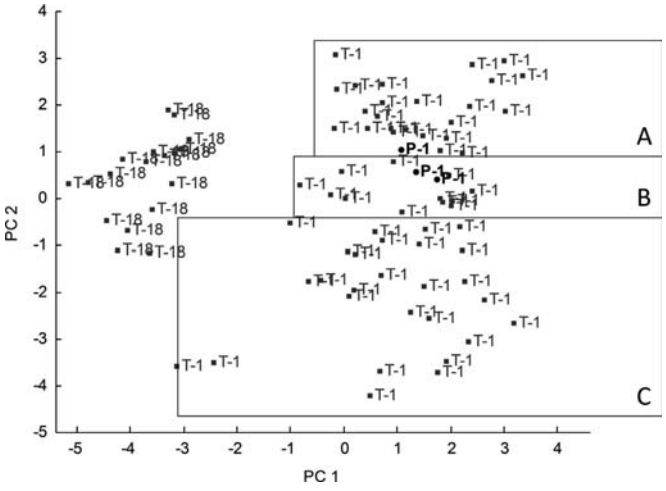


Fig. 7. PC plot of the two largest principal components of the 164 IR spectra of the training set and the 33 wavelet coefficients identified by the pattern recognition GA. Each clear coat paint sample is represented as a point in the PC plot of the data. (T-1 or P-1 = Arlington TX, Doraville GA, Fairfax KS, Fort Wayne IN, Lansing MI, and Pontiac MI and T-18 = Moraine OH.) Blind samples (P-1) are in bold. A = Arlington TX, Doraville GA, Fairfax KS, Fort Wayne IN, Lansing MI, and Pontiac MI (2000–2003); B = Arlington TX, Doraville GA, Fairfax KS, Fort Wayne IN, Lansing MI, and Pontiac MI (2000–2006); C = Doraville GA, Fairfax KS, Fort Wayne IN, Lansing MI (2004–2006).

that have the same production year range and class label. This result suggests that search prefilters developed from IR spectra of clear coats can be used to characterize automotive paint samples by assembly plant or a limited number of plants and can specify a limited production year range for these samples.

Fig. 8 shows a plot of the two largest principal components of the 54 IR spectra and the 23 wavelet coefficients identified by the pattern recognition GA for clear coats from Plant Group 2 (see Table 2). Again, each IR spectrum is represented as a point in the PC plot. All 3 assembly plants (Bowling Green KY, Hamtramck MI, and Orion MI) are well separated from each other in the PC plot of the data.

Fig. 9 shows the five blind samples assigned to Plant Group 2 projected onto the PC plot of the second plant group. Four of the 5 projected (blind) samples lie in a region of the map, which contain clear coat paint samples from the same assembly plant. Blind sample 4, which is from the Hamtramck Michigan Plant, was

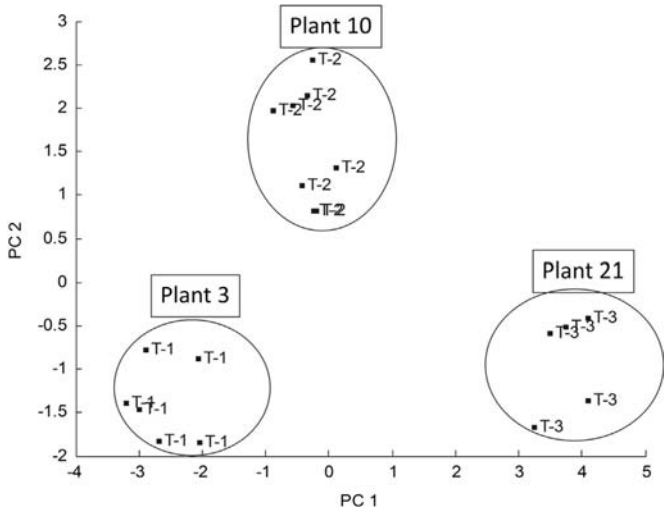


Fig. 8. PC plot of the 54 IR spectra and 23 wavelet coefficients identified by the pattern recognition GA for spectra from Plant Group 2 (T-1 = Bowling Green KY, T-2 = Hamtramck MI, and T-3 = Orion MI).

misclassified as an Orion Michigan Plant sample. There is only one IR spectrum (see Fig. 10) of this model (2006 Buick Lucerne) in the PDQ database; so this model was not well represented in the training set. A comparison of the misclassified Hamtramck Michigan Plant blind sample to the only IR spectrum of the same model, year, and assembly plant in the database (see Fig. 10) shows a peak present in the library spectrum (2006 Buick Lucerne), which is not present in the blind sample. This nullified the match.

Figs. 11 and 12 show the misclassified Hamtramck Michigan plant blind sample compared to the average IR spectrum from the Hamtramck MI plant and from the Orion Michigan plant. Although the match is better for Orion Michigan (the plant to which the blind sample has been assigned by the search prefilter), the similarity of these IR spectra underlies the challenges encountered in differentiating automotive clear coats by assembly plant for GM vehicles from Plant Group 2. Nevertheless, the search prefilters were able to correctly classify 4 of the 5 blind samples assigned to Plant Group 2.

Fig. 13 shows a plot of the two largest principal components of the 141 IR spectra and 13 wavelet coefficients identified by the pattern recognition GA for clear coats from Plant Group 3. Clustering of the spectra by assembly plant and model in the PC plot is evident for the paint samples comprising this training set. Fremont California (Plant 9) and Lordstown Ohio (Plant 17) form distinct clusters in the PC plot of the data as do the trucks from Oshawa (Plant 22). The Buicks from Oshawa Ontario lie in another cluster with SUVs from the Oklahoma City Plant. Chevrolets from the Oklahoma City Plant and from Oshawa, GMC trucks from Shreveport Louisiana and the Flint Michigan Plant, and GMC and Chevrolet trucks from Linden, NJ form another cluster. The lone blind sample assigned to Plant Group 3 is projected onto the PC plot in a region that contains clear coat paint samples from the same assembly plant.

Applying the search algorithm in OMNIC (Thermo Nicolet) to the 10 blind samples, only 4 blind samples were correctly identified compared to 8 using the search prefilters. To achieve the best results, the correlation mode was used to perform the matching, and the spectral region searched was restricted to the extended fingerprint region, which included the carbonyl band. The blind samples correctly classified by OMNIC were also correctly classified by the search prefilters. A summary of the results obtained for the 10 blind samples is shown in Table 4.

Eight of the 10 blind samples were correctly classified by the search prefilters. One misclassified sample is a clear coat paint

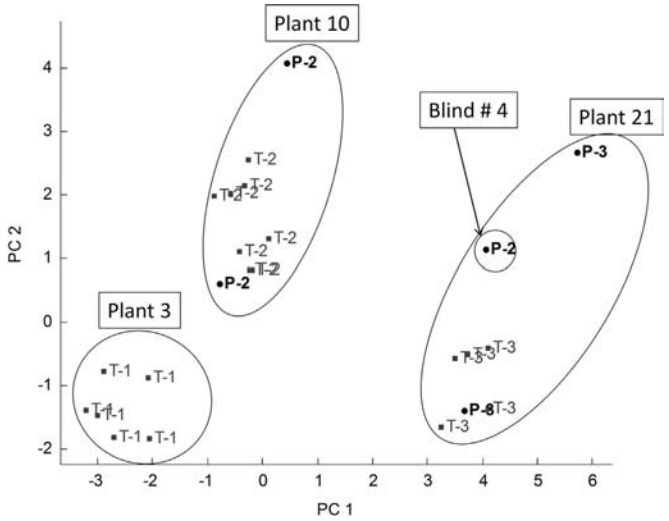


Fig. 9. Five blind samples (P-2=Hamtramck MI and P-3=Orion MI) assigned to Plant Group 2 are projected onto the PC plot of the 23 wavelet coefficients and 54 IR spectra from the second plant group (T-1=Bowling Green KY, T-2=Hamtramck MI, and T-3=Orion MI).

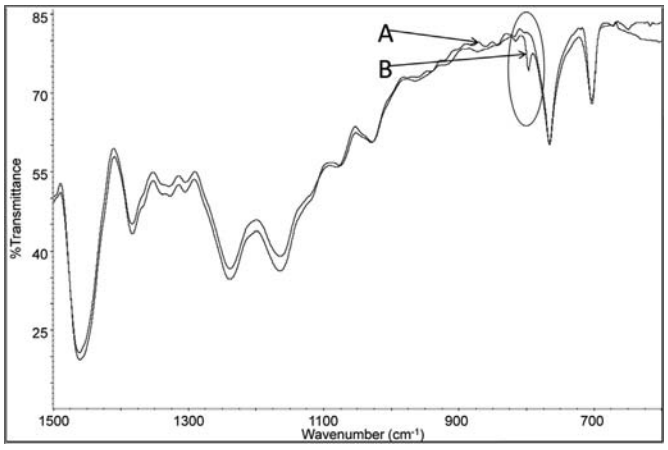


Fig. 10. IR spectrum of (a) the misclassified Hamtramck Michigan Plant blind sample compared to (b) the only IR spectrum of the same model, year and assembly plant in the PDQ database.

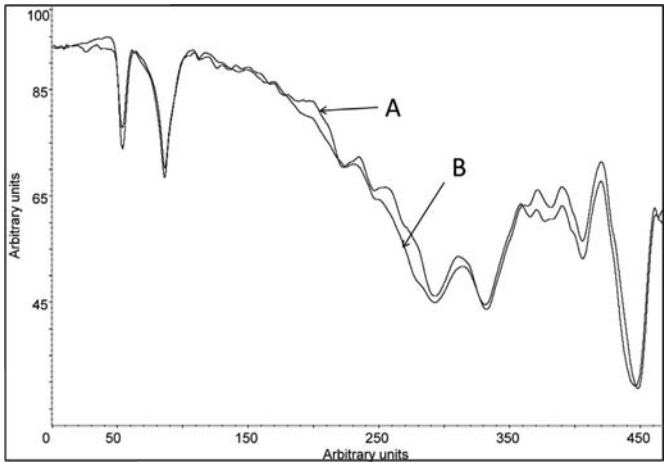


Fig. 11. (a) Misclassified Hamtramck Michigan plant blind sample compared to (b) the average IR spectrum from the Hamtramck MI plant.

sample from a plastic bumper and the other misclassified sample is from an assembly plant not well represented in the PDQ database. The search prefilters were developed from Bio-Rad and Thermo Nicolet IR spectra of paint samples aligned along both the *x* and *y*-

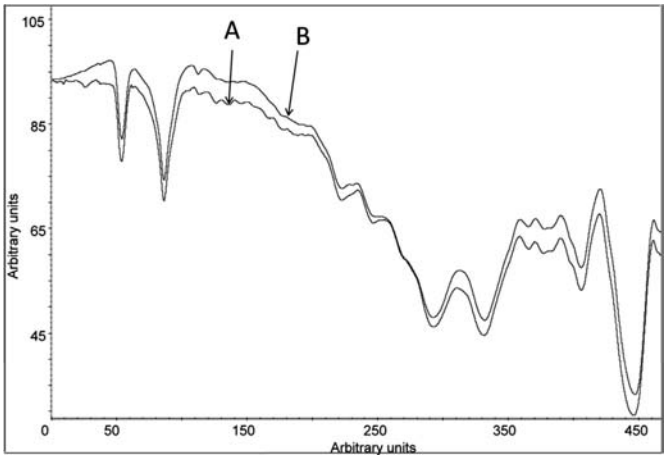


Fig. 12. (a) Misclassified Hamtramck Michigan plant blind sample compared to (b) the average IR spectrum from the Orion Michigan plant.

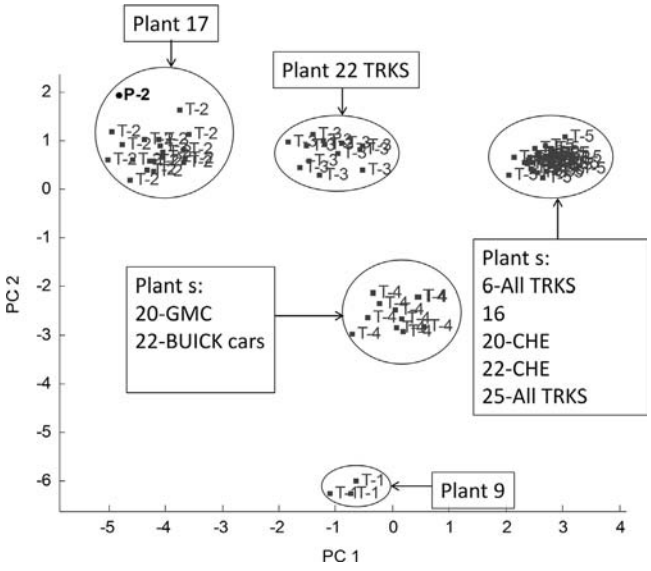


Fig. 13. Plot of the two largest principal components of the 141 IR spectra and 13 wavelet coefficients identified by the pattern recognition GA for clear coats from Plant Group 3. Lone blind sample (P-2) assigned to Plant Group 3 is projected onto the PC plot of the 141 IR spectra and 13 wavelet coefficients identified by the pattern recognition GA. Training set samples are designated by T.

axes using OMNIC software. This allowed for all spectra to be compared even if they were collected on different spectrometers.

Selection of the appropriate mother wavelet was crucial in the development of the search prefilters as it ensured that information about the assembly plant of the vehicle could be extracted from the wavelet transformed spectra. In our previous studies [11–16], we have observed that a decrease in the ability of the pattern recognition GA to correctly classify mid IR spectra occurred when other mother wavelets were used for preprocessing. This result should not come as a surprise. For spectra that contain sharp peaks or discontinuities, it is well known among workers in the field that the Haar wavelet would be indicated for denoising [18]. When the spectra are comprised of broader peaks, the use of a smoother mother wavelet such as the Coiflet is strongly recommended. For mid IR spectra whose peaks are situated between these two extremes, either the Symlet or Daubechies mother wavelets would be expected to give good results for resolving overlapping bands and denoising data. However, the pattern recognition GA generally performed better when the mid IR spectra were preprocessed with Symlets than Daubechies [26], which can be attributed to the

shape of the mother wavelet relative to the shape of the IR peaks. Symlets are more symmetrical than Daubechies.

The purpose of this study is to demonstrate proof of concept, not to develop an on line fully operational pattern recognition based library search system. For this reason, the search problem was intentionally made more challenging through selection of samples from the same manufacturer within a limited production year range. This would test the capability of the search prefilers to differentiate between similar IR spectra. To use these GM search prefilters in an automated library search system, it will be necessary to develop a search prefilter to differentiate paint samples by automobile manufacturer. To demonstrate that GM automotive clear coats can be discriminated from those of other manufacturers, a search prefilter was developed to discriminate GM clear coats from Chrysler and Ford clear coats. For this study, 1314 IR spectra of clear coat paint smears (464 g, 433 Chrysler, and 417 Ford) within a limited production year range (2000–2006) were employed. To develop this search prefilter, the 1314 IR spectra were divided into a training set of 1183 clear coats and a validation set of 131 clear coats. Members of the validation set were chosen by random lot from the 1314 automotive clear coat paint samples. The IR spectra were standardized using spectral line functions previously developed for the GM automotive paint samples with the standardized spectra wavelet transformed prior to pattern recognition analysis. Fig. 14 shows a PC plot of the 53 wavelet

Table 4
Summary of the results obtained for the 10 blind samples.

Blind sample	Assigned plant group	Plant group	Assigned plant (s) search prefilters	Assigned plant OMNIC	Sample ID
1	2	2	10	10	10
2	1	1	4,5,8, or 14 (2004–2006)	18	14 (2004)
3	2	2	21	10	21
4	2	2	21	10	10
5	2	2	21	17	21
6	3	3	17	17	17
7	1	1	1, 4, 5, 8, 14 or 23	20	5
8	2	1	NA	9	14
9	2	2	10	10	10
10	1	1	1, 4, 5, 8, 14, 23	8	14

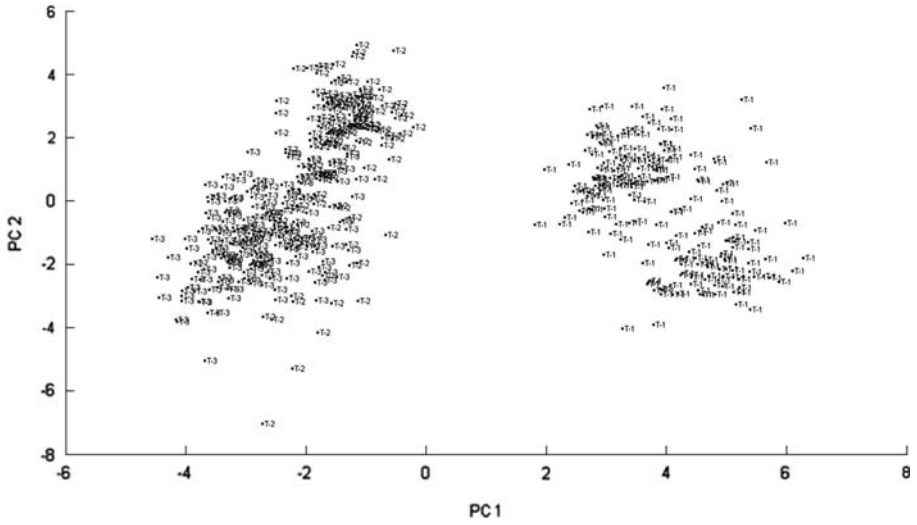


Fig. 14. Plot of the two largest principal components of the 1183 training set samples and 53 wavelet coefficients identified by the pattern recognition GA to differentiate clear coats by automobile manufacturer. T-1=GM, T-2=Chrysler, and T-3=Ford.

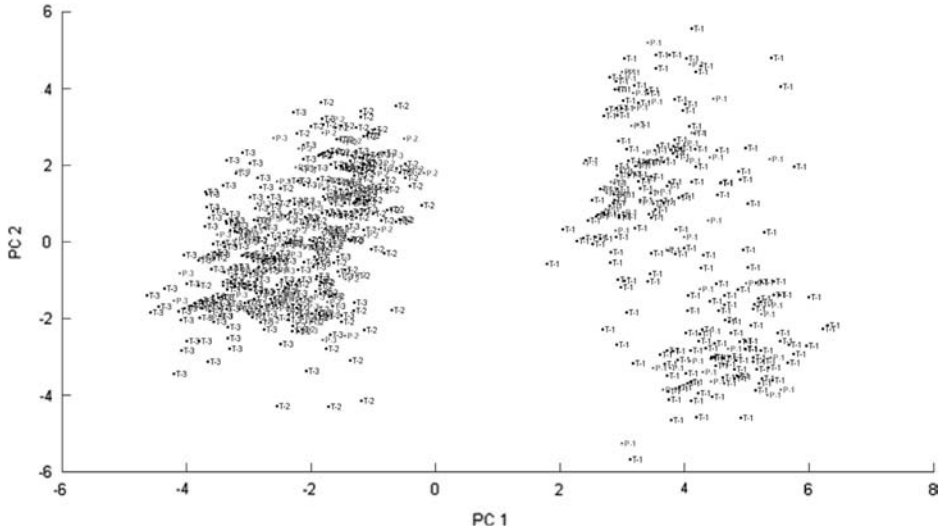


Fig. 15. Validation set samples (P-1=GM, P-2=Chrysler, and P-3=Ford) projected onto the PC plot developed from the 1183 training set samples and 53 wavelet coefficients identified by the pattern recognition GA. For the training set, T-1=GM, T-2=Chrysler, and T-3=Ford.

coefficients identified by the pattern recognition GA to differentiate clear coats by automobile manufacturer. GM clear coats can be readily differentiated from Chrysler and Ford clear coats using the wavelet transformed spectra.

To assess the predictive ability of the 53 wavelet coefficients identified by the pattern recognition GA, we chose to map the 131 clear coat IR spectra from the validation set directly onto the PC map developed from the 1183 training set samples and the 53 wavelet coefficients identified by the pattern recognition GA (see Fig. 15). Every GM clear coat plant sample in the validation set was correctly classified, i.e., each projected GM plant sample lies in a region of the map with clear coat paint samples that have the same class label. By comparison, several Chrysler and Ford validation set samples were misclassified. Evidently, spectral features correlated to the automobile manufacturer can be identified by the pattern recognition GA. This suggests that a search prefilter can be developed to discriminate GM automotive clear coats from those of other automobile manufacturers. When used in tandem with search prefilters developed for GM plant groups and for assembly plants, it should be possible to identify the assembly plant of a GM clear coat paint sample recovered from a hit and run accident where death or injury to a pedestrian has occurred.

4. Conclusions

Search prefilters have been developed to investigate the IR spectral libraries of the PDQ automotive database to differentiate between similar but nonidentical IR paint spectra. Crucial to the success of this study was the use of variable selection methods for the development of search prefilters to facilitate spectral library searching. The methodology used for the development of search prefilters in this study has not been widely reported in the literature. The search prefilters described here have the potential to facilitate spectral library searching of automotive clear coats because the size of the spectral library is truncated to those spectra corresponding to the assembly plants identified by the discriminants. Currently, the inability of PDQ to identify paint samples consisting of only the clear coat paint layer is a significant limitation to the use of PDQ to obtain trace evidence from automotive paint samples.

Information derived from the searches described in this paper can also serve to assess the general discrimination power of original automotive clear coat paint comparisons encountered in casework, and to succinctly communicate the significance of the evidence to the courts. Addressing these concerns is a direct response to a recommendation by the National Academies of Sciences report on strengthening forensic science in the United States [27].

Acknowledgements

Parts of this study were presented at the 2012 Southwest Regional Meeting of the ACS in the Dennis C. Shelly Memorial Symposium. The authors acknowledge the work of Tamara Hodgins, Andrew Ho, and Edmund Leung, who collected, coded and entered in the PDQ database the FTIR spectra used in this study. This research was supported by Award no. 2010-DN-BX-K217 awarded by the National Institute of Justice, Office of Justice Programs, United States Department of Justice. The opinions, findings, and conclusions or recommendations expressed in this publication/program/exhibition are those of the author(s) and do not necessarily reflect those of the Department of Justice.

References

[1] G.A. Bishea, J.L. Buckle, S.G. Ryland, International Forensic Automotive Paint Database, in: Proceedings—Investigation and Forensic Science Technologies, International Society of Optical Engineering (SPIE), vol. 3576, 1999 February, pp. 73-80.
[2] G. Fettis, Automotive Paints and Coatings, VCH Publications, New York, NY, 1995.
[3] J.L. Buckle, D.A. MacDougal, R.R. Grant, Can. Soc. Forensic Sci. J 30 (1997) 199–212.
[4] P.G. Rodgers, R. Cameron, N.S. Cartwright, W.H. Clark, J.S. Deak, E.W. Norman, Can. Soc. Forensic Sci. J 9 (1976) 1–14.
[5] B.B. Hubbard, Barbara Burke, The World According to Wavelets, second ed., A. K. Peters, Natick, MA, 1998.
[6] J.S. Walker, Primer on Wavelets and Their Scientific Applications, Chapman & Hall/CRC, Boca Raton, FL, 1999.
[7] G.A. Eiceman, M. Wang, S. Pradad, H. Schmidt, F.K. Tadjimukhamedov B.K. Lavine, N. Mirjankar, Anal. Chim. Acta 579 (2006) 1–10.
[8] J.S. Karasinski, S.O. Andreescu, A. Sadik, B. Lavine, M.N. Vora, Anal. Chem. 77 (2005) 7941–7949.
[9] B.K. Lavine, K. Nuguru, N. Mirjankar, J. Chemom. 25 (2011) 116–129.
[10] M. Gaye, S.J. Valentine, Y. Hu, Y. Mechref, B.K. Lavine, N. Mirjankar D.E. Clemmer, J. Proteome Res. 11 (2012) 6102–6110.
[11] B.K. Lavine, A. Fasasi, N. Mirjankar, M. Sandercock, S.D. Brown, J. Chemom. 28 (2014) 385–394.
[12] B.K. Lavine, K. Nuguru, N. Mirjankar, J. Workman, Microchem. J. 103 (2012) 21–36.
[13] B.K. Lavine, K. Nuguru, N. Mirjankar, J. Workman, Appl. Spectrosc 66 (8) (2012) 917–925.
[14] B.K. Lavine, A. Fasasi, N. Mirjankar, M. Sandercock, Talanta 119 (2014) 331–340.
[15] B.K. Lavine, A. Fasasi, N. Mirjankar, C. White, Microchem. J. 113 (2014) 30–35.
[16] B.K. Lavine, N. Mirjankar, S. Ryland, M. Sandercock, Talanta 87 (2011) 46–52.
[17] C. Zhu, P.R. Griffiths, Appl. Spectrosc. 52 (1998) 1403–1408.
[18] F. Chau, Y. Liang, J. Gao, X. Shao, Chemometrics—From Basics to Wavelet Transform, pp1, Wiley Interscience, NY (2004) 01–108.
[19] T.R. Stouch, P.C. Jurs, Quant. Struct.—Act. Relat. 5 (2) (1986) 57–61.
[20] T.R. Stouch, P.C. Jurs, J. Chem. Inf. Comput. Sci. 25 (1985) 92–98.
[21] E.M.D. Santos, R. Sabourin, P. Maupin, Inf. Fusion 10 (2009) 150–162.
[22] B.K. Lavine, C.E. Davidson, A.J. Moores, P.R. Griffiths, Appl. Spectrosc 55 (8) (2001) 960–966.
[23] B.K. Lavine, C.E. Davidson, A.J. Moores, Chemom. Intell. Lab. Syst. 60 (1) (2002) 161–171.
[24] J.E. Jackson, A User's Guide to Principal Components, John Wiley & Sons, NY, 1991.
[25] D.L. Massart, L. Kaufman, The Interpretation of Analytical Chemical Data by the use of Cluster Analysis, John Wiley & Sons, New York, NY, 1983.
[26] B.K. Lavine, M. Sandercock, A. Fasasi, Improving Investigative Lead Information and Evidential Significance Assessment for Automotive Paint and the PDQ Database, in: Final Report, National Institute of Justice , 2013.
[27] Strengthening Forensic Science in the United States: A Path Forward, National Research Council of the National Academies Press, Washington, DC, February 2009.

Talanta 132 (2015) 191–196

Contents lists available at ScienceDirect

Talanta

journal homepage: www.elsevier.com/locate/talanta

A sensitive and selective chemosensor for ascorbic acid based on a fluorescent nitroxide switch

Tian Yang [a], Baozhan Zheng [a], Hengxing Liang [c], Yuping Wan [c], Juan Du [a,*], Dan Xiao [a,b,*]

[a] College of Chemistry, Sichuan University, No. 29 Wangjiang Road, Chengdu, PR China
[b] College of Chemical Engineering, Sichuan University, No. 29 Wangjiang Road, Chengdu, PR China
[c] Chengdu Product Quality Supervision and Inspection Institute, Chengdu 610041, PR China

ARTICLE INFO

Article history:
Received 15 June 2014
Received in revised form
20 August 2014
Accepted 27 August 2014
Available online 6 September 2014

Keywords:
Chemosensor
Nitroxide
Fluorescence
AsA

ABSTRACT

Ascorbic acid (AsA), also known as vitamin C, is a vital small-molecule antioxidant with multiple functions in vivo. It's the major natural antioxidant found in plants and is also an essential component of human nutrition. AsA plays a key role in many diseases-related biological metabolism. Therefore, sensitive and selective detection of AsA is greatly important in pharmaceutical, clinical and food industry. Here a sensitive and selective sensor for ascorbic acid detection based on the recovered fluorescence of NAPS-NO (*N*-propyl-triethoxysilane-4-(4-ylamino-1-oxy-2,2,6,6-tetramethylpiperdine)-naphthalimide) probe is described. The fluorescence of the naphthalimide moiety of NAPS-NO is inhibited by the nitroxide group, which is covalently linked to the fluorophore. Then, ascorbic acid reacts rapidly with the nitroxide moiety of NAPS-NO to form hydroxylamine, and the fluorescence properties of the naphthalimide moiety are recovered and the ESR signal decayed. Over a wide range from 80 nM to 50 μM, a good linear relationship between the fluorescence intensity and the concentration of ascorbic acid was found and the detection limit was estimated to be as low as 20 nM. To confirm the practical usefulness of the fluorophore–nitroxide probe, we demonstrated the use of NAPS-NO for the measurement of AsA in human blood serum and also successfully determined the concentration of AsA in HEK 293 cell lysate. Results from confocal laser scanning microscopy experiments demonstrated that this chemosensor is cell permeable and can be used as a fluorescent probe for monitoring ascorbic acid in living cells.

© 2014 Elsevier B.V. All rights reserved.

1. Introduction

Ascorbic acid (AsA), which cannot be synthesized in the human body, is used in large scale as an antioxidant in food, animal feed, beverages, pharmaceutical formulations and cosmetic applications [1]. AsA is the major natural antioxidant found in plants and is also an essential component of human nutrition [2,3]. It plays a key role in biological metabolism and has been commonly used for the prevention and treatment of common cold, mental illness, infertility, cancer and AIDS, etc [4]. Thus, the development of a simple and rapid method for the determination of AsA with high selectivity and sensitivity is desirable for diagnostic and food safe applications [5].

A wide variety of analytical methods is available for the determination of ascorbic acid, such as titrimetric [6,7], spectrophotometric [8,9] and chromatographic [10–12] methods. These methods rely on different phenomena and registration techniques suffering from several limitations. The spectrophotometric methods measure either the resultant color of products of certain reactions involving ascorbate [13] or absorbance of ascorbic acid itself [14]. However, the low selectivity of the reactions involved decreases the accuracy of the ascorbate analysis. Thereby, the reliability of these methods is limited by relatively low specificity. A number of specific assays for reductants including ascorbic acid, uric acid, tocopherol etc. have been developed based on high performance liquid chromatography (HPLC) [15,16]. These techniques require several complicated preliminary steps. In addition, HPLC separations would consume relatively long time, therefore, could not be considered as an express-method. Early methods utilizing nitroxide radicals for ascorbate quantifications were based on measurements of only ESR signal from nitroxide, therefore, suffered from general drawbacks of ESR spectroscopy. Although this technique permits investigations in high optical density substance, the ESR measurements are limited by high cost and complexity of equipments and difficulties in acquiring and processing experimental data. At present, electrochemical approaches become

* Corresponding authors at: College of Chemical Engineering, Sichuan University, No. 29 Wangjiang Road, Chengdu, PR China. Tel.: +86 28 85415029; fax: +86 28 85416029.
E-mail addresses: lxdj@vip.sina.com (J. Du), xiaodan@scu.edu.cn (D. Xiao).

http://dx.doi.org/10.1016/j.talanta.2014.08.066
0039-9140/© 2014 Elsevier B.V. All rights reserved.

the major analytical methods for AsA determination because of their convenience and speediness. Nevertheless, the interference from other similar redox potential molecules can be serious, such as uric acid and dopamine [17]. What's more, the detection limit is always higher than that of fluorescence methods. Particularly, attempts have been made to detect ascorbic acid using nanoparticles. Wang et al. [17] developed a simple fluorescence sensor for sensitive turn-off detection of ascorbic acid by using protein-modified Au nanoclusters in aqueous media. Zhang et al. [18] fabricated an electrochemical sensor for selective detection of ascorbic acid in the presence of dopamine and uric acid by modifying the glassy carbon electrode with carbon-supported $NiCoO_2$($NiCoO_2$/C) nanoparticles. Wang et al. [19] prepared a palladium nanoparticle/graphene/chitosan/glassy carbon electrode which displayed excellent electrochemical catalytic activities towards ascorbic acid, dopamine and uric acid. But these methods have relatively high detection limit towards ascorbic acid. Fluorometric sensing is a preferable approach for detection of AsA due to its comparatively high selectivity, sensitivity, rapidity, operational simplicity, nondestructive methodology and direct visual perception [20].

In recent years, many fluorescent chemosensors were designed for ascorbic acid. Matsuoka et al. [21] synthesised several fluorescent nitroxide compounds based on naphthalene which were sensitive to ascorbic acid. They also demonstrated the use of Naph-DiPy nitroxide for the measurement of ascorbic acid in the plasma of osteogenic disorder Shionogi rats to confirm the practical usefulness of the fluorophore–nitroxide probe. Zheng et al. [22] demonstrated a fluorescent carbon dot probe, its fluorescence was quenched by Cr(VI) through inner filter effect, but Cr(VI) can be reduced to low valent chromium species easily by ascorbic acid, and then resulting in the elimination of the IFE and recovery of CD fluorescence. Therefore the CD – Cr(VI) mixture could behave as an off-on type fluorescent probe for ascorbic acid. Biqing et al. [23] developed a fluorescent turn-on detection for ascorbic acid based on hyperbranched conjugated polyelectrolyte. The fluorescence was superquenched by Cu^{2+} ions, upon addition of ascorbic acid, the paramagnetic Cu^{2+} ions can be transformed into diamagnetic Cu^{1+} ions, which inhibit the quenching and thus lead to fluorescence enhancement of the hyperbranched conjugate polymer. These fluorescent probes all have sensitive response to ascorbic acid, but none of them were used in intracellular environment.

Fluorophore-linked nitroxides represent examples of such fluorescent sensors. The standard redox potential of nitroxides is high enough (E° = 0.54 V vs SHE for piperidine) to oxidize ascorbic acid which have been the only significant reducing agent studied and used in earlier applications of nitroxide radicals to blood and food product [24]. The fluorescence is intramolecular quenched by the linked nitroxide through electron exchange interactions [25–27], but can be recovered when the nitroxide moiety reacts with certain types of radicals, such as methyl radicals and some reducing agents, such as ascorbic acid [28]. Because of this, fluorophore-linked nitroxides have been used for the determination of reducing agents as well as radicals [29–32]. Nitroxide can shuttle between the nitroxyl radical form, the reduced hydroxylamine, and the oxidized oxoammonium cation form with one- and two-electron transfer reactions [21,26]. When the hydroxyl radical or superoxide reacts with the nitroxyl radical, the oxoammonium cation is produced. Most nitroxides are reduced to the corresponding hydroxylamine by reacting with ascorbic acid [24,33–35]. At the same time, the quenching effect of nitroxides disappeared, thus creating a decay of the ESR signal and enhancement of the fluorescence. This indicates that fluorophore–nitroxide coupled systems can act as promising reagents for the rapid and convenient fluorometric detection of ascorbic acid.

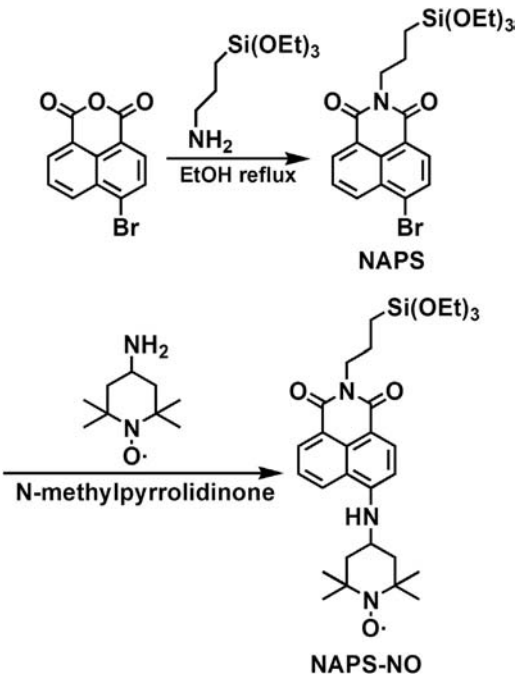
Because of the strong yellow–green fluorescence and good photostability of 1,8-naphthalimide derivatives, they have found wide application in spectral area [36–38]. Here, we describe a new naphthalimide-linked nitroxide probe (NAPS-NO) with high sensitivity and selectivity for the detection of ascorbic acid. According to the previous reports [39,40], the introduction of 3-aminopropyltriethoxysilane can increase the hydrophilicity of the probe, thus resulting in favorable biocompatibility. At the same time, the silane structure can provide a suitable binding site for the further construction of inorganic–organic complex probes, which have the obvious advantage in the efficient separation and analysis of the targets.

A modified previously reported procedure [41,42] was employed for the synthesis of NAPS-NO. It was synthesized from the reaction of 4-Br-1,8-naphthalimide and APTES, followed by reaction with 4-amino-tempo (Scheme 1). The structure of NAPS-NO was characterized by ESR, ESI-MS, FT-IR, and fluorophotometry. The fluorescent intensity of NAPS could be inhibited by the linked nitroxide through electron exchange interactions. When AsA reacted with NAPS-NO, the fluorescent intensity could be recovered. The as-prepared chemosensor exhibited a linear response to AsA concentrations ranging from 80 nM to 50 μM with a detection limit of about 20 nM. The concentration of AsA in human blood serum and HEK 293 cell lysate was determined respectively by the internal standard addition method. Moreover, results of confocal laser scanning microscopy experiments demonstrated that NAPS-NO could be used for monitoring ascorbic acid in living cells.

2. Experimental section

2.1. Apparatus

ESR determination was performed with a Bruker A300 ESR Spectrometer. Fluorescence spectra were measured on a Hitachi F-4500 spectrophotometer equipped with a 1 cm quartz cell. Mass spectra were obtained with MAT-261 spectrometer. FT-IR was recorded on a Thermo Scientific Nicolet 6700 FT-IR spectrometer (Sugar Land, TX, USA). Confocal fluorescence imaging was taken using a Leica TCS SP5 laser scanning confocal microscope (excitation wavelengths 468 nm).



Scheme 1. Synthetic routes to NAPS and NAPS-NO.

2.2. Reagents

We purchased 4-Bromo-1,8-naphthalimide from Adamas Reagent Co., Ltd. 4-amino-1-oxy-2,2,6,6-tetramethylpiperidine was purchased from TCI. 3-aminopropyl-triethoxysilane was purchased from Alfa Aesar. The human serum samples were obtained from Wangjiang Hospital of Sichuan University. HEK 293 cell lysate (2×10^6 cells) was provided by the state key laboratory at Sichuan University. All solvents used for synthesis and measurements were redistilled before use. All the other chemicals were of analytical-reagent grade and used without further purification.

2.3. Cell culture and cell imaging

Hela cells were provided by the state key laboratory at Sichuan University (Sichuan, China). Confocal fluorescence imaging was performed with a Leica TCS SP5 laser scanning confocal microscope (excitation wavelengths 468 nm). Before the experiments, the Hela cells were exposed to 40 μmol L^{-1} ascorbic acid for 30 min at room temperature to allow the AsA to permeate into the cells. The cells were then centrifuged to remove excess AsA, and the treated cells were then incubated with 40 μmol L^{-1} NAPS-NO for another 30 min. Following incubation, the cells were imaged.

2.4. Synthesis of intermediates and probes (Scheme 1)

2.4.1. Synthesis of NAPS (N-propyl-triethoxysilane-4-Br-naphthalimide)

NAPS was synthesized according to Jozef et al. [39,40]. Under nitrogen, a solution of 4-Br-1,8-naphthalimide (0.6 g, 2 mmol) and 3-aminopropyl-triethoxysilane (APTES) (560 μL, 2.4 mmol) in EtOH (40 mL) was refluxed for 5 h, 4-Br-1,8-naphthalimide was almost no more left. In this type of reaction, EtOH was widely used as solvent [39,40]. The mixture was evaporated by rotary evaporation and the intermediate was directly investment in the next reaction. As shown in Fig. S1, ^{1}H-NMR (400 MHz, $CDCl_3$): δ=0.72–0.76 (m, 2*H*), 1.21 (t, *J*=7.0 Hz, 9*H*), 1.80–1.89 (m, 2*H*), 3.81 (q, *J*=7.0 Hz, 6*H*), 4.16 (t, *J*=7.6 Hz, 2*H*), 7.81–7.86 (m, 1*H*), 8.01–8.04 (m, 1*H*), 8.39–8.41 (m, 1*H*), 8.54–8.57 (m, 1*H*), 8.63–8.65 (m, 1*H*) ppm.

Synthesis of NAPS-NO

2.4.2. (N-Propyl-triethoxysilane-4-(4-ylamino-1-oxy-2,2,6,6-tetramethylpiperdine)-naphthalimide)

NAPS (0.48 g, 1 mmol) and 4-amino-1-oxy-2,2,6,6-tetramethylpiperidine (0.34 g, 2 mmol) was dissolved in 20 mL of 1-methyl-2-pyrrolidone. The mixture was heated for 24 h at 100 °C and excess of 4-amino-2,2,6,6-tetramethylpiperidine and 1-methyl-2-pyrrolidone were recovered by vacuum distillation. The crude product was purified by column chromatography on silica gel using a mixture of ethyl acetate and petroleum ether (1:1) yielding 0.2 g (37%) of orange crystals. As shown in Fig. S3, the HPLC spectra indicated that no obvious impurities were observed. HRMS (ESI^+) calcd for $C_{30}H_{44}N_3SiO_6$ $[M+H]^+$: 571.3078. Found: 571.3077. FTIR, cm^{-1}: υ(N–H) 3440, υ(C=O) 1700, υ(C–N) 1386, $\upsilon(SiO^{sym})$ 816, $\upsilon(SiO^{asym})$ 1119 (Fig. S4).

2.5. X-band ESR measurement

To determine the reaction between N–O groups and ascorbic acid, NAPS-NO (10 μM) was mixed with ascorbic acid solutions (0–50 μM). X-band ESR spectra were recorded at room temperature using a Bruker A300 ESR spectrometer (Germany; microwave power 9 mW, amplitude of 100-kHz field modulation 0.6 mT, time constant 2.56 ms) and were analyzed using an ESR data analyzer.

3. Results and discussion

3.1. Chemical properties of spin-labeled fluorescence probe

Reduction of the fluorophore–nitroxide probe by ascorbic acid has been monitored by two independent spectroscopic techniques: ESR and fluorescence. When NAPS-NO was mixed with ascorbic acid, its ESR signal decayed and the fluorescence intensity gradually recovered with different concentrations of ascorbic acid (Fig. 1a and b). As shown in the inset of Fig. 1b, the fluorescence enhanced a lot with the addition of ascorbic acid. This increase in fluorescence intensity clearly validated that NAPS-NO can serve as a highly sensitive sensor for AsA. As expected, the fluorescence intensity at approximately 540 nm increased with increasing AsA concentrations. Fig. 1b inset illustrated that this chemosensor exhibited a linear response toward negative logarithm of AsA concentration from 80 nM to 50 μM, the linear equation was $y=2915-381.4x$ and the linear relative coefficient was $R^2=0.993$. The detection limit of AsA was estimated to

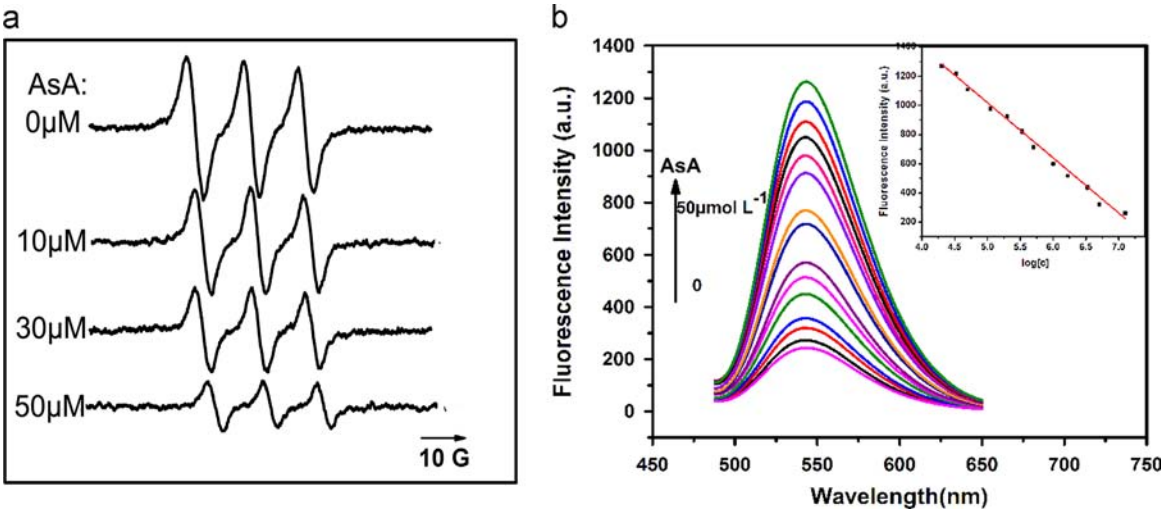


Fig. 1. (a) ESR signal decay and (b) fluorescence spectra of NAPS-NO (10 μM) in aqueous solution (50 mM PBS buffer, pH 7.0) upon addition of various concentrations of AsA (0–50 μM). Inset: plot of fluorescence intensity of NAPS-NO versus the negative log concentration of AsA (λ_{ex}=468 nm).

20 nM, which is lower than the AsA concentration detected by previous researches [15,28] in physiological sample. We also compared our technique with other methods (Table S1), and the results showed that our chemosensor provided lower detection limit and wider line range for the detection of AsA.

3.2. Evaluation of the response to other reductants and oxidants in vitro

NAPS-NO showed no fluorescence enhancement in response to glucose and BSA. In the case of other reductants, such as cysteine, dopamine etc., there were only slightly fluorescence enhancements could be detected (Fig. 2a). The oxoammonium cation is generated when a hydroxyl radical or superoxide reacts with the nitroxyl group at almost the diffusion-controlled rate [21]. Hence, we examined the reactivity of NAPS-NO towards ROS by fluorescence spectrometry (Fig. 2b). NAPS-NO did not show any obvious fluorescence enhancement in response to hydrogen peroxide, hydroxyl radical or high selectivity towards AsA over the other coexisting competitive species is a very important feature to evaluate the performance of NAPS-NO. Therefore, the competition experiments were also conducted. AsA was respectively added into the NAPS-NO solution containing different reductants or ROS. Relative fluorescence intensity was calculated by F/F_0, where F_0 and F were the fluorescence intensity of NAPS-NO containing AsA without and with the presence of reductants or ROS, respectively. As shown in Fig. 2c and d, glucose and BSA have almost no effect, whereas cysteine, dopamine, uric acid and GSH have relatively small effect on the fluorescence intensity of NAPS-NO-AsA system. H_2O_2 and ClO^- play no role, whereas · OH has a little impact on AsA detection. Fig. 2c and d showed that the extra addition of other reductants or ROS produced no obvious interference for AsA detection. These results indicated that NAPS-NO can act as a sensitive and selective AsA-specific fluorescent sensor, and it is expected to find potential applications in selectively and efficiently detecting AsA in biological to the previous reports [21,32], the fluorescence of fluorophore is quenched by the linked nitroxide through intramolecular electron exchange interactions, but can be recovered when the nitroxide moiety reacts with certain reactive oxygen species, such as hydroxyl radicals and some reducing agents, such as ascorbic acid. But they react in a different mechanism. Nitroxide can either accept one electron to be reduced to its diamagnetic counterpart hydroxylamine or donate one electron to be oxidized to its diamagnetic counterpart oxoammonium cation (Scheme S1) [43]. Based on the results of selectivity experiment, we proposed that the short life time of ROS species may result in its lower possibility of reaction with nitroxide than that of the reductants, which resulted in the selectivity of nitroxide towards reactive oxygen species. As for the selectivity towards other reductants, further research works are needed, and we are studying the reasonable mechanism constantly.

In this paper, phosphate buffer solution (PBS) was used throughout because it has been proved to be a good buffer for application of chemosensor in organism. The influence of pH value on the fluorescence intensity of NAPS-NO within the pH range of 5.5–9.0 was evaluated. As shown in Fig. S5, the fluorescence intensity increased with increasing pH until it reached the maximum at

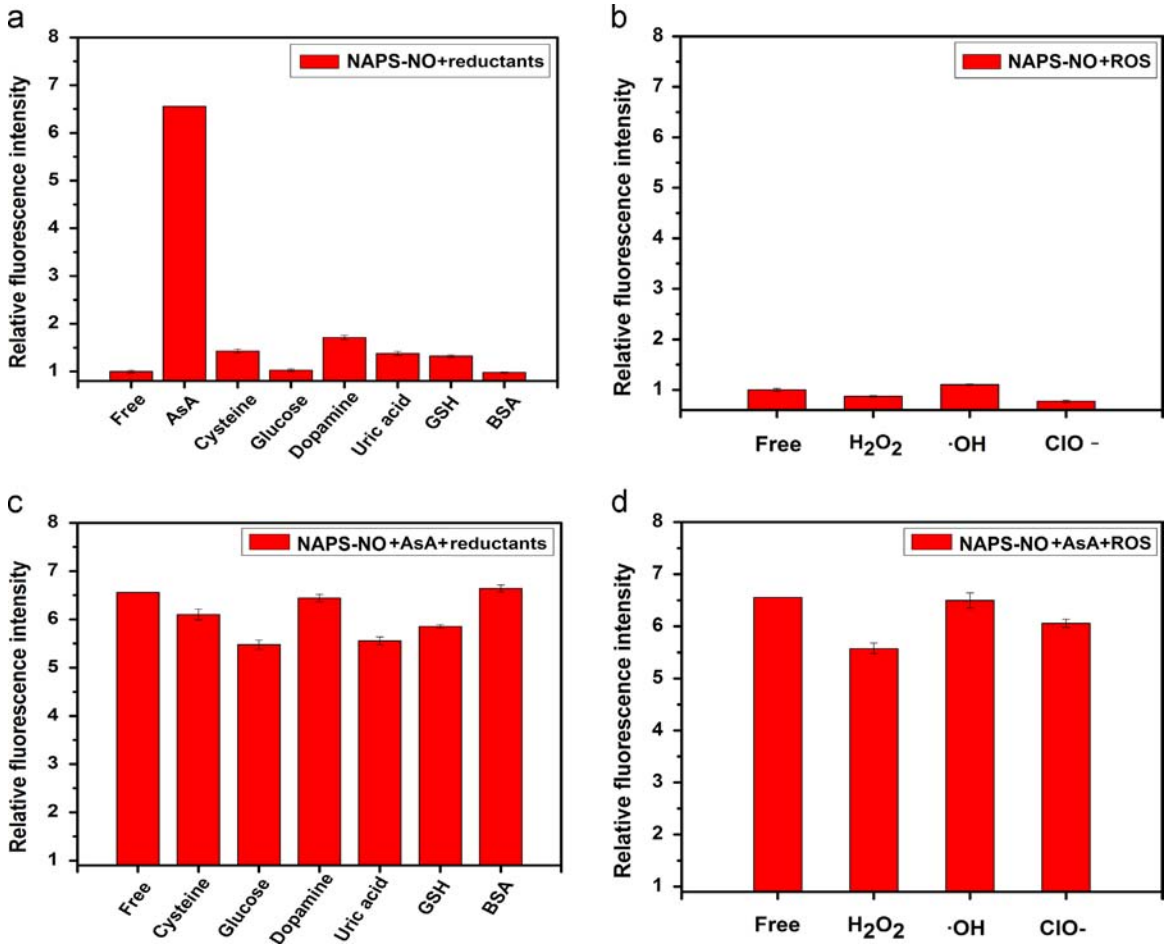


Fig. 2. Fluorescence responses of NAPS-NO (10 μM) to (a) various reductants (5 equiv.), AsA (5 equiv.) and (b) ROS (5 equiv.); fluorescence responses of NAPS-NO (10 μM) to AsA (5 equiv.) in the presence of (c) other reductants (5 equiv.) and (d) ROS (5 equiv.) (λ_{ex}=468 nm). Reductants including cysteine, glucose, dopamine, uric acid, GSH, BSA. ROS including hydrogen peroxide, hydroxyl radical, hypochloride.

pH 7.0 and thereafter decreased, thus we chose pH 7.0 as the optimal pH value to accord with that of neutral media and biological samples.

3.3. Determining the concentration of AsA in blood serum and recovery test

With the purpose of illustrating the reliability and accuracy of the proposed method, the developed sensor was applied to determine AsA in blood serum samples. Herein, 5 μL of blood serum was added to 500 μL of 10 μM NAPS-NO in PBS (50 mM, pH 7.0). Different concentrations of AsA standards were then added to the sample and the mixtures were measured. The fluorescence intensity of NAPS-NO with blood serum was enhanced following additions of different amounts of AsA. After linearly fitting the fluorescence intensity with the concentration of added AsA (Fig. S6), we successfully determined the concentration of AsA in blood serum to be 25 μM, which matched with that of the previous report [44]. Recovery experiments were also carried out by adding known amounts of AsA to the human serum sample. As shown in Table 1, the recovery of AsA was between 96 and 104% with RSD < 5%, which showed that the sensor was suited to detect AsA in blood serum samples.

Table 1
Recoveries of AsA from spiked blood serum samples.

Sample	Level added (μM)	Level found (μM)	Recovery (%)	RSD (%)
1	5	4.95	98.9	1.1
		4.84	96.8	3.2
		4.96	99.2	0.8
2	6	6.14	102.3	2.3
		6.17	102.9	2.9
		6.23	103.9	3.9
3	8	7.86	98.3	1.7
		7.89	98.6	1.4
		7.81	97.6	2.4
4	9	9.09	101.0	1.0
		9.05	100.5	0.5
		9.04	100.4	0.4

3.4. Determining the concentration of AsA in cell lysate

To further show the potential utility of NAPS-NO in biological samples, the probe was studied to detect AsA in cell lysate. A volume of 1 mL of HEK 293 cell lysate was transferred to a centrifuge tube and the large biomolecules were separated from the cell lysate by centrifugation at 12,000 rpm for 10 min. Then, 2 μL of cell lysate supernatant was added to 500 μL of 10 μM NAPS-NO in PBS (50 mM, pH 7.0). Different concentrations of AsA standards were added to the sample and the mixtures were measured. The fluorescence intensity of NAPS-NO with cell lysate was enhanced after additions of different amounts of AsA (Fig. S7). After linearly fitting, we successfully determined the concentration of AsA in cell lysate to be 1.51 μM, which accord with that of former report [45].

3.5. Cell labeling and imaging

We also proposed that NAPS-NO would permeate into cells because of its favorable amphiphilic properties. Laser scanning confocal microscopy was used to investigate this proposition.

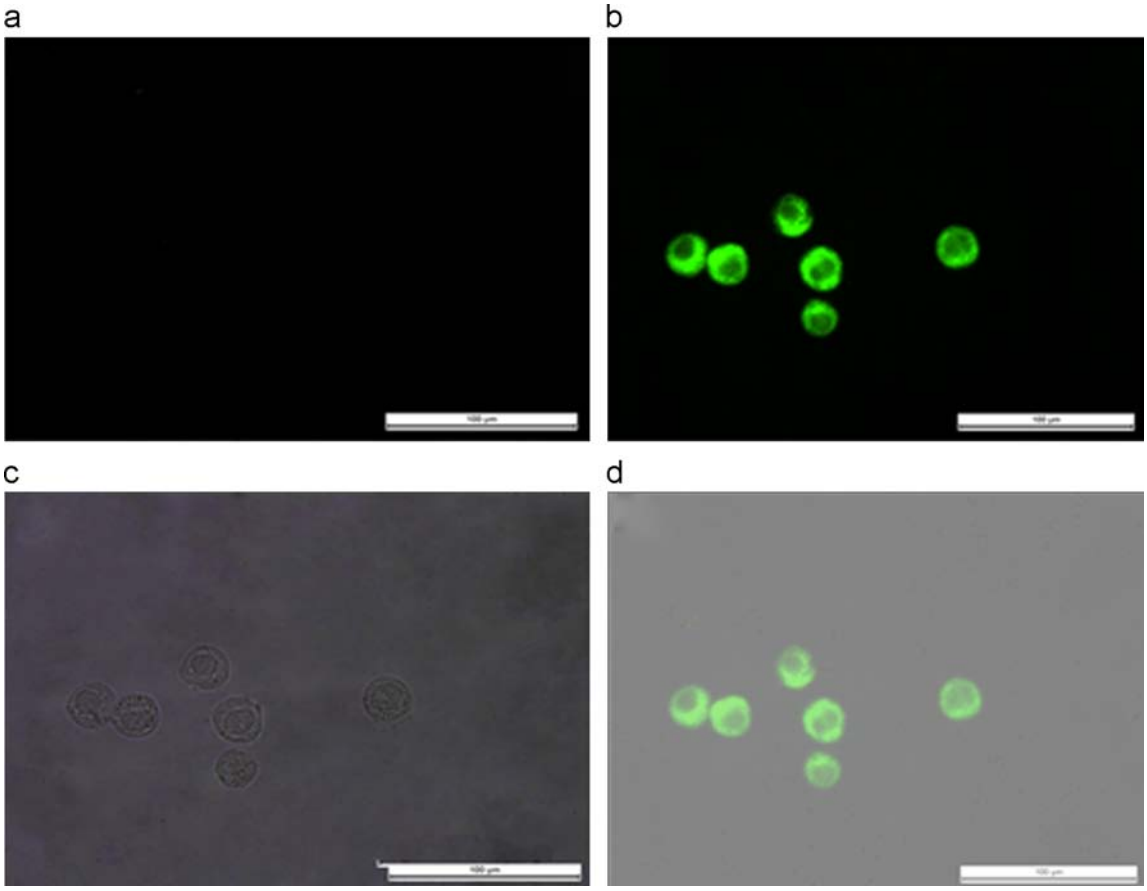


Fig. 3. Confocal fluorescence and brightfield images of Hela cells. (a) Fluorescence image of Hela cells stained with 40 μmol L^{-1} AsA for 30 min at 37 °C. (b) Confocal image of Hela cells that were further incubated with 40 μmol L^{-1} NAPS-NO for another 30 min. (c) Bright field image of cells shown in panel b. (d) The overlay image of b and c. The excitation wavelength was 468 nm.

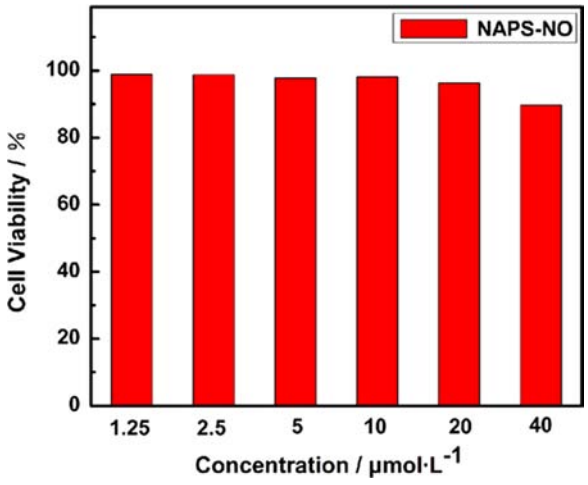


Fig. 4. Cellular toxicity of NAPS-NO determined by MTT assay. Effect of different concentration of NAPS-NO on viability of Hela cells.

Cultured Hela cells were incubated with 40 μmol L^{-1}AsA for 30 min at 37 °C, and an insignificant amount of AsA fluorescence was detected in the cells' interior (Fig. 3a). However, when the cells were supplemented with 40 μmol L^{-1} NAPS-NO for another 30 min, an enormous fluorescence increase from the intracellular area was observed (Fig. 3b). Bright field microscopic images (Fig. 3c) confirmed that the cells were viable throughout the imaging experiments. An overlay of fluorescence and bright field images revealed that the fluorescence signals were localized in the perinuclear region of the cytosol (Fig. 3d), indicating the subcellular distribution of AsA. These results demonstrated that NAPS-NO was cell permeable and might be used for monitoring AsA within biological samples. For future biological applications, the inherent cytotoxicity of NAPS-NO was tested using Hela cells by MTT assay. As shown in Fig. 4, the viability of Hela cells retained more than 90% after treated with NAPS-NO at 20 μmol L^{-1} for 48 h, even at 40 μmol L^{-1} cell viability remained 89%. The results suggested low cytotoxicity and good biocompatibility of NAPS-NO.

4. Conclusion

In conclusion, we proposed a new and simple fluorescent turn-on sensor to detect ascorbic acid in aqueous solution with very high sensitivity and wide detection range by using naphthalimide linked nitroxide as probe. The coordination of nitroxide with AsA was formed more easily, therefore, a recovered fluorescence intensity of naphthalimide moiety was observed. A good linear relationship was obtained from 80 nM to 50 μM for AsA and the detection limit was 20 nM. The chemosensor was successfully used to determine the concentration of AsA in human serum sample and HEK 293 cell lysate by using of standard addition methods. Furthermore, the excellent biological value of NAPS-NO was demonstrated by the fluorescence imaging with Hela cells. The developed method is expected to design new chemosensors based on organic fluorescent molecules and inorganic materials and applicate in clinical diagnostics and oxidative stress monitoring.

Acknowledgments

The work described in this paper was supported by the National Natural Science Foundation of China (21377089, 20927007 and 21177090). We would like to express our sincere thanks to Analytical & Testing Centre of Sichuan University for the MS measurements.

Appendix A. Supporting information

Supplementary data associated with this article can be found in the online version at http://dx.doi.org/10.1016/j.talanta.2014.08.066.

References

[1] S.A. Kumar, P.-H. Lo, S.-M. Chen, Biosens. Bioelectron. 24 (2008) 518–523.
[2] Z. Chen, T.E. Young, J. Ling, S.-C. Chang, D.R. Gallie, Proc. Natl. Acad. Sci. U.S.A. 100 (2003) 3525–3530.
[3] L. Zhang, Z.N. Wang, Y. Xia, G.Y. Kai, W.S. Chen, K.X. Tang, Crit. Rev. Biotechnol. 27 (2007) 173–182.
[4] A. Sevanian, K.J.A. Davies, P. Hochstein, Am. J. Clin. Nutr. 54 (1991) S1129–S1134.
[5] D. Wen, S. Guo, S. Dong, E. Wang, Biosens. Bioelectron. 26 (2010) 1056–1061.
[6] D.E. Hughes, J. Pharm. Sci. 72 (1983) 126–129.
[7] B. Vahid, J. Chem. Soc. Pak. 34 (2012) 1510–1512.
[8] L. Kukoc-Modun, M. Biocic, N. Radic, Talanta 96 (2012) 174–179.
[9] B. Shyla, G. Nagendrappa, Food Chem. 138 (2013) 2036–2342.
[10] M.A. Kutnink, W.C. Hawkes, E.E. Schaus, S.T. Omaye, Anal. Biochem. 166 (1987) 424–430.
[11] S.P. Sood, L.E. Sartori, D.P. Wittmer, W.G. Haney, Anal. Chem. 48 (1976) 796–798.
[12] A.J. Speek, J. Schrijver, W.H. Schreurs, J. Chromatogr. 305 (1984) 53–60.
[13] S. Moore, K.A. Calder, N.J. Miller, C.A. Rice-Evans, Free Radical Res. 21 (1994) 417–425.
[14] G.R. Buettner, Free Radical Res. Commun. 10 (1990) 5–9.
[15] R. Ferin, M.L. Pavao, J. Baptista, Clin. Biochem. 46 (2013) 665–669.
[16] P.A. Motchnik, B. Frei, B.N. Ames, Methods Enzymol 234 (1994) 269–279.
[17] X.X. Wang, P. Wu, X.D. Hou, Y. Lv, Analyst 138 (2013) 229–233.
[18] X. Zhang, S. Yu, W.Y. He, H. Uyama, Q.J. Xie, L. Zhang, F.C. Yang, Biosens. Bioelectron. 55 (2014) 446–451.
[19] X. Wang, M. Wu, W.R. Tang, Y. Zhu, L.W. Wang, Q.J. Wang, P.G. He, Y.Z. Fang, J. Electroanal. Chem. 695 (2013) 10–16.
[20] D. Karak, A. Banerjee, A. Sahana, S. Guha, S. Lohar, S.S. Adhikari, D. Das, J. Hazard. Mater. 188 (2011) 274–280.
[21] Y. Matsuoka, M. Yamato, T. Yamasaki, F. Mito, K.-i. Yamada, Free Radical Biol. Med 53 (2012) 2112–2118.
[22] M. Zheng, Z. Xie, D. Qu, D. Li, P. Du, X. Jing, Z. Sun, ACS Appl. Mater. Interfaces 5 (2013) 13242–13247.
[23] B. Biqing, T. Nanjiao, M. Mingfeng, Z. Lei, Y. Lihui, F. Quli, W. Lianhui, H. Wei, Soft Mater. 12 (2014) 73–78.
[24] R.J. Mehlhorn, J. Biol. Chem. 266 (1991) 2724–2731.
[25] J.P. Blinco, K.E. Fairfull-Smith, B.J. Morrow, S.E. Bottle, Aust. J. Chem. 64 (2011) 373–389.
[26] S.A. Green, D.J. Simpson, G. Zhou, P.S. Ho, N.V. Blough, J. Am. Chem. Soc. 112 (1990) 7337–7346.
[27] G.I. Likhtenshtein, Appl. Biochem. Biotechnol. 152 (2009) 135–155.
[28] T. Maki, N. Soh, K. Nakano, T. Imato, Talanta 85 (2011) 1730–1733.
[29] G.G. Borisenko, I. Martin, Q. Zhao, A.A. Amoscato, Y.Y. Tyurina, V.E. Kagan, J. Biochem. 279 (2004) 23453–23462.
[30] J.L. Chen, S.J. Zhuo, Y.Q. Wu, F. Fang, L. Li, C.Q. Zhu, Spectrochim. Acta, Part A 63 (2006) 438–443.
[31] M. Jia, Y. Tang, Y.F. Lam, S.A. Green, N.V. Blough, Anal. Chem. 81 (2009) 8033–8040.
[32] E. Lozinsky, V.V. Martin, T.A. Berezina, A.I. Shames, A.L. Weis, G.I. Likhtenshtein, J. Biochem. Biophys. Methods 38 (1999) 29–42.
[33] R.D. Kornberg, H.M. McConnell, Biochemistry 10 (1971) 1111–1120.
[34] A. Sienkiewicz, A.M.D. Ferreira, B. Danner, C.P. Scholes, J. Magn. Reson. 136 (1999) 137–142.
[35] B.S. Winkler, S.M. Orselli, T.S. Rex, Free Radical Biol. Med 17 (1994) 333–349.
[36] G.R. Bardajee, A.Y. Li, J.C. Haley, M.A. Winnik, Dyes Pigm 79 (2008) 24–32.
[37] V.B. Bojinov, I.P. Panova, Dyes Pigm 80 (2009) 61–66.
[38] Y.G. Shi, J.H. Yao, Y.L. Duan, Q.L. Mi, J.H. Chen, Q.Q. Xu, Bioorg. Med. Chem. Lett. 23 (2013) 2538–2542.
[39] T. Jesionowski, A. Krysztafkiewicz, Appl. Surf. Sci. 172 (2001) 18–32.
[40] Q.T. Meng, X.L. Zhang, C. He, P. Zhou, W.P. Su, C.Y. Duan, Talanta 84 (2011) 53–59.
[41] J. Kollar, P. Hrdlovic, S. Chmela, J. Photochem. Photobiol., A 195 (2008) 64–71.
[42] J. Kollar, P. Hrdlovic, S. Chmela, J. Photochem. Photobiol., A 204 (2009) 191–199.
[43] F. Lin, D. Pei, W. He, Z. Huang, Y. Huang, X. Guo, J. Mater. Chem. 22 (2012) 11801–11807.
[44] K.R. Dhariwal, W.O. Hartzell, M. Levine, Am. J. Clin. Nutr. 54 (1991) 712–716.
[45] A. Levin, C. DeSouza, C. Zaarour, W. Walsh, M.K. Chan, Z. Verjee, S. McIntyre, K. Adeli, Clin. Biochem. 43 (2010) 1411–1414.

Talanta 132 (2015) 197–204

Contents lists available at ScienceDirect

Talanta

journal homepage: www.elsevier.com/locate/talanta

Determination of pesticide residues in samples of green minor crops by gas chromatography and ultra performance liquid chromatography coupled to tandem quadrupole mass spectrometry

Stanisław Walorczyk*, Dariusz Drożdżyński, Roman Kierzek

Institute of Plant Protection-National Research Institute, Władysława Węgorka 20, 60-318 Poznań, Poland

ARTICLE INFO

Article history:
Received 21 June 2014
Received in revised form
19 August 2014
Accepted 28 August 2014
Available online 8 September 2014

Keywords:
Pesticide residue analysis
Chromatography
Tandem mass spectrometry
Dispersive solid phase extraction
Minor crops

ABSTRACT

A method was developed for pesticide analysis in samples of high chlorophyll content belonging to the group of minor crops. A new type of sorbent, known as ChloroFiltr, was employed for dispersive-solid phase extraction cleanup (dispersive-SPE) to reduce the unwanted matrix background prior to concurrent analysis by gas chromatography and ultra-performance liquid chromatography coupled to tandem quadrupole mass spectrometry (GC–MS/MS and UPLC–MS/MS). Validation experiments were carried out on green, unripe plants of lupin, white mustard and sorghum. The overall recoveries at the three spiking levels of 0.01, 0.05 and 0.5 mg kg^{-1} fell in the range between 68 and 120% (98% on average) and 72–104% (93% on average) with relative standard deviation (RSD) values between 2 and 19% (7% on average) and 3–16% (6% on average) by GC–MS/MS and UPLC–MS/MS technique, respectively. Because of strong enhancement or suppression matrix effects (absolute values $>20\%$) which were exhibited by about 80% of the pesticide and matrix combinations, acceptably accurate quantification was achieved by using matrix-matched standards. Up to now, the proposed method has been successfully used to study the dissipation patterns of pesticides after application on lupin, white mustard, soya bean, sunflower and field bean in experimental plot trials conducted in Poland.

© 2014 Elsevier B.V. All rights reserved.

1. Introduction

A particular crop may be called “minor” if such small amounts are grown that it will provide a limited market for pesticides. If the crop is considered to be of low economic importance at a national level, the pesticide manufacturers have little interest to do expensive research and development work needed for the registration of pesticides for use on the crop, and as a consequence of such a situation, the crop will have limited options for protection against pests and pathogens. Therefore, there are little data, or effectively no data available, about efficacy and residue behaviour of candidate pesticides having potential to be applied for the protection of minor crops. For authorization of pesticides on minor crops, or for minor use, it is preferable to explore other possibilities for determining the efficacy and crop safety of pesticides than those based on the amount of data required for authorization on major crops [1,2].

Although minor crops are grown in relatively small amounts compared with major crops, they are of substantial economic importance in many countries. Which crops are minor largely depends on the specific country and region. In Poland, the list of the plants classified as minor crops is published by the Ministry of Agriculture and Rural Development, and it comprises various crop groups including vegetables, fruit and berry plants, industrial plants and cereals, herbaceous plants and forest nurseries plants [3]. In this work, we focus on the analysis of pesticide residues in green crops of various plants including lupin, white mustard, soya, sunflower, and field bean by using gas chromatography and ultra performance liquid chromatography coupled with tandem quadrupole mass spectrometry (GC–MS/MS and UPLC–MS/MS)-based methods.

It must be highlighted, that the majority of up to now published pesticide residue methods were mainly focused on analysis of less complicated matrices such as fruit and vegetables [4]. The main reason might be the fact that fresh fruits and vegetables are consumed in larger amounts than other crops, so there is a risk for high intake of pesticide residues, especially when they are present above their legislative maximum residue levels (MRLs) [5]. However, another reason is that multiresidue pesticide analysis in matrices of high chlorophyll content is more difficult owing to matrix interferences and complicated extraction procedures [6]. In pesticide analysis, green matrices, high in chlorophyll, represent a particular challenge due to a massive load of co-extractives in the extract. The co-extracted

* Corresponding author: Tel.: +48 618649181; fax: +48 618679180.
E-mail addresses: s_walorczyk@tlen.pl, s.walorczyk@iorpib.poznan.pl (S. Walorczyk).

http://dx.doi.org/10.1016/j.talanta.2014.08.073
0039-9140/© 2014 Elsevier B.V. All rights reserved.

chlorophyll is one of the most problematic matrix interferences in pesticide residue analysis because of its non-volatile characteristics. It may hinder identification of the pesticides of interest by contamination of the chromatographic systems, causing downtime, and reducing the overall analytical performance [7,8].

The use of graphitized carbon black (GCB) as a sorbent has been shown to be effective for removal of co-extracted chlorophyll and other pigments from extract of plant crops [9–15]. On the other hand, GCB is well-known to adsorb pesticides with planar functionality leading to unsatisfactory recoveries of a number of pesticides susceptible to this adsorption, e.g. chlorothalonil, cyprodinil, fenazaquin, mepanipyrim, pirymethanil, prochloraz, quinoxifen, quintozene and thiabendazole [16–18].

The main objective of this work was to investigate the possibility of application of a new type of sorbent, known as ChloroFiltr, in order to reduce the content of chlorophyll from extracts of green plants belonging to the category of minor crops, and thereby reduce the unwanted background while not affecting the recovery of the target pesticides. For the final determination, concurrent analyses were carried out by using a programmable temperature vaporization injector (PTV) gas chromatography–tandem quadrupole mass spectrometry (GC–MS/MS) and ultra-performance liquid chromatography–tandem quadrupole mass spectrometry (UPLC–MS/MS) to achieve improved selectivity and high accuracy. Comprehensive method validation was carried out to evaluate fitness for the intended application, and it involved determination of recovery, precision, linearity, assessment of matrix effects and estimation of measurement uncertainty.

The developed and validated method was applied to the study of dissipation patterns of pesticides in experimental plot trials after application to minor crops including lupin, white mustard, soya bean, field bean and sunflower.

2. Material and methods

2.1. Chemicals and reagents

Acetonitrile and acetone (for residue analysis) were obtained from Witko (Łódź, Poland). Anhydrous magnesium sulphate (reagent grade) and Supel Que Citrate (EN) tubes containing 4 g magnesium sulphate, 1 g sodium chloride, 0.5 g sodium citrate dibasic sesquihydrate, 1 g sodium citrate tribasic dehydrate, water with 0.1% formic acid (LC–MS Chromasolv) and methanol with 0.1% ammonium acetate were obtained from Sigma-Aldrich Sp.z o. o. (Poznań, Poland). Enviro Clean extraction tubes containing 900 mg magnesium sulphate, 300 mg PSA and 150 mg ChloroFiltr were obtained from UCT (Bristol, PA, USA). Deionized water of resistivity 18.2 MΩ cm was prepared with a Milli-Q Plus system from Millipore (Billerica, USA).

2.2. Pesticide analytical standards

Certified pesticide standards and internal standards triphenylphosphate (TPP) and simazine-d10 were obtained from Dr. Ehrenstorfer (Augsburg, Germany). Stock solutions (approximately 1000 μg mL^{-1}) were prepared in acetone. Purities of the standards were accounted for when calculating the concentration of each stock solution. A blend stock solution of all pesticides at a concentration of 10 μg mL^{-1} was prepared in acetone. The working standards at 0.005, 0.01, 0.02, 0.05, 0.2, 0.5 and 1.0 μg mL^{-1} were prepared by diluting this stock solution with acetonitrile and 0.1% ammonium acetate in methanol/0.1% formic acid in water (1:1, v/v) for the GC–MS/MS and UPLC–MS/MS analysis, respectively.

Matrix-matched standards were prepared differently for GC–MS/MS and UPLC–MS/MS analysis. For the GC–MS/MS analysis, a volume (1.5 mL) of the standard at appropriate concentration was evaporated under nitrogen and reconstituted in acetonitrile sample extract at a concentration of 0.5 g mL^{-1}. While for the UPLC–MS/MS analysis, a volume (1 mL) of the standard at appropriate concentration and 2 mL acetonitrile sample extract at a concentration of 0.5 g mL^{-1} were evaporated under nitrogen then reconstituted in 1 mL methanol with 0.1% ammonium acetate/water with 0.1% formic acid (1:1, v/v).

2.3. GC–MS/MS conditions

The GC–MS/MS analysis of was carried out using a Varian CP-3800 gas chromatograph coupled with a Varian 1200 triple quadrupole mass spectrometer (Varian Inc., Middelburg, The Netherlands). The analyte separation was obtained on a DB-5 30 m × 0.25 mm × 0.5 μm capillary column, protected by a deactivated guard column (2 m × 0.53 mm). Helium (purity 99.9999%) at a flow rate of 1.2 mL min^{-1} was used as the carrier gas. The column oven temperature programme was as follows: 80 °C (held for 3 min), programmed at 30 °C $min^{-1}$to 150 °C, then programmed at 10 °C min^{-1} to 300 °C (held for 10 min). Large volume injection (LVI) with programmed temperature vaporization (PTV) was used. The injection volume was 10 μL of sample extract in acetonitrile using a 100 μL syringe. The injector temperature programme was as follows: 70 °C (held for 0.5 min), programmed at 200 °C $min^{-1}$to 300 °C (held for 15 min). The injector split ratio was initially set at 100:1, the splitless mode was enabled at 0.5 min, at 4 min the split ratio was set at 50:1, and it was reduced to 20:1 at 10 min.

The mass spectrometer was operated in electron impact ionization mode (EI, 70 eV) with the filament current of 50 μA and electron multiplier voltage at 300 V above the voltage determined by automatic tuning with perfluorotribulylamine (PFTBA). The manifold ion source and transfer line temperatures were 40, 270 and 290 °C, respectively. The collision gas (argon, 99.9998% purity) was set at the collision cell pressure of 1.7 mTorr. Multiple reaction monitoring (MRM) transitions and other acquisition parameters can be found in supplementary data included with this article. Instrument control, data acquisition and evaluation was performed by using a Varian MS Workstation software, version 6.6.

2.4. UPLC–MS/MS conditions

The UPLC–MS/MS analysis was carried out using a Waters ACQUITY UPLC ultra-performance liquid chromatography system (Milford, USA) coupled with a triple quadrupole mass spectrometer (Waters Inc., Micromass, Quattro Premier XE). The nebulizer and desolvation gas was obtained from a nitrogen generator model NM30-LA (Peak Scientific, Renfrewshire, Scotland, UK). The analyte separation was achieved using a BEH C18 100 mm-× 2.1 mm × 1.7 μm UPLC column protected by a VanGuard Pre-Column 5 mm × 2.1 mm × 1.7 μm. The temperature of the column was thermostated at 40 °C. The column was eluted with the mobile phase: water with 0.1% formic acid (A) and methanol with 0.1% ammonium acetate (B) at the flow rate of 0.3 mL min^{-1} using gradient mode. Gradient was programmed to increase the amount of B from an initial content of 10–100% in 6 min, held for 1 min and returned to the initial conditions (10% B) in 1 min (from 7 to 8 min), held for 1 min. The total run time was 9 min. Sample extract volumes of 5 μL were injected into the system. The temperature of the autosampler was thermostated at 25 °C.

For the MS/MS data acquisition, the interface conditions were optimized for maximum intensity of the precursor ions: nebulizer and desolvation gas (nitrogen) flows were 100 L h^{-1} and 700 L h^{-1}, respectively, source block and desolvation temperatures were 120 °C

and 350 °C, respectively. Argon (99.9998% purity) was used as the collision gas at the pressure of 6.9×10^{-3} mbar. The optimization of multiple reaction monitoring (MRM) transitions was performed individually for each analyte on the instrument used in this work. All the compounds were analysed using positive electrospray ionization mode (ESI+) except for bentazone which was analysed in the negative electrospray ionization mode (ESI−). Multiple reaction monitoring (MRM) transitions and other acquisition parameters can be found in supplementary data included with this article. The instrument was controlled using Waters MassLynx 4.0 software and data evaluation was carried out using Waters TargetLynx software.

2.5. Sample preparation procedure

A 5 g homogenized sample was weighted into a polypropylene centrifuge tube (50 mL), internal standards (50 µL TPP at 150 µg mL^{-1} and 100 µL simazine-d10 at 87 µg mL^{-1}) were added and the sample was and extracted with 5 mL deionized water (Milli-Q) and 10 mL acetonitrile on a laboratory shaker (Heidolph Promax 2020, Schwabach, Germany) for 10 min. Then 0.5 g disodium hydrogencitrate sesquehydrate, 1 g trisodium citrate dihydrate, 4 g anhydrous magnesium sulphate, and 1 g sodium chloride were added and immediately shaken for 1 min, and then centrifuged for 2.5 min at 4500 rpm. A 6 mL aliquot of the acetonitrile supernatant was transferred to a polypropylene centrifuge tube (15 mL) containing 0.9 g anhydrous magnesium sulphate, 0.3 g PSA, and 0.3 g ChloroFiltr. The contents were vortexed for 1 min and centrifuged for 2.5 min at 4500 rpm. For the GC–MS/MS analysis, an aliquot (~0.4 mL) of the supernatant was transferred into an autosampler vial with a fixed insert. For the UPLC–MS/MS, 2 mL of the supernatant were evaporated to dryness under nitrogen, reconstituted with 1 mL 0.1% ammonium acetate in methanol/0.1% formic acid in water (1:1, v/v), and filtered using a 13 mm, 0.2 m GHP membrane into an autosampler vial. The final concentration of sample was 0.5 g mL^{-1} and 1 g mL^{-1} in the case of GC–MS/MS and UPLC–MS/MS analysis, respectively.

2.6. Validation study

The scope of the developed method comprises 25 pesticides (including 15 herbicides, nine fungicides and two herbicides). These are candidate pesticides having potential to be applied for control of the most important pests and pathogens affecting the production of the minor crops under study (i.e. field bean, lupin, sorghum, soya bean, sunflower and white mustard). Data on pesticides, matrices and conducted field experiments are detailed in Supplementary information included with this article.

The developed method was subjected to validation study using green, unripe plants of lupin, white mustard and sorghum samples (previously checked to be free of the target pesticides) in order to determine linearity, matrix induced effects, recovery, precision, limit of quantification (LOQ) and measurement uncertainty.

The calibration was carried out by internal standard method with reference to TPP and simazine-d10 which served as the internal standard for the GC–MS/MS and UPLC–MS/MS analytes, respectively. Linearity was studied by injecting standards at pesticide concentrations 0.005–1.0 µg mL^{-1} and 0.01–1.0 µg mL^{-1} in acetonitrile (GC–MS/MS) or 1 mL methanol with 0.1% ammonium acetate/water with 0.1% formic acid, 1:1, v/v (UPLC–MS/MS), and in matrix extracts of lupin, white mustard and sorghum. These concentration ranges corresponded to pesticide content in real samples between 0.01 and 2.0 mg kg^{-1} (GC–MS/MS) and 0.01 and 1.0 mg kg^{-1} (UPLC–MS/MS).

The percentage of matrix effect (%ME) was obtained for each analyte from the slopes of the calibration curves and was determined by comparing solvent and matrix-matched (lupin, white mustard and sorghum) slopes by using the formula: $\%ME = 100\% \times (1 - slope_{solvent}/slope_{matrix})$ [19].

The recoveries were studied at the three spiking levels of 0.01, 0.05 and 0.5 mg kg^{-1} ($n=6$) on lupin and additional recovery tests at 0.05 mg kg^{-1} ($n=6$) were carried out on white mustard and sorghum. Repeatability precision was expressed in terms of relative standard deviation (RSD) and calculated for each spiking level ($n=6$). The samples were spiked with the pesticides before proceeding with the extraction and the results from the recovery study were assessed for compliance with the European Union guidelines SANCO/12571/2013, according to which the average recovery should fall in the range of 70–120% with an associated RSD less or equal 20% [20].

The LOQ was defined as the lowest spiking level validated with satisfactory values of recovery (70–120%) and RSD ($\leq 20\%$).

The measurement uncertainty was estimated based on the data obtained in the validation study. The major uncertainty sources included in the uncertainty budget were the repeatability of recoveries from spiked samples and uncertainty of the average recovery calculated from rectangular distribution. The relative expanded uncertainty was calculated by using the coverage factor $k=2$ at the confidence level of 95% [21].

3. Results and discussion

3.1. GC–MS/MS and UPLC–MS/MS conditions

MRM-based data acquisition methods with two or three MS/MS transitions for each analyte were developed on both instruments in order to carry out reliable quantification and identification of the pesticides in samples. Optimization of the conditions was started by using pesticide standards with the mass spectrometer operating in full scan mode to obtain the single stage MS spectrum. Then the fragmentation pattern of the selected precursor ions was studied in product ion scan mode at different collision energies (5–50 eV). In the case of UPLC–MS/MS, the pseudo-molecular ion $[M+H]^+$ (and $[M-H]^+$ for bentazone) was present as the peak base of the MS spectrum for all the compounds except for desmedipham and phenmedipham. The $[M+H]^+$ ion was used as the precursor for the MS/MS fragmentation. In the case of desmedipham and phenmedipham, due to lack of sensitivity of $[M+H]^+$ ion, the ammonium adduct $[M+NH_4]^+$ was chosen as the precursor ion. For each target compound, the most selective and sensitive transitions were determined and used for the detection and quantification of the target analytes. To avoid chances of matrix interferences, two or three transitions were used except for internal standards (TPP and simazine-d10). The GC–MS/MS and UPLC–MS/MS acquisition conditions including precursor and product ions, collision energies and other parameters are detailed in Supplementary information included with this article.

3.2. Sample preparation and method validation

Plant pigments including chlorophyll may contribute to high background in chromatograms and occurrence of matrix effects and thereby affect identification and quantification of the compounds of interest. The pigments can thermally degrade in the injection liner or accumulate in the columns which can lead to increased maintenance of the instrument. Thus, routine analysis of pesticide residues in chlorophyll containing matrices might be difficult and the proper choice of sorbent(s) is critical to remove

co-extracted matrix interferences, while assuring good recoveries of the target analytes.

To prepare samples before chromatographic analysis, we employed the well-known and currently widely used quick, easy, cheap, effective, rugged and safe (QuEChERS) strategy to sample extraction and cleanup as this is a very flexible approach and offers many options for analysis depending on the range of pesticides and matrices being tested [22]. But we applied mechanical shaking for an extended time of 10 min (compared with 30 s of manual shaking in some other versions of the QuEChERS) [23]. Also, we lowered the sample amount (to 5 g) and added water (5 ml) before proceeding with the acetonitrile extraction to enable the extraction solvent penetrate better the plant tissues and ensure complete transfer of the analytes from naturally contaminated samples [24].

The QuEChERS technique inherently involves a dispersive-solid phase extraction (dispersive-SPE) step, for which the base sorbent is primary and secondary amine (PSA) which primarily removes fatty acids and other organic acids, sugars, and some pigments. The matrix constituents that might adversely affect the chromatographic analysis. In addition, a new type of sorbent, known as ChloroFiltr, was evaluated to help the dispersive-SPE performance and complement the PSA cleanup by reduction of the content of chlorophyll from green plant extracts [25,26].

Once the sample preparation method was selected, it was subjected to comprehensive validation study to prove its fitness for purpose through the assessment of analytical performance parameters including linearity, matrix effects, recovery, precision and estimation of measurement uncertainty.

3.3. Study of linearity and matrix effect

Generally, the linearity parameters were highly satisfactory. The calibration curves were studied by using internal standardization in solvent solutions and matrix-matched in extracts of lupin, white mustard and sorghum, and gave the coefficients of determination (R^2) of the least squared linear calibration curves >0.99. The exceptions occurred only for desmedipham, flufenacet, phenmedipham and prochloraz in the case of solvent-only calibration (GC–MS/MS), and bentazone in the case of solvent-only, lupin- and sorghum-matched calibration (UPLC–MS/MS). Detailed linearity data (equations and R^2 values) obtained by using solvent-only and matrix-matched standards can be found in Supplementary information included with this article.

The percentage of matrix effect (%ME) was calculated as the difference between the slope of the matrix-matched and solvent-only calibration curves divided by the slope of solvent-only calibration curve. %ME in the range between −20 and 20% can be considered as insignificant because such variability is close to the repeatability RSD values [27,28]. But for most of the compounds under study, much higher values of %ME were present and both enhancement as well as suppression effects could be observed (Table 1).

In the case of UPLC–MS/MS, the analyte responses produced by matrix-matched standards were nearly always substantially higher than the responses obtained for the equivalent standards in solvent, so the matrix enhancement effect occurred predominantly. Otherwise, in the case of GC–MS/MS analysis, the matrix effects occurred in a larger extent (−116 to 82%) but no consistent pattern with respect to different analytes could be observed, i.e. enhancement, suppression, or negligible matrix effects <20% (absolute value) occurred for different compounds.

The prevailing occurrence of enhancement effect in the case of UPLC–MS/MS technique was contrary to our expectation, because the ion suppression effect tend to be more common in positive electrospray mode (ESI+) [29]. A possible explanation for the phenomenon we observed might be a specific suppression of the internal standard (simazine-d10) occurring due to co-eluting matrix compounds which resulted in analytes overestimation. However, this was not a major concern due to consistency of this effect among the matrices which led to sufficiently accurate quantification, provided that matrix-matched calibration would be used.

Table 1
Matrix effects of the pesticides in the GC–MS/MS and UPLC–MS/MS analysis of lupin, white mustard and sorghum extracts, determined as $100\% \times (1 - \text{slope}_{\text{solvent}}/\text{slope}_{\text{matrix}})$.

Pesticides	Lupine		White mustard		Sorghum	
	GC	UPLC	GC	UPLC	GC	UPLC
Acetochlor	−76	43	−88	53	−72	43
Azoxystrobin	24	42	12	51	20	43
Bentazone	–	62	–	57	–	64
Boscalid	2	46	4	53	5	43
Clomazone	−88	38	−44	48	−59	32
Cyproconazole_1	−29	38	−19	43	−19	37
Cyproconazole_2	–	43	–	51	–	40
Deltamethrin 1	68	–	70	–	56	–
Deltamethrin 2	20	–	30	–	9	–
Desmedipham	75	39	77	47	73	38
Dimethenamid-P	−70	48	−62	55	−70	46
Dimoxystrobin	−19	39	−15	49	−15	39
Fluazifop-P-butyl	−22	1	−16	38	−16	20
Flufenacet	44	38	−48	49	37	41
Linuron	–	38	–	50	–	38
Metamitron	–	52	–	59	–	50
Metconazole	−31	39	−25	47	−28	35
Metolachlor-S	−45	42	−48	52	−48	61
Pendimethalin	−39	−91	−39	−5	−33	−50
Phenmedipham	79	37	82	46	77	34
Picoxystrobin	−26	30	−20	46	−20	35
Prochloraz	−11	27	−116	41	−2	28
Propiconazole 1	−40	41	−25	53	−30	41
Propiconazole 2	−45	–	−26	–	−36	–
Prosulfocarb	–	23	–	45	–	28
Quizalofop-P-ethyl	−4	−8	−4	31	−4	8
Tebuconazole	−23	40	−23	49	−14	38
Thiacloprid	–	46	–	51	–	40

By using either techniques (GC–MS/MS or UPLC–MS/MS), the matrix effects were relatively consistent among studied matrices for the majority of the pesticides, so application of matrix-matched standards in any matrix would give acceptably accurate results for quantification of pesticide residues in other matrices, as will be presented further in this section. The exceptions, in the case of GC–MS/MS technique, were flufenacet and prochloraz. Flufenacet exhibited positive effect in lupin and sorghum but negative in white mustard whereas prochloraz exhibited considerable stronger negative matrix effect in white mustard (−116%) than in lupin (−11%) and sorghum (−2%). In the case of UPLC–MS/MS technique, inconsistencies in the occurrence of matrix effects were observed for fluazifop-P-butyl, quizalofop-P-ethyl and pendimethalin. In the case of fluazifop-P-butyl and quizalofop-P-ethyl, stronger positive matrix effects was observed in white mustard than in lupin and sorghum. In contrast, in the case of pendimethalin, stronger negative matrix effects were observed in lupin (−91%) and sorghum (−50%) than in white mustard (−5%). Whereas negligible matrix effects, with absolute values <20% in all matrices, were only observed in the case of boscalid, dimoxystrobin and quizalofop-P-ethyl when using the GC–MS/MS technique.

Because of common occurrence of matrix effects in analysis of pesticide residues in chlorophyll containing matrices under this study, the use of matrix-matched calibration was necessary as a practical approach to compensate for matrix effects and achieve

Table 2
Average recoveries, RSDs and expanded uncertainties U, % ($k=2$, confidence level 95%) in the GC–MS/MS and UPLC-MS/MS analysis of pesticides in green lupin.

Pesticides	Recovery, %								U, %	
	0.01		0.05		0.5		Overall		($k=2$, $\alpha=0.05$)	
	GC	UPLC	GC	UPLC	GC	UPLC	GC	UPLC	GC	UPLC
Acetochlor	122 (2)	97 (18)	120 (3)	79 (7)	119 (1)	98 (1)	120 (2)	91 (9)	13	18
Azoxystrobin	107 (8)	129 (7)	99 (8)	85 (3)	100 (1)	94 (3)	102 (7)	103 (4)	14	9
Bentazone	–	–	–	89 (9)	–	60 (5)	–	75 (9)	–	23
Boscalid	101 (4)	102 (5)	84 (1)	78 (3)	84 (1)	91 (3)	90 (10)	90 (4)	20	9
Clomazone	111 (6)	128 (9)	122 (3)	84 (2)	120 (1)	94 (2)	118 (6)	102 (4)	15	9
Cyproconazole_1	91 (8)	–	91 (1)	98 (7)	96 (3)	109 (1)	92 (5)	104 (7)	11	15
Cyproconazole_2	–	114 (7)	–	72 (1)	–	94 (1)	–	93 (3)	–	7
Deltamethrin 1	106 (13)	–	105 (8)	–	96 (4)	–	102 (9)	–	19	–
Deltamethrin 2	82 (6)	–	87 (5)	–	81 (2)	–	83 (5)	–	14	–
Desmedipham	–	92 (8)	78 (4)	68 (5)	81 (3)	84 (5)	80 (4)	81 (6)	14	16
Dimethenamid-P	81 (10)	–	122 (2)	94 (11)	120 (1)	92 (4)	108 (19)	93 (8)	39	16
Dimoxystrobin	113 (3)	116 (8)	97 (5)	86 (2)	103 (1)	98 (2)	104 (7)	100 (4)	15	8
Fluazifop-P-butyl	94 (4)	107 (14)	103 (4)	84 (3)	102 (2)	92 (4)	100 (5)	94 (7)	10	14
Flufenacet	94 (18)	123 (6)	84 (4)	85 (2)	85 (4)	98 (1)	88 (11)	102 (3)	24	6
Linuron	–	112 (10)	–	77 (4)	–	89 (1)	–	93 (5)	–	11
Metamitron	–	130 (7)	–	82 (4)	–	93 (2)	–	102 (4)	–	9
Metconazole	–	105 (12)	92 (10)	75 (4)	96 (4)	89 (4)	94 (7)	90 (7)	14	15
Metolachlor-S	109 (7)	126 (9)	118 (1)	87 (2)	115 (2)	96 (1)	114 (5)	103 (4)	13	8
Pendimethalin	119 (3)	75 (22)	117 (4)	62 (13)	117 (1)	79 (13)	118 (3)	72 (16)	11	36
Phenmedipham	119 (3)	100 (7)	79 (6)	70 (4)	80 (3)	84 (4)	83 (9)	85 (5)	21	16
Picoxystrobin	101 (19)	110 (7)	101 (4)	89 (4)	101 (1)	99 (2)	101 (10)	99 (4)	20	9
Prochloraz	–	103 (4)	67 (6)	74 (7)	69 (2)	86 (9)	68 (4)	88 (7)	20	15
Propiconazole 1	106 (5)	112 (5)	110 (6)	79 (3)	94 (1)	92 (4)	104 (8)	94 (4)	16	9
Propiconazole 2	109 (8)	–	105 (13)	–	92 (1)	–	102 (11)	–	21	–
Prosulfocarb	–	100 (8)	–	76 (2)	–	90 (5)	–	89 (12)	–	12
Quizalofop-P-ethyl	86 (5)	87 (20)	94 (3)	79 (4)	93 (1)	85 (6)	91 (5)	84 (10)	11	22
Tebuconazole	90 (5)	134 (8)	90 (1)	85 (5)	95 (1)	94 (3)	92 (4)	104 (5)	9	11
Thiacloprid	–	124 (10)	–	86 (4)	–	96 (3)	–	102 (6)	–	11

acceptably accurate quantificative results in both GC–MS/MS and UPLC–MS/MS analyses.

3.4. Recovery study and estimation of measurement uncertainty

For the purpose of evaluating the accuracy (trueness and precision) of the proposed method, a recovery study was carried out by spiking lupin, white mustard and sorghum samples with the target pesticides. The recovery and repeatability RSD values were determined by the analysis of six replicate spiked samples at each level (0.01, 0.05 and 0.5 mg kg^{-1}). The results for calculation of recoveries were obtained by using matrix-matched standards prepared in lupin extracts.

As can be seen in Table 2, most of the compounds presented satisfactory recoveries from lupin in the range between 70% and 120% with RSD values $\leq 20\%$, i.e. compliant with the EU criteria of SANCO/12571/2013 [20]. For a limited number of compounds, especially at the lowest spiking level of 0.01 mg kg^{-1}, the recovery and RSD results were slightly outside the acceptance criteria. The most problematic compound was bentazone which generally did not present satisfactory results. But the overall recoveries of the target pesticides at the three spiking levels of 0.01, 0.05 and 0.5 mg kg^{-1} fell in the range between 68 and 120% (98% on average) and 72–104% (93% on average) with RSD values between 2 and 19% (7% on average) and 3–16% (6% on average) by GC–MS/MS and UPLC–MS/MS techniques, respectively.

Additional recovery evaluation was carried out on white mustard and sorghum (spiking level 0.05 mg kg^{-1}, $n=6$). In this experiment, the results for calculation of recoveries were also obtained by using matrix-matched standards prepared in lupin extracts. Generally, the results were very satisfactory and fulfilled the recovery and precision requirements of SANCO/12571/2013 (Table 3). Flufenacet and

Table 3
Average recoveries and RSDs in the GC–MS/MS and UPLC–MS/MS analysis of pesticides in white mustard and sorghum (spiking level 0.05 mg kg^{-1}, $n=6$).

Pesticides	Recovery (%)			
	White mustard		Sorghum	
	GC	UPLC	GC	UPLC
Acetochlor	70 (14)	93 (6)	102 (11)	91 (3)
Azoxystrobin	78 (6)	85 (4)	87 (7)	88 (3)
Bentazone	–	25 (24)	–	56 (17)
Boscalid	91 (7)	77 (4)	100 (10)	79 (5)
Clomazone	93 (9)	91 (1)	107 (10)	88 (2)
Cyproconazole_1	101 (10)	96 (6)	105 (13)	103 (4)
Cyproconazole_2	–	75 (4)	–	79 (6)
Deltamethrin 1	97 (17)	–	–	–
Deltamethrin 2	87 (4)	–	–	–
Desmedipham	106 (9)	78 (3)	76 (8)	79 (2)
Dimethenamid-P	86 (7)	91 (10)	109 (6)	99 (11)
Dimoxystrobin	109 (6)	88 (2)	103 (14)	91 (3)
Fluazifop-P-butyl	96 (2)	91 (3)	99 (11)	89 (3)
Flufenacet	22 (23)	84 (2)	113 (8)	88 (4)
Linuron	–	106 (2)	–	90 (4)
Metamitron	–	105 (1)	–	107 (2)
Metconazole	110 (10)	79 (4)	100 (20)	76 (3)
Metolachlor-S	79 (11)	92 (4)	99 (6)	94 (2)
Pendimethalin	100 (11)	87 (7)	98 (18)	74 (7)
Phenmedipham	99 (17)	79 (3)	88 (12)	78 (1)
Picoxystrobin	90 (9)	100 (2)	102 (12)	98 (1)
Prochloraz	45 (33)	89 (2)	97 (5)	90 (5)
Propiconazole 1	102 (12)	84 (3)	108 (10)	81 (2)
Propiconazole 2	95 (13)	–	96 (17)	–
Prosulfocarb	–	89 (1)	–	84 (3)
Quizalofop-P-ethyl	96 (5)	94 (3)	101 (5)	92 (1)
Tebuconazole	96 (3)	75 (1)	104 (13)	74 (4)
Thiacloprid	–	94 (2)	–	95 (1)

prochloraz were the exceptions, which presented lower recoveries in white mustard in the case of GC–MS/MS analysis and so was bentazone which presented lower recoveries in white mustard and sorghum in the case of UPLC–MS/MS analysis. These phemomena were likely caused by the occurrence of strong matrix effects, as it was discussed previously in this section. Matrix-matching in the same matrix will be needed to obtain more accurate quantification for these problematic compounds.

The limit of quantification (LOQ) was determined as the lowest spiking level at which the validation criteria were satisfied with average recovery 70–120% and RSD $\leq$20%, and it was 0.01 mg kg^{-1} (except for bentazone and metamitron).

The data derived from the validation study (recovery and RSD) were used to estimate the measurement uncertainty associated with the analytical results when using the developed method to analyse real samples. Precision was identified as the main contribution to the uncertainty, but the uncertainty associated with the recovery, as calculated from rectangular distribution, was also included in the uncertainty budget to avoid underestimation of the total uncertainty [21]. Taking into account the overall recovery and RSD data (Table 2), the calculated measurement uncertainty values ranged from 9% to 39% (17% on average) and from 6% to 36% (13% on average), by using GC–MS/MS and UPLC–MS/MS techniques, respectively (coverage factor k=2, confidence level 95%). These values were lower than a default value of $\pm$50% recommended by the SANCO/12571/2013 document, demonstrating fitness for purpose of the developed and validated method.

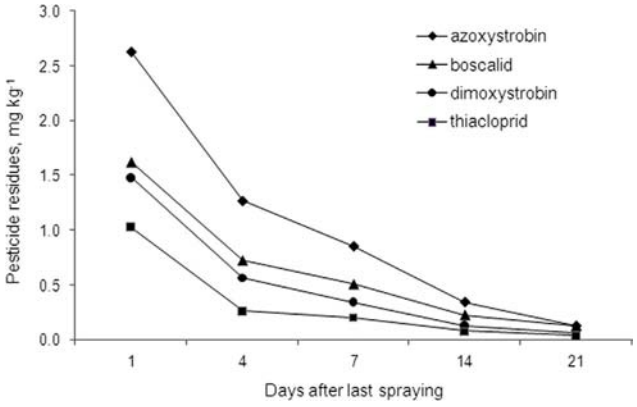


Fig. 1. Dissipation patterns of pesticides after application on lupin.

It must be highlighted that most of the pesticides under this study could be analysed by either techniques, GC–MS/MS or UPLC–MS/MS, therefore the one to offer better analytical performance parameters for the particular pesticide and matrix combination was used when analysing real samples.

3.5. Application to real samples

In this work, we focused on the study of dissipation rates of selected pesticides after application to lupin, white mustard, soya bean, sunflower and field bean. These plants were classified by the Polish Ministry of Agriculture and Rural Development as minor crops, for which there are limited options for protection against pests and pathogens. Our studies entailed the use of candidate pesticides having potential to be applied for the protection of these minor crops in field trials, followed by laboratory analysis for pesticide residues. Detailed data on tests that we have been conducted in experimental plots can be found in Supplementary information included with this article.

The aim of our work was to increase the knowledge in the residue behaviour and dissipation study of the pesticides, which have recently been proposed for the use in comprehensive protection of selected minor crops by means of extension of authorization of pesticides which are already registered for use in Poland on other crops (i.e. major crops).

The dissipation patterns of the pesticides were different probably due to the different chemical structures of the compounds, applied doses and preharvest times but the terminal pesticide residues, i.e. determined in the samples collected in the last sampling time, were always below the maximum residue levels (MRLs) [30]. Pesticide MRLs apply to edible plant parts but in this work unripe green plants were analysed in order to determine the dissipation patterns of the target pesticides and reassure preharvest intervals on the crops under study. Effectively, there was no need to analyse the final crops (seeds) because the target pesticides disappeared on the plants before harvest, and in most cases they fell below the method LOQ in the samples collected in the last sampling time.

We can conclude that the proposed pesticide application schedules were correct and the data concerning the pesticide residue dissipation suggest that the proposed pesticides can be safely used on the studied minor crops, without the risk of the presence of problematic residues, provided that good agricultural practices have been followed. Examples of pesticide dissipation

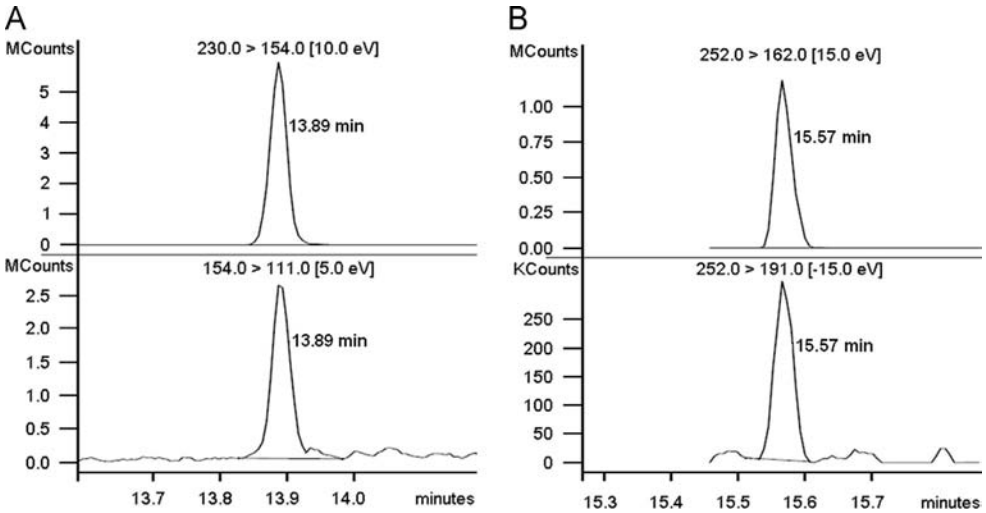


Fig. 2. GC–MS/MS chromatogrrasams of a sample of lupin containing residues of (A) dimethenamid-P (0.016 mg kg^{-1}), and (B) pendimethalin (0.028 mg kg^{-1}). The sample was collected 32 days after spraying with Wing P 462.5 EC.

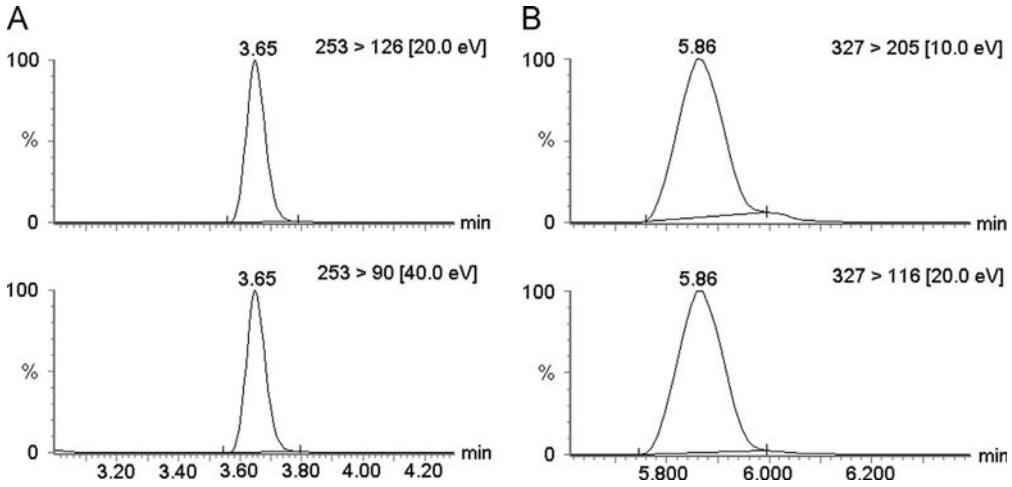


Fig. 3. UPLC–MS/MS chromatograms of (A) a sample of field bean containing thiacloprid (0.057 mg kg^{-1}, 21 days after spraying with Proteus 110 OD), and (B) a sample of sunflower containing dimoxystrobin (0.236 mg kg^{-1}, 14 days after spraying with Pictor 400 SC).

over time plots, showing concentration versus days after the last spraying, for different pesticides applied to lupin in a field experiment are shown in Fig. 1. Whereas, Fig. 2 shows GC–MS/MS chromatograms of a sample of lupin containing residues of dimethenamid-P (0.016 mg kg^{-1}) and pendimethalin (0.028 mg kg^{-1}) and Fig. 3 shows UPLC–MS/MS chromatograms of thiacloprid in field bean (0.057 mg kg^{-1}) and dimoxystrobin in sunflower (0.236 mg kg^{-1}).

The results obtained in this work will aid in the establishment of safe and proper use of pesticides for extension of authorization on minor crops in Poland.

4. Conclusions

Matrices high in chlorophyll present a special difficulty in pesticide residue analysis owing to interferences which can negatively affect the method performance characteristics and create an analytical challenge. As a solution to these problems, we investigated the use of a new QuEChERS-based method of sample preparation and report it for the first time. We used a new sorbent, known as ChloroFiltr, which served for selective reduction of chlorophyll from green plant extracts, and was used in combination with PSA to keep the sample cleanup as straightforward as possible in the dispersive-SPE mode.

The final analysis was carried out by using concurrent determinations by both GC–MS/MS and UPLC–MS/MS, and in the case of both techniques, the importance of using matrix-matched calibration was demonstrated as being of key importance for achieving accurate results. An important conclusion is also that relative consistency of matrix effects in both GC–MS/MS and UPLC–MS/MS analysis for a given pesticide between different matrices, makes it possible to quantify pesticide residues in different matrices using only one matrix-matched calibration curve.

After validation, the developed method was successfully applied to study the dissipation patterns of pesticide residues after application on crops belonging the group of minor crops (lupin, white mustard, soya bean, sunflower and field bean).

Acknowledgements

This work was supported by Ministry of Agriculture and Rural Development (Ministerstwo Rolnictwa i Rozwoju Wsi) under Long-Term Programme of IPP–NRI for 2011–2015 “Protection of cultivated plants with the consideration of food safety, reduction of yield losses and threat to humans, farm animals and the environment” (contract No. HORkor.0660/IOR 2011-2015/2/2013), task No. 1.2. “Assessment of possible complex protection of minor crops”, and by Ministry of Science and Higher Education (Ministerstwo Nauki i Szkolnictwa Wyższego), project ID: POZ-07.

Appendix A. Supplementary information

Supplementary data associated with this article can be found in the online version at http://dx.doi.org/10.1016/j.talanta.2014.08.073.

References

[1] Regulation (EC) no. 1107/2009 of the European Parliament and of the Council of 21 October 2009 concerning the placing of plant protection products on the market and repealing Council Directives 79/117/EEC and 91/414/EEC. Available online: ⟨http://eur-lex.europa.eu/LexUriServ/LexUriServ.do?uri=OJ:L:2009:309:0001:0050:EN:PDF⟩, (accessed 10.06.14).
[2] Available online: ⟨http://www.eppo.int/PPPRODUCTS/minor_uses/minor_uses.htm⟩, (accessed 10.06.14).
[3] Available online: ⟨http://isap.sejm.gov.pl/DetailsServlet?id=WDU20130000659⟩, (accessed 10.06.2014).
[4] H.V. Botitsi, S.D. Garbis, A. Economou, D.F. Tsipi, Mass Spectrom. Rev. 30 (2011) 907–939.
[5] European Food Safety Authority, The 2010 European Union report on pesticide residues in food, EFSA J. 11 (2013) 808 pp. Available online: ⟨http://www.efsa.europa.eu/en/efsajournal/doc/3130.pdf⟩, (accessed 10.06.14).
[6] Y. Wang, H.Y. Jin, S.-C. Ma, J. Lu, R.-C. Lin, J. Chromatogr. A 1218 (2011) 334–342.
[7] E. Muñoz, G. Muñoz, L. Pineda, E. Serrahima, F. Centrich, J. AOAC Int. 95 (2012) 1777–1796.
[8] B. Łozowicka, M. Jankowska, E. Rutkowska, I. Hrynko, P. Kaczyński, J. Miciński, J. Nat. Med. 68 (2014) 95–111.
[9] R.M. González-Rodríguez, R. Rial-Otero, B. Cancho-Grande, J. Simal-Gándara, J. Chromatogr. A 1196–1197 (2008) 100–109.
[10] L. Li, W. Li, D. Qin, S. Jiang, F. Liu, J. AOAC Int. 92 (2009) 538–547.
[11] L.-J. Qu, H. Zhang, J.-H. Zhu, G.-S. Young, H.Y. Aboul-Enein, Food Chem. 122 (2010) 327–332.
[12] R. Xu, J. Wu, Y. Liu, R. Zhao, B. Chen, M. Yang, J. Chen, Chemosphere 84 (2011) 908–912.
[13] M.Á. González-Curbelo, J. Harnández-Borges, L.M. Ravelo-Pérez, M.Á. Rodríguez-Delgado, Food Chem. 125 (2011) 1083–1090.
[14] G. Chen, R. Cao, R. Liu, Food Chem. 125 (2011) 1406–1411.
[15] M. Słowik-Borowiec, E. Szpyrka, S. Walorczyk, Bull. Environ. Contam. Toxicol. 89 (2012) 633–637.
[16] H.G.J. Mol, A. Rooseboom, R. van Dam, M. Roding, K. Arondeus, S. Sunarto, Anal. Bioanal. Chem. 389 (2007) 1715–1754.
[17] C.C. Leandro, P. Hancock, R.J. Fussell, B.J. Keely, J. Chromatogr. A 1166 (2007) 152–162.
[18] S. Walorczyk, Rapid Commun. Mass Spectrom. 22 (2008) 3791–3801.
[19] H. Kwon, S.J. Lehotay, L. Geis-Asteggiante, J. Chromatogr. A 1270 (2012) 235–245.

[20] Document no. SANCO/12571/2013 (2014), Guidance document on analytical quality control and validation procedures for pesticide residues analysis in food and feed. Available online: ⟨http://ec.europa.eu/food/plant/plant_protection_products/guidance_documents/docs/qualcontrol_en.pdf⟩, (accessed 10.06.14).
[21] S. Walorczyk, D. Drożdżyński, J. AOAC Int. 94 (2011) 1625–1642.
[22] S.J. Lehotay, Methods Mol. Biol. 747 (2011) 65–91.
[23] S.J. Lehotay, K. Ae Son, H. Kwon, U. Koesukwiwat, W. Fu, K. Mastovska, E. Hoh, N. Leepipatpoboon, J. Chromatogr. A 1217 (2010) 2548–2560.
[24] O. Lacina, M. Zachariasova, J. Urbanova, M. Vaclavikova, T. Cajka, J. Hajslova, J. Chromatogr. A 1262 (2012) 8–18.
[25] Available online: ⟨https://www.unitedchem.com/catalog/sample-prep/solid-phase-extraction-columns/enviro-clean/quechers-chlorofiltr⟩, (accessed 19.07.14).
[26] ⟨https://www.unitedchem.com/sites/default/files/docs/posters-and-papers/SOFT_MarijuanaPoster_002_Lo-Res.pdf⟩, (accessed 19.07.14).
[27] S. Walorczyk, Talanta 120 (2014) 106–113.
[28] C. Ferrer, A. Lozano, A. Agüera, A.J. Girón, A.R. Fernández-Alba, J. Chromatogr. A 1218 (2011) 7634–7639.
[29] H. Stahnke, S. Kittlaus, G. Kempe, L. Alder, Anal. Chem. 84 (2012) 1474–1482.
[30] Regulation (EC) no. 396/2005 of the European Parliament and of the Council of 23 February 2005 on maximum residue levels of pesticides in or on food and feed of plant and animal origin and amending Council Directive 91/414/EEC. Available online: ⟨http://eur-lex.europa.eu/LexUriServ/LexUriServ.do?uri=OJ:L:2005:070:0001:0016:en:PDF⟩, (accessed 17.06.14).

Talanta 132 (2015) 205–214

Contents lists available at ScienceDirect

Talanta

journal homepage: www.elsevier.com/locate/talanta

Electrochemical detection of ractopamine at arrays of micro-liquid | liquid interfaces

Masniza Sairi [a,b], Damien W.M. Arrigan [a,*]

[a] Nanochemistry Research Institute, Department of Chemistry, Curtin University, GPO Box U1987, Perth 6845, WA, Australia
[b] Mechanization and Automation Research Centre, Malaysian Agricultural Research and Development Institute (MARDI), PO Box 12301, 50774 Kuala Lumpur, Malaysia

ARTICLE INFO

Article history:
Received 4 July 2014
Received in revised form
22 August 2014
Accepted 23 August 2014
Available online 3 September 2014

Keywords:
Ractopamine
Ion transfer
Micro-ITIES
Voltammetry
Stripping voltammetry

ABSTRACT

The behaviour of protonated ractopamine ($RacH^+$) at an array of micro-interfaces between two immiscible electrolyte solutions (micro-ITIES) was investigated via cyclic voltammetry (CV) and linear sweep stripping voltammetry (LSSV). The micro-ITIES array was formed at silicon membranes containing 30 pores of radius 11.09 ± 0.12 μm and pore centre-to-centre separation of 18.4 ± 2.1 times the pore radius. CV shows that $RacH^+$ transferred across the water | 1,6-dichlorohexane μITIES array at a very positive applied potential, close to the upper limit of the potential window. Nevertheless, CV was used in the estimation of some of the drug's thermodynamic parameters, such as the formal transfer potential and the Gibbs transfer energy. LSSV was implemented by pre-concentration of the drug, into the organic phase, followed by voltammetric detection, based on the back-transfer of $RacH^+$ from the organic to aqueous phase. Under optimised pre-concentration and detection conditions, a limit of detection of 0.1 μM was achieved. In addition, the impact of substances such as sugar, ascorbic acid, metal ions, amino acid and urea on $RacH^+$ detection was assessed. The detection of $RacH^+$ in artificial serum indicated that the presence of serum protein interferes in the detection signal, so that sample deproteinisation is required for feasible bioanalytical applications.

© 2014 Elsevier B.V. All rights reserved.

1. Introduction

Ion transfer across the interface between two immiscible electrolyte solutions (ITIES) [1–4] has received increasing interest in the field of electrochemistry, liquid | liquid extraction and membrane transport. Electrochemistry at liquid | liquid interfaces has moved from the transfer of model ions such as tetraalkylammonium ions to the detection of molecules of biological importance such as proteins, peptides, amino acids, drugs, neurotransmitters, food additives and DNA [5]. Thus it plays a potentially important role in new bioanalytical methods.

Ractopamine (Rac) (Fig. 1(a)) is a phenyl β-ethanolamine, with β-adrenergic agonist properties [6–9]. It is primarily used as a therapeutic drug for treatment of pulmonary diseases such as asthma in human and veterinary medicine [6,7]. Unfortunately, this substance is also illegally applied in the livestock industry as a nutrient repartitioning agent. Research shows that β-agonists divert fat deposition to the production of muscle tissues by increasing nitrogen retention, protein synthesis and lipolysis [6,7,9–11]. It also improves growth rate and feed conversion when fed to livestock (such as calves, poultry etc.) [8,9,12]. Recently, veterinary drug residues have become a public food safety concern where ractopamine-treated animals may pose adverse effects on human health, especially in the cardiovascular and central nervous systems [6,7,9,12,13]. Thus, it is banned in many countries, including within the European Union and China, although it is approved by the United States' Food and Drug Administration (U.S. FDA) [12,14–16]. As a result, rapid, simple and sensitive analytical methods for the detection of ractopamine residues are required.

To date, various analytical methods have been reported for the detection of ractopamine, such as immunoassays [9,10,17], electrochemical methods [6,7,13,16], gas chromatography–mass spectrometry [11], liquid chromatography tandem mass spectrometry [12,18] and high performance liquid chromatography [8,14,15]. Electrochemical methods offer the advantages of low instrumental cost and fast analysis, and thus may be the preferred methods in ractopamine detection [7]. Despite the fact that many electrochemical methods have been developed, those studies focused on solid | liquid interfaces, using primarily cyclic voltammetry (CV) [6,7,16]. The two phenolic groups in ractopamine are easily oxidised [6,7,13]. Differential pulse voltammetry (DPV) has also been employed for the detection of ractopamine [6,7,13].

To the best of our knowledge, no studies have been reported on the electrochemical detection of ionised ractopamine based on transfer across the ITIES. Thus, this study opens up the possibilities

* Corresponding author. Tel.: +61 8 9266 9734; fax: +61 8 9266 2300.
E-mail address: D.Arrigan@curtin.edu.au (D.W.M. Arrigan).

http://dx.doi.org/10.1016/j.talanta.2014.08.060
0039-9140/© 2014 Elsevier B.V. All rights reserved.

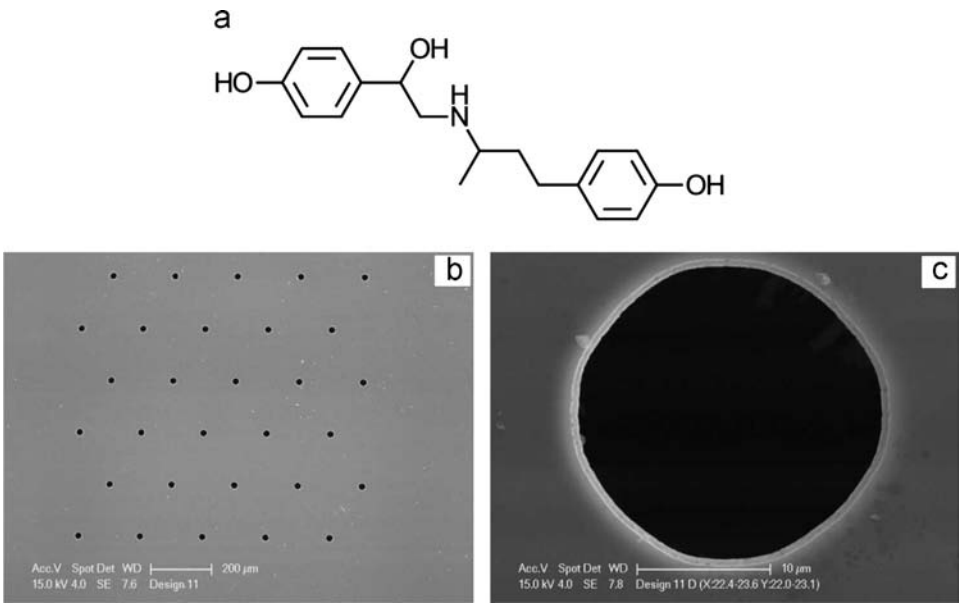


Fig. 1. (a) Molecular structure of ractopamine (b) SEM image of the full micropore array silicon membrane, and (c) SEM of a single micropore within the array.

for the detection of ractopamine based on charge transfer across micro-ITIES. However, the detection of other drugs at the ITIES via various electrochemical methods has been reported in the literature, namely the anticancer drug daunorubicin at a microporous polyethylene terephthalate (PET) membrane-supported ITIES [19], catamphiphilic drugs at a solvent polymeric membrane [20], and β-blocker drugs (propranolol, timolol and sotalol) at a microporous silicon membrane-supported ITIES [21]. Besides analytical studies, the ability of the ITIES to mimic the drug transfer across biological membranes has offered insight into mechanisms of drug action [19]. Voltammetry at the ITIES has been used to investigate the transfer characteristics of charged drug molecules, for example, the Galvani potential difference ($\Delta_o^w\varnothing$) for the ion transfer and the Gibbs energy of transfer, which is directly related [22]. Previous studies by Girault and co-workers [23,24] have shown that the ITIES is a suitable platform for the determination of the partition coefficient of the ionised species, which in turn defines the drug's lipophilicity in biological systems [19,20,22].

Direct drug detection in physiological matrices, such as blood and blood-derived samples, is important because it offers information regarding circulating levels. Yet, this can be hindered due to drug–protein binding [25]. The drug–protein interaction in blood plays an important role in determining drug transportation, absorption, distribution, metabolism and excretion [26–28]. Serum albumins are present at the highest abundance in blood (ca. 60% of the total albumin) [29,30], and these proteins exhibit high affinity towards drugs [26–28,31]. In addition, the pharmacological activity of drugs relates to their free concentration in blood [25]. The measurement of drug–protein interactions has seen the emergence of a number of novel label-free strategies [32]. In this study, albumin from bovine serum (BSA) is employed due to the fact that human and bovine serum albumins are homologous proteins [29,33,34]. BSA is a highly water-soluble globular protein, which has a molar mass of 69,000 amu and a hydrodynamic radius of ca. 3.25 nm [25,35]. BSA also has a low isoelectric point (pI of 5.4) and high negative net charge at neutral pH [36].

In this report, emphasis is placed on the electrochemical behaviour of protonated ractopamine ($RacH^+$) at the micro-ITIES array. Quantitative methods that involve the detection of $RacH^+$ by simple ion transfer at the water | 1,6-dichlorohexane (DCH) micro-interface array are presented, using CV and linear sweep stripping voltammetry (LSSV). Stripping analysis at micro-liquid | liquid interface arrays is appropriate for analyte detection in media such as biological fluids, soil extracts and water [37], thus this technique is examined in this study. The thermodynamic parameters for the transfer of ionisable ractopamine are discussed. In addition to the analytical parameters, the influence of the interfering substances, including serum protein, towards $RacH^+$ detection are also reported.

2. Materials and methods

2.1. Reagents

All reagents used were purchased from Sigma-Aldrich Pty. Ltd., Australia and used without further purification, unless stated otherwise. D-Glucose and sodium chloride (NaCl) were purchased from Ajax Finechem Pty. Ltd., Australia, L-ascorbic acid and potassium phosphate monobasic (KH_2PO_4) from BDH Laboratory Supplies, Australia, and sodium sulfate (Na_2SO_4) from Chem-Supply Pty. Ltd, Australia.

The aqueous phase solution of 10 mM lithium chloride (LiCl) was prepared in ultrapure water (resistivity of 18 MΩ cm) from a Milli-Q water purification system (Millipore Pty. Ltd., North Ryde, NSW, Australia). The organic electrolyte salt was prepared by metathesis of bis(triphenylphosphoranylidene)ammonium chloride (BTPPACl) and potassium tetrakis(4-chlorophenyl)borate (KTPBCl). The organic phase was mechanically stabilized as a polymer gel [38–41] and was composed of the supporting electrolyte (10 mM BTPPATPBCl) and low molecular weight poly(vinylchloride) (PVC) (10% w/v), dissolved in 1,6-dichlorohexane. Prior to the experiments, both the aqueous and organic phase solvents were mutually pre-saturated. The organic reference solution consisted of 10 mM BTPPACl dissolved in 10 mM LiCl (aqueous). Ractopamine hydrochloride and tetrapropylammonium chloride (TPrACl) served as the drug and model analyte species studied, respectively. A stock solution of TPrACl was prepared in 10 mM LiCl while the stock solution of ractopamine hydrochloride was prepared in methanol (MeOH) due to its low solubility in water [15].

In the interfering substances study, the interferents were prepared in 1 mM PBS solution as the supporting electrolyte, which contained 1 mM phosphate buffer, 0.27 mM potassium chloride (KCl) and 13.7 mM NaCl. D-Glucose, L-ascorbic acid, KCl, NaCl, Na_2SO_4, glycine and urea were the interfering substances studied, and the

concentration of each of these was fixed at 5.0 mM. The effect of artificial serum matrix [25,42,43] on the detection of $RacH^+$ was also investigated. The artificial serum used was composed of 1.5 mM KCl, 5.0 mM calcium chloride ($CaCl_2$), 1.6 mM magnesium chloride ($MgCl_2$), 4.7 mM D-glucose, 1.0 mM sodium phosphate monobasic (NaH_2PO_4), 1.0 mM KH_2PO_4, 2.5 mM urea and 0.6 mM bovine serum albumin, prepared in ultrapure water.

2.2. Preparation of micro-interface arrays

The micropore arrays used for micro-ITIES patterning were fabricated in 100 μm thick silicon membrane by lithographic patterning and wet and dry silicon etching methods at Tyndall National Institute, University College Cork, Cork, Ireland [41]. The micropores are depicted in Fig. 1(b) and (c), with 11.09 ± 0.12 μm radius, r_a, 30 pores in a hexagonal close-packed arrangement, and with pore centre-to-centre separation, r_c, of 18.4 ± 2.1 times the pore radius, r_a (i.e. $r_c = 18.4 r_a$). The silicon chip (5 mm × 5 mm) was sealed onto the lower orifice of a cylindrical glass tube ($d_{inner} = 2.5$ mm, $d_{outer} = 4.0$ mm) using silicone rubber sealant (Selleys, Australia and New Zealand) and allowed to cure for 72 h before use. The membrane was cleaned with acetone and dried in air before and after each electrochemical experiment. All the experiments were conducted at room temperature (20 °C).

2.3. Experimental procedure at the micro-ITIES array

The electrochemical techniques were performed using an Autolab PGSTAT 302N (Metrohm, The Netherlands) together with the Nova 1.7 or Nova 1.8 software supplied with the instrument. The electrochemical cell was housed in a Faraday cage for the duration of the experiment to minimize electrical noise. A two-electrode electrochemical cell was employed in this study since the *IR* drop effect at micro-ITIES system is not too high as compared to macro-ITIES system [44]. Both Ag|AgCl electrodes served as reference and counter electrodes in either phase. The applied potential, *E*, is defined as the potential difference between the two electrodes, with positive current due to the transfer of cations from the aqueous to the organic phase [20].

The borosilicate glass tube with membrane sealed to one end with silicone sealant contained 100 μL of the gellified-organic phase and 200 μL of the organic reference solution. This was then immersed in 6 mL of the aqueous phase solution in a 10 mL glass beaker. The electrochemical cells employed in this study can be schematically summarized as follows:

Ag|AgCl|*x* M ractopamine HCl + 10 mM $LiCl_W$||10 mM $BTPPATPBCl_{DCH}$|10 mM BTPPACl in 10 mM $LiCl_W$|AgCl|Ag	Cell 1
Ag|AgCl|0.1 mM ractopamineHCl + 5 mM interfering substance + 10 mM $LiCl_W$||10 mM $BTPPATPBCl_{DCH}$|10 mM BTPPACl in 10 mM $LiCl_W$|AgCl|Ag	Cell 2
Ag|AgCl|*x* M ractopamine HCl + artificial $serum_W$||10 mM $BTPPATPBCl_{DCH}$|10 mM BTPPACl in 10 mM $LiCl_W$|AgCl|Ag	Cell 3

where *x* is the concentration of ractopamine in the aqueous phase. In every electrochemical cell, $TPrA^+$ was spiked into the aqueous phase after the final $RacH^+$ or interferent injection, as a control of the potential axis.

Prior to the injection of analyte into the aqueous phase with a micropipette to achieve the required concentration, a background CV at 5 mV s^{-1} was recorded over a wide potential range so as to establish the limits of the available potential window. A quiet time of 5 s at the initial potential of each scan was implemented. In LSSV, the parameters pre-concentration potential, pre-concentration time and sweep rate were explored to determine the optimum values, and these were implemented in subsequent experiments.

3. Results and discussion

3.1. CV at the micro-ITIES array

CV profiles of 20 to 100 μM $RacH^+$ at the gelled micro-ITIES arrays (Cell 1) are presented in Fig. 2(a) and (b), in the form of experimental data and background-subtracted voltammograms, respectively. The p*K*a of the amine group in ractopamine is 9.4 [8], so that in the aqueous phase used in this work, 10 mM LiCl (pH ~ 6) [19,21], the drug is cationic. The CVs show that $RacH^+$ ions, which are initially present in the aqueous phase, are transferred into the gelled organic phase under potential control, on the forward CV sweep. These ions are transferred back from the organic into the aqueous phase, during the reverse scan.

The shape and magnitude of the voltammetric response are highly dependent on factors such as the diffusion regime shape, the position of the ITIES within the pores, the properties of the electrolyte solutions and of the transferring ion species, and the magnitude of the diffusion zone extension (δ) [45,46]. The interfaces employed here were inlaid so that each pore was filled with the organic electrolyte solution and the interface was at the aqueous side of the membrane [45]. Generally, for an inlaid micro-ITIES array, steady-state voltammograms are obtained in the forward CV sweep, indicating establishment of radial diffusion fields, while peak-shaped voltammograms are obtained on the reverse scans, attributed to linear diffusion control.

However, in this study, the CVs on the forward scan show that the foot of the ion transfer wave was at a very positive applied potential difference (0.8 V), close to the upper limit of potential window (Fig. 2(a)). The current increased steadily with applied potential up to the switching potential, so that a fully-develop stead-state wave shape was not obtained. On the reverse scan, a peak-shaped feature was observed, due to the transfer of $RacH^+$ ions which had been retained within the micropores. The incorporation of PVC in the organic phase increases the viscosity, and hence slows down rate of diffusion of ions in the organogel [45], so that the diffusion coefficient of a target analyte in the gelled organic phase may be ca. nine-times lower than in the aqueous phase [45].

The background-subtracted currents on the forward and reverse scans (Fig. 2(b)) increased linearly with $RacH^+$ concentration in the aqueous phase, with the maximum currents chosen to construct the calibration graphs of the forward scan (Fig. 2(c)). Theoretically, the current of the forward scan can be modelled by the Saito equation [47,48] if a steady-state current (radial diffusion control) had been achieved. At the ITIES, the potential window is restricted by the transfer of background electrolyte ions [5]. However, in this study it was found that $RacH^+$ transfer occurred at a potential just below the transfer of the background electrolytes and steady-state current for $RacH^+$ transfer was not achieved.

Following the final $RacH^+$ experiment, 100 μM $TPrA^+$ was spiked into the aqueous phase (Fig. 2(a) inset—top, and (b) inset) as a model ion and a potential axis reference ion [19,49]. The resulting CV showed a steady-state behaviour on the forward scan, while the reverse scan demonstrated a peak shape, in agreement with previous experiments and computer simulations [45]. This micro-ITIES array thus displayed the expected mass-transport behaviour. The foot of the ion transfer wave, and the half-wave potential were observed at approximately 0.45 and 0.52 V,

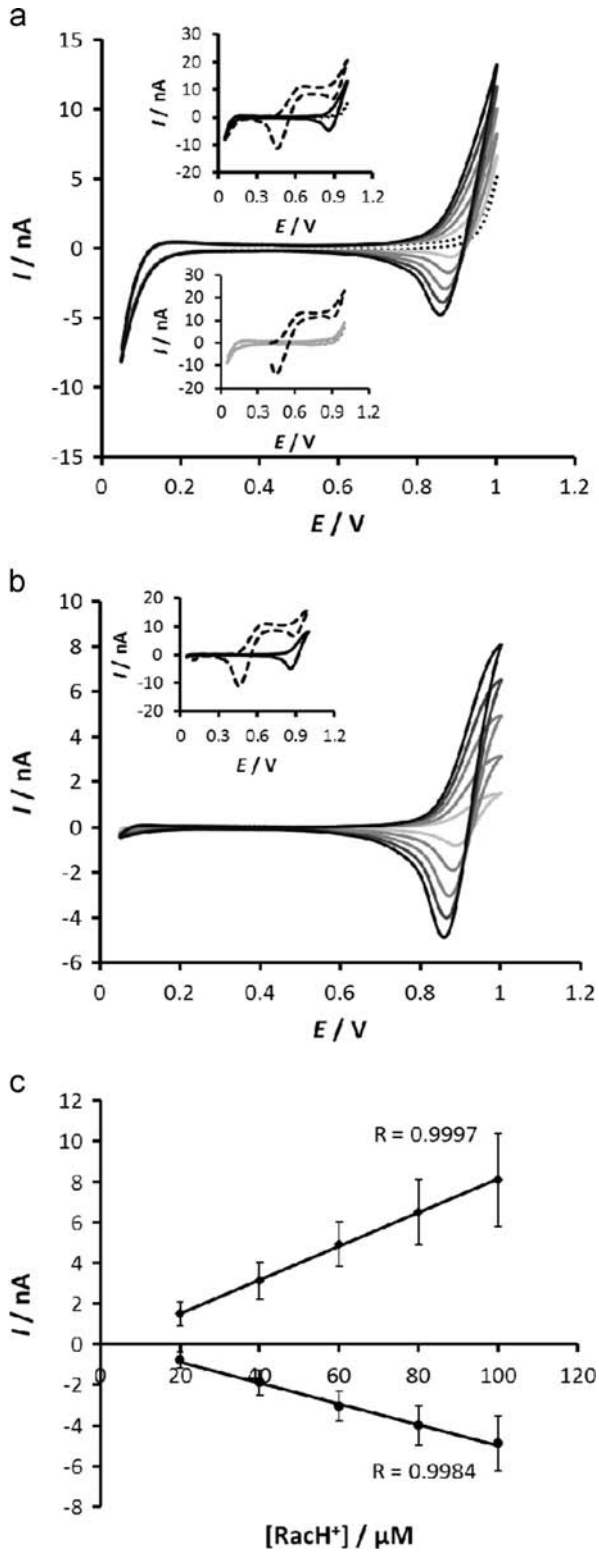


Fig. 2. Cyclic voltammograms of 20 (light gray) to 100 μM (black) $RacH^+$ transfer, in increment of 20 μM (a) and its corresponding background-subtracted CV (b) at 5 mV s^{-1} sweep rate. Inset (a—upper) and (b): voltammograms of blank (dotted line) and 100 μM $RacH^+$ with (dashed line) and without (solid black line) the addition of $TPrA^+$. Inset (a—lower) is a control experiment with 100 μM MeOH (solid gray line) added to the aqueous phase. (c) The corresponding calibration curve of the maximum currents (forward scan) and peak currents (reverse scan) against $RacH^+$ concentrations.

respectively, in agreement with previous studies [25,48]. The formula to calculate the steady-state current (limiting current) for ion transferring from the aqueous to the organic phase is given by the Saito equation modified for the number of micropores in the membrane [47]:

$$I_{ss} = 4zFDCr_aN_p \quad (1)$$

where I_{ss} is the steady-state current, z, D and C are the charge, diffusion coefficient and bulk concentration, of the transferring ions in the aqueous phase, correspondingly. F is the Faraday constant (96,487 C mol^{-1}) and N_p is the number of micropores. The steady-state experimental current was within ca. 10% of the current obtained from Eq. (1). This may indicate that the interfaces formed at the micropore mouths were not flat, in turn enhancing the radial diffusion to the interfaces so that the current is increased. The steady-state current for radial diffusion to an array of hemispherical micro-ITIES is given by [50,51]:

$$I_{ss} = 2\pi zFDCr_aN_p \quad (2)$$

However, in this case the experimental current was ca. 30% lower than that calculated from Eq. (2). This indicates that the μITIES were closest to inlaid microinterface behaviour.

There is a lack of information in the literature on the diffusion coefficient of ractopamine. Attempts to determine this from the oxidation response at glassy carbon electrode were not successful, due to the problems associated with fouling of the surface, probably by the adsorption of either the drug or its oxidation products. A similar fouling problem was reported previously for salbutamol oxidation at glassy carbon electrodes [52]. Therefore, an assumption of the diffusion coefficient value was made based on the published data for salbutamol sulfate ($D = 3.3 \times 10^{-6}$ cm^2 s^{-1}) [53], since ractopamine and salbutamol are a group of β-adrenergic agonist which possess similar chemical structures and functions [16]. Use of this value in Eq. (1) produced a steady-state current for the transfer of $RacH^+$ across microITIES array that was lower than the maximum current in the forward scan, suggesting the need for an accurate diffusion coefficient value.

A final control experiment was the impact of methanol on the CV, because the ractopamine stock solution was prepared in MeOH (see lower inset in Fig. 2(a)). The same injection volume used to prepare 20 to100 μM of analyte was applied. It was observed that the addition of MeOH had no observable effect on the analyte CV.

3.2. Thermodynamic parameters of $RacH^+$ transfer at the water | DCH interface

A number of thermodynamic parameters for the drug transfer were determined from the CV data. These are listed in Table 1.

The value of the formal transfer potential of an ionised drug is obtained by transposing the measured experimental value to the Galvani potential scale, as given by the following expression [54–58]:

$$E_{1/2}\,(\text{drug}) - \Delta_o^w\varnothing^{0'}(\text{drug}) = E_{1/2}\,(\text{TPrA}^+) - \Delta_o^w\varnothing^{0'}(\text{TPrA}^+) \quad (3)$$

where $\Delta_o^w\varnothing^{0'}(\text{TPrA}^+)$ is the formal transfer potential of the $TPrA^+$ ion. $E_{1/2}$ (drug) and $E_{1/2}$ ($TPrA^+$) are the experimental half-wave potentials of the drug and $TPrA^+$ transfer, respectively. In this study, a value of −0.086 V was used for $\Delta_o^w\varnothing^{0'}(\text{TPrA}^+)$ [59]. $TPrA^+$ ion was selected as a model ion since the transfer potential differs from that of $RacH^+$ and there is no mutual interference.

The Gibbs energy of transfer is directly related to the formal transfer potential of the ion transfer [60]. The ability to measure this value depends on the condition that the transferring ion has a lower magnitude of the Gibbs transfer energy than the ions of the supporting electrolytes [58,61]. However, for $RacH^+$, the ion of interest transfers at the upper limit of the potential window so that the experimental measurement of the half-wave potential ($E_{1/2}$ (drug)) was not possible. A similar observation was reported

Table 1
Thermodynamic data for the transfer of cationic β-agonist drug, protonated ractopamine ($RacH^+$) at the micro-water | DCH interface arrays.

Parameter	Value
p*K*a	9.4[a]
$\Delta_0^w\varnothing^{0'}$	~0.29 V (in DCH)
$\Delta G_{tr}^{0',w\to DCH}$	27.88 kJ mol^{-1}
log P_{DCH}^0 (ionised)	−4.89
log P_{n-oct}^0	2.4[b]

[a]Data obtained from Ref. [8].
[b]Data obtained from Ref. [74].

by Osborne and Girault [58] for the transfer of ammonium ions across a water | 1,2-dichloroethane (DCE) interface and by Cacote et al. [62] for the direct transfer of Ag^+ ions across a water | DCE interface. A method to determine the $E_{1/2}$ of the species limiting the potential window was developed by Shao et al. [61], which was based on a set of simulated CVs in which the switching potential is set prior to the forward peak potential. The half-wave potential of the species limiting the potential window was then determined from the resultant working curve, which was a plot of I_{eos}/I_{rp} versus $E_{rp}-E_{1/2}$, where I_{eos} and I_{rp} are the current at the end of the forward scan and the return peak current, respectively, E_{rp} is the return peak potential and $E_{1/2}$ is the half-wave potential. However, the published working curve applied was developed for an ITIES subjected to linear diffusion on both forward and reverse transfer processes and hence is not applicable to the present situation. Our approach was to compare the shape of the experimental CV for $RacH^+$ transfer to that for $TPrA^+$ transfer recorded with different switching potentials [63,64]. Finding a shape for the model ion transfer process which match to that for $RacH^+$, by visual comparison, allowed the $E_{1/2}$ for the ionised drug transfer to be determined by assuming that similar current ratios and potential ratios apply to both ions (i.e. that they have similar transfer kinetics and are not distorted by experimental variables such as cell resistance and capacitance). The $E_{1/2}$ of the $RacH^+$ ion was estimated in this way to be 0.9 V. Taking into account the assumption that Walden's rule ($D^o/D^w=\eta^w/\eta^o$) applies to the transfers of $RacH^+$ and $TPrA^+$, the Galvani transfer potential of $RacH^+$ is obtained using Eq. (3) to be 0.29 V (Table 1) [58].

The formal Gibbs energy of transfer of any ionic species is expressed as [24,44,58]:

$$\Delta_o^w\varnothing^{0'}=\frac{\Delta G_{tr}^{0',w\to o}}{zF} \quad (4)$$

where $\Delta G_{tr}^{0',w\to o}$ is the formal Gibbs transfer energy of ion from the aqueous (w) to the organic (o) phase. The calculated value is presented in Table 1. The formal Gibbs energy of transfer of $RacH^+$ was 27.9 kJ mol^{-1} across a water | DCH interface. Values of 18.3 and 7.7 kJ mol^{-1} have been reported previously for protonated pyridine (PyH^+) transfer across a water | 2-nitrophenyl octyl ether (NPOE) interface, and protonated quinidine (QH^+) transfer across a water | DCE interface, respectively.

Another important thermodynamic parameter is the partition coefficient (log P) of a given solute between two immiscible solvents. This is a measurement of its relative affinity for the two phases, and is related to the free energy of transfer of the solute between the two solvents [24,65]. The measurement of the ionised drug partition coefficient is vital since most drugs (>70%) are ionisable under physiological conditions [44]. In this case, the partition coefficient of $RacH^+$ between water and DCH is obtained from Eq. (5) [19,44,60]:

$$\log P_{DCH}^0(\text{ionised})=-\frac{\Delta G_{tr}^{0',w\to o}}{2.3RT} \quad (5)$$

where R is the gas constant (R=8.31 J K^{-1} mol^{-1}) and T is the temperature in kelvin. The partition coefficient of the $RacH^+$ was −4.9 (Table 1), while the value for $DNRH^+$ was −8.0 [19], both for the water | DCH system. Comparison of the partition coefficients of the neutral form of both drugs in *n*-octanol–water systems shows that the log P_{n-oct}^0 value for daunorubicin was higher than that for ractopamine, meaning that ractopamine is more hydrophilic, since a lower partition coefficient value indicates a more hydrophilic property [19]. A review of the electrochemical investigations made on the transfer of ionisable drugs at ITIES to determine their partition coefficients employing voltammetric methods for water | nitrobenzene (NB), water | NPOE, and water | DCE systems does not include any data for the water | DCH system [22], as this has been introduced only relatively recently [59].

3.3. Optimisation of the LSSV parameters for the detection of $RacH^+$

In order to detect lower concentrations, LSSV was employed, as this entails a pre-concentration step that enhances sensitivity. In the pre-concentration step, $RacH^+$ was extracted from the aqueous to the organogel phase under potential control. Then, the pre-concentrated analyte was stripped out of the organogel using a voltammetric scan [21,37]. The pre-concentration step is important in LSSV as it enables the detection of lower concentrations relative to CV. This stripping analysis method is reported to offer greater sensitivity and lower detection limits, down to nanomolar and parts per billion levels [37]. As a result, the optimisation of LSSV parameters, namely the sweep rate, the pre-concentration potential and the pre-concentration time, was explored, employing Cell 1. Voltammetric scans were conducted in the negative direction, from 1.0 to 0.4 V.

To assess the impact of sweep rate on the results (figure not shown), the sweep rate value was varied between 5 and 100 mV s^{-1}, using 100 μM $RacH^+$. The pre-concentration potential was fixed at 1.0 V while the pre-concentration time was set at 60 s. A blank LSSV was recorded in the absence of analyte, so that background-subtracted LSSV could be obtained by subtracting the blank response from that of the analyte. The stripping peak current was found to be linearly-dependent on the square root of the sweep rate, indicating a linear diffusion-controlled organic phase to aqueous phase transfer process [41]. Despite this result, it was found that lower sweep rates produced a more clearly-defined peak shape, consistent with peak distortion by cell resistance and capacitance at the higher sweep rates. Consequently, all subsequent experiments employed a sweep rate of 5 mV s^{-1} since this sweep rate produced a well-defined peak shape with less sensitivity to these distortions.

The influence of the pre-concentration potential was studied by employing 20 μM $RacH^+$ with a 60 s pre-concentration time, while varying the pre-concentration potential from 0.60 to 1.00 V in increment of 0.05 V (Fig. 3). From the inset graph, it can be seen that the stripping peak current only appeared when the pre-concentration potential was higher than 0.85 V. As observed earlier by CV, $RacH^+$ transfers at an applied potential very close to upper limit of the potential window. The maximum stripping peak current was observed when the pre-concentration potential was 1.00 V, thus this potential was applied for all subsequent experiments.

The influence of pre-concentration time was studied at 1.00 V pre-concentration potential using 100 μM $RacH^+$, with variations in the pre-concentration time from 15 to 180 s. Over the time range of 0–1 min, the increment was 15 s, while in the range 1–3 min, the time increment was increased to 30 s (Fig. 4). The stripping peak

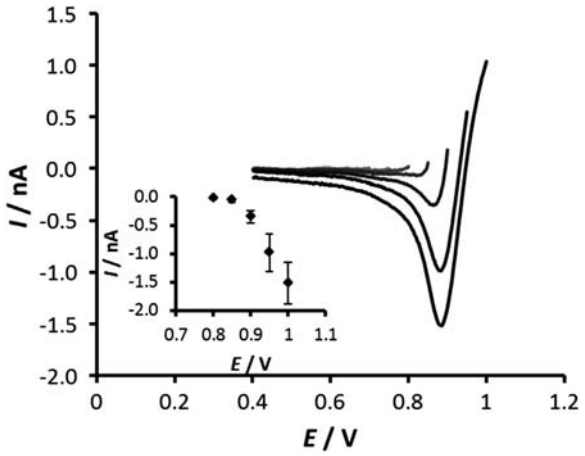


Fig. 3. Influence of pre-concentration potentials from 0.6 V (light gray) to 1.0 V (black) in increment of 0.05 V on the LSSV (background-subtracted) of 20 μM $RacH^+$. The pre-concentration time and sweep rate were fixed at 60 s and 5 mV s^{-1}, respectively. Inset: graph of current at selected pre-concentration potentials of 0.80, 0.85, 0.90, 0.95 and 1.00 V.

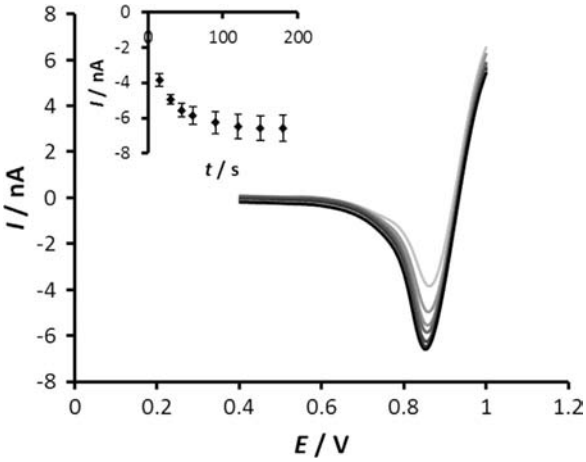


Fig. 4. Influence of pre-concentration times on the LSSV (background-subtracted) of 100 μM $RacH^+$. The pre-concentration potential and sweep rate were fixed at 1.0 V and 5 mV s^{-1}, respectively. LSSV response of 15 (light gray), 30, 45, 60, 90, 120, 150 and 180 s (black) pre-concentration times. Inset: calibration graph of peak current versus pre-concentration times.

current increased as the pre-concentration time increased, eventually reaching a constant value, as illustrated in the inset graph. This effect was reported previously for the detection of propranolol [21] and oligopeptides [39] at the micro-ITIES array, and was attributed the diffusion of analyte away from the interface to the bulk organic phase during the longer pre-concentration times. Therefore, during stripping step, these analytes are not stripped back to the aqueous phase and do not contribute to the stripping peak [37]. The optimum pre-concentration time of 120 s was selected and applied in all subsequent experiments.

3.4. LSSV analysis at the micro-ITIES array

Employing all of the optimised parameters (5 mV s^{-1} sweep rate, 1.00 V pre-concentration potential, 120 s pre-concentration time), low concentrations of $RacH^+$ in the range 0.1–1.0 μM were analysed and a calibration graph was plotted of stripping peak current versus concentration of $RacH^+$ (Fig. 5). The increase in $RacH^+$ concentration resulted in an increase of the stripping peak current, with a linear concentration dependence observed within the range studied, ($I_p = -0.2718$ (nA μM^{-1}) (concentration) -0.0974 (nA), $R = 0.9964$, $n = 6$). The calculated limit of detection

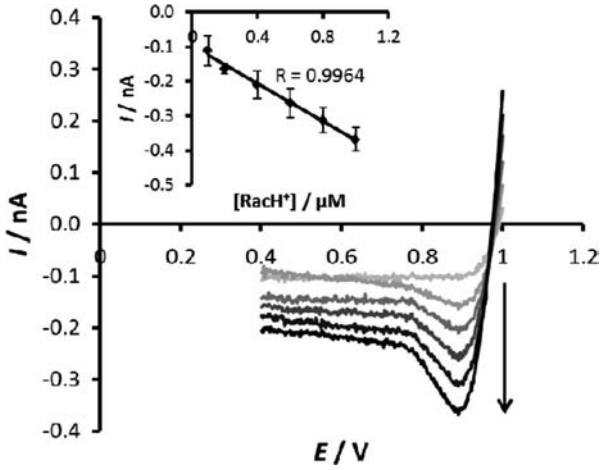


Fig. 5. Background-subtracted LSSV scans of increasing $RacH^+$ concentrations in the aqueous phase (indicated by arrow) at the micro-ITIES arrays at 5 mV s^{-1} sweep rate. LSSV response of 0.1 (light gray), 0.2, 0.4, 0.6, 0.8 and 1.0 μM (black) drug concentrations. Inset is the calibration curve of stripping peak current versus concentration.

(LOD) is 0.1 μM (34 ng mL^{-1}), based on 3 times the standard deviation of the blank ($3s_b$) [66]. This compares well with previously published values. LODs of 1.17 μM (CV and electrochemical impedance spectroscopy at a modified electrode) [67], 0.06 μM (DPV at a carbon nanotube-modified glassy carbon electrode (GCE)) [6], 0.05 μM (DPV at a graphene oxide-modified GCE) [13], and 0.06 μM (DPV at an ordered mesoporous carbon-modified GCE) [7] have been reported for ractopamine.

3.5. Influence of potentially interfering substances

Possible interferences in the detection of $RacH^+$ were investigated using substances such as a sugar, ascorbic acid, metal ions, an amino acid and urea [6,7,19,68]. These substances were selected since they are all models of substances likely to be present in a biological sample. This study was conducted using CV. The aqueous phase of the electrochemical cell (setup as in Cell 2) was spiked with the $RacH^+$ and individual interference substances at concentrations of 0.1 and 5.0 mM, respectively. The current signal for 0.1 mM $RacH^+$ was individually measured in the absence and presence of the interfering substances, and the current change was then determined. In addition, $TPrA^+$ was spiked to every aqueous test phase as a model ion and a potential axis reference ion. The results obtained are summarised in Fig. 6 and in Table 2.

Glucose was chosen as a model of possible sugar interference. Since it is an uncharged molecule and hence does not provide a current for transfer across the water | DCH interface, it is not expected to impact on the detection of $RacH^+$ since no ion transfer signal was detected (Fig. 6(a)). The potential interference of ascorbic acid was also investigated, and no transfer of ascorbate was observed (Fig. 6(b)). Ascorbic acid (p*K*a of 4.17 [19]) was de-protonated in the aqueous phase. The possible interference of metal ions such as K^+ and Na^+ were also evaluated. Metal ions, in particular K^+ and Na^+, are expected to transfer at the positive end of the potential window, which results in a decrease of the potential window [19,49,69]. Additions of KCl (Fig. 6(c)), NaCl (Fig. 6(d)) and Na_2SO_4 (Fig. 6(e)) to the aqueous phase did alter the $RacH^+$ ion transfer signal, in agreement with previous reports [19,69], with KCl having the greatest impact. Glycine was used as a model amino acid interferent and is widely reported in interference studies [6,7,19]. At physiological pH, glycine is a net neutral molecule hence it should not show any ion transfer behaviour at the interface (Fig. 6(f)) [19]. However, there was a slight increase in current at the positive end of the potential window when glycine was added. Note that although amino acids can be

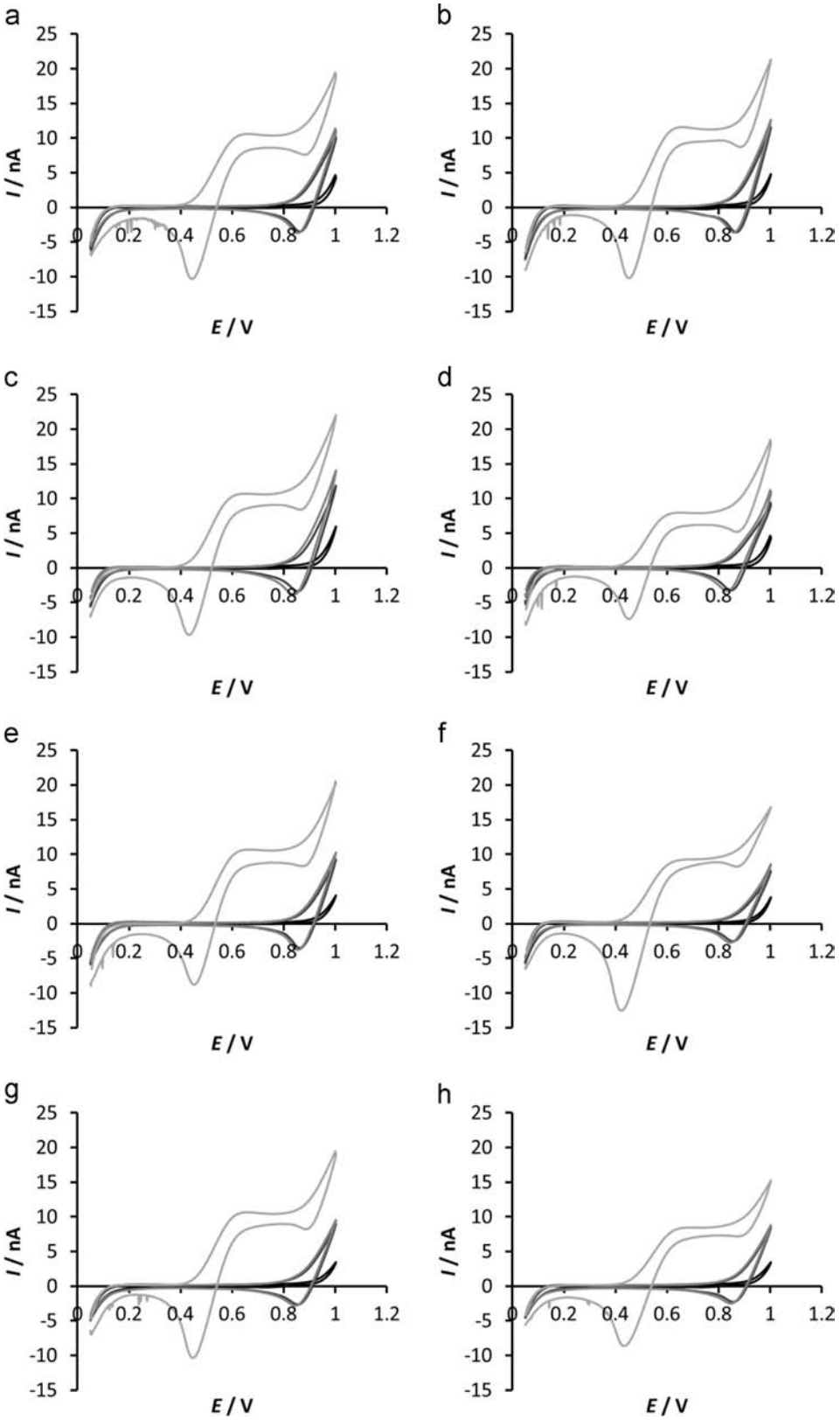


Fig. 6. Electrochemistry of the individual interfering substances at the micro-ITIES arrays. Cyclic voltammograms of the blank aqueous phase solution (10 mM LiCl) (black line), the aqueous phase spiked with 100 μM $RacH^+$ (dark gray line), the aqueous phase spiked with 100 μM $RacH^+$ and the interfering substances (medium gray line), and the aqueous phase spiked with 100 μM $RacH^+$, the interfering substances and 100 μM $TPrA^+$ (light gray line). The interfering substances studied: (a) D-glucose (b) L-ascorbic acid (c) KCl (d) NaCl (e) Na_2SO_4 (f) glycine (g) urea, and (h) PBS solution in the absence of the interfering substance (control). The interfering substance concentration in all cases was 5.0 mM, and run at 5 mV s^{-1} sweep rate.

Table 2
Influence of potentially interfering substances on the detection of protonated ractopamine ($RacH^+$) at the micro- water | DCH interface array. The concentration of $RacH^+$ and interfering substance in all cases were 0.1 mM and 5.0 mM, respectively. In the forward scan, the current was measured at the end of the scan, while in the reverse scan the minimum peak current was selected.

Interfering substance	Forward scan			Reverse scan		
	I_{RacH^+}/nA ($\pm$ s; n=3)	$I_{(RacH^+ + Interferent)}$/nA ($\pm$ s; n=3)	Relative difference (%)[a]	I_{RacH^+}/nA ($\pm$ s; n=3)	$I_{(RacH^+ + Interferent)}$/nA ($\pm$ s; n=3)	Relative difference (%)[a]
Glucose	9.9 $\pm$ 0.17	10.9 $\pm$ 0.10	10.3	3.5 $\pm$ 0.09	3.7 $\pm$ 0.03	6.0
Ascorbic acid	11.6 $\pm$ 0.12	12.6 $\pm$ 0.13	9.2	3.5 $\pm$ 0.05	3.6 $\pm$ 0.02	0.7
KCl	11.9 $\pm$ 0.07	14.1 $\pm$ 0.07	19.2	3.4 $\pm$ 0.05	3.9 $\pm$ 0.01	16.1
NaCl	9.1 $\pm$ 0.10	10.8 $\pm$ 0.04	18.9	3.2 $\pm$ 0.04	3.3 $\pm$ 0.01	3.4
Na_2SO_4	9.3 $\pm$ 0.16	10.3 $\pm$ 0.07	10.7	3.5 $\pm$ 0.06	3.8 $\pm$ 0.02	7.6
Glycine	7.6 $\pm$ 0.08	8.6 $\pm$ 0.01	13.1	2.5 $\pm$ 0.06	2.7 $\pm$ 0.03	8.8
Urea	9.0 $\pm$ 0.10	9.5 $\pm$ 0.08	6.2	2.6 $\pm$ 0.08	2.8 $\pm$ 0.05	6.1
PBS	8.4 $\pm$ 0.05	8.8 $\pm$ 0.03	4.4	2.3 $\pm$ 0.05	2.5 $\pm$ 0.03	9.6
Mean ($\pm$ s; n=8)	9.6 $\pm$ 1.47	–	–	3.1 $\pm$ 0.52	–	–

s=Standard deviation.
[a]Relative difference (%) $= \frac{I_{(RacH^+ + Interferent)} - I_{RacH^+}}{I_{RacH^+}} \times 100\%$

transferred across the ITIES [70], a low pH (pH $\leq$ 1.0) is required to ensure complete protonation of the amino acid, and an ionophore must be used to facilitate the transfer process. The possible interference of urea was also investigated (Fig. 6(g)). Urea did not show a transfer signal at the interface, since it is a neutral compound [71]. In addition, a control experiment to assess the impact of the PBS solution on the interfering substance CVs was conducted, since all the interfering substance stock solutions were prepared in PBS solution (Fig. 6(h)). The same injection volume as used to prepare 5.0 mM of interfering substance was applied. The addition of PBS was observed to have a minimal impact on the interfering substance's CV.

The current changes in the presence of interfering substances (% Relative difference, Table 2) were in the range of 6.2 to 19.2%, and 0.7 to 16.1%, based on the forward and reverse scan currents of $RacH^+$, respectively. The forward current is more sensitive to the presence of potentially-interfering substances than the reverse scan. Substances not expected to interfere produced a ~10% current increase in the forward scan. For both scans, KCl (Fig. 6(c)) demonstrated the highest current change. In all cases, the results exhibited 3% relative standard deviation (% RSD) from repeated measurements on a single electrochemical cell (n=3). Table 2 also summarises the total variation in the $RacH^+$ signal in the absence of potentially interfering substances (% RSD of 15.3 and 16.9% for the forward and reverse scans, respectively), which reflects the experimental day-to-day reproducibility of the experiments.

In addition, the background current signal demonstrated % RSD of 16.3, 19.3 and 10.3%, measured at the minimum, maximum and within the 'polarisation range' (at 0.6 V) potentials, respectively, based on the blank CVs shown in Fig. 6. On the other hand, the $TPrA^+$ current signal demonstrated % RSD of 15.8 and 12.7%, measured at the minimum reverse peak and maximum forward current for this ion (~0.6 V), respectively. Again, the variation in signals reflects the day-to-day reproducibility within the experiments.

Based on these observations, only potassium was seen to have a major impact on the detection of $RacH^+$, and none of the other substances produced ion transfer peaks. Furthermore, since the reverse peak is less impacted than the forward current, use of a stripping voltammetry approach is suggested.

3.6. Determination of $RacH^+$ in artificial serum

The determination of $RacH^+$ in artificial serum as the aqueous phase electrolyte solution was conducted using Cell 3. In this study, two types of artificial serum solutions were prepared; the first contained no BSA, while the second contained BSA at physiological concentration. These solutions were utilised to investigate the possibility that BSA can impede the detection of $RacH^+$, as reported previously for other ionised drugs at the ITIES [25,35].

Several ways have been identified for BSA to hinder the detection process: potential window shortening, drug–protein binding [25,72] or protein adsorption at the interface [25,35]. BSA is a water-soluble globular protein which has a net charge of ~ −17 at physiological pH (of 7.4) [36], while $RacH^+$ has a charge of +1. These opposite charges contribute to ractopamine-albumin binding, although the binding effect will reduce through shielding from the electrolyte ions. Zhang et al. [72] reported that ractopamine bound to BSA mainly by electrostatic and hydrophobic interactions. The formation of the ractopamine-albumin complex was spontaneous and the strong interactions indicated that the drug has a long residence time in blood plasma. Additionally, BSA may adsorb to the ITIES. Collins et al. reported that BSA diminished the signal of ionised propranolol in artificial serum, although detection was still possible [25]. Vanysek and Sun demonstrated that the transfer of Cs^+ ion across a water | NB interface was inhibited by the adsorption of BSA on the interface [35]. Plasma proteins such as albumin have been reported to be a major source of interference in plasma measurement at the ITIES [19,73].

CV of the two artificial serum matrices was carried out with the addition of 100 μM $RacH^+$. Prior to that, a background CV was run over a wide potential range to establish the limits of the available potential window (Fig. 7(a) and (b)). Incorporation of BSA in the artificial serum decreased the width of the potential window to 850 mV, from 950 mV in its absence. Since BSA shortened the potential window at the upper limit (Fig. 7(b)), the detection of ractopamine might be hindered as $RacH^+$ transfers at a very positive applied potential difference, close to the upper limit of the potential window, in the LiCl solution. It was observed that the $RacH^+$ transfer was possible in artificial serum without BSA. The protonated drug transferred close to the positive limit of the potential window on the forward scan, while on the reverse scan, a peak-shaped feature was obtained (Fig. 7(c)). A calibration curve in artificial serum solution without BSA was obtained by plotting the background-subtracted current (both forward and reverse scans) versus the $RacH^+$ concentration. The background-subtracted currents on both the forward and reverse scans increased proportionally with $RacH^+$ concentrations over the range studied (Fig. 7(c) inset).This is in agreement with the result obtained in aqueous LiCl electrolyte.

In contrast, no $RacH^+$ transfer was observed in artificial serum containing BSA (0.6 mM). A small current increment was observed on the forward scan, however no peak-shape feature was observed on the reverse scan (Fig. 7(d)). Since the current signal varied

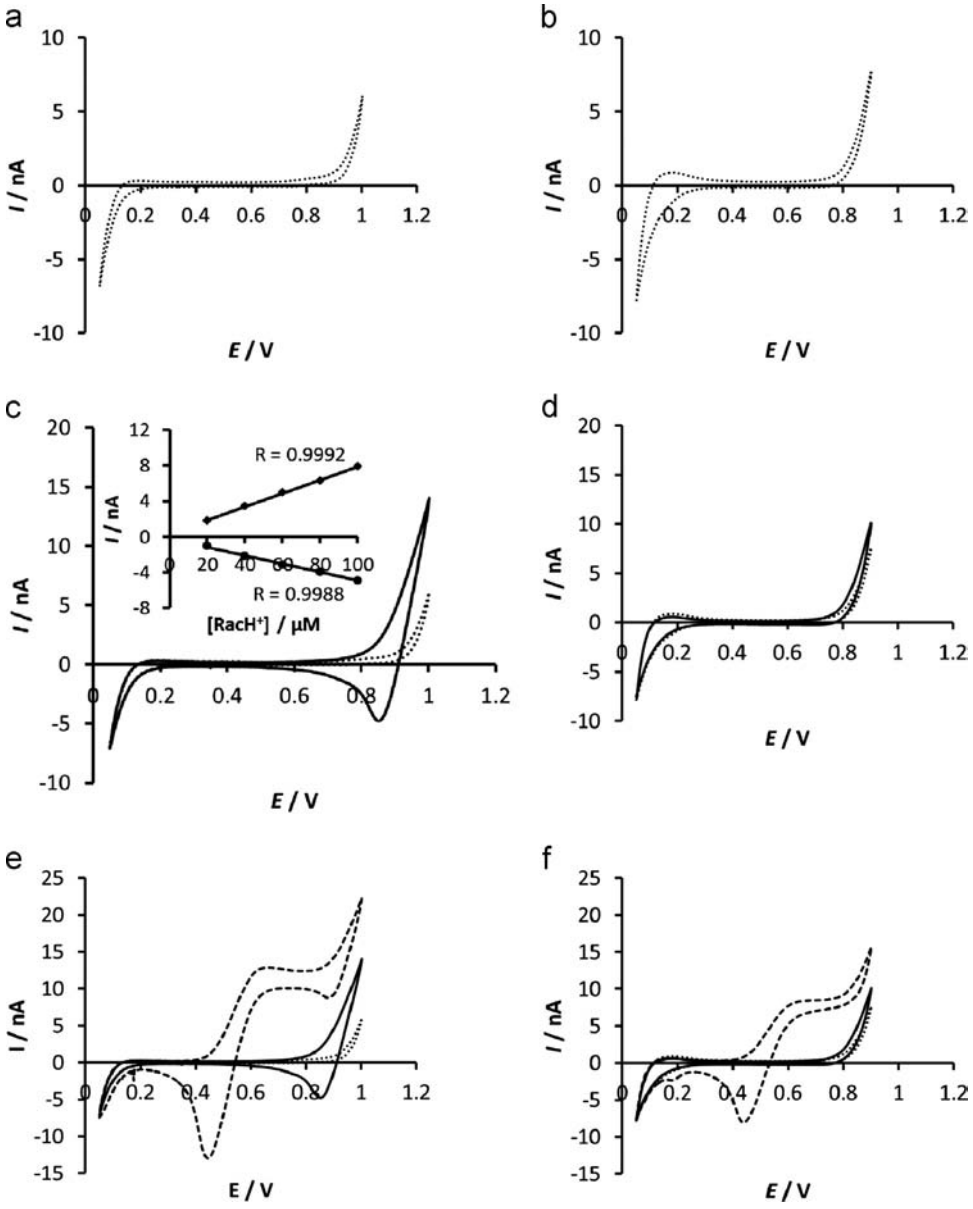


Fig. 7. Cyclic voltammetry at the micro-ITIES array of an artificial serum solution in the aqueous phase ((a) and (b)), 100 μM $RacH^+$ in an artificial serum solution ((c) and (d)), and an artificial serum solution of 100 μM $TPrA^+$ and 100 μM $RacH^+$ ((e) and (f)). Figures (a), (c) and (e) represent cyclic voltammetry of an artificial serum without BSA, while figures (b), (d) and (f) represent cyclic voltammetry in the presence of 0.6 mM BSA. Sweep rate applied was 5 mV s^{-1}. Inset in (c) is the corresponding calibration curve obtained for $RacH^+$ transfer on the forward and reverse scans.

linearly with the transferring analyte concentration, these results showed that the concentration of free $RacH^+$ in the aqueous phase was extremely low. This result is in agreement with previous studies which demonstrated that the presence of 1 mM BSA in artificial serum decreased the propranolol transfer current signal to ~6.4 nA, from ~9.7 nA in its absence [25].

In addition, $TPrA^+$ was also spiked into each artificial serum solution (Fig. 7(e) and (f)). No significant shift of the half-wave potential for the $TPrA^+$ ion was observed ($E_{1/2}$ of ~0.52 V) [25]. However, the steady-state current for $TPrA^+$ in the presence of BSA decreased from ~12.5 (no BSA present) to ~8.5 nA. A similar observation was also made on the reverse scan, where the peak current decreased from ~12.9 to ~7.9 nA in the absence and presence of BSA, respectively. This indicated that BSA adsorbed at the interface and inhibited ion transfer.

The results presented in this section demonstrate that reduction of the available potential window, complexation of the $RacH^+$ by BSA and adsorption of the BSA to the liquid | liquid interface, are the possible interference mechanisms for the detection of ractopamine in serum via ion-transfer voltammetry. Hence, deproteinisation of samples is necessary for this voltammetric analysis to be viable.

4. Conclusion

The voltammetric behaviour of the β-agonist drug, protonated ractopamine, at a water | DCH micro-interface array was investigated. The results show that protonated ractopamine can be detected via CV and LSSV. However, this drug transfers at a very positive potential, close to the positive limit of the available potential window; nevertheless, estimation of the half-wave potential enabled determination of some thermodynamic parameters for this drug, such as the Gibbs energy of transfer and the partition coefficient. In addition, a stripping voltammetry approach was employed successfully to detect

lower concentrations of the drug. The LOD was calculated to be 0.1 μM, which is suitable for applications to drug detection in real samples. Of a range of potentially interfering substances studied, only potassium ions were found to interfere in $RacH^+$ detection, due to its transfer at a potential close to the positive potential limit. Additionally, it was found that BSA diminished the ractopamine signal via potential window reduction, drug–protein complexation and protein adsorption at the ITIES. The results presented here indicate that voltammetry at the micro-ITIES array can be used for detection and characterisation of ionised drugs that transfer at high applied potentials but that analysis of biological samples will require deproteinisation. In the future, an improved performance, such as a lower detection limit, might be achieved with an electrochemical cell that provides a wider potential window, which will enable a more efficient pre-concentration reaction to be implemented.

Acknowledgements

This work was supported by Curtin University and Malaysian Agricultural Research and Development Institute (MARDI), Malaysia. The authors thank Tyndall National Institute, Cork, Ireland, for the gift of the silicon microporous membranes. The authors acknowledge the use of equipment, scientific and technical assistance of the John de Laeter Centre, Curtin University which has been partially funded by the University, and by the State and Commonwealth Governments. Elaine Miller (Curtin University) is acknowledged for her assistance with SEM imaging.

References

[1] H.H. Girault, Charge transfer across liquid–liquid interfaces, in: J.O.M. Bockris (Ed.), Modern Aspects of Electrochemistry, Plenum Press, New York, NY, 1993, pp. 1–62.
[2] P. Vanysek, TrAC, Trends Anal. Chem. 12 (1993) 357–363.
[3] Z. Samec, Pure Appl. Chem. 76 (2004) 2147–2180.
[4] H.H. Girault, Electrochemistry at liquid–liquid interfaces, in: A.J. Bard, C.G. Zoski (Eds.), Electroanalytical Chemistry: A Series of Advances, CRC Press, Boca Raton FL, 2010, pp. 1–104.
[5] D.W.M. Arrigan, G. Herzog, M.D. Scanlon, J. Strutwolf, Bioanalytical applications of electrochemistry at liquid–liquid microinterfaces, in: A.J. Bard, C.G. Zoski (Eds.), Electroanalytical Chemistry: A Series of Advances, CRC Press, Boca Raton FL, 2013, pp. 105–178.
[6] Z. Liu, Y. Zhou, Y. Wang, Q. Cheng, K. Wu, Electrochim. Acta 74 (2012) 139–144.
[7] X. Yang, B. Feng, P. Yang, Y. Ding, Y. Chen, J. Fei, Food Chem. 145 (2014) 619–624.
[8] M.E. Turberg, J.M. Rodewald, M.R. Coleman, J. Chromatogr. B 675 (1996) 279–285.
[9] L. Shen, P. He, Electrochem. Commun. 9 (2007) 657–662.
[10] J. Pleadin, N. Perši, A. Vulić, D. Milić, N. Vahčić, Meat Sci. 90 (2012) 755–758.
[11] L. He, Y. Su, Z. Zeng, Y. Liu, X. Huang, Anim. Feed Sci. Technol. 132 (2007) 316–323.
[12] E.I. Shishani, S.C. Chai, S. Jamokha, G. Aznar, M.K. Hoffman, Anal. Chim. Acta 483 (2003) 137–145.
[13] C. Wu, D. Sun, Q. Li, K. Wu, Sens. Actuators, B 168 (2012) 178–184.
[14] W. Du, G. Zhao, Q. Fu, M. Sun, H. Zhou, C. Chang, Food Chem. 145 (2014) 789–795.
[15] W. Xiu-Juan, Z. Feng, D. Fei, L. Wei-Qing, C. Qing-Yu, C. Xiao-Gang, X. Cheng-Bao, J. Chromatogr. A 1278 (2013) 82–88.
[16] H. Wang, Y. Zhang, H. Li, B. Du, H. Ma, D. Wu, Q. Wei, Biosens. Bioelectron. 49 (2013) 14–19.
[17] X. Lu, H. Zheng, X.-Q. Li, X.-X. Yuan, H. Li, L.-G. Deng, H. Zhang, W.-Z. Wang, G.-S. Yang, M. Meng, R.-M. Xi, H.Y. Aboul-Enein, Food Chem. 130 (2012) 1061–1065.
[18] J. Blanca, P. Munoz, M. Morgado, N. Mendez, A. Aranda, T. Reuvers, H. Hooghuis, Anal. Chim. Acta 529 (2005) 199–205.
[19] J.A. Ribeiro, F. Silva, C.M. Pereira, Anal. Chem. 85 (2013) 1582–1590.
[20] J.A. Ortuno, A. Gil, C. Serna, A. Molina, J. Electroanal. Chem. 605 (2007) 157–161.
[21] C.J. Collins, D.W.M. Arrigan, Anal. Chem. 81 (2009) 2344–2349.
[22] H. Alemu, Pure Appl. Chem. 76 (2004) 697–705.
[23] F. Reymond, P.-A. Carrupt, B. Testa, H.H. Girault, Chem. Eur. J. 5 (1999) 39–47.
[24] G. Bouchard, P.-A. Carrupt, B. Testa, V. Gobry, H.H. Girault, Chem. Eur. J. 8 (2002) 3478–3484.
[25] C.J. Collins, C. Lyons, J. Strutwolf, D.W.M. Arrigan, Talanta 80 (2010) 1993–1998.
[26] P. Zhao, G. Zhu, W. Zhang, L. Zhang, Z. Liang, Y. Zhang, Anal. Bioanal. Chem. 393 (2009) 257–261.
[27] R. Mallik, M.J. Yoo, S. Chen, D.S. Hage, J. Chromatogr. B 876 (2008) 69–75.
[28] Q. Zhang, Y. Huang, R. Zhao, G. Liu, Y. Chen, Biosens. Bioelectron. 24 (2008) 48–54.
[29] Y.-J. Hu, Y. Liu, T.-Q. Sun, A.-M. Bai, J.-Q. Lu, Z.-B. Pi, Int. J. Biol. Macromol. 39 (2006) 280–285.
[30] X.M. He, D.C. Carter, Nature 358 (1992) 209–215.
[31] T.J. Su, J.R. Lu, Z.F. Cui, R.K. Thomas, J. Membr. Sci. 173 (2000) 167–178.
[32] P. Fechner, O. Bleher, M. Ewald, K. Freudenberger, D. Furin, U. Hilbig, F. Kolarov, K. Krieg, L. Leidner, G. Markovic, G. Proll, F. Pröll, S. Rau, J. Riedt, B. Schwarz, P. Weber, J. Widmaier, Anal. Bioanal. Chem. 406 (2014) 4033–4051.
[33] D.C. Carter, B. Chang, J.X. Ho, K. Keeling, Z. Krishnasami, Eur. J. Biochem. 226 (1994) 1049–1052.
[34] Y.-J. Hu, Y. Liu, Z.-B. Pi, S.-S. Qu, Bioorg. Med. Chem. 13 (2005) 6609–6614.
[35] P. Vanysek, Z. Sun, Bioelectrochem. Bioenerg. 23 (1990) 177–194.
[36] Q. Shi, Y. Zhou, Y. Sun, Biotechnol. Prog. 21 (2005) 516–523.
[37] G. Herzog, V. Beni, Anal. Chim. Acta 769 (2013) 10–21.
[38] J.A. Ortuño, C. Rueda, Sensors 7 (2007) 1185–1192.
[39] M.D. Scanlon, G. Herzog, D.W.M. Arrigan, Anal. Chem. 80 (2008) 5743–5749.
[40] M.D. Scanlon, J. Strutwolf, D.W.M. Arrigan, Phys. Chem. Chem. Phys. 12 (2010) 10040–10047.
[41] R. Zazpe, C. Hibert, J. O'Brien, Y.H. Lanyon, D.W.M. Arrigan, Lab Chip 7 (2007) 1732–1737.
[42] M. Cretin, L. Alerm, J. Bartroli, P. Fabry, Anal. Chim. Acta 350 (1997) 7–14.
[43] S. Makarychev-Mikhailov, A. Shvarev, E. Bakker, Anal. Chem. 78 (2006) 2744–2751.
[44] H.-T. Lam, C.M. Pereira, C. Roussel, P.-A. Carrupt, H.H. Girault, Anal. Chem. 78 (2006) 1503–1508.
[45] J. Strutwolf, M.D. Scanlon, D.W.M. Arrigan, Analyst 134 (2009) 148–158.
[46] T.J. Davies, R.G. Compton, J. Electroanal. Chem. 585 (2005) 63–82.
[47] Y. Saito, Rev. Polarogr. 15 (1968) 177–187.
[48] M. Sairi, J. Strutwolf, R.A. Mitchell, D.S. Silvester, D.W.M. Arrigan, Electrochim. Acta 101 (2013) 177–185.
[49] C.J. Collins, A. Berduque, D.W.M. Arrigan, Anal. Chem. 80 (2008) 8102–8108.
[50] K.B. Oldham, J. Electroanal. Chem. 122 (1981) 1–17.
[51] J. Heinze, Angew. Chem. Int. Ed. Engl. 32 (1993) 1268–1288.
[52] M.S.M. Quintino, L. Angnes, Talanta 62 (2004) 231–236.
[53] G. Wei, W. Lu, J. Zheng, Acta Pharm. Sin. 39 (2004) 232–235.
[54] E.S. Ferreira, A. Garau, V. Lippolis, C.M. Pereira, F. Silva, J. Electroanal. Chem. 587 (2006) 155–160.
[55] F. Reymond, V. Chopineaux-Courtois, G. Steyaert, G. Bouchard, P.-A. Carrupt, B. Testa, H.H. Girault, J. Electroanal. Chem. 462 (1999) 235–250.
[56] F. Reymond, G. Steyaert, P.-A. Carrupt, B. Testa, H.H. Girault, Helv. Chim. Acta 79 (1996) 101–117.
[57] G. Bouchard, P.-A. Carrupt, B. Testa, V. Gobry, H.H. Girault, Pharm. Res. 18 (2001) 702–708.
[58] M.D. Osborne, H.H. Girault, Electroanalysis 7 (1995) 425–434.
[59] H. Katano, M. Senda, Anal. Sci. 17 (2001) 1027–1029.
[60] R. Gulaboski, M.N.D.S. Cordeiro, N. Milhazes, J. Garrido, F. Borges, M. Jorge, C.M. Pereira, I. Bogeski, A.H. Morales, B. Naumoski, A.F. Silva, Anal. Biochem. 361 (2007) 236–243.
[61] Y. Shao, A.A. Stewart, H.H. Girault, J. Chem. Soc., Faraday Trans. 87 (1991) 2593–2597.
[62] M.H.M. Cacote, C.M. Pereira, L. Tomaszewski, H.H. Girault, F. Silva, Electrochim. Acta 49 (2004) 263–270.
[63] Z. Samec, V. Marecek, M.P. Colombini, J. Electroanal. Chem. 257 (1988) 147–154.
[64] A.-K. Kontturi, K. Kontturi, L. Murtomaki, D.J. Schiffrin, J. Chem. Soc., Faraday Trans. 86 (1990) 819–822.
[65] T. Nogrady, Medicinal Chemistry: A Biochemical Approach, second ed., Oxford University Press, Inc., New York, NY, 1988.
[66] J.C. Miller, J.N. Miller, Statistics for Analytical Chemistry, second ed., Ellis Horwood Limited, England, 1988.
[67] L.-J. Kong, M.-F. Pan, G.-Z. Fang, X.-l. He, Y.-k. Yang, J. Dai, S. Wang, Biosens. Bioelectron. 51 (2014) 286–292.
[68] J. Duan, D. He, W. Wang, Y. Liu, H. Wu, Y. Wang, M. Fu, S. Li, Talanta 115 (2013) 992–998.
[69] H. Katano, H. Tatsumi, M. Senda, Talanta 63 (2004) 185–193.
[70] Y. Chen, Y. Yuan, M. Zhang, F. Li, P. Sun, Z. Gao, Y. Shao, Sci. China, Ser. B Chem. 47 (2004) 24–33.
[71] M.D. Osborne, H.H. Girault, Electroanalysis 7 (1995) 714–721.
[72] Q. Zhang, Y. Ni, S. Kokot, J. Pharm. Biomed. Anal. 52 (2010) 280–288.
[73] J. Guo, Y. Yuan, S. Amemiya, Anal. Chem. 77 (2005) 5711–5719.
[74] National Institutes of Health, Hazardous Substances Data Bank: Ractopamine, ⟨http://toxnet.nlm.nih.gov⟩ (23/03/2014).

Talanta 132 (2015) 215–221

Contents lists available at ScienceDirect

Talanta

journal homepage: www.elsevier.com/locate/talanta

A carboxylated graphene and aptamer nanocomposite-based aptasensor for sensitive and specific detection of hemin

Ling Gao, Yinghong Xiao *, Yanping Wang, Xue Chen, Bo Zhou, Xiaodi Yang **

Jiangsu Key Laboratory of New Power Batteries, Jiangsu Collaborative Innovation Center of Biomedical Functional Materials, College of Chemistry and Material Science, Nanjing Normal University, Nanjing 210097, China

ARTICLE INFO

Article history:
Received 12 May 2014
Received in revised form
3 September 2014
Accepted 7 September 2014
Available online 16 September 2014

Keywords:
Carboxylated grapheme
Functionalized electrode
Nanocomposite aptasensor

ABSTRACT

A unique nanocomposite was crafted by grafting hemin-binding-aptamer (HBA) onto carboxylated graphene (COO-GR). Infrared spectroscopy, Raman spectroscopy and diffuse reflectance spectra suggested that –NHCO– covalent bonds were formed between HBA and COO-GR. The resulting COO-GR/HBA functionalized electrode was used as a novel label-free biosensor. The square wave voltammetry was employed to realize the selective and specific detection of hemin. The obtained aptasensor possessed excellent performance with a detection limit of 0.64 nmol L^{-1} ($S/N=3$) and a linear range from 1 to 150 nmol L^{-1}. Moreover, COO-GR was shown to be a promising candidate in making aptasensors, carrying advantages over graphene in terms of the simplicity of sensor preparation and the reduction of background noise.

© 2014 Elsevier B.V. All rights reserved.

1. Introduction

Aptamers are capable of binding specific target molecules with high selectivity and affinity. Due to the ease of production in vitro, wide target range, modification ease, reversible thermal denaturation and unlimited shelf life, aptamers are believed to be excellent alternatives to antibodies for recognizing proteins [1–3]. During the past decades, aptamers have been widely studied and exploited for disease diagnoses, biological assay and aptamer-based sensors [4–7]. To monitor the aptamer–target molecule interactions, a label-free method for aptamer-based analysis would make the process simple and easy. However, the sensitivity and electrochemical stability of aptamer-modified electrodes are usually unsatisfactory. To this end, aptamers have to be immobilized onto a variety of solid substrates with large specific surface areas to improve their sensing performances [8–12].

Graphene is a two-dimensional (2D) sheet of covalently bonded carbon atoms, with the highest surface-to-volume ratio, excellent electrical and mechanical performance and thermal stability [13–15]. Graphene and its derivatives offer possibilities for highly sensitive detection with the advantageous large specific surface areas, and have been used as substrates in electroanalytical chemistry [16–18].

Hemin, a well-known natural porphyrinatoiron complex, is an important compound and has been applied in pharmacy, environmental science, food industry and bioscience and technology [19–21]. While there are many studies on the high electrocatalytic activity of hemin for peroxidation reactions in analytical applications as well as in the application of determination of H_2O_2 and related compounds [22–25], studies regarding the detection of hemin as a target are relatively scarce. In this context, it is of great importance to develop a new method for the determination of hemin with high sensitivity and selectivity.

Herein, we report a novel method to develop a highly sensitive label-free electrochemical aptasensor for hemin detection. The proposed method is based on a nanocomposite composed of hemin-binding-aptamer (HBA) and carboxylated graphene (COO-GR), as shown in Scheme 1. In particular, HBA and COO-GR composite was prepared by simply mixing the aqueous solutions of both components. The resulting nanocomposite was immobilized on the surface of glassy carbon electrode (GCE) to construct a sensing platform. The introduction of nanomaterials greatly improved the specific surface area and electrochemical stability of the aptamer-modified electrode. As a result, the modified electrode exhibited high performances on electrochemical sensing of hemin. We note that instead of graphene, COO-GR was employed due to its better dispersibility in water and ease of preparation of the COO-GR/HBA nanocomposite.

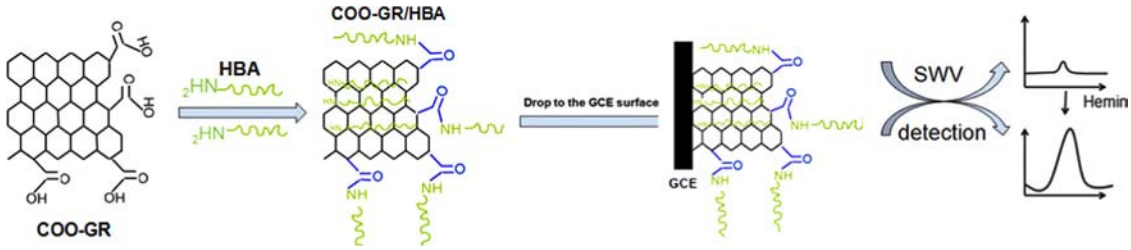
2. Experimental

2.1. Materials and reagents

HBA was purchased from Bioneer Trade Co., Ltd. (Shanghai, China). The sequence of HBA is 5′-NH_2-GTG GGT AGG GCG GGT

* Corresponding author. Tel./fax: +86 25 85891536.
** Corresponding author. Tel.: +86 25 83598648; fax: +86 25 83598280.
E-mail addresses: yhxiao@njnu.edu.cn (Y. Xiao), yangxiaodi@njnu.edu.cn (X. Yang).

http://dx.doi.org/10.1016/j.talanta.2014.09.010
0039-9140/© 2014 Elsevier B.V. All rights reserved.



Scheme 1. Schematic diagram for the preparation of the aptasensor based on COO-GR/HBA nanocomposite for sensitive hemin detection.

TGG-3′ and complementary oligonucleotide sequence is 5′-NH_2-CAC ACA CAC ACA CAC ACA CAC-3′. Hemin was obtained from RED Chemical Co., Ltd. (Shanghai, China). Human serum was supplied by Nanjing Maternity and Child Health Care Hospital (Nanjing, China). COO-GR was purchased from Nanjing XFNANO Materials Tech Co., Ltd. (Nanjing, China). 1-Ethyl-3-(3-dimethy-aminopropyl) carbodiimide hydrochloride (EDC) and N-hydroxysuccinimide (NHS) were purchased from Sigma-Aldrich (Spain). All other chemicals were of analytical grade and purchased from Sigma-Aldrich (Netherlands). Double-distilled water (DDW) was used in making all aqueous solutions.

2.2. Characterizations

Zeta Potential was determined using Zetasizer Nano 90 (Malvern, Britain). The samples were dispersed in water with sonication at ambient temperature. Cyclic voltammetry (CV), differential pulse voltammetry (DPV), electrochemical impedance spectroscopy (EIS) and square wave voltammetry (SWV) were conducted using CHI660B electrochemical analyzer (CH Instruments, Chenhua Inc., Shanghai, China). A three-electrode system was employed consisting of a modified GCE working electrode, a platinum wire counter electrode and a Ag/AgCl (saturated with KCl) reference electrode. Fourier transform infrared (FTIR) spectroscopy was recorded with a Cary 5000 spectrophotometer (Varian Co., USA). 2 mg mL^{-1} COO-GR and 10 μmol L^{-1} HBA were mixed at a volume ratio of 4:1. An aliquot of the mixture (COO-GR/HBA), 2 mg mL^{-1} COO-GR and 10 μmol L^{-1} HBA were dropped on the cleaned KBr disks, respectively and dried under an Infrared lamp. Diffuse reflectance spectra were obtained with the same Cary 5000 spectrophotometer and samples were dropped on the cleaned quartz plates for characterization. Raman spectra were measured on a LabRAM HR800 confocal spectrometer (Jobin Yvon, France), with 514.5 nm Ar laser excitation.

2.3. Fabrication of COO-GR modified electrode

GCE was sequentially polished to a mirror finish with 0.3 μm and 0.5 μm alumina slurry and washed with absolute alcohol followed by rinsing thoroughly with DDW. Finally, the polished electrode was allowed to dry at room temperature after ultrasonication cleaning for 5 min in DDW. 10 μL of 1.6 mg mL^{-1} COO-GR was coated on a cleaned GCE surface and dried in air. The electrode was rinsed thoroughly with 0.1 mol L^{-1} phosphate buffer solution (PBS, pH 7.4) and DDW before application.

2.4. Fabrication of COO-GR/HBA modified electrode

2 mg mL^{-1} COO-GR and 10 μmol L^{-1} HBA were mixed at a volume ratio of 4:1. 10 μL of the mixture (COO-GR/HBA) was blended with 2 μL chitosan adhesive, coated on the cleaned GCE surface and dried in air. The electrode was rinsed thoroughly with 0.1 mol L^{-1} PBS (pH 7.4) and DDW before application.

2.5. Fabrication of graphene/HBA modified electrode

Graphene/HBA modified electrode was fabricated for comparison. Graphene coated GCE was prepared using the same method reported in our previous study [4]. The thus obtained graphene–GCE was activated with 0.5 mL of 0.1 mol L^{-1} PBS containing 10 mmol L^{-1} EDC and 10 mmol L^{-1} NHS for 16 h. Subsequently, the electrode was immersed in 1 mL of 1 μmol L^{-1} HBA containing 0.1 mol L^{-1} NaCl and 4 mol L^{-1} EDTA for at least 24 h at ambient temperature. Finally, the electrode was rinsed with copious DDW to remove any unfixed aptamer molecules.

2.6. Electrochemical measurements

The electrochemical performances of the modified electrodes were investigated by CV, DPV and EIS in a 0.1 mol L^{-1} PBS solution (pH 7.4) containing 10 mmol L^{-1} $[Fe(CN)_6]^{3-/4-}$ and 0.1 mol L^{-1} KCl. CV was swept within potential scanning range from 0.6 to −0.1 V with different scan rates. DPV was conducted with pulse amplitude of 0.05 V, pulse width of 0.05 s and pulse period of 0.2 s. For EIS measurements, an AC sinusoid of 5.0 mV in amplitude was applied as input signal, with the DC potential set to 0.28 V over a wide frequency range from 10^0 to 10^5 Hz.

2.7. Detection of target hemin

Fresh hemin solutions were prepared prior to each experiment by dissolving hemin with a few microliters of 0.1 mol L^{-1} NaOH and subsequent addition of PBS to the requested concentrations. Highly pure N_2 was bubbled through the cell solution for about 20 min prior to each experiment. Detection of hemin was carried out by immersing the COO-GR/HBA modified electrode into a 0.1 mol L^{-1} PBS containing hemin with different concentrations. The resulting change of peak current upon the binding of HBA with hemin was monitored using SWV. SWV was performed with potential scanning from 0.8 to −0.1 V with quiet time of 120 s, scan increment of 4 mV, amplitude of 25 mV and frequency of 15 Hz.

3. Results and discussion

3.1. Chemical structure of COO-GR/HBA

FTIR, diffusion reflectance spectra and Raman spectroscopy were employed to examine the covalent bond formation between HBA and –COOH. Fig. 1A (a) exhibits the characteristic absorption peaks of COO-GR. A broad band ranging from 3600 to 3250 cm^{-1} indicates the presence of –OH groups. –COOH groups in COO-GR is evidenced by the C=O stretching vibration at 1725 cm^{-1}, the –COO asymmetric stretching shoulder peak at 1570 cm^{-1}, and –COO symmetric stretching vibration at 1415 cm^{-1}. A C=C aromatic ring stretching vibration is present at 1635 cm^{-1} [26]. Spectrum of HBA displays a broad band around 3166 cm^{-1}

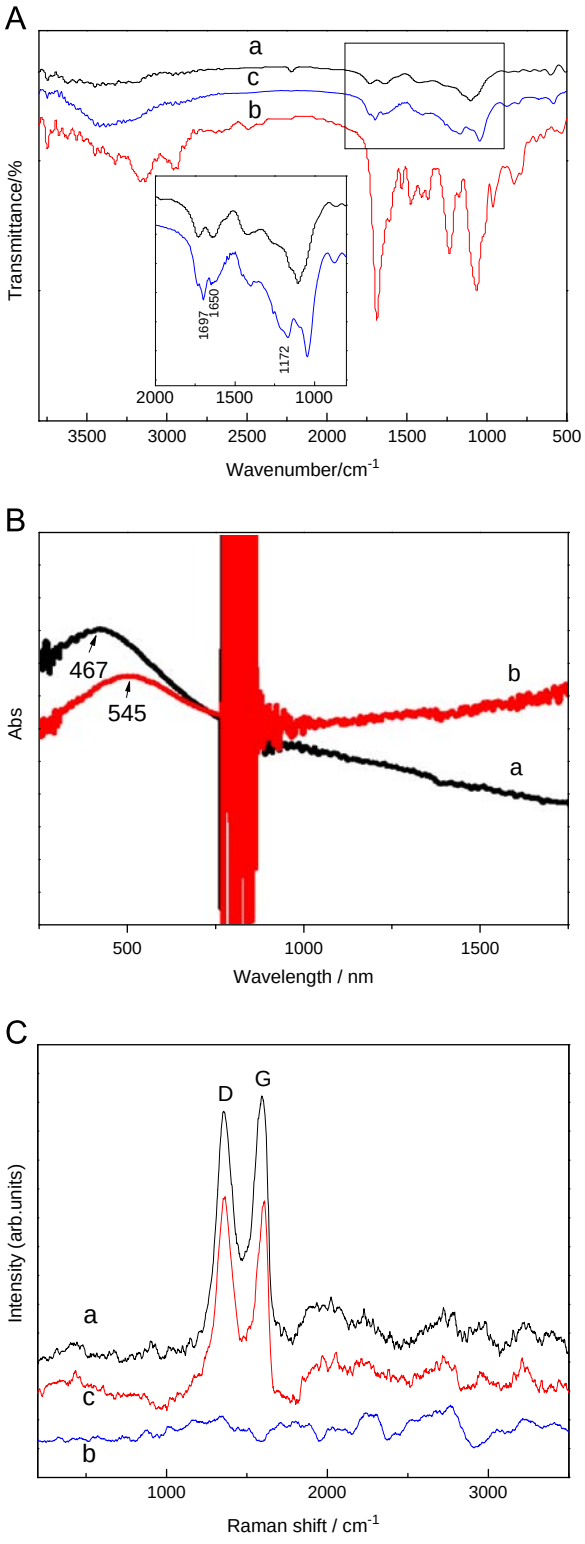


Fig. 1. (A) FTIR of COO-GR (a), HBA (b), and COO-GR/HBA (c). (B) Diffusion reflectance spectra of COO-GR (a) and COO-GR/HBA (b). (C) Raman spectra of COO-GR (a), HBA (b), and COO-GR/HBA (c).

of –N–H stretching vibration, an absorption peak of C=O at 1685 cm^{-1}, a stretching peak at 1228 cm^{-1} of –CN and a dissymmetric stretching vibration of phosphate radicals at 1066 cm^{-1} (b). In the spectrum of the COO-GR/HBA composite, the increase in the intensity of the band around 3400 cm^{-1} is assigned to the presence of –OH groups in COO-GR and –N–H in HBA. The new absorption peaks at 1697 cm^{-1}, 1650 cm^{-1} and 1172 cm^{-1} are attributed to the C=O vibration in –NHCO–, in-plane bending mode of –N–H, and –CN vibration, respectively (c). Diffuse reflectance also reveals the covalent binding of COO-GR and HBA. The noise around 800 nm was caused by the change of the detector from UV to visible light. The featured change of C=O absorbance band from 467 nm in COO-GR to 545 nm in COO-GR/HBA indicates a conversion from –COOH to –NHCO– (B). Raman spectroscopy is a powerful tool to characterize the bonding, ordering, and crystallite size of carbon materials. It is well known that the Raman band at ~1590 cm^{-1} (the G-band) is due to the in-plane phonon modes of graphene, showing the sp^2 bonding. The band around ~1360 cm^{-1} is due to disorder in the graphene layers caused by the presence of sp^3 bonding (the D-band). As can be seen in Fig. 1C, COO-GR also exhibits the two bands with the G band being higher (a), which is in agreement with the previous report [26]. It is reasonable that HBA does not show any featured bands in Raman spectroscopy (b). After binding with HBA, however, the D band of the COO-GR/HBA becomes prominent (c). The HBA molecules decorated on COO-GR cause the sp^2 delocalization due to their strong negativity. sp^2 structures close to the decorated points convert to sp^3 structures, leading to the increase of the D/G intensity ratio for COO-GR/HBA.

3.2. Comparison of COO-GR and graphene for the construction of aptasensors

To clearly show the advantage of COO-GR over graphene in this study, both COO-GR/HBA and graphene/HBA modified electrodes were prepared and characterized as follows. As shown in Fig. 2A, DPV reveals that the peak current of COO-GR/HBA increases compared with COO-GR–GCE; while the peak current of graphene/HBA decreases in comparison with graphene–GCE. In addition, both graphene and graphene/HBA modified electrodes present high background current while the COO-GR and COO-GR/HBA modified electrodes nearly have no background noise, indicating a higher signal to noise ratio (S/N) of the COO-GR based electrodes. EIS measurements (Fig. 2B) suggest that after binding with HBA the charge transfer resistance (R_{et}) of graphene increases by 196 Ω (from a to b) while the R_{et} of COO-GR decreases by 358 Ω (from c to d). The phenomenon is reasonable as graphene is known for its excellent electrical conductivity and immobilization of HBA on graphene will form an organic layer, thus unambiguously increases the surface resistance. As for COO-GR, the existence of carboxylic groups anchoring at the edges of graphene molecules destroys the sp^2 hybridization conjugation of the backbone, thereby inhibiting the electron transfer and resulting in a poor conductivity as well as a high impedance of the coated electrode. Interestingly, the R_{et} of COO-GR/HBA greatly decreases instead. We assume that the R_{et} at electrode/electrolyte interface is determined by two factors: (1) the electrical conductivity of the coating, and (2) the charges of the coating surface. A possible explanation to this phenomenon is that after binding with HBA, –NH_2 groups decorated on HBA are covalently bonded with –COOH to form strong amide bonds, leading to a change in charges of the resulting surface. This assumption is verified by Zeta potential measurements. In a solution with pH=7.4, the Zeta potentials of COO-GR and COO-GR/HBA are −7.65 mV and −0.905 mV, respectively. Another advantage of the current strategy is that the preparation of COO-GR/HBA is relatively simple in comparison with that of graphene/HBA due to the better water solubility of COO-GR (see Section 2).

3.3. Electrochemical characterization of the modified electrodes

Electrochemical properties of the modified electrodes investigated by CV, DPV and EIS are shown in Fig. 3. Compared with the

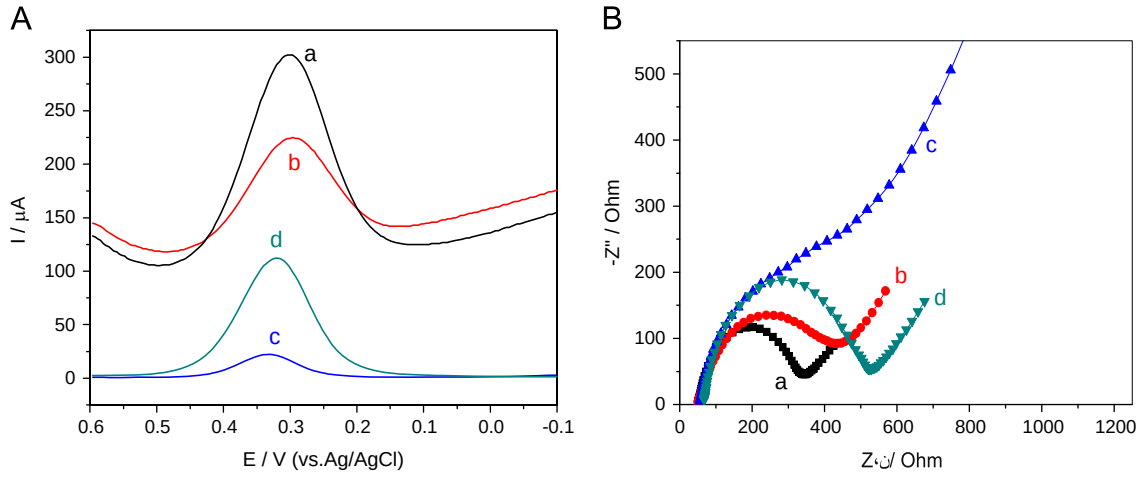


Fig. 2. DPV (A) and EIS (B) of GR (a), GR/HBA (b), COO-GR (c) and COO-GR/HBA electrode (d) in 0.1 mol L^{-1} PBS (pH 7.4) containing 10 mmol L^{-1} $[Fe(CN)_6]^{3-/4-}$ and 0.1 mol L^{-1} KCl.

bare GCE, the COO-GR modified electrode exhibits relatively poor electrochemical performance. In particular, (1) the enclosed area in CV largely decreases, indicating its low charge capability; (2) the peak current in DPV decreases, implying its decreased conductivity; and (3) the R_{et} greatly increases. As discussed above, the existence of carboxylic groups anchoring at the edges of graphene molecules causes the destruction of sp^2 hybridization conjugation of the carbon backbone, leading to poor conductivity of the COO-GR coated electrode. However, after binding with HBA, the electrochemical performance improves as clearly evidenced by the enlarged enclosed area in CV, the increased peak current in DPV, and the decreased R_{et} in EIS. This is due to the fact that $-NH_2$ groups decorated on HBA are covalently bonded with –COOH to form strong amide bonds, and thus the amount of carboxyl groups on the electrode surface is greatly reduced, leading to less negative charges on the surface as confirmed by Zeta potential. The variation of the surface charges has a key influence on the R_{et} at the electrode/electrolyte interface.

3.4. Relationship between peak current and scan rate of CV

To understand the redox kinetics of the functionalized electrode, CV measurements of the COO-GR/HBA electrode at various scan rates were performed. The resulting plots are shown in Fig. 4A. Theoretically, when electron transfer at the interface is fast enough and redox reactions are totally reversible, the difference of peak current (ΔE_p) will remain constant and will not change with scan rate. However, in our study we note that with increasing scan rate from 10 to 200 mV s^{-1}, the anodic peak shifts to more positive positions, while the cathodic peak shifts to more negative positions. As a result, ΔE_p changes from 20 to 80 mV. Meanwhile, both anodic and cathodic peak currents increase with increasing scan rate. Fig. 4B displays the relationship between peak current (I_{pa} and I_{pc}) and square root of the scan rate $\nu^{1/2}$. The linear relationship is expressed by $I_{pa} = -3.807 \times 10^{-5}\nu^{1/2} + 1.341 \times 10^{-5}$ ($R^2_{pa}=0.9939$) and $I_{pc}=3.414 \times 10^{-5}\nu^{1/2} - 1.307 \times 10^{-5}$ ($R^2_{pc}=0.9920$), respectively. The results reveal a quazi-reversible electrochemical kinetics and diffusion-controlled process of the electrochemical reaction at the electrode surface.

3.5. Quantitative detection of hemin

As it is well known, COO-GR on its own can form molecular π–π conjugations with hemin molecules. In the meantime, COO-GR exhibits good electrocatalytic reducibility towards hemin. Thus, a COO-GR coated electrode was applied to directly detect hemin with SWV. Interestingly, the current peaks appear at 0.22 V and the peak current varies with hemin concentrations from 0.1 to 5 μmol L^{-1} (Fig. 5), indicating the responsibility of the COO-GR coated electrode to hemin. It is reasonable because more hemin molecules will be immobilized on to COO-GR when its concentration gets higher. However, no linear relationship was found between peak currents and hemin concentrations, which hinders the application of COO-GR modified electrodes in the quantitative detection of hemin.

To explore an ideal approach for quantitatively detect hemin, HBA was immobilized onto the COO-GR coated electrode to yield an aptasensor. Clearly, when the aptasensor was incubated in hemin solution, the peak current at 0.22 V in SWV increased with increasing hemin concentration, a same phenomenon observed for the COO-GR coated electrode. When the concentration of the hemin solution increases, more hemin molecules are immobilized on the electrode surface due to the specific recognition of HBA to hemin, leading to an increased peak current (Fig. 6A). The different phenomenon from that of the COO-GR coated electrode is as follows: there is a linear relationship between the peak currents and hemin concentrations from 1 to 150 nmol L^{-1}, after which the current reaches a plateau, implying the saturation of hemin on the electrode surface (Fig. 6B). The regression equation is $I=0.4685c+30.9130$, with a linear coefficient of $R^2=0.9940$ and a detection limit of 0.64 nmol L^{-1} ($S/N=3$). The resulting aptasensor exhibits better performance than the reported nano-ZnO-carbon paste electrode with a linear range from 3.07×10^{-9} to 3.07×10^{-7} mol L^{-1} and the fluorescence aptasensor with a linear range of 0.31–2.50 μmol L^{-1}. Furthermore, the detection limit of 0.64 nmol L^{-1} is lower than that of the reported electrochemical sensor (1.5×10^{-9} mol L^{-1}) as well as the fluorescence aptasensor (50 nmol L^{-1}) [27,28].

3.6. Specificity of the COO-GR/HBA aptasensor

Specificity is another important performance for aptasensors to accurately detect analytes in real applications. To evaluate the specificity of the fabricated COO-GR/HBA aptasensor to hemin, standard recoveries were determined based on the calibration curve in the presence of serum. We found that the peak currents at 0.22 V are almost the same for the blank solution and the serum solution (Fig. 7). Moreover, when the concentration of hemin in the mixture of serum and hemin was increased, the peak current increased accordingly, in spite of the presence of serum. This

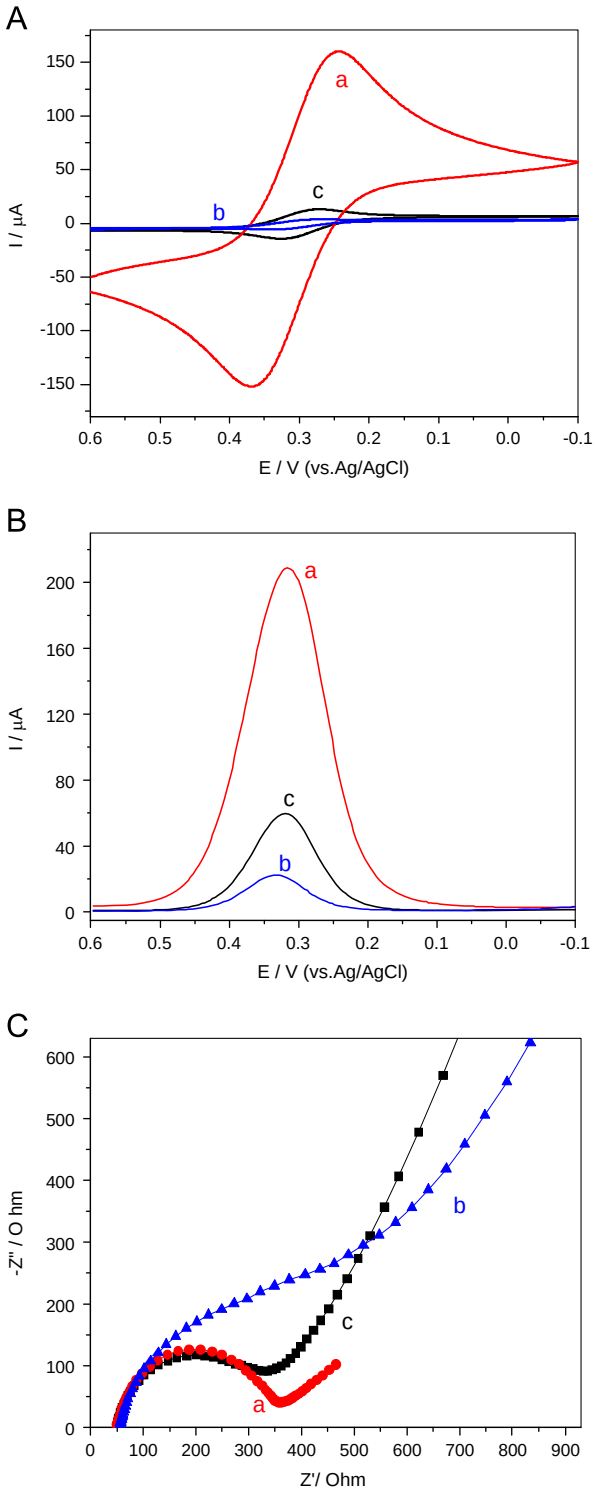


Fig. 3. Electrochemical characterization of bare GCE (a), COO-GR modified electrode (b) and COO-GR/HBA modified electrode (c) in 0.1 mol L^{-1} PBS (pH 7.4) containing 10 mmol L^{-1} $[Fe(CN)_6]^{3-/4-}$ and 0.1 mol L^{-1} KCl. (A) CV, (B) DPV and (C) EIS.

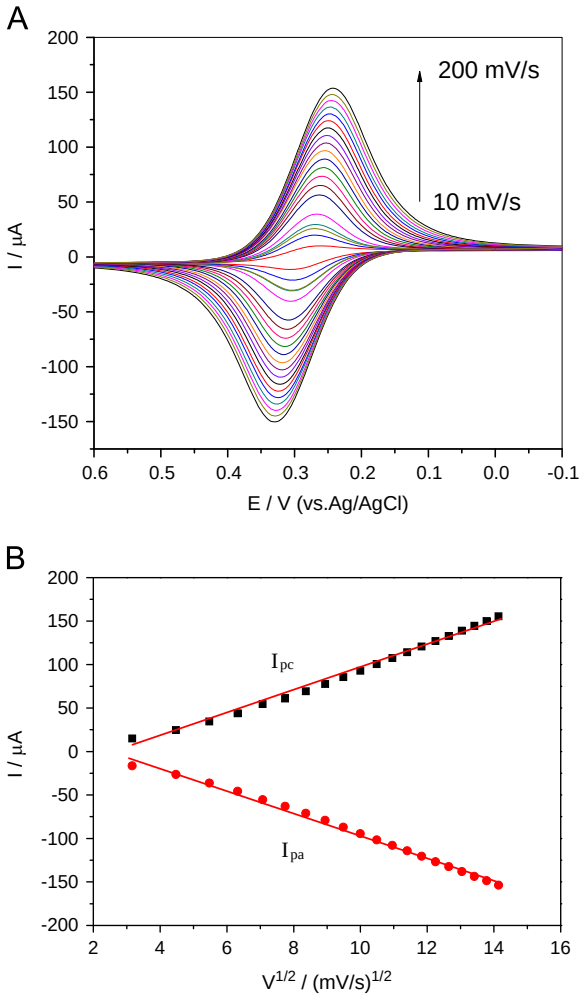


Fig. 4. (A) CVs of the COO-GR/HBA modified electrode with different scan rates in 0.1 mol L^{-1} PBS (pH 7.4) containing 10 mmol L^{-1} $[Fe(CN)_6]^{3-/4-}$ and 0.1 mol L^{-1} KCl. (B) A Randles–Sevik plot of the electrode.

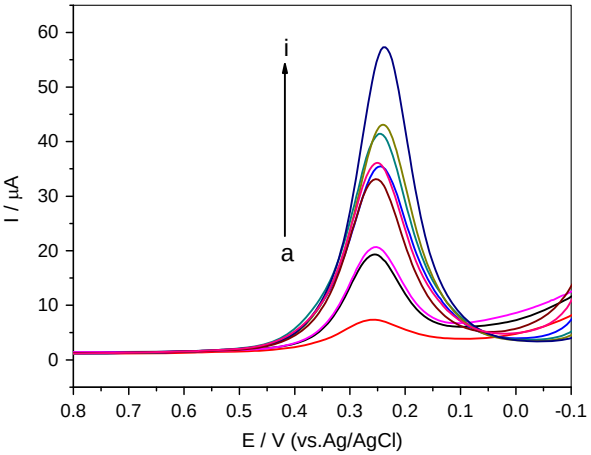


Fig. 5. SWV of the COO-GR coated electrode incubated in hemin with concentrations of 0 (a), 0.1 (b), 0.3 (c), 0.5 (d), 0.7 (e), 2 (f), 3 (g), 4 (h) and 5 μmol L^{-1} (i). Hemin was in 0.1 mol L^{-1} PBS containing 0.1 mol L^{-1} KCl.

demonstrates that the currents change only with hemin concentrations rather than other bio-substances in the mixture. The corresponding data shown in Table 1 indicate that all recoveries turn out to be 97.2–101.9% and fall in the confidence interval of 95–105%, indicating the reliability of the COO-GR/HBA aptasensors in the detection of hemin.

Furthermore, to evaluate the anti-interference property of the fabricated COO-GR/HBA aptasensor, possible interfering species such as K^+, Na^+, Ca^{2+}, NO_3^-, thrombin, adenosine, uridine, cytidine, lysozyme and glucose, which may be present in real samples, were examined in 0.1 mol L^{-1} PBS containing 50 nmol L^{-1} hemin. We found that 50.0-fold of the above species did not show remarkable interference to hemin determination.

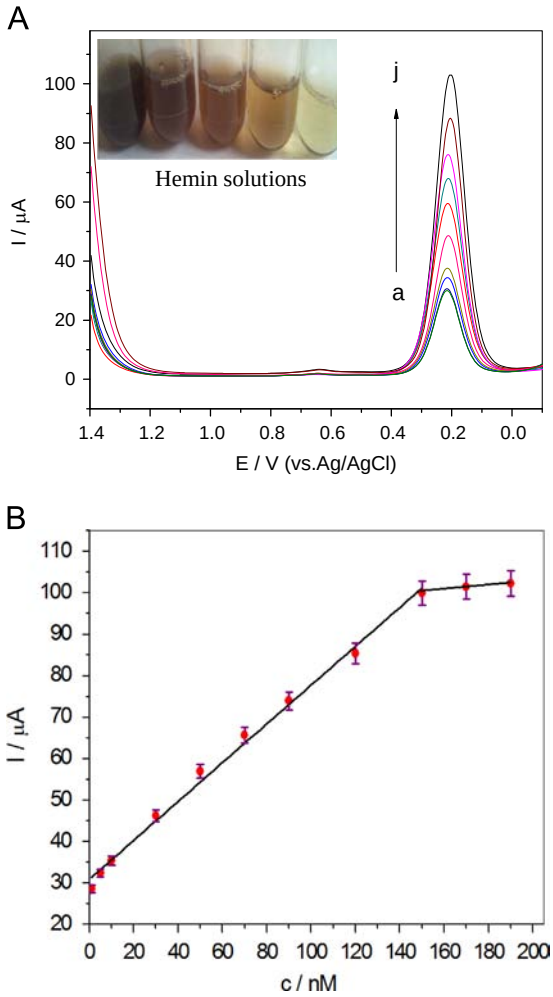


Fig. 6. (A) SWV of the COO-GR/HBA modified electrode incubated in hemin with concentrations of 0 (a), 1 (b), 5 (c), 10 (d), 30 (e), 50 (f), 70 (g), 90 (h), 120 (i) and 150 nmol L^{-1} (j) in 0.1 mol L^{-1} PBS (pH 7.4) containing 0.1 mol L^{-1} KCl. Inset in A is a digital image of hemin solutions with different concentrations. (B) Calibration curve showing the relationship between peak current and hemin concentration. The measurements were repeated 3 times to obtain the standard deviation.

The anti-interference of the COO-GR/HBA aptasensor is acceptable, ensuring its promising application in real sample analysis.

3.7. Analytical performance – repeatability, reproducibility and stability

The repeatability of the sensor response was tested by 10 times successive measurements with the COO-GR/HBA modified electrodes in 0.1 mol L^{-1} PBS containing 50 nmol L^{-1} hemin, giving a satisfying relative standard deviation (RSD) of 1.87%. The reproducibility was examined by six individual determination performed with different COO-GR/HBA modified electrodes in the above solution and the RSD was obtained as 3.69%. Moreover, the proposed aptasensor was stored in 0.1 mol L^{-1} PBS and kept at 4 °C in a fridge. After two weeks, we found that the sensor retained 90.94% of its initial activity. The above results indicated good analytical performance of the proposed aptasensor.

4. Conclusions

Graphene–HBA- and COO-GR–HBA-modified electrodes were crafted and their electrochemical properties were investigated. Although the COO-GR electrode has lower electrical conductivity than that of the graphene electrode, a large number of carboxylic groups in its structure provide active sites for binding with aminated aptamers, HBA. Redox kinetics of the resulting COO-GR–HBA aptasensor is demonstrated to be quazi-reversible and displays a diffusion-controlled process of the electrochemical reaction at the electrode surface. Using SWV as sensing technique, the proposed aptasensor is able to quantitatively detect the analyte of hemin and a detection limit as low as 0.64 nmol L^{-1} can be achieved. Moreover, COO-GR is shown to be a promising candidate in making aptasensors, possessing the advantageous attributes in terms of simplicity of sensor construction and reduction of background noise.

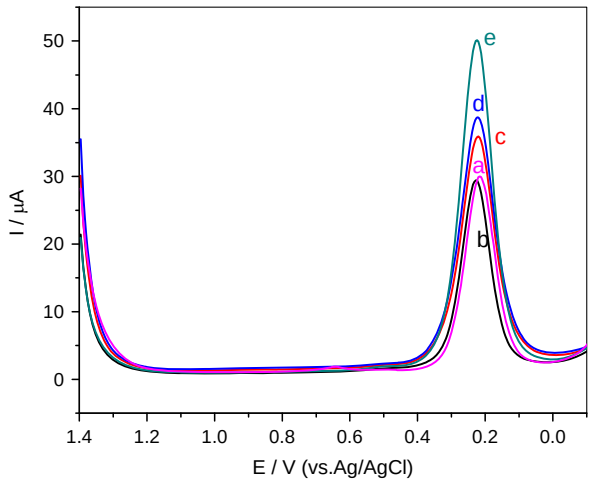


Fig. 7. Specificity analysis of aptasensor tested in blank (a), serum (b) and serum–hemin mixture (c–e). Hemin concentration in serum–hemin mixture is 5 (c), 10 (d) and 35 nmol L^{-1} (e).

Table 1
Standard recovery.

No.	Solution	Concentration of hemin (nmol L^{-1})	Peak current (μA)	Hemin concentration obtained from calibration curve (nmol L^{-1})	Recovery (%)
a	Blank	0	28.12	/	/
b	Serum	0	27.30	/	/
c	Mixture 1 (V_{serum}: V_{hemin}=1:1)	5	33.19	4.86	97.2
d	Mixture 2 (V_{serum}: V_{hemin}=1:2)	10	35.51	9.81	98.1
e	Mixture 3 (V_{serum}: V_{hemin}=1:7)	35	47.63	35.68	101.9

Acknowledgments

The project was funded by the Natural Science Foundation of Jiangsu Province, China (Grant no. BK2012845), the Specialized Research Fund for the Doctoral Program of Higher Education of China (20123219110010), the National Natural Science Foundation of China (21175068), the Foundation of the Jiangsu Education Committee (13KJB150024) and the Priority Academic Program Development of Jiangsu Higher Education Institutions (PAPD).

References

[1] S. Tombelli, M. Minunni, M. Mascini, Biosens. Bioelectron. 20 (2005) 2424.

[2] M. Famulok, J.S. Hartig, G. Mayer, Chem. Rev. 107 (2007) 3715.
[3] P. Zhang, N. Zhao, Z. Zeng, Y. Feng, C.-H. Tung, C.-C. Chang, Y. Zu, Lab. Invest. 89 (2009) 1423.
[4] Y. Wang, Y.H. Xiao, X. Ma, N. Li, X. Yang, Chem. Commun. 48 (2012) 738.
[5] W. Shan, Y. Pan, H. Fang, M. Guo, Z. Nie, Y. Huang, S. Yao, Talanta 126 (2014) 130.
[6] G. Yan, Y. Wang, X. He, K. Wang, J. Liu, Y. Du, Biosens. Bioelectron. 44 (2013) 57.
[7] A. Erdem, G. Congur, Talanta 128 (2014) 428.
[8] X. Jiang, K. Huang, D. Deng, H. Xia, X. Hou, C. Zheng, Trends Anal. Chem. 39 (2012) 38.
[9] G. Jin, L. Lu, X. Gao, M. Li, B. Qiu, Z. Lin, H. Yang, G. Chen, Electrochim. Acta 89 (2013) 13.
[10] M. Pumera, Mater. Today 14 (2011) 308.
[11] X. Dong, Y. Shi, W. Huang, P. Chen, L. Li, J. Adv. Mater. 22 (2010) 1649.
[12] Y.H. Xiao, Y. Wang, M. Wu, X. Ma, X. Yang, J. Electroanal. Chem. 25 (2013) 1922.
[13] K.I. Bolotin, K.J. Sikes, Z. Jiang, M. Klima, G. Fudenberg, J. Hone, P. Kim, H. L. Stormer, Solid State Commun. 146 (2008) 351.
[14] J. Che, L. Shen, Y.H. Xiao, J. Mater. Chem. 20 (2010) 1722.
[15] M.J. Allen, V.C. Tung, R.B. Kaner, Chem. Rev. 110 (2010) 132.
[16] C. Guo, S.R. Ng, S.Y. Khoo, X. Zheng, P. Chen, C.M. Li, ACS Nano 6 (2012) 6944.
[17] M. Pumera, A. Ambrosi, A. Bonanni, E.L.K. Chng, H.L. Poh, Trends Anal. Chem. 29 (2010) 954.
[18] S. Song, Y. Qin, Y. He, Q. Huang, C. Fan, H. Chen, Chem. Soc. Rev. 39 (2010) 4234.
[19] G. Ran, W. Yi, Y. Li, H. Luo, N. Li, Anal. Methods 4 (2012) 2929.
[20] C. Zhou, H. Wang, Y. Chen, C. Chen, Food Sci. Biotechnol. 21 (2012) 669.
[21] J.Y. Wang, Y.T. Lee, P.F. Chang, L.Y. Chau, J. Cell. Physiol. 219 (2009) 617.
[22] M. Zhang, R. Yuan, Y. Chai, S. Chen, X. Zhong, H. Zhong, C. Wang, RSC Adv. 2 (2012) 4639.
[23] S. Xie, Y. Chai, R. Yuan, L. Bai, Y. Yuan, Y. Wang, Anal. Chim. Acta 755 (2012) 46.
[24] A.M. Toader, E. Volanschi, M.F. Lazarescu, V. Lazarescu, Electrochim. Acta 56 (2010) 863.
[25] L. Zhang, J. Zhu, S. Guo, T. Li, J. Li, E. Wang, J. Am. Chem. Soc. 135 (2013) 2403.
[26] K.-W. Park, J. Mater. Chem. A 2 (2014) 4292.
[27] Y. Wang, P. Li, G. Zhan, Chin. J. Appl. Chem. 27 (2010) 1204.
[28] Y. Shi, W. Huang, H. Luo, N. Li, Chem. Commun. 47 (2011) 4676.

Talanta 132 (2015) 222–227

Contents lists available at ScienceDirect

Talanta

journal homepage: www.elsevier.com/locate/talanta

Quantitative lead determination in coating paint on children's outwear by LA-ICP-MS: A practical calibration strategy for solid samples

Selda Mercan*, Sevinç Zeynep Ellez, Zeynep Türkmen, Murat Yayla, Salih Cengiz

Istanbul University, Institute of Forensic Sciences, Forensic Toxicology Laboratory, Cerrahpasa, 34303 Istanbul, Turkey

ARTICLE INFO

Article history:
Received 3 April 2014
Received in revised form
17 August 2014
Accepted 27 August 2014
Available online 4 September 2014

Keywords:
Textile
Coating paint
Lead
Laser ablation
Calibration
Child outwear

ABSTRACT

Lead is a hazardous compound that affects the central nervous system in people, particularly children, and may cause some reversible and irreversible diseases. Legal regulations try to prevent the exposure from products especially produced for children such as coating paints, jewelry, toys, bed linen, textile, etc. The aim of this study was to determine the lead levels of coating paints on children's outwear selling in district bazaar by laser ablation inductively coupled plasma mass spectrometry (LA-ICP-MS) and to specify the percent of non-complying samples. Here we described the solid matrix calibration method and confirmed the results with the microwave-assisted acid digestion method. Both comparative methods were validated by analysis of the certified reference materials (NIST SRM-612 glass matrix, NIST SRM-2582 powdered paint and ERM-EC681k) and bias% for accuracy and RSD% for precision were calculated lower than 6.8% and 7.3%, respectively. The recovery ranges of laser ablation and microwave-assisted acid digestion method for Pb were found to be between 88.2–98.1% and 95.3–101.3%, respectively. The limits of detection values were determined as 0.162 mg kg^{-1} for direct sampling in the ablation chamber and 0.002 ng mL^{-1} for aqueous solutions. Correlation result of 16 samples (r=0.99) examined in both methods was satisfactory. In coating paint samples, 14.65% of 198 (n=29) did not comply with the 90 mg kg^{-1} lead limit according to regulation. Validated quantitative laser ablation method may be preferred to quickly and reliably determine the Pb levels in other solid samples as well as coating paints.

© 2014 Elsevier B.V. All rights reserved.

1. Introduction

Lead (Pb) is known as a common environmental pollutant with long half life and its high levels accumulated in the body may cause intoxication in many organs and tissues. Chronic Pb exposure affects the central nervous system (CNS) and results in serious inhibition in learning and severe changes in behaviors, especially in children. Lead absorption may constitute a serious risk to public health, since it may cause slow cognitive development, impair intellectual performance in children and also increase blood pressure and cardiovascular diseases in adults [1–3]. Handling and mouthing of consumer products such as toys, clothing, and drawstring by children especially in 0–2 years old are the major ways of lead exposure via dermal contact and ingestion [4]. A study conducted showed a high proportion of recalls as well as a high number of deaths/injuries related to strangulation, lead paint or falls and these recalled products included hooded sweatshirts with drawstrings, baby cribs and children's jewelry [5].

Declared acute or chronic lead poisoning cases after oral or dermal exposure items like toys, batteries, fishing sinkers, jewelry, paints, etc. revealed the importance of prevention from lead exposure of children [6–9] and the regulatory limits of lead in consumer products are often lowered [10].

According to the Consumer Product Safety Improvement Act (CPSIA) by Consumer Safety Product Commission (CPSC) of the U.S. definition; "children's products that are designed or intended primarily for use by children 12 years of age or younger cannot contain greater than 100 mg kg^{-1} of total lead content in any accessible component part of the children's product as of the date of 2011 and the maximum limits of total lead that may be present in paint or any similar surface coatings produced for children as 90 mg kg^{-1}" since August 14, 2009. This limit applies to both paints and paint on toys and other articles intended for children and to certain household furniture items [11]. Also British standards about safety of toys (BS-EN71-3) determined similar limits for lead migration [12].

Regulations related to the use of hazardous chemicals in Turkey have recently been re-examined and adjusted to resolve some of the country's health and environmental issues to improve the quality of life and also for the adaptation to EU rules and regulations during the EU accession process. Over the last few years the public authorities

* Corresponding author. Tel.: +90 212 4143000/4122839.
E-mail address: mercans@istanbul.edu.tr (S. Mercan).

http://dx.doi.org/10.1016/j.talanta.2014.08.062
0039-9140/© 2014 Elsevier B.V. All rights reserved.

have been trying to meet the world standards and have taken concrete steps in this regard in Turkey.

A number of analytical methods about textile products including hazardous compounds conducted by atomic absorption spectrometry (AAS) or inductively coupled plasma mass spectrometry (ICP-MS) techniques in aqueous samples have been reported [13,14]. Over the last few decades, solid samples are being preferred to study by laser ablation inductively coupled plasma mass spectrometry (LA-ICP-MS), which is a developmental technique for in situ sampling. Although LA-ICP-MS is powerful for multi-element analysis and is easy to sample [15], in some cases, especially for specific matrices such as textile, coating surfaces, etc., studies are limited by the lack of standard reference materials (SRMs) in the case of a problem about elemental fractionation sources such as aerosol transport, vaporization, atomization, ionization, etc [16,17]. Several study results have been obtained by calibration curves generated from standard addition, direct liquid ablation or matrix-matched standard methods or in situ analysis without applying an internal standard by laser ablation in different sample types such as blood, rat brain tissue, anhydrous minerals and glasses [18–21]. Besides, numerous quantitatively validated reports and reviews have been published especially in geological and forensic fields explaining the technique in detail [22,23].

Researches on inorganic contents of textile products for both children and adults are limited while no published report is available about coating paints conducted either in Turkey or in other countries. A study determined the concentrations of some elements in textile samples such as Cu, Cd, Ni, Mn, etc. by flame and graphite furnace AAS after microwave digestion on textile products and they found concentrations of Cu and Cd in samples higher than the permitted values [24]. A study result of some elements with textile samples manufactured in Turkey was reported in another study conducted by AAS; the levels of Pb and Ni ions in textile material were found to be over the values for baby clothing according to Oeko-Tex [25]. Mataso and Cadore obtained validation results by an acid microwave closed vessel digestion method for textile products used as sports T-shirts and they found chromium in black fabrics as the major inorganic contaminant [14].

Children are exposed to Pb or other similar hazardous substances coming from environment or materials due to daily contact with clothes, bed linen, paints, toys, jewelry and similar products. In recent years, studies have investigated the presence of inorganic contamination in such kinds of consumables for children [26,27].

Guney and Zagury determined the total concentrations of As, Ba, Cd, Cr, Cu, Mn, Ni, Pb, Sb, and Se in toys and jewelry ($n=72$) for children bought on the North American market and compared these results to regulatory limits. According to their results, metallic toys and children's jewelry ($n=24$) 20 items had total concentrations exceeding migratory concentration limits of the European Union. High Pb levels (65%) were also found in some samples [28].

Revealing the hazardous compounds over the restricted limits in products is important, especially in terms of safety for the environment and health of citizens, and safety for workers exposed during the production process as well as for end users [10].

The aim of this study was determination of the Pb levels in coating paints on textile products produced for children and sold in district bazaars in Istanbul and to emphasize their compliance with regulations in our country with a new calibration strategy for LA-ICP-MS.

2. Experimental

2.1. Instrumentation

Measurements were conducted by a Thermo Electron X Series II ICP-MS (Germany), coupled to Nd:YAG laser ablation (LA) unit operating at 213 nm wavelength (New Wave Research Laser Ablation System, Merchantek, USA). For treatment of the samples a microwave acid digestion (CEM, Mars5, Matthews, NC, USA) was used. Water used was deionized (Millipore Direct-Q3 System, 18.2 MΩ cm).

2.2. Reagents and standards

Argon gas with $>99.999\%$ purity was used for the ICP-MS system (Okser, Turkey). Also used were 65% (w/w) HNO_3 and 35% (w/w) H_2O_2 solutions, purchased from Merck with supra pure quality. Certificated calibration solution (10 μg mL^{-1}) used was purchased from High-Purity Standards, Charleston; Indium (In) and Gallium (Ga) (1000 μg mL^{-1}) were used as internal standards (IS) (Absolute Standards, Inc., Hamden, CT, USA). Standard Reference Materials (SRMs) used for Pb were as follows: (i) National Institute of Standards and Technology (NIST) SRM 612 glass matrix (Gaithersburg, MD); (ii) NIST-SRM 2582 Powdered Paint (Gaithersburg, MD); (iii) European Reference Material, ERM-EC681k, low density polyethylene (Geel, Belgium). NIST-SRM 610 (Gaithersburg, MD) was also used as the external calibration standard.

2.3. Optimization

Preliminary optimization of instrumental parameters was conducted using aqueous standards (10 ng mL^{-1}) for an initial quality control of the instrumental performance to conduct both liquid nebulization and laser ablation ICP-MS methods. Afterwards, a second optimization with glass standard (NIST-SRM 612) was accomplished for laser ablation system. All the double charges and oxide levels were checked out. As an external standard, NIST-SRM 610 was analyzed at the beginning and the end of the sequence of the sample to correct for drift and variation during the experiment and to evaluate the capability of a laser ablation technique for the analysis of coatings.

2.4. Sample selection

Child outwear (0–12 years) containing coating paints and manufactured in Turkey were collected from four different district bazaars of Istanbul, ten samples from each bazaar were bought inexpensively and at least three different stallholders were chosen to buy samples. Totally 198 different colored coatings were obtained from forty products (Fig. 1). All these 198 samples were analyzed for ^{208}Pb by LA-ICP-MS and the selected 17 samples were verified by microwave-assisted acid digestion followed by liquid-based ICP-MS analysis.

2.5. Sample treatment and validation

2.5.1. Laser ablation

Each coating paint in different colors was cut into parts with approximately 0.5×0.5 cm dimensions from child outwear as shown in Fig. 2 (left side) and adhered on laminas with the cyanoacrylate adhesive which was also used as blank. NIST-SRM 2582 powdered one was converted to pellet form as follows: a 0.5 g portion of the pre-dried powder material was pressed with a manual hand press tool into a disk-shaped pellet 1.3 cm diameter with a thickness of approximately 3 mm.

NIST-SRM 610 and 612 are universal standards used for any kind of laser ablation applications, but the analysis parameters such as laser energy, scan speed, frequency, etc. applied to the glass matrix are different from coating paint surfaces. For this reason and for the lack of coating paint reference material, a calibration study was conducted in three different matrices, glass, polyethylene and powder, which have decreasing rigidity and increasing lead



Fig. 1. Child (0–12 years) outwear samples bought from district bazaars with several coating paint colors. (For interpretation of the references to color in this figure legend, the reader is referred to the web version of this article.)



Fig. 2. Samples adhered on a lamina for ablation method to the chamber (left side), coated and stripped form of a sample prepared to microwave-assisted acid digestion method (right side).

concentration, respectively, after optimizing the analysis parameters with raster-type ablation. At the beginning of the calibration and linearity studies, all SRMs were analyzed with the same ablation conditions. Signals and ablation patterns were evaluated and proper energies were applied per SRMs until acceptable correlation coefficient was obtained for the calibration curve.

All three SRMs were also placed in the ablation chamber appropriately. We developed a new calibration strategy using three different SRMs including glass, polyethylene and powder matrices to quantitate Pb levels on coating paint textile samples produced for children. SRMs containing Pb certified values as 38.5, 98 and 208.8 mg kg^{-1} respectively were used to obtain the calibration curve in the Laser Ablation method. Three different laser energies were used to obtain a linear calibration curve as the structures and surfaces of SRMs were different from each other as detailed in Table 1. Ablation and analysis conditions of samples are also shown in Table 2. The limit of detection (LOD) and quantification (LOQ) of Pb were calculated as three times and ten times the blank (adhesive agent) deviation. Validation studies were conducted by sampling of SRMs and selected samples close to the regulatory limit (90 mg/kg^{-1}) with six replicates.

2.5.2. Microwave-assisted acid digestion

The calibration curve was prepared in 2% HNO_3 by incremental amount as 0, 0.1, 0.5, 1, 2, 5, 10, 25, 50, 100 and 150 ng mL^{-1}. Calculation of LOD and LOQ was the same with the LA method. To check out the contamination from vessel and fabric, a blank acid mix sample and uncoated fabric sample were separately digested. Additionally, two of SRMs (NIST-SRM 2582 and ERM-EC681k)

Table 1
Laser ablation conditions of SRMs used for calibration curve.

	Depth (μm)	Frequency (Hz)	Spot size (μm)	Scan speed (μm s^{-1})	Fluence (J/cm^2)
Blank (Adhesive agent)	10	10	75	70	1.02
NIST-SRM 612 Glass	20	20	50	250	2.30
EC681k SRM Polyethylene	10	10	75	70	1.21
NIST-SRM 2582 Powder paint	0	5	100	70	0.94

Table 2
Instrumental conditions of ICP-MS and LA-ICP-MS analysis.

ICP-MS conditions	
Radio frequency power	1200 W
Plasma gas flow	13 L min^{-1}
Auxiliary gas flow	0.75 L min^{-1}
Nebulizer gas flow	0.87 L min^{-1}
Additional gas flow (He)	208 mL min^{-1}
Sampling depth	110
Sweeps/replicate	100
Replicates/sample	3
Spray chamber temp.	3 °C
Sample, skimmer cones	Ni
Dwell time	0.01 s
Sample uptake	60 s
LA parameters	
Transport gas	Helium
Scan speed	70 μm s^{-1}
Spot size	75 μm
Pulse frequency	10 Hz
Ablation type	Raster
Focus	On sample surface (autofocus)
Uptake	20 s
Washout	90 s

were treated six times with the same procedure with samples for quality control and validation.

The developed quantitative ablation method was confirmed by an acid microwave closed vessel digestion method with 17 samples and SRMs. First of all, a few drops of acetone were applied onto the coated area of the sample to facilitate the removing of paint and stripped with the aid of a lancet as shown in Fig. 2 (right side). Stripped coatings were weighed (approx. 0.05–0.1 g) after drying at 100 ± 3 °C for a minimum of 3 h and placed in microwave vessels. Ten mL 65% (w/w) HNO_3 and 2 mL 35% (w/w) H_2O_2 were added. Sample preparation and treatment conditions are detailed in Table 3. The final solution was diluted to 25 mL volumetric flask after filtration. Samples were diluted tenfold using 2% HNO_3 and the added internal standards (20 ng mL^{-1} of Ga and In) before analysis. The analyzed conditions are also listed in Table 2.

In the statistical evaluation of the study, Spearmans's correlation test was used to determine the correlation of both methods.

3. Results and discussion

3.1. Laser ablation results

Tuning was performed using NIST-SRM 612 to achieve high and stable ion beam intensities and low oxidation rates. On the other hand, NIST-SRM 610 was used periodically as an external standard to control the variations as well as polyethylene SRM EC681k during the experiment. Also raster type ablation made it easier to achieve repetitive results for ^{208}Pb isotope. Samples were automatically calculated according to the calibration curve after treating the raw data for ablation time vs. gas blank time. The time-resolved spectra were treated to apply background correction and each sample was replicated three times in a run.

A linear calibration curve was plotted using SRMs by Laser Ablation with $R > 0.999$ correlation coefficient with calibration points of blank (adhesive agent), 38.5, 98 and 208.8 mg kg^{-1} of Pb and shown in Fig. 3 after optimization of laser parameters as described

Table 3
Acid digestion procedures of coating paints on textile products for microwave accelerated reaction system.

Sample preparation				
Vessel type	**Sample amount**	**HNO_3 (65%)**	**H_2O_2 (35%)**	
XP1500	50–100 mg	10 mL	2 mL	
MW program (Ramp to temperature)				
Power%	**Ramp** (min)	**Pressure (psi)**	**Temperature** (°C)	**Hold** (min)
100	10	300	230	15

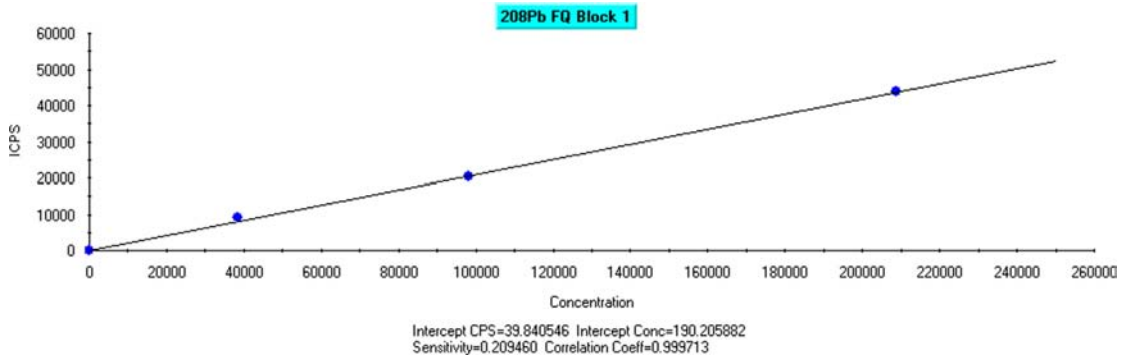


Fig. 3. Calibration curve of lead obtained by LA-ICP-MS with R=0.999 correlation coefficient.

above. Laser energy used for samples was the same with blank and SRM EC681k because of the surface similarity of coating paint matrix with polyethylene.

According to the results, 125 of 198 coating paint samples were found below 10 mg kg^{-1} (63.13%), 44 samples were found between 10 and 90 mg kg^{-1} (22.22%) and 29 of 198 coating paint samples were found over the 90 mg kg^{-1} limit level (14.65%). Numbers of samples found above 90 mg kg^{-1} Pb signified in regulations are listed in Table 4 regarding colors. Mean and median Pb concentrations of these unsuitable samples were 2357.6 and 579.0 mg kg^{-1}, respectively. Mostly yellow and its color tones such as orange, skin tone, brown, red and green were determined as positive in terms of lead. Percent of child outwear over the limitations was found to be 40.0% with 16 among 40 products collected from four different bazaars, whereas in the distribution by bazaars, almost equal distribution was observed as listed in Table 5.

3.2. Microwave-assisted acid digestion results

According to linear calibration ($R > 0.999$) in the range of 0–150 ng mL^{-1}, acceptable recovery and accuracy results of SRMs are shown in Table 6. LOD and LOQ of Pb were found to be 0.002 and 0.005 ng mL^{-1}, respectively.

Comparing the results in Table 6, validation performance of both methods were applicable with the obtained values. LOD and LOQ values and linearity range for both methods were also proper to determine Pb in terms of the accepted level. Seventeen samples were analyzed by both methods and 0.988 correlation (significant at the level 0.01; $n=16$) was found except for one sample with a result of 1539.9 and 274.2 mg kg^{-1} Pb for microwave-assisted acid digestion and laser ablation methods, respectively. Difference of this result might be caused by the heterogeneity of sampling area in the raster ablated [29]. Correlational plot comparing both methods is presented in Fig. 4.

Numbers of quantitative studies conducted by laser ablation in several types of sample are gradually increasing in recent years. Hsieh et al. reported four calibration curves built from aqueous standard solution and blood SRM applied onto membrane filter surface via pipette. Results were satisfactory for laser ablation [18]. In the other study conducted by Jurowski et al. by means of standard solution addition to the rat brain and a long established calibration method was developed [19]. Günther et al. also used standard solutions to direct liquid ablation and found the method suitable both for analyzing small volumes of complex aqueous solutions and for microanalysis of solids [20]. Additionally, matrix-matched quantitative studies to analyze forensic samples, glass, paint, etc. using laser ablation have become a powerful and flexible analytical technique for direct elemental and isotopic analysis of solids [22,23]. As a case in point, Latkoczy et al. produced inter-laboratory tests improved results for nearly all elements with a deviation of $<10\%$, and demonstrated that LA-ICP-MS can deliver absolute quantitative measurements on major, minor and trace elements [30].

To the best of our knowledge, developed and comparable quantitative laser ablation method for coating paints on textile products in this presented method is the first reported study to check the limited lead values specified in regulations. Calibration by SRMs in our study demonstrates a new approach among other calibration techniques in the area of direct analysis of solid certified standards. Besides, coated surface of samples which were

Table 4
Distribution by colors of results found over the 90 mg kg^{-1} Pb limit.

Colors	Number of colors over the limit	Total number of colors	Percentage of colors over the limited value
Beige	0	3	–
Blue/dark blue	0	29	–
Orange	3	8	37.5%
White	0	24	–
Yellow	11	27	40.7%
Red	4	16	25.0%
Black	0	30	–
Gray	0	4	–
Green	3	14	21.4%
Skin tone	6	12	50.0%
Brown	2	4	50.0%
Pink	0	18	–
Silvery	0	4	–
Purple/lilac	0	3	–
Dore	0	2	–
Total	29	198	**%14.65**

Table 5
Distribution of samples over the limit by bazaars.

Bazaar no.	Number of samples over the limit	Number of total products
1	4	10
2	3	10
3	4	10
4	5	10
Total	**16**	**40**

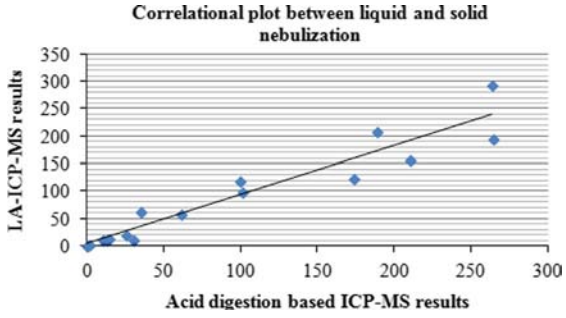


Fig. 4. Correlation plot between microwave-assisted acid digestion ICP-MS and LA-ICP-MS results of 16 coating paint samples.

Table 6
Validation results of both laser ablation and microwave-assisted acid digestion method.

Method	Linear range	LOD	LOQ	According to CRMs		
				Recovery (%)	Accuracy (Bias %)	Precision (RSD%)
Laser ablation	0–208.8 mg kg^{-1}	0.162 mg kg^{-1}	0.54 mg kg^{-1}	gls: 88.19 pe=94.58 pw=98.05	< **6.76**	< **7.29**
Microwave acid digestion	0–150 ng mL^{-1}	0.002 ng mL^{-1}	0.005 ng mL^{-1}	pe=101.3 pw=95.3	< **3.37**	< **4.67**

gls: NIST-SRM 612 (glass); pe: EC681k (polyethylene); pw: NIST-SRM 2582 (powder).

similar with polyethylene SRM ablated with the same laser energy to close the trueness. Correlation results between laser ablation and microwave-assisted acid digestion methods proved the accuracy of the selected ablation method parameters as well.

In comparison, both methods were applicable to determine the Pb level in coating paint samples in any textile product. But the LA-ICP-MS method developed in this study offers several analytical advantages. The method is less time consuming, has easy sample preparation, and has less contamination risk points. Additionally, laser ablation method made it possible to rapidly determine Pb levels of a large number of samples in the same ablation chamber. Moreover, it should not be forgotten that replication of samples is important to ensure the homogeneity of ablation surface.

4. Conclusions

The inter-comparisons presented in this paper demonstrate that both laser ablation and microwave-assisted acid digestion methods were proper to determine Pb level in a coating paint according to the validated result. And both methods could be applied not only to the textile industry but also to other consumer products such as toys, jewelry, hand tools, etc. to check the safety level of restricted inorganic compound besides Pb for children. In this study, developed full quantitative laser ablation method for coating paint on textile products is firstly published obtaining a calibration curve from solid certified materials.

Determination of trace metals such as Ni, Cd, Mn, Cu, Cr as well as Pb in textile productions is a substantial issue not only for the safety of consumers but also for the textile industry in terms of export and import control. This is also important to meet the world standards to protect the human health, to prevent environmental pollution and also to take a better place in the globalized world of trade business. In addition, primary prevention is a strategy that emphasizes the prevention of lead exposure, rather than a delayed response to exposure after it has taken place.

Acknowledgment

Authors would like to thank the Scientific Research Fund of Istanbul University, Turkey for support of this work with a Project number 39090. The authors declare that they have no conflict of interest.

References

[1] A. Castaño, J.E. Sánchez-Rodríguez, A. Cañas, M. Esteban, C. Navarro, A.C. Rodríguez-García, M. Arribas, G. Díaz, J.A. Jiménez-Guerrero, Int. J. Hyg. Environ. Health 215 (2012) 191–195.
[2] P. Heitland, H.D. Köster, Clin. Chim. Acta 365 (2006) 310–318.
[3] G.G. Rhoads, Low level lead exposure harms children: a renewed call for primary prevention, Report of the Advisory Committee on Childhood Lead Poisoning Prevention, 2012.
[4] M. Guney, G.J. Zagury, Environ. Sci. Technol. 46 (2012) 4265–4274.
[5] P. Norum, J. Ha-Brookshire, Int. J. Fashion Des. Technol. Educ. 5 (2012) 25–31.
[6] G.J. Cohen, W.E. Ahrens, J. Pediatr. 54 (1959) 271–284.
[7] E. Mowad, I. Haddad, D.J. Gemmel, Arch. Pediatr. Adolesc. Med. 152 (1998) 485–488.
[8] D. Fassin, A.J. Naudé, Am. J. Public Health 94 (2004) 1854–1863.
[9] T.A. Merritt, Pediatrics 116 (2005) 1050–1051 (author reply 1051).
[10] D. Povey, in: Anne Roberts (Ed.), The Global Lead Advice and Support Service (GLASS), The LEAD Group Inc., Summer Hill, Australia, 2010, pp. 1–6.
[11] CPSIA (U.S. Consumer Product Safety Improvement Act) Web site: Section 101. Children's Products Containing Lead, Lead Paint Rule ⟨http:/www.cpsc.gov/ABOUT/Cpsia/sect101.html⟩ (accessed 20.03.14).
[12] EN (British Standard). Safety of Toys – Part 3: Migration of Certain Elements. BS EN 71-3. European Committee of Standardization, Brussels, Belgium, 2006.
[13] C. Tonetti, R. Innocenti, AUTEX Res. J. 9 (2009) 66–70.
[14] E. Matoso, S. Cadore, Talanta 88 (2012) 496–501.
[15] C.A. Heinrich, T. Pettke, W.E. Halter, M. Aigner-Torres, A. Audétat, D. Günther, B. Hattendorf, D. Bleiner, M. Guillong, I. Horn, Geochim. Cosmochim. Acta 67 (2003) 3473–3496.
[16] D. Günther, B. Hattendorf, Trends Anal. Chem. 24 (2005) 255–265.
[17] B. Fernández, F. Claverie, C. Pécheyran, O.F.X. Donard, Trends Anal. Chem. 26 (2007) 951–966.
[18] H.F. Hsieh, W.S. Chang, Y.K. Hsieh, C.F. Wang, Talanta 79 (2009) 183–188.
[19] K. Jurowski, S. Walas, W. Piekoszewski, Talanta 115 (2013) 195–199.
[20] D. Günther, R. Frischknecht, H.J. Müschenborn, C.A. Heinrich, Fresenius J. Anal. Chem. 359 (1997) 390–393.
[21] Y. Liu, Z. Hu, S. Gao, D. Günther, J. Xu, C. Gao, H. Chen, Chem. Geol. 257 (2008) 34–43.
[22] F.A. Orellana, C.G. Gálvez, M.T. Roldán, C. García-Ruiz, Trends Anal. Chem. 42 (2013) 1–34.
[23] I. Horn, R.L. Rudnick, W.F. McDonough, Chem. Geol. 164 (2000) 281–301.
[24] M. Tuzen, A. Onal, M. Soylak, Bull. Chem. Soc. Ethiop. 22 (2008) 379–384.
[25] S. Saracoglu, U. Divrikli, M. Soylak, L. Elci, M. Dogan, J. Trace Microprobe Tech. 21 (2003) 389–396.
[26] L.J. Yost, J.D. Weidenhamer, Sci. Total Environ. 393 (2008) 348–350.
[27] J.D. Weidenhamer, M.L. Clement, Chemosphere 67 (2007) 961–965.
[28] M. Guney, G.J. Zagury, Environ. Sci. Technol. 47 (2013) 5921–5930.
[29] D. Günther, S.E. Jackson, H.P. Longerich, Spectrochim. Acta Part B 54 (1999) 381–409.
[30] C. Latkoczy, S. Becker, M. Dücking, D. Günther, J.A. Hoogewerff, J.R. Almirall, J. Buscaglia, A. Dobney, R.D. Koons, S. Montero, G.J.Q. van der Peijl, W.R. S. Stoecklein, T. Trejos, J.R. Watling, Vincent S. Zdanowicz, J. Forensic Sci. 50 (2005) 1–15.

Talanta 132 (2015) 228–233

Contents lists available at ScienceDirect

Talanta

journal homepage: www.elsevier.com/locate/talanta

Electrodialytic matrix isolation for metal cations

Shin-Ichi Ohira [a,*], Yuri Hiroyama [a], Koretaka Nakamura [a], Takumi Koda [a], Purnendu K. Dasgupta [b], Kei Toda [a]

[a] Department of Chemistry, Kumamoto University, 2-39-1 Kurokami, Kumamoto 860-8555, Japan
[b] Department of Chemistry and Biochemistry, The University of Texas at Arlington, 700 Planetarium PL, Arlington, TX 76019-0065, USA

ARTICLE INFO

Article history:
Received 19 July 2014
Received in revised form
5 September 2014
Accepted 6 September 2014
Available online 16 September 2014

Keywords:
Ion transfer device
Heavy metals
Serum
Matrix isolation

ABSTRACT

Electrodialytic ion transfer was studied as a matrix isolation tool for heavy metal determinations. An ion transfer device (ITD) was used for the transfer of heavy metal cations. Under optimized flow rates applied voltage and receptor composition, heavy metal ions were quantitatively transferred at concentrations spanning $\mu g\,L^{-1}$ to $mg\,L^{-1}$. As long as the sample pH was acidic, there was no significant sample pH effect on the transfer efficiencies. Significant salt concentrations (> 1 mM NaCl), however, decreased the transfer efficiency. This could be ameliorated (up to 5 mM NaCl) by transient instead of continuous sample introduction. The device was applied to the determination of Fe, Cu and Zn in equine and bovine serum; the reproducibility was better than conventional digestion method.

© 2014 Elsevier B.V. All rights reserved.

1. Introduction

Metals play important biologic functions in all living systems but nearly all are toxic in excess [1]. Thus, metals in various matrices, e.g., drinking and environmental waters, biofluids etc., are of wide interest. Typical analysis techniques include atomic spectrometry, induction coupled plasma mass spectrometry (ICP-MS), and ion chromatography (IC) coupled with post column reaction (IC-PCR). In particular, ICP-MS is widely used because it can provide rapid simultaneous multi element analysis with very good limits of detection [2]. If analyte concentrations are relatively high, biological samples can be directly introduced after dilution to keep matrix interferences manageable. However, this is not possible in many cases: injection of the neat or even diluted sample can cause clogging of the interface, loss of atomizing efficiency, polyatomic interferences etc. [3]. The problems are not unique to ICP-MS. In IC, IC-ICP-MS, or IC-PCR, which are particularly well suited for speciation analysis, suspended/colloidal material cause clogging while proteins exhibit strong adsorption on ion exchange columns [4].

Sample pretreatment strategies used to address these problems typically involve conventional or microwave-assisted [5] wet digestion [6–8], deproteinization [9,10], conventional or microchip based solid phase extraction (SPE) [11–13] etc. Occasionally, matrix effects can be corrected by a matrix-matched blank solution [14] or on-line standard addition [15,16]. Wet digestion is not without pitfalls; the use of large amounts of acids and chemicals invariably raise the blank [17]. Similarly in SPE, the absorption efficiency is strongly affected by the sample pH and on the specific metal of interest [18,19].

We recently reported on-line electrodialytic ion transfer devices (ITDs) for matrix isolation [20,21]. The targeted ionic solutes, small inorganic cations (alkali and alkaline earths) or anions [20], and organic acids [21] were quantitatively transferred from the sample to a deionized water acceptor leaving behind particles, proteins, and non-ionic compounds. The device design isolated the acceptor stream from the electrodes to avoid bubbles or redox conversion in the acceptor stream. While charge of ions, strongly affect their electrophoretic mobility, quantitative transfer under the optimized conditions was still possible regardless of the charge on the ion. However, detailed examination shows that multiply charged ions require slightly less applied voltage for quantitative transfer [20]. Obviously, a deionized water receptor cannot be used for transferring metal ions that form insoluble hydroxides but the use of an acidic receptor will also result in reverse transfer of the acid anion from the receptor, the net outcome being uncertain.

We optimized an ITD and its operating conditions for matrix isolation of metal ions such as Cd^{2+}, Co^{2+}, Cu^{2+}, Fe^{2+}, Fe^{3+},Ni^{2+}, Cr^{3+}, and Zn^{2+} and evaluated their transfer efficiencies in different matrices. We show here successful application of this technique for the determination of Fe, Cu, and Zn in human serum and compare them with results obtained by conventional wet digestion.

* Corresponding author. Tel.: +81 96 342 3384.
E-mail address: ohira@sci.kumamoto-u.ac.jp (S.-I. Ohira).

http://dx.doi.org/10.1016/j.talanta.2014.09.013
0039-9140/© 2014 Elsevier B.V. All rights reserved.

2. Experimental

2.1. Reagents

Chloride salts, $FeCl_3 \cdot 6H_2O$, $NiCl_2 \cdot 6H_2O$, $ZnCl_2$, $CdCl_2$ (www.wako-chem.co.jp), $CuCl_2 \cdot 6H_2O$, $CoCl_2 \cdot 6H_2O$, $CrCl_3 \cdot 6H_2O$ and $FeCl_2 \cdot 4H_2O$ (www.nacalai.co.jp) were used. As a receptor and an isolator solution, 50 mM HNO_3 was prepared daily with trace metal analysis grade nitric acid. Ultrapure water ($>$ 18.2 MΩ cm) was used throughout.

2.2. Electrodialytic metal ion transfer device

Basic ITD structure, same as that was previously described [20], consisted of five flow streams layered atop each other and isolated by membranes. All channels had dimensions of 5×40 mm wide $\times$ long and were fabricated with gaskets constructed of Parafilm® pressure-imbedded in a nylon mesh with an overall thickness of 0.13 mm. Membranes separated the different channels. The central channel is intended for the sample to flow through, atop this is a regenerated cellulose dialysis membrane (DM, SpectraPor® Biotech regenerated cellulose dialysis membrane 129 020, molecular weight cutoff 8 kDa, www.spectrumlabs.com) through which the cation receptor solution flows. This channel is bounded atop by an anion exchange membrane (MAEM, Selemion® ASV, 0.13 mm thickness); the negative electrode is placed above the MAEM. The MAEM does not allow cation transfer; despite the electric field, cations that have been transported into the cation receptor channel cannot therefore further migrate to the cathode channel. The central channel is bounded on the bottom by the same type of dialysis membrane as the one on top, the anion receptor channel follows and this is separated from the anode channel by a cation exchange membrane (MCEM, Selemion® CSO, 0.10 mm thickness, both ion exchange membranes from www.agec.co.jp). The entire assembly was held together between two poly(vinyl)chloride (PVC) end plates and a number of screws. Each PVC plate also contained a 0.2 mm deep machined flow channel for placement of the platinized titanium mesh (0.1 mm thickness) electrodes. Five pairs of fluid inlet/outlet ports served the five flow channels.

2.3. Flow system

Fig. 1 shows the system schematically. Five independently adjustable miniature peristaltic pumps (PPs, WPX1-P1/16S4, www.welco.net) coupled with Pharmed® pumping tube (0.5 mm i.d. $\times$ 3.7 mm o.d.) served the flow channels. All pump voltages were adjusted to obtain a flow rate of 150 μL min^{-1} as measured by a liquid mass flow meter (LF-F30M-A, www.horiba.com). Except as stated, the sample (0.1 mL) was introduced into the ITD by a 6-port injector (I1) into the carrier stream. The acceptor solution receiving the metal ions was directly introduced respectively into the ICP-MS nebulizer or the IC system sample loop. The influent was ultrapure water in all the channels except for the cation receptor and cathode isolator channel. Except as stated the influents for the cation receptor and cathode isolator channel were 50 mM HNO_3 and a 10 mM pH 2.1 phosphate buffer solution, respectively.

2.4. Heavy metal determination by IC-PCR, ICP-MS and AAS

Metal ion concentrations were determined with IC-PCR, ICP-MS, or Atomic Absorption spectrometry (AAS).

Ion chromatographic determination was performed with post-column derivatization with 4-(2-Pyridylazo)resorcinol (PAR) and visible absorbance detection following manufacturer recommended procedure using Ionpac® CG5A (GC, 4×50 mm^2) and CS5A (SC, 4×250 mm^2, both from www.dionex.com). The eluent containing 1.17 g of dipicolinic acid, 0.976 g of K_2SO_4, 3.70 g of KOH and 2.8 mL of HCOOH in 1 L was pumped by a double plunger pump (P1, KP12-13, www.eyela.co.jp) at 1.0 mL min^{-1}. The sample (30 μL) was injected via a 6-port injector (I2, Cheminert C2-2346EH, www.vici.com). The postcolumn reagent (0.15 g PAR, 89 mL 2-dimethylaminoethanol, 25.2 g $NaHCO_3$, and 30.4 mL NH_4OH in 1 L) was teed in at 0.7 mL min^{-1} by a second double plunger pump (P2). The effluent was put through a serpentine-II pattern knitted reactor (RC, 0.5 mm i.d., 500 μL) [22] for good mixing ($\sim$0.3 min reaction time) and the absorbance was then monitored at 530 nm by an absorbance detector (D, Kratos Spectroflow 757). Both column and postcolumn reactor were kept in a column oven (HIC-6A, www.shimadzu.co.jp) at 50 °C. The IC-PCR system could separate and determine Fe^{3+}, Cu^{2+}, Ni^{2+}, Zn^{2+}, Co^{2+}, Cd^{2+}, and Fe^{2+} with limits of detection (LODs) ranging between 3–30 μg L^{-1}.

ICP-MS (Elements, www.thermofisher.com) measurements were made with 1300 W RF power, 16.7 L min^{-1} of total argon flow, and a mass resolution of 300. The masses used for Cr, Mn, Co, Ni, Cu, Zn, and Cd were 53, 55, 59, 60, 65, 66, and 111, respectively.

Atomic absorption spectrometry (AAnalyst100, www.perkinelmer.com) was also used to determine higher levels of Cr, Mn, Cu, Zn, and Fe. Acetylene and air flows were 2 and 4 L min^{-1}, respectively. A multi-element hollow cathode lamp (Lumina®, N3050217, and N3050208 also form Perkin-Elmer) was used.

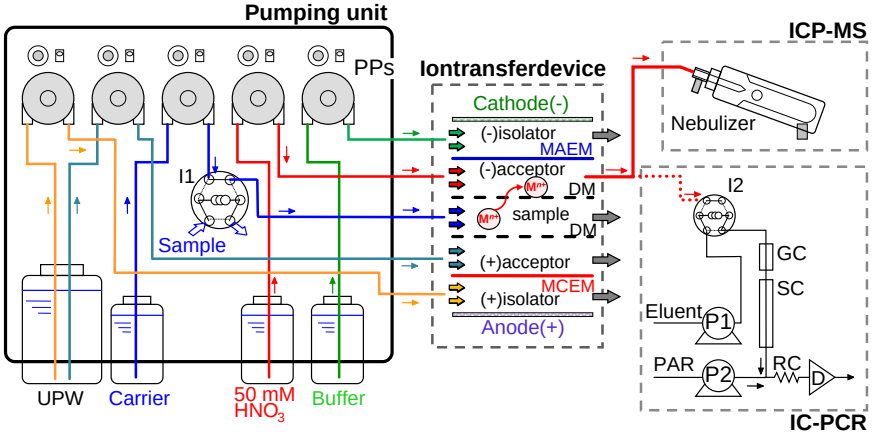


Fig. 1. Schematic flow diagram. UPW: ultrapure water, PPs: peristaltic pumps, MAEM: monovalent selective anion exchange membrane, MCEM: monovalent selective cation exchange membrane, P1, P2: plunger pumps, GC: guard column, SC: separation column, RC: reaction coil, D: absorbance detector, I1, I2: Injectors.

The wet digestion procedure used for comparative analysis was as follows: Sample (5.0 mL), H_2O_2 (2.5 mL) and concentrated HNO_3 (1.0 mL) were heated in a 15 mL polytetrafluoroethylene container until volume was reduced to 1.5–2.0 mL. After cooling, 1.0 mL conc. H_2SO_4 was added. The solution was heated again to fumes. The residue was then diluted with water, made up to volume and analyzed.

3. Results and discussion

3.1. Establishments of ITD for cationic metal ion transfer

Although alkali and alkaline earth metals have been successfully transferred from sample solution into the acceptor solution with an ITD using water in all channels, these ions form soluble hydroxides in the receptor channel. This is not possible for metals other than the alkali and alkaline earths, as the corresponding hydroxides are insoluble. Indeed, the continuous passage of a solution containing 100 μM ea. of Fe^{3+}, Cu^{2+}, Ni^{2+}, Zn^{2+}, Co^{2+}, Cd^{2+}, and Fe^{2+} in 1 mM HNO_3 and water in all other channels with the application of voltage removed significant amounts of the metals from the sample stream, the metal concentrations in the receptor stream were below the LOD of the IC-PCR system (Table 1) but none of the transferred metals were detected in the receptor stream. Most likely insoluble hydroxides are adsorbed on the membrane(s).

Acids (50 mM HNO_3) and buffer (pH 2.1, 10 mM phosphate buffer) were, respectively, used as (−)acceptor and (−)isolator to avoid formation of insoluble hydroxides. The transfer efficiencies, which is defined as the response ratio with and without ITD treatment, improved dramatically and except for Fe^{3+}, near-quantitative transfer was achieved. The receptor acidity was high enough to avoid formation of hydroxides and keep it acidic despite the unavoidable transfer of some of the NO_3^- to the central compartment and hence to the anode receptor. In addition, the highly conductive (−)acceptor and (−)isolator solution decreased the electrical resistance of acceptor channel, and as a result at a constant applied voltage, the electric field strength on the sample channel increased, promoting the desired metal ion transport rate. Thus most of targeted metal ions were quantitatively transferred from a sample to an acceptor solution. However sufficient loss of nitrate towards the sample and the (+)isolator channels and its replacement by the phosphate buffer ion in the receptor channel occurred, causing the receptor pH to increase from ~1.3 to 3.03 during passage through the ITD. Even though at pH 2.1 $H_2PO_4^-$ is the dominant anionic form in solution in a phosphate system, phosphate is not necessarily transported through an AEM as the singly charged species. Ion exchange membranes can be made selective towards monovalent ions by incorporating a very thin layer of an oppositely charged layer atop a conventional ion exchange membrane [23]. For example, incorporating a very thin, highly cross-linked cation exchanger layer atop a standard anion exchange membrane greatly inhibits passage of multivalent anions and such a membrane is available as a monovalent selective anion exchange membrane (MAEM); a monovalent selective cation exchange membrane (MCEM) is correspondingly made of highly cross-linked anion exchange membrane atop a conventional CEM (www.selemion.com). We found it advantageous to use the MAEM and the MCEM, rather than the conventional ion exchange membranes; the pH of the (−)acceptor solution in this case increased barely over that of the initial 50 mM HNO_3.

While other ions were transferred near-quantitatively, ion transfer efficiency for Fe^{3+} was poor. Curiously, replacing HNO_3 with either trifluoroacetic acid (TFA) or $HClO_4$ as the (−)acceptor solution provided near-quantitative transfer for Fe^{3+}. Nitrate forms a complex with Fe^{3+} with the first formation constant being ~10 [24] while it is known that no complexation occurs with perchlorate [25]. There is no available data on the solution phase association of Fe^{3+} with CF_3COO^-; triflate is not known for its complexing properties – we presume that no complexation occurs here either. We ascribe the better performance of $HClO_4$ or CF_3COOH acceptors because the corresponding anions readily move through the dialysis membrane to the sample channel. If they form a lower mobility adduct than the form in which the cation was initially present, transfer will be inhibited.

3.2. Parameter optimizations

Acceptor acid concentration, applied voltage, and solution flow rates were optimized.

The effect of acceptor acid concentration was further examined for HNO_3 and TFA (Fig. 2a). The transfer efficiencies for all tested metal ions increased with increasing (−)acceptor acid concentration. All metal ions tested except Fe^{3+} were quantitatively transferred with 50 mM HNO_3. Higher HNO_3 concentrations resulted in excessive Joule heating ($i > \sim 0.15$ A) and were not pursued. All tested metal ions, including Fe^{3+}, were quantitatively transferred with 50 mM TFA. TFA was only used for IC-PCR detection as the metal background of our particular TFA reagent was too high for ICP-MS.

The applied voltage (V_{app}) provides the motive force for metal ion transport. The effect of varying V_{app} between 0 and 20 VDC is shown in Fig. 2b (100 μM ea. metal ion in a mixture, 50 mM TFA acceptor). Predictably, transfer efficiency increased with increasing

Table 1
Device configurations and observed metal ion concentrations.

	Experimental conditions				Observed concentration (μM)[a]								pH
	CEM	Acceptor (−)	AEM	Isolator (−)	Solutions	Fe^{3+}	Cu^{2+}	Ni^{2+}	Zn^{2+}	Co^{2+}	Cd^{2+}	Fe^{2+}	
1	Normal	DIW	Normal	DIW	Acceptor (−)	ND	ND	ND	0.4	ND	ND	ND	9.851
					Sample	ND	0.18	ND	0.7	ND	ND	ND	2.994
2	Monovalent	DIW	Monovalent	DIW	Acceptor (−)	2.2	4.3	3.8	4.7	3.2	3.3	0.9	8.122
					Sample	20.9	28.3	37.5	29.4	28.1	25.4	26.8	3.096
3	Monovalent	50 mM HNO_3	Monovalent	pH 2.1 buffer	Acceptor (−)	48.4	99.1	97.2	101	100	99.8	96.6	1.740
					Sample	4.3	ND	ND	ND	ND	ND	ND	2.148
4	Monovalent	50 mM TFA	Monovalent	pH 2.1 buffer	Acceptor (−)	93.9	97.7	98.5	97.2	98.7	97.6	98.1	1.612
					Sample	ND	ND	ND	ND	ND	ND	ND	2.181
5	Normal	50 mM HNO_3	Normal	pH 2.1 buffer	Acceptor (−)	46.9	99.5	103	99.2	103	99.4	97.6	3.032
					Sample	5.2	ND	ND	ND	ND	ND	ND	2.018

[a] The introduced ion concentration was 100 μM ea., ND: not detected.

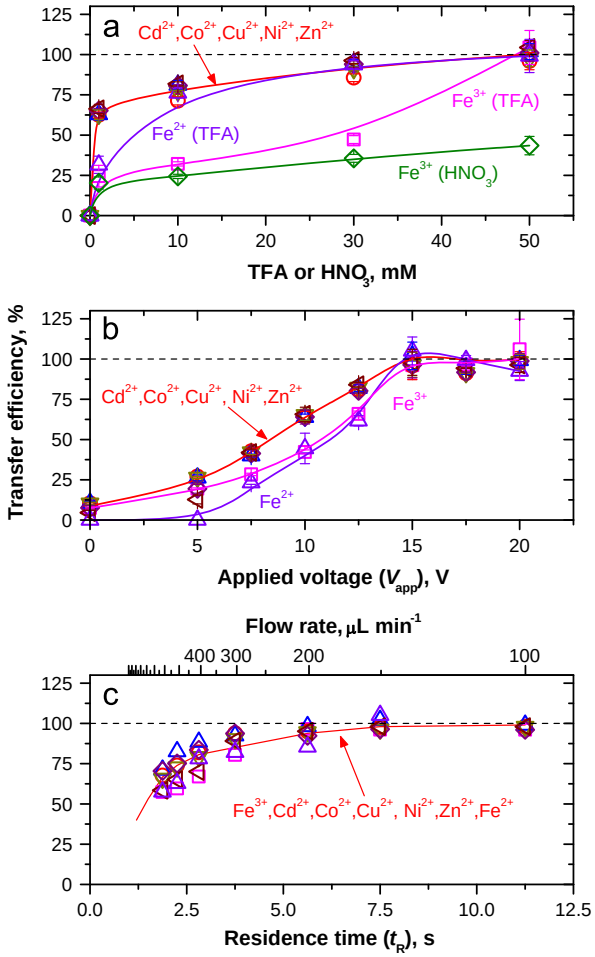


Fig. 2. Optimization of the effective factors. Optimization of the effective factors, acid concentrations (a), applied voltage (b), and residence time (c). The experimental conditions were (a) applied voltage: 15 V, solution flow rates:100 μL min^{-1}, (b) acceptor solution: 50 mM TFA, solution flow rates: 100 μL min^{-1}, and (c) acceptor solution: 50 mM TFA, applied voltage: 15 V.

V_{app}, reaching ≥95% for all tested metals by ~15 V. Transfer efficiency actually decreased slightly at V_{app} > 15 V because of back transport from acceptor to sample solution with larger Joule heating caused by larger currents [20]. V_{app}=15 V was used for all further studies.

The sample solution flow rate controls the ITD residence time. The transfer efficiencies as a function of residence times/flow rates are shown in Fig. 2c. For convenience, all flow rates were changed at the same time. Quantitative transfer was asymptotically approached with decreasing flow rate. We conducted all further experiments with a flow rate of 150 μL min^{-1} (t_R=7.5 s).

Metal ions mixture standards from μg L^{-1} to mg L^{-1} concentration levels were introduced into the ITD and analyzed by ICP-MS and AAS. Transfer efficiencies, obtained from the slopes of calibration curves are summarized in Table 2. At μg L^{-1} concentration levels, all metal cations studied were transferred with 97–104% efficiency. All but Fe^{2+}, Co^{2+}, and Ni^{2+} were tested at the 1–5 mg L^{-1} concentration as well and exhibited 97–99% transfer efficiency.

3.3. Effects of sample pH on ITD

Sample pH greatly affects chelating resin-based SPE of trace metals as the conditional formation constants are strongly pH-dependent. Sample pH must be preadjusted and often auxiliary weak complexing agents added to prevent precipitation [18,19]. In practice, sample pretreatment prior to chelating resin SPE must be optimized for each sample type. As the present ITD does not depend on chelation or ion exchange selectivities, it was of particular interest to examine the pH effects on the transfer efficiencies for different metals in the present device (Fig. 3). The sample standard (2.5 mg L^{-1}) pH was adjusted with acid or buffers: nitric acid for pH 1–3, 1 mM CH_3COOH/CH_3COONH_4 for pH 4–6, 1 mM K_2HPO_4/KH_2PO_4 for pH 6 and 7, 1 mM NH_3/NH_4Cl for pH 8–10. The sample was then introduced into the ITD. Both the pH-adjusted standard and the ITD-processed acceptor solutions were analyzed by AAS. The response ratio was considered as the recovery. Predictably, at pH < 2, recovery was subquantitative (~70–95% at pH 1), due to

Table 2
Transfer efficiencies under optimized conditions.

Ions	Transfer efficiency, %	
	Low levels (10–50 μg L^{-1})	High levels (1–5 mg L^{-1})
Cr^{3+}	99.6 ± 4.2	99.3 ± 1.8
Mn^{2+}	102 ± 5.3	98.3 ± 4.2
Co^{2+}	99.6 ± 4.2	–[a]
Ni^{2+}	104 ± 3.8	–[a]
Cu^{2+}	104 ± 2.7	96.3 ± 4.8
Zn^{2+}	101 ± 2.5	97.4 ± 6.2
Cd^{3+}	96.7 ± 2.9	–[a]
Fe^{2+}	–[a]	98.3 ± 4.2

[a] Not tested.

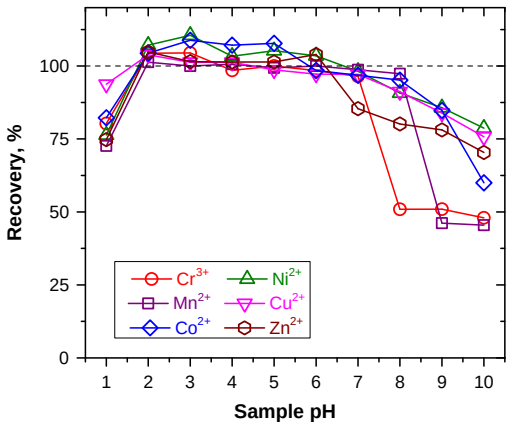


Fig. 3. Sample pH effects on the transfer efficiencies. Solution pH effects on the transfer efficiencies. Experimental conditions were applied voltage: 15 V, acceptor solution: 50 mM TFA, and solution flow rates: 100 μL min^{-1}.

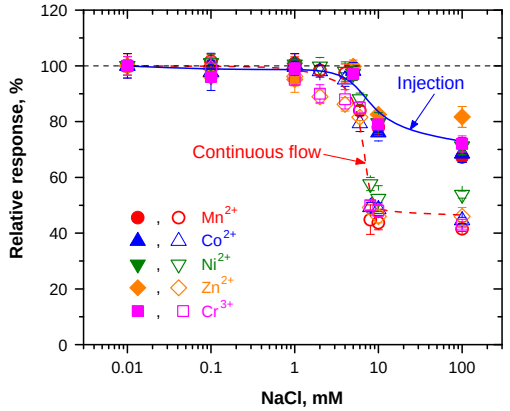


Fig. 4. Effects of sample salt concentration on transfer efficiency. Effects of sample salt concentration on transfer efficiency Experimental conditions were as same as Fig. 3.

Table 3
Comparison of the obtained metal ion concentrations with wet decomposition and present sample pretreatment method.

Serum sample	Fe^{2+}				Cu^{2+}				Zn^{2+}			
	Wet decomposition		Present method		Wet decomposition		Present method		Wet decomposition		Present method	
	Conc. ($mg\ L^{-1}$)	RSD (%)	Conc. ($mg\ L^{-1}$)	RSD (%)	Conc. ($mg\ L^{-1}$)	RSD (%)	Conc. ($mg\ L^{-1}$)	RSD (%)	Conc. ($mg\ L^{-1}$)	RSD (%)	Conc. ($mg\ L^{-1}$)	RSD (%)
Bovine	1.85 ± 0.18	9.7	2.43 ± 0.07	3.0	2.53 ± 0.80	32	2.54 ± 0.08	3.0	2.89 ± 0.31	11	2.15 ± 0.08	3.7
Bovine	1.95 ± 0.46	24	1.96 ± 0.09	4.6	2.60 ± 0.63	24	3.04 ± 0.11	3.6	6.32 ± 0.55	8.7	7.05 ± 0.34	4.9
Equine	2.89 ± 0.26	8.9	2.13 ± 0.11	5.1	2.80 ± 0.62	22	3.78 ± 0.19	5.1	1.88 ± 0.24	13	2.07 ± 0.08	4.1

competition with the large amount of H^+ present. But in the important practical pH range of 2–7, ITD recovery was essentially quantitative except for Zn^{2+} at the higher pH end, likely due to the formation of neutral oxide/hydroxide. The immunity to pH dependence is all the more remarkable in comparison to iminodicarboxylate resins where the recoveries of alkaline earth metals, as well as those Cr, Co, and Ni are reportedly strongly affected by sample pH in this range [18,19]. At $pH > 7$, the recovery of all metals studied predictably began to be affected to varying degrees, the recovery generally decreasing with increasing pH due to the formation of oxides/hydroxides.

3.4. Effects of salts in sample solution

We have previously observed that the ITD could quantitatively transfer common inorganic ions up to ~20 meq/L [20]. The present device is not intended for concentrating trace metals from highly saline matrices, e.g., seawater but to perform matrix cleanup, e.g., in biological samples, rather than having to digest them. Additionally, in biological samples it may have the potential to distinguish free metal ions from those that are covalently bound, e.g., as the metal center in a metalloenzyme molecule. Nevertheless, even most such samples will contain significant amounts of alkali or alkaline earth cations aside from trace metal ions of interest. These cations, of higher mobility and generally present in greater concentrations, are expected to decrease trace metal recoveries. The objective was to determine to what extent of salt can be tolerated before the transfer efficiencies suffers markedly.

The recovery of 100 $\mu g\ L^{-1}$ Mn^{2+}, Co^{2+}, Ni^{2+} and Zn^{2+} were studied in varying concentrations of NaCl as the matrix. The dominant ions in biological fluids were selected as the analytes in this study. The recoveries began to decrease markedly at NaCl concentration > 1 mM (Fig. 4). Several factors may be responsible for this degraded performance: (i) competition from Na^+ (ii) decreased field strength from increasing sample conductivity, and formation of chloro complexes.

In the mode of operation described above, the membranes operate in a steady state transfer mode. It is well known for ion exchange membrane based electrodialytic suppressors used in IC that they will handle a much larger concentration and perform quantitative ion transfer when the same substance is injected as a transient plug rather than in a continuous basis. Injection of a discrete sample is also a more realistic test because sample availability may preclude steady state operation in many cases. We explored 100 µL injection of the trace metals in a saline matrix into a 1 mM HNO_3 carrier stream; the acceptor solution was directly introduced into the ICP-MS nebulizer, resulting in a response peak. Greater tolerance to salt was indeed observed; recoveries in this case were unchanged up to a 5 mM NaCl matrix. We have not explored if higher matrix concentrations can be tolerated with a smaller sample volume.

3.5. Application to serum samples

To evaluate and validate the present method, serum samples were (a) pretreated with the ITD or (b) digested; both were then analyzed by IC-PCR. A prescribed wet digestion method [26] was followed in modified form (see Section 2). The analytical results from the two methods (Table 3) statistically indistinguishable based on a *t*-test [27]. Relatively poor reproducibility of wet digestion methods has previously been reported [28]; the repeatability of the present method (3–5% RSD) was clearly much better.

4. Conclusions

An electrodialytic ion transfer device for heavy metal cations was introduced for matrix isolation and its successful use demonstrated. In the absence of large concentrations of other cations (equivalent to ≤ 5 mM NaCl), trace metal cations can be quantitatively transferred from the sample to an acidic acceptor solution that can be directly introduced to most analysis systems. The device will be particularly applicable to isolating metal ions from matrix components such as proteins, cells, particulate material, and non-ionic compounds.

Acknowledgments

The part of this study was supported by the Japan Science and Technology, Development of Systems and Technology for Advanced Measurement and Analysis program (SENTAN) and Steel Foundation for Environmental Protection Technology. The participation of PKD was made possible through NASA grant NNX11A066G.

References

[1] G. Jarzyńska, J. Falandysz, Environ. Int. 37 (2011) 882–888.
[2] D. Beauchemin, Anal. Chem. 74 (2002) 2873–2894.
[3] T.W. May, R.H. Wiedmeyer, At. Spectrosc. 19 (1998) 150–155.
[4] J.S. Fritz, D.T. Gjerde, Ion chromatography, fourth ed., Wiley-VCH, Weinheim, Germany, 2009.
[5] C.-C. Huang, M.-H. Yang, T.-S. Shih, Anal. Chem. 69 (1997) 3930–3939.
[6] M. Krachler, K.J. Irgolic, J. Trace Elem. Med. Biol. 13 (1999) 157–169.
[7] M.-A. Vaughan, A.D. Baines, D.M. Templeton, Clin. Chem. 37 (1991) 210–215.
[8] R. Forrer, C. Wenker, K. Gautschi, H. Lutz, Biol. Trace Elem. Res. 81 (2001) 47–62.
[9] C.-S. Hsiung, J.D. Andrade, R. Costa, K.O. Ash, Clin. Chem. 43 (1997) 2303–2311.
[10] T. Kita, H. Morita, M. Umeno, S. Kita, S. Shimomura, Bunseki Kagaku 38 (1989) 547–552.
[11] Y. Sohrin, S. Urushihara, S. Nakatsuka, T. Kono, E. Higo, T. Minami, K. Norisuye, S. Umetani, Anal. Chem. 80 (2008) 6267–6273.
[12] T.-T. Shih, W.-Y. Chen, Y.-C. Sun, J. Chromatogr. A 1218 (2011) 2342–2348.
[13] S. Kagaya, Y. Saeki, D. Morishima, R. Shirota, T. Kajiwara, T. Kato, M. Gemmei-Ide, Anal. Sci. 29 (2013) 1107–1112.
[14] H. Vanhoe, C. Vandecasteele, J. Versieck, R. Dams, Mikrochim. Acta 99 (1989) 373–379.
[15] C. Huang, D. Beauchemin, J. Anal. At. Spectrum 18 (2003) 951–952.
[16] D. Beauchemin, Anal. Chem. 57 (1995) 1553–1557.

[17] S.-H. Nam, H. Chung, J.-J. Kim, Y.-I. Lee, Bull. Korean Chem. Soc. 29 (2008) 2237–2240.
[18] S. Hirata, T. Kajiya, M. Aihara, K. Honda, O. Shikino, Bunseki Kagaku 52 (2003) 1091–1104.
[19] Y. Furusho, M. Ono, M. Yamada, K. Ohashi, T. Kitade, K. Kuriyama, S. Ohta, Y. Inoue, S. Motomizu, Bunseki Kagaku 57 (2008) 969–989.
[20] S. Ohira, K. Kuhara, M. Kudo, Y. Kodama, P.K. Dasgupta, K. Toda, Anal. Chem. 84 (2012) 5421–5426.
[21] S. Ohira, K. Kuhara, A. Shigetomi, T. Yamasaki, Y. Kodama, P.K. Dasgupta, K. Toda, On-line electrodialytic matrix isolation of organic acid analytes for chromatographic determination, J. Chromatogr. A (2014) (submitted for publication).
[22] S. Waiz, B.M. Cedillo, S. Jambunathan, S.G. Hohnholt, P.K. Dasgupta D.K. Wolcott, Anal. Chim. Acta 428 (2001) 163–171.
[23] H.-Y. Lu, C.-S. Lin, S.-C. Lee, M.-H. Ku, J.-P. Hsu, S. Tseng, S.-H. Lin, AIChE J. 57 (2011) 1033–1042.
[24] B.N. Mattoo, Z. Phys. Chem. 19 (1959) 156–167.
[25] H. Coll, R.V. Nauman, P.W. West, J. Am. Chem. Soc. 81 (1959) 1284–1288.
[26] Application note 108, Determination of Transition Metals in Serum and Whole Blood by Ion Chromatography, ⟨www.dionex.com⟩.
[27] G.D. Christian, P.K. Dasgupta, K.A. Schug, Analytical Chemistry, seventh ed., Wiley, New York (2013) 93–94.
[28] H. Altundag, M. Tuzen, Food Chem. Toxicol. 49 (2011) 2800–2807.

Talanta 132 (2015) 234–238

Contents lists available at ScienceDirect

Talanta

journal homepage: www.elsevier.com/locate/talanta

An in-situ electropolymerization based sensor for measuring salt content in crude oil

Rashed M. Aleisa, Naim Akmal *

Saudi Aramco Research and Development Center (R&DC), Dhahran 31311, Saudi Arabia

ARTICLE INFO

Article history:
Received 28 May 2014
Received in revised form
8 September 2014
Accepted 9 September 2014
Available online 18 September 2014

Keywords:
Crude oil
Electropolymerization
Salt sensor
Salt in crude oil
Polymer

ABSTRACT

Determining salt content is a vital procedure in the petroleum industry during the process of crude oil transportation, refining and production. Monitoring the salinity value using a fast and direct technique can substantially lower the cost of crude oil in its processing and its production stages. In the present work, a novel analytical method was developed to detect the amount of salt present in crude oil in a quick and reliable manner. The measurement is based on the rate of in-situ electropolymerization of a monomer such as aniline in association with the salt content in the crude oil. The salt dispersed in the hydrocarbon matrix is used as an electrolyte in the electrolytic system to induce an electropolymerization reaction upon the induction of voltages, in which the salt content is measured corresponding to the polymeric film formation on the working electrode surface. Acetonitrile and N-methylpyrrolidone (NMP) were used in the electrochemical cell as solvents, and cyclic voltammetry tests were performed for Arabian crude oil solutions in the presence of aniline. The method has shown an excellent detection response for very low concentrations of salt. Four Arabian crude oils with salt concentrations of 34.2, 28.5, 14.3 and 5.71 mg L^{-1} have produced current intensity of 180.1, 172.6, 148.1 and 134.2 μA at an applied current potential of 1.75 V (vs. Ag/AgCl), respectively. A Calibration curve was obtained in the range of 5–35 mg L^{-1}, giving limits of detection and quantitation at 1.98 and 5.95 mg L^{-1}, respectively. The in-situ electropolymerization based sensor has significant advantages over the existing techniques of salt monitoring in crude oil such as fast response, temperature independency, electrode stability, and minimum sample preparation.

© 2014 Elsevier B.V. All rights reserved.

1. Introduction

In the oil and gas industry, the concentration of salt in crude oil produced depends mainly on the production source such as a drilling well and a reservoir [1]. Interaction of hydrochloric acid and dolomitic limestone with the contents of the well during its treatment causes the formation of sodium, magnesium, and calcium chlorides in the crude oil [2]. Additionally, the injection of seawater into the wellhead for enhancing oil recovery leads to crude oil contamination mostly by sodium chloride [1,3]. Salinity in crude oil creates problem for the petroleum industry. Large quantities of salt in crude oil may cause severe corrosion in pipelines, storage tanks, preheat exchangers, and condensers [1–5]. Additionally, deactivation and fouling of catalysts may take place during the refining process due to the high salinity of the hydrocarbons [4]. The salt content also negatively impacts the market price of crude oil per barrel which ultimately lowers net return on investment [5]. The total amount of salt present in crude oil can vary dramatically, wherein it can be as high as 200,000 mg L^{-1} or as low as 10 mg L^{-1} [3]. Refining plants are equipped with a desalting process that is capable of reducing the amount of salts to a predefined level. Hence, the crude oil is analyzed before and after the desalting process to monitor the salt value and determine the efficiency of the desalting process.

Measurement of salt in crude oil is generally based on indirect techniques i.e., by measuring the electrical property of the hydrocarbon mixture [3]. This technique measures the difference in the electrical potential between conducting electrodes in a mixture of crude oil and solvents, wherein the salinity of the solution mixture is tied to the conductivity values reported [3]. Various analyzers utilizing such sensing techniques have been developed and are commercially available [1]. However, this sensing technique poses significant limitations such as reliability, long life-span, and accuracy during real-time analysis. Furthermore, electrode surface in these sensors is prone to corrosion, which changes its surface characteristics leading to erroneous readings. The physical deterioration of the electrode surface produces a larger error, especially during the measurement of low salt concentrations.

* Corresponding author. Tel.: +966 13 876 8334; fax: +966 13 876 8565.
E-mail address: naim.akmal@aramco.com (N. Akmal).

http://dx.doi.org/10.1016/j.talanta.2014.09.016
0039-9140/© 2014 Elsevier B.V. All rights reserved.

In addition, the laboratory method based on the ASTM method (D-3230) for measuring salt content in crude oil requires prior extraction of salt and extensive use of solvents [3].

We present in this paper, the development of an indirect and novel method based on electro-initiated polymerization via the controlled potential method to monitor the amount of salt present in crude oil [6]. The electropolymerization reaction is based on a free radical mechanism as the monomer polymerizes through applied potentials (i.e., voltages) in the presence of electrolytes. The mechanism and kinetics of many electropolymerizable monomers have received great attention in the past [7–10]. Various monomers can be used in electropolymerization methods including aromatic benzoid compounds such as aniline and phenylenediamine. The reaction of these monomers is usually an oxidative coupling polymerization with a small possibility of reductive polymerization [6]. The analytical solution described below utilizes this technique which involves the basic elements of an electrolytic chemical cell. In essence, the salt present in the crude oil can be utilized as a conductive solution for an electropolymerizable monomer, which on contact with electrical applied voltages, will start the polymerization process. The relationship between solution conductivity and the produced amount of polymeric material has been previously studied [11]. It is expected that an increase in electrolyte concentration will increase the rate of electropolymerization reaction [11]. Hence, the salt concentration in an electrolytic system can be measured by calculating the rate of electropolymerization (i.e., amount of the produced polymer on the working electrode). This hypothesis is intended to be used to measure the salt concentration in crude oil with a similar electrolysis method. This technique is expected to provide a direct readout of the salt value in a real-time analysis of crude oil without extensive sample preparation, leading to an enhanced capability of salt monitoring during crude oil transportation and processing.

2. Experimental

2.1. Materials and apparatus

Acetonitrile, thiophene, aniline, NMP, methanol, butanols, dibenzothiophene (DBT), sodium chloride (powder), dichloromethane, and hexane were purchased from Sigma-Aldrich, and methyl-tetra-butyl-ether (MTBE) was purchased from Burdick and Jackson (Honeywell). Arabian crude oil samples were obtained from the Abqaiq oil field in Saudi Arabia. Deionized water (DI) with 18 $M\Omega\,cm^{-1}$ was obtained by the Milli-Q system in our laboratory. The silver/silver chloride reference electrode (Ag/AgCl), platinum disk electrodes, and polishing kit were purchased from (BASi) Bioanalytical Services. Cyclic voltammetry experiments were performed on the EG&G potentiostat (Model 263A). The reference electrode (Ag/AgCl) was fitted with a flexible connector. All chemicals were used as received without any further purification.

2.2. Electropolymerization of aniline, DBT, and thiophene

The electropolymerization reaction was conducted using a similar procedure described in the literature [6–9]. Initially, 0.25 g of sodium chloride was dissolved in 1.0 mL of DI water to be used as the electrolyte solution. The mixture was then added to a 0.5 mL solution of aniline in the presence of 2.0 mL of acetonitrile. The prepared mixture was stirred using a magnetic stirrer for 15 min at an ambient temperature. Counter, reference and working electrodes were placed inside the mixture, and cyclic voltammetry was performed on the solution using an EG&G potentiostat. The potentiostat was scanned in the range of −3.0 to 4.0 V (vs. Ag/AgCl) electrode at a sweeping rate of 10 mV/s. The solution stirring rate during the cyclic voltammetry was kept low because a high stirring rate can hinder the rate of electropolymerization [10]. The experiment was repeated for other monomers as well (i.e., DBT and thiophene) under the same experimental conditions.

2.3. Electropolymerization of aniline in the presence of crude oil

The electropolymerization of aniline in the presence of crude oil was carried out using the same procedure as described before. However, NMP was added to the solution to enhance the electroconductivity of the mixture. 1.0 mL of aniline was initially dissolved in 5 mL of acetonitrile using a magnetic stirrer under an ambient temperature. In a separate container, 3.0 μl of crude oil was dissolved in 5 mL of NMP under the same conditions. Both solutions were then mixed together and stirred for 15 min with a magnetic stirrer. A standard amount of aqueous sodium chloride solution with a concentration of 3.4×10^{-6} mol L^{-1} was added to the mixture while stirring to ensure a standard concentration of salt present in the mixture. The final solution was placed inside a small glass vessel fitted with three electrodes. Once the electrodes were connected to the potentiostat, a sweeping potential was applied across the counter and working electrodes in the reaction cell using the same cyclic voltammetry parameters. These steps were repeated for four different Arabian crude oil samples, with four different quantities of salt ranging from 4 to 35 mg L^{-1}. The actual amount of salt present in the crude oil was determined by the ASTM Standard Method (D-3230).

3. Results and discussion

3.1. Electrolysis of monomers using cyclic voltammetry

A platinum disk electrode,with a small surface area (1 cm^2), was used as the working electrode so that very small quantities of analyte (i.e., crude oil) in micro liters are sufficient for the in-situ electropolymerization, while a platinum electrode with a larger surface area (1.5 cm^2) was employed as a counter electrode. Electrodes and solution were placed in a specially designed vessel, in which the electrode surface and the reference electrode junction area were completely immersed in the mixture to sustain electrical interference without noise or abnormalities. The sweeping of electrical voltages, at the monomer specific electropolymerization potential, induces the formation of a thin layer of polymeric film on the working electrode surface. The final output of the electrical scanning potentials represents the voltammogram of current vs.voltage; where the peak current (intensity) reflects the amount of the produced polymer on the working electrode. The intensity of the peak can be then correlated to the amount of salt present in the hydrocarbon matrix.

The first stage of the analytical method development consists of selecting an appropriate monomer for the in-situ electropolymerization reaction. DBT, thiophene, and aniline were therefore tested as potential monomers. The reaction was conducted without the crude oil mixture using only a 1.2×10^{-5} mol L^{-1} of aqueous sodium chloride solution. The resulting voltammograms of each monomer are shown in Figs. 1–3 for DBT, thiophene, and aniline, respectively. An electropolymerization reaction was not observed in the DBT solution as seen from the absence of a current peak in Fig. 1. This could be due to the steric hindrance effect present in the DBT structure that impedes the initiation of free radicals in a low salt content. Electrolysis of thiophene has produced a polymeric film as apparent from the current peak in Fig. 2. The thiophene monomer was electropolymerized at a current potential of 1.6 V (vs. Ag/AgCl), which produced a current intensity of 135 μA. However, a further repetition of the

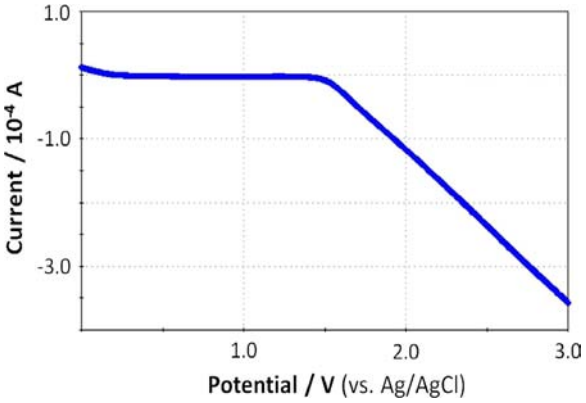


Fig. 1. Voltammogram of DBT in acetonitrile with 1.2×10^{-5} mol L^{-1}aqueous sodium chloride solution at a scan rate of 10 mV/s.

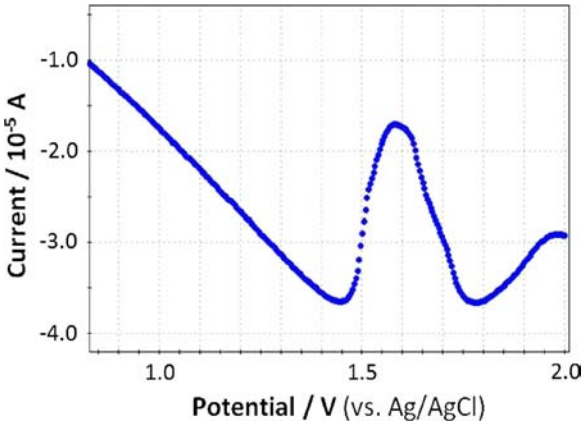


Fig. 2. Voltammogram of thiophene in acetonitrile with 1.2×10^{-5} mol L^{-1}aqueous sodium chloride solution at a scan rate of 10 mV/s.

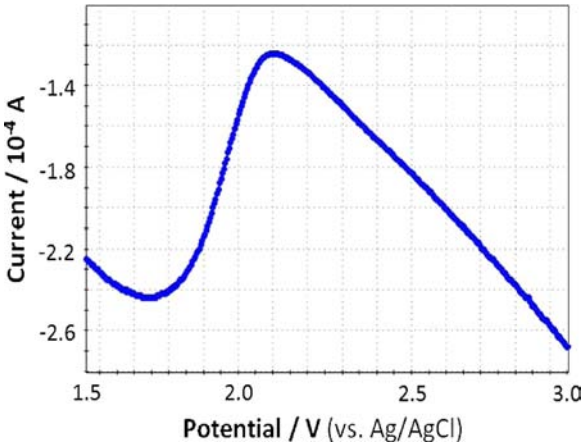


Fig. 3. Voltammogram of aniline in acetonitrile with 1.2×10^{-5} mol L^{-1}aqueous sodium chloride solution at a scan rate of 10 mV/s.

experiment was performed which revealed the non reproducibility of the thiophene electropolymerization. The inconclusive result failed to provide a basis for thiophene to be used as a monomer for this analytical technique. In contrast, electrolysis of the aniline solution has produced a distinguished peak as seen in Fig. 3, which indicates the presence of an electropolymerization reaction at a current potential 2.1 V (vs. Ag/AgCl). The resulting current intensity was reproducible and the polyaniline film was found to be very stable. The reproducibility of the current intensity and stability of the polymeric film were the basis for incorporation of aniline in the analytical technique. The peak height of the aniline monomer is sufficient for crude oil analysis, considering the small amount of salts usually present in the hydrocarbon matrix after an effective desalting process.

3.2. *Effect of aqueous salt concentration on the electropolymerization rate of aniline*

The concept of measurement suggests that an increase in the polymerization rate is due to an increase in the amount of electrolyte present in the solution. To prove this hypothesis, the effect of sodium chloride concentration on the rate of aniline electropolymerization has to be initially studied without the presence of crude oil. The electrolysis of aniline was repeated using aqueous sodium chloride solutions with various concentrations ranging from 2.0×10^{-7} to 8.6×10^{-6} mol L^{-1}. Current intensities of the formation of polyaniline were measured at the same current potential 2.1 V (vs. Ag/AgCl). The peak heights for each solution were then plotted against the salt concentration in Fig. 4. The linearity of the graph illustrates that the rate of electropolymerization (amount of polyaniline produced) is directly proportional to the salt concentration in the solution. The results indicate that the electrolyte concentration in the aqueous solution controls the polymerization rate in an isothermal condition. This is in complete match with the conclusion of the previous results [11]. The previous study also concluded that an increase in concentration of sodium chloride will increase the electropolymerization rate of aniline in an aqueous solution [11]. This is mainly due to the presence of the anions in the system upon dissolution of the electrolytes that are involved in the polymerization reaction. This conclusion was assumed for aniline electropolymerization, since the produced polyaniline contains counter anions [11].

3.3. *Measurement of salt concentration in Arabian crude oil*

The relationship between salt concentration and the rate of aniline electropolymerization presented in Fig. 4 shows that at low concentrations of salt present in the solution, specifically below 1.1×10^{-6} mol L^{-1}, electropolymerization reaction was not induced in the hydrocarbon mixture. This may indicate that a very low amount of salt present in the crude oil cannot be detected using the in-situ electropolymerization method, which counts as a major obstacle for its reliability and effectiveness. However, a standard addition technique can be employed to resolve this limitation. A calculated amount of sodium chloride solution that has a concentration higher than 1.1×10^{-6} mol L^{-1}can be added

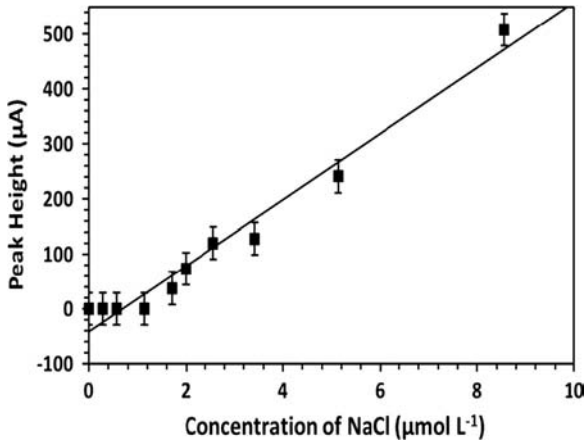


Fig. 4. The relationship between the salt amount in different concentration of sodium chloride solutions and the produced amount of polyaniline film on the working electrode represented by the peak height (current intensity).

during the solution and solvent mixing steps to set a measurable value beyond the limitations of the technique. In this manner, any concentration of salt in crude oil lower than 1.1×10^{-6} mol L^{-1}can be detected. The standard addition amount used here for the analysis of Arabian crude oil samples was 3.4×10^{-6} mol L^{-1} aqueous solution of sodium chloride. This amount was added to the acetonitrile solvent during the sample preparation steps.

In order to measure the salt amount present in crude oil, the same experimental scheme cannot be followed because of the complex nature of the inorganic materials present in the hydrocarbon matrix. The inorganic contents of crude oil are not fully dislodged upon its dissolving with a normal solvent leading to the absence of electrolytes in the system. Therefore, using a compatible solvent that dissolves the hydrocarbon mixture and the aqueous solution is mandatory for the proposed in-situ system. Furthermore, the selected solvent should be capable of enhancing the conductivity of the mixture, since the electrical properties of crude oil are known to be very poor [3]. After experimenting with numerous solvents, such as NMP, MTBE and methanol; NMP was found to be the most suitable solvent for the method. NMP had the ability to fully dissolve the crude oil in the mixture while dislodging the inorganic salts (mostly sodium chloride) present in the crude oil and enhanced the conductive properties of the hydrocarbon mixture. Therefore, the described method of electropolymerization reaction was modified by dissolving the crude oil in NMP prior to its addition into the reaction mixture. This modification ensures accurate measurement of the salt present in crude oil.

Four Arabian crude oils with salt concentrations of 34.2, 28.5, 14.3, and 5.71 mg L^{-1} (based on ASTM Method D-3230) were tested using the in-situ electropolymerization method. The overlaid voltammograms are shown in Fig. 5. The current intensities of each sample were calculated and the results are summarized in Table 1. The findings reveal the direct correlation between the salt content in crude oil and the produced current intensity. This well-matched correlation confirms the reliability of this technique, where an increase of salt content in crude oil increases the conductivity of the solution system paving the way for a thicker polymeric film on the working electrode. A calibration curve was obtained for the Arabian crude oil in the range of 5–35 mg L^{-1} of salt concentrations, as shown in Fig. 6, where the calculated R^2 for the fitted line is 0.998. The detection limit was calculated at 1.98 mg L^{-1} and the limit of quantitation was found to be 5.95 mg L^{-1}. The limit of detection (LOD) and limit of quantitation (LOQ) were calculated using the formulas (LOD= 3.3∗(standard deviation of measurements/slope of calibration curve)) and (LOQ= 3∗LOD), respectively. A solution of 5 mg L^{-1} was used to prepare a diluted solution of salt in crude oil and then was analyzed using the described technique to calculate the standard deviation for multiple measurements.

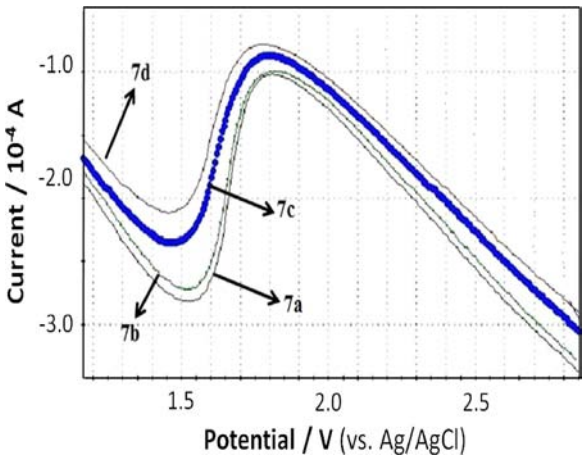


Fig. 5. Overlay of voltammograms of four Arabian crude oils with different salt concentrations at a scan rate of 10 mV/s. The different peak heights indicate the inducing of different polymerization rates when varying the salt amounts.

Table 1
Results of four Arabian crude oils analyzed by the in-situ electropolymerization sensor.

Crude oil	Salt concentration (mg L^{-1}) by ASTM D-3230	Current intensity (μA)	Electropolymerization voltage (V)
a	34.2	180.1	1.75
b	28.5	172.6	1.75
c	14.3	148.1	1.75
d	5.71	134.2	1.75

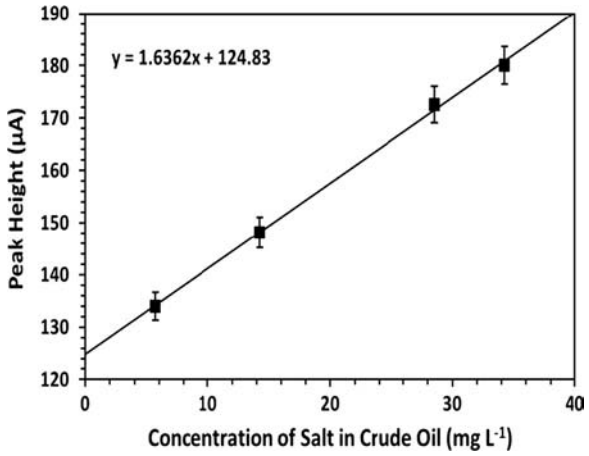


Fig. 6. Calibration curve of Arabian crude oil salt concentrations vs. the peak heights (current intensity) in the cyclic voltammograms.

It has to be mentioned here that the technique developed for monitoring the presence of salt in crude oil and hydrocarbon media is independent of many variables such as temperature, pressure, surface conditions, and flow rate of crude oil. There is no prerequisite to recalibrate the developed analytical method, as the physical surface area of the working electrode remains constant, in contrast to the existing methods. This technique does not require salt extraction prior to measurement and extensive sample preparation as the standard ASTM based test methods. Furthermore, the electrode surface is not exposed to corrosion and deterioration due to the small amount of crude oil needed for the analysis and the type of electrode material used. Table 2 summarizes the key differences between the developed in-situ electropolymerization sensor and the standard lab-scale test methods for measuring the salt content in crude oil [3]. These advantages make this new analytical method a promising tool in the petroleum industry to measure a critical property of crude oil.

4. Conclusions

An in-situ electropolymerization based sensor was developed to measure the salt concentration in crude oil. Aniline, DBT, and thiophene were initially tested as potential monomers for the analytical method. The electropolymerization of aniline was found to produce a measurable and reproducible amount of polymeric film on the working electrode. The amount of polyaniline produced on the electrode surface was directly proportional to the amount of sodium chloride, indicating that the rate of electropolymerization is

Table 2
Characteristics of the in-situ electropolymerization sensor in comparison to the standard test methods for measuring the salt concentration in crude oil.

In-situ electropolymerization sensor.	Standard lab-scale test methods [3].
Does not require salt extraction.	Requires salt extraction in Mohrs' and potentiometric tests.
Only two solvents are used in very small quantities.	Extensive use of solvents such as toluene, xylene, and mixed alcohols.
Robust stability of the electrode condition.	Corrosion of electrode surface is prone in the electrometric method due to the high amount of water in the sample.
No influence of sample viscosity on the measurement procedure.	Increase in the sample viscosity affects the mixing procedure.
The water content in the crude oil has no implication on the measurement due to the insignificant amount of analyte.	Large content of water in the crude oil influences the conductivity measurement leading to erroneous readings of salt.

influenced by the electrolyte content ranging from 2.0×10^{-7} to 8.6×10^{-6} mol L^{-1}. This approach was used with different salt concentrations of Arabian crude oil solutions, where a standard addition of 3.4×10^{-6} mol L^{-1}sodium chloride solution was employed during the sample preparation. Current intensities of 180.1, 172.6, 148.1 and 134.2 μA were calculated for four Arabian crude oils with salt concentrations of 34.2, 28.5, 14.3 and 5.71 mg L^{-1}, respectively. A calibration curve in the range of 5–35 mg L^{-1} was produced with a limit of detection and limit of quantitation at 1.98 and 5.95 mg L^{-1}, respectively. This analytical technique was able to measure the salt concentration in crude oil at very low levels without extensive sample preparation and prior extraction of salt.

Acknowledgments

The authors would like to thank Saudi Aramco for their financial support and permission to publish this work.

References

[1] A. Bahadori, Prediction of Salinity of Salty Crude Oil Using Arrhenius-Type Asymptotic Exponential Function and Vandermonde Matrix, (n.d.). http://dx.doi.org/10.2118/132324-PA.
[2] G. Egloff, M. A.I.M.E, E. Nelson, C. Maxutov, C. Wirth III, Desalting Crude Oils, in: Oklahoma City Meet, Oklahoma, 1937.
[3] M. Fortuny, E.B. Silva, A.C. Filho, R.L.F.V Melo, M. Nele, R.C.C. Coutinho, et al., Fuel 87 (2008) 1241–1248. http://dx.doi.org/10.1016/j.fuel.2007.07.013.
[4] Z.S. Bai, H.L. Wang, Chem. Eng. Res. Des. 85 (2007) 1586–1590. http://dx.doi.org/10.1016/S0263-8762(07)73203-3.
[5] L. Vafajoo, K. Ganjian, M. Fattahi, J. Pet. Sci. Eng. 90–91 (2012) 107–111. http://dx.doi.org/10.1016/j.petrol.2012.04.022.
[6] G. Inzelt, Conduct. Polym.: N. Era Electrochem. (2012), http://dx.doi.org/10.1007/978-3-540-75930-0.
[7] P.K. Sharma, G. Gupta, V.V. Singh, B.K. Tripathi, P. Pandey, M. Boopathi, et al., Synth. Metals 160 (2010) 2631–2637, http://dx.doi.org/10.1016/j.synthmet.2010.10.016.
[8] M. Pagels, J. Heinze, B. Geschke, V. Rang, Electrochim. Acta 46 (2001) 3943–3954. http://dx.doi.org/10.1016/S0013-4686(01)00716-2.
[9] J. Lee, K. Lim, J. Ind. Eng. Chem. 6 (2000) 157–162.
[10] E. Kalaycioglu, L. Toppare, Y. Yagci, Des. Monomers Polym. 1 (1998) 245–250. http://dx.doi.org/10.1163/156855598 × 00350.
[11] S. Mu, J. Kan, Synth. Metals 92 (1998) 149–155, http://dx.doi.org/10.1016/S0379-6779(98)80104-5.

Talanta 132 (2015) 239–244

Contents lists available at ScienceDirect

Talanta

journal homepage: www.elsevier.com/locate/talanta

Mercury fractionation in dourada (*Brachyplatystoma rousseauxii*) of the Madeira River in Brazil using metalloproteomic strategies

C.P. Braga [a], A.C. Bittarello [b], C.C.F. Padilha [a], A.L. Leite [c], P.M. Moraes [a], M.A.R. Buzalaf [c], L.F. Zara [d], P.M. Padilha [a,*]

[a] UNESP – Institute of Biosciences, Botucatu, SP, Brazil
[b] UNESP – FMVZ – Graduate Program in Animal Sciences, Botucatu, SP, Brazil
[c] USP – University of São Paulo, Bauru, SP, Brazil
[d] UNB – University of Brasília, College of Planaltina, Distrito Federal, Brazil

ARTICLE INFO

Article history:
Received 15 July 2014
Received in revised form
9 September 2014
Accepted 11 September 2014
Available online 19 September 2014

Keywords:
Mercury in amazon fish
Metallomics
2D PAGE
GFAAS
ESI–MS/MS

ABSTRACT

This paper presents the results of mercury fractionation in muscle samples of dourada (*Brachyplatystoma rousseauxii*) from the JIRAU Hydroelectric Power Plant in the Madeira River Basin in the Amazon region of Brazil. The proteome of the dourada muscle was separated by two-dimensional polyacrylamide gel electrophoresis (2D PAGE). The mercury present in the protein spots was determined by graphite furnace atomic absorption spectrometry (GFAAS) after acid mineralisation in an ultrasound bath. The protein spots in which the presence of mercury was detected were characterised by electrospray ionisation tandem mass spectrometry (ESI–MS/MS) after tryptic digestion. The GFAAS determinations indicated that 65% of the mercury was linked to the protein fraction with a molar mass (Mm) of less than 90 kDa. The mercury concentrations in the seven spots in which this protein fraction was present were in the range of 11.40–35.10 μg kg^{-1}. Based on the mercury concentrations, it was possible to estimate that the protein spots contained approximately 1–3 mercury atoms per protein molecule. The ESI–MS/MS analysis allowed characterisation of the seven protein spots as the following proteins: protein NLRC5 (molar mass=18.10, pI=6.30); 39S ribosomal protein L36 mitochondrial (molar mass=15.40, pI=8.23); N-alpha-acetyltransferase 20 (Mm=15.95, pI=8.80); Mth938 domain-containing protein (Mm=15.01, pI=9.60); ubiquitin-40S ribosomal protein S27a (Mm=9.80, pI=7.60); parvalbumin alpha (Mm=12.40, pI=3.80) and parvalbumin beta (Mm=13.10, pI=3.45).

© 2014 Elsevier B.V. All rights reserved.

1. Introduction

The Amazon region has a great diversity of water bodies, including not only large rivers and lakes but also numerous streams, which further increase the water volume and the diversity of the ecosystems. These are key factors in maintaining a high diversity of fish in this region. The freshwater fish fauna of the Amazon is considered the richest in the world, with more than 1.300 described species. This diversity of fish from different regions within the Brazilian Amazon is still difficult to assess because the existing studies from several research institutes are sparse [1].

Commercial fishing is concentrated on approximately 40 exploited species, and among the most commonly caught are the following: dourada (Brachyplatystoma rousseauxii); pacu (Mylossoma sp, sp Myleus); jaraqui (Semaprochilodus spp.); tucunaré (Cichla spp.); filhote (*Brachyplathystoma filamentosum*); sardinha (*Triportheus* spp.); jatuarana (*Brycon* spp.); and curimatã (*Prochilodos vimboides*). These species represent 75% of the production of commercial fishing towns in the middle Madeira River of the Amazon in Brazil [2]

Mercury contamination by gold mining activity scarred the Amazon from the 1980s until the middle of the 1990s. The annual emission of mercury into the Amazon basin may have reached approximately 200 t, with Brazil, Bolivia, Venezuela, Guyana and Colombia as the largest emitters. The upper basin of the Madeira River was the second most productive region for gold mining in the Amazon, and this activity contributed to an average emission factor of Hg calculated by Pfeiffer et al. of approximately 1.3 kg of Hg per kg of gold produced in this basin [3,4].

Changes in land use due to agriculture, deforestation, fires, the annual dredging that occurs in some parts of the Madeira River waterway and the construction of hydroelectric plants can accelerate the process of remobilising the mercury in soil and river sediments and, furthermore, particular features of Amazonian environments can also create ideal conditions for mercury methylation, generating

* Correspondence to: Department of Chemistry and Biochemistry, Institute of Biosciences, São Paulo State University (UNESP), Rubião Junior District, 18618-970 Botucatu, São Paulo, Brazil. Tel.: +55 14 3880 0609.
E-mail address: padilha@ibb.unesp.br (P.M. Padilha).

http://dx.doi.org/10.1016/j.talanta.2014.09.021
0039-9140/© 2014 Elsevier B.V. All rights reserved.

methylmercury, which is a more toxic chemical form of this element [2]. Studies have shown that mercury concentrations have remained within natural levels in Amazonian rivers; however, it is known that transformations and processes occurring in the context of remobilising hitherto unavailable mercury species may change their chemical form, making them available for entry into aquatic ecological cycles [4,5].

In the Amazon, fish are the main source of food for coastal communities. Thus, the consumption of predatory fish may pose a risk to the health of these populations, particularly for women of reproductive age and children. The biological half-life of mercury in fish, depending on the species, may be several years. High concentrations of mercury in fish are commonly found in those species that occupy the top of the food chain. However, the extent of the food chain, the individual growth rate and the age of the fish are all factors influencing the variability of mercury levels in predators. Other variables to consider are changes in eating habits, which often vary depending on the stage of development and may also vary significantly between individuals of the same species [5–7]. Thus, mercury from natural and/or anthropogenic sources entering aquatic ecosystems participates in biogeochemical cycles mediated by microorganisms in which it is chemically transformed, undergoing biomagnification and bioaccumulation in the food chain. Thus, predatory fish, which accumulate high levels of mercury, can act as vehicles by which their consumers, such as reptiles, birds and humans, are exposed to this chemical form of mercury [8–10].

To evaluate the resource contamination in a region such as the Madeira River basin and its people, we must not only determine the amount of mercury in environmental components but also necessary biogeochemical knowledge about these ecosystems, which are already complex biogeochemical processes that control the bioavailability of this metal [2,11]. In this context, the synthesis and metabolic functions of some genes and proteins do not occur without the presence of metal ions and metalloenzymes, which are metalloproteins that act as catalysts in biological reactions to regulate biological and physiological functions in cells and organs. Thus, in the last decade interest in metallomics, a field of research in symbiosis with genomics and proteomics, has grown. Metallomics studies allow for determination of the distribution of a metal and/or metalloid species as well as elucidation of the physiological and functional characteristics of biomolecules that contain metal ions in their structures, such as metalloproteins and metal-bound proteins. In metallomics, the metallomes of metal ions or metalloid species present in a biological system (cells, tissues, or body fluids) in the free or complexed form are defined [2,12–14].

Based on the above information, this paper presents results obtained in a quantitative metallomics study of samples of dourada muscle (*Brachyplatystoma rousseauxii*) using 2D PAGE to obtain proteome samples, graphite furnace atomic absorption spectrometry (GFAAS) for quantitative determination of the mercury in the protein spots obtained from the proteins' fractionation and electrospray ionisation tandem mass spectrometry for characterisation of the protein spots in which the presence of mercury was detected.

2. Materials and methods

2.1. Sample collection

The two fish species used in this metallomics study of mercury were chosen based on their trophic levels and because they are among the species most widely consumed by the local riverine population. These fish species were dourada (*Brachyplatystoma rousseauxii*) because, by being a predator species, it has a greater tendency to accumulate mercury due to its feeding on fish that are omnivores and herbivores. A total of three individuals of this species were collected in the Jirau region of the Madeira River (Lat W – 64°43′36″ and Long S – 09°16′21″). The fish were anaesthetised with a benzocaine solution (100 mg L^{-1}) and euthanized to remove muscle samples. A pooled sample of muscle was ground in a Turrax homogeniser, transferred to 15 mL polypropylene flasks and stored in a freezer at −80 °C.

2.2. Sample preparation

Approximately 2.00 g of the pooled muscle samples of each species (weighed in triplicate) was macerated in deionised water using a mortar and pestle. The extracts containing the proteins were separated from the solid portion, centrifuged at 13,000*g* and stored at 4 °C in a refrigerated centrifuge. The protein extracts obtained from these samples were transferred to Eppendorf® tubes and then submitted to the fractional protein precipitation process.

2.3. Fractional precipitation and resolubilisation of protein pellets

To obtain proteins of low molecular weight, precipitation of the proteins contained in the protein extracts was done in two steps (fractional precipitation) [12,13]. In the first step, aliquots of 1 mL of ethanol–chloroform (ratio of 12.5:1 v/v) and the protein extract solution were transferred to 2 mL microtubes in a 1:1 (v/v) ratio. The homogeneous mixture was kept in the refrigerator for 15 min, which was long enough for the formation of a protein precipitate. After this time, the heterogeneous mixture was centrifuged for 10 min at 10,000*g* at 4 °C. The supernatant was then separated for further precipitation, and the obtained precipitates (pellets with proteins of high molecular weight >90 kDa) were kept in microtubes and stored at −20 °C for later determination of their total mercury contents.

In the second precipitation step, 1 mL of the supernatant obtained in the first precipitation stage and 400 μL of hydrochloric acid–ethanol solution (2.5:1 ratio) were added to 2 mL microtubes. This precipitation step was conducted at −20 °C for 3 h, thereby ensuring that the precipitation occurred quantitatively. Then, the heterogeneous mixture was centrifuged at 10,000*g* at 4 °C in a refrigerated centrifuge for 10 min and the supernatant was discarded. The protein precipitate (pelleted proteins of interest with low molecular weights <90 kDa) was washed four times with 1 mL of ice-cold ethanol (−20 °C) to remove traces of hydrochloric acid. This procedure was conducted with replicates ($n=3$) to ensure pellets were obtained that could be used both for quantification of the total protein and the total mercury in the 2D PAGE runs. For quantification of the total protein, the protein pellet was resolubilised in 0.50 mol L^{-1} NaOH and the Biuret method was used [14–17].

2.4. Determination of Hg in the total and in protein spots

Samples of muscle tissue from each fish species studied and/or protein spots were mineralised as follows: 250 mg samples of fish muscle tissue and/or three protein spots cut from polyacrylamide gels for electrophoresis runs of 2D PAGE were transferred to digestion flasks. To each flask was then added 3 mL of concentrated sulphuric acid and 1 mL of hydrogen peroxide 30% (w/w). The set of vials was placed in a UNIQUE ultrasound bath at a temperature of 40 °C and 135 W to complete mineralisation of the sample (clear extract). Then, the acid extracts were transferred to 5 mL volumetric flasks and supplemented up to volume with ultrapure water. To validate the method of mineralisation, standard certified fish protein NRC DORM 4 containing 410 ± 55 mg kg^{-1} of total mercury was also used. The total mercury determination was carried out by GFAAS after acidic mineralisation of the protein pellet and/or the protein spot. This determination was carried out with a SHIMADZU AA-6800 atomic absorption spectrometer equipped with background absorption correction with a self-reverse (SR) system, a pyrolytic graphite

tube with an integrated platform and an ASC-6100 autosampler. Argon was used as the inert gas and the flow rate was kept constant at 1 L min^{-1} throughout the heating program except in the atomisation stage, when the gas flow was interrupted. The absorbance signals were measured for the peaks [3].

2.5. Electrophoretic runs – 2D PAGE

The electrophoretic runs were carried out using 13-cm strips of premade gel containing immobilised ampholytes with a pH range from 3 to 10 in the first dimension of the electrophoretic process (isoelectric focusing electrophoresis, IEF PAGE). In the second dimension of the electrophoretic process, a (SDS PAGE) polyacrylamide gel with a concentration of 15% (w/v) was used. The 2D PAGE runs were carried out using only the low molar mass protein pellets (pellets obtained in the second stage of precipitation). The two steps of the electrophoretic runs were carried out according to the procedure described by Lima et al., Santos et al., Neves et al., Silva et al. [15–18].

After the run, which lasted approximately 250 min, the proteins were revealed using a colloidal Coomassie stain reagent consisting of a solution of ammonium sulphate 8% (m/v), phosphoric acid 1.6% (v/v), Coomassie blue G-250 0.08% (m/v) and methanol 25% (v/v). Before staining, the proteins were fixed for 60 min using a solution containing acetic acid 10% (v/v) and ethanol 40% (v/v). The dye was allowed to remain in contact with the gel for 72 h, after which it was removed through successive washes with deionised water [15–18].

The resulting muscle gels were digitised in a scanner (GE Healthcare, Uppsala, Sweden) and analysed using ImageMaster 2D Platinum 7.0 scanner software (GE Healthcare, Uppsala, Sweden). The image processing was always performed for four gels obtained from the same electrophoretic separation process per aliquot of protein extract. The gels were correlated by matching the spots of the four gels and then comparing them in terms of their distribution, volume, relative intensity, isoelectric point (pIs), molar mass (Mm) and the estimation of the mass of protein per spot [2,15–19].

2.6. Tryptic digestion of protein spots for characterisation by ESI–MS/MS

The protein spots selected for the characterisation step were extracted from the gel using a scalpel and cut into segments of approximately 1 mm^3. The segments were transferred to 2 mL microcentrifuge tubes containing 1% (v/v) acetic acid, and then were subjected to the following steps: removal of the dye, reduction and alkylation, tryptic digestion (using a trypsin solution containing 10 ng μL^{-1} of this enzyme) and elution of peptides [20]. Extracts were dried in a vacuum centrifuge (Eppendorf, Hamburg, Germany) and peptides were dissolved in 10 μL 3% CAN with 0.1% formic acid [20].

2.7. Characterisation of proteins by ESI–MS/MS

Aliquots of the solutions containing the peptides identification was performed on a nanoAcquity UPLC-Xevo QTof MS system (Waters, Manchester, UK). The peptides were separated with a linear gradient of 7–85% mobile phase B (0.1% formic acid in ACN) for 31 min at a flow rate of 0.4 μL/min. The Xevo® G2 Q-TOF mass spectrometer was operated in positive mode, and data were collected in the MS^E method in elevated energy (19–45 V). Source conditions: capillary voltage, 2.5 kV; sample cone, 30 V; extraction cone, 5.0 V and source temperature, 80 °C. ProteinLynx Global Server (PLGS) version 3.0 was used to process and search the continuum LC–MS^E data, setting carbamidomethylation of cysteines as fixed modification and oxidation of methionines as variable modification, allowing one missing cleavage and maximal error tolerance of 10 ppm. Protein identification was performed by homology using the UniprotKB database (http://www.uniprot.org/). At this stage, it is important to know the taxonomic classification of the fish species studied. Thus, the species used in the search was the "Otophysi" series, which is within the superorder Ostariophysi and includes the Siluriformes order to which the dourada belongs [21].

3. Results and discussion

3.1. Determination of total protein

Determination of the total protein concentration in the extracts obtained from the resolubilisation of protein pellets from dourada muscle tissue was obtained with the aim of applying a known amount of protein mass on the IEF strips for the electrophoretic runs. The total protein concentration in the extracts from the low molecular mass pellets (< 90 kDa) was 11.20 ± 0.30 g L^{-1}.

Based on the results of the total protein concentration present in the muscle tissue samples, it was possible to calculate the sample volume of protein extract to be used in the IEF strips in the hydration step prior to isoelectric focusing (separation of proteins in 1D) in order to obtain a protein mass of 375 mg, which, based on the IEF manual system, might favour a better separation of proteins using the 3–10 pH gradient [15,16].

3.2. Protein fractionation by 2D PAGE

The 2D PAGE electrophoresis experiments were performed using extracts from the resolubilisation of the lower molecular weight mass protein pellets from dourada muscle tissue samples. In the protein spots on the gels obtained in the electrophoretic runs, mercury mapping by GFAAS was carried out, and in spots in which the presence of mercury was determined, the proteins were characterised by ESI–MS/MS.

The 2D PAGE electrophoresis experiments on dourada muscle tissue were performed with four replicates. Fig. 1 shows a representative gel obtained in the 2D PAGE electrophoresis run replicates. The protein spots highlighted with circles are those in which mercury was detected, and the concentration of this element was determined by GFAAS. As seen in Fig. 1, the dourada gel shows good resolution, demonstrating the efficiency of the protein fractionation process. Correlation analysis between gels showed that, on average, over 70% of the protein spots were present in all four replicate 2D PAGE runs. It should be noted that the average number of spots found in the gels and the matching gels (correlation gels) showed a relative standard deviation of less than 5%, and these results are much more robust compared with results from the literature [22–26], demonstrating that the optimised conditions of the 2D PAGE were efficient.

3.3. Quantitative evaluation of total mercury

In addition to being determined in samples of muscle tissue of the fish species and in the protein spots, total mercury was also determined in the low and high molecular eight mass protein pellets obtained in the fractional protein precipitation process. The objective of this procedure was to make a mercury mass balance in relation to the concentration of this element in the tissue samples and extracts of the protein pellets. The NRC DORM 4 certificate standard was used to validate the optimised method for the determination of mercury [3]. The concentrations of mercury in the samples and certified standard determined by GFAAS were as follows (μg kg^{-1}): muscle tissue = 331 ± 7, molar mass < 90 kDa = 215 ± 3, molar mass > 90 kDa = n.d. (not detected), and NRC

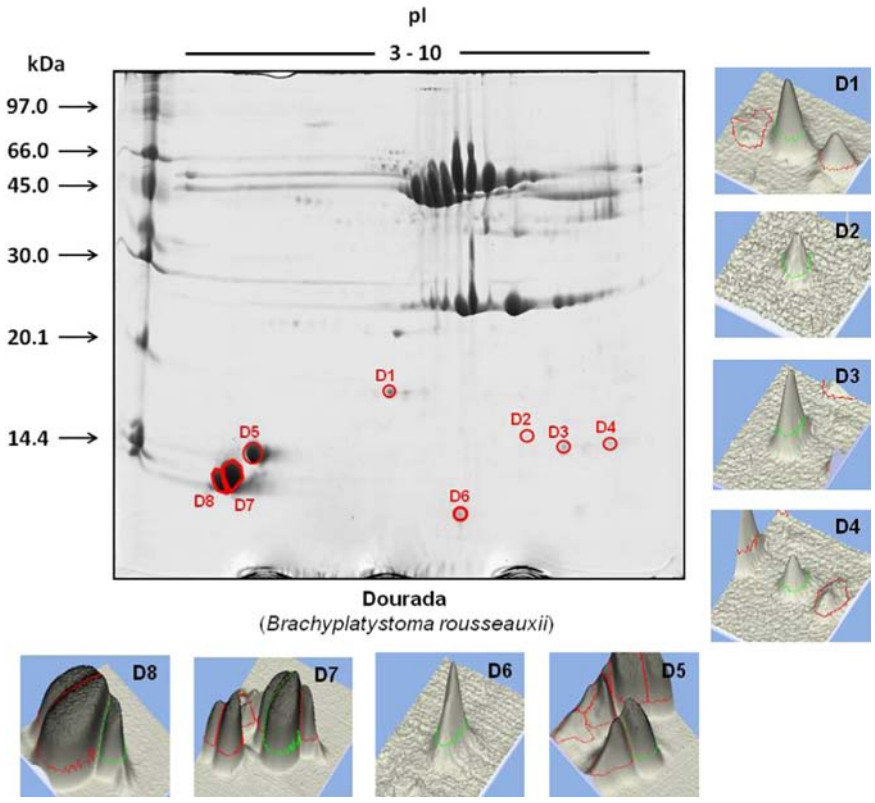


Fig. 1. 15% gel (w/v) obtained by 2D PAGE (pH range 3–10) for muscle tissue samples of dourada. The numbers and circles in red indicate the spots that have been identified for the presence of mercury, were characterised by ESI–MS/MS, and are also presented in 3D. (For interpretation of the references to color in this figure legend, the reader is referred to the web version of this article.)

DORM 4=408 ± 3. Analysing these results, it was observed that approximately 65% of the mercury in muscle tissue samples was linked to the lower molecular weight protein pellets (< 90 kDa), while in the protein extracts of the higher molecular weight pellets (> 90 kDa), the presence of mercury was not detected. From these results, it can be inferred not only that the extraction process was effective but also that most of the mercury present in the dourada muscle samples is really linked to the protein fraction, and the remainder (approximately 35%) may be linked to other macromolecules present in the muscle tissue (e.g., lipids). The data presented are considered fairly robust because they were validated based on results obtained in the mercury determination of the NRC DORM 4 certified standard (protein of fish muscle). It can be seen that the experimental value of the standard deviation obtained for the samples is less than 1%, and the experimental absolute value of the certificate standard (408 μg kg^{-1}) is approximately 0.5% less than the absolute value of the certificate (410 mg kg^{-1}), which proves the accuracy and precision of the optimised method for the determination of mercury.

The mercury concentrations in protein spots obtained in the 2D PAGE runs of the lower molecular weight pellets were also determined using the optimised GFAAS method [3]. These determinations indicated the presence of mercury in the protein spots highlighted with circles in the polyacrylamide gels shown in Fig. 1. Table 1 shows the values of the mercury concentrations determined for each protein spot with their respective molar masses (Mm) and isoelectric points (pI) in addition to the protein mass estimated using ImageMaster 2D Platinum 7.0.

Analysing the results shown in Table 1, it can be observed that the mercury concentrations in the protein spots have values in the range from 11.40 to 35.10 mg g^{-1}. However, the results presented in Table 1 do not provide much information without the characterisation of the proteins in these protein spots. Thus, the estimates of the protein masses in the protein spots (the mass of protein per spot was based on calculating the volume of each protein spot in the polyacrylamide gel – as determined by the

Table 1
Values obtained in the determination of the mercury concentrations in the protein spots of muscle tissue of dourada by GFAAS.

Protein spots	Molar mass (kDa)	pI	Protein mass (μg)	Concentration of Hg (mg g^{-1})
D1	18.10	6.30	0.90	33.30
D2	15.40	8.20	0.20	25.50
D3	15.00	8.80	0.40	13.20
D4	15.00	9.60	0.50	13.30
D5	14.20	4.20	3380	11.40
D6	9.90	7.30	3.80	35.10
D7	11.40	3.70	197.50	16.80
D8	10.80	3.60	19.00	18.30

D1–D8: protein spots of muscle tissue of dourada.

Table 2
Estimates of the number of mercury atoms per protein molecule of the protein from the muscle tissue samples of dourada.

Protein spots	Number of molecules in the protein spot $.10^{15}$	Number of mercury atoms $.10^{15}$	Ratio (Hg/protein)
D1	0.03	0.09	3.00
D2	0.008	0.015	1.88
D3	0.016	0.014	0.88
D4	0.019	0.020	1.05
D5	1.12	1.16	1.04
D6	0.23	0.40	1.74
D7	10.40	9.96	0.96
D8	1.06	1.04	0.99

D1–D8: protein spots of muscle tissue of dourada.

image processing software) and the mass amounts of mercury were converted into the number of protein molecules and moles of mercury. These calculations allowed for an estimate of how many mercury atoms were present per protein molecule [15–18]. The results obtained in these calculations are shown in Table 2 in terms of the number of mercury atoms per protein molecule in the protein spot under consideration.

Based on the results presented in Table 2, it is possible to estimate the proportion of mercury atoms per protein molecule in a protein spot by dividing one value by the other. Thus, the following can be inferred: spots D3–D5 and D7–D8 have approximately one mercury atom per protein molecule in the protein spot; spots D2 and D6 have approximately two mercury atoms per protein molecule; and spot D1 has three mercury atoms per protein molecule. These results, although estimates, suggest that there may be a stoichiometric relationship between the number of mercury atoms and the number of protein molecules in the spots, which would be a possible indication that these spots include metalloproteins and/or metal-binding proteins.

3.4. Characterisation of the protein spots by ESI–MS/MS

Characterisation of the protein spots in which the mercury was identified and quantified (spots highlighted with circles in the polyacrylamide gels shown in Fig. 1) was performed using ESI–MS/MS as a tool in the structural component of the metallomics study. In characterising the protein spots, it is normal to find more than one protein in the database search [27]. However, a condition of engagement in the closure of the protein class was made using that with the highest score and/or coverage and especially considering the pI and molecular weight data obtained by 2D PAGE (experimental data) in relation to the theoretical molar mass obtained from the *Uniprot* database. Table 3 shows the characterisation data obtained from the ESI–MS/MS analysis of the likely protein identified considering the engagement conditions described above. With regard to no proteins being identified in the D5 protein spot, the difficulty of the characterisation process can be related to some failure in the tryptic digestion step or a low protein concentration generating peptides that it is impossible to sequence, or it can be due to limited information available in the databases on the proteins of fish; in this case the applicable database is the database on Amazon fish species.

The results presented in Table 3 show that it was possible to characterise six different types of protein by ESI–MS/MS and that one of these proteins may be a mixture of isoforms (D7 and D8 spots, D7 – *parvalbumin-2*, *parvalbumin alpha and parvabulmin beta*). *Protein NLRC5*, which is a protein that acts in the homeostatic control of innate immunity and mechanisms of antiviral defence, was identified. This protein consists of peptide sequences containing leucine, which has an amino group and a carboxylic acid group, as the primary amino acid [28]. The incorporation of metal ions by this protein has not been reported in the literature. However, spot D1, which features, based on the data of the GFAAS determination, three mercury atoms per molecule of protein, was characterised as protein NLRC5. Thus, based on the data obtained by ESI–MS/MS and GFAAS, it can be inferred, in this case, that the mercury is bound to coordination sites in the protein by nonspecific binding and is not acting as a metal cofactor forming a *metal-binding* protein [14]. The *39S ribosomal protein L36 mitochondrial*, which addresses a protein component of the mitochondrial ribosome subunit and actively participates in the synthesis of other proteins inside the mitochondria, was also identified. This protein is not associated with metal ions considering the information obtained in the literature so far [29]. However, any other protein present in chains with terminal nitrogen atoms may have non-specific binding with divalent metal ions, such as mercury. Moreover, the data of the GFAAS determination showed that this protein has three mercury atoms per protein molecule, which allows the inference that this protein may be a *metal-binding* protein [14]. *N-alpha-acetyltransferase 20*, an enzyme that is part of the catalytic subunit of the NatB complex (alpha-N-acetyltransferase B) and helps catalyse the acetylation of methionine residues of N-terminal peptides beginning with Met–Asp–Glu–Met, Met–Met–Gln and Asn, was another protein identified. It is necessary in order to maintain the structure and function of complex fibres of actomyosin and proper cell migration [30]. Through the methionine residues present in its structure, it can act on a molar basis and form stable complexes with Hg^{2+} ions [31]. Spot D3 of dourada muscle tissue was characterised as the enzyme with mercury attached to its structure, presenting a strong connection with this element, which qualifies this spot as a possible biomarker candidate. It should also be noted that the data obtained by GFAAS indicated a stoichiometric ratio of one mercury atom per N-alpha-acetyltransferase 20 molecules, which reinforces the hypothesis that this enzyme can act as a mercury biomarker. *Mth938 domain/containing protein* was also identified, a cytoplasmic protein component that acts in fat cell differentiation and in the positive and negative regulation of apoptotic processes [30]. An association of this protein with metal ions has not been reported in the literature. However, by presenting peptide sequences with proline and leucine residues with terminal amino and carboxylic groups, it can have non-specific binding with divalent metal ions such as mercury. The data obtained by GFAAS indicated a stoichiometric ratio of one mercury atom per *Mth938 domain/containing protein* molecule, which allows the inference that this protein may be a *metal-binding* protein [14]. In addition, *ubiquitin −40S ribosomal protein S27a*, which is a protein that when covalently linked

Table 3
Proteins identified in samples of the muscle tissue of dourada using ESI–MS/MS.

Spot	Protein	Access	Score	Spot pI/Mm (kDa)	Mm theoretical (Da)	Coverage (%)	Sequenced peptides
D1	Protein NLRC5	NLRC5_ICTPU	35.9502	6.30/18.100	6.12/19.298	0.41	AIGPRDR ISLNKTISK
D2	39S ribosomal protein L36. mitochondrial	RM36_DANRE	47.3535	8.20/15.000	11.6712.944	11.21	SLVGSLTR SALKK
D3	N-alpha-acetyltransferase 20	NAA20_DANRE	18.1279	8.80/15.000	4.95/20.358	6.18	VSNQVAVNMYK
D4	Mth938 domain-containing protein	AAMDC_DANRE	1571.07	9.60/15.000	7.75/13.360	7.38	GVQTLVIGR VWPGGSR TLVIGR VIGR GVQTL QTLVIGR GVQTLV GVQTLVI
D5	Not identified	–	–	4.20/14.200	–	–	–
D6	Ubiquitin-40S ribosomal protein S27a	RS27A_ICTPU	1328.94	7.29/9.900	9.68/17.999	5.77	ESTLHLVLR TLHLVLR STLHLVLR ESTLHL
D7	Parvalbumin-2	PRV2_DANRE	988.761	3.70/11.400	4.46/11.622	36.73	LFLQNFSAGAR IGVDEFALLVK NFFAKVGLSAK IGVDEFALLVKA
	Parvalbumin alpha	PRVB_CYPCA	221.718		4.67/11.451	16.67	LFLQNFSAGAR
D8	Parvalbumin beta	PRVB_SQUCE	134.81	3.60/10.800	4.88/11.263	9.43	AFGLKEADITAALEACK IGIDEFAALVKA

may be involved in DNA repair, cell cycle regulation, endocytosis and lysosomal degradation, was identified. It may also be involved in signalling processes, leading to activation of the NF-kappa-B factor and, in its free form, can activate protein kinases and play a role in cellular signalling. This protein has domains with specific groups for binding of zinc (zinc-finger metal binding domains) [32]. Due to possessing specific domains linked to zinc atoms, which has similar characteristics to mercury (both soft acids), it can also bind other divalent ions such as copper, cadmium and mercury [8,31]. Spot D6 was characterised as being this protein with mercury atoms linked to its structure. The data obtained by GFAAS showed that the D6 spot had a stoichiometric ratio of two mercury atoms per *ubiquitin −40S ribosomal protein S27a* molecule, so it can be inferred that this protein may act as a biomarker of this element. *Parvalbumin*, which is a protein of low molecular weight (11–12 kDa) and has the isoforms *parvalbumin-2*, *parvalbumin alpha and parvalbumin beta*, was the final protein identified. Usually all three isoforms bind calcium ions. This protein is directly involved in the process of muscle relaxation after contraction. It is basically formed by peptide sequences containing serine and alanine, which have amino acid structures with carboxylic, amino and hydroxyl groups susceptible to complexation with divalent metal ions, especially calcium and magnesium [32,33]. *Parvalbumin* linked to mercury was the protein most identified in the protein spots analysed, and different isoforms of this protein were characterised in spots D7 and D8 of dourada muscle tissue. The literature, so far, does not include any paper that discusses the possibility of mercury and/or other potentially toxic metals being bound to parvalbumin or its isoforms. However, the beta isoform of this protein has a cysteine residue in the peptide sequence that can form specific linkages with metal ions with soft acid features such as Hg^{2+} [14,31]. Thus, protein spots D7 and D8 could be potential candidates for mercury biomarkers.

4. Conclusions

With optimisation of the experimental conditions in the developed components of selectivity (2D PAGE) and sensitivity (GFAAS) in the metalloproteomic study proposed, it was possible to characterise eight protein spots by ESI–MS/MS in which the presence of mercury was confirmed by GFAAS. Based on the results obtained so far, it is possible to draw the following conclusions. The protein pellet fraction with a molar mass <90 kDa has approximately 65% of the mercury concentration determined in the dourada muscle tissue samples (the fish species studied). Mercury was not detected in the protein pellet fraction with a molar mass >90. With the data on mercury concentrations determined in the protein spots, it was possible to predict a stoichiometric relationship between the number of mercury atoms per molecule of protein in the protein spot. This ratio presented itself in the range of 1–3 mercury atoms per molecule of protein in the protein spot. The characterisation data on the protein spots allowed the identification of proteins and/or enzymes in eight protein spots, among which two proteins, parvalbumin (with alpha and beta isoforms) and *ubiquitin −40S ribosomal protein S27a*, as well as the *N-alpha-acetyltransferase 20* enzyme, may be candidate mercury biomarkers due to their inclusion of groups with characteristics of soft bases and specific domains linked to zinc atoms, which have similar characteristics to mercury (soft acid). In general terms, the preliminary results obtained can be considered unpublished for the Amazon fish studied, constituting a starting point for metalloproteomic studies related to mercury toxicity in fish from this region of Brazil.

Acknowledgments

The authors thank the Brazilian research funding agency ANEEL/ESBR – P&D: 6631-0001/2012/Contract Jirau 004/2013 and FAPESP (Processes: 2010/51332-5 and 2009/54856-8) for their financial support.

References

[1] R.S. Cardoso, C.E.C. Freitas, A pesca de pequena escala no rio Madeira pelos desembarques ocorridos em Manicoré (Estado do Amazonas), Brasil, Acta Amazonica 38 (2008) 781–788.
[2] P.M. Moraes, F.A. Santos, C.C.F. Padilha, J.C.S. Vieira, L.F. Zara, P.M. Padilha, Biol. Trace Elem. Res. 150 (2012) 195–199.
[3] P.M. Moraes, F.A. Santos, B. Cavecci, C.C.F. Padilha, J.C.S. Vieira, P.S. Roldan, P.M. Padilha, Food Chem. 141 (2013) 2614–2617.
[4] W.C. Pfeiffer, L.D. Lacerda, W. Salomons, O. Malm, Environ. Rev. 1 (1993) 26–37.
[5] P.J. Lechler, J.R. Miller, L.D. Lacerda, D. Vinson, J.C. Bonzongo, W.B. Lyons, J.J. Warwick, Sci. Total Environ. 260 (2000) 87–96.
[6] M. Meili, Water Air Soil Pollut. 56 (1991) 333–347.
[7] H. Akagi, O. Malm, Y. Kinjo, M. Harada, F.J.P. Branches, W.C. Pfeiffer, H. Kato, Sci. Total Environ. 175 (1995) 85–95.
[8] A.C. Barbosa, A.A. Boischio, G.A. East, I. Ferrari, A. Gonçalves, P.R.M. Silva, T.M. Cruz, Water Air Soil Pollut. 80 (1995) 109–121.
[9] E.D. Bidone, Z.C. Castilhos, T.J.S. Santos, T.M.S. Souza, L.D. Lacerda, Water Air Soil Pollut. 97 (1997) 9–15.
[10] J. Lebel, D. Mergler, F. Branches, M. Lucotte, M. Amorim, F. Larribe, J. Dolbec, Environ. Rev. 79 (1998) 20–32.
[11] J. Dolbec, D. Mergler, F. Larribe, M. Roulet, J. Lebel, M. Lucotte, Sci. Total Environ. 271 (2001) 87–97.
[12] A. Viarengo, E. Ponzano, F. Dondero, R. Fabbri, Mar. Environ. Res. 44 (1997) 69–84.
[13] M. Erk, D. IVankovic, B. Raspor, J. Pavicic, Talanta 57 (2002) 1211–1218.
[14] L.S. Garcia, C.S. Magalhães, M.A.Z. Arruda, Talanta 69 (2006) 1–15.
[15] P.M. Lima, R.C.F. Neves, F.A. Santos, C.A. Pérez, M.A.O. Silva, M.A.Z. Arruda, G.R. Castro, P.M. Padilha, Talanta 82 (2010) 1052–1056.
[16] F.A. Santos, P.M. Lima, R.C.F. Neves, P.M. Moraes, A.A. Pérez, M.A.O. Silva, M.A.Z. Arruda, G.R. Castro, P.M. Padilha, Microchim. Acta 173 (2011) 43–49.
[17] R.C.F. Neves, P.M. Lima, W.A. Baldassini, F.A. Santos, P.M. Moraes, G.R. Castro, P.M. Padilha, Quim. Nova 35 (2012) 493–498.
[18] F.A. Silva, B. Cavecci, W.A. Baldassini, P.M. Lima, P.M. Moraes, P.S. Roldan, C.C.F. Padilha, P.M. Padilha, J. Food Meas. Charact. 7 (2013) 158–165.
[19] G.E. Healthcare, Manual do usuário, ImageMaster 2D Platinum 7.0 Edition AA, 2007.
[20] A. Shevchenko, H. Tomas, J. Havlis, J.V. Olsen, M. Mann, Nat. Protoc. 1 (2006) 2856–2860.
[21] G.Z. Li, J.P. Vissers, J.C. Silva, D. Golick, M.V. Gorenstein, S.J. Geromanos, Proteomics 9 (2009) 1696–1719.
[22] A. Sussulini, J.S. Garcia, M.F. Mesko, D.P. Moraes, E.M. Flores, C.A. Pérez, M.A.Z. Arruda, Microchim. Acta 158 (2007) 173–180.
[23] J.S. Garcia, G.H.M.F. Souza, M.N. Eberlin, M.A.Z. Arruda, Metallomics 1 (2009) 107–113.
[24] A.R. Brandão, H.S. Barbosa, M.A. Arruda, J. Proteomics 73 (2010) 1433–1440.
[25] M.A. Silva, J.S. Garcia, G.H.M.F. Souza, M.N. Eberlin, M.A.Z. Arruda, Talanta 80 (2010) 1545–1551.
[26] L.R.V. Mataveli, P. Pawel, S. Mounicou, M.A.Z. Arruda, J. Szpunar, Metallomics 2 (2010) 800.
[27] S. Beranova-Giorgianni, Trends Anal. Chem. 22 (2003) 273–281.
[28] A.G. Poth, H.C. Deeth, P.F. Alewood, J.W. Holland, J. Proteome Res. 7 (2008) 5017–5027.
[29] G. Picariello, P. Ferranti, G. Mamone, P. Roepstorff, F. Addeo, Proteomics 8 (2008) 3833–3847.
[30] P. Giron, L. Dayon, J. Sanchez, Mass Spectrom. Rev. 30 (2011) 366–395.
[31] R.G. Pearson, J. Am. Chem. Soc. 85 (1963) 3533–3539.
[32] E. Hoffman, V. Stroobant, Ion sources, in: E. Hoffman, V. Stroobant (Eds.), Spectrometry: Principles and Applications, 3rd ed., John Wiley and Sons, England, 2007, pp. 15–84.
[33] J. Gross, Introduction, in: J. Gross (Ed.), Mass Spectrometry: A Textbook, 2nd ed., Springer, Germany, 2011, pp. 1–20.

Talanta 132 (2015) 245–251

Contents lists available at ScienceDirect

Talanta

journal homepage: www.elsevier.com/locate/talanta

A novel approach for high sensitive determination of sulfur mustard by derivatization and isotope-dilution LC–MS/MS analysis

Bin Xu, Cheng Zong, Zhiyong Nie, Lei Guo*, Jianwei Xie*

State Key Laboratory of Toxicology and Medical Countermeasures, and Laboratory of Toxicant Analysis, Institute of Pharmacology and Toxicology, Academy of Military Medical Sciences, 27 Taiping Road, Haidian District, Beijing 100850, PR China

ARTICLE INFO

Article history:
Received 29 May 2014
Received in revised form
6 September 2014
Accepted 9 September 2014
Available online 21 September 2014

Keywords:
Derivatization
LC–MS/MS
Quantification
Sulfur mustard
Water
Soil

ABSTRACT

A new isotope-dilution liquid chromatography–tandem mass spectrometry (LC–MS/MS) method for determination of sulfur mustard (SM) has been developed using a direct chemical derivatization method by nucleophile potassium thioacetate (PTA) in aqueous solution. The reaction conditions for derivatization, such as reaction temperature, time, solvent and concentration of PTA, were optimized for high performance. Reversed phase liquid chromatography was suitable for analysis of such a PTA derivatized SM in complex environmental samples. Compared with other conventional gas chromatography or gas chromatography–mass spectrometry methods for direct detection on SM, better sensitivity and selectivity were achieved by this direct derivatization and LC–MS/MS method, where SM can be detected as low as 0.05 ng/mL in acetonitrile. The linear range was from 0.1 to 1000 ng/mL. The relative standard deviation (RSD) of the intra-day precision was less than 11.8%, and RSD of the inter-day precision was less than 12.3%. The whole procedure for both derivatization and analysis was quick and simple, and the total time was less than 1 h. This established method has been successfully employed for determination of spiking samples both in water and soil. A detection limit of 0.1 ng/mL was achieved for river water, while the SM in soil sample could be detected at 0.1 ng/g.

© 2014 Elsevier B.V. All rights reserved.

1. Introduction

Sulfur mustard (SM) is an alkylating chemical agent and known as a major class of chemical warfare agents (CWAs). SM was massively used in World War I and the Iraq–Iran war in 1980s. It is reported that over 100,000 Iranians (military or civilian) were exposed to SM during the Iraq–Iran war, and a large proportion are still suffering with long-term consequences of exposure [1]. It should be noted that great concern related to SM has arisen up to now, i.e., a large amount of CWAs, including SM, was dumped into the ocean areas [2] or buried underground [3] from World War II, and these abandoned chemical weapons or CWAs have caused serious environmental contamination and many casualties or fatalities [4,5]. Thus, it is of great importance to develop a sensitive and robust analytical method for determination of SM in aqueous or soil samples, in light of verification purposes and environmental concerns.

Determination of SM and related chemicals in aqueous or soil samples can present reliable evidence of the original existence of SM as well as the abuse and abandonment of CWAs. When dissolved in water, the hydrolysis of SM is completely prevented or slowed down because of low aqueous solubility as well as formation of oligomeric and polymeric layers by the degradation products [6]. Thus, if existed in abandoned munitions on the seabed, SM would remain intact for a long time. Another most employed sample for the examination of SM is soil, in which organic compounds including SM can be preserved for a long time as a result of high adsorption capacity [7]. Hence, SM can be kept as its original formation in soil for several years [8]. In 1994, Black et al. [9] reported that traces of SM can still be detected in several soil samples collected from a village in northern Iraq attacked by chemical weapons years ago.

However, there is inevitably a variety of degradation products of SM in environmental samples because of its relative high activity. Thus, determination of common degradation products may act as a proof of the original existence of SM. But, there are also some disadvantages with the detection of degradation products, for example, it cannot tell whether the sample still contains intact SM, not to mention the amount of intact SM it contains; and some non-specific degradation products such as thiodiglycol (TDG) cannot confirm the presence of SM individually [10]. As we know, the detection of intact CWAs is the most solid and direct evidence for verification of CWAs, however, the concentration of CWAs like SM was usually very low in environmental samples. So if there is

* Corresponding authors. Tel./fax: +86 10 68225893.
E-mail addresses: guolei@bmi.ac.cn (L. Guo), xiejw@bmi.ac.cn (J. Xie).

http://dx.doi.org/10.1016/j.talanta.2014.09.015
0039-9140/© 2014 Elsevier B.V. All rights reserved.

no method with a sufficiently high sensitivity, then analyzing the degradation products of SM for retrospective detection would be the second choice.

So far, gas chromatography (GC) or gas chromatography–mass spectrometry (GC–MS) are still the preferred analytical technologies for detection of SM and its degradation products [9], but these recommended methods are time-consuming due to complicated preparation procedures for aqueous samples and relatively low sensitivity. Recently, several types of enrichment technology combined with GC–MS have been applied to SM detection, such as solid phase micro-extraction [11], single drop micro-extraction [12], and static headspace-trap [13] technique, and a limit of detection (LOD) of 1 ng/mL in water was achieved. However, these new techniques all require specialized systems or modified absorbent matrices for the determination of SM, which are both expensive and highly professional. Furthermore, some decontamination and enrichment procedures, involving in heating processes [6,13], would easily lead to the degeneration of SM in aqueous environment.

Nowadays, it has been shown that liquid chromatography–mass spectrometry (LC–MS) technique with atmospheric pressure ionization (API) has been increasingly used for detection of water-soluble or non-volatile CWAs and degradation products, in light of its feasibility for aqueous samples, and high sensitivity and selectivity, especially with tandem mass spectrometry [14,15]. And the Organization for the Prohibition of Chemical Weapons (OPCW) has already realized the prospects of LC–MS techniques, so its designated laboratories were encouraged to employ LC–MS analysis as a complementary technique with GC or GC–MS in Proficiency Test with environmental samples, as well as the Confidence Building Exercise on Biomedical Sample Analysis organized by OPCW. However, LC–MS(/MS) method has never been considered for analysis of SM, because of its high alkylation reaction activity with LC column packing material and protic solvent used in common, as well as instability with high temperature and voltage in ESI ion source. Replacement of the halogen groups of SM and related halogen preserved compounds by nucleophiles groups would be a good concept, as by that way it can efficiently prevent SM from alkylation reaction with the matrix and significantly improve the sensitivity in LC–MS. Reversed phase liquid chromatography (RPLC) can then be adopted for quantitative determination of such a SM derivative with MS/MS.

In this article, we developed a direct chemical derivatization method through a covalent reaction between nucleophile potassium thioacetate (PTA) and SM in water, as a direct derivatization approach, so as to detect such a SM derivative by LC–MS/MS analysis. The key point in this derivatization is the higher electronegativity of PTA, its thioacetate anion prior to hydroxide can attack episulfonium cation formatted by SM in water solution and replace chloride readily. The final product bis-(thioacetate) ethyl thioether (BTAETE) was verified with good chromatographic behaviors and excellent mass spectrometric intensity. It makes the determination of SM in water-soluble samples by LC–MS/MS become possible, which greatly reduces pretreatment procedures and improves the detection sensitivity. The reaction conditions for derivatization were optimized for better sensitivity and repeatability. Quantitative analysis with isotope-dilution LC–MS/MS method and the applications on environmental samples were then followed.

2. Experimental

2.1. Caution

SM is a highly reactive alkylation vesicant and cytotoxic agent. Handling of this agent should be carried out in the well-ventilated fume hoods. The use of gloves and stringent protective measures must be adopted.

2.2. Materials and reagents

All reagents were of analytical reagent grade. SM (the purity is over 96%) was supplied by the Institute of Chemical Defense of Chinese People's Liberation Army, and deuterated internal standard d_4-SM as the internal standard (IS) was home-synthesized with a purity of 98% and a deuterated ratio of ca. 100% [16]. Mustard sulfone and mustard sulfoxide were synthesized in house according to previously published procedures [17] and their purities were determined to be more than 95%. Acetonitrile and methanol (HPLC grade) was purchased from J&K Scientific Ltd (Beijing, China). Formic acid (for mass spectrometry, purity is 98%) and potassium thioacetate were obtained from Sigma-Aldrich Inc. (MO, USA). Dichloromethane and n-hexane were purchased from Sinopharm Chemical Reagent Co., Ltd (Beijing, China). Ultrapure water was generated by Milli-Q A10 purification system (Millipore, Billerica, MA, USA).

2.3. Preparation of BTAETE

The stock aqueous solution of PTA was prepared at 100 mg/mL, while SM solution in acetonitrile was at 5% (v/v). For SM derivatization, 1.0 mL PTA stock solution and 1.0 mL 5% SM stock solution (ca. 61 mg) were transferred into a 20 mL headspace vial, then sealed with a polytetrafluoroethylene (PTFE) cap and heated at 100 °C for 1 h.

The reaction solution was extracted with 2 mL of dichloromethane, and then the extracted solution was loaded onto a silica gel column and eluted by an n-hexane/dichloromethane solution at a ratio of 1:3 (v/v). Solvents were removed from collected fractions using rotary evaporation under reduced pressure to give refined product with a pale yellow oil appearance. It was identified as bis-(thioacetate) ethyl thioether (BTAETE) by high resolution MS (HRMS) and NMR, and its purity was greater than 98% by HPLC-Ultraviolent Vis detection. The reaction yield was ca. 44%. ^{1}H NMR ($CDCl_3$): δ3.09 (4H, t), 2.75 (4H, t), 1.58 (6H, s). MS (ESI-HRMS m/z): 239.0229 $[M+H]^+$.

2.4. Preparation of solutions

Standard stock solutions of SM, BTAETE, mustard sulfone and mustard sulfoxide were prepared in acetonitrile, and all stored at −20 °C. A series of standard working solutions of SM at concentrations of 1, 5, 20, 100, 500 ng/mL, and 2, 10 μg/mL were prepared by serial dilution of the stock solution with acetonitrile. Quality control (QC) working solutions were prepared at concentrations of 2.5, 100, 7500 ng/mL. The IS working solution of d_4-SM at a concentration of 370 ng/mL was prepared by dilution of the stock solution. An aliquot of 5 μL of standard or QC working solution and 5 μL of IS working solution were spiked into 40 μL acetonitrile, making the final concentrations at 0.1, 0.5, 2, 10, 50, 200, 1000 ng/mL to establish standard curve of BTAETE and evaluate precision and trueness. The LOD was defined as the lowest concentration at which the signal of the analyte peak from background noise (signal to noise ratio, S/N, is greater than 3) can be reliably differentiated, while the lower limit of quantification (LLOQ) is greater than 10 [18]. The working solutions of BTAETE at concentrations of 1.0, 5.0, 20, 100, 500 ng/mL were prepared by dilution of the stock solution for evaluation of the recovery as well as derivatization efficiency.

2.5. Sample preparation

The stock solution of PTA in water was prepared at 50 mg/mL and stored at 4 °C, then diluted at concentrations of 0.1, 1 and 5 mg/mL with water. For the determination of SM in samples, 50 μL of the spiking sample solution containing IS and 50 μL PTA solution were transferred into a 2 mL headspace vial, then capped the vial and shaken, following heated at 50 °C for 0.5 h. When investigating the most suitable reaction conditions for derivatization, the temperature, time, solvent, pH and concentration of PTA were varied.

Natural water samples were collected from the Yongding River in Beijing with a relative equivalent of mud, and kept at 4 °C. Prior to analysis, the river water samples were centrifuged at 14,000*g* for 10 min, and then transferred the supernatant into a clean vial. An aliquot of 1 mL sample was spiked with a solution of SM in acetonitrile to the concentration of 100 ng/mL. Immediately and individually, 45 μL triplicates of the spiking solution were transferred to headspace vials, 5 μL IS and 50 μL PTA in 50% acetonitrile solutions at a concentration of 1 mg/mL were added for derivatization reaction. After that the supernatant at a volume of 50 μL was transferred into the injection vial insert for LC–MS/MS analysis. LC–MS/MS analysis was performed within the same day, and the recoveries of the spiked SM in the natural water samples were calculated from calibration curve established with a series of standard working solutions prepared in Section 2.4.

Natural soil samples were collected from one suburban area of Beijing, China. Prior to detection, the soil samples were homogenized and freeze-dried at −40 °C for 24 h in order to reduce degradation by endogenous microbials. Triplicates of 0.2 g soil sample were weighted directly into headspace vials, then spiked by 5 μL SM solution at the concentration of 100 ng/mL and shaken for 1 min. Subsequently, 5 μL IS and 90 μL PTA in 50% acetonitrile solutions at a concentration of 1 mg/mL were added for derivatization reaction. After that, the aliquot of samples were transferred into clean vials, and centrifuged at 14,000 *g* for 10 min, and then the supernatant at a volume of 50 μL was transferred into the injection vial insert for LC–MS/MS analysis. The recoveries of the spiked SM in the natural soil samples were calculated.

2.6. Isotope-dilution LC–MS/MS analysis

Separation was performed using an ACQUITY UPLC system (Waters Co., Manchester, UK) consisting of a binary pump and an autosampler. The analytical column is a 2.7 μm particle size CAPCELL CORE C18 column (SHISEIDO, Kyoto, Japan) with a length of 100 mm and i.d. of 2.1 mm. Mobile phase A was water containing 0.1% formic acid, while phase B was acetonitrile. The mobile phases were run at 20% B in the first 1 min, followed by a 4 min linear gradient run to 95%B, then returned to its initial setting and the column was conditioned for 2 min. The flow rate was 0.3 mL/min, and an injection volume was 5 μL. The LC elutes were directly delivered to a 5500 QTrap tandem mass spectrometer (AB Sciex, Framingham, MA, USA) except elutes in the first 1 min to avoid possible contamination of the Turbo V™ source.

In MS/MS analysis, the transitions of the analytes were selected based on their full scan mass spectra obtained by direct electrospray ionization-MS of standard solutions without LC separation. MS equipment was operated in a positive MS/MS mode at a unit resolution for both *Q*1 and *Q*3 using multiple reaction monitoring (MRM) with a dwell time of 100 ms for BTAETE and d_4-BTAETE. The transition of precursor to product ion was monitored at *m*/*z* 238.7→103.0 for BTAETE, *m*/*z* 242.7→107.0 for d_4-BTAETE. Meanwhile, the derivatization products of hemisulfur mustard (*m*/*z* 181.0→103.0), mustard sulfone (*m*/*z* 271.0→103.0) and mustard sulfoxide (*m*/*z* 255.0→213.0), as well as unchanged mustard sulfoxide (*m*/*z* 175.0→63.0), were also monitored. All analytes' parent ions and primary fragment ions with attribution are listed in Table 1. The collision energy was all set at 20 eV, the declustering potential was 80 eV, and the collision cell exit potential was 16 eV. The source conditions were: source temperature, 550 °C; pressures for gas 1 and gas 2, 50 kPa; for curtain gas, 20 kPa. The data were analyzed using Analyst® (version 1.5.1, AB Sciex, Framingham, MA, USA). SPSS software package v15.0 (SPSS Inc., Chicago, USA) was used for orthogonal experimental design and results analysis.

3. Results and discussion

3.1. Mechanism of PTA derivatization of SM

In general, the derivatization reaction should be fast and complete preferable for analytical purpose. Since SM is a highly reactive electrophile, it tends to form an episulfonium ion by an internal S_N2 type mechanism when interacting with other molecules. As shown in Fig. 1, substitution reaction is then completed by an external S_N2 type mechanism, via thioacetate anions attacking episufonium ions. In this reaction, formation of the episulfonium ion is the rate-limiting process and can occur rapidly in the polar solvents [19].

Through the replacement of chloride atoms with two thioacetate groups by S_N2 mechanism, the derivatization can overcome the shortcoming that LC–MS technique is unfavorable for analysis

Table 1
The parent ions and primary fragment ions with attribution of derivatization products of SM, d4-SM, hemisufur mustard, sulfone mustard, sulfoxide mustard, as well as unchanged sulfoxide mustard in ESI.

Compounds	Formula	Parent ion	Fragment ion	Attribution
Derivatization of SM (BTAETE)	$C_8H_{14}O_2S_3$	238.7	103.0	$[M+H\text{-}HSC_2H_4SCOCH_3]^+$
			163.1	$[M+H\text{-}HSCOCH_3]^+$
			196.9	$[M+H\text{-}COCH_2]^+$
Deribatization of d4-SM (d4-BTAETE)	$C_8D_4H_{10}O_2S_3$	242.7	107.0	$[M+H\text{-}HSC_2H_4SCOCH_3]^+$
			167.0	$[M+H\text{-}HSCOCH_3]^+$
Derivatization of hemisulfur mustard	$C_6H_{12}O_2S_2$	181.0	102.9	$[M+H\text{-}HSC_2H_4OH]^+$
			162.9	$[M+H\text{-}H_2O]^+$
Derivatization of sulfone mustard	$C_8H_{14}O_4S_3$	271.1	102.9	$[M+H\text{-}HSO_2C_2H_4SCOCH_3]^+$
			229.1	$[M+H\text{-}COCH_2]^+$
Derivatization of sulfoxide mustard	$C_8H_{14}O_3S_3$	255.0	213.0	$[M+H\text{-}COCH_2]^+$
			103.0	$[M+H\text{-}HSOC_2H_4SCOCH_3]^+$
Unchanged sulfoxide mustard	$C_4H_8OSCl_2$	175.0	63.0	$[M+H\text{-}SOC_2H_4Cl]^+$

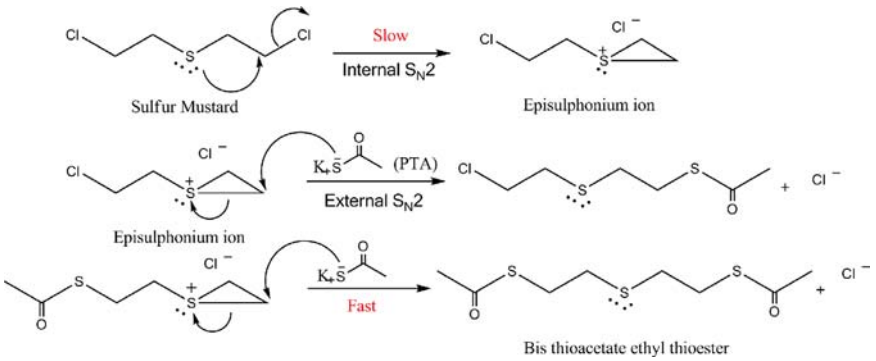


Fig. 1. The derivatization reaction mechanism of SM with PTA.

of SM and related chemicals, because of their high alkylation activity with LC column packing material or protic solvents used in LC. BTAETE of non-alkylation activity is very suitable for LC–MS/MS analysis. The expected mass of the derivative of alkylating agent is $M_w - nX + n$TA, for example in SM, where M_w is the molecular weight of SM, X is Cl (atomic weight 35), TA is thioacetic acid (molecular weight 75), and n is equal to 2, a result is 238.

With regard to two major mustard oxidation products, mustard sulfoxide and sulfone, the sulfur in SM is believed to be lower oxidative reactive because of the presence of two large electron-withdrawing chlorine atoms [20]. Likewise, SM is apt to be relatively oxidized to the sulfoxide, which converts more slowly to the sulfone [21]. The rate of alkylation runs faster for SM than mustard sulfoxide or sulfone, in accordance with the effect of acute exposure to SM or related chemicals [22], as mustard sulfoxide and sulfone also own vesicant toxicity by their alkylation activity [8], and this oxidation of SM is a useful decontamination procedure as a result of formation of crystalline solids without percutaneous adsorption by the skin [23]. The derivatization experiments in tube also showed that it needs more severe conditions for mustard sulfoxide and sulfone than for SM (see Fig. 2). Because of inconsistent reaction conditions, we only developed the derivatization method for SM in this paper.

3.2. Parameters for derivatization

A series of parameters such as reaction temperature, time, pH, solvent and concentration of PTA, and matrix composition were optimized for highest sensitivity and intensity in analysis. As known, the derivatization reagent PTA is water-soluble and can slightly dissolve in organic solvents, while SM is preferred to be dissolved in an aprotic polar solvent to match its lipophilicity and slow down its hydrolyzation. A series of miscible solvents were investigated to check their feasibility for derivatization. Water and DMSO were suitable for preparation of PTA solution in higher concentration than acetonitrile and isopropanol, and SM in acetonitrile showed 20–30% higher response than DMSO and isopropanol after derivatization. Finally, water was chosen for dissolution of PTA and acetonitrile for SM. Because, first, although SM would slowly hydrolyze in water by S_N2 mechanism, it was noted that PTA more easily attacks episulfonium cation formed by SM than hydroxide ion; second, acetonitrile could disperse SM into water as well as its compatibility with LC analysis and "cleaner" background in MS.

In this study, an experimental design by orthogonal array (a Latin square $L_9(3^4)$) was constructed to evaluate the effects of derivatization by the following factors: reaction time (A), temperature (B), concentration of PTA (C), and Blank (D), (D) was setup for calculation of error. The data were analyzed using SPSS statistical software (SPSS for Windows version 16.0; SPSS Inc, Chicago, USA). Then the range analysis was applied to the data

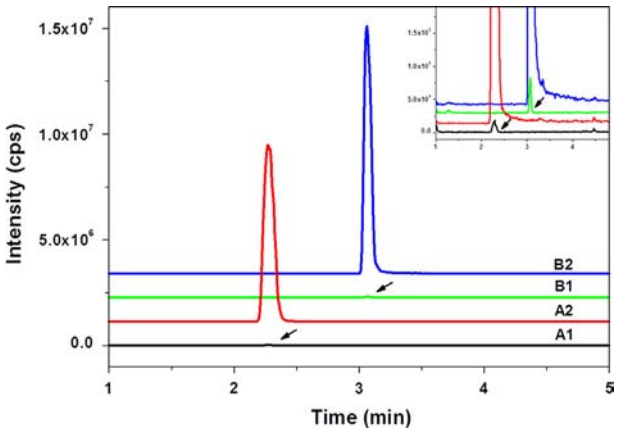


Fig. 2. The extracted ion chromatograms of mustard sulfoxide (A) and mustard sulfone (B) by derivatization with two different reaction conditions at the same concentration of 10 μg/mL. Condition 1, heated at 50 °C for 30 min, and condition 2, heated at 100 °C for 60 min. Inset shows a partially enlarged view.

Table 2
Parameters for derivatization of SM with PTA.

Parameter	Level		
	1	2	3
PTA (mg/mL)	0.1	1	5
Temperature (°C)	R.T.[a]	50	80
Reaction time (min)	10	30	60

[a] R.T. represents room temperature at ca. 25 °C.

analysis, and the setup parameters and obtained results were shown in Table 2 (for data details see Supplementary material). It was shown that 30 min of reaction time, 50 °C of reaction temperature, and 5.0 mg/mL of PTA concentration were the optimal derivatization conditions, and the rank order of the three parameters was $R_C > R_B > R_A$, as well as no unignorable interaction effect was found in such a design. However, it was discovered that the poor resolvability of PTA at higher concentration in organic solvent would affect the derivatization reaction and its stability. Eventually, derivatization of SM in acetonitrile using 1 mg/mL of PTA in water at equal volume, and heated at 50 °C for 30 min were adopted as the most favorable conditions.

The ratio of acetonitrile to water (v/v) and the effect of pH were also tested for optimization of this derivatization. When using the same concentration of SM at 100 ng/mL in acetonitrile and PTA solution at the concentration of 1 mg/mL in water, the response intensity of derivatization product BTAETE could achieve a relatively

1.2 or 4.7 times higher value when the ratio of acetonitrile to water was 1:1 rather than 1:2 or 1:4 by mixing different amounts of SM and PTA solution. It demonstrates that decreasing the volume of PTA solution can improve sensitivity in the case of a far excess of PTA than SM in the acetonitrile–water mixture. To illustrate potential pH effects, the robustness of the derivatization was measured at different apparent pH values by adding formic acid or 1 M NaOH to a mixture of acetonitrile–water at 50:50 (v/v). A lower response was observed at low pH (pH 3) compared with neutral or weak basic pH and almost undetectable at extreme high pH (pH 12), as a result of inhibition of formation of cationic episulfonium compound at low pH and appearance of elimination reaction at extreme high pH value [21]. PTA solution at the concentration of 1 mg/mL was tested in neutral pH value, so the pH value of derivertization reaction was under control at pH 7 more or less.

3.3. Method validation

Under the optimized parameter conditions for UPLC–MS/MS analysis, the examples of chromatograms including SM in natural water and soil at different concentrations are shown in Fig. 3. The developed method was validated with samples spiked with SM in acetonitrile, and was also successfully employed for determination of spiking samples both in water and soil by isotope-dilution LC–MS/MS. The selectivity was assessed by evaluating the unequivocal chromatographic separation and comparison among blank reaction solution, IS spiked blank, and standard spiked samples. Data from the method validation are given in Table 3.

The results show the established method can overcome the shortcoming of low repeatability caused by instability of sulfur mustard in a variety of matrices samples, because through derivatization it can greatly improve stability of analyte in the operation process by transferring the molecules of sulfur mustard with high alkylation activity into the form of BTAETE with non-alkylation activity. And the optimized direct derivatization is more convenient and universal since no decontamination or enrichment apparatus was necessary, no equilibrium time between sample and analyte was needed, only addition of common chemicals into samples at mild condition without solvent exchanging.

3.4. Limit of quantification, linearity and reproducibility

In this work, the LOD of SM was determined as 0.05 ng/mL by giving a S/N ratio greater than 3, whereas LLOQ was 0.1 ng/mL by S/N ratio greater than 10. In typical GC or GC–MS method for direct detection of SM with the recommended pretreatment procedure such as liquid–liquid extraction or solid-phase extraction, the reported LOD was ca. 50 ng/mL [24,25].

Table 3
Method validation for the determination of SM.[a]

Parameter		Value	
LOD (ng/mL)		0.05	
LLOQ (ng/mL)		0.10	
Linearity (R^2)		0.1–1000 ng/mL (0.995)	
Precision and trueness ($n=6$)		(RSD%)	(RE%)
LLOQ (0.1 ng/mL)	Intra-day	11.8	6.9
	Inter-day	12.3	3.4
Low (0.25 ng/mL)	Intra-day	3.9	−4.3
	Inter-day	5.3	−1.2
Medium (10 ng/mL)	Intra-day	7.1	−1.3
	-river	5.4	1.1
	-soil	7.4	−2.4
	Inter-day	9.3	−0.3
High (750 ng/mL)	Intra-day	7.3	4.1
	Inter-day	9.7	1.5
% Matrix effects ± SD ($n=3$)			
BTAETE (10 ng/mL)	River	87 ± 3.9	
	Soil	92 ± 3.3	
% Recovery ± SD ($n=3$)			
SM (10 ng/mL)	Acetonitrile	95 ± 2.5	
	River	80 ± 3.7	
	Soil	83 ± 10	

[a] Except for special annotation, data are obtained in acetonitrile solvent.

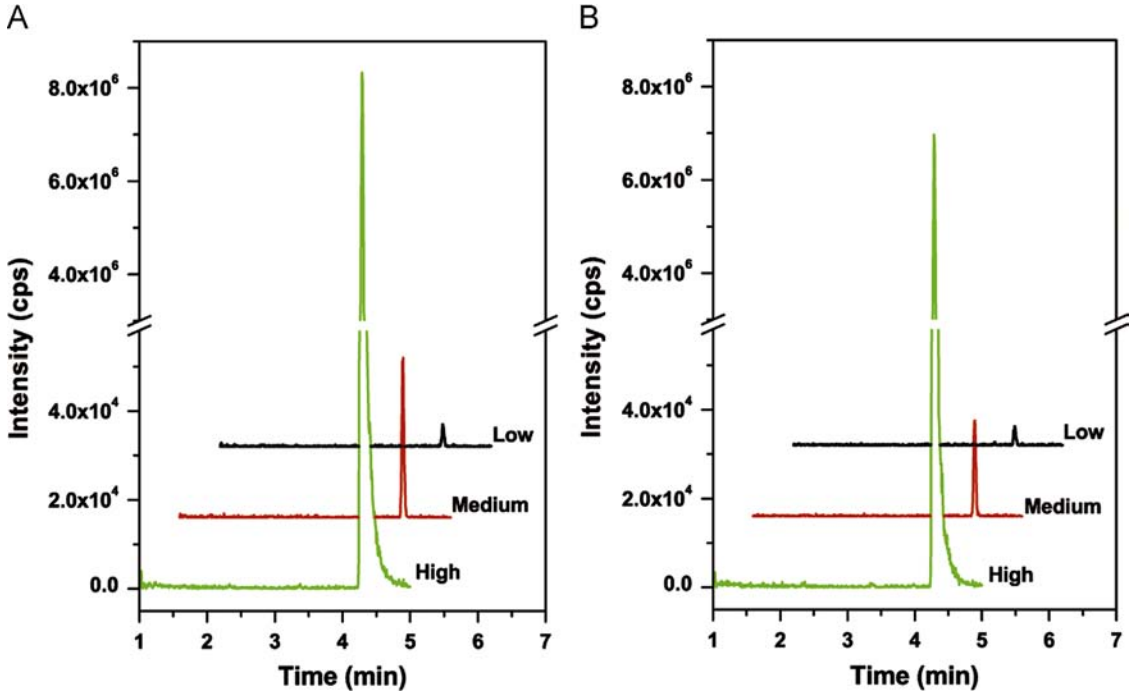


Fig. 3. The extracted ion chromatograms of SM in river water (A) and soil (B) at low (0.25 ng/mL), medium (10 ng/mL) and high (750 ng/mL) concentration.

The linearity and precision of method were investigated within the concentration range from 0.1 ng/mL to 1 μg/mL. Good linearity and method repeatability were obtained in the investigated range. Precision and trueness were measured at LLOD and three QC concentration levels, 0.25, 10, 750 ng/mL. As shown in Table 3, all inter-day and intra-day precisions were less than 12.3%, while the trueness represented by relative error (RE) was from −4.3% to 6.9%, showing our LC–MS/MS coupled with a derivatization procedure has a good feasibility for determination of SM.

3.5. Matrix effects and recovery

The matrix effects was observed at 87% and 92% respectively with river and soil samples by applied post-extraction spiking BTAETE procedure [26], which was evaluated by comparing the BTAETE in matrix and in acetonitrile at concentration of 10 ng/mL.

As it involves the derivatization reaction in our method, we also took the reaction efficiency into consideration by evaluation of the recovery of SM in different matrices. The recovery was investigated by spiking SM into different matrices, then derivatized and quantified BTAETE through the established standard curve of BTAETE in blank reaction system, and the result was calculated by

$$\%\ \text{Recovery} = \frac{C_{\text{BTAETE}}}{C_{\text{SM SPIKING}}} \times \frac{Mw_{\text{SM}}}{Mw_{\text{BTAETE}}} \times 100 \quad (1)$$

where C_{BTAETE} and $C_{SM\ spiking}$ represent the calculated concentration of BTAETE and spiking concentration of SM, while Mw_{BTAETE} and Mw_{SM} mean the molecular weight of BTAETE and SM.

Here this recovery, combining reaction efficiency, matrix effects, extraction efficiency and other factors, and the results were shown as 95%, 80% and 83% separately in acetonitrile, river and soil samples as shown in Table 3. In light of the data of matrix effects presented above, it concludes that the majority of SM molecules in the reaction system were transformed into BTAETE. As shown in Fig. 4, when derivatization of SM at relatively high concentration, for example 1.0 μg/mL, some reaction by-products within very small amounts have been monitored, such as hemisulfur mustard and mustard sulfoxide, as well as the BTAETE's mono-oxidation product bis-(thioacetate) ethylsulfinyl ethane (BTAESE). Although BTAESE can be formed by either derivertization of mustard sulfoxide or oxidation of BTAETE, actually the main contribution of the peak intensity was from partial oxidation of overdosed BTAETE. Since it was not convenient for the reaction of mustard sulfoxide under current conditions, especially unchanged mustard sulfoxide existed at a very low concentration.

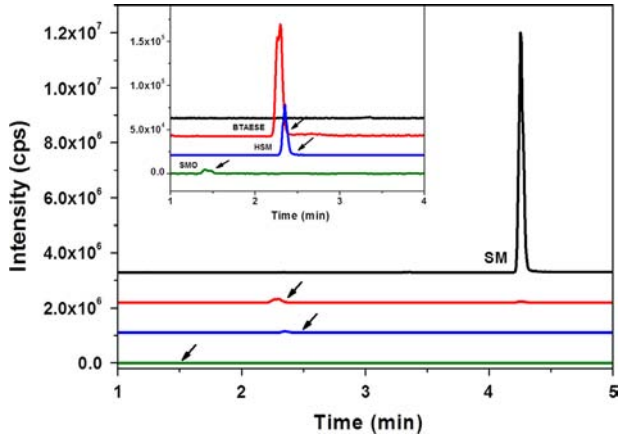


Fig. 4. The extracted ion chromatograms of derivatives of SM and hemisulfur mustard (HSM), mono-oxidation product of BTAETE (BTAESE) and unchanged mustard sulfoxide (SMO) in acetonitrile at the concentration of 1.0 μg/mL. Inset shows a partially enlarged view.

3.6. Determination of SM

Considering the hydrolysis problem of SM, the analysis for water or soil samples were operated immediately after spiking SM, then IS and PTA were added at once. And the selectivity was assessed by comparison among blank matrices reaction solution, IS spiked blank matrices, and standard spiked samples.

This established method with good validation was applied for quantitative determination of spiked natural water and soil samples. A detection limit of 0.1 ng/mL was achieved for the river sample, whereas the SM in soil sample could be detected at 0.1 ng/g. In light of application of stable isotope dilution, the trueness was 1.1% and −2.4% (RE), while the precision was 5.4% and 7.4% (RSD) for spiked river and soil samples respectively, shown in Table 3. Thus, the derivatization method was proved to be well applicable for different environmental samples, including natural water and soil samples.

4. Conclusion

In this work, we developed an isotope-dilution LC–MS/MS method with direct derivatization for determination of SM in aqueous samples, which would be a complementary technique with traditional GC or GC–MS. This method has obtained a good sensitivity lower to 0.05 ng/mL and a wide linear range from 0.1 ng/mL to 1 μg/mL. The total analysis time including sample preparation and instrument analysis was less than 1 h, and the method was easy to handle and has been successfully employed for trace SM determination in environmental samples, such as river water or soil samples. It is of great importance that via such a direct derivatization approach, LC–MS/MS technique can be applied for detection of SM, and it also has good prospects in bioanalysis of SM *in vivo* to meet the challenge of toxicological research.

Acknowledgment

This research was supported by National Science & Technology Major Project of the Ministry of Science and Technology of China (Grant no. 2012ZX09301003-001-010).

Appendix A. Supporting information

Supplementary data associated with this article can be found in the online version at: http://dx.doi.org/10.1016/j.talanta.2014.09.015.

References

[1] G.O. Bizzigotti, H. Castelly, A.M. Hafez, W.H. Smith, M.T. Whitmire, Chem. Rev. 109 (2008) 236–256.
[2] T. Missiaen, M. Söderström, I. Popescu, P. Vanninen, Sci. Total Environ. 408 (2010) 3536–3553.
[3] J.B. Tucker, Bull.-At. Sci. 57 (2001) 51–56.
[4] M.R. Zafarghandi, M.R. Soroush, M. Mahmoodi, K.H. Naieni, A. Ardalan, A. Dolatyari, F. Falahati, M. Mirmohammadkhani, B. Mousavi, M. Ghanei, Cancer Causes Control 24 (2013) 99–105.
[5] J.B. Tucker, Polit. Life Sci. (1996) 167–183.
[6] B.T. Røen, E. Unneberg, J.A. Tørnes, E. Lundanes, J. Chromatogr. A 1217 (2010) 2171–2178.
[7] C.T. Chiou, T.D. Shoup, Environ. Sci. Technol. 19 (1985) 1196–1200.
[8] N.B. Munro, S.S. Talmage, G.D. Griffin, L.C. Waters, A.P. Watson, J.F. King, V. Hauschild, Environ. Health Perspect. 107 (1999) 933–974.
[9] R.M. Black, R.J. Clarke, R.W. Read, M.T. Reid, J. Chromatogr. A 662 (1994) 301–321.
[10] R.M. Black, D. Noort, in: M. Mesilaakso (Ed.), Chemical Weapons Convention Chemicals Analysis: Sample Collection, Preparation and Analytical Methods, John Wiley & Sons, Ltd, Chichester, UK, 2005, pp. 403–432.
[11] G.L. Kimm, G.L. Hook, P.A. Smith, J. Chromatogr. A 971 (2002) 185–191.
[12] M. Palit, D. Pardasani, A. Gupta, D. Dubey, Anal. Chem. 77 (2005) 711–717.
[13] B.T. Røen, E. Unneberg, J.A. Tørnes, E. Lundanes, J. Chromatogr. A 1217 (2010) 761–767.

[14] P. D'Agostino, L. Provost, J. Hancock, J. Chromatogr. A 808 (1998) 177–184.
[15] R.W. Read, R.M. Black, J. Chromatogr. A 862 (1999) 169–177.
[16] Z. Nie, Q. Liu, J. Xie, Talanta 85 (2011) 1154–1159.
[17] R.M. Black, K. Brewster, J.M. Harrison, N. Stansfield, Phosphorus Sulfur Silicon Relat. Elem. 71 (1992) 31–47.
[18] FDA, Guidance for Industry: Bioanalytical Methods Validation, 2001.
[19] P.D. Bartlett, C.G. Swain, J. Am. Chem. Soc. 71 (1949) 1406–1415.
[20] Y.C. Yang, L.L. Szafraniec, W.T. Beaudry, F.A. Davis, J. Org. Chem. 55 (1990) 3664–3666.
[21] Y.C. Yang, J.A. Baker, J.R. Ward, Chem. Rev. 92 (1992) 1729–1743.
[22] W.P. Anslow, D.A. Karnofsky, B.V. Jager, H.W. Smith, J. Pharmacol. Exp. Ther. 93 (1948) 1–9.
[23] S. Popiel, Z. Witkiewicz, A. Szewczuk, J. Hazard. Mater. 123 (2005) 94–111.
[24] P.A. D'Agostino, L.R. Provost, Biol. Mass Spectrom. 15 (1988) 553–564.
[25] P.K. Kanaujia, D. Pardasani, A. Gupta, D. Dubey, J. Chromatogr. A 1139 (2007) 185–190.
[26] B.K. Matuszewski, M.L. Constanzer, C.M. Chavez-Eng, Anal. Chem. 75 (2003) 3019–3030.

Talanta 132 (2015) 252–257

Contents lists available at ScienceDirect

Talanta

journal homepage: www.elsevier.com/locate/talanta

Fluorescent carbon nanodots for sensitive and selective detection of tannic acid in wines

Gaber Hashem Gaber Ahmed [a,b], Rosana Badía Laíño [b], Josefa Angela García Calzón [b], Marta Elena Díaz García [b,*]

[a] Chemistry Department, Faculty of Science, Damanhur University, Damanhur, Egypt
[b] Department of Physical and Analytical Chemistry, Faculty of Chemistry, University of Oviedo, c/JuliánClavería, 8, Oviedo 33006, Spain

ARTICLE INFO

Article history:
Received 22 July 2014
Received in revised form
11 September 2014
Accepted 13 September 2014
Available online 30 September 2014

Keywords:
Carbon nanodots
Tannic acid
Wines

ABSTRACT

Herein we describe an easy one step synthesis of carbon nanodots (C-dots) by thermal carbonization of 6-bromohexylboronic acid using two different amine compounds, polyethyleneglycol bis(3-aminopropyl (PEGA) and 1,2-aminopropane (DPA), at 180 °C in atmospheric oxygen. The as-synthesized C-dots were characterized by FTIR, HRTEM, NMR and fluorescence. The C-dots prepared using PEGA showed a strong emission at 440 nm with excitation at 362 nm. These C-dots exhibited analytical potential as sensing probes for tannic acid (TA) determination. pH effect, interferences, and analytical performance of the method were investigated. The method was found effective in the linear concentration range from 0.1 to 10 mg L^{-1} TA achieving a limit of detection equal 0.018 mg L^{-1} TA. The applicability of the method was demonstrated by direct measurements of TA in red and white wine samples. Validation of the method was achieved by spiking the wine samples with different standard TA concentrations obtaining recoveries in the range (90–112.5%). A probable mechanism by which TA quenched the C-dots fluorescence was proposed.

© 2014 Elsevier B.V. All rights reserved.

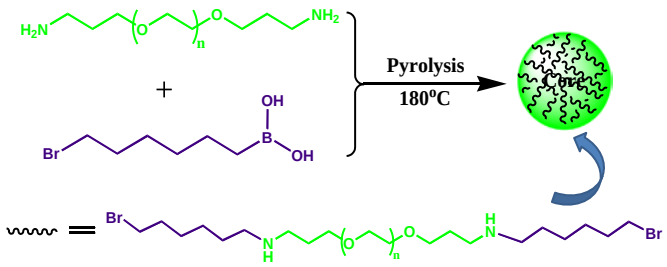
1. Introduction

Tannic acid (TA) is a natural hydrolysable polyphenol compound present in fruits and different kinds of vegetables and, along with other condensed polyphenols, can be found in several beverages including wine, beer, coffee, black tea and white tea. TA is composed of a polyol residue derived from D-glucose, which hydroxyl groups may be partially or fully substituted with galloyl units (gallotannins) [1]. It is used as a food additive (code number E-181) as clarifying agent, flavor adjunct and flavoring agent [2] as well as additive in medicinal products due to its astringent, diuretics and anti-inflammatory activities [3,4]. Moreover, TA has also applications in the tannery industry to transform animal skins to leather and for re-tanning with Cr(III) to prevent leather putrefaction [5]. As an organic pollutant associated with the tanning industry, TA has been found to be toxic to aquatic microorganisms and may form metal complexes that alter the aquatic ecosystem [6,7]. Due to its wide range of applications, analysis of tannic acid is of importance not only in food but also in the medical and environmental fields. Many analytical methods are based on the overall oxidation properties of polyphenols and, consequently, devoted to the determination of total phenolic content rather than specific determination of each component [8–12]. However, many efforts were attempted to measure TA in several kinds of food and beverage samples, as well as in industrial waters. So, a number of methods are available to quantitatively determine tannic acid content in waters, pharmaceuticals and foods, including spectrophotometry [13], electrochemical methods [14–16], luminescence [17–19] and chromatography [20,21]. Each method has its advantages and drawbacks. For example, the determination of tannic acid in wines by the traditional spectrophotometric Folin–Ciocalteu method, based on the formation of a blue phosphotungstic phosphomolybdenum complex, is simple but lacks selectivity as many other compounds in wine interfere. Chromatographic methods allow the determination of tannic acid along other polyphenols but are time consuming and expensive. Electroanalytical methods with different types of electrodes were used for TA determination, but the presence of ascorbic acid limits the use of some of these methods, or laborious sample pretreatments are needed to remove ascorbic acid before analysis [15,16]. These examples demonstrate that sensitive, selective and rapid TA detection is still a challenge.

Recent developments in analytical nanotechnology open the opportunity to develop new sensitive and selective methods for tannic acid determination. Carbon nano dots (C-dots) were found recently to be promising materials in analytical and bioanalytical

* Corresponding author.
E-mail addresses: rbadia@uniovi.es (R.B. Laíño), medg@uniovi.es (M.E.D. García).

http://dx.doi.org/10.1016/j.talanta.2014.09.028
0039-9140/© 2014 Elsevier B.V. All rights reserved.



Scheme 1. Schematic representation of PEGA-C-dots synthesis .

applications, due to their unique optical properties, such as broad excitation spectra, tunable emission wavelength and stable photoluminescence [22]. Exploiting C-dots in analytical chemistry is relatively recent and most methods depend on the C-dots surface functional groups and/or their surface passivation effects. The number of analytical assays using C-dots has been increasing, but in the best of our knowledge, no work has been described for TA determination in real samples using carbon nanodots.

Herein we report a straightforward synthesis of passivated C-dots in one step via thermal carbonization method (Scheme 1), using two different amino precursors, polyethyleneglycol bis(3-aminopropyl) (PEGA) and 1,2-aminopropane (DPA). Those C-dots prepared with PEGA were found sensitive and selective fluorescent nanosensors for TA and were successfully applied to direct TA detection in real red and white wine without sample pretreatment. The synthesis reaction process as well as the mechanism for the selective sensing are also proposed.

2. Experimental

2.1. Materials

All the reagents used were highly pure analytical grade chemicals and used without further purification. The following reagents were used in this study: polyethylene glycol bis(3-aminopropyl) (PEGA), 6-bromohexylboronic acid (BrHBA), glucose, fructose, sucrose, gallic acid, citric acid, calcium chloride, and disodium hydrogen phosphate, all purchased from Sigma-Aldrich. Ascorbic acid, sodium fluoride, potassium chloride, and sodium sulfite were purchased from Merck. 1,2-diaminopropane, tartaric acid and caffeine were purchased from Fluka. NaOH, and HCl were purchased from Prolabo. TA was purchased from Hopkin & Williams chemicals (England).

2.2. Synthesis of C-dots

PEGA-C-dots and DAP-C-dots were synthesized by a thermal carbonization method, using PEGA and DAP, respectively. Typically, 1 mmol of PEGA was dissolved in about 25 mL of milli-Q water. To this solution, 0.25 mmol of BrHBA was added. The solution was then stirred and heated at 150 °C. The heating was continued until near dryness, after which 1 mL of milli-Q water was added. The process was repeated 5 times. Finally the temperature was raised to 180 °C. A yellow solution was formed and heating continued until obtaining a reddish-brown color solution to ensure the formation of the C-dots. The obtained PEGA-C-dots solution was then completed to 25 mL of milli-Q water filtered by nylon filters (0.45 μm) and purified through dialyzer tube (MWCO, 3.5 kDa) for 3 days. The purified solution was divided into two aliquots, the first one was dried completely for characterization analysis while the second was used for the analysis experiments of tannic acid. The pH of the aqueous PEGA-C-dots solution resulted to be 6.43. The same procedure was carried out to prepare DAP-C-dots using DAP instead of PEGA.

2.3. Spectrofluorimetric measurements

In a typical pH effect determination procedure, 100 μL of TA (so that the final concentration is 5 mg L^{-1}) were diluted by about 4 mL of universal buffer (in the range 3–11.5) and then 100 μL of C-dots solution was added. Finally, the solution was completed by the same buffer until a final volume of 5 mL. The fluorescence was measured immediately after the preparation in a 1-cm quartz cuvette 3 times at 440 nm with excitation at 362 nm and slit widths of excitation and emission as 20 and 10 nm, respectively. The average fluorescence data were calculated and presented as a graph. Similarly, for interference measurements, 100 μL of TA (final concentration is 5 mg L^{-1}) was mixed with the interference material (final concentration is 10 mg L^{-1}) and diluted by about 4 mL of universal buffer solution pH=9. Then, 100 μL of C-dots solution was added and finally the solution was completed to 5 mL using the same buffer solution. The subsequent fluorescence was measured as mentioned above with the same instrumental conditions.

2.4. Fluorescence quantum yield measurement

The fluorescence quantum yield was calculated through the well-established comparative method using quinine sulfate as a reference. The following equations were used in the quantum yield measurement:

$$\Phi_C = \Phi_{st}\frac{F_C}{F_{st}}\frac{A_{st}}{A_C}\frac{{n_C}^2}{{n_{st}}^2} \quad (1)$$

$$\Phi_C = \Phi_{st}\frac{G_C}{G_{st}}\frac{{n_C}^2}{{n_{st}}^2} \quad (2)$$

where ϕ is the quantum yield, F is the calculated integrated fluorescence intensity, n is the refractive index, A is the optical density (measured with a UV–Vis spectrophotometer, Perkin Elmer, Lambda 900), and G is the gradient of F vs A linear plot. The subscripts C and st refer to C-dots and the reference fluorophore, respectively. Quinine sulfate dissolved in 0.1 M H_2SO_4 (n=1.33) of quantum yield equal 0.54 at λ_{ex}=350 nm was used as a reference. C-dots were dissolved in milli-Q water (n=1.33).

2.5. Analysis of wine samples

The white wine sample (Soldepeñas, www.felixsolis.com) and red wine samples (Don Mendo, www.sanvelro.com) were used in the application experiment. The pHs of the wines were found 3.31 and 3.43, respectively. TA standards were prepared in 10% ethanol solution to avoid the effect of alcohol and sample pretreatment. Wine samples were diluted so that the alcoholic content was reduced to 10%. In a typical procedure, 100 μL of sample were spiked by 100 μL standard TA (0, 1, and 3 mg L^{-1}) followed by 4 mL buffer solution pH=9 (Na_2HPO_4 and NaOH and/or HCl) and 100 μL of the PEGA-C-dots solution. Finally, the solution was diluted to 5 mL by the same buffer. Fluorescence was measured at 440 nm with excitation at 362 nm. TA was quantified by running a calibration curve using standard solutions. All determinations were carried out in triplicate.

2.6. Instrumentation

HRTEM (JEOL JEM-2100F, 200 kV) was used to determine the size and morphology of the synthesized C-dots. A Varian 620-IR instrument was used to analyze FTIR spectra in the range 600 to 4000 cm^{-1}. ^{1}HNMR and ^{13}CNMR (NAV400 with 9.0 T magnet shielded, 600 MHz) were used for structural analysis of the synthesized C-dots in D_2O

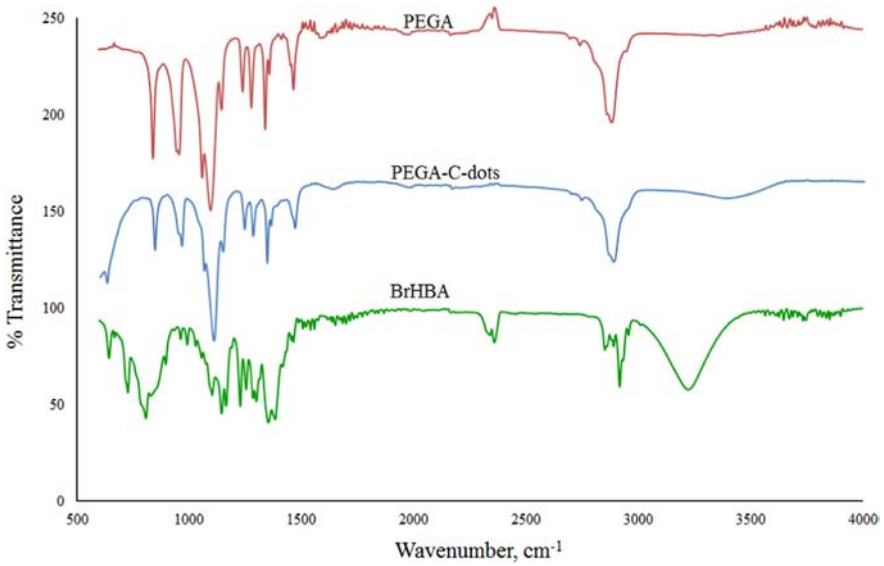


Fig. 1. FTIR spectra of PEGA-C-dots and their precursors.

solvent. Fluorescence spectra were measured using a Cary Eclipse Varian spectrofluorimeter.

3. Results and discussion

3.1. Synthesis and characterization of C-dots

The up-down strategy was used to synthesize C-dots via thermal carbonization method. It is well known that the reaction between the amine group and the alkyl halides proceeds easily and does not need extreme conditions. Higher temperatures than 180 °C were avoided in order to prevent product decomposition. According to the Scheme 1, it was expected that upon heating the long chain product formed between PEGA and BrHBA adhered to the C-dots surface. To confirm this reaction route, the same strategy of synthesis was performed using DAP, a small molecular weight amine, as precursor (Fig. S1).

3.2. FTIR analysis

Fig. 1 shows the spectra of the synthesized PEGA-C-dots and that of reaction precursors for comparison. Two characteristic peaks were identified in the synthesized PEGA-C-dots, the first at 1290 cm^{-1} ascribed to C–H wag (observed only in terminal alkyl halides) and a second at 650 cm^{-1} ascribed to C–Br stretching vibration. Similarly, the same two characteristic peaks were observed in DPA-C-dots (Fig. S2). The absence of characteristic peaks of B–O deformation at 500–550 cm^{-1}, B–O rocking at 725 cm^{-1}, B–OH deformation (at 1210 and 1305 cm^{-1}) and B–N stretching at 780 cm^{-1} in both types of C-dots suggested a pyrolytic deboronation mechanism according reaction route depicted in Scheme 1.

3.3. HRTEM and NMR analysis

The size and the morphology of the as-synthesized PEGA-C-dots and DPA-C-dots are spherical with size range 5 ± 3 nm as demonstrated by the HRTEM images (Fig. S3). Typical ^{13}C NMR spectra of PEGA-C-dots (Fig. S4) showed no signals in the range of 165 to 180 ppm corresponding to sp^2 carbons; however, signals in the range of 40 to 80 ppm revealed the presence of aliphatic sp^3 carbons [23]. On the other hand, ^{13}C NMR spectra of DAP-C-dots (Fig. S5) showed signals in the range of 165 to 170 ppm due to sp^2 carbons that could be ascribed to graphite carbons/planes and signals in the range of 40 to 80 ppm corresponding to aliphatic sp^3 carbons. The ^{1}HNMR spectra of PEGA-C-dots and DPA-C-dots are displayed in Figs. S6 and S7, respectively. Peaks in the range 3.4–3.5 ppm for RCH_2-Br and 0.5–5.0 ppm for R_2NH [23] for both types of C-dots confirmed the information obtained by FTIR.

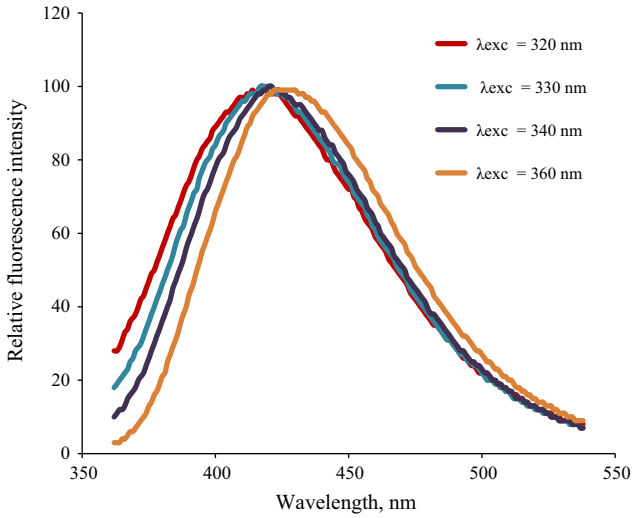


Fig. 2. PEGA-C-dots emission fluorescence as a function of excitation wavelength. (For interpretation of the references to color in this figure legend, the reader is referred to the web version of this article.)

3.4. Fluorescence features of the as-synthesized carbon nanodots

The fluorescence emission peak of PEGA-C-dots at pH 3 (0.2 M Na_2HPO_4/0.1 M citric acid) was blue shifted with the change of excitation wavelength (Fig. 2), a phenomenon frequently observed in C-dots which origin still remains unclear. Notwithstanding, it is frequently ascribed to different functional groups that create surface defects with the result of different energy levels [24]. In further experiments, excitation and emission wavelengths of 362 and 440 nm, respectively, were used. The full width at a half maximum at the different excitation wavelengths demonstrated a narrow size distribution of as-prepared PEGA-C-dots (90 ± 5 nm), thus confirming the absence of fluorescence color-dot size relationship.

On the other hand, the fluorescence quantum yield of the C-dots excited at 362 nm in milli-Q water was calculated to be 0.3%, a value similar to that found for other C-dots obtained from combustion soot of candles [25] or by using a plasma-induced method [26].

3.5. pH effect

The effect of pH is very important in this investigation, as the fluorescence of PEGA-C-dots in the absence and presence of TA is pH dependent. The influence of pH in the range 3–11.5 was investigated for TA interaction with PEGA-C-dots and results shown in Fig. 3. In the acidic pH range 3–6 a white precipitate was formed in presence of TA, particularly at concentrations of TA higher than 5 mg L^{-1}. Maximum quenching effect took place in basic media and a pH=9 was taken as the optimum value for further experimental measurements.

3.6. Analytical figures

Under the optimum experimental conditions, the sensitivity, the linear response range and the limit of detection of TA by PEGA-C-dots fluorescence quenching were determined. Calibration curve, obtained from a Stern–Volmer semilog plot, was linear within the range 0.1 to 10 mg L^{-1} TA being the calibration equation $\log(F^{\circ}/F)=0.0597$ C {mg L^{-1}}, ($R^2=0.994$), where F° and F account for the fluorescence intensities of PEGA-C-dots in the absence and presence of TA, respectively and C represents the concentration of TA in mg L^{-1}. A detection limit of 0.018 mg L^{-1} TA was calculated (%RSD=0.2). As far as we know, no fluorescence methods for TA based on the use of C-dots have been described to date. From Table 1, it is apparent that the present method, exhibits high sensitivity and low detection limit when compared with some electrochemical and optical methods. Among them, that based on the TA oxidation by chitosan capped silver nanoparticles has been recently published for TA determination [27].

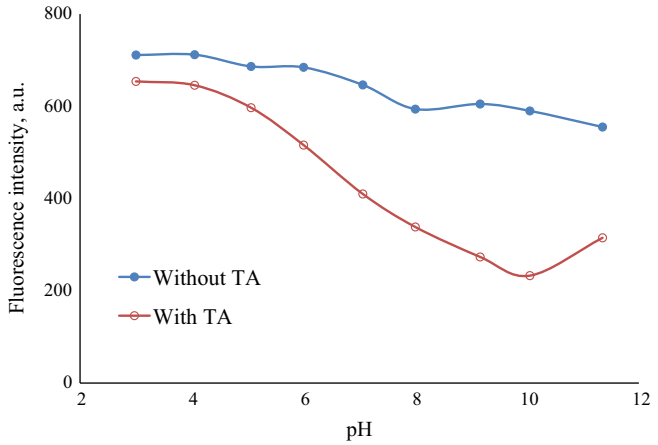


Fig. 3. pH influence on PEGA-C-dots fluorescence in absence and presence of TA (5 mg L^{-1}) at $\lambda_{ex}=362$ nm.

The effect of coexisting compounds on the PEGA-C-dots fluorescence quenching detection of 5 mg L^{-1} TA at pH 9 was investigated. The concentration of all compounds used was 10 mg L^{-1}. The tolerance limit was estimated with a ±5% relative error in fluoresence intensity. The major interference compounds chosen were ascorbic acid, sulfite, caffeine, Mg^{+2} and Ca^{+2} in addition to some abundant components in wine such as gallic acid, sucrose, glucose, fructose, tartaric acid and Na^{+}. It was found that these compounds have no significant effect on the fluorescence emission of PEGA-C-dots by TA. These analytical figures offer a high potential of sensitivity and selectivity for TA in wine samples with no need of sample treatment and it could be comparable to other analytical techniques used for TA determination in such samples.

3.7. Interaction of PEGA-C-dots with TA

The above experimental results showed that the fluorescence quenching observed on adding TA to a C-dots solution at pH=9 remained stable over a long time, indicating that a stable method could be optimized for TA. On the other hand, it was observed that gallic acid did not quench the PEGA-C-dots fluorescence. Carbon dots are known to be excellent electron acceptors and donors [28]; so, a possible mechanism for TA quenching may be attributed to an electron transfer process from the photo excited C-dots to the aromatic groups in TA. The PEGA-C-dots may be wrapped by the TA mimicking dendrimers, so allowing an effective non-radiative energy transfer process (Fig. 4).

On the contrary, in presence of gallic acid such interaction with PEGA-C-dots was not possible and fluorescence quenching did not take place.

3.8. Real sample analysis

Under the optimum experimental conditions described, TA determination in red and white wine samples was performed to validate the method. No sample pre-treatments were made but dilution with buffer. The fluorescence spectra of PEGA-C-dots without and with wine samples spiked by different concentrations (0, 1, and 3 mg L^{-1}) are illustrated in Fig. S8. Table 2 shows the results of TA obtained in wine samples after their dilution. Each result was the average of three samples. It is obvious that satisfactory recoveries were achieved for the spiked samples and results demonstrated that the method offers potential for quantitative determination of TA in wine samples.

4. Conclusions

In summary, we have been successfully synthesized passivated C-dots in an easy one step in which a deboronation process took

Table 1
Figures of merit of different analytical methods for tannic acid determination.

Method	Detection limit (μM)	Linear range (μM)	Samples	Ref.
Inhibition of luminol electrochemiluminescence	0.02	0.05 to 100	Chinese gall, hop pellet	[19]
Chemiluminescence/FIA	0.06	0.06 to 17	Pharmaceuticals, human urine, surface waters	[17]
Quenching of the 3-aminophthalate fluorescence	0.58	3 to 180	Tea beverages	[18]
Anodic stripping voltammetry	0.01	0.01 to 1	–	[14]
Colorimetric: oxidation by chitosan capped Ag nanoparticles	1	1–100	Water	[27]
Spectrophotometric	0.08	1 to 10	Ayurvedic formulation	[21]
Carbon dots fluorescence quenching	0.01	0.05 to 0.6	Wines	This method

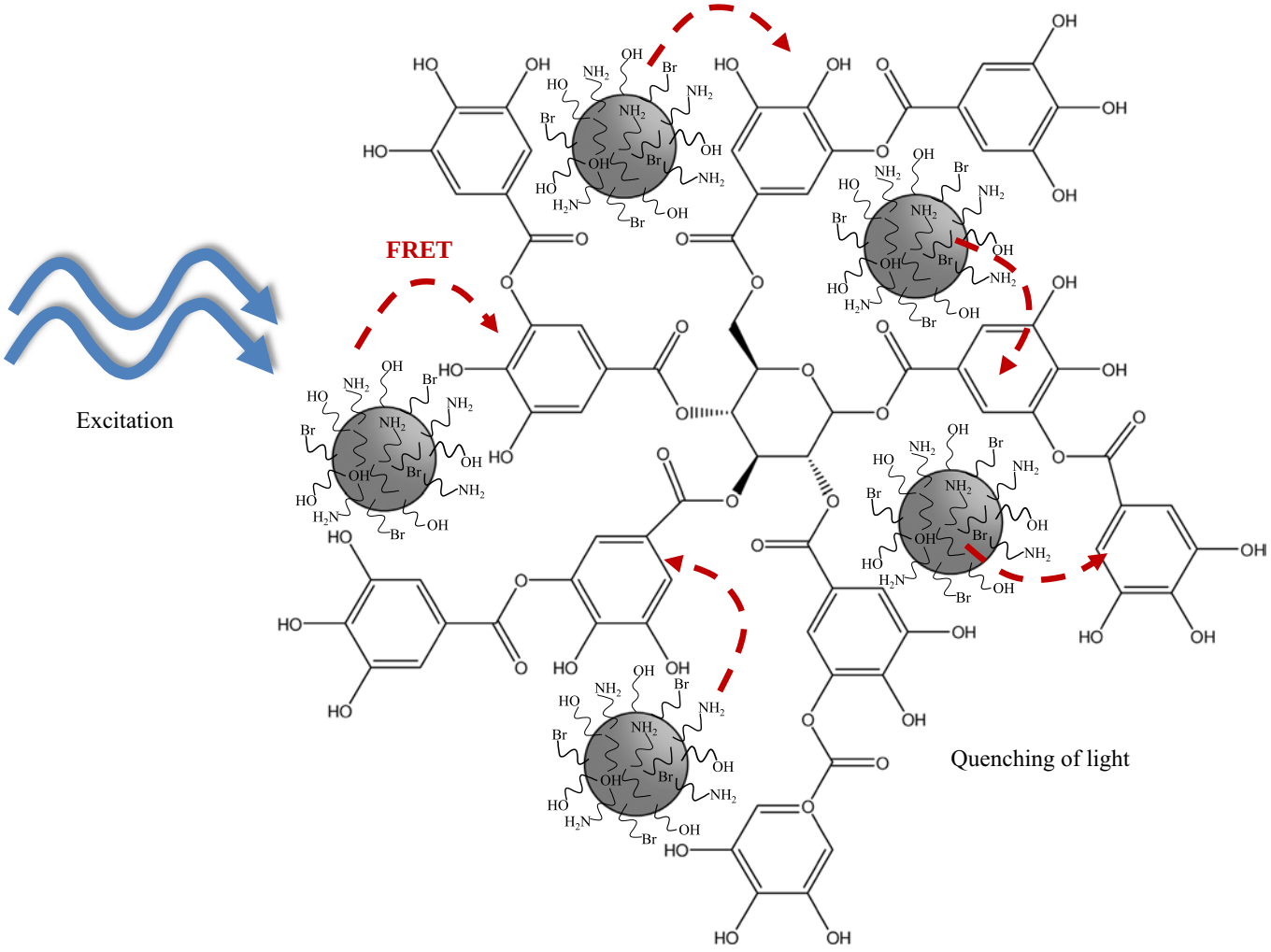


Fig. 4. PEGA-C-dots non-radiative energy transfer to tannic acid dendrimers under excitation wavelength λ_{ex}=362 nm, at pH=9.

Table 2
Results for TA determination in raw and spiked wines.

Spiked conc. (mg L^{-1})	Red wine			White wine		
	Found conc. (mg L^{-1})	% RSD	Recovery (%)	Found conc. (mg L^{-1})	% RSD	Recovery (%)
0	2.69	0.1	–	0.055	0.13	–
1	3.81	0.25	112.2	1.18	0.1	112.5
3	5.4	0.34	90.2	2.95	0.36	96.6

place. The as-synthesized PEGA-C-dots were found sensitive and selective towards TA, so that a promising fluorescence sensing system for TA detection in wines has been developed. The probe system of TA based on PEGA-C-dots fluorescence quenching showed analytical advantages such as rapid detection, high sensitivity and selectivity, wide linear response range, and low cost. A possible mechanism for TA sensing was attributed to a wrapping of the PEGA-C-dots by the TA mimicking dendrimers, so allowing an effective non-radiative energy transfer process.

Acknowledgments

Authors gratefully acknowledge financial support from the Science and Innovation Spanish Ministry (Projs # MICINN-09-CTQ2009-09595 and MAT2012-099). Also, G.H. Gaber Ahmed thanks an Erasmus Mundus Medastar grant.

Appendix A. Supporting information

Supplementary data associated with this article can be found in the online version at http://dx.doi.org/10.1016/j.talanta.2014.09.028.

References

[1] K. Khanbabaee, T. van Ree, Nat. Prod. Rep. 18 (2001) 641–649.
[2] ⟨http://www.fao.org/food/food-safety-quality/scientific-advice/jecfa/jecfa-additives/en/⟩.
[3] N. Aelenei, M.I. Popa, O. Novae, G. Lisa, L. Balaita, J. Mater. Sci.—Mater. Med. (2009), http://dx.doi.org/10.1007/s10856-008-3675-z.
[4] A. Ren, W. Zhang, H.G. Thomas, A. Barish, S. Berry, J.S. Kiel, A.P. Naren, Dig. Dis. Sci. 57 (1) (2012) 99–108.
[5] K.J. Sreeram, T. Ramasami, Resour. Conserv. Recycl. 38 (2003) 185–212.
[6] N.L. Kruthika, G.B. Raju, S. Prabhakar, J. Nanosci (2014), http://dx.doi.org/10.1155/2014/481023.
[7] K.T. Chung, G. Zhao, E. Stevens Jr., B.A. Simco, J. Aquat. Anim. Health 7 (1995) 46–49.

[8] X. Cetó, J.M. Gutiérrez, M. Gutiérrez, F. Céspedes, J. Capdevila, S. Mínguez, C. Jiménez-Jorquera, M. del Valle, Anal. Chim. Acta 732 (2012) 172–179.
[9] Q. Chen, J. Zhao, X. Huang, H. Zhang, M. Liu, Microchem. J. 83 (2006) 42–47.
[10] J. González-Rodríguez, P. Pérez-Juan, M.D. Luque de Castro, Talanta 56 (2002) 53–59.
[11] M. Šeruga, I. Novak, L. Jakobek, Food Chem. 124 (2011) 1208–1216.
[12] B. Lorrain, I. Ky, L. Pechamat, P. Teissedre, Molecules 18 (2013) 1076–1100.
[13] S.P. Gupta, G. Garg, Int. J. Pharmacogn. Phytochem. Res 6 (2014) 190–193.
[14] L. Xu, N. He, J. Du, Y. Deng, Z. Li, T. Wang, Anal. Chim. Acta 634 (2009) 49–53.
[15] D.L. Vu, B. Ertek, L. Červenka, Y. Dilgin, Int. J. Electrochem. Sci. 8 (2013) 9278–9286.
[16] H. Wan, Q. Zou, R. Yan, F. Zhao, B. Zeng, Microchim. Acta 159 (2007) 109–115.
[17] B. Gómez-Taylor Corominas, J.V. García Mateo, L. Lahuerta Zamora, J. Martínez Calatayud, Talanta 58 (2002) 1243–1251.
[18] R.L.C. Chen, C.H. Lin, C.Y. Chung, T.J. Cheng, J. Agric. Food Chem. 53 (2005) 8443–8446. http://dx.doi.org/10.1021/jf051077f.
[19] Y.G. Sun, H. Cui, Y.H. Li, H.Z. Zhao, X.Q. Lin, Anal. Lett. 33 (2000) 2281–2291.
[20] J. Zhu, J. Ng, L.J. Filippich, J. Chromatogr. 577 (1992) 77–85.
[21] S.P. Gupta, G Garg, Der Pharm. Lett. 6 (2014) 31–36.
[22] S.N. Baker, G.A. Baker, Angew. Chem. Int. Ed. 49 (2010) 6726–6744.
[23] ⟨http://www.rsc.org/learn-chemistry/wiki/Introduction_to_NMR_spectroscopy⟩.
[24] L. Tang, R. Ji, X. Cao, J. Lin, H. Jiang, X. Li, K.S. Teng, C.M. Luk, S. Zeng, J. Hao, S.P. Lau, ACS Nano 6 (2012) 5102–5110.
[25] H. Liu, T. Ye, C. Mao, Angew. Chem. Int. Ed. 46 (2007) 6473–6475.
[26] J. Wang, C.-F. Wang, S. Chen, Angew. Chem. Int. Ed. 51 (2012) 9297–9301.
[27] Z Chen, X. Zhang, H. Cao, Y. Huang, Analyst 138 (2013) 2343.
[28] Y.H. Wang, L. Bao, Z.H. Liu, D.W. Pang, Anal. Chem. 83 (2011) 8130–8137.

Talanta 132 (2015) 258–268

Contents lists available at ScienceDirect

Talanta

journal homepage: www.elsevier.com/locate/talanta

The analysis of animal faeces as a tool to monitor antibiotic usage

Bjorn J.A. Berendsen*, Robin S. Wegh, Joost Memelink, Tina Zuidema, Linda A.M. Stolker

RIKILT, Wageningen University and Research Centre, Akkermaalsbos 2, 6708WB, P.O. Box 230, 6700AE Wageningen, The Netherlands

ARTICLE INFO

Article history:
Received 22 July 2014
Received in revised form
4 September 2014
Accepted 11 September 2014
Available online 19 September 2014

Keywords:
Antibiotics
Faeces
Tetracyclines
Sulfonamides
Quinolones
Macrolides
Bacterial resistance

ABSTRACT

The analysis of antibiotics in animal faeces is important to obtain more insight in the possible formation of bacterial resistance in the animals' gut, to learn about the dissemination of antibiotics to the environment, to monitor trends in antibiotic usage and to detect the illegal and off-label use of antibiotics. To facilitate these studies a comprehensive method for the analysis of trace levels of 44 antibiotic compounds including tetracyclines, quinolones, macrolides and sulfonamides in animal faeces by liquid chromatography in combination with tandem mass spectrometric (LC–MS/MS) detection is reported. The method is fully validated according to European regulation and showed satisfactory quantitative performance according to the stringent criteria adopted, with the exception of some of the macrolide compounds, which can be analysed with somewhat high measurement uncertainty. A large survey was carried out monitoring swine and cattle faeces and the outcomes were striking. In 55% of the swines, originating from 80% of the swine farms and in 75% of the calves, originating from 95% of the cattle farms, antibiotics were detected. Oxytetracycline, doxycycline and sulfadiazine were the most detected antibiotics, followed by tetracycline, flumequine, lincomycin and tylosin. Over 34% of the faeces samples contained two or more different antibiotics with a maximum of eight. Possible explanations for these findings are given and the effects are discussed.

© 2014 Elsevier B.V. All rights reserved.

1. Introduction

Antibiotics are medical agents that either kill bacteria or inhibits their growth. Antibiotics can be produced by microorganisms but also be synthetically produced and can be used for both human and veterinary purposes. Antibiotics are excessively used in both human and animal health and as a negative side-effect, bacteria become resistant. Nowadays, bacterial resistance is a major threat for human healthcare: in the USA, 23,000 people per year are dying due to bacterial infections which cannot be cured by antibiotic treatment [1]. Therefore, policies on the use of antibiotics have become more stringent within most countries aiming to decrease bacterial resistance and its dissemination. The focus is mainly on the decrease of antibiotic usage in human health as well as in veterinary practices, because resistant bacteria are easily transferred from animal to human [2]. In The Netherlands, a specific measure was the implementation of mandatory registration of antibiotics delivered to and used by farmers to prevent off-label usage.

After administration of antibiotics, 30–90% of the dose given is excreted in non-metabolized form or as active metabolites [3–5] and as a result high levels of antibiotics and active metabolites are expected to be present in faeces [6]. As a matter of fact, the presence of veterinary antibiotics in liquid waste from swines was previously confirmed [7]. Because slurry is used to optimise the growth and harvest in agriculture, antibiotics are unwillingly disseminated throughout the environment and are found in surface water, soil and crops [8–15] which is expected to contribute to adverse ecotoxicological effects [4,5,16,17] and the emergence of microbial resistance [18–23].

Analysing antibiotics in animal faeces is expected to be effective in several ways. First to obtain more insight in the possible formation of bacterial resistance in the animals' gut, leading to valuable information on the relation between residues and resistance. Second to learn about the dissemination of antibiotics to the environment and possible ecotoxicological effects. Third to monitor trends in antibiotic usage at the farms using non-invasive sampling and last to enforce policies on the use of antibiotics and thus to prevent the illegal and off-label use of antibiotics. We conclude that the analysis of antibiotics in faeces could be very informative and therefore a multi-method to detect a wide range of veterinary antibiotics in faeces is needed.

Multiple analytical methods for the analysis of antibiotics are available focussing on regulatory limits established for food products. Only a few multi-analyte methods on the analysis of antibiotics in faeces are published [12,24–31]. Most of these

* Corresponding author. Tel.: +31 317 480256.
E-mail address: bjorn.berendsen@wur.nl (B.J.A. Berendsen).

http://dx.doi.org/10.1016/j.talanta.2014.09.022
0039-9140/© 2014 Elsevier B.V. All rights reserved.

studies solely focussed on samples taken in Asia and they cover only a minor part of the relevant veterinary antibiotics, up to 17 in total. No fully validated multi-methods applying liquid chromatography (LC) coupled to tandem-mass spectrometry (MS/MS) for the analysis of a wide range of antibiotics in animal faeces is available and no data is available on the antibiotic content of faeces of swines and calves in Dutch animal breeding.

We present a multi-method for the analysis of veterinary antibiotics in faeces aiming for the detection, quantification and confirmation of 4 tetracyclines, 18 sulfonamides, 14 macrolides and 10 quinolones using LC–MS/MS. The method was fully validated for swine faeces according to Commission Decision 2002/657/EC [32]. Using this method 340 different swine faeces samples and 340 calf faeces samples obtained from 20 swine respectively 20 cattle farms were monitored for the presence of antibiotics. Results are presented here.

2. Material and methods

2.1. Reagents and equipment

HPLC grade methanol (MeOH) and acetonitrile (ACN) was obtained from Biosolve (Valkenswaard, The Netherlands). Milli-Q water was prepared using a Milli-Q system at a resistivity of at least 18.2 MΩ cm^{-1} (Millipore, Billerica, MA, USA). Formic acid, ammonium formate, citric acid monohydrate, disodiumhydrogenphosphate (Na_2HPO_4) dihydrate and disodium ethylenediaminetetraacetate (Na_2EDTA) were obtained from VWR International (Darmstadt, Germany) and lead acetate from Sigma Aldrich (St. Louis, MO, USA).

The reference standard of oxytetracycline hydrate, tetracycline HCl, chlortetracycline HCl, doxycycline hyclate, ciprrofloxacin, danofloxacin, enrofloxacin, flumequine, marbofloxacin, nalidixinic acid, norfloxacin, oxolinic acid, sarafloxacin HCl trihydrate, dapsone, sulfacetamide, sulfachloorpyridazine, sulfadiazine, sulfadimidin, sulfadimethoxin, sulfadoxin, sulfamerazine, sulfamethoxazole, sulfamethizole, sulfamethoxypyridazine, sulfamonomethoxin, sulfaphenazole, sulfapyridin, sulfaquinoxalin Na, sulfathiazole, sulfisoxazole, erythromycin, gamithromycin, josamycin, lincomycin HCl, natamycin, pirlimycin HCl, spiramycin, tildipirosin, tulathromycin, tylosin tartrate, valnemulin, amoxicillin, ampicillin, penicillin G Na, penicillin V K, cloxacillin Na hydrate, dicloxacillin Na H_2O, nafcillin Na hydrate, oxacillin Na hydrate were obtained from Sigma-Aldrich, gamithromycin from Hovione (Loures, Portugal), tylvalosin tartrate from ECO Animal Health (London, United Kingdom), tilmicosin and tiamulin fumarate from LGC standards (Teddington, Middlesex United Kingdom) and tildipirosin from MSD Animal Health (Boxmeer, The Netherlands).

Ciprofloxacin d_8 HCL hydrate, difloxacin d_3 HCl hydrate, enrofloxacin d_5 HCl, nalidixic acid d_5, norfloxacin d_5, oxolinic acid d_5, sarafloxacin d_8 HCl, lincomycin d_3, spiramycin d_3, sulfachloropyridazine $^{13}C_6$, sulfadimidine $^{13}C_6$, sulfadimethoxine d_6, sulfadoxine d_3, sulfamerazine $^{13}C_6$, sulfamethoypyridazine d_3, sulfapyridine $^{13}C_6$, sulfaquinoxaline $^{13}C_6$, sulfathiazole $^{13}C_6$, sulfisoxazole $^{13}C_6$, penicillin G d_7 and penicillin V d_5 were obtained from Witega (Beril, Germany), danofloxacin d_3 mesylate, flumequin $^{13}C_3$, gamithromycin d_4, sulfadiazine d_4, sulfamethoxazole d_4, dapson d_8, from Toronto Research Chemicals (Toronto, ON, Canada), erythromycin ^{13}C d_3 from Cachesyn (Mississauga, ON, Canada), tetracycline d_6 from Santa Cruz Biotechnology (Santa Cruz, CA, USA), and demeclocycline and lomefloxacin from Sigma Aldrich.

Stock solutions of the tetracyclines, sulfonamides, penicillins were prepared in MeOH, of the quinolones in ammoniated MeOH and of the macrolides in ACN at 1000 mg L^{-1}. Mix solutions of the individual antibiotic groups were prepared at 10 mg L^{-1} in MeOH and a spiking solution was prepared containing 0.25 μg L^{-1} of the individual sulfonamides 1.0 μg L^{-1} of the individual quinolones, macrolides and sulfonamides, and 2.5 μg L^{-1} of the individual penicillins in MeOH. A mixture of the internal standards was prepared at 5 μg L^{-1} in MeOH.

Citric acid solution (0.1 M) was prepared by dissolving 21 g citric acid monohydrate in 1 L of water. Phosphate solution (0.2 M) was prepared by Na_2HPO_4 in 1 L of water. EDTA solution (0.2 M) was prepared by dissolving 74.4 g Na_2EDTA in 1 L of water. McIlvain–EDTA buffer (0.1 M, pH 4.0) was prepared by mixing 500 ml citric acid solution with 280 ml phosphate solution. 74.4 g Na_2EDTA was added. Stir using a magnetic bar for 30 min. Check the pH and if needed set to pH 4.0 by adding either citric acid solution or phosphate solution. Add water to a total volume is 2 L. Lead acetate solution was prepared by dissolving 100 g lead acetate in 500 mL of water. Ammonium formate solution (1 M) was prepared by dissolving 6.3 g ammonium formate in 100 mL water. Mobile phase A was prepared by diluting 2 ml ammonium formate solution, 160 μL formic acid to 1 L with water. Mobile phase B was prepared by diluting 2 ml ammonium formate solution, 160 μL formic acid to 1 L with MeOH.

2.2. Sample preparation

The faeces samples were homogenised by stirring with a disposable wooden rod, 2.0 g was weighted into a 50 mL poly propylene (PP) centrifuge tube and 80 μL internal standard solution was added. 4 mL of McIlvain–EDTA buffer and 1 mL ACN were added to the sample. The sample was vigorously shaken by hand and placed in a rotary tumbler for 15 min. After shaking 2 mL of lead acetate solution was added and again the sample was vigorously shaken by hand. After centrifugation (3500 g, 10 min) the extract was transferred into a clean test tube and diluted by adding 13 ml 0.2 M EDTA solution. A Phenomenex (Torrance, CA, USA) Strata-X RP 200 mg/6 mL reversed phase solid phase extraction (SPE) cartridge was conditioned with 5 mL MeOH and 5 mL water. The complete extract was applied onto the SPE cartridge which was subsequently washed with 5 mL of water and dried by applying vacuum for 5 min. The antibiotics were eluted from the cartridge using 5 mL MeOH followed by evaporation of the solvent (40 °C, N_2). The residue was redissolved in 200 μL MeOH and subsequently 300 μL water was added before transferring the final extract into an LC–MS/MS sample vial.

2.3. LC–MS/MS

The LC system consisted of a Waters (Milford, MA, USA) model Acquity with a Phenomenex Kinetex C_{18} analytical column of 2.1 × 100 mm^2, 1.7 μm, placed in a column oven at 40 °C. The gradient was: 0–0.5 min, 1% mobile phase B, 0.5–5.0 min, linear increase to 100% B with a final hold of 1.0 min and an equillibration time of 3.5 min, operating at a flow rate of 0.3 mL min^{-1}. The injection volume was 10 μl. Detection was carried out by LC–MS/MS using an AB Sciex (Ramingham, MA, USA) Q-Trap 6500 mass spectrometer in the positive electrospray ionisation (ESI) mode. The operating parameters were: capillary voltage, 2.0 kV; cone voltage, 25 V; source offset, 20 V; source temperature, 150 °C; desolvation temperature, 550 °C; cone gas flow, 150 L h^{-1}; and desolvation gas, 600 L h^{-1}. The antibiotics were fragmented using collision induced dissociation (N_2) and the scheduled Selected Reaction Monitoring (SRM) transitions (20 s window) are presented in Table 1. Data was processed using Multiquant software V2.1.1 (AB Sciex).

Table 1
SRM transitions of the antibiotics and their internal standards.

Component	Precursor ion (m/z)	Product ion (m/z)	DP	CE (eV)	CXP
Amoxicillin	366.0	349.0	40	12	12
		114.0		25	12
Amoxicillin-d_4	370.0	113.9	51	35	6
Ampicillin	350.0	106.1	51	23	10
		160.1		19	14
Ampicilline-d_5	355.0	111.1	51	23	10
Ciprofloxacin	332.0	288.0	66	25	22
		231.0		49	20
Ciprofloxacin-d_8	340.0	235.0	50	51	18
Chlortetracycline	478.9	462.1	40	25	12
		444.1		30	12
Cloxacilline	436.0	276.9	51	19	22
		160.0		19	14
Danofloxacin	358.0	255.0	116	55	20
		82.0		83	12
Danofloxacin-d_3	361.0	255.0	61	53	20
Dapson	249.0	155.9	51	19	14
		107.9		29	12
Dapson-d_8	257.0	160.0	36	21	14
Demeclocycline	465.0	448.0	50	25	32
Dicloxacilline	470.0	159.9	61	21	16
		310.7		19	24
Dicloxacilline-$^{13}C_4$	473.8	160.0	36	17	14
Difloxacin	400.0	299.0	46	39	24
		356.0		27	26
Difloxacin-d_3	403.0	359.0	66	29	26
Doxycycline	444.9	427.9	40	25	12
		410.0		35	12
Enrofloxacin	360.0	286.0	61	47	22
		316.0		27	24
Enrofloxacin-d_5	365.0	321.0	56	27	22
Erythromycin	734.1	98.0	111	111	12
		158.0		45	14
Erythromycin-^{13}C-d_3	738.2	162.0	50	37	16
Flumequine	262.0	201.9	36	43	16
		126.0		61	8
Flumequine-$^{13}C_3$	265.0	204.9	46	45	16
Gamithromycin	777.9	619.2	56	45	48
		158.0		47	14
Gamithromycin-d_4	781.2	623.3	41	47	44
Josamycin	828.1	174.0	56	41	14
		109.0		83	16
Lincomycin	407.0	126.1	81	33	12
		359.0		25	32
Lincomycin-d_3	410.1	129.1	71	35	12
Lomefloxacin	352.0	265.0	50	33	20
Marbofloxacin	363.0	319.9	56	21	24
		72.0		49	10
Nafcilline	414.9	199.0	40	22	12
		179.0		45	12
Nalidixic acid	233.0	159.0	41	43	14
Nalidixic acid-d_5	238.0	188.0	21	37	14
Natamycin	666.0	503.2	40	51	13
		648.3		17	13
Norfloxacin	320.0	231.0	61	29	22
		282.0		41	20
Norfloxacin-d_5	325.0	231.0	56	55	18
Oxacilline	401.9	243.0	50	19	20
		160.0		19	12
Oxolinic acid	261.9	215.9	36	39	16
		160.0		49	12
Oxolinic acid-d_5	267.0	216.9	21	41	16
Oxytetracycline	460.9	426.0	61	27	12
		443.9		23	34
Penicilline G	334.9	176.1	50	17	12
		160.0		19	22
Penicilline G-d_7	342.0	159.9	46	17	12
Penicilline V	351.0	160.0	50	15	10
		114.0		45	10
Penicilline V-d_5	355.9	160.0	31	17	10
Pirlimycin	411.0	112.0	76	31	14
		363.1		23	28
Sarafloxacin	386.0	299.0	81	37	26
		342.0		27	26
Sarafloxacin-d_8	394.0	350.0	56	27	26

Table 1 (*continued*)

Component	Precursor ion (m/z)	Product ion (m/z)	DP	CE (eV)	CXP
Spiramycin	422.2	174.1	46	27	14
		174.3		30	15
Spiramycin-d_3	423.7	174.0	36	27	14
Sulfacetamide	215.0	155.9	41	23	12
		92.0		27	10
Sulfachloropyridazine	284.9	155.9	36	21	10
		91.9		39	10
Sulfachloropyridazin-$^{13}C_6$	290.9	161.9	36	21	14
Sulfadiazine	251.0	156.0	46	21	14
		91.9		35	12
Sulfadiazin-d_4	255.0	160.0	41	23	14
Sulfadimidin	278.9	186.0	66	23	16
		124.0		31	8
Sulfadimidin-$^{13}C_6$	285.0	185.9	56	25	16
Sulfadimethoxin	311.0	156.1	41	27	12
		92.0		45	12
Sulfadimethoxin-d_6	317.0	162.1	51	31	14
Sulfadoxin	311.0	155.9	56	25	12
		107.9		33	14
Sulfadoxin-d_3	313.9	155.9	50	25	12
Sulfamerazine	265.0	155.9	46	23	14
		171.9		23	16
Sulfamerazin-$^{13}C_6$	270.9	97.9	56	37	12
Sulfamethizole	270.9	155.9	41	19	14
		92.0		37	12
Sulfamethizole-$^{13}C_6$	276.9	162.0	36	21	12
Sulfamethoxazole	254.0	155.9	46	21	14
		92.0		27	12
Sulfamethoxazole-d_4	258.0	160.0	46	23	12
Sulfamethoxypyridazine	280.9	156.0	66	23	12
		108.0		39	14
Sulfamethoxypyridazin-d_3	283.9	155.9	41	23	14
Sulfamonomethoxin	281.0	155.9	51	25	12
		92.0		41	14
Sulfaphenazole	315.0	92.0		29	12
		108.0		37	8
Sulfapyridin	250.0	155.9	51	23	14
		92.0		35	10
Sulfapyridin-$^{13}C_6$	256.0	162.0	46	23	14
Sulfaquinoxalin	300.9	155.9	56	23	12
		92.0		41	10
Sulfaquinoxalin-$^{13}C_6$	306.9	161.9	51	23	14
Sulfathiazole	255.9	155.9	41	21	14
		91.9		35	12
Sulfathiazole-$^{13}C_6$	261.9	161.9	36	21	12
Sulfisoxazole	268.0	156.0	41	19	12
		113.0		21	12
Sulfisoxazole-$^{13}C_6$	273.9	162.0	31	19	14
Tetracycline	445.1	410.0	56	27	12
		154.0		37	12
Tetracycline-d_6	451.0	416.0	50	27	34
Tiamulin	494.1	192.1	81	27	14
		119.0		55	8
Tildipirosin	367.9	347.9	191	35	26
		319.9		41	22
Tilmicosin	435.0	695.3	80	25	12
		174.1		35	12
Tulathromycin	403.9	72.1	40	50	12
		577.5		20	12
Tylosin	916.1	174.0	126	47	14
		772.2		43	52
Tylvalosin	1042.1	814.1	31	45	20
		174.0		30	13
Valnemulin	565.1	263.0	56	25	34
		164.1		43	14

2.4. Method validation

A full validation for swine faeces was carried out according to Commission Decision 2002/657/EC [32]. The following parameters were determined: linearity, trueness, repeatability, within-laboratory reproducibility, decision limit (CCα), detection capability (CCβ), selectivity and stability. For each compound a target level was set based on the expected detection limits obtained from method optimisation data: for sulfonamides 5 μg kg^{-1}, for the tetracyclines, quinolone and macrolides 20 μg kg^{-1} and for the penicillins 50 μg kg^{-1}. The validation was carried out at three different levels (0.5, 1.0 and 1.5 ∗ target level), on three different occasions, by two different technicians and including swine faeces samples from different origin ($n=21$).

Quantitative results were obtained using isotopically labelled internal standards. If available corrections were carried out using the corresponding labelled internal standard. Josamycin, tilmicosin and tylvalosin were corrected using spiramycin-d_3, pirlimycin using lincomycin-d_3, tulathromycin and valnemulin using gamithromycin-d_4, natamycin using sulfisoxazole, tiamulin and tylosin using nalidixic acid-d_5, tildipirosin and marbofloxacin using lomefloxacin, oxytetracycline using tetracycline-d_6, chlorotetracycline and doxycycline using demeclocycline, sulfacetamide using sulfadiazine-d_4 and sulfamonomethoxine using sulfamethoxypoiridazine-d_3, sulfaphenazole using sulfadoxin-d_3,

2.4.1. Linearity

On three different days a matrix matched calibration line was prepared including 0, 0.5, 1, 2 and 3 * target level by adding solutions of the antibiotics to aliquots of a blank swine faeces sample. Calibration lines were constructed by plotting the peak areas, corrected by the corresponding internal standard, versus the added concentration and carrying out least squares linear regression. The linearity was considered acceptable if the coefficient of correlation was at least 0.990.

2.4.2. Trueness, repeatability and within-lab reproducibility

On each of the days seven different blank swine faeces samples were selected and analysed as such and spiked at 0.5, 1.0 and 1.5 * target level. Of one batch, similar to the batch used for the calibration samples, an additional six spikes were performed at target level. For each sample the antibiotic's concentration was calculated using the calibration line constructed on the same day. The trueness was calculated by dividing the average calculated level by the nominal concentration. According to 2002/657/EC [32] the trueness should be between 70% and 110% for validation levels between 1.0 μg $kg^{-1}$and 10.0 μg kg^{-1} and between 80% and 110% for validation levels from 10.0 μg kg^{-1}.

Note that because different faeces samples were used within one day, the repeatability is not the pure repeatability as stated in 2002/657/EC [32]. However, using different faeces samples a better understanding of the between sample variation is obtained and the validation better reflects a routine analysis situation. To obtain information on the true repeatability (within a single batch of faeces) the variation of seven aliquots originating from a single batch, at target level on each of the validation days ($n=3$) is evaluated using the same criteria. For clarity this parameter is indicated as RSD_r and the repeatability including matrix variation is indicated by RSD_{r*}.

According to 2002/657/EC [32] the relative within-lab reproducibility (RSD_{RL}) and RSD_r are considered acceptable if they are below the value calculated from the Horwitz equation [33] respectively two third of this value, i.e. below 31.7% respectively 21.1% at a validation level of 10 μg kg^{-1}. Thompson [34], demonstrated that the Horwitz equation is not applicable to the lower concentration range (<120 μg kg^{-1}) and suggested a complementary model. However, these findings are based upon data from products of animal origin and because we consider faeces a more difficult matrix, we did not adopt these more stringent criteria and applied the criteria established in 2002/657/EC [32]. Based on this the RSD_{RL} and RSD_r are acceptable if they do not exceed the values mentioned in Table 2. For RSD_{r*} the same criteria as for RSD_r are adopted.

2.4.3. Decision limit and detection capability

Because there are no legal limits for antibiotics in faeces, here the decision limit, CCα, is the limit at and above which it can be concluded with an error probability of 0.05 that a sample contains the antibiotic compound indicated. The detection capability, CCβ, is the lowest concentration of a compound that, with an error probability of 0.05, will result in a positive finding (above CCα) [32]. For the antibiotics CCα and CCβ were calculated according to the procedure described in 2002/657/EC [32] for banned substances using the linearity approach as stated in ISO 11843 [35], to reflect the lowest levels that can still be determined. This procedure results in a value for CCα and CCβ on each validation day. The reported values are the highest values found on the different days, reflecting a worse case situation. Because CCα and CCβ are calculated from the within-laboratory reproducibility, no specific criteria are set for these parameters.

Table 2
Adopted performance criteria according to 2002/657/EC [24].

Concentration level (μg kg^{-1})	Trueness (%)	RSD_r (%)	RSD_{r*} (%)	RSD_{RL} (%)
2.5	70–110	26.0	26.0	39.0
5	70–110	23.4	23.4	35.2
7.5	70–110	22.1	22.1	33.1
10	80–110	21.1	21.1	31.7
20	80–110	19.0	19.0	28.6
30	80–110	17.9	17.9	26.9

2.4.4. Selectivity

The selectivity of the method was studied based on a practical and a theoretical study. Firstly, the 21 analysed blank samples were checked for interferences at the retention times corresponding to the β-lactam reaction products. Secondly, the procedure previously described for validation of selectivity was applied to estimate the probability of interfering substances [36].

2.4.5. Stability

Stability data for the antibiotics in solution were reported previously [37]. The stability of final extracts was determined by storing these extracts at −18 °C after analysis. After 8 days, the matrix matched calibration standards, the blank samples and the samples spiked at target level ($n=7$) were defrosted and injected in the LC–MS/MS system again. The linearity, the trueness and the repeatability of this series was evaluated based on the established validation criteria to determine whether quantitative analysis is still possible after storing the sample extracts at −18 °C for eight days.

2.5. Faeces sampling

Twenty swine farms and 20 cattle farms were randomly selected. At the slaughterhouse, of each of these farms, 17 animals were selected and faeces was taken directly from the gut. These samples ($n=680$) were immediately transported to the laboratory and stored at <-18 °C. The samples were analysed in batches of 40–80–80 samples using the presented method. Quantification was carried out by preparing a matrix calibration line by adding the antibiotics to blank animal faeces at levels ranging from 0–200 to 200 μg kg^{-1} for tetracyclines, quinolones and macrolides and 0–50–50 μg kg^{-1} for sulfonamides. Of samples that showed peak intensities exceeding the calibration line, the antibiotic concentration was estimated by extrapolation.

3. Results & discussion

3.1. Extraction

The extraction of faeces samples was performed by shaking in McIlvain buffer, pH 4.0/acetonitrile (4:1 v/v). To assess if this extraction procedure is appropriate, it was compared to extraction

Table 3
Summary of the validation study results.

Compound	Validation level ($\mu g\ kg^{-1}$)	Trueness (%) $n=21$	RSD_r (%) $n=3$	RSD_{r^*} (%) $n=21$	RSD_{RL} (%) $n=21$	CCα ($\mu g\ kg^{-1}$)	CCβ ($\mu g\ kg^{-1}$)	Linearity (r^2) ($n=3$)
Doxycycline	10	103		17.7	18.4			
	20	101	7.0	13.5	13.9	8.8	18	> 0.997
	30	97.9		9.4	12.5			
Oxytetracycline	10	102		21.5	29.5			
	20	103	6.2	10.5	16.2	12	24	> 0.995
	30	105		9.6	15.5			
Tetracycline	10	100		11.6	12.3			
	20	97.5	4.5	5.4	6.7	4.1	8.1	> 0.998
	30	97.6		3.8	6.1			
Dapson	2.5	100	5.2	8.0	14.0	1.8	3.6	> 0.997
	5.0	96.2		6.1	10.3			
	7.5	94.3		6.3	11.3			
Sulfacetamide	2.5	92.9		10.6	11.2			
	5.0	93.4	3.5	10.7	11.3	2.1	4.3	> 0.998
	7.5	94.7		7.8	8.1			
Sulfachloropyridazine	2.5	97.8		16.2	18.1			
	5.0	100	9.6	11.2	14.3	1.9	3.9	> 0.991
	7.5	99.9		8.0	8.5			
Sulfadiazine	2.5	101		6.8	10.0			
	5.0	102	1.6	3.3	5.2	0.7	1.3	> 0.995
	7.5	102		3.1	4.1			
Sulfadimethoxin	2.5	104		4.1	6.3			
	5.0	103	2.0	3.8	5.7	0.7	1.4	> 0.999
	7.5	102		3.6	5.4			
Sulfadimidin	2.5	101		4.2	4.3			
	5.0	99.8	2.4	2.6	2.9	0.5	1.0	> 0.996
	7.5	100		2.8	3.1			
Sulfadoxin	2.5	97.5		6.9	8.7			
	5.0	96.3	3.4	3.1	5.8	0.7	1.4	> 0.996
	7.5	94.0		3.7	5.6			
Sulfamerazine	2.5	94.0		7.3	7.6			
	5.0	97.1	2.7	4.8	6.7	0.9	1.8	> 0.999
	7.5	95.0		4.6	7.0			
Sulfamethizole	2.5	103		6.6	6.7			
	5.0	99.6	6.2	6.0	6.0	0.8	1.7	> 0.998
	7.5	100		4.2	5.7			
Sulfamethoxazole	2.5	101		5.8	5.9			
	5.0	98.2	5.6	4.6	5.2	0.9	1.9	> 0.995
	7.5	99.1		5.9	6.3			
Sulfamethoxypyridazine	2.5	101		5.6	5.8			
	5.0	99.4	4.1	3.4	3.9	0.8	1.6	> 0.998
	7.5	100		3.8	3.9			
Sulfamonomethoxin	2.5	97.3		11.0	13.2			
	5.0	94.5	6.0	5.2	8.1	1.2	2.4	> 0.998
	7.5	96.1		6.9	10.8			
Sulfaphenazole	2.5	100		12.8	13.8			
	5.0	104	9.1	11.7	13.6	2.2	4.3	> 0.998
	7.5	97.6		10.0	13.2			
Sulfapyridine	2.5	98.7		6.3	7.4			
	5.0	98.6	3.6	3.2	4.9	0.6	1.2	> 0.998
	7.5	99.2		2.5	4.1			
Sulfaquinoxaline	2.5	104		11.5	16.8			
	5.0	100	4.1	6.1	8.4	1.8	3.6	> 0.999
	7.5	100		6.8	8.4			
Sulfathiazole	2.5	105		4.0	4.9			
	5.0	102	2.7	3.8	6.6	0.6	1.2	> 0.998
	7.5	101		2.8	5.8			
Sulfisoxazole	2.5	97.0		7.7	13.0			
	5.0	98.8	4.7	4.1	5.2	0.9	1.7	> 0.998
	7.5	96.8		4.1	4.3			
Sulfamoxole	2.5	103.1		11.4	12.3	1.5	3.1	> 0.998
	5.0	99.9	4.3	9.0	10.2			
	7.5	99.1		9.2	11.5			

Table 3 (*continued*)

Compound	Validation level (μg kg^{-1})	Trueness (%) $n=21$	RSD_r (%) $n=3$	RSD_{r*} (%) $n=21$	RSD_{RL} (%) $n=21$	CCα (μg kg^{-1})	CCβ (μg kg^{-1})	Linearity (r^2) ($n=3$)
Ciprofloxacin	10	101		12.4	15.2			
	20	99.5	5.0	2.4	4.7	6.2	12.4	> 0.999
	30	103		4.1	5.6			
Danofloxacin	10	87.2		17.3	18.9			
	20	87.5	15.1	20.7	21.0	15	30	> 0.999
	30	87.3		14.5	14.5			
Difloxacin	10	104		9.9	10.4			
	20	101	6.1	5.6	6.9	7.3	15	> 0.999
	30	97.9		6.1	7.0			
Enrofloxacin	10	95.3		10.9	13.9			
	20	95.0	9.8	7.7	10.4	7.8	16	> 0.998
	30	96.9		9.2	10.0			
Flumequine	10	98.1		2.9	4.4			
	20	98.7	1.2	2.1	3.5	5.1	10.2	> 0.999
	30	99.6		2.3	4.6			
Marbofloxacin	10	94.7		16.0	16.1			
	20	97.4	3.9	14.3	14.9	11	22	> 0.997
	30	94.9		12.6	13.0			
Nalidixic acid	10	104		4.4	6.2			
	20	103	2.8	3.3	6.6	6.6	13	> 0.999
	30	103		5.5	7.4			
Norfloxacin	10	101		8.6	8.8			
	20	97.8	7.6	5.4	8.1	6.0	12	> 0.993
	30	100		5.6	10.7			
Oxolinic acid	10	91.8		10.4	14.5			
	20	95.2	3.1	3.8	5.5	5.4	11	> 0.996
	30	95.5		4.0	6.1			
Sarafloxacin	10	91.7		10.0	13.3			
	20	96.9	8.4	10.4	10.5	7.8	16	> 0.998
	30	93.9		7.4	7.5			
Erythromycin	10	110		10.3	16.8			
	20	100	11.3	7.2	7.6	6.1	12	> 0.999
	30	105		8.0	8.1			
Gamithromycin	10	96.4		6.6	9.4			
	20	99.1	2.6	5.6	9.5	6.4	13	> 0.999
	30	101		4.5	11.1			
Josamycin	10	107		16.4	17.9			
	20	108	8.0	13.9	14.1	12	25	> 0.996
	30	108		18.4	18.7			
Lincomycin	10	98.4		5.2	6.6			
	20	98.0	2.0	3.2	3.9	5.2	10	> 0.999
	30	98.7		2.2	2.2			
Natamycin	10	94.3		15.0	20.5			
	20	96.8	10.1	12.4	18.1	15	30	> 0.988
	30	86.2		19.6	25.8			
Pirlimycin	10	94.1		30.3	31.4			
	20	94.8	6.3	29.8	31.6	20	41	> 0.996
	30	96.8		30.0	31.7			
Spiramycin	10	102		7.6	8.9			
	20	104	5.6	6.5	7.8	6.3	13	> 0.998
	30	103		5.2	7.6			
Tiamulin	10	91.2		10.4	15.4	8.9	18	> 0.992
	20	93.4	5.6	10.1	10.5			
	30	92.0		12.5	13.1			
Tildipirosin	10	89.1		27.7	41.4			
	20	83.7	16.5	14.9	18.1	13	26	> 0.975
	30	92.1		15.0	16.0			
Tilmicosin	10	99.8		11.5	17.5			
	20	104	5.0	8.3	16.1	6.3	13	> 0.994
	30	105		8.0	17.7			
Ulathromycin	10	93.3		31.0	32.3			
	20	91.1	3.9	28.9	32.3	32	64	> 0.999
	30	93.0		38.3	39.2			

Table 3 (*continued*)

Compound	Validation level ($\mu g\ kg^{-1}$)	Trueness (%) $n=21$	RSD_r (%) $n=3$	$RSD_{r'}$ (%) $n=21$	RSD_{RL} (%) $n=21$	CCα ($\mu g\ kg^{-1}$)	CCβ ($\mu g\ kg^{-1}$)	Linearity (r^2) ($n=3$)
Tylosin	10	111		27.4	32.9			
	20	127	58.5	34.4	46.8	32	65	> 0.994
	30	147		59.4	64.7			
Tylvalosin	10	119		23.5	29.7			
	20	112	11.5	27.3	27.5	18	36	> 0.986
	30	109		24.4	25.6			
Valnemulin	10	95.0		15.2	16.0			
	20	95.3	5.2	16.2	17.2	19	38	> 0.997
	30	94.3		20.7	22.1			

Validation parameters that do not comply with the criteria for products of animal origin as established by 2002/657/EC [24] are underlined.

using ultrasonification. Three incurred faeces samples were selected: one containing oxytetracycline, one with sulfadiazine and one with tylosin. These samples were homogenised by stirring and eight aliquots were transferred to seperate tubes. Four tubes were extracted according to the described procedure, the other four were extracted by ultrasonification (15 min). The results are presented in Fig. 1. The data was evaluated by an *F*-test and Student's *t*-test. Ultrasonification does not yield higher extraction efficiency and because of ease and sample throughput, it was chosen to extract samples by shaking.

3.2. LC–MS/MS

To find the most optimal LC-system, five analytical columns were compared (all 2.1 × 100 mm^2), being a Phenomenex Kinetex C_{18} and C_{18} XB, a Waters Acquity UPLC BEH and HSS-T3, all 1.7 μm particles, and a Waters Cortecs C_{18}+ 1.6 μm. Using the presented LC system the retention times of all antibiotics showed a similar pattern, with the HSS-T3 column yielding slightly larger retention. More striking differences were observed for the peak width: the Kinetex C_{18} XB and the Cortecs C18+ showed severely broader peaks for especially the tetracyclines. Tildipirosin, the first eluting compound showed broad peaks for the Kinetex C_{18} XB, Acquity UPLC BEH and the Acquity UPLC HSS-T3 column. For tulathromycin especially the Acquity UPLC HSS-T3 column showed significant broader peaks and for oxolinic acid and nalidixic acid, significantly broader peaks were observed using the Kinetex C_{18} XB. Clearly the column materials that are especially developed to enhance peak shapes for basic drugs (Kinetex C_{18} XB and Cortecs C_{18}+) showed relatively poor results for zwitterionic compounds like tetracyclines and some acidic acids. Therefore these column materials can be considered less suitable for multi-antibiotic applications. Overall, the best results were obtained using the Kinetex C_{18} column, however clear limitation in the injection volume in relation to the percentage of organic modifier in the injected solvent were observed. Finally the Kinetex C_{18} column was selected with an injection volume of 10 μL and a maximum of 40% MeOH in the injected solvent.

As the number of SRM transitions is relatively large an insufficient number of scans over a peak is obtained when monitoring all SRMs during the whole run time. Therefore scheduled SRM was used applying ± 20 s intervals around the programmed retention times, which resulted in > 10 scans per peak. A representative chromatogram of a faeces sample spiked at target level is presented in Fig. 2. For clarity extracted ion chromatograms of the individual ion transitions are presented in Supplementary data (S1).

3.3. Internal standard selection

Because for some antibiotics included no isotopically labelled internal standards are available, a study was carried out to determine the most suitable internal standards for each antibiotic compound. Peak areas obtained from the first validation run were subjected to a statistical correlation analysis. For each antibiotic the internal standard that showed the highest correlation with it was selected as the most suitable. In most cases the combination of an antibiotic compound with a structurally related internal standard proved to be optimal. In some cases however, an internal standard belonging to a different compound group was selected, usually based on it having a similar retention time. Internal standards selected for each compound are presented in the experimental section.

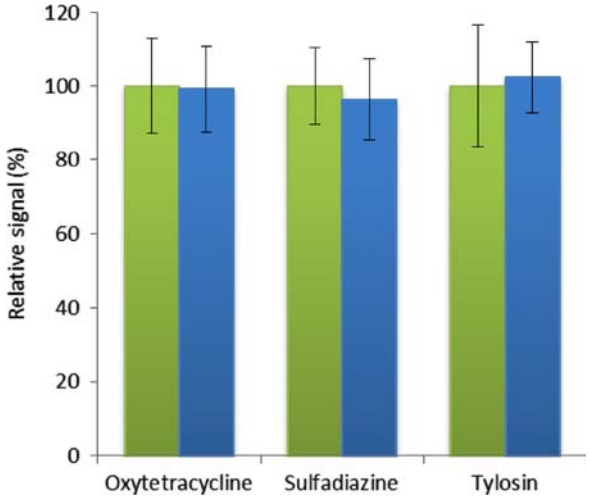


Fig. 1. Comparison of extraction by (green, left bar) shaking and (blue, right bar) ultrasonification for three incurred samples containing either oxytetracycline, sulfadiazine or tylosin ($n=4$). Vertical bars indicate the least significant difference. (For interpretation of the references to colour in this figure legend, the reader is referred to the web version of this article.)

3.4. Matrix effects

The aim of the method was to include tetracyclines, quinolones, macrolides, sulfonamides and penicillins. However, during the method optimisation and validation it was observed that some penicillins were not recovered in specific faeces samples. As a result the between matrix variation was extremely large. It is suggested that these effects are not the result of low recovery of the extraction or clean-up procedure applied, but that these penicillins degrade in the faeces matrix, having a high bacterial activity, directly after spiking. This is supported by the fact that these effects were primarily observed for amoxicillin, ampicillin, penicillin G and penicillin V, the penicillins that are most sensitive towards β-lactam ring structure hydrolysis. To test this hypothesis,

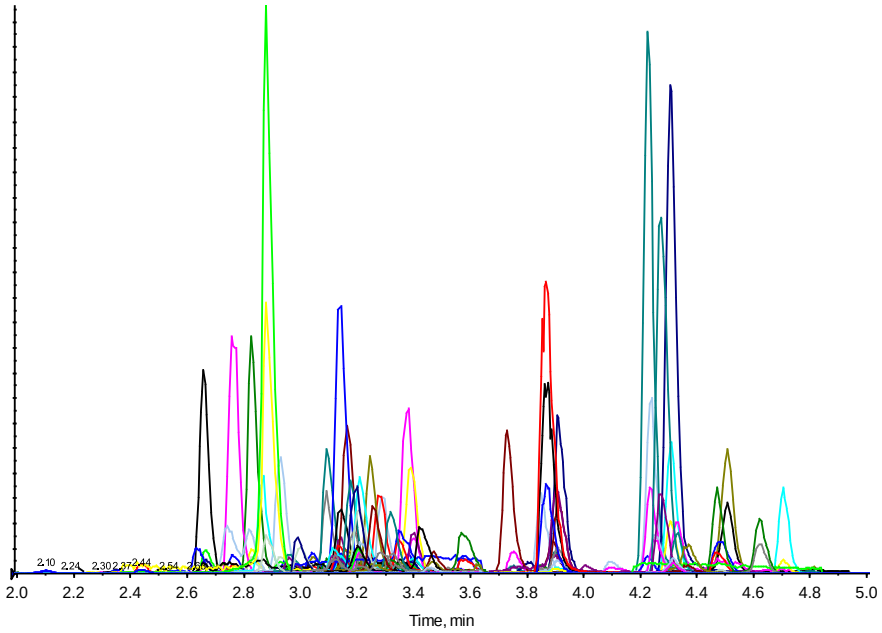


Fig. 2. Representative extracted ion chromatograms of a blank swine faeces sample spiked at target level with the antibiotics.

we applied a previously published method [38] for the analysis of, among others, penicillins in muscle to swine faeces. This method encompasses a forced hydrolysis, to include degradation products of the β-lactams. This method showed satisfactory results for all penicillins, supporting the hypothesis that penicillins are unstable in the faeces matrix. Similar effects were observed for chlortetracycline, which is a naturally occurring antimicrobial compound and also has a short half-life in faeces [39]. The quick degradation of chlortetracycline in faeces has been reported previously [21,40] and might be explained by the presence of resistant bacteria in some faeces samples. These effects were in our laboratory previously observed in soil samples. As a result, the penicillins and chlortetracycline were not included in the validation study.

3.5. Validation

3.5.1. An overview of the validation results is presented in Table 3

For all compounds the trueness is between 87% and 110% and thus complies with the adopted performance criteria. The RSD_r complied with the criteria for all compounds except for tylosin. The results for RSD_{r*} and RSD_{RL} complied with the criteria for most substances. The following compounds did not comply with the adopted criteria for RSD_{r*} and/or RSD_{RL} at or above target level: danofloxacin, josamycin, natamycin, pirlimycin, tulathromycin, tylosin, tylvalosin and valnemulin. Because the precision within a single batch of faeces is acceptable (low RSD_r), clearly the matrix is the main factor influencing the final quantitative result. Thus, if a sample is found to be a suspected positive for these compounds, exact quantification can be carried out using multiple level standard addition. For these antibiotics the target level of 20 $\mu g\ kg^{-1}$ proved to be quite challenging, as can be also be seen from the calculated values for CCα, which directly results in a relatively high variation.

Also for oxytetracycline the target concentration proved to be challenging. This results in high standard deviations at the lower validation levels, but the quantitative performance of the method proved to comply with set criteria for quantitative analysis at concentrations at or above the target level.

For all other compounds the RSD_r is below 11.3%. Taking into account matrix variation, the RSD_{r*} is below 14.3% and the RSD_{RL} is below 21%. Based on these results it is concluded that the presented method is suitable for quantification of the antibiotics present in swine faeces at relevant levels. For danofloxacin, josamycin, natamycin, pirlimycin, tulathromycin, tylosin, tylvalosin and valnemulin and slightly higher measurement uncertainty should be taken into account when performing a quantitative analysis.

The calculated decision limits (CCα), indicating the limit of detection, vary from 0.5–65 to 65 $\mu g\ kg^{-1}$. Based on the samples spiked at the lowest level included in the validation, the calculated values of CCα are realistic and sufficiently low to detect relevant concentrations of antibiotics in swine faeces.

3.5.2. Selectivity

For each antibiotic compound, two product ions were selected and based on those the probability of an interfering signal (P(I)) was calculated [36]. In all cases the selected ion transitions, in combination with their chromatographic separation were considered sufficiently selective which was also apparent from the absence of interfering signals in the blank swine faeces samples.

3.5.3. Stability

Stability data on the antibiotic solutions were previously reported [37]. It was found that the sulfonamide and macrolide solutions are stable for at least 12 months and quinolone solutions at least 6 months at $< 4\ ^{\circ}C$. Storage of the tetracycline solutions is more critical: these should be kept $< -18\ ^{\circ}C$ for a maximum of 2 months.

The stability of swine faeces extracts showed that even if extracts are stored at $-18\ ^{\circ}C$ for 8 days, results similar to those of fresh extracts are obtained. It is concluded that faeces e extracts obtained with the described method are stable for at least 8 days when stored at $-18\ ^{\circ}C$.

3.6. Swine and calf faeces analysis

Twenty pig farms and 20 cattle farms in The Netherlands were randomly selected. Of each of these farms 17 animals were selected in the slaughter phase directly from the gut which indicates that withdrawal periods are taken into account. Because the presented method proved to be sufficient for the analysis of cattle faeces as well, all 680 samples were analysed using the presented method. The

results of the individual farms are presented in Tables 4 and 5 for swine and cattle respectively. Concentrations above the calibration line were calculated based on extrapolation and are therefore rough estimates. Also results for tylosin should be considered indications because the measurement uncertainty for tylosin is relatively high as discussed above.

A large number of antibiotics was detected in the faeces samples. In 55% of the swines, originating from 80% of the swine farms, antibiotics were detected. For the calves in 75% of the faeces samples, originating from 95% of the cattle farms, antibiotics were detected. Oxytetracycline, doxycycline and sulfadiazine were most frequently detected, followed by tetracycline, flumequine, lincomycin and tylosin. All antibiotics detected are registered for swine and/or calve production, but ciprofloxacin (also enrofloxacin detected in this sample but its identity was not confirmed) and flumequine are considered last resort antibiotics and should be used sparingly.

For some compounds detected, the concentrations indicate recent use. Possibly, withdrawal periods were not taken into account which could suggest illegal and/or off-label use of antibiotics. Another plausible option is a delayed excretion due to re-adsorption (from e.g. bones) but there is no scientific data available showing this could explain these high concentrations. Low concentrations could either point at recent use in combination with a high excretion rate, or administration of the antibiotic at an earlier time. Other possibilities are that these levels are the result of contamination at the farm or from re-adsorption or recirculation.

Furthermore, it is noteworthy that in many cases several antibiotics were detected in a single sample (34% of the faeces samples

Table 4
Overview of antibiotics found in swine faeces.

Stable #	Antibiotic detected	Number of positive animals	Concentration ($\mu g\ kg^{-1}$)		
			Lowest	Highest	Median
1	Doxycycline	17	139	750	330
2	Oxytetracycline	10	4	29	13
3	Oxytetracycline	2	6	12	9
	Tiamulin	4	4	4	4
4	Doxycycline	16	50	95,000	1900
	Tylosin	1	28	28	28
5	Doxycycline	1	147	147	147
	Oxytetracycline	6	9	104	21
	Sulfadiazine	3	1	4	1
6	Doxycycline	12	47	520	131
	Sulfadiazine	3	1	14	3
	Tylosin	14	2	16	5
7	Oxytetracycline	7	4	172	46
	Sulfadimethoxin	1	6	6	6
	Sulfadiazine	2	1	1	1
8	Doxycycline	17	16	1500	130
9	–				
10	–				
11	–				
12	Oxytetracycline	9	4	106	38
	Lincomycin	2	1	2	2
13	–				
14	Doxycycline	10	6	32	21
	Oxytetracycline	1	155	155	155
	Tylosin	1	241	241	241
15	Doxycycline	2	8	9	9
	Sulfadiazine	1	7	7	7
	Tylosin	16	43	7700	285
16	Tylosin	1	10	10	10
17	Doxycycline	13	2	200	15
	Oxytetracycline	13	6	1500	105
	Tiamulin	3	1	4	3
18	Oxytetracycline	1	25	25	25
19	Doxycyline	16	324	4500	1500
	Sulfadiazine	16	80	216	126
20	Tylosin	17	10	516	67
	Sulfadiazine	6	1	5	1

Table 5
Overview of antibiotics found in cattle faeces.

Stable	Antibiotic detected	Number of positive animals	Concentratiom (μg/kg)		
			Lowest	Highest	Median
1	Oxytetracycline	16	5	104	16
2	Oxytetracycline	17	90	5200	1200
	Doxycycline	7	5	97	20
	Tetracycline	15	3	29	9
	Tilmicosin	10	3	218	10
	Sulfadiazine	1	16	16	16
	Flumequine	6	trace		
3	Oxytetracycline	11	4	1500	18
	Doxycycline	5	6	152	8
	Tetracycline	1	9	9	9
	Sulfadiazine	7	1	81	1
	Sulfadimidin	1	24	24	24
4	Oxytetracycline	17	3500	21,000	8000
	Tetracycline	17	22	112	44
	Sulfadiazine	2	2	2	2
5	Doxycycline	3	8	63	10
	Oxytetracycline	3	11	583	109
	Tetracycline	1	5	5	5
	Sulfadiazine	6	1	38	3
	Lincomycin	10	1	2	1
6	Lincomycin	14	1	17	6
	Oxytetracycline	15	6	150	38
7	Tilmicosin	2	4	10	6
8	–				
9	Oxytetracycline	17	215	17,000	1500
	Tetracycline	16	5	102	16
	Doxycycline	1	10	10	10
	Sulfadiazine	3	1	5	4
10	Oxytetracycline	15	9	2700	230
	Doxycycline	10	8	120	23
	Tetracycline	2	6	14	10
	Tilmicosin	13	1	63	9
11	Oxytetracycline	13	14	550	71
	Doxycycline	11	5	62	9
	Tetracycline	2	4	4	4
	Sulfadiazine	5	2	4	3
	Flumequine	3	1	11	3
	Tilmicosin	2	2	4	3
	Ciprofloxacin	1	13	13	13
	Enrofloxacin	1	4[a]		
12	Oxytetracycline	17	61	882	450
	Tetracycline	16	3	6	5
13	Oxytetracycline	3	19	33	26
	Flumequine	2	1	2	2
14	Oxytetracycline	7	30	234	61
	Doxycycline	3	11	22	13
	Sulfadiazine	6	1	2	1
	Tilmicosin	4	11	49	15
	Flumequine	1	3	3	3
15	Oxytetracycline	17	138	3049	890
	Tetracycline	16	5	28	10
	Doxycycline	7	5	15	9
	Sulfadiazine	3	1	2	1
16	Sulfadiazine	1	2	2	2
17	Oxytetracycline	16	68	909	217
	Flumequine	15	1	91	4
	Doxycycline	3	17	177	42
	Sulfadiazine	3	1	4	1
	Tilmicosin	1	10	10	10
18	Oxytetracycline	16	406	4848	1700
	Tetracycline	16	8	31	15
	Tilmicosin	1	9	9	9
19	Oxytetracycline	15	5	235	93
	Tilmicosin	4	24	149	67
	Sulfadoxin	2	1	5	3
	Sulfadiazine	2	1	2	2
	Doxycycline	1	27	27	27
20	Flumequine	17	43	1803	321
	Sulfadiazine	11	1	5	2
	Oxytetracycline	2	148	272	210
	Doxycycline	2	18	22	20

[a] Identity not confirmed according to 2002/657/EC [24] due to low signal of second ion transition.

contained two or more different antibiotics), up to three for swine and eight for cattle. It is unlikely that such a diversity of antibiotics was administrated to a single animal. A theoretical explanation could be that the mixtures present at high concentration (mainly observed for the tetracyclines) are the result of the administration of illegal, non-purified preparations. Low concentrations might be the result of contamination within the farm.

Finally it is important to notice that the concentrations of some antibiotics found can select for resistant bacteria [41], especially if the sum of the concentration of different antibiotics within a single sample is considered. Furthermore the effect the combination of antibiotic residues found in relation to the selection of resistant bacteria remains unknown and is a risk factor. Note that only the native antibiotic was searched for and that antimicrobially active metabolites might be present in the samples as well [6] (e.g. N4-acetylsulfonamides [42]), increasing the level of antimicrobial activity in the faeces samples even further. By using faeces as fertilizer in agricultural practices, antibiotic residues as well as resistant bacteria are unintendedly disseminated throughout the environment [43], which is a serious risk for human health.

4. Conclusions

A comprehensive analysis method for the analysis of 44 antibiotics belonging to the tetracyclines, quinolones, macrolides and sulfonamides was successfully developed and fully validated for swine faeces according to 2002/657/EC [32]. The validation showed good trueness, repeatability and within-lab reproducibility for all compounds except for some macrolides and is considered adequate for the detection of antibiotics in animal faeces at relevant levels. The method was applied to the analysis of antibiotics in an extensive monitoring study of swine and cattle faeces and the outcomes were striking. The incidence of antibiotics in the faeces samples was high: in 55% of the swine faeces and 75% of the calve faeces samples at least one antibiotic compound was detected. Also mixtures of antibiotics were found (up to eight in a single animal) and in some cases the concentrations were severe (some exceeding 1 mg kg^{-1}). These results suggest that antibiotics are used off-label and that carry-over of antibiotics on the farm could be of importance. The analysis of faeces is a simple and non-invasive strategy to successfully monitor for antibiotic use in animal breeding and to obtain knowledge on the dissemination of antibiotic residues and resistant bacteria throughout the environment.

Acknowledgements

This project was financially supported by the Dutch Ministry of Economic Affairs (Project 1217259401). We thank Michel Buijsman, Michael Schoeman, Jeroen van de Brink and Sanne Wilmsen for the analysis of the swine and cattle faeces samples.

Appendix A. Supporting information

Supplementary data associated with this article can be found in the online version at http://dx.doi.org/10.1016/j.talanta.2014.09.022.

References

[1] U.S. Department of Health and Human Service Centers for Disease Control and Prevention, Antibiotic resistance threats in the United States, 2013.
[2] C. Novais, A.R. Freitas, E. Silveira, P. Antunes, R. Silva, T.M. Coque, L. Peixe, J. Antimicrob. Chemother. 68 (2013) 2746–2754.
[3] A. Pinheiro, R.M.R. Albano, T.C. Alves, V. Kaufmann, M.R.d. Silva, Agric. Water Manag. 129 (2013) 1–8.
[4] A.K. Sarmah, M.T. Meyer, A.B.A. Boxall, Chemosphere 65 (2006) 725–759.
[5] K. Kumar, S.C. Gupta, Y. Chander, A.K. Singh, L.S. Donald, Adv. Agron., Volume no. 87 (Publisher is Elsevier Inc.) (2005) 1–54.
[6] D. Massé, N. Saady, Y. Gilbert, Animals 4 (2014) 146–163.
[7] G. McCarthy, P.G. Lawlor, M. Gutierrez, G.E. Gardiner, Sci. Total Environ. 463–464 (2013) 712–719.
[8] R. Hirsch, T. Ternes, K. Haberer, K. Kratz, Sci. Total Environ. 225 (1999) 109–118.
[9] L. Migliore, G. Brambolla, P. Casoria, C. Civitareale, S. Cozzolino, L. Gaudio, Fresenius Environ. Bull. 5 (1996) 735–739.
[10] L. Migliore, G. Brambilla, S. Cozzolino, L. Gaudio, Agr. Ecosyst. Environ. 52 (1995) 103–110.
[11] Y. Awad, S.-C. Kim, S. Abd El-Azeem, K.-H. Kim, K.-R. Kim, K. Kim, C. Jeon, S. Lee, Y. Ok, Environ. Earth Sci. 71 (2014) 1433–1440.
[12] X. Hu, Q. Zhou, Y. Lou, Environ. Pollut. 158 (2010) 2992–2998.
[13] B. Berendsen, M. Pikkemaat, P. Römkens, R. Wegh, M. van Sisseren, L. Stolker, M. Nielen, J. Agric. Food Chem. 61 (2013) 4004–4010.
[14] B. Berendsen, L. Stolker, J. Jong, M. Nielen, E. Tserendorj, R. Sodnomdarjaa, A. Cannavan, C. Elliott, Anal. Bioanal. Chem. 397 (2010) 1955–1963.
[15] D.H. Kang, S. Gupta, C. Rosen, V. Fritz, A. Singh, Y. Chander, H. Murray, C. Rohwer, J. Agric. Food Chem. 61 (2013) 9992–10001.
[16] A.d.l. Torre, I. Iglesias, M. Carballo, P. Ramirez, M.J. Munoz, Sci. Total Environ. 414 (2012) 672–679.
[17] Y.-x. Li, X.-l. Zhang, W. Li, X.-f. Lu, B. Liu, J. Wang, Environ. Monit. Assess. 185 (2013) 2211–2220.
[18] H. Heuer, H. Schmitt, K. Smalla, Curr. Opin. Microbiol. 14 (2011) 236–243.
[19] S. Jechalke, A. Focks, I. Rosendahl, J. Groeneweg, J. Siemens, H. Heuer, K. Smalla, FEMS Microbiol. Ecol. 87 (2014) 78–88.
[20] A.A. Pourcher, A. Jadas-Hércart, P. Cotinet, P. Dabert, C. Ziebal, S.L. Roux, R. Moran, D. Heddadj, I. Kempf, Sci. Total Environ. (2014) 482–483.
[21] S.R. Joy, X. Li, D.D. Snow, J.E. Gilley, B. Woodbury, A.L. Bartelt-Hunt, Sci. Total Environ. 481 (2014) 69–74.
[22] H. Fang, Y. Han, Y. Yin, X. Pan, Y. Yu, Chemosphere 96 (2014) 51–56.
[23] S.R. Joy, S.L. Bartelt-Hunt, D.D. Snow, J.E. Gilley, B.L. Woodbury, D.B. Parker, D.B. Marx, X. Li, Environ. Sci. Technol. 47 (2013) 12081–12088.
[24] l. Zhao, Y.H. Dong, H. Wang, Sci. Total Environ. 408 (2010) 1069–1075.
[25] Y.L. Zhao, S. Chen, L.N. Sun, L.S. Jin, L. Chao, Appl. Mech. Mater. 368–370 (2013) 496–500.
[26] Y.B. Ho, M.P. Zakaria, P.A. Latif, N. Saari, Sci. Total Environ. 488–489 (2014) 261–267.
[27] Y. Chen, H. Zhang, Y. Luo, J. Song, Chin. Sci. Bull. 184 (2012) 2205–2217.
[28] E. Martínez-Carballo, C. González-Barreiro, S. Scharf, O. Gans, Environ. Pollut. 148 (2007) 570–579.
[29] A. Jacobsen, B. Halling-Sørensen, Anal. Bioanal. Chem. 384 (2006) 1164–1174.
[30] X. Pan, Z. Qiang, W. Ben, M. Chen, J. Environ. Sci. 23 (2011) 1729–1737.
[31] Y. Huang, M. Cheng, W. Li, L. Wu, Y. Chen, Y. Luo, P. Christie, H. Zhang, Anal. Methods 5 (2013) 3721–3731.
[32] 2002/657/EC, in: Off. J. Europ. Commun., 2002, pp. 8–36.
[33] W. Horwitz, L.R. Kamps, K.W. Boyer, J. Assoc. Off. Anal. Chem. 63 (1980) 1344–1354.
[34] M. Thompson, Analyst 125 (2000) 385–386.
[35] B.I. 11843-7:2012, Capability of Detection, 2012.
[36] B.J.A. Berendsen, A.A.M. Stolker, M.W.F. Nielen, J. Am. Soc. Mass Spectrom. 24 (2013) 154–163.
[37] B.J.A. Berendsen, I.J.W. Elbers, A.A.M. Stolker, Food Addit. Contam. A 28 (2011) 1657–1666.
[38] B.J.A. Berendsen, H.W. Gerritsen, R.S. Wegh, S. Lameris, R. Sebille, A.A.M. Stolker, M.W.F. Nielen, Anal. Bioanal. Chem. 405 (2013) 7859–7874.
[39] S.R. Joy, X. Li, D.D. Snow, J.E. Gilley, B. Woodbury, S.L. Bartelt-Hunt, Sci. Total Environ. 481 (2014) 69–74.
[40] H. Dolliver, S. Gupta, S. Noll, J. Environ. Qual. 37 (2008) 1245–1253.
[41] E. Gullberg, S. Cao, O.G. Berg, C. Ilbäck, L. Sandegren, D. Hughes, D.I. Andersson, PLoS Pathog. 7 (2011) e1002158.
[42] M. Lamshöft, P. Sukul, S. Zühlke, M. Spiteller, Anal. Bioanal. Chem. 388 (2007) 1733–1745.
[43] M. Lamshöft, P. Sukul, S. Zühlke, M. Spiteller, Sci. Total Environ. 408 (2010) 1563–1568.

Talanta 132 (2015) 269–277

Contents lists available at ScienceDirect

Talanta

journal homepage: www.elsevier.com/locate/talanta

Proficiency testing for determination of pesticide residues in soybean: Comparison of assigned values from participants' results and isotope-dilution mass spectrometric determination

Takashi Yarita *, Takamitsu Otake, Yoshie Aoyagi, Takayoshi Kuroiwa, Masahiko Numata, Akiko Takatsu

National Metrology Institute of Japan (NMIJ), National Institute of Advanced Industrial Science and Technology (AIST), AIST Tsukuba Central 3, Umezono, Tsukuba, Ibaraki 305-8563, Japan

ARTICLE INFO

Article history:
Received 1 August 2014
Received in revised form
30 August 2014
Accepted 2 September 2014
Available online 16 September 2014

Keywords:
Proficiency testing (PT)
Candidate reference material
Certified reference material (CRM)
Organophosphorus pesticide
Pyrethroid pesticide
Assigned value
z-Score
Primary method of measurement

ABSTRACT

Proficiency testing (PT) for the determination of pesticide residues in soybean samples was organized by the National Metrology Institute of Japan (NMIJ). The candidate certified reference material, NMIJ CRM 7509-a, that was prepared from the raw soybeans containing target pesticides (diazinon, fenitrothion, chlorpyrifos, and permethrin) was used as the test sample. Forty participants submitted two sets of analytical results along with the details of the analytical method and conditions they applied. Two types of assigned values were established for each target pesticide: one was derived from the analytical results of the participants, and the other was provided from the analytical results by isotope-dilution mass spectrometry (IDMS). The latter values were 7.4–16% higher than the former values, plausibly because the analytical values from the IDMS measurements were not affected by the recovery ratio of the target pesticides during the analytical process. Thus, two kinds of *z*-scores were calculated for individual participants using the corresponding assigned values: one (z_1-score) showed the relative performance score for the present PT and the other (z_2-score) could be used for evaluation of the trueness of their analytical methods.

© 2014 Elsevier B.V. All rights reserved.

1. Introduction

Various pesticides are used worldwide to protect foods against pests and diseases [1]. However, high levels of residual pesticides in foods may result in adverse effects on human health. In Japan, the Positive List System for Agricultural Chemicals Remaining in Foods was introduced in 2006 to prohibit the distribution of foods that contain agricultural chemicals above a certain level, even if the maximum residue limits (MRLs) have not been established [2]. Under this system, analysis of a wide variety of residual pesticides in foods that are under quarantine or in the market is routinely performed.

Analytical protocols for determining the presence of pesticide residues in food samples usually involve complex extraction of the target pesticides, multi-step clean-up of the obtained extracts, and sensitive and selective quantification via a chromatographic technique [3–5]. Ensuring the reliability of the results is crucial to control the risk associated with pesticide residues. Proficiency testing (PT) is one of the key elements in the implementation of an appropriate quality assurance program and performance monitoring procedure for chemical analysis laboratories [6,7]. Consequently, a number of PT programs for the determination of pesticide residues in food samples have already been organized [8–15].

The National Metrology Institute of Japan (NMIJ) has recently undertaken the development of crop certified reference materials (CRMs) for the validation/verification and quality assurance of pesticide residue analysis. The candidate materials used for development of the CRMs were prepared from raw crops containing the target pesticides. Characterization of the target pesticides was carried out by isotope-dilution mass spectrometry (IDMS), which has the potential to be a primary method of measurement [16–19]. To date, we have issued five kinds of CRMs in this field [20–23].

Another recent undertaking of the NMIJ is the organization of PTs for inorganic-constituent analysis of food samples to support skill upgrading of food analysis laboratories [24,25]. In 2012, the NMIJ initiated another PT program for pesticide-residue analysis of food samples. The first round PT was carried out using the candidate soybean powder material, NMIJ CRM 7509-a [23], as a test sample. In this PT, two kinds of assigned values were

* Corresponding author. Tel.: +81 29 861 9416; fax: +81 29 861 6866.
E-mail address: t-yarita@aist.go.jp (T. Yarita).

http://dx.doi.org/10.1016/j.talanta.2014.09.001
0039-9140/© 2014 Elsevier B.V. All rights reserved.

established: one was derived from the analytical results of the participants, and the other was provided from the analytical result used in the certification of CRM 7509-a. In this article, the process and the results of the PT are reported and the difference between the two assigned values is discussed.

2. Experimental

2.1. Test samples

An outline of the preparation of the test samples is presented as follows: the raw soybeans (*Glycine max*, cv. Enrei) were cultivated so as to contain *O*,*O*-diethyl-*O*-2-isopropyl-6-methyl-pyrimidin-4-yl phosphorothioate (diazinon), *O*,*O*-dimethyl-*O*-4-nitro-*m*-tolyl phosphorothioate (fenitrothion), *O*,*O*-diethyl-*O*-3,5,6-trichloro-2-pyridyl phosphorothioate (chlorpyrifos), and 3-phenoxybenzyl (1*RS*, 3*RS*, 1*RS*, 3*RS*)-3-(2, 2-dichlorovinyl)-2, 2-dimethylcyclopropanecarboxylate (permethrin). The soybeans were air-dried, freeze pulverized, mixed, bottled into amber glass bottles (10 g each), sterilized by γ-irradiation (15 kGy), and then the prepared samples were stored at ca. −80 °C until use. The homogeneity of the prepared samples was evaluated by the Japan Food Research Laboratories (Tokyo, Japan) by quantifying the target pesticides. The relative standard uncertainties related to the inhomogeneity were evaluated according to ISO Guide 35 [26] with values of 1.89% for diazinon, 4.00% for fenitrothion, 3.10% for chlorpyrifos, and 3.16% for permethrin. The details of the preparation and the homogeneity evaluation of the test samples have been described elsewhere [23].

2.2. Determination of pesticides in the test samples by NMIJ

The analytical results used in the certification of NMIJ CRM 7509-a were utilized in the present PT. These results were obtained by three analytical methods (Method 1, Method 2, and Method 3) conducted at NMIJ, the flow diagrams and the corresponding target pesticides of which are shown in Fig. 1. These methods consisted of extraction and clean-up processes that were based on the Analytical Methods for Residual Compositional Substances of Agricultural Chemicals, Feed Additives, and Veterinary Drugs in Food [3] and IDMS quantification by GC/MS measurements. Specifically, the initial analytical results (0 month) of the long-term stability assessment that were obtained by Method 1, and the analytical results of the characterization that were obtained by Method 2 or Method 3 were used to obtain the assigned values 2 (described in Section 2.4.). These analyses were performed in Nov. 2011, which was about four months prior to distribution of the samples to the participants. Additionally, the analytical results of the short-term stability monitoring that were obtained by Method 1 were used to evaluate the stability of the PT samples. These analyses were performed two weeks before distribution of the sample (April 2012) and three weeks after the deadline for submission of the participant results (August 2012).

2.3. Analysis by the participants

This PT round was announced to food manufacturers, agricultural producers, testing laboratories, public research institutes, etc., in Japan and was subscribed by 43 participants. On May 8, 2012, the test samples (2 bottles) and working instructions were sent to each participant by a delivery company using a refrigerated transport. The participants were asked to store the samples at −30 to −20 °C in the dark, and then to perform duplicate analysis of the target pesticides (the target pesticides to be determined were selectable by each participant). The participants were also asked to report the details of the analytical method and quantification conditions (such as the purity or concentration of primary calibrants, linear range of the calibration curves, the extraction and clean-up procedure, and the quantification method and its conditions) as well as the analytical results with observed chromatograms using a prescribed sheet in Excel format. The deadline was set to July 31, 2012.

2.4. Establishment of assigned values

For each target pesticide, two kinds of assigned values were established. The assigned value 1 (X_m) was obtained from the analytical results of the participants as follows: the outliers of the results were excluded by Cochran's test and Grubbs' test, and the median of the included results was then calculated. The normalized interquartile range (*NIQR*) was also calculated by multiplying the interquartile range (the difference of quartile 3 and quartile 1) of the included analytical results by 0.743. The assigned value 2 (X_{NMIJ}) was the weighted mean of the NMIJ analytical results obtained by the corresponding analytical methods (Method 1 and either Method 2 or Method 3). Simultaneously, the predicted reproducibility standard deviation ($PRSD_R$), which is the expected inter-laboratory precision for each target pesticide, was calculated using the modified Horwitz equation [27].

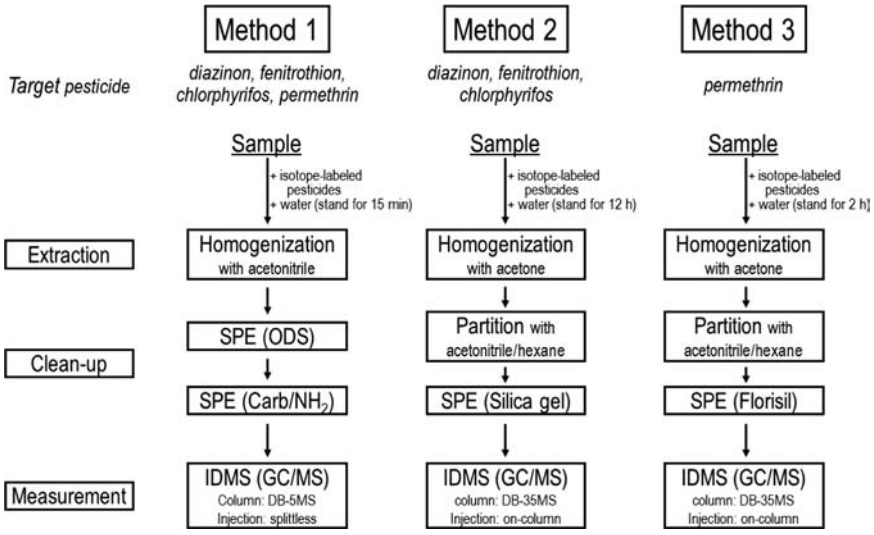


Fig. 1. Flow diagrams of the analytical methods for respective target pesticides used by NMIJ.

2.5. Calculation of z-scores

The performance of each participant was evaluated via the z-score approach in accordance with the ISO/IEC 17043 [28], ISO 13528 [29], and the International Harmonized Protocol for the Proficiency Testing of Analytical Chemistry Laboratories [7] methods. Because two kinds of assigned values were established in this PT, the corresponding z-scores (z_1 and z_2) were calculated using the following equations:

$$z_1 = \frac{x_i - X_m}{NIQR} \quad (1)$$

$$z_2 = \frac{x_i - X_{NMIJ}}{PRSD_R} \quad (2)$$

where x_i represents the analytical result for the target pesticide of the individual participants.

3. Results and discussion

3.1. Stability assessment of the test samples

The target pesticides of the test samples were assayed on three occasions (in November 2011, April 2012, and August 2012) by the NMIJ using Method 1. A one-way analysis of variance (ANOVA) test ($p < 0.05$) indicated that for each target pesticide, the difference in these three data points were not significant. These results suggested that the concentrations of the target pesticides in the PT samples stored at NMIJ remained unchanged during the period from the measurements to obtain assigned value 2 to the deadline for submission of the analytical results by the participants. Furthermore, the pesticide concentrations should remain constant if the participants stored the samples under the instructed conditions (at −30 to −20 °C in the dark). The relative standard deviation of the concentration for permethrin during the stated period was 6.87%, whereas the standard deviation for the other target pesticides was calculated to be below 0.

3.2. Analytical methods and results of the participants

Analytical results were submitted by 40 participants. Answers to the questionnaire on the analytical method and quantification conditions (matrix-matching of the calibration solutions, collection of the observed analytical values with the recovery ratio) that the participants applied are summarized in Fig. 2. More than half of the participants utilized the Multiresidue Method for Agricultural Chemicals by GC/MS (Agricultural Products) (hereafter referred to as “Multiresidue Method”) as the extraction and clean-up method; this is an analytical method established by the Analytical Methods for Residual Compositional Substances of

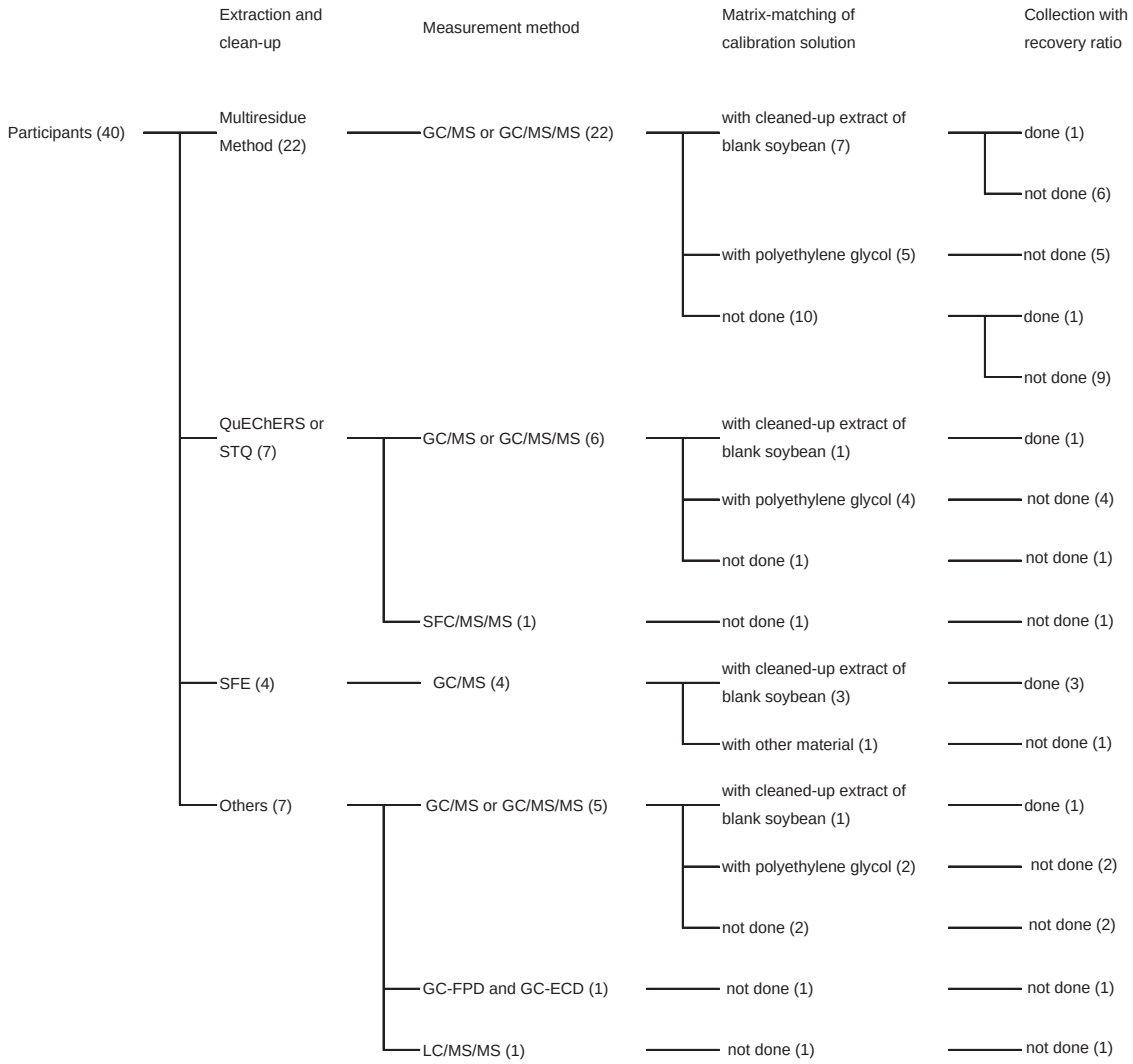


Fig. 2. Summary of the analytical methods and quantification conditions used by the participants. Numbers in parentheses indicate the frequencies of the participants.

Agricultural Chemicals, Feed Additives, and Veterinary Drugs in Food [3]. This method was verified by the Ministry of Health, Labour, and Welfare, Japan, and is intended for use in the Positive List System for Agricultural Chemical Residues in Foods [2]. The procedure is almost the same as that of Method 1, in which the target pesticides are extracted with acetonitrile followed by clean-up using SPE (see Fig. 1). In a spike and recovery test, as a criterion, the recovery ratio of each target pesticide should be in the range 70–120% [30]. If this criterion is met, the observed analytical results from the "Multiresidue Method" can be used without collection of the data based on the corresponding recovery ratio. Therefore, most participants who used this method in the present PT did not collect their analytical values. On the other hand, seven participants applied either the QuEChERS method [5,31] or the STQ [32] method; in both methods, acetonitrile was used as the extraction medium. The latter method consisted of extraction of the target pesticides by the QuEChERS method and clean-up of the extracts using small-size SPE cartridges. Supercritical fluid extraction (SFE), which can shorten the analytical time in comparison with the classical solvent extraction [5,33], was used by four participants. In all cases, carbon dioxide was used as the extraction medium without any modifier. Three participants cleaned up the extracts using SPE cartridges. Moreover, three participants collected the observed analytical values with the recovery ratios of the target pesticides, given that the trapping efficiency of some target pesticides by the collection solvent, which was placed at the end of the system, was not close to 100%.

The results of analysis of the concentration of fenitrothion were submitted by all the participants, whereas those for diazinon and

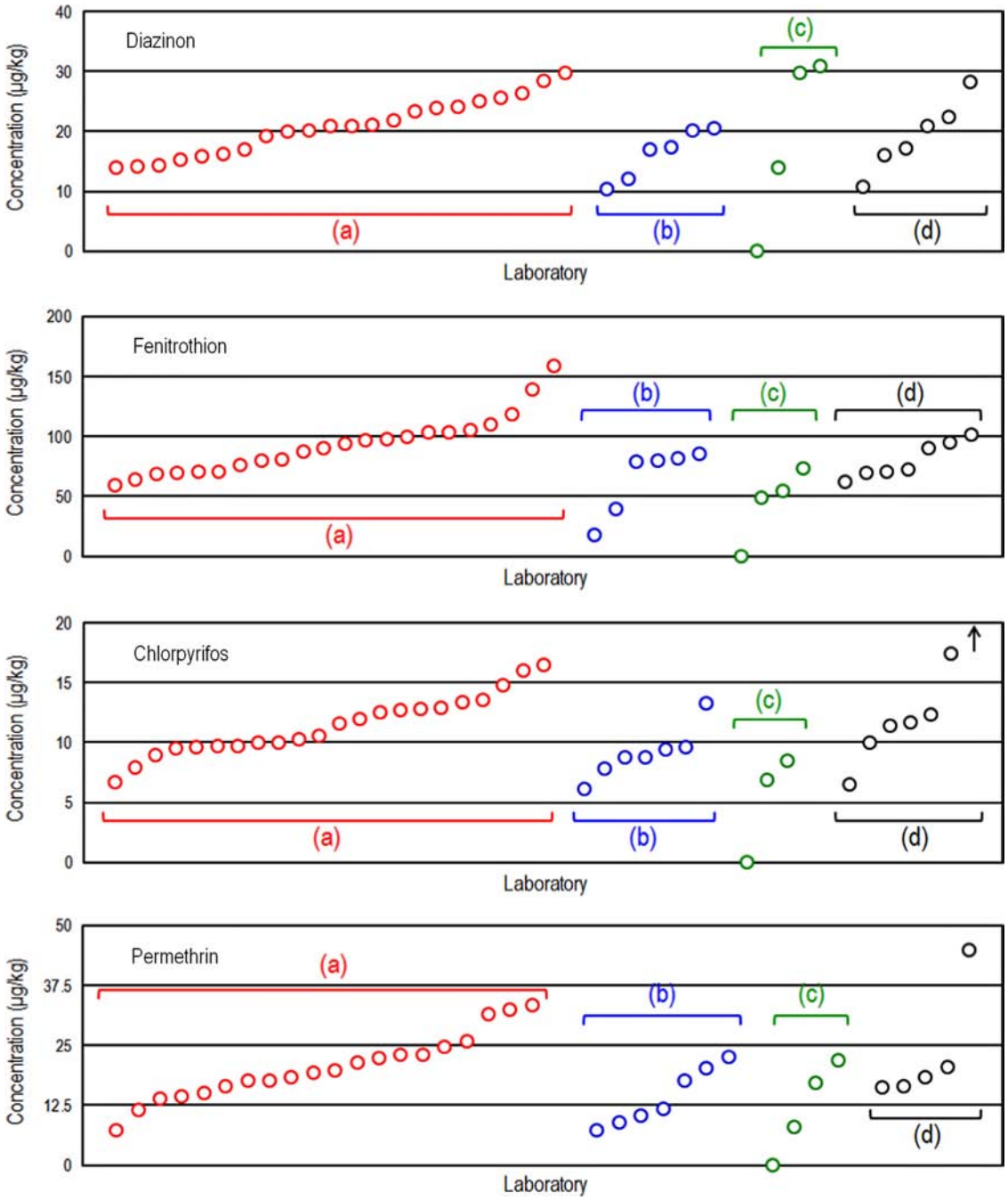


Fig. 3. Effect of the extraction and clean-up method on the analytical results of the participants. (a) Multiresidue Method for Agricultural Chemicals by GC/MS (Agricultural Products), (b) QuEChERS method or STQ method, (c) SFE method, and (d) other methods.

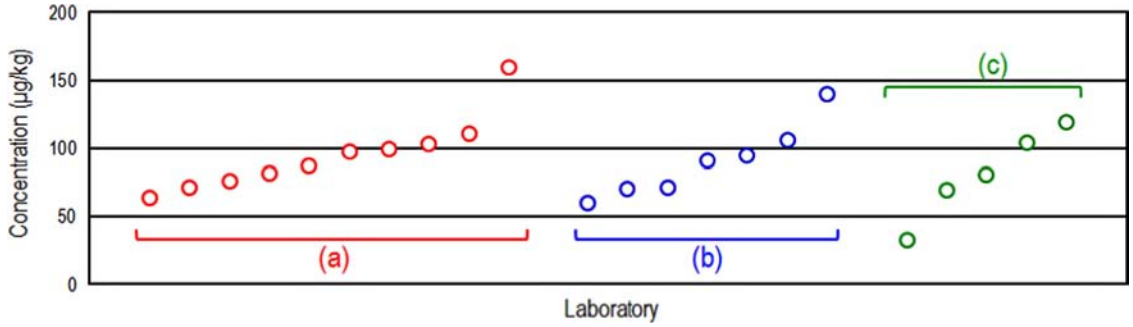


Fig. 4. Effect of matrix-matching of the calibration solution on the analytical results of the participants for assay of fenitrothion. The results obtained by the Multiresidue Method for Agricultural Chemicals by GC/MS (Agricultural Products) are indicated. (a) Without matrix-matching, (b) with matrix-mating using cleaned-up extract of blank soybean, and (c) with matrix-matching using polyethylene glycol.

Table 1
Assigned value 1 and other fundamental statistics.

Pesticide	Quartile 1	Assigned value 1 (median)	Quartile 3	*NIQR*
Diazinon	16.0	20.3	24.1	6.0
Fenitrothion	69.5	80.7	98.3	21.3
Chlorpyrifos	8.9	10.0	12.9	2.9
Permethrin	14.5	18.1	22.5	6.0

The unit of the values is μg/kg.

chlorpyrifos were submitted by 39 participants, and that for permethrin was submitted by 37 participants. Fig. S1 shows histograms of the analytical results. For each target pesticide, an unimodal distribution was obtained for the relationship between the analytical concentration and the number of participants (frequency). A Kolmogorov–Smirnov test ($p > 0.05$) was performed to evaluate the distribution of the analytical results, in which the normality of the distribution was supported for all target pesticides.

The analytical results were plotted based on the method employed, as shown in Fig. 3. One participant that applied SFE obtained results below 0.05 μg/kg for all of the target pesticides, probably due to an error in the conversion of the units. Fig. 3 indicates that even with the use of the same analytical method, there was considerable variation of the observed analytical values among the laboratories. Thus, the effect of the analytical method on the results was not significant. Similar consideration was given to the effect of the matrix-matching of the calibration solution on the analytical values. It is well known that the response of analyte of the sample solution (which was prepared from a real food sample herein) in GC/MS measurement is sometimes higher than that of the calibration solution [34–36]. To avoid this effect, 12 participants used calibration solutions that were matrix-matched using the cleaned-up extract of the blank soybean, and the other 11 participants employed calibration solutions containing polyethylene glycol. As an example, the analytical results of fenitrothion obtained by the Multiresidue Method were plotted based on the type of calibration solution, as shown in Fig. 4. The effect of matrix-matching of the calibration solution on the observed values was much less significant than the variation of the values among laboratories. Note that both the target pesticides and matrix used in the present PT were quite limited, further investigation is required for a more general evaluation of these effects.

3.3. Evaluation of the participants' performance using assigned value 1

3.3.1. Assigned value 1

The median of the analytical results of the participants was used as the X_m value given that this approach is considered robust and has been widely adopted by Japanese PT providers [37]. Initially, the analytical result from the participant that had made an error in the conversion of the units was rejected as an outlier. Subsequently, Cochran's test and Grubbs' test were carried out, in which one result was rejected for diazinon and chlorpyrifos, and three results were rejected for permethrin in the latter test. Using the remaining results, the fundamental statistics (including the X_m and *NIQR* values) were obtained, as shown in Table 1. When compared with the MRLs [38], the X_m values were 20% for diazinon, 40% for fenitrothion, 3.3% for chlorpyrifos, and 36% for permethrin, expressed as relative concentrations. These concentrations were deemed suitable for evaluation of the performance of the individual participants.

3.3.2. Assessment using z_1-scores

For each participant, the z_1-scores for the respective target pesticides were calculated using Eq. (1). The distribution of the participants' z_1-scores is shown in Fig. 5. Based on the ISO/IEC 17043 protocol, the participants' performance was ranked into the following classes:

(1) $|z_1| \leq 2.0$, "satisfactory" performance,
(2) $2.0 < |z_1| < 3.0$, "questionable" performance, and
(3) $3.0 \leq |z_1|$, "unsatisfactory" performance.

The number of participants in the individual classes is summarized in Table 2. If the participants' $|z_1|$ values follow the normal distribution, the ratio of the participants having $|z_1|$ values ranking in the second or third classes should comprise almost 5% of the entire participants. The observed ratios in the present PT were 5% for diazinon, 13% for fenitrothion, 13% for chlorpyrifos, and 16% for permethrin, where the ratio was slightly higher for target pesticides other than diazinon.

3.4. Evaluation of the participants' performance using assigned value 2

3.4.1. Assigned value 2

For each target pesticide, the weighted mean of the analytical results obtained by Method 1 and either Method 2 or Method 3 was calculated, and the result was used as the X_{NMIJ} value. The analytical methods used here were based on IDMS, and independent extraction and clean-up procedures were applied to avoid any possible analytical bias. The uncertainty corresponding to the Assigned value 2 was then estimated according to the ISO Guide 35 by combining the standard uncertainty of the analytical results and those corresponding to the inhomogeneity and instability of the PT samples. The details of these processes are described in the Supplementary material, and the results are summarized in

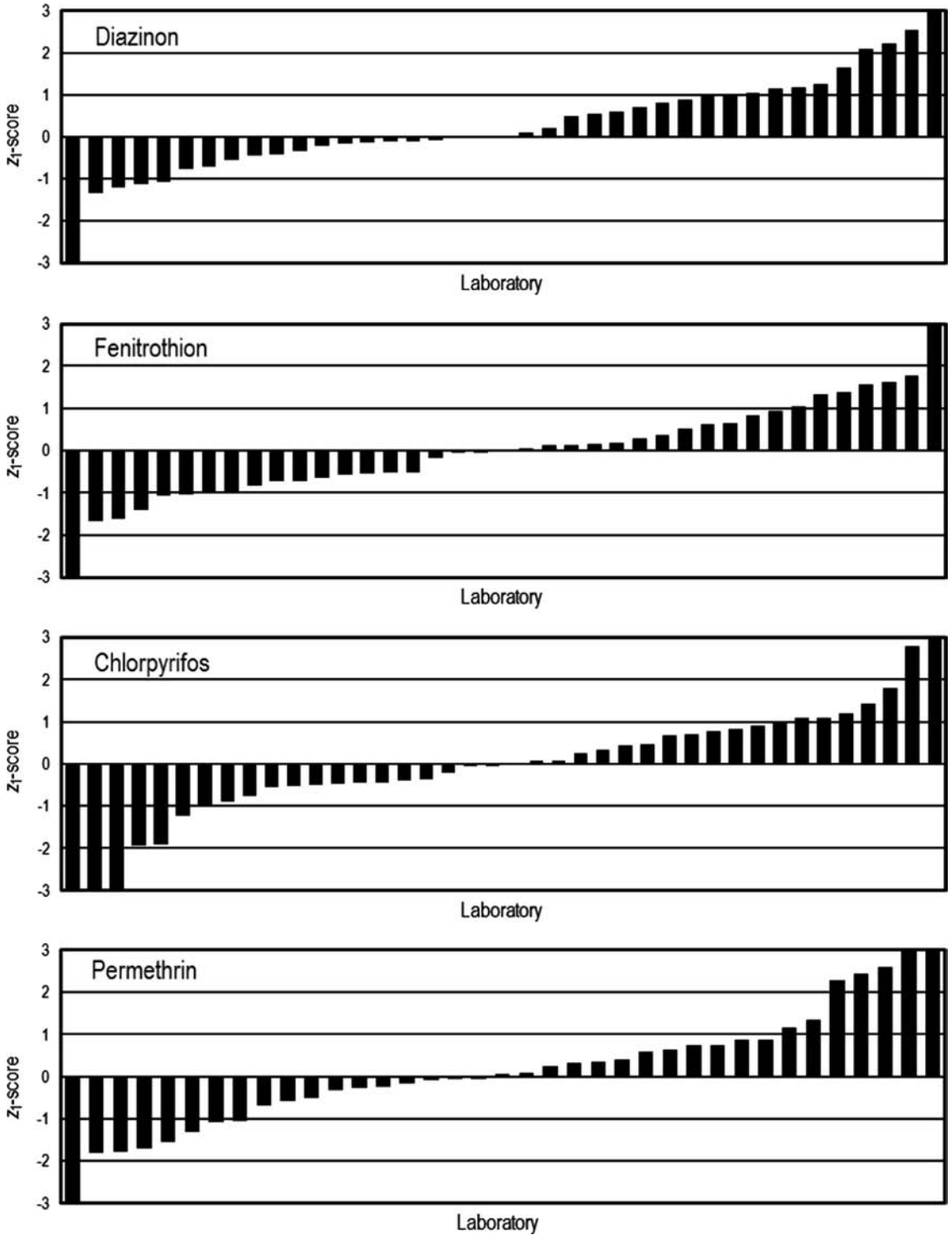


Fig. 5. Distribution of the participants' z_1-scores.

Table 2
Classification of the participants' z_1- and z_2-scores.

Pesticide	Number of participants	$\|z_1\| \leq 2.0$	$2.0 < \|z_1\| < 3.0$	$3.0 \leq \|z_1\|$	$\|z_2\| \leq 2.0$	$2.0 < \|z_2\| < 3.0$	$3.0 \leq \|z_2\|$
Diazinon	39	37	0	2	34	3	2
Fenitrothion	40	35	3	2	33	3	4
Chlorpyrifos	39	34	3	2	35	2	2
Permethrin	37	31	3	3	26	7	4

Table 3
Assigned value 2 with corresponding combined standard uncertainty and $PRSD_R$.

Pesticide	Assigned value 2	Combined standard uncertainty of assigned value 2	$PRSD_R$
Diazinon	21.8	0.6	4.8
Fenitrothion	87.9	5.6	19.3
Chlorpyrifos	11.6	0.6	2.5
Permethrin	19.9	1.9	4.4

The unit of the values is μg/kg.

Table 3. The strategy to obtain the Assigned value 2 and the corresponding uncertainty is the same as that used to certify the NMIJ CRMs [39], and the obtained X_{NMIJ} values seemed highly reliable and traceable to SI units.

3.4.2. Assessment using z_2-scores

If the participants submitted the analytical results with the corresponding uncertainties, their performance could be assessed using Assigned value 2 via the E_n-number approach [28]. However, at present, it is not easy for most food-analysis laboratories in Japan to estimate the uncertainties of their analytical results. In the present PT, therefore, participants were asked only to submit two sets of the analytical results without uncertainties. Thus, the performance of the participants using Assigned value 2 was also assessed by the z-score approach. For this purpose, the $PRSD_R$ value was calculated for each target pesticide using the modified Horwitz equation. Table 3 shows the results, where the relative

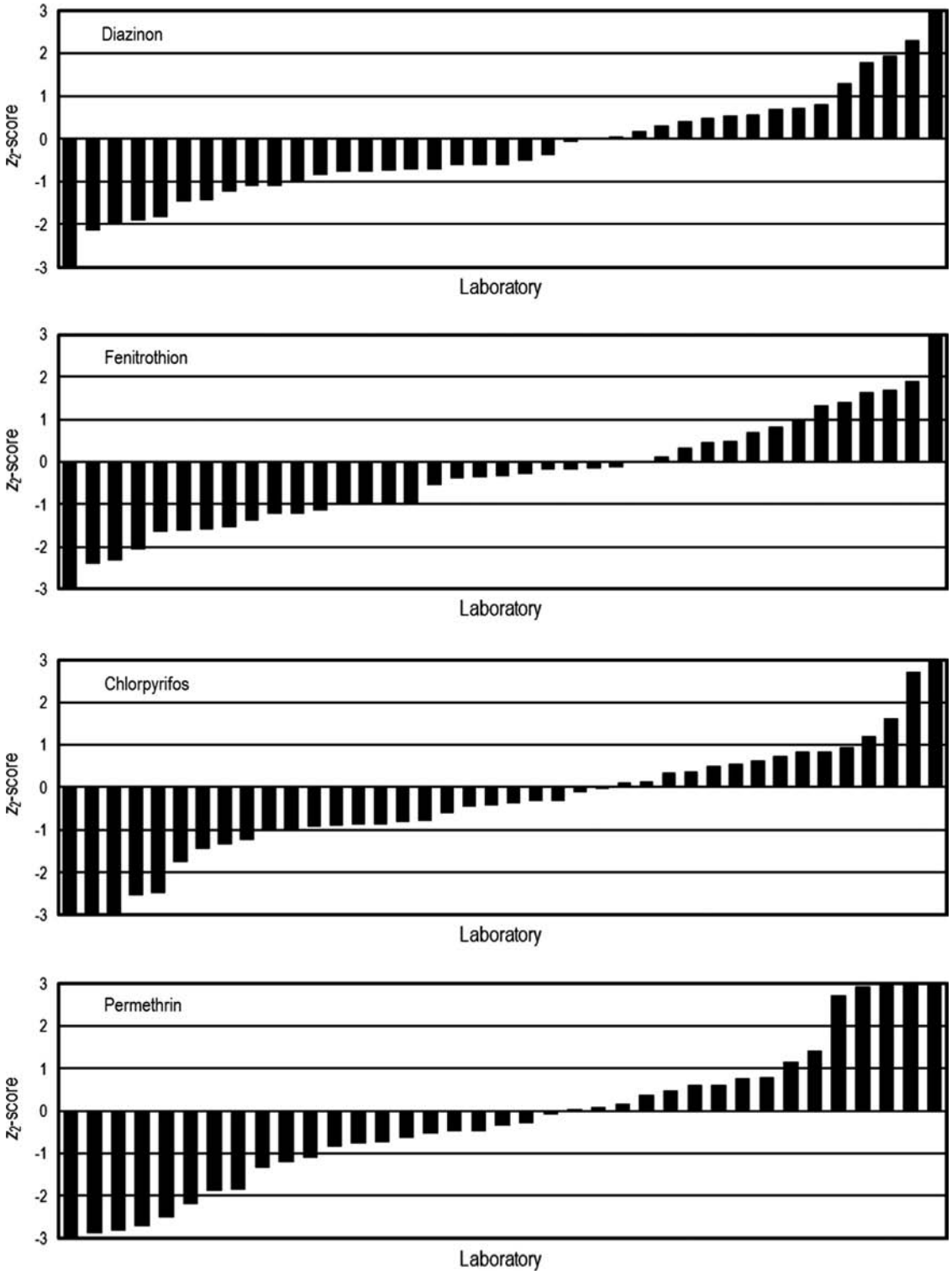


Fig. 6. Distribution of the participants' z_2-scores.

percentage of the respective $PRSD_R$ values was 22% in relation to the corresponding X_{NMIJ} values, and the $PRSD_R$ was much larger than the combined standard uncertainty of the Assigned value 2.

The z_2-scores for the individual target pesticides were then calculated for each participant using Eq. (2). Fig. 6 shows the distribution of the participants' z_2-scores. The performance of the participants was ranked into the following classes:

(1) $|z_2| \leq 2.0$, "satisfactory" performance,
(2) $2.0 < |z_2| < 3.0$, "questionable" performance, and
(3) $3.0 \leq |z_3|$, "unsatisfactory" performance.

The number of participants in the individual classes is also summarized in Table 2. The ratio of the participants having $|z_2|$ values ranking in the second or third classes was 13% for diazinon, 18% for fenitrothion, 10% for chlorpyrifos, and 30% for permethrin. Most participants quantified permethrin according to the following process: *cis*- and *trans*- isomers were individually quantified using corresponding calibrants and the observed concentrations were then summed. This might result in a higher ratio of permethrin in comparison with the other pesticides.

3.5. Comparison of two assigned values

Because assigned value 1 was obtained using the analytical results of the participants, this value possibly depended on the analytical method and quantification conditions used by the participants, the participants' skill, etc. Therefore, the analytical methods and quantification conditions of all participants were listed in the final report of the present PT. On the other hand, assigned value 2 was obtained by the analytical methods based on IDMS at NMIJ. The observed X_{NMIJ} values were 7.4–16% higher than the corresponding X_m values. As described above, most participants did not correct their observed analytical values with the recovery ratios of the target pesticides during the analytical process. At NMIJ, the recovery ratios of isotope-labeled pesticides spiked onto the samples were monitored. The recovery ratios were 79–91% in Method 1. In the IDMS measurement, the recovery ratios of the target pesticides did not affect the analytical values if equilibrium between the target and isotope-labeled pesticides was achieved. The differences between the two assigned values may be due to the difference in the impact of the recovery ratio during the two processes. In previous PTs for the determination of pesticide residues in food samples, the assigned values (concentration) obtained using the participants' analytical results were lower than the spiked concentrations employed for preparation of the test samples [15,40]: these results support our previous conclusion that the differences between the two assigned values may be due to the difference in the impact of the recovery ratio during the two processes.

Because assigned value 2 was higher than the corresponding assigned value 1, the z_2-score tended to be higher than the corresponding z_1-score (if the *NIQ*R and $PRSD_R$ values were not significantly different). This difference between the two scores might be confusing to the participants; therefore, the participants were advised that the z_1-scores showed the relative performance score for the present PT. They were also advised to use the z_2-scores in their evaluation of the trueness of their analytical methods.

4. Conclusion

A new PT program for pesticide-residue analysis of food samples was initiated, and the first round of the program was carried out using the candidate soybean material, NMIJ CRM 7509-a, as the test sample. Two kinds of assigned values were established using either the participants' analytical results or the NMIJ's IDMS analytical results, and the corresponding *z*-scores were calculated for individual participants. The participants could select the appropriate score according to the purpose of their assessment. The effects of the analytical method and quantification conditions on the participants' analytical results were also cursorily considered; further investigation is required to evaluate these effects more generally.

Acknowledgments

The authors thank KANSO Technos for preparing the test samples and Japan Food Research Laboratories for evaluating their homogeneity. Gratitude is extended to the Korea Research Institute and the National Institute of Metrology, China, for analysis of test samples to ensure the analytical results of the NMIJ. This work was partly supported by the Research and Development Projects for Application in Promoting New Policy of the Agriculture Forestry and Fisheries (No. 21044) of the Ministry of Agriculture, Forestry and Fisheries, Japan, and the Health and Labour Science Research Grant of the Ministry of Health, Labour, and Welfare, Japan.

Appendix. Supplementary material

Supplementary data associated with this article can be found in the online version at http://dx.doi.org/10.1016/j.talanta.2014.09.001.

References

[1] F.P. Carvalho, Environ. Sci. Policy 9 (2006) 685–692.
[2] Ministry of Health, Labour and Welfare, Japan, Introduction of the Positive List System for Agricultural Chemical Residues in Foods, ⟨http://www.mhlw.go.jp/english/topics/foodsafety/positivelist060228/introduction.html⟩, 2006.
[3] Ministry of Health, Labour and Welfare, Japan, Annex of the Director Notice (Syoku-An No 124001) Analytical Methods for Residual Compositional Substances of Agricultural Chemicals, Feed Additives, and Veterinary Drugs in Food, 2005 (Amendment in 2006) (in Japanese).
[4] B. Jin, L. Xie, Y. Guo, G. Pang, Food Res. Int. 46 (2012) 399–409.
[5] L. Zhang, L. Shaowen, X. Cui, C. Pan, A. Zhang, F. Chen, Cent. Eur. J. Chem. 10 (2012) 900–925.
[6] I. Taverniers, M. De Loose, E. Van Bockstaele, Trends Anal. Chem. 23 (2004) 535–552.
[7] M. Thompson, S.R. Ellison, R. Wood, Pure Appl. Chem. 78 (2006) 145–196.
[8] M.E. Poulsen, H.B. Christensen, S.S. Herrmann, Accredit. Qual. Assur. 14 (2009) 477–485.
[9] F.G.M. Violante, M.H.W.M. Cardoso, J.M. Rodrigues, A.V. Gouvèa, C.N. Borges, P.R. da, F. Santos, D. da, S. Santos, H.C. de A Góes, V. Souza, A. de S. José, R.D.C. C. Bandeira, V. Cunha, A. Nóbrega, J. Chromatgr. Sci. 47 (2009) 833–839.
[10] K.M. Chan, S.T.C. Cheung, Y.-L. Wong, A.L.S. Cheng, C.-s. Mok, W.-w. Wong, D.W. Tholen, Y.-c. Wong, Trends Anal. Chem. 29 (2010) 562–576.
[11] P. Medina-Pastor, M. Mezeua, C. Rodríguez-Torreblanca, A.R Fernández-Alba, Anal. Bioanal. Chem. 397 (2010) 3061–3070.
[12] M. Okihashi, M. Osakada, K. Uchida, H. Nagayoshi, T. Yamaguchi, K. Kamimoto, Y. Nakayama, H. Obana, Shokuhin Eiseigaku Zasshi, J. Food Hyg. Soc. Jpn. 51 (2010) 253–257 (in Japanese).
[13] B. Kim, S. Ahn, Y. Mitani, Accredit. Qual. Assur. 16 (2011) 499–505.
[14] T. Watanabe, Shokuhin Eiseigaku Zasshi, J. Food Hyg. Soc. Jpn. 52 (2011) J315–J320 (in Japanese).
[15] M. Sykes, M. Thompson, S. Reynolds, J. Agric. Food Chem. 61 (2013) 4205–4209.
[16] T.J. Quinn, Metrologia 34 (1997) 61–65.
[17] W. Richter, Accredit. Qual. Assur. 2 (1997) 354–359.
[18] P. De Bièvre, H.S. Peiser, Fresenius J. Anal. Chem. 359 (1997) 523–525.
[19] M.J.T. Milton, T.J. Quinn, Metrologia 38 (2001) 289–296.
[20] T. Otake, N. Itho, Y. Aoyagi, M. Matsuo, N. Hanari, S. Otsuka, T. Yarita, J. Agric. Food Chem. 57 (2009) 8208–8212.
[21] T. Otake, T. Yarita, Y. Aoyagi, Y. Kuroda, M. Numata, H. Iwata, K. Mizukoshi, M. Nakamura, M. Watai, H. Mitsuda, T. Fujikawa, H. Ota, J. Agric. Food Chem. 59 (2011) 8568–8574.
[22] T. Otake, T. Yarita, Y. Aoyagi, Y. Kuroda, M. Numata, H. Iwata, M. Watai, H. Mitsuda, T. Fujikawa, H. Ota, Food Chem. 138 (2013) 1243–1249.
[23] T. Yarita, T. Otake, Y. Aoyagi, Y. Kuroda, M. Numata, H. Iwata, M. Watai, H. Mitsuda, T. Fujikawa, H. Ota, Talanta 119 (2014) 255–261.

[24] Y. Zhu, T. Kuroiwa, T. Narukawa, K. Inagaki, K. Chiba, Trends Anal. Chem. 34 (2012) 152–160.
[25] S. Miyashita, K. Inagaki, S. Naito, K. Shindoh, T. Narukawa, Y. Zhu, T. Kuroiwa, A. Hioki, T. Fujimoto, K. Chiba, Anal. Bioanal. Chem. 405 (2013) 8347–8362.
[26] ISO Guide 35, Reference Materials – General and Statistical Principles for Certification, International Organization for Standardization, Geneva, 2006.
[27] M. Thimpson, Analyst 125 (2000) 385–386.
[28] ISO/IEC 17043, Conformity Assessment – General Requirements for Proficiency Testing, International Organization for Standardization, Geneva, 2010.
[29] ISO 13528, Statistical Methods for Use in Proficiency Testing by Interlaboratory Comparison, International Organization for Standardization, Geneva, 2005.
[30] Ministry of Health, Labour and Welfare, Japan, Annex of the Director Notice (Syoku-An No 1224-1) Guidelines for the Validation of Analytical Methods for Agricultural Chemical Residues in Food, 2010 (in Japanese).
[31] A. Wilkowska, M. Bizink, Food Chem. 125 (2011) 803–812.
[32] S. Hiramatsu, K. Nishiyama, S. Tokuhashi, T. Ashida, A. Kageyama, M. Takamiya, A. Nakamura, N. Takuma, K. Nishimori, Rep. Publ. Health Kochi, 59 (2013) 47–52 (in Japanese).
[33] K. Uranishi, H. Yamashita, K. Yamamoto, Shokuhin Eiseigaku Zasshi, J. Food Hyg. Soc. Jpn. 53 (2012) 63–74 (in Japanese).
[34] K. Sugitate, S. Nakamura, N. Orikata, K. Mizukoshi, M. Nakamura, A. Toriba, K. Hayakawa, J. Pestic. Sci. 37 (2012) 156–163.
[35] K. Sugitate, M. Saka, T. Serino, S. Nakamura., A. Toriba, K. Hayakawa, J. Agric. Food Chem. 60 (2012) 10226–10234.
[36] S. Walorczyk, Talanta 120 (2014) 106–113.
[37] M. Kubota, Y. Takata, K. Koizumi, Y. Ishibashi, R. Matsuda, Y. Matsumoto, K. Shikakume, A. Ono, M. Sakata, K. Kakita, Bunseki Kagaku 57 (2008) 393 (in Japanese).
[38] The Japan Food Chemical Research Foundation, Maximum Residue Limits (MRLs) List of Agricultural Chemicals in Foods, ⟨http://www.m5.ws001.squarestart.ne.jp/foundation/search.html⟩, 2014.
[39] T. Yarita, A. Takatsu, K. Inagaki, M. Numata, K. Chiba, K. Okamoto, Accredit. Qual. Assur. 12 (2007) 156–160.
[40] Hatano Research Institute, Food and Drug Safety Center, Summary Report of the External Quality Control for Food Hygiene 2013, Hatano, 2014, pp. 67–101 (in Japanese).

Talanta 132 (2015) 278–284

Contents lists available at ScienceDirect

Talanta

journal homepage: www.elsevier.com/locate/talanta

Highly selective visual monitoring of hazardous fluoride ion in aqueous media using thiobarbituric-capped gold nanoparticles

Jyoti Boken [a], Sheenam Thatai [b], Parul Khurana [b], Surendra Prasad [c,*], Dinesh Kumar [b,**]

[a] Department of Physics, Banasthali University, Banasthali-304022, Rajasthan, India
[b] Department of Chemistry, Banasthali University, Banasthali-304022, Rajasthan, India
[c] School of Biological and Chemical Sciences, Faculty of Science, Technology and Environment, The University of the South Pacific, Private Mail Bag, Suva, Fiji

ARTICLE INFO

Article history:
Received 17 June 2014
Received in revised form
14 August 2014
Accepted 14 August 2014
Available online 16 September 2014

Keywords:
Gold nanoparticles
2-Thiobarbituric acid
Fluoride ion sensor
Naked-eye detection
Colorimetric

ABSTRACT

The rapid, selective and sensitive measurement and monitoring of hazardous materials as analytes are the central themes in the development of any successful analytical technique. With this aim, we have synthesized the thiobarbituric-capped gold nanoparticles (TBA-capped Au NPs) involving chemical reduction of $HAuCl_4$ using 2-thiobarbituric acid (TBA) as a reducing and capping agent. The morphology of the TBA-capped Au NPs was confirmed using transmission electron microscope images. For the first time this article reports that the developed TAB-capped Au NPs displays selective, ultrafast and sensitive colorimetric detection of fluoride ion in aqueous samples. The detection of fluoride ion was confirmed by the disappearance of the localized surface plasmon resonance (LSPR) band at 554 nm using UV-vis spectroscopy. The interaction of F^- with TBA-capped Au NPs in aqueous solution has also been confirmed by Raman and FTIR spectroscopy. One of the most exciting accomplishments is the visual detection limit for fluoride ion has been found to be 10 mM at commonly acceptable water pH range 7–8. The whole detection procedure takes not more than 40 s with excellent selectivity providing sample throughput of more than 60 per hour.

© 2014 Elsevier B.V. All rights reserved.

1. Introduction

Metal nanoparticles such as gold nanoparticles (Au NPs) have attracted much attention with wide applications in highly sensitive chemical sensors due to their optical and electrical properties [1,2]. These properties of Au NPs are precisely determined by their dimension [2], shape [3], composition of materials [4,5], surrounding media [6] and relative distance between the particles [7–9]. Therefore, NPs show the intense plasmon resonance band in the visible region [10,11] which is exquisitely sensitive to their aggregation states [12,13].

Fluoride is commonly added to drinking water and toothpaste because of their beneficial effects on dental health. The deficiency of fluoride causes poor dental health and osteoporosis [14,15], while over exposure to fluoride ion causes fluorosis and urolithiasis [16–19]. Even small excess amount of fluoride consumed from tap water can damage bones, teeth, brain, disrupt thyroid function, lower intelligence quotient and/or cause cancer [14–19]. Thus, the Environmental Protection Agency (EPA) has set a maximum level of fluoride ion in water as 1 ppm and that over 2 ppm is considered a health risk [20]. Therefore, the accuracy in detection and determination of fluoride ion in aqueous samples is an extremely important aspect in the public interest. Recently, the colorimetric sensors or nanoprobes have been widely used for selective and sensitive detection for several analytes including alkali metal ions [21,22], heavy metal ions [23,24], oxo anions [25–27], fluoride ion [24,28–37], iodide ion [38], DNA and biomolecules [39–42], hydrogen peroxide [43], organophosphates [44], etc. However, there is still need to develop methods for sensing of fluoride ion due to its various applications.

Fluoride has unique properties compared to other elements as a result of its relative by small size and highest electronegativity. Thus, a number of compounds that are able to bind fluoride ion with high affinity and selectivity have been reported, but only a few reports are available in the literature for fluoride ion probes that utilize the unique optical properties of Au NPs [30,35]. However, the sensitivity and selectivity of this probe were poor compared to the properties of the other probes based on fluorescence and colorimetric probes [35]. The disadvantage on nanoprobes development is that the limited Au NPs are acquirable. In most cases Au NPs have been synthesized by citrate, which dispersed in an aqueous solution through the ionic repulsion of the surface-adsorbed ions. In the presence of electrolytes, due to the charge shielding, the ionic stabilized NPs undergo uncontrolled aggregation. The stabilized Au NPs are protected with non-ionic hydrophilic molecules, but the

* Corresponding author. Tel.: +679 3232416; fax: +679 2321512.
** Corresponding author. Tel.: +91 9928108023; fax: +91 1438 228365.
E-mail addresses: prasad_su@usp.ac.fj (S. Prasad), dschoudhary2002@yahoo.com (D. Kumar).

http://dx.doi.org/10.1016/j.talanta.2014.08.043
0039-9140/© 2014 Elsevier B.V. All rights reserved.

thick protecting layers preventing the core metals to be close together, which are responsible for the change in color in the solution [45]. Therefore, it is essential to develop Au NPs protected with a monolayer of hydrophilic molecules.

Mostly sensors are fluorescent sensors containing quinoline [46], coumarin [47], anthracene [48], fluorescein fluorophores [49–55], pyrroles [56], quinoxalies [57–59] and azophenols [60,61]. Although, fluorescent sensors are widely used in biological studies, they usually require complicated synthesis involving various reaction condition and expensive chemicals. On the other hand, detection method used often required expensive equipment. Thus, it is of great interest to develop new chemical sensors which use easily synthesized chemicals and possesses good selectively and high sensitivity. Fluoride ion sensors are in great demand due to the involvement of fluoride in a variety of environmental issues and healthcare [36,62]. Therefore, a variety of fluoride sensors have been developed [24,28–37]. A selective and sensitive chemosensor that makes use of transition between Au NPs agglomeration states to develop a signal in the presence of fluoride ion is an attractive approach to fabricate fast usability fluoride ion probes [30,35]. With the aim to obtain more sensitive and selective chemosensors, an increasing number of papers have recently appeared, in which the chemosensor have been anchored to different supports [49]. In addition, the application of Au NPs as colorimetric sensors have usually been based on detecting the peak shifts in surface plasmon resonance (SPR) either due to the change in the dielectric constant around the NPs as a result of analyte molecule adsorption or to the analyte induced agglomeration of the NPs [13]. Both effects have provided the selectivity in detection by the functionalized capping agents, highlighting the importance of the synthesis by chemical reduction methods and their stabilization of NPs for use a solution based sensors [63].

In continuation of our interest on developing analytical methods for fluoride removal [15,16] and development of nanosensor for the detection of cations using Au nano-rods [17], and with continuous report on hazardous fluoride contamination in drinking water in rural habitations of Central Rajasthan, India [16], we continued our work towards the development of novel rapid, selective and sensitive method for visual detection and monitoring of hazardous fluoride ion. Thus, herein we introduce an easy, simple and quantitative preparation of the modified Au NPs with 2-thiobarbituric acid (TBA) where UV–vis absorption study has demonstrated that the fluoride selective aggregation is associated with dramatic color change in aqueous solution which leads to rapid, selective and sensitive method for visual detection and monitoring of hazardous fluoride ion. The different agglomeration states of Au NPs produce a different color in the solution. This study has also demonstrated that TBA is a potential candidate to devise the reliable ultrafast colorimetric sensor for the naked-eye visualization of fluoride ion detection at trace level.

2. Materials and methods

2.1. Chemicals

Tetrachloroauric acid and 2-thiobarbituric acid purchased from Sigma-Aldrich (USA) were used as received without any further purification. The regents for all anions (sodium fluoride, potassium

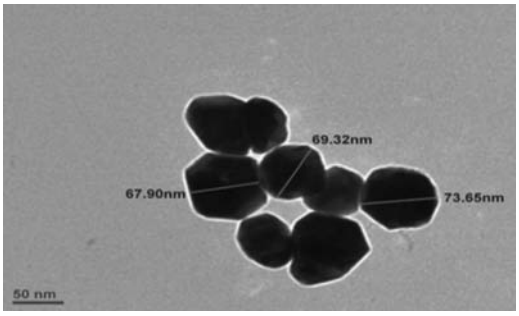


Fig. 2. TEM image of 2-thiobarbituric-capped gold nanoparticles.

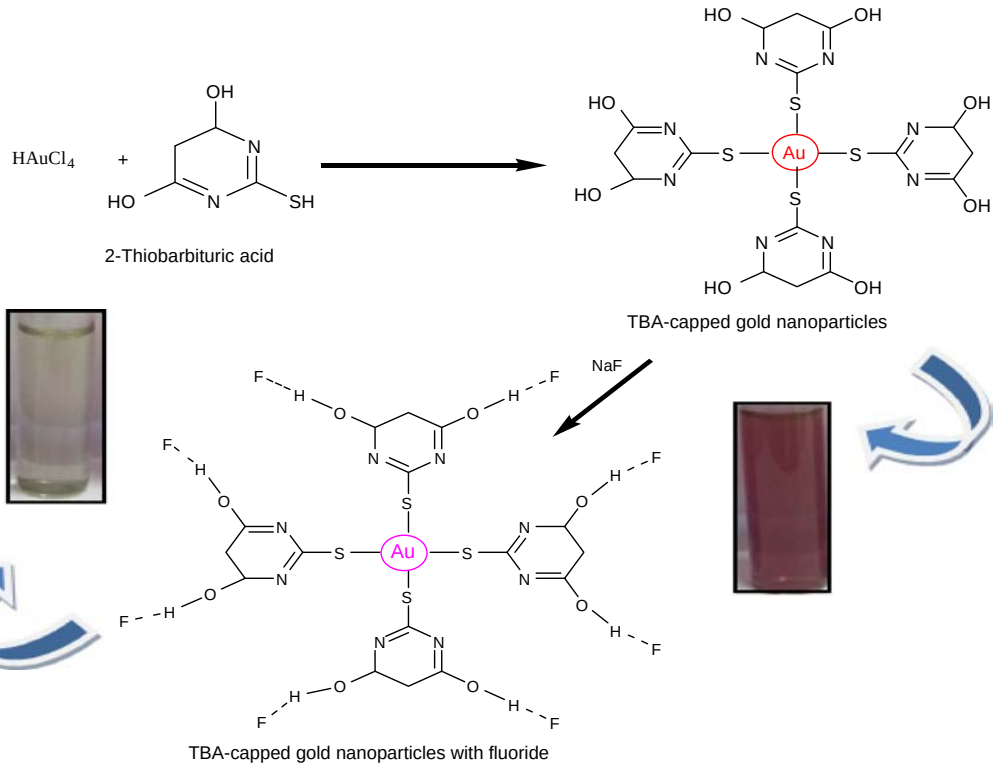


Fig. 1. A schematic representation for fabrication of 2-thiobarbituric capped gold nanoparticles and sensing of fluoride ions.

bromide, sodium chloride, potassium iodide, potassium carbonate, acetic acid, sodium nitrate, potassium dihydrogen phosphate) were purchased from E. Merck Ltd, Mumbai, India. All the solutions were freshly prepared for the synthesis of nanoparticles. Distilled water passed through a Millipore system (resistivity 18 MΩ. cm) was used in the preparation of all the solutions and throughout the experiments. All glassware used were first rinsed with aqua regia and then thoroughly washed with distilled water followed by Millipore water.

2.2. Synthesis of TBA-capped Au NPs

Thiobarbituric-capped Au NPs was synthesized by a wet chemical reduction method where TBA acts as reducing agent as well as capping agent [64]. In synthesis of TBA-capped Au NPs, the aqueous TBA solution (20 mL, 2–20 mM) was added to the boiling solution of $HAuCl_4$ (50 mL, 0.2 mM) under vigorous stirring in a round bottom flask equipped with a condenser. On addition of TBA to tetrachloroauric acid solution a transition in color of the reaction mixture was observed from red to colorless within 10 s. The reaction mixture was further boiled for 30 min under reflux and then cooled with stirring to room temperature i.e. 25 °C. The pH of the TBA-capped Au NPs solutions was adjusted to desired pH 5–8 with 0.1 M NaOH solution.

2.3. Characterization technique

Optical absorption measurements were performed using (Perkin-Elmer Lambda 750) UV–vis-NIR spectrophotometer. The particle size and morphology of the NPs were examined using transmission electron microscope (FEI Tecnai G20) operated at an accelerating voltage of 220 keV. All the samples for transmission electron

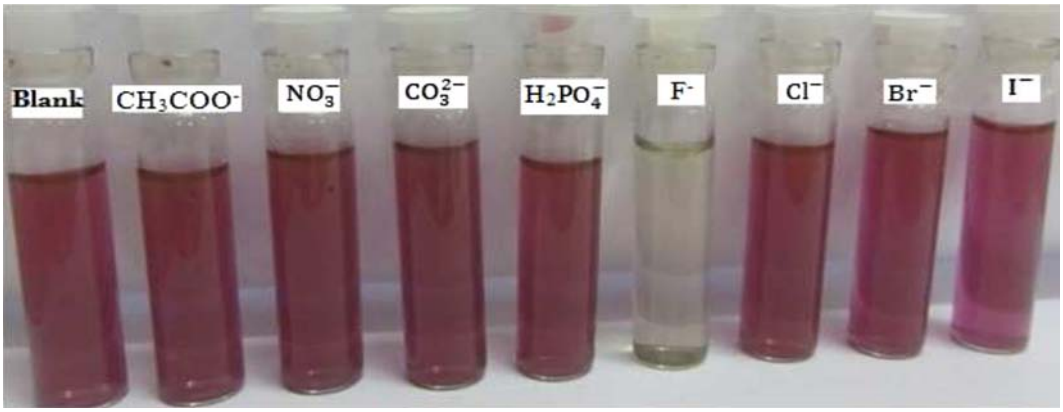


Fig. 3. Color changes of the 2-thiobarbituric-capped gold nanoparticles having 10 mM concentration in the presence of 10 mM anions concentration.

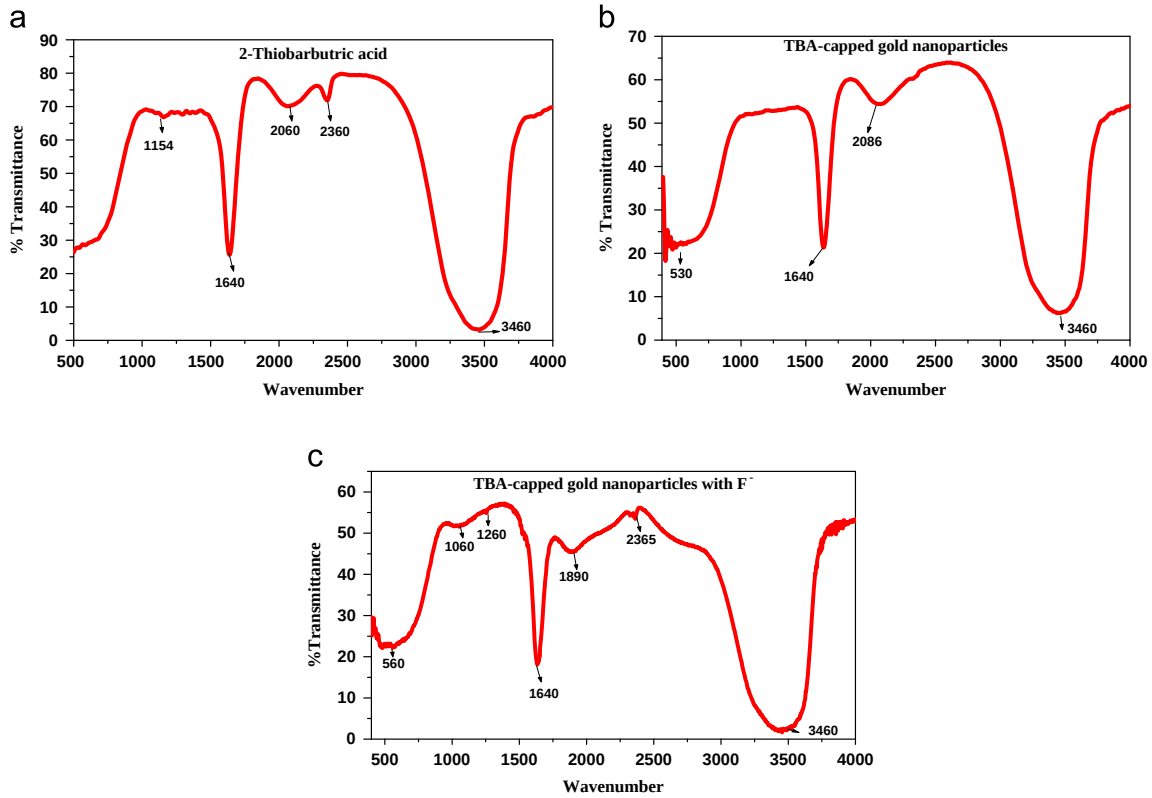


Fig. 4. FTIR spectra of (a) 2-thiobarbituric acid (b) 2-thiobarbituric-capped gold nanoparticles and (c) TBA-capped gold nanoparticles with fluoride ion.

microscope (TEM) were deposited on carbon coated copper grid by placing the drops of diluted samples of TBA-capped Au NPs. Fourier transformation infrared (FTIR) spectrometer (Agilent Cary 660, USA) and Raman spectrometer (Deltanu Advantage 532) were used to obtain information of an element to element bonding or interaction.

3. Results and discussion

The absorption spectrum of Au NPs showed the maximum peak at 554 nm attributed to the localized surface plasmon resonance (LSPR) band. The thiol group is essential to synthesize well dispersed TBA-capped Au NPs. In the synthesis of TBA-capped AuNPs, the position of thiol group plays an important role in the reaction mixture. The analytical method developed herein is novel, rapid, very simple and highly selective which involves the use of sodium fluoride in the presence of TBA-capped Au NPs for the visual detection of hazardous fluoride ion.

3.1. TBA-capped Au NPs fluoride interaction

A schematic representation of synthesis of TBA-capped Au NPs and its interaction with fluoride ion is shown in Fig. 1. The typical LSPR absorbance band of TBA-capped Au NPs at 554 nm provided red color in the absence of fluoride ion and the solution was stable under the experimental conditions. When the fluoride was added to TBA-capped Au NPs solutions, the color dramatically changed from red to colorless and the absorption bands were red shifted i.e. at longer wave length within mixtures which indicated the aggregation of TBA-capped Au NPs [65]. The color transformation was completed within 40 s. On the other hand, other anions did not induce any color change at 10 mM concentration. The UV–vis spectra of the reaction mixture remained unchanged in the presence of fluoride ion over several hours. This observation concluded the formation of H–F hydrogen bonding in the reaction mixture of TBA-capped Au NPs and fluoride ion. It may be attributed to the high charge density and small size of fluoride ion which enabled the formation of hydrogen bonding by interaction with the hydroxyl groups of TBA moieties (Fig. 1). The color change occurred in the reaction was easily monitored by the naked eye.

3.2. Morphological study of TBA-capped Au NPs

The morphology of the TBA-capped Au NPs was studied using TEM images. Fig. 2 shows a typical TEM image of TBA-capped Au NPs. The shape of the gold nanoparticle was slightly irregular. The average particle size (68–74 nm) can be tuned over a size range of 1–20 nm by varying the concentration of TBA in the reaction mixture.

3.3. Visual color change studies

The sensing of halide anions such as F^-, Cl^-, Br^-, I^- and oxo anions such as CH_3COO^-, NO_3^-, CO_3^{2-}, $H_2PO_4^-$ was studied using UV–vis spectroscopy in aqueous solution. The effect of the addition of these anions to TBA-capped Au NPs solutions is shown in Fig. 3 as photographic images which clearly shows that the color changes only after the addition of F^- (10 mM) to the solution and causes a red shift in the LSPR band. It is remarkable to note that the color changes occurred only when F^- was added while of addition other anions such as CH_3COO^-, NO_3^-, CO_3^{2-}, $H_2PO_4^-$, Cl^-, Br^- and I^- failed to cause any significant change in color. This study confirmed that the addition of 10 mM of fluoride ion solution induces the appearance of color change in the reaction mixture.

3.4. FTIR study of TBA-capped Au NPs

Fourier transformation infrared spectroscopy (FTIR) was performed to find the fluoride binding with TBA-capped Au NPs in the samples and related infrared spectra are shown in Fig. 4(a, b and c). The FTIR spectrum for the Au NPs was compared with corresponding surfactant i.e. TBA and it was found that the S-H stretching frequency (2360 cm^{-1}) of bound surfactants disappeared (Fig. 4a and b). This suggests that the bonding of the thiobarbituric to the gold surface takes place through the S-H end. Further the S-H bond cleaved upon S-Au chemisorption is in good agreement with the study done by Hasan et al. on the fate of sulfur bound hydrogen during the formation of a thiol monolayer on gold [66]. The S-H absorption is typically weak and occurs at a lower wave number (frequency) than the corresponding O-H vibration because of the higher atomic mass of sulfur [67]. Due to a high atomic number of gold its vibrational feature is also expected to appear at lower wave number and appeared at 530 cm^{-1} (Fig. 4b) [68]. The appearance of a new weak band at 2365 cm^{-1} (Fig. 4c) was assigned to the H—F hydrogen bond formation in fluoride ion treated TBA-capped Au NPs solution [67]. It may be due to the weak interaction of fluoride ion with hydroxyl group of TBA as shown in Fig. 1. It was found that the band at 1640 cm^{-1} remained unchanged in all the cases which is consistent with the greater affinity of Au for S-H bond compared with C=N. This observation was consistent with earlier reports that the rigid chain conformation on the nanoparticle surface generates

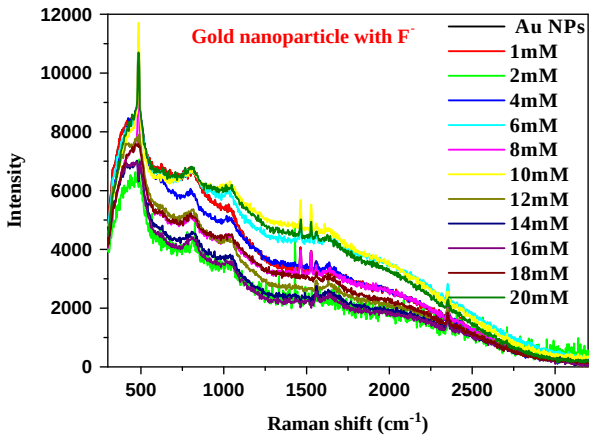


Fig. 5. Raman spectra of 2-thiobarbituric-capped gold nanoparticle with the addition of 1–20 mM of NaF.

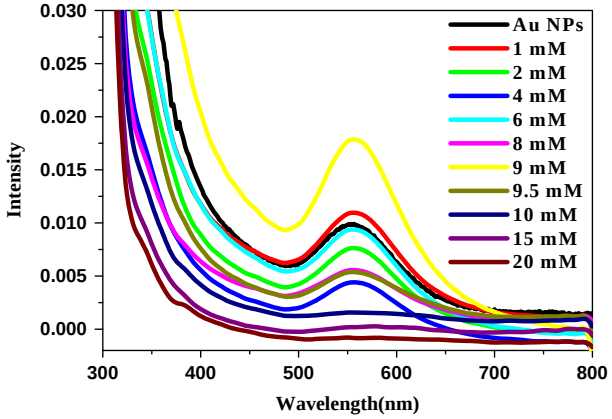


Fig. 6. UV–vis spectra of 2-thiobarbituric-capped gold nanoparticles solution having 10 mM concentration with the addition of different fluoride ion concentrations in the range 1–20 mM in the solution.

a crystalline-like state of chains and restricted their mobility [69]. The band at 3460 cm^{-1} appeared due to O-H stretching present in TBA moieties, which remained same in all the spectra [70].

3.5. Raman spectroscopy study of TBA-capped Au NPs

The Raman spectroscopy has frequently been used to detect vibrations in molecules based on the processes of infrared absorption and Raman scattering which provides information on chemical structure. Raman spectra of TBA-capped Au NPs in presence of different concentration of F^- (1–20 mm) are shown in Fig. 5 which are dominated by the bands around 1030 cm^{-1} and 1530 cm^{-1} attributed to C-S and C-C stretching vibrations respectively. The behavior of other peaks in Raman spectra is consistent with colloidal states [71]. The S-H stretching at 2580 cm^{-1} and S-H bending at 917 cm^{-1} in the Raman spectrum disappeared, indicating dissociative chemisorption of TBA onto Au by rupturing S-H bond [72]. The appearance of a sharp peak at 1470 cm^{-1} evidenced the formation of Au-S bond. These features generally appeared in Raman spectra of thiol [73].

3.6. Sensing assay of fluoride ion

To verify practicality, the proposed method was applied to detect the fluoride ion on the aggregation of Au NPs. 1 mL portion of different concentrations (1–20 mM) of fluoride ion were added individually to 2 mL of TBA-capped Au NPs solutions. The resulting mixtures were allowed to react for 1–5 min. The absorption changes between 550–700 nm were monitored. The extinction at a wavelength above 600 nm was similar to the collective plasmon resonance of closely spaced Au NPs which indicated the anion i.e. F^- induced aggregation of NPs. At certain threshold concentration

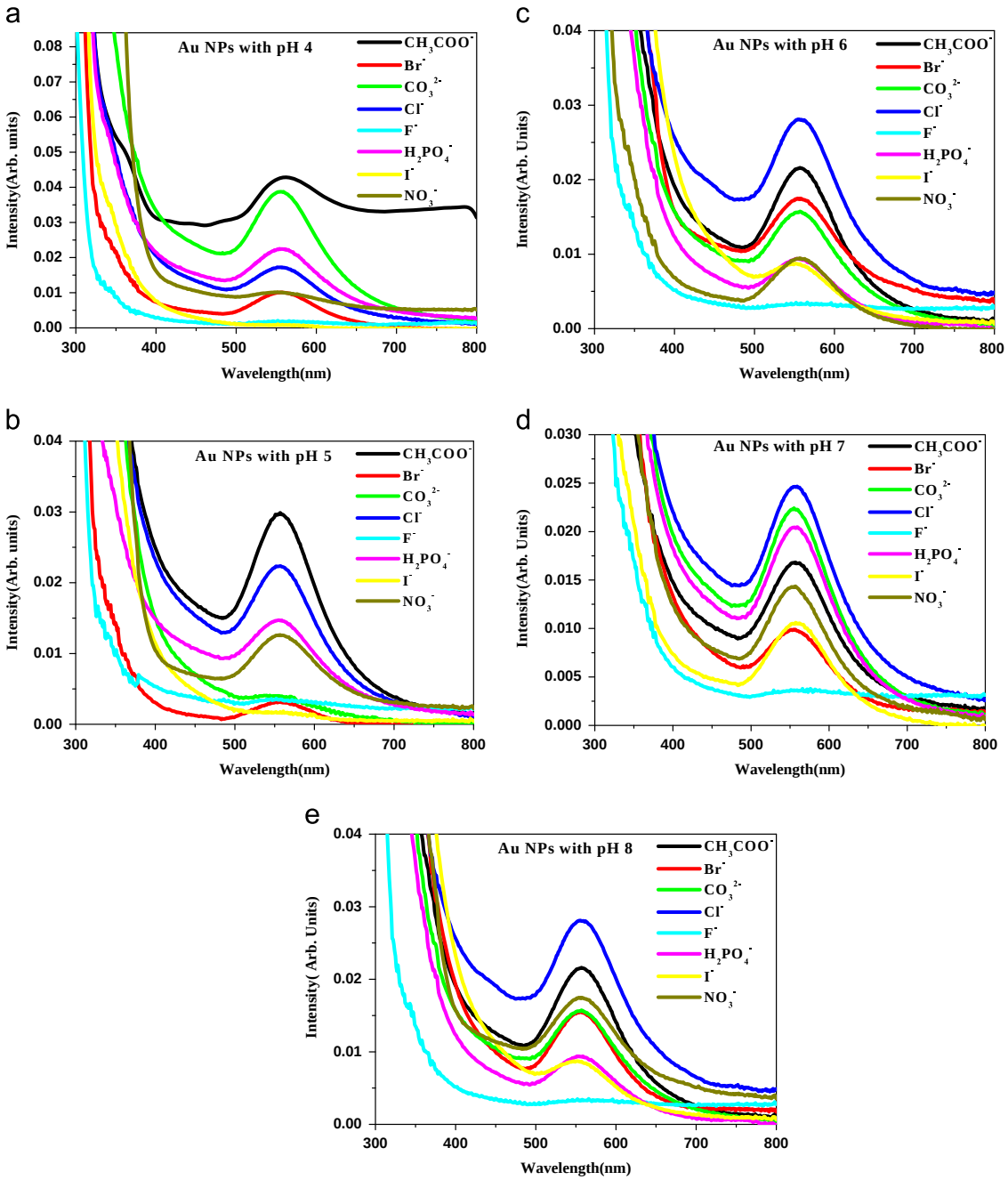


Fig. 7. UV–vis spectra of TBA–capped Au NPs solution having 10 mM concentration at different pH: (a) pH 4, (b) pH 5, (c) pH 6, (d) pH 7 and (e) pH 8.

of F^-, difference in the concentration can be detected by the naked-eye as the color change from red to colorless [35].

The UV–vis spectra of TBA-capped Au NPs solution upon addition of increasing fluoride ion concentrations in the range of 1–20 mM is shown in Fig. 6. Fig. 6 clearly shows that with increasing the amount of fluoride ion in the solution, the intensity of peaks decreased and at the certain concentration peak just disappeared. The peak width was also increased with the addition of higher concentration of fluoride ion in the solution. The changes observed in both parameters revealed the aggregation of NPs [13,65]. The addition of fluoride ion to the TBA-capped Au NPs solution caused dramatic changes in the plasmon band while the interaction was very strong at 10 mM F^- concentration. This concentration displays the colorimetric detection of F^- where the characteristic peak at 554 nm i.e. LSPR disappeared. UV–vis spectra at different concentrations of fluoride showed that with increased concentration of F^- in the reaction mixture, the peak position remained same while decreased in its intensity as well as broadening in the spectra occurred.

3.7. Effect of pH and TEM study

To investigate the effect of pH on the aggregation, the pH of TBA-capped Au NPs solution was varied by using 0.1 M NaOH from 4 to 8 [74]. The UV–vis spectra in the presence of different anions, obtained at different pH, are shown in Fig. 7 (a-e). With increasing pH i.e. increasing density of OH^- in the solution, the nucleophilicity of F^- increased to bind with protective surface of NPs. This result also indicates that the sensing process of F^- is govern by hydrogen bonding and by adsorption phenomenon, otherwise at pH 8, I^- ions could have also bonded with the hydrogen of capping agent i.e. TBA. With an increasing pH of the solution, the efficiency of interaction of larger anions decreases due to their decreased interaction [75]. At pH 8 almost all anions were stable due to their larger size while smaller F^- has strong tendency to disperse its excess charge through the formation of hydrogen bond with the capping agent. This study concluded that the selectivity of F^- ion detection increased with increasing pH of the solution.

The variation of pH from 4 to 8 of Au NPs did not show any change in the red color of the solution which confirmed the stability of the disperse state of TBA-capped Au NPs in the studied pH range. Initially, the pH of TBA-capped Au NPs solution was monitored to be around 2.7–3.0. On decreasing the pH of the solution, the position of the absorption peak remained same while changes observed in their shape and intensity. Very low pH decreases the electrostatic stability of Au NPs by decreasing hydroxyl (–OH) group concentration. The low intensity as well as very broad peaks indicated that the number of Au NPs at the surface significantly decreased by the aggregation of Au NPs or due to decrease in particle to particle distance.

The aggregation of Au NPs at pH 5 to 8 was further confirmed by TEM analysis. The TEM micrographs of Au NPs solution at pH 5, 6, 7 and 8 are shown in Fig. 8(a-d) which clearly show high aggregation at pH 5 and least at pH 8. The TEM images of Au NPs at various pH show that the aggregation occurs maximum at pH 5 while the particles are still dispersed without signs of aggregation at pH 6–8. The maximum aggregation at pH 5 is attributed to the fact that aggregation takes place due to the closer confinement of the particles [65]. TEM images of TBA-capped Au NPs after addition of fluoride ion indicate the formation of aggregated Au

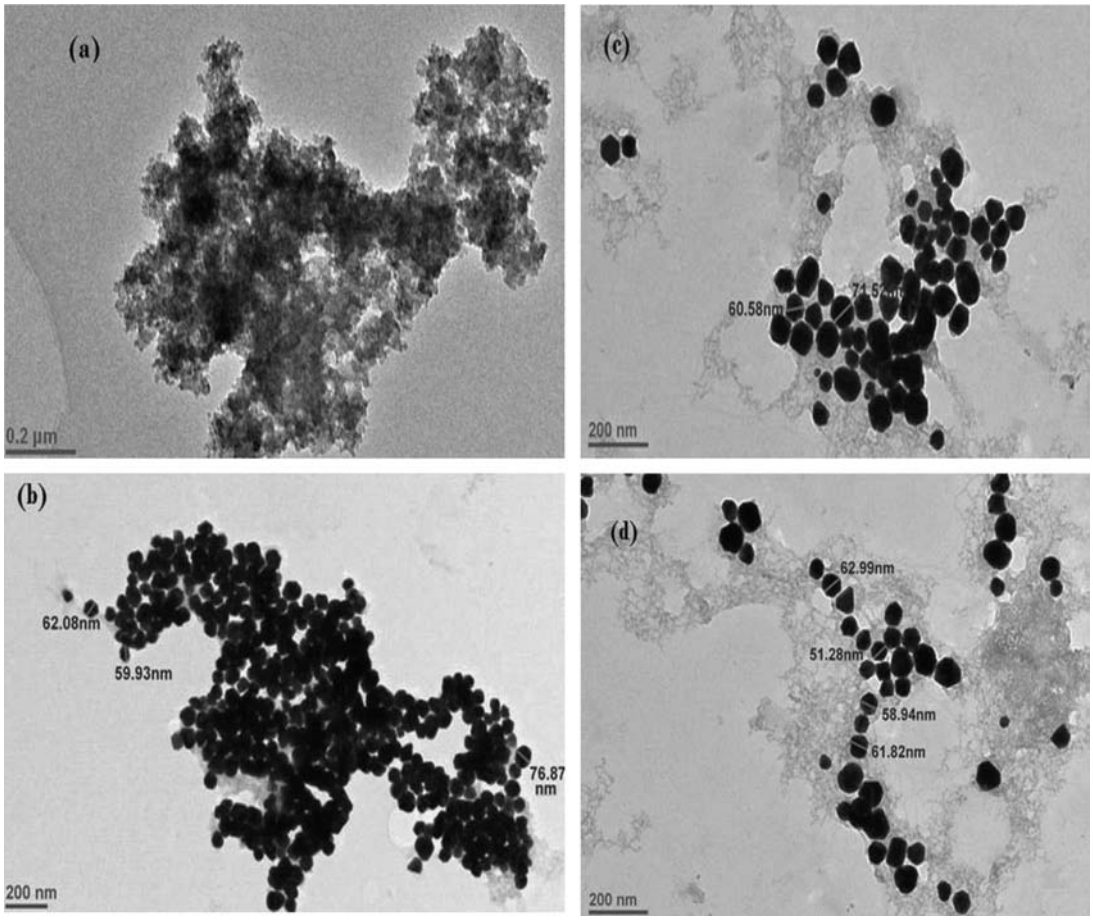


Fig. 8. Transmission electron microscope images of gold nanoparticles at different pH: (a) pH 5, (b) pH 6, (c) pH 7 and (d) pH 8.

NPs as shown in Fig. 8(a). This is attributed to the reduction of interparticle distance. When the distance among the aggregated particles decreases to less than the average particle diameter, the electric dipole-dipole interaction and coupling between the Plasmon's of neighboring particles into the aggregates leads to the formation of a new absorption band at longer wavelengths i.e. red shift the same was observed in Section 3.1 [65,76,77] while the broadening is attributed the slow rate of interaction [65,77].

4. Conclusions

In summary, we have demonstrated a simple way for the development of TBA-capped Au NPs by the chemical reduction method and used as platform for the detection of fluoride ion. In aqueous solution, halide anions (except fluoride) and oxoanions did not induce the aggregation with TBA-capped Au NPs. The color change associated with F^- aggregation has successfully been used for the naked eye detection of F^- at 10 mM concentration in aqueous solution. The reaction of F^- with TBA-capped Au NPs in aqueous solution has also been confirmed by Raman and FTIR spectroscopy.

Acknowledgments

J. Boken is thankful to the Department of Science and Technology (DST), Government of India, New Delhi for financial assistance via grant no. F.No.SR/WOS-A/PS-35/2010. The authors are thankful to Professor Aditya Shastri, Vice Chancellor, Banasthali University, Banasthali for kindly extending the facilities of 'Banasthali Centre for Education and Research in Basic Sciences' sanctioned under CURIE programme of the DST, Government of India, New Delhi, India.

References

[1] Z. Altintas, S.S. Kallempudi, Y. Gurbuz, Talanta 118 (2014) 270–276.
[2] R. Domínguez-González, L.G. Varela, P. Bermejo-Barrera, Talanta 118 (2014) 262–269.
[3] C.L. Haynes, R.P. Van Duyne, Phys. Chem. B 105 (2001) 5599–5611.
[4] R.C. Jin, Y.W. Cao, C.A. Mirkin, K.L. Kelly, G.C. Schatz, J.G. Zheng, Science 294 (2001) 1901–1903.
[5] R. Jin, Y.C. Cao, E. Hao, G.S. Metraux, G.C. Schatz, C.A. Mirkin, Nature 425 (2003) 487–490.
[6] A.D. McFarland, R.P.V Duyne, Nano Lett. 3 (2003) 1057–1062.
[7] J.J. Mock, D.R. Smith, S. Schultz, Nano Lett. 3 (2003) 485–491.
[8] M.D. Malinsky, K.L. Kelly, G.C. Schatz, R.P. Van Duyne, J. Am. Chem. Soc. 123 (2001) 1471–1482.
[9] W.A. Murray, B. Auguie, W.L. Barnes, Phys. Chem. C 113 (2009) 5120–5125.
[10] M.M. Maye, L. Han, N.N. Kariuki, N.K. Ly, W.B. Chan, J. Luo, C.J. Zhong, Anal. Chim. Acta 496 (2003) 17–27.
[11] I. Hussain, M. Brust, A.J. Papworth, A.I. Cooper, Langmuir 19 (2003) 4831–4835.
[12] L. Zhao, K.L. Kelly, G.C. Schatz, Phys. Chem. B 107 (2003) 7343–7350.
[13] A.A. Lazarides, K.L. Kelly, T.R. Jensen, G.C. Schatz, J. Mol. Str. Theochem 529 (2000) 59–63.
[14] Meenakshi, R.C. Maheshwari, J. Hazar. Mat. 137 (2006) 456–463.
[15] V. Tomar, S. Prasad, D. Kumar, Microchem. J. 111 (2013) 116–124 (and references cited therein).
[16] V. Tomar, S. Prasad, D. Kumar, Microchem. J. 112 (2014) 97–103 (and references cited therein).
[17] S. Thatai, P. Khurana, S. Prasad, D. Kumar, Microchim. J. 113 (2014) 77–82 (and references cited therein).
[18] P. Singh, M.K. Barajatiya, S. Dhing, R. Bhatnagar, S. Kothari, V. Dhar, Urol. Res. 29 (2001) 238–244.
[19] G.E.J. Poinern, M.K. Ghosh, Y.-J. Ng, T.B. Issa, S. Anand, P. Singh, J. Hazar. Mat 185 (2011) 29–37.
[20] J.M. Kauffman, J. Am. Phys. Surg. 10 (2005) 38–44.
[21] S.O. Obare, R.E. Hollwell, C.J. Murphy, Langmuir 18 (2002) 10407–10410.
[22] S.Y. Lin, S.W. Liu, C.M. Lin, C.H. Chen, Anal. Chem. 74 (2002) 330–335.
[23] J. Liu, Y. Lu, Fluorescence 14 (2004) 343–354.
[24] N. Kumari, N. Dey, S. Bhattacharya, Analyst 139 (2014) 2370–2378.
[25] Y. Kubo, S. Uchida, Y. Kemmochib, T. Okubob, Tetrahedron Lett. 46 (2005) 4369–4372.
[26] A. Pandya, K.V. Joshi, N.R. Modi, S.K. Menon, Sensor Actuator B 168 (2012) 54–61.
[27] W.L. Daniel, M.S. Han, J.S. Lee, C.A. Mirkin, J. Am. Chem. Soc. 131 (2009) 6362–6363.
[28] L. Xiong, J. Feng, R. Hu, S. Wang, S. Li, Y. Li, G. Yang, Anal. Chem. 85 (2013) 4113–4119.
[29] Z.H. Lin, S.J. Ou, C.Y. Duan, B.G. Zhang, Z.P. Bai, Chem. Commun. 6 (2006) 624–626.
[30] J.A. Gu, Y.J. Lin, Y.M. Chia, H.Y. Lin, Microchim. Acta 180 (2013) 801–806.
[31] F. Du, Y. Bao, B. Liu, J. Tian, Q. Li, R. Bai, Chem. Commun. 49 (2013) 4631–4633.
[32] D.A. Jose, D.K. Kumar, B. Ganguly, A. Das, Org. Lett. 6 (2004) 3445–3448.
[33] A. Satheshkumar, E.H. El-Mossalamy, R. Manivannan, C. Parthiban, L.M. Al-Harbi, S. Kosa, K.P. Elango, Spectrochim. Acta A 128 (2014) 798–805.
[34] A.B. Sarıgüney, A.Ö. Saf, A. Coşkun, Spectrochim. Acta A 128 (2014) 575–582.
[35] S. Watanabe, H. Seguchi, K. Yoshida, K. Kifune, T. Tadaki, H. Shiozaki, Tetrahedron Lett. 46 (2005) 8827–8829.
[36] J.M. Liu, L.P. Lin, X.X. Wang, L. Jiao, M.L. Cui, S.L. Jiang, W.L. Cai, L.H. Zhang Z.Y. Zheng, Analyst 138 (2013) 278–283.
[37] S.Y. Kim, J. Park, M. Koh, S.B. Park, J.I. Hong, Chem. Commun. (2009) 4735–4737.
[38] S.S.R. Dasary, P.C. Ray, A.K. Singh, T. Arbneshi, H. Yu, D. Senapati, Analyst 138 (2013) 1195-1203.
[39] H. Li, L. Rothberg, Proc. Natl. Acad. Sci. USA 101 (2004) 14036–14039.
[40] V. Kattumuri, M. Chandrasekhar, S. Guha, K. Raghuraman, K.V. Katti, K. Ghosh, R.J. Patel, App. Phys. Lett. 88 (2006) 153114.
[41] S. Rho, S.J. Kim, S.C. Lee, J.H. Chang, H.G. Kang, J. Choi, Curr. App. Phys. 9 (2008) 534–537.
[42] D.J. Maxwell, J.R. Taylor, S. Nie, J. Am. Chem. Soc. 124 (2002) 9606–9612.
[43] Z.S. Wu, S.B. Zhang, M.M. Guo, C.R. Chen, G.L. Shen, R.Q. Yu, Anal. Chim. Acta 584 (2007) 122–128.
[44] A.L. Simonian, T.A. Good, S.S. Wang, J.R. Wild, Anal. Chim. Acta 534 (2005) 69–77.
[45] N. Nerambourg, R. Praho, M.H.V. Werts, D. Thmas, M.B. Desce, Int. J. Nanotech. 5 (2008) 722–740.
[46] X. Zhou, B. Yu, Y. Guo, X. Tang, H. Zhang, W. Liu, Inorg. Chem. 49 (2010) 4002–4007.
[47] S. Mizukami, S. Okada, S. Kimura, K. Kikuchi, Inorg. Chem. 48 (2009) 7630–7638.
[48] H.G. Lee, K.B. Kim, G.J. Park, Y.J. Na, H.Y. Jo, S.A. Lee, C. Kim, Inorg. Chem. Commun. 39 (2014) 61–65.
[49] L.N. Neupane, J.Y. Park, J.H. Park, K.H. Lee, Org. Lett. 15 (2013) 254–257.
[50] M. Seydack, Biosens. Bioelectron. 20 (2005) 2454–2469.
[51] Q. Qian, J. Deng, D. Wang, L. Yang, P. Yu, L. Mao, Anal. Chem. 84 (2012) 9579–9584.
[52] V.M. Chauhan, R.H. Hopper, S.Z. Ali, E.M. King, F. Udrea, C.H. Oxley, J.W. Aylott, Sensor Actuator B 192 (2014) 126–133.
[53] D.A. Pearce, N. Jotterand, I.S. Carrico, B. Imperiali, J. Am. Chem. Soc. 123 (2001) 5160–5161.
[54] T. Hirano, K. Kikuchi, Y. Urano, T. Nagano, J. Am. Chem. Soc. 124 (2002) 6555–6562.
[55] K. Komatsu, K. Kikuchi, H. Kojima, Y. Urano, T. Nagano, J. Am. Chem. Soc. 127 (2005) 10197–10204.
[56] S. Schutting, S.M. Borisov, I. Klimant, Anal. Chem. 85 (2013) 3271–3279.
[57] T. Ghosh, B.G. Maiya, J. Chem. Sci. 116 (2004) 17–20.
[58] C.B. Black, B. Andrioletti, A.C. Try, C. Ruiperez, J.L. Sessler, J. Am. Chem. Soc. 121 (1999) 10438–10439.
[59] T. Mizuno, W.H. Wei, L.R. Eller, J.L. Sessler, J. Am. Chem. Soc. 124 (2002) 1134–1135.
[60] D.H. Lee, K.H. Lee, J.I. Hong, Org. Lett. 3 (2001) 5–8.
[61] K.H. Lee, H.Y. Lee, D.H. Lee, J.I. Hong, Tetrahedron Lett. 42 (2001) 5447–5449.
[62] F.M. Hinterholzinger, B. Ruhle, S. Wuttke, K. Karaghiospff, T. Bein, Sci. Rep. 3 (2013) 2562.
[63] A. Sugunan, C. Thanachayanont, J. Dutta, J.G. Hiborn, Sci. Technol. Adv. Mater. 6 (2005) 335–340.
[64] J. Turkevich, P.C. Stevenson, J. Hillier, Discuss. Faraday Soc. 11 (1951) 55–75.
[65] N.T.K. Thanh, Z. Rosenzweig, Anal. Chem. 74 (2002) 1624–1628.
[66] M. Hasan, D. Bethell, M. Brust, J. Am. Chem. Soc. 124 (2002) 1132–1133.
[67] L. Andrews, S.R. Davis, J. Chem. Phys. 83 (1985) 4983.
[68] I.R. Moraes, M.C.P.M. daCunha, F.C. Nart, J. Braz. Chem. Soc. 7 (1996) 453–460.
[69] P. Pandey, S.P. Singh, S.K. Arya, V. Gupta, M. Dutta, S. Singh, B.D. Malhotra, Langmuir 23 (2007) 3333–3337.
[70] U.J. Kim, C.A. Furtado, X. Liu, G. Chen, P.C. Eklund, J. Am. Chem. Soc. 127 (2005) 15437–15445.
[71] S.W. Han, S.J. Lee, K. Kim, Langmuir 17 (2001) 6981–6987.
[72] H.Y. Jung, Y.K. Park, S. Park, S.K. Kim, Anal. Chim. Acta 602 (2007) 236–243.
[73] D. Maniu, V. Chis, M. Baia, F. Toderas, S. Astilean, J. Optoelectron. Adv. Mater. 9 (2007) 733–736.
[74] E. Carbonell, E. Delgado-Pinar, J. Pitarch-Jarque, J. Alarcón, E. García-España J. Phys. Chem. C 117 (2013) 14325–14331.
[75] G. Zhou, C. Zhao, C. Pan, F. Li, Anal. Methods 5 (2013) 2188–2192.
[76] A. Mocanu, I. Cernica, G. Tomoaia, L.D Bobos, O. Horovitz, M.T. Cotisel, Colloid Surf. A 338 (2009) 93–101.
[77] A.A. Abo-Alhasan, S.A. El-Daly, M.M. El-Hendawy, S.H. El-Khalfy, M.E. El-Zeiny, J. Nanomater. Mol. Nanotechnol. 3 (2014) 1–7.

Talanta 132 (2015) 285–293

Contents lists available at ScienceDirect

Talanta

journal homepage: www.elsevier.com/locate/talanta

Evaluation of analytical performance based on partial order methodology

Lars Carlsen [a,b,*], Rainer Bruggemann [c], Olga Kenessova [d], Erkin Erzhigitov [d]

[a] Awareness Center, Linkøpingvej 35, Trekroner, DK-4000 Roskilde, Denmark
[b] Kazakh British Technical University, Department of Chemical Engineering, Almaty, Kazakhstan
[c] Leibniz – Institute of Freshwater Ecology and Inland Fisheries, Department Ecohydrology, Müggelseedamm 310, D-12587 Berlin, Germany
[d] RSE Kazakh Institute of Metrology, Almaty, Kazakhstan

ARTICLE INFO

Article history:
Received 27 June 2014
Received in revised form
27 August 2014
Accepted 5 September 2014
Available online 19 September 2014

Keywords:
Analytical performance
Partial order
Posets
Hasse diagram
Multi-indicator systems

ABSTRACT

Classical measurements of performances are typically based on linear scales. However, in analytical chemistry a simple scale may be not sufficient to analyze the analytical performance appropriately. Here partial order methodology can be helpful. Within the context described here, partial order analysis can be seen as an ordinal analysis of data matrices, especially to simplify the relative comparisons of objects due to their data profile (the ordered set of values an object have). Hence, partial order methodology offers a unique possibility to evaluate analytical performance. In the present data as, e.g., provided by the laboratories through interlaboratory comparisons or proficiency testings is used as an illustrative example. However, the presented scheme is likewise applicable for comparison of analytical methods or simply as a tool for optimization of an analytical method. The methodology can be applied without presumptions or pretreatment of the analytical data provided in order to evaluate the analytical performance taking into account all indicators simultaneously and thus elucidating a "distance" from the true value. In the present illustrative example it is assumed that the laboratories analyze a given sample several times and subsequently report the mean value, the standard deviation and the skewness, which simultaneously are used for the evaluation of the analytical performance. The analyses lead to information concerning (1) a partial ordering of the laboratories, subsequently, (2) a "distance" to the Reference laboratory and (3) a classification due to the concept of "peculiar points".

© 2014 Elsevier B.V. All rights reserved.

1. Introduction – the need for several indicators

Evaluating analytical performance may be assessed, e.g., through interlaboratory comparisons and/or proficiency testings or comparisons of analytical methods or through the optimization process of an analytical method. In the following we will apply the analytical performance of a series of laboratories as an illustrative example how analytical performance advantageously can be evaluated beyond the restrictions imposed by a single-quantity-approach such as the evaluation by checking only the accuracy (see below). Participation in interlaboratory comparisons or proficiency testings and a satisfying result from these are typically a prerequisite for obtaining accreditation to perform a given analysis.

Result of the single laboratory maybe expressed of the *z*-score (see below) only, which measure of how "far away" the single analytical result is from the accepted value, i.e., the *z*-score [1,2]. The *z*-score of the reference laboratory by definition being 0 (Eq. (1)). Obviously, the *z*-score does not as such tell the full story and other measures should be considered simultaneously. These (in the present case three) measures will a priori form a grid in the three-dimensional space and laboratories can be represented as a point in the space spanned by the three coordinates. The projection to each of these three coordinates bears information of its own right and it seems to be careless to aggregate the three quantities in order to obtain an easy to handle scale for ranking purposes. Various approaches for aggregating the indicators have been reported [3,4]. However, such aggregation of the indicators may unequivocally lead to compensation effects where high values in one indicator may compensate low values in another [5].

Taking all three indicators into account simultaneously is a bit more complicated than the use of a single scalar as we are facing a multi-indicator system (MIS). Partial order theory applied in multi-indicator systems is also known as Hasse diagram technique (HDT) [6,7] and appears in this connection as a highly advantageous tool. The visual representation of a partial order can be performed by a so-called Hasse diagram. In the Hasse diagram comparable objects are connected by a sequence of lines [6] and the diagram is characterized by its structure that comprises levels, chains and antichains (see

* Corresponding author at: Awareness Center, Linkøpingvej 35, Trekroner, DK-4000 Roskilde, Denmark.
E-mail address: LC@AwarenessCenter.dk (L. Carlsen).

http://dx.doi.org/10.1016/j.talanta.2014.09.009
0039-9140/© 2014 Elsevier B.V. All rights reserved.

below). An often heard criticism of partial order ranking approaches is that the method is lacking of a unique or absolute ranking, i.e., the presence of incomparabilities. In a Hasse diagram incomparabilities are causing that the Hasse diagram (cf. Fig. 2) has not only a vertical (ranking) but also a horizontal geometrical configuration. Hence, applying partial ordering implies comparison among different objects. The consequent application of this concept leads to figures, which are known in algebra as (directed) graphs.

2. Theory and methods

2.1. Indicators

The z-score denotes the standard score [2] or accuracy [1,8] of the measurements, which enables a comparison between two scores from different normal distributions.

$$z = (m - \mu_a)/s_a \quad (1)$$

where m is the reported value from the laboratory and μ_a and s_a are the accepted value (mean) and standard deviation, respectively, as generated by the Reference laboratory, i.e., the laboratory assigned to perform the interlaboratory comparisons and proficiency testings [9]. In other words: a Reference laboratory is by definition considered as the "best". Also the standard deviation of the laboratory measurements is important to judge the laboratory performance, i.e., the precision of the measurements [1]. Finally a further possible factor to bring into play to elucidate the laboratory performance is the skewness of the distribution of the laboratory measurements [10]. This factor (indicator) tells about the shape of the distribution and thus to what extent the measurements are in analytical or statistical control [11]. The three parameters are all standard output from statistical treatment of the results from a series of replicate measurements (vide infra)

Obviously these factors – or indicators – for evaluating laboratory performance on an individual basis can be easily compared and thus each of them then may constitute the basis for ranking of the laboratories, i.e. the performance of the laboratory relative to each other as well as to the Reference laboratory. As such this may constitute an evaluation tool for selecting laboratories for specifics task. However, only part of the story is told and the information basis is obviously limited.

In the present study the absolute values of the z-score, |z|, and the skewness, |skew|, together with the standard deviation, s, are applied as indicators. The [0, 1] normalized indicators are called r_i (i=1, 2, 3) and any possible triple of values of a certain laboratory is consequently called r. Thus, each laboratory is characterized by a data profile, i.e., an ordered set of indicator values (|z|,s,|skew|).

Generally indicators r_i can be normalized to a [0, 1]-scale (called rn_i) by

$$rn_i(x) = (r_i(x) - r_i\ \mathrm{min})/(r_i\ \mathrm{max} - r_i\ \mathrm{min}) \quad (2)$$

where $r_i$max and $r_i$min being the maximum, minimum value with respect to the objects. Here the indicators r_i are assumed to be already normalized and we consider r as the triple (r_1, r_2, r_3)=(normalized z-score, normalized standard deviation, normalized skewness).

2.2. Partial order

2.2.1. Overview

In this paper the numerical aggregation for example by calculating a composite indicator CI is avoided.

$$\mathrm{CI} = \sum g_1 \cdot rn_i \quad g_i : weights, \quad i = 1, \ldots, 3 \quad (3)$$

The alternative is based on partial order methodology. The subject "Partial Order" is of increasing interest in the mathematical field as well as in many other applied fields. Here a pretty simple variant of partial order is applied to study MIS, according to a recent paper by Bruggemann and Carlsen [12]. This methodology can be applied, whenever a MIS and a data matrix are available and a ranking is of interest. For example partial order was applied in environmental sciences, in biology, in economy and social sciences. Good overviews can be found in Refs. [7,13]. Partial ordering can be considered as a non-parametric method as, in contrast to standard multidimensional analyses no assumptions about linearity or distribution of the indicators are made and are necessary.

2.2.2. The basical equation of Hasse diagram technique

In Partial Ordering the only mathematical relation among the objects is "$\leq$" [6,7,14]. The "$\leq$"-relation is the basis for a comparison of laboratories and constitutes a graph. A laboratory x is connected with laboratory y if and only if the relation $x \leq y$ holds. The crucial question is, under which conditions it can be claimed that $x \leq y$. Here, a system is described by a series of indicators r_j, the MIS. A laboratory, x, characterized by the a set of indicators $r_j(x)$, j=1, …, m can be compared to another laboratory y, characterized by the indicators $r_j(y)$, when

$$\mathrm{r}_i(x) \leq r_i(y) \quad for \quad all \quad i = 1, \ldots, m \quad (4)$$

Eq. (4) is a very hard and strict requirement for establishing a comparison. It demands that all indicators of laboratory x should be better (or at least equal) than those of laboratory y through comparison of the single indicators, respectively. To be still a little bit more technically: Let X be the group of laboratories studied, i.e., X={REF, lab1, lab2, …., lab20}, the laboratory lab$x$ will be ranked higher than laboratory lab$y$, i.e., lab$x$ > lab$y$ or still more condensed $x > y$, if at least one of the indicator values for lab$x$ is higher than the corresponding indicator value for lab$y$ and no indicator for lab$x$ is lower than the corresponding indicator value for lab$y$. However, if r_j(lab$x$) > r_j(lab$y$) for some indicator j and r_i(lab$x$) < r_i(lab$y$) for some other indicator i, lab$x$ and lab$y$ will be called incomparable (notation: lab$x$||lab$y$) expressing the mathematical contradiction due to conflicting indicator values. A set of mutual incomparable objects is called an antichain. When all indicator values for lab$x$ are equal to the corresponding indicator values for lab$y$, i.e., r_j(lab$x$)=r_j(lab$y$) for all j, the two objects will have identical rank and will be considered as equivalent, i.e., lab$x$∼lab$y$.

Eq. (4) is the basic for the Hasse diagram technique (HDT) [6,7,14], which is a special (statistically oriented part of partial order theory). Hasse diagrams are visual representation of the partial order. In the Hasse diagram comparable objects are connected by a sequence of lines [14–17]. For construction of the Hasse diagram, a uniform orientation of the indicators should be secured, i.e., high indicator values correspond to "bad" objects and low values to "good" objects. In Fig. 2 (Section 3) the Hasse diagram based on the data given in Table 1 is shown. Thus, in the present case the higher a laboratory is placed in the Hasse diagram the farther away from the performance of the Reference laboratory it is.

2.2.3. Structure of a Hasse diagram

A Hasse diagram is characterized with it structure that comprises levels, chains and antichains (cf. Fig. 2).

Level: The horizontal arrangement of objects within a Hasse diagram. The level structure gives a first approximation to a weak order (i.e. tied ranks are not excluded: thus, for example in the ordering of four objects $a < b = d < e$ there is a tie, i.e., the equivalence of b and d with respect to the rank.) of the objects from "good" (bottom) to "bad" (top). Unfortunately, this will often give rise to many tied ranks as all objects in a level automatically will be assigned identical ranks. Typically, it is desirable that the degree of tied ranks should be as low as possible, i.e., there is a need for a linear

Table 1
Summary statistics of the laboratories.

Laboratory	*z-Score*	*s*	*Skewness*	$r_1=\|z\|$	$r_2=s$	$r_3=\|skew\|$
lab1	−2.1	0.24	0.9	0.724	0.519	1.000
lab2	0.9	0.25	−0.46	0.310	0.556	0.511
lab3	1.4	0.28	0.28	0.483	0.667	0.311
lab4	−0.3	0.22	0.01	0.103	0.444	0.011
lab5	2.5	0.21	0.16	0.862	0.407	0.178
lab6	−0.1	0.31	0.15	0.034	0.778	0.167
lab7	1.2	0.37	−0.42	0.414	1.000	0.467
lab8	−0.7	0.1	0.64	0.241	0.000	0.711
lab9	−1.6	0.18	0.1	0.552	0.296	0.111
lab10	1.2	0.24	0.7	0.414	0.519	0.778
lab11	−0.3	0.31	0.21	0.103	0.778	0.233
lab12	−0.4	0.2	−0.17	0.138	0.370	0.189
lab13	0.4	0.3	−0.54	0.138	0.741	0.600
lab14	2.6	0.19	−0.04	0.897	0.333	0.044
lab15	1.4	0.19	0.34	0.483	0.333	0.378
lab16	1.9	0.18	−0.89	0.655	0.296	0.989
lab17	2.9	0.18	0.1	1.000	0.296	0.111
lab18	0.9	0.22	0.41	0.310	0.444	0.456
lab19	−0.1	0.37	0.07	0.034	1.000	0.078
lab20	1.8	0.36	−0.76	0.621	0.963	0.844
REF	0	0.1	0	0.000	0.000	0.000

ranking of the single objects. This is obtained looking at chains only. However, it is not immediately obtainable when incomparable objects are included.

Chain: Chains are a subset of X, i.e., $X' \subseteq X$, where all objects in X' fulfill Eq. (4). Chains are characterized by their height that equals the number of objects in X'. Chains are of interest as they can be regarded as a complete order, or ranking of the objects of X', which means that for objects within a given chain all indicators are monotonously varying, i.e. simultaneously decreasing from top (start vertex) to bottom (end vertex).

A maximal chain is a chain for which no other objects can be found as a member of the chain.

A maximum chain is a chain, where the height equals the number of levels.

Between a start vertex and an end vertex there may be several chains of different heights. We call such chains "parallel" chains.

2.2.4. Average ranks

Beyond weak orders, derived from the level structure, partial order methodology provides a weak order by calculating the average rank of the single objects [18]. In cases where only a relatively low number of objects are studied (typically < 25) an exact method for calculating average ranks is available, based on lattice theory [19–21]. Lattice theory avoids the computational difficult combinatorial problem of finding every linear order compatible with the partial order. For example the partial order of three objects a, b, c as $a < b$, $a < c$ would have two compatible linear orders, namely $a < b < c$ and $a < c < b$. However, when the number of objects is n then at maximum n! linear orders must be found, which makes special algorithms, such as those based on lattice theory necessary. A detailed explanation is outside the scope of the present study and appropriate references should be consulted [19–21]. For larger systems, approximations have been presented [18,22–24].

2.2.5. Peculiarity of a data profile

The Hasse diagram in Fig. 2 shows that the following equation is sufficiently often fulfilled:

$$r_i(x) > r_i(y) \Rightarrow r_j(x) > r_j(y). \quad (5)$$

Eq. (5) expresses qualitatively that most often an increase in one of the indicators is implying an increase in another indicator. In the picture of mainstream this means that the elements typically are located within a slim ellipsoid ranging from (0, 0, 0) to (1, 1, 1). Ideally the column wise [0, 1]-normalized tuples r would be expected as points in an ellipsoid-like manifold. Thus, in the present 3-dimensional case it can a priori be expected that the majority of points representing the single laboratories are located around a straight line starting in (0, 0, 0), corresponding to the Reference laboratory, REF, and ending in (1, 1, 1). However, since the Hasse diagram in Fig. 2 is neither completely flat (complete antichain) nor completely thin (complete chain, i.e., a total order) deviations from the line through (0, 0, 0) and (1, 1, 1) obviously are envisaged [25]. Hence, some of the laboratories may be better represented by a pattern, generally described by the set $h(m)$.

$$h(m) = \{0,1\}^m - \{(0,0,\ldots,0),\ (1,1,\ldots,1)\} \quad (6)$$

Here $m=3$. In other words, we want to disclose which labs are located closer to one of the other 6 corners of $h(3)$, for example to (1, 0, 0) or (0, 1, 0). We define such element as peculiar as a verbal expression for deviating from the "main stream" [25].

In more mathematical terms a "near-enough-factor", f, was introduced [25]. In the m-dimensional case the maximum squared Euclidian distance between (0, 0,…, 0) and (1, 1,…, 1) in $h(m)$ is $D_{max}=m$ meaning that the distance between two given points is found on a scale from 0 to m. Hence, we regard laboratories as peculiar, where the distance, d, to one of the corners in $h(m)$, $d < f \bullet D_{max}$. These peculiar labs are represented by an indicator pattern that appears unbalanced relative to laboratories exhibiting more balanced patterns, i.e., being located around the (0, 0, 0) to (1, 1, 1) line. Thus, if f is selected as 0.05 only laboratories with highly unbalanced indicator profiles will be found, i.e., very close to one of the 6 corners of interest.

The term "very close" refers to a relative distance to the maximal distance of 3 within the cube. Thus, $f=0.05$ can be interpreted as 5% of the maximal distance, i.e., $d \leq 0.15$ to one of the peculiar corners and will consequently be denoted as extreme or peculiar due to the significant unbalance in the indicator profile. In other words it can be said this corresponds to a 95% level, meaning that laboratories not being found as extreme on a 95% level are found located around the (0, 0, 0)–(1, 1, 1) straight line. The limit would analogously be 0.3 for an f value equal to 0.1, corresponding to a 90% level.

2.2.6. Sensitivity

The sensitivity determines the relative importance of the single parameters on the structure of partially ordered sets [26]. The leading idea is to find distances between partial ordered sets (posets), where one poset is the original one including all indicators and the others are such posets where one indicator is left out. The indicator, whose elimination from the data matrix leads to the maximal distance to the original one, i.e., leading the highest degree of changes in the Hasse diagram is most important for the structure of the partial order. This kind of sensitivity analysis may be called "indicator-related sensitivity", because the effect of one indicator is studied.

2.2.7. Scanning analysis

Due to the very nature of the partial order methodology, even small differences in the [0, 1]-normalized indicator values may lead to incomparabilities and thus the lack of fulfillment of Eq. (4), i.e., lab$x$ appears incomparable to lab$y$ (vide supra). However, in that analysis all incomparabilities were displayed without regard to the possible importance of the single incomparabilities. In total there are 145 pairs of laboratories lab$x$, lab$y$ with lab$x \parallel$ lab$y$. In contrast a $\leq$ relation could only be found for 65 pairs (lab$x$, lab$y$). Hence a somewhat more nuanced view is necessary. Only if

the differences in indicator values are larger than Δ, the incomparability between two laboratories is considered as relevant. This idea can be expressed in mathematical terms be expressed as Eq. (7).

$$|r_i(labx) - r_i(laby)| > \Delta \text{ and } |r_j(labx) - r_j(laby)| > \Delta, \quad (7)$$

and

$$sgn(r_i(labx) - r_i(laby)) \neq sgn(r_j(labx) - r_j(laby)) \text{ with } sgn(\ldots) \neq 0 \quad (8)$$

with sgn(x) = −1, 0, +1 according to $x < 0$, $= 0$, > 0, respectively.

Note, by the notation r_i(lab$x$) the value of laboratory x with respect to the ith indicator is meant.

In practice this is calculated applying the module scan_incomp4.py in the PyHasse software package, applying the values of the scanning parameter Δ (min, max, steps from min to max) as input [25]. The lower the Δ values the smaller differences between the indicators values will be regarded as real. Thus, only if the differences in indicator values are larger than Δ, the two indicators will be regarded as incomparable, with remarkable data differences and therefore are to be contextually be interpreted as exerting a real conflict.

2.2.8. Tripartite graphs

A systematic introduction to the concept of tripartite graph has previously been reported by Bruggemann and Voigt [27]. Here an intuitive approach is presented. Imagine that lab$x$ has worse values (i.e. higher values) in comparison to laby in the first and second indicator, but better value (i.e. lower value) in the third indicators. This fact can graphically represented as follows (Fig. 1).

Graphs, such as that shown in Fig. 1 are helpful to explain the role of the indicators. In the case, shown in Fig. 1 we see that the pairs of indicators ($r1$, $r3$) or ($r2$, $r3$) are causing the incomparability of lab$x$ with laby. This logical "or" relation with respect to the role of indicators can be applied in several ways. Either one can search for the minimum number of indicators leading to the observed incomparabilities, or – as is done here – to check for numerical discrepancies in indicator values as in Eq. (7) and focus on those pairs of indicators, which not only cause an incomparability, but also, where the numerical differences are greater than Δ (Eq. (7)).

2.2.9. Software

All partial order analyses were carried out using the PyHasse software [28]. PyHasse is programmed using the interpreter language Python (version 2.6) [29–33] Today, the software package contains more than 100 modules and is available upon request from the developer, Dr. R. Bruggemann (brg_home@web.de). A simplified version of PyHasse operating on a web-based browser is under development and will soon be available.

Statistical analyses in connection with the data generation were carried out applying the freely available software R [34].

2.3. Data

The present study is of methodological nature. To this purpose a hypothetical group of 20 laboratories are supposed, each of them "analyzing" an identical sample 5 times. The "results" of the analyses were randomly generated. Based on these 5

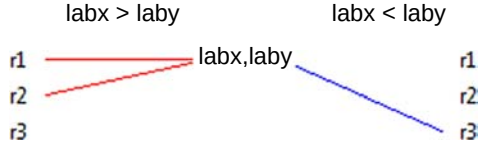


Fig. 1. Example of a tripartite graph.

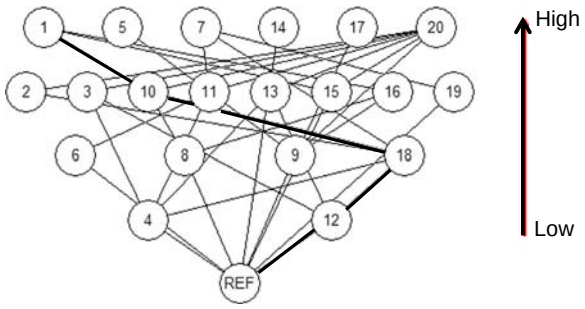


Fig. 2. Hasse diagram constructed based on the data shown in Table 1, the indicators being the absolute z-value,|z|, the standard deviation, s, and the absolute skewness,|skew|. The low to high designation refers the distance of the Reference laboratory (REF) to the single laboratories (here given by their respective numbers). Bold line: Visualization of one of the two possible chains connecting REF and lab1.

"measurements" 3 indicators, i.e., z-score, standard deviation and skewness were estimated by conventional statistics [34] and Eq. (1) and subsequently used for input in the partial order analyses (vide infra) to obtain additional insight in the performance of the laboratories. The z-score and the skewness for the Reference laboratory, REF, were per definition both set to 0 and the standard deviation to 0.1. In Table 1 the z-score, the standard deviation and the skewness derived from the individual laboratories are given.

A look at the data (Table 1) discloses that a given laboratory may report too low or too high z-scores as well as positively or negatively skewed data. However, In order to keep the presentation as simple as possible the absolute values of the z-score and the skewness are applied as indicators for an absolute "distance" from the Reference laboratory, without judging if positive or negative is good or bad, respectively.

3. Results and discussion

A simple linear ordering of the laboratory performance in proficiency testings may be obtained using the absolute value of the z-score as single indicator and thus obtaining a measure for the "distance" of the single laboratory from the Reference laboratory. Likewise also orderings based on the standard deviation and the skewness may be applied. However, it is immediately clear from the data (Table 1) that these orderings, which all offer important information, do not coincide and consequently, in order to obtain the complete picture it is necessary to consider all three indicators simultaneously. As an alternative to the classical aggregation methods applied for MIS we proposed to use partial ordering. The resulting ordering based on the three indicators applied in the present study, i.e., the absolute z-score, |z|, the standard deviation, s, and the absolute skewness, |skew|, can be visualized in a Hasse diagram (Fig. 2).

It is immediately seen that the Hasse diagram (Fig. 2) are characterized by

- Levels (in the present case 5), cf. Section 3.2, Table 3
- Chains (vertically comparable laboratories), cf. Section 3.1, Table 2 (one chain marked, cf. Fig. 2)

The presence of the relatively high number of incomparabilities (145) is often the cause for dismissing partial ordering approaches. However, in the following it will be demonstrated that important information may be retrieved from these incomparabilities.

3.1. Chains

Chains are structures within the Hasse diagram where all indicators weakly monotonously increase upward in the diagram.

Table 2
Number, height and composition of chains between REF and the laboratories in the. top level – level 5 – of the Hasse diagram, providing chains of maximal length.

Chain	Number of chains	Height	Chain composition	Characterization
REF→lab1	2	5	REF, lab4, lab18, lab10, lab1 REF, lab12, lab18, lab10, lab1	Maximum chains
REF→lab5	1	3	REF, lab9, lab5	Maximal chain
REF→lab7	4	4	REF, lab4, lab11, lab7, REF, lab4, lab18, lab7, REF, lab6, lab11, lab7, REF, lab12, lab18, lab7	Maximal chains
REF→lab14	1	2	REF, lab14	Maximal chain
REF→lab17	1	3	REF, lab9, lab17	Maximal chain
REF→lab20	4	5	REF, lab4, lab18, lab2, lab20, REF, lab4, lab18, lab10, lab20, REF, lab12, lab18, lab2, lab20, REF, lab12, lab18, lab10, lab20	Maximum chain

The presence of chains is interesting as the single chains are realizations of a unique ordering for a subset of objects. Thus, the laboratories within a chain can be seen as an absolute linear ordering of these laboratories with respect to all three indicators simultaneously. However, due to the very nature of the partial ordering several chains may lead from one laboratory, e.g., the Reference laboratory (REF) to a laboratory placed higher in the diagram. In Fig. 2 one of the possible chains of maximal height, 5, (a maximum chain) connecting the Reference laboratory to Laboratory 1 (lab1) is shown.

It is worthwhile to note that in the present case with only one minimal element, REF, we find that REF is comparable to all 20 laboratories included in the study. Thus, it is possible to find absolute ordering for all laboratories relative to REF, but obviously not between all laboratories. To illustrate this Table 2 gives the number of maximal/maximum chains for all the connections between REF and the 6 laboratories in the top level of the Hasse diagram as well as the chain composition that states the absolute ordering between the included laboratories. It should be noted that several other maximal chains of varying heights between selected elements exist. It is further noted that due to the level structure (cf. Fig. 2) the maximum heights of a chain will be 5.

It can immediately be seen that not all laboratories are represented in the chain structures given in Table 2. Thus, the laboratories 3, 8, 13, 15, 16 and 19 are not found. These are still comparable to REF and as such an absolute ordering to REF can be established. However, they are members of parallel chains between REF and a top-level element, where another chain of a greater height exists. As an example REF and lab1 are also connected through the chain REF, lab8, lab10, lab1 of only height 4. However, as Table 2 shows, there are parallel chains of larger height.

Taken Table 2 and the chain REF < lab4 < lab18 < lab10 < lab1 as an example, there is a simultaneous increase of all three indicator values. In that sense a graph–theoretical distance can be introduced. The laboratory lab1 has the maximum possible distance from REF. In contrast the laboratories lab4, lab12, lab9, lab6 and lab14 have a minimum distance to the reference laboratory REF. The laboratories lab1 and lab20 have the same graph-theoretical distance to REF (cf. Table 2 and Fig. 2; chain: REF, lab4, lab18, lab10, lab20), nevertheless the pattern of their data values is different. Beside the fact that the graph-theoretical distance as an ordinal concept gives no information about the proximity of two laboratories another deficiency is to be noted: Any additional laboratory, measured by the triple of indicators may be located in one of these chains. Nevertheless it is not known, how to classify it. This task will be discussed in Section 3.3.

3.2. Average ranks

In cases like the here studied a typical request is a linear ordering of the studied objects (here laboratories). Partial order methodology offers attractive alternatives. The level structure as derived from the Hasse diagram (Fig. 2) a priori offers a ranking, although rather rough and with many ties, of the single laboratories. (cf. Table 3).

Table 3
Level structure (cf. Fig. 2).

Level	Level composition
5	lab1 lab5 lab7 lab14 lab17 lab20
4	lab2 lab3 lab10 lab11 lab13 lab15 lab16 lab19
3	lab6 lab8 lab9 lab18
2	lab4 lab12
1	REF

In addition to the rough ranking based on the level structure we have different models to get linear orders of the laboratories, such as single-indicator based ranking, a ranking based on an aggregated indicator value applying weighted sums (Eq. (3)) or an average ranking based on the exact lattice theoretical method (cf. Section 2.2.4), which for a subsequent comparison is assumed as the ideal ranking.

The more detailed approach is to derive average ranks of the single laboratories [22–24]. The average rank of a lab*x* is called Rkav(x). The resulting ranking is in general a weak linear order as several laboratories may have identical Rkav-values. In Table 4 the average ranks are calculated based on the exact method [19–21]. The necessary calculations can be performed by the PyHasse software. The ranking due to Rkav-values can be compared to the ranking obtained based on the |z| score. The significant differences are obvious. In some cases, e.g., lab11 major disagreements are seen. Hence, this strongly supports the hypothesis that a ordering solely based on the |z| score does not reveal the complete picture.

In order to quantify the comparison of the different ranking methods the Sum of Ranking Differences (SRD) may be applied [35–37]. Supposing the average rank (Table 4) as the ideal ranking, it turns out that neither the single-indicators ranks (as e.g. based on |z|, cf. Table 4) nor those of based on *s* or |skew| are getting close (SRD of Rkav, |z|, of Rkav, *s* and Rkav,|skew is estimated to 100, 111 and 82, respectively). The comparison of Rkav-values to a ranking, based on an aggregated indicator value, applying equal weights (Eq. (3)) leads to a SRD of 32. It should be noted [35–37] that the lower the SRD value the better the ranking. To judge the SRD values they should be compared to the maximum SRD value, SRDmax. In the present case with 21 elements (laboratories) SRDmax is calculated to 220 [36]. With this in mind the ranking based on the aggregated values (equal weight) appears reasonable satisfying, whereas the single-indicator based rankings appear rather unsatisfactory.

Table 4
Average rank of the 21 laboratories for comparison the ranking based on the absolute *z*-score, |z|, is given.

Laboratory	Rkav	|z|rank
lab20	19.8	16
lab1	19.0	18
lab7	18.1	11
lab2	14.3	10
lab10	14.0	12
lab5	13.6	19
lab17	13.6	21
lab16	13.4	17
lab3	12.6	14
lab13	12.6	7
lab11	12.5	4
lab15	9.7	13
lab19	9.5	3
lab18	8.8	9
lab6	6.7	2
lab8	6.4	8
lab9	5.3	15
lab12	4.4	6
lab4	4.2	5
lab14	11.5	20
REF	1.0	1

3.3. Classification

The basic idea is to measure labs by a multidimensional system of rules.

So far the Hasse diagram, shown in Fig. 2 reveals only the set of all comparisons among the 21 laboratories. As the data are randomly generated an additional real laboratory will be just an extra vertex in the Hasse diagram. However, in order to classify this additional laboratory rules are needed, i.e. a membership to classes must be established. The most simple rule is to accept the system of randomly generated data where the single indicators have values in the closed interval [0, 1] and to consider a strong proximity (as expressed by *f*, see below) of a real lab to points of $h(3)$ as classifier. Hence, the extreme points, such as (0, 0, 0) (as the best one (Reference lab)) or (1, 0, 0) as a point where the *z*-score is the worst possible, but skewness and standard-deviations are as good as the values of the Reference lab, are of interest. As outlined in the former section there are 2^m extreme points. In our case with three indicators ($m=3$) a classification will be performed by 2^3, i.e. by 8 extreme points (corresponding to the corners of a cube, Fig. 3).

The mainstream of data may be considered as a cloud of points (i.e. cloud of points representing the objects, the labs) in a 3D-space which is oriented in the way that there are labs near the line from (0, 0, 0) to (1, 1, 1) (cf. Fig. 3). As an increase of one indicator value does not necessarily imply an increase of the value of another indicator, the cloud of points will encompass points which are considered as mutually incomparable. A realization of tuples having simulated data such as (1, 0, 0) or (0, 1, 0) does not necessarily appear. Therefore the reasoning is the other way round: Are there realized tuples which can be considered as near to extreme patterns which are not representative for the main stream start and end, i.e., (0, 0, 0) or (1, 1, 1). Here for demonstration purposes we arbitrarily selected $f=0.05$ (Section 2.2.5). The results are shown in the Table 5. It is seen that applying $f=0.05$ six laboratories, i.e., 28.57% of the 21 laboratories included in the study appear to extreme, or peculiar.

It can be deduced that the pattern [0, 1, 0] is approximately (due to $f=0.05$) realized 3 times, the pattern [0, 0, 1] only once, and the pattern [1, 0, 0] appears two times. No simultaneous appearance of two 1's in the extremal pattern is observed. The simultaneous appearance of 0 and 1 indicates that some labs are unbalanced: Good values in two, but a bad value in another aspect. These data fits nicely with the 3D plot depicted in Fig. 4.

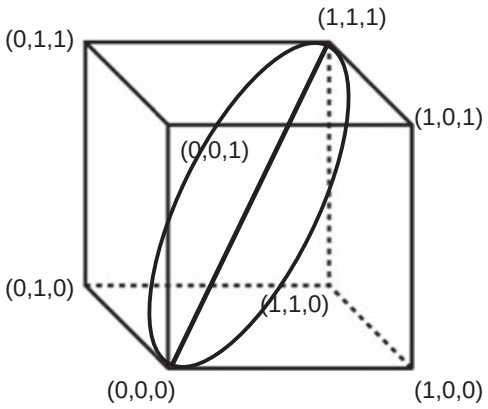


Fig. 3. The extreme points of $h(3)$ (Eq. (6)) themselves provide the structure of a partial order, applying Eq. (4).

Table 5
Extreme, or peculiar laboratories on a 95% level.

Laboratory	Pattern	Interpretation
lab6	[0, 1, 0]	This lab is close in |z| and skew but far away in *s*
lab8	[0, 0, 1]	This lab is close in |z| and *s* but far away in |skew|
lab11	[0, 1, 0]	This lab is close in |z| and skew but far away in *s*
lab14	[1, 0, 0]	This lab is close in *s* and skew but far away in |z|
lab17	[1, 0, 0]	This lab is close in *s* and skew but far away in |z|
lab19	[0, 1, 0]	This lab is close in |z| and |skew| but far away in *s*

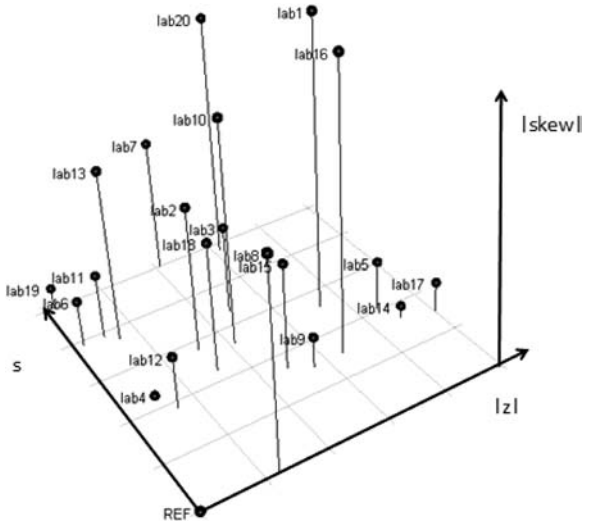


Fig. 4. 3D plot of the 21 laboratories based on the 3 indicators |z|, *s* and |skew|.

An additional laboratory can now be measured by a multirule-system, corresponding to the MIS, introduced: After selection of an f-value it will be associated to one of the 8 points and gets its classification according to Table 5.

3.4. Sensitivity

Three different indicators have been included and a priori they all provide information on the performance of the single laboratory. However, they may not be equally important in their impact

on the structure of the Hasse diagram. In order to elucidate the relative importance of the three indicators a sensitivity study of the partial ordering was conducted [26].

In Fig. 5 the relative importance of the |z|, *s* and |skew| indicators are visualized as calculated applying the PyHasse software.

The relative importance of the three indicators was calculated to be |z|=0.397, *s*=0.444 and |skew|=0.159, respectively, clearly substantiating the primary importance of |z| and *s* when discussing laboratory performance whereas the skewness apparently plays a somewhat secondary, but not negligible role.

3.5. "Real" incomparable elements

Obviously partial ordering may be considered hampered by the fact that even minute differences in indicator values may lead to incomparabilities. However, it may be appropriate to look only at numerically relevant discrepancies (cf. Section 2.2.7).

To illustrate the effect of varying Δ-values, Table 6 summarizes the results for two values of Δ (out of a systematic variation of Δ from 0.1 to 1), i.e., a low value (Δ=0.35) and a larger value (Δ=0.6), respectively. In Table 6 it is displayed which indicator pair exceeds this limit (cf. Eqs. (7) and (8)) and how often this exceeding is realized in terms of incomparable laboratories.

Table 6 can be read as follows using the second row (0.35, |z|, |skew|, 16) as an example: Here for 16 cases within the poset, the Hasse diagram is showing, the indicators |z| and |skew| lead to incomparabilities, whose numerical values are $>=$0.35. Here the focus is on the role of the indicators. In order to obtain further insights into the incomparabilities, it is of obvious interest to disclose which laboratories are representing for example incomparabilities due to large discrepancies of their indicator values. Such information has been compiled in Table 7 using the case with Δ=0.6 as an illustrative example. Table 7 should be read as follows using the second row (lab8,lab17, |z|,|skew| −0.759, 0.607) as an example: Immediately it can be realized that the differences in the indicator values, according to Eq. (7) are larger than Δ=0.6.

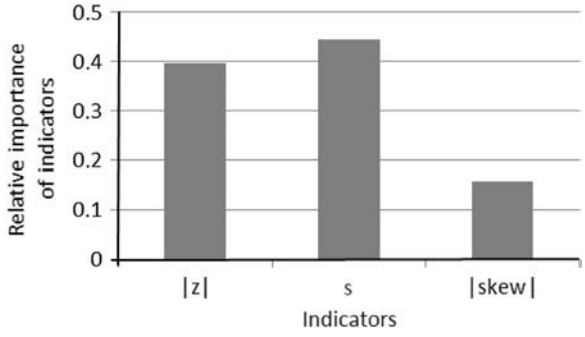


Fig. 5. Relative importance (sensitivity) of the |z|, *s* and |skew| indicators.

Table 6
Incomparabilities as function of the Δ-value.

Δ	Indicator pair	Realizations by the labs
0.35	|z|, *s*	29
0.35	|z|, |skew|	16
0.35	*s*, |skew|	18
Sum of realizations		63
0.6	|z|, *s*	3
0.6	|z|, |skew|	2
0.6	*s*, |skew|	2
Sum of realizations		7

Table 7
Incomparabilities between pairs of laboratories for Δ=0.6 and the involved indicator values.

Pairs of laboratories	Indicators causing the incomparability	Difference in indicator values
lab8, lab14	|z|, |skew|	−0.656, 0.667
lab8, lab17	|z|, |skew|	−0.759, 0.600
lab8, lab19	*s*, |skew|	−1.000, 0.633
lab14, lab19	|z|, *s*	0.863, −0.667
lab16, lab19	|z|, *s*	0.621, −0.704
lab16, lab19	*s*, |skew|	−0.704, 0.911
lab17, lab19	|z|, *s*	0.966, −0.704

Table 8
Incomparabilities between pairs of laboratories for Δ=0.7 and the involved indicator values.

Pairs of laboratories	Indicators causing the incomparability	Difference in indicator values
Lab16, lab19	*s*, |skew|	−0.704, 0.911
Lab17, lab19	|z|, *s*	0.966, −0.704

Especially this is true for |z| and |skew| for the labs lab8, lab17 (second row) and lab8, lab14 (first row).

A systematic variation of Δ from 0.1 to 1 showed that Δ=0.7 is the largest value for the discrepancies appearing in the 21 laboratories. The correspondingly striking lab- and indicator-pairs are given in Table 8

3.6. Tripartite graphs

In order to elucidate the incomparabilities between single laboratories two groups are selected from the top level (Fig. 2), where the most striking laboratories are located in the ranking due to the partial order theory. For each of these two groups three laboratories are for illustrative purposes arbitrarily selected, i.e., group 1: lab1, lab5 and lab7, and group 2: lab14, lab17, lab20. It should be emphasized that any other two groups, in which the laboratories apparently are not connected, could be selected for such a study. From the Hasse diagram (Fig. 2) it is clear that the objects of the first group are not connected with those of the second group. Technically the two groups are "separated subsets" [7] and their separation can be explained by the concept of a tripartite graph, Fig. 6A.

In Fig. 6A three labs on the one side (1, 5, 7) and three labs on the other side (7, 14, 20) are displayed. Hence, 3×3 pairs are possible and these 9 pairs are shown in the middle of the figure. The incomparability can be caused by different indicator pairs. For example (lab1, lab17) is incomparable due to conflicts in data with respect to |z|, *s* or |z|, |skew|. To understand the role of indicators it is of interest to trace back the role of |s| and |skew|. A closer look at Fig. 6A reveals that |skew| (on the left side) is connected with seven pairs of lab, meaning that lab1, lab7, lab5 in seven cases have larger values in |skew|, whereas |z| or |sd| are causing larger values for lab17, lab20 or lab14. Furthermore, one can see that almost everywhere where |skew| is responsible for a larger value of the objects of the first subset also *s* is responsible. An exception is (lab7, lab20) where only *s* is responsible. Hence, it is a fair approximation to visualize the peculiarity of the two subsets by a scatterplot (Fig. 7).

However, Figs. 6A and 7 do not take into account that a relation lab$x$ > lab$y$ with respect to some indicators and lab$x$ < lab$y$ with respect to some others may numerically be irrelevant. Hence, the

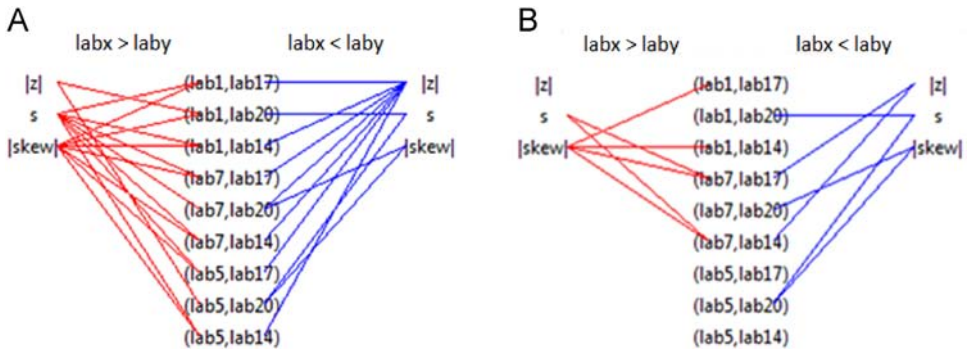


Fig. 6. (A) Tripartite graph of two groups of objects, taken from the top level of the Hasse diagram, Fig. 2. (B) Tripartite graph, where all indicator – (lab*x*, lab*y*) – connections with absolute numerical differences below 0.3 are filtered out (cf. text).

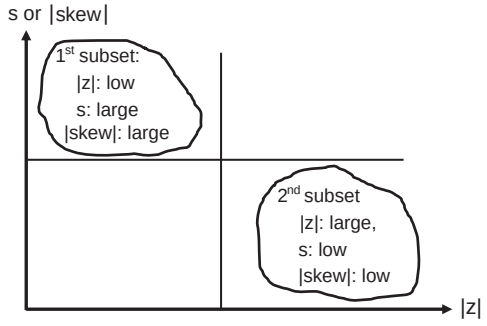


Fig. 7. Approximate graphical model, explaining why the two subsets are not connected. Here the two subsets are {lab1, lab5, lab7} and {lab14, lab17, lab20}.

analysis with tripartite graphs can be performed by filtering out too low values, when the single indicators have a metric.

In Fig. 6B only those indicator pairs are taken into regard whose absolute numerical differences are larger than 0.3. The value 0.3 is here arbitrarily selected to illustrate the concept. When a statistical analysis is performed, usually an idea about numerical noise would be disclosed. Subsequently, the limiting values should be selected accordingly.

This filtering out procedure results in a far clearer diagram, which is easier to be interpreted. It is immediately disclosed that now some incomparabilities can be resolved into comparabilities. See for example the pair (lab7, lab20). This pair is only connected with |skew| (on the right side of the tripartite graph). It can be deduced that the incomparability lab7||lab20 is caused by values less 0.3 in *s* and/or in |z|.

Similarly the pair lab5, lab17 is not connected at all with any of the indicators. Thus, the originally seen incomparability between those two laboratories was apparently caused by only slight and eventually irrelevant data differences. To sum up, it appears clear that only two pairs of laboratories (one taken from the first, the other from the second subset) remains with a "relevant" incomparability (lab7,lab17) and (lab7,lab14). Subsequently these three laboratories, lab7, lab14 and lab17, maybe placed in the scatter plot depicted in Fig. 7. Thus, lab7 would be located in the upper left part, whereas lab17 and lab20 would be located in the lower right part.

Note, that the replacement of $x\|y$ by $x > y$ or $x < y$ obviously may lead to a cascade of changes in a Hasse diagram, due to the axioms of partial order theory. Therefore, the obvious step to construct an enriched Hasse diagram is here not performed.

4. Conclusions and outlook

The present paper demonstrates that partial order methodology offers some tools to evaluate laboratory performance in interlaboratory comparisons or proficiency testings without making any presumptions or pretreatment (apart from a normalization which automatically is done by the appropriate PyHasse modules) of the analytical data provided by the laboratories. The methodology makes it possible to take into account a series of indicators reflecting the performance of the single laboratory. Hence, the method constitutes an alternative to the typical evaluation that is based on single-indicator orderings ore aggregation methods such as described by the simple Eq. (3). The average ranking method has been compared to single-indicator rankings as well as to a ranking based on an aggregated indicator value applying the SRD method.

In the present study the *z*-score, the standard deviation and the skewness have been chosen as indicators. However, the methods described are in no way limited to these indicators. Other additional indicators could be kurtosis or, when talking method development chromatographic conditions like temperature and flow rate. Note, however that the number of indicators should be carefully studied, as too many indicators tend to enhance the number of incomparabilities without inferring essential information.

Several rules to measure objects within the context of relevance applied, allow the identification of laboratories and their relative position. In order to perform a classification, the concept of peculiar points of a set $\{0, 1\}^m$ is of interest. A mainstream of points in the m-dimensional space may form a cloud from (0,…,0) to (1,…,1) points. Thus, the laboratories are of interest, which significantly deviate from this mainstream. Within the simulation study 6 laboratories out of totality of 21 ones turned out to be peculiar, i.e., not belonging to the mainstream. In no case an extreme deviation occurs, where two indicators are large and only one strikingly low.

The relative importance of the single indicators for the overall ordering is derived clearly demonstrating the *z*-score and the standard deviation are of major importance whereas the skewness apparently is only of secondary importance in relation to the overall evaluation of the laboratory performance.

A priori incomparability expresses a conflict in data. However, this does not take into account that such data conflicts may be caused by even very low numerical difference in indicator values and may thus lead to a confusing and even misleading picture. To deal with this the concept, a so-called scanning analysis was introduced in order to filter out such possibly insignificant differences in indicator values. In the illustrative example presented in this paper it was shown that accepting only numerical differences indicator values larger than 0.35 ($\Delta \geq 0.35$) reduced the number of incomparabilities from the original 145 to only 63 (cf. Table 6). Subsequently the focus was directed towards which laboratories are in mutual conflict with respect to which indicator pairs. This was analyzed applying the concept of the tripartite

graphs. Again, a clearer and less confusing picture developed, when only incomparabilities whose numerical discrepancies were considered as significant were included.

Although incomparabilities are often the reason, why modern decision support tools do not consider partial order, we have shown that the discussion of partial order with its inherent incomparabilities allow a refined view on data. Hence, a four step-procedure for data evaluation is suggested:

(1) Construct the partial order and visualize it by a Hasse diagram. The Hasse diagram informs the evaluator about relative ordering of the single objects, here laboratories.
(2) Perform a classification, by allocating laboratories to the points of the partially ordered space of $\{0,1\}^m$. This leads not only to a relative ordering, but also a measurement of distances to the reference object, here the Reference laboratory.
(3) Check, how far a weak order, provided by techniques of partial order theory is in coincidence with the ordering due to single indicators. Here a sensitivity analysis can be helpful, to select the most important (with respect to the ordering) indicator as a ranking index.
(4) Consider those laboratories that are mutually incomparable and whose conflicts in data are thought of as relevant. Apply techniques, such as scanning analyses and tripartite graphs to disclose the reasons for the incomparability. This information may then constitute the basis for advising the laboratories how to improve the performance.

Hence, the present paper has demonstrated that the presence of incomparabilities (being an inherent feature in partial order ranking) may disclose important characteristics.

Ongoing work focuses on a further elucidation of incomparabilities as an information source possibly through an active interplay between partial order methodology and multivariate statistics. Thus, discussion of data discrepancy has shown that it should be possible to combine multivariate statistical techniques with partial order theory [26]. The research in that field is pretty active and it should be noted that the combination of Kohonen networks [38,39] and cluster analysis [40,41], will provide important advices in this field.

Finally it should be emphasized that the methodologies applied in this paper, are generally applicable in cases dealing with the analyses of multi-indicator systems, which in the present context comprise comparisons of analytical methods as well as optimization of an analytical procedure.

Appendix A. Supporting information

Supplementary data associated with this article can be found in the online version at http://dx.doi.org/10.1016/j.talanta.2014.09.009.

References

[1] JCGM 200, International Vocabulary of Metrology – Basic and General Concepts and Associated Terms (VIM), ⟨http://www.bipm.org/utils/common/documents/jcgm/JCGM_200_2008.pdf⟩, 2008 (accessed August 2014).
[2] Standard Score, ⟨https://statistics.laerd.com/statistical-guides/standard-score.php⟩ (accessed August 2014).
[3] J. Figueira, S. Greco, M. Ehrgott, Multiple Criteria Decision Analysis, State of the Art Surveys, Springer, Boston, 2005.
[4] S. Hajkowicz, A. Higgins, Eur. J. Oper. Res. 184 (2008) 255–265.
[5] G. Munda, Social Multi-criteria Evaluation for a Sustainable Economy Operation, Springer, Heidelberg, New York (2008) 227.
[6] Partial Order in Environmental Sciences and Chemistry, in: R. Bruggemann, L. Carlsen (Eds.), Springer, Berlin, 2006.
[7] R. Bruggemann, G.P. Patil, Ranking and Prioritization for Multi-indicator Systems – Introduction to Partial Order Applications, Springer, New York, 2011.
[8] Aim of Statistics in Analytical Chemistry, ⟨http://www.chem.utoronto.ca/coursenotes/analsci/stats/AimStats.html⟩ (accessed August 2014).
[9] Reference Laboratories, ⟨http://www.oie.int/our-scientific-expertise/reference-laboratories/introduction/⟩ (accessed August 2014).
[10] C. Taylor, What is Skewness, ⟨http://statistics.about.com/od/Descriptive-Statistics/a/What-Is-Skewness.htm⟩, 2013 (accessed April 2014).
[11] ASTM, Standard Practice for Verification and Use of Control Charts in Spectrochemical Analysis, ASTM E1329-10, ASTM International, 2013.
[12] R. Bruggemann, L. Carlsen, Sci. Total Environ. 425 (2012) 293–295.
[13] Multi-Indicator Systems and Modelling in Partial Order, in: R. Bruggemann, L. Carlsen, J. Wittmann (Eds.), Springer, New York, 2014.
[14] R. Bruggemann, L. Carlsen, in: R. Bruggemann, L. Carlsen (Eds.), Partial Order in Environmental Sciences and Chemistry, Springer, Berlin, 2006, pp. 61–110.
[15] R. Brüggemann, B. Münzer, Chemosphere 27 (1993) 1729–1736.
[16] R. Brüggemann, K. Voigt, Chemosphere 31 (1995) 3585–3594.
[17] R. Bruggemann, K. Voigt, Comb. Chem. High Throughput Screen. 11 (2008) 756–769.
[18] R. Bruggemann, P. Annoni, MATCH – Commun. Math. Comput. Chem. 71 (2014) 117–142.
[19] J. Morton, L. Pachter, A. Shiu, B. Sturmfels, O. Wienand, SIAM J. Discrete Math. 23 (2009) 1117–1134.
[20] O. Wienand, Lcell, ⟨http://bio.math.berkeley.edu/ranktests/lcell/⟩, 2006 (accessed August 2014).
[21] K. De Loof, H. De Meyer, B. De Baets, Fundam. Inf. 71 (2006) 309–321.
[22] D. Lerche, P.B. Sørensen, R. Brüggemann, J. Chem. Inf. Comput. Sci. 43 (2003) 1471–1480.
[23] R. Brüggemann, P.B. Sørensen, D. Lerche, L. Carlsen, J. Chem. Inf. Comput. Sci. 44 (2004) 618–625.
[24] R. Bruggemann, L. Carlsen, MATCH – Commun. Math. Comput. Chem. 65 (2011) 383–414.
[25] R. Bruggemann, L. Carlsen, MATCH – Commun. Math. Comput. Chem. 71 (2014) 694–716.
[26] R. Bruggemann, E. Halfon, G. Welzl, K. Voigt, C.E.W. Steinberg, J. Chem. Inf. Comput. Sci. 41 (2001) 918–925.
[27] R. Bruggemann, K. Voigt, MATCH – Commun. Math. Comput. Chem. 66 (2011) 231–251.
[28] R. Bruggemann, L. Carlsen, K. Voigt, R. Wieland, in: R. Bruggemann, L. Carlsen, J. Wittmann (Eds.), Multi-Indicator Systems and Modelling in Partial Order, Springer, New York, 2014, pp. 389–423.
[29] J. Ernesti, P. Kaiser, Python – Das umfassende Handbuch, Galileo Press, Bonn, 2008.
[30] M.L. Hetland, Beginning Python – From Novice to Professional, Apress, Berkeley, 2005.
[31] H.P. Langtangen, Python Scripting for Computational Science, Springer-Verlag, Berlin, 2008.
[32] M. Weigend, Objektorientierte Programmierung mit Python, mitp-Verlag, Bonn, 2006.
[33] ⟨https://www.python.org/⟩ (assessed August 2014).
[34] R Core Team, R: A language and environment for statistical computing. R Foundation for Statistical Computing, Vienna, Austria, ISBN: 3-900051-07-0, ⟨http://www.R-project.org/⟩, 2012 (accessed August 2014) (the 3D plot applied the package 'rgl').
[35] K. Héberger, Trends Anal. Chem. 29 (2010) 101–109.
[36] K. Héberger, K. Kollár-Hunek, Chemometrics 25 (2011) 151–158.
[37] B. Škrbić, K. Héberger, N. Đurišić-Mladenović, Anal. Bioanal. Chem. 405 (2013) 8363–8375.
[38] S. Tsakovski, V. Simeonov, J. Chemom. 25 (2011) 254–261.
[39] M. Fattore, Rev. Colomb. Estad. (2014) (in press).
[40] R. Bruggemann, H.-J. Mucha, H.-G. Bartel, MATCH – Commun. Math. Comput. Chem. 69 (2013) 433–462.
[41] R. Bruggemann, L. Carlsen, Qual. Quant. (2014), http://dx.doi.org/10.1007/s11135-014-0076-x.

Talanta 132 (2015) 294–300

Contents lists available at ScienceDirect

Talanta

journal homepage: www.elsevier.com/locate/talanta

Characterisation of biosynthesised silver nanoparticles by scanning electrochemical microscopy (SECM) and voltammetry

Dario Battistel [a,*], Franco Baldi [b], Michele Gallo [b], Claudia Faleri [c], Salvatore Daniele [b,**]

[a] Dipartimento di Scienze Ambientali, Infomatica e Statistica, University Cà Foscari Venice. Calle Larga Santa Marta 2137. 30127 Venice, (I)
[b] Dipartimento di Scienze Molecolari e Nanosistemi, University Cà Foscari Venice. Calle Larga Santa Marta 2137. 30127 Venice, (I)
[c] Dipartimento Scienze della Vita, Siena University, via Mattioli 4, 53100 Siena (I)

ARTICLE INFO

Article history:
Received 17 July 2014
Received in revised form
5 September 2014
Accepted 11 September 2014
Available online 19 September 2014

Keywords:
Silver nanoparticles
Bacteria
Biosynthesis
Scanning electrochemical microscopy
Anodic stripping voltammetry

ABSTRACT

Silver nanoparticles (AgNPs) were biosynthesised by a *Klebsiella oxytoca* strain BAS-10, which, during its growth, is known to produce a branched exopolysaccharide (EPS). *Klebsiella oxytoca* cultures, treated with $AgNO_3$ and grown under either aerobic or anaerobic conditions, produced silver nanoparticles embedded in EPS (AgNPs-EPS) containing different amounts of Ag(0) and Ag(I) forms. The average size of the AgNPs-EPS was determined by transmission electron microscopy, while the relative abundance of Ag (0)- or Ag(I)-containing AgNPs-EPS was established by scanning electrochemical microscopy (SECM). Moreover, the release of silver(I) species from the various types of AgNPs-EPS was investigated by combining SECM with anodic stripping voltammetry. These measurements allowed obtaining information on the kinetic of silver ions release from AgNPs-EPS and their concentration profiles at the substrate/water interface.

© 2014 Elsevier B.V. All rights reserved.

1. Introduction

Recently, a number of novel materials containing silver nanoparticles (AgNPs) have been introduced [1–3]. Their usage in commercial goods, such as cosmetics, apparels, medical and electrical devices [4,5], prompted researchers to investigate on AgNPs toxicity towards human cells, aquatic organisms [6] and, more in general, bacterial strains [7–10]. On the other hand, because of the latter property, AgNPs have received increasing attention as antimicrobial agents towards many Gram-positive and Gram-negative bacteria, fungi and viruses [11].

Nowadays, various methodologies are available for the synthesis of AgNPs [7,12–15], and are based on either chemical or biological approaches. The latter have received increasing attention due to the growing need of developing environmental-friendly technologies in material synthesis [12–14]. To this purpose, several microorganisms have been explored as potential cell-factories for both intra- and extracellular synthesis of nanoparticles of various metals [14]. For the biological synthesis of AgNPs, a variety of microorganisms, coming from bacteria and fungi, have been reported [16–19]. The mechanism is related to multiple phenotypic characteristics of the microorganisms, which can produce polymers, such as polysaccharides [20], which can, consequently, embed and stabilise the metal nanoparticles. These AgNPs-containing materials, in view of their biocompatibility, have potential applications as antimicrobials, especially in biomedical fields and food packaging [6,10,20].

The toxicity of AgNPs depends on several properties of the nanoparticles such as size and shape, surface area and charge, capping agents, bioavailability of the individual particles or silver forms [21–23]. With regard to the latter aspect, it is not yet clear whether the AgNPs toxic effects are due to the release of free Ag^+, the nanoparticles themselves or a combination of both species [24–27]. Therefore, investigations on the AgNPs redox properties and their reactivity at interfaces with aqueous environments is highly desirable.

Scanning electrochemical microscopy (SECM) is gaining increasing applications for the in situ investigation of localised phenomena and reactivity of substrates with high spatial resolution [28]. SECM is a scanning probe microscopy technique, which is based on the amperometric signal generated at a microelectrode by redox-active species in solution, which can perform quantitative local electrochemical experiments for studying heterogeneous and homogeneous reactions [29], for high-resolution imaging of the chemical reactivity and topography of various interfaces and surfaces [30,31]. In the field in which the present work falls, SECM has been used to characterise antimicrobial silver films [32], to

* Corresponding author. Tel.: +39 041 234 8506.
** Corresponding author.
E-mail addresses: dario.battistel@unive.it (D. Battistel), sig@unive.it (S. Daniele).

http://dx.doi.org/10.1016/j.talanta.2014.09.023
0039-9140/© 2014 Elsevier B.V. All rights reserved.

evaluate the interaction between Ag(I) ions and fibroblast cells [33] and to establish the effect of AgNPs on HeLa cells activity [34]. Aspects concerning the characterisation of pristine biosynthesised AgNPs in terms of oxidation state of silver and release of silver ions at interfaces have been less investigated. In fact, AgNPs could contain Ag(0), Ag(I) or both forms, this implying a different reactivity upon their contact with water [35].

Recently, it has been reported that *Klebsiella oxytoca (KO)* cultures, treated with $AgNO_3$ solutions, are able to synthesise AgNPs [36], which are embedded in branched exopolysaccharides (EPS) (AgNPs-EPS) [37]. These materials, produced under aerobic ($AgNPs^{aer}$-EPS) or anaerobic ($AgNPs^{anaer}$-EPS) conditions, could contain various forms of silver species and therefore could manifest different reactivity.

In this article, we report an SECM-voltammetric investigation devoted at establishing the oxidation state and reactivity of AgNPs-EPS biosynthesised by a strain of *KO*, and evaluating the amount of diffusable Ag(I) released at the substrate/solution interface.

2. Materials and methods

2.1. Materials and microbial strain

All chemicals were of reagent-grade and used as received, unless otherwise stated. Potassium hexachloroiridate(III) (Sigma Aldrich) was used as redox mediator in SECM investigations. The Nutrient Broth was purchased from Difco. Glycerol, sodium hydrogen carbonate, ammonium nitrate, magnesium sulphate heptahydrate, sodium dihydrogen phosphate, potassium acetate, sodium citrate, sodium hydroxide and silver nitrate were purchased from Sigma Aldrich. The chloride-free NAC medium, used for cell cultures, contained: 2.5 g l^{-1} sodium hydrogen carbonate, 1.2 g l^{-1} ammonium nitrate, 1.5 g l^{-1} magnesium sulphate heptahydrate, 0.6 g l^{-1} sodium dihydrogen phosphate, 0.132 g l^{-1} potassium acetate and 14.7 g l^{-1}sodium citrate. *Klebsiella oxytoca* was isolated from acid mine drainage of pyrite mines as reported in detail elsewhere [38].

2.2. Cultivation of K. oxytoca BAS-10 and production of AgNPs-EPS

Aerobic and anaerobic AgNPs-EPS were prepared as follows. 200 μL of a suspension containing *KO* BAS-10 cells, kept in cryovials at −80 °C in 25% glycerol and Nutrient Broth, were finally inoculated in chloride-free NAC medium. The pH of the NAC medium was previously adjusted to pH 7.6, by adding NaOH [39]. The *KO* BAS-10 cultures were grown both in aerobic and anaerobic conditions, at a controlled temperature of 30 °C. Aerobic conditions were ensured by stirring the cultures with an orbital stirrer under air-exposed media. For the anaerobic growth, the cultures were placed in a pirex bottle that had been previously saturated with nitrogen, then sealed and maintained under nitrogen blanket. At stationary phase of growth, $AgNO_3$ (to provide 50 mg L^{-1} of total Ag) was added to both types of *KO* BAS-10 cultures. These were left for 24–48 hours, till the metal-enriched polysaccharide flocculated in the bottom of the flask. AgNPs-EPS obtained in both aerobic and anaerobic conditions were subsequently separated by centrifugation and then treated with cooled ethanol in order to obtain a final hydroalcoholic solution 70% v/v. The colloidal materials were kept at 5 °C overnight, dried out under vacuum and grinded in a mortar.

2.3. TEM measurements on AgNPs-EPS

For the analysis of TEM, 1 mg each of $AgNPs^{aer}$-EPS and $AgNPs^{anaer}$-EPS was suspended in 1 ml of milli-Q water and sonicated for 10 min. Then, a 5 μl aliquot of each suspension was placed on a platinum grid coated with Formovar resin and then allowed to dry prior to TEM observations. The TEM images of the AgNPs were obtained using a JEOL JEM 100b (Tokyo, Japan) operating under standard conditions. The size distribution of the AgNPs was determined by image analyses of micrographs using the free source software Image J64 (NIH, USA).

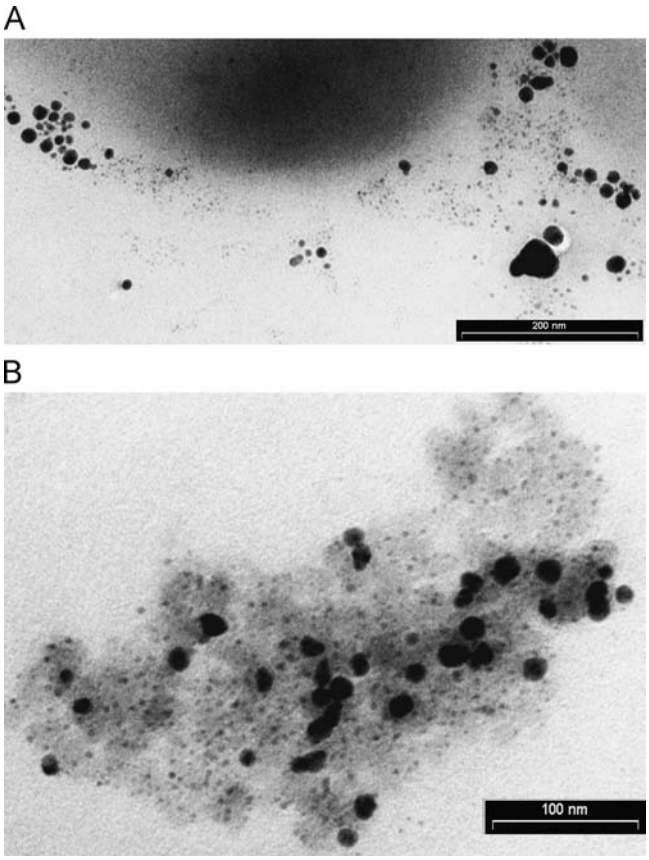


Fig. 1. TEM micrographs obtained on AgNPs-EPS obtained in anaerobic **(A)** and aerobic conditions **(B)**.

2.4. SECM and voltammetric experiments on AgNPs-EPS

SECM and voltammetric experiments were performed in a two-electrode cell, which comprised a working (or SECM tip) electrode and a reference/counter electrode. Platinum disk microelectrodes with nominal radius of 12.5 μm were employed as tip/working electrodes in either SECM or voltammetric measurements. They were prepared by sealing platinum wires within glass capillaries [40]. Afterward, they were tapered to a conical shape, polished with graded alumina powder (5, 1 down to 0.3 μm) and then characterised by cyclic voltammetry at low scan rates and by SECM to evaluate the actual electrode radius of the microelectrode and the overall tip radius to the electrode radius ratio (*RG*) [28,40]. The tips employed here had *RG* values over the range of 8–10. In all electrochemical measurements, a reference/counter electrode Ag/AgCl in saturated KCl was used. A CHI920B workstation (CH Instruments) was employed for both SECM and voltammetric experiments. Measurements, for establishing the oxidation state of the various types of AgNPs (immobilised onto a glass substrate as described below) by SECM, were performed in solutions containing 1 mM K_3IrCl_6 as redox mediator, and 0.1 M KNO_3 as supporting electrolyte. Diffusion controlled oxidation of $IrCl_6^{3-}$ at the SECM tip (vide infra) was achieved by applying a constant potential (E_{tip}) of +0.9 V (see inset in Fig. 2). Current against tip to substrate distance plots (i.e., approach curves) were constructed using normalised currents, $I_N = I/I_{bulk}$, (I is the actual tip current; I_{bulk} is the current

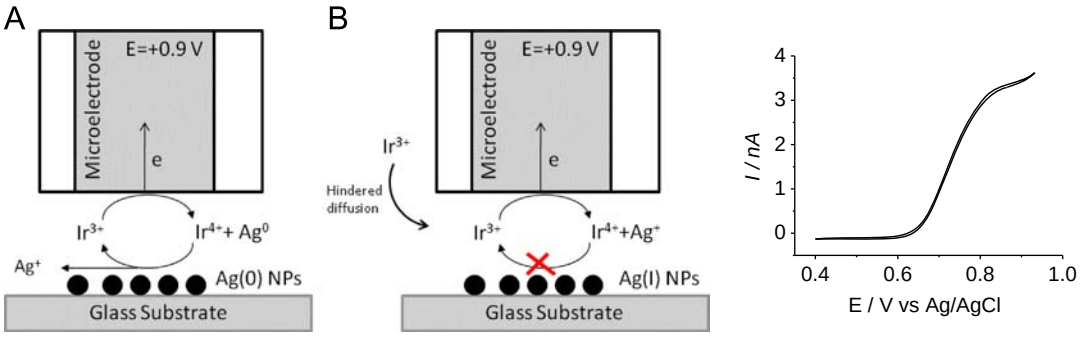


Fig. 2. Schematics of the operating principle for SECM measurements involving: **(A)** negative feedback on Ag(I)NPs and **(B)** positive feedback on Ag(0)NPs. Inset: cyclic voltammetry recorded with a Pt microdisc 12.5 μm radius in a 1 mM K_3IrCl_6+0.1 M KNO_3 solution. Scan rate 10 mV s^{-1}.

measured in the bulk of the solution), against normalised distances $L=d/a$ (d is the tip-substrate distance and a is the microdisc radius). Normalised currents were also used for drawing SECM line scans. For voltammetric and SECM measurements of Ag(I) species, the electrolyte solution consisted of 0.1 M KNO_3. In this measurements, the tip-substrate distance was determined by using the negative feedback approach curves recorded employing oxygen, dissolved in the aerated solution, as redox mediator [41]. The release of silver ions was monitored by using anodic stripping voltammetry (ASV) [42]. Unless otherwise stated, all electrochemical measurements were performed in aerated solutions.

2.5. Immobilisation of the AgNPs-EPS for SECM and voltammetric experiments

For both SECM and voltammetric measurements, $AgNPs^{aer}$-EPS and $AgNPs^{anaer}$-EPS were immobilised onto glass slides. The latter were first washed with ethanol, rinsed with distilled water and dried with nitrogen. The clean slides were afterward soaked in 10% poly-L-lysine (Sigma Aldrich) solutions for 5 min and then dried under chemical hood at 60 °C for 1 h. 20 μL of aqueous suspensions containing 10 mg ml^{-1} AgNPs-EPS were placed on the poly-L-lysine layer [33] and dried at 30 °C overnight. This procedure allowed obtaining several series of three spots (each about 3 mm diameter) of each type of AgNPs-EPS samples.

3. Results and discussion

3.1. TEM analysis

Fig. 1 shows typical TEM micrographs of the $AgNPs^{aer}$-EPS (Fig. 1 A) and $AgNPs^{anaer}$-EPS (Fig. 1B) samples investigated. The high electron-dense spots, due to AgNPs, are embedded on the polysaccharide matrix, and display, predominantly, a spherical shape. Digital analysis provided an average size of 11 ± 5 nm. This value is within those obtained for AgNPs produced by using other bacterial exopolysaccharides [20].

3.2. SECM investigation

The oxidation state of the silver species present in the AgNPs-EPS was investigated by using SECM, operating in the feedback mode in a solution containing K_3IrCl_6 as redox mediator. With this procedure, two phenomena could be observed depending on whether the sample examined was unreactive (or insulating) or reactive (or conducting) [28]. In the first case, the current decreased as the microelectrode, from the bulk solution, was brought towards the substrate (negative feedback); in the second case, the current increased due to the recycling of the redox mediator at the SECM tip (positive feedback). Under our conditions, negative or positive feedback occurred depending on whether the AgNPs-EPS substrates contained Ag(I)NPs or Ag(0) NPs, respectively. This can be understood by considering the scheme shown in Fig. 2. When the substrate contains Ag(0)NPs (Fig. 2 A), the following electrochemical reactions can occur:

$$IrCl_6^{3-} \rightarrow IrCl_6^{2-} + e- \quad (1)$$

reaction at the tip

$$IrCl_6^{2-} + Ag(0) \rightarrow IrCl_6^{3-} + Ag^+ \quad (2)$$

reaction at the substrate

Reaction (2) represents a heterogeneous bimolecular electron transfer process, which is shifted towards the right hand side because the standard redox potential of the $IrCl_6^{2-}/IrCl_6^{3-}$ couple is higher than that of the Ag(I)/Ag(0) species. Thus, when the tip is close to the substrate, the redox mediator is regenerated and the current increases. On the other hand, in the presence of Ag (I) species, reaction (2) does not occur and the substrate hinders the diffusion of the redox mediator (Fig. 2B) [28]. Fig. 3A shows typical normalised current against normalised distance plots recorded while approaching the microelectrode to the $AgNPs^{aer}$-EPS or $AgNPs^{anaer}$-EPS spots. For comparison, approach curves recorded above a clean glass surface, at an EPS sample produced by *KO* cells untreated with $AgNO_3$, and theoretical diffusion controlled approach curves for either positive (red straight line) or negative feedback (blue dashed line) are shown. It is evident that above both the $AgNPs\text{-}EPS^{aer}$ and $AgNPs\text{-}EPS^{anaer}$ spots, positive feedback is recorded. On the other hand, above either the clean glass surfaces or the Ag-free EPS, negative feedback responses are obtained. These results indicate that in both types of materials reaction mechanism (1)–(2) is operative, thus denoting the presence of Ag(0) species. However, the extent of positive feedback, at a given tip to substrate distance, depends on the specific sample investigated, it being larger above the $AgNPs^{anaer}$-EPS. This is conceivably due to a higher amount and readily available Ag(0)NPs in the latter sample with respect to the $AgNPs^{aer}$-EPS. Instead, as expected, negative feedback responses were recorded above either the clean glass surface or the AgNPs-free EPS samples, where reaction (1)–(2) cannot occur. It must be considered that negative approach curves (as those for the glass slide) were also recorded in some zones of the AgNPs-EPS spots investigated, indicating that, locally, either AgNPs-EPS rich of Ag(I) NPs or no AgNPs-EPS material was present.

The distribution and density of Ag(0) in the AgNPs-EPS materials was evaluated by SECM operating in line-scanning mode. These experiments were performed by positioning the SECM tip at ~10 μm above the sample and then recording the current along

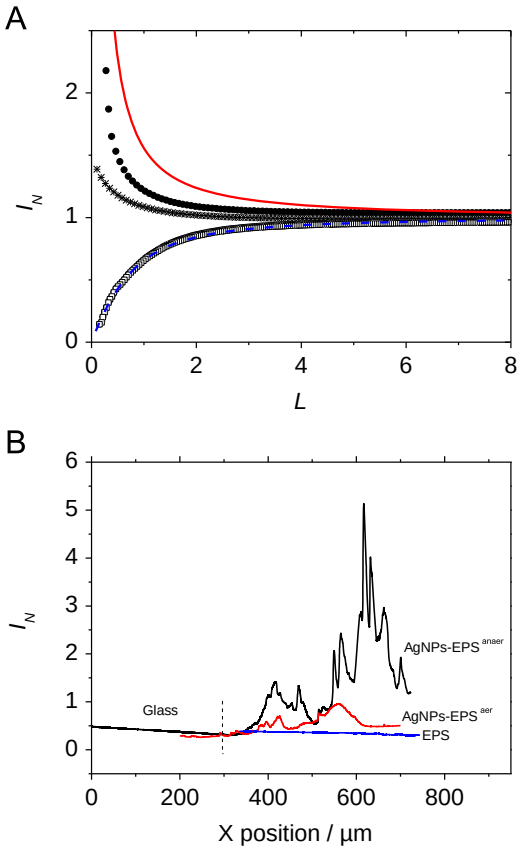


Fig. 3. **(A)** Approach curves recorded above: (∗) AgNPs^{aer}-EPS; (•) AgNPs^{aenaer}-EPS; (⋄) a clean glass surface; (○) EPS untreated with $AgNO_3$; theoretical for (red line) positive and (black line) negative feedback approach curves. **(B)** SECM line-scans recorded above a border region between the clean glass slide and (black line) Ag-NPs^{anaer}-EPS, (red line) Ag-NPs^{aer}-EPS; (blue line) Ag-free EPS.

the x (or y) direction. Fig. 3B shows typical SECM line scans recorded above a border region between the clean glass slide and the AgNPs^{anaer}-EPS (black line) or AgNPs^{aer}-EPS (red line) spots. As is evident, current increments, conceivably due to the positive feedback effect, were recorded when the microelectrode travelled above both types of spots (from 350 to 700 μm in Fig. 3B). Instead, low and almost constant currents were recorded as long as the microelectrode was moved above the glass slides (from 0 to 350 μm in Fig. 3B). Line scans with similar features and low current changes were also obtained above the AgNPs-free EPS samples (see blue line in Fig. 3B). In this case, the current change was essentially due to the roughness of the samples investigated, which could also affect the tip current responses [44]. The latter finding also indicates that the topography of the investigated samples is flat enough and does not affect significantly the overall current responses due to the AgNPs-EPS film.

Comparing the line scans recorded above the AgNPs-EPS samples, it is evident that normalised currents were, in general, higher above the AgNPs^{anaer}-EPS spot, confirming that the latter sample contained larger amounts of Ag(0)NPs as previously observed comparing the positive feedback approach curves. Form TEM images and considering that the EPS matrix provided images of quite flat surfaces, at this level of resolution, it is reasonable to assume that the roughness of the AgNPs-EPS samples does not affect the feedback current responses.

Considering again Fig. 3A, it is evident that the approach curves, recorded above both types of AgNPs-EPS spots, in no case fit that for diffusion controlled positive feedback. This could be attributed to several factors, including the facts that the Ag(0)NPs, embedded in the polysaccharide matrix, do not form large interconnected silver clusters, or that the kinetic of the heterogeneous bimolecular electron transfer process, involved in reaction (2), is not fast. At this stage, we are unable to differentiate among the various factors.

3.3. Study of the release of Ag(I) species

Information on reactivity of AgNPs and the release of Ag(I) species at the AgNPs-EPS/water interface was obtained by combining SECM and voltammetric experiments. The measurements were performed on AgNPs-EPS modified glass-slide spots immersed in a 0.1 M KNO_3 aerated-aqueous solution. Under these conditions, Ag(I) species, eventually present in the samples, or formed by corrosion of Ag(0)NPs, could diffuse to the aqueous solution and thereby collected at the microelectrode tip (scheme in Fig. 4). In these experiments, the tip-substrate distances were established using oxygen (from the air saturated solution) as redox mediator. Oxygen was used in order to avoid any possible interference due to the oxidising action of the $IrCl_6^{2-}/IrCl_6^{3-}$ couple towards Ag(0)NPs.

Evidences for the formation of Ag(I) species or the presence of soluble Ag(0)NPs were, initially, gained by using cyclic voltammetry (CV) with the microelectrode positioned at 10 μm above the substrates. Cyclic voltammograms were recorded in the potential window from 0.05 to 0.80 V, where both reduction of Ag(I) species and oxidation of Ag(0), accumulated at the microelectrode surface, could occur [43]. Fig. 5 shows a typical CV recorded at 50 mV s^{-1} with the Pt microdisc positioned above a AgNPs^{aer}-EPS spot, after 2 hours the introduction of the 0.1 M KNO_3 solution. The potential was initially scanned from the rest potential (0.25 V) towards

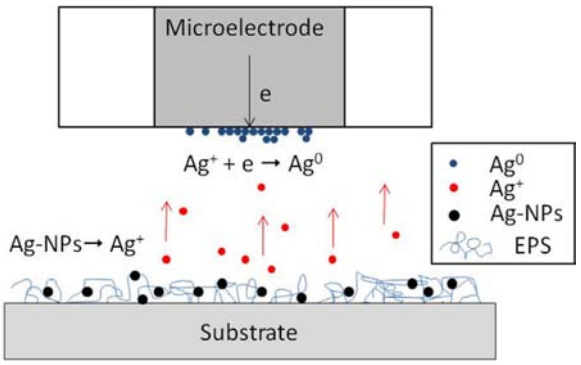


Fig. 4. Schematic of the Ag(I) species release from the AgNPs-EPS substrate and collection at the SECM tip.

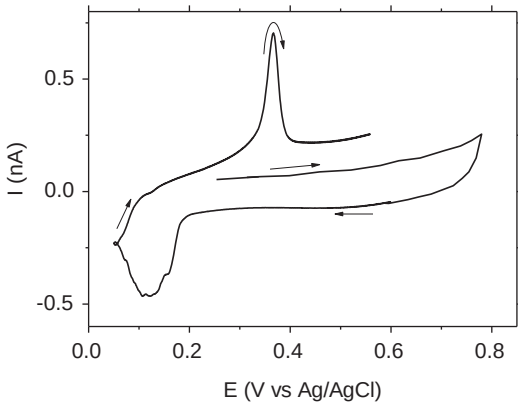


Fig. 5. Cyclic voltammograms recorded by using a 12.5 μm Pt microelectrode placed 10 μm above a Ag-EPS^{aer} spot after two hours immersion in a 0.1 M KNO_3 aqueous solution. Scan rate: 50 mV s^{-1}

positive potentials, to oxidise, eventually, soluble or colloidal Ag(0) NPs-containing compounds; then from the anodic limit the potential was scanned towards negative potentials where Ag (I) species could be reduced; afterwards, the potential was scanned again towards positive values to oxidise Ag(0) accumulated at the electrode surface. As is evident from Fig. 5, no wave is observed during in first anodic scan, indicating that no or negligible amount of Ag (0) was present within the microelectrode/substrate gap. Instead, a cathodic peak at 0.2 V and an anodic one at 0.4 V, due to the reduction of the Ag(I) species and the oxidation of Ag(0) accumulated onto the electrode surface, respectively, were obtained during the subsequent negative and positive scans. The peak shaped response, obtained in the cathodic scan, instead of a steady-state (or pseudo-steady state, typical for microelectrodes) [45], suggested a thin layer behaviour [46] and that almost all Ag(I) species, present within the tip/substrate gap, were depleted.

CVs similar to that shown in Fig. 5 were also obtained above a AgNPs^{anaer}-EPS sample (not shown). However, in the latter case, valuable voltammograms could be obtained only after longer (i.e. 4–5 h) immersion times of the sample in the water solution. This finding suggested that the Ag(I) species released from AgNPs^{anaer}-EPS, which is richer of Ag(0)NPs, involved a more complex pathway, including the metal corrosion process.

To achieve a better sensitivity in the measurements, and for quantitative determination of silver(I) species released from the AgNPs-EPS samples, anodic stripping voltammetry was employed [47,48]. A first series of ASVs was carried out for obtaining information on the dissolution rate of the Ag(I) species. To this purpose, the Pt microelectrode was positioned at 10 μm above the samples and ASVs were recorded with time. The ASVs were performed using a deposition time of 60 seconds, a deposition potential equal to −0.1 V vs. Ag/AgCl and linear sweep voltammetry at 50 mV s^{-1} during the stripping step. Fig. 6A B show typical ASVs thus recorded for different elapsed times after the samples had been immersed in the water solution. For both samples, the stripping peak height increases with time, confirming that increasing amounts of Ag(I) species dissolved to the water phase. The concentration (C^b_{Ag+}) was estimated by comparing the anodic charge involved in the ASV peaks, recorded above the AgNPs-EPS samples, to those obtained in $AgNO_3$ solutions of known concentrations. Fig. 6C shows plot of C^b_{Ag+} against immersion time (t_i). It is evident that the Ag(I) concentration increases with time for both AgNPs-EPS samples; however, after about 20 and 25 min for the AgNPs-EPS^{aer} and AgNPs-EPS^{anaer} sample, respectively, the concentration levels off. This is probably due to the achievement of an equilibrium between soluble Ag(I) and Ag(I)

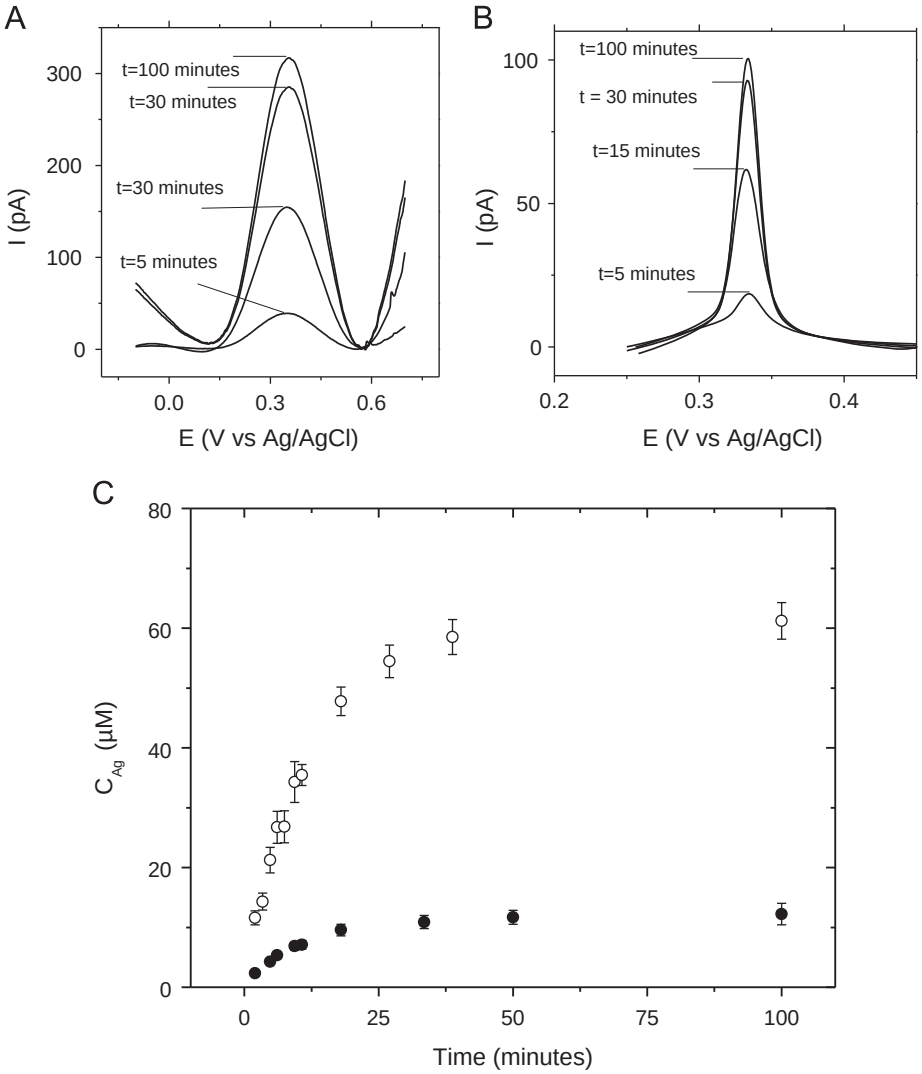


Fig. 6. ASVs recorded at different times with a Pt microdisc positioned at 10 μm above **(A)** Ag^{aer}NPs-EPS and **(B)** Ag^{anaer}NPs-EPS. **(C)** Concentration against elapsed time after immersion in the 0.1 M KNO_3 solution of (○) Ag-NPs^{aer}-EPS and (●)Ag-NPs^{anaer}-EPS samples. ASVs parameters: deposition time 60 s, deposition potential −0.1 V and, 50 mV s^{-1}during the stripping step. Error bars are established on the basis of three consecutive ASVs.

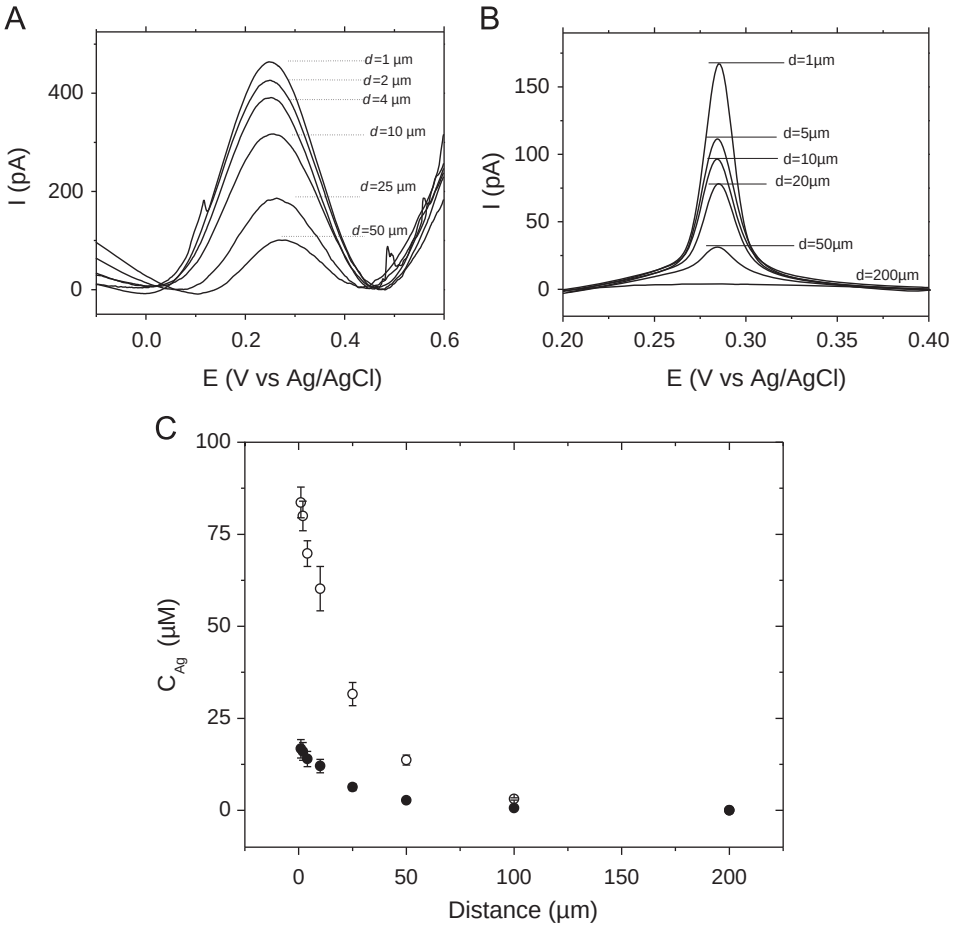


Fig. 7. ASVs recorded at different tip-substrate distances with a Pt microdisc after the samples had been immersed in 0.1 M KNO_3 for 30 minutes. **(A)** for $AgNPs^{aer}$-EPS and **(B)** $AgNPs^{anaer}$-EPS. **(C)** Concentration profiles for (○) $AgNPs^{aer}$-EPS and (●) $Ag\text{-}NPs^{anaer}$-EPS. ASVs parameters: deposition time 60 s, deposition potential -0.1 V and scan rate, during the stripping step, 50 mV s^{-1}. Error bars are calculated on the basis of three consecutive ASVs.

NPs-EPS bound species. It is interesting to note that the amount of Ag(I) released from $AgNPs^{aer}$-EPS is sensibly higher (4–6 times) than that of $AgNPs^{anaer}$-EPS. These results therefore, once again, confirm that the composition of the AgNPs-EPS materials are differently rich of Ag(I)NPs or Ag(0)NPs.

The concentration profiles of Ag(I) species at the samples samples/solution interface at equilibrium (i.e., at the time where C^b achieved the plateau region, in the present case 30 min) were also evaluated by performing a further series of measurements in which ASVs were recorded at different tip to substrate distances (Fig. 7A,B). Fig. 7C shows concentration against distance plots, and, as is evident, for both samples the amount of Ag(I) species in the solution decreases as the tip-substrate distance increases. For distances greater than 100 μm, the amount of Ag(I) was not detectable under the above ASV conditions. These results, again, support the circumstance that multiple equilibria involving Ag(I)-bound to AgNPs-EPS or sparingly soluble species affect the overall dissolution process. Also in these measurements, the amount of Ag(I) released from $AgNPs^{aer}$-EPS is higher than that of $AgNPs^{anaer}$-EPS.

4. Conclusion

In this work, AgNPs, embedded in an exopolysaccharide matrix, biosynthesised using a *K. oxytoca* BAS-10 strain, have been characterised to establish their chemical properties and reactivity at the sample/solution interface. This information has been gathered by using scanning electrochemical microscopy and voltammetry. This study has proven that Ag(0) or Ag(I) forms are present in the AgNPs-EPS materials and their abundance depends on whether the materials were prepared under aerobic or anaerobic conditions. As expected, Ag(I) forms predominate in the $AgNPs^{aer}$-EPS material, conceivable due to the presence of oxygen, which could promote the oxidation of Ag(0)NPs to provide easier diffusable Ag(I) species. This could imply a potentially higher antimicrobial activity of the $AgNPs^{aer}$-EPS composite. The antibacterial activity of both $AgNPs^{aer}$-EPS and $AgNPs^{aner}$-EPS towards both Gram-positive and Gram-negative bacteria is currently under investigation in our laboratory.

Acknowledgement

Financial support of the Ministry of University and Scientific Research (MIUR) (PRIN-2010AXENJ8) is gratefully acknowledged.

References

[1] S. Siripattanakul-Ratpukdi, M. Fürhacker, Water Air Soil Poll 225 (2014) 1–18.
[2] N. Vigneshwaran, A.A. Kathe, P.V. Varadarajan, R.P. Nachane, R.H. Balasubramanya, J. Nanosci. Nanotechnol. 7 (2007) 1893–1897.
[3] A. Goyal, A. Kumar, P.K. Patra, S. Mahendra, S. Tabatabaei, P.J.J. Alvarez, G. John, P.M. Ajayan, Macromol. Rapid Commun. 30 (2009) 1116–1122.
[4] N. Singh, B. Manshian, G.J. Jenkins, S.M. Griffiths, P.M. Williams, T.G. Maffeis, C.J. Wright, S.H. Doak, Biomaterials 30 (2009) 3891–3914.
[5] G. Oberdorster, E. Oberdorster, J. Oberdorster, Environ. Health Persp. 113 (2005) 823–839.
[6] A.K. Suresh, D.A. Pelletier, M.J. Doktycz, Nanoscale 5 (2013) 463–474.

[7] A. Hebeish, M.E. El-Naggar, M.G.M. Fouda, M.A. Ramadan, S.S. Al-Deyab, S. Salem S., M.H. El-Rafie, Carbohydr. Polym 86 (2011) 936–940.
[8] V.K. Sharma, R.A. Yngard, Y. Lin, Adv. Coll. Interf. Sci. 145 (2009) 83–96.
[9] J.R. Morones, J.L. Elechiguerra, A. Camacho, K.B. Holt, J.B. Kouri, J.T. Ramirez, M.J. Yacaman, Nanotechnology 16 (2005) 2346–2353.
[10] A.M. Fayaz, K. Balaji, M. Girilal, P.T. Kalaichelvan, R. Venkatesan, J. Agric. Food Chem. 57 (2009) 6246–6252.
[11] M. Sureshkumar, D.Y. Siswanto, C.K. Lee, J. Mat. Chem 20 (2010) 6948–6955.
[12] N. Vigneshwaran, R.P. Nachane, R.H. Balasubramanya, P.V.A. Varadarajan, Carbohydr. Res. 341 (2006) 2012–2018.
[13] A. Panacek, L. Kvitek, R. Prucek, M. Kolar, R. Vecerova, N.J. Pizurova, J. Phys. Chem. B 110 (2006) 16248–16253.
[14] K.B. Narayanan, N. Sakthivel, Adv. Coll. Interf. Sci. 156 (2010) 1–13.
[15] D. Wei, W. Sun, W. Qian, Y. Ye, X. Ma, Carbohydr. Res. 344 (2009) 2375–2382.
[16] A.K. Gade, P. Bonde, A.P. Ingle, P.D. Marcato, N. Duran, M.K. Rai, J. Biobased Mater. Bioenerg. 3 (2008) 123–129.
[17] G. Li, D. He, Y. Qian, B. Guan, S. Gao, Y. Cui, Int. J. Mol. Sci. 13 (2012) 466–476.
[18] V. Deepak, K. Kalishwaralal, S.R.K. Pandian, S. Gurunathan, in Metal Nanoparticles in Microbiology, Berlin (2011).
[19] G. Yang, J. Xie, Y. Deng, Y. Bian, F. Hong, Carbohydr. Polym 87 (2012) 2482–2487.
[20] P. Kanmani, S.-T. Lim, Process Biochem. 48 (2013) 1099–1106.
[21] A. Yu, X. Jiang, Q. Zeng, Chapter 17: Silver Nanoplates: Synthesis, Growth and Functional Properties, in: A. Barrañón (Ed.), New Nanotechnology Developments, Nova Science Publishers, UK, 2009.
[22] B. Fubini, I. Fenoglio, M. Ghiazza, Nanotoxicology 4 (2010) 347–363.
[23] R. Tantra, J. Tompkins, P. Quincey, Coll. Surf. B Biointer. 75 (2010) 275–281.
[24] N. Lubick, Environ. Sci. Technol. 42 (2008) 8617 8617.
[25] H.J. Johnston, G. Hutchison, F.M. Christensen, S. Peters, S. Hankin, V. Stone, Crit. Rev. Toxicol. 40 (2010) 328–346.
[26] M. Ahamed, M.S. AlSalhi, M.K.J. Siddiqui, Clin. Chim. Acta. 411 (2010) 1841–1848.
[27] M. Hadioui, S. Leclerc, K.J. Wilkinson, Talanta 105 (2013) 15–19.
[28] A.J. Bard, M.V. Mirkin, Scanning Electrochemical Microscopy, Marcel Dekker, New York, 2001.
[29] C.G. Zoski (Ed.), Handbook of Electrochemistry, Elsevier, Amsterdam, 2007.
[30] S. Bergner, P. Vatsyayan, F.-M. Matysik, Anal. Chim. Acta 775 (2013) 1–13.
[31] K. Kranz, Analyst 139 (2014) 336–352.
[32] F.-R.F. Fan, A.J. Bard, J. Phys. Chem. B 106 (2002) 279–287.
[33] K.B. Holt, A.J. Bard, Biochemistry 44 (2005) 13214–13223.
[34] Z. Chen, S.B. Xie, L. Shen, Y. Du, S.L. He, Q. Li, Z.W. Liang, X. Meng, B. Li, X.D. Xu, Analyst 133 (2008) 1221–1228.
[35] G.A. Sotiriou, A. Meyer, J.T.N. Knijnrnburg, S. Panke, S.E. Pratsinis, Langmuir 28 (2012) 15929–15936.
[36] F. Baldi, D. Battistel, S. Daniele, M. Gallo, S. Paganelli, O. Piccolo, C. Faleri, G. Gallo, A.M. Puglia, *In preparation*.
[37] S. Leone, C. De Castro, M. Parrilli, F. Baldi, R. Lanzetta, Eur. J. Org. Chem. 31 (2007) 5183–5189.
[38] F. Baldi, A. Minacci, M. Pepi, A. Scozzafava, FEMS Microbiol. Ecol. 36 (2001) 169–174.
[39] F. Baldi, D. Marchetto, S. Paganelli, O. Piccolo, New Biotechnol 29 (2011) 74–78.
[40] D. Battistel, S. Daniele, R. Gerbasi, M.A. Baldo, Thin Solid Films 518 (2010) 3625–3631.
[41] R.M. Souto, Y. Gonzalez-Garcia, D. Battistel, S. Daniele, Corros. Sci 55 (2012) 401–406.
[42] S. Daniele, I. Ciani, M.A. Baldo, C. Bragato, Electroanalysis 19 (2007) 2067–2076.
[43] D. Battistel, G. Pecchielan, S. Daniele, Chem. Electrochem 1 (2014) 140–146.
[44] D. Battistel, S. Daniele, D. Fratter, Electochim. Acta 78 (2012) 557–562.
[45] M.I. Montenegro, M.A. Queirós, J.L. Daschbach Microelectrodes, Theory and Applications, Kluwer, 1991.
[46] A.J. Bard, L.R. Faulkner, Electrochemical Methods, ed., Wiley, New York, 2001.
[47] J.V. Macpherson, P.R. Unwin, J. Phys. Chem. 100 (1996) 19475–19483.
[48] M.E. Abdelsalam, G. Denuault, S. Daniele, Anal. Chim. Acta 452 (2002) 65–75.

Talanta 132 (2015) 301–314

Contents lists available at ScienceDirect

Talanta

journal homepage: www.elsevier.com/locate/talanta

Immobilized β-cyclodextrin-based silica *vs* polymer monoliths for chiral nano liquid chromatographic separation of racemates

Ashraf Ghanem [a,*], Marwa Ahmed [a], Hideaki Ishii [b], Tohru Ikegami [b]

[a] Chirality Program, Biomedical Science, University of Canberra, Canberra, ACT, Australia
[b] Department of Biomolecular Engineering, Graduate School of Science and Technology, Kyoto Institute of Technology, Matsugasaki, Sakyo-ku, Kyoto, Japan

ARTICLE INFO

Article history:
Received 23 June 2014
Received in revised form
2 September 2014
Accepted 3 September 2014
Available online 16 September 2014

Keywords:
β-Cyclodextrin methacrylate
Silica monolith
Polymer monolith
Chiral separation
Nano-LC
Reversed phase chromatography

ABSTRACT

The enantioselectivity of immobilized β-cyclodextrin phenyl carbamate-based silica monolithic capillary columns was compared to our previously described polymer counterpart. 2,3,6-Tris(phenylcarbamoyl)-β-cyclodextrin-6-methacrylate was used as a functional monomer for the preparation of β-cyclodextrin (β-CD)-based silica and polymer monoliths. The silica monoliths were prepared via the sol–gel technique in fused silica capillary followed by modification of the bare silica monoliths with an anchor group prior to polymerization with β-CD methacrylate using either 2,2′-azobis(isobutyronitrile) or benzoylperoxide as radical initiators. On the other hand, the polymer monoliths were prepared via the copolymerization of β-CD methacrylate and ethylene glycol dimethacrylate in different ratios *in situ* in fused silica capillary. The prepared silica/polymer monoliths were investigated for the chiral separation of different classes of pharmaceuticals namely; α- and β-blockers, anti-inflammatory drugs, antifungal drugs, dopamine antagonists, norepinephrine-dopamine reuptake inhibitors, catecholamines, sedative hypnotics, diuretics, antihistaminics, anticancer drugs and antiarrhythmic drugs. Baseline separation was achieved for alprenolol, bufuralol, carbuterol, cizolertine, desmethylcizolertine, eticlopride, ifosfamide, 1-indanol, propranolol, tebuconazole, tertatolol and *o*-methoxymandelic acid under reversed phase conditions using mobile phase composed of methanol and water. The silica-based monoliths showed a comparative enantioselectivity to the polymer monoliths.

Crown Copyright © 2014 Published by Elsevier B.V. All rights reserved.

1. Introduction

The interest in chirality and its consequences has risen significantly in the last two decades due to scientific and economic reasons. Chiral drugs constitute approximately one-third of all drug sales worldwide and it is expected that nearly 95% of the pharmaceutical drugs will be chiral by 2020 [1]. This imposed strict regulations in approving new chiral entities that include full documentation of the separate pharmacological, toxicological and pharmacokinetic profiles for the individual enantiomers as well as their racemates (mixture of enantiomers) [2]. Accordingly, pharmaceutical companies are yet shifting toward the development of single pure enantiomer drugs via preparative chiral separation techniques rather than the time-consuming chiral syntheses [3]. This raises the need for a high throughput, robust, reliable, environmentally benign and relatively cheaper separation technique of chiral pharmaceuticals to allow their commercialization [4,5].

Miniaturization of the analytical techniques reduces the total analysis time, reagents consumption and is able to handle small samples. Nano-LC is one of the microfluidic techniques where reduction in both column inner diameter (10–300 μm) and flow rate (200–1000 nL/min) are combined [6]. The advantages of miniaturization also include the reduced cost of the packing stationary phase; this is of particular interest when costly chiral stationary phases (CSPs) are used [7]. However, packing the capillaries with small particles (usually 3–5 μm diameter) require high level of experience because of the need of retaining frits [8]. This problem can be overcome using monolithic materials [9–15].

Silica-based monoliths are prepared by sol–gel process which involves the hydrolysis of a mixture of silane oxides followed by condensation and polycondensation reactions [16]. They have a characteristic bi-continuous structure providing mesopores with high surface area (several hundred square meters per gram) which makes it highly efficient for the separation of small molecules [17]. The polar surface of silica-based monolith renders it useful for normal phase liquid chromatography (NPLC) and hydrophilic interaction liquid chromatography (HILIC). Alternatively, silica skeleton needs to be derivatized to be suitable for reversed phase liquid chromatography (RPLC) [16]. On the other hand, polymer-based monoliths are prepared via the *in situ* copolymerization of

* Correspondence to: Professor of Organic Chemistry, President of the Royal Australian Chemical Institute (RACI) ACT, Biomedical Science Program, University of Canberra, ACT 2601 Australia. Tel.: +61 2 6201 2089.
E-mail address: ashraf.ghanem@canberra.edu.au (A. Ghanem).
URL: http://www.chiralitygroup.com (A. Ghanem).

http://dx.doi.org/10.1016/j.talanta.2014.09.006
0039-9140/Crown Copyright © 2014 Published by Elsevier B.V. All rights reserved.

one or more monovinyl monomer with a divinyl cross linker in suitable porogenic solvents (binary or trinary) in a single step process [9]. Free radical polymerization is the common mechanism and the polymer is formed within the capillary to form a continuous porous bed. Polymer monoliths are not only considered for the separation of macromolecules (proteins and peptides) but also for small organic molecules. Remarkable amount of research has been done to increase the surface area of the polymer monolith to ensure adequate separation of small organic molecules [18,19].

The ease and speed of preparation of polymer-based monoliths compared to the technically challenging procedures for silica-monoliths preparation render polymer monoliths an attractive tool in the field of separation science. Nonetheless, polymer monoliths tend to swell or shrink upon exposure to organic solvents compared to silica monoliths, while silica monoliths show lower stability at temperature higher than 60 °C and pH higher than 8.5 compared to the higher temperature and chemical stability of the polymer monoliths. Therefore, both polymer and silica monoliths have their own merits and drawbacks and each of the stationary phases could be tailored to obtain the optimum separation according to the sample nature. To introduce chirality in silica-based monolith, the CS is immobilized on the activated silica skeleton [20] or encapsulated during the sol–gel procedure [21]. On the other hand, to introduce chirality in polymer-based monoliths, the chiral selector (CS) is copolymerized as a functional monomer [22] or immobilized after the monolith preparation [23], [24] in a one pot polymerization procedure or post-polymerization surface modification of reactive groups, respectively [25]. Various classes of CSs are available for enantioselective separation of racemic mixtures, such as, molecularly imprinted polymers, ligand exchange, brush-type, macrocyclic antiobiotics-based, protein/glycoprotein- based, cellulose/amylose derivatives and cyclodextrin (s) derivatives [26–35]. Bonding of β-CD into monoliths has been previously achieved via the copolymerization or post modification approaches. The former is considered a simple and less time consuming compared to the latter. However, due to diversity of monomers precursors, it is time and laborious consuming to prepare different kinds of monolithic columns to establish a robust monolithic backbone. Thus, post modification of raw monoliths with high robustness, tailorability and column efficiency becomes a good alternative [36,37].

The purpose of this study is to compare the enantioselectivity of β-CD-based silica monoliths prepared via the post modification approach to that of β-CD-based polymer monoliths previously prepared via the one pot copolymerization approach [38]. Whether the two approaches would display similar, broader or complimentary chiral discrimination ability is another raised question.

2. Experimental

2.1. Reagents and materials

Benzoyl peroxide (BOP, >97%), ethylene glycol dimethacrylate (EDMA, 98%), 3-(trimethoxysilyl)propyl methacrylate (98%), 1-propanol (99%), 1,4-butanediol (99%), methacryloyl chloride (97%), phenyl isocyanate (>98%), trifluoroacetic acid (TFA, ≥99.5%), sodium hydroxide, toluene, tetramethoxysilane (TMOS), methyltrimethoxysilane (MTMS), poly(ethylene glycol) with molecular weight of 10,000, urea, hydrochloric acid and acetic acid were purchased from Aldrich (Milwaukee, WI, USA). β-Cyclodextrin was purchased from TCA (Tokyo, Japan). Acetone (AR grade), ethanol (HPLC grade) were purchased from BDH (Kilsyth, Vic., Australia). Acetonitrile (HPLC grade) was purchased from Merck (Darmstadt, Germany). Methanol (HPLC grade) was purchased from Scharlau (Sentmenat, Spain). All other reagents were of the highest available grade and used as received. The fused-silica capillaries (100 μm and 150 μm inner diameter) were purchased from Polymicro Technologies (Phoenix, AZ, USA). 2,2′-azobis(isobutyronitrile) (AIBN) was obtained from Wako (Osaka, Japan). (3-Aminopropyl)triethoxysilane, tetrahydrofuran, pyridine and uracil were purchased from Sigma Aldrich (St. Louis, MO, USA). Pyridine and toluene were dried before use over molecular sieves (4 Å) also from Sigma Aldrich (St. Louis, MO, USA), toluene was distilled from calcium hydride (Sigma Aldrich, USA). Tetrahydrofuran was distilled prior to use. Water used for dilutions and experiments was purified by Nanopure Infinity water system (NJ, USA). Racemic analytes were mostly purchased from sigma Aldrich.

2.2. Preparation of the monolithic columns

β-CD functional monomer (Fig. 1) was prepared according to the previously described method [38]. The hybrid-type monolithic silica columns were prepared from a mixture (9 mL) of TMOS and MTMS in a 3:1 ratio, poly(ethylene glycol) (0.9 g), and urea (2.025 g) in 0.01 M acetic acid (20 mL) as described previously [39] resulting in a monolithic silica having through-pore size of 2.0 μm and skeleton size of 1.5 μm. Briefly, TMOS (9 mL) was added to a solution of poly(ethylene glycol) (PEG, 0.9 g, *Mwt*=10,000) and urea (2.025 g) in 0.01 M acetic acid (20 mL) and stirred at 0 °C for 45 min. The resultant homogeneous solution was charged into a fused–silica capillary tube (100 μm ID, Polymicro, AZ), which had

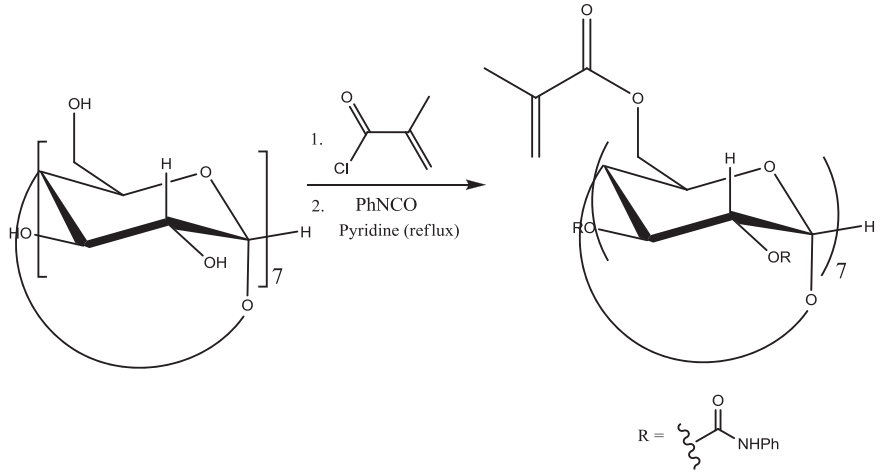


Fig. 1. Schematic diagram showing the preparation of 2,3,6-tris(phenylcarbamoyl)-β-CD-6-methacrylate [38].

been treated in advance with 1 M NaOH solution at 40 °C for 2 h, and allowed to react at 40 °C. Gelation occurred within 2 h, and the gel was subsequently aged in the capillary overnight at the same temperature. Then, temperature was raised, and the monolithic silica column was treated for 4 h at 120 °C to complete the formation of the mesopores with ammonia generated by the hydrolysis of urea, followed by methanol wash. After drying, heat treatment was carried out at 330 °C for 24 h, resulting in the decomposition of organic moieties in the capillary [40]. Usually, 4-m capillary columns were prepared from the same reaction mixture. After preparation, both ends (10–15 cm) of the capillary were trimmed, and several 50-cm long columns were obtained.

Before modification of the surface silanol groups, the monolithic silica capillary columns were evaluated using methanol/water: 80/20 (v/v) as a mobile phase and uracil as the test analyte. The columns exhibited the plate heights in the range of 18–27 μm and a theoretical plate numbers in the range of 16,000–76,000. After the evaluation, the monolithic silica columns were used for modification with 3-methacrylamidopropyltriethoxysilane (MAS) (Fig. 2) followed by polymerization with 2,3,6-tris(phenylcarbamoyl) β-cyclodextrin-6-methacrylate. The anchor group MAS was prepared via previously reported method [41]. *In situ* polymerization of the CS onto the MAS-modified silica surface

Columns were prepared *in situ* as illustrated in Fig. 3; 0.40 μL (0.38 mmol) methacryloyl chloride was added to 0.42 g (0.37 mmol) β-CD dissolved in 9 mL pyridine. The solution was stirred for 6 h at room temperature then 1.9 mL phenyl isocyanate was added and the solution was refluxed for 18 h. 20 mg/mL AIBN or BOP in dioxan was then prepared separately and added to the reaction mixture at a concentration of 0.1 g/mL. The mixture was then filtered through Sartorius Minisart RC 15 0.2 μm pore size filters (Goettingen, Germany), the MAS modified silica columns were then filled with the mixture using a syringe pump or via N_2 gas, the capillaries were placed into 80 °C oven for 24 h to complete the polymerization reaction. Finally the modified columns were washed with dioxan for 24 h and conditioned with the mobile phase prior to use.

The surface modification in fused silica capillaries (150 μm ID) was done by using the same procedure of Schaller et al. [42]. As previously described, only the two permeable polymer-based monolithic capillary columns were prepared via *in situ* copolymerization of binary monomer mixtures consisted of β-CD derived functional monomer and EDMA as a crosslinker along with three porogens namely; 1-propanol, 1,4-butanediol and water in the presence of 1 wt% AIBN (with respect to monomers) [38]. The filled capillaries were then sealed with a septum, placed in 70 °C water bath for 18 h for the polymerization reaction to take place. The unreacted monomers were removed from the monolithic columns by pumping with methanol at a flow rate of 100 μL/h for 4 h before being conditioned with water and mobile phase, both for 1 h at 30 μL/h. Polymer composition in the prepared columns is shown in Table 1.

2.3. Instrumentation

The nano liquid chromatographic system was from Dionex Corporation (UltiMate® 3000 capillary LC system) which featured an integrated flowsplitter connected to a continuously monitored flow meter and control valve to maintain a constant flow rate in the range from 0.1 to 1.0 μL/min. It also comprised a binary pump, a vacuum degasser, an autosampler and a UV detector. The Chromeleon® Chromatography Management System version 7.00 was used for the data processing and control of the HPLC system.

2.4. Standard solutions and sample preparation

Stock solutions of the racemic analytes at concentrations of 1 mg/mL in filtered HPLC grade methanol were prepared. Prior to injection, the stock solutions were further diluted 10× and filtered through Sartorius Minisart RC 15 0.2 μm pore size filters (Goettingen, Germany).

Tested compounds—β-blockers: alprenolol, celiprolol, metoprolol, pindlol, propranolol, acebutolol, carbuterol, bufuralol, tertatolol, atenolol. *α-blockers:* naftopidil. *Antiinflammatory drugs:* ketoprofen, ibuprofen, naproxen, flurbiprofen, indoprofen, cizolirtine, cizolirtine carbinol, carprofen, etodolac, desmethylcizolirtine, glafenine. *Antifungal drugs:* hexaconazole, cyproconazole, tebuconazole, miconazole, diniconazole, sulconazole. *Dopamine antagonists:* eticlopride. *Norepinephrine–dopamine reuptake inhibitor:* nomifensine. *Catecholamines:* arterenol, normetanephrine. *Sedative hypnotics:* aminoglutethimide, phenylglutethimide, *N*-acetylaminoglutethimide, 4-bromogluthethimide, pentobarbital, *p*-hydroxyphenobarbital. *Diuretics:* etozoline. *Antihistaminics:* chlorpheneramine. *Anticancer drugs:* ifosfamide. *Antiarrhythmic drugs:* tocainide. *Miscellaneous:* 1-acenaphthenol, *o*-methoxy mandelic acid, 4-hydroxy-3-methoxymandelic acid, 1-indanol, 1-(2-chlorophenyl)ethanol, 1-phenyl-2-propanol. Chemical structures of the investigated racemates and their suppliers are listed in Table 2.

2.5. HPLC conditions

The mobile phase A and B consisted of 0.1% TFA in water (v/v) and methanol (v/v) or 0.1% TFA in water (v/v) and acetonitrile. For all samples, the injected volume was 0.2 μL. Preliminary UV analyses were performed at several different wavelengths (219–270 nm) for each compound, in order to select the optimum wavelength for all the analytes and best utilise a single wavelength UV detector.

3. Results and discussion

3.1. Silica monoliths: Preparation and characterization

In order to attach the β-CD derivative on silica monolith via the copolymerization approach, surface activation of the bare silica is required. Hence, at the first step of modification, an anchor, *N*-(3-trimethoxysilylpropyl)methacrylamide, was chemically bonded to the silica skeleton at 80 °C. At that temperature, no thermal polymerization of the anchor was detectable by a ^{1}H-NMR measurement of the residue [41]. Surface coverage of the anchor group was evaluated by injecting toluene/benzanilide mixture into MAS-modified capillaries to compare the dead volume (toluene retention) to benzanilide retention time. Columns showed retention

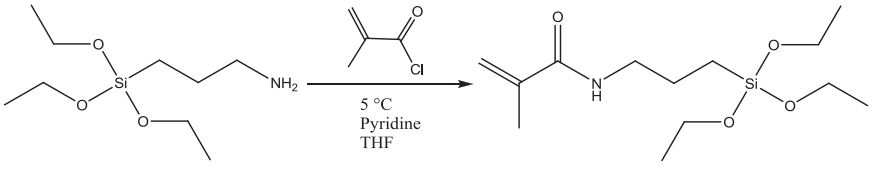


Fig. 2. Schematic preparation of the anchor group (MAS).

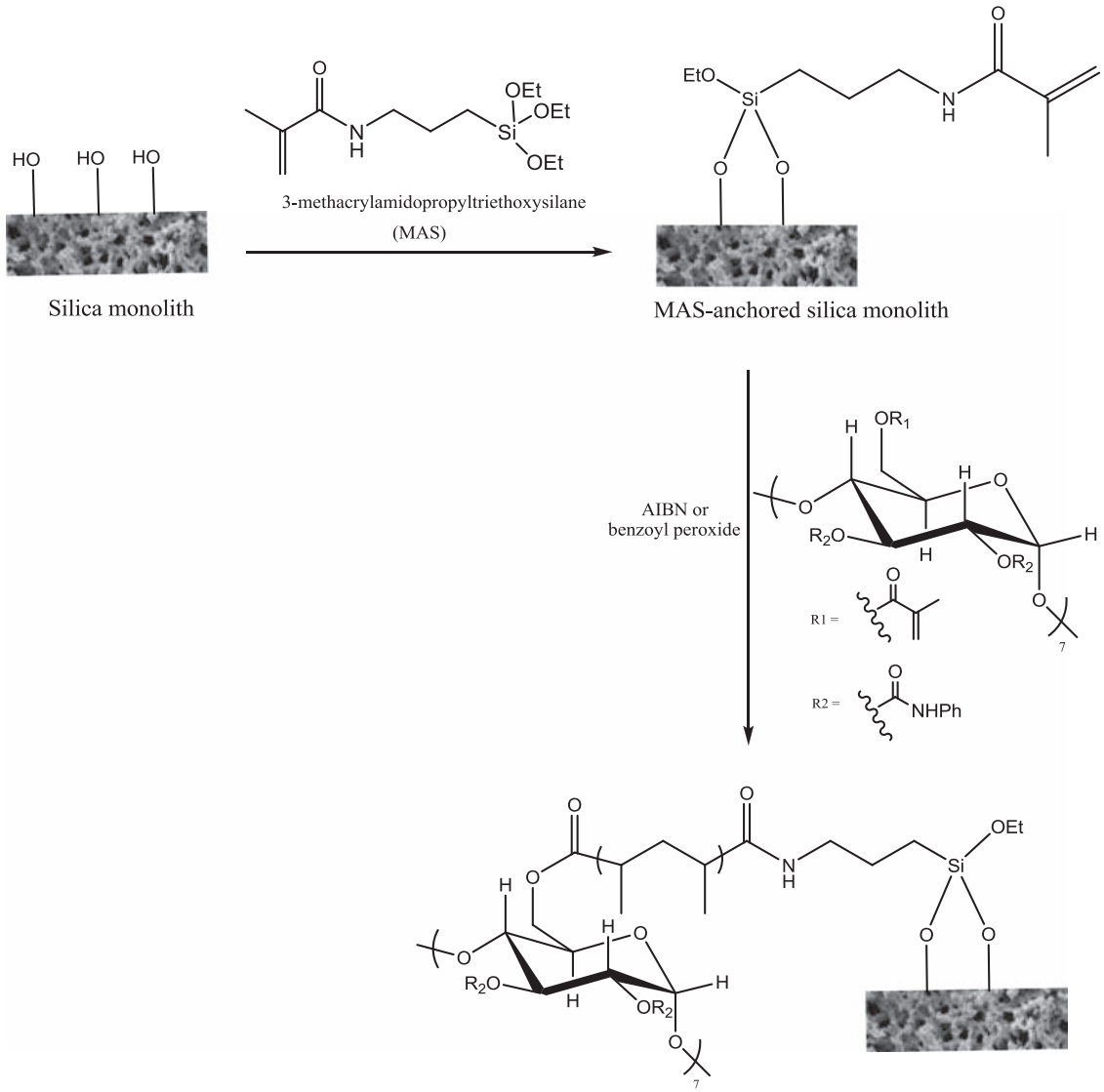


Fig. 3. Schematic diagram for the preparation of β-cyclodextrin-modified silica monolith.

Table 1
Polymer composition in the prepared monoliths [38].

Entry	β-CD monomer (wt%)	EDMA (wt%)	1-Propanol (wt%)	1,4-Butanediol (wt%)	Water (wt%)
A1	10	30	48	6	6
A2	20	20	48	6	6

factors in the range of 1.5–2 were used for the β-CD copolymerization to ensure optimum coverage of the chiral selector. SEM was used to examine anchor-modified silica monoliths for agglomeration of the silane solution during modification. Fig. 4 shows SEM of the silica monolith before (left) and after (right) MAS modification. The capillaries showed homogenous porous structure (Fig. 4).

3.2. Polymer monoliths: Preparation and characterization

For comparison purposes, the previously described polymer monoliths [38] were prepared via *in situ* copolymerization of 2,3,6-tris(phenylcarbamoyl)-β-CD-6-methacrylate as a functional monomer and EDMA as a cross linker in the presence of ternary porogenic system composed of 1-propanol (48%), 1,4-butanediol (6%) and water (6%) (Fig. 5). While the porogen composition was kept constant, the ratio of the functional monomer to the cross linker was varied in attempt to study the effect of CS concentration and column porosity on the enantioselective separation of rcaemates (Table 1).

SEM for A1 and A2 showed homogenous porous structures with interconnecting channels allowing the flow of mobile phase under low column backpressure (Fig. 6).

3.3. Enantioseparation of different classes of pharmaceutical racemates using silica- and polymer-based monoliths

Four columns; AIBN, BOP, A1 and A2, were investigated for the enantioselective nano liquid chromatographic separation of a set of different classes of racemic pharmaceuticals namely: β-blockers, α-blockers, antiinflammatory drugs, antifungal drugs, dopamine antagonists, norepinephrine-dopamine reuptake inhibitors, catecholamines, sedative hypnotics, diuretics, antihistaminics, anticancer drugs and antiarrhythmic drugs. The choice of compounds was arbitrary and guided by our previous investigations [25,38]. A mobile phase composed of acetonitrile and water mixture ranged from 10 to 90% (v/v) was initially tested for the enantioselective separation. No enantioselective separation was observed under

Table 2
Chemical structures and suppliers of the investigated racemates.

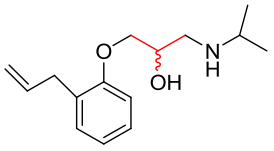
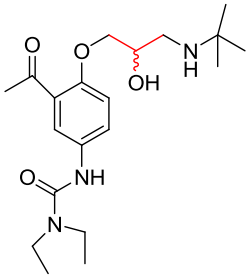
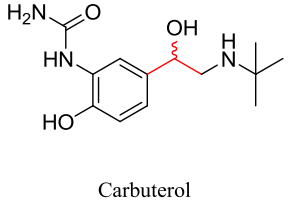
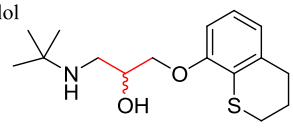
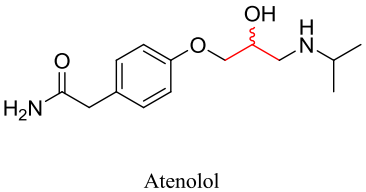
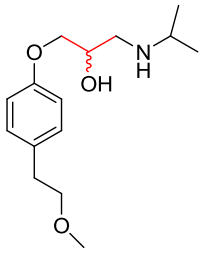
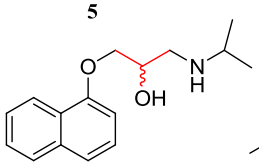
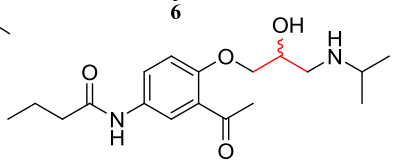
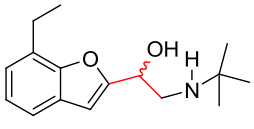
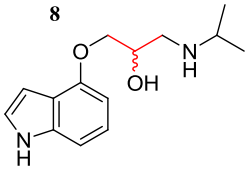
Class	Compound name	Structure	Supplier
β-Blockers	Alprenolol and L-alpenolol	 Alprenolol **1**	3B Scientific Corporation, USA
	Celiprolol and *S*-celiprolol, carbuterol, tertatolol	 Celiprolol **2**  Carbuterol **3**  Tertatolol **4**	American Custom Chemicals Corp., USA
β-Blockers	Atenolol, metoprolol, propranolol, acebutolol, bufuralol, pindolol	 Atenolol **5**  Metoprolol **6**  Propranolol **7**  Acebutolol **8**  Bufuralol **9**  Pindolol **10**	Sigma (St. Louis, MO, USA)

Table 2 (*continued*)

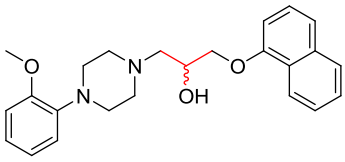
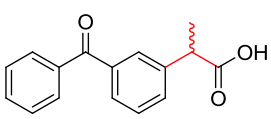
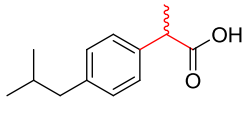
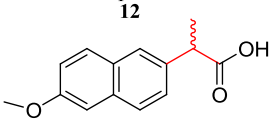
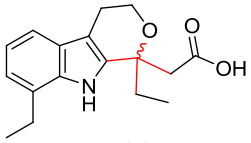
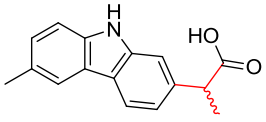
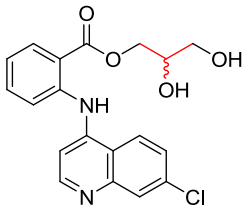
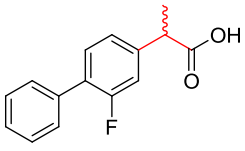
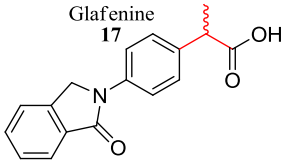
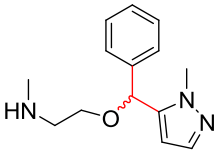
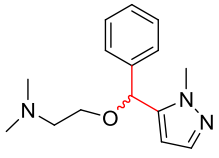
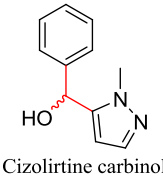
Class	Compound name	Structure	Supplier
α-Blockers	Naftopidil	 Naftopidil **11**	Sigma (St. Louis, MO, USA)
Anti-inflammatories	Ketoprofen, ibuprofen, naproxen, carprofen, etodolac, glafenine, flurbiprofen, indoprofen	 Ketoprofen **12**  Ibuprofen **13**  Naproxen **14**  Etodolac **15**  Carprofen **16**  Glafenine **17**  Flurbiprofen **18**  Indoprofen **19**	Sigma (St. Louis, MO, USA
Anti-inflammatories	Desmethylcizolirtine, cizolirtine, *S*-cizolirtine, cizolirtine carbinol	 Desmethylcizolirtine oxalate **20**  Cizolirtine **21**  Cizolirtine carbinol **22**	American Custom Chemicals Corp., USA
Antifungals	Hexaconazole, cyproconazole, tebuconazole, miconazole, diniconazole, sulconaole		3B Scientific Corporation, USA

Table 2 (*continued*)

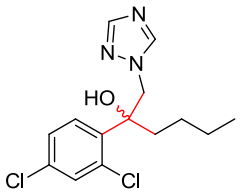
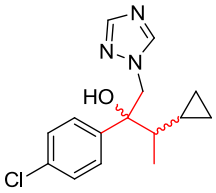
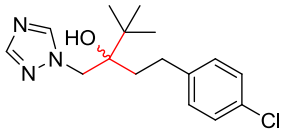
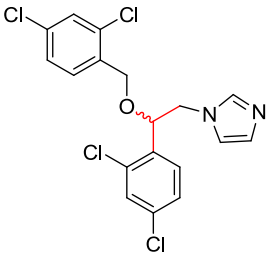
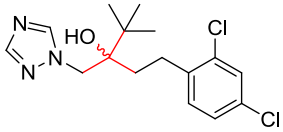
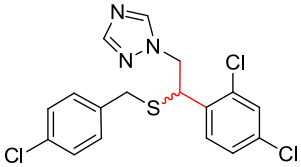
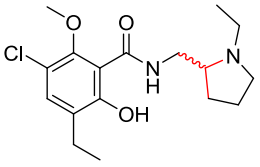
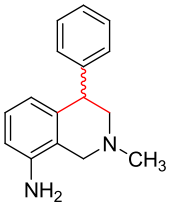
Class	Compound name	Structure	Supplier
		 Hexaconazole **23**	
		 Cyproconazole **24**	
		 Tebuconazole **25**	
		 Miconazole **26**	
		 Diniconazole **27**	
		 Sulconazole **28**	
Dopamine antagonists	Eticlopride	 Eticlopride **29**	American Custom Chemicals Corp., USA
Norepinephrine-dopamine reuptake inhibitors	Nomifensine	 Nomifensine **30**	Sigma (St. Louis, MO, USA
Sedative hypnotics	Aminoglutithimide, phenylglutethimide, 4-bromoglutethimide, *N*-acetylglutethimide, pentobarbital, *p*-hydroxyphenobarbital		American Custom Chemicals Corp., USA

Table 2 (*continued*)

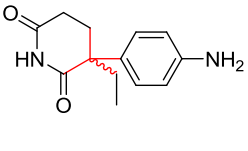
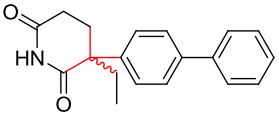
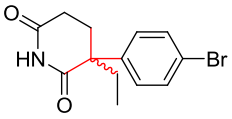
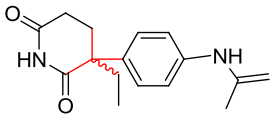
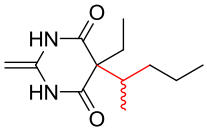
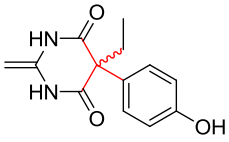
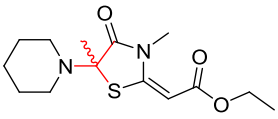
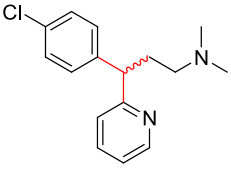
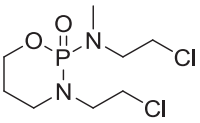
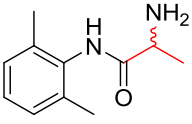
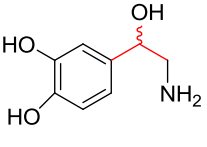
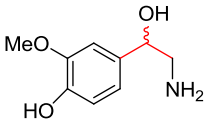
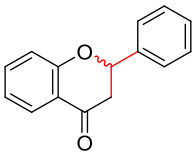
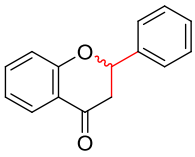
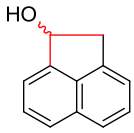
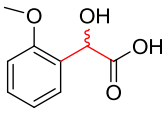
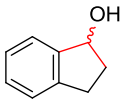
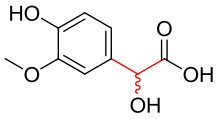
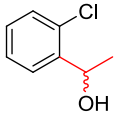
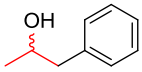
Class	Compound name	Structure	Supplier
		 Aminoglutethimide **31**	
		 Phenylglutethimide **32**	
		 4-bromoglutethimide **33**	
		 *N*-acetylaminoglutethimide **34**	
		 Pentobarbital **35**	
		 *p*-hydroxyphenobarbital **36**	
Diuretics	Etozoline	 Etozoline **37**	American Custom Chemicals Corp., USA
Antihistaminics	Chlorpheniramine	 Chlorpheniramine **38**	Sigma (St. Louis, MO, USA
Anticancers	Ifosfamide	 Ifosfamide **39**	Sigma (St. Louis, MO, USA
Antiarrhythmics	Tocainide	 Tocainide **40**	Sigma (St. Louis, MO, USA
Catecholamines	Arterenol	 Arterenol **41**  Normetanephrine **42**	Sigma (St. Louis, MO, USA

Table 2 (*continued*)

Class	Compound name	Structure	Supplier
Flavonoids	Flavanone, 6-hydroxyflavanone	 Flavanone **43**  6-Hydroxyflavanone **44**	3B Scientific Corporation, USA
Miscellaneous	1-Acenaphthenol, *o*-methoxy mandelic acid, 1-indanol, 4-hydroxy-3-methoxymandelic acid, 1-(2-chlorophenyl)ethane, 1-phenyl-2-propanol	 1-acenaphthenol **45**  *o*-methoxy mandelic acid **46**  1-indanol **47**  4-hydroxy-3-methoxymandelic acid **48**  1-(2-chlorophenyl)ethanol **49**  1-phenyl-2-propanol **50**	Sigma (St. Louis, MO, USA

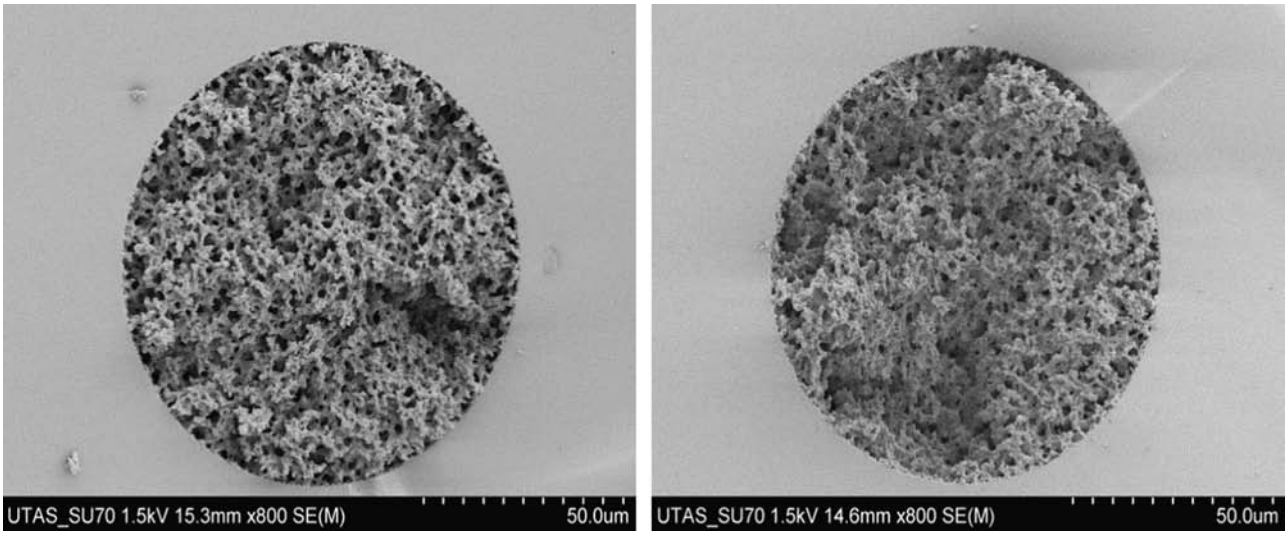


Fig. 4. Scanning electron micrograph of bare silica monolithic column (left) *vs* MAS-modified monolithic column (right) showing homogenous porous monolithic structure in both without any apparent agglomeration.

this condition. However, when aqueous methanol-based mobile phase was used, baseline separation ($Rs \geq 1.5$) was achieved for propranolol **7**, ifosfamide **39**, alprenolol **1**, tertatolol **4**, 1-indanol **47**, tebuconazole **25**, *o*-methoxymandelic acid **46**, celiprolol **2**, cizolirtine **21** and eticlopride **29** while acceptable resolution (*Rs* 1–1.5) was achieved for diniconazole **27**, ketoprofen **12**, metoprolol **6**, desmethylcizolertine **20**, carbuterol **3**, normetanephrine **42** and 6-hydroxyflavanone **44**. Separation (α) and resolution (*Rs*) factors for the baseline/acceptable resolved compounds are listed in Table 3 (cf. Table 3). Comparative chromatograms showing the enantioselective separation on polymer monoliths (A1 and A2 columns) *vs* silica monoliths (AIBN and BOP columns) are also shown in Figs. 7–10. It is worth pointing out that some analytes were resolved on either of the polymer (A1/A2) or silica (AIBN/BOP) monoliths. It was also observed that the silica-based monoliths showed broader enantioselctivities toward diverse chemical

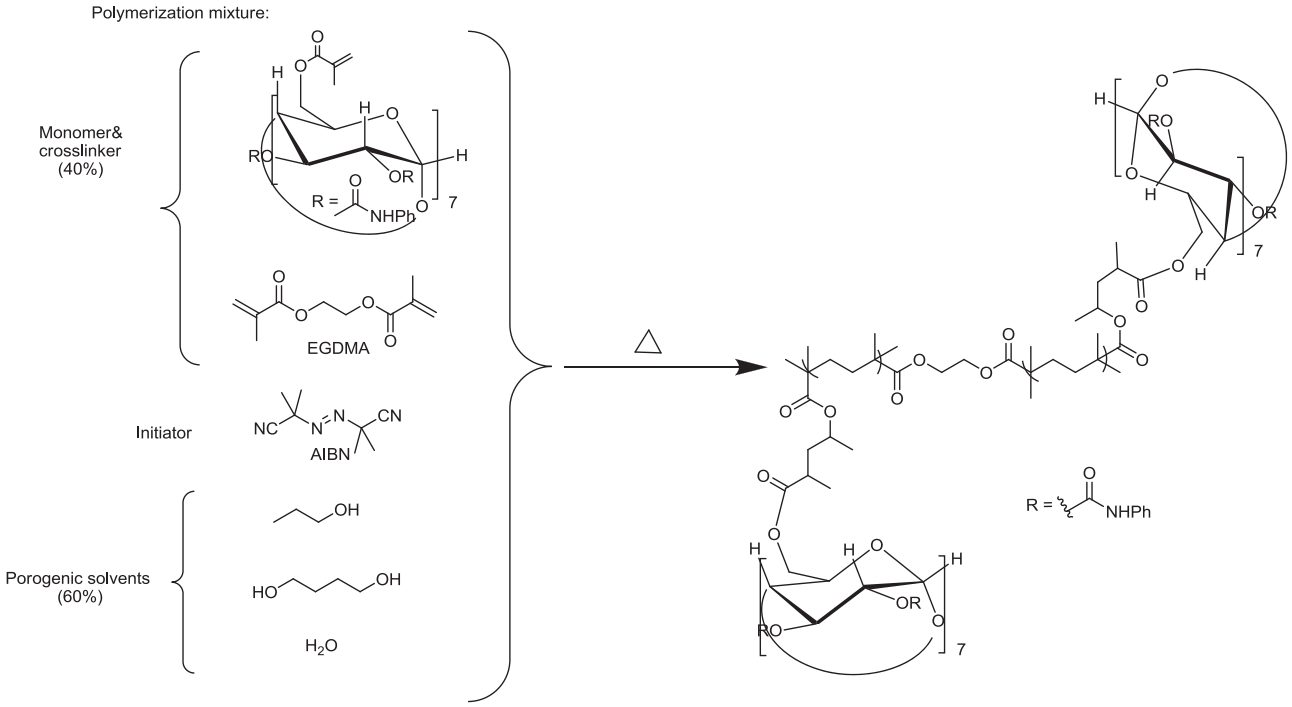


Fig. 5. Schematic diagram showing the preparation of β-CD functionalized polymer monolith [38].

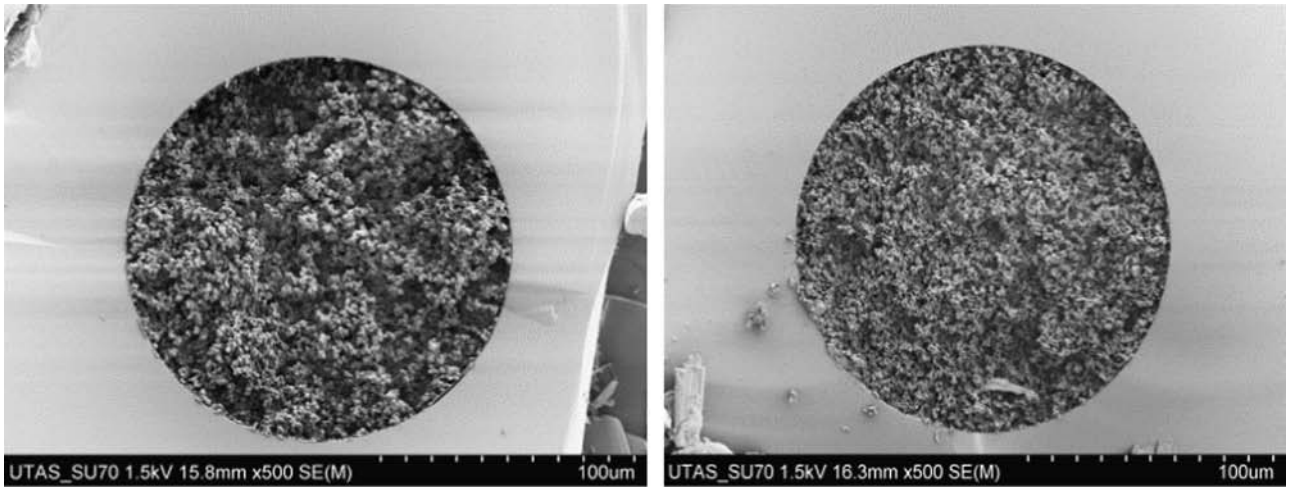


Fig. 6. Scanning electron micrograph of A1 (left) and A2 (right) at 500 × showing homogenous porous monolithic structure [38].

classes of pharmaceutical racemates for example polyhalogenated aromatics such as miconazole **26** and aromatic amides such as eticlopride **29** (Figs. 11 and 12, respectively). Interestingly, the sympathomimetic arternol **41** and its metabolite normetanephrine **42** were acceptably resolved using the silica-based β-CD columns (Figs. 13 and 14) which was not achievable using the polymer monoliths.

It is worth mentioning that the enantioselective separation was achieved under reversed phase conditions which allow the use of less costly solvents and provide easier sample preparation from serum or plasma [43]. Moreover, it eliminates the use of health hazardous solvents such as *n*-hexane. The capillary columns prepared in this study are 10,000 less in internal diameter and operate with one million time less solvent volume than the conventional columns. Consequently, they consume less solvent and produce faster and reproducible separations.

3.4. Insights into the chiral recognition mechanism

The prediction of the chiral recognition mechanisms of CSPs has mainly been based on empirical rules or speculations due to the complexity of the enantioselective separation [44]. Racemates of homologous series of closely related chemical structures tend to interact differently with the chiral selectors resulting in large differences in both enantioselectivities and elution order [45]. It is well established that CDs form transient diastereomeric inclusion complexes with enantiomers by means of the cavity under reversed phase chromatographic conditions. Additionally, derivatization of the external rim hydroxyl groups affords CD derivatives with higher solubility and variable cavity depth with multiple interaction sites [8]. Phenyl carbamate derivatives have been widely explored for the enantioselective separation, their enantioselectivity can be further modulated by introduction of groups

Table 3
Chromatographic parameters, separation and resolution factors for the baseline resolved compounds.

Column	Separated compound	Separation factor (α)	Resolution (*Rs*)
A1	Propranolol	1.39	2.22
	Ifosfamide	1.44	1.65
	Alprenolol	1.89	2.2
	Diniconazole	1.65	1.26
	Ketoprofen	1.46	1.32
	Tertalol	1.67	2.56
	1-Indanol	1.76	2.46
A2	Propranolol	1.52	2.53
	Metoprolol	1.54	1.23
	Tebuconazole	1.45	2.5
	6-Hydroxyflavanone	1.67	1.18
	o-Methoxymandelic acid	1.71	1.58
	Cizolertine	1.72	2.62
	Celiprolol	1.52	1.93
	Tertalol	1.65	2.56
AIBN	Arterenol	1.65	1.36
	Alprenolol	2.1	1.79
	Celiprolol	2.12	2
	Cizolirtine	1.68	2.04
	Eticlopride	2.28	2.44
	Metoprolol	1.62	1.67
BOP	Alprenolol	1.67	1.4
	Miconazole	1.92	1.26
	Bufuralol	1.7	1.46
	Carbuterol	2.44	1.3
	Celiprolol	2.61	1.42
	Cizolirtine	2.28	1.68
	Desmethyl cizolirtine	2.03	1.45
	Methoxymandelic acid	2.1	1.41
	Metoprolol	1.75	1.39
	Normetanephrine	2.43	1.28

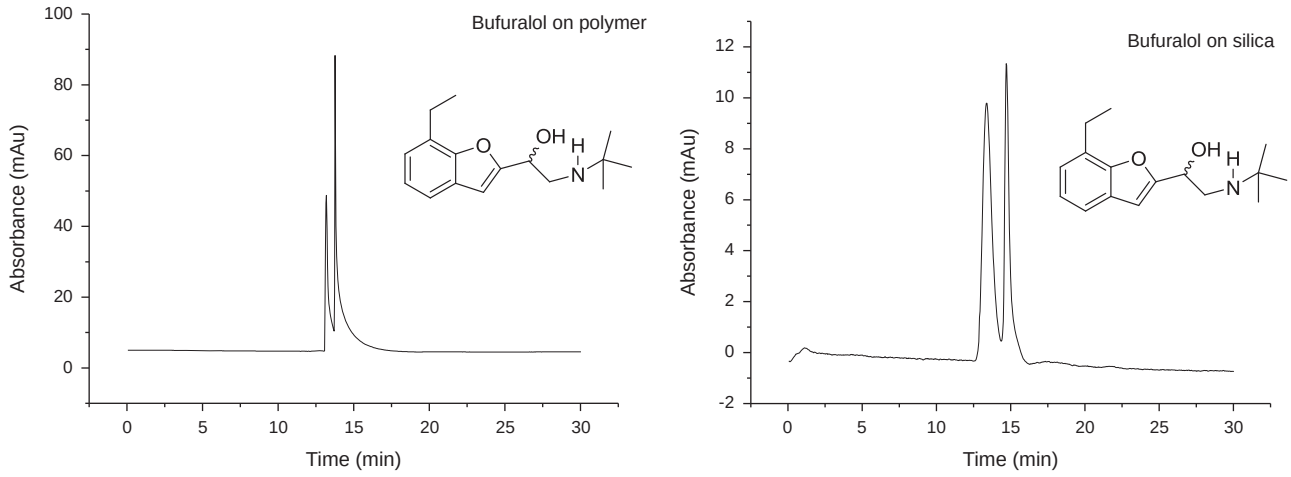


Fig. 7. Enantioselective nano-LC separation of bufuralol: Left: on A1 capillary column (150 μm ID, 25 cm length). Mobile phase: methanol/water (0.1% TFA) 10:90 v/v, UV: 270 nm, flow rate: 0.3 μL/min, Right: BOP capillary column (100 μm, 15 cm), mobile phase: methanol/water (0.1% TFA) 80:20 v/v.

with different electronic effects on the phenyl ring. This suggests that the most important adsorbing sites for the chiral discrimination of on phenyl carbamate derivatives is the polar carbamate group [46]. As demonstrated from testing 50 racemates from different chemical and pharmaceutical classes on four 2,3,6-tris (phenylcarbamoyl)-β-CD-based CSPs, 7 out of the 11 baseline resolved racemates were for chiral centers with secondary alcohols with adjacent electronegative nitrogen bearing alkyl side chain; this underlines the importance of these groups in providing three points of interactions which is required for the chiral recognition as the side chain on the chiral carbon is also thought to be concerned in the chiral recognition mechanism [47]. We postulate that the chiral separation was achieved via the formation of hydrogen bond-stabilized inclusion complexes within the β-CD cavity and the carbamate moiety. It was also observed that the enantioselective separation was mostly achieved at high water content mobile phase; this indicates that water improved the magnitude of interaction between the racemates and the CSP. Aqueous mobile phases allow the inclusion of the whole molecule or just its lipophilic part into the hydrophobic cavity of CD, it has been previously reported that the resolution of this kind of CSP is improved by increase in water content [47]. Interestingly, mobile

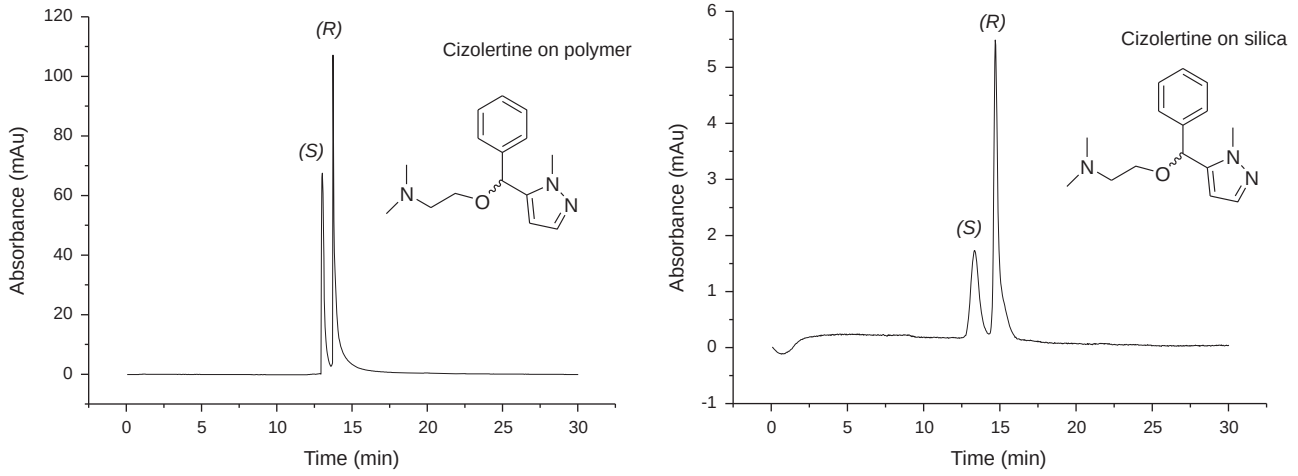


Fig. 8. Enantioselective nano-LC separation of cizolertine: Left: on A2 capillary column (150 μm ID, 25 cm length). Mobile phase: methanol/water (0.1% TFA) 10:90 v/v, UV: 240 nm, flow rate: 0.3 μL/min, Right: BOP capillary column (100 μm, 15 cm), mobile phase: methanol/water (0.1% TFA) 55:45 v/v.

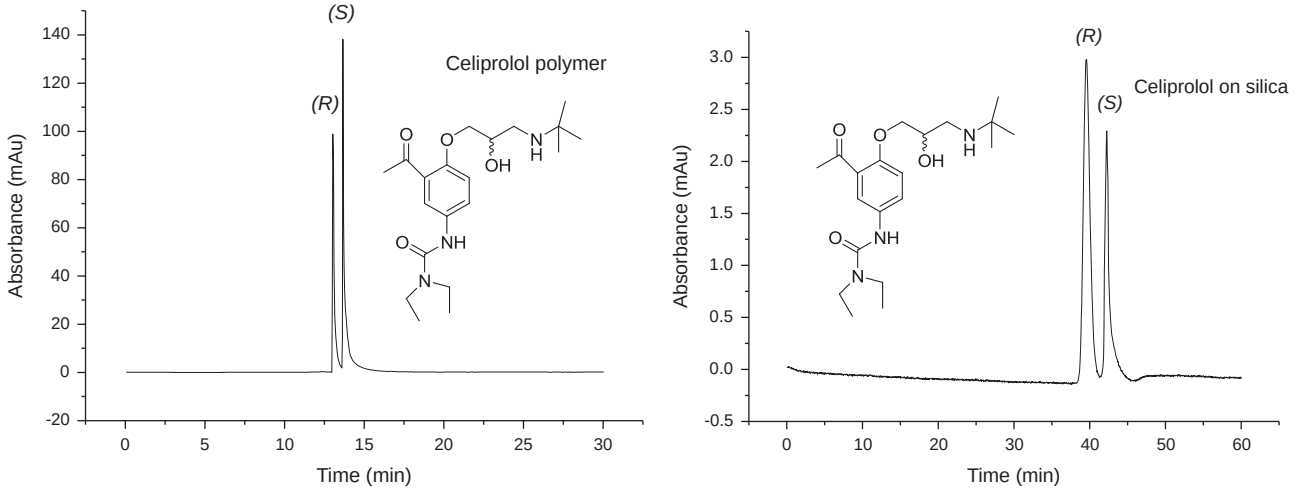


Fig. 9. Enantioselective nano-LC separation of celiprolol: Left: on A2 capillary column (150 μm ID, 25 cm length). Mobile phase: methanol/water (0.1% TFA) 10:90 v/v, UV: 254 nm, flow rate: 0.3 μL/min, Right: AIBN capillary column (100 μm, 25 cm), mobile phase: methanol/water (0.1% TFA) 55:45 v/v.

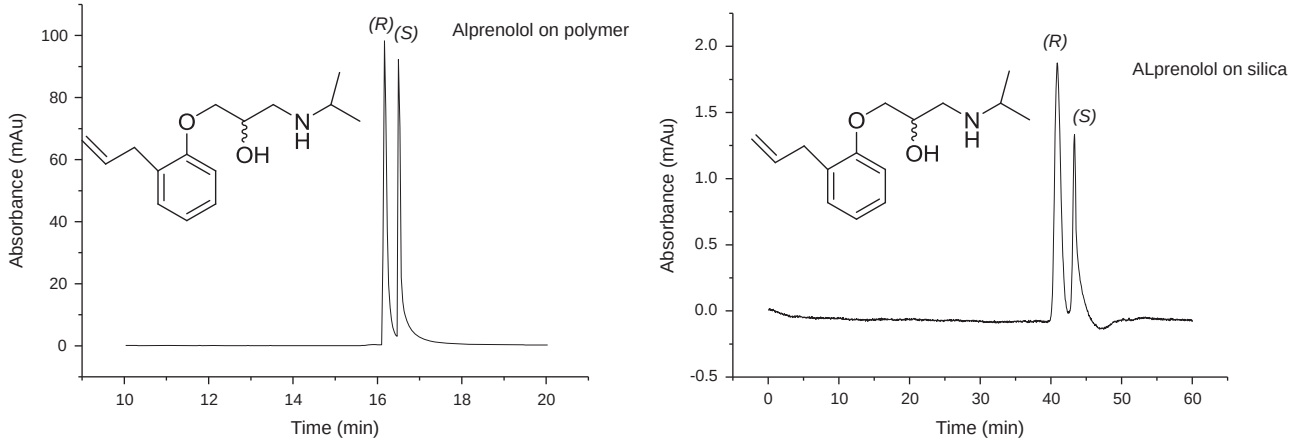


Fig. 10. Enantioselective nano-LC separation of alprenolol: Left: on A2 capillary column (150 μm ID, 25 cm length). Mobile phase: methanol/water (0.1% TFA) 10:90 v/v, UV: 254 nm, flow rate: 0.3 μL/min, Right: AIBN capillary column (100 μm, 25 cm), mobile phase: methanol/water (0.1% TFA) 55:45 v/v.

phase composed of mixture of acetonitrile and water in the range of 10–90% v/v did not furnish any enantioselective separation. On the other hand, when methanol-based mobile phase was used, enantioselective separation was observed; this underlines the importance of solvent polarity in determining retention and chiral separation mechanism in terms of the inclusion complex stability.

It was also demonstrated that the monolith backbone did not play a major role in the chiral separation as mostly the same racemates were resolved on silica or polymer backbone. It is worth

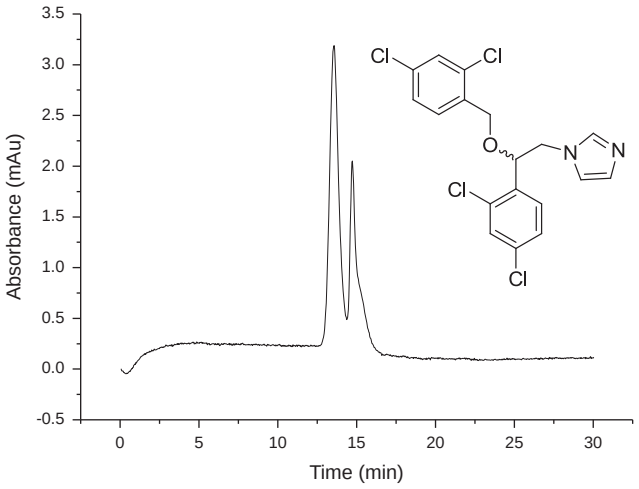


Fig. 11. Enantioselective nano-LC separation of miconazole on BOP capillary column (100 μm, 15 cm), mobile phase: methanol/water (0.1% TFA) 80:20 v/v, UV: 240 nm, flow rate: 0.3 μL/min.

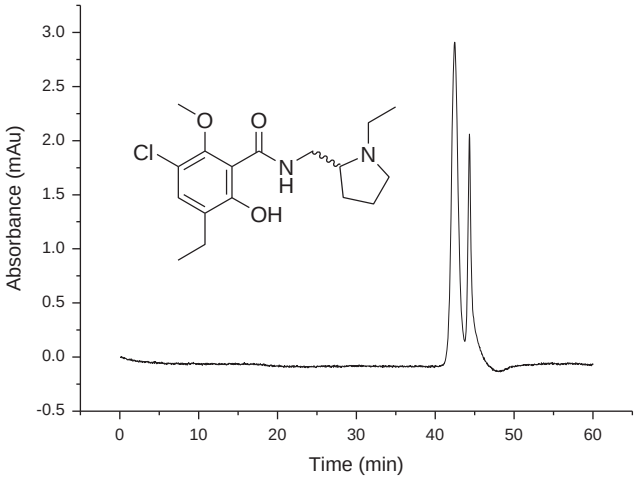


Fig. 12. Enantioselective nano-LC separation of eticloprode on AIBN capillary column (100 μm, 25 cm), mobile phase: methanol/water (0.1% TFA) 55:45 v/v, UV: 270 nm, flow rate: 0.3 μL/min.

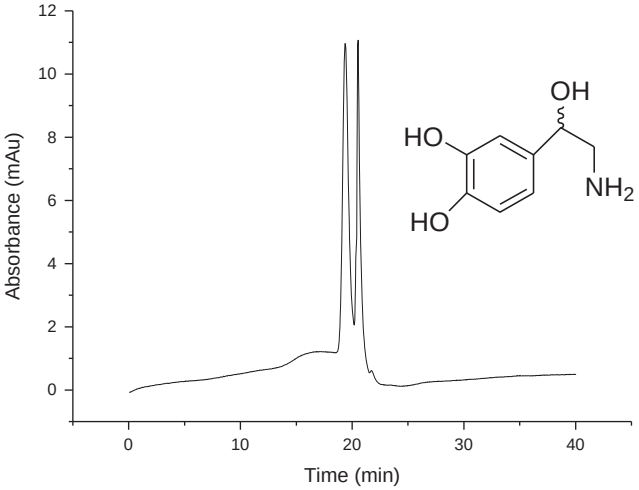


Fig. 13. Enantioselective nano-LC separation of arterenol on AIBN capillary column (100 μm, 25 cm), mobile phase: methanol/water (0.1% TFA) 15:85 v/v, UV: 219 nm, flow rate: 0.5 μL/min.

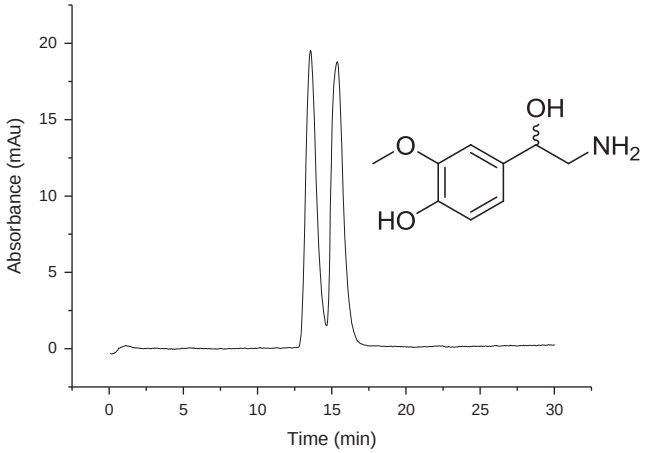


Fig. 14. Enantioselective nano-LC separation of noremetanephrine on BOP capillary column (100 μm, 15 cm), mobile phase: methanol/water (0.1% TFA) 85:15 v/v, UV: 219 nm, flow rate: 0.3 μL/min.

mentioning that polymer monoliths are of smaller surface area and bigger pore size compared to the silica monolith and this had affected the retention times of the racemates but not the enantioselectivity.

4. Conclusions

New β-CD-based CSPs were prepared via the copolymerization of β-CD methacrylate either in one pot or post modification approaches. The prepared columns were investigated for the enantioselective separation of racemates from twelve pharmaceutical classes. β-CD-based silica monolithic capillary columns displayed broader enantioselectivities, nonetheless, the polymer monolith is less time consuming and can be easily reproduced compared with the technically challenging silica monolith preparation. With further option of variation of the porogens/functional monomers ratio composition, tailoring of polymer skeleton will be possible for each separation problem which is still a time consuming process. The enantioselective separation was conducted under reversed phase conditions which augments the environmentally benign nano-liquid chromatographic separations.

Acknowledgements

The authors gratefully acknowledge The Endeavour Program/ Australia Research Award (Project no. ERF_PDR_3853_2014) and the Japan Society for promotion of Science (JSPS) for sponsoring Dr Ghanem's stay at KIT, Kyoto, Japan. Dr. Karsten Gömann, Central Science Laboratory, University of Tasmania (UTAS) for the SEM imaging and the W.J. Weeden scholarship program at the University of Canberra, Australia, for the PhD scholarship offered to Ms. Marwa Ahmed.

References

[1] Global Industry Analysts, Inc., Global Industry Analysts, Inc., San Jose, CA, 2012.
[2] N.M. Maier, P. Franco, W. Lindner, J. Chromatogr. A 906 (2001) 3–33.
[3] E.R. Francotte, J. Chromatogr. A 906 (2001) 379–397.
[4] B. Chankvetadze, J. Sep. Sci. 33 (2010) 305–314.
[5] K.C. Saunders, A. Ghanem, W. Boon Hon, E.F. Hilder, P.R. Haddad, Anal. Chim. Acta 652 (2009) 22–31.
[6] J.P. Chervet, M. Ursem, J.P. Salzmann, Anal. Chem. 68 (1996) 1507–1512.
[7] K. Si-Ahmed, Z. Aturki, B. Chankvetadze, S. Fanali, Anal. Chim. Acta 738 (2012) 85–94.

[8] A. Rocco, A. Maruška, S. Fanali, J. Sep. Sci. 36 (2013) 421–444.
[9] E.A. Arriaga, J. Am. Chem. Soc. 126 (2004) 9874 (9874).
[10] S. Hjerten, J.L. Liao, R. Zhang, J. Chromatogr. 473 (1989) 273–275.
[11] S. Hjerten, J. Mohammad, K.i. Nakazato, J. Chromatogr. 646 (1993) 121–128.
[12] T.B. Tennikova, B.G. Belenkii, F. Svec, J. Liq. Chromatogr. 13 (1990) 63–70.
[13] T.B. Tennikova, M. Bleha, F. Svec, T.V. Almazova, B.G. Belenkii, J. Chromatogr. 555 (1991) 97–107.
[14] H. Minakuchi, K. Nakanishi, N. Soga, N. Ishizuka, N. Tanaka, Anal. Chem. 68 (1996) 3498–3501.
[15] G. Guiochon, J. Chromatogr. A 1168 (2007) 101–168.
[16] R.G.C. Silva, C.B.G. Bottoli, C.H. Collins, J. Chromatogr. Sci. 50 (2012) 649–657.
[17] J. Urban, P. Jandera, Anal. Bioanal. Chem. 405 (2013) 2123–2131.
[18] J. Urban, F. Svec, J.M.J. Fréchet, J. Chromatogr. A 1217 (2010) 8212–8221.
[19] Z. Jiang, N.W. Smith, P.D. Ferguson, M.R. Taylor, J. Sep. Sci. 31 (2008) 27742783.
[20] A. Ghanem, T. Ikegami, N. Tanaka, Chirality 23 (2011) 887–890.
[21] M. Kato, K. Sakai-Kato, N. Matsumoto, T. Toyo'oka, Anal. Chem. 74 (2002) 1915–1921.
[22] W. Bragg, S.A. Shamsi, J. Chromatogr. A 1267 (2012) 144–155.
[23] A. Messina, M. Flieger, F. Bachechi, M. Sinibaldi, J. Chromatogr. A 1120 (2006) 69–74.
[24] R. Mallik, T. Jiang, D.S. Hage, Anal. Chem. 76 (2004) 7013–7022.
[25] M. Ahmed, A. Ghanem, Chirality (in press, DOI 10.1002/chir.22290).
[26] R. Healey, A. Ghanem, Chirality 25 (2013) 314–323.
[27] Y. Xiao, S.-C. Ng, T.T.Y. Tan, Y. Wang, J. Chromatogr. A 1269 (2012) 52–68.
[28] S.M. Han, Biomed. Chromatogr. 11 (1997) 259–271.
[29] Y. Sun, L. Su, Huagong Shikan 25 (2011) 15.
[30] K.K. Chandrul, J. Chem. Pharm. Res. 3 (2011) 822–828.
[31] K. Si-Ahmed, F. Tazerouti, A.Y. Badjah-Hadj-Ahmed, Anal. Bioanal. Chem. 395 (2009) 507–518.
[32] X.-H. Lai, S.-C. Ng, J. Chromatogr. A 1031 (2004) 135–142.
[33] X. Zhang, Y. Zhang, D.W. Armstrong, Module in Chemistry, Molecular Sciences and Chemical Engineering, from Comprehensive Chirality 8 (2012) 177–199.
[34] H. Wikström, L.A. Svensson, A. Torstensson, P.K. Owens, J. Chromatogr. A 869 (2000) 395–409.
[35] C. Karlsson, L. Karlsson, D.W. Armstrong, P.K. Owens, Anal. Chem. 72 (2000) 4394–4401.
[36] M. Wu, Y. Chen, R.a. Wu, R. Li, H. Zou, B. Chen, S. Yao, J. Chromatogr. A 1217 (2010) 4389–4394.
[37] H. Lin, J. Ou, S. Tang, Z. Zhang, J. Dong, Z. Liu, H. Zou, J. Chromatogr. A 1301 (2013) 131–138.
[38] M. Ahmed, A. Ghanem, J. Chromatogr. A 1345 (2014) 115–127.
[39] N. Tanaka, H. Kobayashi, K. Nakanishi, H. Minakuchi, N. Ishizuka, Anal. Chem. 73 (2001) 420A–429A.
[40] O. Nunez, K. Nakanishi, N. Tanaka, J. Chromatogr. A 1191 (2008) 231–252.
[41] T. Ikegami, H. Fujita, K. Horie, K. Hosoya, N. Tanaka, Anal. Bioanal. Chem. 386 (2006) 578–585.
[42] D. Schaller, E.F. Hilder, P.R. Haddad, Anal. Chim. Acta 556 (2006) 104–111.
[43] K. Tachibana, A. Ohnishi, J. Chromatogr. A 906 (2001) 127–154.
[44] X. Bao, R.Q. Snurr, L.J. Broadbelt, Microporous Mesoporous Mater 172 (2013) 44–50.
[45] J.L. Anderson, J. Ding, R.D. McCulla, W.S. Jenks, D.W. Armstrong, J. Chromatogr. A 946 (2002) 197–208.
[46] L. Peng, S. Jayapalan, B. Chankvetadze, T. Farkas, J. Chromatogr. A 1217 (2010) 6942–6955.
[47] J.W. Ryu, D.W. Kim, K.-P. Lee, D. Pyo, J.H. Park, J. Chromatogr. A 814 (1998) 247–252.

Talanta 132 (2015) 315–320

Contents lists available at ScienceDirect

Talanta

journal homepage: www.elsevier.com/locate/talanta

Flow-through, viral co-infection assay for resource-limited settings

Marina Cretich *, Marcello Torrisi, Serena Daminelli, Paola Gagni, Lauren Plavisch, Marcella Chiari

Consiglio Nazionale delle Ricerche (CNR), Istituto di Chimica del Riconoscimento Molecolare (ICRM), Milano, Italy

ARTICLE INFO

Article history:
Received 20 June 2014
Received in revised form
10 September 2014
Accepted 13 September 2014
Available online 3 October 2014

Keywords:
Paper
Nitrocellulose
Resource limited settings
Flow-through immunoassay

ABSTRACT

Here we present a new and rapid immunofiltration assay for simultaneous detection of HIV p24 and hepatitis B virus antigens. The assay platform is composed of a 13 mm nitrocellulose filter spotted with capturing bioprobes and inserted in a Swinnex® syringe filter holder. Samples and reagents are flown through the nitrocellulose filter by manual pressure on the syringe. A colorimetric detection allows for naked eye results interpretation. The assay provides sensitivity in the picomolar range in just 5 min, even using low volumes of sample in complex matrix. Probe deposition by spotting allows for flexible combinations of different capturing agents and multiple diagnoses; furthermore, the very simple and inexpensive set-up makes the syringe-based immunoassay on paper microarray a suitable diagnostic system for resource-limited settings.

© 2014 Elsevier B.V. All rights reserved.

1. Introduction

Conventional and standard methods for pathogen detection include cell culture, PCR and enzyme immunoassays, which are often laborious, require well-equipped dedicated laboratories and take from several hours to several days to perform. Conversely, increased access to diagnostic products requires the development of tests that can be used in remote areas (with no or minimal laboratory infrastructures) by people with little or no laboratory training and that meet the ASSURED criteria [1]. Ideally, for these applications, the detection platform should be simple to use and interpret, stable under a wide range of operating conditions (such as temperature and humidity), portable, disposable and able to perform multiplex tests. Many attempts have been focused on the development of tests based on microfluidic immunoassays targeted at low resource settings (LRSs) [2–4]. However, only a few are complete sample-to-result systems capable of testing blood samples [5–8]. Lateral flow tests (LFTs) may be seen as the gold-standard microfluidic platform in terms of cost, handling simplicity, robustness, market presence and number of lab-on-a-chip applications [9]. The amount of sample and the reagent consumption are moderate, and the concept is mainly used for qualitative and semi-quantitative assays, intended for untrained users. However, the simplicity of LFT is also its main drawback. Assay protocols within capillary driven, flow-through cellulose strips follow a fixed process scheme with limited number of unit operations. Moreover, the highly precise liquid handling and metering is extremely challenging. Other severe drawbacks of LFTs lie in the fact that multiple screening applications, though possible, are difficult to implement.

In LFTs, samples flow in a horizontal direction through a nitrocellulose (NC) membrane towards the adsorbent pad. The horizontal flow causes three major limitations [9,10]: assay time (determined by NC flow rate), "hook effect" (interference due to excess of antigen) and line interference, which makes it difficult to use multiple lines due to the front-line reaction interfering with the behind-line reaction. In immunofiltration assays, the sample and reagents are filtered sequentially through a porous membrane containing spots or lines of capturing antibodies. Succesful examples of immunofiltration assays for detection of small molecules were demonstrated for methamphetamine [11] and the herbicide simazine [12] using water-soluble polyelectrolytes as carriers for the assay reactants. Though highly sensitive, the proposed assays detect only single analytes.

Multiplexed flow-through immunoassays were developed for IgM and antigens specific to *Salmonella typhi* using a 96 well plate connected to a vacuum manifold [13] and a microfluidic cartridge driven by a pneumatic system [14]. Recently, a vertical flow immunoassay was introduced [9] simply by vertically stacking all the components of an LFT, resulting in the detection of C-reactive protein (CRP) concentrations from 0.01 to 10 μg/mL in 2 min. An immunoflow protein platform that actively pumps the sample through an NC membrane was developed, demonstrating detection by fluorescence of 1 pM CRP. Comparing the flow assay to protein microarrays with

* Correspondence to: ICRM - CNR, Via Mario Bianco, 9, 20131 Milano,Italy. Fax: +39 0228500039.
E-mail address: marina.cretich@icrm.cnr.it (M. Cretich).

http://dx.doi.org/10.1016/j.talanta.2014.09.027
0039-9140/© 2014 Elsevier B.V. All rights reserved.

conventional incubation by shaking method the rate of binding is increased by a factor of 10, allowing reduction of assay time without compromising sensitivity. However, all of the above cited works use external actuators like vacuum manifolds or pumps to flow liquids through the membranes.

Here we present a new and rapid immunofiltration assay, suitable for LRSs, for simultaneous detection of HIV p24 and hepatitis B virus (HBV) antigens with sensitivity in the picomolar range. The assay platform is composed of a 13 mm nitrocellulose filter spotted with capturing bioprobes and inserted into a Swinnex® syringe filter holder. Samples and reagents are flown through the nitrocellulose filter by manual pressure on the syringe; alternatevely, liquids can be actuated by a programmable syringe pump. A colorimetric detection enables naked eye results interpretation. Probe deposition by spotting allows for flexible combinations of different capturing agents and multiple diagnosis; furthermore, the very simple and cheap set-up make the syringe-based immunoassay on paper microarray a suitable diagnostic system for resource limited settings.

2. Materials and methods

2.1. Materials

Several filter papers were evaluated: Nitrocellulose Protran BA85 (0.45 μm porosity), Protran BA83 (0.20 μm porosity), PVDF Westran S (0.20 μm porosity) and Westran CS (0.45 μm porosity) from Whatman (GE HealthCare Europe GmbH, Milano, Italy) nitrocellulose BioTrace NT-Blotting, Biotrace NT-transfer (0.20 μm porosity) and PVDF-transfer (0.45 μm porosity) were from Pall Corporation (Pall Italia SRL, Milano, Italy). Biotrace NT-transfer (0.20 μm porosity) was selected for bioassay development. Swinnex® filter holders were from Millipore (Merck KGaA, Darmstadt, Germania). Luer-lok syringes were purchased from Becton Dickinson and Company (Becton Dickinson Italia, Milano, Italy). PBS (phosphate buffered saline), trizma base, bovine serum, tween 20, BSA (bovine serum albumin), and streptavidin–alkaline phosphatase from *Streptomyces avidinii* were purchased from Sigma (St. Louis MO). NBT/BCIP stock solution was purchased from Arrayit Corporation (Sunnyvale CA). HIV p24 antigen, hepatitis B virus (HBV) superficial antigen, corresponding capture and detection biotinilated-antibodies were kind gifts from Dia.Pro., Milano, Italy. The antibody pairs for sandwich immunoassays of HIV p24 and HBV antigens are mouse monoclonal antibodies providing limits of detection in the low pg/mL range when used in proprietary ELISA tests commercialised by Dia.Pro.

2.2. Spotting protocols

Capture antibodies for HIV p24 antigen and hepatitis B superficial antigen (1 mg/mL in PBS) were spotted on Biotrace-NT membranes using a SciFlexArrayer S5 spotter from Scienion (Berlin, Germany). For each replicated spot, 20 droplets (400 pL each) were deposited using a dot-pitch of 800 μm. Streptavidin–alkaline phosphatase (1 U/mL) was spotted as the positive control, and anti-α lactalbumin antibody was used as the negative control. After overnight binding, membranes were washed with PBS and passivated by BSA 2% w/v in PBS for 1 h.

2.3. Incubation protocols

The membranes were inserted on a 13 mm diameter Swinnex® syringe filter holder. Samples containing a mixture of HIV p24 antigen and HBV superficial antigen (HBV-SAg) at different concentrations from 0 to 50 ng/mL either in incubation buffer (Tris/HCl 0.05 M, pH 7.6, NaCl 0.15 M, Tween 20 0.02% w/v, BSA1% w/v) or in pure bovine serum were manually injected through the spotted membranes for 45 s. The sample was then allowed to stay in contact with the membrane for a total incubation time of 5 min. The membranes were then washed with 2 mL washing buffer (0.05 M Tris/HCl, pH 9, 0.25 M NaCl, 0.05% *v*/*v* Tween 20) and 2 mL PBS and then incubated for 10 min with a mixture of biotinylated detection antibodies for HIV p24 antigen and HBV-SAg (1 μg/mL each in incubation buffer) followed by colorimetric detection.

2.4. Colorimetric reaction and detection/quantification protocol

For colorimetric development, the arrays were incubated with streptavidin–AP, 0.1 U/mL in PBS for 10 min at room temperature and washed with PBS. They were then incubated in dark with an NBT/BCIP stock solution in 10 mL Tris–HCl, 0.1 M, pH 9.5 and 0.1 M NaCl for 10 min at 37 °C to speed up the colorimetric reaction and then washed with water. Room temperature incubation for 20 min provides similar results.

The results were visible with naked eye. Pictures of the arrays were taken using a stereo-microscope equipped with a Nikon SMZ 1500 camera and the Infinity Capture software from Lumenera Corporation. ImageJ software was used to analyse the images as follows: luminosities of spots and background were evaluated through the “Measure” function designing circular areas whose colour intensity was calculated by subtracting the backgroud around the spots. The relative intensity (*RI*) of the signals corresponding to the analytes and reported in the graphs was then calculated with the equation

$$RI = (A - N)/P$$

where *A* is the average intensity of analyte corresponding to spots; *N* is the average intensity of negative control spots and *P* is the average intensity of positive control spots. The relative intensities of 6–8 replicate spots were averaged.

2.5. Determination of the limits of detection

For detection limit experiments, the membranes were incubated with a mixture of HIV p24 and HBV-SAg at 100, 50, 20, 5, 2, 1, and 0 ng/mL in PBS or pure bovine serum. The membranes were then incubated with a mixture of biotinylated detection antibodies for HIV p24 and HBV-SAg followed by colorimetric detection and quantification as described above. Calibration curves (dose–response curves) were generated using a three-parameter equation in the OriginLab software. The detection limit was defined as the analyte concentration corresponding to a signal 3 times the standard deviation (SD) above the background signal as calculated from the linear range of the calibration curves.

3. Results and discussion

3.1. Selection of the porous membrane

Seven types of porous membranes, commonly used for western blotting, were tested to perform a colorimetric microarray assay for the detection of HBV superficial antigen (HBV-SAg) as described in Section 2. Relative intensity (*RI*) of spots was detected for a blank sample and for 10 ng/mL HBV-SAg. Fig. 1 reports the quantification of the average intensity of spots and the pictures of the microarray test for 10 ng/mL HBV-SAg performed on different membranes. The Pall nitrocellulose BioTrace membrane with a porosity of 0.2 μm was selected as the object of this study based on the higher intensity of signals, better morphology of spots and lower background intensity.

3.2. Operational set-up

The assay set-up is depicted in Fig. 2. It is composed of a 13 mm diameter nitrocellulose filter spotted with bioprobes inserted in a Swinnex® syringe filter holder. Probe deposition by spotting allows for flexible combinations of different capturing agents and multiple diagnose on the same filter. The sample and the reagents of a sandwich immunoassay are flown through the nitrocellulose filter by manual pressure; alternatively, liquids can be actuated by a programmable syringe pump. After removing the filter from the syringe, a colorimetric detection enables naked eye results interpretation and/or analysis by a camera. This assay set-up differs from available point-of-care platforms in that it is a combination of microarrays and immunofiltration allowing multiplex colorimetric detection of viral antigens in a short assay time. Due to the filtration process, the mass transfer of analytes and reagents to the immobilised antibodies is very efficient, resulting in an assay time of only 5 min (the sample is pushed through the filter for 45 s, and allowed to stay in contact with the membrane for 4 min more). Microarraying probes allow for flexible combinations of different capturing agents and multiple diagnosis. Furthermore, the sequential manual application of assay reagents, the naked eye visible results and the very simple and inexpensive set-up make the syringe-based immunoassay on paper microarray a suitable diagnostic system for resource limited settings.

3.3. Optimisation of sample volume

In order to verify the effect of sample volume on the sensitivity, the assay for the detection of HIV p24 antigen was performed by pushing through the membrane 0.5, 1.0 and 1.5 mL of sample and

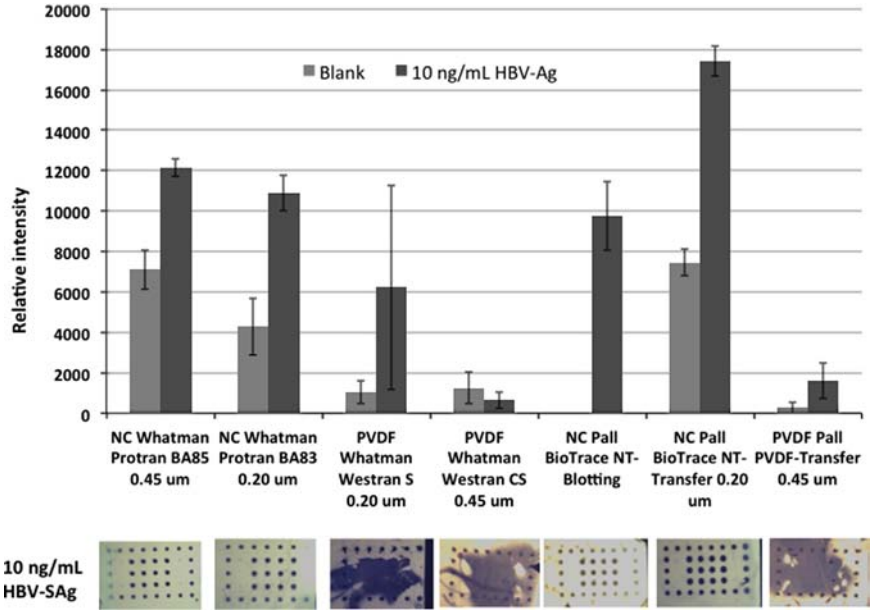


Fig. 1. Microarray test for the detection of HBV superficial antigen performed on seven types of porous membranes, commonly used for western blotting. Relative intensity of spots was detected for a blank sample and for 10 ng/mL HBV-SAg on the central 4×4 array surrounded by an 8×5 frame array as the positive control (streptavidin conjugated to alkaline phosphatase). Lower panel: pictures of the microarray test for 10 ng/mL HBV-SAg performed on the different membranes. The Pall nitrocellulose BioTrace membrane with a porosity of 0.2 μm was selected as the object of this study based on the higher intensity of signals, better morphology of spots and lower background intensity.

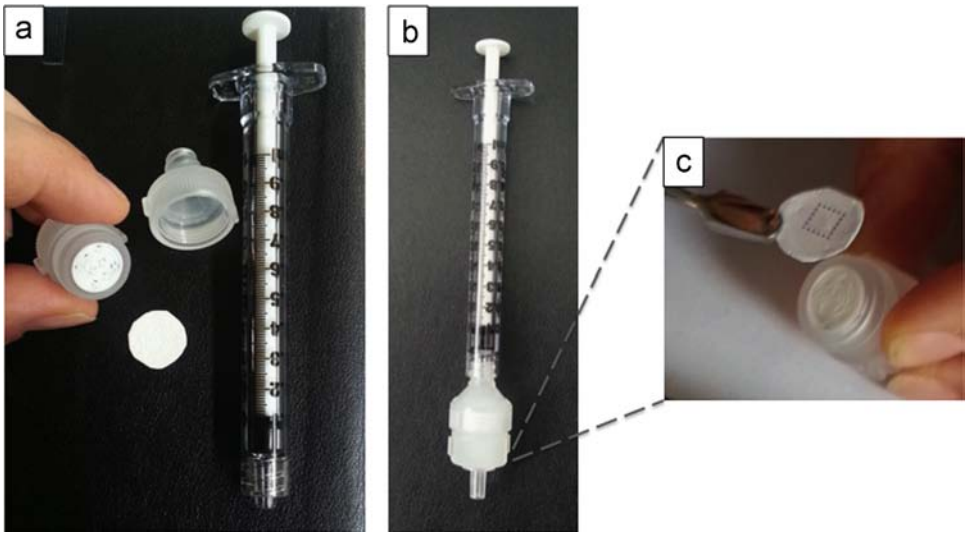


Fig. 2. (a) The assay set-up is composed of a 13 mm nitrocellulose filter spotted with bioprobes and inserted into a Swinnex® syringe filter holder; (b) sample and reagents of a sandwich immunoassay are flown through the nitrocellulose filter by manual pressure; and (c) colorimetric detection allows for naked eye results interpretation.

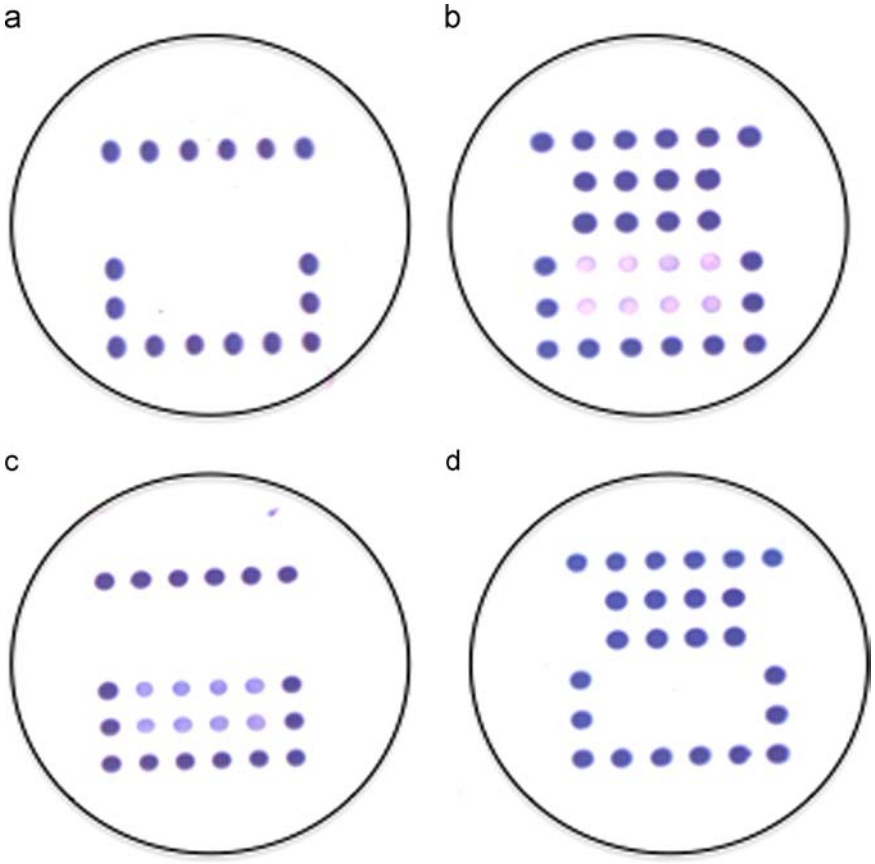
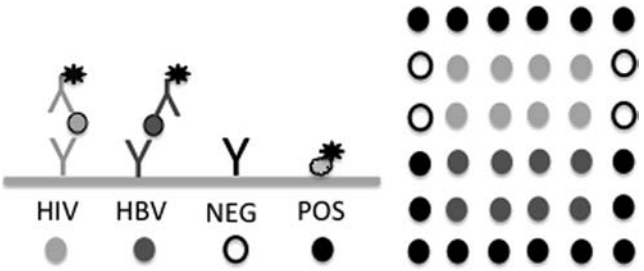


Fig. 3. Detection of HIV p24 antigen (concentrations ranging from 0 to 50 ng/mL) when using different sample volumes: 20 μL, 0.5, 1 and 1.5 mL. The average relative intensity of spots is reported.

Table 1
Limits of detection (LOD) of HIV p24 antigen when using different sample volumes. The assay was performed as described in Section 2.

Sample volume (mL)	0.02	0.5	1	1.5
LOD p24 (ng/mL)	2.79	2.64	0.67	0.42

allowed to stay in contact for an additional 4 min. Furthermore, an experiment was performed using only 20 μL of sample deposited by a pipette and incubated on the membrane for 5 min. Several concentrations of antigen spiked in the buffer were tested (0, 1, 2.5, 5, 10 and 50 ng/mL) in order to determine the limits of detection (LODs) in each of the tested conditions. After incubation with a mixture of the AP-labelled detection antibodies, naked eye visible microarrays were developed by colorimetry for easy detection of the spots. Fig. 3 reports the average relative intensity obtained for each antigen concentration when the four volume amounts were used. A common trend is clearly observable: the larger the sample volume used, the higher the intensity detected in almost every condition. The LODs for HIV p24 antigen using the different sample volumes were calculated as described in Section 2 and are reported in Table 1. The minimum amount of sample used, 20 μL, resulted in a LOD of 2.79 ng/mL whereas the maximum amount of volume tested, 1.5 mL, provided a LOD of 0.42 ng/mL. Provided the assay is not limited by the amount of capturing probe, we observed that keeping the incubation time constant, the higher the volume tested, the better the sensitivity performance. However, the higher LOD of the smaller volume test remains a remarkably low LOD; therefore, the sample volume in the flow through assay can be adjusted, depending on the type of test, to use the minimum sample amount to reach the required sensitivity.



Scheme 1. Spotting scheme. A sandwich immunoassay for the diagnosis of HIV and HBV co-infection is carried out by spotting monoclonal capturing antibodies for HIV p24 antigen and HBV superficial antigen (HBV-SAg); negative control is a non-correlated antibody and positive control streptavidin labelled by alkaline phosphatase (AP). The presence of HIV p24 and HBV-SAg in the sample is detected by biotin-labelled monoclonal detection antibodies and revealed by AP–streptavidin in a colorimetric, naked eye visible microarray.

3.4. Co-infection assay format

Monoclonal capturing antibodies for HIV p24 and HBV-SAg were spotted on the membrane as reported in Scheme 1; a non-correlated capturing antibody is used as negative control whereas streptavidin conjugated to alkaline phosphatase (AP) is the positive control. A scheme of the sandwich immunoassay is reported in Scheme 1. Section 2 reports the optimised assay conditions that were chosen in order to minimise assay time and reagent consumption while keeping the sensitivity performance high. In the first assay step, the sample (500 μL) is manually pushed through the filter in 45 s and allowed to stay in contact with the membrane for 4 min with a total incubation time of less than 5 min. Injection velocity (11 μL/s) and total incubation time were

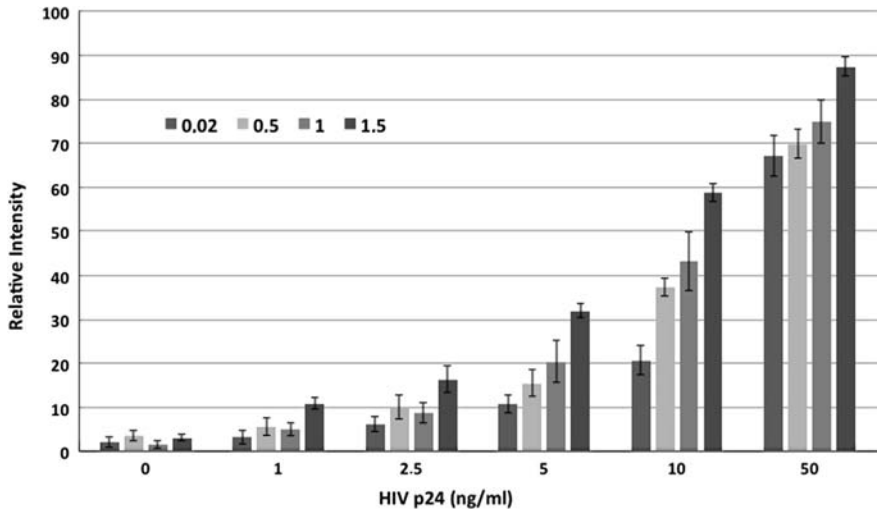


Fig. 4. Pictures of the paper array after colorimetric assay. (a) Detection of blank sample; (b) detection of 10 ng/mL HIV p24 and 10 ng/mL HBV-SAg; (c) detection of 10 ng/mL HBV-SAg and (d) detection of 10 ng/mL HIV p24.

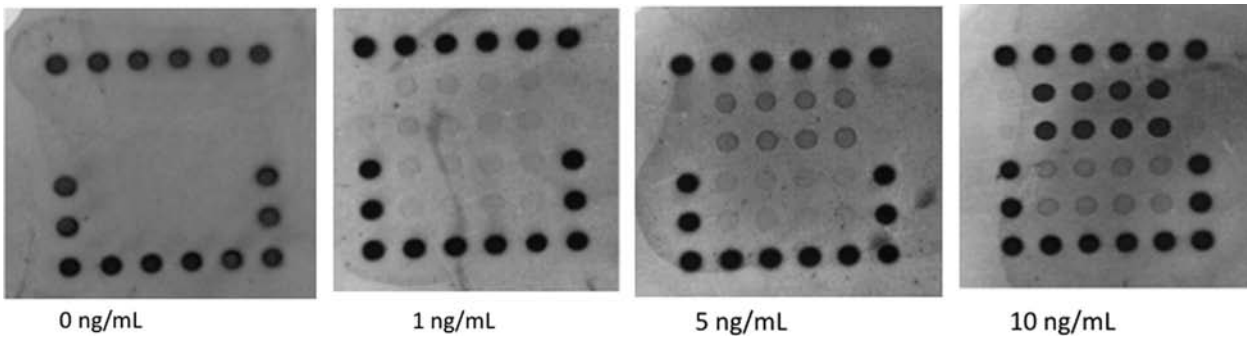


Fig. 5. Pictures of the flow through assay for detection of HIV p24 and HBV-SAg at 0, 1, 5 and 10 ng/mL performed in pure bovine serum. Spots corresponding to the detection of 1 ng/mL are distinguishable from the blank. The assay provided a limit of detection of 0.95 ng/mL for HIV p24 and 1.12 ng/mL for HBV-SAg in 5 min incubation when 1 mL of sample was used.

optimised to strike a balance among ease of manual operation, sample volume consumption, total assay time and performance. After incubation with a mixture of the AP-labelled detection antibodies, naked eye visible microarrays are developed by colorimetry for easy detection of viral antigens resulting in co-infection diagnosis. Typical results are shown in Fig. 4, where detections of a blank sample (Panel a) and a mixture of 10 ng/mL of HIV p24 and HBV-SAg (Panel b) are shown. Panels (c) and (d) show the detection of 10 ng/mL HBV-SAg and HIV p24 antigen respectively. The assay described above was performed using a mixture of 0, 1, 2.5, 5, 10 and 50 ng/mL HIV p24 antigen and HBV-Sag; the co-infection assay resulted in a limit of detection of 1.27 ng/mL for HIV p24 and 2.21 ng/mL for HBV-SAg. Considering a molecular weight of 24 kDa for the HIV p24 antigen and 98 kDa for the HBV-SAg, the limits of detection obtained with 500 μL sample and 5 min incubation are 90 pM for HIV p24 and 13 pM for HBV-SAg.

The effects of a real sample matrix on the membrane background and sensitivity were investigated performing the assay on a bovine serum in which different concentrations of antigens were spiked. Specifically, the assays were performed using a mixture of 0, 1, 2.5, 5, 10 and 50 ng/mL HIV p24 antigen and HBV-SAg spiked in pure bovine serum; 1 mL of serum was incubated for 5 min and the assay was performed as described in Section 2. Fig. 5 reports the pictures of the assay performed at 0, 1, 5 and 10 ng/mL. Spots corresponding to 1 ng/mL antigens spiked in the bovine serum are clearly distinguishable from the blank sample in accordance with the limits of detection provided by the test: 0.95 ng/mL for HIV p24 and 1.12 ng/mL for HBV-SAg. Despite the higher background found when using serum the limits of detection are in the picomolar range even using a complex matrix, thus demonstrating the applicability of the flow through assay in real samples.

4. Conclusions

In the context of pathogen detection, a recurring challenge is to diagnose the diverse co-infections that account for a significant fraction of HIV-associated morbidity and mortality [14]. Standard care at the time of HIV diagnosis includes testing for related opportunistic infections such as those caused by hepatitis C virus (HCV) and hepatitis B virus (HBV) [15]. These multiple diagnoses typically require extensive use of serological diagnostic tools, often in diverse formats, costly and functionally too complex for most LRSs where disease burden is high. The ability to rapidly and inexpensively discriminate HIV mono-infections from more complex co-infections using a simple platform would be a significant advance in the field [16]. A sensitive and multiplex rapid test for HIV co-infection diagnostics would be useful in mobile clinics, correctional facilities, displaced population camps, counselling centres and for immigrant screening, to name a few highly burdened LRSs. Furthermore, military personnel and medical professionals in pre-hospital trauma management require multiplexed tests for use in emergency screening for transfusion transmitted diseases (where no FDA-approved donor screening tests are available) to mitigate risk when emergency blood collections are necessary in austere environments. A microarray for multiplexed detection of HIV p24

and HBV superficial antigen has been recently developed leading to LODs of 54 pg/mL and 45 pg/mL respectively [17]. However, the assay uses silicon chips and a fluorescence scanner for detection with a sample incubation time of 2 h. On the contrary, the flow-through assay presented here, due to manual sequential application of reagents, naked eye visible results and the very simple and cheap set-up makes the syringe based immunoassay on paper microarray a suitable diagnostic system for RLSs. Furthermore, microarraying probes allow for flexible combinations of different capturing agents to develop multiple diagnosis dedicated to specific disease burden.

Acknowledgements

This work was partially supported by the Italian Ministry of University and Research through FIRB “Futuro in Ricerca” project RBFR12OO1G – NEMATIC and CLAN Safe&Smart, and by Regione Lombardia through Project LOCSENS ID 30071637.

References

[1] A.M. Foudeh, T.F. Didar, T. Veres, M. Tabrizian, Lab Chip 12 (2012) 3249–3266.
[2] B. Weigl, G. Domingo, P. LaBarre, J. Gerlach, Lab Chip 8 (2008) 1999–2014.
[3] P. Yager, G.J. Domingo, J. Gerdes, Annu. Rev. Biomed. Eng. 10 (2008) 107–144.
[4] L. Lafleur, D. Stevens, K. McKenzie, S. Ramachandran, P. Spicar-Mihalic, M. Singhal, A. Arjyal, J. Osborn, P. Kauffman, P. Yager, B. Lutz, Lab Chip 12 (2012) 1119–1127.
[5] W.C. Yang, M. Yu, X. Sun, A.T. Woolley, Lab Chip 10 (2010) 2527–2533.
[6] G.A. Messina, N.V. Panini, N.A. Martinez, J. Raba, Anal. Biochem. 380 (2008) 262–267.
[7] K.H. Engler, A. Efstratiou, D. Norn, R.S. Kozlov, I. Selga, T.G. Glushkevich, M. Tam, V.G. Melnikov, I.K. Mazurova, V.E. Kim, G.Y. Tseneva, L.P. Titov, R.C. George, Clin. Microbiol. 40 (2002) 80–83.
[8] T.R. Talbot, K.A. Poehling, T.V. Hartert, P.G. Arbogast, N.B. Halasa, M. Ed, W. Schaffner, A.S. Craig, K.M. Edwards, M.R. Griffin, Vaccine Clin. Infect. Dis. 39 (2004) 641–648.
[9] Y.K. Oh, H.A Joung, S. Kim, M.G. Kim, Lab chip 13 (2013) 768–772.
[10] B.B. Dzantiev, C.M. Ja, J. Park, J. Choi, O.G. Romanenko, A.V. Zherdev, S.A. Eremin, V.A. Izumrudov, Immunol. Lett. 41 (1994) 205–211.
[11] E.V. Yazynina, A.V. Zherdev, B.B. Dzantiev, V.A. Izumrudov, S.J. Gee, B.D. Hammock, Anal. Chem. 71 (1999) 3538–3543.
[12] S. Ramachandran, M. Singhal, K.G. McKenzie, J.L. Osborn, A. Arjyal, S. Dongol, S.G. Baker, B. Basnyat, J. Farrar, C. Dolecek, G.J. Domingo, P. Yager, B. Lutz, Diagnostics 3 (2013) 244–260.
[13] L. Lafleur, D. Stevens, K. McKenzie, S. Ramachandran, P. Spicar-Mihalic, M. Singhal, A. Arjyal, J. Osborn, P. Kauffman, P. Yager, B. Lutz, Lab Chip 12 (2012) 1119–1127.
[14] J.E. Kaplan, et al., Guidelines for Prevention and Treatment of Opportunistic Infections in HIV-Infected Adults: Recommendation from CDC, NIH, MMWR Recommendation Report 58 (2009) 1–207.
[15] S.M. Hammer, J.J. Eron, P. Reiss, et al., J. Am. Med. Assoc. 300 (2008) 555–570.
[16] M.J. Lochhead, K. Todorof, M. Delaney, et al., J. Clin. Microbiol. 49 (2011) 3584–3590.
[17] M. Cretich, M. Bagnati, F. Damin, L. Sola, M. Chiari, Anal. Biochem. 418 (2011) 164–166.

Talanta 132 (2015) 321–326

Contents lists available at ScienceDirect

Talanta

journal homepage: www.elsevier.com/locate/talanta

Microfabricated three-electrode on-chip PDMS device with a vibration motor for stripping voltammetric detection of heavy metal ions

Wen Zhang, Han Zhang, Spencer E. Williams, Anhong Zhou *

Department of Biological Engineering, Utah State University, 4105 Old Main Hill, Logan, UT 84322, USA

ARTICLE INFO

Article history:
Received 10 July 2014
Received in revised form
27 August 2014
Accepted 28 August 2014
Available online 6 September 2014

Keywords:
Microfabricated three-electrode
on-chip device
Vibration motor
Stripping voltammetric detection
Heavy metal ions

ABSTRACT

A microfabricated three-electrode on-chip device with a vibration motor for stripping voltammetric detection of Cd^{2+} and Pb^{2+} ions is introduced. Gold electrodes on a glass substrate are utilized as the counter electrode directly, as well as the working electrode with bismuth coating. The reference electrode is achieved by painting silver/silver chloride layer on the gold layer. Polydimethylsiloxane (PDMS) cover is bonded onto the glass substrate, organizing a compact module. A vibration motor in the device provides vibration as the alternate for stirring to improve detection limits and decrease deposition time. Cyclic voltammetry (CV) is performed with the on-chip reference electrode and a commercial liquid electrolyte Ag/AgCl electrode, showing that the potential shift is less than 20 mV. Differential pulse stripping voltammetry (DPSV) is used to detect Cd^{2+} and Pb^{2+} ions. Linearity is well defined from 10 μg/L to 80 μg/L for both ions. Detection limits for Cd^{2+} and Pb^{2+} ions are 0.7 μg/L and 1.2 μg/L, respectively, at 325 s deposition without vibration; the limits are 0.11 μg/L and 0.25 μg/L at 120 s deposition with vibration. The reliability is verified by detecting Cd^{2+} and Pb^{2+} concentrations of natural water samples and comparing with the results obtained from inductively coupled plasma mass spectrometry (ICP-MS).

© 2014 Elsevier B.V. All rights reserved.

1. Introduction

Heavy metal ions, such as Cd^{2+}, Pb^{2+} and Cu^{2+}, cannot be metabolized in vivo, and they stay in the ecological system [1]. Due to their toxicity and cumulative behaviors, they are of considerable ecological hazard and detrimental effect on human health [2]. Atomic absorption spectrometry (AAS) and inductively coupled plasma mass spectrometry (ICP-MS), which have good precision, high sensitivity and low detection limits, are two typical methods to monitor concentrations of heavy metal ions in the laboratory. However, they are expensive and not suitable for field application because of their complex operations and complicated reagent preparations [3,4].

Electrochemical methods, such as stripping voltammetry, are extensively applied for field measurements of heavy metal ions due to their sensitivity, selectivity, portability and low cost [5,6]. In electrochemical detection, the working electrode often performs an important role because all the reactions occur on its surface. Electrodes with mercury film are often utilized as working electrodes in stripping voltammetry. However, due to the application of highly toxic mercury, new potential pollution will take place [7].

Nowadays there are a number of studies on mercury-free microfabricated electrodes, whose range include new electrode material, novel structure, module package and disposable application [8,9]. In contrast to traditional electrodes, the microfabricated electrodes have special advantages such as increase of mass transport, high signal-to-noise ratio, low cost and good uniformity [10]. Therefore, microfabricated electrodes with different types, such as micro-wire electrode, metal-film electrode and screen-printed electrode, have been applied to detection of heavy metal ions [11,12]. Among the microfabricated electrodes mentioned above, the electrodes with bismuth modification play an important role and are recognized as one of the most powerful tools in heavy metal ion analysis [13]. In brief, two main strategies are often adopted in preparing bismuth-modified electrodes: simultaneous depositing of bismuth and heavy metal onto the working electrode surface (*in situ* bismuth coating) and pre-coating bismuth film (*ex situ* bismuth coating) [14]. By *in situ* bismuth coating, impurities formed on the surface of working electrode can be removed with each cycle, as well as bismuth film can be renewed for each detection; however, this method may bring coating issues in detecting natural samples, and the performances of the *in situ* bismuth coating may be affected by the properties of

* Corresponding author. Tel.: +1 435 213 8716.
E-mail address: Anhong.Zhou@usu.edu (A. Zhou).

http://dx.doi.org/10.1016/j.talanta.2014.08.075
0039-9140/© 2014 Elsevier B.V. All rights reserved.

the samples, worsening the accuracy, precision and sensitivity [14,15]. By *ex situ* bismuth coating, electrodes often show better precision in measurements for natural samples with periodic bismuth-coating renewal or disposable application [16].

There are increasing demands for the microfabricated electrodes with bismuth modification or other modification methods in detection of heavy metal ions. However, the microfabricated electrodes in those applications still suffer from some disadvantages. In some measurements, traditional electrodes are often used as the reference and counter electrodes, so the maintenance for the traditional electrodes, especially for the liquid electrolyte Ag/AgCl electrode, is still needed [17]. Besides, typical detection limits of the microfabricated electrodes are about 1–2 μg/L, which are insufficient for the detection of trace heavy metal ions with less than 1 μg/L concentration [18,19]. Moreover, long deposition time, which may be 300–500 s, is often required to get better signal-to-noise ratio and lower detection limits [20].

In this study, we introduce a novel microfabricated three-electrode on-chip device with a vibration motor; the integration of all three electrodes contributes to simplification of the instrumentation; vibration produces stable convection conditions and thin diffusion layer for the working electrode [21,22], which help to achieve quick measurement and improve the detection limits of Cd^{2+} and Pb^{2+} ions. Thermal evaporation is utilized to deposit gold layer with specialized shapes and connections on a glass substrate. Two 2 × 2 mm square gold electrodes, which are parallel connected externally, are adopted as the working electrode with *ex situ* bismuth coating. In this configuration, each of two gold working electrodes is also possible to be separated and modified with different coatings for detection of more ions in the future. Silver/silver chloride layer is painted onto a rectangular gold surface thus resulting in a solid on-chip reference electrode. A U-shape gold electrode is used as the counter electrode, which surrounds the reference electrode and provides shielding from possible electromagnetic interference. A compact module and an integrated measurement cell are organized by bonding a master-mold-based polydimethylsiloxane (PDMS) cover layer onto the glass substrate. Furthermore, a coin-size vibration motor installed in the module provides vibration function as the alternate for stirring (Fig. 1).

2. Experiments

2.1. Reagents and materials

Silver/silver chloride paste was purchased from Gwent group, United Kingdom. Dow Corning PDMS (Sylgard 184) and silicone adhesive were purchased from Krayden, Inc. (Westminster, Colorado, USA). Coin-size vibration motor was purchased from Digikey, USA. Standard solutions (1000 mg/L Zn^{2+}, Cd^{2+}, Pb^{2+} or Cu^{2+} in 2% HNO_3), acetate buffer (0.1 M, pH 4.6) and phosphate buffered saline (PBS, 0.01 M, pH 7.4) were purchased from Fisher Scientific, USA. Standard solutions (1000 mg/L Sn^{2+} in 2% HNO_3, 1000 mg/L Sb^{3+} in 10% HNO_3) were purchased from Ultra Scientific, USA. Potassium ferri(III)cyanide ($K_3[Fe(CN)_6]$), potassium ferro(II)cyanide ($K_4[Fe(CN)_6]$), bismuth nitrate ($Bi(NO_3)_3 \cdot 5H_2O$), KCl and HNO_3 were purchased from Sigma-Aldrich, USA and of guaranteed reagent (GR) grade. All solutions were prepared with 18 M Ohm cm deionized water from Milli-Q ultrapure water purification system.

2.2. On-chip device fabrication

Fabrication procedures for the microfabricated three-electrode on-chip device are presented in Fig. 2. Firstly, a polytetrafluoroethylene (PTFE) master mold for TE is designed with AutoCAD software and manufactured with a computerized numerical control (CNC) machine. A PDMS mask is acquired by replicating from the PTFE master mold, exposing areas for TE process. Secondly, a 25 × 50 × 1 mm glass substrate, which is covered by the PDMS mask, is prepared. Chromium layer with 15 nm thickness is deposited onto the glass substrate as the adhesive layer with TE instrument (Auto E306, Edwards, United Kingdom), and then 200 nm gold layer is deposited onto the adhesive layer accordingly. In the next step, the PDMS mask is removed, and the glass substrate is rinsed with isopropyl alcohol and deionized water.

A PDMS cover master mold is fabricated with similar process, and a PDMS cover layer with 10 mm thickness is prepared. A 10 × 12 mm hollow area in the PDMS cover layer is reserved for

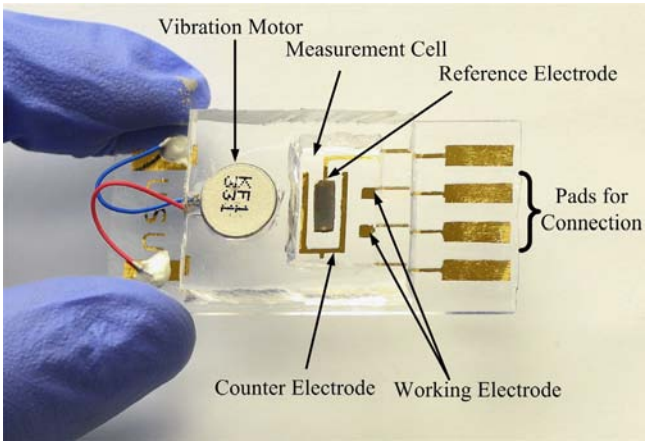


Fig. 1. Photo of the microfabricated three-electrode on-chip device.

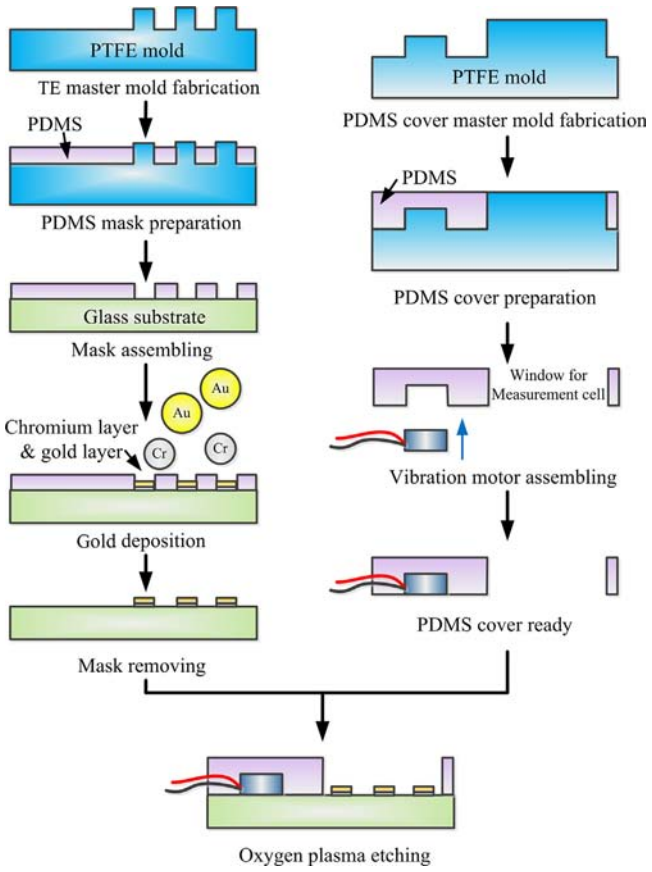


Fig. 2. Basic process flow for the fabrication of the on-chip device.

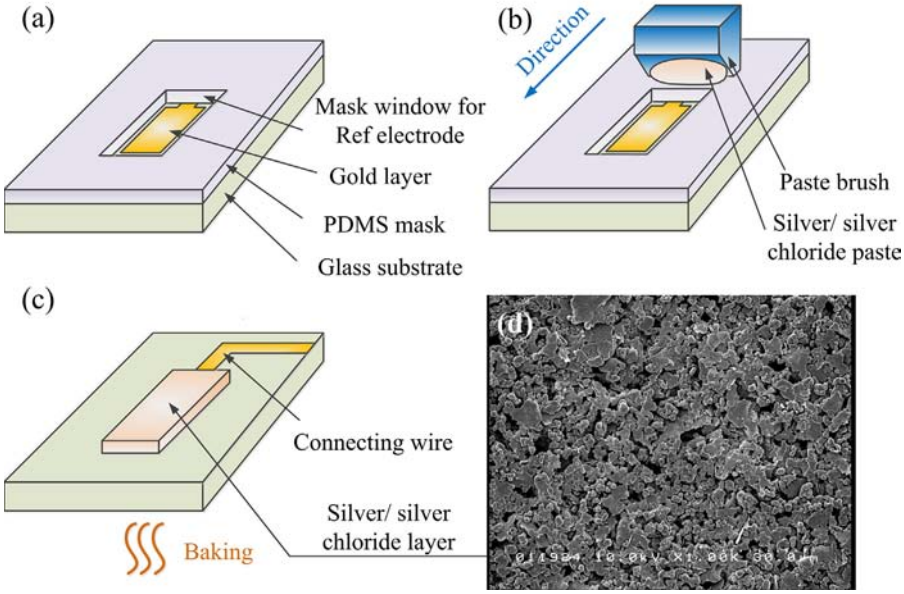


Fig. 3. Schematic representation of the on-chip reference electrode preparation: (a) a PDMS mask exposes the reference electrode area, (b) silver/silver chloride film is painted, (c) the PDMS mask is removed and the device is baked, (d) to form a solid silver/silver chloride layer, whose microstructure is shown by an SEM image.

the measurement cell, as well as the space with 10 mm diameter and 5 mm thickness is reserved for the vibration motor. After that, the motor is assembled into the PDMS cover layer. Finally, the glass substrate and the PDMS cover layer are bonded with oxygen plasma etching (45 s).

2.3. Fabrication of Ag/AgCl reference electrode

To fabricate a solid on-chip reference electrode, film painting process is introduced. It is important to do this step after the PDMS bonding to avoid undesirable influence from oxygen plasma etching. The fabrication procedures are illustrated in Fig. 3. Firstly, ethanol is used to clean the electrodes in the measurement cell, and then the electrodes are dried in nitrogen steam. Secondly, the area in the measurement cell is covered by a 0.2 mm thickness PDMS mask, exposing a window for the reference electrode (Fig. 3a). Then silver/silver chloride paste is painted into the window (Fig. 3b). This step can be fulfilled by either a machine for surface-mount technology (SMT) or manual operation. After the painting step the PDMS mask is removed, and the device is baked at 75 °C (Isotemp oven, Fisher, USA) for 150 s to organize a solid silver/silver chloride layer. A scanning electron microscope (SEM; S-4000, Hitachi, Japan) image of the solid silver/silver chloride layer is given in Fig. 3d, showing uniform microstructures. Moreover, the bare wire of the reference electrode in the cell is covered and protected by silicone adhesive. Finally, cyclic voltammetry (CV) experiments are conducted to assess the performance of the on-chip reference electrode.

2.4. Working electrode preparation

Bismuth coating on the working electrode is performed after reference electrode validation. Firstly, the electrodes, as well as the measurement cell, are rinsed with deionized water. After that, bismuth-coating solution, which contains 0.02 M Bi^{3+} and 0.1 M KCl, is put into the measurement cell. A constant deposition potential of −0.95 V is applied to the working electrode for 300 s. The vibration motor is disabled in the bismuth-coating process. Finally, the electrodes in the measurement cell are rinsed with deionized water and ready for further experiments.

2.5. Electrochemical experiments

A commercial potentiostat analyzer (CHI-1220, CH instruments, USA) is utilized in all electrochemical experiments. To assess the performance of the on-chip reference electrode, CV experiments are performed in solution which contains 0.05 M $K_3[Fe(CN)_6]$, 0.05 M $K_4[Fe(CN)_6]$ and 0.01 M PBS, as well as 0.1 M KCl as supporting electrolyte. Besides, a commercial liquid electrolyte Ag/AgCl electrode (CHI-111, CH instruments, USA) is used for comparison experiments to evaluate the performance of as-fabricated Ag/AgCl reference electrode. Moreover, the effect of vibration on electrochemical responses is evaluated by detecting heavy metal ions, such as Cd^{2+} and Pb^{2+} in water sample, with differential pulse stripping voltammetry (DPSV).

2.6. ICP-MS detection of natural water samples

The ion profiles of natural water samples are detected by Agilent 7700 ICP-MS in Utah Water Research Laboratory. Fifty milliliter of each sample is digested using an Environmental Express hotblock and refluxed at 115 °C with 5 mL trace metal grade nitric acid. Once samples evaporate to 10 mL, they are cooled and ultrapure water is used to fill back to 50 mL volume. Samples are filtered with a 0.45 μm plunger filter and then ready for ICP-MS analysis.

3. Results and discussions

3.1. Evaluation of the fabricated on-chip reference electrode

CV is a popular technique which is widely used for studying electrochemical performance of electrodes. In the CV experiments, the counter electrode, working electrode (without bismuth coating) and reference electrode in the on-chip device are used firstly. Ferri(III)cyanide/ferro(II)cyanide redox couple is chosen to evaluate the performance of the on-chip reference electrode. The potential scan window is of −0.2 V − 0.4 V. Ferro(II)cyanide is oxidized to ferri(III)cyanide in the forward scan, as well as ferri(III) cyanide is reduced to ferro(II)cyanide in the backward scan. The

redox peaks can be achieved in both forward and reverse scans. The performance of the on-chip reference electrode can be evaluated by the shapes and positions of the redox peaks [23]. A group of CV curves are obtained by measuring the current of the working electrode at different scan rates (25 mV/s, 50 mV/s, 75 mV/s and 100 mV/s). The shapes of all the CV curves are nearly identical and show clear redox peaks (supplementary Fig. S1a). The peaks show regular gradient slopes with increasing scan rates, and there is no obvious potential shift between the peaks. The reduction peak and oxidation peak can be found at around 0.105 V and 0.2 V, respectively. The potential difference of redox peaks is about 95 mV due to the microfabricated structure of the working electrode, which is larger than approximate 60 mV for traditional gold working electrode [24].

Comparison of CV experiments is performed accordingly by using a commercial liquid electrolyte Ag/AgCl electrode as well as the counter electrode and working electrode in the on-chip device. The comparison of CV experiments are with the same setting for electrochemical parameters. CV curves for the contrast experiments (supplementary Fig. S1b) are similar to the curves for the on-chip reference electrode. The reduction peak and oxidation peak at around 0.09 V and 0.185 V can be viewed. It can be deduced that the potential shift between the on-chip reference electrode and commercial reference electrode is less than 20 mV.

3.2. Evaluation of the vibration function

DPSV experiments are performed for detection of Cd^{2+} and Pb^{2+} ions. Deposition potential is −1.0 V and scan window is −1.0 V - −0.4 V; amplitude of pulse is 25 mV; step potential change is 5 mV; period of pulse wave is 50 ms. Solution containing 0.1 M acetate buffer (pH=4.6), 50 μg/L Cd^{2+} and 50 μg/L Pb^{2+} ions is adopted in this stage. The above initial setting for DPSV is similar to recent studies [25]. The counter electrode, reference electrode and working electrode in the on-chip device are used. Before the measurements, bismuth coating is carried out on the surface of the gold working electrode. With and without vibration, the DPSV responses are recorded and compared to each other.

Firstly, the vibration condition is optimized. Suggested working voltage of the motor is ranged from 1 V to 3 V DC. The vibrating frequencies are monitored by using an oscilloscope (MSO 2024 A, Tektronix, USA) with a current probe in this working range, as well as the DPSV current peaks for 50 μg/L Cd^{2+} and 50 μg/L Pb^{2+} ions are recorded with 50 s deposition time (Fig. 4). The peaks for Cd^{2+} ion reach saturation when the motor voltage is over 2.4 V, and the peaks for Pb^{2+} ion drop down when the motor voltage exceeds 2.2 V. As a result, the optimized working voltage for the motor is confirmed as 2.2 V.

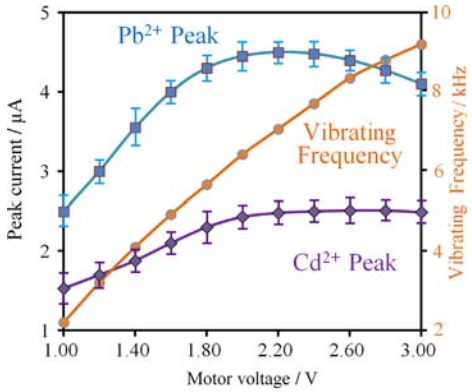


Fig. 4. DPSV current peaks for solution containing 50 μg/L Cd^{2+} and 50 μg/L Pb^{2+} ions (50 s deposition) vs. motor voltage (n=3).

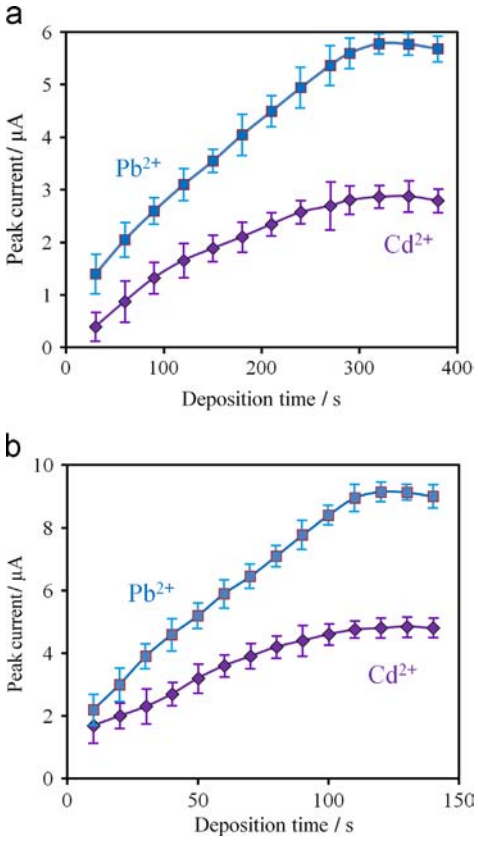


Fig. 5. Effect of the deposition time on the DPSV current peaks of Cd^{2+} and Pb^{2+} (a) without vibration and (b) with vibration for solution containing 50 μg/L Cd^{2+} and 50 μg/L Pb^{2+} ions (n=3). (a) w/o vibration and (b) w/ vibration.

After that, comparison DPSV experiments is carried out accordingly. During the experiments, all parameter settings remain unchanged except the deposition time and vibration condition. The current peaks for Cd^{2+} and Pb^{2+} ions are about 0.6 μA and 1.4 μA with 50 s deposition time when the vibration motor is disabled. The peaks increase to about 1.2 μA and 2.5 μA with 120 s deposition time. In contrast to results without vibration, the peaks more than 2 μA and 4 μA for Cd^{2+} and Pb^{2+} ions, respectively, can be obtained with vibration and 50 s deposition time (supplementary Fig. S2).

Furthermore, the effects of deposition time on current peaks are investigated by two groups of experiments as shown in Fig. 5. In the first group, the vibration is disabled, and the range of deposition time is 25 s–375 s. The current peaks for Cd^{2+} and Pb^{2+} ions increase obviously in the range of 25 s–325 s, and they drop down with more than 325 s deposition time (Fig. 5a). Maximum current peaks for Cd^{2+} and Pb^{2+} ions are approximately 2.8 μA and 5.7 μA with 325 s deposition time, respectively. Vibration is enabled during deposition step in the second group, and the range of deposition time is 10 s–140 s. The maximum current peaks, as much as 4.3 μA and 8.9 μA for Cd^{2+} and Pb^{2+} ions, respectively, are acquired with 120 s deposition time (Fig. 5b).

Moreover, solution containing 0.1 M acetate buffer, 5 μg/L Cd^{2+} and 5 μg/L Pb^{2+} ions is prepared. The detection limits of the on-chip device are calculated as three times of the standard deviation (3σ) of the analytical results for this low concentration solution [18]. The detection limits for Cd^{2+} and Pb^{2+} ions are 0.7 μg/L and 1.2 μg/L without vibration (325 s deposition time), respectively; the detection limits for Cd^{2+} and Pb^{2+} ions can reach as low as 0.11 μg/L and 0.25 μg/L with vibration and 120 s deposition time, which are noticeable better than recent reports [18,19]. It can be

concluded that vibration function brings quicker deposition, higher sensitivity and lower detection limits for Cd^{2+} and Pb^{2+} ions detection.

3.3. Measurements for multi-concentration samples

Eight solutions containing 0.1 M acetate buffer, 10 μg/L–80 μg/L of Cd^{2+} and Pb^{2+} ions (10 μg/L step) are prepared. DPSV experiments are with vibration and 120 s deposition time. Typical DPSV curves for these solutions are shown in Fig. 6a. Current peaks for Cd^{2+} and Pb^{2+} ions are well defined, showing regular increment over the concentration range. The calibration plots of current peak versus ion concentration are presented in Fig. 6b, which show that the linearity is well defined from 10 μg/L to 80 μg/L. The calibration curves and correlation coefficients are $y=0.121x - 0.82$, $r=0.996$ for Cd^{2+} and $y=0.192x - 0.37$, $r=0.991$ for Pb^{2+}, respectively.

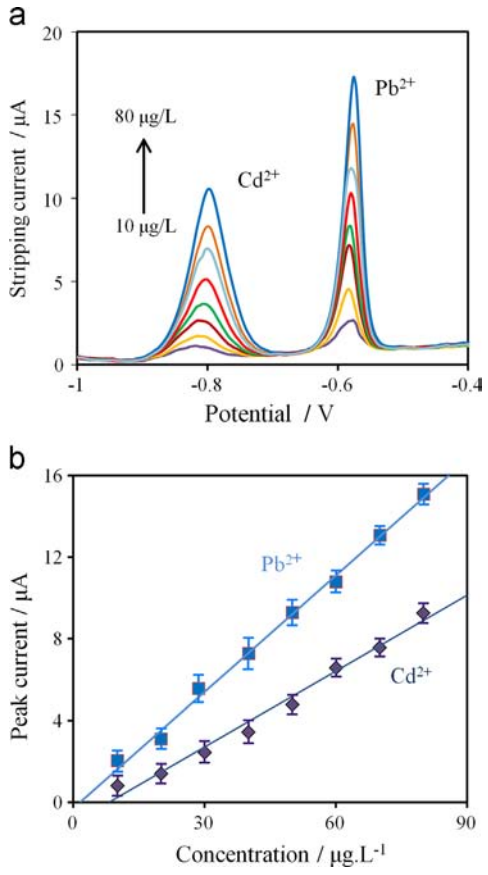


Fig. 6. (a) Typical voltammograms and (b) calibration plots for the microfabricated three-electrode on-chip device in simultaneous detection of Cd^{2+} and Pb^{2+} ions ($n=3$).

Table 1
Tolerated ratios to 5 μg/L Cd^{2+} and 5 μg/L Pb^{2+} in 0.1 M acetate buffer (±5 % deviation).

Foreign Substance	Tolerated Ratio to Cd^{2+}	Tolerated Ratio to Pb^{2+}
Zn^{2+}	45	36
Cu^{2+}	3.5	6
Sn^{2+}	25	8
Sb^{3+}	30	28

3.4. Interference study

The interference of foreign substances, such as Zn^{2+}, Cu^{2+}, Sn^{2+} and Sb^{3+}, is studied in the DPSV measurements with solution containing 0.1 M acetate buffer, 5 μg/L Cd^{2+} and 5 μg/L Pb^{2+} ions. Each substance is considered as interfering agent when the current peak for Cd^{2+} or Pb^{2+} exhibits a deviation more than ±5% [26]. The tolerated ratios to concentrations for Cd^{2+} or Pb^{2+} ions are presented in Table 1. Cu^{2+} ion is found to have an obvious influence on the stripping response for Cd^{2+} and Pb^{2+} ions. The result is in compliance with previous report, and the influence may be caused by the inter-metallic compounds formed in deposition process [27]. Moreover, Sn^{2+} ion also performs a noticeable effect on Pb^{2+} ion, since the stripping potentials for Sn^{2+} and Pb^{2+} ions are close [28].

3.5. Analysis of natural samples

Measurements for natural water samples are also performed. Two natural samples were acquired from Logan River, Logan City, USA, on March 10, 2014. The first sample was from the upstream part ahead of the city. The second sample was from the downstream part in the city. To avoid the interference of sample background, method of standard additions (MSA) is introduced and executed twice. In each MSA stage, diluted standard solution containing 500 μg/L Cd^{2+} and Pb^{2+} ions with adequate volume is added into the samples, keeping 1 μg/L concentration increment for Cd^{2+} and Pb^{2+} ions. Current peaks for the original samples, 1st MSA and 2nd MSA are recorded, respectively, and the concentrations can be calculated according to the original peaks and the MSA peaks [29]. The data are presented in Table 2. The DPSV results meet with standard ICP-MS measurements with less than 15% relative error except Cd^{2+} concentration of the first sample, because it is below the detection limits of the on-chip device.

3.6. Stability and renewal procedure for the device

The stability for the on-chip device is studied with solution containing 0.1 M acetate buffer, 50 μg/L Cd^{2+} and 50 μg/L Pb^{2+} ions. After each bismuth coating, the device shows good stability in approximate 50–60 DPSV measurements, and the relative standard deviations are less than 2.4% and 2.8% for Cd^{2+} and Pb^{2+}, respectively. After that, a renewal procedure is required due to the loss of bismuth

Table 2
Cd^{2+} and Pb^{2+} measurements for natural water samples based on DPSV and ICP-MS.

(a) Sample 1	Original Peak	1st MSA Peak	2nd MSA Peak	Calculated Concentration	ICP-MS Concentration	Relative Error
Cd^{2+}	Not detected	N/A	N/A	N/A	0.04 μg/L	N/A
Pb^{2+}	9.8×10^{-8} A	2.4×10^{-7} A	3.7×10^{-7} A	0.71 μg/L	0.83 μg/L	14%
(b) Sample 2	Original Peak	1st MSA Peak	2nd MSA Peak	Calculated Concentration	ICP-MS Concentration	Relative Error
Cd^{2+}	9.6×10^{-9} A	8.7×10^{-8} A	1.6×10^{-7} A	0.13 μg/L	0.12 μg/L	8%
Pb^{2+}	1.4×10^{-7} A	2.8×10^{-7} A	4.0×10^{-7} A	1.04 μg/L	1.18 μg/L	12%

Sample 1 was from the upstream of Logan River. Sample 2 was from the downstream of Logan River.
Detailed calculation process based on original peaks and MSA peaks is introduced in previous study [29].

coating. During the renewal procedure, the bismuth film on the working electrode is removed with filter paper firstly; and then the device is rinsed with isopropyl alcohol and deionized water; finally the bismuth coating is performed on the working electrode.

The life- cycle for the on-chip device is more than 500 measurements, which is acceptable considering the relative low cost (less than 7 US dollars) for the device. After that, the gold layer for the working electrode and counter electrode may drop off from the substrate. The reference electrode keeps stable and needs no special maintenance in the life cycle.

4. Conclusion

In this study, we introduce a microfabricated three-electrode on-chip device with a vibration motor for stripping voltammetric detection of Cd^{2+} and Pb^{2+} ions in standard and natural water samples. The counter electrode, reference electrode and working electrode are fabricated in the on-chip device. A coin-size vibration motor is also integrated in the device, providing vibration function as the alternate for stirring to improve detection limits and reduce deposition time.

The performance of the on-chip reference electrode is evaluated by CV experiments. Redox peaks for the on-chip reference electrode keep relatively stable at different scan rates. The potential shift of redox peaks between the on-chip reference electrode and commercial reference electrode is less than 20 mV. DPSV experiments validate that higher current peaks, less deposition time and lower detection limits for Cd^{2+} and Pb^{2+} ions can be achieved synchronously from vibration.

The microfabricated three-electrode on-chip device is also used to detect Cd^{2+} and Pb^{2+} ions for both laboratorial standard water samples and natural water samples. The DPSV current peaks exhibit good linearity from 10 μg/L to 80 μg/L for Cd^{2+} and Pb^{2+} ions, respectively, in laboratorial standard water samples. The concentrations for natural samples are calculated based on MSA in DPSV measurements and compared with ICP-MS results, which validate the measurement reliability for the on-chip device.

Acknowledgments

This work was supported by Utah Water Research Laboratory. The authors would like to thank Ms. Tessa Guy for the help in ICP-MS measurements and Dr. Fen-Ann Shen for SEM imaging.

Appendix A. Supporting information

Supplementary data associated with this article can be found in the online version at http://dx.doi.org/10.1016/j.talanta.2014.08.075.

References

[1] A. Jang, Y.W. Seo, P.L. Bishop, Environ. Pollut. 133 (2005) 117–128.
[2] R.A. Goyer, Health Persp 104 (1996) 1050–1054.
[3] D. Buzica, M. Gerboles, A. Borowiak, P. Trincherini, R. Passarella, V. Pedroni, Atmos. Environ. 40 (2006) 4703–4710.
[4] Z.S. Bi, C.S. Chapman, P. Salaun, C.M.G. van den Berg, Electroanalysis 22 (2010) 2897–2907.
[5] R.H. Ouyang, Z.Q. Zhu, C.E. Tatum, J.Q. Chambers, Z.L. Xue, J. Electroanal. Chem. 656 (2011) 78–84.
[6] A. Giacomino, O. Abollino, M. Malandrino, E. Mentasti, Talanta 75 (2008) 266–273.
[7] Z. Zou, A. Jang, E. Macknight, P. Wu, J. Do, P.L. Bishop, C. Ahn, Sens. Actuator B-Chem 134 (2008) 18–24.
[8] G.J. Lee, H.M. Lee, Y.R. Uhm, M.K.u. Lee, C.K. Rhee, Electrochem. Commun. 10 (2008) 1920–1923.
[9] S.B. Hocevar, I. Svancara, K. Vytras, B. Ogorevc, Electrochim. Acta. 51 (2005) 706–710.
[10] K. Stulik, C. Amatore, K. Holub, V. Marecek, W. Kutner, Pure Appl. Chem. 72 (2000) 1483–1492.
[11] G.H. Hwang, W.K. Han, J.S. Park, S.G. Kang, Sens. Actuator B-Chem 135 (2008) 309–316.
[12] I. Cesarino, C. Gouveia-Caridade, R. Pauliukaite, E.T.G. Cavalheiro, C.M.A. Brett, Electroanalysis 22 (2010) 1437–1445.
[13] J. Wang, J.M. Lu, S.B. Hocevar, P.A.M. Farias, B. Ogorevc, Anal. Chem. 72 (2000) 3218–3222.
[14] A. Economou, TrAC Trends Anal. Chem 24 (2005) 334–340.
[15] C.H. Lien, C.C. Hu, K.H. Chang, Y.D. Tsai, D.S. Wang, Electrochim. Acta. 105 (2013) 665–670.
[16] S.B. Hocevar, S. Daniele, C. Bragato, B. Ogorevc, Electrochim. Acta. 53 (2007) 555–560.
[17] D. Asbahr, L.C.S. Figueiredo-Filho, F.C. Vicentini, G.G. Oliveira, O. Fatibello-Filhoa, C.E. Banks, Sens. Actuator B-Chem 188 (2013) 334–339.
[18] Q.M. Feng, Q. Zhang, C.G. Shi, J.J. Xu, N. Bao, H.Y. Gu, Talanta 115 (2013) 235–240.
[19] P.K. Sahoo, Bharati Panigrahy, S. Sahoo, A.K. Satpati, D.a.n. Li, D. Bahadur, Biosens. Bioelectron. 43 (2013) 293–296.
[20] C. Kokkinos, A. Economou, Sens. Actuator B-Chem 192 (2014) 572–577.
[21] V. Aumond, M. Waeles, P. Salaün, K. Gibbon-Walsh, C.M.G. van den Berg, P. M. Sarradin, R.D. Riso, Anal. Chim. Acta. 753 (2012) 42–47.
[22] C.S. Chapman, C.M.G. van den Berg, Electroanalysis 19 (2007) 1347–1355.
[23] A. Määttänen, U. Vanamo, P. Ihalainen, P. Pulkkinen, H. Tenhu, J. Bobacka, J. Peltonen, Sens. Actuator B-Chem 177 (2013) 153–162.
[24] A. Baraket, M. Lee, N. Zine, M. Sigaud, N. Yaakoubi, M.G. Trivella, M. Zabala, J. Bausells, N. Jaffrezic-Renault, A. Errachid, Sens. Actuator B-Chem 189 (2013) 165–172.
[25] Y. Wei, R. Yang, J.H. Liu, X.J. Huang, Electrochim. Acta. 105 (2013) 218–223.
[26] J.H. Luo, X.X. Jiao, N.B. Li, H.Q. Luo, J. Electroceram. Chem 689 (2013) 130–134.
[27] R.O. Kadara, I.E. Tothill, Anal. Bioanal. Chem. 378 (2004) 770–775.
[28] C. Locatelli, G. Torsi, Microelectron. J. 78 (2004) 175–180.
[29] W. Zhang, H. Wan, Q.Y. Sun, D. Ha, P. Wang, D. Kirsanov, A. Legin, Meas. Sci. Technol. 24 (2013) 045801.

Talanta 132 (2015) 327–333

Contents lists available at ScienceDirect

Talanta

journal homepage: www.elsevier.com/locate/talanta

Effective identification of $(NH_4)_2CO_3$ and NH_4HCO_3 concentrations in $NaHCO_3$ regeneration process from desulfurized waste

Muthuraman Govindan [1], Kannan Karunakaran [1], Palanisami Nallasamy [1], Il Shik Moon *

Department of Chemical Engineering, Sunchon National University, 315 Maegok Dong, Suncheon 540-742, Chonnam, South Korea

ARTICLE INFO

Article history:
Received 6 June 2014
Received in revised form
13 August 2014
Accepted 14 August 2014
Available online 28 August 2014

Keywords:
Flue Gas Desulfurization
Sodium sulfate
Ammonium sulfate
Ammonium carbonate
Ammonium bicarbonate
Titration

ABSTRACT

This work describes the quantitative analysis of $(NH_4)_2CO_3$ and NH_4HCO_3 using a simple solution phase titration method. Back titration results at various $(NH_4)_2CO_3$–NH_4HCO_3 ratios demonstrated that 6:4 ratio caused a 3% error in their differentiation, but very high errors were found at other ratios. A similar trend was observed for the double indicator method, especially when strong acid HCl was used as a titrant, where still less errors (2.5%) at a middle ratio of $(NH_4)_2CO_3$–NH_4HCO_3 was found. Remaining ratios with low $(NH_4)_2CO_3$ (2:8, 4:6) show high +ve error (found concentration is less) and high $(NH_4)_2CO_3$ (7:3, 8:2, and 9:1) show high –ve error (found concentration is higher) and vice versa for NH_4HCO_3. In replacement titration using Na_2SO_4, at both higher end ratios of $(NH_4)_2CO_3$–NH_4HCO_3 (2:8 and 9:1), both –ve and +ve errors were minimized to 75% by partial equilibrium arrest between $(NH_4)_2CO_3$ and NH_2COONH_4, instead of more than 100% observed in back titration and only double indicator methods. In the presence of $(NH_4)_2SO_4$ both –ve and +ve error% are completely reduced to 3 ± 1 at ratios 2:8, 4:6, and 6:4 of $(NH_4)_2CO_3$–NH_4HCO_3, which demonstrates that the equilibrium transformation between NH_2COONH_4 and $(NH_4)_2CO_3$ is completely controlled. The titration conducted at lower temperature (5 °C) in the presence of $(NH_4)_2SO_4$ at higher ratios of $(NH_4)_2CO_3$–NH_4HCO_3 (7:3, 8:2, and 9:1) shows complete minimization of both –ve and +ve errors to 2 ± 1%, which explains the complete arresting of equilibrium transformation. Finally, the developed method shows 2 ± 1% error in differentiation of CO_3^{2-} and HCO_3^- in the regeneration process of $NaHCO_3$ from crude desulfurized sample. The developed method is more promising to differentiate CO_3^{2-} and HCO_3^- in industrial applications.

© 2014 Elsevier B.V. All rights reserved.

1. Introduction

Growing awareness of the risks of climate change has generated public concerns, and over the last two decades the sequestering of air pollutants has been of major research interest. As the world's population and energy demand increase, continued industrialization will undoubtedly increase levels of atmospheric pollutants like NO_x, SO_x, and CO_2. In particular power plant and steel plant furnaces emit SO_x and NO_x (called flue gases), which are removed using wet or dry sorbent methods [1]. Flue Gas Desulfurization (FGD) is performed using the wet sorbent method. However, due to the large amount of space required for installation, the large volume of water required and high capital and operating costs [2], research has shifted toward dry methods of SO_2 removal. Various types of solid sorbent/catalysts are being used for dry FGD, such as, calcium based [3], sodium based [4], activated carbon [5], metal oxide [6], and zeolite sorbents [7], waste-derived siliceous materials [8], and mediated electrocatalytic oxidation (MEO) [9,10]. Many of these methods have limitations in terms of their commercialization. Among these methods, sodium-based sorbents are considered more effective for FGD, especially for SO_x. These processes are conducted mainly using sodium carbonate (Na_2CO_3), sodium bicarbonate ($NaHCO_3$), and trona ($Na_2CO_3 \cdot NaHCO_3 \cdot 2H_2O$). In this process, either sodium bicarbonate ($NaHCO_3$) (or) sodium carbonate (Na_2CO_3) reacts with SO_2 to form Na_2SO_3 which is further converted to sodium sulfate (Na_2SO_4) in the presence of excess oxygen, as explained by the following equation sequences [1–4]:

$$2NaHCO_3 + SO_2 \rightarrow Na_2SO_3 + 2CO_2 + H_2O \quad (1)$$

$$2NaHCO_3 \rightarrow Na_2CO_3 + CO_2 + H_2O \quad (2)$$

$$Na_2CO_3 + SO_2 \rightarrow Na_2SO_3 + CO_2 \quad (3)$$

$$Na_2SO_3 + 1/2O_2 \rightarrow Na_2SO_4 \quad (4)$$

However, it had a few drawbacks: (i) sodium bicarbonate is expensive; (ii) the resulting by-product from the sodium

* Corresponding author. Tel.: +82 61 750 3581; fax: +82 61 750 3581.
E-mail address: ismoon@sunchon.ac.kr (I.S. Moon).
[1] These authors contributed equally to this work.

http://dx.doi.org/10.1016/j.talanta.2014.08.044
0039-9140/© 2014 Elsevier B.V. All rights reserved.

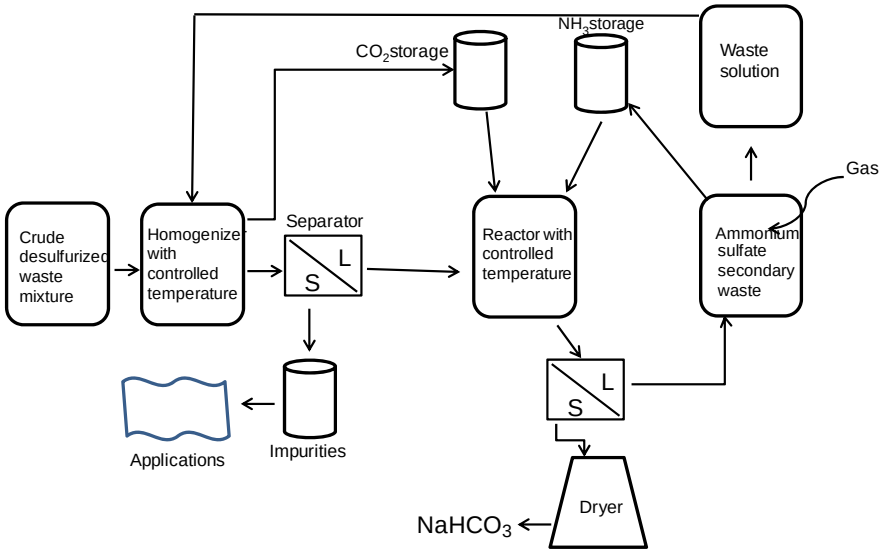


Fig. 1. Schematic representation for the regeneration pathway of $NaHCO_3$ from desulfurized waste sample.

bicarbonate–SO_x reaction (sodium sulfate) is of limited economic value; and (iii) sodium sulfate disposal is expensive and poses significant environmental challenges. To regenerate sodium bicarbonate from secondary waste Na_2SO_4 (SS) provides an efficient way of avoiding the above mentioned drawbacks [11]. The regeneration of sodium bicarbonate from sodium sulfate is schematically presented in Fig. 1.

The regeneration of sodium bicarbonate involves three steps: (i) separation of the sodium sources from their impurities, (ii) regeneration of $NaHCO_3$ (SBC) using NH_4HCO_3 (ABC) or gases of NH_3 and CO_2, and (iii) utilization of secondary waste solution $(NH_4)_2SO_4$ (AS). In these regeneration processes, analysis of each ion plays a crucial role in finalizing the experimental conditions such as the molar ratio of reactants and water content. Particularly the secondary waste AS containg solution, which includes additionally $(NH_4)_2CO_3$ (AC) and ABC, should be exactly analyzed to perfect the minimization of error. Identifications of CO_3^{2-} and HCO_3^- ions are very difficult through analysis by titration due to their complex equilibrium process as follows [5–9,12,13]:

$$NH_{4(aq)}^+ + H_2O_{(l)} \rightleftharpoons NH_{3(aq)} + H_3O_{(aq)}^+ \quad (5)$$

$$CO_{3(aq)}^{2-} + H_2O_{(aq)} \rightleftharpoons HCO_{3(aq)}^- + OH_{(aq)}^- \quad (6)$$

$$CO_{3(aq)}^{2-} + NH_{4(aq)}^+ \rightleftharpoons HCO_{3(aq)}^- + NH_{3(aq)} \quad (7)$$

$$HCO_{3(aq)}^- + NH_{3(aq)} \rightleftharpoons H_2NCOO_{(aq)}^- + H_2O_{(l)} \quad (8)$$

$$H_2NCOO_{(aq)}^- + H_2O_{(l)} \rightleftharpoons CO_{3(aq)}^{2-} + NH_{4(aq)}^+ \quad (9)$$

First, the differentiation of CO_3^{2-} and HCO_3^- by a back titration method using $BaCl_2$ as a precipitant for $CaCO_3$ has been identified to be infeasible [14]. They found more restriction in minimizing the error in quantification of each compound and no detailed studies about various concentration ratios of CO_3^{2-} and HCO_3^- [15]. Later, double indicator Warder's titration method was used to differentiate the CO_3^{2-} and HCO_3^- as a next level [16,17]. However, quantifying the CO_3^{2-} and HCO_3^- is difficult due to lack of endpoint identification; color change is very feeble in case of AC and ABC [18,19], and no detailed study has been performed by the titration method. In the late 1990s, it was reported that FT-IR, NIR, Raman spectroscopies and powder-XRD can differentiate AC and ABC quantitatively and qualitatively [20–22]. The XRD 2θ peaks of ABC and AC are at 16.5 and 34.4, respectively, and can be used to analyze the solid state compositions of mixtures [21]. In the case of FT-IR analysis, there is a possibility of quantitative differentiation of ABC ($1200-1450\ cm^{-1}$ for asymmetric CO stretch and $\sim 1600\ cm^{-1}$ for symmetric CO stretch) and AC ($\sim 1300-1600\ cm^{-1}$ for asymmetric CO stretch). The FT-IR spectra of both solid and solution phases of AC and ABC are quite similar and difficult to distinguish because of broad peaks due to both carbonate and bicarbonate between 1200 and $1700\ cm^{-1}$ and the same peak at $3098\ cm^{-1}$, which is due to the ammonium ion [22]. As reported by Meng et al., by variation of oxygen – hydrogen (OH) bond of ABC at 1450 nm, which is not present in the carbonate, one can differentiate quantitatively in solid state samples [21]. However, it is difficult to distinguish the bicarbonate from carbonate ion in aqueous solution due to interference of hydroxyl (OH) groups in the water, which restricts the NIR analysis in solution samples. ^{13}C NMR studies have demonstrated the qualitative differentiation of ABC and AC at room temperature [23]. Even the fast equilibrium of HCO_3^-/CO_3^{2-} anions results in their two NMR peaks, which permits identifying the HCO_3^-/CO_3^{2-} ions quantitatively. Through the Raman spectra, the ABC and AC in solution phase have been differentiated quantitatively using scattered light of the peaks at $\sim 1015\ cm^{-1}$ (for bicarbonate) and $\sim 1065\ cm^{-1}$ (for carbonate) [24]. However, Raman analysis needs an internal standard for exact differentiation of both ABC and AC. The mixture of our secondary waste contains internal standard compound Na_2SO_4, which should be analyzed additionally using another method. Accordingly several issues must be resolved for the quantitative analyses of ABC and AC in the solution phase, especially in samples obtained during the regeneration of SBC from desulfurized crude waste.

There are some models to control the reaction and its coordinates to get a high yield and purity in regeneration of SBC from desulfurized waste [25,26]. Currently there are no reports on controlling the reaction based on analysis of ions present in the crude waste (before reaction) and secondary product waste (after reaction). In the present work a method is developed based on analysis of ions present in crude waste and secondary waste, to control the reaction in the SBC regeneration process. Herein, validations of back titration at different ratios of AC ad ABC were performed for its confirmation. Then, the double indicator method was repeated with different ratios of AC and ABC to check its applicability for their differentiation. Additionally replacement titration, by SBC, was studied. In order to check the equilibrium of CO_3^{2-} and HCO_3^-, AS and temperature effect were studied.

Finally, the developed method was tested on a real sample from desulfurized crude waste regeneration process of the SBC.

2. Experimental section

2.1. Chemicals

Ammonium bicarbonate and ammonium carbonates were purchased from Aldrich. Phenolphthalein, methyl orange, bromocreasol green, phenol red, sodium carbonate, barium chloride dehydrate, sodium hydroxide, and phosphoric acid were purchased from Daejung Chemicals, Korea. Hydrochloric acid and acetic acid were purchased from OCI, and Duksan Korea respectively.

2.2. Reagents

0.1 M stock solutions of hydrochloric acid, acetic acid and phosphoric acid were prepared by dissolving approximately 8.4 ml of 11.6 M hydrochloric acid in 1 L of deionized water, 5.8 ml of 17.4 M acetic acid in 1 L of deionized water, and 6.8 mL of 14.6 M phosphoric acid in 1 L of deionized water respectively. These solutions were standardized by titration against standard sodium carbonate.

2.3. Back titration

This method is the oldest method to differentiate two components by precipitating one component [14]. In order to differentiate AC and ABC, various ratios such as (2:8), (4:6), (5:5), (6:4), (7:3), (8:2), (9:1) were chosen. The back titration was performed using two steps. In the first step, total alkalinity was determined by placing a 5 ml sample in a 100 ml conical flask, adding methyl orange indicator and titrating against standardized 0.1 M HCl, as shown in Eq. (10). The end point change from yellow to red was considered as a measure of total alkalinity. This procedure was repeated till concordant values were obtained and the average value was taken. In the second step, 5 ml of sample was taken in a 100 ml conical flask, then 16 ml of NaOH and 0.88 ml of 10% $BaCl_2$ solution were added along with a few drops of phenolphthalein indicator. Instantly, the white precipitate ($BaCO_3$) generated in the sample mixture solution was then immediately titrated against standardized 0.1 M HCl solution after using a high speed centrifuge for a short time (30 s), as shown in Eq. 11. The disappearance of pink color is an indication of end point. The volume of consumed HCl was recorded and the test was repeated for concordant values.

Step 1: Total alkalinity:

$$NH_2COONH_4 \text{ and } (NH_4)_2CO_3 + NH_4HCO_3 + 3HCl \rightarrow 3NH_4Cl + 2H_2O + 2CO_2 \quad (10)$$

Step 2: Differentiate HCO_3^- and CO_3^{2-}

$$(NH4)_2CO_3 + NH_4HCO_3 + NaOH + BaCl_2 \xrightarrow{2HCl} 3NH_4Cl + BaCO_3 + H_2O + NaCl + H_2CO_3 \quad (11)$$

2.4. Double indicator method

There are some reports for differentiation of sodium carbonate and bicarbonate in the reaction mixture [16,17], and a few reports for ABC and AC without detailed experimental conditions [15]. The same method has been adopted to identify ammonium carbonate and ammonium bicarbonate [27]. Briefly, ammonium carbonate and ammonium bicarbonate mixture was dissolved in 100 ml of water. 5 ml of this solution was transferred into a conical flask. 2 drops of phenolphthalein were added and pink color appeared. When titrated against 0.1 M acids the pink color disappeared, which is the endpoint of ammonium carbonate solution. To the same solution 2 drops of phenol red were added and the solution became yellow. After titration again with acetic acid the yellow turned into red, which is the ammonium bicarbonate endpoint. For phosphoric acid and hydrochloric acid, methyl orange is used for ammonium bicarbonate and the end point is orange to red. In all titration experiments, the titration time was 0.5–3 min for all titrations at all ratios of AC and ABC. In the AC determination step, the time spent is between 0.5 and 1.5 min. The error% of ABC was calculated by substracting the AC value obtained from the phenolpthalein indicator by total alkalinity (ACl) value obtained from the second indicator (methyl orange). As shown in Eqs. (12)–(14). to cross check, the AC value added with ABC, which is equal to carbamic acid (CAm) or carbonic acid (CA) that developed during titration. Then, the CAm or CA was subtracted by ACl to get right ABC.

$$C_{ACl} - C_{AC} \text{ or } C_{ACm} = C_{ABC} \quad (12)$$

$$C_{AC} + C_{ABC} = C_{CAm \text{ or } CA} \quad (13)$$

$$C_{ACl} - C_{CAm \text{ or } CA} = C_{ABC} \quad (14)$$

In the replacement titration, two times the concentration of Na_2SO_4 was added and repeated as a double indicator method of titration. In stabilization experiments, $(NH_4)_2SO_4$ and temperature were included as two times higher molar concentration and 25 to 5 °C variation respectively. The room temperature experiments were carried out at 20 ± 2 °C. All the experiments were repeated until the results were reproducible.

2.5. Analysis of real regeneration process samples

First, an industrial desulfurized sample 10 g was dissolved in 250 ml of deionized water and filtered to remove impurities, and separated the salt solution for analysis. The Na^+ and NH_4^+ ions were estimated using ion selective electrodes (ISE) that purchased from VAN LONDON Phoenix.CO (No.: NA715XX for Na+ and No.: NH415XX) with the help of iSTEK multimeter (Model No.: pH-240 L) from USA. Prior to the analysis, the electrodes and instruments were calibrated as per the instruction that given by a manufacturing company. In another way, the NH_4^+ was cross checked with standard procedure by UV-Visible spectroscopy (Shimadzu, UV160A) from Japan, by the indophenol blue method at 630 nm [28].

The sulphate ion in the sample was estimated in the form of Barium sulphate by the addition of Barium chloride precipitating agent along with Conditional reagent followed by UV–vis spectrophotometric absorption at 420 nm [29]. All metal ions that present in the real sample was analyzed by ICP-MS (model ELANDRCe, Perkin Elmer) from USA.

3. Result and discussion

3.1. Conventional back titration on differentiation of $(NH_4)_2CO_3$/$(NH_4)HCO_3$

As evidenced in previous reports, SBC and SC can be differentiated effectively by back titration with an error of less than 5%. However, they never considered ACm equilibrium in back titration to differentiate ABC and AC in CO_2 absorption process using ammonia [14]. In the present case, desulfurized waste contains many salts that including SBC and SC in different ratios, which

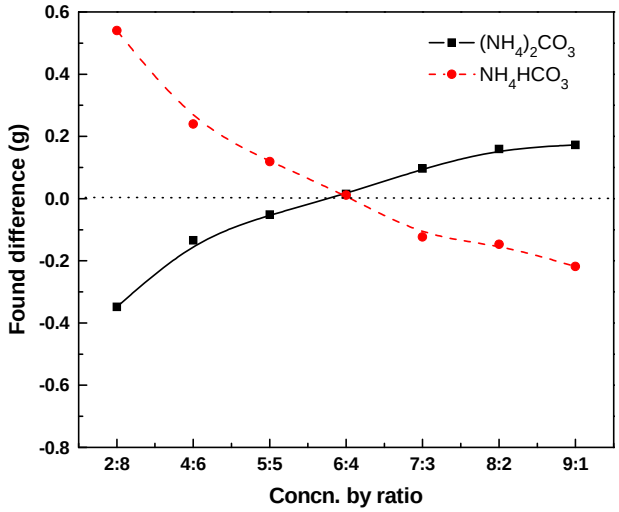


Fig. 2. Effect of different concentration ratios on found concentration differences of $(NH_4)_2CO_3$ and $(NH_4)HCO_3$ in their identification through back titration.

must be accurately identified for further reaction with ABC to regenerate SBC. After reaction or to control the reaction, differentiation of ABC and AC is important. By keeping all in mind, we have started optimizing conditions in back titration such as the effect of NaOH and $BaCl_2$ addition time in particular of AC to ABC ratio 6:4. The obtained results are presented in supporting information Table S1. There appears minimized error% during the both NaOH and $BaCl_2$ addition time in 30 s. Using these selected conditions, the back titrations to identify the ABC and AC in different ratios at room temperature was performed and the obtained results are depicted in Fig.2. At high concentration of AC, the found concentration of AC increased to 0.35 g than (+ve error) the actual input value. At the same time, the found ABC is very decreased to 0.54 g (-ve error) than the originally added in 8:2 ratio. The found difference of both ABC and AC increased and decreased in a similar manner with increasing ratio up to 6:4, where the found difference is almost 0.01 g which equal to less than 3% +ve error. Further increasing the ratios beyond 6:4 of AC and ABC, the found difference shows a reverse trend which means, the found AC is decreased than the originally added and ABC is increased than the input concentrations. The overall found difference explains that the highest concentration of AC or ABC are tended to convert to another form chemically. The chemical equilibrium may dominate more at high end concentration ratios. It is reported that the ABC is converted to AC at high temperature and excess of CO_2 [27]. In a similar way, AC converted to ABC in excess CO_2 and H_2O [30]. But only containing of both ABC and AC, how the conversion has occurred? Instead of conversion, we suggest the possibility of equilibrium stabilization, as shown in the following eqs. (15 and 16). Another possible way for high error % is the formation of ACm from AC in water as shown in eqs. 8 and 9. It is evidenced that the ACm will not precipitate in precipitation step upon addition of $BaCl_2$ [31] to remove the AC from the titer solution in related to avoid its interference during the back titration of the consumed NaOH with HCl. In case ACm remains in titer solution, the consumed HCl volume will vary which in turn leads high error% in determination of AC, as shown in eq. (17)

At High $(NH_4)_2CO_3$: $(NH_4)_2CO_3 \rightleftharpoons NH_4HCO_3$ (15)

At high NH_4HCO_3: $(NH_4)_2CO_3 \rightleftharpoons NH_4HCO_3$ (16)

$$NH_2COONH_4 + NH_4HCO_3 + NaOH + BaCl_2 \xrightarrow{HCL} 2NH_4Cl + BaCO_3 + H_2O + NaCl + NH_2COOH \quad (17)$$

3.2. Double indicator method

Because of defined differences in the pH value of ABC (8.3), and AC (9), the two indicator method could possibly provide accurate ABC and AC concentrations. In consideration of ACm, the pH of ACm 8.9 [32], which is very close to the pH of AC, it clearly helps to differentiate ABC even if it exists because of phenolpthalein used as indicator. Since ABC, ACm, and AC are weak bases, acid selection could minimize errors. We selected three different acids, that is, acetic acid (weak base vs weak acid) and phosphoric and hydrochloric acids (weak base vs strong acid). As evident in literature, In order to know the time dependent equilibrium of AC, ACm, and ABC, the sample titration time at minimum (1 min) and maximum (720 min) were done and the results are tabulated and presented in supporting information Table S2. After 1 min, the error% has increased to only 7 to 10 at AC to ABC of 75:25 ratio. In consideration of practical difficulties, 1 min sampling time was selected for all the titrations. During analysis, we found difficulties in end point measurements, especially for AC and ACm determinations, when only a pale pink was obtained after adding phenolphthalein. This color change behavior just contrary to the SBC and SC differentiation, there was able to judge a clear difference in end point and correct value. The titration results obtained for ABC and AC are depicted in Fig. 3. In plot (b) of Fig.3 illustrates the titration of acetic acid with $(NH_4)_2CO_3/(NH_4)HCO_3$ mixture. During titration, AC or ACm becomes ABC or CAm and carbonic acid (CA) at second endpoint while the use of methyl orange indicator as shown in eqs. 18–20' in case of ACm. The % errors were calculated using eqs. (12–14).

$$(NH_4)_2CO_3 + NH_4HCO_3 + HCl \rightarrow 2NH_4HCO_3 + NH_4Cl \quad (18)$$

$$NH_2COONH_4 + NH_4HCO_3 + HCl \rightarrow NH_4HCO_3 + NH_2COOH + NH_4Cl \quad (18')$$

$$2NH_4HCO_3 + 2HCl \rightarrow 2NH_4Cl + 2H_2CO_3 \quad (19)$$

$$NH_4HCO_3 + NH_2COOH + HCl \underset{\leftrightarrow}{\longrightarrow} NH_2COOH + H_2CO_3 + NH_4Cl \quad (19')$$

$$NH_2COOH + HCl \rightarrow NH_4Cl + CO_2 \quad (20')$$

Depending upon the acid, which we used, the error% is varying for both the ABC and AC or ACm that can be defined as the -ve error% (found value is higher than originally taken) and +ve error%

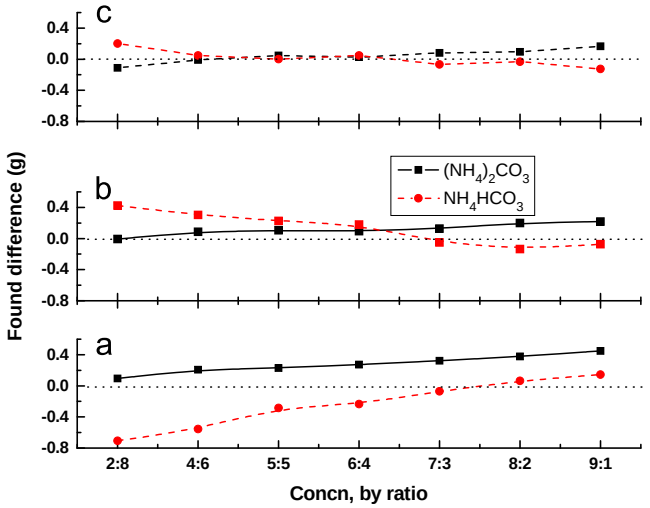


Fig. 3. Effect of acids on titration of different concentration ratios of $(NH_4)_2CO_3/(NH_4)HCO_3$ mixture in their identification by double indicator method: (a) Phosphoric acid; (b) Acetic acid; (c) Hydrochloric acid.

(found value is less than originally taken). The $(NH_4)_2CO_3$ error was a minimum of 5.2 +ve% when carbonate to bicarbonate ratio is 2:8 and with increasing AC ratio –ve error% increases to > 10.0%. Except titration using phosphoric acid, the other two acids CH_3COOH (plot (b) in Fig.3) and HCl (plot (c) in Fig.3) shows a similar trend and vice versa for ABC. The titration of $(NH_4)_2CO_3$/$(NH_4)HCO_3$ mixture with phosphoric acid (plot (a) in Fig.3) shows ABC of 8.7 +ve error% when carbonate to bicarbonate ratio is 2:8, which increases with decreasing of ABC ratio. In a similar way, AC shows –ve error% at lower ratio that increases with decreasing AC, as shown in Fig.3(plot (a)). Among three acids, titration using HCl shows (Fig.3(plot (c)) –ve error% in both AC and ABC differentiation with the existence of a similar equilibrium error problem as found in back titration method. The error% of the both AC and ABC might have also from ACm formation in the first step using phenolpthalein titration where ACm converted to CAm directly, instead of ABC formation, as seen in equation 18'. This ABC and ACm equilibrium (eqn. 19') at high end ratios of AC and ABC might have influenced to receive this high error% in the both –ve and +ve. In higher ABC, more of ACm might have formed and vice versa at lower ABC that makes an equilibrium variation depending upon the concentration of ABC, which leads high error% in their determination. Further works can be carried out using HCl acid.

3.3. Identification through replacement titration by Na_2SO_4

It is known that alkali salts reacts with ABC and AC form alkali carbonate and bicarbonate [11]. Using this approach, sodium sulfate was added accordingly to the concentrations of ABC and AC to convert them to SBC and SC, as shown in the eqs. 21, and 22, this facilitates the accurate differentiation of ABC and AC.

$$Na_2SO_4+(NH_4)_2CO_3 \rightarrow Na_2CO_3+(NH_4)_2SO_4 \quad (21)$$

$$Na_2SO_4+2(NH_4)HCO_3 \rightarrow 2NaHCO_3+(NH_4)_2SO_4 \quad (22)$$

Even the all salts are dissolved in the reaction mixture, due to the high association constant of SBC (0.72) and SC (8.3) [33] makes remain intact and makes easy to differentiate the carbonate and bicarbonate via SBC and SC and the obtained results are depicted in Fig.4. The AC both +ve and –ve error% is controlled within 75% in high end ratios. It is believed that the Na^+ ion effectively replaces the NH_4^+ of AC. In the case of ABC determinations, the excess Na_2SO_4 shows controlled error percentages at most ratios

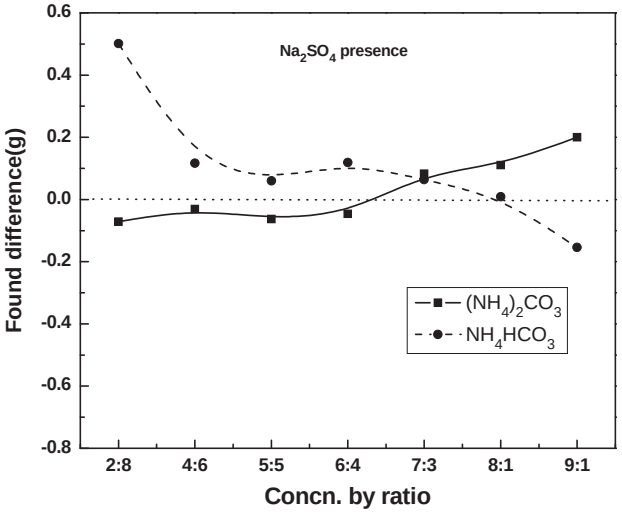


Fig. 4. Replacement titration with Na_2SO_4 on different ratios of $(NH_4)_2CO_3$/$(NH_4)HCO_3$ mixture on their differentiation by double indicator method. Added Na_2SO_4 concentration = 0.14 M.

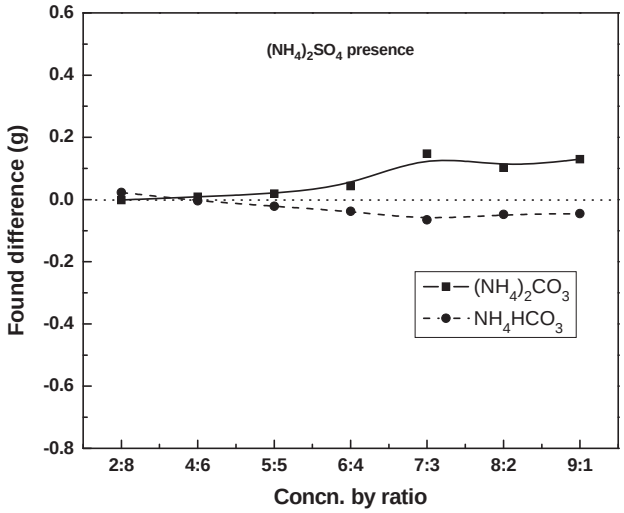


Fig. 5. Effect of $(NH_4)_2SO_4$ with different ratios of $(NH_4)_2CO_3$/$(NH_4)HCO_3$ mixture on their identification by double indicator method. Added $(NH_4)_2SO_4$ concentration = 0.15 M.

except high end ratio of 9:1, indicating effective replacement of the Na^+ ion in ABC. The reason why the minimized error occurred is, only a small amount of AC becomes ACm that might not converted to SC while addition of SS due to sodium ammonium carbamate and double salt formation as shown in eq. 23. But one positive effect of the presence of sodium sulfate is that it enables the differentiation of ABC and AC without its interference. Nonetheless, more accurate differentiation is required regardless of ABC/AC ratio.

$$Na_2SO_4+NH_2COONH_4 \rightarrow NH_2COONa+NH_4.Na.SO_4 \quad (23)$$

3.4. Approach through the effect of equilibrium control by addition of salt and temperature

As explained by eqs. 1 and 2, a common ion in the equilibrium change is sodium ion. One possibility of minimizing equilibrium change involves the addition of excess ammonium ion to the titration solution, here ammonium sulfate is probably a good choice, as shown by eq. 25. Ammonium sulfate added titration results to identify the ABC and AC are depicted in Fig. 5. There appears the error% for both +ve and –ve errors has controlled within in 3 ± 1% upto the ratios of 2:8 to 6:4 of AC and ABC. Also, there might be an equilibrium arrest between AC and ACm if add the AS (eqn. 24) for this both +ve and –ve error% minimization. Beyond these ratios, the both -ve and +ve error% were not controlled within the error limit. These results explain higher the AC concentration in the reaction mixture makes higher the both –ve and +ve error%, which means the equilibrium only between AC and ABC at high concentration. In other words, at high ratios of AC, AS is not able to control the conversion to ABC, as shown in eq. 25. But, the both –ve and +ve error% are almost controlled in all the ratios of AC and ABC when compared with no salt addition and in presence of Na_2SO_4, as shown in Fig.7.

$$NH_2COONH_4 \xrightarrow{(NH_4)_2SO_4} (NH_4)_2CO_3 \quad (24)$$

At higher AC ratio:

$$(NH_4)_2CO_{3(n)}+H_2O+NH_4HCO_{3(n)} \rightarrow (NH_4)_2CO_{3(n-1)}+(NH_4)HCO_{3(n+1)}+NH_4OH_{(n)} \quad (25)$$

It is seen from eq. 13 that there is a possibility of AC decomposition to ABC via H_2O at high concentration ratios and forms NH_4OH in

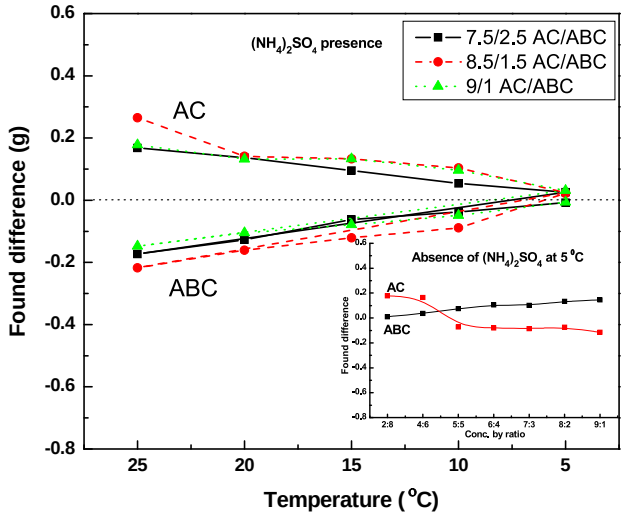


Fig. 6. Effect of temperature with high ratios of $(NH_4)_2CO_3/(NH_4)HCO_3$ mixture on their differentiation in presence of $(NH_4)_2SO_4$ by double indicator method. Added $(NH_4)_2SO_4$ concentration = 0.15 M. Insert figure: Concentration difference effect in absence of $(NH_4)_2SO_4$ at 5 °C on different ratios of $(NH_4)_2CO_3/(NH_4)HCO_3$.

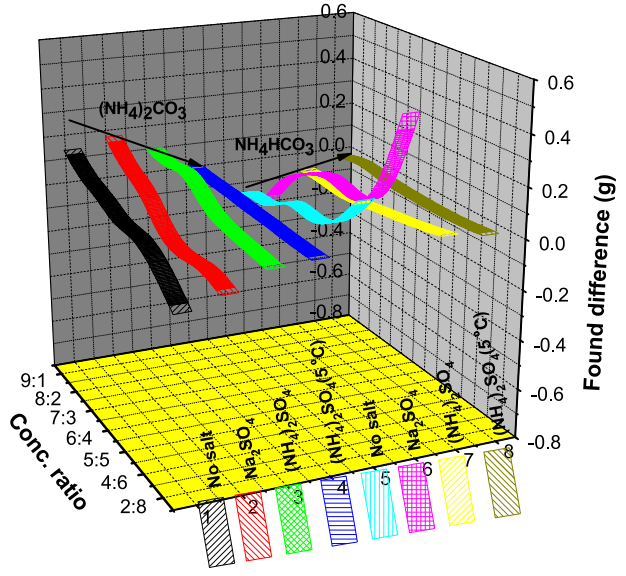


Fig. 7. Overall comparitive plot on differentiation of $((NH_4)_2CO_3/(NH_4)HCO_3$ ratios with different experimental conditions using double indicator method: (a) without addition of salts; (b) With Na_2SO_4; (c) With $(NH_4)_2SO_4$; (d) At 5 °C with $(NH_4)_2SO_4$.

solution or NH_3 might have liberated from solution. Moreover, the concentration we took is very less (0.1 M) for titration, which makes no loss of NH_3 by liberation. We tried to check the pH value after phenolpthalein titration, but found no change or high pH value. It is well known that the reaction can be arrested at low temperature [34], and thus, there is a possibility that the conversion of AC could be controlled by decreasing temperature. As a first trial, the higher AC ratios were considered to check temperature effect and the obtained results are presented in Fig. 6. The five different temperatures examined from 25 to 5 °C shows a clear decrease in the both –ve and +ve error%. Irrespective of the higher three ratios, the both –ve and +ve error% decreased with decreasing temperature to within an error% of (3 ± 1). Nonetheless, only low temperature (5 °C) with absence of AS shows ca. 20% error in both +ve and –ve in all the ratios, as shown in the insert figure of Fig.6. At lower ratios.

2:8 and 4:6, the ABC differentiation is very effective (within 3% error) at 5 °C in the absence of AS and it starts increase with



Scheme 1. Equilibrium arrest between AC, ACm, and ABC at different conditions.

increasing AC to ABC ratios, the differentiation error% is increased up to 20%, which indicates AS is the only component responsible to arrest or control the equilibrium transfer between AC to ACm, and AC to ABC, as shown in Scheme 1. The both AS presence (AC and ACm equilibrium arrested) and low temperature (AC and ABC equilibrium arrested) give highly synergistic effect for clear differentiation of AC and ABC at all ratios. For clear differentiation, comparative results are plotted and presented in Fig. 7, here shown how the error trend of AC and ABC is minimized at different experimental conditions. It clearly explains the accurate identification ABC and AC is only possible by titration in the presence of AS at 5 °C, especially along with impurities. We believe that this present condition may support to get more accurate identification when analyze through an instrument.

At 5 °C in presence of AS in all ratios:

3.5. Validation through real sample

The desulfurized crude sample was first purified by adding water and then reacted with NH_3 and CO_2 to produce $NaHCO_3$. In order to finalize the reaction conditions, ABC and AC determination are important in a secondary waste solution of AS, as shown in reaction 26. The total reaction process was carried out as shown in Fig.1. In brief, 11.1 Kg of crude desulfurised waste were dissolved in 24.12 L of water. The slurry solution heated to 45°C along with stirring about 30 min. Then the slurry was then transferred to filter press machine, which was operated at 45°C and 4 atm pressure. Typically ~11 wt% of insoluble impurities were collected from the filter press. The filtered solution has analyzed by titration for carbonate and bicarbonate, ISE for sodium ion, IC for both cations and anions. In these given conditions, approximately 90 wt% (obtained salt weight/(total raw waste weight-impurities weight) x 100) sodium sources through filter press method have been recovered. The exact weight and volume that obtained were depicted in row 7 in Table 1. The analyzed filtered desulfurized solution was then sent to carbonation tank to produce $NaHCO_3$ using ammonia solution and CO_2 gas. Based on the analysis value of sodium source, the ammonia solution 0.9 mol ratio against sodium source was taken for the production of sodium bicarbonate. Under optimized conditions of temperature, water volume, and pressure, sodium bicarbonate production process were done using the carbonation tank. Then the reaction slurry sent to peeler type decanter modified with the overhead temperature controller. The peeler type decanter was operated at 45 °C temperatures both on overhead and reactants slurry, 800 mesh filter and 3500 rpm. The product error was predicted based on the analyses of both solid and secondary waste liquid by titration, UV-Visible spectroscopy, and ISE methods. The total ions of both solid and liquid that found are displayed in row 11–12 in Table 1. The found difference of BC and C in the presence of all is $2 \pm 0.5\%$. This indicates validation of the present method and very crucial to finalize the further modification in perfection process.

$$\text{Crude waste} + NH_3 + CO_2 + H_2O \rightarrow NaHCO_3 + (NH_4)_2SO_4 \quad (26)$$

4. Conclusions

The AC and ABC were identified within an error% successfully by simple titration. Back titration results confirm it will differentiate

Table 1
Analysis results from regeneration reaction process of $NaHCO_3$ in desulfurized waste.

Raw sample weight(Kg)		11.1			
Water volume (L)		24.12			
Separation temperature		45 °C			
Impurity weight (Kg) and %		1.21; 10.92%			
Filtrate soln. obtained (L)		23.12			
Sodium sources wt (Kg) and wt%		Na_2SO_4=7.66			
		Na_2CO_3=0.99			
		$NaHCO_3$=0.33			
		Total weight=8.98			
		Yield in %=8.98/9.89(11.1-1.21=9.89)=90.78			
For preparation of $NaHCO_3$					
Water volume for $NaHCO_3$ production (L)		23.12			
Reaction tempr. (°C) and Time ($_{min}$)		35–38 and 60 min			
Needed CO_2 (Kg) ammonia (Kg) and vol. (L)		NH_3 (4.519 Kg) or NH_4OH solution (8.319 L): Need CO_2 (11.677 Kg)			
Product weight (Kg) and wt%		8.34; 84.33(8.34/9.89)			
Analysis results	Ions name	Reactants weight (Kg)	Found weight in solid (Kg)	Found weight in solution (Kg)	% error
	SO_4^{2-}	5.178	0.119	4.904	3.08
	CO_3^{2-}	0.559	0.018	0.531	**1.85**
	HCO_3^-	6.157	5.585	0.559	**2.28**
	NH_4^+	2.324	0.022	2.161	5.24
	Na^+	2.999	2.177	0.805	1.83

only one ratio of AC and ABC (6:4) and leave a high error to all other ratios makes unsuitable in their complete identification. Also, the double indicator titration method confirms, similar as the back titration method, not suitable to identify the AC and ABC except one ratio (5:5). In a replacement titration through the addition of Na_2SO_4 minimizes the identification of AC and ABC error% a less than the only double indicator method confirms partial equilibrium arrest between ACm and SC and conversion of AC and ABC to SC and SBC. Instead of SS, AS addition give 3 ± 1 error% up to the ratios of 6:4 confirms the effective minimization in complete equilibrium arrest between ACm and AC, and conversion of AC to ABC. Beyond this 6:4 ratio, the error% has increased with increase in ABC concentration, which concludes only equilibrium between AC and ABC conversion. Finally, at low temperature 5 °C, the error% is completely arrested all equilibriums and minimized the error%, even at high ratios 7:3 of AC and ABC. The validation of the present method in real sample analysis is perfectly working to identify the BC and C in the presence of excess AS within an allowed error%. These results conclude that low temperature in the presence of excess AS is more suitable to differentiate the AC and ABC by titration analysis.

Acknowledgements

This study was supported by the Korea Research Foundation and the Korean Federation of Science and Technology Societies funded by Korea Government (MOEHRD, Basic Research Promotion Fund) and the National Research Foundation of Korea (NRF) funded by the Korean government (MEST) (Grant Nos. 2010-0027330 & 2014001974).

Appendix A. Supporting information

Supplementary data associated with this article can be found in the online version at http://dx.doi.org/10.1016/j.talanta.2014.08.044.

References

[1] I. Dahlan, K.T. Lee, A.R. Mohamed, J. Sci. Ind. Res 163 (2013) 83–87.
[2] R.-B. Lin, S.-M. Shih, C.-F. Liu, Chem. Eng. Sci. 58 (2003) 3659–3668.
[3] C.F. Liu, S.-M. Shih, Ind. Eng. Chem. Res. 45 (2006) 8765–8769.
[4] C. Wu, S.-J. Khang, T.C. Keener, S.-K. Lee, Adv. Environ. Res. 8 (2004) 655–666.
[5] L. Xu, J. Guo, F. Jin, H. Zeng, Chemosphere 62 (2006) 823–826.
[6] R. Sundararaman, C. Song, Energ. Fuel. 27 (2013) 6372–6376.
[7] H. Deng, H. Yi, X. Tang, H. Liu, X. Zhou, Ind. Eng. Chem. Res. 52 (2013) 6778–6784.
[8] I. Dahlan, K.T. Lee, A.H. Kamaruddin, A.R. Mohamed, Environ. Sci. Technol. 40 (2006) 6032–6037.
[9] G. Muthuraman, S.J. Chung, I.S. Moon, J. Ind. Eng. Chem. 51 (2012) 2697–2703.
[10] K.C. Pillai, S.J. Chung, T. Raju, I.S. Moon, Chemosphere 76 (2009) 657–664.
[11] J. Bichel, S. Stephen, Method for recovering purified sodium bicarbonate and ammonium sulfate. U.S. Patent, 0156775 A1, Aug. 12, 2004.
[12] F. Christensson, H.C.S. Koeford, A.C. Petersen, K. Rasmussen, Acta Chem. Scand. A 32 (1978) 15–17.
[13] W.C. Femelius, in: W.C. Femelius (Ed.), Inorganic Syntheses, Vol. II, McGraw-Hill Book Company Inc, New York, 1946, pp. 85–86 (Chapter 4).
[14] J.T. Yeh, K.P. Resnik, K. Rygle, H.W. Pennline, Fuel Process. Technol. 86 (2005) 1533–1546.
[15] J.F.I. Thomas, J.J. Lynch, J. Amer. Water Works Assoc 52 (1960) 259.
[16] A.A.B. Pichle, M. Cefola, Ind. Eng. Chem 6 (1939) 327–332.
[17] A. Suchier, Angew. Chem. 44 (1931) 534–536.
[18] R Belcher, A.J. Nutten, A.M.G. Macdonald, Quantitative Inorganic Analysis, Third ed., Butterworths, London, 1970.
[19] C.L. Wilson, D.W. Wilson, Comprehensive Analytical Chemistry, Elsevier, London, 1960 (Classical Analysis).
[20] N. Wen, M.H. Brooker, J. Phys. Chem. 99 (1995) 359–368.
[21] L. Meng, S. Burris, H. Bui, W.P. Pan, Anal, Chem 77 (2007) 5947–5952.
[22] Q. Zhao, S. Wang, F Qin, C. Chen, Ind. Eng. Chem. Res. 50 (2011) 5316–5325.
[23] F. Mani, M. Peruzzini, P. Stoppioni, Green Chem. 8 (2006) 995–1000.
[24] R. Bosco, B. Grandjean, Using raman spectroscppy to control carbonate/bicarbonate concentrations, U.S. 2011, 0125326 A1, May 26, 2011.
[25] P.L. Fosbøl, K. Thomsen, E.H. Stenby, Ind. Eng. Chem. Res. 48 (2009) 4565–4578.
[26] M. Laliberte, J. Chem. Eng. Data. 52 (2007) 321–335.
[27] H. Huang, S.G. Chang, Energ. Fuel. 16 (2002) 904–910.
[28] W.T. Bolleter, C.J. Bushman, P.W. Tidwell, Anal. Chem. 33 (1961) 592–594.
[29] S.A. Ben Mussa, H.S. Elferjani, F.A. Haroun, F.F. Abdelnabi, Int. J. Pharm.Tech. Res 1 (2009) 598–604.
[30] F. Qin, S. Wang, I. Kim, H.F. Svendsen, C. Chen, Int. J. Green. Gas Con 5 (2011) 405–412.
[31] G.G. Wildgoose, A.T. Masheter, A. Crossley, J.H. Jones, R.G. Compton, Int. J. Electrochem. Sci. 2 (2007) 809–819.
[32] M. Gronvald, C. Faurhold, Acta Chem. Scand. 14 (1960) 1374–1380.
[33] P.D. Wimberley, O. Siggaard-Anderson, N. Fogh-Anderson, A.B.T. Boink, Scand. J. Lab. Inv. 45 (1985) 7–10.
[34] G. Beck, J. Janek, Solid State Ionics 170 (2004) 129–133.

Talanta 132 (2015) 334–338

Contents lists available at ScienceDirect

Talanta

journal homepage: www.elsevier.com/locate/talanta

Electrochemical detection of nitromethane vapors combined with a solubilization device

Sébastien Delile [a], Adeline Aussage [a], Thierry Maillou [a,*], Pascal Palmas [a,*], Virginie Lair [b], Michel Cassir [b]

[a] CEA DAM le Ripault, F-37260 Monts, France
[b] Institut de Recherche de Chimie Paris, CNRS – Chimie ParisTech, 11 rue Pierre et Marie Curie, F-75005 Paris, France

ARTICLE INFO

Article history:
Received 4 April 2014
Received in revised form
11 September 2014
Accepted 13 September 2014
Available online 22 September 2014

Keywords:
Electrochemistry
Explosive sensor
Vapor phase detection
Nitromethane reduction
Prototyping
Screen-printed electrode

ABSTRACT

During the past decade, the number of terrorism acts has increased and the need for efficient explosive detectors has become an urgent worldwide necessity. A prototype, Nebulex™, was recently developed in our laboratory. Basically, it couples the solubilization of an analyte from the atmosphere by a nebulization process and *in-situ* detection. This article presents the development and integration of an electrochemical sensor for the detection of nitromethane, a common chemical product that can be used to make an improvised explosive device. A gold screen-printed electrode was used in a flow-cell and a detection limit of 4.5 μM was achieved by square wave voltammetry. The detection method was also determined to be selective toward nitromethane over a large panel of interfering compounds. Detection tests with the Nebulex™ were thus carried out using a custom-made calibrated nitromethane vapor generator. Detection times of less than one minute were obtained for nitromethane contents of 8 and 90 ppm_v. Further measurements were performed in a room-measurement configuration leading to detection times in the range of 1–2 min, clearly demonstrating the system's efficiency under quasi-real conditions.

© 2014 Elsevier B.V. All rights reserved.

1. Introduction

In a context of terrorism menace, the use of canine corps still represents the most sensitive and reliable solution to detect explosive traces [1–3]. However, dog-handler teams involve high costs for training and maintenance. Moreover, the effective time a dog can be used is limited to less than 1 h [3,4]. Hence, extensive interest has in recent years been devoted to developing artificial systems able to surpass these limitations [4–6]. Beside the purpose of global security, these developments also have implications on environmental protection depending on the impact of explosive compounds on human health and ecosystems [7,8].

Nitromethane (NM) is a common chemical compound used for example as a solvent in chemical laboratories or as a fuel in motor sports. But it can also be utilized in the fabrication of an improvised explosive device [9]. According to the high availability of this compound, NM can be classed as a very significant target for explosive detectors. This compound is highly volatile with a vapor pressure of 37 000 ppm_v at 20 °C and explosion limits of 7.3–63% (v/v) in air [10]. NM is also classified as a hazardous substance for human health with occupational exposure limits fixed to 20 ppm_v in the United States of America and 100 ppm_v in France [11].

NM is detectable with most commercially available combustible gas sensors (semiconductor or metal oxide sensor technology) or volatile organic compound detectors (photoionization technology). Although sensitive, these devices aim at detecting a large panel of chemical species and do not allow the recognition of one specific target substance. Thus, several investigations have been performed in order to produce a more selective response to the presence of NM both in liquid or gaseous phases. Recent developments include dog sniffers [12], photometric titration [13], fluorescence spectroscopy [14,15], laser-induced fluorescence [16], thermal analysis [17], gas chromatography [18,19], conductometric gas sensors [20] and electronic noses [21,22]. The best performances for gas sensors are in the range of 2–30 ppm_v with times of detection close to few seconds. Better detection limits have been obtained with gas chromatography (0.02 and 0.4 ppm_v) but using several experimental steps and long-time exposures (4 h and 10 min, respectively).

Finally, electrochemistry is a particularly suitable method for the detection of NM as it potentially combines several advantages including high sensitivity, a short measuring time, low costs,

* Corresponding authors. Tel.: +33 2 4734 4000.
E-mail addresses: thierry.maillou@cea.fr (T. Maillou), pascal.palmas@cea.fr (P. Palmas).

http://dx.doi.org/10.1016/j.talanta.2014.09.024
0039-9140/© 2014 Elsevier B.V. All rights reserved.

compactness and possibilities of miniaturization for integration. Some interesting approaches have been proposed [23–26] but have important limitations that preclude any further developments, *i.e.* mainly the use of a complex working electrode made of multi-materials and an atmosphere free of oxygen.

We have re-evaluated the potential of this technique for the detection of NM but our investigations were restricted to the development of an easily integrable system, *i.e.*, with constraints of a low-cost material, possible miniaturization and air containing oxygen. In a first investigation [27], we performed a screening of several experimental parameters that govern the electrochemical response in aqueous solution. Finally, square wave voltammetry (SWV) was selected with a gold working electrode in a phosphate buffer solution of pH 7.5. We also evaluated the use of a screen-printed electrode immersed in a custom-made bubbling vapor solubilization unit to detect NM vapors. Even if detection times of 30 s were obtained for NM vapor contents of 100 ppm_v, the efficiency of this assembly was mainly limited because of the heterogeneous stirring of the solution produced by the bubbling process, which resulted in noisy voltammograms.

The major problem has here been solved by using a portable detection device, Nebulex™, which was developed in our laboratory a few years ago [28]. This device is based on an original concept coupling the solubilization of analytes present in the atmosphere (vapors or particles) *via* a nebulization process instead of bubbling and the continuous detection of analytes within the solution. Initially, applications of Nebulex™ were focused on the detection of peroxide and nitroaromatic compounds by an optical measurement (absorbance or fluorescence) [29].

In the present study, we have investigated the possibilities of extending this concept to the detection of NM vapors.

The integration of miniaturized screen-printed electrodes with a flow-cell linked to the nebulization tank of Nebulex™ was evaluated. The efficiency of this assembly was determined by performing vapor detection tests, first under calibrated laboratory conditions and, subsequently, in a room-measurement environment that represents quasi-real conditions of use.

2. Experimental section

All the chemicals were of analytical grade and were used without further purification. All the solutions were prepared with deionized water with a resistivity above 18.2 MΩ at 25 °C (Milli-Q direct UV3, Millipore).

Nitromethane (NM) stock solutions were prepared on a monthly basis by dissolving liquid NM (Aldrich) in water. These solutions were stored in the dark at room temperature. Buffer solutions were prepared by dissolving KCl salt (Sigma-Aldrich) and K_2HPO_4 salt (Fluka) to obtain final concentrations of 1 M and 0.1 M, respectively. The pH was measured with a pH-meter (PHM201, Meterlab) and a combined electrode (XC161, Radiometer). It was adjusted to 7.5 by addition of aliquots of 1 M HCl (Fluka).

The NM concentration in air during the detection tests was determined by high performance liquid chromatography (HPLC) titration of the content of bubblers exposed to NM vapors. The experimental assembly comprised a vessel containing a determined amount of NM (pure or in solution), three bubblers containing water, a flow regulator and a pump. The vacuum created by the pump enabled to suck ambient air into the vessel thus carrying NM vapors into the bubblers. Then, the content of the bubblers was titrated by HPLC (Alliance 2695, Waters). A C-18 column of 150 mm length with an internal diameter of 4.6 mm and a pore size of 5 μm was used. The mobile phase was a mixture of water and methanol with a 50/50 ratio (v/v), the liquid flow rate was 1 mL min^{-1} and the detection was made by UV–vis absorbance at 215 nm. Vapor detection tests performed in the laboratory with Nebulex™ were realized under experimental conditions previously evaluated with this titration assembly and thus, the precise NM concentration in air was known. In the case of untested conditions for NM vapor generation, the concentration was estimated by extrapolation of known conditions.

The electrochemical measurements were performed using a portable potentiostat (PalmSens, Palm Instrument BV) with disposable screen-printed electrodes (SPE) consisting of a gold working electrode, a platinum counter electrode and a silver pseudo-reference electrode (DS250BT, Dropsens). The gold working electrode was pretreated and the silver of the pseudo reference electrode was converted to silver chloride according to the literature [27]. The voltammetric detection of NM was performed using square wave voltammetry with a 4 mV potential step, a 20 Hz frequency and a pulse amplitude of 30 mV. This set of parameters was selected following several optimizations to obtain the best compromise between sensitivity and speed of measurement. All voltammetric experiments were performed without removal of atmospheric oxygen.

The influence of interfering compounds towards the NM detection was studied by inserting an SPE in a flask containing 25 mL of the buffer solution. Five interfering compounds (25 μL of each one) were successively introduced, followed by 3 aliquots of 25 μL of a diluted NM solution (corresponding to 25 μM of NM for each added aliquots). Thus, the ratio of each interfering compounds toward one aliquot of NM was about 1000/1 in weight depending on the density of each compound. Repetitive SWV scans were performed during all the experiment and the current at the NM reduction peak potential was plotted *vs.* the time. The same experiments, in which NM was added before the aliquots of interfering compounds, were also performed to easily check the impact of these compounds on the NM reduction peak intensity (not shown). Three sets of interfering compounds were tested: a set of solvents (acetone, ethanol, toluene, dichloromethane and acetonitrile); a set of cleaning products (multi-use cleaning product, floor cleaning product, liquid soap for hand washing and 2 sorts of shower gels) and a set of various products (*eau de Cologne*, 2 sorts of fragrances, dogs and cats repulsive spray and an aniseed aperitif).

A schematic representation of how the Nebulex™ functions is given in Fig. 1(A). A vacuum is created in the nebulization tank which enables to suck ambient air into the device. The transit of air in the system of nozzles allows the formation of an aerosol by the Venturi effect. The droplets in this aerosol are very small conducing to a very efficient solubilization of analytes from the atmosphere due to the large exchange area between the air and the liquid. A vapor condenser was disposed between the nebulization tank and the pump to reduce the loss of nebulized solution. The flow rate of air used in the following experiments was about 3.5 L min^{-1} and the volume of nebulized solution was 30 mL.

The electrochemical detection system was integrated in the Nebulex™ device by inserting the SPE in a flow cell (Dropsens, *cf.* Fig. 1(B)). A flow of the nebulized solution was generated between the tank and the cell in a closed circuit by using a peristaltic pump (KNF). A short tube with a larger cross-section was added in the circuit before the flow-cell to absorb pressure pulses produced by the pump, resulting in a steady flow of solution and smooth voltammograms. However, this module has also induced a large pressure loss which reduces the flow to a maximum value of 3 mL min^{-1}. This flow-rate was used during the detection tests in order to obtain the lowest time of transit for the nebulized solution between the tank and the measurement cell.

The detection time during the vapor detection assays was defined as the duration separating the beginning of the exposure and the moment at which the current was shifted outside of the noise area. This noise area is calculated as the average current value

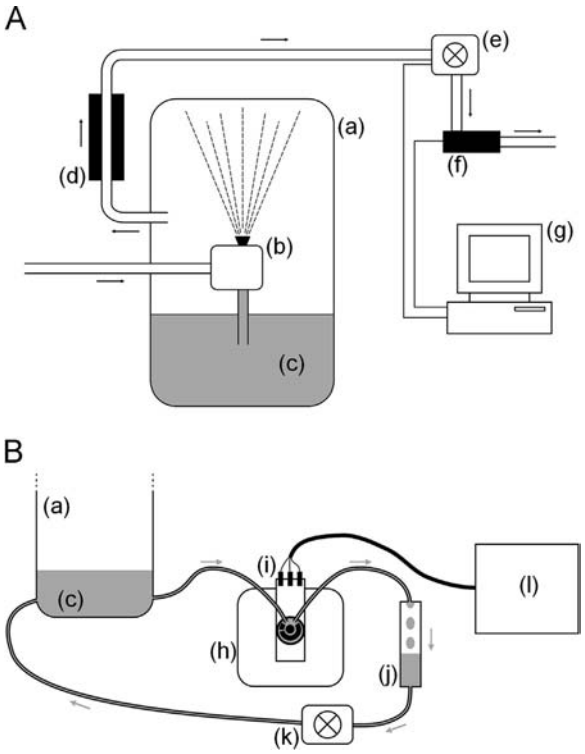


Fig. 1. Principle of the Nebulex™ device (A) and scheme of the electrochemical measurement assembly (B). (a) Nebulization tank; (b) system of nozzles; (c) nebulized solution; (d) vapor condenser; (e) pump; (f) flow-meter; (g) computer; (h) electrochemical flow cell; (i) SPE; (j) tube with larger cross-section; (k) peristaltic pump and (l) potentiostat. The black arrows show the direction of air in the device and the gray arrows show the direction of the nebulized solution in the measurement circuit.

over a set of blank measurements, more or less 3 times the standard deviation (3σ).

For the vapor detection tests in room-measurement conditions, a small amount of NM (5 mL) was deposited at the center of a clean room (32 m^3 in volume), corresponding to a theoretical vapor concentration of about 50 ppm_v. However, only 2 mL were vaporized as about 3 mL of residual liquid NM were left after detection. This shows that a maximum NM concentration of about 20 ppm_v in the gas phase was reached during the experiments. The Nebulex™ device was positioned in the next room and the suction pipe was inserted in the measurement room through the wall. The distance between the end of the suction pipe of the Nebulex™ and the NM source was about 1.2 m and the duration between placing the NM in the room and the beginning of the vapor detection measurement was 30 minutes.

3. Results and discussion

In our first study [27], performances and repeatability of SPEs towards electrochemical detection of NM were evaluated. It was first found that the potential of the NM reduction peak was highly reproducible ($\pm$ 4 mV with 12 different SPEs) due to the transformation of the Ag pseudo-reference to the AgCl pseudo-reference. The gold activation procedure also gave rise to a very stable NM peak intensity with a relative standard deviation of 4.5% on the slope of the current *vs.* NM concentration with 12 different SPEs. The repeatability and performances of the SPEs were also evaluated in the experimental flow-cell assembly used in the present study and similar results were obtained. NM was determined with a sensitivity of 210 nA/μM and a limit of detection (LOD) of 4.5 μM was calculated on the basis of three times the signal-to-noise ratio (3 S/N).

In the present study, the impact of several common interfering compounds on the detection performances was investigated to evaluate the selectivity of our detection method toward NM. These measurements were carried out directly in the electrolytic solution instead of working in the vapor phase *via* the solubilization device in order to maximize the influence of the interfering compounds, and mainly to avoid the false negative results due to poor volatility or poor water solubility.

As can be seen in Fig. 2, only the multi-use cleaning product and the liquid soap for hand washing had a slight impact on the detection curve. Additional measurements were performed on these two isolated compounds to have a better insight into their specific response. The first one produced a negative shift of the base-line all over the examined potential range. Such an effect can be easily identified by checking the root voltamograms (no reduction peak, no NM). The impact of the liquid soap for hand washing is more troublesome because of the appearance of a reduction peak at exactly the same potential than the NM reduction peak. However, this peak remained tiny (*ca.* 0.5 μA) and did not shift the current curve outside of the noise area, even if more soap was added. Moreover, all the interfering compounds were added in a very large proportion compared to each NM aliquot (about 1000/1 in weight). Thus, the interfering impact with respect to the detection performances of these two compounds, as well as the others, can be reasonably neglected. These results allow appreciating the robustness of the method in a realistic environment of use.

The content of NM vapors used in the detection assays was calibrated beforehand. In all the experiments, the NM concentration fraction in the bubblers was about 90% for the first bubbler, 10% for the second and under the HPLC LOD (3.2 μM) for the last. It could thus be deduced that the sum of the amount of NM titrated in the first two bubblers corresponded to the total amount of NM carried by air. Consequently, the NM concentration in air could be calculated taking into account the sum of the titrated amount of NM in the bubblers divided by the total volume of air passing through the bubblers during the experiment. This was expressed as a partial pressure using the ideal gas law.

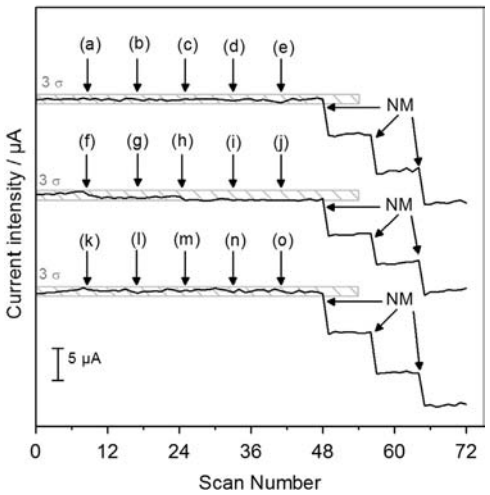


Fig. 2. Plot of the current at the NM reduction potential *vs.* the time during the additions of 25 μL aliquots of (a) acetone; (b) ethanol; (c) acetonitrile; (d) toluene; (e) dichloromethane; (f) multi-use cleaning product; (g) floor cleaning product; (h) liquid soap for hand washing; (i) and (j) 2 sorts of shower gels; (k) eau de Cologne; (l) and (m) 2 sorts of flagrances; (n) dogs and cats repulsive spray and (o) aniseed aperitif. "NM" corresponds to a 25 μM increase of the NM content of the solution. The gray area corresponds to the noise area and constitutes three times the standard deviation obtained from a set of blank measurements.

The experimental parameters governing the NM concentration in air are the amount of NM in the vessel and the vessel geometry. Varying these two parameters enabled to establish an NM vapor concentration range from 0.7 to 8.2 ppm_v. This range was deliberately much lower than the vapor pressure of NM as the purpose of this study was the detection of trace amounts.

The NM solubilization efficiency of the Nebulex™ was also evaluated. Experiments were carried out under previously calibrated conditions for NM vapor generation, but by using the Nebulex™ instead of the bubblers. The content of the nebulization tank after exposure to the NM vapors was titrated by HPLC and compared to the NM concentration in air. A solubilization yield of about 50% was obtained without any prior optimization of the system. An improvement of this efficiency will be possible in the future by performing numerical simulations of both aerosol formation and condensation of droplets from the aerosol to the tank.

The detection of NM vapors with the Nebulex™ device was first attempted under laboratory conditions using an NM concentration in air of 8.2 ppm_v. The resulting voltammograms as a function of time are shown in Fig. 3(A). The measurement of ambient air produced a repeatable base-line with a low level of noise. The reduction peak appeared after a few scans following the exposure to NM vapors. The device was also evaluated to detect NM at a concentration of 90 ppm_v (Fig. 3(B)), which corresponds to the French occupational exposure limit for this compound [11]. In this case, the reduction peak of NM appeared with a higher intensity but was still not observed directly after the beginning of the exposure.

The detection time was determined for each experiment by plotting the current at the NM reduction potential *vs.* the time (*cf.* Fig. 4). Detection times were 36 s and 48 s for the exposures to 90 ppm_v and 8 ppm_v of NM, respectively. Thus, even if the NM concentration in air was decreased by a factor ten or more, giving a less intense NM reduction peak, the detection time was only increased by the duration of one scan. As can be seen in Fig. 4, a short time after the exposure to NM vapors, the reduction current increased linearly with the duration of the experiment. For low NM gas concentrations, the slope of the linear domain was weak. In this case, the detection time can be improved by increasing the NM concentration in the solution. This can be achieved by an

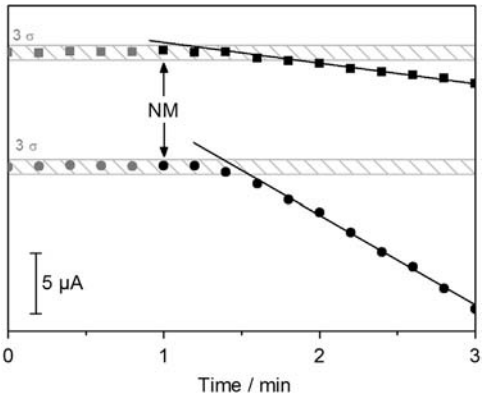


Fig. 4. Plot of the NM reduction current *vs.* the time during the detection tests of NM vapors at concentrations of 8 ppm_v (squares) and 90 ppm_v (dots). Gray squares/dots correspond to the exposure to NM free air (blank measurement) and black squares/dots correspond to the exposure to NM containing air. The gray area corresponds to the noise area and constitutes three times the standard deviation obtained from a set of blank measurements. Only the points outside of the noise area are considered to constitute the linear regressions.

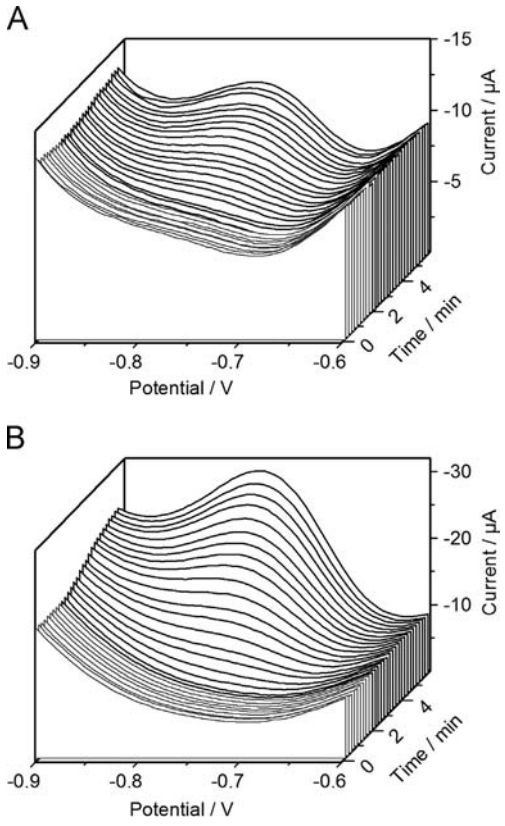


Fig. 3. Voltammograms as a function of the time during detection tests of NM vapors at concentrations of 8 ppm_v (A) and 90 ppm_v (B). The gray curves correspond to measurements of ambient air and the black curves correspond to measurements of NM vapors.

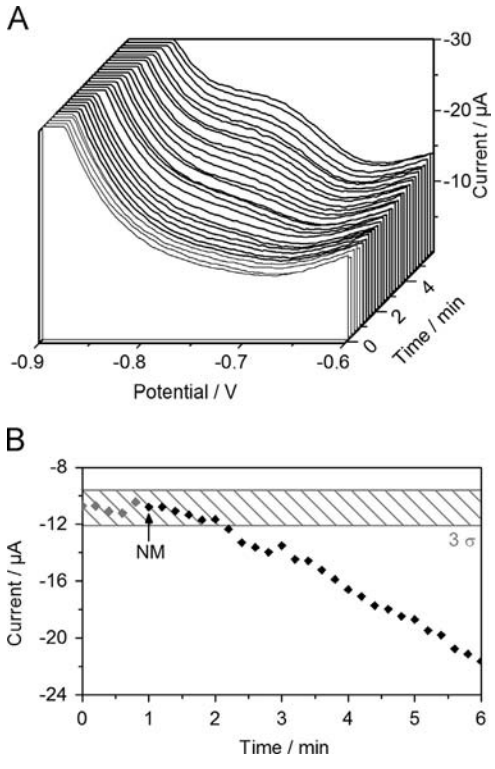


Fig. 5. (A) Voltammograms as a function of the time during a detection test of NM vapors in a room-measurement configuration. The gray curves correspond to the measurement of ambient air and the black curves correspond to the measurement of NM vapors. (B) Plot of the NM reduction current *vs.* time during the same experiment. Gray diamonds correspond to the exposure to NM free air (blank measurement) and black diamonds correspond to the exposure to NM containing air. The gray area corresponds to the noise area and constitutes three times the standard deviation obtained from a set of blank measurements.

optimization of the nebulization process. The initial transient period corresponds to the time the NM takes to reach the SPE from the aerosol. This short period gives a limit of the detection time that cannot be overpassed even at high gas concentrations. A reduction of this delay is possible by an optimization of the measurement circuit from the nebulization tank to the SPE with regard to fluid flow concepts.

Finally, the Nebulex™ device was evaluated in conditions of room-measurements. Liquid NM was left in an empty room and the vapors were sucked into the Nebulex™ device in the adjacent room. The results of one of these experiments are shown in Fig. 5. Measurement conditions were in this case not as ideal as in the laboratory: the base-line corresponding to the measurement of air without NM was not as repeatable and the noise area was broader. The NM reduction peak was nevertheless observable from about 1 min after the beginning of the exposure to the NM vapors. The detection slope (reduction intensity *versus* the time) is closed to two times higher than the one obtained for the experiment at 8 ppm_v of NM vapor concentration. This data is coherent with the maximum theoretical average NM vapor concentration of 20 ppm_v that can be reached in the room (see experimental section).

A detection time of 1 min 20 s after the beginning of the exposure to NM vapors was determined according to the method described above. In addition to the broader noise area, the detection time was also extended because of the use of a longer suction pipe passing through the wall. Even though performances were degraded in unclean (but real) conditions of use, the possibility of detecting NM in a room-measurement configuration within a reasonably short time (*i.e.*, in a one-minute range) was here demonstrated. The next step will be the evaluation of environmental conditions on the system performances. Several parameters can be varied, including the amount of NM, the distance between the NM source and the suction pipe, the presence of obstructing objects, *etc.*

4. Conclusion

This article has described a novel system for the detection of NM vapors with the Nebulex™ device. Electrochemistry was selected as the analytical technique because of its low cost, high sensitivity and fast measurement capability. A flow-cell and an SPE were used to integrate the detection system in the device leading to an LOD of 4.5 μM for NM. Moreover, no significant perturbation of the detection signal was noted after exposure to 15 potential interfering compounds showing the robustness of the method in a realistic environment. The vapor generation used for the detection was calibrated and the solubilization efficiency of the nebulization process was determined.

Finally, the feasibility of electrochemical detection of NM vapors with the Nebulex™ device was successfully demonstrated. Detection times of less than one minute were obtained even for an NM vapor content below 10 ppm_v. The detection of NM vapors in a room-measurement configuration, which is more representative of real conditions of use, was also achieved. In this case, the detection time was slightly longer, due to the experimental conditions not being as clean as in laboratory tests, but was still in the 1 min range.

The LOD obtained with the present system is in the same order than those of other gas sensors. However, this limit can be improved by accumulating analyte vapors over several minutes. Moreover, the presence of NM can be confirmed *a posteriori* by chemical analysis of the nebulized solution.

Routes of improvement were identified to enhance the efficiency of the Nebulex™ device which will eventually be tested in more realistic conditions.

Acknowledgments

The authors gratefully acknowledge the Région Centre (France) for the grant allocated to this subject.

References

[1] K.G. Furton, L.J. Myers, Talanta 54 (2001) 487–500. http://dx.doi.org/10.1016/S0039-9140(00)00546-4.
[2] L. Lazarowski, D.C. Dorman, Appl. Anim. Behav. Sci. 151 (2014) 84–93. http://dx.doi.org/10.1016/j.applanim.2013.11.010.
[3] J.C. Oxley, L.P. Waggoner, Chapter 3 – Detection of explosives by dogs, in: M. Marshall, J.C. Oxley (Eds.), Aspects of Explosives Detection, Elsevier, Amsterdam, 2009, pp. 27–40. http://dx.doi.org/10.1016/B978-0-12-374533-0.00003-9.
[4] S. Singh, J. Hazard. Mater. 144 (2007) 15–28. http://dx.doi.org/10.1016/j.jhazmat.2007.02.018.
[5] J.S. Caygill, F. Davis, S.P.J. Higson, Talanta 88 (2012) 14–29. http://dx.doi.org/10.1016/j.talanta.2011.11.043.
[6] S. Singh, M. Singh, Signal Process. 83 (2003) 31–55.
[7] J. Pitchel, Appl. Environ. Soil Sci. 2012 (2012) 1–33. http://dx.doi.org/10.1155/2012/617236.
[8] D.R.S. Lima, M.L.S. Bezerra, E.B. Neves, F.R. Moreira, Rev. Environ. Health 26 (2011) 101–110. http://dx.doi.org/10.1515/reveh.2011.014.
[9] H. Schubert, The terrorist pallet of liquid explosives and flammable fuels, in: H. Schubert, A. Kuznetsov (Eds.), Detection of Liquid Explosives and Flammable Agents in Connection with Terrorism, Springer, Dordrecht, 2008, pp. 1–5. http://dx.doi.org/10.1007/978-1-4020-8466-9_1.
[10] International Program for Chemical Safety (IPCS), Nitromethane, ICSC 0522, ⟨http://www.inchem.org/documents/icsc/icsc/eics0522.htm⟩ (accessed 19.07.14).
[11] International Agency for Research on Cancer (IARC), Nitromethane, in: World Health Organization, IARC Monographs on the evaluation of carcinogenic risks to human – some industrial chemicals, Lyon, vol. 77, 2000, pp. 487–501.
[12] E. Lotspeich, K. Kitts, J. Goodpaster, Forensic Sci. Int. 220 (2012) 130–134. http://dx.doi.org/10.1016/j.forsciint.2012.02.009.
[13] C.A. Reynolds, D.C. Underwood, Anal. Chem. 40 (1968) 1983–1986. http://dx.doi.org/10.1021/ac60269a047.
[14] J.V. Goodpaster, V.L. McGuffin, Anal. Chem. 73 (2001) 2004–2011. http://dx.doi.org/10.1021/ac001347n.
[15] M.S. Meaney, V.L. McGuffin, Anal. Chim. Acta 610 (2008) 57–67. http://dx.doi.org/10.1016/j.aca.2008.01.016.
[16] C.M. Wynn, S. Palmacci, R.R. Kunz, M. Rothschild, Opt. Express 18 (2010) 5399–5406. http://dx.doi.org/10.1364/OE.18.005399.
[17] A. Nazarian, C. Presser, Thermochim. Acta 576 (2014) 60–70. http://dx.doi.org/10.1016/j.tca.2013.10.036.
[18] A. Takeuchi, Y. Nishimura, Y. Kaifuku, T. Imanaka, S. Natsumeda, H. Ota, S. Yamada, I. Kurotani, K. Sumino, S. Kanno, J. Occup. Health 52 (2010) 194–197. http://dx.doi.org/10.1539/joh.M9014.
[19] K.U. Alwis, B.C. Blount, L.K. Silva, M.M. Smith, K.H. Loose, Environ. Sci. Technol. 42 (2008) 2522–2527. http://dx.doi.org/10.1021/es702733k.
[20] J.R. Sohn, J. Ind. Eng. Chem. 8 (2002) 386–392.
[21] A. Kalach, N. Klochkov, Sens. Transducers 43 (2004) 240–247.
[22] W.J. Peveler, R. Binions, S.M.V. Hailes, I.P. Parkin, J. Mater. Chem. A 1 (2013) 2613–2620. http://dx.doi.org/10.1039/c2ta01027e.
[23] W. Chen, Y. Wang, C. Bruckner, C.M. Li, Y. Lei, Sens. Actuators B: Chem. 147 (2010) 191–197. http://dx.doi.org/10.1016/j.snb.2010.03.046.
[24] L. Wang, X. Zhang, H. Xiong, S. Wang, Biosens. Bioelectron. 26 (2010) 991–995. http://dx.doi.org/10.1016/j.bios.2010.08.027.
[25] Y. Wang, H. Xiong, X. Zhang, Y. Ye, S. Wang, J. Electroanal. Chem. 674 (2012) 17–22. http://dx.doi.org/10.1016/j.jelechem.2012.04.004.
[26] J. Boutros, M. Bayachou, Inorg. Chem. 43 (2004) 3847–3853. http://dx.doi.org/10.1021/ic035173e.
[27] S. Delile, T. Maillou, P. Palmas, V. Lair, M. Cassir, Electrochim. Acta 99 (2013) 94–101. http://dx.doi.org/10.1016/j.electacta.2013.03.052.
[28] P. Charrue, G. Thevenot, G. Cavalin, R. Delmas, Apparatus and method for extracting gaseous, liquid and/or solid elements from a gaseous medium and concentrating same in a liquid medium, World Patent, 2005, WO 2005/025721.
[29] A. Bry, M. Bousquet, L. Hairault, T. Maillou, Method for detecting in situ the presence of explosives in a gaseous medium, World Patent, 2012, WO 2012/072582.

Talanta 132 (2015) 339–353

Contents lists available at ScienceDirect

Talanta

journal homepage: www.elsevier.com/locate/talanta

Review

Electrochemically assisted solid based extraction techniques: A review

Shahram Seidi [a], Yadollah Yamini [b,*], Maryam Rezazadeh [b]

[a] Department of Analytical Chemistry, Faculty of Chemistry, K.N. Toosi University of Technology, Tehran, Iran
[b] Department of Chemistry, Tarbiat Modares University, P.O. Box 14115-175, Tehran, Iran

ARTICLE INFO

Article history:
Received 8 July 2014
Received in revised form
20 August 2014
Accepted 21 August 2014
Available online 18 September 2014

Keywords:
Sample preparation
Electrical driving force
Solid phase extraction
Microextraction.

ABSTRACT

The complexity of the matrices of the analytes from a biological sample or environmental origin can disturb the separation and data analysis steps. Thus, the major incentive of recent research trends in environmental and bioanalysis research is to achieve faster, simpler, inexpensive, and more environmental-friendly sample preparation techniques. Application of auxiliary energies is one of the efficient strategies to reach the aforementioned purposes. Among these, application of electrical driving force in different extraction techniques has found remarkable consideration in recent years attributed to its ability in control of different properties of an extraction system such as selectivity, clean-up, rate, and efficiency by imposition of a variable potential difference. This review attempts to explain the principles of electrically assisted solid based extraction techniques as well as different roles of electrical field in these methods in more details. Also, advantages, disadvantages, and limitations of these techniques are discussed providing coherent information and useful insights for future researches.

© 2014 Elsevier B.V. All rights reserved.

Contents

1. Introduction . . . 339
2. Solid based extraction techniques . . . 340
 2.1. Electrokinetic trapping . . . 340
 2.2. Solid-phase extraction . . . 341
 2.3. Solid-phase microextraction . . . 345
  2.3.1. Types of electrochemical setup used for SPME . . . 345
  2.3.2. Application of electrical driving force in synthesis of SPME fiber . . . 345
  2.3.3. Sorption mechanism of EA-SPME . . . 349
3. Solid based extraction techniques as lab-on-a-chip . . . 350
4. Concluding remarks and future trends . . . 352
Acknowledgments . . . 352
References . . . 352

1. Introduction

Sample preparation is of vital importance in analysis of trace amounts of target analytes or their analysis in complicated matrices. Some sample cleanup, analyte isolation from the interferences, and their preconcentration to a suitable level may be required before instrumental analysis. Sample preparation could be explained as the experimental steps required making a sample ready for analysis. A good sample preparation method should be as fast as possible, reproducible, involve minimum number of steps, has relatively low cost, be environmental friendly, and offer high recoveries, and also have the potential to become automated [1].

Abbreviations: CE-MS, Capillary electrophoresis–mass spectrometry; CV, cyclovoltammetric; EA-SPME, electrically assisted solid phase microextraction; EC-SPE, electrochemical solid-phase extraction; EC-SPME, electrically controlled SPME; EMLC, electrochemically modulated liquid chromatography; EM-SPME, electromembrane surrounded solid phase microextraction; ES-SPME, electrosorption SPME; EQCM, electrochemical quartz crystal microbalance; ESI, electrospray ionization; FIA, flow injection analysis; ICP-MS, inductively coupled plasma mass spectrometry; LLE, liquid–liquid extraction; MIP, molecular imprinted polymer; PGC, porous graphitic carbon; PPy, polypyrrole; QRE, silver quasireference electrode; SCE, saturated calomel electrode; SEM, scanning electron microscopy; SPE, solid phase extraction; SPME, solid phase microextraction

* Corresponding author. Tel.: +98 21 82883417; fax: +98 21 88006544.
E-mail address: yyamini@modares.ac.ir (Y. Yamini).

http://dx.doi.org/10.1016/j.talanta.2014.08.059
0039-9140/© 2014 Elsevier B.V. All rights reserved.

Solid phase based extraction techniques are well-known sample preparation methods, which have been associated with many advances in the past few years. Liquid–solid extraction or solid phase extraction (SPE) was first introduced as a replacement for liquid–liquid extraction (LLE). The technique utilizes a solid support to isolate and preconcentrate the analyte of interest [2–4]. A typical SPE has four processing steps; including conditioning, sample application, washing impurities, and elution of target analytes. Pawliszyn et al. have presented for the first time the miniaturized format of SPE; named solid-phase microextraction (SPME), in which sampling, isolation, and enrichment of analytes and its introduction into the analysis instrument can be done in one step [5]. SPME requires a small amount of extraction phase coated on a solid support. Selectivity of this technique is determined by composition of the extraction phase.

Electrical field induced extraction technique is a topic that is less investigated. A significant growing trend can be observed in the annual number of publications related to the electrically assisted extraction techniques as well as the number of citations to these works in the literature. Thus, it can be concluded that these methods are gradually becoming a quite common place in the analysis of various environmental and biological samples.

In this review, the focus is centered on the electrically assisted solid based extraction techniques to present a general vision of the effect of electric fields on carrying out sample treatment and also to evaluate the real potential of these methods. Advantages, disadvantages, and limitations of these techniques are discussed. These points can be helpful in future scientific researches to overcome current problems and improve electrical induced solid based extraction methods.

For this purpose, a comprehensive survey of past and present novelties and applications of the electrically assisted solid based extraction techniques will be provided. Also, a conceptual clustering method was applied for investigation of different aspects of various electrically assisted techniques and a powerful and innovative way was employed to keep information in the mind for a long period of time.

2. Solid based extraction techniques

Electrochemical techniques have found remarkable applications in SPE and SPME techniques including synthesis of sorbents and enhancement of extraction [6–9]. In the case of synthesis of sorbents, the electrochemical method provides tailoring of key characteristics including thickness, conductivity, degree of oxidation, color, and morphology [10]. This fact has propelled various research groups toward synthesis of new coatings [11–14]. Among the newest, there has been growing interest in conducting polymers due to their multifunctional properties [11].

The idea of application of electrical field in solid-phase extraction originates from a technique termed electrochemically modulated liquid chromatography (EMLC) [15]. EMLC was first reported by Fujinaga et al. in 1963 [16]; then by Blaedel and Strohl [17] and independently by Roe in 1964 [18]. Generally, an electrical field has two effects in the solid based extraction techniques; it directly affects the surface of solid sorbents and provides manipulation possibility of extraction [7–9,19–21], or has an indirect effect so that only provides an electrokinetic migration of charged analytes toward solid sorbent [22] or facilitates elution of the analytes [6]. Electrically assisted solid-phase extraction/microextraction and electrokinetic trapping are the instances for direct and indirect effects of electrical field in solid based extraction techniques, respectively.

According to the literature, the substantial increasing trend in application of the electrical field in solid based extraction techniques can be attributed to several reasons;

1. Properties of the conducting polymer can be modified by varying the conditions during the electropolymerization step to enable extraction of analytes with different sizes and charges.
2. Compared to conventional solid based extraction techniques, in which a material with a fixed number of exchange sites is employed, electrically assisted one offers higher flexibility. This is because the properties of the material and thus the number of exchange sites can be externally controlled by electrochemically controlling the charge of the material [23,24].
3. The use of polymer based fiber films in solid based extraction techniques can be extended to the analysis of neutral, electroinactive analytes by taking the advantage of electrochemically controlled hydrophobic/hydrophilic ‘switching’ [25].
4. Electrically assisted solid based extraction techniques can be used to extract ions and analytes that normally need to be derivatized prior to traditional solid based extractions [26,27].
5. In electrically assisted solid based extraction techniques, the extraction and desorption steps are performed merely by altering the potential of the conducting polymer coated electrode. In this approach, there is thus no need for changes of the solvent in order to enable desorption of the compounds [28].
6. By altering the electrochemical potential of the polymer, desorption of electrostatically held analytes may also be faster compared to the desorption techniques normally used in traditional solid based extractions [29]. This makes the technique particularly interesting for use in conjunction with miniaturized analytical systems.

2.1. Electrokinetic trapping

Electrokinetic trapping is a technique, in which charged species migrate in opposite direction of their net charge under electrical field and are trapped by different strategies such as solid sorbent [30], ion selective membrane [31], hydrogel plug [32], and microporous polymer network material (monolith) [33]. The retained charged species are released from the trap by a pressure driven flow in the absence of the electric field. This technique has drawn much attention due to its potential application in biological sciences; especially for preconcentration of proteins and DNA [30–33].

Singh et al. used silica sorbents as trapping materials for preconcentration and determination of chicken egg albumin so that preconcentration values greater than 1000-fold were achievable by this way [30]. Schematic presentations of the setup used are shown in Fig. 1A and B. About 10 cm of a 30-cm fused silica capillary column was packed with porous silica particles as the stationary phase. The capillary column was conditioned at a pH of about 8.3 using 50 mM tris(hydroxymethyl)aminomethane (TRIS) buffer. A sample containing 100 mg L^{-1} of chicken egg albumin as well as caffeine in 50 mM TRIS was electrokinetically injected onto the stationary phase by applying a voltage of about 50 kV through the stationary phase by means of power supply and electrodes.

It should be noted that albumin species were labeled with fluorescein to permit detection possibility by laser induced dispersed fluorescence. Albumin has a negative charge at pH 8.3, whereas caffeine is a neutral compound in this pH and therefore, can be used as an evidence for electrokinetic trapping of albumin. The electrodes are disposed on either side of the stationary phase and preferably in inlet and outlet reservoirs. The voltage was applied for about 10 min, during which the uncharged caffeine was eluted from the column.

Under the influence of the applied electric field, only neutral caffeine was eluted in about 8 min from the packed column (Fig. 1C) and no evidence was observed for elution of negatively charged albumin species during different investigated times

(60 min and 12 h) of maintaining the voltage. After confirmation of no elution of albumin, application of the voltage was stopped and pressure was applied to the inlet end of the column by a pump (Fig. 1B) to force fluid through the column; thereby eluting the charged molecules retained on the stationary phase (Fig. 1D).

Other applications including selective modification of protein, the use of retained proteins as immobilized catalyzers, and preconcentration of DNA can be considered for this technique. As can be seen, the electrical field has no direct effect on solid based extraction procedure (trapping) here and only helps the migration of charged species toward trapping materials.

2.2. Solid-phase extraction

As it was mentioned in Section 2, the idea of application of electrical field in solid-phase extraction originates from EMLC [15,34–36]. Briefly, EMLC is a unique combinatory technique that simultaneously has the advantages of both electrochemistry and liquid chromatography. A three-electrode electrochemical cell configured as a HPLC column is used in EMLC (Fig. 2) [37]. The working electrode is a conductive material such as porous graphitic carbon (PGC) or glassy carbon coated with conductive materials such as polypyrrole (PPy) that acts as the stationary phase [37]. This characteristic makes it possible to manipulate analyte retention and enhance separation efficiencies through changing the potential applied to a conductive stationary phase. Electrochemical alteration of the stationary phase is similar to the gradient elution in conventional liquid chromatography.

It should be noted that EMLC not only can be used as a separation technique but also can be applied as an extraction method. For example, EMLC coupled with inductively coupled plasma-mass spectrometry (ICP-MS) detection has been employed by Hasan et al. [38] in the extraction mode for removal of some metal ions from deionized water or diluted acids to clean up blank solutions. Implementation of EMLC in chip based device and application of molecular imprinted polymer (MIP) coated conductive stationary phases to create selective phases may be innovative and interesting directions in this field.

SPE can be classified into two general groups; including conventional and electrochemically ones (Fig. 3). Each of the above-mentioned groups is subdivided into two planar and non-planar types and each type can be carried out in various formats. The focus in this review is on electrochemical solid-phase extraction (EC-SPE) and the conventional one has been reviewed by several other authors [2,39–42].

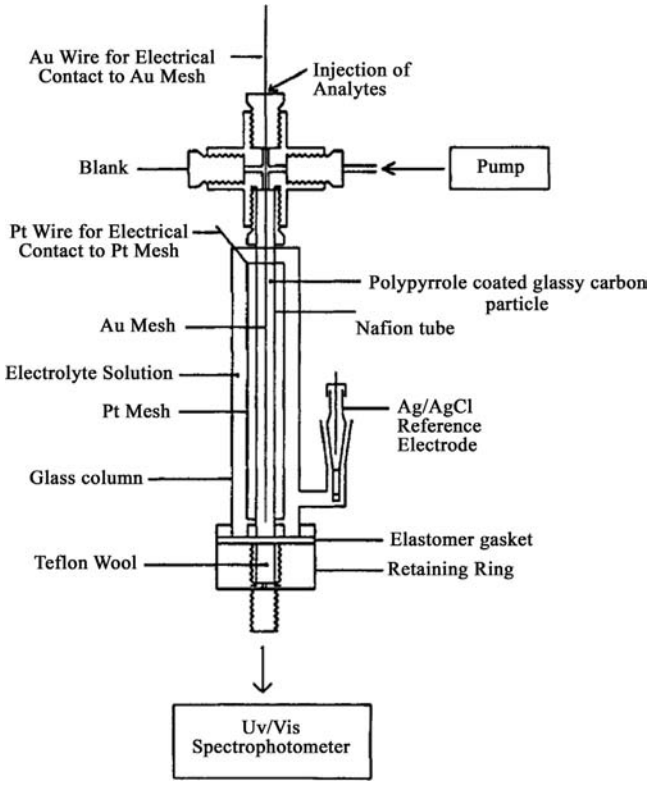


Fig. 2. A schematic presentation of an electrochemically modulated liquid chromatography (reproduced with permission of ACS-Ref. [37]).

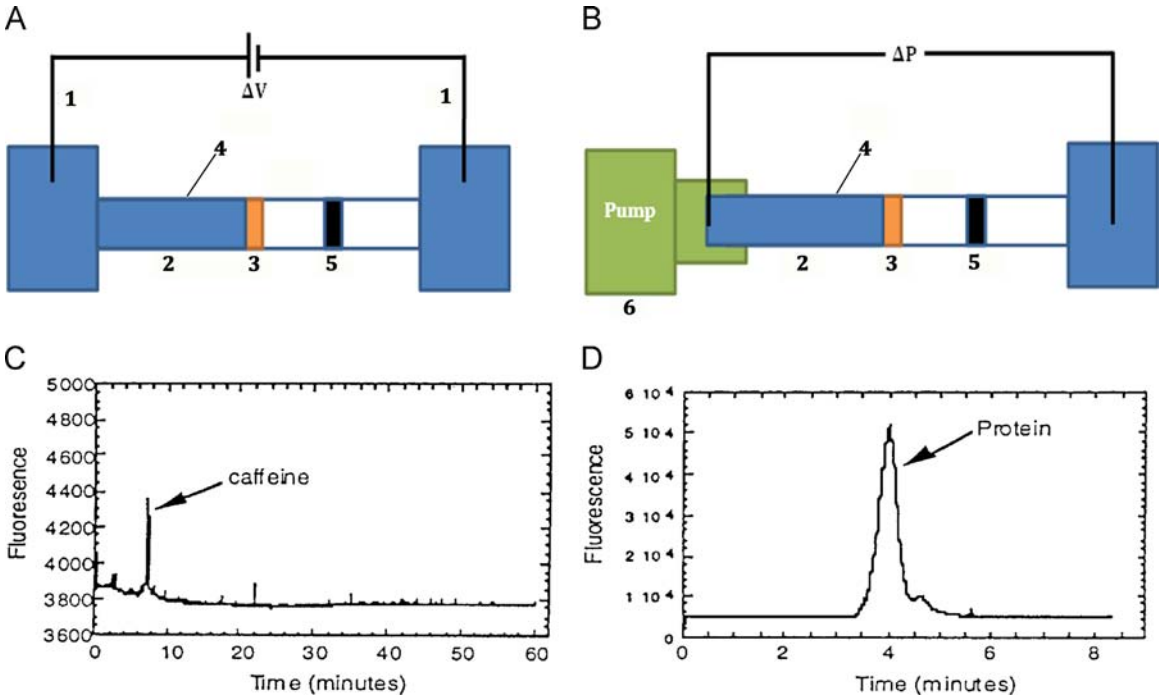


Fig. 1. (A) and (B) An embodiment of the setup used for electrokinetic trapping by Singh et al. (C) and (D) Elution curves for caffeine as uncharged and protein as charged species, respectively; (1) electrodes, (2) stationary phase, (3) frits, (4) fused silica capillary column, (5) laser induced dispersed fluorescence, and (6) pump [30].

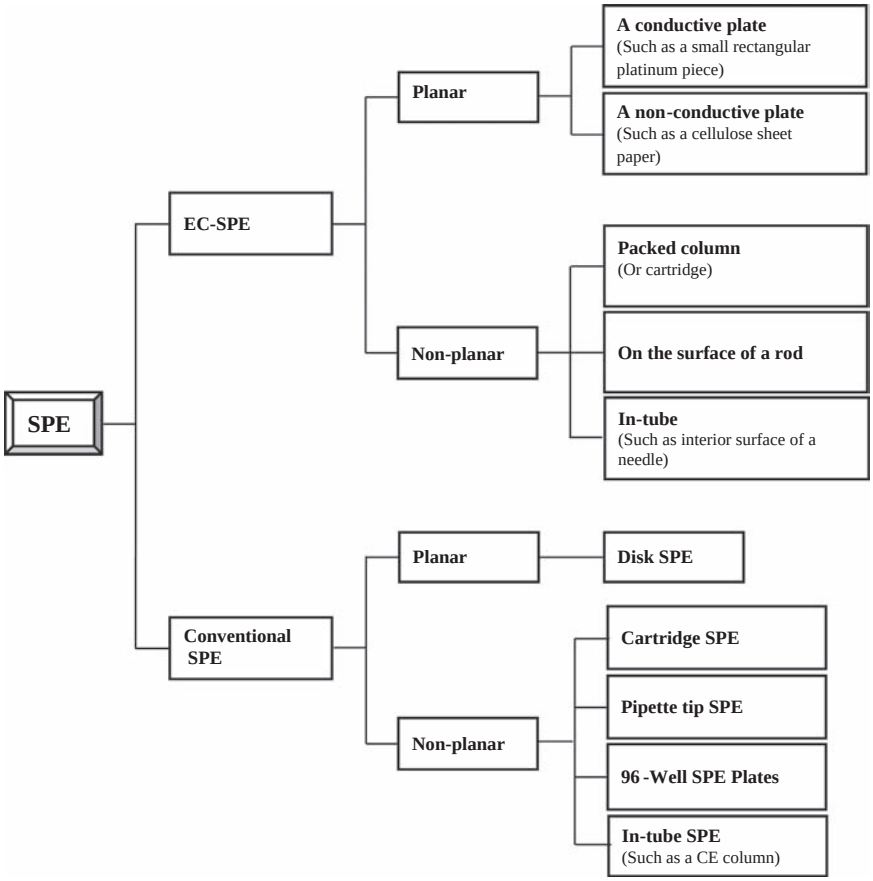


Fig. 3. General classification of solid-phase extraction techniques.

Electrical field has been used in EC-SPE for both assisted extraction and synthesis of solid sorbent aims, solely or simultaneously [6,43–50]. Electrosynthesis of solid sorbent in SPE depends on conductivity of the sorbent substrate. Some examples are interior needle electropolymerization of pyrrole at a constant potential of +1.5 V within 20 min for headspace solid-phase dynamic extraction of some polycyclic aromatic hydrocarbons (PAHs) by Bagheri et al. [50], EC-SPE and amperometric determination of nitrite with PPy nanowire modified electrode deposited on the surface of a graphite rod with diameter of 8 mm under the condition of applied potential of 0.8 V for 300 s by Wang et al. [43], and in-situ EC-SPE of anions and cations using PPy and over-oxidized sulfonated polypyrrole deposited on the surface of a $1.0 \times 0.5\ cm^2$ platinum foil at a constant potential of +0.80 V during 8 min by Şahin et al. [45]. In the first example, electrical field has only been used for electrosynthesis of SPE coating, while in the two subsequent cases both electrosynthesis and assisted extraction can be seen during SPE procedure. In EC-SPE, the extraction is obtained by oxidizing/reducing the conductive polymer, which caused movement of counterions (dopants) in and out of the conductive polymer to maintain its electroneutrality. An introduction to conductive polymers and their different applications, the most commonly used materials to synthesize conductive polymers, and the extraction mechanism by these polymers will be presented in the next section.

An important aspect of EC-SPE, which is almost ignored in comparison with conventional SPE, is on-line combination of this technique with analytical instruments such as chromatography and spectrometry apparatus. In 2005, an on-line EC-SPE using PPy coated electrodes and a thin-layer electrochemical flow cell interfaced to electrospray ionization (ESI-MS) and ICP-MS was developed for determining trace levels of bromide ions in tap water by Liljegren et al. [49]. Determination of bromide at the concentration level of 3 μM was possible using a modified thin-layer electrochemical flow cell coupled with ICP-MS in the tap water sample. The interference effects of various anions were investigated and the results indicated that their impacts can be reduced by electropolymerization of PPy in the presence of bromide ions. Also, different desorption techniques namely stopped-flow desorption and desorption in flowing solutions were examined and the first system exhibited substantial supremacy in comparison with the second one. Regarding the results obtained and possibility of electrochemical control of both extraction and desorption steps in EC-SPE, this technique could be a well-suited candidate for inclusion in miniaturized Lab-on-a-Chip (LOC) systems.

One of the recent advances in EC-SPE is utilization of PPy-modified surface cellulose paper sheets derived from *Cladophora* sp. algae for electrically assisted planar solid based extraction, introduced by Mihranyan et al. [46]. They showed that composites of PPy with cellulose in the form of paper sheets can function as ion exchange membranes by applying an electrical potential to the composite and switching the PPy between its oxidized and reduced states. This novel composite exhibited excellent mechanical stability and could be bent, twisted, or folded without disrupting its mechanical integrity. Also, a high surface area is obtained by this strategy, which improves the ion exchange capacity of conductive paper. More extraction efficiency is expected for a large surface area material with a relatively thin coating of conducting polymer in comparison with a rather thick conductive coating covered a substrate with small surface area. In this work, the PPy-cellulose composite was prepared by oxidative chemical polymerization of pyrrole monomers on cellulose paper sheet in the presence of iron (III) chloride at the room temperature. It was

observed that electrical field only accelerates extraction step and has no effect on the synthesis procedure due to non-conductivity of cellulose paper sheet substrate. Therefore, electrical field in SPE can be used in synthesis, extraction, or both steps.

It should be noted that conductive polymers can be synthesized either chemically or electrochemically [47]. The supremacy of chemical methods to electrochemical ones is that they do not need a conductive substrate for synthesis.

A few attempts have been so far made in this filed [44,46–48]. Gelin et al. investigated the anion absorption properties of this new composite as a function of anion size (nitrate, chloride, and *p*-toluene sulfonate) and anion concentration. Also, they studied how the material behaves in solutions containing more than one anionic species (*p*-toluene sulfonate as a large anion and chloride as a small anion) [44]. It was found that nitrate ions have a slight difference with chloride ions to incorporate in the composite. This is while the composite capacity to host large *p*-toluene sulfonate ions is about 50% compared to the values for the smaller ions at the same oxidation conditions in this study. The results also indicate that anions at electrolyte solution with high concentrations can physically cover most of the composite surface before diffusing into the bulk of the polymer so that the distance between surface sites closely matched the sizes of the anions. Moreover, anomalous behaviors were observed in mixtures containing both chloride and *p*-toluene sulfonate ions. In mixtures with high concentrations of the larger anion, the transport of small ions into the composite was hindered while facilitated transport was observed for small ions at low concentrations of *p*-toluene sulfonate ions.

Also, the authors claimed that no loss of capacity during repeated oxidation and reduction of the polymer indicating that trapping of anions in the reduced polymer did not limit the electroactivity of the present material [44]. However, in the first article in this field, it was reported that after 60 cycles incorporation ability of the film was retained about 85%, which was corresponding to almost 10 h of continuous use [46].

Razaq et al. studied the effects of two different oxidizing agents, iron(III) chloride and phosphomolybdic acid (PMo), in four different electrolyte solutions containing anions with various sizes (chloride, aspartate, glutamate, and *p*-toluene sulfonate) on anion exchange properties of fibrous PPy/Cladophora composites [47]. The results showed larger number of absorbed ions per sample mass for iron (III) chloride in comparison with PMo in all four electrolyte solutions. The highest extraction efficiency was obtained for larger anions in the presence of PMo whereas this result was achieved using iron (III) chloride for small anions. Also, high ion exchange capacities and extraction and desorption rates were observed for large anions using high surface area composites coated with relatively thin layers of PPy.

In another work, Razaq et al. evaluated high-capacity conductive nanocellulose paper sheets for electrochemically controlled solid phase extraction of three DNA oligomers [48]. The ion exchange capacity of the synthesized nanocomposite was at least two orders of magnitude higher than previous reported composite. It was shown that all three oligomers could be straightforwardly extracted from a solution containing an excess of buffer ions with a release efficiency of 40% for the smallest oligomer; indicating that the present material is very promising for development of inexpensive and efficient electrochemically controlled ion-exchange membranes for batch-wise extraction of biomolecules.

Morales-Cid et al. presented a new role of electrical field for SPE technique in a flow system coupled on-line to capillary electrophoresis–mass spectrometry (CE-MS) equipment via a horizontal split-flow interface, which is electrical assisted elution; an indirect effect [6]. Strata X and C_{18} minicolumns were used to preconcentrate the tetracyclines and amines, respectively. Minicolumns of both sorbents were constructed by packing 14 mg of the material in 3 mm id Teflon tubing.

In such system, two major effects are theoretically expected by applying a voltage during the elution step; electrical attraction of the analytes and their subsequent stacking in the flow system immediately before the eluent–buffer interface, and more facilitated analyte elution [6]. Decreasing the eluent volume, need to employ unusual eluents, increasing the determination sensitivity, and decreasing the peak width are the expected impacts of the aforementioned effects. All these advantages were experimentally observed [6]. For example, Fig. 4A shows electropherogram obtained for determination of a 5 mg L^{-1} concentration of tetracycline (1), 2-chlortetracycline (2), and oxycycline (3) without a voltage (A) and a 3 ng L^{-1} concentration using a 10 kV voltage to assist elution-SPE (B). As can be seen, a substantial improvement was obtained for determination sensitivity. However, in spite of the advantages reported, this technique has not been extensively investigated probably due to complicated manifold for this system.

The indirect effect of electrical driving force on SPE with different sorbent materials has been known as a powerful method for improvement of sensitivity of separation techniques such as CE [51]. Fig. 4B shows a schematic representation of this kind of preconcentrator setup. The proposed method allows preconcentration

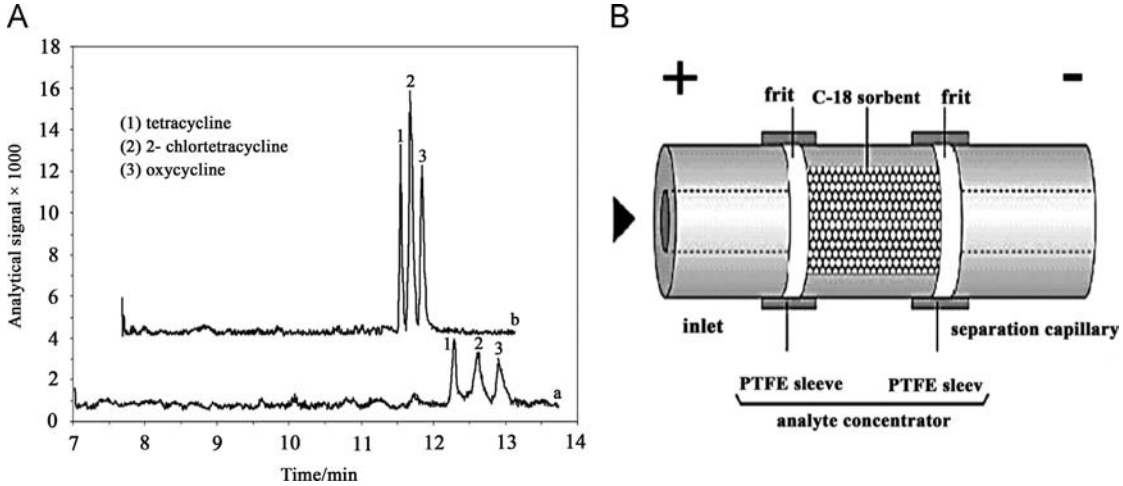


Fig. 4. (A) Electropherogram obtained in determination of a 5 mg L^{-1} concentration of each tetracycline without a voltage (a), a 3 ng L^{-1} concentration using a 210 kV voltage to assist elution-SPE (b), (B) schematic representation of an in-line pre-concentration SPE cartridge (reproduced with permission of Wiley and Elsevier-modified-Refs. [6,51]).

and separation with greater selectivity and higher sensitivity (100- to 200-fold) with respect to CE without in-line preconcentration [51–57].

Generally, elution of an analyte without need to organic solvents, as well as possibility to control analyte retention/elution, more facilitated preconcentration and kinetics due to orientation of charged analytes trajectories toward the pores of the stationary phase, and more rapidity of electrophoretic mobility in comparison with diffusion are the effects that can be counted for electrical field in SPE [58].

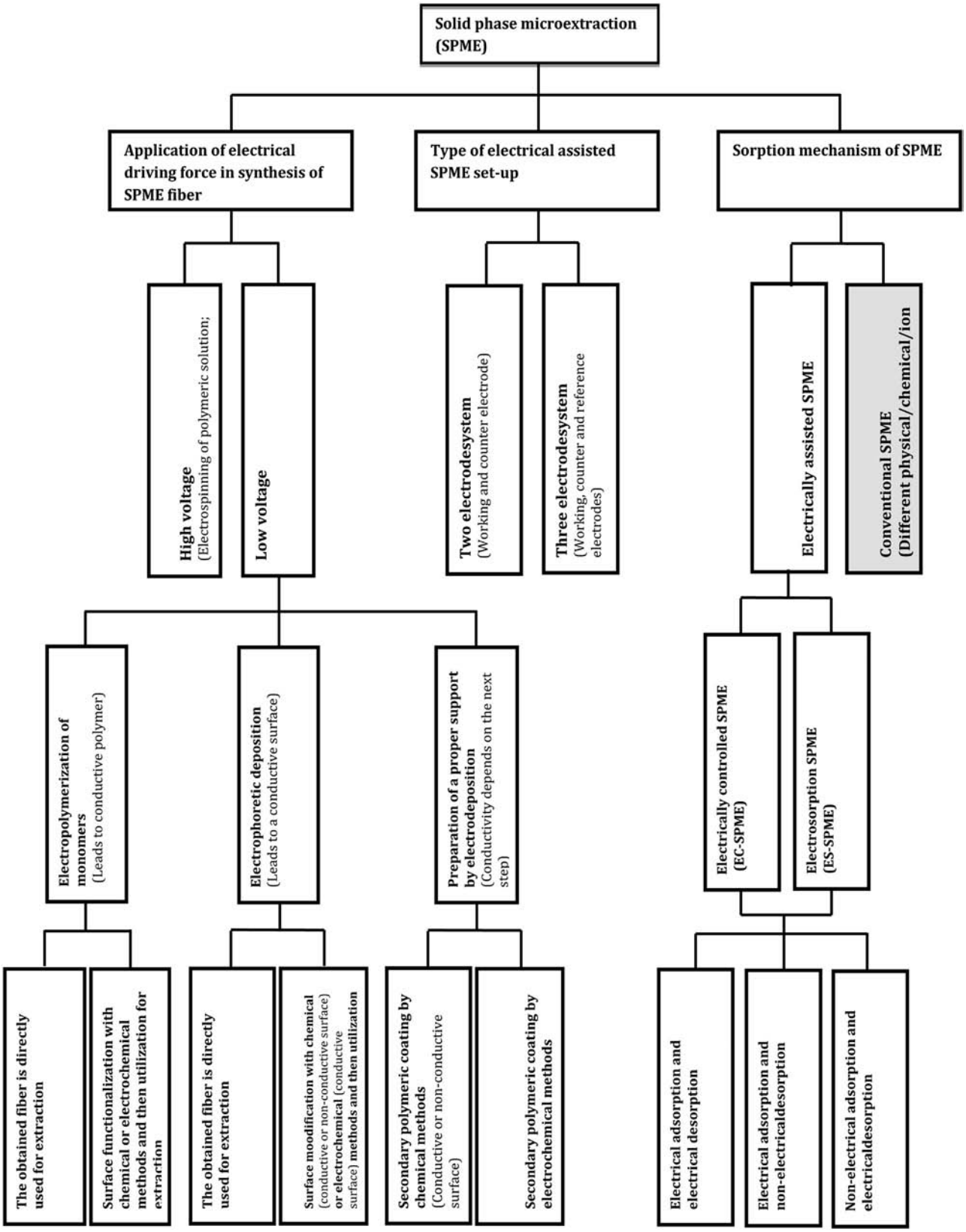


Fig. 5. A general classification for different aspects of electrically assisted solid-phase microextraction including synthesis, type of setups used, and sorption mechanisms (the gray box is related to non-electrically based techniques to give a more comprehensive insight).

Also, detection of extracted analytes in EC-SPE can be carried out either by electrochemical techniques [43,44,46,47] or by different analytical approaches such as chromatographic [45,50] or spectrometry techniques [49].

2.3. Solid-phase microextraction

Nowadays, SPME, a solvent-free miniaturized extraction technique, which was invented by Pawliszyn in 1989, is known as a simple and efficient sample preparation method and has been widely used in different fields including environment, food, natural products, pharmaceuticals, biology, toxicology, and forensic medicine [5,59,60]. As the scope of SPME grew, new improvements were achieved in different aspects of SPME such as appearance of new coatings and application of auxiliary energies that allowed an increase in the specificity of this extraction technique. The main objective of this section is to describe the principles of electrically assisted solid-phase microextraction (EA-SPME) and the recent developments associated with this concept. The discussion covers fundamental understanding about types of EA-SPME setup, application of electrical driving force in synthesis of SPME fibers, and sorption mechanism in EA-SPME (Fig. 5).

2.3.1. Types of electrochemical setup used for SPME

This subject can be viewed from two different perspectives; the setup used for carrying out EA-SPME and the ones for synthesis of SPME coating [61–86].

The most commonly used setup for EA-SPME is the one-compartment three-electrode system consisting of a working electrode, a counter electrode, which is chiefly a platinum wire and a reference electrode, which is chiefly a saturated calomel electrode (SCE) or Ag/AgCl [62,87–89]. In 2008, Öpik et al. introduced an interesting three-electrode system coupled with electrochemical quartz crystal microbalance (EQCM) for EA-SPME as well as electrosynthesis, overoxidation, and characterization of L-aspartic acid-imprinted PPy films [68]. Enantioselectivity of the fabricated film was determined either under stationary conditions with externally applied potential control or in a flow injection analysis (FIA) system.

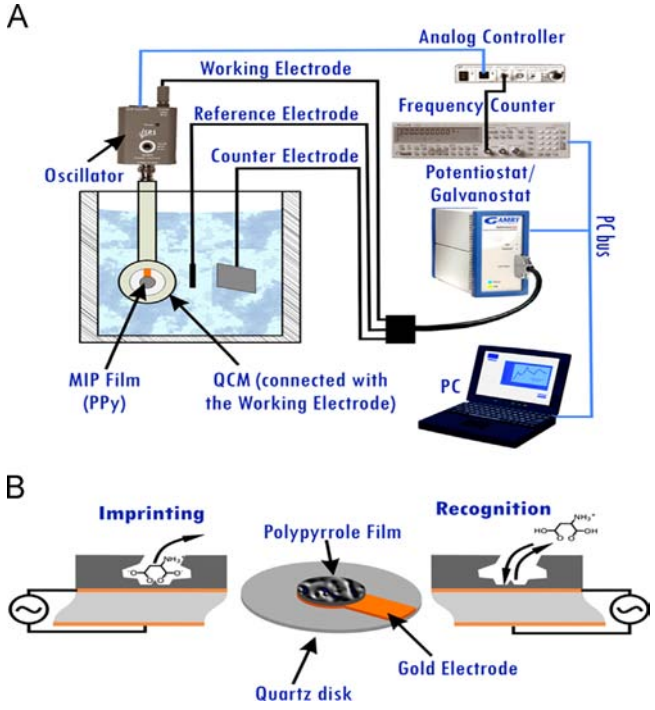


Fig. 6. (A) Simplified diagram of the electrochemical setup used for EQCM experiments. (B) Schematic representation of the chiral recognition of L-aspartic acid by L-aspartic imprinted OPPy films (reproduced with permission of Elsevier-modified-Ref. [68]).

A custom-made Teflon electrochemical cell was used for synthesis and electrochemical measurements (Fig. 6). The face of a 1-in. diameter, polished, gold-coated, 5-MHz crystal served as the working electrode while a rectangular-shaped platinum plate (4×1.5 cm^2) was used as the auxiliary electrode and Ag/AgCl (3 M KCl) as the reference electrode. The results suggest feasibility of preparing molecularly imprinted films by electropolymerization for enantioselective recognition of amino acids and suitability of EQCM for both monitoring the selective recognition as well as electrochemical modulation of the binding process. This method provided a controllable thickness for the fabricated film according to the density of the growing film and the Sauerbrey equation [68].

However, two-electrode system can also be found for EA-SPME in the literature [74,77,81]. Wu et al. developed EA-SPME technique using the lab-made carbonic fiber to determine phenol, *p*-chlorophenol, nitrobenzene, and chloroform in water [81]. The EA-SPME cell was composed by two electrodes; carbonic fiber as the working electrode, and a piece of platinum as the counter-electrode. Different electric voltages were applied to explore the feasibility and applicability of the method. Also, Lee et al. used a pencil lead electrode in a two-electrode system to extract parathion onto the electrode surface with a reductive potential applied of -600 mV for 60 s [77]. However, it should be noted that a three-electrode EA-SPME method with a pencil lead as working electrode was developed for determination of methamphetamine by Djozan et al. [74].

It is worth mentioning that electrode distance is an effective parameter that affects both synthesis and EA-SPME procedures and should be optimized. For instance, it has been understood that the narrowed electrode distances create more efficient adsorption [81]. This phenomenon may be attributed to more heat generation on the surface of electrodes by applying voltage in longer distances, which causes depletion of adsorbed analytes due to exothermic nature of the adsorption process [81].

In another work, Yamin et al. introduced electromembrane surrounded solid-phase microextraction (EM-SPME), in which a carbonaceous pencil lead was simultaneously acted as the cathode and the sorbent inside the lumen of a piece of hollow fiber [90]. The hollow fiber was used as the support for liquid organic membrane around the sorbent. Using organic liquid membrane not only increases the selectivity, but also highly improves sample cleanup and makes it possible to apply high voltages that increase the extraction recovery. It was shown that EM-SMPE has a great potential for analysis of nonvolatile or ionizable compound in complicated matrices [90].

Different coatings were electrically synthesized for SPME by electropolymerization of various types of monomers, mostly PPy [61,64,69,91,92], or electrodeposition of non-polymeric materials such as single-wall or multiwall carbon nanotubes [62,70,72]. According to the literature, a three-electrode system has been used for electropolymerization [61,64,79,91,92], whereas electrodeposition of non-polymeric materials was carried out using a two-electrode system [62,70,72]. In recent years, new two-electrode systems have been developed [83,85,86], which will be discussed in the next section.

2.3.2. Application of electrical driving force in synthesis of SPME fiber

As it is known, the fiber coating is the key part of the SPME; so that this fact has propelled various research groups toward synthesis of new coatings [62,64,65,72]. Among the newest, growing interest has been in conducting polymers due to their

multifunctional properties [64]. Both chemically and electrochemically methods can be applied for synthesis of conductive polymers [47,93]. Although the electrochemical method should be carried out on the surface of a conductive substrate, it has substantial supremacies in comparison with regular SPME in the case of aromatic, polar, and charged analyte species [64]. For these types of analytes, extra steps such as use of complexing agents may be needed. These reagents in the most cases are toxic and expensive [64]. Also, the electrochemical method provides tailoring of key characteristics of conducting polymers including thickness, conductivity, degree of oxidation, color, and morphology [94]. Unlike the chemical method, which has a limited choice domain for dopant ions, an extensive range can be selected for electrochemical polymerization. The limitation of the chemical method originates from the fact that in contrast to the electrochemical method, a neutral polymer is firstly synthesized in the chemical method and subsequently a strong oxidant/reductant, which must be generated from the chemical oxidants/reductants, is used to produce the conductive form of the polymer [95].

The parameters with key roles in electrosynthesis are the solvent, type of dopants [94], type of monomer, applied potential range, electropolymerization time, deposition method [96], and the number of cycles, as well as the scan rate when a cyclovoltammetric (CV) technique is used [64]. For instance, the results of the study by Batina et al. showed that a supporting electrolyte containing KI yields relatively thick and highly conductive films whereas KF produces little conductive, very thin films [94].

In EA-SPME, the ion-exchange capacity of conductive film was generally controlled by the film thickness. Beyond a certain thickness value, diffusion limitation starts to limit the extraction amount. It is shown that as the film thickness increases, the sensitivity will also increase. Thicker coatings have therefore higher ion exchange capacity and result in larger dynamic range before the coatings become saturated [45,97]. Therefore, this issue has an important effect on the success of extraction and should be controlled during the fabrication process. Growth of the films can be controlled based on the charge amount passed during electrosynthesis and determined by scanning electron microscopy (SEM) technique [45,75,97]. Also, a controllable thickness can be achieved using the combination of EQCM and electropolymerization according to the density of the growing film and the Sauerbrey equation [68]. An alternative to improve the ion-exchange capacity of the electrode is increasing the surface area of the electrode, while keeping the film thickness constant. This strategy has recently been applied by Mihranyan et al. [46].

Stability of the synthesized polymeric film is an important issue affected by several factors. The substrate properties may have a great impact on the stability of the deposited thin film [96]. Different electrode materials including gold, glassy carbon, and ink-made carbon composite electrodes were investigated for PPy deposition by Li et al. [96]. Some composite carbon substrate materials demonstrate the best performance. This observation has been attributed to roughness and large surface area of carbon substrate, which can enhance adhesion and enforce the stability of the PPy film structure [96].

As shown in Fig. 5, both low voltage and high voltage electrical fields can be utilized for electropolymerization purposes. However, a completely different story exists between high voltage and low voltage synthesis methods. In the low voltage method, an electrochemical cell consisting of two or three electrodes is used and polymerization is carried out in electrolyte solution containing dopant ions and monomers. Different deposition techniques such as CV, galvanostatic (constant current) and potentiostatic (constant voltage) methods can be used during low voltage electropolymerization that influence the electrochemical activity of the films. Li et al. demonstrated creation of PPy films by galvanostatic deposition with more electrochemical activity compared with the films produced by CV and potentiostatic methods [96]. Also, an insulated film will be created instead of a conductive film by applying potentials in the region required for overoxidation [94].

Application of the high voltage method termed electrospinning in SPME dates back to its appearance as an attractive patterning technique [85,98–100]. By definition, electrospinning is an authoritative method that can draw fibers from polymer solutions and simultaneously integrating them onto microfabricated structures [85]. This technique is based upon the same principle as ESI-MS. However; the fiber jet production is the dominant phenomenon comparing with the formation of charged droplets mist in ESI-MS [101].

Polymeric solution that is used in electrospinning consists of polymers with high molecular weights and accordingly high viscosity and surface tension. This solution is filled into a syringe connecting to a pump to create regular injection during the electrospinning process. Applying voltage between syringe and collector, which is rotated by a rotor, leads to overcoming the surface tension by electrostatic repulsion, deformation of spherical droplets to Taylor conical form, and finally ejection of the polymer jet from the Taylor cone toward collector [83,102]. During coating progress, formation of polymeric droplets is prevented by entanglement of polymer chains as well as the surface tension [83,102]. Diameter of polymer jets becomes smaller within their flying toward collector electrode. This leads to formation of nonwoven nanofibers mat with diameters in the range of micro to nano [83,102]. Various materials with different shapes can be used as the collector electrode [103]. Fig. 7A is a schematic view illustrating an electrospinning device [83].

Electrospinning has been utilized in different fields of science [83,104]. However, it is not a long time this field has been presented in the analytical chemistry. This methodology has been used in solid phase extraction [105,106], affinity membranes [107], semi-micro solid phase extraction [108], and more recently as a SPME fiber [83,102].

As can be seen in the high voltage method, electropolymerization is carried out in the space between two electrodes by applying excessively high voltages in the ranges of 4000–25000 V and no electrolyte solution is utilized here [85]. The other difference between high and low voltage methods is that in the first one, polymer solution is used instead of monomer solution to produce polymeric films.

The conductivity of synthesized films by electrospinning depends on the composition and conductivity of the prepared polymeric solution as well as the diameter of electrospun nanofibers. Fabrication of nanofibers with sub-30-nm diameter has been reported using electrospinning of polyaniline/polyethylene-oxide mixture [99,100]. The results demonstrated polyethylene-oxide, as an insulating impurity, leads to substantially lower conductivity in comparison with pure bulk materials and intensity of this behavior increases by decreasing the diameter of nanofibers; so that nanofibers with 15 nm were found to be insulating [100].

As shown in Fig. 5, the low voltage method can be utilized for synthesis of SPME fibers by electropolymerization of monomers [88,89], electrophoretic deposition of some special materials such as carbon nanotubes [62,70,72], and preparation of a proper substrate for next coating step using electrodeposition [82].

Synthesis of SPME fibers with low voltage electropolymerization of monomers has been reported by different research groups [62,64,87–92,97]. As shown in Fig. 5, a conductive fiber is obtained by this method, which can directly be used for extraction. Also, the nature of its surface can be modified using an extra functionalization step either chemically or electrochemically and subsequently be used for extraction [109]. The functionalization of PPy film electrodes [109] can be achieved by electrostatic

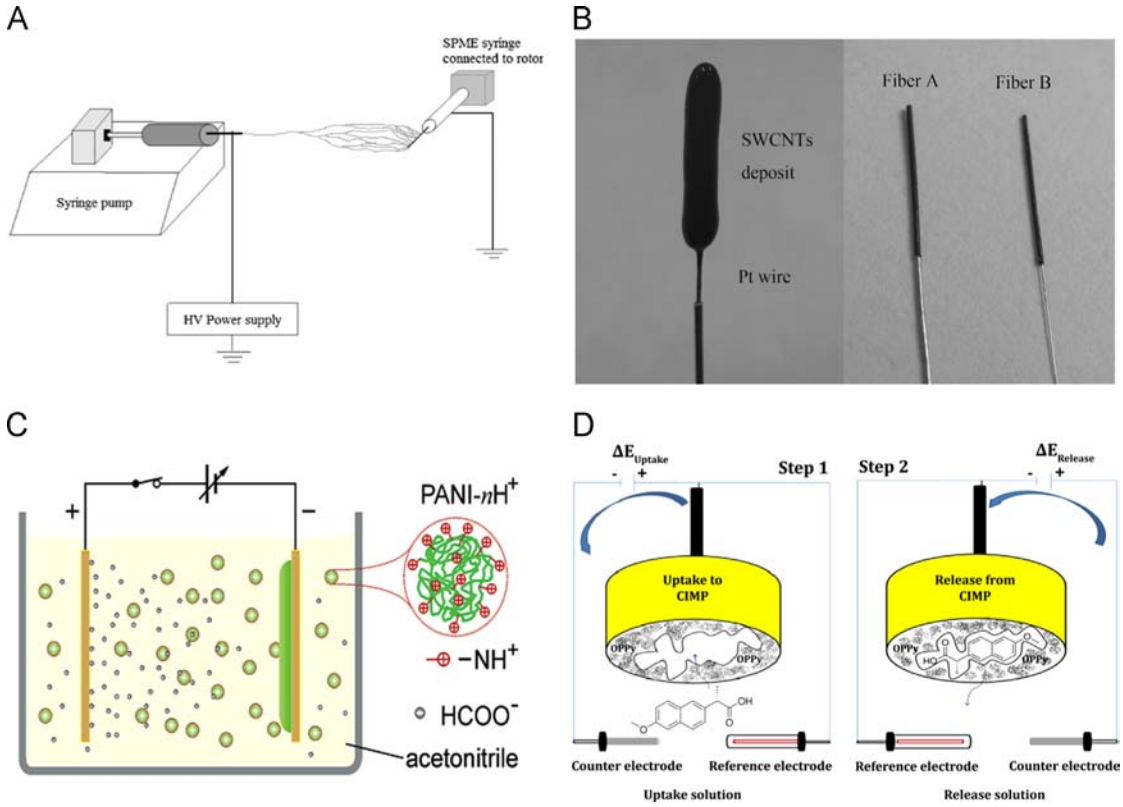


Fig. 7. (A) Scheme of the electrospinning setup, (B) deposition of SWCNTs on Pt wire (left) and the prepared fibers coated with SWCNTs (right), (C) a schematic illustration of the setup used for electrophoretic deposition of polyaniline from its colloidal suspension, (D) selective uptake/release of naproxen to MIP by electrochemically controlled solid-phase sorbent (reproduced with permission of Elsevier and ACS-modified-Refs. [72,83,85,91]).

incorporation of multi-charged anionic complexing ligands during the electropolymerization step, or using active groups that are covalently attached to the polymeric skeleton. These complexing film materials have been synthesized in two steps by chemical derivatization moieties of conducting polymer films previously coated by electropolymerization onto electrodes, and then applied as a cation-exchange film that might be useful for electrosorption SPME (ES-SPME).

An extensive range of monomers including pyrrole [89], sulfonated pyrrole [97], aniline [80,85], *p*-phenylenediamine-co-aniline [78], 3-methylthiophene [76], 3-octylthiophenone [66], 3-dodecylthiophene [63], 3-hexadecylthiophene [66] have so far been used to fabricate conductive SPME fibers. However, among them, pyrrole is the most frequently investigated monomer due to its relative ease of synthesis on various substrates from organic or aqueous media by electrochemical or chemical methods, environmental stability of its polymeric film, and ability to interact with different compounds due to its multifunctional properties including hydrophobicity, acid–base character, π–π interaction, polar functional groups, ion exchange property, hydrogen bonding, and electroactivity [91,92,110]. Pyrrole has been used not only to synthesize SPME sorbents, but also in other fields of analytical chemistry such as preparation of modified electrodes [111,112].

In 2004, Su et al. demonstrated polymerization of pyrrole between an electrode gap (5 μm) when a 10 V dc voltage is applied to the saturated vapor of pyrrole at 24 °C and the relative humidity of 35% [86]. Occurrence of chemical reaction is signaled by the decreasing gap resistance, with 95% reduction in the first hour. In control experiments without any voltage applied, there is no deposition and the resistance does not change when other conditions are kept identical; this indicates that the electric field in the gap directs and facilitates the growth of PPy.

The strength threshold of electric field for the polymerization reaction is about 10^4 V m^{-1} at the relative humidity of 35%. The existence of thin water layers on ionic surfaces in the ambient environment is well known [113,114]. When high electric field ($> 10^5$ V m^{-1}) is generated across the gaps, the polymerization would likely occur within the tiny hydrous environment similar to electrochemical polymerizations in solution. This electrical polymerization method is a simple and robust method that can provide deposition of the conducting polymers. However, this technique has not yet utilized for preparation of SPME coatings; however, it seems that this potential application would open a new window to the world of extraction science.

Electrophoretic deposition of some special materials to fabricate new fiber coatings is of the recent progresses in SPME [62,70,72]. Electrophoretic deposition is usually employed in processing of ceramics, coatings, and composite materials. In this technique, charged particles, which are dispersed in a proper solvent, migrate toward a conductive substrate under electrical field [72,115], accumulate there, and form a homogeneous and rigid deposit. It should be noticed that unlike electrochemical deposition, in this technique, deposition occurs by particle coagulation instead of electrochemical reaction [62,70,72,115].

For the first time in 2009, electrophoretic deposition was utilized for fabrication of new conductive SPME fibers by Li et al. [72]. A platinum wire was electrophoretically coated with single-walled carbon nanotubes (SWCNTs@Pt) and applied to determine phenols in aqueous samples. Fig. 7B shows the electrophoretically deposited SWCNTs on the surface of a platinum wire which has been removed from the SWCNTs/ dimethylformamide (DMF) suspension [72]. Vaporization of DMF in the deposit by subsequent heating leads to closer assembling of SWCNTs and enormously increasing their interaction and finally fabrication of a stable film.

The fabricated coatings showed high durability; so that neither swell in organic solvents nor strip off from the substrate surface. This can be attributed to the strong Van der Waals attractions between the surfaces of the SWCNTs [72].

The prepared fiber showed similar or superior efficiency in comparison with polyaniline fiber due to the high surface area of SWCNTs as well as the presence of oxygenated groups in the structure of nanomaterials. In another work by the same group, SWCNTs@Pt was used for microextraction of trace anions including F^-, Cl^-, Br^-, NO_3^-, and SO_4^{2-} in deionized water [70]. In the second work, a platinum plate was used as the substrate for the working electrode instead of a platinum wire and also, an electrically assisted extraction procedure was carried out compared with conventional SPME procedure in the first work. Regarding the above-mentioned points, different durability was reported during analysis of phenols and anions (more than 80 and 50 times, respectively) for a unique fiber.

Tan et al. used the method presented by Li et al. [72] for deposition of multi-walled carbon nanotubes on the surface of a platinum wire (MWCNTs@Pt) [62]. Subsequently, a surface modification was carried out using PPy, producing a molecularly imprinted polymer to create selective extraction of fluoroquinolone antibiotics. The fabricated coating showed an excellent mechanical stability so that no falling was observed from platinum wire with gentle scrape by a piece of paper. The peak area of the fiber after more than 50 successive electrically assisted extractions was more than 90% of the value obtained for the first extraction, indicating high durability of the fiber.

In 2004, Li et al. presented an interesting method for controlled deposition of polyaniline from colloidal suspensions [85]. First, polyaniline was electrochemically synthesized from aniline using CV, then converted into its emeraldine base form by soaking in a concentrated ammonium hydroxide solution, filtered, washed, and then dried in a vacuum oven. The polyaniline colloidal suspension was prepared by first dissolving the emeraldine base form of polyaniline in formic acid, and subsequently dispersing the polyaniline/formic acid solution into acetonitrile. The key aspect of generating a polyaniline colloidal suspension lies in the unique combination of formic acid and acetonitrile. As illustrated in Fig. 7C, by applying an electric field, the positively charged polyaniline colloids are collected onto the electrode that has a negative bias, and, as a result, a thin film of polyaniline can be formed on the electrode surface. This method has not yet been used in any of the chemically or electrochemically SPME techniques. However, it may open a new horizon toward generation of modern SPME coatings.

If conductive materials such as carbon nanotubes are used during electrophoretic deposition, a conductive SPME fiber will be obtained that can directly be utilized for extraction [70,72], or its surface could be modified either electrochemically [62] or chemically for subsequent analysis. A conductive film is created by an electrochemical modification again whereas the conductivity of SPME fiber using a secondary chemical step depends on application of a strong oxidant/reductant during the fabrication process. As mentioned before, in chemical methods, a neutral polymer is firstly synthesized and to produce the conductive form of the polymer, a strong oxidant/reductant should be used. Electrochemical modification of an electrophoretically prepared surface was reported by Tan et al. [62], but no chemical modification was reported so far.

The results show that electrophoretic deposition offers advantages of low cost, process simplicity, uniformity of deposits, no need to use adhesive, control of deposit thickness, and production of films with high mechanical stability and durability [72,115].

The other application of low voltage electrical fields in synthesis of SPME fibers is preparation of an appropriate substrate for next fabrication step by electrodeposition of a special material (Fig. 5). In this case, conductivity of the coating prepared depends on the final synthesis step and a behavior the same as the one mentioned for electrophoretic deposition method related to chemically or electrochemically modifications is expected here (Fig. 5).

Kanatharana et al. developed a new SPME fiber by electrodeposition of porous Zn film on the surface of an Ag wire followed by coating with polyethylene glycol sol–gel (Ag/Zn/PEG sol–gel) [82]. It provides a powerful analytical tool in terms of simple preparation, low cost, flexibility, robustness, high thermal stability, and long lifetime; up to 359 extractions compared with commercial fibers. Furthermore, the proposed fabricated fiber provides good repeatability as well as fiber-to-fiber reproducibility and therefore, recalibration is omitted during replacement of a new fabricated fiber with the old one.

In this work, Ag/Zn/PEG sol–gel fiber was applied to determine styrene residues in cooked rice sample using a conventional SPME procedure and no electrical field was utilized during the extraction. As can be seen here and also in other reports [62–86], electrosynthesized fibers can be used for both EA-SPME and conventional SPME techniques. However, it should be noted that in the first case the fiber should certainly be conductive while it is not important for the second technique.

Although most conductive SPME fibers used in electrically assisted solid based extraction technique have been prepared electrically [63,64,87–92,97], some works have reported chemical fabrication of conductive polymers and subsequently application in an electrically assisted extraction procedure [65,89]. As mentioned before, conductive polymers can be synthesized either chemically or electrochemically. For instance, Chen et al. chemically prepared a conductive MWCNTs/Nafion coated fiber and applied it as the working electrode in a three-electrode system to determine cationic (protonated amines) and anionic (deprotonated carboxylic acids) compounds in aqueous samples [65] by applying suitable negative and positive potentials, respectively. In another work, this electrode was utilized for determination of some basic drugs using a mild negative potential in urine samples [89].

Therefore, one can have an electrochemically synthesized SPME fiber and electrical extraction, an electrochemical synthesis and non-electrical extraction or a non-electrochemical synthesis and electrical extraction. However, it should be noted that it is possible to use a combination of chemical and electrochemical processes during each of the synthesis and extraction steps of SPME. For instance, in a SPME extraction procedure consisting of two sorption and desorption steps, sorption can be carried out electrically and desorption chemically or vice versa [63,65]. This will be explained in more details in the next section.

Selectivity has always been an important issue to evaluate the efficiency of an extraction technique. In SPME, in order to increase selectivity, a lot of effort has been placed on development of either the preparation method or the material used as the fiber coating phase. For instance, it is possible to control selectivity in the microextraction process using a cation exchange conductive SPME fiber due to dependency of polymer morphology on the size of the dopant ions and the interactions between irreversibly incorporated dopants and ions. However, these strategies showed poor selectivity. To overcome this difficulty, in recent years, new materials such as MIPs were synthesized and used as the coating [61,62,64,68,91,92]. MIPs are synthetic materials that are prepared in the presence of a template molecule, and are identical with the target molecule the polymer should later selectively bind [68].

Both chemical and electrochemical methods can be utilized for removal of templates from the synthesized polymeric film [61,62,64,69,91,92]. For instance, Şahin et al. used 0.05 M phosphate buffer to remove ascorbic acid templates from a molecularly imprinted PPy-modified pencil graphite electrode [61]. Tan et al.

immersed the MIPPy/MWCNTs/Pt fiber into methanol–acetic acid (80:20, v/v) washing solution (at least 5 times) to remove the fluoroquinolone template molecules [62]. Nagaoka et al. developed electrodes coated with overoxidized polypyrrole films for chiral discrimination of glutamic acid in its cationic form with the goal of improving selectivity and sensitivity of currently used MIPs [64]. The overoxidation was performed by scanning the potential repeatedly in a range of −0.3 to +1.0 V (or +1.4 V) at a rate of 40 mV s^{-1} until the background current attained a value below 50 nA cm^{-2}. This method was also applied for determination of two types of anionic species including naproxen and salicylate by Alizadeh et al. in two subsequent papers [91,92]. A schematic presentation of an electrically controlled SPME (EC-SPME) system for selective uptake/release of naproxen using a conductive MIP fiber based on PPy is shown in Fig. 7D.

Generally, the use of MIPs, as a selective solid-phase for sample preparation, may be potentially attractive because they mainly afford selectivity, robustness, and long shelf-life [62,64].

2.3.3. *Sorption mechanism of EA-SPME*

As shown in Fig. 5, SPME technique can be classified into conventional and electrically assisted ones. In conventional SPME, there are different sorption mechanisms depending on the nature of coating and analytes that lead to physical, chemical, or ion exchange interactions. However, the chemical one is not proper because it is seldom reversible and so it should be avoided by selection of an appropriate fiber.

The sorption mechanism in EA-SPME can be subdivided into EC-SPME and ES-SPME. In ES-SPME, the extraction is primarily driven by electrophoresis and complementary charge attraction, in which negative or positive potential can be easily altered to enhance the extraction of cationic or anionic analytes [65]. When an electric field is applied, the charged ions move towards the fibers with an opposite charge and an electrical double layer is formed on the fiber surface. Charged species are therefore concentrated and kept on the double layer. When the electric field is removed or reversed, the ions in the fiber are released back to the bulk solution. No reduction or oxidation of coating occurs during ES-SPME [70]. Furthermore, EC-SPME is carried out using a conductive polymer film, which provides movement of counter ions in and out of the conductive polymer to maintain its electroneutrality by applying a suitable voltage [65].

Generally, incorporation of a dopant with high mobility into the structure of a conductive polymeric film leads to formation of an anion exchanger whereas a cation exchanger coating will be produced when a dopant with low mobility is used during synthesis [116]. A schematic illustration of EC-SPME mechanism for a cation exchanger conductive PPy film is presented in Fig. 8A. Here, poly(styrenesulfonate), (PSS), has been used as the low mobility dopant [116]. When a negative potential is applied, the PPy chain is reduced and results to appearance of negative charges into the film structure due to the presence of the anionic sulfonyl groups of PSS. To compensate the negative charges, cations existing into the surrounding solution adsorb on the surface of the polymeric film. Applying a positive potential leads to oxidation of PPy chain and formation of positive charges, compensated by anionic sulfonyl groups. In this case, the cations adsorbed are desorbed back into the solution.

The EC-SPME mechanism for extraction of anions is shown in Fig. 8B. Similarly, anions are adsorbed by applying a suitable positive potential and consequently oxidation of the conductive film, whereas a negative potential reduces the polymer and results in the expulsion of the previously incorporated anions to return polymer neutrality.

In ES-SPME, instead of using a conductive polymer as the stationary phase, carbonaceous materials, such as pencil lead [74,79], activated carbon fiber [73], and carbon nanotubes [62,70,72] are used as coatings to prepare the SPME fiber. Carbonic fibers may be good choices as working electrodes in EA-SPME due to high conductibility and resistance against temperature elevation as well as chemical corrosion in water [81].

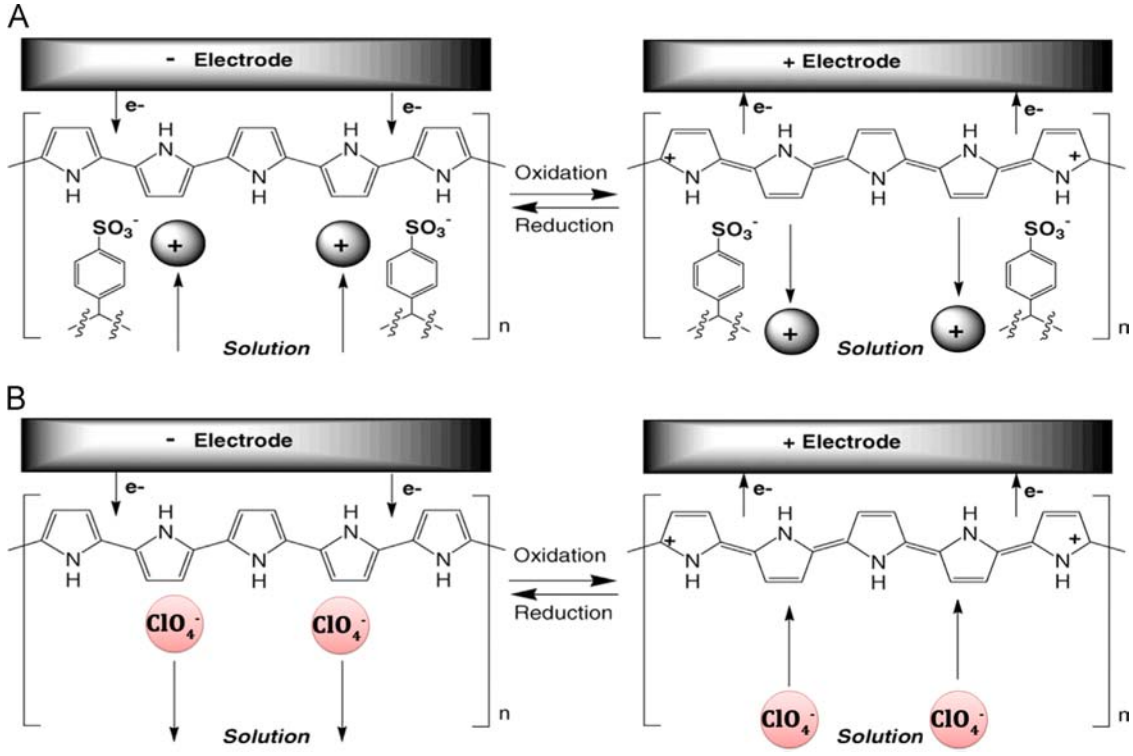


Fig. 8. (A) Scheme of the electrochemically switchable cation exchanger process and (B) anion exchanger procedure (reproduced with permission of Elsevier-modified-Ref. [116]).

As can be seen in Fig. 5, during an EA-SPME procedure, electrical field can be used for both adsorption/desorption steps [64,88], only used for adsorption and a non-electrical desorption is utilized for analysis [62,65], or only used for desorption and adsorption is carried out non-electrically [63,66]. The latter case is one of the most interesting applications of electrical field in EA-SPME, which was for the first time introduced by Mark et al. in two subsequent papers [63,66]. In the first step, neutral arsenobetaine were adsorbed on the surface of poly(3-dodecylthiophene) film due to hydrophobic interactions and under the diffusion controlled extraction process. Then, a positive potential was applied to oxidize the fabricated conductive polymer to its hydrophilic state, which provides a sufficient driving force for desorption of the analyte from the extraction phase into an aqueous solution for subsequent analysis.

Interestingly, it has been claimed that electrical field can affect adsorption of non-ionized compounds [81]. Wu et al. utilized an ES-SPME system to examine the effect of different voltages in the range of −1.5 to +1.5 V on the adsorption efficiency of phenol and *p*-chlorophenol as ionizable compounds and nitrobenzene and chloroform as neutral species [81]. The results showed that different effects of voltage on adsorption processes are attributed to the molecular structure of the investigated compounds. For instance, −1.0 V voltage increased nitrobenzene adsorption about 33%, and +1.5 V raised the amount to 122%, while −1.5 V decreased the adsorption of phenol to 91.1%. To the best of our knowledge, it is the first report of electrically assisted adsorption of neutral compounds and may be an interesting topic for the future researches in the field of electrical induced extraction techniques.

Conductive polymeric films can be used not only for extraction purposes in analytical chemistry, but also as electrochemically switchable ion exchangers for industrial aims such as softening the drinking water. For instance, Weidlich et al. designed a special cell arrangement containing two cation exchanger electrodes based on modified PPy nanoparticles separated by an anion exchanger membrane for continuous operation of the water softening process [116].

Şahin and coworkers have recently reported simultaneous extraction of cationic and anionic species in trace levels including chloride, nitrate, sulfate, calcium, and magnesium using a PPy electrode and an overoxidized sulfonated polypyrrole (OSPPy) electrode [45]. Both PPy and OSPPy electrodes were immersed in the same target solution to act as anode and cathode, respectively. They also used these electrodes as a potentiometric detector in ion chromatography, to determine some anions and cations in water samples [87]. This idea can be extended as a novel interesting technique for industrial applications and will provide many advantages like low cost, ease of modification, renewal, and miniaturization. For instance, its application for water softening instead of the method utilized by Weidlich et al. [116] removes the need for dividing membrane and reduces the process cost.

A summary of recent papers in EA-SPME for determination of various anions, cations, and neutral compounds is presented in Table 1. As shown here, electrical field has found an important position in solid based extraction techniques so that a substantial increasing trend is observed in the literature after the first suggestion by Pawliszyn et al. [110,118]. This can be attributed to several reasons;

1. The properties of the conducting polymer can be modified by varying the conditions during the electropolymerization step to enable extraction of analytes of different sizes and charges.
2. Compared to conventional SPME, in which a material with a fixed number of exchange sites is employed, EA-SPME offers higher flexibility owing to the material properties and thus the number of exchange sites can be externally controlled by electrochemical controlling of the material charge [48,119].
3. The use of polymer based fiber films in SPME can be extended to analysis of neutral, electro-inactive analytes by taking the advantage of electrochemically controlled hydrophobic/hydrophilic 'switching' [63].
4. EA-SPME can be used to extract ions and analytes that normally need to be derivatized prior to traditional SPME extractions [120,121].
5. In EA-SPME, the extraction and desorption steps are merely performed by altering the potential of the conducting polymer coated electrode. In this approach, there is thus no need for changes of the solvent to enable desorption of the compounds [28].
6. Desorption of electrostatically held analytes, by altering the electrochemical potential of the polymer may also be faster compared to the desorption techniques normally used in SPME [29]. This makes the technique particularly interesting for use in conjunction with miniaturized analytical systems.

On the other hand, difficulties in obtaining reproducible extractions as well as high preconcentration factors are the main problems encountered by EA-SPME. The first problem results from morphological changes in conducting polymer coating due to successive oxidation and reduction of the stationary phase during every measurement [76], and the second one is caused by requiring the solution at milliliter volumes to desorb the analytes as well as low adsorption capacity of SPME fiber [28,29]. However, some efforts have recently been carried out to overcome the problems such as synthesis of new fiber coatings, fabrication of polymeric coatings with high surface area, and development of integrated electrode device proving desorption into low microliter volumes [28,29,46]. Also, as can be deduced from the information in Table 1, EA-SPME has rarely been investigated in real samples with complicated matrices such as biological fluids. Surrounding SPME fiber utilizing a porous membrane may be a suitable solution to this issue. Abilities of porous membranes in sample pretreatment techniques, which were addressed in Section 2.3.1, could be a suitable reason for the claim.

3. Solid based extraction techniques as lab-on-a-chip

Recently, downsized installations or LOC systems have been developed to perform laboratory analyses of chemistry, biology, and medicine over a miniaturized chip. Separation techniques were highly benefited from the LOCs. Electrophoretic techniques are perfectly suited for downscaling due to their smaller separation lengths, which is following by increase in electrical fields.

Nyholm et al. have employed an integrated three-electrode device as a new method for controlling the potential conditions to extract, transfer, and desorb anions and cations [29]. This SPME system containing a glassy carbon rod ($40 \times 1.0\ mm^2$), a silver tube (o.d. 2.0 mm, i.d. 1.6 mm), and a stainless steel tube (o.d. 5.0 mm, i.d. 4.0 mm), which operates as the working, pseudo-reference and counter electrode, respectively. A glassy carbon rod and a silver tube were insulated by heat-shrinkable PTFE tube (o.d. 3.1 mm, wall thickness 0.05 mm) and then both electrodes were inserted into a stainless steel tube. PPy coating was electrodeposited on the surface of the glassy carbon working electrode to obtain the required ion exchange capacity. Both the working and reference electrodes are able to vertically move with respect to the stainless steel counter electrode.

As the device is lifted out of a solution after an extraction, a small amount of the solvent, which is held by the capillary force, remains between the electrodes. The potential control over the whole extraction process increases using the device designed by Nyholm; since this design offers potential controlling at all times. Also, potential controlled desorption into vials containing as little

Table 1
Electrically assisted solid phase microextraction (EA-SPME) technique for determination of different anions, cations, and neutral compounds.

Electrochemically controlled solid-phase microextraction (EC-SPME) technique

Type of polymeric film[a]	Analyte	Matrix	Type of adsorption[b]	Type of desorption[b]	Detection system[a]	LOD ($\mu g\ L^{-1}$)	RSD%	Ref.
PPy-ClO_4	Cl^-	Water	E	E	Electrochemical determination	625 nM	< 14	[28]
PPy-ClO_4	Cl^-, NO_2^-, Br^-, NO_3^-, SO_4^{2-}, PO_4^{3-},	Water	E	E	Electrochemical determination	–	< 29	[29]
PPy-TSO	Co(II), Cd(II), Zn(II)					–	< 9.4	
OSPPy	Ni(II),	Sea water	E	E	ETAAS	3.1	< 8.71	[97]
	Cd(II)					0.74		
OPPy	Ni(II), Cd(II)	Sea water	E	E	ETAAS	–	–	[88]
PPy–ClO_4	Dopamine	Water	E	E	FIA-MS	–	< 5	[89]
PPy–Cl	Perchlorate							
PPy–PSS	Glutamate							
	Methylarsonate							
PPy–ClO_4	Cl^-, SO_4^{2-}, NO_3^-,	Water	E	E	IC-	1–4	< 8	[45]
OSPPy	Ca^{2+}, Mg^{2+}				Electrochemical detector	2		
P3DDT	Arsenobetaine	Water	N.E	E	HPLC-ICP-MS	–	–	[63]
P3OT	Arsenic species	Water	N.E	E	HPLC-ICP-MS	14	4.1	[66]
PPy–SβCD	Na^+, K^+	Water	E	E	HPLC-UV	–	–	[67]
PPy–ECB	Ni(II), Co(II), Zn(II), Pb(II),	Water	E	E	ICP-OES	4.3–17.3	4.4–7.4	[69]
	Cu(II), Cd(II), Cr(III)							
PPy–ClO_4	Cl^-, NO_2^-, NO_3^-	Water	E	E	IC-electrochemical detector	–	< 4.5	[71]
P3MT–TBATFB	Arsenate ions	Water	E	E	FIA-ICP-MS	–	–	[76]

Molecularly imprinted polymer based electrochemically controlled solid phase microextraction (MIP-EC-SPME) technique

Type of polymeric film[c]	Analyte	Matrix	Type of adsorption[d]	Type of desorption[d]	Detection system[c]	LOD ($\mu g\ L^{-1}$)	RSD%	Ref.
PPy	Ascorbic acid	Tablets,	E	E	Differential pulse voltammetry,	7.4×10^{-5} M	< 1.62	[61]
		Sirup			IC-electrochemical detector	–	< 0.9	
OPPy	Naproxen	Serum	E	E	Spectrofluorometry	3	< 4	[91]
		Tablet						
OPPy	Salicylate	Serum	E	E	Spectrofluorometry	4×10^{-8} M	< 3.5	[92]
		Cow urine						
		Tablet						
PPy/MWCNTs composite	Fluoroquinolones	Water	E	N.E	HPLC-DAD	0.5–1.9	< 6.5	[62]
		Urine				–		
		Soil				–		
OPPy	L- & D-glutamate	Water	E	E	Spectrofluorometry	–	–	[64]
OPPy	L- & D-aspartic acid	Water	E	E	EQCM	–	–	[68]

Electrosorption solid-phase microextraction (ES-SPME) technique

Type of fiber coating[e]	Analyte	Matrix	Type of adsorption[f]	Type of desorption[f]	Detection system[e]	LOD ($\mu g\ L^{-1}$)	RSD%	Ref.
MWCNTs/Nafion composite	Amphetamine	Urine	E	N.E	GC-FID	0.26	< 8	[117]
	Methamphetamine,					0.12		
	Other basic drugs					–		
MWCNTs/Nafion composite	Amines	Water	E	N.E	GC-FID	0.048–0.070	< 10.9	[65]
	Carboxylic acids							
SWCNTs@Pt plate	F^-, Cl^-, Br^-	Water	E	E	IC-Electrochemical detector	0.06–0.26	2.1–8	[70]
	NO_3^-, SO_4^{2-}							
Activated carbon fiber	Aniline	Water	E	N.E	GC-FID	0.02	6.15	[73]
Pencil lead	Methamphetamine	Street drug	E	N.E	GC–MS	34	< 8	[74]
Pencil lead	Parathion	Water	E	N.E	LC-MS	0.3	< 11.4	[77]
Carbonic fiber	Phenol	Water	E	N.E	GC-FID	–	–	[81]
	p-Chlorophenol,							
	nitrobenzene, chloroform							

[a] **ECB**: eriochrome blue, **ETAAS**: electrothermal atomic absorption spectrometry, **FIA**: flow injection analysis, **HPLC-UV**: high performance liquid chromatography-ultraviolet detector, **IC**: ion chromatography, **ICP-OES**: inductively coupled plasma-optical emission spectrometry, **MS**: mass spectrometry, **OPPy**: overoxidized polypyrrole, **OSPPy**: overoxidized sulfonated polypyrrole, **P3DDT**: poly(3-dodecylthiophene), **P3MT**: Poly(3-methylthiophene), **P3OT**: poly(3-octylthiophene), **PPy**: polypyrrole, **PPy-SβCD**: poly(pyrrole-sulfated β-cyclodextrin), **PSS**: poly(styrenesulfonate), **TBATFB**: Tetrabutylammonium tetrafluoroborate, **TSO**: *p*-toluenesulfonic acid.

[b] **E**: electrically, **N.E**: non-electrically.

[c] **EQCM**: electrochemical quartz crystal microbalance, **HPLC-DAD**: high performance liquid chromatography-diode array detector, **IC**: ion chromatography, **MWNTs**: multi-walled carbon nanotubes, **OPPy**: overoxidized polypyrrole, **PPy**: polypyrrole.

[d] **E**: electrically, **N.E**: non-electrically.

[e] **GC-FID**: gas chromatography-flame ionization detection, **IC**: ion chromatography, **LC**: liquid chromatography, **MS**: mass spectrometry, **MWNTs**: multi-walled carbon nanotubes.

[f] **E**: electrically, **N.E**: non-electrically.

as 200 μL of the solution is possible. All potentials are given with respect to the silver quasi-reference electrode (QRE). The working and reference electrodes are extended during the extraction, desorption, and washing steps while both electrodes are in the transfer mode during the device movement from one solution to another. The capillary held sample solvent was replaced with an analyte-free solution during the washing step by fully extending the working and reference electrodes and repeatedly moving the electrodes with respect to the stainless steel counter electrode for 15 s in a stirred 500-mL volume of the washing solution. The results demonstrated that using an integrated three-electrode device effectively facilitated the electrochemical solid-phase extraction and 1.5–2 orders of magnitude higher extraction efficiencies were obtained compared to conventional SPME. Also, the risk of sample loss during different analysis steps was decreased using this downscaled installation. Therefore, electrochemical SPE was introduced as an interesting miniaturized analytical device.

Also, Nyholm et al. have used PPy coated microarray electrodes for EC-SPME as a preconcentration step in downsized flow systems on individually addressable gold microband electrodes [28]. In this study, a capillary was positioned in a vertical position over the electrode array during both the extraction process and the detection of the desorbed compounds to maintain a flow of analyte solution over the band electrodes. On the other hand, the silicon chip was positioned in a vertical position at the electrolyte surface to enable a flow of analyte solution over the microband electrodes and to perform suitable conductivity between these electrodes and the reference and counter electrodes. Therefore, any contact between the microband electrodes and contamination of the electrolyte are avoided and potentiostatic control of the working electrodes is enabled due to the flow of analyte solution emerging from the capillary.

In comparison with the traditional SPME, significant preconcentration by a factor of approximately 210 and low limit of detection (LOD) of about 625 nmol L^{-1} were obtained by performing the extraction process for only a few minutes and good linearity between the extraction time and detection response at both mmol L^{-1} and μmol L^{-1} concentrations of chloride as the model analyte was achieved.

In another work, a three dimensional microporous polymer network material, or monolith, cast-to-shape in a microchannel was introduced by Shepodd et al. [33]. A system for separation of charged compounds from uncharged species was designed. A fused silica capillary column with an internal diameter of about 110 μm and a porous polymer monolith, prepared by photopolymerization, disposed along a protein of its length. To condition the capillary column, it was perfused with 20 mmol L^{-1} Tris buffer at a pH of about 8.3 (also other suitable buffer materials can be used). Then, about 1–5 kV electrical potential was applied to the porous polymer monolith using a power supply and electrodes. The electrodes were disposed on either side of the stationary phase while the presence of the eluted molecules was detected by laser induced dispersed fluorescence as they passed the detection window. An ultra-microporous material can be interposed between the electrodes and the capillary column, which carries the current. Therefore, it can be used to introduce the fluid into the capillary column and the electrodes. It should be noted that the pores are fine enough that the pressure-driven or electroosmotic flow is negligible.

Using polymer monolith, charged proteins are trapped and retained from a mixture of charged and uncharged species in an electric field. Then, the electrical field eliminates and the retained charged proteins are released from the porous polymer monolith by a pressure-driven flow. Since the pressure-driven flow is independent of direction (i.e., neither reverse fluid flow nor a multi-directional flow field is required), unlike prior art systems, a single flow through the porous polymer monolith can be employed. This invented monolithic polymer material can act as a chromatographic medium. Also, the porous polymer monolithic can be used for preconcentration of charged proteins in a dilute solution by retaining these charged species.

4. Concluding remarks and future trends

Different applications of electrical field were overviewed consisting of its roles as the extraction and elution driving force and electrochemical synthesis. Following that, advantages and disadvantages of proposed methods were discussed and new installations were introduced in this review. The most prominent application of electrical driving force is seen in SPME methods including fiber synthesis and extraction processes. However, some techniques such as EA-SPE that have not found remarkable attention in analytical chemistry are the staircases to development and emerging of subsequent sample preparation methods. In the field of extraction, electrical driving force has some positive effects in selectivity and sample cleanup as well as extraction recovery and speed and offers the possibility of having precise control over the beginning and termination of the extraction. Also, noticeable potential of electrical driving force is not only restricted to extraction and sample preparation techniques and they have shown high efficiency to synthesize various types of coating films. Another interesting field in electrical field stimulated extraction techniques is their application in designing microchip-based devices or LOCs. However, there are limited reported works in solid-phase based LOC systems. Therefore, further studies are required for development of this new aspect to make it a known and useful device in the real world. Limitation of solid-phase based installations for on-line coupling to analysis instruments is also one of the drawbacks of this type of extraction methods, which needs more work and serious efforts.

Acknowledgments

The support provided by the Grant Agency of the Iran's National Elites Foundation (Shahid Chamran's Scientific Prize, Grant no. 15/37651, Tehran, Iran) is highly appreciated.

References

[1] M. Abdel-Rehim, M. Andersson, E. Portelius, C. Norsten-Höög, L.G. Blomberg, J. Microcolumn Sep. 13 (2001) 313–321.
[2] M.-C. Hennion, J. Chromatogr. A 856 (1999) 3–54.
[3] I. Liška, J. Chromatogr. A 885 (2000) 3–16.
[4] J. Henion, E. Brewer, G. Rule, Anal. Chem. 70 (1998) 650A–656A.
[5] C.L. Arthur, J. Pawliszyn, Anal. Chem. 62 (1990) 2145–2148.
[6] G. Morales-Cid, B.M. Simonet, S. Cárdenas, M. Valcárcel, Electrophoresis 29 (2008) 2033–2040.
[7] D. Zhan, S. Mao, Q. Zhao, Z. Chen, H. Hu, P. Jing, M. Zhang, Z. Zhu, Y. Shao, Anal. Chem. 76 (2004) 4128–4136.
[8] F. Kivlehan, Y.H. Lanyon, D.W.M. Arrigan, Langmuir 24 (2008) 9876–9882.
[9] S. Amemiya, X. Yang, T.L. Wazenegger, J. Am. Chem. Soc. 125 (2003) 11832–11833.
[10] C. Gavach, F. Henry, J. Electroanal. Chem. 54 (1974) 361–370.
[11] F. Guo, T. Gorecki, D. Irish, J. Pawliszyn, Anal. Commun. 33 (1996) 361–364.
[12] F. Reymond, D. Fermín, H.J. Lee, H.H. Girault, Electrochim. Acta 45 (2000) 2647–2662.
[13] D.W.M. Arrigan, Anal. Lett. 41 (2008) 3233–3252.
[14] Z. Samec, Pure Appl. Chem. 76 (2004) 2147–2180.
[15] C.J. Collins, D.W.M. Arrigan, Anal. Bioanal. Chem. 393 (2009) 835–845.
[16] P. Vanýsek, L.B. Ramírez, J. Chil. Chem. Soc. 53 (2008) 1455–1463.
[17] C.J. Collins, A. Berduque, D.W.M. Arrigan, Anal. Chem. 80 (2008) 8102–8108.
[18] A. Berduque, D.W.M. Arrigan, Anal. Chem. 78 (2006) 2717–2725.
[19] C. Gavach, Experientia 18 (Suppl.) (1971) S321–S331.
[20] C. Gavach, A. Savajols, Electrochim. Acta 19 (1974) 575–581.
[21] C. Gavach, P. Seta, F. Henry, Bioelectrochem. Bioenerg. 1 (1974) 329–342.
[22] Y. Zhu, L. Cao, J. Hao, Q. Qu, S. Xin, H. Zhang, Microchim. Acta 170 (2010) 121–126.
[23] H. de L. Lira, R. Paterson, J. Membr. Sci. 206 (2002) 375–387.
[24] X.Y. Han, W.Z. Shen, J. Electroanal. Chem. 655 (2011) 56–64.
[25] A.Jani, E. Anglin, S. McInnes, D. Losic, J. Shapter, N. Voelcker, Chem. Commun. 21 (2009) 3062–3064.

[26] H.G.L. Coster, Membr. Sci. Technol. 10 (2004) 1–23.
[27] W. Ya-Rong, L. Jing-Jing, W. Zhi-Yong, F. Jun-Gang, F. Fang, Chin. J. Anal. Chem. 36 (2008) 879–884.
[28] G. Liljegren, L. Nyholm, Analyst 128 (2003) 232–236.
[29] G. Liljegren, J. Pettersson, K.E. Markides, L. Nyholm, Analyst 127 (2002) 591–597.
[30] A.K. Singh, D.W. Neyer, J.S. Schoeniger, M.G. Garguilo, Electrokinetic Concentration of Charged Molecules, US006428666B1.
[31] J. Dai, T. Ito, L. Sun, R.M. Crooks, J. Am. Chem. Soc. 125 (2003) 13026–13027.
[32] R. Dhopeshwarkar, L. Sun, R.M. Crooks, Lab. Chip 5 (2005) 1148–1154.
[33] T.J. Shepodd, E. Franklin, Z.T. Prickett, A. Artau, Cast-to-Shape Electrokinetic Trapping Medium, US20040251205A1.
[34] T. Fujinaga, T. Nagai, C. Takagi, S. Okazaki, Study of the Electrolytic Chromatography. A New Separation Method of Several Metal Ions, Nippon Kagaku Zasshi, vol. 84, 1963, pp. 941–942.
[35] W.J. Blaedel, J.H. Strohl, Anal. Chem. 37 (1965) 64–67.
[36] D.K. Roe, Anal. Chem. 36 (1964) 2369–2370.
[37] R.S. Deinhammer, K. Shimazu, M.D. Porter, Anal. Chem. 63 (1991) 1889–1894.
[38] T. Hasan, D. Gazda, M.D. Porter, R.S. Houk, Anal. Chim. Acta 537 (2005) 63–68.
[39] A. Żwir-Ferenc, M. Biziuk, Pol. J. Environ. Stud. 15 (2006) 677–690.
[40] D.T. Rossi, N. Zhang, J. Chromatogr. A 885 (2000) 97–113.
[41] C.W. Huck, G.K. Bonn, J. Chromatogr. A 885 (2000) 51–72.
[42] C.F. Poole, A.D. Gunatilleka, R. Sethuraman, J. Chromatogr. A 885 (2000) 17–39.
[43] Y. Tian, J. Wang, Z. Wang, S. Wang, Sens. Actuators B 104 (2005) 23–28.
[44] K. Gelin, A. Mihranyan, A. Razaq, L. Nyholm, M. Strømme, Electrochim. Acta 54 (2009) 3394–3401.
[45] Y. Şahin, B. Ercan, M. Şahin, Talanta 75 (2008) 369–375.
[46] A. Mihranyan, L. Nyholm, A.E.G. Bennett, M. Strømme, J. Phys. Chem. B 112 (2008) 12249–12255.
[47] A. Razaq, A. Mihranyan, K. Welch, L. Nyholm, M. Strømme, J. Phys. Chem. B 113 (2009) 426–433.
[48] A. Razaq, G. Nyström, M. Strømme, A. Mihranyan, L. Nyholm, Plos One 6 (2011) 1–9.
[49] G. Liljegren, N. Forsgard, C. Zettersten, J. Pettersson, M. Svedberg, M. Herranen, L. Nyholm, Analyst 130 (2005) 1358–1368.
[50] H. Bagheri, E. Babanezhad, F. Khalilian, Anal. Chim. Acta 634 (2009) 209–214.
[51] N.M. Vizioli, M.L. Rusell, C.N. Carducci, Anal. Chim. Acta 514 (2004) 167–177.
[52] F.W. Tempels, J. Teeuwsen, I.K. Kyriakou, G. Theodoridis, W.J. Underberg, G. W. Somsen, G.J. de Jong, J. Chromatogr. A 1053 (2004) 263–268.
[53] F.W. Tempels, W.J. Underberg, G.W. Somsen, G.J. de Jong, Anal. Chem. 76 (2004) 4432–4436.
[54] G.M. Janini, M. Zhou, L.R. Yu, J. Blonder, M. Gignac, T.P. Conrads, H.J. Issaq, T.D. Veenstra, Anal. Chem. 75 (2003) 5984–5993.
[55] K. Sandra, F. Lynen, B. Devreese, J. Van Beeumen, P. Sandra, Anal. Bioanal. Chem. 385 (2006) 671–677.
[56] W.M. Stoggl, C.W. Huck, G. Stecher, G.K. Bonn, Electrophoresis 27 (2006) 787–792.
[57] V. Kasicka, Electrophoresis 27 (2006) 142–175.
[58] G. Morales-Cid, S. Cárdenas, B.M. Simonet, M. Valcárcel, Trends Anal. Chem. 29 (2010) 158–165.
[59] R.G. Belardi, J. Pawliszyn, Water Pollut. Res. J. Can. 24 (1989) 179–191.
[60] H. Kataoka, H.L. Lord, J.J. Pawliszyn, Chromatogr. A 880 (2000) 35–62.
[61] L. Özcan, M. Şahin, Y. Şahin, Sensors 8 (2008) 5792–5805.
[62] X. Liu, X. Wang, F. Tan, H. Zhao, X. Quan, J. Chen, L. Li, Anal. Chim. Acta 727 (2012) 26–33.
[63] B.J. Yates, K.R. Temsamani, Ö. Ceylan, S. Öztemiz, T.P. Gbatu, R.A. LaRue, U. Tamer, H.B. Mark, Talanta 58 (2002) 739–745.
[64] B. Deore, Z. Chen, T. Nagaoka, Anal. Chem. 72 (2000) 3989–3994.
[65] J. Zeng, J. Chen, X. Song, Y. Wang, J. Ha, X. Chen, X. Wang, J. Chromatogr. A 1217 (2010) 1735–1741.
[66] U. Tamer, B. Yates, A. Galal, T. Gbatu, R. LaRue, C. Schmiesing, K. Temsamani, Ö. Ceylan, H.B. Mark, Microchim. Acta 143 (2003) 205–215.
[67] K.R. Temsamani, Ö. Ceylan, B.J. Yates, S. Öztemiz, T.P. Gbatu, A.M. Stalcup, H.B. Mark, W. Kutner, J. Solid State Electrochem. 6 (2002) 494–497.
[68] V. Syritski, J. Reut, A. Menaker, R.E. Gyurcsányi, A. Öpik, Electrochim. Acta 53 (2008) 2729–2736.
[69] E. Shamaeli, N. Alizadeh, Anal. Sci. 28 (2012) 153–158.
[70] Q. Li, Y. Ding, D. Yuan, Talanta 85 (2011) 1148–1153.
[71] Y. Şahin, B. Ercan, M. Şahin, J. Appl. Polym. Sci. 108 (2008) 3298–3304.
[72] Q. Li, X. Wang, D. Yuan, J. Chromatogr. A 1216 (2009) 1305–1311.
[73] X. Chai, Y. He, D. Ying, J. Jia, T. Sun, J. Chromatogr. A 1165 (2007) 26–31.
[74] D.J. Djozan, T. Baheri, M.H. Pournaghi-Azar, Chromatographia 65 (2007) 45–50.
[75] A. Mohammadi, Y. Yamini, N. Alizadeh, J. Chromatogr. A 1063 (2005) 1–8.
[76] T.P. Gbatu, O. Ceylan, K.L. Sutton, J.F. Rubinson, J.A. Caruso, H.B. Mark, Anal. Commun. 36 (1999) 203–205.
[77] T.-J. Yang, M.-R. Lee, Talanta 82 (2010) 766–770.
[78] X. Rong, F. Zhao, B. Zeng, Talanta 98 (2012) 265–271.
[79] D. Svirskis, B.E. Wright, J. Travas-Sejdic, A. Rodgers, S. Garge, Electroanalysis 22 (2010) 439–444.
[80] H. Bagheri, A. Mir, E. Babanezhad, Anal. Chim. Acta 532 (2005) 89–95.
[81] F. Luo, X. Ma, T. Ping, L. Bian, Z. Wu. The 2nd International Conference on Bioinformatics and Biomedical Engineering, ICBBE 2008, 10.1109/ICBBE.2008.418, p. 3666.
[82] S. Sungkaew, C. Thammakhet, P. Thavarungkul, P. Kanatharana, Anal. Chim. Acta 664 (2010) 49–55.
[83] H. Bagheri, A. Aghakhani, M. Baghernejad, A. Akbarinejad, Anal. Chim. Acta 716 (2012) 34–39.
[84] B.B. Prasad, M.P. Tiwari, R. Madhuri, P.S. Sharma, J. Chromatogr. B 879 (2011) 364–370.
[85] G. Li, C. Martinez, S. Semancik, J. Am. Chem. Soc. 127 (2005) 4903–4909.
[86] M. Su, L. Fu, N. Wu, M. Aslam, V.P. Dravid, Appl. Phys. Lett. 84 (2004) 828–830.
[87] M. Şahin, Y. Şahin, A. Özcan, Sens. Actuators B 133 (2008) 5–14.
[88] T. Uğur, S. Yücel, E. Nusret, U. Yasemin, P. KadirY. Attila, J. Electroanal. Chem. 570 (2004) 6–12.
[89] J. Wu, W.M. Mullett, J. Pawliszyn, Anal. Chem. 74 (2002) 4855–4859.
[90] M. Rezazadeh, Y. Yamini, S. Seidi, B. Ebrahimpour, J. Chromatogr. A 1280 (2013) 16–22.
[91] A. Ameli, N. Alizadeh, Anal. Biochem. 428 (2012) 99–106.
[92] A. Ameli, N. Alizadeh, Anal. Chim. Acta 707 (2011) 62–68.
[93] J. Heinze, B. Frontana-Uribe, S. Ludwigs, Chem. Rev. 110 (2010) 4724–4771.
[94] U. Páramo-García, J.G. Ibanez, N. Batina, Int. J. Electrochem. Sci. 6 (2011) 5172–5188.
[95] K. Gurunathan, A.V. Murugan, R. Marimuthu, U.P. Mulik, D.P. Amalnerkar, Mater. Chem. Phys. 61 (1999) 173–191.
[96] C.M. Li, C.Q. Sun, W. Chen, L. Pan, Surf. Coat. Technol. 198 (2005) 474–477.
[97] Ü. Tamer, N. Ertas, Y.A. Udumd, Ý. Şahin, K. Pekmez, A. Yıldız, Talanta 67 (2005) 245–251.
[98] J. Kameoka, R. Orth, Y.N. Yang, D. Czaplewski, R. Mathers, G.W. Coates, H.G. Craighead, Nanotechnology 14 (2003) 1124–1129.
[99] A.G. Mac Diarmid, W.E. Jones, I.D. Norris, J. Gao, A.T. Johnson, N.J. Pinto, J. Hone, B. Han, F.K. Ko, H. Okuzaki, M. Llaguno, Synth. Met. 119 (2001) 27–30.
[100] Y.X.Zhou, M. Freitag, J. Hone, C. Staii, A.T. Johnson, N.J. Pinto, A.G. Macdiarmid, Appl. Phys. Lett. 83 (2003) 3800–3802.
[101] G.C. Rutledge, S.V. Fridrikh, Adv. Drug Deliv. Rev. 59 (2007) 1384–1391.
[102] J.W. Zewe, J.K. Steach, S.V. Olesik, Anal. Chem. 82 (2010) 5341–5348.
[103] W.E. Teo, S. Ramakrishna, Nanotechnology 17 (2006) R89–R106.
[104] S. Ramakrishna, K. Fujihara, W.E. Teo, T.C. Lim, Z. Ma, An Introduction to Electrospinning and Nanofibers, World Scientific, Singapore, 2005.
[105] X. Kang, C. Pan, Q. Xu, Y. Yao, Y. Wang, D. Qi, Z. Gua, Anal. Chim. Acta 587 (2007) 75–81.
[106] Q. Xu, S.Y. Wu, M Wang, X.Y. Yin, Z.Y. Wen, W.N. Ge, Z.Z. Gu, Chromatographia 71 (2010) 487–492.
[107] K. Yoshimatsu, L. Ye, J. Lindberg, I.S. Chronakis, Biosens. Bioelectron. 23 (2008) 1208–1215.
[108] S. Chigome, G. Darko, U. Buttner, N. Torto, Anal. Methods 2 (2010) 623–626.
[109] M. Heitzmann, C. Bucher, J.C. Moutet, E. Pereira, B.L. Rivas, G. Royal, E. Aman, Electrochim. Acta 52 (2007) 3082–3087.
[110] J.C. Wu, J. Pawliszyn, Anal. Chem. 73 (2001) 55–63.
[111] F.-Y. Song, K.-K. Shiu, J. Electroanal. Chem. 498 (2001) 161–170.
[112] M.B. Gholivand, M. Amiri, J. Electroanal. Chem. 676 (2012) 53–59.
[113] J. Hu, X.-D. Xiao, D.F. Ogletree, M. Salmeron, Science 268 (1995) 267–269.
[114] F.-R.F. Fan, A.J. Bard, R. Guckenberger, M. Heim, Science 270 (1995) 1849–1852.
[115] A.R. Boccaccini, J. Cho, J.A. Roether, B.J.C. Thomas, E.J. Minay, M.S.P. Shaffer, Carbon 44 (2006) 3149–3160.
[116] C. Weidlich, K.-M. Mangold, K. Jüttner, Electrochim. Acta 50 (2005) 5247–5254.
[117] J.Zeng, J. Zou, X. Song, J. Chen, J. Ji, B. Wang, Y. Wang, J. Ha, X. Chen, J. Chromatogr. A 1218 (2011) 191–196.
[118] L. Pan, M. Adams, J. Pawliszyn, Anal. Chem. 67 (1995) 4396–4403.
[119] J. Pawliszyn, Solid Phase Microextraction Theory and Practice, Wiley-VCH, Chichester, 1997.
[120] L. Moens, T. Smaele, R. Dams, Anal. Chem. 69 (1997) 1604–1611.
[121] Z. Zhang, M.J. Yang, J. Pawliszyn, Anal. Chem. 66 (1994) 844A–853A.

Talanta 132 (2015) 354–365

Contents lists available at ScienceDirect

Talanta

journal homepage: www.elsevier.com/locate/talanta

Chemometrics: An important tool for monitoring interactions of vitamin B7 with bovine serum albumin with the aim of developing an efficient biosensing system for the analysis of protein

Mohammad-Bagher Gholivand [a,*], Ali R. Jalalvand [a,b], Hector C. Goicoechea [b], Raimundo Gargallo [c], Thomas Skov [d]

[a] Faculty of Chemistry, Razi University, Kermanshah 671496734, Iran
[b] Laboratorio de Desarrollo Analítico y Quimiometría (LADAQ), Cátedra de Química Analítica I, Universidad Nacional del Litoral, Ciudad Universitaria, CC 242 (S3000ZAA), Santa Fe, Argentina
[c] Solution Equilibria and Chemometrics Group, Department of Analytical Chemistry, University of Barcelona, Diagonal 645, E-08028 Barcelona, Spain
[d] Quality & Technology, Department of Food Science, Faculty of Science, University of Copenhagen, Copenhagen, Denmark

ARTICLE INFO

Article history:
Received 24 July 2014
Received in revised form
9 September 2014
Accepted 11 September 2014
Available online 28 September 2014

Keywords:
Vitamin B7
Bovine serum albumin
Binding
Chemometrics
Protein analysis

ABSTRACT

For the first time, interaction of vitamin B7 (VB7) with bovine serum albumin (BSA) was investigated with the aim of developing a method for the analysis of BSA. The interaction of VB7 with BSA was investigated by cyclic voltammetry (CV), linear sweep voltammetry (LSV), and differential pulse voltammetry (DPV) at a multi-walled carbon nanotubes-modified glassy carbon electrode (MWCNTs/GCE). The recorded electrochemical data was combined with UVvis and fluorescence (F) spectroscopic data into a row- and column-wise augmented matrix and resolved by multivariate curve resolution-alternating least squares (MCR-ALS) as an efficient chemometric tool, and this assisted in the further elucidation of the above interaction. Also, with aid of MCR-BANDS method, the absence of rotational ambiguity was verified in the obtained results and we confirmed that the obtained results were unambiguous and reliable. The binding of VB7 to BSA was also modeled by molecular docking methods. Excellent agreement was found between the experimental and computational results. The differences of DPV responses of VB7 in the absence and presence of BSA (ΔI) were found to be linearly related to BSA concentration between 0.5×10^{-9} mol L^{-1} and 35.0×10^{-9} mol L^{-1}, and a limit of detection (LOD, $3S_b/b$) of 0.22×10^{-9} mol L^{-1} was calculated. Finally, the DPV method was further applied to the determination of serum albumin (SA) in serum samples obtained from Holstein cows and the results were in good agreement with those obtained by a medical diagnostic laboratory whose method was based on traditional cellulose acetate electrophoresis. The MWCNTs/GCE showed enhanced electron transfer kinetics, large electroactive surface area, and was highly sensitive, selective, and stable towards SA determination. The satisfactory analytical performance of the proposed method would make it potentially advantageous for a broad range of biosensing and clinical applications.

© 2014 Elsevier B.V. All rights reserved.

1. Introduction

In living organisms, there are a variety of small molecules with various biological and pharmaceutical functions. Vitamin B7 (VB7, also called vitamin B8 or H, Fig. 1) is a water-soluble vitamin and an essential co-factor for five biotin-dependent carboxylase enzymes. It is synthesized in a wide variety of bacteria and plants. However, several microorganisms as well as higher animals are notable to synthesize it and their needs in this vitamin are met by dietary intake [1]. Besides the typical clinical features, recent evidence indicates that the pregnant women develop biotin deficiency during normal pregnancy [2,3].

Abbreviations: VB7, vitamin B7; BSA, bovine serum albumin; Trp, tryptophan; SA, serum albumin; CV, cyclic voltammetry; LSV, linear sweep voltammetry; DPV, differential pulse voltammetry; MWCNTs, multi-walled carbon nanotubes; GCE, glassy carbon electrode; F, fluorescence; MCR-ALS, multivariate curve resolution-alternating least squares; MD, molecular dynamic; LOD, limit of detection; TBS, Tris–HCl buffer solution; MVD, molegro virtual docker; EFA, evolving factor analysis; PCA, principal component analysis; SIMPLISMA, simple to use self-modeling mixture analysis; ITTFA, iterative target transformation factor analysis

* Corresponding author. Tel.: +98 8314274557; fax: +98 8314274559.
E-mail addresses: mbgholivand2013@gmail.com, mbgholivand@yahoo.com (M.-B. Gholivand).

http://dx.doi.org/10.1016/j.talanta.2014.09.019
0039-9140/© 2014 Elsevier B.V. All rights reserved.

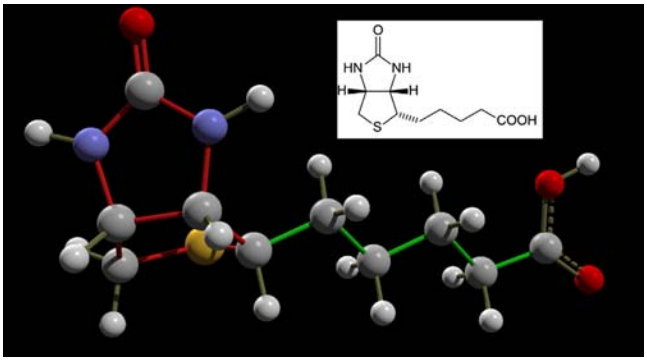


Fig. 1. Molecular structure of VB7.

Among biomacromolecules, serum albumin (SA) is a soluble protein, which is a major constituent of the circulatory system, and it commonly serves as a depository and a transport molecule for many exogenous compounds [4,5]. Consequently, simple, rapid and low cost analysis for SA proteins would be useful [6,7]. Studies on the binding of small molecules with plasma proteins will facilitate the interpretation of the metabolism and transport processes of such substances, and the binding of small molecules with bovine serum albumin (BSA) is a typical example of such interactions. Thus, it is an appropriate protein to use for such investigations, partly because of its structural homology with human serum albumin (HSA) [8].

There are a variety of techniques currently available for obtaining information about protein–ligand interactions such as the measurement of kinetics and binding affinities. Two traditional methods, X-ray diffraction and NMR spectroscopy, employed to obtain structural information of proteins and protein–ligand complexes. Both of these methods have disadvantages: X-ray diffraction requires the preparation of a crystal, which can be time consuming or even impossible; and NMR spectroscopy is not easily applied to larger proteins of more than a few hundred amino acids. Other analytical techniques that can be applied to proteins in solution are spectrophotometry, chemiluminescence, resonance light scattering [9–12]. Compared with spectroscopic methods, electrochemical assay is simple, easily implemented, and has low-cost and fast response. On the other hand, the interpretation of electrochemical data can contribute to elucidation of the interaction of ligand with biomacromolecules.

Chemometrics methods of data analysis, such as multivariate curve resolution-alternating least squares (MCR-ALS), are well known for their ability to resolve different kinds of data and extract profiles of individual chemical components from composite responses. Such results generate valuable information, which other-wise cannot be obtained by conventional methods, and which consequently, enable further analysis of the problem under investigation as is the case with the biosystems in this work.

To the best of our knowledge there is no report on the interactions between VB7 and BSA in the literature, and this work reports a detailed study on the mentioned system for the first time. The main aims of this study were: 1. Investigation of interaction of VB7 with BSA at a MWCNTs/GCE at physiological conditions by CV, LSV, and DPV and also in combination with UV–vis and fluorescence (F) techniques by the use of MCR-ALS. 2. Research and development of an electrochemical method for BSA analysis in conjunction with VB7 which could be suggested for biosensing and clinical applications.

2. Experimental and theoretical details

2.1. Chemicals and solutions

BSA, and VB7 were purchased from Sigma Chemical Company (St. Louise, MO). Multi-walled carbon nanotubes were purchased from io-li-tec, Ionic Liquid Technologies. All other reagents were of analytical grade, and doubly distilled water was used throughout. All solutions used in this work were prepared in Tris–HCl buffer solution (TBS, 0.05 mol L^{-1}, pH 7.4, containing 0.1 mol L^{-1} sodium chloride to maintain the ionic strength of solution). Stock solutions of VB7, and BSA was prepared by dissolving proper amount of their solid powder in the TBS (0.05 mol L^{-1}, pH 7.4) and were kept at dark in a refrigerator for about a week only.

2.2. Instruments and softwares

Electrochemical experiments were performed using a μ-AutolabIII/FRA2 driven by the Nova 1.8 software. A conventional three-electrode cell was used with a saturated calomel electrode (SCE) as reference electrode, a Pt wire as counter electrode and a bare or modified GCE as working electrode. The SEM experiment was made on a KYKY-EM 3200 scanning electron microscope. All fluorescence spectra were measured on a Cary Eclipse fluorescence spectrophotometer equipped with a water bath and a 1.0 cm quartz cell. The UVvis spectra were measured on an Agilent 8453 UVvis Diode-Array spectrophotometer controlled by the Agilent UVvis ChemStation software. A JENWAY-3345 pH-meter equipped with a combined glass electrode was used to pH measurements. The chemical structure of the VB7 was constructed by Hyperchem package (Ver. 8.0), and energy minimization for VB7 was performed by AM1 semi empirical method with Polak-Ribiere algorithm until the root mean square gradient of 0.01 kcal mol^{-1}. The known crystal structure of BSA (PDB Id: 3V03) was obtained from the Brookhaven Protein Data Bank. Water molecules were removed, and hydrogen atoms were added. The molegro virtual docker (MVD) software was employed to generate a docked conformation of VB7 with BSA. LIGPLOT [13], a program for automatically plotting protein–ligand interactions, was used to analyze the interactions between BSA and VB7. MCR-ALS and MCR-BANDS were implemented using the graphical interfaces provided by Prof. Tauler in his web page [14]. The recorded experimental data was smoothed, when necessary, and converted to matrices by means of several homemade MATLAB (Version 7.14) programs. A simple homemade MATLAB program was used for computing the concentrations of VB7 and BSA and their ratio in all voltammetric and spectroscopic experiments. All calculations were run on a DELL XPS laptop (L502X) with Intel Core i7-2630QM 2.0 GHz, 8.0 GB of RAM and Windows 7-64 as its operating system. The MD simulations were performed on a computer with a Linux Fedora 15 as its operating system.

2.3. Fabrication of MWCNTs/GCE and BSA/MWCNTs/GCE

Prior to the electrode modification, the GCE surface was polished with PK-4 polishing kit, BASi MF-2060 successively followed by rinsing thoroughly with redistilled deionized water until a mirror like finish was obtained. It was then dipped in a beaker containing 0.2 mol $L^{-1}H_3PO_4$ solutions to remove the adhered powder, rinsed with distilled water and dried at room temperature for 10.0–15.0 min. The MWCNTs (4.0 mg) was added to 1.0 mL dimethylformamide. A homogeneous and stable suspension of 4.0 mg mL^{-1} MWCNTs was obtained with the aid of ultrasonic agitation for about 30.0 min. A known volume (40.0 μL) of this solution was adsorbed onto the surface of the clean and dried GCE using a micropipette and dried under room temperature. The BSA/MWCNTs/GCE was prepared with the following procedure: an 8.0 mL of the BSA solution (0.40 mg mL^{-1} dissolved in TBS (0.05 mol L^{-1}, pH 7.4)) was dripped on the MWCNTs/GCE surface and dried by passing very slow rate of air for 10.0 min to

form a stable gel-like film. Then BSA/MWCNTs/GCE was kept at 4.0 °C in a refrigerator until use.

2.4. Procedures

Solutions used in the F and UVvis experiments were prepared in TBS (0.05 mol L^{-1}, pH 7.4) containing appropriate amounts of BSA or VB7. The total added volume (BSA or VB7) was less than 0.2 mL. Titrations were performed manually using suitable micropipettes. A mixed solution was shaken thoroughly and equilibrated for 5.0 min. F or UVvis spectra were then recorded.

Solutions used in the voltammetric experiments were prepared in TBS (0.05 mol L^{-1}, pH 7.4) containing appropriate amounts of BSA or VB7. The total added volume (BSA or VB7) was less than 0.4 mL. A given VB7–BSA system was stirred for 10.0 s, and then the sample was analyzed as required.

2.5. Development of the augmented matrix for MCR-ALS

Experiment 1 ($\boldsymbol{D}_{DPV}^{VB7}$): The concentration of VB7 was kept constant (5.5×10^{-4} mol L^{-1}), and BSA was added to the solution in the range of 0.0–5.5×10^{-4} mol L^{-1}.
Experiment 2 ($\boldsymbol{D}_{DPV}^{BSA}$): The concentration of BSA was kept constant (2.5×10^{-4} mol L^{-1}), and VB7 was added to the solution in the range of 0.0–12.5×10^{-3} mol L^{-1}.
Experiment 3 ($\boldsymbol{D}_{LSV}^{VB7}$): The concentration of VB7 was kept constant (4.0×10^{-4} mol L^{-1}), and BSA was added to the solution in the range of 0.0–4.0×10^{-4} mol L^{-1}.
Experiment 4 ($\boldsymbol{D}_{LSV}^{BSA}$): The concentration of BSA was kept constant (2.0×10^{-4} mol L^{-1}), and VB7 was added to the solution in the range of 0.0–1.0×10^{-3} mol L^{-1}.
Experiment 5 ($\boldsymbol{D}_{CV}^{VB7}$): The concentration of VB7 was kept constant (6.0×10^{-4} mol L^{-1}), and BSA was added to the solution in the range of 0.0–6.0×10^{-4} mol L^{-1}.
Experiment 6 ($\boldsymbol{D}_{CV}^{BSA}$): The concentration of BSA was kept constant (1.0×10^{-4} mol L^{-1}), and VB7 was added to the solution in the range of 0.0–5.0×10^{-4} mol L^{-1}.
Experiment 7 ($\boldsymbol{D}_{F}^{VB7}$): The concentration of VB7 was kept constant (6.0×10^{-7} mol L^{-1}), and BSA was added to the solution in the range of 0.0–6.0×10^{-7} mol L^{-1}.
Experiment 8 ($\boldsymbol{D}_{F}^{BSA}$): The concentration of BSA was kept constant (1.0×10^{-7} mol L^{-1}), and VB7 was added to the solution in the range of 0.0–5.0×10^{-7} mol L^{-1}.
Experiment 9 ($\boldsymbol{D}_{UVvis}^{VB7}$): The concentration of VB7 was kept constant (1.0×10^{-6} mol L^{-1}), and BSA was added to the solution in the range of 0.0–1.0×10^{-6} mol L^{-1}.
Experiment 10 ($\boldsymbol{D}_{UVvis}^{BSA}$): The concentration of BSA was kept constant (1.0×10^{-6} mol L^{-1}), and VB7 was added to the solution in the range of 0.0–5.0×10^{-6} mol L^{-1}.

2.6. Foundations in applying MCR-ALS

The MCR-ALS method for the analysis of electroanalytical data is summarized elsewhere [15,16], and here only a working summary is provided. The goal of MCR is to decompose composite measured profiles such as voltammograms or spectra into the different pure profiles for each species in a mixture. The resulting extracted information for the pure components may be in the form of single bands or more complex profiles. Such data can be arranged into $\boldsymbol{D}$ (M × N) matrix with M objects and N variables e.g. wavelength or potential. The MCR decomposition of a matrix is carried out according to the following equation:

$$\boldsymbol{D}=\boldsymbol{C}\boldsymbol{S}^{T}+\boldsymbol{E} \tag{1}$$

where $\boldsymbol{D}$ is the matrix of the experimental data, with dimensions of $M\times N$. The matrix, $\boldsymbol{C}$ (M × P), describes the concentration profiles of the P species involved in the given measured profiles. The matrix, $\boldsymbol{S}^{T}$ (P × N), is then the contribution of the measured profiles of these P species in the N columns of the data matrix (pure signals' profiles). $\boldsymbol{E}$ ($M\times N$) is the matrix of residuals, which contains the data variance unexplained by the product, $\boldsymbol{C}\boldsymbol{S}^{T}$. One important and frequently used iterative approach to solve Eq. (1) is MCR by alternating least squares (ALS). The optimization process starts from initial guesses of $\boldsymbol{C}$ and $\boldsymbol{S}^{T}$, and these are then refined to yield profiles with chemical meaning.

When the same chemical system is monitored using more than one technique, e.g. DPV, LSV, CV, F and UVvis, a matrix is constructed, which consists of row- and column-wise augmented data, i.e. five types of information are presented. The individual data matrices corresponding to the five types of technique are placed side-by-side. The related model for MCR-ALS analysis is shown below:

$$\begin{bmatrix}\boldsymbol{D}_{DPV}^{VB7}\boldsymbol{D}_{LSV}^{VB7}\boldsymbol{D}_{CV}^{VB7}\boldsymbol{D}_{F}^{VB7}\boldsymbol{D}_{UVvis}^{VB7}\\ \boldsymbol{D}_{DPV}^{BSA}\boldsymbol{D}_{LSV}^{BSA}\boldsymbol{D}_{CV}^{BSA}\boldsymbol{D}_{F}^{BSA}\boldsymbol{D}_{UVvis}^{BSA}\end{bmatrix}=\begin{bmatrix}\boldsymbol{C}^{VB7}\\ \boldsymbol{C}^{BSA}\end{bmatrix}$$

$$\left[\boldsymbol{S}_{DPV}^{T}\boldsymbol{S}_{LSV}^{T}\boldsymbol{S}_{CV}^{T}\boldsymbol{S}_{F}^{T}\boldsymbol{S}_{UVvis}^{T}\right]+[\boldsymbol{E}_{DPV}\boldsymbol{E}_{LSV}\boldsymbol{E}_{CV}\boldsymbol{E}_{F}\boldsymbol{E}_{UVvis}] \tag{2}$$

If $\boldsymbol{D}_{\mathrm{DPV}}$, $\boldsymbol{D}_{\mathrm{LSV}}$, $\boldsymbol{D}_{\mathrm{CV}}$, $\boldsymbol{D}_{\mathrm{F}}$, and $\boldsymbol{D}_{\mathrm{UVvis}}$ are the data obtained with the five techniques, there are two matrices of concentration profiles, $\boldsymbol{C}^{\mathrm{VB7}}$ and $\boldsymbol{C}^{\mathrm{BSA}}$, and five row-wise augmented matrices of measured profiles, $\boldsymbol{S}_{\mathrm{DPV}}^{\mathrm{T}}$, $\boldsymbol{S}_{\mathrm{LSV}}^{\mathrm{T}}$, $\boldsymbol{S}_{\mathrm{CV}}^{\mathrm{T}}$, $\boldsymbol{S}_{\mathrm{F}}^{\mathrm{T}}$, and $\boldsymbol{S}_{\mathrm{UVvis}}^{\mathrm{T}}$, which contain the pure signals for the techniques used to obtain $\boldsymbol{D}_{\mathrm{DPV}}$, $\boldsymbol{D}_{\mathrm{LSV}}$, $\boldsymbol{D}_{\mathrm{CV}}$, $\boldsymbol{D}_{\mathrm{F}}$, and $\boldsymbol{D}_{\mathrm{UVvis}}$, respectively.

When the augmented matrix of the five data matrices is being built, the number of analyte species, P, can be obtained with the aid of Evolving Factor Analysis (EFA) [17] or Principal Component Analysis (PCA) or other methods based on factor analysis. The EFA method provides an estimation of the regions or windows where the concentration of different components is changing or evolving, and it also provides an initial estimation of how these concentration profiles change during the experiment. This method is based on the evaluation of the magnitude of the eigenvalues associated with all the submatrices of a matrix built up by adding successively all the rows of the original data matrix. The calculation is performed in two directions: forward (in the direction of the experiment) and backward (in the opposite direction of the experiment), e.g. Abdollahi and Mahdavi illustrate how concentration profiles obtained from EFA may be used as initial estimates for the concentration matrix input in the constrained ALS optimization [18]. PCA, an alternative approach to EFA, is a common chemometrics tool; it yields the number and direction of the relevant sources of variation in a bilinear data set [19]. Once the PCs, P, are determined and an initial estimate of their concentration profiles is obtained, it becomes easier to obtain improved estimates of either the concentration values or pure signals' profiles. Constraints in ALS optimization are implemented to facilitate the finding of pure or most representative contributions to the data matrix using real variables. The resolution methods start with initial estimates of $\boldsymbol{C}$ and work by optimizing iteratively the concentration, while introducing the available information about the system [19]. During the optimization, the suitable constraints are applied to ensure that the final solution is chemically meaningful [20]. The lack of fit (lof) [21], which is defined as the difference between the input data, $\boldsymbol{D}$, and the data reproduced from the $\boldsymbol{C}\boldsymbol{S}^{T}$ product obtained by MCR-ALS, was used as a parameter to evaluate the goodness of fit of the model according to the following expression:

$$lof\ (\%)=100\sqrt{\frac{\sum_{i,j}e_{i,j}^{2}}{\sum_{i,j}d_{i,j}^{2}}} \tag{3}$$

where d_{ij} is an element in the raw data and e_{ij} is the corresponding residual after the model variation is removed.

However, the solutions to Eq. (1) obtained by MCR-ALS are not unique. They can have rotational and intensity ambiguities. To solve this limitation, column- and row-wise augmentation schemes (Eq. (2)) can be used for simultaneous resolution. This kind of simultaneous data analysis is more powerful compared to that described by Eq. (1) and allows for improved resolution of very complex data structures. In general, this method should be useful to overcome some uncertainties in the analysis of the data related to coincidental processes or small signal shifts. Thus, in this work, an augmented data matrix, was constructed and resolved by the MCR-ALS approach.

However, because of the combination of completely different types of data, e.g. voltammetric and spectroscopic data some considerations must be performed in the analysis of the augmented matrix:

1. Due to the fact that voltammetric and spectroscopic signals are of very different magnitude, submatrices must be scaled in order to have a similar weight on the iterative ALS optimization of the augmented data matrix; in a first approach, this is done by dividing submatrices by their maximum values prior to their combination into an augmented data matrix.
2. The concept of component is a critical point. For spectroscopic data component is associated to pure chemical species in solution [22,23], but for electrochemical data component must be associated to a single electrochemical process giving a signal, including not only redox processes but also some other possible phenomena like, for instance, electrode adsorption of a species [15,16] or capacitive currents due to the charging of the electrical double layer at the electrode surface. Anyway, in many situations, a single electrochemical process is produced by a single species.
3. Taking into account the impossibility of applying a closure constrain (i.e., the mass balance) to the matrices obtained at different concentration levels, a normalization of the signals has been made along the MCR-ALS iterations. Considering that such normalization should be common to DPV, LSV, CV, F, and UVvis parts of each pure signal, it has been made by dividing the pure signal by its maximum absolute value (alternative normalization procedures have been tested but the results were similar).
4. To combine voltammetric and spectroscopic sub-matrices into an augmented matrix, all sub-matrices must contain the same number of rows and columns and must share the same distribution of the chemical species along the experiments. Ideally, this condition can be fulfilled using exactly the same total concentrations of VB7 and BSA in all titrations, but this is not possible because the concentrations required for voltammetric experiments are higher than those for spectroscopic ones. Thus, in the present work, voltammetric and spectroscopic experiments have been performed at different total concentrations but at the same values of ratio.

3. Results and discussion

3.1. Morphological studies of the composite electrodes

Fig. 2A and B shows the SEM images of MWCNTs/GCE and BSA/MWCNTs/GCE, respectively. The SEM image of MWCNTs/GCE (Fig. 2A) shows the MWCNTs twining around each other and attached to the GCE. It is clear that MWCNTs almost homogeneously distributed on the electrode surface by forming a thin layer. When BSA was immobilized on the electrode surface the clear MWCNTs image became dim and the protein adsorbed and aggregated onto the surface of the tubes (Fig. 2B); therefore, it demonstrated that MWCNTs were wrapped by BSA.

3.2. Voltammetric studies of VB7–BSA interactions

3.2.1. Cyclic voltammetric studies

Useful information about the interaction of ligands and biomacromolecules usually can be acquired from the cyclic voltammetry (CV) that is one of the most important electroanalytical techniques due to the similarity among various redox chemical and biological processes [24]. Therefore, CV was used to study the interactions of VB7 with BSA. Fig. 3A compares the CVs of VB7 in TBS (0.05 mol L^{-1}, pH 7.4) at GCE (curve a) and MWCNTs/GCE (curve b). As can be seen, MWCNTs exhibited excellent electrocatalytic behavior towards irreversible oxidation of VB7 as evidenced by enhancement of the VB7 oxidation peak current and shift in its oxidation potential to lower values in comparison with the bare GCE. From the CV of the VB7 at MWCNTs/GCE (Fig. 3A, curve b), the E_p and $E_{p/2}$ values were 653 and 572 mV, respectively. When irreversible oxidation occurs at an electrode, at $E_{p/2}$, the corresponding current, i, is given by $(I_d/2)$, and at 25 °C, $|E_p - E_{p/2}| = 47.7/\alpha n$ [25], where n is the electron transfer number, and α of an irreversible electrode process is generally assumed to be 0.5 [26]. Thus, n was calculated to be 1.17 i.e. ~1.

BSA did not exhibit any observable peak at the MWCNTs/GCE at pH 7.4, when BSA was added to the VB7 solution, the oxidation peak shifted towards higher potentials and a decreasing oxidation current was observed (Fig. 3B, curves b–s). This shift may be attributed to the changes of the molecular environment around the VB7 molecule as a result of its interaction with BSA [27]. This observation is consistent with the view that the VB7–BSA interaction occurred between the most hydrophobic segments of the VB7 molecule and the hydrophobic region of the BSA cavity.

Since binding of VB7 to BSA may influence the major electrochemical kinetic parameters of VB7 (such as α (transfer coefficient) and k_s (electrochemical rate constant)) the CVs of VB7 at various scan rates (υ) were recorded at the surface of both BSA/MWCNTs/GCE (VB7–BSA) and MWCNT/GCE (free VB7). Fig. 4A shows the typical cyclic voltammograms of VB7 at various scan rates on the surface of BSA/MWCNTs/GCE. A linear relationship between peak current (I_p) and υ revealed that VB7 oxidation was an adsorption-controlled process (Fig. 4B). Furthermore, from the slopes of the linear plots of I_p vs. υ the surface concentrations of electroactive species (Γ) were estimated as 5.71×10^{-3} and 4.76×10^{-3} mol cm^{-2} for the free VB7 and the bound VB7–BSA, respectively, according to the following equation [28]:

$$I = n^2F^2A\Gamma\upsilon/4RT \quad (4)$$

where n represents the number of electrons involved in reaction (one electron), A is the surface area (0.05 cm^2) of the GCE, T is temperature (25 °C), Γ (mol cm^{-2}) is the surface coveraged and other symbols have their usual meaning. As it is shown by increasing the scan rate, the shifted to a more positive potential. For a totally irreversible and an adsorption-controlled process, the relationship between E_P and υ can be expressed by the Laviron's equation [29]

$$E_p = E^0 - 2.3RT/\alpha nF[\log(RTK_s/nF) - \log \upsilon] \quad (5)$$

where E^0 (V) was the formal potential, and other symbols have their usual meaning. k_s and αn values can be obtained from the intercept and the slope of the linear plot of E_p vs. log υ (Fig. 4C), if the E^0 is known. The E^0 value can be deduced from the intercept of E_p vs. υ (Fig. 4D) plot by extrapolating the line to $\upsilon = 0$ V s^{-1}. By knowing E^0 and graphical representations of E_p vs. log υ for VB7 in the absence and presence of BSA, the α and k_s were obtained from the slope and intercept, respectively. On the assumption that the number of electrons involved in the VB7 oxidation is 1 the values of α for an

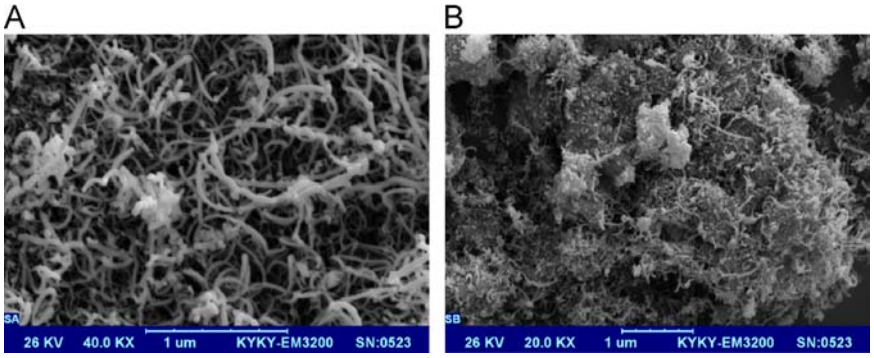


Fig. 2. The SEM images of (A) MWCNTs/GCE, and (B) BSA/MWCNTs/GCE.

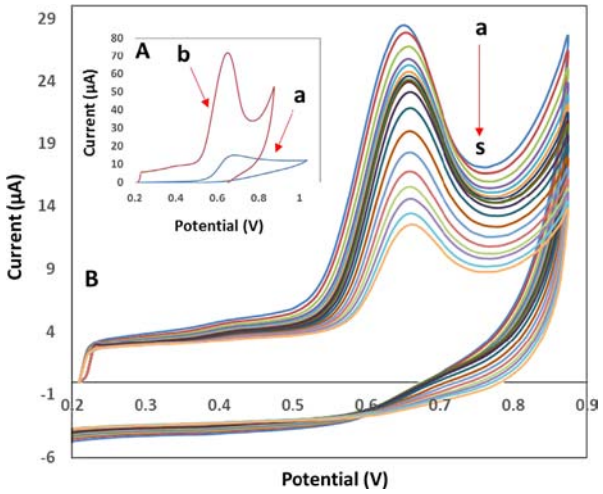


Fig. 3. (A) Cyclic voltammograms of 0.10 mM VB7 in TBS (0.05 mol L^{-1}, pH 7.4) at (a) bare GCE, and (b) MWCNTs/GCE, and (B) cyclic voltammograms of 6.0×10^{-4} M VB7 in TBS (0.05 mol L^{-1}, pH 7.4) at MWCNTs/GCE with different concentrations of BSA (a-s): 0.0–6.0×10^{-4} mol L^{-1} (in steps of 3.33×10^{-5} mol L^{-1}), In all cases scan rate was 50.0 mV s^{-1}.

irreversible surface reaction can be obtained as 0.374 and 0.371 for the free VB7 (at MWCNTs/GCE) and the bound VB7–BSA (at BSA/MWCNTs/GCE), respectively. Also, k_s can be obtained as 3.00 and 2.74 for the free VB7 (at MWCNTs/GCE) and the bound VB7–BSA (at BSA/MWCNTs/GCE), respectively. As can be seen, the values of α and k_s are decreased in the presence of BSA. Decreasing of α may be due to higher absorption of VB7–BSA complex at the electrode surface and decreasing of k_s may be attributed to the lower rate of electron transfer of VB7 in the form of VB7–BSA complex.

3.2.2. Linear sweep and differential pulse voltammetric studies

The LSVs (Fig. 5A) and DPVs (Fig. 5B) of VB7/BSA mixtures in a TBS (0.05 mol L^{-1}, pH 7.4) collected at a MWCNTs/GCE, indicated that the anodic peak current decreased continually and the peak potential shifted a little to more positive values with the addition of BSA. The peak current from this VB7 reaction did not disappear completely with the increase of the BSA concentration; this is unexpected if a competitive adsorption occurred at the electrode. It has been observed, that when an interaction of some biopolymers such as hemoglobin, albumin and DNA with small molecules takes place at quite a low protein concentrations and a short accumulation time, only about 10% of the electrode surface may be covered; this implies that very little competitive adsorption of small molecules can occur [30]. The decrease in peak current without any changes in the electrochemical parameters suggested the formation of an electroinactive VB7–BSA complex because VB7 becomes embedded within the BSA structure, which results in the decrease of the equilibrium concentration of VB7 in solution. However, there is another possible explanation for these observations, and it involves the possible unfolding of the BSA protein as the concentration of the ligand increases. As a result, the protein structure unravels, and this provides pathways for ligands to access the tryptophan or tyrosine residues, which then can be oxidized at MWCNTs/GCE [31].

3.2.3. Determination of binding constant of VB7 to BSA

In this section, the binding behavior of VB7 to BSA/MWCNT/GCE was measured by recording the cyclic voltammograms of VB7 at various concentrations (not shown). It was observed that the peak current increased by increasing the VB7 concentration (C_{VB7}) and then trended to saturation values, as expected with the shape of Langmuir adsorption. Thus the adsorption thermodynamics follows equation [32]:

$$C_{VB7}/I = (1/K_b I_{max}) + (C_{VB7}/I_{max}) \quad (6)$$

where I, I_{max}, and K_b are the peak current, maximum peak current, and the binding constant at BSA/MWCNT/GCE surface, respectively. Regression of C_{VB7}/I on C_{VB7} at BSA/MWCNT/GCE obeyed the following equation: $C_{VB7}/I = 7.416 + 5555.56\ C_{VB7}$ and K_b value can be obtained from the intercept of this equation as 4.12×10^4 mol^{-1} L.

3.3. Analysis of fluorescence quenching mechanism of BSA by VB7

BSA has two tryptophan (Trp) residues that possess intrinsic fluorescence: Trp-212, located within a hydrophobic binding pocket of the protein, and Trp-134, located on the surface of the molecule. Tryptophan emission dominates the BSA fluorescence spectrum in the UV region. When other molecules interact with BSA, Trp fluorescence may change depending on the impact of such interaction on the fluorophore–quencher complex [33]; this is often manifested in the decrease of the quantum yield of fluorescence from the fluorophore i.e. the BSA, and can be induced by a variety of molecular interactions with the quencher molecule. Fluorescence quenching refers to any process, which decreases the fluorescence intensity of a sample, and quenching mechanisms are usually classified as dynamic or static. They are distinguished by their different temperatures and viscosities dependence; thus, dynamic quenching depends on diffusion, and therefore, the biomolecular quenching constants are expected to increase with increasing temperature. In contrast, increased temperature is likely to result in lower values of the static quenching constants.

For fluorescence quenching, the decrease in intensity is usually described by the well-known Stern–Volmer equation [34]

$$F_0/F = 1 + K_{SV}[Q] \quad (7)$$

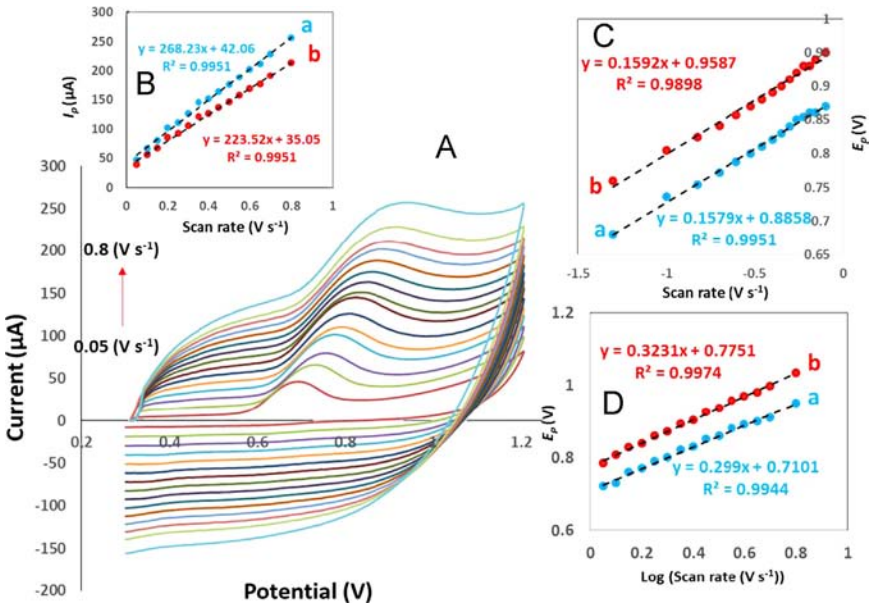


Fig. 4. (A) Cyclic voltammograms of 0.10×10^{-3} mol L^{-1} VB7 at BSA/MWCNTs/GCE in TBS (0.05 mol L^{-1}, pH 7.4) at different scan rates, and (B) The plots of peak currents vs. scan rate for (a) free VB7 (at MWCNT/GCE) and (b) bound VB7–BSA (at BSA/MWCNTs/GCE). (C) and (D) The variations of peak potential vs. υ and log υ for (a) free VB7 and (b) bound VB7–BSA, respectively.

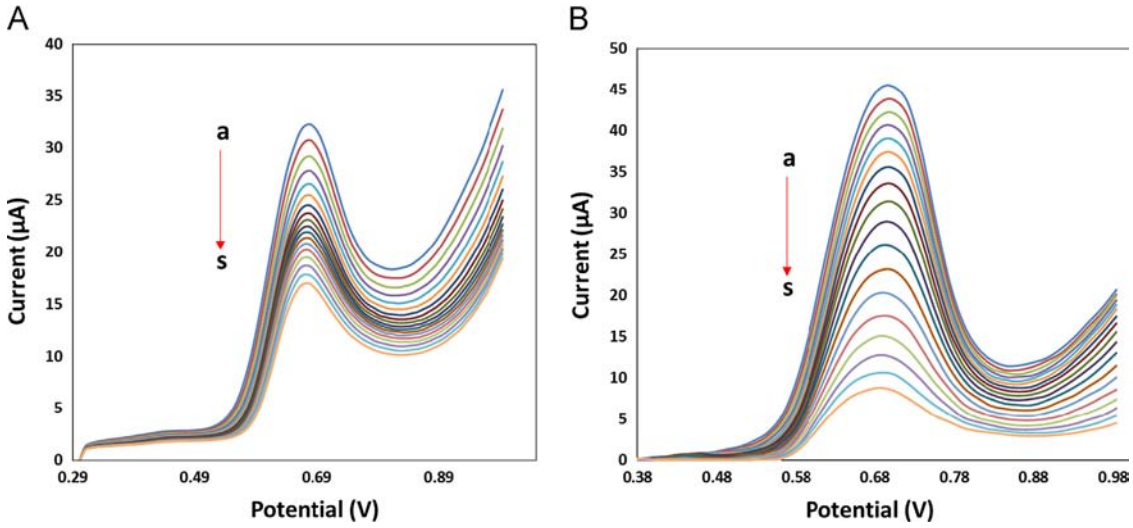


Fig. 5. (A) The LSVs of VB7 (4.0×10^{-4} mol L^{-1}) in TBS (0.05 mol L^{-1}, pH 7.4) in the presence of increasing concentrations of BSA in the range of 0.0–4.0×10^{-4} mol L^{-1}, and (B) Typical DPVs of VB7 (5.5×10^{-4} mol L^{-1}) in TBS (0.05 mol L^{-1}, pH 7.4) in the presence of increasing concentrations of BSA in the range of 0.0–5.5×10^{-4} mol L^{-1}.

where F_0 and F denote the steady-state fluorescence intensities in the absence and in the presence of the quencher. K_{SV} is the Stern–Volmer quenching constant, and [Q] is the concentration of the quencher. The degree of fluorescence quenching as a function of temperature when VB7 was added to BSA, was clearly discernable (Fig. 6A). The values of K_{SV} (Table 1) decreased with increase in temperature, which indicated that the probable quenching mechanism of this interaction was initiated by the formation of a complex rather than by dynamic collision.

3.4. UV–vis studies of VB7–BSA interactions

The interaction of VB7 with BSA was also investigated by UV–vis absorption titration in TBS (0.05 mol L^{-1}, pH 7.4) by maintaining the VB7 concentration constant but changing the BSA concentration. As shown in Fig. 6B, an absorbance peak at 280 nm is shown by VB7 in TBS (0.05 mol L^{-1}, pH 7.4) with the addition of BSA into VB7 solution, the absorption at 280 nm is increased gradually (hyperchromism), and two new absorption peaks at 254, 324 nm is remarkably forming. Based on the above results, we suggested that the alterations in UVvis spectra maybe related to interactions of VB7 with BSA.

Further discussion of the VB7/BSA interaction on the basis of direct observations of the measured profiles was difficult, and multivariate analysis previously discussed was applied to extract further information, especially as function of concentration of the VB7 and BSA reactants.

3.5. Interpretation of the MCR-ALS results

As previously discussed in detail (Section 2.6), the ten individual data matrices obtained from DPV, LSV, CV, F, and UVvis in Figs. 3 and 5–7 were combined into an augmented data matrix (first term of Eq. (2)), and then this augmented matrix was submitted for simultaneous resolution by the MCR-ALS (Eq. (2)) as a powerful chemometric tool. The intention was to extract

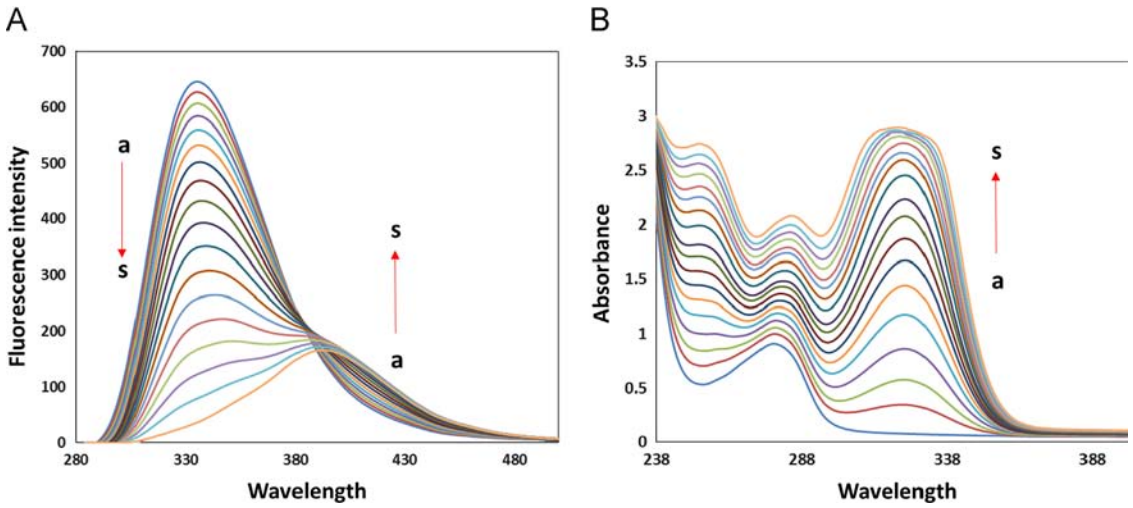


Fig. 6. (A) Fluorescence emission spectra of BSA (1.0×10^{-7} mol L^{-1}) in TBS (0.05 mol L^{-1}, pH 7.4) in the presence of increasing concentrations of VB7 in the range of 0.0–5.0×10^{-7} mol L^{-1}, λ_{ex}= 270.0 nm, and (B) UVvis absorption spectra of 1.0×10^{-6} mol L^{-1} VB7 in TBS (0.05 mol L^{-1}, pH 7.4) in the presence of increasing concentrations of BSA in the range of 0.0–1.0×10^{-6} mol L^{-1}.

Table 1
Stern–Volmer quenching constants at different temperatures for the interaction of VB7 with BSA.

T (K)	K_{SV}($\times10^4$ L mol^{-1})	R^a
298	4.78	0.9988
304	4.23	0.9991
310	3.88	0.9961

[a] Linear correlation coefficient.

information regarding: (i) any BSA–$VB7_m$ complex, and (ii) the relative concentrations of the various reactant and product species. First, the number of contributions to the augmented matrix was determined by SVD and here, the SVD detected four components. These four components may be related to free VB7, free BSA and two BSA–$VB7_m$ complex spices. The second step in the MCR-ALS method, is finding an initial estimate for either pure spectra or voltammograms, which can be obtained by the use of EFA or simple-to-use interactive self-modeling mixture analysis (SIMPLISMA) [35,36]. EFA is usually used to estimate the concentration profiles of the species involved in an evolutionary chemical process whereas SIMPLISMA is mainly used to obtain an estimate of the pure instrumental responses such as pure spectra or pure voltammograms. Since the data matrices in this study do not possess variables in both directions and concentration profiles apply here, initial estimates for MCR-ALS were obtained here by EFA. EFA was basically designed to work with full rank two-way data sets and straightforward analysis of rank-deficient matrix does not provide useful information. To overcome this limitation, de Juan et al. [37] have proposed an evolution of the original algorithm. This new approach is based on a two-step strategy. First, rotational ambiguity is reduced by matrix augmentation. The augmented data matrix, is formed row- and column-wise augmented matrix. Then, EFA is applied to the unfolded full rank augmented data set eventually providing information about contributions that are otherwise hidden. PCA was also employed to select the appropriate number of components to describe the four systems, and it was found that the first four PCs explained 99.9% of the total data variance in the combined matrix. Thus, both the EFA and PCA methods estimate the same number of factors or chemical species involved.

One of the advantages of MCR-ALS rather than the other iterative methods such as iterative target transformation factor analysis (ITTFA) is that in iteration process some constraints should be applied on the data matrix, which results in obtaining more reliable results. It should be noted that due to the presence of CV data which contain negative values, the non-negativity constraint was only employed on concentration profiles. Unimodality constraint was applied to signal profiles. Applying a closure constraint to the matrices obtained at different concentration levels is impossible.

By applying the mentioned constraints, the ALS optimization was started. As previously mentioned, the lof which is defined as the difference between the input data ($\boldsymbol{D}$) and the data reproduced from the product ($\boldsymbol{CS}^T$) obtained by the MCR-ALS, was used as a parameter to evaluate the goodness of fit of the model. In this work, the best lof value was found to be 6.61% which implies that almost all of the variability in the experimental data presented as a product of the extracted signals and the concentration profiles, is explained.

The results of MCR-ALS are shown in Fig. 8. Fig. 8A shows that concentration of VB7 is decreasing and two new complex species are forming upon the addition of BSA. As can be seen, the concentration of one of these complex spices (red dashed line) increased sharply and reached to a maximum at the ratio, $r_{BSA/VB7}\sim1$. Therefore, it may be concluded that this species is a 1:1 BSA–VB7 complex species. On the other hand, Fig. 8A shows that with the mole-ratio method, the concentration of the second BSA-VB7 complex spices (dark blue dashed line) increased slowly to $r_{BSA/VB7}\sim0.5$ and reached equilibrium position as the concentration of BSA increased. Thus, these results indicated that the second spices is a 1:2 BSA–VB7 complex species. The same conclusions about stoichiometries of the complex spices could be obtained from Fig. 8B.

The pure voltammetric and spectral profiles extracted by the application of the MCR-ALS (Fig. 8C–G) provided new qualitative information about the nature of the complex spices. From these figures the valuable information about the nature of the involved complex species in each technique could be obtained. According to these results, it is clear that both complex species are electroactive at the MWCNTs/GCE. The measured and extracted pure spectral and voltammetric profiles agreed reasonably well. The extraction of the voltammetric profiles and their reasonable agreement with the measured data indicated that the MCR-ALS method was applied successfully. The BSA measured curve suggested that the protein in its original structural format was electroinactive, and the extracted profile approximated this profile no obvious extracted bands were evident. However, the complexes' curves, unlike that for the BSA, indicated the presence of electroactive species. To achieve this result

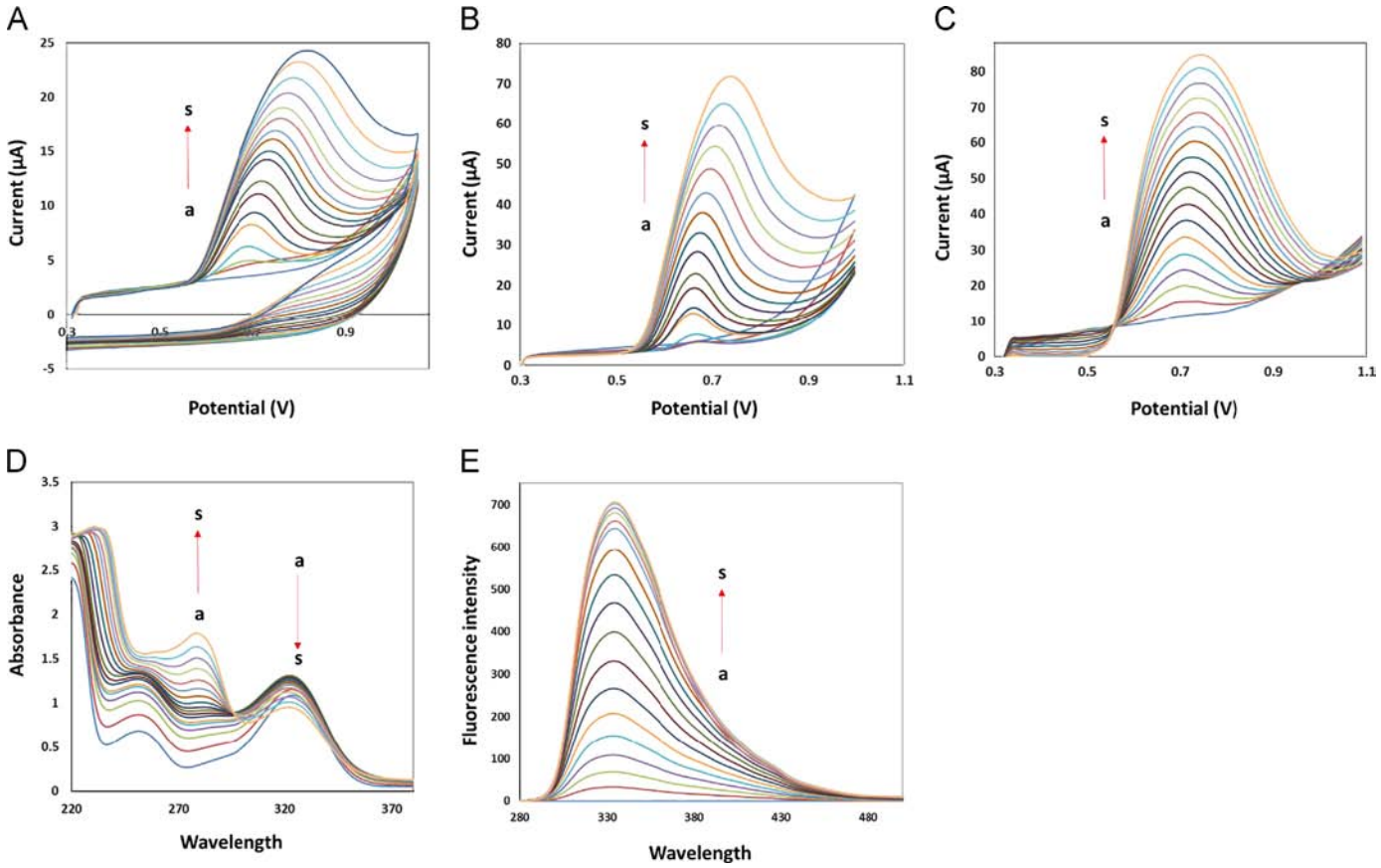


Fig. 7. Response profiles obtained from different experiments described in Section 2.5. (A) Experiment 6, (B) Experiment 4, (C) Experiment 2, (D) Experiment 10, and (E) Experiment 7.

for the reaction occurring at electrode's surface, it is necessary for the potentially oxidizable tryptophan and tyrosine side chain residues to be accessible. This would be facilitated somewhat by an unfolded rather than the originally folded structure of the BSA protein. Therefore, it seemed reasonable to suggest that the binding of the three VB7 molecules facilitated the unfolding of the BSA structure. The plot with coincided experimental and theoretical absorbance data that has been represented in Fig. 8H which is a strong evidence for high quality of fitting process.

3.6. MCR-BANDS analysis to study the extent of rotational ambiguities

One of the advantages of MCR rather than the other bilinear methods like principle component analysis (PCA) and SVD, is its physical meaningful solution due to the use of "natural" constraints [38]. However, in some data analysis, unfortunately MCR method suffers from the existence of ambiguities in the solution. Because of this fact, instead of a unique solution, a band of feasible solutions fitting equally well the experimental data can be obtained [39]. Thus, an important point when using MCR methods is finding a unique solution with interpretable and reliable means to explain the measured experimental data. In 2001, Tauler proposed the method of MCR-BANDS, which was closed to Gemperline's concept to estimate the feasible solutions [40]. This method is based on the calculation of maximum and minimum of relative contribution of every component in the mixture [38,40]. Although Tauler-Gemperline method could not measure correctly the rotational ambiguity [41] MCR-BANDS can provide a good indication of the extent of the rotational ambiguity [42].

In the present study, the MCR-ALS method assisted to obtain reliable results which were in agreement with experimental observations. However, to evaluate the existence of rotational ambiguities in the obtained results, the MCR-BANDS method was used. MCR-BANDS was applied to the data matrix described by the profiles of MCRALS results. Also, the same constraints as those used in MCR-ALS were applied for MCR-BANDS. The maximum and minimum values of the relative contribution function (f^{max} and f^{min}, respectively) were obtained for BSA (f^{max}= 0.271 and f^{min}= 0.271), VB7 (f^{max}=0.6907 and f^{min}=0.6907), BSA-VB7 (f^{max}=0.4289 and f^{min}=), and BSA-$VB7_2$ (f^{max}=0.2521 and f^{min}=0.2521). Interestingly, there is no difference between the f^{max} and f^{min} values for all the resolved components. It means that practically there is no remaining rotation ambiguity [38]. Elimination of rotational ambiguity could be attributed to the application of appropriate constraints and augmentation. When matrix augmentation was ignored, significant differences between the corresponding f^{max} and f^{min} values were observed (the data were not shown). Based on previous reports, one of the approaches can be used to avoid rotational ambiguity in MCR methods is the use of local rank and selective constraints apart from "natural" constraints [35,43]. It seems that, for these electrochemical data, the use of this kind of constraints, i.e. selectivity in the iterative procedure leads to a unique solution.

3.7. Hard-modeling approach

In the case of hard-modeling approaches, a model is applied to guide the decomposition of matrix $\boldsymbol{D}$ following Eq. (1). As an example, in the case of protein-drug interaction, the model

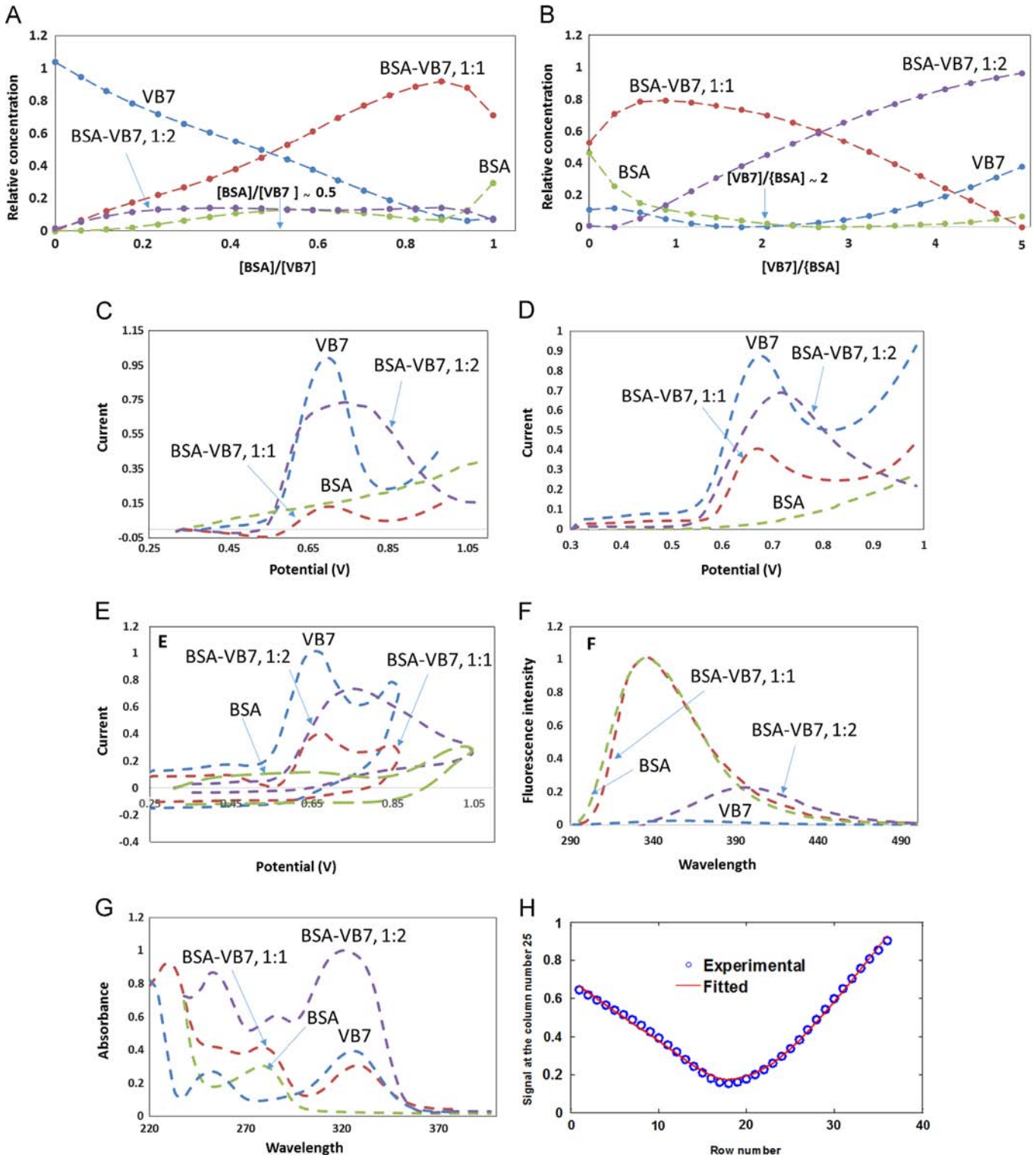


Fig. 8. The results of applying MCR-ALS to augmented matrix: (A and B) Extracted concentration profiles. (C-G) Extracted signal profiles of different species involved in DPV, LSV, CV, F and UVvis experiments, respectively. (H) The plot of experimental (points) and fitted (calculated) data (line).

includes the stoichiometry of the species formed, as well as initial trial value for the binding constant. This value is used to build an initial estimation of the concentration profiles included in ***C***. Once this estimation is obtained, a least squares fit is performed to obtain the pure spectra in $\boldsymbol{S}^{T}$ that best match the concentration profiles in ***C*** and the data in ***D***. A residual matrix ***E*** is then calculated from the difference between the data in ***D*** and the reproduced data matrix. The optimization procedure continues by tuning the stoichiometry of the proposed species until a desired level of residuals ***E*** is reached. A more detailed explanation of the mathematical basis of the algorithms used in these calculations can be found in Dyson et al. [44].

EQUISPEC, a hard-modeling algorithm, was applied to an augmented matrix (combined spectroscopic and voltammetric

data) to compute the binding constants and also verify the results of Section 3.2.3. The results of this study are shown in Table 2. As can be seen, there is a good agreement between the binding constant values computed by EQUISPEC and also with the results reported at Section 3.2.3.

3.8. Molecular docking studies

In this study, the MVD software was used to realize the binding mode of VB7 at the active site of BSA (see Fig. 9A–C). The main aspect for the ligand docking postures was considering the effective interaction of the drug with the various amino acid residues in the active site. The binding site were obtained as Val 546, Phe 550, Leu 574, Phe 508, Thr 578, Ala 527, Leu 582, Leu 531, Val 575, Phe 506, Gln 579, Lys 535, His 534, and Phe 501. LIGPLOT was used to explore the hydrogen bonds interactions between BSA and VB7 as shown in Fig. 9D. Two hydrogen bonding interactions are observed between VB7 and Thr 578 and Gln 579 of BSA, with a distance of 2.99 and 3.00 Å, respectively.

3.9. Analytical applications

3.9.1. Analytical characterizations

The BSA measured curve suggested that the protein in its original structural format was electroinactive, and the extracted profile approximated this profile no obvious extracted bands were evident. Therefore, developing an electroanalytical method for its determination is sensible. Since DPV has a much higher sensitivity than CV, it was used to estimate a lower limit of detection (LOD). Under the optimized conditions for DPV (step potential 0.005 V, modulation amplitude 0.025 V, modulation time 0.05 s, interval time 0.5 s, and scan rate 0.01 $V\,s^{-1}$), the MWCNTs/GCE in the presence of 0.5×10^{-6} mol L^{-1} VB7 in TBS (0.05 mol L^{-1}, pH 7.4) (Fig. 10, curve a) detects BSA in a concentration range of 0.5–35.0×10^{-9} mol L^{-1} (Fig. 10, curves b-l) with a limit of detection (LOD, $3S_b/b$, S_b is the standard deviation ($n=6$) of the blanks, and b is the slope value of the respective calibration graph) of 0.22×10^{-9} mol L^{-1}. Moreover, the sensitivity for BSA detection calculated from the slope of the respective calibration graph was to be 0.0404 μA nM^{-1}, indicating the high sensitivity of the proposed biosensing system.

3.9.2. Stability, repeatability, and reproducibility

Stability of the MWCNTs/GCE was tested by keeping the electrode in TBS (0.05 mol L^{-1}, pH 7.4) for 10 days and then the CVs were recorded and compared with the CVs obtained before immersion. The results indicated that the peak current changed only slightly which indicates that it has good stability. The stability of MWCNTs/GCE over time was checked during a period of 2 months. In between measurements the sensor was kept at room temperature in the dry state. A graph of I_p vs. days reveals that a small change in the DPV signal (approx. 5%) was observed after 2 months of storage. These results indicate that MWCNTs/GCE is significantly stable and has good capacity to perform repeated measurement for 2 months. In order to study the repeatability of the electrode preparation procedure, six modified electrodes based on the same fabrication procedure were prepared and used for the determination of 20.0×10^{-9} mol L^{-1} BSA. The *RSD* for the peak currents for all the six electrodes was calculated to be 3.1%. The reproducibility of the proposed method was checked by determining the *RSD* for 10 replicate measurements on a single electrode in 20.0×10^{-9} mol L^{-1} BSA. It was found out to be 2.3%. These results indicate that the modified electrode has high repeatability and reproducibility in both the preparation procedure and the DPV determinations.

Table 2
Results of applying EQUISPEC.

Analyzed matrix	$K_b(\times10^4$ L $mol^{-1})$
$\left[\boldsymbol{D}^{VB7}_{DPV}\boldsymbol{D}^{VB7}_{LSV}\boldsymbol{D}^{VB7}_{CV}\boldsymbol{D}^{VB7}_{F}\boldsymbol{D}^{VB7}_{UVvis}\right]$	5.98×10^4
$\left[\boldsymbol{D}^{BSA}_{DPV}\boldsymbol{D}^{BSA}_{LSV}\boldsymbol{D}^{BSA}_{CV}\boldsymbol{D}^{BSA}_{F}\boldsymbol{D}^{BSA}_{UVvis}\right]$	4.01×10^4
$\begin{bmatrix}\boldsymbol{D}^{VB7}_{DPV}\boldsymbol{D}^{VB7}_{LSV}\boldsymbol{D}^{VB7}_{CV}\boldsymbol{D}^{VB7}_{F}\boldsymbol{D}^{VB7}_{UVvis}\\ \boldsymbol{D}^{BSA}_{DPV}\boldsymbol{D}^{BSA}_{LSV}\boldsymbol{D}^{BSA}_{CV}\boldsymbol{D}^{BSA}_{F}\boldsymbol{D}^{BSA}_{UVvis}\end{bmatrix}$	4.66×10^4

3.9.3. Interference study

Possible interference for the detection of BSA at the MWCNTs/CCE was investigated by the addition of various ions to TBS (0.05 mol L^{-1}, pH 7.4) in the presence of 0.5×10^{-6} mol L^{-1} VB7 and 10.0 nM BSA. Common interference such as L-arginine (10-fold), D-tryptophan (15-fold), L-glutamine (8-fold), L-leucine (10-fold), Citronensaure-1-hydrate (12-fold), glucose (20-fold), vitamin B_6 (10-fold), tyrosine (12-fold), and cysteine (15-fold) had no effective interference with the current response of 10.0 nM BSA (signal change $<7\%$), suggesting that this proposed method has good selectivity toward determination of BSA in biological samples.

3.9.4. Validation of the proposed method

The validity of the method was demonstrated by the analysis of both synthetic and real samples. Synthetic samples were prepared based on the interferences of foreign substances and BSA. The analytical results of the determination of BSA in synthetic samples are summarized in Table 3. The present method also demonstrates the capability to detect and quantify BSA in biological samples such as serum samples obtained from Holstein cows. The results in Table 3 showed close agreement to those obtained by our method and the cellulose acetate electrophoresis method. Compared with the cellulose acetate electrophoresis method, the proposed sensor is simple, easily implemented, and has low-cost and fast response. Thus, accurate and successful determination of BSA in biological fluids as demonstrated here may allow one to propose the present sensor as a promissory, cheap and accessible alternative for the clinical analysis of protein.

4. Conclusion

In this study, the interaction of VB7 with BSA was investigated at a GCE modified with MWCNTs for the first time. The voltammetric studies revealed a remarkable decrease in anodic current of VB7 upon the addition of BSA with positive shift in peak potentials which indicates the interaction of VB7 with BSA. The MWCNTs/GCE showed an effective electrocatalytic activity towards VB7 oxidation as well as enhancement of the microscopic area and currents in voltammetric investigations. The binding of VB7 to BSA results in a series of changes in electrochemical behavior and spectral characteristics, confirming that the interaction between VB7 and BSA. The application of the MCR-ALS for the resolution of the expanded data matrix produced the estimates of the pure signals of VB7 and BSA which were in good agreement with the measured responses. The results showed that the MCR-ALS is a powerful chemometric tool to resolve complex combined data and showed significant potential for investigating the mechanism of the interaction of BSA with targeting small compounds at the molecular level. Combination of voltammetric and spectroscopic methods is of potential importance in understanding the mechanism of binding of small molecules to biological macromolecules. Finally, DPV technique was applied for determination of BSA in biological

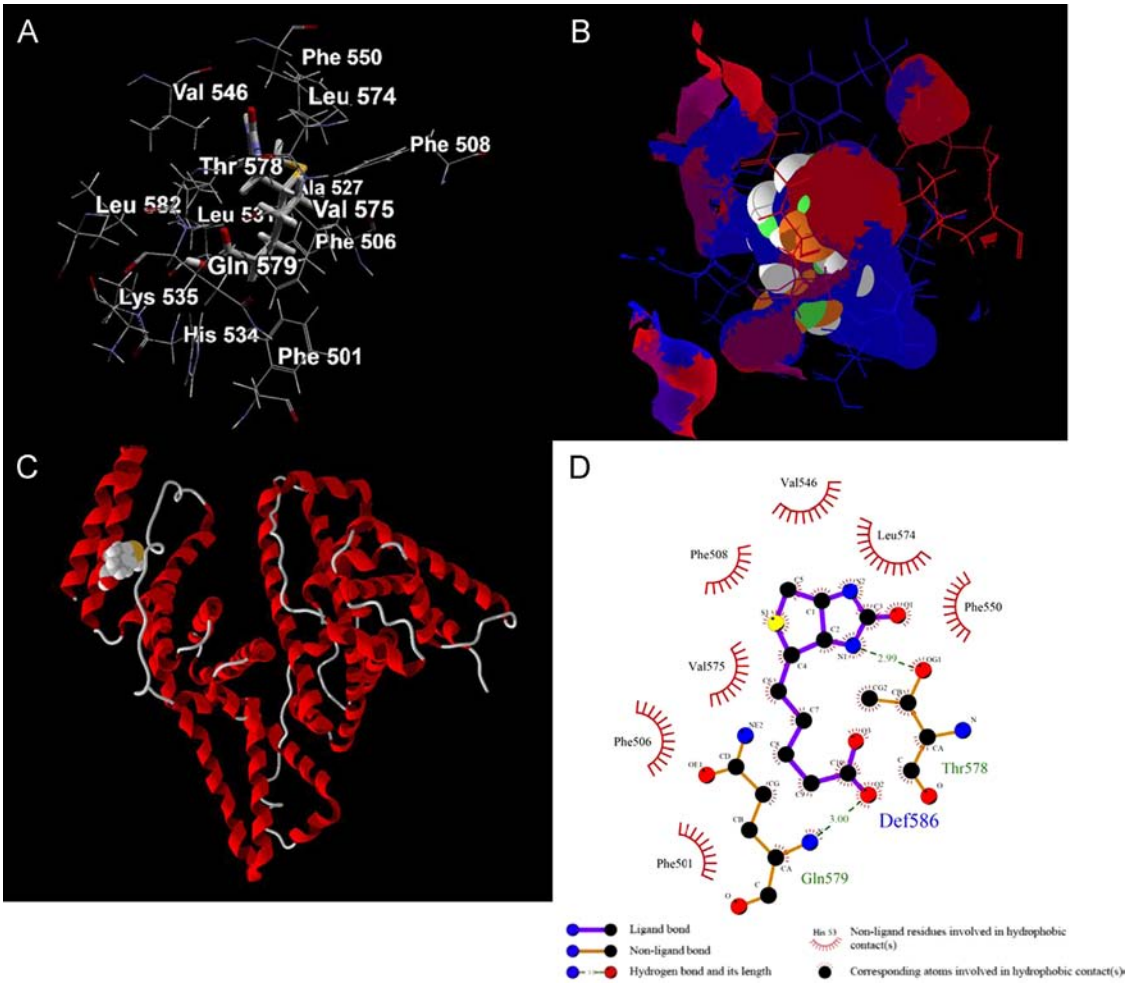


Fig. 9. Computer-generated models of VB7 bound to BSA: (A) The residues of BSA are represented by sticks (thin) and the VB7 is represented by sticks, (B) The binding pocket of protein is represented by hydrophobic interaction and VB7 is shown as CPK model, (C) The VB7 is shown as CPK and BSA is represented by solid ribbon, and (D) The output of LIGPLOT program.

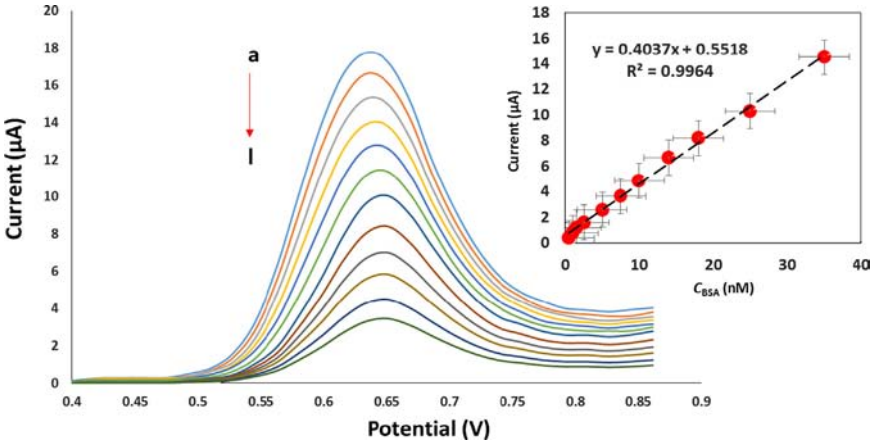


Fig. 10. Differential pulse voltammograms of 0.5×10^{-6} mol L^{-1} VB7 (curve a) in TBS (0.05 mol L^{-1}, pH 7.4) at MWCNTs/GCE in the presence of increasing concentration of BSA (curves b-l: 0.5–35.0×10^{-6} mol L^{-1}). Inset: Variation of the peak current (I) vs. BSA concentration.

samples such as serum samples. The proposed methodology provided a new, sensitive, selective electrochemical sensor utilizing unique properties of MWCNTs such as high specific surface area, electrocalytic and adsorptive properties. MWCNTs modified GCE resulted in catalytic effects toward the electro-oxidation of VB7 since it enhances the oxidation peak currents and lowers the oxidation potential. Therefore, simple and applicable electrochemical sensor allowed the successful determination of BSA in biological samples.

Table 3
The results for the determination of BSA in serum samples obtained from Holstein cows.

Sample	This study	Cellulose acetate electrophoresis
1	$1.4\ (\pm 0.03)\times 10^{-7}$ mol L^{-1}	$1.45(\pm 0.02)\times 10^{-7}$ mol L^{-1}
2	$2.1(\pm 0.06)\times 10^{-7}$ mol L^{-1}	$2.14(\pm 0.05)\times 10^{-7}$ mol L^{-1}
3	$1.8(\pm 0.04)\times 10^{-7}$ mol L^{-1}	$1.88(\pm 0.04)\times 10^{-7}$ mol L^{-1}

Total value was obtained by multiplying the detected value by 100 (dilution factor).

Acknowledgments

The authors gratefully acknowledge the financial support of this study by Razi University Research Council, UNL, CONICET and ANPCyT.

References

[1] E. Livaniou, D. Costopoulou, I. Vassiliadou, L. Leondiadis, J.O. Nyalala, D.S. Ithakissios, G.P. Evangelatos, J. Chromatogr. A 881 (2000) 331–343.
[2] C.G. Staggs, W.M. Sealey, B.J. McCabe, A.M. Teague, D.M. Mock, J. Food Compos. Anal. 17 (2004) 767–776.
[3] R.J. Stratton, T.R. Smith, Best Pract. Res. Clin. Gastroenterol. 20 (2006) 441–466.
[4] H. Malonga, J.F. Neault, H.A. Tajmir-Riahi, DNA Cell Biol. 25 (2006) 393–398.
[5] C. Mancuso, A. Bonsignore, C. Capone, E. Di Stasio, G. Pani, Antioxid. Redox Signal. 8 (2006) 487–494.
[6] C.H. Lu, H.H. Yang, C.L. Zhu, X. Chen, G.N. Chen, Angew. Chem. Int. Ed. 48 (2009) 4785–4787.
[7] H.X. Chang, L.H. Tang, Y. Wang, J.H. Jiang, J.H. Li, Anal. Chem. 82 (2010) 2341–2346.
[8] C. Bertucci, S. Cimitan, A. Riva, P. Morazzoni, J. Pharm. Biomed. Anal. 42 (2006) 81–87.
[9] N. Li, K.A. Li, S.Y. Tong, Anal. Lett. 28 (1995) 1763–1774.
[10] H.S. Soedjak, Anal. Biochem. 220 (1994) 142–148.
[11] N. Li, K.A. Li, S.Y. Tong, Anal. Biochem. 233 (1996) 151–155.
[12] C.Q. Ma, K.A. Li, S.Y. Tong, Anal. Lett. 30 (1997) 739–752.
[13] A.C. Wallace, R.A. Laskowski, J.M. Thornton, Protein Eng. 8 (1995) 127–134.
[14] ⟨http://www.ub.es/gesq/mcr/mcr.htm⟩.
[15] M. Esteban, C. Arino, J.M. Dıaz-Cruz, M.S. Diaz-Cruz, R. Tauler, Trends Anal. Chem. 19 (2000) 49–61.
[16] M. Esteban, C. Arino, J.M. Dıaz-Cruz, Trends Anal. Chem. 25 (2006) 86–92.
[17] H. Gampp, M. Maeder, C.J. Meyer, A.D. Zuberbühler, Talanta 32 (1985) 1133–1139.
[18] H. Abdollahi, V. Mahdavi, Langmuir 23 (2007) 2362–2368.
[19] S. Perez, M.J. Culzoni, G.G. Siano, M.D. Gil Garcia, H.C. Goicoechea, M.M. Galera, Anal. Chem. 81 (2009) 8335–8346.
[20] M. Vives, R. Gargallo, R. Tauler, Anal. Chem. 71 (1999) 4328–4337.
[21] C.B. Zachariassen, J. Larsen, F. Van den Berg, R. Bro, A. De Juan, R. Tauler, Chemom. Intell. Lab. Syst. 83 (2006) 13–25.
[22] R. Tauler, A. Izquierdo-Ridorsa, E. Casassas, Chemom. Intell. Lab. Syst. 18 (1993) 293–300.
[23] R. Tauler, A.K. Smilde, B.R. Kowalski, J. Chemometr. 9 (1995) 31–58.
[24] R.N. Goyal, A.B. Toth, G. Dryhurst, N.T. Nguyen, Bioelectrochem. Bioenerg. 9 (1982) 39–60.
[25] A.J. Bard, L.R. Faulkner, Electrochemical Methods: Fundamentals and Applications, Second ed., Wiley, New York, 2001.
[26] E. Laviron, J. Electroanal. Chem. 52 (1974) 355–393.
[27] Y.N. Ni, X. Zhang, S. Kokot, Spectrochim. Acta A 71 (2009) 1865–1872.
[28] M. Shap, M. Petersson, K. Edstrom, J. Electroanal. Chem. 95 (1979) 123–130.
[29] E. Laviron, J. Electroanal. Chem. 101 (1979) 19–28.
[30] S.S. Kalanur, U. Katrahalli, J. Seetharamappa, J. Electroanal. Chem. 636 (2009) 93–100.
[31] B. Ojiha, G. Das, J. Phys. Chem. B 114 (2010) 3979–3986.
[32] X. Ju, Y.K. Ye, Y.L. Zhu, Electrochim. Acta 50 (2005) 1361–1367.
[33] D.M. Charbonneau, H.A. Tajmir-RIAHI, J. Phys. Chem. B 114 (2010) 1148–1155.
[34] J.R. Lakowicz, Principles of Fluorescence Spectroscopy, Second ed., Plenum Press, New York, 1999.
[35] J. Jaumot, R. Gargallo, A. Juan, R. Tauler, Chemom. Intell. Lab. Syst. 76 (2005) 101–110.
[36] A. Juan, R. Tauler, Crit. Rev. Anal. Chem. 36 (2006) 163–176.
[37] A. de Juan, A. Izquierdo-Ridorsa, R. Tauler, G. Fonrodona, E. Casassas, Biophys.J. 73 (1997) 2937–2948.
[38] J. Jaumot, R. Tauler, Chemom. Intell. Lab. Syst. 103 (2010) 96–107.
[39] H. Abdollahi, R. Tauler, Chemom. Intell. Lab. Syst. 108 (2011) 100–111.
[40] R. Tauler, J. Chemom. 15 (2001) 627–646.
[41] R. Rajkó, Anal. Chim. Acta 645 (2009) 18–24.
[42] H. Parastar, M. Jalali-Heravi, R. Tauler, Trends Anal. Chem. 31 (2012) 134–143.
[43] R. Manne, Chemom. Intell. Lab. Syst. 27 (1995) 89–94.
[44] R.M. Dyson, S. Kaderli, G.A. Lawrance, M. Maeder, A.D. Zuberbühler, Anal. Chim.Acta 353 (1997) 381–393.

Talanta 132 (2015) 366–372

Contents lists available at ScienceDirect

Talanta

journal homepage: www.elsevier.com/locate/talanta

Dispersive solid-phase microextraction and capillary electrophoresis separation of food colorants in beverages using diamino moiety functionalized silica nanoparticles as both extractant and pseudostationary phase

Feng-Jie Liu, Chuan-Ting Liu, Wei Li, An-Na Tang*

Research Center for Analytical Sciences, College of Chemistry, Nankai University, 94 Weijin Road, Tianjin 300071, China

ARTICLE INFO

Article history:
Received 27 June 2014
Received in revised form
2 September 2014
Accepted 7 September 2014
Available online 28 September 2014

Keywords:
Dispersive solid-phase microextraction
Capillary electrophoresis
Diamino moiety functionalized silica nanoparticles
Food colorants

ABSTRACT

In this work, a new method for the determination of food colorants in beverage samples is developed, using diamino moiety functionalized silica nanoparticles (dASNPs) as both adsorbents in dispersive solid-phase microextraction (dSPME) and pseudostationary phases (PSPs) in capillary electrophoresis (CE) separation. dASNPs were firstly used as adsorbents for the preconcentration of four colorants by the dSPME process. After that, colorants were efficiently separated by CE using 30 mM phosphate buffer (pH 6.0) containing 2 mM β-CD and 0.9 mg/mL dASNPs as additives. All factors influencing dSPME and CE separations were optimized in detail. The investigated analytes showed good linearities with correlation coefficients (R^2) higher than 0.9932. The limits of detection for the four food colorants were between 0.030 and 0.36 mg/L, which are lower than those reported previously. The established method was also used to analyze four colorants in beverage samples with recoveries ranging from 82.7% to 114.6%. To the best of our knowledge, this is the first time to use NPs both as extractants in dSPME and pseudostationary phases in CE for the analytical purpose.

© 2014 Elsevier B.V. All rights reserved.

1. Introduction

Food colorants, natural or synthetic, are commonly added to foods to compensate for the loss of natural colors that are destroyed during processing and storage, and to provide the desired colored appearance. However, some synthetic colorants may be pathogenic, especially when they are consumed in excess. At present, about ten kinds of synthetic colorants are permitted to be used as food additives in some countries including China, and their maximum permissible amounts in food are rigidly specified [1] to safeguard consumers' interests. As a result, the analysis of trace colorants in food is of great importance.

Several methods have been widely used to analyze the colorants in food, such as thin-layer chromatography (TLC) [2], gas chromatography (GC) [3], high-performance liquid chromatography (HPLC) [4,5] and HPLC–mass spectrometry (LC–MS) [6]. Among them, HPLC is the most widely used method because it can offer good repeatability and acceptable sensitivity with the traditional UV–vis detection. However, most HPLC methods established for colorant analysis suffer from limited separation ability, and are time consuming especially when the simultaneous determination of a broad range of food colorants is needed. As an alternative method, capillary electrophoresis (CE) has also been used for the analysis of food colorants due to its many advantages, such as high column efficiency, short analysis time and minimal amounts of samples [7–12]. However, lower detection sensitivity, limited selectivity and severe matrix interferences are still drawbacks of the traditional CE technique, which greatly restrain its further use in real sample analysis.

In the past decade, nanoparticles (NPs) have been used in conjunction with CE [13,14], in which they usually worked as pseudostationary phases (PSPs). When NPs are used as PSPs, they are suspended in the electrolytes and are continuously pumped through the capillary by the electro-osmotic flow (EOF) during separation, which guarantees that an entirely fresh dynamic stationary phase is used for every analysis. NPs can also serve as efficient platforms with large surface area for multiple interactions, leading to enhanced separation selectivity and column efficiency. NPs used in CE usually include polymer NPs [15], gold NPs [16], molecularly imprinted polymer NPs [17], latex NPs [18], carbon nanotubes [19] and silica NPs [20–22] etc.

Dispersive solid-phase microextraction (dSPME) [23] is based on the solid-phase extraction (SPE) methodology. In dSPME, the extraction of the analytes is fulfilled by the addition of small

* Corresponding author.
E-mail address: tanganna@nankai.edu.cn (A.-N. Tang).

http://dx.doi.org/10.1016/j.talanta.2014.09.014
0039-9140/© 2014 Elsevier B.V. All rights reserved.

amount of dispersive solid adsorbents in bulk solution. After extraction, the adsorbents containing the retained analytes are settled by centrifugation or filtration, which are later washed with a small volume of solvent for the desorption of analytes. In the dSPME process, it is much easier for the target analytes to interact fully with the adsorbents, so higher adsorption capacities could be obtained in comparison with those in the traditional SPE. Furthermore, the dSPME method is simple, rapid and cost-effective. Since its emergence, dSPME has received considerable attention and has been recognized as a promising sample pretreatment technique [24–26].

NPs have attracted much attention of the analytical scientists recently due to their higher specific surface area when used as the sorbent materials [27,28]. The introduction of NPs in dSPME will present additional advantages such as quicker mass transfer and shorter equilibrium time [29]. Recently, several kinds of NPs including gold nanoparticles [30,31], carbon nanoparticles [24,32,33], molecular imprinting nanoparticles [34,35] and magnetic nanoparticles [25,29,36] have been used as sorbent materials in dSPME.

In this work, we used dASNPs as sorbent materials in dSPME for the extraction of representative four food colorants: carminic acid, tartrazine, sunset yellow, brilliant blue. The four food colorants are water-soluble dyes with two or three sulfonic groups in their structures (Fig. S1). The pretreated samples were then separated by CE still using dASNPs as PSPs. Under optimized experimental conditions, four food colorants were baseline separated within 8 min. The obtained enrichment factors were 18.6, 18.7, 13.6 and 20.8 for carminic acid, tartrazine, sunset yellow and brilliant blue respectively. The present method was also applied for the determination of colorant additives in some fruit juice beverages with satisfactory results. Some articles concerning the electrophoretic analysis of sulfonated dyes were reported [37,38]. To the best of our knowledge, this is the first report on the use of NPs as both extractants and PSPs for the preconcentration and separation of analytes in real samples.

2. Experimental

2.1. Reagents and materials

All chemicals were analytical grade unless noted otherwise. Double-distilled water (DDW) purified by a Nanopure II system (Barnstead, NH, USA) was used throughout the experiment. Thiourea was purchased from Tianda Kewei (Tianjin, China). Phosphoric acid, sodium hydroxide, sodium dihydrogen phosphate, hydrochloric acid were purchased from Tianjin Guangfu Chemicals (Tianjin, China). Tetraethoxysilane (TEOS) (98%), N-(β-aminoethyl)-γ-aminopropyl triethoxysilane (dATES) were purchased from Guotai-Huarong New Chemical Materials (Zhangjiagang,China). Citric acid, ascorbic acid and benzoic acid were from Heowns Biochemical Technologies (Tianjin, China). β-CD was purchased from Shandong Xinda chemicals (Shandong, China). Malic acid, succinic acid, tartaric acid, tartrazine, sunset yellow, carminic acid and brilliant blue standard solutions were from National information center (Beijing, China).

dASNPs were synthesized according to the method reported previously by our lab [39]. Briefly, a total amount of 1.2 mL of ammonia was added to a conical flask in the presence of 25 mL of EtOH and 2.0 mL TEOS (~9 mmol) by slow stirring. After 24 h of reaction under stirring at 30 °C in thermostatic water bath, the functionalized reagents were added with extra TEOS with the volume ratio of dATES: TEOS=1:1 for particle co-condensation. The amount of functionalized reagents (dATES) added corresponds to approximately 5% (0.45 mmol) of the initial amount of TEOS. The reaction continued for another 24 h, and the particles thus formed were centrifuged and washed with ethanol and DDW repeatedly, then vacuum-dried at 80 °C for 6 h.

dASNPs thus formed are sphere-like, monodisperse and uniform in shape, with an average size of approximately 110 nm. as shown in Fig. 1A.

2.2. Apparatus and operating conditions for CE

TEM tests were carried out on a Philips Tecnai G20 at 200 kV (PHG, Amsterdam, Netherlands). A KH-50B ultrasonic cleaner (Kunshan Hechuang Instrumental, Kunshan, Jiangsu, China) and a QL-901 vortex (Haimen Kylin-Bell Lab Instruments Co., Jiangsu, China) were used to disperse dASNPs in background electrolyte or sample solutions. A TG16-WS centrifuge (Hunan Xiangyi Lab Instruments Co., Changsha, China) was used to centrifuge the samples. The zeta potential of dASNPs was determined with Zetasizer Nano ZS equipments (Malvern Instruments, Worces-tershire, UK). All CE experiments were carried out on a TH-3000 HPCE–HPLC amphibious system equipped with a UV detector and CXTH-3000 data handling software (Tianhui Instruments, Baoding, China). The detection wavelength was set at 220 nm unless noted otherwise. Fused-silica capillaries of 375 μm o.d. and 75 μm i.d. (Yongnian Optic Fiber Co, Hebei, China) were used throughout the experiment.

A capillary with the total length of 36 cm and the effective length of 27 cm was made by scraping off 3–5 mm of the polymer outside the capillary at an appropriate place. Prior to the first use, the capillary was successively rinsed by methanol, DDW, 1 mol/L NaOH, DDW, 1 mol/L HCl, DDW and phosphate buffer solution (PBS) for 20 min each. The EOF was determined by using thiourea as the neutral marker.

Separation voltage was set at 8 kV or −8 kV and current is 40 μA. Electrokinetic injection (−7 kV × 3 s) was selected as the injection mode throughout the experiment. 30 mM PBS (pH 6) with 0.9 mg/mL dASNPs and 2 mM β-CD was employed as background electrolyte solution.

2.3. Preparation of standard solution and food samples

Standard solutions of tartrazine (0.5 mg/mL), sunset yellow (0.5 mg/mL), brilliant blue (0.5 mg/mL) and carminic acid (1.0 mg/mL) were prepared in DDW and stored away from light at 4 °C in refrigerator. The working standard solutions with different concentration were prepared by stepwise diluting the standard solutions with PBS just before use. PBS was prepared by dissolving a certain amount of sodium dihydrogen phosphate in DDW and then adjusted to the appropriate pH value with 1 mol/L NaOH or concentrated

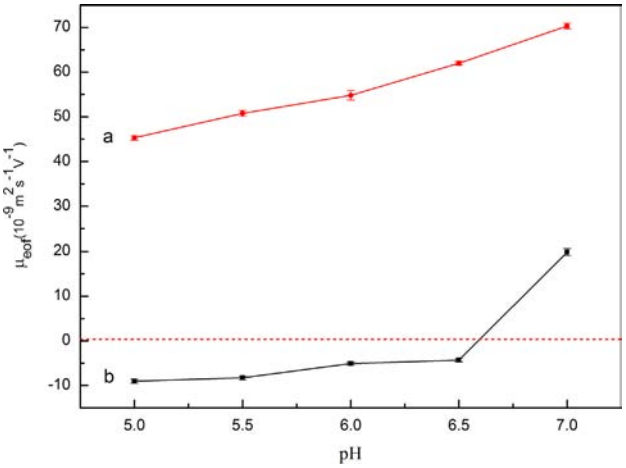


Fig. 1. The effect of buffer solution pH on EOF without dASNPs (a) and with dASNPS (b), (n=3).

H_3PO_4. Background electrolyte solutions were prepared by dissolving β-CD and dASNPs in PBS. Before use, all solutions were filtered through a 0.45 μm Nylon filter and degassed by ultrasonication.

The proposed method was applied to determine the food colorants in four beverage samples (Fruit juice 1–4) produced in Tianjin, China. All the samples were purchased from local supermarkets. The beverages were previously filtered through a 0.45 μm Nylon filter to remove the potential suspended particulate matter, and then diluted with DDW to 1:10, then adjusted to pH 2.5 with concentrated H_3PO_4 or 1 mol/L NaOH after degassed by ultrasonication.

2.4. dSPME procedure

The proposed extraction process is as follows: an aliquot of 9 mL of the aqueous standard solution (or the beverage sample) which was adjusted to pH 2.5 with concentrated H_3PO_4 was placed in a 10 mL plastic centrifuge tube. Then 18 mg amount of dASNPs was added and the mixture was ultrasonicated for 2 min, and vortexed for 8 min. dASNPs enriched with the analytes were centrifuged (10,200 r/min) for 10 min. Next, the analytes were desorbed by 1 mL PBS (10 mM, pH 7) with 15 min ultrasonic agitation. After the mixture was centrifuged (10,200 r/min) for 10 min, the elution solution was collected in a sample tube for subsequent CE analysis.

3. Results and discussion

3.1. Capillary separation

3.1.1. EOF characteristic

EOF is a very important factor in CE separation because analytes move through the capillary by EOF drive, as well as self-electrophoretic mobility if they are charged. Both of the magnitude and direction of the EOF have direct effect on separation efficiency. Knowing the characteristics of the EOF will be helpful to select optimal separation conditions for different analytes. From Fig. 1a, we can see the direction of EOF is cathodic (i.e., from anode to cathode) in the investigated pH range. It was experimentally found that the addition of dASNPs in the background electrolyte can significantly alter the curve of EOF vs pH (as shown in Fig. 1b). From Fig. 1b, we can see that the direction of EOF is anodic (i.e., from cathode to anode) in the pH range of 5–6.7, and the magnitude of EOF decreases as the pH increases. At pH above 6.7, cathodic EOF is regained and the magnitude increases as the pH increases.

As is well known, the EOF in CE system is determined by the net charges on the inner wall of capillary column. For bare silica capillary column, cathodic EOF will be obtained in ordinary pH range because the ionization of silanol groups on capillary wall. When dASNPs are dispersed in the acidic electrolyte, they are positively charged because of the primary and secondary amino groups on their surface. These positively charged NPs tend to be adsorbed on the inner surface of capillary column, mainly through electrostatic interactions with the negatively charged silanol groups. Thus an anodic EOF will be obtained. With the pH of buffer solution increases, the protonation degree of amino groups decreases accordingly. At the same time, however, the ionization degree of silanol groups increases. As a result, cathodic EOF will regenerate and increase with the increasing of pH of buffer solution.

3.1.2. Effect of the concentrations of dASNPs and β-CD on separation

Among the papers previously published on the determination of colorants by CE [11,12,40–43], β-CD was commonly used as background electrolyte additive to improve the resolution. Furthermore, higher pH buffer solutions (usually alkaline) were usually used to produce higher cathodic EOF to surpass the anodic electrophoretic mobility of analytes [11,12,41]. Even so, longer analysis times were usually needed.

As shown in Fig. 1b, the addition of dASNPs in lower pH background electrolyte would result in a reversed EOF, which has been verified to be favorable for the separation of acidic compounds in our previously published paper [39]. The influences of the concentration of dASNPs and β-CD on the separation of four colorants are shown in Fig. 2A. In the absence of dASNPs in background electrolyte, the time needed for the separation was long and wide peaks were obtained for the last eluted compounds (Fig. 2A.c). The addition of β-CD has proved to be beneficial to the separation. When no β-CD was added in the background electrolyte, carminic acid and tartrazine could not be baseline resolved (Fig. 2A.b). When β-CD was added into the carrier electrolyte, a change in the elution order of the colorants was observed probably due to a stronger interaction between β-CD and tartrazine. Fig. 2A. a shows the satisfactory separation of all the colorants within 8 min in the background electrolyte containing both β-CD and dASNPs, which is faster than those previously reported by CE [11,29,41].

The amount of dASNPs in the buffer solution was gradually increased and their impact on separation was investigated. As shown in Fig. 2B inserted, the reversed EOF increased with the increasing concentration of the dASNPs. As a result of this, the migration times of the analytes were shortened at higher concentration dASNPs. However, when the concentration of dASNPs was increased to 1.2 mg/mL, the electrophoretic peaks of most analytes overlapped. At the same time, baseline noise was gradually elevated and capillary blockage happened much frequently, which would result in inconvenient operation. To achieve higher resolution and shorter analysis time, the concentration of dASNPs was chosen to be 0.9 mg/mL.

The effect of β-CD with the concentration ranging from 1 to 4 mM on separation was investigated. As shown in Fig. 2C, better resolution and longer migration windows of analytes could be obtained with the increasing of concentration of β-CD in buffer solution. However, higher concentration β-CD would result in higher viscosity of the background electrolyte solution, which would result in inconvenient operation. So 2 mM β-CD was finally selected for further experiment.

3.1.3. Effect of buffer solution pH on separation

The buffer solution pH plays a significant role in the separation process, because it has multiple effects on several factors influencing separation, such as EOF, the ionization of analytes, the net charges on NPs and the stability of the suspension. To investigate the influence of pH on separation, pH values ranging from 5 to 7 were examined in this work and the results are as shown in Fig. 2D. From Fig. 2D, we can see that carminic acid and tartrazine could not be baseline resolved when pH was 5. All the colorants could be well resolved when pH was above 5, but the migration time increased with the increasing of pH. One probable reason for the extended migration time is the decrease in both the electrophoretic flow of analytes and the EOF of the separation system (as shown in Fig. 1b). pH 6.0 was chosen as the optimum pH to achieve good resolution and short analysis time for subsequent experiments.

3.1.4. Effect of concentration of background electrolyte on separation

The ionic strength of the buffer solution also has effect on the resolution. Different buffer concentrations in the range of 10–40 mM were investigated and the results are shown in Fig. S2. It was experimentally showed that the resolution between

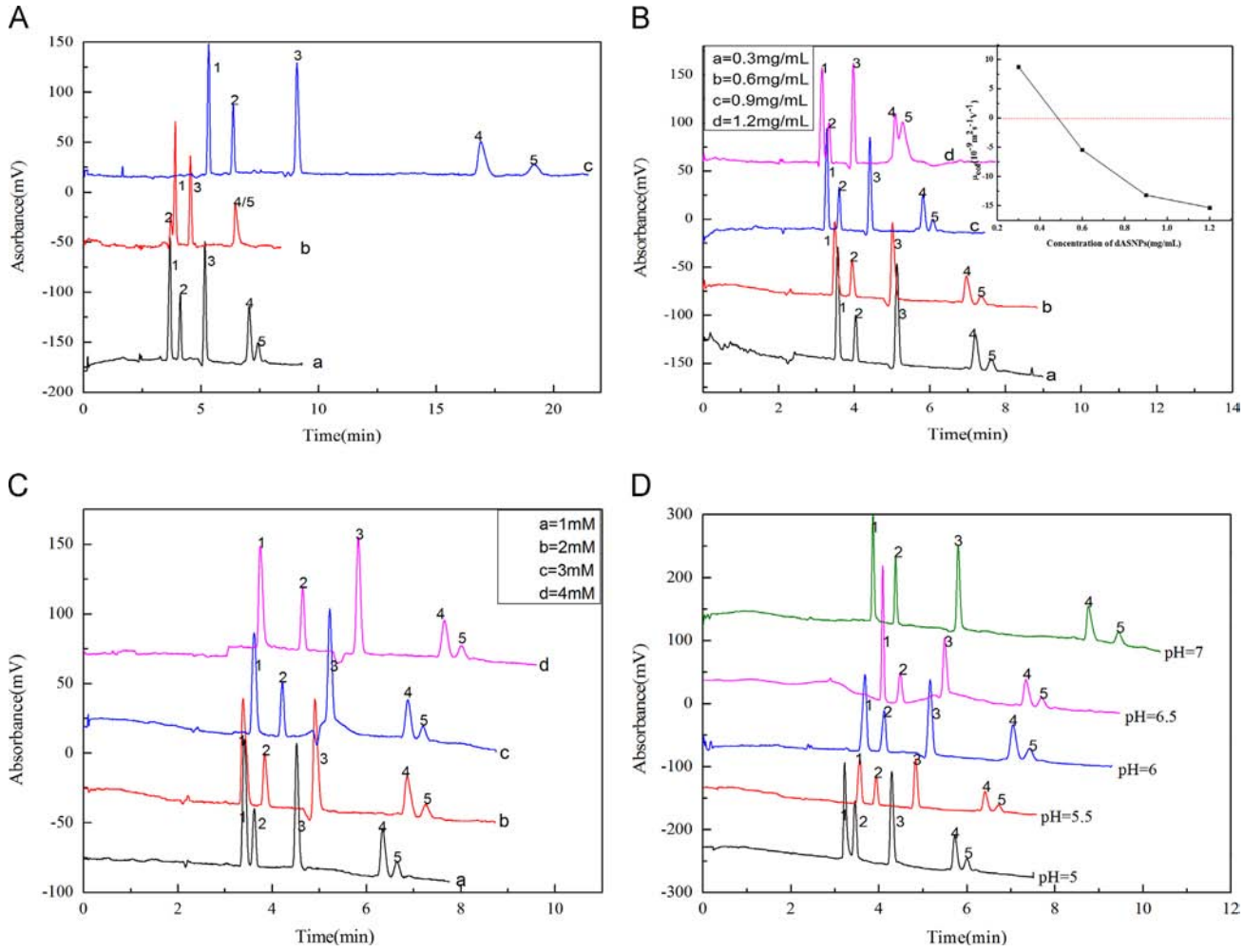


Fig. 2. The electropherograms of four colorants under different experimental conditions. Experimental conditions: (A.a) 30 mM PBS (pH 6.0) with 0.9 mg/mL dASNPs and 2 mM β-CD; (A.b) 30 mM PBS (pH 6.0) with 0.9 mg/mL dASNPs; (A.c) 30 mM PBS (pH 6.0) with 2 mM β-CD; (B) 30 mM PBS (pH 6.0) with 2 mM β-CD and different concentrations of dASNPs; (C) 30 mM PBS (pH 6.0) with 0.6 mg/mL dASNPs and different concentrations of β-CD; (D) 30 mM PBS with 0.6 mg/mL dASNPs and 2 mM β-CD under different pH conditions. The other conditions are mentioned in Section 2.2. Peak identities: (1) carminic acid; (2) tartrazine; (3) sunset yellow; (4) brilliant blue isomer I; (5) brilliant blue isomer II. (For interpretation of the references to color in this figure legend, the reader is referred to the web version of this article.)

carminic acid and tartrazine was moderately improved with the increasing of PBS concentration. The best resolution occurred when the PBS concentration was 40 mM. However, higher buffer concentration would result in less stable baseline due to the production of more Joule heat. As a compromise, the concentration of buffer was finally chosen to be 30 mM.

3.2. Optimization of dSPME

Many parameters would affect the extraction efficiency during the extraction process. Therefore, various conditions such as sample solution pH, the amount of dASNPs, extraction time, and the composition of desorption solvent were optimized to achieve optimal extraction efficiency.

3.2.1. Effect of sample solution pH

The acidity of sample solution is a critical parameter affecting extraction efficiency, since it determines the analytes ionic state as well as the surface charge of the adsorbent. Since the surface of dASNPs is modified by amino groups (–NH-, $–NH_2$), it will be different charged at different pH. Generally, the amino groups are more easily protonated under acidic conditions than basic conditions. Under the investigated pH range from 2 to 5, the signals for food colorants increased first and then decreased, best results were obtained at pH of 2.5 (as shown in Fig. 3A). Under lower pH, the electrostatic interaction between dASNPs and colorants would decrease because colorants were not fully ionized. With pH increasing above 2.5, the electrostatic interaction between dASNPs and colorants also decreased because deprotonation of amine groups of dASNPs. Optimum pH of 2.5 was so selected for the further work.

3.2.2. Effect of the amount of dASNPs

The amount of adsorbent also affects extraction efficiency. The amount of sorbent was also studied. The concentration of dASNPs in the extractant phase was examined in the range of 1–6 mg/mL. As shown in Fig. 3B, the best results were obtained when a concentration of 2 mg/mL (total of 18 mg) was used. Further increasing the amount of sorbent would result in an obvious decrease in analyte signals because higher volume of desorption solvent would be needed. Therefore, the concentration of 2 mg/mL was chosen as the optimal amount.

3.2.3. Effect of ionic strength of sample solution

Increasing the ionic strength in aqueous sample is beneficial to salting out effect generally and may alter the diffusion rate of analytes from aqueous solution to solid phase. So the salt

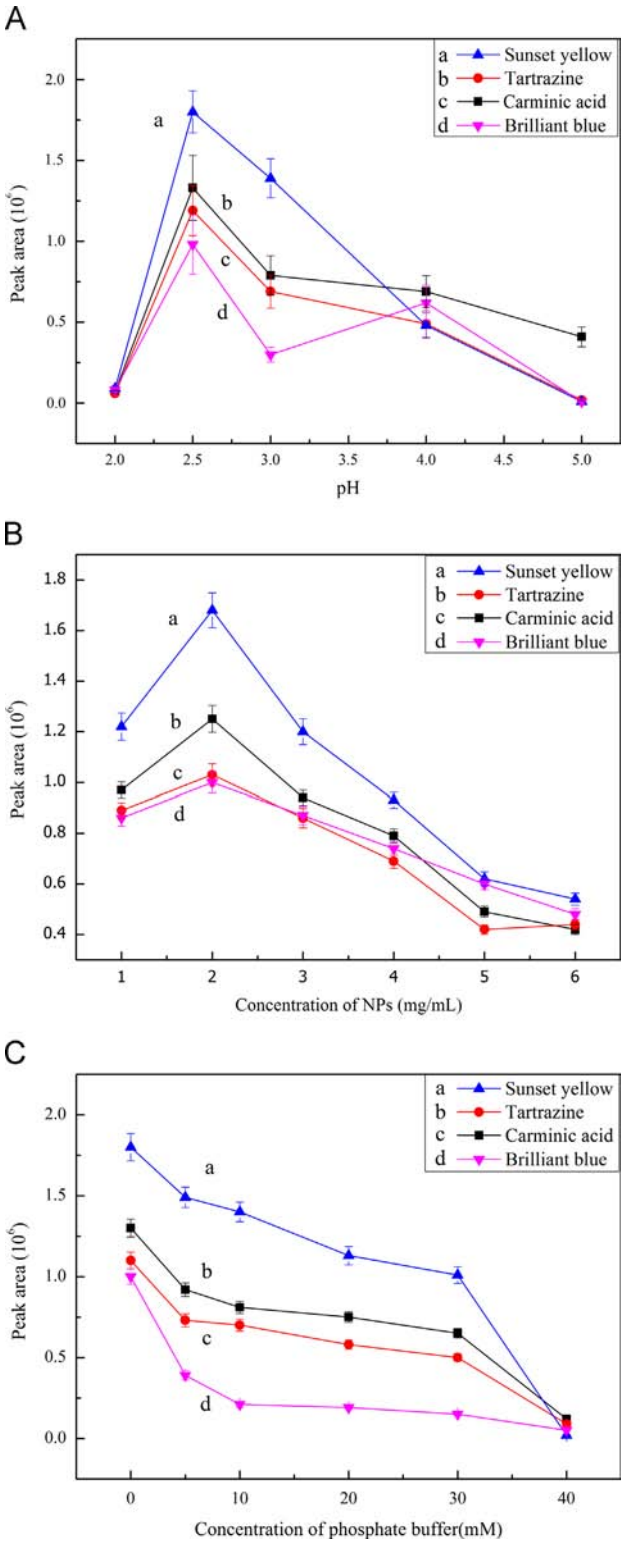


Fig. 3. The effects of the sample pH (A), concentration of dASNPs (B) and ionic strength of sample solution (C) on the extraction of the four food colorants from standard solution samples (carminic acid 2 ppm, tartrazine 1.5 ppm, sunset yellow 1 ppm, brilliant blue 2.5 ppm) ($n=3$ for all extraction and separation). Experimental conditions: (A) adsorption conditions: 2 mg/mL of dASNPs, 9 mL DDW with different pH; desorption conditions: 1 mL of 10 mM PBS (pH 7) as elution solvent; (B) adsorption conditions: 9 mL DDW (pH 2.5) with different concentration of dASNPs; desorption conditions: 1 mL of 10 mM PBS (pH 7) as elution solvent; (C) adsorption conditions: 2 mg/mL of dASNPs, 9 mL PBS with different concentrations; desorption conditions: 1 mL of 10 mM PBS (pH 7) as the elution solvent. The other conditions are mentioned in Section 2.2. Peak identities are the same as Fig. 2. (For interpretation of the references to color in this figure legend, the reader is referred to the web version of this article.)

concentration on extraction efficiency was investigated by adjusting the concentrations of PBS solution from 0 to 40 mM. The results showed that the extraction efficiency of four food colorants decreased with the increased concentrations of PBS (as shown in Fig. 3C). The main reason might be that high ionic strength was disadvantageous to the dispersion of dASNPs in sample solution. Therefore, no additional salt was added during the dSPME process.

3.2.4. The effect of extraction time and mode

The effect of extraction time on the extraction efficiency for food colorants was studied from 5 to 30 min. Results indicated that extraction efficiency increased when the extraction time increased from 5 to 10 min. However, when time was longer than 10 min, the extraction efficiency decreased slightly. It seems the analytes bind strongly with the sorbent and the distribution equilibrium was easy to achieve in 10 min. However, the analytes could not be pulled down easily from the sorbent by desorption solvent with the further increase in extraction time. Therefore, the extraction time was selected as 10 min.

Three different processes for sample agitation during the extraction step were evaluated. Experiment results showed that extraction efficiency obtained only by ultrasonication or vortex was lower than that by a mix of them. Ultrasonication is beneficial to the homogeneous dispersion of NPs in solution, which enables the analytes to interact fully with the sorbent. However, too long ultrasonication will result in the increase in temperature of sample solution, and so the desorption of analytes from sorbents. Ultimately, a procedure of ultrasonication for 2 min and then vortex for 8 min was selected.

3.2.5. Optimization of desorption conditions

Two different buffer solutions including 10 mM PBS and Tris–HCl were evaluated as desorption solvents. The experimental results showed that PBS offered the best recoveries, and so it was selected as desorption solvent in the following work.

The effect of the pH of desorption solvent was studied in the pH range of 6–10 and the results are shown in Fig. 4. It was experimentally found that the best results were obtained at about pH 7. There would be two main types of interactions between colorants and the surface of dASNPs: (1) electrostatic interaction and (2) hydrogen bonding. Zeta potential (ζ) measurement showed that the isoelectric point of dASNPs was about 7.0 (as shown in Fig. S3). When the pH of desorption solvent was lower than 7.0, dASNPs would be positively charged. Colorants would be retained on dASNPs through electrostatic interaction, and so they were not easily be desorbed. When the pH of desorption solvent was higher than 7.0, electrostatic interaction between colorants and dASNPs would decrease gradually. However, hydrogen bonding interaction between them would increase and gradually become the dominant interaction. Furthermore, higher pH would change the surface property of silica-based dASNPs, which would also be disadvantageous for desorption of analytes.

The amount of desorption solvent is another important factor to obtain reliable and reproducible analytical results. In comparison with lower recovery by small amount of desorption solvent, too much desorption solvent would definitely decrease preconcentration factor and so the sensitivity of analytical method. For this purpose, different volumes of desorption solvents from 0.2 to 2 mL were investigated. The experimental results showed that 1.0 mL of PBS (10 mM, pH 7) was sufficient for desorption of colorants from dASNPs.

The effect of desorption time was investigated at 5, 10, 15, 20 and 30 min by ultrasonication. It was found that the desorption efficiency reached maximum at 15 min. Therefore, 15 min was selected as optimum time.

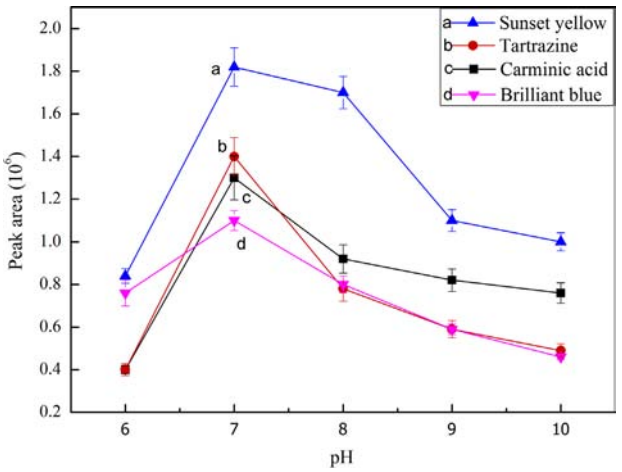


Fig. 4. Effect of the pH of desorption solvent ($n=3$). Experimental conditions: adsorption conditions: 2 mg/mL of dASNPs, 9 mL sample solution (pH 2.5), desorption conditions: 1 mL of 10 mM PBS with different pH as desorption solvent; the concentration of four colorants are the same as in Fig. 3. Peak identities are the same as in Fig. 2.

3.3. Effect of coexisting species in beverage

Citric acid, ascorbic acid and benzoic acid are commonly used as additives in beverages. Malic acid, succinic and tartaric acid are the most likely existing organic acid in apples and grapes. The influences of these organic acids on the analysis were then investigated in detail. The experimental results showed that citric acid, malic acid, succinic and tartaric acid could not be detected after the preconcentration process. The main reason is that these acids have very weak UV absorption at 220 nm. Another reason is associated with the dSPME procedure, during which the pH of sample solution is adjusted to 2.5. Under pH 2.5, it is not easy for the electrostatic interactions to happen between these acids and positively charged dASNPs because the carboxyl groups in these organic acids rarely dissociate. Ascorbic acid and benzoic acid can be separated completely from the studied four food colorants under optimal experimental conditions for beverage samples, so both of them do not interfere with the determination (see Figs. S4–5 in the supplementary files).

3.4. Analytical features of merit of the proposed dSPME method

The features of merit of the dispersive solid-phase microextraction method proposed in this paper are summarized in Table 1. The analytes were quantified with peak areas, and the peak area of brilliant blue was the total area of the two isomers. The corresponding calibration graphs for the four colorants were then constructed using aqueous standards under the optimized extraction procedure. The coefficient of determination were found to be in the range of 0.9932–0.9988. The limits of detection were calculated as the concentration providing an analytical signal three times the background noise (Table 1), which varied between 0.030 and 0.36 mg/L. The intra-day RSDs for five replicate separations of a standard mixture solution were 1.40–2.67% for the migration time and 3.18–7.65% for peak area. Fig. 6S shows the electropherograms of the analytes before and after preconcentration. The concentration factor was defined as the concentration ratio of the analyte after and before preconcentration [44,45].

In Fig. S6a and b, the sample matrix (30 mM PBS for Fig. S6a and b) is the same. We can get the preconcentration factors of 8.4, 6.9, 6.7 and 8.9 for the four colorants separately, which are mainly due to the dSPME process. In Fig. S6a and c, the sample matrix (10 mM PBS for Fig. S6a and 30 mM PBS for Fig. S6c) is different. The preconcentration factors of 18.6, 18.7, 13.6 and 20.8 were obtained for the four colorants separately. Besides the dSPME process, electrostacking effect also took effect in the injection process due to the conductance difference between sample matrix and background electrolyte, which would definitely further improve the preconcentration factor.

Table 1
Analytical figures of merit of the proposed method.

Analytes	Linear range (mg/L)	R^2	Detection Limit (mg/L) ($S/N=3$)	Peak area (RSD %) ($n=5$)	Migration time (RSD %) ($n=5$)
Carminic acid	0.31–10	0.9958	0.060	5.46	1.40
Tartrazine	0.31–10	0.9943	0.072	4.23	2.12
Sunset yellow	0.16–5	0.9932	0.030	3.18	1.32
Brilliant blue	0.63–10	0.9988	0.36	7.65	2.67

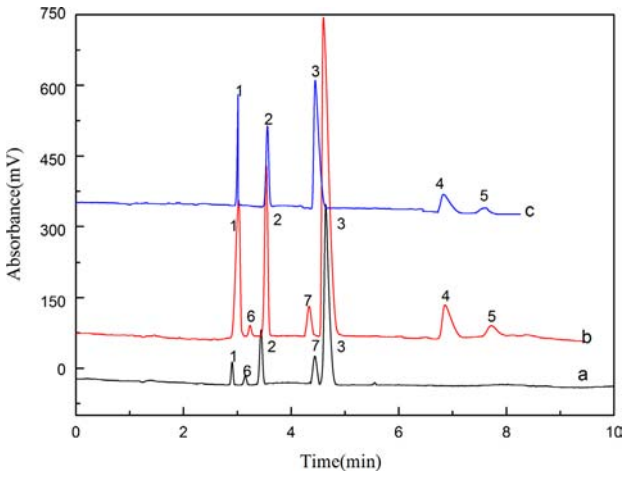


Fig. 5. The electropherograms of fruit juice 4 before (a) and after (b) being spiked with four colorants, and four colorants standard solution (c). Experimental conditions are mentioned in Section 2.2. Peak (1–5) identities are the same as in Fig. 2. Peak (6) and (7): unknown.

3.5. Application to beverage samples

The proposed method was applied to determine the content of the four colorants in four kinds of beverages (Fruit juice 1–4) (Fig. 5). The beverage samples were previously filtered through a 0.45 μm Nylon filter to remove the potential suspended particulate matter, and then diluted with DDW (pH 2.5) to 1:10 after degassed by ultrasonication. Fig. 5 shows the electropherograms of beverage samples before (a) and after (b) being spiked with four colorants, and aqueous standard solutions (c) under the optimum experimental procedure. As can be seen from Fig. 5, no interferences from the sample matrix overlapped with the target analytes. The recoveries of beverage samples spiked with the four colorants were determined in the range of 82.7–114.6%. Analytical results of four colorants in food samples are listed in Table 2. Therefore, the dSPME procedure described in this work has double functions of cleanup and preconcentration that can be applied to real sample analysis.

4. Conclusions

In this work, dASNPs were successfully used as both adsorbent in dSPME and PSPs in CE for the preconcentration and chromatographic separation of four food colorants in beverages. The results indicate that dSPME is an efficient sample preparation technique for the extraction of food colorants in complex matrix. Under optimum conditions, four

Table 2
Analytical results of food colorants in beverage samples.

Food colorants	Beverage samples (concentration/mg/L)			
	Fruit juice 1 ($n=3$)	Fruit juice 2 ($n=3$)	Fruit juice 3 ($n=3$)	Fruit juice 4 ($n=3$)
Carminic acid	ND*	ND	ND	0.87 ± 0.025
Tartrazine	0.99 ± 0.041	0.91 ± 0.039	0.66 ± 0.03	1.40 ± 0.11
Sunset yellow	ND	ND	1.36 ± 0.041	9.28 ± 0.45
Brilliant blue	ND	ND	ND	ND

* ND, not detected.

colorants can be well separated by CE in 8 min, which is faster than those previously reported. The LODs for four colorants are in the range of 0.030–0.36 mg/L after dSPME process, which are over 60-fold lower than those achieved with direct CZE analysis [41]. The proposed method promises simplicity, less organic solvent consumption and high sensitivity. Also, it allows determination of food colorants in beverage with good accuracy and repeatability.

Conflict of interest

The authors have declared no conflict of interest.

Acknowledgments

Financial support from the National Natural Science Foundation of China (21275081) and National Basic Research Program of China (2011CB707703) is gratefully acknowledged.

Appendix A. Supporting information

Supplementary data associated with this article can be found in the online version at http://dx.doi.org/10.1016/j.talanta.2014.09.014.

References

[1] Ministry of Health of the People's Republic of China, 2011, in: 12th ed. Hygienic standards for uses of food additives.
[2] O.M. Andersen, G.W. Francis, J. Chromatogr. 318 (1985) 450–454.
[3] L. Gao, G. Mazza, J. Agric. Food Chem. 42 (1994) 118–125.
[4] V. Hong, R.E. Wrolstad, J. Agric. Food Chem. 38 (1990) 708–715.
[5] J.T. Hann, I.S. Gilkson, J. Chromatogr. 395 (1987) 317–322.
[6] M. Ma, X.B. Luo, B. Chen, S.P. Su, S.Z. Yao, J. Chromatogr. A 1103 (2006) 170–176.
[7] J. Sádecká, J. Polonský, J. Chromatogr. A 880 (2000) 243–279.
[8] M. Pérez-Urquiza, J.C. Beltrán, J. Chromatogr. A 898 (2000) 271–275.
[9] M.C. Boyce, Electrophoresis 22 (2001) 1447–1459.
[10] T. Watanabe, S. Terabe, J. Chromatogr. A 880 (2000) 311–322.
[11] H.Y. Huang, Y.C. Shih, Y.C. Chen, J. Chromatogr. A 959 (2002) 317–325.
[12] H.Y. Huang, C.W. Chiu, S.L. Sue, C.F. Cheng, J. Chromatogr. A 995 (2003) 29–36.
[13] C. Nilsson, P. Viberg, P. Spégel, M. Jo1rntén-Karlsson, P. Petersson, S. Nilsson, Anal. Chem. 78 (2006) 6088–6095.
[14] P. Spégel, L. Schweitz, S. Nilsson, Anal. Chem. 75 (2003) 6608–6613.
[15] N. Na, Y.P. Hu, J. Ouyang, W.R.G. Baeyens, J.R. Delanghe, T.D. Beer, Anal. Chim. Acta 527 (2004) 139–147.
[16] F.K. Liu, Y.T. Hsu, C.H. Wu, J. Chromatogr. A 1083 (2005) 205–214.
[17] P. Spégel, L. Schweitz, S. Nilsson, Electrophoresis 22 (2001) 3833–3841.
[18] C.P. Palmer, E.F. Hilder, J.P. Quirino, P.R. Haddad, Anal. Chem. 82 (2010) 4046–4054.
[19] X. Xiong, J. Ouyang, W.R.G. Baeyens, J.R. Delanghe, X.M. Shen, Y.P. Yang, Electrophoresis 27 (2006) 3243–3253.
[20] Y.Q. Wang, W.R.G. Baeyens, C.G. Huang, G.T. Fei, L. He, J. Ouyang, Talanta 77 (2009) 1667–1674.
[21] H. Li, G.S. Ding, J. Chen, A.N. Tang, J. Chromatogr. A 1217 (2010) 7448–7454.
[22] H. Li, G.S. Ding, C.Y. Yue, A.N. Tang, Electrophoresis 33 (2012) 2012–2018.
[23] S.C. Fu, S.H. Tzing, H.C. Chen, Y.C. Wang, W.H. Ding, Anal. Bioanal. Chem. 402 (2012) 2209–2216.
[24] J.M. Jiménez-Soto, S. Cárdenas, M. Valcárcel, J. Chromatogr. A 1245 (2012) 17–23.
[25] K.M. Giannoulis, G.Z. Tsogas, D.L. Giokas, A.G. Vlessidis, Talanta 99, 2012, pp. 62–68.
[26] J.M. Jiménez-Soto, S. Cárdenas, M. Valcárcel, Anal. Chim. Acta 714 (2012) 76–81.
[27] M. Cruz-Vera, R. Lucena, S. Cárdenas, M. Valcárcel, Anal. Methods 3 (2011) 1719–1728.
[28] R. Lucena, B.M. Simonet, S. Cárdenas, M. Valcárcel, J. Chromatogr. A 1218 (2011) 620–637.
[29] I.P. Román, A. Chisvert, A. Canals, J. Chromatogr. A 1218 (2011) 2467–2475.
[30] H.Y. Wang, A.D. Campiglia, Anal. Chem. 80 (2008) 8202–8209.
[31] W.B. Wilson, A.D. Campiglia, Analyst 136 (2011) 3366–3374.
[32] A.V. Herrera-Herrera, L.M. Ravelo-Pérez, J. Hernández-Borges, M.M. Afonso, J.A. Palenzuela, M.A. Rodríguez-Delgado, J. Chromatogr. A 1218 (2011) 5352–5361.
[33] X.D. Du, Y.L. Wu, H.J. Yang, T. Yang, J. Chromatogr. A 1260 (2012) 25–32.
[34] C. Chen, X.F. Zhang, Z. Long, J.Y. Zhang, C.B. Zheng, Microchim. Acta 178 (2012) 293–299.
[35] Y. Peng, Y. Xie, J. Luo, L. Nie, Y. Chen, L.N. Chen, S.H. Du, Z.P. Zhang, Anal. Chim. Acta 674 (2010) 190–200.
[36] D. Pardasani, P.K. Kanaujia, A.K. Purohit, A.R. Shrivastava, D.K. Dubey, Talanta 86 (2011) 248–255.
[37] X. Wang, Y. Xiong, T. Xie, V.K. Sharma, Y. Tu, J. Yang, S. Tian, C. He, Talanta 111 (2013) 54–61.
[38] Y.S. Al-Degs, A.H. El-Sheikh, M.A. Al-Ghouti, B. Hemmateenejad, G.M. Walker, Talanta 75 (2008) 904–915.
[39] F.J. Liu, G.S. Ding, A.N. Tang, Food Chem. 145 (2014) 109–114.
[40] H.W. Liu, T. Zhu, Y.N. Zhang, S.Z. Qi, A.J. Huang, Y.L. Sun, J. Chromatogr. A 718 (1995) 448–453.
[41] K.L. Kuo, H.Y. Huang, Y.Z. Hsieh, Chromatographia 47 (1998) 249–256.
[42] J. Fischer, P. Jandera, P. Česla, V. Staněk, J. Sep. Sci. 26 (2003) 1035–1044.
[43] P. Česla, J. Fischer, E. Tesařová, P. Jandera, V. Staněk, J. Chromatogr. A 1149 (2007) 358–367.
[44] J. Nan, Y. Jiang, X.P. Yan, J. Anal. At. Spectrom. 18 (2003) 946–950.
[45] A.N. Tang, D.Q. Jiang, X.P. Yan, Anal. Chim. Acta 507 (2004) 199–204.

Talanta 132 (2015) 373–381

Contents lists available at ScienceDirect

Talanta

journal homepage: www.elsevier.com/locate/talanta

Development of an extraction and purification method for the determination of multi-class pharmaceuticals and endocrine disruptors in freshwater invertebrates

B. Huerta [a], A. Jakimska [b], M. Llorca [a], A. Ruhí [a], G. Margoutidis [a], V. Acuña [a], S. Sabater [a,c], S. Rodriguez-Mozaz [a,*], D. Barcelò [a,d]

[a] Catalan Institute for Water Research (ICRA), H_2O Building, Scientific and Technological Park of the University of Girona, Emili Grahit 101, 17003 Girona, Spain
[b] Department of Analytical Chemistry, Chemical Faculty, Gdansk University of Technology, 11/12 Narutowicza Street, 80-233 Gdansk, Poland
[c] Institute of Aquatic Ecology, University of Girona, Campus de Montivili, 17071 Girona, Spain
[d] Water and Soil Quality Research Group, Department of Environmental Chemistry, IDAEA-CSIC, Jordi Girona 18-26, 08034 Barcelona, Spain

ARTICLE INFO

Article history:
Received 26 May 2014
Received in revised form
3 September 2014
Accepted 11 September 2014
Available online 22 September 2014

Keywords:
Invertebrates
Pharmaceuticals
Endocrine disruptor
UPLC–MS/MS
Bioaccumulation
Diclofenac

ABSTRACT

Aquatic organisms from freshwater ecosystems impacted by waste water treatment plant (WWTP) effluents are constantly exposed to constant concentrations of pharmaceuticals, endocrine disruptors and related compounds, among other anthropogenic contaminants. Macroinvertebrates inhabiting freshwater ecosystems might be useful bioindicators of exposure to contaminants, since their lives are long enough to bioaccumulate, but at the same time may integrate short-term changes in the environment. However, studies about potential bioaccumulation of emerging contaminants in these organisms are very scarce. The objectives of this study were to develop an analytical methodology for the analysis of 41 pharmaceuticals and 21 endocrine disruptors in freshwater invertebrates. In addition, bioaccumulation of these contaminants in three macroinvertebrate taxa inhabiting a waste water treatment plant -impacted river was evaluated. The method for the simultaneous extraction of both families of compounds is based on sonication, purification via removal of phospholipids, and analysis by ultra performance liquid chromatography coupled to a mass spectrometer (UPLC–MS/MS) in tandem. Recoveries for pharmaceuticals were 34–125%, and for endocrine disruptors were 48–117%. Method detection limits (MDLs) for EDCs were in the range of 0.080–2.4 ng g^{-1}, and for pharmaceuticals, 0.060–4.3 ng g^{-1}. These pollutants were detected in water samples taken downstream the waste water treatment plant effluent at concentrations up to 572 ng L^{-1}. Two non-esteroidal anti-inflammatory drugs, diclofenac and ibuprofen, and four endocrine disruptors – estrone, bisphenol A, TBEP, and nonylphenol – were detected in at least one macroinvertebrate taxa in concentrations up to 183 ng g^{-1} (dry weight). An isobaric interference was identified during the analysis of diclofenac in *Hydropsyche* samples, which was successfully discriminated via accurate mass determination by TFC-LTQ Orbitrap.
© 2014 Elsevier B.V. All rights reserved.

1. Introduction

Numerous anthropogenic chemicals have been detected in wastewater treatment plants (WWTP) effluents and surface water in recent years, including pharmaceuticals (PhACs) and endocrine disrupting compounds (EDCs) [1–4]. This situation is of special concern in the Mediterranean region, where WWTP effluents often represent a high proportion of stream flow (particularly under water scarcity scenarios [5,6]), and pollutants such as PhACs and EDCs may be present at relatively high concentrations and cause adverse effects to aquatic organisms [7]. For instance, PhACs have been designed to modify specific biochemical pathways in target organisms [8]. On the other hand, EDCs are compounds that belong to different chemical families, characterized by their capability to alter the endocrine system of exposed organisms by mimicking or counteracting natural hormones, which could have severe consequences even at very low concentrations [9,10]. Several examples support the potential effects of these compounds on the river fauna: the feminisation of male fish in effluent-dominated rivers closely related to the presence of the synthetic hormone 17α-ethinylestradiol (EE2) [11,12], altered fish reproduction by some anti-inflammatory compounds, and altered behaviour and endocrine functions due to exposure to antidepressants [13,14]. Within this context, the recent Directive on the review of priority substances in surface water bodies has selected three of these

* Corresponding author. Tel.: +34 972183380.
E-mail address: srodriguez@icra.cat (S. Rodriguez-Mozaz).

http://dx.doi.org/10.1016/j.talanta.2014.09.017
0039-9140/© 2014 Elsevier B.V. All rights reserved.

compounds (diclofenac, ethinylestradiol, β-estradiol) as candidates for the "watch list" in the European priority compounds list [15].

A better understanding of how these compounds are transferred from water to biota could help determining the potential of ecosystem damage associated with the discharge of WWTP effluent containing these contaminants [16]. Among freshwater organisms exposed to these bioactive compounds, invertebrates have been less frequently studied than vertebrate species (i.e. fish) [17,18]. However, these organisms are susceptible of being affected by these compounds, and because of their sedentary life, they are representative of the local conditions in freshwater ecosystems [10,19]. Benthic macroinvertebrates are prey of other consumers, constituting a secondary contaminant entry for upper trophic levels. Their relatively long lives facilitate the incorporation of contaminants in their bodies, whereas they also integrate short-term changes in the environment. Therefore, aquatic macroinvertebrates appear to have the potential to be useful biomonitors of pollution [20]. Trichoptera (caddisflies) are already considered a bioindicator group, and these insects are frequently used to assess the ecological status of basins in Mediterranean rivers (e.g. [21]).

Many pollutants have been recurrently detected in macroinvertebrates (invertebrates large enough to be seen without the use of a microscope), and these organisms have been used as bioindicators of a wide variety of compounds, such as pesticides, PCBs, hormones, and metals [18,22–26]. The capability of macroinvertebrates to bioaccumulate PhACs and EDCs has also been established under controlled exposure conditions (see Table S1). However, information about bioaccumulation of PhACs and other EDCs under natural conditions is still non-existent for the great majority of these compounds. A first critical step to understand the bioaccumulation dynamics of these compounds is to develop and validate analytical methods for their extraction and determination in biota matrices [6,27]. Therefore, the objectives of this study were two-fold: (i) to develop an efficient analytical methodology for the simultaneous analysis of PhACs and EDCs in aquatic invertebrates, and (ii) to assess persistence, distribution, and bioaccumulation of these trace contaminants in macroinvertebrate communities affected by WWTP effluents.

2. Materials and methods

2.1. Standards and solutions

A list of the target analytes, their physico-chemical properties and purity of standards and reagents can be found in the supplementary material (Table S2). Individual stock standards and isotopically labeled internal standards were prepared in methanol at a concentration of approximately 1000 mg L^{-1}. Stock solutions and 20 mg L^{-1} mixtures in methanol were stored at −20 °C. Working standard solutions (1 mg L^{-1}) of all compounds, and mixtures of isotopically labelled internal standards were prepared in methanol/water (1:9, v/v for PhACs; 1:1, v/v for EDCs) before each analytical run.

2.2. Sample collection and pre-treatment

The study was conducted in a section of the River Segre, a tributary to the River Ebro in the Pyrenees (NE Iberian Peninsula). Although industrial and agricultural activities are scarce in this area, the river receives the discharge of a WWTP effluent (29 742 population equivalents). Water and invertebrate samples were collected in two sites, respectively: upstream (500 m) and downstream (1500 m) of the local WWTP in October of 2012. Invertebrate samples from three different taxa were collected, namely the gastropod *Ancylus fluviatilis* (*Planorbidae* family), which are air-breathing limpets that graze on biofilms, the filterer trichopteran *Hydropsyche* spp., (*Hydropsychidae* family), in larval and pupal (aquatic) stages, and the predator flatworm *Phagocata* spp. (*Planariidae* family).

River water (100 mL) was collected to determine the presence of PhACs and EDCs in the aqueous phase. River samples were filtered through 1 μm glass fiber filters followed by 0.45 μm nylon membrane filters and kept at −20 °C until analysis. Macroinvertebrates were collected and placed in a 50 mL Falcon tube filled with river water. Individuals were kept for 24 h in filtered stream water to allow for gut clearance. Approximately 70–120 individuals of each taxon were collected per sampling point and composited Composites were freeze-dried, homogenized with a mortar, and kept at −20 °C until analysis. A prior test was performed to determine the water content in the three taxa, which ranged between 77% (*Hydropsyche*) and 90% (*Ancylus*).

2.3. Extraction and purification optimization

Water samples were analyzed for PhACs and EDCs according to Gros et al. [28] for the analysis of PhAC, and also applied for the analysis of EDCs. Ultra-pure water (100 mL) was spiked with a mixture of the target analytes and subsequently subjected to the extraction method described next. Briefly, 3 mL of EDTA 1 M (4%, v/v) were added to water samples. A Baker vacuum system (J.T. Baker, The Netherlands) was used to pre-concentrate the samples in Oasis HLB cartridges (60 mg, 3 mL). They were loaded with 100 mL of water samples and eluted with 6 mL of methanol. The extracts were evaporated under a gentle nitrogen stream and reconstituted with 1 mL of methanol–water mixture (50:50, v/v for EDCs; 10:90, v/v for PhACs), and 10 μL of IS mixture (1 mg L^{-1}) was added to the final extract.

Macroinvertebrates samples were spiked with a mixture of both families of analytes and subsequently subjected to the chosen extraction methodologies described next to obtain the best recovery results for the target compounds. Sonication (Branson Digital Sonifier, model 102C) was the chosen method for extraction following preliminary studies. Samples were placed in a 50-mL Falcon tube in an ice bath, where 3 mL of solvent were added to the samples and vortexed. Ultrasonic probe was plunged in the solution and sonication was applied in 3 cycles of 120 s, with amplitude (intensity) of 30%. Sample size and extraction solvent were tested: 50, 100 and 200 mg of freeze-dried biomass, whereas extraction solvents tested were methanol (100%) and water/acetonitrile (1:3, 1% formic acid, v/v). Samples were centrifuged at 11000 rpm, for 5 min. Supernatant was collected and 1.5 mL of the extract was taken for further purification.

Four procedures were tested during cleanup optimization on the basis of the analytes recovery and the purity of the extract: solid-phase extraction (SPE) performed in a J.T. Baker® vacuum system with (i) Florisil cartridges (1 g, 6 mL), (ii) Oasis HLB (60 mg, 3 mL), and (iii) an Oasis HLB 96-well plate (30 μm, 30 mg). Another technique for the removal of phospholipids and proteins in plasma and serum, common matrix interferences in biological analysis, was also tested: (iv) an Ostro™ 96-well plate, which exhibits selective affinity towards phospholipids while remaining non-selective towards a range of basic, acidic and neutral compounds. Extracts were subjected to different treatments using each of the four clean-up strategies above mentioned:

(i) Extracts were redissolved in 10 mL of acetonitrile and loaded to the cartridge at 1 mL min^{-1} after conditioning with 10 mL of *n*-hexane and 10 mL of acetonitrile.
(ii) Extracts were redissolved in 200 mL of water with EDTA at 1%. After conditioning the cartridges with 6 mL of methanol and 6 mL of water, they were loaded into the cartridges and the eluted in 6 mL of methanol.

(iii) Extracts were redissolved in 1.5 mL of water 1% EDTA. Oasis HLB 96-well plate was placed in a manifold and wells were conditioned with 1.5 mL of methanol and 1.5 mL of water consecutively applying a vacuum extraction. Extracts were loaded and then eluted in 1.5 mL of methanol.
(iv) Extracts were redissolved in 750 μL of water/acetonitrile (1:3, 1% Formic acid, v/v). Ostro™ 96-well plate was placed in a manifold and wells were added 750 μL of fresh solvent and then carefully mixed with the extract in the well. After extraction by vacuum, purified extracts were collected.

All purified extracts were then evaporated and redissolved in 1 mL of methanol-water mixture (50:50, v/v for EDCs; 10:90, v/v for PhACs), and 10 μL of IS mixture (1 mg L^{-1})was added to the final extracts.

2.4. Instrumental analysis

2.4.1. UPLC–QqQ–LIT

For the analysis of PhACs, water and biota extracts were analysed according to Gros et al. [28] using a ultra performance liquid chromatography (UPLC) system (from Waters Milford, MA, USA) coupled to a hybrid quadrupole linear ion trap mass spectrometer Qtrap 5500 (Applied Biosystems, Foster City, CA, USA), equipped with an electrospray ionization source (ESI). Chromatographic conditions for the positive ionization mode were an Acquity HSS T3 column with methanol and 10 mM formic acid/ammonium formate (pH 3.2) as the mobile phase at a flow rate of 0.5 mL min^{-1}. For the negative ionization mode, an Acquity BEH C18 column was applied using acetonitrile and 5 mM ammonium acetate/ammonia (pH=8) at a flow rate of 0.6 mL min^{-1}. For the analysis of EDCs, extracts were analysed using the method developed by Jakimska et al. [29] in the same instrumental set up, using the Acquity BEH C18 column for both positive and negative modes. The chromatographic separation was achieved with methanol and water (pH 9) as mobile phase at a flow rate of 0.4 mL min^{-1}. The acquisition of the compounds into the analyser Qtrap was done in selected reaction monitoring (SRM) mode with the monitoring of two transitions. The most intense transition was used for quantification purposes when it was possible, whereas the second one was used to confirm the identity of the target compounds. Besides the monitoring of the SRM transitions and their retention time, the relative abundance of the two SRM transitions in the sample were compared with those in the standards, and the relative abundances in the samples must be within ± 20% of the two SRM ratios in the analytical standards. Pharmaceutical diclofenac was quantified with the second SRM transition for the insect *Hydropsyche*, as the first SRM transition was overlapped by an isobaric interference.

2.4.2. HPLC–HRMS

For the confirmation of the presence of diclofenac in *Hydropsyche*, a turbulent flow chromatograph coupled to a hybrid linear ion trap—Orbitrap mass spectrometer (TFC-LC-LTQ Orbitrap Velos) equipped with an ESI was used. The chromatographic system operating in off-line was equipped with a Hypersil Gold PFP column (10 mm × 2.1 mm id, 1.9 μm, ThermoFisher Scientific Company; Villebon-France). The LC eluents were solvent A: acetonitrile and solvent B: HPLC-grade water. The mobile phase gradient was programmed as follows: 0 min 5% A, 0.02–1.50 min 60% A, 1.5–2.0 min 100% A, 2.0–3.0 min 100–5% A, 3.0–3.7 min 5% A. The total chromatographic run time was 3.70 min. The analyser was working in negative ionization mode, and all the data was acquired and processed with Xcalibur 2.1 software (Themo Fisher Scientific, River Oaks Parkway, San Jose, USA). The mass spectrometer was operated with the following parameter settings: spray voltage, 2.5 kV; sheath gas, 60 arbitrary units; auxiliary gas, 20 arbitrary units; sweep gas, 0 arbitrary units, capillary temperature, 350 °C; S-lens RF level, 60; heater temperature, 400 °C. Optimal normalized collision energy (NCE) was set at 30 during all the analysis. Two experiments were performed in two corresponding chromatographic runs. First experiment consisted in two scan events. Scan event 1 performed by full scan from 100 to 350 Da with nominal mass resolving power of 60,000 FWHM in order to detect the accurate mass measurements of the [*M*–*H*] ions of diclofenac. Scan event 2 was a "Dependent Scan" at 30,000 of resolution and allowed the fragmentation of peak of diclofenac found in Scan Event 1 into the ion trap and then analysed into the Orbitrap in order to obtain the fragment ions (MS^2). Second experiment consisted in the fragmentation of the product ions from the first experiment obtaining the MS^3 at a resolution of 7500 FWHM. Identification of diclofenac was based on different criteria: the retention time, the isotopic pattern, the fragmentation pattern, the double bound equivalent (DBE) and the accurate mass (with errors below ± 2 ppm at the time of matching the theoretical mass with the measured mass). All the experiments were performed with a diclofenac standard (25 ng mL^{-1}), a sample extract (spiked also at 25 ng mL^{-1}) and the environmental samples taken upstream and downstream the WWTP.

3. Results and discussion

3.1. Extraction and purification optimization

Sonication was selected as extraction method according to preliminary studies. Energy was transmitted from the probe directly into the sample with high intensity and the sample was quickly processed. Two solvent mixtures were considered during the optimization: methanol (100%) and 0.1% formic acid in water/acetonitrile (1:3, v/v). Higher recoveries were obtained using 100% methanol for the majority of the compounds (see Fig. 1). Sample size (50, 100 and 200 mg, always referred as dry weight) was evaluated as an important parameter, due to the small size of the considered organisms, which is usually a limiting factor during sampling. A compromise was reached in between limit of detection and matrix effect, and 100 mg was selected as the final biomass.

For the purification of the extracts, florisil cartridges were discarded as a viable option, despite being commonly used for the elimination of matrix interferences such as lipids [30,31], due to the low recoveries for most of the target compounds. Oasis HLB cartridges have been widely applied for the analysis of pharmaceuticals [32–34]. A comparison between normal 6 mL cartridges and a 96-well microplate with Oasis HLB stationary phase was performed. Recoveries were similar for the majority of the compound, and significant differences were not be detected between both techniques. Finally, OSTRO™ plate was applied, as it was developed to remove phospholipids and precipitate proteins from small volumes of sample [35]. OSTRO™ resulted as the most appropriate technique, with the highest recoveries for the majority of the target compounds and good reproducibility (see Fig. 2).

Presented results led to the selection of an extraction protocol method based on extraction with ultrasonic probe (120 s, 3 cycles, 30% amplitude) of 100 mg (dry weight) of sample homogenized in 3 mL of methanol. Extract (1.5 mL) was the evaporated to dryness and redissolved in 0.75 μL of a mixture of water/acetonitrile containing 0.1% formic acid. Extract was passed through the OSTRO™ plate, followed by 0.75 μL of the same fresh solvent. Purified extract was divided in two aliquots for the analysis of both families of compounds by UPLC–MS/MS. Aliquots were evaporated to dryness and redissolved in: (a) methanol/water (1:1, v/v) for EDCs; (b) methanol/water (1:9, v/v) for PhACs.

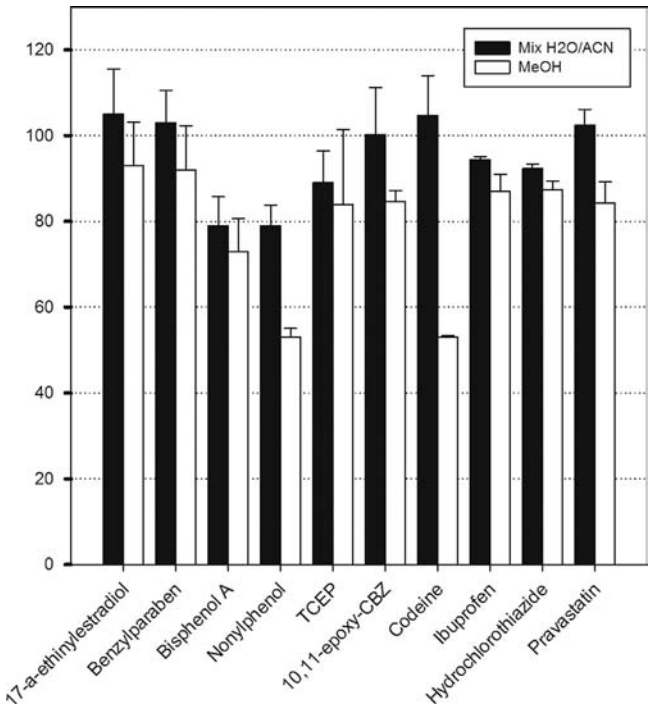


Fig. 1. Comparison of extraction efficiencies (%) of some EDCs and PhACs by sonication using two solvents: a mixture of water/acetonitrile (1:3) and 100% methanol ($n=3$).

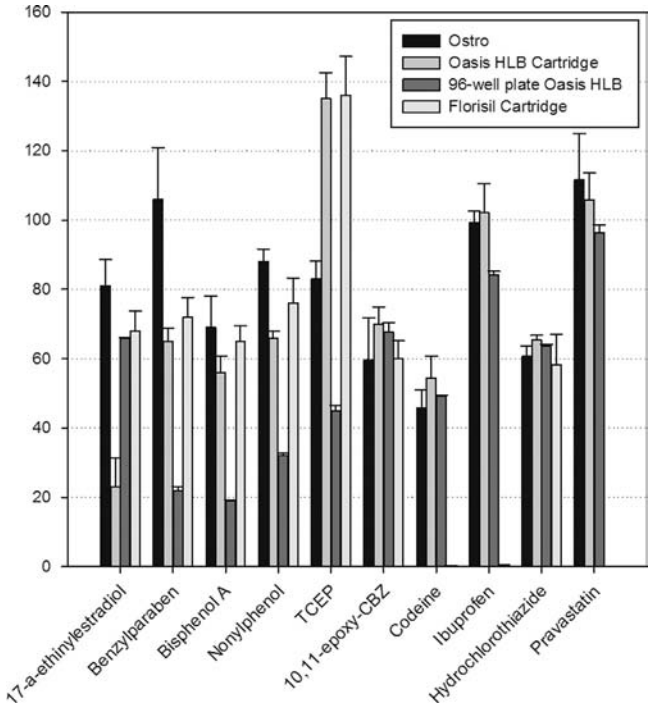


Fig. 2. Comparison of cleanup efficiencies (%) of some EDCs and PhACs by solid phase extraction (SPE) with Oasis HLB and Florisil cartridges, a 96-well-plate Oasis HLB stationary phase, and with Waters OSTRO™ plate ($n=3$).

3.2. Method validation

Method detection limits (MDLs) and method quantification limits (MQLs) in macroinvertebrates for both contaminant families are presented in Tables 1 and 2. Both, MDLs and MQLs, were considered as the minimum amount of analyte with a signal-to-noise ratio of 3 and 10, respectively and were determined in samples spiked at 10 ng g^{-1} ($n=3$). MDLs for EDCs were in the range of 0.08–2.4 ng g^{-1}, and for PhACs, 0.06–4.3 ng g^{-1}.

Calibration curves were generated using linear regression analysis ($r^2 > 0.98$) in the concentration range from 0.1–100 ng g^{-1}. Ion suppression was measured in 20% of the target compounds (data not shown), so isotopically-labelled compounds were used to compensate possible matrix effects with ESI. Accuracy of the instrumental method was calculated from three repeated injections of a spiked sample at 10 ng g^{-1} in the same day as the deviation of the measured mean concentration from the spiked concentration, expressed in percentage, as described by Bogialli et al. [36]. The instrumental precision (intra-day and inter-day) was calculated from five repeated injections in the same day and in five consecutive days. Both values were lower than 20% for EDCs and PhACs.

3.3. Application to environmental samples

3.3.1. Determination of PhACs and EDCs in water

A total of 81 multiple-class human and veterinary PhACs and 19 EDCs and related compounds, as well as some transformation products, were analysed. PhAC and EDCs water concentrations are presented in Table S3. Recovery percentages and method detection limits for EDCs in water samples are presented in Table S4. Twenty-two PhACs and 6 EDCs were detected downstream the WWTP, in concentrations ranging from non-detected to 573 ng L^{-1} and 261 ng L^{-1}, respectively. In contrast, only a PhAC (2-hydroxy-ibuprofen) and 3 EDCs (caffeine, nonylphenol and 1-*H*-benzotriazole) could be quantified upstream the WWTP. Overall, a clear increase in PhACs & EDCs concentrations was observed in the downstream over upstream sites, indicating that the WWTP effluent is a source of contaminant inputs to the River Segre.

Regarding PhACs, non-steroidal anti-inflammatory drugs (NSAIDs) were the most abundant compounds. The highest value was found for 2-hydroxy-ibuprofen (573 ng L^{-1}) followed by acetaminophen (222 ng L^{-1}) and ibuprofen (193 ng L^{-1}). Lower but still considerable levels were found for the diuretic hydrochlorothiazide (311 ng L^{-1}), and the lipid regulator gemfibrozil (285 ng L^{-1}). Other significant groups were the β-blocking agent atenolol (28 ng L^{-1}) and psychiatric drugs such as carbamazepine and venlafaxine. These concentrations are in agreement with a previous study carried out in the same area, where concentrations of some of these PhACs were between 10 and 500 ng L^{-1} [37]. In similar studies performed in surface waters affected by the effluent of a WWTP, concentrations for the majority of these PhACs were in the range from non-detected to 600 ng L^{-1} [28,38], including ibuprofen metabolites, which have been detected at significant concentrations (up to 1 μg L^{-1}) and higher than the values found for the parent compound [39,40].

In the case of EDCs, the triazoles tolyltriazole (261 ng L^{-1}) and 1-*H*-benzotriazole (194 ng L^{-1}) were the most abundant compounds. Other significant groups were: the stimulant caffeine (207 ng L^{-1}), the flame retardants TBEP and TCPP (65 and 71 ng L^{-1}, respectively), and nonylphenol (116 ng L^{-1}). Similar levels of concentrations for TBEP, caffeine and nonylphenol have been detected by several research groups in river and groundwater from Europe, USA, and Australia [41–44].

3.3.2. Determination of PhACs and EDCs in macroinvertebrates

Several compounds were detected in three species of macroinvertebrates (Table 3). PhACs were not detected in the upstream samples in any species, whereas three EDCs – TBEP, estrone and nonylphenol – were measured in upstream samples in at least one of the three taxa., Two NSAIDs drugs (diclofenac and ibuprofen) were detected downstream of the WWTP in *Hydropsyche*. Four

Table 1
Mean percent recoveries ($n=3$) of EDCs at two spiking levels in macroinvertebrates. Method detection and quantification limits (MDL, MQL) in macroinvertebrate composite (ng g^{-1}, dry weight).

	% Recoveries (± RSD)				Precision (%RSD)		
	100 ng g^{-1}	500 ng g^{-1}	MDL (ng g^{-1})	MQL (ng g^{-1})	Intra-day	Inter-day	Accuracy (%)
1*H*-benzotriazole	48 (± 11)	74 (± 14)	0.41	1.4	16	20	−0.10
17α-Ethinylestradiol	40 (± 10)	77 (± 5.9)	2.4	8.0	4.5	19	22
17β-Estradiol	43 (± 13)	83 (± 1.4)	0.34	1.1	5.1	13	9.1
Benzylparaben	40 (± 3.7)	59 (± 19)	0.50	1.6	3.6	9.4	−0.10
Bisphenol A	79 (± 13)	87 (± 11)	0.32	1.1	2.0	8.4	4.8
Caffeine	61 (± 16)	84 (± 18)	0.75	2.5	12	18	−9.7
Estriol	59 (± 12)	117 (± 4.8)	1.1	3.7	0.70	4.6	−3.8
Estrone	46 (± 17)	82 (± 6.1)	0.43	1.4	2.8	11	2.9
E1-3S	69 (± 15)	64 (± 1.0)	0.57	1.9	5.1	8.2	0.80
E1-3G	56 (± 19)	48 (± 13)	1.4	4.5	13	20	5.4
E2-17G	56 (± 22)	54 (± 7.9)	1.6	5.3	4.7	5.4	2.6
Ethylparaben	42 (± 14)	82 (± 7.9)	0.25	0.85	3.1	6.6	−10
Levonorgestrel	48 (± 15)	59 (± 22)	1.1	3.7	11	14	−3.5
Methylparaben	52 (± 6.5)	78 (± 3.0)	0.42	1.4	2.4	5.8	13
Nonylphenol	69 (± 13)	53 (± 12)	0.40	1.3	2.9	4.0	−11
Progesterone	64 (± 10)	80 (± 16)	0.26	0.88	5.3	15	−25
Propylparaben	50 (± 5.9)	79 (± 16)	0.13	0.42	3.4	5.5	2.3
Tolyltriazole	76 (± 0.1)	105 (± 14)	0.31	1.0	8.0	12	11
TCEP	40 (± 13)	56 (± 17)	0.25	0.84	4.2	8.1	8.9
TBEP	61 (± 18)	98 (± 0.4)	0.10	0.27	3.1	13	7.2
TCPP	55 (± 9.0)	87 (± 18)	0.20	0.67	3.5	15	3.7

Table 2
Mean percent recoveries ($n=3$) of PhACs at two spiking levels in macroinvertebrates.

	% Recoveries (± RSD)				Precision (% RSD)		
	100 ng g^{-1}	200 ng g^{-1}	MDL (ng g^{-1})	MQL (ng g^{-1})	Intra-day	Inter-day	Accuracy (%)
Acetaminophen	68 (± 16)	57 (± 7.4)	1.9	6.4	2.5	14	6.9
Acridone	74 (± 0.2)	82 (± 21)	0.78	2.6	1.7	2.4	−17
Alprazolam	96 (± 19)	121 (± 17)	0.71	2.3	1.2	2.5	−11
Atenolol	45 (± 5.1)	65 (± 12)	0.45	1.0	1.1	2.5	13
Azaperone	73 (± 18)	91 (± 13)	1.6	5.3	1.9	2.3	−4.0
Bezafibrate	47 (± 15)	47 (± 6.3)	0.070	0.24	4.5	14	10
Carbamazepine	61 (± 1)	79 (± 9.9)	0.060	0.21	0.80	1.3	0.10
2-OH-CBZ	51 (± 14)	70 (± 16)	1.4	4.6	2.3	2.7	3.3
10,11-epoxy-CBZ	54 (± 2.1)	97 (± 19)	1.1	3.5	4.3	4.4	0.10
Citalopram	66 (± 19)	94 (± 16)	0.10	0.31	0.5	2.0	−12
Codeine	51 (± 15)	71 (± 20)	2.0	6.8	3.3	8.9	−16
Dexamethasone	43 (± 7.4)	41 (± 18)	0.28	0.94	3.3	10	0.10
Diclofenac	44 (± 15)	51 (± 0.7)	0.51	1.7	1.7	15	4.9
Diltiazem	77 (± 7.2)	93 (± 4.6)	0.83	2.8	0.6	1.1	−8.4
Fluoxetine	37 (± 7.5)	68 (± 7.8)	0.44	1.5	1.7	3.8	−0.10
Gemfibrozil	85 (± 16)	85 (± 18)	0.15	0.50	14	18	0.10
Hydrochlorothiazide	70 (± 15)	58 (± 13)	0.10	0.34	8.5	9.4	6.8
Ibuprofen	88 (± 11)	87 (± 3.4)	0.64	2.1	6.9	12	−14
1-OH-ibuprofen	81 (± 15)	125 (± 18)	1.0	3.4	9.0	12	−4.7
2-OH-ibuprofen	90 (± 14)	93 (± 20)	1.3	4.3	6.8	9.0	0.10
Levamisol	37 (± 14)	55 (± 18)	2.5	8.2	2.4	3.7	1.4
Metronidazole	99 (± 12)	99 (± 21)	2.1	6.9	2.0	2.7	−16
Metoprolol	66 (± 17)	75 (± 5.2)	0.080	0.25	1.4	3.2	−0.1
Nadolol	41 (± 17)	58 (± 3.6)	0.35	1.2	1.6	3.1	−4.8
Naproxen	104 (± 15)	109 (± 17)	0.21	0.69	4.8	20	0.10
Norverapamil	58 (± 8.0)	77 (± 11)	0.79	2.6	1.4	1.6	0.10
Paroxetine	103 (± 17)	133 (± 16)	1.6	5.4	1.8	4.3	−12
Piroxicam	59 (± 3.2)	66 (± 16)	2.8	9.5	2.7	4.8	−0.10
Pravastatin	46 (± 16)	37 (± 14)	4.3	14	3.2	5.1	−24
Propanolol	23 (± 19)	34 (± 20)	2.9	9.5	0.60	1.2	0.10
Propyphenazone	60 (± 17)	83 (± 14)	0.16	0.54	1.3	3.8	16
Ronidazole	46 (± 4.5)	56 (± 18)	0.41	1.3	2.3	2.7	15
Salbutamol	45 (± 16)	59 (± 17)	0.21	0.69	3.7	4.2	11
Sotalol	31 (± 11)	46 (± 9.0)	1.1	3.6	3.4	4.1	−0.10
Sulfamethoxazole	59 (± 10)	49 (± 11)	0.71	2.3	3.6	4.4	−11
Tamsulosin	50 (± 12)	64 (± 6.6)	0.20	0.68	3.0	3.5	−0.10
Torasemide	118 (± 7.6)	113 (± 5.1)	0.10	0.31	3.5	8.2	−3.4
Venlafaxine	63 (± 18)	89 (± 16)	0.10	0.30	0.50	1.9	−3.5
Verapamil	79 (± 20)	118 (± 0.3)	0.71	2.3	1.3	2.0	11
Warfarin	57 (± 4.2)	64 (± 17)	0.15	0.50	1.1	1.9	0.10
Xylazine	43 (± 15)	65 (± 10)	0.54	1.8	1.3	1.6	−14

Table 3
PhACs & EDCs concentration (ng g^{-1}, dry weight) in macroinvertebrates from the Segre River (NE Spain).

	Hydropsyche		Ancylus		Hirudo	
	Upstream	Downstream	Upstream	Downstream	Upstream	Downstream
PhACs						
Ibuprofeno	n.d.	183	n.d.	n.d.	n.d.	n.d.
Diclofenac	n.d.	12.4	n.d.	n.d.	n.d.	n.d.
EDCs						
Estrone	n.d.	n.d.	n.d.	n.d.	17.6	12.4
Bisphenol A	n.d.	8.70	n.d.	n.d.	n.d.	n.d.
TBEP	17.9	31.1	7.70	31.8	22.3	20.6
Nonylphenol	n.d.	n.d.	75.5	96.3	76.7	130

EDCs (estrone, bisphenol A, TBEP, and nonylphenol) were detected overall across the three taxa.

It is generally accepted that substances with a logarithm of octanol–water partition coefficient (log K_{ow}) values equal or higher than 3 have the potential to bioaccumulate in organisms, and particularly in lipid tissues [45]. EDCs detected in macroinvertebrates in this study have a log K_{ow} ranging from 3.9 (TBEP) to 5.7 (nonylphenol) (see Table S2), which could make them susceptible for bioaccumulation in aquatic organisms according to this concept [46]. This seems a plausible hypothesis, as the other three EDCs detected in water (1*H*-benzotriazole, tolyltriazole and caffeine), detected at concentrations around 200 ng L^{-1} but with log $K_{ow} < 2$, were not detected in macroinvertebrates. In fact, TBEP was the most ubiquitous compound, as it was detected in samples upstream and downstream for the three macroinvertebrate taxa in concentrations up to 32 ng g^{-1}. TBEP has previously been detected in other organisms, such as herring gull eggs, flathead gray mullet, common carp and Mediterranean barb in similar concentrations [29,47,48]. Nonylphenol was also detected both upstream and downstream the WWTP effluent in *Ancylus* and *Phagocata*, with maximum concentrations for *Phagocata* of 77 ng g^{-1} in the upstream sample and 130 ng g^{-1} downstream the WWTP. This compound has also been detected in concentrations between 206 and 435 ng g^{-1} in mysid shrimps, a crustacean found in marine and freshwaters in the Netherlands [49]. In Italy, concentrations of nonylphenol up to 240 ng g^{-1} were measured in Mediterranean mussel (*Mytilus galloprovincialis*) in a coastal water ecosystem receiving industrial and municipal WWTP effluents [50]. The natural hormone estrone was only detected in *Phagocata* both upstream and downstream the WWTP at 12–18 ng g^{-1}. Estrone has also been detected in fish muscle elsewhere [29,47,51]. However, the likelihood that this hormone was endogenous of *Phagocata* individuals cannot be dismissed. For example, in the polychaete *Nereis virens*, estradiol has been detected in male and female coelomic fluid [52]. There also evidence that indicates that some mollusks are able to synthesize sex steroids, including estrone [46,53,54]. Estrone, estradiol, testosterone, and progesterone have been found in gastropods [55], cephalopods [56], and various bivalves such as Pacific oysters (*Crassostrea gigas*), Yesso scallops (*Patinopecten yessoensis*) [57], and Blue mussels (*Mytilus edulis*) [54,58,59]. However, some authors affirm that there is no convincing evidence for biosynthesis of vertebrate steroids by invertebrates, for example mollusks [60], which might suggest that the presence of estrone in *Phagocata* could be due to uptake from water. Finally, Bisphenol A was only detected in the downstream sample in *Hydropsyche* at 8.7 ng g^{-1}. Although it was detected in biota samples, this compound was below detectable concentrations in the corresponding water sample, which may suggest that this compound could be more persistent in the macroinvertebrate tissue compared to water. Bisphenol A has been detected in fish tissues of several countries in concentrations up to more than 200 ng g^{-1} [29,47,50,51,61].

In the case of PhACs, four of the analyzed compounds had a log $K_{ow} > 3$. However, only two of them, ibuprofen and diclofenac, were detected in macroinvertebrates, whereas gemfibrozil and bezafibrate, present at relatively high concentrations and with log K_{ow} between 3.9 and 4.3, were not detected in the samples. This suggests that accumulation of PhACs is not only regulated by their log K_{ow}. Pharmaceuticals are, in general, hydrophilic compounds and quite often ionized at the pH of surface waters, with acidic and/or basic chemical functional groups, which affects the lipophilicity of these compounds, and thus, the bioaccumulation in aquatic organisms [62]. For instance, accumulation of fluoxetine in fish and algae is significantly affected by variation in pH [63,64]. Ibuprofen and diclofenac have p*K*a < 5, thus would be primarily ionized at the pH ~7.8 of the river water, and the anions would be more soluble than the neutral molecule, leading to a reduction of the sorption by hydrophobic partition onto organic matter [65]. Actually, their log *D* is 0.85 at pH ~7.8 (calculated by ChemAxon), much lower than for the detected EDCs, which suggests that other mechanisms other that lipophilicity are influencing bioaccumulation in *Hydropsyche*. In this study, concentrations of PhACs ibuprofen and diclofenac in *Hydropsyche* were in the range from non-detected to 183 ng g^{-1}, similar to those detected in fish bile [66], and tissues [67]. Sorption of these compounds to colloids in water may occur, act as a long-term storage and being a sink for PhACs [62]. A recent study estimated calculated that the colloidal phase contributed between 22–33% of diclofenac and 9–28% of ibuprofen in the aquatic system, highlighting the important role of colloids as carrier of contaminants [68]. An increased exposure to these compounds could take place due to the filter-feeding habits of *Hydropsyche* [69], which could enhance its uptake.

3.4. Presence of diclofenac in trichopterans

Extremely high concentrations of the anti-inflammatory diclofenac were measured in the *Hydropsyche* extracts when quantifying with the first transition (SRM_1) (see Section 2), both in the upstream and downstream sample. However, SRM_2 was not detected in the upstream sample, and ratio could not be calculated. According to EU Commission Decision 2002/657/EC [70], a requisite to confirm a compound by low resolution mass spectrometry is that the relative intensities of the detected fragment ions have to correspond to those of the calibration standard at comparable concentrations within a minimum of tolerance: 20%. Since diclofenac is known to have low intensity of the second transition produced during the fragmentation (294→214) [66], as the relative intensity (% of base peak) in a standard is ≤10%, thus this tolerance can reach 50%. In both the upstream and downstream *Hydropsyche* samples, SRM_1 was detected at similar intensity. SRM_2 was detected in the downstream sample but the ratio was 30 times higher than the ratios obtained with the diclofenac standard. Extracts of

Phagocata and *Ancylus* from the upstream site were spiked with 25 ng mL^{-1} of diclofenac to calculate the SRM_1/SRM_2 ratio of diclofenac in a complex matrix. Ratios of diclofenac in *Phagocata* and *Ancylus* spiked extracts did comply with the aforementioned rule. However, when the upstream *Hydropsyche* sample was spiked with 25 ng mL^{-1} of diclofenac, the ratio was still much higher than in the standard. Based on these results, the presence of an isobaric interference in *Hydrophsyche* was postulated. In order to confirm this hypothesis and to ensure the correct quantification of diclofenac in the environmental samples, further measures and analytical strategies were taken. A Hypersil Gold PFP column, which provides an alternative selectivity to C_{18} columns to resolve mixtures of halogenated compounds and non-halogenated compounds, was tested to achieve the separation of diclofenac and the suspected interference. The upstream *Hydropsyche* extract spiked with diclofenac at 25 ng mL^{-1} and the non-spiked downstream sample were injected and two peaks were indeed resolved in both cases with the Hypersil Gold PFP column – RT: 1.3 min and 1.6 min (see Fig. 3a) – while in the C_{18} column only one peak appeared. SRM_1 was detected in both peaks separated by Hypersil Gold column, whereas SRM_2 was only detected in the second peak, and the SRM_1/SRM_2 ratio in the second peak confirmed that it was diclofenac. An isobaric interference was assumed to co-elute with the target compound using C18 column, and that interference was only separated with the Hypersil Gold PFP column.

The probability of having an interfering isobaric ion largely decreases with increases in mass resolution and mass accuracy. Therefore, on a second step for confirmation purposes, the accurate mass of the parent compounds in the two resolved chromatographic peaks were determined by injection of the downstream sample in the TFC-LTQ Orbitrap using the same Hypersil Gold PFP column. Measured accurate mass was *m/z*: 294.1714 at RT: 1.3 min and *m/z*: 294.0090 at RT: 1.6 min. Comparing these values with the theoretical mass of diclofenac (*m/z*: 294.0089 and formula $C_{14}H_{11}NCl_2O_2$), an error of 552 ppm and 0.34 ppm was calculated for the isobaric interference (RT: 1.3 min) and suspected diclofenac (RT: 1.6 min), respectively. The low error (< 5 ppm) at RT: 1.6 min added one more confirmation criteria for the identification of diclofenac. In contrast, the most plausible molecular formula suggested by the software for the interfering isobaric mass (ion *m/z*: 294.17069) was $C_{16}H_{25}NO_4$, with a low error (2.8 ppm) and did not include Cl, which is very distinctive for diclofenac.

Accurate mass of the daughter ions was also calculated. The mass spectrometer was operated in a data-dependent-acquisition (DDA) mode in this study, which means that the full-scan analysis with the Orbitrap analyser was followed by a MS–MS scan when the accurate *m/z* of diclofenac was detected. Accurate mass of the product ion (SMR_1) of diclofenac was thus determined in the upstream spiked sample as *m/z*: 250.0190. This mass was detected in the downstream non-spiked sample at the RT: 1.6 min with an error of 1.129 ppm for the calculated molecular formula $C_{13}H_{11}NCl_2$. Conversely, the isobaric interference (*m/z*: 294.1714 and RT: 1.3 min) formed ions with different *m/z* values to those of diclofenac. Product ion of that interfering mass was identified as *m/z*: 250.1453 and the

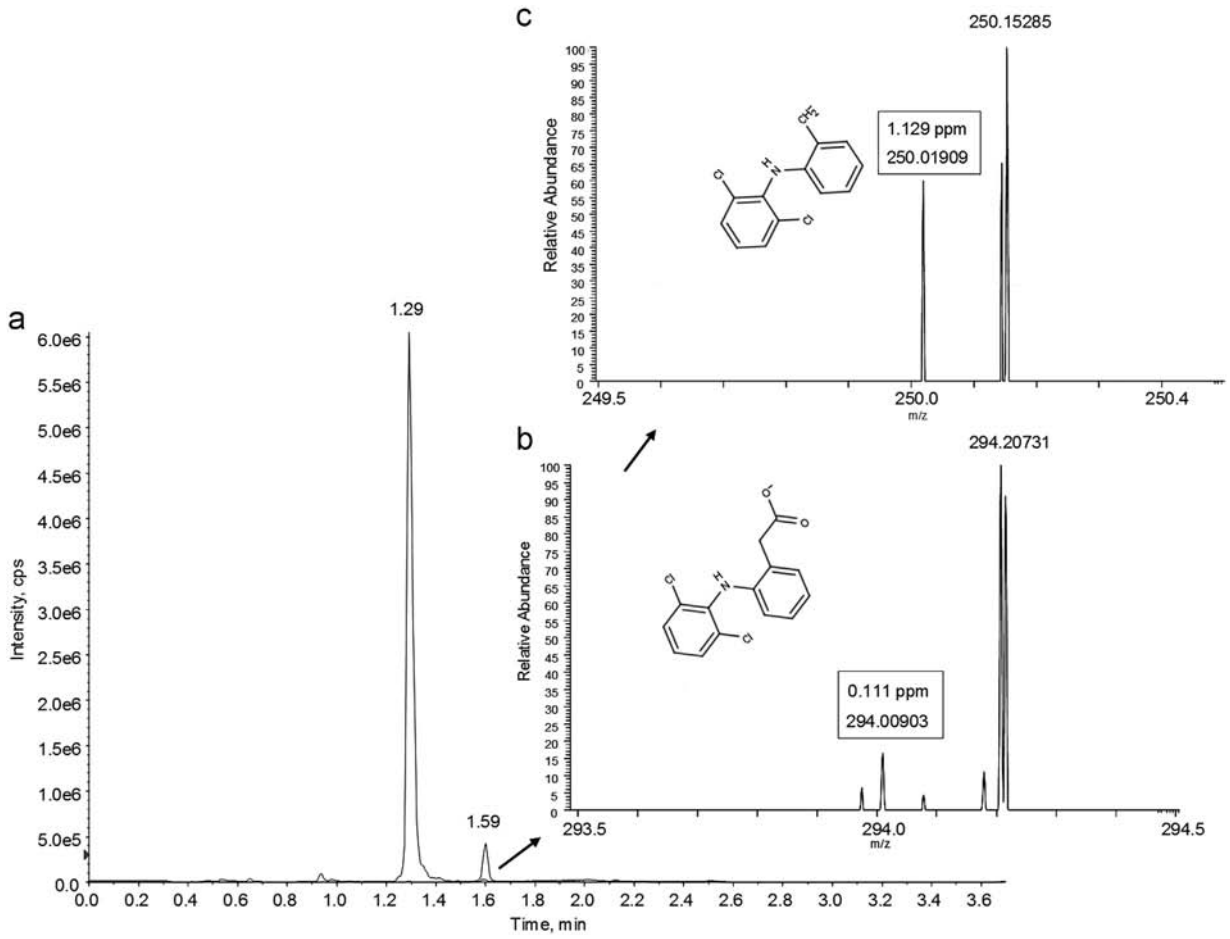


Fig. 3. (a) Chromatographic separation of diclofenac and matrix interference in a *Hydropsyche* sample performed in the Acquity UPLC tandem Qtrap MS; (b) accurate mass of diclofenac, *m/z* 294.009, determined in the Orbitrap MS: (c) Accurate mass of main product ion, *m/z* 250.019, was present in the data dependant scan of this *Hydropsyche* sample which confirmed that diclofenac was present.

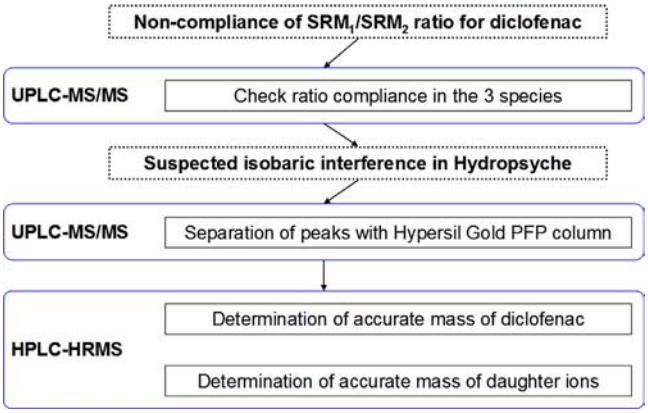


Fig. 4. Workflow applied for the interference discrimination in *Hydropsyche* samples.

molecular formula was $C_{14}H_{20}NO_3$ with an error of 1.092 ppm, being different to the daugher ion of diclofenac.

Other than RTs and accurate mass determination, fragmentation of the ionized molecule can also provide additional information for identification and improve specificity. Product ion of SMR1 of diclofenac (*m/z*: 250.0190 and RT: 1.6 min) was further fragmented in a MS^3 scan event, and gave the ion *m/z*: 214.0430, whose molecular formula was $C_{13}H_{11}NCl$.

According to EU Commission Decision 2002/657/EC, a precursor ion and a product ion at high resolution can achieve the minimum requirement for identification for high resolution mass spectrometry. Both, the accurate mass of *m/z* 250.0190 acquired at 60,000 FWHM, as described in Fig. 3c, and the accurate mass of the precursor ion *m/z*: 294.0090 were determined in the *Hydropsyche* downstream sample. Throughout the experiments, Orbitrap analyser provided excellent accuracy, which means that the matrix components were discriminated drastically. Thus, we were able to determine the presence of diclofenac in *Hydropsyche* samples at the downstream sampling site using SMR2 for quantification and the accurate mass of precursor ion and a product ion at high resolution for confirmation purposes. The workflow applied for the discrimination of the interference is shown in Fig. 4.

4. Conclusions

A simple, rapid, sensitive and efficient analytical method was developed for the determination of 41 PhACs and 21 EDCs in aquatic macroinvertebrates. The final multi-residue procedure consisted of an extraction by sonication, followed by purification of extract lipids, and the analysis was performed by UHPLC–MS/MS, which provided the necessary sensitivity and selectivity for these trace contaminants. The procedure was validated and it is characterized by good accuracy and precision, providing low quantification limits for macroinvertebrates. The method was applied to assess the bioaccumulation of these contaminants in three macroinvertebrate taxa (*Ancylus, Phagocata* and *Hydropsyche*) from a WWTP-impacted river. Two NSAIDs drugs, diclofenac and ibuprofen, and four EDCs – estrone, bisphenol A, TBEP, and nonylphenol – were detected in at least one macroinvertebrate taxa in concentrations up to 183 ng g^{-1}, which seems to indicate that invertebrates have the potential to be useful bioindicators of exposure to PhACs and EDCs.

Acknowledgments

This study has been financed by Spanish Ministry of Economy and Competitiveness through the project SCARCE (Consolider- Ingenio 2010 CSD2009-00065). This work was partly supported by the Generalitat de Catalunya (Consolidated Research Group: Catalan Institute for water Research 2014 SGR 291). We want to thank Jeremías Bodo for his contribution with the graphical abstract. Anna Jakimska has been financially supported for the preparation of a doctoral dissertation within the funding of a doctoral scholarship awarded by Polish National Science Centre on the basis of the decision number 2013/08/T/ST4/00637. We also thank Nuria Cáceres for her help during sampling.

Appendix A. Supporting information

Supplementary data associated with this article can be found in the online version at http://dx.doi.org/10.1016/j.talanta.2014.09.017.

References

[1] M. Gros, M. Petrovic, A. Ginebreda, D. Barceló, Environ. Int. 36 (2010) 15–26.
[2] A. Jelic, M. Gros, A. Ginebreda, R. Cespedes-Sanchez, F. Ventura, M. Petrovic, D. Barcelo, Water Res. 45 (2011) 1165–1176.
[3] A. Joss, E. Keller, A.C. Alder, A. Gobel, C.S. McArdell, T. Ternes, H. Siegrist, Water Res. 39 (2005) 3139–3152.
[4] M. Petrovic, M. Sole, M.J. Lopez de Alda, D. Barcelo, Environ. Toxicol. Chem. 21 (2002) 2146–2156.
[5] V. Osorio, R. Marcé, S. Pérez, A. Ginebreda, J.L. Cortina, D. Barceló, Sci. Total Environ. 440 (2012) 3–13.
[6] M.A. Coogan, R.E. Edziyie, T.W. La Point, B.J. Venables, Chemosphere 67 (2007) 1911–1918.
[7] S.N. Garcia, M. Foster, L.A. Constantine, D.B. Huggett, Ecotoxicol. Environ. Saf. 84 (2012) 207–211.
[8] G. Vernouillet, P. Eullaffroy, A. Lajeunesse, C. Blaise, F. Gagné, P. Juneau, Chemosphere 80 (2010) 1062–1068.
[9] R. Céspedes, S. Lacorte, D. Raldúa, A. Ginebreda, D. Barcelò, B. Piña, Chemosphere 61 (2005) 1710–1719.
[10] D. Pascoe, W. Karntanut, C.T. Müller, Chemosphere 51 (2003) 521–528.
[11] S. Jobling, M. Nolan, C.R. Tyler, G. Brighty, J.P. Sumpter, Environ. Sci. Technol. 32 (1998) 2498–2506.
[12] S. Jobling, R. williams, A. Johnson, A. Taylor, M. Gross-Sorokin, M. Nolan, C. Tyler, Environ. Health Perspect. 114 (Suppl. 1) (2006) 32–39.
[13] T.W. Valenti Jr., G.G. Gould, J.P. Berninger, K.A. Connors, N.B. Keele, K.N. Prosser, B.W. Brooks, Environ. Sci. Technol. 46 (2012) 2427–2435.
[14] J. Corcoran, M.J. Winter, C.R. Tyler, Crit. Rev. Toxicol. 40 (2010) 287–304.
[15] European Commision, in: 2011/0429 (COD), Brussels, 2012.
[16] C.A. Kinney, E.T. Furlong, D.W. Kolpin, M.R. Burkhardt, S.D. Zaugg, S.L. Werner, J.P. Bossio, M.J. Benotti, Environ. Sci. Technol 42 (2008) 1863–1870.
[17] L.B. Barber, S.H. Keefe, R.C. Antweiler, H.E. Taylor, R.D. Wass, Environ. Sci. Technol. 40 (2005) 603–611.
[18] E.B. Dussault, V.K. Balakrishnan, U. Borgmann, K.R. Solomon, P.K. Sibley, Ecotoxicol. Environ. Saf. 72 (2009) 1635–1641.
[19] D.P. Batzer, A. Ruhí, Freshwater Biol. 58 (2013) 1647–1659.
[20] K.L. Goodyear, S. McNeill, Sci. Total Environ. 229 (1999) 1–19.
[21] A. Ruiz-García, J. Márquez-Rodríguez, M. Ferreras-Romero, Ecol. Indic. 14 (2012) 114–123.
[22] E.C. Bizzotto, S. Villa, M. Vighi, Environ. Pollut. 157 (2009) 3192–3198.
[23] D.T. Rhea, D.D. Harper, A.M. Farag, W.G. Brumbaugh, Environ. Monit. Assess. 115 (2006) 381–393.
[24] J. Chetelat, M. Amyot, E. Garcia, Environ. Pollut. 159 (2011) 10–17.
[25] H.A. de Wit, M.J. Kainz, M. Lindholm, Environ. Pollut. 164 (2012) 235–241.
[26] M. Liebig, P. Egeler, J.r. Oehlmann, T. Knacker, Chemosphere 59 (2005) 271–280.
[27] E.B. Dussault, V.K. Balakrishnan, K.R. Solomon, P.K. Sibley, Can. J. Chem. 87 (2009).
[28] M. Gros, S. Rodríguez-Mozaz, D. Barceló, J. Chromatogr. A 1248 (2012) 104–121.
[29] A. Jakimska, B. Huerta, Z. Barganska, A. Kot-Wasik, S. Rodriguez-Mozaz, D. Barcelo, J. Chromatogr. A 1306 (2013) 44–58.
[30] J. Hong, H.-Y. Kim, D.-G. Kim, J. Seo, K.-J. Kim, J. Chromatogr. A 1038 (2004) 27–35.
[31] A. Dirtu, L. Roosens, T. Geens, A. Gheorghe, H. Neels, A. Covaci, Anal. Bioanal. Chem. 391 (2008) 1175–1181.
[32] M.J. Gómez, M. Petrovic, A.R. Fernández-Alba, D. Barcelò, J. Chromatogr. A 1114 (2006) 224–233.
[33] M. Huerta-Fontela, M.T. Galceran, F. Ventura, J. Chromatogr. A 1217 (2006) 4212–4222.
[34] M. Gros, M. Petrovic, D. Barceló, Talanta 70 (2006) 678–690.
[35] Waters Corporation, in, 2010.
[36] S. Bogialli, R. Curini, A. Di Corcia, M. Nazzari, R. Samperi, Anal. Chem. 75 (2003) 1798–1804.

[37] V. Acuña, D. vonSchiller, M.J. García-Galán, S. Rodríguez-Mozaz, L. Corominas, M. Petrovic, M. Poch, D. Barceló, S. Sabater, Sci. Total Environ. 2014, http://dx.doi.org/10.1016/j.scitotenv.2014.05.067, in press.
[38] B. Kasprzyk-Hordern, R.M. Dinsdale, A.J. Guwy, Water Res. 42 (2008) 3498–3518.
[39] L. Ferrando-Climent, N. Collado, G. Buttiglieri, M. Gros, I. Rodriguez-Roda, S. Rodriguez-Mozaz, D. Barcelo, Sci. Total Environ. 438 (2012) 404–413.
[40] S. Weigel, U. Berger, E. Jensen, R. Kallenborn, H. Thoresen, H. Huhnerfuss, Chemosphere 56 (2004) 583–592.
[41] M. Gorga, M. Petrovic, D. Barcelo, J. Chromatogr. A 1295 (2013) 57–66.
[42] R.A. Trenholm, B.J. Vanderford, J.C. Holady, D.J. Rexing, S.A. Snyder, Chemosphere 65 (2006) 1990–1998.
[43] K. Quednow, W. Püttmann, Environ. Pollut. 152 (2008) 476–483.
[44] U. Bolz, H. Hagenmaier, W. Körner, Environ. Pollut. 115 (2001) 291–301.
[45] C. Franke, G. Studinger, G. Berger, S. Böhling, U. Bruckmann, D. Cohors-Fresenborg, U. Jöhncke, Chemosphere 29 (1994) 1501–1514.
[46] C. Riva, C. Porte, A. Binelli, A. Provini, Comp. Biochem. Physiol. C: Toxicol. Pharmacol. 152 (2010) 175–181.
[47] W.-L. Chen, G.-S. Wang, J.-C. Gwo, C.-Y. Chen, Talanta 89 (2012) 237–245.
[48] J.-W. Kim, B.R. Ramaswamy, K.-H. Chang, T. Isobe, S. Tanabe, J. Chromatogr. A 1218 (2011) 3511–3520.
[49] T.A. Verslycke, A.D. Vethaak, K. Arijs, C.R. Janssen, Environ. Pollut. 136 (2005) 19–31.
[50] G. Pojana, A. Gomiero, N. Jonkers, A. Marcomini, Environ. Int. 33 (2007) 929–936.
[51] J. Liu, R. Wang, B. Huang, C. Lin, J. Zhou, X. Pan, Environ. Pollut. 162 (2012) 325–331.
[52] J. Keay, J.W. Thornton, Endocrinology 150 (2009) 1731–1738.
[53] J.W. Thornton, E. Need, D. Crews, Science 301 (2003) 1714–1717.
[54] M. Kajiwara, S. Kuraku, T. Kurokawa, K. Kato, S. Toda, H. Hirose, S. Takahashi, Y. Shibata, T. Iguchi, T. Matsumoto, T. Miyata, T. Miura, Y. Takahashi, Gen. Comp. Endocrinol. 148 (2006) 315–326.
[55] D. Le Guellec, M.C. Thiard, J.P. Remy-Martin, A. Deray, L. Gomot, G.L. Adessi, Gen. Comp. Endocrinol. 66 (1987) 425–433.
[56] A. D'Aniello, A. Di Cosmo, C. Di Cristo, L. Assisi, V. Botte, M.M. Di Fiore, Biochem. Biophys. Res. Commun. 227 (1996) 782–788.
[57] T. Matsumoto, M. Osada, Y. Osawa, K. Mori, Comp. Biochem. Physiol. B: Biochem. Mol. Biol. 118 (1997) 811–817.
[58] M.A. Reis-Henriques, D. Le Guellec, J.P. Remy-Martin, G.L. Adessi, Comp. Biochem. Physiol. B: Biochem. Mol. Biol. 95 (1990) 303–309.
[59] W. Zhu, K. Mantione, D. Jones, E. Salamon, J.J. Cho, P. Cadet, G.B. Stefano, Neuroendocrinol. Lett. 24 (2003) 137–140.
[60] A.P. Scott, Steroids 78 (2013) 268–281.
[61] C. Miège, J.M. Choubert, L. Ribeiro, M. Eusèbe, M. Coquery, Environ. Pollut. 157 (2009) 1721–1726.
[62] A. Zenker, M.R. Cicero, F. Prestinaci, P. Bottoni, M. Carere, J. Environ. Manage. 133 (2014) 378–387.
[63] Y. Nakamura, H. Yamamoto, J. Sekizawa, T. Kondo, N. Hirai, N. Tatarazako, Chemosphere 70 (2008) 865–873.
[64] J. Neuwoehner, B.I. Escher, Aquat. Toxicol. 101 (2011) 266–275.
[65] J.C. Durán-Álvarez, B. Prado, A. Ferroud, N. Juayerk, B. Jiménez-Cisneros, Sci. Total Environ. 473-474 (2014) 189–198.
[66] J.-M. Brozinski, M. Lahti, A. Meierjohann, A. Oikari, L. Kronberg, Environ. Sci. Technol. 47 (2013) 342–348.
[67] B. Huerta, A. Jakimska, M. Gros, S. Rodriguez-Mozaz, D. Barcelo, J. Chromatogr. A 1288 (2013) 63–72.
[68] Y.-P. Duan, X.-Z. Meng, Z.-H. Wen, R.-H. Ke, L. Chen, Sci. Total Environ. 447 (2013) 267–273.
[69] Tachet H, Richoux P, Bournaud M, U.-P. P, Invertebrés d'Eau Douce (2nd corrected impression) ed. CNRS Editions, Paris, 2002.
[70] Council Directive 96/23/EC. Off. J. Union, 2002, L 221/8-36.

Talanta 132 (2015) 382–386

Contents lists available at ScienceDirect

Talanta

journal homepage: www.elsevier.com/locate/talanta

Three-phase solvent bar micro-extraction as an approach to silver ultra-traces speciation in estuarine water samples

José Antonio López-López *, Belén Herce-Sesa, Carlos Moreno

Department of Analytical Chemistry. Faculty of Marine and Environmental Sciences, University of Cádiz, Puerto Real, 11510 Cádiz, Spain

ARTICLE INFO

Article history:
Received 29 April 2014
Received in revised form
15 September 2014
Accepted 18 September 2014
Available online 26 September 2014

Keywords:
Silver
Trace analysis
Speciation
Estuary
Three-phase solvent bar micro-extraction

ABSTRACT

Silver ion inputs into the environment due to human activities have been increased in the last years because it has been used as a bactericide with application in medical, homecare and self-care products. In addition, it is toxic at low concentration for aquatic organisms. In estuarine waters, salinity and dissolved organic matter (DOM) regulate Ag^+ concentration by the formation of complexes as $AgCl_n^{(n-1)-}$ and Ag-DOM.

Difficulties of Ag^+ analysis in estuaries are associated to its low concentration level and interferences of sample matrix. Liquid and solid phase extraction methods have been used for speciation of silver in waters; however, miniaturized methods that offer a better environmental profile are desirable. Hollow fiber liquid phase micro-extraction (HFLPME) allows obtaining higher pre-concentration factors with a reduction of waste generation. Notwithstanding, some operational improvements are needed to permit their use as a routine method that can be afforded using a configuration of three-phase solvent bar micro-extraction (3PSBME).

In this work, tri-isobutylphosphine sulphide (TIBPS) has been used as an extractant for Ag^+ pre-concentration in estuarine waters by 3PSBME. Under optimized conditions, Ag^+ has been pre-concentrated 60 times and the method presents a limit of detection of 1.53 ng L^{-1}. To evaluate which Ag species is transported by TIBPS, Cl^- and DOM have been added to synthetic samples. As a result, a decrease in Ag pre-concentration efficiency after additions has been observed and quantified. Results showed that Ag^+ is selectively transported by TIBPS from estuarine water samples after comparison of the results with those obtained by the reference method of liquid extraction with APDC/DDDC.

© 2014 Elsevier B.V. All rights reserved.

1. Introduction

During the last years, silver inputs into natural water resources have been increased and diversified due to the use of silver and silver compounds in several applications and everyday-used products, such as home and self-care products, fabrics recovery, additives for paints, etc [1–4]. All of them are based on silver capability as a bactericide and fungicide [5]. In particular Ag^+ has been identified as the main reason for its toxicity for aquatic organisms [6]. Ag^+ analysis normally requires pre-concentration and/or separation of the metal from the sample due to its low concentrations and matrix effects on analytical methods [7,8]. In the case of natural waters and in particular for estuarine waters, Ag speciation is ruled by salinity and dissolved organic matter (DOM) being mainly in the form of $AgCl_2^-$ and $AgCl_3^{2-}$ [9,10].

Complexation of silver by Cl^- and DOM affects Ag^+ concentration in estuaries, modifying availability of the metal for aquatic organisms [11,12]. For this reason, different alternatives have been proposed for selective analysis of Ag^+ in natural waters that are based on sample pre-treatment using liquid-liquid extraction and solid phase extraction [9,13]. Also bulk liquid membranes (BLM) have been applied for selective transport of Ag^+ in natural water with the objective of simplifying sample preparation [14]. In general, these techniques present drawbacks associated to solvents and reagents consumption and the need of highly sensitive instrumental techniques for quantification of the metal [9,15].

In order to overcome these drawbacks, sample preparation processes can be miniaturized using micro-extraction methods. Among others, hollow fiber liquid phase micro-extraction (HLFPME) has gained increasing attention in the last years for trace metals analysis, due to its pre-concentration capability and stability [16]. It can be used in a three-phase (3HFLPME) configuration in which simultaneous extraction and re-extraction can be carried out [17]. 3HFLPME consists in the transport of the metal ion from the sample to a small volume of aqueous acceptor solution located inside the fiber. Transport takes place through an organic solution of an extractant agent that is placed in the fiber pores [8,16]. This methodology has been applied for selective pre-concentration of

* Corresponding author. Tel.: +349566165.
E-mail address: joseantonio.lopezlopez@uca.es (J.A. López-López).

http://dx.doi.org/10.1016/j.talanta.2014.09.030
0039-9140/© 2014 Elsevier B.V. All rights reserved.

the free ion of Pb, Cd, and Ni in seawater analysis using kriptofix-22DD as extractant [18].

In spite of the advantages it presents, HFLPME has not been established as a routine technique because it normally needs a support for the fiber, special devices are required to set up fiber's modules, and leaks may appear in the connection with the support [17]. These limitations can be overcome using a three-phase solvent micro-extraction bar (3PSBME), in which the ends of the fiber are thermally sealed [19]. This way, the fiber can be left free into the sample without needing any support, making the 3HFLPME portable and easy to handle, without diminishing features related with high pre-concentration factors and chemical selectivity [16,20].

The aim of this work was the application of 3PSBME to selectively pre-concentrate Ag^+ for Ag speciation in estuarine water samples. In this work, tri-isobutylphosphine sulphide (TIBPS) has been selected as an extractant due to its capability, for selective transport of Ag^+ through liquid membranes from estuarine water samples, offering an approach to silver speciation [14].

2. Materials and methods

2.1. Reagents and solutions

All reagents were analytical-reagent grade unless otherwise stated. Potassium nitrate (99%) and sodium chloride (99,5%) were obtained from Scharlau (Barcelona, Spain). Kerosene and ammonia (30%) were obtained from Panreac (Barcelona, Spain). Sodium thiosulphite (100%), 1-pyrrolidine-dithiocarbamate (APDC) and diethylammonium-diethyldithiocarbamate (DDDC) were purchased from Merck (Darmstadt, Germany). Tri-isobutylphosphine sulphide (TIBPS) was provided by Cytec Industries Inc. (NJ, USA) and humic acids were obtained from Aldrich (Steinheim, Germany). Aqueous solutions of silver were prepared from a 1000 mg L^{-1} standard solution obtained from Merck (Darmstadt, Germany) and samples for optimization studies contained 0.1 mg L^{-1} of silver. Deionized water of resistivity lower than 18.2 MΩ cm was obtained by a Millipore Quantum Ultrapure water supplier (Millipore, USA). Acetylene, air, and argon for atomic spectrometry were obtained from Air Liquid (Madrid, Spain).

2.2. Apparatus

Polypropylene Accurel PP S6/2 hollow fibers of 0.2 μm pore size and 1800 μm internal diameter were used in this study (Membrana, Germany). Samples were stirred using an IKA-Big Squid magnetic stirrer (Ika-Werke, Germany). Silver concentration in the aqueous solutions was quantified using a continuum source atomic absorption spectrometer model ContrAA (Analytikjena, Germany), using a flame atomizer (FAAS) for optimization studies and graphite furnace atomizer for application to real samples (GFAAS). Graphite furnaces used were made in pyrolitic graphite (Analytikjena, Germany). Humic acids were measured as dissolved organic carbon (DOC) in a total carbon analyzer Analytik Jena multi N/C 3100 (Analytikjena, Germany).

2.3. Set-up of hollow fiber membranes: three-phases solvent bar micro-extraction (3PSBME)

In order to set up the three phase solvent bars, 5 cm of fiber was cut and one of its ends was thermally sealed using a hot tip and flat ended tweezers. The internal part of the fiber was filled with the acceptor solution containing $S_2O_3^{2-}$ and the other end of the fiber was thermally sealed. This solvent bar was immersed into the organic solution of kerosene containing TIBPS as extractant to impregnate the fiber pores. Finally the excess of organic solution on the fiber was rinsed with deionized water and the fiber was placed into the sample. After extraction time, the acceptor solution inside the fiber was recovered and measured by atomic absorption spectroscopy. In all cases, three aliquots of each sample were extracted. Additionally, internal replicates were carried out adding three solvent bars to every aliquot of sample [21].

2.4. Optimization

Silver pre-concentration by 3PSBME using TIBPS as extractant agent takes place by coupled cotransport [15]. For this type of mechanism, a cationic complex is formed by Ag and TIBPS. For this reason, the use of a counter-ion (NO_3^-) is needed to form a neutral ion pair $\{(AgTIBPS)^+NO_3^-\}$, which can be solubilized in the organic solution, to be transported until the organic-acceptor solution interface. Thus, the ion pair reacts with the acceptor agent ($S_2O_3^{2-}$) and the metal is retained in the acceptor solution. Therefore, NO_3^- concentration in the sample, TIBPS concentration in the organic solution impregnating the fiber pores, $S_2O_3^{2-}$ in the acceptor, and stirring rate were optimized. Univariate optimization was conducted, varying one of the parameters each time while the rest were kept constant.

The extent of silver transport from samples into the acceptor solution was measured as enrichment factor (*EF*) of Ag in the acceptor. This factor is calculated by the ratio between the concentration of silver in the acceptor phase at a certain experiment time (t) ($[Ag^+]_t$) and the initial concentration of silver ion in the sample ($[Ag^+]_0$) (Eq. (1)).

$$EF = \frac{[Ag^+]_t}{[Ag^+]_0} \quad (1)$$

2.5. Instrumental determination of silver

Instrumental analysis of silver concentration in the acceptor solution was carried out by atomic absorption spectroscopy at a wavelength of 328.1 nm and setting up the spectrometer detector between pixels 98 and 102.

For optimization studies, 100 μg L^{-1} Ag was used as initial concentration in the sample. For this reason, analysis of initial Ag^+ concentration in the sample as well as in the acceptor solution was carried out by FAAS using acetylene as fuel and air as oxidizer. To ensure that enough amount of sample was available for measurement in FAAS, the recovered acceptor solution was diluted into 1.5 mL of deionized water. Besides, calibration standards were prepared with the same matrix as the acceptor solution samples by addition of the corresponding amount of $Na_2S_2O_3$.

In the case of silver at natural concentration levels graphite furnace atomic absorption spectroscopy was used for quantification, applying Ar as inert gas. In this case, the acceptor solution was

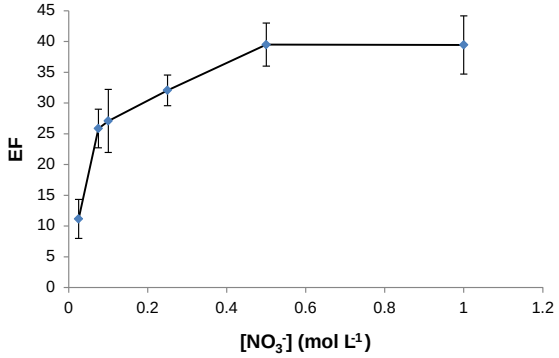


Fig. 1. Optimization of NO_3^- concentration in the sample at 0.1 M TIBPS in the organic phase, 1 M $Na_2S_2O_3$ in the acceptor and 800 rpm stirring speed.

directly recovered from the fiber into a vial and analyzed by GFAAS. Measurements were carried out using ash temperature 1200 °C and atomization temperature 1800 °C in the presence of 5 μg of Pd

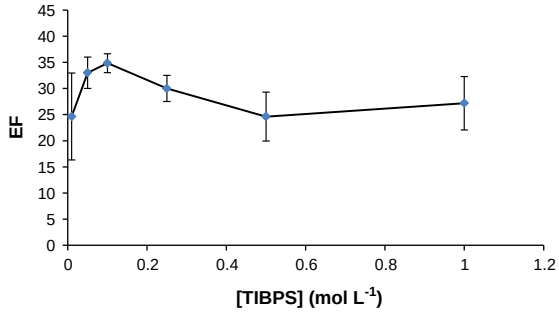


Fig. 2. Optimization of TIBPS concentration in the organic phase at 0.1 M NO_3^-, 1 M $Na_2S_2O_3$ in the acceptor and 800 rpm stirring speed.

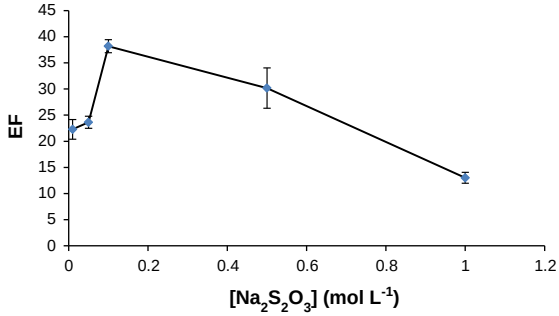


Fig. 3. Optimization of $Na_2S_2O_3$ concentration at 0.1 M NO_3^- in the acceptor, 0.5 M TIBPS in the organic phase, and 800 rpm stirring speed.

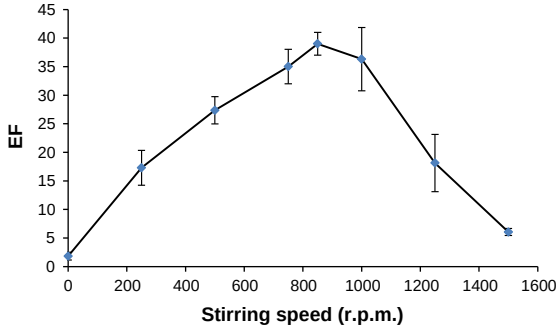


Fig. 4. Effect of stirring speed on enrichment factor under optimized chemical conditions.

$(NO_3)_2$ as matrix modifier [8]. Volume of sample injected was 20 μL and three replicates of each sample of acceptor solution were analyzed. Under these conditions, a limit of detection (LOD) of 0.09 μg L^{-1}, measured as the concentration that offers a signal equal to three times the standard deviation, for the blank signal divided by the slope of the calibration curve was obtained. Linear range of the GFAAS method was 0.1–5 μg L^{-1} [22].

3. Results and discussion

3.1. Optimization of silver pre-concentration by 3PSBME

The first step was the selection of a solvent to impregnate the fiber pores. In this work, different solutions of TIBPS in kerosene and dihexylether were compared for impregnation of the fiber pores. Dihexylether was reported to present higher impregnation capability of Accurel PP 50/280 fibers [8]. In the case of the Accurel PP S6/2 fibers used in this work, kerosene offered similar results as dihexylether. Therefore, kerosene was selected for further experiments because it presents lower cost and better environmental profile.

Initial conditions for optimization were those previously optimized for silver pre-concentration in fibers Accurel PP 50/280: 0.1 M NO_3^- in the sample, 0.1 M TIBPS in the organic phase, 1 M $S_2O_3^{2-}$ in the acceptor, and time of experiment of 4 hours [8]. During optimization, initial concentration of 100 μg L^{-1} of Ag was used in all cases. The effect of nitrate anion concentration was evaluated in the range 0.01–1 M. As it can be observed, enrichment factor was increased by the increasing concentration of nitrate in the sample until it was stabilized at 0.5 M NO_3^- (Fig. 1). Following, the effect of TIBPS concentration on *EF* was studied from 0.1 M to 1 M. Fig. 2 shows that *EF* was improved by the increasing concentration of TIBPS up to 0.1 M, but a decrease in the enrichment factor and poorer reproducibility can be observed at higher concentration. This could be consequence of a loss of diffusion through the organic phase due to an increase in the viscosity of the organic solution. For this reason, 0.1 M TIBPS was used for further experiments. Finally, concentration of the acceptor agent was evaluated in the range 0.01–1 M and a maximum enrichment factor was obtained at 0.1 M $S_2O_3^{2-}$ (Fig. 3).

Evolution of the enrichment factor with stirring speed was also evaluated. As a result, *EF* was improved with the increasing stirring rate up to 900 rpm. At higher stirring speed, transport efficiency decreased because the organic phase was removed from the fiber pores (Fig. 4). Besides, experiment time was studied and a linear increase of the enrichment factor was observed with time until it was stabilized at 120 min. Finally optimized conditions

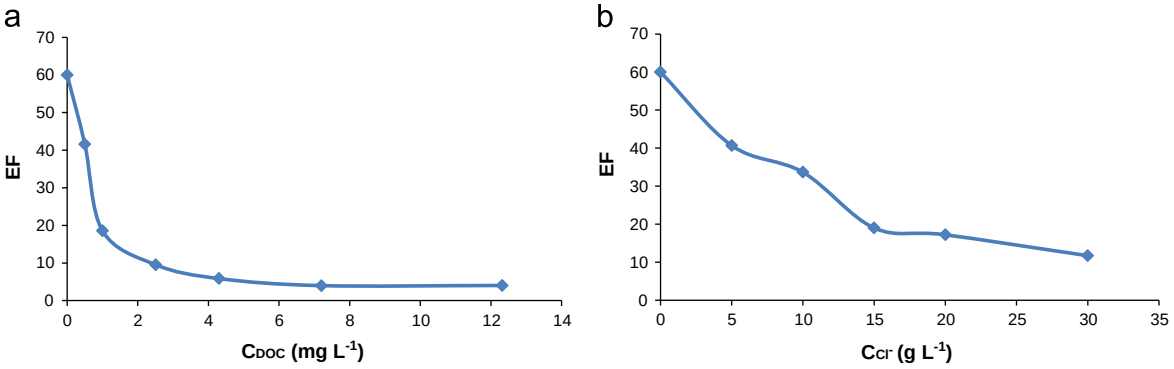


Fig. 5. Effect of a) dissolved organic carbon and b) chloride concentration on Ag^+ enrichment factor.

were 0.5 M NO_3^- in the sample, 0.1 M TIBPS in the organic phase, 0.1 M $S_2O_3^{-2}$ in the acceptor, and 120 min of experiment.

After optimization, samples containing concentrations in the range 0.1–100 μg L^{-1} Ag were analyzed and an average enrichment factor in the whole range of concentration of 60.0 ± 3.2 times was obtained. This fact supports the idea that *EF* is not affected by initial Ag^+ concentration.

3.2. Selective transport of free silver through 3PSBME

In the case of silver, it has been described that Ag^+ is responsible of its toxicity [6,14,19]. Concentration of Ag^+ in estuarine waters is controlled by salinity and dissolved organic matter concentration [9,10]. As a consequence, total silver concentration can be expressed as the sum of Ag^+ and complexes formed with Cl^- and dissolved organic matter in the form of $AgCl_n^{(n-1)-}$ and Ag-DOM, respectively. In order to evaluate which silver species is pre-concentrated by the proposed system, known concentrations of Cl^- and organic matter were added to samples containing 100 μg L^{-1} of Ag. On the one hand, humic acids (HA) were used as a source of DOM, and they were measured as dissolved organic carbon (DOC). On the other hand, NaCl was used as a source of chloride ion.

As it can be seen in Fig. 5a, addition of HA in the range 0.5–12 mg L^{-1} DOC resulted in decreased *EF*, being the slope of the curve higher in the range 0.5 to 2.5 mg L^{-1} DOC. In the case of addition of Cl^- from 1 to 30 g L^{-1}, a decrease in the transport efficiency was also observed, being more regular than in the case of HA (Fig. 5b). These results support the hypothesis that silver species formed after addition of Cl^- and AH were not transported from the sample using TIBPS as extractant. Besides, the combined effect of the HA and Cl^- on *EF* was evaluated and the result was represented by a response surface (Fig. 6). Linear relationship between the logarithm of the enrichment factor and Cl^- concentration and the logarithm of DOC in the samples was observed, offering a fit of 94.82% to the experimental data (Eq. (2)). Therefore, the enrichment factor for silver in samples of known concentration of Cl^- and DOC could be predicted.

$$Log(EF) = 1.4806 - 0.0116C_{Cl^-} - 0.09331Log(C_{DOC}) \quad (2)$$

Taking into account that Ag^+ was assumed to be selectively pre-concentrated, its concentration was directly estimated by 3PSBME, using the *EF* obtained for samples without addition of Cl^- and HA. Additionally, knowing the predicted enrichment factor (EF_p) for known concentration of *HA* and Cl^-, the total concentration of silver Ag_t was estimated by Eq. (3).

$$Ag_t = \frac{Ag^+_{Acceptor}}{EF_p} \quad (3)$$

Finally, total silver (Ag_t) could be considered as the sum of an inert fraction (Ag_i) constituted by $AgCl_n^{(n-1)-}$ and Ag-HA, which were not transportable through the organic phase (Eq. (4)), and Ag^+ that could be transported into the fiber.

$$Ag_t = Ag^+ + Ag_i \quad (4)$$

3.3. Application to real samples

Before application to real samples, a study of methodological blanks was carried out. Blank samples were pre-concentrated using the 3PSBME system and the concentration of Ag in the acceptor solution was measured by GFAAS. Limit of detection of the proposed method was calculated as the average concentration of ten independent blanks samples plus three times their standard deviation, offering a LOD of 1.53 ng L^{-1} [22].

In order to check the capability of the proposed method for predicting total concentration of silver in estuarine conditions of salinity and organic matter, synthetic samples of known total Ag concentration were spiked with different concentrations of DOC and Cl^- and then analyzed. Results of predicted Ag_t by the proposed method were compared with direct measurement of Ag by FAAS in samples prior to the addition of Cl^- and HA. As it can be observed in table 1, no significant differences could be observed between both results after comparison by a *t* test ($n=2$, $\alpha=0.05$) [22].

Finally, real samples from the Guadalquivir River estuary (Spain) with salinities in the range 0–15 and seawater samples from the Bay of Cádiz (Spain) were analyzed by the proposed method. Samples were filtered on-line during sampling and stored frozen in low density polyethylene flasks until they were utilized.

Reference method of liquid-liquid extraction with APDC/DDDC was used to evaluate the accuracy of the proposed method [23]. This method is used for analysis of total silver concentration and results were compared with those of the estimation of total silver in the samples by the proposed method using a *t* test ($n=2$, $\alpha=0.05$). As it can be seen in Table 1, no significant differences were observed for the analysed samples between the reference and the proposed method [22].

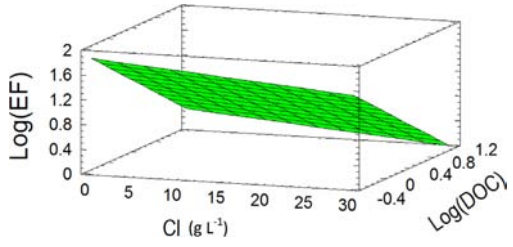


Fig. 6. Surface of response for log(EF) in different DOC and Cl^- concentrations in the sample.

Table 1
Application of 3PSBME to analysis of silver in synthetic and real samples.

Sample	DOC (mg L^{-1})	Cl^- (g L^{-1})	Ag^+	Ag_t (this method)	Ag_t (ref. method)	[c]t	H_0
Synthetic 1	0	0	74,1 μg L^{-1}	74.1 μg L^{-1}	[a]70.4 μg L^{-1}	0.73	Accepted
Synthetic 2	5.0	5.0	19,4 μg L^{-1}	51.0 μg L^{-1}	[a]56.7 μg L^{-1}	−1.68	Accepted
Synthetic 3	5.0	12.0	27,1 μg L^{-1}	86.2 μg L^{-1}	[a]92.5 μg L^{-1}	−1.52	Accepted
Guadalquivir River estuary 1	4.7	2.3	7,4 ng L^{-1}	18.1 ng L^{-1}	[b]16.8 ng L^{-1}	0.75	Accepted
Guadalquivir River estuary 2	4.8	12.6	2,4 ng L^{-1}	7.6 ng L^{-1}	[b]8.0 ng L^{-1}	−0.53	Accepted
Bay of Cádiz 1	3.9	28.1	1,8 ng L^{-1}	6.6 ng L^{-1}	[b]6.3 ng L^{-1}	0.52	Accepted
Bay of Cádiz 2	4.2	29.0	1,6 ng L^{-1}	6.9 ng L^{-1}	[b]7.5 ng L^{-1}	−1.47	Accepted

[a] Flame atomic absorption spectroscopy.
[b] Liquid-liquid extraction with APDC/DDDC and ICP-MS determination [23].
[c] $t_c=4.30$, $n=2$, $\alpha=0.05$.

4. Conclusion

Three-phases solvent bar micro-extraction appears as a reliable and simple alternative for routine application of hollow fiber micro-extraction in the speciation ultra-traces of Ag^+ in estuarine waters. The extractant agent tri-isobutylphoshine sulphide has proved to be selective for transporting Ag^+ in the presence of Cl^- and humic acids. The effect of addition of Cl^- and HA to samples, to simulate estuarine conditions has allowed estimating silver fractions as Ag^+ and Ag associated to Cl^- and organic matter.

Acknowledgments

The present work was financed by the Spanish Ministry of Economy and Competitiveness (CTM-2010–15618).

References

[1] L. Rizzello, P.P. Pompa, Chem. Soc. Rev 43 (2014) 1501–1518.
[2] J.W. Alexander, Surg. Infect. 10 (2009) 289–292.
[3] J. Farkas, H. Peter, P. Christian, J.A. Gallego, M. Hassellov, J. Tuoriniemi, S. Gustafsson, E. Olso., K. Hylland, K.V. Thomas, Environ. Int. 37 (2011) 1057–1062.
[4] L. Geranio, M. Heuberger, B. Nowack, Eviron. Sci. Technol 43 (2009) 8113–8118.
[5] N. Hadrup, H.R. Lam, Regul. Tox. Pharma 68 (2014) 1–7.
[6] S.N. Luoma, Y. Ho, G.W. Bryan, Mar. Pollut. Bull. 31 (1995) 44–54.
[7] Y. Sohrin, K. Bruland, TRAC-Trend 30 (2011) 1291–1307.
[8] J.A. López-López, J.A. Jonsson, M. García-Vargas, C. Moreno, Anal. Method 6 (2014) 1462–1468.
[9] K. N'dungu, M.A. Ranville, R.P. Franks, A.R. Flegal, Mar. Chem. 98 (2006) 09–120.
[10] V.S. Savenko, B.R. Tagirov, Oceanology 36 (1996) 212–215.
[11] J. Wang, X. Wang, Environ. Tox. Chem. 3 (2014) 632–640.
[12] F. Ribeiro, J.A. Gallego-Urrea, K. Jurkschat, A. Crossley, M. Hassellov, C. Taylor, A.M.V.M. Soares, S. Loureiro, Sci. Tot. Environ 466 (2014) 232–241.
[13] I. Miller, K.W. Bruland, Environ. Sci. Tecnol. 29 (1995) 2616–2621.
[14] J.A. López-López, M. García-Vargas, C. Moreno, Talanta 108 (2013) 7–10.
[15] J.A. López-López, M. García-Vargas, C. Moreno, Inter. J. Environ. Anal. Chem. 92 (2012) 636–643.
[16] A.N. Anthemidids, C. Mitani, Curr. Anal. Chem. 9 (2013) 250–278.
[17] A.K. Pabby, A.M. Sastre, J. Mem. Sci. 430 (2013) 263–303.
[18] V. Slaveykova, I. Karadjova, M. Karadjov, D. Tsalev, Environ. Sci. Technol. 43 (2009) 1798–1803.
[19] L. Guo, H.K. Lee, J. Chromatogr. A 1218 (2011) 4299–4306.
[20] A. Spietelun, L. Marcinkowski, M. de la Guardia, J. Namiesnik, Talanta 119 (2014) 34–45.
[21] J.A. López-López, J.J. Pinto, C. Mendiguchía, C. Vergel, M.V. Manuel, C. Moreno, Spanish Patent Application: 201300122 (2013).
[22] J.N. Miller, J.C. Miller, Estadísitca y Quimiometría para Química Analítica, fourth ed., Pearson Education, Madrid, 2002.
[23] K.W. Bruland, R.P. Franks, G. Knauer, J. Martin, Anal. Chim. Acta 105 (1979) 233–245.

Talanta 132 (2015) 387–391

Contents lists available at ScienceDirect

Talanta

journal homepage: www.elsevier.com/locate/talanta

Label-free triple-helix aptamer as sensing platform for "signal-on" fluorescent detection of thrombin

Nan Xu, Quanbo Wang, Jianping Lei*, Lin Liu, Huangxian Ju

State Key Laboratory of Analytical Chemistry for Life Science, School of Chemistry and Chemical Engineering, Nanjing University, Nanjing 210093, PR China

ARTICLE INFO

Article history:
Received 7 August 2014
Received in revised form
13 September 2014
Accepted 18 September 2014
Available online 28 September 2014

Keywords:
Triple-helix aptamer
label-free
fluorescent detection
graphene oxide
thrombin

ABSTRACT

The design of a label-free aptamer for separation of recognition sequence from signal reporter is significant to ensure the high-efficiency affinity between aptamer and target. This work develops a label-free triple-helix aptamer (THA) as sensing platform for "signal-on" fluorescent detection of thrombin. THA was composed of aptamer sequence and help DNA 1 (H1), which contained the complementary sequence of hexachloro-fluorescein (HEX) labeled help DNA 2 (H2). The specific recognition event between aptamer and thrombin triggered the dismission of THA to release H1. The released H1 then reacted with the signal probe of H2/graphene oxide (GO) nanocomposite to form H1-H2 duplex, leading to the fluorescence recovery of H2 due to the detachment of H1-H2 duplex from the surface of GO. With employment of THA as a signal transducer and GO as a "superquencher", this method shows a sensitive response to thrombin with a wide concentration range from 5 to 1200 nM. The limit of detection is 1.8 nM (S/N=3) with excellent selectivity. Considering the universality of THA, the proposed aptasensor would provide a platform for homogeneous fluorescent detection of a wide range of analytes.

© 2014 Elsevier B.V. All rights reserved.

1. Introduction

Triple-helix DNA (THD) is one of nontraditional nucleic acid structures, which involves a third strand in the major groove of a Watson-Crick duplex via Hoogsteen hydrogen bonding [1–4]. Based on groove recognition of THD towards biomolecules, the THD has been extensively employed as therapeutic agents in biomedical and biotechnological applications [5–6]. Recently, THD has been used as template for preparation of site-specific silver nanoclusters with high-stability [7]. By modifications of its nuclear acid structure, THD as signaling probe has been applied in detection of double-stranded DNA (dsDNA) [8,9], microRNA [10], DNA [11], Hg^{2+} [12], and adenosine triphosphate [13], in combination with the techniques of fluorescence and chemiluminescence. The above methods are on the basis of spatial change of THD structure after target recognition for fluorescent signal readout with THD labeling. However, such structural alteration may not induce the enhanced signal for sensitive detection. Therefore, the further functionalization of THD is a promising way in the design of new molecular biology tools, especially for integrating with aptamer as a recognition element.

Aptamers are single-stranded DNA or RNA nucleic acids isolated from random-sequence nucleic acids libraries by SELEX [14,15]. By reason of their high affinity, aptamers are considered to be promising recognition elements for biosensor applications in a wide range of targets including small molecules, ions, and proteins [16–30]. For example, a silver nanocluster functionalized aptamer as sensing platform was designed for multiplexed analysis of pathogenic DNAs via fluorescence resonance energy transfer (FRET) between silver nanocluster and graphene oxide [31]. A sensitive aptasensor was constructed by using two-photon dye labeling aptamer as molecular probe for quantitative detection of adenosine triphosphate [32]. However, due to the requirement of labeling fluorophores or quenchers on the aptamers, these methods are expensive, time-consuming and inconvenient. Meanwhile, another significant problem arises that modifications of dyes on aptamer will influence aptamer's affinity and specificity to target [33]. In order to solve these problems, a triple-helix molecular switch was developed by using a hairpin-shaped aptamer sequence and a dual-labeled oligonucleotide serving as a signal transduction probe [34]. In this work, we design a label-free triple-helix aptamer (THA) as sensing platform for "signal-on" fluorescent detection of thrombin.

Thrombin plays a key role in regulation of tumor growth, metastasis, and angiogenesis [35] and thus it is worth to develop a sensitive and specific method for detection of thrombin in biological samples. Here, by integrating with the advantages of graphene oxide (GO) as efficient supporter and quencher [36], a

* Corresponding author. Tel./fax: +86 25 83593593.
E-mail address: jpl@nju.edu.cn (J. Lei).

http://dx.doi.org/10.1016/j.talanta.2014.09.031
0039-9140/© 2014 Elsevier B.V. All rights reserved.

label-free THA was developed as sensing platform for convenient and homogeneous fluorescent detection of thrombin (Fig. 1). First, the label-free THA and signal probe were conveniently synthesized by the mixing of Apt29 and help DNA 1 (H1), and the hexachloro-fluorescein labeled help DNA 2 (H2) and GO, respectively. After aptamer-thrombin recognition event, the released H1 could react with signal probe of GO/H2 to form H1-H2 duplex, leading to the detachment of H2 from the surface of GO, and thus an enhanced fluorescence was realized for readout. Based on the distinguishment of GO towards single-stranded DNA against double-stranded DNA [37,38] and high affinity between aptamer and target, a fluorescent strategy is achieved for specific detection of thrombin. The label-free THA provides a convenient way for constructing the powerful sensing platform towards the versatility of target in bioanalysis and clinical diagnosis.

2. Experimental

2.1. Materials and reagents

The oligonucleotides along with hexachloro-fluorescein (HEX) labeled DNA were synthesized and HPLC-purified by Sangon Biological Engineering Technology & Co. Ltd. (Shanghai, China). The oligonucleotide sequences were shown in Table 1. Thrombin (Tmb) and horseradish peroxidase (HRP) were purchased from Sigma-Aldrich (Shanghai) Trading Co. Ltd. Bovine serum albumin (BSA) was obtained from Nanjing Sunshine Biotechnology Co. LTD. Human immunoglobulin G antibody (IgG) was obtained from Sangon Biological Engineering Technology & Co. Ltd. (Shanghai, China). Graphene oxide (GO) was obtained from XFNano Materials Tech Co. Ltd. (Nanjing, China). Inorganic metal salts were obtained from Sinopharm Chemical Reagent Co. Ltd. (Shanghai, China). All other reagents were of analytical reagent grade and used as purchased without further purification. Phosphate buffer solution (PBS) (10 mM, containing 20 mM KCl and 2.5 mM $MgCl_2$, pH 6.2) was used for homogeneous fluorescence detection of thrombin. Tris–HCl buffer (20 mM, containing 100 mM NaCl, 5 mM KCl, 1 mM $CaCl_2$, 1 mM $MgCl_2$, and 8.5% glycerol (v/v), pH 7.4) was used to dissolve thrombin. Human blood serum samples were obtained from Jiangsu Province Tumor Hospital (Nanjing, China). Ultrapure water obtained from a Millipore water purification system ($\geq$ 18 MΩcm, Milli-Q, Millipore) was used in all experiments.

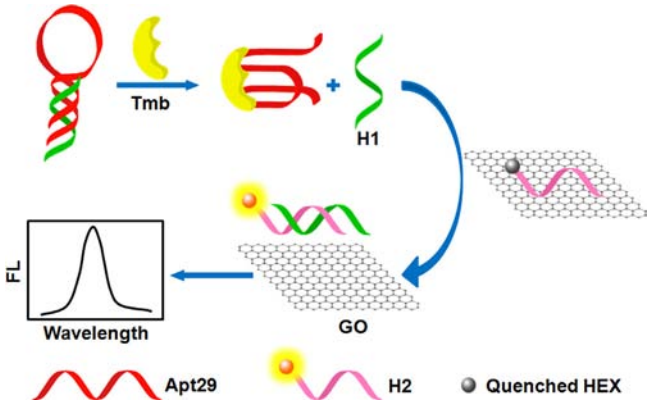


Fig. 1. Schematic illustration of label-free triple-helix aptamer as sensing platform for fluorescent detection of thrombin.

2.2. Apparatus

The synchronous scanning fluorescence spectra were recorded from 500 to 620 nm with a step of 1 nm at the excitation wavelength of 482 nm on a RF-5301PC spectrofluorometer (Shimadzu Co., Japan) equipped with a xenon lamp. The slit width was 5 nm, and the stokes shift ($\Delta\lambda$) was 18 nm for HEX.

2.3. Preparation of triple-helix aptamer and signal probe

The DNA stock solutions of Apt29 (1 μM) and help DNA 1 (H1, 1 μM) were first heated at 90 °C for 10 min, and gradually cooled down to room temperature. Subsequently, THA (0.5 μM) was prepared by mixing the same volume of Apt29 (1 μM) and H1 (1 μM) in 10 mM PBS, and then incubated at room temperature for 30 min.

To obtain the optimal performance, a series of GO dispersions were involved in the preparation of signal probe (GO/H2). The optimal ratio of GO (150 μg mL^{-1}), H2 (1 μM) and PBS was 5:2:43 in volume. The final concentration of the signal probe of GO/H2 was 15.2 μg mL^{-1}.

2.4. Homogenous fluorescence detection of thrombin

4 μL THA (0.5 μM) were mixed with different concentrations of thrombin in a certain volume of PBS to form 50 μL of reaction mixture. After the mixture was incubated at 37 °C for 40 min, 50 μL GO/H2 and 100 μL PBS were added to the reaction mixture at room temperature for 50 min. Subsequently, the final solution was used for fluorescent detection.

3. Results and discussion

3.1. Principle of sensing platform

The mechanism of label-free THA as fluorescent sensing platform for detection of thrombin based on GO is shown as Fig. 1. The work employed THA as a signal trigger which was composed of Apt29 and H1 by Watson-Crick and Hoogsteen base pairings [5]. In the absence of Tmb, H2 was absorbed on GO surface by π-π stacking, and its fluorescence was quenched though FRET [39], that is, the fluorescence of GO/H2 was turned off. Upon the introduction of Tmb, THA structure was dismissed and thus released H1 due to the specific recognition between Apt29 and Tmb. Afterwards, the released H1 reacted with signal probe of GO/H2 to form H1-H2 duplex that was desorbed from surface of GO, leading to the recovery of the fluorescence of signal probe. Therefore, the "signal-on" fluorescence strategy was simply achieved for the sensitive detection of Thrombin with high specificity.

Table 1
Oligonucleotide sequences used in this work.

Oligonucleotide	Sequence
Apt29	5'–CTCTCTTT***AGTCCGTGGTAGGGCAGGTTGGGGTGACT***TTTCTCTC-3'
help DNA 1 (H1)	5'–AAAGAGAGCGTA-3'
help DNA 2 (H2)	5'–TACGCTCTCTTT-HEX-3'

HEX is hexachloro-fluorescein. The aptamer sequence is bold in italic type.

3.2. Feasibility of strategy

The feasibility of the proposed method was demonstrated by fluorescence emission spectra of signal probe under different conditions (Fig. 2). The fluorescence spectrum of GO/H2 exhibited extremely weak fluorescence intensity owing to the strong adsorption of H2 on the surface of GO and the high fluorescence quenching efficiency of GO by FRET (curve a). The introduction of THA brought about no change of fluorescence intensity, because THA was bond up by Watson-Crick and Hoogsteen base pairings (curve b). Once THA was mixed with Tmb followed by GO/H2, the fluorescence intensity increased 37.4 times than that of GO/H2 (curve c). When mixing GO/H2 with free H1, an obvious fluorescence restoring of HEX labeled to H2 was obtained (curve d). These results indentified that THA could release H1 to trigger the fluorescence recovery of HEX in the presence of Tmb, leading to a "signal-on" fluorescence of sensing platform for detection of the target.

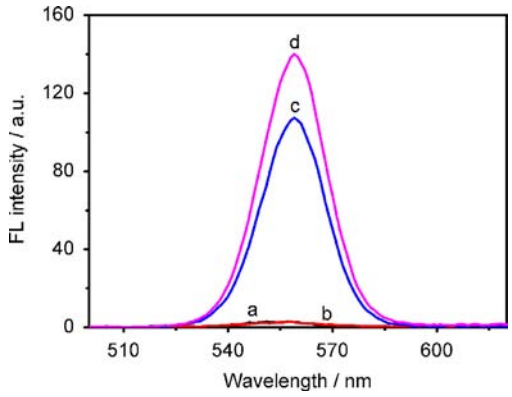


Fig. 2. Fluorescence emission spectra of GO/H2 (a), THA+GO/H2 (b), THA+Tmb+GO/H2 (c), and GO/H2+H1 (d). The concentrations of THA, Tmb, H1 and GO/H2 were 10, 1000, 100 nM and 3.8 μg mL^{-1}, respectively.

3.3. Optimization of conditions

In order to achieve the optimal performance, the concentration of GO as a critical factor for detection efficiency was optimized. As shown in Fig. 3A, the fluorescence intensity ratio of sensing platform, F/F_0, first increased and subsequently decreased as the concentration of GO increased. The results demonstrated that small amount of GO was insufficient to quench the HEX labeled on H2, and by contrast excess GO provided spare area to absorb THA or released H1 resulting in that low fluorescence intensity was recovered. Therefore, the corresponding concentration of GO (3.75 μg mL^{-1}) was chosen as the optimal value for the next experiments.

The effects of reaction time between Apt29 and H1, THA and Tmb, as well as THA/Tmb and signal probe on fluorescence intensity ratio of F/F_0 were investigated step by step. After mixing Apt29 with H1 at the same molar, 30 min was identified as the optimal time to ensure that THA was completely formed (Fig. 3B). For incubation time of THA and Tmb, the value of F/F_0 increased and reached a plateau at 40 min (Fig. 3C), which indicated the THA fully reacted with Tmb and liberated H1. When addition of GO/H2 into the mixture, the F/F_0 ratio first increased and subsequently reduced (Fig. 3D). The phenomena could be explained that the liberated H1 from THA couldn't completely react with signal probe within a short time. But a long reaction time could result in fluorescence enhancement of background due to

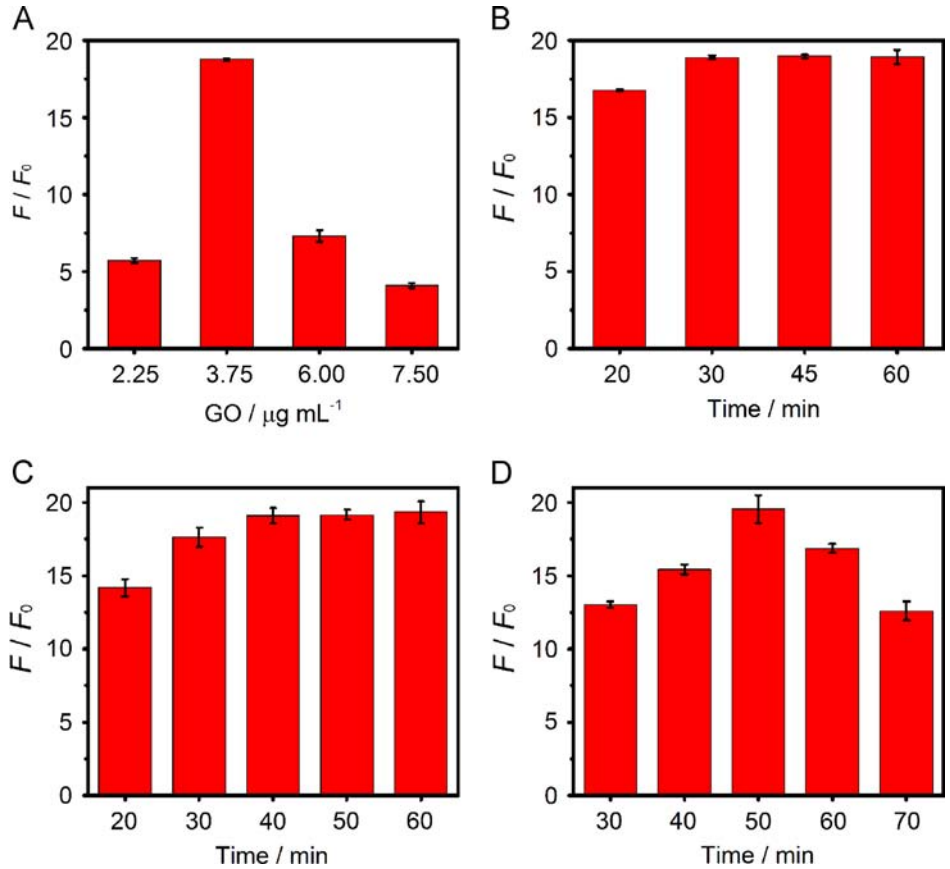


Fig. 3. Effects of (A) GO concentration, incubation time for (B) Apt29+H1, (C) THA+Tmb, and (D) THA+Tmb+GO/H2 on the fluorescence ratio of F/F_0. F and F_0 are the fluorescence intensities of sensing system in the presence and absence of Tmb, respectively. All assays were carried out in 10 mM PBS with 500 nM Tmb, 10 nM THA, while the other parameters were under their optimal conditions.

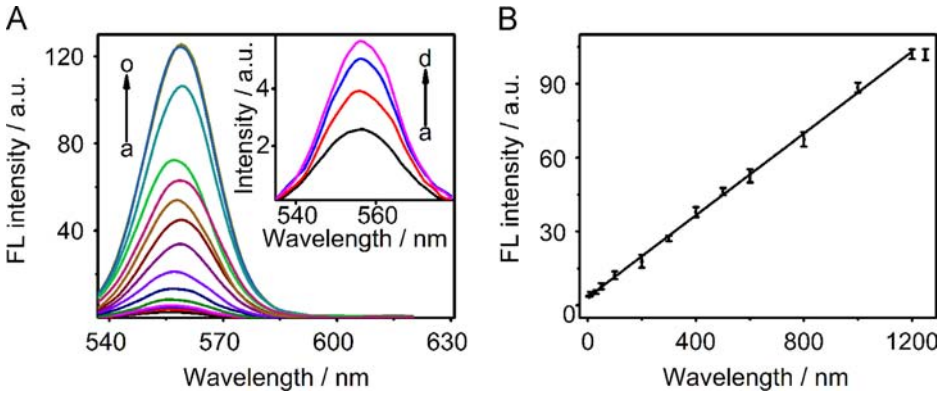


Fig. 4. (A) Fluorescence emission spectra of sensing platform in response of Tmb at 0, 5, 10, 30, 50, 100, 200, 300, 400, 500, 600, 800, 1000, 1200 and 1250 nM (from a to o). Inset: Amplified fluorescence emission spectra in response of Tmb at 0, 5, 10, 30 nM (from a to d). (B) Calibration curve for Tmb detection.

Table 2
Comparison of the fluorescent label-free aptamer-based biosensors for thrombin.

Detection method	LOD (nM)	Linear range (nM)	Ref
Fluorescent detection using triple-helix aptamer	1.8	5–1200	This work
Fluorescent aptasensor based on multi-branched pyrazine derivative	50	5–2500	41
Fluorescent detection based on H_2O_2-catalyzed oxidation via hemin/G-quadruplex DNAzyme	10	0–100	42
Fluorescent detection based on QDs/Ru complex photoinduced charge transfer	50	200–1600	43
Fluorescent detection based on inhibition of polymerase reaction	62.5	0–500	44

the competition of THA with the absorbed H2 onto GO, and thus the F/F_0 ratio reduced [40]. Hence 50 min was chosen as the optimal reaction time for fluorescence detection.

3.4. Tmb detection

Under the optimal concentration of GO and reaction time, the fluorescence intensity of sensing platform enhanced dramatically with the increasing concentration of Tmb in the wide range from 5 to 1200 nM (Fig. 4). The linear regression equation was $I=3.30+0.08\times c$ ($R^2=0.9989$), where I is the fluorescence intensity and c is the Tmb concentration. The detection limit was estimated to be 1.8 nM at 3σ. As shown in Table 2, the detection limit of the proposed aptasensor for thrombin was lower than those of the previous fluorescent label-free aptamer-based methods [41–44]. The high sensitivity and the wide detection range of our method are attributed to the high-efficiency affinity between label-free THA and Tmb, and the strong fluorescence quenching effect of GO on fluorophore labeled on single-stranded DNA. In addition, a relative standard deviation was calculated to be 4.2% for 300 nM thrombin with 6 different aptasensors, indicating acceptable reproducibility.

3.5. Selectivity of sensing platform

To evaluate the selectivity of our strategy for Tmb, the fluorescence responses of sensing platform to Tmb and other proteins containing HRP, BSA and IgG were individually investigated at the same concentration (500 nM). As shown in Fig. 5, the fluorescence intensity of Tmb was approximately 5.9 times higher than that of IgG. For BSA and HRP, the fluorescence intensity of target was 3.4 times and 3.8 times higher than negative controls, respectively. The results could be attributed to that nonspecific adsorption of interference proteins onto GO caused a fraction of H2 to be discharged from surface of GO. The selectivity of the sensing platform resulted from the specific recognition of aptamer to Tmb and the specific hybridization of H1 with H2. It could be summarized that THA as fluorescent sensing platform is promising

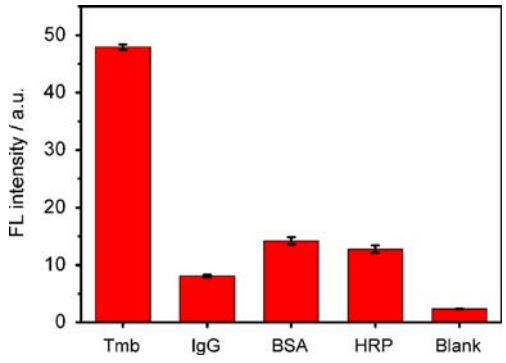


Fig. 5. Fluorescence intensity changes of the aptasensor toward Tmb and other proteins under the same condition. The concentrations of Tmb, IgG, BSA and HRP were 500 nM.

to be applied in homogeneous fluorescent detection of Tmb and related analytes.

3.6. Tmb detection in serum samples

Considering sensitive detection of thrombin in real sample is of great importance for disease diagnosis and drug discovery, thrombin in serum samples was detected by the proposed aptasensor. A series of samples were prepared by spiking the standard solution of 500 nM to different human blood serum samples. All of recoveries were from 97.7% to 92.9%, indicating the proposed strategy could be promising for thrombin detection in real biological samples.

4. Conclusions

The novel label-free triple-helix aptamer was successfully constructed as sensing platform for homogeneous fluorescent detection of target. THA is composed of aptamer sequence and help DNA 1, which functions as the recognition element for specific recognition of Tmb, and the trigger for fluorescence recovery of signal probe,

respectively. Taking advantages of the specific recognition of aptamer to Tmb and the specific hybridization of H1 with H2, the THA-based sensing platform could selectively detect thrombin with a wide linear range and a low detection limit. Moreover, the separation of aptamer from signal reporter ensures the high affinity between aptamer sequence and target. Besides, this method possesses some merits such as convenient operation and low cost. The label-free triple-helix aptamer as a universal signal transducer can provide a simple, sensitive, selective homogeneous protocol in bioanalysis.

Acknowledgements

This work was financially supported by the National Basic Research Program of China (2010CB732400), and National Natural Science Foundation of China (21375060, 21121091, 21135002).

References

[1] P. Zhang, T. Beck, W.H. Tan, Angew. Chem. Int. Ed. 40 (2001) 402–405.
[2] E. Golub, R. Freeman, I. Willner, Anal. Chem. 85 (2013) 12126–12133.
[3] Z.G. Wang, Q.W. Xue, W.Z. Tian, L. Wang, W. Jiang, Chem. Commun. 48 (2012) 9661–9663.
[4] O. Doluca, J.M. Withers, V.V. Filichev, Chem. Rev. 113 (2013) 3044–3083.
[5] K. Hoogsteen, Acta Cryst. 12 (1959) 822–823.
[6] D.P. Arya, Accounts Chem. Res. 44 (2010) 134–146.
[7] L.Y. Feng, Z.Z. Huang, J.S. Ren, X.G. Qu, Nucleic Acids Res. 40 (2012) e122.
[8] Z.Y. Xiao, X.T. Guo, L.S. Ling, Chem. Commun. 49 (2013) 3573–3575.
[9] F. McKenzie, K. Faulds, D. Graham, Chem. Commun. 20 (2008) 2367–2369.
[10] S. Bi, J.L. Zhang, S.Y. Hao, C.F. Ding, S.S. Zhang, Anal. Chem. 83 (2011) 3696–3702.
[11] T.N. Grossmann, L. Röglin, O. Seitz, Angew. Chem. Int. Ed. 46 (2007) 5223–5225.
[12] J. Zheng, Y.H. Nie, Y.P. Hu, J.S. Li, Y.H. Li, Y. Jiang, R.H. Yang, Chem. Commun. 49 (2013) 6915–6917.
[13] S.S. Zhang, Y.M. Yan, S. Bi, Anal. Chem. 81 (2009) 8695–8701.
[14] C. Tuerk, L. Gold, Science 9 (1990) 505–510.
[15] L. Gold, B. Polisky, O. Uhlenbeck, M. Yarus, Annu. Rev. Biochem. 64 (1995) 63–97.
[16] N.K. Navani, Y.F. Li, Curr. Opin. Chem. Biol. 10 (2006) 272–281.
[17] X.J. Chen, Y.Z. Wang, Y.Y. Zhang, Z.H. Chen, Y. Liu, Z.L. Li, J.H. Li, Anal. Chem. 86 (2014) 4278–4286.
[18] S.F. Liu, Y. Lin, L. Wang, T. Liu, C.B. Cheng, W.J. Wei, B. Tang, Anal. Chem. 86 (2014) 4008–4015.
[19] E. Farjami, R. Campos, J.S. Nielsen, K.V. Gothelf, J. Kjems, E.E. Ferapontova, Anal. Chem. 85 (2013) 121–128.
[20] J.H. Liu, C.Y. Wang, Y. Jiang, Y.P. Hu, J.S. Li, S. Yang, Y.H. Li, R.H. Yang, W.H. Tan, C.Z. Huang, Anal. Chem. 85 (2013) 1424–1430.
[21] Z. Zhu, C.C. Wu, H.P. Liu, Y. Zou, X.L. Zhang, H.Z. Kang, C.Y.J. Yang, W.H. Tan, Angew. Chem. Int. Ed. 49 (2010) 1052–1056.
[22] C.C. Wu, L. Yan, C.M. Wang, H.X. Lin, C. Wang, X. Chen, C.Y.J. Yang, Biosens. Bioelectron. 25 (2010) 2232–2237.
[23] K. Hu, Y. Huang, S.E. Wang, S.L. Zhao, J. Pharm. Biomed. Anal. 95 (2014) 164–168.
[24] J.H. Chen, X. Zhang, S.X. Cai, D.Z. Wu, M. Chen, S.H. Wang, J. Zhang, Biosens. Bioelectron. 57 (2014) 226–231.
[25] Y.X. Yuan, R.Q. Li, Z.H. Liu, Anal. Chem. 86 (2014) 3610–3615.
[26] Y. Wang, Z.H. Li, T.J. Weber, D.H. Hu, C.T. Lin, J.H. Li, Y.H. Lin, Anal. Chem. 85 (2013) 6775–6782.
[27] J.W.J. Li, X.H. Fang, W.H. Tan, Biochem. Biophys. Res. Commun. 292 (2002) 31–40.
[28] Z.W. Tang, P. Mallikaratchy, R.H. Yang, Y.M. Kim, Z. Zhu, H. Wang, W.H. Tan, J. Am. Chem. Soc. 130 (2008) 11268–11269.
[29] J. Huang, Z. Zhu, S. Bamrungsap, G.Z. Zhu, M.X. You, X.X. He, K.M. Wang, W. H. Tan, Anal. Chem. 82 (2010) 10158–10163.
[30] D. Li, B. Shlyahovsky, J. Elbaz, I. Willner, J. Am. Chem. Soc. 129 (2007) 5804–5805.
[31] X.Q. Liu, F. Wang, R. Aizen, O. Yehezkeli, I. Willner, J. Am. Chem. Soc. 135 (2013) 11832–11839.
[32] M. Yi, S. Yang, Z.Y. Peng, C.H. Liu, J.S. Li, W.W. Zhong, R.H. Yang, W.H. Tan, Anal. Chem. 86 (2014) 3548–3554.
[33] S. Jhaveri, M. Rajendran, A.D. Ellington, Nat. Biotechnol. 18 (2000) 1293–1297.
[34] J. Zheng, J.S. Li, Y. Jiang, J.Y. Jin, K.M. Wang, R.H. Yang, W.H. Tan, Anal. Chem. 83 (2011) 6586–6592.
[35] M.L. Nierodzik, S. Karpatkin, Cancer Cell 10 (2006) 355–362.
[36] F. Li, H. Pei, L.H. Wang, J.X. Lu, J.M. Gao, B.W. Jiang, X.C. Zhao, C.H. Fan, Adv. Funct. Mater. 23 (2013) 1–9.
[37] Y.Q. Wen, F.F. Xing, S.J. He, S.P. Song, L.H. Wang, Y.T. Long, D. Li, C.H. Fan, Chem. Commun. 46 (2010) 2596–2598.
[38] J.H. Huang, X. Gao, J.J. Jia, J.K. Kim, Z.G. Li, Anal. Chem. 86 (2014) 3209–3215.
[39] C.H. Lu, H.H. Yang, C.L. Zhu, X. Chen, G.N. Chen, Angew. Chem. Int. Ed. 48 (2009) 4785–4787.
[40] B.W. Liu, Z.Y. Sun, X. Zhang, J.W. Liu, Anal. Chem. 85 (2013) 7987–7993.
[41] S.Y. Yan, R. Huang, Y.Y. Zhou, M. Zhang, M.G. Deng, X.L. Wang, X.C. Weng, X. Zhou, Chem. Commun. 47 (2011) 1273–1275.
[42] E. Golub, R. Freeman, A. Niazov, I. Willner, Analyst 136 (2011) 4397–4401.
[43] W.L. Sun, T.M. Yao, S. Shi, Analyst 137 (2012) 1550–1552.
[44] C.F Zhu, Y.Q. Wen, D. Li, L.H. Wang, S.P. Song, C.H. Fan, I. Willner, Chem. Eur. J. 15 (2009) 11898–11903.

Talanta 132 (2015) 392–397

Contents lists available at ScienceDirect

Talanta

journal homepage: www.elsevier.com/locate/talanta

Ultrasensitive 4-methylumbelliferone fluorimetric determination of water contents in aprotic solvents

Katarzyna Kłucińska, Rafał Jurczakowski, Krzysztof Maksymiuk, Agata Michalska *

Department of Chemistry, Warsaw University, Pasteura 1, 02-093 Warsaw, Poland

ARTICLE INFO

Article history:
Received 14 July 2014
Received in revised form
9 September 2014
Accepted 12 September 2014
Available online 19 September 2014

Keywords:
Water determination
Karl Fischer
4-methylumbelliferone
Aliphatic solvents
Fluorometry

ABSTRACT

A novel approach to the quantification of relatively small amounts of water present in low polarity, aprotic solvents is proposed. This method takes advantage of protolitic reaction of 4-methylumbelliferone dissolved in the solvent with water, acting as a base. The low emission intensity neutral 4-methylumbelliferone is transformed in reaction with water to a highly fluorescent anionic form. Thus the increase in emission intensity is observed for increasing water contents in aprotic solvents. For low water contents and highly lipophilic solvents, this method yields (in practical conditions) higher sensitivity compared to biamperometric Karl Fischer titration method in volumetric mode.

It is also shown that organic compounds of protolitic character (amines, acids) not only interfere with water contents determination but increase the sensitivity of emission vs. water contents dependence. Introduction of aqueous solution of strong acid or base (HCl or NaOH) has similar effect on the system as introduction of pure water.

© 2014 Elsevier B.V. All rights reserved.

1. Introduction

Determination of water contents, particularly in the case of organic solvents is essential for many practical applications, especially in industrial processes. Clearly, there is an interest in methods allowing quick and easy access to information on water contents in different organic media. The golden standard for water determination is coulometric Karl Fischer titration, for example [1]. In general, this is the most reliable method, however, in the case of minute water concentrations and especially highly lipophilic, aprotic solvents problems related to sampling and especially tendency of water to spontaneously accumulate close to more hydrophilic surfaces – e.g. glassware, may result in inaccurate determination results [1,2]. In aprotic and non-alcoholic solvents Karl Fischer method is less sensitive because the Bunsen reaction is favored and water/iodine molar ratio changes toward 2:1 in contrast to the 1:l molar ratio found in the protic Karl Fischer environment [3]. For oil samples the results obtained by volumetric and coulometric Karl Fischer methods usually considerably differ even after correcting for the instrumental bias. Thus it was suggested that the volumetric method should be preferred over coulometric method to measure all of the water content in oil samples [4,5]. Moreover, Karl Fischer titration can hardly be performed as an integral part of technological process, or be used to continuously monitor any occurrence of water in the sample media. Thus, different alternative methods of water quantification have been proposed, including advanced techniques like NMR [6], infrared spectrometry [7,8], UV/Vis spectrometry [9,10]. Many of them tried to apply fluorometry for determination of water contents in organic solvents as well for example [11–14]. The latter approach, however, requires application of fluorophore of emission spectra dependent on the presence of water in the studied system. Different compounds have been proposed/tested in this respect, most of them were tailor made (synthesized) for water determination purpose. Moreover, in most cases the increase of water contents in the sample was accompanied with decrease (quenching) of emission signal (e.g. [11,13]). For practical analytical applications, however, commercially available fluorophores probes, and optimally leading to increase of the emission signal with increasing analyte (water) concentrations are preferred. Among widely available, cost-effective ligands 4-methylumbelliferone (4-MU), pH-sensitive, widely used, bright fluorophore is known to be soluble in variety of organic solvents. It was also shown that the emission spectrum of 4-MU probe is dependent on the solvent used and on the presence of acid/bases in the sample, for example [15,16]. The dependence of emission intensity on water contents in ethanol in the presence of constant concentration of hydrochloric acid was also reported [15]. Nevertheless, to our best knowledge, the above-mentioned reports have not led to analytical application of 4-MU as water-sensitive probe for organic media.

The herein proposed approach is based on assumption that in the lipophilic solvents (*even in the absence of acid or bases in the system*) dissolved neutral 4-MU can spontaneously undergo

* Corresponding author. Tel.: +4822 8220211; fax: +48 22 8225996.
E-mail address: agatam@chem.uw.edu.pl (A. Michalska).

http://dx.doi.org/10.1016/j.talanta.2014.09.018
0039-9140/© 2014 Elsevier B.V. All rights reserved.

protolitic reaction with water leading to formation of highly fluorescent species, especially deprotonated 4-MU, a bright fluorophore [15]. It is rational to expect that fluorescence intensity in this case should be dependent on the amount of water present, thus allowing quantification of water in the sample, especially in emulsion. The herein proposed approach was used to quantify amount of water present in the sample of a model organic medium: hexadecane. The effect of other (model) protolitic agents present in the sample on the resulting emission signal was also studied. The proposed method was also applied for toluene and cyclohexane model solvents. Application of 4-MU to quantify minute contents of water in aprotic, lipophilic solvents to our best knowledge has not been proposed in literature.

Results of 4-MU-based water quantification using herein proposed method have been compared with water determination results performed using the classical approach – biamperometric Karl Fischer titration in volumetric mode, showing that especially for low amounts of water present in the sample, herein proposed method offers higher sensitivity.

2. Experimental

2.1. Reagents

Hexadecane (HD), 4-methylumbelliferone (4-MU), HYDRANAL® - Composite 5 K (Titration), HYDRANAL® - Medium K, HYDRANAL® - Water Standard 10.0, toluene, cyclohexane, hexanoic acid, palmitic acid, octanoic acid, isopentyl amine, octadecyl amine and molecular sieves were from Aldrich (Germany). Octylamine, hydrochloric acid and NaOH were of analytical grade and were obtained from POCh (Gliwice, Poland).

Doubly distilled and freshly deionized water (resistance 18.2 MΩcm, Milli-Qplus, Millipore, Austria) was used throughout this work. All solvents were dried over freshly activated molecular sieves (MS 4A).

2.2. Apparatus

Fluorimetric experiments were performed using a spectrofluorimeter Cary Eclipse (Varian). After exposure at an excitation wavelength, unless otherwise stated, equal to 320 nm, emission intensity was observed within the range from 350 nm (or 370 nm) to 600 nm. The slits used were 5 nm both for excitation and emission, while the detector voltage was maintained at 800 V.

Biamperometric Karl Fischer titration in volumetric mode was performed using Titration Equipment: 716 DMS Titrino (Metrohm) and 728 Stirrer (Metrohm), platinum electrodes (400 mV) were used. Chloroform was added to the working solution as a solubility promoter so that the KF titration was conducted in the homogeneous solution. This procedure was found to give more reproducible results. The requirements of complete dissolution in KF method was also discussed earlier [5]. Emulsions were prepared using homogenizer Hielscher, model UP 200 S.

2.3. Preparation of 4-MU stock solutions

4-MU stock solutions in tested solvents were prepared by dissolving 2 mg of 4-MU in 80 ml of a solvent (either hexadecane, toluene or cyclohexane) under sonication (cycle 0.5, power 70%) yielding a concentration 0.025 mg/ml. Sonication was continued for another 5 min. Then the mixture was left for 24 hours to complete dissolution of the fluorophore. Thus prepared solutions were used for fluorimetric measurements.

2.4. Preparation of the samples

Water was introduced to one of the tested solvents (hexadecane, cyclohexane, toluene) containing 4-MU. To assure that introduced water is mixed with dry solvent, the sample was sonicated for 60 seconds. Samples for Karl Fischer titration control experiment were prepared in the same manner.

3. Results and discussion

4-MU is a well-known fluorescent pH indicator, showing strong emission at about 450 nm in aqueous alkaline solutions, this emission is characteristic for deprotonated form of 4-MU – when it is present as anion, Fig. S1 [15,16]. Analytical usefulness of this reagent has been proven in numerous applications, including those where the enzymatic reaction leads to formation of highly fluorescent 4-MU anion, from optically silent enzymatic substrates (for example using alkaline phosphatase, glucuronidase, β-glucosidase and other enzymes).

Fig. 1. presents excitation and emission spectra obtained for 4-MU dissolved in concentration 0.025 mg/ml in hexadecane. As it

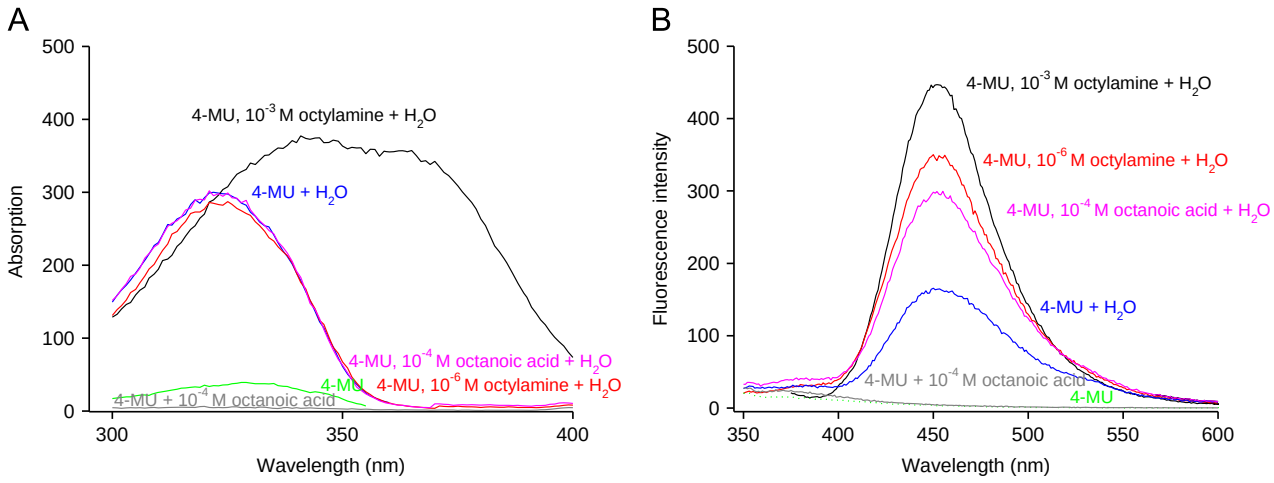


Fig. 1. (A) Excitation and (B) emission spectra (excitation wavelength 320 nm) recorded for 4-MU (0.025 mg/ml) in HD, in the absence and in the presence of model additives tested: (green line) 4-MU in HD, (navy line) 4-MU in HD in the presence of 0.16% v/v water in HD, (red line) 4-MU in HD in the presence of 10^{-6} M octylamine and 0.16% v/v water in HD, (black line) 4-MU in HD in the presence of 10^{-3} M octylamine and 0.16% v/v water in HD, (grey) 4-MU in HD in the presence of 10^{-4} M octanoic acid, (magenta) 4-MU in HD in the presence of 10^{-4} M octanoic acid and 0.16% v/v water in HD.

can be seen in Fig. 1, for 4-MU dissolved in HD weak absorption (at about 320–330 nm) and practically no emission is observed. It should be stressed that 0.025 mg/ml concentration of 4-MU is the highest practically achievable for HD solutions. The emission intensities observed at about 380 nm for the same concentration of 4-MU in toluene were yet lower compared to HD, Fig. S2, and were very weak for cyclohexane (the latter are not included in Fig. S2). It should be stressed that the presence of emission peak at 380 nm confirms, that as expected, neutral 4-MU is present in dry tested solvents [15] (structure A in Fig. S1).

As 4-MU is known to be sensitive to the presence of protolitic agents in sample, the effect of presence of model compounds of this nature was tested. The introduction of protolitic reagents to the model solvent tested, HD, results in only small changes in the emission spectra, Fig. S3. The presence of tested acids: hexanoic, octanoic or palmitic in 10^{-3} M concentration results in 4-MU emission observed at about 380 nm, suggesting that still neutral 4-MU is present in the system, regardless acid added. For higher concentrations of acid added to HD, 10^{-1} M, apart from significant increase of peak at 380 nm, additional peak is formed at about 490 nm, Fig. S3, inset. The latter is typical for neutral tautomer form of 4-MU, structure C, Fig. S1 [15]. This behavior is similar to that reported earlier for strong acid (HCl) introduced to protolitic solvents as water or ethanol [15]. Thus, it is probable that, in the absence of other protolitic agents, even relatively weak (in aqueous environment) acids are able to induce the change of the structure of neutral 4-MU molecule, leading to formation of above mentioned neutral tautomer characterized with emission at about 490 nm.

On the other hand, introduction of a base: isopentylamine, octylamine or octadecylamine in low concentrations, $< 10^{-6}$ M, did not affect the emission spectra obtained. Regardless of the amine used, similar behavior was observed, the exemplary results obtained for octylamine are shown, Fig. 2. For low concentration of amine present in the sample, both excitation and emission spectra recorded resemble those of 4-MU in HD recorded in the absence of amine. However, for higher concentration of amine ($> 10^{-5}$ M) the intensity of emission of 4-MU dissolved in HD was significantly dependent on concentration of amine, as shown on example of octylamine, Fig. 2. For the amine concentration equal to 10^{-5} M a small shoulder is formed on 4-MU emission spectra with a maximum at 450 nm, at wavelength typical for deprotonated form of 4-MU, Fig. S1 B. Further increase of amine contents to 10^{-4} M and 10^{-3} M results in formation of a well-developed emission peak with maximum at 450 nm (excitation 330 nm), clearly pointing out to deprotonation of 4-MU as expected for presence of a base in the sample [15].

Introduction of water to (net) HD containing 4-MU (5 μl to 3 ml, corresponding to 0.17% v/v or 0.093 M concentration) leads to similar change of 4-MU emission spectra as introduction of any amines in 10^{-4} M concentration, Fig. 1. On the excitation spectra a pronounced absorption peak is formed with maximum at about 320 nm. On the emission spectra a strong peak is formed with a maximum at about 450 nm, suggesting the presence of deprotonated form of 4-MU in HD. Thus, it can be assumed that in the absence of other deprotonating agents, water as a base reacts with 4-MU and this reaction leads to deprotonation of 4-MU and formation of structure depicted in Fig. S1 B. This process can be accompanied by partition of 4-MU anion to the water phase, due to its higher (compared to neutral 4-MU) solubility in water. Thus the protolitic reaction of 4-MU with water in aliphatic environment is promising for the analytical, fluorimetric water determination.

Fig. 3. presents emission spectra of 4-MU dissolved in HD, recorded for changing water concentration in the sample from $1.7.10^{-2}$% v/v ($9.3.10^{-3}$ M) to 0.6% v/v (0.37 M). As it can be seen from Fig. 3 introduction of even relatively small amount of water, reaching $1.7.10^{-2}$% v/v, to 4-MU containing HD results in formation of emission peak at wavelength typical for deprotonated form of 4-MU, at 450 nm (excitation wavelength 320 nm). Increase of the amount of water introduced to the sample results in clear increase of the intensity of emission observed at 450 nm. The linear dependence of emission intensity on water contents was observed within the range from $1.7.10^{-2}$% to 0.33% v/v, that is up to 0.185 M water in HD, Fig. 4. Within this range the correlation coefficient, R^2, of the dependence of emission intensity on water contents was equal to 0.987, Table 1. Further increase of water contents in the sample to 0.67% v/v (0.37 M) resulted in some increase in the recorded emission, yet not linear. In this range also the magnitude of error increases, Fig. S4. The plateau of the signal obtained can be attributed to different effects; however, it should be stressed that for these water contents the amount (mole) of water was more than 2000 times higher compared to amount (mole) of 4-MU present in the sample. It can also result from the protolitic reaction, and from acid–base equilibrium prevailing in the sample.

The advantage of herein proposed approach is clearly seen when comparing the results of fluorimetric evaluation of water

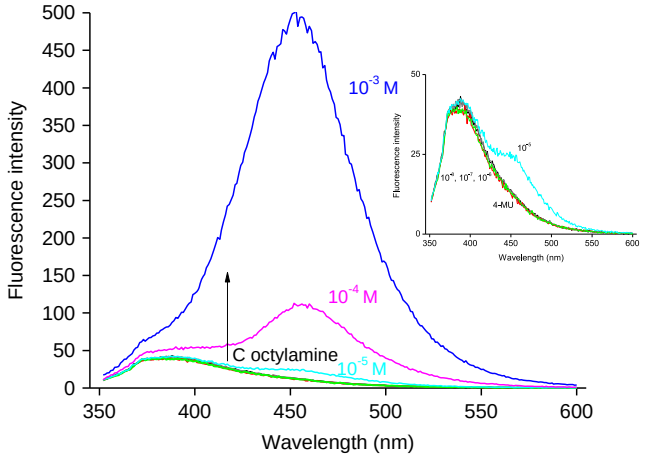


Fig. 2. Emission spectra recorded in different concentrations of octylamine in HD: (black line) 4-MU in HD, and gradually increasing octylamine concentration (grey line) 10^{-8} M, (red line) 10^{-7} M, (green line) 10^{-6} M, (cyan line) 10^{-5} M, (magenta line) 10^{-4} M and (blue line) 10^{-3} M. Inset – magnification of spectra obtained for low concentration of octylamine in HD, excitation wavelength 330 nm.

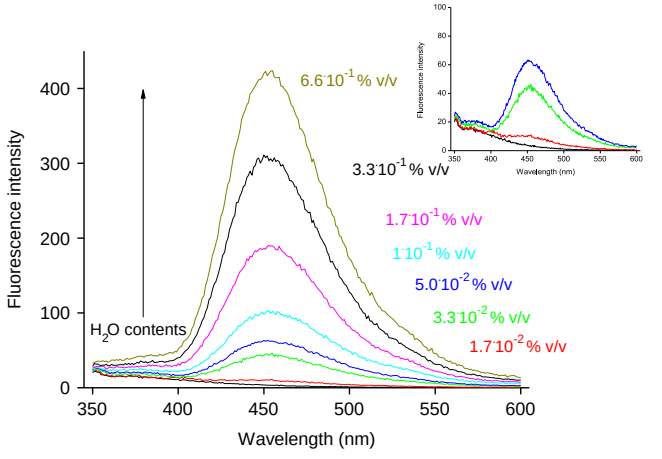


Fig. 3. Emission spectra recorded in different concentrations of water in HD: (black line) 4-MU in HD and gradually increasing water contents from $1.7.10^{-2}$% v/v ($9.3.10^{-3}$ M) to 0.6% v/v (0.37 M). Inset: magnification of spectra obtained for low concentration of water in HD: (black line) 4-MU in HD, (red line) $1.7.10^{-2}$% v/v ($9.3.10^{-3}$ M) water, (green line) $3.3.10^{-2}$% v/v ($1.8.10^{-5}$ M), (blue line) 5.10^{-2}% v/v ($2.8.10^{-2}$ M).

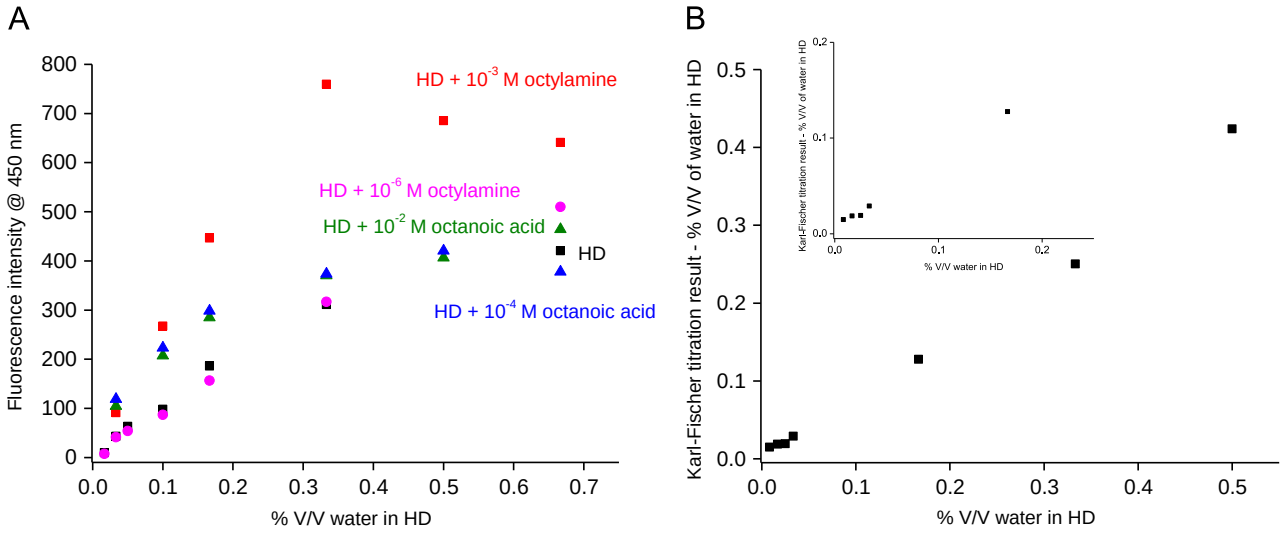


Fig. 4. Dependence of intensity of emission read at 450 nm on the change of water contents in HD sample obtained (A) from fluorimetric experiment, in HD sample (■) in the absence of octylamine, (●) in the presence of 10^{-6} M octylamine, (▲) in the presence of 10^{-4} M octanoic acid, (▲) in the presence of 10^{-2} M octanoic acid and (■) in the presence of 10^{-3} M octylamine (using excitation equal to 360 nm); (B) amount of water determined plotted against amount of water added for Karl Fischer titration of HD samples, inset: magnification of the low water contents range of Karl Fischer titration.

Table 1
Summary of analytical performance of 4-MU as water sensitive fluorescent indicator

System	Hexadecane	Hexadecane $+10^{-2}$ M octanoic acid	Hexadecane $+10^{-6}$ M octylamine	Hexadecane $+10^{-3}$ M octylamine	Toluene	Cyclohexane
$\lambda_{excitation\ (nm)}$	320	320	320	360	320	320
$\lambda_{emission\ (nm)}$	450	450	450	450	450	450
Water contents (%, v/v)	$1.7.10^{-2}$–0.33	< 0.2	$1.7.10^{-2}$–0.33	< 0.3	$1.7.10^{-2}$–20	< 0.2

contents changes using 4-MU as indicator, with results of Karl Fischer titration, Fig. 4. For Karl Fischer titration, as it can be seen from Fig. 4, introduction of relatively small amounts of water to the sample, below 0.1% v/v, yields negligible changes of estimated water amount pointing out to significant negative error of water contents estimation. It should be stressed that Karl Fischer titration is dependent on the sampling procedure, and in the case of relatively low water contents, e.g. accumulation of water introduced to lipophilic HD at the interface of the sample and used vessel, significantly affects obtained results. Herein described approach takes the advantage of emission changes, resulting from 4-MU spontaneous protolitic reaction with water. As 4-MU is dissolved in whole volume of HD, any contact of the sample with water results in change of the emission spectra. Thus, as seen in Fig. 4, fluorimetric approach is significantly more sensitive for relatively low water contents. On the other hand, for higher water contents, > 0,5% v/v, Karl-Fischer method offers higher sensitivity, without limitation on high water contents.

Taking into account that fluorimetric response of 4-MU dye for different water contents in HD originates from protolitic reaction with water acting as a base, it seems justified to check how the presence of base or acid in the sample influences the analytical performance of this system.

As discussed above (Fig. 2), the presence of base (amine) at the concentration 10^{-6} M, in the absence of water, does not affect the emission spectra of 4-MU in HD. Similarly the presence of 10^{-6} M octylamine in HD did not affect the dependence of emission on changes of water contents in the sample. Both the excitation and emission spectra were comparable within the range of experimental error with that recorded in the absence of amine in solution (Fig. S5). Similarly, the dependence of emission intensity at 450 nm on water contents in the sample was linear within the range from $1.7.10^{-2}$% to 0.33% v/v with R^2 equal to 0.988, Table 1.

Increase of octylamine concentration in HD to 10^{-3} M results, in the presence of water, in a significantly broader peak observed on the excitation spectra of 4-MU, Fig. 1. Thus in this case the excitation wavelength used was equal to 360 nm. The emission intensities recorded in the presence of water (0.17% v/v) were significantly higher compared to that recorded for water containing samples in the absence of amine or in the presence of 10^{-6} M octylamine. The emission intensity vs. water contents dependence recorded in the presence of 10^{-3} M octylamine, Fig. S6, for low water contents (< 0.3% v/v) was linear with R^2=0.991, Table 1. The sensitivity of determination was not only higher than for Karl Fischer titration, but also it was the highest among tested model systems. The sensitivity obtained for 10^{-3} M amine present was more than two times higher compared to the system tested in the absence or in the presence of low octylamine concentration in HD, Fig. S5 and Fig S6. Moreover, in the presence of amine in HD the error measured as SD of three replicates is significantly smaller, except for the highest water content tested, which is already at plateau of the dependence, Fig. S4. Thus introduction of amine in 10^{-3} M gives possibility of fine tuning of sensitivity of fluorimetric water contents determination in aprotic solvents, offering significantly higher sensitivity within this region compared to Karl Fischer titration, Fig. 4. However, the linear range of the dependence of emission on contents of water was shorten compared to above-described cases, for higher water contents the decrease of fluorescence intensity was observed, Fig. 4.

The significant increase of sensitivity of water contents determination, especially at low water contents, observed for the 10^{-3} M amine presence in the sample results from the properties

of amine – which is stronger base than water. Thus amine influence on 4-MU deprotonation and concomitant formation of emission signal is potentially stronger than that of water. With increasing water contents in the sample hydrophilicity of the medium increases, protolitic reaction between 4-MU and amine, resulting in protonation of amine on expense of creating of 4-MU anion, is facilitated, resulting in higher sensitivity of water contents determination. The strong emission signal observed can be also to some extent related to formation of structures resembling reversed micelles, containing water in their cores and being stabilized by protonated amine oriented with protonated amine group toward hydrophilic environment of water and with the alkyl chain oriented toward HD. It is probable that the anionic, deprotonated and water-soluble form of 4-MU formed will be present inside the reverse micelles resembling structures, being stabilized with positive charges of the protonated amine, this will ultimately yield higher emission intensity. This effect is probably of low importance for low (10^{-6} M) amine contents in the sample as the population of positive charges that may be created is relatively low, whereas at higher amine contents the enhancement of sensitivity of water determination is clearly seen.

Introduction of acid, as a model compound octanoic acid was used, in 10^{-4} or 10^{-2} M concentration, did not affect the emission or absorption peak positions. The excitation and emission spectra and their maxima, recorded in the presence of octanoic acid, at two concentrations used, were not affected compared to spectra recorded for similar system, yet in the absence of acid, Fig. 1. Introduction of water to HD-containing octanoic acid resulted in increase of emission at 450 nm, similarly as for net HD-containing 4-MU (the maximum of excitation peak was observed at about 320 nm), Fig. 1. The effect of presence of octanoic acid in the system predominantly was observed on the emission intensity vs. water contents dependence. Although for increase of water contents $<0.1\%$ v/v the increase of intensity was slightly higher compared to HD system containing 4-MU in the presence of 10^{-3} M octylamine, the further increase of water contents resulted in much smaller increase of intensity of emission and the dependence was reaching plateau, regardless the concentration of acid present in the HD. Formation of plateau can be related to the fact that octanoic acid is stronger acid than 4-MU, thus deprotonation of 4-MU in this case is not enhanced by water addition. On the other hand, dissociation of octanoic acid, if occurs, leads to formation of water containing reversed micelles resembling structures with anionic charge at the water/HD interface. Thus due to electrostatic repulsion, incorporation of negatively charged 4-MU anion is less likely compared to positively charged water/HD interface in the case of amine reversed micelle resembling structures formed.

Thus although the presence of carboxylic acid in the model solvent HD limits possibility of analytical quantification of the water contents to the low amounts only, the proposed method is robust enough to clearly distinguish samples containing water from those free from water additions.

For analytical application of herein proposed system the information on response time of the system for water addition as well as stability of emission signal in time was collected, Fig. S7, using HD as model solvent. As shown above the intensity of emission recorded in the presence of 10^{-3} M octanoic acid was much lower compared to signals recorded in the presence of water, moreover the intensity of emission was fluctuating in time especially in the presence of octanoic acid in HD.

Introduction of water to the sample leads to pronounced increase of emission, Fig. S7, regardless of the system tested. In the absence of protolitic compounds in HD stable signal was obtained after about 3 min. For sample containing amine or acid emission signal was increasing faster, the stable signal was achieved after about 2 min time. The fastest response was observed for system containing octylamine, regardless of concentration of water tested ($3.4.10^{-2}$% v/v or $1.7.10^{-1}$% v/v), the maximum intensity of emission signal was observed after 1 min. This result is supporting the thesis that presence of amine and possible formation of reverse micelle-like structures favors reaction of 4-MU with water added to the system. It should be stressed that regardless of the system studied (either without additives or containing acid or base) emission signal in the presence of water was stable in experiment time.

Last, but not the least, the above-described experiments confirm, that the proposed system is not only highly sensitive for low water contents but also the results are not interfered by the presence of organic impurities of protolitic character in the sample. This effect is due to spontaneous and beneficial effect of reverse micelles resembling structures formation (provided that the concentration of impurities is high enough) and was not observed for introduction of aqueous solution of acid (HCl) or base (NaOH) solution to the sample. In the latter case, the effect observed was equivalent within the range of experimental error, to that of addition of (neutral) water to the sample, Fig. S8.

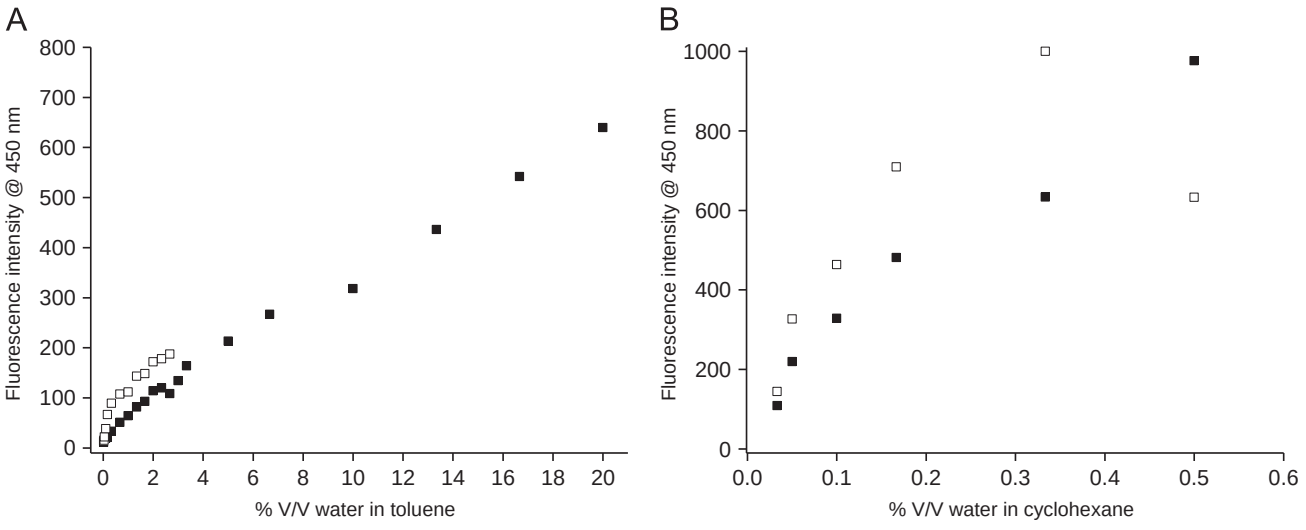


Fig. 5. Dependence of intensity of emission read at 450 nm on the change of water contents in (A) toluene and (B) cyclohexane: (■) 4-MU in tested solvent, (□) in the presence of 10^{-6} M octylamine in tested solvent.

The herein proposed simple method of water quantification using protolitic reaction of 4-MU was also tested on example of other solvents – toluene and cyclohexane.

For 4-MU dissolved in toluene introduction of water resulted in formation of emission peak at 450 nm, of intensity dependent on water contents, Fig. 5. As it can be seen in Fig. 5, similarly as for HD, a linear dependence of intensity of emission on contents of water in the sample was recorded; however, for toluene the linear range of responses was much broader compared to HD. For tested range 0.017% v/v to 20% v/v of water in toluene, it was characterized with R^2 equal to 0.991, Table 1. As it can be seen in Fig. 5, especially for low water contents, $< 0.7\%$ v/v, a further increase of sensitivity is observed if the octylamine is present in the toluene in concentration 10^{-6} M, that is at the concentration of no beneficial effect in the case of hexadecane. Probably the advantageous effect of already low concentration of amine present in toluene is related to higher polarity of this solvent compared to HD. Toluene partially participates in stabilization of water droplets within, thus even low contents of amine actively increases deprotonation of 4-MU molecules and their partition into aqueous phase.

For cyclohexane containing 4-MU, similarly as for above discussed examples, introduction of water resulted in formation of emission peak at 450 nm, of intensity dependent on water contents in the sample, Fig. 5. The linear dependence of emission intensity on water contents was however, limited to about 0.2% v/v of water ($R^2 = 0.967$), Table 1. Similarly as for toluene, introduction of amine in 10^{-6} M concentration to the cyclohexane has resulted in increased emission, however recorded dependence was not linear. Increase of water contents above 0.33% v/v resulted in decrease of recorded emission.

4. Conclusions

The herein presented results clearly show that minute water contents, especially in highly lipophilic, nonpolar solvents like hexadecane, can be determined with high sensitivity due to protolitic reaction of 4-methylumbelliferone with water, acting as a base. The emission intensity of deprotonated 4-MU anion well correlates with water contents in the nonpolar solvent. For low concentrations, this system offers higher sensitivity compared to Karl Fischer titration. Moreover, presence of organic acid and especially organic base leads to further increase of sensitivity, with increasing concentration of this additive in the solvent. This effect can be attributed to formation of structures resembling reversed micelle within the low-polarity solvent – with water core and stabilized with protonated (in the case of amine) or deprotonated (in the case of acid) organic ion located at the water – solvent interface. This spontaneous process in the case of added base (amine) supports partition of ionized 4-MU into the minute water phase.

Acknowledgment

Financial support from National Centre of Science (NCN, Poland), project 2011/03/B/ST4/00747, in the years 2012–2015, is gratefully acknowledged.

Appendix A. Supporting information

Supplementary data associated with this article can be found in the online version at http://dx.doi.org/10.1016/j.talanta.2014.09.018.

References

[1] N. Dantan, W. Frenzel, S. Küppers, Talanta 52 (2000) 101–109.
[2] I. Gergen, F. Radu, D. Bordean, H.-D. Isengard, Food Control 17 (2006) 176–179.
[3] S.K. MacLeod, Anal. Chem. 63 (1991) 557A–566A.
[4] S.A. Margolis, Anal. Chem. 69 (1997) 4864–4871.
[5] S.A. Margolis, Anal. Chem. 67 (1995) 4239–4246.
[6] H. Sun, B. Wang, S.G. DiMagno, Org. Lett. 10 (2008) 4413–4416.
[7] M. Li, G.E. Paecy, Talanta 44 (1997) 1949–1958.
[8] S. Garrigues, M. Gallignani, M. de la Guardia, Anal. Chim. Acta 281 (1993) 259–264.
[9] H. Langhals, Anal. Lett. 23 (1990) 2243–2258.
[10] C. Pinheiro, J.C. Lima, A.J. Parola, Sens. Actuat. B 114 (2006) 978–983.
[11] C. Yunxiang, J. Xin, Talanta 31 (1984) 556–558.
[12] L. Ding, Z. Zhang, X. Li, J. Su, Chem. Commun. 49 (2013) 7319–7321.
[13] F. Gao, F. Luo, X. Chen, W. Yao, J. Yin, Z. Yao, L. Wang, Microchim. Acta 166 (2009) 163–167.
[14] W. Liu, Y. Wang, W. Jin, G. Shen, R. Yu, Anal. Chim. Acta 383 (1999) 299–307.
[15] M. Nakashima, J.A. Sousa, R.C. Clapp, Nat. Phys. Sci. 235 (1972) 16–19.
[16] E. Bardez, P. Boutin, B. Valeur, Chem. Phys. Lett. 191 (1992) 142–148.

Talanta 132 (2015) 398–405

Contents lists available at ScienceDirect

Talanta

journal homepage: www.elsevier.com/locate/talanta

Fabrication and NO_2 gas-sensing properties of reduced graphene oxide/WO_3 nanocomposite films

Pi-Guey Su *, Shih-Liang Peng

Department of Chemistry, Chinese Culture University, Taipei 111, Taiwan

ARTICLE INFO

Article history:
Received 20 July 2014
Received in revised form
23 September 2014
Accepted 24 September 2014
Available online 5 October 2014

Keywords:
Tungsten oxide (WO_3)
Reduced graphene oxide (RGO)
Nanocomposite
Polyol
Metal organic decomposition (MOD)
Room-temperature gas sensor

ABSTRACT

One-pot polyol process was combined with the metal organic decomposition (MOD) method to fabricate a room-temperature NO_2 gas sensor based on tungsten oxide and reduced graphene oxide (RGO/WO_3) nanocomposite films. Fourier Transform infrared spectrometer (FTIR), X-ray diffractometry (XRD), scanning electron microscopy (SEM) and atomic force microscopy (AFM) were used to analyze the microstructure and morphology of the fabricated films. The electrical and NO_2 gas-sensing properties of WO_3 to which various amounts of RGO were added were measured in detail as a function of concentration of NO_2 gas at room temperature, to elucidate the contribution of RGO to the NO_2 gas-sensing capacity. The NO_2 gas-sensing mechanism of the RGO/WO_3 nanocomposite films were explained by considering their composition and microstructures. The sensor that was based on a nanocomposite film of RGO/WO_3 exhibited a strong response to low concentrations of NO_2 gas at room temperature, satisfactory linearity and favorable long-term stability.

© 2014 Elsevier B.V. All rights reserved.

1. Introduction

Nitrogen oxides generated by combustion facilities and automobiles are known to be extremely harmful to the human body and are also a main cause of acid rain. Traditional, the detection of NO_2 gas has been carried out by using chemiluminescent or non-disperse infrared (NDIR) analysis. But these instruments are large, expensive and need a sampling system and complicated maintenance. Therefore, many researchers have been searching for a suitable NO_2 gas sensor for the exhaust monitoring.

Graphene consists of a two-dimensional (2D) array of carbon atoms that are covalently connected via sp2 bonds to form a honeycomb sheet [1]. Graphene exhibited intriguing properties such as high electron mobility at room temperature (250,000 cm^2/Vs), exceptional thermal conductivity (5000 $W\,m^{-1}\,K^{-1}$), and superior mechanical properties [2,3]. The electrical properties make it to be attractive candidates for new materials. Graphene oxide (GO) sheets have recently become attractive as possible intermediates in the manufacture of graphene [4]. In GO, carboxyl groups locate at the carbon sheet edges, and epoxy and hydroxyl functional groups decorate the surface of carbon sheets [5]. However, the oxygen functional groups of GO render it too electrically insulating for use as a conductance-based sensors. Moreover, GO can be chemically or thermally reduced to restore its conductivity several orders of magnitude by removal some of oxygen functional groups [6,7]. Therefore, reduced GO (RGO) exhibited conductive and chemically active defect sites making it an active material for sensor applications. Moreover, the RGO sheets have been used for chemiresistive sensors and exhibit great potential for gas sensing applications [8–12]. Moreover, in order to improve the sensing performance of these graphene-based sensors, the conducting polymers, metals, and metal oxides have been anchored on the surface of graphene sheets to improve the sensitivity of the resultant gas sensors [13–16].

Recently, metal oxide/graphene composite materials have attracted a great deal of attention due to potential applications in optoelectronics, energy conversion devices and gas sensors [1,17,18]. Many methods have been used to prepare metal oxide/graphene composite materials, including the hydro/solvothermal method, solution mixing method, the in-situ growth method and the photoreduction method, all of which have their own advantages and particular conditions of application [17,19–21]. Among these methods, hydro/solvothermal method is the most widely used to prepare metal oxide/graphene composite because chemical bonds form between metal oxides and graphene, which can improve the electric properties of the composite over those of the same metal oxides or graphene alone. Recently, composite films that are based on WO_3 nanopowders and graphene have been reported to be as new gas-sensitive materials to reduce further the operating temperature and to improve the sensitivity of sensors based on these materials [22,23]. Yu et al. fabricated WO_3 nanorodes/graphene nanocomposites using the hydrothermal

* Corresponding author: Tel.: +886 2 28610511x25332; fax: +886 2 28614212.
E-mail address: spg@faculty.pccu.edu.tw (P.-G. Su).

http://dx.doi.org/10.1016/j.talanta.2014.09.034
0039-9140/© 2014 Elsevier B.V. All rights reserved.

method for sensing NO_2 [22]. Senguttuvan et al. fabricated a more rapidly responding NO_2 gas sensor based on WO_3/graphene nanocomposites that were made by the hydrothermal method [23]. The sensing characteristics of these WO_3/graphene-based NO_2 gas sensors depend on their microstructure, which are determined by their fabrication process. Most NO_2 gas sensors have been fabricated by synthesizing graphene that is decorated with WO_3 nanomaterial and drop-coating it on a substrate.

Polyol-based synthesis route has been used for preparing nano-metal oxide materials, because the reaction conditions are easily established, and yield nano-sized particles in the form of dimensionally stable colloidal suspensions. Briefly, this approach uses a polyol with a high boiling point, including diethylene glycol, glycerol, glycol and others, as the reaction medium in the preparation of oxide materials. The polyols act as stabilizers, limiting particle growth and prohibiting agglomeration. Therefore, suitable reactants from homogenous solution (metal acetates/chlorides/alkoxides) are hydrolyzed at elevated temperature, forming nano metal oxides/precursors in suspension in polyol [24–26]. Additionally, the metal organic decomposition (MOD) method for depositing a metal oxide thick film is easily and inexpensively applied [27,28]. Briefly, a metal alkoxide is spin-coated on a substrate, and then MOD forms a strongly adhesive and homogeneous film of metal oxide. Tsai et al. [29–31] used the MOD method to prepare a SnO_2 film to detect amounts of alcohol and CO gases. No attempt has been made to fabricate an NO_2 gas sensor that is based on RGO/WO_3 nanocomposite films by combining the one-pot polyol process with the MOD method. Additionally, the pure WO_3 film typically must usually be used at temperatures from 200 to 500 °C [32,33]. To improve the high resistance and weak response of the WO_3 film operating at room-temperature for practical use, nanocomposite films of RGO and WO_3 were fabricated in this study by such a combination of methods. These films have the advantages of being highly effective, inexpensive and suitable for industrial for mass production. The key step in the fabrication of the RGO/WO_3 nanocomposite film was that the reduction of GO to RGO and the conversion of WO_3 nanoparticles from H_2WO_4 precursors were produced simultaneously in the one-pot polyol approach. The structural characteristics of the RGO/WO_3 nanocomposite films were investigated by X-ray diffraction (XRD) and Fourier Transform infrared spectrometer (FTIR). The surface characteristics of the RGO/WO_3 nanocomposite films were observed using atomic force microscopy (AFM) and scanning electron microscopy (SEM). The NO_2 sensing performance of RGO/WO_3 nanocomposite films with various amounts of the RGO loaded into the WO_3 matrix was studied as the function of concentration of NO_2 gas at room-temperature. Differences in the composition and microstructure were adopted to explain the effect of adding RGO on the sensing mechanism of the RGO/WO_3 nanocomposite films.

2. Experimental

2.1. Preparation of GO

GO was prepared from natural graphite by the Hummers method [34]. Briefly, 0.5 g graphite powder was reacted with a mixture of 2 g $NaNO_3$, 12 mL concentrated H_2SO_4 and 3 g $KMnO_4$; then 40 mL deionized water (DIW) and 10 mL H_2O_2 (30%) were added. The product was filtered and washed with 5% HCl solution and deionized water to yield a brown power. An exfoliated aqueous GO dispersion was produced after sonication for 2 h. The resultant mixture was filtered and washed with DIW by centrifuging until the solution attained a pH of 6, and was then sonicated to form a stable suspension of GO in aqueous media. The resulting aqueous GO solution had a concentration of 0.85 mg/mL.

2.2. Fabrication of gas sensors based on WO_3 films

Fig. 1 displays a picture of the structure of NO_2 sensors fabricated on an alumina substrate. The interdigited gold electrodes were made by screen printing. The electrode gap was 0.2 mm. Tungstic acid (H_2WO_4) (3.0 g) (99.9%, 5.59 g/cm^3, Merck) was added to 10 g of glycerol (99.5%, 1.259 g/cm^3, Merck) and the solution was heated to 190 °C for 1 h with vigorous magnetic stirring. The reaction can be easily followed by observing its distinctive color changes. Within minutes after the reaction's reaching 190 °C, the yellow solution turned pale green and then slowly changed to a deep blue suspension, indicating the formation of tungsten oxide nanoparticles in glycerol. The blue precursor was spin-coated on an alumina substrate with a pair of comb-like electrodes. Then, it was dried by heating to 170 °C in air for 2 h; MOD was then performed in a furnace at 500 °C for 4 h in the ambient atmosphere to form a film of WO_3. During the MOD process, the temperature was increased from the ambient temperature to 500 °C at a heating rate of 5 °C/min. Therefore, a gas sensor based on WO_3 film was obtained (Fig. 1).

2.3. Fabrication of gas sensors based on RGO/WO_3 nanocomposite films

The RGO/WO_3 nanocomposites were synthesized as follows. Tungstic acid (H_2WO_4) (3.0 g) and the required amounts of GO were added to 10 g of glycerol and the resultant solution was heated to 190 °C for 1 h with vigorous magnetic stirring. The solution was continuously stirred until a stable suspension was obtained. The level of doping with GO was varied among 1.6 wt%, 3.2 wt% or 11.8 wt% (of H_2WO_4). The RGO/WO_3 nanocomposite films were formed by MOD in the same manner as used in the fabrication of a gas sensor based on a WO_3 film. For fabricating the RGO/WO_3 nanocomposite films, an MOD temperature of 500 °C was maintained for 4 h.

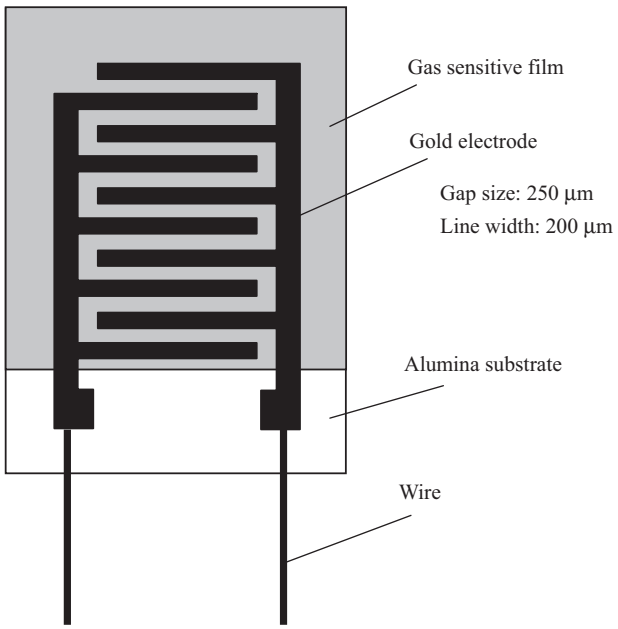


Fig. 1. Structure of NO_2 gas sensor.

2.4. Instruments and analysis

A Fourier Transform infrared spectrometer (FTIR, Nicolet 380) was used to obtain the IR spectra of the GO and RGO. The surface microstructure of the WO_3 film and RGO/WO_3 nanocomposite films coated on an alumina substrate was investigated using a field emission scanning electron microscope (FEI company, Nova Nano-SEM™ 230) quipped with an energy dispersive spectrometer (EDS) and an atomic force microscope (AFM, Ben-Yuan, CSPM 4000) in tapping mode which the horizontal and vertical resolution are 0.26 and 0.10 nm, respectively. The XRD powder pattern of the WO_3, GO and RGO/WO_3 nanocomposite films were measured using Cu K_α radiation (Shimadzu, Lab XRD-6000). The electrical and sensing characteristeristics were measured using a static state system at room temperature, as shown in Fig. 2. Each sensor was connected in series with a load resistor and a fixed 5V tension (DC mode) was continuously supplied to the sensor circuit from a power supply (GW, PST-3202). The resistance of the sensor was determined from the voltage at the ends of the load resistor using a DAQ device (NI, USB-6218) in various concentrations of gas. The standard NO_2, NH_3, and H_2S gases were purchased from Shen Yi Gas Co. (Taiwan). The concentration for standard NO_2, NH_3, and H_2S gases were 100,000, 1000 and 1000 ppm, respectively. The required various gas concentrations were produced by diluting the known volume of standard gas with dry air and then were injected into the chamber. The desired various gas concentrations were measured using a calibrated gas sensor system (Dräger, Mini-Warn). The interfering experiment was performed by measuring the resistance of the sensor exposure to NH_3, H_2S and H_2O gases, respectively. The volume of the chamber is 18 l. The gas inside the chamber was uniformly distributed using a fan. After some time, the chamber was purged with air and the experiment was repeated for another cycles. All experiments were performed at room temperature, which was about 23.0 ± 1.5 °C and the relative humidity was 40% RH.

3. Results and discussion

3.1. Preparation and structural characteristics of RGO/WO_3 nanocomposite films

3.1.1. IR spectra

GO was used as the precursor to prepare the RGO/WO_3 nanocomposite was prepared by the one-pot polyol reaction of H_2WO_4 in glycerol because that the GO had hydrophilic property to be homogenously dispersed in a H_2WO_4 matrix and easily reduced to RGO. To confirm the feasibility of the polyol method for reducing GO to RGO in the one-pot polyol synthesis of RGO/WO_3 nanocomposite, GO was the first reduced in the absence of H_2WO_4 in glycol. The IR spectrum of the GO in Fig. 3(a) includs a peak at 3350 cm^{-1} attributable to the O–H stretching vibration, peaks at 1740 and 1630 cm^{-1} attributable to the C=O stretching vibrations, and a peak at 1357 cm^{-1} attributable to the deformation of O–H. The one-pot polyol synthesis process reduced the heights of the peaks at 1740, 1630 and 1357 cm^{-1} (Fig. 3(b)), suggesting the successful reduction of GO in the one-pot polyol reaction. Therefore, partially reduced GO was formed in the RGO/WO_3 nanocomposite. Additionally, W(VI) was partially reduced to W(V) in polyol to yield a deep blue non-stoichiometric precursor because W(VI) is a moderate oxidizing agent [35]. Therefore, polyol acted as a reducing agent for W(VI), and GO was simultaneously reduced to RGO in the one-pot polyol reaction of H_2WO_4. Additionally, no new peak was observed from the RGO/WO_3 samples, indicating that no new bonding formed between the RGO and WO_3 matrix.

3.1.2. XRD characterization

Fig. 4 shows the XRD spectra of the GO, WO_3 film and RGO/WO_3 nanocomposite films that were prepared by the combined one-pot polyol and MOD method. For GO, a sharp diffraction peak (002) appears at 10.75°, which indicates that most of the graphite powder was oxidized into GO by expanding d-spacing of 6.70 Å [36]. The XRD patterns of WO_3 film show three main peaks at 2θ=23.1, 23.6 and 24.3°, which are identified as corresponding to (002), (020) and (200) orientations, respectively. The XRD patterns showed the formation of monoclinic WO_3, as in the Joint

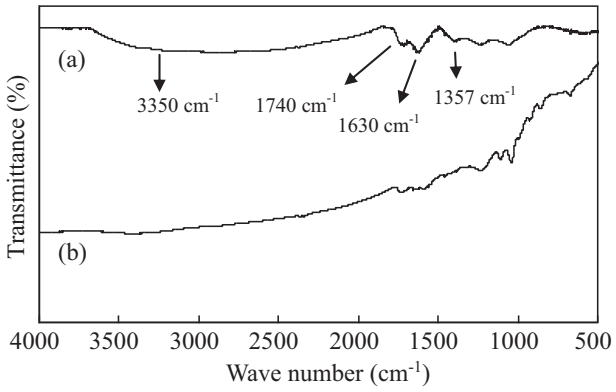


Fig. 3. IR spectra of (a) GO and (b) RGO was fabricated by one-pot polyol process.

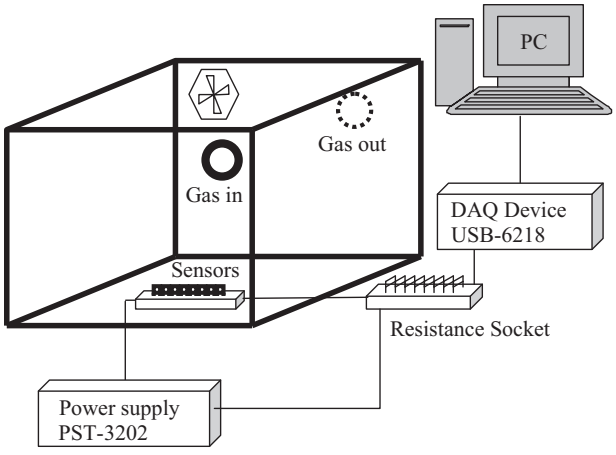


Fig. 2. Measurement system for testing gas sensors.

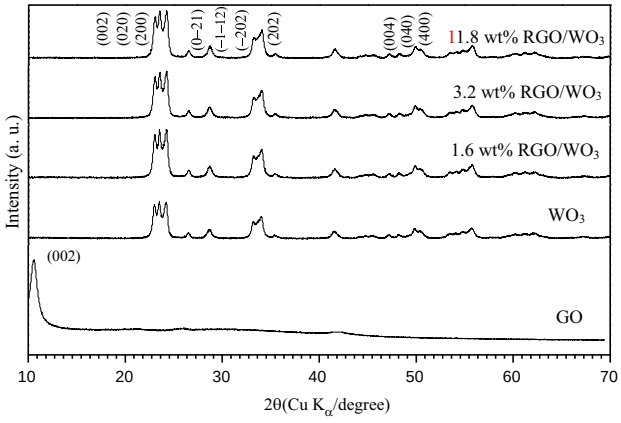


Fig. 4. XRD patterns of WO_3 film and RGO/WO_3 nanocomposite films that were fabricated by one-pot polyol process and MOD at 500 °C for 4 h.

Table 1
Crystallite size of RGO/WO_3 prepared by one-pot polyol process combined with MOD at 500 °C.

Sample	Crystallite size (nm)
WO_3	61.59
1.6 wt% RGO/WO_3	61.60
3.2 wt% RGO/WO_3	61.61
11.8 wt% RGO/WO_3	61.61

Committee of Powder Diffraction Standards (JCPDS 00-020-1324) [37]. For the RGO/WO_3 nanocomposite, by increasing the doping amount of GO in the precursor solution from 1.6 to 11.8 wt%, the XRD patterns showed no appreciable difference between the orientations and phases of WO_3 and RGO/WO_3 samples, probably due to the reduction of GO by glycerol or RGO was embedded in the WO_3 matrix and so could not be easily detected by X-ray diffraction. The crystallite size of WO_3 and RGO/WO_3 samples after MOD at 500 °C for 4 h was estimated from XRD peaks according to Scherrer's equation,

$$D = \frac{0.9\lambda}{(B\ \cos\ \theta)} \quad (1)$$

where D represents mean grain size; B represents the full width at half maximum of the peak; λ is the wavelength of the X-rays, and θ is the angle of the center of the peak. The crystallite size was estimated from the half width of the (200) peak. Table 1 shows the estimated sizes of the crystallite of the WO_3 and RGO/WO_3 samples. By increasing the doping amount of GO in the precursor solution from 1.6 to 11.8 wt%, no appreciable difference between the crystallite size of WO_3 and RGO/WO_3 samples was observed.

3.1.3. AFM and SEM analyses

Fig. 5 presents the surface morphology of the WO_3 film and 3.2 wt% RGO/WO_3 nanocomposite film that were prepared by the combined one-pot polyol and MOD method, determined using tapping-mode AFM. The size of each image is 5 μm × 5 μm. Both WO_3 film (Fig. 5(a)) and 3.2 wt% RGO/WO_3 nanocomposite film (Fig. 5(b)) exhibited a uniform granular morphology. The surface roughness of the WO_3 film and 3.2 wt% RGO/WO_3 nanocomposite film were 21.2 and 19.2 nm, respectively. Fig. 6 presents SEM images and EDS spectra of the WO_3 film and 3.2 wt% RGO/WO_3 nanocomposite film that were prepared by the combined one-pot polyol and MOD method. Both WO_3 film (Fig. 6(a)) and 3.2 wt% RGO/WO_3 nanocomposite film (Fig. 5(b)) exhibited a flat surface. In Fig. 6(b), a local dark region was clearly observed. Comparing the EDS spectra of the WO_3 film and the 3.2 wt% RGO/WO_3 nanocomposite film reveals that the RGO was doped into the WO_3 matrix. Additionally, no naked RGO was present on the surface of the RGO/WO_3 nanocomposite film, even when the amount of added RGO was 11.8 wt%.

3.2. Electrical and Gas sensing properties of RGO/WO_3 nanocomposite films

3.2.1. Effect of RGO content on the electrical properties and sensing mechanism

The sensor response (S) was calculated by the following equation:

$$S(\%) = \frac{(R_{gas} - R_{air})}{R_{air}} \times 100\% = \frac{(\Delta R)}{R_{air}} \times 100\% \quad (2)$$

where R_{gas} and R_{air} are the electrical resistances of the sensor in the tested gas and air, respectively. Fig. 7 plots the responses of the sensors that were based on WO_3 film and RGO/WO_3 nanocomposite films that were prepared using various amounts of GO, to

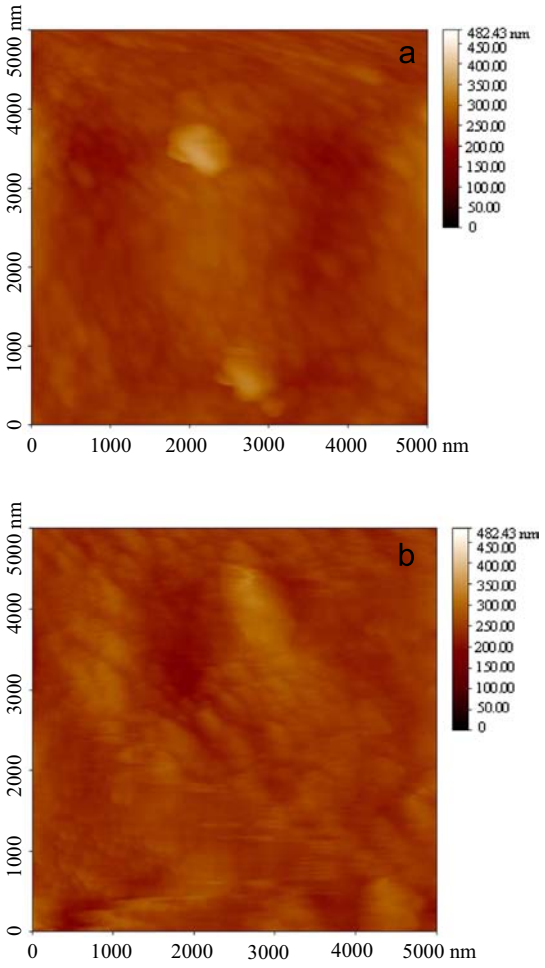


Fig. 5. AFM images of (a) WO_3 film and (b) 3.2 wt% RGO/WO_3 nanocomposite film that were fabricated by one-pot polyol process and MOD at 500 °C for 4 h.

various concentrations of NO_2 gas at room temperature. Clearly, the responses (S) of the sensors that were made of the RGO/WO_3 nanocomposite films were significantly stronger than that of the sensor that was made of the pure WO_3 film. When the amount of RGO added was below 3.2 wt%, the response (S) of the sensors increased and the concentration of NO_2 gas-sensing increased with increasing the amount of RGO added. However, when the mass of RGO added was increased to 11.8 wt%, the RGO/WO_3 nanocomposite film exhibited a small response (S) in the NO_2 gas range studied. When less than 3.2 wt% of RGO were added, as described in Section 3.1.3, the surface morphology of the WO_3 film did not obviously differ from that of the RGO/WO_3 nanocomposite film. Additionally, BET analysis reveals that the difference between the surface area of WO_3 and RGO/WO_3 films was very small. Therefore, differences in surface morphology may not be directly responsible for the improved in the NO_2 gas-sensing of the RGO/WO_3 nanocomposite films compared to that of the pure WO_3 film. Therefore, two main effects are proposed to the improvement in the response (S) of the sensors of the WO_3 film doped with RGO. First, the resistance of pure WO_3 film was around 800 kΩ. When the doping amount of RGO was 1.6 wt%, the resistance of the RGO/WO_3 nanocomposite film was reduced to ~98 kΩ. When the doping amount of RGO was increased to 3.2 wt%, the resistance of the RGO/WO_3 nanocomposite film was reduced further to ~9 kΩ. Therefore, revealing that the added GO was reduced to conductive RGO which formed new electrical paths in the WO_3 matrix in the one-pot polyol reaction. In this situation, a new conductive path was formed by the embedded RGO, and thus the

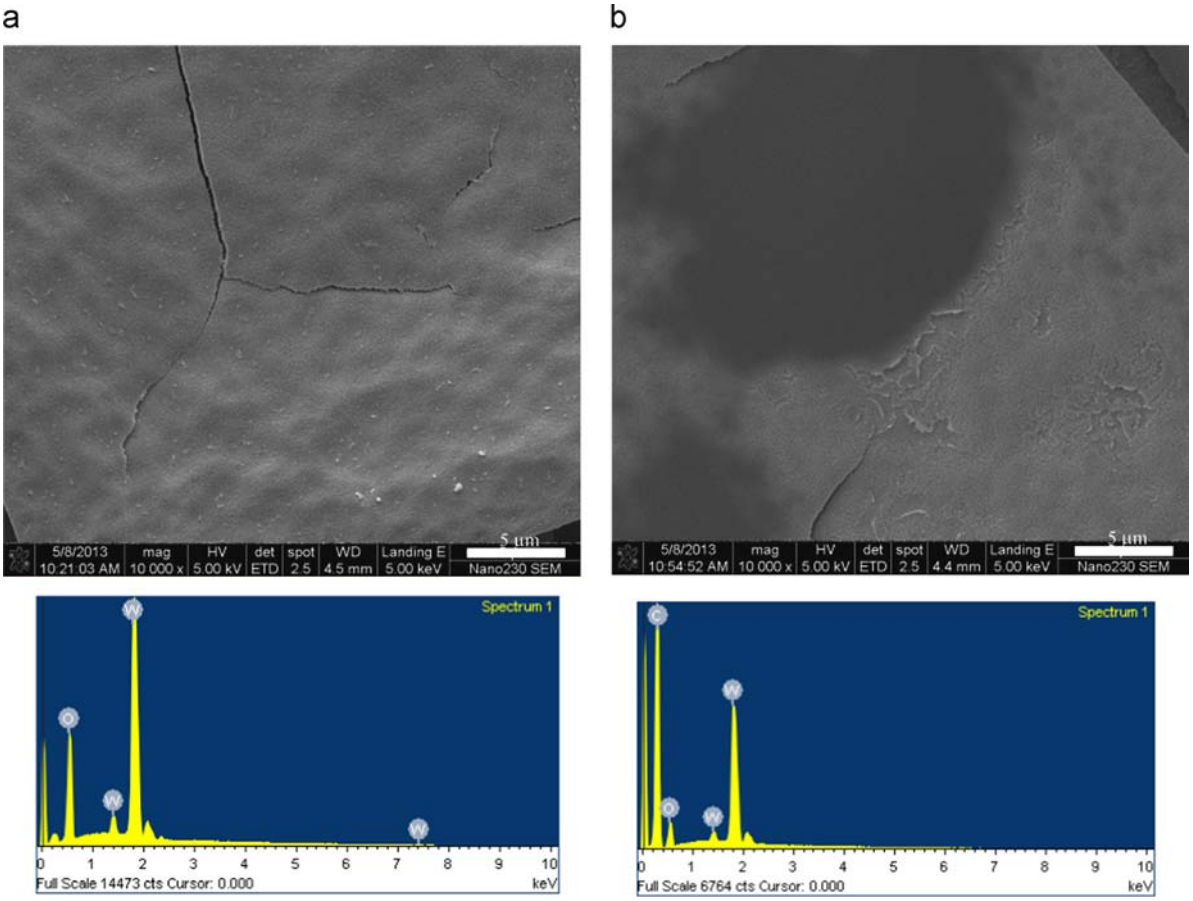


Fig. 6. FE-SEM images and EDS spectra of (a) WO_3 film and (b) 3.2 wt% RGO/WO_3 nanocomposite film that were fabricated by one-pot polyol process and MOD at 500 °C for 4 h.

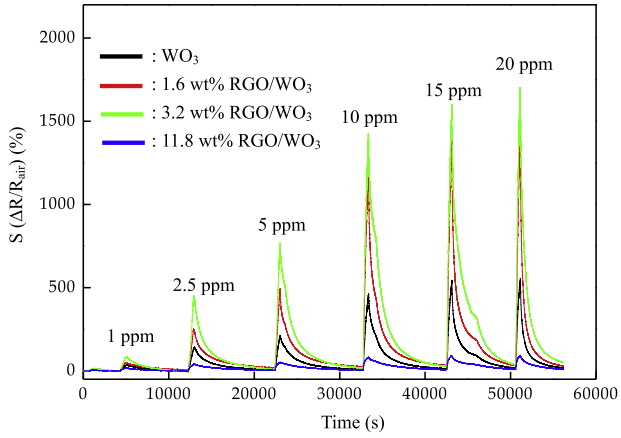


Fig. 7. Response (S) of NO_2 gas sensors based on RGO/WO_3 nanocomposite films that were prepared by one-pot polyol process and MOD at 500 °C for 4 h with various amounts of added RGO, as function of time (s) for various concentrations of NO_2 gas at room temperature.

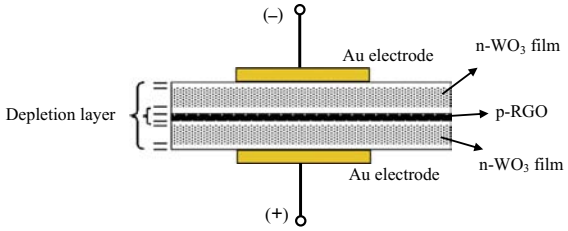


Fig. 8. Equivalent cross-sectional views of a NO_2 gas sensor based on RGO/WO_3 nanocomposite film with hetero-structure (Au/n-WO_3/p-RGO/n-WO_3/Au).

sensitivity of the RGO/WO_3 nanocomposite film was better than that of the WO_3 film. When the amount of added RGO was increased to 11.8 wt%, the amount of added RGO exceeded the percolation threshold so that the change in conductance of the sensing material due to adsorption of NO_2 gas molecules was not obvious. Second, the WO_3 behaved as an n-type semiconductor, and RGO behaved as a p-type semiconductor. Therefore, from the results of XRD and SEM analyses, the WO_3 matrix surrounds the RGO, the p–n hetero-junction that was formed by WO_3 and RGO, as presented in Fig. 8. This hetero-structure was associated with the co-existence of two depletion layers (and associated potential barriers). The first depletion layer was located at the surface of the WO_3 film and the second was at the interface between the RGO and the WO_3 film. Therefore, the p–n heterojunctions were responsible for the fact that the sensor that was based on WO_3/RGO nanocomposite film was much more sensitive than that based on WO_3 film [38,39]. Therefore, the RGO/WO_3 nanocomposite film easily detected the gas at room temperature, owing to the effects of by the combination of the percolation effect and its hetero-structure.

3.2.2. Gas-sensing properties

Fig. 9 plots the responses (S) of the sensor that was made of the 3.2 wt% RGO/WO_3 nanocomposite film to various concentrations of NO_2. The sensor had a response of 16.8% even at a low NO_2 testing concentration of 0.5 ppm. Therefore, the NO_2 gas sensor that was made of the RGO/WO_3 nanocomposite film that was doped with 3.2 wt% of RGO was chosen to study further its other

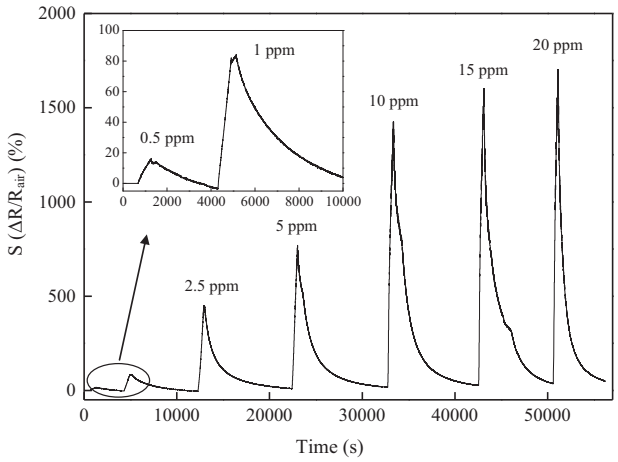


Fig. 9. Response (S) of NO_2 gas sensors based on 3.2 wt% RGO/WO_3 nanocomposite film, as function of time (s) for various concentrations of NO_2 gas at room temperature.

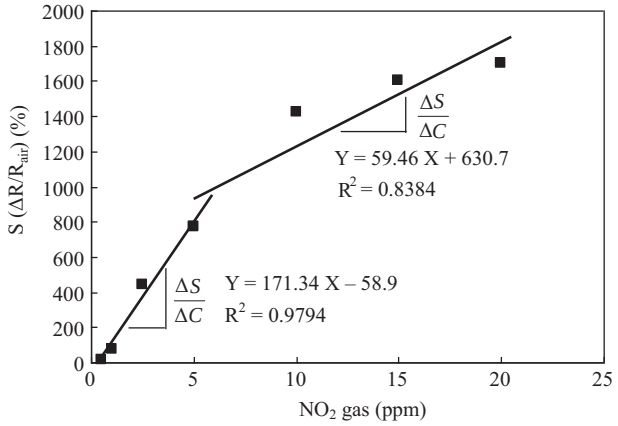


Fig. 10. Linear dependence of response of NO_2 gas sensor based on 3.2 wt% RGO/WO_3 nanocomposite film that was fabricated by one-pot polyol process and MOD at 500 °C for 4 h on concentration of NO_2 gas at room temperature. Sensitivity ($\Delta S/\Delta C$) is determined from the slope of the linear curve.

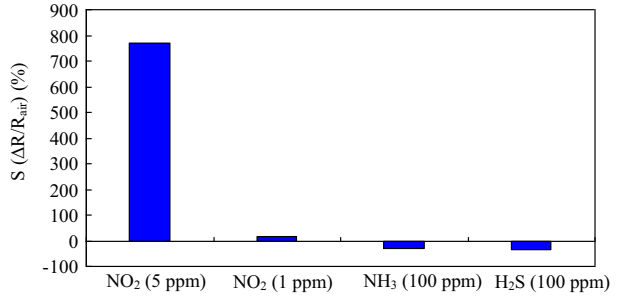


Fig. 11. Response (S) of NO_2 gas sensors based on (a) RGO/WO_3 nanocomposite films that were prepared by one-pot polyol process and MOD at 500 °C for 4 h to various gases.

gas sensing properties. Fig. 10 plots the response (S) as a function of concentration of NO_2 gas for the sensor that was made of the 3.2 wt% RGO/WO_3 nanocomposite film. The sensitivity ($\Delta S/\Delta C$) is determined from the slopes of the plots of response vs. gas concentration. A steep decrease in the slope was observed at from 5 to 20 ppm of NO_2 gas. Therefore, the sensitivity at 0.5 to 5 ppm NO_2 gas was higher than that at 5 to 20 ppm. Fig. 11 plots the results concerning the interfering effects of NH_3 and H_2S gases on the NO_2 gas sensor. NH_3 and H_2S gases may be regarded as having unobvious interference effects with NO_2 at a testing NO_2 concentration of 5 ppm. However, NH_3 and H_2S gases may be regarded having interference effects with NO_2 at a testing NO_2 concentration under 1 ppm. Additionally, from the results in Fig. 11, the sign of the response (S) for the considered adsorbates can be understood as indicating one of two charge transfer mechanisms. In this work, NO_2 doped the RGO/WO_3 film with holes, while NH_3 and H_2S doped it with electrons. Accordingly, the prepared RGO/WO_3 film exhibited the electrical behavior of an n-type semiconductor. During the sensing process, the adsorption of electron-withdrawing NO_2 molecules compensates for the hole carriers in the n-type RGO/WO_3, causing the electrical resistance of the RGO/WO_3 nanocomposite film to increase with concentration of NO_2. The electrical resistance of the RGO/WO_3 nanocomposite film decreased when the film was exposed to NH_3 and H_2S gases because NH_3 and H_2S are electron-donating gases. Fig. 12 plots the effect of ambient humidity on the response (S) of the NO_2 gas

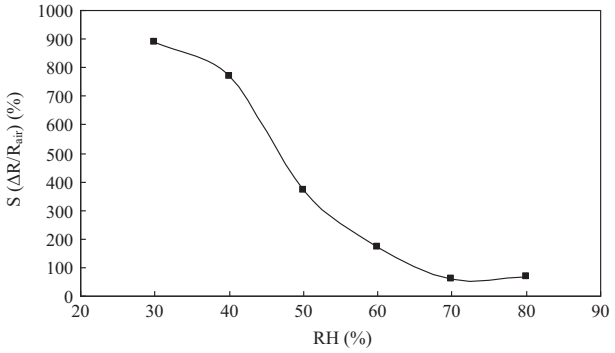


Fig. 12. Effect of ambient humidity on response of the NO_2 gas sensor based on 3.2 wt% RGO/WO_3 nanocomposite film that was fabricated by one-pot polyol process and MOD at 500 °C for 4 h to 5 ppm of NO_2 gas at room temperature.

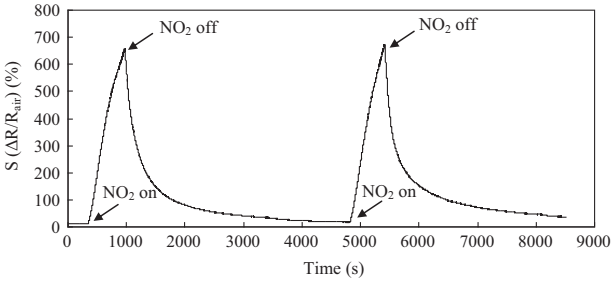


Fig. 13. Reproducibility of response of NO_2 gas sensor based on 3.2 wt% RGO/WO_3 nanocomposite film that was fabricated by one-pot polyol process and MOD at 500 °C for 4 h to 5 ppm of NO_2 gas at room temperature.

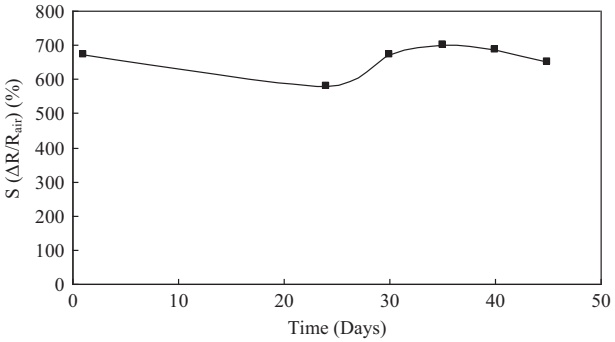


Fig. 14. Long-term stability of response of the NO_2 gas sensor based on 3.2 wt% RGO/WO_3 nanocomposite film that was fabricated by one-pot polyol process and MOD at 500 °C for 4 h in 5 ppm of NO_2.

Table 2
Comparison of performance of NO_2 gas sensor developed herein with the literature.

Sensing material	Fabrication method	Response (%)	Response/recovery times	References
RGO/WO_3 nanocomposite	one-pot polyol process combined with MOD	769[a]	9/18 min	This work
WO_3 nanorods decorated on graphene	hydrothermal method	202[b]	—[c]	[22]
WO_3/RGO nanocomposite	hydrothermal method	135[d]	25/200 s	[23]
MWCNTs/WO_3 nanocomposite	one-pot polyol process combined with MOD	77[e]	10.5/20	[39]

[a] The sensor in response to 5 ppm NO_2 gas at room temperature.
[b] The sensor in response to 20 ppm NO_2 gas at 300 °C.
[c] No explanation in the literature.
[d] The sensor in response to 5 ppm NO_2 gas at 250 °C.
[e] The sensor in response to 5 ppm NO_2 gas at room temperature.

sensor at a testing NO_2 concentration of 5 ppm. The response (S) of the NO_2 gas sensor decreased as the ambient humidity increased, because the physisorbed water occupied the active sites of the sensing materials. Fig. 13 plots the real-time response of the NO_2 gas sensor at a testing concentration of NO_2 of 5 ppm. The response of the sensor increases significantly when the NO_2 gas was introduced into the chamber. However, we did not observe the saturated state of the NO_2 gas sensor, even when the exposure time was prolonged to 10 min. Additionally, two gas on/off cycles produced similar responses, indicating that the NO_2 gas sensor exhibited excellent reproducibility even when the exposure time was prolonged to 10 min. Therefore, we defined the exposure time of about 10 min as the effective response time for the NO_2 gas sensor. The recovery time is defined as the time required for the sensor to recover 90% of the decrease in resistance after the sensor is exposed to a dry gas. The recovery time of the NO_2 gas sensor was 18 min at a testing concentration of NO_2 of 5 ppm. Fig. 14 plots the long-term stability. The response (S) of the NO_2 gas sensor did not significantly vary for at least 45 days in a testing NO_2 concentration of 5 ppm. Table 2 compares the NO_2 gas sensing properties of the NO_2 gas sensor proposed herein with those of sensors in our previous work [39] and elsewhere in the literatures [22,23]. The response of the NO_2 gas sensor that was proposed herein was stronger than that of the NO_2 gas sensor that was fabricated by the hydrothermal method. Additionally, the NO_2 gas sensor that was made of RGO/WO_3 nanocomposite film exhibited higher response than that of the NO_2 gas sensor made of MWCNTs/WO_3 nanocomposite film because that the RGO had high electron mobility, favoring the transport process of electron easily in the RGO/WO_3 nanocomposite film at room temperature [2]. However, the response/recovery times of the NO_2 gas sensor that was proposed herein were longer than that of the NO_2 gas sensor that was fabricated by the hydrothermal method, perhaps because the former sensor had a compact sensing-film.

4. Conclusions

RGO/WO_3 nanocomposite film was fabricated on an alumina substrate by combining the one-pot polyol process with the MOD method. It was found that the introduction of RGO was effective for increasing the conductance of RGO/WO_3 nanocomposite film especially at low concentration of NO_2 gas. Therefore, the response of the RGO/WO_3 nanocomposite film to NO_2 gas increased dramatically when a few RGO was added to the WO_3 film. However, the amount of RGO added exceeded the percolation threshold, no variation in response versus concentration of NO_2 gas was clearly observed.

The NO_2 gas sensor that was based on a RGO/WO_3 film that was doped with 3.2 wt% of RGO responded more strongly than any of the tested sensors that were based on such films with different degrees of doping. The NO_2 gas sensor was very sensitive with acceptable linearity ($Y=171.34X-58.9$; $R^2=0.9794$) between 0.5 and 5 ppm, good reversibility and long-term stability (at least 45 days) when used at room temperature. NH_3 and H_2S gases may be regarded as having unobvious interference effects with NO_2 at a testing NO_2 concentration of 5 ppm. Ambient humidity significantly affected the NO_2 gas sensor. The response and recovery times were 9 and 18 min, respectively.

Acknowledgments

The authors thank the Ministry of Science and Technology (grant no. MOST 103-2113-M-034-001) of Taiwan for support.

References

[1] K.S. Novoselov, A.K. Geim, S.V. Morozov, D. Jiang, Y. Zhang, S.V. Dubonos, I.V. Grigorieva, A.A. Firsov, Science 306 (2004) 666–669.
[2] K.S. Novoselov, A.K. Geim, S.V. Morozov, D. Jiang, M.I. Katsnelson, I.V. Grigorieva, S.V. Dubonos, A.A. Firsov, Nature 438 (2005) 197–200.
[3] A.A. Balandin, S. Ghosh, W. Bao, I. Calizo, D. Teweldebrhan, F. Miao, C.N. Lau, Nano Lett. 8 (2008) 902–907.
[4] C. Daniela, V.D. Marcano, J.M. Kosynkin, J.M. Berlin, A. Sinitskii, Z. Sun, A. Slesarev, L.B. Alemany, W. Lu, M.J.M. Tour, Nano 4 (2010) 4806–4814.
[5] A. Lerf, H. He, M. Forster, J. Kilnowski, J. Phys. Chem. B 102 (1998) 4477–4482.
[6] S.F. Pei, H.M. Cheng, Carbon 50 (2012) 3210–3228.
[7] G. Lu, L.E. Ocola, J. Chen, Appl. Phys. Lett. 94 (2009) 083111-3.
[8] J.T. Robinson, F.K. Perkins, E.S. Snow, Z. Wei, P.E. Sheehan, Nano. Lett. 8 (2008) 3137–3140.
[9] V. Dua, S.P. Surwade, S. Ammu, S.R. Agnihotra, S. Jain, K.E. Roberts, S. Park, R.S. Ruoff, S.K. Manohar, Angew. Chem. Int. Ed. 49 (2010) 2154–2157.
[10] N. Hu, Y. Wang, J. Chai, R. Gao, Z. Yang, E.S.W. Kong, Y. Zhang, Sens. Actuators B 163 (2012) 107–114.
[11] Z. Yang, R. Gao, N. Hu, J. Chai, Y. Cheng, L. Zhang, H. Wei, E.S.W. Kong, Y. Zhang, Nano-Micro Lett. 4 (2012) 1–9.
[12] N. Hu, Z. Yang, Y. Wang, L. Zhang, Y. Wang, X. Huang, H. Wei, L. Wei, Y. Zhang, Nanotechnology 25 (2014) 025502.
[13] X. Huang, N. Hu, R. Gao, Y. Yu, Y. Wang, Z. Yang, E.S.W. Kong, H. Wei, Y. Zhang, J. Mater. Chem. 22 (2012) 22488–22495.
[14] A. Gutés, B. Hsia, A. Sussman, W. Mickelson, A. Zettl, C. Carraro, R. Maboudian, Nanoscale 4 (2012) 438–440.
[15] Q. Huang, D. Zeng, H. Li, C. Xie, Nanoscale 4 (2012) 5651–5668.
[16] P.A. Russo, N. Donato, S.G. Leonardi, S. Baek, D.E. Conte, G. Neri, N. Pinna, Angew. Chem. Int. Ed. 51 (2012) 11053–11057.
[17] J. Chen, J. Shi, X. Wang, H. Cui, M. Fu, Chin. J. Catal. 34 (2013) 621–640.
[18] S. Bai, X.P. Shen, RSC Adv. 2 (2012) 64–98.
[19] Y. Si, E.T. Samulski, Chem. Mater. 20 (2008) 6792–6797.
[20] J.W. Qin, M.H. Cao, N. Li, C.W. Hu, J. Mater. Chem. 21 (2011) 17167–17174.
[21] T.S. Wu, S. Liu, Y.L. Luo, W.B. Lu, L. Wang, X.P. Sun, Nanoscale 3 (2011) 2142–2144.
[22] X. An, J.C. Yu, Y. Wang, Y. Hu, X. Yu, G. Zhang, J. Mater. Chem. 22 (2012) 8525–8531.
[23] S. Srivastava, K. Jain, V.N. Singh, S. Singh, N. Vijayan, N. Dilawar, G. Gupta, T.D. Senguttuvan, Nanotechnology 23 (2012) 205501.
[24] C. Feldmann, Scr. Mater. 44 (2001) 2193–2196.
[25] C. Feldmann, C. Metzmacher, J. Mater. Chem. 11 (2001) 2603–2606.
[26] C. Feldmann, Adv. Funct. Mater. 2 (2003) 101–107.
[27] G.M. Vest, Mater. Res. Soc. Symp. Proc. 60 (1986) 35.
[28] P. Van Geloven, J. Moons, M. Honore, J. Roggen, Sens. Actuators 17 (1989) 361.
[29] P.P. Tsai, I.C. Chen, M.H. Tzeng, MRL Bull. Res. Dev. 6 (1992) 67–72.
[30] P.P. Tsai, I.C. Chen, M.H. Tzeng, Sens. Actuators B 13–14 (1993) 610–612.
[31] P.P. Tsai, I.C. Chen, M.H. Tzeng, Tin oxide (SnOx) carbon monoxide sensor fabricated film methods,, Sens. Actuators B 24–25 (1995) 537–539.

[32] H.T. Sun, C. Cantalini, L. Lozzi, M. Passacantando, S. Santucci, M. Pelino, Thin Film Devices, Sensors and Actuators, Thin Solid Films 287 (1996) 258–265.
[33] Y.G. Choi, G. Sakai, K. Shimanoe, N. Miura, N. Yamazoe, Sens. Actuators B 95 (2003) 258–265.
[34] W.S. Hummers, R.E. Offeman, J. Am. Chem. Soc. 80 (1958) 1339.
[35] P. Porkodi, V. Yegnaraman, D. Jeyakumar, Mater. Res. Bull. 41 (2006) 1476–1486.
[36] A.B. Bourlinos, D. Gournis, D. Petridis, T. Szabó, A. Szeri, I. Dékány, Langmuir 19 (2003) 6050–6055.
[37] ⟨http://www.icdd.com/products/overview.htm⟩.
[38] B.Y. Wei, M.C. Hsu, P.G. Su, H.M. Lin, R.J. Wu, H.J. Lai, Sens. Actuators B 101 (2004) 81–89.
[39] P.G. Su, T.T. Pan, Mater. Chem. Phys. 125 (2011) 351–357.

Talanta 132 (2015) 406–415

Contents lists available at ScienceDirect

Talanta

journal homepage: www.elsevier.com/locate/talanta

Developing electrochemical sensor for point-of-care diagnostics of oxidative stress marker using imprinted bimetallic Fe/Pd nanoparticle

Ekta Roy [a], Santanu Patra [a], Rashmi Madhuri [a,*], Prashant K. Sharma [b]

[a] Department of Applied Chemistry, Indian School of Mines, Dhanbad 826 004, Jharkhand, India
[b] Functional Nanomaterials Research Laboratory, Department of Applied Physics, Indian School of Mines, Dhanbad 826 004, Jharkhand, India

ARTICLE INFO

Article history:
Received 24 July 2014
Received in revised form
22 September 2014
Accepted 23 September 2014
Available online 2 October 2014

Keywords:
Bimetalic Fe/Pd nanoparticle
Surface imprinting
3-Nitrotyrosine
ELISA
Electrochemical sensor

ABSTRACT

A novel electrochemical-sensing platform based on imprinted bimetallic Fe/Pd (BI-Fe/Pd) nanoparticle has been fabricated for point-of-care diagnostics of oxidative stress marker (3-nitrotyrosine) in biological fluids. Herein, BI-Fe/Pd nanoparticles are used as a platform on which 3-nitrotyrosine imprinted cavities are created using acrylamide as monomer and *N*-*N*′-methylene bisacrylamide as cross-linker. The performance of the obtained imprinted sensor is investigated by cyclic, differential pulse, and square wave voltammetry in stripping mode. The imprinted sensor exhibits high recognition ability and affinity for 3-nitrotyrosine in comparison with the non-imprinted one. In addition, the proposed sensor is capable of measuring 3-nitrotyrosine in aqueous as well as in human blood serum, plasma, and urine samples within the range of 4.90–867.57 $\mu g\ L^{-1}$ and 9.90–867.57 $\mu g\ L^{-1}$ with detection limit of 1.20 $\mu g\ L^{-1}$ and 3.25 $\mu g\ L^{-1}$ by square wave and differential pulse stripping voltammetry, respectively. Imprinted BI-Fe/Pd nanoparticle modified sensor shows high affinity and no interference from blood or urine components. Modified sensor was stored for 45 days at room temperature without any detrimental effects to their binding properties. The high affinity of proposed sensor and the lack of requirement for cold chain logistics make them an attractive alternative to the enzyme-linked immunosorbent assay (ELISA) technique.

© 2014 Elsevier B.V. All rights reserved.

1. Introduction

Nitration of tyrosine residue is a common post-translational modification to proteins that occurs *in vivo* especially under conditions of oxidative and nitrosative stress [1]. Tyrosine nitration of proteins (in *ortho* position to the phenolic hydroxyl group) is generated by reactive nitrogen species (peroxynitrite, nitrogen dioxide, nitrous acid, nitryl chloride *etc.*) either from the inflammatory cell defense mechanism or from a combination of nitric oxide synthase activity with a high rate of oxidative metabolism [2]. Tyrosine nitration can dramatically change protein structure and conformation. Subsequently it alter the biological half-life, inactivate enzymes and receptors that depend on tyrosine residues for their activity. This prevents phosphorylation of tyrosine residues, which is important for signal transduction. This modification is also associated with a number of pathologies [1], including neurodegenerative disorders such as Alzheimer's [2], atherosclerosis [3], osteoarthritis [4], rheumatoid arthritis [5], Parkinson's [6] and cardiovascular disease [7].

Now-a-days, 3-nitrotyrosine (3-NT) has been suggested and used as a biomarker for diagnosis of oxidative stress-induced pathological conditions. The predictive value of 3-NT was independent of other measures such as C-reactive protein, an inflammatory marker. Because of its utility in monitoring disease pathology and therapeutic intervention, a sensitive, specific and reliable method for measuring nitrotyrosine is crucial. Several analytical methods have been developed and used to measure free nitrotyrosine and/or nitrated proteins. Among all these methodologies reported so far, three major methodological approaches have been regularly used to measure 3-NT levels in biological matrices. The first methodology, mass spectroscopy (MS) technique, is usually coupled to either gas chromatography (GC–MS) [8] or liquid chromatography (LC–MS) [9]. Second, HPLC coupled with electrochemical detection has been widely used for the measurement of free and protein bound 3-NT [10]. The third and commercialized method reported for 3-NT detection is ELISA. According to the literature, more than five ELISA kits are available for 3-NT determination (Table 1). Based on the reaction with reactive nitrogen species, two forms of 3-NT are found *in vivo*, *i.e.* free

* Corresponding author.
Tel.: +91 9471191640, +91 326 2235935; fax: +91 326 2296563.
E-mail address: rshmmadhuri@gmail.com (R. Madhuri).

http://dx.doi.org/10.1016/j.talanta.2014.09.033
0039-9140/© 2014 Elsevier B.V. All rights reserved.

Table 1
List of commercially available ELISA techniques reported for determination of 3-nitrotyrosine.

S. nos.	Company name	Range ($\mu g\ L^{-1}$)	LOD ($\mu g\ L^{-1}$)	Detection technique
1.	Abcam-ab116691	8.0–1000.0	0.001	Spectrophotometer
2.	HycultBiotech-HK501	0.45–339.28	0.45	Spectrophotometer
3.	USCN	3.7–3000	1.38	Spectrophotometer
5.	MyBiosourse.Com	0–20	0.001	Spectrophotometer
6.	Milipore	$0–12 \times 10^5$	–	Chemiluminescence
7.	This method	(a) 9.90–867.57 (b) 4.90–867.57	(a) 3.25 (b) 1.20	Electrochemical

and protein-bound. Typically, identification and quantification of 3-NT has involved measuring the free 3-NT either in plasma or urine sample [11] and only ELISA techniques are able to detect protein bound 3-NT. All the ELISA kits are based on monoclonal and/or polyclonal natural antibodies against 3-NT. Although natural antibodies are highly selective and sensitive to their target molecule, they exhibit poor stability; require long production time, difficult handling, low temperature storage, and high costs.

For these reasons, today, the research is focusing on the production of artificial antibodies which are capable of selectively binding target analyte with the same sensitivity of the natural antibodies but with simple steps and low cost of production. In this respect, molecularly imprinted polymers (MIPs) are in demand, in place of antibody, to design robust molecular receptors that are capable in recognizing target biological molecules at molecular level. Such MIPs can also mimic natural recognition entities, such as antibodies and biological receptors.

Mergola et al., have prepared 3-NT imprinted polymer as solid-phase extraction (SPE) sorbent material by bulk polymerization with methacrylic acid as functional monomer and acetonitrile as porogen [12]. Although their result showed high selectivity, but their application in real sample analysis (human blood) is not explored, which is the major agenda in 3-NT detection. Similarly, Schöneich et al., have done the 3-NT labeling with fluorogenic compound to visualize the cellular protein 3-NT by confocal microscopy [13]. But how much protein got converted or nitrated at tyrosine residue, *i.e.* the quantitative study, is not explored.

Bimetallic nanoparticles are of wide interest since they lead to many interesting size-dependent electrical, chemical, and optical properties. Recently, zero-valent iron (ZVI, Fe^0) is commonly utilized in biotechnological and biomedical industry, due to its nontoxic, paramagnetic behavior. According to the literature, the reductive activity of ZVI nanoparticles get enhanced in combination with some other metals [14]. A number of combinations has been reported so far to produce bimetallic ZVI systems like Pd/Fe [14], Cu/Fe [15], Ni/Fe [16], and Ag/Fe [17]. Among these alloys, Fe/Pd nanoparticle modification was preferred due to their biocompatibility, high electrical conductivity and inexpensiveness [14].

In this work, first time, we have synthesized 3-NT imprinted polymer as artificial receptor onto the surface of bimetallic nanoparticle for the fabrication of electrochemical sensor. The main aim of this study was to apply artificial receptor modified electrochemical sensor for detection of 3-NT as well as nitrated tyrosine residues in biologically available protein molecules. We have synthesized (*in situ*) a vinyl group modified bimetallic Fe/Pd nanoparticle (BI-Fe/Pd), using acrylic acid as stabilizing agent. The vinyl group modified BI-Fe/Pd was used as a platform for synthesis of 3-NT imprinted polymer in the presence of acrylamide (co-monomer), *N-N′*-methylene bisacrylamide (cross-linker) and ammonium peroxodisulphate (initiator), resulting in a biocompatible polymer matrix. Furthermore, the imprinted BI-Fe/Pd nanoparticles were used for fabrication of electrochemical sensor by drop coating onto the pencil graphite electrode (PGE) surface. The proposed sensor is to be used for the *in vitro* quantitative determination of free amino acid and/or total 3-NT levels in biological samples, without any acid hydrolysis or pronase digestion to release nitrotyrosine from nitrated proteins and peptides. Since the sensor can detect the modified amino acid present in protein, the assay is useful for proteins of all species. Moreover, the comparative study of proposed sensor with popular ELISA technique was also performed and it was found that the proposed sensor is much better than ELISA in terms of cost, time of analysis, handling, storage and reusability.

1.1. Materials and instruments

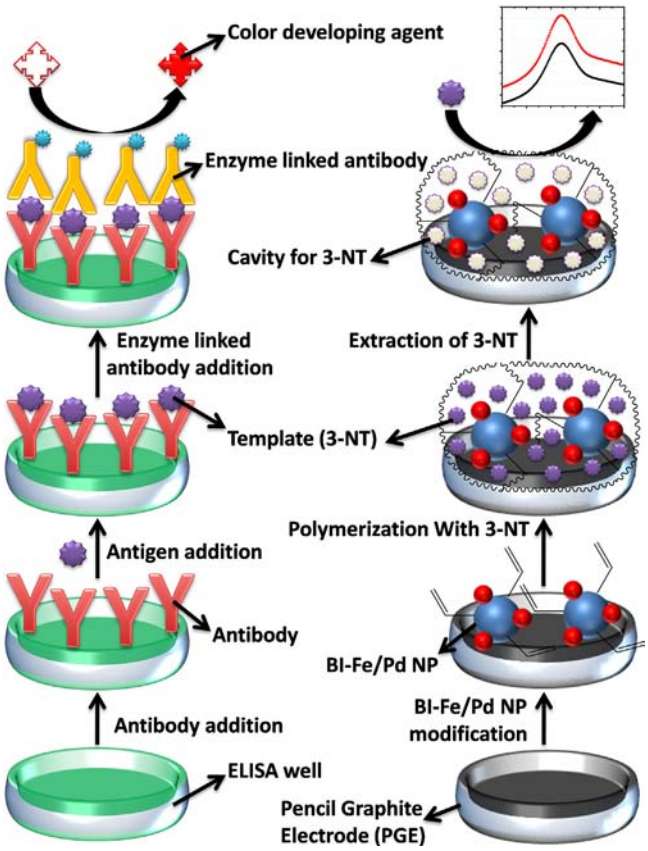
Acryl amide, acrylic acid, ammonium peroxodisulphate (APS), 3-NT, ferrous sulfate heptahydrate ($FeSO_4 \times 7H_2O$) ($>99.0\%$), sodium borohydride ($NaBH_4$) ($>98.0\%$), palladium acetate ($PdCl_2$), *N-N′*-methylene bisacrylamide (MBAA), and other interferents were purchased from Aldrich (Steinheim, Germany) and Fluka (Steinheim, Germany). Solvents, dimethyl sulphoxide (DMSO) and ethanol, were procured from Spectrochem Pvt. Ltd., (Mumbai, India). Standard stock solution of 3-NT ($5.0\ mg\ L^{-1}$) and interferents were prepared in double distilled water. For the binding characterization between imprinted nanoparticle and template, Fourier transform infrared spectroscopy (FT-IR) analysis was carried out on Varian FT/IR (USA) spectrometers. Morphological images and EDAX spectra of bare and modified SPE surfaces and BI-Fe/Pd nanoparticles were recorded using scanning electron microscope (SEM), Hitachi, model S-3400N. For BI-Fe/Pd nanoparticle characterization, UV–vis, X-ray diffraction (XRD), and high resolution transmission electron microscopy (HRTEM) analyses were performed on Perkin Elmer Lambda-35 spectrophotometer, Bruker D8 Focus X-ray diffractometer, and Tecnai T-30 (300 kV FEG TEM), respectively. Three kinds of biological fluids; human plasma, human serum, and human urine; were used to confirm the applicability of the proposed MIP sensor. All the pathological samples were obtained from the local pathology and were used as obtained. All the experiments were performed at room temperature ($25 \pm 1\ ^\circ C$).

1.2. Nitration of protein molecules

To explore the applicability of proposed sensor for protein bounded 3-NT analysis, bovine serum albumin (BSA) and ferritin molecules were nitrated in the laboratory by an earlier reported method [18]. First, protein was dissolved in 50 mM NH_4HCO_3 ($1\ mg\ mL^{-1}$) and nitrated with peroxynitrite ($ONOO^-$) by injecting the nitrating reagent into the protein solution while vortex mixing for 30 s at room temperature. Peroxynitrite was prepared, method described previously [19], by ozonolysis of sodium azide in 0.1 M NaOH and was stored at $-80\ ^\circ C$ until it was used. After nitration, the protein samples were dialyzed overnight against 50 mM NH_4HCO_3 buffer and stored at $-4\ ^\circ C$, before use.

1.3. Preparation of BI-Fe/Pd nanoparticle

Bimetallic Fe/Pd NPs were synthesized by earlier reported method with some modification [14]. Initially, dispersed solutions of acrylic acid with two different concentrations (0.5 v/v % and 1 v/v %) were prepared by deionized double distilled water. For preparation of BI-Fe/Pd nanoparticle, 10.0 mL of dispersant solution was added into 100.0 mL $FeSO_4$ solution ($0.05\ mol\ L^{-1}$). The resultant solution was homogenously mixed by vigorous magnetic stirring for 30 min. Then 125.0 mL of $NaBH_4$ solution (0.1 M) was drop wise added into the mixture for the formation of vinyl group modified zero-valent iron. The reaction mechanism is shown below for clarity:



Scheme 1. Comparative study between working methodology of ELISA and proposed method.

$$Fe^{2+} + 2BH_4^- + 6H_2O \rightarrow Fe^0\downarrow + 2B(OH)_3 + 7H_2\uparrow$$

The prepared, zero-valent iron NPs were washed by deionized water for 2 to 3 times followed by vacuum drying at room temperature. For Fe/Pd bimetallic NPs preparation, the above prepared zero-valent iron NPs were immersed into the solution of $PdCl_2$ (1 mmol, 10 mL ethanol) for 30 min, resulting, the deposition of Pd onto the surface of zero-valent iron NPs.

$$Pd^{2+} + Fe^0 \rightarrow Pd^0 + Fe^{2+}$$

Finally, the modified BI-Fe/Pd NPs were rinsed with ethanol and acetone, followed by vacuum drying at room temperature.

1.4. Fabrication of 3-NT imprinted BI-Fe/Pd NP based sensor

The surface of the PGE was polished with 1.0 μm and 0.05 μm wet alumina slurry followed by 5 min ultrasonication in distilled water. Then the electrode was subjected to drop coating of 5.0 μL of BI-Fe/Pd nanoparticle suspension prepared in THF solvent and kept for 12 h at room temperature for drying (Schemes 1 and 2). Later on, the pre-polymer mixture (purged with 99.999% pure N_2 for 10 min) containing optimized amount of template (3-NT, 0.05 mmol, 11.3 mg in 0.5 ml of DMSO), monomer (acryl amide, 0.1 mmol, 14.2 mg in 120 μL DMSO), cross-linker (MBAA, 0.1 mmol, 11.8 μl), and initiator (APS, 0.05 mmol, 11.4 mg) was casted on the bimetallic NP modified PGE. Finally, the modified PGE was placed in a pre-heated electric oven for 2 h at 50 °C. This results in the formation of polymer (adduct polymer) onto the surface of BI-Fe/Pd NPs modified PGE. For preparation of imprinted polymer, template molecule was extracted from adduct polymer. The adduct polymer modified PGE was placed in 1.0 M NaOH solution for 30 min. Complete template extraction was confirmed by no DPSV response for 3-NT. For control analysis, non-imprinted polymer (NIP) was also prepared by adopting the same procedure, but in the absence of template molecule.

1.5. Electrochemical measurements

All the electrochemical analysis [cyclic voltammetry (CV), differential pulse stripping voltammetry (DPSV), square wave stripping voltammetry (SWSV) and chronocoulometry (CC)] were performed on CH instrument (USA, model number 660C) with three electrode assembly in a electrochemical cell containing 10 mL KCl solution as supporting electrolyte (pH=8.0). Here imprinted nanoparticle modified PGE was used as working, Ag/AgCl as reference and Pt wire was used as counter electrode. Before any eletrochemical analysis, the blank run was taken in the absence of target analyte (3-NT). For qualitative and electrochemical study of 3-NT, CV and CC analyses were performed. CV was recorded in the potential window of +1.8 V to −0.2 V at different scan rates (50–200 mV s^{-1}). Moreover, for quantitative study, DPSV and SWSV were performed. Before DPSV and SWSV analyses, analyte was deposited at electrode for 60 s at −2.5 V vs. Ag/AgCl. Then, DPSV runs were recorded in the potential range varying from +1.3 V to +0.4 V (vs. Ag/AgCl) at a scan rate 10 mV s^{-1}, pulse amplitude 50 mV, and pulse width 50 ms. SWSV were recorded in the potential range varying from +1.3 V to +0.4 V (vs. Ag/AgCl) at a scan rate 10 mV s^{-1}, pulse amplitude 25 mV, and frequency 15.0 Hz.

The peak currents observed in SWSV and DPSV analysis were used for the quantitative measurement of 3-NT in real samples. The limit of detection (LOD) was calculated as three times the standard deviation for the blank measurement in the absence of template, divided by the slope of the calibration plot between 3-NT concentration and DPSV/SWSV current [20].

2. Results and discussions

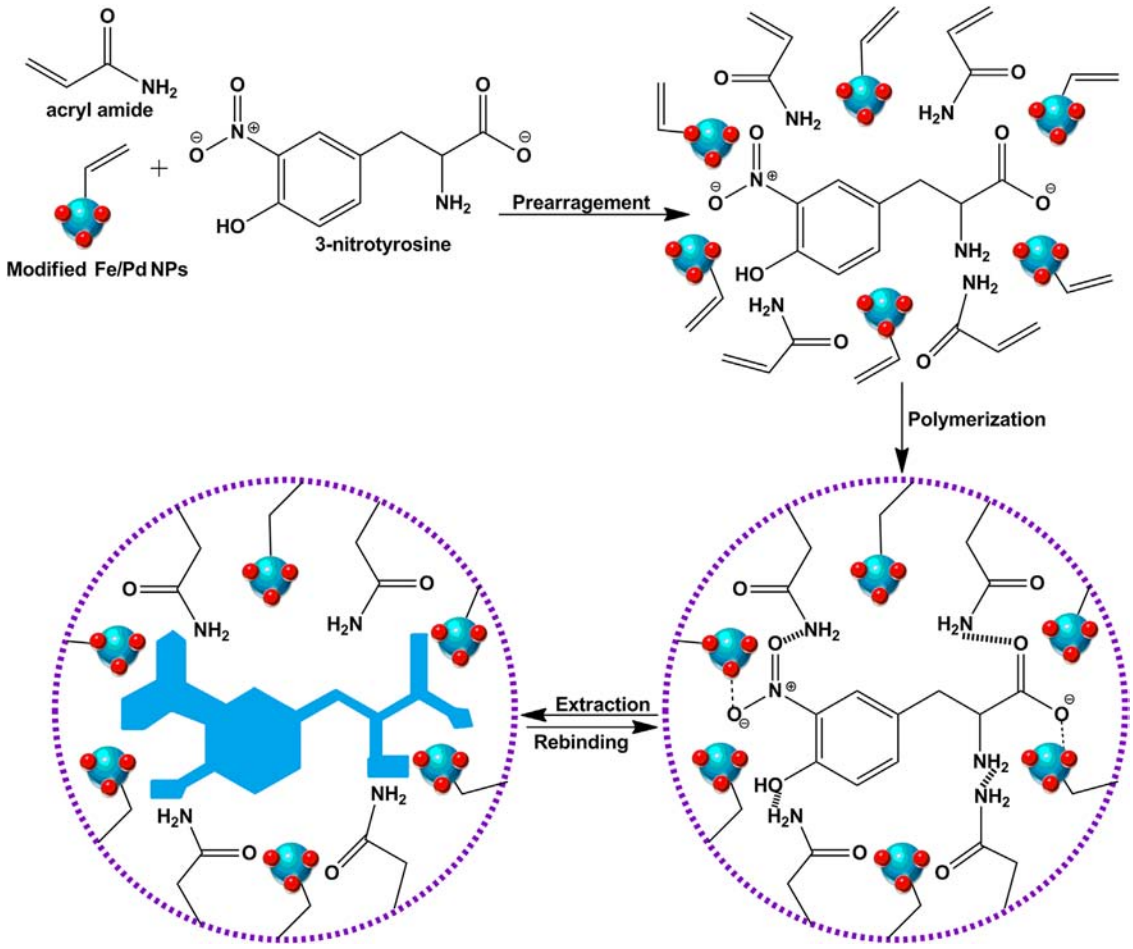
2.1. Characterization of bimetallic Fe/Pd NPs

2.1.1. Composition and morphological characterization

UV–vis, XRD, FT-IR, FE-SEM, EDAX and TEM analyses were performed for characterization of modified BI-Fe/Pd NPs. Fig. 1 (A) shows UV−vis spectrum for the as-formed Fe/Pd bimetallic nanoparticles. Only one SPR band (λ_{max}=365 nm) is observed for the Fe/Pd nanoparticles, rather than two SPR bands. This observation indicates that the nanoparticles were basically an alloy structure with a homogeneous composition, rather than a physical mixture of monometallic Fe and Pd nanoparticles. In order to confirm the compositional homogeneity of the nanoparticles, XRD studies were also carried out. Fig. 1(B) shows the powder XRD spectra of the Fe and BI-Fe/Pd nanoparticles synthesized in the present work. XRD spectra show main peaks at the positions of 30.1°, 35.4°, 43.1°, 57.1° and 62.60°, which are in good agreement with the standard JCPDS file for Fe_3O_4 (JCPDS 89–0691, $a=b=c=8.38$ Å) and can be indexed as the face centered cubic structure of Fe_3O_4 having space group *Fd*3*m* (277). Furthermore, because of low concentration of Pd, no additional peaks related to Pd, were observed for BI-Fe/Pd nanoparticles. All available reflections of the present XRD phases have been fitted with a Gaussian distribution. The broadening of XRD peaks (*i.e.* Scherrer's broadening) attributes nanosized formation of Fe and BI-Fe/Pd nanoparticles. The particle size, *d*, of the synthesized Fe and BI-Fe/Pd nanoparticles were estimated by Debye–Scherrer's equation [21]:

$$d = \frac{0.9\lambda}{B\cos\theta} \quad (1)$$

where, *d* is the particle size, λ is the wavelength of X-rays, θ is the Bragg angle and B is the full width at half maxima (FWHM) on 2θ



Scheme 2. Binding mechanism between monomer, template and bimetallic Fe/Pd nanoparticle.

scale. The average particle size using Debye–Scherrer's equation was of the order of ~4 nm. The morphology and size of the synthesized BI-Fe/Pd nanoparticles are shown using SEM and TEM studies, Fig. 1 (C) and (D), respectively. As evident from Fig. 1(C), spherical microstructures of BI-Fe/Pd nanoparticles were observed in FE-SEM studies. The closure observation reveals that these microstructures are eventually composed of very tiny spherical nanoparticles of size 4–8 nm. In order to confirm the XRD and FE-SEM observations, HRTEM studies were also carried out. HRTEM studies, Fig. 1(D), confirm that the synthesized BI-Fe/Pd nanoparticles were spherical in shape and had average size ~4 nm. These observations are in good agreement with XRD and FE-SEM studies. Fig. 1(E), shows the EDAX spectra for the Fe/Pd bimetallic nanoparticles. The compositions of Fe and Pd are 92.49% and 7.51%, respectively. The uniformity in the particle-to-particle composition, and the concurrent presence of both Fe and Pd in each particle, confirmed that the particles had a Fe/Pd bimetallic structure. To study the vinyl group modification of BI-Fe/Pd NP, FT-IR spectrum was recorded (Fig. 1(F)). In the spectrum, three characteristic bands of vinyl group (–C=C–, 1680 cm^{-1}; =C–H, 3100 cm^{-1}; and =C–H (bend), 1000 cm^{-1}) were observed, which confirms the vinyl group generation on the surface of BI-Fe/Pd NPs.

2.1.2. Electrochemical characterization

The electrocatalytic behavior of the bimetallic NPs were studied in KCl solution (pH=8.0) containing 5.0 mmol L^{-1} $K_3Fe(CN)_6$, which acts as an electro-chemical probe. As shown in Fig. S1A, the cyclic voltammogram of $K_3Fe(CN)_6$ at bare PGE, shows an oxidation peak at +0.158 V and a reduction peak at +0.251 V. The peak current increased four-fold when ZVI NPs were immobilized on the electrode. This is attributed to an increase in effective working electrode surface area by coating of nanoparticles. However, two-fold increase in peak current was observed on BI-Fe/Pd NPs modified electrode as compared to ZVI NPs modified electrode. Similar results are obtained in the DPSV and SWSV analyses (S1 B and C), which confirm that the deposition of Pd onto the surface of ZVI enhanced the electrocatalytic activity.

2.2. Characterization of imprinted polymer

2.2.1. UV–vis spectroscopic evaluation for the template–monomer interaction

To study the binding interaction between monomer and template, UV–vis spectroscopic study was performed in aqueous medium (Fig. 2(A)). Herein, different concentrations of acryl amide monomer were added to the fixed concentration of template. Nitrotyrosine showed an absorption band with λ_{max}=625 nm, which decreases with increase in concentration of monomer (up to 2:1 ratio). But after this ratio, with increase in concentration of monomer, the absorbance peak remains constant (Fig. 2(A)). The decrease in absorbance value can be attributed due to the non-covalent interactions (mainly the hydrogen bonding interaction) between the functional group of monomer and template molecule (Scheme 2). So, the optimized molar ratio of 2:1 (monomer:template) is used for further studies.

2.2.2. Binding interaction between polymer and template by FT-IR analsis

FT-IR spectra of nitrotyrosine (B), adduct (C) and MIP (D) were shown in Fig. 2. As depicted in curve A, after binding with monomer in adduct polymer, the characteristic bands of nitrotyrosine

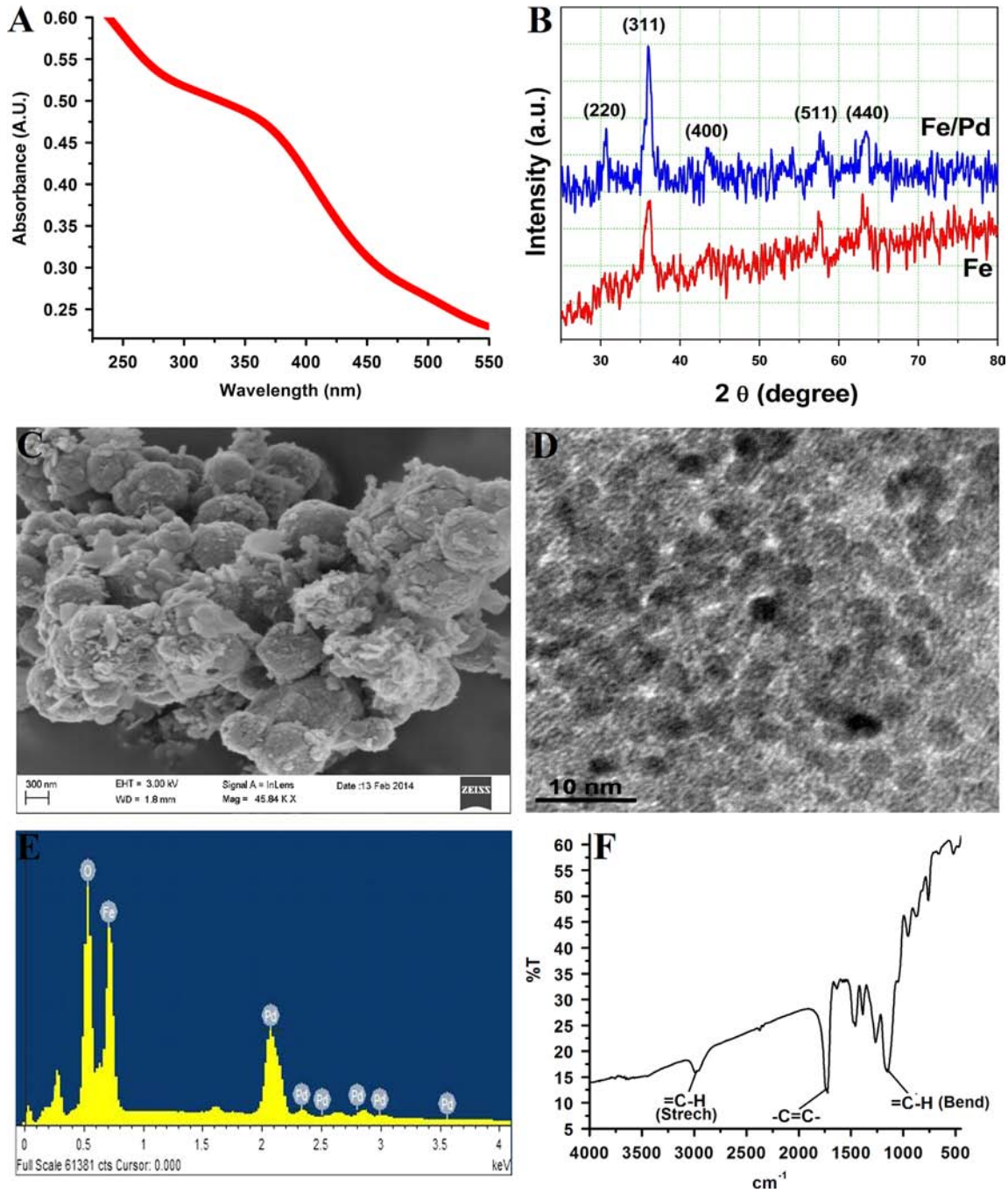


Fig. 1. Characterization of bimetallic Fe/Pd nanoparticle by: (A) UV, (B) XRD, (C) FE-SEM, (D) HR-TEM, (E) EDAX, and (F) FT-IR analyses.

[–CO (asym), 2000 cm^{-1}; –NO, 1440 cm^{-1}; –CO (Sym), 1120 cm^{-1}; and –OH, 3000 cm^{-1}] shifts to lower wavelengths side (1850 cm^{-1}, 1490 cm^{-1}, 1000 cm^{-1} and 2980 cm^{-1}). The bands due to the monomer skeleton remain constant at their original positions (1590 cm^{-1} and 3500 cm^{-1}) in adduct as well as in the spectrum of MIP (curve C and D). In the MIP spectrum (curve D), the template related band was absent. This suggests the complete removal of template from polymer cavity, after extraction.

2.2.3. *Morphological characterization of imprinted polymer by SEM and EDAX analyses*

The morphological differences between adduct and MIP-modified PGEs were studied by SEM analysis (Fig. 3(A) and (B)). As shown, adduct-modified PGE surface is uniform and very compact in comparison to the MIP-modified PGE, which shows a rough surface with clearly visible cavities. The cavities present at the MIP-modified PGE are generated after template extraction; suggest the successful imprinting of 3-NT in the polymer matrix. In order to explore compositional information about the polymer matrix, EDAX spectra of adduct (Fig. 3(C)) and MIP (Fig. 3(D)) modified PGEs were also recorded. Theoretically, both adduct and MIP has similar elemental composition but the intensity varies after template extraction. As observed, the characteristic peak for 'C', 'N', 'O' element are present in both adduct and MIP-modified PGEs surface but their percentage is less in MIP-modified surface (Table shown in Fig. 3(C) and (D)). The data obtained from both SEM and EDAX analysis confirms the successful imprinting of 3-NT.

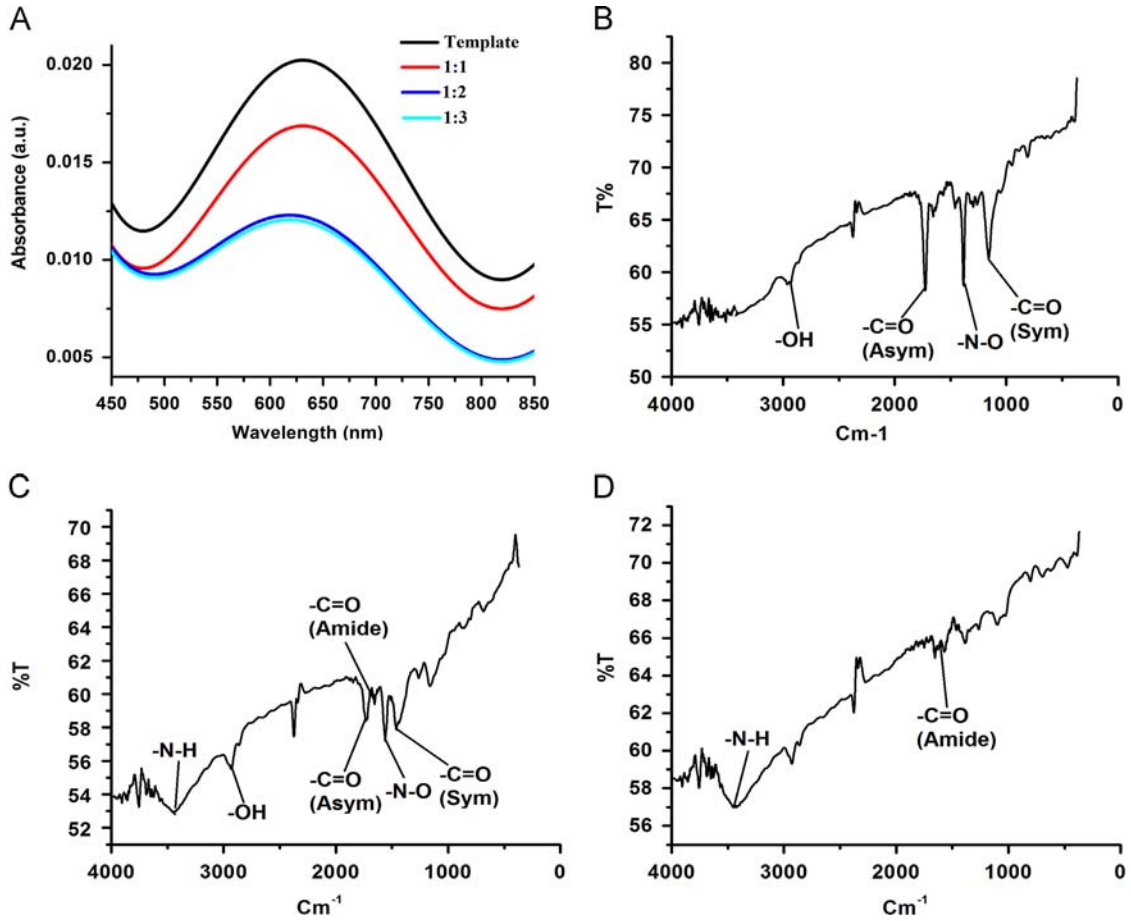


Fig. 2. (A) UV–vis spectra of template and monomer in different molar ratio and FT-IR spectra of (B) template (3-nitrotyrosine), (C) adduct, and (D) MIP.

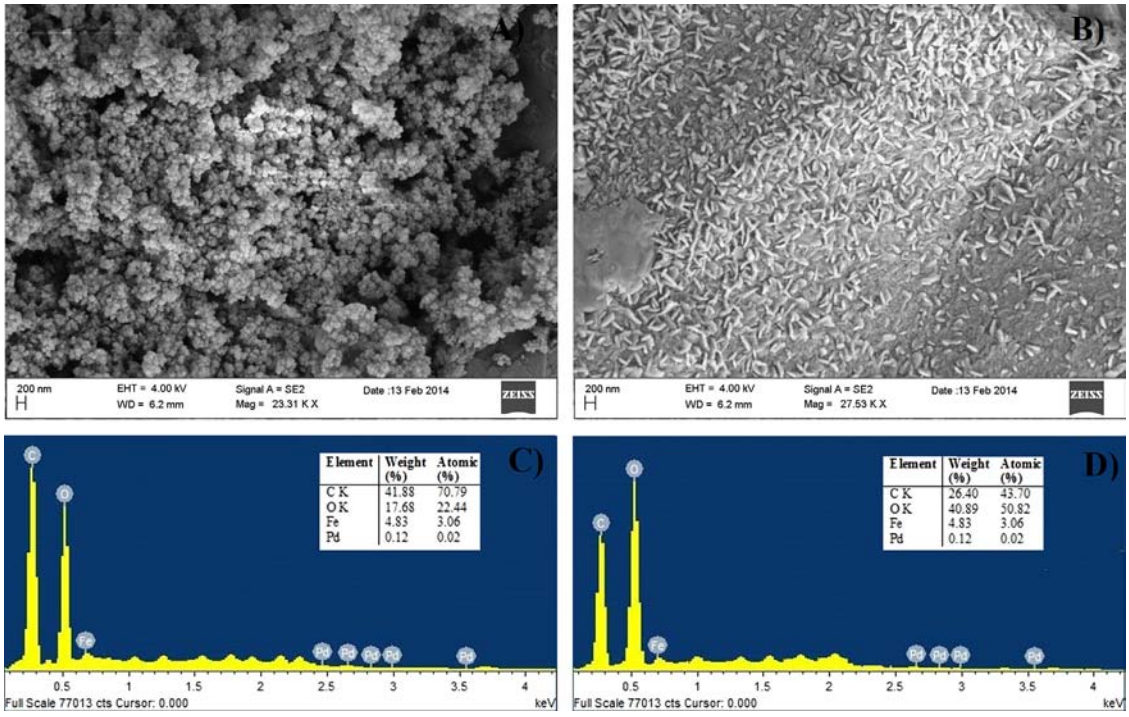


Fig. 3. SEM images and EDAX spectra of adduct ((A) and (C)) and MIP ((B) and (D)).

2.3. Electrochemical behavior of nitrotyrosine

Cyclic voltammety and chronocoulometric experiments were carried out to study the electrochemical behavior of nitrotyrosine at the bare, MIP, and NIP modified-PGE. Irreversible cathodic waves with reduction peak potential at +0.80 V can be observed on the surface of the PGE and MIP-modified PGE (Fig. S2). The reduction peak current (I_p) at MIP/PGE was significantly higher than that of bare PGE, indicating the significantly enhanced efficiency of the MIP nanoparticles modification on the PGE surface (Fig. S2). On the other hand, a weak current was observed on the NIP/PGE, which may be due to the non-specific adsorption of 3-NT (Fig. S2).

The reduction system was characterized by a cathodic peak at the negative-moving step but the anodic peak was absent on the reverse scan. This indicates the ir-reversible reduction of 3-NT molecule (Fig. 4(A)). The reduction reaction process was attributed to the four electrons reduction of the nitro group of 3-NT to generate the related hydroxylamine according to the currently accepted mechanism for the electro-reduction of aromatic and hetero-aromatic nitro compounds [22–24].

The effect of potential scan rate on the reduction peak current of 3-NT was investigated at the MIP/PGE. As can be been seen from Fig. 4(A), the I_p increased gradually with the increasing scan rate and there was a linear relationship between I_p (μA) and scan rate (50–200 mV s^{-1}) as shown in the linear regression equation:

I_p (μA)=(1.401 ± 0.085) ν+(119.87 ± 8.38); n=6; R^2=0.99, which suggests that the reduction of 3-NT on the MIP/PGE electrode is a controlled surface-adsorption process. The influence of pH value on the current response of 50.0 μg L^{-1} 3-NT was examined by DPSV with KCl solution in the pH range from 2.0 to 12.0. As can be seen in Fig. S4, initially, the I_p increases with an increase in pH from 2.0 to 8.0, and then decreases for further increasing pH values (8.0 to 12.0). Therefore, the optimum pH of KCl solution was set at 8.0 for further experiments. The number of protons, which participated during the reduction of 3-NT on a MIP-modified PGE, was evaluated through the relationship between peak potentials and pH. A linear shift of E_p toward negative potential with increasing pH from 2.0 to 12.0 indicates that protons are directly involved in the reduction of 3-NT and it follows following equation: $E_p = -0.412 - 0.0509$ pH (R^2=0.99). According to the Nernst equation:

$$E = E^0 - \left[\frac{(2.303mRT)}{(nF)}\right] \text{pH}$$

(where m and n are corresponding to the transference numbers of proton and electron, respectively) [25], the ratio of m/n was calculated nearly to be 1, suggesting the numbers of the involved protons and electrons were equal in the electro-reduction of 3-NT. Since it is known that four electrons (n=4) and four protons participated in electrocatalytic reduction of 3-NT, the diffusion coefficient (D) of 3-NT can be estimated from the known values of electrode surface area (A) and of anodic peak currents (I_p) at various scan rates (ν) in a 3-NT solution with fixed concentration (C^*) by Eq. (2) [26]:

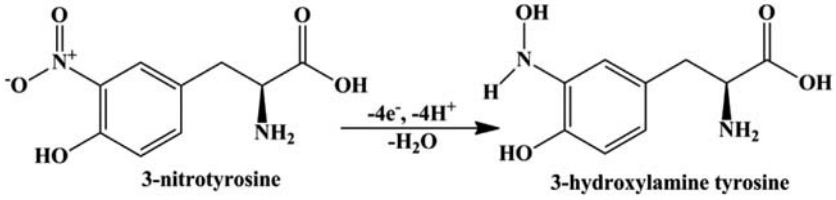
$$I_p = 0.4463\, nF\, C^* A \nu^{1/2} D^{1/2} \left(\frac{nF}{RT}\right)^{1/2} \quad (2)$$

where the terms of F, R, and T have their universal meanings, C^*=50.0 μg L^{-1}. With the relation between peak current and square root of scan rate [I_p(μA)=(24.67 ± 1.08) $\nu^{1/2}$+(30.82 ± 9.38); n=6; R^2=0.99], diffusion coefficients of 3-NT were estimated to be 2.12×10^{-12} and 2.32×10^{-10} $cm^2\, s^{-1}$ (Table S1) on bare and modified PGE, respectively.

Chronocoulometry was also employed to measure the diffusion coefficient of 3-NT in solution. Fig. 4(B) shows the charge as a function of time with increase in concentration of 3-NT. Herein, the total charge is directly proportional to the current produce in the system, as expected, charge increases with increase in concentration of analyte (Fig. 4(B)). In CC, the net charge (Q) was also proportional to the inverse of the square root of transition time (t), known as Anson plot (Fig. S3). Since the mass transfer of 3-NT to electrode surface is diffusion controlled, the diffusion coefficient for 3-NT on MIP-modified PGE surface was calculated according to Eq. (3) [26]:

$$Q = 2nFA\, C(Dt)^{1/2}\pi^{1/2} \quad (3)$$

where the parameters have it meanings as described above, the diffusion coefficient was found 2.87×10^{-10} $cm^2\, s^{-1}$ (Table S1). Similarly, the value of diffusion coefficient of 3-NT was also calculated for bare PGE and was found to be 2.92×10^{-12} $cm^2\, s^{-1}$. Other kinetic parameters were also calculated to study the electrochemical behavior of 3-NT, the detailed calculation was given in supporting information and results are portrayed in Table S1.



2.4. Performance of the imprinted sensor

2.4.1. Calibration curve and detection limit

Under the optimal analytical conditions (accumulation potential of −2.5 V and 30 s deposition time, Fig. S4), determination of 3-NT was performed by DPSV and SWSV techniques. As can be seen from Fig. 4(C) and (D), the sharp and well-defined reduction peak current increased linearly with increasing concentration of 3-NT in both type of analyses but the current sensitivity is higher in case of SWSV. The calibration graph of the prepared sensor shows a linear relationship over 3-NT concentration in the range of 9.90 μg L^{-1} to 867.57 μg L^{-1} (for DPSV) and 4.90 μg L^{-1} to 867.57 μg L^{-1} (for SWSV). The linear regression equations are (Fig. S5):

$$I_p(\mu A) = (0.059 \pm 0.002)C + (4.042 \pm 0.753); \quad n = 9; \quad R^2 = 0.99,$$

$$\text{LOD} = 1.20\ \mu g\ L^{-1} (\text{SWSV})$$

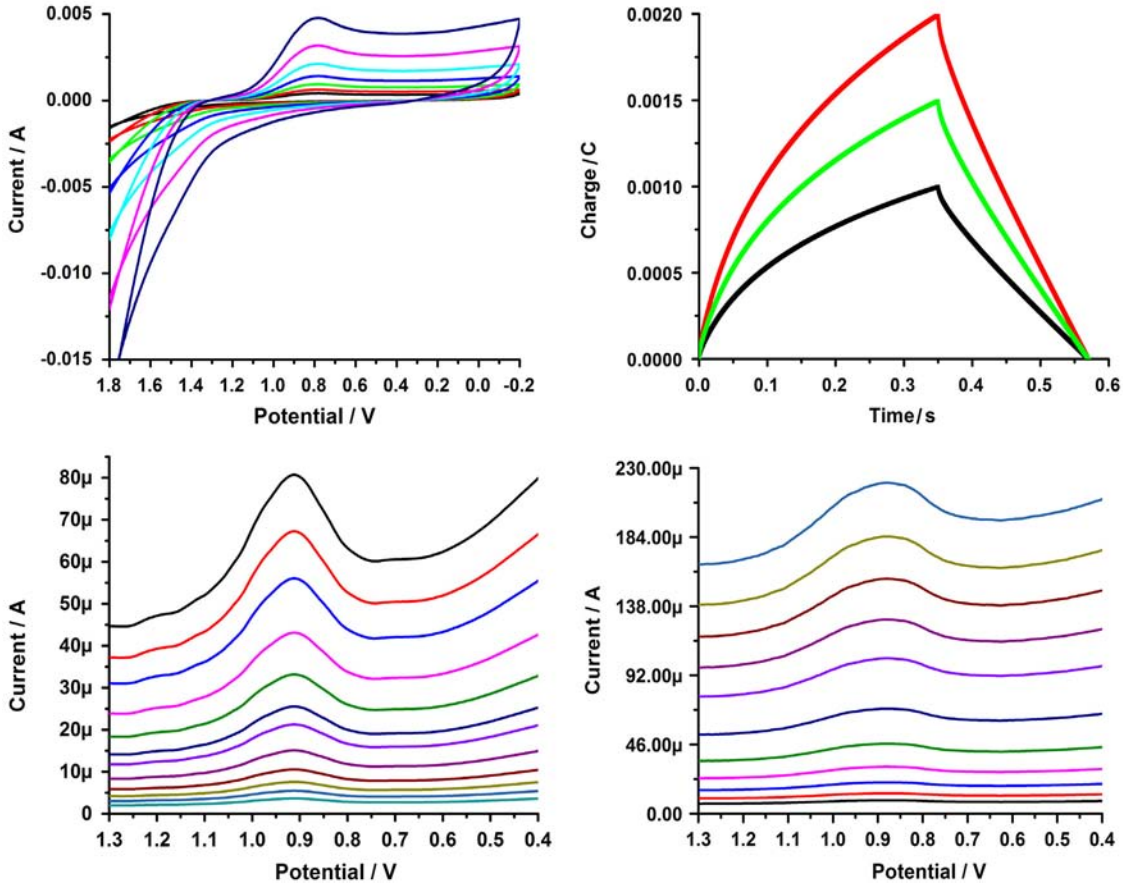


Fig. 4. (A) CV runs of 3-nitrotyrosine (50.0 μg L^{-1}) at different scan rates ranging from 50.0 mV s^{-1} to 200 mV s^{-1}; (B) chronocoulometry runs (Q–*t* curves) for differenet concentration of 3-nitrotyrosine; (C) DPSV response of nitrotyrosine on MIP-modified PGE with increasing concentration (9.90 μg L^{-1} to 867.57 μg L^{-1}), and (D) SWSV response of nitrotyrosin on MIP-modified PGE with increasing concentration (4.90 μg L^{-1} to 867.57 μg L^{-1}) in optimized conditions. Accumulation time 30 s, accumulation potential −2.5 V, in KCL solution at pH=8.0.

$$I_p(\mu A) = (0.037 \pm 0.002)C + (3.101 \pm 0.621); \quad n = 9; \quad R^2 = 0.99,$$

$$\text{LOD} = 3.25\ \mu g\ L^{-1}(\text{DPSV})$$

The proposed electrode is compared with a known solid phase microextraction method [12], by means of Student's *t*-test, where $t_{calculated}$ (1.13) is found to be less than $t_{tabulated}$ (2.77) at the confidence level of 95%. This revealed that, although, a similar order of precision is observed for both the methods, our proposed method is comparatively simple, selective, and cost-effective.

To study the recognition ability of MIP, the DPSV response of MIP and NIP-modified PGE were also tested for different concentration of 3-NT. We observed that the response of MIP-PGE was significantly increased with increasing the concentration of nitrotyrosine (Fig. S5). On the other hand, no significant change was observed with NIP-PGE (Fig. S5). This curtailed the chance of any non-specific adsorption and false positive results during analysis.

2.4.2. Selectivity of the imprinted sensor

To ensure selectivity of the imprinted sensor, SWSV response of 3-NT and various concentration of structural analogs including tyrosine, nitrophenol, nitroaniline, phenylalanine, tryptophan, histidine, aniline, and bisphenol were compared and the results are shown in Fig. 5. As depicted in Fig. 5, sensor shows negligible current response for any concentration of the individual interfering compounds ((A) 0 μg L^{-1}; (B), 200 μg L^{-1}; (C) 400 μg L^{-1}; (D) 600 μg L^{-1}; (E) 800 μg L^{-1}, and (F) 1000 μg L^{-1}). However, in the binary mixture of interferents and 3-NT (50.0 μg L^{-1}), the sensor shows 100% current response for target analyte (3-NT). The

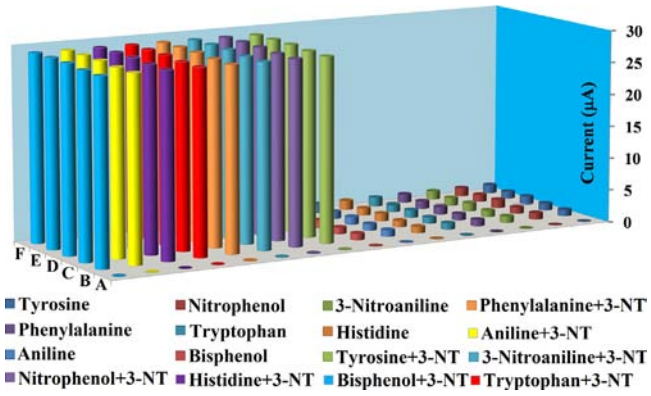


Fig. 5. Effect of structural analogues/interferents on the SWSV response of 3-nitrotyrosine on the MIP-modified PGEs.

result showed that the excess concentration of interfering compounds had no influence on the current response of 3-NT (Fig. 5). So, it can be easily concluded that the interference of the structural analouge compounds were negligible on the 3-NT determination, which clearly proved the reasonable selectivity of the proposed sensor.

2.4.3. Reproducibility and stability of imprinted PGE

To investigate the reproducibility of the as-prepared sensor, three different concentrations of 3-NT (low, 10.0 μg L^{-1}; middle, 50.0 μg L^{-1} and high, 500.0 μg L^{-1}) were measured using six MIP-modified PGEs

Table 2
Determination of 3-nitrotyrosine in the human serum, plasma, and urine samples by imprinted BI-Fe/Pd nanoparticle modified PGE and commercially available ELISA kit.

Spiked ($\mu g\ L^{-1}$)	Human serum				Human plasma				Human urine			
	Detected[a] ($\mu g\ L^{-1}$)	Detected ($\mu g\ L^{-1}$)	Recovery (%)	RSD[b] (%)	Detected[a] ($\mu g\ L^{-1}$)	Detected ($\mu g\ L^{-1}$)	Recovery (%)	RSD[b] (%)	Detected[a] ($\mu g\ L^{-1}$)	Detected ($\mu g\ L^{-1}$)	Recovery (%)	RSD[b] (%)
Sample 1												
10.00	10.10	10.20	102.0	1.0	10.00	10.00	100.0	1.2	9.99	10.05	100.5	1.1
50.00	–	50.10	100.2	1.2	–	50.45	100.9	1.4	–	50.15	100.3	2.5
100.0	–	99.9	99.9	1.5	–	100.3	100.3	1.1	–	100.1	100.1	1.6
Sample 2												
10.00	10.00	9.98	99.8	1.2	9.99	9.90	99.0	2.0	10.00	10.00	100.0	1.1
50.00	–	50.05	100.1	1.3	–	49.80	99.6	1.8	–	50.05	100.1	1.2
100.0	–	98.9	98.9	2.4	–	100.1	100.1	2.1	–	100.1	100.1	1.5
Sample 3												
10.00	10.00	10.10	101.0	1.8	10.00	9.89	98.9	1.3	10.10	10.00	100.0	1.9
50.00	–	49.95	99.9	2.1	–	50.10	100.2	1.3	–	50.30	100.6	2.7
100.0	–	99.7	99.7	1.1	–	100.4	100.4	1.9	–	100.05	100.0	1.9

[a] Detected by ELISA kit (RAB0389 SIGMA, human NT-3 ELISA kit).
[b] RSD was calculated for three replicate determinations.

prepared independently under the identical experimental conditions. All the six electrodes (prepared independently) use the same standard curve and the relative standard deviation (RSD) was found in the rage from 1.1% to 1.8%. A good repeatability was also observed with relative standard deviation (RSD) of 2.0%, forthree parallel detection. The used MIP-modified PGE could be easily regenerated (25 times) by the method of template extraction. In the cycle of pre-concentration, determination, regeneration, and rinsing, the RSD for five replicate measurements was 1.5%. For evaluating the stability of the electrode, the peak current change of 50.0 $\mu g\ L^{-1}$ 3-NT was measured from day to day. When stored in air at room temperature, the sensor can retain 95.5% of its initial response even after 15 days, and decreased to 87.5% after 30 days. These results indicate that the prepared sensor has acceptable reproducibility and good stability for the detection of 3-NT.

2.5. Real sample analysis

2.5.1. Aanalysis of human blood and urine sample

Biological applicability of the imprinted sensor was investigated by measuring the 3-NT concentration in human blood plasma, serum as well as in urine samples using the standard addition method. Urine and blood samples of healthy volunteers were used for this analysis. The samples were used as obtained, without any pre-treatment. First, 0.1 mL of real sample was added to the electrochemical cell having 10.0 mL of supporting electrolyte. Then, samples were spiked with known concentration of standard 3-NT ranging from 10.0 $\mu g\ L^{-1}$ to 100.0 $\mu g\ L^{-1}$, and their square wave voltammograms were recorded using the MIP-modified PGE. A well-defined peak for the reduction of 3-NT was observed at the peak potential of +0.95 V, similar to the peak obtained in standard solutions. No other peaks were found in entire measurements. These measurements further confirmes the selectivity of imprinted sensor for 3-NT determination. To further explore the clinical applicability of the proposed sensor, the same sample obtained from local pathological laboratory were also analyzed by a commercially available ELISA kit (RAB0389 SIGMA, Human NT-3 ELISA Kit). The comparative data obtained from ELISA kit and proposed method was portrayed in Table 2. As shown in Table 2, almost similar results were obtained by both the methods and the recoveries were obtained in ranges of 98.9–100.9%. The recovery data showed acceptable range, which indicated that the proposed method can be utilized successfully for the detection of free and/or bound 3-NT in human biological fluids with adequate accuracy and reliability.

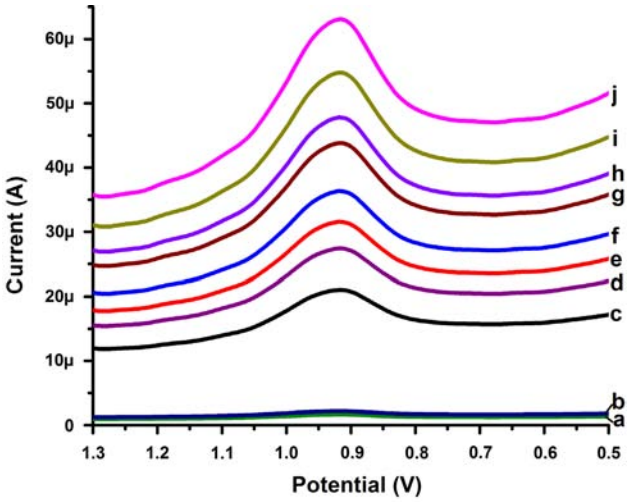


Fig. 6. SWSV runs for BSA (a), ferritin (b), nitrated BSA (c), nitrated ferritin (e), nitrated BSA+3-nitrotyrosine ((d) 135.0 $\mu g\ L^{-1}$; (f) 200.0 $\mu g\ L^{-1}$; (g) 255.0 $\mu g\ L^{-1}$) and nitrated ferritin+3-nitrotyrosine ((h) 280.0 $\mu g\ L^{-1}$; (i) 340.0 $\mu g\ L^{-1}$; (j) 400.0 $\mu g\ L^{-1}$).

2.5.2. Analysis of nitrated protein

To further explore the applicability of the proposed sensor, nitrated proteins BSA and ferritin were also analyzed. As shown in the Fig. 6, the sensor does not show any SWSV current response for unmodified proteins *i.e.* normal BSA and ferritin (curve a, b). But a clear response was obtained for nitrated BSA and ferritin molecules (curve c, e). Whereas, when a known concentrations of 3-NT was spiked in the above solution, 100% recovery was obtained (curve d, f, g, and h, i, j). This suggests that the proposed sensor is able to detect free as well as protein-bound nitrotyrosine.

2.6. Comparison with commercialy available 3-NT determination technique

The proposed method was also compared at several points and factors with comercially available ELISA technique for 3-NT determination. All the points considered during comparison were portrayed in Table 3. As proposed, our sensor is highly selective and low-cost device. It does not require any highly skilled professional for operation and also takes very less analysis time. So, the proposed sensor can be easily used for commercial analysis of 3-

Table 3
Comparative study between proposed BI-Fe/Pd modified molecularly imprinted sensor and commercially available ELISA techniques for 3-nitrotyrosine determination.

S. nos.	Comparative data	ELISA kit	Our technique
1.	Storage temperature	Individual components have to be store between 2 and 8 °C, samples have to be store preferably at −70 °C	Not necessary, all the experiments and reagents are performed and stored at room temperature
2.	Use of antigen and antibody	Biotinylated tracer antibody, streptavidin–peroxidise solution, TMB solutions, stop solutions are associated with this assay	All these are replaced by using a synthetic antibody: molecularly imprinted polymer (MIP)
3.	Detection technique	UV–vis study	More selective electrochemical study
4.	Analytical handling	Many more complicated step are associated with this technique like reagent preparation, standard preparation, qualified laboratory staff *etc.*	It is less complicated and very easy in operation and handling. No need of operator
5.	Cost	Highly expensive	Very cost-effective
6.	Analysis time	Very high, reported 3.5 h for hycult ELISA kit	Short, maximum 10 min
7.	Mode of determination	Indirect	Direct
8.	Storage ability	Expiration date, which is very less	It can be used after 6 month from the date of preparation
9.	Reusability	It has to be thrown away after the 1st use	A single sensor can be used 25times for analysis
10.	Dilution	Most important, used only in highly diluted samples. Requires 10,000 times dilution, some times	It can be measured in a wide range of concentration for high to more diluted solution. Without diluted or pre-treated blood sample can also be analyzed by this technique

NT as a replacement of costly, difficult and time-cumbersome ELISA techniques.

3. Conclusion

In this study, we have demonstrated a fresh role of BI-Fe/Pd nanoparticle as a platform for imprinting of 3-NT molecule. The resulting imprinted BI-Fe/Pd nanoparticles revealed higher selectivity for 3-NT in aqueous medium and their high molecular recognition ability was maintained in a complex environment of human serum, plasma, and urine. Unlike other reported methods, the proposed sensor can detect free as well as protein-bound nitrotyrosine. Furthermore, the imprinted nanoparticle was applied for fabrication of electrochemical sensor, which shows good recognition capacity, high sensitivity and selectivity, broad linearity, good stability, and excellent reproducibility during 3-NT determination. The proposed sensor is very well compared with ELISA, a commercially available technique for 3-NT detection and it was found that the proposed sensor is much better than ELISA in terms of cost, time of analysis, handling, storage and reusability. So the high affinity of proposed sensor and the lack of requirement for cold chain logistics make them an attractive alternative to the enzyme-linked immunosorbent assay (ELISA) technique.

Acknowledgments

Authors are thankful to Department of Science and Technology, Government of India for sanction of Fast Track Research Project for Young Scientists to Dr. Rashmi Madhuri (Ref. no.: SB/FT/CS-155/2012) and Dr. Prashant K. Sharma (Ref. no.: SR/FTP/PS-157/2011). Dr. Sharma (FRS/34/2012-2013/APH) and Dr. Madhuri (FRS/43/2013-2014/AC) are also thankful to Indian School of Mines, Dhanbad for grant of Major Research Project under Faculty Research Scheme. Authors are also thankful to Board of Research in Nuclear Sciences (BRNS), Department of Atomic Energy, Government of India for granting a major research project (no. 34/14/21/2014-BRNS). E.R. & S.P are also thankful to Indian School of Mines, Dhanbad for Junior Research Fellowship.

Appendix A. Supporting information

Supplementary data associated with this article can be found in the online version at http://dx.doi.org/10.1016/j.talanta.2014.09.033.

References

[1] K.M. Boje, Front. Biosci. 9 (2004) 763–776.
[2] H. Tohgi, T. Abe, K. Yamazaki, T. Murata, E. Ishizaki, C. Isobe, Neurosci. Lett. 269 (1999) 52–54.
[3] T.J. Anderson, Heart Fail. Rev. 8 (2003) 71–86.
[4] R.F. Loeser, C.S. Carlson, M.D. Carlo, A. Cole, Arthritis Rheum. 46 (2002) 2349–2357.
[5] H. Kaur, B. Halliwell, FEBS Lett. 350 (1994) 9–12.
[6] G.T. Liberatore, V. Jackson-Lewis, S. Vukosavic, A.S. Mandir, M. Vila, W.G. McAuliffe, V.L. Dawson, T.M. Dawson, S. Przedborski, Nat. Med. 5 (1999) 1403–1409.
[7] M.H. Shishehbor, R.J. Aviles, M.-L. Brennan, X. Fu, M. Goormastic, G.L. Pearce, N. Gokce, J.F. Keaney Jr., M.S. Penn, D.L. Sprecher, J.A. Vita, S.L. Hazen, JAMA 289 (2003) 1675–1680.
[8] D. Tsikas, A. Mitschke, M.-T. Suchy, F.-M. Gutzki, D.O. Stichtenoth, J. Chromatogr. B 827 (2005) 146–156.
[9] L.F. Marvin, T. Delatour, I. Tavazzi, L.B. Fay, C. Cupp, P.A. Guy, Anal. Chem. 75 (2003) 261–267.
[10] J.S. Althaus, K.R. Schmidt, S.T. Fountain, M.T. Tseng, R.T. Carroll, P. Galatsis E.D. Hall, Free Radical Biol. Med. 29 (2000) 1085–1095.
[11] J. Jin, C. Wang, Y. Tao, Y. Tan, D. Yang, Y. Gu, H. Deng, Y. Bai, H. Lu, Y. Wan, Z. Lu, Y. Li, Sens. Actuators, B 153 (2011) 164–169.
[12] L. Mergola, S. Scorrano, R.D. Sole, M.R. Lazzoi, G. Vasapollo, Biosens. Bioeletron. 40 (2013) 336–341.
[13] V.S. Sharov, R. Pal, E.S. Dremina, E.K. Michaelis, C. Schoneich, Free Radical Biol. Med. 53 (2012) 1877–1885.
[14] X. Wang, M. Zhu, H. Liu, J. Ma, F. Li, Sci. Total Environ. 449 (2013) 157–167.
[15] J. Cao, R. Xu, H. Tang, S. Tang, M Cao, Sci. Total Environ. 409 (2011) 2336–2341.
[16] H. Chen, H. Luo, Y. Lan, T. Dong, B. Hu, Y. Wang, J. Hazard. Mater. 192 (2011) 44–53.
[17] Y. Han, W. Li, M. Zhang, K. Tao, Chemosphere 72 (2008) 53–58.
[18] G. Nikov, V. Bhat, J.S. Wishnok, S.R. Tannenbaum, Anal. Biochem. 320 (2003) 214–222.
[19] J.C. Niles, S. Burney, S. Singh, J.S. Wishnok, S.R. Tannenbaum, Proc. Nat. Acad. Sci. U.S.A. 96 (1999) 11729–11734.
[20] D.A. Skoog, F.T. Holler, T.A. Neiman, Principles of Instrumental Analysis, fifth ed., Harcourt Brace College Publishers, Orlando, 1998.
[21] A.L. Patterson, Phys. Rev 56 (1938) 978–982.
[22] B. Rezaei, S. Damiri, Electrochim. Acta 55 (2010) 1801–1808.
[23] A El. Jammal, J.C. Vire, G.J. Patriarche, O.N. Palmeiro, Electroanalysis 4 (1992) 57–64.
[24] S.F. Lv, K.B. Wu, X.P. Dang, S.S. Hu, Talanta 63 (2004) 653–657.
[25] C.L. Zhou, Z. Liu, Y.M. Dong, D.M. Li, Electroanalysis 21 (2009) 853–858.
[26] A. Bard, L.R. Faulkner, Electrochemical Methods Fundamentals and Application, second ed., John Wiley and Sons, New York, NY, 1980.

Talanta 132 (2015) 416–423

Contents lists available at ScienceDirect

Talanta

journal homepage: www.elsevier.com/locate/talanta

Development of gold nanoparticles modified screen-printed carbon electrode for the analysis of thiram, disulfiram and their derivative in food using ultra-high performance liquid chromatography

Kanokwan Charoenkitamorn [a], Orawon Chailapakul [a,c,*], Weena Siangproh [b,**]

[a] Electrochemistry and Optical Spectroscopy Research Unit, Department of Chemistry, Faculty of Science, Chulalongkorn University, 254 Phayathai Road, Patumwan, Bangkok 10330, Thailand
[b] Department of Chemistry, Faculty of Science, Srinakharinwirot University, Sukhumvit 23, Wattana, Bangkok 10110, Thailand
[c] National Center of Excellent of Petroleum, Petrochemicals and Advanced Materials, Chulalongkorn University, Patumwan, Bangkok 10330, Thailand

ARTICLE INFO

Article history:
Received 16 July 2014
Received in revised form
10 September 2014
Accepted 11 September 2014
Available online 30 September 2014

Keywords:
Dithiocarbamates
Fungicides
Screen-printed carbon electrode
Gold nanoparticles
Simultaneous determination
Ultra-high performance liquid chromatography

ABSTRACT

For the first time, gold nanoparticles (AuNPs) modified screen-printed carbon electrode (SPCE) was developed as working electrode in ultra-high performance liquid chromatography (UHPLC) coupled with electrochemical detection (UHPLC-ED) for simultaneous determination of thiram, disulfiram, and *N,N*-diethyl-*N',N'*-dimethylthiuram disulfide, their derivative compound. The separation was performed in reversed-phase mode using C18 column, mobile phase consisting of 55:45 (v/v) ratio of 0.05 M phosphate buffer solution (pH 5) and acetonitrile at a flow rate of 1.5 mL min^{-1}. For the detection part, the amperometric detection was chosen with a detection potential of 1.2 V vs. Ag/AgCl. Under the optimal conditions, the good linear relationship was obtained in the range of 0.07–15, 0.07–12, and 0.5–15 μg mL^{-1} (correlation coefficient more than 0.9900) for thiram, *N,N*-diethyl-*N',N'*-dimethylthiuram disulfide, and disulfiram, respectively. The limits of detection (LODs) of thiram, *N,N*-diethyl-*N',N'*-dimethylthiuram disulfide, and disulfiram were 0.022, 0.023, and 0.165 μg mL^{-1}, respectively. Moreover, this method was successfully applied for the detection of these compounds in real samples (apple, grape and lettuce) with the recoveries ranging from 94.3% to 108.8%. To validate this developed method, a highly quantitative agreement was clearly observed compared to standard UHPLC–UV system. Therefore, the proposed electrode can be effectively used as an alternative electrode in UHPLC-ED for rapid, selective, highly sensitive, and simultaneous determination of thiram, disulfiram, and *N,N*-diethyl-*N',N'*-dimethylthiuram disulfide.

© 2014 Elsevier B.V. All rights reserved.

1. Introduction

Nowadays, the designing of electrochemical sensor has been developed in the field of electrochemistry to improve the analytical efficiency in the terms of sensitivity, selectivity, reliability, ease of fabrication and use, and low cost. Screen printing is the technology used for fabrication of biosensors and chemical sensors instead of using large-scale electrode. Their various advantages such as miniaturization, versatility, and low cost of production are really attractive [1]. In addition, many laboratories use the screen-printing for in-house production of sensors. Screen-printed carbon electrode (SPCE) is an alternative material used instead of using the traditional electrodes based on economic substrate. Recently, SPCE have been successfully used as the electrochemical sensor for various researches due to the simplicity to produce and still give the rapid responses [2]. Moreover, the main advantage of SPCE is able to use only once and then is discarded. This advantage can be used to solve the problems of surface fouling compared with those of conventional electrodes. However, the limitation of SPCE is small surface area of working electrode leading to the lack of sensitivity [3]. Therefore, electrode modification is necessary to solve this problem.

For electrode modification, metal-nanoparticles modified SPCE is focused to improve the electrochemical efficiency. Metal-nanoparticles are attractive catalyst in the electrochemical applications. Transition metals, especially precious metals, show very high catalytic abilities for catalyzing the redox process of some interested molecules, making the use of electroanalytical techniques for applications are extended [4]. Particularly, gold nanoparticles (AuNPs) have received significant attention in recent years. AuNPs are widely used in many fields due to their unique optical and physical properties, such as surface plasmon oscillations for labeling, imaging, and sensing [5]. For the electrochemical fields, AuNPs have been widely used for modification of electrode because of their benefits including catalysis, mass

* Corresponding author. Tel.: +662 218 7615.
** Corresponding author. Tel.: +662 249 5000x18208.
E-mail addresses: corawon@chula.ac.th (O. Chailapakul), weenasi@hotmail.com (W. Siangproh).

http://dx.doi.org/10.1016/j.talanta.2014.09.020
0039-9140/© 2014 Elsevier B.V. All rights reserved.

transport, and high effective surface area [1]. AuNPs have the ability to improve the detection signal, electron transfer, which make the limit of detection in electrochemical sensor is reduced. Moreover, the most importance is AuNPs showed strong specific interaction with the sulfur-containing compounds [6]. Therefore, AuNPs became an interesting nanomaterial used as modifier onto working electrode for electrochemical detection of sulfur-containing compounds.

Thiram (tetramethyl thiuram) and disulfiram (tetraethyl thiuram) are oraganosulfur compounds in the group of dithiocarbamates (DTCs) fungicides. DTCs have been used in agriculture as fungicides in foliage vegetable and fruit [7]. Besides these agricultural applications, DTCs are also used in industry such as vulcanization accelerator and antioxidant in rubber. The use of DTCs results in their release into the environment causing the contamination in food and water which leads to hazardous effect in the living organisms through diverse pathways [8]. Environmental problem resulting from uncontrollable use of fungicides in agriculture is one of the most important evidence. Therefore, it is necessary to continuously develop simple, selective, and sensitive methods for analysis of fungicides [9].

Various methods have been developed for analysis of DTCs. Spectrometry [10–12] and head space gas chromatography [13] have been used as the methods for the determination of DTCs after their decomposition to carbon disulfide (CS_2). From these methods, most of DTCs can degrade to CS_2. Therefore, they are unable to distinguish among different DTCs. Moreover, gas chromatography [14,15], capillary electrophoresis [16–20], and high performance liquid chromatography (HPLC) were used for simultaneous determination of DTCs coupled with UV detection. Especially, HPLC is the simple technique used for easy separation of the disulfide substance. However, the drawback of the UV detection is low sensitivity. Therefore, HPLC coupled with electrochemical detection became an important choice for the determination of disulfides [21]. The main advantage of electrochemical detection compared to those of spectrometry is that the derivatization step is not needed, which makes the analysis time and cost reduced. In addition, the use of electrochemical detection after the separation by HPLC can provide more sensitive detection than UV [22].

Recently, ultra-high performance liquid chromatography coupled with electrochemical detection (UHPLC-ED) is a high potential alternative method for various analysis. UHPLC concerns to the development of short column packed with small particles for working at high pressures (>400 bar). The use of UHPLC can enhance chromatographic performances in terms of efficiency, resolution, and analysis time [23]. In the detection part, AuNPs modified electrode was used as amperometric detection. Amperometry is an attractive potential technique because of its fast response, high sensitivity, relatively low cost of equipment, no need for complicated operation, and simplicity for direct sulfur assay [24].

With such benefits from the mentioned background, the objective of this work is to develop AuNPs modified SPCE in UHPLC-ED system for simultaneous determination of DTCs with high sensitivity, specificity, and rapid analysis. Thiram (tetramethyl thiuram) and disulfiram (tetraethyl thiuram) are chosen as representative compounds of DTCs because they are importantly applied to control a variety of pest [25]. Typically, when thiram and disulfiram are mixed together, the intermediate of *N,N*-diethyl-*N',N'*-dimethylthiuram disulfide (DEDMTDS) appears as the derivative of thiram and disulfiram. This compound is one of DTCs that affects human health and has the same effect of thiram and disulfiram. The presence of *N,N*-diethyl-*N',N'*-dimethylthiuram disulfide can also use to monitor thiram and disulfiram in samples. Therefore, the detection of *N, N*-diethyl-*N', N'*-dimethylthiuram disulfide is important. This derivative compound is also determined along with the measurement of thiram and disulfiram.

To the best of our knowledge, there is no publication report about the use of AuNPs modified SPCE as working electrode for ED after the UHPLC separation to simultaneously determine thiram, DEDMTDS, and disulfiram. Moreover, this developed UHPLC-ED using AuNPs modified SPCE was applied for the first time to analyze thiram, DEDMTDS, and disulfiramthe DTCs in fruits and vegetables collected from local markets.

2. Materials and methods

2.1. Chemicals and reagents

All chemicals used in this work were of analytical grade, and all solutions were prepared using Milli-Q water from Millipore ($R \geq 18.2$ M Ω cm^{-1}). Acetonitrile (HPLC-grade), chloroform, and sulfuric acid were obtained from Merck (Darmstadt, Germany). Potassium dihydrogen phosphate (KH_2PO_4) was acquired from BDH laboratory supplies (VWR International Ltd., England). Disodium hydrogen phosphate (Na_2HPO_4) and sodium hydroxide (NaOH) were purchased from Merck (Darmstadt, Germany). Standard thiram (tetramethyl thiuram) was obtained from Chem Service (West chester, PA, USA). Standard disulfiram (tetraethyl thiuram) and gold (III) chloride solution were obtained from Sigma-Aldrich (St. Louis, MO, USA).

All of stock standard solutions (1000 μg mL^{-1}) were prepared by dissolving 10 mg of each analyte in acetonitrile. The solutions were then placed in an amber bottle and stored at 4 °C. To prepare working standard solution, the standard solution was mixed and diluted in suitable proportions of acetonitrile:Milli-Q water (50:50; v/v), and kept for 5 min before measurement. All solutions and solvents were filtered by 0.22 μm nylon membranes prior to use in UHPLC separation.

2.2. Fabrication and modification of screen-printed carbon electrode

The working electrode was fabricated using screen printing and modified by electrodeposition techniques. The Ag/AgCl electrode and Pt wire was used as reference and auxiliary electrodes, respectively. To fabricate the in-house screen-printed carbon electrode (Fig. S1), the Ag/AgCl ink was first printed on the PVC substrate for using as a conductive pad. Then, the carbon ink was printed to create a working electrode. The each step of printing electrode was allowed to dry in an oven at 55 °C for 1 h. The screen-printed carbon electrode was ready to modify in the next step.

For the electrodes modification, the 10 mM of gold (III) solution was used to modify onto electrode surface by electrodeposition technique. The three-electrode system was placed into cell containing 2 mL of solution of 10 mM of gold (III) solution in 0.5 M H_2SO_4 followed by deposition of gold onto the SPCE at a deposition potential of −0.6 V (vs. Ag/AgCl) for 50 s while the solution was stirred (by means of a mechanical stirrer bar). The gold nanoparticles (AuNPs) were obtained onto the electrode surface. After the modification, the AuNPs modified SPCE was carefully rinsed with distilled water and dried under N_2 gas prior to use.

2.3. Cyclic voltammetry

The electrochemical reaction and optimal parameters for electrodeposition step were studied by cyclic voltammetry (CV) using a CH instrument potentiostat 1232 A (CH Instrument, Inc., USA). The working electrodes used in this work were bare SPCE and AuNPs modified SPCE. The reference and auxiliary electrode were silver/silver chloride electrode and Pt wire, respectively. All experiments were done at room temperature.

2.4. UHPLC experiment and apparatus

The UHPLC system was performed in reversed-phase mode using an LC-20ADXR solvent deliver unit (Shimadzu Corporation,

Japan), an autosampler (SIL-20 A) with 0.1–100 mL loop and a Kinetex™ core-shell C18 column (50 mm x 4.6 mm i.d.; particle size, 2.6 μm, Phenomenex). The UHPLC-electrochemical measurement was carried out in 45:55 (v/v) ratio acetonitrile: 0.05 M phosphate buffer solution (pH 5), which was adjusted to pH 5 with 0.1 M sodium hydroxide solution, as mobile phase with an applied potential of 1.2 V vs. Ag/AgCl, an injection volume of 50 μL, and a flow rate of 1.5 mL min^{-1}. All chromatographic separations were performed at room temperature.

2.5. Electrochemical measurement

The thin-layer flow cell consisted of a working AuNPs modified SPCE, a reference Ag/AgCl electrode (Bioanalytical system Inc., USA), and a stainless steel tube counter electrode. The geometric area of the AuNPs modified SPCE in the flow cell was estimated to be 0.40 cm^2 with 1 mm thick silicon rubber gasket as a spacer. An electrochemical measurement for amperometric control and signal processing was performed using CH instrument potentiostat 1232 A.

2.6. Sample preparation

The three real samples including apple, grape and lettuce were obtained from local markets in Thailand. For analysis, 50 g of cut sample was weighted accurately and transferred to a blender. Then 50 μL of 500 μg mL^{-1} of standard mixture solution and chloroform were added. The mixture was homogenized with blender and transferred into centrifuge tubes. After centrifugation at 4000 rpm for 10 min, all of the organic phases were filtered through a Buchner funnel with Whatman filter paper No. 4 and transferred to 250 mL vessel of the rotary vacuum evaporator for evaporation to dryness at room temperature. The residues were dissolved in 4.5 mL of acetonitrile using ultrasonic stirring, filtered through the 0.2 μm pore size of nylon membrane, and collected in 5 mL of volumetric flask. After that, acetonitrile filtered through the 0.2 μm pore size of nylon membrane was added to adjust volume to 5 mL of solution. Finally, 50 μL of the solution was injected into the UHPLC system. The determination of DTCs in samples was analyzed within the linear dynamic range that obtained by adding different volume of 500 μg mL^{-1} of standard mixture solution into the blank sample and prepared following the above treatment.

2.7. Method validation

Standard solutions and samples were analyzed, and the currents were integrated. A calibration curve of standard solutions was performed under optimal conditions and treated with linear least square regression analysis using the Excel software package. The limit of detection (LOD) and limit of quantification (LOQ) were determined from the 3 S_{bl}/S and 10 S_{bl}/S, respectively, where S_{bl} is standard deviation of blank ($n=10$), and S is sensitivity of method, obtained from the slope of the linearity. For the precision of intra-day and inter-day, three concentrations of DCTs (1, 6, and 12 μg mL^{-1}) were observed for three times within a day and three different days. To validate the developed method, UHPLC-ED was compared to the standard method of UHPLC coupled with ultraviolet detection (UHPLC–UV) using the paired *t*-test.

3. Results and discussion

3.1. Surface morphology of AuNPs modified SPCE

Gold (III) solution was used to generate the AuNPs on the electrode surface by electrodeposition. The surface morphology of bare SPCE and AuNPs modified SPCE was investigated using scanning electron microscope (SEM) as shown in Fig. 1A and B, respectively. After the modification, the well dispersed gold particles in nanoscale was observed (Fig. 1B). The distribution of AuNPs on the electrode surface led to increase the surface area and improve the electrochemical sensitivity of the modified electrode.

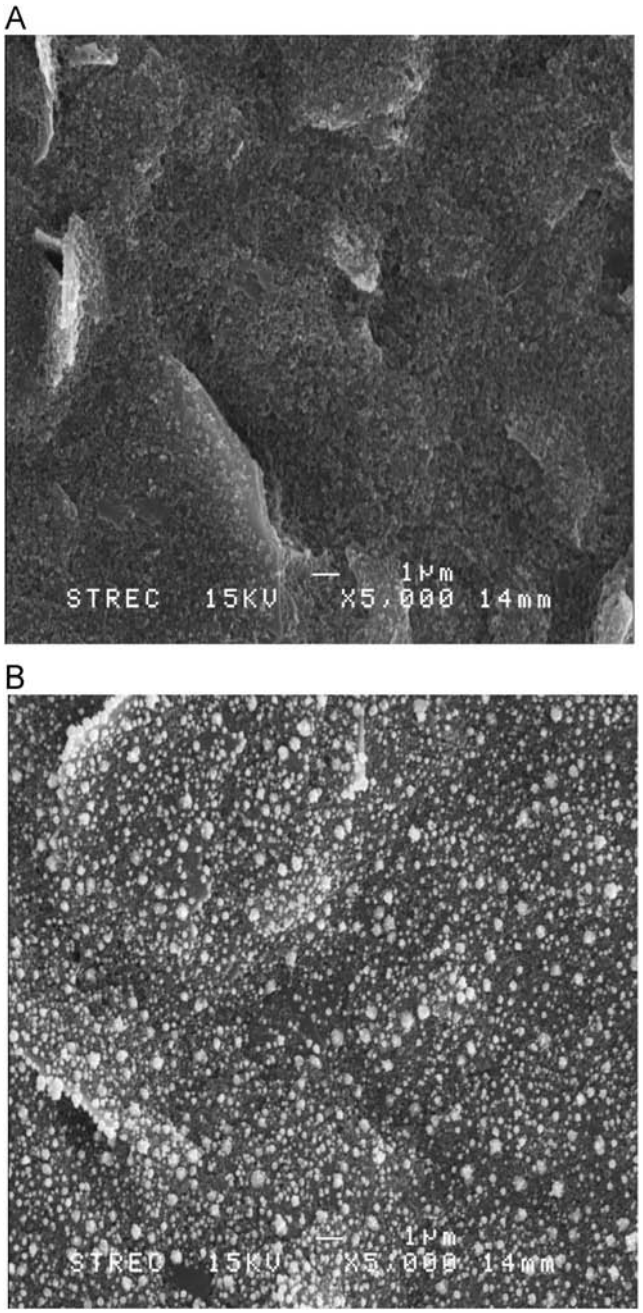


Fig. 1. SEM images of (A) bare SPCE and (B) AuNPs modified SPCE prepared by electrodeposition of 10 mM gold (III) solution at applied potential of -0.6 V for 50 s.

3.2. Optimization of the electrode modification

For the electrode modification using electrodeposition technique, the deposition potential and deposition time were optimized because these factors can effect to the analytical results. First, thiram was selected as the representative compounds because it is the best electrochemically active species at bare carbon electrode. Therefore, it is easy to observe the signal obtained from modified and unmodified electrode. To obtain the optimal condition of AuNPs modified SPCE, the dependence of deposition potential and

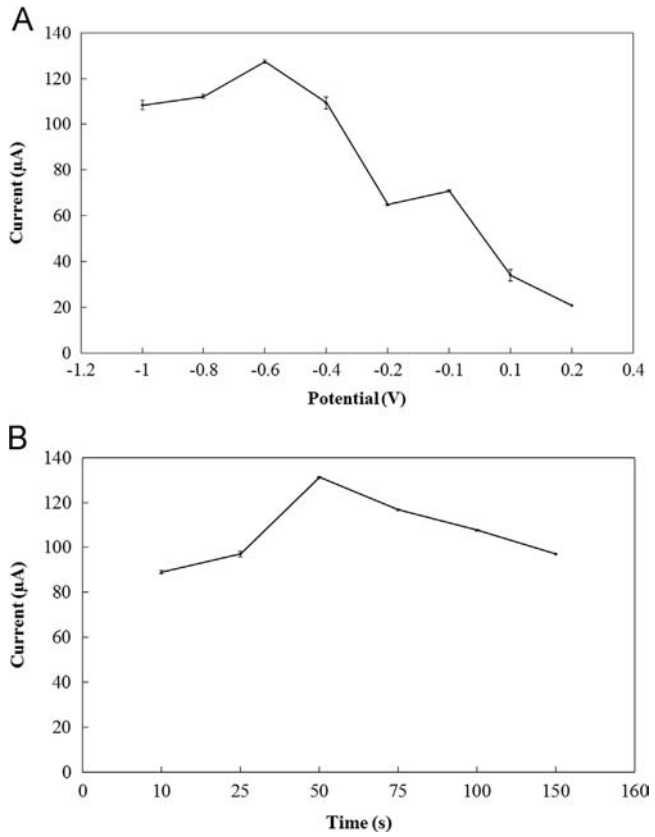


Fig. 2. Effect of the (A) deposition potential and (B) deposition time of thiram at AuNPs modified SPCE. Data are shown as the mean ± SD derived from three replicates.

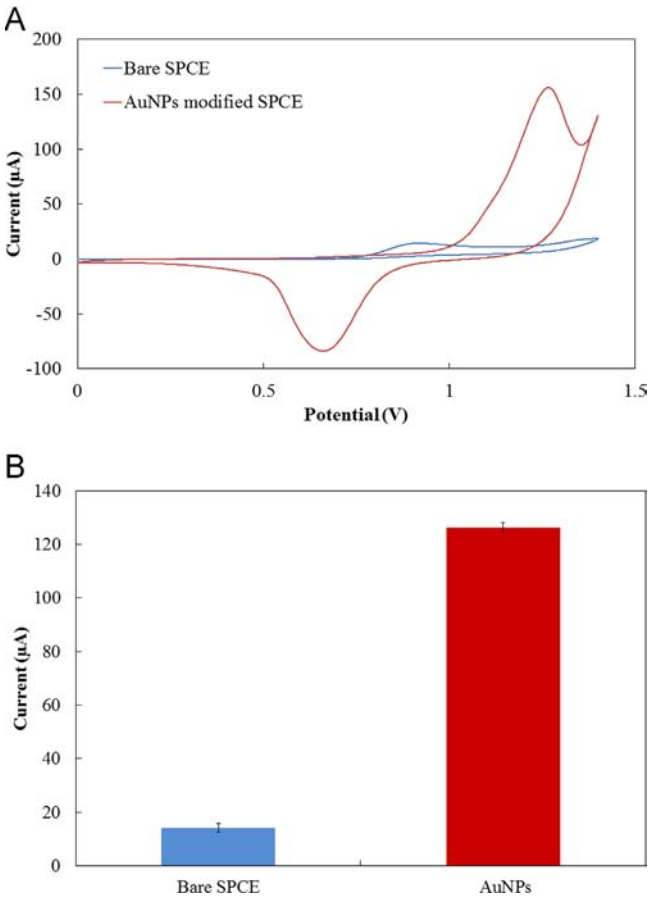


Fig. 3. (A) Cyclic voltammogram of thiram at the AuNPs modified SPCE (red line) compared to bare SPCE (blue line) and (B) comparison of oxidation current density between AuNPs modified SPCE (red rod) and bare SPCE (blue rod) vs. Ag/AgCl at the concentration of 10 μg mL^{-1} in 55:45 of 0.05 M phosphate solution pH 5: acetonitrile, scan rate 100 mV s^{-1}.

deposition time were studied using cyclic voltammetry, and the relationship between the studied parameter and current response of thiram was plotted. The deposition potential was studied in the range of −1.0 to 0.2 V. The current signal of thiram was initially increased as the function of deposition potential from −1.0 to −0.6 V and then decreased (Fig. 2A). For the deposition time, the current signal of thiram increased from 10 s to 50 s and then decreased (Fig. 2B). Therefore, the deposition potential of −0.6 V and the deposition time of 50 s were chosen as optimal parameters for modification of AuNPs onto the electrode surface.

3.3. Electrochemical response of thiram at AuNPs modified SPCE

As mentioned above, thiram is the best electrochemically active species. Thus, it was used as the representative of DTCs to study the electrochemical response. The cyclic voltammogram (CV) of 10 μg mL^{-1} of thiram obtained from bare SPCE and AuNPs modified SPCE at the potential range of 0.0 to 1.4 V was shown in Fig. 3. From CV results, the anodic current of thiram was investigated, and the current at AuNPs modified SPCE was significantly higher than the current obtained from bare SPCE due to the distribution of AuNPs on the electrode surface. We believe that the AuNPs on the electrode surface can enhance electron transfer and also improve the electrochemical determination of DTCs. For the comparison of oxidation current density between AuNPs modified SPCE and bare SPCE (Fig. 3B), the higher current density about nine times was observed at AuNPs modified SPCE. This result indicated that the AuNPs modified SPCE can be assuring electrode for the detection of thiram, disulfiram, and DEDMTDS. Therefore, this modified electrode can be an alternative electrode for using as working electrode with the advantages of low-cost material, simple fabrication and high sensitivity in case of detection DTCs.

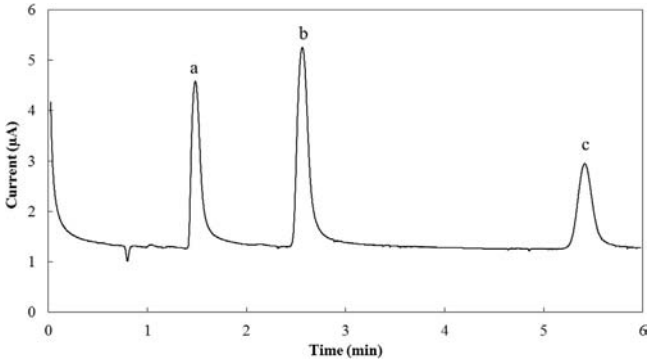


Fig. 4. Representative UHPLC-ED chromatogram of 12 μg mL^{-1} of thiram (a), DEDMTDS (b), and disulfiram (c) in a mobile phase (0.05 M phosphate solution (pH 5): acetonitrile), the detection potential of 1.2 V vs. Ag/AgCl using AuNPs modified SPCE, the injection volume of 50 μL, and the flow rate of 1.5 mL min^{-1}. Chromatograms are representative of at least three independent repetitions.

3.4. UHPLC separation

In this work, C18 column was used to separate thiram, DEDMTDS, and disulfiram by isocratic elution. The effect of percentage of acetonitrile used in the mobile phase on the

retention characteristics was first evaluated. When the percentage of acetonitrile ≤ 40 was used, the separation time was higher than 20 min and peak broadening of disulfiram was observed. On the other hand, at higher content of acetonitrile in mobile phase, the current signal of thiram, DEDMTDS, and disulfiram were decreased due to the low of diffusion coefficient with changing ionic strength of the medium. Therefore, the acetonitrile of 45% was selected as compromise to achieve the completely separated them within 6 min with good sensitivity. In addition, 0.05 M phosphate buffer solution (pH 5) was chosen as the electrolyte solution because the high concentration of salt in buffer solution was not suitable for the UHPLC system. The chromatogram for the separation of standard mixture solution was shown in Fig. 4. The retention time of thiram, DEDMTDS, and disulfiram was 1.5, 2.6, and 5.4 min, respectively, and the retention time stability was found in the range of 0.1% to 1.5%. The peak widths were 11.6 s for thiram, 14.2 s for DEDMTDS, and 18.8 s for disulfiram. Therefore, this proposed system offers the rapid time for separating DTCs.

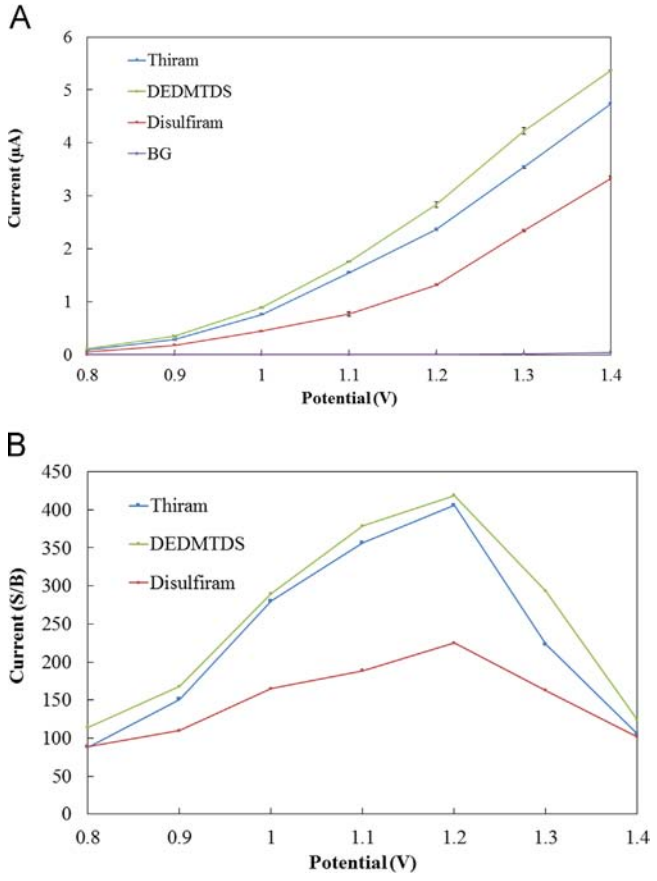


Fig. 5. Hydrodynamic voltammetric results at the AuNPs modified SPCE for a 10 μg mL^{-1} each mixture (50 μL total) of thiram and disulfiram. (A) thiram (blue line), DEDMTDS (green line), disulfiram (red line), and background (purple line); (B) hydrodynamic voltammogram of signal-to-background ratios. The other conditions are the same as in Fig. 4. Data are shown as the mean ± 1 SD derived from three independent repetitions.

3.5. Hydrodynamic voltammetry

Hydrodynamic voltammetry was used to optimize the detection potential. The potential was studied in the range of 0.8 to 1.4 V. The peak current after each injection at different potential was recorded corresponding to the background current. These data were plotted as a function of applied potential to obtain the hydrodynamic curves as shown in Fig. 5. The detection potentials significantly affected the oxidation current of the thiram, DEDMTDS, and disulfiram as well as the background current (Fig. 5A). Therefore, the net current after background subtraction was studied, and signal-to-background (S/B) ratios were plotted corresponding to the detection potential. It was found that the current increased when the potential increased up to 1.2 V for all compounds (Fig. 5B). Therefore, the detection potential of 1.2 V was selected as optimal detection potential for amperometric detection of thiram, DEDMTDS, and disulfiram after their separation with UHPLC.

3.6. Method validation

3.6.1. Analytical performance

The analytical performance of this proposed system was studied. The calibration curve between the concentration and current response of analytes was plotted as shown in Fig. 6. Under the optimal conditions, the linearity was observed in the range of 0.07 to 15 μg mL^{-1} for thiram, 0.07 to 12 μg mL^{-1} for DEDMTDS, and 0.5 to 15 μg mL^{-1} for disulfiram. The limit of detection (LOD) and limit of quantification (LOQ) were calculated from 3 S_{bl}/S and 10 S_{bl}/S, where S_{bl} is the standard deviation of blank measurements ($n=10$), and S is the sensitivity of the method or the slope of linearity. Good linearity value with $r^2 > 0.99$ was obtained. LODs and LOQs were summarized in Table 1. In addition, when the performance of AuNPs

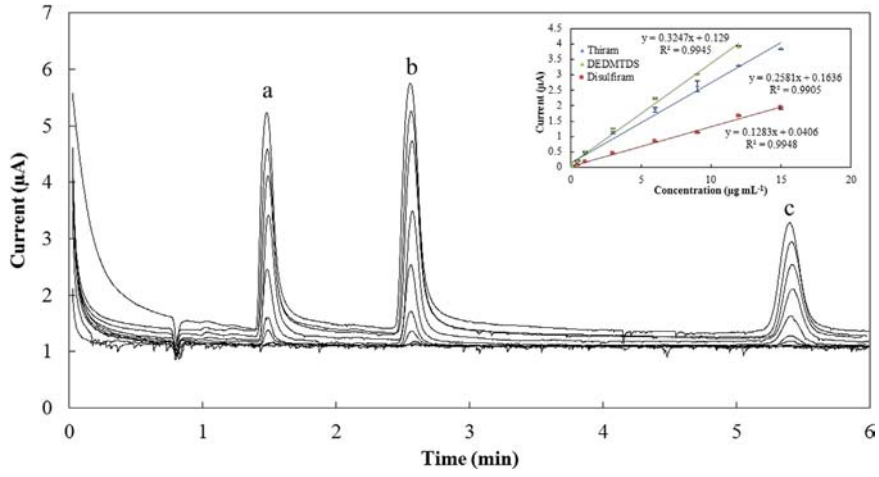


Fig. 6. The amperometric voltammogram for different concentrations of thiram (a), DEDMTDS (b), and disulfiram (c) (0.07 to 15 μg mL^{-1}) using AuNPs modified SPCE and the corresponding calibration plots (inset). Measurements were performed under the optimal conditions.

Table 1
Linearity, limit of detection (LOD) and limit of quantitation (LOQ) of the UHPLC-ED method ($n=3$).

Analyte	Linear range (μg mL^{-1})	Slope (peak height) (μA/μg mL^{-1})	Intercept (μA)	r^2	LOD (μg mL^{-1})	LOQ (μg mL^{-1})
Thiram	0.07–15	0.2585	0.1636	0.9905	0.022	0.074
DEDMTDS	0.07–12	0.3247	0.129	0.9945	0.023	0.076
Disulfiram	0.5–15	0.1283	0.0406	0.9948	0.165	0.551

Table 2
Recent report using different types of electrodes for electrochemical determination of DTCs.

Modified electrode	Detection method	Linearity range (μg mL^{-1})	LOD (μg mL^{-1})	Analyte	Real sample	Reference
Cylindrical carbon fiber microelectrode	Square-wave voltammetry	0.24–144	0.10	Thiram	Grape	[7]
Graphite-poly (tetrafluoroethylene)	Amperometry	2–100	0.14–1.0	Thiram and disulfiram	Apple	[26]
Hanging mercury drop electrode	Differential pulse voltammetry	0.01–0.6	0.01	Ziram	rice	[27]
Hanging mercury drop electrode	Square-wave voltammetry	0.01–0.19	0.0072	Ziram	Potato, cabbage and tomato	[28]
AuNPs modified SPCE	Amperometry	0.07–15	0.022–0.165	Thiram, DEDMTDS and disulfiram	Grape, apple and lettuce	This work

Table 3
The intra- and inter-precisions and recoveries of the UHPLC-ED method ($n=3$).

Samples	Spiked level (μg mL^{-1})	Analyte	Intra-day		Inter-day	
			Recovery (%)	RSD (%)	Recovery (%)	RSD (%)
Apple	1	Thiram	97.1	1.1	99.0	3.7
		DEDMTDS	101.5	0.2	100.6	1.0
		Disulfiram	104.1	3.3	100.6	4.9
	3	Thiram	102.7	0.1	100.7	5.7
		DEDMTDS	102.7	0.3	102.0	1.4
		Disulfiram	108.5	0.3	103.3	4.4
	6	Thiram	109.0	0.9	104.0	4.4
		DEDMTDS	109.2	1.3	104.8	4.0
		Disulfiram	97.4	0.6	98.1	2.4
	9	Thiram	109.3	0.6	107.0	1.8
		DEDMTDS	109.2	0.3	107.7	1.7
		Disulfiram	103.6	0.6	104.2	4.9
	12	Thiram	101.5	0.2	101.9	0.7
		DEDMTDS	106.5	0.4	102.5	3.4
		Disulfiram	102.6	0.2	101.4	2.5
Grape	1	Thiram	100.1	0.2	102.3	3.3
		DEDMTDS	101.5	2.3	99.7	1.9
		Disulfiram	108.8	0.7	104.2	7.7
	3	Thiram	103.9	0.6	100.7	2.8
		DEDMTDS	105.2	0.2	102.2	2.5
		Disulfiram	107.9	0.3	104.7	2.7
	6	Thiram	103.5	1.0	103.3	2.9
		DEDMTDS	98.9	1.5	102.6	4.9
		Disulfiram	98.4	0.2	100.6	3.4
	9	Thiram	107.4	0.5	107.2	0.1
		DEDMTDS	100.4	1.0	102.6	4.7
		Disulfiram	97.5	0.4	98.0	2.6
	12	Thiram	106.1	0.4	103.3	2.4
		DEDMTDS	102.1	0.7	101.9	0.8
		Disulfiram	100.5	0.3	100.9	5.0
Lettuce	1	Thiram	98.8	0.8	101.9	3.4
		DEDMTDS	102.6	1.4	101.6	1.4
		Disulfiram	102.4	1.7	100.8	4.3
	3	Thiram	105.1	0.9	99.7	4.8
		DEDMTDS	102.4	1.0	103.4	3.6
		Disulfiram	104.1	1.9	99.0	4.9
	6	Thiram	98.9	0.2	96.7	4.4
		DEDMTDS	98.7	0.5	101.7	4.7
		Disulfiram	106.0	0.5	101.3	4.1
	9	Thiram	108.0	1.8	105.8	2.5
		DEDMTDS	100.5	3.7	101.8	3.8
		Disulfiram	103.1	0.8	102.6	4.2
	12	Thiram	102.6	1.3	101.6	2.5
		DEDMTDS	100.5	2.9	101.1	0.8
		Disulfiram	100.1	0.6	102.5	2.3

Table 4
Determination of DTCs level in different samples ($n=3$) by traditional UHPLC-UV method and the developed UHPLC-ED method reported here.

Samples	Spiked level (μg mL^{-1})	Analyte	Amount found (μg mL^{-1}) (x ± SD)		% recovery	
			UHPLC-ED	UHPLC-UV	UHPLC-ED	UHPLC-UV
Apple	1	Thiram	0.99 ± 0.04	1.02 ± 0.03	99.0	102.2
		DEDMTDS	1.01 ± 0.01	1.01 ± 0.02	100.6	101.1
		Disulfiram	0.98 ± 0.05	1.01 ± 0.05	97.5	100.6
	6	Thiram	6.24 ± 0.27	5.79 ± 0.26	104.0	96.5
		DEDMTDS	6.15 ± 0.10	6.12 ± 0.19	102.5	101.9
		Disulfiram	5.89 ± 0.14	5.72 ± 0.13	98.1	95.4
	12	Thiram	12.23 ± 0.50	11.90 ± 0.36	101.9	99.2
		DEDMTDS	12.30 ± 0.49	11.78 ± 0.62	102.5	98.1
		Disulfiram	12.42 ± 0.25	12.26 ± 0.23	103.5	102.1
Grape	1	Thiram	1.02 ± 0.03	1.02 ± 0.02	102.3	102.2
		DEDMTDS	1.01 ± 0.02	1.00 ± 0.01	100.8	99.7
		Disulfiram	1.04 ± 0.08	0.99 ± 0.01	104.2	98.7
	6	Thiram	6.20 ± 0.18	5.92 ± 0.19	103.3	98.7
		DEDMTDS	6.15 ± 0.30	6.01 ± 0.22	102.6	100.1
		Disulfiram	6.04 ± 0.21	6.04 ± 0.12	100.6	100.7
	12	Thiram	12.17 ± 0.34	12.09 ± 0.41	101.4	100.8
		DEDMTDS	12.23 ± 0.60	12.00 ± 0.60	101.9	100.0
		Disulfiram	12.40 ± 0.41	12.30 ± 0.20	103.3	102.5
Lettuce	1	Thiram	1.02 ± 0.03	0.98 ± 0.03	101.9	98.1
		DEDMTDS	1.02 ± 0.01	1.02 ± 0.04	102.2	101.6
		Disulfiram	1.01 ± 0.04	0.97 ± 0.09	100.8	97.1
	6	Thiram	5.80 ± 0.26	5.75 ± 0.25	96.7	95.8
		DEDMTDS	6.10 ± 0.28	5.99 ± 0.22	101.7	99.8
		Disulfiram	6.08 ± 0.25	5.99 ± 0.13	101.3	99.8
	12	Thiram	12.20 ± 0.41	11.98 ± 0.27	101.6	99.9
		DEDMTDS	12.13 ± 0.47	11.94 ± 0.62	101.1	99.5
		Disulfiram	12.30 ± 0.20	12.11 ± 0.35	102.5	100.9
Paired two-tail test	t values (at 1 μg mL^{-1})	Thiram	0.104			
		DEDMTDS	0.898			
		Disulfiram	0.792			
	t values (at 6 μg mL^{-1})	Thiram	2.293			
		DEDMTDS	3.029			
		Disulfiram	1.747			
	t values (at 12 μg mL^{-1})	Thiram	2.808			
		DEDMTDS	2.989			
		Disulfiram	−0.243			
	t critical		4.303			

modified SPCE was compared to the other previous electrodes for the detection of DTCs as shown in Table 2. It was found that the LODs obtained from the proposed electrode were lower than using cylindrical carbon fiber [7] and graphite-poly (tetrafluoroethylene) composite electrode [26]. However, few researches used the mercury electrode to provide lower LOD than this method but the mercury is toxic [27,28]. Therefore, the proposed electrode offers less toxicity, uncomplicated, and low cost. Additionally, the proposed electrode shows good electrocatalytic properties for DTCs detection to obtain a high electrochemical sensitivity.

3.6.2. *Application to real samples*

To assess the applicability of the proposed method, target compounds in samples from local supermarkets were investigated. The proposed method was applied for the detection of three different samples, including apple, grape, and lettuce. The standard addition method was chosen to investigate the reliability of this proposed system. The precision of the analytical process was evaluated by the repeatability of the process. The spiked concentrations in the dynamic linearity between 1 to 15 μg mL^{-1} were studied to calculate the RSD percentage. The summary of intra- and inter-day precision, and recovery that obtained from the proposed method was shown in Table 3. The RSDs and recoveries of intra-day were found in the range of 0.1–3.7% and 94.3–108.8%, respectively, while the inter-day RSDs and recoveries were found in the range of 0.1–5.7% and 95.8–107.7%, respectively. Therefore, this method is an alternative and suitable for rapid separation and simultaneous determination of DTCs.

To validate the proposed method, UHPLC-UV was used as a standard method to compare the acceptable and reliable. The results obtained from UHPLC-ED and UHPLC-UV were compared by a paired *t*-test at the 95% confidence for three samples that spiked with three standard concentrations (1, 6, and 12 μg mL^{-1} to represent the low, medium, and high level, respectively). The critical *t*-value was significantly higher than calculated *t*-values between two assays. From the results shown in Table 4, the calculated *t*-values of three concentrations were found in the range of –0.243 to 3.029 and lower than critical *t*-values (4.303). It can be concluded that there is no significant difference between UHPLC–ED and conventional UHPLC–UV method. Therefore, the results obtained from UHPLC coupled with amperometric detection using AuNPs modified SPCE is acceptable and reliable for applying to simultaneous determination of DTCs in food.

4. Conclusions

AuNPs modified SPCE was firstly developed for the determination of thiram, disulfiram, and DEDMTDS after their separation with UHPLC system. Under the optimal conditions, the separation was complete within 6 min, and the high current response signal was obtained at AuNPs modified SPCE. The main advantages for the use of AuNPs modified SPCE are in term of high sensitivity, low-cost and simple fabrication-based material. Reproducible signal from %RSD for intra- and inter-day were below 5%. These

results indicated that the high reproducibility was obtained using this system for long time. Moreover, the proposed UHPLC-ED system is an acceptable and reliable method compared to standard UHPLC-UV system using paired *t*-test. Ultimately, the UHPLC coupled with AuNPs modified SPCE amperometry is successfully applied for real samples. This proposed electrode could be a novel or an alternative electrode in UHPLC-ED system for the simultaneous determination of DTCs in fruits and vegetables with low cost material, simple fabrication, and high sensitivity.

Acknowledgments

KC gratefully acknowledges the partially financial supports from Thailand Research Fund (TRF) through the Royal Golden Jubilee Ph.D. program (Grant Number PHD/0049/2553). OC and WS greatly thank the Thailand Research Fund through Research Team Promotion Grant (RTA5780005), the Thai Government Stimulus Package 2 (TKK2555), under the Project for Establishment of Comprehensive Center for Innovative Food, Health Products and Agriculture, Chulalongkorn University. We also thank the financial support from the 90th Anniversary of Chulalongkorn University Fund (Ratchadphiseksomphot Endowment Fund).

Appendix A. Supporting information

Supplementary data associated with this article can be found in the online version at http://dx.doi.org/10.1016/j.talanta.2014.09.020.

References

[1] M. Albareda-Sirvent, A. Merkoci, S. Alegret, Sensor Actuat. B-Chem. 69 (2000) 153–163.
[2] J. Li, H. Xie, L. Chen, Sensor Actuat. B-Chem. 153 (2011) 239–245.
[3] K.C. Honeychurch, J.P. Hart, TrAC, Trends Anal. Chem. 22 (2003) 456–469.
[4] D. Hernandez-Santos, M.B. Gonzalez-Garcia, A.C. Garcia, Electroanalysis 14 (2002) 1225–1235.
[5] M. Das, K. Shim, S. An, D. Yi, Toxicol. Environ. Health Sci 3 (2011) 193–205.
[6] L. Agüí, C. Peña-Farfal, P. Yáñez-Sedeño, J.M. Pingarrón, Talanta 74 (2007) 412–420.
[7] M.A. Hernández-Olmos, L. Agüí, P. Yáñez-Sedeño, J.M. Pingarrón, Electrochim. Acta 46 (2000) 289–296.
[8] S. Rastegarzadeh, S. Abdali, Talanta 104 (2013) 22–26.
[9] L.G. Shaidarova, G.K. Budnikov, S.A. Zaripova, J. Anal. Chem. 56 (2001) 748–753.
[10] E.D. Caldas, M.H. Conceicao, M.C.C. Miranda, L. de Souza, J.F. Lima, J. Agr. Food Chem. 49 (2001) 4521–4525.
[11] S. Heise, H. Weber, L. Alder, Fresen. J. Anal. Chem. 366 (2000) 851–856.
[12] W. Schwack, S. Nyanzi, Z. Lebensm, Unters.-Forsch 198 (1994) 8–10.
[13] O.H.J. Szolar, Anal. Chim. Acta. 582 (2007) 191–200.
[14] N. Ahmad, L. Guo, P. Mandarakas, S. Appleby, J. AOAC Int. 78 (1995) 1238–1243.
[15] R.C. Perz, H. van Lishaut, W. Schwack, J. Agric. Food Chem. 48 (2000) 792–796.
[16] A. Kumar Malik, W. Faubel, Talanta 52 (2000) 341–346.
[17] A.W.M. Lee, W.F. Chan, F.S.Y. Yuen, C.H. Lo, R.C.K. Chan, Y. Liang, Anal. Chim. Acta. 339 (1997) 123–129.
[18] A.K. Malik, W. Faubel, Crit. Rev. Anal. Chem. 31 (2001) 223–279.
[19] A.K. Malik, B.S. Seidel, W. Faubel, J. Chromatrogr. A. 857 (1999) 365–368.
[20] M. Rossi, D. Rotilio, HRC-J. High Res. Chrom 20 (1997) 265–269.
[21] W.A. Kleinman, J.P. Richie Jr, J. Chromatogr. B. 672 (1995) 73–80.
[22] M.D. da Silva, J.R. Procopio, L. Hernandez, J. Liq. Chromatogr. R. T. 22 (1999) 463–475.
[23] D.T.T. Nguyen, D. Guillarme, S. Rudaz, J.L. Veuthey, J. Sep. Sci. 29 (2006) 1836–1848.
[24] P.Y. Chen, C.H. Luo, M.C. Chen, F.J. Tsai, N.F. Chang, Y. Shih, Int. J. Mol. Sci. 12 (2011) 3810–3820.
[25] C. Fernández, A.J. Reviejo, J.M. Pingarrón, Anal. Chim. Acta. 305 (1995) 192–199.
[26] C. Fernández, A.J. Reviejo, L.M. Polo, J.M. Pingarrón, Talanta 43 (1996) 1341–1348.
[27] L. Mathew, M.L.P. Reddy, T.P. Rao, C.S.P. Iyer, A.D. Damodaran, Talanta 43 (1996) 73–76.
[28] P. Qiu, Y.N. Ni, Chin. Chem. Lett. 19 (2008) 1337–1340.

Talanta 132 (2015) 424–432

Contents lists available at ScienceDirect

Talanta

journal homepage: www.elsevier.com/locate/talanta

Characterization of monovarietal virgin olive oils by phenols profiling

Verónica Sánchez de Medina [a,b,c], Feliciano Priego-Capote [a,b,c,*], María Dolores Luque de Castro [a,b,c]

[a] Department of Analytical Chemistry, Annex C-3, Campus of Rabanales, University of Córdoba, E-14071 Córdoba, Spain
[b] University of Córdoba, Agroalimentary Excellence Campus, ceiA3, E-14071 Córdoba, Spain
[c] Institute of Biomedical Research Maimónides (IMIBIC), Reina Sofía Hospital, University of Córdoba, E-14071 Córdoba, Spain

ARTICLE INFO

Article history:
Received 22 May 2014
Received in revised form
23 September 2014
Accepted 28 September 2014
Available online 7 October 2014

Keywords:
Monovarietal virgin olive oil
Phenolic compounds
LC–MS/MS
Secoiridoids
Data dependent methods
Precursor ion scanning
Neutral loss scanning

ABSTRACT

The phenolic profiles of seven monovarietal virgin olive oils (VOOs) – *viz.* Arbequina, Arbosana, Cornicabra, FS-17, Hojiblanca, Picual and Sikitita – were characterized by using a quantitative strategy based on LC–MS/MS and the selected reaction monitoring (SRM) mode. Data dependent methods, based on precursor ion scanning, product ion scanning and neutral loss scanning, were developed for confirmatory analysis of secoiridoid derivatives. The observed phenolic profiles were used to find correlation between pairs of phenols and similarity trends among the monovarietal VOOs. A Pearson analysis revealed several correlations among phenols with p-value < 0.01 and correlation coefficient (R) > 0.75 in the seven monovarietal VOOs. Cluster analysis showed two main clusters between VOOs, formed by Arbequina/Hojiblanca/Cornicabra/Picual and Sikitita/Arbosana/FS-17. High correlations ($R > 0.7$) were observed for the following pairs of VOOs: Arbequina/Hojiblanca ($R=0.77$), essentially supported on levels of hydroxytyrosol acetate (3,4-DHPEA-AC) and dialdehydic forms of secoiridoids; Cornicabra/FS-17 ($R=0.81$) and Picual/FS-17 ($R=0.79$), by correlation of flavonoids and secoiridoid derivatives in general. The highest correlation was observed for the pair Picual/Cornicabra ($R=0.99$). This preliminary study allowed setting similarities and dissimilarities between monovarietal VOOs by analysis of the phenolic profile. The observed connections between phenols for different varieties have been tentatively interpreted according to the main pathways for phenols biosynthesis.

© 2014 Elsevier B.V. All rights reserved.

1. Introduction

The minor fraction of virgin olive oil (VOO), formed by a chemically heterogenous group that includes more than 230 compounds, represents about 2% (w/w) of VOO. This fraction encompasses non-polar compounds such as phytosterols, waxes or hydrocarbons, and a polar or mid-polar sub-fraction [1] mostly constituted by volatile and phenolic compounds. Phenols present in VOO are also characterized by a chemical diversity of families such as phenolic alcohols and derivatives, phenolic acids, hydroxy-isochromans, flavonoids, lignans and secoiridoids. Among them, secoiridoids, the most concentrated phenols present in VOO, are specific compounds of *Oleaceae* plants [2]; in fact, secoiridoids differentiate VOO as unique among other vegetable oils.

Phenolic compounds have been widely studied because of their nutraceutical effects, relevant contribution to the sensory properties of VOO with special emphasis on bitterness and pungency, and their stabilizing role to ensure the long shelf-life of VOOs as compared to other vegetable oils [3]. The nutraceutical and stability properties of phenolic compounds have been linked to the capability of the phenolic structure for inhibiting oxidation processes. Numerous studies have evaluated the oxidation inhibition capability of phenols present in VOO, which allowed identifying hydroxytyrosol as the VOO phenol with the highest oxidation inhibition power by the DPPH test, followed by oleuropein aglycon (3,4-DHPEA-EA) and decarboxymethyloleuropein aglycon (3,4-DHPEA-EDA) [4]. The EFSA (European Food Safety Authority) report has emphasized the inhibition activity of hydroxytyrosol and secoiridoids against the oxidation of phospholipids and LDL cholesterol [5]. In fact, the antioxidant capability of hydroxytyrosol is responsible for its prevention role against tumoral diseases, cardiovascular diseases such as atherosclerosis [6], and diabetic neuropathies [7]. Secoiridoids also possess several health properties such as their implication in the inhibition of blood platelet aggregation, involvement in the synthesis of thromboxane in human cells and protection of erythrocytes from oxidative damage [8]. Additionally, anti-inflammatory activity of decarboxymethyl ligstroside

* Corresponding author at: Department of Analytical Chemistry, Annex C-3, Campus of Rabanales, University of Córdoba, Córdoba, Spain.
Tel./fax: +34 957218615.
E-mail address: q72prcaf@uco.es (F. Priego-Capote).

http://dx.doi.org/10.1016/j.talanta.2014.09.039
0039-9140/© 2014 Elsevier B.V. All rights reserved.

aglycon (*p*-HPEA-EDA [9], and recent evidences about its action on Alzheimer's disease [10] have been reported. Complementarily, Lozano-Sánchez et al. have developed a study on the influence of the phenolic composition of five monovarietal VOOs on the cytotoxic activity against human breast cancer cells [11]. These authors deduced that the sensitivity of breast cancer cells to phenolic extracts from VOOs was up to 12 times higher when the extracts were from VOOs with high content of secoiridoids as compared to other with low/nil content of these phenolic compounds.

One other particular family of phenols such as flavonoids has also been associated to health benefits related with cancer and coronary heart diseases [12–14].

Also organoleptical properties of VOOs have been correlated with the level of individual phenols [15–17]; thus, bitter intensity has been mainly related to hydroxytyrosol derivatives [18,19]; pungency character associated to two other secoiridoids such as 3,4-DHPEA-EDA and *p*-HPEA-EDA [20]; and also a negative correlation has been found between the vanillin content of VOO and their bitter sensory attributes [21].

Numerous studies have been published dealing with the quantitative and qualitative analysis of phenols in VOO. However, few of them have been focused on determination of phenols in monovarietal VOOs despite all the benefits – in terms of health, sensory properties and stability – associated to this family of compounds. In this sense, there is a demand for the quantitative characterization of phenols in monovarietal VOOs in order to evaluate the presence of the most significant compounds such as hydroxytyrosol, tyrosol, secoiridoids, phenolic acids and flavonoids. A deep characterization of the phenolic content of monovarietal VOOs could aid consumers to select the optimum VOO according to their preferences. The aim of this study was to characterize the phenolic composition of seven monovarietal VOOs by using a quantitative strategy based on LC–MS/MS analysis in selected reaction monitoring (SRM) mode. The observed phenolic profiles were then used to find statistical correlations between pairs of phenols and define tentative similarity trends among the monovarietal oils.

2. Materials and methods

2.1. Monovarietal virgin olive oil samples

The monovarietal VOO samples used in this work were obtained from olive fruits collected from 15th to 22nd November 2013 at intermediate ripening from different cultivars located in different areas of the South of Spain: Arbequina (Sevilla), Arbosana (Córdoba), Cornicabra (Toledo), Hojiblanca (Málaga), Picual (Jaén), Sikitita (Córdoba) and FS-17 (Córdoba). Oils samples were stored in darkness at −20 °C.

2.2. Reagents

The solvents used for analysis of phenols from VOOs were LC–MS grade methanol and *n*-hexane both from Scharlab (Barcelona, Spain). MS-grade formic acid as ionization agent in the chromatographic mobile phases was also from Scharlab. Deionized water (18 MΩ cm) from a Millipore Milli-Q water purification system (Bedford, MA, USA) was used to prepare the aqueous chromatographic phase.

Standards of target phenols (*viz.* hydroxytyrosol and tyrosol as simple phenols, verbascoside as phenyletanoid, oleuropein representing secoiridoids; luteolin, apigenin, apigenin-7-glucoside, luteolin-7-glucoside, diosmetin, quercetin and rutin as flavonoids; and vanillin, caffeic acid, *p*-coumaric acid, ferulic acid and vanillic acid as phenolic aldehydes and acids) for quantitative analysis of these metabolites in VOO were from Extrasynthese (Genay, France). Syringic acid, used as internal standard (IS), was from Extrasynthese (Genay, France). Individual stock standard solutions and multistandard solutions were prepared by dilution of each compound in methanol. The solutions were stored at −20 °C.

2.3. Apparatus and instruments

An MS2 minishaker from Ika (Wilmington, USA) was used to enhance the transfer of phenols from oil to a methanol–water solution for individual quantitation of the target compounds. Phenols extracts were analyzed by an Agilent 6410 triple quadrupole (QqQ) detector furnished with an electrospray ionization (ESI) source.

2.4. Extraction of phenols from VOO

Phenolic compounds were extracted from VOO by shaking 1 g of oil with 1 mL of hexane and 1 mL of 60:40 methanol–water mixture for 1 min in the MS2 minishaker. The hydroalcoholic phase was directly injected into the LC–QqQ. This approach has been widely validated in previous research and is accepted as sample preparation strategy for analysis of phenolic compounds in VOO [22–24].

2.5. LC–MS/MS analysis of phenols extracts

Analyses were performed by reversed-phase liquid chromatography followed by negative electrospray ionization (ESI) and tandem mass spectrometry (MS/MS) detection. 10 μL of extract was injected in triplicate into the LC system for chromatographic separation of the target compounds using a Mediterranea C18 analytical column (150 mm × 0.46 mm i.d., 3 μm particle size) from Teknokroma (Barcelona, Spain). The column compartment was kept at 30 °C. The mobile phases were: phase A (0.1% formic acid in water) and phase B (0.1% formic acid in methanol). The gradient program, at 0.8 mL min^{-1} constant flow rate, was as follows: initially 96% phase A and 4% phase B kept for 2 min; from 2 to 17 min, the mobile phase A was from 96 to 34%; from 17 to 35 min, mobile phase A was from 34 to 0% A, while B ranged from 66 to 100% B. This last composition was kept for 5 min. After each analysis, the column was equilibrated for 7 min up to the initial conditions.

The entire eluate was electrosprayed and ionized in negative mode and monitored by MS/MS in Selected Reaction Monitoring (SRM) mode by monitoring selective transitions from precursor to product ions. The flow rate and temperature of the drying gas (N_2) was 10 L min^{-1} and 300 °C, respectively. The nebulizer pressure was 50 psi and the capillary voltage 3000 V. The dwell time was set at 200 μs. Identification and quantitation of the phenols were performed using commercial standards, except for hydroxytyrosol acetate (3,4-DHPEA-AC) and secoiridoid derivatives, for which commercial standards were not available. For this reason, these compounds were relatively quantified as oleuropein equivalents.

2.6. Statistical analysis

After LC–MS/MS analysis, a data set was built with the concentrations of phenols found in each analytical sample. Normalization by logarithmic transformation was used as preprocessing step. The definitive data set was exported to Statgraphic software (Centurion XV.I) for statistical analysis by Pearson correlation analysis. Additionally, the data set was also exported into the Mass Profiler Professional (MPP) software package (version 2.0, Agilent Technologies, Santa Clara, CA, USA)

Table 1
Optimization of the MS/MS step for qualitative and quantitative determination of phenols.

Phenol	Fragmentor (V)	Precursor ion	Collision energy (eV)	Quantitative transition (*m/z*)	Product ion confirmation (*m/z*)
Hydroxytyrosol	110	153.1	10	153→123	108
Tyrosol	110	137	10	137→119	81
Caffeic acid	110	179	13	179→135	107
***p*-Coumaric acid**	80	163	10	163→119	93
Ferulic acid	110	193	13	193→134	178
Oleuropein	170	539	23	539→307	275
Luteolin	170	285	35	285→133	175
Apigenin	170	269	35	269→117	151
Vanillic acid	80	167	11	167→151	108
Vanillin	80	151	14	151→136	108
Diosmetin	170	299	20	299→284	256
Quercetin	170	301	20	301→179	151
Apigenin-7-glucoside	220	431	35	431→268	225
Luteolin-7-glucoside	230	447	35	447→285	284
Verbascoside	80	623	35	623→161	179

for Clustering Analysis, which allowed organizing samples into clusters based on similarity of their abundance profiles.

3. Results and discussion

3.1. Parameters of the selected reaction monitoring method

A panel of 16 phenols, which can be considered among the most important phenols in VOO with available commercial standards, was selected for determination purposes [22,25,26]. The monitored compounds were hydroxytyrosol and tyrosol, caffeic acid, *p*-coumaric acid, ferulic acid, vanillic acid, vanillin, verbascoside, apigenin, luteolin and their corresponding glucosides, diosmetin, quercetin, rutin and oleuropein.

The most sensitive transitions from precursors to product ions were used for quantitation of phenols, whereas secondary transitions were used as qualifiers for confirmatory analysis. The SRM transitions and the corresponding acquisition parameters such as isolation voltage of the first quadrupole and collision energy were optimized by using standard solutions resulting in the values listed in Table 1. SRM transitions with quantitative purposes agreed with those reported in methods previously published, which have also identified the chemical structure associated to product ions formed after MS/MS fragmentation [27,28].

Quantitation was carried out using the ratio between the peak area of each phenol and that of the IS. Calibration models were developed for each phenol using multistandard solutions. Nine concentration levels from 0.25 ng mL^{-1} to 5 μg mL^{-1} were analyzed in triplicate to obtain the calibration curves. The calibration equations, coefficients of regression (R^2) and quantitation limits (LOQs) are listed in Table 2.

Table 2
Calibration equations, regression coefficients and limits of quantification for analysis of phenolic compounds.

Phenol	Calibration equations	Regression coefficient (R^2)	LOQ (μg mL^{-1})
Hydroxytyrosol	$y=15.938x-0.5866$	0.993	0.25×10^{-3}
Tyrosol	$y=0.0108x-0.0128$	0.981	1
Caffeic acid	$y=31.8938x-0.6562$	0.995	0.25×10^{-3}
***p*-Coumaric acid**	$y=20.2813x+0.6944$	0.998	0.05
Ferulic acid	$y=7.1723x-0.6368$	0.991	0.01
Oleuropein	$y=4.1947x-2.0536$	0.995	0.25×10^{-3}
Luteolin	$y=33.6232x-0.7341$	0.998	0.25×10^{-3}
Apigenin	$y=40.7716x-19.5034$	0.993	0.25×10^{-3}
Vanillic acid	$y=0.7035x-0.0135$	0.994	0.01
Vanillin	$y=2.2616x-0.0659$	0.993	0.01
Diosmetin	$y=21.9695x-1.1352$	0.997	0.25×10^{-3}
Quercetin	$y=0.4437x-0.0163$	0.994	0.25×10^{-3}
Apigenin-7-glucoside	$y=33.3276x-1.2567$	0.992	0.25×10^{-3}
Luteolin-7-glucoside	$y=11.2851x-0.2514$	0.991	0.25×10^{-3}
Verbascoside	$y=2.3377x-0.0526$	0.992	0.25×10^{-3}

3.2. Confirmatory analysis of secoiridoid derivatives by data-dependent methods

Oleuropein is the major secoiridoid found in the pulp of olives [29], where its concentration reaches relatively high levels in immature fruits (around 2.7 mg g^{-1}) [30]. However, its concentration declines with progression of the maturation process of the fruit to form secoiridoid derivatives such as 3,4-DHPEA-EDA, *p*-HPEA-EDA, 3,4-DHPEA-EA and *p*-HPEA-EA as well as hydroxytyrosol, 3,4-DHPEA-AC, tyrosol and elenolic acid glucoside, which can be considered as indicators of the extent of olives maturation [31–33]. The formation of these secoiridoid derivatives and that of phenolic alcohols is significantly enhanced during the process for production of VOO by action of β-glucosidases, which are released during the pressing step. For this reason, these compounds are massively found in VOO instead of oleuropein. Among these compounds, it is worth mentioning the presence of secoiridoid derivatives such as 3,4-DHPEA-AC, *p*-HPEA-EDA and 3,4-DHPEA-EDA 3,4-DHPEA-EA and ligstroside aglycon (*p*-HPEA-EA) due to their relevance in VOO in terms of concentration as well as nutraceutical properties and sensory contribution.

Quantitative analysis of secoiridoid derivatives is critical to offer a comprehensive overview of the phenolic composition of VOOs. However, they were not preliminary included in the development of the SRM method due to the unavailability of commercial standards. Thus, confirmatory analysis was previously required to prove their presence in monovarietal VOO samples included in this study. For this purpose, data-dependent methods were used to scan the presence of these target metabolites by taking benefit from the versatility of the triple-quad mass analyzer, particularly, precursor ion scanning, product ion scanning and neutral loss scanning, which are selective tools to confirm the presence of derivatives that can be structurally associated to hydroxytyrosol and tyrosol. Thus, 3,4-DHPEA-EDA, 3,4-DHPEA-EA and 3,4-DHPEA-AC are esters of hydroxytyrosol, while *p*-HPEA-EDA and *p*-HPEA-EA are esters of tyrosol since the two sets of compounds are formed by hydrolysis of oleuropein and ligstroside, respectively. With these premises, a precursor ion scanning method by monitoring representative ions found for hydroxytyrosol and tyrosol

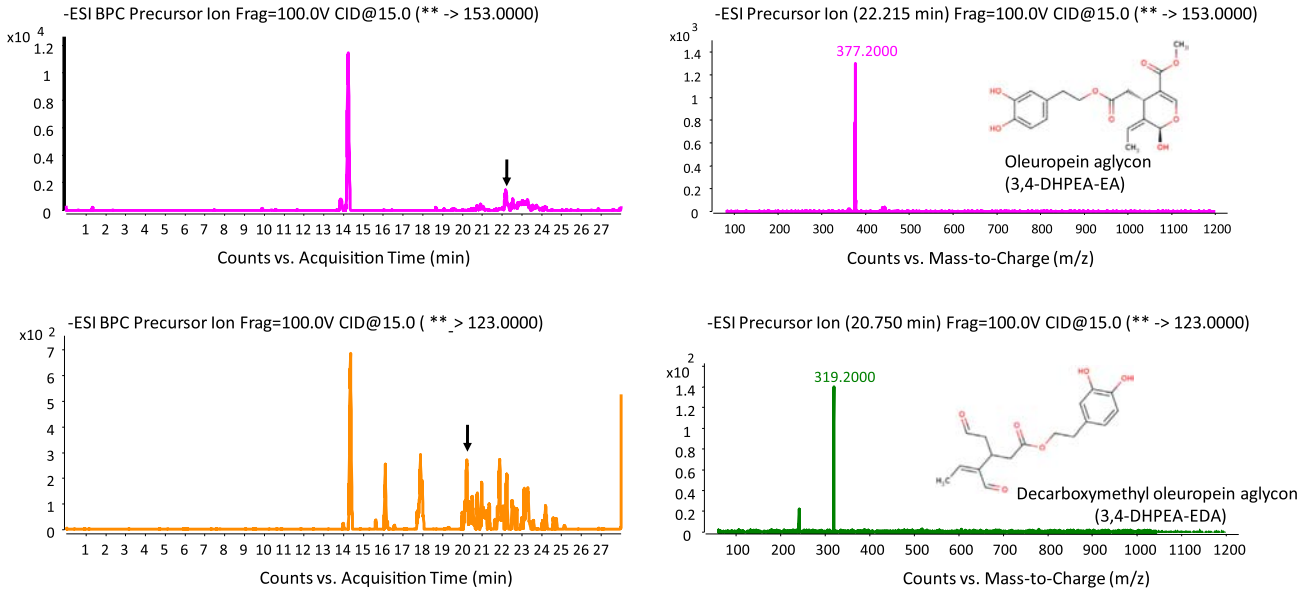


Fig. 1. Precursor ion scanning for qualitative analysis of 3,4-DHPEA-EA and 3,4-DHPEA-EDA.

(identified as molecular ions or stable fragments) at the third quadrupole (Q3) could scan compounds formed by condensation reaction of the two phenolic alcohols in the first quadrupole (Q1). Precursor ion scanning by monitoring the precursor ion for hydroxytyrosol *m/z* 153 at Q3 allowed detecting an ion with precursor ion *m/z* 377 at 22.2 min elution time as Fig. 1 shows, which fit to the $[M–H]^-$ ion of 3,4-DHPEA-EA. Similarly, one other compound with precursor ion *m/z* 319, which corresponded to 3,4-DHPEA-EDA, was detected by monitoring the *m/z* 123 at Q3 (20.75 min), which is the most stable product ion formed by fragmentation of hydroxytyrosol (Fig. 1). Product ion scanning for *m/z* 377 and 319 revealed two selective transitions with quantitative purposes for 3,4-DHPEA-EA and 3,4-DHPEA-EDA by monitoring product ions at *m/z* 275 and 59, respectively, which had previously been detected [27,28]. Neutral loss scanning analysis by monitoring 102 and 260 mass units allowed confirming the presence of these two secoiridoid derivatives, as Supplementary Fig. 1 shows.

The two derivatives obtained by hydrolysis of ligstroside, *p*-HPEA-EA and *p*-HPEA-EDA, were identified by the same strategy. The presence of the two derivatives was detected by precursor ion scanning by monitoring *m/z* 137 at Q3, which fits with the cleavage of tyrosol by the ester bound. Thus, two precursor ions with *m/z* 361 and 303 were detected at retention time 24.1 and 21.9 min (as Fig. 2 shows), which were identified as *p*-HPEA-EA and *p*-HPEA-EDA, respectively. Product ion scanning for both precursors enabled to find quantitative transitions from *m/z* 361 and 303 to product ions at *m/z* 291 and 59. Neutral losses observed for these transitions, 70 and 244 mass units, were scanned by tuning Q1 and Q3 to confirm the presence of both ligstroside derivatives (Supplementary Fig. 2).

The presence of 3,4-DHPEA-AC was verified by precursor ion scanning by monitoring *m/z* 59 at Q3, which provided a chromatographic peak at 19.9 min with precursor *m/z* 195. The identity of this secoiridoid derivative was confirmed by neutral loss scanning of 136 Da, which fit the fragment formed by hydrolysis of the ester bound. These results are illustrated in Fig. 3.

After verification and confirmatory analysis of oleuropein derivatives in monovarietal VOOs, an optimization study for selection of the SRM transitions for tentative quantitation of secoiridoid derivatives was developed to include them in the LC–MS/MS method. The optimization method was also carried out by using phenolic extracts from the analyzed VOOs. Table 3 summarizes the main results obtained by data-dependent methods, as well as qualitative and quantitative MS/MS parameters.

3.3. Statistical description of phenolic profiles in monovarietal VOOs

Despite the phenolic characterization of VOOs had been widely addressed, no special attention had been paid to profiling of this family of compounds in monovarietal VOOs. Thus, although several monovarietal VOOs had been analyzed, the studies were limited to quantitation of a reduced number of phenols. This is the case of the research developed by Oliveras-López et al., who quantified only nine representative phenols in three Spanish monovarietal VOOs [34]. In a lesser extent, other authors have focused their attention on a small number of VOO varieties (usually one to three) in which they have quantified up to 15 phenolic compounds [35–37].

It is quite difficult to compare the results of phenolic concentrations provided by different studies owing to the great variety of factors (including genetic, pedo-climatic, geographical origin, agronomic and technological factors) that influence the chemical composition of VOO [38–41]. Nevertheless, some trends can be visualized by overall evaluation of monovarietal VOOs. The averaged concentrations found for 16 target phenolic compounds in each monovarietal VOO and standard deviation (SD) values are listed in Table 4. Hydroxytyrosol, the most representative phenol in VOO [42], was found at levels below 5 $\mu g\, g^{-1}$ in all monovarietal VOO, which practically agrees with results provided by previous authors [11,44,45], except in FS-17 that provided very high levels of this phenol – around 25 $\mu g\, g^{-1}$ – (Fig. 4A). To the authors' knowledge, there are not other studies reporting such high levels of hydroxytyrosol in VOO. This monovarietal VOO also gave the highest concentration of tyrosol (23.6 $\mu g\, g^{-1}$), followed by Arbosana with 18.7 $\mu g\, g^{-1}$, while the resting varieties gave levels below 6 $\mu g\, g^{-1}$ (Fig. 4B). The high concentration of tyrosol found in this study for some varieties is more usual than for hydroxytyrosol since Gómez-Rico et al. found similar concentration of this simple phenol in Picual VOO [43].

One other variety such as Arbequina was clearly outstanding in terms of 3,4-DHPEA-AC, 3,4-DHPEA-EDA and *p*-HPEA-EDA, which is clearly correlated to the bitter character of VOOs from Arbequina fruits (Fig. 4C). These data agree with the study of García-González

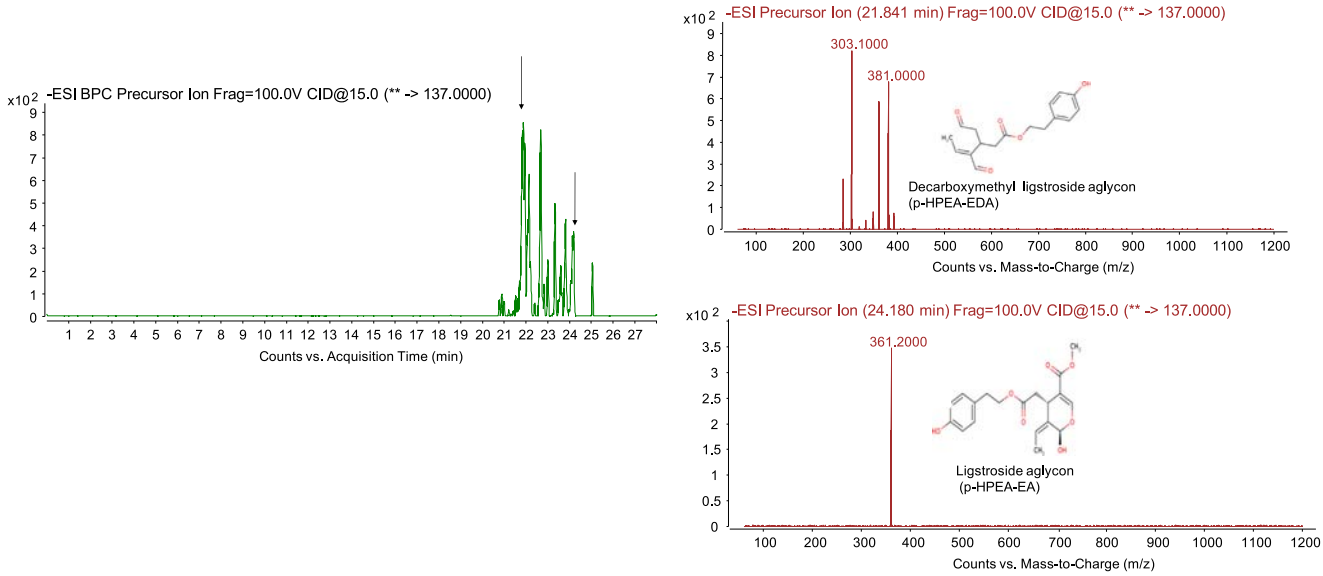


Fig. 2. Precursor ion scanning for qualitative analysis of *p*-HPEA-EA and *p*-HPEA-EDA.

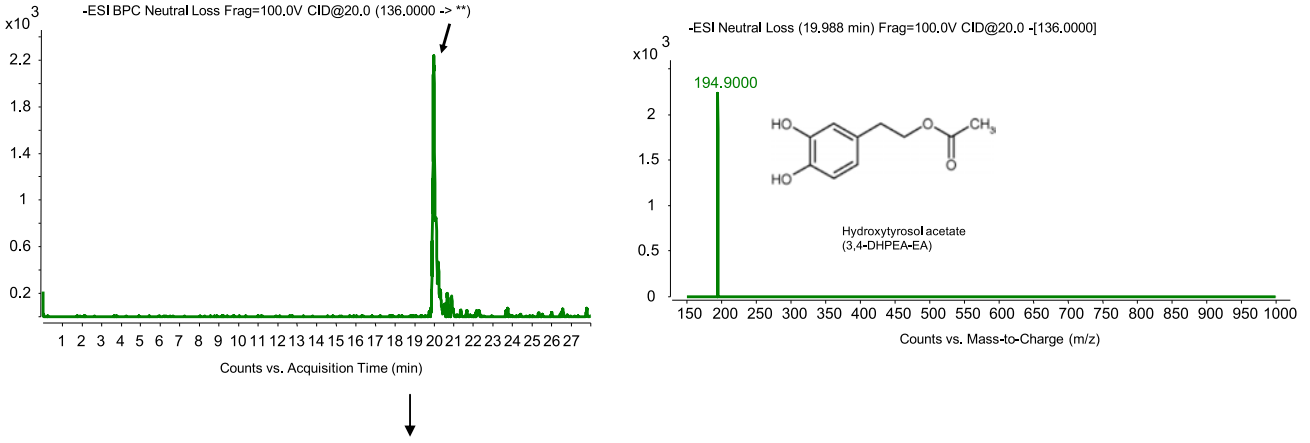


Fig. 3. Neutral loss scanning for qualitative analysis of 3,4-DHPEA-AC.

Table 3
Optimization of the MS/MS step for qualitative and quantitative determination of oleuropein derivatives.

Phenol	Precursor ion	Neutral loss	Fragmentor (V)	Collision energy (eV)	Quantitative transition (*m/z*)	Product ion confirmation (*m/z*)
3,4-DHPEA-AC	195.1	136	110	12	195→59	135
3,4-DHPEA-EDA	319.1	260	110	12	319→59	139
***p*-HPEA-EDA**	303.1	244	110	12	303→59	137
3,4-DHPEA-EA	377	102	110	12	377→275	307
***p*-HPEA-EA**	361.1	70	110	12	361→291	101

et al. and Lozano-Sánchez et al., who also found higher values of 3,4-DHPEA-AC and EDA secoiridoids for Arbequina VOO as compared to Picual VOOs from different zones [37,11]. Apart from Arbequina, the study proposed here also revealed extra levels of these secoiridoid derivatives in Hojiblanca VOO as compared to the resting VOO varieties.

On the other hand, four varieties (*viz.* Cornicabra, FS-17, Hojiblanca and Picual) reported VOOs with high levels of the aglycon forms of oleuropein and ligstroside, 3,4-DHPEA-EA and *p*-HPEA-EA, respectively (Fig. 4D). Levels of these two derivatives are strongly related to the pungent character of VOOs. Previous studies also offered similar results for these two relevant EA secoiridoids; thus, Gómez-Rico et al. found the highest concentrations of 3,4-DHPEA-EA and *p*-HPEA-EA in Cornicabra and Picual VOOs [43], and García-González et al. detected higher levels of both phenols in Picual VOO as compared to Arbequina VOO [37].

One other secoiridoid such as oleuropein, which is highly concentrated in olive pulp, did not exceed 0.03 $\mu g\, g^{-1}$ in the different varieties, while verbascoside was only detected in Arbequina and Sikitita VOOs.

Ferulic, *p*-coumaric and caffeic acids are synthesized through the phenylpropanoid pathway, by which *p*-coumaric acid is hydroxylated to caffeic acid, and that methoxylated to ferulic acid. As Supplementary Fig. 3shows, these phenolic acids were more concentrated in FS-17, Arbequina and Sikitita VOOs, which could

Table 4
Concentration ($\mu g\ mL^{-1}$) and standard deviation (SD) of individual phenols in monovarietal VOOs.

	Arbequina	SD	Arbosana	SD	Cornicabra	SD	FS-17	SD	Hojiblanca	SD	Picual	SD	Sikitita	SD
Hydroxytyrosol	1.76	0.01	2.07	0.02	1.43	0.02	33.89	1.86	1.98	0.03	1.42	0.08	1.82	0.30
Tyrosol	2.28	0.12	18.69	6.42	4.28	0.09	23.59	8.02	4.39	0.36	4.42	0.13	5.49	0.55
Caffeic acid	0.031	0.001	0.026	< 0.001	0.030	< 0.001	0.105	0.002	0.025	< 0.001	0.029	0.001	0.039	0.001
***p*-Coumaric acid**	1.15	0.01	0.24	0.02	0.22	0.01	0.98	0.01	0.55	0	0.22	0.01	1.06	0.06
Ferulic acid	0.125	0.004	0.152	0.002	0.105	0.001	0.283	0.009	0.130	0.003	0.104	0.001	0.331	0.021
Oleuropein	0.023	0.001	0.022	nd	0.022	0.001	0.023	nd	0.022	0.001	0.023	0.001	0.026	0
Luteolin	3.74	2.24	4.14	1.06	0.84	0.02	0.17	0.01	3.94	2.53	0.93	0.02	4.93	3.07
Apigenin	1.17	0.01	2.91	0.12	0.77	0	0.51	0	1.31	0.04	0.79	0.00	1.04	0.00
Vanillic acid	0.62	0.02	0.80	0.02	0.16	0	0.51	0.02	0.85	0.09	0.14	0.01	1.06	0.03
Vanillin	0.19	0.01	0.10	0	0.42	0.01	0.10	0	0.21	0.01	0.43	0	0.17	0
Diosmetin	3.06	1.61	1.05	0.01	0.48	0.01	0.17	0.01	0.52	0.03	0.53	0.01	4.89	2.83
Quercetin	0.064	< 0.001	0.045	0.006	nd	nd	0.043	< 0.001	0.042	< 0.001	0.038	nd	0.092	0.005
Apigenin-7-glucoside	0.038	< 0.001	0.038	< 0.001	0.038	< 0.001	0.038	< 0.001	0.038	< 0.001	0.038	< 0.001	0.038	< 0.001
Luteolin-7-glucoside	0.025	< 0.001	0.027	< 0.001	0.024	< 0.001	0.023	< 0.001	0.023	< 0.001	0.025	< 0.001	0.024	< 0.001
Rutin	0.040	0.001	0.040	0.003	0.040	nd	0.037	nd	0.040	nd	0.038	nd	0.038	< 0.001
Verbascoside	0.031	< 0.001	nd	nd	nd	nd	nd	nd	nd	nd	nd	nd	0.026	0.001
3,4-DHPEA-AC	56.48	12.84	1.09	0.01	7.66	1.23	9.60	2.69	17.20	8.27	8.16	1.84	9.14	2.66
3,4-DHPEA-EDA	439.67	159.08	6.96	0.62	10.04	2.36	9.94	2.92	82.15	29.18	11.20	3.68	9.03	2.78
***p*-HPEA-EDA**	56.70	11.61	10.40	1.72	15.69	4.82	9.22	2.62	18.47	9.30	17.18	6.94	7.72	1.84
3,4-DHPEA-EA	9.65	2.95	8.55	1.08	51.06	25.14	60.40	20.34	66.72	21.43	51.65	18.52	9.32	3.08
***p*-HPEA-EA**	1.58	0.01	2.23	0.07	39.27	12.50	16.91	7.04	17.03	9.33	42.90	12.66	1.59	0.00

be attributed to a higher activity of the enzymes involved in this pathway. These results are in agreement with those obtained by García et al., who also found the highest level of phenolic acids in Arbequina VOO, followed by Hojiblanca, Picual and Cornicabra VOOs [44].

Vanillin and vanillic acid presented an opposite behavior. Thus, Cornicabra and Picual VOOs reported the lowest concentration of vanillic acid, whereas vanillin was high-concentrated in these VOOs as compared to the resting varieties (Supplementary Fig. 4). The activity of the oxidation enzyme involved in the pathway to convert vanillin into vanillic acid could be responsible for this result.

Concerning flavonoids, Arbequina, Arbosana, Hojiblanca and Sikitita VOOs provided higher levels of luteolin, apigenin and diosmetin than the other varieties (Supplementary Fig. 5). This trend was also found by García et al. [44]. Levels of quercetin were slightly higher in Arbequina and Sikitita monovarietal oils as compared to the resting varieties. Finally, no critical differences were observed between levels of glucoside flavonoids such as luteolin-7-glucoside, apigenin-7-glucoside and rutin.

3.4. Statistical correlation between phenolic compounds

Considering the data set formed by concentrations of phenols in the seven monovarietal VOO, a Pearson correlational analysis was carried out to find statistical correlations between phenolic compounds. Few studies have been focused on correlation analysis among phenolic compounds present in VOO. Pérez et al. studied the relationship among four groups of phenols in VOOs from Picual × Arbequina crosses [45]. However, this statistical evaluation has not been applied to different monovarietal VOOs. In the present work, several correlations were found between pairs of phenols with p-value < 0.01 and correlation coefficient $(R) > 0.75$, which are indicative of at least a moderate relationship between them (Supplementary Table 1). A strong positive correlation was found between p-HPEA-EA and 3,4-DHPEA-EA ($R=0.93$, p-value$=0.002$) as well as between p-HPEA-EDA and 3,4-DHPEA-EDA ($R=0.89$, p-value$=0.007$). These correlations could be tentatively explained according to the main pathways involved in the biosynthesis of phenolic compounds. Thus, in the synthesis of oleosides, ligstroside is converted into oleuropein by hydroxylation [46]. This process is quite active at the early stages of maturation through which fruits are highly-concentrated in oleuropein. However, it can be assumed that ripening as well as crushing and malaxation of olive fruits during oil production contribute to release β-glucosidases, which produce the aglycon forms of ligstroside and oleuropein (p-HPEA-EA and 3,4-DHPEA-EA) [29]. This fact would support the positive observed correlation. Additionally, the aglycon forms are hydrolyzed and turned into the dialdehydic form of secoiridoids (p-HPEA-EDA and 3,4-DHPEA-EDA) by action of a decarboxymethylase, which also tentatively justifies the positive correlation found for the two dialdehydic secoiridoid forms. Supplementary Fig. 6 shows the biosynthetic pathways of secoiridoids.

Consistent positive correlations were also found within the flavonoids class. The highest correlation was detected for apigenin and luteolin glucosides ($R=0.91$, p-value$=0.003$). Both compounds are formed through the flavone and flavonols biosynthesis from their respective aglycone by glycosyltransferase. This common pathway could explain the strong positive correlation. A significant negative correlation was observed between quercetin and vanillic acid ($R=-0.91$, p-value$=0.004$). Vanillic acid is synthesized through the phenylalanine pathway, whereas quercetin is obtained by biosynthesis of flavonoids. There is a connection between both pathways: the p-caffeoyl-CoA; therefore, depending on the activity of enzymes using p-caffeoy-CoA as substrate the prevalence of vanillic acid or quercetin would be tentatively justified. High activity of methyltransferase enzyme would imply the formation of vanillic acid, while the synthesis of quercetin would be supported on the activity of chalcone synthase (Supplementary Fig. 7).

Significant correlations with p-value between 0.01 and 0.05 were also found for some pairs of phenols. Thus, 3,4-DHPEA-EDA and 3,4-DHPEA-AC exhibited positive correlation ($R=0.89$, p-value$=0.03$) that could be explained because 3,4-DHPEA-AC is obtained by cleavage of 3,4-DHPEA-EDA [8]. Luteolin was also positively correlated to other two aglycon flavonoids such as diosmetin and apigenin ($R=0.81$, p-value$=0.03$ and $R=0.79$, p-value$=0.03$, respectively). Apigenin is the substrate for the synthesis of luteolin in the flavonoids pathway by action of a hydroxylase, which allows explaining this positive correlation. As previously mentioned, diosmetin is a methoxyderivative of luteolin and, for this reason, their concentrations in VOO could be correlated. Apigenin was also positively correlated with apigenin-7-glucoside ($R=0.82$, p-value$=0.02$), which could be ascribed to

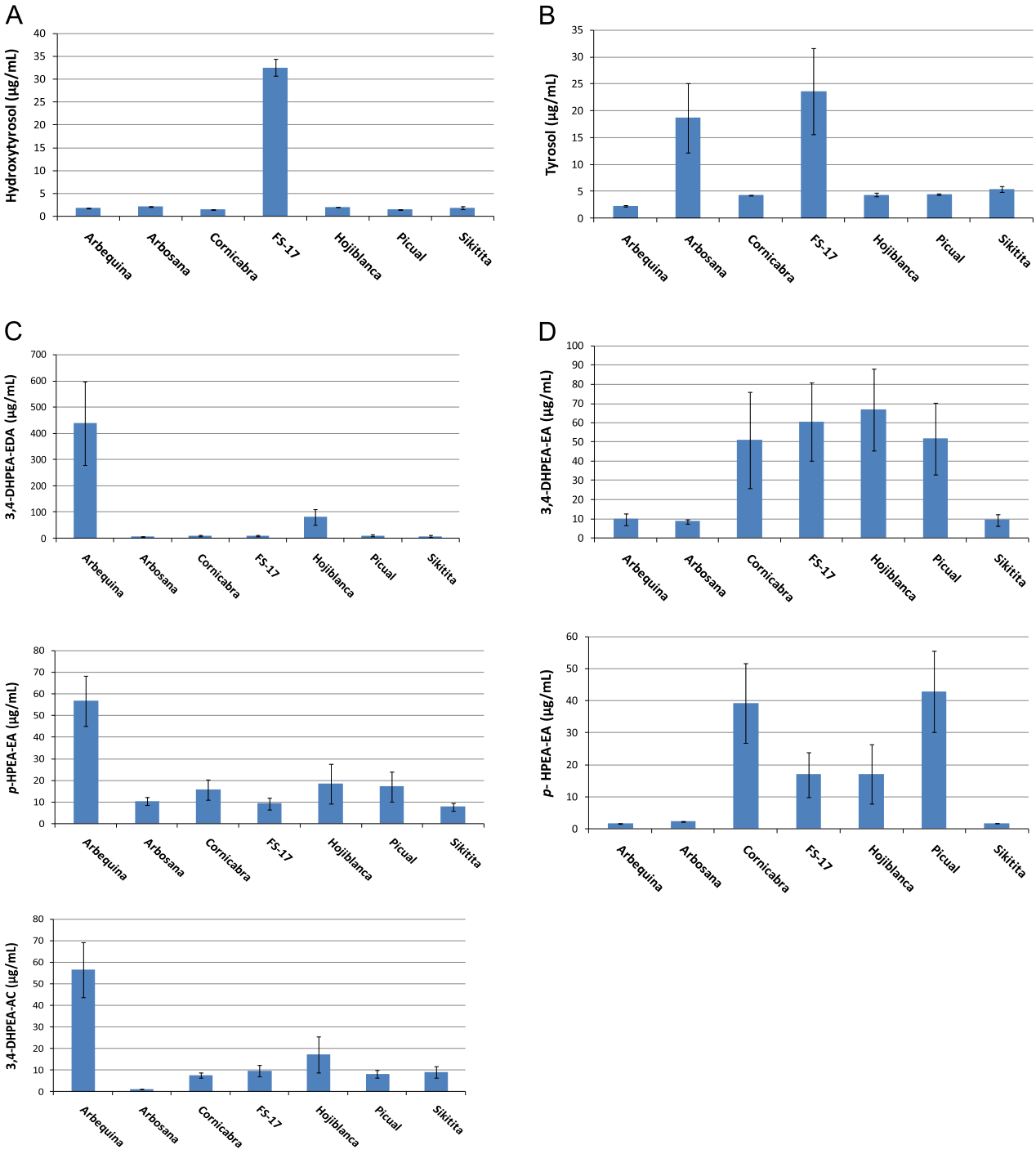


Fig. 4. Concentration plots corresponding to: (A) hydroxytyrosol (B) tyrosol; (C) 3,4-DHPEA-AC, 3,4-DHPEA-EDA and *p*-HPEA-EDA; (D) 3,4-DHPEA-EA and *p*-HPEA-EA.

the glycosylation step that favors storage of certain phenols in VOOs.

Other remarkable correlations were those between vanillin–vanillic acid and luteolin–caffeic acid ($R=-0.79$, p-value$=0.03$ and $R=-0.76$, p-value$=0.05$, respectively). The former correlation could be explained because vanillic acid is obtained by oxidation of vanillin. Luteolin and caffeic are produced in two different pathways: the flavonoids and phenylpropanoid pathways, respectively. However, there is a nexus between them through *p*-coumaric acid. Consequently, the degree of concentration of each compound should depend on the enzymatic activity. In this manner, higher concentration of caffeic acid would involve a high hydroxylase activity. On the other hand, high levels of luteolin could assume an increased activity of the flavonoids biosynthesis pathway (Supplementary Fig. 8).

3.5. Differences in the phenolic profiles of monovarietal VOOs

The next step was to find similarities and differences between the phenols profiles of the analyzed monovarietal VOOs by Clustering analysis. This analysis was applied to the complete data set. Supplementary Fig. 9 shows the cluster graph obtained by comparing phenolic profiles of monovarietal VOOs. The dendrogram reveals the relationships between phenols in one dimension and between VOO samples in the other dimension. Two main clusters can be observed in the graph: Arbequina, Hojiblanca,

Table 5
Correlation values between monovarietal VOO pairs.

VOO	Arbequina	Arbosana	Cornicabra	FS-17	Hojiblanca	Picual	Sikitita
Arbequina	–	0.24	0.10	0.06	**0.77**	0.11	0.52
Arbosana	0.24	–	0.36	0.56	0.41	0.36	0.63
Cornicabra	0.10	0.36	–	**0.81**	0.65	**0.99**	0.51
FS-17	0.06	0.56	**0.81**	–	0.62	**0.79**	0.58
Hojiblanca	**0.77**	0.41	0.65	0.62	–	0.65	**0.74**
Picual	0.11	0.36	**0.99**	**0.79**	0.65	–	0.51
Sikitita	0.52	0.63	0.51	0.58	**0.74**	0.51	–

Cornicabra and Picual were classified within the same cluster, whereas the second one was formed by Sikitita, Arbosana and FS-17. Each cluster was divided into subclusters, which were constituted by VOO pairs, except for Sikitita VOO. The detected subclusters were Arbequina/Hojiblanca, Cornicabra/Picual and Arbosana/FS-17. Among them, the higher similarity was observed between Cornicabra and Picual VOOs since a parallelism was found in the levels of most phenols both with positive and negative correlation. García et al. also found a high similarity in the phenolic profile of Picual and Cornicabra VOOs [44].

The main differences between VOO monovarietal samples were observed in the levels of certain groups of phenols. Thus, it was clear that levels of secoiridoids and derivatives are critical to establish differences between VOOs. In particular, levels of 3,4-DHPEA-AC, 3,4-DHPEA-EDA and *p*-HPEA-EDA followed an opposite trend to those observed for 3,4-DHPEA-EA and *p*-HPEA-EA. This was clearly detected in Arbequina and Hojiblanca VOOs, which provided high levels of EDA phenols and 3,4-DHPEA-AC (particularly Arbequina VOO) as compared to the other varieties. The opposite situation was observed for Sikitita and Arbosana VOOs, which were characterized by low levels of the EA secoiridoid derivatives, and for Cornicabra and Picual, which provided relatively high levels for these compounds. The described trends for secoiridoids have been discussed in other studies as mentioned in the previous sections, with special emphasis on Arbequina, Picual, Cornicabra and Hojiblanca VOOs [11,34,37,43,44].

One other aspect to be emphasized was the high concentrations of phenolic alcohols, hydroxytyrosol and tyrosol, and phenolic acids observed in FS-17. Table 5 shows the correlation between the pairs of VOO samples according the measured concentration of phenolic compounds. As can be seen, high correlations ($R > 0.7$) were observed for the following pairs of VOO: Arbequina/Hojiblanca ($R=0.77$), essentially supported on levels of 3,4-DHPEA-AC and EDA derivatives; Cornicabra/FS-17 ($R=0.81$), Picual/FS-17 ($R=0.79$) and Picual/FS-17 ($R=0.74$), by correlation of flavonoids and secoiridoid derivatives in general. The highest correlation was observed for the pair Picual/Cornicabra ($R=0.99$), which agrees with the parallelism between phenolic levels previously described.

4. Conclusions

This preliminary study allowed setting similarities and dissimilarities between monovarietal VOOs by analysis of the phenolic profile. The observed connections between phenolic compounds for different varieties have been interpreted according to the main pathways for phenols biosynthesis.

Acknowledgements

The Spanish Ministerio de Economía y Competitividad (MINECO) through Project CTQ2012-37428 and FEDER program are thanked for financial support. F.P.C. is sponsored by Ministerio de Ciencia e Innovación (MICINN) through a Ramón y Cajal Contract (RYC-2009-03921). Luis Rallo and Diego Barranco (Agronomy Department, University of Córdoba) and Deoleo, S.A. (Córdoba, Spain) are acknowledged for providing the oils.

Appendix A. Supplementary material

Supplementary data associated with this article can be found in the online version at http://dx.doi.org/10.1016/j.talanta.2014.09.039.

References

[1] M. Murkovic, S. Lechner, A. Pietzka, M. Bratacos, E. Katzogiannos, J. Biochem. Biophys. Methods 61 (2004) 155–160.
[2] A. Bendini, L. Cerretani, A. Carrasco-Pancorbo, A. Gómez-Caravaca, A. Segura-Carretero, A. Fernández-Gutiérrez, G. Lercker, Molecules 12 (2007) 1679–1719.
[3] A. Segura-Carretero, J. Menéndez-Menéndez, A. Fernández-Gutiérrez, Polyphenols in olive oil: the importance of phenolic compounds in the chemical composition of olive oil, in: V.R. Preedy, R.R. Watson (Eds.), Olives and Olive Oil in Health and Disease Prevention, Elsevier, Oxford, 2010, pp. 167–174.
[4] A. Carrasco-Pancorbo, L. Cerretani, A. Bendini, A. Segura-Carretero, M. Del Carlo, T. Gallina-Toschi, G. Lercker, D. Compagnone, A. Fernandez-Gutierrez, J. Agric. Food Chem. 53 (2005) 8918–8925.
[5] European Food Safety Authority (EFSA), EFSA J. 9 (2011) 2033–2058.
[6] K. Hagiwara, T. Goto, M. Araki, H. Miyazaki, H. Hagiwara, Eur. J. Pharmacol. 662 (2011) 78–84.
[7] S.N. El, S. Karakaya, Nutr. Rev. 67 (2009) 632–638.
[8] F. Visioli, C. Galli, J. Agric. Food Chem. 46 (1998) 4292–4296.
[9] G.K. Beauchamp, R.S. Keast, D. Morel, J. Lin, J. Pika, Q. Han, C.H. Lee, A.B. Smith, P.A. Breslin, Nature 437 (2005) 45–46.
[10] A.H. Abuznait, H. Qosa, B.A. Busnena, K.A. El Sayed, A. Kaddoumi, ACS Chem. Neurosci 6 (2013) 973–982.
[11] J. Lozano-Sánchez, A. Segura-Carretero, J.A. Menendez, C. Oliveras-Ferraros, L. Cerretani, A. Fernández- Gutiérrez, J. Agric. Food Chem. 58 (2010) 9942–9955.
[12] L. Le March, Biomed. Pharmacother. 56 (2002) 296–301.
[13] C. Kanadaswami, L.T. Lee, P.P.H. Lee, J.J. Hwang, F.C. Ke, Y.T. Huanh, M.T. Lee, In Vivo 19 (2005) 895–909.
[14] P. Nestel, Curr. Opin. Lipidol. 14 (2003) 3–8.
[15] F. Gutiérrez-Rosales, J. Ríos, M. Gómez-Rey, J. Agric. Food Chem. 51 (2003) 6021–6025.
[16] F. Gutiérrez, S. Perdiguero, R. Gutiérrez, J.M. Olías, J. Am. Oil Chem. Soc 69 (1992) 394–395.
[17] R. Mateos, A. Cert, C.M. Pérez-Camino, J.M. García, J. Am. Oil Chem. Soc 81 (2004) 71–75.
[18] O. Frank, H. Ottinger, T. Hofmann, J. Agric. Food Chem. 49 (2001) 231–238.
[19] F. Favati, N. Condelli, F. Galgano, M.C. Caruso, Food Chem. 139 (2013) 949–954.
[20] P. Andrewes, J.L. Busch, T. De Joode, A. Groenewegen, H. Alexandre, J. Agric. Food Chem. 51 (2003) 1415–1420.
[21] M.J. Tovar, M.J. Motilva, M.P. Romero, J. Agric. Food Chem. 49 (2001) 5502–5508.
[22] M. El Riachy, F. Priego-Capote, L. Leon, M.D. Luque de Castro, L. Rallo, J. Sci. Food Agric. 92 (2012) 2524–2533.
[23] V. Sánchez de Medina, F. Priego-Capote, C. Jiménez-Ot, M.D. Luque de Castro, J. Agric. Food Chem. 59 (2011) 11432–11441.
[24] A. Rotondi, A. Bendini, L. Cerretani, M. Mari, G. Lercker, G.T. Toschi, J. Agric. Food Chem. 52 (2004) 3649–3654.
[25] R. García-Villalba, A. Carrasco-Pancorbo, C. Oliveras-Ferraros, A. Vázquez-Martín, J.A. Menéndez, A. Segura-Carretero, A. Fernández-Gutiérrez, J. Pharm. Biomed. Anal. 51 (2010) 416–429.
[26] Y. Ouni, A. Taamalli, A.M. Gómez-Caravaca, A. Segura-Carretero, A. Fernández-Gutiérrez, M. Zarrouk, Food Chem. 127 (2011) 1263–1267.
[27] R. Japón-Luján, F. Priego-Capote, A. Marinas, M.D. Luque de Castro, Rapid Commun. Mass Spectrom. 22 (2008) 855–864.

[28] M. Becerra-Herrera, M. Sánchez-Astudillo, R. Beltrán, A. Sayago, LWT Food Sci. Technol. 57 (2014) 49–57.
[29] D. Ryan, M. Antolovich, P. Prenzler, K. Robards, S. Lavee, Sci. Hort. 92 (2002) 147–176.
[30] S.M. Cardoso, S. Guyot, N. Marnet, J.A. Lopes-da-Silva, J.A. Renard, C.M. Coimbra, J. Sci. Food Agric 85 (2005) 21–32.
[31] M.J. Amiot, A. Fleuriet, J.J. Macheix, J. Agric. Food Chem. 34 (1986) 823–826.
[32] M.J. Amiot, A. Fleuriet, J.J. Macheix, Phytochemistry 28 (1989) 67–69.
[33] A. Bianco, R.L. Scalzo, M.L. Scarpati, Phytochemistry 32 (1993) 455–457.
[34] M.J. Oliveras-López, M. Innocenti, C. Giaccherini, F. Ieri, A. Romani, N. Mulinacci, Talanta 73 (2007) 726–732.
[35] S. Kesen, H. Kelebek, S. Selli, J. Am. Oil Chem. Soc 90 (2013) 1685–1696.
[36] A. Bakhouche, J. Lozano-Sánchez, R. Beltrán-Debón, J. Joven, A. Segura-Carretero, A. Fernández-Gutiérrez, Food Res. Int. 50 (2013) 401–408.
[37] D.L. García-González, N. Tena, R. Aparicio, J. Agric. Food Chem. 58 (2010) 8357–8364.
[38] J.M. García, S. Seller, M.C. Pérez-Camino, J. Agric. Food Chem. 44 (1996) 3516–3520.
[39] M.D. Salvador, F. Aranda, G. Fregapane, Food Chem. 73 (2001) 45–53.
[40] S.B. Temime, T. Wael, B. Bechir, A. Leila, D. Douja, Z. Mokhtar, J. Food Lipids 13 (2006) 88–99.
[41] R. Zamora, M. Alaiz, F.J. Hidalgo, J. Agric. Food Chem. 49 (2001) 4267–4270.
[42] C. Manna, P. Galletti, V. Cucciolla, G. Montedoro, V. Zappia, J. Nutr. Biochem 10 (1999) 159–165.
[43] A. Gómez-Rico, G. Fregapane, M.D. Salvador, Food Res. Int. 41 (2008) 433–440.
[44] A. García, M. Brenes, P. García, C. Romero, A. Garrido, Eur. Food Res. Technol. 216 (2003) 520–525.
[45] A.G. Pérez, L. León, M. Pascual, C. Romero-Segura, A. Sánchez-Ortiz, R. de la Rosa, C. Sanz, PLoS One (2014), http://dx.doi.org/10.1371/journal.pone.0092898.
[46] S. Damtoft, H. Franzyk, S.R. Jensen, Phytochemistry 34 (1993) 1291–1299.

Talanta 132 (2015) 433–442

Contents lists available at ScienceDirect

Talanta

journal homepage: www.elsevier.com/locate/talanta

Development of a new sorptive extraction method based on simultaneous direct and headspace sampling modes for the screening of polycyclic aromatic hydrocarbons in water samples

Sara Triñanes, Mª Teresa Pena, Mª Carmen Casais*, Mª Carmen Mejuto

Departamento Química Analítica, Nutrición y Bromatología, Instituto de Investigación y Análisis Alimentario, Universidad de Santiago de Compostela, 15782 Santiago de Compostela, Spain

ARTICLE INFO

Article history:
Received 18 June 2014
Received in revised form
16 September 2014
Accepted 18 September 2014
Available online 7 October 2014

Keywords:
Polycyclic aromatic hydrocarbons
Silicone sorbents
Sorptive extraction
Ultra-high performance liquid chromatography
Water analysis

ABSTRACT

A new straightforward and inexpensive sample screening method for both EPA and EU priority polycyclic aromatic hydrocarbons (PAHs) in water has been developed. The method is based on combined direct immersion and headspace (DIHS) sorptive extraction, using low-cost disposable material, coupled to ultraperformance liquid chromatography with fluorescence and UV detection (UPLC-FD-UV). Extraction parameters, such as the sampling mode, extraction time and ionic strength were investigated in detail and optimized. Under optimized conditions, water samples (16 mL) were concentrated in silicone disks by headspace (HS) and direct immersion (DI) modes simultaneously, at room temperature for 9 h for the majority of the 24 studied compounds. Ultrasound-assisted desorption of extracted analytes in acetonitrile was carried out also at room temperature. The optimized chromatographic method provided a good linearity ($R \geq 0.9991$) and a broad linear range for all studied PAHs. The proposed analytical procedure exhibited a good precision level with relative standard deviations below 15% for all analytes. Quantification limits between 0.7 and 2.3 $\mu g\ L^{-1}$ and 0.16 and 3.90 $ng\ L^{-1}$ were obtained for compounds analyzed by UV (acenaphtylene, cyclopenta[c,d]pyrene and benzo[j]fluoranthene) and fluorescence, respectively. Finally, the proposed method was applied to the determination of PAHs in different real tap, river and wastewater samples.

© 2014 Elsevier B.V. All rights reserved.

1. Introduction

Polycyclic aromatic hydrocarbons (PAHs) constitute a broad group of organic compounds which have received much attention over the years because of their wide distribution in the environment as well as their well-known carcinogenic and mutagenic properties [1,2]. Due to the ubiquity of PAHs and their potential deleterious effects on human health, these compounds have been often monitored in air, soil, water, foods and beverages [3]. On the basis of risk assessment, 15 PAHs have been identified as priority hazardous substances by the European Union (EU) [4]. Moreover, in 2005, the Joint FAO/WHO Experts Committee on Food Additives appended to the list a 16th compound (benzo[c]fluorene, B[c]F) also considered as genotoxic. To distinguish this list from the set of 16 US EPA PAHs [5], the term "15+1 EU priority PAHs" is commonly used. The list of these PAHs comprises of B[c]F, cyclopenta[c,d]pyrene (CP[c,d]P), benz[a]anthracene (B[a]A), chrysene (Chry), 5-metylchrysene (5-MC), benzo[j]fluoranthene (B[j]F), benzo[b]fluoranthene (B[b]F), benzo[k]fluoranthene (B[k]F), benzo[a]pyrene (B[a]P), dibenzo[a,l]pyrene (DB[a,l]P), dibenzo[a,h]anthracene (DB[a,h]A), benzo[g,h,i]perylene (B[g,h,i]P), indeno[1,2,3-c,d]pyrene (I[1,2,3-c,d]P), dibenzo[a,e]pyrene (DB[a,e]P), dibenzo[a,i]pyrene (DB[a,i]P) and dibenzo[a,h]pyrene (DB[a,h]P). Because of the continued development of European legislation in this area, analytical methodology for multiple PAHs in water and other types of samples is required in order to get a clearer picture of human exposure.

A variety of analytical methods have been used for determining trace concentrations of PAHs in water samples. Aside from the classical liquid–liquid extraction (LLE), alternative sampling methods like solid phase extraction (SPE) [6], solid phase microextraction (SPME) [7], stir bar sorptive extraction (SBSE) [8] and silicone rods and tubes sorptive methods [9] have been developed. These procedures, based on equilibrium extraction, exhibit several advantages over LLE, regarding sample preparation speed and allows for improved sample throughput by parallel analyses [10].

The most widely used sorptive extraction phase is polydimethylsiloxane (PDMS). Absorptive interactions are much weaker compared to adsorption on active surfaces. Therefore, analyte desorption can be performed under softer conditions, such as

* Corresponding author. Tel.: +34 881814265; fax: +34 981547141.
E-mail address: carmela.casais@usc.es (M.C. Casais).

http://dx.doi.org/10.1016/j.talanta.2014.09.044
0039-9140/© 2014 Elsevier B.V. All rights reserved.

lower temperature and shorter desorption times and the degradation of unstable analytes is significantly impaired as compared to adsorptive processes [9,11].

Among the PDMS extraction techniques, solid-phase microextraction (SPME) has been widely used to extract PAHs from water samples [12–14]. Stir bar sorptive extraction (SBSE) which is more recent, has also been used for that kind of extraction [15–17]. In addition to PDMS coated fibers and stir bars (Twisters), PDMS is also available in bulk formats (sheets, tubes and rods). Silicone materials in form of rods (SRs) and tubes (STs) for the enrichment of organic compounds have been employed by Popp et al. [18,19]. In terms of analyte extraction the SRs and STs are similar to SPME and SBSE. Additional advantages of using bulk PDMS or equivalent materials as sorbent are the possibility of customizing the volume of polymer for each particular application, the availability of different formats and the very low cost of the sorbent in comparison with SPME fibers and Twisters. The latter feature makes it possible to use a new piece of sorbent for each extraction, which avoids problems associated with carry-over and cross contamination, allowing simultaneously processing as many samples as desired, and providing the possibility of considering the disposable sorbent material for analyte storage purposes [9].

The aim of this work was to develop and optimize a new one shot procedure based on sorptive extraction coupled with UPLC-FD-UV for determination of the 16 EPA priority PAHs and the "15+1" EU priority PAHs in water samples. The 24 PAHs are naphthalene (Naph), acenaphthylene (Acy), acenaphthene (Ace), fluorene (Flu), phenanthrene (Phe), anthracene (Anth), fluoranthene (Flt), pyrene (Pyr), B[c]F, CP[c,d]P, B[a]A, Chry, 5-MC, B[j]F, B[b]F, B[k]F, B[a]P, DB[a,l]P, DB[a,h]A, B[g,h,i]P, I[1,2,3-c,d]P, DB[a,e]P, DB[a,i]P and DB[a,h]P.

Disposable silicone in disks format, sampling simultaneously in direct immersion and headspace (DIHS) modes, was chosen as extractant phase and the influence of different experimental parameters (e.g. sampling mode, stirring rates, extraction time, etc.) on the analyte recoveries was investigated optimizing the operating conditions. Chromatographic conditions have been also optimized in order to obtain the satisfactory separation of 24 studied PAHs. Finally, the applicability of the developed procedure was tested for the determination of PAHs in some real tap, river and wastewater samples.

2. Materials and methods

2.1. Reagents, standards and materials

The disposable silicone sorbent was purchased from Goodfellow (Bad Nauheim, Germany) in sheets with a thickness of 0.6 mm. Silicone provided by Goodfellow is not pure PDMS but a phenyl-vinyl-methyl-polysiloxane (so-called PVMQ silicone Rubber). Disks (5 mm diameter × 0.6 mm thickness, 12 μL volume) were obtained by cutting the silicone sheet with a sharp hollow punch (internal diameter 5 mm). The obtained pieces were weighed and those differing by more than 2% in weight were discarded. Before being used for analytes extraction, disks were sonicated three times (5 min each) with methanol–acetone (1:1, v/v) mixture and then were conditioned overnight at 200 °C. Finally the pieces of silicone were sonicated three times (5 min each) with acetonitrile (ACN) and stored dry in sealed bags before use.

ACN and methanol (gradient-grade, Lichrosolv), and 2-propanol (analysis grade), were supplied by MercK (Darmstadt, Germany). Ultrapure water was produced by means of a Milli-Q Gradient A-10 system (Millipore, Billerica, MA, USA). Potassium carbonate and potassium hydrogenum carbonate were purchased from Sigma-Aldrich (Madrid, Spain). Sodium chloride (NaCl) was supplied by Prolabo (Fontenay-Sous-Bois, France). EPA-610 Polycyclic aromatic hydrocarbons mixture was supplied by Supelco (Bellefonte, PA, USA). 5-MC (10 μg mL^{-1}), DB[a,l]P (10 μg mL^{-1}), CP[c,d]P (10 μg mL^{-1}), B[c]F (10 μg mL^{-1}), DB[a,e]P (10 μg mL^{-1}), DB[a,i]P (10 μg mL^{-1}) and DB[a,h]P (10 μg mL^{-1}) were from Dr. Ehrenstorfer GmbH (Augsburg, Germany). Durapore filters (Millex GV, 13 mm, 0.22 μm) were supplied by Millipore.

2.2. Samples and sample preparation

Spiked and non-spiked ultrapure, tap, and river waters samples, and both raw (influent) and treated (effluent) wastewater samples were used in this study. All samples were used directly without preliminary filtration. Ultrapure and tap waters were obtained directly in the laboratory when needed. River water samples were collected in different points in Galicia (northwest Spain). Sewage water samples were obtained from the inlet and outlet of an urban wastewater treatment plant in operation near Santiago de Compostela (~100,000 inhabitants), equipped with a primary and aerobic secondary treatment, and which receives mostly municipal non-industrial wastewaters. Spiked samples were prepared by adding a standard solution of analytes at levels between 0.12 ng mL^{-1} and 2.5 ng mL^{-1}, depending on the considered compound.

Extractions were carried out in 22 mL capacity glass vials furnished with PTFE-lined septa (covered with aluminum foil) and aluminum caps. Vials and caps were supplied by Sugelabor (Madrid, Spain).

Under optimized conditions, 16 mL of water was transferred to extraction vials containing 4 g (25%w/v) of sodium chloride, 1 mL of 2-propanol (i-prOH) and a PTFE covered stirrer (6 mm × 3 mm). Analytes were extracted by night (c.a. 15 h approximately) at room temperature, with 5 silicone disks immersed directly in the stirred sample (900 r.p.m) and a sixth silicone disk in the headspace of the sample, fixed to the septum of the vial with a stainless steel pin (i.d. 0.4 mm). After extraction, the silicone disks were removed with clean tweezers, rinsed with ultrapure water and transferred into a small vial containing 0.25 mL of ACN and desorbed during 5 min in an ultrasonic (US) bath. Then, 0.1 mL of the obtained ACN extract was taken and diluted with 0.1 mL of water to match the initial mobile phase composition in the UPLC separation program. This diluted solution was filtered through a 0.22 μm Durapore filter and 5 μL was injected into the UPLC system.

2.3. Chromatographic method (UPLC-FD-UV)

UPLC chromatographic separations were developed in a system comprising a quaternary pump (Acquity H Class, Waters), an UV–vis diode array and a fluorescence detector (FD) in series (Waters, Singapore). The autosampler has a temperature controller for the samples and is fitted with a flow through needle system. Analytical column temperature was controlled with an integrated oven module. The analytical column was a 50 mm × 2.1 mm I.D. Zorbax Eclipse PAH Rapid Resolution HT C_{18} column, (particle size 1.8 μm). A filter guard cartridge (2.1 mm × 0.2 μm) was used to protect the analytical column (Waters, USA). Empower 2.1 Software was used for data acquisition.

A binary solvent system made of ACN and water was used for chromatographic separations. The gradient elution program was as follows: initial conditions, 47% ACN for 0.5 min, then a linear ramp to 80% ACN in 4.9 min and finally another linear ramp to 100% ACN in 1.9 min, holding in 100% ACN for 3.7 min.

The flow rate was also programmed. Initially it was set at 0.6 mL min^{-1} during 7.3 min, and then increased to 0.9 mL min^{-1} for 0.2 min, holding at 0.9 mL min^{-1} for 3.5 min. The column

Table 1
Experimental domain and significance of the main effects associated to each factor and second order interactions in the 2^3 factorial design.

Factors	i-PrOH (% v/v)	NaCl (% w/v)	Silicone disks number			
Low level	0	0	2			
Central Level	5.3 (0.85 mL)	11 (1.75 g)	3			
High level	10.6 (1.75 mL)	22 (3.50 g)	4			
Relative effects	A	B	C	AB	AC	BC
Naph	***(+)	***(+)	***(+)	**(−)	**(+)	**(−)
Acy	(+)	(+)	(−)			
Ace	***(+)	***(+)	(+)			**(−)
Flu	***(+)	**(+)	***(+)		**(−)	***(−)
Phe	***(+)	***(+)	(+)			
Anth	***(+)	***(+)	(+)			
Fluor	(+)	(+)	(+)			
Pyr	(+)	(+)	(+)			
B[c]F	(+)	(+)	(+)			
CP[c,d]P	(+)	(+)	(+)			
B[a]A	(+)	(−)	***(+)			
Chry	(+)	(−)	***(+)			
5-MC	(+)	(−)	***(+)			
B[j]F	(+)	(−)	(+)		(+)	
B[b]F	(+)	(−)	***(+)			
B[k]F	(+)	(−)	***(+)			
B[a]P	**(+)	(−)	***(+)			
DB[a,l]P	(+)	(−)	***(+)			
DB[a,h]A	***(+)	(−)	***(+)			
B[g,h,i]P	***(+)	(−)	***(+)			
I[1,2,3-cd]P	**(+)	(−)	***(+)			
DB[a,e]P	***(+)	**(−)	***(+)		***(+)	
DB[a,i]P	*(+)	(−)	***(+)			
DB[a,h]P	**(+)	(−)	***(+)			

*Indicates a statistically significant effect at 95% level (greater the number of asterisks the more important is the effect). A negative or positive sign points out that, factor affects negatively or positively the extraction efficiency for analytes.

Table 2
Experimental domain and significance of the main effects associated to each factor and second order interactions in the CCD design. Sample volume: 16 mL

Factors	i-prOH (% v/v)	NaCl (% w/v)	Silicone disks number						
Low level	6.2 (1 mL)	8.1 (2 g)	3						
Central level	12.5 (2 mL)	18.7 (3 g)	5						
High level	18.8 (3 mL)	25 (4 g)	6						
Relative effects	A	B	C	AB	AC	BB	AA	CC	BC
Naph	*(−)	(−)	(+)			**(−)			
Acy	***(−)	(+)	(+)			*(−)			
Ace	*(−)	(−)	(+)						
Flu	*(−)	(−)	(+)						
Phe	***(−)	(−)	*(+)						
Anth	***(−)	(−)	(+)						
Fluor	*(−)	(−)	(+)						
Pyr	*(−)	(−)	(+)						
B[c]F	(−)	(−)	(+)						
CP[c,d]P	(−)	(−)	(+)	*(−)					
B[a]A	(−)	(−)	(+)						
Chry	(−)	(−)	(+)						
5-MC	(−)	*(−)	*(+)						
B[j]F	(−)	*(−)	**(+)			*(−)			
B[b]F	(−)	(−)	*(+)			*(−)			
B[k]F	(−)	*(−)	**(+)						
B[a]P	(−)	(−)	**(+)						
DB[a,l]P	(+)	(−)	***(+)			*(−)			
DB[a,h]A	(+)	**(−)	***(+)		*(−)				
B[g,h,i]P	(−)	(−)	**(+)			*(−)			
I[1,2,3-cd]P	(+)	**(−)	***(+)						
DB[a,e]P	(+)	**(−)	***(−)	*(−)	*(−)	**(−)	**(−)	*(−)	
DB[a,i]P	(+)	(−)	**(+)						
DB[a,h]P	(+)	(−)	**(+)						

*Indicates a statistically significant effect at 95% level (the greater the number of asterisks the more important is the effect). A negative or positive sign indicates that factor affects negatively or positively the extraction efficiency for analytes.

temperature was set at 30 °C. Detection was performed using a fluorescence wavelength programming developed to obtain the better sensitivity and minimal interference by adapting detection conditions from a previously reported procedure [20]. The excitation/emission wavelengths pairs (nm) were set as follows: 267/330 for Naph; 275/315 for Ace and Flu; 247/357 for Phe; 238/418 for Anth, Flt, Pyr and B[c]F; 270/393 for B[a]A, Chry and 5-MC; 294/425 for B[b]F, B[k]F, B[a]P, DB[al]P, DB[ah]A and B[ghi]P; 245/500 for I[1,2,3-cd]P; 306/398 for DB[a,e]P; 290/434 for DB[a,i]P and 300/452 for DB[a,h]A. Acy, CP[c,d]P and B[j]F were analyzed by UV detection (254 nm) because these compounds do not exhibit fluorescence. Retention times and the characteristic UV absorbance spectrums of each PAH were used to confirm the identity of the chromatographic signals. The separation of the 24 PAHs was carried out in 9 min.

2.4. Experimental design analysis and software

Experimental designs were applied to carry out the optimization process of extraction using the extraction yield for the 24 PAHs as the objective function. Firstly, a full factorial design, 2^3, with 3 central points (11 runs) was developed to evaluate the significance of three operational factors. Levels for factors were (see Table 1): i-PrOH addition (0–10.6% v/v (0–1.75 mL)), NaCl concentration (0–22% w/v (0–3.5 g)), and silicone disks number (2–4, maintaining one of them always in the HS mode). Table S1 presents the experimental design matrix.

Later a central composite design (CCD) was developed moving the variable levels in the direction suggested by the former and were as follows (see also Table 2): i-PrOH addition (6.2–18.8% v/v (1–3 mL)), NaCl concentration (12.5–25% w/v(2–4 g)), and silicone disk number (3–6, one of them always at HS). The CCD was performed in 18 experiments, including 4 replicated central points. Table S2 presents the experimental plan for runs.

Finally a multi-objective optimization study using desirability functions [21] was carried out. By the evaluation of the responses with the help of desirability functions, the procedure finds for the best conditions to get better results in the extraction efficiency for the whole ensemble of PAHs. This function penalizes the decrease of this efficiency for each peak and finally, individual desirability functions are combined (geometric mean) in a global desirability function.

Experimental design analysis was performed with the software Statgraphics Centurion XVI.II for Windows (Statpoint technologies, Warrenton, VA, USA).

3. Results and discussion

3.1. Optimization of the chromatographic method (UPLC-FD-UV)

Reversed phase chromatography with C_{18} as stationary phase was employed to achieve the separation of 24 studied PAHs. ACN and water were selected as mobile phases. Chromatographic conditions, such as mobile phase gradient program, temperature column and flow rate, were evaluated in order to obtain the best resolution in the shortest analysis time.

Different proportions of ACN and water were tested. The mobile phase gradient was optimized until a satisfactory resolution of the 24 PAHs was achieved. Then, the influence of temperature on the PAHs resolution was investigated by setting the oven at 25, 30, 35, 40 and 45 °C. The best separation of the considered compounds was obtained at 30 °C. Good chromatographic profile with minimum runtime was obtained at 0.6 mL min^{-1}.

The optimized chromatographic conditions led to a suitable separation of 24 studied PAHs (Fig. 1), maintaining a good resolution and peak shape quality in a reasonable analysis time (9 min).

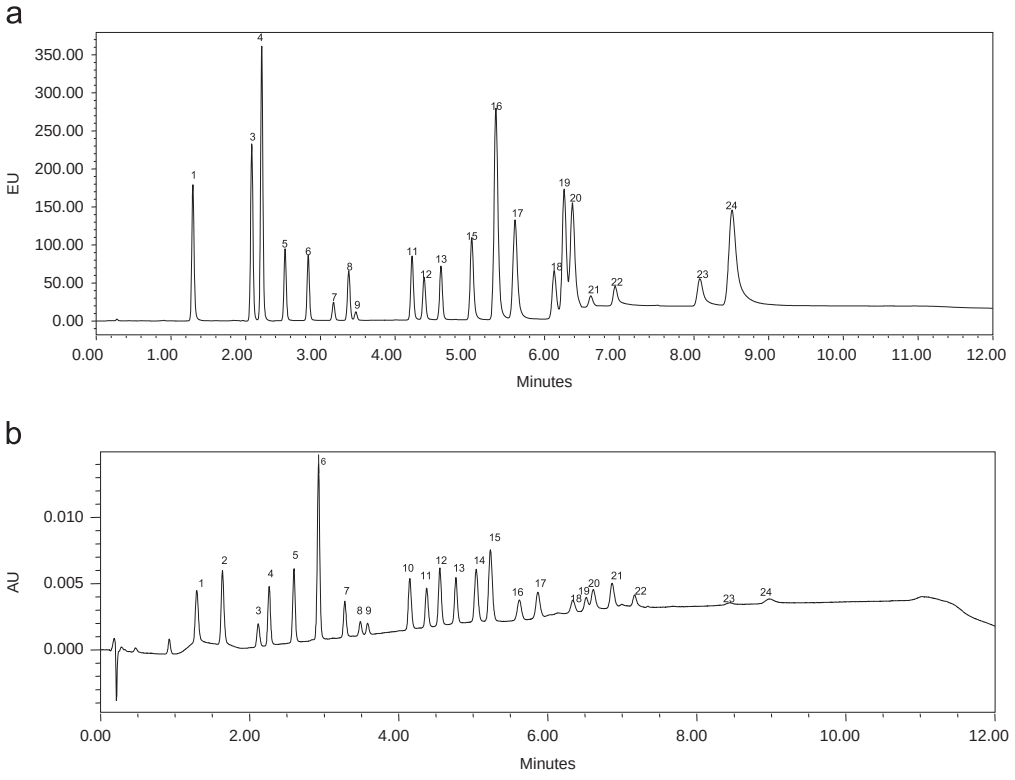


Fig. 1. Chromatograms obtained by UPLC: (a) Fluorescence and (b) UV–vis. Peak assignment:1) Naph; 2) Acy; 3) Ace; 4) Flu; 5) Phe; 6) Anth; 7) Flt; 8) Pyr; 9) B[c]F; 10) CP[c,d]P; 11) B[a]A; 12) Chry; 13) 5-MC; 14) B[j]F; 15) B[b]F;16) B[k]F);17) B[a]P); 18) DB[a,l]P, 19) DB[a,h]A; 20) B[g,h,i]P; 21) I[1,2,3–c,d]P; 22) DB[a,e]P; 23) DB[a,i]P; 24) DB[a,h]P.

3.2. Operating parameters

The extraction efficiency is usually affected by the stirring speed in sorptive extraction methods, since stirring favors migration of the analytes from the sample to the silicone phase. As expected, higher responses were measured for stirred samples versus non-stirred ones; however, significant differences were not observed when the extractions were carried out at three different stirring rates: 700, 900 and 1100 r.p.m. An intermediate value of 900 r.p.m. was selected as the best option.

3.2.1. Desorption conditions

In order to investigate the PAHs desorption, silicone disks were firstly desorbed with 250 μL of ACN for 5 min using an ultrasonic bath. ACN was chosen as desorption solvent on the basis of their compatibility with further LC reversed-phase separation. To verify the volume of ACN as well as the desorption time, the procedure was repeated twice using fresh solvent, but the recovery values in the second desorption stage represented in all experiments less than 5% of the analyte present (data not shown). Taking into account that silicone disks were considered as single-use sorbents, there was no risk of cross contamination problems, and therefore a single desorption step of 5 min was chosen.

Then, to evaluate the US influence, silicone disks were left to stand for 5 min with 250 μL of ACN helping or not the desorption process with the aid of US. Improved results (in the range 5–11% depending on the particular analyte) were obtained for US-assisted processes so a single US-assisted desorption step of 5 min using 250 μL of ACN was employed in all subsequent experiments.

3.2.2. Sampling mode arrangement and temperature

Kinetics of sorptive extraction processes change depending on the relative position of the sorbent and the bulk of sample (headspace (HS) and/or direct immersion (DI) in the sample). The choice of extraction mode will be dependent on the analyte volatility and/or sample complexity. Both modes (HS or DI) have been proposed for the extraction of PAHs from aqueous and solid samples with SPME fibers [22] or by cold-fiber solid phase microextraction(CF-SPME) [23]. The sample temperature is also an important factor, since temperature will influence the volatilization of the analytes and their subsequent pass to the HS. However, it is well known that the sorption of the analytes by the coating is an exothermic process and thus this variable has a double effect on the extraction yield. Previously reported approaches using CF-SPME [24] and conventional SPME [25] for the extraction of PAHs and other more volatile analytes in soil and water samples adopt a two stages procedure based on the successive (DI mode followed by HS extraction) sampling employing different temperatures in each stage which complicates the operational setup significantly. On the other hand, for SBSE, some studies have reported that extraction periods of 11–14 h (usually at room temperature) can be considered optimal for most of analytes to reach steady state [26,27]. That, it was decided to develop a one-shot procedure aiming at the quantitative extraction of all analytes of interest in a single sampling operation, preferably at room temperature that can be performed easily without special equipment requirements.

To do that, a series of assays were carried out in order to evaluate the sampling mode arrangement. In these experiments, aliquots of a water sample spiked with target compounds were transferred to extraction vials containing a fixed amount of salt. Comparative extractions were performed using only one silicone disk (in DI or HS sampling mode) or two silicone disks (configured to perform simultaneously DI and headspace (HS) sampling modes). As expected, the presence of one disk in the HS led, in general, to better response for the low molecular weight (lighter) PAHs, such as Naph, Acy, Ace, Flu, Phe or Ant (Fig. 2) but no improvement was observed for the heavier PAHs. The opposite behavior is observed for the direct immersion mode, which provided higher extraction efficiency for the high molecular weight PAHs. This behavior is in agreement with reported results for CF-SPME [24]. As can be clearly observed in Fig. 2, the combination of direct and HS sampling modes simultaneously did led to a satisfactory extraction for all the PAHs, opening a new approach for the one shot extraction of a large variety of PAHs, including all those currently considered in safety international regulations.

The influence of sampling temperature and the addition of i-PrOH to the samples before the extraction has been summarized in Fig. 3. As can be expected, at room temperature the efficiencies of the extraction for lighter PAHs are better than those at 100 °C and the opposite behavior was observed for the heavier PAHs. Moreover, the extraction efficiency of heavier PAHs at room temperature was improved by the addition of small percentages of i-PrOH to the water samples, so in the first instance 10% (v/v) of i-PrOH content was selected because of its positive effect on recovery. It should be noted that usually water samples for the analysis of PAHs contain appreciable proportions of i-PrOH, or another organic solvent, to compensate the natural tendency of PAHs to adhere to the glass walls [28]. Thus this unintended effect of i-PrOH in the extraction recoveries was considered a fortunate but positive result. Additionally, when extractions were performed at 100 °C some interferences appeared in the chrysene peak (probably due to degradation products of other PAHs at high temperature), in addition Ghiasvand et al. [23] reported a very high pressure in the extraction vial due to water evaporation at high temperatures (150 °C), which clearly represents a high source of inaccuracy in results due to leaking, so room temperature was selected for subsequent experiments.

The conclusion of these preliminary experiments was that combining both direct immersion and head space sampling (DIHS)

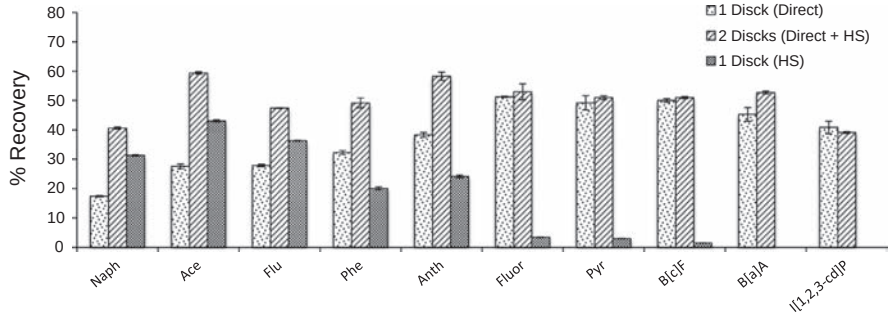


Fig. 2. Influence of the sampling mode on the efficiency of the sorptive microextraction process for some representative PAHs, $n=3$ replicates. Experiments at room temperature for 15 h. Sample volume: 9 mL with 10% (w/v) of NaCl and 10% (v/v) of i-PrOH.

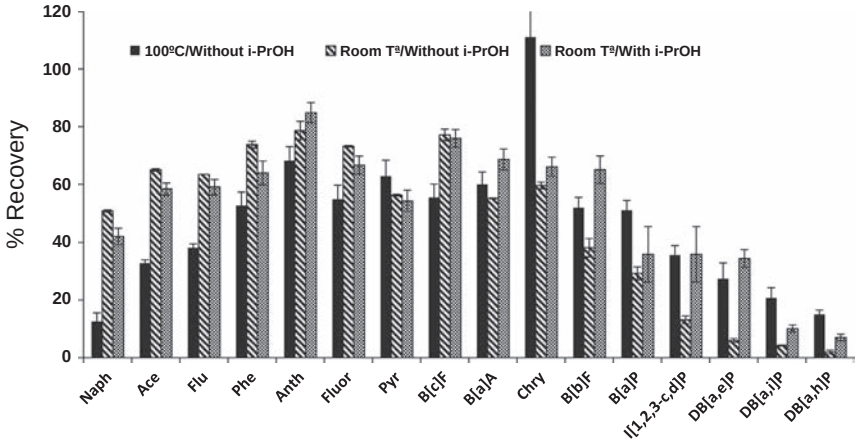


Fig. 3. Influence of temperature and i-PrOH on the efficiency of the DIHS microextraction process, $n=3$ replicates. Number of silicone disks: 2 (HS and DI). Sample: 9 mL of ultrapure water with 10% (w/v) of NaCl and 10% (v/v) of i-PrOH (only for experiments with i-prOH). Extraction time: 15 h at room temperature and 2 h at 100 °C.

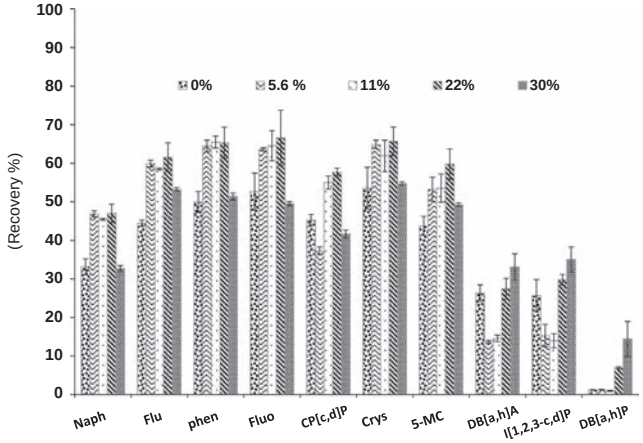


Fig. 4. Effect of ionic strength in the efficiency of the DIHS microextraction process, $n=3$ replicates.

modes simultaneously at room temperature could be a novel and advantageous approach in the development of an efficient sampling mode for PAHs in water samples.

Some additional preliminary tests were carried out in order to define the sampling format for combined DIHS extraction. In some of these tests, silicone disks were kept in fixed positions (separated approximately by 50 mm) relative to the sample by means of a stainless steel pin (i.d. 0.4 mm) fixed to the septum, in such a way that one of the disks kept immersed in the sample and the other remain in the headspace when the vial is closed. The other format consisted in placing one silicone disk in the headspace attached to the stainless steel pin while the other was loose into the sample. Comparison of results (data not shown) revealed better results for the heavier PAHs with the last option so this sampling mode was adopted in further experiments

3.2.3. Ionic strength

Adding a small amount of salt often improves extraction efficiency in most conventional extraction and microextraction procedures for PAHs [14,29]. The presence of salts in the samples increases the distribution coefficient of the non-ionized analytes thus improving recoveries. This effect could be explained by the decrease of the PAHs solubility in the aqueous sample, especially for high molecular weight PAHs.

To evaluate the influence of the ionic strength on the efficiency of the sorptive extraction, samples in triplicate with NaCl (0–30% (w/v)) were analyzed. Series of experiments were performed with 9 mL aliquots of spiked ultrapure water, and 2 silicone disks (DIHS mode). A relationship between ionic strength and extraction efficiency was observed and it is shown for representative analytes in Fig. 4. The addition of salt affects positively the recovery of the low molecular weight (lighter) PAHs. For the heavier PAHs higher responses were attained for samples containing 22% (w/v) of NaCl. This behavior could be probably related to a significant diminution of the solubility of the compounds in the aqueous phase. However, at high concentrations of NaCl (about 30% v/v) the efficiencies of the extraction for the PAHs were decreased except for the heavier PAHs such as DB[a,h]A, B[g,h,i]P or DB[a,h]P. As detailed later, the influence of the ionic strength was further examined during the optimization process.

3.2.4. Sample volume

Operating at the maximum levels imposed for PAHs by European directives constitutes a challenge for laboratories developing routine water analysis [30]. One obvious option to tackle this difficulty is to increase the sample volume. Different water volumes (9 and 16 mL) were compared and tested for triplicate. To do this, water samples containing about 22% (w/v) of sodium chloride and 10% (v/v) of i-PrOH were transferred to the extraction vial. The number of silicone disks was adapted proportionately to the sample volume. For 16 mL three silicone disks were exposed directly to the stirred sample and a fourth silicone disk was placed at the HS. With 9 mL of sample, one silicone disk was on HS and the second one loose in the solution. The results of these experiments (data not shown) showed that there are no significant differences between extraction efficiencies for 9 or 16 mL of sample, so a sample volume of 16 mL was adopted to achieve a reduction of the detection limits.

3.3. Optimization of the variables affecting the extraction

Once the amount of sample was fixed (16 mL), and on the basis of the preliminary studies, other operational parameters (NaCl concentration, i-PrOH addition, and sorbent area and volume) should be studied and optimized. A chemometrical approach based on experimental designs was applied to carry out this optimization process. Firstly, a full factorial design, 2^3, with 3 central points was developed to evaluate the significance of the three operational factors. The experimental domain of that design and the standardized main effects and multiplicative terms

for each compounds are summarized in Table 1; Table S1 shows the experimental design matrix.

Fig. S1 (Supplementary material) shows some effect's standardized Pareto charts for the above-mentioned parameters in representative analytes among the considered group. The length of depicted bars is proportional to the absolute effect of the considered factor (or two factor interactions) in the recovery of the particular analyte to which the chart belongs. A positive sign points out to an improvement in the efficiency of the extraction when the factor changes from the low to the high level, within the domain of the design and, a negative one indicates the opposite behavior. The vertical dotted line in the graphs represents the statistical significance bound, established at 95% confidence level. Considering Naph and Phen as representative compounds for the lighter PAHs, we can observe that factors A (i-prOH) and B (salt) had a statistically positive effect in the extraction efficiency. Factor C (disks number) appears significant for a few analytes. This can be explained because the addition of salt to the samples and the incorporation of some i-prOH favor the displacement of lighter PAHs to the head space. The variable influence of the number of disks in these results can be interpreted because all experiments were developed situating only one silicone disk in the HS, no matter the total number of disks considered. Also some interaction factors appear significant for lighter PAHs.

On the other hand, for heavier compounds such as B[ghi]P and DB[ah]A factors A and C exhibit a statistically significant positive effect while no statistical significance for factor B was observed. Also in that case, the observed results can be justified quite easily. Heavier PAHs are sampled essentially in the bulk liquid sample so the number of disks (the sorbent volume and exposed area) influences the extraction capacity and kinetics of the process. Also, the presence of larger amounts of i-PrOH favors the extraction by limiting the tendency of heavier PAHs to adhere to glass vial walls. Salt addition, on the contrary is less significant for heavier highly hydrophobic PAHs.

Table 1 shows clearly that the number of silicone disks, or in other words, the sorbent surface and volume, appears as the most important factor for the majority of considered analytes. Also, the i-prOH amount added to samples is significant for many analytes, especially for the heavier and the lighter ones. Finally, salt addition appears only critical for the lighter PAHs.

The above factorial design can only be used to fit a first order linear model to the experimental results. However, data at replicated central points indicated the existence of curvature for the response surface and response gradient pointing outside the experimental region actually explored. Consequently, a central composite design (CCD) was developed moving the variable levels in the direction suggested by the gradient. The experimental domain and the summary of conclusions obtained for the CCD design have been summarized in Table 2 and, main effects for some representative PAHs are shown in Fig. S2.

The amount of salt added to samples appears significant only for a few analytes (among the heavier PAHs) but practically in all cases the effect is negative so, taking into account results in Table 1, this means that some salt is needed to favor the extraction of the lighter PAHs although its level should be maintained at intermediate values to avoid the negative effect in the extraction of the remaining analytes of interest. The lower extraction efficiency for hydrophobic compounds when ionic strength increases have been explained by their adsorption tendency onto glass walls [27] and due to the increase in the viscosity of the sample, leading to slower extraction kinetics for lipophilic species [31], as well as the decrease of PAHs solubility in the aqueous sample, especially for the heavier PAHs [14,30]. Since they are repulsed to the water/headspace interface (the so-called oil effect), they cannot interact with the PDMS disk, fully immersed into the sample matrix, and therefore, lower extraction efficiencies were achieved.

Regarding the i-PrOH addition, its influence inhibiting the adsorption of analytes in glass walls appears mostly significant for the lighter PAHs but an excess of i-PrOH (see Fig. S2, for fluorene which can be considered a representative example of lighter PAHs) negatively affects the extraction. On the other hand, for heavier PAHs, the effect is not significant in the range 1–3 mL. Thus, water samples must contain a minimum level of 6% (1 mL if the alcohol is added to the sample portion analyzed) of i-PrOH.

Finally, for the number of disks factor (see Table 2 and Fig. S2) the influence is positive and significant for the heaviest PAHs.

Departing from the data obtained with CCD design, a multi-objective optimization study using desirability functions [21] was carried out. The 24 analytes were split into two groups (the primary motivation was that the statistical software used can only manage 16 response functions simultaneously): the more volatile PAHs (Naph, Acy, Ace, Flu, Phe, Anth, Flt, Pyr, B[c]F, CP[c,d]P, B[a]A, Chry, 5-MC, B[j]F, B[b]F on one side, and the less volatile (CP[c,d]P, B[a]A, Chry, 5-MC), B[j]F, B[b]F, B[k]F, B[a]P, DB[a,l]P, DB[a,h]A, B[g,h,i]P, I[1,2,3-c,d]P, DB[a,e]P, DB[a,i]P, DB[a,h]P on the other. This procedure finds a compromise overall optimum aiming at the quantitative extraction of each individual considered analyte and finally combining those individual desirability functions in a global desirability (D) which is the geometric mean of the individual ones. Fig. 5 shows the global desirability for each group of analytes, showing that quite similar operating conditions can be applied to both groups so it is possible finding a good compromise operating procedure for the extraction of the 24 PAHs in samples. For the first group (more volatile PAHs) the maximum appears when the extraction is developed using a volume of 0.32 mL (c.a. 2% v/v) of i-PrOH and 3.5 g (c.a. 22% w/v) of salt and 6 silicone

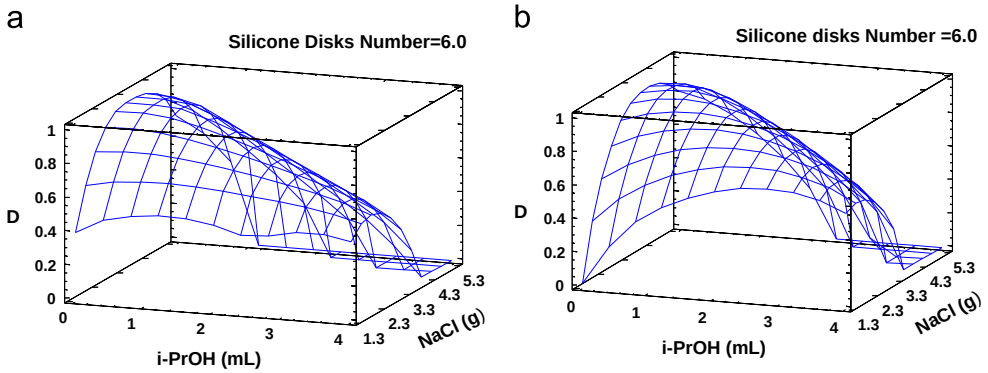


Fig. 5. Estimated global desirability response surface for PAHs: a) with low molecular weight and b) with high molecular weight.

disks. For the less volatile PAHs, the maximum involved extraction also with 6 silicone disks and 3.7 g (23%) of salt, but using 0.76 mL of isopropanol (5% v/v). Thus, a fine tune optimization of the added amounts of i-PrOH and salt amounts was carried out concluding that optimum extraction of 24 analytes can be performed employing 1 mL of i-PrOH, 4 g of NaCl and 6 silicone disks (one in the HS and five immersed in the water sample).

3.4. Extractions kinetics

The time-course for the sorptive extraction at room temperature was investigated with spiked aliquots (16 mL) of ultrapure water considering variable sampling times ranging from 1 to 24 h. As frequently occurs with sorptive techniques, the extraction process showed slow kinetics [32]. As illustrated in Fig. 6 for a number of representative PAHs of lower and higher volatility, maximum responses were obtained after 9 h for the majority of analytes except for the heaviest compounds (DB[ah]A, B[ghi]P, I[123-cd]P, DB[a,e]P, DB[a,i]P, DB[a,h]P), which needed 15 h to reach the extraction equilibrium. Taking this last value (15 h) allows for the unattended overnight extraction of several samples in parallel using a multiposition magnetic stirrer. Moreover, this sampling time is usual in SBSE protocols [27], although cost of extraction elements is not comparable.

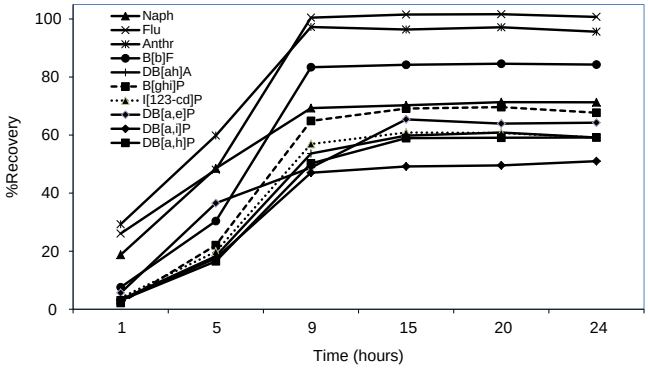


Fig. 6. Kinetics of the DIHS extraction procedure for selected compounds. Average responses for duplicate extractions.

3.5. Performance of the analytical procedure

The quality parameters of the developed chromatographic method were studied in terms of linearity, linear range, repeatability, reproducibility, detection limits (LODs) and quantification limits (LOQs). A signal-to-noise ratio of 3 and 10 was used to determine LODs and LOQs, respectively. Table 3 summarizes the performance of UPLC-FD-UV system for target species using the optimized conditions. As can be seen the proposed method exhibits excellent linearity ($R \geq 0.9991$) in the studied calibration ranges. RSD for injections of standards at different concentration levels was maintained below 6% for injections on successive days. Instrumental LOQs varied between 0.004 and 0.082 $\mu g\ L^{-1}$ in the case of PAHs determined by UPLC-FD, ranging from 17 to 57 $\mu g\ L^{-1}$ for compounds analyzed by UV, with recoveries between 46% and 103%. Recoveries in different types of water samples as well as LODs and LOQs for individual analytes have been summarized in Table 4.

Possible matrix effects of the extraction procedure were evaluated by extracting different kinds of real water samples. All the samples were spiked with the target compounds (0.12–2.5 $\mu g\ L^{-1}$) and also a parallel sample of ultrapure water was performed in order to compare the results. For wastewater and River B and C samples the response for each compound was corrected with that corresponding to non-spiked aliquots of the same sample. Spiked and non-spiked fractions were processed in triplicate and the extraction efficiency was compared with that achieved for ultrapure water (Table 4). Obtained results indicated that the efficiency of the

Table 3
Linearity, precision and instrumental LODs and LOQs of the developed UPLC-FD-UV method.

Compound	Linearity		Precision (RSD%)[a]		LOD S/N=3 $\mu g\ L^{-1}$	LOQ S/N=10 $\mu g\ L^{-1}$
	Calibration ($\mu g\ L^{-1}$)	R	Low level[b]	High level[c]		
Naph	0.5–100	0.9992	3.5	1.3	0.014	0.048
Acy	60–800	0.9995	2.9	2.2	17.0	56.7
Ace	0.5–100	0.9999	3.8	1.0	0.009	0.031
Flu	0.1–20	1	2.8	0.6	0.001	0.004
Phe	0.05–10	0.9999	1.2	0.9	0.003	0.010
Anth	0.05–10	0.9999	1.9	0.7	0.018	0.059
Fluor	0.1–20	0.9998	4.6	2.7	0.025	0.082
Pyr	0.05–20	0.9999	1.7	2.8	0.006	0.021
B[c]F	0.05–10	0.9998	1.6	3.6	0.020	0.068
CP[c,d]P	20–160	0.9991	4.5	2.0	5.1	16.86
B[a]A	0.05–10	1	2.3	0.5	0.003	0.011
Chry	0.05–10	0.9999	1.6	2.4	0.004	0.013
5-MC	0.05–10	0.9999	4.4	1.3	0.003	0.010
B[j]F	30–160	0.9992	1.8	2.1	6.8	22.6
B[b]F	0.2–20	0.9999	3.9	0.8	0.010	0.035
B[k]F	0.05–10	0.9999	2.3	1.3	0.002	0.005
B[a]P	0.05–10	0.9999	1.1	1.5	0.004	0.012
DB[a,l]P	0.05–10	0.9996	3.0	1.0	0.007	0.025
DB[a,h]A	0.1–20	0.9998	1.8	1.3	0.005	0.018
B[g,h,i]P	0.1–20	0.9994	3.3	1.3	0.006	0.018
I[1,2,3-cd]P	0.05–10	0.9998	5.2	2.5	0.013	0.045
DB[a,e]P	0.05–10	0.9998	5.1	2.6	0.021	0.070
DB[a,i]P	0.05–10	0.9994	2.7	2.6	0.009	0.031
DB[a,h]P	0.05–10	0.9992	2.6	1.8	0.008	0.026

[a] $n=5$ replicates.
[b] Concentrations from 0.05 to 80 $\mu g\ L^{-1}$.
[c] Concentrations from 0.5 to 800 $\mu g\ L^{-1}$.

Table 4
Recoveries from spiked tap and river water, and treated and raw wastewater samples extracted by the proposed HSDI extraction procedure and further analyzed by UPLC-FD-UV. LOD and LOQ values for the proposed method.

Compound	Water					Wastewater		LOD S/N=3 (ng L^{-1})	LOQ S/N=10(ng L^{-1})
	Ultrapure[a]	River A	River B	River C	Tap	Treated	Raw		
Naph	65.1 ± 6.2	71.1 ± 0.6	69.3 ± 0.6	69.4 ± 0.4	65.6 ± 1.5	76.2 ± 1.9	66.3 ± 1.9	0.70	2.30
Acy	77.3 ± 4.2	87.5 ± 1.3	71.4 ± 0.8	65.3 ± 0.7	82.5 ± 0.6	74.4 ± 0.8	72.4 ± 1.1	680	2300
Ace	84.2 ± 12.2	99.5 ± 2.3	93.8 ± 0.8	92.5 ± 1.0	94.5 ± 2.0	73.6 ± 2.8	67.8 ± 0,7	0.36	1.20
Flu	87.1 ± 9.2	98.5 ± 1.2	92.3 ± 0.7	93.2 ± 0.7	99.9 ± 3.2	84.0 ± 0.4	70.8 ± 13.9	0.05	0.16
Phe	103.1 ± 4.7	110.3 ± 3.1	103.7 ± 1.3	97.8 ± 0.5	96.7 ± 1.4	86.7 ± 2.2	84.3 ± 1.5	0.09	0.31
Anth	90.8 ± 6.0	98.2 ± 11.7	98.6 ± 1.5	100.8 ± 4.5	94.3 ± 0.9	93.7 ± 4.2	87.2 ± 2.2	0.62	2.10
Fluor	87.6 ± 5.1	96.1 ± 6.9	88.5 ± 0.2	87.0 ± 2.2	93.4 ± 4.2	84.5 ± 0.7	78.1 ± 2.4	0.90	3.00
Pyr	85.6 ± 6.2	100.5 ± 5.0	98.0 ± 2.8	100.4 ± 2.6	95.0 ± 2.0	73.0 ± 4.8	69.1 ± 3.8	0.23	0.70
B[c]F	76.2 ± 7.9	87.5 ± 0.1	82.0 ± 0.7	83.8 ± 2.8	83.6 ± 2.0	77.9 ± 0.8	70.5 ± 3.7	0.85	2.80
CP[c,d]P	79.2 ± 3.1	79.9 ± 1.8	83.3 ± 1.0	84.2 ± 1.2	80.1 ± 0.5	69.3 ± 0.8	71.6 ± 1.3	200	670
B[a]A	83.8 ± 9.6	90.9 ± 3.7	88.8 ± 1.8	90.0 ± 0.1	96.8 ± 0.7	75.8 ± 2.9	68.4 ± 2.6	0.12	0.42
Chry	84.7 ± 4.5	83.1 ± 7.7	81.2 ± 2.0	81.4 ± 2.2	88.8 ± 1.0	79.4 ± 0.8	69.4 ± 3.6	0.14	0.47
5-MC	71.2 ± 5.6	76.4 ± 2.1	71.7 ± 0.9	71.8 ± 0.8	82.0 ± 4.2	70.3 ± 1.4	58.4 ± 1.6	0.14	0.46
B[j]F	73.8 ± 7.1	78.9 ± 0.5	83.1 ± 0.4	83.4 ± 0.3	70.3 ± 0.3	83.6 ± 0.2	78.8 ± 0.3	300	990
B[b]F	78.1 ± 6.5	73.6 ± 3.9	74.6 ± 1.0	75.3 ± 0.4	85.3 ± 4.3	70.7 ± 1.7	55.0 ± 1.9	0.43	1.40
B[k]F	86.3 ± 6.3	93.0 ± 0.9	92.1 ± 0.4	91.7 ± 0.2	94.3 ± 1.9	72.3 ± 1.1	57.2 ± 0.8	0.06	0.20
B[a]P	88.8 ± 4.5	93.1 ± 1.5	84.7 ± 1.1	84.4 ± 0.5	95.6 ± 1.3	78.5 ± 1.5	62.4 ± 1.5	0.13	0.42
DB[a,l]P	67.7 ± 2.8	68.6 ± 0.8	74.9 ± 2.1	67.1 ± 0.4	74.3 ± 1.2	67.1 ± 1.8	41.7 ± 3.6	0.35	1.20
DB[a,h]A	64.0 ± 2.9	54.2 ± 2.1	57.3 ± 1.5	58.2 ± 0.9	59.8 ± 1.2	41.5 ± 2.8	38.3 ± 2.7	0.26	0.87
B[g,h,i]P	69.4 ± 2.9	74.5 ± 1.1	62.7 ± 1.5	65.8 ± 0.9	65.6 ± 1.3	55.9 ± 2.2	36.4 ± 2.1	0.25	0.83
I[1,2,3-cd]P	56.4 ± 7.2	55.6 ± 1.3	58.0 ± 0.5	58.1 ± 0.1	58.0 ± 6.0	43.8 ± 7.4	26.1 ± 0.7	0.76	2.50
DB[a,e]P	57.8 ± 4.0	61.7 ± 1.1	57.5 ± 1.2	54.0 ± 1.2	59.1 ± 4.1	48.6 ± 1.8	30.9 ± 1.2	1.20	3.90
DB[a,i]P	45.9 ± 3.8	44.9 ± 5.6	46.5 ± 1.1	46.5 ± 1.3	45.6 ± 1.3	26.2 ± 5.4	16.7 ± 4.3	0.65	2.20
DB[a,h]P	60.4 ± 4.2	66.5 ± 0.5	63.2 ± 8.7	58.0 ± 04	56.9 ± 2.2	19.0 ± 2.0	11.9 ± 2.3	0.40	1.30

Addition level 0.12–2.5 μg L^{-1}; $n=3$ replicates.
[a] $n=15$ replicates for ultrapure water.

Table 5
Comparative data of the developed sorptive extraction method with other similar procedures described in the literature for the determination of PAHs in water samples.

Parameters	Silicone rod-SE [18][a]	SBSE [27][b]	Kevlar filament-SE[33][c]	SPME[25][d]	Proposed method
Sample amount (mL)	10	100 (River) 25 (Wastewater diluted to 100)	20	25	16
Sorbent volume (μL)	8	47	8 cm length × 9.23 μm i.d. × 1000 filaments=5.43 μl	No data	72
Solvent addition effect (% solvent optimized)	Not studied	Yes (10% MeOH)	Not studied	Not studied	Yes (6% i-PrOH)
Salt addition effect (% salt optimized)	Not studied	Yes (20% NaCl)	Not studied	Yes (24% NaCl)	Yes (25% NaCl)
Desorption solvent	ACN:Water (4:1)	No (Thermal desorption)	ACN	None (Thermal desorption)	ACN
Solvent desorption consumption (mL)[e]	0.1 mL	No	0.1 mL	None	0.25 mL
Extraction time (h)[f]	3 h	14 h	0.5 h	1.3 h (48 min DI+32 min HS)	15 h (9 h for the majority of the compounds)
Determination technique	HPLC-FD	GC × GC-TOF-MS	HPLC-FD	GC–MS	UPLC-FD-UV
Extraction efficiency (%)	53–77	48–100	No data	60–110 (1 μg/L) 60–115 (5 μg/L)	46–103
Precision (%)	< 10	≤ 26 (Wastewater)	< 13	0.6–24.9 (1 μg/L) 1.6–12.6 (5 μg/L)	< 15
LOQs (ng L^{-1})	0.3–4	0.05–5 (River) 0.06–3.9 (Wastewater)	1.3–15	LODs (170–310 ng L^{-1})	0.2–3 (FD) 668–2226 (UV)
Number of analyzed PAHs	14	16	7	13	24

[a] Direct sorptive extraction with silicone rod.
[b] PDMS stir bar sorptive extraction.
[c] Direct sorptive extraction with Kevlar filament.
[d] SPME consecutive extractions with PDMS/DVB (65 μm).
[e] Solvent consumption only in the desorption stage; solvent consumption in clean-up, solvent exchanges and cartridges activation not included.
[f] Time employed in extraction stage; any other operations were not included. GC × GC-TOFMS, two-dimensional gas chromatography time-of-flight mass spectrometry.

extraction process was not much affected by the nature of water samples except for wastewater and the heavier PAHs. For ultrapure, tap and river waters, the efficiency of the extraction procedure remained the same. Therefore, simple external calibration can be used in the determination. On the contrary, for wastewater samples the standard addition method should be recommended.

Table 6
Concentrations of PAHs found in different water samples.

Compound	River B	River C	Treated wastewater	Raw wastewater
Flu	1.20 ± 4.1	1.20 ± 6.7	n.d	n.d
Phe	4.90 ± 0.3	111.0 ± 1.8	7.50 ± 7.5	11.00 ± 3.4
Anth	n.d	1.40 ± 11	n.d	n.d
Pyr	n.d	1.70 ± 1.1	n.d	n.d
Chry	1.80 ± 3.3	5.40 ± 5.5	n.d	n.d
5-MC	2.10 ± 9.3	2.00 ± 1.7	n.d	n.d
B[b]F	4.20 ± 2.3	4.50 ± 8.5	n.d	n.d

Average (ng L^{-1}) ± relative standard deviation (RSD %); $n=3$ replicates per sample; n.d., not detected.

Finally, Table 5 compares the analytical characteristics of similar previously published methodologies for the determination of PAHs in water samples. Comparison with the results of SBSE procedure shows that precision, recoveries and detection limits do no greatly differ. The obvious advantage of the described extraction method as compared with SBSE is that the silicone sorbent is very cheap. Kevlar sorptive extraction and SPME exhibit poorer quantification limits, while the silicone rod method provides lower recovery values for some PAHs. Additionally, the present procedure has the important advantage of enabling the determination of all 16 EPA and 15+1 EU priority PAHs.

3.6. Analysis of water samples

The applicability of the proposed extraction method was tested by the determination of PAHS in different water samples (tap, river, treated and raw wastewater). Table 6 summarizes the responses obtained for each sample. It is important to emphasize that the regions close to River B and River C were recently affected by a forest burning, so the appearance of some studied compounds was quite foreseeable. In fact, for those rivers we could determine the presence of some PAHs such as Flu, Phen, Chry or B[b]F among others. The studied PAHs were not detected in River A as well in tap water. Only phenantrene was quantified in wastewater.

4. Conclusions

An analytical procedure allowing the one-shot analysis of 24 priority PAHs as established both by the US EPA and the EU has been developed by resorting to a novel strategy based on the simultaneous combination of headspace and direct immersion sampling modes in the same water sample by means of the use of cheap, single-use silicone disks, which avoids cross-contamination and clean up processes. Desorbed analytes are separated and determined by UPLC coupled to UV/FD in only 9 min. The procedure appears very simple and many samples can be prepared simultaneously providing adequate sample throughput. The procedure appears free of interferences even for wastewater samples with recoveries in the range 46–103% and quantification limits allowing its application under international regulations. Combined use of HS and DI sampling modes appears clearly advantageous as compared to both individual modes in terms of analysis time, sample consumption, cost and manipulation.

Acknowledgments

This work has been supported by the Spanish Ministry of Economy and Competitiveness and by E.U. FEDER funds (project CTQ2012-33080). All authors explicitly declare not having any conflict of interest regarding this article.

Appendix A. Supplementary material

Supplementary data associated with this article can be found in the online version at http://dx.doi.org/10.1016/j.talanta.2014.09.044.

References

[1] S.K. Samanta, O.V. Singh, R.K. Jain, Trends Biotechnol. 20 (2002) 243–248.
[2] P.E.T. Douben, PAHs: An Ecotoxicological Perspective, John Wiley & Sons Ltd., England, 2003.
[3] P. Plaza-Bolaños, A. Garrido Frenich, J.L. Martínez Vidal, J. Chromatogr. A 1217 (2010) 6303–6326.
[4] European Union, Commission Recommendation 2005/108/EC, Off. J. Eur. Union L34 (2005) 43-45.
[5] United States Environmental Protection Agency (US EPA), Appendix A to 40 CFR Part 423, November (2010). Available from: ⟨http://www.epa.gov/waterscience/methods/pollutants.htm⟩.
[6] J. Ruana Urbe, J. Chromatogr. A 778 (1997) 337–345.
[7] B. Tang, U. Isacsson, Energy Fuel 22 (2008) 1425–1438.
[8] F. David, P. Sandra, J. Chromatogr. A 1152 (2007) 54–69.
[9] M. van Pinxteren (née Schellin), A. Paschke, P. Popp, J. Chromatogr. A 1217 (2010) 2589–2598.
[10] O. Krüguer, G. Christoph, U. Kalbe, W. Berger, Talanta 85 (2011) 1428–1434.
[11] E. Baltussen, C.A. Cramers, P.J.F. Sandra, Anal. Bioanal. Chem. 373 (2002) 3–22.
[12] R. Doong, S. Chang, Y. Sun, J. Chromatogr. A 879 (2000) 177–188.
[13] M.S. García-Falcón, M. Pérez-Lamela, J. Simal-Gándara, J. Agric. Food Chem. 52 (2004) 6897–6903.
[14] A.J. King, J.W. Readman, J.L. Zhou, Anal. Chim. Acta 523 (2004) 259–267.
[15] P. Popp, C. Bauer, L. Wennrich, Anal. Chim. Acta 436 (2001) 1–9.
[16] M. Bourdat-Deschamps, J.J. Daudin, E. Barriuso, J. Chromatogr. A 1167 (2007) 143–153.
[17] A. Prieto, O. Telleira, N. Etxebarria, L.A. Fernandez, A. Usobiaga, O. Zuloaga, J. Chromatogr. A 1214 (2008) 1–10.
[18] P. Popp, C. Bauer, A. Paschke, L. Montero, Anal. Chim. Acta 504 (2004) 307–312.
[19] L. Montero, P. Popp, A. Paschke, J. Pawliszyn, J. Chromatogr. A 1025 (2004) 17–26.
[20] M.T. Pena, M.C. Casais, M.C. Mejuto, R. Cela, J. Chromatogr. A 1216 (2009) 6356–6364.
[21] G. Derringer, R. Suich, J. Qual. Technol. 12 (1980) 214–219.
[22] R. Doong, S. Chang, Y. Sun, J. Chromatogr. Sci. 38 (2000) 528–534.
[23] A.R. Ghiasvand, S. Hosseindazadeh, J. Pawliszyn, J. Chromatogr. A 1124 (2006) 35–42.
[24] E. Martendal, E. Carasek, J. Chromatogr. A 1218 (2011) 1707–1714.
[25] J. Nunes Bianchin, G. Nardini, J. Merib, A. Neves Dias, E. Martendal, E. Carasek, J. Chromatogr. A 1233 (2012) 22–29.
[26] A. Prieto, O. Zuloaga, A. Usobiaga, N. Etxebarria, L.A. Fernández, J. Chromatogr. A 1174 (2007) 40–49.
[27] M.J. Gómez, S. Herrera, D. Solé, E. García-Calvo, A.R. Fernández-Alba, Anal. Chem. 83 (2011) 2638–2647.
[28] L.H. Keith, Environmental Sampling and Analysis: A Practical Guide, Lewis publishers, NY, 1991 (Chapters 2 and 4).
[29] V. Fernández-González, E. Concha-Graña, S. Muniategui-Lorenzo, P. López-Mahía, D. Prada-Rodríguez, J. Chromatogr. A 1176 (2007) 48–56.
[30] Directive 2008/105/EC of the European Parliament and the Council, of 16 December 2008, on environmental quality standards in the field of water policy, Off. J. Eur. Union 348 (2008) 84–97.
[31] A. Prieto, R. Rodil, J.B. Quintana, I. Rodríguez, R. Cela, Anal. Chim. Acta 716 (2012) 119–127.
[32] Y. Naude, M. Van Aardt, E.R. Rohwer., J. Chromatogr. A 1216 (2009) 2798–2804.
[33] T.M. Hii, C.H. Basheer, H.K. Lee, J. Chromatogr. A 1216 (2009) 7520–7526.

Talanta 132 (2015) 443–450

Contents lists available at ScienceDirect

Talanta

journal homepage: www.elsevier.com/locate/talanta

Analytical quality assurance in veterinary drug residue analysis methods: Matrix effects determination and monitoring for sulfonamides analysis

Rodrigo Barcellos Hoff [a,b,*], Gabriel Rübensam [b], Louise Jank [a,b], Fabiano Barreto [b,c], Maria do Carmo Ruaro Peralba [a], Tânia Mara Pizzolato [a], M. Silvia Díaz-Cruz [d], Damià Barceló [d,e]

[a] Instituto de Química, UFRGS, Porto Alegre, RS, Brazil
[b] Ministério da Agricultura, Pecuária e Abastecimento, Laboratório Nacional Agropecuário—LANAGRO/RS, Porto Alegre, RS, Brazil
[c] Faculdade de Farmácia, UFRGS, Porto Alegre, RS, Brazil
[d] Department of Environmental Chemistry, IDAEA, CSIC, Jordi Girona 18-26, 08034 Barcelona, Spain
[e] Catalan Institute for Water Research (ICRA), Parc Científic i Tecnològic de la Universitat de Girona, C/Emili Grahit, 101 Edifici H2O, E-17003 Girona, Spain

ARTICLE INFO

Article history:
Received 4 June 2014
Received in revised form
15 August 2014
Accepted 17 August 2014
Available online 27 August 2014

Keywords:
Quality control
Veterinary drug residues
Matrix effects
Validation
Ion suppression
Control charts
Antibiotics
Sulfonamides

ABSTRACT

In residue analysis of veterinary drugs in foodstuff, matrix effects are one of the most critical points. This work present a discuss considering approaches used to estimate, minimize and monitoring matrix effects in bioanalytical methods. Qualitative and quantitative methods for estimation of matrix effects such as post-column infusion, slopes ratios analysis, calibration curves (mathematical and statistical analysis) and control chart monitoring are discussed using real data. Matrix effects varying in a wide range depending of the analyte and the sample preparation method: pressurized liquid extraction for liver samples show matrix effects from 15.5 to 59.2% while a ultrasound-assisted extraction provide values from 21.7 to 64.3%. The matrix influence was also evaluated: for sulfamethazine analysis, losses of signal were varying from −37 to −96% for fish and eggs, respectively. Advantages and drawbacks are also discussed considering a workflow for matrix effects assessment proposed and applied to real data from sulfonamides residues analysis.

© 2014 Elsevier B.V. All rights reserved.

1. Introduction

Food containing veterinary drug residues above maximum residue limit (MRL) is of major concern, since it is related directly to public health as well as international trade relationships. The demand in food regulatory control has expanded dramatically in recent decades, and residues surveillance became an important factor to be considered in international trade of commodities [1,2].

In Brazil, veterinary drug and pesticide residues analysis in animal (and also in vegetable) products are under the Ministry of Agriculture, Livestock and Supply (MAPA) management [3]. Routine analysis and methods development and validation are attributed to MAPA official laboratories network – National Agricultural Laboratories (Lanagro) – and MAPA accredited private laboratories [4]. MAPA's demand on method development and validation in residue analysis has been increased in the last decade due to the increased role of the Brazilian livestock products in national and international markets and meanly to ensure that the products traded are compliant with the safety and quality criteria required by consumers [4,5]. Wherefore, our laboratory has absorbed one important fraction of this demand in developing, validating, and submitting for accreditation methods for analysis of antimicrobial and non-antimicrobial residues in different matrices, such as milk and edible tissues of different animal species including cattle, pork, poultry, and even fish [6–10]. For these purposes, international guidelines, such as Commission Decision 2002/657/EC concerning the performance of analytical methods and the interpretation of results, and others from the US Food and Drug Administration (FDA) and the International Conference on Harmonization (ICH), are used in order to obtain methods validated according to the most stringent international criteria [11–14]. Within this issue, especial attention is paid to matrix effect (ME), which is a fundamental parameter to be determined, assessed and minimized especially when

* Corresponding author at: Ministério da Agricultura, Pecuária e Abastecimento, Laboratório Nacional Agropecuário—LANAGRO/RS, Estrada da Ponta Grossa, 3036 CEP, 91780-580 Porto Alegre, RS, Brazil. Tel.: +55 51 3248 2133; fax: +55 51 3248 2690.
E-mail address: rodrigo.hoff@agricultura.gov.br (R.B. Hoff).

http://dx.doi.org/10.1016/j.talanta.2014.08.046
0039-9140/© 2014 Elsevier B.V. All rights reserved.

liquid chromatography–mass spectrometry (LC–MS) and/or tandem mass spectrometry (LC–MS/MS) methods are used [15–19]. The conceptualization of this phenomenon has been comprehensively reviewed by a number of authors [15,16,20,21]. Briefly, ME is related to the alteration of ionization efficiency in the ionization source by the presence of coeluting substances: the occurrence of endogenous substances originally present in the sample itself and that remains in the final extract, are appointed as the major source. A wide scope of molecules can lead to signal suppression or enhancement, especially when occurs in high concentration in the extract and elute in the same retention time window than the analyte [22]. A secondary cause are substances not originally present in the samples but able to migrate to extracts during sample preparation process as polymer and phthalates or material released by stationary phases, in bulk or in solid phase extraction (SPE) cartridges, for instance [20]. Normally, this alteration affects dramatically the method accuracy and precision and has been regarded as a critical validation item by most guidelines consulted. However, there is no consensus on how this phenomenon should be assessed during method validation. Beside, different experienced approaches of ME evaluation, based on procedures published in the scientific literature such as post-column infusion, calibration curves comparison, quantitative estimation based in standards, spiked samples and matrix-matched control comparison and control charts evaluation, has been experienced [23–27].

Although the knowledge on ME in mass spectrometry analysis has been improved in recent years, only few practical approaches has been reported for routine analysis [28–31]. In the present work, practical approaches to detect and estimate the occurrence of ME in qualitative and quantitative terms in LC–MS/MS methods for veterinary drugs residues analysis are presented and discussed. Tools for monitoring ME along the execution of routine methods are also reported. Without the purpose to exhaust the issue, the present study is proposed as a walkthrough based in relatively simple and easy techniques to be applied to analytical chemistry laboratories to deal with the critical theme of matrix effects in residues analysis.

2. Materials and methods

2.1. Analytical standards and reagents

Analytical standards with high purity ($\geq$99%) were obtained from Sigma-Aldrich (St Louis, MO, USA) namely sulfamerazine (SMR), sulfamethazine (SMZ), sulfamethoxazole (SMA), sulfamethoxypyridazine (SMPZ), sulfadiazine (SDZ), sulfapyridine (SPY), sulfadimethoxine (SDMX), sulfaguanidine (SGA), sulfacetamide (SCA), sulfabenzamide (SBZ), sulfisomidin (SIM), sulfamethizole (SMTZ), sulfaquinoxaline (SQX), sulfathiazole (STZ), sulfaisoxazole (SIX) and sulfadoxin (SDX). The metabolite N^4-acetyl-sulfamerazine (N^4-SMR) and the isotopically labelled compounds d^4-sulfamethoxazole (d^4-SMA), d^4-sulfamethazine (d^4-SMZ) and d^4-sulfadiazine (d^4-SDZ), used as surrogate and/or internal standards, were purchased from Toronto Research Chemicals (North York, Ontario, Canada).

Methanol (MeOH), acetonitrile (ACN), hexane and acetone of HPLC-grade were supplied by J. T. Baker (Deventer, The Netherlands). Diatomaceous earth was supplied by Agilent Technologies. Acetic acid and water (HPLC grade) were purchased from Merck (Darmstadt, Germany).

Individual stock standard solutions were prepared in MeOH: acetone (50:50) at 1 mg mL^{-1} and stored at −4 °C until use. Standard solutions of the mixtures of all compounds in appropriate concentrations were prepared by stock solutions dilutions using MeOH or acetone. Aliquots of each stock standard solution were diluted to obtain final concentrations of 10 μg mL^{-1} and 1 μg mL^{-1} and were stored at −20 °C.

2.2. Samples and sample preparation

Liver of different food production animals, chicken eggs, and fish muscle were obtained from Federal Inspection Service (SIF) or collected from treated animals in a farm. Liver and muscle samples were manual and finely chopped and homogenized in order to avoid slurring. Egg samples were manual and gently homogenized in order to avoid protein denaturation. After these processes, all samples were stored at −20 °C before extraction step.

Liver and fish samples were extracted by two different methods based on pressurized liquid extraction (PLE) and by ultrasounds-assisted extraction (US). A detailed discussion about these methods and validation results were submitted to publication. For PLE, an ASE 350 accelerated solvent extractor (Dionex, Sunnyvale, CA, USA) was used. Prior to extraction, d^4-SMA, d^4-SMZ and d^4-SDZ were added as surrogate standards in a concentration of 100 ng g^{-1}. Samples (0.5 g) were mixed into the PLE cells with diatomaceous earth as dispersing agent. Prior to extraction, the cells were submitted to a clean up method in order to remove lipids from the samples using hexane as solvent. PLE parameters were as follows: temperature 60 °C, 4 cycles of 5 min each one. Total flush volume of 80% and 300 s of purge with nitrogen flow were applied.

After that, the same PLE cells were submitted to a second extraction process using ACN with 0.2% acetic acid as extraction solvent. In this case, the extraction temperature was optimized at 90 °C. A preheating period of 8 min was selected and 3 cycles of 7 min each were carried out. A total flush volume of 80% and 60 s of purge with nitrogen flow were applied. Pressure was set at 1500 psi as it has been demonstrated that this parameter is not decisive in PLE.

The extracts were maintained in freezer by 1 h (at −18 °C) in order to promote protein precipitation. Following, samples were centrifuged at 1500 × *g* for 10 min in a 5810R centrifuge (Eppendorf). The supernatant was evaporated at 40 °C under nitrogen flow using a Turbo-Vap system (Zymark) until dryness. Extracts were redissolved in 1.0 mL of mobile phase mixture (water-ACN, 85:15) and transferred to a HPLC vial.

In ultrasound-assisted extraction, samples (0.5 g) were weighted in 15 mL polypropylene tubes and spiked as described for the PLE method. Following, 10 mL ACN were added and tubes were mixed in a mechanical vortex by 10 s. Afterwards all samples were placed into an ultrasonic bath for 1 h. and then stored in freezer (−18 °C) for 1 h. to promote protein precipitation. Then, samples were centrifuged at 1500 × *g* for 10 min. Supernatant was brought to dryness at 40 °C under a gentle nitrogen stream. The extracts were redissolved in 2.0 mL of the mobile phase mixture. An aliquot of 2 mL of hexane was added to remove the fat content. Afterwards, tubes were mixed in a vortex for 5 s followed by centrifugation (3500 rpm for 10 min). The lower layer was carefully transferred to a HPLC vial.

Sulfonamides analysis in eggs samples was performed as described elsewhere [32]. Briefly, samples were extracted with ACN and concentrated before reconstitution with mobile phase.

2.3. Instrumentation

LC analysis was performed with a Symbiosis™ Pico System (Spark Holland, Emmen, The Netherlands), equipped with a HPLC system consisting of an Alias™ autosampler, a loop injector and two binary pumps with a four-channel solvent selector for each one. Chromatographic separation was performed using a HPLC column Purospher® STAR (C18, ec, 150 × 4.6 mm, 5 μm) preceded by a guard column with the same packing material. The flow rate was set to 0.2 mL min^{-1}, being eluent (A) HPLC grade water acidified with 10 mM of formic acid, and eluent (B) ACN with

10 mM of formic acid. The elution gradient started with 25% of eluent (B), increasing to 80% in 10 min and to 100% in 11 min. During the next 2 min the column was kept at 100% (B), readjusted to the initial conditions in 3 min and equilibrated for 7 min. MS/MS analyses were carried out in a 4000 QTRAP hybrid triple quadrupole-linear ion trap mass spectrometer (Applied Biosystems, Foster City, CA, USA) equipped with a turbospray ionization source (ESI) working in the positive mode (ESI+).

For fish and egg analysis, the LC–MS/MS system was an Agilent 1100 series LC (Santa Clara, CA, USA) with a quaternary pump, a vacuum degasser, and an auto sampler, coupled with an API 5000 triple quadrupole mass spectrometer (Applied Biosystems, Foster City, CA, USA) with an electrospray ionization source (ESI).

The optimization of the MS/MS experimental conditions was performed in previous studies and are presented in our work published elsewhere (OR: in this same issue) [33]. For increased sensitivity and selectivity, MS/MS data acquisition was performed in the selected reaction monitoring (SRM) mode, recording the two most intense transitions from the precursor ions to the product ions.

2.4. Post-column infusion method

Post-column infusions of individual standards into the MS system were performed to verify the ME of the extracts obtained for all methods, in order to verify if the whole extract or some elution fraction of the extract cause signal suppression/enhancement. This procedure was based on the experiments described by Bonfiglio et al. [23]. Briefly, blank samples extracted by the above-mentioned methods were injected into the LC–MS/MS system under the chromatographic conditions optimized for each methodology. For each injection, a standard solution of individual compound was infused into the MS system using an infusion pump, at a flow rate of 10 μL min^{-1}, through a tee-joint installed post-column. Standard solution concentration was 100 ng mL^{-1}. ME were evaluated observing signal attenuation or signal enhancement on the response of the infused analyte.

2.5. Calibration curves evaluation method

A calibration curve was prepared using standard solutions diluted in pure solvent or in mobile phase (external Standard calibration curve or "*S*"). A second calibration curve was prepared spiking a blank matrix and following with the extraction and/or cleanup procedure (Recovery calibration curve or "*R*"). Finally, a third calibration curve was made using a extract of a blank sample, which was submitted to the whole extraction and/or cleanup procedure and was spiked with standard solution at the end of the protocol, generally in the final dilution, immediately before injection (Tissue Standard calibration curve (matrix-matched) or "*TS*"). These calibration curves were prepared with the same number of points or replicates to obtain the same expected concentration in the three kinds of curve. Usually, the MRL is the central point and are constructed with a minimum of 6 point. For a MRL value of 100 μg kg^{-1} (as in the case of sulfonamides in liver), calibration curves comprehends 0, 25, 50, 100, 150 and 200 μg kg^{-1} levels. All curves were prepared and analyzed in the same batch for a more accurate comparison. After analysis, the curves were plotted and inspected visually and statistically.

Alternatively, ME was evaluated using slope ratios comparison according to the approach proposed by Romero-Gonzáles et al. [34] and Sulyok et al. [35] in a modified application of the quantitative approach of Matuszewski et al. [24]. Slopes are compared between each pair of curves obtained in the linear calibration curves prepared by spiking mobile phase (*S*), blank sample (*R*), and extract of blank sample (*TS*). Slope ratios below 0.9 or above 1.1 were associated with ion suppression and ion enhancement, respectively. For values inside that range, ME was considered negligible.

To differentiate between extraction efficiency and matrix-induced signal suppression/enhancement, the slope ratios of the linear calibration functions were calculated to yield the recovery (RE), the signal suppression/enhancement due to ME and the relative recovery, i.e. the recovery of the extraction step (RE_R) as follows:

$$RE(\%) = 100 \times slope_{spikedsamples}/slope_{liquidstandards} \quad (1)$$

$$ME(\%) = 100 \times slope_{matrix-matched\ standard}/slope_{liquidstandards} \quad (2)$$

$$RE_R(\%) = 100 \times slope_{spikedsamples}/slope_{matrix-matched\ standard} \quad (3)$$

2.6. Matrix effect quantitative estimation

The quantitative estimation of a ME, when present, was performed using a modification of the equations previously proposed by Matuszewski et al. [24]. This procedure allows determination of the ME along with the RE_R and overall "process efficiency" or method overall recovery (RE) by comparing the absolute peak areas of 3 sets of samples. Set A is composed by standard solutions (*S*). Set B is composed by samples spiked after extraction (*TS*) and set C is prepared with samples spiked before extraction (*R*). Since the values have been obtained, ME, RE_R, and RE values can be calculated as follows:

$$ME(\%) = (B/A \times 100) - 100 \quad (4)$$

$$RE_R(\%) = C/B \times 100 \quad (5)$$

$$RE(\%) = C/A \times 100 = (ME \times RE_R)/100 \quad (6)$$

2.7. Control chart

Control charts are a useful tool for the monitoring of the analytical method behavior along with-in-batch and batch-to-batch variations including those due to ME. Within this purpose, for each analysis batch, 6 quality control samples (QC) spiked at the MRL concentration level for all compounds analyzed in each method were obtained. These QC samples, as described above, are composed by 3 samples spiked after (*TS*) and 3 samples spiked before extraction (*R*). Analyte peak area of each QC sample plus standards in pure solvent are plotted in a spreadsheet using Excel software. The cells include a formula to provide average, relative standard deviation and the upper and lower limits for ME, calculated according to the control chart parameters.

3. Results and discussion

As aforementioned, there is no consensus on how ME should be evaluated during method validation, neither on the criteria that should be adopted in establish when these effects are or not occurring [36]. However, according to recent literature, two main procedures have been used to determine ME on LC–ESI–MS/MS analysis: post-column infusion, which is a dynamic technique that provides qualitative information on where ME occur along the chromatographic run; and post extraction addition, which is a static technique that quantitatively provides the ME degree at the analyte retention time [20,37]. The last technique has been preferentially used to evaluate and compare ME of different matrices in terms of relative ME. In order to evaluate the most reported approaches to ME estimation, data of two in-house developed and validated methods were used as an example.

3.1. Case study: Determination of sulfonamides (SAs) in liver, muscle and fish using two extraction procedures

Two extraction methods were developed and validated for analysis of SAs residues in liver, muscle and fish. The complete development, optimization and validation data for both methods were recently submitted to publication. Both, the PLE and the US methods were previously evaluated by their potential ME using all the described approaches.

3.2. Post-column infusion method

First, blank extracts from each extraction method were injected in a post-column apparatus for comparison with pure mobile phase in order to evaluate the variation of the standards mixture signal.

The chromatographic separation of SAs was achieved using a modification of the method published elsewhere [33,38]. Some SAs had very similar chromatographic retention time (coeluting), but were well resolved as individual peaks in the MS/MS SRM mode. The detailed optimization and discussion about the chromatography method are presented in our report published in that same issue.

To evaluate ME, first we investigated if the extraction methods could contribute with co-extractive substances that might suppress selectively the different temporal regions of the chromatogram.

As can be observed in Fig. 1, both PLE and US extracts presented signal suppression in some regions of the chromatogram. This suppression effect is more intense in the 5–6 min region. Mobile phase signal (MP, grey line) shows a standard solution infused in a post-column "*T*" connection, over a mobile phase injection. PLE (black line) and US (dashed black line) represent the signal of the respective blank extracts. The standard solution was a mixture of all analytes at a concentration level of 100 ng mL^{-1}. Any line represents a TIC signal for all monitored SRM transitions (> 36). *TS* signal is a TIC chromatogram for a blank sample spiked at 100 ng mL^{-1} injected in normal mode. The signal was multiplied by a factor of 20 times for a better comparison with the post-column infusion chromatograms. PLE and US showed very similar matrix effects over the standard signal. In the region 11–22 min both signals were virtually overlaid. In summary, analytes do not elute in the most critical suppression zones. Thus, the chromatographic conditions could be used without modifications.

3.3. Calibration curves approach

As explained before, the use of calibration curves to estimate ME can be performed in many ways. Herein, examples of each interpretation mode are demonstrated.

3.4. Graphical plot—Visual and statistical analysis

Once the 3 curves are analyzed and plotted, the following situations are considered:

Situation 1. A similar slope, non-similar intercepts. Similarity between slopes show that matrix do not interfere in the linearity of the responses. The difference between intercepts is given by the losses caused by the sample preparation process. It is expected a lower response for *R* curve. If *TS* and *S* curve could be overlapped, there is no ME. If those curves have non-similar behaviour, ME is present, but it is affecting only the signal, not the linearity. Any kind of curve can be used in this method, if an appropriate correction is applied to adjust response losses. Fig. 2 shows an example of this situation.

Situation 2. Non-similar slopes: linearity is distinct between curves. If *TS* and *R* curves had similarity in the slopes, this means that the presence of the matrix itself change the responses. In this case, only *TS* or *R* calibrations curves may be used in this method. Fig. 3 gives an example.

Situation 3. TS and *S* curves are totally overlapped. There is no ME. However, if *R* curve shows differences in intercept and slope, this means that sample preparation process change significantly the response. Thus, *R* curves may be used. See Fig. 4 for an experimental data example.

Situations 4. All curves are perfectly overlapped. No ME and recovery equals or very closely to 100%. Presumably this is just a theoretical possibility.

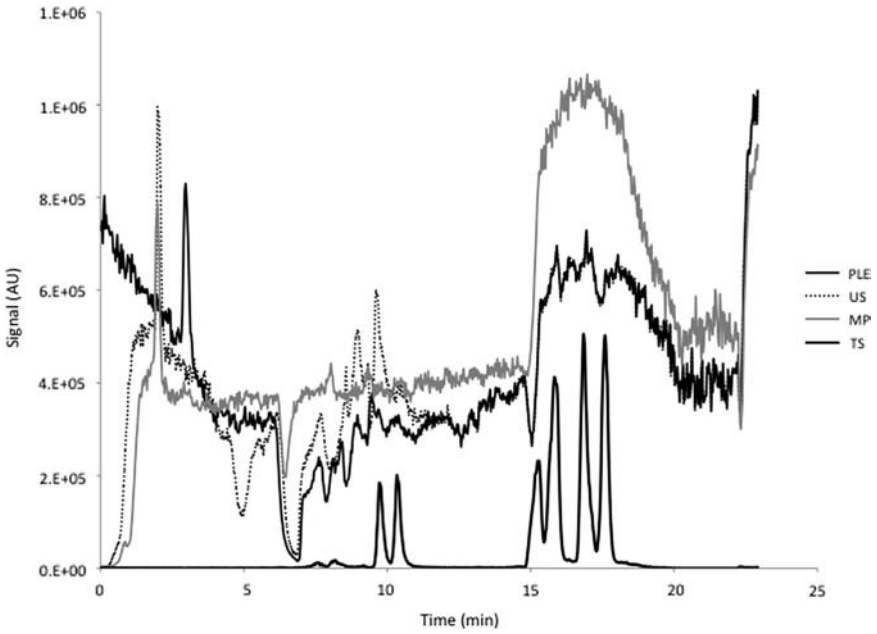


Fig. 1. Total ion chromatograms of post-column experiments. Continuous black line is a pressurized liquid extraction (PLE) blank extract; dashed black line is a ultrasound-assisted extraction (US) extract; grey line is mobile phase injection (MP) and the lower chromatogram in bold black line is a spiked tissue extract injected without post-column infusion in order to identify the elution window of the target analytes (*TS*).

In some cases, a matrix can exhibit high heterogeneity from sample to sample, which can cause significant alterations in ME [39]. This situation must be also evaluated in method development and validation. The simple superposition of plot is useful to distinguish between each calibration curve. But in some cases statistical analysis must be performed to elucidate the variation. For slope variation values, a *F*-test is applied. If $F_{cal} < F_{tab}$, the *F*-test is not significant (5% significance level), and it can be considered that the variances are similar.

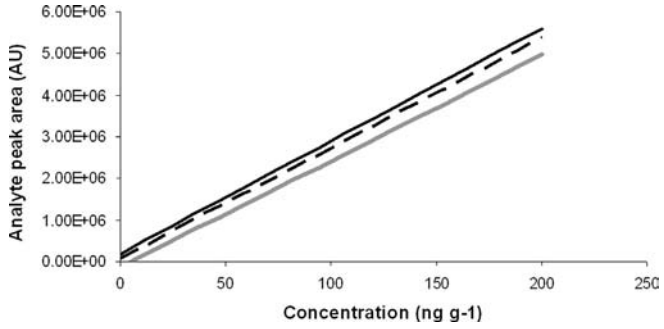


Fig. 2. Calibration curves comparison for ME evaluation: similar slopes, non-similar intercepts. Continuous line is *S* curve; dashed line is a *TS* curve and grey line represents an *R* curve.

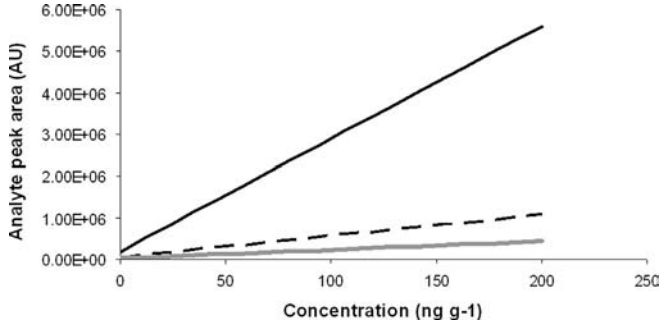


Fig. 3. Calibration curves comparison for ME evaluation: non-similar slopes. Continuous line is *S* curve; dashed line is a *TS* curve and grey line represents an *R* curve.

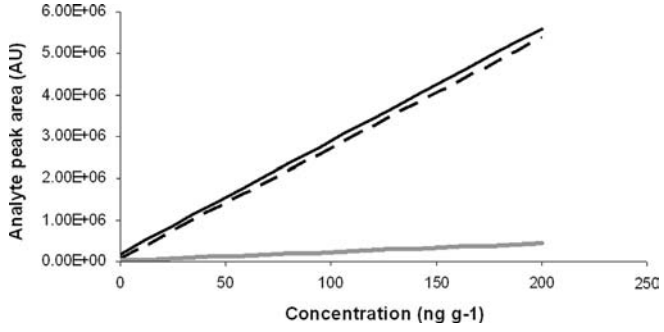


Fig. 4. Calibration curves comparison for ME evaluation: absence of ME. Continuous line is *S* curve; dashed line is a *TS* curve and dotted line represents an *R* curve.

For instance, from statistical comparison for sulfamerazine analysis in liver using matrix-matched calibration curves prepared by 2 distinct extraction methods (PLE and US) we obtained $F_{cal} < F_{tab}$ (F_{cal}=0.10 and F_{tab}=12.22 (0.05, 1, 4)) which means that the variation difference between extraction methods (PLE and US) is not significant. The slope, intercept and respective variances of both curves were calculated by the ordinary least squares method. Based on the results it was possible to conclude that PLE and US extraction methods gave equivalent responses for this analyte. In other words, matrix effects between these sample preparation methods are similar. In practical terms, it is possible to use a calibration curve prepared by US to quantify samples prepared by both methods or conversely. Similar behaviour was observed for other sulfonamides. Notwithstanding, a group of analytes was considered statistically distinct. Results are shown in Table 1.

3.5. Slope ratio and mathematical model for slopes comparison

Using Eqs. (1)–(3), quantitative values for ME and recovery were obtained (see Table 2). The slopes obtained in the calibration curve using matrix-matched samples were compared with the values obtained with standards in pure solvent. Besides the equations, slope ratio was calculated for each pair of curves to the 17 SAs included in the experiment. In this case, an acceptable range must be previously established. In the present study, a range from 0.9 to 1.1 was selected as lower and upper limits, respectively. The data were also demonstrated in Table 2.

As can be observed, using Eqs. (1)–(3), ME was very high varying from 9.4 to 73.5 % to PLE method and from 8.5 to 76.2% when US method was applied. That means an ion suppression extension as high as 91.6% in the case of SIZ, for instance. In general terms, both PLE and US methods presented very intense and highly similar ME. The use of slope ratio with acceptance limits of 0.9–1.1 shows agreement with the data obtained using the equations: an extremely intense ME for both PLE and US methods and a high degree of agreement between ME produced by PLE and US methods. When slopes of *R* and *TS* curves, some analytes showed a ratio value between tolerance range indicating no significant difference between those curves. The only analyte that showed a selective behaviour was SCA, which was the sulfonamide that suffered less effects of the matrix.

3.6. Quantitative estimation

Several degrees of ME were demonstrated, highlighting the huge variability among matrices. Depending on matrix nature, co-extractives can produce ion suppression or enhancement. For instance, Table 3 shows the quantitative ME data for some sulfonamides in fish and eggs. In the case of fish method, ME is present in the range of 30 to 40% of signal losses. RE and RE_R were in the ranges 25–41% and 46–79%, respectively. In other words, only ME can be responsible for approximately half of losses, if recovery will be considered as losses of extraction method plus

Table 1
F-test results for equality of variances between matrix-matched calibration curves prepared by PLE or US methods. F_{tab}=12.22 (0.05, 1, 4).

	SMR	SMZ	SMA	SMPZ	SDZ	SPY	SDMX	SCA	SMTZ	SQX	STZ	SIZ	SDX	N4-SMR
F_{cal}	0.10	3.76	11.42	26.79	56.73	167.26	213.88	3.04	49.27	5.03	565.65	1.51	1.17	2.06
F_{tab}	12.22	12.22	12.22	12.22	12.22	12.22	12.22	12.22	12.22	12.22	12.22	12.22	12.22	12.22
Results	$F_{cal} < F_{tab}$	$F_{cal} < F_{tab}$	$F_{cal} < F_{tab}$	$F_{cal} > F_{tab}$	$F_{cal} > F_{tab}$	$F_{cal} > F_{tab}$	$F_{cal} > F_{tab}$	$F_{cal} < F_{tab}$	$F_{cal} > F_{tab}$	$F_{cal} < F_{tab}$	$F_{cal} > F_{tab}$	$F_{cal} < F_{tab}$	$F_{cal} < F_{tab}$	$F_{cal} < F_{tab}$
Variation not significant	True	True	True	False	False	False	False	True	False	True	False	True	True	True

Table 2
Relative (RE_R) and absolute recoveries (RE), matrix effect (ME) estimated using slopes data for PLE and USE extraction methods for sulfonamides analysis in liver.

	SMR	SMZ	SMA	SMPZ	SDZ	SPY	SDMX	SGA	SCA	SBZ	SIM	SMTZ	SQX	STZ	SIZ	SDX	N4-SMR
PLE																	
RE (%)	8.8	8.1	4.7	7.6	6.0	7.8	8.3	4.2	25.2	1.5	9.2	3.0	5.0	6.7	3.0	11.7	13.9
ME (%)	23.9	25.7	13.5	28.7	16.4	24.1	29.3	12.9	73.5	6.7	30.8	19.2	20.0	11.3	9.4	34.7	24.5
RE_R (%)	36.7	31.5	35.1	26.5	36.5	32.6	28.2	32.7	34.4	23.0	29.8	15.5	25.3	59.2	31.5	33.7	56.8
USE																	
RE (%)	13.0	14.2	7.7	13.2	11.6	15.8	12.8	5.1	33.5	2.4	15.1	4.5	8.7	8.1	3.9	19.6	16.6
ME (%)	21.7	23.6	13.5	23.9	20.3	28.0	24.8	16.5	76.2	4.4	25.0	20.8	17.8	23.0	8.5	32.2	25.8
RE_R (%)	59.9	60.1	57.2	55.3	57.4	56.5	51.6	31.2	43.9	54.1	60.3	21.7	48.9	35.4	46.3	60.7	64.3
PLE slope ratio																	
TS/*S*	0.24	0.26	0.13	0.29	0.16	0.24	0.29	0.13	0.73	0.07	0.31	0.19	0.20	0.11	0.09	0.35	0.25
R/*S*	0.09	0.08	0.05	0.08	0.06	0.08	0.08	0.04	0.25	0.02	0.09	0.03	0.05	0.07	0.03	0.12	0.14
R/*TS*	0.37	0.31	0.35	0.26	0.37	0.33	0.28	0.33	0.34	0.23	0.30	0.16	0.25	0.59	0.32	0.34	0.57
USE slope ratio																	
TS/*S*	0.22	0.24	0.13	0.24	0.20	0.28	0.25	0.16	0.76	0.04	0.25	0.21	0.18	0.23	0.09	0.32	0.26
R/*S*	0.13	0.14	0.08	0.13	0.12	0.16	0.13	0.05	0.33	0.02	0.15	0.05	0.09	0.08	0.04	0.20	0.17
R/*TS*	0.60	0.60	0.57	0.55	0.57	0.56	0.52	0.31	0.44	0.54	0.60	0.22	0.49	0.35	0.46	0.61	0.64
Ratio USE/PLE																	
R/*R*	1.49	1.75	1.63	1.74	1.94	2.02	1.55	1.22	1.33	1.55	1.64	1.51	1.73	1.22	1.33	1.67	1.19
TS/*TS*	0.91	0.92	1.00	0.83	1.24	1.16	0.85	1.28	1.04	0.66	0.81	1.08	0.89	2.04	0.91	0.93	1.05

Table 3
ME quantitative estimation for sulfonamides residue analysis in fish and eggs ($n=3$ for each value).

	Sample type	Sulfonamides in fish (peak area)			Sulfonamides in eggs (peak area)		
		SMR	SMZ	SMA	STZ	SMZ	SQX
A	Standard in solvent	6.43E+05	4.09E+05	4.88E+05	7.01E+06	3.39E+06	7.56E+06
B	Matrix-matched	3.46E+05	2.56E+05	2.53E+05	2.56E+05	1.29E+05	2.49E+05
C	Spiked sample	1.59E+05	1.66E+05	2.00E+05	2.14E+05	1.22E+05	2.19E+05
	Equation						
	$ME(\%)=(B/A\times 100)-100$	−46	−37	−48	−96	−96	−97
	$RE_R(\%)=C/B\times 100$	46	65	79	84	95	88
	$RE(\%)=(ME\times R_R)/100$	25	41	41	3	4	3

ME=matrix effects; RE=Recovery; RE_R=Relative recovery.

losses by ion suppression. In the case of eggs, matrix is characterized by the intense presence of phospholipids, which are also related with a highly intense ME, causing analytes losses from 95 to 97% [40]. However, in the case of sulfonamides in eggs, recoveries were satisfactory, from 80 to 102%. The selected cases demonstrate a common profile of ME (fish) besides an extreme case (eggs), but are useful to exemplify the co-existence between intense ME and high recovery values (> 80%). The data corroborate that ME is independent of the recovery. For the eggs case, another extraction protocols should be evaluated, in order to remove the co-extractives [32].

3.7. ME continuous monitoring using control charts

The estimation of the ME during a validation procedure is mandatory, because it is used for several matrices more or less distinct those used during validation. A method for ME behavior monitoring intra-batch and inter-batch will be always necessary. Moreover, monitoring itself is not the complete task: if ME are changing, QC samples must reflect this change and procedures to assess these modifications must be available to the analyst.

Using the same kind of QC samples (*S*, *R* and *TS*) in every batch, all necessary information about the method accuracy will be available at any moment, for any batch. Accuracy data for QC samples will provide data to build a control chart to monitor ME, recovery and method accuracy.

Control charts are very useful tools to monitor analytical methods behaviour. Over time, minor and major changes were naturally occurring in routine methods. Thus, ME could be suffering changes and method adjustments will be necessary to guarantee the adequate fitness to purpose. For ME monitoring, quality control samples were inserted in each analysis batch and the results were calculated according to the quantitative ME estimation. Control charts present lower and upper limits. These limits are based on the standard deviation observed in the series. Lower and upper limits can be used as warning limits (using the average multiplied by 2 times the standard deviation), to observe trends in the results and apply preventive action before the method exceed the upper or lower limits based in 3 standard deviation values.

Table 4
Accuracy acceptability criteria.

Concentration level	Range
$\leq 1\ \mu g\ kg^{-1}$	$-50a+20\%$
$>1\ \mu g\ kg^{-1}\ a<10\ \mu g\ kg^{-1}$	$-30a+10\%$
$\geq 10\ \mu g\ kg^{-1}$	$-20a+10\%$

Acceptance criteria follow those described in 2002/657/EC Commission Decision and Brazilian analytical quality assurance guidelines [11,41]. To evaluate accuracy obtained by routine data, a critical analysis of QC samples results is performed for every batch in accordance with limits showed in Table 4.

QC samples data ($n=3$ by batch) were plotted on control charts and critically analyzed. Results for each routine analysis should be reviewed, and in case of non-compliance with criteria, it must be recorded. For a batch, if the review of QC samples shows non-

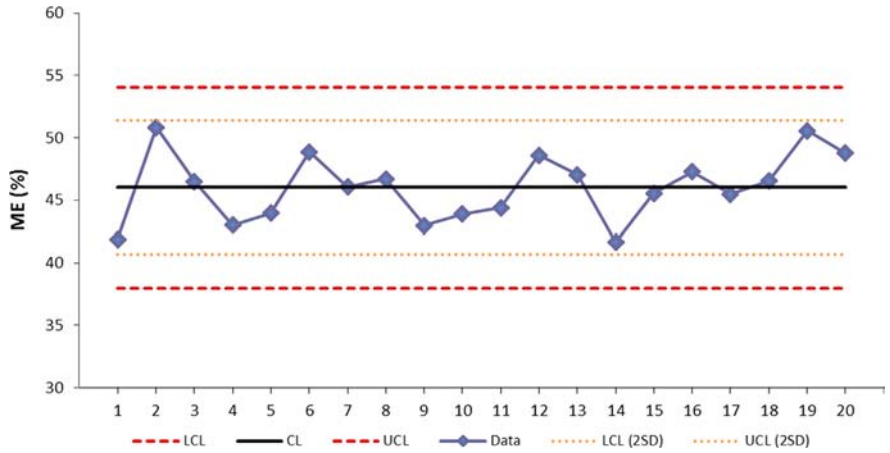


Fig. 5. Plot for matrix effects monitoring for sulfadiazine determination in liver. ME=Matrix effect; CL=central limit; UCL (2SD)=upper control limit based on 2 standard deviation; UCL=upper control limit; LCL (2SD)=lower control limit based on 2 standard deviation; LCL=lower control limit.

compliances in relation to acceptance criteria, appropriate corrective actions must be taken. Fig. 5 shows an example for ME monitoring to a sulfonamide residue analysis in liver samples. In that example, data of ME (in %) for SDZ obtained from 20 batches were plotted. The central limit (CL) was 46.4%, with an average standard deviation of 2.6%. Lower and upper control limits were obtained by adding or reducing the standard deviation value (multiplied by 2 or 3) from CL.

3.8. General remarks: Matrix effect assessment in routine methods

Concisely, in our laboratory, the following workflow is used to evaluate, minimize and monitor ME:

i. In method development, qualitative and/or quantitative approaches for ME determination can be used for analytes and surrogates/internal standards: the results can help to decide what kind of calibration curve could be used, depending on the extension of ME observed.
ii. Extraction protocols can be modified or improved to avoid co-extraction of matrix compounds: a SPE method could be more adequate than LLE, for instance. Different solvents or solvent mix can be critical to minimize ME.
iii. Once ME is observed, the post-infusion protocol is used to determine in what chromatogram region the suppression occurs.
iv. Mobile phase gradient and/or additives can be modified in order to provide analytes elution in a region with absence of suppression. Generally, just simple changes in the gradient composition are adequate to promote separation of the analytes elution window form zones with intense signal suppression. In extreme cases, solvent and even column change could be necessary.
v. Extract injection volume can be reduced in order to decrease ME, except when the analyte responses does reduce in the same extent.
vi. Evaluate the effect of surrogate/internal standards in the correction of ME.
vii. If even with these changes, ME still remain relevant, the magnitude of the effect can be monitored during routine analysis, using an accuracy control chart.

In validation data, a differentiation between recovery and ME must be clear. In mass spectrometry analysis, recovery can be deeply affected by ME although the sample preparation process showed high efficiency. As ME directly affects the yield of analytes ionization, method overall recovery have a correlation with the ME extension. In the present work, we refer to the IUPAC's recovery concept, which is the analyte yield obtained after the extraction procedure [42]. The "apparent recovery", according to IUPAC, is the degree of agreement between the nominated and calculated concentration. We use the term "relative recovery" to express the recovery value discounting the ME. Relative recovery represents the analyte losses caused only by the extraction procedure. Thus, this term should not be confused with the term "apparent recovery".

Summarizing, recovery includes losses of target compounds throughout the whole sample preparation process (extraction, concentration, derivatization, etc) plus the eventual ME. RE_R is the loss of analytes caused by the sample preparation but not include the ME.

Several approaches were considered to ME evaluation. Clearly, the methods that can be used before the method validation are more useful. The obtained data can be used to make changes or adjustments in the extraction and/or chromatography conditions to avoid or minimize the impact of ion suppression/enhancement. Once adequate conditions were established, remaining ME could be estimate using a simple approach as those based in calibration curves or QC samples. If ME is relevant in a routine method, ME could be monitored using a control chart in order to detect advance changes in method behaviour.

4. Conclusions

ME is a very frequent issue in bioanalytical methods, especially in LC–MS and LC–MS/MS based methods. Despite the fact that currently there are no established acceptable limits for ME, it is a consensus that their magnitude must be estimated and, if possible, minimized. Thus, analytes extraction procedures and/or chromatographic conditions changes could be carried out. In literature, several approaches to estimate ME were reported. Herein, we report our experience with ME estimation, minimization and continuous monitoring, applying several ME estimation strategies for analytical methods which are used in routine analysis in our laboratory. Each technique was discussed and their advantages and/or drawbacks were appointed, in order to provide a practical guide for researchers interested in assessment of ME. Based on the experience with these several techniques, the ME evaluation must be performed before the validation, using the quantitative estimation and post-column infusion, concomitantly. Using this procedure, all necessary changes and adjustments could be assessed before the validation process, improving the quality of the results and overcoming the undesirable ME.

Acknowledgements

This research was funded by the Brazilian Ministry of Agriculture (MAPA) and was also partly supported by the Generalitat de Catalunya (Consolidated Research Group: Water and Soil Quality Unit 2014-SGR-418). Rodrigo Barcellos Hoff acknowledges his doctoral scholarship from CAPES (Project PVE 163/2012). Merck is acknowledged for the gift of one of the HPLC columns used.

References

[1] A. Anadón, D. Arnold, A. Boobis, R. Ellis, A. Fernández Suárez, K. Greenlees, et al., in: Sixty-sixth Meeting of the Joint FAO/WHO Expert Committee on Food Additives, 2006.
[2] P.A. Blackwell, A.B.A. Boxall, P. Kay, H. Noble, J. Agric. Food Chem. 53 (2005) 2192–2201. http://dx.doi.org/10.1021/jf049527b.
[3] A. de Queiroz Mauricio, E.S. Lins, Food Addit. Contam. Part A 29 (2012) 482–489. http://dx.doi.org/10.1080/19440049.2011.620987.
[4] A.d.Q. Mauricio, E.S. Lins, M.B. Alvarenga, Anal. Chim. Acta 637 (2009) 333–336. http://dx.doi.org/10.1016/j.aca.2008.09.061.
[5] E.S. Lins, E.S. Conceição, A.D.Q. Mauricio, Food Addit. Contam. Part A 29 (2012) 490–496. http://dx.doi.org/10.1080/19440049.2011.653988.
[6] G. Rübensam, F. Barreto, R.B. Hoff, T.L. Kist, T.M. Pizzolato, Anal. Chim. Acta 705 (2011) 24–29. http://dx.doi.org/10.1016/j.aca.2011.02.041.
[7] R. Hoff, T.B.L. Kist, J. Sep. Sci. 32 (2009) 854–866. http://dx.doi.org/10.1002/jssc.200800738.
[8] R. Hoff, F. Ribarcki, I. Zancanaro, L. Castellano, C. Spier, F. Barreto, et al., Food Addit. Contam. Part A 29 (2012) 577–586. http://dx.doi.org/10.1080/19440049.2011.641508.
[9] F. Barreto, C. Ribeiro, R.B. Hoff, T.D. Costa, Food Addit. Contam. Part A 29 (2012) 550–558. http://dx.doi.org/10.1080/19440049.2011.641160.
[10] M.S. Bittencourt, M.T. Martins, F.G.S. de Albuquerque, F. Barreto, R. Hoff, Food Addit. Contam. Part A 29 (2012) 508–516. http://dx.doi.org/10.1080/19440049.2011.606228.
[11] Brasil. Ministério da Agricultura Pecuária e Abastecimento, Manual de garantia da qualidade analítica, 1st ed., MAPA/ACS, Brasília, 2011.
[12] P. Gowik, J. Chromatogr. A 1216 (2009) 8051–8058. http://dx.doi.org/10.1016/j.chroma.2009.06.059.
[13] R. Companyó, M. Granados, J. Guiteras, M.D. Prat, Anal. Bioanal. Chem. 395 (2009) 877–891. http://dx.doi.org/10.1007/s00216-009-2969-4.
[14] J.A.R. Paschoal, S. Rath, F.P.D.S. Airoldi, F.G.R. Reyes, Quim. Nova 31 (2008) 1190–1198.
[15] A. Cappiello, G. Famiglini, P. Palma, H. Trufelli, J. Liq. Chromatogr. Related Technol. 33 (2010) 1067–1081. http://dx.doi.org/10.1080/10826076.2010.484314.
[16] Y. Huang, R. Shi, W. Gee, R. Bonderud, Bioanalysis 4 (2012) 271–279. http://dx.doi.org/10.4155/bio.11.315.
[17] J. O'Mahony, L. Clarke, M. Whelan, R. O'Kennedy, S.J. Lehotay, M. Danaher, J. Chromatogr. A 1292 (2013) 83–95. http://dx.doi.org/10.1016/j.chroma.2013.01.007.
[18] B.J.A. Berendsen, L.A.A.M. Stolker, M.W.F. Nielen, M.W.F. Nielen, TrAC, Trends Anal. Chem. 43 (2013) 229–239. http://dx.doi.org/10.1016/j.trac.2012.09.019.
[19] M. Bourdat-Deschamps, S. Leang, N. Bernet, J.-J. Daudin, S. Nélieu, J. Chromatogr. A 1349 (2014) 11–23. http://dx.doi.org/10.1016/j.chroma.2014.05.006.
[20] P.J. Taylor, Clin. Biochem. 38 (2005) 328–334. http://dx.doi.org/10.1016/j.clinbiochem.2004.11.007.
[21] C. Côté, A. Bergeron, J.N. Mess, M. Furtado, F. Garofolo, Bioanalysis 1 (2009) 1243–1257.
[22] J.-P. Antignac, K. De Wasch, F. Monteau, H. De Brabander, F. Andre, B. Le Bizec, Anal. Chim. Acta 529 (2005) 129–136. http://dx.doi.org/10.1016/j.aca.2004.08.055.
[23] R. Bonfiglio, R.C. King, T.V. Olah, K. Merkle, Rapid Commun. Mass Spectrom. 13 (1999) 1175–1185 (10.1002/(SICI)1097-0231(19990630)13:12 < 1175::AID-RCM639 > 3.0.CO;2-0).
[24] B.K. Matuszewski, M.L. Constanzer, C.M. Chavez-Eng, Anal. Chem. 75 (2003) 3019–3030. http://dx.doi.org/10.1021/ac020361s.
[25] J. Smeraglia, S.F. Baldrey, D. Watson, Chromatographia 55 (2002) S95–S99.
[26] N.R. Srinivas, Biomed. Chromatogr. 23 (2009) 451–454. http://dx.doi.org/10.1002/bmc.1152.
[27] Y. Zou, J. Zhao, J. Zhang, G. Wang, B. Tang, X. Li, et al., Anal. Methods 5 (2013) 5662–5668. http://dx.doi.org/10.1039/c3ay41115j.
[28] A. González-Antuña, J.C. Domínguez-Romero, J.F. García-Reyes, P. Rodríguez-González, G. Centineo, J.I. García Alonso, et al., J. Chromatogr. A 1288 (2013) 40–47. http://dx.doi.org/10.1016/j.chroma.2013.02.074.
[29] F. Li, M. Ewles, M. Pelzer, T. Brus, A. Ledvina, N. Gray, et al., Bioanalysis 5 (2013) 2409–2441. http://dx.doi.org/10.4155/bio.13.201.
[30] S.V. Malysheva, J. Diana Di Mavungu, I.Y. Goryacheva, S. De Saeger, Anal. Bioanal. Chem. 405 (2013) 5595–5604. http://dx.doi.org/10.1007/s00216-013-6948-4.
[31] E. Saar, D. Gerostamoulos, O.H. Drummer, J. Beyer, Anal. Bioanal. Chem. 393 (2009) 727–734. http://dx.doi.org/10.1007/s00216-008-2498-6.
[32] R.B. Hoff, F. Barreto, J. Melo, M.T. Martins, T.M. Pizzolato, M.C.R. Peralba, Food Addit. Contam. Part A 31 (2014) 39–47. http://dx.doi.org/10.1080/19440049.2013.861082.
[33] R.B. Hoff, F. Barreto, T.B.L. Kist, J. Chromatogr. A 1216 (2009) 8254–8261. http://dx.doi.org/10.1016/j.chroma.2009.07.074.
[34] R. Romero-González, A. Garrido Frenich, J.L. Martínez Vidal, O.D. Prestes, S.L. Grio, J. Chromatogr. A 1218 (2011) 1477–1485. http://dx.doi.org/10.1016/j.chroma.2011.01.034.
[35] M. Sulyok, R. Krska, R. Schuhmacher, Anal. Bioanal. Chem. 389 (2007) 1505–-1523. http://dx.doi.org/10.1007/s00216-007-1542-2.
[36] K. de C. Mariotti, G. Rübensam, F. Barreto, V.C. Bica, L.Z. Meneghini, R.S. Ortiz, et al., Chromatographia. (n.d.) 1–8. 10.1007/s10337-013-2569-5.
[37] A. Van Eeckhaut, K. Lanckmans, S. Sarre, I. Smolders, Y. Michotte, J. Chromatogr. B 877 (2009) 2198–2207. http://dx.doi.org/10.1016/j.jchromb.2009.01.003.
[38] R.B. Hoff, F. Barreto, J. Melo, L. Jank, M.D.C.R. Peralba, T.M. Pizzolato, Anal. Methods 4 (2012) 2822–2830. http://dx.doi.org/10.1039/c2ay25197c.
[39] B. Álvarez-Sánchez, F. Priego-Capote, M.D. Luque de Castro, TrAC, Trends Anal. Chem. 29 (2010) 111–119. http://dx.doi.org/10.1016/j.trac.2009.12.003.
[40] S. Ahmad, H. Kalra, A. Gupta, B. Raut, A. Hussain, M.A. Rahman, J. Pharm. Bioallied Sci. 4 (2012) 267–275. http://dx.doi.org/10.4103/0975-7406.103234.
[41] Commission of the European Communities, Commission Decision 2002/657/EC, (2002).
[42] D.T. Burns, K. Danzer, A. Townshend, Pure Appl. Chem. 74 (2002) (2002) 2201–2205.

Talanta 132 (2015) 451–456

Contents lists available at ScienceDirect

Talanta

journal homepage: www.elsevier.com/locate/talanta

Short communication

Rapid geographical differentiation of the European spread brown macroalga *Sargassum muticum* using HRMAS NMR and Fourier-Transform Infrared spectroscopy

Tanniou Anaëlle[a], Vandanjon Laurent[b,d], Gonçalves Olivier[b], Kervarec Nelly[c], Stiger-Pouvreau Valérie[a,*]

[a] LEMAR UMR CNRS UBO IRD IFREMER 6539, Université de Bretagne Occidentale (UBO), Institut Universitaire Européen de la Mer (IUEM), Technopôle Brest-Iroise, Rue Dumont d'Urville, Plouzané 29280, France
[b] GEPEA UMR CNRS 6144, Université de Nantes, Laboratoire GEPEA, CRTT, 44602 Saint-Nazaire, France
[c] Service RMN-RPE, UFR Sciences et Techniques, Université de Bretagne Occidentale (UBO), Avenue Le Gorgeu, 29200 Brest, France
[d] LBCM EA 3884, Université de Bretagne Sud (UBS), IUEM, Campus de Tohannic, 56000 Vannes, France

ARTICLE INFO

Article history:
Received 23 October 2013
Received in revised form
21 August 2014
Accepted 2 September 2014
Available online 22 September 2014

Keywords:
HRMAS NMR
FTIR spectroscopy
Sargassum muticum
Geographical origin discrimination
Latitudinal gradient

ABSTRACT

Two recent techniques based on chemical footprinting analysis, HRMAS NMR and FTIR spectroscopy, were tested on a brown macroalgal model. These powerful and easily-to-use techniques allowed us to discriminate *Sargassum muticum* specimens collected in five different countries along Atlantic coasts, from Portugal to Norway. HRMAS NMR and FTIR permitted the obtaining of an overview of metabolites produced by the alga. Based on spectra analysis, results allowed us to successfully group the samples according to their geographical origin. HRMAS NMR and FTIR spectroscopy respectively point out the relation between the geographical localization and the chemical composition and demonstrated macromolecules variations regarding to environmental stress. Then, our results are discussed in regard of the powerful of these techniques together with the variability of the main molecules produced by *Sargassum muticum* along the Atlantic coasts.

© 2014 Elsevier B.V. All rights reserved.

1. Introduction

Sargassum muticum is a brown macroalga native from Japan and widely spread along the European Atlantic coasts [1–6]. Distributed from Northward to Southward of Europe, it can be found nowadays from Norway to Portugal, demonstrating its large capability to adapt to different climate conditions (temperature, irradiance, hydrodynamism). This large sustainable biomass could represent a viable biotechnological asset in the European resource development programs. For this reason, *S. muticum* was collected in three sites of five countries (Portugal, Spain, France, Ireland and Norway). The present study is integrated in a global approach to find applications of the huge biomass of *S. muticum* observed along the Atlantic coasts. Previous works carried out on French populations highlighted interesting properties such as anti Reactive Oxygen Species (ROS), i.e. antioxidative [7–11] or antibacterial, antibiotic or antifouling, properties [12–15] of polar and apolar extracts and semi-purified fractions from *S. muticum*. The aim of our present study was then to obtain an overview of the global biochemical composition of specimens from different countries using new techniques for this purpose, and for the end, to know if *S. muticum* populations present or not a chemical adaptation along Atlantic coasts. Results on the lipid, protein or glucid macromolecules quantification are very used as indicators in biotechnology, especially in having information about the physiological state of the studied organism, reflecting for example the metabolic changes in answer to a given environmental stress.

In this context, we were interested in studying the biochemical composition of *S. muticum* populations collected along a latitudinal gradient, by using two non invasive techniques: the *in vivo* ^{1}H HRMAS NMR (High Resolution Magic Angle Spinning Nuclear Magnetic Resonance) and the infrared (IR) spectroscopy in order to pointing out or not the sources of chemical profile differences. These two techniques are used for about twenty years in various domains; the HRMAS NMR was already used in chemotaxonomy on various marine models to point out the differences between bacterial strains or algal species for example [16–20]. But this technique had only rarely used to follow physiological processes, in particular on seaweeds. Fourier Transform IR spectroscopy (FTIR) was still never used on macroalgae but was previously used to differentiate species of microorganisms or even strains [21–24]. These two rapid techniques are convenient as they use small

* Corresponding author. Tel.: +33 2 98 49 88 06; fax: +33 2 98 49 87 72.
E-mail address: valerie.stiger@univ-brest.fr (V. Stiger-Pouvreau).

http://dx.doi.org/10.1016/j.talanta.2014.09.002
0039-9140/© 2014 Elsevier B.V. All rights reserved.

amount of sample thus permitting repeated manipulations (allowing a better reproductibility of the results). Finally, these two techniques allowed studying a wide range of molecules, and thus, pointing out very fine differences between samples. We selected then these two interesting techniques as a source of complementary information, FTIR allowing a global chemical variations analysis and the possibility to access to the content in the main macromolecules while HRMAS NMR allows to point out complementary chemical fingerprinting for a species or a given sample [17,19–20].

2. Materials and methods

2.1. Sampling sites and sample preparation

Thalli of *Sargassum muticum* were collected between March and May 2011 in three sites of five countries along a latitudinal gradient in Europe. Samples were collected, from South (March) to North (May), in respectively Portugal, Spain, France, Ireland and finally Norway (Table 1). Sampling period was chosen according to the physiological state of the alga in all the countries. During these periods, *Sargassum muticum* was still immature [1,6]. During collection, only the apical and median parts of the thalli were retained and the holdfast was left in place to allow regrowth and thus minimize collecting impact. Immediately after collection and epiphytes removal, specimens were firstly washed with filtered seawater then with distilled water in order to get rid of residual sediments and salts. The cleaned algal materials were then surface dried with blotting paper towel, chopped into fragments, freeze-dried, powder reduced with a Waring Blender and finally sieved at 250 μm.

2.2. HRMAS-NMR spectroscopy

All HRMAS NMR spectra were obtained using a Bruker DRX 500 spectrometer (Bruker BioSpin, Wissembourg, France) equipped with an indirect HRMAS $^{1}H/^{31}P$ probehead with gradient Z at 25 °C. A typical proton ^{1}H HRMAS spectrum consisted of 64 scans and it was performed with presaturation of the water peak. Each spectrum was phased and baseline-corrected using a polynomial function. Spectra data processing was performed using the software MestReNova 6.0.2 for Windows (Mestrelab Research S.L., Spain). Afterwards the data were subjected to statistical analysis using the Statistica 8 (StatSoft ®) software for PC. For HRMAS NMR, three independent samples per site were analyzed, which represent then a pool of 45 samples analyzed. About 5 mg of each sample were put in a zirconium oxide vial and set into a 4 mm MAS rotor. Around 30 μL of D_2O were added into the rotor with the sample for 2 H field locking (depending on the quantity of the freeze-dried powder). The sample was placed in a rotor spinning around an axis, which is oriented at the so-called magic angle of 54°7 with respect to the magnetic field B_0. Good homogenization and synchronization were obtained at a spinning rate of 5000 Hz. In this study, three HRMAS NMR spectra, corresponding to three independent records for each sample, were obtained by sample.

The statistical procedure used in this study was based on a cluster analysis to illustrate *S. muticum* geographical origin discrimination using HRMAS NMR analysis. Variables used to perform this analysis were the form of the peak (single, double, triple or massive peaks) together with the peak position (δ). These variables were determined for each HRMAS NMR spectrum (three for each site) between 0 and 7 ppm, since some chemical shifts appeared to be different in the samples depending on sites and countries all along this spectral region. We took into account only positive peaks with a noise factor of 4.00. The cluster analysis was then made using a matrix of absence/presence of the observed signals in order to summarize the *in vivo* chemical diversity of the samples.

2.3. FTIR spectroscopy

Infrared spectra were recorded in reflection mode directly on the single reflexion diamond crystal of the ATR (Attenuated Total Reflexion) accessory loaded with few milligrams of freeze-dried algal powder. The Bruker tensor 27 FTIR spectrometer equipped with the ATR platinum module, with a deuterated triglycine sulfate detector RT-DLaTGS and the OPUS v7.0.122 software (Bruker Optics, Germany) was set up with the following parameters. The spectral resolution was fixed to 1 cm^{-1}, the number of scans to 32, the selected spectral range between 4000 and 400 cm^{-1}. Background spectra were collected using the same instrument settings as those employed for the samples and was performed against air. Spectra were recorded for 3 technical replicates, i.e. 3 biological replicates, per site, representing a total of 45 samples analyzed for all studied countries. The recorded spectra were treated in group to compensate the CO_2/H_2O and the base-line effects and with the correction tools integrated into the OPUS software. The spectra were then smoothed using the Savitzky–Golay algorithm [25] but for presentation purpose only. For the multivariate analysis, the spectra pre-processing sequence was different and excluded the smoothing step, since it could

Table 1
List of sampling data (sites localization) for each country and hydrodynamism conditions.

Country	Region	Sampling date	Locality	Site	Latitude	Longitude	Exposition
Norway	Øygarden	May 17, 2011	Solberg	1	60°35' N	4°47' W	Sheltered
	Øygarden	May 17, 2011	Krækjebærholmen	2	60°35' N	4°50' W	Semi-exposed
	Øygarden	May 17, 2011	Sauøyna	3	60°35' N	4°51' W	Semi-exposed
Ireland	Connaught	April 17, 2011	Clifden	1	53°24' N	10°7' W	Exposed
	Munster	April 18, 2011	Spanish Point	2	52°51' N	9°26' W	Semi-exposed
	Munster	April 18, 2011	Miltown Malbay	3	52°50' N	9°26' W	Semi-exposed
France	Bretagne	April 18, 2011	Fort du Dellec	1	48°21' N	4°34' W	Semi-exposed
	Bretagne	April 18, 2011	Le Minou	2	48°20' N	4°36' W	Semi-exposed
	Bretagne	April 18, 2011	Pointe du Diable	3	48°21' N	4°33' W	Exposed
Spain	Galicia	March 18, 2011	Museo del Mar	1	42°13' N	8°46' W	Semi-exposed
	Galicia	March 18, 2011	Cabo Estay	2	42°11' N	8°48' W	Exposed
	Galicia	March 21, 2011	Cabo Udra	3	42°20' N	8°49' W	Exposed
Portugal	Algarve	April 1, 2011	Queimado	1	37°49' N	8°47' W	Semi-exposed
	Algarve	April 1, 2011	Almograve	2	37°39' N	8°48' W	Semi-exposed
	Algarve	April 1, 2011	Zambujeira	3	37°33' N	8°47' W	Semi-exposed

impact the resolution of the data, and therefore decrease the detection of putative important vibrators and their contribution to the FTIR signature. The CO_2/H_2O and base-line effects corrected replicate spectra were averaged to generate a new spectrum from the three original spectra of the same type, i.e. the new spectrum intensities were calculated by averaging original spectra intensities. Then, mean spectra were vector normalized first to account for differences in samples thickness commonly found when working on powders, and second derivative transformed to detect a maximum of vibrators (peak position) and enhance their contribution to the FTIR signature on the whole spectral range [26–29].

Multivariate analysis was performed on the mean, vector normalized, second derived spectra using the Metaboanalyst 2.0 pipeline [30]. Principal component analysis (PCA) and Cluster analysis were performed on those pre-processed spectra. Then the replicate spectra were averaged to generate a new spectrum from the three original spectra of the same type, i.e. the new spectrum intensities were calculated by averaging original spectra intensities. Afterwards the data were subjected to cluster analysis employing the Ward's algorithms and using the second derivative and vector normalization preprocessing method to calculate inter-spectral distances (Euclidian distance).

3. Results and discussion

The ^{1}H HRMAS NMR spectra comparison shown on Fig. 1A (only one spectrum was selected for each country) revealed some differences between the five different sampled countries. As visible on the Fig. 1B, countries presenting the least homogeneous grouping are Spain and Ireland, where the site 1 is different from the two others. This corresponds to the measured geographical distances between the different sites (Table 1). In every case we can notice a clear distinction between the five countries. Some areas present a larger variability, as for example: the aromatic domain towards 5.5 and 6.5 ppm, the edge of peaks between 3.0–5.5 ppm, which corresponded to polyols described as mannitol in *S. muticum* [19], the proportions of the amino acid glutamine/glutamates (carboxylate anions and salts of glutamic acid), against the malic acid/malates (esters and salts of malic acid) (peaks around 2.0–2.5 ppm As N. Kervarec is a co-author of this paper) and some unsaturated fatty acids towards 1.0–1.5 ppm (Fig. 1A). Some countries are recognizable rather easily thanks to certain characteristic peaks, as for example the peak towards 2.6 ppm very marked in Spain and the peak at 2.91 ppm very marked in Ireland (Fig. 1A). We can also observe in a general way that sugars (3.0 to 5.5 ppm) are more plentiful and diversified in Norway, France and Portugal while more lipidic compounds (0.8 to 3.0 ppm) are found in Ireland, France and Spain. In view of spectrum it would be rather saturated lipids; even if some unsaturated ones are visible in France and Spain for example towards 4.8 ppm. Differences of composition in fatty acids were already observed in other *Sargassum* species collected from two different geographical zones but never within the same genus [31]. Fig. 1 shows that chemically closed populations resulted from places geographically closed, which is not the case of FTIR dendogram presented on Fig. 3, where the grouping is different. Indeed, populations in Spain and France are the most similar while populations in Norway present the "most original" profile compared with those of the other countries. Samples providing from Norway contained a great amount of malate and sugars (3.5 and 4.5 ppm). The geographical position of populations belonging to the same species has a real effect on chemical composition and this effect is adequately important for allowing their differentiation according to their origin. However, some authors affirm that, in brown algae, geographical variations of marine algae metabolites composition were non-significant [32–33] and could be further due to seasonal variations in *S. muticum* metabolites content [34]. This bias was avoided by

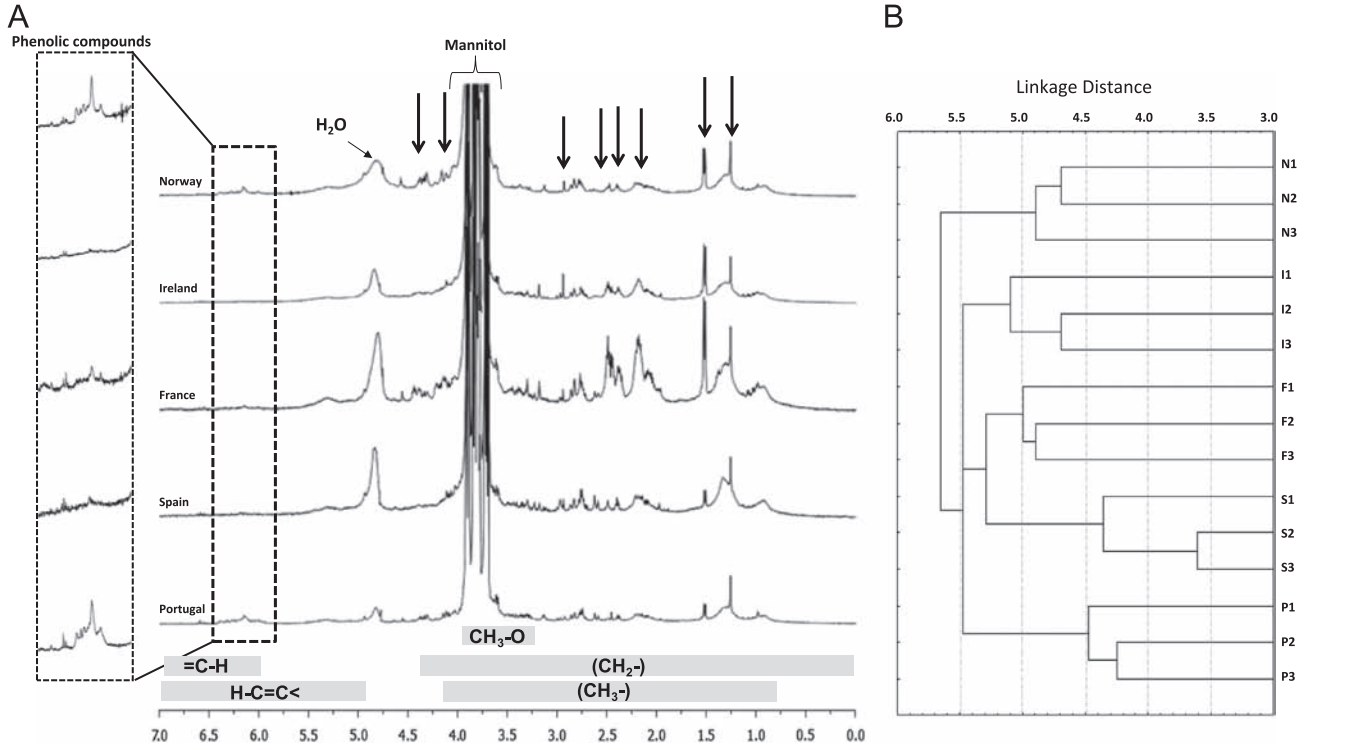


Fig. 1. (A) Typical ^{1}H HRMAS NMR spectra of *Sargassum muticum* sampled in five different countries (only one spectrum is represented by country as the three spectra by site were all identical). Spectral regions are indicated in gray at the bottom and specific differences between countries by arrows at the top. (B) Cluster analysis based on 45 spectral observations issued from Norway (N), Ireland (I), France (F), Spain (S) and Portugal (P) with the numbers 1,2,3 representing the three sites sampled by country, regrouping the triplicate per site.

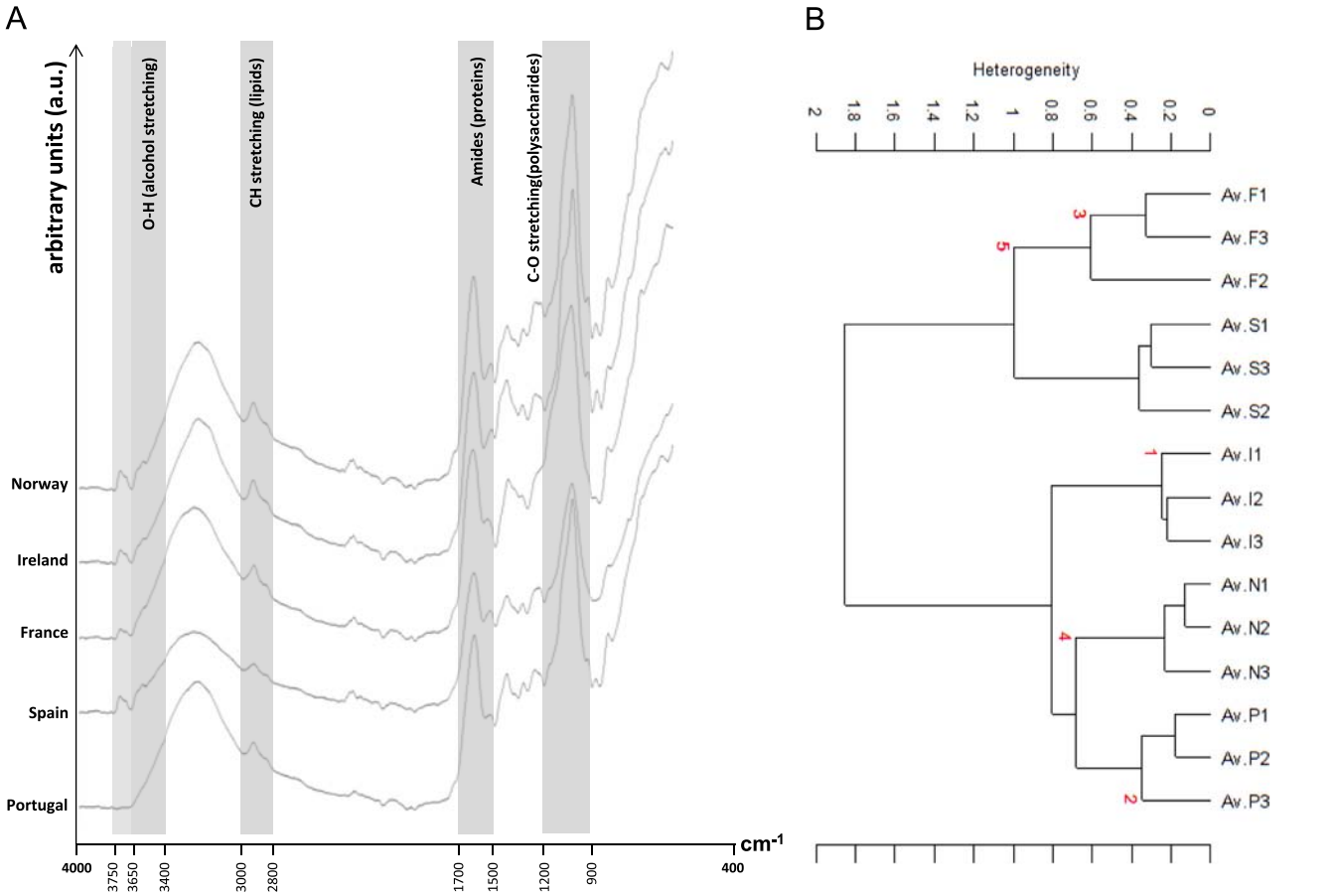


Fig. 2. (A) Spectra from analysis in FTIR of samples of *Sargassum muticum* (averaged spectra calculated by averaging the 3 sites spectra intensities for each country). (B) Cluster analysis performed using the second derivative and vector normalization of the spectra from 400 to 4000 cm^{-1}. The Ward's algorithm was used to build the dendrogam. Letters and numbers as on Fig. 1.

harvesting seaweeds in the various countries at the same physiological state during spring 2011 (Table 1). Nevertheless, the same experiment should be carried out during the other seasons to test the seasonality effect on the chemical contents. In addition, it would be also interesting to pursue this experiment on seaweeds collected at the same period the following years to see if the tendencies are confirmed from one year to the next. This technique showed that seaweeds coming from different geographical places could be differentiated by their biochemical profile. Blind assays were realized on spectra of unknown origin allowing to recognize their geographical origin (country and site) with 100% success except for samples resulting from Ireland where sites can be confused; the success rate was then 60% (data not shown). Those scores are upper than those obtained for similar studies [35–36] for food applications on aliment origin.

Fig. 2 permitted to obtain an overview of the intensity of peaks in specific areas of FTIR spectra. The highlighted areas corresponded to the major macromolecules spectral region [37]. Thus, few peaks are characteristic of a single sample. On the other hand, we can quote for example: a peak at 2965 cm^{-1} only visible in France and Spain; at 688 and 3594 cm^{-1} present for samples originated from Norway, Ireland and Spain. A great variability between countries was observed between 800 and 950 cm^{-1} and 1930–2560 cm^{-1}. The intensity of the vibrators bands composing an IR spectrum is proportional to the abundance of the chemical groupings in the analyzed sample (Beer–Lambert law). It is thus possible to obtain, besides the usually exploited qualitative data, quantitative or rather semi-quantitative information. FTIR spectroscopy permitted then to distinguish samples by their geographical origins (Fig. 2). The vector normalized second derivative spectral data were qualitatively analyzed using principal component analysis (PCA) for each algal sample, taking also into account the location of the collection in the considered country. In Fig. 3, results indicated that the five algal samples were clustered into five distinct groups, clearly associated to each geographical origin (axis 2, with a contribution superior to 17% of the total variability). Inside each cluster, it was moreover possible to distinguish subgroups according to the specific location of collection in a considered country (axis 1, with a contribution superior to 36% of the total variability). The clustering results clearly revealed that each algal sample could be distinguished according to its FTIR spectrum, exhibiting moreover differences for the three tested sampling sites for a considered country. Those observations suggested that each algal sample presented its own FTIR signature, depending on its particular chemical composition. Indeed, according to the work of [27–29] this spectral signature could be directly related to the relative amount of the matrix main constitutive molecules (at least lipids, proteins and carbohydrates), which were moreover in our case geographical/climate dependent.

Actually, numerous approaches are developed for the estimation of the relative or absolute intracellular metabolites abundance on the whole cell [38–39]. IR spectroscopy expresses here all its analytical potential compared with classical dosage techniques, because it is not invasive, fast and requires only some milligrams or even micrograms of biomass [40]. The recent works of [41] demonstrated in particular the possibility to estimate the effect of the light intensity variations or the nitrogen and sulfur concentrations on the lipids accumulation for the microalga *Chlamydomonas reinhardtii*. These spectral data immediately inform on the

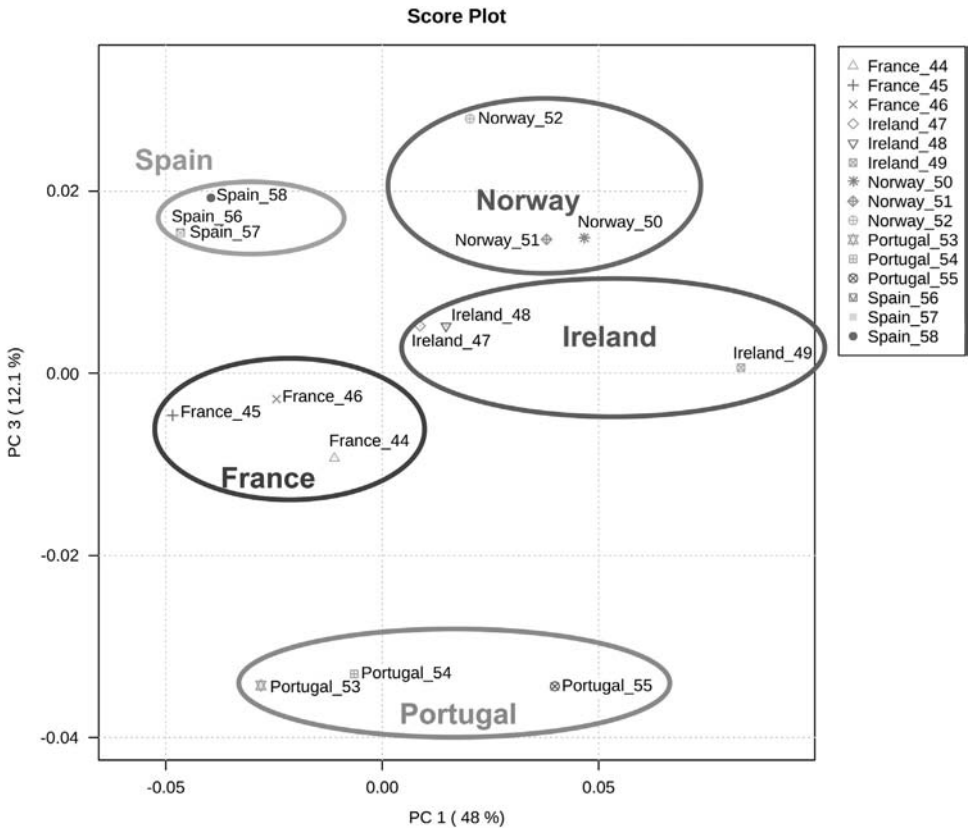


Fig. 3. PCA score plot of the vector normalized second derivative FTIR signatures of the various sample of *Sargassum muticum* collected in Norway, Ireland, France, Spain and Portugal. The legend in the upright corner details the name of the algal samples together with their site of collection and the geographical clusters are highlighted on the score plot.

presence or the absence (of detection) of a family of macromolecules with regard to another one for a given sample. It is also possible to compare the relative abundances of these molecules (since the concentration of one of them does not vary during the studied process) [38]. On the other hand, the exploitation of the bands intensity in the quantification applications absolved from these macromolecules requires taking precautions because the sources of IR spectra variations are numerous and they may modify the recorded intensities. Here, we can see on Fig. 3 that the proteins compartment (1400–1800 cm^{-1}) did not vary between samples while polysaccharides (1000–1200 cm^{-1}) and lipids (2800–3000 cm^{-1}) area were very variable [37]. Thus, polysaccharides were more present in Norway and France and lipids more present in France, Norway and Portugal. Except for the lipids compartment where the Spanish samples seemed to contain a lot of lipids in HRMAS NMR and not in FTIR, the results were close between the HRMAS NMR and the FTIR method. The fact is that for present Spanish samples, lipids were saturated for the greater part and thus very visible in HRMAS NMR while the IR gives us an image of total lipids content. But numerous factors influence the appearance of the recorded IR spectra. The relevant works of [42] underlined clearly the importance of these effects, which were widely ignored in numerous studies previous to their investigations. According to these authors, the spectral variations for a succession of samples can be attributed to four different factors: (i) the dispersal effect of a radiation produces wide fluctuations which overlap on the spectra [43] (ii) the presence of a nucleus is also going to modify and to amplify this distortion effect [42] (iii) the variations of intensity observed on the whole IR spectra can be attributed to the heterogeneousness of thickness of the sample and finally, (iv) the significant contribution of the signal of the water on the amide I (primary amide) area (3300–3400 cm^{-1}) [44] which can make difficult the interpretation of the obtained results. To get away from this type of problem it seems thus essential to choose bands with the least possible covering or when it is not possible, because of the complexity of the sample for example, to use more global processing methods which will thus exploit the influence of all the spectral contributions for a given sample. We found recently approaches of relative estimations of macromolecular microalgal contents using IR spectrometry as a routine technique. Stehfest et al. [45] were among the first ones to study the effect of nitrogenous and phosphorous stresses on phytoplanktonic species with IR spectrometry. Recently, Di Giambattista et al. [46] used FTIR as an efficient method to diagnostic the presence of tumor cell death, showing the great potential of this technique also in medical studies.

We can thus admit that whatever the used technique and the observed variations, no specific major molecule seems to be really produced by the seaweeds from the different studied countries, along our chosen latitudinal gradient (Portugal to Norway). Only the relative proportions of each molecule seem to evolve along the latitudinal gradient, as it was already shown in the particular phenolic compounds studied in a previous study [47]. Complementary analyses carried out at the laboratory allowed, thanks to chemical analysis techniques, to validate the variations and the tendencies observed in HRMAS NMR and FTIR. Indeed the colorimetric tests used for the determination of protein and carbohydrates contents for example, show a weak variability of the protein compartment following countries while, on the other hand, lipids and polysaccharides are subjected to big variations in *S. muticum* populations collected along Atlantic coasts [48].

4. Conclusion

In our study both HRMAS NMR and FTIR appeared as two quick and reliable methods for geographical origin discrimination studies together with the obtaining of an overview of biochemical composition of samples. These two relevant techniques provided results analogous to those obtained by standard chemical tests. Their main advantages are that they are quick and easy to use methods, which need low biomass consumption (some milligrams). These techniques are then promising for this type of investigation because they would allow, without preliminary extraction, the simultaneous and fast qualitative overview of macromolecules for a given species with the possibility of connection with the environmental variations. These results are exciting as no DNA polymorphism could be highlighted in populations of *Sargassum muticum* collected in Europe (Viard, pers. comm.). Our chemical procedure could then represent a real tool of traceability for further studies of *S. muticum* in Europe.

Acknowledgments

This study is part of the Ph.D. thesis work carried out by the first author within the Laboratoire des Sciences de l'Environnement Marin (LEMAR UMR 6539) set at the IUEM (UBO-UEB). It was supported by the Ministère de l'Education Nationale, de l'Enseignement Supérieur et de la Recherche (UBO allocation for the first author). This study is part of the BIOTECMAR project contract no. 2008-1/032 for the collection of samples in Europe, and was co-financed with the support of the European Union ERDF – Atlantic Area Program. This study is also related to the research projects INVASIVES (Era-net Seas-era, 2012–2016) and COSELMAR for the analysis of samples.

References

[1] E. Plouguerné, K. Le Lann, S. Connan, G. Jechoux, E. Deslandes, V. Stiger-Pouvreau, Aquat. Bot. 85 (2006) 337–344.
[2] A. Engelen, C. Espirito-Santo, T. Simoes, C. Monteiro, E.A. Serrao, G.A. Pearson, R.O.P. Santos, Eur. J. Phycol. 43 (2008) 275–282.
[3] S. Kraan, J. Appl. Phycol. 20 (2008) 825–832.
[4] M. Incera, C. Olabarria, J.S. Troncoso, J. Lopez, Mar. Ecol. Prog. Ser. 377 (2009) 91–101.
[5] C. Olabarria, I.F. Rodil, M. Incera, J.S. Troncoso, Mar. Env. Res 67 (2009) 153–158.
[6] K. Le Lann, S. Connan, V. Stiger-Pouvreau, Mar. Env. Res 80 (2012) 1–11.
[7] M. Nakai, N. Kagayama, K. Nakahara, W. Miki, Mar. Biotechnol. 8 (2006) 409–414.
[8] T. Kuda, T. Kunii, H. Goto, Jpn. Food Chem. 103 (2007) 900–905.
[9] S. Kumar Chandini, P. Ganesan, N. Bhaskar, Food Chem. 107 (2008) 707–713.
[10] K. Le Lann, C. Jegou, V. Stiger-Pouvreau, Phycol. Res. 56 (2008) 238–245.
[11] A Tanniou, E. Serrano Leon, L. Vandanjon, E. Ibanez, J.A. Mendiola, S. Cerantola, N. Kervarec, S. La Barre, L. Marchal, V. Stiger-Pouvreau, Talanta 104 (2012) 44–52.
[12] C. Hellio, J.P. Marechal, B. Véron, G. Bremer, A. Clare, Y. Le Gal, Mar. Biotechnol. 6 (2004) 67–82.
[13] E. Plouguerné, C. Hellio, E. Deslandes, B. Véron, V. Stiger-Pouvreau, Bot. Mar. 51 (2008) 202–208.
[14] E. Plouguerné, P. Georgantea, E. Ioannou, C. Vagias, V. Roussis, C. Hellio, E. Kraffe, V. Stiger-Pouvreau, Mar. Biotechnol. 12 (2010) 52–61.
[15] A. Bazes, A. Silkina, P. Douzenel, F. Faÿ, N. Kervarec, D. Morin, J.-P. Bergé, N. Bourgougnon, J. Appl. Phycol. 21 (2008) 395–403.
[16] S. Gudlavalleti, C.M. Szymanski, H.C. Jarrell, D.S. Stephens, Carbohydr. Res. 341 (2006) 557–562.
[17] S. Salaün, N. Kervarec, P. Potin, D. Haras, M. Piotto, S. La Barre, Talanta 80 (2010) 1758–1770.
[18] W. Li, Analyst 131 (2006) 777–781.
[19] K. Le Lann, N. Kervarec, C.E. Payri, E. Deslandes, V. Stiger-Pouvreau, Talanta 74 (2008) 1079–1083.
[20] C. Jégou, G. Culioli, N. Kervarec, G. Simon, V. Stiger-Pouvreau, Talanta 83 (2010) 613–622.
[21] D. Helm, H. Labischinski, D. Naumann, J. Microbiol. Methods 14 (1991) 127–142.
[22] D. Naumann, D. Helm, H. Labischinski, Nature 351 (1991) 81–82.
[23] C. Kirschner, K. Maquelin, P. Pina, N.A. Ngo Thi, L.P. Choo-Smith G.D. Sockalingum, C. Sandt, D. Ami, F. Orsini, S.M. Doglia, P. Allouch, M. Mainfait, G.J. Puppels, D. Naumann, J. Clin. Microbiol. 39 (2001) 1763–1770.
[24] C.A. Rebuffo, J. Schmitt, M. Wenning, F. von Stetten, S. Scherer, Appl. Environ. Microbiol. 72 (2006) 994–1000.
[25] A. Savitzky, M.J. E. Golay, Anal. Chem. 36 (1964) 1627–1639.
[26] A. Domenighini, M. Giordano, J. Phycol. 45 (2009) 522–531.
[27] M.K. Kim, K.H. Jeune, J. Microbiol. Biotechnol. 19 (2009) 1206–1212.
[28] M. Mecozzi, M. Pietroletti, A. Tornambe, Spectrochim. Acta A Mol. Biomol. Spectrosc. 78 (2011) 1572–1580.
[29] M. Pietroletti, A. Capobianchi, E. Ragosta, M. Mecozzi, Spectrochim. Acta A Mol. Biomol. Spectrosc. 77 (2010) 673–679.
[30] J. Xia, R. Mandal, I.V. Sinelnikov, D. Broadhurst, D.S. Wishart, Nucleic Acids Res. 40 (2012) W127–W133.
[31] V.E. Vaskovsky, S.V. Khotimchenko, B. Xia, L. Hefang, Phytochemistry 42 (1996) 1347–1356.
[32] A. Praud, R. Valls, L. Piovetti, B. Banaigs, J.-Y. Benaïm, Phytochemistry 40 (1995) 495–500.
[33] R. Valls, L. Piovetti, Biochem. Syst. Ecol. 23 (1995) 723–745.
[34] G.V. Joshi, C.A. Gowda, Ind. J. Mar. Sci. 4 (1975) 165–168.
[35] L. Shintu, S. Caldarelli, J. Agric. Food Chem. 54 (2006) 4148–4202.
[36] L. Shintu, S. Caldarelli, B.M. Franke, Meat Sci. 76 (2007) 700–707.
[37] J. Coates, A practical Approach Encyclopedia of Analytical Chemistry, John Wiley & Sons, Ltd., Chichester (2006) 10815–10837.
[38] A.P. Dean, D.C. Sigee, B. Estrada, J.K. Pittman, Bioresour. Technol. 101 (2010) 4499–4507.
[39] H. Wagner, Z. Liu, U. Langner, K. Stehfest, C. Wilhelm, J. Biophoton. 3 (2010) 557–566.
[40] R. Davis, L.J. Mauer, in: A. Mendez-Vilà (Ed.), Current Research, Technology and Education Topics in Applied Microbiology and Microbial Biotechnology, 2, Formatex Research Center, 2010, pp. 1582–1594.
[41] T. Cakmak, P. Angun, Y.E. Demiray, A.D. Ozkan, Z. Elibol, T. Tekinay, Biotechnol. Bioeng. 109 (2012) 1947–1957.
[42] M. Romeo, B. Mohlenhoff, M. Diem, Vib. Spectrosc. 42 (2006) 9–14.
[43] G. Mie, Ann. Phys. (Leipzig) 25 (1908) 377–445.
[44] C. Berthomieu, R. Hienerwadel, Photosynth. Res. 101 (2009) 157–170.
[45] K. Stehfest, J. Toepel, C. Wilhelm, Plant Physiol. Biochem. 43 (2005) 717–726.
[46] L. Di Giambattista, D. Pozzi, P. Grimaldi, S. Gaudenzi, S. Morrone A.C. Castellano, Anal. Bioanal. Chem. 399 (2011) 2771.
[47] A. Tanniou, L. Vandanjon, M. Incera, E. Serrano Leon, V. Husa, J. Le Grand J.L. Nicolas, N. Poupart, N. Kervarec, A. Engelen, R. Walsh, F. Guérard, N. Bourgougnon, V. Stiger-Pouvreau, J. Appl. Phycol. 26 (2014) 1215.
[48] A. Tanniou, Océanologie Biologique, Université de Bretagne Occidentale (2014) 217–237 (PH.D. Thesis).

Talanta 132 (2015) 457–462

Contents lists available at ScienceDirect

Talanta

journal homepage: www.elsevier.com/locate/talanta

Nitrite sensing based on the carbon dots-enhanced chemiluminescence from peroxynitrous acid and carbonate

Zhen Lin [a,b], Xiangnan Dou [b], Haifang Li [b], Yuan Ma [b], Jin-Ming Lin [b,*]

[a] Department of Pharmaceutical Analysis, Faculty of Pharmacy, Fujian Medical University, Fuzhou 350004, China
[b] Beijing Key Laboratory of Microanalytical Methods and Instrumentation, Department of Chemistry, Tsinghua University, Beijing 100084, China

ARTICLE INFO

Article history:
Received 31 July 2014
Received in revised form
14 September 2014
Accepted 16 September 2014
Available online 7 October 2014

Keywords:
Chemiluminescence
Carbon dots
Peroxynitrous acid
Carbonate

ABSTRACT

In this work, chemiluminescence (CL) from peroxynitrous acid (ONOOH)–carbonate system greatly amplified by carbon dots was observed. The CL mechanism of the ONOOH–carbonate–carbon dots system has been investigated and the results reveal that the carbon dots could serve as the energy acceptor, which gives us new insight into the optical properties of the new emerging carbon nanomaterial. There is a good linear relationship between the CL signal and the concentration of the nitrite using for ONOOH formation, which provides us a nitrite sensing method with sensitivity as high as 5.0×10^{-9} M (S/N=3). The method has been successfully applied to the determination of nitrite in tap water with the recovery of 98%. The standard deviations are within 2.5%.

© 2014 Elsevier B.V. All rights reserved.

1. Introduction

Peroxynitrite is a powerful oxidizing agent of biological importance, which exists in many forms, such as *trans*-peroxynitrous acid (ONOOH), *cis*-ONOOH, activated form of ONOOH, and peroxynitrous anion [1–3]. ONOOH, as a weak acid with a pKa of 6.8, is an important form of peroxynitrite [4]. In acid solution, ONOOH is an unstable compound with lifetime less than 1 s [5]. In basic solution, ONOOH could be converted to peroxynitrous anion ($ONOO^-$) that is fairly stable and can decompose slowly to nitrite and superoxide anion radical. The oxidation reaction by peroxynitrite is beneficial for destroying invading organism. However, peroxynitrite is also involved in protein and lipid nitration, which has been found to be an early event in the etiology of some pathologies. The study concerning peroxynitrite has attracted many attractions.

Certain chemical reactions released their energy through light emission, which was called as chemiluminescence (CL). Large amount of excited species with short life are involved in CL reaction. Hence, CL could be a useful tool in reactive species investigation. Since 1999, Starodubtseva et al. had reported weak CL emission from excited ONOOH. ONOOH/$ONOO^-$ also oxidized pholasin [6], chloroquine [7,8] and bilirubin [9] to produce strong CL. There are some reports concerning the CL from the decomposition of $ONOO^-$, which is enhanced by some energy acceptors, such as fluorescent compounds [10], CdTe quantum dots [11]. Materials, including Mg–Al–carbonate layered double hydroxides [12] and gold nanoparticles [13], could increase the CL from ONOOH related system. Carbonate solution was reported to react with $ONOO^-$ to produce $ONOOCO_2^-$ that had a lifetime less than 3 ms and decomposed rapidly into $\bullet NO_2$ and carbonate radical ($\bullet CO_3^-$)[14,15]. $\bullet CO_3^-$ changed to carbon dioxide in its excited form that brought in the CL emission [16].

Carbon dots, as a new type of fluorescent carbonaceous nanoparticle, owned lots of advantages, such as environmental benign, optical stability, low cost and easy preparation. Nowadays, fluorescent carbon dots have been successfully applied in bioimaging for cells [17,18]. The new properties of carbon dots, such as catalytic activity [19,20], fluorescent probe [21,22] and photocatalyst [23,24], have been reported recently by several groups. The CL enhanced role of carbon dots was firstly reported in our group and the CL mechanism was revealed. There are several possible mechanisms explaining the enhancing effect of carbon dots: (1) Carbon dots have catalysis effect on the reaction [25]. (2) Carbon dots concentrated the excited CL emitter, which facilitated the CL emission [26]. (3) Carbon dots were involved in the CL reaction and the CL emission was through the annihilation of hole-injected and electron-injected carbon dots [27].

We firstly found that carbon dots had enhancing effect on the ONOOH system [27]. In the present work, we further find that carbon dots could greatly amplify the CL from ONOOH–carbonate system. Furthermore, the carbon dots–ONOOH–carbonate CL system has higher CL intensity than that from carbon dots–ONOOH system. More interestingly, a linear relationship between the

* Corresponding author. Tel./fax: +86 10 62792343.
E-mail address: jmlin@mail.tsinghua.edu.cn (J.-M. Lin).

http://dx.doi.org/10.1016/j.talanta.2014.09.046
0039-9140/© 2014 Elsevier B.V. All rights reserved.

nitrite for the formation of ONOOH and CL signal produced from the carbon dots–ONOOH–Na_2CO_3 system was found. Hence, the proposed method can be employed for the determination of nitrite with improved sensitivity. The CL enhanced mechanism of carbon dots on ONOOH–Na_2CO_3 system was also illustrated in details, and its role of energy acceptor was further discussed.

2. Experimental

2.1. Reagents and materials

All chemicals were of analytical grade and were used as received. Sodium nitrite ($NaNO_2$) was from Sinopharm Chemical Reagent Co., Ltd (Shanghai, China). Hydrogen peroxide (H_2O_2, 35%) was obtained from Alfa Aesar China Ltd. Serine and polyethylene glycol 1500 (PEG 1500) were purchased from Merck Company (Darmstadt, Germany). 5, 5-Dimethyl-1-pyrroline N-oxide (DMPO) was from Sigma-Aldrich Chemical Co. (St. Louis, USA). Sulfuric acid (H_2SO_4, 98%) and glycerine were bought from Beijing Chemical Reagent Co. (Beijing, China).

2.2. Apparatus

Flow injection experiments were performed with a LumiFlow LF-800 detector (NITI-ON, Funabashi, Japan). Batch CL experiment was performed with a BPCL ultraweak CL analyzer (Institute of Biophysics, Chinese Academy of Science, Beijing, China). Two peristaltic pumps (SJ-1211, Atto, Tokyo, Japan) were used to deliver the solution into the spiral flow CL cell, which was installed in front of the photomultiplier tube (PMT). The fluorescent spectra were performed using a FL-7000 spectrofluorometer (Hitachi, Japan). Electron paramagnetic resonance (EPR) spectra were measured on a JEOL spectrometer (JES-FA200, Japan).

2.3. CL system

Carbon dots were prepared by microwave heating of serine in the presence of 15 mL glycerine and 1.0 g PEG 1500 by microwave oven for 10 min. Carbon dots were dialyzed against pure water before the batch experiment. While in the flow injection experiment, carbon dots were used without any further treatment. CL kinetic curves were obtained by batch experiments, which were carried out in the glass cuvette. The CL profiles were displayed and integrated for 0.1 s interval. A microliter syringe was used for the injection of the solution from the upper injection port. The addition orders of the reagent were changed to investigate the interaction of the reagent and design the CL flow injection analysis system.

The manifolds of the flow injection system were shown in Fig. S1. The solution of $NaNO_2$ and H_2O_2 was mixed at the three-way channel, where HNOOH was produced and reached the flow cell through channel AB. Carbon dots and Na_2CO_3 were pumped by pumps 1 and 2 to mix with HNOOH in the flow cell. The CL signal was collected by the LF-800 detector. The peak height of the signal recorded was measured as CL intensity.

2.4. Sample preparation

For the determination nitrite in tap water, the water was firstly filtered by 0.25 μm and then was passed through a cation-exchange resin to eliminate interferences from metal cation.

3. Results and discussions

3.1. CL from carbon dots–$NaNO_2$–H_2O_2–Na_2CO_3 system by flow injection system

Flow injection system with precise control of the sample volume, flow rate and mixing time of the reagent has been employed to compare the CL intensity from several systems. The manifolds of the flow injection system were shown in Fig. S1. The interaction of $NaNO_2$ and H_2O_2 in acid medium produced ONOOH [28]. The solution of $NaNO_2$ and H_2O_2 was mixed at the three way channel AB to generate HNOOH. Carbon dots enhanced the CL from ONOOH system, and its CL has been recorded in Fig. 1a. The baseline of curves b and c in Fig. 1 stands for the CL intensity caused by the reaction of ONOOH–NaOH and ONOOH–Na_2CO_3 systems. The introduction of carbon dots further increased the CL intensity from ONOOH–NaOH and ONOOH–Na_2CO_3 system (Fig. 1b and c). ONOOH, as a weak acid with pKa of 6.8 [4], is suggested to be turned to $ONOO^-$ related species in alkaline medium. The CL enhancement of carbon dots in alkaline medium is suspected to be attributed to the interaction between carbon dots and $ONOO^-$ related species [29]. Compared with the CL from carbon dots–$NaNO_2$–H_2O_2–Na_2CO_3 system (Fig. 1d), the CL from carbon dots–H_2O_2–Na_2CO_3 system in the absence of $NaNO_2$ was rather low, which confirmed the main role of nitrite and its related species (ONOOH, $ONOO^-$, and $ONOOCO_2^-$) in the CL reaction.

3.2. CL from carbon dots–$NaNO_2$–H_2O_2–Na_2CO_3 system by batch experiment

The CL dynamic curves under different reagent injection orders have been obtained by batch experiment. The injection of solution of Na_2CO_3 and carbon dots together into ONOOH was accompanied by very strong CL (Fig. 2), which was stronger than the CL intensity obtained when Na_2CO_3 and carbon dots were added in that order into ONOOH. In the absence of nitrite, very weak CL emission as low as 120 count was observed in Fig. 2, which further verified the important role of ONOOH, $ONOO^-$ and $ONOOCO_2^-$ in the CL system.

$$HNO_2 + H_2O_2 \rightarrow ONOOH + H_2O \quad (1)$$

$$ONOOH + OH^- \rightarrow ONOO^- + H_2O \quad (2)$$

$$ONOO^- + CO_2 \rightarrow ONOOCO_2^- \quad (3)$$

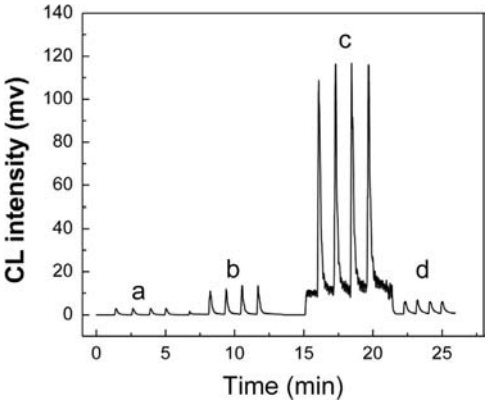


Fig. 1. The CL signal in the flow injection system for carbon dots–$NaNO_2$–H_2O_2, carbon dots–$NaNO_2$ H_2O_2 NaOH, carbon dots–$NaNO_2$–H_2O_2–Na_2CO_3 and carbon dots–H_2O_2–Na_2CO_3 systems. Conditions: 0.1 M H_2O_2 in 0.025 M H_2SO_4, 1.0×10^{-5} M $NaNO_2$, 0.1 M Na_2CO_3, carbon dots with a dilution of 1: 1000.

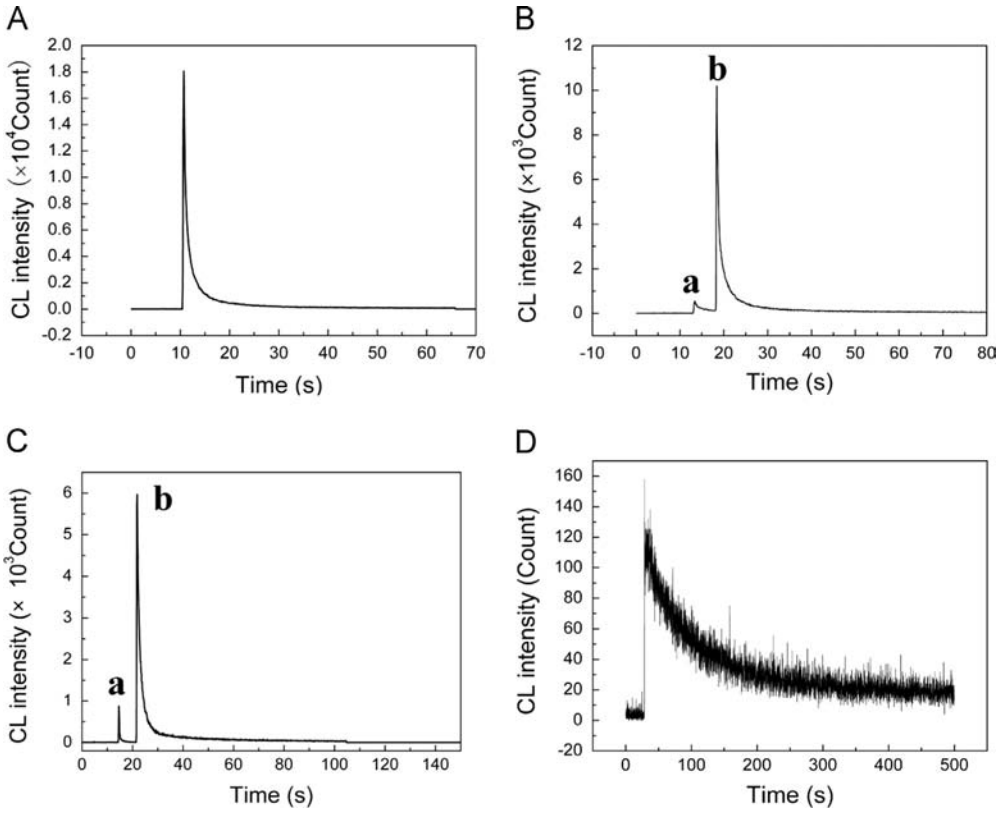


Fig. 2. CL kinetic curves of carbon dots–$NaNO_2$–H_2O_2 system with different reagent mixing orders: (A) injecting Na_2CO_3 and carbon dots solution together into the mixture of H_2O_2 and $NaNO_2$, (B) injecting carbon dots and Na_2CO_3 successively to $NaNO_2$–H_2O_2 solution, (C) injecting Na_2CO_3 and carbon dots successively to $NaNO_2$–H_2O_2 solution, and (D) Na_2CO_3 and carbon dots were injected simultaneously into H_2O_2 solution. Curve a in (B) stands for the CL caused by injecting Na_2CO_3 into $NaNO_2$–H_2O_2 solution. Curve b in (B) is the CL resulting from the injection of carbon dots into the solution containing Na_2CO_3–$NaNO_2$–H_2O_2. Conditions: 0.1 M H_2O_2 in 0.025 M H_2SO_4, 1.0×10^{-5} M $NaNO_2$, 0.1 M Na_2CO_3, carbon dots with a dilution of 1: 1000.

3.3. The determination of nitrite

The batch CL signals increased with the concentration of nitrite. Hence, this system can be developed as a flow injection analysis method for the determination of nitrite. To establish the optimal conditions for the analysis of nitrite, the effects of the pH on the CL reaction, the length of the channel as well as the flow rate of the solution on the CL analysis were investigated. It has been found that maximum CL intensity is observed in solution with pH value around 7.0, which is slightly higher than the pKa of ONOOH (6.8). It is known that ONOOH is generated from $NaNO_2$ and H_2O_2 in acid medium. While only ONOOH in its anion ($ONOO^-$) form could react with CO_2 to form $ONOOCO_2^-$ [30]. Solution with the pH value around 7.0 is not only beneficial for the formation of $ONOO^-$ but also facilitates the generation of CO_2.

ONOOH is generated from $NaNO_2$ and H_2O_2 in channel AB (Fig. S1). Short mixing channel could reduce the decomposition of ONOOH and brought in higher CL intensity. The flow rate of the solution affected the mixing efficiency of the reagent, the decomposition of unstable compound as well as the detection time in spiral CL detection cell. Fig. 3A showed that $NaNO_2$ and H_2O_2 solution with flow rate as high as 4.5 mL min^{-1} could greatly reduce the decomposition of ONOOH and obtain optimal signal. The optimized flow rate for Na_2CO_3 and carbon dots solution is 2.4 mL min^{-1} (Fig. 3B).

The CL intensity increased linearly with the nitrite concentration in the range of 1.0×10^{-7} to 1.0×10^{-5} M and the correlation coefficient is 0.9956 (Fig. 4). The relative standard deviations (R. S. D) (n=10) of the analysis were 1.8 %, 2.5 %, and 1.9 % for 1.0×10^{-7}, 1.0×10^{-6}, and 5.0×10^{-6} M nitrite, respectively. The limit of detection (S/N=3) for nitrite was 5.0×10^{-9} M. The flow-injection CL analysis has been applied successfully to detect nitrite in tap water. The concentration of nitrite in the tap water from Haidian district (Beijing, China) is 1.8×10^{-7} M and the result is in good agreement with the value obtained by spectrophotometric method (1.9×10^{-7} M)[31]. The recovery calculated by spiking the tap water with 1.0×10^{-6} M nitrite is 98%. Some metal cations have positive interference on the CL detection. Cation-exchange resins could effectively eliminate the interferences from cations. With the using of cation-exchange resins, ions such as 1000-fold Na^+, Ca^{2+}, F^-, Cl^-, Br^-, NO_3^-, SO_4^{2-}, 200-fold Mg^{2+}, Fe^{2+}, Fe^{3+}, Zn^{2+} and 100-fold Co^{2+} have no interferences on the CL detection of 1.0×10^{-6} M nitrite.

3.4. CL mechanism

Carbon dots could greatly enhance the CL in $NaNO_2$–H_2O_2–carbonate system. In order to identify the enhanced mechanism of carbon dots, CL spectrum was measured by a fluorescence spectrometer with the xenon lamp turned off. The maximum CL spectrum for carbon dots–$NaNO_2$–H_2O_2–carbonate system presented in Fig. 5A is around 500 nm, which is blue-shifted compared with maximum CL spectrum for carbon dots–$NaNO_2$–H_2O_2 system (520 nm). $ONOOCO_2^-$ and its related radical, $\bullet CO_3^-$, is suggested to be generated and is also confirmed by using DMPO as the trapping reagent (Fig. 6A) [32] in carbon dots–$NaNO_2$–H_2O_2–Na_2CO_3 system. Carbon dioxide in its excited form, $(CO_2)_2^*$ is suggested to be formed through $\bullet CO_3^-$ (Reactions 4 and 5) [33,34]. $(CO_2)_2^*$ could release to its basic ground with CL emission in 440 nm (Reaction 6). It could be found from the fluorescence spectrum of carbon dots whose emission wavelength was located at 500 nm with 440 nm as the excitation wavelength. Hence, it is

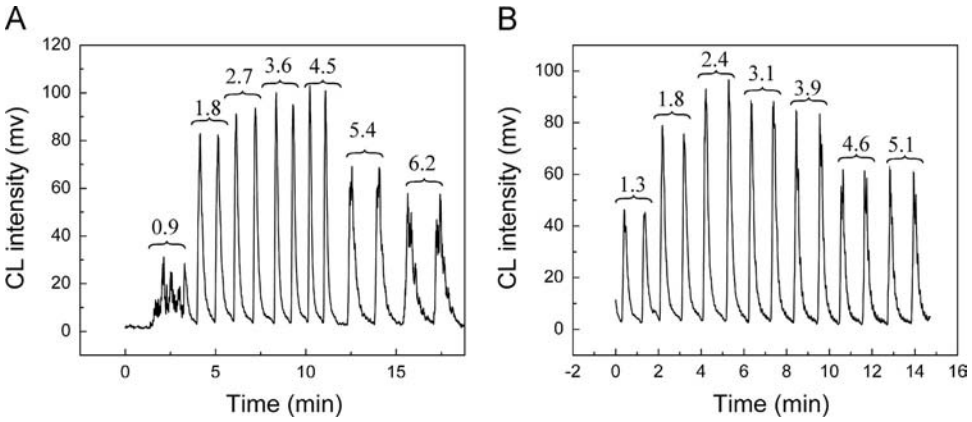


Fig. 3. The effects of the flow rate of $NaNO_2$ and H_2O_2 solution (A), Na_2CO_3 and carbon dots solution (B) on the flow-injection CL detection system.

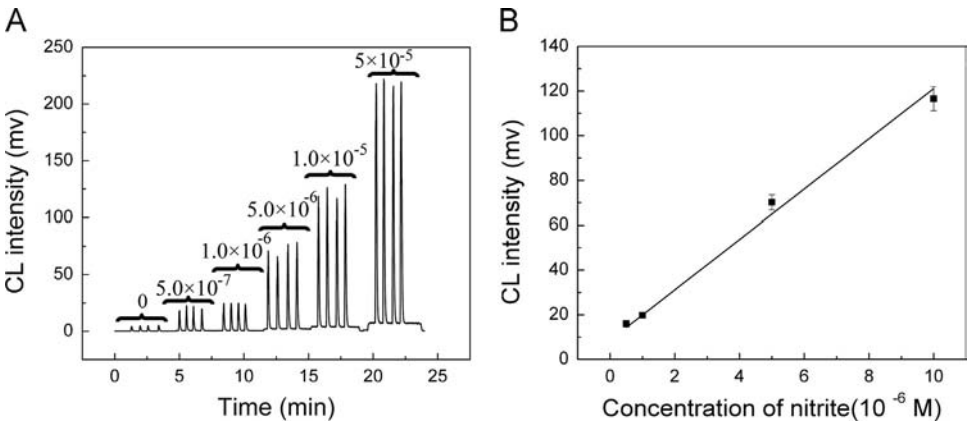


Fig. 4. Flow injection signals (A) and standard curve (B) for the nitrite concentration ranging from 1.0×10^{-7} to 1.0×10^{-5} M. Experimental conditions: 0.5 M H_2O_2 in 0.05 M H_2SO_4, 0.1 M Na_2CO_3, carbon dots in a dilution of 1: 1000, high voltage: −800 V, and 100 μL samples were injected.

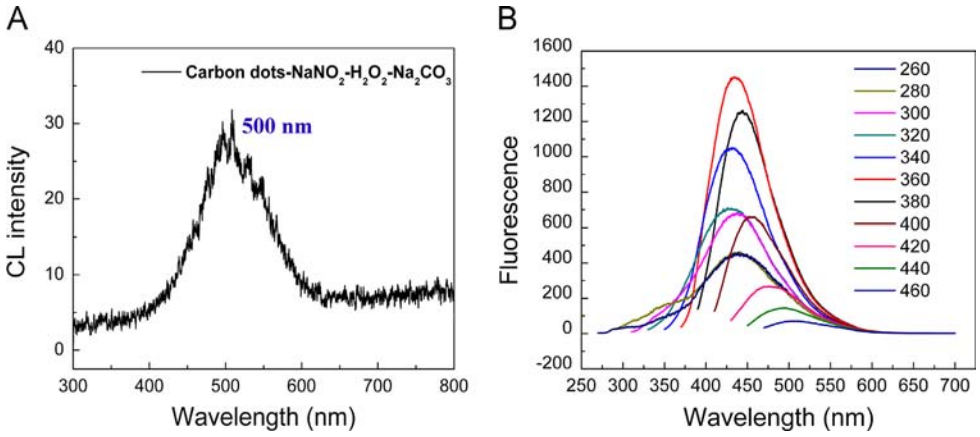


Fig. 5. (A) The CL spectrum of carbon dots–$NaNO_2$–H_2O_2–Na_2CO_3 system and (B) the fluorescent spectra for carbon dots excited at wavelengths from 260 nm to 460 nm with 20 nm increment.

reasonable to deduce that carbon dots partially serve as the energy acceptor in the CL system (Reactions 7 and 8), which gives us new insight into the role of carbon dots. The EPR signal of carbon dots changed greatly in the presence of $NaNO_2$–H_2O_2. The presence of carbonate in carbon dots-$NaNO_2$-H_2O_2 system decreased the EPR signal changing of carbon dots, which further confirmed its energy acceptor role (Fig. 6B).

$$ONOOCO_2^- \rightarrow \bullet CO_3^- + \bullet NO_2 \quad (4)$$

$$2(\bullet CO_3^-) \rightarrow (CO_2)_2^* + O_2^{2-} \quad (5)$$

$$(CO_2)_2^* \rightarrow 2CO_2 + h\nu\ (440\ \text{nm}) \quad (6)$$

$$(CO_2)_2^* + R \rightarrow CO_2 + R_a^* \quad (7)$$

$$R_a^* \rightarrow R_a + h\nu(500\ \text{nm}) \quad (8)$$

It is noted that CL spectrum for carbon dots–$NaNO_2$–H_2O_2–carbonate system is partially overlapped with that from carbon dots–$NaNO_2$–H_2O_2 system (520 nm). The overlapping indicated that the CL is partially aroused from the radiative electron–hole annihilation between hole-injected and electron-injected carbon dots ($R^{\bullet+}$ and $R^{\bullet-}$) [35,36] (Reactions 13 and 14). Oxidant species

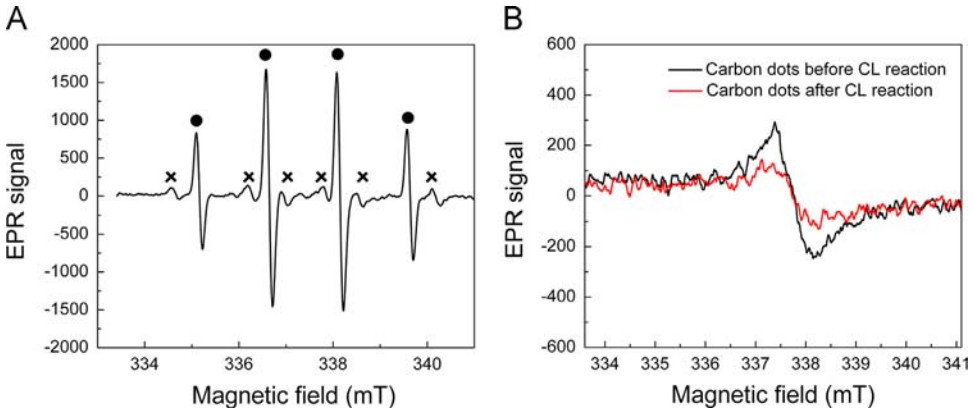


Fig. 6. (A) EPR spectra of carbonate and hydroxyl radicals generated by reaction of DMPO probe in carbon dots–$NaNO_2$–H_2O_2–Na_2CO_3 system and (B) EPR spectra of the carbon dots before and after the CL reaction.

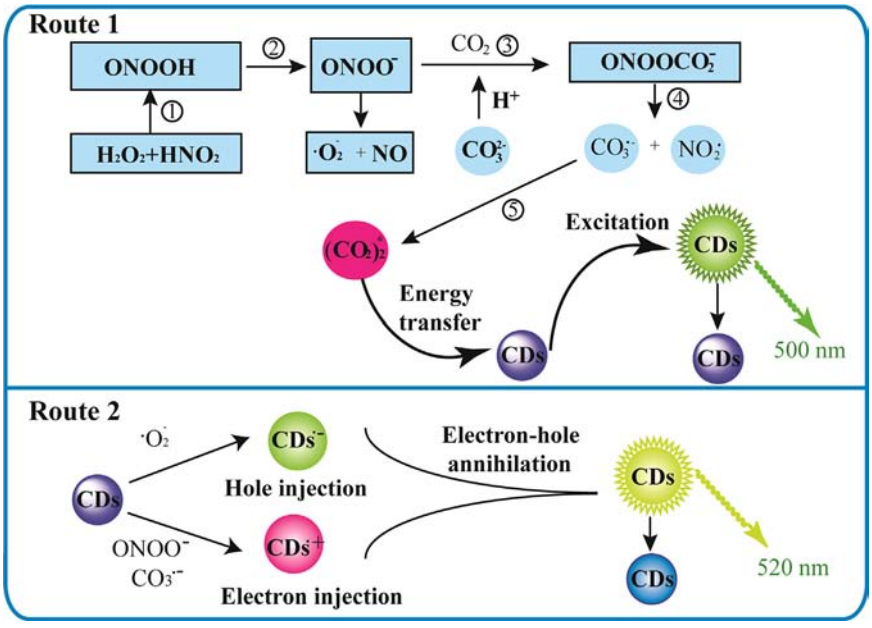


Fig. 7. Schematic illustration of CL mechanism of carbon dots–$NaNO_2$–H_2O_2–Na_2CO_3 system. CDs stand for carbon dots.

that existed in the carbon dots–$NaNO_2$–H_2O_2–carbonate system, including $ONOO^-$, OH● and $\bullet CO_3^-$, could serve as the hole injector and convert carbon dots into $R^{\bullet+}$ (Reactions 11and 12). $O_2^{\bullet-}$ generated from the decomposition of $ONOO^-$could donate its electron to carbon dots to produce carbon dots with negative charge (Reactions 9 and 10) [37].

$$ONOO^- \rightarrow \bullet O_2^- + NO \quad (9)$$

$$R + \bullet O_2^- \rightarrow R^{\bullet-} + O_2 \quad (10)$$

$$R + ONOO^- \rightarrow R^{\bullet+} + \text{product} \quad (11)$$

$$R + OH\bullet \rightarrow R^{\bullet+} + OH^- \quad (12)$$

$$R^{\bullet-} + R^{\bullet+} \rightarrow R_b^* \quad (13)$$

$$R_b^* \rightarrow R_b + h\nu\ (525\ \text{nm}) \quad (14)$$

The discussion above indicated that carbon dots could enhance the CL from $NaNO_2$–H_2O_2–Na_2CO_3 system through two pathways (Fig. 7). Firstly, carbon dots acts as the energy acceptor in carbon dots–$NaNO_2$–H_2O_2–Na_2CO_3 system. This kind of enhancement in the system is related with the excited species generated from $ONOOCO_2^-$ and $\bullet CO_3^-$. With pH value above the pKa of ONOOH, ONOOH converted to its anion form ($ONOO^-$). $ONOO^-$ reacted with CO_2 that was generated from the protonation of carbonate to produce $ONOOCO_2^-$. The decomposition of $ONOOCO_2^-$ resulted in the formation of $\bullet CO_3^-$ and $(CO_2)_2^*$. $(CO_2)_2^*$ acted as the energy donor and donated its energy to carbon dots and excited the carbon dots, whose energy releasing brought in the CL emission (Route 1 in Fig. 7). CL is also partially generated from the radiative electron–hole annihilation between hole-injected and electron-injected carbon dots (Route 2 in Fig. 7).

4. Conclusion

Carbon dots were found to have CL enhancement on $NaNO_2$–H_2O_2–Na_2CO_3 system. The CL mechanism has been investigated. $(CO_2)_2^*$ is suggested to be existing in the system and donates its energy to excite carbon dots to its excited form, which released their energy to ground-state by CL emission. The radiative electron–hole annihilation between hole-injected and electron-injected carbon dots also had contribution for the CL. The investigation not only gave us new insight into the characteristic of carbon dots but also showed a broad prospect for the application of carbon dots in CL system. With the advantage of the CL from carbon dots–$NaNO_2$–H_2O_2–Na_2CO_3 system, a sensitive and

simple flow-injection CL method for nitrite sensing has been developed. The established method has been successfully applied to the determination of nitrite in tap water with good recoveries and precision.

Acknowledgments

This work was supported by National Natural Science Foundation of China (Nos. 91213305, 21305015) and China Equipment and Education Resources System (No. CERS-1-75).

Appendix A. Supporting information

Supplementary data associated with this article can be found in the online version at http://dx.doi.org/10.1016/j.talanta.2014.09.046.

References

[1] B. Alvarez, H. Rubbo, M. Kirk, S. Barnes, B.A. Freeman, R. Radi, Chem. Res. Toxicol. 9 (1996) 390–396.
[2] Y.D. Liang, J.F. Song, J. Pharm. Biomed. Anal. 38 (2005) 100–106.
[3] Y. Zhao, K. Houk, L.P. Olson, J. Phys. Chem. A. 108 (2004) 5864–5871.
[4] W. Koppenol, J. Moreno, W.A. Pryor, H. Ischiropoulos, J. Beckman, Chem. Res. Toxicol. 5 (1992) 834–842.
[5] M.N. Hughes, Biochimica et Biophysica Acta (BBA)-Bioenergetics. 1411 (1999) 263–272.
[6] J. Glebska, W.H. Koppenol, Free Radical Biol. Med. 38 (2005) 1014–1022.
[7] Y.D. Liang, J.F. Song, X.F. Yang, W. Guo, Talanta 62 (2004) 757–763.
[8] Y.D. Liang, J.F. Song, X.F. Yang, Anal. Chim. Acta 510 (2004) 21–28.
[9] C. Lu, J.M. Lin, C.W. Huie, Talanta 63 (2004) 333–337.
[10] C. Lu, F. Qu, J.M. Lin, M. Yamada, Anal. Chim. Acta. 474 (2002) 107–114.
[11] H. Zhang, L. Zhang, C. Lu, L. Zhao, Z. Zheng, Spectrochim. Acta Part A 85 (2011) 217–222.
[12] Z. Wang, X. Teng, C. Lu, Analyst 137 (2012) 1876–1881.
[13] J. Li, Q. Li, C. Lu, L. Zhao, Analyst 136 (2011) 2379–2384.
[14] S.V. Lymar, J.K. Hurst, J. Am. Chem. Soc. 117 (1995) 8867–8868.
[15] M.G. Bonini, R. Radi, G. Ferrer-Sueta, A.M.D.C. Ferreira, O. Augusto, J. Biol. Chem. 274 (1999) 10802–10806.
[16] C. Lu, J.-M. Lin, C.W. Huie, M. Yamada, Anal. Chim. Acta. 510 (2004) 29–34.
[17] L. Cao, X. Wang, M.J. Meziani, F. Lu, H. Wang, P.G. Luo, Y. Lin, B.A. Harruff, L.M. Veca, D. Murray, J. Am. Chem. Soc. 129 (2007) 11318–11319.
[18] S.T. Yang, L. Cao, P.G. Luo, F. Lu, X. Wang, H. Wang, M.J. Meziani, Y. Liu, G. Qi, Y.P. Sun, J. Am. Chem. Soc. 131 (2009) 11308–11309.
[19] W. Shi, Q. Wang, Y. Long, Z. Cheng, S. Chen, H. Zheng, Y. Huang, Chem. Commun. 47 (2011) 6695–6697.
[20] Y. Song, K. Qu, C. Zhao, J. Ren, X. Qu, Adv. Mater. 22 (2010) 2206–2210.
[21] L. Zhou, Y. Lin, Z. Huang, J. Ren, X. Qu, Chem. Commun. 48 (2012) 1147–1149.
[22] Y. Dong, R. Wang, H. Li, J. Shao, Y. Chi, X. Lin, G. Chen, Carbon 50 (2012) 2810–2815.
[23] H. Li, X. He, Z. Kang, H. Huang, Y. Liu, J. Liu, S. Lian, C.H.A. Tsang, X. Yang, S. T. Lee, Angew. Chem. Int. Ed. 49 (2010) 4430–4434.
[24] L. Cao, S. Sahu, P. Anilkumar, C.E. Bunker, J. Xu, K.A.S. Fernando, P. Wang, E.A. Guliants, K.N. Tackett, Y.P. Sun, J. Am. Chem. Soc. 133 (2011) 4754–4757.
[25] M.L. Zhang, Q.F. Yao, W.J. Guan, C. Lu, J.-M. Lin, J. Phys. Chem. C. 118 (2014) 10441–10447.
[26] Z. Lin, X.N. Dou, H.F. Li, Q.S. Chen, J.-M. Lin, Microchim. Acta. 181 (2014) 805–811.
[27] Z. Lin, W. Xue, H. Chen, J.-M. Lin, Anal Chem. 83 (2011) 8245–8251.
[28] M. Anbar, H. Taube, J. Am. Chem. Soc. 76 (1954) 6243–6247.
[29] S. Goldstein, G. Czapski, J. Am. Chem. Soc. 120 (1998) 3458–3463.
[30] S. Goldstein, G. Czapski, J. Lind, G. Merenyi, Chem. Res. Toxicol. 14 (2001) 1273–1276.
[31] N.V.N. Sreekumar, B. Hegde, P. Manjunatha, B.R. Sarojini, B.K, Microchem. J. 74 (2003) 27–32.
[32] R.G. Wolcott, B.S. Franks, D.M. Hannum, J.K. Hurst, J. Biol. Chem. 269 (1994) 9721–9728.
[33] J.-M. Lin, M. Yamada, Anal. Chem. 71 (1999) 1760–1766.
[34] S.X. Liang, L.X. Zhao, B.T. Zhang, J.M. Lin, J. Phys. Chem. A. 112 (2008) 618–623.
[35] Z. Ding, B.M. Quinn, S.K. Haram, L.E. Pell, B.A. Korgel, A.J. Bard, Science 296 (2002) 1293–1297.
[36] L. Zheng, Y. Chi, Y. Dong, J. Lin, B. Wang, J. Am. Chem. Soc. 131 (2009) 4564–4565.
[37] P. Di Mascio, E.J.H. Bechara, M.H.G. Medeiros, K. Briviba, H. Sies, FEBS Lett. 355 (1994) 287–289.

Talanta 132 (2015) 463–468

Contents lists available at ScienceDirect

Talanta

journal homepage: www.elsevier.com/locate/talanta

An ultra-sensitive colorimetric Hg^{2+}-sensing assay based on DNAzyme-modified Au NP aggregation, MNPs and an endonuclease

Chao Li, Peiqing Dai, Xinyi Rao, Lin Shao, Guifang Cheng*, Pingang He, Yuzhi Fang

Department of Chemistry, East China Normal University, Shanghai 200241, PR China

ARTICLE INFO

Article history:
Received 12 July 2014
Received in revised form
18 September 2014
Accepted 28 September 2014
Available online 7 October 2014

Keywords:
Endonuclease
Au nanoparticle aggregation
Magnetic nanoparticles
DNAzyme
Mercury ions

ABSTRACT

This paper reports the development of an ultra-sensitive colorimetric method for the detection of trace mercury ions involving DNAzymes, Au nanoparticle aggregation, magnetic nanoparticles and an endonuclease. DNAzyme-sensing elements are conjugated to the surface of Au nanoparticle-2, which can crosslink with the T-rich strands coated on Au nanoparticle-1 to form Au nanoparticle aggregation. Other T-rich stands are immobilized on the surface of MNPs. The specific hybridization of these two T-rich strands depends on the presence of Hg^{2+}, resulting in the formation of a T-Hg^{2+}-T structure. Added endonuclease then digests the hybridized strands, and DNAzyme-modified Au NP aggregation is released, catalysing the conversion of the colourless ABTS into a blue-green product by H_2O_2-mediated oxidation. The increase in the adsorption spectrum of $ABTS^+$ at 421 nm is related to the concentration of Hg^{2+}. This assay was validated by detecting mercury ion concentrations in river water. The colorimetric responses were not significantly altered in the presence of 100-fold excesses of other metal ions such as Zn^{2+}, Pb^{2+}, Cd^{2+}, Mn^{2+}, Ca^{2+} and Ni^{2+}. The inclusion of both Au NP aggregation and an endonuclease enables the assay to eliminate interference from the magnetic nanoparticles with colorimetric detection, decrease the background and improve the detection sensitivity. The calibration curve of the assay was linear over the range of Hg^{2+} concentrations from 1 to 30 nM, and the detection limit was 0.8 nM, which is far lower than the 10 nM US EPA limit for drinking water.

© 2014 Elsevier B.V. All rights reserved.

1. Introduction

Mercury is a highly toxic global pollutant with an environmental residence time from 0.5 to 2 years [1,2]. This kind of persistent toxic substance occurs naturally and releases into the environment through both natural and anthropogenic processes. Mercury has a strong affinity to organic substances, which plays an important role in mobilization and transportation of mercury from forest ecosystems to water ecosystems [3,4]. Consumption of polluted water or seafood can lead to the accumulation of mercury in the human body, leading to some serious illnesses, including neuropsychological dysfunction and chronic mercury poisoning syndrome. Among various mercury pollutants, Hg^{2+} is the most stable inorganic form in water environments [5]. Moreover, methyl mercury, the most common organic source and bioaccumulative form of mercury, is generated from Hg^{2+} by microbial biomethylation [6]. Hence, the sensitive and specific detection of Hg^{2+} is important for water pollution control and drinking water safety.

The determination of trace amounts of mercury has commonly been carried out using cold vapor atomic absorption spectrometry (CVAAS) or inductively coupled plasma mass spectrometer (ICP-MS). These instrumental analysis of Hg require that all chemical forms of mercury are needed to reduce to elemental mercury (Hg^0) [4]. However, these extra pretreatment steps can lead to increased risk of contamination and/or mercury volatilization from sample. Therefore, it is very urgent to develop the novel and sensitive methods for the detection of Hg avoiding the environmentally hazardous pretreatment steps. Hg sensors based on T-Hg^{2+}-T conjugation have been developed to meet the requirement [7–10]. These electrochemical [11–13], fluorescence [14] and optical sensors [15–17] have been used to monitor aqueous Hg^{2+}. Due to its high sensitivity and low production costs, electrochemical sensing is one of the most popular Hg^{2+} detection system designs. However, its unstable performance, poor reproducibility, and high non-specific absorption lead to imperfect detection. While fluorescence is another attractive detection method, it requires sophisticated instrumentation, an expensive and complicated labelling procedure, and it tends to result in a high background. Compared with the methods described above, colorimetric systems are stable and easy to control, but less sensitive. Hence, to meet the requirements of Hg ion detection in drinking water (within the 10 nM US EPA limit), the sensitivity of the colorimetric method should be improved. In this work, we use Au nanoparticle aggregation modified with DNAzymes as signal amplification elements and demonstrate that this approach reduces the detection limit.

* Corresponding author. Tel./fax: +86 021 54340047.
E-mail address: gfcheng@chem.ecnu.edu.cn (G. Cheng).

http://dx.doi.org/10.1016/j.talanta.2014.09.037
0039-9140/© 2014 Elsevier B.V. All rights reserved.

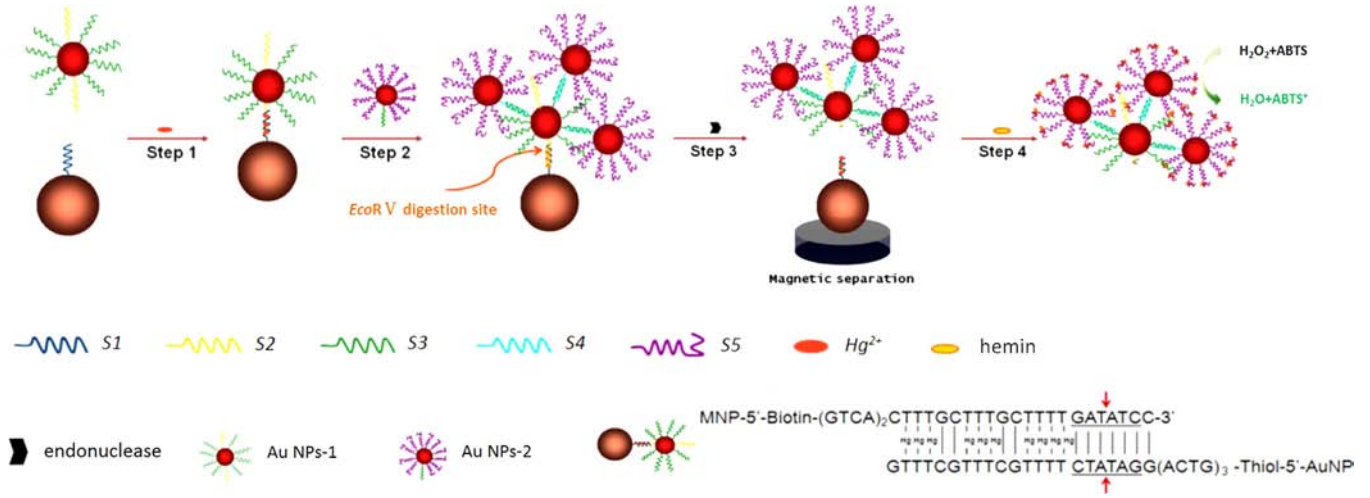


Fig. 1. A schematic illustration of the amplified Hg^{2+}-sensing assay.

Due to their favourable biocompatibility, it is easy to modify magnetic nanoparticles (MNPs) with biologically active groups to achieve the enrichment and separation of components of interest [18]. MNPs have been employed in this way to powerful effect in a number of applications [19–21]. However, MNPs have been reported to exhibit an intrinsic peroxidase-like activity, which could cause a background signal in colorimetric assays [22]. Moreover, the use of MNPs in an optical detection system could lead to uneven scattering, leading to some bias in the results. To eliminate these disadvantages, this assay uses an endonuclease with a specific recognition and hydrolysis ability to release the sensing element into the liquid phase for UV-visible spectrophotometric detection. This paper reports the development of a novel, selective and sensitive colorimetric Hg^{2+}-sensing assay based on Au NP aggregation coated with DNAzyme, MNPs and an endonuclease (*Eco*RV). As illustrated in Fig. 1, this strategy uses several DNA strands and consists of four main steps. First, in the presence of Hg^{2+}, MNPs coated with the T-rich S1 strands (S1/MNPs) specifically hybridize with AuNP-1s modified with the T-rich strands (S2) and with AuNP-1s modified with cross-linking strands (S3). Second, the Au NP-2s covered with a different type of cross-linking strand (S4) and with DNAzyme strands (S5) are added to the Au NP aggregation formed in the first step. The excess AuNP-1s, AuNP-2s and interfering substances are then removed by magnetic separation. Then, *Eco*RV is used to digest the DNA double-strand to release Au NP aggregation, contributing to the amplification of the optical signal. After incubating the supernatant of the digested Au NP aggregation with hemin, the colorimetric measurement is carried out, with the optical signal of $ABTS^+$ at 421 nm directly related to the concentration of the Hg ion in solution.

2. Experimental procedures

2.1. Materials

An HZQ-C Swing bed machine (Donglian Electrical Technology Co. Ltd., China) was used to assemble the oligonucleotide strands onto the surfaces of the Au NPs and MNPs. Colorimetric measurements were performed on a Cary 50 UV–visible Spectrophotometer (Varian, Palo Alto, USA). A JEM-2100F field emission electron microscope (JEOL, Japan) was used to observe the structure of the nanoparticles.

Tris-(2-carboxyethyl) phosphine (TCEP), saline sodium citrate (SSC) buffer (15 mM SSC, 150 mM NaCl, pH 7.0), bovine serum albumin (BSA) and hemin were purchased from Sigma Chemical Co. (Shanghai, China). Chloroauric acid and 2,2′-azino-bis(3-ethylbenzo-thiazoline-6-sulfonic acid) diammonium salt (ABTS) were obtained from Sangon Biotechnology Co. (Shanghai, China). *Eco*RV and 100 × BSA were purchased from New England Biological Technology Co. Ltd. (Beijing, China). Streptavidin-coated magnetic nanoparticles (MNPs, hydrodynamic diameter of 100 nm, 10 mg/mL) were obtained from Chemicell GmbH (Germany). All oligonucleotides were synthesized by Shanghai Sangon Biotechnology Co. and purified by HPLC. The oligomer sequences and the buffers used are listed in the supporting information.

2.2. Preparation of oligonucleotide-modified MNPs

A 100-μL solution of MNPs modified with streptavidin (10 mg/mL) was washed three times with SSC buffer to remove sodium azide. Then, 0.38 nmol S1 in 200 μL of SSC buffer was added to the collected MNPs. After 1 h of gentle shaking at room temperature, the mixture was washed to remove free DNA. A 1% BSA solution was used to block the MNP surface and eliminate further non-specific adsorption. After 1 h of blocking treatment, these S1/MNPs were stored in 200 μL of Hg^{2+} capture buffer at 4 °C.

2.3. Preparation of oligonucleotide-modified Au NPs

Au NPs with an average diameter of 13 nm (estimated by TEM) were prepared by the citrate reduction method [23]. S2 and S3 (0.36 nmol and 3.6 nmol, respectively) were treated with TCEP (2.5 mM, dissolved in 0.1 M Tris-HAc, pH 7.4) for 1 h. Then, 200 μL Au NPs (10.4 nM) were added to the reduced S2 and S3 solution. The mixture was gently stirred at room temperature for 42 h while the salt concentration was gradually adjusted to a final value of 0.3 M NaAc. The solution was centrifuged (13000 rpm, 15 min) and rinsed with water twice to remove the excess oligonucleotides. Then, 10 μL of 20% BSA was added for 1 h to block the surface of the Au NPs. The resulting solution was suspended in 200 μL capture buffer and named Au NPs-1. The Au NPs-2 (S4 to S5 ratio of 1:100) and Au NPs-3 (S2 to S5 ratio of 1:10) were prepared by the same procedure and dispersed in hybridization or capture buffer, respectively. All of the Au NPs were stored at 4 °C until further use.

2.4. Hg^{2+} recognition

The recognition of Hg^{2+} was carried out by following steps. Briefly, 10 μL S1/MNPs, 40 μL S2/S3/Au NPs and certain volumes of Hg^{2+} were added to a tube and gently shaken at room

temperature for 30 min. Then, 1200 μL S4/S5/Au NPs was added to form Au NP aggregation. The hybridization was carried out at 37 °C for 40 min. The aggregations were washed with water and then resuspended in 20 μL 10 × NE buffer 3, 1 μL of 100 × BSA and 4 U *Eco*RV in a final volume of 100 μL. After vigorous shaking at 37 °C for 2 h, the aggregations were washed twice with water. The supernatants from all washes were collected and diluted with 2 × HEPES to a final volume of 1 ml. Then, 500 μL of hemin (190 nM) was added, and the mixtures were incubated with gentle shaking to form the DNAzyme complexes.

2.5. Colorimetric measurements

After 5.6 μmol of ABTS and 0.6 μmol of H_2O_2 were added to the above solutions, the absorption spectrum of $ABTS^+$ was measured from 380 to 520 nm. The $A_{421\ nm}$ recorded after a 10-min reaction was used for quantitative analysis.

3. Results and discussion

3.1. The characteristics of the Hg^{2+}-sensing assay

Several experiments were conducted to test the feasibility of the proposed Hg^{2+} assay. First, only S1/MNPs and Au NPs-3 were used to confirm the ability of the assay to capture Hg^{2+} (Fig. 2a). The assay gave out a very lower response ($A_{421\ nm}$) while no Hg^{2+} existed (curve a). When Hg^{2+} ions were introduced into this system, they induced the two strands of DNA (S1 and S2) to intertwist by forming T-Hg^{2+}-T bonds; meanwhile, an *Eco*RV digestion site was formed by complementary base-pairing reactions [24,25]. After *Eco*RV treatment, the absorbance at 421 nm (A_{421}) was progressively higher when the concentration of Hg^{2+} in the solution increased from 100 nM to 500 nM (curves b and c, respectively). This result demonstrates that the immobilization of T-rich strands on the surface of nanoparticles such as Au NPs and MNPs does not disturb the specific recognition of Hg^{2+} or the endonuclease activity. The increased A_{421} of curve c illustrates that the colorimetric responses of the assay depends on the mercury ions by formation of T-Hg-T structure. However, further signal amplification was limited by the number of active sites on the Au NP surface, restricting the detection limit.

As in our previous work, the Au NP surface influences the efficiency of target recognition and the signal amplification ability [26]. That is, higher S5 (the sensing strands) to S2 (the capture strands) ratios on individual Au NPs will enhance the absorbance signal at the expense of target capture efficiency, which ultimately restricts the amplification of signal intensity. Au NP aggregation was introduced to overcome this problem. The lowest signal in Fig. 2b is the response of the assay with only S1/MNPs (curve a), representing the background signal with no sensing element. Although the Au NPs-3 coated with an S2 to S5 ratio of 1:100 produce a clear signal (curve b), the limited number of active sites due to the low S2 to S5 ratio limits Hg^{2+} capture, resulting in a low signal. Curve c is the result of the assay using Au NP aggregation as the sensing element, with a S2 to S5 ratio on the Au NP aggregation of 1:100. The increase in the catalytic absorbance signal indicates the superiority of the Au NP aggregation in amplifying the absorbance signal and effectively capturing the target at the same S2 to S5 ratio.

In contrast with the individual Au NP-3s, in the Au NP aggregation, the capture strands (S2) and the DNAzyme sensing strands (S5) are immobilized on different Au NPs. To maximize the signal amplification, the S5:S4 ratio on the surface of the sensing Au NPs was increased while controlling the S3:S2 ratio at a lower level (10:1) to ensure effective target capture. A large absorbance signal was observed when the S5:S4 ratio on the sensing Au NPs

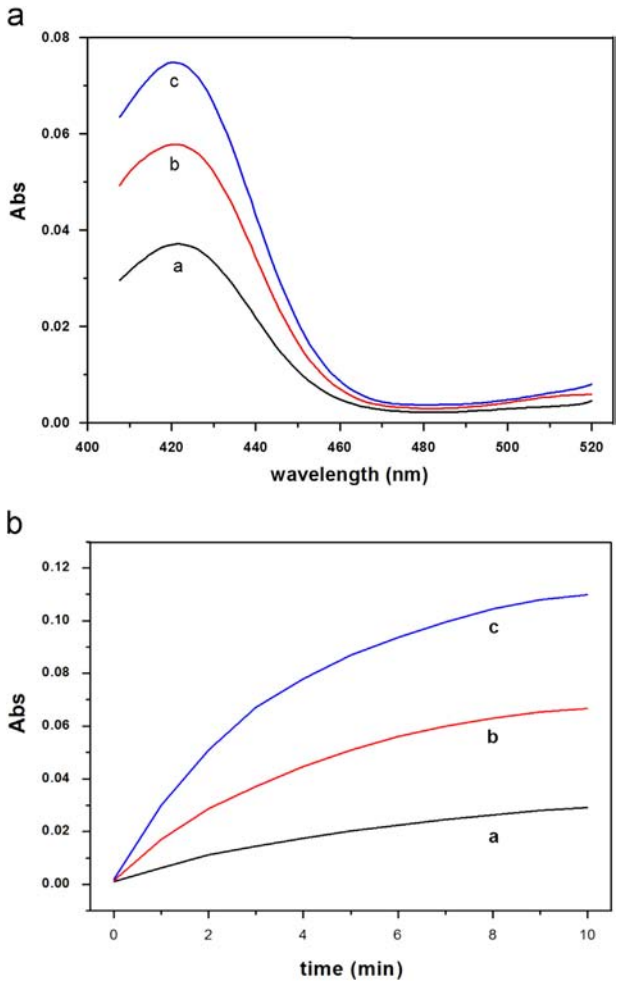


Fig. 2. (a) Spectra produced by assays performed with S1/MNPs and Au NPs-3 without target (a), with 100 nM Hg^{2+} (b) and 500 nM Hg^{2+} (c) in the presence of 63 nM hemin and 60 U *Eco*RV after 10 min of catalysis. (b) Kinetic absorbance *vs.* time curves of assays with different sensing elements: (a) none, (b) Au NPs-3 and (c) Au NP aggregation in the presence of 500 nM Hg^{2+}, 63 nM hemin and 60 U *Eco*RV, with an S2 to S5 ratio of 1:100.

was fixed at 100:1 (Fig. 3, curve c). This almost fourfold increase in the response (compared with Fig. 3, curve b) enabled ultrasensitive detection of Hg^{2+} in drinking water.

TEM was used to monitor the deposits after magnetic separation and confirm the formation of Au NP aggregation. Fig. 4a presents the results without Hg^{2+} ions, which lead to the collection of MNPs alone. Compared with Fig. 4a, several darker particles representing DNAzyme-modified Au NPs are observed in Fig. 4b after discarding the free Au NPs, thus demonstrating the success of the MNP-Hg^{2+}-Au NP sandwich structure. The abundant deposits of Au NPs on MNPs due to the binding between S1/MNPs and Au NP aggregation, yielding a lot of relatively dark spots (Fig. 4c) [27,28]. It confirms the feasibility of assay in efficient capture of the target and sensitive amplification of the signal. After *Eco*RV treatment, the DNA duplex between MNPs and Au NP aggregation was digested. Most Au NPs are separated from the deposit, leading to a dramatic decrease in the presence of darker particles in the TEM image as shown in Fig. 4d. The results of this TEM experiment verify the ability to detect trace mercury ions by the strategy discussed above.

3.2. Optimization

To determine the optimal conditions for the colorimetric Hg^{2+}-sensing assay, several key parameters were varied, including

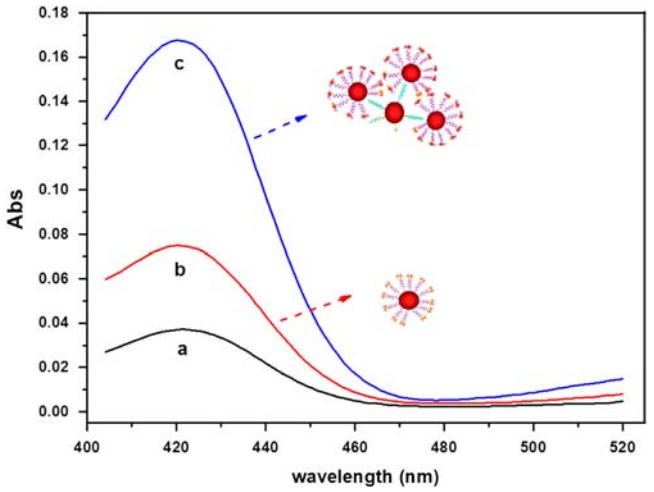


Fig. 3. The catalysis spectra of the assay consisting of S1/MNPs and Au NPs-3 without target (a) and with 500 nM Hg^{2+} (b), and of the assay consisting of S1/MNPs and Au NP aggregation (with a S5:S4 ratio of 100:1) (c) in the presence of 63 nM hemin and 60 U *Eco*RV recorded after a 10 min catalysis period.

mercury ions capture time, the dosages of *Eco*RV and the salinity in target capture and the formation of Au NP aggregation respectively. Fig. 5a presents data on capture time determination over the range from 10 to 60 min at room temperature. These data reveal that the $\Delta A_{421\ nm}$ of the supernatant increases sharply as capture time increases up to 40 min, with further increases in capture time having no effect. Therefore, we deduce that 40 min ensures adequate combination between Hg^{2+} and the two capture elements. The incubation time was also varied. The salinity in the Au NP aggregation and mercury ions capture has been shown to affect the optical signal (S1 and S2). After comparing the results under different conditions, the salinity of each Hg^{2+} capture and Au NP aggregation was fixed at 0.6 M and 1 M.

We observed that adding *Eco*RV has a dampening effect on the catalytic reaction, suggesting that this step should be optimized. The effect of adding different concentrations of *Eco*RV on $\Delta A_{421\ nm}$ is shown in Fig. 5b. The $\Delta A_{421\ nm}$ first increased as the amount of *Eco*RV increased, reaching a peak at 60 U. We expect that less than 60 U of *Eco*RV is insufficient to completely digest the DNA duplex. However, adding more than 60 U of *Eco*RV interferes with the catalytic reaction rather than influencing digestion.

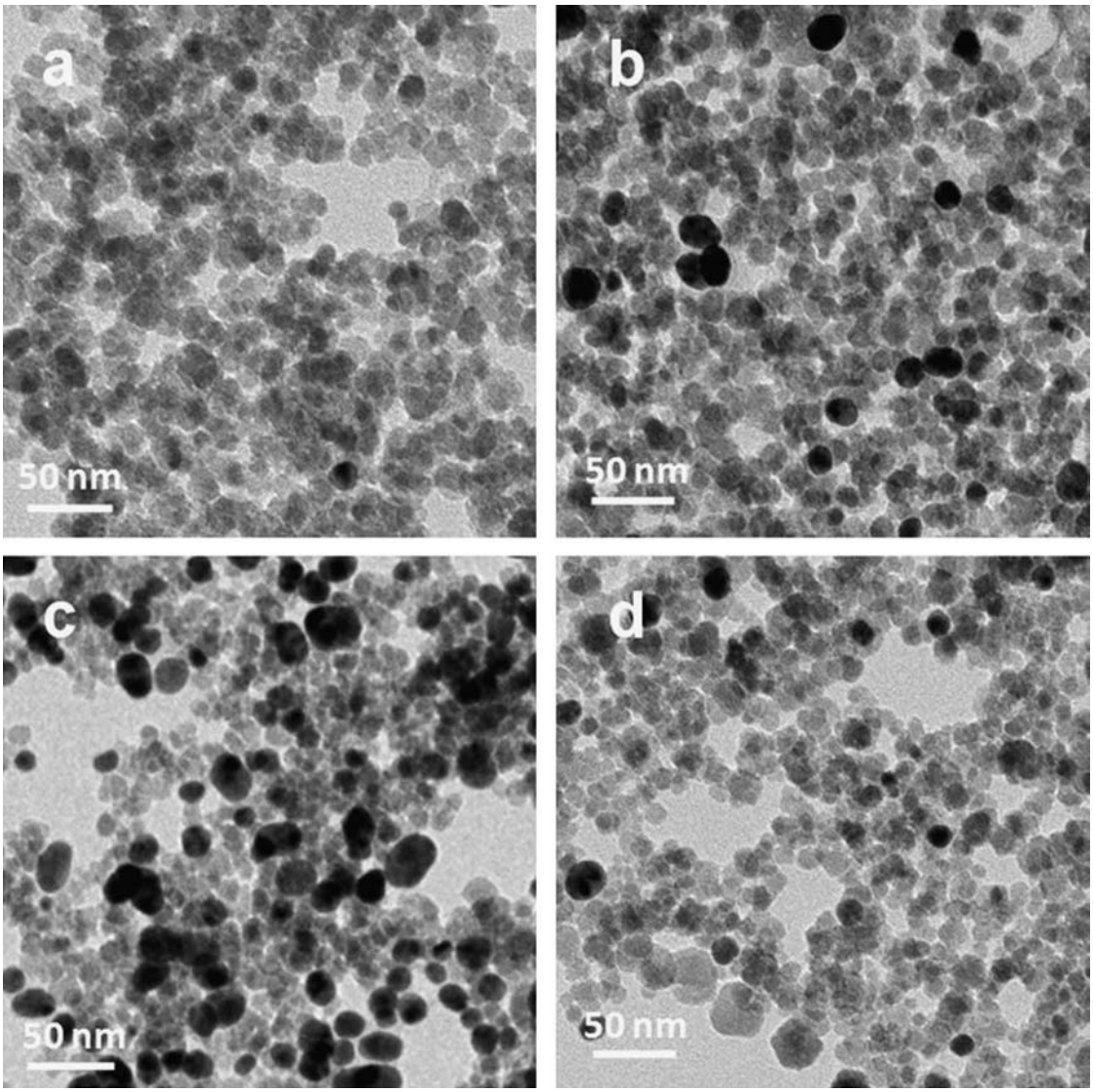


Fig. 4. TEM images of deposits for the assay consisting of S1/MNPs and Au NP-3 s without Hg^{2+} (a) and in the presence of 500 nM Hg^{2+} (b); the deposits for the assay consisting of S1/MNPs and Au NP aggregation (with S4:S5 = 100:1) before (c) and after (d) *Eco*RV digestion in the presence of 500 nM Hg^{2+}.

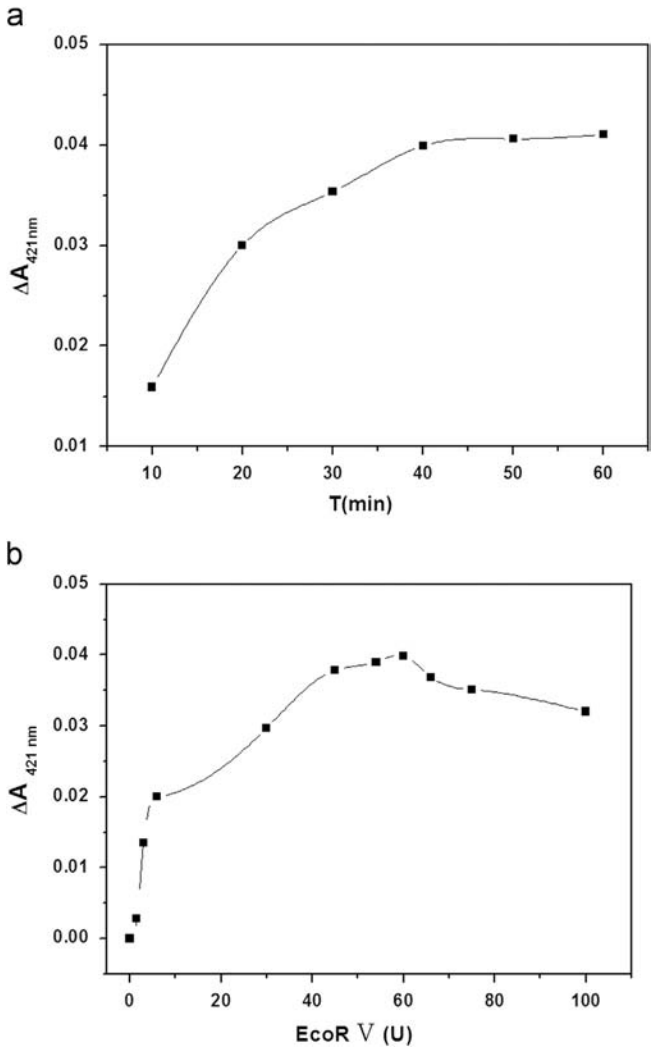


Fig. 5. (a) Influence of the Hg^{2+} capture time on the $\Delta A_{421\ nm}$ of the assay and (b) influence of the amount of *Eco*RV on $\Delta A_{421\ nm}$ in the presence of 63 nM hemin and 25 nM Hg^{2+}.

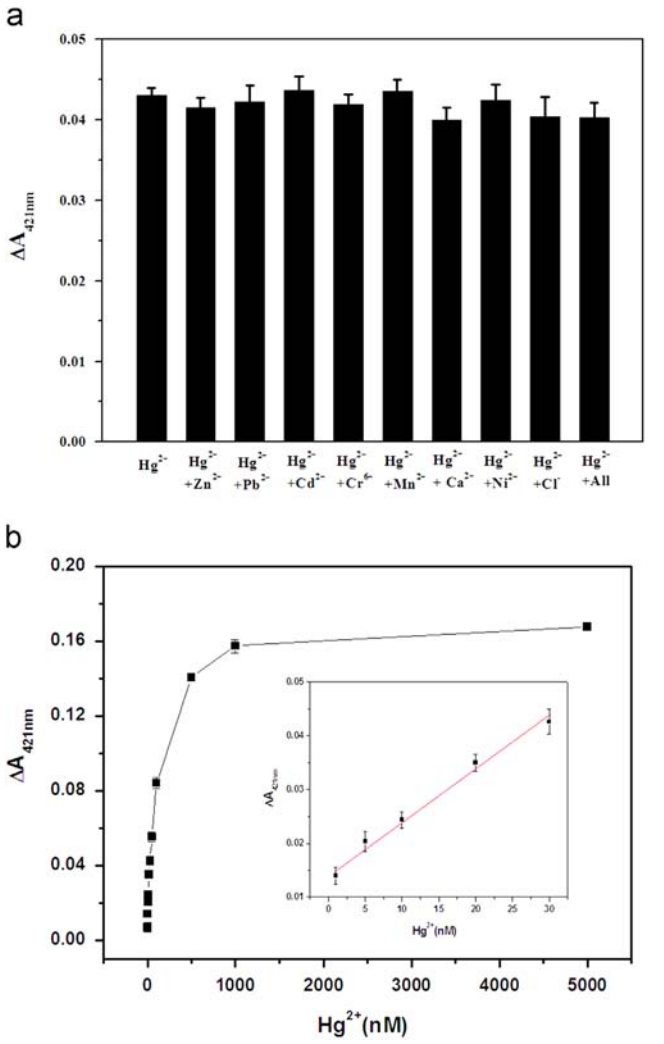


Fig. 6. (a) The selectivity of the Hg^{2+} sensing assay in the presence of 25 nM Hg^{2+} and 2.5 μM of other metal ions. (b) The calibration curve corresponding to the $\Delta A_{421\ nm}$ of the Hg^{2+} sensing assay with different Hg^{2+} concentrations after 10 min catalytic reactions. The inset presents the amplification of the linear range from 1 nM to 30 nM with a correlation coefficient of 0.9923. All data were obtained from five independent experiments, and the error bars denote standard deviations.

3.3. Selectivity of the Hg^{2+}-sensing assay

To test the selectivity of the Hg^{2+}-sensing assay, 2.5 μM aliquots of other metal ions including Zn^{2+}, Pb^{2+}, Cd^{2+}, Cr^{2+}, Mn^{2+}, Ca^{2+}, Ni^{2+} and Cl^- were added individually or in combination to the detection solution together with 25 nM Hg^{2+}. The $\Delta A_{421\ nm}$ signal was measured, and the results are reported in Fig. 6a. It can be seen that only slight effects of co-existent ions has been observed on the UV absorption of the Hg^{2+} sensor. Even when all of the metal ions were present in the detection solution together, little interference was exhibited. This result verifies the high selectivity of the assay for Hg^{2+} against interfering materials and demonstrates its applicability in complex aqueous systems.

3.4. Quantitative detection of mercury ions

Various amounts of Hg^{2+} (1 nM-5 μM) were incubated under the optimal conditions to obtain the calibration curve. The data in Fig. 6b presented that the increase in $\Delta A_{421\ nm}$ depends on the increase in the Hg^{2+} concentration. However, when Hg^{2+} concentration is higher than 1 μM, the absorbance intensity was not obviously enhanced and a plateau is reached, because the interaction between the thymine residues and Hg^{2+} reaches a balance and saturation. A liner response was obtained for Hg^{2+} concentrations ranging from 1 nM to 30 nM, according to the equation $\Delta A_{421\ nm} = 0.0147 + 1.0 \times 10^{-3} c_{Hg2+}$ (nM) with correlation coefficient 0.9923 and P-value 0.037 at 95% confidence level. A detection limit of 0.8 nM Hg^{2+} was determined by evaluating the average response of the blank plus three times the standard deviation, and this limit is far lower than the 10 nM US EPA limit for drinking water. In comparison with previous colorimetric sensors [16], the use of Au NP aggregation significantly improves the sensitivity of Hg^{2+} detection.

3.5. Application to sample analysis

As the quantitative analysis and effective detection of Hg^{2+} in practical aqueous systems is of great importance for human health and the environment, our sensor was applied to analyse three real samples (tap water, river water and industrial wastewater) before and after the addition of certain amounts of Hg^{2+}. The analytical results corresponding to the determination of Hg^{2+} in the three samples are shown in Table 1. The concentration of mercury ions in the first two samples was too low to be detectable. However, when 10 nM of Hg^{2+} standard solution was added, the readable signals were observed. The response of industrial wastewater

Table 1
Detection of Hg^{2+} in aqueous samples.

Sample	Hg^{2+} measured (nM)[a]	CVAAS (nM)[b]	Addition of Hg^{2+} (nM)	Detection of Hg^{2+} (nM)[a]	Recovery (%)
Tap water	Not found	Not found	10.0	10.4	104.0
River water	Not found	Not found	10.0	9.3	93.0
Industrial wastewater	12.3	12.5	12.0	25.4	109.2

[a] All data were obtained from three independent experiments.
[b] All data were obtained by cold vapor atomic absorption spectrometry.

sample was measurable and the addition of 12 nM Hg^{2+} showed about twice signal enhancement more than the original indicating that interfering materials in the samples did not influence Hg^{2+} detection. Compared with the data of cold vapor atomic absorption spectrometry (CVAAS) the results obtained by proposed Hg^{2+}-sensor were satisfied. The recovery values between 93.0 and 109.2% clearly manifest the potential of this sensing assay to detect Hg^{2+} in real aqueous samples.

4. Conclusion

The colorimetric detection strategy proposed here demonstrates the feasibility of specific, sensitive and convenient detection of trace amounts of mercury ions in drinking water. The application of Au NP aggregation, MNPs and an endonuclease results in efficient amplification of the colorimetric signal of Hg^{2+}, elimination of the interference from co-existing substances and reduction of the background. Compared with individual Au NPs, the use of Au NP aggregation almost quadruples the catalytic capacity. Moreover, the endonuclease digestion and the separation of MNPs enable convenient detection of Hg^{2+} in the liquid phase. This assay enabled the measurement of absorbance signals of Hg^{2+} from 1 nM to 30 nM with a detection limit of 0.8 nM, which is much lower than the US Environmental Protection Agency (EPA) limit of Hg^{2+} for drinkable water (10 nM). The sensing assay can also be applied in practical aqueous systems to determine the Hg^{2+} content. Given the sensitivity and specificity of this method, we expect that it will be a promising tool for practical Hg^{2+} analysis.

Acknowledgements

This work was supported by the National Natural Science Foundation of China (grant no. 21175045) and the National Ministry of Science and Technology (grant no. 2011YQ150078-6).

Appendix A. Supporting information

Supplementary data associated with this article can be found in the online version at http://dx.doi.org/10.1016/j.talanta.2014.09.037.

References

[1] P. Li, X.B. Feng, G.L. Qiu, L.H. Shang, Z.G. Li, J. Hazard. Mater. 168 (2009) 591–601.
[2] L.C. Chasar, B.C. Scudder, A.R. Stewart, A.H. Bell, G.R. Aiken, Environ. Sci. Technol. 43 (2009) 2733–2739.
[3] H. Cheng, Y. Hu, Environ. Sci. Technol. 46 (2012) 4695–4696.
[4] H. Pyhtilä, P. Perämäki, J. Piispanen, M. Niemelä, T. Suoranta, M. Starr, T. Nieminen, M. Kantola, L. Ukonmaanaho, Microchem. J. 103 (2012) 165–169.
[5] F.A. Cotton, G. Wilkinson, C.A. Murillo, M. Bochmann, Advanced Inorganic Chemistry, Wiley, New York, 1999.
[6] T.W. Clarkson, L. Magos, G.J. Myers, N. Engl. J. Med. 349 (2003) 1731.
[7] Z. Zhao, X.M. Zhou, Biosens. Bioelectron. 26 (2011) 2666–2669.
[8] D.M. Kong, J Wu, N. Wang, W. Yang, H.X. Shen, Talanta 80 (2009) 459–465.
[9] R. Kavitha, T. Stalin, J. Lumin. 149 (2014) 12–18.
[10] J. Ge, X.P. Li, J.H. Jiang, R.Q. Yu, Talanta 122 (2014) 85–90.
[11] D. Han, Y.R. Kim, J.W. Oh, T.H. Kim, R.K. Mahajan, J.S. Kim, H. Kim, Analyst 134 (2009) 1857–1862.
[12] P. Miao, L. Liu, Y. Li, G.X. Li, Electrochem. Commun. 11 (2009) 1904–1907.
[13] J.K. Wu, L.Y. Li, B.J. Shen, G.F. Cheng, P.G. He, Y.Z. Fang, Electroanalysis 22 (2010) 479–482.
[14] P. Travascio, P.K. Witting, A.G. Mauk, D. Sen, J. Am. Chem. Soc. 123 (2001) 1337–1348.
[15] T. Li, B.L. Li, E.K. Wang, S.J. Dong, Chem. Commun. 24 (2009) 3551–3553.
[16] C.J. Yu, T.L. Cheng, W.L. Tseng, Biosen. Bioelectron. 25 (2009) 204–210.
[17] J.K. Wu, L.Y. Li, D. Zhu, P.G. He, Y.Z. Fang, G.F. Cheng, Anal. Chim. Acta. 694 (2011) 115–119.
[18] Y. Du, B.L. Li, S.J. Guo, Z.X. Zhou, M. Zhou, E.K. Wang, S.J. Dong, Analyst 136 (2011) 493–497.
[19] J. Zheng, G.F. Cheng, P.G. He, Y.Z. Fang, Talanta 80 (2010) 1868–1872.
[20] Y. Guo, X. Jia, S. Zhang, Chem. Commun. 47 (2011) 725–727.
[21] Y.H. Tennico, D. Hutanu, M.T. Koesdjojo, C.M. Bartel, V.T. Remcho, Anal. Chem. 82 (2010) 5591–5597.
[22] S. Centi, S. Tombelli, M. Minunni, M. Mascini, Anal. Chem. 79 (2007) 1466–1473.
[23] L. Gao, J. Zhuang, L. Nie, Nature Nanote. 2 (2007) 577–583.
[24] Z. Guo, J. Duan, F. Yang, M. Li, T. Hao, S. Wang, D. Wei., Talanta 93 (2012) 49–54.
[25] M. Zhu, Y. Wang, Y. Deng, L. Yao, S.B. Adeloju, D. Pan, F. Xue, Y. Wu, L. Zheng, W. Chen, Biosen. Bioelectron. 61 (2014) 14–20.
[26] X. Rao, J. Zhang, J. Cui, Y. Hu, T. Liu, J. Chai, G. Cheng, P. He, Y. Fang, Chem. Res. Chin. Univ. 29 (2013) 868–873.
[27] G.K. Darbha, A.K. Singh, U.S. Rai, E. Yu, H. Yu, P.C. Ray, J. Am. Chem. Soc. 130 (2008) 8038–8043.
[28] I. Ojea-Jime´nez, X. Lo´pez, J. Arbiol, V. Puntes, ACS Nano 6 (2012) 2253–2260.

Talanta 132 (2015) 469–478

Contents lists available at ScienceDirect

Talanta

journal homepage: www.elsevier.com/locate/talanta

Fast and simple screening for the simultaneous analysis of seven metabolites derived from five volatile organic compounds in human urine using on-line solid-phase extraction coupled with liquid chromatography-tandem mass spectrometry

Wen-Chieh Chiang [a], Chao-Yu Chen [a], Ting-Chen Lee [a], Hui-Ling Lee [a,*], Yu-Wen Lin [b]

[a] Department of Chemistry, Fu Jen Catholic University, Xinzhuang Dist, New Taipei City 24205, Taiwan
[b] Department of Public Health, Fu Jen Catholic University, Xinzhuang Dist, New Taipei City 24205, Taiwan

ARTICLE INFO

Article history:
Received 30 July 2014
Received in revised form
16 September 2014
Accepted 17 September 2014
Available online 7 October 2014

Keywords:
On-line SPE
LC–MS/MS
Seven metabolites derived from five VOCs
Human urine

ABSTRACT

Recently, the International Agency for Research on cancer classified outdoor air pollution and particulate matter from outdoor air pollution as carcinogenic to humans (IARC Group 1), based on sufficient evidence of carcinogenicity in humans and experimental animals and strong mechanistic evidence. In particular, a wide variety of volatile organic compounds (VOCs) are volatized or released into the atmosphere and can become ubiquitous, as they originate from many different natural and anthropogenic sources, such as paints, pesticides, vehicle exhausts, cooking fumes, and tobacco smoke. Humans may be exposed to VOCs through inhalation, ingestion, or dermal contact, which may increase the risk of leukemia, birth defects, neurocognitive impairment, and cancer. Therefore, the focus of this study was the development of a simple, effective and rapid sample preparation method for the simultaneous determination of seven metabolites (6 mercaptic acids+*t*,*t*-muconic acid) derived from five VOCs (acrylamide, 1,3-butadiene, acrylonitrile, benzene, and xylene) in human urine by using automated on-line solid-phase extraction (SPE) coupled with liquid chromatography–electrospray tandem mass spectrometry (LC–MS/MS). An aliquot of each diluted urinary sample was directly injected into an autosampler through a trap column to reduce contamination, and then the retained target compounds were eluted by back-flush mode into an analytical column for separation. Negative electrospray ionization tandem mass spectrometry was utilized for quantification. The coefficients of correlation (r^2) for the calibration curves were greater than 0.995. Reproducibility was assessed by the precision and accuracy of intra-day and inter-day precision, which showed results for coefficient of variation (CV) that were low 0.9 to 6.6% and 3.7 to 8.5%, respectively, and results for recovery that ranged from 90.8 to 108.9% and 92.1 to 107.7%, respectively. The limits of detection (LOD) and limits of quantification (LOQ) were determined to within 0.010 to 0.769 ng mL^{-1} and 0.033 to 2.564 ng mL^{-1} in this study. A stability study test included 3 freeze/thaw cycles during short-term storage at room temperature for 36 h and long-term storage at −20 °C for 1 month, and the CV (coefficient of variation) showed less than 8.4, 7.4 and 9.7%, respectively. To the best of our knowledge, this is the first study to provide simple, small injection volumes (40 μL) and a rapid LC–MS/MS method combined with an on-line SPE step for the simultaneous detection, identification, and quantification of seven metabolites derived from five VOCs in human urine for evaluation of the future risk of human exposure to volatile organic compounds.

© 2014 Elsevier B.V. All rights reserved.

1. Introduction

Recently, the International Agency for Research on cancer classified outdoor air pollution and particulate matter from outdoor air pollution as carcinogenic to humans (IARC Group 1), based on sufficient evidence of carcinogenicity in humans and experimental animals and strong mechanistic evidence [1]. Air pollutants belong to diverse groups of chemical compounds that are generally grouped into four categories: gaseous pollutants (volatile organic compounds (VOCs), including benzene); persistent organic compounds (polycyclic aromatic hydrocarbons (PAHs), including benzo[a]pyrene (BaP); heavy metals; and, particulate matter (PM).

* Corresponding author at: Department of Chemistry, Fu Jen Catholic University, No. 510 Zhongzheng Rd. Xinzhuang Dist, New Taipei City 24205, Taiwan.
Tel.: +886 2 29053573; fax: +886 2 29023209.
E-mail address: 076308@mail.fju.edu.tw (H.-L. Lee).

http://dx.doi.org/10.1016/j.talanta.2014.09.029
0039-9140/© 2014 Elsevier B.V. All rights reserved.

In particular, volatile organic compounds (VOCs) are high-production chemicals with several common industrial applications such as chemical intermediates, dry-cleaning chemicals, and solvents, and also are present in cigarette smoke, gasoline, factory fumes and automobile exhaust [2]. According to EPA reports, several VOCs are mutagenic, neurotoxic, genotoxic, and/or carcinogenic and may increase the risk of leukemia, birth defects, neurocognitive impairment, and cancer from both short- and long-term exposure to humans [2–5]. Examples such as benzene and 1,3-butadiene all are proven carcinogens [6]. Acrylamide and acrylonitrile are IARC class 2 carcinogens [7,8]. Xylene has been classified by the IARC as group 3, but it is an important industrial chemical and is a constituent of tobacco smoke [9]. These findings strongly suggest a potential link between exposure to VOCs and diseases in humans.

Over the past few years, exposure to VOCs has often been assessed by the determination of VOC metabolites in urine, and the main advantages of monitoring urinary VOC metabolites are as follows: non-invasive, longer physiological half-life of metabolites compared with parent compounds, and the specificity of mercapturic acid (MAs) metabolites. MAs can be regarded as the final product of the mercapturate metabolic detoxification pathway, and also have been recognized as *N*-acetyl-L-cysteine-*S* conjugates. MAs are released into circulation and removed from the blood by the kidneys for excretion in urine [10,11]. In the present study, we monitored urinary VOC metabolites as biomarkers of exposure to acrylamide, 1,3-butadiene, acrylonitrile, benzene, and xylene. These seven metabolites (Fig. 1) were included: *N*-acetyl-*S*-(2-carbamoyl-2-hydroxyethyl)-L-cysteine (GAMA), *N*-acetyl-*S*-(3,4-dihydroxybutyl)-L-cysteine (DHBMA), *N*-acetyl-*S*-(4-hydroxy-2-buten-1-yl)-L-cysteine (MHBMA3), *N*-acetyl-*S*-(2-cyanoethyl)-L-cysteine (CYMA), trans,trans-muconic acid (*t,t*-MA), *S*-phenylmercapturic acid (PMA), and *N*-acetyl-*S*-(2,4-dimethylphenyl)-L-cysteine (2,4-DPMA).

Various traditional analytical approaches with different sensitivities and specificities can be used to measure VOC metabolites in urine samples. These approaches include gas chromatography with flame ionization detection (GC–FID) [12], gas chromatography with electron capture detection (GC–ECD) [13], gas chromatography with mass spectrometry (GC–MS) [14], high-performance liquid chromatography with ultraviolet absorption detection (HPLC–UV) [15], and high-performance liquid chromatography with fluorescence (HPLC–FD) [16]. All those approaches have specificity for individual VOC metabolites, but a sample preparation protocol such as that used for chemical derivatization reactions is needed or the result could be a lack of sensitivity for low concentrations of VOC metabolites. E-nose analysis of exhaled breath is a new method for assessing VOC profiles in humans [17,18]. Recently, liquid chromatography tandem mass spectrometry (LC–MS/MS) methods have proven to be highly selective, sensitive, accurate, and with the capacity to simultaneously quantify VOC metabolites in human urine [2,11,19,20].

Most published methods for the determination of VOC metabolites in urine involve a labor-intensive and time-consuming procedure that requires purification by solid-phase extraction (SPE) [21–25], such as molecularly imprinted polymers (MIPs) [26] and C18 [27] or liquid–liquid extraction (LLE) [28,29]. To avoid the drawbacks of the extraction method, therefore, we developed a simple, quick and cheap sample preparation method and combined it with on-line SPE-LC–MS/MS, which was rapid, automated, and required only a small sample volume with a decreased matrix effect that provided an accurate, precise and simultaneous determination of these seven metabolites derived from five VOCs (acrylamide, 1,3-butadiene, acrylonitrile, benzene, and xylene.) in human urine samples. Combining these two technologies not only enhanced the signal but also improved the sensitivity compared with other existing methods currently in use. To the best of our knowledge, this is the first study to provide simple, small-injection volumes (40 μL), and a rapid LC–MS/MS method combined with an on-line SPE step that was developed for the simultaneous detection, identification, and quantification of these seven metabolites derived from five VOCs in human urine for an estimation of the possible risk of human exposure to volatile organic compounds.

2. Experimental

2.1. Chemical and reagents

N-acetyl-*S*-(2-hydroxy-3-propionamide)-L-cysteine dicyclohexylammonium salt (GAMA), *N*-acetyl-*S*-(2-hydroxy-3-propionamide)-L-cysteine-d_3 dicyclohexylammonium salt (GAMA-d_3),

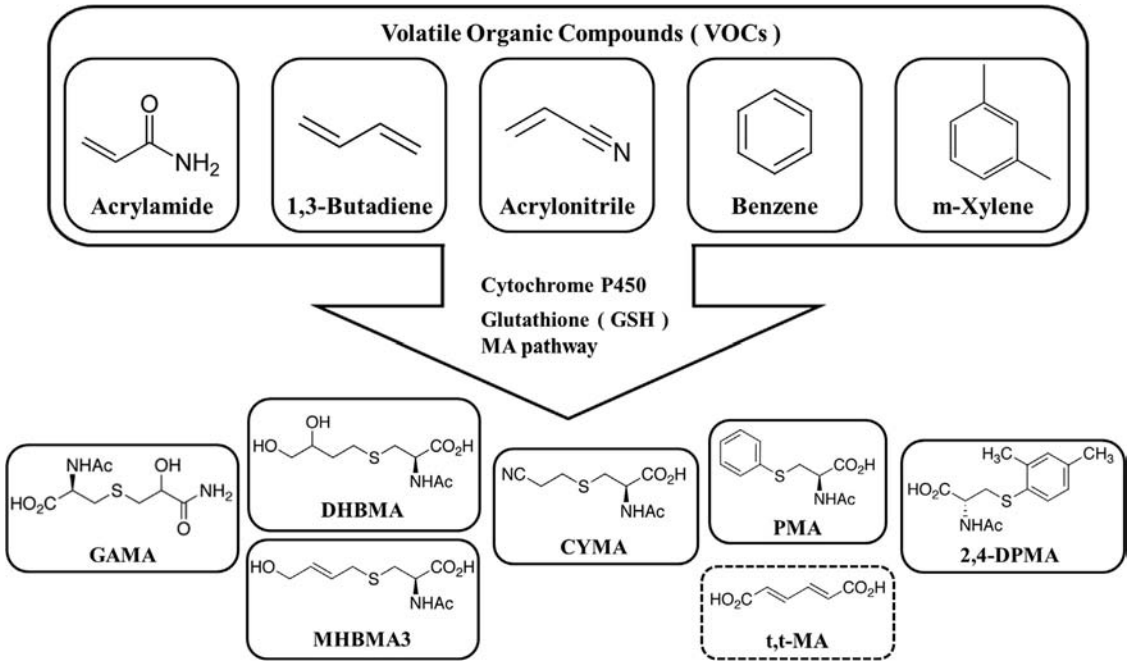


Fig. 1. Metabolic pathway of seven metabolites derived from five VOCs (6 mercapturic acids + *t,t*-muconic acid) in this study.

trans, trans-muconic acid (*t,t*-MA), trans, trans-muconic acid-d_4 (*t,t*-MA-d_4), *S*-phenylmercapturic acid (PMA), *S*-phenyl-d_5-mercapturic acid (PMA-d_5), *N*-acetyl-*S*-(2-cyanoethyl)-L-cysteine (CYMA), *N*-acetyl-*S*-(2-cyanoethyl)-L-cysteine-d_3 (CYMA-d_3), *N*-acetyl-*S*-(3,4-dihydroxybutyl)-L-cysteine (DHBMA), *N*-acetyl-*S*- (3,4-dihydroxybutyl) -L-cysteine-d_7 (DHBMA-d_7), *N*-acetyl-*S*-(4-hydroxy-2-buten-1-yl)-L-cysteine (MHBMA3), *N*-acetyl-*S*-(4-hydroxy-2-buten-1-yl)-L-cysteine-d_3 (MHBMA3-d_3), *N*-acetyl-*S*-(2,4-dimethylphenyl)-L-cysteine (2,4-DPMA) and *N*-acetyl-*S*-(2,4-dimethylbenzene)cysteine-d_3 (2,4-DPMA-d_3) were obtained from Toronto Research Chemicals.

HPLC-grade methanol (MeOH) and HPLC-grade acetonitrile (ACN) were purchased from J.T. Baker. Formic acid (FA) and Ammonium acetate (AA) were purchased from Sigma-Aldrich. Acetic acid (HOAc) was purchased from Merck.

2.2. Sample preparation method

The urinary samples were thawed from −20 °C and immediately centrifuged at 3000 rpm and 4 °C for 10 min. To a 40 μL aliquot of each urinary sample supernatant after centrifugation was added 10 μL 20% HOAc (v/v), the sample was allowed to acidify, and then it was diluted with 350 μL 5% ACN (v/v)+10 mM AA. Finally, a 25 μL aliquot of diluted sample was spiked with 25 μL of internal standards (IS) solution (400 ng mL^{-1} *t,t*-MA-d_4, 50 ng mL^{-1} DHBMA-d_7, and 100 ng mL^{-1} PMA-d_5, 2,4-DPMA-d_3, MHBMA3-d_3, CYMA-d_3, GAMA-d_3) prior to vortex mixing, and then the sample was kept frozen at −20 °C until it could be analyzed. A 40 μL aliquot of diluted urine sample was injected into the analytical system.

2.3. Automated on-line SPE

The column-switching system used in the present study is described in detail elsewhere [30]. This system consisted of a switching valve (10-port, 2-position microelectric actuator from Valco Instrument Co., Ltd.) and an Inertsil ODS (33 mm × 4.6 mm, 5 μm) column. The switching valve function was controlled by Analyst 1.4.2™ software (AB SCIEX, Canada). The column-switching operation, including the LC gradients, used during the online cleanup and the analytical procedures are summarized in Table 1. When the switching valve was at position A, 40 μL of the prepared urine sample was loaded onto the trap column via an autosampler (Agilent 1200 Series; Agilent Technology, U.S.A.), and a binary pump (Agilent 1200; Agilent Technology) delivered 100% solvent A (100% H_2O) at a flow rate of 1 mL min^{-1} as the loading and washing solvent (Eluent I). After the trap column was flushed with the loading solvent for 1.5 min, the valve was switched to the injection position (position B) to inject the sample into the analysis column. At 3.0 min after injection, the valve was switched back to position A, and the column again was eluted with solvent A (Eluent I) using a linear gradient from 100% solvent A to 100% solvent B (90% ACN, v/v with 0.1% formic acid) for 6.0 min, followed by 100% solvent A for 1.9 min for equilibration of the trap column and preparation for the next analysis. The total run time was 11 min.

2.4. LC–MS/MS analysis

40 μL aliquots of diluted urine were separated on an Inertsil ODS-80 Å (150 mm × 4.6 mm, 5 μm) column at a flow rate of 1.0 mL min^{-1} using the Agilent 1200 HPLC system. The optimized mobile phase gradient involved the following alternations of mobile phase A (5% ACN, v/v with 0.1% formic acid) and mobile phase B (90% ACN, v/v with 20 mM ammonium acetate). The gradient was started at 100% mobile phase A, which was maintained for 3 min, then changed to 90% mobile phase A in 0.1 min. This composition was held for 5.0 min then ramped to 0% mobile phase A for 3.5 min, then ramped again to 100% mobile phase A in 0.1 min, and held for 2.4 min at 100% mobile phase A to finish the 11 min cycle of analysis before the next sample was injected. The mass spectrometric data were collected using a triple–quadrupole mass spectrometer, API 3000 (Applied Biosystem, MDS SCIEX, Concord, Ontario, Canada), operating with a TurboIonSpray source. The mass spectrometer coupled with electrospray ionization (ESI) interfaces was operated in negative ion mode at an ion spray voltage of −4200 V. The turbospray settings were as follows: nebulizer and curtain gas at 15 psi, collision-assisted dissociation (CAD) at 6 psi, and the source heater probe temperature at 550 °C.

2.5. Method validation

The aim of this study was to develop a sensitive, precise, and accurate method, so we discussed the parameters as follows and obeyed the criteria from the US FDA [31]. The urine was collected and then pooled from 5 healthy volunteers (nonsmoker) and analyzed by LC–MS/MS for the presence of the seven metabolites derived from five VOCs; three of the VOC metabolites revealed no signals, ($S/N < 3$). The exceptions were GAMA, DHBMA, CYMA and DHBMA (the level close to $S/N \leq 10$), and the pooled urine was also used as the blank urine matrix for the matrix effect test.

2.5.1. Stock solution and calibration curve

The seven stock standard solutions were prepared in MeOH, and they were stored in polypropylene screw-top tubes at −20 °C.

Table 1
Chromatographic conditions of the on-line SPE LC–MS/MS.

Time (min)	Flow rate (mL min^{-1})	Eluent I[a] (trap column)		Time (min)	Flow rate (mL min^{-1})	Eluent II[b] (analytical column)		Time (min)	Valve position	Remarks
		Solvent A	Solvent B			Solvent A	Solvent B			
0	1.0	100	0	0.0	1.0	100	0	0	A	Injection and washing of sample
3.0	1.0	100	0	3.0	1.0	100	0	1.5	B	Start of elution of analyte to the analytical column
9.0	1.0	0	100	3.1	1.0	90	10	3.0	A	End of elution; trap column cleanup and reconditioning
9.1	1.0	100	0	5.0	1.0	90	10	11.0	A	
11.0	1.0	100	0	8.5	1.0	0	100			
				8.6	1.0	100	0			
				11.0	1.0	100	0			

[a] Eluent I:Solvent A: 100% H_2O; Solvent B: 90% ACN (v/v) with 0.1% FA.
[b] Eluent II: Solvent A: 5% ACN (v/v) with 0.1% FA; Solvent B: 95% ACN (v/v) with 20 mM AA.

In order to evaluate the amounts of analytes in the urine, a set of nine concentrations of standard solutions were diluted from 0.1 to 50.0 ng mL^{-1} (2.5 to 50.0 ng mL^{-1} for *t,t*-MA) with 5% ACN (v/v)+ 10 mM AA and blank urine matrix, and were spiked with a fixed amount of 400 ng mL^{-1} *t,t*-MA-d_4, 50 ng mL^{-1} DHBMA-d_7, and 100 ng mL^{-1} PMA-d_5, 2,4-DPMA-d_3, MHBMA3-d_3, CYMA-d_3, and GAMA-d_3 as internal standards (IS). The reagent blank (5% ACN, v/v with 10 mM AA) and quality control (QC) samples were also injected after every twenty sample injections to test the total analytical process. The QC sample was prepared daily at 10 ng mL^{-1} standard solution containing IS in a solvent.

2.5.2. Precision and accuracy

Precision and accuracy were investigated at four spike levels (1, 5, 10, and 20 ng mL^{-1}) of the standard solutions into the pooled urine samples. The accuracy and precision of the assay was determined by analyzing replicates ($n=5$) spiked with 1, 5, 10 and 20 ng mL^{-1} in the pooled urine samples and by calculating the CV (coefficient of variation).

2.5.3. Intra-day and inter-day analysis

Experiments on intra-day and inter-day variations were assessed by identical analyses of pooled urine samples. The intra-day accuracy and precision of the assay was determined by analyzing replicates ($n=5$) spiked with 1, 5, 10 and 20 ng mL^{-1} in the pooled urine samples and calculating the accuracy and CV (coefficient of variation). The inter-day was assessed by analyzing replicates of the pooled urine samples ($n=5$) obtained on different days (replicates per day for 6 days) from the same subject.

2.5.4. Matrix effect

Matrix effects were assessed at two concentrations for each of the seven metabolites derived from five VOCs by comparing the peak areas of quintuplicate runs at each concentration for analyte standards in a neat solvent and in the spiked pooled urine samples. The relative matrix effect was established according to the following formula:

$$\mathrm{ME}\% = A_{(\text{analyte standards (in diluted urine)})}/A_{(\text{analyte standards (neat solvent)})} \times 100\%.$$

2.5.5. Freeze–thaw and stability

Stability was investigated by spiking with four levels (1, 5, 10, and 20 ng mL^{-1}) of standard solutions into pooled urine samples, and the accuracy were calculated to check the stability in the replicates under different conditions: (1) three freeze–thaw cycles, (2) short-term storage in an autosampler for 36 h, and (3) long-term storage at −20 °C for one month.

2.6. Statistical analysis

Data were analyzed using SPSS software (Version 17.0 for Windows; SPSS Inc., Chicago, IL, USA), and were compared using a Student's *t*-test ($p<0.05$ significance level).

2.7. Subjects

The present study was approved by the Institutional Review Board of the Fu Jen Catholic University. Spot urine samples were collected at randomly time in the morning and stored at −20 °C until analysis. The average age of the 55 male smokers was 38.67 ± 7.83 years and the average age for the 55 male nonsmokers was 40.20 ± 9.26 years.

3. Results and discussion

3.1. Optimization of the LC–MS/MS condition

The enzymatic pathways for metabolism (GSH, CYP 450, and MA pathway) in humans were used to select the target VOC metabolites in the present study [7,32–34]. Our goal was to develop an effective and rapid method with demonstrated validity for the quantification of VOC metabolites in urine samples. Herein, to achieve a more sensitive product ion, the optimal mass fragmentations of target compounds for the achievement of a multiple reaction monitoring (MRM) mode were investigated by directly infusing 1 μg mL^{-1} each of the standard solutions and the internal standard solutions (IS) at 10 μL min^{-1} into a mass spectrometer using a syringe pump (KD Scientific, KDS 100). The negative electrospray ionization mode was most efficient at generating the $[M-H]^-$ precursor ions that provided the best sensitivity for all target analytes. Under these conditions, the tandem mass spectrometry parameters were optimized for the sensitive and selective isolation of the precursor ions and their fragmentations, and all the parameters were summarized for this study (Table 2): quantitative pair (Q1/Q3), declustering potential (DP), focusing potential (FP), collision energy (CE), and collision cell exit potential (CXP).

Six of the seven metabolites (except for *t,t*-MA) are known to have similar structures (Fig. 1), and another consideration was the testing of different mobile phases and columns that would lead to the selection of a chromatographic method that could achieve higher retention, the greatest intensity, and peak shapes for all compounds. For example, we evaluated mobile phase compositions such as acetonitrile with either ammonium acetate (10 or 20 mM AA) or formic acid (0.1% FA). The addition of ammonium acetate improved the peak shape and intensity, and all the VOC metabolites achieved the highest peak responses and the greatest peak shapes using acetonitrile with ammonium acetate (95% ACN+20 mM AA (v/v)) rather than with formic acid (95% ACN+0.1% FA (v/v)). As a result, the optimal separation of VOC metabolites occurred using (A) 5% ACN+0.1% FA (v/v) and (B) 95% ACN+20 mM AA (v/v) in a total run of 11 min, as shown in Fig. 2. Moreover, in order to solve the matrix effect problem, we developed an automated on-line C18 SPE column-switch technique for the measurement of VOC metabolites. The composition of the

Table 2
Optimized MS/MS parameters for the analysis of seven metabolites derived from five VOCs.

Analyte	MW	Q1/Q3	DP	FP	CE	CXP
Acrylamide						
GAMA	250.2	249.0/120.0	−9	−170	−24	−10
GAMA-d_3	253.2	252.0/120.0	−9	−170	−24	−10
1,3-Butadiene						
DHBMA	251.3	250.0/121.0	−21	−180	−23	−10
DHBMA-d_7	258.3	257.1/128.0	−21	−180	−23	−10
MHBMA3	233.2	232.0/103.0	−18	−188	−18	−10
MHBMA3-d_3	236.3	235.0/103.0	−21	−203	−19	−10
Acrylonitrile						
CYMA	216.2	215.0/86.0	−21	−180	−20	−10
CYMA-d_3	219.2	218.0/86.0	−21	−180	−20	−10
Benzene						
t,t-MA	142.1	141.0/97.0	−30	−200	−15	−10
t,t-MA-d_4	146.1	145.0/100.0	−30	−200	−15	−10
PMA	239.2	238.0/109.0	−20	−200	−15	−10
PMA-d_5	244.3	243.0/114.0	−18	−157	−22	−10
Xylene						
2,4-DPMA	267.3	266.0/137.0	−11	−201	−16	−10
2,4-DPMA-d_3	270.3	269.0/137.0	−7	−157	−19	−10

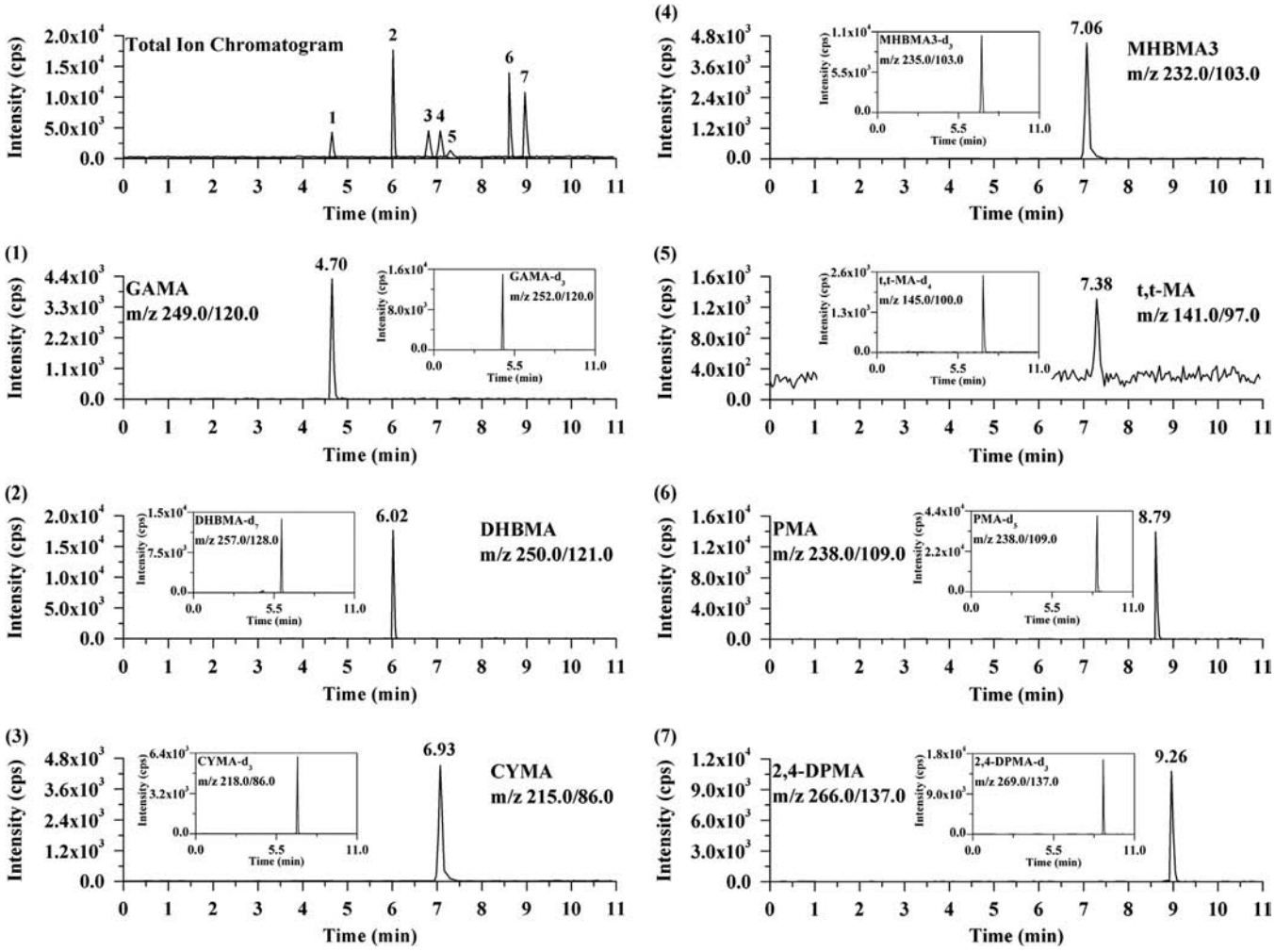


Fig. 2. MRM chromatograms of on-line SPE LC-MS/MS analysis of 10 ng mL^{-1} standards: (1) GAMA, (2) DHBMA, (3) CYMA, (4) MHBMA3, (5) *t,t*-MA, (6) PMA, and (7) 2,4-DPMA.

whole system included the mobile phase, an on-line SPE trap column and an analytical column, which enhanced the chromatographic selectivity and reproducibility, as shown in Table 1. However, when the on-line C18 SPE column-switch technique and the off-line (by direct injection to the analytical column) chromatogram were compared, the latter resulted in matrix effects that led to either the suppression or the enhancement of the analyte response, as shown in Fig. 3. When comparing the signal-to-noise (*S*/*N*) ratio for the seven analytes, the *S*/*N* ratio signals using the on-line C18 SPE column-switch technique were 1.03- to 7.81-fold (data not shown) more sensitive than the off-line method.

To the best of our knowledge, this is the first study to determine the seven metabolites derived from five VOCs using on-line SPE coupled with LC–MS/MS, this method can indeed reduce the endogenous contaminants and offers a new analytical approach to the identification of selected metabolites in human urine for an estimation of the possible risk of human exposure to volatile organic compounds.

3.2. Optimization of the sample preparation method

A rapid and simple sample preparation method played an important role in the present study. In order to assess whether the acidification procedure affected the signal response we only spiked the solvent blank with an IS solution (5% ACN (v/v)+ 10 mM AA). The results showed that the seven metabolites derived from five VOCs had no signal ($S/N < 3$) during the analytical process. Thus, we used identical sample preparation methods to evaluate three different acids, 20% HOAc, 20% FA, and 20% HCl (v/v) to determine the optimal acidification conditions, as described in Section 2.2. When the data were compared (Fig. 4), it was apparent that the best recovery was provided from 20% HOAc. A non-acidified urinary sample may cause a high matrix effect for all metabolites from the addition of acid into a urinary sample and the resultant precipitation of protein and the need for centrifuge to remove interferences. To investigate this acidification effect, working solution with different percent values ranging from 5% to 20% (v/v) were studied and indeed found increased DHBMA and PMA levels. The results showed that by increasing the percentage of HOAc, the recovery was satisfied in (Fig. 4B). As mentioned above, the optimal sample preparation method involved adding10 μL 20% HOAc (v/v) to 40 μL of a urinary sample in order to acidify it, followed by dilution. Finally, the diluted sample was spiked with a specific amount of IS solution prior to analysis.

3.3. Calibration curves and limits of quantitation

There are two significant considerations in the development of any analytical method: the linearity range and the sensitivity of the method. Calibration curves were calculated by plotting a peak-area ratio of the standards and IS against the concentration, according to the following formula: Ratio$=(A_{\text{STD in neat solvent}})/(A_{\text{IS in neat solvent}})$.

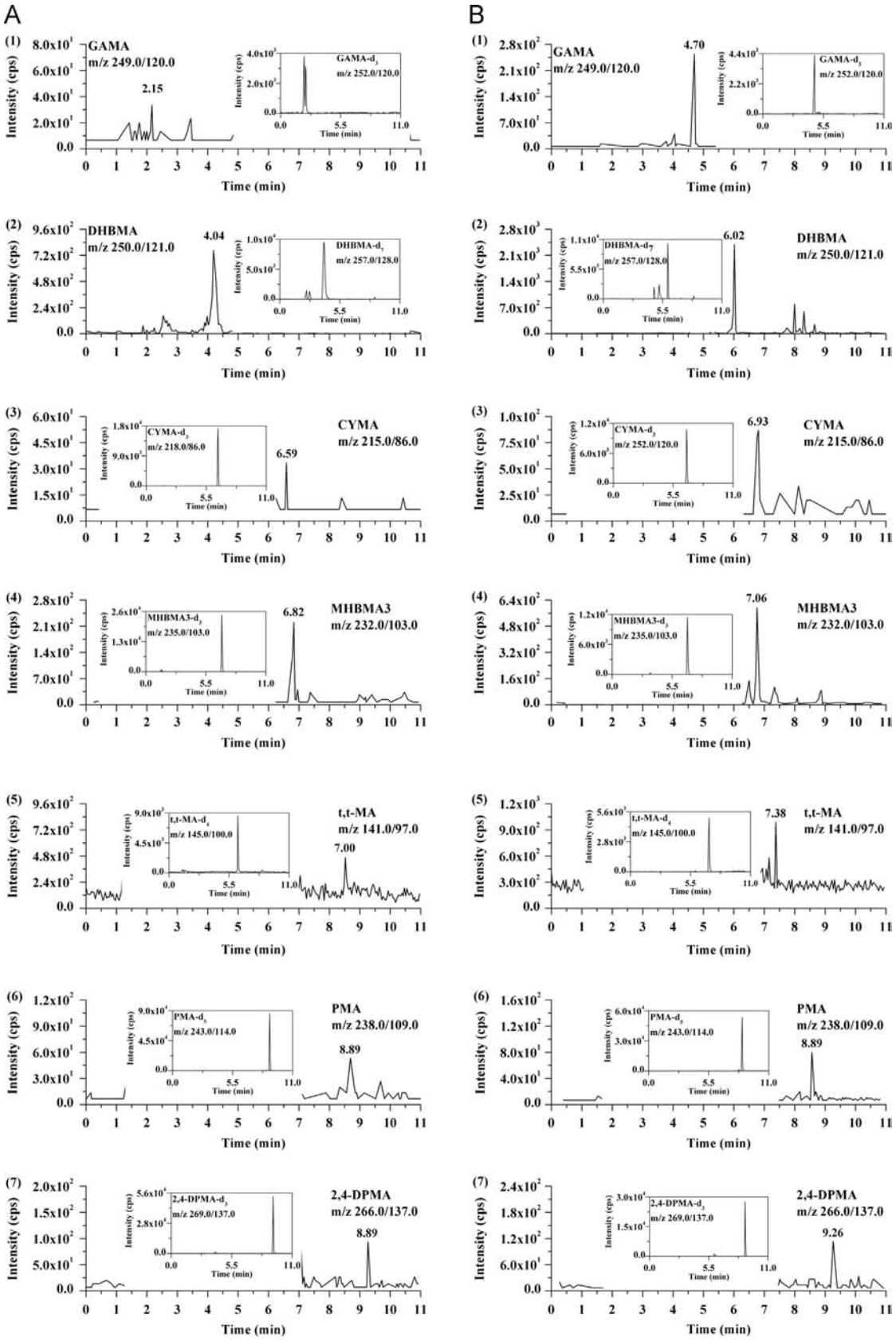


Fig. 3. Representative MRM chromatograms of (A) off-line SPE (B) on-line SPE LC-MS/MS analysis for the 10 ng mL^{-1} spike of seven metabolites derived from five VOCs in a blank urine sample.

Our calibration curves ranged from 0.1 to 50.0 ng mL^{-1}, except for *t*, *t*-MA, which ranged from 2.5 to 50.0 ng mL^{-1}, and the calibration curves had correlation coefficients higher than 0.995, with the neat solvent as well as with the blank urine matrix.

A comparison of the slopes showed no significant differences and the calibrators in the neat solvent had slopes that were similar to those prepared with the blank urine matrix (slopes were 0.92 to 1.18 for the seven metabolites derived from five VOCs, respectively). Therefore, since no analyte-free matrix is available, the limits of detection (LOD) and the limits of quantification (LOQ) were calculated using the lowest concentration of the calibration curve methodology with signal-to-noise ratios of 3 and 10 in neat solvent, which were found within 0.010 to 0.769 ng mL^{-1} (on column 0.40 to 30.76 pg in an injection volume of 40 μL) and 0.033 to 2.564 ng mL^{-1}(on column 1.32 to 102.56 pg in an injection volume of 40 μL), respectively. The performances found in this study were compared with those of the other methods reported in the literature, and the results are shown in Table 3. The advantages of the on-line SPE/LC–MS/MS over the other methods included lower LOD, LOQ and smaller sample volumes, it was relatively fast, and it was simple.

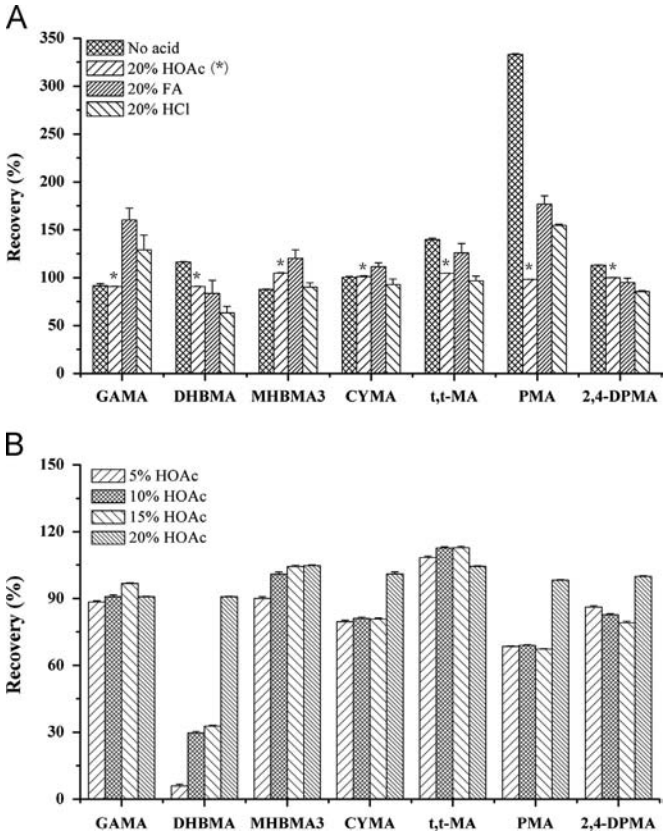


Fig. 4. (A) Effect on the recovery of the seven metabolites derived from five VOCs in human urine with different sample pretreatments by spiking of the seven internal standard solutions. (B) Effect of the different percent acetic acid (HOAc) on the recovery of the seven metabolites derived from five VOCs in human urine.

3.4. Method validation

Method validations were performed using blank urine as a sample matrix. Precision, accuracy, matrix effect, freeze/thaw, and stability were determined in Sections 3.4.1–3.4.4. Based on the results, the precision and accuracy were satisfactory, and this analytical method achieved robustness and was suitable for the simultaneous analysis of the seven metabolites derived from five VOCs in human urine.

3.4.1. Precision and accuracy

Using on-line SPE for the determination of the seven metabolites derived from five VOCs was effective and rapid. The precision and accuracy were calculated by spiking at four different known levels (1, 5, 10, and 20 ng mL^{-1}) into a blank urine matrix, and the accuracy was expressed as accuracy (%)=[(measured concentration − blank urine matrix concentration)/spiked concentration] × 100%. The detection accuracy (n=5) of the seven metabolites derived from five VOCs ranged from 90.8 to 108.9%, and the precision ranged from 0.9 to 6.6%. More than 200 urinary samples were assayed continuously without a significant occurrence of contamination to the curtain plate (data not shown). The results are summarized in Table 4.

Table 3
Comparison of the analytical methods and LODs found in the literature and used in the present study.

Analyte	Analytical method	Sample volume	Sample preparation	LOD (ng mL^{-1})	Reference
GAMA	LC–MS/MS	4 mL	SPE (ENV^+, Isolute)	1.5	[36]
	UPLC–MS/MS	50 μL	Dilution	9.4	[11]
	LC–MS/MS	40 μL	Dilution	0.014	This study
DHBMA	LC–APCI–MS/MS	5 mL	SPE (Strata X, Phenomenex)	23.0	[21]
	LC–MS/MS	100 μL	Dilution	0.05	[2]
	UPLC–MS/MS	50 μL	Dilution	5.0	[11]
	LC–MS/MS	40 μL	Dilution	0.033	This study
MHBMA3	UPLC–MS/MS	50 μL	Dilution	0.6	[11]
	LC–MS/MS	40 μL	Dilution	0.06	This study
CYMA	LC–MS/MS	0.5 mL	Dilution	0.5	[19]
	UPLC–MS/MS	50 μL	Dilution	0.5	[11]
	LC–MS/MS	40 μL	Dilution	0.077	This study
t,*t*-MA	LC–UV	50 μL	SPE (MAX, Oasis)	5.0	[25]
	UPLC–MS/MS	50 μL	Dilution	20.0	[11]
	LC–MS/MS	40 μL	Dilution	0.769	This study
PMA	HPLC–FD	2 mL	Derivatization	1.0	[16]
	LC–MS/MS	100 μL	Dilution	0.01	[2]
	UPLC–MS/MS	50 μL	Dilution	0.3	[11]
	LC–MS/MS	40 μL	Dilution	0.024	This study
2,4-DPMA	LC–MS/MS	0.5 mL	On-line RAM (C18)	0.10	[27]
	UPLC–MS/MS	50 μL	Dilution	0.5	[11]
	LC–MS/MS	40 μL	Dilution	0.01	This study

Table 4
Accuracy and precision of intra- and inter-day assay for the detection seven metabolites derived from five VOCs in human urine.

Analyte	Spiked level (ng mL^{-1})	Intra-day ($n=5$)[a]		Inter-day ($n=30$)[b]		ME (%)[c]	CV (%)[d]
		Accuracy (%)[e]	CV (%)[d]	Accuracy (%)[e]	CV (%)[d]		
GAMA	Blank (5.14 ± 0.63 [c]/4.88 ± 0.64 [d])						
	1.0	92.5	4.1	98.8	8.9	87.0	12.0
	5.0	106.0	6.6	106.7	8.8	n.r.	n.r.
	10.0	108.9	4.3	103.3	8.7	n.r.	n.r.
	20.0	104.7	5.4	101.7	8.6	n.r.	n.r.
DHBMA	Blank (2.53 ± 0.18[a]/2.59 ± 0.17[b])						
	1.0	101.4	4.4	100.7	7.3	n.r.	n.r.
	5.0	97.1	4.1	95.9	7.4	120.1	1.3
	10.0	90.8	2.1	95.8	8.3	90.0	2.2
	20.0	94.0	2.6	92.1	5.0	n.r.	n.r.
MHBMA3	Blank (2.03 ± 0.06[a]/2.07 ± 0.10[b])						
	1.0	103.4	2.1	99.5	5.6	n.r.	n.r.
	5.0	102.0	2.5	99.0	4.5	105.3	6.8
	10.0	104.8	2.8	100.7	5.2	99.3	2.9
	20.0	101.0	3.0	95.5	5.8	n.r.	n.r.
CYMA	Blank (0.52 ± 0.04[a]/0.52 ± 0.05[b])						
	1.0	101.4	2.9	107.9	8.3	n.r.	n.r.
	5.0	100.6	2.7	101.3	6.9	108.8	8.4
	10.0	101.0	0.9	96.1	4.6	110.2	4.1
	20.0	98.6	2.1	96.1	5.9	n.r.	n.r.
t,t-MA	Blank (N.D)[f]						
	1.0	102.8	3.3	107.7	7.4	n.r.	n.r.
	5.0	100.1	2.8	99.7	4.5	102.0	8.2
	10.0	104.4	3.0	101.4	4.8	110.2	5.4
	20.0	103.3	1.5	101.6	4.0	n.r.	n.r.
PMA	Blank (N.D)[f]						
	1.0	106.9	1.5	105.2	6.3	n.r.	n.r.
	5.0	101.0	3.5	103.6	4.7	86.7	1.6
	10.0	98.2	2.5	100.9	6.4	86.7	4.7
	20.0	101.0	4.4	99.6	5.0	n.r.	n.r.
2,4-DPMA	Blank (N.D)[f]						
	1.0	106.1	2.8	103.8	4.7	n.r.	n.r.
	5.0	100.6	2.5	100.3	4.8	105.2	4.8
	10.0	99.9	2.5	99.6	3.8	99.7	6.6
	20.0	100.6	2.2	99.1	3.7	n.r.	n.r.

n.r.: Not reported.

[a] $n=5$, 5 replicates per day.
[b] $n=30$, 5 replicates per day for 6 days.
[c] ME%$=A_{(\text{analyte standards (in diluted urine)})}/A_{(\text{analyte standards (neat solvent)})} \times 100\%$.
[d] CV: coefficient of variation.
[e] Expressed as [(measured concentration − blank urine matrix concentration)/spiked concentration] × 100%.
[f] N.D: not detected, $S/N < 3$.

3.4.2. Intra-day and inter-day analysis

The accuracy of the procedure was demonstrated by spiking blank urine matrix samples with four concentrations (1, 5, 10, and 20 ng mL^{-1}) of standards to evaluate inter-day and intra-day assay precision. These preparations were also used as quality control samples to monitor the day-to-day performance of the assays. The intra-day ($n=5$) and inter-day ($n=30$) assay variations were 0.9–6.6% and 3.7–8.9%, respectively, as shown in Table 4.

3.4.3. Matrix effects

There was a need to assess the possibility of a matrix effect caused by ionization competition between the analytes and coeluting compounds during on-line SPE LC–MS/MS analysis. Two concentration levels of the seven metabolites derived from five VOCs standards were compared according to the peak areas of quintuplicate runs at each concentration for analyte standards for a solvent and for spiked pooled urine samples. The observed concentrations due to either ion suppression or ion enhancement ranged from 86.7 to 120.1% for spiked concentrations of two of the seven metabolites derived from five VOCs standards showing a matrix effect in the pooled human urine samples (Table 4). The CV ranged from 1.3 to 8.4%, so it was concluded that the matrix effect did not influence the method reliability. Therefore, the use of a stable istotope-labelled internal standard compensated for by internal standards is one of the best approaches to correct for a matrix effect.

3.4.4. Freeze/thaw stability

We evaluated the stability of the seven metabolites derived from five VOCs in a blank urine matrix based on three parameters: (1) three freeze/thaw cycles, (2) short-term stability in an autosampler for 36 h, and (3) long-term stability at −20 °C for one month. We measured the accuracy after adding four concentrations into a blank urine matrix. The data showed that all of the seven metabolites derived from five VOCs were stable under different conditions, and the accuracy ranged from 80.5 to 116.8%, as shown in Table 5.

3.5. Application of the method

The optimized methodology was applied to the determination of the seven metabolites derived from five VOCs by analyzing

Table 5
Stability study of the seven metabolites derived from five VOCs in human urine after three different conditions (long-term storage, short-term storage, and freeze–thaw three cycles).

Analyte	Spiked level	Long-term ($n=10$)		Short-term ($n=10$)		Freeze–thaw[a] ($n=15$)	
	(ng mL^{-1})	Accuracy (%)[b]	CV (%)[c]	Accuracy (%)[b]	CV (%)[c]	Accuracy (%)[b]	CV (%)[c]
GAMA	1.0	80.5	8.9	81.5	6.1	116.8	6.0
	5.0	98.9	9.7	102.4	5.7	105.6	1.8
	10.0	103.6	7.5	102.8	5.3	106.9	3.2
	20.0	103.6	4.5	106.2	4.1	103.2	2.9
DHBMA	1.0	99.9	7.6	100.2	4.2	99.7	0.8
	5.0	98.8	5.6	95.5	3.9	94.6	4.1
	10.0	101.1	9.7	90.9	3.1	89.3	8.4
	20.0	97.5	5.2	92.1	3.5	91.3	8.4
MHBMA3	1.0	100.5	2.7	101.1	2.6	99.0	4.3
	5.0	100.6	3.3	102.5	3.0	98.8	2.0
	10.0	103.3	3.5	105.5	2.7	102.9	2.9
	20.0	100.0	3.9	99.4	2.6	100.2	3.6
CYMA	1.0	98.7	4.9	101.1	4.6	106.6	6.2
	5.0	98.7	2.7	100.9	3.9	100.5	4.4
	10.0	100.9	2.4	100.7	2.7	97.8	5.3
	20.0	98.7	2.4	98.3	3.3	96.3	1.3
t,*t*-MA	1.0	103.9	4.7	103.9	3.0	103.3	7.0
	5.0	98.4	4.0	101.4	2.9	100.4	4.4
	10.0	102.1	3.7	102.7	3.6	102.6	1.4
	20.0	103.4	3.3	101.7	2.7	103.0	1.8
PMA	1.0	105.7	2.7	108.6	4.4	108.1	6.7
	5.0	101.1	2.5	99.8	4.2	103.2	0.8
	10.0	99.3	3.0	102.6	7.4	104.5	3.0
	20.0	99.4	4.6	102.3	3.8	99.2	2.5
2,4-DPMA	1.0	102.8	4.5	106.4	2.8	104.3	1.9
	5.0	100.7	1.7	100.2	3.0	99.4	2.6
	10.0	99.7	2.2	99.3	3.1	99.4	4.1
	20.0	100.8	3.9	100.1	1.7	100.7	4.1

[a] $n=15$, 5 replicates per day for 3 days.
[b] Expressed as [(measured concentration − blank urine matrix concentration)/spiked concentration] × 100%.
[c] CV: Coefficient of variation.

Table 6
Concentration of seven metabolites derived from five VOCs in the urine of smokers and non-smokers by on-line SPE LC–MS/MS.

Analyte	Smoker (ng mL^{-1}) ($n=55$) mean ± SD[a]	Nonsmoker (ng mL^{-1}) ($n=55$) mean ± SD[a]	p Value[b]
GAMA	53.6 ± 44.3	29.5 ± 16.9	< 0.001***
DHBMA	274.8 ± 110.4	133.8 ± 70.8	0.003**
MHBMA3	129.2 ± 99.2	52.3 ± 36.8	< 0.001***
CYMA	68.2 ± 57.6	30.5 ± 36.1	0.024*
t,*t*-MA	155.6 ± 112.9	64.1 ± 42.7	< 0.001***
PMA	7.0 ± 4.4	0.6 ± 0.4	0.031*
2,4-DPMA	4.9 ± 4.1	1.1 ± 0.3	0.058[c]
DHBMA/(DHBMA+MHBMA3)	0.7 ± 0.2	0.7 ± 0.2	0.460 [c]

[a] SD: standard deviation.
[b] Probability (Student *t*-test).
[c] No significant difference.
* $p < 0.05$.
** $p < 0.01$.
*** $p < 0.001$.

human urine (Table 6). The average age of the 55 male smokers was 38.67 ± 7.83 years and the average age for the 55 male nonsmokers was 40.20 ± 9.26 years. In general, the formation of the seven metabolites derived from five VOCs is complicated, involving occupational and environmental exposures, life style, stress, genetic polymorphisms of the metabolizing enzymes and physiological factors [2,7,11]. Therefore, a large intra-individual variation in the seven metabolites derived from excretion of the five VOCs was found, with RSDs ranging from 40.2–84.5% to 29.0–118.5% for smokers and nonsmokers, respectively. Many reports have shown the MHBMA consisted of three isomers (MHBMA1, MHBMA2, and MHBMA3, with the same mass (common transitions, 232/103), which were similar in chemical structure [2,11]. Thus, an appropriate chromatographic optimization was crucial for the correct quantification of all the MHBMA (Table S1 and S2). According to Alwis et al. [11] as mentioned earlier among MHBMA isomers, MHBMA3 was detected in a majority of the samples (99.0%) tested, MHBMA1 and MHBMA2 were not (< LOD) found in nonsmokers. Therefore, we monitored urinary VOC metabolites as biomarkers of exposure to 1,3-butadiene major focused on the MHBMA3, which acted as a target compound. Simultaneously, we have indicated that MHBMA3 existed and also there was no detection of either MHBMA1 or MHBMA2 in human urine for this study (Fig S1A–C). The metabolic ratio DHBMA/(DHBMA+ MHBMA), excretion of these two metabolites is mainly influenced by the activity of epoxide hydrolase (DHBMA) and glutathione-*S*-transferase (MHBMA) after 1,3-butadiene exposure [2,9,11]. However, comparisons of previous studies have found to be about 0.88–0.98 for humans [19,21], as shown in (Table S3). As a result, metabolic ratios for our subjects are somewhat lower were 0.72 ± 0.15 (0.38–1.00) in nonsmoker and 0.70 ± 0.16 (0.35–1.00) in smoker, respectively (Table 6). Although *t*,*t*-MA and DHBMA were not specific biomarker of tobacco smoke, led to lack of specificity resulting from the multiple sources of exposure can perplex the interpretation of experimental data. However, determining multiple biomarkers of different parent compounds can provide complementary information and also further get a stronger data set for assessing the potential health risk of exposure to a mixture of environmental chemicals [7,11]. For examples, both DHBMA and *t*,*t*-MA have been used as biomarkers of exposure in a large occupational study [2,11] and also distinguish groups with different exposure conditions such as environmental, occupational and cigarette smoking [6]. However, before the excretion of *t*,*t*-MA might be influenced by the uptake of sorbic acid (a popularly used food preservative), *S*-PMA is considered to be a more specific biomarker for low-level exposures to benzene [2]. According to Pouli et al.'s [35] report has shown that GC analysis of the tobacco smoke gas phase passing through acetate or 3C filter. Values are reported in 5.4 μg/Cigarette (*m*-xylene) and also information has shown the composition of xylene produced from petroleum is a mixture containing approximately 1:2:1 ratio of the *o*-xylene, *m*-xylene and *p*-xylene, respectively [27]. It is noteworthy that Gonzalez-Reche et al.'s [27] report was demonstrated the ratios of DMPA isomers (2,5 DPMA 3.3 ng mL^{-1}, 2,4 DPMA 9.9 ng mL^{-1} and 3,4 DPMA 3.7 ng mL^{-1}) in human metabolism are reflect in the ratios of xylene isomers in the air [27]. Therefore, 2,4 DPMA was major amount and easier to be examined for biological monitoring of xylene exposed workers. Thus, our method can develop a powerful tool for the estimation of internal exposure to these substances. Despite the relatively small number of samples analyzed, these data were broadly consistent with the values previously reported using different approaches (Table S3) [11]. The results of the present study found GAMA, DHBMA, MHBMA3, CYMA, *t*,*t*-MA, and PMA VOC metabolite levels that were signifcantly higher in smokers than in nonsmokers. The methods will be combined with environmental monitoring and should be useful for future epidemiological studies of exposure to VOCs in the general population.

4. Conclusion

A simple, rapid LC–MS/MS method combined with an on-line SPE step was developed for the simultaneous detection, identification, and quantification of seven metabolites found in human urine. Due to low sample consumption (40 μL of urine), the pretreatment procedure was extremely simple and involved neither costly time- nor labor-consuming sample preparation steps. The method accuracy for intra-day and inter-day assays ranged from 90.8 to 108.9% and precision was measured at 0.9 to 8.9% for the seven metabolites in human urine samples. The high selectivity and sensitivity of this method during the simultaneous measurement of the seven metabolite profiles in human urine samples offers a new analytical approach to the identification of selected metabolites in human urine for an estimation of the possible risk of human exposure to volatile organic compounds.

Acknowledgments

This work was supported by grants number NSC102-2113-M-030-005-MY2 and NSC101-2632-B-030-001-MY3 from the Ministry of Science and Technology, Taiwan, ROC.

Appendix A. Supporting information

Supplementary data associated with this article can be found in the online version at http://dx.doi.org/10.1016/j.talanta.2014.09.029.

References

[1] D. Loomis, Y. Grosse, B.a. Lauby-Secretan, F.E. Ghissassi, V.r. Bouvard, L. Benbrahim-Tallaa, N. Guha, R. Baan, H. Mattock, K. Straif, Lancet Oncol. 14 (2013) 1262–1263.
[2] Y.S. Ding, B.C. Blount, L. Valentin-Blasini, H.S. Applewhite, Y. Xia, C.H. Watson, D.L. Ashley, Chem. Res. Toxicol. 22 (2009) 1018–1025.
[3] Y.-F. Huang, K.-Y. Wu, S.-H. Liou, S.-N. Uang, C.-C. Chen, W.-C. Shih, S.-C. Lee, C.-C. Huang, M.-L. Chen, Int. Arch. Occup. Environ. Health 84 (2011) 303–313.
[4] T. Schettgen, A. Musiol, A. Alt, E. Ochsmann, T. Kraus, Anal. Bioanal. Chem. 393 (2009) 969–981.
[5] Y. Li, A.C. Li, H. Shi, H. Junga, X. Jiang, W. Naidong, J.H. Lauterbach, Biomed. Chromatogr. 20 (2006) 597–604.
[6] Y.M. Kim, S. Harrad, R.M. Harrison, Environ. Sci. Technol. 36 (2002) 5405–5410.
[7] E. Minet, F. Cheung, G. Errington, K. Sterz, G. Scherer, Biomarkers 16 (2011) 89–96.
[8] E. Hartmann, J. Latzin, B. Schindler, H. Koch, J. Angerer, Arch. Toxicol. 85 (2011) 601–606.
[9] L. Sabatini, A. Barbieri, P. Indiveri, S. Mattioli, F.S. Violante, J. Chromatogr. B 863 (2008) 115–122.
[10] C.A. Hinchman, N. Ballatori, J. Toxicol. Environ. Health 41 (1994) 387–409.
[11] K.U. Alwis, B.C. Blount, A.S. Britt, D. Patel, D.L. Ashley, Anal. Chim. Acta 750 (2012) 152–160.
[12] M. Jakubowski, I. Linhart, G. Pielas, J. Kopecky, Br. J. Ind. Med. 44 (1987) 834–840.
[13] T. Einig, L. Dunemann, W. Dehnen, J. Chromatogr. B Biomed. Appl. 687 (1996) 379–385.
[14] T. Renner, M. Baer-Koetzle, G. Scherer, J. Chromatogr. A 847 (1999) 127–133.
[15] G. Marrubini, T. Coccini, L. Manzo, J. Chromatogr. B Biomed. Sci. Appl. 758 (2001) 295–303.
[16] T. Einig, W. Dehnen, J. Chromatogr. A 697 (1995) 371–375.
[17] P. Montuschi, N. Mores, A. Trové, C. Mondino, P.J. Barnes, Respiration 85 (2013) 72–84.
[18] P.M. Félix, S.M. Almeida, C. Franco, A.B. Almeida, C. Lopes, M.I. Claro, E. Fragoso, C. Teles, H.T. Wolterbeek, T. Pinheiro, Int. J. Environ. Health Res. (2014) 1–14.
[19] T. Schettgen, J. Bertram, T. Kraus, Talanta 98 (2012) 211–219.
[20] C.-F. Wu, S.-N. Uang, S.-Y. Chiang, W.-C. Shih, Y.-F. Huang, K.-Y. Wu, Anal. Bioanal. Chem. 402 (2012) 2113–2120.
[21] M. Urban, G. Gilch, G. Schepers, E. van Miert, G. Scherer, J. Chromatogr. B Anal. Technol. Biomed. Life Sci. 796 (2003) 131–140.
[22] M. Urban, D. Kavvadias, K. Riedel, G. Scherer, A.R. Tricker, Inhalation Toxicol. 18 (2006) 831–839.
[23] A. Sapkota, R.U. Halden, F. Dominici, J.D. Groopman, T.J. Buckley, Chem. Biol. Interact. 160 (2006) 70–79.
[24] A. Barbieri, L. Sabatini, A. Accorsi, A. Roda, F.S. Violante, Rapid Commun. Mass Spectrom. 18 (2004) 1983–1988.
[25] B.L. Lee, H.Y. Ong, Y.B. Ong, C.N. Ong, J. Chromatogr. B Anal. Technol. Biomed. Life Sci. 818 (2005) 277–283.
[26] M. Mudiam, A. Chauhan, K. Singh, S. Gupta, R. Jain, R. Ch, R.C. Murthy, Anal. Bioanal. Chem. 405 (2013) 341–349.
[27] L. Gonzalez-Reche, T. Schettgen, J. Angerer, Arch. Toxicol. 77 (2003) 80–85.
[28] G. Marrubini, E. Terulla, G. Brusotti, G. Massolini, J. Chromatogr. B 822 (2005) 209–220.
[29] G. Scherer, M. Urban, H.-W. Hagedorn, R. Serafin, S. Feng, S. Kapur, R. Muhammad, Y. Jin, M. Sarkar, H.-J. Roethig, J. Chromatogr. B 878 (2010) 2520–2528.
[30] C.-J. Wang, N.-H. Yang, C.-C. Chang, S.-H. Liou, H.-L. Lee, J. Chromatogr. B 879 (2011) 3538–3543.
[31] Guidance for Industry: Bioanalytical Method Validation, U.S. Dept. of Health and Human Services, Food and Drug Administration, Center for Drug Evaluation and Research: Center for Veterinary Medicine, Rockville, MD, 2001.
[32] S. Kotapati, B.A. Matter, A.L. Grant, N.Y. Tretyakova, Chem. Res. Toxicol. 24 (2011) 1516–1526.
[33] A.A. Melikian, R. O'Connor, A.K. Prahalad, P. Hu, H. Li, M. Kagan, S. Thompson, Carcinogenesis 20 (1999) 719–726.
[34] M.I. Boettcher, T. Schettgen, B. Kutting, M. Pischetsrieder, J. Angerer, Mutat. Res. 580 (2005) 167–176.
[35] A.E. Pouli, D.G. Hatzinikolaou, C. Piperi, A. Stavridou, M.C. Psallidopoulos, J.C. Stavrides, Free Radical Biol. Med. 34 (2003) 345–355.
[36] M. Boettcher, H. Bolt, H. Drexler, J. Angerer, Arch. Toxicol. 80 (2006) 55–61.

Talanta 132 (2015) 479–485

Contents lists available at ScienceDirect

Talanta

journal homepage: www.elsevier.com/locate/talanta

Label-free electrochemical immunoassay of Bcl-2 protein expression on tumor cells

Lina Chen [a], Yiqun Luo [a], Tong Liu [a], Yanhong Yuan [b], Huoliang Gu [b], Yong Yang [b], Ling Li [b], Liang Tan [a,b,*]

[a] Key Laboratory of Chemical Biology and Traditional Chinese Medicine Research (Ministry of Education of China), College of Chemistry and Chemical Engineering, Hunan Normal University, Changsha 410081, PR China
[b] Department of Chemistry, College of Chemistry and Chemical Engineering, Hunan Normal University, Changsha 410081, PR China

ARTICLE INFO

Article history:
Received 28 July 2014
Received in revised form
14 September 2014
Accepted 18 September 2014
Available online 7 October 2014

Keywords:
Tumor cells
Drug-resistance
Bcl-2 protein
Electrochemical impedance spectroscopy
Competitive immunoassay

ABSTRACT

Bcl-2 protein is one of the anti-apoptotic members in Bcl-2 family proteins. It can regulate apoptosis in response to a wide variety of toxic agents, which has a close relationship with drug-resistance of tumor cells. Electrochemical impedance spectroscopy measurements were employed to quantify the cell concentration and analyze the expression of Bcl-2 protein on tumor cells and drug-resistant tumor cells based on the competitive immunoassay. Bcl-2 antibody and bovine serum albumin were adsorbed on Au nanoparticles to construct nanocomposites that could be captured on the Bcl-2 protein modified electrode. The binding of the nanocomposites resulted in a great increase of the charge-transfer resistance (R_{ct}) due to the strong steric hindrance effect and this effect was inhibited in the presence of MCF-7 cells and MCF-7/ADR cells owing to the competitive immunoreaction between the nanocomposites and Bcl-2 proteins on cells. Under the optimal conditions, the charge-transfer resistance change (ΔR_{ct}) is proportional to the logarithm of the cells concentration from 5×10^2 to 1.6×10^6 cell mL^{-1} with a detection limit of 170 cell mL^{-1}. The expression of Bcl-2 protein on MCF-7/ADR cells was found to be significantly higher than that in MCF-7 cells, indicating that the up-regulation of Bcl-2 protein is one of characteristics of drug-resistant tumor cells.

© 2014 Elsevier B.V. All rights reserved.

1. Introduction

One of the major obstacles to successful chemotherapy is that tumors frequently are resistant to certain forms of chemotherapy or develop resistance during the course of initial therapy. Three main categories of chemotherapy resistance, such as agent-specific resistance, multidrug resistance and comprehensive resistance, which influence each other, are regarded to be active on the cellular level [1]. The comprehensive resistance theory attempts to explain resistance with mechanisms that induce or prevent apoptosis. Apoptosis is a programmed death program and it can be induced by a multitude of stimuli, including growth factor withdrawal, DNA damage, and oncogene activation [2]. It is known that apoptosis plays a vital role in normal development, tissue homeostasis, and the removal of damaged and infected cells. Disruption of the normal apoptotic process is implicated in a variety of human diseases [3]. An imbalance between pro- and anti-apoptotic proteins leads to the accumulation of cells and the inability to respond correctly to apoptotic stimuli in many forms of cancer. As a result, these cancers do not respond well to cancer therapies that rely on the induction of apoptosis for their effect [4]. The Bcl-2 family of proteins are known to regulate apoptosis in response to a wide variety of toxic agents [5,6]. Bcl-2 family members possess up to four conserved Bcl-2 homology (BH) domains designated BH1, BH2, BH3, and BH4, which correspond to α-helical segments. Some proteins contain BH1–BH4 domain, and some contain only one or several of such domains [7,8]. Bcl-2 family members are given the different biological functions due to the difference between domains. This family includes both death antagonists such as Bcl-2, Bcl-xL, Mcl-1, Bcl-w and A-1 which suppress cell death, and death agonists such as Bax, Bak, Bik, Bad and Bid which promote cell death [9]. They have attracted intensive interest in both basic research to understand the fundamental principles of cell survival and cell death and drug discovery to develop a new class of anticancer agents. It is now generally accepted that the anti-apoptotic member Bcl-2 protein can protect cancer cells from apoptosis induced by a variety of anticancer agents [10,11] although the precise mechanism is unclear. Several

* Corresponding author at: Key Laboratory of Chemical Biology and Traditional Chinese Medicine Research (Ministry of Education of China), College of Chemistry and Chemical Engineering, Hunan Normal University, Changsha, 410081, PR China. Tel./fax: +86 731 88872531.
E-mail address: liangtan@hunnu.edu.cn (L. Tan).

http://dx.doi.org/10.1016/j.talanta.2014.09.047
0039-9140/© 2014 Elsevier B.V. All rights reserved.

studies have demonstrated that high Bcl-2 expression in cancers (particularly lymphomas) correlates with poor response to chemotherapy [12,13].

The classical techniques for analysis on gene and protein expression on cells in molecular biology and cytobiology research include enzyme-linked immunoassay [14], western blotting [15], immunohistochemistry [16], flow cytometry [17], and so on. Although these methods are valid and sensitive, most of them require special equipment, talented operator and the use of labels including fluorescein and isotope. Electrochemical impedance spectroscopy (EIS) has become a very popular method in fundamental and applied electrochemistry and materials science in recent years. It is now applied to the characterization of electrode processes and complex interfaces. Moreover, this label-free technique has found its wide application in the bioanalysis and the detected objects include antigen [18], DNA [19], bacteria [20], cells [21], and so on. The most common Nyquist plot of impedance spectroscopy consists of a semicircle at higher frequencies and a line at lower frequencies that are characteristic of a kinetic controlled process and a mass-transfer controlled process at the electrode interface, respectively. The typical electrochemical interface can be represented as an electrical circuit including four parameters, in which the ohmic resistance of the electrolyte solution (R_s) and the Warburg impedance (Z_w) represent bulk properties of the electrolyte solution and diffusion features of the redox probe in solution while the double-layer capacitance (C_{dl}) and the charge-transfer resistance (R_{ct}) reveal interfacial properties of the electrode [22]. The information of surface-modification and -assembly on an electrode can be effectively obtained by EIS measurement at a proper frequency.

In the present work, the nanocomposites composed of Au nanoparticles, Bcl-2 antibody and bovine serum albumin were prepared and characterized by transmission electron microscope, UV–vis and infrared spectrophotometry, respectively. Bcl-2 proteins were immobilized on the modified glassy carbon electrode with poly-L-lysine using a covalent crosslinking method. The EIS measurements were performed to analyze the modification process and the binding of nanocomposites on the electrode surface. Tumor cells and drug-resistant tumor cells were introduced in the process of capture of the nanocomposites and their effect on the charge-transfer resistance was studied. A sensitive and label-free electrochemical method for the quantitative detection of tumor cells and analysis on Bcl-2 protein expression on cells was developed based on the competitive immunoreaction.

2. Experimental

2.1. Materials and apparatus

Rabbit anti-human Bcl-2 antibody (Ab) and Bcl-2 protein (antigen, Ag) were purchased from Beijing Bio synthesis Biotechnology Co., Ltd. (China). L-lysine was obtained from Jill Biochemical Company (China). Bovine serum albumin (BSA, Sigma-Aldrich) was used as received. $HAuCl_4$ and trisodium citrate were purchased from Shanghai Chemical Reagent Co., Ltd. (China). Phosphate buffer solution (PBS, pH 7.4) consisting of 136.8 mmol L^{-1} NaCl, 9.7 mmol L^{-1} Na_2HPO_4, 2.7 mmol L^{-1} KCl and 1.5 mmol L^{-1} KH_2PO_4 was used in the experiments. Doxorubicin hydrochloride (adriamycin, ADR) was obtained from Zhejiang Hisun Pharmaceutical Co., Ltd. (China). Other chemicals were of analytical reagent grade and all aqueous solutions were prepared and diluted with doubly-distilled water.

EIS detections were performed with a CHI660 electrochemical workstation (CH Instruments, China) by using a conventional three-electrode system. Glassy carbon electrode (GCE, 3 mm in diameter) acted as the working electrode. A KCl saturated calomel electrode (SCE) served as the reference electrode. A platinum plate served as the counter electrode. The absorption spectra were recorded on a UV-2450 UV–vis spectrophotometer (Shimadzu, Japan). The sizes of gold nanoparticles (Au NPs) and BSA-Au NPs-Ab nanocomposites were characterized ex situ by a Tecnai G2 20ST transmission electron microscope (TEM, FEI, USA). The images of modified electrode surface were obtained with a JSM-6700F field emission scanning electron microscope (FESEM, JEOL, Japan). The cell-modality observation was performed with an inverted optical microscope (OLYMPUS CKX41, Japan).

2.2. Preparation of gold nanoparticles and BSA-Au NPs-Ab nanocomposites

Colloidal gold nanoparticles were prepared by a classic citrate-reduction method according to literature [23]. In brief, a 50 mL aqueous solution of 0.01% $HAuCl_4$ (w/w) was heated to boiling in a conical flask. 2 mL of 1% trisodium citrate was added to this solution drop by drop under vigorous stirring. The color of the solution changed from gray, purple, to wine red, indicating the formation of gold nanoparticles. Then, the mixed solution was stirred continuously until it was cooled to room temperature and was stored in a brown glass bottle at 4 °C for further use.

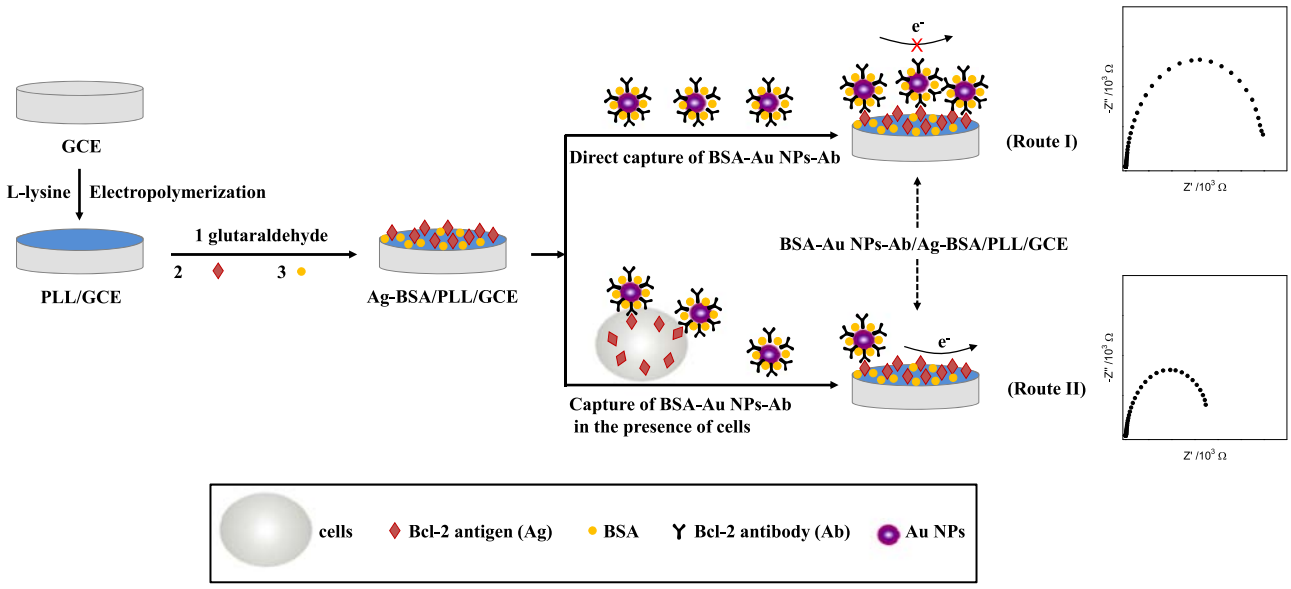
The preparation of BSA-Au NPs-Ab nanocomposite suspension was performed as following: while gently stirring, 1 mL of Ab (100 μg mL^{-1}) was added into 2.0 mL Au NPs suspension (adjusted to pH 7.4 with 0.1 M NaOH) and continuously stirred for at least 5 h. The mixed solution was centrifugated at 13,000 rpm for 20 min and the precipitate was dispersed with 1 mL pH 7.4 PBS. Then 200 μL of 5% BSA solution was added to cover the nonspecific sites. After stirring for at least 2 h, the solution was centrifugated at 13,000 rpm for 20 min. The red precipitate was re-dispersed in 1 mL pH 7.4 PBS. The such-made composite suspension could be stored at 4 °C for more than 1 month without significant decrease in activity.

2.3. Cell culture

Human breast cancer MCF-7 cells and adriamycin-resistant human breast cancer MCF-7 cells (MCF-7/ADR) were obtained from XiangYa Central Laboratory of Central South University, China. They were cultured using RPMI-1640 growth medium (from Gibco) supplemented with 10% newborn calf serum in the absence and presence of 1 mol L^{-1} ADR, respectively, in an incubator (5% CO_2, 37 °C). When the adherent cells spread over the bottom of the culture bottle, they were trypsinized and collected, then washed for three times with a sterile pH 7.4 PBS. The sediments were re-suspended in pH 7.4 PBS and then employed in the assembly processes of BSA-Au NPs-Ab nanocomposites. The density of resuspended cells was determined with a hematocytometer.

2.4. Fabrication of biosensor and measurement procedures

As shown in Scheme 1, an indirect competitive immunoassay of the expression of Bcl-2 protein on tumor cells is presented in this work. Prior to modification, GCE was polished with 0.05 μm α-Al_2O_3 power slurries until a mirror shiny surface appeared, and it was sonicated sequentially in acetone, HNO_3 (1:1, v/v), NaOH (1 mol L^{-1}) and double-distilled water for 3 min. The treated electrode was scanned between −1.0 and 1.0 V vs. SCE in 0.5 M H_2SO_4 aqueous solution for sufficient cycles to obtain reproducible cyclic voltammograms. And then the electrode was thoroughly rinsed with double-distilled water and dried with a stream of nitrogen gas. The electropolymerization of L-lysine was performed



Scheme 1. The assembly processes on the GCE surface and the measurement principle.

in 0.1 M pH 9.0 PBS containing 5 mM L-lysine by cyclic potential scanning from −1.0 to 2.2 V for 5 cycles with a scan rate of 100 mV s^{-1}. The obtained electrode was denoted as PLL/GCE. The modified electrode was then immersed in 2.5% glutaraldehyde aqueous solution for 1 h at room temperature (25 °C). A 5 μL 100 μg mL^{-1} Bcl-2 protein solution was dropped on the PLL/GCE surface and allowed to dry in refrigerator at 4 °C for overnight. Next, 5% BSA was employed to block the non-specific sites, which produced Ag-BSA/PLL/GCE. These antigen-modified electrodes were stored at 4 °C when not in use. Finally, Ag-BSA/PLL/GCEs were dipped into the BSA-Au NPs-Ab solution for 3 h at room temperature in the absence and presence of pH 7.4 PBS containing freshly trypsinized cells, respectively, which achieved the capture of the nanocomposites based on the immunoreaction. The prepared electrode was marked as BSA-Au NPs-Ab/Ag-BSA/PLL/GCE. The electrode was gently washed with pH 7.4 PBS after each step in the assembly processes. The EIS measurements were carried out in pH 7.4 PBS containing 1 mM $K_3Fe(CN)_6$, 1 mM $K_4Fe(CN)_6$, and 0.2 M NaCl at room temperature. The working electrode potential was fixed at the formal potential of the ferricyanide/ferrocyanide couple and the amplitude was 10 mV. The impedance spectrograms were collected within the frequency range between 1 mHz and 100 kHz.

3. Results and discussion

3.1. Characterization of BSA-Au NPs-Ab nanocomposites

Fig. 1A shows the UV–vis spectra of Au NPs, Bcl-2 Ab, BSA and BSA-Au NPs-Ab nanocomposites in aqueous solution from 200 to 800 nm. Au NPs had an obvious peak at about 523 nm that is regarded as a characteristic absorbance peak of Au NPs [24]. Two prominent absorption peaks at 217 nm and 280 nm, which were derived from peptide bonds [25] and Tyr and Trp residues [26], respectively, were presented on the spectrum of Bcl-2 Ab. One can find the similar absorption peaks at 213 nm and 280 nm on the spectrum of BSA. The above characteristic absorption peaks of Au NPs and proteins could be all observed in the spectrum of BSA-Au NPs-Ab nanocomposites with red shifts of some peaks. It suggests that proteins were successfully assembled on Au NPs surface. FTIR spectra of Au NPs, Bcl-2 Ab, BSA and BSA-Au NPs-Ab nanocomposites in the range of 4000-500 cm^{-1} are shown in Fig. 1B. The characteristic peaks of Au NPs at ~673, ~1402 and ~1610 cm^{-1} were ascribed to the out-of-plane bending vibration, the symmetric and asymmetric stretching vibration of $-COO^-$, respectively [27], which means that citrate was adsorbed on Au NPs that were prepared based on the redox reaction using $HAuCl_4$ and trisodium citrate. Bcl-2 Ab had two bands at ~1647 and ~1532 cm^{-1} corresponding to the absorption bands I and II of amino acids, respectively [27]. The two similar absorption bands at ~1656 and ~1532 cm^{-1} were presented on the spectrum of BSA. The absorption bands at ~1647, ~1532, ~1402 and ~673 cm^{-1} could be all found in the spectrum of BSA-Au NPs-Ab nanocomposites, indicating that the prepared nanocomposites were composed of Bcl-2 Ab, Au NPs and BSA.

Fig. 2A and B shows the TEM images of Au NPs and BSA-Au NPs-Ab nanocomposites, respectively. The average size of prepared Au NPs, which were linked each other, was measured to be around 20 nm. BSA-Au NPs-Ab nanocomposites were highly monodispersed and their mean diameter was increased in comparison with that of Au NPs, suggesting that Bcl-2 Ab and BSA were successfully assembled on the surface of Au NPs and the electrostatic repulsion was presented between the nanocomposites due to the electronegativity of the adsorbed proteins.

3.2. Capture of BSA-Au NPs-Ab nanocomposites on the antigen-modified electrode

It is known that the EIS measurement is a sensitive technique for investigating the changes of interfacial properties at electrode surfaces. Fig. 3 illustrates the Nyquist plots of the impedance spectra of the different modified electrodes. GCE exhibited almost a straight line, which indicates the excellent conductivity of the bare electrode (curve a). A low-frequency linear response and a high-frequency semicircle in the Nyquist plot, which were characteristic of a mass-transfer controlled electrode process and a kinetic controlled process at the electrode interface, respectively, could be found in the impedance spectra of PLL/GCE (curve b). The typical electrochemical interface can be represented as an electrical circuit shown in the inset of Fig. 3, which consisted of four parameters. The charge-transfer resistance, R_{ct}, was calculated to be 1500 Ω, indicating that the PLL film on the GCE surface was conductive though its conductivity was inferior to the bare GCE. The

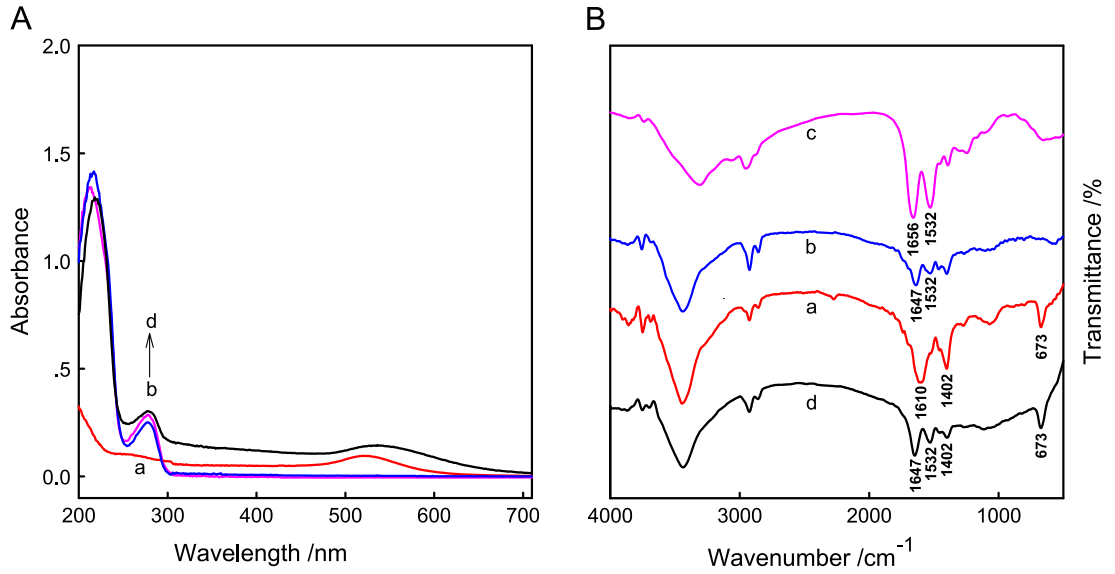


Fig. 1. UV–vis absorption spectra (A) and FTIR spectra (B) of Au NPs (a, red line), Bcl-2 Ab (b, blue line), BSA (c, pink line) and BSA-Au NPs-Ab nanocomposites (d, black line). (For interpretation of the references to color in this figure legend, the reader is referred to the web version of this article.)

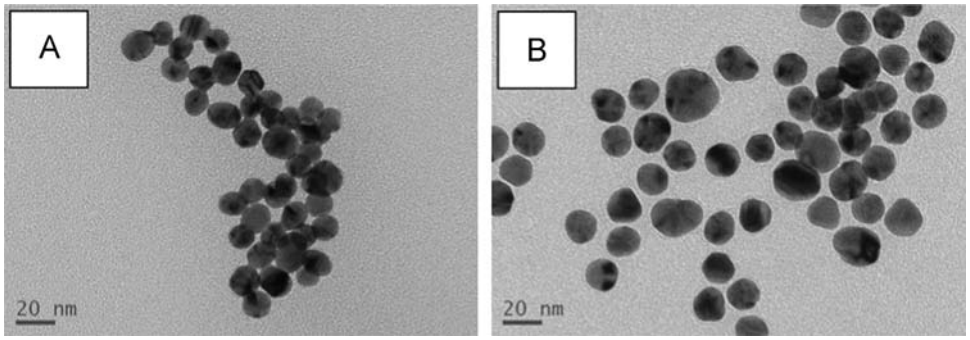


Fig. 2. TEM images of Au NPs (A) and BSA-Au NPs-Ab nanocomposites (B).

immobilization of Bcl-2 protein resulted in the increased charge-transfer resistance on Ag/PLL/GCE (R_{ct}=36,000 Ω, calculated from curve c), suggesting that the antigen was successively assembled onto PLL/GCE. The semicircle diameter of the Nyquist plot was increased to 77,000 Ω with the addition of BSA (calculated from curve d), proving that BSA could block the non-specific sites on the antigen-modified electrode. A further increased R_{ct} value (R_{ct}=128,000 Ω) after the introduction of BSA-Au NPs-Ab nanocomposites in the absence of MCF-7 cells was noticed (calculated from curve e). It proves the serious steric hindrance effect of the captured nanocomposites, on which Bcl-2 antibodies could be bound to Bcl-2 proteins on the electrode surface, leading to the result that the charge transfer between solution and electrode was significantly inhibited (as shown by Route I in Scheme 1). In addition, the charge-transfer resistance of BSA-Au NPs-Ab/Ag-BSA/PLL/GCE assembled in the presence of MCF-7 cells (calculated from curve f) was larger than that of Ag-BSA/PLL/GCE but it was much smaller than that of BSA-Au NPs-Ab/Ag-BSA/PLL/GCE assembled in the absence of MCF-7 cells. It means that a competition occurred between the cells and Bcl-2 proteins immobilized on the electrode surface for binding with the nanocomposites. Once the tumor cells were introduced in the assembly process of nanocomposites, some nanocomposites could automatically react with Bcl-2 proteins on the tumor cells and suffered sedimentation with these cells under gravity. As shown by Route II in Scheme 1, only the partial nanocomposites were linked on Ag-BSA/PLL/GCE, which would weaken the steric hindrance effect on electrode surface and result in the decline of the charge-transfer resistance. Hence, it is feasible to develop an EIS method for measuring Bcl-2 protein expression on cells based on the negative effect of the cells on the assembly of BSA-Au NPs-Ab nanocomposites.

SEM measurement was also employed to testify the proposed scheme. Fig. 4A and B shows the FESEM images of Ag-BSA/PLL/GCE surface and BSA-Au NPs-Ab/Ag-BSA/PLL/GCE surface, respectively. It was observed that a rough and thick protein coating was presented on the PLL modified GCE electrode. Obviously some BSA-Au NPs-Ab nanocomposites were distributed on Ag-BSA/PLL/GCE, indicating the immunoreaction of Bcl-2 antibodies with Bcl-2 proteins immobilized on the electrode surface and the capture of the nanocomposites.

3.3. Condition optimization of the EIS measurements

It is concluded from Fig. 3 that the binding of BSA-Au NPs-Ab nanocomposites and the introduction of tumor cells had influence on the charge-transfer resistance of the modified electrode. Some factors, which were closely related to the assembly processes on the electrode surface and could affect the EIS signals, were investigated. Here the charge-transfer resistance of BSA-Au NPs-Ab/Ag-BSA/PLL/GCE assembled in the absence of cells and that assembled in the presence of cells were represented as $R_{ct(a)}$ and $R_{ct(p)}$, respectively, and $R_{ct(a)} > R_{ct(p)}$. Fig. 5A shows the effect of the dilution times of BSA-Au NPs-Ab nanocomposites on $R_{ct(a)}$. One can find that the $R_{ct(a)}$ value was remained almost unchanged

when the dilution times of the nanocomposites was increased from 1 to 5, and then decreased at the higher dilution times. It indicates that the steric hindrance effect, which could dominate the charge-transfer resistance, depended on the adequate amount of BSA-Au NPs-Ab nanocomposites on the electrode surface. Thus, the optimal dilution times was selected at 5 in order to obtain the maximum $R_{ct(a)}$ value and save the nanocomposites. Fig. 5B shows the effect of the incubation time of BSA-Au NPs-Ab nanocomposites with cells on the charge-transfer resistance change (ΔR_{ct}), which is the difference between $R_{ct(a)}$ and $R_{ct(p)}$. The ΔR_{ct} value was enhanced with the increasing incubation time from 30 to 180 min and then suffered a little decrease when the incubation time was further prolonged. Enough incubation time was beneficial to the effective capture of the nanocomposites but too long time might lead to cell lysis or breakdown in the absence of growth medium since the tumor cells was suspended in pH 7.4 PBS. So the optimal condition for the incubation time was chosen at 180 min.

3.4. Analysis on Bcl-2 protein expression on tumor cells

Fig. 6A and B shows the microscopic images of MCF-7 cells and MCF-7/ADR cells in logarithmic growth phase, respectively. The drug-resistant MCF-7 cells on the substrate, presenting vague cellular outline, were closely interconnected and owned the increased contact area in contrast with MCF-7 cells that were regular polygon- or spindle-shaped. The nucleus and vesicles in MCF-7/ADR cells could be dimly observed. The above observation results indicate that apparent characteristic distinction exists between the tumor cells and the drug-resistant tumor cells. It can lead to the difference in the expression of some proteins such as cellular adhesion molecules on cells [28].

The analysis on the expression of Bcl-2 protein on MCF-7 cells and MCF-7/ADR cells based on a competitive immunoreaction using the EIS measurements were performed. Fig. 7A and B shows electrochemical impedance spectra of BSA-Au NPs-Ab/Ag-BSA/PLL/GCE assembled in the presence of MCF-7 cells and MCF-7/ADR cells with different concentrations, respectively. The high-frequency semicircle in the Nyquist plot was decreased when the cell concentration was enhanced, which suggests that the amount of the captured BSA-Au NPs-Ab composites on the electrode surface was diminished due to the competitive immunoreaction between the nanocomposites and the Bcl-2 proteins on cells and the steric hindrance effect on electrode surface was inhibited. In addition, MCF-7/ADR cells exerted more remarkable influence on the R_{ct} responses than MCF-7 cells with the same concentration, indicating that less nanocomposites were immobilized on BSA-Au NPs-Ab/Ag-BSA/PLL/GCE in the presence of MCF-7/ADR cells. It also suggests that the expression of Bcl-2 protein on MCF-7/ADR cells was significantly higher than that on MCF-7 cells. As we know, drug-resistant tumor cells can survive in the presence of anti-tumor drugs, upregulating the level of anti-apoptotic protein or downregulating the expression of pro-apoptotic protein. Bcl-2 protein is a gene protein inhibiting cell apoptosis. Surely the up-regulation of Bcl-2 protein can improve the survivability of MCF-7/ADR cells in the presence of the anti-tumor drug adriamycin.

Fig. 8 exhibits the plot of the ΔR_{ct} value (its definition is shown in Section 3.3 and $\Delta R_{ct}=R_{ct(a)}-R_{ct(p)}$) vs. the concentration of MCF-7 cells and MCF-7/ADR cells (c_{cell}). The measurements were performed three times to assess the reproducibility of the developed immunosensor using the three independently prepared Ag-BSA/PLL/GCE based on the same fabrication procedure. The RSD of the detection results was all lower than 7%, showing acceptable performance. Obviously the ΔR_{ct} value was increased with the enhancement of the cells concentrations and gradually reached a plateau at higher c_{cell}. In addition, the ΔR_{ct} value responding to MCF-7/ADR cells was higher than that responding to MCF-7 with the same concentration. As shown in the inset of Fig. 8, ΔR_{ct} exhibited a linear response with respect to $\lg c_{cells}$ over the range of cell concentration from 5×10^2 to 1.6×10^6 cells mL^{-1}. The regression equations were $\Delta R_{ct}=1.188\times10^4 \lg c_{cells}-3.166\times10^3$ with a correlation coefficient of 0.993 for MCF-7 cells and $\Delta R_{ct}=1.234\times10^4 \lg c_{cells}+5.280\times10^3$ with a correlation coefficient of 0.977 for MCF-7/ADR cells, respectively, and the detection limit for cells, based on three times of the standard deviation of the reagent blank (3σ), was

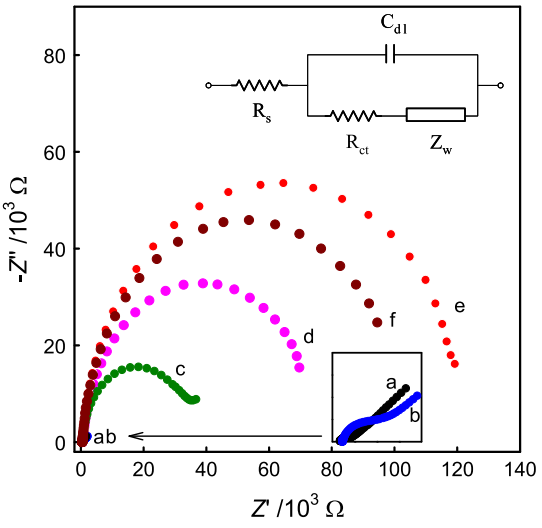


Fig. 3. Electrochemical impedance spectra of GCE (a), PLL/GCE (b), Ag/PLL/GCE (c), Ag-BSA/PLL/GCE (d), BSA-Au NPs-Ab/Ag-BSA/PLL/GCE assembled in the absence of MCF-7 cells (e) and BSA-Au NPs-Ab/Ag-BSA/PLL/GCE assembled in the presence of MCF-7 cells (f) in a pH 7.4 PBS containing 1 mM $K_3Fe(CN)_6$, 1 mM $K_4Fe(CN)_6$ and 0.2 M NaCl. 100 kHz~5 mHz, 10 mV rms, 0.20 V vs. SCE. Inset: the equivalent circuit.

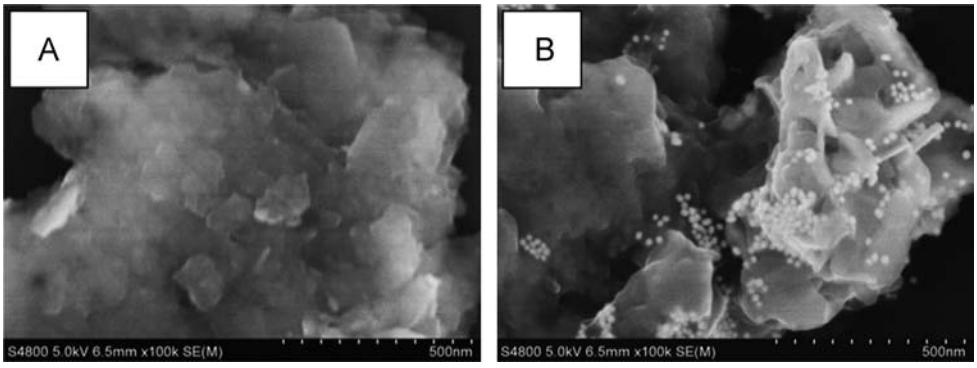


Fig. 4. FESEM images of Ag-BSA/PLL/GCE surface (C) and BSA-Au NPs-Ab/Ag-BSA/PLL/GCE surface (D). Magnification: 10,0000 × .

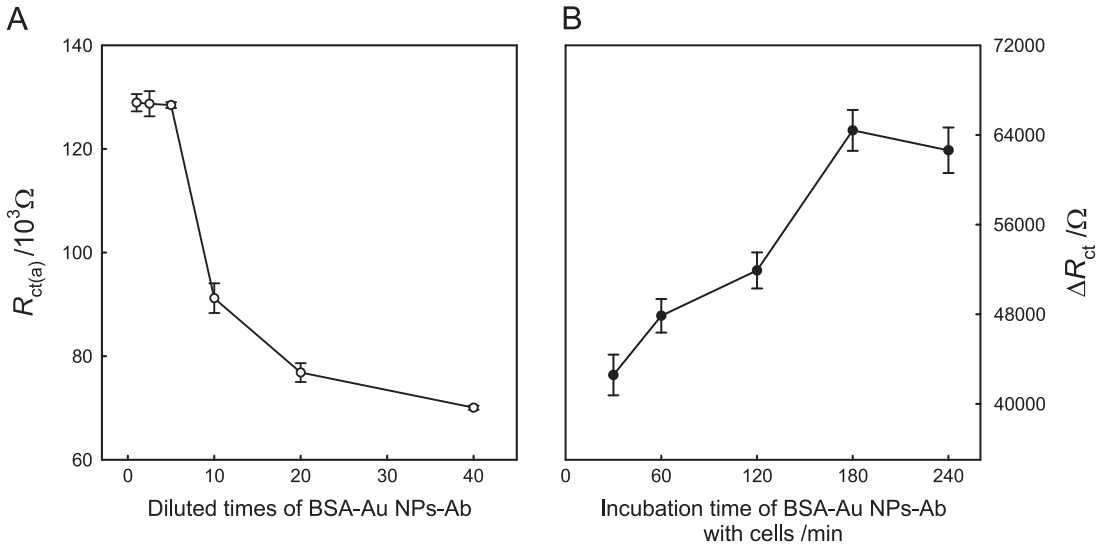


Fig. 5. (A) Effect of the dilution times of BSA-Au NPs-Ab nanocomposites on the charge-transfer resistance of BSA-Au NPs-Ab/Ag-BSA/PLL/GCE assembled in the absence of cells ($R_{ct(a)}$). (B) Effect of the incubation time of BSA-Au NPs-Ab nanocomposites with cells on the difference between the charge-transfer resistance of BSA-Au NPs-Ab/Ag-BSA/PLL/GCE assembled in the absence of cells and that assembled in the presence of cells (ΔR_{ct}).

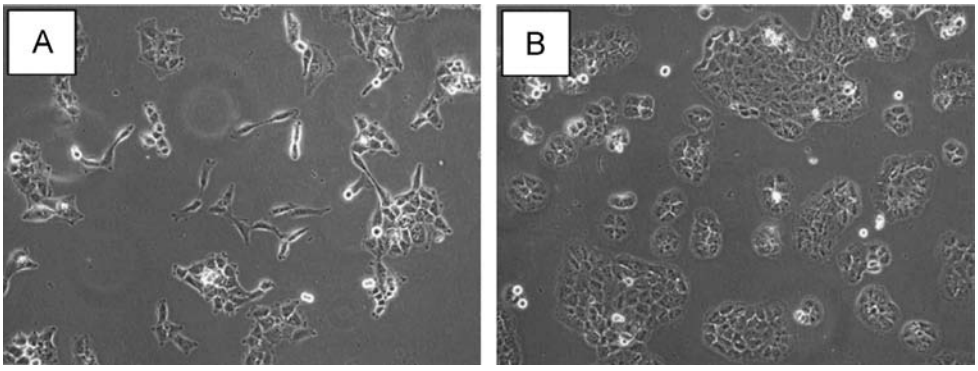


Fig. 6. Microscope images (200 ×) of MCF-7 cells (A) and MCF-7/ADR cells (B).

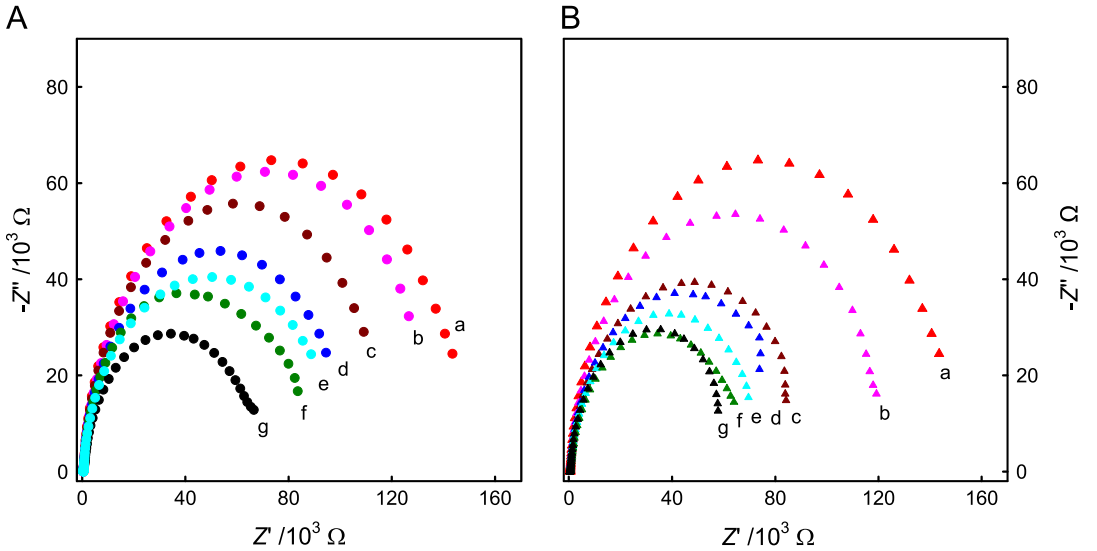


Fig. 7. Electrochemical impedance spectra of BSA-Au NPs-Ab/Ag-BSA/PLL/GCE assembled in the presence of MCF-7 cells (A) and MCF-7/ADR (B) with different concentrations at 0 (a), 5×10^2 (b), 2.5×10^3 (c), 1.25×10^4 (d), 6.25×10^4 (e), 3.2×10^5 (f), 1.6×10^6 (g) cells mL^{-1}.

170 cells mL^{-1}. Compared with other electrochemical cyto-sensors (as shown in Table 1), the developed method presents the relatively wide linear range and low detection limit. Moreover, no labels were used in this work. The above results indicate that the developed method provide a sensitive and label-free method for quantitative measurement of cells.

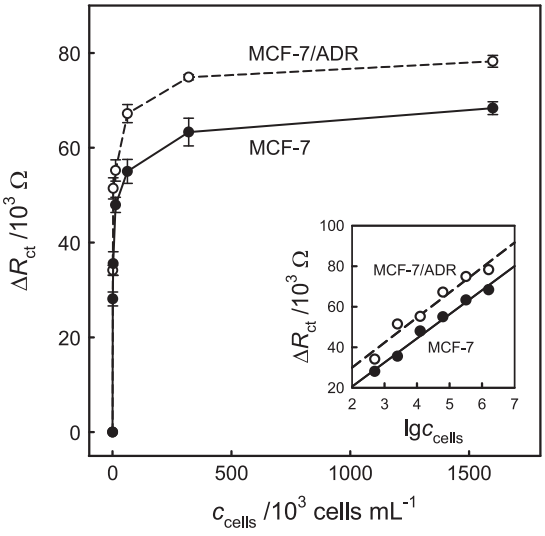


Fig. 8. Plot of ΔR_{ct} vs. c_{cells} of MCF-7 cells (•) and MCF-7/ADR cells (○). Inset: plot of ΔR_{ct} vs. lgc_{cells}. Results are presented as mean ± SD (error bar) of triplicate experiments.

Table 1
Comparison of quantitative detection of cells using electrochemical methods.

Measuring method	Linear range (cells mL^{-1})	Detection limit (cells mL^{-1})	References
QCM	7.5×10^2–7.5×10^7	750	[29]
Amperometry	1.0×10^3–1.0×10^7	620	[30]
Amperometry	2.0×10^3–2.0×10^6	1500	[23]
EIS	1.0×10^4–2.0×10^6	3500	[31]
Amperometry	1.6×10^3–2.0×10^6	700	[28]
Amperometry	2.5×10^3–1.6×10^5	800	[32]
EIS	5.0×10^2–1.6×10^6	170	This work

QCM: quartz crystal microbalance.

4. Conclusion

Nanocomposites consisted of Au NPs, Bcl-2 antibody and BSA were successfully prepared and they could be captured on the Bcl-2 protein-modified electrode based on the immunoreaction, leading to a great increase of the charge-transfer resistance on the electrode surface due to the serious steric hindrance effect. This binding was inhibited in the presence of tumor cells owing to the competitive immunoreaction between the nanocomposites and the Bcl-2 proteins on cells, which resulted in the retraction of R_{ct}. The change extent of the charge-transfer resistance was found to be closely related to the concentration of cells. It developed a sensitive and label-free electrochemical method for the quantitative detection of tumor cells. MCF-7/ADR cells exerted more remarkable influence on the R_{ct} responses than MCF-7 cells with the same concentration, suggesting that the expression of Bcl-2 protein on the drug-resistant tumor cells was significantly higher than that on the tumor cells. The research results support the conclusion that the up-regulation of Bcl-2 protein is one of important factors leading to drug resistance of tumor cells.

Acknowledgments

This work was supported by the Hunan Provincial Natural Science Foundation (12JJ3015), the Scientific Research Fund of Hunan Provincial Education Department (14A095), the Program for Excellent Talents in Hunan Normal University (ET12203) and Aid Program for Science and Technology Innovative Research Team in Higher Educational Institutions of Hunan Province.

References

[1] V. Nuessler, O. Stötzer, E. Gullis, R. Pelka-Fleischer, A. Pogrebniak, F. Gieseler, W. Wilmanns, Leukemia 13 (1999) 1864–1872.
[2] M.K.L. Collins, G.R. Perkins, G. Rodriguez-Tarduchy, M.A. Nieto, A. López-Rivas, Bioessays 16 (1994) 133–138.
[3] J.C. Reed, Am. J. Pathol. 157 (2000) 1415–1430.
[4] S.W. Fesik, Cell 103 (2000) 273–282.
[5] J.C. Reed, T. Miyashita, S. Takayama, H.G. Wang, T. Sato, S. Krajewski, C. Aimé-Sempé, S. Bodrug, S. Kitada, M. Hanada, J. Cell. Biochem. 60 (1996) 23–32.
[6] Q.L. Lu, G. Elia, S. Lucas, J. Alero Thomas, Int. J. Cancer 53 (1993) 29–35.
[7] Y. Tsujimoto, J. Cell. Physiol. 195 (2003) 158–167.
[8] S. Shangary, D.E. Johnson, Biochemistry 41 (2002) 9485–9495.
[9] Z. Huang, Oncogene 19 (2000) 6627–6631.
[10] J.A. Pietenpol, N. Papadopoulos, S. Markowitz, J.K. Willson, K.W. Kinzler, B. Vogelstein, Cancer Res. 54 (1994) 3714–3717.
[11] S. Haldar, A. Basu, C.M. Croce, Cancer Res. 57 (1997) 229–233.
[12] L. Campos, J.P. Rouault, O. Sabido, P. Oriol, N. Roubi, C. Vasselon, E. Archimbaud, J.P. Magaud, D. Guyotat, Blood 81 (1993) 3091–3096.
[13] A. Bonetti, M. Zaninelli, R. Leone, G.L. Cetto, G. Pelosi, S. Biolo, A. Menghi, E. Manfrin, F. Bonetti, Q. Piubello, Clin. Cancer Res. 4 (1998) 2331–2336.
[14] V. Chauhan, M. Howland, Toxicol. In Vitro 28 (2014) 1222–1229.
[15] K. Arii, T. Suehiro, Y. Ikeda, Y. Kumon, M. Inoue, S. Inada, H. Takata, A. Ishibashi, K. Hashimoto, Y. Terada, Metabolism 59 (2010) 1287–1293.
[16] M.D. Begnami, J.H.T.G. Fregnani, S. Nonogaki, F.A. Soares, Hum. Pathol. 41 (2010) 1120–1127.
[17] M. Vaskova, M. Kovac, P. Volna, P. Angelisova, E. Mejstrikova, J. Zuna, T. Brdicka, O. Hrusak, Leuk. Res. 35 (2011) 1111–1113.
[18] H. Chen, J. Jiang, Y. Huang, T. Deng, J. Li, G. Shen, R. Yu, Sens. Actuators B 117 (2006) 211–218.
[19] H. Gong, T. Zhong, L. Gao, X. Li, L. Bi, H.B. Kraatz, Anal. Chem. 81 (2009) 8639–8643.
[20] M. Labib, A.S. Zamay, O.S. Kolovskaya, I.T. Reshetneva, G.S. Zamay, R.J. Kibbee, S.A. Sattar, T.N. Zamay, M.V. Berezovski, Anal. Chem. 84 (2012) 8966–8969.
[21] A. Venkatanarayanan, T.E. Keyes, R.J. Forster, Anal. Chem. 85 (2013) 2216–2222.
[22] E. Barsoukov, J.R. Macdonald, Impedance Spectroscopy: Theory, Experiment, and Applications, second ed., John Wiley & Sons, Inc., Hoboken, New Jersey, 2005.
[23] L. Ding, Q. Ji, R. Qian, W. Cheng, H. Ju, Anal. Chem. 82 (2010) 1292–1298.
[24] C. Cao, S.J. Sim, Biosens. Bioelectron. 22 (2007) 1874–1880.
[25] A.R. Goldfarb, Leo J. Saidel, E. Mosovich, J. Biol. Chem. 193 (1951) 397–404.
[26] D.L. Nelson, M.M. Cox, Principles of Biochemistry, fifth ed., W.H. Freeman and Company, New York, 2008.
[27] Y. Ke, H. Dong, Handbook of Analytical Chemistry, the Third Part—Spectroscopic Analysis, second ed., Chemical Industry Press, Beijing, 1998.
[28] B. Zhou, X. Xiao, L. Xu, L. Zhu, L. Tan, H. Tang, Y. Zhang, Q. Xie, S. Yao, Biosens. Bioelectron. 38 (2012) 389–395.
[29] Z. Shen, M. Huang, C. Xiao, Y. Zhang, X. Zeng, P. Wang, Anal. Chem. 79 (2007) 2312–2319.
[30] W. Cheng, L. Ding, J. Lei, S. Ding, H. Ju, Anal. Chem. 80 (2008) 3867–3872.
[31] X. Jiang, L. Tan, B. Zhang, Y. Zhang, H. Tang, Q. Xie, S Yao, Sens. Actuators B 149 (2010) 87–93.
[32] L. Xu, L. Zhu, N. Jia, B. Huang, L. Tan, S. Yang, H. Tang, Q. Xie, S. Yao, Sens. Actuators B 186 (2013) 506–514.

Talanta 132 (2015) 486–493

Contents lists available at ScienceDirect

Talanta

journal homepage: www.elsevier.com/locate/talanta

endoProteoFASP: A novel FASP approach to profile salivary peptidome and disclose salivary proteases

Fábio Trindade [a], Francisco Amado [b], Pedro S. Gomes [c,d], Rui Vitorino [a,*]

[a] QOPNA, Mass spectrometry center, Department of Chemistry, University of Aveiro, 3810-193 Aveiro, Portugal
[b] School of Health Sciences, University of Aveiro, Portugal
[c] Laboratory for Bone Metabolism and Regeneration–Faculty of Dental Medicine, U. Porto, Porto, Portugal
[d] MedInUP–Center for Drug Discovery and Innovative Medicines, University of Porto, Porto, Portugal

ARTICLE INFO

Article history:
Received 2 July 2014
Received in revised form
11 September 2014
Accepted 13 September 2014
Available online 22 September 2014

Keywords:
FASP
Saliva
Peptidome
Proteolysis
Protease

ABSTRACT

The salivary peptidome, which can represent up to 20% of total secreted proteins in human saliva, is highly influenced by proteolytic events. However, the development of strategies to understand the dynamics underlying the generation of salivary peptides has been a challenging task. In order to disclose in more detail the proteolytic events taking place in saliva, we aimed to characterize salivary peptidome and predict salivary proteases by applying, for the first time, a filter-aided sample preparation (FASP) approach to saliva. Thus, as a proof-of-concept of this application, harvested saliva samples from healthy individuals were incubated in 30 kDa cut-off spin filters for 18 or 115 h, at 37 °C, to promote saliva autolysis and the attained peptidome was characterized and compared with the naturally occurring one. In *ex vivo* conditions, proline-rich proteins, P-B peptide, histatin 1 and statherin were found to be the most susceptible salivary proteins to proteolysis. Peptide fragments were mainly attributed to the activity of cathepsin L1 and *K* at 18 h, whereas at 115 h, the attained peptide fragments were attributed to the activity of cathepsins *K* and L1, and MEP1A. Overall, the described endoProteoFASP approach makes the most of saliva's own protease pool and avoids the use of synthetic peptides and exogenous proteases to understand the proteolytic events occurring in the oral fluid. Hence, it could be very helpful in future studies targeting the characterization of salivary proteases and peptidome from different pathophysiological conditions.

© 2014 Elsevier B.V. All rights reserved.

1. Introduction

Human whole saliva (WS) is a complex body fluid which bathes the oral hard and soft tissues. Its constituents are responsible for essential functions such as food tasting and initiation of digestion, as well as protecting the oral mucosa from pathogenic microbiota, in order to maintain a healthy oral condition [1]. From the proteinaceous composition of WS, several enzymes were already identified, including amylase, carbonic anhydrase, catalase and proteases [2,3]. Indeed, proteases present in oral fluid effectively modulate the structure and function of some salivary proteins and have been implicated in tissue destruction in oral disease, e.g. salivary neutrophil collagenase, lactotransferrin and MMP-9 were associated to periodontal destruction [4]. As a consequence of such modulation, low-molecular-weight (LMW) proteins and peptides become a relevant fraction of the salivary proteome. Thus, characterization of salivary peptidome and identification of the salivary proteases represent pivotal steps towards molecular comprehension of the oral microenvironment equilibrium, as well as regarding proteolysis-associated, inflammatory and infectious diseases [5,6]. Moreover, those approaches allow the development of molecular tools for disease diagnosis, to establish accurate prognosis and to follow-up available therapies for the disease [5,7]. Thus, efforts have been made in an attempt to characterize salivary peptidome, resulting up to date, in the identification of over 2000 peptides [7]. Despite all attempts to achieve an accurate identification, the proteolytic cleavage is currently regarded as a complex and not well known process, involving a set of endo- and exo-proteinases that generate a multitude of small peptides, which might be seen as an individual "fingerprint" [3,6,8]. Previous studies performed on saliva showed that the majority of proteolytic fragments belong to proline-rich proteins (PRPs) family, histatin family and statherin. Aiming to disclose the protease activity of the saliva and the consequent peptide formation, different strategies have been developed. For instance, through the analysis of cleavage sites on the main salivary peptide classes, generation of small peptides has been sugested to

* Corresponding author.
E-mail address: rvitorino@ua.pt (R. Vitorino).

http://dx.doi.org/10.1016/j.talanta.2014.09.026
0039-9140/© 2014 Elsevier B.V. All rights reserved.

emerge from cathepsin D activity [9] or from enzymes with activity resembling those of the gastrointestinal tract, namely trypsin, chymotrypsin or elastase [10]. A different strategy using histatin 5 as a substrate in zymography allowed the identification of a total of 13 proteases with cleavage specificities towards arginine and lysine residues [11]. Neverthless, the identification of glutamine endoproteinase that recognizes KPQ↓ as the main consensus sequence remains unconclusive, though being suggested that it probably derives from dental plaque and it is likely of microbial origin [12].

Conventionally, proteomic approaches pointing the identification of salivary proteins follow one of two main strategies. A SDS-PAGE approach proceeded by "in-gel" digestion can be pursued. This decreases the complexity of the sample and simultaneously, confers robustness against impurities. Alternatively, a *shotgun* approach may be utilized with proteins being digested "in-solution". This reduces sample manipulation and, therefore, eases protocol automation. The combination of such advantages is provided by filter-aided sample preparation (FASP) method [13,14], which confers proper sample clean-up, minimizing the risk of interfering substances; provides a reactor environment for protein digestion; and guarantees the separation of the digestion products. Nonetheless, the FASP protocol is associated with significant sample loss, a drawback that can be overcome by prepassivating the filter unit with a detergent, such as Tween®-20, which may reduce peptide loss by 300%. This and other modifications have been proposed by Erde et al. [15] to achieve better sensitivity, and increase peptide recover and proteomic coverage. An example of other adaptations is provided by Wiśniewski and Mann, which developed a multienzyme digestion FASP (MED-FASP) approach that increases the proteome coverage, due to consecutive proteolysis of the retained material with two or more proteases [16]. The combination of FASP with isobaric mass tagging (iFASP) was also proven possible with higher peptide labeling efficiency than the conventional protocols provided by manufacturers [17]. The versatility of FASP is notorious in numerous studies, which describe protocol adaptations to attain different purposes. For instance, an *N*-glyco-FASP approach was developed to enrich *N*-glycopeptides, retrieving over 6000 *N*-glycosylation motifs in proteins from mouse brain, kidney, liver, heart and plasma [18]. Posterior studies were performed following the same approach in other biological samples such as mouse microglial cells [19], human spermatozoa [20] and supernatants of cultured breast cancer cell lines [21]. The combination of FASP with size-exclusion chromatography was also performed to map another posttranslational modification, the phosphorylation. A previous report has addressed the expression of phosphorylated peptides in the mouse brain proteome [22]. In the same study, another FASP variation is described, the filter aided antibody capturing and elution (FACE), in which a monoclonal phosphotyrosine antibody is added to the FASP filter, to obtain an enriched mixture of peptides displaying phosphotyrosine sites. Those two approaches combined resulted in over 12,000 mapped phosphorylation sites [22].

Overall, while the FASP approach seems to be an effective methodology for peptide-related research, to the best of our knowledge, the use of FASP approach for saliva processing and analysis has not been conducted before. In this way, we hypothesize that FASP allow an effective enrichment of salivary peptidome and, simultaneously, can assure the retention of high-molecular weight (HMW) material with valuable information with regard to proteolytic activity taking place in the oral fluid. We believe that FASP represents a potential technique to establish the referred connection between saliva degradome and salivary proteases. Hence, as a proof-of-concept, we aim to characterize the salivary peptidome and to predict human salivary proteases activity in two healthy individuals, by making use, for the first time, of the FASP technique.

2. Experimental section

2.1. Saliva sampling and processing

Unstimulated whole saliva (UWS) was collected from two healthy men, aged 22 and 32 years, reporting the absence of systemic or oral pathologic conditions. Samples were collected one hour after breakfast by passive drooling and were immediately centrifuged at 12000*g* for 30 min at 4 °C to remove insoluble material, cell debris, bacteria and possible food remnants. Samples from each individual were randomly designated as S1 and S2. UWS supernatants were collected carefully and stored at −80 °C. Protein from processed saliva samples was quantified with a colorimetric assay from BioRad® (DC kit). The following procedures were performed in duplicate.

2.2. FASP–collecting natural peptidome

Saliva samples were divided into two fractions. One fraction from each sample was incubated with 20 mM dithiothreitol (DTT) at 100 °C, for 45 min, to prevent proteolysis (control). The other fraction was kept intact. Spin filters (30 kDa cut-off) were washed and conditioned with 200 μL of ammonium bicabornate (ABC) solution, by centrifugation at 14000*g* for 10 min at 20 °C. Filtrates were discarded. Then, spin filters were loaded with 150 μg of protein and natural occurring peptides were eluted by washing the filter system 5 times with 500 μL of ABC solution. All filtrates were vacuum-dried in SpeedVac®.

2.3. FASP–collecting peptides originated by saliva autolysis

In order to retrieve peptides originated by saliva autolysis, filters were incubated 18 or 115 h at 37 °C, acting as proteomic reactors (Fig. 1). To prevent filter drying and possible damage, 500 μL of ABC solution was added to the reactors before incubation. Generated peptides were then collected by centrifugation at 14,000*g* for 10 min at 20 °C. Filters were washed once more with 500 μL of ABC solution and the filtrates were saved. Then, filters were successively washed with 400 μL of SDS 1% and with 400 μL of ABC solution. A final trifluoroacetic acid (TFA) 0.1% wash was performed. All filtrates were vacuum-dried in SpeedVac®. Final retentates were resuspended in 20 μL of MiliQ water and stored at −80 °C.

2.4. Peptide separation by nanoHPLC

Dried peptide extracts were resuspended in 5 μL of a 50:49.7:0.3 acetonitrile/water/TFA (v/v/v) solution and then sonicated for 3 min. Then, 25 μL of a 0.1% trifluoroacetic acid solution was added and the samples were, once again, sonicated for 3 min. 10 μL of each sample was separated onto a 150 mm × 75 μm Pepmap100 capillary analytical C18 column with 3 μm particle size (Dionex, LC Packings) at a flow rate of 300 nL/min. The mobile phases A and B were 2% ACN 0.1% TFA in water and 95% ACN, 0.045% TFA, respectively. The gradient started at 10 min and ramped to 60% B till 50 min and 100% B at 55 min and retained 100% B till 65 min. The chromatographic separation was monitored at 214 nm using a UV detector (Dionex/LC Packings) equipped with a 3 nL flow cell. The eluted peptides were collected directly on a MALDI plate in 20 s fractions using an automatic fraction collector Probot (Dionex, Amsterdam), with addition of 270 nL of α-cyano-4-hydroxycinnamic acid matrix (3 mg/mL α-cyano-4-hydroxycinnamic acid in 70% acetonitrile and 0.1% TFA, spiked with Glu–Fib (15 fmol)).

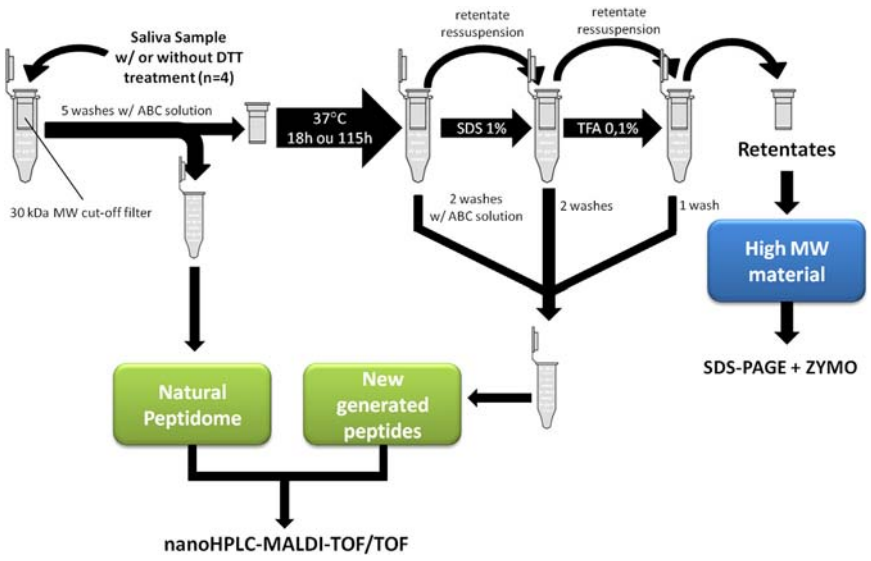


Fig. 1. Experimental Workflow. Natural peptidome from two saliva samples was washed away taking advantage of a 30 kDa cut-off filter. Then, samples were incubated at 37 °C for 18 hours or 115 hours and the newly generated peptides were retrieved with subsequent washes of ABC solution, SDS 1% and TFA 0,1%. A parallel protocol was followed were samples were pre-treated with DTT to prevent proteolysis. Peptides were separated and identified using an offline nanoHPLC-MALDI-TOF/TOF strategy. Retentates were subjected to electrophoretic and zymographic analysis.

2.5. Mass spectrometry analysis and identification of peptides

Mass spectra were acquired on a MALDI-TOF/TOF mass spectrometer (4800 Proteomics Analyzer, Applied Biosystems, Foster City, CA, USA) in the positive ion reflector mode and in the 700–4100 Da mass range. A data-dependent acquisition method was created to select the 16 most intense peaks in each samples spot for subsequent tandem mass spectrometry (MS/MS) data acquisition. Internal pattern Glu-Fib peak (m/z 1570.68 Da) was used as an internal caliber for the MS device. MS/MS data was searched against the Swissprot protein database for *Homo Sapiens* (release date 21032013) using Mascot software (v.2.1.0.4., Matrix Science Ltd., UK). Search parameters included the "none" option for enzyme selection, MS tolerance for precursor ions was set at 40 ppm and 0.4 Da for fragment ions. Positive identification was considered for individual ion scores above 40 and default significance threshold $p < 0.05$.

2.6. Protease prediction

Prediction of proteases was conducted with Proteasix[beta] software [23]. The peptide list to be processed was created accordingly to the significant proteins identified and admitting the unique peptides for a given experimental condition, i.e., sample, time of incubation and presence/absence of DTT treatment.

2.7. Protein retentate separation by SDS-PAGE

The HMW material retained in the filters was separated by gel electrophoresis under reducing and denaturing conditions, applying a 200 V electric current and making use of 12.5% SDS-PAGE gels prepared accordingly to Laemmli [24]. Prior to this, HMW retentates were precipitated in acetone and resuspended in Laemmli loading buffer to be boiled at 100 °C for 5 min, for subsequent gel electrophoresis. After finishing the run, the gels were incubated with fixation solution (methanol/acetic acid, 40:10 v/v) for 45 min. Then, the gels were stained with colloidal coomassie blue overnight and destained with 20% methanol until the background color was removed.

2.8. Protein retentate zymography

From the total retentate, 5 µL of sample was saved for zymography, before protein precipitation. In order to perform gelatin zymography, 10% SDS-PAGE gels were prepared with 0.1% (w/v) gelatin incorporated. Then, 10 µL of sample buffer, containing 0.5 M Tris–HCl pH 6.8, 5% (w/v) SDS, 20% (w/v) glycerol and 0.1% bromophenol blue, were added to each aliquot of retentate. Samples were incubated 10 min at room temperature. Gel electrophoresis was performed applying a constant voltage of 120 V. After finishing the run, the gels were incubated with renaturation buffer, with 2.5% (w/v) Triton X-100, for 2×30 min. Next, gels were placed in developing buffer, containing 50 mM Tris–HCl pH 7.4, 5 Mm NaCl, 100 mM $CaCl_2$, 1 µM $ZnCl_2$ and 0.06% (w/v) Triton X-100, and allowed to incubate overnight. Finally, the gels were stained with colloidal coomassie blue for, at least, 3 h. SDS-PAGE and zymogram gels were scanned with the Molecular Imager® Gel Doc™ XR+ System (Bio-Rad®).

3. Results

In order to characterize salivary peptidome and to disclose the potentially associated human salivary proteases, we reasoned that FASP approach would give a valuable contribute since it guarantees proper peptide separation, providing, at the same time, a reactor-like environment for the proteolytic activity. Thus, we enrolled two healthy individuals as biological replicates, in order to conduct a proof-of-concept experimental workflow based on the classic FASP approach, the endoProteoFASP. This allowed the collection and comparison of both naturally occurring peptides and those generated after saliva autolysis, as outlined in Fig. 1. A prior centrifugation was performed before sample filtration, in order to exclude bacterial material from saliva. In this way, only the soluble proteases, present within the saliva supernatant were the target of the analysis. Two incubation times were selected, a short (18 h) and extended (115 h) which produced minimal and significant alterations, respectively, in saliva SDS-PAGE profile. In this sense, natural peptidome ($t=0$ h, T0) was washed away from whole saliva samples taking advantage of the 30 kDa cut-off filter, which prevented the elution of the HMW material, containing

endogenous proteases. Then, saliva samples were incubated at 37 °C, for 18 h (T18) or 115 h (T115) to promote saliva autolysis. The newly created peptides were then eluted by subsequent washes with ABC solution, SDS 1% and TFA 0.1%. A SDS wash was included to increase the probability of recovering peptides of higher hydrophobicity, since it was demonstrated that the use of a SDS spin column retrieves more hydrophobic species when compared to FASP [25]. Moreover, the use of a detergent seems to reduce the probability of peptide loss [15]. In the end of the experimental protocol, over 500 salivary peptides were identified, of which 225 unique peptides were found in untreated sample 1 (S1) and 588 in untreated sample 2 (S2), distributed along T0, T18 and T115, as depicted in Venn diagrams (Fig. 2), created by Venny web tool [26], and listed in Supplemental Table S1.

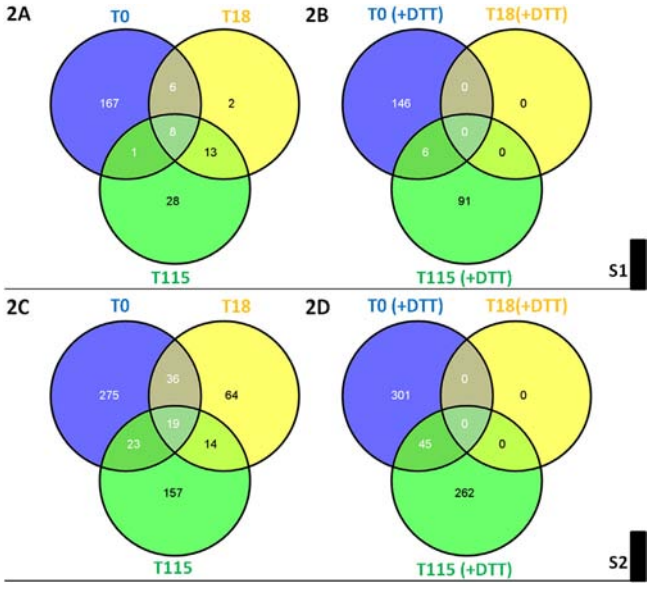


Fig. 2. Distribution of the number of identified peptides before autolysis (T0, blue), after 18 hours of incubation (T18, yellow) and after 115 hours of incubation (T115, green) for untreated sample 1(2A) and 2 (2C) and DTT-treated sample 1(2B) and 2 (2D).

Naturally occurring peptides (T0) identified from S1 and S2, covered several salivary proteins, mainly PRPs, which represented almost 50% of all assigned peptides. P-B peptide (SMR3B), statherin, histatin 1 and mucin 7 followed as the proteins with higher peptide identification, with an average of 17%, 13%, 12% and 5% of the overall set of assigned peptides (Table 1 and Supplemental Table S2). A high variability is noticeable in the individual peptidome, as in S1 and S2, only 27.7% of the identified peptides were shared, as depicted in Fig. 3A.

Following the first cleanup, samples were incubated at 37 °C for 18 h in order to attain a new peptidome following autolysis (T18). To assure that the new set of peptides was a consequence of the activity of the endogenous proteases, parallel protocols were performed in an attempt to completely inhibit salivary autolysis. Firstly, whole saliva samples were boiled at 100 °C, for 10 min, in the presence of SDS 1% (w/v). However, retentates displayed gelatinolytic activity, after 18 h, regardless of the denaturing conditions (Fig. S1). This data shows that salivary proteases are resistant to heat and to SDS, in a concentration similar to Laemmli loading buffer. In a second attempt, samples were boiled at 100 °C, for 45 min in the presence of DTT, a well-known reducing agent, at a final concentration of 20 mM. In this case, the proteolytic activity was completely inhibited, as shown by the absence of gelatinolytic activity (Fig. S1) and by the absence of peptides, at T18, in DTT-treated samples (Fig. 2B and D).

At T18, saliva autolysis resulted in the formation of 29 more peptides for S1 and 133 for S2, which further highlights the differences between individuals (only 8% of the peptides were shared at T18, see Fig. 3B). Comparing T0 to T18 peptidome, we detected that more than half of the set of peptides at T18 had not been identified at T0 (Fig. 2A and C). Indeed, at T18, the vast

Table 1
Number of peptides identified for each protein identified, before autolysis, after 18 h autolysis, after 115 h autolysis, for untreated and DTT-treated samples.

Protein ID	Protein Name	Before Autolysis				After Autolysis 18h				After Autolysis 115h			
		S1		S2		S1		S2		S1		S2	
		Unt.	DTT	Unt.	DTT	Unt.	DTT	Unt.	DTT	Unt.	DTT	Unt	DTT
ACTB_HUMAN	Actin, cytoplasmic 1	0	3	0	0	0	0	0	0	0	0	0	0
AMYP_HUMAN	Pancreatic alpha-amylase	0	0	1	7	0	0	0	0	0	0	2	0
FIBB_HUMAN	Fibrinogen beta chain	0	0	4	1	0	0	3	0	0	0	0	0
FYB_HUMAN	FYN-binding protein	0	0	0	0	0	0	0	0	1	0	0	0
H4_HUMAN	Histone H4	0	5	0	0	0	0	0	0	0	0	0	0
HIS1_HUMAN	Histatin-1	13	26	87	90	0	0	0	0	0	0	0	0
HIS3_HUMAN	Histatin-3	7	2	9	0	0	0	0	0	0	0	0	0
IQEC3_HUMAN	IQ motif and SEC7 domain-containing protein 3	0	0	0	5	0	0	0	0	0	0	0	0
MUC7_HUMAN	Mucin-7	12	14	22	21	0	0	0	0	0	0	0	0
PIGR_HUMAN	Polymeric immunoglobulin receptor	5	6	5	0	1	0	0	0	1	0	0	0
PRB2_HUMAN	Basic salivary proline-rich protein 2	26	24	113	114	0	0	65	0	0	42	0	115
PRB3_HUMAN	Basic salivary proline-rich protein 3	14	2	19	20	6	0	24	0	26	28	92	86
PRB4_HUMAN	Basic salivary proline-rich protein 4	0	0	14	31	0	0	16	0	0	0	100	16
PRP1_HUMAN	Basic salivary proline-rich protein 1	50	22	124	114	9	0	60	0	29	81	107	234
PRPC_HUMAN	Salivary acidic proline-rich phosphoprotein 1/2	32	19	42	32	10	0	20	0	24	24	80	72
SC31A_HUMAN	Protein transport protein Sec31A	0	0	0	0	0	0	0	0	0	0	0	10
SMR3B_HUMAN	Submaxillary gland androgen-regulated protein 3B	56	44	64	66	3	0	0	0	0	0	0	0
STAT_HUMAN	Statherin	22	30	89	73	0	0	0	0	0	0	0	0
TRFL_HUMAN	Lactotransferrin	3	2	0	0	0	0	0	0	0	0	0	0
WIPF2_HUMAN	WAS/WASL-interacting protein family member 2	0	0	0	0	0	0	0	0	0	0	0	9

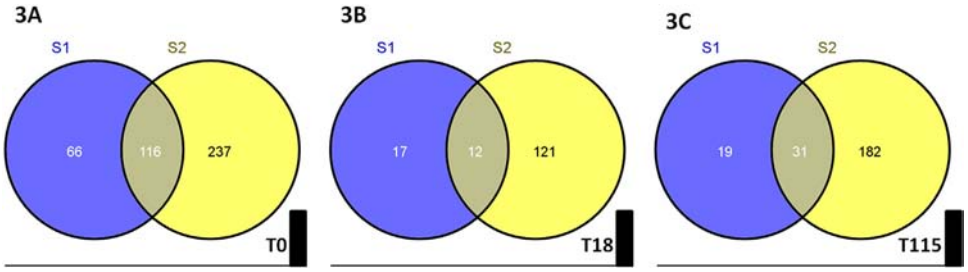


Fig. 3. Venn diagrams depicting inter-individual variability in salivary peptidome, at T0 (3A), at T18 (3B) and at T115 (3C).

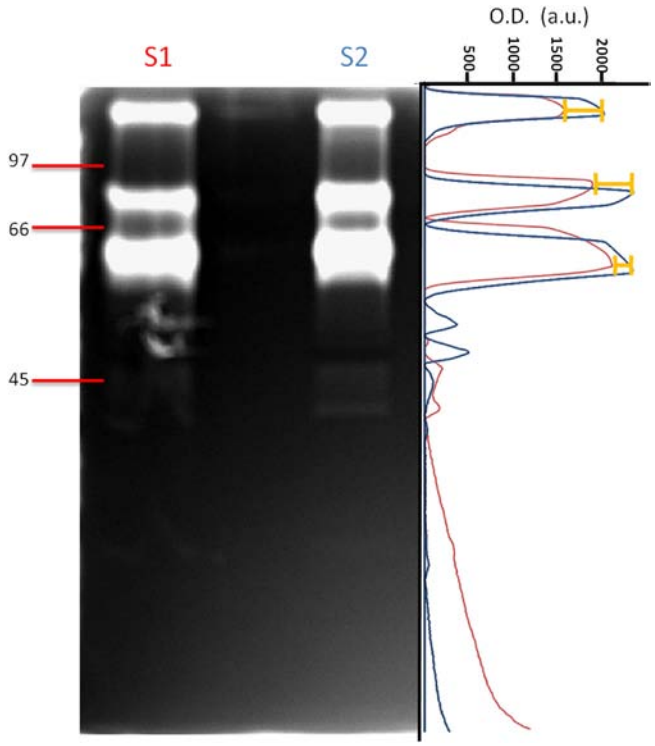


Fig. 4. Gelatin zymograms of the samples after 115 hours of incubation. At the left, zymographic profile of samples 1 (S1) and 2 (S2). At the right, optical density (in arbitrary units) profile of samples 1 and 2, showing higher gelatinolytic activity of sample 2 (yellow symbols).

majority of the attained peptides seems to result from proteolysis of PRPs, mostly basic PRPs 1 (PRP1) and 2 (PRB2), while at T0, peptides derived from a wide range of proteins (Table 1). This data suggests that PRPs are the group of salivary proteins more prone to proteolysis *ex vivo*. When samples were subjected to 115 h of incubation (T115), a larger set of peptides was obtained. In this case, 50 more peptides were eluted from S1, whereas 213 more peptides were eluted from S2. Again, a high inter-individual variability was observed, with only 13.4% of the peptides being detected in both samples (Fig. 3C). At T115 (Table 1), PRPs were again the main source of peptides, though, with a larger group of PRP isoforms being responsible for the generation of new peptides (i.e., PRP1, PRB2, PRB3, PRB4 and PRPC).

Interestingly, in all experimental time points (T0, T18 and T115) a higher production of peptides was verified in S2, in spite of the fact that all experiments were conducted with the same starting protein mass (150 μg). This apparent higher rate of peptide formation is also suggested by the higher gelatinolytic activity of S2, when compared to the one of S1, as depicted in the gelatin zymogram in Fig. 4.

As a consequence of the activity of endogenous proteases, some differences were expected to be found in the SDS-PAGE profile of the salivary proteins. Those differences are evident in Fig. 5. When comparing the electrophoretic profile of the sample retentates at T18 and T115, it is notorious the appearance of new bands between 35 and 45 kDa, around 25 kDa, 17–18 kDa (only in S1) and below 15 kDa, at T115. These new bands can be attributed to the fragments of HMW proteins that underwent proteolysis. Surprisingly, those differences were more expressive in DTT-treated samples, after 115 h of incubation.

An extensive proteolysis was observed in PRPs, with proteases attacking preferably between Gln–Gly residues, but also between Pro–Gln, Pro–Pro, Arg–Ser residues, at the N-terminal of the peptides, and between Arg–Ser and Tyr–Gly, at the C-terminal of the peptides (Supplemental Tables S3 and S4). Indeed, the common peptide sequences among T0, T18 and T115, in both samples, were ^{49}GPPPPPGKPQ^{58}, ^{70}GPPPPPGKPQ^{79} and ^{92}SPPGKPQGPPPQ GGNQPQ^{109}, ^{52}SPPGKPQGPPPQGGNQPQ^{69}, which belong to PRP1 and PRB2, respectively; ^{148}GPPPQGGRPQGPPQGQSPQ^{166} which belong to PRPC and ^{268}GPPPPGGNPQQPLPPPAGKPQ^{288} and ^{17}QSLN EDVSQEESPSVISGKPEGR^{39} to PRB3. Taking the above sequences as an example, 122 out of 185 cleavage sites took place between Gln–Gly, and the remaining 63 occurred between Arg–Ser, Arg–Gln, Gln–Gln and Pro–Ser. In order to predict the salivary proteases responsible for the production of the identified peptides, a Proteasix^{BETA} [23] analysis was performed, accordingly to the particular peptide set of each experimental group. As depicted in Table 2, the proteases cathepsin L1 (CTSL1) and meprin A (subunit alpha, MEP1A), a cysteine and a metalloprotease, respectively, were predicted ubiquitously in the different experimental conditions, except in the presence of DTT, at T18 (due to the absence of peptides). Hence, these data suggest that these proteases are the most resistant to time and to reducing conditions. In fact, CTSL1 and CTSK have specificity for substrates displaying Gln in position P1 and Gly in P1', thus explaining the higher frequency of cleavage sites between Gln–Gly. At T18, in untreated samples, which yielded 150 peptides, cleavage sites appeared to result from the activity of a large range of predicted proteases, including cysteine-, serine- and metalloproteinases (Table 2). At T115, samples were further decomposed, regardless of the treatment with DTT. Nevertheless, a minor set of proteases remained active, comprising cathepsins K and L1, MMP9, MEP1A and a disintegrin and metalloproteinase with thrombospondin motifs 5 (ADAMTS5), the later only figuring in DTT-treated samples.

4. Discussion

This work describes, for the first time, the use of a FASP approach to profile salivary peptidome and to disclose potentially associated human salivary proteases. The dual use of a 30 kDa cut-off filter as a sample cleaner device and as a "proteomic reactor" allowed proper separation of peptides and, at the same time, an increase in the activity of soluble salivary proteases. Thus, we provided the proof-of-concept of a novel peptidomic approach, the endoProteo-FASP, to understand the dynamics of the salivary peptidome, making

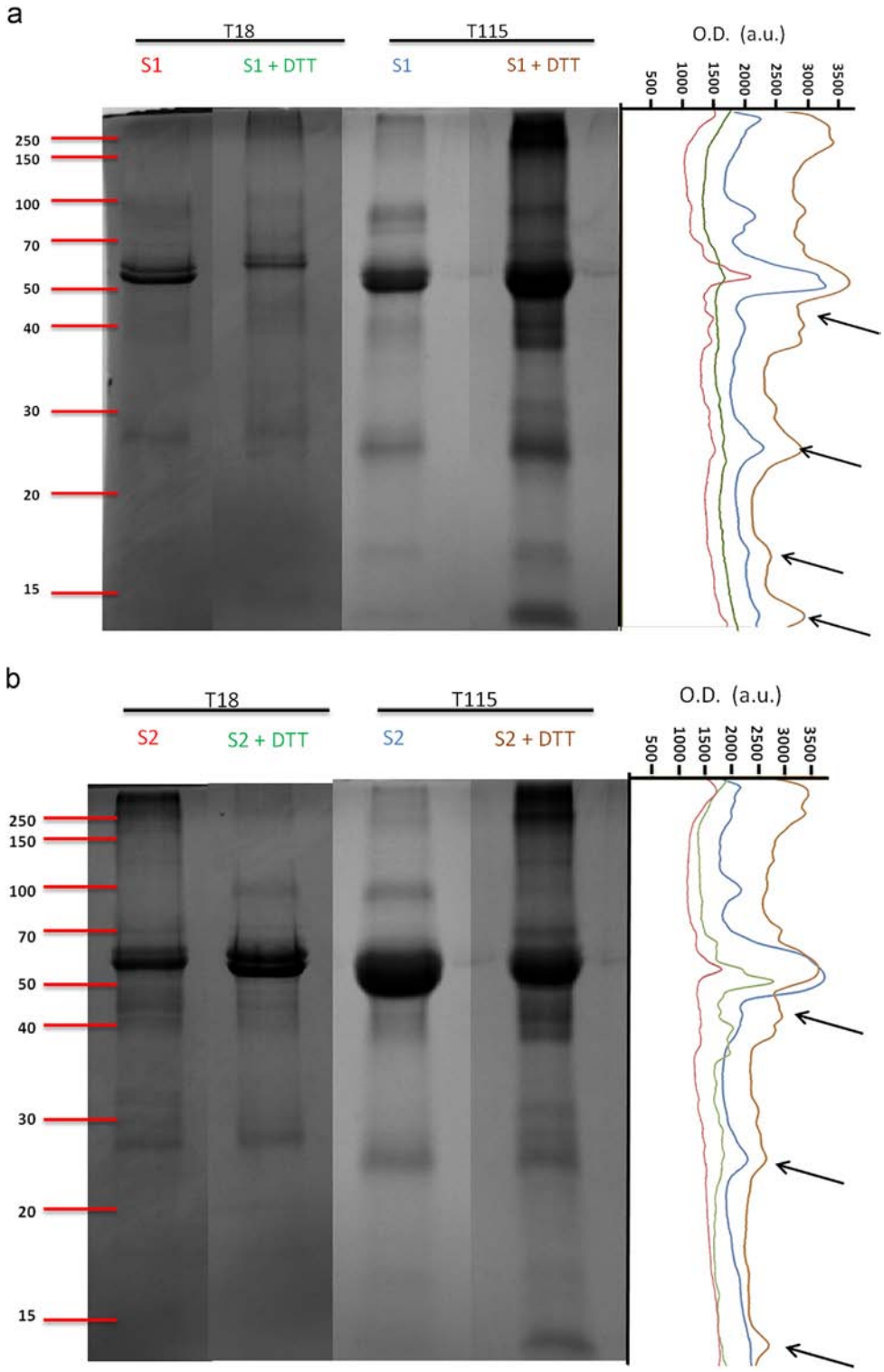


Fig. 5. SDS-PAGE of the retentates for sample 1 (a) and 2 (b), after 18 and 115 hours of incubation. At the left, red lines identify molecular weight ladders. At the right, optical density (in arbitrary units) profile of sample 1 in the different experimental conditions (red, untreated sample at T18; green, DTT-treated sample at T18; blue, untreated sample at T115 and brown, DTT-treated sample at T115). Black arrows indicate prominent changes in the electrophoretic profile from T18 to T115.

the most of saliva's own protease pool and avoiding the use of synthetic peptides and exogenous proteases, as previously reported in the literature [12,15–22,27]. Additionally, our work confirmed the utility of the combination of the ammonium bicarbonate extraction method with sample filtration in order to enrich salivary peptides, as reported previously by our group [28].

With the endoProteoFASP approach we provided a novel time-based experimental approach that gives valuable information with regard to the process of saliva autolysis. If, on one hand, we could identify the susceptible proteins to proteolysis in a time-course manner, on the other hand, we were able to understand which endogenous proteases may be involved in those proteolytic events.

Table 2
Predicted proteases by Proteasix[BETA] software (> 15% of cleavage) derived from unique peptides identified before autolysis, after 18 h autolysis and after 115 h autolysis, in untreated and DTT-treated samples.

Experimental Condition		**Predicted proteases** (UniProt gene name)
Before autolysis	Untreated samples	CTSL1, MEP1A
	DTT-treated samples	CTSL1, MEP1A
After 18 h autolysis	Untreated samples	CTSL1, CTSB[a], CTSK, CTSS[a], KLK2[a], KLK4[a], MEP1A[b], MMP12[b], MMP9[b], NLN[a], PLG[a], PREP[b], THOP1[a]
	DTT-treated samples	None (there was not any peptide identified)
After 115 h autolysis	Untreated samples	CTSK, CTSL1, MEP1A, MMP9[b]
	DTT-treated samples	ADAMTS5, CTSK, CTSL1, MEP1A, MMP9[b]

[a] Predicted only in sample 1.
[b] Predicted only in sample 2.

A major concern with this approach was to guarantee proper sample clean-up before incubation and, therefore, to assure that the new peptides, identified at different times, resulted from saliva autolysis, rather than being part of the natural peptidome. Indeed, the identified peptides could be attributed to the activity of proteases in the oral fluid, as evidenced by the absence of shared peptides before and after sample incubation (Fig. 2B and D). Moreover, the inexistence of peptides at T18 corroborates an effective clean-up of the samples and a successful inhibition of the proteolytic activity.

Despite inter-individual variability, PRPs, P-B peptide, histatin 1 and 3, mucin 7, polymeric immunoglobulin receptor and statherin represented the most susceptible salivary proteins to proteolysis *in vivo*, as proven by the number of peptides identified to these proteins at T0 (Table 1) which is corroborated by the LC-MS/MS-based characterization of whole salivary peptidome [29–31]. Protein fragments at T0 were attributed to the activity of CTSL1 and MEP1A. To date, CTSL1, but not MEP1A, was already identified in saliva through the combination of histatin 5 zymography and LC-ESI-MS/MS [11]. The presence of MEP1A in saliva remains to be confirmed, though it seems a relevant protease in saliva autolysis, as confirmed by its prediction in all incubation time points. After 18 h and 115 h of incubation, the majority of the eluted peptides belonged almost exclusively to the different PRP isoforms, suggesting that these proteins display the highest susceptibility to *ex vivo* proteolysis. Cleavage site analysis showed that the peptide bond between Gln–Gly residues was the preferential site for proteolysis, which is in agreement with previous findings [29–32]. Interestingly, the formation of the new PRPs peptides is associated with a time-dependent profile of proteases, a variation never reported so far, to the best of our knowledge. At T18, a wide range of cathepsins (K, S, L and B), serine proteases (kallikreins 2 and 4, plasminogen and prolyl endopeptidase) and metalloproteinases (MMP 9 and 12, MEP1A, neurolysin and thimet oligopeptidase) seems to be responsible for PRPs degradation. At T115, however, only CTSL1 and K, MMP9 and MEP1A were predicted, a factor that can be explained due to irreversible denaturation or due to proteolysis of susceptible proteases. The association of PRPs fragments with different sets of proteases (T18 *vs* T115) highlights the dynamism underlying saliva autolysis, with proteases being permanently active (CTSL1 and MEP1A) and others being active at particular periods.

The consistent prediction of CTSL1 and MEP1A at T0 (reflecting the proteolytic events before secretion) and at T18 and T115 (reflecting the proteolytic events in the soluble fraction of saliva) suggest that human proteases are largely responsible for proteome modulation. Nonetheless, taking into account that Proteasix software is based on the prediction of human proteases, we acknowledge that proteolysis may also result, to some extent, from the activity of bacterial proteases with the same substrate specificity as the proteases covered by this software. The activity of microbial proteases might help to explain inter-individual variability regarding the number of peptides of each salivary protein. This whole hypothesis is supported by the findings of Helmerhorst et al. [11], who found that histatin degradation is 7.5 times faster in whole saliva's pellet, where bacteria is deposited, than in whole saliva supernatant. Nonetheless, care was given to harvest saliva samples from healthy individuals that did not shown any form of periodontal disease or active caries lesions. While differences may still exist between the oral microbiota of the participants, the absence of oral inflammation or infectious processes minimizes the risk of sample contamination with proteases from pathogenic microbiota.

As one may notice, at T115, the electrophoretic profile of the samples changed, due to the appearance of new LMW bands. This is particularly true for DTT-treated samples (4th lane of the gels, Fig. 5A and B). In these samples 91 new peptides were identified for S1, and 262 for S2. This data suggests that DTT enhanced protein hydrolysis due to the denaturation of salivary proteins. Although, at this time point, the eluted peptides resulted mainly from PRPs and from only 3 novel proteins, namely, FYN-binding protein (85.4 kDa), protein transport protein Sec31A (133 kDa) and WAS/WASL-interacting protein family member 2 (46.3 kDa). Probably, by increasing the incubation time of the samples, one would address interesting information with respect to saliva's most resistant proteins to endoprotease activity. Additionally, our data evidences the resistance of salivary proteases to denaturing conditions. This resilience was found when saliva samples depicted gelatinolytic activity after being boiled in the presence of SDS and also when DTT-treated samples yielded peptides, after 115 h of incubation. This particular robustness of salivary proteases has also been observed by other authors. For instance, Thomadaki et al. [12] showed that the addition of an inhibitor cocktail to whole saliva (containing AEBSF, aprotinin, pancreatic trypsin inhibitor, leupeptin, antipain and EDTA), spiked with histatin 5, statherin or PRP1, did not prevent the degradation of these susceptible proteins. Robinson and colleagues [27] demonstrated, through a PALeO (proteinase activity labeling employing ^{18}O-enriched water) experiment, that sample freezing, *per se*, is not effective to inhibit proteolysis. Another example is provided by Xiao et al. [33], which showed that salivary proteome is stable only for two weeks, if stored at 4 °C with protease inhibitors, or at room temperature with addition of ethanol, when comparing to samples stored at −80 °C with protease inhibitors. de Jong et al. [34] also provided evidence for proteome instability, pointing the freezing rate as an additional concern with regard to the peptidome composition and demonstrating a decrease in the abundance of peptides in samples kept at room temperature, for 24 h. Therefore, our work along with the above referred studies [12,27,33,34] contributes to the body of evidence of the great resilience of salivary proteases, an important factor that should be stressed in future works where inhibition of those enzymes is pointed. Moreover, this work emphasizes the huge importance of sample pre-treatment to assure the quality of the samples over time, given that, despite the initial denaturation, salivary proteases may, most certainly, restore their activity, which can lead to sample degradation.

In spite of the similar zymographic profile of S1 and S2 retentates, optical density analysis suggests a higher gelatinolytic

activity of the latter. Indeed, S2 autolysis attained to a bigger set of eluted peptides, regardless of the time of incubation. This data provides an evidence of inter-individual variability, which might be attributed to differential activity of the proteases present in the oral fluid. Indeed, MMP9 and MMP2, two proteases with gelatinolytic activity, were predicted exclusively from S2 peptidome. Furthermore, several proteases were predicted in S1, whilst absent in S2, namely cathepsins B and S, neurolysin, kallikrein 2 and 4, plasminogen and thimet oligopeptidase. Future validation of the differential activity of such proteases should be performed, to ensure the conformity of the peptidome data (sample filtrates) with proteome data (sample retentates). Nevertheless, these observations point at the potential application of the endoProteoFASP approach to clinical research, with regard to biomarker discovery, since it is possible to address variations in individual peptidome and attribute those changes to the variation of a protease profile.

5. Concluding remarks

This work addresses the first exploratory study regarding salivary proteases and peptidome with a FASP approach. A remarkable dynamism of salivary peptidome was notorious and could be attributed to the differential participation of proteases with substrate specificities close to human cathepsins, serine proteases and metalloproteinases, in a time-course. Several hallmarks of proteolytic events taking place in saliva were confirmed with this approach, such as the identification of PRPs, P-B peptide, histatin 1 and statherin, as proteolysis-susceptible proteins, instead of other salivary proteins. Furthermore, the relative higher abundance of Gln–Gly cleavage site can be attributed for the first time to cathepsins L1 and K. Additionally, it seems that there is a correlation between the intensity of the gelatinolytic activity and the number of identified peptides, with this methodology. Therefore, this optimized endoProteoFASP approach to saliva samples could be useful in future studies aiming not only the characterization of salivary proteases, but also other biological fluids and peptidome from different pathophysiological conditions.

Acknowledgments

This study was supported by QOPNA: Fundação para a Ciência e a Tecnologia (FCT, Portugal), European Union, QREN, FEDER and COMPETE for funding the QOPNA research unit (project PEst-C/QUI/UI0062/2013), RNEM (Portuguese Mass Spectrometry Network) and EXPL/BBB-BEP/0317/2012 (FCOMP-01-0124-FEDER-027554) and COST action BM1307. The authors would like to acknowledge Dr. Julie Klein for her help in processing data with Proteasix^{beta} software.

Appendix A. Supporting information

Supplementary data associated with this article can be found in the online version at http://dx.doi.org/10.1016/j.talanta.2014.09.026.

References

[1] G.H. Carpenter, Annu. Rev. Food Sci. Technol. 4 (2013) 267–276. http://dx.doi.org/10.1146/annurev-food-030212-182700.
[2] H.H. Chauncey, F. Lionetti, R.A. Winer, V.F. Lisanti, J. Dent. Res. 33 (1954) 321–334. http://dx.doi.org/10.1177/00220345540330030501.
[3] M. Castagnola, T. Cabras, A. Vitali, M.T. Sanna, I. Messana, Trends Biotechnol. 29 (2011) 409–418. http://dx.doi.org/10.1016/j.tibtech.2011.04.002.
[4] M.G. Salazar, N. Jehmlich, A. Murr, V.M. Dhople, B. Holtfreter, E. Hammer, et al., J. Clin. Periodontol. 40 (2013) 825–832. http://dx.doi.org/10.1111/jcpe.12130.
[5] E.J. Helmerhorst, Ann. N. Y. Acad. Sci. 1098 (2007) 454–460. http://dx.doi.org/10.1196/annals.1384.013.
[6] T. Cabras, F. Iavarone, B. Manconi, A. Olianas, M.T. Sanna, M. Castagnola, et al., Bioanalysis 6 (2014) 563–581. http://dx.doi.org/10.4155/bio.13.349.
[7] F. Amado, M.J.C. Lobo, P. Domingues, J.A. Duarte, R. Vitorino, Expert Rev. Proteomics 7 (2010) 709–721. http://dx.doi.org/10.1586/epr.10.48.
[8] F.M.L. Amado, R.P. Ferreira, R. Vitorino, Clin. Biochem. 46 (2013) 506–517 http://dx.doi.org/10.1016/j.clinbiochem.2012.10.024.
[9] R. Vitorino, A. Caseiro, P. Domingues, F. Amado, Proteomics Clin. Appl. 3 (2009) 528–540. http://dx.doi.org/10.1002/prca.200800183.
[10] G. Lucchi, C. Chambon, C. Truntzer, D. Pecqueur, P. Ducoroy, C. Schwartz, et al., Int. J. Pept. Res. Ther. 15 (2009) 177–185. http://dx.doi.org/10.1007/s10989-009-9167-2.
[11] X. Sun, E. Salih, F.G. Oppenheim, E.J. Helmerhorst, Proteomics Clin. Appl. 3 (2009) 810–820. http://dx.doi.org/10.1002/prca.200800242.
[12] K. Thomadaki, E.J. Helmerhorst, N. Tian, X. Sun, W.L. Siqueira, D.R. Walt, et al., J. Dent. Res. 90 (2011) 1325–1330. http://dx.doi.org/10.1177/0022034511420721.
[13] J.R. Wiśniewski, A. Zougman, N. Nagaraj, M. Mann, Nat. Methods 6 (2009) 359–362.
[14] L.L. Manza, S.L. Stamer, A.-J.L. Ham, S.G. Codreanu, D.C. Liebler, Proteomics 5 (2005) 1742–1745. http://dx.doi.org/10.1002/pmic.200401063.
[15] J. Erde, R.R.O. Loo, J.A. Loo, J. Proteome Res. 13 (2014) 1885–1895. http://dx.doi.org/10.1021/pr4010019.
[16] J.R. Wiśniewski, M. Mann, Anal. Chem. 84 (2012) 2631–2637. http://dx.doi.org/10.1021/ac300006b.
[17] G.S. McDowell, A. Gaun, H. Steen, J. Proteome Res. 12 (2013) 3809–3812 http://dx.doi.org/10.1021/pr400032m.
[18] D.F. Zielinska, F. Gnad, J.R. Wiśniewski, M. Mann, Cell 141 (2010) 897–907. http://dx.doi.org/10.1016/j.cell.2010.04.012.
[19] D. Han, S. Moon, Y. Kim, H. Min, Y. Kim, BMC Genomics 15 (2014) 1–17.
[20] G. Wang, Y. Wu, T. Zhou, Y. Guo, B. Zheng, J. Wang, et al., J. Proteome Res. 12 (2013) 5750–5759. http://dx.doi.org/10.1021/pr400753f.
[21] P.J. Boersema, T. Geiger, J.R. Wiśniewski, M. Mann, Mol. Cell. Proteomics 12 (2013) 158–171. http://dx.doi.org/10.1074/mcp.M112.023614.
[22] J.R. Wiśniewski, N. Nagaraj, A. Zougman, F. Gnad, M. Mann, J. Proteome Res. 9 (2010) 3280–3289. http://dx.doi.org/10.1021/pr1002214.
[23] J. Klein, J. Eales, P. Zürbig, A. Vlahou, H. Mischak, R. Stevens, Proteomics 13 (2013) 1077–1082. http://dx.doi.org/10.1002/pmic.201200493.
[24] U.K. Laemmli, Nature 227 (1970) 680–685.
[25] M.S. Bereman, J.D. Egertson, M.J. MacCoss, Proteomics 11 (2011) 2931–2935.
[26] J.C. Oliveros, VENNY. An interactive tool for comparing lists with Venn Diagrams, (2007).
[27] S. Robinson, R.K. Niles, H.E. Witkowska, K.J. Rittenbach, R.J. Nichols, J. a Sargent, et al., Proteomics 8 (2008) 435–445. http://dx.doi.org/10.1002/pmic.200700680.
[28] R. Vitorino, A.S. Barros, A. Caseiro, R. Ferreira, F. Amado, Talanta 94 (2012) 209–215. http://dx.doi.org/10.1016/j.talanta.2012.03.023.
[29] N. Le Yondre, H. Tammen, R. Hess, P. Budde, M. Jürgens, Open Proteomics J. 1 (2008) 99–105.
[30] M. Morzel, A. Jeannin, G. Lucchi, C. Truntzer, D. Pecqueur, S. Nicklaus, et al., J. Proteomics (2012), http://dx.doi.org/10.1016/j.jprot.2012.04.028.
[31] A. Caseiro, R. Vitorino, A.S. Barros, R. Ferreira, M.J. Calheiros-Lobo, D. Carvalho, et al., Biomed. Chromatogr. 26 (2012) 571–582. http://dx.doi.org/10.1002/bmc.1677.
[32] A. Caseiro, R. Ferreira, A. Padrão, C. Quintaneiro, A. Pereira, R. Marinheiro, et al., J. Proteome Res. 12 (2013) 1700–1709. http://dx.doi.org/10.1021/pr3010343.
[33] H. Xiao, D.T.W. Wong, Anal. Chim. Acta 722 (2012) 63–69.
[34] E.P. de Jong, S.K. van Riper, J.S. Koopmeiners, J.V. Carlis, T.J. Griffin, Clin. Chim. Acta. 412 (2011) 2284–2288. http://dx.doi.org/10.1016/j.cca.2011.08.023.

Talanta 132 (2015) 494–502

Contents lists available at ScienceDirect

Talanta

journal homepage: www.elsevier.com/locate/talanta

Comparison of the performance of different silicon-based SALDI substrates for illicit drug detection

T. Guinan [a], M. Ronci [a], R. Vasani [a], H. Kobus [b], N.H. Voelcker [a,*]

[a] Mawson Institute, University of South Australia, Mawson Lakes, SA 5095, Australia
[b] School of Physical and Chemical Sciences, Flinders University, Bedford Park, SA 5042, Australia

ARTICLE INFO

Article history:
Received 2 September 2014
Received in revised form
24 September 2014
Accepted 25 September 2014
Available online 7 October 2014

Keywords:
NALDI™
NIMS
DIOS
SALDI
Drug detection

ABSTRACT

Surface-assisted laser desorption ionization mass spectrometry (SALDI-MS) is an emerging technique used for the detection of small molecules (< 700 Da) such as illicit drugs. In recent times, this technique has been employed for the detection of illicit drugs in various body fluids including saliva. Three common SALDI techniques, desorption ionization on porous silicon (DIOS), nanostructure-initiator mass spectrometry (NIMS) and nanostructured laser desorption ionization (NALDI™) are compared for the detection of four drug classes, amphetamines, benzodiazepines, opiates and tropane alkaloids. We focus in our comparison on structural and chemical characteristics, as well as analytical performance and longevity.

© 2014 Elsevier B.V. All rights reserved.

1. Introduction

Matrix-assisted laser desorption ionization time of flight mass spectrometry (MALDI-TOF-MS) is a soft ionization technique which is typically used for the analysis of organic molecules (> 700 Da) such as peptides, proteins and oligonucleotides [1–3]. The analyte is typically dissolved into a UV-absorbing organic acid matrix, which vaporizes upon irradiation with a pulsed UV laser. A limitation of MALDI-TOF-MS is the difficulty to detect small organic molecules (< 700 Da) in the noisy spectra produced in the low mass range as a result of matrix adduct formation [4,5]. Matrix-free techniques, referred to as surface-assisted laser desorption ionization mass spectrometry SALDI-MS have been introduced for the detection of small molecules [6–9]. Successful implementations of SALDI-MS include those based on nanostructured silicon such as desorption ionization on porous silicon (DIOS) [10], nanostructure-initiator mass spectrometry (NIMS) [11] and nano-assisted laser desorption ionization (NALDI™) [12]. DIOS and NIMS substrates are both based on porous silicon but differ in wafer dopant, pore size, depth and surface chemistry. DIOS substrates are macroporous with pore depths (< 500 nm) whereas NIMS fall into the mesoporous regime with pore depths in excess of 10 μm. Furthermore, DIOS substrates are generally functionalized with a perfluorinated silane [13], whilst NIMS is functionalized with a heavily fluorinated siloxane in 1,3-bis(heptadecafluoro-1,1,2,2-tetrahydrodecyl)tetramethyldisiloxane ($BisF_{17}$) [11,14].

NALDI™, on the other hand is a commercially available – and recently discontinued – substrate from Nanosys, Inc. and Bruker Daltoniks, Inc [12]. The substrates comprise of silicon nanowires (SiNWs) grown from vapor liquid solid deposition on silicon or steel [4]. The SiNWs are parallel to the surface, 100 to 500 nm in length and 10 to 20 nm in diameter [15]. The nanostructures are functionalized with pentafluorophenylpropyldimethylchlorosilane (F_5PhPr). The NALDI™ surface has a high nanostructure density (> 100 /μm^2), which has been shown to cause dramatic increases in observed signal intensities for small molecule analysis [4]. NALDI™ has been used for the detection of low molecular weight compounds between 50–1500 Da [12,15,16].

One potential application for SALDI is for the detection of illicit drugs at the roadside [17,18]. Since 2004, countries including Australia, Finland and France have introduced screening procedures for a range of illicit drugs including amphetamines and tetrahydrocannibinol [19] at the roadside. The use of oral fluid testing allows for non-invasive screening of drugs, which have been administered within a 24 h time frame [20]. Furthermore, the majority of drug molecules (with the exception of benzodiazepines) are found in oral fluids at higher concentrations in comparison to blood, serum or urine [19,21,22]. However, current immunoassays for saliva in use on the roadside are only presumptive and samples providing positive results are submitted for confirmatory laboratory analysis using gas chromatography mass spectrometry (GC–MS) or high performance liquid chromatography-mass spectrometry (HPLC-MS).

* Correspondence to:Mawson Institute, University of South Australia, GPO Box 2471, Adelaide, SA 5001,Australia.
Tel.: +61 (08) 8302 5508; fax: +61 (08) 8302 5613.
E-mail address: nico.voelcker@unisa.edu.au (N.H. Voelcker).

http://dx.doi.org/10.1016/j.talanta.2014.09.040
0039-9140/© 2014 Elsevier B.V. All rights reserved.

In this paper, we compare the characteristics of DIOS, NIMS and NALDI™ and their analytical performance in relation to the detection of four different drug classes, amphetamines, opiates, benzodiazepines and tropane alkaloids at concentrations relevant to body fluid testing. Quantitative SALDI analysis on the three substrates is also presented for oxycodone in both water and PBS. Finally, the longevity of the three substrates was investigated by comparing the average signal-to-noise (S/N) produced for flunitrazepam on fresh and six-month old samples. This was done since nanostructured substrates often have high surface areas that can be contaminated upon exposure to air, which causes strong interferences in the mass spectra.

2. Materials and methods

2.1. Reagents

Hydrofluoric acid (HF) (48%) was obtained from Fischer Scientific (United Kingdom). Ethanol (EtOH) (100% undenatured), methanol (99.9%), acetone and DCM were purchased from Chem Supply (Australia). Water was purified using a Labconco water purifier (USA) (referred to as milliQ water). Tridecafluoro-1,1,2,2-tetrahydrooctyldimethylchlorosilane (F_{13}) and $BisF_{17}$ were purchased from Gelest Inc (USA). α-Cyano-4-hydroxycinnamic acid (CHCA) was purchased from Bruker-Daltonics (Germany). Phosphate buffered saline (PBS, pH 7.4, 1 X) was purchased from Sigma Aldrich (Australia).

Certified standard solutions of methadone, flunitrazepam, oxycodone, 3,4-methylenedioxymethamphetamine (MDMA) and cocaine were kindly provided by Forensic Science South Australia (Australia).

2.2. DIOS fabrication

Monocrystalline (0.008–0.02 Ωcm) antimony doped n-type Si (1 0 0) wafers from Silicon Quest International (CA, USA) were cut with a diamond cutter into 3.5 cm x 3.5 cm squares. The cleaning processes were carried out by sonicating the wafers in 99.9% methanol and drying under a stream of nitrogen. Porous silicon (pSi) was fabricated by light-assisted anodic etching of cut Si wafers using a photomask. The photomask was 2.4 cm x 2.4 cm containing 100 spots approximately 1 mm in diameter. In brief, photopatterned pSi arrays were clamped into a custom-built Teflon anodization cell contacting a gold foil anode (Space Products International, CA, USA). A 0.5 mm diameter platinum wire (99.9%, Aldrich, WI, USA) formed into a ring was used as a cathode. A 1:1 HF:EtOH electrolyte solution was filled into the Teflon well. The Si wafer was illuminated using a fiber optic light source which passed through a photomask and then through a set of two aspheric lens, $f=80$ mm (OptoSigma, CA, USA) for collimation. A constant current of 3.2 mA/cm^2 was then applied across the cell for 2 min using a source meter program, created in LabView 6.1 to control a 2425 current source meter (Keithley, Ohio, USA). The generated pSi films were then subjected to several methanol washes, before being dried under a stream of nitrogen gas.

2.3. Oxidation and functionalization

The freshly etched pSi was ozone-oxidized at a flow rate of 3.25 g/h using an Ozone-Generator 500 (Fischer, Germany). Following oxidation, the wafer was subjected to a second pore broadening etch using 5% HF/H_2O for 30 s. Subsequently, the double etched surface was ozone oxidized (as above) for a second time. The hydroxyl-terminated surface was then silanized via the addition of 80 μL of neat F_{13} for 15 min at 90 °C. After silanization, the pSi arrays were washed with methanol, dried under a stream of nitrogen gas and then stored in a desiccator until required.

2.4. NIMS fabrication

Monocrystalline (0.01–0.02 Ωcm) boron doped p-type Si (1 0 0) wafers from Silicon Quest International (CA, USA) were etched in a 2:1 HF:EtOH electrolyte solution at a constant current of 27 mA/cm^2 for 5 min. The freshly etched pSi was ozone-oxidized at a flow rate of 3.25 g/h using an Ozone-Generator 500 (Fischer, Germany). The hydroxyl-terminated surface was then functionalized via the addition of 80 μL of neat $BisF_{17}$ for 60 min at room temperature. To assist removal of excess derivitizing agent the NIMS substrate was placed in the oven for 3–5 s and then blown off with a stream of nitrogen gas.

NALDI™ target plates, purchased from Bruker Daltonics (Germany) were used as supplied.

2.5. Preparation of drug solutions

Stock solutions of each drug at 0.1 mg/mL were prepared by diluting the content of each certified standard ampoule to a final volume of 10 mL in a volumetric flask. Solutions were stored at −20 °C. Working solutions at 1000 ng/mL were obtained by diluting the stock solutions with milliQ. Working solutions were kept at +4 °C and prepared fresh every two weeks. Illicit drug solutions at varying concentrations (~0.5–100 ng/mL in water) were prepared from the working solutions immediately prior to analysis. For salt analysis, oxycodone was diluted at various concentrations (5–500 ng/mL) in PBS.

2.6. Sample deposition method for illicit drug solutions in water

Aliquots of drug solutions (1 μL) were deposited onto SALDI-MS substrates. The solvent was allowed to completely evaporate under ambient conditions. Upon evaporation, pSi chips were mounted on a modified MALDI target plate (MTP384, Bruker Daltonics, Germany) and analyzed. The NALDI™ chip was attached to a MTP NALDI™ adapter (Bruker Daltonics, Germany).

2.7. SALDI-MS analysis

Mass spectra were collected using an Autoflex Series III Bruker MALDI-TOF-TOF mass spectrometer equipped with a SmartBeam (337 nm, Nd:YAG) 200 Hz pulsed laser, operated at 200 Hz frequency. The laser attenuator offset was optimized for each drug on the NIMS, NALDI™ and DIOS surface so as to maximize the productions of protonated species whilst reducing background noise. Briefly, the laser attenuator offset was set to approximately 40%, 55% and 60% for NALDI™, NIMS and DIOS respectively in reflectron positive (RP) mode unless otherwise stated. Mass spectra were generated by averaging 500 individual laser shots. Data acquisition used flexControl 3.3 (build 85) software and data analysis was performed using flexAnalysis version 3.3. Instrumental parameters for the RP acquisition were set as follows: 19.00 and 16.80 kV for the ion source 1 and 2, respectively, 8.25 kV for the lens and 21.00 and 9.40 kV for reflector 1 and 2, respectively. Quadratic external calibration of the TOF tube was performed before each acquisition on the monoisotopic masses of CHCA adducts, namely $CHCA[M+H\text{-}H_2O]^+$, $CHCA[M+H]^+$, $CHCA[M+Na]^+$, $CHCA[2M+H\text{-}CO_2]^+$, $CHCA[2M+H]^+$ and $CHCA[3M+Na_2]^+$.

2.8. Scanning electron microscopy (SEM) analysis

For DIOS, NIMS and NALDI™ SEM micrographs, in-plane and cross sectional surface morphologies were investigated using a FEI

Quanta 450 FEG environmental SEM fitted with an SSD detector operated at an accelerating voltage of 30 kV.

2.9. Infrared (IR) spectroscopy

Transmission IR spectroscopy was performed using a Nicolet Avatar 370MCT spectrometer (Thermo Electron Corporation, USA). IR spectra were recorded and analyzed using OMNIC version 7 software (Thermo Electron Corporation, USA). Spectra were recorded over a range of 650–4000 cm^{-1} at a resolution of 4 cm^{-1} and taken as an average of 64 scans.

2.10. X-ray photoelectron spectroscopy (XPS)

XPS analysis was used to confirm surface functionalization of DIOS, NIMS and NALDI™ substrates. The XPS spectra were recorded on a SPECS SAGE XPS spectrometer using Mg Kα radiation source (hv = 1253.6 eV) operating at 10 kV and 20 mA. The elements present in the sample surface were identified from a survey spectrum recorded over the energy range of 0–1000 eV at a pass energy of 100 eV and a resolution of 0.5 eV and take off angle of 90° with respect to the sample surface. The areas under the selected photoelectron peaks in the spectrum were used to calculate the percentage of atomic concentrations. All the binding energies (BEs) were referenced to the C 1 s neutral carbon peak at 285.0 eV to compensate for the effect of surface charging. The analysis area was circular with a diameter of 3 mm. CasaXPS software was used to process spectra.

2.11. Water contact angle measurements

Water contact angle (WCA) using the sessile drop method was performed by placing a 1 μL droplet of milliQ water on the sample surface in ambient atmosphere. A Panasonic Super Dynamic wv-BP550 Closed Circuit TV camera was used to obtain images of the droplet. This was done on two separate surfaces and on six different spots per surface. The WCAs were measured using ImageJ version 1.41 using the Drop Analysis-DropSnake plug in.

2.12. Statistical analysis

The statistical significance of the difference between the performances of the three different SALDI substrates was assessed by performing a Three Way Analysis of Variance (ANOVA). The chosen factors were substrate, type of drug and level of concentration and the response data was the average signal intensity ratio from three experimental replicates. G*Power 3.1 was used to run the analysis setting the confidence to 95% and the TukeyHSD method was used for the pairwise multiple comparison procedures.

All precision measurements (coefficient of variation) were expressed as the percentage relative standard deviation (% RSD).

3. Results and discussion

3.1. Characterization of SALDI substrates

SEM micrographs of NIMS, DIOS and NALDI™ substrates are depicted in Fig. 1A-C respectively. For NIMS substrates, SEM analysis showed that homogeneous pSi pores with approximately 10 nm in diameter (Fig. 1A) and 13 μM in depth (Fig. S-1A) were consistently obtained via electrochemical etching.

In contrast, DIOS substrates had pore diameters and cross sections of approximately 100 nm (Fig. 1B) and 450 nm (Fig. S-1B), respectively. Etching conditions for the pSi-based NIMS and DIOS substrates were highly consistent from etch to etch. The NALDI™ surface is covered by SiNWs that are 10 nm in diameter with lengths ranging from 100–500 nm.

DIOS and NIMS substrates were functionalized with F_{13} and $BisF_{17}$, respectively. NALDI™ substrates on the other hand are reportedly functionalized with F_5PhPr which is a common silane used to functionalize silicon based SALDI substrates [12]. The chemical composition of the nanostructures hydrophobic coating was investigated using XPS and spectra are shown in Fig. S-2. A summary of the chemical composition from XPS survey spectrum for DIOS, NIMS and NALDI™ is presented in Table 1. As expected, each of the substrates investigated had a high fluorine content consistent with the perfluorinated silanes and the siloxane used during functionalization, respectively.

Infrared (IR) spectroscopy was used to characterize NIMS and DIOS pSi surfaces. Fig. S-3 displays a series of IR spectra for each surface modification. In the case of Fig. S-3A, the hydride terminated pSi surface displays vibrations at 900 cm^{-1} and 2100 cm^{-1} attributed to the SiH_2 scissor vibration and Si-H stretching vibrations in SiH_2-SiH or Si_3-SiH, respectively. Upon ozone oxidation these peaks disappeared and new peaks were observed, in particular the characteristic silicon oxide vibrational modes at 1100 cm^{-1} and 3500 cm^{-1}, corresponding

Table 1
Elemental composition (in atomic percentage, Atom. %) as determined by XPS for functionalized DIOS, NIMS and NALDI™ substrates.

Substrate	O 1s Atom. %	C 1s Atom. %	F 1s Atom. %	Si 2p Atom. %
DIOS-F_{13}	28.5	14.3	13.8	43.4
NIMS-$BisF_{17}$	20.9	23.3	25.6	30.2
NALDI™-F_5PhPR	16.1	28.1	31.2	24.6

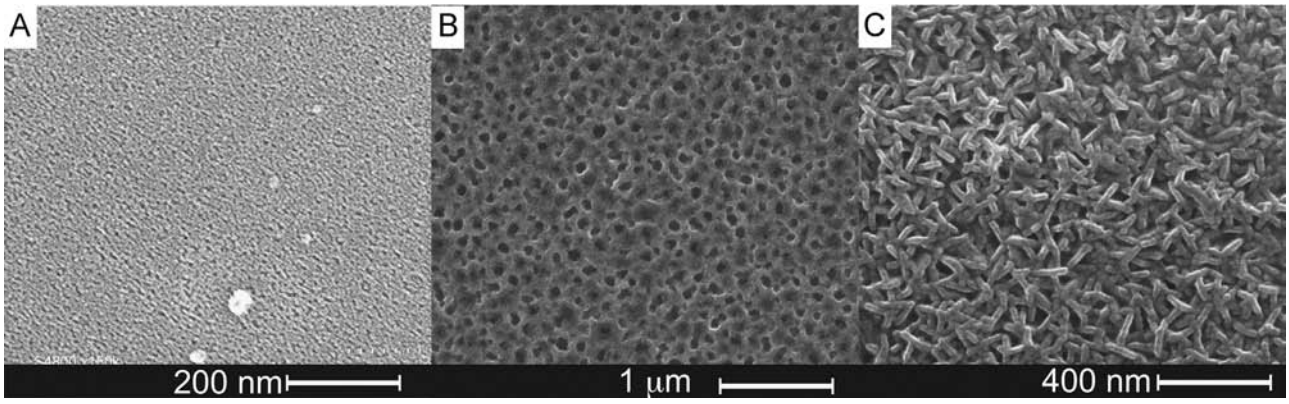


Fig. 1. SEM micrographs showing top view of a) NIMS, b) DIOS and c) NALDI™ substrates.

to stretching vibrations of the silicon oxide (Si-O) and silanol (SiO-H) functional groups, respectively (Fig. S-3B). Once the oxidized pSi surface was reacted with $BisF_{17}$ for NIMS (Fig. S-3C) and F_{13} for DIOS (Fig. S-3D), overtones were observed at 1140 cm^{-1} and 1220 cm^{-1} attributed to CF_2 stretching and at 1280 cm^{-1} for CF_3 asymmetric stretching vibrations. Additional peaks were observed for the F_{13}

Table 2
Comparison of S/N values with SD ($n=3$) and % RSD for four drug molecules at 100 ng/mL concentration using SALDI analysis on DIOS, NIMS and NALDI™ substrates.

Drug	DIOS	NIMS	NALDI™	% RSD	% RSD	% RSD
Methadone	91.6 ± 9.6	98.7 ± 8.1	139.2 ± 63.8	10.5	8.2	45.8
Oxycodone	460.8 ± 33.1	489.8 ± 29.9	232.6 ± 14.2	7.2	6.1	2.5
Flunitrazepam	10.1 ± 2.9	34.6 ± 11.5	11.8 ± 2.7	29.5	33.3	22.8
MDMA	480.9 ± 61.5	200.9 ± 105.3	229.0 ± 33.2	12.8	52.4	14.5
Cocaine	1713.0 ± 215.8	2715.0 ± 66.0	1235.0 ± 199.4	12.6	2.4	20.2

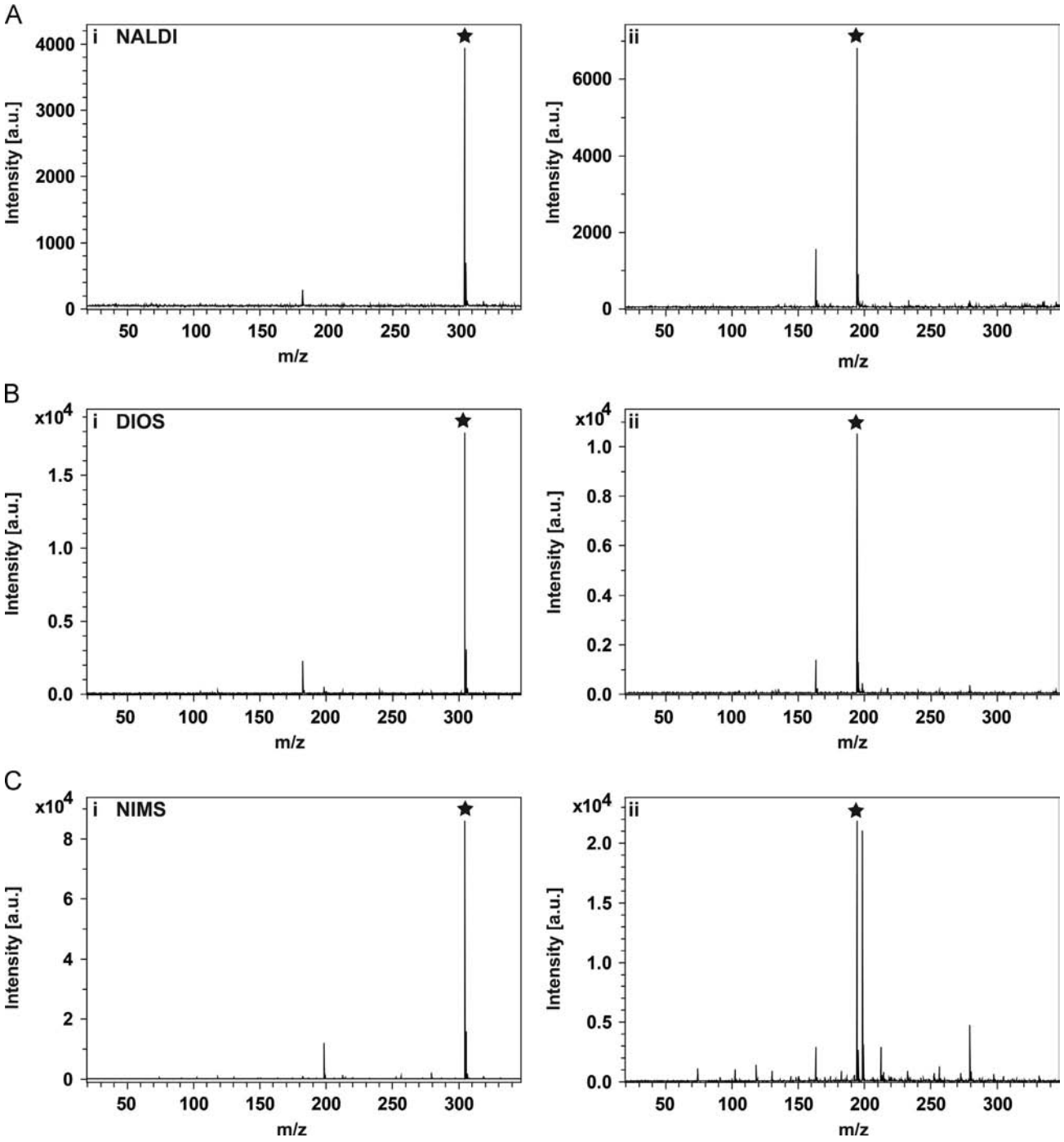


Fig. 2. Comparison of SALDI mass spectra on A) NALDI™, B) F_{13}-DIOS and C) $BisF_{17}$-NIMS substrates for i) cocaine and ii) MDMA at 100 ng/mL using optimized laser energies for each substrate. Star represents the m/z for each drug detected.

functionalized pSi in the region of 2850–3000 cm^{-1} (See Fig. S-3D), corresponding to CH_2 stretching vibrations.

The WCAs for NALDI™, NIMS and DIOS were 138°, 110° and 124° showing that all three surfaces are very hydrophobic (Fig. S-4). Hydrophobic surfaces are desirable since a drop of body fluid is confined on a small footprint of the chip, instead of spreading out, as would be the case for hydrophilic surfaces. This results in concentration of the analyte within a small area and translates into higher sensitivity.

3.2. Analytical performance

The analytical performance of each substrate was investigated for four drug classes: amphetamines, benzodiazepines, opiates and cocaine. Each of the substrates (NIMS, NALDI™ and DIOS) generated good quality SALDI mass spectra for methadone, oxycodone, MDMA, flunitrazepam and cocaine, as representative of different classes of drugs, at forensically relevant concentrations (100 ng/mL), with the exception of flunitrazepam. On each SALDI substrate, the drug molecules were predominately detected as the molecular ion $[M+H]^+$ due to their proton affinities (PA)[23].

Average S/N was recorded in replicates of three and averaged for comparison (Table 2). DIOS and NIMS substrates produced average S/N that were not statistically different for the opiates, methadone and oxycodone. The S/N for oxycodone (100 ng/mL) on the NALDI™ substrate was half that of DIOS and NIMS, and was statistically different ($P < 0.01$). For MDMA, DIOS produced

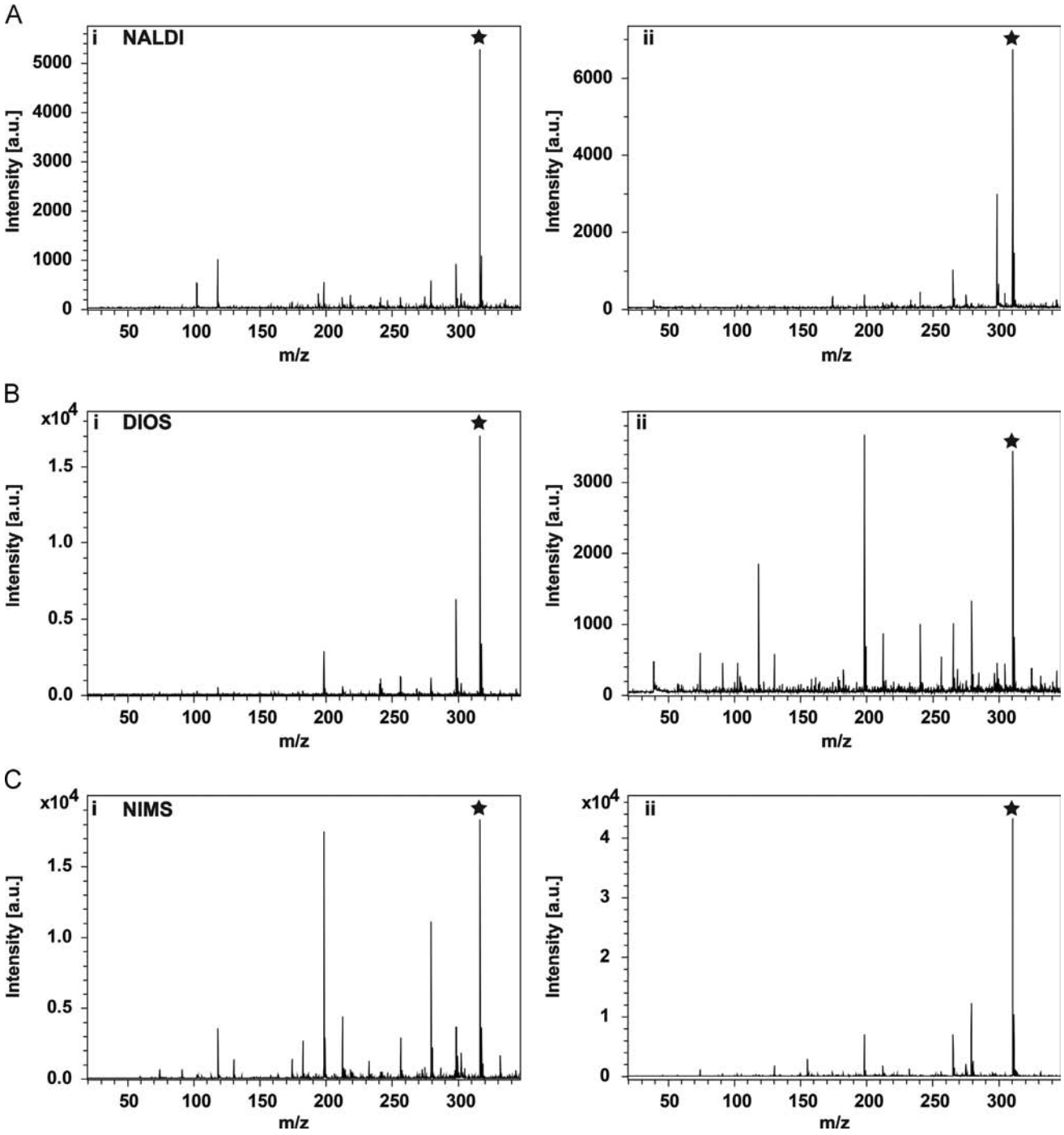


Fig. 3. Comparison of SALDI mass spectra on A) NALDI™, B) F_{13}-DIOS and C) $BisF_{17}$-NIMS substrates observed for i) oxycodone and ii) methadone at 100 ng/mL using optimized laser energies for each substrate. Star represents the m/z for each drug detected.

statistically significant ($P < 0.01$) higher S/N in contrast to NIMS and NALDI™ which both produced similar S/N on average. As a result of the average S/N for MDMA observed on DIOS substrates (Table 2) and the clean spectra generated, DIOS would therefore be considered more appropriate for amphetamine detection. In contrast, NIMS produced higher S/N for flunitrazepam in comparison to NALDI™ and DIOS but this difference was not statistically significant. For cocaine on the other hand, NIMS produced average S/N that were statistically higher in comparison to both NALDI and DIOS with a 95% confidence interval (Table S-1).

The precision of each substrate was also assessed using the % RSD for the observed S/N. For RSD % values of $< 20\%$ the average S/N are considered precise [24]. For each of the drugs, with the exception of flunitrazepam, the DIOS and NIMS surfaces both showed

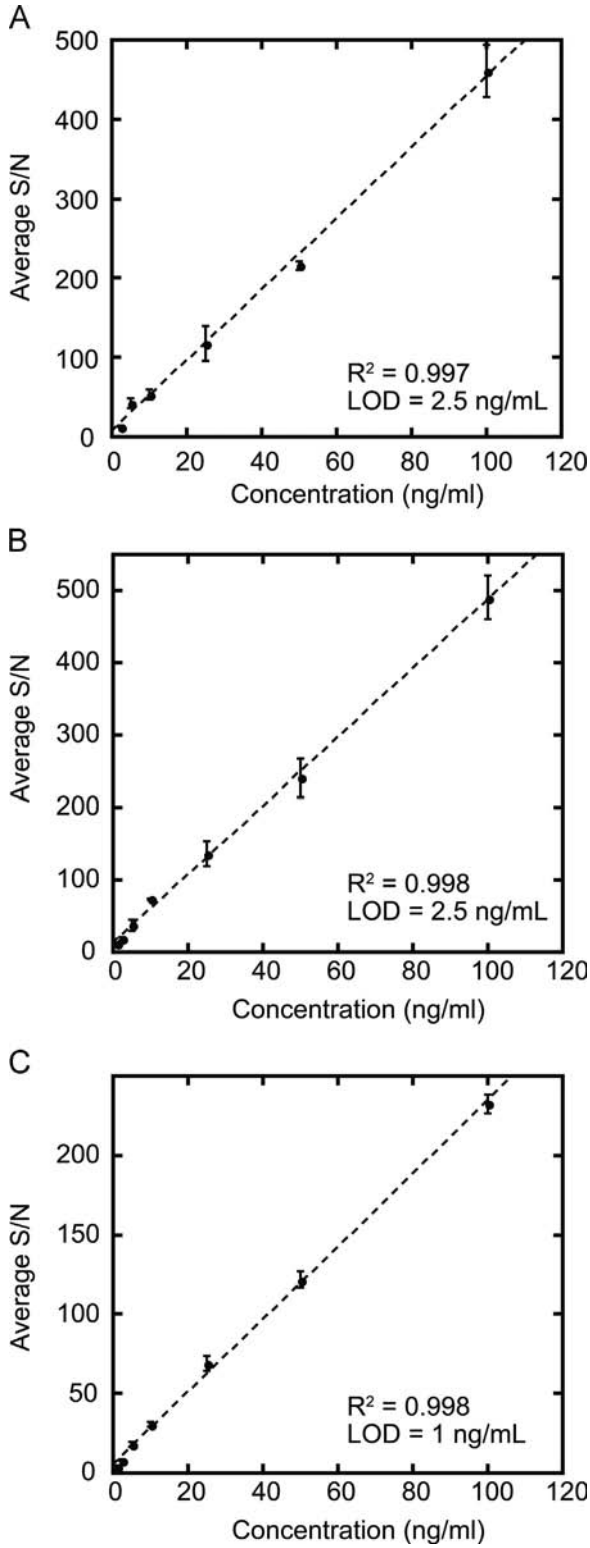


Fig. 4. Average S/N for oxycodone (0–100 ng/mL) in water on A) NALDI™, F_{13}-DIOS and C) $BisF_{17}$-NIMS substrates.

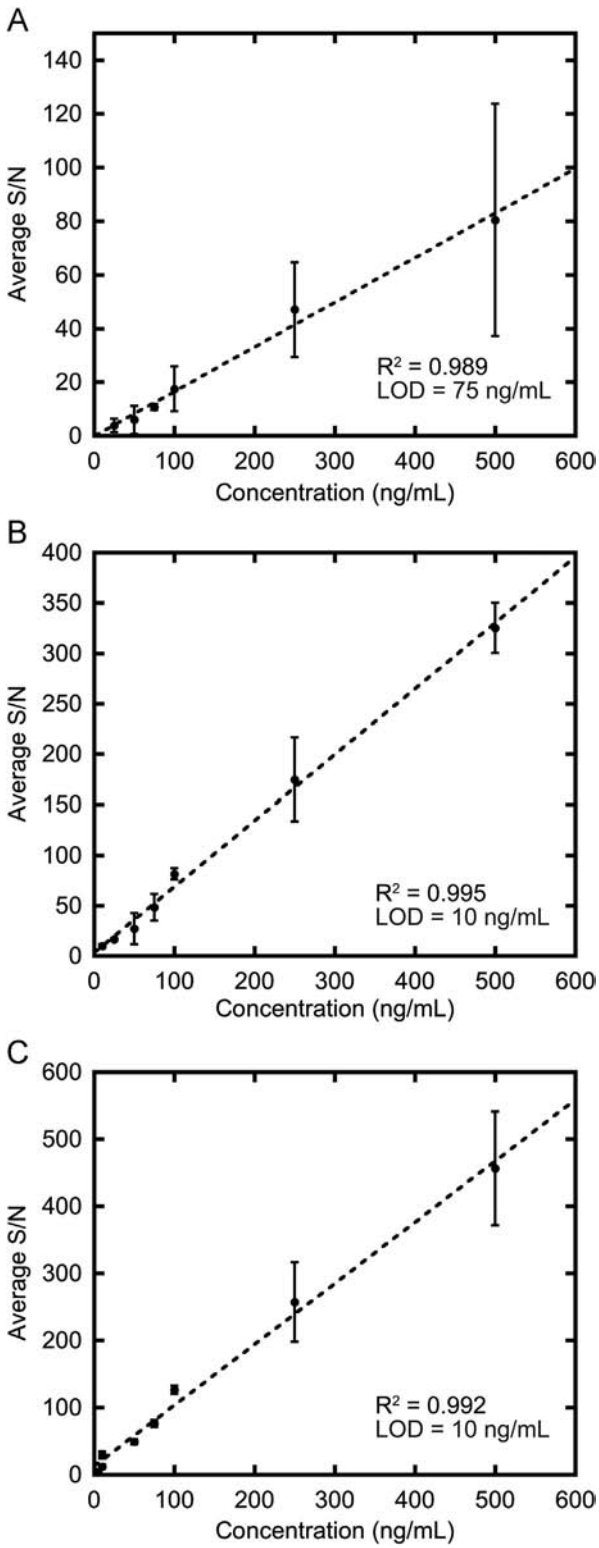


Fig. 5. Average S/N for oxycodone (0–500 ng/mL) in PBS on A) NALDI™, B) F_{13}-DIOS and C) $BisF_{17}$-NIMS substrates.

good precision (Table 2). However, for the detection of MDMA on the NIMS substrate the RSD % was 52.4, which suggests a high variability in S/N. The NALDI™ surface had higher RSD % in comparison to both DIOS and NIMS for the detection of each drug molecule except for oxycodone (RSD % 2.5) and MDMA (RSD % 14.5).

Fig. 2 shows representative positive ion NALDI™, DIOS and NIMS mass spectra for cocaine and MDMA at 100 ng/mL, respectively. For cocaine at 100 ng/mL, the mass spectra did not suffer any interferences or contaminants on any of the substrates. Fragment ions were present for NALDI™ and DIOS alongside the protonated molecular ion for cocaine at 304 m/z. The loss of $C_6H_5CO_2$ results in the fragment peak at 182 m/z being observed in good agreement with the literature [25].

For MDMA (molecular ion at 194 m/z, fragment ion ($-CH_3NH_2^+$) at 163 m/z), on the other hand, a high signal intensity background peak at 198 m/z was observed for the NIMS surface. This peak is present on all three substrates, but its intensity appears to be dependent on the efficiency of desorption/ionization of the analyte. At lower MDMA concentrations, this peak and other background peaks become more prominent and may obscure the MDMA signal. The presence of this peak was also observed on the DIOS and NALDI substrate during MDMA analysis but to a lesser degree.

Fig. 3 shows representative positive ion DIOS, NALDI™ and NIMS mass spectra for oxycodone, and methadone at 100 ng/mL. For oxycodone, high intensity background ions were present in the spectra for NALDI™, NIMS, and to a lesser extent DIOS, due to the difference in sensitivity of the three substrates for the detection of oxycodone. High signal intensities were observed for NALDI™ and NIMS with minimal background ions present within the spectra for methadone (Fig. 3Aii and Fig. 3Cii). However, for DIOS, as a result of high intensity background peaks in and around methadone the spectrum was convoluted (Fig. 3Bii). A peak observed at 265 m/z on NIMS and DIOS substrates can be attributed to the loss of $C_2H_5N^+$. This peak was not observed on the NALDI™ substrate perhaps as a result of the lower laser energy required to desorb/ionize methadone from the NALDI™ target. Interestingly, for both of the opiates, methadone and oxycodone, many background ions were present in the spectra which is due to the increase in laser energy required to desorb and ionize the opiates from each of the SALDI substrates.

The limit of detection (LOD) [26] for oxycodone in water was evaluated for NIMS, NALDI™ and DIOS substrates (Fig. 4A-C). The LOD was defined as the minimum concentration giving a S/N > 10. For NIMS, NALDI™ and DIOS, the LOD was determined to be approximately 1 ng/mL (S/N 12.1 ± 2.9), 2.5 ng/mL (12.3 ± 1.3) and 2.5 ng/mL (13.0 ± 0.9), respectively. All of the substrates showed good linearity ($R^2 > 0.99$) over the concentration range tested, demonstrating that analyte quantitation can be achieved [26].

The LOD for oxycodone in PBS was calculated on NALDI™, DIOS and NIMS substrates (Fig. 5A-C) to simulate the detection of oxycodone from human body fluids and to assess each substrate for salt resistance. Interestingly, the observed LOD on the NALDI™ substrate was > 75 ng/mL, 30 times higher than in water, perhaps due to salt interference/intolerance. The observed LOD for oxycodone on NIMS and DIOS was approximately 10 ng/mL with S/N of 11.9 ± 3.5 and 9.7 ± 1.9, respectively.

For NALDI™, the % RSD (Table S-2) was calculated to assess and compare the precision of the observed S/N values for oxycodone in PBS. A summary of the results is displayed in Table S-2. At each concentration, except for 75 ng/mL (% RSD 10.1) a high % RSD was observed ranging from 37.5–88.2%, which suggests a lack of precision. In contrast, % RSD values for DIOS (Table S-3) were below 19.8% demonstrating good precision with the exception of 250 ng/mL, 75 ng/mL and 50 ng/mL with % RSD 23.8%, 27.5% and 56.6%, respectively. Better overall precision was observed for NIMS substrates (Table S-4) at all oxycodone concentrations except for 250 ng/mL and 10 ng/mL (% RSD 22.9% and 29.6%, respectively).

For NIMS and DIOS good linearity ($R^2 > 0.99$) was observed and the LOD only decreased by one order of magnitude suggesting better desalting capabilities. A poorer linear fit was observed for NALDI™, suggesting that quantitation may be difficult to achieve for more complex mixtures. The technical note for the NALDI™ target suggests that desalting of samples is necessary prior to analysis [27]. Unlike DIOS and NIMS substrates, processing steps are therefore required for NALDI™. Furthermore, the technical note suggests that the entire chip should be immersed in 200 mL of deionized water, which may lead to cross contamination on sample spots.

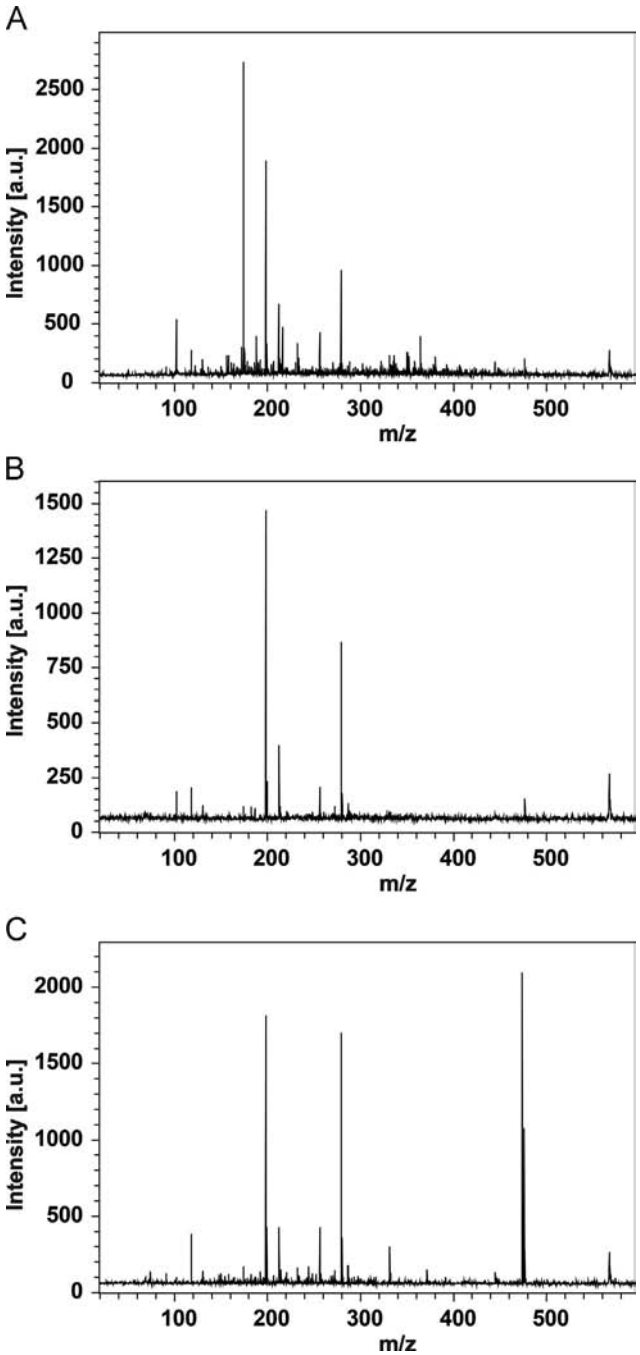


Fig. 6. Background spectra observed for freshly opened or prepared A) NALDI™, B) F_{13}-DIOS and C) $BisF_{17}$-NIMS substrates.

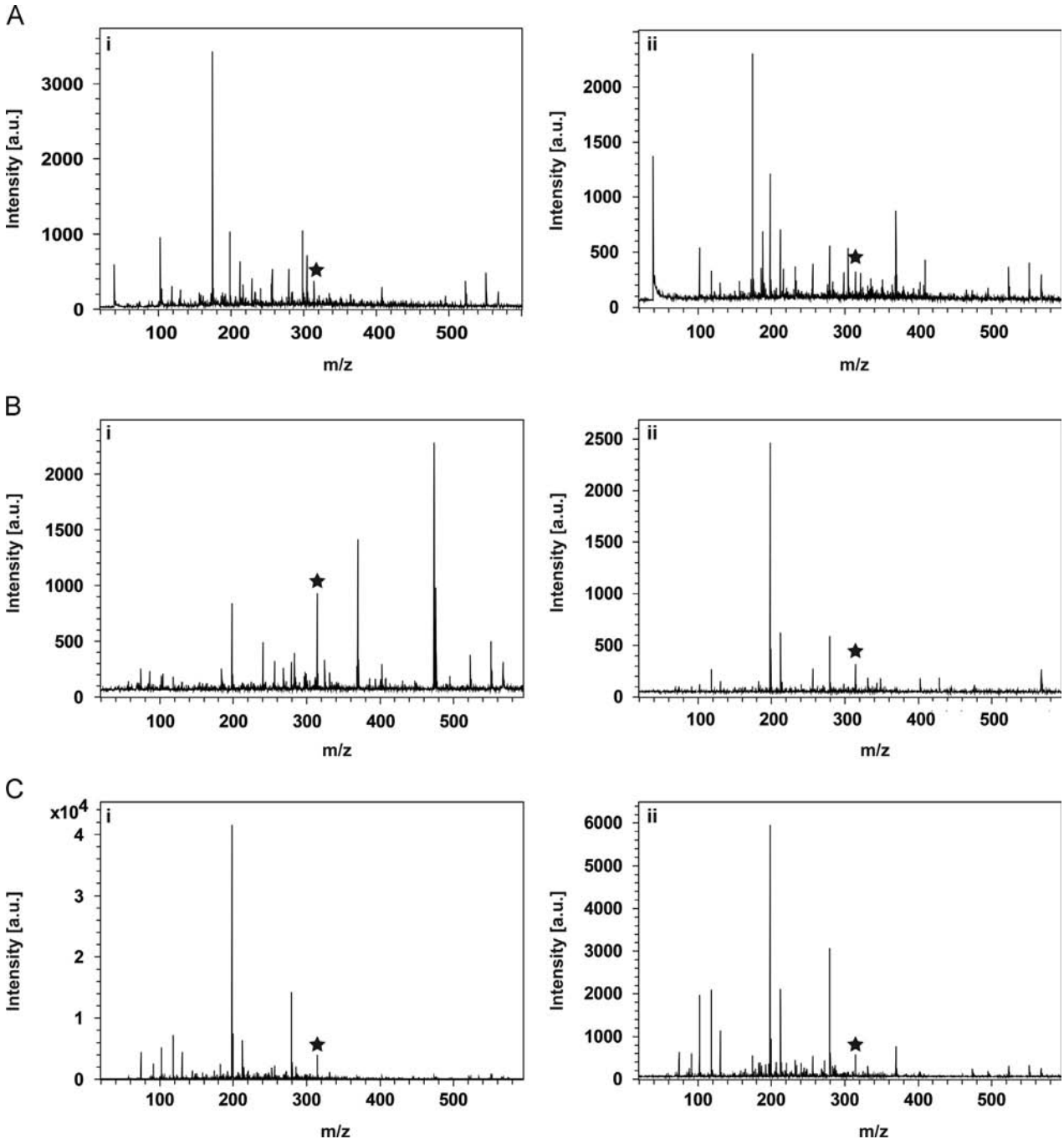


Fig. 7. Mass spectra for flunitrazepam (100 ng/mL) on A) NALDI™, B) F_{13}-DIOS and C) BisF_{17}-NIMS on i) freshly opened or prepared substrates and ii) six-month old substrates. Star represents the m/z for each drug detected. The laser attenuator offset required for detection of flunitrazepam on NALDI™, F_{13}-DIOS and BisF_{17}-NIMS was 42%, 58% and 62%, respectively.

3.3. *Background ions and long-term storage of the SALDI substrates*

Fig. 6 displays background spectra observed for NALDI™, NIMS and DIOS substrates on sample spotted with water without the presence of any illicit drug molecules. Interestingly, similar high intensity peaks at 102, 130, 198, 212, 279 and 567 m/z were observed for each of the three functionalized substrates. A comparison of spectra for the freshly etched and oxidized DIOS and NIMS substrates revealed that the majority of background peaks observed are due to the oxidation step since none of these peaks were observed for the freshly etched pSi substrates (Fig. S-5). This presence of background ions was attributed to the restructuring of the nanostructured silicon surfaces (NALDI™, NIMS and DIOS), which results in the formation of surface ion (Si_n^+ and $OSiH^+$), previously investigated by Northern et al. [28]. In any case, F_{13} functionalized DIOS chips produced the lowest number and intensity of background signals.

The longevity of each substrate was investigated for flunitrazepam since each of the substrates showed similar S/N (Table 2) at 100 ng/mL (Fig. 7). Several background peaks were present for NALDI™ on both the freshly opened substrate (Fig. 7A-i) and a six-month old target (Fig. 7A-ii). We also observed a high intensity peak (38.96 m/z) for both the freshly opened and six-month old NALDI™ target, potentially corresponding to potassium. This peak was only present during the detection of flunitrazepam and not in background spectra (Fig. 6). Since DIOS and NIMS required no increase in laser fluence to desorb/ionize flunitrazepam the potassium peak was not observed (Fig. 7B-C).

Upon further investigation it became clear that the presence of this peak was a result of an artifact that occurred upon increasing the laser energy. Fig. S-6 displays overlaid mass spectra for flunitrazepam (zoomed into the mass region for potassium) on NALDI, DIOS and NIMS substrates at increased laser energies all of which show the presence of potassium. Another disadvantage of NALDI™ for the detection of flunitrazepam was the presence of numerous peaks ranging from 300–350 Da that obscured the signal of the target analyte in the freshly opened and six-month old NALDI target. For both DIOS and NIMS, no significant decrease in S/N from freshly etched to six-month old samples was observed. Furthermore, contaminant peaks close to the protonated mass of flunitrazepam (314 m/z) were not observed. Whilst DIOS and NIMS produced relatively clean mass spectra for flunitrazepam, NIMS produced higher signal intensities compared with NALDI™ and DIOS, suggesting a better sensitivity for benzodiazepine detection.

3.4. Ease of fabrication and use

An advantage of DIOS and NIMS (pSi-based substrates) is the ease and cost of fabrication. DIOS and NIMS chips can be fabricated using simple electrochemical etching processes that require minimal equipment. As a result automated assemblies for etching pSi have been developed for mass production [29]. However, since DIOS is fabricated using photo electrochemical etching an additional light source and lens set-up is required, which limits up scaling procedures [29, 30]. In any case, within our laboratory the current cost of fabrication is approximately AUS $9 for chips of similar dimensions to NALDI™.

Unlike pSi based SALDI, NALDI™ is fabricated via complex chemical vapor deposition techniques. These complex fabrication procedures, whilst allowing for large-scale fabrication result in a costly product, up to AU $900 for five NALDI™ target plates.

4. Conclusions

We have compared three common SALDI substrates (NALDI™, NIMS and DIOS) for their analytical performance for specific drug classes, namely amphetamines (MDMA), opiates (methadone and oxycodone), benzodiazepines (flunitrazepam) and tropane alkaloids (cocaine). NIMS was observed to produce better LODs for oxycodone in both water and PBS in comparison with DIOS and NALDI™. Each of the substrates produced similar low intensity background spectra, which did not obscure the drug molecules investigated. Finally, this study showed that each of the substrates could be used for the detection of illicit drugs after six months of storage in ambient conditions. All three substrates show strong potential for illicit drug detection, but our study shows that the performance of the substrates depends on the nature of the drug, the medium and the storage term.

Acknowledgments

We would like to acknowledge Forensic Science South Australia (FSSA) and the Australian Research Council (ARC LP110200446) for financial support. We would like to acknowledge the valuable technical assistance of internship students Frank Adolf and Markus Riese from Mannheim University.

Appendix A. Supporting information

Supplementary data associated with this article can be found in the online version at http://dx.doi.org/10.1016/j.talanta.2014.09.040.

References

[1] W.C. Chang, L.C.L. Huang, Y. Wang, W.P. Peng, H.C. Chang, N.Y. Hsu, W.B. Yang, C.H. Chen, Anal. Chim. Acta 582 (2007) 1–9.
[2] K. Dreisewerd, Am. Chem. Soc 103 (2003) 395–425.
[3] E. Hoffmann, V. Stroobant, Mass Spectrometry, Principles and Applications, John Wiley and Sons, England, 2001.
[4] E.P. Go, J.V. Apon, G. Luo, A. Saghatelian, R.H. Daniels, V. Sahi, R. Dubrow B.F. Cravatt, A. Vertes, G. Siuzdak, Anal. Chem. 77 (2005) 1641–1646.
[5] E.P. Go, J. Prenni, J. Wei, A. Jones, S.C. Hall, H.E. Witkowska, Z. Shen, G. Siuzdak, J. Anal. Chem. 75 (2003) 2504–2506.
[6] T. Guinan, P. Kirkbride, P.E. Pigou, M. Ronci, H. Kobus, N.H. Voelcker, Mass Spectrom Rev (2014), http://dx.doi.org/10.1002/mas.21431.
[7] G.l. Piret, H. Drobecq, Y. Coffinier, O. Melnyk, R. Boukherroub, Langmuir 26 (2009) 1354–1361.
[8] M. Dupre, Y. Coffinier, R. Boukherroub, S. Cantel, J. Martinez, C. Enjalbal J Proteomics 75 (2012) 1973–1990.
[9] M. Dupre, C. Enjalbal, S. Cantel, J. Martinez, N. Megouda, T. Hadjersi, R. Boukherroub, Y. Coffinier, Anal. Chem. 84 (2012) 10637–10644.
[10] J.J. Thomas, Z. Shen, R. Blackledge, G. Siuzdak, Anal. Chim. Acta 442 (2001) 183–190.
[11] T.R. Northen, O. Yanes, M.T. Northen, D. Marrinucci, W. Uritboonthai, J. Apon S.L. Golledge, A. Nordstrom, G. Siuzdak, Nature 449 (2007) 1033–1036.
[12] R.H. Daniels, S. Dikler, E. Li, C. Stacey, J. Assoc. Lab. Automat 13 (2008) 314–321.
[13] S.A. Trauger, E.P. Go, Z. Shen, J.V. Apon, B.J. Compton, E.S.P. Bouvier, M.G. Finn, G. Siuzdak, Anal. Chem. 76 (2004) 4484–4489.
[14] O. Yanes, H.-K. Woo, T.R. Northen, S.R. Oppenheimer, L. Shriver, J. Apon, M. N. Estrada, M.J. Potchoiba, R. Steenwyk, M. Manchester, G. Siuzdak, Anal. Chem. 81 (2009) 2969–2975.
[15] M.F. Wyatt, S. Ding, B.K. Stein, A.G. Brenton, R.H. Daniels, J. Am. Soc. Mass Spectrom. 21 (2010) 1256–1259.
[16] C. Yoo, M. Ronk, D. Semin, S. Fu, J. Fox, G. Shi, in: 57th ASMS Conference, Philadelphia, PA, 2009.
[17] T. Guinan, M. Ronci, H. Kobus, N.H. Voelcker, Talanta 99 (2012) 791–798.
[18] R.D. Lowe, G. Guild, P. Harpas, G. Siuzdak, P. Kirkbride, P. Hoffman N.H. Voelcker, H. Kobus, Rapid Commun. Mass Sp. 23 (2009) 3543–3548.
[19] O.H. Drummer, Ther. Drug. Monit. 30 (2008) 203–206.
[20] S.W. Toennes, S. Steinmeyer, H.-J. Maurer, M.R. Moeller, G.F. Kauert, J. Anal. Toxicol. 29 (2005) 22–27.
[21] A. Verstraete, L. Labat, Ann. Toxicol. Anal. 21 (2009) 3–8.19.
[22] S.M.R. Wille, E. Raes, P. Lillsunde, T. Gunnar, M. Laloup, N. Samyn A.S. Christophersen, M.R. Moeller, K.P. Hammer, A.G. Verstraete, Ther. Drug. Monit. 31 (2009) 511–519.
[23] P. Östman, J.M.H. Pakarinen, P. Vainiotalo, S. Franssila, R. Kostiainen, T. Kotiaho, Rapid Commun. Mass Sp. 20 (2006) 3669–3673.
[24] M. Persike, M. Karas, Rapid. Commun. Mass Sp. 23 (2009) 3555–3562.
[25] R.M. Smith, J.F. Casale, Microgram J. 7 (2010) 16–41.
[26] K. Pihlainen, K. Grigoras, S. Franssila, R. Ketola, T. Kotiaho, R. Kostiainen J. Mass. Sp. 40 (2005) 539–545.
[27] NALDI nanostructured laser desorption ionization targets, Bruker Daltonics, 2012, pp 4. url: www.care-bdal.com.
[28] T.R. Northen, H.-K. Woo, M.T. Northen, A. Nordström, W. Uritboonthail K.L. Turner, G. Siuzdak, J. Am. Soc. Mass Sp 18 (2007) 1945–1949.
[29] C. Garman, P. Sines, S.P. McGinnis, B. Das, Rev. Sci. Instrum. 72 (2001) 275–277.
[30] M.J. Sailor, Chemistry of porous silicon, Porous Silicon in Practice, Wiley-VCH Verlag GmbH & Co. KGaA, Weinheim, Germany, 2011, http://dx.doi.org/10.1002/9783527641901.ch6.

Talanta 132 (2015) 503–512

Contents lists available at ScienceDirect

Talanta

journal homepage: www.elsevier.com/locate/talanta

Determination of traces of several pesticides in sunflower oil using organic phase immuno electrodes (OPIEs)

Elisabetta Martini, Mauro Tomassetti *, Luigi Campanella

Department of Chemistry, "Sapienza" University of Rome, P.le Aldo Moro 5, 00185 Rome, Italy

ARTICLE INFO

Article history:
Received 9 June 2014
Received in revised form
22 August 2014
Accepted 2 September 2014
Available online 22 October 2014

Keywords:
Pesticides analysis
Sunflower oil
Immunosensors
Competitive step
Enzyme reaction
Organic phase

ABSTRACT

Testing for traces of different pesticides (triazinic, organophosphates and chlorurates), present in hydrophobic matrices such as sunflower oil was checked using new immunosensors working in organic solvent mixtures (OPIEs). The competitive process took place in an n-hexane–chloroform 75% (V/V) mixture, while the subsequent final enzymatic measurement was performed in decane using tert-butylhydroperoxide as substrate of the enzymatic reaction. A Clark electrode was used as transducer and peroxidase enzyme as marker. A linear response of between about 10 nM and 4 μM was usually obtained in the presence of sunflower oil. Immunosensors show satisfactory selectivity and precision and recovery tests carried out on commercial sunflower oil samples gave excellent results. Lastly, theoretical confirmation of the possibility that immunosensors can act positively in organic solvent mixtures was discussed on the basis of Hill's coefficient values.

© 2014 Elsevier B.V. All rights reserved.

1. Introduction

In recent years several authors [1–4] discovered that some antibodies were capable of retaining activity and selectivity in the non-aqueous phase, while, until recently, it was believed possible only in aqueous environment. Consequently a start was made also on the development of immunosensors working in the organic phase [5–7]. Even though the field of organic phase immunosensing is still not highly developed, the potential benefits of this approach for the measurement of poorly water-soluble analytes in organic solvent are manifold [6]; indeed many analytical methods involving non-polar analytes require solvent extraction prior to measurement. The analytical assay is therefore greatly simplified if the method is able to function effectively in non-polar solvent extract. However, several phytopharmaceutical compounds are more soluble in organic solvent than in aqueous solutions (see Table 1), and can therefore be rightly included in the category of compounds described above; also testing for them thus encounters difficulties linked to the low solubility of several pesticides in aqueous medium. These difficulties increased further when the low solubility in water solution of the analyte to be determined was coupled with the very low solubility of the real matrix in which the analyte was contained, as in the case of edible oily matrices. To overcome these difficulties, in the last two years, immunodevices were fabricated that are capable of operating in organic solvent, i.e. organic phase immuno electrodes (OPIEs) [8]. To this end, in a first investigation [8], in accordance with what is reported in literature [9–11], several different aspects of the new type of immunosensor were optimized. In particular different competitive formats [8,12] were tested and the results confirmed as the ELISA type format was found to be quite suitable [12]. Furthermore, the practicality of immobilizing the antibody used on the polymeric membrane support was confirmed [8,12]. However, the choice of the organic phase solvent was the most important and difficult point, although the factors governing antibody–antigen binding in organic solvent were clearly more complex and required further elucidation. Solvent properties such as hydrophobicity, molecular mass and fraction can all affect the binding process [6], but also the antigen and the real matrix solubility in the selected solvent play an important role. Furthermore, of equal importance is the fact of whether also the last enzymatic reaction involved in the enzyme immunoassay method was performed in the organic solvent or not. It is actually surprising that greater efforts appear not to have been made in this area [6], although basic research is not lacking [9–11,13–18]. Studies reported in literature concerning choice of solvent refer above all to alcoholic and hydroalcoholic solutions [19–22] and often do not agree among themselves [6,19–22] also because of the different antibody systems used in these studies. For this reason the organic phase immunoassay development has continued to rely on an empirical rather than mechanistic approach [6]. Also our approach to this problem was therefore of this type in our first research [8] involving the analysis of traces of triazinic pesticides in olive oil. A series of tests were thus carried out by

* Corresponding author. Tel.: +39 0649913722; fax: +39 0649913601.
E-mail address: mauro.tomassetti@uniroma1.it (M. Tomassetti).

http://dx.doi.org/10.1016/j.talanta.2014.09.004
0039-9140/© 2014 Elsevier B.V. All rights reserved.

Table 1
Comparison of solubility of several pesticides in chloroform and in water.

Pesticide	Solubility in chloroform ($g\,L^{-1}$)	Solubility in water ($g\,L^{-1}$)
Atrazine	52.0	0.028
Simazine	0.9	0.006
Carbaryl	200	0.040
Parathion	0.50	0.060
2,4-D	32	0.9
2,4,5-T	32	0.2

the present authors in previous work [8] using different solvents, different electrochemical transducers and different immunosensor constructions, or operating measurement format. This series of trials led to the development of suitable amperometric immunosensors for the analysis of triazinic, organophosphate and chlorurate pesticides in olive oil and olive oil by-products [8,23], with the competitive format of the immunological test (ELISA type) performed in 50% (V/V) chloroform n-hexane mixture, which was found [8] to be the best compromise among the different solubility requirements mentioned above, using as transducer a classical Clark electrode for oxygen with the external cup and the gas permeable membrane both made of PTFE and a pesticide–BSA conjugated hapten marked using horseradish peroxidase enzyme. These devices were certainly innovative compared to what had previously been reported in literature, but produced good results also for the applications in real olive oil samples and derivatives [8,23]. The success obtained in these researches involving pesticide measurement in olive oil matrices using the new OPIE aroused our interest in this field and so in the present research also the possibility of testing for the above pesticides in other kinds of edible oils was investigated. Since the literature contains several reports concerning the presence of traces of several pesticides such as atrazine, simazine, 2,4-D, 2,4,5-T and parathion in sunflower oil [24–29], it was decided to apply the OPIEs developed also to determine these pesticides in sunflower oil. Of course our approach was very similar to that successfully used for pesticide analysis in olive oil. However, also in this case the choice of solvent was a central point, considering that sunflower oil does not have exactly the same solubility as olive oil in the different organic solvents. For this reason measurements in the present work were performed in n-hexane–chloroform 75% (V/V) mixture instead of in the same 50% (V/V) mixture as used in the previous research aimed at measuring pesticide traces in olive oil [8].

2. Materials

2.1. Apparatus

The amperometric measurements were performed in a 5 mL thermostated glass cell at 23 °C under constant stirring. The Clark electrode, supplied by Universal Sensor Inc., New Orleans (U.S.A.), was connected to an amperometric biosensor detector provided by the same firm and to an analogue recorder mod. 868 Amel (Milan, Italy). In all experiments performed in the organic phase, the plastic cap of the electrodes was replaced by a PTFE cap.

2.2. Reagents and materials

Anti-atrazine monoclonal antibody, anti-dichloro-phenoxyacetic acid and anti-trichloro-phenoxyacetic acid antibodies, as well as atrazine and simazine carboxyderivative, dichloro-phenoxyacetic acid (i.e. 2,4-D) and trichloro-phenoxyacetic acid (i.e. 2,4,5-T), were provided by Dr. S. Eremin (Department of Chemical Enzymology, Faculty of Chemistry, Moscow State University, Russia). Anti-parathion was a commercial antibody and was obtained from Acris (Acris Antibodies, Herford, Germany). 1-Chloro-3-ethylamino-5-isopropylamino-2,4,6-triazine (i.e. Atrazine), 6-chloro-N,N′-diethyl-1,3,5-triazine-2,4-diamine (i.e. simazine), N-tert-butyl-6-chloro-N′-ethyl-1,3,5-triazine-2,4-diamine (i.e. tert-buthylazine), 2-amino-4-chloro-6-(isopropylamino)-s-triazin (i.e. atrazine desethyl), 1-naphthyl methylcarbamate (i.e. carbaryl), 2-methyl-2-(methylthio)propanal O-(N-methylcarbamoyl)oxime (i.e. aldicarb), diethyl 4-nitrophenyl phosphate (i.e. Parathion) were supplied by Pestanal Sigma-Aldrich (Sigma-Aldrich, Milan, Italy). Potassium chloride, dibasic and monobasic anhydrous potassium phosphate RPE, chloroform RPE, dichloromethane RPE and diethyl ether RPE were supplied by Carlo Erba Reagents (Carlo Erba, Milan, Italy). Ny+ Immobilon Affinity membrane (porosity 0.65 μm) was provided by Millipore (Millipore Corporation, Vimodrone, Milan, Italy). The biotinylation kit, supplied by Sigma Immunochemicals (Sigma, Milan, Italy), was composed of biotinylation reagent (BAC-SulfoNHS, namely biotinamido hexanoic acid 3-sulfo-N-hydroxysuccinimide ester), 5 M sodium chloride solution, micro-spin column (2 mL) (in practice, a small empty cylindrical vessel prepackaged with Sephadex G-50), 0.1 M sodium phosphate buffer pH 7.2, 0.01 M phosphate buffer saline (PBS) pH 7.4 (reconstituted with 1 L of deionised water to give 0.01 M phosphate buffer, 0.138 M NaCl, 2.7 mM KCl, pH 7.4); lastly extravidin® peroxidase (containing 0.2 mL of extravidin Peroxidase conjugate at 2.0 $mg\,mL^{-1}$, with 0.01% thimerosal). Phenol, dialysis membrane (art. D-9777), 1-ethyl-3 (3-dimethylaminopropyl) carbodiimide, albumin (from bovine serum) (BSA) and TRIS (hydroxymethyl-aminomethane), tert-butylhydroperoxide solutions in decane solvent and TWEEN® 20, provided by Sigma-Aldrich (Sigma-Aldrich, Milan, Italy).

2.3. Samples

Edible sunflower oil samples, produced by the most important industrial Italian sunflower oil producer firms, were purchased from a local shop and stored in sealed glass bottles.

3. Methods

3.1. Immunosensor assembly and electrochemical format

The electrochemical transducer used was an amperometric gaseous diffusion amperometric electrode for O_2 determination (see Fig. 1). The transducer consisted of a Clark type electrode, equipped with PTFE cup and a gas permeable membrane of the same material. For the immunosensor assembly, in practice, three membranes were mounted on the PTFE cap of the Clark electrode, in the following order: the gas-permeable membrane, the dialysis membrane and the Immobilon membrane with the antibody immobilized on it. The membranes were kept in place by a nylon net and a PTFE O-ring. A constant potential of −650 mV with respect to an $Ag/AgCl/Cl^-$ anode was applied to the Pt cathode of the oxygen electrode. Horseradish peroxidase enzyme was used as marker for immunocomplex detection. The cathode and anode of the Clark type amperometric electrode were immersed in an internal solution of phosphate buffer saline (PBS), pH 7.4 (reconstituted with 1 L of deionized water to give 0.01 M phosphate buffer, 0.138 M NaCl and 2.7 mM KCl). The current, which was measured and flowed in the external circuit, was obviously a function of the concentration of dissolved oxygen present in the internal solution. This concentration was regulated (through the diffusion of the oxygen across the gas permeable membrane) by the enzymatic reaction, which took place in decane (see Fig. 1); in this enzymatic reaction the reduction in the oxygen consumed was a function of the reduction in the concentration of the peroxidase enzyme present in the antibody complex formed on the Immobilon membrane as a result of the competitive process

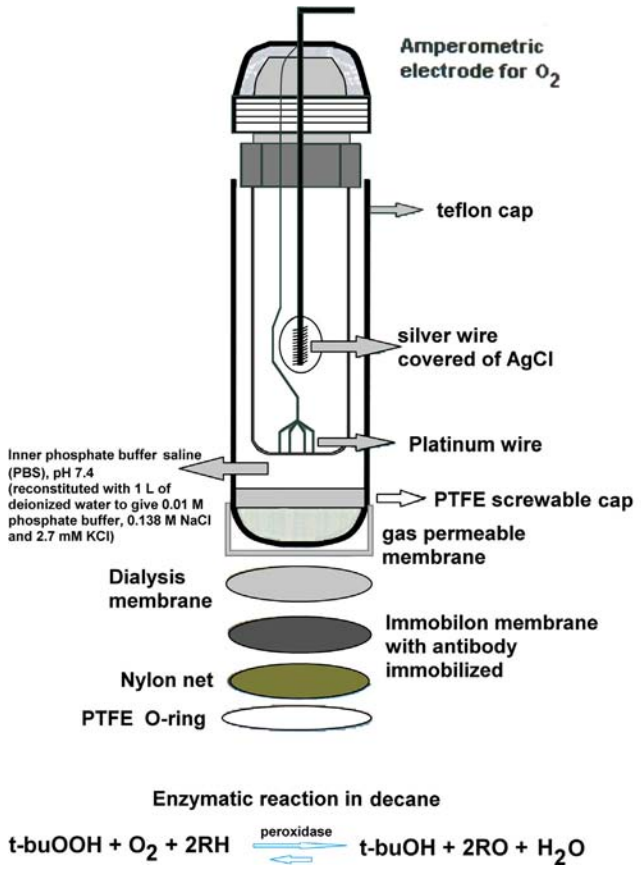


Fig. 1. Amperometric immunosensor used for pesticide determination in organic solvent using a Clark electrode as transducer and horseradish peroxidase as marker.

performed in the 75% (V/V) chloroform–hexane mixture. Of course, the higher the concentration of the antigen to be determined the lower the quantity of enzyme remaining fixed in the antibody complex on the Immobilon membrane, and therefore the less the enzymatic reaction was shifted to the right and so the less oxygen was consumed, that is, the greater the quantity of oxygen passing through the gas permeable membrane into the internal buffer solution. As a result the greater the quantity of oxygen reduced at the cathode the higher the intensity of the circulating current and the stronger the amperometric signal.

3.2. Antibody immobilization on Immobilon membrane

A commercial Immobilon membrane was used for antibody immobilization. It consisted of a positively charged nylon membrane with polyester reinforcement optimized for reliable and reproducible transfer, immobilization, hybridization, and subsequent reprobing. The Immobilon Ny+ membrane was cut into 1 cm^2 surface area disks and 50 μL of a 0.01 M antibody solution was directly deposited on the membrane surface. The membrane was then dried at room temperature for about 24 h and stored at 4 °C.

3.3. Atrazine pesticide carboxylation

To a stirred heterogeneous mixture of 1.01 g of atrazine (i.e. 5.01 mM) in 100 mL of absolute ethanol a solution of 0.574 g of 3-mercaptopropanoic acid was added (i.e. 5.40 mM) together with 0.714 g of 85% KOH (i.e. 10.8 mM) in 10 mL of absolute ethanol, under N_2. At reflux the mixture became homogeneous and soon a precipitate (KCl) began to form. Reflux was continued (4 h). The hot mixture was filtered, and the filtrate concentrated to a white solid. The solid was triturated with 25 mL of 5% $NaHCO_3$ and filtered [30].

3.4. Parathion carboxylation

A solution of 3.0 g of 4-nitrophenol (i.e. 21.6 mM) in 15 mL of acetonitrile was added dropwise to a stirred solution containing 4.59 g (i.e. 27.8 mM) of methyldichlorothiophosphate, 20 g of finely ground K_2CO_3 and 20 mL of acetonitrile. After stirring for 1 h at room temperature the mixture was filtered through celite and the solvent removed. The following format was applied to obtain the synthesis of the hapten: to a stirred solution of 500 mg of O-methyl-O-(4-nitrophenyl)phosphorochloridothioate (i.e. 1.87 mM) in 3 mL of MeOH cooled in an ice–water bath, a solution of 274 mg (i.e. 4.88 mM) of KOH and 229 mg of 4 aminobutyric acid (i.e. 2.22 mM) in 1.7 mL of MeOH was added dropwise. After stirring for 5 min, the reaction mixture was filtered and extracted with 1 M HCl–chloroform. The extract was dried over $MgSO_4$, and the solvent was evaporated [31].

3.5. Albumin–pesticide conjugation

The carboxylate pesticide was dissolved in 5 mL of dichloromethane to which 38 mg (i.e. 0.33 mM) of N-hydroxysuccinimide ester, 68 mg (i.e. 0.33 mM) of N,N-dicyclohexylcarbodiimide and 3.7 mg (i.e. 0.03 mM) of 4-dimethylaminopyridine were added. The mixture was stirred for 3 h and filtered, and the solvent removed. The format for coupling the carboxylate pesticide, for example the carboxylated atrazine, to the carrier protein to prepare hapten–BSA conjugates was as follows: 20 mg (i.e. 0.3×10^{-3} mM) of BSA were dissolved in 2 mL of borate buffer (0.2 M, pH 8.7) to which 0.4 mL of DMF was added. A solution of active ester (0.018 mM) in 0.1 mL of DMF was then added to the stirred protein solution, and stirring was continued for one day at 4 °C [31,32].

3.6. Albumin–pesticide biotinylation and peroxidase conjugation scheme

The avidin–biotin peroxidase technique is based on the use of a biotinylated antigen and of avidin horseradish peroxidase conjugate as part of the labelling system [33,34]. The technique exploits the high affinity binding of biotin to avidin. The BiotioTag kit is specially designed for the small scale labelling of antibodies using biotinamido hexanoic acid 3-sulfo-N-hydroxysuccinimide ester (BAC-SulfoNHS) as the labelling reagent. This reagent is particularly useful when mild reaction conditions are required for the biotinylation of sensitive biomolecules such as antibodies, enzymes and surface proteins. After the labelling reaction, the biotinylated protein is separated from the unreacted or hydrolyzed reagent by a fast gel-filtration step using G-50 microspin columns. BAC-SulfoNHS reacts with free amino groups of proteins to form stable amide bonds. In brief: 0.1 mL of 4.5×10^{-4} M pesticide-albumin solution in sodium phosphate buffer (pH 7.2; 0.1 M) was prepared. BAC-SulfoNHS solution 5 mg mL^{-1} was also prepared separately by dissolving 5 mg of biotinamido hexanoic acid 3-sulfo-N-hydroxysuccinimide ester in 30 μL DMSO (dimethylsulphoxide) and adding sodium phosphate buffer (pH 7.2; 0.1 M) for a final volume of 1 mL. 10 μL of BAC-SulfoNHS solution were immediately added to the pesticide-albumin solution with gentle stirring and the mixture incubated under stirring for 30 min at 2–8 °C. Then the resin contained in a micro-spin G-50 column was re-suspended in the column by vortexing and equilibrated with 0.2 mL of PBS, (pH 7.40; 0.01 M); this buffer was needed also for the elution of the labelled protein from the column. The biotinylation reaction mixture was applied to the top-center of the resin and the column was centrifuged for 5 min at 700g. The purified sample was then collected at the bottom of an Eppendorf test tube.

This step was repeated twice more and a total of three fractions were collected. As extravidin binds to biotin with a high affinity and specificity, an extravidin peroxidase solution (20 μL, 2.0 mg mL^{-1}), diluted 1:100 in PBS containing 1% BSA solution, was added to the collected fractions and incubated for 1 h at room temperature, then gently rinsed with PBS, (pH 7.4; 0.01 M).

3.7. Determination of pesticide by immunosensor. (Competitive format between pesticide biotin–avidin–peroxidase conjugated and non-conjugated, both free in n-hexane–chloroform 75% (V/V) mixture, for the respective antibody immobilized in membrane).

For this purpose, the Immobilon membrane, on which the antibody was immobilized, was fixed to the head of the amperometric Clark type electrode as described in Section 3.1. Before measurement, the immunosensor was dipped into a Tris–HCl buffer solution, (pH 8.0; 0.1 M), containing 0.05% Tween-20 by weight and 2.5% BSA by weight (bovine albumin was used to minimize non specific adsorption on the membrane). The pesticide to be determined was added in 5 mL of n-hexane–chloroform mixture 75% (V/V) contained in the measurement cell, together with a fixed supply of pesticide Biotin-Avidin-peroxidase conjugated, i.e. 20 μL (0.01 M solution) of conjugated pesticide in the same solvent mixture. The peroxidase-conjugated pesticide was allowed to compete for 30 min with the non-conjugated pesticide, both free in solution, in binding with the antibody immobilized on the Immobilon membrane. After washing with the same solvent mixture to remove all the unbound labelled pesticide, the specific substrate of the enzyme, i.e. 20 μL of tert-buthylhydroperoxide solution 1% (V/V) in decane was added to 5 mL of the selected organic solvent, i.e. decane, in which the immunosensor was dipped, under stirring. The measured signal (as nA) of the transducer correlated directly with the pesticide concentration to be measured. The higher the pesticide concentration to be measured, the lower the O_2 consumed in the enzymatic reaction, the higher the signal of the O_2 reduced at the Clark electrode (see the enzymatic reaction in decane illustrated in Fig. 1) [35–39]. The sequence for measuring the pesticide using the above format is schematized in Fig. 2. Using this format a calibration curve was constructed by plotting the current variation ΔI (nA) as a function of the log of pesticide concentration (as M) and employed to determine the unknown concentration of pesticide contained in the sample. In this way the original data of the immunosensor response to increasing antigen concentration, which always display logarithmic trends, take on a sufficiently linear trend. Moreover, the application of other, even more complex, methods, described in the literature to obtain the same result, for instance the so-called logit–log method, or equations with three-four parameters [40,41], do not provide better results than those described above. The enzymatic reaction response took about 15–20 min. A membrane already used in a previous test can be regenerated by suitably rinsing it in a solution of glycine 0.1 M and MgCl 2.5 M, at pH 2. This solution was apparently capable of splitting the antibody complex [12]. However, it was found that the immunosensor response when using a regenerated membrane may be up to 15% lower than in the previous measurement. This would of course affect the sensitivity and the repeatability of the measurement and thus the method's precision. Therefore all individual measurements reported in this paper were performed each time using a new (not regenerated) immunological membrane.

3.8. Pesticides measurement in sunflower oily samples and recovery tests

Immunosensors described in this paper were used first of all to measure respectively the triazinic (atrazine, simazine), organophosphate (i.e. parathion) and chlorurate (i.e. 2,4-D and 2,4,5-T) pesticides possibly present in commercial sunflower oil samples examined “as is” using the respective calibration curves. To this end, 0.5 mL of the oily sample were added in 4.5 mL of n-hexane–chloroform 75% (V/V) mixture and the measure was performed as described above in the paragraph 3.7, using the respective pesticide calibration curves to obtain the final concentration of pesticides. In addition, recovery tests were carried out on the oily samples spiked with known concentrations of each pesticide in order to obtain a final pesticide concentration of about 10^{-7} M. For this purpose 200 μL of the organic phase mixture solution of pesticide 10^{-5} M was dissolved in 4.5 mL of n-hexane–chloroform 75% (V/V) mixture, to which 0.5 mL of commercial sunflower oil samples were added. Also in this case the measurements were performed as described in paragraph 3.7 and using the respective calibration curves to obtain the concentrations of spiked solutions.

4. Results and discussion

As explained in the introduction of the present paper, the choice of the organic solvent in which to perform the competitive format involved taking multiple factors into consideration, and an ad hoc table, Table 2, shows how the n-hexane–chloroform 75% (V/V) mixture used in the present work represents a good compromise between all the various requirements set out in the “Introduction”. Indeed, both the checked analyte and the oily samples are completely soluble in this solvent mixture, as is also the marked antigen. The hydrophobicity value of this mixture ($\log P$ is about 2.5) is still satisfactory; lastly, the dielectric constant ($\xi = 2.92$) is neither too high nor too low. In other words the choice fell on an organic but non-alcoholic mixture, very similar to the one that had previously proved to be particularly suitable also when enzymatic OPEEs were being developed [42]. Lastly, other tests, performed in the previous research [8] and in similar conditions, evidenced that also the signal obtained from the final peroxidase enzymatic reaction was more satisfactory when performed in organic solvent, particularly in decane and using tert-butylhydroperoxide as substrate, than in aqueous solution, since, as reported in the literature [8,11,24,42], the enzymatic sensor's response may be better when operating in organic solvent (or solvent mixture) than in aqueous buffer (owing to the lower interference from hydrophilic ionic species, lower microbial contamination, enhanced thermostability, and so on). Furthermore, the difference in the behaviour of the catalase and peroxidase enzymatic reactions taking place in a non-polar hydrophobic solvent like decane (see Fig. 1), instead of in aqueous buffer, was extensively discussed in previous papers [8,35–37,42] and biosensor features were compared with those of biosensors working in more polar organic [43] or aqueous [44] solvents. With regard to the fabrication of the labelled pesticide required in the functioning of the immunosensors constructed, it should be noted that, in the case of atrazine, as described in the preceding Section 3.3, it had first to be carboxylated. The latter could thus be conjugated with the BSA (see Section 3.5). Lastly, as far as the enzymatic labeling is concerned, the classical method involving avidin and extravidin was used [34,40], as described in Section 3.6. Also in the case of the parathion it was necessary to follow the same reaction formats, as described in Sections 3.4 and 3.5, to obtain the enzyme labeled BSA hapten. Of course, the reactions to achieve carboxylation were slightly different [30,31] from those used to carboxylate the atrazine. Lastly, in the case of the 2,4-D and the 2,4,5-T, it was naturally not necessary to perform pesticide carboxylation, as their molecule already possesses a carboxyl group. It was therefore sufficient directly to perform the conjugation with BSA, and thus the customary enzymatic labeling with avidin and extravidin as illustrated in Sections 3.5 and 3.6. The optimization of other factors such as the ELISA type measurement format, or the concentration of the labelled antigen used free in solution, or

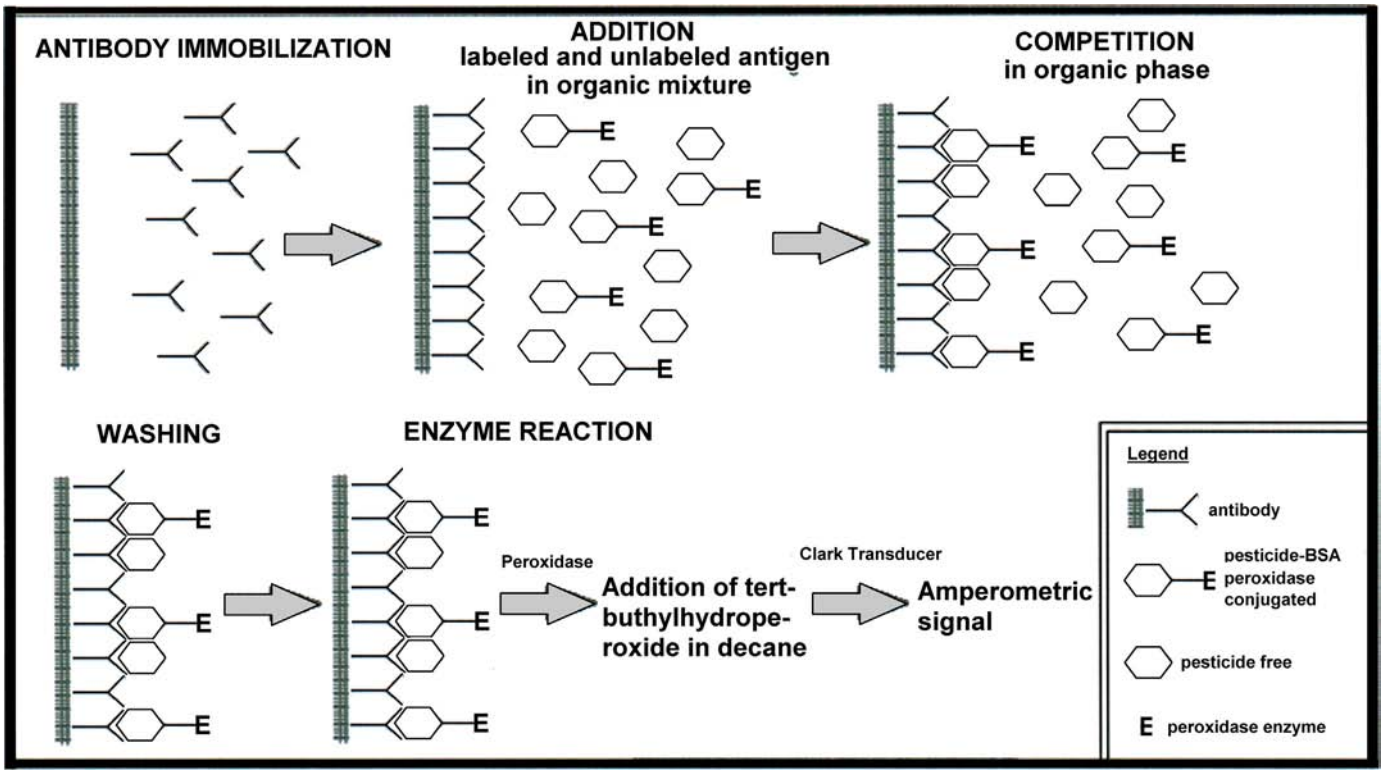


Fig. 2. Measurement: competitive format between the pesticide to be measured and a fixed concentration of peroxidase-pesticide conjugated, both free in organic phase solution, for the antibody immobilized in immobilon membrane.

Table 2
Comparison of solubility of sunflower oil samples, analyte and enzyme substrate in different solvents or solvent mixtures and values of some properties of these solvents. In this case the best compromise is found to be the n-hexane–chloroform 75% (V/V) mixture.

Solubility of (a) → (g) Properties (h) → (i)	Chloroform	Solution n-hexane–chloroform 50% (V/V) mixture	Solution n-hexane–chloroform 75% (V/V) mixture	Hexane
(a) Sunflowers oil (1 mL in 5 mL of solvent)	Opaque	Not completely clear	Clear	Clear
(b) Atrazine (10^{-5} M)	Clear ($S=52$ g L^{-1})	Clear	Clear	Suspension
(c) Simazine	Soluble ($S=0.9$ g L^{-1})	Clear	Clear	Low soluble ($S=3.1\times10^{-3}$ g L^{-1})
(d) 2,4-D (10^{-5} M)	Soluble ($S=32$ g L^{-1})	Clear	Clear	Low soluble ($S=30\times10^{-3}$ g L^{-1})
(e) Parathion (10^{-5} M)	Low soluble ($S=50\times10^{-1}$ g L^{-1})	Clear	Clear	Soluble ($S=20$ g L^{-1})
(f) 2,4,5-T (10^{-5} M)	Soluble ($S=32$ g L^{-1})	Clear	Clear	Low soluble ($S=30\times10^{-3}$ g L^{-1})
(g) Substrate: tert-butylhydroperoxide in decane (0.038 M)	Partially miscible	Miscible	Miscible	Miscible
(h) Log P (hydrofobicity)	2.0	2.6	2.5	3.5
(i) Relative dielectric constant	4.81	3.70	2.92	1.89

the choice of substrate and its concentration, used in the final enzymatic reaction, the competitive step time and so on, were optimized in previous investigations [8,12,23]. As far as transducer choice is concerned, the classical Clark type electrode was used as, in practice, the gas-permeable membrane of this probe protects the working and reference inner electrodes. This ensures that the system is more repeatable and the method more 'robust' [45]. The decision to use an amperometric transducer of this type, i.e. classical, and certainly not particularly modern, compared for instance with more recent transducers based on silica chips, or screen-printed devices and so on, was based precisely on the simplicity with which the classical Clark type gas diffusion amperometric electrode can operate also in organic solvent provided that its outside cap and gas permeable membrane are made for example of PTFE. While more modern transducers, such as those mentioned above, in order to be used in organic solvents, must be completely coated with hydrophobic resin, which, however wisely selected, are usually unlikely to remain fully intact when immersed in organic solvent, especially during the competition step which necessarily cannot be too short in an immunological method of the ELISA type.

Fig. 2 shows the scheme of the measurement used and the competitive format between the pesticide and a fixed concentration of peroxidase pesticide conjugated, both free in the organic phase mixture, for the antibody immobilized in the membrane. The new OPIE response as a function of increasing 2,4-D, 2,4,5-T, or parathion pesticide concentration, the corresponding calibration curves and the confidence intervals for three pesticide determinations, obtained using a semilogarithmic scale, are shown in Fig. 3, while the analytical data obtained for the respective calibration

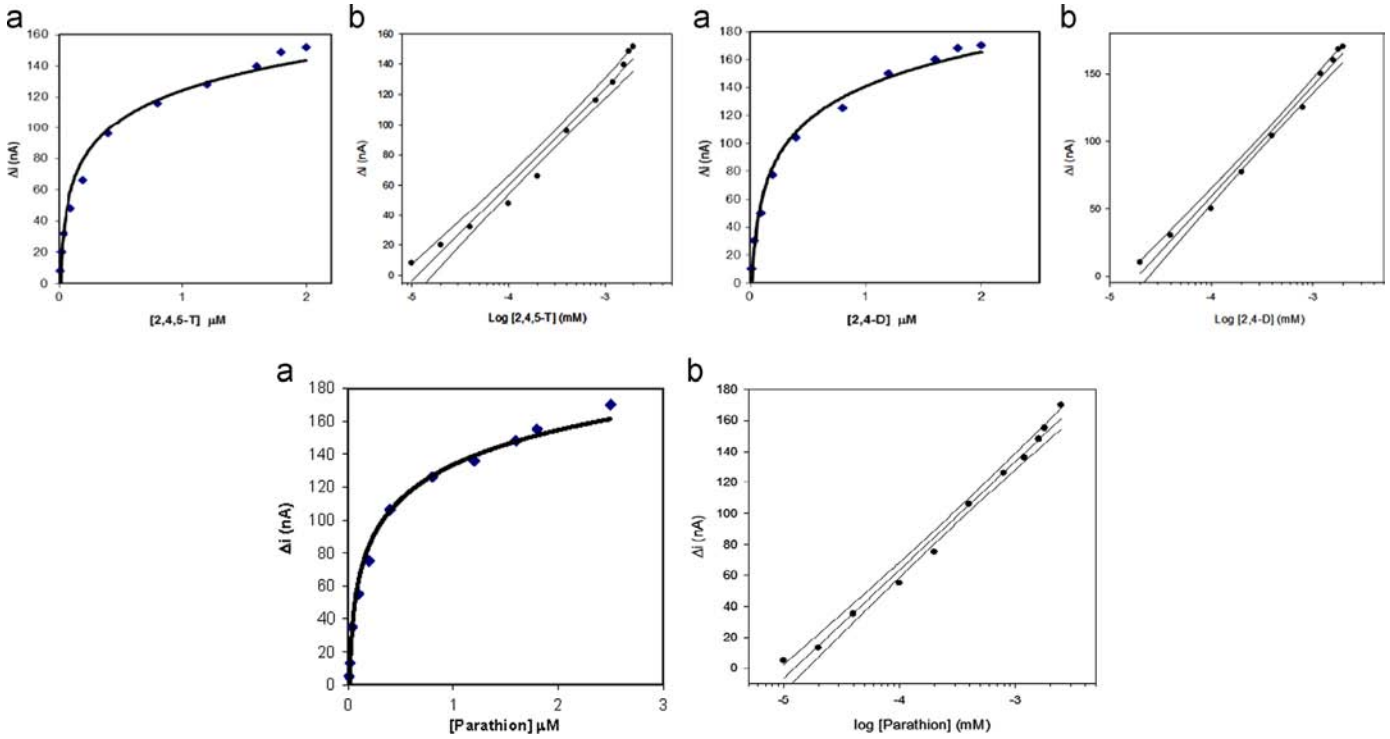


Fig. 3. (a) Trends in the response to 2,4,5–T, 2,4-D and parathion of respective OPIEs, as a function of growing pesticide concentration in sunflower oil. Competition in n-hexane–chloroform 75% (V/V); final enzymatic measurement in decane; and (b) corresponding calibration curve and confidence interval for the same pesticides determination, obtained using a semilogarithmic scale.

Table 3
Analytical data of new OPIEs obtained for calibration curves of different pesticides, for the measurement of 2,4-D, 2,4,5-T and parathion, in the presence of sunflower oil, using: in all cases n-hexane–chloroform mixture 75% (V/V) in the competitive step of the immunoassay, decane as solvent and tert-butylhydroperoxide in decane as substrate for the final enzymatic reaction, and Clark electrode as transducer.

Pesticide	2,4,5-T	2,4-D	Parathion
Regression equation ($y=\Delta i$ (nA), $x=M$)	$Y=64.3\ (\pm 1.4)\log X+124.2\ (\pm 10.1)$	$Y=98.1\ (\pm 1.9)\log X+468.6\ (\pm 14.9)$	$Y=70.0\ (\pm 1.8)\log X+343.2\ (\pm 10.2)$
Linear range (M)	1.0×10^{-8}–2.5×10^{-6}	1.2×10^{-8}–6.0×10^{-6}	1.0×10^{-8}–2.5×10^{-6}
Correlation coefficient	0.9779	0.9896	0.9887
Repeatability of the measurement (as pooled SD%)	7.5	6.6	6.8
Low limit of detection (LOD) (M) (RSD% ≤ 5.0)	0.5×10^{-8}	0.6×10^{-8}	0.5×10^{-8}

curves in the analysis of these pesticides in sunflower oil are summarized in Table 3. Conversely, the same data for the analysis of atrazine and simazine are displayed in Table 4 and in Fig. 4. Significantly, the linear range is very similar in all cases (between about 10–20 nM and 2–4 μM, respectively) as well as the LOD (between about 8 and 12 nM, respectively). The highest calibration sensitivity was found to be that of the immunosensor for atrazine towards atrazine itself (≈ 104 nA/log *M*), i.e. almost double that of the same immunosensor to simazine. However, also in the case of the other immunosensors, the sensitivity towards the respective pesticides was always found to be good (lying between about 64 and 98 nA/log *M*). Generally speaking, the precision was of the same order and always acceptable (the pooled SD was found to lie between 6.6% and 7.5%, in any case). Lastly, Table 5 illustrates some selectivity data of the immunosensor devices developed with regard to different pesticides (i.e. triazinic, chlorurate and organophosphate), comparing the % response of each respective immunosensor to different pesticides. It may be observed that the selectivity among pesticides of the same class is only appreciable and poor for the cases in which the structural formula of the pesticide being tested is very similar to that of the specific antigen of the antibody used (for instance, this is the case for simazine versus atrazine, or of 2,4,5-T versus 2.4-D), but it is noteworthy that the antibody response to antigens belonging to different classes of pesticide, (i.e. paraoxon and carbaryl) is very low or even negligible. This means that each of the immunosensors constructed possesses a good selectivity versus other classes of pesticide that differ from the class of pesticides for which it was constructed. Lastly, it was decided to test the validity of new immunodevices also from the point of view of immunological methods. For this purpose, a comparison is made in Table 6 between the k_{aff} and IC_{50} values obtained for the different pesticides tested using the Langmuir curve [46,47] for the respective immunosensors. In Table 6 the k_{aff} values obtained by performing the competitive process in n-hexane–chloroform 75% (V/V) mixture are compared, for the reader's convenience, with those obtained in previous research [8] performing the same process but in 50% (V/V) mixture. It is noteworthy that the k_{aff} values all lie between about (3.3×10^6 and 5.6×10^6) M^{-1}; in the case of simazine, the value is slightly lower (about 2.4×10^6), which is only to be expected as it was determined using the immunosensor constructed for atrazine. It is only logical that, although having obtained a k_{aff} value again of the same order as atrazine, it should be slightly lower. Moreover, this is in agreement with the results reported in Table 4, observing different calibration sensitivity values. Lastly a series of tests were run on real samples

Table 4
Analytical data of atrazine OPIE, obtained for calibration curves of atrazine and simazine pesticides in the presence of sunflower oil, using: in all cases n-hexane–chloroform mixture 75% (V/V) in the competitive step of the immunoassay, decane as solvent and tert-butylhydroperoxide in decane as substrate for the final enzymatic reaction, and Clark electrode as transducer.

Analytical data	Atrazine	Simazine
Regression equation ($y=\Delta i$ (nA), $x=M$)	$Y=103.9\ (\pm 3.9)\ \log X+531.4\ (\pm 28.6)$	$Y=57.1\ (\pm 2.2)\ \log X+282.4\ (\pm 30.8)$
Linear range (M)	2.0×10^{-8}–2.0×10^{-6}	1.5×10^{-8}–4.0×10^{-6}
Correlation coefficient	0.9730	0.9736
Repeatability of the measurement (as pooled SD%)	7.1	7.5
Low limit of detection (LOD) (M) (RSD% ≤ 5.0)	1.2×10^{-8}	0.8×10^{-8}

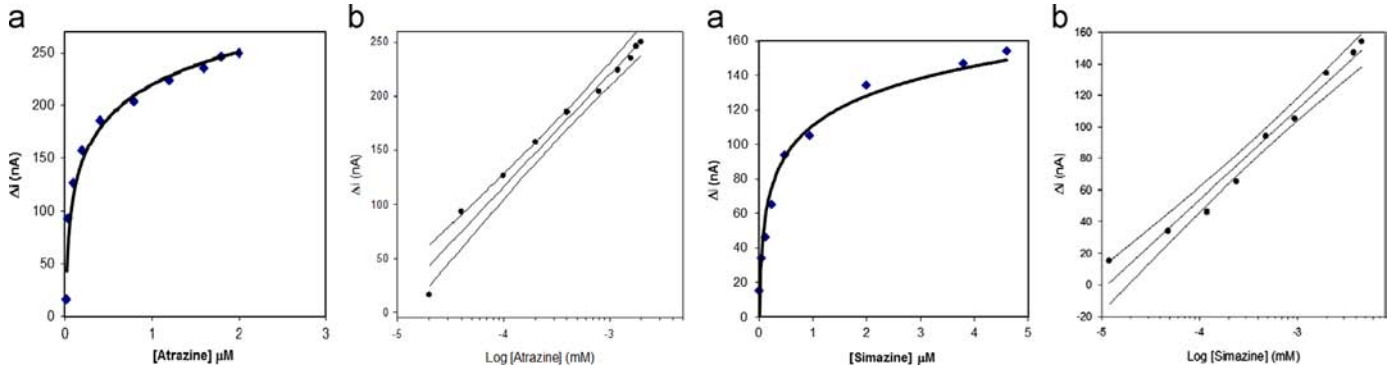


Fig. 4. (a) Trends in the response to atrazine or simazine of triazinic OPIE as a function of growing pesticide concentration in sunflower oil. Competition in n-hexane–chloroform 75% (V/V); final enzymatic measurement in decane; and (b) corresponding calibration curve and confidence interval for the same pesticides determination, obtained using a semilogarithmic scale.

Table 5
Selectivity of immunosensors for different pesticides: comparison of the per cent response to different pesticides using each of the immunosensor devices developed. Final concentration in 5 mL of the organic solvent mixture of each pesticide tested = 2.5×10^{-6} M.

Atrazine immunosensor		2,4-D immunosensor		Parathion immunosensor	
Compound	Selectivity to atrazine (checked as 100%) (percentage of response) (RSD % ≤ 5.5)	Compound	Selectivity to 2,4-D (checked as 100%) (percentage of response) (RSD % ≤ 5.5)	Compound	Selectivity to parathion (checked as 100%) (percentage of response) (RSD % ≤ 5.5)
Atrazine	100	2,4-D	100	Parathion	100
Simazine	55	2,4,5-T	66	Atrazine	20
Atrazine-desethyl	32	Atrazine	24	Simazine	11
Tert-buthylazine	36	Simazine	12	2,4-D	22
2,4-D	28	Parathion	30	2,4,5-T	15
Paraoxon	25	Aldicarb	25	Aldicarb	24
Carbaryl	18	Carbaryl	10	Carbaryl	19

Table 6
Comparison of k_{aff} and IC_{50} values obtained for different pesticides found by measurements carried out in n-hexane–chloroform 75% (V/V) mixture and in the presence of sunflower oil, or in 50% (V/V) mixture and in the presence of olive oil.

Pesticide tested	Organic solvent mixture used and edible oil tested	k_{aff} (M^{-1}) RSD% ≤ 5.0	IC_{50} (M) RSD% ≤ 5.0
Atrazine	Measurement in n-hexane–chloroform mixture 75% (V/V); (competition in presence of sunflower oil and final enzymatic measurement in decane)	4.65×10^{6}	2.15×10^{-7}
Simazine		2.38×10^{6}	4.20×10^{-7}
2,4-D		3.84×10^{6}	2.60×10^{-7}
2,4,5-T		3.33×10^{6}	3.00×10^{-7}
Parathion		5.56×10^{6}	1.83×10^{-7}
Atrazine	Measurement in n-hexane–chloroform mixture 50% (V/V); (competition in presence of olive oil and final enzymatic measurement in decane)	5.71×10^{6}	1.75×10^{-7}
Simazine		2.63×10^{6}	3.80×10^{-7}
2,4-D		5.00×10^{6}	2.00×10^{-7}
2,4,5-T		4.00×10^{6}	2.50×10^{-7}
Parathion		6.67×10^{6}	1.50×10^{-7}

of sunflower oil. Table 7 shows the results found in the search for different pesticides when analysing commercial sunflower oil samples using newly developed OPIEs; the values expressed in M are sufficiently in agreement with relative literature reports [2–5,25–29]. In practice, in the commercial samples tested, any traces of pesticide were so low as to be equal to, or lower, than the

Table 7
Testing for traces of different pesticides in several commercial sunflower oil samples, and recovery tests of the same pesticides in the same spiked sunflower oil samples using developed immunosensor methods.

Pesticide tested	Concentration found in the sample "as is" in the oily matrix (M)	Concentration range reported in the literature [references]	Nominal concentration of spiked oil samples (value $\times 10^8$) (M)	Found experimental concentration (value $\times 10^8$) (M)	% Recovery
Atrazine	$\leq 1.2\times10^{-7}$	4.6×10^{-7}–1.4×10^{-6} [25]	10.0	9.8 ± 0.4	98.2 ± 0.8
Simazine	$\leq 1.0\times10^{-7}$	5.0×10^{-7}–2.0×10^{-6} [26]	10.0	9.6 ± 0.5	96.4 ± 0.9
2,4-D	$\leq 0.6\times10^{-8}$	1.4×10^{-9}–2.5×10^{-3} [27]	10.0	10.3 ± 0.2	103.0 ± 0.6
2,4,5-T	$\leq 0.5\times10^{-8}$	1.4×10^{-9}–2.5×10^{-3} [28]	10.0	9.9 ± 0.5	99.0 ± 0.9
Parathion	$\leq 0.5\times10^{-8}$	3.4×10^{-9}–8.6×10^{-6} [25,29] 1.7×10^{-7}–3.0×10^{-6} [25,29]	10.0	10.1 ± 0.6	101.3 ± 0.8

Table 8
Hill's coefficients in different tests for the analysis of all the pesticides to be determined in sunflower or olive oils. The first five tests were obtained using a competitive format, in the presence of sunflower seeds oil, in n-hexane–chloroform 75% (V/V), while the second five tests used a competitive format, in the presence of olive oil, in chloroform–n-hexane 50% (V/V); for both tests the final enzymatic measurements were carried out in decane and tert-butylhydroperoxide in decane was used as substrate.

Solvent mixture	Oily matrix	Pesticide tested	Hill's coefficient (n) using Eq. (1). In all cases RSD% $\leq$ 5.0	Hill's coefficient (x) using Eq. (2). In all cases RSD% $\leq$ 5.5
75% (V/V)	Sunflowers	Atrazine	Slope = 0.89	Slope = 1.96
75% (V/V)	Sunflowers	Simazine	Slope = 0.87	Slope = 1.68
75% (V/V)	Sunflowers	2,4-D	Slope = 0.91	Slope = 1.87
75% (V/V)	Sunflowers	2,4,5-T	Slope = 0.81	Slope = 1.83
75% (V/V)	Sunflowers	Parathion	Slope = 0.95	Slope = 1.88
50% (V/V)	Olive	Atrazine	Slope = 0.85	Slope = 2.35
50% (V/V)	Olive	Simazine	Slope = 0.91	Slope = 2.05
50% (V/V)	Olive	2,4-D	Slope = 0.86	Slope = 2.72
50% (V/V)	Olive	2,4,5-T	Slope = 0.75	Slope = 2.15
50% (V/V)	Olive	Parathion	Slope = 0.83	Slope = 2.02
Aqueous buffer	Olive	Atrazine	Slope = 0.60	Slope = 1.51

Table 9
Iwuoha–Smith function (I.S.F.): $1/\eta\xi$ (where η is the absolute viscosity of the solvent and ξ its dielectric constant). The higher the I.S.F. value, the greater the diffusion of the analyte from the solvent to the enzymatic membrane.

Final enzymatic reaction performed in:	η (mPa s)	ξ	I.S.F. value ($1/\eta\xi$)
Aqueous buffer solution	0.89	78.4	0.014
n-Hexane–chloroform 50% (V/V) solution	0.65	3.70	0.42
n-Hexane–chloroform 75% (V/V) solution	0.36	2.92	0.95
n-Hexane solution	0.29	2.02	1.70
Decane solution	0.92	2.00	0.54

method's detection limit, i.e. about $< 10^{-8}$ M. However, also several recovery tests were carried out on spiked sunflower oil samples. In this case the tests were performed alternatively using both atrazine and simazine, or else 2,4-D or 2,4,5-T, or the parathion pesticide. The same Table 7 illustrates how recoveries always lie between about 96.4% and 103%, and are thus quite satisfactory. Lastly, even though the results obtained in the present and previous researches [8,23] are a positive indication of the possibility of being able to work in organic solvents, a theoretical confirmation, as it were, was sought by applying well-known equations for this purpose reported in the literature. In particular, as far as the value of Hill's coefficient (n) is concerned, in its original acceptance [48]:

$$\text{Log } Y/(1-Y) = n \log [A]/K \quad (1)$$

(where, Y represents the ratio of the immunocomplex formed on the membrane and the total immobilized antibody; [A] the unlabeled pesticide concentration and K the dissociation constant); (n) theoretically indicates the number of binding sites per molecule, that is, in the present case, the number of binding pesticide molecules per molecule of antibody. As may be observed in Table 8, it is evident that, if the competition takes place in an n-hexane–chloroform 75% or 50% (V/V) mixture, the value found in all tests lies between 0.75 and 0.95, in practice generally close to one (i.e. the theoretical value), while, if the competition (as well as the final enzymatic measure) takes place in aqueous buffer solution (see the last line of Table 8), the coefficient is found to have a value of about 0.6. It thus seems that, when operating in organic solvent, this value comes closest to the theoretical behaviour of the Hill plot.

It is also quite apparent from Table 8 that the value found in the various tests with different pesticides is never an integer. This of course is due partly to experimental error, but also to the fact that, as reported in the literature, [48,49], the Hill coefficient (n) can evidence any type of deviation from normal saturation behaviour in which the value of the slope would theoretically tend towards one [50].

On the other hand, in view of literature reports [51] and applying Hill's equation in the form used by Adeyoju et al. [52]:

$$\log Y/(1-Y) = x \log (\Delta I/I_{50}) \quad (2)$$

(where, ΔI is the change in the current caused by the immunocomplex formed for a given concentration of pesticide and I_{50} is the current when the immunocomplex formed is 50%). It can be seen (Table 8) that the Hill coefficient (x), if the competition takes place in organic solvent mixture, is generally greater than 1 (equal to, very close to, or higher than 2), whereas, if the competition takes place in aqueous solution it amounts to about 1.5. This would mean [53,54] that the immunosensor is more sensitive if the competition between free antigen and enzyme labelled antigen takes place in the organic solvent mixture, in which the deviation from unit value is greater than in aqueous solvent [53]. However, none of this is surprising as the same thing had been observed in previous research [8,23,24]. Nevertheless, in the present case something that did not emerge in previous work was observed: Table 8 itself, for instance, also shows the Hill coefficient values found using Eqs. (1) and (2), both when the competition is performed in an n-hexane–chloroform mixture 75% (V/V) and in the 50% (V/V) mixture.

It is interesting to observe that, using Eq. (1), the (n) coefficients found working in the 75% mixture do not differ substantially from those found using the 50% (V/V) mixture, whereas in the case of Eq. (2), working with the 75% (V/V) mixture, the coefficient (x), although always greater than 1, is systematically lower than the corresponding value observed when the 50% (V/V) mixture is used. In the latter case, the coefficient is actually found to be always greater than 2. This is in good agreement with findings both in the case of the k_{aff} values (see Table 6), for which it is observed that, although of the same order as and indeed very similar to, those obtained using the 50% (V/V)

Table 10
Comparison of main analytical data among some organophosphate, or atrazine OPIEs and OPEEs, or classical inhibition enzyme electrodes.

Solvent	Sensor type	Pesticide	Linearity range (M)Ref.	Reference	LOD (M)	RSD (%)	Selectivity
Chloroform–hexane 50% (V/V)	OPIE	(a) Parathion	1.0×10^{-8}–2.5×10^{-6}	[23]	8.0×10^{-9}	7.0	Good selectivity to
		(b) Atrazine	1.2×10^{-8}–5.0×10^{-6}	[8]	8.0×10^{-9}	6.1	all other classes of pesticides
Chloroform–hexane 50% (V/V)	OPEE	(c) Malathion	3.0×10^{-8}–1.2×10^{-7}	[42]	1.4×10^{-8}	13.2	Poor selectivity to
		(d) Paraoxon	3.5×10^{-8}–2.0×10^{-7}	[42]	1.6×10^{-8}	7.5	all classes of pesticides
		(b) Atrazine	2.0×10^{-9}–2.0×10^{-4}	[43]	1.0×10^{-9}	8.0	
Water–glycine buffer 0.1 M; pH= 8	Classical inhibition	(c) Malathion	3.0×10^{-8}–3.0×10^{-7}	[44]	1.8×10^{-8}	2.8	Poor selectivity to
	enzyme electrode	(d) Paraoxon	1.8×10^{-8}–$1.8\times10^{-}$	[44]	7.0×10^{-9}	1.7	all classes of pesticides

mixture, they are always slightly higher than those found with the 75% (V/V) mixture. Furthermore, the same is observed even when comparing the values of the respective calibration sensitivities, displayed in the calibration straight line equations set out in Tables 3 and 4 of this paper and obtained when operating with the 75% (V/V) mixture, with the corresponding values reported in the previous research [8], obtained using the 50% (V/V) mixture of n-hexane–chloroform. All this, while also confirming the internal consistency of the various data obtained in the present work, would allow us to conclude that the properties of the solvent mixture actually play a non negligible role in the sensitivity of the immunosensor method and that, at least as far as organic solvents (and mixtures thereof) are concerned, a given increase in the polarity of the organic solvent (and thus of its dielectric constant) favours the sensitivity of the immunological method. Moreover, this appears to be in agreement with the results reported in the literature by several authors [5,6]. Of course this argument appears not to be valid on going from organic to aqueous solvents. In this case other factors probably outweigh the simple polarity of the solvent. Lastly, if the Iwuoha and Smith (I.S.F.) function [51,52] $1/\eta\xi$ is applied (where η is the absolute viscosity of the solvent and ξ is the dielectric constant) to estimating the solvent effect on the diffusion of the substrate to the enzyme, in the final enzymatic reaction, according the results reported in Table 9, the higher the value of the I.S.F. function (that is, the lower the value of the viscosity η and/or of the dielectric constant ξ of the solvent), the greater the diffusion of the analyte from the solvent to the enzymatic membrane [24,54]. However, the viscosity and dielectric constant values are very low for organic solvents, for instance, for n-hexane at room temperature ($\eta=0.29$ mPa s; $\xi=2.02$, respectively) when compared with the corresponding value for water ($\eta=0.89$ mPa s; $\xi=78.4$); therefore diffusion is more favourable in n-hexane and in all the other organic solvents considered than in water and therefore, on going from aqueous solvents to organic solvents, there is a considerable increase in the I.S.F. index which therefore enhances the diffusion of the substrate towards the enzyme. On the other hand, the use of decane, which also has a slightly lower I.S.F. index than the 75% (V/V) mixture, is certainly preferable in view of the very high solubility of tert-butylhydroperoxide in decane. Lastly, it is interesting to note that even if also the final enzymatic reaction is performed in an n-hexane–chloroform mixture the diffusion of the analyte from the solvent to the enzymatic membrane would be enhanced by performing the reaction in water and that moreover, going from the n-hexane–chloroform 50% (V/V) to the 75% (V/V) mixture, the I.S.F. index increases and therefore, as far as the final enzymatic reaction is concerned, the 75% (V/V) solvent would work better (as expected) than the 50% (V/V) mixture. It must nevertheless be pointed out that no absolute value can be attributed to the equations and mathematical relations discussed above. However, all authors agree that their 'indicative' value is undeniable [24,48–51,54]. Lastly, if the principal analytical data obtained in the present work are compared with those obtained using inhibition enzymatic sensors, as we investigated in the past [8,23,42,43,44] and not just involving triazinic pesticides but also organophosphates, observing Table 10 it may be concluded that (even if the linearity range and the calibration sensitivity [8,23] are generally found to be better in the case of the OPIEs), on the whole, important analytical data, such as the LOD are not much different in the case of the immunosensor or inhibition enzymatic biosensors. What is found to be substantially different is the selectivity (much better for the immunosensor than for the inhibition enzymatic biosensors).

5. Conclusions

Several immunosensors operating in an n-hexane–chloroform 75% (V/V) solvent mixture were developed for the purpose of determining traces of atrazine, simazine, parathion, 2,4-D and 2,4,5-T in sunflower oil. Good results were obtained using a Clark type transducer and performing not only the competitive assay but also the actual final enzymatic reaction in organic solvent instead of in aqueous solution, i.e. in practice carrying out the final electroenzymatic measurement by a classical OPEE, using as substrate for the peroxidase catalyzed enzymatic reaction a solution of tert-buthylhydroperoxide in decane. Therefore the experimental conditions were practically the same as used by us to determine atrazine traces in olive oil [8], although with the important difference of performing the test in n-hexane–chloroform 75% (V/V) mixture instead of in the 50% (V/V) mixture. The simplicity of the method, the relatively low cost and the possibility of using these new immunodevices to easily detect traces of different types of pesticide in such an important food oil as sunflower oil, means that the method is of great practical interest to the modern food industry. Fresh research is therefore already under way to extend the method also to other types of food seed oil, in which for instance the detection of several of the pesticides tested, such as 2,4-D and 2,4,5-T, is generally even much more frequent than in sunflower and olive oil.

Acknowledgements

Authors are indebted to Prof. S. Eremin (Moscov State University), who supplied antibodies of atrazine, 2,4-D and 2,4,5-T. This work was funded by "La Sapienza" University of Rome, "Ateneo and University Projects".

Appendix A. Supporting information

Supplementary data associated with this article can be found in the online version at http://dx.doi.org/10.1016/j.talanta.2014.09.004.

References

[1] A.J. Russell, L.J. Trudel, P.L. Skipper, J.D. Groopman, S.R. Tannenbaum A.M. Klibanov, Biochem. Biophys. Res. Commun. 158 (1989) 80–85.
[2] W. Stöcklein, A. Gebbert, R.D. Schmid, Anal. Lett. 23 (1990) 1465–1476.
[3] W. Stöcklein, F.W. Scheller, R. Abuknesha, Sens. Actuators B 24–25 (1995) 80–84.
[4] W. Stöcklein, A. Warsinke, F.W. Scheller, Organic solvent modified enzyme-linked immunoassay for the detection of triazine herbicides, in: D.S. Aga,

E.E. Thurman (Eds.), Immunochemical Technology for Environmental Applications, ACS Symposium Series 657, American Chemical Society, Washington, DC, 1997, pp. 373–381.
[5] J. Penalva, R. Puchades, A. Maquieira, Anal. Chem. 71 (1999) 3862–3872.
[6] S.J. Setford, S. Kroger, A.P.F. Turner, Analusis 27 (7) (1999) 600–609.
[7] A. Abad, A. Montoya, J. Agric. Food Chem. 45 (1997) 1495–1501.
[8] M. Tomassetti, E. Martini, L. Campanella, Electroanalysis 24 (4) (2012) 842–856.
[9] S. Saini, G.F. Hall, M.E.A. Downs, A.P.F. Turner, Anal. Chim. Acta 249 (1991) 1–15.
[10] L. Braco, Mikrochim. Acta 120 (1995) 231–242.
[11] B. Lu, E.I. Iwuoha, M.R. Smyth, R. O'Kennedy, Biosens. Bioelectron. 12 (1997) 619–625.
[12] L. Campanella, S. Eremin, D. Lelo, E. Martini, M. Tomassetti, Sens. Actuators B 147 (2011) 78–86.
[13] S. Kröger, S.J. Setford, A.P.F. Turner, Anal. Chem. 70 (23) (1998) 5047–5053.
[14] S. Kröger, A.P.F. Turner, Anal. Chim. Acta 347 (1997) 9–18.
[15] S.F. White, A.P.F. Turner, R.D. Schmid, U. Bilitewski, J. Bradley, Electroanalysis 6 (1994) 625–632.
[16] J. Wang, N. Naser, D. Lopez, Biosens. Bioelectron. 9 (1994) 225–230.
[17] J. Penalva, J.A. Gabaldon, A. Maquieira, R. Puchades, Food Agric. Immunol. 12 (2000) 101–114.
[18] M.A. González-Martinez, J. Penalva, J.C. Rodriguez-Urbis, E. Brunet, A. Maquieira, R. Puchades, Anal. Bioanal. Chem. 384 (2006) 1540–1547.
[19] K.S. Goh, J. Hernandez, S.J. Powell, C.D. Greene, Contam. Toxicol. Bull. Environ. 45 (1990) 208–214.
[20] S. Matsuura, Y. Hamano, H. Kita, Y. Takagaki, J. Biochem. 114 (1993) 273–278.
[21] S. De Lauzon, K.M. Rajkowski, N. Cittanova, Steroid Biochem. Mol. Biol. 48 (1994) 225–233.
[22] K. Beyer, D. Knopp, R. Niessner, Food Technol. Biotechnol. 35 (1997) 215–223.
[23] E. Martini, Mauro Tomassetti G., Merola, L., Campanella, Agent orange herbicides, organophosphate and triazinic pesticides analysis using new organic phase immunosensors, in: Atti del XXIV Congresso della Divisione di Chimica Analitica della Società Chimica Italiana, A. Rossi, S. Lanteri, E.Magi (Eds.), Genova, 2013, p. 118.
[24] E.I. Iwuoha, M.R. Smyth, M.E.G. Lyons, Biosens. Bioelectron. 12 (1) (1997) 53–75.
[25] B. Gilbert-Lopez, J.F. Garcia-Reyes, A. Molina-Diaz, Talanta 79 (2009) 109–128.
[26] S. Walorczyk, J. Chromatogr. A 1165 (2007) 200–212.
[27] O. Lacina, M. Zachariasova, J. Urbanova, M. Vaclavikova, T. Cajka, J. Hajslova J. Chromatogr. A 1262 (2012) 8–18.
[28] A.M. Gillespie, S.M. Walters, Anal. Chim. Acta 245 (1991) 259–265.
[29] R.C. Prados-Rosales, J.L. Luque García,, M.D. Luque de Castro, J. Chromatogr. A 993 (1–2) (2003) 121–129.
[30] M.H. Goodrow, R.O. Harrison, B.D. Hammock, J. Agric. Food Chem. 38 (1990) 990–996.
[31] M.J. Kim, H.S. Lee, D.H. Chung, Y.T. Lee, Anal. Chim. Acta 493 (2003) 47–62.
[32] Y.H. Liu, M.J. Jin, W.J. Gui, J.L. Chen, Y.R. Guo, G.N. Zhu, Anal. Chim. Acta 591 (2007) 173–182.
[33] M. Duk, E. Lisowska, J.H. Wu, A.M. Wu, Anal. Biochem. 221 (1994) 266–272.
[34] S.V. Rao, K.W. Anderson, L.G. Bachas, Biotechnol. Bioeng. 65 (1999) 389–396.
[35] L. Campanella, G. Spuri Capesciotti, M.V. Russo, M. Tomassetti, Curr. Enzyme Inhib. 4 (2008) 86–92.
[36] M. Tomassetti, G. Spuri Capesciotti, T. Gatta, L. Campanella, Catalase OPEE operating in highly hydrophobic solvent: mechanism and applications, in: F. Baldini, et al., (Eds.), Sensors: Proceedings of the First National Conference on Sensor, Rome, 162, Springer, New York, USA, 15–17 February 2012, pp. 113–117 (lecture notes in electrical engineering).
[37] N.V. Ivanova, P.P. Gladyshew, M.I. Goryaev, (e)N.V. Ivanova, P.P. Gladyshew M.I. Goryaev, Seriya Khimicheshaya 25 (3) (1975) 28–34.
[38] J. Hernandez-Ruiz, M.B. Arnao, A.N.P. Hiner, F. Garcia-Canovas, M. Acosta, Biochem. J. 354 (2001) 107–114.
[39] D.P. Barr, S.D. Aust, Arch. Biochem. Biophys. 303 (2) (1993) 377–382.
[40] M.R. Flynn, Ann. Occup. Hyg. 48 (7) (2004) 617–622.
[41] B. Nix, D. Wild, Calibration curve-fitting, The Immunoassay Handbook, second ed., David Wild, Nature Publishing Group, New York (2001) 198.
[42] L. Campanella, S. De Luca, M.P. Sammartino, M. Tomassetti, Anal. Chim. Acta 385 (1999) 59–71.
[43] L. Campanella, A. Bonanni, E. Martini, N. Todini, M. Tomassetti, Sens. Actuators B 111–112 (2005) 505–514.
[44] L. Campanella, R. Cocco, M.P. Sammartino, M. Tomassetti, Sci. Total Environ. 123/124 (1992) 1–16.
[45] A. Sassolas, B. Prieto-Simón, J.L. Marty, Am. J. Anal. Chem. 3 (2012) 210–232.
[46] P. Önnerfjord, S. Eremin, J. Emnéus, G. Marko-Varga, J. Immunol. Methods 213 (1) (1998) 31–39.
[47] E. Valera, J. Ramón-Azcón, F.J. Sanchez, M.P. Marco, Á. Rodríguez, Sens. Actuators B: Chem 134 (1) (2008) 95–103.
[48] R. Chang, Physical Chemistry with Application to Biological Systems, Macmillan, New York (1990) 248.
[49] M.L. Coval, J. Biol. Chem. 245 (1970) 6335–6336.
[50] J. Yon-Kahn, G. Hervè, Molecular and Cellular Enzymology, Springer Verlag, Berlin (2010) 33.
[51] O. Adeyoju, E.I. Iwuoha, M.R. Smyth, Talanta 41 (9) (1994) 1603–1608.
[52] O. Adeyoju, E.I. Iwuoha, M.R. Smyth, Anal. Lett. 27 (11) (1994) 2071–2081.
[53] Q. Deng, S. Dong, Analyst 121 (1996) 1979–1982.
[54] E.I. Iwuoha, M.R. Smyth, M.E.G. Lyons, J. Electroanal. Chem. 390 (1995) 35–45.

Talanta 132 (2015) 513–519

Contents lists available at ScienceDirect

Talanta

journal homepage: www.elsevier.com/locate/talanta

Dinuclear copper(II) octaazamacrocyclic complex in a PVC coated GCE and graphite as a voltammetric sensor for determination of gallic acid and antioxidant capacity of wine samples

B.B. Petković [a,*], D. Stanković [b], M. Milčić [b], S.P. Sovilj [b], D. Manojlović [b]

[a] Department of Chemistry, Faculty of Natural Sciences and Mathematics, University of Priština, 38220 Kosovska Mitrovica, Serbia
[b] Faculty of Chemistry, University of Belgrade, P.O. Box 51, 11058 Belgrade 118, Serbia

ARTICLE INFO

Article history:
Received 19 June 2014
Received in revised form
10 September 2014
Accepted 13 September 2014
Available online 22 September 2014

Keywords:
Gallic acid
Dinuclear copper(II) octaazamacrocyclic complex
PVC matrix
Voltammetric sensor

ABSTRACT

A novel efficient differential pulse voltammetric (DPV) method for determination gallic acid (GA) was developed by using an electrochemical sensor based on $[Cu_2tpmc](ClO_4)_4$ immobilized in PVC matrix and coated on graphite (CGE) or classy carbon rod (CGCE). The proposed method is based on the gallic acid oxidation process at formed $[Cu_2tpmcGA]^{3+}$ complex at the electrode surface. The complexation was explored by molecular modeling and DFT calculations. Voltammograms for both sensors, recorded in a HNO_3 as a supporting electrolyte at pH 2 and measured in 2.5×10^{-7} to 1.0×10^{-4} M of GA, resulted with two linear calibration curves (for higher and lower GA concentration range). The detection limit at CGE was 1.48×10^{-7} M, while at CGCE was 4.6×10^{-6} M. CGE was successfully applied for the determination of the antioxidant capacity based on GA equivalents for white, rosé and red wine samples.
© 2014 Elsevier B.V. All rights reserved.

1. Introduction

Gallic acid, a type of phenolic acid, is occurring in plants in the form of free acids, esters, catechin derivatives and hydrolysable tannins [1]. As one of the most biologically-active phenolic compounds of plant origin, gallic acid is commonly used in the pharmaceutical and food industry. Plant polyphenols are multifunctional and can be reducing agents, hydrogen donating antioxidants, singlet oxygen quenchers and in some cases metal chelating agents [2]. Gallic acid is used as a standard for determining the phenol content of various analytes by the Folin–Ciocalteau spectrophotometric method and the results are reported in gallic acid equivalents. The measurement of "total phenols" is a good indication of the level of antioxidants present in the sample [3].

The importance of the phenolic compounds has led to the development of various methods for their determination in various types of samples, including chemiluminescence [4] spectrophotometry [5] and capillary electrophoresis [6,7] as well as chromatography [8]. Electrochemical methods were also employed for this purpose. Gallic acid and other phenolic compounds were determined in wine samples and plant extracts at a glassy carbon electrode [9–13], at hanging mercury drop electrode [14,15] and at carbon paste electrode modified with nanotubes [16,17]. Electrodes with polyphenols at carbon-polyvinil chloride [18], polyepinephrine modified glassy carbon electrode [19] and a natural bentonite, modified with different quaternary ammonium cations [20] have also been described and successfully analytically applied. Cyclyc, diferential pulse and adsorptive stripping voltammetric techniques were mostly used in those reported works [21]. Recently, a photoelectrochemical sensor applied to sense gallic acid has been designed with polyaniline–reduced graphene oxide–titanium dioxide [22], while a voltammetric electronic tongue system (ET) made from an array of modified graphite-epoxy composites plus a gold microelectrode was used in qualitative and quantitative analysis of polyphenols found in wine [23].

Bearing in mind the most of past research in electrochemical determination of GA and other phenols, the main disadvantage of GCE was polymerization and adsorption of investigated and other species on the electrode itself. Therefore, GCE should be polished to provide new active surface before any electrochemical measurement. Inability for determination of more samples in a row with the same electrode without previous preparation and better electrode sensitivity were the reasons for the taken electrode modifications [16–20]. Polymer modified electrodes however, have many advantages such as improved electro catalysis, absence of

* Correspondence to: Department of Chemistry, Faculty of Natural Sciences and Mathematics, University of Priština, 38220 Kosovska Mitrovica, Lole Ribara 29, Serbia. Tel.: +381 28 425 396; fax: +381 28 425 399.
E-mail addresses: bedpet@orion.rs, branka.petkovic@pr.ac.rs (B.B. Petković), dalibors@chem.bg.ac.rs (D. Stanković), mmilcic@chem.bg.ac.rs (M. Milčić), ssovilj@chem.bg.ac.rs (S.P. Sovilj), manojlo@chem.bg.ac.rs (D. Manojlović).

http://dx.doi.org/10.1016/j.talanta.2014.09.025
0039-9140/© 2014 Elsevier B.V. All rights reserved.

surface fouling and prevention of undesirable reactions competing kinetically with the desired electrode process. On the other hand, DPV technique has many advantages compared with conventionally used CV, e.g. a better sensitivity, selectivity and response [24].

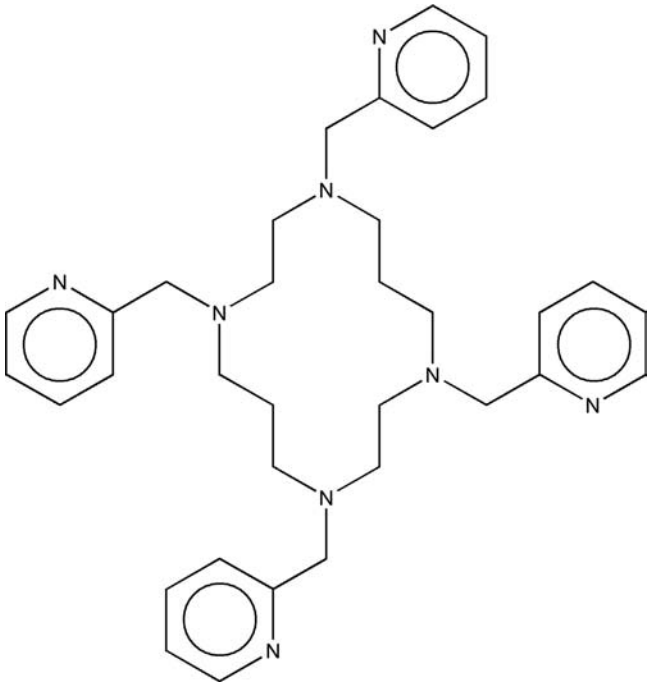
It is important to mention biosensors as powerful specific analytical devices that also have been used for the detection of phenolic compounds. Biosensors based on several types of copper-containing enzymes which catalyze the oxidation of a wide range of phenolic compounds by utilizing molecular oxygen, such as tyrosinase [25,26] and laccase [27,28] were coupled to electrochemical or optical techniques for this purpose.

The general idea of this work was to examine application possibility of simple and efficient sensor for rapid differential pulse voltammetric determination of GA at low concentrations, based on previously synthesized $[Cu_2tpmc](ClO_4)_4$ complex immobilized in a PVC matrix. To the best of our knowledge, there is no report which relates to the application of complexation agent immobilized in PVC matrix as a modifier for graphite or classy carbon rod and the determination of gallic acid or antioxidant capacity of real samples. Similarly as in the case of copper containing enzymes, it could be very useful and interesting to examine the possibility of polyphenols oxidation in a presence of synthetic copper macrocyclic complex. Also, modification of the electrode surface should prevent polymerization on the electrode itself. Furthermore, the probability of formation of GA sensitive reversible $[Cu_2tpmcGA]^{3+}$ complex could be investigated by molecular modeling and Differential Function Theory (DFT) calculations. The determination of structural parameters obtained by molecular modeling is a powerful tool to add chemical and physical information to those obtained by other techniques.

2. Experimental

2.1. Chemical and reagents

The initial macrocyclic ligand *N,N′,N″,N‴*-tetrakis(2-pyridylmethyl)-1,4,8,11-tetraazacyclotetradecane (*tpmc*) (Scheme 1) and the next synthesized $[Cu_2tpmc](ClO_4)_4$ complex which was electroactive sensor material, were prepared by the procedure described in literature [29,30]. 1,4.8.11-tetraaza-cyclotetradecane 98%, as a starting compound, was used as received from Aldrich Chemical Company. The purity of synthesized ligand and complex were tested by elemental analyses performed by standard micromethods (Anal. Calcd. for ($C_{34}H_{44}N_8$) (%): C, 72.30; H, 7.85; N, 19.84. Found: C, 72.48; H, 7.89; N, 19.68). Poly(vinyl chloride), PVC, was used as Pevicon made by Fostatbolaget, Sweden. Dibutyl phthalate (DBP) and gallic acid (GA) were used as received from Fluka. Nitrite and sulfuric acid, potassium nitrate (all p.a.) and appropriate mixture of acetic acid and sodium hydroxide for acetate buffer, all purchased from Merck and Sigma-Aldrich, were used in supporting electrolyte investigations. Tetrahydrofuran (THF) was available from Merck and distilled before use and high purity water (Millipore, 18 MΩ cm resistivity) were used as solvents.



Scheme 1. *N,N′,N″,N‴*-tetrakis(2-pyridylmethyl)-1,4,8,11-tetraazacyclotetradecane (*tpmc*).

2.2. GA standard

Gallic acid (p.a) was used for preparation test solutions and as standard for measurement of the antioxidant capacity. The stock solution of gallic acid (1×10^{-3} M) was prepared in methanol (HPLC grade). Once prepared standard was protected from light with aluminum foil and kept in refrigerator. It was stable for at least 1 month. The working standards were prepared freshly from the stock solutions for each new measurement.

2.3. Electrode preparation

The PVC membrane contained 5 % (w/w) $[Cu_2tpmc](ClO_4)_4$, 38 % PVC and 57 % dibutyl phthalate. A total of 0.270 g of these reagents was mixed with 2.5 mL THF. A glassy carbon (GC) rod (ϕ 3 mm) (Sigardur-Sigri Electrographite, GmbH, Germany) was directly coated by dipping two times in the mixture. The same procedure was used for coating graphite rod (ϕ 6 mm) made by Sigma Aldrich. The formed coating bead on the GC and graphite was allowed to dry in air over night and then, electrode was kept in 10^{-4} M GA solution for about 24 h. This modified GC and graphite electrodes were finally used as voltammetric sensors for determination of GA. The voltammetric responses of the electrodes were measured in the series of standard GA solutions within the range of 2.5×10^{-7} to 1.0×10^{-4} M in a 10^{-2} M solution of HNO_3 as a supporting electrolyte.

2.4. Electrochemical measurements

Cyclic and differential pulse voltammetric measurements were recorded on a Metrohm 797 VA Computance instrument (Herisau, Switzerland). The triple-electrode system was consisted of a working electrode, GC or graphite electrode modified with PVC membrane with activated dinuclear Cu(II)/*tpmc* complex as sensor component, a reference Ag/AgCl, KCl (3 M) (Model 6.0728.010) and anauxiliary separate platinum rod electrode (Model 6.0340.000). The cyclic and the differential pulse voltammograms of standard GA solutions were recorded in the potential range from 0.0 to 1.0 V, using a scan rate of 100 mV/s (for CV) and 10 mV/s (for DPV). A modulation time was varied from 20 to 80 ms, and pulse amplitude was changed in range of 10 to 90 mV. The measurements were performed in unaerated solutions. The pH measurements were carried out using a Hanna Instruments pH-meter with a Hanna Instruments combined pH reference electrode. All of the experiments were done at room temperature (25 °C).

2.5. Sample preparation

Determination antioxidant capacity presented as mg/L of GA in white, rosé and red wine samples were done using an extremely

simple procedure involving the direct addition of a sample aliquot in the electrochemical cell without any sample pretreatment. The wine samples in triplicate, commercially available in Serbia were analyzed by the proposed voltammetric method used as a standard for determination of antioxidant capacity. An aliquot of 1 mL of wine was added to 9 mL of 10^{-2} M HNO_3 solution in electrolytic cell and homogenized with a magnetic stirrer before voltammetric measures described in previous section.

2.6. Spectrophotometric determination of total phenolic content

The total phenolic content (TP) of the wines was determined using the Folin–Ciocalteu micro method (F–C) as adapted for wine analysis [31]. Gallic acid was used to obtain the calibration curve and results were expressed as mg gallic acid equivalents per litre of wine (mg/L of GA). Red and rosé wine samples required dilution.

2.7. Computation details

Based on Cambridge Structural Database search published in our previous paper [32] starting structure for optimization copper complexes with *tpmc* ligand were chosen. Geometries of all structures were fully optimized with DFT (Differential Function Theory) method, according to procedure described before [32]. Reaction energies were calculated as a difference between ZPE corrected electronic energies of reaction products and reactants [33].

3. Results and discussion

For better understanding the general idea of this work, the attention should be drown to several issues regarding the construction and operation of working electrode. Polymer modified electrodes are often prepared by casting solution droplet containing dissolved polymer onto the surface and allowing the solvent to evaporate, by dip or spin coatings, or via electropolymerization in the presence of the dissolved monomer. The purpose of polymer film, from the chemical point of view is to immobilize sensor component, promote electron transfer and to prevent electrode surface contamination by other species presented in the sample [34]. This electrode was prepared by simple coating technique using PVC matrix as carrier of active component. The more conductive polymer nafion was not compatible with $[Cu_2tpmc](ClO_4)_4$ complex, so less conductive but more durable polymer matrix consisted from PVC and DBP as plasticizer was used instead. Membrane was coated on a GCE and graphite for comparison. $[Cu_2tpmc](ClO_4)_4$ complex immobilized in PVC matrix is activated by GA solution. The probable operation mechanism of the sensor involved complexation between dinuclear Cu(II)/tpmc complex immobilized in membrane and GA determined in the solution, and two step electrochemical oxidation of captured GA, probably in the complex ion $[Cu_2tpmcGA]^{3+}$.

A number of dinuclear metal(II) complexes with *tpmc* and additional bidentate ligand are known [35,36], but there is no evidence of dinuclear copper *tpmc* complex with GA. Assuming that reversible formation of this complex on the surface of the membrane is sensitive to different concentration of GA in solution, the next step was to investigate formation possibility of proposed dinuclear copper *tpmc* complex with GA.

3.1. Structure of $[Cu_2tpmcGA]^{3+}$ complex ion and DFT calculations

Based on the results of the extensive CSD search [32] and molecular modeling, the structure of optimized $[Cu_2tpmcGA]^{3+}$ complex ion was obtained (Fig. 1). Details are given in Supplementary materials. This structure is in agreement with other structures found in CSD [30,37–39].

Complex stability was examined by calculation of value for the energy of reaction (please see Supplementary material) which is 10.4 kcal/mol in favor of $[Cu_2tpmcGA]^{3+}$complex. The results of energy calculations clearly indicated that gallic acid would have high preference for binding to $[Cu_2tpmc]^{4+}$ complex in aqueous solution, and that the $[Cu_2tpmcGA]^{3+}$complex will be formed even in the case of very low concentration of gallic acid.

3.2. Electrochemical investigation

Electrochemical behavior of GA on the surface of bare and coated glassy carbon and graphite electrode was investigated by CV technique. Cyclic voltammograms of 10^{-4} M GA in HNO_3 solution as supporting electrolyte (pH about 2) at graphite (a) and glassy carbon electrode (b) (GE and GCE) are presented in Fig. 2. CV at modified both electrodes with activated $[Cu_2tpmc](ClO_4)_4$ complex immobilized in PVC matrix (CGE and CGCE) (Fig. 3) were recorded under the same conditions. Voltammograms exhibited two anodic oxidation peaks on both bare electrodes (both parts of Fig. 2). The first peak of GA appeared in the region of 0.5–0.6 V and it originated primarily from the oxidation of the ortho-hydroquinone group in the ring of the molecule. The second oxidation peak about 0.9 V was caused by the oxidation of the third –OH group of GA [40]. On the basis on analysis of the voltammograms it could be noticed that the peak current decreased in every next cycle due to absorption and polymerization of GA on the bare electrodes surfaces. On the other hand, coating of the membrane over the GCE and GE decreased a current density on the electrode, but prevent polymerization Fig. 3. In both coated electrodes cycling barely changed the shape of the cyclovoltammograms. The most significant changes were observed between the first and second cycles. Further cycling led to stabilization of the electrodes, which achieved steady state already after 2–3 cycles.

Differential pulse voltammetry (DPV) was selected for determination of GA as a suitable electroanalytical technique due to its low background currents and low detection limits. Working conditions were studied by variation of modulation time and modulation amplitude in order to provide lowest detection limit. After

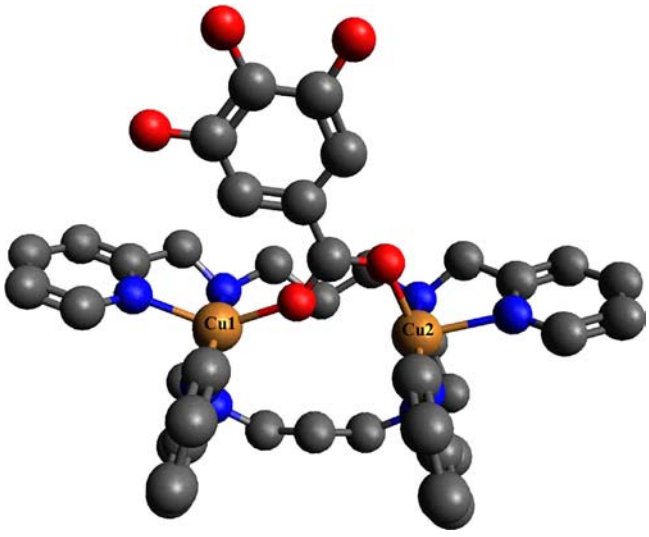


Fig. 1. Optimized structure of $[Cu_2tpmcGA]^{3+}$ complex ion. Colors: yellow-copper; red-oxygen; blue-nitrogen; grey-carbon. Hydrogen atoms are omitted for clarity. (For interpretation of the references to color in this figure legend, the reader is referred to the web version of this article.)

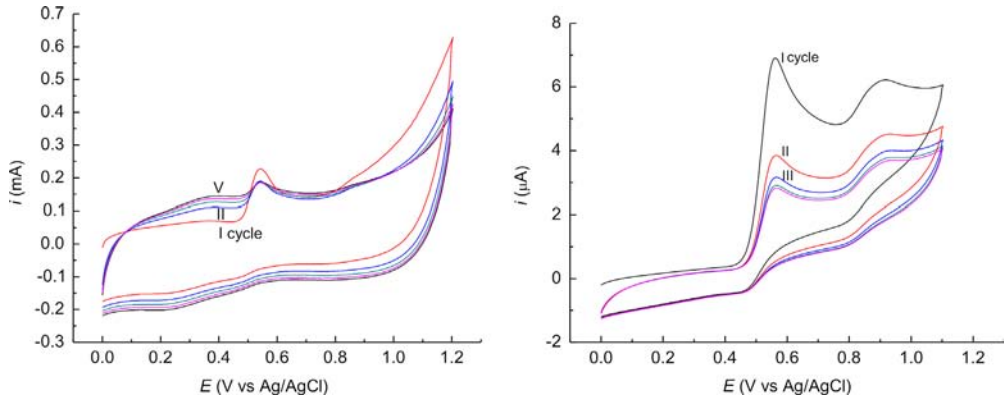


Fig. 2. Cyclic voltammetric profiles for the electrochemical oxidation of 10^{-4} M gallic acid in HNO_3 solution (pH about 2) at GCE (a) and CGCE (b); scan rate of 100 mV/s.

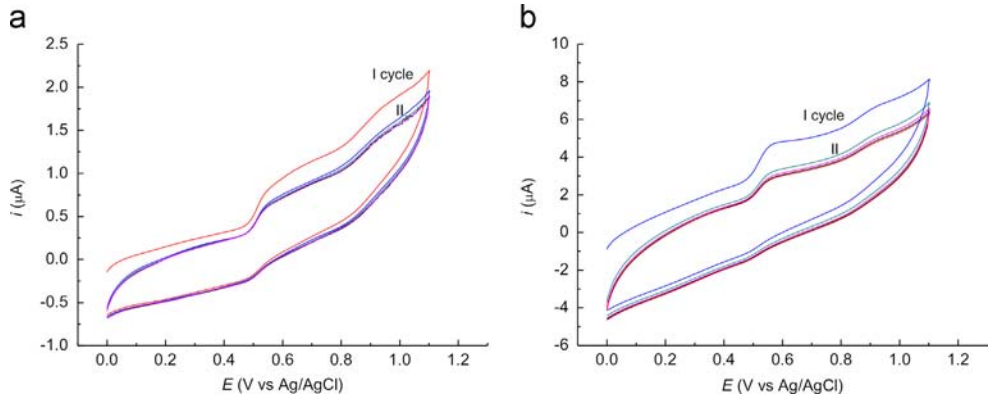


Fig. 3. Cyclic voltammetric profiles for the electrochemical oxidation of 10^{-4} M gallic acid in HNO_3 solution (pH about 2) at GE (a) and CGE (b); scan rate of 100 mV/s.

variation of modulation time from 20 to 80 ms, and changing pulse amplitude in range of 10 to 90 mV, the optimal modulation time of 40 ms and pulse amplitude of 50 mV were chosen taking into account the distortion and height of the peak of quantification, and also forego peak.

3.3. Selecting of supporting electrolyte and optimal pH

Bearing in mind that the sensory component, dinuclear Cu/*tpmc* complex could be blocked at higher pH values where the smaller OH^- ion could easily bridge two copper centers in macrocyclic complex and form $[Cu_2OH(tpmc)]^{3+}$ ion [30], the acidic environment was selected for GA determination.

Different supporting electrolytes were tested: HNO_3, H_2SO_4 and acetate buffer. All voltammetric features exhibited small shoulder before the first oxidation peak of GA (Fig. 4(a)) and the origin of forego peak is described to oxidation of obtained nitrate, sulfate or acetate bridged dinuclear copper complex itself, obtained by complexation of dinuclear copper/*tpmc* complex and anion from supporting electrolyte. These and similar structures were already reported in literature [30,37,38]. The highest and well pronounced signal for GA was recorded in H_2SO_4 and HNO_3, with better baseline and smaller forego peak in HNO_3. Therefore, the nitric acid was chosen for supporting electrolyte in following investigations. Differential pulse voltammograms in HNO_3 solution with different pH values were analyzed by construction of diagram of the influence of the pH on peak potential and peak current (Fig. 4(b)). The previous assumption that GA oxidation became difficult with an increase in pH was confirmed by those results. The value of pH=2 was chosen for further studies.

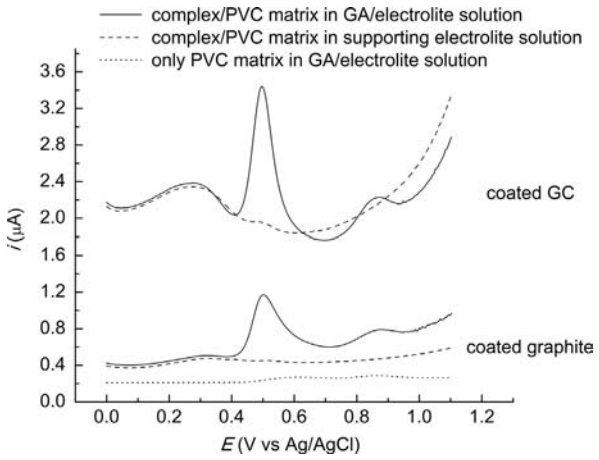


Fig. 4. Differential pulse voltammograms of 10^{-5} M GA in HNO_3, H_2SO_4 and acetate buffer as supporting electrolyte at CGE (a); the influence of the pH on peak potential and peak current obtained from differential pulse voltammograms of 10^{-6} M GA in aqueous solution of different concentrations of HNO_3 (b).

3.4. DPV study with different electrodes

In order to investigate impact of PVC matrix and different electrode material on voltammetric response, DPV was recorded at coated graphite and GC with and without complex in the polymer matrix (Fig. 5). It was obvious that supporting electrolyte in absence of GA gave a good baseline and electrode coated with PVC matrix without sensory component - $[Cu_2tpmc](ClO_4)_4$ respond barely even to large amounts of GA in the standard

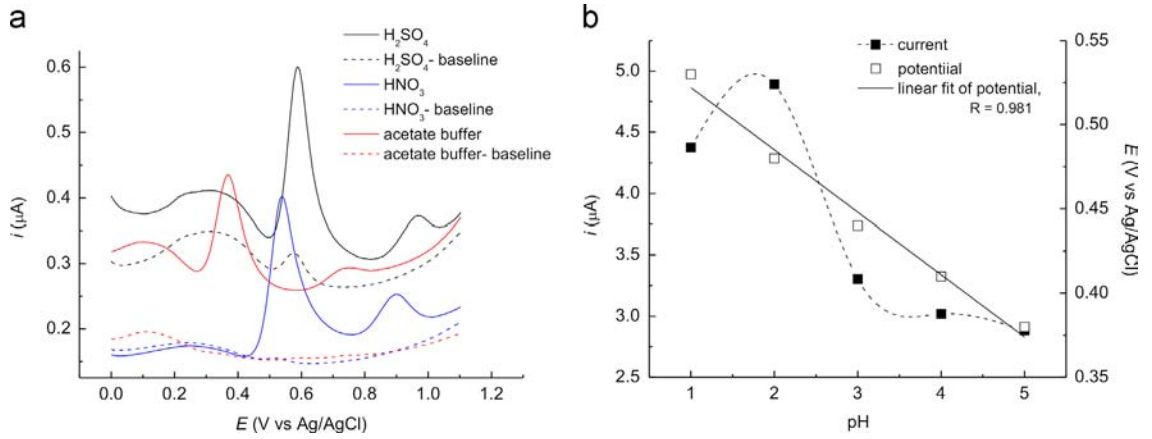


Fig. 5. Comparison of voltammetric responses provided by GC and graphite electrodes modified with/without copper complex: $[Cu_2tpmc](ClO_4)_4$ complex incorporated in polymer matrix, recorded in 10^{-4} M GA and supporting electrolyte (solid line); $[Cu_2tpmc](ClO_4)_4$ complex incorporated in polymer matrix, recorded only in a HNO_3 as a supporting electrolyte, pH about 2 (dash line); polymer matrix without $[Cu_2tpmc](ClO_4)_4$ complex, recorded in 10^{-4} M GA (doth line); scan rate, 10 mV/s.

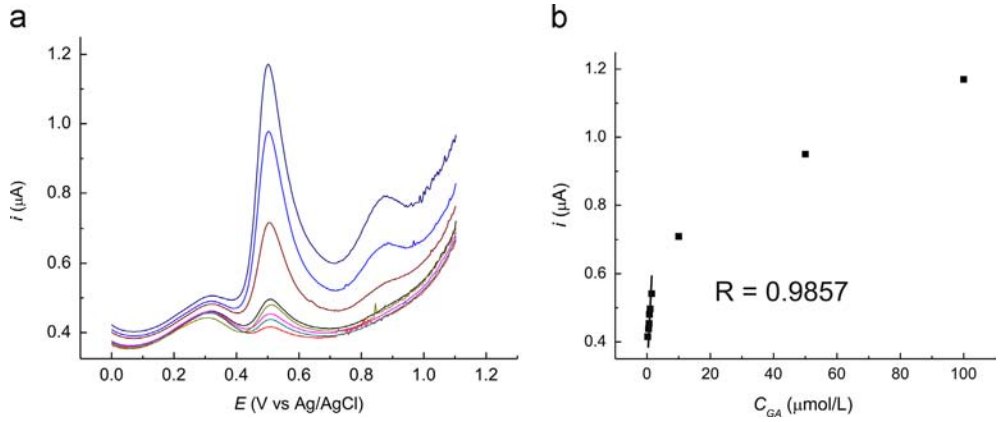


Fig. 6. DPV of CGE with GA added in concentration of 2.5×10^{-7}–1×10^{-4} M, pH=2 (a); calibration curves for GA (b).

solution. In such way, DPV response of the CGE and also CGCE came only from the dinuclear copper/*tpmc* complex immobilized in a polymer matrix. The peaks were now well-defined (Fig. 5). The origin of forego peak as a consequence of oxidation of obtained nitrate bridged dinuclear copper complex itself, made by complexation of $[Cu_2tpmc](ClO_4)_4$ and nitrate from supporting electrolyte, is confirmed due to absence of this peak in voltammogram of CGE coated only with PVC matrix. The first oxidation peak of GA on both electrodes was recorded on 0.50 V, while second less expressive oxidation peak appeared on 0.87, but it was lost for GA concentrations smaller than 10^{-6} M for CGE and 10^{-5} M for CGCE. Although CGCE exhibited higher peak current, it was found that faster loses its response to GA concentrations (limit was about 10^{-6} M), while with CGE it was possible to detect concentrations of 10^{-7} M order of magnitude. Larger surface and porosity of the graphite electrode could be a possible reason for that behavior.

3.5. Construction of the calibration curve

Differential pulse voltammograms of various concentrations of GA from 2.5×10^{-7} to 1.0×10^{-4} M recorded on more sensitive CGE (compared with CGCE) were shown in Fig. 6(a). The first anodic peak of GA was chosen for quantification of GA due to its reversibility, very good reproducibility and linear dependence on current density of this peak vs. the concentration of gallic acid. The calibration curve was constructed by plotting the current density of first anodic peak vs. the concentration of GA. There were two resulting calibration linear plots (Fig. 6(b)). The higher concentration range is described by the regression equation: *Ip* (10^{-7} A)= $5.06\times10^{4}\times C_{GA}+6.8209$, where *Ip* is the current density of first anodic peak and C_{GA} is the concentration of gallic acid expressed in mol/L. The lower concentration range is expressed by the relationship: *Ip* (10^{-7} A)=$3.895\times C_{GA}+1.14\times10^{6}$ (R=0.9857), and with detection limit (LOD) of GA determination of 1.48×10^{-7} M. Detection limit was estimated from three times the standard deviation. The limiting point, 2.63×10^{-6} M vs. 6.9310^{-7} A, obtained by extrapolating of the linear plots, determined which of these two mentioned equations should be used. Standard deviations of 0.025 μA in the oxidation peak current and 0.006 V in the peak potential for three repeated detections of GA concentration of 5×10^{-5} M as well as the decrease in peak current to 23.5% of the initial current after three months, suggests good reproducibility and stability of results when the modified electrode was used.

Two regression equations were obtained from voltammograms for CGCE: *Ip* (μA)=$4.4\times10^{3}\times C_{GA}+0.93$ for higher concentration range, and *Ip* (μA)=$2.4\times10^{5}\times C_{GA}+0.03$ for lower concentration range, with LOD of 4.6×10^{-6} M of GA.

For comparative purposes, relevant characteristics of some of the modified electrodes [16–19] were listed with data of the proposed electrode for GA determination (Table 1). The proposed CGE is comparable in LOD and in linear range with reported ones. In some cases it had better characteristics.

Table 1
Some response characteristics of different modified electrodes for GA determination.

Electrode	Technique	Supporting electrolytes and working pH	Linear range	Detection limit (LOD)	Ref.
CPE modified with carbon nanotubes	DPV	Phosphate buffer solution, pH 2.5	0.5–15 μM	0.3 μM	[16]
CPE modified with multi-walled carbon nanotubes	DPV	Britton–Robinson buffer solution, pH 2	1.00–6.25 μM,	0.27 nM	[17]
Carbon–poly(vinyl chloride) composite electrode	DPV	Phosphate buffer solutions, pH 5.0	29 μg/L–0.45 mg/L	0.16 μg/L	[18]
Polyepinephrine/GCE	AdSV	Phosphate buffer solution, pH 1.88	1.0–20.0 μM	0.663 μM	[19]
Graphite modified with $[Cu_2tpmc](ClO_4)_4$ immobilized in PVC matrix	DPV	Nitric acid, pH 2	0.25–1 μM 5 μM–0.1 mM	0.148 μM	Proposed electrode

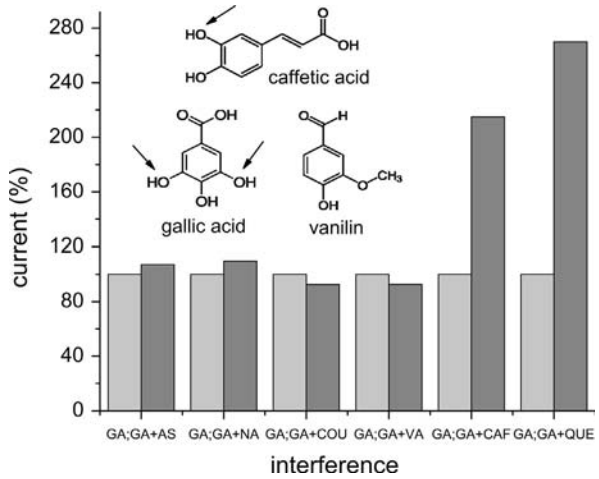


Fig. 7. Histogram of influence of the interfering compounds on current obtained for determination of GA under optimized experimental conditions. Some molecule structures are with and without electroactive OH^- groups.

3.6. Interference study

The potential interfering agents for electrochemical determination of gallic acid are phenolic acids, flavonoids and other organic molecules in minor amounts such as ascorbic acid. The studied compounds (ascorbic acid—AS, naringin—NA, *p*-coumaric acid—COU, vanillin—VA, caffetic acid—CAF and quercetin—QUE) were chosen due to differences and complexity in structure. The influence of possible interfering compound was examined by comparing peak current produced by GA and peak current of GA and studied compound mixture (1:1, concentrations of 10^{-5} M). Higher interferences were obtained in presence of caffeic acid and quercetin while the other substances (vanillin, naringin, ascorbic and *p*-coumaric acid) produced smaller change of the signal (Fig. 7). According to the literature [3,10], the first anodic peak could be ascribed to the oxidation of different polyphenolic compounds that had a structure with orthodiphenol (catechol) groups at B-ring, like catechin, gallic, caffeic, quercetin and some others.

3.7. Determination of the antioxidant capacity of the wine samples

In the present study, the estimation of the antioxidant capacity of the wine samples was based of gallic acid current oxidation using DPV technique. As the first anodic peak could be ascribed to the oxidation of different polyphenolic compounds present in wines that had a structure with orthodiphenol groups at B-ring, thus, these compounds were the major contributors to the antioxidant capacity in wine determined by electrochemical method. Five different wine samples were analyzed with proposed CGE. The results of antioxidant properties of the wine samples were presented as mg/L of GA calculated from calibration curve and presented in Table 2. The same wine samples were determined at a bare GCE by CV technique. The surface of GC was refreshed before each experiment because surface polymerization, while the same CGE electrode was used for all determinations. The total phenols were determined by Folin–Ciocalteu method and results were not comparable with those obtained by the electrochemical methods. The reason is detection of all phenols by spectrophotometric method (not only polyphenols with orthodiphenol groups at B-ring). Furthermore, F–C reagent may react with many non-phenolic organic substances (sugars, proteins, ascorbic acid, etc.) and inorganic substances (Fe(II), metabisulfite, sodium phosphite, etc.), giving an overestimation of the phenolic content [41].

Table 2
The antioxidant capacity of wine samples determined by electrochemical and spectrophotometric methods.

Samples	DPV on CGE (mg/L of GA)	CV on GCE (mg/L of GA)	F–C (mg/L of GA)
White wine	406.58	437.38	748.34
Rosé wine	406.58	445.20	671.75
Red wine 1	420.17	448.37	534.19
Red wine 2	365.76	368.99	578.88
Red wine 3	581.81	611.41	701.42

4. Conclusion

The application of complexation agent $[Cu_2tpmc](ClO_4)_4$ immobilized in PVC matrix as a modifier for coating graphite or classy carbon rod and the determination of gallic acid and antioxidative capacity of wine samples was presented in this paper. Electrode with synthesized macrocyclic complex showed the same effect on oxidation of polyphenols as a biosensors based on natural macrocycles in copper-containing enzymes. Electroactive $[Cu_2tpmcGA]^{3+}$ was used as a sensor material for determination of low concentrations of GA at simple coated CGE and CGCE by sensitive DPV technique. The practical usefulness of the CGE was demonstrated by the estimation of the antioxidant capacity, expressed as gallic acid equivalents, in white, rosé and red wine samples, using an extremely simple procedure without any sample pretreatment.

The proposed electrode had advantages such as simple preparation, good reproducibility and electrochemical surface stability. Its detection limit is quite comparable with reported modified and unmodified electrodes for determination of GA. CGE was chosen for real sample analysis due to better voltammetric response and lower LOD, which is 1.48×10^{-7} M. Still, we rightly assumed that application of more conductive polymer matrix coated on transducer surface could provide lower LOD of the electrode. Hence, the next task would be to find suitable and compatible CP for better adopting

of complexation agent $[Cu_2tpmc](ClO_4)_4$ and to provide electrode which might have better analytical characteristics.

Acknowledgment

Financial support for this study was provided by the Ministry of Education, Science and Technical Developmentof the Republic of Serbia, Projects Number 45022 and 172030.

Appendix A. Supporting information

Supplementary data associated with this article can be found in the online version at http://dx.doi.org/10.1016/j.talanta.2014.09.025.

References

[1] M Naczk, F Shahidi, J. Pharm. Biomed. Anal. 41 (2006) 1523–1542.
[2] C.A. Rice-Evans, B.J. Miller, G. Paganga, Free Radic. Boil. Med 20 (1996) 933–956.
[3] P.A Kilmartin, H. Zou, A.L. Waterhouse, J. Agric. Food Chem 49 (2001) 1957–1965.
[4] R.L.C Chen, C.H. Lin, C.Y. Chung, T.J. Cheng, J. Agric. Food Chem 53 (2005) 8443–8446.
[5] L.M. Magalhães, M. Santos, M.A. Segundo, S. Reis, J.L.F.C. Lima, Talanta 77 (2009) 1559–1566.
[6] M.S. Fernandez-Pachon, D. Villano, A. M Troncoso, M.C. Garcıa-Parrilla, Anal. Chim. Acta 563 (2006) 101–108.
[7] F. Berli, J. D'Angelo, B. Cavagnaro, R. Bottini, R. Wuilloud, M.F. Silva, J. Agric. Food Chem. 56 (2008) 2892–2898.
[8] X. Shao, L.S Lv, T. Parks, H. Wu, C.T. Ho, S.M. Sang, J. Agric. Food Chem. 58 (2010) 12608–12614.
[9] P.A. Kilmartin, H. Zou, A.L. Waterhouse, J. Agric. Food Chem. 49 (2001) 1957–1965.
[10] P.A. Kilmartin, H. Zou, A.L. Waterhouse, Am. J. Enol. Vitic 53 (2002) 294–302.
[11] M. Šeruga, I. Novak, L. Jakobek, Food Chem. 124 (2011) 1208–1216.
[12] P.A. Kilmartin, Antioxid. Redox Signal. 3 (2001) 941–955.
[13] A.J. Blasco, A. González Crevillén, M.C. González, A. Escarpa, Electroanalysis 19 (2007) 2275–2286.
[14] E. Giannakopoulos, Y. Deligiannakis, G. Salahas, J. Electroanal. Chem. 664 (2012) 117–125.
[15] S. Abbasi., A. Daneshfar, S. Hamdghadareh, A. Farmany, Int. J. Electrochem. Sci 6 (2011) 4843–4852.
[16] L.P. Souza, F. Calagari, A.J. Zarbin, L.H. marcolino-Junior, M.F. Begramini, J. Agric. Food Chem 59 (2011) 7620–7625 (J).
[17] S.M. Ghoreishi, M. Behpour, M. Khayatkashani, M.H. Motaghedifard, Anal. Methods 3 (2011) 636–645.
[18] M.M. Davila, M. Marino, F. Ahuatl, M. Elizalde, J. Mattusch, R. Wennrich, ESC Trans 3 (2006) 69–80.
[19] R. Abdel-Hamid, E.F. Newair, J. Electroanal. Chem. 704 (2013) 32–37.
[20] A. Abu Rabi-Stanković, Z. Mojović, A. Milutinović-Nikolić, N. Jović-Jovičić, P. Banković, M. Žunić, D. Jovanović, Appl. Clay Sci. 77–78 (2013) 61–67.
[21] A. Sánchez Arribas, M. Martínez-Fernández, M. Chicharro, Trends Anal. Chem. 34 (2012) 78–96.
[22] W. Ma, D. Han, S. Gan, N. Zhang, S. Liu, T. Wu, Q. Zhang, X. Dong, L. Niu, Chem. Commun 49 (2013) 7842–7844.
[23] X. Cetóa, J.M. Gutiérrezb, M. Gutiérrezc, F. Céspedesa, J. Capdevilad, S. Mínguezd, C. Jiménez-Jorquerac, M. del Vallea, Anal. Chim. Acta 732 (2012) 172–179.
[24] C.M.A. Brett, A.M.O. Brett, Electrochemistry—Principles, Methods and Applications, Oxford Science Publications, 1993.
[25] J. Yu, H. Ju, Electroanalysis 16 (2004) 1305–1310.
[26] R.S. Freire, N. Durana, L.T. Kubota, J. Braz. Chem. Soc 13 (2002) 119–123.
[27] S.A.S.S. Gomes, M.J.F. Rebelo, Sensors 3 (2003) 166–175.
[28] J. Abdullah, M. Ahmad, N. Karuppiah, L.Y. Heng, H. Sidek, Sensors 7 (2007) 2238–2250.
[29] S. Chandrasekhar, W.L. Wallz, L. Prasad, J.W. Quail, Can. J. Chem. 75 (1997) 1363–1374.
[30] E. Asato, H. Toftlund, S. Kida, M. Mikuriya, K. Murray, Inorg. Chim. Acta 165 (1989) 207–214.
[31] A Waterhouse,. Folin–Ciocalteau Micro Method for Total Phenol in Wine, (2009). (⟨http://www.waterhouse.ucdavis.edu/phenol/folinmicro.htm⟩).
[32] B.B. Petković, M. Milčić, D. Stanković, I. Stambolić, D. Manojlović, V.M. Jovanović, S.P. Sovilj, Electrochim. Acta 89 (2013) 680–687.
[33] A.V. Marenich, C.J. Cramer, D.G. Truhlar, J. Phys. Chem B113 (2009) 6378–6396.
[34] J. Wang, Analytical Electrochemistry, second ed., Wiley, 2000.
[35] G. Vučković, D. Opsenica, S.P. Sovilj, D. Poleti, M. Avramov-Ivić, J. Coord. Chem. 42 (1997) 241–251.
[36] S.P. Sovilj, G. Vučković, K. Babić, N. Matsumoto, M. Avramov-Ivić, V.M. Jovanović, J. Coord. Chem. 31 (1994) 167–179.
[37] A.M. Appel, R. Newell, D.L. Du Bois, M.R. Du Bois, Inorg. Chem. 44 (2005) 3046–3056.
[38] G.A. Bogdanović, Z.M. Miodragović, G. Vučković, R. Marković, A. Spasojević-de Bire, Synth. React. Inorg. Met.-Org. Chem. 31 (2001) 1189–1203.
[39] G. Vučković, M. Antonijević-Nikolić, T. Lis, J. Mrozinski, M. Korabik, D.D. Radanović, J. Mol. Struct. 872 (2008) 135–144.
[40] B. Yang, A. Kotani, K. Arai, F. Kusu, Chem. Pharm. Bull. 49 (2001) 747–751.
[41] A. Escarpa, M.C. González, Anal. Chim. Acta 427 (2001) 119–127.

Talanta 132 (2015) 520–527

Contents lists available at ScienceDirect

Talanta

journal homepage: www.elsevier.com/locate/talanta

A low-cost autonomous optical sensor for water quality monitoring

Kevin Murphy [a], Brendan Heery [a], Timothy Sullivan [a], Dian Zhang [a,b], Lizandra Paludetti [a,c], King Tong Lau [b], Dermot Diamond [b], Ernane Costa [c], Noel O'Connor [b], Fiona Regan [a,*]

[a] Marine and Environmental Sensing Technology Hub (MESTECH), NCSR, Dublin City University (DCU), Glasnevin, Dublin 9, Ireland
[b] CLARITY, Centre for Sensor Web Technologies, NCSR, Dublin City University (DCU), Glasnevin, Dublin 9, Ireland
[c] LAFAC Applied and Computational Physics Laboratory, University of São Paulo, Pirassununga, São Paulo 13635-900, Brazil

ARTICLE INFO

Article history:
Received 27 May 2014
Received in revised form
16 September 2014
Accepted 18 September 2014
Available online 7 October 2014

Keywords:
Optical sensor
Environmental monitoring
Low-cost sensors
Water quality
In-situ sensing

ABSTRACT

A low-cost optical sensor for monitoring the aquatic environment is presented, with the construction and design described in detail. The autonomous optical sensor is devised to be environmentally robust, easily deployable and simple to operate. It consists of a multi-wavelength light source with two photodiode detectors capable of measuring the transmission and side-scattering of the light in the detector head. This enables the sensor to give qualitative data on the changes in the optical opacity of the water. Laboratory tests to confirm colour and turbidity-related responses are described and the results given. The autonomous sensor underwent field deployments in an estuarine environment, and the results presented here show the sensors capacity to detect changes in opacity and colour relating to potential pollution events. The application of this low-cost optical sensor is in the area of environmental pollution alerts to support a water monitoring programme, where multiple such sensors could be deployed as part of a network.

© 2014 Elsevier B.V. All rights reserved.

1. Introduction

The monitoring of European water bodies has historically been limited but there has been a step change owing to the adoption of the Water Framework Directive (WFD) in Europe [1]. In response to this as well as other legislations including the Bathing Water Directive [2], the Birds Directive [3] and the Habitats Directive [4], the monitoring of water within Europe will increase in coming years. Additionally the pressures of climate change, which will lead to resource scarcity and water quality changes, give a strong scientific and economic argument for the expansion of aquatic monitoring. All of these factors will drive the increase in environmental monitoring by regulatory agencies, although it should be noted that the high cost associated with physical sample collection and the transportation to, and subsequent analyses in, laboratories is one of the reasons for the low level of monitoring over the years [5]. The precision and accuracy of these techniques, along with their adherence to standard techniques for legal and regulatory procedures has maintained the need for these methodologies. The initiative for more monitoring has not necessarily been matched by an increase in funding for these activities, which means that new technology should be employed to meet the desired increase in spatial and temporal monitoring.

The use of *in-situ* sensors, capable of continuously monitoring chemical and physical parameters, has been increasing in the recent past and offers a potential solution to some of the challenges outlined above. They can also provide real-time information and contribute to a better representation of long-term trends in aquatic environments [6]. It is now technologically conceivable to envision a network of sensors being deployed at key spatial locations, capable of autonomous operation in the field for a year or more and providing real-time alerts for key events [7]. The area of wireless networked sensors is fast becoming one of the most dynamic and important areas of multi-disciplinary research [8,9]. The communications and data gathering abilities of the network need to be of a high quality and suit the tasks at hand. The data from remote continuous monitoring of the environment can be, and is already being, used for a variety of applications, in addition to environmental protection [10,11]. Despite the promise of such a system many challenges remain using currently available technology, including a limitation in the analytes measurable, interferences, bio-fouling issues, expense, power requirements and the need for frequent calibrations. In essence the major issue for environmental sensing remains, in some instances, being able to accurately measure and detect environmental pollutants in laboratory conditions, but struggling to reproduce these results in the field with continuous *in-situ* monitors [12].

If these networks of sensors are to become not only a reality but commonplace it is necessary to produce reliable, inexpensive *in-situ* sensors. This means costs need to be considerably reduced

* Corresponding author.
E-mail address: fiona.regan@dcu.ie (F. Regan).

http://dx.doi.org/10.1016/j.talanta.2014.09.045
0039-9140/© 2014 Elsevier B.V. All rights reserved.

but also, and as importantly, retain and increase the accuracy of the measurements. Some of the recent developments in the this field have included *in-situ* fluorometers for the measurement of phytoplankton [13], chemical sensors for pH measurements [14], and the use of optical refractive index measurements for generic water event detection [15]. While some of these sensors are less precise than laboratory techniques or some existing continuous monitoring sensors they can produce extremely useful data. A barrier to deployment of successful monitoring networks up to now has been cost and availability of analyte specific sensors. The sensor described here proposes to address the cost issue – enabling the development of a low-cost network to provide valuable qualitative information on water quality that can lead to more informed decisions. These devices can be used to inform grab sampling and lead to the desired quantitative analytical approaches at appropriate times and locations. They can give indications of pollution, as early warning systems, or observe trends in environmental conditions.

This paper presents a low-cost, robust and easily deployable sensor for the monitoring of aquatic environments. This multi-wavelength optical sensor has been designed so that it can be operated on an autonomous basis or in a network of sensors and thus is equipped with telecommunications. The sensor is capable of measuring the transmission of light emitted by five separate LED light sources through water, while simultaneously measuring the side-scattering of the light measured at right angles to the transmission path. The optical colorimetric sensor (OCS) is devised to give data on bulk water property changes, particularly opacity and colour changes.

The OCS is not a turbidimeter or a chlorophyll sensor, though it can clearly provide valuable data relating to turbidity events and primary productivity events. The analytical objectives of the OCS are the determination of qualitative variations in water quality based on opacity or colour changes due to pollution events or temporal environmental events. By qualitative it is meant that the optical responses observed using the system are related to opacity changes in the aquatic environment. This qualitative response is confirmed by co-deploying and correlating the trends of the OCS with a sensor sonde measuring multiple environmental parameters over the test period. The target water quality parameters are water opacity based on transmission measurements of different coloured LEDs. The advantages over existing devices include its autonomous nature, low cost and environmental robustness that could lead to multi-sensor deployments for a sensor network. The device can be used to detect pollution events that result in an increase in suspended solids, algal blooms or other environmental events.

Commercial water sensing equipment, in the form of either multi-parameter sondes or single parameter sensors, dominate the environmental sensing market. The cost of these sensors can be prohibitive and when anti-fouling measures and logging systems are taken into the account purchase costs can be further elevated. All sensors require cleaning and maintenance at regular intervals by well trained personnel, which makes the cost of ownership sometimes prohibitively expensive – particularly during the summer. The OCS described here would reduce the purchase and maintenance costs of the sensor (including anti-fouling and logging systems). This makes it possible to build a sensor network over a large spatial area of an interesting aquatic system with a high spatial resolution thereby allowing for the creation of a real-time pollution alert system.

This paper is structured as follows; an introduction of the topic of low-cost optical monitoring in a marine environment is given in this section. The Experimental section gives the details of all the materials and methods used in the construction and testing of the sensor in the laboratory and in field deployments. The Results and discussion section analyses and presents the data gathered in the laboratory and in the environment and discusses the outcomes. The Conclusions section reviews the paper, highlighting the ability of the low-cost sensor to detect shifts in water colour and opacity in both the laboratory tests and field trials.

2. Experimental

This section describes how the optical sensor is designed and built, as well as outlining all key elements of the sensor. Sections 2.3 and 2.4 delineate the tests carried out both in the laboratory to characterise the sensor and the field trials undertaken to observe the performance under real-life conditions.

2.1. Materials

The photodiodes were manufactured by Texas Instruments (OPT101P) and were purchased from Farnell electronics (www.farnell.com), as was the Raspberry Pi (Model B) and its accessories. The LEDs were obtained from Radionics via RS-online (www.rs-online.com) and were manufactured by Avago Technologies (Amber; HLMP-3850), Kodenshi (IR; OPE5685) and Knightbright (Red; L-7113EC, Blue; L-53MBC and Green; L-7113VGCK). The Wixel module was from Pololu Robotics and Electronics and was purchased via Cool Components (www.coolcomponents.co.uk).

The PVC-U tubing for the body of the sensor, the stainless steel parts and the copper plating were acquired from local hardware and marine boating suppliers. The clamps and O-rings were purchased from Alfa Laval (http://www.alfalaval.com/). The enclosures for the electronics were obtained through Radionics Ireland and Dexgreen (http://www.dexgreen.com/).

The food dyes used were E133 Brilliant Blue FCF (blue), E124 Ponceau 4R (red), E102 Tartrazine and E142 Green S (green) and E110 Sunset Yellow (yellow), from Goodall's of Ireland. The two turbidity standards were a Formazin solution (246142) from HACH and a Styrenedivinylbenzene copolymer solution (6073G) from YSI (a Xylem brand).

2.2. Design and construction

The complete sensor system, illustrated in Fig. 1, has the following features: an LED array light source, two photodiode detectors (90° and 0° to the light source), a low cost (Table 1), a robust re-deployable design, flexible electronic control, in-built antifouling measures, optional GSM communications, an optional integrated temperature sensor and a custom built data logger. Table 1 gives a breakdown of the components cost at the time of manufacture.

2.2.1. Sensor body

The OCS is constructed using low cost, robust materials (stainless steel 308 and 304, PVC-U, copper, rubber and IP 67 and IP 68 rated enclosures). It consists of a stainless steel sensor head protected by copper, a foam-filled floatation chamber, double sealed electronics housing, stainless steel mooring point and ballast chain.

Fig. 1(a) gives an exploded view of the device with the numbering corresponding to Table 2 which lists all of the labelled components and materials. Fig. 1(b) presents a schematic of the sensor head showing the configuration of the LED array, along with relative locations of photodiodes. The OCS can be moored in various ways, including standalone (floating), buoy integrated or pier attached. The OCS is positively buoyant; with the ballast chain attached and connected as a single point mooring, it floats at the surface. In this configuration the sensing elements are submerged to a depth of 1 m, with the electronic and communication housing above the surface.

2.2.2. Sensor head design and Optics

The sensor head is the part of the sensor which houses the optics and the detection abilities of the sensor. As the sensor is

designed to be deployed in marine and other aquatic environments, biofilms will most likely form on all components [16]; to minimise this effect the sensor head is constructed of copper which has strong anti-fouling properties [17]. This includes a copper shroud around the light source and detectors and electroplating any exposed stainless steel housing with copper.

The schematic in Fig. 1(b) shows the sensor head consisting of a light source containing five LEDs of differing wavelengths: IR (λ_{PEAK}=850 nm, FWHM=45 nm), red (λ_{PEAK}=627 nm, FWHM=45 nm), amber (λ_{PEAK}=583 nm, FWHM=36 nm), green (λ_{PEAK}=515 nm, FWHM=30 nm) and blue (λ_{PEAK}=430 nm, FWHM=60 nm). The schematic also illustrates the configuration of the various LEDs within the array. Two silicon photodiode detectors (PDs), having a >20% efficiency spectral response ranging from 410 to 1080 nm, are used to detect the light. These photodiodes are placed at 90° and 0° to the optical path of the light emitted from the LEDs. The pathlength between the LED array and the 0° PD is approximately 6 cm, with the 90° PD placed 3 cm from the optical path at right angles to it midway along the path. This enables the transmission of light from multiple optical wavelengths through the water and the side-scattering of the light from the water (and from particulate matter in the water) to be measured simultaneously. The LEDs and the photodiodes are held in place by an epoxy resin and left exposed to the environment with no additional interfaces to the water; they are then encased within a piece of T-shaped copper tubing to prevent non-scattered light from entering the 90° PD. These specific LEDs have been chosen as they are readily and inexpensively available, while providing good coverage across the majority of the visible spectrum.

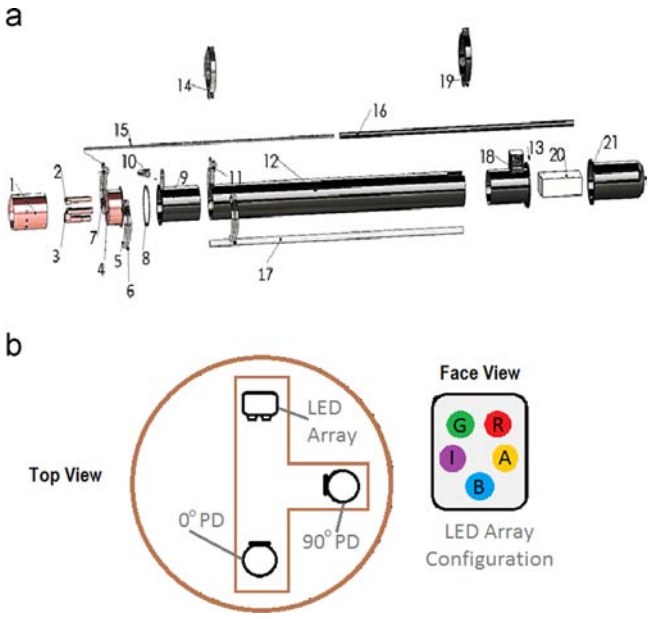


Fig. 1. (a) An exploded view of the mechanical components making up the sensor, with the numbering relating to Table 2. (b) Schematic of the sensor head showing the orientation of the LED array and photodiodes relative to each other and the configuration of the five LEDs (green [G], red [R], amber [A], blue [B] and IR [I]) within the array. (For interpretation of the references to color in this figure legend, the reader is referred to the web version of this article.)

Table 1
System component costs at time of manufacture (not including R&D costs).

Components	Approximate cost (€)
Mechanical	150
Opto-electronics	250
Logger box	150
Mooring	<100
Total	**<650**

2.2.3. Electronics

The OCS system is controlled by a Texas Instruments CC2511F32 micro-controller programmed in a variant of C. This is achieved using a Wixel, a general-purpose programmable module, mounted on a board with additional inputs and outputs. In the current configuration the sensor is programmed to read the signals from the two photodiodes for each LED and the ambient light level (*i.e.* the signal level for the photodiodes with all LEDs off) every 10 s. Light levels are recorded by the PDs connected via trans-impedance amplifiers to the 12 bit analogue to digital convertor of the microcontroller. Individual measurements are produced by averaging a number of readings, to reduce electronic noise. The data is outputted via an RS232 and captured by the logger detailed below. The system can be reprogrammed to use USB, GSM or low-power RF communications and to vary the optical sampling rate and sensitivity. A circuit schematic of the key components is shown in Fig. 2, including the Wixel, the LEDs, the PDs, the array of amplifiers and the power regulator.

The sensor can be powered from any rechargeable, on-board 6 V lead acid battery or using a power cable to connect the mains via an adaptor. During a measurement cycle the OCS draws approximately 250 mW of power while communication via GSM can draw up to 2.5 W. The system is programmed to sleep outside of the measurement and communication cycles, reducing the power consumption to below 1 mW. If the OCS is configured to measure and transmit, using GSM, every minute it can operate off battery power for approximately 85 h.

Table 2
Mechanical components list.

Part no. (Fig. 1)	Component	Material	Supplier
1	Detector shroud	Formed copper plate	Hardware store
2	Optical detector	Photodiodes in copper tube	Farnell Electronics
3	Light source	Five LEDs in copper tube	Radionics Ireland
4, 9, 14	Sensor housing & clamp	Copper plated stainless steel (308)	Hardware store
5,6,7,11	Clamp	Stainless steel (304)	Alfa Laval
8	O-ring seal	Rubber	Alfa Laval
10,13	Mooring point	Stainless steel ring	Boating supplier
12	Floatation chamber	PVC-U tube, foam filled	Hardware store
15	Reinforcing rod	Stainless steel (308)	Hardware store
16	Reinforcing rod sheath	Polythene tube	Hardware store
17	Electronics conduit	PVC tube	Hardware store
18, 19, 21	Electronics housing & clamp	Neptune 100 PVC enclosure (IP 68 rated)	Dexgreen
20	Electronics enclosure	ABS enclosure (IP 67 rated)	Radionics Ireland

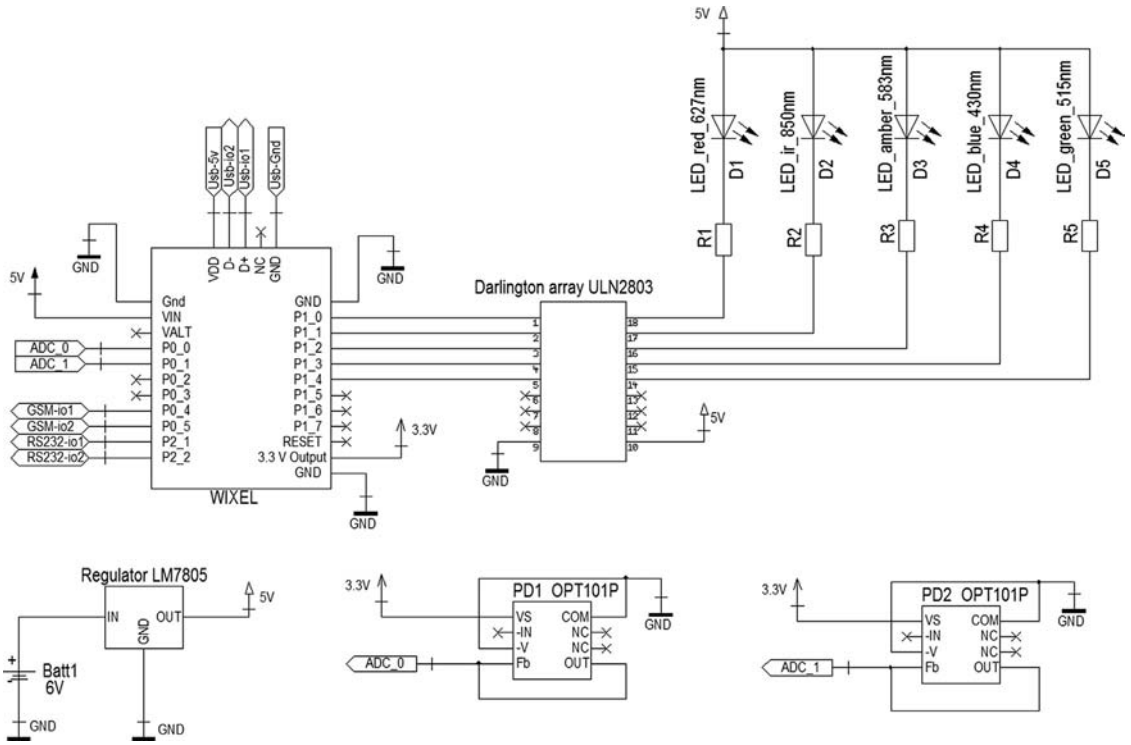


Fig. 2. A simplified circuit diagram showing the keys elements of the electronic control system for the sensor.

2.2.4. Data logger

To record the data obtained by the OCS a low-cost prototype data logger, based on an off-the-shelf single board computer (SBC) called "Raspberry Pi® (R-Pi)," was built. R-Pi consists of a 700 MHz ARM11 processor, Broadcom VideoCore IV GPU, 512 MB RAM, 2 × USB 2.0 ports, general purpose input–output (GPIO) interface, RJ-45 LAN connector and an SD card slot for on-board storage. The board can be powered by a 5 V DC power supply via a Micro USB or GPIO header. The power consumption of the R-Pi is 3.5 W maximum depending on the peripherals attached.

One limitation of the R-Pi is that it does not have a real time clock (RTC) module on-board; to solve this issue a RasClock® was purchased and installed on the R-Pi. The cost of the logger and its housing amounts to under €150, when all parts are purchased separately without economy of scale.

Fig. 3 shows the structure of the system. A data tunnel between the logger and OCS is established through a USB to Serial converter. The USB Wi-Fi access point (AP) allows the operator to download data onto a mobile device such as a smart phone or laptop wirelessly within a range of up to 45 m, through HTTP protocol. The unit is also compatible with a GSM/3G dongle, which can send data back to a data centre in real-time. In addition the data is saved onto the SD card on-board the logger. The R-Pi is powered by a 5 V external power source. The AP module (Edimax ew-7711uan) is powered directly from power supply to increase the system stability.

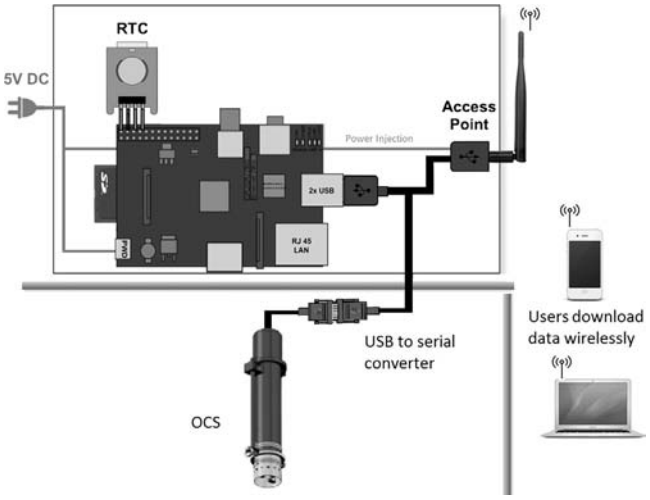


Fig. 3. Block diagram of the structure of the logger and its communication with the sensor and users.

2.3. Laboratory characteristics of the OCS

Communication between the computer and the laboratory test sensor was established using a terminal program, via a USB port. 230 V mains electricity was used as the power source via a 12 VDC convertor. The sensor was positioned in the sample solution and data logged via the PC terminal. All of the laboratory experiments were made using a black container in 1.5 L of water, as this covered the head of the sensor. The tests were performed in triplicate, collecting the data for 5 min, obtaining 25 measurements for each sample. Deionised water was used to dilute the food dyes and the turbidity standards.

In order to test the response of the sensor to different colours, food dyes were used in various concentrations diluted in water. Food dyes were chosen to mimic the colour effects of impurities in the water in an effective and cost efficient manner. All of the dyes listed above were extracted using an electronic micro-pipette and mixed with water in concentrations of 0, 10, 20, 30, 40, 50, 60 and 70 μL of food dye per L of water.

The effect of opacity on the sensor was also investigated. For these experiments turbidity standards were diluted in water and the turbidity of the sample was quantified. Inhomogeneous mixing of the turbidity standard in water necessitated that the turbidity

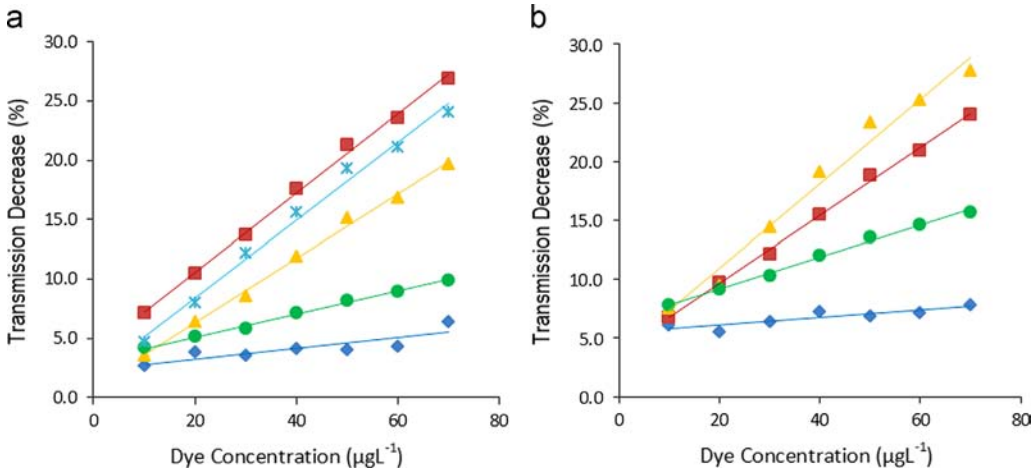


Fig. 4. Average attenuation data ($n=3$) recorded for the red (squares), amber (triangles), green (circles), blue (asterisk) and IR (diamonds) LEDs in the green dye solution for (a) 0° photodiode and (b) 90° photodiode.

level was cross-checked using a commercial turbidimeter (a TURB 430 IR/T from WTW). Five turbidity measurements were taken for each dilution and an average was calculated to give the final concentration. The concentrations of the standards prepared were 2.2, 3.1, 4.3, 5.2, 5.9, 8.1, 14.7, 21.4, 42.4 and 54.2 NTU.

2.4. Field deployments

Two sites in the Dublin vicinity have been used to perform field trials of the OCS; Malahide estuary (lat.: 53° 27' 14'', long.: −6° 9') and Poolbeg marina (lat.: 53° 20' 39', long.: −6° 13'). These trials have been carried out beside commercial sensors for turbidity, chlorophyll and other parameters to enable a true comparison of results and validation of the OCS.

In Malahide, north of Dublin city, the deployment took place in a typical estuarine body characterised by an elongated shallow channel. The inner estuary is fed with freshwater from a river and does not drain at low tides. The outer estuary is mainly influenced by the Irish Sea, which drains almost completely at low tides. The average water movement is towards the sea as with all estuaries, but it is a mixed estuary as the river flow is less dominant than the tidal flow. The main pressures affecting the estuarine catchment water quality is the presence of waste water treatment plants and sewer overflows.

Poolbeg Marina is in a busy port environment on the lower Liffey estuary, with the deployment site located in an area of less intense ship traffic. The topography of the estuary is heavily modified, being walled for its whole length and undergoing regular dredging. At the site the water depth is approximately 8 m and the width of the channel from wall-to-wall is approximately 260 m. The area acts as a buffer zone for the freshwater input from the river upstream and the tidal flow. Anthropogenic effects have an influence also, with the input of pollutants (run-off, storm drains, sewage treatment discharges, industrial discharges, port activity and recreational boating) and the modification of water flow (upstream dam releases).

The deployments at Poolbeg and Malahide consisted of the OCS and a commercial sonde which were deployed off a pontoon in the marina. The commercial system was a YSI sonde (V4 6600) and measured temperature, conductivity, pH, depth, chlorophyll, turbidity, dissolved oxygen and blue-green algae concentration. The OCS sensor and the YSI system were deployed at a depth of approximately 1 m.

3. Results and discussions

3.1. Laboratory tests

The results obtained from the laboratory tests on the food dyes and turbidity standards are presented here. The response of the OCS to water opacity trends, and hence water quality, can be observed by evaluating it with known turbidity standards in the laboratory and subsequently with a turbidity sensor in the field. Fig. 4 shows the percentage change in the optical signal recorded on the PD for each LED *versus* the concentration of colour dye, compared to water, with the ambient light subtracted to correct for light pollution and dark current effects. All of the proceeding results for the 90° PD exclude the blue LED data sets as the signal recorded by the photodiode for this particular LED is extremely weak and subject to large variations, producing potentially inaccurate data. The low light levels of the LED are exacerbated by the fact that the 90° PD universally returns a lower signal than the 0° PD due to the right-angled optical path and the blue LED is spectrally situated where the PD response is the weakest, meaning that a much lower percentage of the light is detected. It should be noted that the amber LED for the 90° PD can give a low signal level and thus a larger than average variance, but the results are included.

In Fig. 4 the response of the 0° PD to the increasing concentration of dye for the LEDs is shown to be linear. The R^2 value for the red, blue, amber and green LEDs is >0.99, with the R^2 value for the IR LED equal to 0.732. The results for the 90° PD are also quite linear with the R^2 value for the red, amber and green LEDs >0.98 and the R^2 value for the IR LED is equal to 0.781. These results highlight that, for the LEDs in the visible range the green is the most transmitted and the red and blue are the least transmitted, when the green dye is used, as expected.

The results from laboratory testing of the OCS with turbidity standards are presented in Fig. 5. The results for the green LED is depicted in Fig. 5, giving the change in optical signal for the (top) 0° PD and the (bottom) 90° PD. It was found that the performance of the OCS differs in its response to the turbidity standards compared to the food dyes. Fig. 5 shows that the response of the 0° PD to turbidity standards was similar to that of the food dyes. The other colour LEDs were also found to be transmitting less light to the PD with increasing concentration of turbidity standard. The results for the 90° PD, however, show a different reaction with a general growth in optical signal recorded for increasing

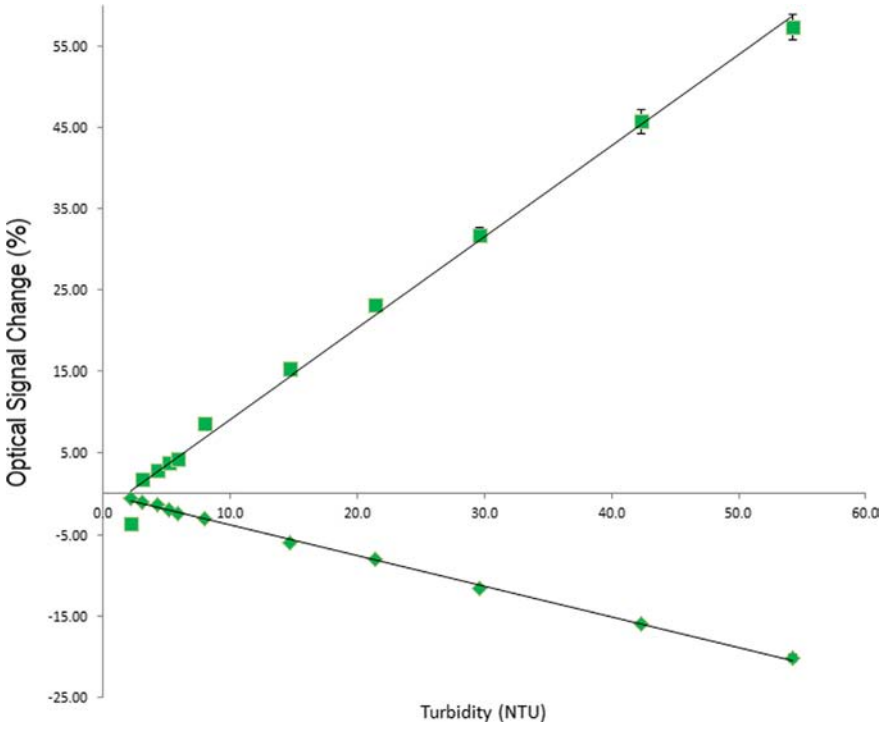


Fig. 5. Average signal response ($n=3$) of the green LED for varying concentrations of turbidity standards for both the 0° (diamonds) and 90° (squares) photodiodes.

concentration of turbidity standard. This figure shows that the response of green LED has a linear relationship with increasing turbidity standards for both the 0° ($R^2=0.9986$) and 90° ($R^2=0.9939$) PDs. This trend is evident also in the other colour LED results, although not in as significant a manner as that of the green LED.

The increase in signal in the 90° PD for turbidity (compared with a decrease for the dyes) is as expected and it indicates that the light is being scattered off particulate matter in the water and some of the side-scattered portion is subsequently detected by the 90° PD. It should be noted that at very low levels of turbidity (<5 NTU) the results become more unstable with standard deviations of greater than 5% being observed. Turbidity is used as a surrogate variable for suspended solids concentration [18] and the levels of both turbidity and suspended solids levels are important drivers of population, community and ecosystem level dynamics of phytoplankton and bacterioplankton in estuarine systems [19]. Sustained and sporadic increases in turbidity levels are associated with fluctuations in microbial populations and concentration of re-suspended contaminants such as heavy metals and other pollutants [20]. In a number of estuarine systems, strong correlations have been found between suspended particle concentration and the number of attached bacteria, an important parameter in estimating microbial population of bacteria such as *E. coli* and faecal coliforms [21]. Re-suspension of benthic sediment leading to higher turbidity levels can create elevated *E. coli* concentrations in estuarine waters.

3.2. Field deployments

During the deployment periods of the sensor in the field it was found that the system performed successfully in terms of measuring, acquiring and logging the data. The data logger recorded all the data onto the SD card while allowing it to be accessed also via Wi-Fi. Although other embedded systems, such as Arduino®, are widely used in marine sensor networks [22,23] the R-Pi provides much more functionalities than these traditional embedded systems. These include the supporting of Linux kernel-based operating systems which provides the capability of communication with a wide range of USB enabled or TCP/IP based devices and support for many programming languages such as C, C++, Java, and Python. The initial cost of R-Pi (€35) is higher than that of the Arduino® (€23–Arduino Due) but add-on devices for internal sensor communications and external data transmission are much cheaper, reducing the overall cost.

A drawback of the R-Pi is that it consumes more power (typically 700 mA) than that of some other embedded systems (as low as 100 mA) but due to its high processing capability only one logger unit would be required for a medium–large scale sensor network, lowering the overall power usage. The Raspberry PI also provides high computation capability which allows for raw sensor data to be processed on board. Anomaly detection and event detection could be performed on-site and alert messages would be sent to the base station only once outliers or abnormal events are detected. The raw sensor data could be stored on site and would not need to be transmitted to the base station. Using the two-way communication capability, the operator can query the raw data associated with the events detected; such a system would reduce the communication (data transmissions) costs which generally consume the majority of the power in a large scale wireless sensor network.

The performance of the sensor in an environmental setting provided further evidence of the ability of the OCS to measure colour and opacity changes in the water. The physical set-up of the light source and the detectors allows for various potential methods of determining turbidity and chlorophyll content, including spectral bands [24,25] and the ratios of the transmitted to side-scattered light detected by the PDs. In the laboratory studies it was found that the green LED gave the strongest signal and most significant response for water opacity and colour changes. Therefore the results presented relate to the green LED data, using two straightforward methods described below.

In Fig. 6, the turbidity recorded by the YSI sonde is shown along with a scaled version of the optical signal response recorded by the 0° PD for the green LED on the OCS. This illustrates clearly the inverse relationship between a rise in turbidity and a fall in optical

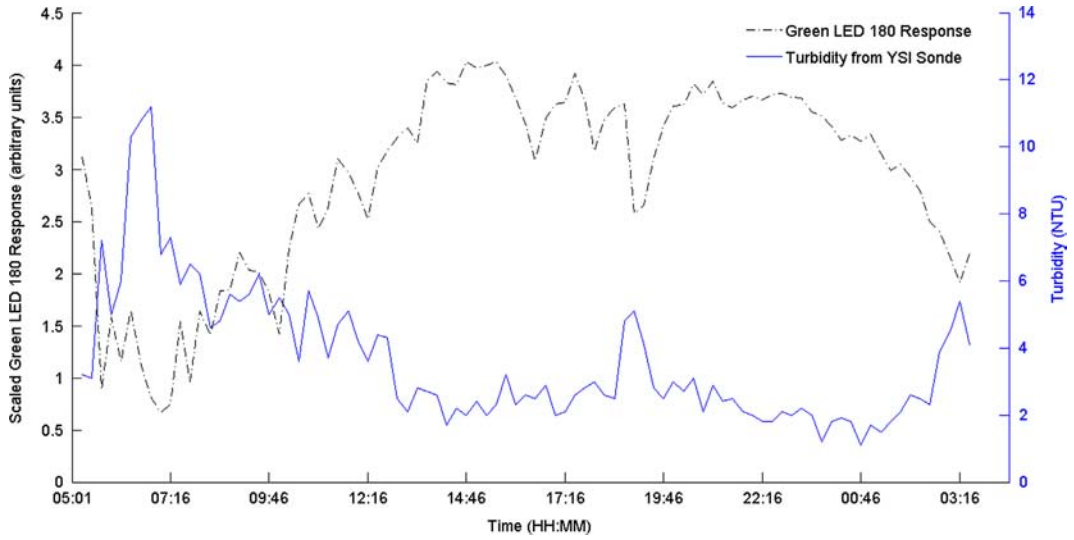


Fig. 6. Turbidity measured at Poolbeg marina by the YSI sonde (solid blue line) over a 26 h period, with the response of the 0° PD to the green led also plotted (dashed line). This response has been scaled to show it on the same plot. (For interpretation of the references to color in this figure legend, the reader is referred to the web version of this article.)

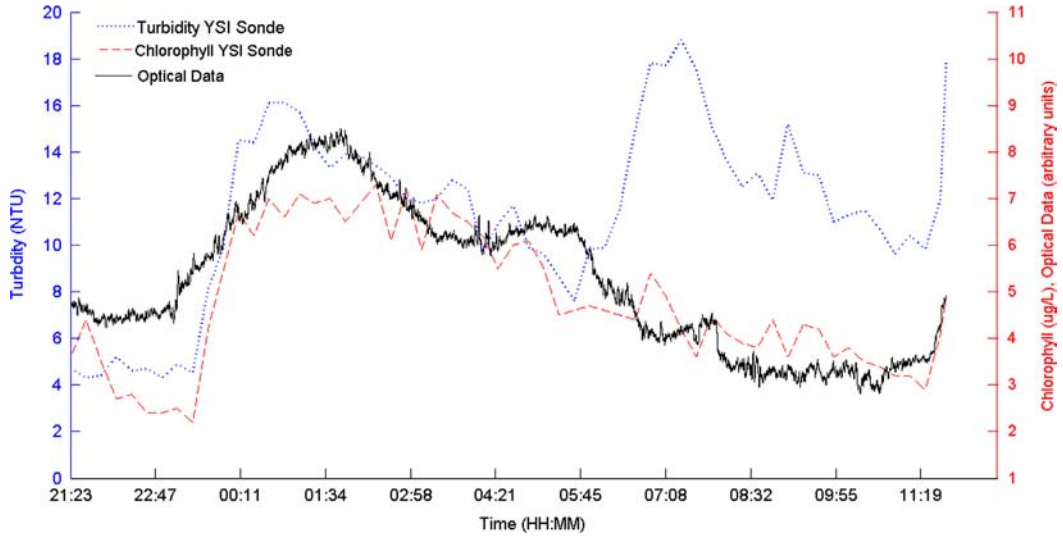


Fig. 7. Turbidity (dotted blue line) and scaled chlorophyll (dashed red line) measured at Malahide by the YSI sonde over a 14.5 h period, along with optical data from the green LED (solid black line). The method for calculating the optical data is given above. (For interpretation of the references to color in this figure legend, the reader is referred to the web version of this article.)

signal for the 0° PD, which is in agreement with the results obtained in the laboratory tests depicted in Fig. 5. The signal response has been corrected for ambient light and has been smoothed using a moving average filter. The optical signal response in Fig. 6 has been scaled and thus has arbitrary units. The correlation between the 0° PD response and the YSI measured turbidity was calculated using the Pearson method to be −0.8322.

The results shown in Fig. 7 illustrate how it may be possible to do the same for the assessment of colour presence in the water; here chlorophyll is used as an example. In Fig. 7 the turbidity and a scaled set of chlorophyll concentrations measured by the YSI sonde are given, along with optical data from the OCS. This data was recorded during the Malahide deployment and the section of the data displayed covers approximately 14.5 h. The optical data shown is for the green LED. The raw signal has been adjusted using the following calculation:

$$G_{\mathrm{LED}} = \left(\frac{G_{90} - D_{90}}{G_0 - D_0}\right) \times S,$$

where G_{LED} is the green LED result, G_0 and G_{90} are the optical signals for the green LED from the 0° and 90° PDs respectively, D_0 and D_{90} are the ambient light signals from the 0° and 90° PDs and S is a scaling factor.

Performing this has the effect of smoothing out the event driven spikes in turbidity, dominated by particulate matter, from the optical data, leaving a more stable signal; the residual optical data tracks the changes in the chlorophyll concentration. A question remains as to whether the parameter being represented by the optical data will always be a reliable indicator of chlorophyll. It is clear from the measurements that there is a relationship between this optical dataset and a surrogate chlorophyll value which gives an indicator of chlorophyll occurrence and variation. A Pearson correlation carried out on the residual optical data and the chlorophyll concentration measured by the YSI sonde gives a value of 0.8123.

Based on the results to date it is believed that this sensor could be employed, within a network of sensors, to identify event changes in the bulk water quality parameters, such as variations in water clarity and primary productivity-related turbidity. The low-cost

nature of the OCS means that multiple sensors could be deployed across a large area, with a high spatial density. It is envisaged that a small number of auto-samplers and/or more expensive, sophisticated sensors could be deployed in tandem with multiple low-cost OCS units to ground truth the data and verify the bulk water property changes. Alternatively the events detected by the low-cost sensor network could inform and drive the location and timing of manual grab sampling for laboratory analysis.

4. Conclusions

The design, building and operation of a low-cost, multi-wavelength optical system for water quality monitoring has been illustrated and described. The OCS is capable of measuring the change in optical signal along two different optical paths (transmitted and side-scattered). The performance of the system has been tested in the laboratory with food dye and turbidity standard solutions of varying concentrations. These results show strong linear correlations between the optical signal response and turbidity concentration, as well as colour change from the food dyes. The system was deployed in the field at different locations and the recorded data correlated well with commercial water quality sensors. The results from the field trials highlight that the system has the ability to detect both sudden and significant changes in water opacity arising from environmental events.

The work presented in this paper has outlined the first generation of the sensor development and results. Further work and potential adaptations are required to produce a sensor that can be easily and quickly calibrated in the field; along with more sophisticated data analysis, this will enable the sensor to produce the most desirable results from the data collected. In order to facilitate this, additional longer term deployments in test locations are planned. It is now possible to gather this type of data over a large spatial area, in real-time, at a reasonable cost; this would make these kinds of systems particularly attractive to lower income countries struggling with the effects of climate change and water related challenges. The intention is to commercialise the OCS as a real-time pollution monitoring system.

Acknowledgements

The authors acknowledge the funding of this research through the Beaufort Marine Research Award, carried out under the Sea Change Strategy and the Strategy for Science Technology and Innovation (2006–2013), with the support of the Marine Institute, funded under the Marine Research Sub-Programme of the National Development Plan 2007–2013 under grant BEAU/SENS/10.

Also, QUESTOR Research Centre under Grant DCU8/10/2013 and Science Foundation Ireland under grant 07/CE/I1147.

The authors also wish to thank the staff at Poolbeg and Malahide Marinas for permission, assistance and access to the deployment location and facilities. Some students have assisted in this work and deserve thanks, Matthew Meagher for producing drawings and Camilla Nardi Pinto for testing and calibration.

References

[1] European Water Framework Directive, Directive 2000/60/EC.
[2] European Bathing Water Directive, Directive 2006/7/EC.
[3] European Birds Directive, Directive 2009/147/EC.
[4] European Habitats Directive, Directive 1992/43/EC.
[5] D. Diamond, K.T. Lau, S. Brady, J. Cleary, Talanta 75 (3) (2008) 606–612. http://dx.doi.org/10.1016/j.talanta.2007.11.022.
[6] R. Greenwood, J. Webster, F. Regan, Royal Society of Chemistry Report 2007.
[7] J. Grath, R. Ward, A. Scheidleder, P. Quevauviller, J. Environ. Monit. 9 (11) (2007) 1162–1175. http://dx.doi.org/10.1039/B710665N.
[8] C. Albaladejo, P. Sanchez, A. Iborra, F. Soto, J.A. Lopez, R. Torres, Sensors 10 (7) (2010) 6948–6968. http://dx.doi.org/10.3390/s100706948.
[9] P.W. Rundel, E.A. Graham, M.F. Allen, J.C. Fisher, T.C. Harmon, New Phytol. 182 (3) (2009) 589–607. http://dx.doi.org/10.1111/j.1469-8137.2009.02811.x.
[10] S.M. Glenn, T.D. Dickey, B. Parker, W. Boicourt, Oceanography 13 (1) (2000) 24–34. http://dx.doi.org/10.5670/oceanog.2000.50.
[11] T.S. Moore, K.M. Mullaugh, R.R. Holyoke, A.S. Madison, M. Yucel, G.W. Luther III, Annu. Rev. Mar. Sci. 1 (2009) 91–115. http://dx.doi.org/10.1146/annurev.marine.010908.163817.
[12] W. Bourgeois, A.C. Romain, J. Nicolas, R.M. Stuetz, J. Environ. Monit. 5 (6) (2003) 852–860. http://dx.doi.org/10.1039/B307905H.
[13] T. Leeuw, E.S. Boss, D.L. Wright, Sensors 13 (6) (2013) 7872–7883. http://dx.doi.org/10.3390/s130607872.
[14] B.H. Tangena, et. al., Water Contamination Emergencies (2011), pp. 13–31 . 10.1039/9781849733199-00013
[15] A. Radu, S. Anastasova, C. Fay, D. Diamond, J. Bobacka, A. Lewenstam, Proceedings of the IEEE Sensors Conference, 2010, pp. 1487–1490. 10.1109/ICSENS.2010.5690357
[16] A. Whelan, F. Regan., J. Environ. Monit.8 (9) (2006) 880–886. http://dx.doi.org/10.1039/B603289C.
[17] L.D. Chambers, et al., Surf. Coat. Technol. 201 (6) (2006) 3642–3652. http://dx.doi.org/10.1016/j.surfcoat.2006.08.129.
[18] W.F. Henley, M.A. Patterson, R.J. Neves, A. Dennis Lemly, Rev. Fish. Sci. 8 (2) (2000) 125–139.
[19] N.K. Goosen, J. Kromkamp, J. Peene, P. van Rijswijk, P. van Breugel, J. Mar. Sys. 22 (2–3) (1999) 151–171.
[20] A. Tremblay, L. Varfalvy, C. Roehm, M. Garneau (Eds.), Environmental Science and Engineering Series, Springer, New York.
[21] Y.A. Pachepsky, D.R. Shelton, Crit. Rev. Environ. Sci. Technol. 41 (12) (2011) 1067–1110.
[22] N.W. Bergmann, M. Wallace, E. Calia, Proceedings of the Sixth International Conference on Intelligent Sensors, Sensor Networks and Information Processing (ISSNIP), 2010, pp. 19–24 . 10.1109/ISSNIP.2010.5706802
[23] J. Trevathan, et al., Sensors 12 (7) (2012) 9711–9748. http://dx.doi.org/10.3390/s120709711.
[24] A.A. Gilerson, et al., Opt. Express 18 (23) (2010) 24109–24125. http://dx.doi.org/10.1364/OE.18.024109.
[25] F.E. Hoge, R.N. Swift, Appl. Opt. 25 (15) (1986) 2571–2583. http://dx.doi.org/10.1364/AO.25.003677.

Talanta 132 (2015) 528–534

Contents lists available at ScienceDirect

Talanta

journal homepage: www.elsevier.com/locate/talanta

Anodic alumina coating for extraction of volatile organic compounds in human exhaled breath vapor

GuoJuan Zhang, LiangYuan Zou, Hui Xu *

Key Laboratory of Pesticide & Chemical Biology, Ministry of Education, Institute of Environmental Chemistry, College of Chemistry, Central China Normal University, Wuhan 430079, People's Republic of China

ARTICLE INFO

Article history:
Received 13 June 2014
Received in revised form
10 September 2014
Accepted 13 September 2014
Available online 5 October 2014

Keywords:
Anodic alumina
Fiber
Solid phase microextraction
Gas chromatography/mass spectrometry
Volatile organic compounds

ABSTRACT

The objective of the study is to develop a facile and highly sensitive solid phase microextraction-gas chromatography/mass spectrometry method for the analysis of volatile organic compounds in human exhaled breath vapor. For the purpose, a highly ordered nanoporous anodic alumina coating was prepared by a two-step anodic oxidization method based on aluminum substrate. To have a good knowledge of the fiber, some features were characterized and the results indicate that the coating has several advantages, including excellent chemical and thermal stability, high mechanical strength, large surface area and good extraction performance. In addition, some parameters related to extraction efficiency were also studied. Under the optimal conditions, the coating was used to quantitatively extract volatile organic compounds. Good linearity and wide linear range were obtained with correlation coefficients (R^2) ranging from 0.9933 to 0.9999. The detection limits of benzene homologues, aldehydes and ketones were between 0.7 and 3.4 ng L^{-1}. Relative standard deviations ($n=5$) ranged from 1.8 to 15.0%. Satisfied recovery (89–115%) was obtained at two spiked concentration levels. Finally, the developed method was successfully applied for the analysis of volatile organic compounds in human exhaled vapor samples of lung cancer patients and the controls, and the results were statistically analyzed with Independent-Sample *T* Test. The proposed method exhibits some outstanding merits, including convenience, non-invasion, low cost and sensitivity. It provides a potential tool for rapid detection of volatile organic compounds in human exhaled breath.

© 2014 Elsevier B.V. All rights reserved.

1. Introduction

As biological terminal metabolites, volatile organic compounds (VOCs), including olfactive and non-olfactive VOCs are the carriers of useful and significant bio-information [1–3]. They contain much important information linked to disease diagnosis [4,5], food security [6,7] and quality test [8]. However, due to its trace μg-to-ng concentration level with strong volatility and liquidity in complicated biological sample matrices, especially in gaseous matrix (air, exhaled vapor), sample preparation is of great necessity before quantitative analysis. The most common sample preparation approaches for VOCs in gaseous matrix are sorbent tube trap [9–11], fibers coated sorbent materials for solid phase microextraction (SPME) [12,13] and direct cryofocusing [14]. As to sorbent tube trap, needle trap is an emerging preconcentration method. It can be used for both active and passive sampling, and extraction capacity can be increased by adding the amount of sorbent inside the needle [15]. However, it is a tough and time-consuming work to pack the sorbent materials and the analytical performance heavily relays on sorbent materials [15,16]. With cooled preconcentration device using a liquid cryogen such as carbon dioxide or nitrogen, the method of cryofocusing can efficiently trap targets. But the disadvantages of high-cost and poor retention of ultra-volatiles limit its application [11].

SPME has been a powerful sample preparation method since introduced by Pawliszyn in the early 1990s, which combines sampling, extraction, pre-concentration and sample introduction in one step [17]. Owing to its time-efficient, simplicity, solvent-free, field usable and linkup with detection instruments (SPME-gas chromatography, SPME-high performance liquid chromatography and SPME-capillary electrophoresis), SPME has been broadly applied in different fields, such as environment [18], food [19], forensics [20] and pharmaceuticals [21]. This technique depends on distribution of analytes between sample matrix (or its headspace) and stationary phase, such as fiber coating. UP to now, some SPME coatings, including polydimethylsiloxane (PDMS), polyacrylate (PA), and some combinations such as PDMS/divinylbenze (DVB),

* Corresponding author. Tel.: +86 27 67867953; fax: +86 27 67867955.
E-mail address: huixu@mail.ccnu.edu.cn (H. Xu).

http://dx.doi.org/10.1016/j.talanta.2014.09.035
0039-9140/© 2014 Elsevier B.V. All rights reserved.

carboxen (CAR)/PDMS, DVB/CAR/PDMS, carbowax (CW)/DVB and CW/template resin, have been applied to commercial SPME fibers [22]. However, they suffer from the drawbacks of high cost and instability at high temperature, for example, the maximum temperature for 100 μm PDMS is 280 °C, 65 μm PDMS /DVB is only 270 °C. The substrate for most commercial fibers is fused silica, which is fragile and should be treated with great care, its lifetime is therefore limited. In addition, the kinds of coating materials for commercial SPME fibers are numbered, restricting the wide application of SPME [23].

In this regard, a number of researches have been devoted to the development of new fiber coating. New materials utilized in fiber coating for SPME include zinc oxide nanorod [6], porous anodized alumina [24–26], molecularly imprinted polymer [27], polymeric ionic liquid [28], metal–organic framework [29] and carbon materials [30]. Of which, nanoporous anodized alumina, a kind of aluminum (Al)-substrate inorganic nanomaterial has attracted increasing attention in recent years, owing to its remarkable properties such as chemical, thermal stability and high surface area. Nanoporous anodic alumina (NPAA) with one dimensional nanostructure is made up of some parallel cylindrical nanopores which are vertical to the surface of Al substrates [31]. It can be obtained by a two-step anodic oxidation method. Pore structures are tunable by changing the anode voltage, anodic oxidation time or electrolyte [31–33]. It has been widely used in different fields, such as the template material for the fabrication of other nanostructured arrays nonmetals [34], the support of sensors [35], functional electrodes [36] and filtration [37]. Due to high surface area, NPAA has drawn the attention of chemists for gas absorption material [24,26]. Li and co-workers fabricated NPAA fibers and applied for the analysis of VOCs in plants [24]. However, to our knowledge, nothing has been reported on the utilization of NPAA coated fibers for the adsorption of VOCs in human exhaled breath vapor (EBV).

Exhaled breath analysis has been one of the important diagnostic methods because of its safety, low cost and non-invasive nature [38,39]. However the sample matrix of human EBV is complex, the existence of nitrogen, oxygen, carbon dioxide, inert gases and water [38,40] may seriously interfere with the analytical signal.

In this work, a simple, rapid, low-cost and sensitive solid phase microextraction–gas chromatography/mass spectrometry (SPME–GC/MS) method was proposed and validated for the analysis of VOCs in human EBV. For the purpose, a highly ordered NPAA SPME fiber coating was fabricated on aluminum substrate by a two-step anodization strategy. VOCs studied in our work include benzene homologues, aldehydes and ketones. Some features of fiber including morphology, extraction selectivity and durability were investigated. Parameters related to extraction and desorption performance were optimized systematically. Finally, the developed method was applied for the quantitative analysis of VOCs in EBV of lung cancer patients and the healthy volunteers.

2. Materials and methods

2.1. Chemicals and materials

Ethanol (HPLC grade) was purchased from Biologic-Reagents (USA). Benzene (99.5%), octanal (98%), undecane (99%), 2-heptanone (98%) and 2-pentanone (99%) were provided from TCI Development Co. LTD (Shanghai, China). Pentanal (98.5%) and ethylbenzene (99.7%) were obtained from Amethyst Chemicals (Beijing, China). Hexanal (98%) and heptanal (97%) were bought from ABCR GmbH & Co. KG (Germany). Decane (99.5%) was purchased from Dr. Ehrenstorfer GmbH (Germany). Nonanal (97%), 2-methylvaleraldehyde (98%) and 2-ethylbutanal (97%) were purchased from Alfa Aesar (Tianjin, China). Oxalic acid, acetone, sodium hydroxide, phosphoric acid, chromium trioxide and perchloric acid were analytical reagent-grade and provided by Sinopharm Chmical Reagent Co. Ltd (Shanghai, China). Ultra-pure water was used in all experiments (arium® pro Ultrapure Water Systems, Sartorius Stedim Biotech, Gottingen, Germany). Five microliter microsyringe was bought from Feige, China. Aluminum wire (99.999% purity, 0.25 mm diameter, annealed) was purchased from Beijing Jiamingboye Yousejinshu Co. Ltd (Beijing, China). Gas-tight syringe (10 mL) was purchased from Agilent Technologies Inc (USA).

2.2. Standard solution and gas calibration sample

Stock solution of 8 analytes (benzene, pentanal, 2-pentanone, hexanal, heptanal, 2-heptanone, octanal and nonanal) was prepared in ethanol at 1650 μg mL^{-1}, stock solution of internal standard (IS, 2-methylvaleraldehyde) was prepared in ethanol at 1650 μg mL^{-1}. In order to investigate extraction selectivity, stock solution of 5 analytes (pentanal, hexanal, heptanal, octanal and nonanal) and stock solution of 7 analytes (2-ethylbutanal, 2-methylpentanal, hexanal, 2-heptanone, heptanal, decane and undecane) were prepared in ethanol at 1650 μg mL^{-1}, respectively. The daily standard working solutions were prepared by diluting the corresponding stock solution. All of them were stored at −20 °C in the dark. The mixed gas calibration samples, involving 8 analytes and known concentrations of IS (5 ng mL^{-1}) were prepared by direct vaporization of 2.0 μL working solution in a 25 mL evacuated sealed vial in water bath (50 °C, 20 min).

2.3. Preparation of NPAA fiber

NPAA fiber was prepared as described in previous literature [24] with a minor modification. The steps are as follows: (1) A straight aluminum wire with the length of 17.0 cm was ultrasonically washed with acetone and ultrapure water for 20 min. (2) To get a fresh aluminum surface, the wire was immersed in a 0.1 mol L^{-1} sodium hydroxide solution until many bubbles were produced. Then it was electropolished under the constant voltage of 9 V in a mixture solution of perchloric acid and ethanol (1:5, v/v) for 1 min, and ultrasonic cleaning in ultrapure water was followed to make the surface smooth. (3) With aluminum wire as anode and graphite bar as cathode, the first anodic oxidization was carried out at a constant 45 V voltage in 0.3 mol L^{-1} oxalic acid solution (10 °C, vigorous stirring), and the process lasted for 2 h. (4) The tip 2 cm of the oxidized aluminum wire was soaked in a mixed acid (6% phosphoric acid + 1.8% chromic acid, 70 °C) for 90 min and ultrasonically cleaned with ultrapure water to get a rough and uneven aluminum matrix. (5) Under the same conditions as step 3, the anodization process was repeated for another 6 h. (6) The prepared fiber was dried in an air tight bag containing desiccant for 10 h (room temperature) and conditioned at GC injector for 30 min with the temperature programming from 65 to 265 °C at a rate of 20 °C min^{-1} and hold at 265 °C for 20 min.

2.4. SPME procedure

The prepared SPME fiber with the effective length of 1.5 cm was installed into a home-made SPME holder (5 μL microinjector) according to literature [17]. Before every usage, the fiber was inserted into GC injector to condition for 20 min (265 °C) in order to remove the possible residues. During exposure, 2 μL working solution was injected into a 25 mL sealed glass vial with a PTFE-lined septum cap, and evaporated in water bath (50 °C, 20 min). Then, the conditioned NPAA SPME fiber coating was pushed out from the holder cartridge and exposed for an appropriate time.

At the end of extraction, the fiber was retracted into needle and injected immediately into GC for thermal desorption at 265 °C for 6 min.

2.5. Instrumentation

The GC–MS QP2010 Plus system (Shimadzu, Japan) coupled with a split/splitless injector was employed for all chromatographic analysis experiments. The mass spectrometry was operated in EI mode at 70 eV. All separations were carried out on a CP-Pora bond Q column (30 m × 0.32 mm × 0.5 μm, Varian Chrompack, USA). Helium was used as carrier gas at a constant velocity of 1.62 mL min^{-1}. GC oven temperature was programmed as follows: initially maintained at 80 °C for 2 min, then up to 140 °C at a rate of 8 °C min^{-1} and held for 2 min, subsequently programmed at 5 °C min^{-1} to 250 °C and held for 12 min. The transfer line and the ion source temperatures were set at 250 °C and 200 °C, respectively. Data acquisition was performed in selected ion monitoring (SIM) mode. The qualitative ions for each analytes were as follows, benzene: *m*/*z* 77, 52; 2-pentanone: *m*/*z* 86, 41; pentanal: *m*/*z* 41, 58; hexanal: *m*/*z* 41, 56; 2-heptanone: *m*/*z* 58, 71; heptanal: *m*/*z* 41, 70; octanal: *m*/*z* 41, 56; nonanal: *m*/*z* 41, 56.

Surface morphology of the proposed fiber was obtained by scanning electron microscope (SEM, JEOL, JSM-6700F, Japan).

2.6. Breath sample collection

Before collection, all Tedlar® bags were cleaned by flushing with nitrogen gas and then filled with nitrogen and heated at 70 °C for 10 h to get rid of any contaminations. Breath samples, involving ten lung cancer patients (Hubei Cancer Hospital, Hubei, China) and ten healthy volunteers (Central China Normal University, Hubei, China) who had fasted overnight were collected in a 1 L Tedlar® bags through a disposable mouthpiece. Then, a 25 mL sample was transferred into a crimped and evacuated glass vial by a gastight syringe.

2.7. Statistical analysis

The samples of controls and patients were statistically analyzed with Independent-Sample *T* Test (*t*-test) by SPSS statistics version 19.0.0 (IBM, New York, NY, USA). The level of significance was determined by two-sided test. A *P* value of < 0.05 was considered statistically significant.

3. Results and discussion

3.1. Preparation and characterization of the fiber

3.1.1. Fabrication of NPAA coating

During the anodizing of metal aluminum wire, two different kinds of films, namely barrier-type oxide films and porous oxide film were generated, of which, the formation of porous oxide layer is a self-organized process [41]. Due to the volume expansion of alumina at the metal/oxide interface, tensile stress which creates repulsive force between the neighboring pores is generated. Moreover, the compressive stress makes the steady-state oxide grow upward in the vertical direction [42,43]. As a result, the porous oxide layer covers all of metal aluminum surface. The whole course is heavily controlled by the type of electrolyte, re-anodization time and anodizing voltage, especially anodization time, because the preparation of anodic alumina is the result of dynamic equilibrium between the oxide growth and the oxide dissolution [43].

In this work, to achieve better extraction efficiency, re-anodization time (4 h, 6 h, 8 h, 11 h) were investigated. The results indicated that extraction efficiency increased with time and reached to the maximum at 6 h, then followed with a plateau. Because the thickness of fiber coating increases with the re-anodization time, better surface morphology and extraction efficiency can be obtained [43]. The stable extraction efficiency after 6 h is ascribed to dynamic equilibrium between the oxide growth and the oxide dissolution. Therefore, 6 h was chosen to be the optimal re-anodization time of the potential application.

3.1.2. Morphology of coating

To obtain the morphology of the prepared fiber, scanning electron microscopy (SEM) analysis was carried out in our work. The anodic alumina is a kind of one dimensional nanomaterial. As shown in Fig. 1(A), the surface of the fiber is almost covered with series of parallel cylindrical nanopores. The uniform nanopores are about 50 nm in diameter, which can provide a relatively large specific surface area for extraction. From Fig. 1(B), we can see that they are perpendicularly grown on the surface of aluminum wire and parallel to each other. The thickness of the coating is about 20 μm. The results indicated that a highly order nanoporous anodic alumina fiber was successfully prepared. The fiber with high area-to-volume ratio can provide abundant adsorption sites for extraction and facilitate fast mass transfer.

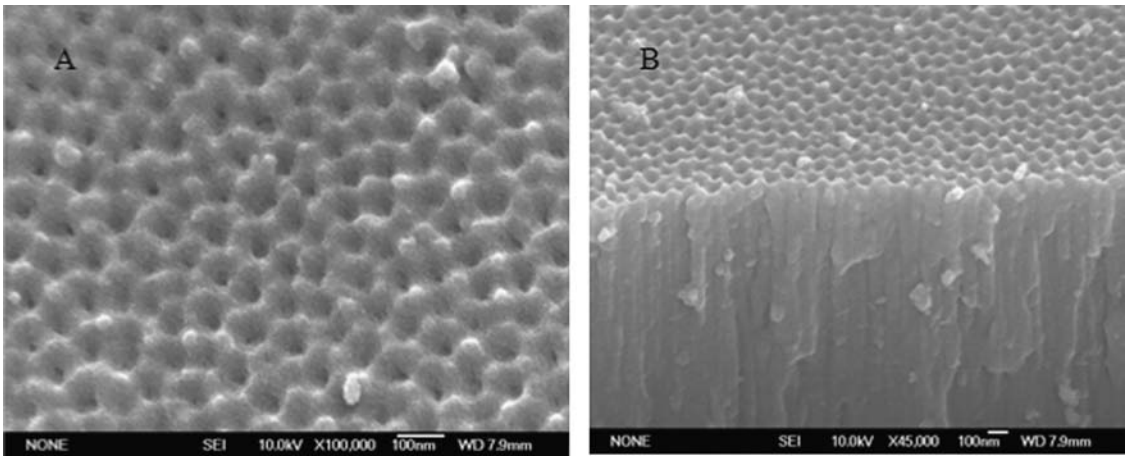


Fig. 1. Scanning electron microscope images of NPAA fiber: (A) top view, 100,000 × ; (B) cross-section view, 45,000 × .

3.1.3. Extraction selectivity

To study the extraction selectivity of the NPAA fiber, enrichment factors (EFs) of five straight chain aldehydes, including pentanal, hexanal, heptanal, octanal and nonanal were investigated with the NPAA coating as extraction phase by direct injecting of 1 μL solution, whose concentration was the same as that of gas calibration samples. EF is defined as the ratio of the peak area of the extracted gaseous analytes to that by direct injection of liquid solution. Octanol-water partition coefficient, log*P* is related to the polarity of analytes and used as an indicator for hydrophobicity. The higher log*P* means the weaker polarity of analytes. The polarity of compound decreases with the growth of carbon chain. The alumina coating is hydrophilic [37], thus, the compound with the strong and medium polarity can be easily captured by the hydrophilic coating. In the study, we find that the value of log*P* increases with the growth of the carbon chain length of aldehyde molecules (from 1.44 to 3.56, not shown), while EFs gradually reduce from pentanal to nonanal (Fig. 2A). In addition, with the increasing of carbon chain, the volatility of analytes decreases, thus the amount of analytes captured by NPAA coating lessens.

Then, EFs of the following two groups of isomers were also studied to evaluate the effect of analyte structure on the extraction selectivity of fiber: (a) 2-ethylbutanal, 2-methylpentanal, hexanal; (b) 2-heptanone, heptanal. The results in Fig. 2B indicate that isomers with larger log*P* values usually have smaller EFs. For example, the EF of hexanal (log*P*, 1.97) is lower than those of 2-ethylbutanal (log*P*, 1.78) and 2-methylpentanal (log*P*, 1.78). Similar result is obtained for heptanal (log*P*, 2.50) and 2-heptanone (log*P*, 1.97). The results indicate that the analyte structure, such as carbon chain and isomerizaiton can directly affects the polarity of analyte and further the extraction selectivity of fiber. From Fig. 2B, we also can find that the EF values of aldehydes and ketones are much higher than that of the *n*-alkanes. The better extraction selectivity to aldehydes and ketones mainly results from their lower log*P* and the relatively strong Lewis acid-base interaction where aldehydes and ketones (electron-pair donor) are acted as Lewis base and the Al surface provides Lewis acid sites [44]. The results indicate that the NPAA fiber is suitable for the extraction of polar and volatile compounds.

3.1.4. Fiber durability

Fiber durability is an important issue when the material is used as extraction phase. It was studied by investigation of the mechanical strength, thermal and chemical stability, and lifespan of the NPAA fiber. Aluminum substrate can provide better mechanical strength than silica substrate, which is commonly used in commercial SPME fiber. And the in-situ anodized alumina is hardly stripped from the substrate when compared with other coatings. In addition, the inorganic oxide coating fiber has relatively better thermal and chemical stability [44] compared with polymer and organic coating prepared by sol–gel or electrodeposition methods. To investigate the reusability of the fiber, numerous extraction-desorption-conditioning cycles were carried out at the VOCs concentration of 5 ng mL^{-1}, and the peak signal was recorded. The results in Fig. 3 indicate that there is no significant difference in extraction efficiency of the NPAA fiber after 140 replicate extractions. Excellent thermal, chemical and mechanical stability and long lifespan (over 140 times usage) demonstrates the robustness of the fiber. Besides the excellent durability, low cost and high precision are also the remarkable advantages of the fiber for analytical application.

3.2. Selection of SPME conditions

The prepared nanoporous fiber was used to extract VOCs, several parameters closely related to extraction performance, such

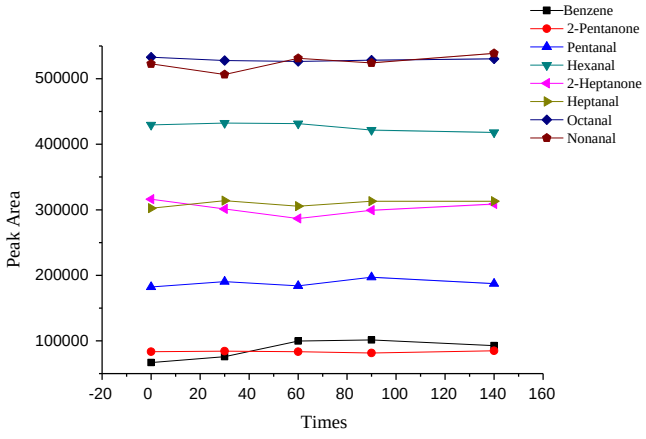


Fig. 3. Use times of the fiber, conditions: concentration of the analytes, 5 μg L^{-1}; extraction temperature, 50 °C; extraction time, 20 min; desorption temperature, 265 °C; and desorption time, 6 min.

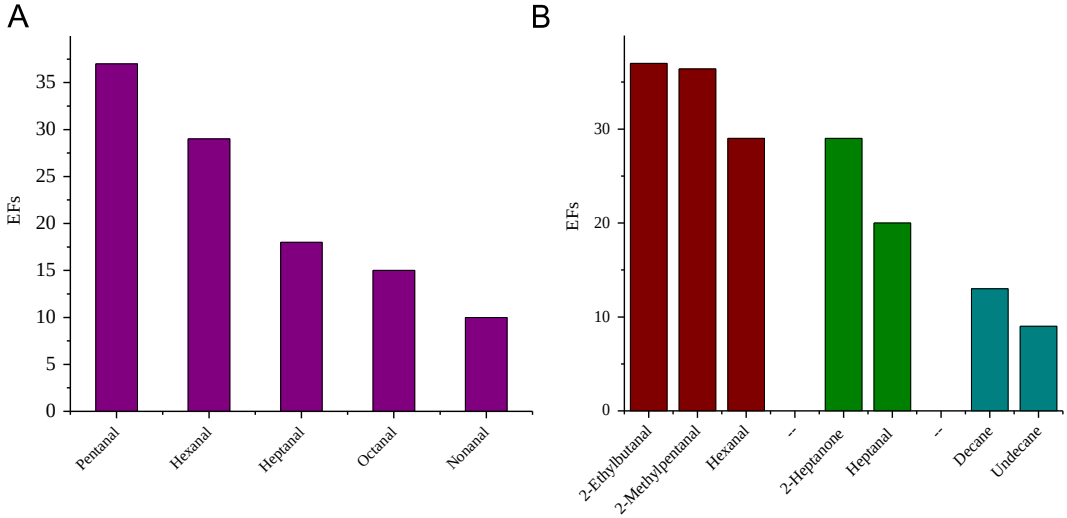


Fig. 2. Extraction selectivity of NPAA SPME fiber coating toward different analytes. (A) five straight chain aldehydes. (B) two groups of isomers and a group of homologous compounds.

as desorption temperature and time, extraction temperature and time were optimized systematically.

In order to achieve better desorption efficiency, thermal desorption temperature was investigated in the range of 230–275 °C. The result in Fig. 4A indicates that the best desorption temperature is 265 °C. Complete desorption can be realized at high desorption temperature. It will take a long time to desorb analytes from the NPAA fiber at low desorption temperature. Thus, the desorption temperature for subsequent experiments was set at 265 °C.

For SPME-thermal desorption model, carryover effect can affect the repeatability of analytical method. Even though desorption is carried out at elevated temperatures, carryover may still exist. Therefore, a relative longer desorption time should be required.

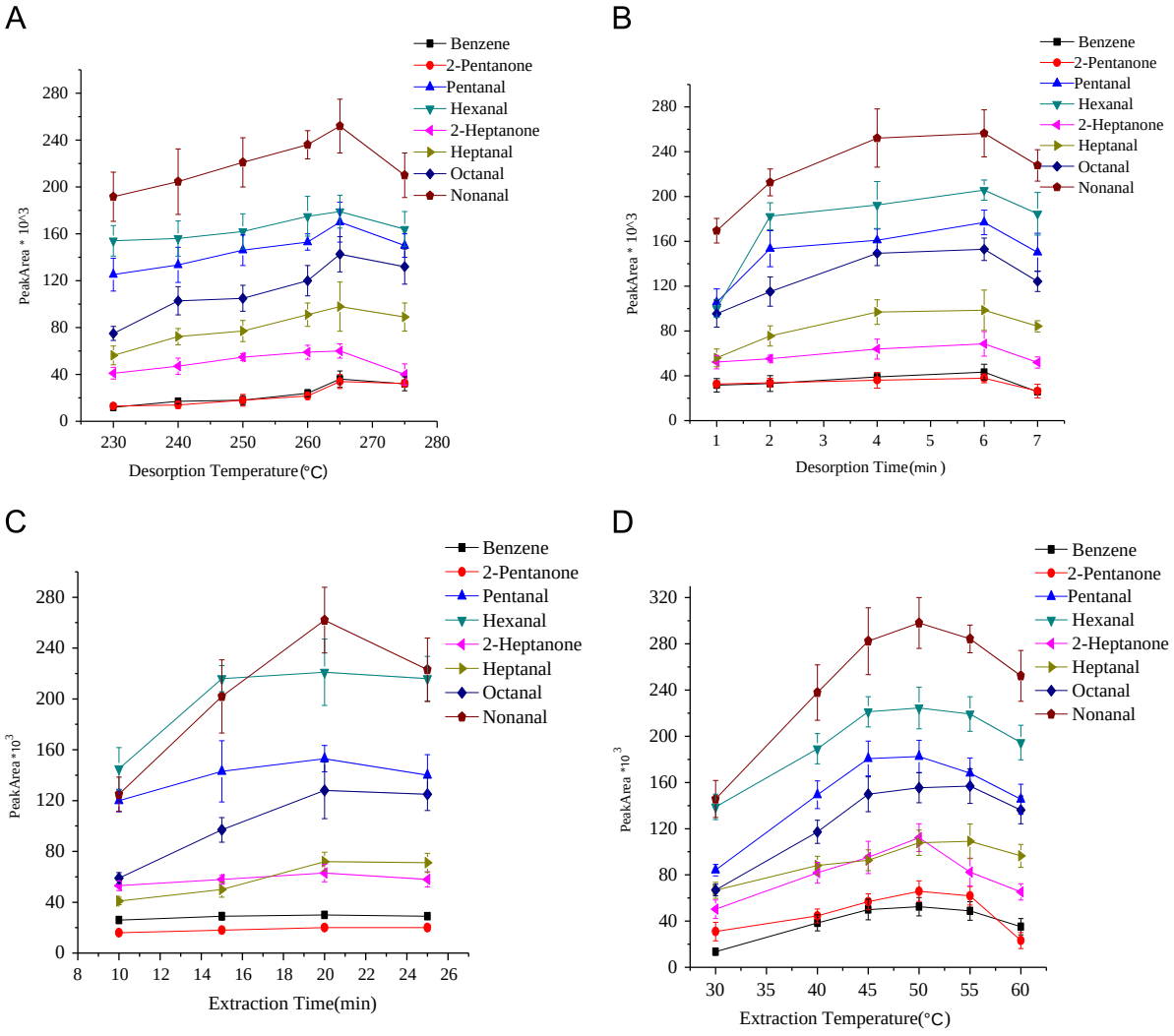


Fig. 4. The selection of (A) desorption temperature, (B) desorption time, (C) extraction time and (D) extraction temperature, concentration of the analytes: 2 μg L^{-1}.

Table 1
Correlation coefficients (R^2), linear ranges, limit of detection (LOD), relative standard deviation (RSD) and recovery of the method.

Analytes	R^2	Linear range (μg L^{-1})	LOD (ng L^{-1})	RSD (%)												Recovery (%)	
				One fiber (n=5)						Fiber-to-fiber (n=5)							
				Intra-day SpikedConc (μg L^{-1})			Inter-day SpikedConc (μg L^{-1})			Intra-day SpikedConc (μg L^{-1})			Inter-day SpikedConc (μg L^{-1})			SpikedConc (μg L^{-1})	
				10	0.1	0.01	10	0.1	0.01	10	0.1	0.01	10	0.1	0.01	1	10
Benzene	0.9933	0.005–10	1.7	13.4	12.4	8.0	3.2	8.9	4.9	9.9	9.5	2.2	8.1	7.0	6.4	94	95
2-Pentanone	0.9998	0.005–40	0.7	11.7	10.0	11.9	4.1	8.0	6.1	6.3	10.8	13.8	7.2	15.0	6.8	114	113
Pentanal	0.9999	0.005–40	1.0	5.8	10.4	3.5	8.1	11.2	12.9	13.8	5.7	11.1	13.9	14.0	9.7	90	97
Hexanal	0.9997	0.005–40	0.7	9.0	3.8	8.3	2.9	8.8	10.9	13.4	9.6	12.0	5.7	9.0	13.4	115	108
2-Heptanone	0.9996	0.005–30	3.3	6.9	9.5	6.1	13.5	5.8	11.3	10.3	6.7	15.0	11.9	4.7	9.2	109	104
Heptanal	0.9999	0.005–30	1.0	8.6	9.8	3.9	9.5	7.0	12.1	14.2	3.0	9.9	10.6	5.3	6.2	114	111
Octanal	0.9988	0.005–40	3.4	8.4	10.9	7.7	10.8	7.5	13.1	13.1	8.4	9.6	14.1	13.4	11.1	102	110
Nonanal	0.9999	0.005–40	1.1	10.4	10.7	1.8	13.5	12.8	10.9	6.3	11.7	12.4	13.0	8.6	11.0	91	89

In this work, thermal desorption time ranging from 1 min to 7 min was investigated. As shown in Fig. 4B, the best desorption time is 6 min. And we also studied the desorption efficiency of the nanoporous fiber, the results showed that after 6 min nearly all of the adsorbed analytes could be desorbed from the fibers. Hence, thermal desorption time of 6 min was selected for the following experiments.

Solid phase microextraction is an equilibrium-based process. Extraction time, a key factor in SPME is closely related to extraction efficiency. The selection of extraction time has direct impact on the sensitivity and repeatability of the proposed analytical method. The influence of the extraction time on extraction efficiency was studied at 10, 15, 20 and 25 min. The extraction time profile is shown in Fig. 4C. We can find that extraction efficiency increases with time within 20 min and slightly decreases in 25 min. Thus, the extraction time of 20 min was selected for the following studies. The relatively short equilibration time is attributed to the porous structure of the NPAA fiber which accelerates mass transfer from and to fiber.

Generally, high temperature can enhance distribution velocity, which is benefit for the diffusion of gaseous analytes to fiber, thereby improving extraction ability of SPME. But adsorption is an exothermic process, high temperature will decrease partition coefficient of analytes towards extraction phase. Fig. 4D demonstrates the extraction temperature profiles for VOCs and we can see that the extracted amount increases with the elevated temperature (from 30 to 60 °C), but decreases obviously after 50 °C. Therefore, 50 °C; was chosen to be the optimum extraction temperature.

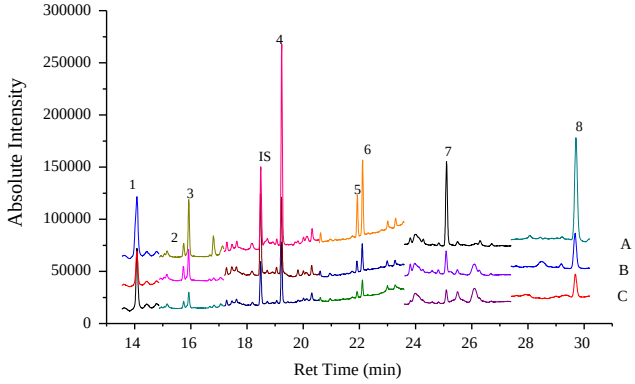


Fig. 5. GC–MS-SIM Chromatograms of VOCs in EBV samples (A: spiked EBV of healthy volunteer (1 μg L^{-1}), B: lung cancer patient, C: healthy volunteer). Peaks: 1. benzene; 2. 2-pentanone; 3. pentanal; 4. hexanal; 5. 2-heptanone; 6. heptanal; 7. octanal; 8. nonanal.

3.3. Analytical validation

The analytical evaluation parameters, including linearity range, correlation coefficients (R^2), limit of detection (LOD), recovery, reproducibility and repeatability of the developed SPME-GC/MS method were investigated by analysis of eight VOCs under the optimized conditions. Calibration curves were plotted using internal standard method. To get a series of gas calibration standards containing known concentrations of IS (5 μg L^{-1}), 2 μL standard working solution was injected into a sealed glass vial. Table 1 illustrates the quantitative analytical results. The proposed method showed good linearity with R^2 ranging from 0.9933 to 0.9999 in relatively wide concentration ranges. The limits of detection (LODs) with signal-to-noise ratio of 3 ($S/N=3$) were between 0.7 and 3.4 ng L^{-1}. The relative standard deviations (RSDs), including intra-day and inter-day of one fiber and fiber-to-fiber were both measured at three spiked concentration levels. The RSDs of one fiber ($n=5$) were in the range of 1.8–13.5%, which showed the good repeatability of the method. The RSDs of fiber-to-fiber ($n=5$) ranging from 2.2 to 15.0% indicated good reproducibility. The recoveries which were determined by the spiked experiments at two concentration levels in the EBV sample of controls were between 89% and 115%. The high recovery indicated the low matrix effect of the method. GC/MS-SIM chromatograms of VOCs in EBV samples are shown in Fig. 5 (A: spiked EBV of healthy volunteer, B: lung cancer patient, C: healthy volunteer). The results show that the NPAA fiber-based analytical method is effective and reliable.

3.4. Comparison with other methods

The intercomparison with several previously reported methods [45,46,16] was also carried out. The analytical results are shown in Table 2. The common methods for the analysis of aldehydes, ketones and benzene series in gaseous matrix are on- fiber-derivatisation solid phase microextraction method (method 1) and needle trap micro-extraction method (method 2). In comparison with method 1, NPAA coating shows relativity higher precision in a much wider linear range. In addition, the process of derivatization is not needed in our proposed method, which provides a rapid and simple analysis. Better sensitivity is obtained when compared with method 2. And it is a tough and time-consuming work to pack the sorbent materials into needles.

3.5. Application to real samples

To assess the viability of the proposed method, the NPAA SPME fiber was used to extract VOCs in EBV from both lung cancer

Table 2
Intercomparison with different methods previously reported.

Detection	Pretreatment	Coatings	Matrix	Analytes	LOD (nM)	Linear range (nM)	R^2	RSD (%)	Reference
GC/MS	On-fiber-derivatisation SPME	65 μm PDMS/DVB	In exhaled breath	Straight aldehydes C3–C9	0.001	0.003–0.3	0.97–0.99	7.2–15.1	45
GC/MS	On-fiber-derivatization SPME	65 μm PDMS/DVB	In human breath	Aldehydes C6–C9	0.001–0.003	0.002–20	0.99	3.0–24.0	46
GC–MS	Needle trap micro-extraction	Polymer DVB/ carbopack/ carboxen DVB/ carboxen PDMS/carbopack/ carboxen PDMS/ carboxen	Environmental monitoring and breath analysis	Benzene aldehydes C5–C9	0.04–1.5	0.003–7.2	0.89–0.99	2.7–61.3	16
GC/MS	SPME	NPAA coating	In exhaled breath	Benzene ketones aldehydes	0.007–0.03	0.03–465	0.99	1.8–15.0	This work

Table 3
The comparison results between the healthy and patient samples.

	Benzene	2-Pentanone	Pentanal	Hexanal	2-Heptanone	Heptanal	Octanal	Nonanal
Means ± SD[a]	3.42 ± 1.41	0.64 ± 0.30	0.28 ± 0.13	0.68 ± 0.37	0.16 ± 0.05	0.13 ± 0.06	0.04 ± 0.02	0.36 ± 0.07
Means ± SD[b]	3.06 ± 1.21	1.81 ± 0.55	0.53 ± 0.16	0.82 ± 0.19	0.34 ± 0.13	0.35 ± 0.10	0.093 ± 0.06	0.48 ± 0.06
t[c]	0.545	5.552	2.989	1.009	4.022	5.474	1.621	3.594
p[d]	0.592	0.001	0.008	0.331	0.002	0.001	0.135	0.002

[a] Healthy people ($n=10$).
[b] Lung cancer patients ($n=10$). Concentrations are presented as Means ± SD, the units are $\mu g\ L^{-1}$ and SD is standard deviation.
[c] The value of t was obtained at the confidence of 95%.
[d] $P<0.05$ was considered significant.

patients ($n=10$) and healthy volunteers ($n=10$). The results were statistically analyzed with Independent-Sample T Test (Table 3). As shown, average concentrations of 2-pentanone, pentanal, 2-heptanone, heptanal and nonanal were overtly higher in patients when compared to the control group ($P<0.05$). In contrast, no significant differences in benzene, hexanal and octanal were found between the two groups. The phenomenon may result from relatively small sample size, different stage of lung cancer patients and so on. Long-term and extensive research with more statistical data is required in further study. In general, the proposed method is feasible and acceptable for the analysis of VOCs in human EBV.

4. Conclusion

In this work, a novel nanoporous anodic alumina fiber was prepared by a simple two-step anodization method. The prepared NPAA fiber features the characteristics of facile preparation, low cost, environment-friendly, thermal, chemical and mechanical stability and long lifetime. Moreover, the porous and ordered structure of the coating exhibits a large surface-to-volume ratio, which enables high extraction efficiency and fast mass transfer. The fiber was successfully applied for the extraction of eight VOCs in EBV samples of lung cancer patients and healthy people. The quantitative results indicate that the proposed method is rapid, sensitive and reliable and robust, it provides a potential tool for rapid detection of VOCs in human exhaled breath.

Acknowledgements

This research was financially supported by National Natural Science Foundation of China (No. 21175052) and self-determined research funds of CCNU from the colleges' basic research and operation of MOE (No. CCNU14A05010).

References

[1] G. Li, Z. Zhang, Microchem. J. 95 (2010) 127–139.
[2] C.A. Zini, F. Augusto, E. Christensen, B.P. Smith, E.B. Caramão, J. Pawliszyn, Anal. Chem. 73 (2001) 4729–4735.
[3] J. Kesselmeier, M. Staudt, J. Atmos. Chem. 33 (1999) 23–88.
[4] M. Phillips, R.N. Cataneo, A.R.C. Cummin, A.J. Gagliardi, K. Gleeson, J. Greenberg, R.A. Maxfield, W.N. Rom, CHEST 123 (2003) 2115–2123.
[5] P.J. Mazzone, J. Thorac. Oncol. 3 (2008) 774–780.
[6] J. Ji, H. Liu, J. Chen, J. Zeng, J. Huang, L. Gao, Y. Wang, X. Chen, J. Chromatogr. A 1246 (2012) 22–27.
[7] Z. Zhang, G. Li, L. Luo, G. Chen, Anal. Chim. Acta 659 (2001) 151–158.
[8] A. Krumbein, P. Peters, B. Brückner, Postharvest Biol. Technol. 32 (2004) 15–28.
[9] K.H. Kim, Y.H. Kim, R.J.C. Brown, Anal. Bioanal. Chem. 405 (2013) 8397–8408.
[10] E. Pierini, L. Sampaolo, A.R. Mastrogiacomo, J. Chromatogr. A 855 (1999) 593–600.
[11] E. Woolfenden, J. Chromatogr. A 1217 (2010) 2674–2684.
[12] M. Giardina, S.V. Olesik, Anal. Chem. 75 (2003) 1604–1614.
[13] H. Yu, L. Xu, P. Wang, J. Chromatogr. B 826 (2005) 69–74.
[14] M.D. Knutson, F.E. Viteri, Anal. Biochem. 242 (1996) 129–135.
[15] M. Heidari, A. Bahrami, A.R. Ghiasvand, F.G. Shahna, A.R. Soltanian, Anal. Chim. Acta 785 (2013) 67–74.
[16] P. Trefz, S. Kischkel, D. Hein, E.S. James, J.K. Schubert, W. Miekisch, J. Chromatogr. A 1219 (2012) 29–38.
[17] C.L. Arthur, J. Pawliszyn, Anal. Chem. 62 (1990) 2145–2148.
[18] C. Martínez, N. Ramírez, V. Gómez, E. Pocurull, F. Borrull, Talanta 116 (2013) 937–945.
[19] C. Blasco, G. Font, J. Mañes, Y. Picó, Anal. Chem. 75 (2003) 3606–3615.
[20] H. Lai, P. Guerra, M. Joshi, J.R. Almirall, J. Sep. Sci. 31 (2008) 402–412.
[21] M.B. Heringa, J.L.M. Hermens, Trends Anal. Chem. 22 (2003) 575–587.
[22] J. Pawliszyn (Ed.), Handbook of Solid Phase Microextraction, Chemical Industrial Press, Beijing, 2009.
[23] C. Dietz, J. Sanz, C. Cámara, J. Chromatogr. A 1103 (2006) 183–192.
[24] Z. Zhang, Q. Wang, G. Li, Anal. Chim. Acta 727 (2012) 13–19.
[25] D. Djozan, Y. Assadi, S.H. Haddadi, Anal. Chem. 73 (2001) 4054–4058.
[26] D. Mombello, N.L. Pira, L. Belforteb, P. Perlo, G. Innocentib, S. Bossia, M.E. Maffei, Sens. Actuators, B 137 (2009) 76–82.
[27] Y. Wang, Y. Gao, P. Wang, H. Shang, S. Pan, X. Li, Talanta 115 (2013) 920–927.
[28] M.J. Trujillo-Rodríguez, H. Yu, W.T.S. Cole, T.D. Ho, V. Pinó, J.L. Anderson, A.M. Afonso, Talanta 121 (2014) 153–162.
[29] Y. Wu, C. Yang, X. Yan, J. Chromatogr. A 1334 (2014) 1–8.
[30] X. Song, Y. Shi, J. Chen, Talanta 116 (2013) 188–194.
[31] A.M.M. Jani, D. Losic, N.H. Voelcker, Prog. Mater. Sci. 58 (2013) 636–704.
[32] K. Nielsch, J. Choi, K. Schwirn, R.B. Wehrspohn, U. Gösele, Nano. Lett. 2 (2002) 677–680.
[33] A.P. Li, F. Müller, A. Birner, K. Nielsch, U. Gösele, J. Appl. Phys. 84 (1998) 6023–6026.
[34] T. Gorisse, L. Dupré, P. Gentile, M. Martin, M. Zelsmann, D. Buttard, Nanoscale Res. Lett. 8 (2013) 1–9.
[35] W.G. Yelton, K.B. Pfeifer, A.W. Staton, J. Electrochem. Soc. 149 (2002) H1–H5.
[36] A. Mozalev, S. Magaino, H. Imai, Electrochim. Acta 46 (2001) 2825–2834.
[37] G. Jeon, M. Jee, S.Y. Yang, B. Lee, S.K. Jang, J.K. Kim, Appl. Mater. Interfaces 6 (2014) 1200–1206.
[38] A. Mashira, R.A. Dweika, Adv. Powder Technol. 20 (2009) 420–425.
[39] A.N. Martin, G.R. Farquar, A.D. Jones, M. Frank, Anal. Bioanal. Chem. 396 (2010) (739-425).
[40] W. Miekisch, J.K. Schubert, G.F.E. Noeldge-Schomburg, Clin. Chim. Acta 347 (2004) 5–39.
[41] G.E.J. Poinern, N. Ali, D. Fawcett, Mater 4 (2011) 487–526.
[42] O. Jessensky, F. Müller, U. Gösele, Appl. Phys. Lett. 72 (1998) 1173–1175.
[43] G.D. Sulka, Nanostruct. Mater. Electrochem. (2008) 1–116.
[44] M. Liu, Y. Liu, Z. Zeng, T. Peng, J. Chromatogr. A 1108 (2006) 149–157.
[45] D. Poli, M. Goldonia, M. Corradia, O. Acampaa, P. Carbognanic, E. Internulloc, A. Casalini, A. Muttia, J. Chromatogr. B 878 (2010) 2643–2651.
[46] S. Svensson, M. Lärstad, K. Broo, A.C. Olin, J. Chromatogr. B 860 (2007) 86–91.

Talanta 132 (2015) 535–540

Contents lists available at ScienceDirect

Talanta

journal homepage: www.elsevier.com/locate/talanta

Rapid extraction of melamine in powdered milk for direct electrospray ionization tandem mass spectrometry analysis

Elisângela do Carmo Domingo [a,*], Aline Auxiliadora Tireli [b], Cleiton Antonio Nunes [a], Alexandre Vieira Batista [a], Mário César Guerreiro [b], Sandra Maria Pinto [a]

[a] Department of Food Science, Federal University of Lavras, Lavras, Minas Gerais, Brazil
[b] Department of Chemistry, Federal University of Lavras, Lavras, Minas Gerais, Brazil

ARTICLE INFO

Article history:
Received 25 March 2014
Received in revised form
25 September 2014
Accepted 1 October 2014
Available online 22 October 2014

Keywords:
Adulteration
Melaminium bis(trichloroacetate) dihydrate
Trichloroacetic acid precipitation
Ethyl acetate extraction

ABSTRACT

A combination of a simple pretreatment for melamine extraction and direct analysis in electrospray ionization tandem mass spectrometry (ESI–MS/MS) is proposed. Three pretreatments were evaluated. The first was based on suppressing interference using acetonitrile. The second used sulphuric acid and trichloroacetic acid to suppress interference and for melamine extraction, respectively. The third used sulphuric acid to suppress milk interference, trichloroacetic acid for melamine precipitation, and ethyl acetate for melamine extraction. However, only the last pretreatment suppressed milk interference in melamine detection and a good linearity (R^2=0.99) was obtained. The presence of MS/MS 85 on melamine fragmentation spectrum showed the selectivity of this method. The limit of detection and limit of quantification were 0.269 μg L^{-1} and 0.897 μg L^{-1}, respectively. The recoveries and relative standard deviation (RDS) of method were lower than 114% and 7.86%, respectively. Further, the research was extended to elucidate the nature of the melamine in the extract through infrared spectroscopy and microscopy analyses. The precipitate was characterized as melaminium bis(trichloroacetate) dihydrate, which is generated through hydrogen bound formation in an interaction between melamine and trichloroacetic acid. Therefore, a simple, fast, and easy method for melamine extraction and direct ESI–MS/MS analysis was developed.

© 2014 Elsevier B.V. All rights reserved.

1. Introduction

Milk is a complete food and source of essential nutrients, including carbohydrate, protein, fatty acids, calcium, phosphorus and magnesium. Moreover, the milk constituents can affect dairy products performance and quality; therefore, the industries usually define milk quality based on the nutrient levels, mainly protein and fat. These parameters have been used to calculate the payout to the supplier [1]. Unfortunately, adding nonauthentic nutrients has been used to adulterate milk and, consequently, increase economic gain [2].

This adulteration is defined as the removal or replacement of milk components and addition of substances without a purchaser's knowledge, including water, whey, sucrose, starch, salt, sodium hydroxide, and formaldehyde [2,3]. Melamine is a nitrogen-rich compound commonly used to manufacture plastics, laminates, glues and adhesives [4]. Although it is not an ingredient in food, it was reported as present in Chinese powdered milk and infant formula in 2008. It was used to falsely increase the apparent milk protein and was not discovered because the routinely used methods could not distinguish between nitrogen from protein and non-protein sources, which resulted in incorrectly high protein measurements [5]. Consuming tainted products by the Chinese population affected 294,000 infants and children with more than 50,000 hospitalizations and at least 6 deaths [6]. This scandal scared the world and created the need for sensitive, specific, rapid, and reliable screening methods.

The Food and Drug Administration (FDA) from the United States of America (USA) established a liquid chromatography–mass spectrometry (LC–MS/MS) method to detect melamine in infant formula. This technique is accurate, but it is time consuming and requires hazardous solvent [7,8]. Many researchers have reported analytical methods for melamine detection and quantification, such as gas chromatography-single quadrupole mass spectrometry [9], a spectrophometric method [10], liquid chromatography tandem mass spectrometry [1,4,11–14], and an enzyme-linked immunosorbent assay [7]. However, these most available methods are time-consuming,

List of abbreviations: ESI–MS/MS, electrospray ionization tandem mass spectrometry; FDA, Food and Drug Administration; HB, hydrogen bond; HMF, 5-hydroxymethylfurfural; HTST, high temperature short time; LOQ, limit of quantification; LOD, limit of detection; LC–MS/MS, liquid chromatography tandem mass spectrometry; R^2, linearity; USA, United States of America

* Corresponding author. Tel.: +55 35 38291324.
E-mail address: elisangela.domingo@posgrad.ufla.br (E.d.C. Domingo).

http://dx.doi.org/10.1016/j.talanta.2014.10.003
0039-9140/© 2014 Elsevier B.V. All rights reserved.

labor-intensive and expensive. Therefore, to simplify the sample preparation and improve the methods for detecting melamine, it is important to monitor contamination and prevent damage to consumer health.

Recent advances in ambient ionization mass spectrometry facilitate direct, rapid, real-time, and high-throughput analyses with little or no sample pretreatment [19,20]; it has been used to characterize food and identify adulterants, and authors report it as a reliable method [21,22]. In this paper, we proposed a simple and rapid sample preparation to detect melamine in powdered milk using electrospray ionization tandem mass spectrometry (ESI–MS/MS). Further, the research was extended to infrared spectroscopy and microscopy analyses to identify the nature of the precipitate formed during extraction.

2. Material and methods

2.1. Sample and reagents

Powdered milk was prepared from pasteurized milk (Grain Lait, Perdões, Brazil; high temperature short time [HTST]). Melamine was obtained from Sigma (St. Louis, USA) with chemical purity of greater than 98% and dissolved in Milli-Q purified water.

2.2. Powdered milk preparation

Triplicates of powdered milk were produced from pasteurized milk concentrated in a rotary evaporator (70 °C, TE-0581, TE-210, Tecnal, Piracicaba, Brasil) until the concentration of 52% of total solids; thereafter, the concentrate was dried in mini spray dryer (MSD 1.0, Labmaq, Ribeirão Preto, Brasil). The temperature for the inward and outward drying air was 160 and 100 °C, respectively, and the feed flow rate was 0.79 L h^{-1} in system with dual fluid nozzle atomization.

2.3. Melamine-added milk standards

Melamine stock solutions (500 mg L^{-1}) were prepared by dissolving melamine in water. The powdered milk was diluted in water and contaminated with melamine at different concentrations (0, 2.5, 5, 10, 15 and 20 mg L^{-1}).

2.4. Melamine extraction

Three extraction procedures were evaluated. The first pretreatment was performed in accordance with the methodology described by Desmarchelier et al. [12]. The powdered milk (1 g) and melamine aliquots were placed into a falcon polypropylene tube that was mixed and allowed to stand for 10 min. The water (5 mL) and acetonitrile (5 mL) were added successively, and the resulting slurry was thoroughly mixed after each solvent was added. The slurry was further diluted with acetonitrile (30 mL) and water (10 mL) and placed onto an automated shaker for 5 min. The tube was then centrifuged at 4000*g* at room temperature for 10 min (Centrifuge, Beckman, GS-15R), and the liquid supernatant was used for direct injection into ESI–MS/MS.

The second pretreatment was performed by adjust to pH 4.6 with 2 mol L^{-1} sulphuric acid (pHmeter, Quimis, Q400AS); thereafter, the samples were filtered. The filtered aliquot (5 mL) was added to 24% trichloroacetic acid (5 mL) and left to stand for 15 min. The mixture was filtered and the permeate was divided in two parts. The first aliquot of extract was used for injection into ESI–MS/MS. The remaining portion (4 mL) was added to ethyl acetate (4 mL) followed by stirring (Vortex, Phoenix-AP56); thereafter, the supernatant was used for direct injection into ESI–MS/MS (the third pretreatment sample). The extraction steps are described in Fig. 1.

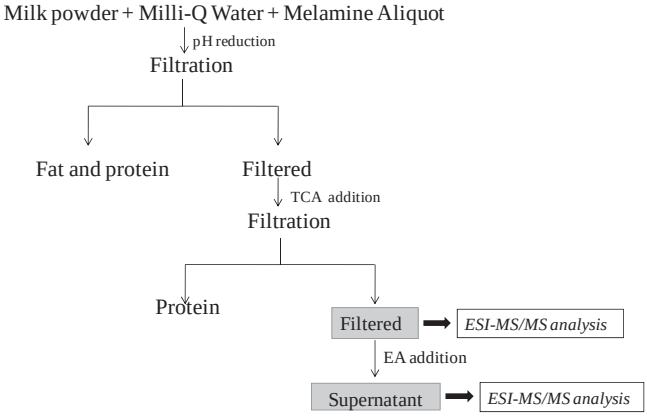


Fig. 1. The second and third pretreatment steps for powdered milk. TCA—trichloroacetic acid; EA—ethyl acetate; ESI–MS/MS—electrospray ionization tandem mass spectrometry.

2.5. ESI–MS/MS analysis

An aliquot of formic acid was added to yield 0.1% as the final concentration in the extract. Sample introduction was performed by using a micro syringe at a flow rate of 10 μL min^{-1}. To avoid cross-interference between samples, HPLC-grade methanol (Merck, Brasil) was injected between each infusion.

ESI–MS/MS analyses were performed using Agilent 1100 Series LC/MSD trap equipment in positive ion mode to identify the melamine. The spectra were obtained through 50 scans at 0.2 s intervals. The MS parameters were as follows: heat capillary temperature 350 °C, dry gas flow 6 L min^{-1}, nebulizer pressure 15 psi, and capillary voltage −3.5 kV. Mass spectra were acquired and accumulated over 60 s.

2.6. Method performance

The linearity (R^2) was evaluated from three calibration curves with six levels of melamine concentrations in powdered milk [23].

The limit of detection (LOD) and limit of quantitation (LOQ) were detected on blank samples ($n=10$) and calculated by Eqs. (1) and (2), respectively:

$$\mathrm{LOD} = 3\frac{sb}{b} \quad (1)$$

$$\mathrm{LOQ} = \frac{10sb}{b} \quad (2)$$

where *sb* is the standard deviation of the areas of the blank samples in mass spectrum, and *b* is the slope of the calibration curve [23]. The recovery and accuracy (%) were calculated according to Eq. (3), using blank matrices spiked with melamine at two fortification levels (8 mg L^{-1}; 12 mg L^{-1}).

$$R(\%) = \frac{(C_1 - C_2)}{C_3} \times 100 \quad (3)$$

where C_1 is the melamine concentration determined in adulterated milk, C_2 is the melamine concentration determined in blank sample, and C_3 is the concentration added [24]. The precision was calculated by the relative standard deviation (Eq. (4)).

$$\mathrm{RSD} = \frac{s}{x} \times 100 \quad (4)$$

where *s* is the standard deviation of replicate, and *x* is the mean of replicate. The selectivity was evaluated by the presence of melamine fragment MS/MS 85 [24].

2.7. Infrared spectroscopy analysis

The infrared spectra were recorded on a Shimadzu FT-IR Prestige 21 spectrometer. The melamine (500 mg L^{-1}) and trichloroacetic acid (24%) solutions were in a 1:1 ratio. The precipitate (2 mg) was dried and mixed with potassium bromide powder (200 mg) and pressed to form a thin, transparent disk. Infrared absorption spectra within the range 4000–400 cm^{-1} at a 2 cm^{-1} resolution using 32 scans were recorded at room temperature.

2.8. Optical and electronic microscopy analysis

The melamine (500 mg L^{-1}) and trichloroacetic acid (24%) solutions were at a 1:1 ratio, and the crystals images were obtained using optical microscopy (Meiji ML 5000, Meiji Techno América, Santa Clara, USA) coupled with a camera (Cle-Palmer 49901-35, Cole-Palmer, Vernon Hills, USA).

The melamine (15 mg L^{-1}) and trichloroacetic acid (24%) solutions were at a 1:1 ratio, and 60 µL of this mixture was added to a blade, to which Poli-L-Lisin was previously added. After 30 min, the Karnovsky solution was added until the blade was covered and stored at 8 °C over 3 h. The sample was washed with cocodilato buffer (0.05 M) three times over 10 min and washed with water three times. Then, the dehydration process began by adding 25, 50, 75, 90% acetone over 10 min then three times in 100% acetone for 10 min each, followed by drying in a critical point dryer. The sample was placed in the gold bath then observed in microscope (LEO Evo 040).

3. Results and discussion

3.1. Melamine extraction and detection

Melamine, 1,3,5-triazine-2,4,6-triamine, has 126.1 Da molecular mass. Detection of this compound in milk can be affected by matrix interference because powdered milk has a compound with similar molecular mass, namely 5-hydroxymethylfurfural (HMF), which has a 126.1 Da molecular mass. HMF is a natural compound formed when milk is heated; its ESI–MS spectrum is characterized by the presence of the *m*/*z* 127.1 [21]. However, HMF fragmentation produces the MS/MS fragments 109, 84, and 71, whereas protonated melamine generated ions with *m*/*z* 110, 85, and 60, showing that fragmentation can be used to differentiate these compounds [25].

To analyse the melamine in powdered milk samples and suppress matrix interference, extraction procedures were performed. First, the extraction procedure by Desmarchelier et al. [12] was performed for samples spiked with melamine. The mass spectrum for this extract is presented in Fig. 2.

The mass spectrum presented a number of *m*/*z* signals related to the presence of disaccharide from milk. Lactose is the main carbohydrate in milk and could be identified by two peaks in the spectrum. The signal detected at *m*/*z* 381 and 365 were generated from lactose association with sodium and potassium, respectively. However, the low 127.1 signal hampers the fragmentation, which does not show whether this signal is from melamine or HMF, indicating that the high lactose signal disrupts the detection; this occurred at all concentrations evaluated. The additional ions in the spectrum arose from the other powdered milk components.

Desmarchelier et al. [12] successfully used this method to detect melamine through liquid chromatography, which separates matrix components from melamine and, consequently, suppresses matrix interferences. On the other hand, ESI–MS/MS does not provide proper separation, which favours matrix effects during melamine detection.

To assess melamine in powdered milk through ESI–MS/MS by suppressing milk interference, another pretreatment procedure was evaluated, which was based on eliminating milk interference; this procedure was performed in two steps. The first step consisted of eliminating the insoluble protein and fat. The decrease in pH for milk from 6.6 to 4.6 promoted protein precipitation; and filtering this mixture formed an extract without casein micelles and fat. The fat was eliminated based on the solubility difference from the extract, and the insoluble protein was eliminated based on the characteristic isoelectric points at pH 4.6 [26]. In the second step, the trichloroacetic acid reacted with melamine to form a precipitate; thereafter, it was filtered to eliminate the soluble protein and directly injection into the ESI–MS/MS. The mass spectrum for this extract is shown in Fig. 3.

Melamine detection is affected by interference from milk compounds, mainly the ions from lactose and mineral interactions. The *m*/*z* 127.1 has a small intensity, which limited the fragmentation and distinction between melamine and HMF, showing that this pretreatment was not efficient to suppress the interference. Many authors have reported interference by the milk matrix during melamine detection. Ibáñez, Sancho and Hernández [27] reported that the matrix interference affected melamine detection in mass spectrometry. Xia et al. [28] reported that the matrix affected melamine determination even using hydrophilic interaction liquid

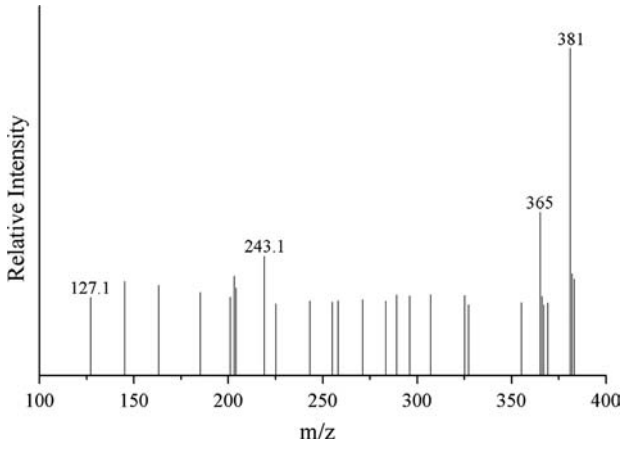


Fig. 2. The mass spectrum for the melamine extract obtained according Desmarchelier et al. [12]. The sample includes 15 mg L^{-1} of melamine, and the peaks show the *m*/*z* 381 $[Lactose+Na]^+$ and *m*/*z* 365 $[Lactose+K]^+$.

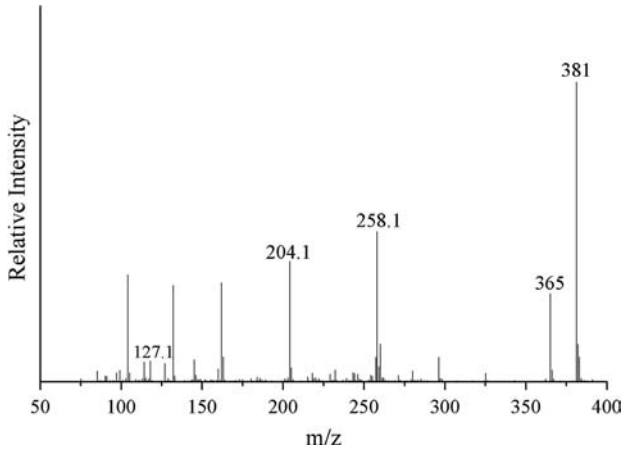


Fig. 3. The mass spectrum for the extract obtained by precipitating melamine using trichloroacetic acid (samples with 15 mg L^{-1} of melamine). *m*/*z* 381 $[Lactose+Na]^+$; *m*/*z* 365 $[Lactose+K]^+$.

chromatography coupled to ESI–MS. He et al. [4] observed that the melamine signal was suppressed by milk compounds. Gonzalez-Antuña et al. [29] described how the matrix interferes with the mass spectrometry, showing that the competition between matrix analyte compounds and modifying the physical properties of the droplets can affect analysis efficiency.

Nevertheless, different solvents have been used to clean the sample for melamine detection, including acetonitrile, methanol, diethyl ether, and dichloromethane [1,9,13,14,30–34]. Thus, an additional step in the extraction procedure was performed to suppress the matrix interference. The sample was prepared over three steps; the first consisted of suppressing the insoluble protein and fat followed by melamine precipitation and ethyl acetate addition to the melamine extract. Thereafter, the supernatant was injected into an ESI–MS/MS, and the results were shown in Figs. 4 and 5.

This extract produced a mass spectrum with high intensity for the *m/z* 127.1 (Fig. 4), which favoured fragmentation (MS/MS) (Fig. 5). As expected for the milk sample spiked with melamine, the fragmentation of *m/z* 127.1 confirms the presence of melamine through identification of the MS/MS 85.2 peak, which is produced through loss of the N_2CH_2 group [12]. Moreover, the MS/MS 99 is formed by ionization of $C_2N_5H_5^+$ which is produced by HNC elimination [35].

Many authors have reported melamine detection in milk and its discrimination from HMF in milk. Yang et al. [25] showed interference by HMF in melamine detection and proposed that the fragment MS/MS 85 can be used to exclude false positive signals. Dane and Cody [21] reported that the low levels of melamine may be difficult to identify in the presence of HMF. Chen and Yan [36] used capillary electrophoresis coupled with diode array detection to differentiate melamine from HMF and demonstrated melamine detection.

In addition, a calibration curve was obtained using five concentrations of milk contaminated with melamine. The response range was discerned, and the calibration curve is represented by the equation shown in Fig. 6.

A linear relationship was observed between the melamine concentration and absolute mass spectral intensity of ion 127, which indicated that the ESI–MS/MS can be efficiently used for melamine detection.

The LOD and LOQ were 0.269 μg L^{-1} and 0.897 μg L^{-1} respectively, showing that the third extraction can be successfully applied to detect and quantify melamine in powdered milk with a limit below 1 μg L^{-1}. The accuracy of this method was found by melamine addition in milk and quantitative analysis, showing

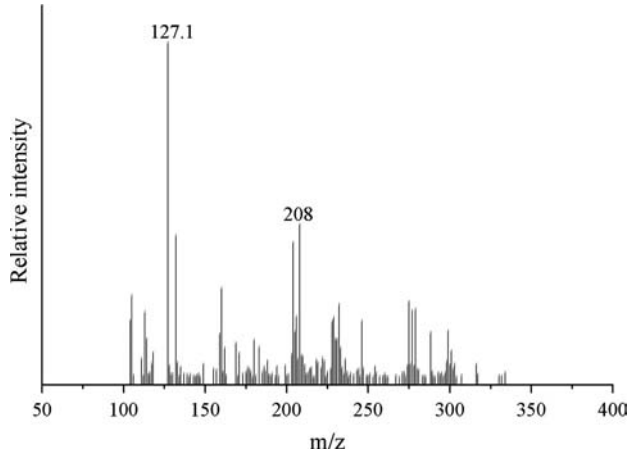


Fig. 4. The mass spectrum for the extract obtained by melamine precipitation with trichloroacetic acid and solubilized in ethyl acetate (sample with 15 mg L^{-1} of melamine) as well as *m/z* 127.1 fragmentation.

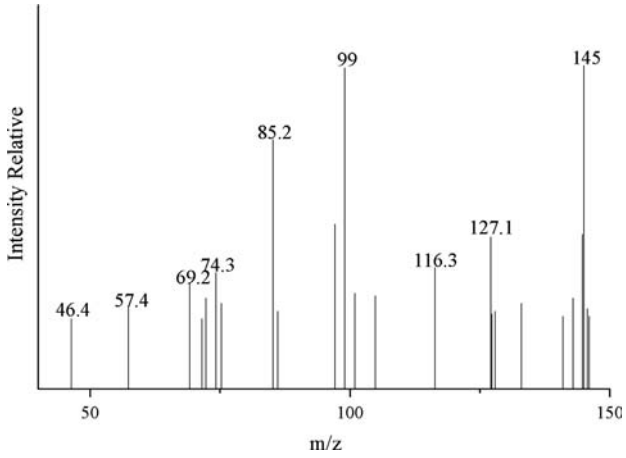


Fig. 5. Mass spectrum of *m/z* 127.1 fragmentation for the extract obtained by the third extraction technique (powdered milk contaminated with 15 mg L^{-1} of melamine).

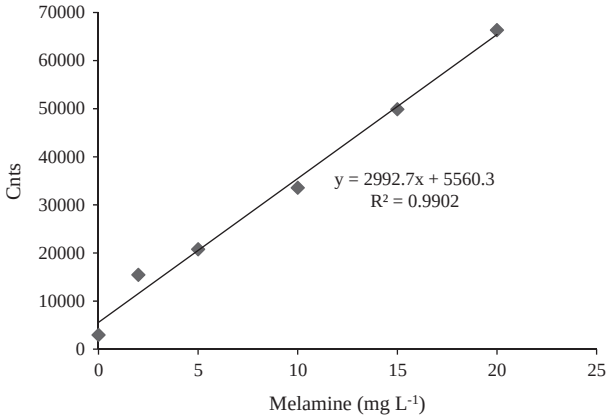


Fig. 6. The relationship between mass intensity and melamine concentration.

acceptable recovery (109 and 114%). Thus, the satisfactory data was obtained, showing the accuracy of the method developed. Cao et al. [7] reported recovery rates of 72.8–123% for melamine detection using enzyme-linked immunosorbent assay (ELISA). Yang et al. [25] using surface desorption atmospheric pressure chemical ionization to detect melamine in milk products showed 97–113% of recovery.

The method precision was lower than 7.86%, showing it can be used to detect melamine in powdered milk. Thus, the extraction followed by ESI–MS/MS is a precise and accurate method to detect melamine in powdered milk. Ibáñez et al. [27] using LC–MS/MS showed good precision (RSD < 5%) for melamine detection and reported that the RSD < 20% is acceptable. Cao et al. [7] showed that the precision of ELISA method was lower than 18.9%. Yang et al. [25] reported that the precision of surface desorption atmospheric pressure chemical ionization mass spectrometry to detect melamine was lower than 11.9%.

The presence of MS/MS 85 on melamine fragmentation spectrum (Fig. 5) showed that the method can remove the interference of milk compounds [12]. These results show that melamine could be simply and rapidly detected by ESI–MS/MS. It can be concluded that the method had a good precision and accuracy for melamine detection.

Many authors reported different methods to detect melamine and showed the sensibility of these, although most of than are time-consuming, labor-intensive and expensive [4,7,13,14,27,28,32,33]. In this sense, the developed method is a promising technique to melamine detection since it is sensitive, simple and practical. In

addition, this method does not require a long extraction procedure and can be applied in routine analysis of powdered milk.

3.2. The nature of the melamine in the extract

Melamine precipitation was based on a reaction with trichloroacetic acid, which forms of melamine salt crystals. The interaction between melamine and trichloroacetic acid facilitates crystal formation, and this complexation adds an interesting aspect to the intramolecular hydrogen bond (HB) system formed [37–41]. Thus, to investigate the nature of the precipitate, infrared spectroscopy was employed. The infrared spectrum of melamine and precipitate were shown in Fig. 7.

The melamine N–H stretching vibrations absorb in an interference-free region (3500–3300 cm^{-1}) of the infrared spectrum; thus, they are suitable bands for HB assignment. The presence of HB moves the N–H stretching band to a lower wavenumber due to a weaker of N–H bond. The strong peak at 3419 cm^{-1} (melamine spectrum) is attributed to NH_2 symmetric stretching (ν_{sym}), which was shifted to 3414 cm^{-1} in the melaminium salt, as observed by Kanagathara et al. [42], while asymmetric stretching (ν_{asym}=3470 cm^{-1}) did not change the wavenumber. In addition, the side chain C–N stretching [39], which occurs at 1439 cm^{-1} is shifted to 1335 cm^{-1}, which provides insight into the presence of HB during formation of the precipitate, melaminium bis (trichloroacetate) dihydrate, as reported by Perpétuo and Janczak [43] and Kanagathara et al. [42]. The melamine salt crystals are shown in Fig. 8.

The melaminium bis(trichloroacetate) dihydrate crystal was detected using different microscopy techniques, which demonstrated the characteristic structure of the salt formed during the second sample pretreatment step, which consists of adding trichloroacetic acid and a reaction with melamine. However, Kanagathara et al. [42] reported a different morphology, which can be explained by the using of trichloroacetic acid at a different concentration.

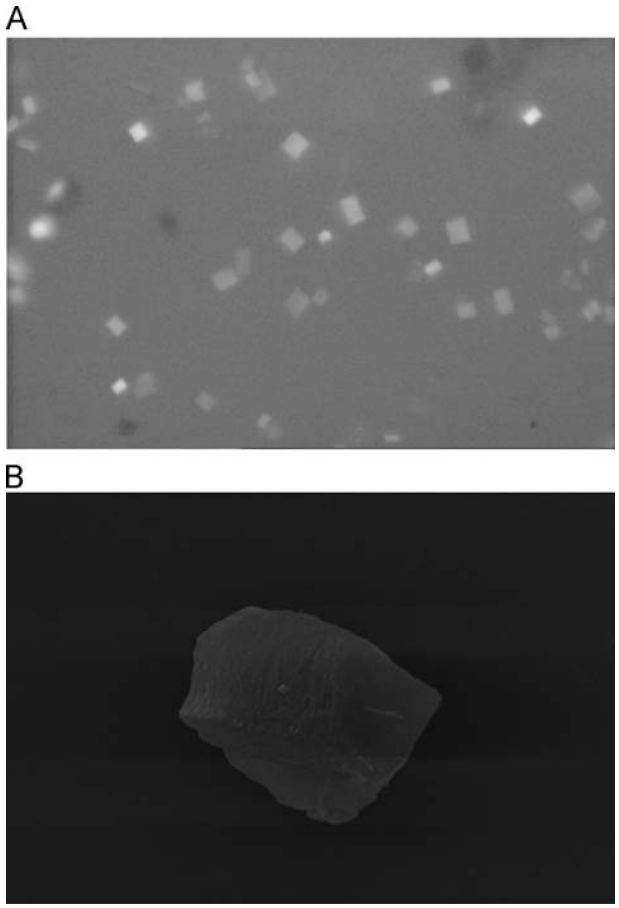


Fig. 8. A melaminium bis(trichloroacetate) dihydrate crystal observed using optical microscopy (A) (500 mg L^{-1} of melamine) and electronic (B) microscopy (15 mg L^{-1} of melamine).

4. Conclusion

The first and second pretreatments were based on melamine extraction using acetonitrile and trichloroacetic acid, respectively. However, these techniques did not efficiently suppress milk interference for melamine detection.

For the third pretreatment sulphuric acid was used to suppress protein and fat, and trichloroacetic acid and ethyl acetate were used for melamine precipitation and extraction, respectively. The ESI–MS/MS analysis showed that the matrix interference was removed, and a linear correlation was observed between the melamine concentration and the mass spectrometry results, showing that the adulteration can be detected and quantified. The recovery and precision were accepted. The LOD and LOQ were below than 1 μg L^{-1}.

The protocol for melamine extraction was based on melaminium bis(trichloroacetate) dihydrate formation by trichloroacetic acid addition and solubilization with ethyl acetate, which was not previously reported; and we showed that it as a simple, fast, and easy method for melamine extraction from powdered milk and direct ESI–MS/MS analysis. Future studies could use this extract for additional analytical methods to extend the sample pretreatment application.

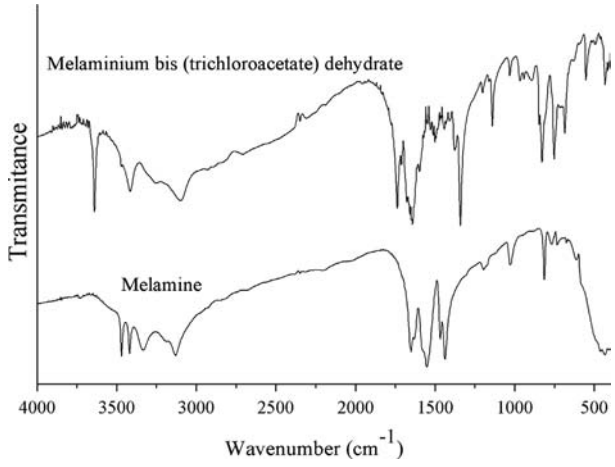


Fig. 7. The near infrared spectrum for melamine and its precipitate using trichloroacetic acid.

References

[1] G. Abernethy, K. Higgs, J. Chromatogr. A 1288 (2013) 10–20.
[2] J.C. Moore, J. Spink, M. Lipp, J. Food Sci. 77 (2012) R118–R126.
[3] P.M. Santos, E.R. Pereira-Filho, L.E. Rodriguez-Saona, J. Agric. Food Chem. 61 (2013) 1205.
[4] D. He, X. Zhang, B. Gao, L. Wang, Q. Zhao, H. Chen, H. Wang, C. Zhao, Food Control 36 (2014) 36–41.
[5] E. Domingo, A.A. Tirelli, C.A. Nunes, M.C. Guerreiro, S.M. Pinto, Food Res. Int. 60 (2014) 131–139.
[6] World Health Organization, Toxicological and Health Aspects of Melamine and Cyanuric Acid: Report of a WHO Expert Meeting, in Collaboration with FAO, 2009, from ⟨http://goo.gl/ko4Sl⟩.
[7] B. Cao, H. Yang, J. Song, H. Chang, S. Li, A. Deng, Talanta 116 (2013) 173–180.
[8] Y.T. Hsieh, W.T. Chen, I. Tomalová, J. Preisler, H.T. Chang, Rapid Commun. Mass Spectrom. 26 (2012) 1393–1398.

[9] P. Lutter, M. Savoy-Perroud, E. Campos-Gumenez, L. Meyer, T. Goldmann, M. Bertholet, P. Mottier, A. Dermarchelier, F. Monard, C. Perrin, F. Robert, T. Delatour, Food Control 22 (2011) 903–913.
[10] W. Chansuvarn, S. Panich, A. Imyim, Spectrochim. Acta, A 113 (2013) 154–158.
[11] A. Khedr, J. Chromatogr. B 930 (2013) 98–103.
[12] A. Desmarchelier, M.G. Cuadra, T. Delatour, P. Mottier, J. Agric. Food Chem. 57 (2009) 7186–7193.
[13] X. Deng, D. Guo, S. Zhao, L. Han, Y. Sheng, X. Yi, Y. Zhou, T. Peng, J. Chromatogr. B 878 (2010) 2839–2844.
[14] B.N. Tran, R. Okoniewski, R. Storm, R. Jansing, K.M. Aldous, J. Agric. Food Chem 58 (2010) 101–107.
[19] M.Z. Huang, S.C. Cheng, Y.T. Cho, J. Shiea, Anal. Chim. Acta 702 (2011) 1–15.
[20] G.B. Savindo, J.S. Garcia, Y.E. Corilo, B.G. Vaz, J.J. Zacca, R.G. Cosso, M.N. Eberlin, M.G. Peter, J. Agric. Food Chem. 58 (2010) 9407–9412.
[21] A.J. Dane, R.B. Cody, Analyst 135 (2010) 696–699.
[22] L. Ming, B. Hu, J. Li, R. Chen, X. Zhang, H. Chen, Anal. Chem. 81 (2009) 7724–7731.
[23] G.L. Long, J.D. Winefordner, Anal. Chem. 55 (1983) 712A–724A.
[24] B.K. Matuszewski, M.L. Constanzer, C.M. Chavez-Eng, Anal. Chem. 75 (2003) 3019–3030.
[25] S. Yang, J. Ding, J. Zheng, B. Hu, J. Li, H. Chen, Z. Zhou, X. Qiao, Anal. Chem. 81 (2009) 2426–2436.
[26] P. Walstra, J.T.M. Wouters, T.J. Geurts, Dairy Science and Technology, second ed., Taylor and Francis, USA, 2006.
[27] M. Ibáñez, J.V. Sancho, F. Hernández, Anal. Chim. Acta 649 (2009) 91–97.
[28] J. Xia, N. Zhou, C. Zhou, B. Chen, Y. Wu, S. Yao, J. Sep. Sci. 33 (2010) 2688–2697.
[29] A. Gonzalez-Antuña, J.C. Domínguez-Romero, J.F. Garcia-Reyes, P. Rodríguez-Gonzalez, G. Centineo, J.I.G. Alonso, A. Molina-Díaz, J. Chromatogr. A 1288 (2013) 40–47.
[30] F.N. Ihunegbo, S. Tesfalidet, W. Jiang, J. Sep. Sci. 33 (2010) 988–995.
[31] R.A. Yokley, L.C. Mayer, R. Rezaaiyan, M.E. Manuli, M.W. Cheung, J. Agric. Food Chem. 48 (2000) 3352–3358.
[32] X.D. Pan, P.G. Wu, D.J. Yang, L.Y. Wang, X.H. Shen, C.Y. Zhu, Food Control 30 (2013) 545–548.
[33] G. Koh, R.S. Chia, Q. Lin, P.S. Cheow, T.L. Teo, T.K. Lee, J. Sep. Sci. 34 (2011) 3043–3052.
[34] K. Zeng, Z. Liu, Y. Ning, J. Li, J. Tang, M. Zhang, Chin. J. Chromatogr 31 (2013) 477–480.
[35] Shan-Shan Ju, Chau-Chung Han, Chung-Jen Wu, Alexander M. Mebel, Yit-Tsong Chen, J. Phys. Chem. B 103 (1999) 582–596.
[36] Z. Chen, X. Yan, J. Agric. Food Chem. 57 (2009) 8742–8747.
[37] M.K. Marchewka, Mater. Lett. 58 (2004) 843–848.
[38] M.K. Marchewka, Mater. Sci. Eng., B 95 (2002) 214–221.
[39] S. Debrus, M.K. Marchewka, M. Drozd, H. Ratajczak, Opt. Mater. 29 (2007) 1058–1062.
[40] V. Sangeetha, K. Gayathri, P. Krishnan, N. Sivakumar, N. Kanagathara, G. Anbalagan, J. Cryst. Growth 289 (2014) 30–38.
[41] Y. Wang, A.M. Mebel, C. Wu, Y. Chen, C. Lin, J. Jiang, J. Chem. Soc. 93 (1997) 3445–3451.
[42] N. Kanagathara, N.G. Renganathan, M.K. Marchewka, N. Sivakumar, K. Gayathri, P. Krishnan, S. Gunasekaran, G. Anbalagan, Spectrochim. Acta, A 101 (2013) 112–118.
[43] G.J. Perpétuo, J. Janczak, Acta Crystallogr., Sect. C: Cryst. Struct. Commun. C62 (2006) o372–o375.

Talanta 132 (2015) 541–547

Contents lists available at ScienceDirect

Talanta

journal homepage: www.elsevier.com/locate/talanta

A new sensitive electrochemical method for the determination of vanadium(IV) and vanadium(V) in Benfield sample

Munawar Saeed Qureshi [a,*], Abdull Rahim bin Mohd Yusoff [a], Afzal Shah [b,c,**], Ayman Nafady [d], Sirajuddin [e]

[a] Institute of Environmental & Water Resource Management (IPASA), Universiti Teknologi Malaysia, Skudai, Johor, Malaysia
[b] Department of Chemistry, University of Science and Technology, Bannu 28100, Khyber Pakhtunkhwa, Pakistan
[c] School of Chemistry, Monash University, Clayton Campus 3800, Melbourne, VIC, Australia
[d] Department of Chemistry, College of Science, King Saud University, Riyadh 11451, Saudi Arabia
[e] National Center of Excellence in Analytical Chemistry, University of Sindh, Jamshoro, Pakistan

ARTICLE INFO

Article history:
Received 19 June 2014
Received in revised form
30 September 2014
Accepted 1 October 2014
Available online 14 October 2014

Keywords:
Differential pulse cathodic stripping voltammetry
Britton–Robinson
Cupferron
Benfield sample
Artificial sample

ABSTRACT

Vanadium(IV) and vanadium(V) can be determined by using differential pulse cathodic stripping voltammetry technique (DPCSV). Cupferron (ammonium *N*-nitrosophenylhydroxylamine) was used as ligand to form complex compounds with vanadium ions in Britton–Robinson buffer (BRB) solution. At concentration lower than 1.0×10^{-6} M, both V(IV) and V(V) cupferron complexes showed a single cathodic peak at −0.576 V in BRB of pH 4; thus V(IV) and V(V) ions cannot be differentiated at low concentration. However, the ionic species of vanadium can be differentiated at high concentration in the presence of cupferron. Parameters including pH of BRB solution, initial potential and accumulation potential were optimized. Under the optimized parameters, the limit of detection (LOD) was 0.09 nM, and the peak current was linear in the concentration range 0.01–0.9 μM total vanadium ions. The determination of V(IV) and V(V) ions was carried out at higher concentration in the sample using calibration plot method. At higher concentration range of 10–60 μM V(IV) and V(V) ions were determined with LOD of 1.2 and 1.1 μM, respectively. The developed method was successfully applied to 10,00,000 fold diluted Benfield sample and 0.6227 M total vanadium ions were determined. The determination of V(IV) and V(V) ions were also successfully carried out in artificial sample as well as Benfield sample (dilution factor, 10,000). The concentration of V(IV) and V(V) ions was 22.52 μM and 38.91 μM, respectively, giving total vanadium concentration of 0.6143 M in Benfield sample.

© 2014 Elsevier B.V. All rights reserved.

1. Introduction

Vanadium(V) is widely used and released into environment from various industrial processes [1]. Natural sources like weathering of soil, marine aerosols and volcanic emissions also contribute their concentration to the atmosphere. Vanadium exists unbound in nature. Various vanadium ores are known but none is mined as such for the metal and generally; vanadium is obtained as byproducts of other ores. Vanadium has been identified in the sun, stars, meteorites, variety of plants and animals [2]. The majority of vanadium release in the atmosphere results from human activity, particularly by the combustion of oil and coal and as by-product of petroleum refining. Vanadium enters water bodies from deposition of airborne particulates, weathering of vanadium rich soils, and direct dumping. Most of the vanadium in aquatic systems is natural and result of soil runoff [3].

The toxicity of vanadium depends on its physico-chemical state; particularly on its valence state and solubility. Pentavalent V_2O_5 has been reported more toxic as compared to trivalent V_2O_3. Vanadium compounds are poorly absorbed through the gastrointestinal system. Inhalation exposures to vanadium and vanadium compounds result primarily in adverse effects to the respiratory system. Quantitative data are, however, insufficient to derive a sub-chronic or chronic inhalation. There is little evidence that vanadium or its compounds are reproductive toxins or teratogens. There is also no evidence that any vanadium compound is carcinogenic [4].

The analytical methods most often used to determine vanadium in environmental samples are; high performance liquid chromatography (HPLC) [5–7], ion chromatography hyphenated with inductively coupled plasma-optical emission spectrometry (ICHICP-OES)

* Corresponding author. Tel.: +60 75531579; fax: +60 75531575.
** Corresponding author at: Department of Chemistry, University of Science and Technology, Bannu 28100, Khyber Pakhtunkhwa, Pakistan.
E-mail addresses: munawar@utm.my (M.S. Qureshi), afzalnm@yahoo.com (A. Shah).

http://dx.doi.org/10.1016/j.talanta.2014.10.005
0039-9140/© 2014 Elsevier B.V. All rights reserved.

[8], atomic absorption spectrometry (AAS) [9,10], spectrofluorimetry [11], atomic emission spectrometry (AES) [12], adsorptive stripping voltammetry (AdSV) with different complexing agents, such as alizarin violet [13], cupferron [14,15], gallic acid/catechol [16] chloranilic acid [17], catalytic effects [18–20] and differential pulse polarography (DPP) [21,22]. Cathodic stripping voltammetry (CSV) has wide range of applications in the determination of metal ions [23,24], organic species [25] and complexes [26].

The main aim of the undertaken study was to develop novel, robust, highly sensitive and selective method for the quantitative determination vanadium ions and to apply the developed method to Benfield sample solutions. Artificial samples were also screened for respective vanadium ions by the currently developed method.

2. Experimental

2.1. Instrumentation and chemicals

Trace analyzer of Metrohm, Autolab with GPES 4.9.005 software has been used for the determination of vanadium(IV) and vanadium(V) ions. The electrochemical cell comprised of Hanging Mercury Drop Electrode (HMDE) as working electrode, Ag/AgCl 3 M KCl_{sat} as reference electrode and Platinum as auxiliary electrode. Cyber Scan 500 pH meter was used for pH measurements. All chemicals; vanadium(IV) oxide sulfate hydrate, ammonium metavanadate, cupferron, boric acid, *ortho* phosphoric acid, sulphuric acid, hydrochloric acid, sodium hydroxide and glacial acetic acid were of analytical grade and purchased from Merck (Germany). Britton–Robinson buffer solution was prepared by dissolving 2.47 g of boric acid in 200 mL deionized water. 2.3 mL of glacial acetic acid and 2.7 mL of *ortho* phosphoric acid were added into the boric acid solution. The mixture was transferred into 1 L volumetric flask and deionized water was added up to the calibration mark. The pH range of buffer from 2–12 was adjusted and maintained with 2 M NaOH and 2 M HCl.

2.2. Methodology

100 μL standard solution of analyte (vanadium ions) in 20 mL BRB solution was taken into the voltammetric cell. The solution in the cell was also treated with sufficient amount of pH adjuster so that we get a pH 4.0 at the end. Nitrogen gas was purged through the solution for 5 min to create an inert gas atmosphere inside the cell and in order to remove the dissolved oxygen from the analyte solution. During pretreatment and accumulation process for 30 s, the solution was stirred at 0 V initial potential. After accumulation for 30 s, stirring was stopped and solution was equilibrated for 2 s used as a quiescent time. Then, the solution was scanned at 200 mV/s and voltammograms were recorded via current-potential measurement using DPCSV electrochemical technique. Similar procedure was employed for standard solutions of V(IV) and V(V) ions. Sensitivity, reproducibility and linearity of response were checked by addition of standard solutions and triplicate analyses.

2.3. Determination of vanadium in Benfield sample solution

In the experiment, a few microliter of Benfield sample mixed with BRB and required amount of cupferron was added into voltammetric cell and scanned. Sample dilution is needed if the voltammograms of vanadium–cupferron complexes are out of range. Such problem may also be caused by high content of carbonate ions in sample or if the sample is too concentrated. If content of carbonate ion is too high, dilution of sample should be done by adding a few microliter of 1.0 M sulphuric acid into sample based on the ratio needed. The pH was adjusted to 4.0 ± 0.1 with 2 M NaOH solution. The rest of the voltammetric procedure is same as true in case of standard vanadium solution. Nearly similar protocol was followed in case of vanadiumV(IV) and V(V) ions determination via developed voltammetric method.

3. Results and discussion

3.1. Effect of pH

Buffer solutions were used as electrolytes to enhance the conductivity, avoid the current shifting and allow the metal ions adsorption on the surface of electrode [27,28]. Due to the limitation of Britton–Robinson buffer solution, HCl and NaOH were used for pH adjustment. The pH range from 2-12 was optimized (Table 1 and Figs. 1–3).

Based on Table 1, the V(IV) ions did not show any peak current after addition of 100 μL of 0.1 mM V(IV). The peak current was found to increase with increasing the cupferron concentration for each pH. As the concentration of cupferron was increased to 50 μM the current increased drastically. Peak current increased from pH 2 to pH 4 and decreased at pH 5. The peak potential shifted towards more negative value i.e. from −0.463 V to −0.601 V. Table 1 also shows the effect of pH on peak shifting. The range of peak potential was found between −0.538 V and −0.626 V. pH 4 gave maximum peak current (592 nA) at peak potential (−0.588 V).

Low peak current values (7–10 nA) were obtained for pH 10 to pH 12 while no peak was recorded at pH 13. Maximum peak current values for both V(IV) and V(V) ions were obtained at pH 4.

Table 1
Effect of pH on peak current values for vanadium ions.

pH	Cupferron (μM)	0.5 μM [V(IV) and V(V)] without cupferron		0.5 μM V(IV) with cupferron		0.5 μM V(V) with cupferron	
		E (V)	*I* (nA)	*E* (V)	*I* (nA)	*E* (V)	*I* (nA)
2	10	–	–	−0.463	−92.48	−0.463	−116.6
	30	–	–	−0.475	−250.3	−0.488	−330.1
	50	–	–	−0.488	−378.4	−0.500	−482.8
3	10	–	–	−0.563	−91.97	−0.563	−126.8
	30	–	–	−0.576	−305.7	−0.576	−322.2
	50	–	–	−0.588	−435.0	−0.588	−425.5
4	10	–	–	−0.563	−157.5	−0.576	−169.2
	30	–	–	−0.576	−409.0	−0.588	−389.5
	50	–	–	−0.588	−592.6	−0.601	−575.2
5	10	–	–	−0.588	−174.0	−0.588	−109.9
	30	–	–	−0.601	−383.1	−0.613	−220.9
	50	–	–	−0.601	−530.2	−0.613	−273.1
6	10	–	–	−0.601	−18.63	−0.601	−22.97
	30	–	–	−0.613	−64.50	−0.613	−65.84
	50	–	–	−0.626	−110.5	−0.626	−100.5
7	10	–	–	−0.601	−6.506	−0.601	−6.928
	30	–	–	−0.613	−24.38	−0.613	−22.85
	50	–	–	−0.613	−43.22	−0.613	−40.47
8	10	–	–	−0.538	−3.853	−0.551	−3.531
	30	–	–	−0.601	−9.042	−0.588	−6.593
	50	–	–	−0.601	−16.80	−0.601	−11.35
9	10	–	–	−0.588	−3.658	−0.588	−3.789
	30	–	–	−0.601	−5.424	−0.601	−4.858
	50	–	–	−0.601	−7.473	−0.601	−6.488
10	10	–	–	−0.638	−3.790	−0.626	−4.037
	30	–	–	−0.638	−5.697	−0.638	−5.122
	50	–	–	−0.638	−7.253	−0.638	−6.520
11	10	–	–	−0.676	−3.955	−0.676	−4.319
	30	–	–	−0.676	−6.006	−0.676	−5.654
	50	–	–	−0.676	−7.741	−0.676	−6.925
12	10	–	–	−0.701	−4.222	−0.701	−3.721
	30	–	–	−0.701	−6.312	−0.688	−5.338
	50	–	–	−0.701	−8.151	−0.688	−6.979

Peak potential = *E* (V), peak current = *I* (nA).

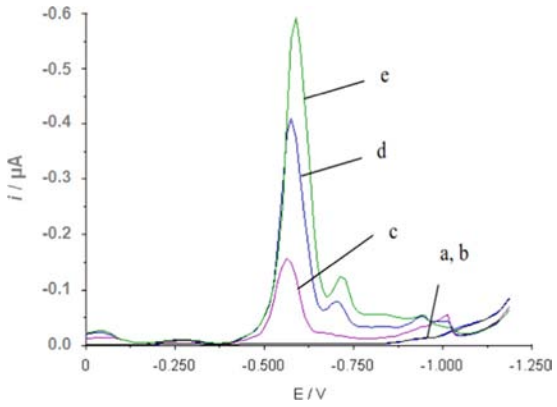


Fig. 1. Voltammogram of vanadium(IV) ions; pH 4; (a) 20 mL of 0.04 M BRB as supporting electrolyte; (b) 100 µL V(IV); (c) 100 µL V(IV)+20 µL cupferron; (d) 100 µL V(IV)+60 µL cupferron, (e) 100 µL V(IV)+100 µL cupferron. E_i=0 mV, E_{acc}=0 mV, t_{acc}=30 s, scan rate=200 mV/s, concentration of BRB=0.04 M; V(IV) ions=0.0001 M, concentration of cupferron=0.01 M.

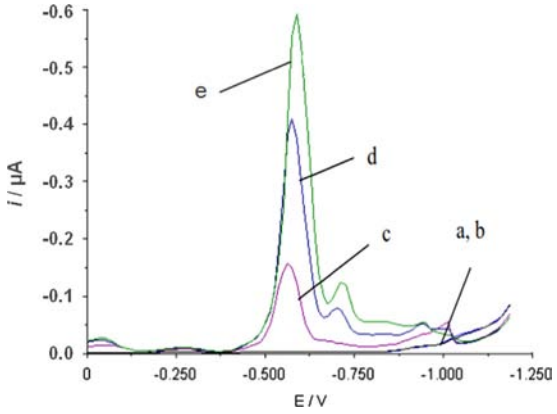


Fig. 2. Voltammogram of V(V) ions at pH 4 with BRB 0.04 M as supporting electrolyte. (a) 20 mL BRB pH 4, (b) 100 µL V(V), (c) 100 µL V(V)+20 µL cupferron, (d) 100 µL V(V)+60 µL cupferron, (e) 100 µL V(V)+100 µL cupferron. E_i=0 mV, E_{acc}=0 mV, t_{acc}=30 s, scan rate=200 mV/s, concentration of V(V) ions=0.0001 M, concentration of cupferron=0.01 M.

The overall peak potential was proportional to pH and shifted towards negative value.

The shape and pattern of voltammograms at different pH values were almost same. However, peak current values at pH 2–pH 5 were higher than pH 6–pH 12. It is evident from Table 1 that peak current decreases with shift of pH from acidic to basic medium. The lower peak current values may be due to the formation of unstable complexes.

3.2. Comparison of electrochemical results obtained for V(IV) and V(V) ions

The shifting of peak potential and variations in magnitude of peak current are highly sensitive to pH change. Fig. 3(a) and (b) show voltammograms for V(IV) cupferron and V(V) cupferron complexes at pH 3 to pH 12, respectively. Fig. 3(a) and (b) show that pH 4 is the optimum parameter, which generates maximum peak currents −592.6 nA and −575.2 nA for both V(IV) and V (V) complexes, respectively. The corresponding peak potential values −0.588 V and −0.601 V were true for V(IV) and V(V), respectively.

It is evident from Fig. 3(c) that variations in pH and application of 0.04 M BRB as supporting electrolyte greatly affect the magnitude of peak currents. The magnitude of peak current −592.6 nA for V(IV) ions is slightly higher than −575.2 nA for V(V) ions.

3.3. Effect of initial potential

Initial potential effect was optimized to get well-resolved and best-shaped voltammograms with maximum peak current values. Initial potential, E_i was used for cleaning the electrode's surface while accumulation potential, E_{acc} was used for the deposition of analyte on the electrode's surface. Electrode potentials control the deposition and stripping of analyte based on oxidation/reduction processes. Peak current is function of stripping process and its magnitude is the measure of analyte concentration [8]. The range of initial potentials from 0 mV to −900 mV was used to study the effect of initial potential for the determination of V(IV) and V(V) ions as shown in Fig. 4(a) and (b). The highest peak current values −28.22 nA at E_{peak}=−0.188 V with E_i=0 mV and −72.61 nA at E_{peak}=−0.963 with E_i=−200 mV were obtained for V(IV) and V (V) ions respectively.

The trend of the peak currents was decreased for the initial potential from −200 mV to −900 mV. Initial potential of −200 mV gave the highest peak current at −73.9 nA, whereas, the 0 mV initial potential gave the second high peak current at −72.61 nA. Since the difference between peak currents in case of -200 mV and 0 mV of initial potential was very small which is less than 1 nA, therefore, initial potential at 0 mV for V(V) ions can be chosen as optimum initial potential.

The range of accumulation potentials from 0 mV to −900 mV was also optimized to get maximum peak currents for the determination of V(IV) and V(V) ions (Fig. 5). The highest peak current values −28.63 nA at E_{acc}=0 mV and −75.5 nA at E_{acc}=0 mV were obtained for V(IV) and V(V) ions, respectively. While, the lowest peak current values −11.12 nA at E_{acc}=−900 mV and −16.58 nA at E_{acc}=−900 mV were obtained for V(IV) and V(V) ions, respectively. However, the trend of the accumulation potential effect for both V (IV) and V(V) ions was almost similar. The graph showed the decreasing of peak currents from 0 mV to −900 mV of accumulation potential for the determination of both V(IV) and V(V) ions. The peak currents obtained for V(V) ions were always greater than V(IV) ions. The maximum peak current values in both cases can be obtained at E_{acc}=0 mV.

3.4. Effect of cupferron concentration on peak current

Variable concentrations of cupferron (ligand) and vanadium species (analyte metal ions) were mixed and electrochemically scanned. The range of volumetric proportions was 20–100 µL while range of molar concentrations was 0.001–0.01 M in each analysis. The addition of V(IV) and V(V) ions into the voltammetric cell without cupferron did not show any voltammogram (peak current). However, after the addition of cupferron, peak currents were obtained (Table 2). In case of V(IV) ions, maximum peak currents for both concentrations (0.001 M and 0.01 M) of cupferron were obtained at E_{peak}=−0.576 V. In case of 0.01 M cupferron, peak currents −171.6 nA, −278.4 nA and −425.2 nA were obtained for 20 µL, 60 µL and 100 µL of cupferron, respectively. However, in case of 0.001 M cupferron, peak currents −10.81 nA, −66.94 nA and −109.5 nA were obtained for 20 µL, 60 µL and 100 µL of cupferron, respectively. Addition of 0.01 M cupferron gave higher results as compared to 0.001 M cupferron. The same trend and pattern of electrochemical results were observed for V (V) ions, (Table 2).

3.5. Analysis of vanadium ions in Benfield samples

The developed method was successfully applied to Benfield samples, which were collected from the oil and gas company in Terengganu, Malaysia. Calibration curves method was used to

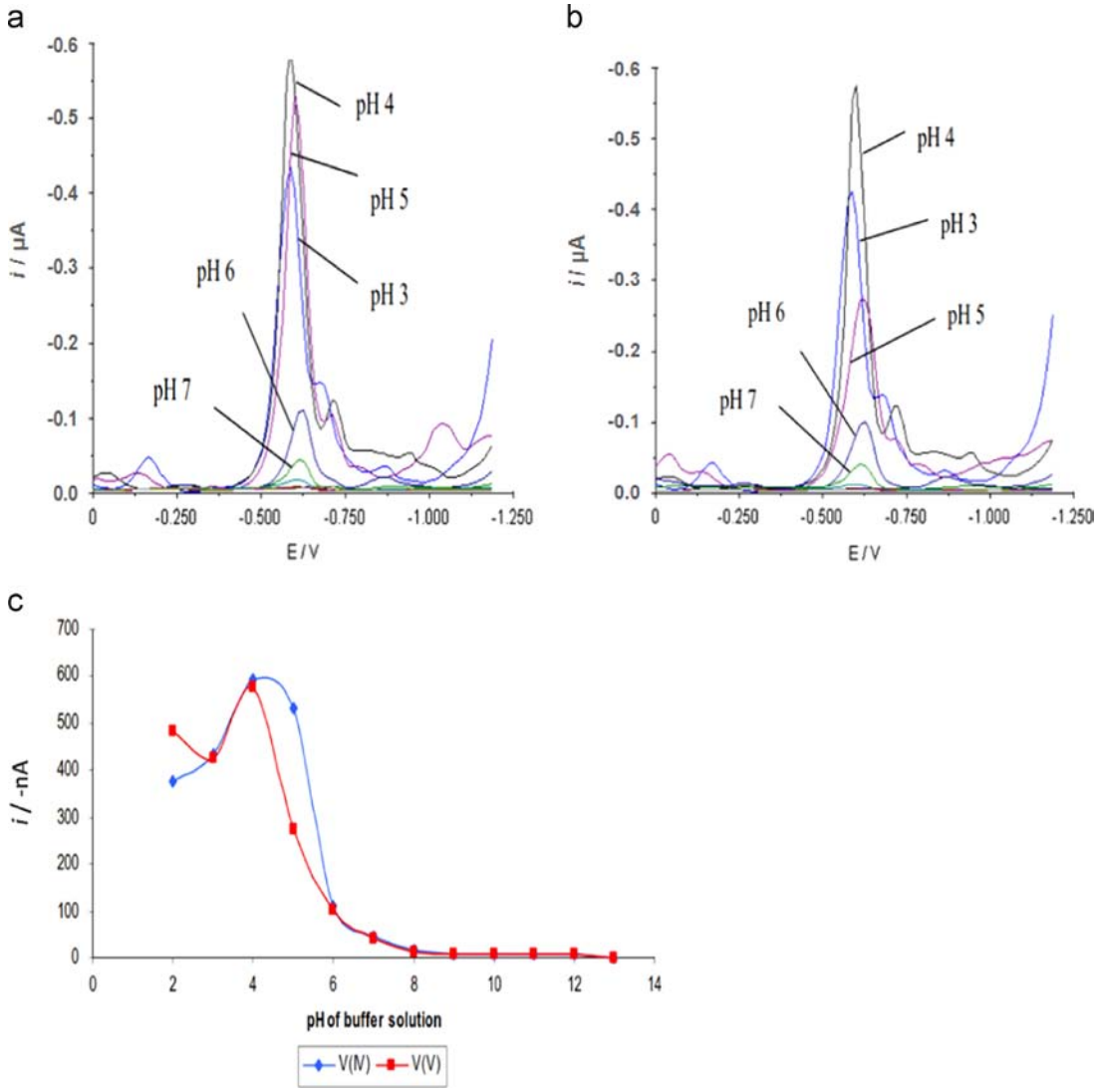


Fig. 3. (a and b) Voltammogram of peak currents for (a) V(IV) and (b) V(V) ions from pH to pH 12 with BRB 0.04 M as supporting electrolyte. E_i=0 mV, E_{acc}=0 mV, t_{acc}=30 s, scan rate=200 mV/s, concentration of V(IV) and V(V) ions=0.0001 M, concentration of cupferron=0.01 M. (c) Comparison for the effect of pH buffer solution from pH 2 to pH 13 with BRB 0.04 M as supporting electrode for the determination of V(IV) and V(V) ions. E_i=0 mV, E_{acc}=0 mV, t_{acc}=30 s, scan rate=200 mV/s, concentration of V(IV)=0.0001 M, concentration of V(V)=0.0001 M, concentration of cupferron=0.01 M.

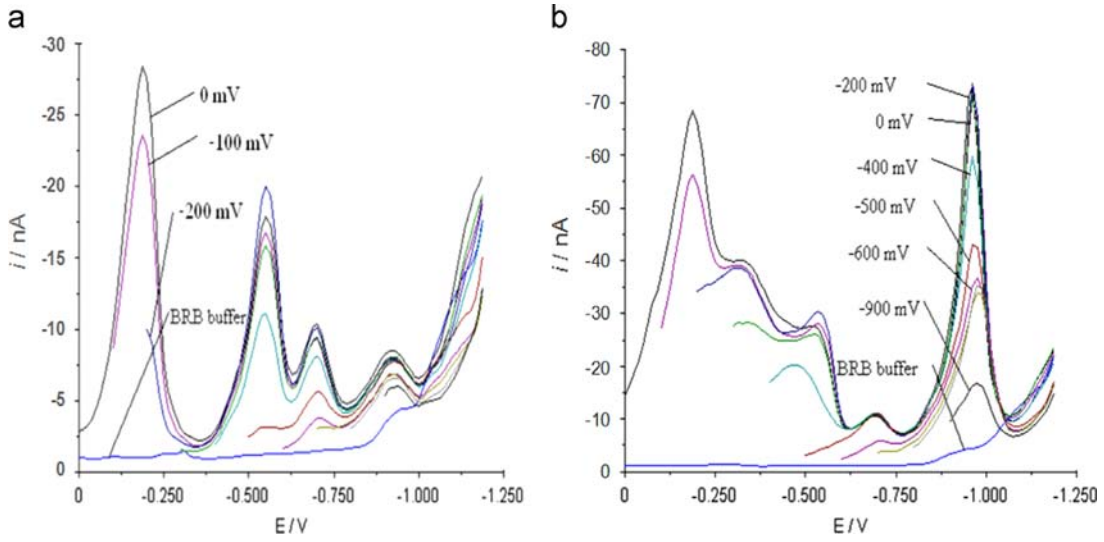


Fig. 4. Voltammogram of peak currents for (a) V(IV) and (b) V(V) ions on different initial potentials, E_i by using pH 4 BRB 0.04 M as supporting electrolyte, scan rate=200 mV/s, E_{acc}=0 mV, t_{acc}=30 s, concentration of V(IV) and V(V) ions in cell=1×10^{-5} M, concentration of cupferron=0.001 M.

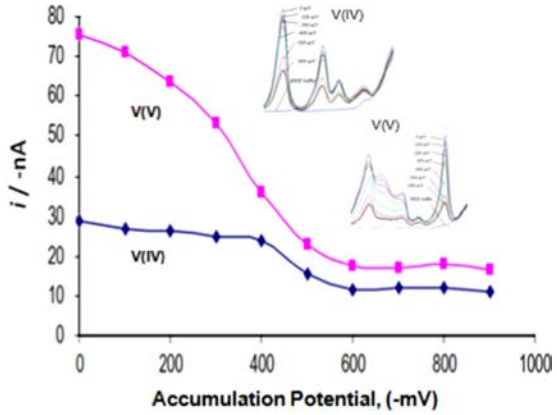


Fig. 5. Comparison of the peak currents obtained from the effect on accumulation potential from 0 mV to −900 mV for determination of V(IV) and V(V) ions. BRB 0.04 M at pH 4 as supporting electrolyte, E_i=0 mV, t_{acc}=30 s, scan rate=200 mV/s, concentration of V(IV) ions in cell=1×10^{-5} M, concentration of V(V) ions in cell=1×10^{-5} M, concentration of cupferron=0.001 M.

Table 2
Peak currents obtained from different concentrations of V(IV), V(V), and cupferron.

Molar concentration	Vanadium [μM]	Cupferron [μM]	Potential E (V)	Current *I* (nA)
0.001 M V(V)+0.01 M cupferron	1	–	–	–
	3	–	–	–
	5	–	–	–
	5	10	−0.551	−154.1
	5	30	−0.563	−283.1
	5	50	−0.576	−390.6
0.001 M V(IV)+0.01 M cupferron	1	–	–	–
	3	–	–	–
	5	–	–	–
	5	1	−0.551	−10.81
	5	3	−0.563	−66.94
	5	5	−0.576	−109.5
0.001 M V(V)+0.001 M cupferron	1	–	–	–
	3	–	–	–
	5	–	–	–
	5	1	−0.551	−10.52
	5	3	−0.576	−64.05
	5	5	−0.576	−112.2
0.01 M V(IV)+0.001 M cupferron	10	–	–	–
	30	–	–	–
	50	–	–	–
	50	1	−0.188	−23.72
	50	3	−0.188	−62.11
	50	5	−0.175	−82.66
0.01 M V(V)+0.001 M cupferron	10	–	−0.976	−58.80
	30	–	−1.001	−291.18
	50	–	−1.013	−383.4
	50	1	−1.013	−385.3
	50	3	−1.013	−377.3
	50	5	−1.013	−374.9

pH 4 BRB 0.04 M buffer solution as supporting electrolyte. E_i=0 mV, E_{acc}=0 mV, t_{acc}=30 s.

determine the unknown concentrations and LOD for vanadium ions.

Under the optimized parameters, the concentration range 0.01–0.9 μM of vanadium ions showed linear relationship to peak currents. The linear regression coefficient R^2=0.9858 and limit of detection 0.09 nM were calculated using calibration plot method, (Fig. 6). In each case, 100 μL of 5000 fold diluted Benfield sample (giving a total dilution factor of 10,00,000) was electrochemically scanned to determine the unknown concentration of vanadium ions. This gives a concentration of 6.227×10^{-7} M vanadium. Using the calibration equation and multiplication by dilution

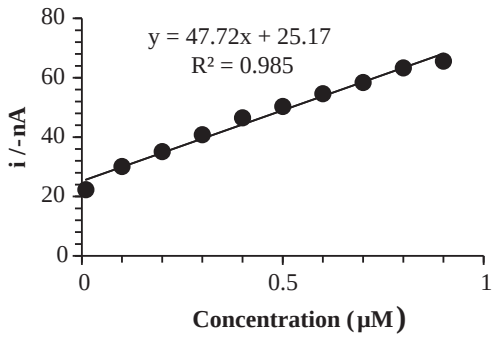


Fig. 6. Caliberation Plot; BRB 0.04 M at pH 4 as supporting electrolyte, E_i & E_{acc}=0 mV, t_{acc}=30 s, scan rate=200 mV/s, concentration range of vanadium ions, 0.01–0.9 μM, concentration of cupferron=0.001 M.

factor, concentrations of total vanadium ions in Benfield sample becomes 0.6227 M. The results of calibration plots were validated by using standard addition method which gave nearly same results. The amount of V(IV) and V(V) ions in Benfield sample was also carried out at higher concentration range in sample with low dilution of 10,000 (see below).

3.6. Calibration of V(IV) and V(V) at higher concentrations

The estimation of V(IV) and (V) ions were also achieved in the concentration range of 10–60 μM at under similar condition as true for calibration curve at lower range as mentioned in Section 3.5. It was noticed that the detection limit of in case of V(IV) was 1.2 μM and 1.1 μM in case of V(V) ions. Calibration plots are displayed in Figs. S1a and S1b (see Supplementary data). In order to verify the determination of V(IV) and V(V) ions by respective linear calibration plots, we analyzed these ions in an artificial sample with different concentration of ions as depicted in Table S1 of supplementary data file. The results show very close recovery among the added and determined values of these ions in the sample, which validate this method very well regarding the separation of V(IV) and V(V) ions in higher concentrations range. In addition we determined the concentration of V(IV) and V (V) ions in Benfield sample by taking 100 μL of 100 fold diluted (giving a total dilution factor of 10,000). The amount V(IV) ions came out to be 22.52 μM which is equal to a concentration of 0.2252 M V(IV) ions while amount of V(V) ions was 38.91 μM in diluted sample giving a total concentration of V(V) ions of 0.3891 M. By adding the amount of V(IV) and V(V) ions in the mixture a total amount of 0.6143 M vanadium is obtained which is nearly equal to total vanadium concentration of 0.6227 M as determined by calibration plot method at lower concentration in Section 3.5. This result further strengthens the validation of developed method.

3.7. Figure of merits

The presently developed voltammetric method in higher concentration ranges for determining V(IV) and V(V) ions was and total V(V) ions determination at lower concentration range was compared with several electrochemical methods for vanadium determination. Table 3 shows the comparison of data regarding the linear ranges of determination of vanadium ions and respective LODs with respect to our developed method shown in Refs. [17,21,32–37].

The data listed in Table 3 clearly indicates the superiority of our methods over the cited method especially in regards to separation and determination of V(IV) and V(V) as illustrated in Fig. S1a and b as well as in Table S1. In other words, this approach is a novel

Table 3
Comparison of results for determination of V(IV) and V(V) by various electrochemical techniques.

Electro-analytical method	V(IV)	V(V)	Refs.
Adsorptive stripping voltammetry	–	LR: 0.25–150 nM LOD: 0.0098 nM	[17]
Catalytic adsorptive stripping voltammetry	–	LR: 0.2–50 nM LOD: 0.009 nM	[21]
Differential pulse polarography	–	LR: 9.8–200 μM LOD: 3.9 μM	[32]
Adsorptive cathodic stripping voltammetry	–	LR: 0–1.47 μM LOD: 0.2 nM	[33]
Catalytic adsorptive stripping voltammetry	–	LR: 0.2–10 nM LOD: 0.07 nM	[34]
Catalytic stripping voltammetry	–	LR:0.05–4 nM LOD: 0.015 nM	[35]
1.5th and 2.5th order derivative adsorption voltammetry	–	LR:0.5–200 nM LOD: 0.0025 nM	[36]
Potentiometric titration	–	LR:0.5–2000 μM LOD: NM	[37]
Differential pulse cathodic stripping voltammetry	LR: 10–60 μM LOD: 1.2 μM	LR:10–60 μM as V(V) with LOD: 1.1 μM LR: 0.01–0.9 μM as total V with LOD: 0.09 nM,	This work

LR, linear range; LOD, limit of detection; NM, not mentioned.

finding where the specific concentration of cupferron plays a crucial role in separation and determination of both the mentioned ions of vanadium. This strategy could be employed to estimate the respective ions of vanadium in other types of samples as well.

4. Conclusions

The differential pulse cathodic stripping voltammetry is the most sensitive voltammetric technique and used for trace level determinations. This technique was used in the determination of vanadium(IV) and vanadium(V) ions. The V(IV) and V(V) ions showed no peak at low concentration without cupferron (a complexing agent). High peak currents were produced when cupferron was added as a ligand. The optimum values of initial potential, final potential and accumulation time (t_{acc}) were 0 mV, −1.2 V and 30 s, respectively. The metal deposition on electrode's surface was held at 0 mV accumulation potential. The electronic structures of metals significantly affect the formation of complexes. Different ionic species of a metal have different affinity for a complexing ligand. When higher amounts of cupferron was added, more cupferron-vanadium complexes may be formed, which produce maximum peak currents. While, at lower amounts of cupferron, less formation of complex may occur, this gives small peak currents and makes it difficult to differentiate ionic species of vanadium. At higher concentration, cupferron may form different complexes with V (IV) and V(V) ions. The variations in the geometrical pattern and electrochemical behavior of these different complexes may affect the shifting of peak potential and magnitude of peak current for the respective ionic specie of vanadium. Hence, peak shifting and variation in the magnitude of peak currents cause the differentiation of V(IV) and V(V) ions. Comparatively, the developed method has high selectivity and sensitivity for vanadium ions. It is highly cost effective and easy in preparation of stable electrochemical cell set-up. In the undertaken study, the LOD was found to be 1.2 μM and 1.1 μM for V(IV) and V(V) ions in the higher range and 0.09 nM for total vanadium in lower range. Such findings highlight a clear edge of developed method over other method cited elsewhere [13,17,21,23,24,29–37].

Acknowledgments

We acknowledge the financial support provided by University of Technology, Malaysia and grateful to Water Research Alliance and Department of chemistry for their valuable technical assistance in this research work. Financial assistance of King Saud University by their Research Project RGP-VPP-236 is equally acknowledged and appreciated.

Appendix A. Supporting information

Supplementary data associated with this article can be found in the online version at http://dx.doi.org/10.1016/j.talanta.2014.10.005.

References

[1] K. Pyrzynska, T. Wierzbicki, Talanta 64 (2004) 823–829.
[2] R.J.H. Clark, The Chemistry of Titanium and Vanadium: An Introduction to the Chemistry of the Early Transition Elements, Publisher Elsevier ASIN: B0000CODRJ, 2007.
[3] J. Rose, Environmental Health: The Impact of Pollutants, New York, USA: Gordon and Breach Science Publishers, ISBN; 2881247385, 9782881247385, 1, 2008.
[4] M. Nordberg, G.F. Nordberg, B.A. Fowler, L. Friberg, Handbook on the Toxicology of Metals, Academic Press, ISBN; 0080546102, 9780080546100, 3, 2011.
[5] G. Li, Q. Wei, Q. Hu, Z. Huang, G. Yang, Microchim. Acta 158 (2007) 95–102.
[6] F. Aureli, S. Ciardullo, M. Pagano, A. Raggi, F. Cubadda, J. Anal. At. Spectrom 23 (2008) 1009–1016.
[7] J. Peng, S. Liu, C. Deng, Anal. Sci. 21 (2005) 259–262.
[8] L. Rostampour, M.A. Taher, Talanta 75 (2008) 1279–1283.
[9] Y. Saavedra, P. Fernández, A. González, Anal. Bioanal. Chem. 379 (2004) 72–76.
[10] K.G. Fernandes, A.R.A. Nogueira, J.A.G. Neto, J.A. Nóbrega., J. Braz. Chem. Soc 15 (2004) 676–681.
[11] J. Gao, X. Zhang, W. Yang, J. Kang, Anal. Chim. Acta 455 (2002) 159–165.
[12] S.E. Dancsak, S.G. Silva, J.A. Nóbrega, B.T. Jones, G.L. Donati, Anal. Chim. Acta 806 (2014) 85–90.
[13] P.H. Deng, J.J. Fei, Y.I. Feng, J. Electroanal. Chem. 648 (2010) 85–91.
[14] S. Abbasi, H. Khani, R. Sahraei., Food Anal. Methods 5 (2012) 272–278.
[15] Q.A. Acton., Issues in General Food Research, Scholarly-Editions, ISBN; 149010951X, 9781490109510, 2013.
[16] R. Dansby-Sparks, J.Q. Chambers, Z.L. Xue, Anal. Chim. Acta 643 (2009) 19–25.
[17] R. Piech, B. Baś, B. Paczosa-Bator, W.W. Kubiak, J. Electroanal. Chem. 633 (2009) 333–338.
[18] I. Povar, T. Cazac, L. Chiriac, R. Sandulescu, J. Electroanal. Chem. 661 (2011) 275–279.
[19] W. Joseph, L. Donglai, T. Sompong, L. Yuehe, S.A. Omowunmi, Talanta 69 (2006) 914–917.
[20] M. Mazlum, Ali A. Ensafi, Int. J. Environ. Anal. Chem 81 (2001) 117–125.

[21] A. Bobrowski, K. Nowak, J. Zarebski, Anal. Chim. Acta 543 (2005) 150–155.
[22] P. Sharma, R. Rajpal, Trans SAEST 39 (2004) 61–65.
[23] E. Espada-Bellido, Z. Bi, C.M.G.V.D Berg, Talanta 105 (2013) 287–291.
[24] C.E. Banks, J. Kruusma, R.R. Moore, P. Tomčík, J. Peters, J. Davis, Š. Komorsky-Lovrić, R.G. Compton, Talanta 65 (2005) 423–429.
[25] T. Spătaru, N. Spătaru, A. Fujishima, Talanta 73 (2007) 404–406.
[26] A.A. Ensaifi, T. Khayamian, M. Taei, Talanta 78 (2009) 942–948.
[27] J. Wang, Analytical Electrochemistry, Wiley-VCH Inc., 2006.
[28] G. Henze, Introduction to Polarography and Voltammetry, Metrohm Ltd., Herisau, Switzerland (2003) 11.
[29] M.Y. Khuhawar, G.M. Arain, Talanta 68 (2006) 535–541.
[30] K. Oguma, O. Yoshioka, J. Noro, H. Sakurai, Talanta 96 (2012) 44–49.
[31] C. Yonga, Proc. Eng 24 (2011) 447–453.
[32] S. Puri, R.K. Dubey, M.K. Gupta, B.K. Puri, Talanta 46 (1998) 655–664.
[33] S.B.O. Adeloju, F. Pablo, Anal. Chim. Acta 288 (1994) 157–166.
[34] M. Vega, C.M.G. van den Berg, Anal. Chim. Acta 293 (1994) 19–28.
[35] H. Li, R.B. Smart, Anal. Chim. Acta 333 (I 996) 131–138.
[36] W. Jin, S. Shi, J. Wang, J. Electroanal. Chem. 291 (1990) 41–47.
[37] S.E. Quintar, J.P. Santagata, V.A. Cortinez, Talanta 67 (2005) 843–847.

Talanta 132 (2015) 548–556

Contents lists available at ScienceDirect

Talanta

journal homepage: www.elsevier.com/locate/talanta

Sorbent-packed needle microextraction trap for synthetic musks determination in wastewater samples

Laura Vallecillos [a], Francesc Borrull [a,*], Juan M. Sanchez [b], Eva Pocurull [a]

[a] Department of Analytical Chemistry and Organic Chemistry, Universitat Rovira i Virgili, Campus Sescelades, Marcel·lí Domingo s/n, Tarragona 43007, Spain
[b] Department of Chemistry, Universitat de Girona, Campus Montilivi, Girona 17071, Spain

ARTICLE INFO

Article history:
Received 8 May 2014
Received in revised form
31 July 2014
Accepted 5 August 2014
Available online 12 August 2014

Keywords:
Gas chromatography–tandem mass spectrometry
Needle trap
Synthetic musk fragrances
Thermal desorption
Wastewater samples

ABSTRACT

A needle trap (NT) device filled with HF Bondesil-C18 as a sorbent material was evaluated for the dynamic headspace analysis of a family of nine synthetic musks compounds that include two nitro musks, six polycyclic musks (with galaxolide and tonalide as the most widespread used polycyclic musks) and the degradation product of galaxolide (galaxolidone) in wastewater samples. Different parameters affecting the adsorption capacity of the sorbent were studied (e.g. extraction mode, extraction temperature, salt concentration, preincubation time fill and ejection speed or fill volume). Furthermore, injection parameters used with the NT device (e.g. desorption mode, desorption temperature and time) were evaluated to optimize the desorption and transfer of the target compounds into the GC column. Method detection limits obtained with gas chromatography–tandem mass spectrometry (GC–MS/MS) detection were found in the low ng L^{-1} range, between 2.5 and 10 ng L^{-1}, depending on the target compounds. Moreover, under optimized conditions, the method gave good levels of intra-day and inter-day repeatabilities in wastewater samples with relative standard deviations ($n=5$, 100 ng L^{-1}) less than 11 and 17%, respectively. The developed method was satisfactorily applied to the analysis of aqueous samples obtained from three wastewater treatment plants. All the polycyclic musks studied were detected in influent samples with cashmeran, galaxolide and tonalide as the most representative compounds. The analysis of effluent wastewater showed a decrease in the concentrations of all of the polycyclic musk detected in influent samples and an increase in the concentration of galaxolidone until a maximum value of 820 ng L^{-1}.

© 2014 Elsevier B.V. All rights reserved.

1. Introduction

Sample preparation is the cornerstone of chemical analysis. Preconcentration is a crucial step when synthetic musk fragrances often occurring in concentrations as low as μg L^{-1} or ng L^{-1} are to be determined in environmental water samples. Some preconcentration techniques such as liquid–liquid extraction (LLE) [1–3], solid-phase extraction (SPE) [4–7], dispersive liquid–liquid extraction (DLLME) [8–10], solid phase microextraction (SPME) [11,12], single drop microextraction (SDME) [13,14], microextraction by packed sorbents (MEPs) [15,16] or dispersive microsolid-phase extraction (D-μ-SPE) [17] have been reported. Of all the extraction techniques mentioned, SPE is the most widely used in the environmental analytical field because it consumes minimal amount of organic solvents and a great diversity of sorbents is commercially available.

Nevertheless the development of economical and ecological small scale sample preparation techniques that are able to meet requirements such as enhanced sensitivity and selectivity, robustness and simple handling are desirable [18,19]. In this way, solvent-free extraction methods based on the partitioning of analytes between gaseous or liquid phase and stationary phase have become important and have been widely applied in research over the last decade, with SPME as one of the most successfully approaches [20,21].

Although Raschdorf [22] developed the first device based on a needle filled with Tenax sorbent in the 1970s, needle trap (NT) extraction devices have only recently become popular due to their combination of advantages of SPME (e.g. solvent-free, fast, sensitive and one-step sample preparation and injection method) and SPE (e.g. sensitivity of the method can be increased by increasing the sample volume) with robustness, easier handling during sampling and desorption, and the fact that they permit a high degree of automation and on-line coupling to GC instruments [23–26]. The literature found up to now can be divided in two categories depending on the NT device used: (a) internally coated needles [27–29] and (b) needles packed with commercially

* Corresponding author. Tel.: +34 977559560; fax: +34 977558446.
E-mail address: francesc.borrull@urv.cat (F. Borrull).

http://dx.doi.org/10.1016/j.talanta.2014.08.016
0039-9140/© 2014 Elsevier B.V. All rights reserved.

available sorbents [26,30–36] or chemically synthesized polymers [37,38]. Regardless of the kind of NT used, the extraction by NT has the advantages of being solvent-free and of having sampling and analysis times that are significantly shorter than most existing methods.

In this study, two different needles packed with 20 mm or 30 mm of HF Bondesil-C18 sorbent were evaluated in order to determine the optimal configuration to extract the synthetic musks fragrances present in wastewater samples prior to analysis by GC–MS/MS. The different parameters affecting the adsorption capacity of the NT as well as the desorption and transferring of the target compounds into the GC were also studied. Once the most appropriate experimental conditions were found, the NT methodology was compared in terms of method validation parameters with other microextraction techniques and was successfully applied for the analysis of synthetic musk fragrances in wastewater samples.

2. Experimental part

2.1. Chemical standards

The nitro musk fragrances 2,4,6-trinitro-1,3-dimethyl-5-tert-butylbenzene (MX, musk xylene) and 1,1,3,3,5-pentamethyl-4,6-dinitroindane (MM, musk moskene) were purchased as 100 μg mL^{-1} solutions in acetonitrile from Sigma-Aldrich (Steinheim, Germany) and Riedel de Haën (Seelze, Germany), respectively. The six polycyclic musks studied were supplied by Promochem Iberia (Barcelona, Spain) and were the following: 6,7-dihydro-1,1,2,3,3-pentamethyl-4(5H)-indanone (DPMI, cashmeran), 4-acetyl-1,1dimethyl-6-tert-butyllindane (ADBI, celestolide), 6-acetyl-1,1,2,3,3,5-hexamethylindane (AHMI, phantolide), 5-acetyl-1,1,2,6-tetramethyl-3-isopropylindane (ATII, traseolide), 1,3,4,6,7,8-hexahydro-4,6,6,7,8,8-hexamethylcyclopenta-(*g*)-2-benzopyran (HHCB, galaxolide), and 7-acetyl-1,1,3,4,4,6-hexamethyl-1,2,3,4-tetrahydronaphthalene (AHTN, tonalide). International Flavors & Fragances Inc. (Barcelona, Spain) provided1,3,4,6,7,8-hexahydro-4,6,6,7,8,8-hexamethylcyclopenta-[*g*]-2-benzopyran-1-one (HHCB-lactone, galaxolidone) and the deuterated analogue ^{2}H15-Musk xylene (^{2}H15-MX, surrogate standard) was supplied as a 100 μg mL^{-1} solution in acetone by Symta (Madrid, Spain). Table 1 shows the boiling point and the octanol/water partition coefficient of each target compound.

Individual standard solutions of the synthetic musks were prepared in acetone at concentrations of 4000 μg mL^{-1} for polycyclic musks and 1000 μg mL^{-1} for HHCB-lactone. A standard mixture solution of 100 μg mL^{-1} was prepared in ethyl acetate. MX, ^{2}H15-MX and MM standards were supplied directly at a concentration of 100 μg mL^{-1} and used as received. Acetone and ethyl acetate were GC grade with purity >99.9% from Prolabo (VWR, Llinars del Vallès, Barcelona, Spain).

Ultrapure water was obtained using an ultrapure water purification system from Veolia waters (Sant Cugat del Vallés, Barcelona, Spain). Helium gas with a purity of 99.999% was used for the chromatographic analysis (Carburos Metálicos, Tarragona, Spain).

2.2. Sampling

Influent and effluent wastewater samples were collected from three urban wastewater treatment plants (WWTPs) located in Tarragona (WWTP A), Reus (WWTP B) and Vila-seca/Salou (WWTP C) between October and December 2013. The WWTPs receive urban sewage and industrial discharges from a population of about 130,000 inhabitants. The three WWTPs use activated sludge for biological treatment and the WWTP C also employs a tertiary treatment based on reverse osmosis (RO). All samples were collected by using pre-cleaned amber glass bottles and were filtered using a 1.2 μm glass fibre filter (Fisherbrand, Loughborough, UK) and a 0.22 μm nylon filter (Scharlab, Barcelona, Spain). Samples were analysed within three days of their collection (stored at 4 °C in the fridge).

Table 1
Boiling point, log K_{ow}, retention times (t_R) and parent and products ions of the target compounds.

No.	Compound	Boiling point (°C)	Log K_{ow}[a]	t_R (min)	Parent ion (m/z)	Product ions (m/z)[b]
1	Cashmeran (DPMI)	286.1	5.9	8.33	191	107, **135**, 173
2	Celestolide (ADBI)	309	5.4	10.24	229	131, **173**, 187
3	Phantolide (AHMI)	336.6	5.9	10.98	229	131, 145, **187**
4	Traseolide (ATII)	350	6.3	12.02	215	131, 171, **173**
5	Galaxolide (HHCB)	326	5.9	12.31	243	171, **213**
6	Tonalide (AHTN)	356.8	6.3	12.36	243	**145**, 159, 187
7	Musk xylene (MX)	392.3	3.8	13.24	282	**265**, 266, 281
8	Musk moskene (MM)	351.1	5.2	13.35	263	187, 201, **211**
9	Galaxolidone (HHCB-lactone)	*	*	16.93	257	183, 201, **239**
10	^{2}H15-musk xylene (^{2}H15-MX)[c]	*	*	13.10	294	170, **276**, 295

* Information not found in the bibliography.
[a] Log K_{OW} values predicted from SRC-K_{OW}Win software.
[b] Quantification ions (m/z) are shown in bold type.
[c] Surrogate standard (SS).

2.3. Preparation of the needle trap

Hamilton (Bonaduz, Switzerland) 22 gauge stainless steel (metal hub) needles (O.D.=0.718 mm, I.D.=0.413 mm and 51 mm length) with point style 5 (Fig. 1) were filled with HF Bondesil-C18 sorbent (120 μm) from Agilent Technologies (Palo Alto, USA). Stainless steel wire (AISI 316L, GoodFellow, Huntingdon, UK) of 100 μm diameter was used to prepare spiral plugs to hold sorbent particles inside the needles. First, a small piece of spiral plug (five turns, ~1.5 mm) was fixed in the tip of the needle to prevent sorbent particles from being fixed in the side hole of the needle. Then, 20 mm or 30 mm of C18 sorbent particles were positioned inside the needle. Finally, another spiral plug was carefully introduced in the upper position of the needle until it reached the end of the sorbent layer to fix the sorbent particles. Using this needle configuration, needle traps were conditioned in the GC injector at 230 °C for 30 min to eliminate any contaminations from the manufacturing process or shipping. Each needle was stored inside a closed vial until analysis.

2.4. Needle trap extraction

A CombiPAL autosampler (CTC Analytics, Zwigen, Switzerland) equipped with a single Magnet Mixer, a 100 μL Hamilton syringe and controlled by the Cyclo Composer Macro Editor 1.4 Software was used for the fully automated needle trap (NT) micorextraction. The general microextraction procedure was as follows: 10 mL of sample or standard solution was introduced into a 20 mL HS glass vial and immediately sealed with a Teflon septum. When the temperature of the heat/stir accessory reached 60 °C, the vial was automatically transported there and the headspace was allow to equilibrate with the sample at the extraction temperature for 15 min. The needle with 30 mm of HF Bondesil-C18 sorbent was inserted in the vial to perform the HS dynamic extraction. 500 μL of headspace vapours

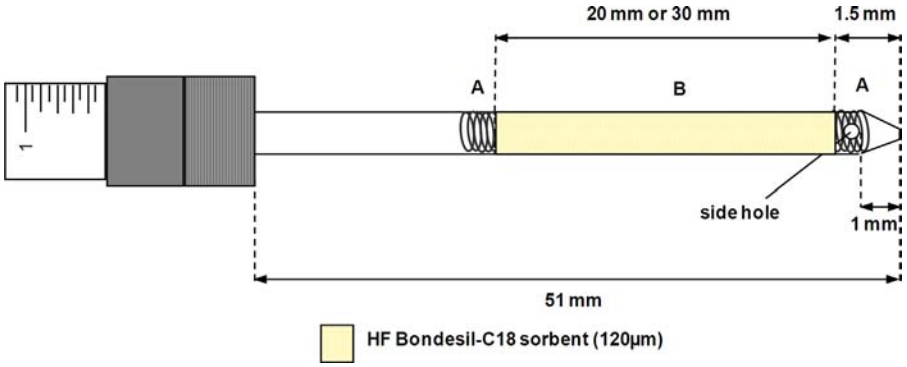


Fig. 1. Sorbent-packed needle trap device: (A) spiral plugs and (B) sorbent material.

were then percolated by pumping up through the sorbent 5 cycles of 100 μL at 10 μL s^{-1} fill and 30 μL s^{-1} ejection speeds. Afterward, the desorption was conducted at 230 °C for 3 min and the compounds were subsequently analysed by GC–MS/MS.

2.5. Gas chromatography–tandem mass spectrometry

GC–MS/MS analyses were performed on a Varian 3800 gas chromatograph (Varian, Walnut Creek, CA, USA) connected to a Varian 4000 ion trap detector. The GC was equipped with a 1079 programmable temperature injector and a 0.8 mm i.d. insert liner (Varian) and a CombiPal autosampler (CTC Analytics, Zwigen, Switzerland). A fused silica capillary column (3 m × 0.25 mm i.d.) from Micron Phenomenex (Torrance, CA, USA) was used as a guard column. The chromatographic separation was done in a midpolarity phase capillary analytical column with 50% diphenyl/50% dimethylpolysiloxane (30 m × 0.25 mm i.d.; 0.25 μm film thickness) from Micron Phenomenex. The oven temperature was programmed as follows: 70 °C hold for 3 min, raised at 40 °C min^{-1} to 180 °C, then 5 °C min^{-1} to 220 °C and finally 20 °C min^{-1} to 280 °C (hold 3.25 min). The carrier gas employed was helium with purity of 99.999%, at a constant flow of 1 mL min^{-1}. During the thermal desorption the injector was operated in splitless mode at 230 °C. Temperatures of transfer line, manifold and trap temperatures were 280 °C, 50 °C and 200 °C, respectively. A filament-multiplier delay of 3 min was established in order to increase filament's service life. The mass spectrometer analysed the substances after electron impact ionization in tandem mass spectrometry mode (MS/MS).

3. Results and discussion

3.1. GC–MS/MS optimization

A mixed solution of 10 μg mL^{-1} of the target musk fragrances and 1 μg mL^{-1} of ^{2}H15-MX as surrogate standard (SS) was prepared in ethyl acetate and 1 μL of this solution was directly injected into the GC–MS, using electron ionization fragmentation in full scan mode. All compounds were separated in just 17 min using the chromatographic conditions described in Section 2.4. Under optimum chromatographic conditions, the chromatogram (Fig. 2a) also shows the separation of two galaxolide stereoisomers (4S, 7S; 4S, 7R). The galaxolide was quantified by integrating the 4S and 7R/S peaks together due to the fact that both stereoisomers are responsible for the musky odour [39]. In order to achieve maximum sensitivity/selectivity of the compounds, the MS/MS method was carried out by selecting appropriate precursor/product ions and the MS/MS parameters optimized in a previous paper [14]. The three product ions selected for a correct identification of the target analytes as well as the retention time and the parent ion of each analyte are summarized in Table 1. Each compound was acquired separately in one segment, except, HHCB and AHTN and the target nitro musks (^{2}H15-MX, MX and MM).

3.2. Needle trap optimization

To optimize needle trap (NT) microextraction conditions, two different NT were tested, the first one contained 20 mm of HF Bondesil-C18 sorbent while the second one was filled with 30 mm of the same sorbent. HFBondesil-C18 sorbent was selected as extraction sorbent due to its ability to extract a wide range of non polar compounds, including synthetic musk fragrances, by establishing nonpolar interactions [4,6,16]. More selective SPE sorbents previously used to extract synthetic musk fragrances from environmental samples, as Oasis HLB [5] or Bond Elut Nexus [7], were discharged because they are not commercially available at higher particle sizes (100–250 μm). The particle size would affect the packing density and consequently affect the capacity, the extraction efficiency and desorption efficiency of the NT device. As has been demonstrated by Zhan and Pawliszyn [40], NTs packed with small particles possess higher extraction capacity and efficiency but much higher resistances to flow as well. In addition, the use of low particle size sorbents could make pneumatic restrictions and generation of bubbles and important factor to take into account.

The main parameters that affect the sorption and desorption process in NT microextraction were optimized for each needle in order to maximize the chromatographic peak area of the compounds by analysing a standard mixed solution of 1 μg L^{-1} of all the target musks and the SS ^{2}H15-MX in 10 mL of ultrapure water. To obtain the best conditions for each needle, such variables as extraction mode, extraction temperature, salt concentration, preincubation time, fill and ejection speed, fill volume and desorption parameters (temperature and time) were optimized because these factors were expected to be the most influential in the extraction process. Taking into account our previous experience in the determination of synthetic musk fragrances in wastewater samples by SDME and previous literature on synthetic musks [12,14,41,42], the initial experimental conditions selected were as follows: 300 g L^{-1} NaCl, 80 °C extraction temperature, 5 min preincubation time, 200 μL fill volume (2 cycles × 100 μL), 30 μL s^{-1} fill and ejection speed, and 3 min of desorption time at 230 °C. In the same way, sample volume and stirring rate were fixed at 10 mL (20 mL HS vials) and 750 rpm, respectively.

Firstly the extraction mode was optimized. As musk fragrances are semi-volatile compounds two extraction modes were tested, immersion [43] and headspace [26,30]. The results showed that immersion mode provided higher peak areas than those obtained by headspace mode for all of the target compounds using both 20 mm and 30 mm NTs (data not shown). However, due to the trap's pneumatic

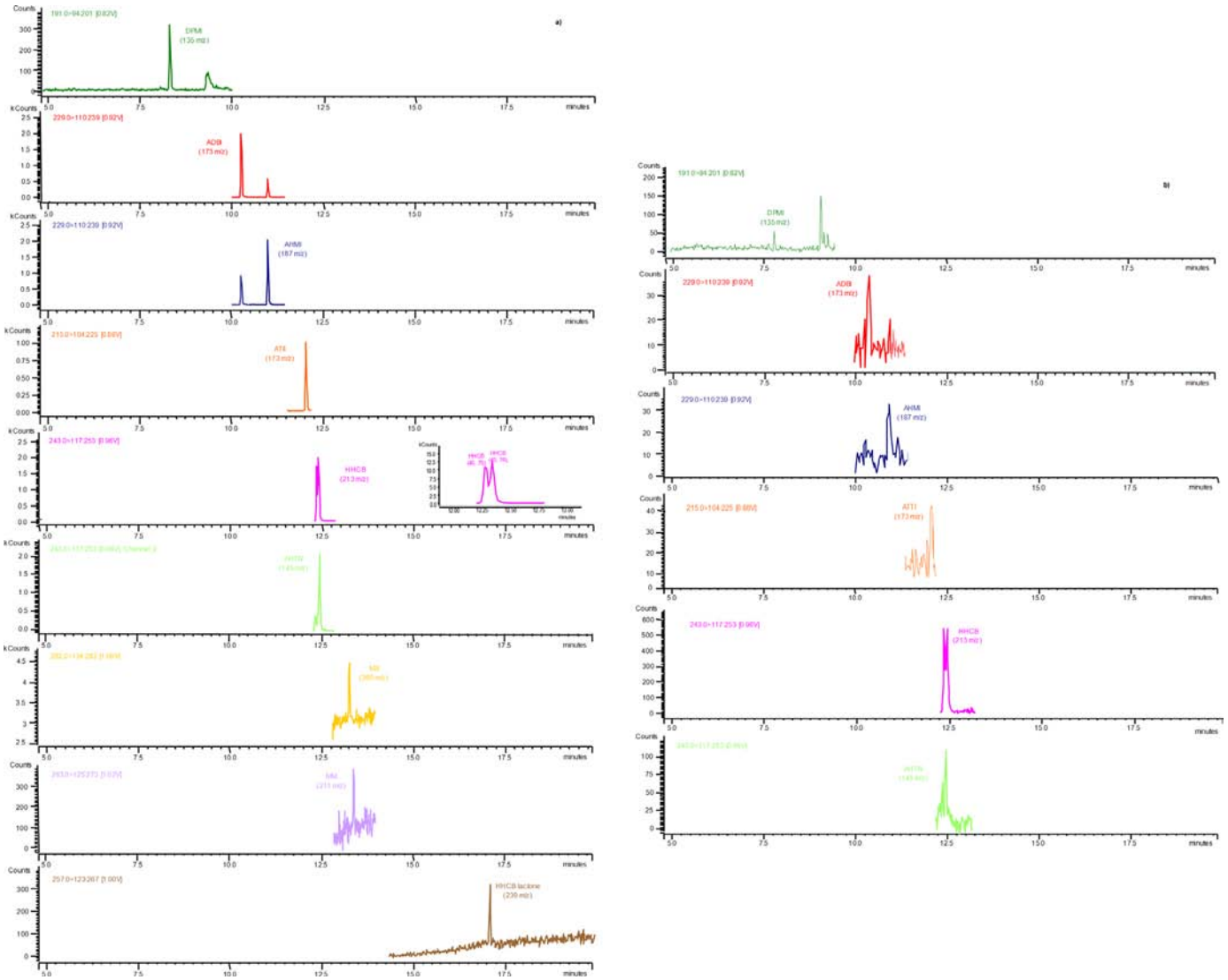


Fig. 2. MRM chromatograms of a influent wastewater sample from WWTP B. (a) Sample spiked with 1 μg L^{-1} of musk fragrances and (b) unspiked sample.

restrictions and the bubble formation it was impossible to ensure a constant flow rate of the sample inside the needle and the exact sample volume that pass through the sorbent, obtaining non reproducible results. So, headspace mode was selected to optimize the NT microextraction. In the same way NT desorption with organic solvent was discarded and replaced by thermal desorption.

Then the extraction temperature was studied by comparison of the peak areas obtained at 30 °C, 45 °C, 60 °C, 80 °C and 100 °C. The other extraction conditions were the same as described previously. Independently of the NT used, a progressive increase in the peak areas was observed for all of the polycylic musks up to an optimum extraction temperature of 60 °C after which there was a decrease when the extraction temperature was extended up to 100 °C (Fig. 3). While nitro musks compounds reached the highest peak areas at 80 °C with slightly better peak areas than those obtained at 60 °C. However, as a compromise 60 °C was chosen as the optimum extraction temperature.

To study the influence of adding salt on the efficiency of NT microextraction, the ionic strength of the ultrapure water solutions was modified by adding NaCl in the range of 0–360 g L^{-1}. 300 g L^{-1} was selected as the optimal salt concentration because maximal peak areas were obtained for most of the target compounds (data not shown). DPMI and HHCB-lactone showed maximal peak areas at 200 g L^{-1} NaCl but only a slight decrease in those analytical signals was observed at 300 g L^{-1} NaCl. It is clear that the addition of NaCl increased the ionic strength and thus promotes the transport of the analytes to the headspace and hence to the NT [44]. Therefore, it is to be expected that this will drive additional analytes into the headspace or gaseous phase and NT.

Regarding the preincubation time, 5, 15 and 30 min were also studied in order to enhance the efficiency of the NT efficiency. The best results were obtained working with 30 min (data not shown). However due to the fact that no statistical differences were observed between 15 and 30 min (differences $<10\%$ of peak areas), 15 min of preincubation time was selected as optimum in order to reduce the analyses time.

Fill and ejection speed were studied in the range of 1–100 μL s^{-1} with a 100 μL Hamilton syringe. Higher fill/ejection speeds were discarded for pneumatic restrictions of the NT that can lead in repeatability problems [23]. Theoretically, lower fill speeds increase the sampling time to help musks to diffuse through the sorbent, so the extraction efficiency of the NT should be better working at low fill speeds than working at high fill speeds [23]. Experimental results (Fig. 4) showed that the highest peak areas and therefore the best extraction efficiency was achieved working at 1 μL s^{-1} fill and 30 μL s^{-1} ejection speeds for all of the target analytes independently of the NT used. However, since no statistical differences were observed between

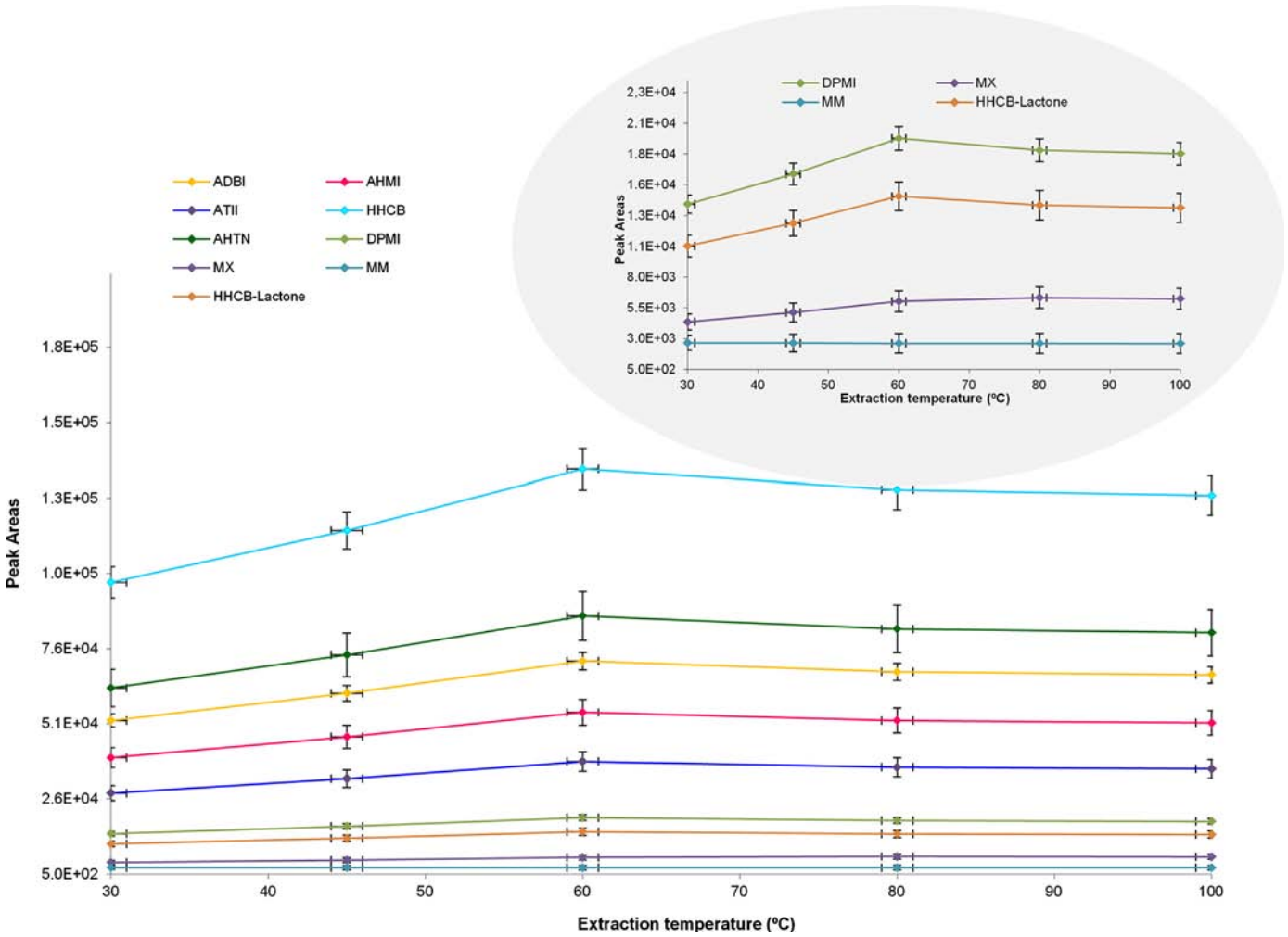


Fig. 3. Effect of the extraction temperature on the chromatographic peak areas obtained with NT microextraction (1 μg L^{-1}, $n=3$). Experimental conditions: 30 mm HF Bondesil-C18 sorbent NT, 10 mL sample volume poured in a 20 mL HS vial stirred at 750 rpm, 30% NaCl addition, preincubation time of 5 min, 200 μL fill volume, 30 μL s^{-1} fill and ejection speed and 3 min desorption time (230 °C).

working at 1 μL s^{-1} or 10 μL s^{-1} fill speeds and not to lengthen the extraction time, 10 μL s^{-1} fill speed was chosen as optimal.

Then, fill volume was optimized under optimal conditions for both 20 mm and 30 mm sorbent NTs. The range of volumes studied was between 100 μL and 1000 μL and were percolated by drawing and discarding between 1 and 10 cycles of 100 μL. In concordance with the results obtained by Eom et al. [35] and Alonso et al. [45] for the determination by NT microextraction of BTEX (benzene, toluene, ethylbenzene and p-xylene) and volatile organic compounds in water and blood, respectively, increasing sampling volume, the extracted amount of analyte was increased; this occurred because sampling more headspace induced the transfer of more target analytes from the solution to the headspace, resulting in higher trapping efficiency. The results show that working with a 20 mm sorbent NT a proportional increase of the response of all of the target compounds up to 300 μL was observed (data not shown). At higher fill volumes the analytical signal remains constant. Whereas the 30 mm sorbent NT reached the highest peak areas at 500 μL or 750 μL depending on the target compounds. Due to the compounds that reached the highest peak areas at 500 μL are the less sensitive ones (nitro musk), 500 μL was chosen to work with a 30 mm sorbent NT.

Finally desorption parameters as desorption time and temperature were tested. Working with a 20 mm sorbent NT the highest peak areas were obtained at holding for 1 min the NT at 230 °C while no statistical differences were observed increasing the desorption time to 3 or 5 min, and carryover problems were not detected. Moreover, with a 30 mm NT the best peak areas were reached at 3 min desorption time and 230 °C desorption temperature. Not statistical differences were observed for the vast majority of the target compounds between 1 or 3 min of desorption time but carryover problems were detected for HHCB and AHTN working at 1 min desorption time.

Under the optimized conditions decribed in Table 2, as can be seen in Fig. 5, the 30 mm sorbent NT presented higher peak areas for all the target analytes, so this was the NT selected to validate the method.

3.3. Method validation

As NT microextraction may be strongly influenced by the sample matrix, before validating the method, the matrix effect was studied by statistically comparing the slopes of the calibration curves for influent and effluent WWTPs samples with that obtained with ultrapure water. As expected, the matrix effect was observed in both kinds of water, especially in influent samples. The feasibility of the microextraction procedure must be demonstrated with real samples spiked at different concentrations.

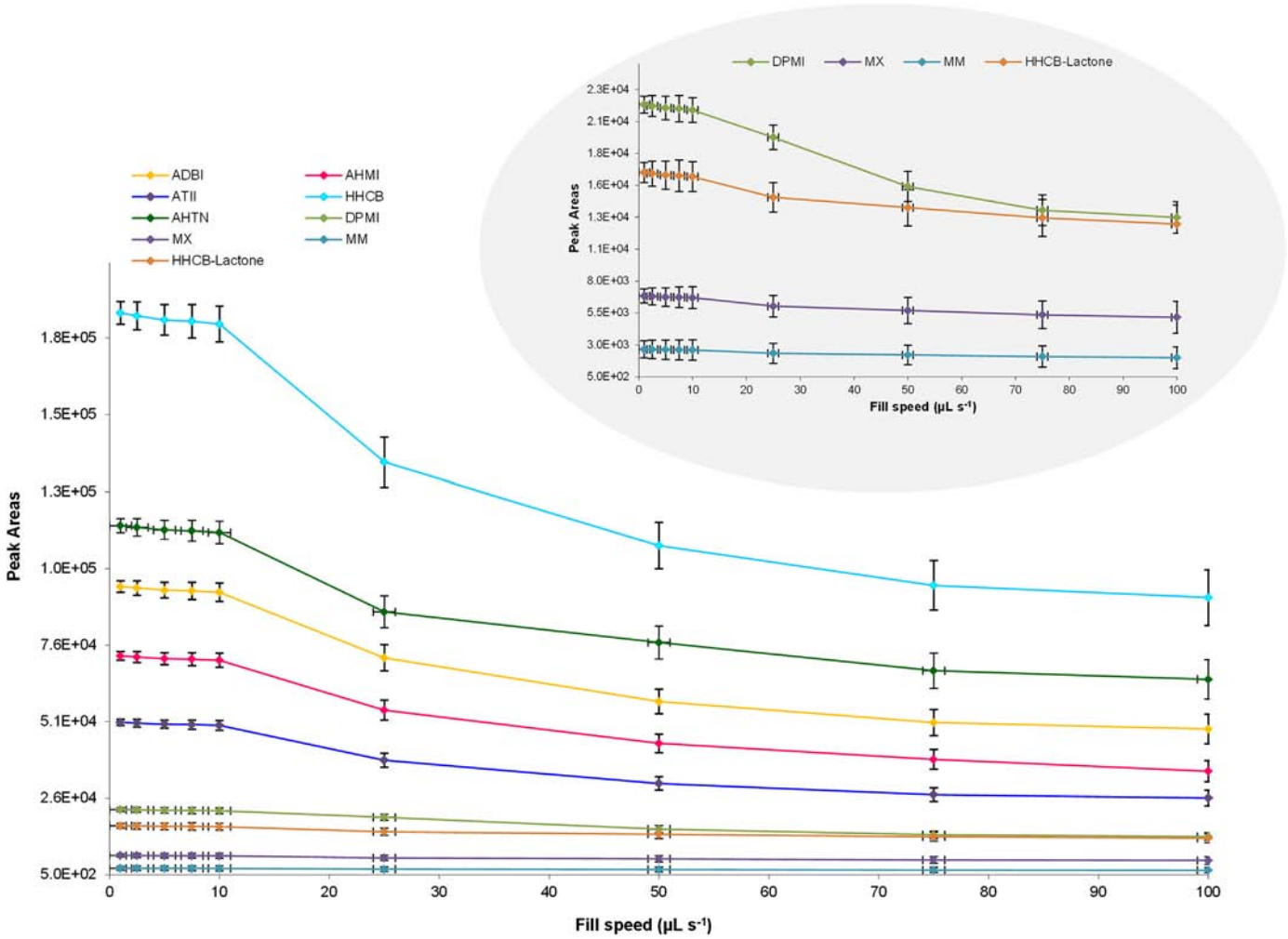


Fig. 4. Effect of the fill speed on the chromatographic peak areas obtained with NT microextraction (1 μg L^{-1}, $n=3$). Experimental conditions: 30 mm HF Bondesil-C18 sorbent NT, 10 mL sample volume poured in a 20 mL HS vial stirred at 750 rpm, 30% NaCl addition, an extraction temperature of 60 °C, preincubation time of 15 min, 200 μL fill volume, 30 μL s^{-1} ejection speed and 3 min desorption time (230 °C).

Table 2
NT microextraction optimum conditions for each HF Bondesil-C18 needle studied.

Process	Parameters	20 mm Sorbent NT	30 mm Sorbent NT
Extraction	Mode	Headspace	Headspace
	Temperature (°C)	60	60
	NaCl (g L^{-1})	30	30
	Preincubation time (min)	15	15
	Fill/ejection speed (μL s^{-1})	10/30	10/30
	Fill volume (μL)	200 (2 cycles × 100 μL)	500 (5 cycles × 100 μL)
Desorption	Mode	Temperature	Temperature
	Temperature (°C)	230	230
	Time (min)	1	3

The method was then analytically validated with an influent and an effluent sample from WWTP A by establishing the linear ranges, method detection limits (MDL), method quantification limits (MQL), intra-day and inter-day repeatabilities (expressed as relative standard deviation (RSD)). Procedural blanks of the conditioned NT were performed before NT microextraction in order to prevent carryover effects and ensure the repeatability of the analytical method.

The WWTP A samples used to validate the method were analysed ($n=5$), and the peaks of t HHCB and AHTN appeared in the chromatogram of the influent sample, while in the effluent sample peaks of HHCB, AHTN and also HHCB-lactone were found. The averaged peak area of each detected compound was subtracted from the corresponding peak area of each spiked sample.

The linear range of the method was obtained by analysing the WWTP A samples spiked with all of the target analytes at concentrations between 2.5 ng L^{-1} and 5000 ng L^{-1} while the SS concentration remained constant at 1000 ng L^{-1}. The method was linear in all ranges between MQL and 5000 ng L^{-1} for all of the target

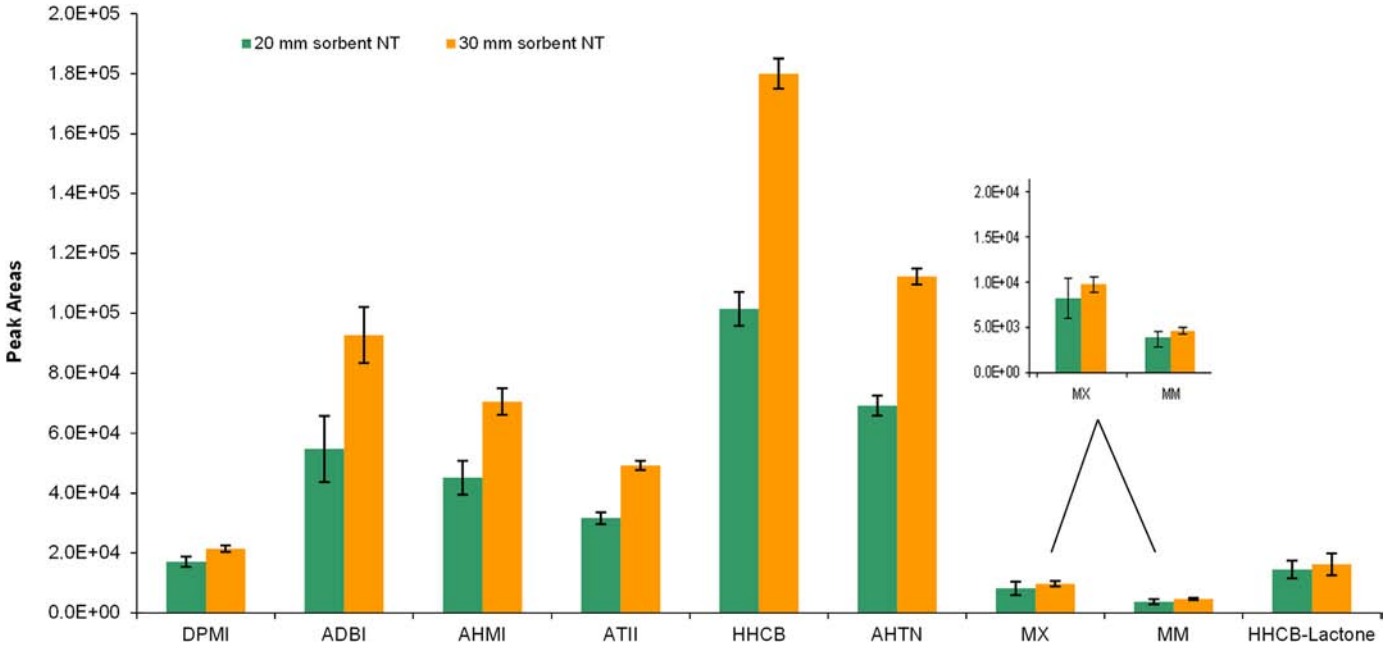


Fig. 5. Comparison of the chromatographic peak areas obtained with the 2 sorbent-packed needle traps in the optimal NT microextraction conditions for extracting the target musk fragrances from 10 mL water samples spiked at 1 μg L^{-1} (n=3).

Table 3
Method linear ranges, MDLs, MQLs, intra-day repeatabilities and inter-day repeatabilities.

Compound	Influent				Effluent			
	Linear range[a] (ng L^{-1})	MDLs (ng L^{-1})	RSD[b] (%)	RSD[c] (%)	Linear range[a] (ng L^{-1})	MDLs (ng L^{-1})	RSD[b]	RSD[c]
DPMI	10-5000	3.5	7	11	7.5-5000	2.5	6	7
ADBI	7.5-5000	3	8	15	5-5000	2.5	6	14
AHMI	7.5-5000	2.5	6	16	5-5000	2.5	5	9
ATII	20-5000	5	11	11	5-5000	2.5	8	11
HHCB	7.5-5000	3*	10	13	7.5-5000	2.5*	3	7
AHTN	7.5-5000	3.5*	8	17	7.5-5000	2.5*	5	10
MX	20-5000	10	7	12	20-5000	10	5	14
MM	25-5000	12	6	13	20-5000	10	9	15
HHCB-lactone	20-5000	10	10	13	10-5000	5*	8	11

[a] MQL (ng L^{-1}) were fixed as the lowest calibration level.
[b] Intra-day repeatability (% RSD): n=5, 100 ng L^{-1}.
[c] Inter-day repeatability (% RSD): n=5, 100 ng L^{-1}.
* Estimated.

analytes and matrices. In addition, the presence of SS enabled us to improve the determination coefficients (r^2) of the calibration curves to values higher than 0.997 for all the target compounds. MQLs were the lowest point of the calibration curve and MDLs were evaluated by spiking WWTP A influent or effluent samples in order to obtain a signal-to-noise ratio higher than three, for the compounds that did not appear in these samples. MDLs for HHCB, AHTN and HHCB-lactone were estimated as the concentration that gave a signal average of plus three times the standard deviation of the influent or effluent sample signal (n=10). These limits are shown in Table 3. Thus, MQLs ranged from 5 ng L^{-1} to 25 ng L^{-1} and MDLs ranged from 2.5 ng L^{-1} to 12 ng L^{-1} depending on the compound and matrix studied. These limits are better than those reported in the literature, which reports MDLs between 5 ng L^{-1} and 63 ng L^{-1} for influent and effluent waters working with microextraction by packed sorbents [16], dispersive liquid–liquid microextraction [9,10] or ultrasound-assisted emulsification-microextraction [8] as extraction techniques. However, slightly better MDLs (from 0.25 ng L^{-1} to 9 ng L^{-1}) were obtained working with solid phase microextraction as the preconcentration technique [41,46].

Intra-day and inter-day repeatability were obtained with five replicates of influent and effluent sample spiked at 100 ng L^{-1} (see Table 3). Intra-day repeatability (%RSD, n=5) was always less than 11% for both influent and effluent samples. Inter-day repeatability was always less than 17% or 15% (%RSD, n=5) for influent and effluent samples, respectively.

3.4. Needle trap extraction versus ionic liquid-based headspace single drop microextraction

The NT methodology was compared in terms of method validation parameters with an ionic liquid-based headspace single drop microextraction (IL-HS-SDME) methodology, which was successfully applied by our research group for the determination of musk fragrances in wastewater samples [14]. Both microextraction techniques are considered environmental friendly because of the use of 1 μL of an ionic liquid as extraction solvent instead of an organic solvent in the case of the IL-HS-SDME or because it is a solventless technique as NT. In addition both extraction procedures were fully automated by a CombiPal autosampler to ensure the repeatability of

Table 4
Concentrations of the target musks found in wastewater samples ($n=8$) in ng L^{-1}.

Compounds	WWTP A		WWTP B		WWTP C	
	Influent	Effluent	Influent	Effluent	Influent RO	Effluent RO
DPMI	260-630	< MQL-10	< MQL-880	n.d.-180	n.d.- < MQL	n.d.- < MQL
ADBI	n.d.-30	n.d.- < MQL	< MQL-40	n.d.- < MQL	n.d.-30	n.d.- < MQL
AHMI	n.d.-20	n.d.- < MQL	< MQL-110	n.d.- < MQL	n.d.-40	n.d.- < MQL
ATII	n.d.-70	n.d.- < MQL	< MQL-180	n.d.-30	n.d.-90	n.d.- < MQL
HHCB	560-600	160-210	20-1160	10-550	70-240	< MQL
AHTN	130-260	40-70	< MQL-430	< MQL-240	< MQL-50	< MQL
MX	n.d.	n.d.	n.d.	n.d.	n.d.	n.d.
MM	n.d.	n.d.	n.d.	n.d.	n.d.	n.d.
HHCB-lactone	n.d.	< MQL-820	n.d.	< MQL-290	n.d.-270	n.d.

n.d.—Not detected.
< MQL—values under the method quantification limit.

the methodology when dispensing a drop of ionic liquid (IL-HS-SPME) or to control the fill/ejection speed (NT).

Method validation parameters were obtained by the analysis of 10 mL influent and effluent samples spiked at different concentrations by using GC–MS/MS as separation and detection technique. The results showed that better MDLs were obtained with NT microextraction with values between 2.5 ng L^{-1} and 12 ng L^{-1}, while IL-HS-SDME MDLs ranging between 10 ng L^{-1} and 30 ng L^{-1}. The main reason of the increase of the MDLs when working with IL-HS-SDME is that because of the low volatility of the ionic liquids, residues could be accumulated in the glass wool placed inside the GC liner. In the same way, higher MQLs were obtained with IL-HS-SDME (50–100 ng L^{-1}). Both methods were linear between the MQLs and 5000 ng mL^{-1} with NT microextraction and up to 10,000 ng mL^{-1} with IL-HS-SDME. On the other hand, slightly better repeatability results were obtained with IL-HS-SDME, with intra-day repeatability values between 2 and 6% and inter-day repeatabilities ranging between 5 and 11%.

Summarizing, both methodologies were successfully applied for the determination of musk fragrances in wastewater samples but the validation results as well as daily work have led me to conclude that the NT microextraction is preferable to IL-HS-SDME.

Furthermore, NT microextraction validation values can also be compared with those obtained by Moeder et al. [15] working with MEPs as extraction technique. MEPs is a microextraction technique that can be considered as a miniaturized solid-phase extraction in which the sorbent (~1 mg) is inserted between the needle and the barrel as a cartridge but not in the needle. Moeder et al. [15] obtained MDLs of 42 ng L^{-1} and 37 ng L^{-1} for HHCB and AHTN, respectively, while working with NT as extraction technique slightly better MDLs, between 2.5 and 3.5 ng L^{-1} for HHCB and AHTN, respectively, were obtained. These values can be explained by the differences in sorbent position. NT design allows working in headspace mode and thermal desorption, and that makes this technique ideal for the extraction of volatile organic compounds from air or wastewater samples. On the other hand, MEPs bin is ideal for work in immersion mode and desorption with organic solvents and is normally used to extract polar compounds from environmental or biological samples [47].

3.5. Method application

To demonstrate the applicability of the NT-GC–MS/MS, influent and effluent wastewater samples from three WWTPs (A, B, C) on different dates were analysed ($n=8$). All the polycyclic musk compounds were detected in some of the influent samples from WWTP A and WWTP B, with HHCB (20–1160 ng L^{-1}) and AHTN (< MQL-430 ng L^{-1}) as the only compounds present in all the samples analysed (Table 4). For instance, Fig. 2b shows MRM chromatograms of the influent from WWTP B for the sample spiked with 1000 ng L^{-1} of musk fragrances (a), and the unspiked sample (b). As expected, the concentrations of polycyclic musk found in effluent WWTP A and B samples were lower than those detected in influent samples and with DPMI (n.d.– 180 ng L^{-1}), HHCB (10–550 ng L^{-1}) and AHTN (< MQL-240 ng L^{-1}) as the compounds that showed the highest concentrations. None of the samples contained detectable traces of nitro musk compounds. HHCB-lactone was only detected in effluent WWTP A and B samples as a result of the degradation of HHCB to HHCB-lactone during the WWTP treatment [48,49].

In the same way, HHCB (70–240 ng L^{-1}) and AHTN (< MQL-50 ng L^{-1}) are the only compounds present in all the influent samples of RO taken from WWTP C. The remaining polycyclic musk as well as HHCB-lactone were detected in some of the samples in minor concentrations. In effluent RO samples all targets musks were detected at values below the MQL or were not detected.

Previous works [4,7,50,51] that have focused on the determination of synthetic musk fragrances in wastewater samples confirms the finding of the present study, i.e. that the most abundant fragrances found in wastewater samples are the polycyclic musks HHCB and AHTN, although other polycyclic musks as DPMI, ADBI or AHMI can also be present in minor concentrations.

4. Conclusions

In this study, a NT microextraction followed by GC–MS/MS procedure was developed for determining nine musk fragrances in water samples. The NT-GC–MS/MS method was shown to be completely automated, simple and environmentally friendly. It also provided low ng L^{-1} MDLs and satisfactory precision (RSD between 3 and 11%) for wastewater samples.

The following main parameters involved in the NT microextraction were evaluated and optimized: sorbent-packed needle trap, extraction mode, extraction temperature, salt concentration, preincubation time, fill and ejection speed, fill volume and desorption parameters (temperature and time). Two sorbent-packed needle traps were tested (20 mm HF Bondesil-C18 sorbent and 30 mm HF Bondesil-C18 sorbent), and the best conditions were found to be the following: 30 mm HF Bondesil-C18 sorbent needle trap, 10 mL sample volume placed in a 20 mL HS vial and stirred at 750 rpm, 30% NaCl addition, an extraction temperature of 60 °C, preincubation of 15 min, 10 μL s^{-1}/30 μL s^{-1} fill and ejection speed, 500 μL fill volume and 3 min desorption time (230 °C).

The applicability of the method was also tested with water samples from influent and effluent WWTPs. The most abundant compounds were found to be DPMI, HHCB and AHTN while the remaining polycyclic musk fragrances were present at lower concentrations. None of the samples analysed contained detectable

traces of nitro musk compounds and HHCB-lactone was only detected in effluent samples as a degradation product of HHCB.

Acknowledgements

L. Vallecillos would like to thank the Department of Innovation, Universities and Enterprises and the European Social Fund for a Predoctoral Grant (FI-DGR 2012).

We would also like to thank the personnel at the wastewater treatment plants for their cooperation with all aspects of this study.

References

[1] A.M. Peck, K.C. Hornbuckle, Environ. Sci. Technol. 38 (2004) 367–372.
[2] P.E. Stackelberg, E.T. Furlong, M.T. Meyer, S.D. Zaugg, A.K. Henderson, D.B. Reissman, Sci. Total Environ. 329 (2004) 99–113.
[3] D.W. Kolpin, M. Skopec, M.T. Meyer, E.T. Furlong, S.D. Zaugg, Sci. Total Environ. 328 (2004) 119–130.
[4] Y. Lv, T. Yuan, J.Y. Hu, W.H. Wang, Anal. Sci. 25 (2009) 1125–1130.
[5] Z. Moldovan, R. Chira, A. Alder, Environ. Sci. Pollut. Res. 16 (2009) 46–54.
[6] D. Bendz, N.A. Paxéus, T.R. Ginn, F.J. Loge, J. Hazard. Mater. 122 (2005) 192–204.
[7] L.I. Osemwengie, S. Steinberg, J. Chromatogr. A 932 (2001) 107–118.
[8] J. Regueiro, M. Llompart, C. Garcia-Jares, J.C. Garcia-Monteagudo, R. Cela, J. Chromatogr. A 1190 (2008) 27–38.
[9] M. López-Nogueroles, A. Chisvert, A. Salvador, A. Carretero, Talanta 85 (2011) 1990–1995.
[10] A.N. Panagiotou, V.A. Sakkas, T.A. Albanis, Anal. Chim. Acta 649 (2009) 135–140.
[11] H. Liu, L. Liu, Y. Xiong, X. Yang, T. Luan, J. Chromatogr. A 1217 (2010) 6747–6753.
[12] L. Vallecillos, F. Borrull, E. Pocurull, Anal. Bioanal. Chem. 405 (2013) 9547–9554.
[13] L. Vidal, A. Canals, N. Kalogerakis, E. Psillakis, J. Chromatogr. A 1089 (2005) 25–30.
[14] L. Vallecillos, E. Pocurull, F. Borrull, Talanta 99 (2012) 824–832.
[15] M. Moeder, S. Schrader, U. Winkler, R. Rodil, J. Chromatogr. A 1217 (2010) 2925–2932.
[16] J. Cavalheiro, A. Prieto, M. Monperrus, N. Etxebarria, O. Zuloaga, Anal. Chim. Acta 773 (2013) 68–75.
[17] W.-H. Chung, S.-H. Tzing, W.-H. Ding, J. Chromatogr. A 1307 (2013) 34–40.
[18] M. Tobiszewski, A. Mechlinska, B. Zygmunt, J. Namiesnik, Trends Anal. Chem. 28 (2009) 943–951.
[19] F. Pena-Pereira, I. Lavilla, C. Bendicho, Trends Anal. Chem 29 (2010) 617–628.
[20] F. David, E. Van Hoeck, P. Sandra, Anal. Bioanal. Chem. 387 (2007) 141–144.
[21] H. Lord, J. Pawliszyn, J. Chromatogr. A 885 (2000) 153–193.
[22] F. Raschdorf, Chimia 32 (1978) 478–483.
[23] M. Alonso, A. Godayol, E. Antico, J.M. Sanchez, J. Sep. Sci. 34 (2011) 2705–2711.
[24] J. De Crom, S. Claeys, A. Godayol, M. Alonso, E. anticó, J.M. Sanchez, J. Sep. Sci. 33 (2010) 2833–2840.
[25] P. Trefz, S. Kischkel, D. Hein, E.S. James, J.K. Schubert, W. Miekisch, J. Chromatogr. A 1219 (2012) 29–38.
[26] P. Prikryl, R. Kubinek, H. Jurdádová, J. Sevcík, I. Ostrovsky, L. Soják, V. Berezkin, Chromatorgaphia 64 (2006) 65–70.
[27] Y. Gong, I.-Y. Eom, D.-W. Lou, D. Hein, J. Pawliszyn, Anal. Chem. 80 (2008) 7275–7282.
[28] S. Shojania, R.D. Oleschuk, M.E. McComb, H.D. Gesser, A. Chow, Talanta 50 (1999) 193–205.
[29] K. Ridgway, S.P.D. Lalljie, R.M. Smith, J. Chromatogr. A 1174 (2007) 20–26.
[30] H. Jurdádová, R. Kubinek, M. Jurcisinová, Z. Krkosová, J. Blasko, I. Ostrovsky, L. Soják, V.G. Berezkin, J. Chromatogr. A 1194 (2008) 161–164.
[31] I.-Y. Eom, A.-M. Tuguela, J. Pawliszyn, J. Chromatogr. A 1196 (2008) 3–9.
[32] A. Wang, F. Fang, J. Pawliszyn, J. Chromatogr. A 1072 (2005) 127–135.
[33] I.-Y. Eom, J. Pawliszyn, J. Sep. Sci. 31 (2008) 2283–2287.
[34] M. Mieth, S. Kischkel, J.K. Schubert, D. Hein, W. Miekisch, Anal. Chem. 81 (2009) 5851–5857.
[35] I.-Y. Eom, V.H. Niri, J. Pawliszyn, J. Chromatogr. A 1196 (2008) 10–14.
[36] V.H. Niri, I.-Y. Eom, F.R. Kermani, J. Pawliszyn, J. Sep. Sci. 32 (2009) 1075–1080.
[37] D.-W. Lou, X. Lee, J. Pawliszyn, J. Chromatogr. A 1201 (2008) 228–234.
[38] Y. Saito, I. Ueta, M. Ogawa, K. Jinno, Anal. Bioanal. Chem. 386 (2006) 725–732.
[39] R. Gatermann, S. Biselli, H. Huhnerfuss, G.G. Rimkus, M. Hecker, L. Karbe, Arch. Environ. Contam. Toxicol. 42 (2002) 437–446.
[40] W. Zhan, J. Pawliszyn, J. Chromatogr. A 1260 (2012) 54–60.
[41] M. Polo, C. Garcia-Jares, M. Llompart, R. Cela, Anal. Bioanal. Chem. 388 (2007) 1789–1798.
[42] J. Regueiro, C. Garcia-Jares, M. Llompart, J.P. Lamas, R. Cela, J. Chromatogr. A 1216 (2009) 2805–2815.
[43] R. kubinek, V.G. Berezkin, R. Górová, G. Addová, H. Mracnová, L. Soják, J. Chromatogr. B 800 (2004) 295–301.
[44] A. Tankeviciute, R. Kazlauskas, V. Vickackaite, Analyst 126 (2001) 1674–1677.
[45] M. Alonso, M. Castellanos, E. Besalú, J.M. Sanchez, J. Chromatogr. A 1252 (2012) 23–30.
[46] C. Garcia-Jares, M. Llompart, M. Polo, C. Salgado, S. Macias, R. Cela, J. Chromatogr. A 963 (2002) 277–285.
[47] C. Duan, Z. Shen, D. Wu, Y. Guan, Trends Anal. Chem. 30 (2011) 1568–1574.
[48] T.G. Poulsen, K. Bester, Environ. Sci. Technol. 44 (2010) 5086–5091.
[49] S. Franke, C. Meyer, N. Heinzel, R. Gatermann, H. Hühnerfuss, G. Rimkus, W.A. König, W. Francke, Chirality 11 (1999) 795–801.
[50] K. Bester, Chemosphere 57 (2004) 863–870.
[51] Y. Lv, T. Yuan, J. Hu, W. Wang, Sci. Total Environ. 408 (2010) 4170–4176.

Talanta 132 (2015) 557–563

Contents lists available at ScienceDirect

Talanta

journal homepage: www.elsevier.com/locate/talanta

One-step synthesis of magnetic graphene oxide nanocomposite and its application in magnetic solid phase extraction of heavy metal ions from biological samples

Jieping Sun, Qionglin Liang, Qiang Han, Xiaoqiong Zhang, Mingyu Ding *

Beijing Key Laboratory for Microanalytical Methods and Instrumentation, Department of Chemistry, Tsinghua University, Beijing 100084, China

ARTICLE INFO

Article history:
Received 25 July 2014
Received in revised form
12 September 2014
Accepted 18 September 2014
Available online 7 October 2014

Keywords:
Tri-iron tetroxide /graphene oxide nanocomposite
Magnetic solid-phase extraction
Heavy metal ions
Biological samples

ABSTRACT

A novel magnetic graphene oxide nanocomposite was synthesized by one-step coprecipitation method and characterized by transmission electron microscopy, X-ray photoelectron spectroscopy and vibrating sample magnetometer. The nanocomposite beard many intriguing properties, including chemical stability, high adsorption capacity, and superparamagnetic. These properties evoked great interest and desire of its exploration in magnetic solid-phase extraction of heavy metal ions from complex samples. Several parameters effecting the analytical performance, such as the sample pH, amounts of adsorbent, sample volumes, elution volumes, and coexisting ions, had been investigated in detail. The adsorbed metal ions were easy eluted by controlling the pH condition and the materials could be reused more than 20 times. Under the optimized conditions, the limits of detection were 0.016, 0.046, 0.395, 0.038, 0.157 μg L^{-1} for Co^{2+}, Ni^{2+}, Cu^{2+}, Cd^{2+}, and Pb^{2+}, respectively. The intra-day relative standard deviations ($n=5$) were in the range of 1.8–5.5% at 10 μg L^{-1}. The proposed method was successfully applied to biological sample analysis and got excellent recoveries in the range of 81–113% even the matrix was complex.

© 2014 Elsevier B.V. All rights reserved.

1. Introduction

The rapid development of industrial production causes serious pollution, especially heavy metal pollution [1]. From both natural and anthropogenic origin, heavy metals have been introduced into the environment and organism. The heavy metals cycle in the living creature chain and eventually endanger human health. The levels of heavy metal ions in human urine and plasma can indicate the existence of environment pollution, which benefits for controlling the pollution in time [2]. Therefore, the simultaneous evaluation for different heavy metals in biological samples is highly demanded. Compared to the technologies for detecting metal ions [3–5], inductively coupled plasma mass spectrometry (ICP-MS) possesses higher sensitivity, accuracy, and the capacity of simultaneously detecting various metal ions [6]. However, the low level of heavy metal ions and the complex matrix of the biological sample restrict its application [7]. Thus, a sample preparation prior to instrumental analysis to separate the matrix is essential [8].

Recently, magnetic solid phase extraction (MSPE) has been proposed from traditional solid phase extraction (SPE) and widely used due to its high recovery and ease of operation [9,10]. By taking advantage of both magnetic and non-magnetic adsorbent material, the MSPE method exhibits excellent adsorption efficiency and rapid separation from the matrix by an external magnetic field. The most important component of the MSPE technique is the adsorbent material, which dominates the sensitivity and selectivity of the method [11,12]. Graphene, a carbon-based material, has attracted considerable research interests in separation application areas due to its ultrahigh specific surface area [13–16]. Some works about its application in separating organic substance by π-π interaction had been reported by our research group [9,17,18]. However, its application in separation of metal ions was rarely reported [19]. Alvand et al. [20] used chelating agent to form stable complex with metal ions, which was separated due to π—π stacking interaction between graphene and the complex. However, as for graphene, there were strong π—π stacking interactions between neighboring sheets which might lead to restacking and agglomeration, resulting the loss of effective surface areas. Ethylene diamine tetraacetic acid (EDTA) was modified to the surface of graphene oxide (GO) by Hou group [21] and the synthesized EDTA-GO was used as an idea adsorbent for metal ions by conjugate action. However, several problems also exist, for instance, lacking of sufficient stability as well as hard to be separated because of the small size. Also, the complex synthesis and operation process will introduce interfering metal ions. In addition, most of the reported methods were applied to simple matrix samples, such as environmental water [22–24]. The separation of

* Tel.: +86 10 62797087.
E-mail address: dingmy@mail.tsinghua.edu.cn (M. Ding).

http://dx.doi.org/10.1016/j.talanta.2014.09.043
0039-9140/© 2014 Elsevier B.V. All rights reserved.

heavy metal ions from complex biological samples required higher selectivity and higher adsorption capacity of the adsorbent material [2,6].

GO, an idea adsorbent material, has abundant active sites and in rich of hydroxyl and carboxyl, which is suit to bind with metal ions. The adsorbed analytes could be easy eluted by acid according to the H^+ competing. However, it is difficult to separate the GO from aqueous solution because of its good dispersibility and high hydrophilicity [25], which restricts its direct application as an adsorbent. As one kind of grapheme hybrid materials, tri-iron tetroxide (Fe_3O_4)/GO possesses high adsorption capacity for heavy metal ions and could be easy separated via an external magnetic field. The preparation methods for Fe_3O_4/GO, including solvothermal reaction and covalent bonding, are complex and require rigorous conditions [9]. In this paper, an easy controlled one-step chemical coprecipitation method [26] was used to introduce the Fe_3O_4 to the surface of GO. It was characterized by transmission electron microscopy (TEM), X-ray photoelectron spectroscopy (XPS), and vibrating sample magnetometer (VSM) and applied to MSPE. The parameters influencing the extract recovery, including the sample pH, amounts of adsorbent, sample volumes, elution volumes, and coexisting ions were optimized in detail. The proposed method was also successfully applied to human urine and plasma for simultaneously detecting five kinds of heavy metal ions.

2. Experimental

2.1. Reagents and materials

Expanded graphite powder (100 mesh) was purchased from the Xinghe Graphite Co. Ltd. (Qingdao, China). The stock standard solutions (1000 mg L^{-1}) of Co^{2+}, Ni^{2+}, Cu^{2+}, Cd^{2+}, and Pb^{2+} (M^{2+}) were supplied by National Research Center for Certified Reference Materials (Beijing, China). The working standard solution was prepared daily by mixing individual standard solution and diluting to obtain a desired concentration. All reagents used in the experiment were of analytical reagent grade. High purity water (18.2 MΩ cm) prepared by Aifeibo Super Water-Purifiend Apparatus (Aifeibo Co. Ltd., China) was used throughout this work.

2.2. Instrumental and analytical conditions

TEM image were taken out using an H-7650B transmission electron microscope (Hitachi, Japan). XPS data were collected using a PHI-5300 ESCA X-ray photoelectron spectrometer (PHI, America). Magnetization curves were recorded using a 7307 Vibrating Sample Magnetometer (LakeShore, America).

A Thermo Scientific iCAP Q ICP-MS instrument (Thermo Fisher Scientific GmbH, Germany) was used for all ICP-MS experiments. Instrument tuning was performed prior to analysis by using a tuning solution according to the recommendation from manufacturer. The plasma power was 1548.6 W. High-purity argon was supplied as the cool gas, nebulizer gas, and auxiliary gas at the flow rates of 13.91 L min^{-1}, 1.03 L min^{-1}, and 0.80 L min^{-1}, respectively. The sample uptake time was set at 60 s and the wash time was set at 120 s.

2.3. Synthesis of GO

GO was prepared from expanded graphite according to the modified Hummers method [9]. About 1 g of sodium nitrate and 6 g of potassium permanganate were added into 46 mL of 98% sulfuric acid in an ice bath. Expanded graphite powder was slowly added with vigorous agitation. Then the mixture was maintained at 4 °C in an ice bath for 24 h. Afterwards, the reaction was transferred to a 35 °C oil bath for 30 min. Subsequently, 92 mL of high purity water was gradually added and the mixture was kept at 98 °C for 15 min. The expanded graphite in the solution was significantly oxidized and became aureate. After the temperature was reduced to 60 °C, 30% hydrogen peroxide was added slowly until visible bubbles were generated. The above mixture was centrifuged to remove the supernatant, and the GO was washed by 5% sufficient hydrochloric acid and high purity water to remove excess acid. Finally, the material was dried in oven at 60 °C for 6 h.

2.4. Synthesis of Fe_3O_4/GO

Fe_3O_4/GO was synthesized by chemical coprecipitation method [26]. The synthesized GO was dispersed in high purity water (1 mg mL^{-1}) and ultrasonicated for 3 h to obtain a clear dispersion of GO. 25 mg ferric chloride and 150 mg ferrous chloride were added slowly to 50 mL of 1 mg mL^{-1} GO at 50 °C under N_2. The ammonia solution was added slowly to precipitate Fe^{2+} and Fe^{3+} ions for synthesis of magnetite particles. After being rapidly stirred for 30 min by constant mechanical stirring, the solution was cooled to room temperature. Then, the dark black colored solution was applied by external magnetic field to separate the Fe_3O_4/GO. Afterwards, the Fe_3O_4/GO was washed with high purity water 5 times and dispersed in high purity water (5 mg mL^{-1}).

2.5. MSPE procedures

First, the adsorbent solution (5 mg mL^{-1}) was shaked fully to make sure the contents of Fe_3O_4/GO were homogeneous. 1.2 mL of the above adsorbent solution (containing 6 mg adsorbent) was placed into a beaker. The solution was magnetically separated via an external magnetic field to isolate the adsorbent. Second, the pH of solution was adjusted to 6.5 and 50 mL of 4 μg L^{-1} aqueous sample solution was transferred into the beaker. The mixture was shaked for 7 min and magnetically separated via an external magnetic field. Third, the adsorbed analytes were desorbed from the isolated adsorbent with 2 mL of 1 mol L^{-1} HNO_3 by shaking for 7 min. Finally, the adsorbent was removed via an external magnetic field and the supernatant was collected for the determination of M^{2+} by ICP-MS. High purity water was chosen as the blank solution and subjected to MSPE as described above.

2.6. Sample preparation

Urine samples were collected from the healthy volunteers. The sample was filtered through a 0.22 μm filter and its pH was adjusted to 6.5. Then, the homogeneous sample was 10 times diluted with high purity water and applied to the MSPE procedure given above.

Human plasma samples were obtained from different healthy volunteers and stored at -20 °C before use. For analysis, the samples were placed in an oven at 37 °C for 3 h. Then, a certain volume of acetonitrile was added into plasma sample to remove the proteins and centrifuged at 3500 rpm for 10 min. Afterwards, the clear supernatant was 10 times diluted and the MSPE procedure was followed under optimum conditions.

3. Results and discussion

3.1. Characterization of the Fe_3O_4/GO

Using dispersable GO as matrix, the Fe_3O_4/GO was prepared by chemical coprecipitation method of iron ions. Fe^{3+} and Fe^{2+} ions were captured by carboxylate anions on the surface of GO sheets and then ammonia solution was added slowly to precipitate Fe_3O_4. Generally the ratio of Fe^{3+} and Fe^{2+} ions for preparation of Fe_3O_4 was controlled

as 2:1. As Fe^{3+} had a much higher affinity than Fe^{2+} for carboxylic groups, a large excess of Fe^{2+} was adopted. Fe_3O_4/GO was characterized with TEM, XPS, and VSM.

3.1.1. TEM

The morphologies of GO and Fe_3O_4/GO were characterized with TEM. As could be seen from Fig. 1a, GO had a typical flake-like shape with some corrugations. Fig. 1b showed that well separated Fe_3O_4 nanoparticles were homogeneously and uniformly decorated on the surface of GO, which indicated that the Fe_3O_4 was successfully prepared [9]. Besides, the studies on the regeneration of the prepared Fe_3O_4/GO in section 3.5 showed the strong interaction between Fe_3O_4 and GO which exhibited excellent stability even in the acidic solution.

3.1.2. XPS

The chemical state of element in Fe_3O_4/GO was further investigated by XPS. As shown in Fig. 2a, the wide scan XPS spectra of the GO and Fe_3O_4/GO showed the same photoelectron lines at binding energies of about 285 and 530 eV, attributed to C1s and O1s, respectively [26]. However, the sharp peaks approximately 710 eV, which corresponded to the characteristic peaks of Fe2p in Fe_3O_4/GO, which indicated the existence of carbon, oxygen and iron in the composite [9]. In the spectrum of Fe2p in Fig. 2b, the peaks of $Fe2p_{3/2}$ and $Fe2p_{1/2}$ were located at 711.12 and 724.79 eV, not at 710.34 and 724.02 eV, which were for γ-Fe_2O_3. The result was in accordance with the reported data of $Fe2p_{3/2}$ and $Fe2p_{1/2}$, which indicated the formation of Fe_3O_4 phase in the composites [26]. Three peaks were present in the O1s spectrum of GO (Fig. 2c), which corresponded to C (O) OH at 531.8 eV, C=O at 532.5 eV and C-OH at 533.4 eV. The discrepancy was the peak at 530.4 eV in the O1s spectra of Fe_3O_4/GO nanocomposite (Fig. 2d), which was the contribution of the anionic oxygen in Fe_3O_4.

3.1.3. VSM

The magnetization curve of Fe_3O_4/GO was measured at room temperature using a supper conducting quantum interference device by cycling the field between -10 and 10 kOe, as shown in Fig. 3. The magnetic hysteresis loop was S-like curves. The magnetic remanence of the sample was 0.785 emu g^{-1}, almost no remaining magnetization when the external magnetic field was removed, suggesting that Fe_3O_4/GO exhibited a superparamagnetic behavior. The specific saturation magnetization (Ms) of the composites was 48.6 emu g^{-1} which was smaller than the reported value of bulk Fe_3O_4 of 92 emu g^{-1} [27]. The reduction in the value of Ms could be attributed to the relatively low amount of Fe_3O_4 loaded on GO [26]. However, Fe_3O_4/GO still could be separated rapidly under the external magnet. What was more, the more amounts of GO could increase the adsorption capacity of Fe_3O_4/GO.

3.2. Adsorption capacity

To investigate the adsorption capacity of the prepared Fe_3O_4/GO, 50 mL solutions of various concentrations of M^{2+} were equilibrated with 1 mL of adsorbent solution (containing 5 mg adsorbent). The adsorption capacity was calculated according to the following equation [28]:

$$Q_e = \frac{(C_i - C_e)V}{m} \quad (1)$$

where Q_e is the adsorption capacity (mg g^{-1}), C_i and C_e are the initial and equilibrium concentrations (mg L^{-1}) of M^{2+} in solution, V is the volume of the aqueous solution in L and m is the weight of the sorbent in g based on the dry weight of Fe_3O_4/GO. The experimental adsorption data were applied to the modified Langmuir equation

$$\frac{C_e}{Q_e} = \frac{C_e}{Q_m} + \frac{1}{K_L Q_m} \quad (2)$$

where K_L is the Langmuir isotherm constant (L mg^{-1}), and Q_m is the maximum adsorption capacity. The plot of C_e/Q_e versus C_e yielded a straight line revealing that the adsorption of five metal ions obeyed the Langmuir isotherm. The Q_m calculated from the slope are 1.28 mg g^{-1} for Co^{2+}, 1.55 mg g^{-1} for Ni^{2+}, 1.64 mg g^{-1} for Cd^{2+}, 6.58 mg g^{-1} for Cu^{2+}, and 9.71 mg g^{-1} for Pb^{2+}, respectively. The higher adsorption capacity of Cu^{2+} and Pb^{2+} was due to the strong complexation ability for Cu^{2+} and Pb^{2+} with carboxylic groups in GO.

3.3. Optimization of the MSPE conditions

Due to the high surface area, superparamagnetism and excellent absorbent ability, the Fe_3O_4/GO was used in MSPE for M^{2+}. The effects of the pH, amounts of adsorbent, adsorption time, sample volume, sedimentation time, HNO_3 concentration, elution volume and elution time were investigated.

3.3.1. Effect of the pH

The pH played an important role to the adsorption due to its influence on the solution chemistry of heavy metals and surface charge of the adsorbent. The sample solutions of pH range of 2–10 containing M^{2+} were investigated and the result was showed in

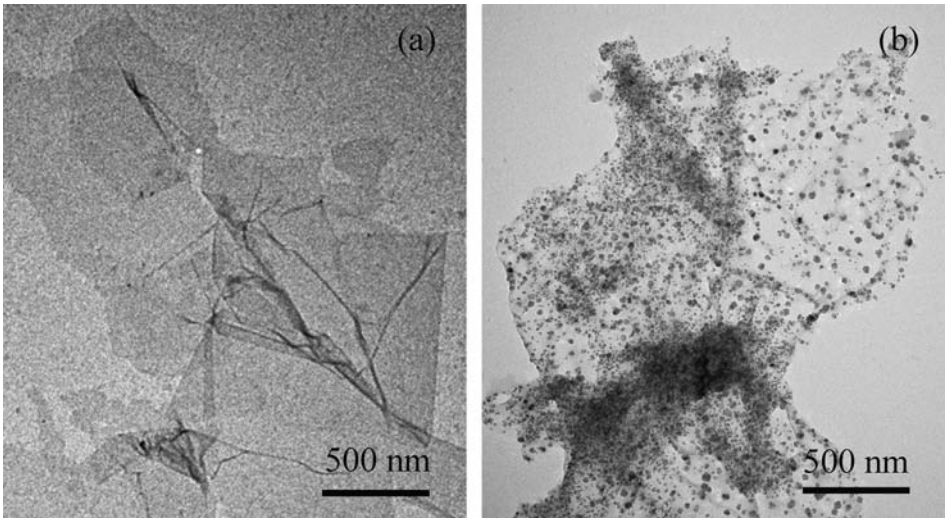


Fig. 1. TEM images of (a) GO, (b) Fe_3O_4/GO.

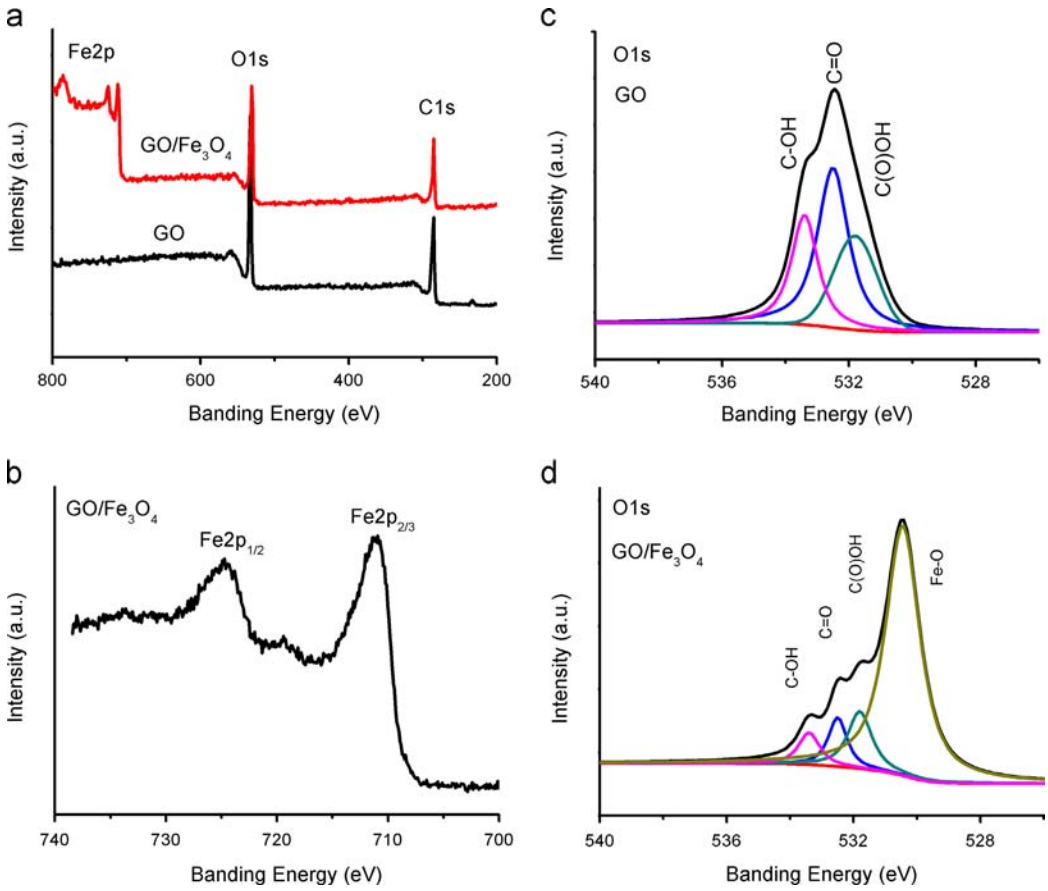


Fig. 2. XPS spectra of (a) wide scan of GO and Fe_3O_4/GO, (b) Fe 2p spectrum, (c) O1s spectrum of GO, (d) O1s spectrum of Fe_3O_4/GO.

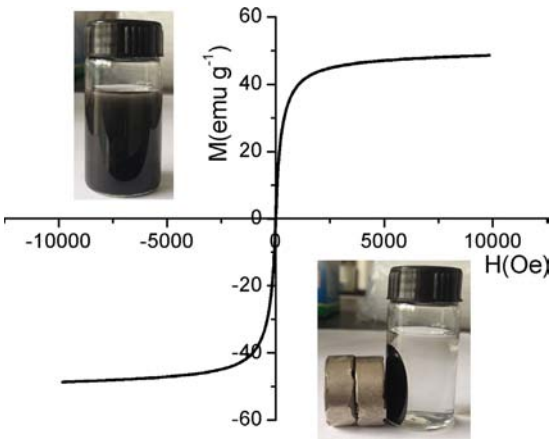


Fig. 3. The magnetization hysteresis loop of Fe_3O_4/GO.

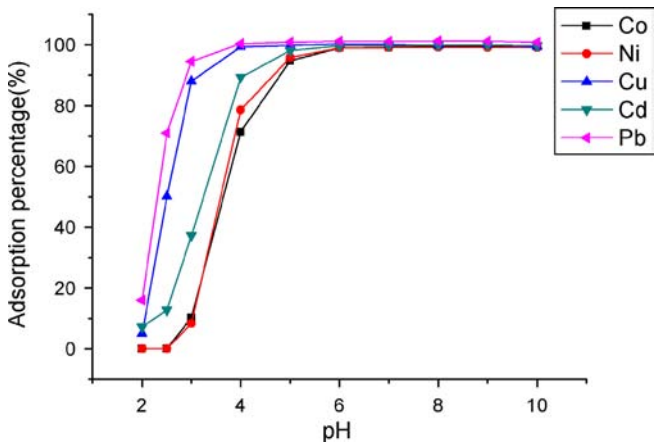


Fig. 4. Effect of pH on the adsorption percentage of the M^{2+} (4 μg L^{-1}) on the Fe_3O_4/GO; sample volume: 50 mL; adsorption time: 7 min.

Fig. 4. When pH was 2, the adsorption percentages were below 20% for all five metal ions. The lower adsorption capacity might be ascribed to the competition of M^{2+} with H^+. In other words, an excess of H^+ tended to occupy the surface active sites and competed effectively with M^{2+} due to electrostatic forces at low pH, which leaded to fewer available binding sites for M^{2+}. With the increase of pH, the –COOH and –OH groups converted to $–COO^-$ and $–O^-$, and surface charge was more negative to adsorb the positively charged metal ions. As can be seen, the adsorption percentages of Cu^{2+} and Pb^{2+} increased rapidly with the increase of pH from 2 to 4 and quantitative adsorption percentages were achieved in the pH range of 4–10. However, the adsorption percentages of Co^{2+}, Ni^{2+}, and Cd^{2+} got quantitative adsorption percentages when pH > 6. That might because of the strong complexation ability for Cu^{2+} and Pb^{2+} with carboxylic groups in GO which also leaded to a relatively high adsorption capacity for Pb^{2+} and Cu^{2+} in section 3.2. In addition, the relative high adsorption percentages at high pH (> 8) were attributed to the precipitation between M^{2+} and OH^-. Finally, a sample pH of 6.5 was selected to guarantee excellent adsorption percentages and used acid solution to elute the M^{2+} for further experiments.

3.3.2. Effect of the volumes of adsorbent solution

The effect of the volumes of adsorbent solutions was investigated by using different volumes of adsorbent solutions (0.3, 0.6, 0.9, 1.2, 1.5, 1.8, 2.1, 2.4 mL of 5 mg mL^{-1}) for 50 mL of 4 μg L^{-1} of heavy metal ions solution. The mixture was applied under the MSPE procedures in section 2.5. As shown in Fig. 5, 1.2 mL of adsorbent solution (containing 6 mg adsorbent) was enough to obtain quantitative recovery. So 1.2 mL of adsorbent solution was selected for further experiments.

3.3.3. Effect of the adsorption and elution time

In order to obtain an appropriate adsorption time, 50 mL of sample solution containing 4 μg L^{-1} of heavy metal ions was adsorbed for 1, 2, 5, 7, 10, and 15 min and the recoveries were studied, respectively. The results showed that 7 min was the appropriate adsorption time which got excellent recoveries with minimal time required for sample processing. Also, the effect of the elution time was examined and the results from Fig. 6 showed that 7 min was the optimizing elution time.

3.3.4. Effect of the sample volume

The effect of the sample volume on the recoveries was studied to obtain a higher enrichment factor. The sample solutions of 5, 10, 20, 50, 100, and 200 mL containing 200 ng of each metal ions were subjected to the general MSPE procedure, respectively. The results showed that the recoveries were excellent when the sample volumes were in the range of 5–50 mL, and then slightly decreased with further increase of sample volume to 200 mL. 50 mL sample volume was used in further experiments.

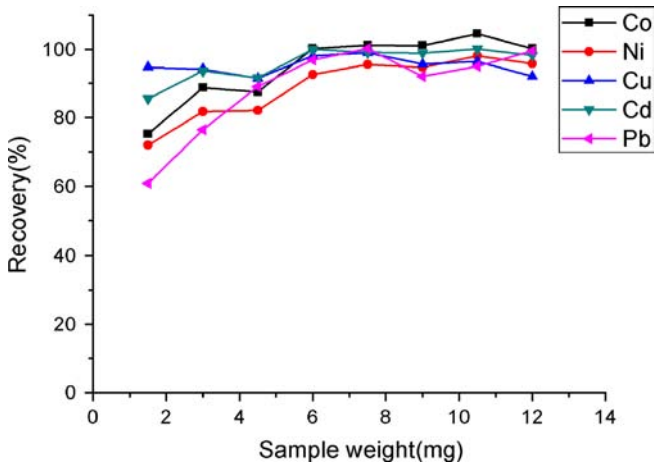


Fig. 5. Effect of the sample weight on the recovery of the M^{2+} (4 μg L^{-1}); sample volume: 50 mL; adsorption time: 7 min; eluent: 2 mL 1 mol L^{-1} HNO_3; eluent time: 7 min.

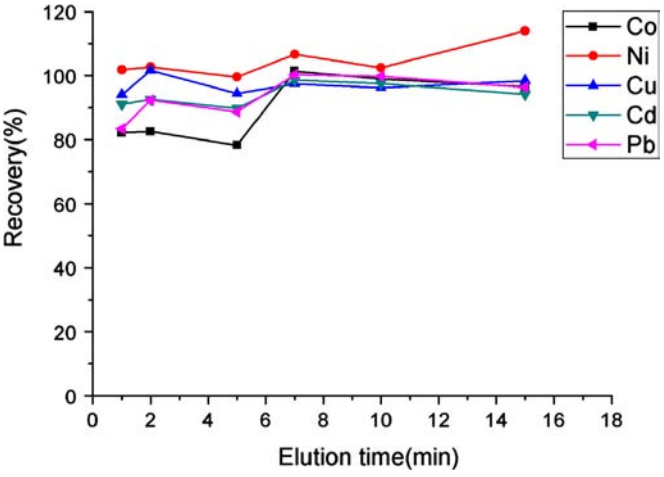


Fig. 6. Effect of the eluent time on the recovery of the M^{2+} (4 μg L^{-1}); sample weight: 6 mg; sample volume: 50 mL; adsorption time: 7 min; eluent: 2 mL 1 mol L^{-1} HNO_3.

3.3.5. Effect of the elution concentration and volume

It could be seen from Fig. 4 that M^{2+} had lower adsorption percentage at lower pH, which indicated that acid could desorb M^{2+} in adsorbent. What is more, HNO_3 is the mostly harmless acid to ICP-MS which was recommended. Therefore, HNO_3 was selected as the eluent and the concentration was investigated in the range of 0.1–2 mol L^{-1}. The results in Fig. 7 showed that the recoveries slightly increased along with the increase of HNO_3 concentrations. Considering that the instrument could not stand too strong acid, 1 mol L^{-1} HNO_3 was selected as eluent in following experiments. 1, 1.5, 2, 2.5, 3, and 4 mL of 1 mol L^{-1} HNO_3 were used to investigate the effect of elution volume, respectively. The results indicated that the recoveries slightly increased along with the increase of elution volumes. In order to achieve high enrichment factor, the volume should be as small as possible. 2 mL of 1 mol L^{-1} HNO_3 was sufficient to quantitatively elute all the metal ions and was employed as the optimum elution volume.

3.4. Effect of coexisting ions

Diverse ions which existed in experimental environment and sample matrix may interfere the recoveries of M^{2+}. To study the effect of coexisting ions, interferences from representative monovalent metal ions K^+, Na^+, bivalent metal ions Mg^{2+}, Ca^{2+}, and trivalent metal ions Al^{3+}, Fe^{3+} were investigated on 50 mL solutions containing 4 μg L^{-1} of M^{2+}. The tolerance limit was set as the largest amount of coexisting ions that reduce the recoveries of M^{2+} to less than 85%. The results indicated 100 mg L^{-1} of K^+, 100 mg L^{-1} of Na^+, 20 mg L^{-1} of Mg^{2+}, 20 mg L^{-1} of Ca^{2+}, 2 mg L^{-1} of Fe^{3+}, and 1 mg L^{-1} of Al^{3+} had no significant interference on the extraction and determination of 4 μg L^{-1} M^{2+}. The results indicated that the sorbent had excellent selectivity to analyte metal ions and was suitable for the analysis of biological samples with complex matrix.

3.5. Regeneration of the prepared Fe_3O_4/GO

In order to examine the regeneration of the prepared Fe_3O_4/GO, it was washed to neutral pH by high purity water and reused for

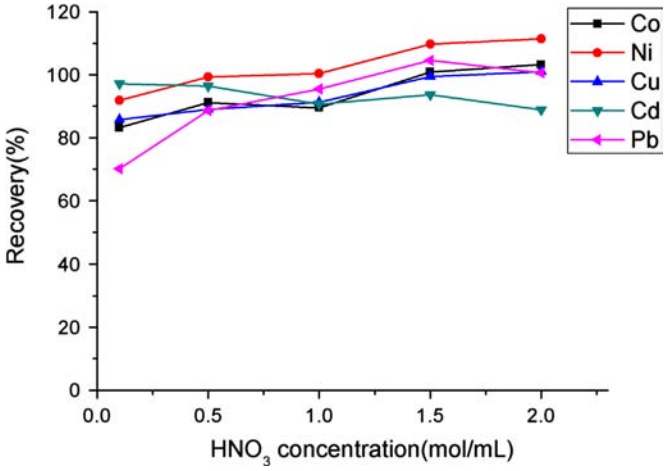


Fig. 7. Effect of the HNO_3 concentration on the recovery of the M^{2+} (4 μg L^{-1}); sample weight: 6 mg; sample volume: 50 mL; adsorption time: 7 min; eluent volume: 2 mL HNO_3; eluent time: 7 min.

proposed MSPF procedures. The results showed that the absorbent could be reused for more than 20 times without a significant decrease of the recoveries.

3.6. Validation of the ICP-MS coupled with the proposed MSPE method

To evaluate the analytical performance of established method, a series solution in the concentration were prepared and applied to the MSPE procedures. Limits of detection (LOD) were determined from the three times of standard deviation of 10 consecutive runs of blank solution. As showed in Table 1, the LODs of this method were 0.016, 0.046, 0.395, 0.038, 0.157 μg L^{-1} for Co, Ni, Cu, Cd, and Pb, respectively. The relative standard deviations (RSDs, $n=5$) were in the range of 1.8–5.5% at 10 μg L^{-1}. The linear range covered 1–150 μg L^{-1} with correlation coefficient (r) higher than 0.9981. The LODs of the developed sorbent in comparison with other sorbents for extraction of heavy metal ions was given in Table 2. As can be seen, the LODs obtained by this work were lower than that reported methods. Besides, compared to these reported methods, the present MSPE method was fast, precise, easy to operate, and had high adsorption capacity.

Table 1
Linear relationships and sensitivities for detection of five metal ions.

Target ions	Linear equation	r	Limit of detection (μg L^{-1})	Intra-day RSD %($n=5$)			Inter-day RSD % ($n=5$)		
				a	b	c	a	b	c
Co	y=270397 x+45286	0.9996	0.016	3.8	1.3	0.8	7.7	4.0	1.3
Ni	y=67108 x+17760	0.9981	0.046	1.8	0.9	0.7	5.0	1.2	0.8
Cu	y=155261x- 60836	0.9992	0.395	3.5	2.6	0.8	6.0	3.5	2.5
Cd	y=29176 x+3770	0.9999	0.038	5.4	4.3	4.3	7.3	6.0	4.6
Pb	y=202759x- 31446	0.9997	0.157	5.5	2.6	2.0	6.1	4.5	3.6

[a] $c=10$ μg L^{-1};
[b] $c=500$ μg L^{-1};
[c] $c=1000$ μg L^{-1}

Table 2
Comparison with previously reported methods of limits of detection (μg L^{-1}).

Target ions	This work	poly (TMAAm-co-DVB-co-AMPS) resin [29]	MnO_2 / MWCNTs [30]	MWCNTs/o-cresolphthalein complexone [3]	chitosan/silica [24]	MWCNTs –APDC [4]
Co	0.016	0.44		5.31		0.40
Ni	0.046	0.71		5.68		0.57
Cu	0.395			1.64	0.30	0.30
Cd	0.038	0.23	1.5		0.05	0.45
Pb	0.157	1.07	4.4	3.52	0.96	0.60

poly (TMAAm – co – DVB – co - AMPS) resin: poly (2 – thiozylmethacrylamide – co – divinylbenzene – co – 2 – acrylamide – 2 - methyl- 1 - propanesulfonic acid)
MnO_2: Manganese dioxide
MWCNTs: multiwalled carbon nanotubes
APDC: ammonium pyrrolidine dithiocarbamate

Table 3
Analytical results of target ions in biological samples (mean ± s.d., $n=5$).

Target ions	Urine			Plasma		
	Added (μg L^{-1})	Found (μg L^{-1})	Recovery (%)	Added (μg L^{-1})	Found(μg L^{-1})	Recovery (%)
Co	0	3.1 ± 0.2	–	0	2.7 ± 0.2	–
	10	13.5 ± 0.6	104	10	11.6 ± 0.6	89
	20	23.5 ± 1.1	102	20	22.9 ± 0.5	101
Ni	0	15.3 ± 0.5	–	0	12.2 ± 0.4	–
	10	24.2 ± 0.7	89	10	22.1 ± 0.7	99
	20	34.1 ± 0.8	94	20	34.8 ± 0.6	113
Cu	0	9.0 ± 0.2	–	0	18.9 ± 0.3	–
	10	17.5 ± 0.7	85	10	28.7 ± 1.6	98
	20	27.4 ± 0.8	92	20	41.3 ± 0.8	112
Cd	0	1.1 ± 0.1	–	0	3.9 ± 0.1	–
	10	11.1 ± 0.7	100	10	13.3 ± 0.3	94
	20	21.1 ± 0.2	100	20	23.3 ± 0.2	97
Pb	0	4.2 ± 0.1	–	0	21.5 ± 0.6	–
	10	13.7 ± 0.5	95	10	29.6 ± 1.1	81
	20	23.6 ± 1.0	97	20	44.1 ± 0.8	113

3.7. Analysis of biological samples

In order to validate the suitability of proposed method, the method was applied to the biological samples (urine and plasma) and the analytical results along with the recoveries at two spiked concentrations (10 and 20 μg L^{-1}) were given in Table 3. It can be seen that the recoveries for the spiked samples were between 81 and 113%.

4. Conclusions

A novel magnetic nanocomposite Fe_3O_4/GO was successfully synthesized through one-step chemical coprecipitation method. The material displayed high adsorption capacity for five heavy metal ions and was stable even in acid solution. The adsorbent ability increased in high pH, which showed higher adsorption capacity for Cu^{2+} and Pb^{2+} due to the strong complexation ability with carboxylic groups. It could be separated rapidly under external magnet, reused at least 20 times, and successfully applied to MSPE. The method was fast, precise, easy to operate, and had low LODs. What was more, the proposed method was successfully applied to biological sample and got the excellent recoveries even the matrix was complex. The detecting results could indicate the existence of environment pollution, which benefited for controlling the pollution in time.

Conflict of interest

The authors have declared no conflict of interest.

Acknowledgements

This project was supported by the National Nature Science Foundation of China (No. 21075074).

References

[1] B. Dai, M. Cao, G. Fang, B. Liu, X. Dong, M. Pan, S. Wang, J. Hazard. Mater. 219-220 (2012) 103–110.
[2] M.H. Mashhadizadeh, M. Amoli-Diva, J. Anal. Atom. Spectrom. 28 (2013) 251.
[3] A. Duran, M. Tuzen, M. Soylak, J. Hazard. Mater. 169 (2009) 466–471.
[4] M. Tuzen, K.O. Saygi, M. Soylak, J. Hazard. Mater. 152 (2008) 632–639.
[5] H.M. Jiang, Z.P. Yan, Y. Zhao, X. Hu, H.Z. Lian, Talanta 94 (2012) 251–256.
[6] J. Wang, X. Ma, G. Fang, M. Pan, X. Ye, S. Wang, J. Hazard. Mater. 186 (2011) 1985–1992.
[7] Z. Zang, Z. Hu, Z. Li, Q. He, X. Chang, J. Hazard. Mater. 172 (2009) 958–963.
[8] S. Sadeghi, H. Azhdari, H. Arabi, A.Z. Moghaddam, J. Hazard. Mater 215-216 (2012) 208–216.
[9] Q. Han, Z. Wang, J. Xia, S. Chen, X. Zhang, M. Ding, Talanta 101 (2012) 388–395.
[10] H. Bagheri, A. Afkhami, M. Saber-Tehrani, H. Khoshsafar, Talanta 97 (2012) 87–95.
[11] Q. Meng, X. Zhang, C. He, P. Zhou, W. Su, C. Duan, Talanta 84 (2011) 53–59.
[12] Z. Zhang, H. Zhang, Y. Hu, X. Yang, S. Yao, Talanta 82 (2010) 304–311.
[13] Q. Liu, J. Shi, J. Sun, T. Wang, L. Zeng, G. Jiang, Angew Chem. Int. Ed. 50 (2011) 5913–5917.
[14] S. Zhang, Z. Du, G. Li, Anal. Chem. 83 (2011) 7531–7541.
[15] Y.B. Luo, Z.G. Shi, Q. Gao, Y.Q. Feng, J. Chromatogr. A 1218 (2011) 1353–1358.
[16] M.M. Wang, X.P. Yan, Anal. Chem. 84 (2011) 39–44.
[17] Z. Wang, Q. Han, J. Xia, L. Xia, M. Ding, J. Tang, J. Sep. Sci. 36 (2013) 1834–1842.
[18] X. Zhang, S. Chen, Q. Han, M. Ding, J. Chromatogr. A 1307 (2013) 135–143.
[19] Y. Wang, S. Gao, X. Zang, J. Li, J. Ma, Anal. Chim. Acta 716 (2012) 112–118.
[20] M. Alvand, F. Shemirani, Microchim. Acta 181 (2013) 181–188.
[21] C.J. Madadrang, H.Y. Kim, G. Gao, N. Wang, J. Zhu, H. Feng, M. Gorring, M.L. Kasner, S. Hou, ACS Appl. Mat. Interfac. 4 (2012) 1186–1193.
[22] W. Zhang, X. Shi, Y. Zhang, W. Gu, B. Li, Y. Xian, J. Mater. Chem. A 1 (2013) 1745.
[23] D. Huang, X. Wang, C. Deng, G. Song, H. Cheng, X. Zhang, J. Chromatogr. A (2013).
[24] D. Chen, B. Hu, C. Huang, Talanta 78 (2009) 491–497.
[25] B. Zawisza, R. Sitko, E. Malicka, E. Talik, Anal. Methods 5 (2013) 6425.
[26] J. Li, S. Zhang, C. Chen, G. Zhao, X. Yang, J. Li, X. Wang, ACS Appl. Mat. Interfac. 4 (2012) 4991–5000.
[27] X. Yang, X. Zhang, Y. Ma, Y. Huang, Y. Wang, Y. Chen, J. Mater. Chem. 19 (2009) 2710.
[28] W. Wang, R. Ma, Q. Wu, C. Wang, Z. Wang, Talanta 109 (2013) 133–140.
[29] Ş. Turan, Ş. Tokalıoğlu, A. Şahan, C. Soykan, React. Funct. Polym. 72 (2012) 722–728.
[30] B. Yang, Q. Gong, L. Zhao, H. Sun, N. Ren, J. Qin, J. Xu, H. Yang, Desalination 278 (2011) 65–69.

Talanta 132 (2015) 564–571

Contents lists available at ScienceDirect

Talanta

journal homepage: www.elsevier.com/locate/talanta

An etched stainless steel wire/ionic liquid-solid phase microextraction technique for the determination of alkylphenols in river water

Meiyu Cui [a], Jinxue Qiu [a], Zhenghua Li [b], Miao He [a], Mingshi Jin [a], Jiman Kim [b], Maurizio Quinto [c], Donghao Li [a,*]

[a] Key Laboratory of Natural Resource of the Changbai Mountain and Functional Molecular (Yanbian University), Ministry of Education, Park Road 977, Yanji City, Jilin Province, China 133002
[b] Department of Chemistry, BK21 School of Chemical Materials Science, Department of Energy Science and SKKU Advanced Institute of Nanotechnology, Sungkyunkwan University, Suwon, Korea
[c] SAFE — Department of Science of Agriculture, Food and Environment, University of Foggia, via Napoli 25, I-71100 Foggia, Italy

ARTICLE INFO

Article history:
Received 29 May 2014
Received in revised form
2 September 2014
Accepted 7 September 2014
Available online 7 October 2014

Keywords:
SPME
Ionic liquids
Alkylphenols
GC–MS
Water

ABSTRACT

In this study, a stainless steel wire/ionic liquid-solid phase microextraction technique was developed for the direct extraction of APs from water samples. Some parameters were optimised, such as selection of the substrate and ILs, extraction time, extraction temperature, stirring rate and sample pH, etc. The experimental data demonstrated that the etched stainless steel wire was a suitable substrate for IL-coated SPME. The coating was prepared by directly depositing the ILs onto the surface of the etched stainless steel wire, which exhibited a porous structure and a high surface area. The $[C_8MIM][PF_6]$ IL exhibited maximum efficiency with an extraction time of 30 min, and the aqueous sample was maintained at 40 °C and adjusted to pH 2 under stirring conditions. The enrichment factor of the IL coating for the four APs ranged from 1382 to 4779, the detection limits (LOD, S/N=3) of the four APs ranged from 0.01 to 0.04 ng mL^{-1} and the RSD values for purified water spiked with APs ranged from 4.0 to 11.8% (n=3). The calibration graphs were linear in the concentration range from 0.5 to 200 ng mL^{-1} ($R^2 > 0.9569$). The optimised method was successfully applied for the analysis of real water samples, and the method was suitable for the extraction of APs from water samples.

© 2014 Elsevier B.V. All rights reserved.

1. Introduction

Alkylphenols (APs) are ubiquitous environmental contaminants resulting from the degradation of alkylphenol polyethoxylates (APnEOs). APnEOs are surface-active agents that are commonly used in household cleaning products, agricultural applications and the chemical industry [1]. The residual surfactants and their degradation products are directly discharged to plants or surface water without any treatment, and the residuals can disperse into different environmental compartments. APs possess lipophilic properties, are stable in the environment and exhibit a tendency to accumulate in living organisms. The European Union (EU) listed APs as endocrine-disrupting chemicals (EDCs) in 1996. Emerging research suggests that APs are widely distributed in various environmental matrices, and an increased awareness of the presence of APs in the environment has led to an intensified interest in the trace analysis of these compounds [2,3].

The determination of APs from environmental samples at low concentrations remains a challenging task, and major studies on APs have focused on the development of rapid and simple extraction methods. The conventional methods for extracting APs from an environmental sample are liquid–liquid extraction (LLE) [4] and solid-phase extraction (SPE) [5,6]. However, these methods are tedious, time-consuming and require large amounts of high-purity organic solvents, which are expensive, toxic and cause additional environmental problems. Over the past decade, special attention has been focused on sample preparation methods that ensure a reduction in the amount of organic solvents required or even eliminate them completely and limit the number of operations and processes to a minimum.

Solid-phase microextraction (SPME) is a sample preparation technique that integrates sampling, isolation, enrichment and injection into one step [7–9]. SPME has sparked great interest in the scientific community because it is solvent-free, sensitive, fast, simple to operate and easily incorporated into chromatographic analysis. A polymer-coated microfibre plays the key role in the SPME procedure; the fibre can adsorb certain organic analytes and concentrate them from the various phases of a sample [10].

* Corresponding author. Tel.: +86 433 2436456; fax: +86 433 2732456.
E-mail address: dhli@ybu.edu.cn (D. Li).

http://dx.doi.org/10.1016/j.talanta.2014.09.012
0039-9140/© 2014 Elsevier B.V. All rights reserved.

The fibre has a crucial effect on the accuracy and selectivity of the SPME procedure. Certain commercial fibres of this have been developed; however, these fibres are expensive, fragile and unstable under extreme thermal and chemical conditions, which limit the applications of SPME for real samples. To meet the requirements of complex analysis, new SPME coatings with remarkable properties, such as enhanced sensitivity [11], high thermal stability [12], mechanical and chemical stability and low cost, have been continually developed using new preparation methods [13] or new materials [14,15]. Moreover, fused silica has the disadvantages of being fragile and expensive. Therefore, recent studies have focused primarily on the development and further extension of supports with a long lifetime [16]. Other materials have been explored to replace silica rods as the SPME substrate [17–20]. Stainless steel, which is flexible and durable and exhibits good mechanical properties, is a suitable SPME substrate [21–23]. Stainless steel is resistant to corrosion in various environments, such as in acidic solutions and under alkaline conditions.

Room-temperature ionic liquids (ILs) are ionic compounds that are liquid over a temperature range near or below room temperature. ILs are non-molecular solvents consisting of a heterocyclic cation and an anion. ILs exhibit good thermal stability, negligible vapour pressure and convenient use. Because the cations and the anions can be integrated in different combinations, we can also obtain ILs with specific functions by specially designing the structure thereof. ILs exhibit good extractability for various organic compounds and metal ions [24–26]. Considering the above mentioned characteristics and advantages, ILs may be potential adsorbents for SPME. Jiang [27] and Amini [28] demonstrated that [C_8MIM][PF_6] can be physically adsorbed on the surface of fused silica tubing or stainless steel wire as the coating for SPME.

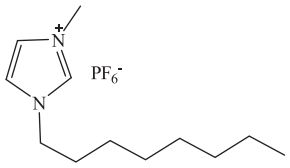
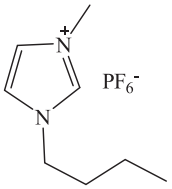
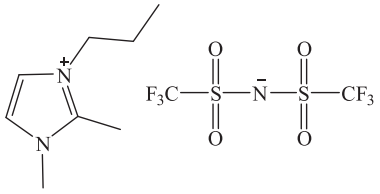
In this study, we prepared a SPME fibre based on the deposition of an ionic liquid on an etched stainless steel wire, instead of a commercial polyacrylate (PA) fibre, to analyse APs in water samples. Four oestrogenic APs (4-*n*-pentylphenol, 4-*n*-hexylphenol, *p*-*tert*-octylphenol and nonylphenols) were used as the target compounds. The goal of this study was to develop a sensitive, robust and inexpensive SPME method that can be used for the analysis of APs in water samples. Therefore, we also investigated the effects of the various experimental parameters that affected the extraction efficiency. Under the optimised conditions, we compared the enrichment factor with that obtained from a commercial PA fibre. Finally, the fibres were applied to extract APs from actual river-water samples to evaluate their applicability in real sample analysis.

2. Experimental

2.1. Chemicals and materials

The alkylphenol standards (4-*n*-pentylphenol, 4-*n*-hexylphenol, *p*-*tert*-octylphenol and nonylphenols), the silylation reagent BSTFA (N,O-bis(trimethylsilyl)trifluoroacetamide) and the internal standard (phenanthelene-d_{10}) used in this study, whose purities were higher than 99%, were purchased from Chem. Service (Hatfield, PA, USA). Standard solutions (1000 mg L^{-1}) of each compound were prepared in HPLC-grade methanol and stored in a refrigerator. A mixture of these alkylphenol compounds was prepared by diluting the standard solution with methanol, and additional diluted working solutions were prepared daily by diluting the standard solution with purified water or river water. The ILs used in this study were 1,2-dimethyl-3-propylimidazolium bis (trifluoromethylsulphonyl)imide [C_3MIM][NTf_2], 1-butyl-3-methylimidazolium hexafluorophosphate [C_4MIM][PF_6] and 1-octyl-3-methylimidazolium hexafluorophosphate ([C_8MIM][PF_6]), which were purchased from Sigma-Aldrich (Bellefonte, PA, USA). The structures and densities of the three ILs are shown in Table 1. The organic solvents used (dichloromethane, acetonitrile, methanol and acetone) were of HPLC grade and obtained from Caledon (Georgetown, Ont., Canada). Trifluoroacetic acid was of HPLC grade and purchased from Sigma-Aldrich (Bellefonte, PA, USA). Purified water was provided by a Milli-Q water purification system. Hydrofluoric acid (40.0%) was purchased from a local chemical reagent agent.

Table 1
Property of the three ILs selected in our experiment.

Abbreviation	ILs structure	Mw	Density (g cm^{-3})
[C_8MIM][PF_6]		340.29	1.24
[C_4MIM][PF_6]		284.18	1.38
[C_3MIM][NTf_2]		419.36	1.47

Solid-phase microextraction fibres composed of polyacrylate with a film thickness of 85 μm (PA, 85 μm) were purchased from Sigma-Aldrich (Bellefonte, PA, USA). The PA fibres were conditioned before every use in the hot injector of a gas chromatography system for 30 min at 230 °C according to the instructions provided by the supplier. A fibre holder for manual use was purchased from Sigma-Aldrich (Bellefonte, PA, USA). The needle core of a 1-μL microsyringe (Zhenhai, Zhejiang, Jiangsu) was used. PTFE stir bars (5 mm × 1 mm × 1 mm) were obtained from Sigma-Aldrich (Bellefonte, PA, USA). All glassware and other equipment were thoroughly washed with methanol and dried in an oven at 400 °C for 12 h after use.

2.2. Instrumentations

The chromatographic conditions of APs analysis were similar to those reported by Yang et al. [29,30]. Specific as follows:

HPLC analysis was performed using an Agilent 1100 series (Palo Alto, CA, USA) HPLC system. The HPLC system consisted of a quaternary pump, a vacuum degasser, a high-performance autosampler and a temperature-controlled column compartment. An Agilent G1315A diode array detector (Palo Alto, CA, USA) was employed. A ZORBAX Eclipse XDB-C_8 analytical column (150 mm × 4.6 mm, 5 μm) was used for chromatographic separation, and the constant flow of the mobile phase was maintained at 1 mL min^{-1}. A 4.6 mm × 12.5 mm Eclipse XDB-C_8 column (4.6 mm × 12.5 mm, 5 μm) drop-in guard cartridge (Agilent, CA, USA) was attached in line after the sample injector port and before the analysis column to trap residual contaminants that may have been contained in the mobile phase and/or the HPLC system. The solvent composition used as the mobile phase

was a mixture of ACN and H_2O (ACN:H_2O=5:5), and the UV detection wavelength was set to 225 nm. The water used in the mobile phase was filtered through 0.45-μm nylon membranes and degassed with ultrasonic waves; the water contained 0.1% trifluoroacetic acid.

GC analysis was performed on a Shimadzu GC 2010 equipped with a DB5 fused-silica capillary column (30 m × 0.25 mm; film thickness 0.25 μm), and detection was performed on a Shimadzu QPMS 2010 mass spectrometer with a quadrupole mass spectrometer system. The column temperature was maintained at 80 °C for 2 min and then programmed to increase by 20 °C min^{-1} to 100 °C, by 10 °C min^{-1} to 200 °C, finally ramped to 280 °C at the rate of 20 °C min^{-1} and then held for 20 min; the column flow was 1.20 mL min^{-1}. The other operating conditions consisted of an injection temperature of 280 °C in the splitless mode and the use of helium (99.99%) as the carrier gas. The GC–MS interface temperature was 280 °C. The electron ionisation-selected ion mode (EI-SIM) was used for quantification of the analytes. The solvent cut time was 8.0 min. The ion source temperature and the energy of the ionising electron were set to 200 °C and 70 eV, respectively. The selected *m*/*z* ratios of the ions used for quantification and identification of the target analytes were 179 and 207.

SEM micrographs of the stainless steel wire before and after etching were recorded on a Hitachi S-3500N scanning electron microscope at 20.0 kV.

2.3. SPME fibre preparation

The SPME device (Fig. 1) used in this study was prepared in our laboratory and modified from a 1-μL gas chromatography microsyringe with a stainless steel needle wire. The stainless steel needle of the microsyringe measured approximately 5 cm in length, from which a 1.5-cm portion was cut, resulting in the exposure of 1.5 cm of the stainless steel wire. The stainless steel wire could be exposed and retracted by pulling the upper end of the handle. Before etching, the needle wire was successively washed with methanol and dichloromethane and then conditioned at 200 °C under nitrogen gas for approximately 30 min. The stainless steel wire was etched by hydrofluoric acid for 20 min; the surface of the stainless steel wire became black and rough after etching. Then, the stainless steel wire was also conditioned at 200 °C to eliminate any possible contaminants. During the coating procedure, we prepared the dichloromethane and ILs mixture as reported by other researchers [27,28] in a ratio of 1:9, which was used as the coating solution. We dipped the etched stainless steel wire directly into the coating solution for 3 min and removed it; the dichloromethane evaporated immediately when the fibre was exposed to the surrounding air, and the ILs formed a thin layer on the etched stainless steel wire. The coating process was repeated three times. The coated stainless steel wire was directly used as the SPME fibre for the extraction of APs from water samples.

2.4. Stainless steel wire/IL–SPME procedures

For the experiment, the standard solution was gradually diluted using triple-distilled water until the concentration of each target compound was 500 ng mL^{-1}. A 1.3-mL aliquot of the APs aqueous samples was placed in a 1.5-mL glass vial. In this study, the SPME sampling method was performed by direct immersion, with the immersion depth and the vial position held constant. During the extraction, the aqueous samples were continuously stirred with a magnetic stir bar on a stir plate. Unless otherwise noted, prior to the extraction step, the pH of the aqueous sample was adjusted to 2 with hydrochloric acid. The temperature of the solution was maintained at 40 °C in a thermostatic water bath, and all of the experiments were conducted for a period of 30 min. After extraction, the compounds retained on the fibre were desorbed using an off-line static-state desorption mode.

Samples of river water were collected from the Buerhatong River (Yianji, Jilin Province), and the water was directly analysed by the optimised SPME process after sampling without any pretreatment. Because the matrix of the real sample was complex and the sensitivity of HPLC–UV is rather low, GC–MS analysis was performed on the real sample to ensure accuracy. Due to the polarity of the APs, a derivatisation procedure was performed before the GC–MS analysis. The derivatisation procedure has been thoroughly studied in our laboratory [31]. The concentration of each target compound after extraction was defined as the ratio of the amount of the target compound to the volume of the ILs. The amount of each IL can be calculated from the peak area of the corresponding liquid chromatograph due to the IL's ultraviolet absorption. A volume of 1 μL for each IL was injected into the liquid chromatography system, and the obtained peak area was used for quantification of the ILs adsorbed on the etched stainless steel wire. A gas chromatographic internal standard, phenanthelene-d_{10}, was added to every sample prior to GC injection.

2.5. Desorption procedures

The optimisation experiments were performed by HPLC. After extraction the fibre was placed into a vial filled with an organic solvent for desorption, and ensuring its total immersion. And desorption for 5 min was carried out at ultrasonic treatment. A subsample was subjected to further analysis by HPLC.

Analytical performance characteristics and real sample analysis were performed by GC–MS. The procedure involved the use of a 50-μL mixture of BSTFA and acetone (1:1), and the headspace (HS) derivatisation was performed on fibre, the derivatisation time was 10 min. The fibre was direct injected into the GC injector, a subsample was subjected to GC–MS for further analysis.

3. Results and discussion

The amount of analytes adsorbed by the ILs at equilibrium is directly related to their concentrations in the sample and can be expressed by the following equation [32]:

$$n_A = K_{fs} V_f V_s C_0 / (K_{fs} V_f + + V_s) \quad (1)$$

where n_A is the amount of analyte A extracted by the coating when equilibrium is reached, V_s and V_f are the volumes of the sample solution and the coating, respectively, C_0 is the initial concentration of the analytes in the sample and K_{fs} is the distribution coefficient. If V_s is very large ($V_s >> K_{fs}V_f$), and the amount of analyte extracted by the ILs coating can be expressed by

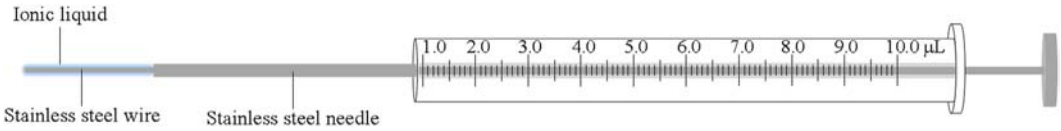


Fig. 1. Schematic representation of the etched stainless steel wire/ionic liquid-solid phase microextraction technique.

the following equation [32]:

$$n_A = K_{fs} V_f C_0 \quad (2)$$

According to the operating principle of SPME, when equilibrium is reached, the amount of the adsorbed target compounds is proportional to the volume of the ILs and K_{fs}. Therefore, the chemical and physical properties of the substrate and the ILs are the primary factors that determine the extraction efficiency. For the quantitative analysis of trace levels of APs in water samples, the extraction efficiency is especially crucial; therefore, selecting a suitable SPME substrate is important in the SPME fibre coating technique. The extraction efficiency of the IL-SPME technique can be improved by increasing the amount of ILs adsorbed on the substrate, which can be achieved by modifying the substrate surface.

3.1. Selection of the substrate

A stainless steel wire was used as the substrate for SPME instead of a commercial fibre due to the former's strong mechanical properties and its ability to be modified easily [14,21,33]. A previous study [27,28] showed that the surface of a stainless steel wire is smooth and the amount of ILs adsorbed on the stainless steel is limited due to the low adsorption interaction between the ILs and stainless steel or fused silica; therefore, the extraction efficiency is limited. The amount of ILs that coat the supporting material depends on the surface properties of the supporting material. To improve the adsorption of the ILs on the stainless steel wire, the wire was etched using hydrofluoric acid for 20 min that partially dissolved the wire and increased the surface area. Physical characteristic of the wire before and after the etching procedure have been studied by SEM: as reported in Fig. 2, etched wire showed more roughness, porosity, and then a greater surface area if compared with non-etched wire (Fig. S1 and Table S1).

To evaluate the adsorption capacity of the stainless steel wire, the two different surfaces of the wire were compared, and the amount of ILs adsorbed on the different surfaces was calculated from the ILs' absorption peak area on the corresponding liquid chromatograph. Fig. 2B shows the peak area of the $[C_8MIM][PF_6]$ IL adsorbed onto the stainless steel wire and the etched stainless steel wire. The amount of the ILs adsorbed onto the etched stainless steel wire was observed to be approximately two times that adsorbed on the unetched wire. This result indicates that the etched stainless steel wire favoured enhanced extraction efficiency because it adsorbed more ILs than the original stainless steel wire. Therefore, the etched wire was selected as the SPME substrate in the following study.

3.2. Selection of ILs

Similarly to the conventional SPME, the extraction efficiency of the IL-coated SPME is dependent on the physiochemical properties of the fibre coating material and the target analytes, such as the functional groups and structure of the chemicals. The different kinds of the ILs can change the partition coefficient (K_{fs}) of the target compounds between the extraction phase and the sample. A preliminary ILs selection was carried out taking in consideration ILs with appropriate physico-chemical characteristics, such as water solubility, viscosity and hydrophobicity. On the base of this preliminary selection, three ILs were candidate as the coating materials: 1,2-dimethyl-3-propylimidazolium bis(trifluoromethylsulphonyl)imide ($[C_3MIM][NTf_2]$); 1-butyl-3-methylimidazolium hexafluorophosphate ($[C_4MIM][PF_6]$) and 1-octyl-3-methylimidazolium hexafluorophosphate ($[C_8MIM][PF_6]$). The coating materials feature a cationic imidazolyl group and anionic $[NTf_2]$ or $[PF_6]$ groups. The purpose of this study was to directly extract the target analytes from water samples; therefore, the fibres were directly immersed in the water phase. To protect the dissolution of the ILs from the coating into the water system, we selected ILs that

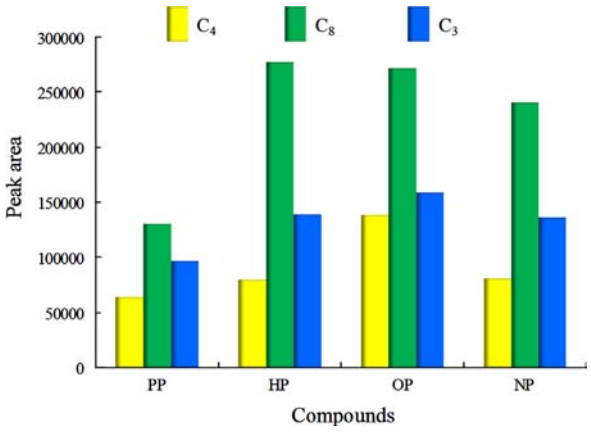


Fig. 3. The effect of the nature of the ILs on the extraction efficiency. Deionised water (1.3 mL) spiked with 500 ng mL^{-1} of each of the four APs, with direct-immersion SPME at 40 °C for 30 min.

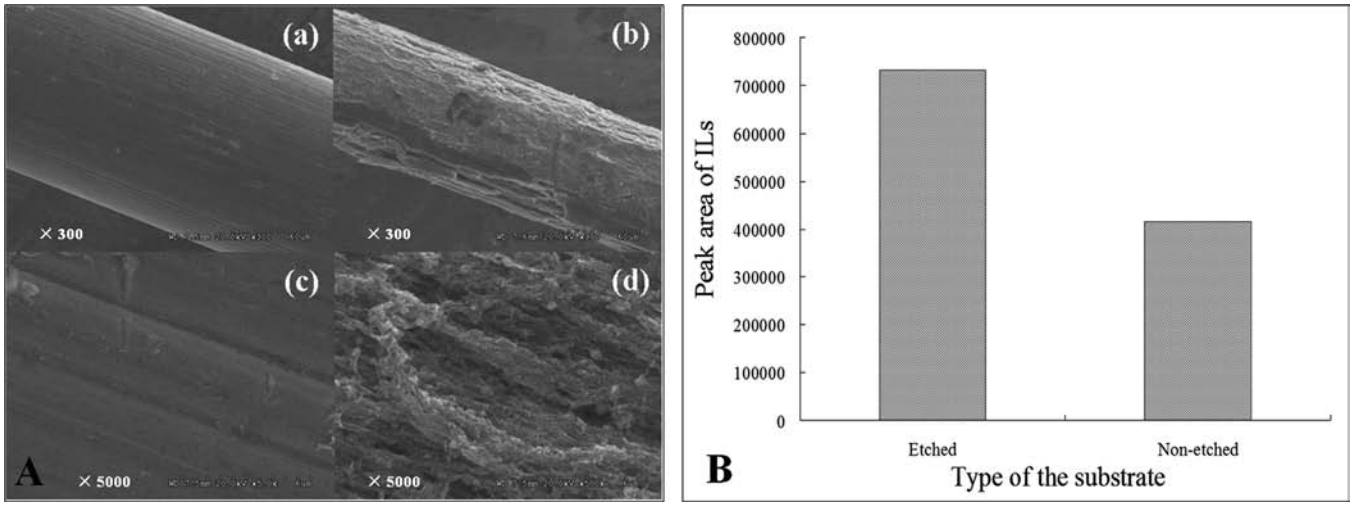


Fig. 2. A) Scanning electron micrographs of the surface of the stainless steel wire before (a and c) and after (b and d) etching. Images a and b were captured at a magnification of 300; images c and d were captured a magnification of 5000. B) The amount of ILs adsorbed onto the SPME fibre with and without etching, as analysed by LC-UV.

contain a hydrophobic anion. The length of the lateral chain linked to the imidazolyl group also affected the physical and chemical properties of the ILs. The ILs with a longer lateral chain exhibit higher viscosity, which can increase the amount of ILs adsorbed onto stainless steel. Furthermore, the different lateral chain lengths of the ILs will affect the extraction efficiency because the K_{fs} values of the ILs are also different. Therefore, we also selected two ILs that contain the same anion but a different cationic lateral chain for comparison. Fig. 3 shows the effect of the different ILs on the extraction efficiency of the four types of APs. Among the three types of ILs selected, [C_8MIM][PF_6] exhibited the best extraction efficiency due to its high viscosity and hydrophobicity; thus, a relatively large amount of ILs can be adsorbed onto the etched stainless steel. Furthermore, the strong interaction between the octyl group in the [C_8MIM][PF_6] and the analytes and the lower solubility of $[PF_6]^{-1}$ than $[NTf_2]^{-1}$ leads to the high viscosity, strong adsorbability and low solubility of the IL. Consequently, [C_8MIM][PF_6] displays higher extractability compared with the other two types of ILs. Therefore, [C_8MIM][PF_6] was chosen as the fibre coating material in the following experiments.

3.3. Optimisation of the SPME parameters

3.3.1. Extraction time

SPME is an equilibrium-based and non-exhaustive extraction technique. The target compounds are then distributed between the matrix and the extraction phases obeying to the partition constant when equilibrium is reached. Under non-equilibrium conditions, EE is dependent from extraction time: in order to study this influence, the EE of the IL-SPME was analysed in a time range of 10–50 min. Results are displayed in Fig. 4A: during the first 30 min, a high dependence from extraction time was observed, while only slight increases (sometimes not noticeable) were recorded for higher times. Thus, 30 min was chosen as the extraction time for further experiments.

3.3.2. Extraction temperature and stirring rate

For the direct-immersion SPME, the diffusion and mass transfer of the target compounds to the extraction phase are vital for obtaining good extraction efficiency and reproducibility. Stirring the sample and increasing the extraction temperature can improve the extraction efficiency by increasing the K_{fs} value by accelerating the diffusion and mass transfer of the analytes to the extraction phase. At a suitable extraction temperature and stirring rate, good extraction efficiency can be obtained within an economic analysis time.

To investigate the effect of the extraction temperature, a temperature range of 20 °C to 80 °C was studied. As shown in Fig. 4B, a higher extraction efficiency was obtained when the temperature increased from 20 °C to 40 °C; however, above 40 °C, the extraction efficiency decreased sharply. A high temperature could accelerate the diffusion and mass transfer and further improve the extraction efficiency. However, when the temperature was higher, the solubility of the analyte and the ILs in water also increased; therefore, the target dissolved in the water phase from the coating materials, and the extraction efficiency decreased. Thus, 40 °C was selected as the extraction temperature in the following experiments.

A series of experiments using different stirring rates was also conducted to investigate the effect of the stirring rate on the extraction efficiency. According to the experimental results, a positive effect was obtained by increasing the stirring rate. The extraction efficiency was satisfactory when the stirring rate was 400 rpm. Above this rate, the magnetic stir bar was difficult to operate. In addition, rapid agitation causes the mass transfer of the analytes from the water phase to the headspace by splatter, which is unfavourable for the direct SPME mode used in the present study.

3.3.3. Sample pH

Phenolic compounds are weak organic acids, and there are different forms of such compounds that occur depending on the acidity of a sample. Thus, in this study, the extraction efficiency was also greatly affected by the form of the target compounds that occurred in the aqueous sample. The compounds dissociated to their ionic form when the pH value of the aqueous sample exceeded the acidic dissociation constant (pKa) values of the compounds, and the compounds primarily existed in their molecular form when the pH value of the aqueous sample was lower than the pKa values of the compounds. The adsorption behaviour of the dissociated form of a molecule is very different from that of the non-dissociated form. It was important to control the pH of the extraction media to enhance the affinity of each compound to the fibre and improve the extraction efficiency. Referring to previous studies [30], the pH of sample solution was set to 2, 5, 7, and the results were compared (the data not shown). The experimental results showed that better extraction efficiency was obtained when the pH value of the sample solution was 2.0. In the following experiments, the pH of the aqueous sample was adjusted to 2.0 with hydrochloric acid.

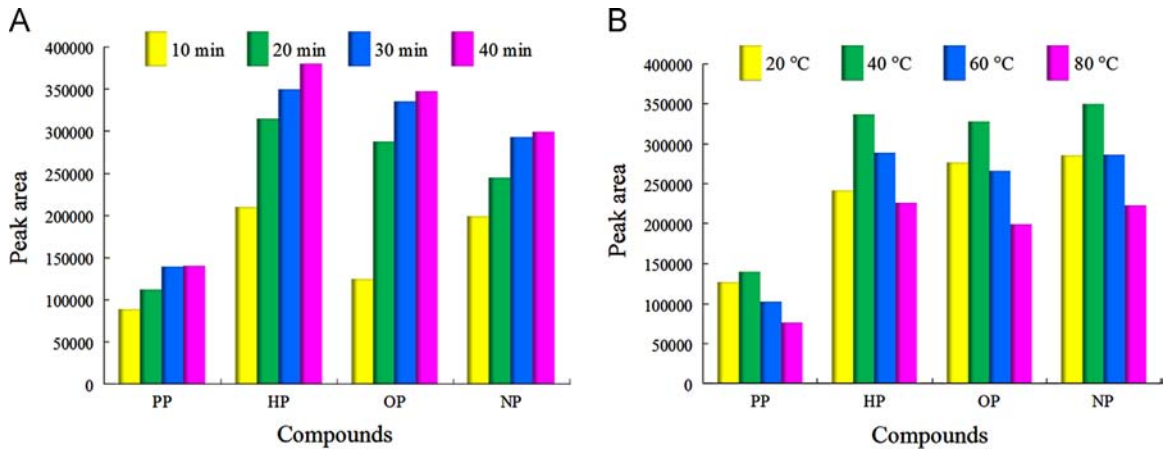


Fig. 4. A) The effect of the extraction time on the extraction efficiency. Deionised water (1.3 mL) spiked with 500 ng mL^{-1} of each of the four APs, with direct-immersion SPME at 40 °C with the [C_8MIM][PF_6] coating. B) The effect of the extraction temperature on the extraction efficiency. Deionised water (1.3 mL) spiked with 500 ng mL^{-1} of each of the four APs, with direct-immersion SPME for 30 min with the [C_8MIM][PF_6] coating.

3.3.4. Desorption procedure

Complete desorption of the analytes from the fibre enhances the reproducibility of the method and ensures that no crossover pollution exists in subsequent analysis. Additionally, the complete desorption of the analytes can minimise damage to the chromatographic instrument; therefore, we carefully investigated the effects of the desorption solvent and desorption time. In this study, a desorption procedure using a fibre-based, etched stainless steel IL substrate in the off-line mode and static state was adopted. The organic solvent used as the desorption solvent was required to have good solubility towards the target compounds and be compatible with the subsequent chromatographic analysis. APs show good solubility in methanol, which is suitable for the mobile phase in liquid chromatography analysis; therefore, methanol was used as the desorption solvent. The experimental results indicated that 5 min was the optimum desorption time, and no carryover was observed.

Table 2
Characterisation of the etched stainless steel wire/ILs SPME method determined by GC–MS.

Compound	Linear range (ng mL^{-1})	R^2	LOD* (S/N=3) (ng mL^{-1})	RSD (%)	logKow[a]	EFs		Increased multiple of EFs
						ILs	PA	
4-*n*-Pentylphenol	0.5–200	0.9734	0.03	11.2	3.747	1382	212	-
4-*n*-Hexylphenol	0.2–200	0.9692	0.01	7.6	4.675	1560	178	8.8
p-tert -Octylphenol	0.1–200	0.9917	0.01	4.0	5.139	4046	372	10.9
Nonylphenols	0.1–200	0.9569	0.04	8.3	5.603	4779	285	16.8

logKow[a] is the indicator for hydrophobicity, namely n-octanol_water partition coefficients. Data taken from ChemExper: (http://www.chemexper.com/).

* The detection limits were obtained at the 30 min extracting time and the 40 °C sample temperature when the pH of the aquatic sample was 2 under stirring 400 rpm.

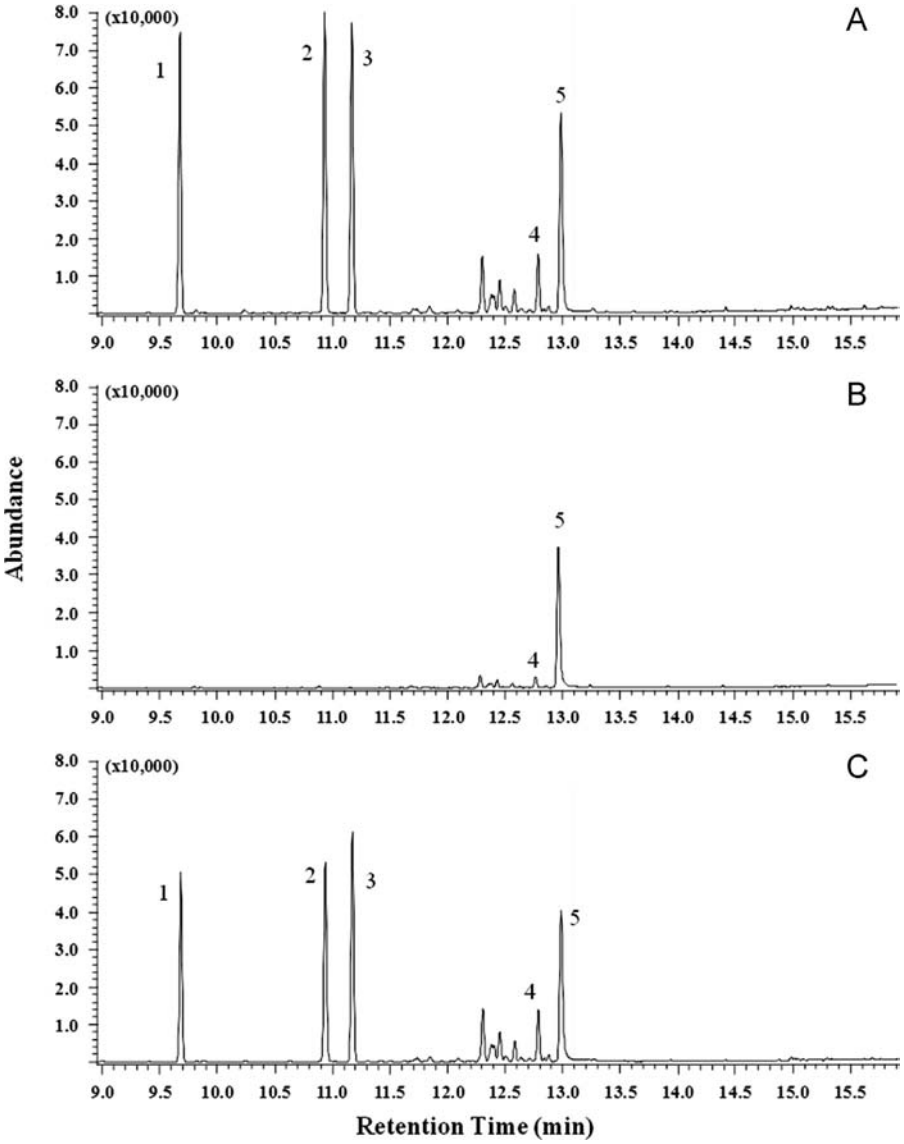


Fig. 5. GC–MS chromatograph of the river samples subjected to SPME and the derivatisation procedure; standard solution (A), river-water sample (B) and spiked river-water sample (C). Peaks: 1: 4-*n*-pentylphenol, 2: 4-*n*-hexylphenol, 3: *p-tert*-octylphenol, 4: nonylphenols, 5: PHE-d_{10}.

3.4. Analytical performance characteristics

The GC–MS method is widely used because of its good selectivity and high sensitivity. In addition, the reliability and accuracy of analysis have been significantly improved by applying highly specific and sensitive instrumentation. The matrix of the real sample analysed in this study was complex, and the sensitivity of the HPLC-UV method is rather low; therefore, GC–MS analysis was performed on the real sample to ensure accuracy. Due to the polarity of the APs, a derivatisation procedure was performed prior to the GC–MS analysis.

In this study, four types of AP standard mixtures were used to evaluate certain analytical performances and validate the proposed method. The linearity and the limits of detection (LODs) were evaluated using purified water spiked with four APs at five different concentration levels. These spiked samples were subjected to all of the stainless steel wire/IL–SPME procedures and the derivatisation experiment. The LODs were verified by analysing the different concentrations of the APs and calculated as three times the signal-to-noise ratio, according to published guidelines. Three replicate analyses were performed for each spiked levels (0.5, 2, 5, 50, 200 ng mL^{-1}) to evaluate the repeatability of the experiment. The figures of merit, including the linear ranges, correlation coefficients, repeatability and the limits of detection (LODs), are listed in Table 2. The linear range reached as wide as 10^3 for all of the analytes, with good correlation coefficients varying from 0.9569 to 0.9917. The LODs for the four alkylphenols ranged from 0.01 to 0.04 ng mL^{-1}. The enrichment factors ranged from 1382 to 4779. The repeatability of the adsorption on the fibre-based etched stainless steel substrate was represented by the relative standard deviation (RSD), which was observed to be less than 11.2% for the three repeated experiments under the optimised conditions.

In this study, a PA fibre was selected to perform the control experiment and to further validate the performance of the IL-coated stainless steel wire prepared in our laboratory. A PA fibre is typically employed in the polar polymer extraction phase used in common SPME. PA exhibited a high extraction efficiency and selectivity towards phenolic compounds in a previous study [23]. Because SPME is a non-exhaustive extraction technique, the EF value was used to evaluate the enrichment ability of the coatings. The EF value was defined as the ratio of the concentration of the target compounds after extraction to that before extraction. The EF values of the four APs obtained from the two coatings are listed in Table 2. As shown, for all of the target compounds, high EF values were recorded for the IL-coated stainless steel wire, and the EF values of the IL coatings were significantly higher than the EF value obtained from the PA fibre. This result demonstrates that the IL-coated etched stainless steel wire exhibited higher enrichment efficiency towards the APs than did the PA fibre, indicating that the IL coating extraction was suitable for the SPME of the APs.

3.5. Real sample

The proposed technique was successfully applied for the determination of the APs in river-water samples (three sites, three samples were collected at each site) from the Buerhatong River, which were collected in Yanji City, China. Among the four types of APs, only the NPs were detected in the river samples (as shown in Fig. 5); the concentration of the NPs was 46.65 ng mL^{-1}, and the RSD of the NPs was between 9.3% and 11.8%. To validate the analytical behaviour of other chemicals in real sample analysis, the river-water sample was spiked with 100 ng mL^{-1} of the AP standard mixture, and the sample was subjected to IL coating extraction and the above-described derivatisation procedures. As shown in Fig. 5, signals associated with all of the chemicals clearly appeared in the spiked real sample chromatograph. The enrichment factors of the APs ranged from 1328 for 4-*n*-pentylphenol to 3925 for nonylphenols, with an average RSD of 10.2%.

4. Conclusions

An economical, simple, rapid, environmentally friendly and highly efficient etched stainless steel/ionic liquid SPME technique was developed. The amount of the ILs adsorbed significantly increased using the etching method due to the formation of a rough surface on the wire substrate. This method favours a high extraction efficiency for stainless steel/ionic liquid SPME. The substrate, IL type, extraction time, extraction temperature and pH value are the main parameters that affect the extraction efficiency. The optimised conditions of the extraction procedure were determined to be as follows: etched stainless steel, [C_8MIM][PF_6], 30 min, 40 °C and pH 2. The enrichment factors and detection limits for the four alkylphenols ranged from 1382 to 4779 and from 0.01 ng mL^{-1} to 0.04 ng mL^{-1}, respectively. The low detection limits of the method allowed for its use in routine analysis. The etched stainless steel/ionic liquid SPME was coupled with the GC–MS method to successfully detect low levels of APs from river-water samples. Relative to the enrichment factor of a commercial PA fibre, the enrichment factors of the coated stainless steel wire reached values 6.5 to 16.8 times as great. The optimised and validated SPME technique was demonstrated to be useful for the qualitative and quantitative analysis of APs in water samples.

Acknowledgments

This study was supported by a grant from the National Natural Science Foundation of China (No. 21165020 and 21265023).M. Quinto is very grateful to the STAR*AgroEnergy Project286269.

Appendix A. Supporting information

Supplementary data associated with this article can be found in the online version at http://dx.doi.org/10.1016/j.talanta.2014.09.012.

References

[1] M. Petrovic, D. Barceló, J. Mass Spectrom. 36 (2001) 1173–1185.
[2] S.C. Laws, S.A. Carey, J.M. Ferrell, G.J. Bodman, R.L. Cooper, Toxicol. Sci. 54 (2000) 154–167.
[3] S. Meier, H.C. Morton, E. Andersson, A.J. Geffen, G.L. Taranger, M. Larsen, M. Petersen, R. Djurhuus, J. Klungsøyr, A. Svardal, Aquat. Toxicol. 105 (2011) 136–150.
[4] A.D. LaFleur, K.A. Schug, Anal. Chim. Acta 696 (2011) 6–26.
[5] J.A. Padilla-Sánchez, P. Plaza-Bolaños, R. Romero-González, N. Barco-Bonilla, J.L. Martínez-Vidal, A. Garrido-Frenich, Talanta 85 (2011) 2397–2404.
[6] Z. Kuklenyik, J. Ekong, C.D. Cutchins, L.L. Needham, A.M. Calafat, Anal. Chem. 75 (2003) 6820–6825.
[7] B. Bojko, E. Cudjoe, G.A. Gómez-Ríos, K. Gorynski, R. Jiang, N. Reyes-Garcés, S. Risticevic, É.A.S. Silva, O. Togunde, D. Vuckovic, J. Pawliszyn, Anal. Chim. Acta 750 (2012) 132–151.
[8] S. Risticevic, V.H. Niri, D. Vuckovic, J. Pawliszyn, Anal. Bioanal. Chem. 393 (2009) 781–795.
[9] C.L. Arthur, J. Pawliszyn, Anal. Chem. 62 (1990) 2145–2148.
[10] S. Endo, S.T.J. Droge, K.U. Goss, Anal. Chem. 83 (2011) 1394–1400.
[11] H.L. Xu, Y. Li, D.Q. Jiang, X.P. Yan, Anal. Chem. 81 (2009) 4971–4977.
[12] F. Bianchi, M. Mattarozzi, P. Betti, F. Bisceglie, M. Careri, A. Mangia, L. Sidisky, S. Ongarato, E. Dalcanale, Anal. Chem. 80 (2008) 6423–6430.
[13] A. Kloskowski, M. Pilarczyk, J. Namieśnik, Anal. Chem. 81 (2009) 7363–7367.
[14] X.Y. Cui, Z.Y. Gu, D.Q. Jiang, Y. Li, H.F. Wang, X.P. Yan, Anal. Chem. 81 (2009) 9771–9777.
[15] Q. Zhao, J.C. Wajert, J.L. Anderson, Anal. Chem. 82 (2009) 707–713.
[16] P. Hashemi, M. Shamizadeh, A. Badiei, P.Z. Poor, A.R. Ghiasvand, A. Yarahmadi, Anal. Chim. Acta 646 (2009) 1–5.
[17] J. Ji, H. Liu, J. Chen, J. Zeng, J. Huang, L. Gao, Y. Wang, X. Chen, J. Chromatogr. A 1246 (2012) 22–27.

[18] B. Chen, B. Hu, M. He, X. Mao, W. Zu, J. Chromatogr. A 1227 (2012) 19–28.
[19] Z. Zhang, Q. Wang, G. Li, Anal. Chim. Acta 727 (2012) 13–19.
[20] Z. Zhang, H. Duan, L. Zhang, X. Chen, W. Liu, G. Chen, Talanta 78 (2009) 1083–1089.
[21] X. Rong, F. Zhao, B. Zeng, Talanta 98 (2012) 265–271.
[22] M. Sun, J. Feng, H. Qiu, L. Fan, X. Li, C. Luo, Talanta 114 (2013) 60–65.
[23] Y. Ma, F. Zhao, B. Zeng, Talanta 104 (2013) 27–31.
[24] P. Sun, D.W. Armstrong, Anal. Chim. Acta 661 (2010) 1–16.
[25] E. Aguilera-Herrador, R. Lucena, S. Cárdenas, M. Valcárcel, TrAC, Trends Anal. Chem 29 (2010) 602–616.
[26] C.F. Poole, S.K. Poole, J. Sep. Sci. 34 (2011) 888–900.
[27] J. Liu, N. Li, G. Jiang, J. Liu, J.Å. Jönsson, M. Wen, J. Chromatogr. A 1066 (2005) 27–32.
[28] R. Amini, A. Rouhollahi, M. Adibi, A. Mehdinia, Talanta 84 (2011) 1–6.
[29] C. Yang, X. Piao, J. Qiu, X. Wang, C. Ren, D. Li, J. Chromatogr. A 1218 (2011) 1549–1555.
[30] C. Yang, J. Zhao, J. Wang, H. Yu, X. Piao, D. Li, J. Chromatogr. A 1300 (2013) 38–42.
[31] D. Li, J. Park, J.-R. Oh, Anal. Chem. 73 (2001) 3089–3095.
[32] G. Ouyang, D. Vuckovic, J. Pawliszyn, Chem. Rev. 111 (2011) 2784–2814.
[33] X. Hu, G. Dai, J. Huang, T. Ye, H. Fan, T. Youwen, Y. Yu, Y. Liang, J. Chromatogr. A 1217 (2010) 5875–5882.

Talanta 132 (2015) 572–578

Contents lists available at ScienceDirect

Talanta

journal homepage: www.elsevier.com/locate/talanta

Fluorophotometric determination of critical micelle concentration (CMC) of ionic and non-ionic surfactants with carbon dots via Stokes shift

Mukesh Lavkush Bhaisare [a], Sunil Pandey [a,e], M. Shahnawaz Khan [d], Abou Talib [d], Hui-Fen Wu [a,b,c,d,e,*]

[a] Department of Chemistry, National Sun Yat-Sen University, Kaohsiung, 70, Lien-Hai Road, Kaohsiung 80424, Taiwan
[b] School of Pharmacy, College of Pharmacy, Kaohsiung Medical University, Kaohsiung 807, Taiwan
[c] Institute of Medical Science and Technology, National Sun Yat-Sen University, Kaohsiung 80424, Taiwan
[d] Doctoral Degree Program in Marine Biotechnology, National Sun Yat-Sen University and Academia Sinica, Kaohsiung 80424, Taiwan
[e] Center for Nanosciences and Nanotechnology, National Sun Yat-Sen University, 70, Lien-Hai Road, Kaohsiung 80424, Taiwan

ARTICLE INFO

Article history:
Received 21 June 2014
Received in revised form
5 September 2014
Accepted 6 September 2014
Available online 16 September 2014

Keywords:
Critical micelle concentration
Stokes shift
Carbon dots
Surfactants
Cetyltrimethyl ammonium bromide
Sodium dodecyl sulfate
Triton X-100
Dodecyldimethyl (3-sulfopropyl) ammonium hydroxide
Fluorescence spectroscopy

ABSTRACT

A new and facile method for the determination of critical micelle concentration (CMC) of ionic and non-ionic surfactants is proposed in this article. Carbon dots exhibited substantial fluorescence and therefore enhanced the sensitivity of this evaluation. Understanding the formation of surfactant micelles is vital for the applications of biomedicine such as drug fabrication and smart molecular vehicles in delivering therapeutic dosage to various molecular sites. The fluorescence property of carbon dots was utilized for the first time to estimate the critical micelle concentration of surfactants. The central concept of the approach is based on the Stokes shift determination of a system composed of constant amount of carbon dots with varying concentrations of ionic and non-ionic surfactants. The synthesized carbon dots were characterized by FTIR, TEM, XRD, Raman, UV, and fluorescence spectroscope. The carbon dots were excited at 280 nm so as to obtain maximum emission for the Stokes shift measurement. The CMC value of cetyltrimethyl ammonium bromide (CTAB), sodium dodecyl sulfate (SDS), Triton X-100, dodecyldimethyl(3-sulfopropyl)ammonium hydroxide (SB-12) evaluated by this approach was found to be 0.98, 7.3, 0.19, and 3.5 mM, respectively. The signals of spectra were assigned and explained in terms of both electron transitions between specific molecular orbital and the interaction with solvent.

© 2014 Elsevier B.V. All rights reserved.

1. Introduction

Surfactant is a unique group of compounds containing both a hydrophobic long-chain (tail) and a hydrophilic polar group (head) in their structures [1,2]. When the concentration reaches a specific narrow range, called critical micelle concentration [3], the molecules tend to self-associate with tails aggregating inward into an assembled micellar structure which is favored thermodynamically in polar solvents [4]. The formed micelles have a center of hydrophobic (tail) moiety and an outward head (hydrophilic) moiety took place in a continuous phase generally observed in aqueous phase. In contrast, when the outer portion of micelles is comprised of tail (hydrophobic) moiety and the head moiety assembled in center of the micelles it is called as the reverse micelle which is formed in oil phase. In this study all the experiments were specifically conducted in aqueous phase. The formed micelle has been described as structure of aggregate; it has characteristically various interactions such as hydrophobic, electrostatic interaction and hydrogen bonding. These micelles comprise unique characteristics such as uniform nanosize, core-shell structure, and being stable thermodynamically in physiological conditions due to their low critical micelle concentration [5,6]. With this amphiphilic structure, surfactants have been extensively employed in applications including the fields of chemistry [7], biotechnology, and pharmacy [8]. A variety of surfactants have been utilized with their capability to enhance the permeability of drugs across biological membranes [9]. In complex systems, surfactants were widely used in membrane protein separation, crystallization, purification and stabilization. Since the physicochemical properties of solutions below and above CMC demonstrate drastic changes, such as surface tension, electrical conductivity,

* Corresponding author at: Department of Chemistry, National Sun Yat-Sen University, Kaohsiung, 70, Lien-Hai Road, Kaohsiung 80424, Taiwan.
Tel.: +886 7 5252000x3955; fax: +886 7 5253908.
E-mail address: hwu@faculty.nsysu.edu.tw (H.-F. Wu).

http://dx.doi.org/10.1016/j.talanta.2014.09.011
0039-9140/© 2014 Elsevier B.V. All rights reserved.

turbidity, osmotic pressure, density, viscosity, and light scattering [10]. Many methods have been proposed to determine the CMC of plethora of surfactants, e.g. spectrophotometry [11], colorimetric [12], potentiometry, refractometry, conductometry, capillary electrophoresis, light scattering [13], pyrene 1:3 ratio method [14], and so forth. Among these methods, spectrophotometry is a simple and reliable tool for determination of CMC. Due to the outstanding fluorescence exhibited by carbon dots (C-dots) [15], the nanodots were introduced in an attempt to enhance the sensitivity for the fluorophotometric determination of CMC.

Most of the methods reported for the determination of critical micelle concentration have several disadvantages such as low sensitivity, the necessity of dye or probe, large volume of sample, tedious experimental techniques as well as the interpretation tools required. Additionally, some methods are particularly applicable to the CMC determination of a specific surfactant which is one of the major drawbacks of those methods [16]. In the present work, in order to solve these problems, we have developed a modified technique based on the fluorescence and the Stokes shift of C-dots, which is one category of highly fluorescent materials based on carbon materials [17] to investigate the CMC of CTAB, SDS, Triton X-100, and SB-12.

C-dots are growing popular among the families of quantum dots because of the excellent optical and biomedical properties [18]. The advantages of being able to emit intense and tunable photoluminescence (PL) have made C-dots to be a favorable ingredient for the applications in the fields of catalysis and energy [19]. Additionally, carbon quantum dots demonstrated special characteristics, e.g. non-blinking, high aqueous solubility, and non-toxicity [20]. There are many established protocols for the synthesis of amorphous as well as crystalline C-dots using facile routes such as thermal cracking of organic compounds [21], microwave mediated synthesis [22], laser ablation of graphite [23], electro-oxidation of graphite, and oxidation of candle soot [24].

The central concept of this work is based on the Stokes shift, the difference of peak maxima in excitation and emission spectra [25], of C-dots in the presence of varying concentration of surfactants. The C-dots decorated with both positive as well as negative charged moieties were found to be efficiently interacting with charged or non-charged head group surfactants. This phenomenon leads to the exhibition of sharp Stokes shift in the presence of the surfactants. Herein, cationic cetyltrimethyl ammonium bromide (CTAB), anionic sodium dodecyl sulfate (SDS), non-ionic Triton X-100, as well as zwitterionic dodecyldimethyl (3-sulfopropyl)ammonium hydroxide (SB-12) surfactants were investigated and the CMC were evaluated. Note that this zwitterionic surfactant has seldom been studied [26]. Since the zwitterionic surfactant is electrically neutral in nature, it is easily to be distinguished from others. For the determination of CMC values, the intersection of the extrapolation of curves in a graph of Stokes shift versus concentration was perceived as a point of change and was typically denoted as the CMC. All of the experiments were performed at room temperature.

2. Materials and methods

Sucrose was purchased from J.T. Baker (USA). Cetyltrimethyl ammonium bromide (CTAB), sodium dodecyl sulfate (SDS), Triton X-100, sulfuric acid and sodium hydroxide were purchased from Sigma-Aldrich (USA). Quinine sulfate was supplied by Alfa Aesar (Great Britain). Dodecyldimethyl(3-sulfopropyl)ammonium hydroxide (SB-12) was supplied by Tokyo Chemical Industry Co., Ltd. (Japan). Ultrapure water from a Milli-Q Plus water purification system (18.2 MΩ, Millipore, and Bedford, MA, USA) was used for all experiments.

2.1. Preparation and purification of fluorescent carbon dots (C-dots)

C-dots were prepared by controlled carbonization of sucrose modified method proposed by Minghong Wu group [27]. 2.5 g of sucrose was weighed and dissolved by adding 2 mL of deionized water. Add 3 mL concentrated sulfuric acid dropwise into the solution with continuous vigorous stirring. The yellowish brown colored reaction mixture was neutralized with sufficient amount of NaOH. The dark brown color reaction mixture was isolated by a centrifuge operated at 18,000 rpm for 10 min. It was further purified by dialysis (MW cutoff 12–14 kD) against Milli-Q water for 24 h under constant stirring condition. In order to concentrate the amount of C-dots the solution was dried in a rotary vacuum evaporator (Büchi, Germany) and frozen dried for the quantification of C-dots.

2.1.1. Quantum yield measurement

The quantum yield (Q) of the C-dots has been calculated using the following equation, Eq. (1). Quinine sulfate (Q is 0.54) was chosen as a reference to determine Q, where Q denotes for quantum yield, I represents measured integrated emission intensity, n denotes the refractive index, and E is the optical density. R represents the fluorophore of known quantum yield for reference [28,29].

$$Q = Q_R \frac{I}{I_R}\frac{E_R}{E}\frac{n^2}{n_R^2} \quad (1)$$

2.2. Determination of critical micelle concentration of surfactants

2 mg of dried C-dots was mixed with varying concentrations of CTAB, SDS and Triton X-100 and make up to 5 mL as the total volume. The stock solutions of all surfactants were prepared and used for further experiments. The concentrations of stock solutions for CTAB, SDS, Triton X-100, and SB-12 were 10 mM, 50 mM, 5 mM, and 25 mM. In case of CTAB, aqueous dilutions were prepared from 0.2 to 2 mM at the interval of 0.2 mM from a stock solution. As for SDS, 2–20 mM diluted solutions were prepared with increment of 2 mM from stock solution. In the case of Triton X-100, various dilutions prepared from 50 to 500 μM with increment of 50 μM from the stock solution. For SB-12, solutions were prepared from 0.5 mM to 6.0 mM with increment of 0.5 mM from the stock solution. 2 mg of highly purified C-dots was added in all the dilutions and make up the volume up to 5 mL. These solutions were sonicated for 5 min in order to equilibrate the solution. Similar procedure was followed for SDS except the dilutions were varied from 2 to 20 mM from a stock of 50 mM. 10 mM Triton X-100 stock solution was prepared and 50 to 500 μM dilutions were prepared from the stock solution. After equilibrating the C-dots-surfactants solution, the excitations as well as the emission spectra were recorded using the fluorescence spectroscope (Hitachi F 2700, Japan). The excitation maxima relative to emission maxima were recorded for each concentration of dilution sample.

The Stokes shift was calculated using the following equation:

$$\Delta\nu(\text{Stokesshift}) = \nu_{ex} - \nu_{em} \quad (2)$$

where ν_{ex} and ν_{em} refer to the excitation and the emission maximum, respectively.

From the graphical representation of the Stokes shift versus concentration, CMC values of the surfactants were evaluated.

2.3. Characterization of carbon dots (C-dots)

The morphology and uniformity of C-dots were measured by a high resolution transmission electron microscope (JEOL, Japan). Spectral properties of C-dots were studied by a UV–vis spectroscope

(Thermo, Evolution 201, USA) and fluorescence spectroscope (Hitachi-2700, Japan) using a standard quartz cuvette having a path length of 1 cm. Functional groups of C-dots were studied using a Fourier transform infrared spectrometer (Perkin Elmer, USA). The crystallinity of C-dots were studied using an X-ray diffraction (XRD) (Phillip, The Netherlands). Raman spectra were recorded from the Horiba, Jobin–Yvon Labram spectrometer with 630 nm laser sources.

3. Results and discussion

3.1. The characterization of C-dots

The brown colour C-dots solution exhibited intense green fluorescence strongly under UV light (λ_{ex}=365 nm), as shown in schematic illustration of Fig. 1. C-dots are spherical in shape and are highly mono-dispersed with uniform size (Fig. 2A). Moreover, the TEM micrograph depicts the nanoscale size of C-dots with average particle diameter ranging from 3 to 6 nm with maximum population of C-dots as 5 nm (diameter), (see Fig. 2B). The UV–vis spectrum (Fig. 2C) of C-dots displayed continuous absorbance increasing from 280 nm to 380 nm which is in agreement with relevant literatures [27]. Fig. 2D showed the combined photoluminescence spectra of aqueous solution of C-dots with different excitation wavelengths. The aqueous C-dots solution was excited at 260–400 nm with 20 nm increment. The maximum intensity for emission spectra observed 387 nm was excited at 280 nm. The emission peak was shifted to a higher wavelength with the increase of the excitation wavelength. All experiments were carried out at 280 nm (excitation wavelength) to determine the critical micelle concentration (CMC) for all surfactant-C-dots dilutions. An FTIR technique was used to identify the functional groups on the surface of C-dots. As shown in Fig. 3A, the band of the ester group appeared at 1719 cm^{-1} and the peak of the C=O group found at 1719 cm^{-1} depict aromatization. The broad peak at 3438 cm^{-1} and the band in the range of 1000–1400 cm^{-1} implied the existence of a large amount of hydroxyl groups and C-O groups. X-ray diffraction (XRD) of C-dots (Fig. 3B) reveals a characteristic peak at 2θ=20.12°, which can be assigned to the plane (002) with an interlayer spacing of 4.2 Å, which is larger than that of bulk graphite (3.3 Å), indicating poor crystallization [30]. The Raman spectrum shown in Fig. 3C reveals the typical graphitic nature of C-dots. C-dots exhibited D- and G-bands corresponding to 1345 and 1540 cm^{-1} with no 2D peak in graphite. It can clearly be seen that the D peak is more prominent than G peak. This indicates the presence of amorphous carbon nanomaterials in the form of C-dots. The ratio of I_D/I_G, which is the characteristic peak of the disorder extent and the ratio of sp^3/sp^2 carbon, implying the extent of structural defects [30]. The I_D/I_G ratio of 2 indicates highly crystalline graphite. We calculated the I_D/I_G ratio for the as-synthesized C-dots and the estimated ratio of 0.873 indicating high purity of C-dots. The quantum yield of C-dots calculated with the reference to Quinine sulfate was found out to be 42%, which was summarized in Table 1.

3.2. The evaluation of critical micelle concentration (CMC) for CTAB, SDS, Triton X-100, and SB-12

Fig. 4A displays the impact of varying concentration of CTAB on the fluorescence properties of C-dots excited at 280 nm, which is the preliminary criterion of the determination of CMC. Generally, cationic surfactants such as CTAB acquire positively charged headgroups that are partially neutralized by anions, while anionic surfactants possess negatively charged head groups that are partially neutralized by cations [31]. As CTAB concentration increases, there was consistent decrease in fluorescence intensity (emission) of C-dots (Fig. 4A). Another noteworthy finding was the comparable intensities of both emission and excitation spectra of C-dots-CTAB mixture. The red shift observed from 375 nm to 425 nm may be due to the surface protection of C-dots with CTAB which may affect the PL properties of C-dots. In the close proximity of miniature scale of C-dots in the solution, due to monomers of surfactants, many thermodynamically favoured reactions are initiated leading to the change of the surface as well as the optical properties of the materials. Due to the negative charge exhibited by the C-dots in aqueous solution [31], as the concentration of CTAB monomers increases, the interaction of

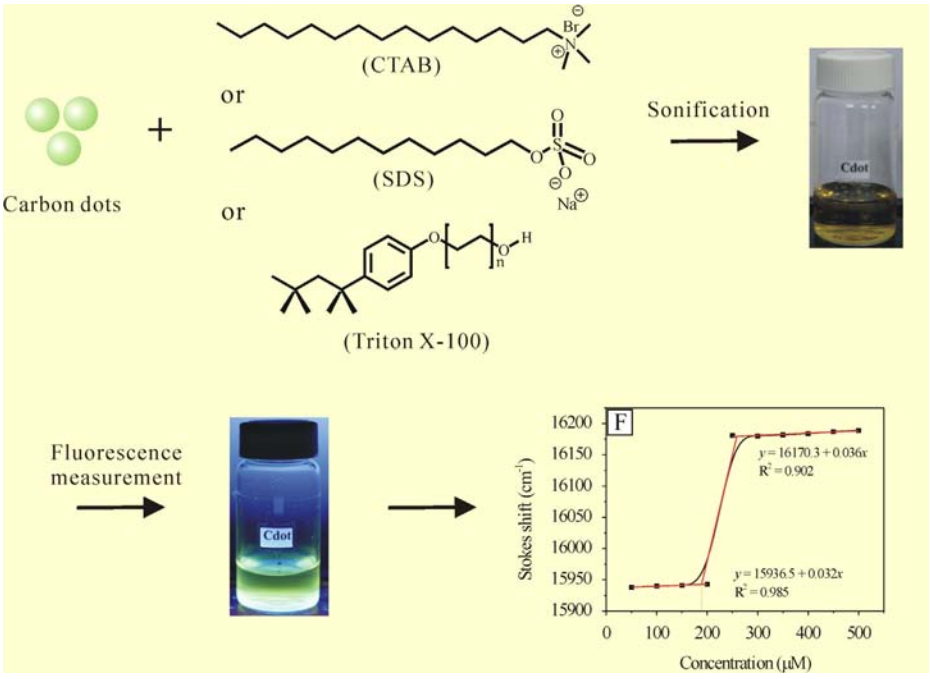


Fig. 1. Schematic illustration of experimental procedures.

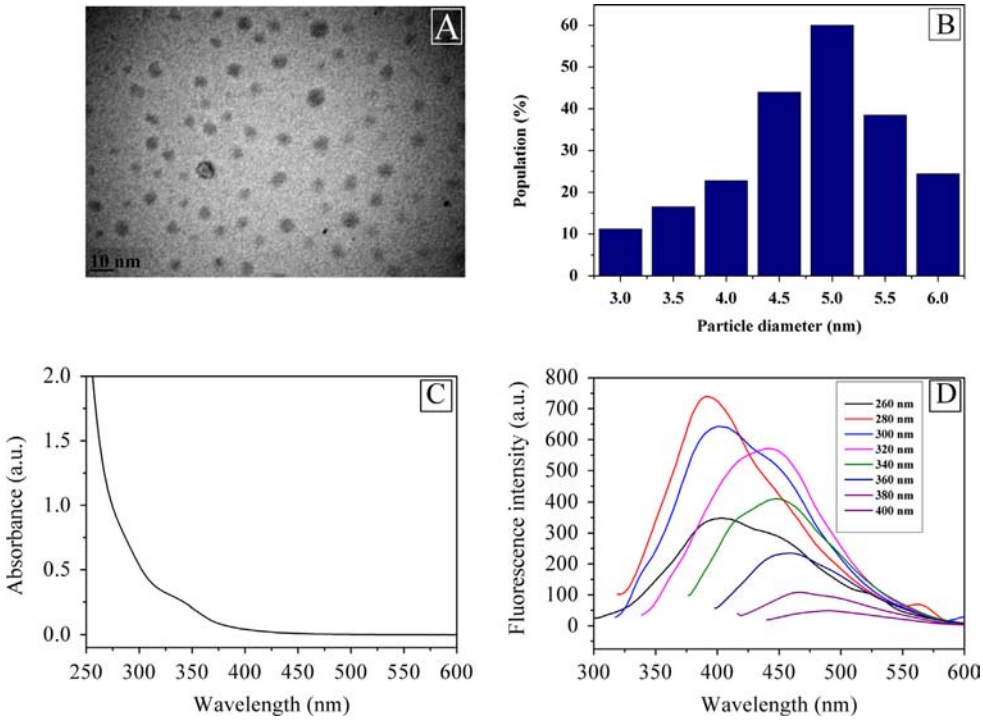


Fig. 2. Characterization of carbon dots: (A) TEM image, (B) histogram of particle diameter distribution, (C) UV–vis spectra, and (D) fluorescence spectra excited at different wavelengths.

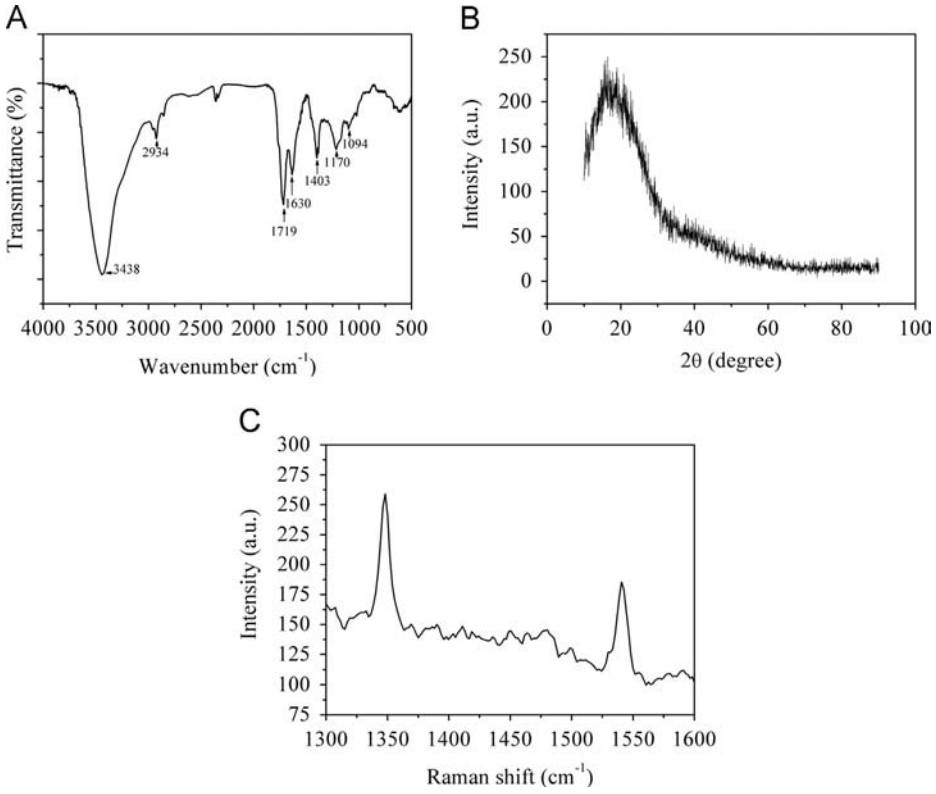


Fig. 3. Continued characterizations of carbon dots: (A) FTIR spectra, (B) XRD pattern, and (C) Raman spectra.

C-dots with positively charged CTAB becomes more frequent and results in greater stability of the C-dots-surfactant aggregate and consequently causing larger Stokes shift [25]. The utilization of the Stokes shift for the evaluation of CMC is based on two key points: higher Stokes shift of monomers compared to micelles and the adsorption of CTAB molecules on C-dots. The surfactant molecules were scattered throughout the aqueous solution at lower concentration of CTAB (below CMC). As the concentration increased, the surfactant molecules began to aggregate at the air-solution interface. There is no sign of monomers remained after the CMC point and the Stokes shift decreased drastically which was shown in Fig. 4B. The capability of C-dots to exhibit such sharp transition

Table 1
Determination of quantum yield of carbon dots with quinine sulfate as the reference.

Sample	Integrated emission intensity (I)	Abs. at 360 nm (A)	Refractive index of solvent (n)	Quantum yield at 360 nm (Q)
Quinine sulfate	41,301	0.07	1.33	0.54
C-dots sample	101,334	0.23	1.33	0.42

reveals their suitability as an excellent molecular sensor for the present work. Due to this magnificent property observed in selected fluoro-probes, there is change in the emission as well as excitation spectrum and hence the considerable Stokes shift.

Fig. 4B explains the Stokes shift with respect to concentration of CTAB. It can be observed that, by virtue of pre-micellar concentration (concentration just before critical micelle concentration), the Stokes shift was found to be less with increasing concentration of CTAB. After a particular concentration of CTAB, there was a steep decrease in the Stokes shift and finally it levels

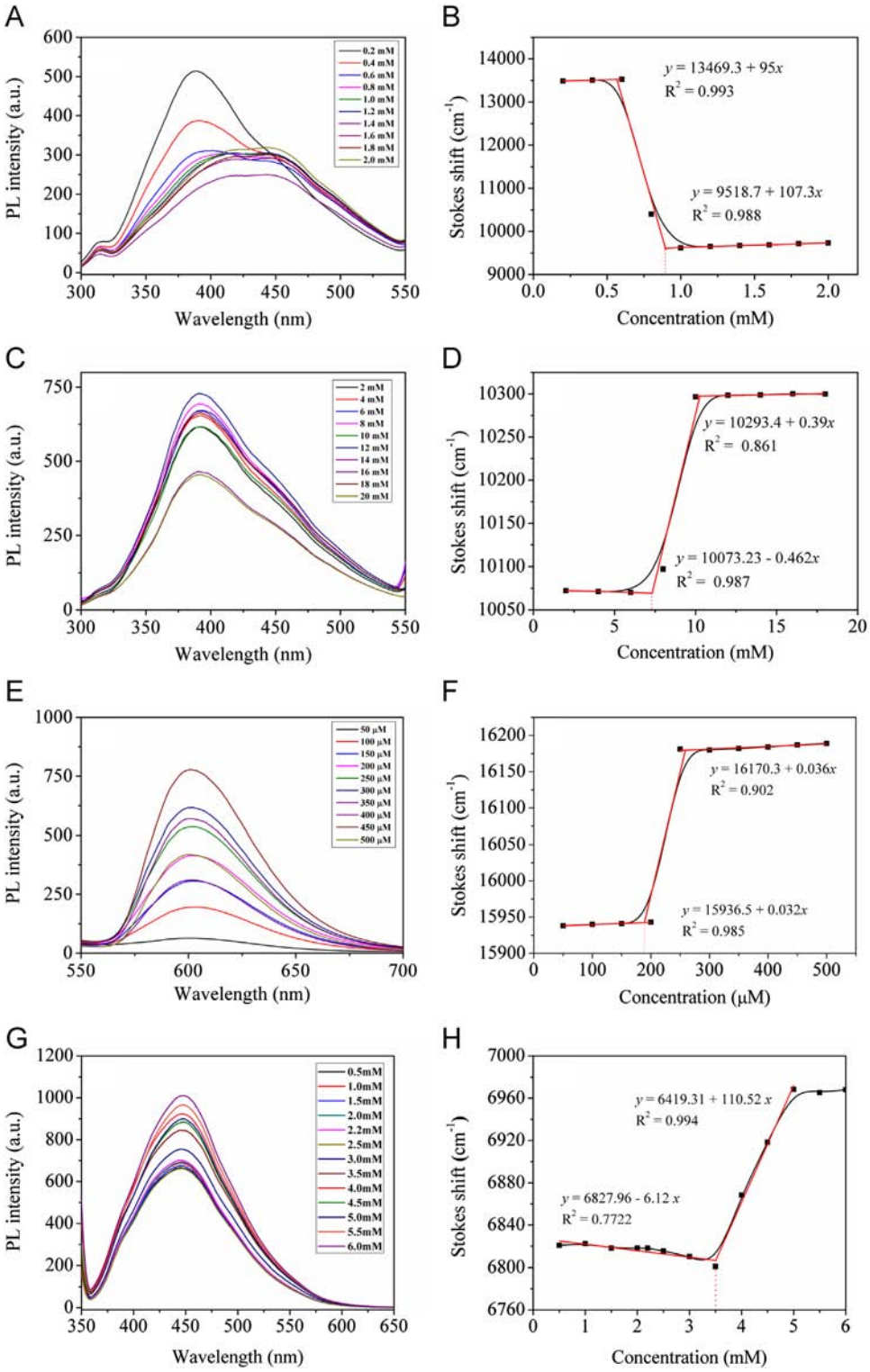


Fig. 4. Excitation and emission fluorescence spectra, and the corresponding relationship of the Stokes shift and the concentration of surfactant CTAB (A and B), SDS (C and D), Triton X-100 (E and F), and SB-12 (G and H), respectively.

Table 2
List of CMC evaluations from some proposed protocols and the approach in this work.

Method	Surfactants	CMC in mM	Condition measured	References
Synchronous fluorescence spectroscopy	Triton X-100	0.2	Aggregation by hydrogen bonding	[16]
Fiber-optic refractive index sensing	Triton X-100, SDS	0.21, 8.10	Refractive index	[33]
UV and fluorescence Spectroscopy	Triton X-100	0.224	Based on Non invasive method-Time-resolved spectroscopy, steady state	[11]
Conductance	SDS	8.1	Pyrene	[34]
Near-infrared spectroscopy	SB-12	2.7	NIR spectroscopic technique	[35]
Fluorescence spectroscopy	CTAB, SDS, Triton X-100, SB-12	0.98, 7.3, 0.19, and 3.5	Stokes shift	This paper

off after a particular concentration indicating the accumulation of the CTAB monomers and this concentration is equivalent to CMC of CTAB. To calculate the critical micelle concentration (CMC), the lines on the plateau were extrapolated as shown in Fig. 4B. The point of intersection of the two lines was considered as the critical micelle concentration. The critical micelle concentration of CTAB was found to be 0.98 mM which was in strong agreement with earlier findings [32].

Fig. 4C explains the impact of anionic surfactant such as sodium dodecyl sulfate (SDS) on PL properties of C-dots. In Fig. 4C, because of the considerable dissipating energy significant Stokes shift between excitation and emission was observed in this figure. This indicated that these Stokes shifts were found to be sensitive to SDS concentration. Since the electrostatic interactions exist predominantly between SDS and C-dots due to the negative charge of the surface head group of SDS, the Stokes shift increased rapidly when the concentration reached CMC at which circular pattern of SDS micelles formed despite the fact that very low Stokes shift of the monomers exhibited initially. This also indicates that very low energy fluorescence was observed for micelles as compared to that of monomers. Therefore, C-dots were unlikely remained and were saturated on micelles which showed nearly straight line in the figure as the concentrations higher than CMC. Fig. 4D displays the relation between the Stokes shift and the concentrations of the SDS. The sharp increase of Stokes shift from low value of SDS monomers to high value of micelles makes the point of change be clearly indicative of CMC value. As the concentration reached to CMC constant Stokes shift was observed from the surfactant and C-dots aggregate even with increased concentration of SDS. Using the aforementioned method, the CMC of SDS was determined to be 7.3 mM which was in good agreement with the earlier findings.

In the case of non-ionic surfactant, Triton X-100 was considered as the model molecule for the CMC evaluation. Due to the absence of charge on the surface of head portion of the surfactant, weak interaction with C-dots was exhibited. Apart from this, the interactions of van der Waals force, steric repulsion or interface may play important roles in intermolecular forces. As shown in Fig. 4E, the minimum fluorescence range was observed from the PL spectra of Triton X-100 despite the change of concentration. Wide disparity in intensity between the excitation and emission spectra was clearly observed from Fig. 4E. Compared to cationic and anionic surfactants, non-ionic counterpart exhibits insignificant interaction between molecules and C-dots. Even with UV excitation a small Stokes shift was displayed demonstrates this weak interaction compare to the charged surfactants. Moreover, the weak fluorescence intensity shown compare to the charged counterparts of surfactants further confirms this hypothesis. As the surfactant is non-ionic the interactions with C-dots is prolonged and hence exhibited the different optical behavior. At low surfactant concentration very large excitation intensity was observed but the emission intensity was very low relatively. As the surfactant concentration increases, reverse excitation intensity was observed and the similar pattern occurred to emission. Fig. 4F demonstrates the relation between the Stokes shift and the concentration of Triton X-100; it reveals that monomers exhibited smaller Stokes shift compared to that of micelles. And very minute change in Stokes shift was observed even at CMC compared to ionic surfactants. The relationship between the variations of the Stokes shift in accordance with the alteration of surfactant concentration was plotted and the CMC value was indicated in Fig. 4F. As the concentration increased the Stokes shift was very small initially and sudden increase occurred as the concentration approached CMC and then the curve levelled off. As the fluorescence property of C-dots was negligibly influenced by the micelles of non-ionic surfactant Triton X-100 which was formed at CMC. Constant Stokes shift was observed above CMC as the concentration increased implying that insignificant change occurred in Stokes shift. Using the aforementioned method, the CMC of Triton X-100 was determined to be 0.19 mM which was in good agreement of the earlier findings.

CMC determination of the zwitterionic surfactant was performed with the model molecule of dodecyldimethyl(3-sulfopropyl)ammonium hydroxide. Different concentrations of surfactant were prepared and were mixed with constant concentration of C-dots. From the measurements of the fluorescence pattern at a particular excitation wavelength of 340 nm, the zwitterionic surfactant displayed distinct behavior. The fluorescence spectrum was recorded in Fig. 4G and the relationship of the Stokes shift vs concentration was demonstrated in Fig. 4H. Since the zwitterionic surfactant contain both cationic [+] and anionic [−] charges on different positions of the same molecule. From the mixing of the C-dots with the zwitterionic surfactant, the fluorescence pattern regarding the excitation wavelength exhibited unexpected consistency which is remarkably different from other surfactants. The maximum of excitation wavelength was fixed at the particular wavelength of 280 nm for all concentrations. Just like other surfactants, the intensity of excitation varies. For greater clarity, the relationship between the Stokes shift, which was calculated from the energy difference of excitation and emission, and the surfactant concentration was illustrated in Fig. 4H. The Stokes shift decreased initially as concentration of surfactant increased, and as, the concentration reached to the particular concentration, namely CMC, the Stokes shift sharply increased and then proceeded to level off on a plateau. CMC of SB-12 was estimated to be 3.5 mM according to the intersection of the extrapolation of curves in the graph of Stokes shift versus concentration in Fig. 4H. The close similarity of this Stokes shift correlation and those of anionic or non-ionic surfactants may result from the mild interaction of the zwitterionic surfactant with the cationic moiety of C-dots. For comparison, Table 2 presented some proposed protocols for CMC evaluation, including the results obtained in this work for CTAB, SDS, Triton X-100, and SB-12. It is clear that the results are in good agreement.

4. Conclusions

We have successfully developed a new and facile fluorophotometric approach for the determination of critical micelle

concentration (CMC) of ionic and non-ionic surfactants with the assistance of C-dots. C-dots exhibited substantial fluorescence and therefore enhanced the sensitivity. The spectra were assigned and explained in terms of both electron transitions between specific molecular orbitals and the interaction with solvent. CMC values of cationic cetyltrimethyl ammonium bromide (CTAB), anionic sodium dodecyl sulfate (SDS), nonionic Triton X-100, and zwitterionic dodecyldimethyl(3-sulfopropyl)ammonium hydroxide surfactant (SB-12) evaluated by this approach was found to be 0.98, 7.3, 0.19, and 3.5 mM, respectively. The CMC values acquired were consistent with those obtained formerly by other methods. By introducing C-dots in the CMC evaluation of surfactants via fluorophotometric method opens new avenues for broader applications in the near future.

Acknowledgments

The authors acknowledge the financial support from the Ministry of Science and Technology of Taiwan. The authors appreciate Mr. Bo-sgum Wu for his help in purchasing the chemicals. We thank the National Sun Yat-Sen University and Kaohsiung Medical University Joint Research Project (NSYSU-KMU JOINT RESEARCH PROJECT, #NSYSU-KMU (103-P 023) for financial support for this publication.

References

[1] H. Noritomi, Y. Kato, S. Kato, J. Surf. Eng. Mater. Adv. Technol. 4 (2014) 9.
[2] D. Kumar, M.A. Rub, M. Akram, J. Colloid Interface Sci. 418 (2014) 324–329.
[3] K.L. Young, M.L. Personick, M. Engel, P.F. Damasceno, S.N. Barnaby, R. Bleher, T. Li, S.C. Glotzer, B. Lee, C.A. Mirkin, Angew. Chem. Int. Ed. 52 (2013) 13980–13984.
[4] E. Ruckenstein, R. Nagarajan, J. Phys. Chem. 79 (1975) 2622–2626.
[5] A. Farvadi, S. Abolmaali, Z. Sobhani, F.G.H. Yousefi, Res. Pharm. Sci. 9 (2013) 1–10.
[6] H. Tian, C. Deng, H. Lin, J. Sun, M. Deng, X. Chen, X. Jing, Biomaterials 26 (2005) 4209–4217.
[7] K. Yan, H. Li, P. Li, H. Zhu, J. Shen, C. Yi, S. Wu, K.W. Yeung, Z. Xu, H. Xu, Biomaterials 35 (2014) 344–355.
[8] W. Chen, P. Zhong, F. Meng, R. Cheng, C. Deng, J. Feijen, Z. Zhong, J. Control. Release 169 (2013) 171–179.
[9] D. Kaushal, D. Rana, S. Chauhan, Fluid Phase Equilib. 360 (2013) 239–247.
[10] G.N. Smith, P. Brown, S.E. Rogers, J. Eastoe, Langmuir 29 (2013) 3252–3258.
[11] U. Anand, C. Jash, S. Mukherjee, J. Colloid Interface Sci. 364 (2011) 400–406.
[12] K.G. Furton, A. Norelus, J. Chem. Educ. 70 (1993) 254.
[13] C.E. Lin, T.Z. Wang, T.C. Chiu, C.C. Hsueh, J. High Resolut. Chromatogr. 22 (1999) 265–270.
[14] J. Aguiar, P. Carpena, J. Molina-Bolıvar, C. Carnero Ruiz, J. Colloid Interface Sci. 258 (2003) 116–122.
[15] S. Pandey, M. Thakur, A. Mewada, D. Anjarlekar, N. Mishra, M. Sharon, J. Mater. Chem. B 1 (2013) 4972–4982.
[16] D. Yu, F. Huang, H. Xu, Anal. Methods 4 (2012) 47–49.
[17] A. Mewada, S. Pandey, S. Shinde, N. Mishra, G. Oza, M. Thakur, M. Sharon, M. Sharon, Mater. Sci. Eng. C 33 (2013) 2914–2917.
[18] J. Tang, B. Kong, H. Wu, M. Xu, Y. Wang, Y. Wang, D. Zhao, G. Zheng, Adv. Mater. 25 (2013) 6569–6574.
[19] S. Zhu, Q. Meng, L. Wang, J. Zhang, Y. Song, H. Jin, K. Zhang, H. Sun, H. Wang, B. Yang, Angew. Chem. 125 (2013) 4045–4049.
[20] A. Zhu, Q. Qu, X. Shao, B. Kong, Y. Tian, Angew. Chem. 124 (2012) 7297–7301.
[21] A.B. Bourlinos, A. Stassinopoulos, D. Anglos, R. Zboril, M. Karakassides, E.P. Giannelis, Small 4 (2008) 455–458.
[22] Q. Wang, X. Liu, L. Zhang, Y. Lv, Analyst 137 (2012) 5392–5397.
[23] S. Hu, J. Liu, J. Yang, Y. Wang, S. Cao, J. Nanoparticle Res. 13 (2011) 7247–7252.
[24] H. YoungáKo, C. HyunáLee, J. Mater. Chem. B 1 (2013) 4438–4445.
[25] M. Halder, Chem. Educ. 12 (2007) 33–36.
[26] H.M. Kwaambwa, F.M. Nermark, Green Sustain. Chem. 2013 (2013) 135–140.
[27] J. Zhang, W. Shen, D. Pan, Z. Zhang, Y. Fang, M. Wu, New J. Chem. 34 (2010) 591–593.
[28] S.-L. Hu, K.-Y. Niu, J. Sun, J. Yang, N.-Q. Zhao, X.-W. Du, J. Mater. Chem. 19 (2009) 484–488.
[29] A.N. Fletcher, Photochem. Photobiol. 9 (1969) 439–444.
[30] H. Li, Z. Kang, Y. Liu, S.-T. Lee, J. Mater. Chem. 22 (2012) 24230–24253.
[31] K. Exall, V.K. Balakrishnan, J. Toito, R. McFadyen, Sci. Total Environ. 461 (2013) 371–376.
[32] Y. Shi, H.Q. Luo, N.B. Li, Spectrochim. Acta Part A: Mol. Biomol. Spectrosc. 78 (2011) 1403–1407.
[33] C.H. Tan, Z.J. Huang, X.G. Huang, Anal. Biochem. 401 (2010) 144–147.
[34] A.M. Khan, S.S. Shah, J. Chem. Soc. of Pakistan 30 (2008) 186–191.
[35] C.D. Tran, S. Yu, J. Colloid Interface Sci 283 (2005) 613–618.

Talanta 132 (2015) 579–582

Contents lists available at ScienceDirect

Talanta

journal homepage: www.elsevier.com/locate/talanta

Short communication

Application of laser microdissection ICP–MS for high resolution elemental mapping in mouse brain tissue: A comparative study with laser ablation ICP–MS

Alessandra Sussulini *, J. Sabine Becker

Zentralinstitut für Engineering, Elektronik und Analytik, Analytik (ZEA-3), Forschungszentrum Jülich, D-52425 Jülich, Germany

ARTICLE INFO

Article history:
Received 19 August 2014
Received in revised form
29 September 2014
Accepted 1 October 2014
Available online 14 October 2014

Keywords:
Laser microdissection
Laser ablation
Inductively coupled plasma mass spectrometry
Mouse brain
Mass spectrometry imaging
Quantification

ABSTRACT

Mapping of elements in biological tissue by laser induced mass spectrometry is a fast growing analytical methodology in life sciences. This method provides a multitude of useful information of metal, nonmetal, metalloid and isotopic distribution at major, minor and trace concentration ranges, usually with a lateral resolution of 12–160 μm. Selected applications in medical research require an improved lateral resolution of laser induced mass spectrometric technique at the low micrometre scale and below. The present work demonstrates the applicability of a recently developed analytical methodology – laser microdissection associated to inductively coupled plasma mass spectrometry (LMD ICP–MS) – to obtain elemental images of different solid biological samples at high lateral resolution. LMD ICP–MS images of mouse brain tissue samples stained with uranium and native are shown, and a direct comparison of LMD and laser ablation (LA) ICP–MS imaging methodologies, in terms of elemental quantification, is performed.

© 2014 Elsevier B.V. All rights reserved.

1. Introduction

Laser microdissection (LMD) is a technology that isolates specific cell populations from heterogeneous tissue sections under direct microscopic visualization by means of a highly focused laser beam [1,2]. The development of laser-based tissue microdissection systems has provided the basis for the rapid acquisition of specific morphologically and/or phenotypically distinct types of cells for different types of molecular analysis. This has permitted the cell-type specific molecular analysis of solid tissues, especially biopsies (samples of tissue taken for determine the presence or extent of a disease), and has provided new insights into both physiological cell mechanisms and pathomechanisms [3]. For example, a specific part of the hippocampus of brain tissue, cornu ammonis (CA1) pyramidal neurone layer, could be isolated for targeted proteome analysis from a transgenic rat carrying a human amyloid precursor protein transgene using LMD [4].

Recently, Becker and coworkers [5–8] proposed the coupling of LMD to an inductively coupled plasma (ICP) mass spectrometer in order to obtain elemental images of thin biological tissues. In this methodology, LMD acts as an ablation system, where a glass chamber is placed over the sample and a flow of a carrier gas transports the ablated material, and the ICP mass spectrometer operates as the detector for metals, semimetals and non-metals that are present in the biological tissue sample [7].

In the pioneer LMD ICP–MS work [5], a lateral resolution of 3 μm was obtained for a brain tissue impregnated with a droplet of highly concentrated copper solution (1000 mg L^{-1}). It is expected that with the insertion of a more powerful laser in the LMD microscope and the coupling to a more sensitive mass spectrometer (sector field ICP–MS instead of the currently used quadrupole ICP–MS), a lateral resolution up to 300 nm range should be possible in future investigations, opening up the field of quantitative single cell analysis and imaging.

The improvement of LMD ICP–MS analytical features can make possible to acquire more precise and detailed information on elemental distribution in brain samples and other biological tissues at low-micrometre and nanometre scale, as a LMD microscope allows the observation and selection of specific structures and single cells, which can be ablated by the focused laser beam with a lateral

Table 1
LMD ICP–MS imaging applications described in the literature.

Detected analytes	Sample	Refs.
^{63}Cu, ^{65}Cu	Mouse brain (Cu-stained)	[5]
^{13}C, ^{23}Na, ^{24}Mg, ^{31}P, ^{39}K, ^{56}Fe, ^{63}Cu, ^{64}Zn	Mouse brain	[6]
^{13}C, ^{23}Na, ^{24}Mg, ^{31}P, ^{39}K, ^{56}Fe, ^{64}Zn	Rat brain	[7]

* Correspondence to: Department of Analytical Chemistry, Institute of Chemistry, Universidade Estadual de Campinas, PO Box 6154, 13083-970 Campinas, SP, Brazil. Tel.: +55 19 35213060.
E-mail address: sussulini@iqm.unicamp.br (A. Sussulini).

http://dx.doi.org/10.1016/j.talanta.2014.10.001
0039-9140/© 2014 Elsevier B.V. All rights reserved.

resolution down to the low and sub-micrometre scale [5,9]. Table 1 illustrates the LMD ICP–MS imaging experiments described in the literature until the present moment.

In this work, the application of LMD ICP–MS to elemental imaging of native and metal-stained mouse brain tissues is shown. Uranium was chosen for tissue staining since it is important when

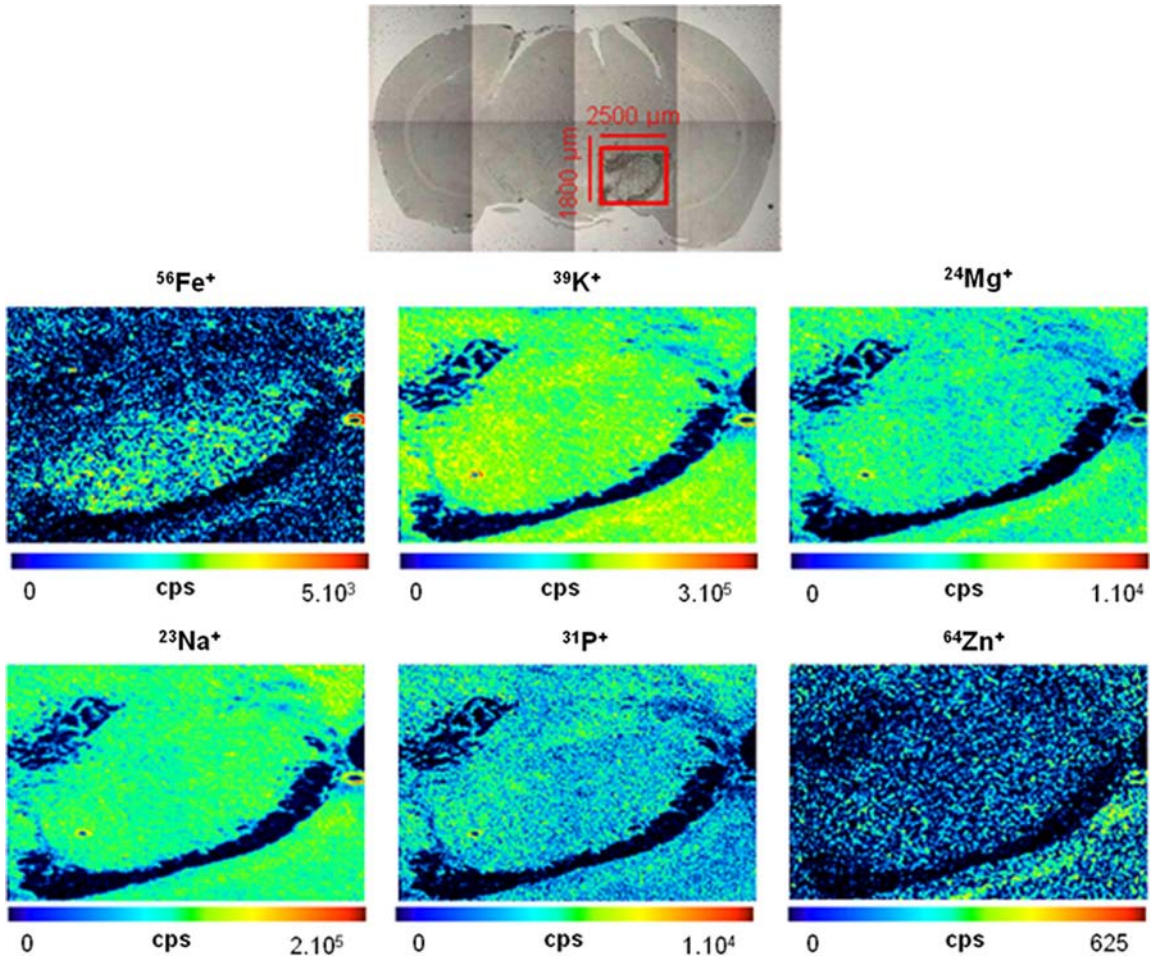


Fig. 1. LMD ICP–MS qualitative images with lateral resolution of 6 µm for a native mouse brain tissue (substantia nigra region).

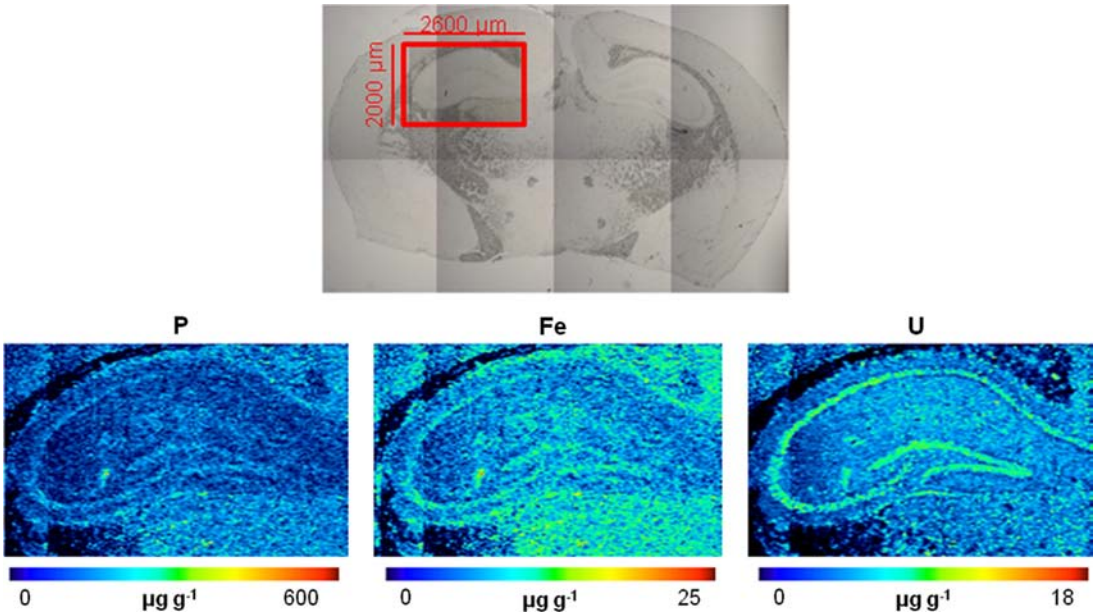


Fig. 2. LMD ICP–MS quantitative images with lateral resolution of 4 µm for a mouse brain tissue (left hippocampus region) stained with ^{238}U solution at 100 µg L^{-1}.

toxicology studies (in extreme conditions) are considered [10]. This methodology provided high resolution images (4 μm) using a low concentrated (100 μg L^{-1}) uranium solution as staining agent. Two interesting brain regions, substantia nigra and hippocampus, were selected for LMD ICP–MS imaging experiments. Substantia nigra plays a role in reward, addiction and movement functions, and is also related to the pathophysiology of Parkinson's disease [11] and schizophrenia [12]. Hippocampus acts in short and long-term memory and is involved in the development of stress, epilepsy [13], schizophrenia [14], and other diseases.

2. Experimental

For LMD ICP–MS experiments, a small laser ablation glass chamber mounted on the microscope glass slide containing the sample and constituting the bottom was inserted in the LMD device (MMI SmartCut Plus, Molecular Machines and Industries, Zürich, Switzerland) and coupled to a quadrupole-based inductively coupled plasma mass spectrometer (XSeries II, Thermo Fischer Scientific, Bremen, Germany) [5,6,8].

For comparative experiments by LA ICP–MS, a laser ablation system (New Wave UP213, Fremont, CA, USA) coupled to the same mass spectrometer previously described was employed [15,16].

Table 2
Figures of merit from the quantification by LMD ICP–MS of mouse brain tissue (hippocampus region) after staining with 100 μg L^{-1} ^{238}U solution.

Analyte	Analytical calibration function	Correlation coefficient (R)	Limit of detection (μg g^{-1})[a]	Limit of quantification (μg g^{-1})[b]
^{31}P	$y=6.0597x+5612$	0.9823	143	476
^{56}Fe	$y=158.2x+2941$	0.9904	7.2	24
^{238}U	$y=384.82x-229.48$	0.9876	0.39	1.3

[a] Calculated as 3 times the standard deviation of the blank sample divided by the slope from the calibration curve.
[b] Calculated as 10 times the standard deviation of the blank sample divided by the slope from the calibration curve.

Schematics and analytical workflows for LMD and LA ICP–MS imaging experiments can be found in previous references from J.S. Becker's working group [5,7,9].

Mouse brain samples were collected, cryo-cutted (thickness of 10 μm) and placed in microscope glass slides. For metal-staining experiments, the brain samples were immersed in the solution of interest for at least 1 h and then dried at room temperature overnight before LMD ICP–MS imaging experiments.

When quantification of the imaging data was performed, metal spiked tissue homogenates were employed. They were prepared from brain homogenates of analogous mice without any treatment and doped with trace elements with defined concentrations, as described elsewhere [15,17]. To validate the ion images, at least two isotopes, if available, were analyzed. Possible isobaric interferences of single-charged analyte ions with polyatomic or double-charged ions were studied systematically and minimized under optimized experimental conditions.

Data treatment was performed as described in reference [18]. Signal normalization in relation to ^{13}C was made for all obtained images, including the qualitative ones, where no quantification was performed and only signal intensities are shown.

3. Results and discussion

LMD ICP–MS qualitative images with lateral resolution of 6 μm for a native mouse brain (substantia nigra region) tissue are shown in Fig. 1. The lateral resolution is improved to 4 μm when brain tissue is stained with ^{238}U solution at 100 μg L^{-1}. Tissue staining

Table 3
Comparison between LA and LMD ICP–MS results and characteristics.

	LMD ICP–MS	**LA** ICP–MS
Detected elements	Fe, P and U	P and U
Lateral resolution	4 μm	13 μm
Tissue thickness	Below 14 μm	10–40 μm
Routine scale	No	Yes
Quantification	Challenging	Using metal spiked tissue homogenates

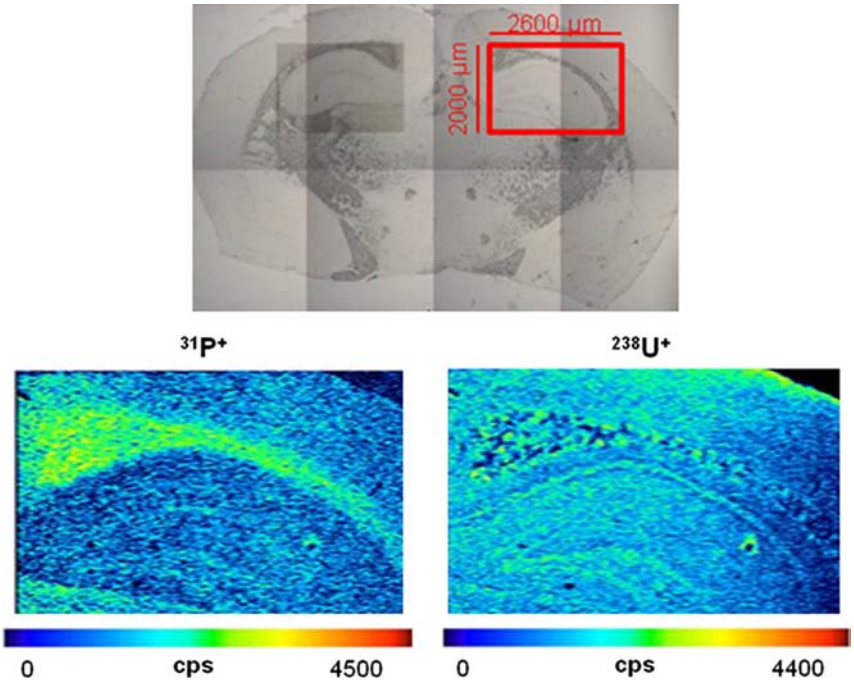


Fig. 3. LA ICP–MS qualitative images with lateral resolution of 13 μm for a mouse brain tissue (right hippocampus region) stained with ^{238}U solution at 100 μg L^{-1}.

allowed the detection of enhanced intensities that provided a very good differentiation of the brain substructures (layers). Fig. 2 shows the LMD ICP–MS quantitative images for the stained mouse brain (left hippocampus region) and Table 2 describes the figures of merit of the quantification procedure for the detected elements in brain: iron, phosphorus and uranium (coming from the staining procedure).

The same stained mouse brain sample, in this case the right hippocampus region, was used for a comparison between LMD and LA ICP–MS. Fig. 3 shows the results obtained by LA ICP–MS. The lateral resolution was worse than when LMD ICP–MS was employed (13 μm in contrast to the 4 μm previously obtained) and it was not possible to detect iron in the sample. In a previous work [10], uranium- and neodymium-stained rat brain tissues were analyzed by LA ICP–MS, but the obtained resolution was only 100 μm and it was not possible to observe brain substructures so clearly as in the case of LMD ICP–MS analyses. Moreover, only the staining agents were quantified in the LA ICP–MS images. These results together demonstrate the potentiality of LMD ICP–MS in obtaining elemental images with high resolution, in the low micrometer range, for metal-stained biological tissues.

Table 3 summarizes a comparison between LA and LMD ICP–MS results and characteristics. It is important to point out that LMD ICP–MS is a methodology still under development and needs to be improved. Future steps involve the improvement of imaging resolution by using a more powerful laser source that allows the enhancement of the ablation process. The laser spot size can be reduced as more material is transported to the ICP source and, then, the lateral resolution is improved. The use of a more sensitive mass spectrometer, such as an ICP–SFMS, is also required in order to analyze elements in single cells. The development of alternative calibration strategies (e.g., solution-based calibration [19] or printed patterns [20]) and/or the improvement of standard samples preparation [21] for obtaining quantitative images is also an important point to be further studied.

Acknowledgements

The authors would like to thank Dr. Andreas Matusch for providing the brain samples and preparing the mouse brain sample standards for quantification of analytical data. A.S. would like to thank the Alexander von Humboldt Foundation (Bonn, Germany) for the post-doctoral fellowship. The last author (J.S.B.) would like to acknowledge to Thermo Scientific (Bremen, Germany) and to Deutsche Forschungsgemeinschaft (DFG grant number BE 2649/5-1) for instrumental support of the BrainMet laboratory.

References

[1] M. Zellner, M. Veitinger, E. Umlauf, Acta Neuropathol. 118 (2009) 181–195.
[2] V. Espina, J.D. Wulfkuhle, V.S. Calvert, A. VanMeter, W. Zhou, G. Coukos, D.H. Geho, E.F. Petricoi, L.A. Liotta, Nat. Protoc. 1 (2006) 586–603.
[3] G.I. Murray, Acta Histochem. 109 (2007) 171–176.
[4] K.E. Wilson, R. Marouga, J.E. Prime, D.P. Pashby, P.R. Orange, S. Crosier, A.B. Keith, R. Lathe, J. Mullins, P. Estibeiro, H. Bergling, E. Hawkins, C.M. Morris, Proteomics 5 (2005) 3851–3858.
[5] J.S. Becker, S. Niehren, A. Matusch, B. Wu, H.F. Hsieh, U. Kumtabtim, M. Hamester, A. Plaschke-Schlütter, D. Salber, Int. J. Mass Spectrom. 294 (2010) 1–6.
[6] B. Wu, S. Niehren, J.S. Becker, J. Anal. At. Spectrom. 26 (2011) 1653–1659.
[7] B. Wu, J.S. Becker, Int. J. Mass Spectrom. 323-324 (2012) 34–40.
[8] B. Wu, J.S. Becker, Int. J. Mass Spectrom. 307 (2011) 112–122.
[9] J.S. Becker, A. Matusch, B. Wu, Anal. Chim. Acta 835 (2014) 1–18.
[10] J.S. Becker, J. Dobrowolska, M. Zoriy, A. Matusch, Rapid Commun. Mass Spectrom. 22 (2008) 2768–2772.
[11] J. Jankovic, J. Neurol. Neurosurg. Psychiatry 79 (2008) 368–376.
[12] Y. Watanabe, H. Tanaka, A. Tsukabe, Y. Kunitomi, M. Nishizawa, R. Hashimoto, H. Yamamori, M. Fujimoto, M. Fukunaga, N. Tomiyama, PLoS One 9 (2014) e104619.
[13] M. Joëls, Epilepsia 50 (2009) 586–597.
[14] I.C. Wright, S. Rabe-Hesketh, P.W. Woodruff, A.S. David, R.M. Murray, E.T. Bullmore, Am. J. Psychiatry 157 (2000) 16–25.
[15] J.S. Becker, A. Matusch, J.Su. Becker, B. Wu, C. Palm, A. Becker, D. Salber, Int. J. Mass Spectrom. 307 (2011) 3–15.
[16] M-M. Pornwilard, R. Weiskirchen, N. Gassler, A.K. Bosserhoff, J.S. Becker, PLoS One 8 (2013) e58702.
[17] K. Jurowski, S. Walas, W. Piekoszewski, Talanta 115 (2013) 195–199.
[18] A. Sussulini, A. Matusch, M. Klietz, A. Bauer, C. Depboylu, J.S. Becker, Biomed. Spectrosc. Imaging 1 (2012) 125–136.
[19] D. Pozebon, V.L. Dressler, M.F. Mesko, A. Matusch, J.S. Becker, J. Anal. At. Spectrom. 25 (2010) 1739–1744.
[20] M. Bonta, H. Lohninger, M. Marchetti-Deschmann, A. Limbeck, Analyst 139 (2014) 1521–1531.
[21] K. Jurowski, M. Szewczyk, W. Piekoszewski, M. Herman, B. Szewczy, G. Nowak, S. Walas, N. Miliszkiewicz, A. Tobiasz, J. Dobrowolska-Iwanek, J. Anal. At. Spectrom. 29 (2014) 1425–1431.

Talanta 132 (2015) 583–590

Contents lists available at ScienceDirect

Talanta

journal homepage: www.elsevier.com/locate/talanta

On-line biosensor for the detection of putative toxicity in water contaminants

Evgeni Eltzov [a,b,c], Vladimir Slobodnik [d], Rodica E. Ionescu [e], Robert S. Marks [a,b,c,f,g,*]

[a] Department of Biotechnology Engineering, Ben-Gurion University of the Negev, Beer-Sheva 84105, Israel
[b] School of Material Science and Engineering, Nanyang Technology University, Nanyang Avenue, 639798, Singapore
[c] CREATE, Singapore
[d] Department of Biotechnology Engineering, Faculty of Engineering Science, Sami Shimon, Ashdod, Israel
[e] Laboratoire de Nanotechnologie et d'Instrumentation Optique, Institute Charles Delaunay, Université de technologie de Troyes, UMR CNRS 6281, 12 rue Marie-Curie BP 42060 10004 TROYES, Cedex, France
[f] The National Institute for Biotechnology in the Negev, Ben-Gurion University of the Negev, Beer-Sheva 84105, Israel
[g] The Ilse Katz, Center for Meso and Nanoscale Science and Technology, Ben-Gurion University of the Negev, Beer-Sheva 84105, Israel

ARTICLE INFO

Article history:
Received 22 June 2014
Received in revised form
17 September 2014
Accepted 20 September 2014
Available online 13 October 2014

Keywords:
Bioluminescence
Sensor
Water pollution
Flow-through monitoring

ABSTRACT

Potential threat on drinking water requires monitoring solutions, such as the one proposed herein, as a real-time, wide ranged, water monitoring system to detect the presence of toxicants in water. We studied the role of a selected number of parameters affecting performance and, thus, improved the prototype into an optimized next-generation device, resulting in enabling increased measurement duration, coupled with increased sensitivity. The chosen parameters in question were the peristaltic flow system, the fiber probe matrix stability through a re-design of the fiber probe holder and flow unit cell, as well as the modulation of bacterial medium concentration to increase bioreporter performance while keeping biofouling in check. Measurements were made with spiked samples and validated with polluted field-collected samples.

© 2014 Elsevier B.V. All rights reserved.

1. Introduction

Increasing population and activities thereof, produce large varieties and quantities of waste chemicals [1], which oftentimes affect drinking water quality [2–4]. In order to safeguard our water supplies, it must be monitored constantly to prevent its contaminated form from reaching the consumers [5–7], while being diverted to processing centers for its remediation.

There are two main forms of water monitoring. One requires the tester to go to the field and make an on-site test or alternatively taking the sample to an accredited test laboratory. The main disadvantage is that the user must go to the place in question. However, the advantage of the first possibility is that the dispatchable equipment includes disposable elements and the answer is quasi-immediate enabling a response. The second form involves use of a continuous monitoring system, with near real-time monitoring, that will give the user continuous feed on the particular point, where the tests are being conducted, such as a chosen river site, which is advantageous as only infrequent human dispatch would then be required. However, the sophisticated mechanics involved complicates the overall system from a number of engineering parameters.

There are two main analytical categories in monitoring water [8], the classical chemical chromatographic ones and the bioassay-based ones. The former (HPLC, GC, GC/MS [9]) is aimed at both identification and quantification. Their disadvantage is their specificity: an unfamiliar toxicant will not be detected. In addition, these are costly and require both sophisticated instrumentation as well as qualified personnel. They are nonetheless very useful and remain today the workhorse of the chemical identification industry. On the other hand, bioassays assess a potential toxic effect on a living organism, however, they lack the ability to measure a specific concentration or even provide most of the times an identification of the monitored toxicant. Despite these disadvantages, those sensing systems have one great advantage: the toxicant monitoring range is very broad [8,10–14]. In this particular area, bacterial-based bioassays, have shown promising applicative results. These consist in using genetically modified bioreporter organisms that generate light as a response to toxic compounds (see Section 2.2).

Bioassays using bacterial bioreporters are used either in their classical liquid-phase bacterial suspension [15–17] or immobilized in biosensor systems [18–20]. In both cases, the tested water

* Corresponding author at: The National Institute for Biotechnology in the Negev, Ben-Gurion University of the Negev, Beer-Sheva 84105, Israel.
Tel.: +972 8 6477182; fax: +972 8 6472857.
E-mail address: rsmarks@bgu.ac.il (R.S. Marks).

http://dx.doi.org/10.1016/j.talanta.2014.09.032
0039-9140/© 2014 Elsevier B.V. All rights reserved.

samples must be disposed of via a septic step according to licensed (MLI or II) laboratory regulations,, so as to prevent contamination of the environment, which is protected by stringent regulations. Disposable bioassays are usually autoclaved, although one may imagine chemical neutralization could also be used, while immobilized-phase on-line biosensors require asceptization of the test effluent, despite the fact that one can create stable immobilized probes with virtual non-leaching of the said bioreporters [10,13,20], while still retaining good levels of sensitivity.

The aim of this study was to improve on some of the limitations found in the earlier system [13]. It was then discovered that the bacterial on-line system required that the user provide growth medium continuously, so as to sustain the immobilized bacteria in a continuous stream of water. Indeed, the signal improved, however, an increase in biofouling occurred, which could affect the overall sensor performance. Therefore, we checked two types of such growth media at different concentrations so as to obtain that concentration of either growth medium, which is really necessary to reduce increased biofouling potential while helping the system increase its performance. We also then noticed that increased sample flow rate had a detrimental mechanical effect on the hydrogel structure that was used to entrap the bacteria, thus we designed herein, a protective proprietary fiber optic probe flow cell. This study therefore looked at improving both sensor sensitivity and increasing measurement time, while retaining simplicity of operation, size, and real-time monitoring capability.

2. Materials and methods

2.1. Chemicals

Tryptone (T7293), Yeast Extract (92144), NaCl (S7653), alginate (B25266), $CaCl_2$ (C1016), p-chlorophenol, copper sulfate (209198), kanamycin (K1377), and ampicillin (A0797) were obtained from Sigma. All stock solutions were diluted with distilled water (dW) and stored at temperatures as suggested by the manufacturers' instructions.

2.2. Bacterial strain

The bioluminescent *Escherichia coli* bioreporter strain TV1061 [21] used in this study is sensitive to metabolic changes, such as with cytotoxic substances. It harbors plasmid-borne fusions with a specific heat-shock *grpE* promoter adjacent to the *luxCDABE* reporter operon, whose activation is detected by light emission (bioluminescence). The *Lux* operon has five promoterless structural genes. These are responsible for both the heterodimeric luciferase units (*lux* A and B) and the synthesis of the luciferase substrate, tetradecanal, by an ATP- and NADPH-dependent multienzyme complex composed of fatty acid reductase, transferase, and a synthetase (*lux* C, D and E) [22]. Strain stocks were stored at −80 °C with 20% (v/v) glycerol as a cell cryoprotectant additive [12]. Stock bioreporter strains were placed on LB-agar plates (NaCl 5 g L^{-1}, yeast extract 5 g L^{-1}, tryptone 10 g L^{-1}, agar 15 g L^{-1}) supplemented with 50 μg mL^{-1} kanamycin and, thereafter, incubated at 37 °C in a rotary thermo-shaker overnight (MaxQ 4450, ThermoScientific, USA). These were then stored at 4 °C for future experimentation.

2.3. Bacterial growth

Bacterial cultivation prior to measurements was performed in 10 mL LB-medium (NaCl 5 g L^{-1}, yeast extract 5 g L^{-1}, tryptone 10 g L^{-1}) supplemented with 50 μg mL^{-1} kanamycin for TV1061. Cells were grown overnight at 37 °C in a rotary thermo-shaker (MaxQ 4450, ThermoScientific, USA) at 120 rpm in the presence of the antibiotic. Cultures were then diluted to approximately 10^7 cells/mL and re-grown in 25 mL LB at 26 °C without shaking and without antibiotics, to an early exponential phase (OD 600_{nm} of 0.2) as determined by an Ultrospec 2100 pro spectrophotometer (Amersham, England).

2.4. Fiber optic probe bioreporter immobilization procedure

The harvested cells were mixed 1:1 (v/v) with a filter-sterilized 2% (w/v) low viscosity sodium alginate solution. Multimode optical fibers, PUV 400 BN (CeramOptec, GmBH, eramOptecBonn), were used in these experiments. They present a pure silica core diameter of 400 μm, with a refractive index of 1.4571 (at 633 nm) and a cladding diameter of 440 μm, with a refractive index of 1.4011 (at 633 nm). Their black nylon jacket was stripped away from a 1-cm long optical fiber proximal tip, which was then used for the immobilization of the bioluminescent bioreporter bacteria [23]. The 1-cm optical fiber tip was first exposed (for a few seconds) to the bacterial alginate suspension, and then dipped (for a few seconds) into a sterile 0.5 M calcium chloride solution [20], thus entrapping the bacteria onto the fiber proximal tip within a hardened calcium alginate matrix. Six to seven layers have been shown to be the optimal number of layers when previously tested [13]. Thereafter, the optical fiber probe, with immobilized bioluminescent bacteria at its tip, was immediately used after preparation for experimentation (Fig. 1C).

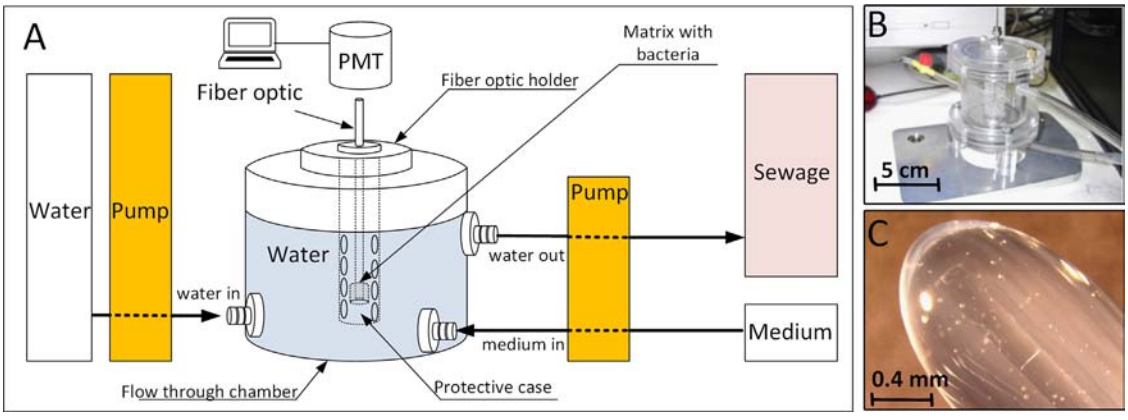


Fig. 1. A. Scheme of the perspex "protective" flow unit holding the fiber optic probe and its connected peristaltic pumps; B. Photo of perspex flow unit; C. Calcium (2% v/v)-polymerized alginate with six adlayers forming the fiber optic probe.

2.5. Instrument setup

A field-operable fiber-optic photodetector device was previously designed [10] and in order to monitor toxicity in a flow-through manner, it was modified in a recent study [13] including improvements, such as an added flow cell, (Fig. 1) which was placed in the light-tight box, so as to prevent any damage to the photon-counting unit by the surrounding light. A Hamamatsu HC135-01 PMT Sensor Module was used for bioluminescence measurements, combining the sensitivity of a photomultiplier tube (PMT) with the intelligence of a microcontroller. The detector was optimized to the blue light region and included a 21-mm diameter active area to gather light radiation without any optical focusing elements.

In order to increase the flow rate of the incoming water sample, while retaining the fiber probe matrix integrity, a new design of its configuration was made (Fig. 1A) due to the fact that a pressure issue was discovered and affected the bacterial performance. In this system, water flows through a workshop-made inner cell, whilst the chamber is made of transparent perspex, thus both protecting the fiber-optic from the water current and also enabling, when needed, a visual supervision of the biosensor probe integrity (Fig. 1B). The cell module design includes two inlets, one for incoming water and the other for supplementary growth medium ($d=3.5$ mm), and one outlet, for the exiting water stream ($d=3.5$ mm), while a separate entrance was made for the fiber optic probe housing the immobilized bacteria. Initially, the water flow in the new setup was conducted with only one peristaltic pump, which brought water into the flow unit; however, we observed a continual underperformance of the immobilized bioluminescent bacteria, which we eventually determined to be due to a pressure build up inside the flow through chamber (Fig. 1A), thus preventing the bioreporters from functioning properly. So as to release the said pressure from developing due to the single peristaltic pump use, an additional pump was connected to the system exit, so as to continually remove the water from the operation unit, with both pumps working at equal flow rates. The upper lid of the fiber optic probe cell includes an inlet for the fiber optic probe, which bathes continually in the water flow, and secured at four different points, so as to prevent it from moving due to the sheer forces caused by the water flow. The said optic fiber probe is thus contained within a porous cylinder. Multiple pores (diameter = 2 mm) were drilled in a regular array over the surface of the cylinder, while the distance between them was 3.5 mm. The main purpose of this structure was to protect the fragile biosensor probe matrix – placed at the proximal end of the fiber – which is exposed to the incoming water sample sheer forces. An added benefit is a decrease in the flow velocity around the matrix. The water flow was measured by a rotometer (1017, Burkert) localized in the inlet water stream. To record and analyze the data, a specific driver was developed using LabView (version 3.1, National Instruments Corporation), which allowed to record and analyze the bioluminescence signal in real time.

2.6. Optimization procedures

2.6.1. Comparative effect of two different growth media and concentrations thereof on bioreporter signal response

Two sterile bacterial media 2 YT (Yeast extract tryptone; composed of 16 g L^{-1} Yeast extract 10 g L^{-1} and 16 g L^{-1} Tryptone) and LB (Luria Bertani broth; composed of Tryptone 10 g L^{-1}, Yeast extract 5 g $L^{-1,}$ and NaCl 10 g L^{-1}) were fed into the on-line system at different concentrations ranging between 0 and 7.5% (v/v), in tap water, through the water flow of a calibrated peristaltic pump (Masterflex® 7754-57, Cole Parmer Instrument Company, USA). The sensor response to the target water pollutant (e.g. 2% (v/v) ethanol) was measured over a period of 4–10 h and any changes or improvements noted.

2.6.2. Effect of the flow system management on sensor activity

As explained above, the original system used one peristaltic pump to bring water into the flow unit, which increased pressure onto the resident immobilized bacteria and therefore prevented the bioreporters from functioning properly. The putative effect of the pressure on bacterial sensor activity was further examined by the addition of another peristaltic pump to the exit of the system, so as to continually remove the water from the operation unit, with both pumps working at equal flow rates. At first, the effect on the bacterial cell activation, when using one working pump, was measured without the addition of any chemicals. Bacterial activity in the flowing tap water (with the addition of medium) was measured with either a working (kinetic mode) or an inactive (static mode) inlet pump. Thereafter, the effect of the addition of a second pump to the flow system was examined. In both approaches (system with one or two pumps), bacteria were exposed (at $t=0$ minutes) to 2% (v/v) ethanol as model toxicant.

2.6.3. Effect of the flow rate on stability of the probe matrix

The stability brought by the protective fiber probe cell module on previously observed matrix erosion to the bacterial immobilization matrix of the fiber probe was examined periodically by visual observation and overall evaluation by light microscopy, before and after a system run of 24 h, occurring at differential flow rates from 0 to 10 L h^{-1}.

2.6.4. Effect of the flow unit design on biosensor sensitivity

Two different architectures of the flow unit (old version (without a flow cell unit) and present version (as described throughout notably in Section 2.5) were tested and compared in this work, so as to evaluate their effect on the sensor probe performance, while being exposed to various concentrations of a positive control (e.g. 0.02, 0.2 and 2% (v/v) of ethanol).

2.7. Increased measurement duration

In order to evaluate the analytical performance of the biosensor device, at a longer measurement duration, bioluminescent bioreporter cells were exposed thrice to water pollutants over a 48-h period (compared to our previous work which was for only a useful 24 h): once at the onset of the experiment, and twice after at 24-h time periods ($t=0$; $t=24$ h; $t=48$ h). Strain TV1061 was exposed to three different model toxicants known to be optimal test concentrations in our previous device (2% (v/v) ethanol, p-chlorophenol (1 mg mL^{-1}) and copper (5 ppm)) in separate experiments.

2.8. Environmental water samples

The 24-h experiments were performed using environmental water from Lakhish River (Israel, Lat.31°48'56.68"N Lon. 34°38'35.66"E) with the TV1061 strain, and the improved experimental prototype setup (Fig. 1B). We only tested 24 h due to the fact that we measured the water in our lab and not on-site so had insufficient amounts of environmental water to increase the monitoring time. Freshly collected Lakhish water was stored at 4 °C and used within five days of collection to reduce field composition changes. In order to determine if any putative effect from water salinity may affect the immobilized cells, bacteria were exposed to synthetic water that was made from deionized water with the addition of 48 mg L^{-1} $NaHCO_3$, 30 mg L^{-1} $CaSO_4 \cdot 2H_2O$, 30 mg L^{-1} $MgSO_4$, and 2 mg L^{-1} KCl, with a hardness of 40 mg L^{-1}.

2.9. Viability measurements

Evaluation of the viability of bioreporter bacterial cells after their exposure to toxicants during each experimental run (24 h) was accomplished via the viable plate counting method [24]. Serial 10-fold dilutions of bacterial samples were made in sterile PBS buffer and 10 μL samples were thereof evenly spread onto non-selective solidified nutrient LB agar surface plates. The number of viable colony forming units (cfu) was enumerated as bacterial colony plaques after 24 h incubation at 37 °C.

3. Results and discussion

3.1. Effect of water pressure on the bacterial response.

The effect of water pressure caused by a single peristaltic pump on the immobilized bacteria was evaluated by observing the bioreporter response in the prototype setup (Fig. 1A), with and without an additional water exit pump (which helps remove the water from the flow unit). In the first mode, we observed that when only one pump (placed before the measuring unit) is used in the sensor system, a high pressure seemed to be created in the measuring unit. In the second mode, where an additional pump was added to the system, and placed after the flow unit, and operated at the same flow rates as those of the input pump, it was observed that bacterial performance increased. Indeed, this step was expected to prevent the generation of pressure inside the measuring unit. Fig. 2 presents the effect of the pressure on the immobilized bacteria. Increased water pressure inside the flow unit housing the immobilized bacteria had an inhibitory effect on the activity of the bioreporter cells (Fig. 2A), exemplified by decreased luminescence in the presence of normally inducing pollutant concentrations in water [25]. Others have shown that increased pressure could affect the membrane integrity [26], fluidity [27], or protein denaturation [28] in bacteria. Fig. 2B shows that the addition of the second pump into the system solved the inhibitory issue. Immobilized bacteria regained their capacity to respond to the toxicant (Fig. 2B) and this dual peristaltic pump mode was adopted in all future experiments.

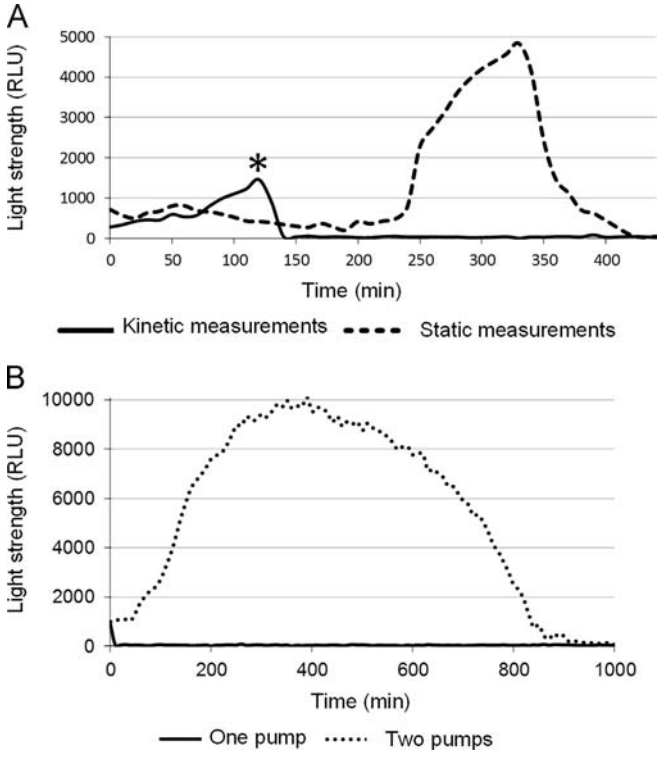


Fig. 2. Effect of pressure on immobilized bacteria in the newly designed instrument. A. Response of the cells once the peristaltic pump is turned on. The solid line represents the flow system with one working pump (*pump operation starts at $t=120$ min) and dash line represents the system without the peristaltic pump. B. Effect of the addition of a second pump to the system, 2% (v/v) ethanol was added at time $t=0$ min.

3.2. Effect of medium type and concentration thereof on bioreporter sensor responsiveness

A living organism needs a continuous source of nutrients to maintain its routine metabolism. The use of bioreporter bacteria as a sensing element raised the issue of the need of supplying any (or enough) nutrients to maintain normal cell functionality when integrated into a continuously operated biosensor device so as to produce reliable measurements. It is known that a sub-minimal amount of nutrients will cause a detrimental effect on natural metabolic processes in the cell, resulting in unreliable responses of the biosensing system [29]. The bioluminescence signals of exposed bio-reporter bacteria to medium-free tap water have already been investigated in previous studies [10,13,23], where exposure to medium-free water resulted in a strong and rapid increase in light induction (without toxicant addition), followed by a sharp decrease which stabilized at a basal level. The proposed flow-through prototype compared two different and popular media (LB and 2 YT) at three different concentrations: 2.5%, 5% and 7.5% (v/v), to which was added 2% (v/v) ethanol as the model toxicant. Ethanol is commonly used as an antimicrobial compound and is known to cause protein damage and to induce a protein damage sensitive *grpE*-dependent bioluminescent response in TV1061 [21].

Fig. 3A represents the different effects on sensor activity, from the nature of the growth medium tested, and this in combination with its various concentrations. The addition of LB to the cells induces the best bioluminescence response. It is important to remember that 2 YT medium differs from LB media in its amino acid concentration (tryptone/yeast extract) (twice lower in LB), while NaCl in LB is twice higher, suggesting that salt may have a more central role in the bacterial bioluminescence response to the toxicants. We will not speculate further here, although this physiological response is worthy of further investigation, just as other parameters would likewise need investigation such as

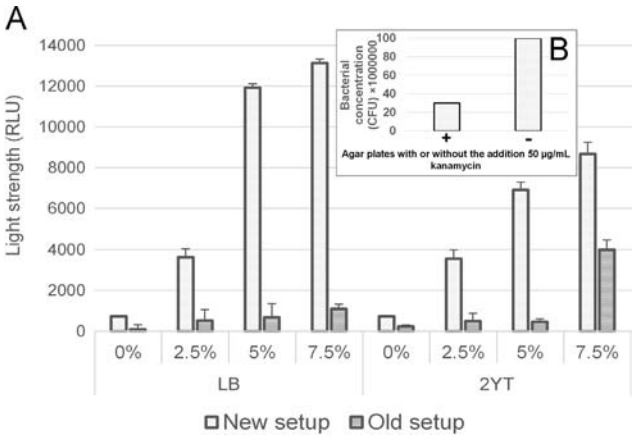


Fig. 3. A. Differential response obtained with TV1061 strain using 2% (v/v) ethanol with the addition of either 2 YT or LB growth media at different concentration. B. Viability count of bacteria (bioreporters versus biofouling bacteria) on agar plates differentiated by the addition or absecence of 50 μg mL^{-1} kanamycin. The previous setup is the tubing mode and new cell unit design.

temperature, pH, incubation time, and matrix composition [30]. The complicated relationship between bioreporter bioluminescence expression on biosensor performance and its bathing medium [31], endogenous aldehyde and internal ions (e.g. potassium, sodium, calcium and magnesium) [32–34] requires careful regulation. Interestingly, there were no significant differences in the cell response, namely in the signal obtained, with the higher concentrations of either 5% or 7.5% (w/v) of LB (Fig. 3A). Possibly the required threshold of essential components are thus satisfied with 5% (w/v). Thus, to help reduce the inevitable bacterial contamination to the system, a lower LB concentration was chosen.

An additional modification brought to the present (dual pump) setup was to add the medium directly into the fiber probe cell unit, unlike previously, when this was done at the onset of the water flow (Fig. 1). This step decreased the contamination rates of the system from biofouling activities on the alginate matrix [35–37], from unwanted bacterial overgrowth, originating in the water tubing and inner cell. These may also cause false positive signals from the inlet stream by reducing toxicant exposure to the immobilized bio-reporter cells, by preventing (or reducing) diffusion of both the nutrients and any putative toxic agents to the immobilized reporter bacteria. This phenomenon is obviously enhanced in systems that are rich with nutrients, thus minimal optimal levels of nutrients need to be carefully controlled. Fig. 3A demonstrates that a good and reliable signal response can still be obtained with a reasonable level of medium (5% (v/v)) maintained in the inlet flow. To determine the ratio between biofouling bacteria (kanamycin sensitive) and those immobilized (genetically engineered bioreporters resistant to kanamycin) in the alginate matrix, a water flow (with the addition of 5% (v/v) LB) was passed for 24 h. Fig. 3B shows the presence of resistant and non-resistant bacteria at the probe matrix. Calcium alginate hydrogel was decomposed and the released cells were grown on agar plates (with or without antibiotic). Indeed, there was an increase in the bacterial concentration on the agar plates without any antibiotic addition (Fig. 3B), suggesting the occurrence of biofouling upon the immobilization matrix. We cannot discard the fact that an additional possible reason for these results is that during long-term exposure some bacteria may remove their plasmid and thus loose their resistance to kanamycin.

3.3. Effect of flow rate on matrix stability

It has been reported that bacteria used in real-time flow experiments cannot afford a flow rate higher than 3 L h^{-1} [17,38] as this may cause an erosion of the probe matrix with a consequent loss of bacterial cells, thus altering the analytical performance of the water-pollutant detection device. Parameters enabling decreased response time and increased sensitivity are important for real-time monitoring of drinking water, using reasonable sampling volumes at a reasonable pace. The ability to work under high flow rates is an elegant solution for this issue. In designing a dual pump device, the effect of the water flow rate on the bacterial probe matrix integrity is evaluated qualitatively by its exposure to a range of different flow rates for 24 h (Table 1). As explained hereabove, the effect of the the water flow was examined by visual observation and overall evaluation by light microscopy, before and after a system run of 24 h. The diameter of the fiber optic was measured before after water exposure. Each (+) logged in the table represents 25% of the initial matrix diameter. It can be clearly seen that the present new design (Fig. 1A) shows higher consistency with a reduced visible damage within the reported range of tested flow rates. The proximal probe matrix in the old setup [13] was partially reduced at 3 and 4.5 L h^{-1}, and vanished totally from 6 L h^{-1}, unlike in the present system, thanks to its new design. In the previously published system, the fiber optic was placed directly into the water flow and was thus exposed to the direct shear stresses made by the passing liquid. In the present configuration, there was no direct pressure from the water flow on the matrix, as the fiber optic was placed in a special protective casing and this reduced the damaging effect of the water flow.

3.4. Effect of the flow unit design on sensor sensitivity

An ideal biosensor has two key properties, i.e. high sensitivity (response to a low concentration of analytes) and high specificity (the ability to discriminate between species according to the immobilized biorecognition elements) [39]. The immobilized bioreporter bacteria confer the biosensor's specificity. Indeed, various strains may be designed to be sensitive to different chemicals and stresses (heavy metals, oxidative compounds, general stresses and antibiotics).

In the present research, the effect of the flow-measurement unit design on sensor sensitivity was determined by exposure of the immobilized bacteria to cytotoxic stress (i.e. ethanol and p-chlorophenol). It was noticed that in the two compared flow units, the immobilized cells responded in different manners (Fig. 4). The possible reasons for this phenomenon are the differences in the design of the water flow unit and, consequently, the important changes in the rate flow. One should mention that in both tested devices, the presence of the toxicants was not constant, i.e. the toxicant was added to the system only for half an hour (as a pulse), while for the rest of the measurement, the immobilized bacteria were exposed to a clear tap water flow, with or without supplementary growth medium. It is assumed that the

Table 1
Effect of water flow rate on the stability of the bacterial matrix. Decrease in the number of (+) symbols implies higher matrix erosion (when (++++) no damage is observed in matrix) and (–) represents the absence of matrix on the fiber.

Flow rate (l/h)	Old setup	New setup
0	++++	++++
1.5	++++	++++
3	++	++++
4.5	+	++++
6	–	+++
8	–	++
10	–	++

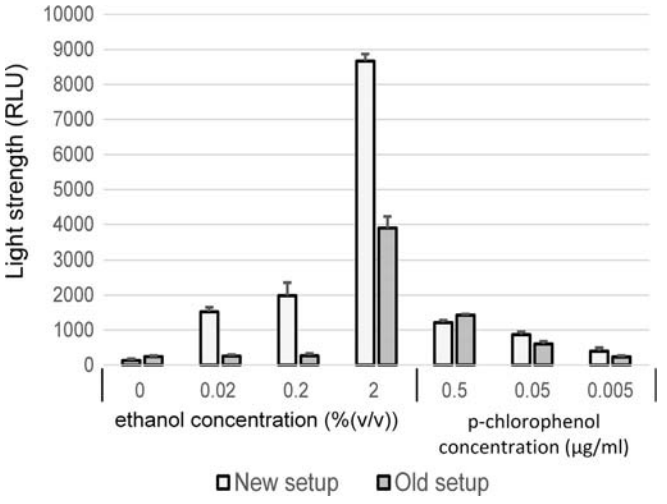


Fig. 4. Improved sensitivity with the use of the new flow unit design tested with different concentrations of ethanol and p-chlorophenol.

diffusion rate of the toxicant into the alginate matrix depended on several main parameters: the concentration of the chemical in the liquid, the time of exposure of the toxicant, as well as, the matrix density. In the tubing-based optical–fiber setup [13], toxicants were passed into the measuring unit much faster and, once simple non-medium containing tap water came as a replacement, they were washed out of the system sooner. In the dual pump setup, the fiber optic is exposed to a reduced toxicant concentration at the beginning, as compared to the previous design. Therefore, it takes longer to reach the same toxicant concentration and the same for nontoxic water to replace it. Thus, immobilized bacteria are exposed to the toxicant for a longer duration, allowing increased diffusion inside the matrix. Our supposition is confirmed by the recent reviews that showed that the longer bacteria are exposed to toxicants, the more material diffuses to its surface and into its cytoplasm [40]. Fig. 4 shows that the new flow cell design allowed an increase in sensor sensitivity (100-fold higher in the case of ethanol) when compared to the previous setup. Ethanol is a model cytotoxic compound that was used as a positive control in many previous publications using TV1061 as the bioreporter bacteria [41–43]. Our probes were also exposed to different concentrations of p-chlorophenol, oftentimes found in wastewaters and sewage [44] and the sensitivity of the previously published setup was roughly comparable to that of the earlier static system [45,46]. However, it was not sensitive enough to detect typical contaminations of surface water in developed countries, which usually range from <1 ng L^{-1} to 1 μg L^{-1}. The new system has, however, demonstrated a higher sensitivity (10-fold higher) compared to the previous setup (Fig. 4) and is now comparable to other methodologies (e.g. electrochemical [47,48]). Obviously solving other engineering issues may help increase further the sensitivity of the system albeit the fact that the bioreporters are themselves limiting. Solving physiological parameters may also help increase their sensitivity.

3.5. Increased on-line measurement duration

The challenge of on-site analysis requires elongated tests [49], during continuous measurements, and this was done here for longer periods of time (two days) using a single optical fiber probe, as compared to previous studies (one day). Experimentally, two setups (previously published one and present one) were operated for 48 h, while the immobilized cells were exposed to different toxicants (copper, ethanol and p-chlorophenol) each for 24 h (at $t=0$, $t=24$ and $t=48$ for 30 min). Indeed, many environmental compounds, such as metal ions, phenols and ethanol, may induce heat shock response in bacteria [50], including toxic copper [51] [52].

It was found that 48-h experiments with the previous setup showed much lower cell response to test controls after 20 h of sensor operation [13], and no activity by 48 h of measurements (data not shown). Many different factors may be responsible for these results, such as biofouling formation on the immobilization matrix, destructive effect of the water flow on the probe matrix, washing out of the matrix calcium, with subsequent loss of alginate polymer and then release of the bacteria from the fiber [13]. In the new setup, on the other hand, bacteria remained active for twice as long (Fig. 5), albeit even longer periods were not yet tested. As immobilized cells respond differently (e.g. time of response, recovery time, strength of the signal) to the pandemonium of possible contaminating compounds due to their available concentration as well as toxic effect, it is suggested that a putative role in the future may be found for the use of data-mining tools to provide analyte detection and identification using panels of bioreporters producing specific fingerprints.

Bioreporter bacteria used in this research were “tailored” to respond in a dose-dependent manner to changes in environmental conditions with luminescence amplitude being proportional to bacterial damage [13,20,53–55]. However, after each exposure (three different times), the responsiveness decreased which could be due to the formation of biofouling (Fig. 3), decrease in their repair mechanism ability or some other reason. An additional and important issue is the recovery capability of the device-based bacteria (i.e. the time required by the system to return back to the unstimulated mode). A faster recovery rate increases the availability of the device for detecting further contaminants, thereby decreasing the possibility of overlooking passing pollutants [49]. In both setups (previous [13] and present), decreasing the toxicant concentration decreases the time needed for recovery, thus lowering the damaging effect of the toxicants on the immobilized cells, which enables faster recovery rate. Furthermore, after the second and third exposure to the same toxicants, there was a further decrease in the recovery time. As explained above, a

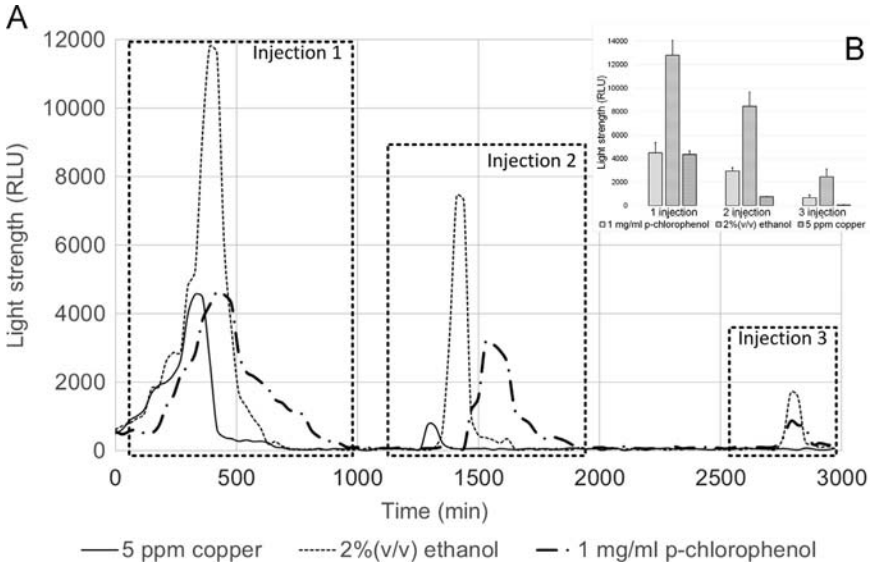


Fig. 5. (A) kinetic response of strain TV1061 to 2% (v/v) ethanol, 5 ppm copper and 1 mg/mL p-chlorophenol. Chemicals were added at $t=0$, $t=1{,}200$ and $t=2{,}680$ min with the addition of 5% (v/v) LB. (B) Summary of results from all experiments ($n=10$) using 2% (v/v) ethanol, 5 ppm copper and 1 mg mL^{-1} p-chlorophenol.

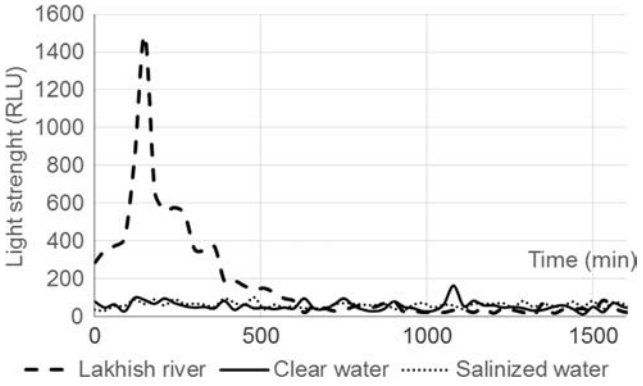


Fig. 6. Response of TV1061 strain to Lachish River water samples with the addition of 5% (v/v) LB.

possible reason is that their defense system may still be active from the first exposure, sensitizing the cells to the next damage.

3.6. *Environmental toxicity*

To evaluate the capability of the newly designed setup (Fig. 1B) to sense the presence of pollutants in environmental samples, bacteria were exposed to Lakhish (Israel) River water. Sewage and waste in the 70-km Lakhish River, which flows through the northern part of Ashdod, have plagued the city's residents over the years. Moreover, rainwater carrying large amounts of contaminations from road surfaces is drawn off into the sea without any treatment and consequently, both the coastal strip and Lachish River are now polluted [56]. Fig. 6 represents a 24-h experiment showing a strong inducing response suggestive of the presence of pollutants. To test the possible salinity effect of river water on immobilized bacteria, cells were exposed to synthetic saline water [57]. In this case the bioreporter bacteria response were similar to clear water, suggesting that the positive signal with the Lakhish samples was indeed due to presence of the contaminating chemicals. Thus, our system can test positive environmental samples, albeit without identification of the actual pollutants, therefore it can only be considered a first line of defense alarm. The kinetics of the response differed from some of the tested chemicals (Fig. 5), surely due to chemical mixtures at various concentrations [58,59].

4. Conclusions

Herein, a further optimized on-line fiber-optic system for monitoring water pollutants is reported after tweaking several engineering parameters. The designed architecture of the fiber-containing measuring unit decreased the shear stress forces, thus preventing its degradation and subsequently, the release of bioreporter bacteria into the tested water sample. Such a system, thus, allows for a higher flow rate of larger volumes of sample to be tested in less time.

Acknowledgments

This publication is supported by the Singapore National Research Foundation under CREATE programme “Nanomaterials for Energy and Water Management” and the Bi-lateral France-Israel Research Networks Programme “Nano-chip platform for water probing pollutants” (2009–2011). Matan Burstin is thanked for an earlier fiber probe design of the cell.

References

[1] J.E. Cohen, Science 302 (2003) 1172–1175.
[2] D.W. Schindler, W.F. Donahue, Proc. Natl. Acad. Sci. USA 103 (2002) 7210–7216.
[3] C.G. Knight, S.B. Velev, M.P. Staneva, Geo. J 35 (1995) 415–423.
[4] P. Aldhous, Nature 422 (2003) 251.
[5] K.A. Kidd, P.J. Blanchfield, K.H. Mills, V.P. Palace, R.E. Evans, J.M. Lazorchak, R.W. Flick, Proc. Natl. Acad. Sci. USA 104 (2007) 8897–8901.
[6] A.C. Belfroid, A. Van der Horst, A.D. Vethaak, A.J. Schafer, G.B.J. Rijs, J. Wegener, W.P. Cofino, Sci. Total Environ. 225 (1999) 101–108.
[7] A. Brouwer, M.P. Longnecker, L.S. Birnbaum, J. Cogliano, P. Kostyniak, J. Moore, S. Schantz, G. Winneke, Environ. Health Perspect. 107 (1999) 639–649.
[8] S. Belkin, D.R. Smulski, S. Dadon, C. Vollmer, K.T.K. Van Dyk, A. LaRossa, Water Res. 31 (1997) 3009–3016.
[9] S. Belkin, Curr. Opin. Microbiol. 6 (2003) 206–212.
[10] B. Polyak, E. Bassis, A. Novodvorets, S. Belkin, R.S. Marks, Water Sci. Technol. 42 (2000) 305–311.
[11] E. Sagi, N. Hever, R. Rosen, A.J. Bartolome, J.R. Premkumar, R. Ulber, O. Lev, T. Scheper, S. Belkin, Sensor Actuat. B-Chem 90 (2003) 2–8.
[12] Z. Hubalek, Cryobiology 46 (2003) 205–229.
[13] E. Eltzov, R.S. Marks, S. Voost, B.A. Wullings, M.B. Heringa, Sensor Actuat. B-Chem 142 (2009) 11–18.
[14] S. Köhler, T.T. Bachmann, J. Schmitt, S. Belkin, R.D. Schmid, Sensor Actuat. B-Chem 70 (2000) 139–144.
[15] S.P. Rupani, M.R. Gu, K.B. Konstantinov, P.S. Dhurjati, T.K. Van Dyk, R.A. LaRossa, Biotechnol. Prog. 12 (1996) 387–392.
[16] M.B. Gu, G.C. Gil, J.H. Kim, J. Biotechnol. 93 (2002) 283–288.
[17] B.M. Gu, C.G. Gil, Biosens. Bioelectron. 16 (2001) 661–666.
[18] A. Heitzer, K. Malachowsky, J.E. Thonnard, P.R. Bienkowski, D.C. White, G.S. Sayler, Appl Environ. Microbiol. 60 (1994) 1487–1494 (Appl. Environ. Microbiol - correct checked in Talanta publications).
[19] Y. Ikariyama, S. Nishiguchi, T. Koyama, E. Kobatake, M. Aizawa, M. Tsuda, T. Nakazawa, Anal. Chem. 69 (1997) 2600–2605.
[20] B. Polyak, E. Bassis, A. Novodvorets, S. Belkin, R.S. Marks, Sensor Actuat. B-Chem 74 (2001) 18–26.
[21] T.K. Van Dyk, W.R. Majarian, K.B. Konstantinov, R.M. Young, P.S. Dhurjati, R.A. LaRossa, Appl. Environ. Microbiol. 60 (1994) 1414–1420.
[22] E.A. Meighen, FASEB J 7 (1993) 1016–1022.
[23] J.R. Premkumar, L. Ovadia, R.S. Marks, B. Polyak, R. Rosen, S. Belkin, Talanta 55 (2001) 1029–1038.
[24] M.T. Madigan, J.M. Martinko, J.P. Brock, Biology of Microorganisms, Prentice-Hall, Inc., New Jersey, 2005.
[25] B.H. Hite, W. Va. Univ 58 (1899) 15–35.
[26] M. Ritz, J.L. Tholozan, M. Federighi, M.F. Pilet, Int. J. Food Microbiol. 79 (2002) 47–53.
[27] M. Yaldagard, S.A. Mortazavi, F. Tabatabaie, Afr. J. Biotechnol. 7 (2008) 2739–2767.
[28] M. Moussa, J.M. Perrier-Cornet, P. Gervais, Appl. Environ. Microbiol. 73 (2007) 6508–6518.
[29] M.T. Madigan, J.M. Martinko, J. Parker, T.D. Brock, Biology of Microorganisms, Prentice Hall, Upper Saddle River, NJ, 1997.
[30] H. Strosnider, Whole-Cell Bacterial Biosensors and the Detection of Bioavailable Arsenic, U.S. Environmental Protection Agency, Washington, DC, 2003.
[31] C.D. Yang, H. Takeyama, T. Tanaka, T. Matsunaga, Enzyme Microb. Tech. 29 (2001) 13–19.
[32] E.S. Kempner, F.E. Hanson, J. Bacteriol. 95 (1968) 975–979.
[33] S.C. Tu, Biochemistry 18 (1979) 5940–5945.
[34] H. Watanabe, H. Inaba, J.W. Hastings, Arch. Microbiol. 156 (1991) 1–4.
[35] L.F. Melo, T.R. Bott, Exp. Therm. Fluid. Sci. 14 (1997) 375–381.
[36] H.C. Flemming, Appl. Microbiol. Biotechnol. 59 (2002) 629–640.
[37] T.E. Cloete, V.S. Brozel, A. Vonholy, Int. Biodeterior. Biodegr 29 (1992) 299–341.
[38] J.H. Lee, M.B. Gu, Biosens. Bioelectron. 20 (2005) 1744–1749.
[39] E. Eltzov, R.S. Marks, in: Thouand G (Ed.), Luminescent Microbial Biosensor: Design, Construction and Implementation, Pan Stanford, 2015.
[40] W. Drost, M. Matzke, T. Backhaus, Chemosphere 67 (2007) 36–43.
[41] E. Eltzov, R.S. Marks, IEEE Instrum. Meas 12 (2009) 10–16.
[42] E. Eltzov, R.S. Marks, Adv. Biochem. Eng. Biotechnol. 117 (2010) 131–154.
[43] B. Polyak, E. Bassis, A. Novodvorets, S. Belkin, R.S. Marks, Sensor Actuat. B-Chem 74 (2001) 18–26.
[44] D.L. Li, Y.Y. Guo, Z.X. Chang, F. Yu, X.L. Feng, J. Chem. Eng. Data. 58 (2013) 731–736.
[45] B. Polyak, E. Bassis, A. Novodvorets, S. Belkin, R.S. Marks, Water Sci. Technol. 42 (2000) 305–311.
[46] R. Pedahzur, B. Polyak, R.S. Marks, S. Belkin, J. Appl. Toxicol. 24 (2004) 343–348.
[47] J. Kochana, A. Gala, A. Parczewski, J. Adamski, Anal. Bioanal. Chem. 391 (2008) 1275–1281.
[48] U. Wollenberger, F. Lisdat, A. Rose, K. Streffer, in: P.N. Bartlett (Ed.) Bioelectrochemistry: Fundamentals, Experimental Techniques and Applications ChichesterWollenberger, John Wiley and Sons, Ulla, 2008, pp. 219-248.
[49] E. Michelini, L. Cevenini, M. Calabretta, S. Spinozzi, C. Camborata, A. Roda, Anal. Bioanal. Chem. 405 (2013) 6155–6163.
[50] T.K. Van Dyk, T.R. Reed, A.C. Vollmer, R.A. LaRossa, J. Bacteriol. 177 (1995) 6001–6004.
[51] J. Charles, G. Crini, F. Degiorgi, B. Sancey, N. Morin-Crini, P.M. Badot, Environ. Sci. Pollut. Res. 21 (2013) 1–13.
[52] S.C.R. Monteiro, G.L.L. Pinho, K. Hoffmann, I.F. Barcarolli, A. Bianchini, Environ. Toxicol. Chem. 32 (2013) 1412–1419.
[53] S. Belkin, Curr. Opin. Microbiol. 6 (2003) 206–212.

[54] S. Yagur-Kroll, C. Lalush, R. Rosen, N. Bachar, Y. Moskovitz, S. Belkin, Appl. Microbiol. Biotechnol. 98 (2013) 1–11.
[55] B. Polyak, E. Bassis, A. Novodvorets, S. Belkin, R. Marks, Water Sci. Technol. 42 (2000) 305–311.
[56] M. Milov, A. Popadin, On rainwater usage in Ashdod, in: N. Manusof (Ed.), Water Crisis in Israel and Ways of its Overcoming Jerusalim, 2009, Jerusalem Immigrant Community House; Jerusalem, pp. 54.
[57] K. Hakkila, T. Green, P. Leskinen, A. Ivask, R. Marks, M. Virta, J. Appl. Toxicol. 24 (2004) 333–342.
[58] E. Eltzov, S. Pennybaker, M. Shanit-Orland, R.S. Marks, A. Kushmaro, Sensor Actuat. B-Chem 174 (2012) 342–348.
[59] T. Xu, D.M. Close, G.S. Sayler, S. Ripp, Ecol. Indic. 28 (2013) 125–141.

Talanta 132 (2015) 591–599

Contents lists available at ScienceDirect

Talanta

journal homepage: www.elsevier.com/locate/talanta

The microwave induced plasma with optical emission spectrometry (MIP–OES) in 23 elements determination in geological samples

P. Niedzielski [a,*], L. Kozak [a,b], M. Wachelka [a,c], K. Jakubowski [a], J. Wybieralska [d]

[a] Adam Mickiewicz University in Poznań, Faculty of Chemistry, Department of Analytical Chemistry, 89B Umultowska Street, 61-614 Poznan, Poland
[b] Poviat Sanitary and Epidemiological Station in Poznań, Department of Food, Nutrition and Food Contact Materials, 10 Sieroca Street, 61-771 Poznan, Poland
[c] Selwa-Lab, 56 Okopowa Street, 01-042 Warsaw, Poland
[d] Adam Mickiewicz University in Poznan, Faculty of Chemistry, Environmental Laboratory of Unique Analytical Instrumentation, 89B Umultowska Street, 61-614 Poznan, Poland

ARTICLE INFO

Article history:
Received 4 July 2014
Received in revised form
28 September 2014
Accepted 8 October 2014
Available online 19 October 2014

Keywords:
Microwave induced plasma optical emission spectrometry
X-ray fluorescence
Atomic absorption spectrometry
Multielemental analysis
Geological samples

ABSTRACT

The article presents the optimisation, validation and application of the microwave induced plasma optical emission spectrometry (MIP–OES) dedicated for a routine determination of Ag, Al, B, Ba, Bi, Ca, Cd, Cr, Cu, Fe, Ga, In, K, Li, Mg, Mn, Mo, Na, Ni, Pb, Sr, Tl, Zn, in the geological samples. The three procedures of sample preparation has been proposed: sample digestion with the use of hydrofluoric acid for determination of total concentration of elements, extraction by aqua regia for determination of the quasi-total element concentration and extraction by hydrochloric acid solution to determine contents of the elements in acid leachable fraction. The detection limits were on the level 0.001–0.121 mg L^{-1} (from 0.010–0.10 to 1.2–12 mg kg^{-1} depend on the samples preparation procedure); the precision: 0.20–1.37%; accuracy 85–115% (for recovery for certified standards materials analysis and parallel analysis by independent analytical techniques: X-ray fluorescence (XRF) and flame absorption spectrometry (FAAS)). The conformity of the results obtained by MIP–OES analytical procedures with the results obtained by XRF and FAAS analysis allows to propose the procedures for studies of elemental composition of the fraction of the geological samples. Additionally, the MIP–OES technique is much less expensive than ICP techniques and much less time-consuming than AAS techniques.

© 2014 Elsevier B.V. All rights reserved.

1. Introduction

The microwave induced plasma optical emission spectrometry (MIP–OES), besides different spectrometric techniques as inductively coupled plasma optical emission spectrometry (ICP–OES), inductively coupled plasma mass spectrometry (ICP–MS), atomic absorption spectrometry (AAS) or atomic fluorescence spectrometry (AFS) techniques has been designed for elements determination in various samples [1]. The relatively short history (the first analytical application in 1963 [2]) and late (2011) commercialization of instruments [3] caused a small popularity of the technique. The application of determination of selected elements as e.g. Na [4], Cu, Cr, Mn, Fe, Cd, Zn, Ni, Au [5], Ag, Pd, Pt [6], Hg [7], K, Ca, Mg, Sr [8], Cl, Br [9], Si [10], Ba, Pb [11] first of all have based on laboratory-made analytical instruments. The different plasma gases has been used in MIP–OES technique: argon [5,6] or helium [7,9], but the use of nitrogen [12] (generating from atmospheric air) allowed significantly decrease the operating costs [10] and made the technique competitive to inductively coupled plasma based techniques [3].

The most of MIP–OES studies were concentrated on the optimisation of the analytical systems to obtain the lowest detection limits with satisfactory precision and accuracy [7]. The more efficient nebulisers (as ultrasonic nebuliser (US)) [13], the hydride generation and introducing in the plasma, connected with the US nebulizer [14,15] or direct solid samples introduction as a slurry [16–18] have been applied.

The MIP–OES spectrometry (besides ICP–OES, ICP–MS, AAS or AFS techniques) has been successfully used as chromatographic detector in hyphenated techniques [19,20]. Both in gas chromatography (GC) [21,22], capillary electrophoresis (CE) [23,24] or high performance liquid chromatography (HPLC) [25] the MIP–OES detectors allowed to determine elements (e.g. Se, [22] Cu, [23] As, [24] Cr [25]) species. Commercialisation of GC–MIP–OES instrumentation made this hyphenated techniques the most popular utilization of MIP–OES technique [26].

The article presents the application of the new analytical technique of MIP–OES to multielemental analysis of geological samples using Agilent 4100 MP-AES spectrometer, the first commercially

* Corresponding author.
E-mail address: pnied@amu.edu.pl (P. Niedzielski).

http://dx.doi.org/10.1016/j.talanta.2014.10.009
0039-9140/© 2014 Elsevier B.V. All rights reserved.

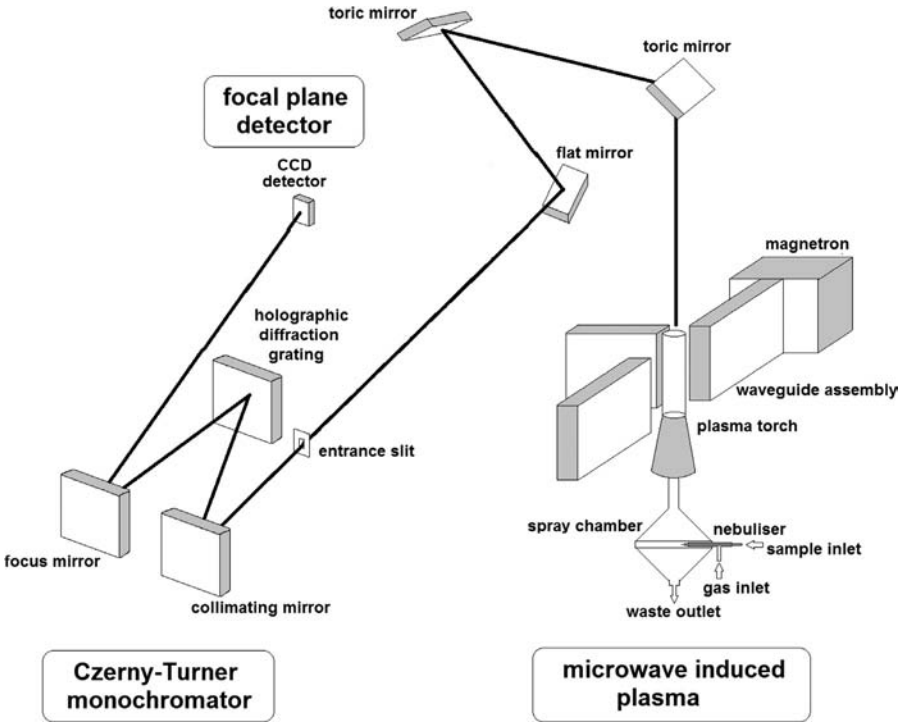


Fig. 1. Schematic diagram of the MP-AED 4100 spectrometer.

available MIP–OES analytical instrument. The validation of proposed samples preparation procedures and spectrometric measurements of real geological samples has been done. The results obtained for MIP–OES technique have been compared with independent methods: XRF and FAAS The compliance of the results obtained by different techniques allows to propose the MIP–OES based analytical procedures for routine analysis.

2. Experimental

2.1. Instruments

The nitrogen (with on-line nitrogen generator) microwave induced plasma optical emission spectrometer MP-AED 4100 (Agilent, USA), with SPS-3 autosampler (Agilent, Australia), worked in multielemental mode has been used (Fig. 1). The wavelengths selected for element determination and relative emission intensity for indicated spectral lines are put together in Section 3.2. The spectrometer was equipped with Czerny-Turner monochromator with 600 mm focal length with fixed entrance slit, holographic diffraction grating with 2400 lines/mm (wavelength range 178–780 nm) and CCD detector (532 × 128 pixel) directly cooled to 0 °C using a thermoelectric Peltier device. The microwave excitation assembly was an aircooled magnetron operating at 2450 MHz (fixed plasma power of 1 kW, vertically-oriented plasma with end-on or axial viewing). The plasma gas flow was fixed at 20 L min^{-1} and the auxiliary gas flow was fixed at 1.5 L min^{-1}. The glass spray chamber, glass concentric Meinhard nebuliser and quartz plasma torch (Agilent, Australia) have been used. For all elements determinations common settings have been used: the uptake time (the time of sample introduction to the plasma) 5 s, the plasma stabilisation time with sample aspiration 5 s, read time 2 s, read in triplicates. The mode of automatic background correction (off-peak left, off-peak right or off-peak left+right) has been used. The operating parameters: viewing position and nebuliser pressure were optimised for each element respectively and discussed in the text. The sequential analysis has been performed automatically with the appropriate (optimized) changes of operating parameters: viewing position and nebulizer pressure while the nebulizer pressure indicates the sequence of analysis (the elements determination has been grouped from the lowest to the highest value of the pressure).

Table 1
The spectral condition for FAAS determination.

element	wavelength (nm)	slit (nm)
Ca	422.7	0.5
Mg	202.6	1.0
Fe	248.3	0.2
Cr	357.9	0.2
Cu	324.8	0.5
Mn	279.5	0.2
Ni	232.0	0.2
Cd	228.8	0.5
Pb	217.0	1.0
Zn	213.9	1.0

As the reference analytical instrument the flame (air-acetylene) atomic absorption spectrometry SpectrAA 240FS (Varian, Australia) equipped with the SIPS-20 automatic system for standard solution preparation and on-line sample dilution (Varian, Australia) has been used in fast-sequention multielemental mode. The following determination conditions were used: a stoichiometric flame (13.5 L min^{-1} air and 2.0 L min^{-1} acetylene) was used except determination of chromium, where a flame with excess of inflammable gas was used (11.5 L min^{-1} air and 4.0 L min^{-1} acetylene), using the hollow cathode lamps (HCL) and background correction with a deuterium lamp (except Ca, Mg and Fe determination). The spectral condition has been placed in Table 1. The lamp current was equal to 7 mA (Ca/Mg lamp), 10 mA (Co/Cr/Cu/Fe/Mn/Ni lamp), and 5 mA (Ag/Cd/Pb/Zn lamp). The detection limits were on the level of 0.01 mg L^{-1}. The uncertainty (understood as a parameter characterizing the dispersion of the values attributed to a measured parameter, the main component of uncertainty was precision) of the entire analytical process (sample preparation and spectrometric measurements) did not

exceed 10% for Ca, Mg, Fe and Mn, and 15% for the other elements determined.

The second reference technique was X-ray fluorescence. The X-ray spectrometer Tracer IV Handheld XRF (Bruker, USA): the voltage range 4–45 kV; current 1–45 μA; the Silicon Drift Detectors (SDD) has been used. The spectrometer was equipped with portable vacuum pomp and worked in quantitate mode (determination of Al_2O_3, SiO_2, P_2O_5, S, K_2O, CaO, TiO_2, V_2O_5, Cr_2O_3, MnO, Fe_2O_3, NiO, ZnO, ZrO_2, SnO_2 with detection limit 0.01%) elaborated by manufacturer for geochemical analysis. The uncertainty of the measurements was below 5.0% for all elements determined.

For sample decomposition two microwave laboratory systems MW500 and MW520 (Merck, Germany) with fixed by manufacturer microwave power, equipped with high-pressure close Teflon units have been used. No temperature or pressure measurement and control have been available. For sample homogenisation the laboratory agate grinder Pulverisette (Fritsch, Germany) and plastic sieves (2.00 mm; 0.20 mm and 0.02 mm (Cisa, Spain)) have been used.

2.2. Reagents

Only reagents of analytical purity and deionised water produced in a Milli-Q device (Millipore, USA) were used. For MIP–OES analysis the 23-elements ICP commercial analytical standard (Merck, Germany) and for FAAS analysis the AAS commercial standards (Merck, Germany) have been used. For sample preparation the hydrochloric acid (diluted to concentration 2 mol L^{-1}), hydrofluoric acid (40%), nitric acid (65%) and boric acid (the 5% (w/v) solution), (Merck, Germany) have been used. For analysis quality control the standard reference materials BCR667 (JRC's Institute for Reference Materials and Measurements, European Commission), NIST2709 (National Institute of Standards & Technology, USA) and IAEA405 (International Atomic Energy Agency, Austria) have been used.

2.3. Methodology

2.3.1. Sample preparation

After initial homogenisation and elimination of coarse material (fractions with a particle diameter larger than 5 mm), the material was divided into laboratory samples weighing approx. 100 g. In the laboratory, the samples were dried at room temperature and the coarse material (particle diameter larger than 1 mm) was removed on a plastic sieve. Next the samples were grinded and sieved on plastic sieve (0.02 mm).

2.3.2. Sample extraction or digestion

2.3.2.1. Hydrofluoric acid digestion. The amount of 0.50 ± 0.01 g of sample were put in Teflon high-pressure unit and 6 mL of concentrated nitric acid were added. After reaction of the nitric acid with carbonates, 3 mL of concentrated hydrofluoric acid were added and unit was closed by Teflon cap. After reaction the unit was opened and 10 mL of boric acid solution were added immediately.

2.3.2.2. Aqua regia extraction. The extractions by aqua regia were prepared in compliance with the ISO 11466.3 procedure. The representative sample of 1.00 ± 0.01 g was extracted with concentrated nitric acid and concentrated hydrochloric acid (3.0 mL of nitric acid to 9.0 mL of hydrochloric acid) using microwave heating with a laboratory microwave unit.

2.3.2.3. Sample hydrochloric acid leaching. The hydrochloric acid extracts (acid leaching) methodology [27] has been prepared follow the previous geochemical studies [28]. The amount of 2.00 ± 0.01 g of the sample was weighed and put in a conical flask to which a hydrochloric acid solution (2 mol L^{-1}) was poured carefully in small portions (20 mL). After the reflux condenser was connected, the flask was heated up to approx. 80 °C. This temperature was then maintained for about 30 min.

The sample obtained after extraction or digestion was drained quantitatively through a paper filter (previously rinsed with 200 mL of distilled water) using polyethylene funnel into a plastic test tube; and finally the water was added up to a volume of 20.0 mL. In the case of hydrofluoric acid digestion 30 mL of boric acid solution were added to the solution and finally the water was added up to a volume of 50.0 mL.

3. Results and discussion

3.1. The stability of wavelength observation (off-set)

The accuracy of wavelength selection was checked for following spectral lines: Zn 213.857 nm; Mn 279.482 nm; Cu 327.395 nm; Sr 407.771 nm; Ba 493.408 nm; Ba 614.171 nm and K 766.491 nm, respectively. The long term stability of wavelength accuracy has been shown in Fig. 2. Generally, the offset value didn't exceed 0.020 nm and the long-time offset changes range was 0.001 nm to 0.004 nm. The highest wavelength deviation from the exact value has been noticed for Cu line 327.395 nm – the 60 days offset mean value 0.021 ± 0.001 nm, the lowest for Ba line 493.408 nm – the 60 days offset mean value 0.001 ± 0.001 nm. The highest offset changes have been observed for instrument zero order (the assumed position of optics by the manufacturer)—the standard deviation for 60 days offset value 0.004 nm.

3.2. Optimisation of MIP–OES spectrometer working condition

3.2.1. The nebuliser gas pressure

To obtain the highest analytical signal the user can optimize the nebulizer pressure for each element. The changes of analytical signal with the increase of gas pressure in nebulizer have been shown in Fig. 3, the optimal values recommended for routine analysis have been specified in Table 2. For most elements (Al, Ba, Ca, Ga, In, K, Li, Mn, Mo, Na, Sr, Tl) the pattern was the signal increase with the increase of nebuliser pressure. However, the changes of signal level with the increase of the nebuliser pressure were inconsiderable. In multielemental analysis the order of the elements determination has been automatically decide based on the results of optimisation of the nebuliser gas pressure: from the lowest to the highest value of the pressure to increase the analytical capability.

3.2.2. The position of plasma observation

The plasma is viewed from the top, and different elements/lines may have a slightly different offset from the centre view. Generally, the highest analytical signal has been obtained for the defined by

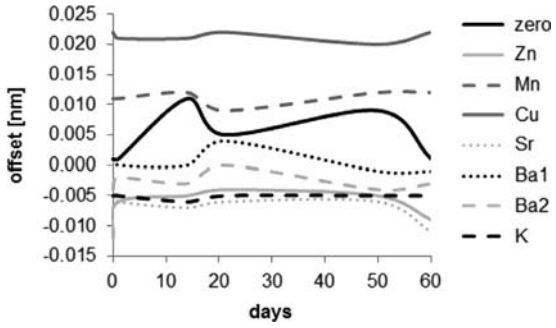


Fig. 2. Long-time offset changes for MIP–OES instrument.

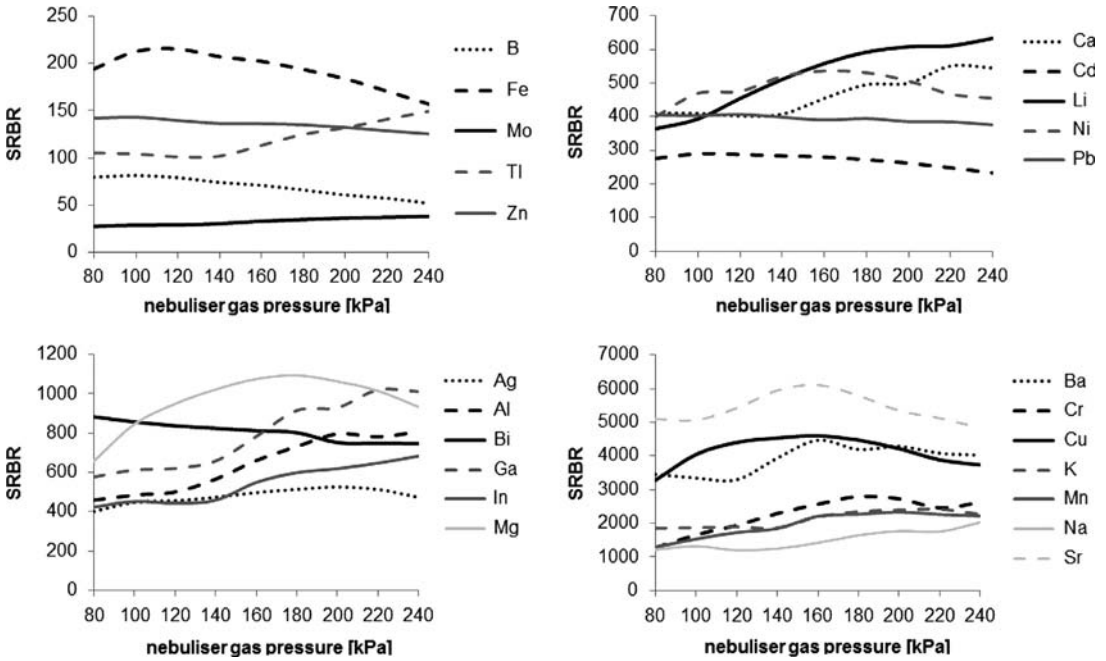


Fig. 3. The analytical signal changes with increasing of MIP–OES nebuliser pressure. SRBR—signal to root background ratio.

Table 2
The optimised parameters and figures of merit for metals determination by MIP–OES ($n=6$).

	Wavelength (nm)	Nebuliser pressure (kPa)	Viewing position	Detection limit (mg L^{-1})	Limit of quantification (mg L^{-1})	Precision (%)	Calibration range (mg L^{-1})	Correlation ceoficient	Accuracy compared to XRF (%)	Accuracy compared to FAAS (%)
Ag	328,068	240	0	0.082	0.164	0.68	20	0.9999	–	–
Al	396,152	200	0	0.002	0.005	0.70	20	0.9986	100.6	–
B	249,772	140	10	0.026	0.052	0.24	20	0.9998	–	–
Ba	455,403	240	10	0.015	0.029	0.41	20	0.9981	–	–
Bi	306,772	240	−120	0.092	0.184	0.53	20	0.9997	–	–
Ca	616,217	80	10	0.090	0.180	0.20	200	0.9993	97.6	95.4
Cd	228,802	180	10	0.090	0.181	0.22	20	0.9998	–	100.4
Cr	425,433	220	−10	0.001	0.003	0.93	20	0.9995	–	109.1
Cu	324,754	220	0	0.005	0.011	0.59	20	0.9998	–	100.2
Fe	238,204	140	10	0.075	0.150	0.49	100	0.9996	104.4	103.5
Ga	417,204	240	10	0.016	0.031	0.23	20	0.9999	–	–
In	451,131	240	10	0.037	0.075	0.69	20	0.9987	–	–
K	769,897	240	10	0.008	0.015	1.27	20	0.9995	106.6	–
Li	610,365	240	−10	0.007	0.015	1.65	20	0.9999	–	–
Mg	383,829	240	0	0.099	0.199	0.54	100	0.9987	–	98.5
Mn	403,076	240	10	0.001	0.003	0.71	20	0.9990	107.1	102.5
Mo	379,825	180	40	0.045	0.091	0.73	20	0.9997	–	–
Na	589,592	240	10	0.121	0.241	1.37	20	0.9996	–	–
Ni	352,454	200	20	0.002	0.004	0.55	20	0.9999	–	102.4
Pb	405,781	80	−130	0.113	0.226	0.78	20	0.9983	–	107.8
Sr	407,771	200	10	0.001	0.003	0.50	20	0.9982	–	–
Tl	535,046	240	20	0.005	0.009	0.81	20	0.9985	–	–
Zn	213,857	200	10	0.020	0.039	0.17	20	0.9997	–	97.5

the manufacturer as the central under the torch (0) or similar to central (± 20) viewing position. For molybdenum and in particular lead and bismuth the viewing position outside the axis of plasma symmetry has given the highest analytical signal. The changes of analytical signal during the shift of viewing position have been shown in Fig. 4. The optimal values recommended for routine analysis have been specified in Table 2.

3.3. The validation of analytical procedure

3.3.1. Analytical figures of merit: Calibration, limits of detection and quantification, precision

Optimized analytical methodology was validated follow ISO17025 criteria. The following parameters were defined: detection limits (defined follow 3 sigma criteria, where sigma is a standard deviation of series of 6 replicates of a blank) and limits of quantification (6 sigma criteria), range of calibration using non-linear algorithm provides a least second order least squares line of best fit in the intensity vs. concentration domain, and instrumental precision of determinations (Table 2). The obtained values of parameters characterising the analytical method showed a real possibility to apply MIP–OES technique in the determinations of elements content in the extracts of environmental samples [29]. Additionally, the uncertainty of the whole analytical procedure (including sample preparation step), involving the repetition of the extraction cycle and measurement of elements content, assuming the values below 20% (that was mainly produced by the sample preparation stage), confirms the possibility to apply the described procedure in the studies of element content in

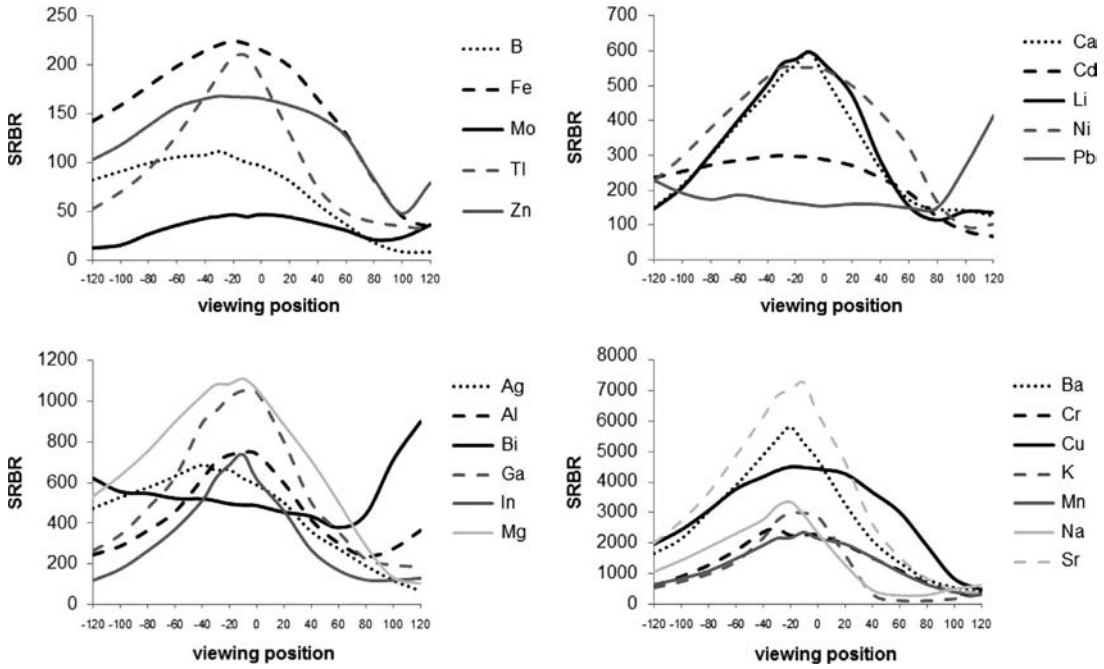


Fig. 4. The analytical signal changes with the changes of plasma viewing position in MIP–OES. SRBR—signal to root background ratio, viewing position in dimensionless manufacturer units.

Table 3
The comparison of the results XRF analysis and MIP–OES analysis after hydrofluoric acid digestion ($n=3$).

Determined by XRF	Sample A		Sample B		Sample C		Sample D		Sample E	
	Mean (mg kg^{-1})	SD (mg kg^{-1})	Mean (mg kg^{-1})	SD (mg kg^{-1})	Mean (mg kg^{-1})	SD (mg kg^{-1})	Mean (mg kg^{-1})	SD (mg kg^{-1})	Mean (mg kg^{-1})	SD (mg kg^{-1})
Al	87,560	6020	80,150	6780	45,350	3240	58,140	4530	105,600	6560
K	5,730	320	5,550	310	6,310	380	6,120	370	3,890	300
Ca	5,170	310	10,000	530	6,140	350	8,860	480	12,960	630
Mn	110	11	100	10	77	8	107	9	141	14
Fe	17,230	890	14,160	780	13,058	790	12,350	800	18,390	920
Determined by MIP–OES	**Mean** (mg kg^{-1})	**SD** (mg kg^{-1})	**Mean** (mg kg^{-1})	**SD** (mg kg^{-1})	**Mean** (mg kg^{-1})	**SD** (mg kg^{-1})	**Mean** (mg kg^{-1})	**SD** (mg kg^{-1})	**Mean** (mg kg^{-1})	**SD** (mg kg^{-1})
Al	87,560	6230	78,470	5460	48,350	3140	62,110	4980	96,860	6340
K	5,850	340	6,070	460	6,700	380	6,610	360	4,180	230
Ca	5,390	320	9,290	670	6,050	450	8,630	550	12,330	670
Mn	120	11	115	12	70	9	116	10	158	15
Fe	16,580	880	15,000	770	13,950	810	13,290	840	19,390	950
Recovery	**Mean (%)**	**RSD (%)**	**Mean (%)**	**RSD (%)**	**Mean (%)**	**RSD (%)**	**Mean (%)**	**RSD (%)**	**Mean (%)**	**RSD (%)**
Al	100.0	7.1	97.9	7.0	106.6	6.5	106.8	8.0	91.7	6.5
K	102.1	5.8	109.4	7.6	106.2	5.7	108.0	5.4	107.5	5.5
Ca	104.3	5.9	92.9	7.2	98.5	7.4	97.4	6.4	95.1	5.4
Mn	109.1	9.2	115	10.4	90.9	12.9	108.4	8.6	112	9.5
Fe	96.2	5.3	105.9	5.1	106.8	5.8	107.6	6.3	105.4	4.9

geological samples [3]. The quality of analysis of the samples series has been controlled by the reslope or "known sample" analysis with the use of Shewhart's control cards. Additionally, the differences of the values of detection limits obtained during validation procedure and calculated for routine analysis were inconsiderable.

3.3.2. *The accuracy studies*

For the accuracy studies for the determination of the total content of element after hydrofluoric acid sample decomposition the independent analytical method has been used. The X-ray fluorescence, as the method designed for total element content determination without sample preparation, has been chosen. The measurements have been performed parallel for five geological samples (A–E) with the use the portable XRF spectrometer and after sample HF decomposition MIP–OES analysis. The results comparison (Table 3) showed the high conformity of results obtained by both analytical methods (the MIP–OES recovery from 91.7% to 115%). Additionally, for selected elements (Ca, Cd, Co, Cr, Cu, Fe, Mg, Mn, Ni, Pb and Zn) the FAAS analysis parallel to MIP–OES have been done. The results obtained by FAAS were similar in the range of uncertainty to the results obtained by MIP–OES. Both methods are complementary (Table 2) and may be

Table 4
The results of analysis of reference certified materials by MIP–OES after aqua regia extraction ($n=6$).

	BCR667						NIST2709						IAEA405					
	Certified		Found		Recovery		Certified		Found		Recovery		Certified		Found		Recovery	
	M (mg kg^{-1})	SD (mg kg^{-1})	Mean (mg kg^{-1})	SD (mg kg^{-1})	Mean (%)	RSD (%)	Mean (mg kg^{-1})	SD (mg kg^{-1})	Mean (mg kg^{-1})	SD (mg kg^{-1})	Mean (%)	RSD (%)	Mean (mg kg^{-1})	SD (mg kg^{-1})	Mean (mg kg^{-1})	SD (mg kg^{-1})	Mean (%)	RSD (%)
Pb	31.9	1.1	31	1	97.2	3.2	17.3	0.1	17	1	98.8	5.8	74.8	3.1	73	4	97.6	5.5
Ca	x	x	31200	3050	x	x	19100	900	20010	1890	105	9.4	x	x	22150	2130	x	x
Fe	44800	1000	44200	1320	98.7	3.0	33600	700	32900	1100	97.9	3.3	37400	990	36300	1000	97.1	2.8
B	x	x	4.3	0.3	x	x	74	x	70	4	94.6	5.7	x	x	11.2	1.1	x	x
Cd	0.67	0.11	0.66	0.05	98.5	7.6	0.371	0.002	0.38	0.03	102	7.9	0.73	0.07	0.69	0.05	94.5	7.2
Mo	x	x	3400	150	x	x	x	x	4230	180	x	x	x	x	3980	176	x	x
Zn	175	13	176	12	101	6.8	103	4	101	6	98.1	5.9	279	10	271	11	97.1	4.1
Ni	128	9	122	11	95.3	9.0	85	2	79	3	92.9	3.8	32.5	2.0	30	2	92.3	6.7
Al	x	x	25340	530	x	x	73700	1600	26540	670	36.0	2.5	77900	7354	28780	720	36.9	2.5
Sr	x	x	302	10	x	x	239	6	228	8	95.4	3.5	118	20	112	6	94.9	5.4
Cu	60	9	58	3	96.7	5.2	33.9	0.5	31	2	91.4	6.5	47.7	1.7	45	3	94.3	6.7
Cr	178	16	159	12	89.3	7.5	130	9	121	8	93.1	6.6	84	6	78	5	92.9	6.4
Bi	x	x	1025	78	x	x	x	x	923	56	x	x	x	x	894	51	x	x
Ag	x	x	6.1	0.5	x	x	x	x	3.2	0.2	x	x	x	x	10.1	0.7	x	x
Mg	x	x	15760	789	x	x	14600	200	12900	720	88.4	5.6	12300	1273	10850	783	88.2	7.2
Mn	920	40	895	54	97.3	6.0	529	18	511	25	96.6	4.9	495	16	467	21	94.3	4.5
Ga	x	x	4.0	0.2	x	x	3.0	0.1	2.7	0.1	90.0	3.7	x	x	4.2	0.2	x	x
In	x	x	<0.1	x	x	x	x	x	<0.1	x	x	x	x	x	<0.1	x	x	x
Ba	x	x	213	12	x	x	979	28	904	32	92.3	3.5	x	x	132	11	x	x
Tl	x	x	<0.1	x	x	x	0.58	0.01	<0.1	x	x	x	x	x	<0.1	x	x	x
Na	x	x	>2000	x	x	x	12200	300	>2000	x	x	x	x	x	>2000	x	x	x
Li	x	x	314	23	x	x	x	x	91	7	x	x	72	10	70	5	97.2	7.1
K	x	x	>2000	x	x	x	21100	600	>2000	x	x	x	24900	10182	>2000	x	x	x

x—Not certified.

Table 5
The results of analysis of reference certified materials by MIP–OES after hydrochloric acid leaching, certified values for leaching available only for NIST2709 ($n=6$).

	BCR667						NIST2709						IAEA405						Leaching	Recovery	NIST2709
	Certified		Found		Recovery		Certified		Found		Recovery		Certified		Found		Recovery		Certified	Found	Recovery
	Mean (mg kg^{-1})	SD (mg kg^{-1})	Mean (mg kg^{-1})	SD (mg kg^{-1})	Mean (%)	RSD (%)	Mean (mg kg^{-1})	SD (mg kg^{-1})	Mean (mg kg^{-1})	SD (mg kg^{-1})	Mean (%)	RSD (%)	Mean (mg kg^{-1})	SD (mg kg^{-1})	Mean (mg kg^{-1})	SD (mg kg^{-1})	Mean (%)	RSD (%)	Mean (mg kg^{-1})	Mean (mg kg^{-1})	Mean (%)
Pb	31.9	1.1	16	1	51.3	5.6	17.3	0.1	11	1	61.0	6.0	74.8	3.1	44	1	58.8	3.2	9	11	115
Ca	x	x	25305	1998	x	x	19100	900	13835	403	72.4	2.9	x	x	16310	811	x	x	12415	13835	111
Fe	44800	1000	27320	178	61.0	0.7	33600	700	27769	773	82.6	2.8	37400	990	19918	577	53.3	2.9	23520	27769	118
B	x	x	2.9	0.2	x	x	74	x	47	4	62.8	7.6	x	x	8.6	0.6	x	x	52	47	89.8
Cd	0.67	0.11	0.51	0.01	75.4	1.4	0.371	0.002	0.31	0.01	86.3	4.4	0.73	0.07	0.59	0.01	80.1	1.2	0.4	0.31	62.5
Mo	x	x	2702	128	x	x	x	x	2237	90	x	x	x	x	2083	5	x	x	x	2237	x
Zn	175	13	152	2	86.6	1.4	103	4	87	3	84.5	3.3	279	10	189	8	67.6	4.1	79	87	110
Ni	128	9	92	4	76.6	5.8	85	2	60	4	70.0	5.9	32.5	2.0	25	1	76.8	4.8	65	60	90.9
Al	x	x	11819	185	x	x	73700	1600	16690	735	22.6	4.4	77900	7354	12273	541	15.8	4.4	16214	16690	103
Sr	x	x	277	19	x	x	239	6	188	1	78.7	0.8	118	20	104	1	87.7	0.7	x	188	x
Cu	60	9	52	1	86.8	2.6	33.9	0.5	29	2	85.8	5.3	47.7	1.7	41	2	85.1	5.6	27	29	106
Cr	178	16	96	6	53.7	6.7	130	9	80	5	44.6	4.9	84	6	49	1	58.3	2.9	53	80	109
Bi	x	x	654	47	x	x	x	x	563	37	x	x	x	x	556	20	x	x	x	563	x
Ag	x	x	xx	xx	x	x	x	x	xx	xx	x	x	x	x	xx	xx	x	x	x	xx	x
Mg	x	x	10116	678	x	x	14600	200	9448	325	64.7	3.4	12300	1273	8038	379	65.4	4.7	10366	9448.0	91.1
Mn	920	40	828	16	89.9	2.0	529	18	433	22	81.8	5.1	495	16	422	28	85.3	6.7	418	433	103
Ga	x	x	2.0	0.1	x	x	3.0	0.1	1.7	0.1	56.7	8.3	x	x	1.9	0.1	x	x	x	1.7	x
In	x	x	<0.1	x	x	x	x	x	<0.1	x	x	x	x	x	<0.1	x	x	x	x	<0.1	x
Ba	x	x	100	9	x	x	979	28	499	28	45.3	4.6	x	x	61	6	x	x	382	499	116
Tl	x	x	<0.1	x	x	x	0.58	0.01	<0.1	x	63.8	7.6	x	x	<0.1	x	x	x	x	<0.1	x
Na	x	x	>2000	x	x	x	12200	300	895	77	7.3	8.6	x	x	>2000	x	x	x	488	895	87.5
Li	x	x	262	25	x	x	x	x	78	6	x	x	72	10	65	5	89.6	7.7	x	78	x
K	x	x	2519	585	x	x	21100	600	1496	141	11.8	5.7	24900	10182	2626	227	10.5	8.6	2954	1496	84.5

x—Not certified, xx—not measured, hydrochloric acid was used for leaching.

Table 6
The results of geochemical analysis by MIP–OES (mg kg^{-1}, $n=3$), the uncertainty below 20% for each measurements.

	Sample 1			Sample 2			Sample 3			Sample 4			Sample 5			Sample 6		
	HF	AR	HCl	HF	AR	HCl	HF	AR	HCl	HF	AR	HCl	HF	AR	HCl	HF	AR	HCl
Pb	23	3	< 1	22	4	< 1	18	3	< 1	20	3	< 1	28	5	< 1	30	3	< 1
Ca	6430	4940	4720	5620	2990	2750	5980	3340	3180	6200	3790	3710	4980	3120	2730	5670	3650	3480
Fe	10300	8760	8150	9870	8670	8430	9780	8270	8060	9230	8890	8620	11700	10800	10000	12300	10800	10400
B	x	5	5	x	7	7	x	7	6	x	8	7	x	8	8	x	8	7
Cd	16	11	10	12	3	2	12	3	2	10	5	3	11	5	3	15	4	3
Mo	10	8	7	10	4	4	9	4	3	9	4	2	6	5	3	11	5	3
Zn	56	22	17	34	12	10	36	11	9	43	11	10	32	11	11	29	12	10
Ni	31	5	< 1	28	3	< 1	43	2	< 1	26	2	< 1	31	3	< 1	33	3	< 1
Al	22300	20800	20000	18300	17100	16700	23200	15600	15000	15600	15800	15100	18500	1300	12100	19700	14200	13700
Sr	15	10	6	15	7	5	12	7	5	17	7	6	14	7	6	15	8	6
Cu	30	25	25	41	8	5	59	3	2	42	3	2	66	4	3	48	4	2
Cr	35	7	2	52	3	1	74	1	1	68	2	1	59	2	1	54	3	2
Bi	12	8	6	12	8	5	11	4	4	14	7	5	9	5	4	7	5	3
Ag	9	4	xx	8	3	xx	6	2	xx	11	2	xx	11	2	xx	9	2	xx
Mg	450	267	253	520	245	223	492	256	212	499	289	275	467	287	232	456	275	226
Mn	135	113	102	87	54	49	115	90	82	123	88	81	103	76	64	82	67	45
Ga	2	< 1	< 1	3	< 1	< 1	1	< 1	< 1	2	< 1	< 1	3	< 1	< 1	1	< 1	< 1
In	1	< 1	< 1	1	< 1	< 1	2	< 1	< 1	2	< 1	< 1	1	< 1	< 1	2	< 1	< 1
Ba	2340	554	516	2200	670	571	1980	556	505	2450	645	590	2970	689	642	3210	734	674
Tl	15	8	6	13	7	6	14	7	6	21	9	8	18	8	7	16	9	7
Na	890	15	12	780	19	9	757	11	7	876	11	8	924	10	9	901	12	8
Li	213	134	125	200	123	114	216	145	132	267	176	158	235	189	154	245	165	149
K	2720	45	36	1510	34	27	2590	29	25	1020	23	21	1810	22	18	1320	26	22

HF—hydrofluoric acid sample digestion, AR—aqua regia sample extraction, HCl—hydrochloric acid sample extraction.
x—Not measured, boric acid was used in digestion procedure, xx—not measured, hydrochloric acid was used for leaching.

alternatively used in analysis of environmental samples [29]. The MIP–OES measurements accuracy was good in comparison with the results obtained (Table 2) by independent techniques XRF and FAAS (the mean value of accuracy obtained from 5 independent analyses). For results obtained by MIP–OES and reference techniques: XRF and FAAS measurements the statistical analysis has been done. The distribution tests: chi2 and Kolmogorow–Smirnow indicate the normal distribution of data (and the need of the use parametric test) and the results have been compared using Student's *t*-test. The results of the *t*-test indicates no statistically significant differences with the level of probability $p < 0.05$. Additionally, the proposed procedure of total element content determination by MIP–OES is safe for glass or quartz parts of analytical instrument.

3.3.3. *The traceability studies*

The traceability studies have been performed with the use of standard reference materials: BCR667 (the estuarine sediment), NIST2709 (the agricultural soil from San Joaquin Valley in the central California) and IAEA405 (the estuarine sediment from Tagus estuary (Portugal)). Additionally five geological samples (described by the letters A–E) have been used as in—laboratory standards.

The traceability studies for aqua regia samples extraction (procedure of quasi-total elements content determination) have been done with the use of three standard certified materials (geological matrix). The results of recovery (Table 4) were high (from 88.4% to 105%). The worst recovery has been found for aluminum determination, it was caused by the lack of decomposition of aluminosilicates by aqua regia. The results conformity allows use the procedure in analysis of environmental samples.

The traceability studies for leaching procedure (hydrochloric acid extraction) have been performed for NIST2709 certified reference material (the certified values of elements content in leachable fraction were available). The obtained recovery values (in the range from 84.5% 118%) were high (Table 5) and the usefulness of acid leaching procedure has been confirmed. To find the recovery level for acid leaching procedure the analysis of three certified materials has been done and the obtained results has been compared with the certified value for total concentration of the elements. The recovery values were in the range from 10.5% to 89.9%, for most elements were under 60%.

The validation procedure was carried out for 66 separately prepared samples and 1374 instrumental measurements (903 (MIP–OES), 396 (FAAS) and 75 (XRF)) have been done. The results of recovery, discussed below, were comparable with the works of different authors [11,13]. Additionally, the good MIP–OES results accuracy and compliance with the results obtained using diffe rent techniques (FAAS and XRF) are evidence of not significant interferences.

3.4. *Application for geological samples*

With the use of prepared application the analyses of geological samples (river sediments: 89–95% SiO_2, 3–5% organic matter) have been done. The MIP–OES technique allows the fast determination of 23 elements content in several hundred of samples with satisfactory accuracy and precision. The results of geochemical analysis have been specified in Table 6.

4. Conclusion

The MIP–OES techniques may become the very useful tool in geochemical analysis. The low cost of instrumentation and operation (comparable with FAAS) and fast and multielemental analysis (comparable with ICP–OES [30]) allow use the MIP–OES technique in the analysis of various geological samples. Good accuracy and precision, obtained in MIP–OES analysis let to recommend this technique both for determination of the total concentration of elements and quasi-total and acid leachable elements concentration. The availability of first commercial MIP–OES analytical instrument may precipitate the use the MIP–OES technique in analytical chemistry.

Acknowledgements

The authors thank to Professor Jan Milecki from Faculty of Chemistry Adam Mickiewicz University in Poznan for the possibility to use the MIP–OES instrument. The studies were partially financed by National Science Centre Poland, based on the decision No. DEC-2013/09/B/ST10/00610 and the described procedure will be used in the geochemical analysis.

References

[1] J. Qinhan, D. Yixiang, J.A. Olivares, Spectrochim. Acta, Part B 52 (1997) 131–161. http://dx.doi.org/10.1016/S0584-8547(96)01553-4.
[2] R. Mavrodineanu, R.C. Hughes, Spectrochim. Acta 19 (1963) 1309–1317. http://dx.doi.org/10.1016/0371-1951(63)80240-4.
[3] W. Li, P. Simmons, D. Shrader, T.J. Herrman, S.Y. Dai, Talanta 112 (2013) 43–48. http://dx.doi.org/10.1016/j.talanta.2013.03.029.
[4] K. Jankowski, Talanta 54 (2001) 855–862. http://dx.doi.org/10.1016/S0039-9140(01)00333-2.
[5] P.G. Brown, D.L. Haas, J.M. Workman, J.A. Caruso, F.L. Fricke, Anal. Chem. 59 (1987) 1433–1436.
[6] K. Jankowski, A. Jackowska, P. Łukasiak, Anal. Chim. Acta 540 (2005) 197–205. http://dx.doi.org/10.1016/j.aca.2004.09.012.
[7] M. Murillo, N. Carrión, J. Chirinos, A. Gammiero, E. Fassano, Talanta 54 (2001) 389–395. http://dx.doi.org/10.1016/S0039-9140(00)00672-X.
[8] H. Matusiewicz, B. Golik, Microchem. J. 76 (2004) 23–29. http://dx.doi.org/10.1016/j.microc.2003.10.007.
[9] B. Koschuh, M. Montes, J.F. Camuña, R. Pereiro, A. Sanz-Medel, Total Organochloride, Mikrochim. Acta. 129 (1998) 217–223.
[10] R.S. Amais, G.L. Donati, D. Schiavo, J.A. Nóbrega, Microchem. J. 106 (2013) 318–322. http://dx.doi.org/10.1016/j.microc.2012.09.001.
[11] H. Matusiewicz, M. Ślachciński, Microchem. J. 115 (2014) 6–10. http://dx.doi.org/10.1016/j.microc.2014.02.002.
[12] Y. Arai, S. Sato, K. Wagatsuma, ISIJ Int. 53 (2013) 1993–1999. http://dx.doi.org/10.2355/isijinternational.53.1993.
[13] H. Matusiewicz, M. Slachcinski, Spectrosc. Lett. 44 (2011) 128–137. http://dx.doi.org/10.1080/00387010.2010.481703.
[14] H. Matusiewicz, M. Ślachciński, Spectrosc. Lett. 43 (2010) 474–485. http://dx.doi.org/10.1080/00387010903360040.
[15] H. Matusiewicz, M. Ślachciński, Microchem. J. 95 (2010) 213–221. http://dx.doi.org/10.1016/j.microc.2009.12.004.
[16] H. Matusiewicz, B. Golik, Spectrochim. Acta, Part B 59 (2004) 749–754. http://dx.doi.org/10.1016/j.sab.2004.01.016.
[17] H. Matusiewicz, M. Ślachciński, Microchem. J. 82 (2006) 78–85. http://dx.doi.org/10.1016/j.microc.2005.08.001.
[18] H. Matusiewicz, M. Ślachciński, Microchem. J. 86 (2007) 102–111. http://dx.doi.org/10.1016/j.microc.2006.12.002.
[19] J.C.A. Wuilloud, R.G. Wuilloud, A.P. Vonderheide, J.A. Caruso, Spectrochim. Acta, Part B 59 (2004) 755–792. http://dx.doi.org/10.1016/j.sab.2004.03.009.
[20] B. Rosenkranz, J. Bettmer, TrAC, Trends Anal. Chem. 19 (2000) 138–156. http://dx.doi.org/10.1016/S0165-9936(99)00189-2.
[21] J. Koch, M. Okruss, J. Franzke, S.V. Florek, K. Niemax, H. Becker-Ross, Spectrochim. Acta, Part B 59 (2004) 199–207. http://dx.doi.org/10.1016/j.sab.2003.12.005.
[22] C. Dietz, J. Sanz Landaluze, P. Ximénez-Embún, Y. Madrid-Albarrán, C. Cámara, Anal. Chim. Acta 501 (2004) 157–167. http://dx.doi.org/10.1016/j.aca.2003.09.027.
[23] H. Matusiewicz, M. Ślachciński, Cent. Eur. J. Chem. 9 (2011) 896–903. http://dx.doi.org/10.2478/s11532-011-0079-6.
[24] H. Matusiewicz, M. Ślachciński, Microchem. J. 102 (2012) 61–67. http://dx.doi.org/10.1016/j.microc.2011.11.010.
[25] G. Heltai, B. Fehér, M. Horváth, Chem. Pap. 61 (2007) 438–445. http://dx.doi.org/10.2478/s11696-007-0059-7.
[26] R.I. Pereiro, C.A. Díaz, Anal. Bioanal. Chem. 372 (2002) 74–90. http://dx.doi.org/10.1007/s00216-001-1139-0.
[27] M.P. Jonathan, S.K. Sarkar, P.D. Roy, M.A. Alam, M. Chatterjee, B.D. Bhattacharya, A. Bhattacharya, K.K. Satpathy, Ecotoxicology 19 (2010) 405–418.
[28] W. Szczuciński, N. Chaimanee, P. Niedzielski, G. Rachlewicz, D. Saisuttichai, T. Tepsuwan, et al., Pol. J. Environ. Stud. 15 (2006) 793–810.
[29] A.E. Croslyn, B.W. Smith, J.D. Winefordner, Crit. Rev. Anal. Chem. 27 (1997) 199–255. http://dx.doi.org/10.1080/10408349708052201.
[30] M.R. Hammer, Spectrochim. Acta, Part B 63 (2008) 456–464. http://dx.doi.org/10.1016/j.sab.2007.12.007.

Talanta 132 (2015) 600–605

Contents lists available at ScienceDirect

Talanta

journal homepage: www.elsevier.com/locate/talanta

Functionalized gold nanorod-based labels for amplified electrochemical immunoassay of *E. coli* as indicator bacteria relevant to the quality of dairy product

Xinai Zhang [a,*], Fan Zhang [b], Hongyin Zhang [a], Jianzhong Shen [a], En Han [a], Xiaoya Dong [a]

[a] School of Food and Biological Engineering, Jiangsu University, Zhenjiang 212013, PR China
[b] Liaocheng People's Hospital, Liaocheng 252002, PR China

ARTICLE INFO

Article history:
Received 31 July 2014
Received in revised form
25 September 2014
Accepted 2 October 2014
Available online 22 October 2014

Keywords:
Electrochemical immunoassay
Silica-functionalized gold nanorods
Ferrocenecarboxylic acid
Signal amplification
E. coli
Dairy product

ABSTRACT

In this paper, we report an amplified electrochemical immunoassay for *Escherichia coli* as indicator bacteria relevant to the quality of dairy product using the functionalized gold nanorod-based labels ({$_d$Ab–AuNR–FCA}). The {$_d$Ab–AuNR–FCA} labels were designed by exploiting silica-functionalized gold nanorods (AuNR@SiO_2) as the carriers for immobilization of detection antibody ($_d$Ab) and ferrocenecarboxylic acid (FCA), in which $_d$Ab was used for recognition of *E. coli* and FCA tags served as signal-generating molecule. Greatly amplified signal was achieved in the sandwich-type immunoassay when enormous FCA linked to AuNR@SiO_2. Compared with the commercially available {$_d$Ab–FCA}, the {$_d$Ab–AuNR–FCA} labels exhibited a better performance for *E. coli* assay due to the advantages of AuNR@SiO_2 as carriers. Under optimal experimental conditions, it showed a linear relationship between the peak current of FCA and the logarithmic value of *E. coli* concentration ranging from 1.0×10^2 to 5.0×10^4 cfu mL^{-1} with a detection limit of 60 cfu mL^{-1} ($S/N=3$), and the electrochemical detection of *E. coli* could be achieved in 3 h. Moreover, the proposed strategy was used to determine *E. coli* in dairy product (pure fresh milk, yogurt in shelf-life, and expired yogurt), and the recoveries of standard additions were in the range of 95.1–106%. This proposed strategy exhibited rapid response, high sensitivity and specificity for *E. coli* assay in dairy product, and could become a promising technique to estimate the quality of dairy product.

© 2014 Elsevier B.V. All rights reserved.

1. Introduction

Dairy product is rich in protein, fat and other nutrients, and could be easily contaminated with pathogenic bacteria during the process of manufacture, storing, transporting and selling [1–3]. Increasing numbers of human infections and outbreaks associated with contaminated dairy product have been reported in China and many other countries. Various investigations demonstrate that these outbreaks are often linked with *Escherichia coli* levels present in dairy product [4,5]. As a consequence, the presence of *E. coli* in dairy product is considered as a possible threat or indicator of microbiological dairy product quality deterioration [6,7]. In many countries, health departments routinely detect *E. coli* in dairy product to protect people from bacterial infections.

Conventional methods for *E. coli* detection are standard plate count, most probable number (MPN), Petrifilm™ aerobic count plate method, etc. [8–10]. Although these methods have the advantage of high accuracy, they are complicated in operation, lack of specificity and time-consuming, which delays the time to market and results in a serious backlog of dairy product. Moreover, other microorganisms potentially present in dairy product could interfere with *E. coli* assay to cause false positive results. Therefore, the development of rapid, sensitive and specific methods for *E. coli* analysis has become a great challenge for in-time estimating the quality of dairy product.

Recently, some microbiological techniques such as polymerase chain reaction [11], immunoassay [12] and in situ hybridization technique [13] have been developed as alternatives to the conventional methods for *E. coli* detection. Among the above techniques, immunoassay-based protocols employing antibody–antigen interaction has been regarded as one of the most important analytical techniques in biological assay [14]. In comparison with other immunological methods such as fluorescence [15], chemiluminescence [16], or surface-plasmon resonance [17], electrochemical immunoassay provides a promising

* Corresponding author. Tel./fax: +86 511 88780201.
E-mail address: zhangxinai@mail.ujs.edu.cn (X. Zhang).

http://dx.doi.org/10.1016/j.talanta.2014.10.013
0039-9140/© 2014 Elsevier B.V. All rights reserved.

approach for specific and rapid analysis because of the advantages of simple instrumentation, easy signal quantification, low cost of the entire assay, and potential ability for real-time and on-site detection [18–20].

In order to achieve a successful electrochemical immunoassay, signal amplification is a critical need for obtaining low detection limit and high sensitivity [21]. At present, the advantages of nanotechnologies have provided alternative approaches for sensitive detection of biological analytes [22]. Various nanomaterials including nano tubes [23], nanorods [24], and nanoparticles [25] have been used as excellent carriers for the preparation of labels by loading numerous signal tags, and the prepared labels can greatly amplify the transduction signal of a recognition event in bioassay. Among these nanomaterials, gold-based nanomaterials [26], especially gold nanorods (AuNRs), have attracted considerable interest in biomolecule analysis due to their variable length–diameter ratio and large surface area [27,28]. However, cetyltrimethylammonium bromide (CTAB), serving as the essential inducer and stabilizer in the fabrication process of AuNRs, could interfere with the biological process because of its toxicity, which results in some limitations to AuNRs in the biocompatibility. Considerable efforts have been made to circumvent these drawbacks [29,30], in which silica-functionalized AuNRs (AuNR@SiO_2) has been proved to be an effective strategy to increase the functional surface area of AuNRs, facilitate the biocompatibility and enrich the practical applications [31].

In this paper, an amplified electrochemical immunoassay was proposed for *E. coli* analysis in dairy product using the functionalized AuNR-based labels ({$_d$Ab–AuNR–FCA}). The {$_d$Ab–AuNR–FCA} labels were fabricated by exploiting AuNR@SiO_2 as the carriers for immobilization of detection antibody ($_d$Ab, anti-*E. coli* polyclonal antibody) and ferrocenecarboxylic acid (FCA), in which $_d$Ab was used for recognition of *E. coli* and FCA tags served as signal-generating molecule. Here, AuNR@SiO_2 had large surface area to load enormous FCA, and thus played important roles in signal amplification to improve detection sensitivity. In the case of the electrochemical assay, L-cysteine was self-assembled on a gold electrode surface through Au–S bonding, which introduced a high density of capture antibody ($_c$Ab, anti-*E. coli* monoclonal antibody). The sandwich-type system was formed by the specific recognition of the electrode surface-confined $_c$Ab to *E. coli*, followed by the attachment of the {$_d$Ab–AuNR–FCA} labels. The analysis of *E. coli* was performed by electrochemical detection of FCA in the bound labels on the electrode surface. The results confirmed that the electrochemical immunoassay gave a useful protocol for *E. coli* analysis with rapid response, high sensitivity and specificity, and thus provided a powerful tool for estimating the quality of dairy product.

2. Experimental

2.1. Reagents and materials

Ferrocenemonocarboxylic acid (FCA), 1-ethyl-3-(3-dimethylaminopropyl) carbodiimide (EDC), N-hydroxysuccinimide (NHS) and bovine serum albumin (BSA) were purchased from Sigma Chemicals (St. Louis, MO, USA). *E. coli* (DH5α) was supplied by School of Food and Biological Engineering, Jiangsu University (Zhenjiang, China). Anti-*E. coli* monoclonal antibody (serving as capture antibody, $_c$Ab), and anti-*E. coli* polyclonal antibody (serving as detection antibody, $_d$Ab) were obtained from Beijing Biosea Biotechnology Co. Ltd. (Beijing, China). 3-Aminopropyltriethoxysilane (APTES, 99%) and tetraethoxysilane (TEOS) were obtained from Aladdin Reagent Database Inc. (Shanghai, China). L-cysteine, $HAuCl_4$ and other chemical reagents were purchased from Shanghai Chemical Reagents Co. Ltd. (Shanghai, China). All the reagents used were of analytical-reagent grade and all solutions were prepared with pure water from Millipore (Milli-Q, 18.2 MΩ cm). The glassware was autoclaved prior to be used.

2.2. Apparatus

All electrochemical measurements were performed on a CHI660 electrochemical working station (CH Instruments Inc., Austin, TX, USA) with a conventional three-electrode system comprised of a platinum wire as the auxiliary, a saturated calomel electrode (SCE) as the reference, and the modified gold working electrode. Electrochemical impedance spectroscopy (EIS) was carried out within frequency range of 0.10 Hz–100 kHz at the amplitude of 5 mV and the applied potential of 0.24 V. Transmission electron microscopy (TEM) was collected on JEM-2100 (JEOL Ltd., Tokyo, Japan). UV–visible spectroscopic data were obtained on a Cary 500 UV–vis-NIR spectrometer (Varian Comp, USA).

2.3. Preparation of the {$_d$Ab–AuNR–FCA} labels

AuNRs were first synthesized by using the seed mediated method (see Supplementary Data) [27,32]. Next, the freshly AuNRs were dispersed in 10 mL Milli-Q water by sonication for 10 min, and 100 μL of 0.10 mol L^{-1} NaOH was added, followed by 60 μL the mixtures of TEOS, APTES and ethanol in the volume ratio of 1:1:5 with stirred effectively for 24 h. The resulting solution was centrifuged at 10,000 rpm for 10 min to obtain the precipitate of AuNR@SiO_2. The precipitate was washed several times with water and redispersed in 5 mL PBS. Then, AuNR@SiO_2 was mixed with 4.0 mg mL^{-1} $_d$Ab and stirred for 2 h. The resulting $_d$Ab–AuNR was centrifuged at 12,000 rpm for 10 min to remove the non-conjugated $_d$Ab and then redispersed in 5 mL PBS. Last, the {$_d$Ab–AuNR–FCA} labels were fabricated by addition of 1.0 mL of saturated FCA solution (dissolved in PBS) to the $_d$Ab–AuNR. After incubation for 2 h under shaking, the labels were isolated by 5000 rpm for 10 min to remove the unbound FCA, and then dispersed in 5 mL PBS to form homogeneous dispersions. The obtained {$_d$Ab–AuNR–FCA} labels were stored in a refrigerator at 4 °C before use.

2.4. Fabrication of the capture antibody ($_c$Ab)-based immunosensor

A gold electrode (3 mm in diameter) was used to fabricate the $_c$Ab-based immunosensor. Prior to surface modification, the electrode was polished with 0.05 μm alumina slurry, followed by successive sonication in anhydrous ethanol and water. Subsequently, the electrode was electrochemically cleaned in 0.50 mol L^{-1} H_2SO_4 solution by cyclic potential scanning between −0.40 V and 1.5 V at 100 mV s^{-1} until a stable cyclic voltammogram was obtained. Afterwards, the cleaned electrode was modified by immersing in 0.02 mol L^{-1} L-cysteine in HAc–NaAc buffer solution (pH 5.0) for 6 h to form a self-assembled membrane (SAM), and the electrode surface was rinsed with water and PBS. Next, 10 μL of 0.40 mol L^{-1} EDC and 0.10 mol L^{-1} NHS in PBS were cast on Au/L-cysteine electrode to activate carboxyl group of L-cysteine for 1 h. The activated electrode was rinsed with PBS and incubated with 1.0 mg mL^{-1} $_c$Ab for 1 h to prepare the $_c$Ab-based immunosensor. The immunosensor was then treated with 1.0% (wt/vol) BSA/PBS for 30 min to block the non-specific adsorption.

2.5. Electrochemical detection of E. coli

After being rinsed and dried, the $_c$Ab-based immunosensor was incubated with *E. coli* sample at a certain concentration for 50 min at 37 °C. Subsequently, 10 μL of the {$_d$Ab–AuNR–FCA} labels were dropped on the *E. coli*-captured electrode and incubated for 50 min. The resulting electrode was rinsed with water, and then immersed in an electrochemical cell containing 5.0 mL of 0.10 mol L^{-1} $KClO_4$ in PBS to detect the immobilized FCA with differential pulse voltammetry

(DPV) from 0.10 to 0.50 V (vs. SCE) with pulse amplitude of 50 mV and width of 50 ms.

3. Results and discussion

3.1. Mechanism of electrochemical immunoassay with the {$_d$Ab–AuNR–FCA} labels

The mechanism of electrochemical immunoassay with the {$_d$Ab–AuNR–FCA} labels for the analysis of *E. coli* is illustrated in Fig. 1. In the preparation process of the electrochemical immunosensor, L-cysteine was first self-assembled on gold electrode surface through Au–S bonding (step a), and the carboxyl group of L-cysteine was activated by using EDC/NHS (step b), which introduced a high density of $_c$Ab through amide bond (step c). After further treated with BSA to block the non-specific adsorption, the $_c$Ab-based immunosensor could effectively capture *E. coli* in sample solution by the first immunoreactions (steps d and e). Finally, the {$_d$Ab–AuNR–FCA} labels were introduced to the electrode surface during the secondary binding event (step f). The anchored FCA tags, serving as signal-generating molecule, were detected by DPV in this immunoassay. Since FCA was only present when the {$_d$Ab–AuNR–FCA} labels reacted with *E. coli*, the peak current reflected the concentration of *E. coli* in sample solution, providing a strategy for estimating the quality of dairy product.

3.2. Characteristics of AuNR@SiO_2

AuNRs were fabricated by using the seed mediated method, and then SiO_2 coating has been accomplished when APTES and TEOS were added to the reaction solution together (Fig. 2, top). Transmission electron microscopy (TEM) was conducted to characterize AuNRs and AuNR@SiO_2. As shown in Fig. 2A, AuNRs exhibited typically rod-like shapes, measuring about 10 nm in mean diameter and about 40 nm in length. After active sites were generated on the surface of AuNRs, TEM image was recorded to depict the size and morphology characterization of AuNR@SiO_2 (Fig. 2B). As can be seen, the shape of AuNRs had no obvious change after surface modification, and each AuNR was coated with a thick SiO_2 shell. UV–vis absorption spectrometry was also used to characterize AuNRs and AuNR@SiO_2 (Fig. 2C). Apparently, AuNRs exhibited two characteristic peaks at 730 nm and 500 nm, which were assigned to the oscillation of electrons along the short and long axis, respectively. When SiO_2 was attached to AuNRs, the slightly red-shifted peak position was probably due to a change of surrounding dielectric function induced by the SiO_2 shell formed on AuNRs.

3.3. Characteristics of the electrochemical immunosensor

The fabrication process of the electrochemical immunosensor was characterized by electrochemical impedance spectroscopy (EIS), which

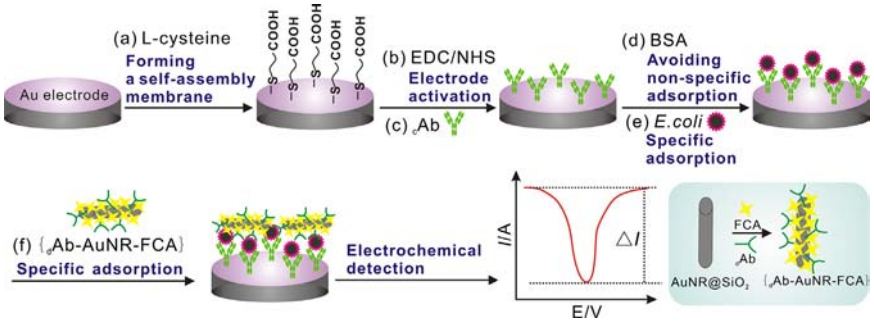


Fig. 1. Schematic illustration of the electrochemical immunoassay of *E. coli* based on the {$_d$Ab–AuNR–FCA} labels.

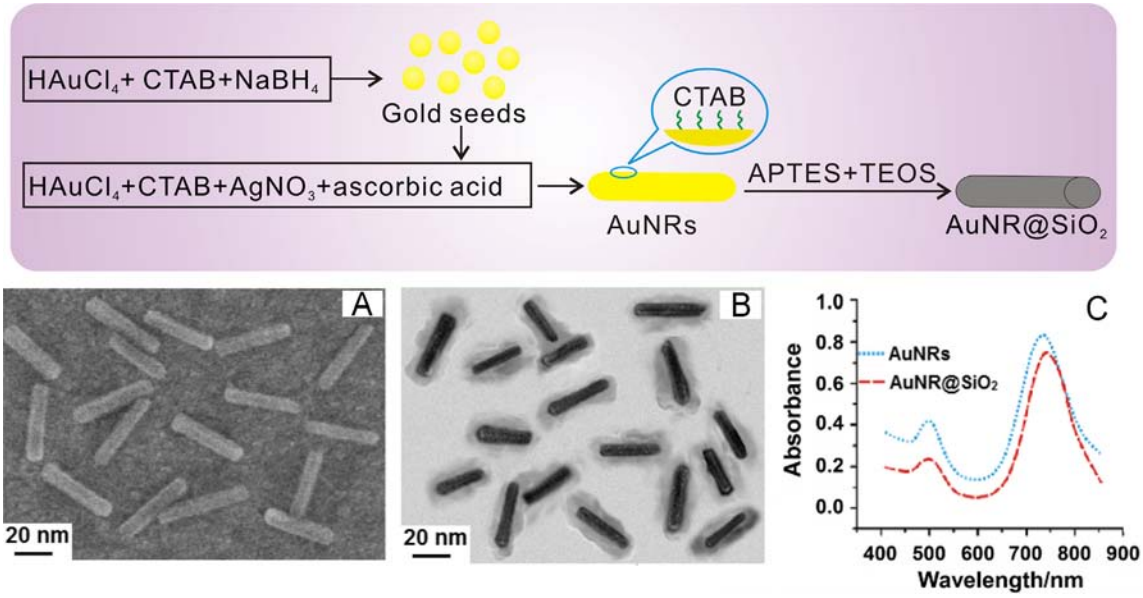


Fig. 2. Top: scheme showing the fabrication steps of AuNRs and AuNR@SiO_2. Bottom: TEM images of AuNRs (A) and AuNR@SiO_2 (B), UV adsorption spectra of AuNRs and AuNR@SiO_2 (C).

was performed in 0.01 moL L^{-1} PBS (pH 7.4) containing 0.10 moL L^{-1} KCl and 2.5 mmoL L^{-1} $Fe(CN)_6^{3-/4-}$ as the redox probe (Fig. 3). As expected, the gold electrode modified with L-cysteine (Au/L-cysteine, curve b) resulted in a great increase in the electron-transfer resistance (R_{et}) value compared to that at the bare gold electrode (bare Au, curve a). This indicated that the self-assembly membrane could inhibit the electron transfer. After $_c$Ab was assembled on the Au/L-cysteine, the R_{et} increased drastically (Au/L-cysteine/$_c$Ab, curve c), indicating that antibody acts as mass-transfer blocking layer and hinders the diffusion of $Fe(CN)_6^{3-/4-}$ toward the electrode surface. As expected, Au/L-cysteine/$_c$Ab modified with BSA resulted in a great increase in the R_{et} value (curve d). Subsequently, the R_{et} increased again once *E. coli* was captured by the immobilized $_c$Ab on the electrode surface (Au/L-cysteine/$_c$Ab/*E. coli*, curve e). Finally, the treatment of the electrode with the {$_d$Ab–AuNR–FCA} labels gave rise to an additional barrier towards the access of the redox probe to the electrode (Au/L-cysteine/$_c$Ab/*E. coli*/{$_d$Ab–AuNR–FCA}, curve f). These observations were consistent with the fact that the electrode was fabricated as expected, which confirmed the success in design of the proposed immunosensor.

3.4. Optimization of detection conditions

Incubation time and temperature were important factors of the immunological reaction. The effect of incubation time on peak current was studied from 20 to 70 min (Fig. 4A). It was found that the peak current increased gradually with increasing incubation time and reached a constant value after 50 min. A longer incubation time did not improve the peak current. Thus, an incubation time of 50 min was used for the immunoassay of *E. coli* in this study.

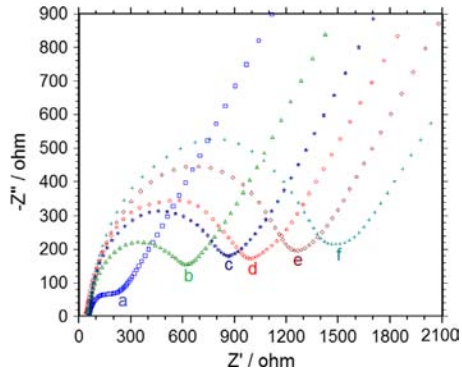


Fig. 3. (A) Electrochemical impedance spectra (EIS) on (a) bare Au electrode; (b) Au/L-cysteine; (c) Au/L-cysteine/$_c$Ab; (d) Au/L-cysteine/$_c$Ab treated with BSA; (e) Au/L-cysteine/$_c$Ab/*E. coli*; (f) Au/L-cysteine/$_c$Ab/*E. coli*/{$_d$Ab–AuNR–FCA} in 0.01 moL L^{-1} PBS (pH 7.4) containing 0.10 moL L^{-1} KCl and 2.5 mmoL L^{-1} $Fe(CN)_6^{3-/4-}$ as the redox probe at the applied potential of 0.24 V.

The relationship of peak current with incubation temperature ranging from 20 to 45 °C is shown in Fig. 4B. The maximum response was obtained at 37 °C and the peak current reduced when the temperature was higher than 37 °C. This might be attributed to the decrease of the biomolecule activity at a high temperature. Thus, 37 °C was chosen as the optimum incubation temperature.

3.5. Electrochemical immunosensor for E. coli assay based on the {$_d$Ab–AuNR–FCA} labels

Under optimal conditions, the electrochemical immunosensor was used for the detection of *E. coli* at different concentrations. As shown in Fig. 5A, the peak current of FCA increased with increasing *E. coli* concentration in the recognition solution, which was attributed to the increasing amount of the {$_d$Ab–AuNR–FCA} labels to bind the electrode surface. The corresponding calibration curve presented a linear relationship between the current response and the logarithmic value of *E. coli* concentration ranging from 1.0×10^2 to 5.0×10^4 cfu mL^{-1} with a slope of 2.03 (curve a, Fig. 5B). The detection limit of the electrochemical immunosensor was 60 cfu mL^{-1} ($S/N=3$) and the electrochemical detection of *E. coli* could be achieved in 3 h.

In order to demonstrate the enhanced sensitivity caused by the application of the {$_d$Ab–AuNR–FCA} labels, the commercially available {$_d$Ab–FCA} was used to replace the labels for performing the same procedure. As shown in curve b (Fig. 5B), the peak current was proportional to the logarithmic value of *E. coli* concentration from 1.0×10^3 to 1.0×10^7 cfu mL^{-1} with a slope of 0.66, and the detection limit was 400 cfu mL^{-1} ($S/N=3$). By comparison between the two slopes, the detection sensitivity of the proposed strategy was much higher than that obtained from {$_d$Ab–FCA}, verifying the advantages of the designed {$_d$Ab–AuNR–FCA}.

The performance of the electrochemical immunosensor has been compared with those reported in the literatures for *E. coli* analysis. Characteristics such as the linear range and detection limit are summarized for all of them in Table 1. As can be observed, the proposed immunosensor exhibited a wide linear range and low detection limit for *E. coli* assay. The reason might be that AuNR@SiO_2 took the advantages of large functional surface area and good biocompatibility, and could be used as efficient carriers for loading enormous FCA and $_d$Ab to design the {$_d$Ab–AuNR–FCA} labels for signal amplification.

3.6. Specificity, accuracy, stability and reusability of the immunosensor

The specificity of the immunosensor for *E. coli* assay was performed by using different microorganisms (e.g. *Staphylococcus aureus*, *Salmonella enteritidis*, and *Microzyme*), which were known

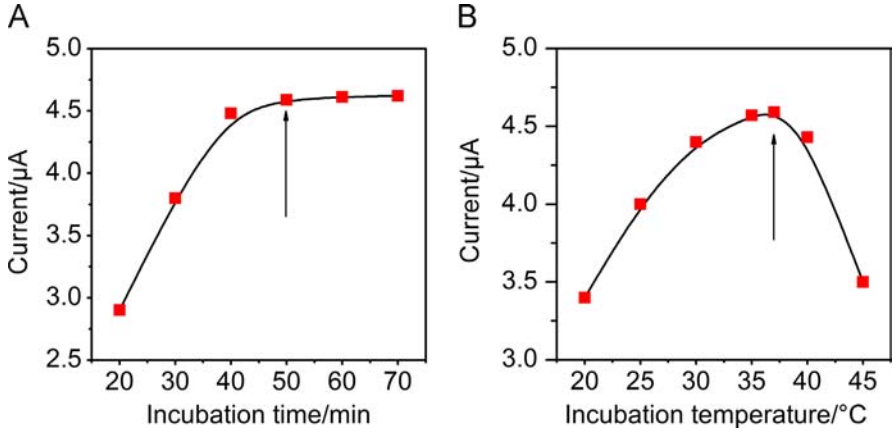


Fig. 4. Effect of incubation time (A) and temperature (B) on peak current of the electrochemical immunosensor for *E. coli* analysis at the concentration of 4.0×10^3 cfu mL^{-1}.

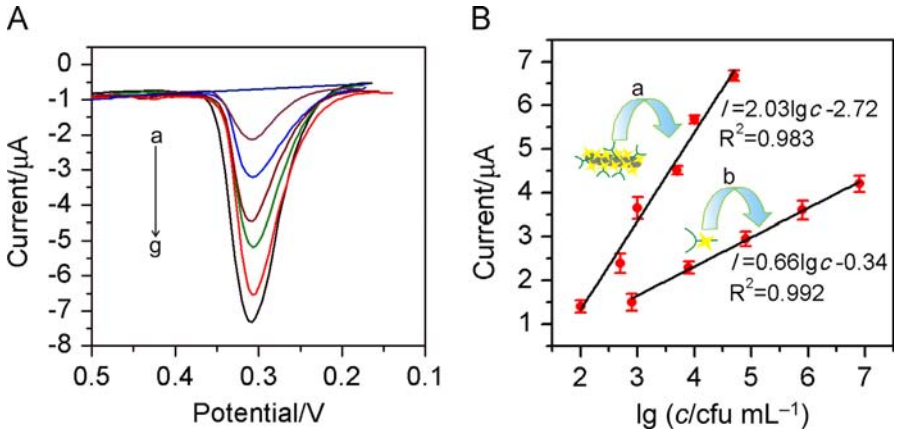


Fig. 5. (A) DPV response of the proposed strategy using the {$_d$Ab–AuNR–FCA} labels for *E. coli* analysis at the concentrations of (a) 0; (b) 1.0×10^2 cfu mL^{-1}; (c) 5.0×10^2 cfu mL^{-1}; (d) 1.0×10^3 cfu mL^{-1}; (e) 5.0×10^3 cfu mL^{-1}; (f) 1.0×10^4 cfu mL^{-1}; (g) 5.0×10^4 cfu mL^{-1}. (B) Calibration curve for *E. coli* detection measured with the electrochemical immunoassay by using (a) the {$_d$Ab–AuNR–FCA} labels and (b) {$_d$Ab–FCA} in 5.0 mL PBS containing 0.10 moL L^{-1} $KClO_4$.

Table 1
Comparisons of linear range and detection limit of different methods for *E. coli* assay.

Methods	Linear range	Detection limit	Reference
Hybrid nanostructure-based electrochemical immunosensing	2.0×10^2–2.0×10^6 cfu mL^{-1}	80 cfu mL^{-1}	[20]
IMS-QD fluorescence method[a]	1.0×10^3–1.0×10^7 cfu mL^{-1}	1.0×10^3 cfu mL^{-1}	[33]
Quartz crystal microbalance DNA sensor	2.67×10^2–2.67×10^6 cfu mL^{-1}	2.67×10^2 cfu mL^{-1}	[34]
Boron doped diamond biosensor	4×10^4–2×10^5 cells mL^{-1}	4×10^4 cells mL^{-1}	[35]
Electrochemical impedance immunosensor	6.0×10^4–6.0×10^7 cells mL^{-1}	6.0×10^3 cells mL^{-1}	[36]
Electrochemical DNA biosensor	1.0×10^3–5.0×10^5 cfu mL^{-1}	$500\pm5\%$ cfu mL^{-1}	[37]
Electrochemical immunoassay by using {$_d$Ab–FCA} labels	1.0×10^3–1.0×10^7 cfu mL^{-1}	400 cfu mL^{-1}	This work
Electrochemical immunoassay by using {$_d$Ab–AuNR–FCA} labels	1.0×10^2–5.0×10^4 cfu mL^{-1}	60 cfu mL^{-1}	This work

[a] IMS, immunomagnetic separation; QD, quantum dots.

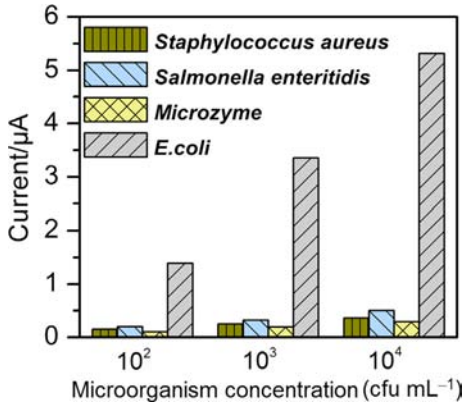


Fig. 6. The specificity diagram to compare the current response of FCA for different microorganisms.

to be potentially present in dairy product. As shown in Fig. 6, the current response obtained from *E. coli* was much higher than that obtained from other microorganisms. The observation signified that the electrochemical immunosensor could be used to detect *E. coli* in the presence of other microorganisms. Therefore, the proposed strategy could reduce the risk of false positive determination caused by other microorganisms. The application of sandwich-type immunoassay of *E. coli* played important roles in improving the specificity.

Five *E. coli* samples were detected to estimate the precision of the electrochemical immunosensor and six repetitive measurements were made for each *E. coli* sample. It was found that the average value was closed to the result obtained from the standard plate count method and the relative error (R.E.) maximum was less than 7.4%. The results confirmed that the proposed strategy exhibited acceptable accuracy for *E. coli* assay.

When the Au/L-cysteine/$_c$Ab-modified immunosensor and the {$_d$Ab–AuNR–FCA} labels were stored in a refrigerator at 4 °C, the current response still remained at 92% of the initial response after a storage period of 2 weeks, showing a quite satisfying stability. The long-term stability might be attributed to the strong interaction between Au/L-cysteine-modified electrode and $_c$Ab, and the strong covalently immobilization of $_d$Ab and FCA molecules on the surface of AuNR@SiO_2.

The reproducibility of the immunosensor was also evaluated from the current response of the Au/L-cysteine/$_c$Ab-modified immunosensor. A series of five measurements from the batch resulted in a relative standard deviations (RSD) of 5.6%, indicating the reproducibility of the proposed immunosensor was acceptable.

The regeneration of the immunosensor was performed by rinsing with 0.10 moL L^{-1} glycine-hydrochloric acid (Gly-HCl, pH 2.8) to dissociate the antigen–antibody complex. After each sandwich immunoassay, the electrode was treated with Gly-HCl for 8 min to remove *E. coli* and the {$_d$Ab–AuNR–FCA} labels. The as-renewed immunosensor could restore 89.6% of the initial value after five assay runs, indicating acceptable reusability.

3.7. Evaluation of E. coli in dairy product

In order to further verify the accuracy of the method for practical analysis of *E. coli*, the electrochemical immunosensor was used to determine *E. coli* in pure fresh milk, yogurt in shelf-life, and expired yogurt by the calibration curve method. For preparation of the dairy product samples, 1 mL of dairy product was diluted to 10 mL with 0.01 moL L^{-1} PBS (pH 7.4), and then spiked with desired concentrations of 5.0×10^2, 1.0×10^3 and 5.0×10^3 cfu mL^{-1} *E. coli*, respectively. Subsequently, the samples were detected by exploiting the proposed strategy. As shown in Table 2, the recoveries of standard additions are in the range of

Table 2
Determination results and recoveries of samples ($n=5$).

Sample	Detected (cfu mL^{-1})	Spiked (cfu mL^{-1})	Found (cfu mL^{-1})	Recovery (%)	RSD (%)
Pure fresh milk	No detected	5.0×10^2	482	96.4	4.25
Yogurt in shelf-life	No detected	1.0×10^3	1060	106	2.76
Yogurt expired for 10 days	216	1.0×10^3	1157	95.1	2.82
Yogurt expired for 20 days	648	5.0×10^3	5885	104.2	3.18
Yogurt expired for 30 days	2695	5.0×10^3	7526	97.8	1.92

95.1–106%, indicating acceptable accuracy of the electrochemical immunosensor. The results demonstrated that the proposed strategy can be applied to real samples and has great potential in practical applications.

4. Conclusions

In this paper, we developed an amplified electrochemical immunosensor for sandwich-type analysis of *E. coli* based on the {$_d$Ab–AuNR–FCA} labels. The prepared AuNR@SiO_2 provided an effective way to improve properties of AuNRs and was used as efficient carriers for loading enormous FCA and $_d$Ab to design the {$_d$Ab–AuNR–FCA} labels. Under optimal experimental conditions, a linear relationship between the current response of FCA and the logarithmic value of *E. coli* concentration was found ranging from 1.0×10^2 to 5.0×10^4 cfu mL^{-1} with a detection limit of 60 cfu mL^{-1} ($S/N=3$), and the electrochemical analysis could be achieved in 3 h. The proposed strategy was also used to determine *E. coli* in dairy product, and the recoveries of standard additions were in the range of 95.1–106%. The results confirmed that the electrochemical immunoassay exhibited good performance for *E. coli* with rapid response, high sensitivity and specificity, and thus could potentially become a promising technique for the assay of *E. coli* in dairy product.

Acknowledgments

This work was supported by the National Natural Science Foundation of China (21205051, 31271967, 21305052, 21205050), China Postdoctoral Science Foundation (2013M541605) and Scientific Research Foundation of Jiangsu University (11JDG144).

Appendix A. Supplementary data

Supplementary data associated with this article can be found in the online version at http://dx.doi.org/10.1016/j.talanta.2014.10.013.

References

[1] Å. Rosengren, A. Fabricius, B. Guss, S. Sylvén, R. Lindqvist, Int. J. Food Microbiol. 144 (2010) 263–269.
[2] K.J. Domig, U. Zitz, S. Macher, A. Kronberger, A. Reiter, W. Kneifel, Int. Dairy J. 29 (2013) 21–27.
[3] P. Belli, A.F.A. Cantafora, S. Stella, S. Barbieri, C. Crimella, Food Control 32 (2013) 366–370.
[4] B.P. Murphy, M. Murphy, J.F. Buckley, D. Gilroy, M.T. Rowe, D. McCleery, S. Fanning, Int. J. Hyg. Environ. Health 208 (2005) 407–413.
[5] J. Rey, S. Sánchez, J.E. Blanco, J. Hermoso de Mendoza, M. Hermoso de Mendoza, A. García, C. Gil, N. Tejero, R. Rubio, J.M. Alonso, Int. J. Food Microbiol. 107 (2006) 212–217.
[6] M.C. Martín, N. Martínez, B. del Rio, V. Ladero, M. Fernández, M.A. Alvarez, J. Dairy Sci. 93 (2010) 860–867.
[7] Y. Gao, D. Li, X. Liu, Food Control 30 (2013) 453–458.
[8] E. Voitoux, V. Lafarge, C. Collette, B. Lombard, Int. J. Food Microbiol. 77 (2002) 213–221.
[9] A. Rompré, P. Servais, J. Baudart, M.R. de-Roubin, P. Laurent, J. Microbiol. Methods 49 (2002) 31–54.
[10] J.S. Van Kessel, J.S. Karns, L. Gorski, B.J. McCluskey, M.L. Perdue, J. Dairy Sci. 87 (2004) 2822–2830.
[11] K. Rantsiou, V. Alessandria, L. Cocolin, Int. J. Food Microbiol. 154 (2012) 37–43.
[12] Y. Zhang, C. Tan, R. Fei, X. Liu, Y. Zhou, J. Chen, H. Chen, R. Zhou, Y. Hu, Anal. Chem. 86 (2014) 1115–1122.
[13] P. Geng, X. Zhang, Y. Teng, Y. Fu, L. Xu, M. Xu, L. Jin, W. Zhang, Biosens. Bioelectron. 26 (2011) 3325–3330.
[14] X. Zhang, P. Geng, H. Liu, Y. Teng, Y. Liu, Q. Wang, W. Zhang, L. Jin, L. Jiang, Biosens. Bioelectron. 24 (2009) 2155–2159.
[15] P. Zhu, D.R. Shelton, S. Li, D.L. Adams, J.S. Karns, P. Amstutz, C.M. Tang, Biosens. Bioelectron. 30 (2011) 337–341.
[16] S. Xu, Y. Liu, T. Wang, J. Li, Anal. Chem. 83 (2011) 3817–3823.
[17] Y. Wang, J. Dostalek, W. Knoll, Anal. Chem. 83 (2011) 6202–6207.
[18] Z. Cui, D. Wu, Y. Zhang, H. Ma, H. Li, B. Du, Q. Wei, H. Ju, Anal. Chim. Acta 807 (2014) 44–50.
[19] D. Lu, J. Wang, L. Wang, D. Du, C. Timchalk, R. Barr, Y. Lin, Adv. Funct. Mater. 21 (2011) 4371–4378.
[20] X. Zhang, W. Lu, E. Han, S. Wang, J. Shen, Electrochim. Acta 141 (2014) 384–390.
[21] G.X. Zhong, P. Wang, F.H. Fu, S.H. Weng, W. Chen, S.G. Li, A.L. Liu, Z.Y. Wu, X. Zhu, X.H. Lin, J.H. Lin, X.H. Xia, Talanta 125 (2014) 439–445.
[22] L.N. Feng, Z.P. Bian, J. Peng, F. Jiang, G.H. Yang, Y.D. Zhu, D. Yang, L.P. Jiang, J.J. Zhu, Anal. Chem. 84 (2012) 7810–7815.
[23] H. Nie, S. Liu, R. Yu, J. Jiang, Angew. Chem. 121 (2009) 10046–10050.
[24] Y. Teng, X. Zhang, Y. Fu, H. Liu, Z. Wang, L. Jin, W. Zhang, Biosens. Bioelectron. 26 (2011) 4661–4666.
[25] Y. Lou, T. He, F. Jiang, J.J. Shi, J.J. Zhu, Talanta 122 (2014) 135–139.
[26] X. Liu, Q. Dai, L. Austin, J. Coutts, G. Knowles, J. Zou, H. Chen, Q. Huo, J. Am. Chem. Soc. 130 (2008) 2780–2782.
[27] C. Deng, J. Chen, M. Yang, Z. Nie, S. Si, Electrochim. Acta 56 (2011) 8851–8856.
[28] G.K. Darbha, U.S. Rai, A.K. Singh, P.C. Ra, Chem. Eur. J. 14 (2008) 3896–3903.
[29] A. Wang, Q. Peng, Y. Li, Chem. Mater. 23 (2011) 3217–3222.
[30] Y. Khalavka, J. Becker, C. Sönnichsen, J. Am. Chem. Soc. 131 (2009) 1871–1875.
[31] J. Pérez-Juste, I. Pastoriza-Santos, L.M. Liz-Marźan, P. Mulvaney, Coord. Chem. Rev. 249 (2005) 1870–1901.
[32] T.K. Sau, C.J. Murphy, Langmuir 20 (2004) 6414–6420.
[33] X.L. Su, Y. Li, Anal. Chem. 76 (2004) 4806–4810.
[34] X. Mao, L. Yang, X.L. Su, Y. Li, Biosens. Bioelectron. 21 (2006) 1178–1185.
[35] E. Majid, K.B. Male, J.H.T. Luong, J. Agric. Food Chem. 56 (2008) 7691–7695.
[36] C. Ruan, L. Yang, Y. Li, Anal. Chem. 74 (2002) 4814–4820.
[37] K. Li, Y. Lai, W. Zhang, L. Jin, Talanta 84 (2011) 607–613.

Talanta 132 (2015) 606–612

Contents lists available at ScienceDirect

Talanta

journal homepage: www.elsevier.com/locate/talanta

A highly sensitive protocol for the determination of Hg^{2+} in environmental water using time-gated mode

Dawei Huang [a,b], Chenggang Niu [a,*], Guangming Zeng [a], Xiaoyu Wang [a], Xiaoxiao Lv [a]

[a] College of Environmental Science and Engineering, Key Laboratory of Environmental Biology and Pollution Control (Hunan University), Ministry of Education, Hunan University, Changsha 410082, China
[b] South China Institute of Environmental Sciences, Ministry of Environmental Protection of PRC, Guangzhou 510655, China

ARTICLE INFO

Article history:
Received 3 August 2014
Received in revised form
28 September 2014
Accepted 2 October 2014
Available online 18 October 2014

Keywords:
Hg^{2+}
Thymine–Hg^{2+}–thymine
Time-gated fluorescent sensing strategy
Mn:CdS/ZnS quantum dots
Graphene oxide

ABSTRACT

In this paper, a sensitive time-gated fluorescent sensing strategy for mercury ions (Hg^{2+}) monitoring is developed based on Hg^{2+}-mediated thymine (T)–Hg^{2+}–T structure and the mechanism of fluorescence resonance energy transfer from Mn-doped CdS/ZnS quantum dots to graphene oxide. The authors employ two T-rich single-stranded DNA (ssDNA) as the capture probes for Hg^{2+}, and one of them is modified with Mn-doped CdS/ZnS quantum dots. The addition of Hg^{2+} makes the two T-rich ssDNA hybrids with each other to form stable T-Hg^{2+}-T coordination chemistry, which makes Mn-doped CdS/ZnS quantum dots far away from the surface of graphene oxide. As a result, the fluorescence signal is increased obviously compared with that without Hg^{2+}. The time-gated fluorescence intensities are linear with the concentrations of Hg^{2+} in the range from 0.20 to 10 nM with a limit of detection of 0.11 nM. The detection limit is much lower than the U.S. Environmental Protection Agency limit of the concentration of Hg^{2+} for drinking water. The time-gated fluorescent sensing strategy is specific for Hg^{2+} even with interference by other metal ions based on the results of selectivity experiments. Importantly, the proposed sensing strategy is applied successfully to the determination of Hg^{2+} in environmental water samples.

© 2014 Elsevier B.V. All rights reserved.

1. Introduction

Hg^{2+} is a highly toxic metallic pollutant as it has strong bioaccumulation. The cell functions will be inhibited when Hg^{2+} is accumulated in the vital organs and tissues, and then causes a variety of human health problems [1]. The exposure to Hg^{2+} even at very low concentrations still has potential risks for human beings [1,2]. The contamination of Hg^{2+} is a serious environmental health problem in the world, especially the contamination of drinking water and other environmental water resources [3]. Therefore, the monitoring of Hg^{2+} levels with highly sensitivity and selectivity in aquatic ecosystems is still an important and urgent issue. Traditional methods including atomic absorption spectroscopy (AAS), atomic fluorescence spectrometry (AFS), inductively coupled plasma mass spectrometry (ICPMS), and X-ray absorption spectroscopy have been widely used for the determination of Hg^{2+} [3–7]. Although these traditional analytical techniques are very sensitive and selective, the development of new and efficient Hg^{2+} detection methods that are cost-effective, rapid, sensitive, selective, and applicable in routine and in situ is also important and necessary. In previously reported works, it is found that T–T mismatches could selectively capture Hg^{2+} to form stable T–Hg^{2+}–T base pairs due to the intrinsic specific interaction between Hg^{2+} and thymine [8,9]. Based on the intrinsic specific interaction between Hg^{2+} and thymine, a series of fluorescent, colorimetric, and electrochemical sensors were proposed for Hg^{2+} quantification [10–29]. As far as fluorescent sensors are concerned, many of them could be applied to the determination of Hg^{2+} in aquatic ecosystems due to the low detection limits which are lower than the toxic level reported by the U.S. Environmental Protection Agency. However, most fluorescent sensors for Hg^{2+} are based on organic dyes or QDs that usually have short lifetime fluorescence. The background noises caused by the scattering light from solid substrates, the luminescence from the optical components, and samples themselves might affect the sensitivity of the methods. Hence, it is of interest to develop a highly sensitive fluorescence method based on luminophor with long lifetime fluorescence, which can use time-gated mode to decrease the background noises. It has been previously reported that Mn-doped QDs have the features of high quantum yield, photostability, size-tunable optical properties, and long lifetime fluorescence [30–34]. What's more, it has been proved that water soluble Mn-doped CdS/ZnS QDs with long lifetime fluorescence (~4.8 ms) and excellent stability in aqueous solution exhibited outstanding performances in our previously reported works [26,27].

* Corresponding author. Tel.: +86 731 88823820; fax: +86 731 8882282.
E-mail addresses: cgniu@hnu.edu.cn, cgniu@hotmail.com (C. Niu).

http://dx.doi.org/10.1016/j.talanta.2014.10.015
0039-9140/© 2014 Elsevier B.V. All rights reserved.

The authors thought that the Mn-doped CdS/ZnS QDs are good choices for time-gated fluorescent methods as a fluorescence label.

In recent years, graphene oxide (GO) has emerged and attracted considerable attention in the biological and medical applications because of its superior surface properties, unique electronic properties, and good biocompatibility [35–39]. Especially, GO is an efficient quencher of an organic fluorophore or inorganic luminescent nanomaterial through either energy transfer or electron transfer process [40–43]. Without any surface modification, GO can strongly adsorb unfolded single-stranded DNA (ssDNA) *via* the π–π stacking interactions while adsorption of well-folded or double-stranded DNA (dsDNA) is disfavored [44]. Therefore, a series of GO-based biosensors have been fabricated due to their superior and unique features [45–50]. What's more, compared with the papers using GNPs as the quencher, there are three main reasons which make us employ graphene oxide (GO) as a new quencher: (1) better quenching efficiency; (2) stronger adsorption for ssDNA; and (3) higher anti-interference ability (such as GO cannot be affected by salt concentration). Based on these advantages, the authors employ GO as an effective quencher and want to propose a method with higher sensitivity and selectivity.

Combining advantages of the Mn-doped CdS/ZnS QDs and GO together, a highly sensitive and selective time-gated fluorescent sensing strategy is designed for Hg^{2+} detection in aqueous solution based on the principle of fluorescence resonance energy transfer (FRET). The Mn-doped CdS/ZnS QDs act as the energy transfer donor while the GO serves as the energy transfer acceptor. Two T-rich ssDNA, which specifically bind to Hg^{2+} to form T–Hg^{2+}–T coordination chemistry, are selected as the Hg^{2+} recognition probes. It is found that the proposed time-gated fluorescent method exhibits highly sensitivity and superior selectivity toward Hg^{2+}. In addition, the determination of Hg^{2+} in spiked environmental water samples is performed to demonstrate the applicability of this kind of method.

2. Experimental section

2.1. Chemicals and apparatus

Two oligonucleotides used in the present study were synthesized and HPLC purified by Shanghai Sangon Biological Engineering Technology & Services Co., Ltd. (Shanghai, China) and dissolved in buffer (0.010 M Tris–acetate, pH=7.6), then stocked at −20 °C for future usage. The sequences of the two oligonucleotides were shown as follows: 5′TTTGTTTGTTGG3′ (ssDNA1); 5′SH-CCTTCTTTCTTA3′ (ssDNA2). 3-mercaptopropionic acid (MPA, 99+%) was purchased from Sigma-Aldrich and used as received without further purification. Tetrabutylammonium chloride was obtained from Tianjin Guangfu Fine Chemical Co., Ltd. (Tianjin, China). Graphite powder was purchased from Tianjin Kemiou Chemical Reagent Co., Ltd. (Tianjin, China). GO was prepared using a modification of Hummers and Offeman's method from environmental graphite powder [51–53]. Mn-doped CdS/ZnS QDs were synthesized according to the previously reported papers, and the characterization and various performance of this kind of quantum dots were also presented in previously reported papers [30,31]. All metal salts used in this work were purchased from Sinopharm Chemical Reagent Co., Ltd. (Shanghai, China). All other chemicals and solvents were of analytical reagent grade and obtained from the commercial sources, and then were used without further purification. Ultrapure water was used throughout the experiments. The time-gated fluorescence intensity was measured and recorded with a Perkin-Elmer LS-55 spectrofluorimeter (United Kingdom). UV/vis absorption spectra were recorded by using a Shimadzu UV Spectrophotometer (UV-2550, Kyoto, Japan). Atomic fluorescence measurements were performed on an Atomic Fluorescence Spectrometer (AFS-9700) (Beijing, China).

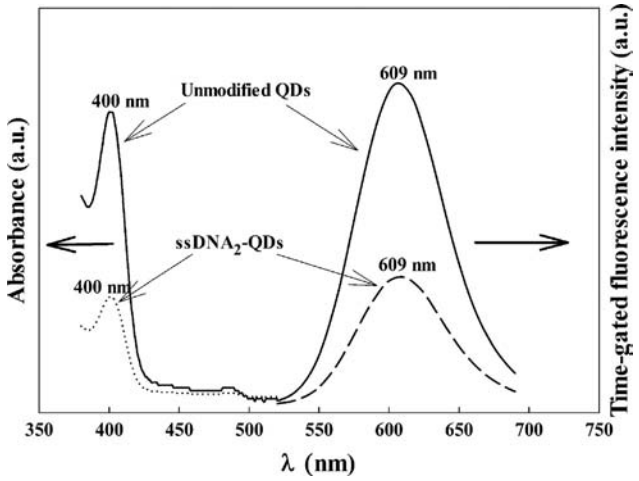


Fig. 1. The absorbance and fluorescence emission spectra of water soluble Mn-doped CdS/ZnS QDs and ssDNA2-modified Mn-doped CdS/ZnS QDs.

2.2. Synthesis of water soluble Mn-doped CdS/ZnS QDs

The Mn-doped CdS/ZnS QDs are hydrophobic. The characteristic of hydrophobic is a stumbling block for the reaction between QDs and the water soluble alkylthiol-capped oligonucleotides. Therefore, the ligand-exchange was carried out using hydrophilic 3-mercaptopropionic acid to prepare the water soluble QDs. The details of the ligand-exchange experiment are as follows. Firstly, 2.0–5.0 mg of Mn-doped CdS/ZnS QDs was dissolved in 1.0 mL of chloroform, and then 1.0 mL MPA solution (1.0 mL of MPA was dissolved in 1.5 mL water which contained 1.0 g KOH) was dropped into the QDs chloroform solution with stirring in a glass bottle with a capacity of 10 mL. Stirring was continued for 8.0 h. After that, 2.0 mL of methanol was added to the mixture and blended well by vortex. After standing for 10 min, a large amount of acetone was added to the mixture, generating a lot of precipitation. To obtain the precipitate, the suspension was centrifuged at 4000 rpm for 5.0 min. After throwing away the supernatant, the precipitate was dissolved in 2.0 mL water, and then the solution was centrifuged at 12,600 rpm for 20 min using Centrifugal Filter Devices (Amicon Ultra-0.5) to remove impurities. Finally, the pure water soluble Mn-doped CdS/ZnS QDs were redispersed into 5.0 mL of Tris–acetate buffer (0.010 M, pH=7.6) by vortex and stored at 4 °C for future usage. The fluorescence excitation and emission of this kind of QDs were 400 nm and 609 nm, respectively. The absorbance spectrum and fluorescence emission spectrum of the resulting QDs are shown in Fig. 1. The concentration of the resulting QDs was about 5.7×10^{-7} M according to the absorbance at 400 nm. The resulting water soluble Mn-doped CdS/ZnS QDs have long lifetime fluorescence (~4.8 ms) and excellent stability in aqueous solution.

2.3. Preparation of ssDNA2-modified Mn-doped CdS/ZnS QDs

ssDNA2 was conjugated to the Mn-doped CdS/ZnS QDs according to a previously reported work with minor modifications [54]. Firstly, the Mn-doped CdS/ZnS QDs solution and ssDNA2 solution were mixed together at a mole ratio of 1:5 (1.0 mL, 5.7×10^{-7} M Mn-doped CdS/ZnS QDs mixed with 30 μL, 0.10 mM ssDNA2). After standing for 12 h, the mixture was brought to 0.15 M NaCl and the particles were aged for an additional 12 h. After that, the NaCl concentration was then raised to 0.30 M, and the mixture was allowed to stand for a further 40 h. The mixture was centrifuged using Centrifugal Filter Devices (Amicon® Ultra-0.5) to remove the unreacted ssDNA2 afterwards. Finally, the ssDNA2-modified Mn-doped CdS/ZnS QDs (ssDNA2-QDs

complex) were redispersed into 5.0 mL Tris–acetate buffer (0.010 M, pH=7.6) by vortex and stored at 4 °C for future usage. The number of ssDNA2 immobilized on the Mn-doped CdS/ZnS QDs was estimated by measuring the absorbance difference at 260 nm before and after modification with ssDNA2. The average ssDNA2 loading was about one ssDNA2 per QD. The final concentration of ssDNA2-modified Mn-doped CdS/ZnS QDs was about 1.0×10^{-7} M according to the absorbance at 400 nm. The absorbance and fluorescence emission spectra of the ssDNA2-modified Mn-doped CdS/ZnS QDs are also shown in Fig. 1, indicating that the spectra remain unchanged compared to the unmodified QDs.

2.4. General procedures for Hg^{2+} monitoring

Briefly, 40 μL of 2.0×10^{-7} M ssDNA1, 40 μL of 1.0×10^{-7} M ssDNA2-QDs complex, 40 μL of different concentrations of Hg^{2+}, and 100 μL of buffer (0.010 M Tris–acetate, 0.10 M $NaNO_3$, pH=7.6) were mixed uniformly by vortex and incubated for 30 min to form T–Hg^{2+}–T coordination chemistry firstly. Then, 50 μL of 0.30 mg/mL GO was added to the mixture to differentiate the unfolded and folded ssDNA. The final step is to monitor the time-gated fluorescence intensity of the mixture above. Similar procedures were used to test the selectivity of the proposed sensing strategy. The concentrations of Hg^{2+} used in the sensitivity experiments were 0, 0.20, 0.40, 0.60, 0.80, 1.0, 2.0, 4.0, 6.0, 8.0, 10.0, 50.0, 100.0, and 1000.0 nM. 1.0 μM of Hg^{2+} was used in the optimization experiments. Various other metal ions of 2.0 μM were used in the selectivity experiments. The other metal ions used in the selectivity experiments are as follows: Ag^{+}, Co^{2+}, Ni^{2+}, Ca^{2+}, Cd^{2+}, Al^{3+}, Fe^{3+}, Au^{3+}, Cr^{2+}, Mn^{2+}, Pb^{2+}, Cu^{2+}, Mg^{2+}, Zn^{2+}, and Ba^{2+}. The lake water samples were taken from Taozi Lake in Hunan University. The river water samples were taken from Xiangjiang River. The spring water samples were taken from the Lush Maple Spring in Yuelu Mountain. The time-gated fluorescence spectra were measured and recorded by a Perkin-Elmer LS-55 spectrofluorimeter. The parameters of the spectrofluorimeter were set as λ_{ex}=400 nm, λ_{em}=609 nm, delay time, 0.10 ms, excitation slit, 15 nm, and emission slit, 20 nm.

3. Results and discussion

3.1. Experimental principle

The proposed sensing strategy was designed based on the principle of FRET from ssDNA2-QDs complex to GO. The fundamental of the proposed sensing strategy is shown in Fig. 2. In this study, the proposed strategy comprises two ssDNA: one is a 12-mer T-rich oligonucleotide (ssDNA1), and the other is a 12-mer T-rich oligonucleotide with an alkanethiol moiety at the 5′-terminus (ssDNA2). Both ssDNA1 and ssDNA2 consist of seven thymine units, which interact specifically with Hg^{2+} to form T–Hg^{2+}–T coordination chemistry. ssDNA2 was functionalized with Mn-doped CdS/ZnS QDs via the alkanethiol moiety at the 5′-terminus. The ssDNA2-QDs complex exhibited strong and stable fluorescence emission at 609 nm when excited at 400 nm. ssDNA1 and ssDNA2-QDs complex could not hybridize each other because of the seven mismatched T–T base pairs in the absence of Hg^{2+}. Upon addition of the Hg^{2+} solution to the mixture of ssDNA1 and ssDNA2-QDs complex, Hg^{2+}-mediated base pairs (T–Hg^{2+}–T) induce ssDNA1 and ssDNA2 with seven T–T mismatches hybridizing each other. It has been previously reported that Hg^{2+} binding to the DNA strand is a synergistic process, and the binding of one Hg^{2+} facilitates the binding of another Hg^{2+} to the same strand [55]. What's more, the T–Hg^{2+}–T pair is more stable than the A–T Watson–Crick pair [8]. The hybridization of ssDNA1 and ssDNA2 formed a stable and rigid structure in aqueous solution. When

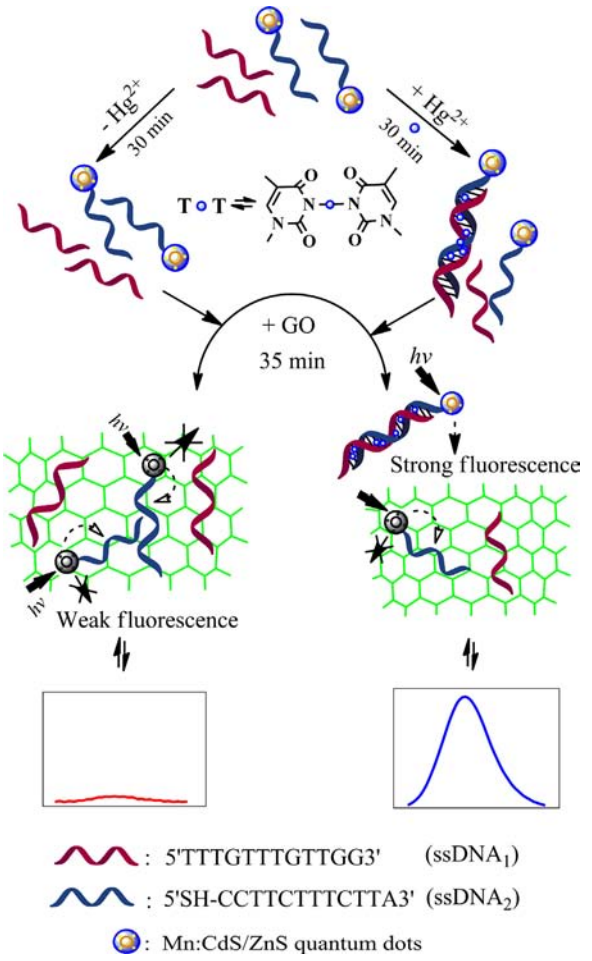


Fig. 2. Schematic description of the proposed sensing strategy for Hg^{2+} monitoring.

the hybridization solution is mixed with GO solution, the well-folded structure after hybridization could not be adsorbed on the surface of GO which makes the Mn-doped CdS/ZnS QDs far away from the surface of GO. As a result, the fluorescence intensity of the Mn-doped CdS/ZnS QDs was observed upon light excitation. The time-gated fluorescence intensity of Mn-doped CdS/ZnS QDs will be changed upon sequential addition of different concentrations of Hg^{2+} and equivalent GO to the mixture of ssDNA1 and ssDNA2-QDs complex. Therefore, we can monitor the concentration of Hg^{2+} according to the change in time-gated fluorescence intensity of Mn-doped CdS/ZnS QDs using the proposed sensing strategy. The time-gated fluorescence spectra with and without the addition of Hg^{2+} are shown in Fig. 3. In addition, a certain amount of Hg^{2+} was added to the solution that only contains ssDNA2-QDs complex to evaluate the effect of Hg^{2+} to Mn-doped CdS/ZnS QDs. The results indicated that the fluorescence performance was not sensitive to Hg^{2+} no matter whether the presence of different concentrations of Hg^{2+} or in the 1.0 μM of Hg^{2+} solution with reaction time increases.

3.2. Optimal conditions for the proposed sensing strategy

The GO concentration was studied firstly because of the intense effect on ssDNA2-QDs complex. Various concentrations of GO were added to the ssDNA2-QDs complex solution. The time-gated fluorescence intensity of the mixture above is monitored and recorded in Fig. 4(A). As shown in Fig. 4(A), the time-gated fluorescence intensity decreased with an increase in the GO concentration, and the complete quenching was observed when 0.30 mg/mL or more GO was added.

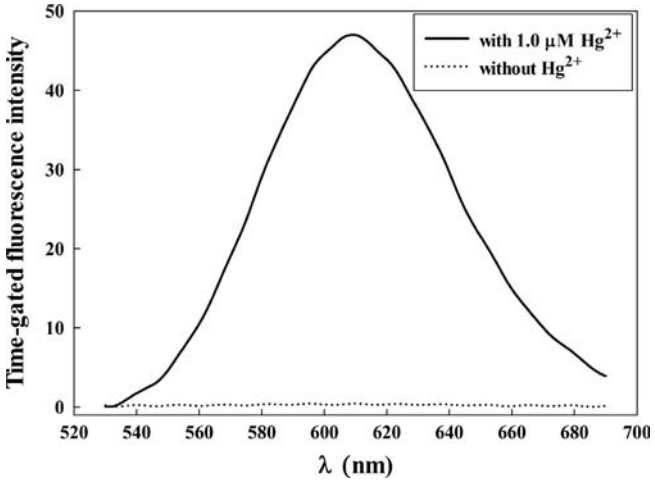


Fig. 3. Time-gated fluorescence emission spectra of the proposed sensing strategy without and with 1.0 μM Hg^{2+}.

The reason may be that all of the ssDNA2-QDs complexes were adsorbed on the surface of GO because of the strong π–π stacking interactions between ssDNA and GO, which resulted in the maximized fluorescence quenching of Mn-doped CdS/ZnS QDs. As a result, the authors chose 0.30 mg/mL as the suitable concentration of GO.

The incubation time after the addition of Hg^{2+} to the mixture of ssDNA1 and ssDNA2-QDs complex to form the T–Hg^{2+}–T pairs was investigated afterwards, and the results are shown in Fig. 4(B). The time-gated fluorescence intensity increased with the increase of incubation time and remained constant after 30 min. Hence, the authors chose 30 min as the optimum incubation time. The adsorption time after the addition of GO to the mixture of ssDNA1, ssDNA2-QDs complex, and ssDNA1/ssDNA2-QDs was also studied due to the important role in the detection sensitivity. As indicated in Fig. 4(C), the time-gated fluorescence intensity decreased with the increase of adsorption time and remained constant over 35 min. Consequently, the authors chose 35 min as the optimum adsorption time. In addition, room temperature (28 °C–30 °C) was selected as the operational temperature for convenience and the media pH of 7.6 (Tris–acetate buffer) was used throughout the experiments. Because PO_4^{3-}, Cl^-, or S^{2-} can react with Hg^{2+} to generate precipitation, it is best to avoid these anions in the buffer used in the system of Hg^{2+} detection. Hence, Tris–acetate buffer is selected as the media buffer. Herein, 1.0 μM was selected as the concentration of Hg^{2+} in all optimal experiments.

3.3. *Determination of Hg^{2+} in buffer using the proposed sensing strategy*

Based on the optimum conditions, various concentrations of Hg^{2+} were introduced to evaluate the sensitivity of the fluorescent sensing strategy. The fluorescent spectra upon addition of various concentrations of Hg^{2+} are recorded in Fig. 5(A). As shown in Fig. 5 (A), it is clear that higher concentration of Hg^{2+} resulted in more fluorescence intensity enhancement. Importantly, even very low concentration of Hg^{2+} can induce perceptible change of the time-gated fluorescence intensity which indicated that the proposed sensing strategy is very sensitive for Hg^{2+}. The calibration curve of time-gated fluorescence intensity as a function of the concentration of Hg^{2+} of the sensing strategy is shown in Fig. 5(B). Fig. 5(C) shows that the time-gated fluorescence intensity was linearly dependent on the concentration of Hg^{2+} in the range from 0.20 to 10 nM. The equation for the linear calibration curve was $y=4.17x+1.89$ (x is the concentration of Hg^{2+}, y is the time-gated fluorescence intensity) with correlation coefficient of 0.9937. According to the standard

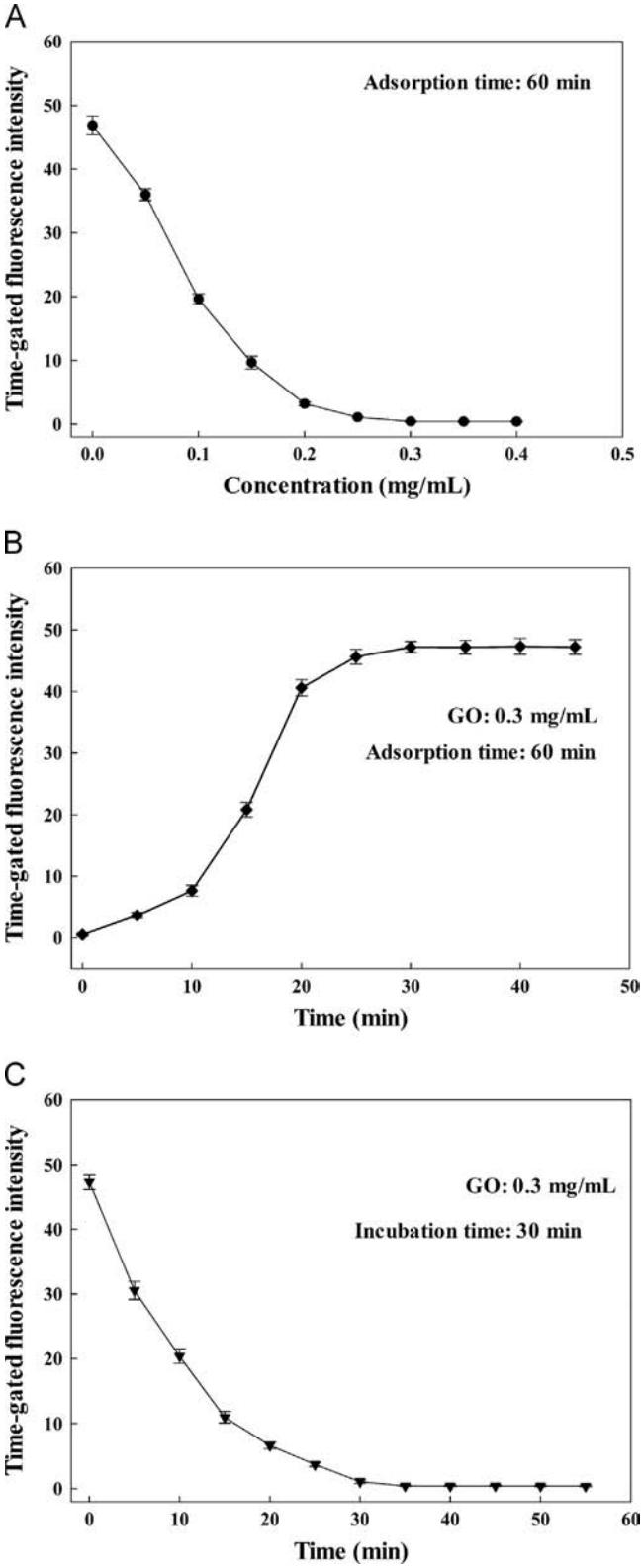


Fig. 4. Optimization experiments of the concentration of GO (A), the incubation time (B), and the adsorption time (C). The error bars are the standard deviation.

deviation of 0.15 for the blank signal with 20 parallel measurements, a limit of detection was estimated to be 0.11 nM based on a $3\alpha/slope$ standard (α is the standard deviation of the blank signal). The detection limit is much lower than the standard of the U.S. Environmental Protection Agency (EPA). The EPA regulates the maximum allowable level of Hg^{2+} in drinking water to be 10 nM. The detection

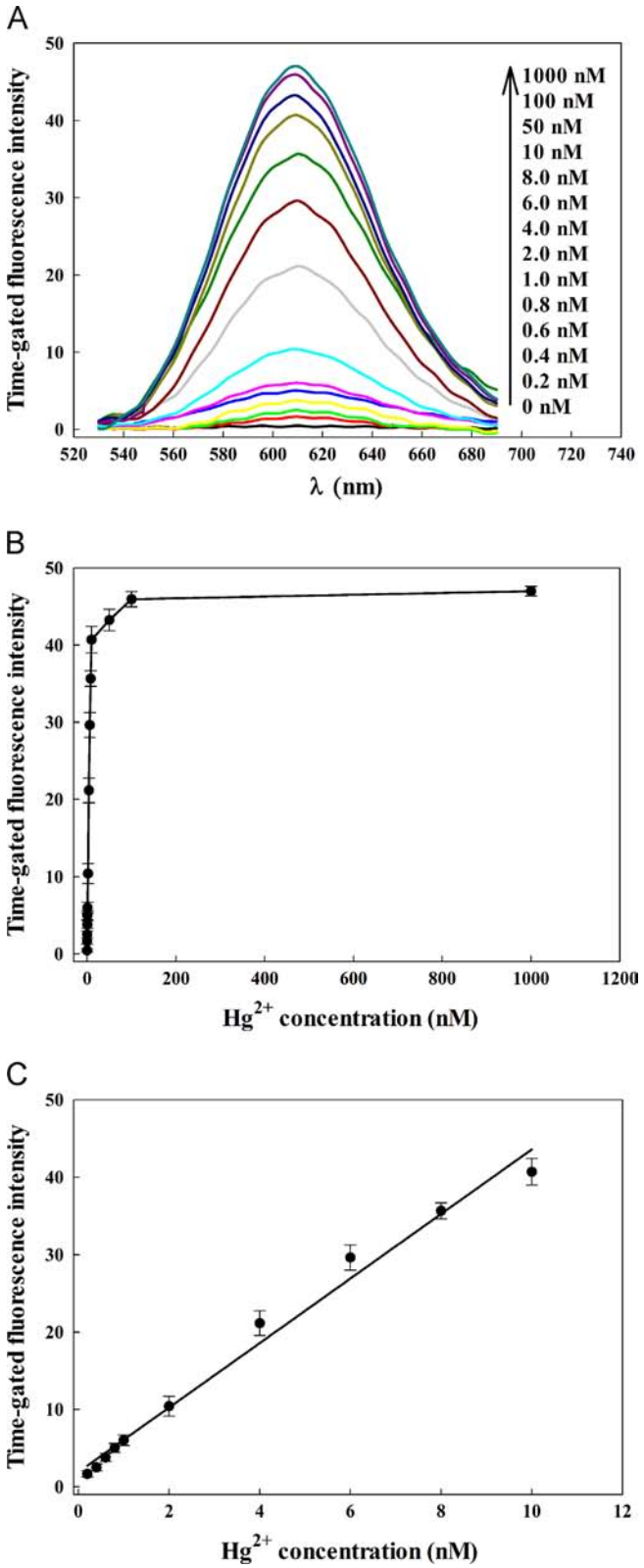


Fig. 5. (A) Time-gated fluorescence spectra of the proposed sensing strategy after addition of different concentrations of Hg^{2+} in buffer. (B) The calibration curve of time-gated fluorescence intensity as a function of the concentration of Hg^{2+}. (C) Linear region of (B). The concentrations of Hg^{2+} in (C) are 0.2, 0.4, 0.6, 0.8, 1.0, 2.0, 4.0, 6.0, 8.0, and 10 nM. Each data point is the mean of three measurements. The error bars are the standard deviation.

limit of the proposed sensing strategy is much improved in comparison to those previously reported colorimetric methods and fluorescent methods for Hg^{2+} [10–12,14,16,18–20,25–29,56]. The results

Table 1
Sensitivity comparison for Hg^{2+} between the proposed sensing strategy and some other previously reported methods.

Methods	No.	Linear ranges	Detection limits	References
Colorimetric methods	1	0.1–2.0 μM	100 nM	[11]
	2	Not mentioned	1.0 nM	[12]
	3	Not mentioned	0.5 μM	[16]
	4	25–500 nM	17 nM	[19]
	5	Not mentioned	1.0 μM	[20]
	6	0.096–6.4 μM	40 nM	[29]
Fluorescent methods	1	10–200 nM	5.0 nM	[10]
	2	2.0–60 nM	2.0 nM	[14]
	3	Not mentioned	2.4 nM	[18]
	4	3.0–800 nM	3.2 nM	[25]
	5	1.0–10 nM	0.49 nM	[26]
	6	1.0–10 nM	0.61 nM	[27]
	7	0–0.5 μM	20 nM	[28]
	8	3.6–10,000 nM	3.6 nM	[56]
	9	0.2–10 nM	0.11 nM	This work

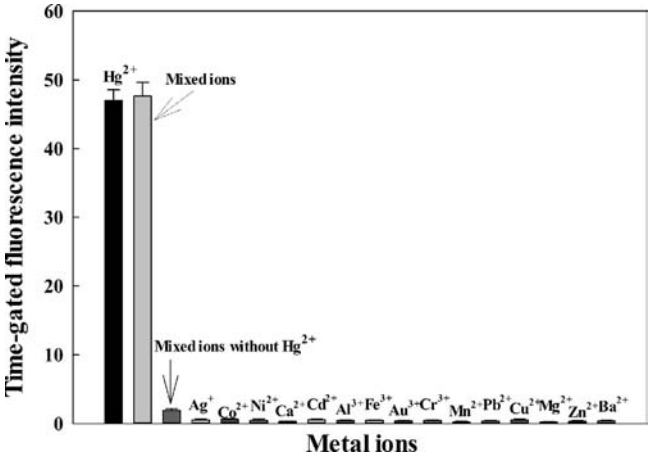


Fig. 6. Selectivity of the proposed sensing strategy towards Hg^{2+} over other metal ions. The concentrations of Hg^{2+} and other metal ions are 1.0 μM and 2.0 μM, respectively. Each data point is the mean of three measurements. The error bars are the standard deviation.

are summarized in Table 1. The exceptionally low detection limit for Hg^{2+} of the proposed sensing strategy may be attributed to four vitally important factors: (1) the super quenching capability of GO; (2) the strong interaction between ssDNA and GO via π–π stacking interactions; (3) the specific interaction between Hg^{2+} and thymine which can form stable T–Hg^{2+}–T coordination chemistry; and (4) the long lifetime fluorescence of Mn-doped CdS/ZnS QDs which can use time-gated mode to reduce the background noises and increase the signal to noise ratio.

To test the repeatability of this sensor, three kinds of modified QDs and GO were prepared with the same procedure and the RSD is about 2.1% for determination of 100 nM Hg^{2+} under the optimum conditions.

3.4. Selectivity of the proposed sensing strategy for Hg^{2+} determination

Excellent selectivity is important and necessary for a robust practical method. Herein, two experiments were conducted to investigate the selectivity of the proposed sensing strategy. First, every metal ion was studied as an independent sample to investigate the selectivity of the sensing strategy. The metal ions are Hg^{2+}, Ag^{+}, Co^{2+}, Ni^{2+}, Ca^{2+}, Cd^{2+}, Al^{3+}, Fe^{3+}, Au^{3+}, Cr^{2+}, Mn^{2+}, Pb^{2+}, Cu^{2+}, Mg^{2+}, Zn^{2+}, and Ba^{2+}. It can be seen from Fig. 6 that only the sample of Hg^{2+} exhibited significant response. Second, Hg^{2+}

and other metal ions were mixed together to form a mixture solution as a sample for selectivity testing. As shown in Fig. 6, the sample also exhibited remarkable response. These results above indicated that these metal ions have little effect on the determination of Hg^{2+}. Hence, the proposed sensing strategy shows excellent anti-jamming capability and selectivity toward Hg^{2+} based on the specific interaction between Hg^{2+} and thymine. 1.0 μM was selected as the concentration of Hg^{2+}, while the concentrations of other metal ions were 2.0 μM in the section.

3.5. Determination of Hg^{2+} in environmental water samples

The proposed sensing strategy was further tested with environmental water samples to demonstrate its applicability. The environmental water samples were spring water, river water, lake water, and tap water samples. These samples were filtered (0.20 μm filter membrane) and then centrifuged for 15 min at 12,000 rpm to remove the visible impurities before use. The concentrations of total mercury in these samples were 0.019, 0.057, 0.041, and 0.021 nM which were measured by the Atomic Fluorescence Spectrometer (AFS). It was found that the concentration of Hg^{2+} in these samples was too low to be detected using the proposed sensing strategy. Hence, extra Hg^{2+} was added to the samples to test the feasibility of the sensing strategy. The environmental water samples were spiked with different concentrations of Hg^{2+} (0, 0.80, 4.0, and 8.0 nM), and then tested according to the general procedure with four replicates using the proposed sensing strategy and AFS. The results are summarized in Table 2 and are in good agreement with the results obtained by AFS. According to the results, the authors think that the present sensing strategy can be applied to detect Hg^{2+} in environmental water samples.

In the experiments of real samples, all the solutions were prepared and diluted with Tris–acetate buffer except water samples, and when all the solutions were mixed together, the pH of the mixture was about 7.6 (the same with the pH of Tris–acetate buffer); hence, the effect of pH is not considered in the paper. If the pH of the environmental water samples is serious acid or alkali polluted, the pH of the samples should be adjusted to 7.6 using Tris–acetate buffer before usage.

Table 2
Determination of Hg^{2+} in environmental water samples using the proposed sensing strategy and AFS.

Samples	Added Hg^{2+} (nM)	Proposed method (mean[a] ± SD[b])	AFS (mean ± SD)	Recovery (%)
Spring water 1	0	c	0.019 ± 0.001	–
Spring water 2	0.80	0.77 ± 0.05	0.79 ± 0.02	96.25
Spring water 3	4.0	3.89 ± 0.15	3.97 ± 0.09	97.25
Spring water 4	8.0	7.90 ± 0.17	8.03 ± 0.10	98.75
River water 1	0	c	0.057 ± 0.006	–
River water 2	0.80	0.75 ± 0.07	0.80 ± 0.03	93.75
River water 3	4.0	4.02 ± 0.15	3.98 ± 0.04	100.5
River water 4	8.0	8.10 ± 0.21	8.03 ± 0.09	101.25
Lake water 1	0	c	0.041 ± 0.005	–
Lake water 2	0.80	0.76 ± 0.06	0.79 ± 0.02	95.0
Lake water 3	4.0	3.90 ± 0.15	4.02 ± 0.05	97.5
Lake water 4	8.0	7.87 ± 0.20	8.10 ± 0.11	98.38
Tap water 1	0	c	0.027 ± 0.002	–
Tap water 2	0.80	0.75 ± 0.05	0.82 ± 0.02	93.75
Tap water 3	4.0	4.10 ± 0.13	4.0 ± 0.06	102.5
Tap water 4	8.0	8.15 ± 0.18	7.95 ± 0.09	101.88

c: No Hg^{2+} concentration could be detected.
[a] Mean of four determinations.
[b] SD, standard deviation.

4. Conclusions

In summary, the authors developed a highly sensitive and selective time-gated fluorescent sensing strategy for Hg^{2+} determination. The proposed method is mainly based on the super quenching capability of GO with strong adsorption function toward ssDNA *via* π–π stacking interactions, the specific and selective T–Hg^{2+}–T coordination chemistry between two neighboring T-rich strands, and the long lifetime fluorescence of Mn-doped CdS/ZnS QDs with unique photophysical properties. Compared to some other previously reported works for Hg^{2+}, this fluorescent sensing strategy exhibited an extremely low detection limit. In addition, the present sensing strategy showed excellent selectivity and a broad linear range from 0.20 to 10 nM. Particularly, the proposed fluorescent sensing strategy can also work very well in environmental water samples. Based on the results of the study, the authors believe that the proposed fluorescent sensing strategy is applicable in routine and in situ Hg^{2+} monitoring in environmental water samples.

Acknowledgments

Special thanks are given to Mr. Y. Charles Cao and his group of the University of Florida, and Dr. Ou Chen for kind assistance in synthesis of Mn-doped CdS/ZnS core/shell QDs. This work was financially supported by the National Environmental Science Foundation of China (20977026), the National 863 High Technology Research Foundation of China (2006AA06Z407), the Hunan Provincial Environmental Science Foundation of China (14JJ2045), and the Scientific Research Fund of Hunan Provincial Education Department (13k017).

References

[1] H.H. Harris, I.J. Pickering, C.N. George, Science 301 (2003) 1203.
[2] P.B. Tchounwou, W.K. Ayensu, N. Ninashvili, D. Sutton, Environ. Toxicol. 18 (2003) 149–175.
[3] L. Järup, Br. Med. Bull. 68 (2003) 167–182.
[4] O.T. Butler, J.M. Cook, C.M. Davidson, C.F. Harrington, D.L. Miles, J. Anal. At. Spectrom. 24 (2009) 131–177.
[5] Y. Li, C. Chen, B. Li, J. Sun, J. Wang, Y. Gao, Y. Zhao, Z. Chai, J. Anal. At. Spectrom. 21 (2006) 94–96.
[6] M. Leermakers, W. Baeyens, P. Quevauviller, M. Horvat, TrAC Trends Anal. Chem. 24 (2005) 383–393.
[7] A. Bernaus, X. Gaona, J.M. Esbri, P. Higueras, G. Falkenberg, M. Valiente, Environ. Sci. Technol. 40 (2006) 4090–4095.
[8] Y. Miyake, H. Togashi, M. Tashiro, H. Yamaguchi, S. Oda, M. Kudo, Y. Tanaka, Y. Kondo, R. Sawa, T. Fujimoto, T. Achinami, A. Ono, J. Am. Chem. Soc. 128 (2006) 2172–2173.
[9] Y. Tanaka, S. Oda, H. Yamaguchi, Y. Kondo, C. Kojima, A. Ono, J. Am. Chem. Soc. 129 (2007) 244–245.
[10] C.W. Liu, C.C. Huang, H.T. Chang, Anal. Chem. 81 (2009) 2383–2387.
[11] J.S. Lee, M.S. Han, C.A. Mirkin, Angew. Chem. 119 (2007) 4171–4174.
[12] D. Li, A. Wieckowska, I. Willner, Angew. Chem. Int. Ed. 47 (2008) 3927–3931.
[13] D.H. Wu, Q. Zhang, X. Chu, H.B. Wang, G.L. Shen, R.Q. Yu, Biosens. Bioelectron. 25 (2010) 1025–1031.
[14] M. Li, Q.Y. Wang, X.D. Shi, L.A. Hornak, N.Q. Wu, Anal. Chem. 83 (2011) 7061–7065.
[15] R. Freeman, T. Finder, I. Willner, Angew. Chem. Int. Ed. 48 (2009) 7818–7821.
[16] N. Kanayama, T. Takarada, M. Maeda, Chem. Commun. 47 (2011) 2077–2079.
[17] A. Ono, H. Togashi, Angew. Chem. Int. Ed. 43 (2004) 4300–4302.
[18] J. Liu, Y. Lu, Angew. Chem. Int. Ed. 46 (2007) 7587–7590.
[19] Y. Wang, F. Yang, X.R. Yang, ACS Appl. Mater. Interfaces 2 (2010) 339–342.
[20] X.J. Xue, F. Wang, X.G. Liu, J. Am. Chem. Soc. 130 (2008) 3244–3245.
[21] X.M. Tang, H.X. Liu, B.H. Zou, D.B. Tian, H. Huang, Analyst 137 (2012) 309–311.
[22] J.Y. Zhuang, L.B. Fu, D.P. Tang, M.D. Xu, G.N. Chen, H.H. Yang, Biosens. Bioelectron. 39 (2013) 315–319.
[23] Z.D. Liu, Y.F. Li, J. Ling, C.Z. Huang, Environ. Sci. Technol. 43 (2009) 5022–5027.
[24] N. Dave, M.Y. Chan, P.J. Huang, B.D. Smith, J.W. Liu, J. Am. Chem. Soc. 132 (2010) 12668–12673.
[25] Z.D. Wang, J.H. Lee, Y. Lu, Chem. Commun. 44 (2008) 6005–6007.
[26] D.W. Huang, C.G. Niu, M. Ruan, X.Y. Wang, G.M. Zeng, C.H. Deng, Environ. Sci. Technol. 47 (2013) 4392–4398.

[27] D.W. Huang, C.G. Niu, X.Y. Wang, X.X. Lv, G.M. Zeng, Anal. Chem. 85 (2013) 1164–1170.
[28] Y.F. Zhang, Q. Yuan, T. Chen, X.B. Zhang, Y. Chen, W.H. Tan, Anal. Chem. 84 (2012) 1956–1962.
[29] H. Wang, Y.X. Wang, J.Y. Jin, R.H. Yang, Anal. Chem. 80 (2008) 9021–9028.
[30] Y. Yang, O. Chen, A. Angerhofer, Y.C. Cao, J. Am. Chem. Soc. 128 (2006) 12428–12429.
[31] Y. Yang, O. Chen, A. Angerhofer, Y.C. Cao, J. Am. Chem. Soc. 130 (2008) 15649–15661.
[32] D.J. Norris, N. Yao, F.T. Charnock, T.A. Kennedy, Nano Lett. 1 (2001) 3–7.
[33] D.J. Norris, A.L. Efros, S.C. Erwin, Science 319 (2008) 1776–1779.
[34] A. Nag, S. Chakraborty, D.D. Sarma, J. Am. Chem. Soc. 130 (2008) 10605–10611.
[35] A.K. Geim, K.S. Novoselov, Nat. Mater. 6 (2007) 183–191.
[36] J.C. Meyer, A.K. Geim, M.I. Katsnelson, K.S. Novoselov, T.J. Booth, S. Roth, Nature 446 (2007) 60–63.
[37] K.S. Novoselov, A.K. Geim, S.V. Morozov, D. Jiang, M.I. Katsnelson, I.V. Grigorieva, S.V. Dubonos, A.A. Firsov, Nature 438 (2005) 197–200.
[38] M. Pumera, Chem. Soc. Rev. 39 (2010) 4146–4157.
[39] Y.B. Zhang, Y.W. Tan, H.L. Stormer, P. Kim, Nature 438 (2005) 201–204.
[40] H.F. Dong, W.C. Gao, F. Yan, H.X. Ji, H.X. Ju, Anal. Chem. 82 (2010) 5511–5517.
[41] C.H. Lu, H.H. Yang, C.L. Zhu, X. Chen, G.N. Chen, Angew. Chem. Int. Ed. 48 (2009) 4785–4787.
[42] S.J. He, B. Song, D. Li, C.F. Zhu, W.P. Qi, Y.Q. Wen, L.H. Wang, S.P. Song, H.P. Fang, C.H. Fan, Adv. Funct. Mater. 20 (2010) 453–459.
[43] M. Liu, H.M. Zhao, X. Quan, S. Chen, X.F. Fan, Chem. Commun. 46 (2010) 7909–7911.
[44] A.J. Patil, J.L. Vickery, T.B. Scott, S. Mann, Adv. Mater. 21 (2009) 3159–3164.
[45] Y. Wang, Z.H. Li, D.H. Hu, C.T. Lin, J.H. Li, Y.H. Lin, J. Am. Chem. Soc. 132 (2010) 9274–9276.
[46] Y.Q. Wen, F.F. Xing, S.J. He, S.P. Song, L.H. Wang, Y.T. Long, D. Li, C.H. Fan, Chem. Commun. 46 (2010) 2596–2598.
[47] M. Li, X.J. Zhou, S.W. Guo, N.Q. Wu, Biosens. Bioelectron. 43 (2013) 69–74.
[48] M. Liu, H.M. Zhao, S. Chen, H.T. Yu, Y.B. Zhang, X. Quan, Chem. Commun. 47 (2011) 7749–7751.
[49] Z.L. Song, X.H. Zhao, W.N. Liu, D. Ding, X. Bian, H. Liang, X.B. Zhang, Z. Chen, W. H. Tang, Small 9 (2013) 951–957.
[50] P.J. Huang, J.W. Liu, Anal. Chem. 84 (2012) 4192–4198.
[51] W.S. Hummers, R.E. Offeman, J. Am. Chem. Soc. 80 (1958) 1339.
[52] N.I. Kovtyukhova, P.J. Ollivier, B.R. Martin, T.E. Mallouk, S.A. Chizhik, E.V. Buzaneva, A.D. Gorchinskiy, Chem. Mater. 11 (1999) 771–778.
[53] L.J. Cote, F. Kim, J.X. Huang, J. Am. Chem. Soc. 131 (2009) 1043–1049.
[54] G.P. Mitchell, C.A. Mirkin, R.L. Letsinger, J. Am. Chem. Soc. 121 (1999) 8122–8123.
[55] A. Ono, Y. Miyake, Nucleic Acids Res. (Suppl. 3) (2003) S227–S228.
[56] J. Du, M.Y. Liu, X.H. Lou, T. Zhao, Z. Wang, Y. Xue, J.L. Zhao, Y.S. Xu, Anal. Chem. 84 (2012) 8060–8066.

Talanta 132 (2015) 613–618

Contents lists available at ScienceDirect

Talanta

journal homepage: www.elsevier.com/locate/talanta

Highly sensitive colorimetric detection of lead using maleic acid functionalized gold nanoparticles

Nalin Ratnarathorn [a], Orawon Chailapakul [b], Wijitar Dungchai [a,*]

[a] Department of Chemistry, Faculty of Science, King Mongkut's University of Technology Thonburi, Prachautid Road, Thungkru, Bangkok 10140, Thailand
[b] Center of Excellence for Petroleum, Petrochemicals, and Advanced Materials, Chulalongkorn University, Patumwan, Bangkok 10330, Thailand

ARTICLE INFO

Article history:
Received 5 August 2014
Received in revised form
6 October 2014
Accepted 10 October 2014
Available online 23 October 2014

Keywords:
Colorimetric sensing
Gold nanoparticles
Lead

ABSTRACT

Highly sensitive colorimetric detection for Pb^{2+} has been developed using maleic acid (MA) functionalized GNP. The –COOH on MA was used to modify GNP surface whereas the other –COOH functional group have strong affinity to coordination behavior of Pb^{2+} allowing the selective formation more than other ions. MA–GNPs solution changed from red to blue color after the addition of Pb^{2+} due to nanoparticle aggregation. The different optical absorption and discriminate of particle size between the MA–GNPs solution with and without Pb^{2+} were characterized by UV–visible spectroscopy and transmission electron microscopy (TEM), respectively. The color intensity as a function of Pb^{2+} concentration gave a linear response in the range of 0.0–10.0 $\mu g\,L^{-1}$ (R^2=0.990). The detection limit was found at 0.5 $\mu g\,L^{-1}$ by naked eye and can be completed the analysis within 15 min. The MA–GNPs aggregated with Pb^{2+} showed high selectivity when was compared to other metal ions (As^{3+}, Ca^{2+}, Cd^{2+}, Co^{2+}, Cu^{2+}, Fe^{3+}, Hg^{2+}, Mg^{2+}, Mn^{2+}, Ni^{2+}, Pb^{2+} and Zn^{2+}) and anions (Cl^-, NO_3^- and SO_4^{2-}). Our proposed method was also applied for the determination of Pb^{2+} in real drinking water samples from 5 sources. The result of real water samples were not statistically significant different from the standard methods at the 95% confidence level (pair *t*-test method). Moreover, we evaluated our proposed method for the determination of trace Pb^{2+} concentration in real breast milk samples. The recoveries were acceptable and ranged from 101 to 104% for spiked Pb^{2+} in real breast milk samples. Thus, MA–GNP colorimetric sensing provides a simple, rapid, sensitive, easy-to-use, inexpensive and low detection limit for the monitoring of Pb^{2+}.

© 2014 Elsevier B.V. All rights reserved.

1. Introduction

The present food and drinking water are often contaminated with harmful substances for humans, either as part of the production process, natural or caused by the additives added to it. Lead (Pb^{2+}) is a major environmental pollutant and ranks second in the list of toxic substances that cause renal malfunction and damage to the brain and kidneys [1]. It has also been classified as carcinogenic agents by the World Health Organization (WHO) and International Agency for Research on cancer. Moreover, the long-term exposure to low concentrations of these metals causes adverse health effects. Therefore, WHO controlled level of lead in drinking water is not over 10 $\mu g\,L^{-1}$ [2]. Several methods have been used for the detection of lead such as atomic absorption spectrometry (AAS) [3–5], inductively coupled plasma mass spectrometry (ICP/MS) [6], inductively coupled plasma atomic emission spectroscopy (ICP/AES) [7], electrochemical method [8] and X-ray fluorescence spectrometry [9]. Although, these methods can detect lead sensitively and accurately, but there are limits in their complicated sample preparation processes, expensive, and required any specialized as well as sophisticated instrumentation [10].

Colorimetric sensors for Pb^{2+} determination attract much attention for their conveniences of visual observation and simple operations. They allow the direct analysis by the naked eyes without costly instruments compared with other methods. In recent year, gold nanoparticles (GNPs) have been widely used for colorimetric assays because their extinction coefficients are high relative to common organic compound [11–13]. GNPs have been extensively employed as colorimetric sensors for the detection of small concentrations of toxic metals such as arsenic, cadmium, cobalt, nickel and lead [14–16]. Kim et al. used GNPs capped with 11-mercaptoundecanoic acid to be capable of detecting Pb^{2+} through the coordination between the carboxylic groups and Pb^{2+} [17]. Moreover, Lu and co-workers reported a colorimetric sensor for Pb^{2+} detection using DNA-functionalized GNPs [18]. In 2010, GNPs capped with gallic acid (GA–GNPs) for the detection of Pb^{2+} has been reported. Huang and

* Corresponding author. Tel.: +66 2 470 9553; fax: +66 2 470 8840.
E-mail address: wijitar.dun@kmutt.ac.th (W. Dungchai).

http://dx.doi.org/10.1016/j.talanta.2014.10.024
0039-9140/© 2014 Elsevier B.V. All rights reserved.

co-workers have also demonstrated the aggregation of GA–GNPs in aqueous solutions and its minimum detectable concentration for Pb^{2+} in drinking water is 10 nM or 2.1 μg L^{-1} [12]. The detection limits of GA–GNPs are lower than the maximum allowable contamination level of Pb^{2+} in drinking water (WHO). However, the European Food Safety Authority (EFSA) reported that even using a low concentration of Pb^{2+} in drinking water (2.1 μg L^{-1}), adverse effect children's intelligence development can be observed [19,20]. In the absence of a safe exposure limit of children to Pb^{2+} and because of its ability to accumulate in the body for a long time, a great interest in the evaluation of the adverse effects of Pb^{2+} in low concentrations has emerged. Moreover, Human Health State of the Science in Canada has studied the trace Pb^{2+} concentration in breast milk because it is good biomarkers of maternal and infant exposure to Pb^{2+}. The Pb^{2+} level in human milk was found in the range from 0.025 to 15.8 μg L^{-1} in 210 mothers cross Canada [21,22]. Therefore, a highly sensitive, selective, simple and rapid method for the detection and quantification of trace Pb^{2+} is still required not only for the acceptance criteria of food safety but also toxicology.

Maleic acid, which has two carboxylic groups ($HO_2CCH=CH-CO_2H$), should be suitable for the modification of nanoparticles surface. In the previous reports, GNPs was modified by thiol compounds such as glutathiol [10], cysteine [23], alkyl phosphate [24] and 11-mercaptoundecanoic acid [25] for the determination of Pb^{2+} in micromole level but maleic acid functionalized GNPs has been not investigated for the colorimetric detection of Pb^{2+}. Thus, the aim of this work was to develop the highly sensitive, selective, simple and rapid colorimetric sensor for trace Pb^{2+} determination using maleic acid modified GNPs. Maleic acid is easy to modify on GNPs surface within 1 h. MA–GNPs solution changed from red to blue color after the addition of Pb^{2+} and can be observed by the naked eye. The pH effect and the reaction time were studied in this work. The low limits of detection for Pb^{2+} at sub μg L^{-1} level with a short analysis time of 15 min were obtained by our proposed assay. Finally, our developed method was successfully applied for determination of trace levels of Pb^{2+} in drinking water samples and the human breast milk samples.

2. Experimental

2.1. Chemicals and materials

All chemicals used in experiment were analytical reagent (AR) grade and solutions were prepared using high pure water with a resistance of 18 MΩ cm^{-1}. Dithiothreitol (DTT), glutathione (Glu), homocysteine (Hcy), L-cysteine (L-cys), maleic acid (MA), metal ions (As^{3+}, Cd^{2+}, Co^{2+}, Cu^{2+}, Fe^{3+}, Hg^{2+}, Mg^{2+}, Mn^{2+}, Ni^{2+}, Pb^{2+}, Zn^{2+} using atomic absorption grade), KCl, KNO_3 and K_2SO_4 were bought from Sigma-Aldrich (St. Louis, Missouri). Whatman No. 1 filter paper was bought from Cole-Parmer (Vernon Hills, IL). All glassware was thoroughly cleaned with freshly prepared 1:1 HCl/HNO_3 and rinsed with high pure water prior to use. All metal ions stock solutions were prepared in 50 mM phosphate buffer pH 5.8.

2.2. Instrumentation

UV–visible absorption spectra were recorded in a quartz cuvette (1-cm pathlength) using a UV–visible spectrometer (Lambda 35, Perkin Elmer Instruments, USA). Size distribution of particles was recorded by Transmission Electron Microscope (TEM, TECNAI T20 G^2, FEI, Netherland). Photographic results were recorded using a digital camera (PowerShot S95, 10.1 Megapixels, Canon). An atomic absorption spectrometer (AAS) with a hollow cathode lamp and standard air/acetylene flame (Analyst 300, Perkin Elmer Instruments, USA) was used for atomic absorbance measurements. A hollow cathode lamp was used under the following operations conditions: wavelength: 283.3 nm; slit-width: 0.7 H nm; lamp current: 10 mA.

2.3. Synthesis of GNPs

100 mL of $HAuCl_4$ (0.01%) was added into a 250 mL Erlenmeyer flask and then boiled. After that, 3.5 mL of trisodium citrate (1%) was added and further rapidly stirred for 15 min. We continually stirred for 30 min without heating. The solution was cooled to room temperature which was stored in the refrigerator 4 °C before further use [15].

The MA–GNPs solution was prepared using self-assembly of the organic compound on the GNP surface. A red of GNP solution (~20 nm in diameter) was first prepared from GNPs stock solution. Then, 0.20 mL of 0.01 M MA was added into 0.40 mL of GNP solution to generate MA–GNPs. Organic compound was self-assembled on to the surface of GNPs by incubating the GNPs with the MA solutions for 1 h at room temperature. After this step, the GNP aggregation was characterized using UV–visible Spectrometry.

2.4. Detection of lead

0.60 mL of MA–GNP solution in the eppendrof was mixed with 0.40 mL of metal ion solutions (As^{3+}, Ca^{2+}, Cd^{2+}, Co^{2+}, Cu^{2+}, Fe^{3+}, Hg^{2+}, Mg^{2+}, Mn^{2+}, Ni^{2+}, Pb^{2+} and Zn^{2+}) and anions solutions (KCl, KNO_3 and K_2SO_4) in 50 mM phosphate buffer at pH 5.8. For background (Bg), 0.40 mL of buffer was mixed 0.60 mL of MA–GNP solution (Bg–MA–GNPs). Then, the mixture was incubated for 15 min at the room temperature and analysis by the spectrometer and TEM.

2.5. Sample preparation for transmission electron microscopy (TEM)

Transmission electron microscope (TEM) measurements were performed on TECNAI T20 G^2 instrument which operated at an accelerating voltage of 120 kV and the 25000× magnification. The sample solutions for TEM studies were prepared by placing a drop of GNPs, MA–GNPs, Bg–MA–GNPs and Pb^{2+}–MA–GNPs on a formvar coated copper grid. The films on the TEM grids were allowed to dry for 1 h. The size of nanoparticle studies was performed in aqueous solution by Center of Nanoimaging, Mahidol University.

2.6. Applications

To evaluate the utility of our proposed method, the Pb^{2+} in the drinking water samples from five different sources was quantified. Our method was validated against AAS. Prior to analysis by AAS, preconcentration was carried out on all samples. 1.5 L of sample was mixed with 1 mL of 0.1 M HCl and then heated to evaporate excess water until 5.0 mL of samples remained. For AAS, samples were adjusted to a final volume of 10 mL with deionized water. For our proposed method, 0.60 mL of MA–GNP solution in the eppendrof was mixed with 0.40 mL of the water sample without any pretreatment. Then, the mixture was incubated for 15 min at the room temperature and analysis by spectrometer. For testing of trace levels of Pb^{2+} in the human breast milk, the sample was divided two parts. The first was analyzed by our method without spiking Pb^{2+} and the second was spiked with the standard Pb^{2+} solution at 10.0, 25.0 and 50.0 μg L^{-1} to obtain the final concentration at 1.0, 2.5 and 5.0 μg L^{-1}, respectively. Prior to analysis, spiked samples were precipitated the protein by adding 0.75 mL of sample with 0.15 mL of 10% w/v TCA (Tri chloroacetic acid). After that, samples were stored at 4 °C for 15 min and then subjected to centrifugation at 14,500 rpm for 10 min. The precipitate was removed from the supernatant and kept only supernatant for analysis.

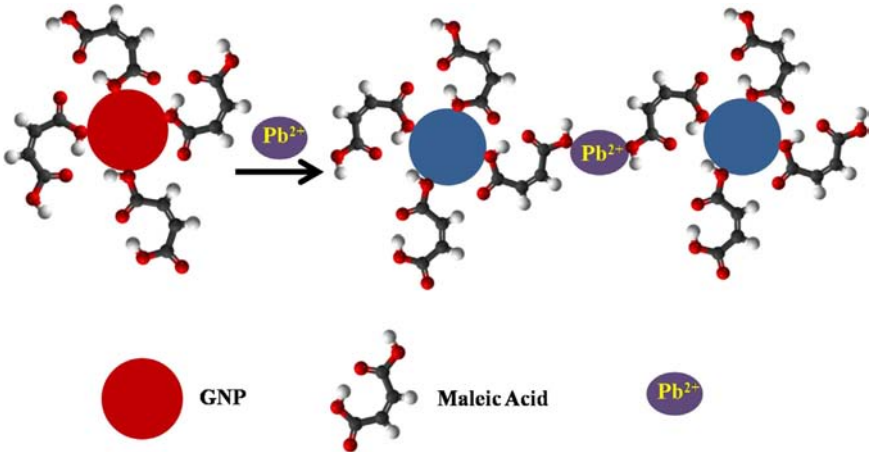
3. Results and discussion

3.1. Characterization of GNP aggregation

Maleic acid has two carboxylic groups ($HO_2CCH=CHCO_2H$) so one carboxylic group should be suitable for the modification of nanoparticles surface and the other carboxylic group can capture Pb^{2+} in aqueous solution as shown in Scheme 1. In this experiment, the color of solution change from dark pink to blue after adding 1.0 μg L^{-1} of Pb^{2+} in the MA–GNPs solution (Fig. 1). MA–GNPs in the presence and absence of Pb^{2+} were characterized by UV–vis Spectroscopy and Transmission Electron Microscope (TEM). A characteristic band of MA–GNPs was observed at approximate 520 nm. After the addition of Pb^{2+}, the wavelength at 520 nm decreased and a new red-shifted change at 600 nm (Fig. 1), so Pb^{2+} can induce aggregation of MA–GNPs. To confirm the mechanism of the interaction between MA–GNPs and Pb^{2+}, the solution of GNPs, MA–GNPs, Bg–MA–GNPs and Pb^{2+}–MA–GNPs were analyzed by TEM as shown in Fig. S1. The prepared GNPs were dispersed an average particle size under ~20 nm in diameter, whereas the nanoparticles remain isolated and randomly distributed in the absence of Pb^{2+} ions (Fig. S1a–c). Upon addition of Pb^{2+}into MA–GNPs, the solution turned blue color. TEM studies clearly indicate that Pb^{2+} induces aggregation of nanoparticles (Fig. S1d). Possible mechanism is the obstructive aggregation of MA–GNPs in the absence of Pb^{2+} due to the electrostatic repulsion against van der Waals attraction of carboxylic of MA on the GNPs surface [13]. After the addition Pb^{2+}, the other –COOH group of MA can binds with Pb^{2+} and it is specificity than other metals (Fig. 1) because of the coordination number of Pb^{2+} more over the other metal cations. Other metal cations interact only with lesser numbers of ligands, leaving the nanoparticles isolated; hence, no spectral change and no color of solution change were observed under the experimental conditions [26].

3.2. Selectivity study

We investigated the change in values of absorption ratio ($A_{600/520}$) for MA–GNPs that measured after 15 min upon the addition of the metal ions. The concentration of other metal ions was studied for 15 min at higher than 100 times of Pb^{2+} concentration (1.0 μg L^{-1} of



Scheme 1. Schematic of aggregating process of MA–GNPs induced by adding Pb^{2+}.

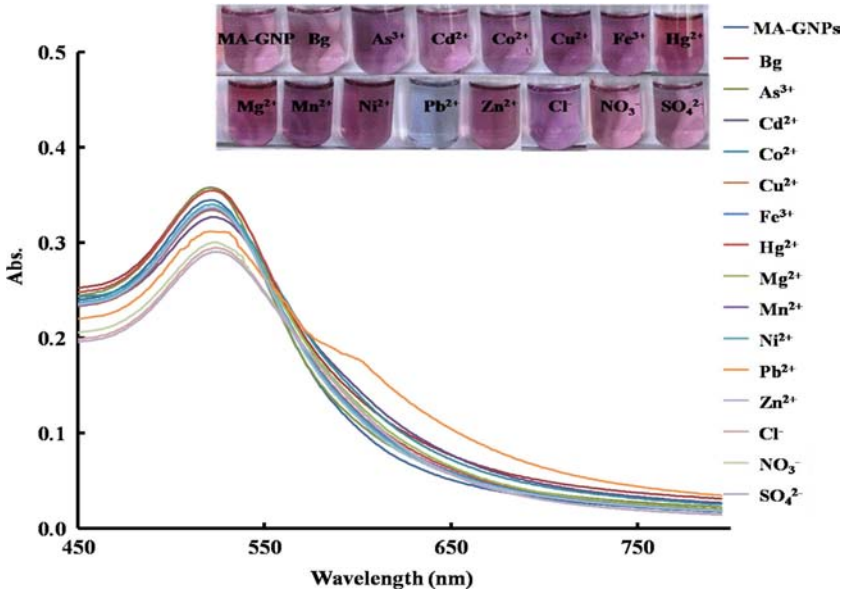


Fig. 1. UV–visible spectra of MA–GNPs solutions with cations (1.0 μg L^{-1} of Pb^{2+} and 0.1 mg L^{-1} of other cations) and anions (250.0 mg L^{-1} Cl^-, 45.0 mg L^{-1} NO_3^- and 200.0 mg L^{-1} SO_4^{2-} following Guidelines for drinking-water quality by [2]). (For interpretation of the references to color in this figure legend, the reader is referred to the web version of this article.)

Pb^{2+} and 0.1 mg L^{-1} of As^{3+}, Cd^{2+}, Co^{2+}, Cu^{2+}, Fe^{3+}, Hg^{2+}, Mg^{2+}, Mn^{2+}, Ni^{2+} and Zn^{2+}). Most interference levels in this study were higher than the permissible limit in the drinking water by WHO (For example; 0.003, 0.05 and 0.02 mg L^{-1} for Cd^{2+}, Co^{2+} and Ni^{2+}, respectively). Moreover, interference effect of anions at the levels containing in drinking-water (250.0 mg L^{-1} Cl^-, 45.0 mg L^{-1} NO_3^- and 200.0 mg L^{-1} SO_4^{2-} by [2]) was studied. The result showed that the color of solution didn't change to blue color after the addition of anions and other metal ions as shown in Fig. 1. The absorbance ratio ($A_{600/520}$) of MA–GNPs with different metal ions and anions is shown in Fig. 2. Only Pb^{2+} can be observed a significant $A_{600/520}$ value. Possible mechanism is the unique coordination behavior of Pb^{2+} as $[Xe]4f^{14}5d^{10}6s^2$ electronic configuration. It appears as a borderline acid, able to bind to wide families of ligands within very flexible bond length and geometry so it allows the formation of a stable supramolecular complex. Other metal cations interact only with lesser numbers of ligands, leaving the nanoparticles isolated because of the rigid coordination geometry or may result from other factors e.g., the change in particle geometry. Hence, no spectral and color change were observed under the experimental conditions [26,27]. On the aforementioned results, MA–GNPs can be utilized to detect Pb^{2+} with high selectivity.

GNPs surface can be typically modified by carboxylic, amino, and thiols group to achieve selective cross-linking (and thus aggregation) therefore we also investigated the effect of cross-linking group in this part. DTT, Hcy, L-Cys and Glu were studied due to the active group in their molecules. All modified GNPs synthesized by our method showed an absorbance at 520 nm wavelength and observed a red solution. After adding 1.00 μg L^{-1} various metals including Pb^{2+}, As^{3+}, Cd^{2+}, Co^{2+}, Cu^{2+}, Fe^{3+}, Hg^{2+}, Mg^{2+}, Mn^{2+}, Ni^{2+} and Zn^{2+} in the solution of DTT–GNPs, Hcy–GNPs and L-Cys–GNPs at pH 5.8, the color of the solution for all metals changes from red to violet and spectra shifts from 520 nm to 600 nm (Fig. S2a–c). Whereas, Glu–GNPs (Fig. S2d) showed no change occurs, the absorption spectrum is still intact. Therefore, Glu–GNPs, DTT–GNPs, Hcy–GNPs and L-Cys–GNPs gave no specificity to Pb^{2+} under this condition.

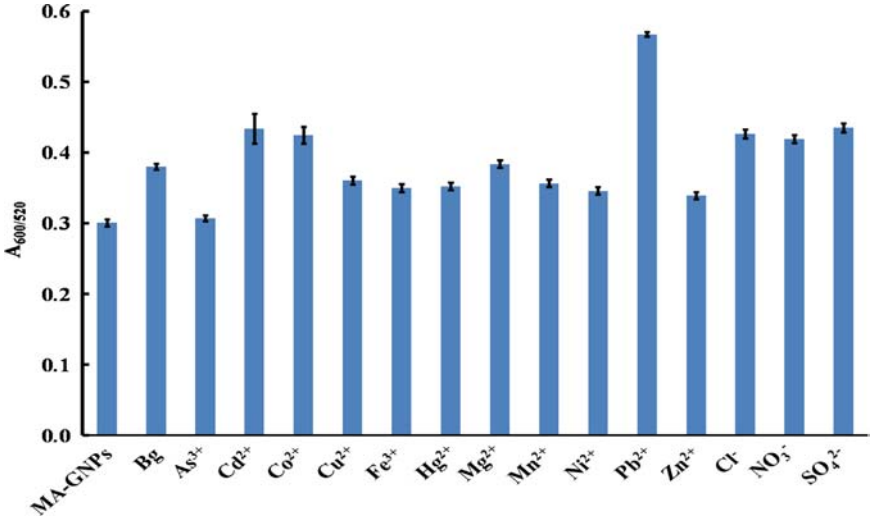


Fig. 2. The values ($A_{600/520}$) of MA–GNPs upon the addition of 1.0 μg L^{-1} Pb^{2+} and 0.1 mg L^{-1} of other cations and 250.0 mg L^{-1} Cl^-, 45.0 mg L^{-1} NO_3^- and 200.0 mg L^{-1} SO_4^{2-}. The error bars represent standard deviations based on three independent measurements.

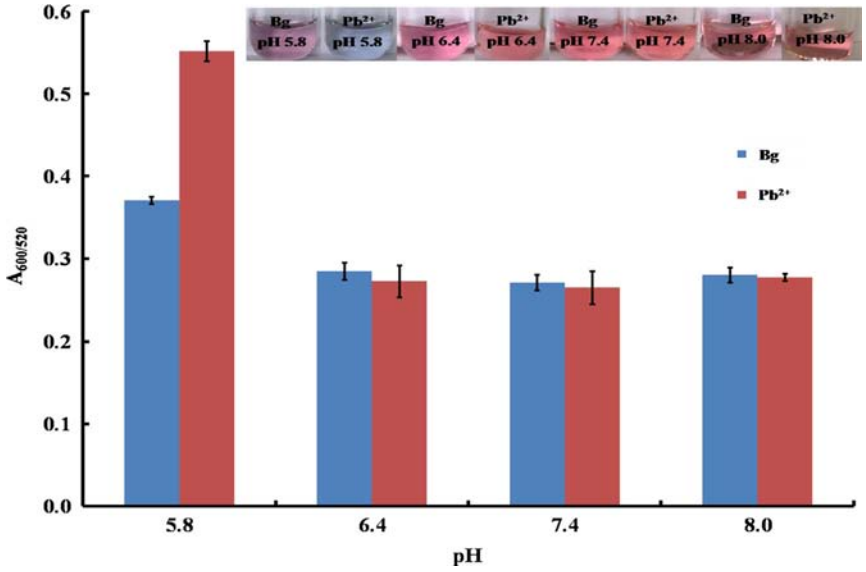


Fig. 3. Effect of pH 0.6 μL of MA–GNPs mixed 0.4 μL of Pb^{2+} (1.0 μg L^{-1}) in phosphate buffer pH 5.8, 6.4, 7.4 and 8.0 for 15 min error bar at $n=3$.

3.3. Effect of pH and reaction time

We investigated the colorimetric response of MA–GNPs with Pb^{2+} at different pH (5.8, 6.4, 7.4 and 8.0). Only MA–GNPs with Pb^{2+} at pH 5.8 showed the color change and higher absorbance ratio ($A_{600/520}$) than buffer (Bg). While at pH 6.4, 7.4 and 8.0 show no significant difference of the absorbance ratio ($A_{600/520}$) and color solution between presence and absence of Pb^{2+} (Fig. 3). Additionally, Bg–MA–GNPs slightly change color at low pH (<6.58) and the absorbance ratio was larger than at high pH (Fig. 3). MA–GNPs ionizable of structure would be affected by the pH value, which was high enough for ionization, taking the pK_{a1} (1.93) and pK_{a2} (6.58) value of MA into consideration. The electrostatic repulsion between the MA–GNPs would increase and disintegrated to all ions at pH more than pK_{a2}, while the electrostatic repulsion between the MA–GNPs would decrease and occur van der Waals attraction between –COOH group of MA with GNPs at pH less than pK_{a2}. The mechanism can be attributed to the function of Pb^{2+} with MA–GNP in a chelating reaction. The aggregation of MA–GNPs was induced by the coordination between Pb^{2+} and carboxylate of MA at pH 5.8. The various metal cations including As^{3+}, Cd^{2+}, Co^{2+}, Cu^{2+}, Fe^{3+}, Hg^{2+}, Mg^{2+}, Mn^{2+}, Ni^{2+}, Pb^{2+} and Zn^{2+} no changed of color occurs after adding into the MA–GNPs at pH 6.4, 7.4 and 8.0 (Fig. S3). Therefore, we selected the optimum pH at pH 5.8 for Pb^{2+} detection by the naked eye.

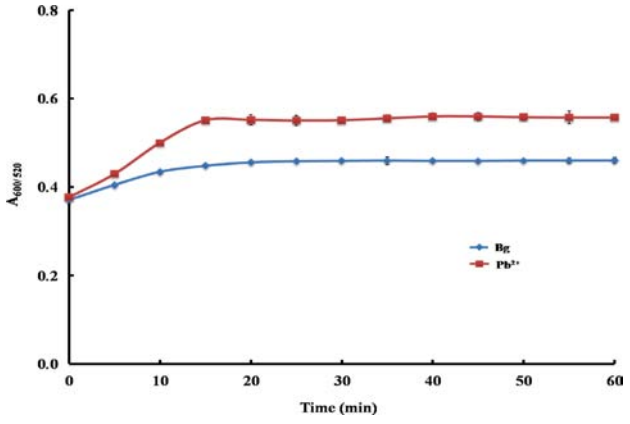


Fig. 4. Effect of reaction time between 0 and 60 min (0.6 μL of MA–GNPs mixed 0.4 μL of Pb^{2+} (1.0 μg L^{-1}) in phosphate buffer pH 5.8) Error bar at $n=3$.

The effect of reaction time between MA–GNPs and Pb^{2+} was investigated. The ratio between the absorbance at a wavelength of 520 nm to 600 nm was used to evaluate as shown in Fig. 4. We found that for low concentration of Pb^{2+} (1.0 μg L^{-1}) absorbance ratio reached reach equilibrium within 15 min. This result represents the fast performance of this assay for Pb^{2+}.

3.4. Calibration

The different concentrations of Pb^{2+} were added to MA–GNPs. The degree of aggregation of MA–GNPs depended on concentration of Pb^{2+}. Fig. 5 shows that the absorbance changed with the addition of different concentrations of Pb^{2+}. The maximal absorption at 520 nm decreased and a new peak at 600 nm increased with increasing Pb^{2+} concentration, which indicated the aggregating between MA–GNPs and Pb^{2+} has a relationship with the concentration. Thus, the MA–GNPs for the detection of different concentrations of Pb^{2+} was processed directly using the UV–vis absorbance ratio ($A_{600/520}$). A linear correlation existed between the absorbance ratio ($A_{600/520}$) and the concentration of Pb^{2+} ranging from 0.0 to 10.0 μg L^{-1} ($R^2=0.990$) as shown in Fig. 5. The detection limit was found at 0.5 μg L^{-1}. In the presence of high concentration of Pb^{2+} more than 10.0 μg L^{-1}, the UV–Vis absorption spectra of Pb^{2+}–MA–GNPs became broader and shifted to much longer wavelength (>600 nm). The value is not in a linear range. Consequently, the concentration of Pb^{2+} ranging from 0.0 to 10.0 μg L^{-1} made this assay suitable for the determination of Pb^{2+} in aqueous solution. Compared with the other colorimetric methods based on nanoparticles (Table 1), our method has the higher sensitivity and more rapid.

3.5. Analytical applications

To validate our assay for the determination of Pb^{2+} in real samples, drinking water samples from 5 sources were analyzed by our assay and the traditional method (Atomic Absorption Spectroscopy, AAS) as shown in Table 2. The data were then compared by a paired *t*-test. Our results were not statistically significant different from the standard methods at the 95% confidence level

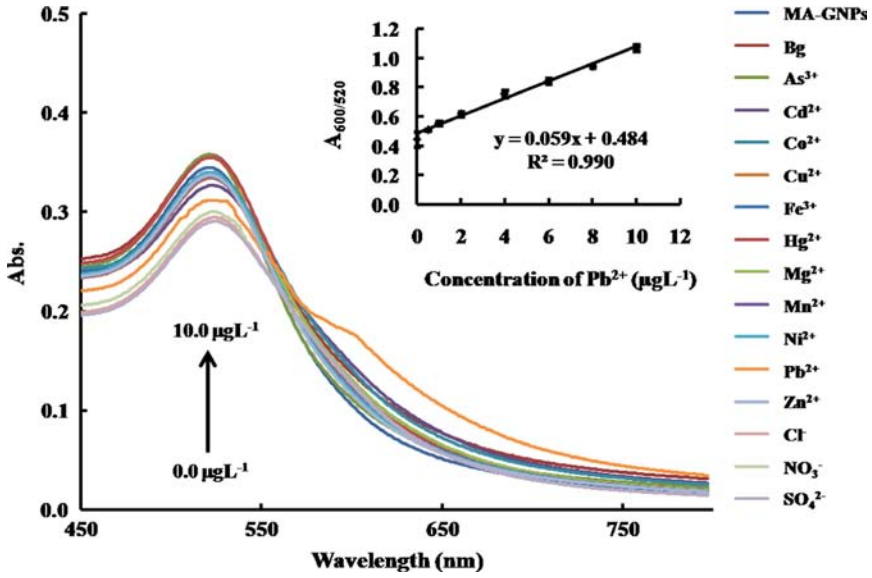


Fig. 5. UV–visible spectra of MA–GNP solutions with various concentrations of Pb^{2+} in the range from 0.0 to 10.0 μg L^{-1} at 15 min.

Table 1
Nanoparticles optical assays for the detection of Pb^{2+}.

Probe unit	LOD	Linear range	Real sample	Time (min)	Refs.
DNAzyme and GNPs	103.6 μg L^{-1}	N/A[a]	N/A[a]	20	[28]
Gallic acid–GNPs	2.1 μg L^{-1}	2.1–207.2 μg L^{-1}	N/A[a]	30	[12]
Gallic acid–GNPs or Gallic acid–AgNPs	N/A[a]	6.2–62.2 mg L^{-1}	N/A[a]	N/A[a]	[26]
Gallic acid–GNPs	5.2 μg L^{-1}	10.4–207.2 μg L^{-1}	Drinking water	N/A[a]	[29]
Papain–GNPs	41.4 μg L^{-1}	N/A[a]	N/A[a]	N/A[a]	[30]
Cysteine–alanine–leacine–asparagine–asparagine–GNPs	20.7 μg L^{-1}	20.7 μg L^{-1}–6.2 mg L^{-1} 10.4–41.4 mg L^{-1}	N/A[a]	N/A[a]	[16]
Alkyl Phosphate–GNPs	621.6 μg L^{-1}	0.0–2.1 mg L^{-1}	N/A[a]	15	[24]
Maleic acid–GNPs	**0.5 μg L^{-1}**	**0.0–10.0 μg L^{-1}**	**Drinking water and milk**	**15**	**Our method**

[a] Not available.

Table 2
Levels of Pb^{2+} in drinking water samples were measured using our method and AAS.

Water samples	Concentration of Pb^{2+} (μg L^{-1})	
	AAS	Our method
Sample 1	6.74+0.02	6.42+0.51
Sample 2	7.71+0.03	7.95+1.38
Sample 3	7.90+0.01	9.21+0.77
Sample 4	7.74+0.03	8.68+0.79
Sample 5	10.20+0.06	11.42+0.04

The standard deviation of water samples at $n=5$.

(t-test value=0.67, t critical value=2.31). Moreover, we also evaluated the utility of our method by analysis low level of Pb^{2+} in human breast milk samples. We found that Pb^{2+} in the human breast milk samples were not detectable under our detection limit (0.5 μg L^{-1}). Thus, known amounts of Pb^{2+} were spiked into milk samples to get the final concentration at 1.0, 2.5 and 5.0 μg L^{-1}. It was found the level of Pb^{2+} at 1.09+0.20, 2.93+0.62, and 5.06+0.29 μg L^{-1}, respectively ($n=7$) and the percentage recovery in the range 101–105%. Therefore, the MA–GNPs can be used to measure the low amount of Pb^{2+} in real samples. It is an easy to measure without the need for analyze complex or expensive, used of less levels and does not require expert analysis.

4. Conclusions

In summary, a simple, rapid, highly sensitive, easy-to-use, inexpensive, and portable alternative point-of-measurement monitoring for Pb^{2+} using MA–GNPs colorimetric assay has been developed. The Pb^{2+}-induced MA–GNPs aggregation results in a marked red shift in the UV–vis absorption spectra and a visible color change from red to blue. The detection limit of this method by the detection of naked eye is 0.5 μg L^{-1} which lower than other GNPs colorimetric probs. Furthermore, Pb^{2+} was clearly distinguish able color change from the other heavy metal ions under the optimum conditions at the critical level of Pb^{2+} in drinking water prescribed by WHO. Finally, our method was successfully applied to analysis of Pb^{2+} in water samples and the human breast milk samples. Therefore, this method should be applicable to detect low level of Pb^{2+} in drinking water and some biological samples.

Acknowledgements

Orawon Chailapakul and Wijitar Dungchai gratefully acknowledge the financial support from Thailand Research Fund through TRF Senior Research Scholar (RTA5780005).

Appendix A. Supporting information

Supplementary data associated with this article can be found in the online version at http://dx.doi.org/10.1016/j.talanta.2014.10.024.

References

[1] L. Fewtrell, R. Kaufmann, A.P. Ustun, Lead, W.H.O. (Environmental Burden of Disease Series) Geneva, 2003, pp. 5–21.
[2] Guidelines for Drinking-Water Quality, third ed., W.H.O. Geneva, 2004, pp. 8–35.
[3] A.A. Jigam, B.E.N. Dauda, T. Jimoh, H.N. Yusuf, Z.T. Umar, Afr. J. Food Sci. 5 (2011) 156–160.
[4] M.H. Shagal, H.M. Maina, R.B. Donatus, K. Tadzabia, Glob. Adv. Res. J. Environ. Sci. Toxicol 1 (2012) 18–22.
[5] K. Bakkali, N.R. Martos, B. Souhail, E. Ballesteros, Food Chem. 2 (2009) 590–594.
[6] H.W. Liu, S.J. Jiang, S.H. Liu, Spectrochim. Acta, Part B 54 (1999) 1367–1375.
[7] E. Pehlivan, G. Arslan, F. Gode, T. Altun, M.M. Ozcan, Grasas Aceites 59 (2008) 239–244.
[8] Z. Zou, A. Jang, E. MacKnight, P.M.i. Wu, J. Do, P.L. Bishop, C.H. Ahn, Sens. Actuators, B 134 (2008) 18–24.
[9] D.H.S. Richardson, M. Shoreb, R. Hartreeb, R.M. Richardson, Sci. Total. Environ. 176 (1995) 97–105.
[10] F. Chai, C. Wang, T. Wang, L. Li, Z. Su, Appl. Mater. Interfaces 2 (2010) 1466–1470.
[11] R. Elghanian, J.J. Storhoff, R.C. Mucic, R.L. Letsinger, C.A. Mirkin, Science 277 (1997) 1997 (1080).
[12] K.W. Huang, C.J. Yu, W.L. Tseng, Biosens. Bioelectron. 25 (2010) 984–989.
[13] Z. Chen, Z. Wang, J. Chen, S. Wang, X. Huang, Analyst 137 (2012) 3132–3137.
[14] J.R. Kalluri, T. Arbneshi, S.A. Khan, A. Neely, P. Candice, B. Varisli, M. Washington, S. McAfee, B. Robinson, S. Banerjee, A.K. Singh, D. Senapati, P.C. Ray, Angew. Chem. Int. Ed. 48 (2009) 1–5.
[15] M. Zhang, Y.Q. Liux, B.C. Ye, Analyst 137 (2012) 601–607.
[16] X.K. Li, Z.X. WANG, Chem. Res. Chin. Univ. 2 (2010) 194–197.
[17] Y. Kim, R.C. Johnson, J.T. Hupp, Nano Lett. 1 (2001) 165–167.
[18] J. Liu, Y. Lu, J. Am. Chem. Soc. 127 (2005) 12677–12683.
[19] Lead Standard in Drinking Water, The SCHER, 2011.
[20] EFSA Panel on Contaminants in the Food Chain (CONTAM), EFSA Journal 8 1147. Available online: ⟨http://www.efsa.europa.eu/en/efsajournal/pub/1570.htm⟩.
[21] The Minister of Health, Final Human Health State of the Science Report on Lead. (2013). Available online: ⟨http://www.hc-sc.gc.ca/ewh-semt/pubs/contaminants/dhhssrl-rpecscepsh/index-eng.php⟩.
[22] G.A.K. Koyashiki1, M.M.B. Paoliello, P.B. Tchounwou, Rev. Environ. Health 25 (2010) 243–253.
[23] Y.P. Zhanga, J. Chena, L.Y. Baib, X.M. Zhoub, L.M. Wang, J. Chin. Chem. Soc. 57 (2010) 972–975.
[24] S.K. Kim, S. Kim, E.J. Hong, M.S. Han, Korean Chem. Soc 31 (2010) 3806–3808.
[25] C. Fan, S. He, G. Liu, L. Wang, S. Song, Sensors 12 (2012) 9467–9475.
[26] K. Yoosaf, B.I. Ipe, C.H. Suresh, K.G. Thomas, J. Phys. Chem. C 111 (2007) 12839–12847.
[27] L.S. Livny, J.P. Glusker, C.W. Bock, Inorg. Chem. 37 (1998) 1853–1867.
[28] H. Wei, B. Li, J. Li, S. Dong, E. Wang, Nanotechnology 19 (2008) 1–5.
[29] N. Ding, Q. Cao, H. Zhao, Y. Yang, L. Zeng, Y. He, K. Xiang, G. Wang, Sensors 10 (2010) 11144–11155.
[30] Y. Guo, Z. Wang, W. Qu, H. Shao, X. Jiang, Biosens. Bioelectron 26 (2011) 4064–4069.

Talanta 132 (2015) 619–624

Contents lists available at ScienceDirect

Talanta

journal homepage: www.elsevier.com/locate/talanta

Ultrasensitive turn-on fluorescent detection of trace thiocyanate based on fluorescence resonance energy transfer

Juan Song, Fang-Ying Wu *[,1], Yi-Qun Wan, Li-Hua Ma *[,1]

Department of Chemistry, Nanchang University, Nanchang 330031, China

ARTICLE INFO

Article history:
Received 13 August 2014
Received in revised form
5 October 2014
Accepted 10 October 2014
Available online 18 October 2014

Keywords:
Gold nanoparticles
Fluorescein
Fluorescence resonance energy transfer
Thiocyanate
Milk
Saliva

ABSTRACT

Thiocyanate (SCN^-) is a small anion byproduct of cyanide metabolism. Several methods have been reported to measure SCN^- above the micromolar level. However, SCN^- is derived from many sources such as cigarettes, waste water, food and even car exhaust and its effect is cumulative, which makes it necessary to develop methods for the detection of trace SCN^-. In this paper, a simple and ultrasensitive turn-on fluorescence assay of trace SCN^- is established based on the fluorescence resonance energy transfer (FRET) between gold nanoparticles (AuNPs) and fluorescein. The detection limit is 0.09 nM, to the best of our knowledge, which has been the lowest detection LOD ever without the aid of costly instrumentation. The fluorescence of fluorescein is significantly quenched when it is attached to the surface of AuNPs. Upon the addition of SCN^-, the fluorescence is turned on due to the competition action between SCN^- and fluorescein towards the surface of AuNPs. Under an optimum pH, AuNPs size and concentration, incubation time, the fluorescence enhancement efficiency $[(I_F-I_0)/I_0]$ displays a linear relationship with the concentration of SCN^- in the range of 1.0 nM to 40.0 nM. The fluorescein–AuNP sensor shows absolutely high selectivity toward SCN^- than other 16 anions. The common metal ions, amino acids and sugars have no obvious interference effects. The accuracy and precision were evaluated based on the recovery experiments. The cost effective sensing system is successfully applied for the determination of SCN^- in milk products and saliva samples.

© 2014 Elsevier B.V. All rights reserved.

1. Introduction

As an important chemical raw material, thiocyanate (SCN^-) is widely employed in many industrial processes such as pesticide production, textile dyeing, electroplating, printing, photofinishing and hydrometallurgy. Compared with the lethal cyanide ion, SCN^- is a less toxic anion that can be found at μM in human bodies through the digestion of glucosinolate-containing brassica vegetables (broccoli, cauliflower, cabbage, etc.), or by ingesting cheese and milk, which contain SCN^- [1]. SCN^- ranks after perchlorate as a potent inhibitor of iodide uptake by the thyroid but may be more concentrated in some food items such as milk products [2]. And it is more serious for pregnant woman, infant or population in iodine deficiency area [3]. Besides, another significant source of SCN^- in the body is from smoker. Cyanide in tobacco, once absorbed, is eliminated through its conversion to SCN^- by the enzyme rhodanese, which is found in the mitochondria of liver and kidney cells [4]. Therefore, the concentration levels of SCN^- in human body liquids are considered to be an important indicator for assessing habitual smoking behavior as well as distinguishing nonsmokers from smokers [1]. For the general population, low levels of serum SCN^- may predispose them to inflammatory or inflammation-mediated diseases [5]. All of these aspects underscore the importance of SCN^- determination.

Several methods for the SCN^- detection have been developed over the recent years, including ion chromatography [6], gas chromatography/mass spectrometry [7], colorimetry [4,8,9], electrophoresis [10], electrochemistry [11], fluorimetry [12], and surface-enhanced Raman scattering (SERS) [13,14]. However, some of these methods lack sufficient sensitivity to detect SCN^- at low levels (5–8.5 mg L^{-1}) [15], which correspond to the SCN^- levels typically found in milk samples. And most of them are time-consuming and costly or require sophisticated instrumentation and professional staffs. Hence, exploring an accurate, rapid, sensitive and low-cost method to detect SCN^- in milk and human body liquids still remains a challenge.

Fluorescence resonance energy transfer (FRET) has been widely exploited as an extremely useful tool in analytical and sensing applications [16,17]. FRET is a kind of non-radiation energy transfer form, and the energy of the donors is transferred to the acceptors by the interaction of electric dipoles. The efficiency of FRET is determined by many factors including the overlap extent between the emission spectrum of the donors and the absorption

* Corresponding authors. Tel.: +86 79183969882; fax: +86 79183969514.
E-mail addresses: fywu@ncu.edu.cn (F.-Y. Wu), lihua2003@gmail.com (L.-H. Ma).
[1] Present address: ALS Ellington, 1414 Lumpkin Road, Houston, TX 77043, USA.

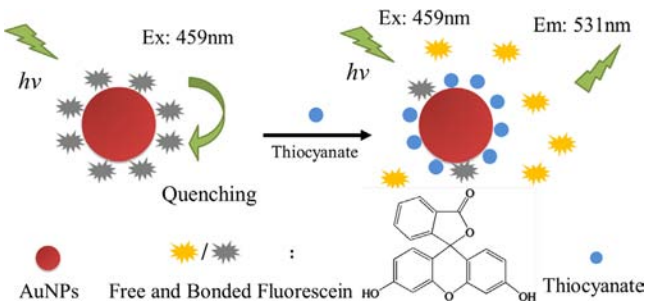
http://dx.doi.org/10.1016/j.talanta.2014.10.023
0039-9140/© 2014 Elsevier B.V. All rights reserved.

spectrum of the acceptors, the distance between the donors and acceptors, the relative orientation of the electric dipoles of the donors and acceptors and so on. Gold nanoparticles (AuNPs) have been widely exploited for chemical and biochemical sensing [18–21] because of their high surface area-to-volume ratios, size-dependent optical properties, and easy to be modified or functionalized chemically. Particularly, AuNPs have been explored as the efficient energy acceptors to substitute for organic acceptors [22] and selected for establishing a FRET system as a fluorescence quencher [23], which have been developed for detection of DNA [24] in the presence of Rhodamine B, protein [25] with aptamer as part of the biosensor, iodide and iodate [26] based on fluorescein-5-isothiocyannate-modified AuNPs, thiols [27] based on Nile Red-Absorbed AuNPs, medicine captopril [28], glyphosate [29] based on the FRET between charged CdTe quantum dots and AuNPs, metallic ions [30] using quantum dots and AuNPs co-sensing system. It was reported that fluorescein can be absorbed on the surface of AuNPs, resulting in fluorescence quenching due to FRET between fluorescein and the AuNPs to detect acetylthiocholine with the aid of enzyme [31] and melamine [32]. Inspired by these works, we have examined the potential of FRET between fluorescein and AuNPs as a novel and sensitive probe for the determination of SCN^- in milk products and saliva. Upon addition of SCN^- that competed with fluorescein molecules to absorb on the surface of the AuNPs, fluorescein molecules were freed from the surface of AuNPs and the fluorescence was recovered (Scheme 1). We have tested another 16 different kinds of anions and only the presence of SCN^- was able to restore fluorescence, allowing the ultrasensitive and selective determination of SCN^- concentration within 5 min. The aim of present work is to propose an alternative methodology with economic aspects, on site, real time and operating simplicity to conventional techniques for SCN^- detection in water, milk products and saliva samples of smokers and nonsmokers.

2. Experimental

2.1. Materials

Chemicals were of analytical grade and used without further purification unless otherwise stated. Hydrogen tetrachloroaurate hydrate ($HAuCl_4 \cdot 4H_2O$) was bought from Sinopharm Chemical Reagent Co. Ltd. (Shanghai, China). Amino acids including L-arginine (Arg), L-histidine (His), L-lysine (Lys), L-tyrosine (Tyr), L-valine (Val) and L-threonine (Thr) were purchased from Shanghai Jingchun Technology Co. Ltd. (Shanghai, China). Na_2SO_4, Na_2SO_3, $Na_2S_2O_3$, Na_2S, Na_2CO_3, $Na_2C_2O_4$, CH_3CO_2Na, $NaNO_3$, $NaNO_2$, $KClO_4$, NaF, NaCl, kBr, KI, $FeCl_3$, $MgCl_2$, $CaCl_2$, $ZnCl_2$, and NH_4Cl were purchased from Shanghai Qingxi Technology Co. Ltd. (Shanghai, China). All the carbohydrates including D-fructose, D-glucose and sucrose were purchased from Shanghai Lanji Technology Co. Ltd. (Shanghai, China). The pH value of the solution was adjusted by mixing different volume ratio of NaH_2PO_4 and Na_2HPO_4.



Scheme 1. Schematic illustration for the sensing of SCN^- based on FRET.

2.2. Apparatus

All fluorescence measurements were carried out on F-4600 spectrofluorimeter (Hitachi, Japan) equipped with a xenon lamp source and a 1.0 cm quartz cell, and the scan speed was 12,000 nm min^{-1}. UV–vis absorption spectra were recorded using UV-2550 spectrophotometer (Shimadzu, Kyoto, Japan) with a 1.0 cm quartz cell at room temperature. Transmission electron microscopy (TEM) was carried out with a JEM-2010 transmission electron microscope (JEOL Ltd. Japan). The samples were prepared by drop-coating the AuNPs solution onto the carbon-coated copper grid and were loaded onto a specimen holder for the purpose of TEM.

2.3. Preparation of colloidal Au NPs

All pieces of the experimental glassware used were cleaned in a bath of freshly prepared aqua regia solution (HCl:HNO_3, 3:1) and then rinsed thoroughly with H_2O and finally dried in the oven at 100 °C prior to use. Citrate capped gold nanoparticles with different sizes was synthesized based on the well-documented Frens' method [33] (trisodium citrate was used as reducing agent). In this method, it was possible to control the size of the particles by varying [Au(III)]/[citrate] ratio during the reduction step as listed in Table S1. A standard procedure for the preparation of AuNPs with size 13 nm was summarized as follows. A 50 mL aqueous solution of $HAuCl_4$ (0.25 mM) was heated to boiling point and 1.3 mL of trisodium citrate (1%) was added. The end point of the reaction was right after the solution reached a wine red color. The obtained wine-red solution was stored at 4 °C for further use. The UV–vis spectral characteristics and sizes for different sets of gold nanoparticles are summarized in Table S1 and results are in agreement with Frens' method. The molar concentration of 13 nm sized AuNPs was calculated according to Beer's law [34] (the molar extinction coefficient for 13 nm AuNPs is 2.78×10^8 $(mol\ L^{-1})^{-1}$ cm^{-1} at 520 nm).

2.4. Preparation of real samples

The pretreatment of liquid milk samples was carried out following the general procedure [35]. Briefly, 2 g milk product was added into 1.5 mL of 10% trichloroacetic acid and 5.0 mL of acetonitrile mixture to remove proteins in milk samples. The mixture solution was transferred to centrifugal tube to undergo sonication for 10 min and then centrifuged at 12,000 rpm min^{-1} for 15 min. The supernatant was filtered through a 0.22 μm membrane filter to remove lipids. The pH of filtrate was adjusted to 6.8, and the filtrate was filtered through 0.22 μm membrane filter again after centrifugation. The filtered liquid was diluted with water to 10 mL for further analysis.

In the case of infant formula, about 0.6 g sample was used for the determination. First, sample was dissolved with 2.0 mL water in a centrifuge tube, 1.5 mL of 10% trichloroacetic acid and 5.0 mL acetonitrile mixture were added to undergo 15 min ultrasonic treatment. Then, the mixture was centrifuged at 12,000 rmp min^{-1} for 15 min. The rest of operation was the same as the pretreatment of liquid milk.

Saliva is a cleaner matrix. Saliva samples from healthy smoking and non-smoking volunteers were collected and refrigerated for 30 min at 4 °C, then centrifuged at 3000 rpm for 10 min. After centrifugation, 100 μL of the supernatant solution was transferred into 10.0 mL volumetric flask and diluted to the mark with deionized water.

2.5. Detection of SCN^-

Typically, a stock solution of 10 μM fluorescein was prepared with Milli-Q water for the further use. 30 μL of 10 μM fluorescein was added into 200 μL AuNPs (15 nM), the resulted mixture was equilibrated at the room temperature for 10 min. Then, 770 μL of

0.01 M (pH 7.0) PBS (NaH_2PO_4–Na_2HPO_4) containing various concentrations of SCN^- was mixed with above mixture solution and further incubated for 10 min. The fluorescence intensities at 531 nm (excitation wavelength was 459 nm) of the mixture in the presence (I_F) and absence (I_0) of SCN^- were recorded, respectively.

2.6. Accuracy and precision

A recovery study was conducted by adding known amounts (5 nM, 10 nM, 15 nM) of the SCN^- to the real samples, followed by pre-treatment. Each concentration was replicated in triplicate. Degree of accuracy expresses the concordance between the accepted value and the value found. The evaluation of inter-day precision (intermediate precision) of the assay was performed on two different days by different analysts. The repeatability was evaluated on the same day for intra-day precision in 3 vessels used for the dissolution test. The relative standard deviation (RSD) and the relative mean square error prediction (RMSEP) from the results was calculated.

3. Results and discussion

3.1. Characterization of AuNPs

Transmission electron microscope datum was used to characterize the size and shape of AuNPs. We synthesized various sized AuNPs and chose the AuNPs sized 13 nm as an example shown in Fig. 1 A, the prepared AuNPs were dispersed uniformly with spherical shape and the sizes were measured to be an average diameter of 13.1 nm with relative standard deviation as 24% (shown in Fig. S1). The characterizations of other sized AuNPs were listed in Table S1.

3.2. Interaction between SCN^- and fluorescein–AuNPs assembly

The fluorescence quenching of fluorophores by AuNPs was dominated by the mechanisms of FRET, the inner filter effect and electron transfer [31]. FRET requires good overlap between the emission of the fluorophores and the SPR band of AuNPs. The emission spectrum of fluorescein (peak at 531 nm) was partially overlapped with the absorption spectrum of AuNPs in different sizes (as shown in Fig. 2A). It has been reported that the fluorescein can be adsorbed onto the surface of citrate-stabilized AuNPs to form a fluorescein–AuNPs assembly due to the electrostatic interaction. The overlap integral areas of absorption spectrum of different sized AuNPs with emission spectrum of fluorescein were shown in Table S2. The fluorescence of fluorescein exhibits a maximum wavelength at 531 nm and the SPR peak of AuNPs with size 13 nm is 520 nm, indicating the largest overlap integral area (4063) between the fluorescence of fluorescein and the SPR band of 13 nm AuNPs. Fig. S2A shows the fluorescence intensity change at 531 nm of the AuNPs–fluorescein system following successive addition of different size AuNPs and Fig. S2B shows the resulting emission spectral change of addition of 13 nm sized AuNPs. It is clear that the fluorescence emission intensity decreased gradually with increasing the AuNPs concentration for all four different sized AuNPs. The fluorescence quenching efficiency can be quantified by the Stern–Volmer equation:

$$\frac{I_0}{I} = 1 + K_{sv}[Q] \quad (1)$$

where I_0 and I are the fluorescence intensity in the absence and presence of the quencher (AuNPs), respectively. K_{sv} is the quenching constant and Q is the concentration of quencher.

The Stern–Volmer plots (see Fig. 2B) show that the different quenching efficiency with the different size of the AuNPs. The quenching constants derived from the slope of the different sized AuNPs were shown in Table S2. It is obvious that the 13 nm sized AuNPs had the largest quenching efficiency. The result is consistent with the conclusion that this type of AuNPs possess maximal FRET overlapping integral area.

We also investigated the effect of the different size of AuNPs on the fluorescent enhancement efficiency with the addition of SCN^- (as shown in Fig. S3). The result indicated that when the SCN^- was added to the fluorescein–AuNPs with different sizes, the 13 nm sized fluorescein–AuNPs showed the maximum level of fluorescence recovery. The results may be due to that SCN^- had good ability to interact with 13 nm sized AuNPs. To sum up, the 13 nm sized AuNPs was selected as the FRET acceptor for the further experiments.

Fluorescein molecules adsorbed on the surface of AuNPs can be released by introducing another compound, which can interact with the AuNPs, resulting in the recovery of the fluorescence [26–28]. To validate the competition between fluorescein and SCN^-, the effect of SCN^- on the fluorescence of the fluorescein–AuNPs mixture was performed and shown in Fig. 2C. The fluorescence spectrum of fluorescein (curve '*a*' in Fig. 2C) was almost identical to that of the mixture of fluorescein and SCN^- (curve '*b*' in Fig. 2C). The results provided clear evidence that there was no interaction between fluorescein and SCN^-. When fluorescein was mixed with AuNPs sized 13 nm, the fluorescence was significantly quenched (curve '*c*' in Fig. 2C) due to the FRET between fluorescein and AuNPs. Upon the addition of SCN^- to the solution of fluorescein–AuNPs, the fluorescein was detached from the AuNPs surface, leading to the recovery or turn-on of the fluorescence (curve '*d*' in Fig. 2C). In addition, we found that the SPR peak was slightly shifted after the addition of 3.0 μM SCN^-

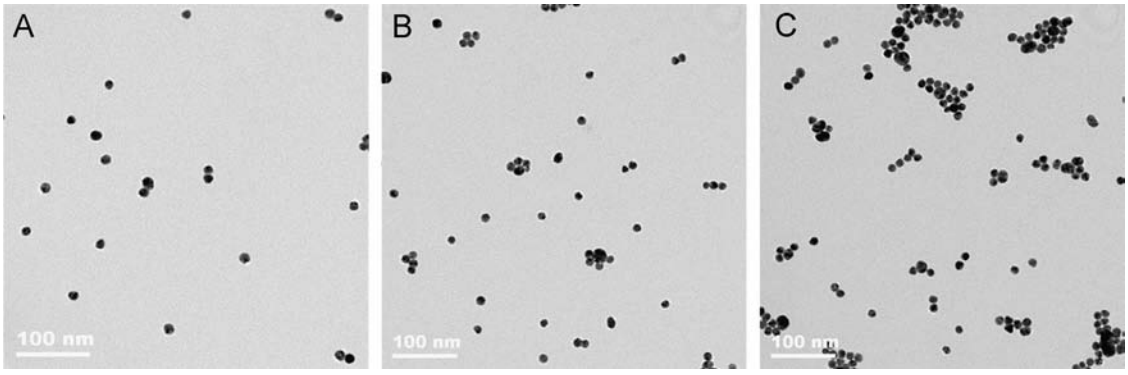


Fig. 1. TEM images of (A) AuNPs, (B) AuNPs with fluorescein (0.3 μM) and low concentration of SCN^- (0.5 μM), and (C) AuNPs with fluorescein (0.3 μM) and a high concentration of SCN^- (3.0 μM). The concentration of AuNPs is 3.0 nM with 13 nm size.

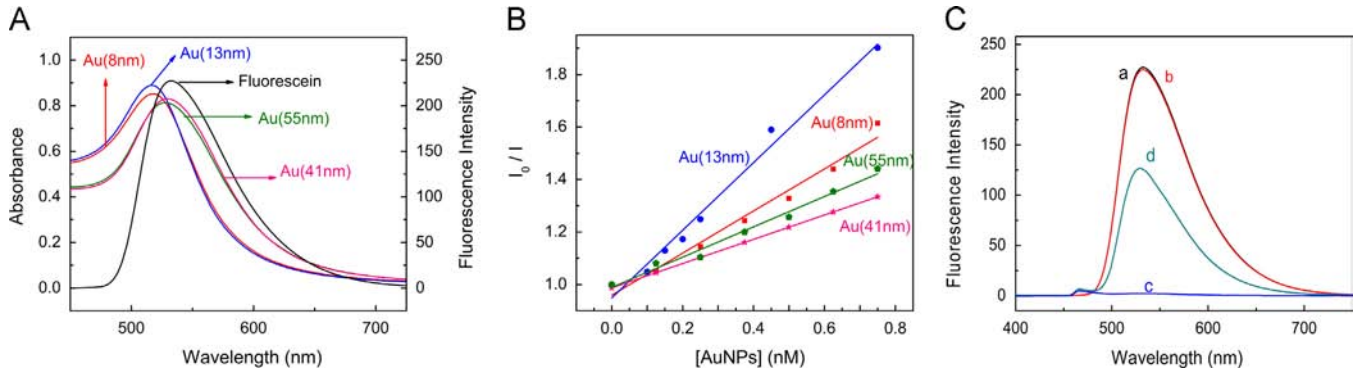


Fig. 2. (A) Emission spectra of fluorescein (0.3 μM) and absorption spectra of AuNPs (3.0 nM) with different sizes (8, 13, 41 and 55 nm), respectively; (B) Stern–Volmer plots. The quenching efficiencies of AuNPs as a function of particle sizes; (C) Fluorescence spectra of (a) fluorescein, (b) fluorescein and SCN^- mixture, (c) fluorescein and AuNPs sized 13 nm, (d) AuNPs sized 13 nm, fluorescein and SCN^- in pH 7.0 buffer (0.01 M Na_2HPO_4–NaH_2PO_4). Fluorescein, 0.3 μM; SCN^-, 0.2 μM; AuNPs, 3 nM.

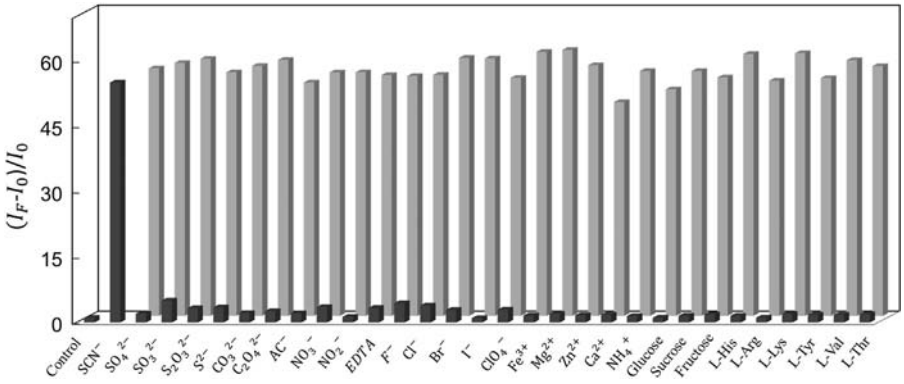


Fig. 3. The fluorescent enhancement efficiency $[(I_F-I_0)/I_0]$ of fluorescein (0.3 μM)–AuNPs (3.0 nM) in the presence of different kinds of foreign ions and compounds (0.1 μM) without (Black bars (Blue in print version)) and with SCN^- (0.1 μM) (Grey bars (Red in print version)) in pH 7.0 buffer (0.01 M Na_2HPO_4–NaH_2PO_4). The concentrations of testing substances were 50 μM for Ca^{2+}, Mg^{2+}, Zn^{2+}, Fe^{3+}, Na^+, K^+, SO_4^{2-}, $S_2O_3^{2-}$, $S_2O_3^{2-}$, S^{2-}, CO_3^{2-}, $C_2O_4^{2-}$, AC^-, NO_3^-, NO_2^-, EDTA, F^-, Cl^-, Br^-, ClO_4^-, glucose, fructose, sucrose, L-tyrosine, L-valine, and L-threonine, 10 μM for L-histidine, L-arginine, L-lysine and 0.1 μM for I^-, respectively.

(Fig. S4). As shown in Fig. 1B and C, 0.3 μM SCN^- can make the AuNPs aggregate slightly, which became stronger in the presence of 3.0 μM of SCN^- (Fig. 1C).

3.3. Effect of AuNPs concentration and pH

To improve the sensitivity of the sensor, we investigated the effect of the AuNPs concentration and the pH of the solution on the displacement of fluorescein from the surface of AuNPs by SCN^-. Fig. S5A shows the fluorescent enhancement efficiency $[(I_F-I_0)/I_0]$ in the presence of 15 nM SCN^- as a function of AuNPs concentration. The efficiency was gradually increased with increasing the concentration of AuNPs and reached maximum when the concentration was up to 3 nM. The fluorescent enhancement efficiency started decreasing when the concentration was beyond 3 nM, which may be attributed to the fact that high concentration of the AuNPs increased the collisional encounter, leading to an enhancement in collisional quenching of released fluorescein. Thus, 3 nM of AuNPs was chosen for the following experiment. The effect of pH was also investigated in the range from pH 5.0 to 9.0. As shown in Fig. S5B, the fluorescent enhancement efficiency is highly dependent on pH value of solution and the highest point was obtained at pH 7.0. Therefore, the optimized pH value for SCN^- detection system is 7.0.

3.4. Effect of incubation time

The effect of the incubation time of SCN^- was investigated as well. Fig. S6 shows the plot of fluorescence intensity variation over the different concentrations of SCN^-. It can be deduced that the fluorescence recovery was almost 90% completed within 10 min. Therefore, all the fluorescence measurements were performed 10 min after initiation of the reaction.

3.5. Effect of potentially interfering ions

To assess the recognition ability of fluorescein–AuNPs probe, the fluorescent enhancement efficiency responses from metal ions (including Ca^{2+}, Mg^{2+}, Zn^{2+}, Fe^{3+}, Na^+, K^+), anions (including SO_4^{2-}, SO_3^{2-}, $S_2O_3^{2-}$, S^{2-}, CO_3^{2-}, $C_2O_4^{2-}$, AC^-, NO_3^-, NO_2^-, $EDTA^{2-}$, F^-, Cl^-, Br^-, I^-, ClO_4^-), sugars (glucose, fructose, sucrose) and amino acid (L-histidine, L-arginine, L-lysine, L-tyrosine, L-valine, L-threonine), which possibly existed in the real samples were performed. As shown in Fig. 3 (blue/black histograms), the addition of SCN^- to a solution of 3.0 nM fluorescein–AuNPs resulted in a dramatic increase in the fluorescent enhancement efficiency $[(I_F-I_0)/I_0]$, while the other ions and compounds exhibited no such change. It turns out that this fluorecein–AuNPs probe showed excellent selectivity of SCN^- over the other ions and compounds. To expand the field of application, the interference from these ions and compounds were further investigated as shown in Fig. 3 (red/gray histograms). This was conducted through the analysis of a standard solution of SCN^- (0.1 μM) in the presence of the excess amounts of coexisting compounds. Ca^{2+}, Mg^{2+}, Zn^{2+}, Fe^{3+}, Na^+, K^+, SO_4^{2-}, SO_3^{2-}, $S_2O_3^{2-}$, S^{2-}, CO_3^{2-}, $C_2O_4^{2-}$, AC^-, NO_3^-, NO_2^-, EDTA, F^-, Cl^-, Br^-, ClO_4^-, glucose, fructose, sucrose, L-tyrosine, L-valine, and L-threonine did not interfere at the concentrations of 50 μM, and L-histidine, L-arginine, L-lysine did not interfere at the concentrations of 10 μM, and 0.1 μM of I^- did not interference. In practical assays, the potential interference from amino acids may

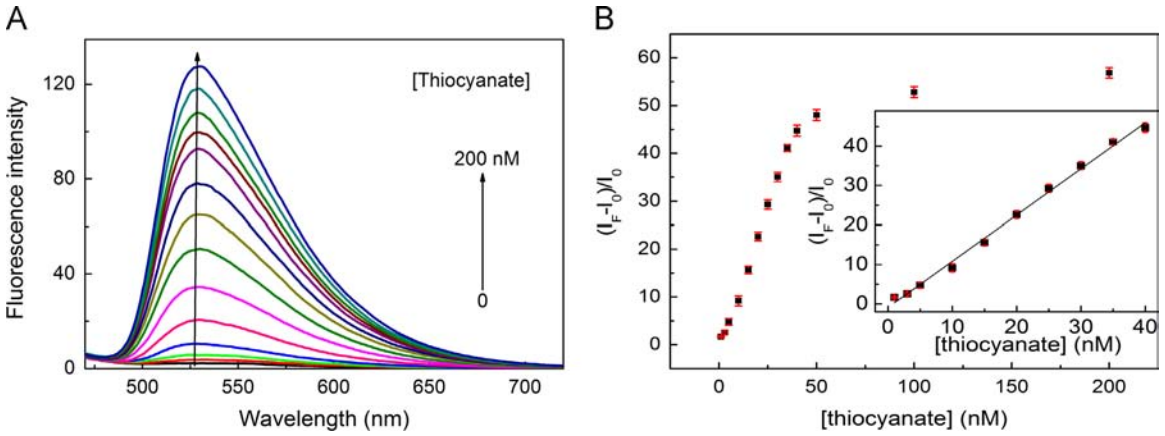


Fig. 4. (A) Fluorescent spectra of fluorescein–AuNPs in the presence of SCN^- at various concentrations in pH 7.0 buffer (0.01 M Na_2HPO_4–NaH_2PO_4). Amounts of SCN^- were 1.0, 3.0, 5.0, 10.0, 15.0, 20.0, 25.0, 30.0, 35.0, 40.0, 50.0, 100.0 and 200.0 nM from bottom to top, respectively. (B) Effect of the SCN^- concentration on the fluorescent enhancement efficiency. Inset is the calibration curve.

be insignificant and could be eliminated during sample pretreatment by removing the protein from the samples.

3.6. The sensitivity for the detection of SCN^-

Under the optimized conditions, the capability of this sensing system for quantitative detection of SCN^- was evaluated. The fluorescent spectra of fluorescein–AuNPs in the presence of different amounts of SCN^- were shown in Fig. 4A. A linear relationship between the fluorescent enhancement efficiency $[(I_F-I_0)/I_0]$ and the concentration of SCN^- ($C_{\overline{SCN}}$, nM) was observed in the range of 1.0 nM to 40.0 nM (as shown in Fig. 4B) with a detection limit of 0.09 nM (3 s/K). The calibration equation was: $Y=-0.8974+1.172C_{\overline{SCN}}$ with the satisfactory correlation coefficient ($R^2=0.998$), where Y referred to the fluorescent enhancement efficiency $[(I_F-I_0)/I_0]$ and X was the concentration of SCN^-.

3.7. Analysis of real samples

In order to validate the applicability of the fluorescein–AuNPs probe for SCN^- sensing, a recovery study was conducted by adding known amounts of SCN^- to the real samples. Each concentration was replicated in triplicate. That is to say, none and various concentration of SCN^- were spiked into the milk and saliva samples according to the procedure described in Section 2.4. The accuracy and precision evaluation of the results of such measurements were then processed with the use of recoveries (%) and the relative mean square error prediction (RMSEP)[36] (Table 1). Degree of accuracy expresses the concordance between the accepted value and the value found. The measured recovery is typically between 90% and 110% with RSD lower than 10%, indicating the good accuracy of the method. The precision results of the proposed method in real samples were evaluated by analyzing repeatability and intermediate precision. The assay evidenced a low RSD ranging from 0.9% to 8.6% for intra-day precision and from 0.3% to 8.5% for inter-day precision performed by the different analysts. The t-value of 2.57 is obtained with 95% significance. Analytical data in Table 1 showed that the recoveries varied from 102% to 104% in the spiked liquid milk sample, 100% to 107% in the spiked infant milk sample, 100% to 101% in the non-smoker saliva sample, and 101% to 108% and 101% to 105% Smoker 1' saliva and Smoker 2' saliva, respectively. The good recoveries, lower RSD and RMSEP (shown in Table 1 and Table S3) demonstrate the accuracy and reliability of the present fluorescence method for detecting SCN^- in practical applications.

Table 1
The application of the proposed method for analysis of milk and saliva samples spiked with different amounts of SCN^-.

Sample	Determination	Added (10^{-9} M)	Amount found (10^{-9} M)[a]	RSD (%, $n=6$)	Recovery (%)	RMSEP[b] (%)
Liquid milk	Not found	5.0	5.1 ± 0.3[c]	5.2	102	3.7
		10.0	10.3 ± 0.4	3.3	103	
		15.0	15.6 ± 1.2	6.4	104	
Infant milk	Not found	5.0	5.0 ± 0.4	7.0	100	5.7
		10.0	10.7 ± 0.7	5.8	107	
		15.0	15.8 ± 1.0	5.5	106	
Non-smoker saliva	Not found	5.0	5.0 ± 0.5	8.6	100	0.5
		10.0	10.1 ± 0.6	5.6	101	
		15.0	15.0 ± 0.4	2.4	100	
Smoker 1′ saliva	Not found	5.0	5.2 ± 0.4	6.2	103	4.5
		10.0	10.7 ± 0.2	1.5	108	
		15.0	15.2 ± 0.2	0.9	101	
Smoker 2′ saliva	Not found	5.0	5.1 ± 0.1	2.0	102	2.9
		10.0	10.5 ± 0.7	5.6	105	
		15.0	15.1 ± 0.9	5.3	101	

[a] The range amount found is evaluated by $\bar{x}\pm t(s/\sqrt{n})$, the value of $t_{0.95,5}$ is 2.57.
[b] RMSEP means relative mean square error prediction, RMSEP $=\sqrt{\left(\sum(x_{found}-x_{added})^2/\sum(x_{added})^2\right)}$.
[c] Average $\pm$ standard deviation (SD) of the three replicate measurements for each test sample.

4. Conclusions

In summary, a sensitive turn-on fluorescent detection method for SCN^- based on FRET from fluorescein to AuNPs is developed. It has been found that the 13 nm sized AuNPs exhibit higher quenching efficiency than other sized AuNPs, which is rationalized that this type of AuNPs shows the maximal overlap between its SPR absorption and the emission of fluorescein. This method offers a couple of advantages over the published SCN^- detection techniques (as shown in Table S4). First, this method can be operated without expensive instrument, which simplifies operations and reduces the associated costs. Second, it allows detection of concentrations as low as 0.09 nM, resulting in the rapid and sensitive detection of SCN^- in milk and saliva samples. Finally, this sensor exhibits unbelievable selectivity for SCN^- over the other ions and

compounds. We will focus on the practical applications in the future research.

Acknowledgments

This work is financially supported by Jiangxi Province Scientific and Technological support major projects planned (no. 20133-ACG70002, Jiangxi Province Natural Science Foundation (no. 20132BAB203011), and Natural Science Foundation of China (no. 21365014).

Appendix A. Supporting information

Supplementary data associated with this article can be found in the online version at http://dx.doi.org/10.1016/j.talanta.2014.10.023.

References

[1] K.A. O'Connell, M.M. Gerkovich, B.A. Fears, M.R. Cook, Addict. Behav. 13 (1988) 383–386.
[2] R.A. Niemann, D.L. Anderson, J. Chromatogr. A 1200 (2008) 193–197.
[3] K.K. Banerjee, P. Marimuthu, P. Bhattacharyya, M. Chatterjee, Br. J. Nutr. 78 (1997) 679–681.
[4] J. Zhang, C. Yang, X. Wang, X. Yang, Anal. Bioanal. Chem. 403 (2012) 1971–1981.
[5] Y. Xu, S. Szép, Z. Lu, Proc. Natl. Acad. Sci. 106 (2009) 20515–20519.
[6] I. Demkowska, Ż. Polkowska, J. Namieśnik, J. Chromatogr. B 875 (2008) 419–426.
[7] J.S. Torano, H.J.M. van Kan, Analyst 128 (2003) 838–843.
[8] Z. Zhang, J. Zhang, C. Qu, D. Pan, Z. Chen, L. Chen, Analyst 137 (2012) 2682–2686.
[9] H.H. Deng, C.L. Wu, A.L. Liu, G.W. Li, W. Chen, X.H. Lin, Sens. Actuators, B 191 (2014) 479–484.
[10] J.E. Prest, S.J. Baldock, M.S. Beardah, S.P. Doyle, P.R. Fielden, N.J. Goddard, B.J. Treves Brown, Analyst 136 (2011) 3170–3176.
[11] M. Sancy, J. Pavez, M.A. Gulppi, I.L. de Mattos, R. Arratia-Perez, C. Linares-Flores, M. Paez, T. Nyokong, J.H. Zagal, Electroanal 23 (2011) 711–718.
[12] A. Banerjee, A. Sahana, S. Lohar, I. Hauli, S.K. Mukhopadhyay, D.A. Safin, M.G. Babashkina, M. Bolte, Y. Garcia, D. Das, Chem. Commun. 49 (2013) 2527–2529.
[13] X. Lin, W.L.J. Hasi, X.T. Lou, S. Lin, F. Yang, B.S. Jia, Y. Cui, D.X. Ba, D.Y. Lin, Z.W. Lu, J. Raman Spectrosc. 45 (2014) 162–167.
[14] P. Pienpinijtham, X.X. Han, S. Ekgasit, Y. Ozaki, Anal. Chem. 83 (2011) 3655–3662.
[15] Report of an FAO/WHO Technical Meeting, Benefits and Potential Risks of the Lactoperoxidase System of Raw Milk Preservation, ⟨http://apps.who.int/iris/handle/10665/43553⟩.
[16] C.A. Chen, C.C. Wang, Y.L. Chen, Y.J. Jong, S.M. Wu, Chem. Commun. 50 (2014) 8069–8072.
[17] C. Wang, Y. Tang, Y. Liu, Y. Guo, Anal. Chem. 86 (2014) 6433–6438.
[18] Z. Chen, G. Zhang, X. Chen, J. Chen, J. Liu, H. Yuan, Biosens. Bioelectron. 41 (2013) 844–847.
[19] X. Liu, Y. Wang, P. Chen, Y. Wang, J. Zhang, D. Aili, B. Liedberg, Anal. Chem. 86 (2014) 2345–2352.
[20] Y. Wu, S. Zhan, L. Wang, P. Zhou, Analyst 139 (2014) 1550–1561.
[21] G. Lu, P. Tan, C. Lei, Z. Nie, Y. Huang, S. Yao, Talanta 128 (2014) 360–365.
[22] M. Li, S.K. Cushing, Q. Wang, X. Shi, L.A. Hornak, Z. Hong, N. Wu, J. Phys. Chem. Lett. 2 (2011) 2125–2129.
[23] H. Zhang, L. Wang, W. Jiang, Talanta 85 (2011) 725–729.
[24] L. Dyadyusha, H. Yin, S. Jaiswal, T. Brown, J.J. Baumberg, F.P. Booy, T. Melvin, Chem. Commun. (2005) 3201–3203.
[25] W. Wang, C. Chen, M. Qian, X.S. Zhao, Anal. Biochem. 373 (2008) 213–219.
[26] Y.M. Chen, T.L. Cheng, W.L. Tseng, Analyst 134 (2009) 2106–2112.
[27] S.J. Chen, H.T. Chang, Anal. Chem. 76 (2004) 3727–3734.
[28] M.R. Hormozi-Nezhad, H. Bagheri, A. Bohloul, N. Taheri, H. Robatjazi, J. Lumin. 134 (2013) 874–879.
[29] J. Guo, Y. Zhang, Y. Luo, F. Shen, C. Sun, Talanta 125 (2014) 385–392.
[30] X. Wang, X. Guo, Analyst 134 (2009) 1348–1354.
[31] S.Y. Lim, J.H. Kim, J.S. Lee, C.B. Park, Langmuir 25 (2009) 13302–13305.
[32] L. Guo, J. Zhong, J. Wu, F. Fu, G. Chen, Y. Chen, X. Zheng, S. Lin, Analyst 136 (2011) 1659–1663.
[33] G. Frens, Nature (Phys. Sci.) 241 (1973) 20–22.
[34] J.R.G. Navarro, M.H.V. Werts, Analyst 138 (2013) 583–592.
[35] Y. Ma, H. Niu, X. Zhang, Y. Cai, Analyst 136 (2011) 4192–4196.
[36] Y. Ni, Z. Xia, S. Kokot, J. Hazard. Mater. 192 (2011) 722–729.

Talanta 132 (2015) 625–629

Contents lists available at ScienceDirect

Talanta

journal homepage: www.elsevier.com/locate/talanta

Reaction-based colorimetric signaling of Cu^{2+} ions by oxidative coupling of phenols with 4-aminoantipyrine

Hong Yeong Kim, Hyo Jin Lee, Suk-Kyu Chang*

Department of Chemistry, Chung-Ang University, Seoul 156-756, Republic of Korea

ARTICLE INFO

Article history:
Received 27 July 2014
Received in revised form
26 September 2014
Accepted 29 September 2014
Available online 14 October 2014

Keywords:
Cu^{2+} signaling
Colorimetry
Oxidative coupling
4-Aminoantipyrine
Phenol
Quinoneimine dye

ABSTRACT

A new Cu^{2+}-selective chromogenic probe system based on the oxidative coupling of phenols with 4-aminoantipyrine was developed. Cu^{2+} ions promoted facile coupling of phenols with 4-aminoantipyrine to yield quinoneimine dyes. Signaling with a number of phenols having no para-substituent, such as *o*-cresol and *m*-cresol, as well as *p*-chlorophenol having para substituent that could be expelled during the oxidation process was possible. The signaling of Cu^{2+} ions was not interfered by the presence of representative metal ions except for Al^{3+} ions. The possible interference from Al^{3+} ions was successfully removed by using fluoride ions as a masking agent. The phenol-4-aminoantipyrine probe system showed chromogenic Cu^{2+} signaling by prominent color change from colorless to pink with a detection limit of 8.5×10^{-7} M. The signaling of Cu^{2+} ions in practical samples using tap water and simulated semiconductor wastewater was also tested.

© 2014 Elsevier B.V. All rights reserved.

1. Introduction

Copper ions are the third most biologically important transition metal ions after iron and zinc [1,2]. It is a key constituent of the copper proteins involved in oxygen transport, oxygenation, electron transport, and antioxidative functions [3]. Copper has also been known as an important environmental pollutant [4]. The copper concentration in the environment varies widely with an average concentration of 0.01 mg/L in surface water and up to 100 mg/L in semiconductor wastewater [5]. Owing to the extensive use of copper in modern industrial applications, sensitive and selective chemosensors for Cu^{2+} ions have attracted much attention in environmental monitoring [6,7].

Recently, chemodosimeters or chemical probes using a reaction-based signaling approach have received much research interest [8]. The advantages of this strategy are cumulative, and specific chemical reactions between the probe molecule and analytes allow high sensitivity and excellent selectivity in signaling [9]. In particular, development of selective reaction-based probes for Cu^{2+} ions has been successfully realized. A number of probes have been devised based on the spirolactam ring-opening process of rhodamine derivatives [10,11]. In addition, Cu^{2+}-induced hydrolysis processes have become another important strategy for the design of Cu^{2+}-selective probes. A classical example reported by Czarnik's group is the spirolactam ring-opening of rhodamine-hydrazide followed by hydrolysis [12]. Other probes are generally based on activated esters, Schiff-bases, and hydrazone function containing dyes [13–16]. Cu^{2+}-mediated oxidation and oxidative cyclization processes have also been successfully used for the development of selective and sensitive probes for Cu^{2+} ions [6,17,18].

4-Aminoantipyrine (AAP) has been used as a useful chromogenic reagent for the determination of various phenols in aqueous solution [19]. The determination is based on the oxidative coupling of phenols with AAP by oxidants such as H_2O_2, persulfate, and $K_3Fe(CN)_6$ to yield highly colored diagnostic quinoneimine dyes [20,21]. On the other hand, coupling reaction of phenols with 4-aminoantipyrine is a well-established process for the determination of oxidants, such as hydrogen peroxide, in industrial analytes [22,23]. The same reaction can also be used for the determination of glucose in blood by using phenol, AAP, and glucose oxidase [24]. Interestingly, Cu^{2+} ions have been reported to act as an oxidant in the coupling of catechol with 4-aminoantipyrine [25]. However, no studies have been carried out on the construction of Cu^{2+}-selective probes employing this useful reaction. In this paper, we report a new colorimetric signaling system for Cu^{2+} ions based on a metal ion-induced coupling of phenols with 4-aminoantipyrine. Upon treatment with Cu^{2+} ions, coupling of phenols with 4-aminoantipyrine smoothly

* Corresponding author. Tel.: +82 2 820 5199; fax: +82 2 825 4736.
E-mail address: skchang@cau.ac.kr (S.-K. Chang).

http://dx.doi.org/10.1016/j.talanta.2014.09.048
0039-9140/© 2014 Elsevier B.V. All rights reserved.

proceeded to form a new quinoid dye with a prominent color change from colorless to pink.

2. Experimental section

2.1. General

4-Aminoantipyrine, 4-(2-hydroxyethyl)-1-piperazineethanesulfonic acid (HEPES), and ammonium persulfate were purchased from Sigma-Aldrich Co. Boric acid was obtained from Wako Co. Phenol, 4-nitrophenol, 2,4,6-trimethylphenol, *m*-cresol, *o*-cresol, and *p*-chlorophenol were obtained from commercial sources. For the spectroscopic studies, perchlorate salts of Li^+, Na^+, K^+, Mg^{2+}, Ca^{2+}, Ba^{2+}, Al^{3+}, Mn^{2+}, Fe^{2+}, Fe^{3+}, Co^{2+}, Ni^{2+}, Cu^{2+}, Zn^{2+}, Ag^+, Cd^{2+}, Hg^{2+}, and Pb^{2+} were obtained from Sigma-Aldrich Co. Chromium(III) nitrate nonahydrate was purchased from Sigma-Aldrich Co. Sodium fluoride and ethylenediaminetetraacetic acid (EDTA) were purchased from Fluka. UV–vis measurements were performed using spectroscopy grade acetonitrile obtained from J.T. Baker. All chemicals and solvents were used without further purification. ^{1}H NMR (600 MHz) and ^{13}C NMR (150 MHz) spectra were acquired on a Varian VNS spectrometer and referenced to the residual solvent signal. UV–vis spectra were acquired using a Jasco V-550 spectrophotometer and Scinco S-3100 equipped with a Peltier temperature controller. Column chromatography was performed using silica gel (240 mesh). Electron-impact (EI) mass spectra (LRMS) were recorded on a Micromass Autospec spectrometer. Compound **1** was prepared following the reported procedure [26].

2.2. Purification of Cu^{2+} signaling compound

Phenol (0.48 g, 5.1 mmol) and copper (II) perchlorate hexahydrate (1.26 g, 3.4 mmol) were dissolved in 100 mL of HEPES-buffered 90% aqueous acetonitrile solution. 4-Aminoantipyrine (70 mg, 0.34 mmol) dissolved in 10 mL of distilled water was added dropwise to the solution. The reaction mixture was stirred at room temperature for 1 h, and 100 mL of dichloromethane was poured in order to extract the Cu^{2+}-signaling product. After separation of the dichloromethane layer, the organic solution was concentrated under reduced pressure. The residue was purified by simply passing through a silica gel plug using dichloromethane/methanol (9:1, v/v) to obtain 52 mg (52% yield) of the Cu^{2+}-signaling compound as a dark orange powder. ^{1}H NMR (600 MHz, $CDCl_3$) δ 8.50 (dd, J=10.3, 2.7 Hz, 1H), 7.53–7.34 (m, 5H), 7.24 (dd, J=9.9, 2.7 Hz, 1H), 6.54 (dd, J=9.9, 2.3 Hz, 1H), 6.44 (dd, J=10.3, 2.3 Hz, 1H), 3.36 (s, 3H), 2.50 (s, 3H); ^{13}C NMR (150 MHz, $CDCl_3$) δ 188.01, 156.88, 153.43, 150.37, 143.72, 133.93, 133.24, 130.40, 129.58, 129.09, 128.52, 126.13, 119.92, 35.18, 10.78; MS (EI): m/z calcd for M^+ ($C_{17}H_{17}N_3O_2$): 295.13, found 295.16.

2.3. Measurement of signaling behaviors

UV–vis signaling behaviors of the probe system towards Cu^{2+} ions and other metal ions were measured in a mixture of CH_3CN and HEPES-buffered solution (pH 7.5) (1:9, v/v). The stock solutions of phenol and 4-aminoantipyrine were prepared in acetonitrile, and metal ions and buffer solutions were made in distilled water. Sample solutions for measurement were prepared by successively adding the stock solutions of metal ions (37.5 μL, 10 mM), HEPES buffer (30 μL, 1.0 M), phenol (225 μL, 5.0 mM), and 4-aminoantipyrine (75 μL, 1.0 mM) in each vial. The solution was diluted with CH_3CN and HEPES-buffer solution to make a final volume (3.0 mL) with a composition of 1:9, v/v. Final concentrations of metal ions, phenol, 4-aminoantipyrine, and HEPES buffer were 1.25×10^{-4} M, 3.75×10^{-4} M, 2.5×10^{-5} M, and 10 mM, respectively.

2.4. pH effects on the signaling towards Cu^{2+}

The effects of pH on the signaling towards Cu^{2+} were elucidated by measuring the responses in a pH range between 4.0 and 10.0 that adjusted with buffer solutions. The buffer solutions used were acetate buffer for pH 4.0–5.8, HEPES buffer for pH 7.0–8.0, and borate buffer for pH 9.0–10.0. Final concentrations of Cu^{2+}, phenol, 4-aminoantipyrine, and each buffer solution were 1.25×10^{-4} M, 3.75×10^{-4} M, 2.5×10^{-5} M, and 10 mM, respectively, under the same measurement conditions.

2.5. Preparation of simulated semiconductor wastewater

Referring to the two relevant literatures on wastewater compositions [27,28], the following metal concentrations were used for the preparation of the simulated semiconductor wastewater: $[Al^{3+}]=8.64\times10^{-5}$ M, $[Fe^{3+}]=5.37\times10^{-5}$ M, $[Pb^{2+}]=7.24\times10^{-6}$ M, $[Mn^{2+}]=1.82\times10^{-6}$ M, $[Zn^{2+}]=1.07\times10^{-5}$ M, and $[Ni^{2+}]=1.36\times10^{-5}$ M.

2.6. Determination of the detection limit for Cu^{2+} ions

Following IUPAC recommendations, the detection limit for the Cu^{2+} ions was determined using the equation $3\times s_{bl}/m$, where s_{bl} denotes the standard deviation of the blank signal (the number of measurements=20) and m represents the slope of the calibration curve [29].

3. Results and discussion

A novel colorimetric signaling system for Cu^{2+} ions based on a metal ion-induced coupling of phenols with 4-aminoantipyrine was developed. The signaling behavior of the probe system toward metal ions was investigated by UV–vis spectrophotometry. A mixture (15:1 mole ratio) of phenol and 4-aminoantipyrine (**PhOH-AAP**) showed no significant absorptions above 400 nm in 90% aqueous acetonitrile solution buffered at pH 7.5 (HEPES buffer). The molar ratio was chosen on the basis of the observation that Cu^{2+} signaling increased proportionally as the phenol concentration increased up to 15:1 mole ratio of phenol and AAP and then became constant (Fig. S1, Supplementary information). Upon treatment of this **PhOH-AAP** system with various metal ions,

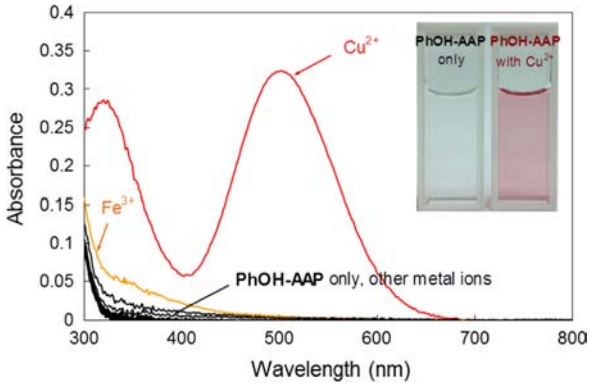
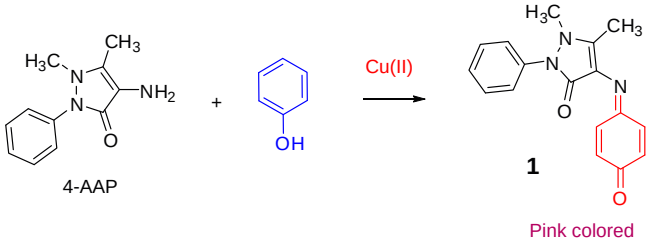


Fig. 1. Changes in UV–vis spectra of the **PhOH-AAP** system in the presence of various metal ions. $[AAP]=2.5\times10^{-5}$ M, $[PhOH]=3.75\times10^{-4}$ M, $[M^{n+}]=1.25\times10^{-4}$ M, $[Pb^{2+}]=2.5\times10^{-5}$ M in a mixture of CH_3CN and HEPES buffer solution (pH 7.5, 10 mM), (1:9, v/v). Spectral data for Cr^{3+} and Fe^{2+} were obtained against a reagent blank.

a pronounced change was observed exclusively with Cu^{2+} ions (Figs. 1 and S2, Supplementary information). In the presence of Cu^{2+} ions, a new strong absorption at 501 nm developed and the solution color of the **PhOH-AAP** system prominently changed from colorless to pink. No significant responses were observed from the other metal ions. On the other hand, meaningful fluorescence properties of **PhOH-AAP** were not observed for the signaling of any surveyed metal ions.

The prominent colorimetric signaling of Cu^{2+} ions by the **PhOH-AAP** system is due to the transformation depicted in Scheme 1. Phenol and AAP were oxidatively coupled to form a highly colored quinoneimine dye **1** promoted by Cu^{2+} ions. The formation of the aminoantipyrine-coupled product of phenols such as **1** by a practical persulfate oxidant was already known [26]. The proposed signaling process was confirmed by ^{1}H and ^{13}C NMR spectroscopy. For this, the ^{1}H NMR spectrum of the Cu^{2+}-signaling **PhOH-AAP** system was measured after purification of the reaction mixture. The resulting spectrum was identical to that obtained for compound **1** prepared independently using persulfate as an oxidant (Fig. 2 and Fig. S3, Supplementary information). In particular, the resonance peaks for the para-H (6.87 ppm) of phenol disappeared and the remaining four protons of the quinoid subunit appeared as two pairs of doublets (8.50 and 6.44 ppm for H-6 and H-5, 6.54 and 7.24 ppm for H-3 and H-2). One of the resonance peaks (H-6), assigned by means of a 2D ^{1}H–^{13}C HSQC spectrum (Fig. S4, Supplementary information), experienced a large shift to the lower field from 7.20 to 8.50 ppm due to a large anisotropic effect of nearby antipyryl group [26]. ^{13}C NMR and UV–vis spectral evidences also confirmed the formation of **1** under the signaling conditions (Fig. S5 and Fig. S6, Supplementary information). Furthermore, treatment of the Cu^{2+}-signaling **PhOH-AAP** system with chelating EDTA did not affect the UV–vis spectrum of the resulting solution, indicating the irreversible nature of the suggested reaction-based signaling process (Fig. S7, Supplementary information).



Scheme 1. Colorimetric signaling of Cu^{2+} ions by phenol and 4-aminoantipyrine pair (**PhOH-AAP**).

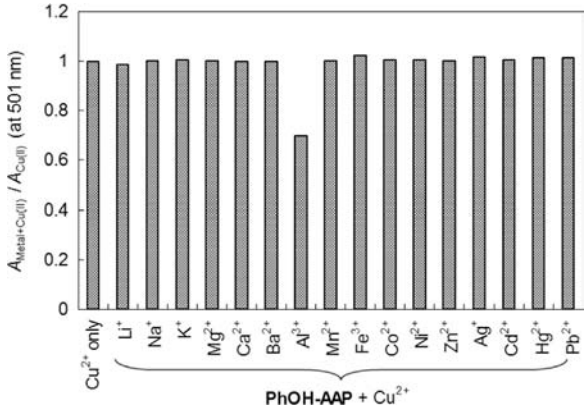


Fig. 3. Competitive signaling of Cu^{2+} ions by the **PhOH-AAP** system in the presence of other metal ions as background. [AAP]$=2.5\times10^{-5}$ M, [PhOH]$=3.75\times10^{-4}$ M, [Cu^{2+}]$=1.25\times10^{-4}$ M, [M^{n+}]$=1.25\times10^{-4}$ M in a mixture of CH_3CN and HEPES buffer solution (pH 7.5, 10 mM), (1:9, v/v). To prevent precipitation, [Pb^{2+}]$=2.50\times10^{-5}$ M.

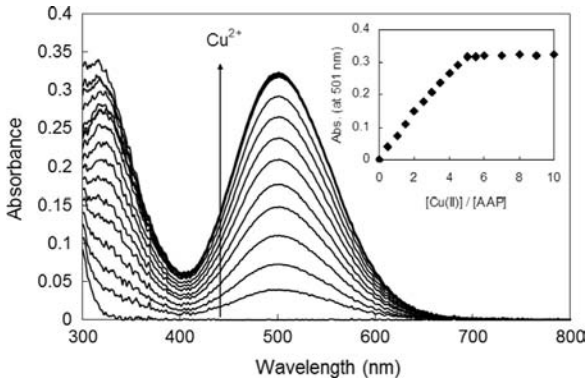


Fig. 4. Changes in absorption spectrum of the **PhOH-AAP** system as a function of Cu^{2+} concentration. Inset: absorbance change at 501 nm as a function of Cu^{2+} ion concentration. [AAP]$=2.5\times10^{-5}$ M, [PhOH]$=3.75\times10^{-4}$ M, [Cu^{2+}]$=0-2.5\times10^{-4}$ M in a mixture of CH_3CN and HEPES buffer solution (pH 7.5, 10 mM), (1:9, v/v).

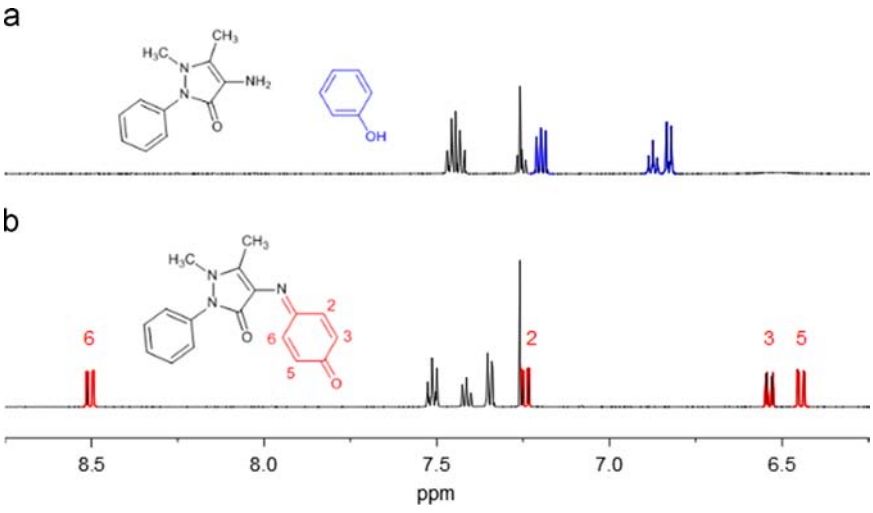


Fig. 2. Partial ^{1}H NMR spectra of (a) PhOH and AAP (1:1 mole ratio) and (b) purified product after Cu^{2+} signaling of the **PhOH-AAP** system. Each compound was dissolved at 3.0×10^{-2} M in $CDCl_3$.

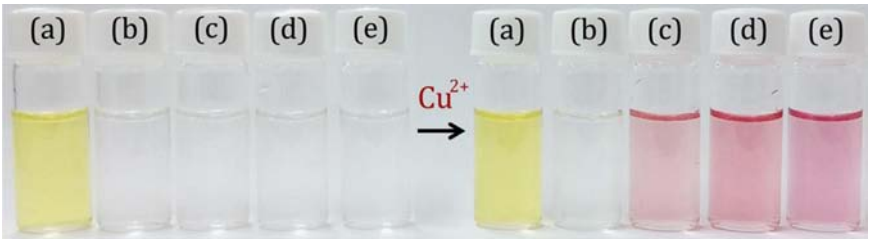


Fig. 5. Photograph of mixtures of various phenols and AAP in the absence or presence of Cu^{2+}. [AAP]$=2.5\times10^{-5}$ M, [phenol]$=3.75\times10^{-4}$ M, [Cu^{2+}]$=1.25\times10^{-4}$ M in a mixture of CH_3CN and HEPES buffer solution (pH 7.5, 10 mM), (1:9, v/v). (a) 4-Nitrophenol, (b) 2,4,6-trimethylphenol, (c) *m*-cresol, (d) *o*-cresol, and (e) *p*-chlorophenol.

The Cu^{2+}-selective signaling was not affected by the presence of common alkali, alkaline earth, and transition metal ions except for Al^{3+}, Cr^{3+}, and Fe^{2+}, as background. The signaling ratio $A_{Metal+Cu(II)}/A_{Cu(II)}$ observed at 501 nm varied across a narrow range, from 0.99 for Li^{+} ions to 1.02 for Fe^{3+} ions (Fig. 3). On the other hand, considerable interference was observed with Al^{3+} ions with a $A_{Al(III)+Cu(II)}/A_{Cu(II)}$ ratio of 0.70. However, the interference from Al^{3+} ions was successfully removed by using fluoride ions as a masking agent [30]; in the presence of 40 equiv of fluoride ions, the interference from Al^{3+} ions disappeared completely (Fig. S8, Supplementary information). In the presence of Fe^{2+} or Cr^{3+}, the Cu^{2+}-signaling of the probe system decreased to 53% by Fe^{2+}, or totally suppressed by Cr^{3+}. These interferences are due to the fact that undesirable interaction of Cu^{2+} ions with redox-active Fe^{2+} and Cr^{3+} ions [31,32]. The reaction of Cu^{2+} ions with Fe^{2+} or Cr^{3+} ions resulted in the decreases in Cu^{2+} level in the analytes, and leads to a significantly reduced signal for Cu^{2+}-triggered oxidative condensation between phenol and AAP. This observation implies that the present system could work as a practically applicable Cu^{2+}-selective probe in commonly encountered environmental systems except for the analytes rich in redox-active metal ions of Fe^{2+} or Cr^{3+}.

To check the quantitative analytical behavior of the **PhOH-AAP** system for Cu^{2+} signaling, a UV–vis titration was carried out in 90% aqueous acetonitrile (buffered at pH 7.5 using HEPES). As the concentration of Cu^{2+} ions increased, the absorption profile of the **PhOH-AAP** system changed progressively to that of **1** while showing a steadily increasing new band at 501 nm (Fig. 4). From the titration data, the detection limit in the determination of Cu^{2+} ions by the **PhOH-AAP** system was estimated to be 8.5×10^{-7} M in 90% aqueous acetonitrile solution (Fig. S9, Supplementary information) [29].

The effects of pH on the signaling were assessed by measuring the responses of the **PhOH-AAP** system as a function of the pH of the medium. As shown in Fig. S10 (Supplementary information), the Cu^{2+} signaling was most pronounced between pH 7 and 8. Signaling speed was fast and the response was completed within 10 min after mixing the analyte solutions (Fig. S11, Supplementary information). Additionally, the **PhOH-AAP** mixture was stable under the ambient temperature and open laboratory atmosphere for more than 1 day. The Cu^{2+}-selective signaling was possible for a number of phenols, such as *o*-cresol and *m*-cresol as well as *p*-chlorophenol (Figs. 5 and S12, Supplementary information). In the case of *p*-chlorophenol, the para-chloro substituent is known to be expelled during the oxidative process to form a quinoid dye [26]. Furthermore, practical applicability of the Cu^{2+}-selective signaling by the **PhOH-AAP** system was confirmed in tap water and simulated semiconductor wastewater (Fig. S13 and S14, Supplementary information). In particular, the interference from Al^{3+} in simulated semiconductor wastewater was successfully removed by using fluoride ions as a masking agent (Fig. S15, Supplementary information). The Cu^{2+} signaling by **PhOH-AAP** system in simulated semiconductor wastewater was possible up to 1.0×10^{-4} M.

4. Conclusion

In summary, a new chromogenic probe system for the selective signaling of Cu^{2+} ions was developed based on the Cu^{2+}-induced oxidative coupling of phenols and 4-aminoantipyrine. The mixture of phenol and 4-aminoantipyrine exhibited pronounced Cu^{2+}-selective chromogenic signaling with a color change from colorless to pink. Interference from Al^{3+} ions was successfully eliminated by using fluoride ions as a masking agent. The detection limit for the determination of Cu^{2+} ions was 8.5×10^{-7} M in 90% aqueous acetonitrile solution. The reported sensing approach would be useful as a convenient and practical colorimetric signaling system for Cu^{2+} ions in chemical and environmental applications, such as preliminary monitoring of Cu^{2+} levels in tap water and semiconductor wastewater.

Acknowledgements

This research was supported by a fund from the Korea Research Foundation of the Korean Government (NRF-2013R1A1A2008574).

Appendix A. Supplementary information

Supplementary information associated with this article can be found in the online version at http://dx.doi.org/10.1016/j.talanta.2014.09.048.

References

[1] J.J.R. Fraústo da Silva, R.J.P. Williams, The Biological Chemistry of the Elements: The Inorganic Chemistry of Life, Oxford University Press, UK, Oxford (1991) 388–399.
[2] R. Uauy, M. Olivares, M. Gonzalez, Am. J. Clin. Nutr. 67 (1998) 952S–959S.
[3] R.-C. Geoff, O. Tina, Descriptive Inorganic Chemistry, 3rd ed., W.H. Freeman, New York (2002) 516.
[4] R. Krämer, Angew. Chem. Int. Ed. 37 (1998) 772–773.
[5] C.L. Lai, S.H. Lin, Chemosphere 54 (2004) 235–242.
[6] J. Jo, H.Y. Lee, W. Liu, A. Olasz, C.-H. Chen, D. Lee, J. Am. Chem. Soc. 134 (2012) 16000–16007.
[7] J.Y. Noh, G.J. Park, Y.J. Na, H.Y. Jo, S.A. Lee, C. Kim, Dalton Trans. 43 (2014) 5652–5656.
[8] K. Kaur, R. Saini, A. Kumar, V. Luxami, N. Kaur, P. Singh, S. Kumar, Coord. Chem. Rev. 256 (2012) 1992–2028.
[9] Y. Yang, Q. Zhao, W. Feng, F. Li, Chem. Rev. 113 (2013) 192–270.
[10] X. Zhang, Y. Shiraishi, T. Hirai, Org. Lett. 9 (2007) 5039–5042.
[11] Y. Zhao, X.-B. Zhang, Z.-X. Han, L. Qiao, C.-Y. Li, L.-X. Jian, G.-L. Shen, R.-Q. Yu, Anal. Chem. 81 (2009) 7022–7030.
[12] V. Dujols, F. Ford, A.W. Czarnik, J. Am. Chem. Soc. 119 (1997) 7386–7387.
[13] X. Qi, E.J. Jun, L. Xu, S.-J. Kim, J.S.J. Hong, Y.J. Yoon, J. Yoon, J. Org. Chem. 71 (2006) 2881–2884.
[14] J. Kovács, A. Mokhir, Inorg. Chem. 47 (2008) 1880–1882.
[15] M.H. Kim, H.H. Jang, S. Yi, S.-K. Chang, M.S. Han, Chem. Commun. (2009) 4838–4840.
[16] N. Li, Y. Xiang, A. Tong, Chem. Commun. 46 (2010) 3363–3365.
[17] D. Wang, Y. Shiraishi, T. Hirai, Chem. Commun. 47 (2011) 2673–2675.
[18] W. Lin, L. Long, B. Chen, W. Tan, W. Gao, Chem. Commun. 46 (2010) 1311–1313.
[19] Y. Fiamegos, C. Stalikas, G. Pilidis, Anal. Chim. Acta 467 (2002) 105–114.
[20] E. Emerson, J. Org. Chem. 8 (1943) 417–428.
[21] E. Emerson, K. Kelly, J. Org. Chem. 13 (1948) 532–534.

[22] V. Vojinović, A.M. Azevedo, V.C.B. Martins, J.M.S. Cabral, T.D. Gibson, L. P. Fonseca, J. Mol. Catal. B Enzym. 28 (2004) 129–135.
[23] J.P.N. Ribeiro, M.A. Segundo, S. Reis, J.L.F.C. Lima, Talanta 79 (2009) 1169–1176.
[24] A.C.A. de Oliveira, V.C. Assis, M.A.C. Matos, R.C. Matos, Anal. Chim. Acta 535 (2005) 213–217.
[25] G.G. Mohamed, M.A. Zayed, F.A. Nour El-Dien, R.G. El-Nahas, Spectrochim. Acta Part A 60 (2004) 1775–1781.
[26] P.F. Jones, K.E. Johnson, Can. J. Chem. 51 (1973) 2860–2868.
[27] Y.C. Wong, V. Moganaragi, N.A. Atiqah, Orient. J. Chem. 29 (2013) 1421–1428.
[28] Y.B. Onundi, A.A. Mamun, M.F. Al-Khatib, M.A. Al-Saadi, A.M. Suleyman, Int. J. Environ. Sci. Tech. 8 (2011) 799–806.
[29] Y.-Q. Wang, Y. Liu, X.-W. He, W.-Y. Li, Y.-K. Zhang, Talanta 99 (2012) 69–74.
[30] D.K. Nordstrom, L.N. Plummer, D. Langmuir, E. Busenberg, H.M. May, B. F. Jones, D.L. Parkhurst, ACS Symp. Ser. 416 (1990) 398–413.
[31] C.J. Matocha, A.D. Karathanasis, S. Rakshit, K.M. Wagner, J. Environ. Qual. 34 (2005) 1539–1546.
[32] K. Ivanov, D. Dimitrov, B. Boyanov, World Acad. Sci., Eng. Technol. 5 (2011) 266–272.

Talanta 132 (2015) 630–634

Contents lists available at ScienceDirect

Talanta

journal homepage: www.elsevier.com/locate/talanta

Phylogenetic analysis of microalgae based on highly abundant proteins using mass spectrometry

Hae-Won Lee [a,b,1], Seong Woon Roh [a,c,1], Kichul Cho [a,c], Kil-Nam Kim [a], In-Tae Cha [a], Kyung June Yim [a], Hye Seon Song [a], Young-Do Nam [d], Tatsuya Oda [e], Young-Ho Chung [f,g], Soo Jung Kim [f], Jong-Soon Choi [f,g,*], Daekyung Kim [a,c,**]

[a] Jeju Center, Korea Basic Science Institute, Jeju 690-756, Republic of Korea
[b] World Institute of Kimchi, Gwangju 503-360, Republic of Korea
[c] Green Chemistry & Environmental biotechnology, University of Science and Technology, Daejeon 305-350, Republic of Korea
[d] Fermentation and Functionality Research Group, Korea Food Research Institute, Sungnam 463-746, Republic of Korea
[e] Division of Biochemistry, Faculty of Fisheries, Nagasaki University, Bunkyo-machi 1-14, Nagasaki 852-8521, Japan
[f] Division of Life Science, Korea Basic Science Institute, Daejeon 305-806, Republic of Korea
[g] Graduate School of Analytical Science and Technology, Chungnam National University, Daejeon 305-764, Republic of Korea

ARTICLE INFO

Article history:
Received 26 March 2014
Received in revised form
21 August 2014
Accepted 23 August 2014
Available online 12 October 2014

Keywords:
Microalgae
Rapid identification
Phylogenetic analysis
MALDI-TOF

ABSTRACT

The blooms of toxic phototrophic microorganisms, such as microalgae and cyanobacteria, which are typically found in freshwater and marine environments, are becoming more frequent and problematic in aquatic systems. Due to accumulation of toxic algae, harmful algal blooms (HABs) exert negative effects on aquatic systems. Therefore, rapid detection of harmful microalgae is important for monitoring the occurrence of HABs. Mass spectrometry-based methods have become sensitive, specific techniques for the identification and characterization of microorganisms. Matrix-assisted laser desorption/ionization (MALDI) with time-of-flight (TOF) mass spectrometry (MS) allows us to measure a unique molecular fingerprint of highly abundant proteins in a microorganism and has been used for the rapid, accurate identification of bacteria and fungi in clinical microbiology. Here, we tested the specificity of MALDI-TOF MS using microalgal strains (*Heterocapsa*, *Alexandrium*, *Nannochloropsis*, *Chaetoceros*, *Chlorella*, and *Dunaliella* spp.). Our research suggested that this method was comparable in terms of the rapid identification of microalgea to conventional methods based on genetic information and morphology. Thus, this efficient mass spectrometry-based technique may have applications in the rapid identification of harmful microorganisms from aquatic environmental samples.

© 2014 Elsevier B.V. All rights reserved.

1. Introduction

Harmful algal blooms (HABs), commonly called red tides [1], result from accumulation of various microalgae and are known to cause outbreaks of shellfish poisoning and death of fish, mammals, and sea plants [2]. HABs affect global coastal regions [1], and some algal toxins can cause diarrheic, paralytic, amnesic, and neurotoxic shellfish poisoning, thereby endangering human health and negatively affecting the tourism industry and fishery resources [3]. Most HABs are formed by blooming microscopic algae, phytoplankton, or specific cyanobacteria and occur when microalgae rapidly proliferate and when a large biomass of toxic or noxious microalgae accumulates in marine ecosystems or freshwater ecosystems [1]. Therefore, in order to respond quickly and appropriately to dissipate HABs, studies are needed to understand the ecology of microalgae as aquatic microbial eukaryotes and for enumeration and identification of harmful microalgae. Traditionally, identification of microalgae in HAB events has been achieved by light or electron microscopy examination. However, these methods may be difficult and time-consuming. Within the last decade, real-time polymerase chain reaction (PCR) assays [3] have been developed for rapid detection of microalgae in HABs. Molecular tools such as real-time PCR are known to be very useful for the detection of microorganisms [3]. However, exact identification of individual strains is nearly impossible using real-time PCR because of the limited availability of specific primer-probe sets.

Mass spectrometry (MS)-based methods have been established as an indispensable technology for interpretation of the information encoded in genomes, complementing DNA-based approaches [4].

* Corresponding author at: Division of Life Science, Korea Basic Science Institute, Daejeon 305-806, Republic of Korea.
** Corresponding author at: Jeju Center, Korea Basic Science Institute, Jeju 690-756, Republic of Korea.
E-mail addresses: jschoi@kbsi.re.kr (J.-S. Choi), dkim@kbsi.re.kr (D. Kim).
[1] Hae-Won Lee and Seong Woon Roh have contributed equally to this work.

http://dx.doi.org/10.1016/j.talanta.2014.08.078
0039-9140/© 2014 Elsevier B.V. All rights reserved.

Currently, MALDI-time-of-flight (TOF) MS has been applied for the detection of ribosomal protein mass patterns for the confirmation of pathogens [5]. Additionally, MALDI-TOF MS provides identification of pathogen and microorganisms and can be used to determine microbial taxonomy [6]. Reproducibility and accuracy of taxonomic identification of microorganisms using MALDI-TOF MS were confirmed by the previous studies under different cultivation conditions [7,8]. In another study, identification of filamentous fungi through spores was carried out using MALDI-TOF MS [9]. Importantly, the use of MALDI-TOF MS can reduce costs and time required for identification of microorganisms [10] and elucidation of microbial taxonomy can be used to determine microbial diversity based on natural relationships without identification of functional taxonomy or isolation of microorganisms [11].

Taxonomic system mirroring 'order in nature' [12] is established by phylogenetic analysis that can identify unknown organisms and classification in taxonomic groups on the bases of relationships. In this study we focused on developing a MALDI-TOF MS-based method for the phylogenetic analysis of harmful microalgal strains belonging to the genus *Alexandrium*, *Chaetoceros*, and *Heterocapsa*, as well as strains of the genus *Nannochloropsis*, *Chlorella*, and *Dunaliella* and we compared identification using MALDI-TOF MS to classical morphological methods and molecular genetic methods based on ribosomal RNA (rRNA) genes.

2. Experimental

2.1. Cultures of microalgal strains

Eight microalgae (*Chlorella* sp. J31 and J37, *Dunaliella* sp. J33, *Chaetoceros* sp. J28 and J32, *Alexandrium tamarense* J18, *Heterocapsa* sp. J3, and *Nannochloropsis granulata* J34) were obtained from the University of Nagasaki in Japan. Each strain was maintained and cultured using Erd-Schreiber modified (ESM) medium in plant growth chambers (VS-3DM, Vision Scientific, Korea). The ESM medium contained the following: 120 mg/L $NaNO_3$, 5 mg/L K_2HPO_4, 0.1 mg/L vitamin B_1, 0.01 mg/L vitamin B_{12}, 0.001 mg/L biotin, 0.26 mg/L EDTA–Fe^{3+}, 0.33 mg/L EDTA–Mn^{2+}, and 1000 mg/L Tris dissolved in artificial seawater; the pH was adjusted to 8.0. The seawater used for ESM medium was prefiltered through a membrane filter with a 0.2-μm pore size made of cellulose acetate. The cultures were stored in sterilized 500-mL Erlenmeyer flasks and inoculated in a plankton chamber under controlled conditions at 26 °C with 60% humidity and a 12/12 h light/dark cycle. The cool-white fluorescent lamp used for incubation supplied approximately 45.8 W/m^2 of light intensity. Each species of microalgae was tested in the exponential growth phase.

2.2. Morphological analysis using microscopy

Morphologies and sizes of the eight microalgae strains were observed on slides using the phase-contrast mode of a fluorescence microscope (FSX100, OLYMPUS, JPN).

2.3. Phylogenetic analysis based on 18S rRNA gene sequences

For phylogenetic analysis based on the 18S rRNA gene sequences, microalgal DNA was extracted using a DNA extraction kit (DNeasy Blood & Tissue Kit, Qiagen, Netherlands) in order to remove PCR inhibitors from the microalgae [13]. Then, the 18S rRNA gene amplification was carried out using a PCR premix (AccuPower, Bioneer, Korea) and two eukaryotic primers (Ecol-7F, 5′-ACCTGGTTGATCCTGCCAG-3′ and Ecol-1534R, 5′-TGATCCTTCYGCAGGTTCAC-3′). The PCR protocol was as follows: initial denaturation for 10 min; 30 cycles of denaturation at 94 °C for 1 min, annealing at 55 °C for 2 min, extension at 72 °C for 3 min, and a final extension for 5 min. The PCR products were sequenced using an automated DNA analyzer system (PRISM 3730xl DNA Analyzer, Applied Biosystems, USA) with a BigDye Terminator Cycle Sequencing Ready Reaction Kit (Applied Biosystems) according to the manufacturer's instructions. The 18S rRNA gene sequences of microalgae, verified using the BLAST search program (http://blast.ncbi.nlm.nih.gov/Blast.cgi), were aligned by CLUSTAL_W. Phylogenetic dendrograms were constructed using MEGA5 and the neighbor-joining method with 1000 randomly selected bootstrap replicates.

2.4. Spectral fingerprinting analysis using MALDI-TOF MS

We carried out the direct transfer method to analyze protein profiling of whole microorganism cells by MALDI-TOF MS without protein extraction and inactivation steps [14]. MALDI-TOF MS samples in triplicate were air-dried and mixed with α-cyano-4-hydroxycinnamic acid (CHCA) in 33% acetonitrile (ACN) and 33% ethanol (EtOH) with 3% trifluoroacetic acid (TFA) at a 1:1 ratio. Prepared samples were then homogenized. Ion spectra providing protein profiles were obtained in linear mode and positive-ion mode (laser frequency of 1000 Hz) with a mass range of 2000–20,000 Da using an UltrafleXtreme TOF/TOF mass spectrometer (Bruker Daltonics, Germany). Extraction delay time, lens, and ion sources 1 and 2 were set to 150 ns, 6.47, 25, and 23 kV, respectively. Adjustment and analysis of obtained MALDI-TOF MS spectra data were carried out using Excel 2010 (Microsoft, USA) and MultiExperiment Viewer (MeV) 4.8.1. Ion spectra of protein profiles from 2000 to 20,000 Da (Fig. 1) for each microalga were used to construct dendrograms by hierarchical clustering analysis (HCA) in MeV. The ordering optimization was sample leaf order, the distance metric was Euclidean distance, and the linkage method was complete linkage clustering. The sensitivity of the MALDI-TOF MS approach was analyzed to determine the amount of cells required for mass spectra analysis using each microalgae strain of *Heterocapsa* sp. J3, *Chaetoceros* sp. J28, and *Dunaliella* sp. J33. We first established the number of cells present in dense cultures using a hemocytometer with direct viable counts of 10-fold serial dilutions. Based on these counts we prepared samples containing 10^1–10^6 cells which were then analyzed using MALDI-TOF MS as previously described.

3. Results and discussion

We rapidly identified a total of eight species of microalgae using MALDI-TOF MS and compared these results with those of other techniques, i.e., morphological observations and phylogenetic analyses. First, we observed microalgal samples using light microscopy to identify morphologies.

3.1. Morphology

The eight microalgae exhibited proper morphologies for each of their species (Fig. S1). However observation of morphology can be easily confusing and is not as accurate as other techniques, such as phylogenetic analysis for taxonomy. Moreover, strains J31, J34, and J37 exhibited similar morphologies; this may cause difficulties in correctly identifying such strains by morphological and taxonomical evaluations. While observation of the ultrastructural morphology of microalgae by transmission electron microscopy has been carried out and can be much more precise in taxonomy analysis, it is costly, time-consuming, and difficult.

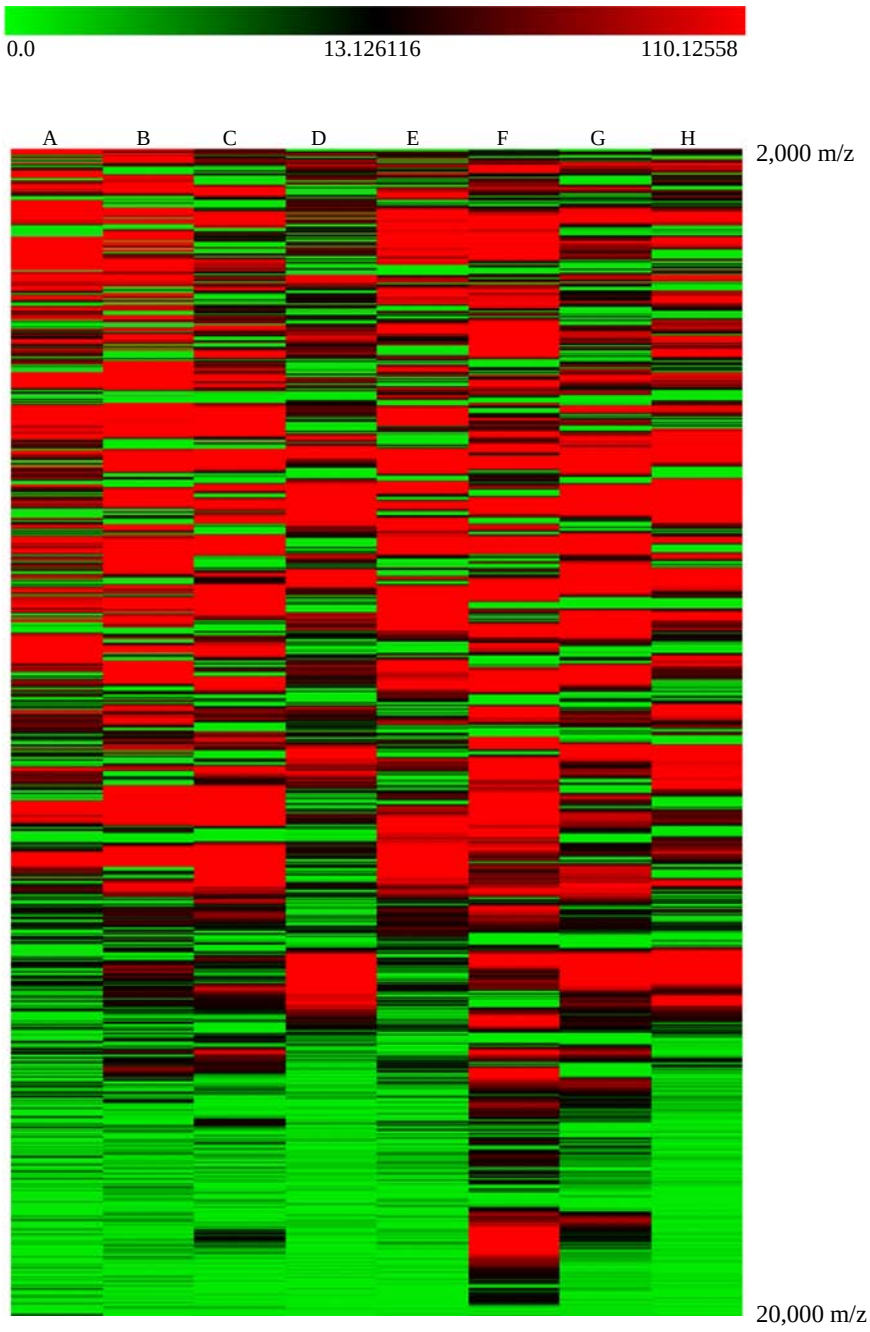


Fig. 1. Mass spectra for proteins in spectra from 2000 to 20,000: A, strain J3; B, strain J18; C, strain J28; D, strain J31; E, strain J32; F, strain J33; G, strain J34; and H, strain J37.

3.2. Phylogenetic analysis

The 18S rRNA genes of microalgae in this study are accessible at the NCBI GenBank; J28 and J32 of *Chaetoceros* sp. are KF289814 and KF289816, J31 and J37 of *Chlorella* sp. are KF289815 and KF289811, J34 of *N. granulata* is KF289818, J33 of *Dunaliella* sp. is KF289817, J3 of *Heterocapsa* sp. is KF289812, and J18 of *A. tamarense* is KF289813. The obtained 18S rRNA gene sequences were used to construct a phylogenetic dendrogram to determine the relationships between microalgae strains and other microalgae genes registered in the NCBI (Fig. S2). The microalgae strains used in our study are identified in Table 1. The phylogenetic dendrogram of 18S rRNA genes of microalgae strains showed that the closely related genera *Nannochloropsis* and *Chaetoceros* corresponded to the class *Stramenopiles*, the closely related genera *Chlorella* and *Dunaliella* corresponded to the class *Viridiplantae*, and the closely related genera *Heterocapsa* and *Alexandrium* corresponded to class *Alveolata*. Accordingly, genomic taxonomy analysis could separate each microalga to taxonomy based on a phylogenetic dendrogram. However, genomic taxonomy analysis is costly and time-consuming compared to mass spectrometric taxonomy analysis.

3.3. Mass spectrometric taxonomy analysis and comparison of taxonomy based on mass spectrometry and the phylogenetic marker gene

Ion spectra of protein profiles obtained from 2000 to 20,000 Da (Fig. 1) that were identical with only minor shifts from triple measurements for each microalga were generated and used to construct a phylogenetic dendrogram (Fig. 2). This dendrogram based on mass spectra was different from the phylogenetic dendrogram

Table 1
Microalgae strains identified from a BLAST search of the NCBI database in our study.

Strain	Taxon	BLAST result (accession number)	Query cover (%)	Identity (%)
J28	*Chaetoceros* sp.	*Chaetoceros* sp. NMBguh003-2 (DQ886407)	100	100
J32	*Chaetoceros* sp.	*Chaetoceros* sp. NMBguh003-1 (DQ886406)	100	100
J31	*Chlorella* sp.	*Chlorella* sp. KMMCC C-185 (GQ122357)	100	99
J37	*Chlorella* sp.	*Chlorella* sp. KMMCC 868 (JQ315773)	100	99
J34	*Nannochloropsis granulata*	*Nannochloropsis granulata* BDH02 (KC128500)	100	100
J33	*Dunaliella* sp.	*Dunaliella* sp. ABRIINW-Sh6.3 (JQ712983)	100	100
J3	*Heterocapsa* sp.	*Heterocapsa* sp. HE04 (FJ549370)	100	99
J18	*Alexandrium tamarense*	*Alexandrium tamarense* ATHK (JF906994)	100	99

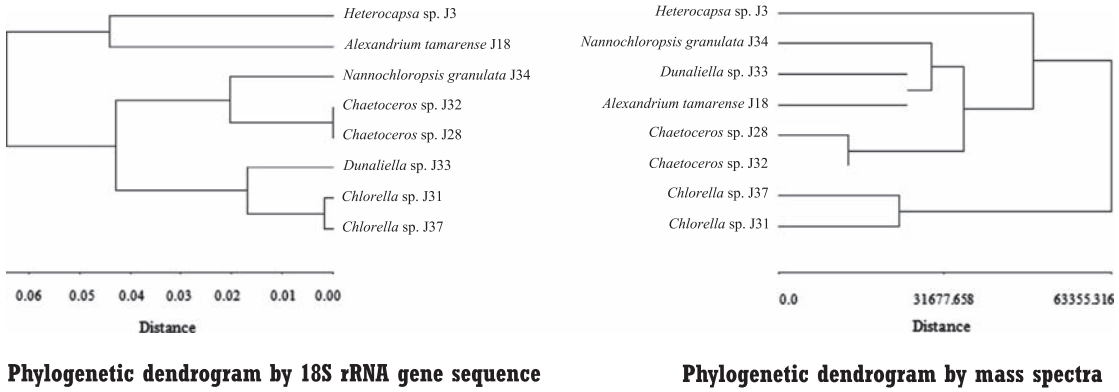


Fig. 2. Comparison between the 18S rRNA gene phylogenetic and mass spectral dendrograms for microalgae.

based on genomic taxonomy using the 18S rRNA gene sequence, and strains of the same genus were shown to be closely related (*Chlorella* sp. J31 and J37; *Chaetoceros* sp. J28 and J32). While genomic taxonomy bound closely related strains corresponding to each class in the phylogenetic dendrogram, MS-based taxonomy did not bind closely related strains corresponding to each class in the sequence-based dendrogram. The dendrograms based on mass spectra and the rRNA gene sequences were compared (Fig. 2). The MS-based dendrogram yielded relationships that were distinguishable at the taxonomic level of the genus. However, the dendrogram based on the rRNA gene sequences yielded relationships that were distinguishable at all taxonomic classification levels. Phylogeny by genotype is known to determine the taxonomy of microorganisms [15], and the restrictions of MS-based taxonomy have been previously described in a mini-review by Welker and Moore [6]. Interestingly our MS-based dendrogram positions the green alga of the genus *Dunaliella* (sample J33) with the dinoflagellate *Alexandrium* (sample J18), rather than in a clade with other green algae of the genus *Chlorella* (samples J31 and J37), as expected based on the sequence analysis. Utilizing MALDI-TOF MS with the construction of diverse microalgae MS profiles may resolve the discrepancy between sequence- and MS-based identification and prove to be an efficient method since it is more rapid and cost-effective than sequence-based identification. Currently, some databases providing protein MALDI-TOF MS libraries for bacteria with some eukaryotes are available, such as SARAMIS (AnagnosTec) and BioTyper (Bruker Daltonics); these databases have been used to rapidly identify bacteria and yeast from clinical samples [16]. Sensitivity tests demonstrated that the MALDI-TOF MS approach requires at least 10^4 cells of *Heterocapsa* sp. J3 and 10^5 cells of either *Chaetoceros* sp. J28 or *Dunaliella* sp. J33 to produce similar MS profiles containing all the abundant peaks.

3.4. Possibility of rapid identification of microalgae during HAB events using MALDI-TOF MS

Next, we sought to investigate the potential application of this method for identification of HABs. Microalgae were analyzed using MALDI-TOF MS to obtain highly abundant protein spectra. The obtained spectra from 2000 to 20,000 Da were used to construct a phylogenetic dendrogram with highly abundant protein profiles of microalgae strains; the strains were rapidly identified using MALDI-TOF MS. Though Lee and colleagues carry out dinoflagellates identification of protein profiling using MALDI-TOF MS [17], their analysis method is slower than our methods due to protein extraction phase. This MS-based method does not necessitate protein extraction and inactivation steps, and requires only a few minutes from sample collection and preparation to MS analysis and identification. Therefore, we suggest that this method can be used for rapid identification of dominant microalgae during HAB events in aquatic environments. MALDI-TOF MS can rapidly detect cyanobacteria and microalgae during HAB events in fresh water and ocean environments more rapidly than morphological and genetic identification. A previous study reported using MALDI-TOF MS to distinguish between pathogenic and non-pathogenic genotypes of the achlorophyllous microalgae species [18]. Thus the MALDI-TOF MS approach can be used to discriminate between toxic and non-toxic strains of the same species, or species of the same genus if MS databases including diverse toxic and non-toxic strains are first established. Additionally, MALDI-TOF MS may be able to provide rapid identification of microalgae or cyanobacteria in wastewater treatment facilities; however, we do not expect that this method would be applicable for complicated aquatic systems where specific microalgae are not dominant.

Identification of microalgae by morphology may be relatively simple, but classification of morphology for identification of microalgae requires expert knowledge of microalgae morphology; therefore, mistakes in the classification and identification of microalgae may occur. Taxonomic classification of microalgae can be performed by genotyping of ribosomal genes; however, this method is more expensive and time-consuming than identification of microorganisms by MALDI-TOF MS. Because MALDI-TOF MS will work only if the target microalga is present in high amounts, samples may be centrifuged and concentrated or the use of a plankton net may be helpful. Otherwise, Jadhav's method [19] to

enrich the target microorganism with specific culture media can be considered in order to increase the detection of specific target microalgae. Additionally classification and identification of microalgae based on the MALDI-TOF MS method can be performed with a user-friendly dedicated equipment and software, such as the BioTyper system. Based on our analysis, we have constructed a flowchart (Fig. S3) for rapid identification of microalgae from environments during HAB events.

4. Conclusion

In this study we described the MALDI-TOF MS-based method for monitoring the occurrence of HABs by rapid identification of harmful microalgae, as shown in previous studies for infectious bacteria [20] and achlorophyllous microalgae [18]. This rapid identification method, in combination with comprehensive profile databases of the highly abundant proteins of diverse toxic and non-toxic strains, could be effectively applied to identify eukaryotic microalgae or cyanobacteria during HAB events in fresh water and ocean environments. Furthermore, the use of MALDI-TOF MS could allow for identification of microalgae in HABs at reduced cost and in shorter times. Additionally MALDI-TOF MS profiling can be combined with other separation techniques, such as high-performance liquid chromatography and capillary electrophoresis, as demonstrated by Horká and colleagues, who analyzed the probiotic bacteria present in cow-milk using a combination of capillary electrophoresis and MALDI-TOF MS [21]. Therefore, MALDI-TOF MS combined with other separation techniques could be a useful tool to rapidly identify many microorganisms (i.e., in addition to microalgae in HABs) in the environment. In conclusion, MALDI-TOF MS can be applied for direct analysis of microalgae during a HAB event in an aquatic system by measurement of harmful microalgae.

Acknowledgments

This work was supported by a grant from the Center for Analytical Research of Disaster Science of Korea Basic Science Institute (C33730) to J.S. Choi and the Basic Science Research Program through the National Research Foundation of Korea (NRF) funded by the Ministry of Education, Science and Technology (2012R1A1A2040922).

Appendix A. Supporting information

Supplementary data associated with this article can be found in the online version at http://dx.doi.org/10.1016/j.talanta.2014.08.078.

References

[1] D.M. Anderson, A.D. Cembella, G.M. Hallegraeff, Annu. Rev. Mar. Sci. 4 (2012) 143–176.
[2] M. Maso, E. Garces, Mar. Pollut. Bull. 53 (2006) 620–630.
[3] L. Galluzzi, A. Penna, E. Bertozzini, M. Vila, E. Garces, M. Magnani, Appl. Environ. Microbiol. 70 (2004) 1199–1206.
[4] R. Aebersold, M. Mann, Nature 422 (2003) 198–207.
[5] S. Sauer, M. Kliem, Nat. Rev. Microbiol. 8 (2010) 74–82.
[6] M. Welker, E.R. Moore, Syst. Appl. Microbiol. 34 (2011) 2–11.
[7] N. Valentine, S. Wunschel, D. Wunschel, C. Petersen, K. Wahl, Appl. Environ. Microbiol. 71 (2005) 58–64.
[8] B.H. Clowers, D.S. Wunschel, H.W. Kreuzer, H.E. Engelmann, N. Valentine, K.L. Wahl, Anal. Chem. 85 (2013) 3933–3939.
[9] M. Horká, A. Kubesová, J. Šalplachta, E. Zapletalová, J. Horký, K. Šlais, Anal. Chim. Acta 716 (2012) 155–162.
[10] A. Bizzini, G. Greub, Clin. Microbiol. Infect. 16 (2010) 1614–1619.
[11] H. Trüper, K. Schleifer, The Prokaryotes, 2nd ed., Springer-Verlag, New York, NY (1992) 126–148.
[12] P. Kämpfer, S.P. Glaeser, Environ. Microbiol. 14 (2012) 291–317.
[13] L.E. Eland, R. Davenport, C.R. Mota, Water Res. 46 (2012) 5355–5364.
[14] A. Freiwald, S. Sauer, Nat. Protoc. 4 (2009) 732–742.
[15] L. Wayne, D. Brenner, R. Colwell, P. Grimont, O. Kandler, M. Krichevsky, L. Moore, W. Moore, R. Murray, E. Stackebrandt, Int. J. Syst. Bacteriol. 37 (1987) 463–464.
[16] E. Carbonnelle, P. Grohs, H. Jacquier, N. Day, S. Tenza, A. Dewailly, O. Vissouarn, M. Rottman, J.L. Herrmann, I. Podglajen, L. Raskine, J. Microbiol. Methods 89 (2012) 133–136.
[17] F.W.-F. Lee, K.C. Ho, S.C.-L. Lo, Harmful Algae 7 (2008) 551–559.
[18] J. Murugaiyan, J. Ahrholdt, V. Kowbel, U. Roesler, Clin. Microbiol. Infect. 18 (2012) 461–467.
[19] S. Jadhav, D. Sevior, M. Bhave, E.A. Palombo, J. Proteomics 97 (2014) 100–106.
[20] Z. Vasileuskaya-Schulz, S. Kaiser, T. Maier, M. Kostrzewa, D. Jonas, Syst. Appl. Microbiol. 34 (2011) 35–39.
[21] M. Horká, P. Karásek, J. Šalplachta, F. Růžička, M. Vykydalová, A. Kubesová, V. Dráb, M. Roth, K. Šlais, Anal. Chim. Acta 788 (2013) 193–199.

Talanta 132 (2015) 635–640

Contents lists available at ScienceDirect

Talanta

journal homepage: www.elsevier.com/locate/talanta

Raman spectroscopy based identification of flame retardants in consumer products using an acquired reference spectral library

Sutapa Ghosal*, Huiting Fang

Environmental Health Laboratory Branch, California Department of Public Health, Richmond, CA 94804, USA

ARTICLE INFO

Article history:
Received 10 September 2014
Received in revised form
1 October 2014
Accepted 4 October 2014
Available online 30 October 2014

Keywords:
Raman spectroscopy
Flame retardants
Molecular identification

ABSTRACT

Flame retardants (FRs), a class of commonly used chemical additives in consumer products such as polyurethane foams, are well known for their persistence in the environment, bioaccumulation and potential toxicity [1]. In order to address the potential health concerns and environmental impacts associated with the wide-spread use these chemicals, it is essential to identify them efficiently in the environment and consumer products. Raman spectroscopy (RS) offers an attractive option for the non-invasive, in-situ identification of flame retardants in a variety of sample formats [2–4]. RS based chemical identification relies on the availability of spectral libraries for identification through spectral matching with reference chemicals. Here we present the application of Raman spectroscopy for identifying FR additives in select consumer products using an acquired spectral library of commonly used FRs. The RS based method described here enables simultaneous identification of multiple components within a sample, which can offer important insights into the sources of FR contamination, in addition to identification of the FR component itself. The availability of Raman spectral library of commercially used FRs, such as the one presented here, will facilitate the identification of these chemicals in consumer products.

Published by Elsevier B.V.

1. Introduction

Since establishment of the Technical Bulletin in 1975 [5], by which the California Bureau of Electronic and Appliance Repair, Home Furnishings and Thermal Insulation (BHFTI) regulated the flammability of upholstered furniture and bedding products, a wide variety of flame-retardants (FR), especially brominated flame-retardants (BFR), have been used by US manufacturers for decades to comply with the flammability standards outlined in the bulletin. Consequently, demand for FR chemicals in the US has increased by 4.6% each year, and is expected to reach 938 million pounds in 2016 according to the Global Information Inc. [6] At the same time, numerous studies have shown that the wide spread use of FRs is not safe as they pose potentially significant health risks [1]. As early as 1973, there were reports of adverse health effects resulting from the contamination of animal feed with polybrominated biphenyls (PBBs) in Michigan, and as a result PBBs were banned from production [7,8]. Over the last decade a number of widely used FRs including polybrominated diphenyl ethers (PBDE) such as penta- and octa-brominated diphenyl ethers (BDE), which are known for their toxicity effects [9], have either been banned by the state government or voluntarily phased out by US manufacturers. To further reduce US manufactures' reliance on synthetic flame retardants, a new flammability standard TB117-2013 was issued recently by BHFTI [10]. TB117-2013 requires all upholstered furniture to pass a smolder resistant test rather than an open flame test [10]. In other words, US foam manufacturers are no longer required to add FR chemicals to pass the flammability test. Despite the restrictions on production and usage of toxic FRs, consumer products previously treated with banned chemicals are still in use. In addition, the proposed alternative FR species, such as tris(1,3-dichloro-2-propyl) phosphate (TDCPP), also pose significant environmental and health hazards [11]. As a result of these concerns, it has become necessary to monitor the prevalence and distribution of these chemicals in various consumer products and the environment in order to better understand and thus mitigate any associated health and environmental impacts.

Numerous studies have been conducted to characterize flame retardants both in the environment and in consumer products using a variety of different techniques. Kierkegaard et al. identified decabromodiphenyl ethane, in sewage sludge, sediment, and indoor air using high-resolution mass spectrometry (MS) and quantified it with low-resolution MS [12]. Guardia et al. have reported a method for determining the concentration of PBDEs in multiple FR mixtures using gas chromatography/mass spectrometry (GC/MS) [13]. Stapleton et al. used GC/MS coupled with a portable X-ray fluorescence analyzer (XRF) to identity FR chemicals in polyurethane foam collected from baby products [14].

* Corresponding author at: Environmental Health Laboratory Branch, California Department of Public Health, 850 Marina Bay Parkway, Mailstop G365/EHLB, Richmond, CA 94804, USA. Tel.: +1 510 620 2815; fax: +1 510 620 2825.
E-mail address: Sutapa.Ghosal@cdph.ca.gov (S. Ghosal).

http://dx.doi.org/10.1016/j.talanta.2014.10.007
0039-9140/Published by Elsevier B.V.

While Webster et al. analyzed the presence of deca-BDE in indoor dust samples using scanning electron microscopy with energy dispersive X-ray spectroscopy (SEM/EDS) as well as a micro-XRF [15]. MS based methods for the identification of FRs are not applicable for chemicals which are thermally labile, such as hexabromocyclododecane (HBCD) [16]. Moreover, MS based techniques often rely on invasive and time consuming sample preparation steps in order to provide molecular level information. Fluorescence and electron microscopy techniques offer elemental and morphological information, but lack FR specific molecular identification. Therefore, an analytical approach that offers direct, non-invasive molecular-level identification of FR chemicals in consumer products and in environmental samples with minimal sample preparation would be of considerable interest.

Raman spectroscopy has been widely used as a non-invasive analytical tool for the characterization of both organic and inorganic materials since its inception in the 1930s [17]. The molecular specificity of Raman analysis can be combined with high spatial resolution afforded by a microscopy platform and the resulting technique is referred to as Raman micro-spectroscopy (RMS), which is a highly versatile tool for a broad range of analytical applications. In particular, access to spatially resolved chemical information without extensive sample preparation or water interference makes the RMS technique appropriate for a variety of sample formats [17,18]. We have previously demonstrated the application of RMS for identifying individual fungal spores [19] as well as FR species in environmental samples [2,3]. Kikuchi et al used Raman spectroscopy for the analysis of brominated FRs in electrical and electronic equipment [4]. Raman spectroscopy based chemical identification involves qualitative/quantitative spectral matching of an unknown spectrum with a spectral library of reference chemicals, and hence relies on the availability of well-documented spectral libraries. Raman spectral libraries related to various applications have been created in order to facilitate the increasing use of Raman spectroscopy in a variety of fields including forensic science, archaeology, art, medicine, solid-state physics, and pharmaceutical chemistry. Given the suitability of RMS for environmental analysis, it is necessary to create tailored spectral libraries for particular applications such as the detection/identification of specific environmental contaminants. Here we present the acquisition of Raman spectral library of FR chemicals commonly used in consumer products. The acquired spectral library is subsequently used to identify of FR additives in representative consumer items. This study illustrates the application of Raman spectroscopy for the identification of FR additives and polymer matrices associated with consumer products through the matching of unique spectral signatures. Simultaneous identification of FR with the associated polymer matrix is essential for linking FR contaminants to specific consumer materials, which is an important step towards source attribution. Creation of a reference spectral library for commonly used FRs is essential for the RS based identification of FRs in a broad range of samples.

2. Material and methods

2.1. FR materials

FR reference chemicals for the creation of FR specific spectral library were acquired from various commercial sources. These include Sigma-Aldrich, St-Louis, MO; Pfaltz and Bauer, Waterbury, CT, and AccuStandard, New Haven, CT. The various FR species analysed in this study are—decabromodiphenyl ether (deca-BDE,); hexabromodiphenyl ether (hexa-BDE); 2-ethylhexyl-2,3,4,5-tetrabromobenzoate (TBB); bis(2-ethylhexyl)-tetrabromophthalate (TBPH); tris(1,3-dichloro-;2-propyl) phosphate (TDCPP); tris(2-chloroethyl) phosphate (TCEP); hexabromocyclododecane (HBCDD); tetrabrom obisphenol A (TBBPA); brominated polystyrene (Br-PS); tris(2-chloropropyl) phosphate (TCPP); triphenyl phosphate (TPP) and antimony trioxide (Sb_2O_3). Reference spectrum of pentabromodiphenyl ether (penta BDE) was acquired from polyurethane foam containing 5.3% Penta-BDE as measured by bulk GC–MS [20] and was validated by comparison with penta-BDE spectrum available in the literature [21]. Melamine spectrum was available from in-house Raman spectral libraries.

2.2. Consumer materials

Representative consumer materials for this study were collected from commonly used consumer items, which are typically known to contain FRs. These included materials from a VCR and a computer monitor (CRT) casings as well as the fabric from a car visor. The exact manufacture dates of these items were not known, but they were estimated to have originated between the years of 1985–2005 and had been subjected to extensive use. Additional consumer materials included several samples of polyurethane foam (PUF)—these samples were kindly provided by Dr. Thomas Webster (Boston University) and Dr. Heather Stapleton (Duke University) and had been collected as part of their study on FR exposure among gymnasts [20]. Approximately 1 mm^2 sized samples were extracted from each material using a clean scalpel blade. The samples were then placed on double-sided adhesive carbon substrates mounted on standard aluminum SEM stubs.

2.3. Confocal Raman spectroscopy

Raman spectroscopy measurements were performed using two commercially available micro-Raman setups, each equipped with a near-infrared 785 nm diode laser—(1) Senterra Dispersive Raman microscope (Bruker Optics Inc., Billerica, MA), and (2) Renishaw inVia Raman microscope (Renishaw Plc., Old Town, Wotton-under-Edge, Gloucestershire, U. K.). On the Senterra Raman microscope, all spectra were recorded and analyzed using OPUS 6.0.72 dll 3.0.1.1 software (Opus Software Inc., San Rafael, CA) with a spectral resolution of $\sim$3–5 cm^{-1}. The Senterra system is equipped with Sure_Cal® function for continuous automated laser and Raman frequency calibration using an integrated neon laser light. On the Renishaw system, GRAMS WiRE software package (Galactic Industries Corp., 395 Main St., Salem, NH) was used for instrument control and data acquisition. The spectral resolution was $\sim$2.5 cm^{-1}. Wavelength calibration was performed periodically using neon laser light. On both systems a silicon wafer spectrum was acquired on a daily basis as a quality control step to monitor and correct for minor wavelength offsets. Samples were excited using 1–100 mW of 785 nm laser light focused onto the sample typically through a 20× or 50× objective. Signal acquisition times varied between 60 and 120 s per measurement. Spectra for the liquid FR samples were acquired using a Macrokit (Renishaw Plc) sample holder coupled to the Renishaw microscope, which enables spectral acquisition in the liquid phase. Raw spectra were processed to eliminate dark noise and contributions from the spectrometer's optical parts. The spectra were baseline corrected using a Fixed Multi-point Baseline Correction algorithm (GRAMS/AI version 9.1) or a Concave Rubberband Correction method (Opus Software Inc., San Rafael, CA) and smoothed using Savtisky–Golay smoothing algorithm (GRAMS/AI version 9.1). Preprocessed spectra of the reference FR samples were compiled into a spectral database using the GRAMS Spectral ID software from Thermo Fisher Scientific Informatics. Molecular identification of sample composition was accomplished through spectral library searches using both commercial and laboratory acquired Raman spectral libraries. Spectral library searches were performed using

an automated correlation based search algorithm (GRAMS Spectral ID, version 9.1). The quality of the match between the sample and the various library spectra was evaluated based on visual inspection of the spectra as well as calculated Hit Quality Index (HQI) values, which ranged from 0 to 1, with 0 representing a perfect match.

3. Results and discussion

3.1. Acquisition of FR spectral library

In order to identify an unknown chemical through spectral library search it is necessary to use a reference spectral library of relevant chemicals against which the unknown spectrum can be evaluated for a potential match. Fig. 1 shows the acquired Raman spectra of a number of FR reference chemicals commonly found in consumer products. The spectral range shown in Fig. 1 extends from 100 to 2000 cm^{-1}, where majority of the FR related spectral features are typically located. Each FR species displays a unique spectral fingerprint, which distinguishes it from other members of the FR family and can be used to identify it. This is true even for closely related FRs such as PBDEs, which differ in terms of the number and arrangement of Br ions per molecule. For example, hexa- and deca-BDE (containing 6 and 10 Br ions, respectively) both have peaks in the 100–250 cm^{-1} region (Fig. 1), typically associated with brominated FRs [22]. However, each can be individually identified based on their unique spectral features. Deca-BDE is characterized by triplet peaks centered at ~224 cm^{-1}, while hexa-BDE has a broad peak at ~212 cm^{-1}. In both cases, the general peak position is indicative of the C-Br bond [22], but the detailed features are representative of their unique molecular structure. Spectral feature corresponds to distinct molecular vibrations and as such are characteristic of the analyte's unique molecular and structural composition.

Since the ban on use of various BFRs, phosphorus based flame retardants (PFRs) have often been proposed as potential alternatives. PFRs can be broadly classified into three groups i.e. inorganic, organic and halogen containing PFRs [23]. Raman spectra of some of the commonly used PFRs are shown in Fig. 1. The three chlorine containing PFRs (TCEP, TCPP, TDCPP) all show prominent peaks in the 600–800 cm^{-1} region typically associated with C–Cl stretching [22]. As with BFRs, the individual PFR species are clearly distinguishable based on their unique spectral signatures. The acquired FR spectral library, shown in Fig. 1, highlights the utility of Raman spectral analysis for distinguishing between broad classes of FRs such as BFR versus chlorinated PFR, as well as identifying individual FR species. This will be illustrated in greater detail in subsequent sections, where we present the identification of FR additives in representative consumer products.

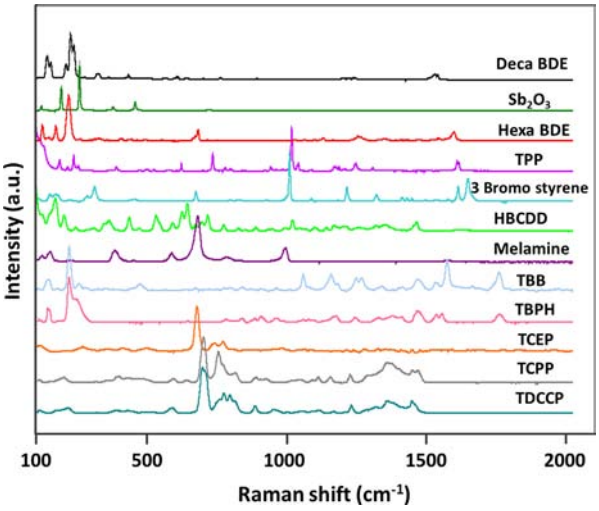


Fig. 1. Reference Raman spectra of FRs commonly present in consumer products.

3.2. Identification of FR additives in polyurethane foam

Polyurethane foam is one of the most extensively used polymer materials, with widespread applications in furniture and a variety of other consumer products. The widespread use of PUF makes it potentially a significant source of PUF related FR contamination in the environment. In recent years, Stapleton et al and Carignan et al. have investigated this particular class of FRs in terms of their presence in consumer products and the environment [14,20]. Here we present RMS based identification of FRs in PUF samples that have been previously characterized by Carignan et al. using gas chromatography negative chemical ionization mass spectrometry (GC/ECNIMS) and X-ray fluorescence spectroscopy (XRF) [20]. Given the detailed analytical information already available about these samples, they represent a unique opportunity for exploring the feasibility of RMS based identification of FRs in consumer products.

Table 1 lists the PUF samples examined in this study along with the associated FRs and their respective concentrations as reported by Carignan et al. [20]. Carignan et al. identified TDCPP to be the primary FR in PUFs 7 and 8, with measured concentrations of 6.6% and 5.6%, respectively [20]. RMS analysis of PUFs 7 and 8 is shown in Fig. 2 along with the reference spectra for melamine and TDCPP. Melamine was identified as a major constituent in both PUF 7 and 8 based on spectral matching analyses. Melamine and its derivatives are classified as non-halogenated flame retardants and have been proposed as viable alternatives to Penta-BDE [23–25]. It is currently used in flexible polyurethane foam in concentration ranging from 30% to 40% melamine per weight of the polyol and is typically applied as a crystalline powder [25]. Strong melamine specific peaks (967.3 cm^{-1}, 984 cm^{-1}) evident in PUF 7 and 8 spectra suggest significant presence of melamine in the foams. This is consistent with the typical concentrations of melamine reported in the literature (30-40%) [25], which is considerably higher than the TDCPP concentrations (< 10%) reported by Carignan et al. [20]. In addition to melamine, PUF 7 spectrum also showed evidence of TDCPP along with peaks related to the polymer matrix (600–1800 cm^{-1}) (Fig. 3). Polymer related peaks representing the PUF matrix were common to all the PUF samples examined in this study.

The two individual PUF 7 spectra shown in Figs. 2 and 3 were acquired at two different locations on the sample and are spectrally distinct. The observed differences in spectral features correspond to differences in molecular composition at these two sites and as such are indicative of spatial heterogeneity in sample composition. The PUF 7 spectrum shown in Fig. 2 is characterized by strong melamine peaks suggestive of a melamine hotspot. The observed heterogeneous distribution of melamine in PUF 7 is

Table 1
List of PUF samples analyzed in this study along with the FR species and the corresponding concentrations as reported by Carignan et al. [20].

PUF	FRs (%)[20]
7	TDCPP (6.6)
8	TDCPP (5.6)
6	TBB (2.8), TPP (1.1), TBPH (1.3)
5	Penta BDE (3.7), TPP (0.3)
4	Penta BDE (5.3), TPP (0.4)
3	Penta BDE (4.8), TPP (0.3), TDCPP (0.1)

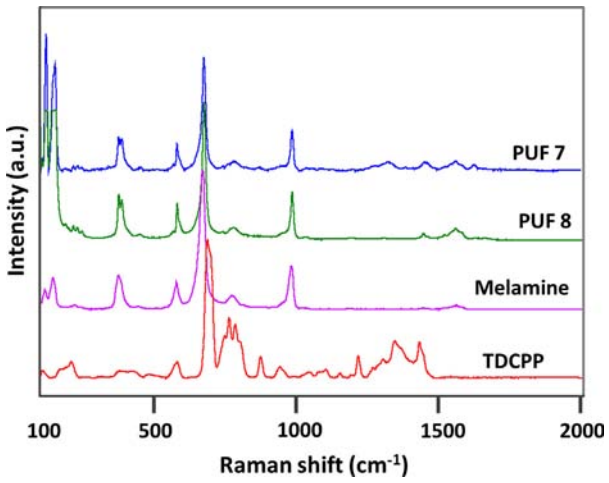


Fig. 2. RMS analyses of two different foam samples (PUF 7 and 8) showing spectral comparison with reference Raman spectra of melamine and tris(1,3-dichloro-2-propyl) phosphate (TDCPP).

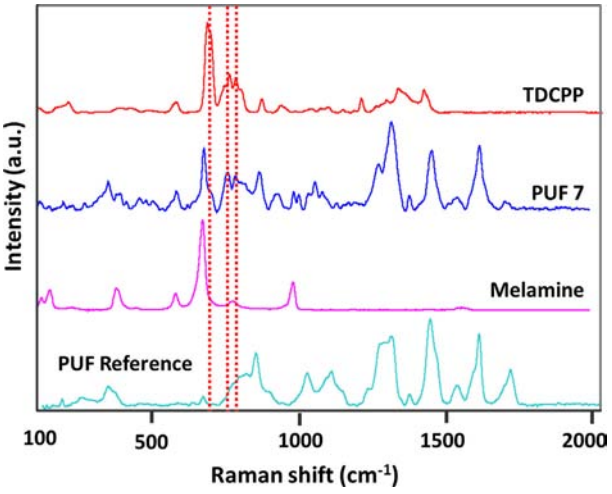


Fig. 3. Raman spectrum of the PUF 7 foam sample showing spectral matches with reference Raman spectra of tris(1,3-dichloro-2-propyl) phosphate (TDCPP), melamine, polyurethane foam (PUF). The red dotted lines identify position of the strongest TDCPP peaks.

consistent with the application of melamine as crystalline powder, which can create localized hotspots.

A particular advantage of RMS analysis is that it enables simultaneous identification of multiple constituents in the sample by probing the entire Raman active compositional profile. For instance, in case of PUF 7, we were able to identify several components including melamine, TDCPP and the polymer matrix based on the acquired spectrum. In Raman analysis, spectral response is determined by concentration and Raman cross-section of the constituent molecular bonds. Therefore, the spectral response can be dominated by signals from constituents with higher concentration and/or Raman cross-section. An example of this can be seen in case of PUF 6, which was reported as containing multiple FR species—TPP, TBB and TBPH [20]. Fig. 4 shows acquired spectrum of PUF 6 along with reference spectra of the three constituent FR species. The PUF 6 spectrum is dominated by peaks arising from the polymer matrix, which is the primary constituent. In comparison, the FR related peaks are less prominent. TPP is identifiable based on two sharp peaks located at 1005 cm^{-1} (P–O–C anti-symmetric stretch in organ-ophosphorus compounds) and 3063 cm^{-1} (=C–H stretch of the benzene ring) [22]. TBB and TBPH

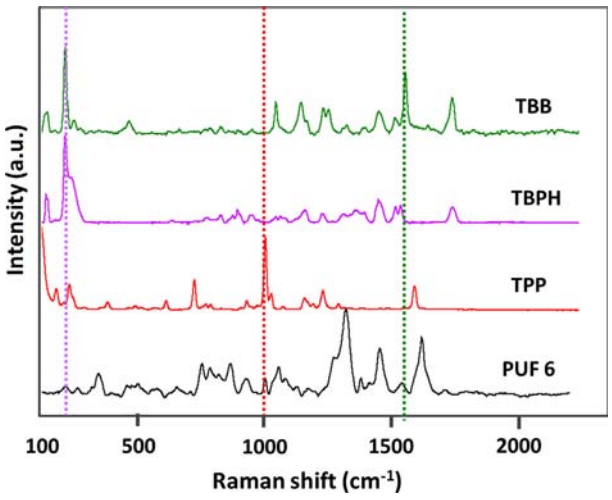


Fig. 4. Raman spectrum of the PUF 6 foam sample showing spectral matches with reference Raman spectra of 2-ethylhexyl-2,3,4,5-tetrabromobenzoate (TBB), bis(2-ethylhexyl)-tetrabromophthalate (TBPH), triphenyl phosphate (TPP). Dotted green, purple and red lines identify positions of the strongest peaks for TBB, TBPH and TPP, respectively. (For interpretation of the references to color in this figure legend, the reader is referred to the web version of this article.)

both show a sharp peak around 216 cm^{-1}, indicative of the C-Br bond [22]. In addition to the 216 cm^{-1} band, TBB also has a sharp peak at 1555 cm^{-1} (benzene ring stretch), which distinguishes it from TBPH [22]. All of these FR related peaks are evident in the PUF 6 spectrum though they are less prominent compared to the PUF peaks. In addition to the above mentioned FR species, PUF 6 also showed some localized presence of melamine.

The three remaining PUF samples (PUF 3, 4, and 5) were all reported as containing TPP and Penta-BDE in varying concentrations, Penta-BDE being the dominant FR species [20]. Fig. 5 shows acquired spectra of the three PUF samples. All three spectra have a sharp peak at 1005 cm^{-1} from TPP. They also contain singlet and doublet peaks in the 100–250 cm^{-1} region, which are characteristic of penta BDE [21]. Similar to PUF 6, these spectra also show strong response from the polymer matrix.

In summary, RMS analysis of the PUF samples confirmed the presence of FR species previously identified by Carignan et al [20]. In addition, RMS analyses also identified the presence of melamine, not reported by Carignan et al [20]. These results also illustrate the simultaneous identification of multiple constituents in a sample, which is a particularly advantageous in terms of contaminant and source attribution in environmental monitoring. This is discussed further in the following section where we present RMS based characterization of select consumer products, simultaneously identifying both the polymer matrix and the associated FR species.

3.3. Identification of FR species and polymer matrices in consumer products

Consumer products are a major source of FR related contamination, particularly in indoor environments [15,26–29] where migration of FRs from consumer items into the surroundings can take place via volatilization and/or physical weathering of products [15,30,31]. Several studies have highlighted the necessity of linking FR contaminants in the environment to their original sources [15,26]. In case of mechanical transfer of FRs via physical weathering of products, FR chemicals are often transferred in association with the product matrix. We have previously reported the identification of FRs together with the associated polymer matrix, in residential dust samples, which is suggestive of

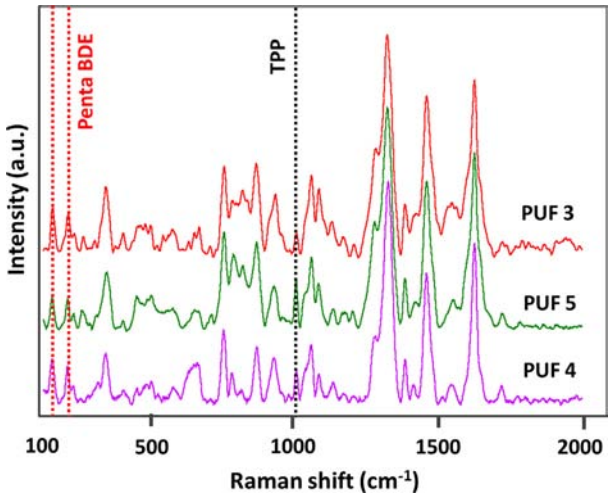


Fig. 5. RMS analyses of foam samples from three different sources with peak assignments for the identified FR species, penta BDE and triphenyl phosphate (TPP). Dotted red and green lines identify positions of the strongest peaks for penta BDE and TPP, respectively. (For interpretation of the references to color in this figure legend, the reader is referred to the web version of this article.)

mechanical transfer of FRs from consumer items into the environment via physical weathering [2,3]. Linking FR contamination to a specific consumer item necessitates knowledge of the product composition i.e. FR species and polymer matrix associated with the item. As mentioned earlier, Raman spectroscopy is well suited for this type of multicomponent analysis. To illustrate this point, we present RMS based characterization of three consumer items (car visor covering and, casing materials from a VCR and a computer monitor) with the goal of identifying the polymer matrices and the associated FR species.

Fig. 6 shows acquired spectra of the three consumer materials along with reference spectra of the polymer and FR constituents identified through spectral library search. In all three cases, both the polymer matrix and the associated FR species are readily identifiable based on their unique spectral signatures. The car visor material consists of two FRs, deca-BDE and antimony trioxide, incorporated into a polyvinyl chloride (PVC) polymer matrix (Fig. 6a). The VCR casing material was identified as high-impact polystyrene (HIPS) with deca-BDE as the FR component (Fig. 6b). The polymer and FR components of the CRT casing were determined to be polycarbonate (PC) and TPP, respectively (Fig. 6c). Product specific spectral fingerprints offered by the RMS method

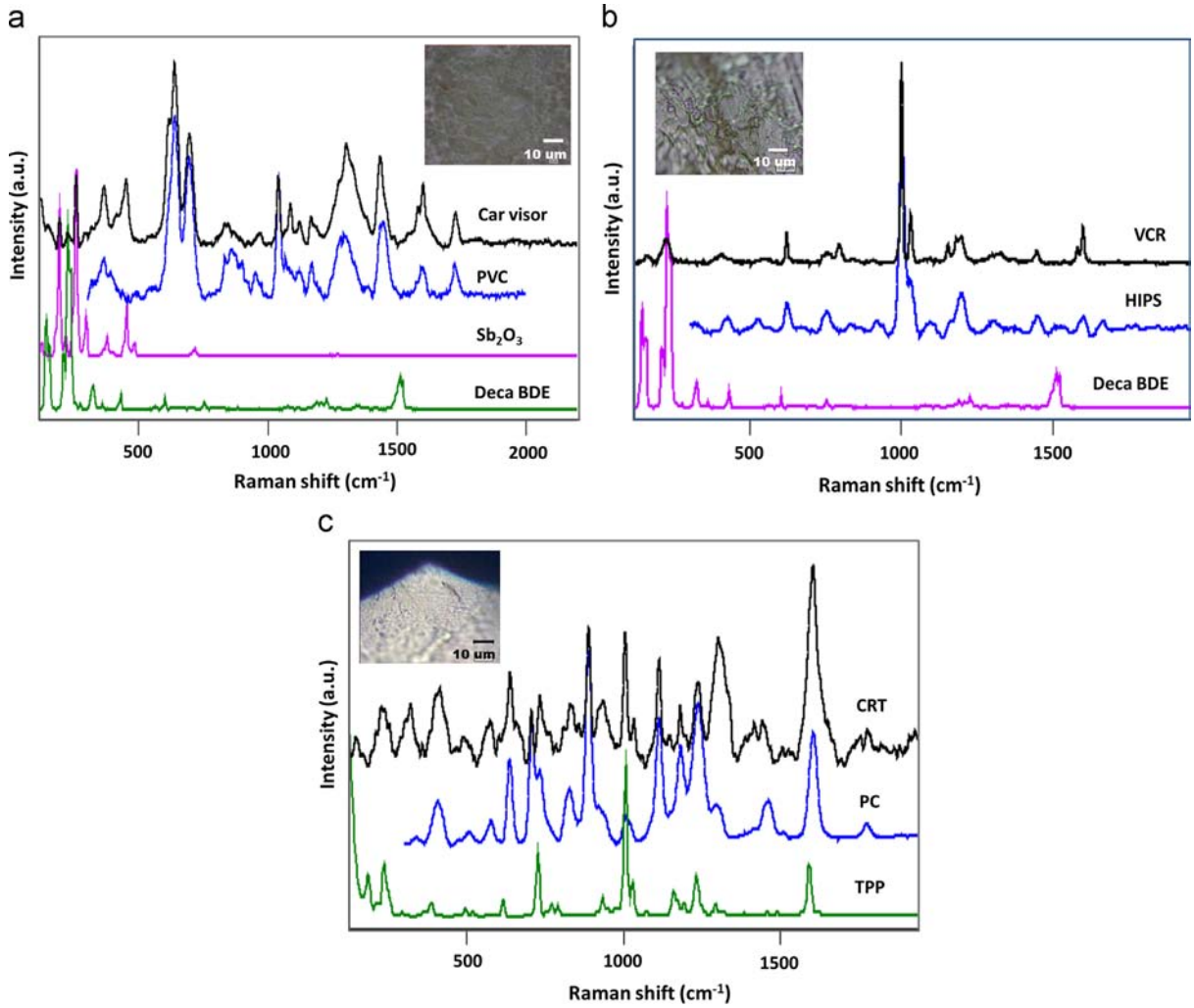


Fig. 6. RMS analyses of consumer products. (a) Raman spectrum of car visor material showing spectral match with reference Raman spectra deca-BDE, antimony trioxide (Sb_2O_3) and polyvinyl chloride (PVC). (b) Raman spectrum of the VCR casing showing spectral match with reference Raman spectra of high impact polystyrene (HIPS) and deca-BDE. (c) Raman spectrum of the CRT casing showing spectral match with reference Raman spectra of poly carbonate (PC) and triphenyl phosphate (TPP). Insets: 50 × reflected light image showing the region of RMS analysis.

described here can be used for FR identification and source attribution in a variety of environmental samples and consumer products.

4. Conclusion

The results presented here highlight the utility of Raman spectroscopy as a non-invasive analytical tool for the identification and source attribution of FRs in consumer products and environmental samples. RS based identification relies on the availability of relevant spectral libraries of reference chemicals in order to accomplish chemical identification through spectral matching. We have compiled a reference spectral library of several commonly used FR chemicals to facilitate the identification process. The acquired spectral library has been used successfully to identify FR additives in a selection of commercially used polyurethane foam samples. The foam samples had been previously characterized by GC–MS as part of a separate study [20]. Our results are in excellent agreement with the previous study and also offer additional information such as the presence of melamine, another FR species. We have also identified polymer matrices and FR species associated with three commonly used consumer items to illustrate the applicability of RS for source characterization.

Acknowledgements

S.G. and H.F. would like to thank Dr. Thomas Webster (Boston University) and Dr. Heather Stapleton (Duke University) for access to the PUF samples. S.G. would also like to thank Dr. Jeff Wagner (CDPH) for access to consumer product samples and Dr. Simon Ip for helpful discussions.

References

[1] S.D. Shaw, et al., Rev. Environ. Health 25 (4) (2010) 261–305.
[2] S. Ghosal, J. Wagner, Analyst (2013) 3836–3844138 (2013) 3836–3844.
[3] Wagner, J., et al., Morphology, Spatial Distribution, and Concentration of Flame Retardants in Consumer Products and Environmental Dusts using Scanning Electron Microscopy and Raman Micro-spectroscopy. 2012.
[4] S. Kikuchi, et al., Anal. Sci. 20 (2004) 1111–1112.
[5] California Bureau of Electronic and Appliance Repair, H.F.a.T.I., Requirements, Test Procedure and Apparatus for Testing the Flame Retardance of Resilient Filling Materials Used in Upholstered Furniture., in Technical Bulletin 117 S.o.C. D.o.C. Affairs, (Ed.), 1975: Sacramento, CA.
[6] Information, G., Flame Retardants (US Market & Forecast), in Advanced Material Market Research Report. 2012, Global Information p. 245.
[7] J.K. Stross, et al., Toxicol. Appl. Pharmacol. 58 (1981) 145–150.
[8] J. Jacobson, et al., Am. J. Public Health 74 (4) (1984) 378–379.
[9] T.A. McDonald, Chemosphere 46 (5) (2002) 745–755.
[10] California Bureau of Electronic and Appliance Repair, H.F.a.T.I., Requirements, Test Procedure and Apparatus for Testing the Flame Retardance of Resilient Filling Materials Used in Upholstered Furniture., S.o.C.D.o.C. Affairs, (Ed.), 2013: Sacramento, CA.
[11] I. van der Veen, J. de Boer, Chemosphere (2012) (Journal Article).
[12] A. Kierkegaard, J. Bjorklund, U. Friden, Environ. Sci. Technol. 38 (12) (2004) 3247–3253.
[13] M.J. Guardia, R.C. Hale, E. Harvey, Environ. Sci. Technol. 40 (2006) 6247–6254.
[14] H.M. Stapleton, et al., Environ. Sci. Technol. 45 (2011) 5323–5331.
[15] T.F. Webster, et al., Environ. Sci. Technol. 43 (9) (2009) 3067–3072.
[16] E. Eljarrat, D. Barceló, TrAC Trends Anal. Chem. 23 (10) (2004) 727–736.
[17] M.J. Pelletier, Analytical Applications of Raman Spectroscopy, Blackwell Science Ltd., Oxford, 1999.
[18] G.J. Puppels, et al., J. Raman Spectrosc. 22 (1991) 217–225.
[19] S. Ghosal, J.M. Macher, K. Ahmed, Environ. Sci. Technol. 46 (11) (2012) 6088–6095.
[20] C.C. Carignan, et al., Environ. Sci. Technol. 47 (23) (2013) 13848–13856.
[21] G.C. Stevens, et al., A new rapid analysis method for fire retardants in polymers, in: InterFlam, Interscience Communications: University of Nottingham, Nottingham, UK, 2010.
[22] J.B. Lambert, H.F. Shurvell, R.G. Cooks, Introduction to Organic Spectroscopy, Macmillan, New York, 1987.
[23] I. van der Veen, J. de Boer, Chemosphere 88 (2012) 1119–1153.
[24] S.L. Waaijers, et al., Rev. Environ. Contam. Toxicol. 222 (2013) 1–71.
[25] U.S.E.P. Agency, Environmental Profiles of Chemical Flame-Retardant Alternatives for Low-Density Polyurethane Foam, U.S.E.P. Agency, 2005.
[26] J.G. Allen, et al., Environ. Sci. Technol. 42 (11) (2008) 4222–4228.
[27] Suzuki, G., et al., PBDEs and PBDD/Fs in House and Office Dust from Japan., in Organohalogen Compounds. 2006: Oslo, Norway. p. 1843–1846.
[28] H.M. Stapleton, et al., Environ. Sci. Technol. 39 (4) (2005) 925–931.
[29] S. Hazrati, S. Harrad, Environ. Sci. Technol. 40 (24) (2006) 7584.
[30] Kose, T., et al., Determination of the Emission Amount of Organic Pollutants from Household Products Using a Model Room., in Organohalogen Compounds. 2008: Birmingham, England. p. 2305–2308.
[31] G. Suzuki, et al., Environ. Sci. Technol. 43 (5) (2009) 1437–1442.

Talanta 132 (2015) 641–647

Contents lists available at ScienceDirect

Talanta

journal homepage: www.elsevier.com/locate/talanta

Boron doped diamond microelectrodes arrays for electrochemical detection in HPLC

Eric Mahé, Didier Devilliers *, François Dardoize

Sorbonne Universités, UPMC Univ Paris 06, CNRS, UMR 8234 PHENIX, Electrochimie et liquides ioniques, 4 Place Jussieu, 75005 Paris, France

ARTICLE INFO

Article history:
Received 10 June 2014
Received in revised form
30 September 2014
Accepted 2 October 2014
Available online 22 October 2014

Keywords:
High performances liquid chromatography
Electrochemical detection
Boron doped diamond
Microelectrodes arrays (MEA)

ABSTRACT

Boron doped diamond microelectrodes arrays (MEA) have been prepared in order to be used as new amperometric sensors in electrochemical cells for HPLC detectors. The following parameters were studied: number and diameter (15–40 μm) of the electrodes, distance between them (50–240 μm), and effect of the flow rate (0.1–3 mL/min). It was thus possible to find the optimum value of the parameters which give a good signal/noise ratio in the chronoamperometric responses, with a size of the electrochemical sensors as small as possible.

© 2014 Elsevier B.V. All rights reserved.

1. Introduction

Electroanalysis is a powerful tool for analytical chemistry, especially considering flow analysis and amperometric HPLC detection. Forty years ago, Adams and Kissinger have started their contributions to the development of the electrochemical (EC) detection associated to liquid chromatography (LC) [1]. The principle of these detectors is based on an electron transfer reaction during the oxidation/reduction process of a target analyte, after its separation in a chromatography column, at a millimetric/centimetric solid electrode for the major part of the modern systems [2,3].

The use of these detectors in HPLC is attractive because of their qualities: selectivity and sensibility. Generally these detectors are not very expensive; they are composed of a simple efficient potentiostatic electronic part, associated with a high gain current follower and a sensor: a three-electrode flow-cell, which is the sensitive part of the detector. The principle of the amperometric detectors is to apply an appropriate electric potential between the reference and the working electrode and to measure the faradaic current resulting from the analyte reaction at the working electrode. This current is proportional to the concentration of the sample after baseline correction of the residual current. Several kinds of materials were used in those cells for the working electrode considering their respective electrochemical window and stability: carbon paste, gold, platinum, silver, glassy carbon, etc. In the active volume of a cell, three mass transport mechanisms exist: convection far from the electrode surface, migration and diffusion close to the active surface of the working electrode. A number of works were done to simulate these mass transfers and provide interesting ways to improve the design of the electrochemical cells [4,5]. In a LC–EC flow-cell, it is assumed that the hydrodynamic regime is controlled by the competition between the convective part and the diffusional part. Péclet adimensional number is the suitable parameter for the quantification of the ratio of the convection transport rate to the diffusion transport rate.

In addition, microelectrodes [6] were widely studied for their use in analytical electrochemistry, because of the increase of the current density by the hemispherical diffusion effect, leading to a better signal/noise ratio and to a short response time [7]. However, if the current density may be high on one microelectrode, when the concentration of the sample is low the total current remains very small and generally arrays of microelectrodes are used to get an amplification of the current measured for signal treatments [8–11]. Theoretical studies were led to propose the best arrangement of the microelectrodes in the arrays. Usually done in static medium, they give a good idea for the distances between microelectrodes to get the different signal regimes for further studies in continuous flow [12].

In 1987, it was shown by Pleskov et al. [13] that synthetic diamond doped with boron (BDD) becomes conductive and offers a high overpotential for oxygen or hydrogen evolution. There is an important focus on the development of this material which could be attributed to its numerous qualities: chemical inertness, mechanical durability, low background current and wide electroactive window.

* Corresponding author. Tel.: +33 144273677; fax: +33 144273856.
E-mail address: didier.devilliers@upmc.fr (D. Devilliers).

http://dx.doi.org/10.1016/j.talanta.2014.10.028
0039-9140/© 2014 Elsevier B.V. All rights reserved.

For that reason, it has been proposed as an anodic material for the oxidation of organic pollutants [14]. In addition, it is easy to clean in situ [15].

The research of the lowest concentration detection is a constant goal in HPLC. This goal can be reached by combining the qualities of the diamond material and the array of microelectrodes in an amperometric detector. The parameters which must be taken into account to manufacture optimized BDD microelectrodes array (MEA) for HPLC amperometric detection are studied in the present work.

To our knowledge, the first operational application of microelectrodes for the use in HPLC was done by Kissinger and colleagues [16]. An interdigitated array of microelectrodes was used to enhance the current obtained in a redox cycling process in a flow stream at the output of an HPLC column. The results show a higher current density and lower noise due to the size effect of the microelectrodes array used, compared to a macro-electrode with the same geometric area.

The interest of microelectrodes has met a fast development, the microdisc electrodes were widely used to study rapid electron transfer processes and theoretical models were proposed for the mass transport on different shapes of microelectrodes in static cells [17,18].

More and more techniques were employed to machine arrays of microelectrodes, for example, sealed wires in epoxy with a polishing of the surface [19], easy to produce but with a poor reproducibility; arrays have been constructed on silicon substrates using electron beam lithography [20], or multilayer systems with conductive carbon ink laid on a polymer surface and covered by an insulator film. The electrodes are obtained by laser drilling, leading to small holes through the insulator down to the carbon ink [21]. This process offers numerous possibilities to modify the diameter of the electrodes, their number and their spacing. It allows the manufacturing of different arrays and so, verifying if the tests are in agreement with the theory.

The first use of these arrays is for cyclic voltammetry with the electrodes in a static cell with fast-scan technique [17]. However, Aixill et al. [22] demonstrated the good agreement between the theory to predict the current at a micro-strip electrode taking into account the lateral diffusion, normal diffusion and axial convection and the experimental results obtained with a home-made cell with platinum strips as working electrodes and the oxidation of tris(4-bromophenyl)amine in continuous flow-cells. The results show an enhanced mass transport characteristic compared with equivalent macro-electrodes. In practical devices, the machining of the micro-arrays introduces a finite thickness of the insulating layer or a recessed geometry of the conductive part, responsible of the local perturbation of the flow. A simulation of the effect was realized [23] for the two cases with the strips across the flow and for different linear speeds of the liquid. For recessed micro-band electrodes, the formation of eddies inside the cavities led to an increase of a stagnant flow at the bottom which prevents the renewal of the electro-active species. The industry of semiconductors has introduced new technologies to produce thin insulating films with hard materials; the applications of these techniques allowed the production of arrays of microelectrodes with the recess depth of 500 nm [24]. In reference with a previous work of Heinze [25] for recessed single microdisc electrodes, a new equation has been proposed [24] for the steady state current:

$$I_{lim} = \pi a^2 nFD\frac{C}{a+h} \quad (1)$$

where a is the radius of the microdisc; n, the number of electrons exchanged; F, the Faraday constant; D, the diffusion coefficient; h, the height of the recess and C the concentration of the electro-active species.

If the electrode may be considered as a single inlaid microdisc, equation can be used as follows:

$$I_{lim} = 4anFDC \quad (2)$$

Several arrays were made with different radii, from 2.5 μm up to 100 μm and distances between the electrodes from 30 μm to 750 μm. In static mode and cyclic voltammetry, larger electrodes produced a current more important than predicted by Eq. (1) because that equation is only valid for microelectrodes. As expected, the current obtained from calculations and from experiments is similar when the distance/radius ratio is large [24].

The chemical vapor deposition (CVD) of diamond and the possibility to introduce a p-type dopant during the growing process of diamond provide a material which becomes conductive with the physical properties of diamond. It was very attractive to use this material in electroanalysis. Several hundreds of reviews [26–28] were published on applications of these electrodes in cyclic voltammetry for the analysis of pesticides, herbicides, pharmaceutical products [29–31]. The conductive diamond was also used to manufacture electrodes for electrochemical detection in HPLC and flow injection [32–38] electrochemical reactions [39].

The applications were extended to arrays of microelectrodes [39,40,41]. The techniques employed for manufacturing the diamond arrays of electrodes where more or less sophisticated, from photolithography up to pattern the isolation surface with a powerful laser beam [42]. Multi-layers arrays were obtained by the deposition of conductive and non-conductive diamond on a solid substrate. 0.6 μm electrodes were obtained by etching with an oxygen/argon plasma process [43].

It was interesting to investigate the possibility to combine the properties of the BDD with the principle of microelectrodes as fabricated by Fujishima and colleagues [36,40] to manufacture new sensors for HPLC.

In this paper, the parameters which drive the responses of the detector were studied to provide a cell for electrochemical detection in HPLC.

2. Experimental

With HPLC, the sensor works in continuous flow, to avoid a mixture of the products separated in the column. The volume of the cell must be as small as possible (less than 5 μL); the classical flow rate was set at 1 mL/min, which roughly led to a velocity of the flow of 1–1.5 m/min in the cell considering the cell geometry.

2.1. Chemicals

The electrochemical tests were mainly realized using hydroquinone as a model analyte related to interesting molecules separated through HPLC.

Quinone/hydroquinone redox functional group is encountered in many natural or synthetic biological, pharmaceutical and environmental important analytes (catecholamine neurotransmitters, ubiquinone coenzymes, emodine pharmaceutical agent, chloranil analog pesticides, etc.). The solutions were prepared with the eluent for chromatography: 8% CH_3CN in a 10^{-3} M solution of $LiClO_4$ (Sigma-Aldrich, France). The solutions were prepared every day and kept in an ice bath. The water (resistivity: 18 MΩ cm) was obtained from a Milli-Q apparatus (Millipore, France).

2.2. Apparatus

Electrochemical experiments were performed with an Eldec 105 (Precision Instruments, Marseille, France) amperometric detection unit. The three-electrode cell of the detector is shown

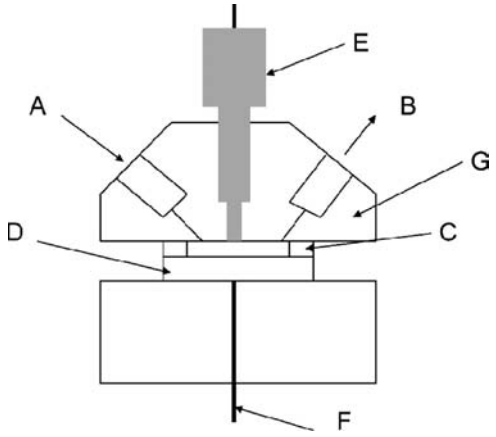


Fig. 1. Electrochemical flow-cell fitted with a BDD microelectrodes array as the working electrode: A: inlet, B: outlet, C: seal, D: diamond microelectrodes array, E: reference electrode, F: contact for working electrode, G: auxiliary electrode.

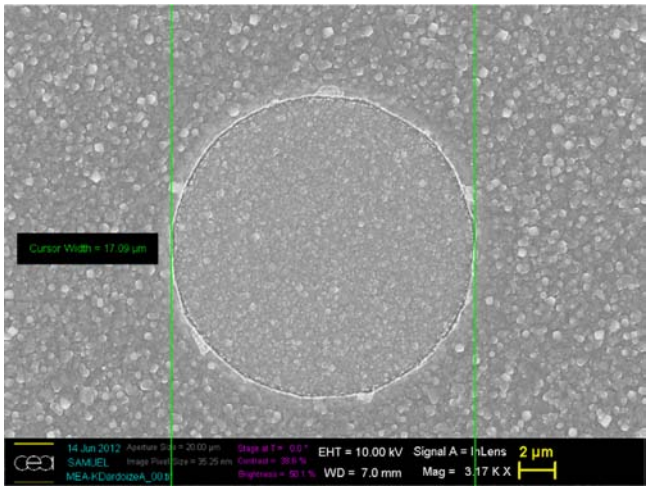


Fig. 2. Electron microscope picture of one microelectrode. Diameter of the BDD electrode: 17 μm, thickness of the insulator: 300 nm.

in Fig. 1. It has been adapted to receive the BDD electrodes array as working electrode, an Ag/AgCl reference electrode and a stainless steel counter electrode. The inlet and outlet of the flow and a hole for inserting the reference electrode are located at the upper part of the cell. The inlet and outlet diameters are: 0.4 mm and the channel height is about 50 μm. The potential of the working electrodes was 0.7 V vs Ref for all the experiments in order to investigate hydroquinone functional group oxidation process (the standard potential of the quinone/hydroquinone redox couple is about 0.5 V vs Ag/AgCl). The chromatography experiments were carried out using a Dionex pump (Montigny le Bretonneux, France), an injection valve Negretti and Zambra (UK), a 15 cm column, 4.6 mm inside diameter, C 18.5 μm Waters Symmetry. The chromatograms were directly recorded on a Kipp and Zonen BD 111 recorder or a Shimadzu CR 6 A integrator.

2.3. Arrays of electrodes

Several arrays of microelectrodes were manufactured in accordance with our drawings by the Commissariat à l'Energie Atomique (CEA, Saclay, France) to investigate the problems which arise with the use of the microelectrodes in a continuous flow. The manufacturing procedure was described elsewhere [44], and may be summarized rapidly: on a p-Si boron-doped substrate, a conductive boron-doped diamond film was grown using microwave plasma chemical vapor deposition. Then, non-conductive diamond was deposited to cover the first film to produce an insulator. Finally, this last layer was patterned with a laser beam to obtain the arrays of microelectrodes through the insulator down to the conductive diamond. The sensor (15×15 mm^2 geometrical area, 1.5 mm thick) was placed in the cell described in Fig. 1. A seal is used to insure the water-tightness between the upper block of the cell and the array, a Kel-F block with a hole to get the contact with the array. A film of indium/gallium alloy was laid on the back of the silicon substrate under the array in order to have an ohmic electric contact. The two parts of the cell were screwed together to compress the seal.

3. Results

3.1. Tests with one microelectrode

A single microelectrode with a diameter of 17 μm was prepared and examined by Scanning Electron Microscopy (see Fig. 2) in order to check the quality of the preparation procedure. From SEM experiments, it was shown that the thickness of the diamond insulator was about 300 nm.

The 17 μm microelectrode was inserted in the cell of the electrochemical detector and a chromatography test was realized by the injection of 20 μL of a solution which contains 18 μg of hydroquinone. A peak of 0.8 nA was obtained with a retention time of 5 min with our conditions, a good signal/noise ratio and a fast equilibration time of the electrode, less than observed on millimetric BDD electrodes.

Another single disc microelectrode with a diameter of 40 μm was prepared for studying its voltammetric response. A 3-dimension AFM picture and a schematic profile of that electrode are given in Fig. 3A. As the ratio h/a is very small (about 0.01), Eq. (2) may be used, instead of Eq. (1). The radius, a, of the inlaid microdisc electrode may be calculated from the measurement of steady state limiting current I_{lim}. The cyclic voltammogram shown in Fig. 3B was performed with ferrocenemethanol 1 mM in phosphate buffer saline solution with a scan rate of 5 mV s^{-1}. From Eq. (2), one can calculate the experimental radius $a \approx 20$ μm, in agreement with the AFM image (Fig. 3A). It can be established from that behavior that the insulating diamond layer has no pinholes defects.

3.2. Tests with arrays of microelectrodes

A simple idea was to increase the number of electrodes in order to inject lower quantities of product and increase the signal.

Several arrays were manufactured, suitable for the geometry of the electrochemical cell. As can be seen from Fig. 4, very regular hexagonal arrangements of electrodes could be obtained. On the center of a multi-layer piece as described previously, an array was machined: about 16,000 electrodes with a diameter $\Phi = 2a = 15$ μm, with a distance $d = 45$ μm between the electrodes ($d/a = 6$), were arranged in a circle with a diameter of 6 mm. This regular arrangement gave an active surface of around 2.8 mm^2. After an equilibration time of 12 min, a sensitivity of 0.1 nA/FS (Full Scale) was reached on the detector with a flat base line; the injection of 90 pg of hydroquinone in 20 μL (corresponding to a concentration of 4×10^{-8} mol L^{-1}) gave a peak of 0.03 nA with a signal/noise ratio of 30/1 (Fig. 5).

3.3. Study of the arrays geometry

In order to enhance the sensibility of electrode arrays and get the best signal/noise ratio, several parameters have to be

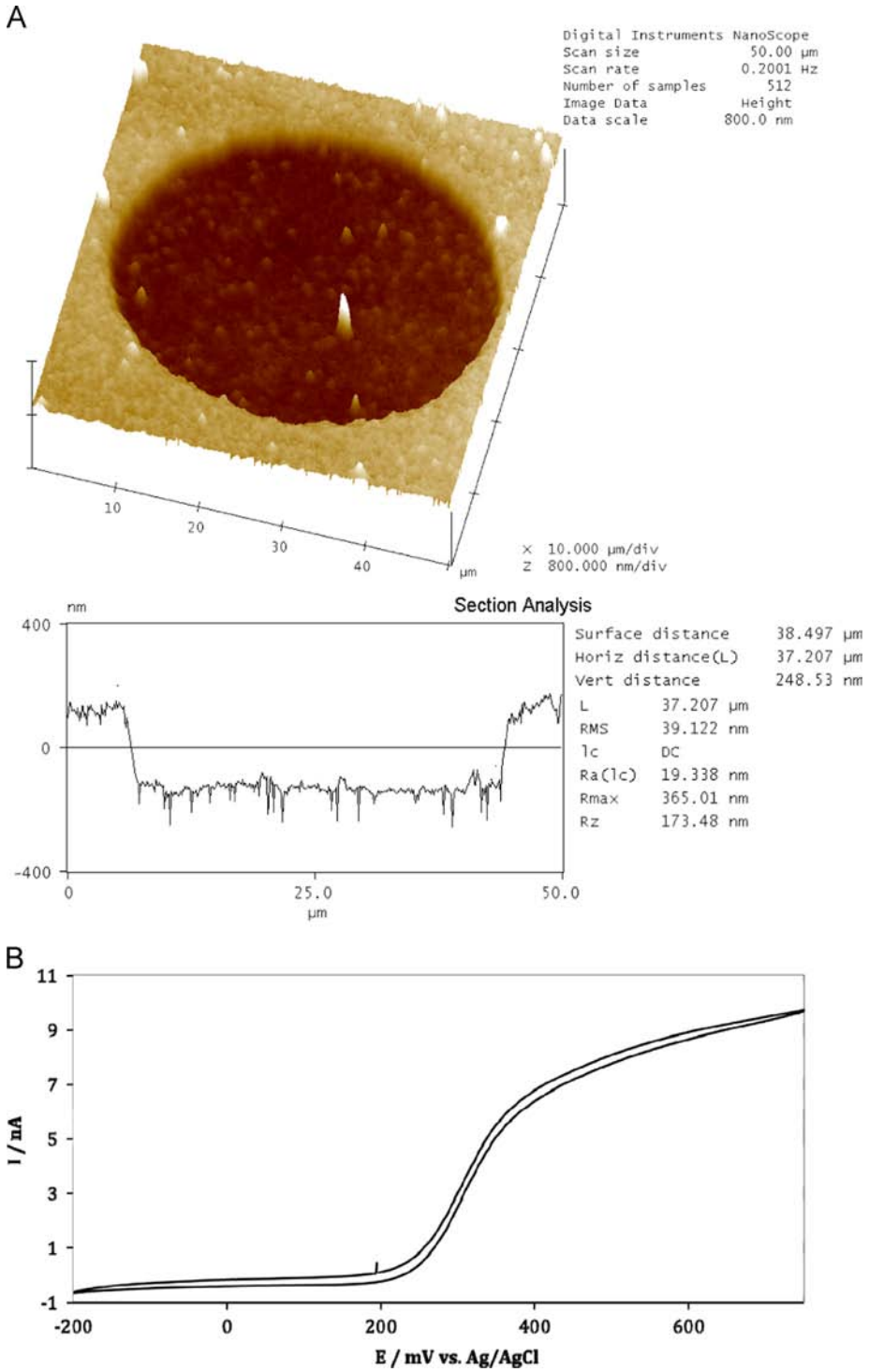


Fig. 3. Study of a single 40 µm BDD microelectrode (A): AFM picture and schematic profile of the recess of the electrode. (B): cyclic voltammetric response. Ferrocenemethanol 1 mM in phosphate buffer saline solution with a scan rate of 5 mV s^{-1}.

studied: number of electrodes, diameter of the electrodes, distance between the electrodes and effect of the flow rate.

3.3.1. *Distance between the electrodes*

In our cell, a flow rate value of 1 mL/min was chosen, corresponding to a velocity of the flow inside of the cell around 1.5 m/min, taking into account its volume (4.5 µL), whilst most of the works on microelectrodes array found in the literature were done without flow. It was necessary to determine the distance between the electrodes which produces the highest signal and exhibits the benefit of microelectrodes. Three arrays were manufactured with 68 disc microelectrodes with a diameter of 15 µm and a depth of 300 nm. The distance between two consecutive electrodes in the flow was 50, 120 or 240 µm, in a hexagonal geometry (d/a=6.7, 16 or 32, respectively). The arrays were successively placed in the cell of the electrochemical detector. After equilibration at a flow rate of 1 mL/min, a solution of 80 ng of hydroquinone in 20 µL was injected (concentration: 3.5×10^{-5} mol L^{-1}). The arrays with a distance between the electrodes of 120 and 240 µm provide a

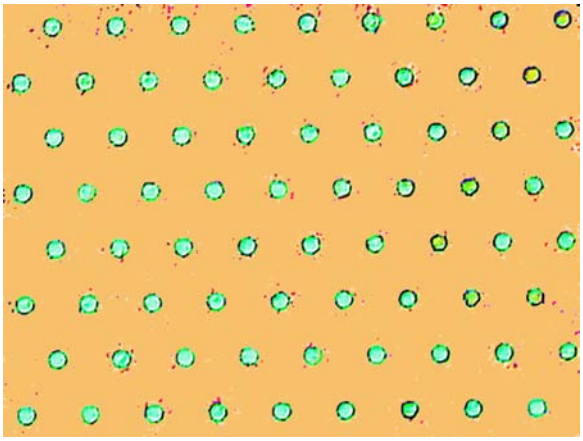


Fig. 4. Array of microelectrodes. The diameter of each microelectrode is 15 μm with a distance of 60 μm between the electrodes. Size of the picture: 542 μm × 407 μm.

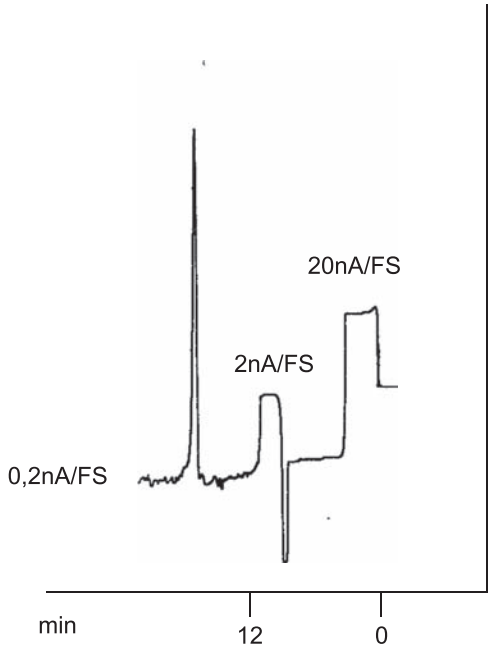


Fig. 5. Chromatogram of the injection of 90 pg of hydroquinone. Quick equilibration time of the cell: 12 min to reach the sensitivity of 0.1 nA/FS. Signal of 0.03 nA with a ratio $S/N=30/1$.

signal of 0.9 nA, while the array with a distance of 50 μm gives a signal of only 0.64 nA (Fig. 6). One can conclude that, for the chosen diameter $\Phi=15$ μm, the value $d/a=6.7$ is not sufficient for optimizing the signal-to-noise ratio for the same number of microelectrodes.

Taking into account the velocity of the flow inside the cell, we think that, due to the depletion, the hydroquinone molecules, oxidized at the electrode, are not completely renewed by forced convection if the electrodes are too close. Hereafter, a ratio $d/a=16$ has been chosen for the subsequent experiments.

3.3.2. *Effects of the flow rate*

The study of the chronoamperometric response of a recessed micro-band electrode was done by other authors by simulation [23]. In this case, it was clearly demonstrated that there is a relation between the chronaoamperometric response of the electrode and the velocity of the flow via the Péclet number. The Péclet number can be calculated from the average flow velocity, u, the channel height, h, and the diffusion coefficient D:

$$Pe = uh/D \quad (3)$$

In our experiments, Pe is in the range 250–5000.

Several arrays were prepared to determine the arrangement of electrodes which provides the best signal/noise ratio in chromatographic conditions with different flow rates.

The electron transfer occurring at the electrode is a function of several parameters. Several tests, reported in Fig. 7, were done using an array of 68 electrodes ($\Phi=15$ μm, $d=120$ μm, and $d/a=16$) increasing the flow rate from 0.1 mL/min up to 3 mL/min. The same samples were injected: 70 ng of hydroquinone in 20 μL (concentration: 3×10^{-5} mol L^{-1}). A decrease of the normalized peak area was observed (black full circles in Fig. 7). It can be attributed to the change of the residence time of the analyte in front of each microelectrode with the variation of the flow rate. For flow rates that have been tested in this work, in the magnitude order of 1 mL/min, the characteristic residence time, τ_r, of analyte flux over each microelectrode surface is shorter than the diffusion time, τ_d, at each microelectrode. The τ_r/τ_d ratio can be understood as an efficiency parameter linked to the amount of analyte detected at the microelectrodes array sensor. τ_r is controlled by the flux rate in the cell and by the thickness of the flow cell, whereas τ_d is controlled by the geometry of the electrodes.

We have calculated the collection efficiency of the microelectrodes array with a standard injection volume of 20 μL of analyte from the experimental measurement of the electric charge consumed for the detected peak. The collection efficiency of the flow-cell detector can be defined as the ratio of the experimental charge to the calculated charge needed to oxidize the whole amount of injected analyte. When the flux rate increases the collection efficiency diminishes (Fig. 7). It means that the amount of analytes reacting at the electrodes diminishes drastically due to the decrease of the residence time of species close to each microelectrode.

From those experiments, it should be noticed that the critical parameter for an HPLC amperometric detector is not the collection efficiency alone, but also the highest possible signal-to-noise ratio compatible with on-line detection at the outlet of the HPLC column.

3.3.3. *Diameter and number of the electrodes*

An important parameter in the detector for HPLC is the void volume of the sensor, the smallest as possible not to lose the quality of the separation by dilution inside the cell. The simplest solution for amplifying the signal is to increase the number of electrodes or/and to increase the size of the electrodes. Taking into account the previous results, an array was manufactured for reaching a good compromise: the electrodes, with $\Phi=30$ μm are placed in staggered rows, at a distance of 100 μm between the electrodes ($d/a=6.7$). The 5800 electrodes are gathered in a circle with a diameter of 8 mm, the active area is around 4.1 mm^2 and the internal volume of the cell is close to 4.5 μL. A typical result is displayed in Fig. 8. After 12 min equilibration time, the detector is set at 0.1 nA/FS, the injection of 16 pg of hydroquinone gave a peak of 0.07 nA with a high signal/noise ratio 55/1. Indeed, the d/a parameter in not the only pertinent criterion. The diameter of the microdisc electrode must also be taken into account for the optimization of the detector.

4. Conclusion

Boron-doped diamond has been used as a highly efficient electrode material for electrochemical detectors in high flow rate conditions. It offers a wide range of electro-activity, a quick equilibration time and an easy in situ cleaning. By combining its

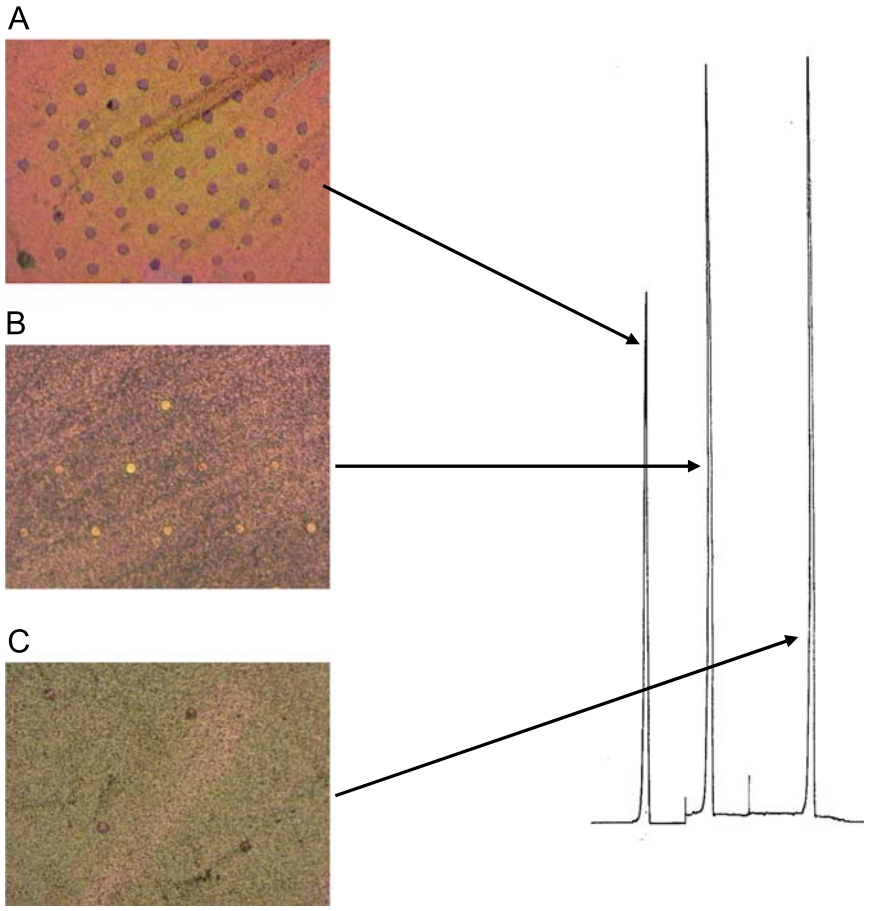


Fig. 6. Chromatograms obtained by the injection of 80 ng of hydroquinone on three different arrays with 68 electrodes of 15 μm of diameter on each array. The electrode spacing was: 50 (A), 120 (B) or 240 (C) μm. A signal of 0.64 nA was recorded for the array A. With the arrays B and C the same signal of 0.9 nA was recorded.

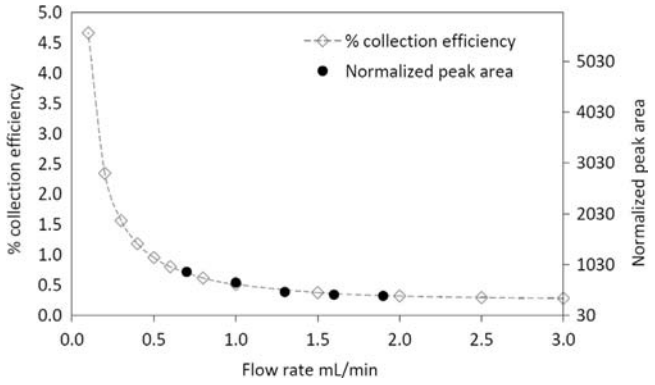


Fig. 7. Correlated variations of the area of the peak and the collection efficiency of the flow-cell versus the flow rate. An array of 68 electrodes was used, with a distance between the electrodes of 120 μm.

remarkable qualities with the particular properties of arrays of microelectrodes, new sensors for the electrochemical detection in HPLC were designed. Several series of arrays were prepared to determine the effect of the size of the electrodes, their spacing, disposition and number. Taking into account these results, a sensor was manufactured to be inserted in the cell of an electrochemical detector, leading to the detection of very small amounts of hydroquinone at the picogram scale, after a short equilibration time, less than 15 min, and a high signal/noise ratio.

Three key parameters have been identified for the optimization of the detection: the flux velocity, which controls the collection

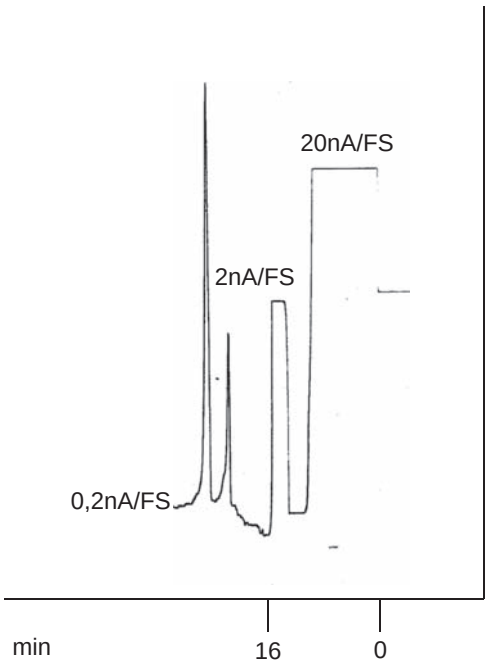


Fig. 8. Chromatogram obtained with the selected array: diameter of the electrodes: 30 μm, distance between the electrodes: 100 μm, active surface area: 4.1 mm^2. Injection of 16 pg of hydroquinone. After equilibration, the change of the sensitivity set on the detector was directly noted on the chromatogram, a peak of 0.07 nA was obtained with a ratio $S/N=55:1$.

efficiency; the d/a ratio, which controls the signal to noise ratio and, at last, the diameter of the microdiscs, which is related to the sensitivity. A more extensive study should lead to the optimal electrochemical detector for HPLC.

Acknowledgements

The authors wish to thank Dr P. Bergonzo and his group of the LIST, CEA (Saclay, France) for the manufacturing of the arrays and the fruitful discussions which have allowed the development of this work. Precision Instruments (Marseille, France) is also acknowledged for financial support and industrial development of the cells fitted with BDD arrays for electrochemical detection in HPLC.

References

[1] P.T. Kissinger, C. Refshauge, R. Dreiling, R.N. Adams, Anal. Lett. 6 (1973) 465–477.
[2] M. Goto, T. Nakamura, D. Ishii, J. Chromatogr. 226 (1981) 33–42.
[3] D.A. Roston, P.T. Kissinger, Anal. Chem. 53 (1981) 1695–1699.
[4] I. Streeter, R.G. Compton, Sens. Actuators B 130 (2008) 620–624.
[5] D. Barak-Shinar, M. Rosenfeld, S. Abboud, J. Electrochem. Soc. 151 (2004) H261–H266.
[6] K. Stulik, C. Amatore, K. Holub, V. Marecek, W. Kutner, Pure Appl. Chem. 72 (2000) 1483–1492.
[7] S. Fletcher, M.D. Horne, Electrochem. Commun. 1 (1999) 502–512.
[8] C. Amatore, in: I. Rubinstein (Ed.), Physical Electrochemistry: Principles, Methods and Applications, Marcel Dekker, New York, 1995, pp. 131–208.
[9] K. Stulik, V. Pacakova, Electroanalytical Mesurements in Flowing Liquids, E. Horwood, Chichester, 1987.
[10] C. Belmont-Hebert, M.L. Tercier, J. Buffle, G.C. Fiaccabrino, N.F. De Rooij, M. Koudelka-Hep, Anal. Chem. 70 (1998) 2949–2956.
[11] R. Feeney, S.P. Kounaves, Anal. Chem. 72 (2000) 2222–2228.
[12] H.J. Lee, C. Beriet, R. Ferrigno, H.H. Girault, J. Electroanal. Chem. 502 (2001) 138–145.
[13] Y.V. Pleskov, A.Y. Sakharova, M.D. Krotova, L.L. Bouilov, B.V Spitsyn, J. Electroanal. Chem. 228 (1987) 19–27.
[14] D. Gandini, E. Mahé, P.A. Michaud, W. Haenni, A. Perret, Ch. Comninellis, J. Appl. Electrochem. 30 (2000) 1345–1350.
[15] E. Mahé, D. Devilliers, Ch. Comninellis, Electrochim. Acta 50 (2005) 2263–2277.
[16] O. Niwa, H Tabei, B.P Solomon, F. Xie, P.T. Kissinger, J. Chromatogr. B 670 (1995) 21–28.
[17] C. Amatore, C.J. Lefrou, J. Electroanal. Chem. 324 (1994) 33–58.
[18] A.M. Bond, P.J. Mahon, K.B. Oldham, C.G. Zoski, J. Electroanal. Chem. 366 (1994) 15–27.
[19] T.W. Sohn, P.W. Stoecker, W. Carp, A.M. Yacynych, Electroanalysis 3 (1991) 763–766.
[20] T. Hepel, J. Osteryoung, J. Electrochem. Soc. 133 (1986) 752–757.
[21] B.J. Seddon, Y. Shao, H.H. Girault, Electrochim. Acta 39 (1994) 2377–2386.
[22] W.J. Aixill, A.C. Fischer, Q. Fulian, J. Phys. Chem. 100 (1996) 14067–14073.
[23] R. Ferrigno, P.F. Brevet, H.H. Girault, J. Electroanal. Chem. 430 (1977) 235–242.
[24] M.E. Sandison, N. Anicet, A. Glidle, J.M. Cooper, Anal. Chem. 74 (2002) 5717–5725.
[25] J. Heinze, Angew. Chem. 32 (1993) 1268–1288.
[26] K. Peckova, J. Musilova, J. Barek, Crit. Rev. Anal. Chem. 39 (2009) 148–172.
[27] Y. Zhou, J. Zhi, Talanta 79 (2009) 1189–1196.
[28] J.H.T. Luong, K.B. Male, J.D. Glennon, Analyst 134 (2009) 1965–1979.
[29] L. Svorc, M. Rievaj, D. Bustin, Sens. Actuators B 181 (2013) 294–300.
[30] L. Bandzuchova, L. Svorc, J. Sochr, J. Svitkova, J. Chyrlkova, Electrochim. Acta 111 (2013) 242–249.
[31] B.C. Lourencao, R.A. Medeiros, R.C. Rocha-Filho, L.H. Mazo, O. Fatibello-Filho, Talanta 78 (2009) 748–752.
[32] I. Martins, F.C. Carreira, L.S. Canaes, I.A. de Souza Campos Jr, L.M. da Silva Cruz, S. Rath, Talanta 85 (2011) 1–7.
[33] Z. Bartosova, D. Jirovsky, A. Horna, J.Chromatogr. A 1218 (2011) 7996–8001.
[34] W. Siangproh, P. Rattanarat, O. Chailapakul, J. Chromatogr. A 1217 (2010) 7699–7705.
[35] R.A. Medeiros, B.C. Lourencao, R.C. Rocha-Filho, O. Fatibello-Filho, Talanta 99 (2012) 883–889.
[36] T.A. Ivandini, B.V. Sarada, C. Terashima, T.N. Rao, D.A. Tryk, H. Ishiguro, Y. Kubota, A. Fujishima, J. Chromatogr. B 791 (2003) 63–72.
[37] L.S. Andrade, M.C. De Moares, R.C. Rocha-Filho, O. Fatibello-Filho, Q.B. Cass, Anal. Chim. Acta 654 (2009) 127–132.
[38] A.F. Azevedo, F.A. Souza, J.T. Matsushima, M.R. Baldan, N.G. Ferreira, J. Electroanal. Chem. 658 (2011) 38–45.
[39] D. Khamis, E. Mahé, F. Dardoize, D. Devilliers, J. Appl. Electrochem. 40 (2010) 1829–1838.
[40] K. Tsunozaki, Y. Einaga, T.N. Rao, A. Fujishima, Chem. Lett. 5 (2002) 502–503.
[41] K.L. Soh, W.P. Kang, J.L. Davidson, S. Basu, Y.M. Wong, D.E. Cliffel, A.B. Bonds, G.M. Swain, Diam. Relat. Mater. 13 (2004) 2009–2015.
[42] M. Pagels, C.E. Hall, N.S. Lawrence, A. Meredith, T.G.J. Jones, H.P. Godfried, C.S. J. Pickles, J. Wilman, C.E. Banks, R.G. Compton, L. Jiang, Anal. Chem. 77 (2005) 3705–3708.
[43] C. Pietzka, A. Denisenko, L.A. Kibler, J. Scharpf, Y. Men, E. Kohn, Diam. Relat. Mater. 18 (2009) 816–819.
[44] E. Vanhove, J. De Sanoit, J.C. Arnault, S. Saada, C. Mer, P. Mailley, P. Bergonzo, M. Nesladek, Phys. Status Solidi A 204 (2007) 2931–2939.

Talanta 132 (2015) 648–652

Contents lists available at ScienceDirect

Talanta

journal homepage: www.elsevier.com/locate/talanta

Determination of fluorine contents in plant samples by means of facilitated extraction with enzyme

Junseok Lee [a], Jinsung An [b], Hye-On Yoon [a,*]

[a] Seoul Center, Korea Basic Science Institute, 6-7, Inchon-ro 22-gil, Seongbuk-gu, Seoul 136-075, Republic of Korea
[b] Department of Civil & Environmental Engineering, Seoul National University, 1 Gwanak-ro, Gwanak-gu, Seoul 151-742, Republic of Korea

ARTICLE INFO

Article history:
Received 24 June 2014
Received in revised form
2 October 2014
Accepted 4 October 2014
Available online 18 October 2014

Keywords:
Fluorine
Facilitated extraction
Enzyme
Protease
Plant sample

ABSTRACT

In this study, facilitated extraction with enzyme was employed for the first time to extract fluorine (F) from plants. Feasibility of the proposed method for F analysis was assessed by comparing with the alkali fusion-ion selective electrode (ISE) method. In the extraction procedure, 30 mg of a protease and 0.1 g of a plant sample were added in 10 mL of deionized water. In the absence of sonication, the solution was mechanically shaken for 10 s. A variety of parameters (i.e., the amounts of enzymes used, physical treatment conditions applied, extraction time, temperature, and pH) were optimized to enhance the extraction efficiency of the proposed method. The suitability of the proposed method for various plant samples (i.e., grass, perilla, peanut, hot pepper, and eggplant) was also evaluated. The proposed method involves decreased operation time, simplified extraction procedures, and minimal consumption of hazardous reagents and solvents in comparison with other existing methods. Experimental results demonstrated that facilitated extraction with enzyme is appropriate for the rapid determination of F content in plant samples.

© 2014 Elsevier B.V. All rights reserved.

1. Introduction

Fluorine (F) as a harmful pollutant in fluoride compounds and soluble fluoride has received considerable attention because of its effects on both ecosystem and human health. Although an appropriate intake of F is known to prevent dental caries, continuous intake of vegetation accumulated with F seems to cause dental and skeletal fluorosis and osteoporosis [1–3].

F present in atmosphere and vegetation is generally determined as tracers following hydrogen fluoride (HF) leakage accidents. The concentration of HF leaked into the atmosphere can be calculated using the concentration of F in plant samples by a reverse tracking method on the basis of the high diffusion velocity of F [4]. In addition, the extent of exposure and environmental pollution was assessed by determining F content of plants in the vicinity of the HF leakage accident area [5]. It is therefore important to determine F concentrations in crops because of their potential to accumulate F in the human body through the dietary pathway.

Various methods for the determination of F concentrations in plants have been extensively studied for decades. The alkali fusion-ion selective electrode (ISE) technique combining the use of filtration under slightly alkaline conditions for the removal of the interfering cations was widely used to determine the F contents in plant samples [6,7]. Pyrohydrolysis and oxygen bomb combustion techniques [8–10] were also employed to determine F contents in coal and plants, respectively. However, these methods were time-consuming and complicated procedures, which generate a large volume of hazardous wastes to extract F from plant samples.

Currently, facilitated extraction with the aid of enzyme has been predominantly applied for the determination of arsenic (As) and selenium (Se) [11–14] present in plant samples. Enzymes are used to catalyze chemical reactions by which plants are formed, and enable the hydrolysis of chemical bonds in plants to dissociate. The α-amylase and protease hydrolyze the peptide bonds of polysaccharide cell membranes of plants [15]. One of the main advantages of the extraction with enzyme is its simplicity and rapidity owing to its high reaction rate through the alleviation of activation energy. In addition, the usage of organic solvents and hazardous chemicals can be avoided. To date, there are no reports on the application of the extraction method with the use of enzyme for the rapid determination of F contents in plant samples.

In this study, extraction conditions (e.g., amounts and combination of enzymes, sonication applied, extraction time, temperature, and pH) of the proposed facilitated extraction with enzyme

* Corresponding author. Tel.: +82 2 6943 4192; fax: +82 2 6943 4149.
E-mail address: dunee@kbsi.re.kr (H.-O. Yoon).

http://dx.doi.org/10.1016/j.talanta.2014.10.016
0039-9140/© 2014 Elsevier B.V. All rights reserved.

were examined and optimized to increase the extraction recovery. The extraction procedure presented in this paper has been derived from a method described by Sanz et al. [11,12], who studied the applicability of the use of enzyme for the analysis of As in plant samples. The proposed method is used to hydrolyze proteins and other components in plant samples by the combined use of α-amylase and protease. Feasibility of facilitated extraction with enzyme proposed in this study was assessed by comparing with alkali fusion-ISE technique as a reference method. It was also applied to analyze F contents in various plant samples to confirm its versatility. The proposed method aims to remove complicated and time-consuming extraction procedures for the rapid determination of F contents in plant samples.

2. Materials and methods

2.1. Reagents

Starch and proteins make up to 80–90% of plant samples. Therefore, α-amylase (*Bacillus* sp.) and protease (*Streptomyces griseus*) (Sigma-Aldrich, St. Louis, MO, USA) were used to degrade cell membranes of the F containing plant samples. The α-amylase breaks down starch into smaller carbohydrate molecules such as maltose and glucose. The protease breaks down certain chemical bonds in proteins into smaller peptides and amino acids. Deionized (DI) water (Milli-Q Element System, Millipore, USA) was used as the extraction solvent. A total ionic strength adjustment buffer (TISAB) solution obtained from Fluka (Sigma-Aldrich, St. Louis, MO, USA) was used to maintain the ionic strength of solutions prior to the analysis of F using ion electrode (pH-270L, Istek, Korea). Sodium hydroxide (NaOH, $\geq$98%, Samchen Chemicals, Korea) and hydrochloric acid (HCl, Dongwoo Fine-Chem, Korea) solutions were used for pH adjustment in the alkali fusion-ISE method.

2.2. Sample collection

Rice was used as a representative sample of plants because of its dietary importance. Rice samples affected and unaffected by HF exposure (leakage accident (2012) in Gumi city, Republic of Korea) [16] were collected in the vicinity of the HF spillage. Rice A was collected from the site that was directly affected by HF exposure. Conversely, Rice B, as the control sample, was collected from the background area unaffected by HF exposure. Rice A* and Rice B* were taken from the aforementioned points, respectively after one year has passed. The samples were naturally dried at room temperature and were ground by a Gyral Grinder (Chemplex, USA). In order to prevent the samples from absorbing moisture, the ground samples were stored in a desiccator.

Other plant samples such as grass, perilla (*Perilla frutescens var. japonica Hara*), peanut (*Arachis hypogaea*), hot pepper (*Capsicum annuum*), and eggplant (*Solanum melongena*) were also used to evaluate the versatility of the proposed extraction method. These plants were representative of crops cultivated in the HF leakage accident area. The plant samples were collected in the vicinity of the sampling point of rice samples and prepared using the same procedure as rice samples.

2.3. Extraction procedures

The extraction procedure for the F analysis in rice samples was followed by Sanz et al. [11,12] with some modifications. 0.1 g of the sample was added to 10 mL of DI water in a 50 mL polyethylene tube followed by the addition of 10 mg of α-amylase. In order to accelerate the extraction reaction of rice samples, an ultrasonic probe was introduced into the sample suspension and the sample was subjected to ultrasound irradiation for 120 s at 20% amplitude. The probe tip was cleaned with DI water between the sonication processes to prevent sample contamination. After preliminary sonication, 30 mg of the protease was added and sonication was repeatedly employed. The suspension was filtered through a 0.4 μm polycarbonate Whatman filter using a vacuum pump and the effluent was collected. The effluent was mixed at 1:1 (v/v) ratio with TISAB solution to maintain the ionic strength and F concentration was determined by ISE.

As the reference values, the alkali fusion-ISE technique developed by McQuaker and Gurney [7] was used to analyze F concentration in a plant sample. Briefly, 0.5 g of sample with 6 mL NaOH solution was incubated at 600 °C and then neutralized using HCl. This solution was filtered through Whatman no. 40 filter paper to remove interfering cations including Fe and Al and the filtrate was subsequently analyzed by ISE for the determination of F. The F concentrations in rice samples determined using both the extraction method with aid of enzyme and alkali fusion-ISE method were compared with each other to calculate the recovery efficiency of facilitated extraction with enzyme method proposed in this study.

2.4. Optimization procedures

The optimized conditions of facilitated extraction with enzyme were determined by assessing the effects of selected parameters on the recovery efficiency of F from the rice sample. Recovery efficiency was defined as the ratio of F concentration determined using the method proposed in this study to pseudo total F concentration determined using the alkali fusion-ISE method. Optimization parameters included the amounts of enzymes used (0–30 mg corresponding to 0–30% enzyme/sample ratio), the combination of different enzymes applied (α-amylase and protease), physical treatment (in the presence and in the absence of sonication), and the extraction time (10–120 s). These various extraction conditions were optimized based on preliminary experiments. Versatility of facilitated extraction with enzyme under the optimized conditions to other plant samples was also tested. All experiments were performed in triplicate.

3. Results and discussion

3.1. Optimization of facilitated extraction with enzyme

3.1.1. The amounts and combinations of enzymes used

The effect of enzyme concentration on the extraction efficiency of F in the rice sample was studied to determine the optimum amounts of α-amylase and protease. Different amounts (0, 10, 20, and 30 mg corresponding to 0%, 10%, 20%, and 30% enzyme to sample ratio) and combinations of α-amylase and protease were separately tested to find optimal conditions. In all experiments, sonication time and wave amplitude of ultrasound were set 120 s and 20%, respectively. F concentrations extracted using different amounts of enzymes are shown in Table 1. It can be inferred that the F concentration is completely recovered with 30 mg of protease. The recovery of the extracted F increased from 44.9% to 98.8% when the amount of the protease increased from 10 to 30 mg. However, there was no effect on the recovery when only α-amylase was used. These results suggested that the major enzyme extracting the F from the rice sample is a protease rather than α-amylase. It supported the fact that F is bound to proteins like other elements despite small total protein content (7–8%) [11,12]. Almost 100% of the F was successfully recovered from the rice samples when using the protease regardless of the addition of α-

Table 1
F concentrations obtained from facilitated extractions with varying amount of enzymes.

Amounts of enzymes (mg)		F concentration (μg g^{-1})[a]	Recovery (%)[b]
α-amylase	Protease		
0	0	4.83 ± 1.31[c]	15.0
0	10	14.5 ± 1.08	44.9
0	20	22.4 ± 0.99	69.3
0	30	31.9 ± 1.07	98.8
10	0	3.13 ± 0.58	9.67
10	30	34.2 ± 1.16	106

[a] Concentration of F is the average of triplicate analysis.
[b] Recovery is defined as (F concentration determined using facilitated extraction with enzyme × 100)/total F concentration obtained from alkali fusion-ISE method.
[c] Mean ± standard deviation (n=3).

Table 2
Recovery of facilitated extraction with enzyme when employing sonication or mechanical shaking with varying extraction time.

Physical treatment	Time (s)	F concentration (μg g^{-1})	Recovery (%)
Sonication	30	31.8 ± 0.39[a]	98.6
	60	33.0 ± 0.87	102
	120	32.7 ± 0.94	101
Mechanical shaking	10	32.5 ± 0.9	101
	120	32.4 ± 1.38	100
	1800	32.2 ± 1.03	99.6

[a] Mean ± standard deviation (n=3).

amylase. In consequence, 30 mg of the protease was selected as the optimum enzyme concentration.

3.1.2. Effects of sonication and extraction time

The efficiency of F extraction in the presence and in the absence of the sonication was investigated. Without the use of sonication, the suspension (containing 0.1 g of rice sample and 10 mL of DI water) was mechanically shaken for 10 s to evenly blend the enzyme. The results obtained from both methods are shown in Table 2. In general, sonication disrupts the cell membrane and thereby enables rapid transfer of extraction solution to the target compounds, resulting in high extraction recovery [17]. On the other hand, there was no effect of sonication on the reaction rate of enzymes for F extraction regardless of sonication time, as shown in Table 2. In the absence of enzymes, F was scarcely extracted during sonication (Table 1). These results demonstrated that sonication could not hydrolyze the proteins associated with F but broke down the cell membranes into smaller products.

It is widely recognized that sonication is capable of decreasing extraction time owing to its physical effects on the cell membrane [17–19]. However, in F analysis, there is no effect of sonication on F extraction. Furthermore, total dissolved solid (TDS) in solutions extracted with sonication was higher than that of solutions extracted without sonication. This could increase the filtration time and make it difficult to filtrate using vacuum pump. As shown in Table 2, F was effectively recovered within a short time (i.e., 10 s) even without sonication. Hence, sonication process was avoided in the proposed extraction method in order to reduce the filtration time.

Extraction time is one of the important parameters for rapid analysis of F contents. Therefore, F concentrations extracted at different extraction times with and without sonication were measured and compared. As shown in Table 2, the recovery of facilitated extraction with enzyme was not influenced by extraction time because overall extraction processes were completed during 10 s without sonication. It indicated that protease immediately reacted with the protein associated with F, indicating that the proposed extraction method is suited for the rapid analysis of F in rice samples. The reaction rate was fairly high when a sufficient amount of protease was used for the hydrolysis of cell membranes. After the addition of protease, mechanical shaking of the solution for 10 s followed by filtration could sufficiently extract F from rice samples and it was used as an optimum condition of the physical treatment.

3.1.3. Temperature and pH

Since enzymes could be significantly affected by temperature and pH of the solution, their effects on F extraction were assessed. In general, the optimum values of temperature and pH of α-amylase and protease were 25–35 °C and 6–8, respectively [20,21]. In our preliminary tests, the difference of recoveries between the solutions incubated at room temperature and at 35 °C was negligible. Furthermore, DI water without adjusting pH (i.e., pH 5.5–6) seemed to have sufficient ability to extract F from the rice sample when employing enzymes concurrently. Hence, there was no need to be taken concerning temperature and pH of solution and consequently the proposed method was performed at room temperature and unaltered pH levels (5.5–6).

3.2. Feasibility of facilitated extraction with enzyme for the determination of F concentration

The proposed method for the determination of total F concentration in the rice samples was compared with the alkali fusion method in order to assess its feasibility. The alkali fusion-ISE method was usually used as a reference method for the analysis of total F concentration in vegetation samples [6,7]. The experimental conditions of facilitated extraction with enzyme are as follows: 0.1 g of sample, 30 mg of protease, 10 mL of DI water as solvent, and mechanically shaking for 10 s without sonication. Results obtained by facilitated extraction with enzyme are in good agreement with those obtained by the alkali fusion method from 0.012 to 0.378 of relative error (defined as the ratio of difference between F concentrations determined using alkali fusion-ISE and the proposed method to total F concentration determined using alkali fusion-ISE) (Fig. 1), indicating the suitability of the proposed

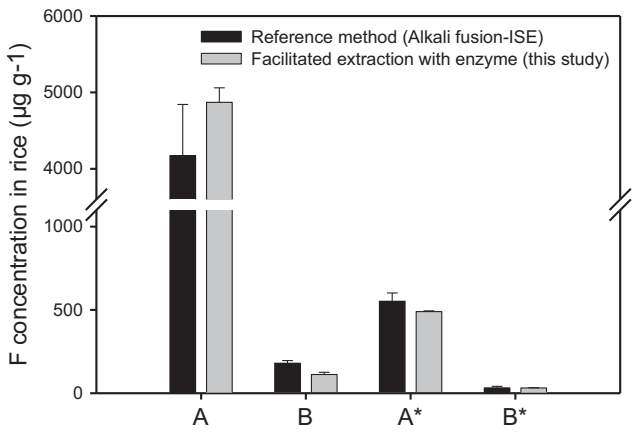


Fig. 1. Comparison of F concentrations in rice samples determined using alkali fusion-ISE and facilitated extraction with enzyme methods. Rice A is collected from the site that is directly affected by HF exposure. Conversely, Rice B, as the control sample, is collected from the background area unaffected by HF exposure. Rice A* and Rice B* are taken from the aforementioned points, respectively after one year has passed.

Table 3
Comparison of several extraction methods for the determination of F concentration in plant samples.

Order	Analytical method	Sample type	Solvent used	Time required (h)[a]	Waste generated (mL sample^{-1})[b]	Source
1	Alkali fusion+ISE	Vegetation	NaOH, HCl	8.0	100	[6,7]
2	Pyrohydrolysis+ISE	Coal	DI water	4.5	100	[8,9]
3	Oxygen combustion+ISE	Coal	$NaHCO_3$, Na_2CO_3	0.5	1000	[10]
4	Facilitated extraction with enzyme+ISE	Rice	DI water	0.5	10	This study

[a] Time required is calculated by adding times for sample preparation, extraction process, and the ISE analysis.
[b] Waste generated is calculated by adding solvent, and acid/alkali solution used.

extraction method for F analysis in rice sample over a wide range of F concentrations (31.9–4870 μg F^-/g sample). The standard deviations of facilitated extraction with enzyme (1.07–190 μg F^-/g sample) were much smaller than those of alkali fusion method (8.70–670 μg F^-/g sample). This result indicated that facilitated extraction with enzyme was more precise method for F analysis in the rice samples. The F concentrations of unaffected rice samples (31.9 and 112 μg F^-/g sample) were comparable to those of other rice samples studied previously [22,23]. On the other hand, owing to the influence of HF exposure, the obtained values from Rice A and Rice A* (4870 and 490 μg F^-/g sample, respectively) were one or two orders of magnitude higher than previously reported values [22,23].

3.3. The figures of merit

Facilitated extraction with enzyme for the analysis of F contents in rice samples is a rapid and simple method compared to conventional methods such as alkali fusion, pyrohydrolysis, and oxygen combustion (Table 3). Although alkali fusion method achieved limit of detection (LOD) of 3 ppm that is quite low to determine F contents in solid samples [7], it necessitates complicated and time-consuming procedures, resulting in the generation of excessive waste. In thermal hydrolysis method, although 3.7–5.1% of standard deviation and 20 ppm LOD were obtained, it requires proficient skills in its application and complex apparatus to meet the condition of high temperature about 1000 °C [8,9]. Oxygen bomb combustion method can prevent the loss of F through volatilization because of using enclosure flask and combustion process is completed within 10 min. Despite these advantages, it has complicated procedures and generates overfull waste about 1000 mL [10].

The proposed method can simplify the extraction procedures and thereby saving the pretreatment time, as shown in Table 3. In the existing methods, the suspension originated from the extraction process is generally centrifuged for at least 10–20 min, and the supernatant is filtered and then analyzed [11,12]. On the other hand, in the proposed method, centrifugation step can be avoided and the suspension is directly filtered by a 0.4 μm polycarbonate filter, resulting in the additional reduction of the extraction time by approximately 5 min. Furthermore, only 10 mL of DI water is used as the extraction solvent, which is a relatively smaller quantity compared to those used in other methods. In addition, the proposed method eliminates acid/base solutions and organic solvents, and consequently diminishes hazardous wastes generated and analytical error.

3.4. Application to various plant samples

30 mg of protease and 0.1 g of sample were added to 10 mL of DI water and the solution was mechanically shaken for 10 s without sonication. F concentrations in different plant samples were determined to evaluate the applicability of the proposed method for a wide range of plant samples. Grass, perilla, peanut, hot pepper, and eggplant samples were used in this study. All the plant samples were analyzed using both the alkali fusion-ISE and the proposed facilitated extraction with enzyme. F concentrations of various plant samples are presented in Table 4. F concentrations in plant samples varied from 28.0 to 121.5 μg F^-/g sample. These values were comparable to the F contents of 9–248 μg F^-/g sample reported in previous studies [24]. As shown in Table 4, results obtained from both the extraction methods are in good agreement with 0.072–0.284 of relative error regardless of plant species. Therefore, it clearly confirmed that facilitated extraction with enzyme for the analysis of F contents is suitable for a wide range of plant samples.

Table 4
F concentration in different plant samples using both alkali fusion-ISE and facilitated extraction with enzyme methods.

Plant samples	Total F concentration (μg g^{-1})		Relative error (RE)[a]
	Alkali fusion-ISE	Facilitated extraction with enzyme	
Grass	169 ± 19.0[b]	122 ± 0.50	0.284
Perilla	30.6 ± 2.24	36.4 ± 4.50	0.190
Peanut	47.2 ± 11.5	54.3 ± 0.50	0.150
Hot pepper	28.2 ± 8.76	30.2 ± 0.20	0.072
Eggplant	25.4 ± 4.60	28.0 ± 3.50	0.102

[a] Relative error is defined as the ratio of the difference between F concentrations determined by alkali fusion-ISE and facilitated extraction with enzyme to F concentration determined by alkali fusion-ISE.
[b] Mean ± standard deviation (n=3).

4. Conclusions

In this study, novel facilitated extraction method with enzyme using protease for the rapid determination of F contents in plant samples was developed. Important parameters including the amounts of enzymes used, physical treatment conditions applied (sonication), extraction time, temperature, and pH were optimized. The feasibility of the proposed method was evaluated by comparing with alkali fusion-ISE technique, which is a reliable method for F analysis. Compared with other methods, facilitated extraction with enzyme is a rapid and simple method, eliminating complicated and time-consuming procedures. In addition, only a small amount of the solvent was used and the use of hazardous chemicals can be avoided. Hence, the proposed method is efficient and environmentally friendly for the rapid determination of F contents in plant samples.

Acknowledgments

This study received substantial support from the Geo-Advanced Innovation Action (GAIA) project (Grant 2012000540014) of the Korea Environmental Industry & Technology Institute (KEITI). The authors also acknowledge the support by a grant from the Korea Basic Science Institute (Project no. C34704).

References

[1] J.A. Camargo, Chemosphere 50 (2003) 251–264.
[2] O. Barbier, L. Arreola-Mendoza, L.M. Del Razo, Chem. Biol. Interact. 188 (2010) 319–333.
[3] S.J. Cronin, V. Manoharan, M.J. Hedley, P. Loganathan, N.Z. J. Agric. Res. 43 (2000) 295–321.
[4] J.S. Jacobson, L.H. Weinstein, D.C. Mccune, A.E. Hitchcock, J. Air Pollut. Control Assoc. 16 (1966) 412–417.
[5] ASTDR, Toxicological profile for fluorides, hydrogen fluoride, and fluorine, Agency for toxic Substances and Disease Registry, 2003.
[6] M.K. Malde, K Bjorvatn, K. Julshamn, Food Chem. 73 (2001) 373–379.
[7] N.R. McQuaker, M. Gurney, Anal. Chem. 49 (1977) 53–56.
[8] I. Sredovic, Lj. Rajakovic, J. Hazard. Mater. 177 (2010) 445–451.
[9] J.C. Warf, W.D. Cline, R.D. Tevebaugh, Anal. Chem. 26 (1954) 342–346.
[10] D.A. Levaggi, W. Oyung, M. Feldstein, J. Air Pollut. Control Assoc. 21 (1971) 277–279.
[11] E. Sanz, R. Munoz-Olivas, C. Camara, Anal. Chim. Acta 535 (2005) 227–235.
[12] E. Sanz, R. Munoz-Olivas, C. Camara, J. Chromatogr. A 1097 (2005) 1–8.
[13] J.L. Guzman Mar, L.H. Reyes, G.M. Mizanur Rahman, H.M. Skip Kingston, J. Agric. Food Chem. 57 (2009) 3005–3013.
[14] J.L. Capelo, P. Ximennez-Embun, Y. Madrid-Albarran, C. Camara, Anal. Chem. 76 (2004) 233–237.
[15] K. Poutanen, Trends Food Sci. Technol. 8 (1997) 300–306.
[16] J. An, H.A Lee, J. Lee, H.-O. Yoon, Chemosphere 119 (2015) 577–582.
[17] M. Toma, M. Vinatoru, L. Paniwnyk, T.J. Mason, Ultrason. Sonochem. 8 (2001) 137–142.
[18] M. Vinatoru, Ultrason. Sonochem. 8 (2001) 303–313.
[19] C. Bendicho, I. De La Calle, F. Pena, M. Costas, N. Cabaleiro, I. Lavilla, TrAC Trends Anal. Chem. 31 (2012) 50–60.
[20] A. Rosenthal, D.L. Pyle, K. Niranjan, S. Gilmour, L. Trinca, Enzyme Microb. Technol. 28 (2001) 499–509.
[21] F. Hostettler, E. Borel, H. Deuel, Helv. Chim. Acta 34 (1951) 2132–2139.
[22] J. Ruan, M.H. Wong, Environ. Geochem. Health 23 (2001) 53–63.
[23] J. Franzaring, H. Hrenn, C. Schumm, A. Klumpp, A. Fangmeier, Environ. Pollut. 144 (2006) 158–165.
[24] J.A. Cooke, M.S. Johnson, A.W. Davison, Environ. Pollut. 11 (1976) 257–268.

Talanta 132 (2015) 653–657

Contents lists available at ScienceDirect

Talanta

journal homepage: www.elsevier.com/locate/talanta

A competitive strategy based on cucurbit[7]uril supramolecular interaction for simple and sensitive detection of dibucaine

Yan Li [a,b], Chang-Feng Li [b,*], Li-Ming Du [a,**], Jian-Xia Feng [a], Hai-Long Liu [a], Yun-Long Fu [b]

[a] Analytical and Testing Center, Shanxi Normal University, Shanxi, Linfen 041004, PR China
[b] School of Chemistry and Materials Science, Shanxi Normal University, Linfen 041004, PR China

ARTICLE INFO

Article history:
Received 8 June 2014
Received in revised form
29 August 2014
Accepted 3 September 2014
Available online 11 September 2014

Keywords:
Dibucaine
Spectrofluorometry
Competitive interaction
Supramolecular chemistry
Cucurbit[7]uril

ABSTRACT

In this work, the competitive interaction between dibucaine and three fluorescent probes (i.e., berberine, palmatine, and coptisine) for occupancy of the cucurbit[7]uril (CB[7]) cavity was studied by fluorescence spectra, UV–visible absorption spectra, ^{1}H NMR spectra, and theoretical calculations in acidic aqueous solution. Based on the fluorescence enhancement of berberine, palmatine, and coptisine upon binding with CB[7], respectively, a series of fluorescence detection methods for dibucaine were proposed. At the optimized conditions, the fluorescence intensity of berberine-CB[7], palmatine-CB[7], and coptisine-CB[7] complexes showed negative correlation to the concentration of dibucaine, which led to a series of simple and sensitive fluorescence methods for the determination of dibucaine for the first time. Linear ranges obtained in the detection of the dibucaine were 0.018–3.34 μmol L^{-1}, 0.032–4.47 μmol L^{-1}, and 0.079–4.42 μmol L^{-1} with detection limits of 6.0 nmol L^{-1}, 12.0 nmol L^{-1}, and 25.0 nmol L^{-1}, respectively. Moreover, the proposed method was successfully applied for the determination of the drug in biological fluids. The competitive mode based on CB[7] superstructure provided a promising assay strategy for fluorescence detection in various potential applications.

© 2014 Published by Elsevier B.V.

1. Introduction

Dibucaine, 2-butoxy-N-(2-diethylaminoethyl)-4-quinolinecarboxamide hydrochloride (DC) (Scheme 1) has attracted great clinical interest for its 15 times more potent than procaine and five times than cocaine in producing local anesthesia, but with considerably more poisonous property [1]. A number of assays have been reported for detection of DC in biological and pharmaceutical samples, including differential-pulse polarographic [1], chromatography [2–9], atomic absorption spectrometry [10] and spectrophotometry [11]. However, chromatography requires the use of organic solvents, expensive instruments, and time-consuming operating steps [2–9]. Though easier to operate, the reported method of spectrophotometry also need the use of haematoxylin in the presence of boric acid to give a reddish-violet chromogen fluorescent product, and showed low sensitivity and limited extending potential [11]. Some other methods are not sensitive enough [1,10]. Therefore, simple and sensitive detection method is in urgent need for determination of DC especially in biological fluids. To the best of our knowledge, no fluorescence analyst method is available for the detection of DC.

Supramolecular chemistry provides a possibility for selective detection of DC due to the steric effect of macrocyclic compounds. Supramolecular complex formation of macrocyclic compounds is widely utilized as molecular-scale devices, sensors, fluorescent probes due to the amphiprotic properties of macrocyclic compounds [12–14]. Specially, the cucurbit[*n*]urils (CB[*n*], *n*=5–8, 10), which are comprised of *n* glycoluril units bridged by 2*n* methylene groups, possess considerable negative charge density in their carbonyl-fringed portals for the binding of metal ions and cationic organic compounds. Meanwhile the extremely nonpolarizable cavity preferably accommodates hydrophobic moieties [15–18]. The CB[7] host (Scheme 1) has been of particular interest in fluorescent assay since its remarkable ability to form host–guest complexes with organic molecules [19–26].

Herein, we employ berberine hydrochloride (BER), palmatine hydrochloride (PAL), and coptisine (COP) as signal probes for the fluorescence detection of DC in biological fluids samples (Scheme 2). When DC was added into the aqueous solution of CB[7], there was no distinct fluorescence change. However, dramatic increase in fluorescence intensity was observed when BER, PAL, or COP was added to CB[7] solution. As such, when DC was mixed with CB[7]–berberine, CB[7]–palmatine, or CB[7]–coptisine complexes, the significant decrease of fluorescence intensity can

* Corresponding author. Tel./fax: +86 357 205 7969.
** Corresponding author.
E-mail addresses: lichangfeng2@aliyun.com (C.-F. Li), lmd@dns.sxnu.edu.cn (L.-M. Du).

http://dx.doi.org/10.1016/j.talanta.2014.09.005
0039-9140/© 2014 Published by Elsevier B.V.

be observed. The fluorescence intensity showed a negative correlation to the concentration of DC with a linear calibration plot in the ranges of 0.018–3.34, 0.032–4.47, and 0.079–4.42 μmol L^{-1}, with detection limits of 6.0 nmol L^{-1}, 12.0 nmol L^{-1}, and 25.0 nmol L^{-1} for the above three complexes, respectively. Moreover, the designed method was successfully applied in the detection of DC in urine samples, which showed promising application in various practical scenarios.

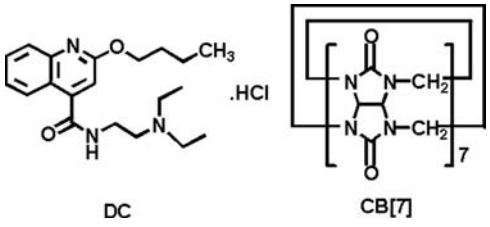
2. Experimental

2.1. Materials and reagents

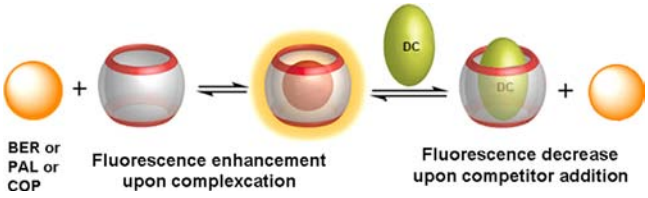
Berberine hydrochloride (BER), palmatine hydrochloride (PAL), coptisine (COP), and DC were obtained from the Chinese National Institute for the Control of Pharmaceutical. CB[7] was prepared and characterized according to the reported procedure [17,18]. CB[7] stock solutions of 1.0 mmol L^{-1} were prepared by dissolving CB[7] in a 100 mL volumetric flask with doubly-distilled water. All the stock standard solutions were stable for several weeks at room temperature. All other reagents used were of analytical grade, and double-distilled water was used thoroughly.

2.2. Apparatus

The fluorescence measurements were performed on a Cary Eclipse spectrofluorometer (America). The slit widths of both excitation and emission monochromators were set to 5 nm. All measurements were performed in a standard 10 mm path-length quartz cell set to a temperature of 25.0 ± 0.5 °C. Absorption spectra were measured on a U-3010 UV–visible spectrophotometer (Hitachi, Japan). ^{1}H NMR spectra were obtained using a Bruker AV-600 MHz spectrometer (Switzerland) in D_2O buffered with DCl (0.10 mol L^{-1}). Molecular modeling calculations were optimized at the B3LYP/6-31 G(d) level of density functional theory with the Gaussian 03 program.



Scheme 1. Structure of DC and CB[7].



Scheme 2. Competitive recognition of CB[7] to DC against BER, PAL, or COP.

2.3. Spectra measurement procedure

The fluorescence measurements were carried out with the excitation wavelength of 345, 344, and 358 nm in the absence or presence of DC solution. In a 10 mL colorimetric flask, 0.5 mL 0.1 mmol L^{-1} CB[7] solution, 0.5 mL 0.1 mmol L^{-1} probe molecular solution (i.e. BER, PAL, or COP), followed by 1.0 mL of 1.0 mol L^{-1} hydrochloric acid, and a given concentration of DC standard solution or sample solution were sequentially added. The mixture was diluted to the volume with water and shaken for 15 min at room temperature.

2.4. Analysis of spiked human urine

Urine samples were handled according to the previous protocol [27]. Briefly, each urine sample (10.0 mL) was placed into a centrifuge tube, spiked with 1.0 mL drug stock solution and then centrifuged at 5000 rpm for 5 min. The clear supernatant of the spiked urine sample was extracted by solid phase extraction (SPE) using 001 × 7 strong-acid cation exchange resin. The procedure was as follows: 1 mL of the spiked urine sample was transferred into the SPE cartridge (with the resin height being 1 cm and the diameter 1 cm). After allowing the sample to pass through to waste under gravity, the resin was washed with 1 mL 1% sodium hydroxide solution and 2 mL double-distilled water (amino acids can be removed). The filtrate was discarded. Finally, the analyte was eluted into a colorimetric flask with 4 mL of methanol/water (1:1, v/v) and then the general procedure was followed.

3. Results and discussion

3.1. Spectral characteristics

Because the same trends showed for three fluorescent probes (i.e., BER, PAL or COP), the following research used the BER as example. The UV–visible spectra of DC and BER showed absorption bands at 202, 246, 321 nm and 228, 263, 345 nm, respectively

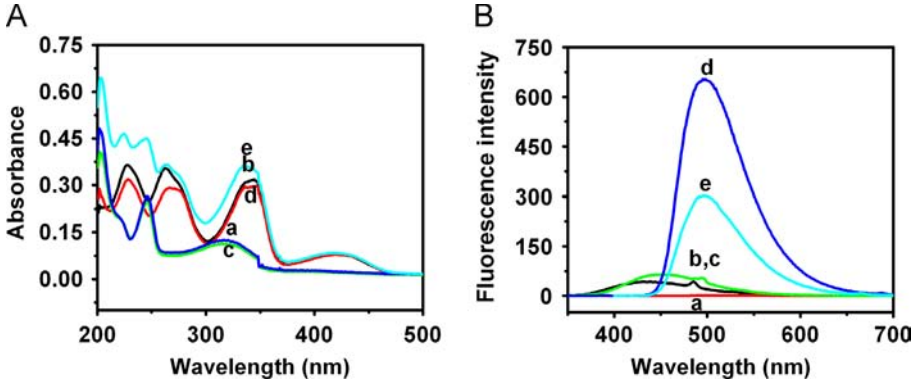


Fig. 1. (A) UV–visible spectra of (a) DC, (b) BER, (c) DC+CB[7], (d) BER+CB[7] and (e) BER+CB[7]+DC. The concentrations of BER, CB[7] and DC are 10.0 μmol L^{-1}, pH=1. (B) Fluorescence spectra of (a) BER, (b) DC, (c) DC+CB[7], (d) BER+CB[7] and (e) BER+CB[7]+DC. The concentrations of BER, CB[7] and DC are 5.0, 5.0, and 3.34 μmol L^{-1}, respectively, pH=1.

(Fig. 1A, curve a and b). After the addition of CB[7] into DC or BER solution, a slight hypochromicity was observed (Fig. 1A, curve c and d). This should be attributed to the inclusion of DC or BER by CB[7] and produce supramolecular complexes. However, a increase in absorption spectra was observed upon addition of DC into BER–CB[7] complex solution (Fig. 1A, curve e). This should be attributed to the BER molecule expelled from the CB[7] cavity because of the introduction of DC.

The solution of BER alone showed undetectable fluorescent emission, meanwhile, DC also exhibited very weak native fluorescence in acidic aqueous solution (Fig. 1B, curve a and b). After the addition of CB[7] into DC solution, no distinct change of fluorescence was observed (Fig. 1B, curve c). However, a dramatic increase in fluorescence intensity was observed upon addition of CB[7] in BER solution (Fig. 1B, curve d). This should be attributed to the inclusion of BER by CB[7] to change the space structure or conformation of BER and produce a fluorescent complex. Interestingly, the addition of DC to the mixture of CB[7] and BER led to significant decrease of fluorescence intensity (Fig. 1B, curve e). Furthermore, with the increasing concentration of DC, the fluorescence intensity became smaller (Supporting information, Figs. S1–S3). The fluorescence intensity decrease to the amount of added DC led to a series of simple and sensitive fluorescence methods for the determination of DC.

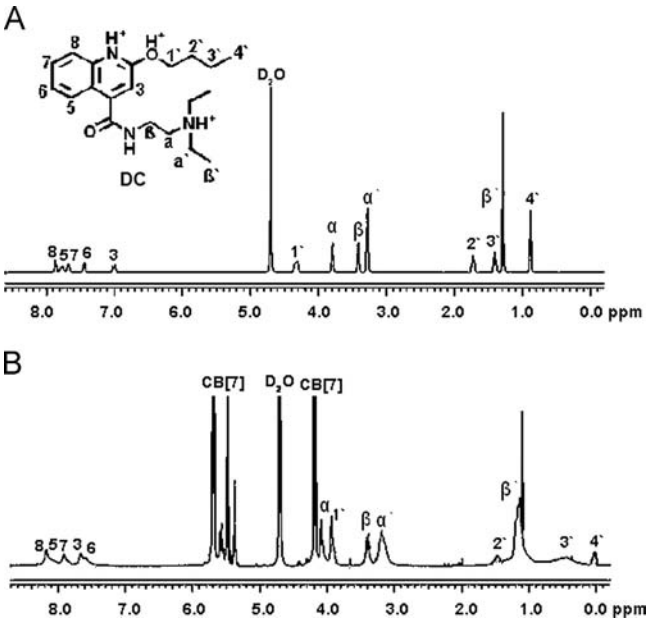


Fig. 2. ^{1}H NMR (600 MHz) spectra of (A) DC and (B) DC in the presents of CB[7] in D_2O buffered with DCl (0.10 mol L^{-1}).

3.2. Interaction mechanism of the fluorescent probe

Although the fluorescent emission of pure BER, PAL, and COP was very weak or undetectable, the fluorescence intensity greatly enhanced after they entered the hydrophobic cavity of CB[7], which showed a good linear relationship between $1/F$ and $1/c_{CB[7]}$, indicating the existence of a 1:1 complex. The binding constant (K) for these complexes were determined to be 9.57×10^4, 4.26×10^4, and 1.86×10^5 L mol^{-1} [19–21].

When DC was added to CB[7]-complexes solution, DC could compete to occupy the CB[7] cavity with BER, PAL and COP. Due to the greater $K_{DC-CB[7]}$ ($1.1 \pm 0.2 \times 10^7$ L mol^{-1}) value [28] than $K_{CB[7]-BER}$, $K_{CB[7]-PAL}$, and $K_{CB[7]-COP}$, which showed the stronger binding of DC with CB[7], BER, PAL, and COP in CB[7] cavity was displaced by DC. As a result, the fluorescent intensity of CB[7]–BER, CB[7]–PAL, CB[7]–COP complex weakened.

The formation of CB[7]–DC inclusion complex could be confirmed by ^{1}H NMR spectroscopy (Fig. 2). Compared with the proton resonance of the unbound DC molecule (Fig. 2A), the resonance of protons $H_{1'}$, $H_{2'}$, $H_{3'}$, and $H_{4'}$ of the bound DC in the ^{1}H NMR spectrum of CB[7]–DC complex experienced a progressively up-field shift (Fig. 2B), indicating that CB[7] binds selectively to the protonated oxygen-terminal butyl residues due to cooperative hydrophobic and ion–dipol interactions. Because of the excellent matched size and morphology, butyloxy residues was enclosed in the cavity of CB[7] more tightly than triethylammonium groups in acidic aqueous solution. The resonance of protons H_3 of DC experienced a slightly down-field shift, indicating this part of the molecule was located just outside the carbonyl portal of the CB[7] host.

Molecular modeling calculations were optimized at the B3LYP/6-31G(d) [29] level of density functional theory [30,31] using the Gaussian 03 program. The results confirmed the partial inclusion of DC in the hydrophobic cavity of CB[7] (Fig. 3). It can be seen from molecular simulation that both butyloxy group and quinolyl group were protonated in acidic solution, giving the cationic form of DC. This indicated that, in the energy-minimized structure, butyloxy group of the molecule located inside the host, however, quinolyl group of the molecule located just outside the carbonyl portal of the CB[7] host.

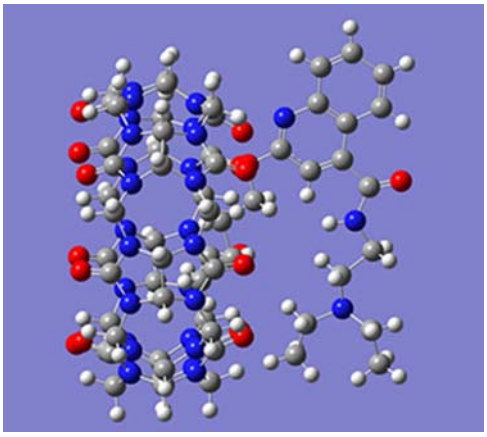


Fig. 3. Energy-minimized structure of CB[7]–DC complex in the ground state using balls and tubes for rendering the atoms. Color codes for DC and CB7: oxygen, red; nitrogen, blue; carbon, dark gray; hydrogen, gray. (For interpretation of the references to color in this figure legend, the reader is referred to the web version of this article.)

3.3. Analytical performance

From Supporting information (Figs. S1–S3), in the solution of 5.0 μmol L^{-1} BER–CB[7], PAL–CB[7], and COP–CB[7] complexes, the plots of fluorescence intensity vs the concentration of DC showed a series of linear relationship in the ranges of 0.018–3.34 μmol L^{-1}, 0.032–4.47 μmol L^{-1}, and 0.079–4.42 μmol L^{-1}, respectively. The linear regression equations were $I = -90.42c + 602.08$, $I = -80.23c + 626.08$, and $I = -86.69c + 819.81$ (c denotes the concentration of DC in μmol L^{-1}) with the correlation coefficients of 0.9997, 0.9991, and 0.9995, and the detection limits of 6.0 nmol L^{-1}, 12.0 nmol L^{-1}, and 25.0 nmol L^{-1} at 3σ for the same order, respectively. A comparison of the results obtained by the proposed method with those obtained by the other spectroscopic approaches shows the sensitive is satisfactory (Table 1).

Prior to the application of the proposed fluorescence method in analysis of the drug in human urine samples, the effect of common ingredients in human urine on the determination of DC was examined. The criterion for interference was fixed at a ±5%

Table 1
Comparison with other proposed methods for the determination of DC.

Technique		Linear range (μmol L^{-1})	LOD (μmol L^{-1})	Application	Reference
Differential-pulse polarographic		1–100	0.5	Pharmaceutical ointment	[1]
HPLC		0.004–0.079	–	–	[3]
HPLC		0.132–13.2	0.034	Human urine	[4]
GC		13.2–105.3	4.42	Biological fluidsand tissues	[5]
GC–MS		1.32–263.2	0.26	Plasma; urine	[6]
LC–MS		–	0.013	Human serum	[7]
CS–LC–MS		0.0263–2.63	0.0086	Plasma	[8]
HIEKC		105.3–289.5	2.63	Commercial ointment	[9]
Atomic absorption spectrometry		152.6–952.6	10.97	Pharmaceutical formulation	[10]
		99.99–999.9	2.13	Ointment	[10]
Spectrophotometry		13.2–78.96	4.42	Pharmaceutical preparations	[11]
Spectrofluorimetry	CB[7]/BER	0.018–3.34	0.006	Human urine	This work
	CB[7]/PAL	0.032–4.47	0.012	Human urine	This work
	CB[7]/COP	0.079–4.42	0.025	Human urine	This work

Table 2
Fluorescence determination of DC in spiked urine ($n=5$, $p=95\%$).

Samples	Spiked urine		
	DC added (μg mL^{-1})	DC found (μg mL^{-1})	Recovery(%) ± S.D.[a]
Urine 1	0.1	0.098	98.0 ± 1.27
Urine 2	0.2	0.197	98.5 ± 1.25
Urine 3	0.4	0.414	103.5 ± 1.30
Urine 4	0.8	0.807	100.9 ± 0.80
Urine 5	1.0	1.025	102.5 ± 1.40

[a] Average of five determination.

variation in the average fluorescence intensity calculated for the established level of DC. The results showed no interference of the common ingredients in urine samples. However, the components such as cysteine, alanine, phenylalanine, and valine could change the fluorescence intensity of the complex to a certain degree. Hence, they should be separated prior to the determination.

3.4. Analytical application

Due to the high sensitivity, good selectivity and stability shown in the proposed fluorescent method, the method was applied in the determination of the DC in spiked samples of human urine. The results are presented in Table 2 (using the CB[7]–BER complex as signal probe). The standard deviations obtained from the proposed method were less than 1.40%. The recoveries examined with a standard addition method were in the range of 98.0–103.5%.

4. Conclusion

In this work, the supramolecular systems of CB[7] were designed for the first time in the determination of DC. The CB[7]–BER, CB[7]–PAL, and CB[7]–COP complexes were indentified to have a greatly enhanced fluorescent emission due to strong coplanar and rigidity of BER, PAL, and COP, respectively. Since the interaction of DC with CB[7] was stronger than BER, PAL, and COP, the CB[7]–BER, CB[7]–PAL, and CB[7]–COP superstructures would be disintegrated upon addition of DC considering the thermodynamic factor, which led to a significant fluorescence reduction, respectively. Based on the competitive mode, a series of novel fluorescence methods for the determination of DC were established with high sensitivity, cost-effectiveness, and easy operation, which was successfully applied in biological fluids. The interaction mechanism between the DC and the CB[7] also confirmed that the butyloxy group of the DC molecule located inside the host in acidic aqueous solution via UV–visible absorption spectra, the ^{1}H NMR spectrum and the theoretical calculations.

Acknowledgments

This work was supported by the National Natural Science Foundation of China (No. 21171110) and the Foundation of Shanxi Normal University (No. ZR1210). Helpful suggestions by anonymous referees are also gratefully acknowledged.

Appendix A. Supporting information

Supplementary data associated with this article can be found in the online version at http://dx.doi.org/10.1016/j.talanta.2014.09.005.

References

[1] M.S.M. Fernández-Marcote, M. Callejón Mochón, J.C. Jiménez Sánchez, A. Guiraúm Pérez, Analyst 121 (1996) 681–685.
[2] M.M.A. Elsayed, Biomed. Chromatogr. 21 (2007) 491–496.
[3] R.D. Barbosa, A. Klassen, P.D. Marcato, M. Franz-Montan, R. Grillo, L.F. Fraceto, E. de Paula, Lat. Am. J. Pharm. 32 (2013) 1362–1369.
[4] K. Igarashi, F. Kasuya, M. Fukui, H. Nanjyou, Chem. Pharm. Bull. 35 (1987) 3033–3036.
[5] M. Culea, N. Palibroda, Z. Moldovan, A.D. Abraham, P.T. Frangopol., Chromatographia 28 (1989) 24–26.
[6] T. Ohshima, T. Takayasu, J. Chromatogr. B 726 (1999) 185–194.
[7] T. Saitoa, S. Moritaa, I. Kishiyamab, S. Miyazakib, A. Nakamotoc, M. Nishidad, A. Namerad, M. Nagaod, S. Inokuchi, J. Chromatogr. B 872 (2008) 186–190.
[8] S. Kawano, H. Murakita, E. Yamamoto, N. Asakawa, J. Chromatogr. B 792 (2003) 49–54.
[9] H. Okamoto, A. Uetake, R. Tamaya, T. Nakajima, K. Sagara, Y. Ito, J. Chromatogr. A 929 (2001) 133–141.
[10] N.T. Abdel-Ghani, A.F.A. Youssef, M.A. Awady, II Farmaco 60 (2005) 419–424.
[11] N.T. Abdel-Ghani, A.F.A. Youssef, M.A. Awady., Anal. Lett. 28 (1995) 2663–2671.
[12] S. Li, W.C. Purdy, Chem. Rev. 92 (1992) 1457–1470.
[13] R. Ludwig, Fresenius J. Anal. Chem. 367 (2000) 103–128.
[14] W.L. Mock, N.Y. Shih, J. Am. Chem. Soc. 111 (1989) 2697–2699.
[15] L. Isaacs, Acc. Chem. Res. 47 (2014) 2052–2062.
[16] S. Liu, C. Ruspic, P. Mukhopadhyay, S. Chakrabarti, P.Y. Zavalij, L. Isaacs, J. Am. Chem. Soc. 127 (2005) 15959–15967.
[17] J. Kim, I.S. Jung, S.Y. Kim, E. Lee, J.K. Kang, S. Sakamoto, K. Yamaguchi, K. Kim, J. Am. Chem. Soc. 122 (2000) 540–541.
[18] A. Day, A.P. Arnold, R.J. Blanch, B. Snushall, J. Org. Chem. 66 (2001) 8094–8100.
[19] Y.P. Li, H. Wu, L.M. Du, Chin. Chem. Lett. 20 (2009) 322–325.
[20] C.J. Li, J. Li, X.S. Jia, Org. Biomol. Chem. 7 (2009) 2699–2703.
[21] C.F. Li, L.M. Du, W.Y. Wu, A.Z. Sheng, Talanta 80 (2010) 1939–1944.
[22] M. del Pozo, L. Hernández, C. Quintana, Talanta 81 (2010) 1542–1546.
[23] Y. Jang, R. Natarajan, Y.H. Ko, K. Kim, Angew. Chem. Int. Ed. 53 (2014) 1003–1007.

[24] L. Cao, M. Šekutor, P.Y. Zavalij, K. Mlinaric′-Majerski, R. Glaser, L. Isaacs, Angew. Chem. Int. Ed. 53 (2014) 988–993.
[25] J.P.D. Silva, R. Choudhury, M. Porel, U. Pischel, S. Jockusch, P.C. Hubbard, V. Ramamurthy, A.V.M. Canarió, ACS Chem. Biol. 9 (2014) 1432–1436.
[26] M.H. Tootoonchi, S. Yi, A.E. Kaifer, J. Am. Chem. Soc. 135 (2013) 10804–10809.
[27] Y.X. Chang, Y.Q. Qiu, L.M. Du, C.F. Li, M. Guo, Analyst 136 (2011) 4168–4173.
[28] I.W. Wyman, D.H. Macartney., Org. Biomol. Chem. 8 (2010) 247–252.
[29] C. Lee, W. Yang, R.G. Parr, Phys. Rev. B 37 (1988) 785–789.
[30] A.D. Becke, J. Chem. Phys. 88 (1988) 2547–2553.
[31] A.D. Becke, Phys. Rev. A 38 (1988) 3098–3100.

Talanta 132 (2015) 658–663

Contents lists available at ScienceDirect

Talanta

journal homepage: www.elsevier.com/locate/talanta

A novel biosensor based on single-layer MoS_2 nanosheets for detection of Ag^+

Kang Mao, Zitong Wu, Yinran Chen, Xiaodong Zhou *, Aiguo Shen, Jiming Hu

Key Laboratory of Analytical Chemistry for Biology and Medicine (Ministry of Education), College of Chemistry and Molecular Sciences, Wuhan University, Wuhan 430072, China

ARTICLE INFO

Article history:
Received 24 July 2014
Received in revised form
10 October 2014
Accepted 13 October 2014
Available online 22 October 2014

Keywords:
Single layer MoS_2
Ag^+
"C–Ag^+–C"
Fluorescence detection

ABSTRACT

In this work, we use for the first time single layer MoS_2 as the fluorescence quencher to design a detection method for Ag^+ with excellent robustness, selectivity and sensitivity. To maintain the ultrathin MoS_2, bulk MoS_2 materials have been exfoliated by intercalation with lithium followed by reaction with water. As-prepared two-dimensional MoS_2 not only has good water-solubility but also obtains high fluorescence quenching efficiency within 5 min. Importantly, the detection limit of this assay for Ag^+ (1 nM) was lower than the maximum limitation guided by the United States Environmental Protection Agency (EPA) and the World Health Organization (WHO). Further, this new Ag^+ probe was demonstrated in monitoring Ag^+ in lake water samples with satisfactory results.

© 2014 Elsevier B.V. All rights reserved.

1. Introduction

As we all know, heavy metals are highly toxic and carcinogenic even at a trace level, which can enter the environment due to increasing industrial activities. They are non-biodegradable and can accumulate in the food chain, posing a severe threat to the environment and human health. Therefore, heavy metal pollution becomes a major concern for global sustainability. Among these heavy metal ions, silver ions (Ag^+) have received considerable attention in recent years because the use of silver, silver nanoparticles, and silver compounds has increased and recent studies emphasized bioaccumulation and the potential negative impact of Ag^+ on aquatic organisms [1–3]. Long term exposure of Ag^+ in water causes the death of exposed organisms such as environmentally benign bacteria [3]. Even nanomolar concentration of Ag^+ in water perturbs Na^+ and Cl^- homeostasis of fishes and invertebrates [2]. It is therefore essential to monitor Ag^+ in the environment, drinking water, food and biological fluids.

Conventional methods for Ag^+ measurement include atomic absorption spectroscopy (AAS), inductively coupled plasma/mass spectrometry (ICP-MS), inductively coupled plasma/atomic emission spectrometry (ICP-AES), ultraviolet–visible (UV–vis) spectroscopy, etc. Although these techniques are highly sensitive and selective, they require tedious sample preparation and preconcentration procedures, expensive instruments, and professional personnel. Moreover, they are inappropriate to be used as portable devices for real-time and on-site detection. In contrast, biosensors, especially fluorescent sensing, have great potential in high throughput detection of Ag^+ on-site [4–7]. Further, rapid development of nanotechnology has provided new opportunities for improved performance of fluorescence sensors in terms of sensitivity, selectivity and reproducibility. Fluorescent sensing is based on analyte-induced changes in the physicochemical properties of fluorophores such as fluorescence intensity, lifetime, and anisotropy, which are related to charge transfer or energy transfer processes [8,9]. However, relatively a few fluorescent sensors for Ag^+ have been reported compared with fluorescent sensors for other metal ions [10–16]. Furthermore, most of the fluorescent sensors for Ag^+ showed limitations in practical application due to low water solubility or other drawbacks. Hence, it remains essential to develop much simple, efficient and robustness methods of silver ion probe that can be used for detection of Ag^+ in complex water samples.

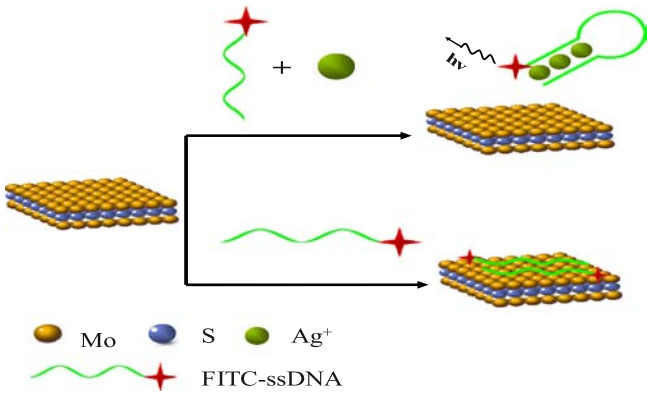
The rise of graphene has recently inspired great research interest in other types of ultrathin nanomaterials due to their attractive properties and various potential applications [17,18]. Therefore, following the same vein on graphene study, researchers have started the exploration of graphene analogs materials comprising stacked atomic or molecular layers. Strong covalent bonds in layers and weak Van der Waals interaction between layers allow the graphene analogs to form a robust two-dimensional (2D) nanostructure. Layered molybdenum disulfide (MoS_2) is one of the typical graphene analogs and a prototypical transition metal dichalcogenide material, which consists of covalently bonded Mo and S atoms [19]. Single-layer MoS_2 can be viewed as an "S–Mo–S" [10] sandwich structure, stacking a positively charged molybdenum plane between two negatively charged sulfur planes. Every

* Corresponding author. Tel.: +86 27 68752439, +86 27 68758116.
E-mail address: zhouxd@whu.edu.cn (X. Zhou).

http://dx.doi.org/10.1016/j.talanta.2014.10.026
0039-9140/© 2014 Elsevier B.V. All rights reserved.

Mo is coordinated in a trigonal prismatic geometry to six S atoms. Owing to the specific 2D confinement of electron motion and the absence of interlayer perturbation, the MoS_2 monolayer possesses a direct band gap, showing dramatic improvement in photoluminescence quantum efficiency [20–22] and leads to an attractive electrocatalytic activity [23].To our surprise, it has been found that some fluorescent dyes underwent drastic quenching in the presence of MoS_2 nanoparticles (MoS_2NCs). Zhu et al. [24] designed single-layer MoS_2 based nanoprobes which have been successfully used as a sensing platform for the detection of DNA and small molecules. Goswami et al. [25] reported that fluorescence of Hoechst 33258 was efficiently quenched in the presence of MoS_2 nanoparticles and estimated the probability of the distance distribution between the donor (Hoechst 33258) and acceptor (MoS_2NCs) by employing a statistical method based on Forster resonance energy transfer (FRET)-based model. Compared with other nano-materials, except high fluorescent quenching efficiency, cheap bulk MoS_2 materials are engineered easily and single layer MoS_2 has good water solubility. Such reports imply that single or fewer layers MoS_2 could also be one of the most valuable quenching materials in environmental, biomedical, and other applications.

Considering all of these mentioned above, to the best of our knowledge, we report for the first time a novel FRET-based method for Ag^+ based on single-layered MoS_2. It is known that oligonucleotides can interact with some types of metal ions with high specificity [26]. It has been previously demonstrated that Ag^+ can selectively bind in between two DNA cytosine (C) bases and promote these C–C mismatches to form stable C–Ag^+–C base pairs. The Ag^+-mediated C–Ag^+–C pairs are more stable and have higher melting temperature than the Watson–Crick C–G pairs. Further, Ag^+ can be incorporated into the DNA duplex without largely altering the double helical structure because the van der Waals radius of silver (≈ 1.44 Å) is smaller than the base pair spacing of the DNA duplex (≈ 3.4 Å) [27,28]. In this work, the excellent quenching performance of single layer MoS_2 was combined with Ag^+-mediated base pairs "C–Ag^+–C" to sensitively and selectively detect Ag^+. Scheme 1 shows the design of fabrication of the assay for Ag^+ on single layer MoS_2. Compared with other reported methods, the proposed method has some advantages of simple instrument, low background and high sensitivity both in aqueous buffer and complex water.



Scheme 1. Schematic representation of fluorescent detection of Ag^+ on single layer MoS_2 platform (a FITC-labeled Ag^+ specific oligonucleotide, rich in cytosine, is employed as the fluorescent probe in sensing targets. When FITC-labeled DNA probe is in the state of random coil ssDNA, FRET from FITC-ssDNA to single layer MoS_2 occurs and fluorescence disappears. However, when the DNA probe is in formation of dsDNA due to the addition of Ag^+, the energy donor FITC is far away from the surface of single layer MoS_2 and fluorescence will be recovered).

2. Materials and methods

2.1. Materials

(5′-FITC-CTCTCTTCTCTTCATTTTTCAACACAACACAC-3′) were purchased from Sangon Biotech (Shanghai, China) Co., Ltd. and purified by HPLC. Bulk MoS_2 and *n*-butyllithium were from Aladdin (Shanghai, China). $AgNO_3$ and other inspected species (including Ni^{2+}, Cu^{2+}, Cr^{3+}, K^+, Na^+, Fe^{3+}, Pb^{2+}, Co^{2+}, Mn^{2+}, Hg^{2+}, Zn^{2+}, Al^{3+}, Fe^{2+}, Mg^{2+}, Cl^-, SO_4^{2-}, NO_3^- HCO_3^- and PO_4^{3-}) were prepared with ultrapure water from a Millipore system (18.2 M resistivity). All the experiments were carried out in phosphate buffer saline (PBS) buffer (0.1 mM PBS, 50 mM $NaNO_3$, 10 μM EDTA [29], pH 8.00).

2.2. Instrumentation

Bulk MoS_2 material was characterized by a scanning electron microscope (SEM). The morphology of single layer MoS_2 was characterized by a JEM-2100 transmission electron microscope (TEM) operated at 200 kV. Subsequently, a confocal laser micro-Raman spectrometer (HR800UV, JOBIN YVON) was used to obtain the Raman spectra of single layer MoS_2 with excitation wavelength being set at 633 nm. Finally, a fluorescence spectrometer (F-4600, Hitachi Co. Ltd., Japan) with a Xenon lamp excitation source was employed to record fluorescence spectra. The excitation was set at 490 nm and the emission was monitored at 518 nm.

2.3. Preparation of single layer MoS_2

Single-molecular-layer MoS_2 was prepared by exfoliation of lithium-intercalated MoS_2 powder in water with some modifications [30–32]. 0.35 g of layered bulk MoS_2 materials were mixed with 100 mL 1 M of *n*-butyl lithium in hexane solution, then the mixtures were stirred and allowed to react in nitrogen environment for 48 h at room temperature. After the mixture was filtrated, washed with hexane several times and dried, the lithium-intercalated MoS_2 powder obtained was exfoliated under ultrasonication for over 0.5 h (120 W) in 100 mL ultrapure water. During the whole experimental process, the lithium ions fulfill several important functions. First, the Li ions are inserted into the interlayer space of the layered bulk MoS_2 material, which expands the interlayer distance and weakens the van der Waals interactions between the layers. Second, the inserted Li^+ ions are subsequently reduced to Li^0 by accepting electrons during the discharge process. The metallic lithium can react with water to form LiOH and produce hydrogen gas. The generated hydrogen gas pushes the layers further apart [33]. Finally, the obtained stable MoS_2 dispersion was centrifuged to remove the unexfoliated monolayer MoS_2 and get the homogeneous single layer MoS_2 suspension (1.0 mg/mL).

2.4. Fluorescence spectra measurements

2.4.1. Selection of optimal MoS_2 concentration

FITC-ssDNA solution (500 nM) was incubated for 5 min at 90 °C and then cooled down slowly to the room temperature. Single layer MoS_2 solution was diluted by PBS buffer (pH 8.00) to a final concentration of 0.05 mg/mL. Different volumes (0–300 μL) of single layer MoS_2 solution (0.05 mg/mL) were mixed with 10 μL 500 nM of FITC-ssDNA in 1.5 mL test tube, and different volumes of PBS buffer were added to make each solution 400 μL, then these mixtures were vibrated and allowed to react for 0.5 h at 30 °C. Finally the fluorescence measurements were done at room temperature. To save the cost and time, kinetic assay is necessary to find turning point that fluorescence quenching and fluorescence recovery. 200 μL of single layer MoS_2 solution (0.5 mg/mL) was mixed with 10 μL 500 nM of FITC-ssDNA in cuvette, after 15 min,

20 μL of 2 μM Ag^+ in aqueous buffer and 170 μL PBS buffer were added. The fluorescence spectra were measured at 30 °C.

2.4.2. Assay for Ag^+ in aqueous buffer

FITC-ssDNA solution (500 nM) was incubated for 5 min at 90 °C, then cooled down slowly to the room temperature. 200 μL of single layer MoS_2 solution (0.05 mg/mL) was mixed with 10 μL 500 nM of FITC-ssDNA in 1.5 mL test tube, then the mixed solution was stirred and allowed to react for 5 min at 30 °C, after that, different volumes of 2 μM Ag^+ in aqueous buffer (0–20 μL) were added; finally, appropriate aliquot of PBS buffer (pH 8.00) was introduced to make each reaction solution 400 μL and final Ag^+ concentration (0, 1, 2, 3, 4, 6, 8, 10, 20, 40, 60, 80, 100 nM). The final mixed solution was stirred and allowed to react for 15 min at 30 °C. The fluorescence spectra were measured at room temperature.

2.4.3. Selectivity assays

In order to ensure the selectivity of the method towards Ag^+, the other 14 common metal ions and 5 common anions in natural water instead of Ag^+ were used to react with the above system and performed in the same manner. 200 μL of single layer MoS_2 solution (0.05 mg/mL) was mixed with 10 μL, 500 nM of FITC-ssDNA in 1.5 mL test tube, then the mixed solution was stirred and allowed to react for 5 min at 30 °C; after that, different metal ions (20 μL, 2 μM) in aqueous buffer were added, and finally, appropriate aliquot of PBS buffer (pH 8.00) was introduced to make each reaction solution 400 μL. The final mixed solution was stirred and allowed to react for 15 min at 30 °C. All the above experiments were conducted in PBS buffer (10 mM, 50 mM $NaNO_3$, 10 μM EDTA, pH 8.00).

2.4.4. Detection of Ag^+ in real samples

Atomic absorption spectrometry (AAS) was applied to detect Ag^+ in East Lake water to verify feasibility of this new Ag^+ probe and obtain real concentration of Ag^+ in lake water. East Lake water was filtered by 0.22 μm microporous membrane.10 μL FITC-ssDNA (500 nM) was incubated with 10 μL single layer MoS_2 (1.0 mg/mL) for 10 min at 30 °C; later, 380 μL of East Lake water was mixed in the above solution. The final mixed solution was stirred and allowed to react for 30 min at 30 °C. Also, the detection of Ag^+ in tap water has been completed. 380 μL tape water was mixed with Ag^+ aqueous solution. Then PBS buffer was added into mixed solution and made up the final volume of 400 μL. Final Ag^+ concentration is (e–a) 0, 5.00, 10.00, 50.00 and 100.00 nM, respectively. And then fluorescence spectra were monitored at room temperature.

3. Results and discussion

3.1. Characterization of single layer MoS_2

According to the method described in literature [30] with some modifications, single layer MoS_2 was synthesized. To confirm the successful formation of 2D MoS_2 nanosheet, the as-prepared MoS_2 was characterized by high resolution transmission electron microscopy (HRTEM) and bulk MoS_2 was characterized by SEM (Fig. S1). As shown in Fig. 1A, the sheet width of single layer MoS_2 was approximately 10 nm exhibiting relatively narrow size distribution [34]. Raman spectrum was used to further confirm the single-layer MoS_2 due to line width and frequency difference of the E^1_{2g} and A_{1g} Raman modes, which confirmed the effective reduction of flake thicknesses from the bulk MoS_2 to the dispersions [21]. Results in Fig. 1B reflect the characteristics of single layer MoS_2. The two peaks at 384 and 409 cm^{-1} are attributed to the in-plane E^1_{2g} and out-of-plane A_{1g} vibrations of single-layer MoS_2, respectively [35]. As the Raman spectra were consistent with those in previously reported literatures [18,21,32,35,36], it was proved that we had successfully prepared single layer MoS_2 in this work.

3.2. FRET between FITC-tagged ssDNA and single layer MoS_2

Single-layered MoS_2 is a kind of two-dimensional surface nanomaterial with favorable water solubility. Charge transfer from the electron donor to single or fewer layer MoS_2 material is substantial and is partially associated with the p-type nature of ultrathin MoS_2 material [37]. FITC-labeled ssDNA was absorbed rapidly when approached the surface of ultrathin MoS_2 via the van der Waals force between nucleobases and the basal plane of MoS_2, and was then quenched owing to charge transfer. Therefore, the fluorescence of FITC was efficiently quenched due to FRET between FITC and single layer MoS_2. According to Scheme 1, a FITC-labeled Ag^+ specific oligonucleotide, rich in cytosine, was employed as the fluorescent probe in sensing targets. The conformation of the probe would be changed from random coil single stranded DNA (ssDNA) to straight stiff double stranded DNA (dsDNA) with "C–Ag^+–C" base pairs followed by the addition of Ag^+. When FITC-labeled DNA probe was in the state of random coil ssDNA, FRET from FITC-ssDNA to single layer MoS_2 occurred, because the distance from the energy donor FITC to the energy acceptor single layer MoS_2 was shortened by the special p-type nature of ultrathin MoS_2 material [37] and Van der Waals force between nucleotide bases and single layer MoS_2. However, when the DNA probe was in formation of dsDNA due to the addition of Ag^+, the energy donor FITC was far away from the surface of single layer MoS_2 and FRET was disappeared. Therefore, the introduction of enough amounts of Ag^+ led to a large degree of fluorescence recovery, and the degree of fluorescence quenching

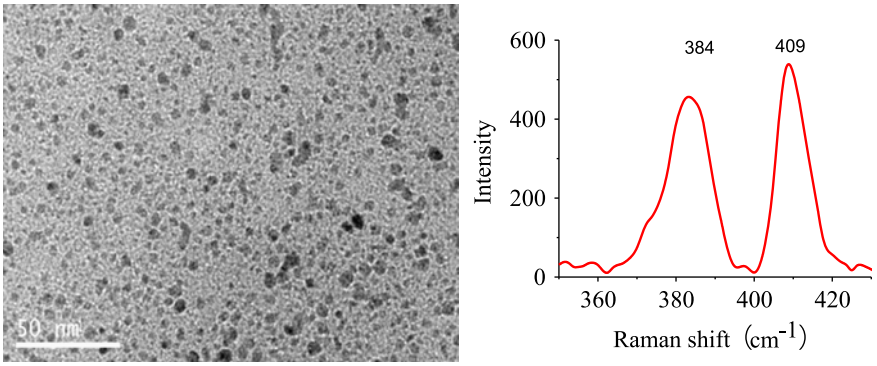


Fig. 1. High resolution transmission emission microscope (HRTEM) image of as-prepared single layer MoS_2 (A) and Raman spectra of single layer MoS_2 (B).

was closely related to the amount of added Ag^+ in certain linear range. The fluorescence of 12.5 nM FITC-ssDNA was effectively quenched by 25 μg/mL single layer MoS_2 (Fig. 2A, curve b), compared with the intensity without MoS_2 (Fig. 2A, curve a), indicating the strong quenching effect of single layer MoS_2 on the fluorescence of dye. The FITC-ssDNA rich in cytosine could capture Ag^+ by forming "C–Ag^+–C" base pairs. In the presence of Ag^+, the random coil ssDNA changed its conformation to rigid dsDNA, thus weakening the interactions between DNA nucleotide bases and single layer MoS_2 due to the hydrophilic force of the phosphoric skeleton in dsDNA, finally leading to the recovery of fluorescence (Fig. 2A, curve c). Results showed that the addition of Ag^+ induced the disappearance of FRET and the fluorescence recovery of FITC-ssDNA (Fig. 2B, curve b). Further, the fluorescence quenching kinetics was very fast, and highest fluorescence quenching efficiency was obtained within 5 min after FITC-ssDNA was mixed with the MoS_2 nanosheet solution. Meanwhile the fluorescence recovery kinetics was with up to best fluorescence recovery efficiency obtained within 15 min when Ag^+ was added into mixture solution (Fig. 3). This suggested that the designed Ag^+ probe system is successful and can be established with high performances.

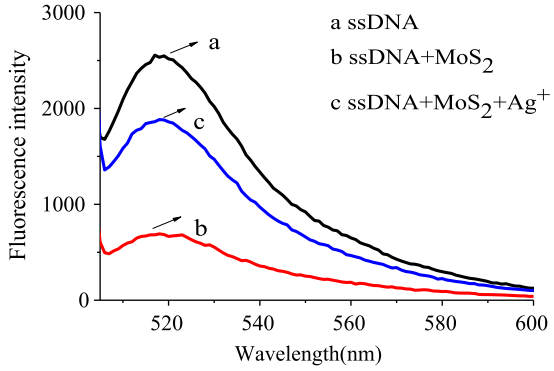


Fig. 2. Fluorescence spectra of before (curve a) and after (curve b) single layer MoS_2 (25 μg/mL) quenched 15 nM FAM-labeled ssDNA, and the change of fluorescence intensity after addition of Ag^+ (100 nM) (curve c). All these fluorescence spectra are carried out in PBS buffer at room temperature. The fluorescence is excited at 490 nm, and given in normalized form.

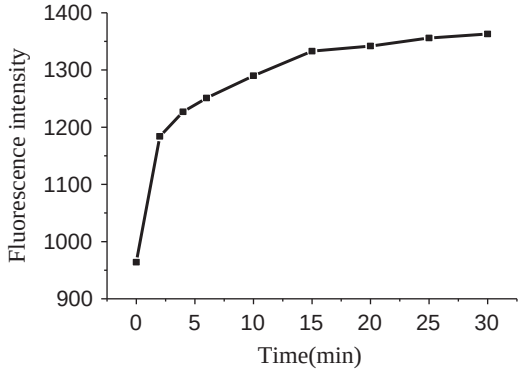


Fig. 3. Real-time fluorescence recovery records of mixtures with FITC-ssDNA (12.5 nM) and 25 μg/mL single layer MoS_2 upon additions of 100 nM Ag^+ (200 μL of single layer MoS_2 solution (0.5 mg/mL) are mixed with 10 μL 500 nM of FITC-ssDNA in cuvette, after 15 min, 20 μL of 2 μM Ag^+ in aqueous buffer and 170 μL PBS buffer is added. The fluorescence spectra are measured at 518 nm.).

3.3. Optimization of concentration of single layer MoS_2

Next, concentration of single layer MoS_2 was optimized as it is crucial in the detection of Ag^+ in aqueous buffer and complex water samples. As can be seen in Fig. 4A, the fluorescence intensity decreased gradually with the increasing concentration of single layer MoS_2, and a platform of fluorescence intensity was observed when the concentration of single layer MoS_2 reached 25 μg/mL (Fig. 4B). It indicated that too low concentration of single layer MoS_2 could lead to low fluorescence quenching efficiency and narrow detection range of Ag^+, while MoS_2 in high concentrations could have a poor effect on fluorescence recovery, and lower the sensitivity of Ag^+ determination. Therefore, an optimized concentration of 25 μg/mL single layer MoS_2 was chosen in the experiments.

3.4. Quantitative analysis of Ag^+ in aqueous buffer

As shown in Fig. 5, a new simple and sensitive assay for Ag^+ was successfully designed. The fluorescence intensity was dependent on the concentration of Ag^+ over a range of 1–100 nM when the concentration of single layer MoS_2 was 25 μg/mL. Fig. 5B shows that the fluorescence intensity increases rapidly as the concentration of Ag^+ increases from 1 nM to 6 nM ($R_1^2=0.996$). However, it exhibited another linear relationship ($R_2^2=0.995$) when the concentration of Ag^+ changed from 10 nM to 100 nM, where the fluorescence intensity increased more slowly as the Ag^+ concentration increased. The reason for this phenomenon was probably that FITC-labeled DNA in the state of random coil single strand was correspondingly abundant when Ag^+ was less than 6 nM in the system, and the plane structure of single layer MoS_2 could strongly adsorb these random coil single-strand

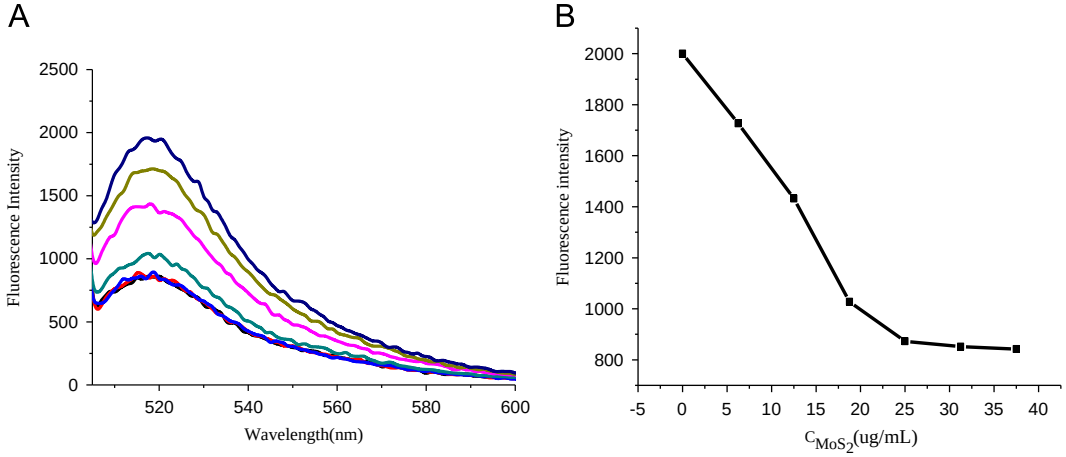


Fig. 4. (A) The fluorescence emission spectra of different concentrations of single layer MoS_2 (0, 6.25, 12.5, 18.75, 25, 31.25, 37.5 μg/mL) upon incubation with 12.5 nM FITC-ssDNA, then reacted with 100 nM Ag^+. (B) The fluorescence intensity at 518 nm changed against single layer MoS_2 concentration. The fluorescence spectra are excited at 490 nm. All experiments are in PBS buffer (10 mM, 50 mM $NaNO_3$, pH 7.4) at room temperature.

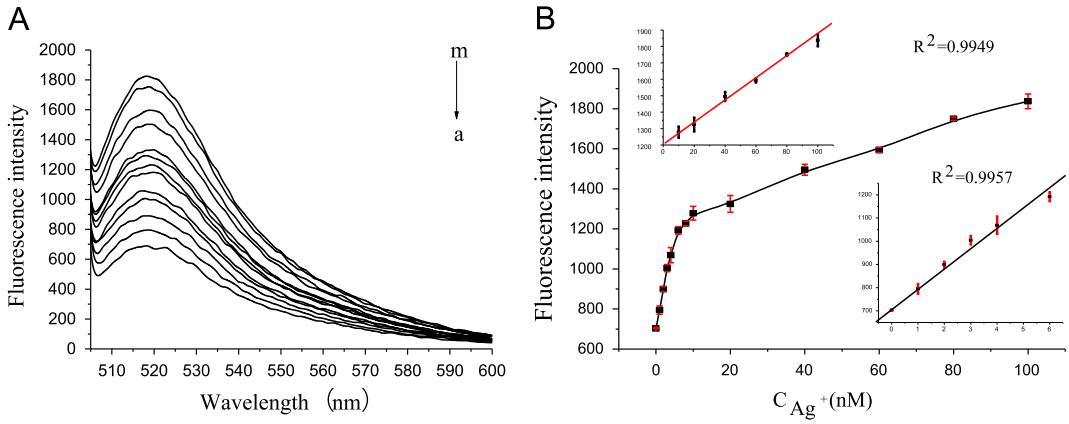


Fig. 5. (A) The normalized fluorescence spectra of 12.5 nM FITC-ssDNA upon incubation with 25 μg/mL single layer MoS_2, then reacted with a series of concentrations of Ag^+ (a–m: (0, 1, 2, 3, 4, 6, 8, 10, 20, 40, 60, 80, 100 nM)). (B) Calibration curve for Ag^+ detection in buffer, data are presented as average ± sd from three independent measurements. All these experiments are operated at room temperature and the fluorescence excitation and emission wavelengths are 490 nm and 518 nm, respectively.

Table 1
The precision of Ag^+ detection. The normalized fluorescence spectra of 12.5 nM FITC-ssDNA upon incubation with 25 μg/mL single layer MoS_2, then reacted with Ag^+ concentrations of 4.00 nM and 40.00 nM, respectively. All these experiments are operated at room temperature and the fluorescence excitation and emission wavelengths are 490 nm and 518 nm, respectively. Every experiment is repeated thrice.

$C(Ag^+)$ (nM)	Fluorescence intensity							RSD(%)
	0	6 h	12 h	24 h (1 d)	2 d	4 d	7 d	
4.00	1069.12	1072.34	1083.52	1104.64	1056.14	1047.87	1045.53	1.82
40.00	1495.41	1503.72	1431.35	1522.28	1436.62	1432.44	1468.36	2.38

Note: h is the abbreviation of the hour and d is the abbreviation of the day.

FITC-DNAs onto its surface, owing to the weak adsorption competition among the free FITC-ssDNA. When Ag^+ exceeded 6 nM in the system, free FITC-DNA in the state of random coil single strand became scarce. Adsorption competition among them became more intense, and so the fluorescence changed more slowly as the Ag^+ concentration increased. This method could be applied to detect as low as 1 nM (3 times the standard deviation rule) Ag^+ in aqueous buffer, and the detection range was wide, ranging from 1 nM to 100 nM. From this perspective, the proposed method towards Ag^+ has its own uniqueness, that is, the present method is much simpler and more effective to detect Ag^+ down to trace levels Table 1.

3.5. Selectivity of the method towards Ag^+

For determination of Ag^+ in natural water, the main interference includes other metal ions, such as Ca^{2+} and Mg^{2+}, because they always coexist with Ag^+. The results are demonstrated in Fig. 6, showing that no other metal ions interfered with the detection of Ag^+ in natural water. Furthermore, the effects of the other 12 common metal ions were taken into account. Typically, under optimum experimental conditions, the Ag^+ detection system was incubated respectively with 100 nM Ag^+ and 10 μM other 12 other metal ions in PBS buffer. As shown in Fig. 6, compared with the Ag^+ system, the existence of the other 12 commonly seen metal ions had almost no influence on detection of Ag^+. This suggested that the binding affinity of Ag^+ to a "C–C" mismatch site appeared to be much stronger than that to all metal ions except for Ag^+. The results clearly illustrated the specificity of the method for Ag^+.

3.6. Detection of Ag^+ in real samples

In order to further investigate the potential application of the sensor in the practical samples, the assay was used to detect Ag^+ in lake water and tap water. The concentration of Ag^+ in lake water

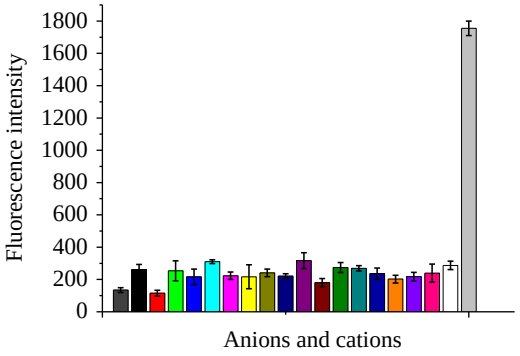


Fig. 6. Selectivity of single layer MoS_2-based method for Ag+. The other 14 common metal ions and 5 common anions in natural water instead of Ag^+ are used to react with above system and performed in the same way. The Ag^+ concentration of 100 nM is tested, while the concentration of other inspected species is 10 μM. All these experiments are operated at room temperature and the fluorescence excitation and emission wavelengths are 490 nm and 518 nm, respectively. Note: from left to right: Cl^-, SO_4^{2-}, NO_3^-, PO_4^{3-}, HCO_3^-, Ni^{2+}, Cu^{2+}, Cr^{3+}, K^+, Na^+, Fe^{3+}, Pb^{2+}, Co^{2+}, Mn^{2+}, Hg^{2+},Zn^{2+}, Al^{3+}, Fe^{2+}, Mg^{2+} and Ag^+.

from the East Lake of Wuhan, Hubei Province, China was chosen to detect Ag^+. To verify the feasibility of this new Ag^+ probe and obtain real concentration of Ag^+ in lake water, atomic absorption spectrometry (AAS) was applied to verify Ag^+ concentration in East Lake water compared with the Ag^+ probe in this work. Real concentration of Ag^+ detected by AAS in lake water is 1.039 nM (SD=0.002, n=3). As shown in Fig. 7, the concentration of detection of Ag^+ in the lake water (Fig. 7, curve b) was approximately equal to 1.04 nM Ag^+ in aqueous buffer (Fig. 7, curve a). It is probably that lake water contained many kinds of metal ions. These complicated materials in lake water could stabilize the fluorescence strength in some way and on the other hand, they might also participate in the nonspecific adsorption competition with each other onto the single

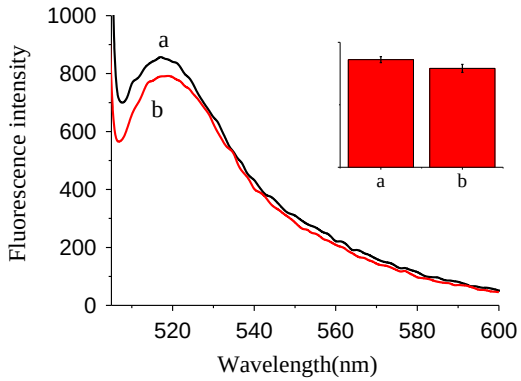


Fig. 7. Detection of Ag^+ in the East Lake water samples using fluorescence spectra of (a) single layer MoS_2+FITC-ssDNA+1 nmAg^+ aqueous buffer (b) single layer MoS_2+FITC-ssDNA+ lake water. Inset: corresponding histograms with error bar (standard deviation from the mean, $n=3$). Excitation wavelength is at 490 nm, and the emission intensity is monitored at 518 nm.

Table 2
Rate of recovery of Ag^+ 0.380 μL lake water mixed with Ag^+ aqueous solution, mixed solution final volume is 400 μL and final Ag^+ concentration are 4.00,8.00 and 12.00 nM, respectively. All these experiments are operated at room temperature and the fluorescence excitation and emission wavelengths are 490 nm and 518 nm, respectively.

Addition concentration of Ag^+ (nM)	Measured concentration of Ag^+ (nM)				Rate of standard addition recovery (%)			
–	$n=1$	$n=2$	$n=3$	Average	$n=1$	$n=2$	$n=3$	Average
0	1.02	0.98	1.04	1.01	–	–	–	–
4.00	4.64	4.62	4.73	4.66	90.75	90.25	93.00	91.33
8.00	8.75	8.31	8.64	8.57	96.75	91.25	95.38	94.46
12.00	12.36	12.44	12.71	12.50	94.58	95.25	97.50	95.78

layer MoS_2 surface. All these reasons led to the comprehensive result. Meanwhile, standard addition recovery experiment has been completed in our work. FromTable 2, good result (more than 90%) for rate of recovery of Ag^+ was obtained. Also, we have show an application of the proposed method in the tap water. According to our experimental data, no Ag^+ can be detected in tap water. So, low and certain concentrations of Ag^+ have been spiked into tap water. The result we detected for the concentrations of Ag^+ is closed to the theoretical concentration (see Fig. S2 in the Supporting information). In addition, the toxic levels for Ag^+ in drinking water are defined by the United States Environmental Protection Agency (USEPA) to be 10 nM [38]. The detection limit of this assay for Ag^+ (1 nM) was lower than the maximum limitation guided by the United States Environmental Protection Agency (EPA) as well as that permitted by the World Health Organization (WHO). Therefore, this sensor demonstrated great potential in practical applications.

4. Conclusion

In summary, a simple and novel approach based on FRET between single layer MoS_2 and FITC-ssDNA for detection of Ag^+ was proposed for the first time in this work. The proposed method exhibits higher sensitivity and selectivity toward Ag^+ even in the presence of other competitive heavy metal ions. Importantly, Ag^+ ion detections in lake water samples are performed to demonstrate the capablility of the sensor in practical applications. The developed sensor with high sensitivity and selectivity may be an alternative method for Ag^+ ion detection in environmental, biomedical, and other applications. Furthermore, we expect that this strategy based on single layer MoS_2 as fluorescent quencher may offer a new approach in sensitive and selective detection of a wide spectrum of analytes, high-through put drug screening and other metal ions.

Acknowledgments

We gratefully acknowledge the support from the Natural Science Foundation of China (NSFC) (Nos. 20927003, 90913013, 41273093 and 21175101), the National Major Scientific Instruments and Device Development Project (2012YQ16000701), and the Foundation of China Geological Survey (Grant no. 12120113015200).

Appendix A. Supporting information

Supplementary data associated with this article can be found in the online version at http://dx.doi.org/10.1016/j.talanta.2014.10.026.

References

[1] V.P. Hiriart-Baer, et al., Aquat. Toxicol. 78 (2006) 136–148.
[2] J.R. Shaw, et al., Environ. Toxicol. Chem. 17 (1998) 594–600.
[3] M.N. Croteau, et al., Environ. Sci. Technol. 45 (2011) 6600–6607.
[4] Y. Yang, et al., Anal. Biochem. (2012) 48–52.
[5] W. Pu, et al., Microchim. Acta 177 (2012) 137–144.
[6] C.X. Tang, et al., Chem. Commun. 47 (2011) 12304–12306.
[7] A. Porchetta, et al., J. Am. Chem. Soc. 135 (2013) 13238–13241.
[8] C.Y. Lin, et al., Anal. Chem. 82 (2010) 6830–6837.
[9] C. Zhao, et al., Chem. Eur. J. 16 (2010) 8147–8154.
[10] I.T. Ho, K.C. Haung, W.S. Chung, Chem.– Asian J. 6 (2011) 2738.
[11] L. Liu, et al., Org. Lett. 10 (2008) 2271–2274.
[12] X. Zhu, et al., Tetrahedron Lett. 49 (2008) 1843–1846.
[13] K.M.K. Swamy, et al., Chem. Commun. (2009) 1234–1236.
[14] L. Liu, et al., Org. Lett. 10 (2008) 4581–4584.
[15] F. Wang, et al., Inorg. Chem. 50 (2011) 2240–2245.
[16] A. Chatterjee, et al., J. Am. Chem. Soc. 131 (2009) 2040–2041.
[17] M. Aliofkhazraei, N. Ali, Two-Dimensional Nanostructures, CRC Press, Boca Raton, FL, USA, 2012.
[18] S.Z. Butler, et al., ACS Nano 7 (2013) 2898–2926.
[19] D. Yang, et al., Phys. Rev. B 43 (1991) 12053–12056.
[20] M. Buscema, et al., Nano Lett. 13 (2013) 358–363.
[21] K. Wang, et al., ACS Nano 7 (2013) 9260–9267.
[22] Q.H. Wang, et al., Nat. nanotechnol. 7 (2012) 699–712.
[23] T. Wang, et al., Anal. Chem. 85 (2013) 10289–10295.
[24] C. Zhu, et al., J. Am. Chem. Soc. 135 (2013) 5998–6001.
[25] N. Goswami, A. Giri, S.K. Pal, Langmuir 29 (2013) 11471–11478.
[26] G.H. Clever, C. Kaul, T. Carell, Angew. Chem. Int. Ed. 46 (2007) 6226–6236.
[27] Y. Tanaka, et al., J. Am. Chem. Soc. 129 (2007) 244–245.
[28] D. Huang, et al., Environ. Sci. Technol. 47 (2013) 4392–4398.
[29] Z. Lin, X. Li, H.B. Kraatz, Anal. Chem. 83 (2011) 6896–6901.
[30] P. Joensen, et al., Mater. Res. Bull. 21 (1986) 457–461.
[31] Z. Zeng, et al., Angew. Chem. Int. Ed. 50 (2011) 11093–11097.
[32] V. Nicolosi, et al., Science 340 (2013) 1226419.
[33] Z. Zeng, et al., Angew. Chem. Int. Ed. 51 (2012) 9052–9056.
[34] S. Ji, et al., Electrochim. Acta 109 (2013) 269–275.
[35] Z. Yin, et al., ACS Nano 6 (2011) 74–80.
[36] H. Li, et al., Small 8 (2012) 682–686.
[37] S. Dey, et al., Chem. Asian J. (2013) 1780–1784.
[38] T. Li, et al., Chem. Eur. J. 15 (2009) 3347–3350.

Talanta 132 (2015) 664–668

Contents lists available at ScienceDirect

Talanta

journal homepage: www.elsevier.com/locate/talanta

A multifunctional label-free electrochemical impedance biosensor for Hg^{2+}, adenosine triphosphate and thrombin

Lifen Chen, Zhong-Ning Chen *

State Key Laboratory of Structural Chemistry, Fujian Institute of Research on the Structure of Matter, Chinese Academy of Sciences, Fuzhou, Fujian 350002, China

ARTICLE INFO

Article history:
Received 10 July 2014
Received in revised form
13 October 2014
Accepted 16 October 2014
Available online 28 October 2014

Keywords:
Electrochemical impedance spectroscopy
Biosensor
Hg^{2+}
Adenosine triphosphate
Thrombin

ABSTRACT

A multifunctional label-free biosensor for the detection of Hg^{2+}, adenosine triphosphate and thrombin has been developed based on the changing of the electrochemical impedance spectroscopy (EIS) from the modified electrodes when nucleic acid subunits interacting with different targets. The modified electrode consists of three interaction sections, including DNA with T–T mismatch recognizing Hg^{2+} to form T–Hg^{2+}–T complex, split DNA chip against ATP, and DNA domin against thrombin to form G-quadruplex. Upon DNA interaction with thrombin or ATP, an increased charge transfer resistance (R_{ct}) had been detected. However, a decreased R_{ct} against Hg^{2+} was obtained. The R_{ct} difference (ΔR_{ct}) has relationship with the concentration of the different targets, Hg^{2+}, ATP and thrombin can be selectively detected with the detection limit of 0.03, 0.25, and 0.20 nmol L^{-1}, respectively. To separately detect the three analytes existing in the same sample, ATP aptamer, G-rich DNA strands and EDTA were applied to mask ATP, Hg^{2+} or thrombin separately.

© 2014 Elsevier B.V. All rights reserved.

1. Introduction

The development of biosensors for specific detection of bioanalyte has attracted particular attention due to their essential roles in clinical diagnostics [1], drug discovery [2] and environmental monitoring [3]. Among various biosensors, DNA-based ones are particularly interesting because of their high sensitivity [4], specificity [5] and easy regeneration capabilities [6]. The structural switching properties of DNA allow the biosensors to mediate target-responsive signal transduction. Over these years, great progresses have been made in developing DNA biosensors for the detection of small molecules [7,8] (e.g. cocaine or adenosine), proteins [9,10] (e.g. thrombin or lysozyme), or metal ions [11,12]. Although most of the biosensors are focused on monitoring single target analyte, many efforts have been taken to develop multifunctional DNA biosensors for the parallel detection of multiple target analytes [13]. For example, Du et al. [14] proposed a electrochemical impedance biosensor based on the integrated aptamer consisting of the adenosine triphosphate aptamer and the thrombin aptamer for the parallel detection of adenosine triphosphate (ATP) and thrombin with the detection limits of 1×10^{-8} and 1×10^{-11} mol L^{-1}, respectively. Deng et al. [15] adopted gold nanoparticles (AuNPs) as the signal amplifier and fabricated a sensitive bifunctional electrochemical biosensor for small molecule and protein. Lin et al. [16] designed a novel DNA-based electrochemical biosensor for the detection of three metal ions based on DNA interaction with Pb^{2+}, Ag^{+} and Hg^{2+}. These biosensors had been applied in real samples detection with satisfied results. However, to the best of our knowledge, no literature about simultaneous detection of metal ions, small molecules and proteins had been reported.

Electrochemical impedance spectroscopy (EIS) is one of the most generally used electrochemical techniques to monitor the properties of electrode surfaces. Any tiny changes on the electrode surfaces can be captured by impedimetric spectroscopy [17–19], which is widely employed in biosensors for monitoring bimolecular interactions or conformational changes. In this work, a sensitive multifunctional label-free electrochemical impedance biosensor is developed for the parallel detection of metal ion, small molecule and protein, and Hg^{2+}, ATP and thrombin were chosen as the example of metal ion, small molecule and protein. The targets could be captured onto the electrodes upon interaction with the sensing elements, in the present of Hg^{2+}, Hg^{2+} can insert into two DNA T–T mismatches, which leads to the formation of a T–Hg^{2+}–T pair, which elimination of the block of the electron-transfer reaction of the redox probe, however when the thrombin and ATP was introduced, the electrode surface formed an analogous insulating layer which retarded the interfacial electron transfer reaction of the redox probe, which further induces the changes of charge-transfer

* Corresponding author. Tel.: +86 591 83792346.
E-mail address: czn@fjirsm.ac.cn (Z.-N. Chen).

http://dx.doi.org/10.1016/j.talanta.2014.10.039
0039-9140/© 2014 Elsevier B.V. All rights reserved.

resistance (ΔR_{ct}). As a result, three different analytes coexisting in a sample could be detected separately by a single biosensor.

2. Experimental

2.1. Materials and reagents

All oligonucletides were synthesized and purchased from Sangon Biotechnology Co. Ltd. (Shanghai, China). The sequences of oligonucleotides used in this study are list as follow:

Capture probe DNA (S1): 5′SH-TCAGACTTTTTTTTACCTGGGG-GAG TATGGTTGGTGTGGTTGGACG-3′.

Detection probe DNA (S2): 3′AGTCTGTTTTTTTTTGGAAGGAGG CGT GGTTGGTGTGGTTGGACG5′.

Linker Probe DNA (S3): 5′CCTGCTTTCGTCC3′.

G-rich DNA: 5′GGTTGGTGTGGTTGG3′.

ATP aptamer DNA: 5′ACCTGGGGGAGTATTGCGGAGGAAGGT3′

The sequences of split DNA against ATP and thrombin aptamer were labeled by wave line and straight line, separately.

6-Mercaptohexano (MCH), cysteine, adenosine triphosphate (ATP), cytidine triphosphate (CTP), guanosine triphosphate (GTP), anduridine triphosphate (UTP), bovine serum albumin (BSA), bovine Hemoglobin (BHb) and immunoglobulin G (IgG) were purchased from Sigma (St. Louis, MO) and used as received. The human serum had been got from the Hospital of Fuzhou University. Other chemicals were of analytical reagent grade and were used directly without further purification. Deionized water from a Millipore Milli-Q system was used throughout this work.

2.2. Sensor preparation

The Au electrodes (2 mm in diameter) were pretreated according to previous procedures [20]. Briefly, they were polished with various particle sizes (1.0 and 0.05 μm) of alumina slurry (Al_2O_3) and sonicated with pure water for 5 min and dried in a nitrogen stream to obtain clean gold electrode surfaces. They were electrochemically activated by consecutive potential scanning between −0.3–1.6 V in a fresh 0.5 mol $L^{-1}H_2SO_4$ solution under until stable cyclic voltammogram were obtained. Finally, they were rinsed with pure water and dried with nitrogen before modification. Capture DNA (S1) (10 μL) was dropped on surface of gold electrodes in a closed container at 37 °C for 2 h to form self-assemble monolayer, then the modified electrode was incubated into detection DNA (S2) (10 μL) at 37 °C for 2 h, and finally the electrodes was incubated into the buffer solution of linker DNA DNA (S3) (10 μL) for another 2 h before next experiment, and the final DNA concentration was 3.33 μmol L^{-1}. during the process, the capture DNA was modified onto the electrode surface first through thiol–Au interaction, then capture DNA was hybridized with detection DNA to form partially hybridized DNA (S1+S2), which was further hybridized with linker DNA (S3), finally the film of DNA (S1+S2+S3) was formed and modified to the electrode surface, then the electrode was incubated in 1 mM 6-mercaptohexanol (MCH) solution for 1 h to remove nonspecific DNA adsorption on the gold surface. The modified electrodes were finally incubated with different concentrations of Hg^{2+}, ATP and thrombin for 1, 2 and 1 h, respectively. For each step of immobilization, the EIS of the modified electrode was recorded while $[Fe(CN)_6]^{3-/4-}$ was used as redox probe. All experiments were carried out at laboratory ambient temperature.

2.3. Measurement

All electrochemical measurements were performed on a CHI Model 660D electrochemical analyzer (Chenhua Instruments, Shanghai, China) with a conventional three-electrode system. Au electrode, Ag/AgCl electrode and Pt wire were used as working electrode, reference electrode and counter electrode, respectively. EIS studies were performed in 5 mmol L^{-1} $[Fe(CN)_6]^{3-/4-}$ solution containing 0.1 mol L^{-1} KCl. The AC (alternating current) voltage amplitude was 5 mV, and the voltage frequency was from 100 kHz to 100 mHz. The applied potential was 250 mV vs Ag/AgCl. A Randles equivalent circuit was used to fit the obtained impedance spectra.

3. Results and discussion

3.1. The principle of the biosensor

The protocol of the proposed biosensor is shown in Fig. 1. The capture probe with an alkanethiol moiety at the 5-terminus covalently immobilized on a gold electrode through Au–S bond, then detection DNA was partly hybridized with the capture probe through the linker DNA, result in the formation of the film of DNA (S1+S2+S3) onto the electrode surface. Both the capture and the detection probes consist of DNA fragments that serve as the sensing elements, in which T-rich DNA sequence, aptamer domain and split ATP aptamer recognize Hg^{2+}, thrombin and ATP, respectively. On the one hand, DNA S1 and S2 can bind with Hg^{2+} to form T–Hg^{2+}–T structure and the formed duplex-like DNA can promote the electron transfer, which results in the reduce of the charge transfer resistance R_{ct}. On the other hand, the addition of ATP can induce recombination of DNA S1 and S2 since both of which contain the sequence of split ATP aptamer fragments, this make the enhancement of the rigid structure of DNA S1+S2+S3, thus resulting in an increase of R_{ct}. In addition, DNA S1 and S2 which contain thrombin aptamer could also specifically recognize thrombin. The hybridized parts among DNA strands S1, S2 and S3 are dehybridized to form thrombin-stabilized G-quadruplex. Although DNA strand S3 is free released from the electrode and may provide an easier penetration channel for the redox probe, the macromolecular protein thrombin can be captured on the electrode surface to increase film thickness, thus resulting in a significant enhancement of R_{ct}.

Simple experiments had been performed to verify the feasibility of the proposed biosensor. Fig. 2 shows the EIS at different conditions. The equivalent circuit (Fig. 2, inset) as the model of the working electrode was applied to fit the EIS data [21], where R_s, Z_w and C_d are

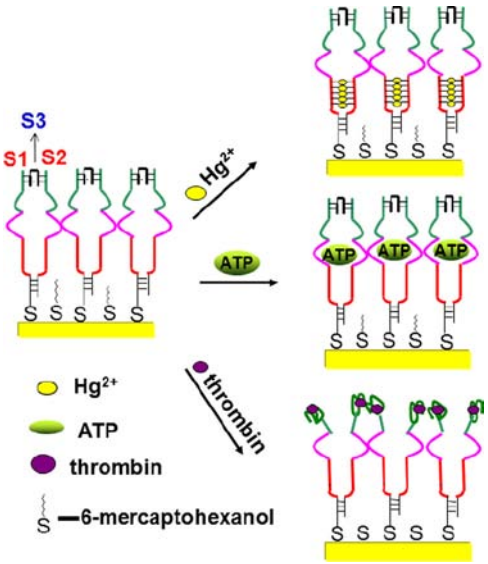


Fig. 1. Principle of the DNA-based EIS biosensor in response to Hg^{2+}, ATP and thrombin.

the electrolyte solution resistance, the Warburg impedance and the double layer capacitance, respectively. The most important parameter is R_{ct}, which reflects the electron transfer kinetics in the surfaces of the different electrodes. As shown in Fig. 2, curve *a* depicts the Nyquist diagram of the DNA S1+S2+S3 film modified gold electrode without analytes with R_{ct} of 2905 Ω. In the presence of Hg^{2+}, R_{ct} decreases to a smaller value (curve *b*, 1405 Ω) due to Hg^{2+} inserting into two DNA T–T mismatch and the formation of DNA(S1)/Hg/DNA (S2) complex as duplex DNA, thus enhancing the electron transfer ability of the redox probe on the electrode surface. Since ATP can induce the association of split aptamer fragments and the formation of DNA(S1)/ATP/DNA(S2) complex, the addition of ATP stabilizes the associated complex so that R_{ct} increases greatly (curve *c*, 5613 Ω). When thrombin is captured on the surface of Au electrode, R_{ct} increases significantly also (curve *d*, 4882 Ω) due to the bind of thrombin to the electrode surface, thus increasing the film thickness.

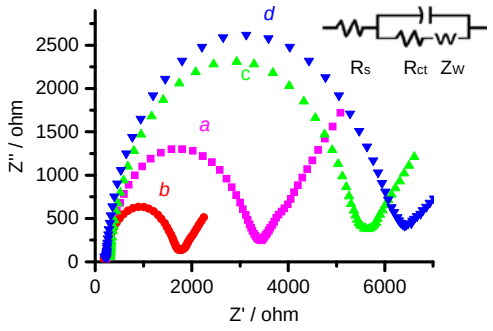


Fig. 2. Representative impedance spectra for the DNA biosensor before (a) and after incubating with 1 μmol L^{-1} Hg^{2+} (b); 1 μmol L^{-1} thrombin (c); 1 μmol L^{-1} ATP (d), respectively. The inset represent the equivalent circuit employed to fit the EIS measured data with 5 mmol L^{-1} $[Fe(CN)_6]^{3-/4-}$ as redox probe.

3.2. Performance of the biosensor

In order to further investigate the analytical application, the biosensor was employed to detect Hg^{2+}, ATP and thrombin with various concentrations, respectively. As shown in Fig. 3A and Table 1, ΔR_{ct} decreased with increasing the concentration of Hg^{2+}, in which the ΔR_{ct} exhibited a linear relationship with the logarithm of Hg^{2+} concentration in the range from 5×10^{-7} to 1×10^{-10} mol L^{-1}. On the other hand, with the increase of the concentration of ATP, the formed DNA(S1)/ATP/DNA(S2) complex is progressively increased (Fig. 3B), which resulted in increased ΔR_{ct}. The linear responses of ΔR_{ct} against the logarithm of ATP concentration is from 1×10^{-6} to 1×10^{-9} mol L^{-1}. For thrombin, as shown in Fig. 3C, the increase of thrombin concentration caused the increase of ΔR_{ct}, until no distinct change in ΔR_{ct} was observed when the concentration of thrombin was decreased to 1 nmol L^{-1}. The ΔR_{ct} increased in line with the logarithm of thrombin concentration within a range from 1×10^{-6} to 1×10^{-9} mol L^{-1}. By the application of the R_{ct} difference (ΔR_{ct}), Hg^{2+}, ATP and thrombin were selectively detected with the detection limit of 0.03, 0.25 and 0.20 nmol L^{-1}, respectively, which was lower than the previous reported EIS sensor for Hg^{2+} [11], ATP [14] and thrombin [22]. The reproducibility of the electrochemical sensor

Table 1
The linear relationship between ΔR_{ct} and the logarithm of the concentrations of Hg^{2+}, ATP or thrombin.

	Linear regression equation (ΔR_{ct})	Regression coefficient (R)	Detection limit (mol L^{-1})
Hg^{2+}	303.78log$C$(Hg^{2+})+ 3208.16	−0.9918	3.0×10^{-11}
ATP	785.73log$C$(ATP)+ 7247.91	−0.9928	2.5×10^{-10}
Thrombin	531.46log$C$(thrombin)+ 5202.32	−0.9854	2.0×10^{-10}

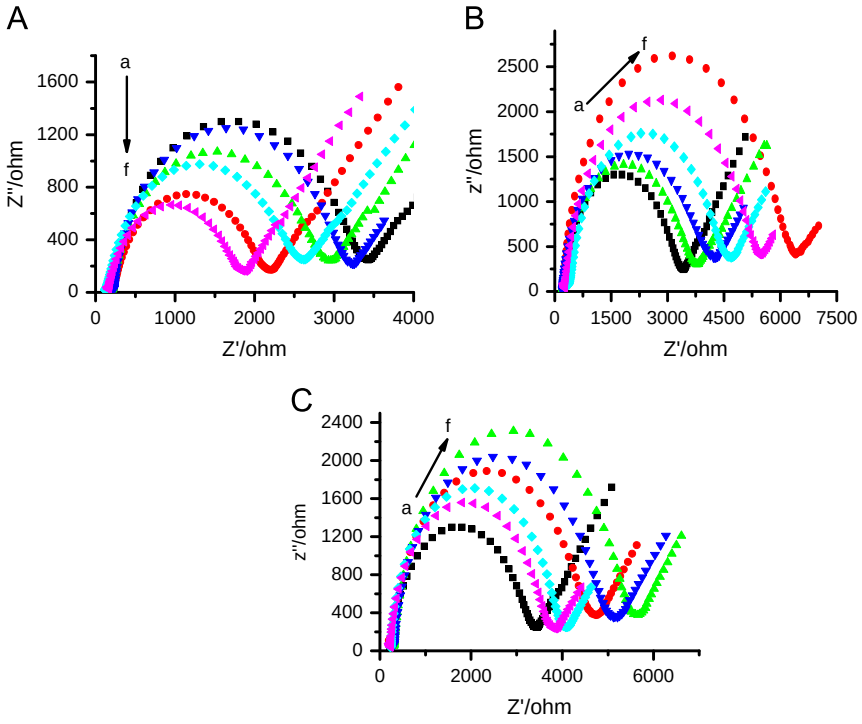


Fig. 3. Impendence spectra upon incubation with various concentrations of Hg^{2+}, ATP and thrombin at ambient temperature, (A) Hg^{2+} (a: 1×10^{-10} mol L^{-1}; b: 1×10^{-9} mol L^{-1}; c: 1×10^{-8} mol $^{-1}$; d: 1×10^{-7} mol $^{-1}$; e: 5×10^{-7} mol $^{-1}$; f: 0 mol L^{-1}); (B) ATP (a: 0 mol L^{-1}; b: 1×10^{-9} mol $^{-1}$; c: 5×10^{-9} mol $^{-1}$; d: 1×10^{-8} mol $^{-1}$; e: 1×10^{-7} mol $^{-1}$; f: 1×10^{-6} mol $^{-1}$); (C) thrombin (a: 0 mol $^{-1}$; b: 1×10^{-9} mol $^{-1}$; c: 5×10^{-9} mol $^{-1}$; d: 1×10^{-8} mol $^{-1}$; e: 1×10^{-7} mol $^{-1}$; f: 1×10^{-6} mol $^{-1}$).

was also investigated. Every five freshly modified electrodes were tested for the targets, respectively. All electrodes showed nearly similar electrochemical response, in which the relative standard deviation is 3.8% for Hg^{2+}, 3.0% for ATP and 4.8% for thrombin detection. The sensor still retained bioactivity after being stored at 4 °C for four weeks and impedance signal reduced less than 5%. These results suggest that the biosensor exhibits good reproducibility.

3.3. Separately detection of analytes

The introduced label-free multifunctional electrochemical biosensor could separately detect three different analytes. As mentioned above, in contrast with a decreased R_{ct} in response to Hg^{2+}, ATP and thrombin could induce an increased R_{ct}. When the signal is reduced upon the addition of the sample, we could first suppose that the sample contains Hg^{2+}, but it is still unable to determine whether the sample is a mixture. In order to exclusively detect Hg^{2+}, ATP or thrombin, masking agents was used to differentiate the electrochemical signals due to different analytes. EDTA, ATP aptamer and G-rich DNA were thus used for masking Hg^{2+}, ATP and thrombin, respectively. The mixture of EDTA and ATP aptamer successfully mask Hg^{2+} and ATP for the detection of thrombin. The mixture of EDTA and G-rich DNA was used for masking Hg^{2+} and thrombin for the detection of ATP, whereas the mixture of G-rich DNA and ATP aptamer was used for masking thrombin and ATP for the detection of Hg^{2+}. As shown in Fig. 4, it is demonstrated that the exclusive detection of Hg^{2+}, ATP and thrombin existing in the buffer solution could be achieved, respectively.

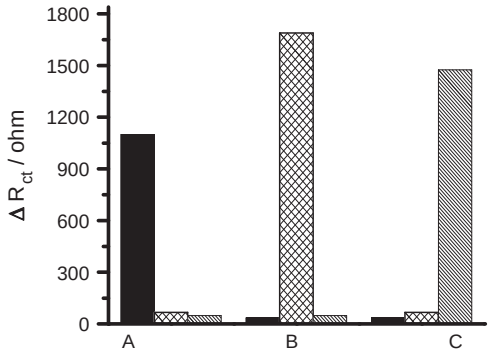


Fig. 4. (A) Specific detection of Hg^{2+}, ATP and thrombin existing in the buffer solution. (A) In the presence of ATP aptamer and G-rich DNA for Hg^{2+} determination; (B) in the presence of G-rich DNA and EDTA for ATP determination; (C) in the presence of ATP aptamer and EDTA for thrombin determination. The concentrations of masking reagents were both 10 μmol L^{-1}, and the targets were 100 nmol L^{-1}.

3.4. Interference study and sample detection

In order to explore the application of this biosensor in practical detection, the specificity of the multifunctional biosensor was also investigated. The interfering experiments were made when the analyte and the interfering species present in the same system. Other metal ions including Mg^{2+}, Ni^{2+}, Zn^{2+}, Cd^{2+}, Cu^{2+}, Ca^{2+}, Fe^{3+}, Ag^{+} and Pb^{2+} were used as the interferents. It was revealed that only Hg^{2+} caused a considerable decrease of the R_{ct} (Fig. 5A). This is due to these metal ions could not insert into a T–T base pair to form a stable structure such as T–Hg^{2+}–T, and T–T base pair is only selective to Hg^{2+}. On the other hand, cytidine triphosphate (CTP), guanidine triphosphate (GTP) and anduridine triphosphate (UTP) were used in the control experiments to assess the specificity of the biosensor for the detection of ATP. As shown in Fig. 5B, significant changes in the EIS response were unobserved in presence of other triphosphates, implying that other nontarget molecules do not interact with the biosensor and thus not interfere with the detection of ATP. As for the detection of thrombin, bovine serum albumin (BSA), bovine hemoglobin (BHb) and immunoglobulin G (IgG) were used as the interferents to examine the selectivity of the sensor (Fig. 5C). It was found that the EIS response in the present of other interferents protein, the EIS response for thrombin was not found significant change. These results demonstrate that this biosensor displays a sufficient

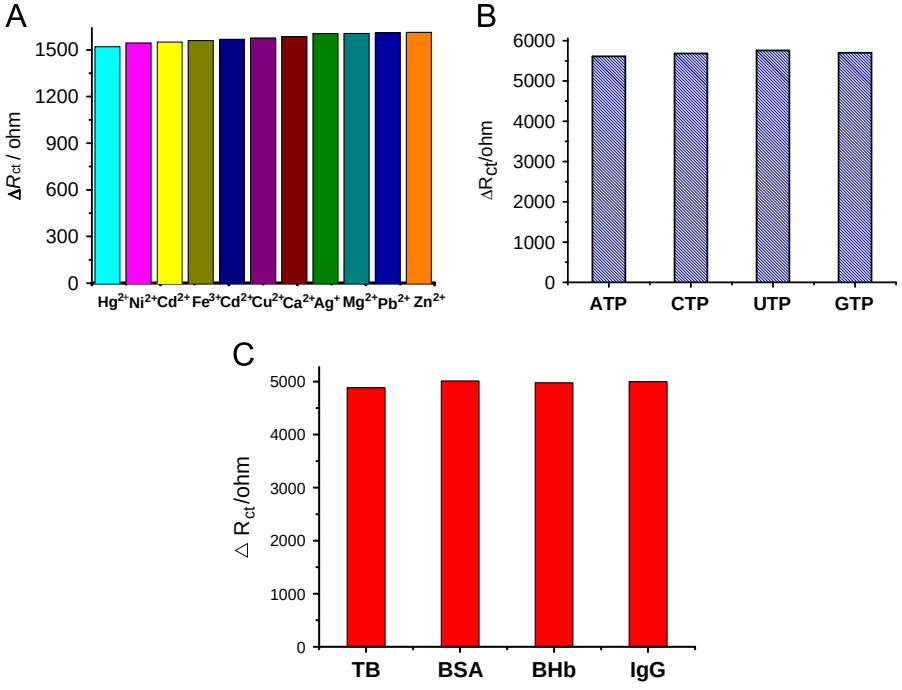


Fig. 5. Selectivity of the electrochemical biosensor. (A) Selectivity of the biosensor toward Mg^{2+}, Ni^{2+}, Zn^{2+}, Cd^{2+}, Cu^{2+}, Ca^{2+}, Fe^{3+}, Ag^{+} and Pb^{2+} in the present of ATP and ATP. (B) EIS response for cytidine triphosphate (CTP), guanosine triphosphate (GTP) and uridine triphosphate (UTP) in the present of ATP and ATP. (C) EIS response for bovine serum albumin (BSA), bovine Hemoglobin (BHb) and immunoglobulin G (IgG) in the present of thrombin and thrombin. All the concentrations of tested molecules were used at 10^{-6} mol $^{-1}$.

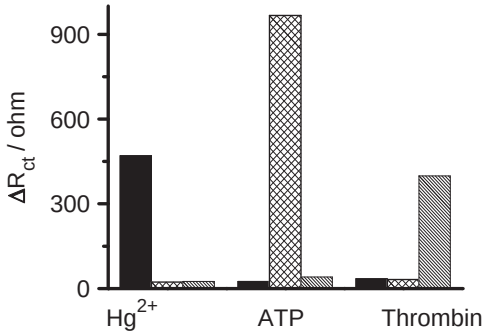


Fig. 6. Specific detection of Hg^{2+}, ATP and thrombin in the human serum in the presence of masking reagents, the concentrations of masking reagents were both 10 μmol L^{-1}, 10^{-8} mol L^{-1} Hg^{2+}, 10^{-8} mol L^{-1}ATP and 10^{-9} mol L^{-1} thrombin.

specificity for the exclusive detection of Hg^{2+}, ATP and thrombin, respectively.

To validate the possibility of the proposed biosensor in a real application, the human serum samples were spiked with different concentrations of Hg, ATP and thrombin, the concentration of Hg^{2+} is 1.5 mg/100 mL (75 nmol L^{-1}) which is defined by American Conference of Governmental Industrial Hygienists (ACGIH). Therefore, the concentrations in human serum were chosen to contain 1×10^{-8} mol L^{-1} Hg^{2+}, 1×10^{-8} mol L^{-1} ATP, and 1×10^{-9} mol L^{-1} thrombin, respectively. As shown in Fig. 6, simultaneous detection of three targets with masking reagents in the human serum was achieved. The results indicated that the biosensor has great potential for practical application.

4. Conclusions

An efficient, label-free DNA-based electrochemical impedance biosensor has been developed for the detection of Hg^{2+}, ATP and thrombin by taking advantage of the unique properties of split DNA fragment/target interaction and the specific aptamer target recognition. Hg^{2+} could interact with T–T mismatch even in the presence of other competitive metal ions to form T–Hg^{2+}–T so that the electron transfer is highly enhanced and the sensor showed high specificity for mercury(II). ATP could bind to partially split aptamer fragment and thrombin interacts with G-rich DNA strands to be preferentially adsorbed on the DNA modified Au electrode, both of which weakens the electron transfer. Based on this principle, we have successfully detected Hg^{2+}, ATP and thrombin at a concentration down to 0.03, 0.25 and 0.2 nmol L^{-1}, respectively. This electrochemical biosensor exhibits obvious advantages over the conventional methods. First, by combining of the unique properties of split aptamer fragment/target interaction and the specific aptamer-target recognition, label-free detection has been developed which makes the fabricating process simple and convenient, it took only 1, 2 and 1 h for the further detection Hg^{2+}, ATP, thrombin, respectively. Second, DNA could be prepared easily at low cost to afford a cheap biosensor. The multifunctional DNA-based biosensor shows good selectivity, reproducibility, and the useful life could retained for weeks for detection, which provides a promising platform for the electrochemical parallel detection of metal ions, small molecules and proteins, respectively. Moreover, the biosensor was applied to analyze targets in human serum with satisfactory results, which provide it could be used in the analysis of targets in complex samples.

Acknowledgements

This project was financially supported by the NSFC (Grant 21305141).

References

[1] D.S. Elenis, P.C. Ioannou, T.K. Christopoulos, Anal. Chem. 79 (2007) 9433.
[2] S. Wang, E.S. Forzani, N. Tao, Anal. Chem. 79 (2007) 4427.
[3] M.S. Wilson, Anal. Chem. 77 (2005) 1496.
[4] M. Famulok, G. Mayer, M. Blind, Acc. Chem. Res. 33 (2000) 591.
[5] S.D. Jayasena, Clin. Chem. 45 (1999) 1628.
[6] S. Tombelli, A. Minunni, A. Mascini, Biosens. Bioelectron. 20 (2005) 2424.
[7] M. Zayats, Y. Huang, R. Gill, C.A. Ma, I. Willner, J. Am. Chem. Soc. 128 (2006) 13666.
[8] B.R. Baker, R.Y. Lai, M.S. Wood, E.H. Doctor, A.J. Hegger, K.W. Plaxco, J. Am. Chem. Soc. 128 (2006) 3138.
[9] K.H. Cheng, B.X. Ge, H.Z. Yu, Anal. Chem. 79 (2007) 5158.
[10] M. Bini, Minunni, S. Tobelli, S. Centi, M. Mascini, Anal. Chem. 79 (2007) 3016.
[11] L. Shi, G. Liang, X.H. Li, X.H. Liu, Anal. Methods 4 (2012) 1036.
[12] X. Zhu, Z.Y. Lin, L.F. Chen, B. Qiu, G.N. Chen, Chem. Commun. (2009) 6050.
[13] J. Elbaz, B. Shlyahovsky, D. Li, I. Willner, Chem. Bio. Chem. 9 (2008) 232.
[14] Y. Du, B.L. Li, H. Wei, Y.u. Wang, E.K. Wang, Anal. Chem. 80 (2008) 5110.
[15] Y. Deng, J.H. Chen, L.H. Nie, Z. Nie, S.Z. Yao, Anal. Chem. 81 (2009) 9972.
[16] Z.Z. Lin, X.H. Li, H.B. Kraatz, Anal. Chem. 83 (2011) 6896.
[17] H. Cai, T.M.H. Lee, I.M. Hsing, Sens. Actuators, B 114 (2006) 443.
[18] E. Radi, J.L.A. Sanchez, E. Baldrich, C.K. O'Sullivan, Anal. Chem. 77 (2005) 6320.
[19] M.C. Rodriguez, A.N. Kawde, J. Wang, Chem. Commun. 34 (2005) 4267.
[20] X. Zhu, Z.Y. Lin, L.F. Chen, B. Qiu, G.N. Chen, Chem. Commun. 46 (2010) 3149.
[21] F. Patolsky, A. Lichtenstein, I. Willner, J. Am. Chem. Soc. 123 (2001) 5194.
[22] Y. Jalit, F.A. Gutierrez, G. Dubacheva, C. Goyer, L. Coche-Guerente, E. Defrancq, P. Labbé, G.A. Rivas, M.C. Rodríguez, Biosens. Bioelectron. 41 (2013) 424.

Talanta 132 (2015) 669–675

Contents lists available at ScienceDirect

Talanta

journal homepage: www.elsevier.com/locate/talanta

Development of a pH sensing membrane electrode based on a new calix[4]arene derivative

H. Elif Kormalı Ertürün [a,*], Ayça Demirel Özel [a], Serkan Sayın [b], Mustafa Yılmaz [b], Esma Kılıç [a]

[a] Department of Chemistry, Faculty of Science, Ankara University, Tandoğan, 06100 Ankara, Turkey
[b] Department of Chemistry, Faculty of Science, Selçuk University, Selçuklu, 42075 Konya, Turkey

ARTICLE INFO

Article history:
Received 28 August 2014
Received in revised form
10 October 2014
Accepted 14 October 2014
Available online 22 October 2014

Keywords:
Calix[4]arene
pH sensing PVC membrane electrode
Potentiometry
pH measurement
Titratable acidity

ABSTRACT

A new pH sensing poly(vinyl chloride) (PVC) membrane electrode was developed by using recently synthesized 5,17-bis(4-benzylpiperidine-1-yl)methyl-25,26,27,28-tetrahydroxy calix[4]arene as an ionophore. The effects of membrane composition, inner filling solution and conditioning solution on the potential response of the proposed pH sensing membrane electrode were investigated. An optimum membrane composition of 3% ionophore, 67% *o*-nitrophenyl octyl ether (*o*-NPOE) as plasticizer, 30% PVC was found. The electrode exhibited a near-Nernstian slope of 58.7 ± 1.1 mV pH^{-1} in the pH range 1.9–12.7 at 20 ± 1 °C. It showed good selectivity for H^+ ions in the presence of some cations and anions and a longer lifetime of at least 12 months when compared with the other PVC membrane pH electrodes reported in the literature. Having a wide working pH range, it was not only applied as a potentiometric indicator electrode in various acid–base titrations, but also successfully employed in different real samples. It has good reproducibility and repeatability with a response time of 6–7 s. Compared to traditional glass pH electrode, it exhibited excellent potentiometric response after being used in fluoride-containing media.

© 2014 Elsevier B.V. All rights reserved.

1. Introduction

Accurate and reliable measurement of the pH in chemical, biological, clinical, industrial and environmental samples is always important [1–3]. The pH measurements are generally carried out by use of glass electrodes. They have become very popular due to their selectivity, reliability and dynamic pH range. Although pH-sensitive glass electrode has distinguished response characteristics and has been in use for such a long period, it has certain setbacks such as its high resistance, fragility, its instability in hydrofluoric acid or fluoride solutions, alkaline and acid errors and its unsuitability to serve as a microelectrode for biological applications [4,5]. Accordingly, the studies to develop non-glass pH-sensitive electrodes such as solid contact electrodes (SCE's) [1,6–13], coated wire electrodes (CWE's) [13,14], field effect transistors (FET's) [15,16], nanorod based electrodes [17,18] and polymeric membrane electrodes [19–33] have gained interest. Among these, PVC membrane electrodes are the preferred ones due to their low electrical resistance and ease of construction [31,32]. In addition, with the membrane supported by a tough material, they are solid and not easily fragile. These properties are critical, especially for in-vivo and in-vitro pH measurements. pH-sensitive membrane electrodes based on PVC are also considered for clinical applications and they are currently under investigation [8,10,22,34].

Many authors have focused on the design of new carriers for hydrogen ions to use as ionophores in the construction of pH sensing membrane electrodes. Among these carriers, hexafluorophosphate [1], diazacyclooctadecane [4], decamethylcyclopentasiloxane [6], hexabutyl-tri-amidophosphate [19], hex-3-ene [20], azole [21], phenoxazine derivatives (chromoionophores) [10,27,28], amines [11–13,22–25], pillar[5]arene [29] and calix[4]arenes [30–33] appear to be promising. Calixarenes are very popular as attractive and excellent ionophores due to their host–guest chemistry and ion-recognition properties [35,36]. It is stated in the literature that some specially designed calixarenes could successfully be used for the construction of pH electrodes [30–33].

Therefore, in this work, we focused on the possibility of us ing recently synthesized 5,17-bis(4-benzylpiperidine-1-yl)methyl-25,26,27,28-tetrahydroxy calix[4]arene (Fig. 1) as ionophore in the construction of a new pH sensing membrane electrode. It is known that calix[4]arene derivatives bearing amine or amide functions were capable of interacting with anions by hydrogen bonds.

* Corresponding author. Tel.: +90 3122126720; fax: +90 3122232395.
E-mail address: kormali@science.ankara.edu.tr (H.E. Kormalı Ertürün).

http://dx.doi.org/10.1016/j.talanta.2014.10.032
0039-9140/© 2014 Elsevier B.V. All rights reserved.

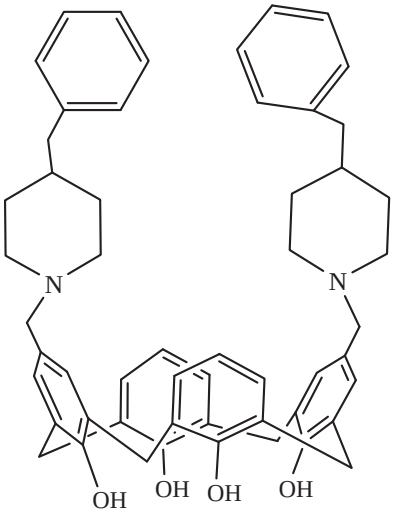


Fig. 1. The structure of 5,17-bis(4-benzylpiperidine-1-yl)methyl-25,26,27,28-tetrahydroxy calix[4]arene.

The studies regarding the removal of arsenate and dichromate ions from the aqueous solutions by using the calix[4]arene studied in liquid–liquid extraction indicated that it was protonated at proton-switchable binding sites in acidic conditions [37]. Hence, facilitating binding of anions at low pH is resulted from electrostatic interactions as well as hydrogen bonding via N atoms in upper piperidine rim and –OH groups in lower rim of the calix[4]arene derivative used in this study. It was considered that the calix[4]arene derivative could be used as suitable ionophore for hydrogen ion due to its possible reversible interaction with piperidine nitrogen or –OH groups of this compound. For this purpose, membranes with various combinations were prepared by changing the ratio of ionophore, PVC, plasticizer and lipophilic additive in order to determine the optimum membrane composition. The selectivity against some anions and cations, response time, lifetime, working range and other performance characteristics of the proposed electrode were investigated. The developed pH sensing membrane electrode worked well under laboratory conditions to determine titratable acidity and pH in real samples.

2. Experimental

2.1. Reagents and solutions

All chemical substances used were of reagent grade and were used without further purification.

High molecular weight poly(vinyl chloride), PVC, *o*-nitrophenyl octyl ether, *o*-NPOE, dibutyl phtalate, DBP, bis-(2-ethylhexylsebacate), BEHS, potassium tetrakis(*p*-chlorophenyl)borate, KT*p*ClPB, sodium tetraphenylborate, NaTPB, cesium tetrakis(3-methylphenyl)borate, CsT(3-Me)PB, and tetrahydrofurane, THF, were obtained from Sigma-Aldrich/Fluka in selectophore purity.

Britton–Robinson, BR, buffer solutions were used to investigate the performance of the pH sensing membrane electrode. BR buffer solutions were prepared by mixing appropriate amounts of boric acid, acetic acid and phosphoric acid; and the pH of these solutions were adjusted with the addition of diluted sodium hydroxide or hydrochloric acid solutions to the stock buffer solutions by the use of a combined glass pH-electrode.

The working solutions were obtained by dilution of 0.1 M stock solutions of ions with deionized water which was supplied from ELGA Purelab Classic Ultrapure Water System.

5,17-Bis-[(4-benzylpiperidine)methyl]-25,26,27,28-tetrahydroxycalix[4]arene was synthesized at the Department of Organic Chemistry of Selçuk University by procedures given in the literature [37].

2.2. Preparation of the electrode

The pH-sensing membrane electrode was prepared as follows: 0.0128 g of ionophore and 0.2851 g of *o*-NPOE were dissolved in 5 mL THF. 0.1276 g of PVC was slowly added to this mixture. The homogenous mixture formed was poured onto a glass disc with a diameter of 3.5 cm attached to a glass plate and was kept at room temperature for 24 h for the evaporation of THF. The 0.7 cm diameter disc of the polymer membrane was cut and fixed to the end of a glass tube with a diameter of 0.5 cm and a length of 10 cm.

An internal filling solution containing 1.0×10^{-3} M $CaCl_2$ was put into this glass tube and an AgCl-coated silver wire was placed into it. The prepared electrode was conditioned in deionized water for 12 h before each use.

2.3. Potential measurements

All potentiometric measurements were performed at 20 ± 1 °C by using the following cell assembly:

Ag/AgCl reference electrode | analyte solution | membrane | 1.0×10^{-3} M $CaCl_2$ | AgCl | Ag.

The potential measurements were made by the use of Mettler-Toledo SevenMulti pH–Ionmeter with Rondolino Sample Changer. The reference electrode was Ag/AgCl electrode (Mettler-Toledo Inlab Reference, catalogue no: 51343190). The pH measurements were carried out with Mettler-Toledo Inlab Routine Pro pH electrode (catalogue no: 51343055). The test solutions were stirred and the potentials were recorded after the equilibrium potentials had been reached.

The potentiometric titrations of hydrochloric, hydrofluoric and phosphoric acids were carried out with automatic titrater, Orion 940 expandable ion analyzer *S*/*N* 5816. The proposed electrode was employed in real samples such as vinegar, red wine, beer, fizzy drinks and fruit juices to demonstrate its applicability.

All electrochemical measurements were carried out with CHI660D Electrochemical Workstation and the experimental data taken under open circuit potential was recorded with three electrode cell in which Ag/AgCl/KCl, 3 M was the reference electrode. The electrode under study was the working electrode and the auxiliary electrode was platinum wire (BASi MW-1032). The impedance spectra were recorded in solutions of acetate buffer and BR buffer containing sodium chloride within the frequency range of 100 kHz to 0.01 Hz at 0.2 V and the amplitude for the sinusoidal excitation signal was 0.05 mV.

3. Results and discussion

3.1. The determination of the membrane composition

In the field of ion-selective electrodes (ISE), the common range of membrane composition was determined as 1–7% ionophore, 28–33% PVC (internal matrix), 60–69% plasticizer (solvent) and 0.03–2% lipophilic anion [38]. Herein, the optimum membrane composition for the proposed pH-sensing membrane electrode was found as 3% ionophore, 67% plasticizer and 30% PVC. The results obtained from the electrodes prepared with different membrane compositions are summarized in Table 1. The SEM images for the membrane of the proposed electrode with and without ionophore were shown in Fig. 2. The surface of both

Table 1
Effect of the membrane composition on the potentiometric response of new calix[4]arene based pH-sensing membrane electrode (Plasticizer/PVC=2.2).

Electrode number	Membrane composition (wt%) (m_T: 425.5 mg)				Slope $\pm tS/\sqrt{N}$ (mV pH^{-1})		Linear pH range
	Ionophore	Plasticizer	Additive[a]	PVC			
1	–	69.2 (*o*-NPOE)	–	30.8	39.5 ± 2.2	$N=3$	3.2–10.7
2	1	69 (*o*-NPOE)	–	30	42.9 ± 0.9	$N=3$	1.9–10.7
3	2	68.3 (*o*-NPOE)	–	29.7	53.3 ± 1.4	$N=3$	1.9–12.7
4	**3**	**67 (*o*-NPOE)**	**–**	**30**	**58.7 ± 1.1**	***N*=10**	**1.9–12.7**
5	3	67 (DBP)	–	30	51.2 ± 1.8	$N=3$	4.8–10.7
6	3	67 (BEHS)	–	30	24.3 ± 1.3	$N=3$	4.8–10.7
7	3	67 (*o*-NPOE)	KT*p*ClPB	30	47.1 ± 2.1	$N=3$	3.2–10.7
8	3	67 (*o*-NPOE)	NaTPB	30	52.2 ± 1.7	$N=3$	4.8–12.7
9	3	67 (*o*-NPOE)	CsT(3-Me)PB	30	40.9 ± 0.6	$N=3$	3.2–12.7

[a] Lipophilic additives were 70% mole ratio relative to the ionophore.

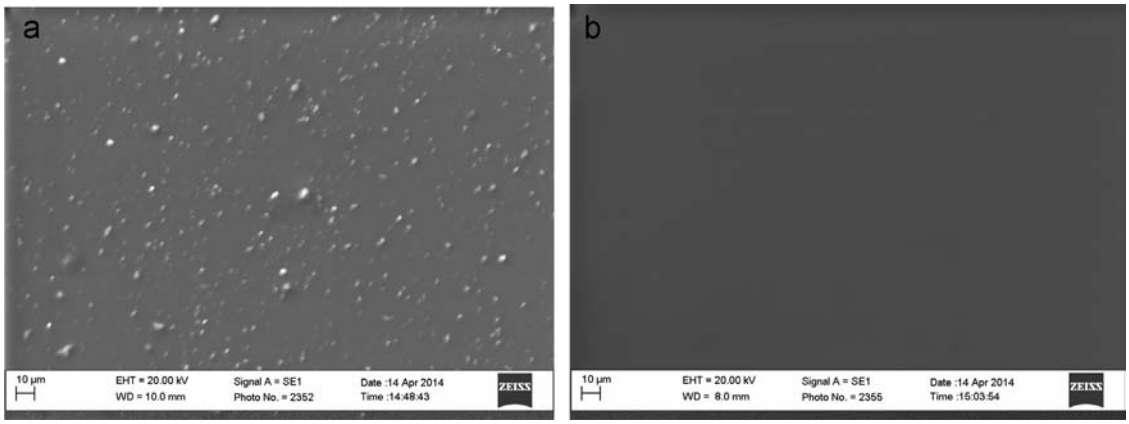


Fig. 2. SEM images of the PVC membranes containing 67 % *o*-NPOE and 30 % PVC (a) with 3% ionophore (b) without ionophore.

membranes was uniform and there were no defect. It can be seen that white spots in Fig. 2a referred as ionophore, which enhanced the sensitivity of H^+ ions of the membrane, was distributed hom ogeneously.

Concerning the effect of concentration of the macrocyclic compounds introduced into the membrane upon the selectivity, working range and the slope of the electrode, it is reported that the interaction between the macrocyclic compound and the species to be determined has a notable influence on these features [38]. Therefore, the preliminary studies were carried out by the membranes prepared by keeping the plasticizer/PVC ratio at 2.2 and changing the ratio of ionophore in the range 1–3%. As can be seen in Table 1, the electrode prepared with polymeric membrane containing 1% ionophore (electrode 2) and without ionophore (electrode 1) showed sub-Nernstian slopes in the linear working range of pH 1.9–10.7 and pH 3.2–10.7, respectively. It is stated in the literature that the complex stoichiometry between the macrocyclic compound and the analyte ion is of great importance regarding the selectivity and the slope of the electrode [38,39].

Therefore, the percentage of the ionophore in the membrane was increased up to 2 and 3% in order to investigate the effect of the ionophore concentration upon the performance. Not only the slopes of electrode 3 (53.3 ± 1.4 mV pH^{-1}) and electrode 4 (58.7 ± 1.1 mV pH^{-1}) were improved but also the linear working ranges were observed to be better than those containing 1% ionophore. We concluded that increasing the ionophore ratio upto 3% provided better response characteristics and the studies related to optimization of the membrane composition were continued by keeping the ionophore ratio at 3%.

Due to the fact that the plasticizers change the dielectric constant of the membrane phase, the type of the plasticizer has a remarkable effect upon the selectivity and the performance characteristics of the ISE membranes [40–42]. Therefore, DBP, BEHS and *o*-NPOE were used to investigate the effect of the plasticizer. It is clear in Table 1 that the electrode containing *o*-NPOE (electrode 4) exhibited higher slope and wider linear working range than that of the electrodes prepared with DBP (electrode 5) and BEHS (electrode 6). This led us to conclude that *o*-NPOE was the best membrane plasticizer for the proposed pH-sensing membrane electrode. That was why all the studies to determine the performance of the electrode and all the analytical applications relating to it were performed by the use of this electrode.

It is well-known that the addition of a lipophilic anion to neutral carrier membranes improved almost all of the electrode characteristics, since it stabilizes the membrane operating conditions, decreases the membrane resistance and significantly reduces the response times [39,43,44]. In our study, the electrodes were prepared by using KT*p*ClPB (electrode 7), NaTPB (electrode 8), and CsT*p* (3-Me)PB (electrode 9) as lipophilic additives. These electrodes showed weaker H^+ selectivity with sub-Nernstian slopes and narrower pH ranges. This is not in accordance with the literature, since it is claimed that the addition of lipophilic sites to the membrane phase improves the performance of the electrodes. It may be attributed to the fact that sodium, potassium and cesium ions which form ion-pairs with tetraphenylborate and tetrakis(*p*-chlorophenyl)borate, settle in the cavity of the calix[4] arene and decrease the number of active sites in the membrane. The adverse effect in our case can also be the result of the nature of the ionophore.

Taking into account both the slopes and the linear pH range of the electrodes, the electrode prepared with the membrane containing 3% ionophore, 67% *o*-NPOE and 30% PVC demonstrated the best Nernstian slope of 58.7 ± 1.1 mV pH^{-1} in the widest pH range

1.9–12.7 (electrode 4). Hence, further studies were performed with the electrode 4.

3.2. The effect of conditioning and inner filling solution

The effect of the conditioning upon the performance of the electrode was investigated by the use of two electrodes with the same membrane composition and 1.0×10^{-3} M $CaCl_2$ as inner filling solution. The electrodes were kept in 1.0×10^{-3} M HCl and in deionized water for 12 h, separately. The results obtained revealed that the performance and the lifetime of the electrode conditioned in deionized water were higher than that of the electrode conditioned in acid solution. Therefore, the electrodes were kept in deionized water prior to each experiment.

The composition and the concentration of the inner filling solution were found to have a significant effect on the potentiometric response of the PVC membrane electrodes by means of changing its selectivity and working range [45]. Either the chloride salts of inert electrolyte or the chloride salt of analyte ion with lower concentration were commonly used as internal solutions [46,47]. For this purpose, the electrode prepared with the membrane containing 3% ionophore, 67% *o*-NPOE and 30% PVC was filled with 1.0×10^{-3} M HCl and 1.0×10^{-3} M $CaCl_2$. From the view point of linear working range, it was determined that the most appropriate inner filling solution was 1.0×10^{-3} M $CaCl_2$. This application also confirmed that inner filling solutions prepared with inert salts have great effect on the working range of the electrodes [47].

3.3. Working range and the slope of the electrode

In order to investigate the working range and the slope of the electrode under study, two different types of calibration graphs were plotted (Fig. 3). The potentials measured were plotted against the pH values to obtain the first calibration curve (Fig. 3a) by using series of buffer solutions in the range of pH 1.9–12.9. The second calibration curve (Fig. 3b) was performed by recording the time elapsed to reach a stable potential value after the addition of diluted NaOH to access the appropriate pH (see Fig. 4). The proposed electrode was found much more suitable than many of the other alternatives given in the literature as regard to the linear working range and slope [1,6–14,16,18–20,22–25,30,32,33]. The comparison of response characteristics of some different type of pH sensing electrodes together with the proposed electrode are given in Table 2.

In this study, the impedance measurements were evaluated in two different buffer solutions containing sodium chloride. Fig. 5 (A) displays the impedance plots of the proposed pH sensing membrane and the same membrane without ionophore immersed into acetic acid/acetate buffer-NaCl solution (pH: 4). This type of spectra shows the behaviour of the membranes in the electrodes. As it can be seen, at high frequencies, the signal is mainly dominated by the electrical resistance and the geometric capacitance in parallel with the membrane which showed well defined semi-cyclic impedances [1,7]. The electrical resistance for the ionophore free membrane (electrode 1) was much lower than the resistance for the ionophore-containing membrane (electrode 4). On the contrary, it was stated in literature that the addition of neutral carriers such as alkyldibenzylamines had no effect on the electrical resistance of the membrane electrodes [24]. This behaviour may be attributed to the introduction of a huge neutral macrocyclic compound as calix[4]arene derivative to the membrane. On the other hand, there is a diffusional component ($\sim45^\circ$ line) at low frequencies which clearly indicates the reversible diffusion of the hydrogen ion from the solution into the proposed electrode membrane [7].

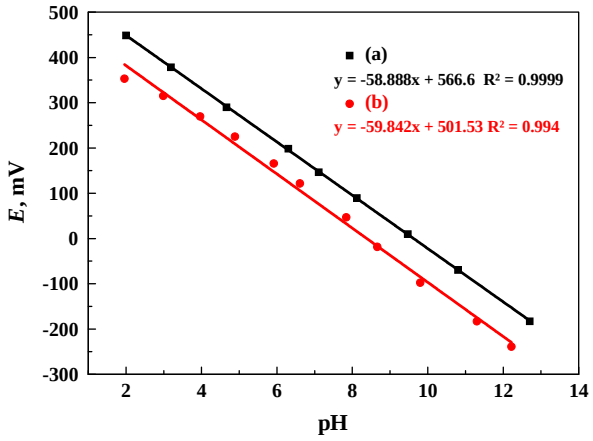


Fig. 3. Typical calibration graphs of the proposed pH sensing membrane electrode (electrode 4) plotted by the data obtained from (a) pH-ion meter and (b) potential-time graph.

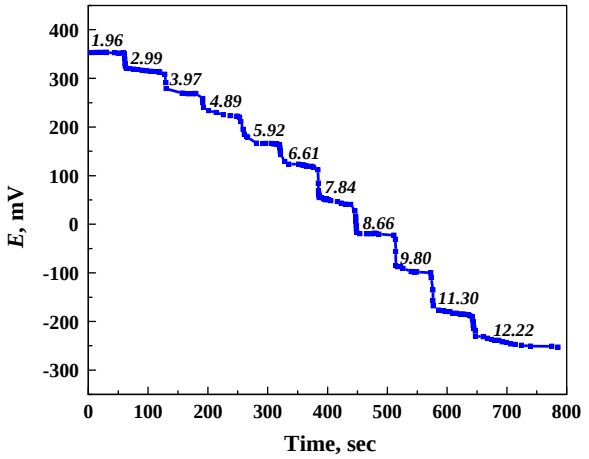


Fig. 4. Dynamic response of the proposed electrode for step changes in pH (electrode 4).

The impedance behavior of the proposed electrode in different pH buffered solutions (pH 3, pH 5 and pH 7) was presented in Fig. 5(B). The electrode displayed nearly the same semi-cyclic impedances at high frequencies. However, the bulk resistance increased with increasing pH values. This phenomenon was related to the transfer of hydrogen ion from solution to the calix [4]arene derivative in polymer layer. Hence, it is in accordance with the literature proposing that the energy of transfer of the hydrogen ion across the polymer membrane increased with increasing pH values [12,13].

3.4. Response time and lifetime of the electrode

The response time of an ion-selective electrode is an important factor for any analytical application. Therefore, the response time required for the electrode to reach 95% of equilibrium mV values after successful immersion in a series of solution each having a 10-fold difference in hydrogen ion concentration was measured. The static response time thus obtained was 6–7 s over the entire pH range (1.9–12.7) and no change was observed in 10 min. This was also confirmed from the potential-time graph in Fig. 4. The response times are comparable to, or even shorter than those reported in literature, that were found to give linear response in the same or narrower working ranges [6–12,30–34].

The lifetime of the electrode was determined by reading its potentials and plotting the calibration curves for a period of 12

Table 2
Comparison of the proposed electrode with some pH sensing electrodes.

Electrode	Sensing material	Linear range (pH)	Sensitivity (mV pH^{-1})	Response time (t_{95})	References
RSE	Quinhydrone	2.0–9.5	57.5 ± 0.2	< 10 s	[1]
SCE	Decamethylcyclopentasiloxane	1.9–9.8	57.6 ± 0.2	< 15 s	[6]
CWE	*N,N*-dioctadecylmethylamine	4.0–11.0	50.2 ± 0.4	< 5 s	[14]
FET	Carbon-nanotube thin film	3.0–13.0	50.9		[16]
MOE	MoO_3 nanorod	1.0–5.0	54 ± 2	< 60 s	[18]
PME	Calix[4]-aza-crown derivative	2.5–11.5	59.2	< 10 s	[30]
PME	Tri-*n*-dodecylamine	4.0–10.0	54 ± 2	< 6 s	[22]
PME	Calix[4]arene derivative	1.9–12.7	58.7 ± 1.1	6–7 s	This work

RSE redox system based electrode; SCE solid contact electrode; CWE coated wire electrode; FET field effect transistor; MOE metal oxide electrode; PME polymeric membrane electrode.

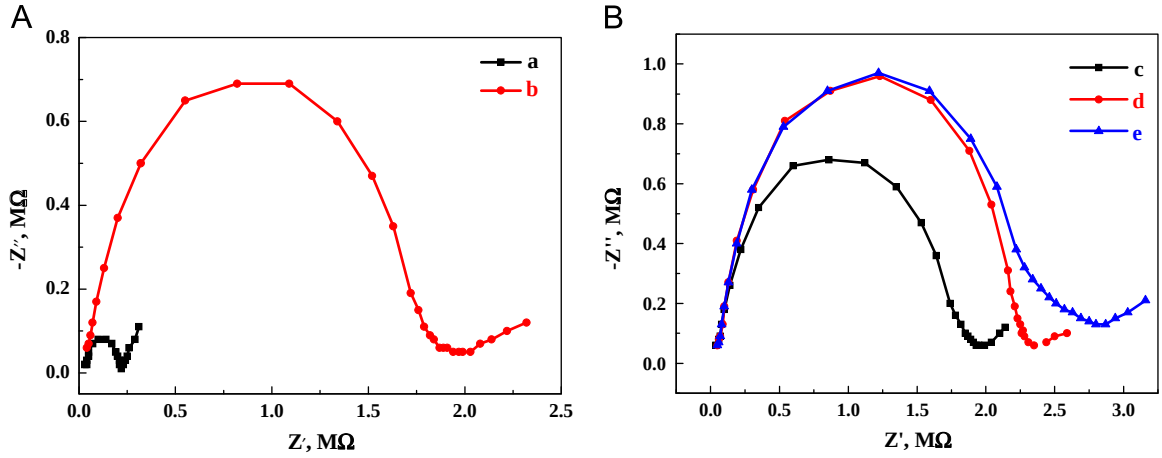


Fig. 5. Typical impedance plots of the membranes containing *o*-NPOE and PVC (A) in acetic acid/acetate buffer–NaCl solution (pH: 4): (a) without ionophore, electrode 1, (b) with 3% ionophore, electrode 4; (B) in BR buffer-NaCl solutions at: (c) pH: 3, (d) pH: 5, (e) pH: 7 for electrode 4.

months. The slope of the electrode was observed to show no significant change even after this period. This shows that the lifetime of the electrode prepared by the use of 5,17-bis(4-benzylpiperidine-1-yl)methyl-25,26,27,28-tetrahydroxy calix[4]arene was longer than the PVC membrane and other non-glass pH electrodes reported in literature with good repeatability and reproducibility [12,20,22,30–32].

3.5. The selectivity of the electrode

It is reported in literature that the working range of macrocyclic compounds-based electrodes was adversely affected by the anions and the cations. It is known that cations decrease the lower detection limit (at high pH) and anions decrease the upper detection limit (at low pH) of the pH electrodes [23,33]. In short, many ionic impurities are expected to narrow the working range of the electrode [13,43]. The interferences of cations such as Na^+, K^+, Li^+, NH_4^+, Mg^{2+}, Ca^{2+} (0.1 M) and anions such as bromide, iodide, chloride, nitrate, thiocyanate, perchlorate (1.0×10^{-3} M) were evaluated by the use of the fixed interference method (FIM).

The effect of the above mentioned anions on the pH response of the electrode was demonstrated in Fig. 6a. Tentatively notwithstanding, in the presence of higher anion concentrations at low pH values, anions form ion pair with hydrogen ions which are bonded to calix[4]arene thereby making the ionophore irresponsible, for the protons, to penetrate into and the system behaves insensitive to hydrogen ions. In this case, the potential is independent of the pH and is a function of the concentration of anions in the solution [31,32]. As it can be seen in Fig. 6a, the anions except from universal impurity chloride affected the working range of the proposed pH sensing membrane electrode. The following sequence of anion interference was observed: $ClO_4^- > SCN^- > I^- > NO_3^- > Br^-$.

Cation interference was also investigated in the region of high pH, where the hydrogen ion concentration is very low, but the above mentioned cation concentration is high, that causes alkaline error in case of some glass pH electrodes. The potentiometric response of the electrode in the presence of these cations indicated that the working range and the Nernstian slope were not changed (Fig. 6b). These results indicated that the corresponding cations would not cause any significant interference unless they present in concentrations > 0.1 M. These results are comparable to and even better than some of the data given for other PVC-based membrane electrodes in the literature [6,14,31–33]. Therefore, this electrode can conveniently be used for pH measurements in the media containing these ions.

3.6. The analytical applications of the electrode

The electrode was used in the titrations of hydrochloric, hydrofluoric and phosphoric acids with standardized sodium hydroxide. The titration curves were plotted in order to elucidate whether the prepared pH sensing membrane electrode can be employed as an indicator electrode in acid–base titrations. The same titrations were also carried out by the use of a commercial combined glass pH electrode. The expected end-points were observed identical for the proposed electrode and combined glass pH electrode. An example of each titration curves is given as supplementary material (Fig. 7). Furthermore, no erosion effect of hydrofluoric acid was observed on the prepared membrane. After a measurement with this electrode in hydrofluoric acid, the working range and the Nernstian slope remained the same. It can be concluded that the electrode prepared could be successfully employed in acid–base titrations and in fluoride containing media.

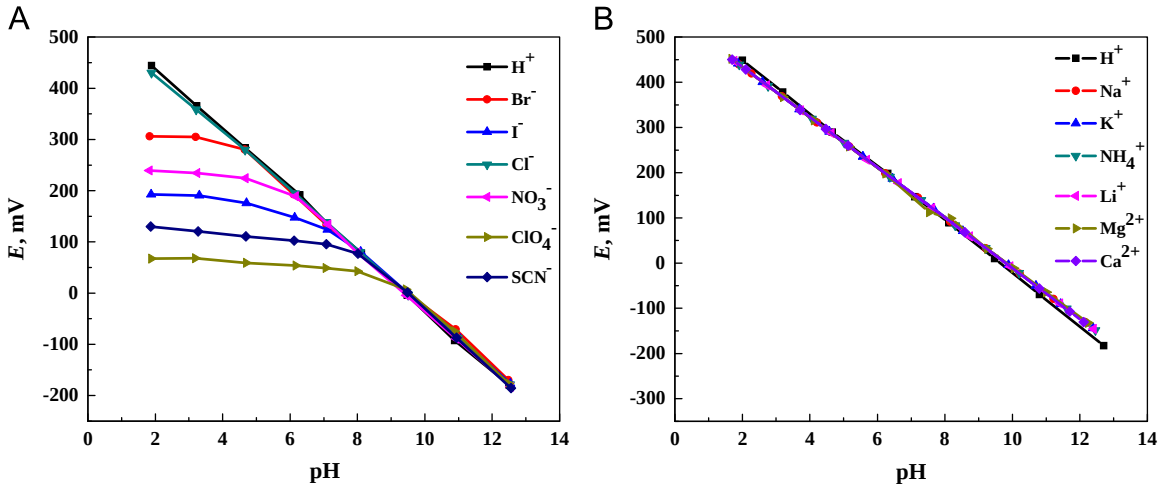


Fig. 6. Potentiometric response of the proposed electrode in the presence of (a) anions ($C=1.0\times10^{-3}$ M), (b) cations ($C=0.1$ M).

Table 3
The titratable total acidity of beverages found with the proposed electrode and commercial combined glass pH electrode (95% CL, $N=5$, $t_{crit}=2.78$, $F_{crit}=6.39$).[a]

Beverages	Glass pH electrode	Proposed electrode	t_{exp}	F_{exp}
Orange juice	13.3 ± 0.6	13.3 ± 0.6	0.1	1.0
Apple juice	9.8 ± 0.3	9.8 ± 0.1	0.4	0.2
Fizzy drink	0.6 ± 0.0	0.7 ± 0.0	2.3	0.2
Beer	0.6 ± 0.0	0.6 ± 0.0	0.1	1.0
Red wine	8.4 ± 0.2	8.1 ± 0.2	2.1	0.4
Vinegar	85.3 ± 4.3	83.6 ± 1.9	0.9	0.2

[a] The results were rounded as one digit beyond the decimal point.

The feasibility of the proposed electrode for the determination of the titratable acidity of some commercial beverages was also investigated [48]. Packaged of beverages were obtained from a local market (Ankara, Turkey). The analytical results obtained by this pH electrode were compared with those obtained by commercial combined glass pH electrode (Table 3). From Table 3, the critical value of t is 2.78 for the 95% confidence level and 4 degree of freedom. Since $t > t_{exp}$, no significant differences between the results obtained with the proposed pH sensing PVC membrane electrode and the commercial combined glass pH electrode was detected. Furthermore, since critical value of $F(6.39) > F_{exp}$, we concluded that the results obtained from the proposed electrode appear to give better precision than those from combined glass pH electrode at the 95% confidence level. It can be suggested that the developed calix[4]arene based PVC membrane electrode could be an effective tool for potentiometric determination of the titratable acidity in real samples.

4. Conclusions

5,17-Bis(4-benzylpiperidine-1-yl)methyl-25,26,27,28-tetrahydroxy calix[4]arene can be successfully used as an ionophore in pH-sensing membrane electrode. The proposed electrode can be a good alternative for a glass electrode. It showed good selectivity for H^+ ions in the presence of some cations and anions and a longer lifetime of at least 12 months. This electrode was also found much more suitable when compared with the other PVC membrane pH electrodes reported in the literature as regard to the linear working range and slope. Due to the fact that the electrode had a wide working pH range, it can be not only employed as an indicator electrode in acid–base titrations, but also can be used for the titratable acidity in different real samples. It was also successfully utilized in fluoride-containing media. The advantages of this electrode are its simplicity of preparation, low-cost, fast response time and long lifetime. Furhermore, it can be possible to prepare a PVC micro-pH electrode using the new calix[4]arene derivative to perform in-vivo pH measurements. We predicted that the proposed electrode could also be used as an anion-selective electrode for some anions due to the ability of protonated calix[4]arene binding anions reversibly to the polymer membrane by hydrogen bonds [49].

Acknowledgements

We gratefully acknowledge the financial support of Ankara University Research Fund (Grant no: 10B4240003).

Appendix A. Supporting information

Supplementary data associated with this article can be found in the online version at http://dx.doi.org/10.1016/j.talanta.2014.10.032.

References

[1] J. Ping, Y. Wang, J. Wu, Y. Ying, F. Ji, Microchim. Acta 176 (2012) 229–234.
[2] I.M. Illyas, H.H. Mohd, S.S. Intan, A.G Sulaiman, Int. J. Electrochem. Sci. 7 (2012) 12045–12053.
[3] X. Ge, Y. Kostov, L. Tolosa, G. Rao, Anal. Chim. Acta 734 (2012) 79–87.
[4] R. Ansari, M. Arvand, L. Heydari, J. Chem. Sci. 126 (2014) 41–48.
[5] L.B. Peng, L.Y. Heng, S.A. Hasbullah, M. Ahmad, J. Anal. Chem. 62 (2007) 884–888.
[6] B. Kim, J. Shim, K.C. Chung, Anal. Lett. 44 (2011) 2138–2149.
[7] G.A. Crespo, D. Gugsa, S. Macho, F.X. Rius, Anal. Bioanal. Chem. 395 (2009) 2371–2376.
[8] A. Michalska, A. Hulanicki, A. Lewenstam, Analyst 119 (1994) 2417–2420.
[9] R.C. Faria, L.O.S. Bulhões, Anal. Chim. Acta 377 (1998) 21–27.
[10] N. Zine, J. Bausells, A. Ivorra, J. Aguiló, M. Zabala, F. Teixidor, C. Masalles, C. Viñas, A. Errachid, Sens. Actuators, B 91 (2003) 76–82.
[11] W.S. Han, K.C. Chung, M.H. Kim, H.B. Ko, Y.H. Lee, T.K. Hong, Anal. Sci. 20 (2004) 1419–1422.
[12] W.S. Han, M.Y. Park, K.C. Chung, K.C. Cho, T.K. Hong, Electroanal 13 (2001) 955–959.
[13] W.S. Han, M.Y. Park, K.C. Chung, K.C. Cho, T.K. Hong, Talanta 54 (2001) 153–159.
[14] P.W. Alexander, T. Dimitrakopoulos, D.B. Hibbert, Electroanalysis 9 (1997) 1331–1336.
[15] J.H. Ahn, J.Y. Kim, M.L. Seol, D.J. Baek, Z. Guo, C.H. Kim, S.J. Choi, Y.K. Choi, Appl. Phys. Lett. 102 (2013) 1–5.
[16] Y.S. Chien, W.L. Tsai, I.C. Lee, J.C. Chou, H.C. Cheng, IEEE Electron Device Lett. 33 (2012) 1622–1624.
[17] M. Kashif, M.E. Ali, S.M.U. Ali, U. Hashim, S.B.A. Hamid, Nanoscale Res. Lett. 8 (2013) 68–77.
[18] G.S. Zakharova, N.V. Podval'naya, J. Anal. Chem. 68 (2013) 50–56.

[19] V.M. Lutov, K.N. Mikhelson, Sens. Actuators, B 18 (1994) 400–403.
[20] M. Arvand, K. Ghaiuri, Talanta 79 (2009) 863–870.
[21] J. Chojnacki, J.F. Biernat, J. Electroanal. Chem. 277 (1990) 159–164.
[22] K. Nurminen, L. Outinen-Y, S. Narkilahti, J. Lekkala, Procedia Eng. 5 (2010) 544–547.
[23] D.H. Cho, K.C. Chung, S.S. Jeong, M.Y. Park, Talanta 51 (2000) 761–767.
[24] D.H. Cho, K.C. Chung, M.Y. Park, Talanta 47 (1998) 815–821.
[25] K.I. Joung, H.J. Yoon, H. Nam, K.J. Paeng, Microchem. J. 68 (2001) 115–120.
[26] G.A. Crespo, M.G. Afshar, E. Bakker, Anal. Chem. 84 (2012) 10165–10169.
[27] E. Lindner, V.V. Cosofret, R.P. Kusy, R.P. Buck, Talanta 40 (1993) 957–967.
[28] J. Langmaier, E. Lindner, Anal. Chim. Acta 543 (2005) 156–176.
[29] R.R. Kothur, J. Hall, B.A. Patel, C.L. Leong, M.G. Boutelle, P.J. Cragg, Chem. Commun. 50 (2014) 852–854.
[30] X.J. Liu, B. Peng, F. Liu, Y. Qin, Sens. Actuators, B 125 (2007) 656–663.
[31] D. Kuruoğlu, E. Canel, S. Memon, M. Yılmaz, E. Kılıc, Anal. Sci. 19 (2003) 217–221.
[32] A. Demirel, A. Doğan, E. Canel, S. Memon, M. Yılmaz, E. Kılıc, Talanta 62 (2004) 123–129.
[33] V.V. Egorov, Y.V. Sin'kevich, Talanta 48 (1999) 23–28.
[34] C. Espadas-Torre, M.E. Meyerhoff, Anal. Chem. 67 (1995) 3108–3114.
[35] E.M. Collins, M.A. McKervey, E. Madigan, M.B. Moran, M. Owens, G. Ferguson, S.J. Harris, J. Chem. Soc., Perkin Trans. 1 (1991) 3137–3142.
[36] C.D. Gutsche, K.C. Nam, J. Am. Chem. Soc. 110 (1988) 6153–6162.
[37] S. Sayin, F. Ozcan, M. Yilmaz, A. Tor, S. Memon, Y. Cengeloglu, Clean—Soil, Air, Water 38 (2010) 639–648.
[38] Y.A. Zolotov, Macrocyclic Compounds in Analytical Chemistry, John Wiley and Sons Ltd., USA, 1997.
[39] U. Schaller, E. Bakker, E. Spichiger, E. Pretsch, Anal. Chem. 66 (1994) 391–398.
[40] Y.W. Choi, N. Minoura, S.H. Moon, Talanta 66 (2005) 1254–1263.
[41] Y.W. Choi, S.H. Moon, Environ. Monit. Assess. 70 (2001) 167–180.
[42] M.M.G. Antonisse, D.N. Reinhoudt, Electroanalysis 11 (1999) 1035–1048.
[43] S. Amemiya, P. Bühlmann, Y. Umezawa, Anal. Chem. 70 (1998) 445–454.
[44] R. Eugster, P.M. Gehrig, W.E. Morf, U.E. Spichiger, W. Simon, Anal. Chem. 63 (1991) 2285–2289.
[45] M. Javanbakht, M.R. Ganjali, H. Eshghi, H. Sharghi, M. Shamsipur, Electroanalysis 11 (1999) 81–84.
[46] J Bobacka, V. Väänänen, A. Lewenstam, A. Ivaska, Talanta 63 (2004) 135–138.
[47] E. Bakker, P. Buhlmann, E. Pretsch, Electroanalysis 11 (1999) 915–933.
[48] Anonim, TS 1125 ISO 750, Meyve ve Sebze Ürünleri Titre Edilebilir Asitlik Tayini, Turkish Standards Institution, Ankara, 2002 (Translated from ISO 750:1998(EN) Fruit and Vegetable Products—Determination of Titratable Acidity).
[49] S. Erden, A. Demirel, S. Memon, M. Yılmaz, E. Canel, E. Kılıç, Sens. Actuators, B 113 (1) (2006) 290–296.

Talanta 132 (2015) 676–679

Contents lists available at ScienceDirect

Talanta

journal homepage: www.elsevier.com/locate/talanta

Short communication

Development of microfluidic-based assays to estimate the binding between osteocalcin (BGLAP) and fluorescent antibodies

Hector Carmona [a], Hector Valadez [a], Yeoheung Yun [b], Jagannathan Sankar [b], Lissette Estala [a], Frank A. Gomez [a,*]

[a] Department of Chemistry and Biochemistry, California State University, Los Angeles, 5151 State University Drive, Los Angeles, CA 90032-8202, USA
[b] Department of Bioengineering, North Carolina Agricultural & Technical State University, 1601 E. Market Street, Greensboro, NC 27411, United States

ARTICLE INFO

Article history:
Received 15 July 2014
Received in revised form
12 October 2014
Accepted 13 October 2014
Available online 22 October 2014

Keywords:
Osteocalcin (BGLAP)
Binding assay
Fluorescent antibodies

ABSTRACT

Osteocalcin (bone gamma-carboxyglutamate protein; BGLAP) is a highly conserved molecule associated with mineralization of bone matrix. It regulates the dynamics of new bone formation and bone resorption. The synthesis of osteocalcin by osteoblasts is regulated by the active form of vitamin D. In this paper, we report the use of two fluorescent-based assays, one bead-based and a second involving an amino-silane surface pre-treatment, to obtain binding constants of $3.53 \times 10^6\ M^{-1}$ and $3.19 \times 10^6\ M^{-1}$, respectively, for the binding of BGLAP to fluorescently labeled monoclonal-anti BGLAP-clone 2D5. These simple microfluidic techniques demonstrate the feasibility of developing microsphere-based and surface electrostatically-attached binding assays to study peptide–antibody interactions. Both techniques utilize sub-microliter volumes of material an important consideration when studying bone turnover markers (BTMs) like BGLAP.

© 2014 Elsevier B.V. All rights reserved.

1. Introduction

The bone is a metabolically dynamic tissue that undergoes continuous remodeling throughout its lifetime. Bone remodeling serves to adjust bone architecture to meet changing mechanical needs and it helps to repair micro-damages in bone matrix preventing the accumulation of old bone [1]. Imbalances between osteoclast-mediated bone resorption and new bone formation causes metabolic bone disorders such as postmenopausal osteoporosis and osteopetrosis [2,3]. In osteoporosis, bone resorption outpaces bone formation resulting in ever porous bones. It is often treated by inhibition of bone resorption; however, bone formation is unfortunately also suppressed by this type of treatment illustrating the tightly coupled processes involved in bone remodeling. In osteopetrosis, the bones become denser due to an imbalance of bone formation over bone resorption [4]. The ability to detect and monitor the enzymes and proteins called bone turnover markers (BTMs), excreted biochemical products formed during bone metabolism would allow better understanding and earlier diagnosis of bone remodeling imbalance [5–7].

Osteocalcin, also known as bone gamma-carboxyglutamate (gla) protein (BGLAP), is a BTM produced primarily by osteoblasts during bone formation [8]. Because it is the most abundant of the non-collagenous proteins in bone it is widely studied as information can be garnered regarding bone formation and resorption. While BGLAP can be measured by a number of immunoassays they are hampered by the minute quantities of the protein in serum, lack of experimental protocols, and degradation in serum limiting analytical approaches to its study [9,10].

There are a myriad of studies espousing the use of bead-based techniques to probe the chemistry of biological systems [11–14]. Specifically, microsphere-based analyses enable facile separation of bound complexes from unbound species without the use of complex techniques and instrumentation. The limits of detection (LOD) are naturally decreased since the use of microspheres increases the surface area-to-volume ratio of the medium allowing for sample concentration. The plethora of microspheres commercially available come in a variety of diameters and surface termini thereby allowing for a paucity of chemistries to be conducted and heretofore immobilization of a wide range of biological species.

Poly(dimethylsiloxane) (PDMS) has for years been the material of choice in many microfluidic applications due to its elastomeric properties, ease of use and cost just to name a few reasons [15]. Unfortunately, unmodified PDMS is hydrophobic and is difficult to wet with aqueous solvents hindering many biochemical applications. In the important area of cell adhesion research, the use of amino-silane and homobifunctional aldehyde reagents has allowed for the covalent modification of PDMS and subsequent immobilization of proteins, antibodies, and other biological species.

In this paper we report the development of two fluorescence-based techniques to analyze the binding of BGLAP to fluorescently

* Corresponding author. Tel.: +1 323 343 2368; fax: +1 323 343 6490.
E-mail address: fgomez2@calstatela.edu (F.A. Gomez).

http://dx.doi.org/10.1016/j.talanta.2014.10.025
0039-9140/© 2014 Elsevier B.V. All rights reserved.

labeled monoclonal-anti BGLAP-clone 2D5. In the first assay, BGLAP was covalently attached to magnetic beads and samples were incubated with increasing concentrations of fluorescently labeled anti-BGLAP clone 2D5 antibodies. The supernatant was extracted and injected into microchannels and the fluorescence measured to assess the extent of binding. In the second assay, 3-aminopropyltriethoxysilane (APTES) was used to modify the microchannel walls converting the –OH termini of the PDMS surface to an amine terminus. Injection of BGLAP into the microchannel caused it to electrostatically attach to the microchannel wall. Subsequent injection of bovine serum albumin to reduce non-specific binding, followed by fluorescently labeled antibody proved quantitatively the effectiveness of the assay. The use of these techniques demonstrate the ease of examining BTMs in a microfluidic platform and provide options to scientists to examine biological interactions where only minute quantities of expensive material may be available.

2. Experimental

2.1. Chemicals and materials

Osteocalcin Fragment 1-49 Human and Mix-n-stain Antibody labeling kit was obtained from Sigma-Aldrich Inc. (St. Louis, MO). Monoclonal Anti-BGLAP clone 2D5 antibodies and APTES were obtained from Sigma-Aldrich Inc. (St. Louis, MO). Negative photoresist SU-8-2025 and SU-8 developer were obtained from Microchem (Newton, MA). PDMS and Sylgard 184 silicone elastomer curing agent were purchased from Dow Corning (Midland, MI). Dynabeads M-270 carboxylic acid terminated magnetic beads were purchased from Invitrogen (Grand Island, NY).

2.2. Microchip fabrication

The master mold was created using the SU-8-2025 negative photoresist poured directly onto a 4 in. silicon wafer and was spun on a spin coater in order to achieve a uniform thickness of approximately 75 μM. A mask-aligner was used with a high-resolution transparency mask to create the channels on the wafer and the master mold. The PDMS and the curing agent were mixed at a ratio of 10:1, degassed, and poured directly onto the master mold. The microchip was cured at 75 °C for 2 h. This resulted in a chip with channels of the following dimensions: 100 μM width × 75 μM depth × 2 cm length. The inlet and outlet to the 10-channel chip were 25 μm in diameter and were made using a manual hole punch (Technical Innovations, Inc., Brazoria, TX). The microchips were then irreversibly sealed to a glass slide using plasma oxidation; the chip and the glass slide are cleaned using ethanol and are exposed to plasma oxidation.

2.3. Surface modification of microchannels

Six microchannels were incubated for 30 min with a 10% APTES in ethanol mixture to allow for silanization. At the conclusion of the incubation time the channels were washed with ethanol in deionized water, which was followed by incubation of osteocalcin in sodium bicarbonate at 1 mg/mL for 30 min. After incubation the channels were washed with deionized water and incubated with bovine serum albumin (BSA) at a concentration of 50 μM in PBS for 30 min. The microchannels were then washed with phosphate buffered solution (PBS) at a pH of 7.4 and channels 2–6 were incubated with fluorescently labeled antibodies ranging in concentration from 0.0 to 1.65 μM for 25 min. Channel 1 was used as a control and was not incubated with antibody. Once the incubation is complete all the channels were washed with PBS and the chips were ready for imaging.

2.4. Derivitization of magnetic beads

100 μL of carboxylic acid terminated magnetic beads was obtained from a stock solution consisting of 2×10^9 beads/mL. The beads were washed (5 ×) with 100 μL of 2-(*N*-morpholino) ethanesulfonic acid (MES) buffer (25 mM, pH 5.0). An external magnet was used at the end of each wash in order to separate the beads from solution and the supernatant was discarded. After the final wash, 200 μL of osteocalcin (1 mg/mL) in MES was added to the beads along with 100 μL of N-(3-Dimethylaminopropyl)-N′-ethyl-carbodiimide hydrochloride EDC (100 mg/mL) in MES and vortexed overnight. After 24 h of incubation the supernatant was removed from the bead solution. The beads were then washed with 100 μL of Tris buffer (50 mM, pH 7.4). Following the addition of Tris buffer, the beads were washed five times with PBS (100 mM, pH 7.4) in 1% BSA to block nonspecific binding. Lastly, the beads were washed once in PBS (100 mM, pH 7.4) and resuspended in PBS buffer. The bead solution was split into five aliquots of 20 μL and the supernatant was extracted. Different concentrations of fluorescently labeled anti-BGLAP clone 2D5 antibodies were made at concentrations of 0.0–1.65 μM and 20 μL of each was incubated with the functionalized beads for 30 min. After incubation the supernatant at each concentration was extracted and injected into channels 2–6 of a PDMS chip. Fluorescence measurements were taken of each channel.

2.5. Fluorescence microscopy and image processing

Fluorescence images were taken with a fluorescence microscope (Nikon Eclipse-2000U) equipped with a CCD camera (IN1820, SPOT Imaging Solutions, Sterling Heights, MI). A 20 × objective lens was used to focus the excitation and emission light. SPOT software was used to control the CCD camera and capture the images at an exposure rate of 105 ms and a gain of 4. ImageJ software was then used to analyze the images to extract intensity data. The background was subtracted from the intensity data for each concentration and plotted against the concentration. The binding isotherms were fitted using nonlinear regression with GraphPad Prism 5.0 (GraphPad Software, Inc., La Jolla, CA) to the Langmuir isotherm to determine the binding constants.

3. Results and discussion

In this work two different types of experiments were conducted to assess the binding of BGLAP to fluorescent antibodies. In the first series of experiments, BGLAP was covalently attached to magnetic beads and increasing concentrations (0.0–1.65 μM) of fluorescently labeled anti-BGLAP clone 2D5 antibodies were added into separate vials of solutions containing the derivatized beads. The supernatant was extracted after incubation for 24 h and injected into microchannels and the fluorescence was measured (Fig. 1). An increased fluorescence intensity is observed in the series of microchannels on increasing the concentration of fluorescent antibody. Subsequently, original antibody solutions were separately injected into a PDMS chip and their fluorescence also measured. The binding isotherm (Fig. 2) was obtained by extracting fluorescence intensity data from images of antibody solutions at different concentrations. The fluorescence intensity of free fluorescently labeled anti-BGLAP clone 2D5 antibody is an indirect method of measuring the amount of antibody bound to BGLAP. The binding constant was determined to be $3.53 \times 10^6 \pm 6.15 \times 10^5\ M^{-1}$ at the 95% confidence level.

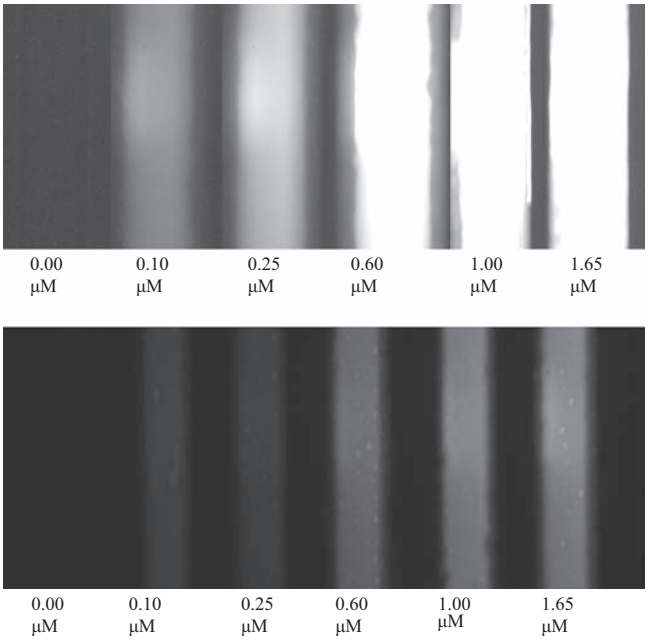


Fig. 1. Fluorescence inside microfluidic device for low to high concentrations of fluorescently labeled anti-BGLAP clone 2D5 antibody (magnetic bead method top image and APTES method bottom image). The images were taken at an exposure rate of 105 ms to avoid photobleaching and then analyzed to determine fluorescence intensity at each concentration.

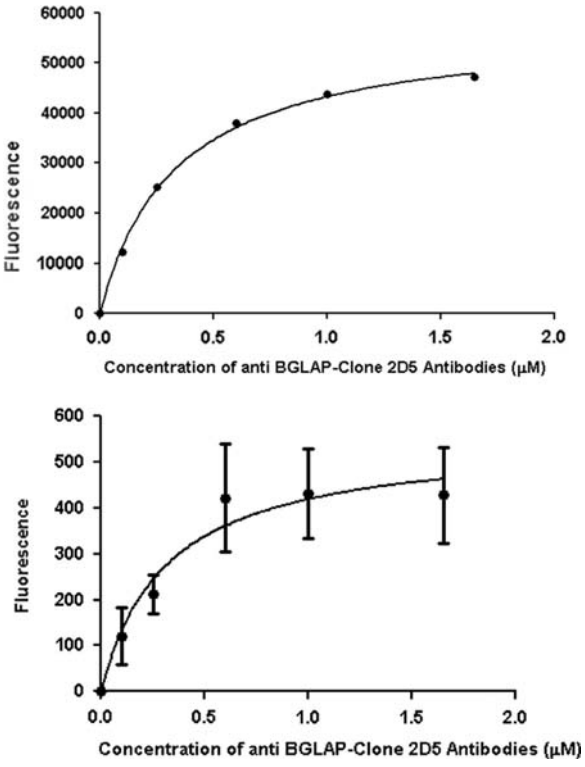


Fig. 2. Binding isotherms for fluorescently labeled anti-BGLAP clone 2D5 antibody from fluorescence microscopy using a bead-based assay (top) and surface modification assay (bottom).

In a second series of experiments, we used a similar surface modification we employed in the analysis of the glycopeptide antibiotics teicoplanin from *Actinoplanes teicomyceticus* and vancomycin from *Streptomyces orientalis* to 5-carboxyfluorescein-D-Ala-D-Ala-D-Ala (FAM-(D-Ala)$_3$ [16]. Here, 3-aminopropyltriethoxysilane (APTES) was used to modify the surfaces of a series of microchannels and each channel was subsequently exposed to a solution of BGLAP for a 25 min followed by washing and addition of BSA to reduce non-specific binding. There is no need for a pre-calibration of the amount of BGLAP electrostatically attached to the functionalized surface based on our earlier work with the glycopeptide antibiotics [16]. The microchannels are subjected to increasing concentrations of fluorescently labeled anti-BGLAP clone 2D5 antibody at room temperature followed by a wash with PBS. As shown in Fig. 1, the microchannels, with immobilized BGLAP, showed fluorescence after incubation with antibody. We speculate that the immobilization of BGLAP onto the microchannel surface results from the electrostatic attraction between the positively charged amine group on the microchannel surface and the negatively charged carboxyl groups on the BGLAP protein. The binding isotherm (Fig. 2) was obtained by extracting fluorescence intensity data from images of the microchannels with BGLAP incubated with antibody at different concentrations ranging from 0.0 to 1.65 µM. The binding constant was determined to be $3.19 \times 10^6 \pm 1.86 \times 10^6\ M^{-1}$ at the 95% confidence level.

Based on the two methods presented, a similarity in binding constants was obtained in both cases. To confirm this, a two-sample independent student *t*-test was utilized in order to determine if there was any statistical difference between the binding constants. When analyzed, it was determined that there was no statistical difference ($p > 0.05$) in the binding constants obtained using magnetic beads and APTES.

While a number of enzyme-linked immunoadsorbent assays (ELISAs) have been reported to detect BGLAP, we believe this report to be the first to actually quantify the binding of BGLAP to an antibody [17–19]. It is important to note, that this type of measurement is not unique in microfluidics as there is much precedent in the literature detailing both study and quantification of affinity constants between ligands and antibodies [20–22]. For example, Holden and Cremer provide a nice review on recent biophysical experiments to obtain mechanistic details of biomacromolecule interactions in microfluidic devices utilizing only nanoliters of analyte [23]. Because BGLAP is found in such small quantities in the body, techniques that offer high sensitivity and requiring minute sample volumes with short measurement times are at a premium.

4. Conclusions

In this study we have examined the binding constants of a fluorescent antibody to osteocalcin via two distinct techniques. The first assay involved the use of magnetic beads derivatized with osteocalcin that were subjected to increasing concentrations of fluorescently labeled anti-BGLAP clone 2D5 antibodies. The supernatant (free-antibody) was examined microscopically in a microchip and its extent of fluorescence could be used to assess the extent of binding between osteocalcin and antibody realizing a binding constant ($3.53 \times 10^6 \pm 6.15 \times 10^5\ M^{-1}$). The second assay first required the application of APTES to the microchannel wall to form a positively charged surface which upon addition of BGLAP electrostatically attached to the wall. Addition of increasing concentrations of fluorescently labeled antibody realized a binding constant $3.19 \times 10^6 \pm 1.86 \times 10^6\ M^{-1}$. The inherent ease of the assays detailed herein demonstrates the future potential of microfluidic-based assays of these types. Given the need for techniques that require minute quantities of materials and that are accurate, simple, inexpensive, and rapid, the development of fluorescent-based methods to analyze interactions like the one described herein are warranted. Future work will focus on expanding the range of interactions to be studied as well as integrating other microfluidic components to the devices.

Acknowledgments

The authors gratefully acknowledge financial support for this research by Grants from the National Science Foundation (EEC-0812348 and HRD-0934146).

References

[1] D.J. Hadjidakis, I.I. Androulakis, Ann. NY Acad. Sci. 1092 (2006) 385–396.
[2] L.A. Kingsley, J.M. Chirgwin, T.A. Guise, Proc. Natl. Acad. Sci. USA 104 (2007) 10753–10754.
[3] L. Pei, P. Tontonoz, J. Clin. Invest. 113 (2004) 805–806.
[4] T.J. Teitelbaum, P.J. Orchard, N. Engl. J. Med. 351 (2004) 2839–2849.
[5] J. Lee, S. Vasikaran, Ann. Lab. Med. 32 (2012) 105–112.
[6] R. Civitelli, R. Armamento-Villareal, N. Napoli, Osteoporos. Int. 20 (2009) 843–851.
[7] Y.H. Yun, A. Bhattacharya, N.B. Watts, M.J. Schulz, Sensors 9 (2009) 7957–7969.
[8] A.N. Kapustin, C.M. Shanahan, Arterioscler. Thromb. Vasc. Biol. 31 (2011) 2169–2171.
[9] E.M. Diaz Diego, R. Guerrero, C. de la Piedra, Clin. Chem. 40 (1994) 2071–2077.
[10] A.J. Lee, S. Hodges, R. Eastell, Ann. Clin. Biochem. 37 (2000) 432–446.
[11] S.H. Yazhi, K.L. Giles, I.M. White, Anal. Chem. 85 (2013) 10605–10611.
[12] Z. Gao, M. Xu, L. Hou, G. Chen, D. Tang, Anal. Chem. 85 (2013) 6945–6952.
[13] N.W. Choi, J. Kim, S.C. Chapin, T. Duong, E. Donohue, P. Pandey, W. Broom, W.A. Hill, P.S. Doyle, Anal. Chem. 84 (2012) 9370–9378.
[14] M.J. McFadden, M.S. Junop, J.D. Brennan, Anal. Chem. 82 (2010) 9850–9857.
[15] C.A. Charitidis, Ind. Eng. Chem. Res. 50 (2011) 565–570.
[16] M.D. Goldberg, R.C. Lo, S. Abele, M. Macka, F.A. Gomez, Anal. Chem. 81 (2009) 5095–5098.
[17] M. Ihara, A. Yoshikawa, Y. Wu, H. Takahashi, K. Mawatari, K. Shimura, K. Sato, T. Kitamori, H. Ueda, Lab Chip 10 (2010) 92–100.
[18] A.J. Lee, S. Hodges, R. Eastell, Ann. Clin. Biochem. 37 (2000) 432–446.
[19] S. Jiang, H.W. Cheng, P.Y. Hester, J.–F. Hou, Poult. Sci. 92 (2013) 1951–1961.
[20] M. Gerardot, F. d'Orlye, S. Descroix, A. Varenne, J. Chromatogr. A 1218 (2011) 4052–4058.
[21] J. Hu, C. Easley, Analyst 136 (2011) 3461–3468.
[22] J. Svobodova, S. Mathur, A. Muck, T. Letzel, A. Svatoš, Electrophoresis 31 (2010) 2680–2685.
[23] M.A. Holden, P.S. Cremer, Annu. Rev. Phys. Chem. (2005) 369–387.

Talanta 132 (2015) 680–684

Contents lists available at ScienceDirect

Talanta

journal homepage: www.elsevier.com/locate/talanta

Selectivity in analytical chemistry: Two interpretations for univariate methods

Zsanett Dorkó [a], Tatjana Verbić [b], George Horvai [a,c,*]

[a] Department of Inorganic and Analytical Chemistry, Budapest University of Technology and Economics, Szent Gellert ter 4., H-1111 Budapest, Hungary
[b] Faculty of Chemistry, University of Belgrade, Studentski Trg 12-16, 11000 Belgrade, Serbia
[c] MTA-BME Research Group of Technical Analytical Chemistry, Szent Gellert ter 4., H-1111 Budapest, Hungary

ARTICLE INFO

Article history:
Received 14 July 2014
Received in revised form
8 October 2014
Accepted 12 October 2014
Available online 22 October 2014

Keywords:
Analytical method
Selectivity
Error
Interference

ABSTRACT

Selectivity is extremely important in analytical chemistry but its definition is elusive despite continued efforts by professional organizations and individual scientists. This paper shows that the existing selectivity concepts for univariate analytical methods broadly fall in two classes: selectivity concepts based on measurement error and concepts based on response surfaces (the response surface being the 3D plot of the univariate signal as a function of analyte and interferent concentration, respectively). The strengths and weaknesses of the different definitions are analyzed and contradictions between them unveiled. The error based selectivity is very general and very safe but its application to a range of samples (as opposed to a single sample) requires the knowledge of some constraint about the possible sample compositions. The selectivity concepts based on the response surface are easily applied to linear response surfaces but may lead to difficulties and counterintuitive results when applied to nonlinear response surfaces. A particular advantage of this class of selectivity is that with linear response surfaces it can provide a concentration independent measure of selectivity. In contrast, the error based selectivity concept allows only yes/no type decision about selectivity.

© 2014 Elsevier B.V. All rights reserved.

1. Introduction

Selectivity is one of the most important features of any analytical measurement. Without selectivity, i.e., if the measuring system responded to every substance in exactly the same way both qualitatively and quantitatively, it would not be possible to determine the concentration of any particular substance in a mixture. It is therefore logical to expect that analytical chemists have a widely accepted definition of selectivity of analytical methods. One would also expect that selectivity can be quantitated in a meaningful way, so that one could compare methods or method variants according to their selectivities.

1.1. Lack of a general definition and of a measure of selectivity

Surprisingly, there is no generally accepted definition of selectivity in analytical chemistry, as shown by a recent review [1] and opinions diverge on its measurability. Some notable sources on the subject may be mentioned here. IUPAC has issued two recommendations and a technical report about the selectivity of general analytical methods [2–4]. It has also published selectivity definitions for particular methods, like potentiometry [5]. Guidelines for good laboratory practice require selectivity tests as part of method validation [6]. Metrological organizations define selectivity of measurements, including chemical ones [7,8]. Clinical chemists appear to avoid the term selectivity and discuss interferences instead [9]. Textbooks of analytical chemistry usually devote very little space to selectivity and either redefine it in an approximate fashion or cite an IUPAC definition as it has been shown in a review [1]. No two of the mentioned sources define selectivity in exactly the same way, and none of them quantitates selectivity (except for some special techniques, like potentiometry).

The common denominator of some of the more recent recommendations by the mentioned professional organizations is that they consider an analytical method selective only if interferences do not influence the measurement result at all or at least not significantly [1]. This is a very strict and therefore quite safe definition but it has some disadvantages. Analytical chemists often develop methods which need to work reliably with a large variety of samples. The question is then how one can prove that a method will be selective (in the above very strict sense) in any future samples to be investigated. Thus the recommendations shift the burden to the analytical chemist who should define the range of future samples which can be selectively analyzed with a particular method. Recommendations for solving this task have been

* Corresponding author at: Department of Inorganic and Analytical Chemistry, Budapest University of Technology and Economics, Szent Gellert ter 4., H-1111 Budapest, Hungary. Tel.: +36 1 4631480.
E-mail address: george.horvai@mail.bme.hu (G. Horvai).

http://dx.doi.org/10.1016/j.talanta.2014.10.018
0039-9140/© 2014 Elsevier B.V. All rights reserved.

published in clinical chemistry [9], where the possible range of samples is more or less known, but similar recommendations are unlikely to be available or even possible for many other analytical problems.

The other disadvantage of the above mentioned definitions of selectivity is that while they may be satisfactory to characterize a fully developed method, they do not provide any quantitative measure of selectivity, not even an approximate one, which could guide the analytical chemist during method development in assessing and improving selectivity.

1.2. Narrowing of the problem

Interferences to an analytical method can be of many different types. One may have sample matrix effects, analytical reagents may undergo side reactions with some sample components, etc. In a frequently encountered type of interference some components of the sample may influence the measured signal in the same way as the analyte. This is a typical problem with sensors, but spectral overlaps are of the same type, and in immunoassays we also have cross sensitivities. Even if we reduce the selectivity problem to such cases (as will be done in this paper), there is no general definition and measure of selectivity available. In individual analytical techniques, though, measures of selectivity have been defined for this type of interference. In absorption spectroscopy at a single wavelength, when the Lambert Beer law is valid for mixtures, the ratio of the respective molar absorbances of the analyte and the interferent, respectively, is an obvious measure of selectivity (see below). In ion selective electrode potentiometry selectivity coefficients have been widely used. Such selectivity concepts are typically based on the response characteristics of a technique or a device in mixed solutions of the analyte and the interferent(s).

This paper investigates if the common selectivity concepts used in analytical chemistry are meaningful, i.e. free of internal contradictions and mutually compatible. This work appears to be the first one to carry out such analysis. It is based among others on our experience with selectivity problems of ion selective electrodes [10–13], numerous method validations following guidelines for Good Laboratory Practice (GLP) [14,15] and investigations about the selectivity of molecularly imprinted polymers [16,17]. An impulse to this work has been given by important recent recognitions about the selectivity of ion selective electrodes [18–21] supported by a large body of experimental data. This study was also motivated by the work of M. Valcarcel and coworkers, who have also recognized the lack of general approaches to analytical selectivity and contributed to the clarification of the term selectivity [22].

2. Selectivity concepts and their properties in the univariate case

The problem discussed here is defined as follows. An analytical output quantity (a signal or an estimate of the analyte concentration, in either case a scalar quantity) is influenced by two components' concentration (Fig. 1). One of these components is considered the analyte, the other the interferent. It is assumed that the response to the analyte alone is a strictly monotonous function of the analyte concentration. The interferent is supposed to affect the measurement in a similar manner to the analyte. This means here that the interferent alone would also give a monotonous calibration line with the same direction as the analyte. For simplicity we shall assume that the calibration lines are both monotonously increasing. It is also assumed that the addition of any of the two components to any mixture of them will increase the output value. All these assumptions are satisfied by many analytical methods.

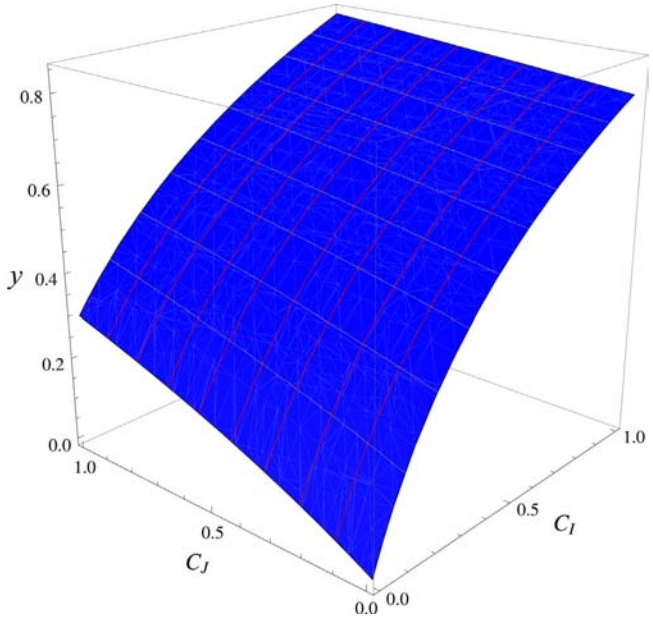


Fig. 1. A general response surface (y: measured signal, c_I: analyte concentration, c_J: interferent concentration).

The main ideas of the paper will be introduced by discussing first the simplest possible case, i.e., that of linear response in both concentration variables.

2.1. Linear response function

Let the measured signal, y, be a homogeneous linear function of the two concentrations, i.e.,

$$y = f(c_I, c_J) = k_I c_I + k_J c_J \tag{1}$$

here I denotes the analyte, J the interferent, c with a subscript stands for the respective concentration. The k-s are constants. (The equation might also include an additive constant. This would, however, not influence the final result.) The analyst wants to estimate the concentration of the analyte from the measured signal, y. Without having any further information, this is not possible, because there are two unknown concentrations but only one equation. As additional information the analyst may know, for example, that the ratio of interferent to analyte concentration is less than a certain value in all future samples. In another scenario the analyst may ascertain by a quick test or by sample preparation that the interferent concentration is less than a certain value. In either case a rational approach is to consider at first the total signal to be due to the analyte alone. By this procedure one obtains the highest possible value of the analyte concentration (because of the monotonicity criteria made above) which is in accordance with the measured signal value and the additional condition at the same time. This estimate of the analyte concentration may be in error, but as will be shown immediately, the maximum of this error may be estimated and compared with the required tolerance level.

The biased estimate, $\hat{c}_I$, of the analyte concentration is calculated, as proposed above, by dividing the signal, y, by k_I, which is the slope of the calibration line in pure I solutions:

$$\hat{c}_I = \frac{y}{k_I} = \frac{k_I c_I + k_J c_J}{k_I} = c_I + \frac{k_J}{k_I} c_J \tag{2}$$

This equation shows that the estimate is biased, it is higher than the true c_I. The relative error of the estimate is:

$$\frac{\hat{c}_I - c_I}{c_I} = k_{IJ}\frac{c_J}{c_I} \tag{3}$$

where

$$k_{IJ} = \frac{k_J}{k_I} \tag{4}$$

The maximum committed relative error can be estimated now from the maximal ratio of the two concentrations if this was the additional information. If this error is higher than the maximum allowed error, the method needs improvement. For example the interferent concentration may be reduced by sample pretreatment. Alternatively, the analytical device may be improved. If in the end the error of the method is less than the predefined error limit, then one may say that the method is selective for I compared to J, at least as long as the additional information about the samples is valid.

Analytical chemists have also other approaches to define selectivity. This is easily discussed for linear response functions [23]. One compares the values of k_I and k_J with each other. The method is considered selective for I if $k_I > k_J$ (which is equivalent to $k_{IJ} < 1$) and selective for J if $k_I < k_J$. If $k_I = k_J$ the method is not selective. These criteria are very reasonable. The relationship between the two constants shows to which compound is the method more sensitive. This type of selectivity may be simply characterized by k_{IJ}, which may therefore be called a selectivity coefficient. One should note that this second type of selectivity depends only on the response surface (which in the linear case is a plane), and does not depend on additional information about the samples.

The two selectivity concepts discussed here, i.e. the one based on error considerations and the one based on sensitivities, are not very simply related to each other. This is immediately seen if one considers the following example. Let there be a linear response surface with $k_{IJ} = 1$. In a particular sample the ratio of the concentrations, c_J/c_I, should be 0.01. The relative error of the c_I measurement is then 1% as predicted by Eq. (3). If this error level is tolerable, then the method will be considered selective (at least in the case of this sample and for any other samples where $c_J/c_I < 0.01$), because the effect of the interferent on the measurement result is negligible. But according to the other, sensitivity based definition of selectivity, the method is not selective at all, since $k_{IJ} = 1$, i.e., $k_I = k_J$.

The conclusion from these considerations is that two commonly used and apparently meaningful selectivity concepts are in conflict with each other even for the simplest possible response surface. This ambiguity may have contributed to the confusion about selectivity definitions.

Another conclusion is that the error based selectivity definition is only meaningful if we apply it either to a single sample instead of a method (which is not very practical in analytical chemistry), or if we make some tacit assumption about the composition of all future samples. Such assumptions may be difficult to check unless the composition of the samples is very restricted. In bioanalysis such restriction often exists for endogenous interferents which have a relatively narrow natural concentration range.

The selectivity concept based on the response surface parameter k_{IJ} has a great advantage: it provides a meaningful measure of selectivity for linear response surfaces in the form of k_{IJ}. It is also independent of assumptions about the sample composition. But it has also some disadvantages. Most importantly it cannot be transferred in a unique way to nonlinear response surfaces. This is so because k_{IJ} of a linear response surface can be interpreted in many different ways, which give the same result for a linear surface but usually different results for a nonlinear one. To give just two examples k_{IJ} can be interpreted as the ratio of the slopes of the separate calibration lines for I and J, respectively, or as the ratio of the two partial derivatives of y with respect to I and J, respectively.

A third approach to selectivity which is also intuitively appealing, consists of comparing the pure I and pure J concentrations, respectively, which belong to the same signal value. From Eq. (1) these are easily obtained for linear response surfaces:

$$c_I = \frac{y}{k_I} \tag{5}$$

and

$$c_J = \frac{y}{k_J} \tag{6}$$

If $c_I < c_J$ then the measurement may be regarded selective for I, since the same signal is caused by a smaller concentration of I than of J (and as assumed above the signal increases with concentration). From Eqs. (5) and (6) this type of selectivity for I occurs if $k_{IJ} < 1$, just like before. However, for nonlinear response surfaces this selectivity definition may have a complex relationship with the others.

2.2. General response function

In case of a more or less general response function (which still maintains monotonicity and smoothness as in Fig. 1) the problems of defining selectivity and of estimating the measurement error become worse. Sensitivity, i.e., the partial derivative of the signal with respect to either concentration, is no more a constant as it was in the form of k_I and k_J, respectively, in the linear case. The ratio of sensitivities for I and J, respectively, is only a local quantity (changing with both c_I and c_J) and not a universal constant.

Nonlinear response surfaces may complicate any statement about method selectivity. It is possible (as has been found, for example, in potentiometry [21]) that in certain ranges of c_I and c_J the method is selective for I and in other ranges for J. Thus one cannot always say that the method is selective for I or J, even if we consider only the response surface.

With some nonlinear surfaces a further type of selectivity has been defined, e.g., in potentiometry [18], which is conceptually different from those discussed so far. An interesting property of such surfaces is that given the parameters of the calibration line for the pure analyte I, the whole response surface (including the response to pure J) can be described by a single additional parameter. In potentiometry this parameter is the difference between the standard potentials measured in I and J solutions, respectively. This parameter (divided by a constant factor) has been called selectivity coefficient, although it does not describe selectivity in any of the above mentioned ways. However, it can be used to calculate any of those measures because it describes (together with the calibration parameters for I) the whole response surface.

2.3. Pseudo linear response functions

Since interpretation of selectivity becomes so difficult with nonlinear response surfaces, it is natural to ask if there are any practically existing nonlinear response surfaces which retain the simple properties of linear ones, with respect to selectivity. Interestingly, such surfaces exist. The Nicholsky equation in potentiometry (Eq. (7)) describes, for example, such a response surface if it is applied to two ions of identical charge.

$$E = E_I^0 + \frac{RT}{z_I F}\ln(a_I + k_{IJ}a_J^{z_I/z_J}) \tag{7}$$

(The notation is well known, only k is not in capital letter as in potentiometry.) It will be shown now that this equation is just one

representative of a special class of functions well-behaved in matters of selectivity.

Let us recall that for linear response surfaces the relative error was expressed by Eq. (3).

After simple rearrangement:

$$\hat{c}_I = c_I + k_{IJ} c_J \tag{8}$$

Similarly to the linear case, even if the response function is nonlinear, the biased estimate for the analyte concentration should be calculated from the measured signal by assuming that the concentration of the interferent is zero. Let us consider now only such response functions where for any (c_I, c_J) pair which gives the same signal y the relationship of Eq. (8) is valid. Then:

$$y = f(c_I, c_J) = f(\hat{c}_I, 0) = f(c_I + k_{IJ} c_J, 0) \tag{9}$$

here f means a general bivariate function. The right hand side of Eq. (9) describes a bivariate response surface which need not be linear. It is special, however, because it is an apparently univariate function of the variable

$$c_I + k_{IJ} c_J \tag{10}$$

with k_{IJ} being a constant. Due to Eq. (9) the error formula of Eq. (3) will be valid for such functions. As a practical example the Nicholsky equation for two ions of equal valency z satisfies this criterion:

$$E = E_I^0 + \frac{RT}{zF} \ln(a_I + k_{IJ} a_J) \tag{11}$$

As immediately seen, for a constant value of E the value of $a_I + k_{IJ} a_J$ is also constant. Note also that this equation is nonlinear.

One may call the response surfaces which satisfy Eq. (9) pseudo-linear surfaces. If a method has such a response surface then it can be characterized by a concentration independent selectivity coefficient. The measurement error is also easily calculated in this case, just like with linear response functions.

If the general condition of Eq. (9) is not satisfied, one can in many practical applications limit the allowed range of the variables c_I and c_J so that in the limited range Eq. (9) is valid, at least approximately. In certain analytical problems the analyte concentration can only move in a narrow range, so that the condition of Eq. (8)

$$\hat{c}_I = c_I + k_{IJ} c_J$$

needs to be satisfied with a k_{IJ} that is not an overall constant but can be considered constant in a narrow range of the analyte concentration. In this range it must be then independent of the interferent concentration.

2.4. The measure of selectivity

The previous discussion has shown that with certain response functions a constant and meaningful selectivity factor can be used. The constant k_{IJ} has been used here for easy comparison with the potentiometric selectivity coefficient. But k_{IJ} has a large value (i.e., much larger than 1) when the effect of the interferent on the signal is larger than that of the analyte. It would be therefore more appropriate to use the reciprocal of k_{IJ} to measure selectivity. In this paper we have used k_{IJ} for easy comparison with the Nicholsky equation (Eq. (11)).

3. Conclusion

Selectivity is an extremely important property of any analytical method but its definition and quantitation have still remained open questions. Many definitions of selectivity are possible and have indeed been used. They have been divided in this paper into two classes: definitions based on measurement error and definitions based on the response surface. Both types have their respective merits and problems. The error based selectivity is very general and very safe but its application to a range of samples (as opposed to a single sample) requires the knowledge of some constraint about the possible sample compositions. The selectivity concepts based on the response surface are easily applied to linear response surfaces but may lead to difficulties and counterintuitive results when applied to nonlinear response surfaces. A particular advantage of this class of selectivity is that with linear response surfaces it can provide a concentration independent measure of selectivity. In contrast, the error based selectivity concept allows only yes/no type decision about selectivity.

The relationship between the two classes of selectivity definitions has been derived for linear response surfaces (and with the necessary assumptions about the constraints of sample composition). It has been shown that the error based selectivity and the response surface based selectivity may be contradicting, i.e., a measurement classified as nonselective by using one definition may be perfectly selective according to the other definition.

If the response surface is nonlinear the selectivity concepts based on the response surface diverge and comparison with the error based selectivity becomes difficult. It has been shown here, however, that a practically relevant class of nonlinear response functions show in this respect the same behavior as the linear response functions. Therefore this type of nonlinear response function allows the use of a simply interpreted concentration-independent selectivity measure. Moreover it follows from our derivations that this is the only kind of nonlinear function making such simple interpretation possible.

Future research should investigate the response function of common analytical techniques and find the typical additional constraints used to limit the uncertainty of the result. From these one should derive, wherever possible, simple relationships between the parameters of the response function and the maximum error of the result. Notably such work has already been very successfully done in ion-selective potentiometry [18]. Interference by more than a single compound needs to be addressed, too. The uncertainty arising from interference should also be related to the uncertainty due to limited precision in measuring the signal and the limited precision of the calibration. One should also clarify the relations to multivariate concepts of selectivity.

Acknowledgments

The financial support of the OTKA, Hungary (Grant No. K104724) and the Ministry of Education, Science, and Technological Development of Serbia (Grant No. 172035) is gratefully acknowledged. Discussions with Dr P. Horvai and help with rendering Fig. 1 by Dr L. Höfler are gratefully acknowledged.

References

[1] T. Verbic, Z. Dorko, G. Horvai, Rev. Roum. Chim. 58 (2013) 569–575.
[2] G. den Boef, A. Hulaniczki, Pure Appl. Chem. 55 (1983) 553–556.
[3] J. Vessman, R.I. Stefan, J.F. Van Staden, K. Danzer, W. Lindner, D.T. Burns, A. Fajgelj, H. Muller, Pure Appl. Chem. 73 (2001) 1381–1386.
[4] M. Thompson, S.L.R. Ellison, R. Wood, Pure Appl. Chem. 74 (2002) 835–855.
[5] R.P. Buck, E. Lindner, Pure Appl. Chem. 66 (1994) 2527–2536.
[6] U.S. Department of Health and Human Services, Food and Drug Administration, Center for Drug Evaluation and Research (CDER), Center for Veterinary Medicine (CVM), Guidance for Industry, Bioanalytical Method Validation, Rockville, 2001, pp. 4–5.
[7] V.J. Barwick, E. Prichard (Eds), Eurachem Guide: Terminology in Analytical Measurement – Introduction to VIM 3, 2011, pp. 20.
[8] JCGM (Joint Committee for Guides in Metrology), International Vocabulary of Metrology – Basic and General Concepts and Associated Terms (VIM), third ed., 2012, pp. 41.

[9] CLSI (Clinical and Laboratory Standards Institute), Interference Testing in Clinical Chemistry; Approved Guideline – second Guideline, second ed., CLSI document EP7-A2, Wayne, Pennsylvania USA, 2005, pp. 6,7.
[10] G. Horvai, V. Horvath, A. Farkas, E. Pungor, Talanta 36 (1989) 403–405.
[11] V. Horvath, G. Horvai, Anal. Chim. Acta 282 (1993) 259–264.
[12] G. Horvai, Trends Anal. Chem. 16 (1997) 260–266.
[13] G. Horvai, Sens. Actuators, B-Chem. 43 (1997) 94–98.
[14] S. Drabant, K.B. Nemes, V. Horvath, A. Tolokan, G. Grezal, M. Anttila, B. Gachalyi, H. Kanerva, S. Al-Behaisi, G. Horvai, I. Klebovich, Eur. J. Pharm. Biopharm. 58 (2004) 689–695.
[15] V. Horvath, A. Tolokan, A. Egresi, T. Pap, G. Horvai, K. Balogh-Nernes, I. Klebovich, J. Chromatogr. B 816 (2005) 153–159.
[16] I. Ferrer, F. Lanza, A. Tolokan, V. Horvath, B. Sellergren, G. Horvai, D. Barcelo, Anal. Chem. 72 (2000) 3934–3941.
[17] T. Pap, G. Horvai, J. Chromatogr. A 1034 (2004) 99–107.
[18] E. Bakker, R.K. Meruva, E. Pretsch, M.E. Meyerhoff, Anal. Chem. 66 (1994) 3021–3030.
[19] E. Bakker, J. Electroanal. Chem. 639 (2010) 1–7.
[20] A. Lewenstam, T. Sokalski, J. Jasielec, W. Kucza, R. Filipek, B. Wierzba, M. Danielewski, ECS Trans 19 (2009) 219–224.
[21] E. Bakker, Anal. Chem. 69 (1997) 1061–1069.
[22] M. Valcarcel, A. Gomez-Hens, S. Rubio, Trends Anal. Chem. 20 (2001) 386–393.
[23] D. Harvey, Modern Analytical Chemistry, The McGraw-Hill Companies, Inc., USA, 2000. pp. 40.

Talanta 132 (2015) 685–689

Contents lists available at ScienceDirect

Talanta

journal homepage: www.elsevier.com/locate/talanta

Pretreatment-free lateral flow enzyme immunoassay for progesterone detection in whole cows' milk

J.V. Samsonova [a,*], V.A. Safronova [a], A.P. Osipov [b]

[a] Department of Chemical Enzymology, Chemistry Faculty, M.V. Lomonosov Moscow State University, 1-11 Leninskie Gory, Moscow, 119991 Russia
[b] National University of Science and Technology "MISiS", 4 Leninsky Ave., Moscow, 119049 Russia

ARTICLE INFO

Article history:
Received 19 August 2014
Received in revised form
12 October 2014
Accepted 18 October 2014
Available online 28 October 2014

Keywords:
Progesterone
Lateral flow enzyme immunoassay
Horseradish peroxidase
Whole cows' milk

ABSTRACT

New rapid method of lateral flow enzyme immunoassay (LFEIA) for progesterone detection in whole cows' milk was developed. The test system utilized horseradish peroxidase as a label along with the substrate solution containing 3,3',5,5'-tetramethylbenzidine and dextran sulfate to obtain an insoluble blue colored product of the enzyme reaction on a surface of analytical membrane (test and control lines). Several aspects of LFEIA were optimized: time of the signal detection, membrane materials and assay conditions. Resulting competitive LFEIA can be performed within 15 minutes with the limit of progesterone detection of 0.8 ng/ml. Progesterone concentration in whole milk samples was determined by LFEIA and enzyme-linked immunosorbent assay (ELISA). The results obtained were in good correlation (R=0.97, n=46). Thus new sensitive LFEIA can be successfully used for on-site monitoring of oestrus status of cows' reproductive system and for early none-pregnancy detection. The method is fast, easy to perform and needs no preliminary sample preparation.

© 2014 Elsevier B.V. All rights reserved.

1. Introduction

Nowadays lateral flow immunoassay (LFIA) is a convenient method for semi-quantitative and quantitative detection of important biologically active substances performed on-site, point-of-care places or for personal testing [1]. The approach is widespread in medical and veterinary diagnostics, food control and many other areas due to short time of analysis (10–15 min) and easy procedure. LFIA test strips contain all necessary reagents in dry form; so to perform a test it is sufficient to add a liquid sample (extract) which migrates along overlying membranes and results in the formation of specific immunocomplexes in different areas of a test strip. The result of analysis is usually presented in a form of colored lines in the test and control zones of analytical membrane. A range of labels is used in LFIA including colloidal gold, latex particles, enzymes, quantum dots etc. [1–3]. It was reported that enzyme labels provided up to 10–30 times higher assay sensitivity compared to conventional LFIA labels such as colloidal gold [3–6]. Enzyme immunochromatography as a form of quantitative immunoassay was pioneered by Zuk et al. in 1985 [7]. The authors used paper test strip totally covered by specific antibodies and the assay was based on the measurement of the height of colored bars formed on strips as a result of immunoreaction with the following enzyme substrate saturation. Later enzyme immunoassay was realized in conventional LFIA format with specific reagents immobilized in a form of narrow bands [8]. In enzyme LFIA the most often used label is horse radish peroxidase (HRP) [3–6], however alkaline phosphatase [8,9] and cholinesterase [10] were also employed. As far as HRP is concerned, colorimetric [3–6], chemiluminescent [11,12] and electrochemical [13] detection modes were reported. Substrate solution contained 3,3',5,5'-tetramethylbenzidine (TMB) was predominantly employed for colorimetric detection in HRP-based LFIA [4,6], however 4-chloro-1-naphthol was also used in few studies [5,7].

In veterinary practice one of important biomarkers which should be checked on-site is sex hormone progesterone (P4). Thus P4 concentration in cows' milk is used to monitor cyclicity and confirm oestrus behavior as well as to perform non-pregnancy diagnosis on day 19–21 after artificial insemination [14,15]. Milk sampling is a convenient way of sample collection because probes are readily available. Moreover P4 concentration in milk is few times higher than in blood and they are closely correlated [16,17]. On day 19–21 (end of the oestrus cycle) P4 level in milk of non-pregnant cow is low (around 1–2 ng/ml) whereas for pregnant cow it is high (> 7 ng/ml) and remains high throughout gestation. Milk P4 test is the earliest proven method of identification of non-pregnant cows with high sensitivity [15].

* Corresponding author. Tel.: +7 495 9393407; fax: +7 495 939 2942.
E-mail addresses: jvs@enz.chem.msu.ru, jvsamsonova@gmail.com (J.V. Samsonova), capreace@inbox.ru (V.A. Safronova), aposipov@mail.ru (A.P. Osipov).

http://dx.doi.org/10.1016/j.talanta.2014.10.043
0039-9140/© 2014 Elsevier B.V. All rights reserved.

Despite the fact that a variety of LFIA–based test systems is in use for a range of applications worldwide the practically important lateral flow immunoassay to measure the level of cows' milk P4 within the required concentration range hasn't been developed yet. Just a few attempts were taken to develop rapid LFIA for P4 [18–21]. The first paper established LFIA for a hapten where P4 was used as a model antigen was published in 1996 [18]. Finnish researchers showed that P4 can be detected with the plain LFIA test strip prepared of nitrocellulose membrane. A sample (milk) was first added and soaked into the membrane followed by the colloidal gold-labeled P4-protein conjugate. The detection limit was from 5 ng/ml (visual detection) to 2 ng/ml (photometric analysis). Later the influence of some LFIA parameters on the performance characteristics was investigated but sensitivity and variability of the method remained a problem [19]. Another LFIA system with an enzyme label was just able to detect mean differences between 5 and 50 ng/ml of P4 but due to large variability the limit of detection could not be determined [20]. A colloidal carbon was also used as a label in another modification of LFIA for P4 [21]. To increase the sensitivity of the assay high coating concentration of a P4-protein conjugate in combination with low concentration of specific antibody was used. As a result an IC_{50} equal to 0.6 μg/l P4 was achieved. However the assay was developed in buffer and did not work in whole cows' milk.

In our previous work the main approaches to a new P4 test based of lateral flow principle and utilized an enzyme as a label were established [22]. The objective of the present study was to develop quick and sensitive lateral flow enzyme immunoassay (LFEIA) for P4 determination in whole cows' milk without preliminary sample preparation.

2. Material and methods

Dextran sulfate MW 8000 (w/v) and P4 were purchased from «Sigma» (USA). Inorganic salts, acids and organic solvents were obtained from «Chimmed» (Russia). Tween 20 was from «MP Biomedicals» (France). Ready-to-use substrate solution containing TMB and H_2O_2 was supplied by "Immunoved" (Russia).

The following buffers were used: 0.01 M K-phosphate (K_2HPO_4-KH_2PO_4), 0.15 M NaCl, pH 7.4 (PBS) and 0.01 M K-phosphate (K_2HPO_4-KH_2PO_4), 0.15 M NaCl, 0.05% Tween 20, pH 7.4 (PBST).

P4 standard solutions were prepared by dilution of the stock solution (1 mg/ml in ethanol) with PBST.

Polyclonal rabbit antiserum obtained against 11α-hydroxy-progesterone hemisuccinate and the synthesis of a conjugate of 3-O-carboxymethyl oxime progesterone (3-CMO-P4) with HRP were described elsewhere [22].

The following membrane materials were used to prepare LFEIA test strips: analytical nitrocellulose membranes CNPC (15 μm), 150CNPH, CNPF (10, 8 and 5 μm) (MDI, India); absorbent pad AP045 (MDI, India) and sample pads MAPDS-0300 (Arista Biologicals, USA), FR1 (0,35; 0,6), R4, R7 and WF1 (MDI, India).

Whole cows' milk samples were kindly provided by SE «Ermolino» (Kaluga region, Russia) and stored at 4 °C.

2.1. Preparation of LFEIA test strips

Test strips (75*4 mm) were assembled according to the scheme shown in Fig. 1. Sample pad and absorbent pad were 27 mm long and overlain the analytical membrane by 2 mm. The specific antibody solution in PBS as test capture reagent was dispensed on the analytical membrane using BioJet Quanti 3000 and BioDot XYZ- 3050 dispensing platform (USA). To form a control zone, the antibodies against HRP were dispensed onto the strip at a distance of 5 mm from the test zone. The following parameters of the pump were applied: droplet size – 30 nl, step – 0.3 mm, speed – 50 mm/s. The strips were dried for 24 hours at 37 °C.

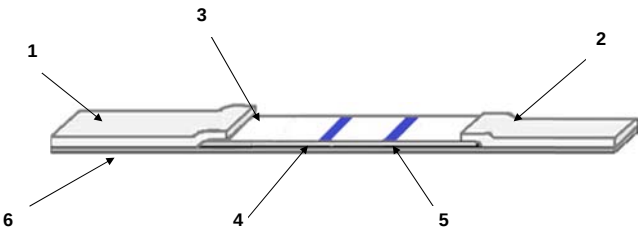


Fig. 1. Construction of LFEIA test strip. 1–sample pad; 2–absorbent pad; 3–analytical membrane; 4–test line; 5–control line; 6–plastic base.

2.2. Sample preparation

Whole milk samples were incubated for 30 min at 37 °C and vortexed before use.

2.3. ELISA procedure

"ELISA-progesterone-milk" kit (Immunoved, Russia) was used to perform P4 measurement in whole cows' milk samples. Briefly, aliquots of 10 μl P4 standard solutions/samples were added to wells of a mictotiter plate followed by 100 μl enzyme tracer (P4-HRP). After incubation and plate washing the substrate solution (100 μl) was added to each well. The color reaction was stopped after 10–15 min with 100 μl stop solution. Result of the reaction was evaluated on spectrophotometer at 450–620 nm ("Molecular Devices", USA). The values of optical densities were converted to $\%B/B_0$ values according to the formula: $B/B_0=(I/I_0) * 100\%$, where I is a value of optical density for a sample, I_0 is the value of optical density for 'zero' standard.

2.4. LFEIA procedure

A test strip was placed on a horizontal surface. The mixture of 10 μl 3-CMO-P4-HRP and 120 μl standard solution or sample was added onto the sample pad, and the solution migrated toward the absorbent pad. In 10 min the test strips were placed into tubes containing 2 ml of substrate solution supplied with 10% dextran sulfate and incubated for 5 minutes while stirring. After staining test strips were dried for 15 minutes at room temperature. Dried strips were scanned (Epson Perfection V700 Photo, Seiko-Epson, Japan) with a resolution of 600 dpi in 24-bit color (RGB). Analysis of the digital images and quantification of color intensity of test and control lines was performed using Scion Image software. Line intensity was corrected by the background subtraction and converted to $\%B/B_0$ mode as described earlier.

3. Results and discussion

In present work HRP with colorimetric detection of an analytical signal was used. As it was shown in our previous article colloidal gold label in LFIA of P4 did not provide required assay sensitivity [22]. So the approach called LFEIA (lateral flow enzyme immunoassay) consisting of the combination of the sensitivity of enzyme immunoassay with the rapidity of lateral flow assay was proposed. Enzyme-based lateral flow immunoassay with visual generation of results in test and control zones requires an additional procedure – coloring of a test strip by substrate solution. In our study to visualize the result of immunoreaction in LFEIA HRP was used in combination with the substrate solution contained

TMB and dextran sulfate. It was found earlier that dextran sulfate dramatically lowers the solubility of the TMB oxidation product which concentrated in the membrane zone where an enzyme conjugate bounded and that allows to develop highly sensitive technique for the detection of HRP [3,23]. TMB coloring can face a problem of background noise and line diffusion [6]. It was reported that after a completion of immunoreaction by vertical flow the best way to pass TMB substrate solution over the test strip in terms of uniformity of signal color and the background noise is the horizontal direction of substrate solution flow [4,6]. For this approach special substrate pads were applied to provide flow across analytical membrane. In our study P4 conjugated to HRP was mixed with a sample (standard solution) and the resulting mixture was applied onto a sample pad and migrated along the test strip (Fig. 1). To perform staining the test strip was immersed in a tube containing a HRP coloring precipitating substrate solution (TMB). This simple approach provided uniform coloring pattern and reduced diffusion of test and control lines. In this case the visual detection can be carried out in 5 minutes.

To develop accurate LFIA for P4 with HRP as a label the color intensity of the precipitating product of TMB oxidation should be proportional to the amount of the enzyme within immunocomplexes concentrated in the test line of analytical membrane, moreover the measured signal (end-point measurement) should be stable during time. Considering these conditions the dependence of the color intensity formed on the surface of analytical membrane during substrate reaction at different concentrations of HRP was studied. The experiment was conducted as follows: HRP solution was spotted on a surface of analytical membrane; after drying a piece of membrane was incubated in TMB solution for 5 minutes then the membrane was taken from substrate solution and quantification of colorimetric analytical signal was carried out by a scanner within 60 min (Fig. 2). The results have shown that the analytical signal (color intensity) remains stable for at least an hour after staining (Fig. 2A). The signal was also proportional to the concentration of HRP absorbed on the membrane in a form of saturation curve (Fig. 2B). Some reduction of signal intensity during initial 15–20 min after staining could be attributed to a membrane drying and to the fact that the background signal increased within the first 10–15 minutes (data not shown). Therefore, visual detection of LFEIA results can be performed immediately after staining and further instrumental detection – in 15 minutes after staining.

In current work direct competitive format of LFEIA was employed where specific antibodies were immobilized on a surface of analytical membrane. Sensitivity of the competitive immunoassay strongly depends on the label concentration, sensitivity of signal registration and antibodies affinity. The next step of the work was the selection of optimal membrane components and reagents concentration for sensitive competitive LFEIA. Five types of commercial analytical membranes with different pore size (15, 10, 8, 5 μm) and capability to bind proteins (CNPF – lower, CNPC – higher and CNPH – the highest protein binding) were considered. A range of lateral flow assay characteristics (assay time, sensitivity etc.) depends on the pore size of analytical membrane used. For example, while the pore size increase the sensitivity of the assay decrease, however the analysis time significantly reduces. Also the visual form of the stained line on the analytical membrane looks different. As shown in Fig. 3 for membranes with larger pore size the test line became less clear and diffused that can complicate visual detection of the results. It was also found that the membrane with a smaller pore size required 3 times less amount of P4 labeled with HRP to produce a line color of the same intensity, thus LFEIA sensitivity can be increased and background signal reduced. On the basis of the above characteristics a membrane with pore size of 8–10 μm was considered as optimal.

To develop lateral flow immunoassay in whole cows' milk a few aspects should be addressed – assay should detect P4 in the required concentration range (1–10 ng/ml) and can be applicable to such complicated matrix as undiluted whole milk. Few sample pads were checked in a combination with analytical membranes to fabricate a test strip. The LFEIA sensitivity (Fig. 4A) and the ability of whole cows' milk to migrate along a test strip were considered (Fig. 4B). As shown on Fig. 4, assay sensitivity was affected by a type of a sample pad used. For example, percent of signal inhibition at P4 concentration equal to 10 ng/ml varied from 80% to 20%. This could be attributed to different components which are used by membrane material producers for the pretreatment of sample pads and quite often are unknown. Among them are detergents, wicking agents etc. The zone of a test strip reached by the front of a whole milk sample also depended on a particular combination of membranes (Fig. 4B). Our aim was to find such combination which allows milk sample to flow up to absorbent

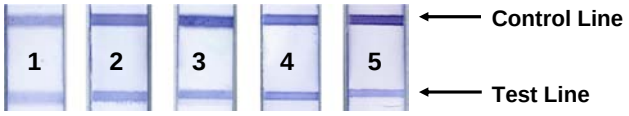


Fig. 3. Appearance of test and control lines on different type of analytical membrane in LFEIA: 1–CNPC 15 μm, 2–150CNPH, 3–CNPF 10 μm, 4–CNPF 8 μm, 5–CNPF 5 μm.

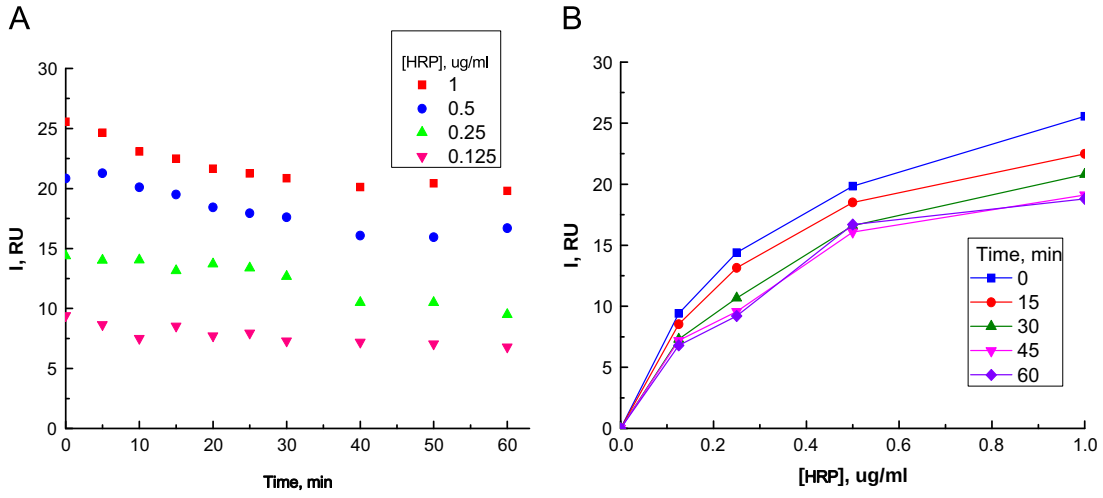


Fig. 2. (A) The dependence of the signal intensity on measuring time and (B) the enzyme concentration (HRP) on the membrane surface after 5 min staining in TMB solution. I, RU – color intensity of the zone with immobilized HRP, relative units.

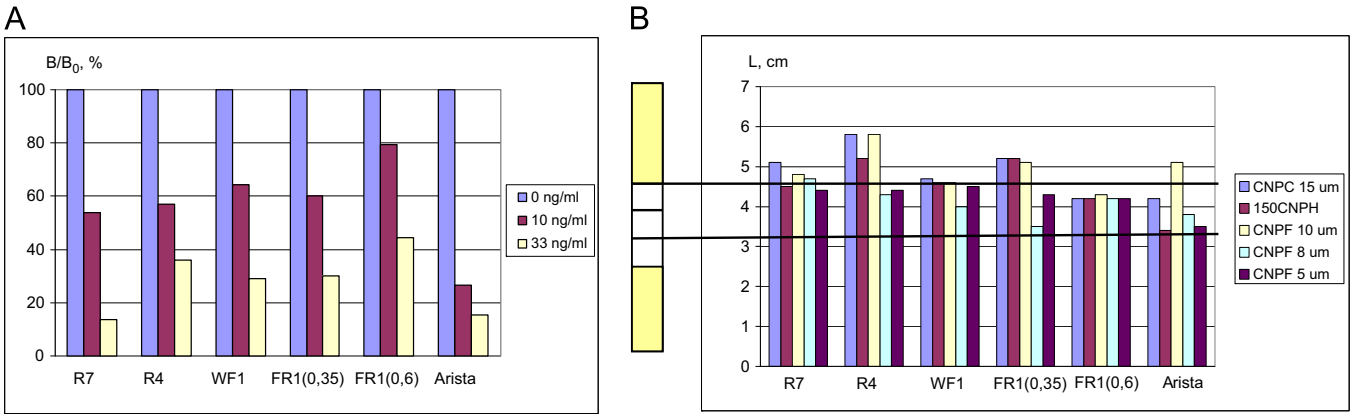


Fig. 4. (A) Analytical signal inhibition at different P4 concentrations (analytical membrane CNPF 10 μm) and (B) length of milk front migration on LFEIA strip (b) for a range of combinations of analytical membrane and sample pad (bottom row).

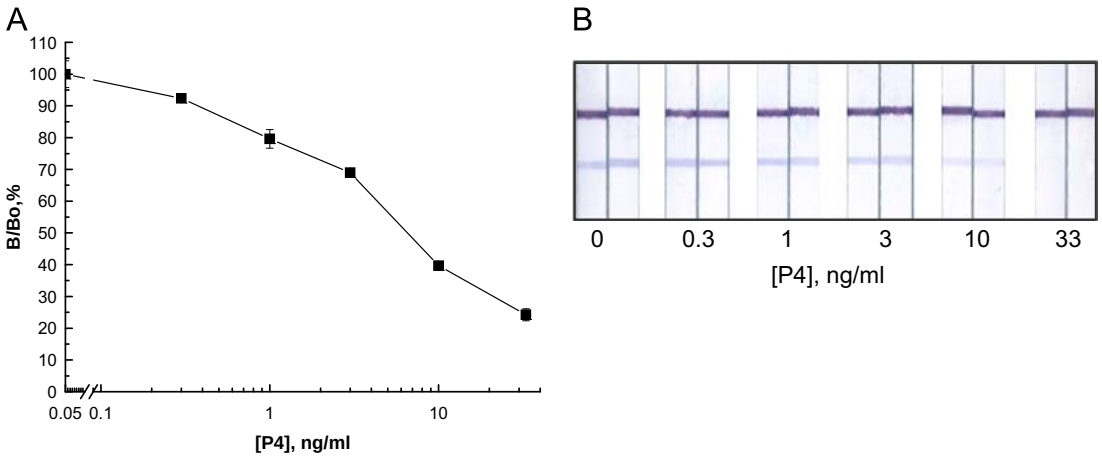


Fig. 5. LFEIA P4: calibration curve and its visualization after substrate staining.

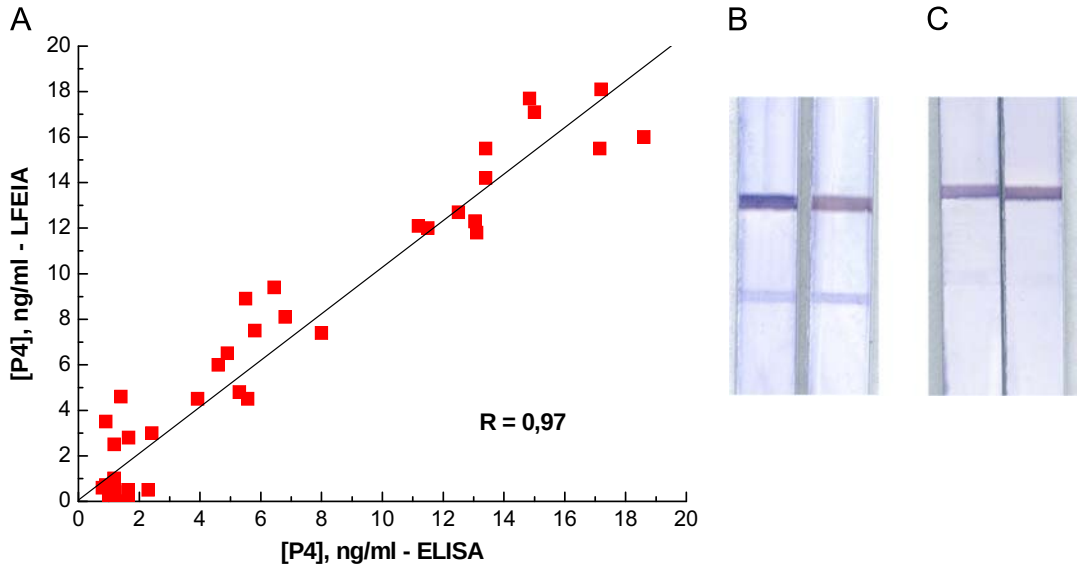


Fig. 6. (A) Correlation of the results of P4 detection in whole cows' milk obtained by ELISA and LFEIA (a) and example of signal visualization for (B) non-pregnant and (C) pregnant cow.

pad and at the same time provides necessary LFEIA sensitivity. On the base of above factors an optimal combination of the sample pad and analytical membrane was chosen for sensitive LFEIA of P4 in whole milk.

As a result of above study rapid LFEIA was designed and carried out as follows: aliquots of standard solution/sample and HRP-labeled P4 were mixed and applied onto the sample pad. When the solution was absorbed, the membrane was immersed in a test

tube with substrate solution and incubated for 5 minutes. Then the strip was taken out and visual result was registered. The instrumental detection was carried out in 15 min. An example of calibration curve and visual appearance of test and control lines are presented on Fig. 5. The detection limit of LFIA P4 was 0.8 ng/ml. Variation of results did not exceed 10%. It could be seen that concentration of P4 about 7–10 ng/ml and higher caused significant color change of a test line and its almost full disappearance.

To evaluate the applicability of this method for whole cows' milk, 46 samples from pregnant cows as well as from non-pregnant animals taken on different days of oestrus cycle were analyzed by the developed LFEIA and ELISA. The results were in good correlation ($R=0.97$) (Fig. 6). Moreover analysis of whole milk samples taken from pregnant cows caused almost complete disappearance of a test line whereas milk samples from non-pregnant cows taken at the beginning or end of oestrus cycle were identified as non-pregnant by visual and quantitative detection. Thus, this method can be used to quantify the level of P4 in whole cows' milk and can be applied for early determination of cows' non-pregnancy on a dairy farm without any special equipment. Quantitative detection of P4 with the help of an available portable device can give valuable information about status of a cow's reproductive system.

4. Conclusions

Here the applicability of LFEIA approach to P4 detection in particular concentration range in such complicated matrix as whole cows' milk was demonstrated. The pretreatment-free test can be used for rapid P4 detection while monitoring status of cows' reproductive system and for early non-pregnancy diagnosis on day 19–21 after artificial insemination. Development of rapid P4 milk test for on-farm use was a complicated task for years [14,21] and LFIA-based test was just recently commercialized. Using enzyme labels in LFIA is new and to some extent underestimated direction of research. "Enzyme immunochromatographic assay", "enzyme-based dry-reagent strip biosensor", "ELISA-on-a-chip", "enzyme-linked immuno-strip biosensor", "lateral flow immunosensor" – these are all names of the same assay principle which combines sensitivity of the enzyme immunoassay with advantages of lateral flow immunoassay (rapidity, low-cost and disposability) [4–6,9,13]. The approach can be considered as rapid ELISA performed in the form of lateral flow format or as an LFIA utilizing an enzyme label. This approach could be a potential substituent of a conventional ELISA as soon as it will be realized in rapid form with minimal manipulation required, particularly in cases when the sensitive on-site detection of a target analyte is needed. For instance, a delayed-release effect of an enzyme substrate by the asymmetric polysulfone membrane described recently by Joung et al. [12] provided one-step mode of chemiluminescent enzyme LFIA. Rapid and sensitive colorimetric, chemiluminescent or electrochemical detection of enzyme labels in visual or quantitative mode with the help of portable devices can be applied for a wide range of enzyme flow immunoassay applications in different areas.

Acknowledgments

The authors gratefully acknowledge dairy farm SE "Ermolino" (Kaluga region) for providing whole milk samples.

References

[1] G.A. Posthuma-Trumpie, J. Korf, A. van Amerongen, Anal. Bioanal. Chem. 393 (2009) 569–582. http://dx.doi.org/10.1007/s00216-008-2287-2.
[2] D.G. Bruno, Pathogens 3 (2014) 341–355. http://dx.doi.org/10.3390/pathogens3020341.
[3] C. Parolo, A. de la Escosura-Muniz, A. Merkoci, Biosens. Bioelec 40 (2013) 412–416. http://dx.doi.org/10.1016/j.bios.2012.06.049.
[4] J.H. Cho, E.H. Paek, I.H. Cho, S.H. Paek, Anal. Chem. 77 (2005) 4091–4097. http://dx.doi.org/10.1021/ac048270d.
[5] A.N. Kawde, X. Mao, H. Xu, Q. Zeng, Y. He, G. Liu, Am. J. Biomed. Sci. 2 (2010) 23–32. http://dx.doi.org/10.5099/aj100100023.
[6] C. Zhang, Y. Zhang, S. Wang, J. Agric. Food Chem. 54 (2006) 2502–2507. http://dx.doi.org/10.1021/jf0531407.
[7] R.F. Zuk, V.K. Ginsberg, T. Houts, J. Rabbie, H. Merrick, E.F. Ullman, M.M. Fischer, S.N. Sizto, D.J. Litman, Clin. Chem. 31 (1985) 1144–1150.
[8] H. Watanabe, A. Satake, M. Matsumoto, Y. Kido, A. Tsuji, K. Ito, M. Maeda, Analyst 123 (1998) 2573–2578.
[9] T. Ono, M. Kawamura, S. Arao, H. Nariuchi, J. Immunol. Methods. 272 (2003) 211–218.
[10] D. Du, J. Wang, L. Wang, D. Lu, Y. Lin, Anal. Chem. 84 (2012) 1380–1385. http://dx.doi.org/10.1021/ac202391w.
[11] I.H. Cho, E.H. Paek, Y.K. Kim, J.H. Kim, S.H. Paek, Anal. Chim. Acta. 632 (2009) 247–255. http://dx.doi.org/10.1016/j.aca.2008.11.019.
[12] H.A. Joung, Y.K. Oh, M.G. Kim, Biosens. Bioelec. 53 (2014) 330–335. http://dx.doi.org/10.1016/j.bios.2013.10.004.
[13] K. Inoue, P. Ferrante, Y. Hirano, T. Yasukawa, H. Shiku, T. Matsue, Talanta 73 (2007) 886–892. http://dx.doi.org/10.1016/j.talanta.2007.05.008.
[14] G.A. Posthuma-Trumpie, A. van Amerongen, J. Korf, W.J. van Berkel, Trend. Biotechnol 27 (2009) 652–660. http://dx.doi.org/10.1016/j.tibtech.2009.07.008.
[15] G. Purohit, Webmed Central Reproduction 1: WMC001305 (2010) http://www.webmedcentral.com/article_view/1305.
[16] J.A. Laing, R.B. Heap, Br. Vet. J. 127 (1971) 19–22.
[17] H. Dobson, S.E. Midmer, R.J. Fitzpatrick, Vet. Rec. 96 (1975) 222–223.
[18] M.P. Laitinen, M. Vuento, Acta Chem. Scand. 50 (1996) 141–145.
[19] M.P. Laitinen, M. Vuento, Biosens. Bioelec 11 (1996) 1207–1214.
[20] K. Sananikone, M.J. Delwiche, R.H. BonDurant, C.J. Munro, Trans. ASAE. 47 (2004) 1357–1365.
[21] G.A. Posthuma-Trumpie, J. Korf, A. van Amerongen, Anal. Bioanal. Chem. 392 (2008) 1215–1223. http://dx.doi.org/10.1007/s00216-008-2362-8.
[22] V.A. Safronova, J.V. Samsonova, V.G. Grigorenko, A.P. Osipov, Moscow Univ. Chem. Bull 67 (2012) 241–248. http://dx.doi.org/10.3103/S0027131412050045.
[23] J.L. McKimm-Breschkin, J. Immunol. Method. 135 (1990) 277–280.

Talanta 132 (2015) 690–697

Contents lists available at ScienceDirect

Talanta

journal homepage: www.elsevier.com/locate/talanta

Online solid-phase extraction–liquid chromatography–mass spectrometry to determine free sterols in human serum

Isabel Mendiara, Karim Bentayeb, Cristina Nerín, Celia Domeño *

Department of Analytical Chemistry, EINA-University of Zaragoza, María de Luna St. 3, E-50018 Zaragoza, Spain

ARTICLE INFO

Article history:
Received 13 August 2014
Received in revised form
8 October 2014
Accepted 14 October 2014
Available online 23 October 2014

Keywords:
Cholesterol precursor
Phytosterol
Human serum
LC–MS
Online
Solid phase extraction

ABSTRACT

An automated method for analyzing free non-cholesterol sterols in human serum using online solid phase extraction–liquid chromatography–mass spectrometry is proposed herein. The method allows the determination of three phytosterols (sitosterol, stigmasterol and campesterol) and two cholesterol precursors (desmosterol and lanosterol). The analysis of sterols in human serum is critical in the study of cholesterol-related disorders, such as inherited familial hypercholesterolemias. Special effort was made to isolate the analytes from the serum lipoproteins, their natural conveyance through the bloodstream. The sample treatment consisted of a Bligh–Dyer extraction followed by dilution of the extract. This treatment allowed the sample to be injected into the online system and ensured the correct detection of the analytes, while avoiding the matrix effects commonly related to serum samples.

The analytical performance showed linear ranges that covered two orders of magnitude, with correlation coefficients above 0.99. Limits of detection and quantification ranged from 0.2 ng/mL to 13 ng/mL and from 1.0 ng/mL to 43 ng/mL, respectively. Recovery when spiking serum with a half or a tenth of the average concentration reported in human serum ranged from 99% to 111% and from 102% to 120%, respectively. Intra-day precision and inter-day precision were below 20%.

© 2014 Elsevier B.V. All rights reserved.

1. Introduction

Sterols are metabolites related to cholesterol metabolism. The analysis of these compounds in human serum is an essential step in the diagnosis of cholesterol-related disorders, such as inherited familial hypercholesterolemias, cerebrotendinous xanthomatosis and sitosterolemia [1]. Cholesterol and related sterols are regulated in the human body *via* a complex set of mechanisms. Cholesterol can be absorbed through diet at intestinal level [2]. The rate of cholesterol consumption can be inferred from the presence of phytosterols such as sitosterol, stigmasterol and campesterol in human serum, since they undergo the same absorption and secretion processes [3]. Cholesterol is also endogenously produced and regulated in the liver. Some sterols such as desmosterol and lanosterol are intermediate products (precursors) in this reaction mechanism. Since these compounds leak into the bloodstream at a rate proportional to their formation in the cholesterol synthetic pathway, the circulating levels of these endogenous precursors reflect the rate of cholesterol synthesis [4,5].

Sterols have a non-polar structure and are carried through the circulatory system by lipoproteins. Lipoproteins are aggregates of lipids surrounded by a 2-nm amphiphilic layer composed of phospholipids, apoproteins and free cholesterol [6]. Therefore, the analysis of sterols involves the breakage of these aggregates.

The extraction of sterols has been typically performed using the Bligh–Dyer method [7,8], where a mixture of chloroform and methanol solubilizes the lipids from the lipoproteins, allowing the apoproteins to be separated. Sterols have been traditionally analyzed using gas chromatography, *via* a time-consuming derivatization step [4,9–11]. Liquid chromatography (LC) coupled to mass spectrometry (MS) avoids this derivatization step, diminishing the sample processing time [8,12]. However, the sample cleanup prior to LC–MS analysis is still strongly recommended and a solid phase extraction (SPE) step is generally performed [8,13].

An interesting choice is the use of hyphenated techniques that couple SPE to LC–MS using a switching valve, which is common in the analysis of biological samples and enables rapid and reliable sample preparation [14–17]. Several publications dealing with online systems are focused on determining drugs in plasma or urine; but scarce literature has been found related to the determination of endogenous metabolites [18,19]. A previous work of the authors aimed at the reduction of the sample processing time for determining free and bonded sterols in human serum [20,21] and another contribution demonstrated the capacity of coupling a Restricted Access Material (RAM) cartridge to LC–MS for determining bile acids

* Correspondence to: Departamento de Química Analítica, Escuela de Ingeniería y Arquitectura (Edificio Torres Quevedo). C/ María de Luna 3, Zaragoza, CP 50018, Spain. Tel.: +34 876 555 296; fax: +34 976 762388.
E-mail addresses: isabelmn@unizar.es (I. Mendiara), karimben@unizar.es (K. Bentayeb), cnerin@unizar.es (C. Nerín), cdomeno@unizar.es (C. Domeño).

http://dx.doi.org/10.1016/j.talanta.2014.10.029
0039-9140/© 2014 Elsevier B.V. All rights reserved.

in human serum [22]. To the best of our knowledge, there is not such a system to determine sterols in human serum, so the present contribution aims at the routine analysis of sterols in a faster way by using an online system.

2. Materials and methods

2.1. Chemicals and reagents

The sterols under study (Fig. 1) were provided by Sigma-Aldrich (Madrid, Spain): desmosterol (purity 85%, Chemical Abstract Service identification number: 303-04-2), campesterol (65%, 474-62-4), stigmasterol (95%, 83-48-7), lanosterol (97%, 79-63-0), sitosterol (95%, 83-46-5), and cholesterol-26,26,26,27,27,27-D6 (internal standard, IS, 97%, 60816-17-3). The solvents used were methanol (supragradient LC–MS grade, 67-56-1), 2-propanol (LC–MS grade, 67-63-0), and chloroform (HPLC grade, 67-66-3). The solvents were supplied by Sharlab (Barcelona, Spain). Water was obtained from a Milli-Q Plus 186 device from Millipore (Billerica, MS, USA).

Stock solutions of 1000 mg/L in methanol were prepared for each analyte. A stock solution of the IS at 100 mg/L was prepared in 2-propanol. A working solution with all of the sterols in methanol, at a concentration of approximately 10 mg/L, was prepared and stored in the dark at 4 °C.

2.2. Pooled serum

The pool of serum was obtained by mixing individual serum samples from 150–200 informed healthy volunteers. The pool was provided by the Lipids Unit of the Aragon Institute of Health Sciences (Zaragoza, Spain), and stored in the dark at −80 °C prior to the analysis.

2.3. Sample preparation

The sample was prepared using the following method: 300 μL of serum were extracted through a modification of the Bligh–Dyer method [23]. A volume of 1 mL of chloroform–methanol (1:2, v/v) was mixed with 30 μL of the IS solution and then added to the serum. The mixture was then centrifuged at 9000 rpm (7500*g*) for 10 min in a Microfuge® 18 Centrifuge, Beckman Coulter™ (Brea, CA, USA). The lower organic phase was recovered using a glass Pasteur pipet and transferred to a 2-mL vial. The extract was then accurately weighed, and 1 mL of methanol was added. The resulting extract was filtered using a 0.22-μm Nylon syringe filter. After this sample treatment, the final serum sample extract was ready to be injected into the online system described below.

2.4. Online system setup

Fig. 2 illustrates the online system. The mobile phases were delivered using three pumps; a 600E Controler Multisolvent Delivery System (pump 1) with a 717 plus Autosampler (Waters, Milford, MS, USA), a Kontron 322 System auxiliary binary pump (Kontron Instruments, Neufahrn, Germany) (pump 2) and an Alliance® 2795 Separations Module (Waters) (pump 3). The fluidic paths were controlled using a Cheminert C72 × 1690ED 10-port valve controlled by microelectric actuators, purchased from VICI® Valco Instruments (Houston, TX, USA). The analytes were detected using a Quattro micro™ API Mass Spectrometer (Waters). All these instruments were connected to operate simultaneously. This is explained in detail in the Supplementary information section S1.

Table 1 shows the steps of the online method, flow rate and composition of pumps 1 and 3, as well as the valve position program. The online method comprises four steps: loading, washing, eluting and detection.

2.4.1. Loading

For loading, 300 μL of the treated serum were injected using the 717 plus Autosampler and transferred to a 20 × 4 mm BioTrap 500C18 cartridge, supplied by ChromTech Ltd. (Cheshire, UK) at a 2.0 mL/min flow of 60% methanol and 40% water. A 2-μm filter was included before the cartridge to prevent clogging. This step lasted 4 min.

2.4.2. Washing

The washing step consisted of a 2.0 mL/min flow of water. The elution of large, non-retained molecules was monitored at 220 nm using a 2487 dual λ absorbance detector (Waters). Their elimination was considered to be complete when the UV signal had fallen below 0.05 absorbance units. Then, the valve was automatically switched to the eluting position.

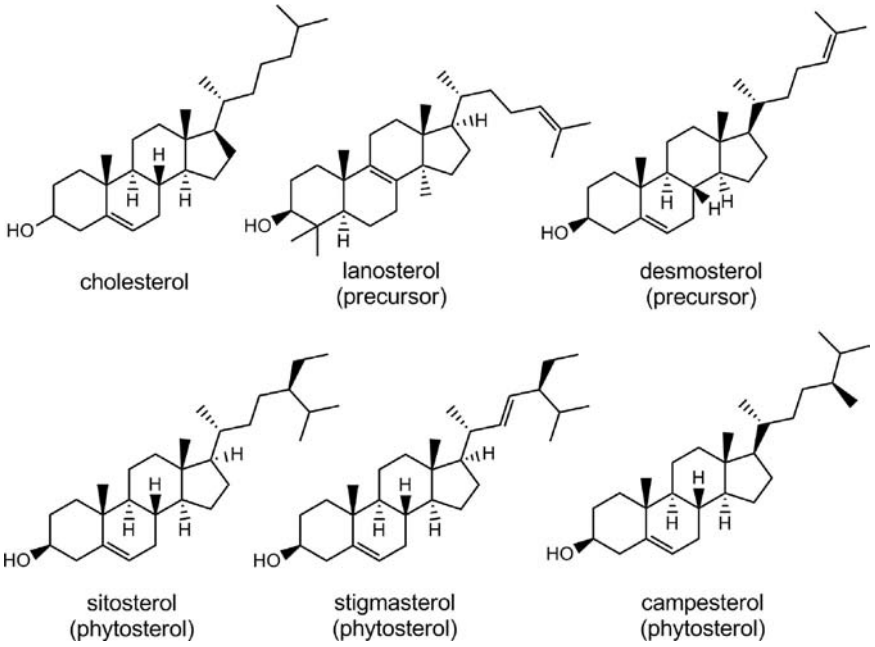


Fig. 1. Chemical structures of the sterols under study and cholesterol.

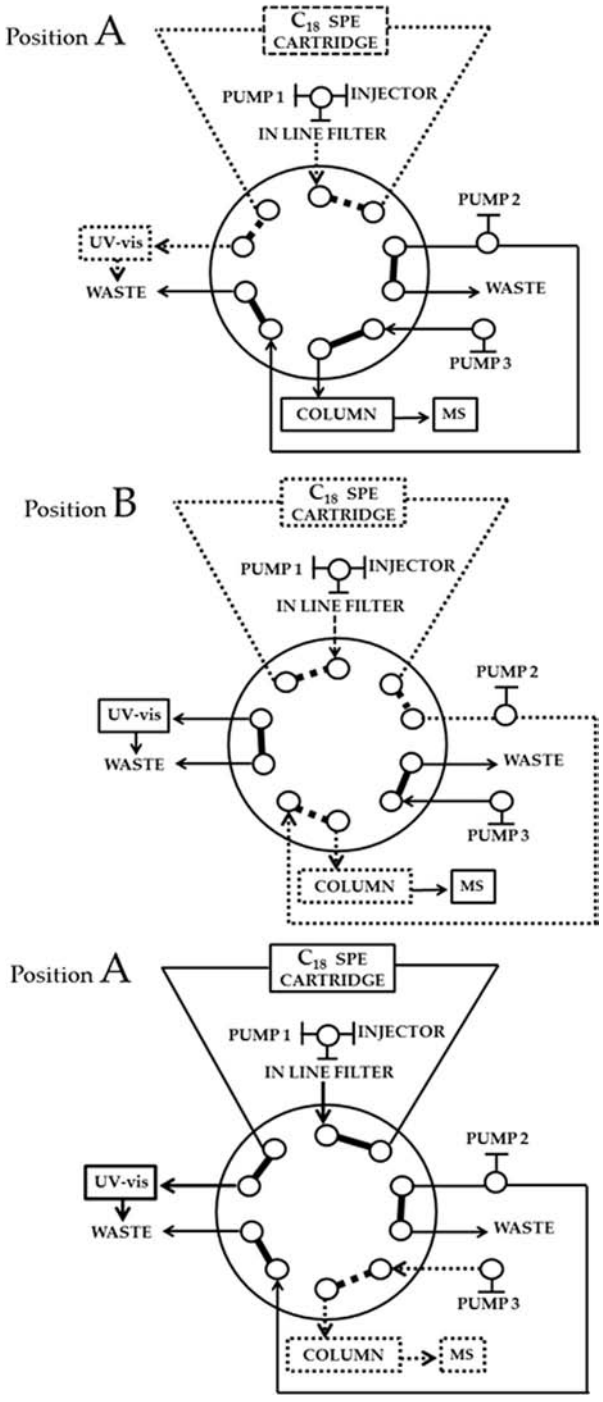


Fig. 2. SPE–LC–MS flowchart scheme. (A) Loading and detection steps. (B) Eluting step.

2.4.3. Elution

From min 9 to 35, the retained compounds were backflushed from the cartridge using 2-propanol at a flow rate of 0.4 mL/min. Before entering the analytical column, a water cross-flow of 0.6 mL/min was added (pump 2), leading to a total flow of 1 mL/min of 60% water and 40% 2-propanol. This flow composition ensured that the sterols were retained at the head of the analytical column.

2.4.4. Detection

The analytes were separated using an XTerra® MS C18 column (4.6 × 100 mm and 3.5 μm particle size, Waters). A guard column of the same stationary phase material and 5 μm particle size was used to protect the analytical column. The column temperature was set at 60 °C. The analytical gradient started at 35 min, using an 85% methanol and 15% water, at a flow rate of 0.7 mL/min. Then, the gradient was increased in 9 min to 100% methanol, where it was held for 5 min. The last compound (sitosterol) was eluted after 13.8 min of chromatography.

The compounds of interest were determined using atmospheric pressure chemical ionization (APCI) detecting in positive mode. The detection parameters were as follows: corona current, 10 μA; source temperature, 130 °C; desolvation temperature, 600 °C and desolvation nitrogen flow, 600 L/h. The optimized cone voltage was +20 V for all the compounds. The chromatograms were registered in selected ion monitoring (SIM) mode. The protonated molecules (m/z) of the target analytes are listed in Table 2. MassLynx v4.1 software from Waters was used to acquire and process the generated data.

Complementary information dealing with the steps of the online system can be found in the Supplementary information, section S2.

2.5. Evaluation of the method performance

The following analytical parameters were studied: calibration curve, limits of detection (LODs) and quantification (LOQs), linear dynamic range, recovery and reproducibility. The linear dynamic range was determined from the response of nine standard solutions spiked with the IS (30 μL of a 100 mg/L 2-propanol solution). The calibration curve was prepared in a 1:2 (v/v) chloroform: methanol solution, coinciding with the composition of the resulting mixture after the sample treatment. These solutions were injected into the system in triplicate. The LOD and LOQ were calculated as three and ten times the standard deviation of the area of the peaks detected, respectively, when processing blank samples (chloroform–methanol, 1:2 v/v). The determination of the intra-day precision ($n=5$), the inter-day precision ($n=3$) and the recovery was carried out by analyzing serum spiked at two concentration levels: half and a tenth of the average concentration of sterols according to the Human Metabolome Database [24].

Matrix effects were investigated by a post-extraction addition experiment, as explained by Trufelli et al. [25]. Four sets of samples were analyzed: a standard solution with a known concentration of the analytes (set A), serum samples spiked with the same amount of analytes after the sample treatment (set B), serum samples spiked with the same amount of analytes before the sample treatment (set C) and serum samples non-spiked (set D) to subtract the endogenous concentration levels. The response of the analytes was used in the following equations to quantify the matrix effects (Eq. (1)), the extraction recovery (Eq. (2)) and the process efficiency (Eq. (3)).

$$\text{Matrix effects}(\%) = \frac{100 \times (B-D)}{A} \quad (1)$$

$$\text{Extraction recovery}(\%) = \frac{100 \times (C-D)}{(B-D)} \quad (2)$$

$$\text{Process efficiency}(\%) = \frac{100 \times (C-D)}{A} \quad (3)$$

3. Results and discussion

3.1. Sample treatment

The Bligh–Dyer method [26] is commonly used with human serum samples to extract the lipids and remove the protein fraction due to sterols are carried through the bloodstream by lipoproteins [7,8]. For this reason, protein precipitation approach,

Table 1
SPE and LC mobile phase flow rates, composition and 10-port switching valve position program. The shaded cells correspond to flows that do not carry analytes; but condition the path for the following injection.

Step	Time (min)	Valve position	Flow through the SPE cartridge (Pump 1)				Flow through the analytical column (Pump 3)		
			Flow rate (mL/min)	Methanol water (60/40) (%)	Water (%)	2-Propanol (%)	Flow rate (mL/min)	Methanol (%)	Water (%)
Loading	0	A	2.0	100	0	0	0.3	0	0[a]
Washing	4		2.0	0	100	0	0.3	100	0
Eluting	9	B	0.4	0	0	100	1.0	0	100
Detection[b]	0	A	0.4	0	0	100	0.7	85	15
	9		0.4	100	0	0	0.7	100	0
	14		0.4	100	0	0	0.7	100	0

[a] From min 0 to 4, the composition was 100% 2-propanol (see section S2).
[b] Time of the chromatographic separation.

Table 2
Detection parameters, linear dynamic range and limits of detection and quantification of the analysis of sterols by the proposed online SPE–LC–MS method.

Sterol	CAS number[a]	Retention time (min)	*m/z*	Linear dynamic range (μg/mL)	Correlation coefficient	LOD (ng/mL)	LOQ (ng/mL)	Concentration in pooled serum (μg/mL)
Desmosterol	303-04-2	11.2	367.5	0.017–2.70	0.991	5.0	17	0.83 ± 0.23
Lanosterol	79-63-0	12.9	409.5	0.001–0.527	0.999	0.2	1.0	0.17 ± 0.04
Stigmasterol	83-48-7	13.0	395.5	0.025–5.22	0.994	7.5	25	1.35 ± 0.42
Campesterol	474-62-4	13.1	383.5	0.025–9.27	0.990	7.5	25	1.49 ± 0.26
Sitosterol	83-46-5	13.8	397.5	0.043–7.03	0.999	13	43	1.28 ± 0.07

[a] Chemical Abstract Service identification number.

results in the undesirable precipitation of the lipoproteins and the subsequent loss of the analytes (Fig. S3). Thus, a lipid extraction step is essential to determine sterols even when using an online system.

The composition of the final organic phase is mainly chloroform, which is not miscible with water and is not suitable for direct injection in reversed-phase liquid chromatography. Thus, the extract needs to be dried and reconstituted in a compatible solvent [8]. The aim of the sample treatment was to obtain a final extract suitable to be directly injected into the system. Herein, we took advantage of the miscibility properties of the water–methanol–chloroform tertiary system (as the Bligh–Dyer method does). First, the composition of the initial mobile phase in the online system was adjusted by increasing the proportion of methanol to the maximum that still allows the analytes to be retained in the C18 SPE cartridge, which is 60% methanol and 40% water. Next, the extract was diluted using methanol in such a way that the mixture with the initial composition of the mobile phase gives a single liquid phase. Fig. S4 shows the composition of the extract along the sample treatment in a ternary diagram for methanol–water–chloroform mixtures.

3.2. Online system setup

3.2.1. Loading and washing steps

In the loading step, the analytes were injected and taken to a C18 SPE cartridge. The strong non-polar properties of sterols permitted the use of C18 cartridges to concentrate them, while other less non-polar compounds (even lipids) were eluted to waste.

The solvent used in the washing step was water. This solvent showed satisfactory results removing interferences in a previous work [20].

3.2.2. Elution step and water cross-flow

Preliminary tests showed that 2-propanol was a powerful solvent for recovering the sterols from a C18 SPE cartridge. The elution profile was determined by collecting 0.4-mL fractions from the SPE cartridge in backflush mode every minute for 40 min. The fractions were later analyzed by direct flow-MS (*i.e.* without using the analytical column) in full-scan mode from 340 to 400 Da. In this way, each fraction appeared as a single peak (Fig. S5). As can be seen, 10 mL (25 fractions × 0.4 mL/fraction) of 2-propanol quantitatively recovered the analytes from the cartridge. Thus, the eluting stage lasted from 9 min to 35 min.

Because the cartridge and the analytical column were C18, the designed system did not have truly orthogonal features. This means that the eluting strength of 2-propanol would prevent the retention of the analytes in the head of the analytical column, compromising the chromatographic step. This problem was overcome by adding water to the 2-propanol eluent after the cartridge. To find out the necessary amount of water required to reduce the eluotropic strength of the flow, the following experiment was carried out. A standard solution of 1 μg/mL of sterols was prepared in 2-propanol. Increasing volumes of water were added to 1 mL of the standard solution and the resulting solutions were manually injected into the LC–MS, using an auxiliary sample loop and the MS divert valve. Fig. 3 shows how the added water reduced the eluotropic strength of the solution, enabling the chromatographic process. From these results, it was concluded that the flow composition entering the column should contain at least 60% (v/v) water.

A flow of 40% 2-propanol and 60% water (v/v) produced high backpressure in the analytical column. Hence, the total flow rate entering the column was cut back to 1.0 mL/min (working backpressure of 200 bar), 0.4 mL/min of 2-propanol were used to backflush the analytes from the cartridge and 0.6 mL/min water cross flow was added to reduce the eluotropic strength of the eluent.

3.3. Detection step

Sterols were detected in SIM mode as $[M+H-H_2O]^+$, which corresponds to the loss of the hydroxy group as a molecule of water (Table 2). This is commonly observed in the chemical ionization of alcohols [27]. Sterols crashed into several daughter

ions when the Multiple Reaction Monitoring (MRM) detection mode was selected (even when using soft collision voltages). The signal/noise values obtained in SIR mode were much higher than those of the MRM mode. In this case, the selectivity provided by the MRM mode was not enough to make up for the loss of sensitivity.

3.4. Cross contamination

The Bligh–Dyer extraction method is intended for removing proteins and simultaneously extracting lipids from blood and other tissues, so it is not sterol-selective. During the development of the method, cross-contamination was detected (blank injections with ghost peaks). Phospholipids and triacylglycerols usually build up in analytical or guard columns, especially when using aqueous mobile phases [28]. This problem was solved by extending the chromatographic gradient for 5 min after the elution of the last compound. Fig. S6 shows the improvement when a column cleaning step with 2-propanol was included. This is consistent with Ismaiel et al., who found that 35% of 2-propanol in the mobile phase was essential to elute lipids from the C18 guard column [28].

3.5. Evaluation of the method performance

One of the major drawbacks in biological analysis is the presence of matrix effects, which affect the recoveries, quantitative performance and the efficiency of the analytical process [15,25,29]. Hence, verifying the absence of matrix effects is advisable. In accordance with Trufelli et al. [25], post-extraction addition experiments were performed to evaluate matrix effects, extraction recovery and process efficiency.

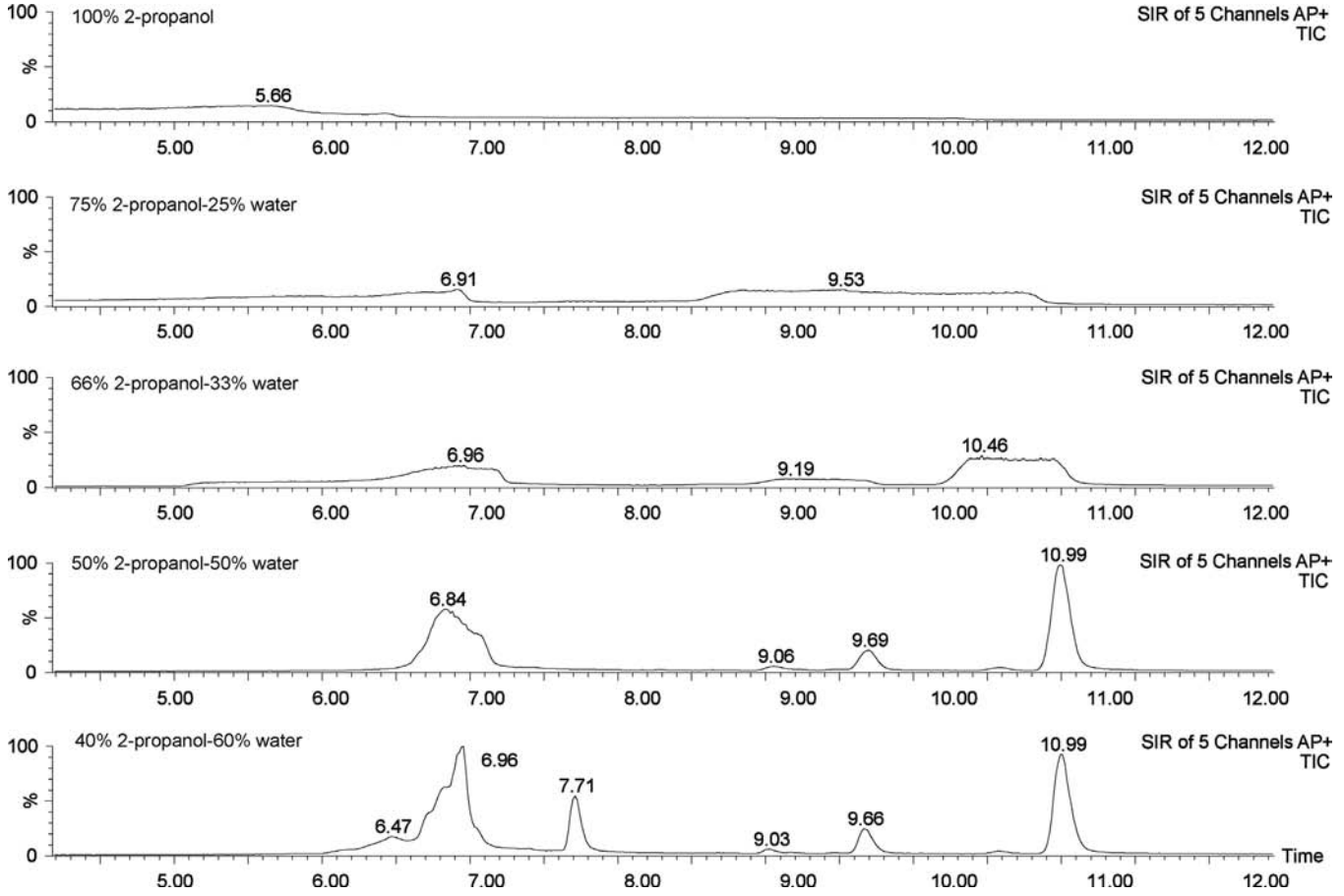


Fig. 3. Study of the eluotropic strength of the flow to be transferred to the LC analytical column. Increasing the ratio 2-propanol/water led to a weaker initial mobile phase. The chromatographic process was possible with at least 1.5 times more of water than 2-propanol.

Table 3
Recovery, intra- and inter-day precision of the analysis of sterols by the proposed online SPE–LC–MS method.

Sterol	Spiked concentration (ng/mL)	Calculated concentration (mean ± std deviation, ng/mL)	Recovery (%)	Intra-day precision (RSD %, $n=5$)	Inter-day precision (RSD %, $n=3$)
Desmosterol	205	210 ± 12	102	6	12
	42	47 ± 5	112	10	18
Lanosterol	38	42 ± 6	111	10	16
	10	12 ± 3	120	15	20
Stigmasterol	398	403 ± 12	101	7	10
	76	80 ± 9	105	11	14
Campesterol	736	730 ± 7	99	5	13
	154	157 ± 9	102	12	19
Sitosterol	440	448 ± 10	102	4	15
	87	92 ± 6	106	11	17

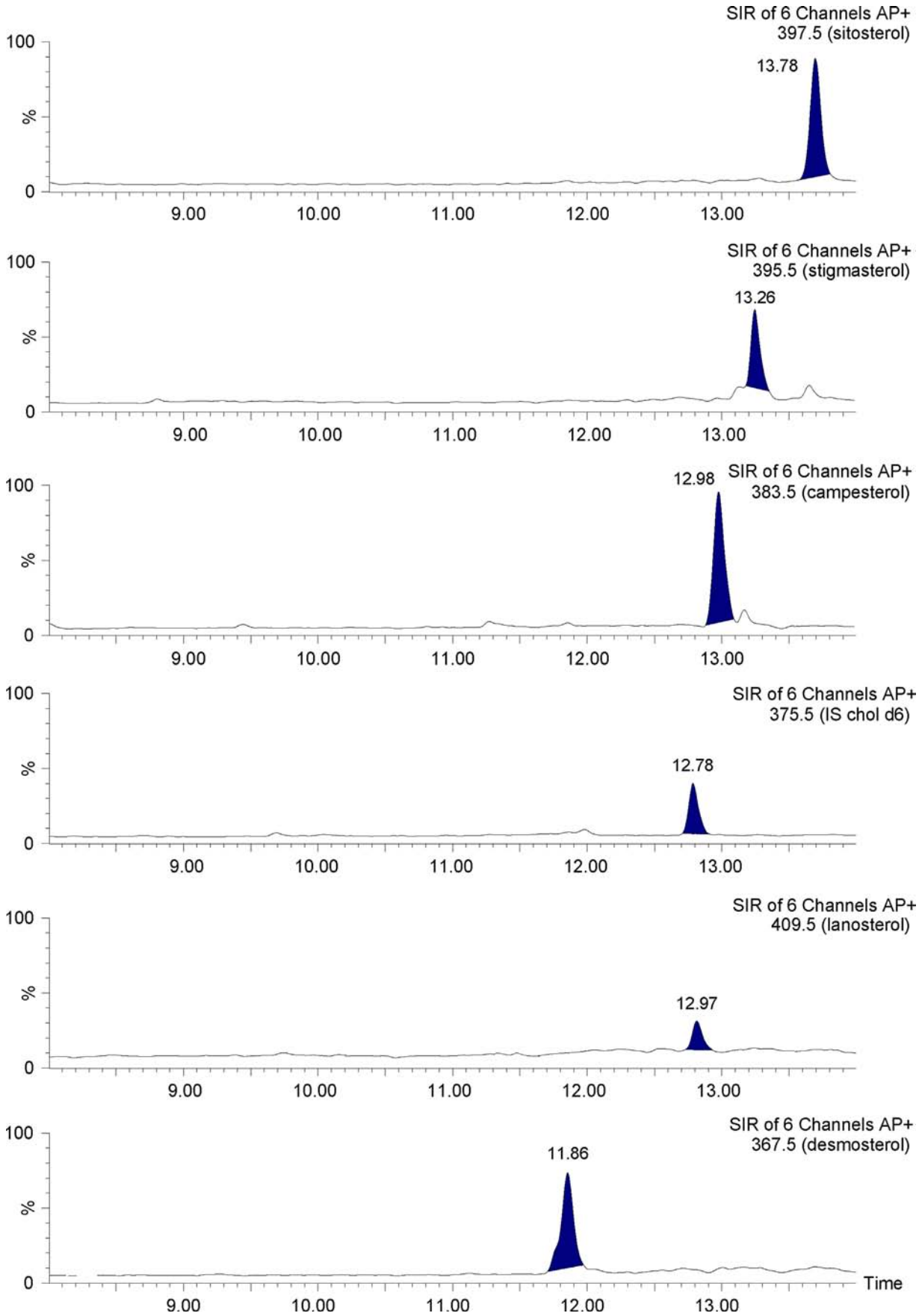


Fig. 4. Chromatograms of the studied sterols obtained after processing pooled serum.

Matrix effects ranged from 89% (stigmasterol) to 106% (lanosterol). This means that the signals observed were slightly affected by other compounds coming from the sample. Thus, there were almost no losses during the sample treatment. Finally, the process efficiency was also determined. The values obtained ranged from 90% (stigmasterol and campesterol) to 99% (desmosterol or lanosterol). These results showed that matrix effects do not hinder the determination of sterols *via* the proposed method. Since the response of the spiked samples was similar to the response of the sterol standard solution, an external calibration could be performed without applying a matrix matched calibration or standard additions.

3.6. Analytical features

The following analytical parameters were determined: linear dynamic range, LODs and LOQs, recovery, intra-day precision and inter-day precision. The results related to the linear dynamic range, limits of detection and quantification are listed in Table 2. Calibration was performed by plotting the ratio of the signal of the analyte and the deuterated IS versus the ratio of \the concentrations. The calibration curves were linear to two orders of magnitude with correlation coefficients that ranged from 0.990 (campesterol) to 0.999 (sitosterol or lanosterol). The LOD ranged from 0.2 ng/mL (lanosterol) to 13 ng/mL (sitosterol), and the LOQ ranged from 1.0 ng/mL (lanosterol) to 43 ng/mL (sitosterol). All of them were low enough to analyze the sterols in human serum.

Recovery and reproducibility (intra-day precision and inter-day precision) were evaluated by spiking the serum samples with standard solutions as it is described in Section 2.5. The results are summarized in Table 3. Recovery of the analytes at two levels of concentration was consistent and reproducible. The values obtained ranged from 99% to 111% when spiking with half of the average concentration in serum, and ranged from 102% to 120% when spiking with one tenth of the average concentration in serum. The results of intra-day precision ($n=5$) and inter-day precision ($n=3$) range from 4 to 20%. These results showed that the method meets the standards required for the study of hypercholesterolemia diseases.

3.7. Analysis of pooled serum

The chromatograms of the analytes in pooled serum are showed in Fig. 4. The concentration of sterols in the pool of serum was also determined (Table 2). It can be seen that the concentrations obtained were in agreement with the values found in literature [2,7]. As said before, serum levels of cholesterol precursors are related to liver cholesterol synthesis and they were found in much less concentration than cholesterol in human serum. The concentration of desmosterol and lanosterol resulted in 0.83 ± 0.23 μg/mL and 0.17 ± 0.04 μg/mL (Table 2), similar to the concentration values reported by McDonald et al. (0.71 μg/mL and 0.20 μg/mL, respectively) [7]. The content of phytosterols is typically higher than the content of cholesterol precursors, and it is more sample-dependant. The concentration of stigmasterol (1.35 ± 0.42 μg/mL), campesterol (1.49 ± 0.26 μg/mL) and sitosterol (1.28 ± 0.07 μg/mL) (Table 2) fall within the ranges reported in the Human Metabolome Database [24]. Due to the association between non-cholesterol sterols with cholesterol absorption, synthesis and metabolism, the determination of these compounds is a useful tool to explore their behavior in the human body.

4. Conclusions

An online SPE–LC–MS system to determine non-cholesterol sterols in human serum has been developed and described herein. The method allows the determination of two cholesterol precursors, desmosterol and lanosterol, and three phytosterols, stigmasterol, campesterol and sitosterol.

This protocol substantially reduces the sample treatment, avoiding the time-consuming evaporation and reconstitution steps. The lipoproteins were extracted using the well-established Bligh–Dyer method, and the losses associated to a protein precipitation step with methanol or acetonitrile were eluded. This was achieved thanks to the careful selection of both the final extract and the initial mobile phase solvent compositions.

Two LC instruments have been coupled to operate simultaneously by using event analog signals. As a consequence, no additional tasks have to be executed by the analyst to run the online system. The use of the C18 cartridge combined with C18 LC was not a problem thanks to a water cross-flow added between both stationary phases. This can be performed by using a 10-port switching valve instead of an ordinary 6-port valve. Matrix effects were thoroughly studied and reduced to an extent that external standard calibration could be used.

All this work led to a sample treatment time reduction of 75%; that is to say, using this protocol, 25 samples can be handled in only 2 h. In previous works, the authors needed a working day (8 h) to handle these samples, using the alternative Bligh–Dyer, evaporation, reconstitution and SPE clean-up protocol based on the work of McDonald et al. [8].

The significant reduction in the analysis time would help in the research of cholesterol related diseases, which demands the processing of high number of samples to infer reliable conclusions.

Acknowledgements

We gratefully acknowledge the Regional Government of Aragon and the European Social Fund for financing this work through funds awarded for the project PI037/09 and also the Regional Government of Aragon and the European Social Fund for the founds given to GUIA Group T-10. K. Bentayeb gratefully acknowledges the Cuenca Villoro Patronato for personal funding. We are also grateful to the Lipids Unit from the Aragon Institute of Health Sciences for providing the pooled serum.

The authors have declared no conflict of interest.

Appendix A. Supporting information

Supplementary data associated with this article can be found in the online version at http://dx.doi.org/10.1016/j.talanta.2014.10.029.

References

[1] A. Kuksis, J. Chromatogr. A 935 (2001) 203–236.
[2] A. Honda, K. Yamashita, H. Miyazaki, M. Shirai, T. Ikegami, G.R. Xu, M. Numazawa, T. Hara, Y. Matsuzaki, J. Lipid Res. 49 (2008) 2063–2073.
[3] K.M. Phillips, D.M. Ruggio, J.A. Bailey, J. Chromatogr. B 732 (1999) 17–29.
[4] H. Gylling, H. Vanhanen, T.A. Miettinen, J. Lipid Res. 34 (1993) 59–67.
[5] T.A. Miettinen, H. Gylling, Eur. J. Clin. Invest. 33 (2003) 976–982.
[6] R.N. Redinger, J. Lab. Clin. Med. 142 (2003) 7–20.
[7] J.G. McDonald, D.D. Smith, A.R. Stiles, D.W. Russell, J. Lipid Res. 53 (2012) 1399–1409.
[8] McDonald, Methods Enzymol. 432 (2007) 145–170.
[9] C. Domeno, B. Ruiz, C. Nerin, Anal. Bioanal. Chem. 381 (2005) 1576–1583.
[10] R.G. Dyer, C.S. Hetherington, K. Alberti, M.F. Laker, J. Chromatogr. B 663 (1995) 1–7.
[11] S. Keller, G. Jahreis, J. Chromatogr. B 813 (2004) 199–207.
[12] C. Schummer, O. Delhomme, B.M.R. Appenzeller, R. Wennig, M. Millet, Talanta 77 (2009) 1473–1482.
[13] N. Kornel, A. Jakab, P. Ferenc, D. Bongiorno, L. Ceraulo, M.R. Averna, D. Noto, V. Karoly, Rapid Commun. Mass Spectrom. 20 (2006) 2433–2440.
[14] C. Moser, D. Zoderer, G. Luef, M. Rauchenzauner, L. Wildt, A. Griesmacher, C. Seger, Anal. Bioanal. Chem. 403 (2012) 961–972.
[15] K. Georgi, K.S. Boos, Chromatographia 63 (2006) 523–531.
[16] Z. Kuklenyik, A.M. Calafat, J.R. Barr, J.L. Pirkle, J. Sep. Sci. 34 (2011) 3606–3618.

[17] K.S. Boos, C.T. Fleischer, Fresenius J. Anal. Chem. 371 (2001) 16–20.
[18] A. Navarrete, M.P. Martinez-Alcazar, I. Duran, E. Calvo, B. Valenzuela, C. Barbas, A. Garcia, J. Chromatogr. B 921 (2013) 35–42.
[19] H. Kataoka, K. Saito, Bioanalysis 4 (2012) 809–832.
[20] I. Mendiara, C. Domeno, C. Nerin, J. Sep. Sci. 35 (2012) 3308–3316.
[21] L. Baila-Rueda, A. Cenarro, M. Cofan, I. Orera, S. Barcelo-Batllori, M. Pocovi, E. Ros, F. Civeira, C. Nerin, C. Domeno, Anal. Methods 5 (2013) 2249–2257.
[22] K. Bentayeb, R. Batlle, C. Sánchez, C. Nerín, C. Domeño, J. Chromatogr. B 869 (2008) 1–8.
[23] E.G. Bligh, W.J. Dyer, Can. J. Physiol. Pharmacol. 37 (1959) 911–917.
[24] D.S. Wishart, T. Jewison, A.C. Guo, M. Wilson, C. Knox, Y.F. Liu, Y. Djoumbou, R. Mandal, F. Aziat, E. Dong, S. Bouatra, I. Sinelnikov, D. Arndt, J.G. Xia, P. Liu, F. Yallou, T. Bjorndahl, R. Perez-Pineiro, R. Eisner, F. Allen, V. Neveu, R. Greiner, A. Scalbert, Nucleic Acids Res. 41 (2013) D801–D807.
[25] H. Trufelli, P. Palma, G. Famiglini, A. Cappiello, Mass Spectrom. Rev. 30 (2011) 491–509.
[26] E.G. Bligh, W.J. Dyer, Can. J. Biochem. Physiol. 37 (1959) 911–917.
[27] F.W. McLafferty, F. Turecek, Interpretation of Mass Spectra, fourth ed., Sausalito, California, 1993.
[28] O.A. Ismaiel, T. Zhang, R.G. Jenkins, H.T. Karnes, J. Chromatogr. B 878 (2010) 3303–3316.
[29] H.P. Nguyen, L. Li, I.S. Nethrapalli, N. Guo, C.D. Toran-Allerand, D.E. Harrison, C.M. Astle, K.A. Schug, J. Sep. Sci. 34 (2011) 1781–1787.

Talanta 132 (2015) 698–704

Contents lists available at ScienceDirect

Talanta

journal homepage: www.elsevier.com/locate/talanta

Homogeneous immunoassays by using photon burst counting technique of single gold nanoparticles

Tao Lan, Jinjie Wang, Chaoqing Dong, Xiangyi Huang *, Jicun Ren *

School of Chemistry & Chemical Engineering, State Key Laboratory of Metal Matrix Composites, Shanghai Jiao Tong University, 800 Dongchuan Road, Shanghai 200240, PR China

ARTICLE INFO

Article history:
Received 27 July 2014
Received in revised form
26 September 2014
Accepted 2 October 2014
Available online 23 October 2014

Keywords:
Gold nanoparticles (GNPs)
Photon burst counting
Homogeneous sandwich immunoassay
Prostate specific antigen (PSA)

ABSTRACT

In this paper, we reported a sensitive single particle method by combining the photon burst counting technique with gold nanoparticles (GNPs) as labeling probes. The photon bursting of single GNPs will be generated in a highly focused laser beam (less than 1 fL) due to the plasmon resonance scattering and Brownian motion of GNPs. We observed an excellent linear relationship between the photon burst counts and the number of particles in GNPs solution. We investigated the statistical behaviors of background noise and photon burst signal of GNPs, and proposed the data processing method based on Gaussian distribution of the background noise. A new homogeneous sandwich immunoassay was developed by using this single particle method. We evaluated the performance of this method by using prostate-specific antigen (PSA) as a model. The linear range of PSA was 1–1000 pmol/L and the detection limit was 0.8 pmol/L. This novel method was successfully used for the direct detection of cancer biomarker PSA in human serum samples. Our results were in good agreement with conventional ELISA assays.

© 2014 Elsevier B.V. All rights reserved.

1. Introduction

The principle of immunoassay is on the basis of the specific reaction of antibody and antigen, and this analytical method is widely used in the fields of medical diagnostics, drug discovery, environmental monitoring, and food safety [1–3]. In current immunoassay, heterogeneous format such as ELISA is widely applied since this format usually has high sensitivity, wide dynamic ranges, and good specificity [4]. However, heterogeneous format relies on physical separation of binding and unbinding species before quantification, which results in nonuniform antibody-binding properties, reduced antibody activity, and makes this assay format laborious and time-consuming [5–7]. By contrast, the single-step and washing-free homogeneous format has attracted considerable interest [8–11]. The key issue in homogeneous immunoassay is how to quantitatively and sensitively distinguish antibodies (or antigens) and antibody–antigen complexes in the reaction solution [12,13]. Various strategies have been reported for this purpose based on different signal-transducer principles, such as colorimetric [14,15], fluorescence [16,17], electrochemistry [18], and chemiluminescence [19]. However, these detection methods still provide unsatisfactory sensitivity, therefore, to develop a sensitive and selective detection technique becomes critical in homogeneous immunoassay.

Single molecule methods provide alternative detection techniques for heterogeneous and homogeneous immunoassays. With the great progress on photoelectric conversion technology, it has been no longer a problem for single molecule detection by using the photon burst method [20,21]. Hirschfeld's group [22] for the first time reported the detection of the photon burst from a single molecule in solution. In their work, a single protein molecule was labeled with 80–100 fluorescent dyes, and the single molecule photon burst phenomenon was observed in solution. Dovichi's group [23–28] did some prospective studies on the photon counting technique, and they used the sheath flow cuvette to form the basis of a detector with a photomultiplier tube for counting the scattering photoelectrons bursts of individual particles eluted from a capillary. These methods provided good sensitivity for single particle detection. Recently, Zhang and co-workers [29,30] did some great works on single molecule detection by photon burst counting technique. They significantly improved the sensitivity and selectivity of the detection method using fluorescent quantum dots as probes and two-color labeling technique. This method has been successfully used in the detection of DNA [31], Micro-RNA [32], protein [33], virus and so on.

Compared to fluorescent dyes and semiconductor quantum dots, GNPs show unique chemical and optical properties such as

* Corresponding author at: School of Chemistry & Chemical Engineering, Shanghai Jiao Tong University, 800 Dongchuan Road, Shanghai 200240, PR China. Tel.: +86 21 54746001; fax: +86 21 54741297.
E-mail address: jicunren@sjtu.edu.cn (J. Ren).

http://dx.doi.org/10.1016/j.talanta.2014.10.004
0039-9140/© 2014 Elsevier B.V. All rights reserved.

strong light absorption and scattering effect, high photothermal conversion rate, excellent photostability, noncytotoxicity and excellent biocompatibility. Up to now, GNPs are widely applied in certain biological fields, such as DNA hybridization detection, immunoassay, bioimaging, single particle tracking, drug delivery, and cancer diagnostics and therapy. Zhang [34–36] proposed a novel single nanoparticle method by the mass spectrometer, and they used the method to detect special sequence DNA and biomarkers targets in one-step homogeneous hybridization solutions. Yan [37–40] developed a single nanoparticle detection method by using a sensitive flow cytometer. The method can quantitatively detect nanoparticles, biomolecules or cells of different sizes by counting the fluorescence or scattering photon bursts of the analytes.

In resonance light scattering correlation spectroscopy (RLSCS), which is similar to fluorescence correlation spectroscopy (FCS), we observed the strong photon bursting phenomenon of single gold nanoparticles due to plasmon resonance scattering and Brownian motion of single GNPs in a highly focused detection volume. In this paper, we described a novel single particle method by using photon burst counting technique of plasmon resonance scattering. The photon burst counts and the number of particles in GNPs solution showed a good linear relationship. We investigated the statistical behaviors of noise and photon burst signal of GNPs and observed that the background noise of photon burst shows Gaussian distribution. Based on the behaviors of noise and photon burst signal of GNPs, we established a method for data processing of the photon burst counting. Based on this single particle method, new homogeneous immunoassays were developed. In the immunoassay, the sandwich strategy was used, and antibody or antigen was covalently conjugated to GNPs surfaces, respectively. The quantitative analysis is based on the linear relationship between the photon burst counts and log antigen concentration. This novel technique was successfully used for the detection of cancer biomarker prostate specific antigen (PSA) in serum samples. Our results obtained were in good agreement with conventional ELISA assays.

2. Experimental

2.1. Chemicals and materials

Mouse monoclonal anti-human PSA antibodies (ab10185 and ab10186), PSA protein (ab119154) were purchased from Abcam (Hong Kong) Ltd (Hong Kong, China). ELISA kits for human PSA were purchased from Beijing North Institute of Biological Technology (Beijing, China). Bovine serum albumin (BSA) and 4, 7, 10, 13, 16, 19, 22, 25, 32, 35, 38, 41, 44, 47, 50, 53-hexadecaoxa-28, 29-dithiahexapentacontanedioic acid di-*N*-succinimidyl ester (NHS-PEG disulfide) were obtained from Sigma-Aldrich Chemical Co. (Milwaukee, U.S.A.). Sodium citrate, disodium hydrogen phosphate, sodium dihydrogen phosphate and hydrogen tetrachloroaurate(III) hydrate ($HAuCl_4$) were purchased from Sinopharm Chemical Reagent Co. Ltd (Shanghai, China). Alexa 647 fluorescent dye was purchased from Invitrogen Co. (California, U.S.A.). Ultrapure water (18.2 MΩ) was obtained from the Millipore Simplicity System (Bedford, MA, U.S.A.). All other reagents were products of Sigma-Aldrich Chemical Co. (Milwaukee, U.S.A.).

Prostate cancer patient serum samples and healthy human serum samples were provided by Shanghai Jiao Tong University Affiliated Shanghai First People's Hospital. Serum samples were clotted for 30 min at room temperature and centrifuged (Beckman Coulter, U.S.A.) at 2500 rpm for 10 min, and the serum samples were stored at 4 °C for further use. All experiments were performed in compliance with the relevant laws and institutional guidelines.

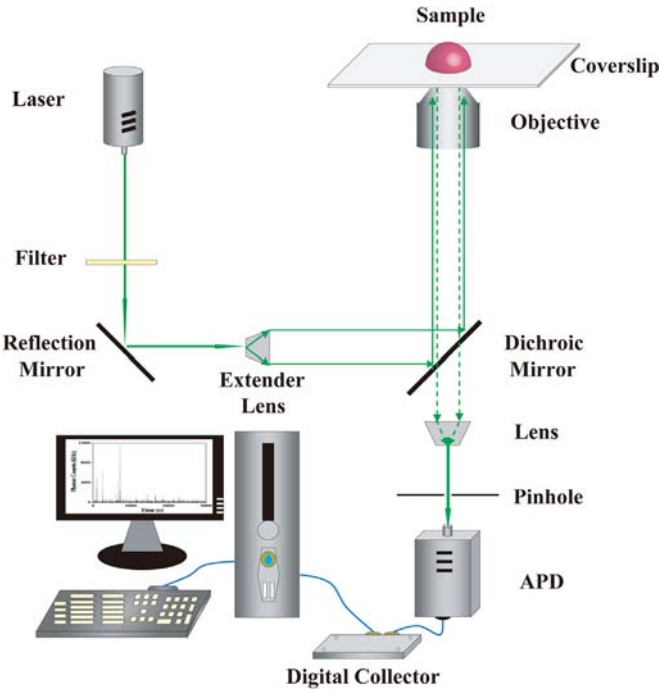


Fig. 1. Schematic diagram of photon burst counting system.

2.2. Instrumentations

The setup of photon burst counting system is similar to resonance light scattering correlation spectroscopy (RLSCS), and is shown in Fig. 1, which is based on an inverted Olympus IX 71 microscope (Japan). The exciting radiation provided by a 532 nm laser beam from an argon ion laser (ILT Technology, Shanghai, China) was attenuated to 20 μW by a neutral density filter. The sample was placed on a cover-slip (thickness: 0.13–0.17 mm), and the laser line was focused on the sample solution by a water immersion objective (UplanApo, 60 × NA1.2, Olympus). The scattering light was collected by the same objective. Then the light passed through the dichroic mirror (505DRLP, Omega Optical, U.S.A.) and the 35 μm pinhole into an avalanche photodiode (SPCM-AQR14, Perkin-Elmer EG&G, Canada). The signals obtained were recorded by a real time digital correlator (Flex02-12D/C, Correlator.com, U.S.A.). The measurement time per sample was 300 s and the time interval was 1 ms.

2.3. Synthesis of GNPs

GNPs were synthesized by reduction of the $HAuCl_4$ solution with sodium citrate according to the method described in the reference [41] with a minor modification, and the synthesis procedure was described in Supporting information.

2.4. Conjugation of antibodies to GNPs

In the conjugation of GNPs with antibodies, anti-human PSA antibodies were first modified with NHS-PEG disulfide through the reaction between the succinimidyl ester and amino group of antibodies, and then linked to the surface of GNPs through the covalent interactions between the disulfide and GNPs, respectively. The procedure was described in Fig. S-1.

Disulfide-functionalized antibodies were prepared by adding 10 μL antibody solution (1 mg/mL antibody) and 40 μL NHS-PEG disulfide solution (0.005 mol/L) into 50 μL 0.01 mol/L PB buffer (pH7.4). The resultant mixture was allowed to react for 8 h at room temperature. To remove excess NHS-PEG disulfide, the disulfide-

functionalized antibodies were purified and washed by ultrafiltration (Millipore ultrafiltration tube, cutoff of 50 kDa) 3 times with the 0.01 mol/L PB buffer. The products were redispersed in the 0.01 mol/L PB buffer and were stored at 4 °C for further use.

Antibody-functionalized GNPs were prepared by adding 5 μL 0.1 M NaOH and 20 μL 134 nmol/L disulfide-functionalized antibody into 300 μL 1.36 nmol/L 20 nm GNPs solution, and the solution were incubated for 8 h at 4 °C. In order to remove excess antibody, the GNP@antibody conjugates were purified and washed by centrifugation at 14,000 rpm for 5 min twice. The centrifuged conjugates were redispersed in 300 μL water for the first time, and 300 μL 0.01 mol/L PBS buffer (containing 0.1% BSA, pH 7.4) for the second time. Then the centrifuged conjugates were stored at 4 °C for further use.

2.5. Homogeneous sandwich immunoassay procedures

In the sandwich immunoassay of PSA, 20 μL of 1.36 nmol/L GNP-antibody-1 solution, 20 μL of 1.36 nmol/L GNP-antibody-2 solution were added into a 200 μL sterilized polypropylene tube respectively, and mixed well. To each mixed solution, 20 μL of standard antigen solution with different concentrations, or human sera, which was first 10 times diluted for sera samples by PBS buffer (containing 0.1% BSA, 10 mmol/L, pH 7.4) are added, and then incubated at 37 °C for 60 min. Finally, the dilution of serum samples was 40 times. The measurements of sample solutions were carried out by a home-built photon burst counting system. The recording time per sample was 300 s, and the assay of each sample repeated three times.

2.6. ELISA method (control experiments)

The ELISA procedures for assays of PSA were described in Supporting information.

2.7. Data processing and analysis

All data files for each measurement were exported as hexadecimal ASCII files. The hexadecimal ASCII files should be changed into decimalized ones by the detection software, and these decimalized files could be calculated and plotted with Origin (OriginLab Corp., MA, U.S.A.) software. The photon burst counts could be obtained by the Pick Peak tools in Origin software. The calibration curve was processed by plotting the photon burst counts against antigen concentrations.

3. Results and discussion

3.1. Photon burst counting detection system

Fig. 1 shows the schematics of photon burst counting system based on the resonance light scattering of noble metal nanoparticles, which is similar to the fluorescence correlation spectroscopy (FCS) system. As shown in Fig. 1, the scattering light intensities can be real time monitored by an avalanche photodiode when single nanoparticles (such as GNPs) diffuse into or out of the highly focused illumination volume due to Brownian motion.

In this study, 40 nm GNPs are used as model samples and their typical photon burst spectrum is displayed in Fig. 2.

As shown in Fig. 2, the strong photon burst of single GNPs is observed due to Brownian motion of single GNPs. However, the differences in the photon burst signal of single GNPs are relatively large, which are within the range of 0–12,000 kHz. This phenomenon mainly attributes to two reasons: the size distribution of nanoparticles and the non-uniform distribution of the focused laser beam. In order to study the effects of GNP sizes on the photon burst signal, variable sizes of GNPs (55 nm, 40 nm, 30 nm, 20 nm) were prepared. The photon burst traces and TEM images of different GNPs are shown in Fig. S-2 (Supporting information). As GNPs used in this study has a good monodispersity, which can be seen from Fig. S-2, the size distribution of GNPs provides a tiny contribution to the differences of photon burst intensity. The confocal configuration of laser beam is the main contributor to the differences in the photon burst. Due to the Gaussian distribution of the focused laser beam intensity, the intensity in the center of the focused laser beam is the strongest. The strong photon burst is generated when a GNPs passes through the center of the focused laser beam, and the weaker photon burst is observed when a GNPs passes through the edge of the focused laser beam.

3.2. The statistical characteristics of photon burst counts

As shown in Fig. 2, the marked differences in the photon burst signal of single GNPs probably result in the difficulty in the data

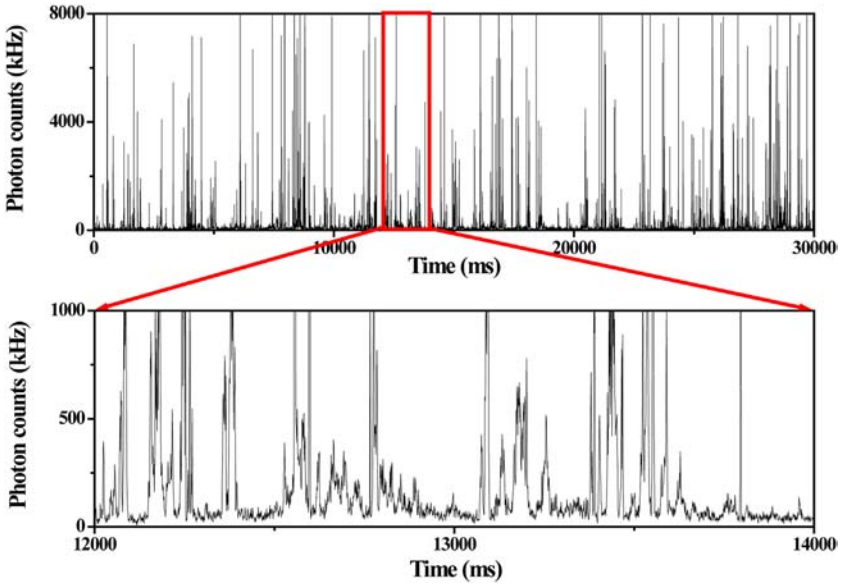


Fig. 2. Typical photon burst spectrum of GNPs. GNPs used was 40 ± 4 nm, the concentration of GNPs was 340 pmol/L, the sampling time was 30 s, and the bin time was 1 ms.

processing. In fact, the signal of photon burst includes two parts, the burst signal of GNPs and background noise. We need to develop a reliable method for efficiently distinguishing the signal and noise in a photon burst spectrum. In fluorescent photon burst counting technique, Christina and Nie [42,43] observed that the relation between the signal intensity and the photon burst counts of corresponding intensity satisfied the Poisson distribution. In order to obtain the relationship between the signal intensities and the numbers of photon burst peaks of the corresponding intensity, we investigated the photon burst of ultra-pure water as a background. As shown in Fig. 3A, the photon burst intensity of water varies around 0–45 kHz with tiny changes, which indicates that the background signal is weak and the detection system is stable.

The relationship between the photon burst intensity and the photon burst counts of corresponding intensity of water were fitted by using Gaussian and Poisson distribution models, respectively, and the results of two fitting methods were compared in Fig. 3B. The curve between the photon burst intensity and the photon burst counts of corresponding intensity is preferably fitted by Gaussian distribution model, and the correlation coefficient is up to 0.992. But, the Poisson model is unsuitable for fitting the data of background signal and the correlation coefficient obtained is only 0.838. Therefore, in the case, we think that the relationship between the intensity and the photon burst counts satisfies Gaussian distribution.

Fig. 4A shows the curve between the photon burst intensity and the photon burst counts of 40 nm GNPs according to the data of Fig. 2. The results show that the distribution between the intensity and the photon burst counts has a certain tailing. Since the noise zone must be a symmetric distribution, as displayed a symmetrical Gaussian distribution from the background of water, the noise zone of GNPs is considered to be a symmetrical profile. Thus the left part of noise distribution from GNPs was symmetrically operated, and the noise of the GNPs was extracted from the photon burst spectrum of GNPs. The noise zone was fitted by both Gaussian and Poisson distribution, and the results of two fitting methods were compared in Fig. 4B. The green line is the Gaussian fitting curve, and the blue one is the Poisson fitting curve. The result is similar to the background of water, and the noise zone of GNPs preferably meets Gaussian fitting and does not fit Poisson distribution. This result demonstrates that Gaussian model is suitable for fitting the noise zone of photon burst.

The photon burst spectrum of silver nanoparticles (SNPs) also can be observed by the same system, and the photon burst spectrum of a 20 nm SNPs and the fitting results of its noise zone were shown in Fig. S-3. In the figure, we found the Gaussian distribution was also suitable for fitting the photon burst noise zone of SNPs. So the introduced photon burst counting technique in this manuscript is also available for SNPs.

3.3. Principle of photon burst counting technique

To separate the signal of GNPs from the background noise in the photon burst spectrum of GNPs, a key parameter called the threshold is introduced. In the processing of data, all of the photon burst peaks, which intensities are above the threshold, are considered to be the signal of GNPs, and the peaks which the peak intensity is below the threshold are treated as the background noise. The photon burst counts can be calculated by using the Pick Peaks tool in Origin 6.1.

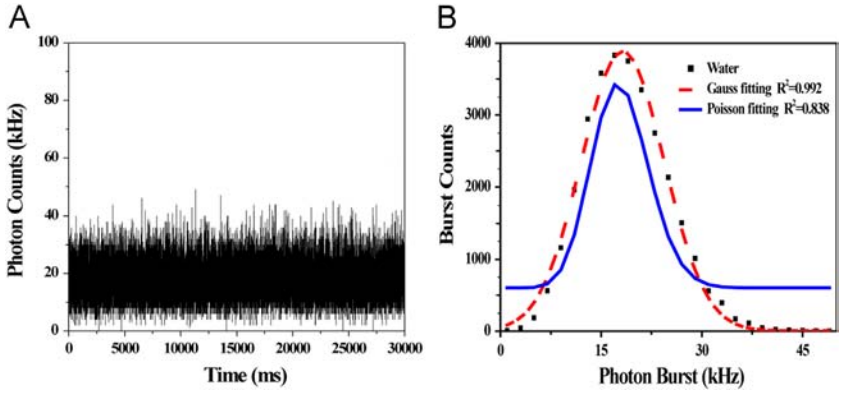


Fig. 3. Photon burst spectrum (A) and the noise distribution spectrum (B) of ultra-pure water. The resistivity of the water was 18 MΩ/cm. The sampling time was 30 s, and the bin time was 1 ms.

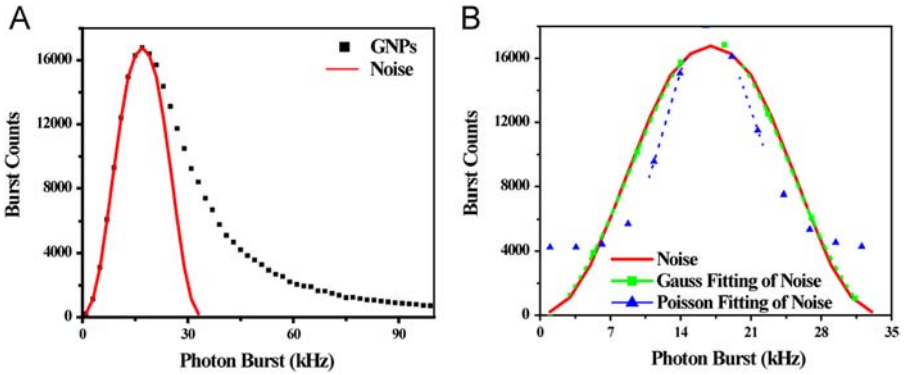


Fig. 4. (A) Photon burst signal distribution of 40 nm GNPs, and (B) the fitting curves of the noise zone. The GNPs used was 40 ± 2 nm, the concentration of GNPs was 340 pmol/L, the measurement time was 30 s, and the bin time was 1 ms. (For interpretation of the references to color in this figure legend, the reader is referred to the web version of this article.)

The threshold value (T) can be described as follows,

$$T = B + K \times F \quad (1)$$

where B is the baseline value, F is the fluctuation value of the baseline (or noise) and K is the coefficient. We can obtain the baseline value and the fluctuation value according to the Gaussian distribution of the background noise mentioned above.

In a Gaussian distribution curve, the mathematical function $f(x)$ was expressed as follows,

$$f(x) = \frac{1}{\sqrt{2\pi}\sigma}\exp\left[-\frac{(x-\mu)^2}{2\sigma^2}\right] \quad (2)$$

where μ is the mathematical expectation of the distribution, and σ represents the standard deviation. In the photon burst distribution of GNPs, the mathematical expectation of the fitting curve reflects the most frequently occurring photon burst intensity, which can be considered as the baseline values (B) in this case. When x falls around $\mu+2\times\sigma$ and $\mu-2\times\sigma$, the confidence level is about 95.45%, that is, there are 95.45% of the data falls in the zone. In this case, the fluctuation value can be chosen as 4σ.

Based on the theory above, the threshold value and the fluctuation value were obtained. We first extract the noise zone of samples, and then fit the noise zone with Gaussian distribution to get the baseline value μ and fluctuation value 4σ of the noise zone. The threshold was defined as $\mu+K\times 4\sigma$.

K is one of the critical parameters in the detection method, and is related to the sensitivity and reproducibility of the method. The photon burst data of 40 nm GNPs with the concentration of 340 pmol/L, 170 pmol/L, 68 pmol/L, 34 pmol/L and 17 pmol/L are recorded in Fig. S-4. The photon burst counts reduce with the decrease in GNPs concentration. The different K values were putted into the threshold Eq. (1), and different thresholds were obtained. Fig. 5 displays the relationship between the concentration of GNPs and the photon burst counts of GNPs, respectively. As shown in Fig. 5, the slopes of the curve gradually reduced with the increase of K, which illustrated the reduction in the sensitivity. But the error becomes larger in the case of low K, because certain noises in the data are not completely eliminated. Under the consideration of both sensitivity and reproducibility, we selected 2 as the value of K, and the threshold were set as $\mu+8\times\sigma$ for the subsequent experiments. As shown in Fig. 5, the errors of each point are very small, which demonstrates that the method has a good reproducibility.

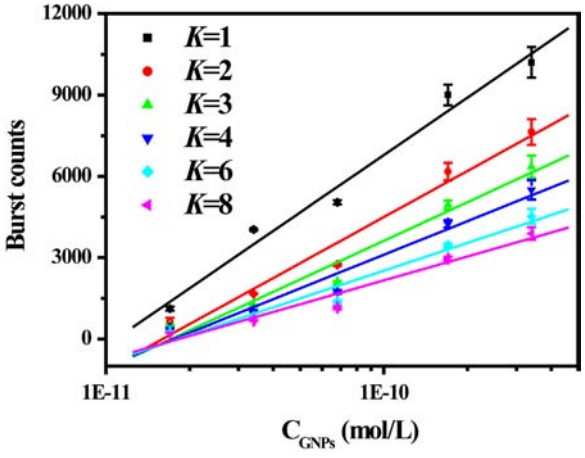


Fig. 5. Linear relationships between the concentration and the photon burst counting of GNPs. The K was 1, 2, 3, 4, 6, and 8, respectively. The GNPs used was 40 nm, the concentrations of GNPs were 340 pmol/L, 170 pmol/L, 68 pmol/L, 34 pmol/L, 17 pmol/L, and the sampling time was 30 s.

The reproducibility of photon burst counting method was investigated. In the intra-day study, the 40 nm GNPs was used as samples, each sample was detected seven times, and the measurement time was 300 s. In the inter-day study, the 40 nm GNPs was also used as samples, each sample was detected three times in the subsequent five days, and the measurement time was 300 s. The photon burst counts was calculated by Origin 6.1. The results are shown in Table S-1. The RSDs of the intra-day and the inter-day are 1.7% and 2.2%, respectively. The results further illustrate that the method described in this study shows a good reproducibility.

In order to obtain the accurate photon burst counts of gold nanoparticles, first the curve between the photon burst intensity and the photon burst counts of the GNPs is obtained based on a photon burst spectrum of GNPs, and the left part of this curve is symmetrically operated to generate the noise distribution curve of GNPs. And then, the mathematical expectation μ and the standard deviation σ of this noise zone can be acquired by fitting this curve with a Gaussian distribution. Finally, the threshold of this spectrum is set as $\mu+8\times\sigma$, the number of peaks which are beyond this threshold is calculated by the Pick Peak tools of Origin software, this number is considered to be the photon burst counts of a GNPs.

3.4. Homogeneous sandwich immunoassay by photon burst counting method

Prostate specific antigen (PSA) is a member of the kallikrein-related peptidase family and is secreted by the epithelial cells of the prostate gland [44,45]. PSA is present in small quantities in the sera of men with healthy prostates, but is often elevated in the presence of prostate cancer or other prostate disorders [46–48].

Fig. 6 illustrates the principle of homogeneous sandwich immunoassay on the basis of photon burst counting technique. As shown in Fig. 6, when GNPs labeled with two different antibodies are mixed in a sample containing antigens, the binding of antigens will cause GNPs to form dimers (or oligomers), which leads to the significant reduction in the number of nanoparticles. To further confirm the successful immunoreactions between the antibodies conjugated GNPs and antigen, TEM images of GNPs before and after the immunoassay were shown in Fig. S-5. In the study, the GNPs was 20 nm, the concentration of GNPs@Ab was 680 pmol/L, a 1:1 mixture solution of the two nanoprobes, GNP@Ab1:GNP@Ab2, was added into the solution of PSA with a concentration of 1 nmol/L. The mixed solution was incubated for 1 h at 37 °C, then drop on a copper grid and examined by TEM. In , few GNPs dimmer in the red circle can be found which may be caused by the aggregation of GNPs themselves. But in Fig S-5B, the increased GNPs dimmers can be seen, which were believed to be formed by the sandwich immunoreactions between antibodies and antigen.

Photon burst counting method can sensitively detect the changes in the photon burst counts of GNPs before and after immune reactions. We reason that the photon burst counts of GNPs reduces with an increase of antigens in solution due to the formation of immunocomplexes. The relationship between the photon burst counts of GNPs and antigen concentration may be used for quantification of antigen level. In this study, the sandwich immune reaction of PSA was used as models to construct homogeneous sandwich immunoassay platforms based on photon burst counting method.

We first investigated the effect of GNPs sizes on sandwich immunoassay of PSA. As we know, the large-sized GNPs are not stable in biological samples, and they are easy to form aggregates, which will affect the accuracy of analytical results. Therefore, the sizes of GNPs used in the assay were 20 nm and 40 nm, respectively. In the assay, the concentration of 20 nm GNPs was 680 pmol/L, and the concentration of 40 nm GNPs was 170 pmol/L. As shown in Fig. S-6A,

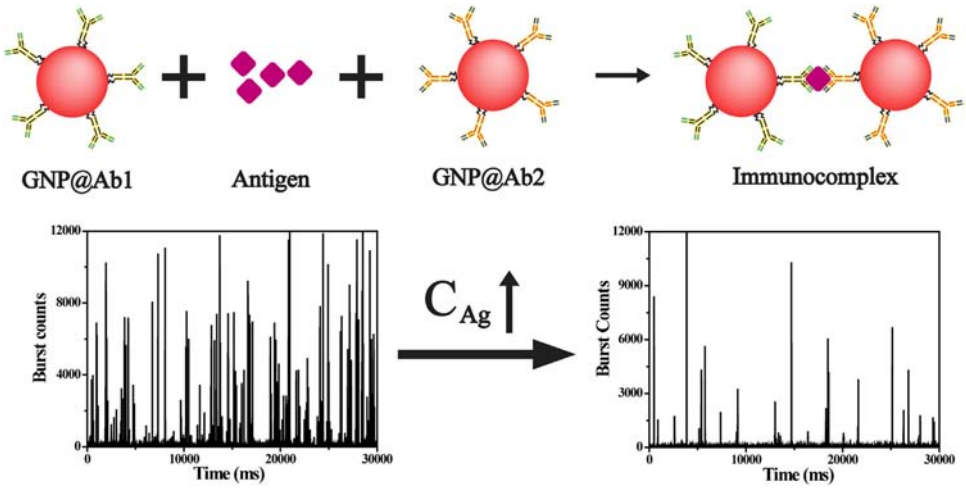


Fig. 6. Principle of homogeneous sandwich immunoassay based on photon burst counting method. GNP@Ab1 and GNP@Ab2 represent the antibodies labeled gold nanoparticles. C_{Ag} means the concentration of antigen.

the photon burst counts reduced with an increase of the probe sizes. The probe size of GNPs provides an obvious effect on the sensitivity and linear range of the sandwich immunoassay of PSA. When the small sized GNPs are used, the linear range is one order of magnitude wider than big sized GNPs, and the slope of the calibration curve is larger, which represents more sensitive in this case. Therefore, the probes size used in the subsequent sandwich immunoassay of PSA was 20 nm.

We also investigated the effects of GNPs concentration on sandwich immunoassay of PSA. The 20 nm GNPs were used in the assay, and their concentrations were 2.72 nmol/L, 1.36 nmol/L and 680 pmol/L, respectively. As shown in Fig. S-6B, the linear range increases with the increase in the concentration of GNPs. When the concentration of GNPs is 2.72 nmol/L, the linear range only has two orders of magnitude. But when the concentration of GNPs reduces to 680 pmol/L, the linear range reaches to three orders of magnitude. In the following research of sandwich immunoassay, the concentration of GNPs we used is 680 pmol/L.

We used the photon burst counting technique to construct a homogeneous sandwich immunoassay for PSA antigens. Under the optimal consideration, a good linear relationship between the photon burst counts and the log PSA concentration was obtained, which was shown in Fig. 7. The calibration curve of PSA has a wide linear range over three orders of magnitude (from 1 pmol/L to 1 nmol/L), and the detection limit is 0.8 pmol/L for PSA.

The method was successfully applied for the direct detection of the PSA level in serum samples from normal subjects and cancer patients. In the sandwich immunoassay measurements, all serum samples were diluted 10 times with a buffer (0.1% BSA/PBS). The photon burst spectrum of a prostate cancer patient serum sample is shown in Fig. S-7. In Fig. S-7, very few peaks are found, which doesn't affect the accuracy of the results. The results of PSA levels in serum samples are shown in Table 1, we observed that the PSA levels in cancer patients were more than one order of magnitude higher than those in healthy subjects. The contrast experiments were performed with ELISA. As shown in Table 1, the RSDs were less than 7%, and this result illustrated that the present method has a good reproducibility. The results obtained from the photon burst counting method were in good agreement with ELISA assays.

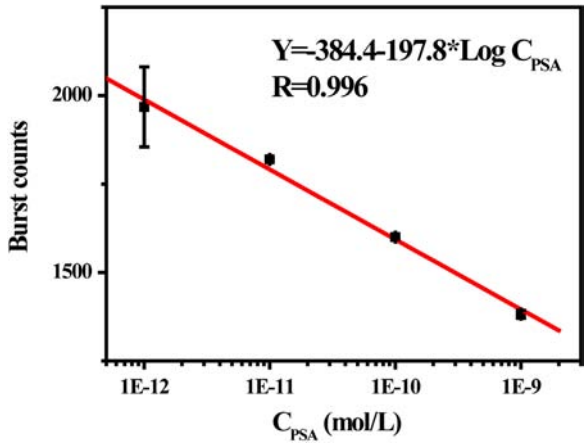


Fig. 7. The linear relationship between the photon burst counts and the concentration of PSA by homogeneous sandwich immunoassay based on the photon burst counting method. In the sandwich immunoassay of PSA, the size of GNPs used was 20 nm, and the concentration of GNPs was 680 pmol/L.

Table 1
The PSA levels in serum samples measured by sandwich immunoassay based on photon burst counting technique and ELISA.

Samples	Photon burst		ELISA (mol/L)
	Concentration (mol/L)	RSD (%)	
Normal 1	4.07×10^{-11}	1.4	3.40×10^{-11}
Normal 2	1.22×10^{-11}	6.5	1.70×10^{-11}
Cancer 1	1.45×10^{-10}	1.5	1.16×10^{-10}
Cancer 2	2.48×10^{-10}	5.9	1.06×10^{-10}

4. Conclusions

In this work, we described a novel photon burst counting method based on the resonance light scattering and Brownian motion of GNPs in a highly focused laser beam. The data processing method was proposed in the photon burst counting technique. This single particle technique was applied to develop homogeneous immunoassays. In the immunoassay, the sandwich strategy was used and the experimental conditions were investigated. This technique was successfully used for the direct detection of biomarker PSA in serum samples, and the results obtained were in good agreement with conventional ELISA assays. Compared with current methods, this method can be characterized as good reproducibility, high sensitivity, and a short analysis time, and it exhibits promising potential applications in clinical diagnosis, environmental and food safety analysis.

Acknowledgements

This work was financially supported by NSFC (20975067, 21075081 and 21135004). J.C.R. thanks Prof. Daode Hu (Shanghai Jiao Tong University Affiliated Shanghai First People's Hospital) for providing healthy human and cancer patient serum samples.

Appendix A. Supporting information

Supplementary data associated with this article can be found in the online version at http://dx.doi.org/10.1016/j.talanta.2014.10.004.

References

[1] R.S Yalow, S.A. Berson, Nature 184 (1959) 1648–1649.
[2] J.H. Lee, S. Park, H. Hyun, M.W. Bordo, R. Oketokoun, K.A. Nasr, J.V. Frangioni, H.S. Choi, Anal. Chem. 85 (2013) 3508–3514.
[3] J. Liu, M. Yu, C. Zhou, S. Yang, X. Ning, J. Zheng, J. Am. Chem. Soc. 135 (2013) 4978–4981.
[4] J.Y. Byun, Y.B. Shin, D.M. Kim, M.G. Kim, Analyst 138 (2013) 1538–1543.
[5] T. Kreisig, R. Hoffmann, T. Zuchner, Anal. Chem. 83 (2011) 4281–4287.
[6] Y. Wang, L.J. Tang, J.H. Jiang, Anal. Chem. 85 (2013) 9213–9220.
[7] A. Ranzoni, G. Sabatte, L.J. Van Ijzendoorn, M.W. Prins, ACS Nano 6 (2012) 3134–3141.
[8] R. Pacheco-Gómez, J. Kraemer, S. Stokoe, H.J. England, C.W. Penn, E. Stanley, A. Rodger, J. Ward, M.R. Hicks, T.R. Dafforn, Anal. Chem. 84 (2011) 91–97.
[9] K. Karns, A.E. Herr, Anal. Chem. 83 (2011) 8115–8122.
[10] X. Liu, Q. Dai, L. Austin, J. Coutts, G. Knowles, J. Zou, H. Chen, Q. Huo, J. Am. Chem. Soc. 130 (2008) 2780–2782.
[11] K. Aurich, S. Nagel, G. Glöckl, W. Weitschies, Anal. Chem. 79 (2007) 580–586.
[12] T. Lan, C. Dong, X. Huang, J. Ren, Talanta 116 (2013) 501–507.
[13] T. Lan, C. Dong, X. Huang, J. Ren, Analyst 136 (2011) 4247–4253.
[14] Y. Jiang, H. Zhao, Y. Lin, N. Zhu, Y. Ma, L. Mao, Angew. Chem. 122 (2010) 4910–4914.
[15] C. Cao, X. Li, J. Lee, S.J. Sim, Biosens. Bioelectron. 24 (2009) 1292–1297.
[16] J. Wang, T.J. Mountziaris, Biosens. Bioelectron. 41 (2013) 143–149.
[17] X. Cui, M. Liu, B. Li, Analyst 137 (2012) 3293–3299.
[18] M. Hervás, M.A. López, A. Escarpa, TrAC, Trends Anal. Chem. 31 (2012) 109–128.
[19] J.S. Lee, H.A. Joung, M.G. Kim, C.B. Park, ACS Nano 6 (2012) 2978–2983.
[20] S.A. Soper, Q.L. Mattingly, P. Vegunta, Anal. Chem. 65 (1993) 740–747.
[21] E.B. Shera, N.K. Seitzinger, L.M. Davis, R.A. Keller, S.A. Soper, Chem. Phys. Lett. 174 (1990) 553–557.
[22] T. Hirschfeld, Appl. Opt. 15 (1976) 2965–2966.
[23] N.J. Dovichi, J.C. Martin, J.H. Jett, M. Trkula, R.A. Keller, Anal. Chem. 56 (1984) 348–354.
[24] F. Zarrin, N.J. Dovichi, Anal. Chem. 57 (1985) 1826–1829.
[25] S. Wu, N.J. Dovichi, J. Chromatogr. A 480 (1989) 141–155.
[26] D. Chen, N.J. Dovichi, Anal. Chem. 68 (1996) 690–696.
[27] O.O. Dada, D.C. Essaka, O. Hindsgaul, M.M. Palcic, J. Prendergast, R.L. Schnaar, N.J. Dovichi, Anal. Chem. 83 (2011) 2748–2753.
[28] J. Zhang, K.O. Voss, D.F. Shaw, K.P. Roos, D.F. Lewis, J. Yan, R. Jiang, H. Ren, J.Y. Hou, Y. Fang, X. Puyang, H. Ahmadzadeh, N.J. Dovichi, Nucl. Acids Res. 27 (1999) 1–7.
[29] C.Y. Zhang, L.W. Johnson, J. Am. Chem. Soc. 130 (2008) 3750–3751.
[30] C.Y. Zhang, L.W. Johnson, Analyst 131 (2006) 484–488.
[31] H. Li, L. Ying, J.J. Green, S. Balasubramanian, D. Klenerman, Anal. Chem. 75 (2003) 1664–1670.
[32] L.A. Neely, S. Patel, J. Garver, M. Gallo, M. Hackett, S. McLaughlin, M. Nadel, J. Harris, S. Gullans, J. Rooke, Nat. Methods 3 (2005) 41–46.
[33] E.A. Nalefski, C.M. D'Antoni, E.P. Ferrell, J.A. Lloyd, H. Qiu, J.L. Harris, D.H. Whitney, Clin. Chem. 52 (2006) 2172–2175.
[34] S. Hu, R. Liu, S. Zhang, Z. Huang, Z. Xing, X. Zhang, J. Am. Soc. Mass Spectrom. 20 (2009) 1096–1103.
[35] G. Han, Z. Xing, Y. Dong, S. Zhang, X. Zhang, Angew. Chem. 123 (2011) 3524–3527.
[36] R. Liu, Z. Xing, Y. Lv, S.C. Zhang, X. Zhang, Talanta 83 (2010) 48–54.
[37] L. Yang, S. Zhu, W. Hang, L. Wu, X. Yan, Anal. Chem. 81 (2009) 2555–2563.
[38] L. Yang, L. Wu, S. Zhu, Y. Long, W. Hang, X. Yan, Anal. Chem. 82 (2010) 1109–1116.
[39] L. Yang, Y. Zhou, S. Zhu, T. Huang, L. Wu, X. Yan, Anal. Chem. 84 (2012) 1526–1532.
[40] S. Zhu, L. Yang, Y. Long, M. Gao, T. Huang, W. Hang, X. Yan, J. Am. Chem. Soc. 132 (2010) 12176–12178.
41] J.J. Storhoff, R. Elghanian, R.C. Mucic, C.A. Mirkin, R.L. Letsinger, J. Am. Chem. Soc. 120 (1998) 1959–1964.
[42] A. Agrawal, C. Zhang, T. Byassee, R.A. Tripp, S. Nie, Anal. Chem. 78 (2006) 1061–1070.
[43] C.M. D'Antoni, M. Fuchs, J.L. Harris, H.P. Ko, R.E. Meyer, M.E. Nadel, J.D. Randall, J.E. Rooke, E.A. Nalefski, Anal. Biochem. 352 (2006) 97–109.
[44] W.J. Catalona, D.S. Smith, T.L. Ratliff, K.M. Dodds, D.E. Coplen, J.J. Yuan, J.A. Petros, G.L. Andriole, N. Engl. J. Med. 324 (1991) 1156–1161.
[45] T.A. Stamey, N. Yang, A.R. Hay, J.E. McNeal, F.S. Freiha, E. Redwine, N. Engl. J. Med. 317 (1987) 909–916.
[46] W.J. Catalona, P.C. Southwick, K.M. Slawin, A.W. Partin, M.K. Brawer, R.C. Flanigan, A. Patel, J.P. Richie, P.C. Walsh, P.T. Scardino, Urology 56 (2000) 255–260.
[47] J.P. Richie, W.J. Catalona, F.R. Ahmann, M.L.A. Hudson, P.T. Scardino, R.C. Flanigan, J.B. Dekernion, T.L. Ratliff, L.R. Kavoussi, B.L. Dalkin, Urology 42 (1993) 365–374.
[48] J. Morote, C. Raventos, J. Lorente, M. Lopez-Pacios, G. Encabo, I. De Torres, J. Andreu, J. Urol. 158 (1997) 502–504.

Talanta 132 (2015) 705–712

Contents lists available at ScienceDirect

Talanta

journal homepage: www.elsevier.com/locate/talanta

Comparative proteomic and transcriptomic profile of *Staphylococcus epidermidis* biofilms grown in glucose-enriched medium

Virginia Carvalhais [a,b,c], Angela França [a,c], Gerald B. Pier [c], Manuel Vilanova [d,e], Nuno Cerca [a], Rui Vitorino [b,*]

[a] CEB—Centre of Biological Engineering, LIBRO - Laboratory of Research in Biofilms Rosário Oliveira, University of Minho, Campus de Gualtar, 4710-057 Braga, Portugal
[b] QOPNA, Mass Spectrometry Center, Department of Chemistry, University of Aveiro, Aveiro, Portugal
[c] Division of Infectious diseases, Department of Medicine, Brigham and Women's Hospital, Harvard Medical School, Boston, MA, USA
[d] ICBAS—Instituto de Ciências Biomédicas de Abel Salazar, Universidade do Porto, Porto, Portugal
[e] IBMC—Instituto de Biologia Molecular e Celular, Rua do Campo Alegre 83, Porto, Portugal

ARTICLE INFO

Article history:
Received 26 July 2014
Received in revised form
1 October 2014
Accepted 8 October 2014
Available online 19 October 2014

Keywords:
LC–MS/MS
EmPAI
Protein extraction methods
RNA-seq
Staphylococcus epidermidis biofilms

ABSTRACT

Staphylococcus epidermidis is an important nosocomial agent among carriers of indwelling medical devices, due to its strong ability to form biofilms on inert surfaces. Contrary to some advances made in the transcriptomic field, proteome characterization of *S. epidermidis* biofilms is less developed. To highlight the relation between transcripts and proteins of *S. epidermidis* biofilms, we analyzed the proteomic profile obtained by two mechanical lysis methods (sonication and bead beating), associated with two distinct detergent extraction buffers, namely SDS and CHAPS. Based on gel electrophoresis-LC–MS/MS, we identified a total of 453 proteins. While lysis with glass beads provided greater amounts of protein, CHAPS extraction buffer allowed identification of a higher number of proteins compared to SDS. Our data shows the impact of different protein isolation methods in the characterization of the *S. epidermidis* biofilm proteome. Furthermore, the correlation between proteomic and transcriptomic profiles was evaluated. The results confirmed that proteomic and transcriptomic data should be analyzed simultaneously in order to have a comprehensive understanding of a specific microbiological condition.
© 2014 Elsevier B.V. All rights reserved.

1. Introduction

When *Staphylococcus epidermidis* establishes biofilms on indwelling medical devices, this may cause an early removal of the implant due to the lack of effective antibiotic therapeutics and risk of eventual systemic infection [1,2]. *S. epidermidis* biofilms grown in glucose-enriched medium were previously associated with an increased proportion of dormant cells within a biofilm [3]. Dormancy is a clinically relevant physiological state, since it has been associated with long-term bacterial survival, increased cellular tolerance to antibiotics [4–6] and evasion of the host immune system [3,7].

The availability of the complete genome of *S. epidermidis* strains RP62A (ATCC 35984) [8] and ATCC 12228 [9] has led to the development of proteomic studies, since it has been suggested that the genome sequence is not sufficient to elucidate the biological functions of an organism [10]. Although there have been major advances in the molecular characterization of the pathogenic mechanisms of *S. epidermidis* biofilms [1], much less is known regarding the proteome. A few proteomic studies, however, have been performed with some *Staphylococcus* spp. in order to identify specific features associated with the pathogenicity and physiology of these microorganisms [11–18]. In *S. epidermidis*, 2-Dimensional Electrophoresis (2-DE) analysis of proteomic patterns showed several differentially expressed proteins when comparing commensal and invasive strains [12]. To ensure high quality and reliable proteomic results, an appropriate sample preparation is fundamental [19,20]. Due to the complex structure of biofilms [21], it is necessary to develop an effective lysis method in order to obtain maximum coverage of the biofilm proteome and minimal protein losses, similar to the approach optimized for total RNA extraction from *S. epidermidis* biofilms [22]. Different protein extraction methods, including enzymatic, chemical, mechanical and other methods available via commercial extraction kits have been tested to obtain the highest number of proteins in *Staphylococcus* spp. [11,14]. Although the majority of these studies were performed with cell suspensions, relatively harsh techniques have been shown to be rapid and efficient to disrupt and lyse biofilms of Gram-positive bacteria, such as mechanical methods like bead beating with glass beads (FastPrep) or sonication [14,23,24]. Often, to optimize protein recovery, enzymes and detergents may be used in conjugation with mechanical lysis. Since lysostaphin efficiently cleaves staphylococcal cell wall peptidoglycan [25,26], it may

* Corresponding author.
E-mail address: rvitorino@ua.pt (R. Vitorino).

http://dx.doi.org/10.1016/j.talanta.2014.10.012
0039-9140/© 2014 Elsevier B.V. All rights reserved.

be used to disrupt staphylococcal biofilms [27]. However, due to high costs of lysostaphin, detergents are frequently used to enhance protein isolation and solubilisation [28].

In an attempt to determine the relation between protein and mRNA levels, several studies have shown that often the correlation is surprisingly low, and differs widely among organisms [29]. Correlation coefficients were found to vary from 0.09 to 0.46 in multi-cellular organisms, from 0.34 to 0.87 in yeasts, whereas in bacteria the correlations ranged from 0.20 to 0.47 (reviewed in [30]). Up to now, no correlation analysis between the transcriptome and proteome of *S. epidermidis* biofilms has been conducted.

Hence, herein, since distinct lysis and extraction methods may yield different protein recoveries, we assessed different lysis methods to obtain proteins from *S. epidermidis* biofilms grown in glucose-enriched medium. Then, we compared the proteomic profile with the gene expression profile obtained by RNA sequencing (RNA-seq) technology., We undertook a gel-based method to determine protein isolation efficiency, using total protein extracted with a detergent-based extraction (SDS or CHAPS) coupled with mechanical lysis (sonication or bead beating). A detailed analysis of proteomic data was performed in each condition. Label-free relative protein abundance index (emPAI) was used for the relative quantitation of the proteome and was compared to transcriptomic profile. The overall goal was to characterize and correlate both proteomic and transcriptomic profiles of *S. epidermidis* biofilm-grown cells.

2. Materials and methods

2.1. Growth conditions

Biofilm forming *S. epidermidis* 9142 strain was used as a model [31]. One colony was inoculated into 1 mL of Tryptic Soy Broth (TSB) (Liofilchem, Roseto degli Abruzzi, Italy) and incubated at 37 °C at 120 rpm for 18 h. The overnight culture was adjusted to an optical density at 640 nm of 0.250 (± 0.05) with TSB and 10 μL of the suspension was transferred into a 24-well plate (Thermo Fisher Scientific, Waltham, MA, USA) containing 1 mL of TSB supplemented with 0.4% glucose (v/v) (TSB 0.4% G) (Thermo Fisher Scientific). The culture plate was then incubated at 37 °C at 120 rpm for 24 h. After this period, the culture medium covering the biofilm was removed and replaced by fresh TSB supplemented with 1% glucose (v/v) (TSB 1% G). Biofilms were allowed to grow in these same conditions for 24 additional hours. Thereafter, biofilm culture medium was removed and biofilms were washed twice with phosphate buffered saline (PBS).

2.2. Protein preparation

The same number of biofilms (12 biofilms for each condition) were directly scraped and suspended in detergent extraction buffers: 25 mM Tris–HCl (pH=7.2) (Pharmacia Biotech, Uppsala, Sweden), 10 mM CHAPS (Sigma-Aldrich, St. Louis, MO, USA, 0.5 M NaCl (VWR, Radnor, PA, USA), 5% glycerol (Sigma-Aldrich) and 1 mM PMSF (Sigma-Aldrich) or 60 mM Tris–HCl (pH=6.8), 10% glycerol, 5% SDS (USB Corporation, Cleveland, OH, USA) and 1 mM PMSF. Mechanical lyses were performed in a sonicator (Cole-Parmer® 750-Watt Ultrasonic Homogenizer, Cole Parmer, Vernon Hills, IL, USA) (10 min, 30 s running, 10 s pause, 40% amplitude) or by bead beating, using glass beads of 0.1 mm (Sigma-Aldrich) in a FastPrep® cell disruptor (BIO 101, ThermoElectron Corporation, Thermo Fisher Scientific) (3 cycles of 30 s and 6.5 m/s). After lyses, cell debris were removed by centrifugation (15,000g for 15 min at 4 °C) and proteins precipitated with cold acetone [32]. Then, protein quantification was performed using the RC-DC assay (Bio-Rad, Hercules, CA, USA), following the manufacturer's instructions.

2.3. One-dimensional gel electrophoresis (SDS-PAGE) in gel protein digestion and protein identification

Forty μg of protein were incubated with SDS 10% (w/v), 0.5 M Tris–HCl (pH 6.8), glycerol, mercaptoethanol and bromophenol blue (w/v) for 5 min at 100 °C. Then, samples were loaded on Novex NuPAGE® 4–12% Bis-Tris gel (Life Tecnologies, Grand Island, NY, USA) and proteins were separated at a constant voltage (200 V). The gel was stained with colloidal Coomassie G-250 and all the lanes were manually excised into 16 gel slices for in-gel digestion with trypsin TPCK (AB Sciex, Framingham, MA, USA). Peptide extraction was made with 10% formic acid/ 50% acetonitrile. Dried peptides were dissolved in 5% acetonitrile (VWR), 0.1% formic acid (Sigma-Aldrich) and 0.1% trifluoroacetic acid (Sigma-Aldrich). Separation of tryptic peptides by nano-HPLC was performed on the module separation Ultimate 3000 (Dionex, Thermo Fisher Scientific) using a capillary column (Pepmap100 C18; 3 μm particle size, 0.75 μm internal diameter, 15 cm in length). A gradient of solvent A, (water/acetonitrile/trifluoroacetic acid (98:2:0.05, v/v/v)) to solvent B (water/acetonitrile/trifluoroacetic acid (10:90:0.045, v/v/v)) was used. The separation of 2 μg/μL sample was performed using a linear gradient (5–50 % B for 30 min, 50–70% B for 10 min and 70–5% A for 5 min) with a flow rate of 0.3 μL/min. The eluted peptides were mixed with a continuous flow of CHCA matrix solution (270 nL/min, 2 mg/mL in 70% ACN/0.1% TFA and internal standard Glu-Fib at 15 ftmol) and applied directly on a MALDI plate in 20 s fractions using an automatic fraction collector Probot (Dionex, Thermo Fisher Scientific). Mass spectra were obtained on a matrix assisted laser desorption/ionization–time of flight MALDI-TOF/TOF mass spectrometer (4800 Proteomics Analyzer, Applied Biosystems, Foster City, CA, USA) in the positive ion reflector mode and obtained over the mass range from 700 to 4500 Da with 900 laser shots. A fragmentation voltage of 2 kV was used throughout the automated runs. The spectra were processed and analyzed by the T2S (v1.0, Matrix Science Ltd, London, U.K) and submitted in Mascot software (v.2.3.0.2, Matrix Science Ltd) for protein/ peptide identification based on MS/MS data using the following criteria: trypsin as enzyme; a maximum of two missed cleavages; mass tolerances of 40 ppm for peptide precursors, mass tolerance of 0.6 Da was set for fragment ions. Simultaneously, phosphorylation of threonine (T), serine (S) and tyrosine (Y) were searched as variable modifications. The local false discovery rate (FDR) was calculated by searching the spectra against SwissProt (Firmicutes, release date 06022013) decoy (random) database. Protein identification was considered reliable when the individual ion score for each peptide had a minimum individual score of 95% and a minimum sequence tag of four aminoacids. Relative quantitation was performed using emPAI. Gene ontology [33] analysis was performed with proteins identified in each extraction condition using STRING database (Search Tool for the Retrieval of Interacting Genes/Proteins) (version 9.1) [34] (statistically significant specific GO terms, FDR adjust $p < 0.05$). Two independent experiments were performed with pools of *S. epidermidis* biofilms.

2.4. RNA sequencing

RNA extraction from *S. epidermidis* biofilms, cDNA library preparation and RNA-seq, were performed as previously described, with some modifications [35]. Briefly, total RNA was extracted using the RNeasy Mini kit (Qiagen, Valencia, CA, USA). To remove genomic DNA, Ambion® TURBO DNA-free™ kit (Life Technologies) was used followed by acid–phenol:chloroform precipitation (Ambion®, Life

Tecnhologies), both following the manufacturer's instructions. RNA integrity was determined using the Bioanalyzer 2100 (Agilent Technologies, Santa Clara, CA, USA), and samples with RNA Integrity Number (RIN) above 8 were selected for complementary DNA (cDNA) library preparation. Ribosomal RNA was depleted from total RNA samples using the Ribo-Zero™ Magnetic kit for Gram-Positive bacteria (Epicentre, Madison, WI, USA), following the manufacturer's specifications. The Illumina® TruSeq™ RNA Sample Preparation kit (Illumina, San Diego, CA, USA) was used with the already purified mRNA, following the manufacturer's protocol. The construction of the libraries was rigorously validated by quantitative PCR and Hi-Sensitivity D1K TapeStation (Agilent 2200 TapeStation). Sequencing data were generated from paired-end reads (2×150 bp) on a MiSeq® system (Illumina) using a RNA-seq library of 10 nM. The mapping to reference genome and normalization of gene expression was performed using CLC Genomics Workbench software (V.5.5.1, CLC Bio.). RNA-seq reads were aligned to the reference genome of *S. epidermidis* strain RP62A (GenBank accession number NC_002976). Gene expression was normalized by calculating Reads per Kilobase per Million Mapped Reads (RPKM) using the methods described by Mortazavi and colleagues [36], in which normalization is adjusted by the counts of reads per kilobase per million mapped and gene length. All genes with RPKM value under 1.00 were not considered for analysis. Three independent experiments, each one from a pool of four biofilms, were performed.

3. Results and discussion

3.1. Proteomic characterization

In the present study, a proteomic and transcriptomic analysis of *S. epidermidis* biofilms grown in glucose-enriched medium was performed using gel-based proteomic separation and LC–MS/MS analysis along with RNA-seq technology, respectively. The proteomic profile obtained is highly dependent on the extraction procedure used, with quickness, handling and robustness of protein extraction methodologies being important criteria [11,37–39]. Before protein concentration, we used SDS-PAGE to compare the lysis efficiency of sonication and glass bead disruption of *S. epidermidis* biofilm cells (Fig. 1). Cellular lysis by the glass bead disruption method produced a higher protein yield compared to the performed sonication cycle. Due to sample and protein properties, precipitation may be required as a treatment to reduce or eliminate substances which could interfere with protein identification, as well as to concentrate proteins [40].

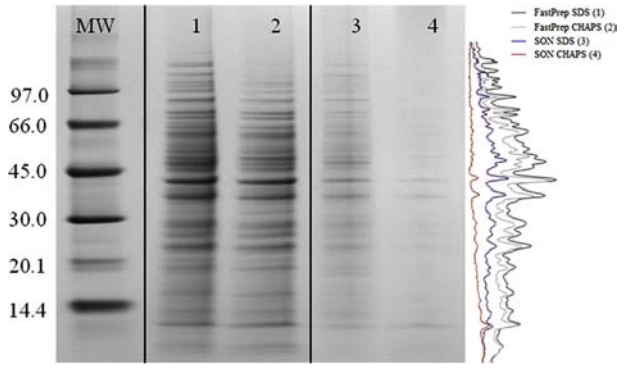


Fig. 1. SDS-PAGE before protein concentration and respective optical density traces. 1—Protein profile obtained with FastPrep and SDS buffer extraction; 2—protein profile obtained with FastPrep and CHAPS buffer extraction; 3—protein profile obtained with sonication and SDS buffer extraction; 4—protein profile obtained with sonication and CHAPS buffer extraction. *MW*—molecular weight (KDa).

However, it is known that protein precipitation leads to specific changes in the protein composition of proteomic samples. These modifications depend, mainly, on the specific structure of the protein rather than the precipitating agent used [41]. Nevertheless, proteins recovered in each extraction method were precipitated, solubilised and quantified, followed by SDS-PAGE (Supplementary Fig. S1) and LC–MS/MS analysis.

A total of 453 *S. epidermidis* proteins were identified, which corresponds to 17.96% of the predicted proteome (total of 2522 for *S. epidermidis* RP62A strain in UniProtKB database, at 29112013) with an increased confidence (FDR was below 5.5% among replicates). Venn diagram [42] demonstrated that 158 proteins were common to all extraction conditions (Supplementary Fig. S2). A total of 361 proteins were identified in FastPrep lysates with SDS, 391 in FastPrep with CHAPS, 359 in sonication lyses with SDS and 175 proteins after sonication in the CHAPS extraction buffer. The FastPrep protocol seemed to be the most efficient to lyse cells within *S. epidermidis* biofilms. Additionally, the CHAPS extraction buffer resulted in the identification of a higher number of proteins, compared to the SDS extraction buffer. Interestingly, this last finding, diverges from the work described by Encheva and colleagues [43], where it was shown that SDS gave a higher protein yield as compared to CHAPS, in an analysis of the *Streptococcus pneumoniae* proteome. SDS is an anionic detergent, used as a surfactant in protein denaturation, breaking lipid–lipid interactions and lipid–protein interactions rather than protein–protein interactions [44]. SDS is known to be very effective at solubilising almost all proteins [45,46]. However, it denatures them, causing loss of their native conformations and functions [47]. Alternatively, zwitterionic detergents such as CHAPS minimize protein–protein interactions [28,48]. Differences in extraction efficiency support the importance of extraction buffer to optimize protein yield or to increase yields of groups of proteins.

Next, Gene Ontology (GO) annotation, incorporating molecular function (Supplementary Table 1), biological processes (Supplementary Table 2) and cellular component (Supplementary Table 3) of proteins recovered from each extraction condition was analyzed. The main differences were observed in molecular function enriched categories (Fig. 2). The GO terms adenyl nucleotide binding (GO:0030554) and nucleic acid binding (GO:0003676) were only found in protein extraction performed with FastPrep lysis. Similarly, the GO terms for metal ion binding (GO:0046872), cation binding (GO:0043169) and ion binding (GO:0043167) were only found enriched in extractions performed with SDS buffer. These findings may be explained by the interaction established by SDS and cationic metal ions, due to the anionic head group of SDS [49]. While some studies showed that mechanical disruption of bacterial cells enhances the identification of cytoplasmic proteins [50,51], a number of cell membrane, secreted and cell surface proteins were also identified here. Membrane proteins are hydrophobic and they are present in low levels, since they are unstable and often aggregate, causing problems in analyzing membrane protein extractions [52]. However, within a heterogeneous protein properties set, it is difficult to find the conditions which will solubilise all proteins, including most membrane proteins, since not all are equally hydrophobic [53].

In an attempt to search for a methodological impact in the intrinsic properties of identified proteins, GRAVY score (grand average of hydropathy), molecular weight and p*I* were analyzed (Fig. 3). Overall, p*I*, protein molecular weight and GRAVY score presented a similar tendency, among the tested conditions, with a few exceptions. Most of the identified proteins had a GRAVY score between -0.5 and -0.25 (Fig. 3A). CHAPS extraction buffer allowed separation of a higher number of hydrophilic proteins (GRAVY score lower than -1.00) compared to SDS extraction buffer. Although gel-based approaches, e.g. SDS-PAGE, may allow

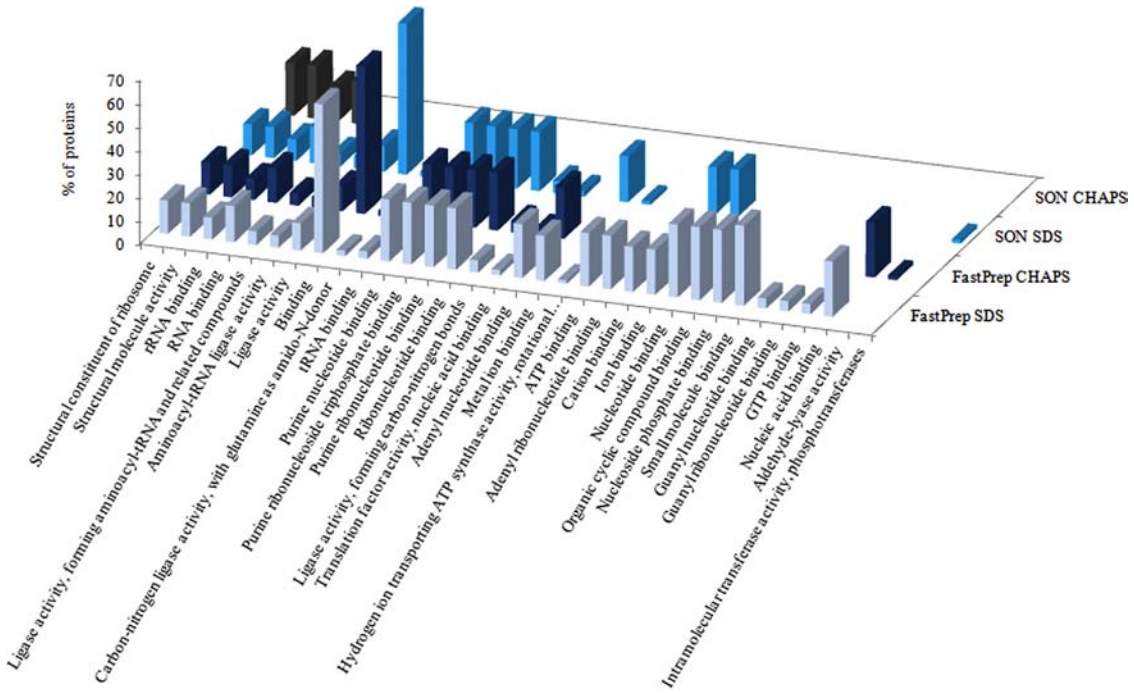


Fig. 2. GO classification. Molecular function specific terms with statistically significant enrichment ($p < 0.05$, FDR-corrected).

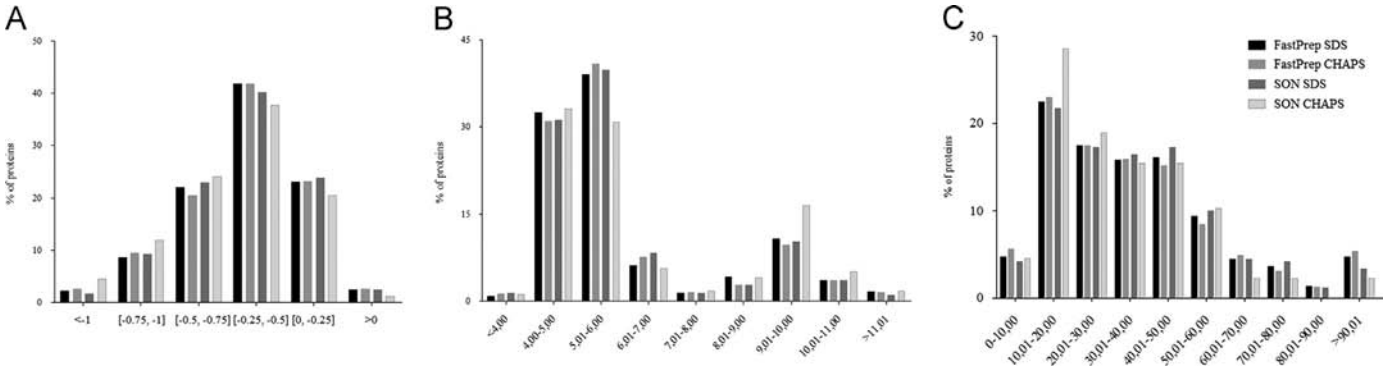


Fig. 3. Intrinsic properties of proteins. GRAVY (A), p*I* (B) and molecular weight (C) for each condition.

recovery of a significantly higher number of hydrophobic proteins, these extraction methods seemed to be less efficient at isolating hydrophobic proteins (positive GRAVY score). However, a few cell membrane proteins were identified, despite having high hydrophobicity. Our approach allowed us to identify only 3.3% of hydrophobic proteins. In proteins inferred from homology or with evidence at protein level (total of 997 proteins in UniProtKB/Swiss-Prot at 29112013), the number of hydrophobic proteins corresponds to 13.04%. Concerning p*I*, most of the isolated proteins showed a value between 4–6 or 9–10, similar to proteins inferred from homology or with evidence at protein level. More than 60% of proteins had a p*I* between 4 and 6 (Fig. 3B). Gumber et al. [54] showed that non-ionic detergents, such as Tween20 and Triton X-100 were more efficient at extracting proteins with high p*I*. Conversely, CHAPS associated with urea was shown to extract more proteins with low p*I* [54]. Regarding molecular weight, most of the proteins presented a mass between 10 and 50 kDa (Fig. 3C), which is also the most common range among the proteins inferred from homology or with evidence at the protein level. The FastPrep protocol allowed separation of higher numbers of proteins with more than 90 kDa compared to sonication. Moreover, the CHAPS extraction buffer combined with FastPrep seemed to be more efficient than SDS in obtaining proteins of less than 10 kDa. Independent of the methodological approach, a predominance of hydrophilic proteins, with 10–50 kDa and a p*I* between 4 and 6 was observed. Overall, major differences were not clearly found in molecular weight, GRAVY and p*I*, and only the GO analysis showed evident differences between SDS and CHAPS detergent extraction buffers.

3.2. Transcriptomic characterization

Whole transcriptomic profile of *S. epidermidis* biofilm cells was obtained by RNA-seq. This methodology represents a valuable method to measure mRNA expression levels, since RPKM normalization allows comparison of transcript levels among and within samples [36]. A total of 2069 genes were found with a RPKM value above 1.00, which corresponds to 77.72% of the *S. epidermidis* genome (total of 2662 for RP62A strain in GenBank). More than 50% of transcripts presented RPKM values up to 250. The most represented GO slim terms in each RPKM group (RPKM < 150, 151 > RPKM < 250 and RPKM > 250) are represented in Fig. 4. Additionally to common GO terms, RPKM values above 250 showed a predominance of catabolic (GO:0009056) and carbohydrate metabolic processes (GO:0005975) within the biological process GO category (Fig. 4A). In contrast, transcripts with RPKM lower than

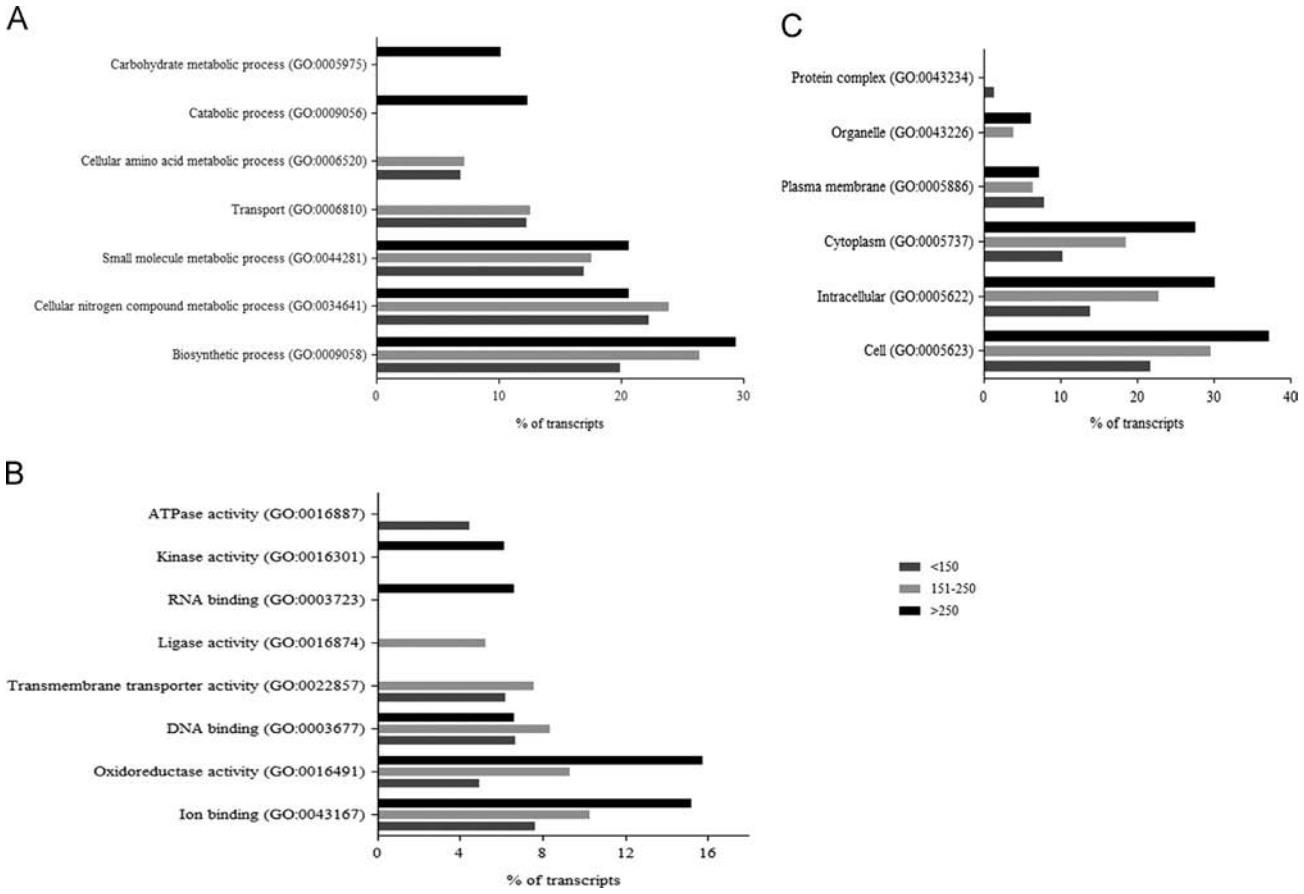


Fig. 4. GO classification of RNA-seq data. Five most represented GO slim terms of biological processes (A), molecular functions (B) and cellular components (C).

Table 1
List of the 10 genes with higher RPKM values found in transcriptomic analysis and respective function.

Gene	RPKM	Gene function
*SERP_SeSRP*1	299,510.4	Non-coding RNA involved in protein export
*SERP_SetmRNA*1	372,738.7	Transfer-messenger RNA
*SERP*1273	28,468.9	Universal stress protein
*SERP*2379	27,311.7	Diacetyl reductase [(S)-acetoin forming] which catalyzes the irreversible reduction of 2,3-butanediol to (S)-acetoin in the presence of NADH
*asp*23	24,019.2	Alkaline shock protein 23 which may play a key role in alkaline pH tolerance
arcC	11,927.2	Carbamate kinase
*SERP*2220	13,204.3	Universal stress protein
*SERP_SernpB*1	15,829.8	Non-coding RNA
spoVG	13,016.0	Septation protein
*SERP*2343	11,865.1	Uncharacterized protein

250 were associated with transport (GO:0006810) and cellular amino acid metabolic processes (GO:0006520), in addition to common GO terms. Molecular functions related to RNA binding (GO:0003723) and kinase activity (GO:0016301) were only found in transcripts with RPKM higher than 250 (Fig. 4B). Regarding cellular components (Fig. 4C), protein complex category (GO:0043234) was amongst the most represented transcripts with RPKM lower than 150. Amongst the 10 most expressed transcripts are genes involved in response to stimulus, translation, catabolic processes and non-coding RNAs (Table 1). These were expected results since during growth, bacteria need to obtain energy. Moreover, increased expression of certain classes of genes may be related to an adaptive response [55–59]. It is well known that glucose has a key role in biofilm physiology since is generally used to promote biofilm growth *in vitro* [7,31]. However, high concentrations of glucose affect biofilm gene expression [31].

3.3. Comparative proteomic and transcriptomic analysis

In order to compare proteomic and transcriptomic profiles, mass spectrometry and RNA-seq data were compared. Large scale proteomic experiments have been conducted using emPAI to determine, in a single LC–MS/MS experiment, the relative quantitation of proteins based on protein coverage by the peptide matches in a database search result [60–62]. Since the emPAI value has a linear correlation with protein concentration, it allows a more accurate estimation of protein abundance, as compared to simple peptide or spectral count [62,63]. In order to obtain an estimation of protein abundance, two independent experiments were performed. Then, emPAI values were compared within each condition (Supplementary Fig. S3). Importantly, emPAI presented the same tendency among proteins found in each extraction condition. Furthermore, reproducibility of experiments was also high, as indicated by Pearson correlation (Pearson's *r*

correlation), which varied between 0.81 and 0.99. Based on these results, we chose to calculate the emPAI average for further analysis. Extremely abundant proteins may affect the efficiency of protein identification because of ionization suppression and detector saturation as well as the limited loading capacity of LC columns [62]. We observed that bead beating lysis led to a lower percentage of identified proteins with low emPAI (0–0.20) compared to those identified following sonication (Supplementary Fig. S4). Moreover, a combination of bead beating and CHAPS extraction buffer showed more proteins with higher emPAI values (>5.00). Protein separation by SDS-PAGE and in-gel digestion decreased sample complexity and, consequently, contributed to avoiding suppression by extremely abundant proteins. Since proteins with similar abundances may functionally be correlated, proteins common to all conditions were further analyzed using CLUSTER 3.0 [64] (Fig. 5). We found four main clusters which resulted from the hierarchical clustering (two main biological processes are represented in Fig. 5). Proteins with lower emPAI tended to be involved in biosynthetic and cellular nitrogen compound metabolic processes (cluster A and D). Clusters B and C include mainly proteins with higher emPAI values. Protein cluster B is mainly related to biosynthetic processes and translation. Protein cluster C is related to biosynthetic and catabolic processes. Catabolic process was also found as one of the most prevalent GO term in transcripts with higher RPKM (Fig. 4A). Interestingly, proteins with the highest emPAI values presented translation among the main biological processes. In accordance, molecular functions, such as structural constituent of ribosome and RNA binding, were found among these proteins. However, these biological functions were not evidenced in transcripts with the highest RPKM. More precisely, instead of translation, response to stress was a biological process found significant in these transcripts, among others. In relation to molecular functions, only oxidoreductase activity was a significant class. Despite a biological condition is not characterized by the most expressed transcripts or proteins, it is of utmost importance to undertake a whole bacteriome analysis using multi-approaches. RPKM obtained by RNA-seq was next compared to emPAI values obtained from protein extraction experiments performed with FastPrep and sonication (Fig. 6). Correlations between mRNA transcripts and protein abundance obtained with FastPrep lyses were 0.37 and 0.36 (Pearson coefficient) in SDS and CHAPS extraction buffer, respectively. A somewhat smaller correlation coefficient was observed in sonication lyses with SDS ($r=0.30$) and CHAPS extraction buffer ($r=0.22$). Although this is not a strong correlation, our results are in agreement with correlation data previously described in bacteria (reviewed by [30]). When we zoomed Fig. 6A and B, we found that several proteins did not correlate with mRNA expression level. The main biological processes of these proteins are translation (when emPAI is higher than RPKM) and response to stress (when emPAI is lower than RPKM). Interestingly, dormancy is associated with low metabolic activity, leading to a decrease expression of transcripts involved in translation [65]. This suggests that these biological processes, in particular, may contribute to a lower correlation between transcriptomic and proteomic data. In almost every organism, transcript abundances only partially predict protein abundances, which suggests that other modes of regulation must be involved to explain how the levels of proteins are set within cells [29]. Also, the localization of proteins may display different correlations when compared to global correlation [66]. Despite direct correlation between proteins and mRNA is lower than 0.50, besides noise and experimental errors [67], several levels of regulation of transcripts and proteins may cause variability, such as transcription, post-transcription and post-translation regulation. Protein folding and post-translational modifications as phosphorylation, glycosylation, acetylation, proteolysis, methylation, lipidation, among others, are the most significant modifications [68–71]. Phosphorylation, such as found in LRTQKIVFS(Phospho)IGLCYSILMALSR peptide (Q5HLC3),

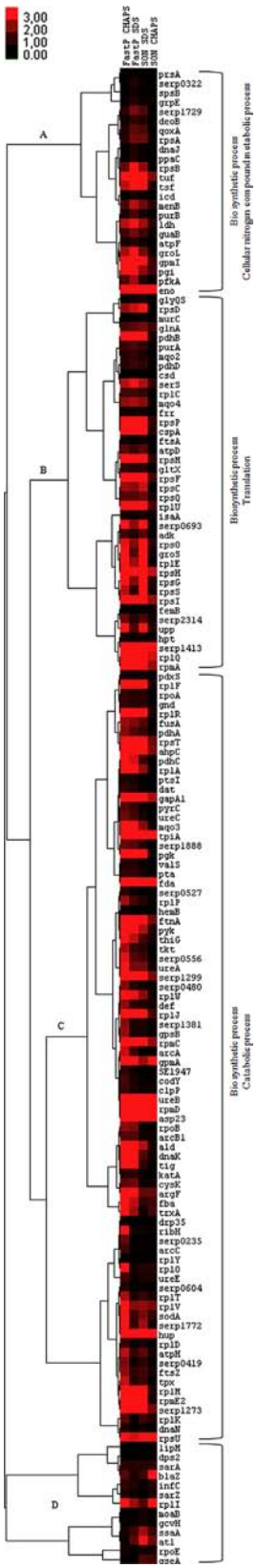


Fig. 5. emPAI hierarchical clustering. Clusters and two most represented biological function of the common proteins in each of the tested conditions generated in CLUSTER 3.0 and based on emPAI average from replicates (Slim terms).

corroborate that protein modifications increase phenotypic variability. These regulation mechanisms may explain why transcripts and proteins levels have a low correlation, among bacteria. Previously, it

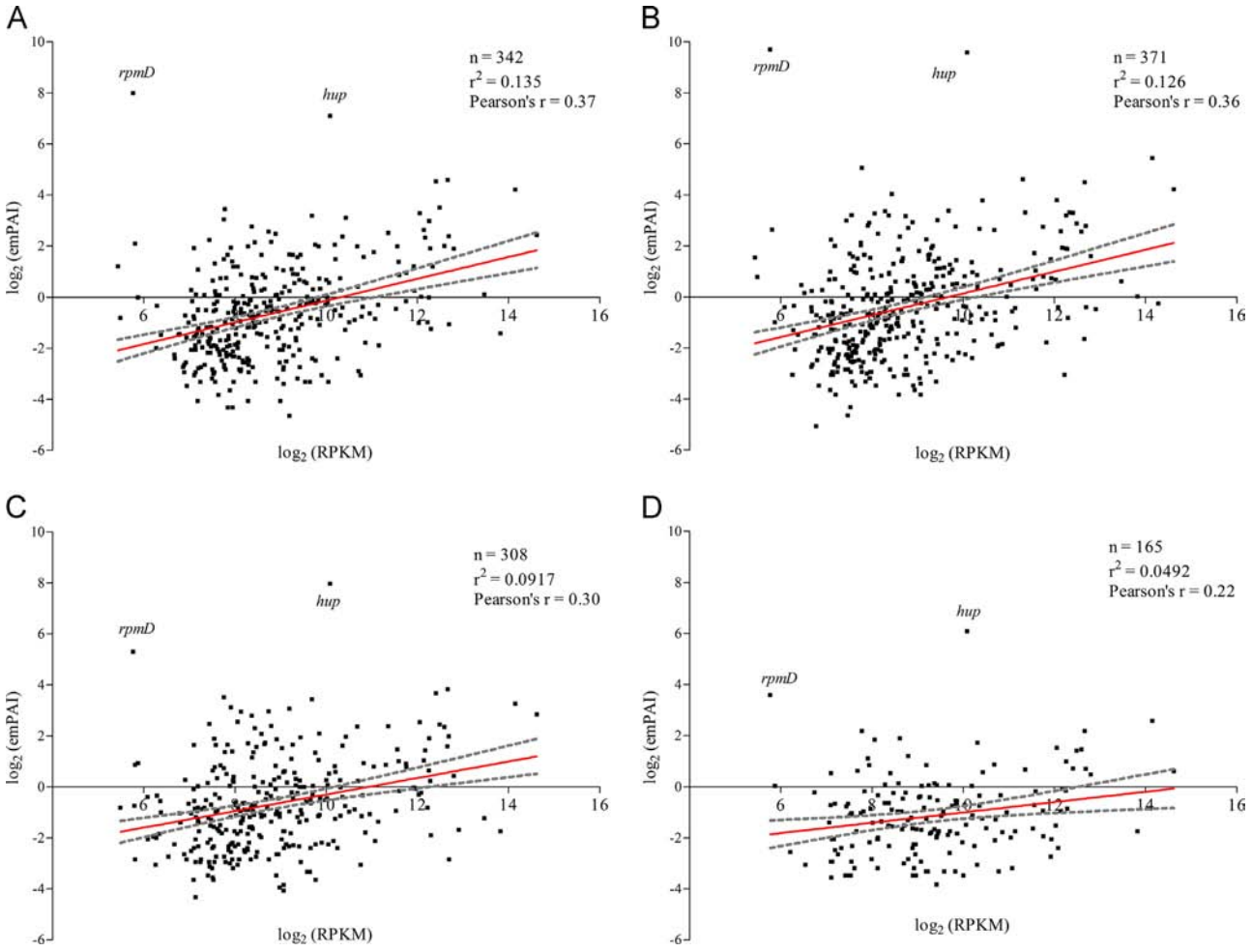


Fig. 6. Protein and transcript correlation in *S. epidermidis* biofilms grown in glucose enriched medium. FastPrep SDS (A), FastPrep CHAPS (B), SON SDS (C), SON CHAPS (D). Linear regression ($R2$), Pearson correlation (Pearson's r) and a number of proteins (n) are shown. The 95% confidence interval is shown is each condition, represented in grey dashed line. All correlations were significant ($p < 0.01$). SON—sonication.

was shown that, in *Staphylococcus aureus*, serine and threonine phosphorylations was associated with metabolic activity, virulence and translation [72]. This addresses the biological importance of regulation processes and modifications over proteins.

4. Conclusion

Similar to other studies, we demonstrated that protein extraction methods affect the proteome characterization of *S. epidermidis* biofilms. It is assumed that an efficient protein extraction method is crucial to ensure successful proteome analysis. A combination of mechanical and chemical lyses or enzymatic lysis provides a better methodology to extract proteins from *S. epidermidis* biofilms. The ideal choice of a detergent is still empirical, although, optimization of sample preparation is fundamental to correctly analyze the cell proteome. Our data suggest that a higher number of total proteins from *S. epidermidis* biofilm can be extracted and recovered by a combination of glass beads mechanical lysis with CHAPS extraction buffer. However, only mildly hydrophobic proteins can be solubilised with SDS or CHAPS. Also, the use of SDS extraction buffer led to an enhancement of metal ion binding proteins. A few lyse buffers have been used to enhance protein extraction, but one buffer is not sufficient for all purposes. This study emphasizes the need for a detailed study over extraction buffers that should be used for each experiment in order to identify the most efficient extraction methodology.

More important, we provide evidences that transcriptomic and proteomic data present a similar correlation to other bacteria, despite the detergent extraction buffer used. Interestingly, proteins involved in translation or response to stress appear to be those which less correlate with the correspondent transcript. Several "omics" may provide useful information instead of individual transcriptome or proteome analysis, since it gives an integrative view of a specific physiological state.

Acknowledgements

The authors thank Stephen Lorry at Harvard Medical School for providing CLC Genomics software. This work was funded by Fundação para a Ciência e a Tecnologia (FCT) and COMPETE grants PTDC/BIA-MIC/113450/2009, FCOMP-01-0124-FEDER-014309, QOPNA research unit (project PEst-C/QUI/UI0062/2013), RNEM (National Mass Spetrometry Network) and CENTRO-07-ST24-FEDER-002034. The following authors had an individual FCT fellowship: VC (SFRH/BD/78235/2011); AF (SFRH/BD/62359/2009). NC is an Investigador FCT. The authors also thank the FCT Strategic Project PEst-OE/EQB/LA0023/2013 and the Project "BioHealth—Biotechnology and Bioengineering approaches to improve health quality", Ref. NORTE-07-0124-FEDER-000027, co-funded by the Programa Operacional Regional do Norte (ON.2-O Novo Norte), QREN, FEDER. The authors also acknowledge the project "Consolidating Research Expertise and Resources on

Cellular and Molecular Biotechnology at CEB/IBB", Ref. FCOMP-01-0124-FEDER-027462.

Appendix A. Supporting information

Supplementary data associated with this article can be found in the online version at http://dx.doi.org/10.1016/j.talanta.2014.10.012.

References

[1] M. Otto, Semin. Immunopathol. 34 (2012) 201–214.
[2] L.G. Harris, R.G. Richards, Injury 37 (Suppl. 2) (2006) S3–14.
[3] F. Cerca, F. Andrade, A. Franca, E.B. Andrade, A. Ribeiro, A.A. Almeida, N. Cerca, G. Pier, J. Azeredo, M. Vilanova, J. Med. Microbiol. 60 (2011) 1717–1724.
[4] K.S. Williamson, L.A. Richards, A.C. Perez-Osorio, B. Pitts, K. McInnerney, P.S. Stewart, M.J. Franklin, J. Bacteriol. 194 (2012) 2062–2073.
[5] J. Kim, J.S. Hahn, M.J. Franklin, P.S. Stewart, J. Yoon, J. Antimicrob. Chemother. 63 (2009) 129–135.
[6] J.A. Shapiro, V.L. Nguyen, N.R. Chamberlain, J. Med. Microbiol. 60 (2011) 950–960.
[7] Y. Yao, D.E. Sturdevant, M. Otto, J. Infect. Dis. 191 (2005) 289–298.
[8] S.R. Gill, D.E. Fouts, G.L. Archer, E.F. Mongodin, R.T. Deboy, J. Ravel, I.T. Paulsen, J.F. Kolonay, L. Brinkac, M. Beanan, R.J. Dodson, S.C. Daugherty, R. Madupu, S.V. Angiuoli, A.S. Durkin, D.H. Haft, J. Vamathevan, H. Khouri, T. Utterback, C. Lee, G. Dimitrov, L. Jiang, H. Qin, J. Weidman, K. Tran, K. Kang, I.R. Hance, K.E. Nelson, C.M. Fraser, J. Bacteriol. 187 (2005) 2426–2438.
[9] Y.Q. Zhang, S.X. Ren, H.L. Li, Y.X. Wang, G. Fu, J. Yang, Z.Q. Qin, Y.G. Miao, W.Y. Wang, R.S. Chen, Y. Shen, Z. Chen, Z.H. Yuan, G.P. Zhao, D. Qu, A. Danchin, Y.M. Wen, Mol. Microbiol. 49 (2003) 1577–1593.
[10] K. Aggarwal, K.H. Lee, Brief. Funct. Genomic. Proteomics 2 (2003) 175–184.
[11] R. Nandakumar, M.P. Nandakumar, M.R. Marten, J.M. Ross, J. Proteome Res. 4 (2005) 250–257.
[12] X.M. Yang, N. Li, J.M. Chen, Y.Z. Ou, H. Jin, H.J. Lu, Y.L. Zhu, Z.Q. Qin, D. Qu, P.Y. Yang, FEMS Microbiol. Lett. 261 (2006) 32–40.
[13] C.L. Gatlin, R. Pieper, S.T. Huang, E. Mongodin, E. Gebregeorgis, P.P. Parmar, D.J. Clark, H. Alami, L. Papazisi, R.D. Fleischmann, S.R. Gill, S.N. Peterson, Proteomics 6 (2006) 1530–1549.
[14] A. Resch, S. Leicht, M. Saric, L. Pasztor, A. Jakob, F. Gotz, A. Nordheim, Proteomics 6 (2006) 1867–1877.
[15] D. Becher, K. Hempel, S. Sievers, D. Zuhlke, J. Pane-Farre, A. Otto, S. Fuchs, D. Albrecht, J. Bernhardt, S. Engelmann, U. Volker, J.M. van Dijl, M. Hecker, PLoS One 4 (2009) e8176.
[16] C. Kohler, S. Wolff, D. Albrecht, S. Fuchs, D. Becher, K. Buttner, S. Engelmann, M. Hecker, Int. J. Med. Microbiol. 295 (2005) 547–565.
[17] R. Monteiro, R. Vitorino, P. Domingues, H. Radhouani, C. Carvalho, P. Poeta, C. Torres, G. Igrejas, J. Proteomics 75 (2012) 2892–2915.
[18] S. Planchon, M. Desvaux, I. Chafsey, C. Chambon, S. Leroy, M. Hebraud, R. Talon, J. Proteome Res. 8 (2009) 1797–1809.
[19] M.M. Shaw, B.M. Riederer, Proteomics 3 (2003) 1408–1417.
[20] M. Fountoulakis, B. Takacs, Methods Enzymol. 358 (2002) 288–306.
[21] H.C. Flemming, J. Wingender, Nat. Rev. Microbiol. 8 (2010) 623–633.
[22] A. Franca, A.I. Freitas, A.F. Henriques, N. Cerca, PLoS One 7 (2012) e37480.
[23] S. Vilain, V.S. Brozel, J. Proteome Res. 5 (2006) 1924–1930.
[24] C. Rathsam, R.E. Eaton, C.L. Simpson, G.V. Browne, V.A. Valova, D.W. Harty, N.A. Jacques, J. Proteome Res. 4 (2005) 2161–2173.
[25] B.L. de Jonge, Y.S. Chang, D. Gage, A. Tomasz, J. Biol. Chem. 267 (1992) 11255–11259.
[26] J.K. Kumar, Appl. Microbiol. Biotechnol 80 (2008) 555–561.
[27] J.A. Wu, C. Kusuma, J.J. Mond, J.F. Kokai-Kun, Antimicrob. Agents Chemother. 47 (2003) 3407–3414.
[28] J.M. Neugebauer, Methods Enzymol. 182 (1990) 239–253.
[29] C. Vogel, E.M. Marcotte, Nat. Rev. Genet. 13 (2012) 227–232.
[30] A.R. de Sousa, L.O. Penalva, E.M. Marcotte, C. Vogel, Mol. Biosyst. 5 (2009) 1512–1526.
[31] D. Mack, N. Siemssen, R. Laufs, Infect. Immun. 60 (1992) 2048–2057.
[32] L. Jiang, L. He, M. Fountoulakis, J. Chromatogr. A 1023 (2004) 317–320.
[33] M. Ashburner, C.A. Ball, J.A. Blake, D. Botstein, H. Butler, J.M. Cherry, A.P. Davis, K. Dolinski, S.S. Dwight, J.T. Eppig, M.A. Harris, D.P. Hill, L. Issel-Tarver, A. Kasarskis, S. Lewis, J.C. Matese, J.E. Richardson, M. Ringwald, G.M. Rubin, G. Sherlock, Nat. Genet. 25 (2000) 25–29.
[34] A. Franceschini, D. Szklarczyk, S. Frankild, M. Kuhn, M. Simonovic, A. Roth, J. Lin, P. Minguez, P. Bork, C. von Mering, L.J. Jensen, Nucleic Acids Res. 41 (2013) D808–D815.
[35] A. Franca, V. Carvalhais, T. Maira-Litran, M. Vilanova, N. Cerca, G. Pier, Pathog. Dis 70 (2014) 444–448.
[36] A. Mortazavi, B.A. Williams, K. McCue, L. Schaeffer, B. Wold, Nat. Methods 5 (2008) 621–628.
[37] J. Blonder, M.B. Goshe, R.J. Moore, L. Pasa-Tolic, C.D. Masselon, M.S. Lipton, R.D. Smith, J. Proteome Res. 1 (2002) 351–360.
[38] M.P. Washburn, D. Wolters, J.R. Yates III, Nat. Biotechnol. 19 (2001) 242–247.
[39] A. Tanca, G. Biosa, D. Pagnozzi, M.F. Addis, S. Uzzau, Proteomics 13 (2013) 2597–2607.
[40] A. Bodzon-Kulakowska, A. Bierczynska-Krzysik, T. Dylag, A. Drabik, P. Suder, M. Noga, J. Jarzebinska, J. Silberring, J. Chromatogr. B 849 (2007) 1–31.
[41] M. Zellner, W. Winkler, H. Hayden, M. Diestinger, M. Eliasen, B. Gesslbauer, I. Miller, M. Chang, A. Kungl, E. Roth, R. Oehler, Electrophoresis 26 (2005) 2481–2489.
[42] J.C. Oliveros. VENNY. An Interactive Tool for Comparing Lists with Venn Diagrams. ⟨www.bioinfogp.cnb.csic.es/tools/venny/⟩. 2007.
[43] V. Encheva, S.E. Gharbia, R. Wait, S. Begum, H.N. Shah, Proteomics 6 (2006) 3306–3317.
[44] A.M. Seddon, P. Curnow, P.J. Booth, Biochim. Biophys. Acta 1666 (2004) 105–117.
[45] M.P. Molloy, Anal. Biochem. 280 (2000) 1–10.
[46] S. Luche, V. Santoni, T. Rabilloud, Proteomics 3 (2003) 249–253.
[47] B. Hames, in: D. Rickwood, B. Hames (Eds.), Gel Electrophoresis of Proteins. A Practical Approach, New York, 1998, pp. 35-40.
[48] DM Bollag, SJ Edelstein, MD Rozycki, in: DM Bollag, SJ Edelstein, MD Rozycki (Eds.), Protein Methods, Wiley-Liss, New-York, 1996, pp. 1–26.
[49] S. Sahu, A. Mishra, G. Krishnamoorthy, Analyst 138 (2013) 5942–5948.
[50] K. Sauer, A.K. Camper, G.D. Ehrlich, J.W. Costerton, D.G. Davies, J. Bacteriol. 184 (2002) 1140–1154.
[51] K. Sauer, A. Camper, J. Bacteriol. 183 (2001) 6579–6589.
[52] M.A. Churchward, R.H. Butt, J.C. Lang, K.K. Hsu, J.R. Coorssen, Proteome Sci 3 (2005) 5.
[53] A.U. Freiburghaus, Mol. Biotechnol. 2 (1994) 281–293.
[54] S. Gumber, D.L. Taylor, R.J. Whittington, J. Microbiol. Methods 68 (2007) 115–127.
[55] S.E. Cramton, M. Ulrich, F. Gotz, G. Doring, Infect. Immun. 69 (2001) 4079–4085.
[56] J.K. Knobloch, K. Bartscht, A. Sabottke, H. Rohde, H.H. Feucht, D. Mack, J. Bacteriol. 183 (2001) 2624–2633.
[57] S. Rachid, K. Ohlsen, W. Witte, J. Hacker, W. Ziebuhr, Antimicrob. Agents Chemother. 40 (2000) 3357–3363.
[58] S. Dobinsky, K. Kiel, H. Rohde, K. Bartscht, J.K. Knobloch, M.A. Horstkotte, D. Mack, J. Bacteriol. 185 (2003) 2879–2886.
[59] T. Dorr, M. Vulic, K. Lewis, PLoS Biol. 8 (2010) e1000317.
[60] S.E. Ong, M. Mann, Nat. Chem. Biol. 1 (2005) 252–262.
[61] A. Kudlicki, PLoS One. 7 (2012) e32339.
[62] Y. Ishihama, Y. Oda, T. Tabata, T. Sato, T. Nagasu, J. Rappsilber, M. Mann, Mol. Cell Proteomics 4 (2005) 1265–1272.
[63] K. Shinoda, M. Tomita, Y. Ishihama, Bioinformatics 26 (2010) 576–577.
[64] M.J. de Hoon, S. Imoto, J. Nolan, S. Miyano, Bioinformatics 20 (2004) 1453–1454.
[65] K. Lewis, Nat. Rev. Microbiol. 5 (2007) 48–56.
[66] D. Greenbaum, C. Colangelo, K. Williams, M. Gerstein, Genome Biol. 4 (2003) 117.
[67] S. Haider, R. Pal, Curr. Genomics 14 (2013) 91–110.
[68] L. Straub, PLoS Biol. 9 (2011) e1001146.
[69] J.A. Cain, N. Solis, S.J. Cordwell, J. Proteomics 97 (2013) 265–286.
[70] T. Maier, M. Guell, L. Serrano, FEBS Lett. 583 (2009) 3966–3973.
[71] M. Guell, E. Yus, M. Lluch-Senar, L. Serrano, Nat. Rev. Microbiol. 9 (2011) 658–669.
[72] K. Ohlsen, S. Donat, Int. J. Med. Microbiol. 300 (2010) 137–141.

Talanta 132 (2015) 713–718

Contents lists available at ScienceDirect

Talanta

journal homepage: www.elsevier.com/locate/talanta

A novel dispersive solid-phase extraction method using metal-organic framework MIL-101 as the adsorbent for the analysis of benzophenones in toner

Ning Li, Quanfei Zhu, Yang Yang, Jianlin Huang, Xueping Dang, Huaixia Chen *

Hubei Collaborative Innovation Center for Advanced Organic Chemical Materials, Ministry-of-Education Key Laboratory for the Synthesis and Application of Organic Functional Molecules & College of Chemistry and Chemical Engineering, Hubei University, Wuhan 430062, China

ARTICLE INFO

Article history:
Received 22 July 2014
Received in revised form
12 October 2014
Accepted 16 October 2014
Available online 28 October 2014

Keywords:
Metal-organic framework (MOFs)
Benzophenone
2,4-Dihydroxybenzophenone
2-Hydroxy-4-methoxy-benzophenone
Dispersive solid-phase extraction (DSPE)
Toner samples

ABSTRACT

Metal-organic frameworks (MOFs) have been paid widespread attention in the field of adsorption and separation materials due to its porosity, large specific surface area, unsaturated metal-ligand sites and structural diversity. In this study, the green powder MIL-101 was synthesized and used for the extraction of benzophenone, 2,4-dihydroxybenzophenone and 2-hydroxy-4-methoxy-benzophenone from toner samples for the first time. The synthesized MIL-101 was characterized by X-ray diffraction, scanning electron microscopy, thermogravimetry and nitrogen adsorption porosimetry. The MIL-101 was applied as the dispersive solid phase extraction (DSPE) adsorbent for the extraction and preconcentration of benzophenone, 2,4-dihydroxybenzophenone and 2-hydroxy-4-methoxy-benzophenone from toner samples. The extraction conditions were investigated. Under the optimized conditions, a DSPE-HPLC method for the determination of benzophenone, 2,4-dihydroxybenzophenone and 2-hydroxy-4-methoxy-benzophenone was developed. The method yielded a linear calibration curve in the concentration ranges from 4.0 to 3500 μg L^{-1} for the three analytes in toner samples with regression coefficients (r^2) of 0.9992, 0.9999 and 0.9990, respectively. Limits of detection were 1.2, 1.2 and 0.9 μg L^{-1}, respectively. Both the intra-day and inter-day precisions (RSDs) were $<10\%$.

© 2014 Elsevier B.V. All rights reserved.

1. Introduction

The daily exposure to sunlight has harmful health effects. So, the use of personal care products containing ultraviolet (UV) filters steadily increased. In general, UV filters are divided in two categories: organic and inorganic filters, and are used in single or combination of both in cosmertics and sunscreens, to protect from UV light. The organic UV filters posses single or multiple aromatic structures, commonly conjugated with different chemical groups, which are able to absorb UV solar radiation and protect human skin from direct exposure. These compounds are used extensively in sunscreens, cosmetic products such as facial day creams, after-shave products, makeup formulations, lipsticks, shampoos, and in plastic based packaging materials.

There are 12 well-known BP-UV filters, namely benzophenone (BP), 2,4-dihydroxybenzophenone (benzophenone-1, BP-1) and 2-hydroxy-4-methoxy- benzophenon (benzophenone-3, BP-3), as well as other less usual compounds as 2-hydroxybenzophenone (2-OH-BP) or 4-hydroxybenzophenone (4-OH-BP). There are increasing evidences that BP-UV filters are able to interfere with the endocrine system. In vitro studies have shown that BPs stimulate the proliferation of the breast cancer cellline MCF-7 due to their estrogenic activity, and that these compounds have antiandrogenic activity too [1-3]. So, in European Union and China, the maximum content of BPs in cosmetics is regulated by the actual legislations, at a usual concentration between 0.1% and 10% (w/w). Therefore, monitoring of BPs in cosmetics samples is important for the quality control of sunscreen products.

Up to now, the main approaches for the detection of BPs included thin layer chromatography (TLC) [4], gas chromatography (GC) [5], high performance liquid chromatography (HPLC) [6,7], gas chromatography–mass spectrometry (GC–MS) [8,9] and liquid chromatography–mass spectrometry (LC–MS) [10]. All of the above reported methods are accurate but somewhat expensive and time consuming or requires complex sample preparation prior to analysis. In these methods, HPLC is a common and useful method for trace determination of analytes in complex samples. Sample preparation techniques, such as liquid–liquid extraction (LLE) [11–14], solid phase extraction (SPE) [15] and solid-phase microextraction (SPME) [16], can enhance the sensitivity and selectivity of HPLC. Compared with LLE and LPME, SPE has the

* Corresponding author at: College of Chemistry and Chemical Engineering, Hubei University, Wuhan 430062, China. Tel.: +86 27 88662747; fax: +86 27 88663043.
E-mail address: hxch@hubu.edu.cn (H. Chen).

http://dx.doi.org/10.1016/j.talanta.2014.10.038
0039-9140/© 2014 Elsevier B.V. All rights reserved.

advantages of simplicity, rapidity and less consumption of organic solvents. SPE has become a routine sample preparation technique for extracting analytes from water samples. Dispersive solid-phase extraction (DSPE) is a procedure which involves single extraction of sample with solid adsorbent and followed by a rapid clean-up process [17]. The advantages of the preparation method are simplicity of operation, efficient, less consumption of organic solvents. So, DSPE is previously used for the determination of pesticides, herbicides, environmental pollutants and veterinary drug residues.

Metal-organic frameworks (MOFs) are a new class of hybrid inorganic-organic microporous crystalline materials self-assembled straightforwardly from metal ions with organic linkers through coordination bonds. The availability of various building blocks of metal ions organic linkers makes it possible to prepare an infinite number of new MOFs with diverse structures, topologies, and porosity, which bear multiple complexing functions [18–21]. The particular interest in MOFs is due to the easy tunability of their pore size and shape from a microporous to a mesoporous scale by changing the connectivity of the inorganic moiety and the nature of organic linkers. Compared with conventional adsorbents, MOFs have diverse compositions and structure types, tunable pore size, large surface area, and coordinative unsaturated or saturated metal sites to regulate the adsorption ability. MOFs have shown great potential in sorption-related fields [22–33]. Recently, researches on the liquid phase adsorption on MOFs have attracted great interests. Unfortunately, to the best of our knowledge, MOFs have not been applied for the DSPE and determination of small molecule drugs in complex matrices.

MIL-101, $Cr_3O(F/OH)(H_2O)_2[C_6H_4(CO_2)_2]_3$, is one of the most widely studied MOFs which has a cubic structure, a huge pore volume and pore sizes. MIL-101 is built up from carboxylate moieties (terephthalic acid PTA) and chromium trimeric octahedral clusters and offers a unique high surface area, large pore windows (12 to 16 Å) and mesoporous pores (29 to 34 Å), and excellent chemical and solvent stability which are very suitable for liquid phase adsorption [34,35].

In this work, MIL-101 was synthesized using the hydrothermal synthesis method, and a novel DSPE method for the extraction and concentration of three commonly used BP-UV filters (benzophenone, 2,4-dihydroxybenzophenone, 2-hydroxy-4-methoxy-benzophenone) in toner samples was developed using MIL-101 as the adsorbent for the first time. The adsorption mechanism of analytes on MIL-101 was discussed. Some important extraction parameters affecting the performance, such as the amount of MIL-101, extraction time, extraction solvent, the solution pH and salt effect were investigated.

2. Experimental

2.1. Reagents and standards

Terephthalic acid (99%, TPA), chromium (III) nitrate $Cr(NO_3)_3 \cdot 9H_2O$ (98%) and hydrofluoric acid (HF) (40.0%) (Aladdin Chemistry Co. Ltd., Shanghai, China) were used to prepare MIL-101. N,N-dimethylformamide (99.5%, DMF) and ethanol (99.7%) (Sinopharm Chemical Reagent Co. Ltd., Shanghai, China) were used as the solvents. Benzophenone (99.5%, BP), 2,4-dihydroxybenzophenone (99.5%, BP1) and 2-hydroxy-4-methoxy-benzophenon (99.5%, BP3) were purchased from Aladdin (Aladdin Chemistry Co. Ltd., Shanghai, China). Methanol and acetonitrile (HPLC grade) were obtained from Tedia Company Inc. (Ohio, USA). Other reagents used were of analytical grade. Ultrapure water was obtained on an Ultrapure Water System (Beijing, China). *Caution: Care should be taken to avoid direct contact with hydrofluoric acid because of its high toxicity and to prepare all the solutions in a well-ventilated hood!*

The stock standard solutions of BP, BP1 and BP3 were prepared in methanol at a concentration of 1.0 mg mL^{-1} and stored at −4 °C in refrigerator. Working standard solutions of BP, BP1 and BP3 were prepared by appropriate dilution of the stock solutions using ultrapure water.

2.2. Apparatus and HPLC conditions

The chromatographic analysis was carried out on a Dionex Summit U3000 HPLC system equipped with a manual injector and a Photodiode Detector Array (PDA) (DionexTechnologies, USA). A personal computer equipped with a Chromeleon Chem-Station program for LC was used to process chromatographic data. An amethyst-C18 column (4.6 mm × 250 mm, 5 μm) from Sepax Technologies Inc. (Newark, USA) was connected with a guard column (cartridge 2.1 mm × 12.5 mm, 5 μm, Agilent Technologies, Palo Alto, CA, USA) filled with the same packing material. The mobile phase was a mixture of methanol-0.04% phosphoric acid solution (80:20, v/v) and the flow rate was 1.0 mL min^{-1}. The column temperature was set at 30 °C by a temperature controller (Nuohai Technologies, China). The UV detector was set at wavelengths of 256 nm (BP), 290 nm (BP1 and BP3) for analytes. All injections were performed manually with a 20.0 μL sample loop. 0.22 μm membrane was obtained from Xingya Scavenging Material Company (Shanghai, China).

The X-ray diffraction (XRD) patterns were recorded with a D/max-2500 diffractometer (Rigaku, Japan) using Cu K_α radiation ($\lambda = 1.5418$ Å) over the angular range from 2° to 50°. The microscopic morphology of the material was examined by a Model X-650 scanning electron microscope (Hitachi, Tokyo, Japan). The TGA experiments were performed on a PTC-10A thermal gravimetric analyzer (Hitachi, Tokyo, Japan) from room temperature to 800 °C at a ramp rate of 10 °C min^{-1}. The surface area, pore volume, and pore size distributions of adsorbents were measured on a NOVA 2000e surface area and pore size analyzer (Quantachrome, Florida, FL, USA) at 77 K in the range $0.02 \le P/P_0 \le 0.20$. The Barrett–Joyner–Halenda (BJH) method was used to calculate the mesopore distribution for the adsorbents.

2.3. Synthesis of MIL-101(Cr)

MIL-101 was synthesized according to Férey et al. [34] with small modifications. Typically, $Cr(NO_3)_3 \bullet 9H_2O$ (1601.1 mg, 4.0 mmol), terephthalic acid (665.2 mg, 4.0 mmol), and hydrofluoric acid (0.2 mL, 1.0 mmol) were mixed with 19.2 mL of ultrapure water in a teflon-lined stainless steel autoclave, sealed, heated to 220 °C for 8 h, and then were cooled down rapidly to 150 °C within 1 h. It was cooled down slowly to room temperature within 12 h. The resultant green crystalline solid was washed thoroughly with DMF and ethanol by Soxhlet extraction. The procedure was repeated at least 4 h to remove the unreacted terephthalic acid and ethanol from MIL-101 pores. The green solid was then evacuated in vacuum at 150 °C for 12 h to form dehydrated MIL-101, which was characterized by X-ray diffraction (XRD) spectrometry, thermogravimetric analysis (TGA), scanning electron microscopy (SEM) and nitrogen adsorption porosimetry.

2.4. Extraction procedure

The MIL-101 was dried overnight at 150 °C before use. Then, 12 mg of MIL-101 was dispersed into sample solution (20 mL) in a 50 mL centrifuge tube. The mixture was vortexed for 40 min. Subsequently, MIL-101 was isolated from the solution by centrifugation at 10000 rpm for 5 min. The supernatant was discarded. 1.0 mL of methanol with acetonitrile (3:7, v/v) was added. The analytes were desorbed under ultrasonication for 5 min (120 W, 100 kHz). The mixture was centrifuged at 10000 rpm for 5 min. The collected eluate was dried with a gentle stream of nitrogen at

30 °C and dissolved in 0.1 mL of methanol and filtered through 0.22 μm membrane for HPLC analysis.

2.5. Sample preparation

Three different toner samples were purchased from a local store. The toner samples were filtered through 0.22 μm millipore cellulose membrane, then, diluted for 10 times using ultrapure water and stored in clean glass containers at 4 °C in darkness before use.

3. Results and discussion

3.1. Characterization of the prepared MIL-101

The prepared MIL-101 was characterized by XRD, TGA, SEM and N_2 adsorption–desorption experiment (Fig. 1). The experimental XRD pattern of the synthesized MIL-101 crystals was in good agreement with the simulated one, showing the successful preparation of MIL-101. The TGA data revealed that the MIL-101 was stable up to 330 °C. The SEM image exhibited cubic shaped crystals

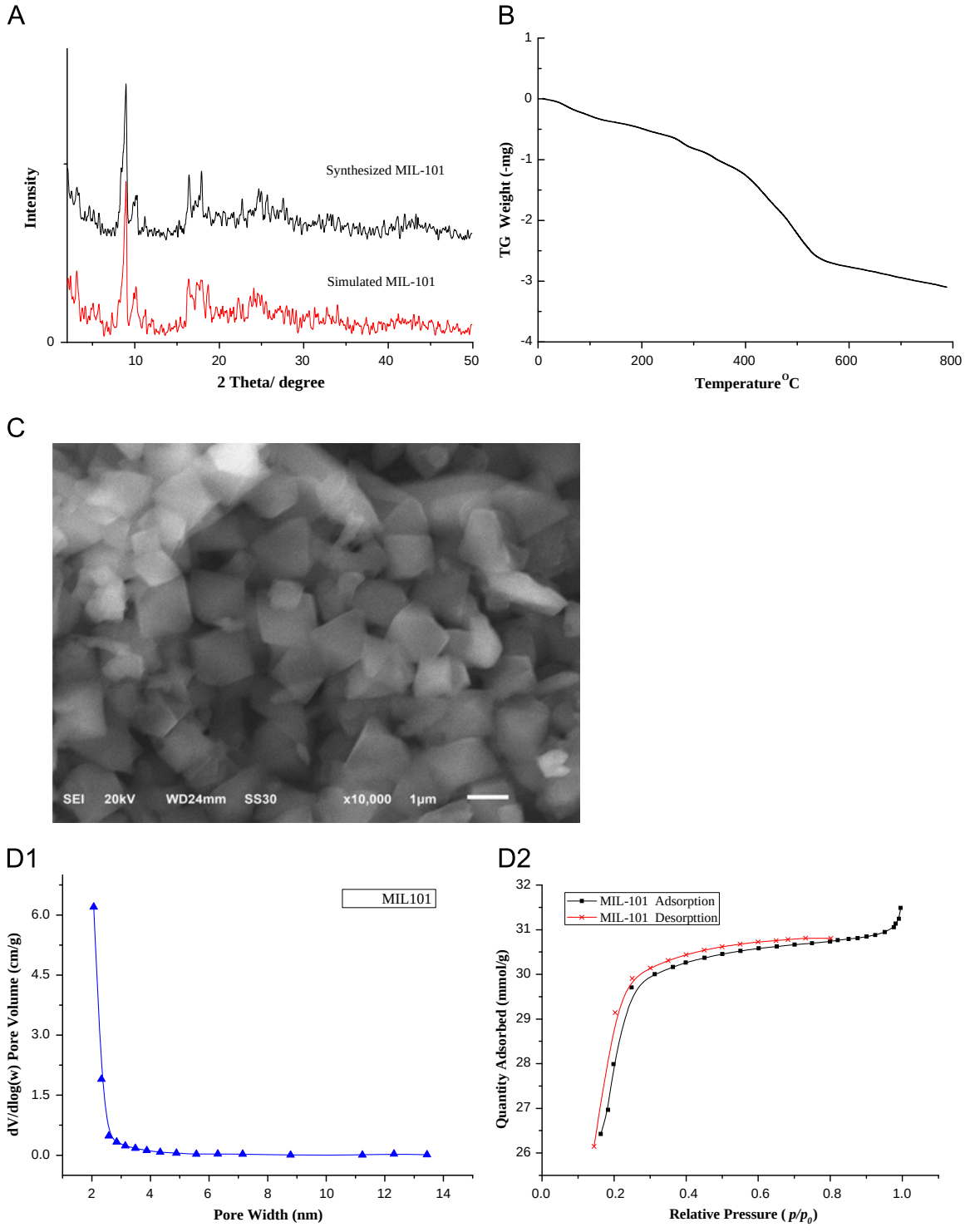


Fig. 1. XRD pattern (A), TGA curve (B), SEM image (C), nitrogen adsorption–desorption isotherms and the pore size distribution (D) of synthesized MIL-101.

of MIL-101 with an average size of 1 μm. The prepared MIL-101 was characterized by surface area and pore size analyzer and gave a BET surface area of 2295 m^2 g^{-1} with a pore volume of 0.53 cm^3 g^{-1}.

3.2. Optimization of the DSPE conditions

In order to optimize the DSPE conditions, several extraction parameters including the amount of MIL-101, desorption solvent, the adsorption time, solution pH and the ionic strength were investigated. Sample solutions (20 mL) were spiked with analytes at 100 μg L^{-1} to perform the experiments.

3.2.1. Effect of the amount of MIL-101

The amount of MIL-101 has a significant effect on the recoveries of target analytes. So, the amounts of MIL-101 were tested from 2.0 mg to 15.0 mg. The experimental results showed that the recoveries of analytes increased with the increase of MIL-101. When 12 mg of MIL-101 was used, the recoveries of BP, BP1 and BP3 were in the range of 80–100%. Subsequently, obtained analyte recoveries remained almost unchanged while increasing the amount of MIL-101. Therefore, 12 mg of MIL-101 was chosen as the final amount.

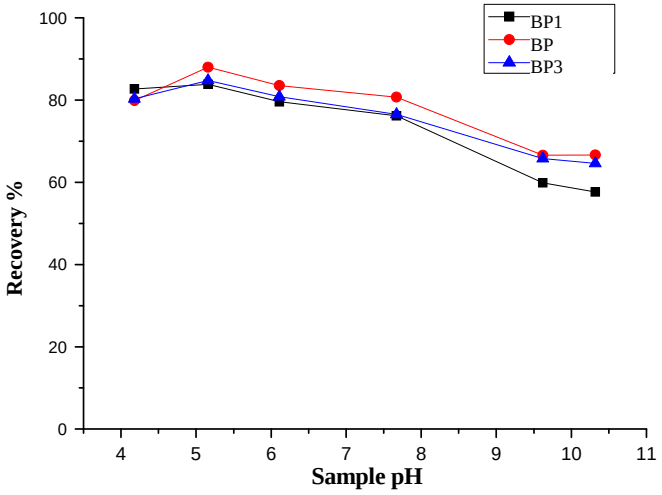


Fig. 2. The effect of solution pH. Other conditions: MIL-101, 12 mg; concentration of BP, BP1 and BP3, 100 μg L^{-1}; extraction time, 50 min; desorption solvent, 1 mL methanol with acetonitrile (3:7, v/v); 0% (w/v) NaCl.

3.2.2. Effect of desorption solvent

Different desorption solvents including methanol, methanol with acetonitrile (7:3, v/v), methanol with acetonitrile (5:5, v/v), methanol with acetonitrile (3:7, v/v) and acetonitrile were tested, respectively. The experimental data indicated that methanol with acetonitrile (3:7, v/v) provided the best desorption efficiency due to its strongest dissolving ability toward analytes. Ultrasonic irradiation enhanced the desorption of the analytes from MIL-101. The experimental results indicated that the 1.0 mL mixture of methanol with acetonitrile (3:7, v/v) as the eluent under ultrasonic irradiation offered the higher recoveries of analytes.

3.2.3. Effect of the adsorption time

The adsorption time had an obvious effect on the recoveries of target analytes. It was necessary to select an exposure time that guarantees the equilibrium between aqueous phase and sorbent. So, the adsorption times were varied from 20 min to 60 min. The experimental results showed that the highest recoveries of these analytes were obtained when the adsorption time was at 50 min. After 50 min, the recoveries of these analytes decreased slightly. Therefore, the adsorption time of 50 min was chosen for further studies.

3.2.4. Effect of solution pH

The sample pH is another important factor that affects the extraction of analytes. The sample pH not only influences the molecular existing form of analytes but also closely affects the charge species and density on the sorbent surface. The effect of solution pH on the recoveries of BP, BP1 and BP3 was investigated in a range of 4.0 to 10.5. As illustrated in Fig. 2, the recoveries of analytes increased slightly when the solution pH increased from 4.0 to 5.0, then further increase of pH from 5.0 to 10.5 led to a

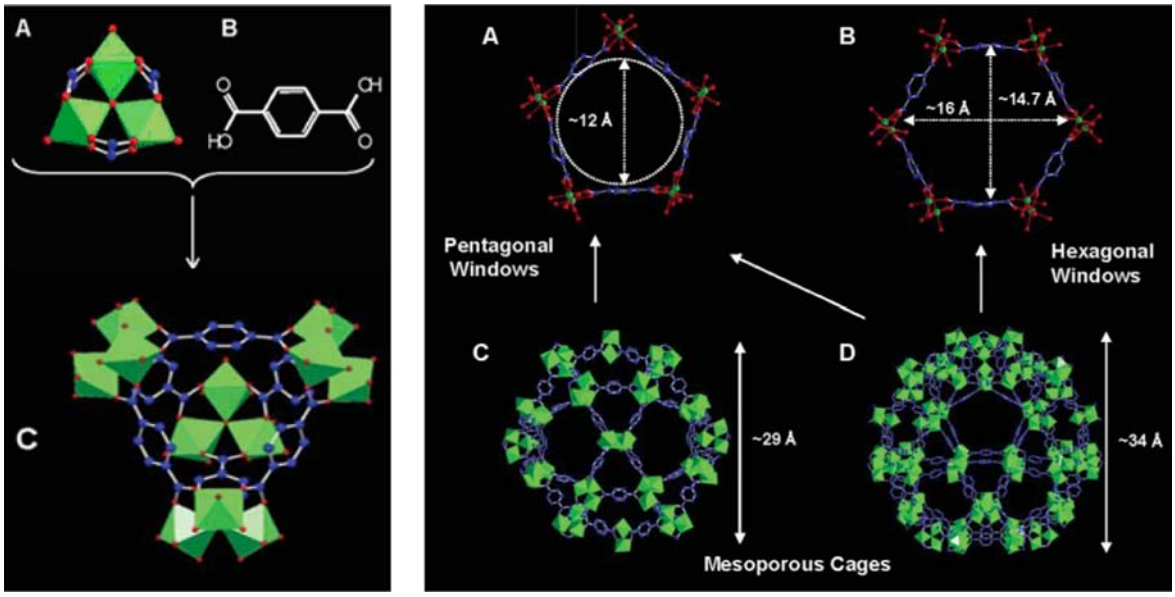


Fig. 3. Structure of MIL-101. Adapted and reproduced with permission from Ref. [33] Copyright 2005 American Association for the Advancement of Science; Left (A) The computationally designed trimeric building block chelated by three carboxylic functions. The ST was constructed with (B) terephthalic acid, which lies (C) on the edges of the ST. Right (A and B) Ball-and-stick view and free dimensions (A°) of the pentagonal and hexagonal windows. (C and D) Ball-and-stick view of the two cages.

decrease of the recoveries. Thus, pH 5.0 was chosen as the optimum sample pH.

Generally, when the solution pH value is higher than pKa of the analyte, the analyte is mostly in an ionic form due to the deprotonation. The dissociation constants (pKa) of BP, BP1 and BP3 are all bigger than 7.5, respectively. As the solution pH $\leq$ 5.0, the three ananlytes were mainly in the forms of molecule state. A significant decrease of the adsorption capacity of MIL-101 for BP, BP1 and BP3 with the pH increased from 5.0 to 10.5 might be resulted from the increase of negative charges on the surface of MIL-101[36]. As revealed in Fig. 3, Cr^{3+} exists in octahedral environment, each of the octahedral is coordinated by one chromium ion and four carboxyl ligand from terephthalic acid. The π-π interaction between the benzene rings in analytes and MIL-101 may also play important role for the extraction. BP, BP1 and BP3 with delocalized π electrons allowed π-π interaction with the terephthalic acid molecules in the framework of MIL-101, and the π-complexation between the π-electrons of benzene rings and Lewis acid sites in the pores of MIL-101. Besides, the molecules of the target analytes can enter the pores of MIL-101 for the kinetic dynamic diameters of BP, BP1 and BP3 are smaller than the pores (29 Å and 34 Å) and their windows (12 Å and 16 Å × 14.5 Å) of MIL-101 [34]. And, large octanol-water partitioning coefficients of the analytes enhance their hydrophobic interaction with the hydrophobic MIL-101 framework. The results showed that the interaction between MIL-101 and the analytes made a principal contribution to extraction.

3.2.5. *Effect of ionic strength*

Addition of salt into the sample solutions could decrease the solubility of organic compounds in the aqueous solution and lead to the salting-out effect. In the extraction procedure, the effect of ionic strength of the sample solution was evaluated by adding 0–25% (w/v) of sodium chloride into the samples. The experimental results showed that the salt concentration have not influence on the extraction efficiency. So, no NaCl was added in the subsequent experiments.

3.3. *Analytical approach*

Under the optimized conditions, the linearity of the calibraton curves was in the range of 4.0–3500 μg L^{-1} for three analytes in toner samples. Satisfactory determination coefficients (r^2) (>0.9990) for analytes were obtained. The limits of detection (LODs, S/N=3) and limits of quantification (LOQs, S/N=10) were found to be 0.9–1.2 μg L^{-1} and 3.1–4.0 μg L^{-1}, respectively (Table 1), which were lower than the maximum possible magnitude of three analytes in toner.

Table 1
Linearity and sensitivity characteristics of the MIL-101-DSPE-HPLC method for BP, BP1 and BP3.

Matrix	Analyte	Regression equation	R^2	LOD (μg L^{-1})	LOQ (μg L^{-1})
Toner	BP	$Y=0.0143X+0.4942$	0.9992	1.2	3.9
	BP1	$Y=0.0132X-0.0644$	0.9999	1.2	4.0
	BP3	$Y=0.0191X-0.4691$	0.9990	0.9	3.1

3.4. *Sample analysis*

The development method was applied to the determination of analytes in toner samples. Three toner samples were purchased from local supermarket. The results showed that these samples were free of BP, BP1 and BP3.

To validate the established method in real samples, the blank toner samples were spiked BP, BP1 and BP3 at three levels of 10, 1000 and 3500 μg L^{-1}, respectively. The recoveries were 93.7–104.8%, as shown in Table 2.

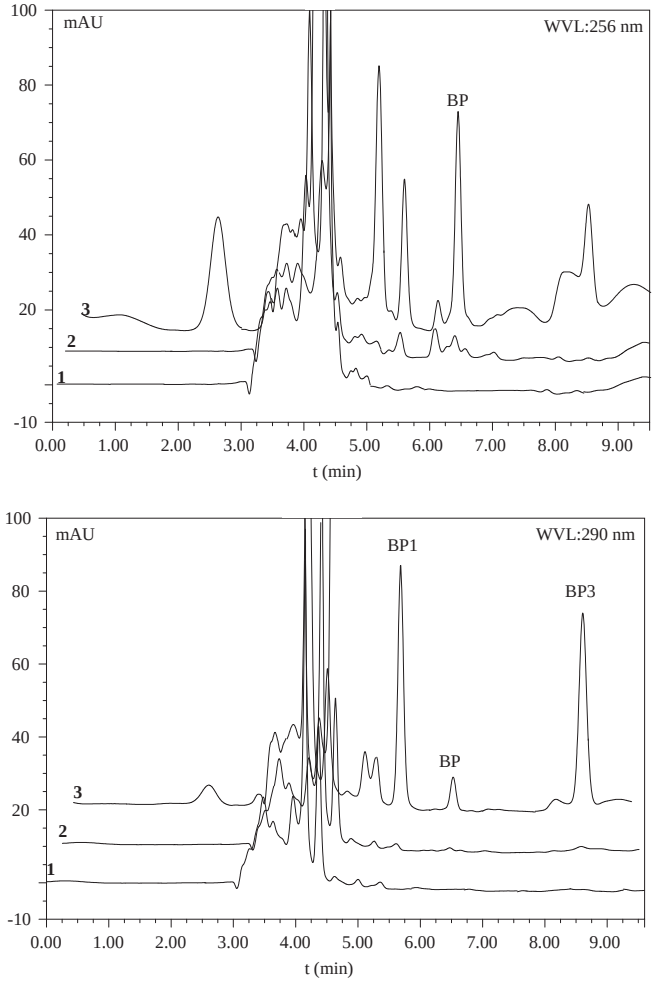


Fig. 4. HPLC chromatograms of BP, BP1 and BP3 in toner. (1) real toner sample; (2) spiked toner at 500 μg L^{-1}; (3) spiked toner at 500 μg L^{-1} after MIL-101.

Table 2
Recoveries and precisions of the method for BP, BP1 and BP3 in toner (n=4).

Matrix	Recovery & RSD (%)		Spiked (μg L^{-1})								
			BP			BP1			BP3		
			10	1000	3500	10	1000	3500	10	1000	3500
Toner	Recovery		93.7	104.8	99.6	104.5	102.4	99.7	100.1	100.7	99.9
	RSD (%)	intraday	6.4	5.9	1.7	1.5	6.2	7.4	2.3	5.9	2.6
		interday	7.6	6.7	7.0	3.3	2.5	5.4	8.9	3.2	7.2

Table 3
Comparison of the MIL-101-DSPE-HPLC method with other analytical techniques for the determination of BPs.

Method	Analyte	Sample	LOD (μg L^{-1})	Linear range (μg L^{-1})	Recoverys (%)	References
LLE [a] –HPLC-MS/MS	BP1	urine	1 (LOQ)	1–100	100–110	[37]
SPME [b] –GC–MS	BP3	urine	5	10–500	90–95	[38]
DLLME [c] –HPLC-MS/MS	BP3	serum	0.2	0.6–40	99–106	[39]
MIL-101-DSPE-HPLC	BP, BP1, BP3	toner	0.9–1.2	4.0–3500	93.7–104.8	This method

[a] Liquid-liquid extraction.
[b] Solid-phase microextraction.
[c] Dispersive lquid-liquid microextraction.

The intra- and inter-day reproducibilities (RSDs) were calculated with BP, BP1 and BP3 spiked at 10, 1000 and 3500 μg L^{-1} in toner. Five parallel extractions of a sample solution over a day gave the intra-day RSDs, and the inter-day RSDs were determined by extracting sample solutions that had been independently prepared for contiguous days. The intra- and inter-day RSDs were in the range of 1.5–7.4% and 2.5–8.9%, respectively, which indicated the acceptable reproducibility.

Chromatograms of real toner sample, spiked toner at 500 μg L^{-1} and spiked toner at 500 μg L^{-1} after MIL-101 were shown in Fig. 4. It can be seen that a dramatic enrichment of the peak height was observed.

Compared with other analytical techniques for the determination of BPs (Table 3), the limit of detection of the MIL-101-DSPE-HPLC for BPs was obviously lower than SPME-GC–MS. And, the sensitivity of the method for BPs was similar to LLE-LC-MS/MS and DLLME-LC-MS/MS. The result revealed that the MIL-101-DSPE-HPLC is a sensitive, rapid, low cost and reproducible technique. The method can be used for selective extraction and sensitive determination of analytes in complex samples.

4. Conclusions

In this work, MIL-101 was synthesized using a hydrothermal synthesis method. The material was characterizated and successfully applied for the dispersive solid-phase extraction of BP, BP1 and BP3 in toner samples. The developed approach offered wide linear range, and good reproducibility. Owing to the diverse structures and unique characteristic, MOFs possesses great potential in the preconcentration and analysis of trace compounds in real aqueous samples.

Acknowledgments

This work was supported by the Natural Science Fund for Creative Research Groups of Hubei Province of China (grant no. 2011CDA111), and the Education Commission of Hubei Province of China (grant no. T201101, D20120106), the National Nature Science Foundation of China (grant no. 20975030, 20835004, 21003034). The authors would like to thank their colleagues for their valuable technical assistance.

References

[1] M.M. Rieger, Cosmet. Toiletries 112 (1997) 65–68.
[2] T. Suzuki, S. Kitamura, R. Khota, K. Sugihara, N. Fujimoto, S. Ohta, Toxicol. Appl. Pharmacol. 203 (2005) 9–17.
[3] M. Schlumpf, B. Cotton, M. Conscience, V. Haller, B. Steinmann, W. Lichtensteiger, Environ. Health Perspect. 109 (2001) 239–244.
[4] K.E. Vanoosthuyze, L.S.G. Van Poucke, A.C.A. Deloof, Anal. Chin. Acta 275 (1993) 177–182.
[5] K. Ikeda, S. Suzuki, Y. Watanabe, J. Chromatogr. A. 513 (1990) 321–326.
[6] X.Y. Ye, Z. Kuklenyik, L.L. Needham, A.M. Calafat, Anal. Chem. 77 (2005) 5407–5413.
[7] S.P. Wang, W.T. Lee, J. Chromatogr. A. 987 (2003) 269–275.
[8] T. Felix, B.J. Hall, J.S. Brodbelt, Anal. Chim. Acta 371 (1998) 195–203.
[9] K.W. Ro, J.B. Choi, M.H. Lee, J.W. Kim, J. Chromatogr. A. 688 (1994) 375–382.
[10] H. Jeon, Y. Chung, J. Ryu, J. Chromatogr. A. 1131 (2006) 192–202.
[11] E.E. Tyrala, W.E. Dodson, Arch. Dis. Child. 54 (1979) 787–800.
[12] S. Stavchansky, A. Combs, R. Sagraves, M. Delgado, A. Joshi, Biopharm. Drug Dispos. 9 (1988) 285–299.
[13] B. Srdjenovic, V. Djordjevic-Milic, N. Grujic, R. Injac, Z. Lepojevic, J. Chromatogr. Sci. 46 (2008) 144–149.
[14] M. Pellegrini, E. Marchei, S. Rossi, F. Vagnarelli, A. Durgbanshi, O. García-Algar, O. Vall, S. Pichini, Rapid Commun. Mass Spectrom. 21 (2007) 2693–2703.
[15] E. Marchei, D. Escuder, C.R. Pallas, O. Garcia-Algar, A. Gómez, B. Friguls, M. Pellegrini, S. Pichini, J. Pharm. Biomed. Anal. 55 (2011) 309–316.
[16] A.R. Khorrami, A. Rashidpur, Anal. Chim. Acta 727 (2012) 20–25.
[17] J. Blanchard, C.W. Weber, L.E. Shearer, J. Chromatogr. Sci. 28 (1990) 640–642.
[18] O.M. Yaghi, M. O' Keeffe, N.W. Ockwig, H.K. Chae, M. Eddaoudi, J. Kim, Nature 423 (2003) 705–714.
[19] M. Eddaoudi, J. Kim, N. Rosi, D. Vodak, J. Wachter, M. O' Keeffe, O.M. Yaghi, Science 295 (2002) 469–472.
[20] Y.K. Hwang, D.Y. Hong, J.S. Chang, S.H. Jhung, Y.K. Seo, J. Kim, A. Vimont, M. Daturi, C. Serre, G. Férey, Angew. Chem. Int. Ed. 47 (2008) 4144–4148.
[21] B.L. Chen, S.C. Xiang, G.D. Qian, Chem. Res 43 (2010) 1115–1124.
[22] J.R. Li, R.J. Kuppler, H.C. Zhou, Chem. Soc. Rev. 38 (2009) 1477–1504.
[23] K.A. Cychosz, R. Ahmad, A.J. Matzger, Chem. Sci 1 (2010) 293–302.
[24] J.R. Li, J. Sculley, H.C. Zhou, Chem. Rev. 112 (2012) 869–932.
[25] M.P. Suh, H.J. Park, T.K. Prasad, D.W. Lim, Chem. Rev. 112 (2012) 782–835.
[26] K. Sumida, D.L. Rogow, J.A. Mason, T.M. McDonald, E.D. Bloch, Z.R. Herm, T. H. Bae, J.R. Long, Chem. Rev. 112 (2012) 724–781.
[27] S. Galli, N. Masciocchi, V. Colombo, A. Maspero, G. Palmisano, F.J. Lopez-Garzon, M. Domingo-Garcia, I. Fernandez-Morales, E. Barea, J.A.R. Navarro, Chem. Mater. 22 (2010) 1664–1672.
[28] K.A. Cychosz, A.J. Matzger, Langmuir 26 (2010) 17198–17202.
[29] E. Haque, J.W. Jun, S.H. Jhung, J. Hazard. Mater. 185 (2011) 507–511.
[30] E. Haque, J.E. Lee, I.T. Jang, Y.K. Hwang, J.S. Chang, J. Jegal, S.H. Jhung, J. Hazard. Mater. 181 (2010) 535–542.
[31] E. Haque, J.W. Jun, S.N. Talapaneni, A. Vinu, S.H. Jhung, J. Mater. Chem. 20 (2010) 10801–10803.
[32] K.A. Cychosz, A.G. Wong-Foy, A.J. Matzger, J. Am. Chem. Soc. 131 (2009) 14538–14543.
[33] Z.Y. Gu, C.X. Yang, N. Chang, X.P. Yan, Acc. Chem. Res. 45 (2012) 734–745.
[34] G. Férey, C. Mellot-Draznieks, C. Serre, F. Millange, J. Dutour, S. Surble, I. Margiolaki, Science 309 (2005) 2040–2042.
[35] O.I. Lebedev, F. Millange, C. Serre, G. Van Tendeloo, G. Férey, Chem. Mater. 17 (2005) 6525–6527.
[36] E. Haque, J.E. Lee, I.T. Jang, Y.K. Hwang, J. Jegal, S.H. Jhung, J. Hazard. Mater. 181 (2010) 535–542.
[37] A.G. Asimakopoulos, L. Wang, N.S. Thomaidis, K. Kannan, J. Chromatogr. A. 1324 (2014) 141–148.
[38] T. Felix, B.J. Hall, J.S. Brodbelt, Anal. Chim. Acta 371 (1998) 195–203.
[39] F Vela-Soria, O Ballesteros, A Zafra-Gómez, L Ballesteros, A Navalón, Talanta 121 (2014) 97–104.

Talanta 132 (2015) 719–726

Contents lists available at ScienceDirect

Talanta

journal homepage: www.elsevier.com/locate/talanta

Direct electrodeposition of cable-like CuO@Cu nanowires array for non-enzymatic sensing

Junping Dong [a,b,*], Linxiao Ren [a], Yuan Zhang [a,b], Xiaoli Cui [c], Pengfei Hu [d], Jiaqiang Xu [a,*]

[a] Department of Chemistry, College of Science, Shanghai University, Shanghai 200444, China
[b] State Key Laboratory of Transducer Technology, Shanghai Institute of Microsystem and Information Technology, Chinese Academy of Sciences, Shanghai, 200050, China
[c] Department of Materials Science, Fudan University, Shanghai, 200433, China
[d] Laboratory of Microstructures, Shanghai University, Shanghai 200444, China

ARTICLE INFO

Article history:
Received 6 July 2014
Received in revised form
8 September 2014
Accepted 6 October 2014
Available online 22 October 2014

Keywords:
CuO@Cu nanowires array
Electrodeposition
Glucose
Non-enzymatic sensor

ABSTRACT

Vertically aligned cable-like CuO@Cu nanowires array was synthesized using a template-directed electrodeposition strategy. The morphology, crystal structure, and surface property of nanowires array were investigated by SEM, HRTEM, XRD, and XPS, respectively. It is found that the free standing namowires are highly dense, and possess about 20 μm in length and 200 nm in diameter. The bulk Cu nanowires are assembled by a number of single crystalline Cu nanoparticles and surface is wrapped by a thin layer of amorphous CuO with size of 2.5 nm. Electrocatalytic activity of the nanowires array towards glucose oxidation was investigated by cyclic voltammetry and amperometry in alkaline media. The nanowires array with 3×3 mm^2 was then used to fabricate a non-enzymatic glucose sensor. The sensor exhibits a wide concentration range of 1×10^{-6} M–1×10^{-2} M for glucose, with an ultra-high sensitivity of 1250.8 μA mM^{-1} cm^{-2} and excellent anti-interference ability. The good sensing performances could be attributed to the integration of the superior electrocatalysis of high density of Cu nanowires array and the outer shell of negatively charged CuO against interferences.

© 2014 Elsevier B.V. All rights reserved.

1. Introduction

In the past few years, one-dimensional (1-D) nanostructures have attracted a considerable amount of attention, because of their potential utilization in electronic, magnetic, optical, energy and chemical sensors [1–6]. As important 1-D nanostructures, nanowires array commonly assembled by numbers of nanowires, possess a high surface area-to-volume ratio, rendering them extremely sensitive to species adsorbed on surfaces and resulting in excellent sensitivity and activity [7].

The ability to precisely prepare nanowires array on a large scale with tailored morphology and geometry is an important goal of the material science. In the last decade, various methods have been developed to prepare high-density and well-aligned nanowires array. The conventional techniques used to fabricate nanowires array include sol–gel method, chemical vapor deposition, direct electrodeposition and so forth [8–11]. Among these methods, template-assisted electrodeposition has been established to be an attractive route for the synthesis of nanowire arrays because of its simplicity, cost-effectiveness, low temperature fabrication, etc [12]. Also, the morphology, nanostructure, and composition of nanowires array could be tuned through selectively controlling deposition parameters. To date, the templates used in the most work were generally entailed to two types of nanoporous template, polycarbonate template and porous anodic aluminum oxide template. For polycarbonate template, it usually contains randomly distribution cylindrical pores with poor density and there are numbers of pores intersect within the template. As a consequence, the nanowires array obtained within polycarbonate template usually suffer from some drawbacks, such as less uniformity and low density of nanowires [13,14]. Anodic aluminum oxide is another type of template which has advantages over polycarbonate template such as high density, highly ordered pore channels and uniform pore size. Thus the nanowires can be well confined in the uniform and parallel hexagonally porous structure of the anodic aluminum oxide membrane. After the post-treatment in phosphoric acid solution or NaOH solution, the nanowires achieved normally possess ordered morphology and high-density (channel density of template is in the range of 10^{10}–10^{12} cm^{-2}). More recently, a lot of works tend to electrodeposition of nanowires array in anodic aluminum oxide template for virous applications. Glennon et al. deposited Au nanowires array in anodic aluminum oxide membrane and utilized this ordered nanowires array as a matrix to immobilize horseradish peroxidase for the biosensing of hydrogen peroxide [15]. Liang and co-workers fabricated Cu nanowire arrays and employed them as effective current collectors in lithium-ion batteries [16]. Jiang et al. introduced the highly ordered Pd nanowire arrays as effective catalysts

* Corresponding authors. Tel.: +86 21 66132930.
E-mail addresses: jpdong@shu.edu.cn (J. Dong), xujiaqiang@shu.edu.cn (J. Xu).

http://dx.doi.org/10.1016/j.talanta.2014.10.027
0039-9140/© 2014 Elsevier B.V. All rights reserved.

for ethanol oxidation in direct alcohol fuel cells [17]. Cheng et al. applied the Pd nanowires array to the detection of formaldehyde in environmental pollution [18].

In the family of one-dimensional metallic nanomaterials, considerable attention has been focused on the Cu nanowires, due to its low cost, excellent electrical conductivity and easy availability. Cu based nanomaterials exhibit the direct electrooxidation to some small molecular organic compounds [19–22]. This will provide a chance for construction of non-enzymatic glucose sensor. Non-enzymatic glucose biosensors are based on the glucose oxidation catalyzed by a variety of electrocatalysts, including metals (Au, Pt, Pd), metal oxides (Co_3O_4, CuO, NiO), alloys (PtPb, PtRu) [23,24]. Non-enzymatic glucose biosensors have alleviated the problems of enzyme-based biosensors such as insufficient stability, lower reproducibility, thermal and chemical instability, sensitivity to temperature, pH, and humidity [25,26]. Hence it will probably become the fourth generation glucose sensors for the future analytical applications.

In the case of sensor device, the well-aligned nanowires array is attractive than those randomly scattered nanowires usually prepared by a wet-chemistry method. The array acts as an excellent current collector to improve the signal-to-noise and mechanical stability is enhanced as well. Besides, nanowires array is easily tailored to various geometry and size for further device fabrication.

In this work, the highly ordered cable-like CuO@Cu nanowires array was synthesized by electrodeposition within anodic aluminum oxide template. The nanowires array with different lengths from 20 μm to 90 μm was obtained. The bulk Cu nanowires are assembled by a number of single crystalline Cu nanoparticles and surfaces are wrapped by a thin layer of amorphous CuO with thickness of 2.5 nm. The nanowires array shows the excellent electrocatalytic activities to glucose oxidation in alkaline media. An enzyme-free glucose sensor based on the cable-like CuO@Cu nanowires array was developed for detection of glucose. The sensor exhibits a wide concentration range of 1×10^{-6} M–1×10^{-2} M for glucose, with an ultra-high sensitivity of 1250.8 μA mM^{-1} cm^{-2} and excellent anti-interference ability.

2. Experimental

2.1. Reagents and materials

H_2SO_4, $CuSO_4\cdot5H_2O$, NaCl and NaOH were purchased commercially from Sinopharm Chemical Reagent Co. Ltd. (Shanghai, China) and used without further purification. L-Ascorbic acid (AA), dopamine (DA), uric acid (UA) and d-(+)-glucose were purchased from Sigma-Aldrich. All the other chemicals used were of analytical grade and all solutions were diluted with doubly distilled water. The porous anodic aluminum oxide (AAO) templates with a nominal pore size of 200 nm were obtained from Whatman Inc.

2.2. Instruments

The electrochemical experiments were performed using an electrochemical workstation (Chenhua, Shanghai, China). Scanning electron microscopy (SEM) (JSM-6700F), transmission electron microscope (TEM) (JSM-200CX) and high-resolution transmission electron microscope (HRTEM) (JEM-2010F) were utilized for the investigation of the morphology and structural properties of the deposited nanowires. The crystal phase, chemical composition and surface property of the prepared nanowires were determined by X-ray diffractometer (XRD) (Bruker AXS) with Cu Ka radiation at 40 kV and 40 mA. X-ray photoelectron spectra (XPS) was conducted on ESCALAB 250Xi using monochromatic Al Ka radiation as the exciting source. The peak at 284.6 eV attributed to the C–C band in the C1s spectrum was used for binding energy reference.

2.3. Synthesis of nanowire array

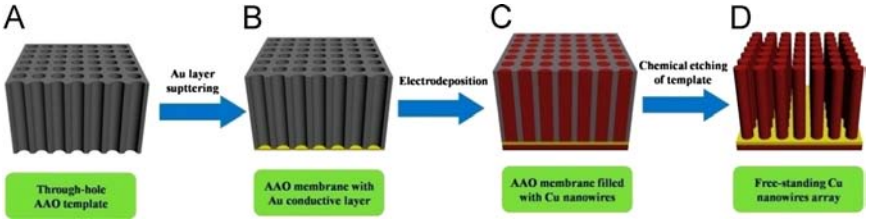
Vertically standing Cu nanowires array were fabricated using a template electrodeposition technique and the experimental procedures used for the preparation of the Cu nanowires array are presented in Scheme 1. Typically a thin layer of Au was first sputtered onto one side of the AAO template which served as the working electrode during the electrodeposition. Electrodeposition of copper nanowires was carried out at a constant current density of 1.0 mA cm^{-2} for 8 h in a copper bath that consisted of 0.5 M $CuSO_4$ and 0.1 M H_2SO_4. Finally, the templates were dissolved with a 5% H_3PO_4 solution for 6 h and carefully rinsed away with deionized water to remove any remaining H_3PO_4. Subsequently, the free-standing Cu nanowires array with an orange–red color was obtained and stored in N_2 atmosphere when not used. It is noteworthy that along with the growth of Cu nanowires array, a thin film of Cu (about 10 μm) was simultaneously deposited onto the back side of the Au layer (Scheme 1C). This back layer is very favorable to prevent the nanowires from collapsing after removal of the templates, which could provide a powerful support for the subsequent preparation of the sensors.

2.4. Sensor fabrication

Firstly nanowires array was rinsed in deionized water and punctured to a size of 3×3 mm^2 of slice. Then the tailored slice was pasted to the surface of 5 mm glassy carbon electrode (GCE) with very small amount of conductive silver paste and left it dry a few of hours before use. Finally the epoxy resin was used to seal the edges of array and the resulting electrode was denoted as NAS (nanowires array sensor).

2.5. Electrochemical experiments

All of the electrochemical experiments were carried out at room temperature in a standard three-electrode system. Before each experiment, the solution was purged by N_2 gas for 20 min and a nitrogen atmosphere was then kept over the solution during measurements. The NAS was evaluated as a glucose sensor in 0.1 M NaOH solution. The cyclic voltammetry (CV) was carried out in the potential range of 0.2–1.0 V vs. Ag/AgCl (3 M KCl). The amperometric curves were recorded by adding the desired amount of glucose into NaOH solution under stirring condition.



Scheme 1. The Schematic diagram of the fabrication of Cu nanowires array.

3. Results and discussion

3.1. Characterization of nanowires array

Fig. 1 records the SEM images of the prepared nanowires array after carefully etching away the AAO template. The plane views of the nanowires array in Fig. 1A and B clearly show that most of the nanowires are running along the pores of the template. The nanowires array is free standing and highly uniform, not lodging or curved to form bundles. The cross-section images (Fig. 1C and D) show that the nanowires are about 20 μm in length and 200 nm in diameter, which is consistent with the channel diameter of AAO template. The length of nanowires can be controlled by varying the deposition time. Fig. S1 shows the SEM images of the nanowires array deposited for 20 min (Fig. S1A) and 24 h (Fig. S1B–D) respectively. When the electrodeposition time was shortened to 20 min, the length of nanowires was 0.5 μm (Fig. S1A). While the nanowires array with a uniform length of approximately 90 μm can be achieved by prolonging the deposition time to 24 h (Fig. S1B–C). Unfortunately, it can be clearly seen that the longer nanowires tend to aggregate into bundles on a large scale after removing of the AAO template (Fig. S1D).

The microstructures of the nanowires array were further investigated by TEM and selected area electron diffraction. Fig. 2A and B shows the TEM images of the discrete nanowires. The morphology and size of nanowires are in accordance with the observation in SEM images. Moreover, the high magnification TEM image of a single nanowire in Fig. 2B clearly shows that the electrodeposited Cu nanowires are assembled by lots of nanoparticles. The corresponding electron diffraction pattern taken from a single nanowire is displayed in Fig. 2C. The continuous bright rings can be indexed as face-centered cubic polycrystalline Cu structure. Additionally, the selected-area electron diffraction pattern (in Fig. 2D) reveals that the nanoparticles near the edge of nanowire exhibit the characteristic single crystalline Cu structure nature, which is useful for biosensing behavior. Therefore, it can be concluded that the bulk Cu nanowires are aggregated of a numbers of single crystalline Cu nanoparticles.

XRD profile of Cu nanowires array is shown in Fig. 3A. The peaks positioned at 43.30°, 50.43°, 74.13°, 89.93°, and 95.14° perfectly match the {111}, {200}, {220}, {311}, and {222} crystalline planes of the face-centered cubic metal Cu (JCPDS 04-0836), respectively. Those results are consistent with the electron diffraction pattern taken from the Cu nanowires in Fig. 2C. No extra peaks of other oxides such as Cu_2O or CuO are visible, suggesting the high purity of Cu nanowires. An obvious peak observed at $2\theta = 38.18°$ was attributed to Au (111) (JCPDS 004-0874).

XPS is a powerful tool for the surface structural analysis. The XPS profile of Cu nanowires array is shown in Fig. 3B. It is found that four main bands are centered at 932.3 eV, 952.4 eV, 934.8 eV and 954.5 eV, which are corresponding to binding energy of Cu $2P_{3/2}$, Cu $2P_{1/2}$, CuO $2P_{3/2}$ and CuO $2P_{1/2}$, respectively (NIST X-ray Photoelectron Spectroscopy Database). XPS results imply the presence of a small amount of CuO. It is generally believed that the copper nanomaterials could be oxidized easily in air due to the high surface energy. Although the characterization of XRD proves the metallic nature of bulk Cu nanowires array, the result of XPS reveals that there is a small amount of CuO existed on the surface of Cu nanowires actually, whose quantity is too small to be quantified by bulk characterization techniques such as XRD. In addition, the HRTEM image in Fig. 3C further confirms that the outer surface of Cu nanowires array is wrapped by a thin shell of amorphous CuO layer. The thickness of CuO shell can also be distinguished to be ~2.5 nm. Moreover, rows of lattice fringes with a space of 0.127 nm are clearly visible, which matches well with the crystal plane {220} of metallic Cu structure. This kind of array with the nanocable-like structure is interesting and has not been reported till now in the open literatures. Even though the shell of CuO is very thin and amorphous, it would make a significant effect on the performance of biosensor and effectively improve the anti-interference ability of NAS.

3.2. Electro-oxidation of glucose on NAS

In order to evaluate the analytical applicability of NAS, the electrocatalytic performance of NAS towards the glucose was

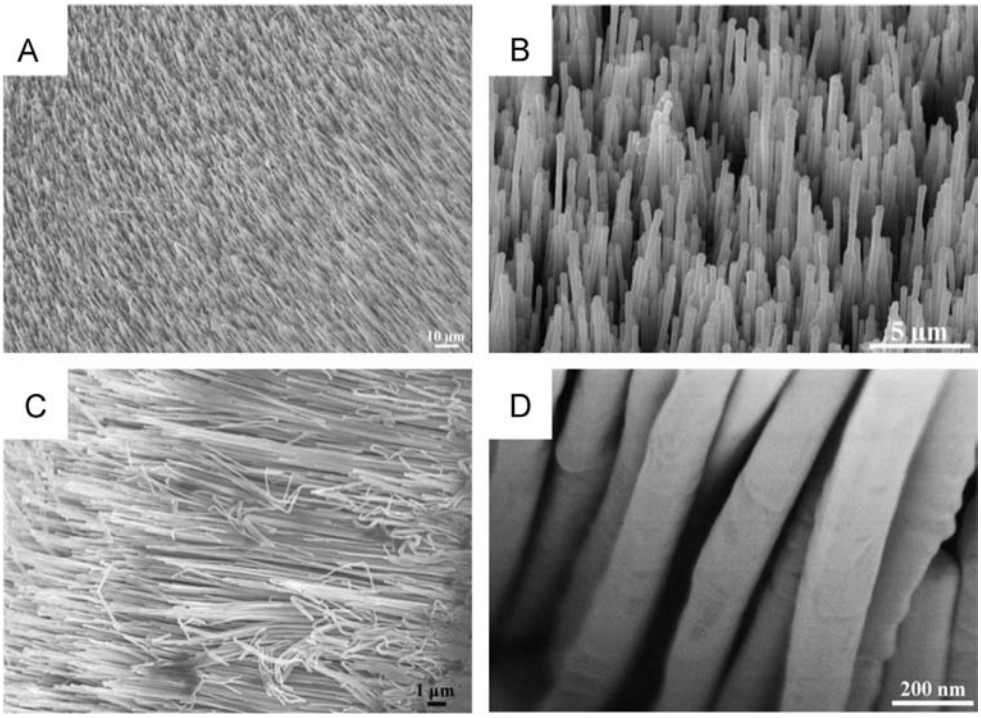


Fig. 1. SEM images of nanowires array after completely dissolving the AAO template.

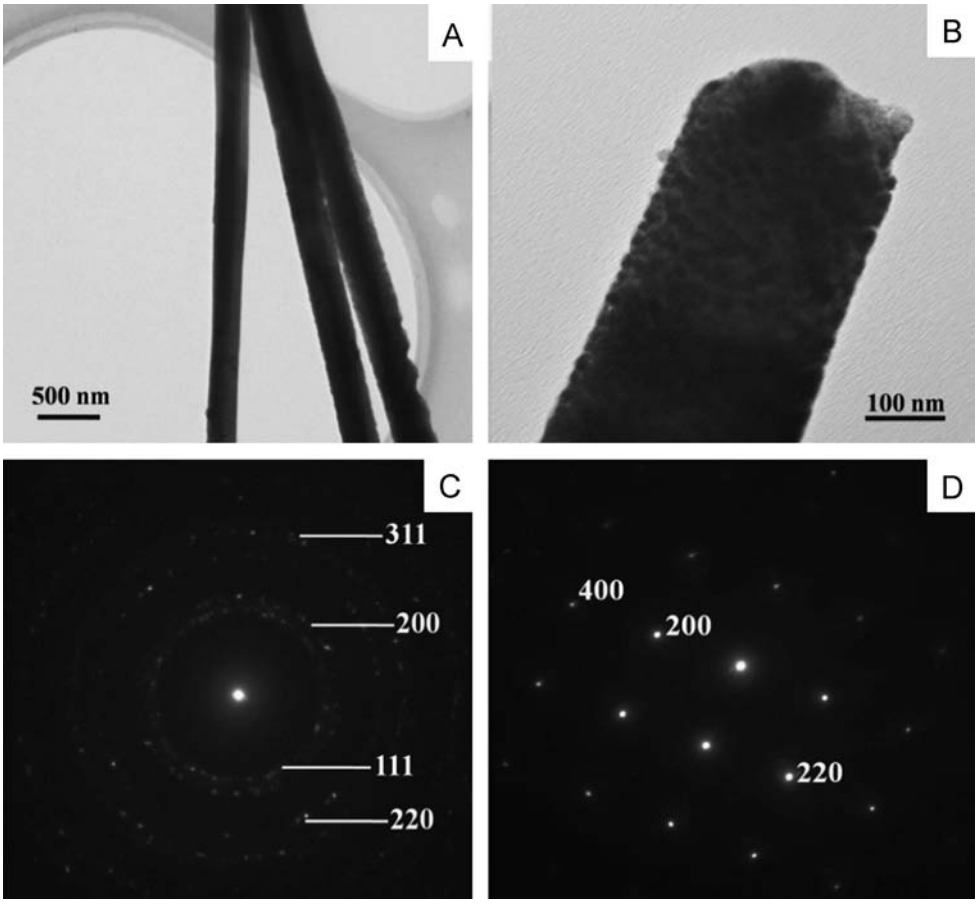


Fig. 2. TEM images of the prepared nanowires after thoroughly remove of template: (A) Low magnification TEM image; (B) High magnification TEM image of a single nanowire; (C) Electron diffraction pattern of a single nanowire; (D) Electron diffraction pattern of the nanoparticles near the edge of nanowire.

investigated extensively in alkaline solution. Fig. 4A shows the cyclic voltammograms of NAS in the presence and absence of the glucose in the potential range of −1.0 to 1.0 V. Some redox transitions appeared and were indicated by peaks I–IV. In the absence of glucose, the peak I and peak II are due to the transition Cu (0) to Cu (I) and Cu (0) to Cu (II), respectively [22,27,28]. The wave at about 0.25 V (peak III) is associated with the formation of soluble species, such as $HCuO_2^-$, from the oxidation of Cu [27]. It is generally thought that the presence of Cu (III) species is crucial to electrocatalytic oxidation of glucose. Unfortunately, this species is rather unstable. The formation of Cu (III) species has been previously reported at about 0.60 V [28], but it is not easily distinguished in Fig. 4A and could only be observed in highly alkaline electrolytes. The reverse scan reveals that the symmetric cathodic peaks of peak IV, peak V and peak VI are assigned to the reduction of Cu (III) to Cu (II), Cu (II) to Cu (I) and Cu (I) to Cu (0), respectively.

Therefore, the electrochemical reaction which occurs on the surface of the Cu nanowires can be described as follow:

$$Cu + OH^- \rightarrow CuOH + e^-$$

$$Cu + 2OH^- \rightarrow Cu(OH)_2 + 2e^-$$

$$Cu + 3OH^- \rightarrow HCuO_2^- + H_2O + 2e^-$$

$$Cu(OH)_2 \rightarrow Cu\ (III)$$

In the presence of the glucose, the peak I and peak II became weaker and even invisible, indicating the interaction between the Cu species and glucose [27]. Moreover, the disappearance of the peak III may be due to the adsorption of glucose on the surface of Cu catalyst to form a passivation film, which blocks the contact of Cu substrate and OH^- [29]. During the cathodic potential sweep, the missing of the peak IV supports the evidence that Cu (III) has been consumed in the electrooxidation of the glucose. Additional, the other peaks of Vand VI diminished proportionally, possibly as a result of the interaction between Cu (I) and glucose [29]. So the electrocatalytic oxidation of glucose to glucolactone in the alkaline solution at NAS can be summarized as:

$$Cu\ (III) + glucose \rightarrow Cu\ (II) + glucolactone$$

In order to investigate the applicability of NAS in non-enzymatic glucose sensing, CVs (Fig. 4B) were recorded in the different concentrations of glucose under the potential range of 0.2–1.0 V. It can be noticed that the oxidation peak currents increase accordingly with the increase of glucose concentration in the potential range of 0.50 V–0.75 V, presenting a pronounced electrocatalytic behavior of Cu catalyst to the oxidation of glucose.

3.3. Optimization for glucose sensing on NAS

To find the optimal conditions for the amperometric sensing of glucose, various factors influencing the response of the sensor were investigated.

The effect of the concentration of NaOH on the response current of the sensor is illustrated in Fig. S2A. With the concentrations of NaOH solution are increased from 10 to 100 mM, the responses to glucose are improved accordingly since glucose is oxidized more easily at higher pH. However, when the concentration of NaOH is above 100 mM, the response current is reduced, and meanwhile,

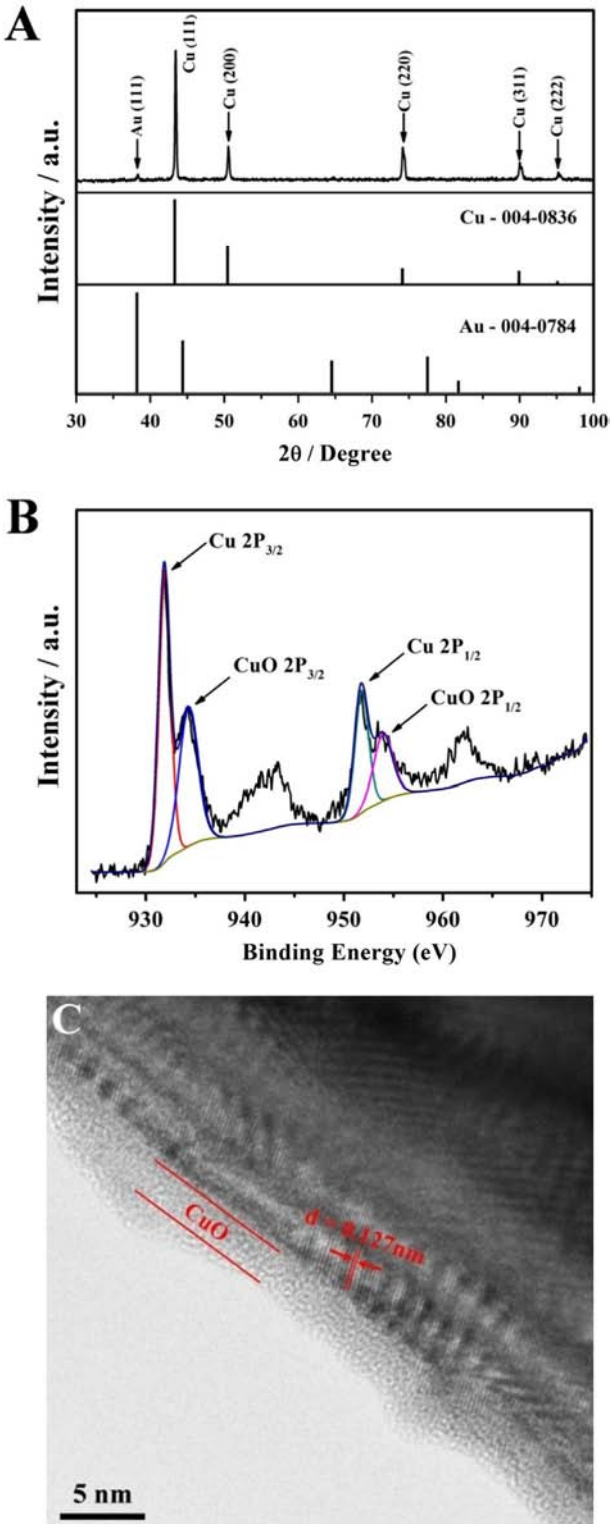


Fig. 3. (A) XRD patterns of the nanowires array; (B) XPS spectra of nanowires array; (C) HRTEM image of a single nanowire.

the noise signal is raised as a result of an increase of background reactions.

Fig. S2B showed the amperometric responses of the NAS to 0.2 mM glucose under different potentials from 0.55 V to 0.7 V in 100 mM NaOH. In the range of 0.55 V–0.65 V, the oxidation currents of glucose increase gradually with increasing potential. The maximum response current is observed at 0.65 V and a good signal/noise ratio can also be offered. While, further increasing the

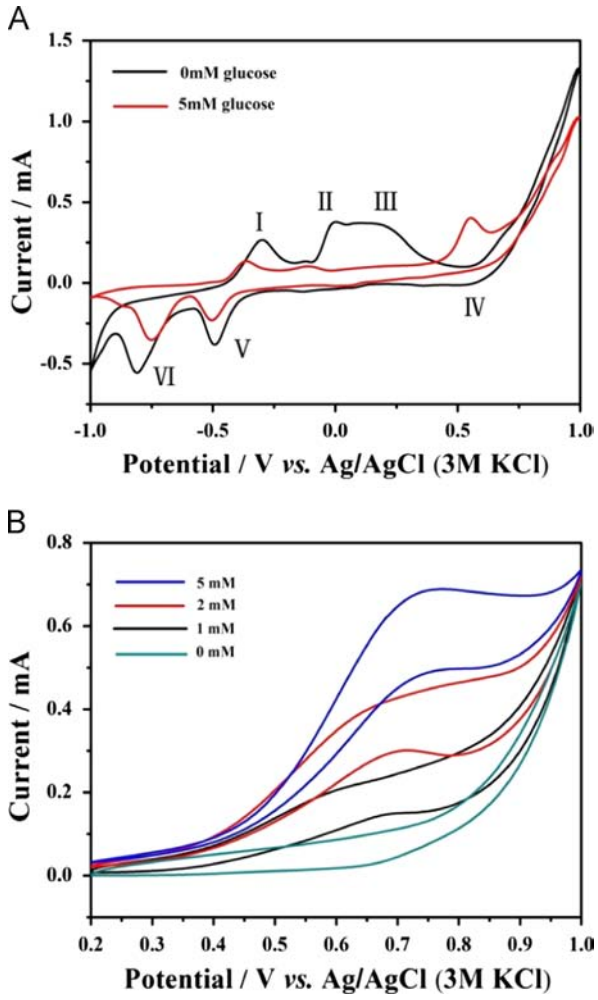


Fig. 4. (A) Cyclic voltammograms of the NAS in the presence and absence of 5 mM glucose in 100 mM NaOH and scan rate at 5 mV/s. (B) CV obtained for the increment of glucose (0 mM to 5 mM) on NAS in 100 mM NaOH and scan rate at 5 mV/s.

potential, the side reactions would take place on the electrode surface, resulting in the increase of the background current. Besides, under the high potential, some interfering species (such as ascorbic acid, uric acid and dopamine) would be oxidized and generate some intermediate products that would probably hinder glucose oxidation. Therefore, an applied potential of 0.65 V and a medium of 100 mM NaOH solution are chosen for subsequent experiments.

Fig. S2C presents the responses of Cu nanowires array with different lengths to glucose. One can observe that the response current of nanowires array with length of 20 μm is higher than that one with 90 μm. This result could be attributed to the less void space between the longer nanowires, which blocking the diffusion of glucose molecules from the bulk solution to the active sites of nanowires surface.

3.4. Analytical application of NAS

NAS were evaluated by measuring the response to glucose under the optimal conditions.

Fig. 5A illustrates the typical amperometric responses to successive increments of glucose concentration at the NAS. It is found that the response currents increase with successive additions of glucose. And the current value achieves 95% of the steady-state current within 5 s. The currents are linear with the concentration of glucose

in the range of 1×10^{-6} M–1×10^{-2} M with the linear equation: I (μA) = 112.57 C_{glu} (mM) + 16.02 and a correlation coefficient of 0.997. The sensitivity of NAS sensor is 1250.8 μA mM^{-1} cm^{-2} and the detection limit is estimated to be 6.9×10^{-7} M ($S/N=3$). This ultra-high sensitivity of NAE sensor is prominent and striking.

The comparison of NAS with different non-enzymatic glucose sensors based on Cu nanomaterial or other metal based on array strategy are summarized in Table 1. As can be seen that the CuO@Cu nanowires array exhibits excellent performance in terms of wide linear range, high sensitivity and low detection limit in contrast with the previous works.

NAS was also used to detect glucose in human serum samples using standard additions method. A rapid and stable amperometric response is obtained when the addition of 25 μL the diluted human serum samples into 25 ml 100 mM NaOH. The amount of glucose in human serum is calculated to be 4.05 mM from calibration curve (average for $n=3$), which is close to 4.2 mM given by a local hospital.

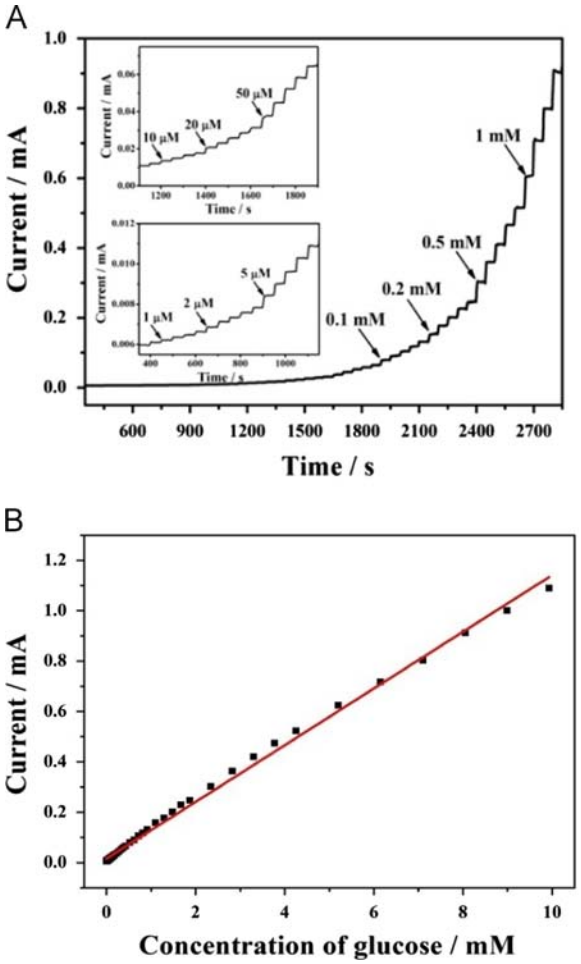


Fig. 5. (A) Typical amperometric responses of the NAS to the successive addition of different amounts of glucose in 0.1M NaOH at applied potential of 0.65V; (B) The corresponding calibration curve.

3.5. Anti-interference study of the NAS

One of the major challenges in non-enzymatic glucose sensor is some electrochemically active interferences (such as ascorbic acid (AA), dopamine (DA) and uric acid (UA)) which generate electrochemical signals at the same potential as glucose. Ordinary, the normal physiological level of glucose is about 3–8 mM in human serum, while those of ascorbic acid, dopamine and uric acid are about 0.1 mM [41]. The interference experiments (Fig. 6A) were carried out by adding 0.01 mM interfering species in 100 mM NaOH.

Compared to glucose, the interfering species of 0.01 mM AA, DA and UA yield current response of ~2.68 %, ~1.26 % and ~0.14 % respectively, indicating the good selectivity of NAS against these interferences. Additionally, chloride ion is also one of the important interferences in human serum. It has been reported that the electrochemical glucose sensors based on Cu electrodes could easily lose their activity due to the chloride poisoning effect. Therefore, the anti-interference performance of the NAS against chloride ion was examined (Fig. 6B). The change of amperometric response is negligible in the presence of 2 mM chloride ion, demonstrating the tolerance of the NAS to the chloride ion. All these excellent anti-interference ability of the NAS could be attributed to the existence of a thin shell of CuO layer on the outer surface of Cu nanowires. Usually, the isoelectric point of CuO is 9.5 [22]. So, the CuO layer on the surface of Cu nanowires could carry a certain amount of negative charge in 100 mM NaOH medium (pH = 13). As a result, those negatively charged species could be excluded out of the negatively charged Cu nanowires surface.

Furthermore, the other saccharide such as fructose and sucrose may also interfere with the accurate determination of glucose. Considering their relatively low concentration in physiological samples [42], Fig. 6C shows that the current responses are 2.79% and 4.47% for 8.1 μM fructose and 10 μM sucrose in contrast to glucose, respectively.

3.6. Reproducibility and stability of NAS

The reproducibility and stability of NAS were also evaluated. The current responses of five newly prepared NAS to 0.2 mM glucose

Table 1
Comparison of the performance of NAS glucose sensor with that of non-enzymatic glucose sensors base on Cu nanomaterial or other metal nanoarray.

Electrode composition	Potential (V)	Liner range ($molL^{-1}$)	LOD (M)	Sensitivity (μA mM^{-1} cm^{-2})	Ref.
Cu nanowires	0.60 vs. Ag/AgCl	up to 3.0×10^{-3}	3.5×10^{-8}	420.3	[22]
Cu nanocubes @ MWCNTS	0.55 vs. Ag/AgCl	up to 7.5×10^{-3}	1.0×10^{-3}	1096	[30]
CuO/Cu electrode	0.70 vs. Ag/AgCl	2.0×10^{-3} –2.0×10^{-2}	1.0×10^{-5}	761.9	[31]
3D macroporous Cu electrode	0.60 vs. Ag/AgCl	8.0×10^{-4} –3.0×10^{-3}	8.0×10^{-7}	3258	[32]
Cu foam	0.35 vs. Ag/AgCl	1.0×10^{-4} –5.0×10^{-3}	9.8×10^{-7}	1810	[33]
Cu nanoparticles @ MWCNTS	0.63 vs. Ag/AgCl	5.0×10^{-4} –7.5×10^{-3}	2.0×10^{-6}	922	[34]
MWCNT/PEI/Cu	0.35 vs. SCE	1.0×10^{-5} – 5.0×10^{-4}	5.0×10^{-7}	714	[35]
Pt nanotubes array	0.40 vs. SCE	2.0×10^{-3} –1.4×10^{-2}	1.0×10^{-6}	0.1	[36]
Au nanowires array	−0.40 vs. Hg/HgO	1.0×10^{-3} –1.0×10^{-2}	5.0×10^{-5}	309	[37]
Au nanotubes array	0.25 vs. SCE	1.0×10^{-3} –4.25×10^{-2}	1.0×10^{-5}	1.13	[38]
Pt–Pb nanowires array	−0.20 vs. SCE	up to 1.1×10^{-2}	8.0×10^{-6}	11.25	[39]
Pt–Ni nanowires array	0.45 vs. SCE	2.0×10^{-6} – 2.0×10^{-3}	1.5×10^{-6}	920	[40]
CuO@Cu nanowires array	0.65 vs. Ag/AgCl	1.0×10^{-6} –1.0×10^{-2}	6.9×10^{-7}	1250.8	This study

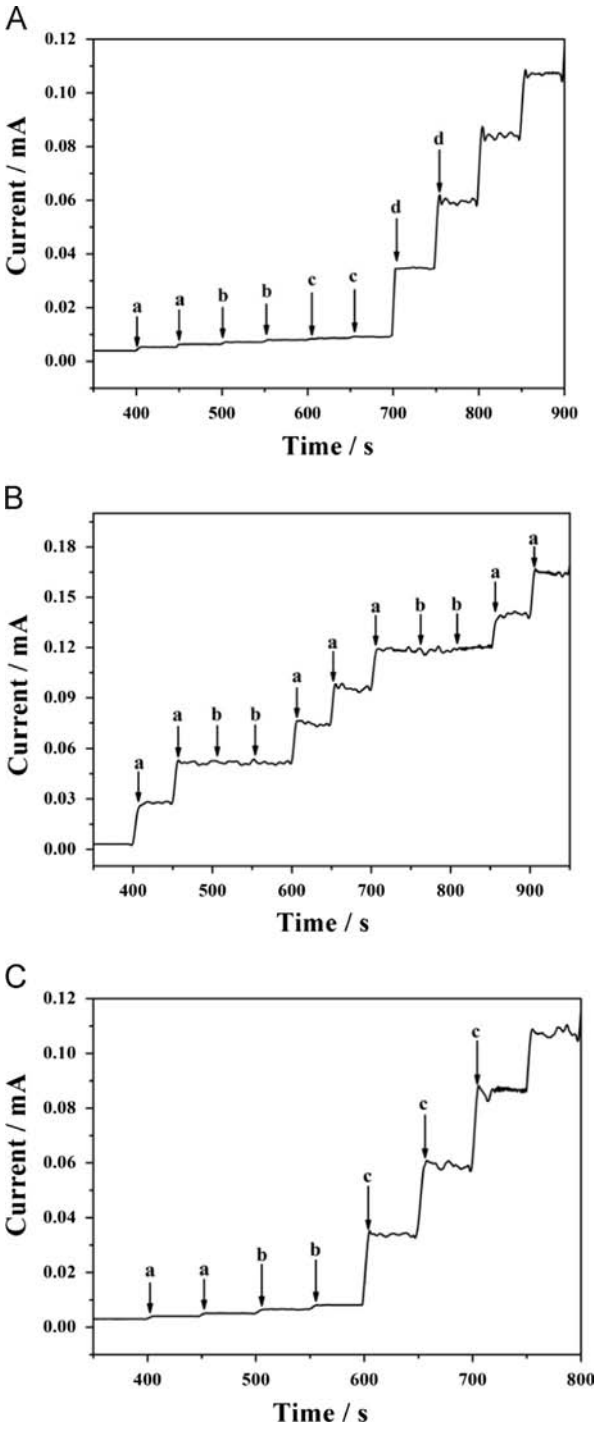


Fig. 6. (A) Amperometric responses of 0.01 mM ascorbic acid (a), 0.01 mM dopamine (b), 0.01 mM uric acid (c) and 0.2 mM glucose (d); (B) Amperometric responses of 0.2 mM glucose (a) and 2 mM NaCl (b); (C) Amperometric responses of 8.1 μM fructose (a), 10 μM sucrose (b) and 0.2 mM glucose (c). Experimental conditions: in 100 mM NaOH medium and at the applied potential of 0.65 V.

were measured (Fig. S3A) and the relative standard deviation (RSD) was 5.3%. The current responses of 10 successive measurements to 0.2 mM glucose at one chosen NAS yielded a RSD of 3.1%, demonstrating that the NAS was stable and suitable for repeated detection of glucose (Fig. S3B). The long term stability was investigated by measuring the responses of glucose over 20 days. Fig. S3C shows the variation of current during the investigated period. For convenience, the response on the first day was set to 100%. The results demonstrated that the responses were almost unchanged over the entire investigated period and the NAS was found to retain 94% of its initial activity within 20 days, implying that the NAS can be used in long term routine applications.

4. Conclusion

In this paper, we constructed the mechanically stable and easily handling cable-like CuO@Cu nanowires array for glucose electrooxidation and further fabricated a non-enzymatic glucose sensor with ultra-high sensitivity.

SEM images reveal that Cu nanowires array is highly dense, thus providing the more active sites for glucose electrocatalytic oxidation. The bulk Cu nanowires are found to have a polycrystalline structure and are assembled by a lot of single crystalline Cu nanoparticles. XPS combined with HRTEM confirm that there is a thin layer of CuO wrapped on the outer surface of Cu nanowires, which could repulse some negatively charged species such as UA, DA, AA, Cl^- in alkaline medium, implying the excellent anti-inference ability. Moreover, metallic Cu nanowires array possesses the excellent unidirectional conductivity along 1-D direction and therefore facilitating the electron transfer of redox reaction. Based on these merits, Cu nanowires array is developed for a non-enzymatic glucose sensor. And it exhibits excellent sensing performances such as a wide linear range, ultra-high sensitivity and selectivity. Besides that, it is also successfully applied to detect glucose in serum samples with good accuracy.

Acknowledgments

This work is financed by National Natural Science Foundation of China (No.51301101 and No. 61071040) and China Postdoctoral Science Foundation (Grant no. 2013M530188).

Appendix A. Supporting information

Supplementary data associated with this article can be found in the online version at http://dx.doi.org/10.1016/j.talanta.2014.10.027.

References

[1] Z.L. Wang, J. Song, Science 312 (2006) 242–246.
[2] X. Duan, Y. Huang, R. Agarwal, C.M. Lieber, Nature 421 (2003) 241–245.
[3] H.Q. Cao, Z. Xu, H. Sang, D. Sheng, C.Y. Tie, Adv. Mater. 13 (2001) 121–123.
[4] Z. Jiang, Q. Zhang, C. Zong, B.J. Liu, B. Ren, Z. Xie, L. Zheng, J. Mater. Chem. 22 (2012) 18192–18197.
[5] I. Hochbaum, P. Yang, Chem. Rev. 110 (2009) 527–546.
[6] P.C. Chen, S. Sukcharoenchoke, K. Ryu, L. Gomez de Arco, A. Badmaev, C. Wang, C. Zhou, Adv. Mater. 22 (2010) 1900–1904.
[7] Y. Wang, Y. Zhu, J. Chen, Y. Zeng, Nanoscale 4 (2012) 6025–6031.
[8] S. Öztürk, N. Taşaltin, N. Kilinç, Z.Z. Öztürk, J. Optoelectron. Biomed. Mater. 1 (2009) 15–19.
[9] Q. Zhao, G. Wen, Z. Liu, Y. Fan, G. Zou, L. Li, R. Zheng, S.P. Ringer, H.K. Mao, Nanotechnology 22 (2011) 125603.
[10] Y. Li, X. Niu, J. Tang, M. Lan, H. Zhao, Electrochim. Acta 130 (2014) 1–8.
[11] E.C. Walter, M.P. Zach, F. Favier, B.J. Murray, K. Inazu, J.C. Hemminger, R.M. Penner, Chem. Phys. Chem. 4 (2003) 131–138.
[12] J.C. Hulteen, C.R. Martin, J. Mater. Chem. 7 (1997) 1075–1087.
[13] K. Krishnamoorthy, C.G. Zoski, Fabrication of 3D gold nanoelectrode ensembles by chemical etching, Anal. Chem. 77 (2005) 5068–5071.
[14] H. Yao, J. Duan, D. Mo, H.Y. Gu, Y. Chen, J. Liu, T. Schapers, J. Appl. Phys. 110 (2011) 094301–094306.
[15] J. Xu, F. Shang, J.H.T. Luong, K.M. Razeeb, J.D. Glennon, Biosens. Bioelectron. 25 (2010) 1313–1318.
[16] H. Duan, J. Gnanaraj, J. Liang, J. Power Sour. 196 (2011) 4779–4784.
[17] C. Xu, H. Wang, P.K. Shen, S.P. Jiang, Adv. Mater. 19 (2007) 4256–4259.
[18] Y. Zhang, M. Zhang, Z. Cai, M. Chen, F. Cheng, Electrochim. Acta 68 (2012) 172–177.
[19] G. Casell, T.R.I. Cataldi, A. Guerrier, E. Desimoni, Anal. Chim. Acta 335 (1996) 217–225.

[20] K.B. Male, S. Hrapovic, Y. Liu, D. Wang, J.H. Luong, Anal. Chim. Acta 516 (2004) 35–41.
[21] J. Huang, Z. Dong, Y. Li, J. Li, J. Wang, H. Yang, S. Li, S. Guo, J. Jin, R. Li, Sens. Actuators B 182 (2013) 618–624.
[22] Y. Zhang, L. Su, D. Manuzzi, H.V.E. de los Monteros, W. Jia, D. Huo, C. Hou, Y. Lei, Biosens. Bioelectron. 31 (2012) 426–432.
[23] P. Si, Y. Huang, T. Wang, J. Ma, RSC Adv. 3 (2013) 3487–3502.
[24] G. Wang, X. He, L. Wang, A. Gu, Y. Huang, B. Fang, B. Geng, X. Zhang, Microchim. Acta 180 (2012) 161–186.
[25] T.W. Tsai, G. Heckert, L.F. Neves, Y. Tan, D.Y. Kao, R.G. Harrison, D.E. Resasco, David W. Schmidtke, Anal. Chem. 81 (2009) 7917–7925.
[26] S. Chen, X. Hai, X.W. Chen, J.H. Wang, Anal. Chem. 86 (2014) 6689–6694.
[27] J. Zhao, F. Wang, J. Yu, S. Hu, Talanta 70 (2006) 449–454.
[28] P.F. Luo, S.V. Prabhu, R.P. Baldwin, Anal. Chem. 62 (1990) 752–755.
[29] J.M. Marioli, T. Kuwana, Electrochim. Acta 37 (1992) 1187–1197.
[30] J. Yang, W. Zhang, S. Gunasekaran, Biosens. Bioelectron. 26 (2010) 279–284.
[31] T.G.S. Babu, T. Ramachandran, B. Nair, Microchim. Acta 169 (2010) 49–55.
[32] B. Qi, H. Yang, K. Zhao, M.M. Bah, X. Bo, L. Guo, J. Electroanal. Chem. 700 (2013) 24–29.
[33] X. Niu, Y. Li, J. Tang, Y. Hu, H. Zhao, M. Lan, Biosens. Bioelectron. 51 (2014) 22–28.
[34] J. Zhao, L. Wei, C. Peng, Y. Su, Z. Yang, L. Zhang, H. Wei, Y. Zhang, Biosens. Bioelectron. 47 (2013) 86–91.
[35] H. Wu, W. Cao, Y. Li, G. Liu, Y. Wen, H. Yang, S. Yang, Electrochim. Acta 55 (2010) 3734–3740.
[36] J. Yuan, K. Wang, X. Xia, Adv. Funct. Mater. 15 (2005) 803–809.
[37] S. Cherevko, C.H. Chung, Sens. Actuators B 142 (2009) 216–223.
[38] Y. Zhou, S. Yang, Q. Qian, X. Xia, Electrochem. Commun. 11 (2009) 216–219.
[39] Y. Bai, Y. Sun, C. Sun, Biosens. Bioelectron. 24 (2008) 579–585.
[40] S.S. Mahshid, S. Mahshid, A. Dolati, M. Ghorbani, L. Yang, S. Luo, Q. Cai, Electrochim. Acta 58 (2011) 551–555.
[41] L. Lu, L. Zhang, F. Qu, H. Lu, X. Zhang, Z. Wu, S. Huan, Q. Wang, G. Shen, R. Yu, Biosens. Bioelectron. 25 (2009) 218–223.
[42] Z. Zhuang, X. Su, H. Yuan, Q. Sun, D. Xiao, M.M.F. Choi, Analyst 133 (2008) 126–132.

Talanta 132 (2015) 727–732

Contents lists available at ScienceDirect

Talanta

journal homepage: www.elsevier.com/locate/talanta

Living cells imaging for copper and hydrogen sulfide by a selective "on–off–on" fluorescent probe

Yong Qian *, Jie Lin [1], Tianbao Liu [1], Hailiang Zhu *

State Key Laboratory of Pharmaceutical Biotechnology, School of Life Sciences, Nanjing University, Nanjing 210093, China

ARTICLE INFO

Article history:
Received 18 July 2014
Received in revised form
11 October 2014
Accepted 15 October 2014
Available online 24 October 2014

Keywords:
Fluorescent probe
Copper ion
Hydrogen sulfide
Displacement approach
Imaging

ABSTRACT

A novel highly selective and sensitive fluorescent probe (NJ1) had been designed and synthesized for Cu^{2+} detection by fluorescence quenching mechanism, and then the enhancement of fluorescence intensity with the addition of hydrogen sulfide in complex NJ1Cu aqueous solution at physiological conditions were described. This "on–off–on" type fluorescence recognition system was a reversible process, which could be utilized to monitor copper ion and hydrogen sulfide based on a complex NJ1Cu formation–Cu^{2+} displacement approach. Importantly, this real-time recognition process of Cu^{2+} and hydrogen sulfide exhibited excellent anti-interference ability. In addition, this new fluorescent probe also has potential utility for Cu^{2+} and hydrogen sulfide detection in living cells, providing a potential tool for investigating copper ion and hydrogen sulfide in living systems or environment.

© 2014 Elsevier B.V. All rights reserved.

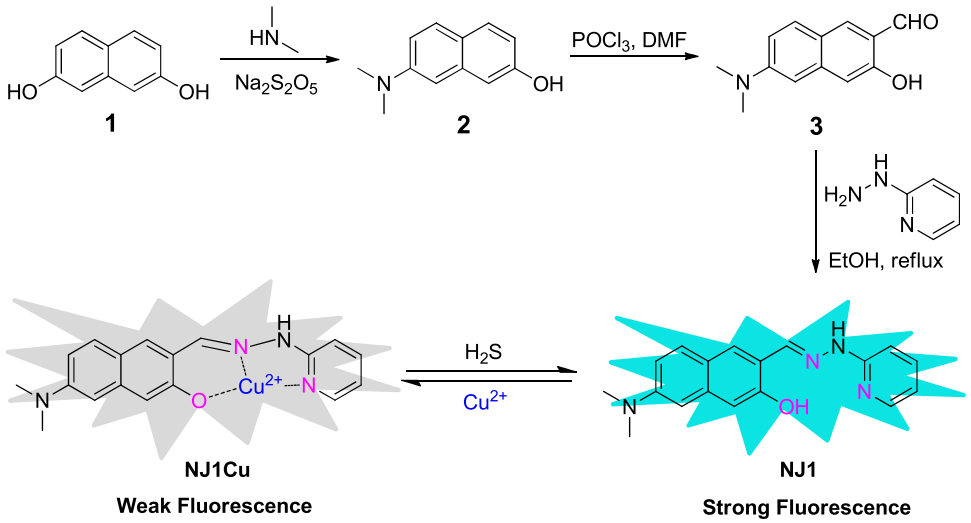
1. Introduction

Developing a sensitive, reliable and selective detection technique for various chemically and biologically pertinent metal cations and anions has attracted many research interests [1]. As the third most abundant transition metal in the human body, copper plays an important role in various physiological processes of organism [2]. However, the excessive exposure to these Cu^{2+} sources could cause imbalance in cellular processes, resulting in various diseases such as Alzheimer's disease and Parkinson's disease [3]. Additionally, copper has also been widely used in the industrial process, which is potentially toxic to environment. Therefore, there is an increasing need to monitor the existence of Cu^{2+} in the live biological samples or aquatic environment [4]. Fluorescent probes have become an important diagnostic tool for biological and environmental concern considering their sensitivity, special selectivity, and real-time monitoring with fast response time [5]. Owning to the notorious paramagnetic nature of Cu^{2+}, it usually leads to fluorescence quenching effect of the bound fluorophore [6]. More interestingly, this Cu^{2+} complex would also be potentially applied to monitor other substances, such as sulfide anion [7].

Hydrogen sulfide (H_2S) is a toxic gas best known for its rotten egg smell. It is slightly soluble in water, giving the hydrosulfide anion HS^- ($pK_a = 6.9$) and the sulfide dianion S^{2-} ($pK_a > 14$). H_2S has been utilized as a reactant or produced as a by-product in industrial process, which is widely spread in the environment. However, the role of H_2S in living organisms has recently received increasing attention. It has been suggested as the third signaling gasotransmitter, along with nitric oxide and carbon monoxide [8]. It is shown to act as a vascular relaxant, an energy regulator, and to be associated with cardiovascular regulation and the inflammation response [9]. Altering the level of hydrogen sulfide in human body or exposure to high-level sulfide can cause various physiological and biochemical problems. Therefore, the detection of hydrogen sulfide in industry, environment, and biological samples has attracted great attention. Several conventional detection strategies have been developed for hydrogen sulfide [10], such as electrochemical methods and ion chromatography. However, these analytic methods usually need complicated equipment and trou blesome sample pretreatment that are unsuitable for the analysis of sulfide in real time. For this reason, more convenient detection tools, such as fluorescent probes, have received significant attention as their easy operability and high sensitivity. To the best of our knowledge, several hydrogen sulfide selective probes based on copper ion displacement approach have been reported [7]. However, most of these probes have some limitations such as poor water solubility, complicated synthesis, poor membrane permeability, and detection systems required much organic co-solvents [7c], which would significantly restrict their practical applications in physiological condition. So far, real-time sulfide selective probes that are applicable in aqueous solution are still limited. It is thus desirable to develop simple and effective fluorescent probes for detection of sulfide in aqueous media that displays high sensitivity and selectivity as well as enables easier accessibility.

* Corresponding authors. Tel.: +86 025 8359 2672.
E-mail addresses: yongqian@nju.edu.cn (Y. Qian), zhuhl@nju.edu.cn (H. Zhu).
[1] These authors contributed equally to the work.

http://dx.doi.org/10.1016/j.talanta.2014.10.034
0039-9140/© 2014 Elsevier B.V. All rights reserved.



Scheme 1. Synthesis of NJ1 and the proposed mechanism of the monitoring system.

With this in mind, we designed and synthesized a novel small fluorescent probe NJ1 (Scheme 1). NJ1 demonstrated obvious fluorescence quenching after the addition of copper ion to form new complex NJ1Cu. This new complex displayed high specificity for hydrogen sulfide that induced copper ion to be released from the dye in the aqueous media, resulting in fluorescence enhancement. Herein, we reported the synthesis, photophysical characterization of NJ1 that was highly sensitive and selective for Cu^{2+}. The subsequent complex NJ1Cu could be developed as a platform for hydrogen sulfide real-time detection that could be potentially utilized in industry, environment, or biological requirements. Furthermore, the imaging of copper ion and hydrogen sulfide in living cells were also successfully developed.

2. Experimental

2.1. Materials and instrumentations

All chemicals were purchased from commercial suppliers and used without further purification. Chromatographic purification of products was accomplished by using forced-flow chromatography on silica gel (300–400 mesh). Thin layer chromatography was performed on EM Science silica gel 60 F254 plates (250 μm). Visualization of the developed chromatogram was accomplished using UV lamp. Nuclear magnetic resonance (NMR) spectra were acquired on Bruker DRX-400 operating at 100 MHz for ^{1}H NMR and ^{13}C NMR; residual protio solvent signals were used as internal standards for calibration purposes. Data for ^{1}H NMR are reported as follows: chemical shift (ppm), multiplicity (s, singlet; d, doublet; t, triplet; q, quartet; and m, multiplet), integration, coupling constant (Hz). TOF EI mass was performed by Mass Spectrometry Facility at Nanjing University. All fluorescence measurements were recorded on a Varian Cary Eclipse Fluorescence Spectrophotometer and Hitachi Fluorescence Spectrophotometer F-7000. The pH measurements were carried out on a HI 2221 calibration check pH/ORP meter.

2.2. General procedure for analysis

Stock solution of metal ions and other anions were prepared in ultrapure H_2O, stock solution of NJ1 (1 mM) were prepared in DMSO, which was diluted to the required concentration for measurement. All fluorescence measurements were carried out at room temperature on a Hitachi Fluorescence Spectrophotometer F-7000. The samples were excited at 360 nm; the emission spectrum was scanned from 425 nm to 650 nm at 1200 nm/min.

2.3. Cell culture and fluorescence imaging

HeLa cells were grown up in DMEM medium with 10% fetal bovine serum/penicillin/streptomycin in a 5% CO_2 atmosphere at 37 °C. Cells were then seeded on Coverglass-Bottom confocaldish and continuously incubated at 37 °C in a 5% CO_2 atmosphere for 24 h. After cells were incubated with 1 μL, 10 mM NJ1(final concentration: 10 μM) for 30 min at 37 °C, media was removed, and cells were washed with HEPES buffer three times again to remove any probe left in solution to optimize the background signal. Then, cells were added to fresh media and incubated with Cu^{2+} (0 μM, 10 μM) for another 20 min at 37 °C before imaging; or NaHS (10 μM) was added into the cells with NJ1 (10 μM) and Cu (10 μM) for another 20 min at 37 °C before imaging. All imaging experiments were performed on a fixed cell DSU spinning confocal microscope (Olympus), excitation at 405 nm. Imaging was performed using X40 objective and captured using Slidebook software. For all experiments, solution of NJ1 was prepared in DMSO (10 mM) and diluted into DMEM to the desired working concentration (10 μM). Cu^{2+}, and NaHS were diluted into ddH_2O to the desired working concentrations (10 μM) from a 10-mM stock solution.

2.4. Synthesis of probe NJ1

2.4.1. (E)-7-(dimethylamino)-3-((2-(pyridine-2-yl)hydrazono) methyl)naphthalene-2-ol

To a mixture compounds 3- (645 mg, 3 mmol) and 2-hydrazinylpyridine (360 mg, 3.3 mmol) was added ethanol under argon. The mixture was stirred at 80 °C for 1 h. The solvent was then evaporated under reduced pressure and the obtained residue was purified by silica gel column chromatography (eluent: 30 ethyl acetate/petroleum ether). (E)-7-(dimethylamino)-3-((2-(pyridine-2-yl)hydrazono)methyl)naphthalene-2-ol (NJ1) was obtained as a brown solid (421 mg, 46). ^{1}H NMR (400 MHz, DMSO-d_6): δ 10.76 (s, 1 H), 9.72 (s, 1 H), 8.54 (s, 1 H), 8.49 (d, J=2.3 Hz, 1 H), 8.12 (d, J=3.8 Hz, 1 H), 7.73 (d, J=8.8 Hz, 1 H), 7.69 (d, J=8.8 Hz, 1 H), 7.73 (d, J=7.4 Hz, 1 H), 7.30 (d, J=8.4 Hz, 1 H), 7.20 (d, J=8.8 Hz, 1 H), 6.96–6.99 (m, 2 H), 2.80 (s, 6 H).^{13}C NMR (100 MHz, DMSO-d_6): δ 157.8, 157.2, 152.7, 148.2, 140.8, 138.3, 133.1, 130.24, 130.22, 125.0, 119.2, 116.9 115.6, 114.8, 107.8, 106.9, 45.6; Ms (TOF MS EI$^+$): (m/z): 304.2.

3. Results and discussion

3.1. Synthesis

The preparation of the fluorescent probe (NJ1) and the possible reaction mechanism of NJ1 toward Cu^{2+} to form NJ1Cu complex, which could be utilized to monitor hydrogen sulfide, are shown in Scheme 1. The synthesis is quite straightforward through a three-step route with 2, 7-dihydroxynaphthalene (1) as the starting material. 7-(Dimethylamino)naphthalen-2-ol (2) was then synthesized by a Bucherer reaction using dimethylamine. The formylation of compound 2 was achieved using $POCl_3$/DMF reaction to afford aldehyde 3 in 83% yields. Finally, the target compound NJ1 was obtained by refluxing with 2-hydrazinylpyridine in EtOH. The final probe was characterized using NMR spectroscopy and mass spectrometry (see the supporting information).

3.2. Effects of the absorption and emission spectroscopic properties of NJ1

With this novel probe in hand, we first investigated its absorption and emission spectra in 20 mM HEPES buffer (pH 7.4, 0.5% DMSO, 25 °C), which could be utilized for studying the binding mechanism of NJ1 with Cu^{2+}. As described in Fig. 1, upon the addition of Cu^{2+} into the solution of NJ1, the absorption bands at 250 and 350 nm decreased, and new absorption bands at 300 and 450 nm emerged simultaneously.

We then evaluated the change of fluorescence emission spectra after the addition of Cu^{2+} into the solution of NJ1. The free probe displayed a strong fluorescence emission at physiological pH. The introduction of Cu^{2+} (1.0 equiv.) to the solution of NJ1 would lead to almost complete fluorescence quenching, revealing that NJ1 could be recognized Cu^{2+} through fluorescence "on–off" behavior. The pH effect studies suggested that the significant fluorescent signals could be observed at the physiological pH (Fig. S1).

We next evaluated the sensitivity of NJ1 for Cu^{2+} through varying concentrations of Cu^{2+} (0–10 μM) (Fig. 2a). The continuous addition of Cu^{2+} resulted in a gradual decrease of fluorescence intensity at 492 nm, and reached the saturation state when 1.0 equiv. of Cu^{2+} was added into NJ1 solution; the detection limit was found to be 0.5 μM. The effective fluorescence quenching of NJ1 was attributed to the coordination to a paramagnetic copper ion to form NJ1–Cu complex. The linear relationship of the fluorescence titration displayed that NJ1 responded to copper ion in 1:1 stoichiometry (Fig. 2b). This result had also been confirmed using TOF EI-MS (see the supporting information).

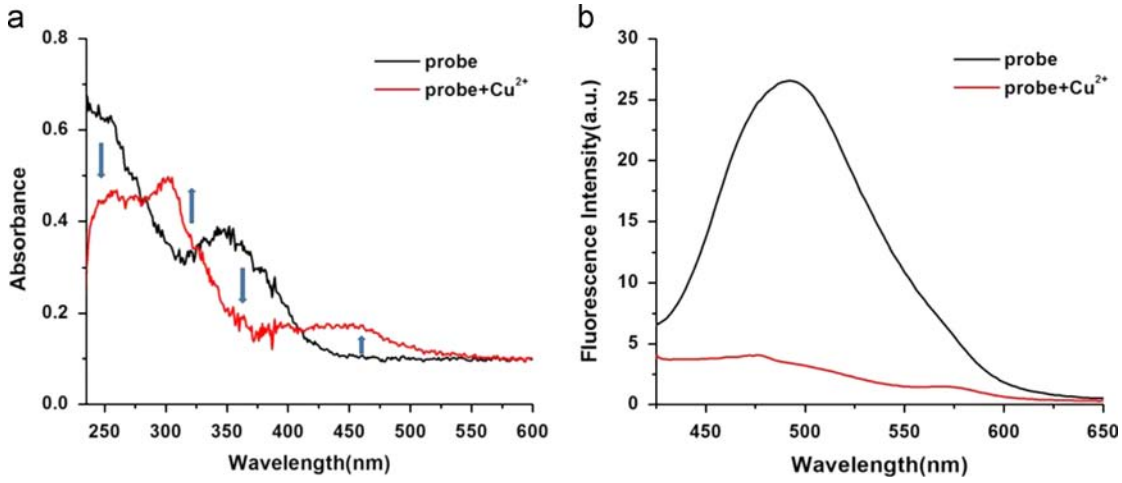


Fig. 1. (a) Absorption spectra of NJ1 (5 μM) in the absence and presence of Cu^{2+} (5 μM) in 20 mM HEPES buffer (pH 7.4, 0.5% DMSO) at 25 °C. (b) Fluorescence spectra of NJ1 (5 μM) in the absence and presence of Cu^{2+} (5 μM) at 25 °C. Excitation wavelength=360 nm. The data represent the average of three independent experiments.

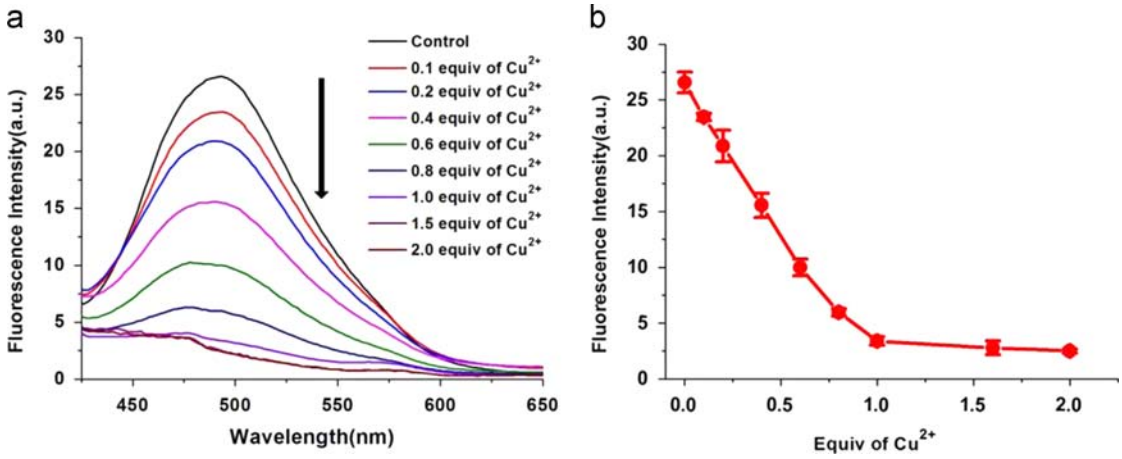


Fig. 2. (a) The fluorescence spectra of NJ1 (5 μM) incubated with different concentrations of Cu^{2+} (0.5–10 μM) in 20 mM HEPES buffer (pH 7.4, 0.5% DMSO) at 25 °C. (b) The fluorescence intensity of NJ1 at 492 nm versus different concentrations of Cu^{2+} (0.5–10 μM). Excitation: 360 nm, emission: 425–650 nm. The data represent the average of three independent experiments.

Then, the specificity of NJ1 toward Cu^{2+} was investigated by monitoring the change of the emission signal of NJ1 upon addition of other metal ions (represented by K^+, Na^+, Ag^+, Cu^+, Pb^{2+}, Pd^{2+}, Zn^{2+}, Mg^{2+}, Mn^{2+}, Fe^{2+}, Cd^{2+}, Al^{3+}, Cr^{3+}, Fe^{3+}, Cu^{2+}). All other metal ions had little quenching effect on the fluorescence spectra of NJ1, which did not induce significant fluorescence spectral changes. Only Cu^{2+} could cause a remarkable fluorescence quenching of NJ1, which demonstrated that NJ1 have high selectivity toward Cu^{2+} ions. To examine the intereference of different metal ions on the Cu^{2+} recognition of NJ1, antiinterference of NJ1 was also carried out. As displayed in Fig. 3, in the absence of Cu^{2+}, other potential competitive metal ions failed to cause significantly fluorescent quenching of NJ1, whereas it would be dramatically quenched after addition of Cu^{2+} ions. Taken together, all these results showed that NJ1 possessed high selectivity toward Cu^{2+}; the other coexiting metal ions could not lead to significant intereference on Cu^{2+} recognition.

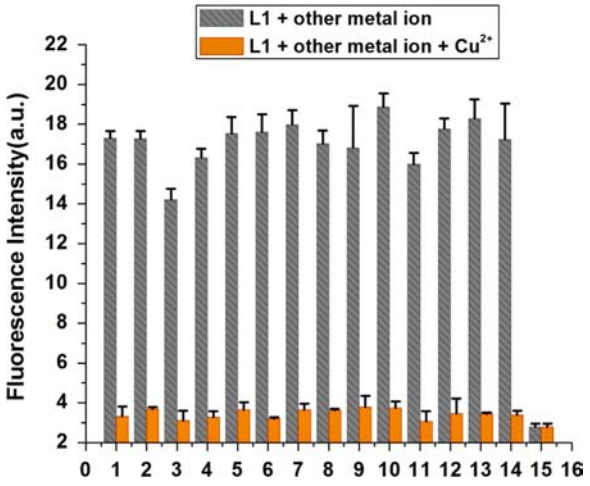


Fig. 3. Fluorescence emission spectra of NJ1 (5 μM) and different metal ions (5 μM) in the absence (gray bar) and presence (orange bar) of Cu^{2+} (5 μM) in 20 mM HEPES buffer (pH 7.4, 0.5% DMSO) at 25 °C. (1) K^+, (2)Na^+, (3) Ag^+, (4) Cu^+, (5) Pb^{2+}, (6) Pd^{2+}, (7) Zn^{2+}, (8) Mg^{2+}, (9) Mn^{2+}, (10) Fe^{2+}, (11) Cd^{2+}, (12) Al^{3+}, (13) Cr^{3+}, (14) Fe^{3+}, (15) Cu^{2+}. All the data represent the fluorescence intensity at 492 nm, excitation: 360 nm. The data represent the average of three independent experiments.

Subsequently, the "off–on" property of NJ1Cu toward H_2S was investigated. As H_2S is a small gas molecule and has a pK_a of around 6.9, we chose NaHS as the sulfide sources. The fluorescence recovered quickly upon the addition of NaHS to the solution of NJ1Cu, so this probe was potentially suitable for real-time monitoring of hydrogen sulfide levels in biological samples. The high selectivity was an important quality for an excellent fluorescent sensor; then selective fluorescence response of NJ1Cu to various anions or sulfur species had also been investigated in physiological conditions. Interestingly, NJ1 could only be regenerated by adding hydrogen sulfide to the NJ1Cu solution. Other anions or sulfur species, such as Cl^-, Br^-, I^-, HSO_3^-, HSO_4^-, $S_2O_5^-$, SO_4^{2-}, SO_3^{2-}, lys, cys, could not result in the significant change of the fluorescence intensity and corresponding fluorescence regeneration. The competitive experiment of NJ1Cu system was also carried out for the selectivity of NJ1Cu toward hydrogen sulfide in the presence of other anions. As shown is Fig. 4a, there were nearly no difference in the absence and presence of other anions; this system indicated remarkably selective "turn on" behavior toward H_2S. Furthermore, an excellent linear response of NJ1Cu versus the concentration of NaHS in the low concentration region (varying between 0 and 5 μM) was observed (Fig. 4b). Thus, the above results strongly proved that NJ1Cu system was a selective and sensitive detection method toward hydrogen sulfide that could not be significantly interfered by the commonly coexistent anions.

3.3. Cellular imaging experiment

We further investigated the potential application of NJ1 in living cells. Hela cells were incubated with 10 μM NJ1 in culture medium for 30 min at 37 °C; then live-cell imaging of the cells were carried out using confocal fluorescence microscopy. As shown in Fig. 5, strong fluorescence in the cells was observed after the cells were incubated with this developed probe. Next, the cells were added to 10 μM Cu^{2+} and further incubated for another 20 min, the fluorescence of the cells was quickly quenched and showed almost no fluorescence. However, the fluorescence of cells could be quickly recovered after incubation with 10 μM NaHS for 20 min at 37 °C. Therefore, these results revealed that NJ1 has the potential to use for the detection of copper ion in living cells and their complex NJ1Cu would also be an excellent monitoring system to visualize sulfide in living cells.

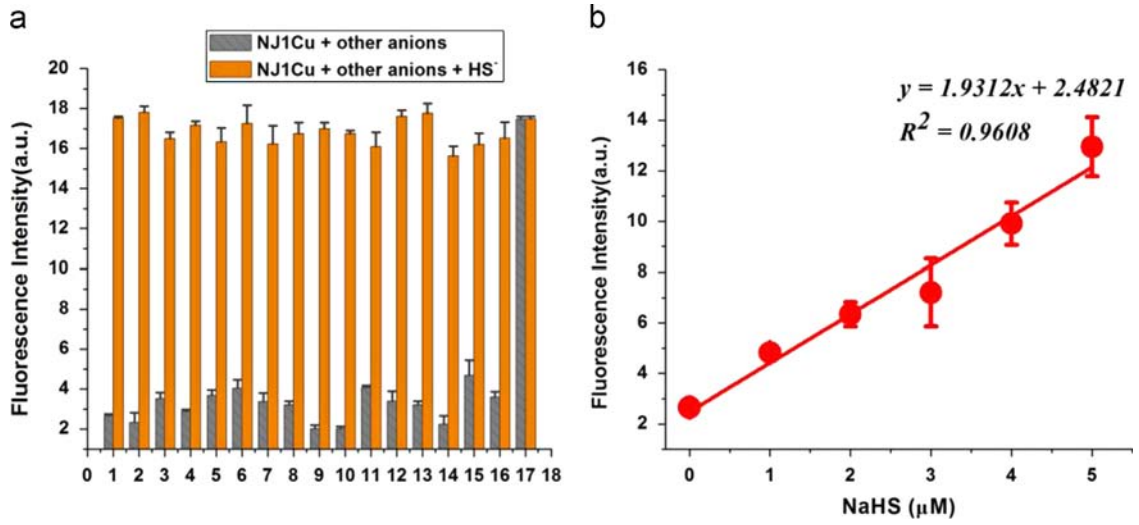


Fig. 4. (a) Fluorescence spectra of NJ1Cu (5 μM) upon addition of different anions (5 μM) in 20 mM HEPES buffer (pH 7.4, 0.5% DMSO) at 25 °C. The gray bars represent the fluorescence intensity of NJ1Cu in the presence of 5 μM anions; the orange bars represent the fluorescence intensity of the above solution on further addition of 5 μM NaHS. (1) Cl^-, (2) Br^-, (3) I^-, (4) $HClO_4^-$, (5) CH_3COO^-, (6) HPO_4^{2-}, (7) HSO_3^-, (8) HSO_4^-, (9) NO_2^-, (10) NO_3^-, (11) OCN^-, (12) $S_2O_5^-$, (13) SO_4^{2-}, (14) SO_3^{2-}, (15) lys, (16) cys, (17) HS^-. (b) Fluorescence spectra of NJ1Cu (5 μM) upon addition of different amounts of HS^- ions (0–5 μM). All the data represent the fluorescence intensity at 492 nm, excitation: 360 nm. The data represent the average of three independent experiments.

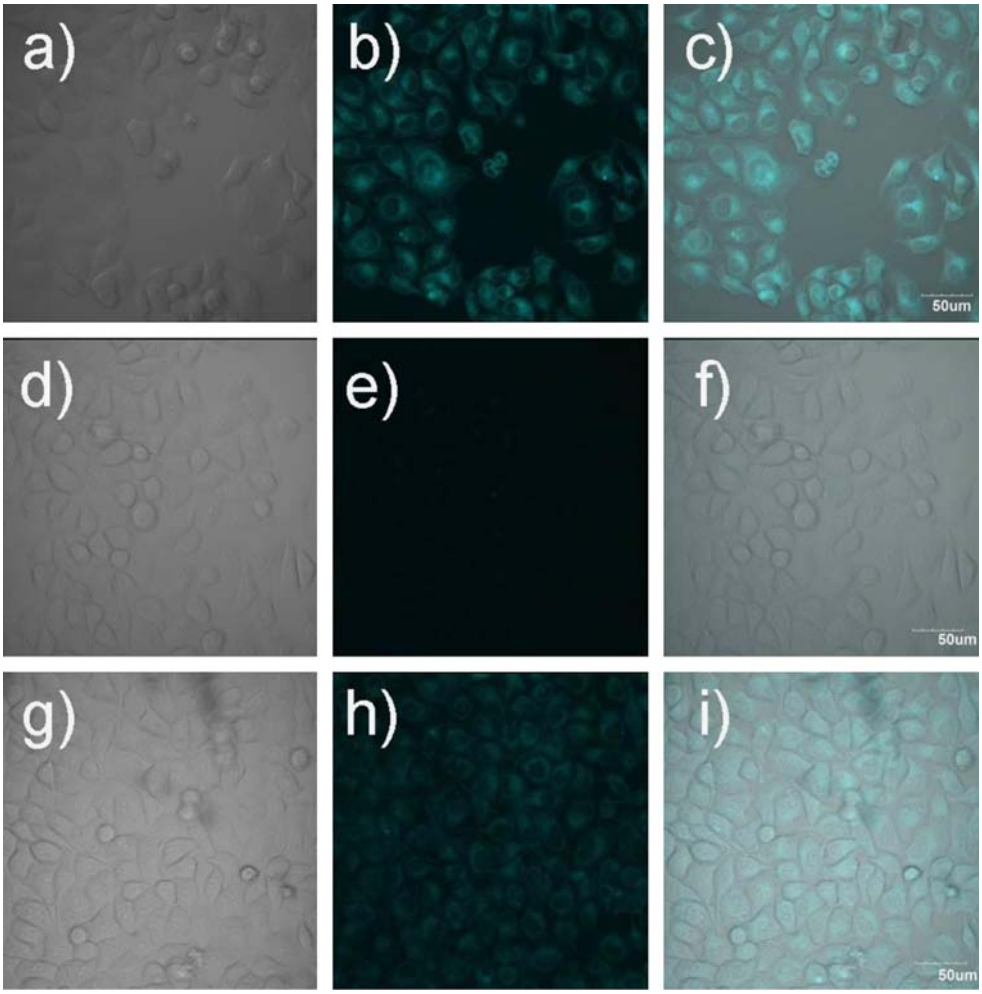


Fig. 5. Confocal fluorescent images of HeLa cells: Cells incubated with NJ1 (10 μM) for 30 min (a–c); Cells incubated with NJ1 (10 μM) for 30 min and subsequent treatment of the cells with Cu^{2+} (10 μM) for 20 min (e–f); Cells incubated with NJ1 (10 μM), Cu^{2+} (10 μM) for 30 min and subsequent treatment of the cells with NaHS (10 μM) for another 20 min (g–i). (a, d, and g) Bright-field images; (b, e, and h) fluorescent images; (c, f, and i) merged images. λ_{ex}=405 nm, scare bar=50 μM.

4. Conclusions

In summary, we have designed and synthesized a novel highly selective and sensitive fluorescent probe NJ1 for Cu^{2+} detection by fluorescence quenching mechanism. The enhancement of fluorescence intensity with the addition of hydrogen sulfide by Cu^{2+} released from the core of the complex NJ1Cu in aqueous solution at physiological conditions were also described. This "on–off–on" type fluorescence recognition system was a reversible process, which could be utilized to detect copper ion and hydrogen sulfide based on a complex NJ1Cu formation–Cu^{2+} displacement approach. More importantly, this real-time recognition process of Cu^{2+} and hydrogen sulfide exhibited excellent antiinterference ability. Furthermore, Preliminary imaging experiments demonstrated that NJ1 also had the potential to be used for imaging in living cells. Therefore, this new, simple, sensitive, and selective fluorescent probe has potential application in biological or environment systems for Cu^{2+} and hydrogen sulfide detection. The development of more specific fluorescent probes for optical imaging in living cells, tissues, and animals is our current interest and ongoing in our laboratory.

Acknowledgments

This work is financially supported by grants of the National Natural Science Foundation of China (21302094 to Y.Q.), the Jiangsu Natural Science Foundation (BK20130552 to Y.Q.), the Fundamental Research Funds for the Central Universities (20620140214 to Y.Q.), the Research Fund for the Doctoral Program of Higher Education of China (20130091120036 to Y.Q.), and Jiangsu Province large scientific instruments shared services platform (BZ201307 to Y.Q.).

Appendix A. Supporting information

Supplementary data associated with this article can be found in the online version at http://dx.doi.org/10.1016/j.talanta.2014.10.034.

References

[1] J. Du, M. Hu, J. Fan, X. Peng, Chem. Soc. Rev. *41* (2012) 4511–4535.
[2] E. Gaggelli, H. Kozlowski, D. Valensin, G. Valensin, Chem. Rev. *106* (2006) 1995–2044.
[3] K.J. Barnham, C.L. Masters, A.I. Bush, Nat. Rev. Drug Discov. *3* (2004) 205–214.
[4] T.Q. Duong, J.S. Kim, Chem. Rev. *110* (2010) 6280–6301.
[5] (a) Y. Qian, J. Karpus, O. Kabil, S.Y. Zhang, H.L. Zhu, R. Banerjee, J. Zhao, C. He, Nat. Commun. *2* (2011) 495;
(b) K. Sasakura, K. Hanaoka, N. Shibuya, Y. Mikami, Y. Kimura, T. Komatsu, T. Ueno, T. Terai, H. Kimura, T. Nagano, J. Am. Chem. Soc. *133* (2011) 18003–18005.

[6] S. Sirilaksanapong, M. Sukwattanasinitt, P. Rashatasakhon, Chem. Commun. (Camb) *48* (2012) 293–295.
[7] (a) F. Hou, J. Cheng, P. Xi, F. Chen, L. Huang, G. Xie, Y. Shi, H. Liu, D. Bai, Z. Zeng, Dalton Trans. *41* (2012) 5799–5804;
(b) F. Hou, L. Huang, P. Xi, J. Cheng, X. Zhao, G. Xie, Y. Shi, F. Cheng, X. Yao, D. Bai, Z. Zeng, Inorg. Chem. *51* (2012) 2454–2460;
(c) M. Xu, C. Yin, F. Huo, Y. Zhang, J. Chao, Sensor. Actuator. B. 204 (2014) 18.
[8] D.J. Lefer, Proc. Natl. Acad. Sci. U S A 104 (2007) 17907–17908.
[9] (a) G.A. Benavides, G.L. Squadrito, R.W. Mills, H.D. Patel, T.S. Isbell, R.P. Patel, V.M. Darley-Usmar, J.E. Doeller, D.W. Kraus, Proc. Natl. Acad. Sci. U S A *104* (2007) 17977–17982;
(b) M. Fu, W. Zhang, L. Wu, G. Yang, H. Li, R. Wang, Proc. Natl. Acad. Sci. U S A *109* (2012) 2943–2948.
[10] (a) B. Divjak, W. Goessler, *J. Chromatogr. A. 582* (1999) 267–274;
(b) B. Vallejo, P. Richter, I. Toral, C. Tapia, M.D. *Anal. Chim. Acta 436* (2001) 301–307.

Talanta 132 (2015) 733–738

Contents lists available at ScienceDirect

Talanta

journal homepage: www.elsevier.com/locate/talanta

Development of a method for total Hg determination in oil samples by cold vapor atomic absorption spectrometry after its extraction induced by emulsion breaking

Priscila de O. Vicentino, Daniel M. Brum, Ricardo J. Cassella *

Departamento de Química Analítica, Universidade Federal Fluminense, Outeiro de São João Batista s/n, Centro, Niterói, RJ 24020-141, Brazil

ARTICLE INFO

Article history:
Received 5 August 2014
Received in revised form
9 October 2014
Accepted 12 October 2014
Available online 23 October 2014

Keywords:
Mercury
Extraction induced by emulsion breaking
Cold vapor atomic absorption spectrometry
Oil

ABSTRACT

This work reports the development of a novel extraction method for total Hg determination in oil samples. After extracting Hg from samples it was quantified in the extracts by cold vapor atomic absorption spectrometry (CV-AAS), employing a laboratory-made gas–liquid separator (GLS) and $NaBH_4$ as reducing agent. The extraction of Hg from samples was carried out by extraction induced by emulsion breaking (EIEB), which is based on the formation and breaking of water-in-oil emulsion between the oil samples and an extractant solution containing an emulsifying agent (surfactant) and nitric acid. Operational parameters of the GLS were evaluated in order to set the best performance of the measurement system. In these studies it was proven that the volume of sample and the concentration of HCl added to the sample extracts had significant influence on Hg response. The best conditions were achieved by adding 0.5 mL of a 0.3 mol L^{-1} HCl solution on 1 mL of sample extract. The extraction conditions were also optimized. The highest efficiency was observed when 4 mL of a solution containing 2.5% triton X-100 and 15% v/v HNO_3 were employed for the extraction of Hg contained in 20 mL of sample. Emulsion breaking was performed by heating at 80 °C and took approximately 20 min. The limit of quantification of the method was 1.9 μg L^{-1} and recovery percentages between 80% and 103% were observed when spiked samples (2 and 10 μg L^{-1}) of diesel oil, biodiesel and mineral oil were analyzed.
© 2014 Elsevier B.V. All rights reserved.

1. Introduction

Nowadays, the determination of trace elements in organic liquids is one of the most challenging tasks in the field of analytical chemistry. The high complexity of samples, that present high carbon content, makes these procedures very laborious and subjected to contamination and losses of analytes during sample preparation. Atomic spectrometric techniques are very popular for the elemental analysis of organic liquids (such as oils), especially because of their high selectivity and suitable sensitivity and precision [1–3]. Besides, atomic spectrometric techniques are well-established and present in the majority of analytical laboratories. Despite these advantages, most times, the use of atomic spectrometric techniques requires a careful preparation of samples in order to avoid or minimize possible interferences.

Different strategies have been employed for sample preparation in the elemental analysis of organic liquids by spectrometric techniques. Total decomposition of samples [4–8] and their introduction in the equipment in the form of emulsions or microemulsions [9–12] are very popular, despite some problems verified in their application. Extraction methods are also available for the determination of trace elements in organic liquids [13–16]. They present some advantages over the other methods, since they make possible the separation of the organic matrix. Besides, in most cases, the calibration can be performed with aqueous standard solutions, thus avoiding the use of unstable and high-cost oil-based standards.

Mercury is one of the metallic elements that arouses the greatest interest in the scientific community, probably due to its toxicity and particular chemistry [17,18]. It is prone to accumulation in biota and represents a serious problem when released to the environment, being recognized as a large scale global pollutant [19,20]. Undoubtedly, the natural occurrence of Hg in crude oil and its presence in fuels [21,22] contribute significantly to the input of this pollutant to the environment. Some spectrometric techniques, such as cold vapor atomic absorption spectrometry (CV-AAS) [23], electrothermal atomic absorption spectrometry (ETAAS) [24], atomic fluorescence spectrometry (AFS) [25], inductively coupled plasma mass spectrometry (ICP-MS) [26] and electrothermal vaporization coupled to ICP-MS (ETV-ICP-MS) [27] were already employed for total Hg determination in oil samples.

A few extraction methods were already proposed for total Hg determination in organic liquids. Liang et al. [28] reported the

* Corresponding author. Tel.: +55 21 2629 2344; fax: +55 21 2629 2143.
E-mail address: cassella@vm.uff.br (R.J. Cassella).

http://dx.doi.org/10.1016/j.talanta.2014.10.019
0039-9140/© 2014 Elsevier B.V. All rights reserved.

development of a method for extraction of total Hg from gasoline and other petroleum-derived products followed by the determination of Hg in the aqueous extracts by cold vapor AFS. The extraction was performed with a mixture of BrCl/HCl. The same mixture was employed by Uddin et al. [29] in the determination of total Hg in crude oils by cold vapor AFS. Nevertheless, in this case, the samples were firstly diluted in toluene in order to decrease their viscosity and allow a convenient shaking with the aqueous extractant solution. Bromine water was employed by Heyward et al. [30] for the oxidation and extraction of Hg from liquid hydrocarbons. In this work, Hg determination in the extracts was carried out by CV-AAS.

The goal of this work was to develop and propose a novel simple approach for the determination of total Hg in different types of oils without using either bromine or any organic solvent. The method employed the extraction induced by emulsion breaking (EIEB) [31–34], which is based on the formation and breaking of detergent emulsions prepared with the samples and an extractant solution (containing triton X-100 and nitric acid only), to enhance the extraction process. The developed method was applied in the determination of trace concentrations of Hg in diesel, biodiesel and mineral oil samples.

2. Experimental

2.1. Apparatus

Absorbance measurements were performed with a Varian AA240FS atomic absorption spectrometer (Mulgrave, Australia) equipped with a hollow cathode lamp of Hg operated at 5 mA. The measurements were made at 253.4 nm wavelength using a 1 nm slit width.

A laboratory-made gas-liquid separator (GLS) was employed for Hg cold vapor generation. The GLS was constructed with a capped 50 mL polyethylene tube and PEEK connections. A scheme of the GLS used in this work is depicted in Fig. 1. Ultrapure Argon (99.99%, Linde Gases, Macaé, Brazil) was employed to transport Hg vapor from GLS to the measurement cell.

Emulsion breaking was carried out by heating the flasks in a water bath maintained at 80 ± 2 °C). A water bath supplied by Nova Técnica (São Paulo, Brazil), model NT-247, was employed for this purpose.

2.2. Reagents and solutions

The water used in this work was deionized in a Direct-Q 3 system from Millipore (Milford, MA, USA). It always had resistivity equal to or higher than 18.2 MΩ cm. All reagents were of analytical grade and used without further purification.

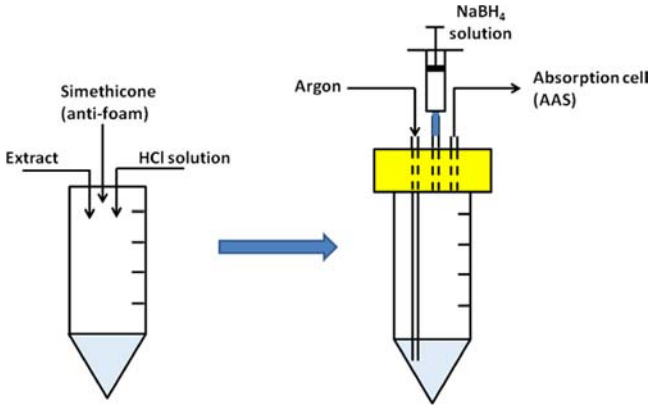


Fig. 1. Gas–liquid separator (GLS) employed in this work.

A 1000 μg mL^{-1} stock solution of Hg(II), supplied by Spex (Metuchen, NJ, USA), was employed for the preparation of aqueous diluted standard solutions of Hg(II). They were prepared from suitable dilution of the stock solution with deionized water just before their use.

The oil-based stock solution of Hg(II) with 100 μg g^{-1} concentration was supplied by Conostan (Bale, Canada). Diluted oil-based solutions employed for spiking the samples in the recovery test were prepared from adequate dilution of the stock solution with HPLC grade hexane (Tedia, Fairfield, OH, USA).

Concentrated nitric and hydrochloric acids from Tedia (Fairfield, OH, USA) were employed to prepare diluted solutions of these acids. Dilution was performed in a volumetric flask with deionized water.

A 0.5% m/v $NaBH_4$ solution was prepared by dissolving 0.5 g of the reagent (Vetec, Rio de Janeiro, Brazil) in approximately 80 mL of a 0.05% m/v NaOH solution. Afterwards, the obtained solution was transferred to a 100 mL volumetric flask and the volume was made up to the mark with the same 0.05% m/v NaOH solution. The $NaBH_4$ solution was prepared daily just before its use.

The 75 mg mL^{-1} simethicone solution employed as antifoam was purchased from the drugstores of the city of Niterói in the form of commercial pharmaceutical formulation.

2.3. General extraction and measurement procedure

Mercury extraction from oil samples was achieved by employing extraction induced by the emulsion breaking technique, which is based on the formation and breaking of water-in-oil emulsions. Emulsions were prepared by vigorous mixing of 20 mL of each oil with 4 mL of a solution containing 2.5% m/v triton X-100 and 15% v/v HNO_3 in a 50 mL capped polyethylene flask. Then the flask containing the emulsion was put on a horizontal mixer, where it was agitated for 30 min at 100 rpm. After the extraction time needed to promote quantitative transference of Hg from the oil to the aqueous dispersed phase the flask containing the emulsion was immersed into the water bath at a temperature of 80 ± 2 °C, where it was maintained until the emulsion breaking was observed, which took approximately 20 min. Emulsion breaking resulted in the formation of two well-defined phases: (i) the upper oil phase and (ii) the lower aqueous acid phase, containing Hg extracted from oil. The oil was removed with the aid of a pipette, and the lower phase (extract) was collected for Hg quantification.

The determination of Hg in the extracts was performed by CV-AAS, using the GLS constructed for this purpose. The main advantages of this GLS were the possibility to use discrete portions of the extracts for analysis and the use of different flasks for the determination of Hg in each aliquot of the extract, which avoided cross contamination. The measurement of Hg in the extracts was performed by transferring 1.0 mL of the extract, 0.5 mL of a 0.3 mol L^{-1} HCl solution and 2 drops of a 75 mg mL^{-1} simethicone solution to the GLS flask, which was adapted to the GLS cap. Then, 0.1 mL of a 0.5% m/v $NaBH_4$ solution was added through the hole in the cap using a syringe. The Hg vapor formed was transported to the spectrometer by the Ar that flowed through the GLS, yielding a transient signal. Peak height was employed as a quantitative variable.

3. Results and discussion

3.1. Optimization of the operational conditions for Hg measurement by CV-AAS

The first step of this work was to evaluate the viability of the use of the laboratory-made GLS (Fig. 1) assembled for Hg vapor generation, aiming its measurement by atomic absorption spectrometry. The main characteristic of the GLS employed in this work

was that it made possible introducing discrete portions of the extracts into the system. The generation of Hg cold vapor was performed through the addition of a given volume of $NaBH_4$ (reducing agent) solution on the mixture of the sample (or standard solution) with HCl solution. Argon was bubbled in the mixture in order to provide Hg vapor release from solution and its transportation to the measurement cell. In order to achieve maximum sensitivity, the influences of chemical variables such as HCl and $NaBH_4$ concentrations and the sample volume introduced into the GLS were investigated. Some parameters such as the volumes of HCl solution mixed with the sample and $NaBH_4$ solution added to the GLS were maintained constant at 0.5 and 0.1 mL, respectively. The carrier gas (Ar) flow rate was also maintained constant at 1000 mL min^{-1}.

The generation of Hg cold vapor depends on the addition of a suitable amount of reducing agent, since mercury is found in solution in the form of Hg(II) ions and needs to be reduced to gaseous elemental Hg. Sodium borohydride was employed for this purpose. As mentioned previously, the volume of $NaBH_4$ solution added was always 0.1 mL and the concentration of the reagent was varied in the range of 0.01–0.2% m/v. All $NaBH_4$ solutions were prepared in the presence of 0.5% m/v NaOH. The highest Hg response was observed when the $NaBH_4$ concentration was 0.1% or 0.2% m/v. Therefore, a 0.1% m/v $NaBH_4$ solution was employed in all further experiments.

The vapor generation of Hg also depends on the acidity of the medium since the decomposition of $NaBH_4$ into hydroboron intermediates, which are responsible for the reduction of Hg(II) ions, is accelerated in acidic medium [35]. Hence, to keep the medium acid sufficient for promoting suitable Hg vapor evolution, HCl solution was added to the sample extract (or standard solution) before addition of $NaBH_4$ solution. As mentioned previously, the volume of HCl solution added to the flask was always 0.5 mL and the concentration of HCl in this solution was varied from 0 to 6 mol L^{-1}. The results obtained in this experiment (Fig. 2) showed that the highest response could be achieved when HCl concentration was in the range of 0.10–0.3 mol L^{-1}. When the HCl concentration was higher than this value, a decrease of Hg signals was verified. In view of these results, a 0.3 mol L^{-1} HCl solution was selected for the method.

The volume of sample added to the GLS controlled the amount of Hg introduced into the measurement system. Theoretically, the increase of the mass of Hg added to the flask would lead to the increase of signals. On the other hand, the magnitude of Hg signals could be limited by the amount of reducing agent added, which could not be enough to promote the evolution of all Hg present in the solution, and also by kinetic effects. Then, an experiment was performed to evaluate the influence of the sample volume employed on Hg measurement. A 50 μg L^{-1} Hg(II) solution was used and the other conditions were those optimized in the previous experiments. The sample volume was varied from 0.5 to 5 mL.

As can be seen in Fig. 3, the Hg response increased linearly with the increase of sample volume. This behavior was already expected, since the increase of the sample volume also increased the amount of Hg inserted into the system for atomization. The signals are registered in terms of peak height and peak area (Fig. 3) and no significant differences are observed in their behavior with the variation of volume, indicating that the release of Hg vapor from aqueous medium is fast and does not suffer from kinetic interferences. Evidently, the increase of volume caused some broadening of the peaks, which must be associated to the higher amount of Hg that must be atomized. As the volume of extract recovered in the extraction induced by emulsion breaking was limited to not more than 4 mL, all further experiments were conducted with 1 mL of solution (extract or standard solution) in order to allow that measurements could be made in triplicate.

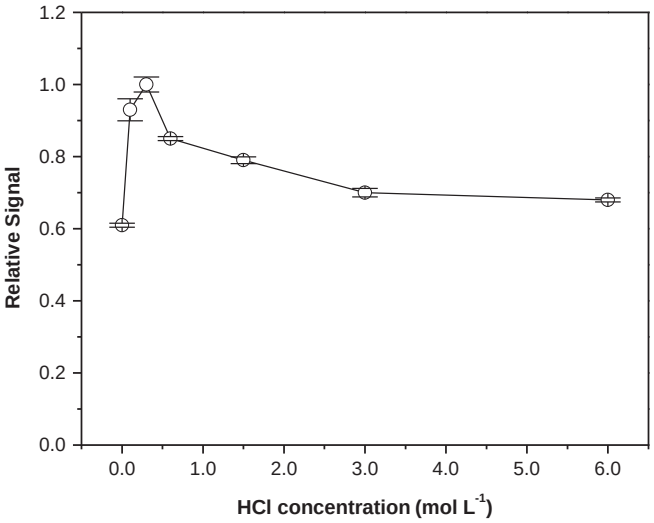


Fig. 2. Effect of HCl concentration in the solution mixed with the extract (or satndard solution) for Hg measurement by CV-AAS. Volume of sample =1 mL and volume of HCl solution =0.5 mL.

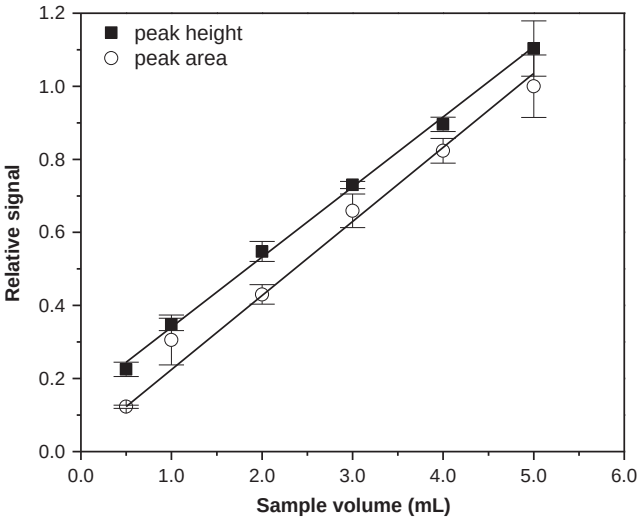


Fig. 3. Effect of sample volume employed for Hg measurement by CV-AAS. Volume of HCl solution =0.5 mL and concentration of HCl in the solution =0.3 mol L^{-1}.

The final conditions used in the measurement of Hg employing the proposed GLS are summarized in Table 1. Mercury signals obtained in the construction of a typical calibration curve are shown in Fig. 4.

3.2. Optimization of extraction induced by emulsion breaking conditions

After establishing suitable conditions for Hg measurement by CV-AAS using the GLS device proposed in this work, the extraction induced by emulsion breaking was optimized. As well known, extraction induced by emulsion breaking is based on the formation and breaking of detergent emulsions. The extraction of the analytes occurs during phases separation (emulsion breaking) due to the stronger affinity of metallic cations by the acid aqueous medium than oil one. In the present work, the extraction conditions were optimized using a diesel oil sample spiked with 10 μg L^{-1} of Hg in organometallic form (oil-based standard). The parameters evaluated were concentration and type of surfactant (triton X-100 and triton X-114), concentration of HNO_3 in the extractant solution, and extraction time.

Table 1
Operational parameters of the GLS employed in the measurement of Hg by CV-AAS.

Parameter	Condition
Sample volume	1 mL
HCl solution concentration	0.3 mol L^{-1}
HCl solution volume	0.5 mL
$NaBH_4$ solution concentration[a]	0.5% m/v
$NaBH_4$ solution volume	0.1 mL
Carrier gas (Ar) flow rate	300 mL min^{-1}

[a] Solution prepared in 0.05% m/v NaOH.

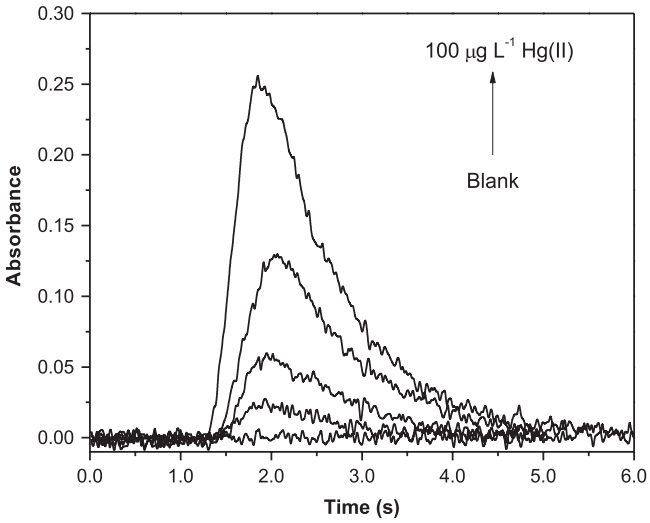


Fig. 4. Hg signals obtained with the GLS constructed in this work at optimized conditions.

The first parameters evaluated were the type and concentration of surfactant in the extractant solution. Both triton X-100 and triton X-114 were tested as emulsifier agents in different ranges of concentrations. Triton X-100 was tested in the range of 0.5–7% m/v, whereas triton X-114 was tested in the range of 0.5–15% m/v. These ranges were chosen taking into account the ability of each surfactant to promote adequate emulsification of the system. The HNO_3 concentration in the extractant solution, in this experiment, was always 15% v/v. Results obtained (Fig. 5) showed that surfactant concentration played an important role on the extraction efficiency of Hg from oil. In both cases, at low concentrations of surfactant, Hg response was low, indicating that the analyte was not satisfactorily extracted from oil. This poor extraction occurred possibly due to the inefficient dispersion of the aqueous phase through the oil. The increase of surfactant concentration resulted in the increase of Hg signals probably because of the formation of emulsions with very small droplets, which increased the contact between the extractant solution and the sample. The highest signals were obtained at 2.5% m/v triton X-100 concentration and 12.5% m/v triton X-114 concentration.

Another aspect considered in this study was the time required to break the emulsions. In general, triton X-114 emulsions are broken in a shorter time than triton X-100 emulsions when the surfactants are present in the same concentration. This difference occurs due to higher stability of triton X-100 emulsions when compared with triton X-114 ones. Nevertheless, when considering optimized concentrations, a 2.5% m/v triton X-100 solution was selected for the method because it was broken in approximately 20 min while the 12.5% m/v triton X-114 emulsion took approximately 35 min to be broken. The presence of triton X-100 in the

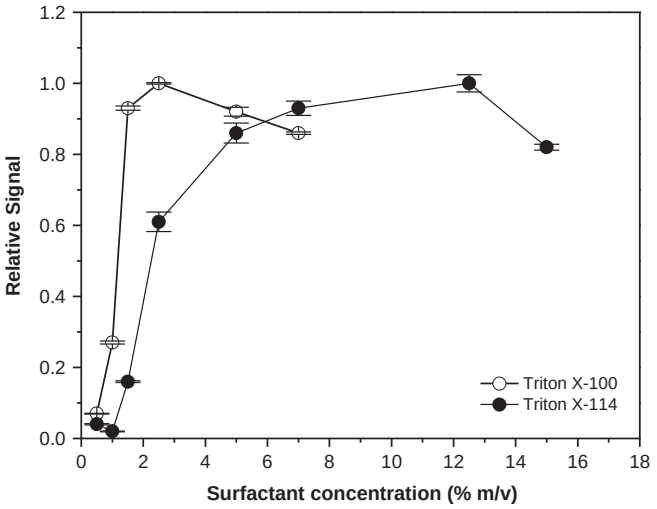


Fig. 5. Effect of surfactant type and concentration in the extractant solution on the extraction of Hg from the diesel oil employed in the optimization studies. HNO_3 concentration = 15% v/v.

extracts from EIEB resulted in the formation of an excessive amount of foam inside the GLS system during Hg measurement. This drawback was overcome by the addition of two drops (approximately 100 μL) of a 75 mg mL^{-1} simethicone solution, which acted as an antifoam agent.

The concentration of HNO_3 in the extractant solution also played fundamental role in the extraction process. According to data obtained in previous works [31–34], the extraction process is enhanced in the presence of mineral acids because H^+ ions compete with metallic cations for the basic sites present in the organic molecules that form the oil sample. Also, nitric acid is able to break covalent bonds between metals and organic structures (oxidation), allowing the release of metals to the medium in the form of free ions. In the present work, the influence of HNO_3 concentration in the extractant solution was investigated in the range of 5–30% v/v. It is important to remember that this solution also contained 2.5% m/v triton X-100, employed as an emulsifier agent. Maximum signals were observed at 15% v/v HNO_3. In concentrations below this value, the amount of acid was not enough to displace Hg from organic structures. At HNO_3 concentrations higher than 15% v/v, the signals decreased probably due to the influence of some substances co-extracted from sample, since this same behavior was not noted when standard solutions of Hg(II) were tested to evaluate the influence of HNO_3 concentration (Fig. 6). Therefore, a 15% v/v HNO_3 concentration was chosen for extracting Hg from samples in the method.

Finally, the last parameter evaluated is the extraction time, which is the time lapse between emulsion formation and breaking. Although the formation of emulsions already enhances the extraction process, since it increases the contact between the oil sample and the aqueous extractant solution, sometimes extraction efficiency can be limited by the time required for displacing metals from organic molecules and achieving satisfactory transference of the analyte from the organic to the aqueous phase.

The influence of extraction time was tested in the range of 0 (emulsion breaking just after its formation)–60 min. The extraction process was carried out maintaining the emulsions under continuous agitation with a horizontal shaking. This agitation was performed to avoid phases separation (emulsion breaking) and allowed aqueous droplets of extractant solution to move through the continuous phase, represented by the oil, thus improving extraction efficiency. The concentrations of HNO_3 and triton X-100 in the emulsifier solutions were those optimized in the previous

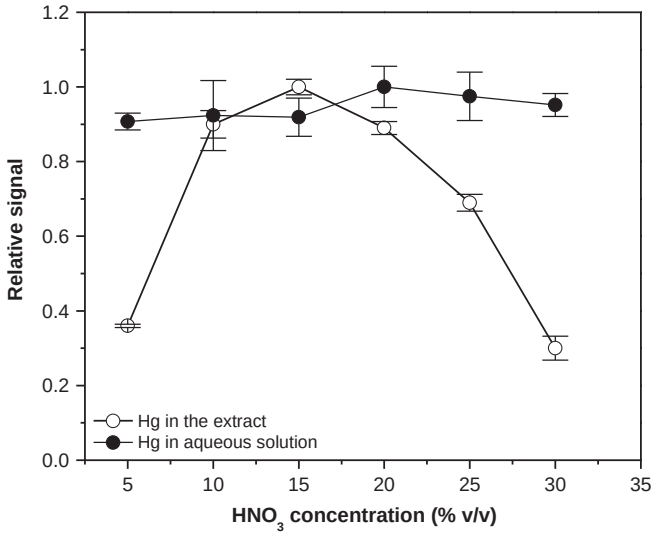


Fig. 6. Effect of HNO_3 concentration in the extractant solution on the extraction of Hg from the diesel oil employed in the optimization studies. Triton X-100 concentration =2.5% m/v.

experiments. The maximum Hg response was observed by agitating the emulsions for 30 min, at least, before emulsion breaking. Therefore, this extraction time was used in the preparation of samples for analysis employing the proposed method.

3.3. Analytical features of the method

The proposed method yielded linear calibration curves in the range of 10–100 $\mu g\,L^{-1}$, with the typical equation $A=0.0014[Hg(\mu g\,L^{-1})]+0.0007$ ($r^2=0.9985$). The limits of detection and quantification of the proposed method were calculated from the calibration graph and took into account the preconcentration factor obtained with the extraction procedure, which was 5 (quantitative extraction of the analyte from 20 mL of sample to 4 mL of extract). The limit of detection (3σ criterion) was 0.6 $\mu g\,L^{-1}$, whereas the limit of quantification (10σ criterion) was 1.9 $\mu g\,L^{-1}$. They were estimated from 10 repetitive measurements of the blank obtained from extraction. The precision of the method was satisfactory for this kind of procedure, being situated in the range of 3.5–5.6% (2 and 10 $\mu g\,L^{-1}$ concentration levels) for within-run analysis and 5.0–11.7% for between-run analysis (2 and 10 $\mu g\,L^{-1}$ concentration levels).

The enhancement factor (EF) was also calculated. It is defined as the ratio of the slope of the standard addition curve obtained when EIEB is applied to a spiked sample to the slope of the calibration curve obtained by direct introduction of the aqueous standards in the system. The derived EF is 5.1, very close to the expected value of 5, which represents the volume ratio of the organic to the aqueous phases. This result confirms that the method is virtually free of non-specific interferences, in relation to Hg measurement in the extracts, and that the analyte is quantitatively extracted from oils.

3.4. Evaluation of calibration strategy and application of the propose method

The application of EIEB to oil analysis resulted in the formation of aqueous extracts with specific characteristics. They contained minor amounts of organic matter extracted from the samples and significant concentrations of HNO_3 and surfactant, which were originally present in the extractant solution composition. The presence of these substances could cause some non-specific interferences on Hg measurement by changing the kinetics and/or efficiency of Hg reduction. In order to verify the possible occurrence of non-interferences on Hg measurement, calibration curves prepared in water were compared with standard addition curves prepared in the extracts obtained from diesel oil, biodiesel and mineral oil samples free of Hg (S_1, S_4 and S_5). The curves were prepared in the range of concentrations of 10–100 $\mu g\,L^{-1}$. As can be seen in Table 2 there were no significant differences between the slopes of the calibrations curves and standard addition curves, indicating that at optimized conditions the method is actually free of non-specific interferences and it is possible to quantify Hg in the extracts obtained from different oil samples by external calibration approach.

Once the calibration strategy was established, the proposed method was applied in the determination of total Hg in five samples of different types of oils. Samples of biodiesel, diesel oil and mineral oil were analyzed. A recovery test was performed to evaluate the accuracy of the method. In a such test, samples were spiked with 2 and 10 $\mu g\,L^{-1}$ of Hg, in the form of organometallic compound, and the EIEB procedure was applied in the optimized conditions. The difference between the Hg concentrations found in non-spiked and spiked samples was employed to estimate recovery rates. Recovery rates between 80% and 103% were achieved (Table 3), indicating that the proposed method is really able to extract and quantify total Hg in oil samples of different origins.

Table 2
Typical calibration curves obtained in the comparison of external calibration and standard addition approaches.

Calibration mode	Equation	Sample type
Calibration curve	$A=0.0014[Hg(\mu g\,L^{-1})]+0.0007$, $r^2=0.996$	
Standard addition curve	$A=0.0014[Hg(\mu g\,L^{-1})]+0.0012$, $r^2=0.998$	Diesel oil
	$A=0.0014[Hg(\mu g\,L^{-1})]+0.0019$, $r^2=0.998$	Biodiesel
	$A=0.0016[Hg(\mu g\,L^{-1})]+0.0006$, $r^2=0.993$	Mineral oil

Table 3
Results obtained in the determination of total Hg in oil samples by the proposed method. Results are expressed as mean ± standard deviation ($n=3$).

Sample	Oil	Hg added ($\mu g\,L^{-1}$)	Hg found ($\mu g\,L^{-1}$)	Recovery (%)
S_1	Diesel	0	< LOD	–
		2.0	2.0 ± 0.1	100
		10	12.0 ± 1.1	100
S_2	Diesel	0	2.6 ± 0.3	–
		2.0	4.4 ± 0.7	90
		10	12.1 ± 0.4	95
S_3	Diesel	0	6.8 ± 0.8	–
		2.0	8.6 ± 0.9	90
		10	17.0 ± 1.7	103
S_4	Biodiesel	0	< LOD	–
		2.0	1.6 ± 0.1	80
		10	10.3 ± 1.2	103
S_5	Mineral	0	< LOD	–
		2.0	1.6 ± 0.1	80
		10	9.6 ± 0.7	96

4. Conclusions

The method proposed (and optimized) in this work was shown to be a good alternative to total digestion for the determination of total Hg in oil samples. It presented remarkable advantages over regular methods based on Hg extraction from organic liquid samples such as the preconcentration of the analyte in the

aqueous phase and the possibility of using aqueous standards in the methodological calibration procedure, instead of high-cost and unstable oil-based standards. Besides, possible interferences due to the high content of carbon in the samples were not seen, which permitted external calibration to be employed in the quantification of Hg in the extracts.

The laboratory-made GLS device proposed in this work was suitable for Hg vapor generation from the extracts. It is easy to construct and can be employed in other applications for Hg determination in different types of samples. Additionally the GLS worked in a way that avoided cross contamination, since different flasks were used in the measurement of Hg in different solutions.

Different types of oils could be analyzed with the developed method, independently of the particular characteristics of the samples tested. This fact shows the versatility of the extraction procedure in relation to Hg extraction and can open new possibilities for the use of EIEB in the analysis of other organic samples.

Acknowledgments

The authors would like to thank CNPq (Conselho Nacional de Desenvolvimento Científico e Tecnológico (Grant no. 472800/2012-4)), Brazil, CAPES (Coordenação de Aperfeiçoamento de Pessoal de Nível Superior), Brazil, and FAPERJ (Fundação Carlos Chagas Filho de Amparo à Pesquisa do Estado do Rio de Janeiro (Grant no. E-26/110.907/2013)), Brazil, for providing grants and fellowships and for financial support.

References

[1] F.G. Lepri, E.S. Chaves, M.A. Vieira, A.S. Ribeiro, A.J. Curtius, L.C.C. Oliveira, R.C. Campos, Appl. Spectrosc. Rev. 46 (2011) 175–206.
[2] R.Q. Aucélio, R.M. Souza, R.C. Campos, N. Miekeley, C.L.P. Silveira, Spectrochim. Acta Part B 62 (2007) 952–961.
[3] M.G.A. Korn, D.S.S. Santos, B. Welz, M.G.R. Vale, A.P. Teixeira, D.C. Lima, S.L.C. Ferreira, Talanta 73 (2007) 1–11.
[4] F.W. Sant'Ana, R.E. Santelli, A.R. Cassella, R.J. Cassella, J. Hazard. Mater. 149 (2007) 67–74.
[5] A. Ulrich, A. Wichser, Anal. Bioanal. Chem. 377 (2003) 71–81.
[6] P.B. Maciel, L.L.S. de Barros, E.C.M. Duarte, M.N.C. Harder, G.G. Bortoleto, C.H. Abreu Jr., F.C.A. Villanueva, J. Radioanal. Nucl. Chem. 297 (2013) 209–213.
[7] A.V. Soin, T.A. Maryutina, T.V. Arbuzova, B.Ya. Spivakov, J. Anal. Chem. 65 (2010) 571–576.
[8] C. Benincasa, J. Lewis, E. Perri, G. Sindona, A. Tagarelli, Anal. Chim. Acta 585 (2007) 366–370.
[9] R.J. Cassella, B.A.R.S. Barbosa, R.E. Santelli, A.T. Rangel, Anal. Bioanal. Chem. 379 (2004) 66–71.
[10] M. Murillo, Z. Benzo, E. Marcano, C. Gomez, A. Garaboto, C. Marin, J. Anal. At. Spectrom. 14 (1999) 815–820.
[11] D.M. Brum, C.F. Lima, N.F. Robaina, T.C.O. Fonseca, R.J. Cassella, Spectrochim. Acta Part B 66 (2011) 338–344.
[12] R.J. Cassella, D.M. Brum, C.F. Lima, T.C.O. Fonseca, Fuel 90 (2011) 1215–1220.
[13] A. de Leonardis, V. Macciola, M. de Felice, Int. J. Food Sci. Technol. 35 (2000) 371–375.
[14] H.J. Sun, J. Am. Oil Chem. Soc. 66 (1989) 549–552.
[15] R. Ooms, W.V. Pee, J. Am. Oil Chem. Soc. 60 (1983) 957–960.
[16] R. Ansari, T.G. Kazi, M.K. Jamali, M.B. Arain, S.T. Sherazi, N. Jalbani, H.I. Afridi, J. Am. Oil Chem. Soc. 91 (2008) 400–407.
[17] N.E. Selin, Annu. Rev. Environ. Resour. 34 (2009) 43–63.
[18] P. Holmes, K.A.F. James, L.S. Levy, Sci. Total Environ. 408 (2009) 171–182.
[19] R.P. Mason, W.F. Fitzgerald, F.M.M. Morel, Geochim. Cosmochim. Acta 58 (1994) 3191–3198.
[20] S.M. Wilhelm, Environ. Sci. Technol. 35 (2001) 4704–4710.
[21] S.M. Wilhelm, N. Bloom, Fuel Process. Technol. 63 (2000) 1–27.
[22] M.Y.A. Shpirt, S.A. Punanova, Solid Fuel Chem. 45 (2011) 330–336.
[23] G.P. Brandão, R.C. de Campos, A.S. Luna, Spectrochim. Acta B At. Spectrosc. 60 (5) (2005) 625–631.
[24] W.N.L. dos Santos, F.S. Dias, M.V. Reboucas, M.G. Pereira, V.A. Lemos, L.S.G. Teixeira, J. Anal. At. Spectrom. 21 (2006) 1327–1330.
[25] A. Shafawi, L. Ebdon, M. Foulkes, P. Stockwell, W. Corns, Analyst 124 (1999) 185–189.
[26] E. Björn, W. Frech, Anal. Bioanal. Chem. 376 (2003) 274–278.
[27] J.P. Snell, E. Bjorn, W. Frech, J. Anal. At. Spectrom. 15 (2000) 397–402.
[28] L. Liang, M. Horvart, P. Danilchik, Sci. Total Environ. 187 (1996) 57–64.
[29] R. Uddin, M.A. Al-Fahad, A.K. Al-Rashwan, M.A. Al-Qarni, Environ. Monit. Assess. 185 (2013) 3681–3685.
[30] M.P. Heyward, R.L. Hurle, B. Sauerhammer, Anal. Commun. 34 (1997) 279–281.
[31] R.J. Cassella, D.M. Brum, C.E.R. de Paula, C.F. Lima, J. Anal. At. Spectrom. 25 (2010) 1704–1711.
[32] R.J. Cassella, D.M. Brum, C.F. Lima, L.F.S. Caldas, C.E.R. de Paula, Anal. Chim. Acta 690 (2011) 79–85.
[33] N.F. Robaina, D.M. Brum, R.J. Cassella, Talanta 99 (2012) 104–112.
[34] F.M. Pereira, R.C. Zimpeck, D.M. Brum, R.J. Cassella, Talanta 117 (2013) 32–38.
[35] A. D'Ulivo, Spectrochim. Acta Part B 59 (2004) 793–825.

Talanta 132 (2015) 739–752

Contents lists available at ScienceDirect

Talanta

journal homepage: www.elsevier.com/locate/talanta

Review

Current trends in green liquid chromatography for the analysis of pharmaceutically active compounds in the environmental water compartments

Heba Shaaban [a,*], Tadeusz Górecki [b]

[a] Department of Pharmaceutical Chemistry, College of Clinical Pharmacy, University of Dammam, Eastern Province, KSA, Dammam 31441, Saudi Arabia
[b] Department of Chemistry, Faculty of Science, University of Waterloo, Waterloo, ON, Canada N2L 3G1

ARTICLE INFO

Article history:
Received 16 June 2014
Received in revised form
24 September 2014
Accepted 29 September 2014
Available online 18 October 2014

Keywords:
Green chromatography
Environmental analysis
Liquid chromatography
Pharmaceuticals
High mobile phase temperature

ABSTRACT

Green analytical chemistry is an aspect of green chemistry which introduced in the late nineties. The main objectives of green analytical chemistry are to obtain new analytical technologies or to modify an old method to incorporate procedures that use less hazardous chemicals. There are several approaches to achieve this goal such as using environmentally benign solvents and reagents, reducing the chromatographic separation times and miniaturization of analytical devices. Traditional methods used for the analysis of pharmaceutically active compounds require large volumes of organic solvents and generate large amounts of waste. Most of them are volatile and harmful to the environment. With the awareness about the environment, the development of green technologies has been receiving increasing attention aiming at eliminating or reducing the amount of organic solvents consumed everyday worldwide without loss in chromatographic performance.

This review provides the state of the art of green analytical methodologies for environmental analysis of pharmaceutically active compounds in the aquatic environment with special emphasis on strategies for greening liquid chromatography (LC). The current trends of fast LC applied to environmental analysis, including elevated mobile phase temperature, as well as different column technologies such as monolithic columns, fully porous sub-2 μm and superficially porous particles are presented. In addition, green aspects of gas chromatography (GC) and supercritical fluid chromatography (SFC) will be discussed. We pay special attention to new green approaches such as automation, miniaturization, direct analysis and the possibility of locating the chromatograph on-line or at-line as a step forward in reducing the environmental impact of chromatographic analyses.

© 2014 Elsevier B.V. All rights reserved.

Contents

1. Introduction . . . 740
2. Recent trends in green liquid chromatography . . . 740
   2.1. Reduction in solvent consumption . . . 740
      2.1.1. Fast chromatography . . . 740
      2.1.2. Reduction in system dimension . . . 745
   2.2. Replacement of existing solvents with green alternatives . . . 747
      2.2.1. Use of ethanol in RP–HPLC . . . 747
      2.2.2. Replacement of organic modifiers with pure water (superheated water chromatography) . . . 747
      2.2.3. Replacement with carbon dioxide . . . 748
3. Green aspects of gas chromatography . . . 749
4. Application of direct chromatographic techniques . . . 749

* Corresponding author. Tel.: +966 54 626 2270; fax: +966 13 333 0290.
E-mail addresses: Hsmohammed@uod.edu.sa, helhussieny79@yahoo.com (H. Shaaban).

http://dx.doi.org/10.1016/j.talanta.2014.09.050
0039-9140/© 2014 Elsevier B.V. All rights reserved.

5. Placing the chromatograph with respect to the investigated medium . . . 749
6. Green aspects of biological techniques . . . 749
7. Conclusions . . . 750
Acknowledgements . . . 750
References . . . 750

1. Introduction

The concept of green chemistry was introduced in the nineties with the aim of minimizing the environmental impact of chemical activities [1]. Green analytical chemistry is an aspect of green chemistry with the aim of minimizing hazardous waste and to use solvents friendly to the environment [2]. Recently, green chemistry has gained increasing attention from many researchers in both industry and academia and the need to make analytical chemistry greener is becoming more widely accepted. The main objectives of green analytical chemistry are to develop new analytical method or to modify an old one to incorporate procedures that need less hazardous chemicals [3]. The crisis of the shortage of acetonitrile (2008–2009) encouraged many chromatographers to develop new analytical methods aiming at reducing the use of acetonitrile as an organic modifier for RP–LC or replacing it with other alternatives. The driving force for decreasing acetonitrile usage at that time was cost rather than the desire to develop green methodologies [4].

In traditional LC, little attention has been given to green aspects of the separation. Traditional LC methods using standard column dimensions and conventional stationary phases require large amounts of organic solvents and generate large volumes of waste. For instance, traditional LC instruments operated with a column of standard internal diameter (4.6 mm) and 25 cm length at a mobile phase flow rate of about 1–1.5 mL min^{-1} generate more than 1L of effluent daily, and this waste has to be disposed of [5]. Common solvents used in LC are volatile organic compounds that can easily disperse in the environment, many of them exhibiting both acute and chronic toxicity; therefore green aspects should be taken into consideration when new analytical method has to be developed.

Chromatographic techniques have the potential to be greener at all steps of the analysis, from sample collection to separation and final determination. Because sample preparation prior to chromatographic analysis cannot be avoided in most case, solventless or miniaturized sample preparation techniques should be used whenever possible. Currently, greening of sample preparation methods has been receiving greater attention aiming at minimizing or eliminating the solvent usage [4]. Green sample preparation techniques include solventless solid phase microextraction (SPME), supercritical fluid extraction (SFE, when only pure carbon dioxide is used), and solid phase extraction (SPE) where a small volume of organic solvent is used [1,6]. The most widespread clean-up method used for the analysis of pharmaceuticals is SPE. It provides many advantages in the green point of view such as low organic solvent consumption, short sample preparation time and the possibility of automation [7]. SFE is also an environmentally-friendly analytical methodology that can be automated easily and completely [1]. Because greening of sample preparation techniques is beyond the scope of this review, readers are advised to refer to other articles for more details e.g. [1,8–10]. The main directions currently explored for transforming chromatography in a green approach are reduction of solvent consumption through reducing columns internal diameters and particle sizes (from 5 to sub-2 μm), replacement of acetonitrile and/or methanol in the mobile phases by less harmful and environmental friendly alternatives such as water, ethanol and carbon dioxide (either in sub-critical or supercritical states) and miniaturization [1,11].

The growing demand for development of environmentally friendly analytical protocols usually results with miniaturization of the existing and well established methods [12]. Miniaturized separation systems offer many advantages such as consuming fewer consumables, producing less waste, minimizing energy consumption and allowing on-line or at-line analysis. All of these advantages make the chromatographic analysis green. For the analysis of pharmaceuticals in environmental samples, very sensitive and highly efficient methods are highly required, especially for wastewater. Because of the polarity of pharmaceuticals, the technique of choice for their analysis is LC, which remains the main tool for the analysis of pharmaceuticals in most commercial and research laboratories. Therefore, recent developments in green LC methodologies will be discussed in this review[1].

2. Recent trends in green liquid chromatography

The direct way to minimize the solvent consumption of an HPLC separation is to reduce the analysis time (without increasing flow rate of the mobile phase) [5]. For a given separation, the volume of the mobile phase consumed (V) can be calculated from the following equation [5]:

$$V = F \times t \quad (1)$$

where F is the volumetric flow rate and t is the analysis time.

However many approaches can be used to achieve fast separations, including the use of monolithic columns, fully porous sub-2-μm particles with UPLC systems, superficially porous particles and elevated mobile phase temperatures, not all of these strategies are considered green separations. The advantages and disadvantages of these approaches will be discussed in details in the following sections.

Another way of reducing the use of solvent in liquid chromatography is to decrease the column volume by shortening its length and/or decreasing the internal diameter [5]. Also, in recent years miniaturization of HPLC systems and columns has gained interest. The use of micro-flow and capillary columns could effectively reduce solvent consumption; however, dedicated systems are highly needed. In addition to solvent reduction strategies, replacing traditional solvents with more benign alternatives such as ethanol, carbon dioxide and pure water has received great attention.

Other chromatographic systems such as GC and SFC are considered green approaches because GC is a solvent-free technique, and SFC is based mainly on using environmentally friendly carbon dioxide, which minimizes the use of toxic organic solvents and additives. This review focuses mainly on liquid chromatographic separations.

2.1. Reduction in solvent consumption

2.1.1. Fast chromatography

High-speed HPLC analysis is highly required in many analytical fields, such as clinical, forensic, toxicological, environmental and pharmaceutical analysis [13]. Speeding up LC method using fast analysis results in reducing the overall solvent consumption and costs. These improvements provide benefits for laboratories in terms of productivity enhancement and economic savings. Recently; new stationary phases, new column geometries and new instruments are introduced in order

[1] Some parts are based on Ref. 11.

to decrease analysis times while maintaining high resolution and efficiency. Various analytical approaches have been proposed to speed up the analysis. These approaches usually include the following strategies, applied individually or in combination(s): reducing the column length, increasing the mobile phase flow rate, decreasing packing particle size, increasing pressure or increasing temperature. In fast LC method development, all factors are usually not changed simultaneously, but step-by-step to optimize the separation and reduce the analysis time without losing resolution.

Gritti and Guiochon proposed different approaches to achieve rapid LC separations without loss in resolution and efficiency [14]. The first strategy is to increase the mobile phase linear velocity, which can be achieved either by operating the column under a higher inlet pressure or by decreasing the solvent viscosity. The eluent viscosity can be reduced by elevating the column temperature, so the diffusion coefficients of the solutes increase, leading to faster mass transfer [14]. Another strategy aiming at increasing the velocity of the mobile phase is to increase the column permeability which allows higher flow rates to be used with the same inlet pressure. This could be accomplished by using monolithic columns. An alternative approach to decrease the analysis time while maintaining efficiency is to reduce the column length while decreasing the plate height, which can be done by using smaller particle size packing (e.g. sub-2 μm). However, in this case column permeability is decreased and very high pressures are mandatory. Finally, analysis time can be shortened by combining the increase in column permeability with an increase in efficiency, which could be achieved by using sub-3 μm superficially porous particles [14]. These different strategies and their application to the analysis of pharmaceuticals in the environmental water samples will be discussed in more details in the following section.

2.1.1.1. Monolithic columns. Monolithic supports consist of a single rod of porous material with unique features in terms of permeability and efficiency. These supports were originally introduced during the 1990s [15]. Different kinds of monoliths can be prepared, both inorganic (silica, zirconia, carbon and titania) and organic (polymethacrylate, polystyrene-divinylbenzene and polyacrylamide). However, the only commercially available kinds are polymethacrylate, polystyrene-divinylbenzene and silica-based monolithic columns [15]. Silica-based monolithic supports are most widely used in HPLC and have been commercially available since 2000 from Merck and Phenomenex under the trademarks Chromolith and Onyx, respectively [15].

Monolithic columns provide many advantages. One of them is their high external porosity due to the relatively large thorough-pores, which imparts high column permeability. Consequently, chromatographic separations can be performed at lower backpressures than with conventional fully porous particle-packed columns [16,17]. Another advantage is the possibility of using high flow rates (up to 10 mL min^{-1}), due to low flow resistance, leading to fast separations using conventional LC systems [18]. Although high speed analysis using monolithic columns is quite common, the amount of waste generated is the same as or greater than with conventional HPLC columns of comparable dimensions [5]. Monolithic columns are used mainly for speeding up the analysis and this approach is not considered a powerful option for greening the analysis, especially that small internal diameter column, e.g. 2.0 or 3.0 mm, are not commercially available in all common column lengths [13]. In addition, the wide use of monolithic columns in the environmental analysis is not common due to the limited commercial availability of different stationary phases [18]. Another drawback of monolithic supports is poor efficiency due to radial heterogeneity of monolithic silica rods, as their external porosity is smaller in the center than close to the wall [19]. In addition, silica-based monoliths have limited chemical stability (pH range) [20]. All these drawbacks limit their applications in environmental analysis.

For environmental analysis, commercial Chromolith columns of 100 mm × 4.6 mm I.D. are typically used. These columns have been reported in the analysis of three fluoroquinolone antibiotics in river water samples using fluorescence detection with analysis time of 14 min [21]. In this study, the mobile phase consumption was quite large because of using high mobile phase flow rate (2.5 mL min^{-1}). The use of coupled monolithic columns was also proposed to increase peak capacity and resolution; however, this increased the analysis time significantly [22]. In this study, two coupled monolithic columns were used to separate 21 pharmaceutical residues in 70 min with Ultra-Violet (UV) detection.

Because of the use of high mobile phase flow rates with monoliths, their use with mass spectrometric detection is limited and few LC–MS methods using monolithic columns were developed for environmental analysis [23]. Green liquid chromatography can sometimes benefit from the use of monolithic stationary phases because these columns offer the possibility of using mobile phases of higher viscosity, for example ethanol/water mixtures [24]. Also, monolithic columns allow the use of high mobile phase flow rates leading to shorter analysis times. However, unless the column diameter is reduced, this does not result in solvent savings [24]. Since large volumes of organic solvents are consumed due to the usage of high mobile phase flow rates, alternatives have been developed aiming at speeding up the analysis but with lower solvent consumption.

2.1.1.2. Fully porous sub-2 μm particles and ultrahigh pressure liquid chromatography (UPLC). The development of fully porous sub-2 μm particles is considered a second leap forward in column technology. Columns packed with these small particles were commercially available since 2004. Fully porous sub-2 μm particles could improve efficiency, optimal velocity and mass transfer compared to conventional particle sizes [25,26]. These particles can be used to decrease the analysis time since the optimal flow rate is inversely proportional to particle diameter according to the equation [27]:

$$\mu = \nu D_m / d_p \quad (2)$$

where ν is the reduced mobile phase velocity, (d_p) is the particle diameter, μ is the optimal velocity and D_m the diffusion coefficient of the solute in the mobile phase. Reducing the particle size allows the use of high flow rates resulting in decreasing the analysis time without loss of resolution and efficiency. Also, the A and C terms of Van Deemter equation can both be decreased by using smaller particle size columns, which leads to a reduction in the plate height and a corresponding increase in efficiency for a given column length. The A term represents the dispersive contribution from the flow profile (eddy diffusion, $A = 2\lambda d_p$) where λ is particle shape with regard to the packing and the C terms are mass transfer terms in mobile and stationary phases [28]. The use of small particle size packing (sub-2 μm) improves the chromatographic performance as these particles provide minimum plate heights nearly four times smaller than those observed with conventional columns packed with 5 μm particles or with monolithic columns [13]. However, the main limitation of using sub-2 μm particles is the induction of high column backpressure. According to Darcy's law, the pressure is inversely proportional to the particle size at the optimum linear velocity [20]:

$$\Delta P = \mu L \eta \phi / d_p^2 \quad (3)$$

where ΔP is the pressure drop, L is column length, η is the viscosity of the solvent and is the flow resistance. The high backpressure generated by these particles prevents these particles to be used with standard HPLC hardware. To overcome this problem, some improvements to the chromatographic systems have been made. In recent years, instruments that can produce pressure above 400 bar

have been commercialized and are known as UHPLC systems. The term UHPLC is used to define the use of columns packed with sub-2 μm particles at pressures exceeding 400 bar [15]. The first commercially available UHPLC system was introduced by Waters Corporation in 2004. Several instruments were also developed by other manufactures and can withstand pressures ranging from 600 to 1200 bar [29]. These systems can speed up LC separations compared with conventional HPLC while maintaining identical performance [20,30]. Liquid chromatographic separations performed in less than 10 min are considered fast, and separations performed in less than 1 min are known as ultrafast [13]. Sub-2 μm particles can provide flat Van Deemter curves which allows high flow rates to be used leading to decreased analysis time even further; however, the mobile phase consumption might be increased and in this case solvent savings might be an issue. Therefore, speeding up the analysis simultaneously with reducing solvent consumption could be achieved by using small particle size particles in a combination with short columns, generating the same number of theoretical plates as with conventional columns, but with shorter analysis time and lower solvent consumption. For example, a 5 cm column packed with sub-2 μm particles is sufficient to obtain approximately the same number of plates as a 15 cm column packed with 5 μm particles according to equation [31]:

$$N \sim L/2d_p \quad (4)$$

When small particles are packed in columns with small diameter, savings in solvent consumption are more obvious than when standard column diameter (4.6 mm) is used. In addition, using small diameter columns could reduce frictional heating which might contribute to efficiency losses [20]. However, it should be mentioned that UHPLC systems are sometimes used with conventional particles (3–5 μm) leading to large solvent consumption, therefore not all

Table 1
Applications of columns packed with sub-2 μm particles in the analysis of pharmaceuticals in environmental water samples.

Analytes	Sample	Stationary phase	Detection	Flow rate	Analysis time	Reference
7 Antidepressants	Wastewater Surface water	Acquity UPLC BEH C18 (50 mm × 2.1 mm, 1.7 μm)	MS-Triple Q mass analyzer	0.4 mL min^{-1}	7.5 min	[33]
74 Pharmaceutically active compounds	Wastewater Surface water Ground water	Acquity UPLC BEH C18 (100 mm × 2.1 mm, 1.7 μm)	MS-Triple Q mass analyzer	0.4 mL min^{-1}	8 min	[34]
28 Basic/neutral pharmaceuticals	Surface water	Acquity UPLC BEH C18 (100 mm × 1 mm, 1.7 μm)	MS-Triple Q mass analyzer	0.07 mL min^{-1}	15.5 min	[35]
9 Pharmaceuticals	Surface water	Acquity UPLC HSS T3 (100 mm × 2.1 mm, 1.8 μm)	MS-Triple Q mass analyzer	0.5 mL min^{-1}	9.6 min	[36]
15 Steroidal oral contraceptives	Surface water	Acquity UPLC BEH C18 (50 mm × 2.1 mm, 1.7 μm)	MS-Triple Q mass analyzer	0.1 mL min^{-1}	8.5 min	[37]
10 Pharmaceuticals	Wastewater	Acquity UPLC BEH C18 (100 mm × 2.1 mm, 1.7 μm)	MS-Triple Q mass analyzer	0.35 mL min^{-1}	7.2 min	[38]
36 Endocrine disrupting chemicals	River water	Acquity UPLC HSS T3 (100 mm × 2.1 mm, 1.8 μm)	MS-Q-TOF mass analyzer	0.5 mL min^{-1}	9.5 min	[39]
11 Illicit drugs	Wastewater Surface water	Acquity UPLC BEH C18 (50 mm × 2.1 mm, 1.7 μm)	MS-Triple Q mass analyzer	0.3 mL min^{-1}	6 min	[40]
65 Illicit drugs	Wastewater Surface water	Acquity UPLC BEH C18 (150 mm × 1 mm, 1.7 μm)	MS-Triple Q mass analyzer	0.04 mL min^{-1}	23.1 min	[41]
160 Pharmaceutical metabolites	Wastewater	Acquity UPLC BEH C18 (100 mm × 2.1 mm, 1.7 μm)	MS-Q-TOF mass analyzer	0.3 mL min^{-1}		[42]
47 Pharmaceuticals	Wastewater	Acquity UPLC HSS T3 (100 mm × 2.1 mm, 1.8 μm)	MS-Triple Q mass analyzer	0.3 mL min^{-1}	10 min	[43]
76 Illicit drugs and metabolites	Wastewater	Acquity UPLC BEH C18 (150 mm × 2.1 mm, 1.7 μm)	MS-Q-TOF mass analyzer	0.3 mL min^{-1}		[44]
20 Pharmaceuticals	Wastewater Surface water	Acquity UPLC BEH C18 (50 mm × 2.1 mm, 1.7 μm)	MS-Triple Q mass analyzer	0.3 mL min^{-1}	9 min	[45]
7 Estrogens	Wastewater Surface water Ground water	Acquity UPLC BEH C18 (50 mm × 2.1 mm, 1.7 μm)	MS-Q-TOF mass analyzer	0.4 mL min^{-1}	13 min	[46]
16 Sulfonamides and trimethoprim	Wastewater Surface water	Acquity UPLC BEH C18 (100 mm × 2.1 mm, 1.7 μm)	MS-Triple Q mass analyzer	0.3 mL min^{-1}	> 6.5 min	[32]
9 Sulfonamides	Wastewater Surface water	Zorbax SB C18 columns (150 mm × 4.6 mm, 1.8 μm)	UV λ=272	1.5 mL min^{-1}	3 min	[47]
9 Pharmaceuticals	Wastewater Surface water	Zorbax SB-AQ column (30 mm × 2.1 mm, 1.8 μm)	UV λ=272, 247	1 mL min^{-1}	1 min	[48]
81 Pharmaceutical residues	Surface and treated waters	Acquity BEH C18 column (50 mm × 2.1 mm, 1.7 μm)	MS-Q-IT mass analyzer	0.5 mL min^{-1}		[49]
27 Pharmaceuticals	Drinking or waste water	Acquity BEH C18 column (100 mm × 2.1mm, 1.7μm)	MS-Triple Q mass analyzer	400 μL min^{-1}.	12 min	[50]
81 Pharmaceuticals	Waste, surface, underground, and drinking water	Acquity HSS T3 column (50 mm × 2.1 mm, 1.8 μm)	MS-Triple Q-LIT mass analyzer	0.5 mL min^{-1}		[51]
10 Anticancer drugs	Hospital and urban wastewaters	Acquity HSS T3 column (50 mm × 2.1 mm, 1.7 μm)	MS-Triple Q-LIT mass analyzer	0.4 mL min^{-1}		[52]
69 Multiclass pharmaceuticals	Surface water	Acquity HSS T3 column (150 mm × 2.1 mm, 1.8 μm)	MS-Q-TOF mass analyzer		19 min	[53]
21 Pharmaceuticals and 6 personal care products	Drinking-water sludge	Acquity BEH C18 column (50 mm × 2.1 mm, 1.7 μm)	MS-Triple Q mass analyzer	0.225 mL min^{-1}		[54]
48 Pharmaceuticals and 6 metabolites	Wastewater and surface water	Acquity BEH C18 column (100 mm × 1.0 mm, 1.7 μm)	MS-Triple Q mass analyzer	100 μL min^{-1}	15 min	[55]
25 Acidic/neutral pharmaceuticals and personal care products	Surface water	Acquity BEH C18 column (100 mm × 1.0 mm, 1.7 μm)	MS-Triple Q mass analyzer	0.05 mL min^{-1}		[56]

UHPLC analytical methods published in the literature are considered green separations. Overall, though, using sub-2 μm particles packed in short narrow bore columns with UHPLC could significantly lower the consumption of the mobile phase compared to using conventional particle sizes with standard HPLC systems [5].

Several recent applications of UPLC–UV, UPLC–MS [Quadrople (Q), time-of-flight (TOF), linear ion trap (LIT) mass analyzer] methods using sub-2 QUOTE μm particle size packed columns in environmental analysis are summarized in Table 1. Most of these applications are based on reversed-phase separations using the Acquity UPLC BEH C18 columns of 1.7 μm particle size with different columns lengths. Other C18 reversed-phase columns such as Zorbax SB C18 (1.8 μm particle size) have also been used.

As an example, Chang et al. reported an UPLC-MS/MS method for the analysis of 16 sulphonamides and trimethoprim antibiotics in influent and effluent wastewater and river water using Acquity UPLC BEH C18 column (100 mm × 2.1 mm, 1.7 μm) [32]. The analytes could be separated in less than 6.5 min at a flow rate of 0.3 mL min^{-1} (Fig. 1). As can be seen in the figure, very sharp peaks were obtained with peak widths of 5–10 s at the base, and the 17 analytes were eluted in less than 6.5 min providing short analysis time and high sample throughput. The method detection limits for the 17 analytes were 20–200 pg L^{-1} for the influent, 16–120 pg L^{-1} for the effluent and 8.0–60 pg L^{-1} for the river water.

2.1.1.3. Superficially porous particles. Superficially porous particles, also known as fused-core particles were originally developed in the 1990s by Kirkland. In 2006, sub-3 μm superficially porous particles became commercially available which is considered a major breakthrough in column technology [57]. Introducing superficially porous particles to the markets has provided an attractive alternative option for high speed analysis using conventional LC systems. The use of columns packed with these particles is another approach aiming at shortening the analysis time. Fused core particles could reduce the analysis times while maintaining column efficiencies with relatively low pressures [58,59]. Typical sub-3 μm superficially porous particles consist of a 1.7 μm solid core surrounded by 0.5 μm layer of porous silica, giving a total particle diameter of 2.7 μm. Columns packed with this kind of particles are available under different brand names, such as Halo (Advanced Materials Technology), Ascentis (Sigma-Aldrich) and Poroshell (Agilent). Also, fused core particles with a 1.9 μm fused core and 0.35 μm layer of porous silica coating (i.e. 2.6 μm diameter) are offered under different brand names such as Kinetex (Phenomenex) and Accucore (Thermo Fisher Scientific) [13]. In addition to sub-3 μm fused core particles, superficially porous sub-2 μm particles are becoming available from an increasing number of manufacturers.

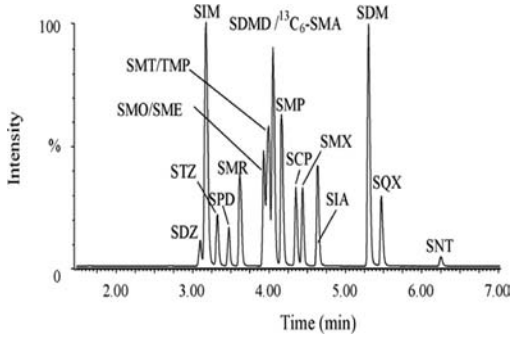


Fig. 1. Chromatogram of 17 analytes separated by LC–MS/MS [32]. Chromatographic conditions: Acquity UPLC BEH C18 column (100 mm × 2.1 mm, 1.7 μm) with a flow rate of 0.3 mL min^{-1}. Peak identification: (sulfamethoxypyridazine (SMP), sulfamoxol (SMO), sulfaquinoxaline (SQX), sulfanitran (SNT), sulfisomidine (SIM), sulfamethoxazole (SMX), sulfamerazine (SMR), sulfathiazole (STZ), sulfadiazine (SDZ), sulfamethizol (SMT), sulfadimidine (SDMD), sulfadimethoxine (SDM), sulfapyridine (SPD), sulfisoxazole (SIA), sulfachloropyridiazine (SCP), sulfameter (SME) and trimethoprim (TMP).

Researchers have conducted many studies aiming at comparing the performance of superficially porous particles to that of fully porous sub-2 μm particles e.g. [18,29,60–62]. From these studies, it can be shown that the use of fused-core silica particles could improve chromatographic column efficiency over fully porous particles. These particles exhibit efficiencies that are comparable to sub-2 μm porous particles, but with lower backpressures. Enhanced efficiency with these particles is due to narrower particle size distribution leading to improvements in the eddy diffusion term. Also, the thin porous shell on fused-core particles allows solutes to diffuse more quickly in and out of the porous structure for interaction with the stationary phase resulting in reduced resistance to mass transfer (the C-term in the van Deemter equation) and allowing operation at higher flow rates without a significant loss in efficiency [60]. Using this kind of column packing in the analysis of pharmaceuticals is limited to food analysis [63–66] and biological fluids [67,68]. Also, several papers describing the use of columns packed with these particles in environmental analysis have been published [69–71]. As an example, Tarcomnicu et al. reported a UHPLC–MS/MS method for the analysis of 15 top-prescribed pharmaceuticals and their metabolites in influent wastewater using a Kinetex C18 column (100 mm × 2.1 mm, 2.6 μm particle size) [69]. By working at a mobile phase flow rate of 0.2 mL min^{-1} under gradient elution, a fast chromatographic separation in 9 min was achieved. In another study, Pedrouzo et al. could separate 10 drugs of abuse and their metabolites in waste and surface waters in 13 min [70]. The analysis was performed on fused-core Ascentis Express C18 column (50 mm × 4.6 mm × 2.6 μm) using a flow rate of 0.4 mL min^{-1}. Bratkowska et al. could separate seven polar pharmaceuticals in wastewater and surface water in less than 13 min using C18 Kinetex column (100 mm × 4.6 mm × 2.6 μm) at a flow rate of 0.6 mL min^{-1}. However, all these studies were limited to few compound classes and/or small numbers of analytes. The use of columns packed with fused core particles was also extended to cover a larger number of pharmaceuticals from a wide range of classes. As an example, Shaaban and Górecki [72] reported a UPLC–UV method for the analysis of 25 emerging contaminants including veterinary antibiotics, CNS stimulants, non-steroidal anti-inflammatory drugs, steroids and preservatives from personal care products in wastewater and surface water in only 10 min (Fig. 2). In this study, all the studied analytes could be fully separated using a C18 Kinetex column (150 mm × 4.6 mm × 2.6 μm) at a flow rate of 1 mL min^{-1}. Achieving the analysis in a short time with low flow rate resulted in solvent savings, making the analysis green. Compared to separations performed on conventional stationary phases, using superficially porous particles can be considered a powerful approach to achieving fast green separations on conventional LC systems.

2.1.1.4. High temperature liquid chromatography. One of the ways to reduce the analysis time when conventional RP–LC systems are used is increasing flow rates while using ambient operating temperatures. Working at high temperature is a promising approach to increase the analysis speed. Elevated column temperature can be used as a tool to overcome the flow rate problem associated with high back pressure, allowing the use of flow rates that otherwise could not be applied [73].

In 1969, the term high temperature liquid chromatography (HTLC) was introduced [74]. HTLC is LC analysis performed at temperatures above ambient and below supercritical [75]. By increasing temperatures, the analysis conditions could be improved because some physical parameters playing an important role in HPLC, such as viscosity, mobile phase polarity or diffusivity depend strongly on temperature [76]. Antia and Horvath showed that increasing the separation temperature is a very efficient tool for large molecule separation [77]. Later on, in 1995, Chen and Horvath presented an extremely high speed separation of four proteins at 120 °C in less than 10 s [78].

Using high temperatures in HPLC offers many significant advantages. By increasing the temperature, the viscosity of the mobile phase will be decreased resulting in reduced backpressure. This allows the use of small particle size packing, long columns and increasing the column length through coupling. Elevating the temperature from ambient (20 °C) to about 50 °C causes a decrease in solvent viscosity by ~50% [79]. Consequently, it becomes possible to double the column length at the same linear velocity to double the efficiency, or to operate the same column at an approximately twice faster flow rate to provide about twice faster analysis with nearly the same efficiency [14]. Also, increasing the temperature leads to an increase in the optimal mobile phase linear velocity. Under the maximum operating pressure, the main benefit of an increase in the temperature is a reduction in the analysis time. In addition to decreasing the analysis time, reduction in mobile phase consumption could also be achieved leading to greener analysis.

Another benefit of using high mobile phase temperature is that the change in the dielectric constant of water makes it less polar and allows reducing the percentage of organic solvent in the mobile phase [75]. Also, by increasing temperature the partition coefficients of the analytes between the mobile phase and the stationary phase is decreased leading to a reduction in the organic solvent percentage in the mobile phase in order to maintain the same retention otherwise, the analytes would elute earlier (but at lower resolution). Both these phenomena make HPLC analysis at elevated temperatures greener than at room temperature. Also, operation at high temperature could enhance the mass transfer of the solutes in the mobile phase due to the increase in the diffusion coefficients of the molecules in the solvent. According to the Wilke–Chang equation, the diffusion coefficient is directly proportional to temperature and inversely proportional to viscosity. Consequently, by increasing the temperature, diffusion of the analytes in the mobile and stationary phases increases, and the minimum plate height (H) in the van Deemter curve shifts to higher linear velocities allowing the use of higher flow rates without compromising the efficiency [75,80]. Other advantages of using high temperature in LC separations are discussed elsewhere [81,82]. On the other hand, using high temperature in LC has some limitations. For example, the availability of packing materials stable at temperatures higher than 80 °C is very limited. Also, potential degradation of thermolabile analytes and the need to have constant temperature along the chromatographic system is of great concern [74]. To successfully implement HTLC, a special instrumentation is required including a mobile phase preheater, column heater and post column effluent cooling system. The use of a specially designed heating system allows the benefits of high eluent temperatures to be accomplished. The instrumental design used for HTLC should minimize both thermal mismatch and extra-column band broadening. Thermal mismatch results from insufficient mobile phase preheating and viscous heat dissipation across the column length, leading to thermal gradients both longitudinally and radially. While radial thermal gradients decrease efficiency, longitudinal thermal gradients affect solute retention factors. Also, in order to minimize extra-column band broadening, the system used should have low dead volume [73].

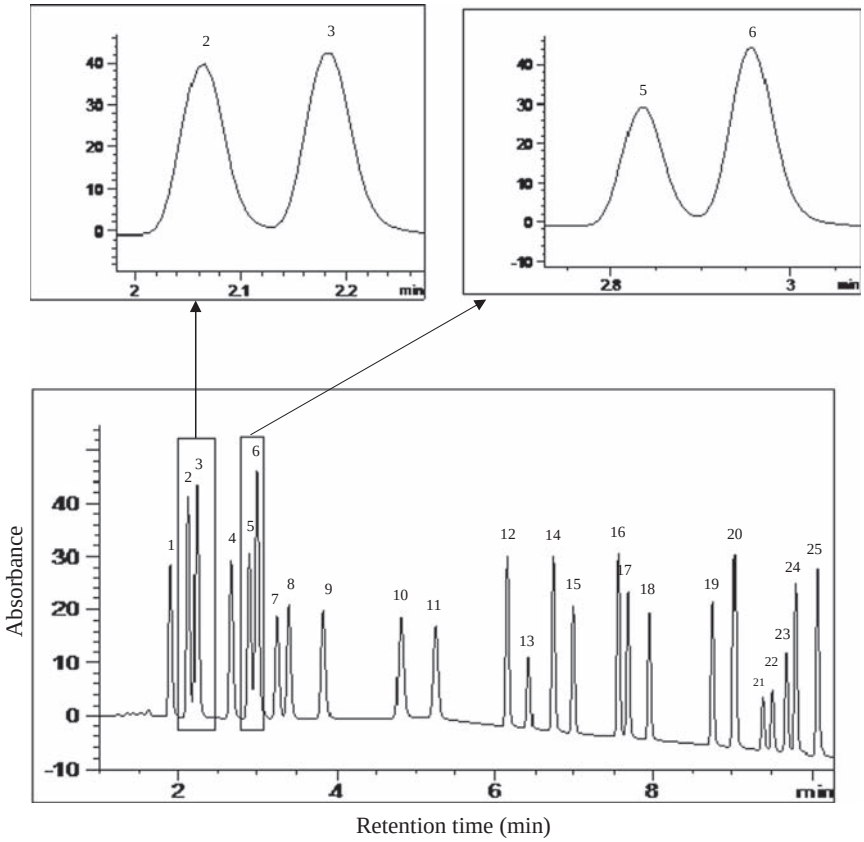


Fig. 2. Chromatogram of analytes separated on a column packed with fused-core particles [72]. Chromatographic conditions: Zorbax Stable Bond C18 columns (150 mm × 4.6 mm × 1.8 μm) at 30 °C using gradient elution. The gradient used for the analysis was 0 min, 15% acetonitrile and flow rate 1 mL min^{-1}; 3 min, 15% acetonitrile and flow rate 1.3 mL min^{-1} then increasing to 82% acetonitrile at 10 min with flow rate 1.3 mL min^{-1}. The equilibrium time was set to 5 min. Peak identification: 1—sulphanilamide, 2—theophylline, 3—acetaminophen, 4—sulfacetamide, 5—caffeine, 6—sulfadiazine, 7—sulfathiazole, 8—sulfapyridine, 9—sulfamerazine, 10—sulfamethazine, 11—sulfamethoxypyridazine, 12—sulfamonomethoxine, 13—acetyl salicylic acid, 14—sulfamethoxazole, 15—methylparaben, 16—sulfadimethoxine, 17—sulfaphenazole, 18—ethylparaben, 19—propylparaben, 20—ketoprofen, 21—17 α-ethinyl estradiol, 22—estrone, 23—fenoprofen, 24—flurbiprofen and 25—diclofenac. The inset shows baseline separation of peaks 2, 3 and 5, 6.

However using elevated mobile phase temperatures provide many advantages, the technique is not routinely used in environmental analysis and its applications have been typically limited to temperatures not exceeding 60–80 °C with conventional solvents. Until now, the approach of using a high mobile phase temperature in pharmaceutical industry is not common in everyday routine analysis. Due to the low availability of packing materials stable at high temperatures and the thermal instability of some analytes, the use of high temperature LC separations in the environmental area is limited. However, some environmental applications at high temperature are described in the literature. For example, an UPLC–UV method for the analysis of nine sulfonamides in surface water and wastewater at elevated temperature was reported [47]. In this study, nine sulfonamides could be fully separated on a single Zorbax SB C18 column (150 mm × 4.6 mm, 1.8 μm particle size) at 60 °C in only 3 min using a flow rate of 1.5 mL min^{-1} (Fig. 3). By increasing temperature to 60 °C, the percentage of the acetonitrile as an organic modifier could be reduced to 20% resulting in reducing solvent consumption and making the analysis green. Also, extending column length through coupling at elevated temperature and its use for the analysis of pharmaceuticals in wastewater has also been reported in the literature. Eight sulfonamides were determined in wastewater samples at 80 °C with very high efficiency in less than 16 min using isocratic elution on three coupled columns (3 × 150 mm × 4.6 mm, 1.8 μm particle size) [83]. Also, coupled columns have been used in a gradient mode of separation for the analysis of a large number of pharmaceuticals. For example, Shaaban & Górecki separated 24 pharmaceuticals (sulfonamides and non-steroidal anti-inflammatory drugs) in a wastewater sample in less than 27 min with very high efficiency using this technique [84].

The use of high mobile phase temperature in combination with ultra-high pressure liquid chromatography is a promising approach aiming at increasing the analysis speed without compromising efficiency and minimizing the organic solvents consumption. To the best of our knowledge the use of temperatures higher than 80 °C for the analysis of pharmaceuticals in aquatic environmental samples has not been reported thus far. Several environmental applications of HT–UPLC with separations performed at temperatures above 100 °C have been described in the literature. As an example, Thomas described the analysis of triazine herbicides in surface, ground and municipal drinking water by UPLC at 160 °C [85]. In this study, 12 herbicides was separated in less than 2.5 min with a flow rate of 0.5 mL min^{-1} using a Hypercarb porous graphitic carbon column (100 mm × 1 mm, 3 μm particle size) (Fig. 4). Only 20% acetonitrile was used as an organic modifier at high temperature (160 °C) leading to a reduction in the consumption of organic solvents. The use of pure water as an eluent for the environmental analysis of pharmaceuticals in water compartments has not been reported in the literature. Development of packing materials stable at very high temperature is highly needed in the near future to enable exploring high temperature liquid chromatography applications in environmental analysis.

2.1.2. Reduction in system dimension

As discussed before, the consumption of organic solvents can be reduced by speeding up the analysis via using monolithic columns, fully porous sub-2 μm particles with very high pressure systems, superficially porous particles and high mobile phase temperatures. However, not all these fast chromatographic approaches allow reduction in solvent use. Other ways to reduce solvent consumption is to decrease the column volume via shortening its length or reducing its internal diameter, and to miniaturize the whole chromatographic system.

2.1.2.1. Reduced column length and diameter. Because of the high cost of UPLC systems, their availability in many laboratories is not common. Therefore, using conventional HPLC systems with reduced column dimensions is another alternative to reduce the solvent consumption. A direct way to shorten the analysis time is decreasing the column length [13]. However, using short columns has some drawbacks such as loss of resolution. In order to compensate for the loss in efficiency resulted from using shorter column lengths, a simultaneous reduction in particle size is necessary.

To obtain the maximum number of plates at the optimal velocity (u_{opt}) when the internal diameter of the column is reduced, the flow rate has to be reduced by a factor (F) according to the following equation [31]:

$$F_2 = F_1 \times \frac{r_2}{r_1} \quad (5)$$

where F_2 and r_2 are the flow rate and the radius for the smaller diameter column, and F_1 and r_1 are the flow rate and the radius for the larger diameter column.

Upon reducing the column diameter from 4.6 to 3 mm, the flow rate has to be reduced by a factor of 0.43 resulting in a 57% reduction in solvent consumption and waste generation [5]. Upon switching from a standard 4.6 mm I.D. column to a narrow bore 2.1 mm I.D. column, F equals 4.8. When a 4.6 mm column is

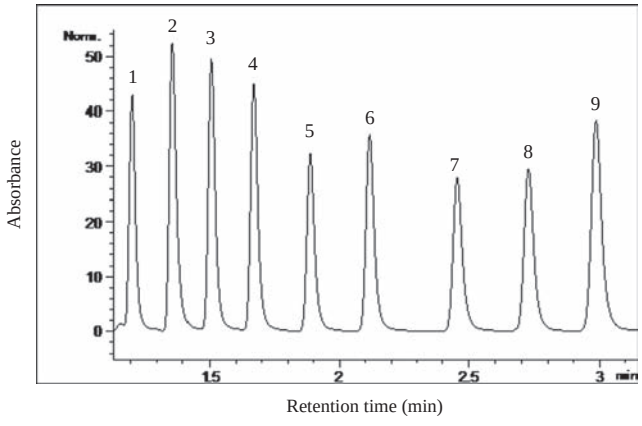


Fig. 3. Chromatogram of separation of the studied sulfonamides [47]. Chromatographic conditions: acetonitrile:water containing 0.5% acetic acid (20:80 v/v) at 60 °C and a flow rate of 1.5 mL min^{-1} with UV detection at 272 nm. Peak identification: 1—sulfanilamide, 2—sulfisomidine, 3—sulfacetamide, 4—sulfadiazine, 5—sulfapyridine, 6—sulfamerazine, 7—sulfamethoxypyridazine, 8—sulfamethazine, 9—sulfamonomethoxine.

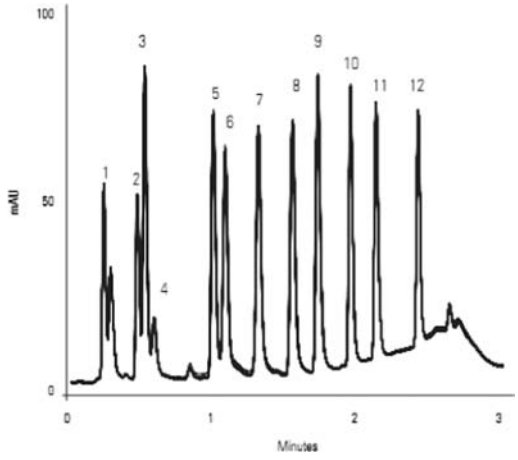


Fig. 4. Chromatogram of separation of 12 triazine herbicides [85]. Chromatographic conditions: a Hypercarb graphitic carbon column (100 mm, 1 mm, 3 μm particle size) at 160 °C. Peak identification: 1. melamine, 2. unknown, 3. deisopropylatrazine, 4. desethylatrazine, 5. cyanazine, 6. propazine, 7. prometryn, 8. atrazine, 9. ametryn, 10. simazine, 11. simetryn, 12. propanil.

operated at 1 mL min^{-1}, the 2.1 mm column should be operated at 0.21 mL min^{-1} [31]. Thus, a narrow bore column of 2 mm I.D. uses approximately one-fifth of the solvent that a wide bore column of 4.6 mm uses when run at the same mobile phase linear velocity; a 1.0 mm microbore column uses 1/20 of the solvent consumed with a 4.6 mm i.d. column [4].

In addition to a reduction in solvent consumption, small diameter columns could increase sensitivity due to the reduction in dilution of the solutes in the mobile phase and the appearance of more concentrated bands at the detector [31]. Another advantage of using narrow bore columns is faster heat dissipation compared to standard columns, so the use of narrow bore columns is highly preferred when very high pressure is used [13].

UPLC fast analysis technologies using short columns with smaller diameter packed with smaller particles and operated at high pressures offer a greener alternative to conventional HPLC. Chen and Kord demonstrated that a UPLC system with a narrow bore column (2.1 mm) offers ~80% solvent savings compared to conventional HPLC [86]. Using narrow bore columns (2 or 2.1 mm) with standard particle size packing (2.5–5 μm) for the pharmaceutical analysis in the aquatic media is well documented in the literature [82,87–95]. The use of UHPLC systems with narrow bore columns packed with small particles (sub-2-μm) has also reported (see Table 1). Because of its high selectivity and sensitivity, MS becomes the technique of choice for detecting pharmaceuticals in environmental samples. Using MS as a detection method provide many advantages such as the confirmation of the identity of the studied compounds, especially when complex matrices such as environmental samples are used. In addition, MS is a greener technique than using UV detection because when MS is used, smaller internal diameter columns ($\leq$2 mm) are preferred due to the increased sensitivity of the instrument and inability to cope with the larger amounts of solvent vapour from larger internal diameter columns ($\geq$4.6 mm) [4]. Among different kinds of mass analyzers, triple quadrupole is the most commonly used mass analyzer in the analysis of pharmaceuticals in the aquatic environment (Table 1). Other MS analyzers such as quadrupole-linear ion traps have also been used for UPLC applications (Table 1). High resolution MS using e.g. hybrid Q-TOF analyzers has also been proposed for the analysis of pharmaceuticals in environmental water samples [42,44,46,67,96,97].

UV detection has also been reported for the analysis of pharmaceuticals in the environmental water samples. For example, the analysis of nine pharmaceuticals in surface water and wastewater using UPLC–UV method in only one minute was reported [48]. In this study, nine pharmaceuticals (sulfonamides, NSAIDs and CNS stimulants) could be fully separated on a short narrow bore Zorbax SB-AQ column (30 mm × 2.1 mm, 1.8 μm particle size) in only 1 min using a flow rate of 1 mL min^{-1} (Fig. 5a). The real chromatogram of waste water sample showing acetaminophen separated from other interferences is presented (Fig. 5b). Unlike LC–MS, LC–UV detection lacks the ability to provide compound confirmation. Therefore in this study the specificity and the selectivity of the method were evaluated by studying the peak purity index values including purity factor (similarity factor), threshold limit, and purity ratio (similarity ratio) for each analyte. Similarity ratio values below unity indicate spectrally pure peaks, while values above unity indicate spectrally impure peaks. For all the studied analytes, similarity ratios were below unity indicating that no significant differences between the spectra could be observed. Consequently, the peaks were considered pure, with no coelution [48]. In this method, a significant reduction in solvent consumption was achieved, as the volume of the mobile phase consumed in each run was only 1 mL. Achieving the LC separation in less than 1 min is widely known as ultrafast analysis [13]. The method could be used as an alternative to traditional approaches, making the analysis of pharmaceuticals greener.

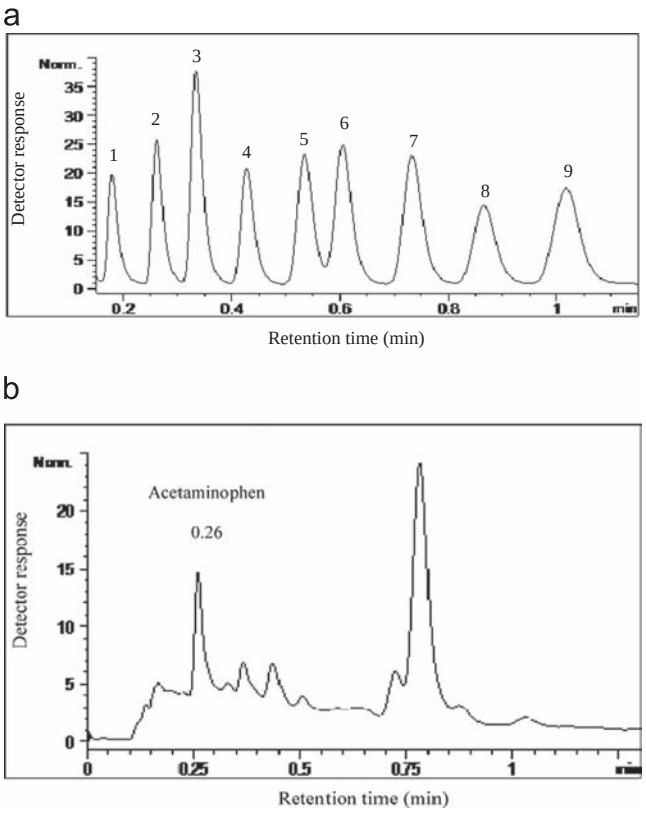


Fig. 5. (a) Chromatogram of separation of the studied pharmaceuticals with UV detection at 272 nm and (b) chromatogram of wastewater sample extract showing detection of AMPH at a detection wavelength of 247 nm [48]. Chromatographic conditions: acetonitrile:water containing 0.5% acetic acid (85:15 *v*/*v*) at 30 °C and a flow rate of 1 mL min^{-1}. Peak identification: 1—sulfanilamide, 2—acetaminophen, 3—theobromine, 4—theophylline, 5—sulfathiazole, 6—sulfamerazine, 7—caffeine, 8—sulfamethoxypyridazine, 9—sulfamethoxazole.

Table 2
classification of LC techniques according to the internal diameter and the impact on the flow rate [31].

LC techniques	Column diameter (mm)	Flow rate (μL min^{-1})
Conventional LC	4.6	1000
	4.0	750
	3.0	430
Narrow-bore LC	2.1	210
	2.0	100
Micro-LC	1.0	47
Capillary LC	0.5	11
Nano-LC	0.1	0.5

2.1.2.2. Micro-flow and capillary HPLC. The substitution of all toxic reagents employed in chemical analysis is not easy, so reduction of the amounts employed should be also considered [1]. Min iaturization is considered a promising approach in solvent savings. Recently, using microflow chromatography to reduce the use of organic solvents has gained great interest [5]. This approach focuses on reducing the overall scale of the analytical instrument. Table 2 shows the classification of LC techniques according to the internal diameter, flow rate and sensitivity [31]. Using microflow chromatography provides many advantages. For example, microflow LC systems allow the use of flow rates of microliters rather than milliliters per minute used with conventional instruments, leading to great reduction in solvent consumption and waste generation. These instruments can be operated automatically resulting in less than 10 mL of waste during 24 h of analysis [5]. Another advantage of

using microflow chromatography is that a small fraction of the chromatographic stationary phase is needed for column packing [5]. Also, micro-LC is preferred when MS is used for the detection. Fast analysis using microflow chromatography with low solvent consumption is well documented in the literature [5] (Fig. 6). In this example, only 39 μL of solvent was used to separate the analyte mixture on a 300 μm I.D. column, whereas 12 mL of solvent per analysis were needed when a standard column of 4.6 mm I.D. was used. While solvent savings of microscale LC has been demonstrated theoretically and experimentally, there are also some drawbacks relates to sensitivity such as lower limit of detection arising from UV-detector limitations [5]. Because of relatively small volumes of injected sample in the ranges of 10–60 nL and 1–50 μL (nano-LC and CLC, respectively), the sensitivity with these techniques can be questionable for the analysis of real samples [98]. It is more problematic for the low level quantitation required in metabolite and trace impurity studies [5]. Several studies have been carried out to solve this problem by using more sensitive detectors such as MS and/or applying sample pre-concentration (off- and on-column) [98].

However micro-LC columns allow great reduction in solvent use, their application in routine analysis is very limited because of the difficulty in column packing, instrumental requirements, and lower plate numbers compared with similar columns in terms of length and particle size [31]. Using columns of 1 mm I.D. in environmental analysis is not widely common. Only few studies were reported for the analysis of pharmaceuticals in the aquatic environment. As an example, Kasprzyk-Hordern et al. could separate 28 pharmaceuticals and illicit drugs in surface water using micro-LC column of 1 mm internal diameter in 15.5 min with a flow rate of 70 μL min^{-1} and resulted in solvent consumption of less than 1.1 mL run^{-1} [35]. In another study, the same author separated 65 stimulants in wastewater and surface water in 23.1 min on a micro-LC column with a flow rate of 40 μL min^{-1} and resulted in the use of ~0.9 mL of solvent per run [41]. Also, using a column of 0.5 mm I.D. with a flow rate of 20 μL min^{-1} is reported for the determination of vitamin E in cosmetic products [99]. Miniaturization to nano-columns and using LC-chip columns have also been reported [4]. These columns can interface directly

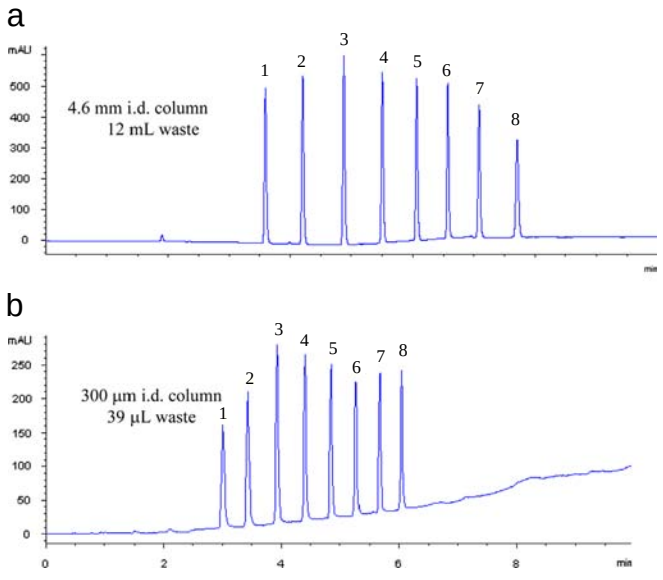


Fig. 6. Chromatogram of separation of an alkyl benzene mixture separated [5] on (a) conventional HPLC using 4.6 mm i.d. column at 1.5 mL min^{-1} requiring 12 mL of solvent per analysis; and (b) microscale HPLC using 0.3 mm i.d. column at 6 μL min^{-1} requiring only 39 μL of solvent per analysis. Chromatographic conditions: Gradient elution 50–95% acetonitrile in water over 5 min, then 95% in 1 min using Agilent SB-18, 150 mm, 3.5 μm particles and UV detection at 220 nm.

to a nanospray LC–MS system. Nano-LC instruments using a few hundred nanoliters of the mobile phase per minute are now commercially available [4]. Capillary and nano-LC columns have been applied mainly to proteomics and food analysis [100]; they found limited applications in environmental analysis. Using nano-LC systems as "green" techniques requires instrument adjustments, including minimizing extra-column volumes through decreasing pump, injector and detector cell volumes, as well as the volumes of all connections between the injector and the detector [4].

2.2. Replacement of existing solvents with green alternatives

Replacing toxic solvents with greener alternatives is another strategy aiming at reducing the solvent consumption. The most commonly used solvent in LC separations is acetonitrile. Because of its unique characteristics, such as the ability to dissolve a wide range of solutes, low acidity, minimal chemical reactivity, low UV cut-off and low viscosity [31], it is considered the solvent of choice for RP–LC separations [101]. Even though the unique characteristics of acetonitrile, it is less preferred as a green solvent because of its flammability, volatility and toxicity. Consequently, HPLC wastes containing acetonitrile must be properly disposed of, which is costly and might be harmful to the environment [5]. Green alternatives such as water, acetone, ethanol and carbon dioxide are environmentally friendly and can replace acetonitrile in some LC applications [31].

2.2.1. Use of ethanol in RP–HPLC

Ethanol has characteristics similar to acetonitrile but with less toxicity, lower disposal costs and less volatility, allowing higher stability of the mobile phase composition upon long [31]. However, the use of ethanol with conventional LC systems (400 bar) is hindered because of its high viscosity. With the development of UPLC instrumentation providing pressures $\geq$1000 bar, the viscosity is no longer considered a critical problem. Replacement of acetonitrile with ethanol as an organic modifier is a new approach aiming at greening the RP–LC analysis where ethanol/water is used as the mobile phase. In this case, all incoming solvents and outgoing waste are compatible with the environment. The tendency to use ethanol in place of acetonitrile or methanol in LC separations has been evidenced by the gradually increasing number of publications [102–108]. Also, substitution of acetonitrile as organic modifier by mixtures of propylene carbonate and ethanol may be considered a greener approach for pharmaceutical applications [109]. Propylene carbonate (R,S-4-methyl-1,3-dioxolan-2-one) is a carbonate ester derived from propylene glycol, synthesized by means of more or less green processes, often used as a polar aprotic solvent in analytical chemistry and organic synthesis. Such a replacement is achievable without any major compromise in terms of elution order, chromatographic retention, efficiency and peak symmetry [109]. Considered in both analytical and sustainable viewpoints, the mixture of ethanol and water is an effective alternative mobile phase for RP–LC methods.

2.2.2. Replacement of organic modifiers with pure water (superheated water chromatography)

Greening the analysis by replacing traditional solvents with green alternatives can also be achieved by replacing the organic modifier with pure hot water. In recent years, the use of pure water as an eluent has been received a great interest and studied by a number of researchers. This approach is known as "Superheated Water Chromatography" (SHWC), "Subcritical Water Chromatography" or "Chromatography in Very Hot Water" [110]. SHWC is a green alternative for conventional RP–LC separations where

the mobile phase used is a mixture of water with acetonitrile or methanol [5].

At elevated temperatures, dielectric constant of water decreases and water becomes a stronger solvent resulting in increasing the solvent strength. Therefore pure water can be used as an eluent in RP–LC [75]. For example, at 150 °C, the dielectric constant of water is reduced to that comparable of a mixture of 50:50 *v*/*v* methanol–water at ambient temperature. Elimination of organic modifier allows LC separations to be completely "green" [111]. Using water as an eluent provides attractive advantages such as non-toxicity and wide availability. In addition, waster is inexpensive, non-flammable and environmentally friendly [5]. Also, using pure water as a solvent allows the possibility of hyphenation with non-conventional detectors, e.g. flame ionization detector (FID), which is desirable for UV-transparent compounds [110]. Furthermore, using pure water allows UV detection to be carried out at very short wavelengths (~190 nm), allowing the detection of many analytes that do not absorb at longer wavelengths [110]. Besides, the compatibility of heated effluents with MS detectors has been shown to increase the ionization efficiency and signal to noise ratio (S/N) for some compounds [75].

To implement SHWC, special instrumentation is required as described before. However, alkyl silane-bonded phases are the most popular in RP–LC; they show thermal and chemical instability [112]. Conventional alkyl silane-bonded silica phases are typically unstable at temperatures above 50 °C since higher temperature accelerates the dissolution of silica in aqueous solutions. At temperatures above 100 °C, silica-based C18 phases are rapidly degraded with water as the mobile phase [113]. Another drawback of these stationary phases is the degradation at pH outside the range of 2.5–8. To overcome the problem of thermal and chemical instability of alkyl silane-bonded silica phases, different approaches have been developed such as grafting an organic protective layer on the silica surface, modifying silica with bonding and endcapping technologies and synthesizing hybrid particles resulting in organic groups incorporated into the silica matrix [110]. Also, alternative packing materials have been developed to withstand high temperatures, including metal oxide-based columns, porous graphitic carbon and organic polymers such as polystyrene-divinylbenzene (PS–DVB). However SHWC has attractive features, this technique has some limitations such as potential on-column degradation of thermally labile compounds and insolubility of hydrophobic compounds in water [5].

Pharmaceutical analysis is an area of particular interest for SHWC. The use of pure water as a mobile phase in pharmaceutical analysis is reported in the literature [114–118]. For example, six anticancer drugs were separated on a polystyrenedivinylbenzene (PS–DVB) column with buffered superheated water as a mobile phase using temperature range from ambient temperature up to 160 °C [114]. Good separation for all analytes is achieved. The use of SHWC in analysis of environmental pollutants is also reported [119–122]. In environmental analysis, analyte stability is important and before any quantitative work is carried out it is necessary to check recoveries and ensure that the high temperatures don't result in artefact peak formation [123].

2.2.3. Replacement with carbon dioxide

Another approach in greening LC separations is the use of carbon dioxide either in a liquid state, or as a supercritical fluid. In supercritical fluid chromatography (SFC), the chromatographic eluent is usually the pressurized carbon dioxide in the supercritical state with a polar modifier, such as methanol or ethanol, and very small amounts of acid or base as additives to improve the peak shapes of the analytes [124,125]. Pressure must be controlled to keep carbon dioxide in the supercritical form. Upon depressurization, carbon dioxide returns to gas phase allowing the recovery of non-volatile analytes [5]. Carbon dioxide provides many advantages as a green alternative such as it is non-toxic and environmentally friendly. Also, in the supercritical state it has low viscosity allowing high flow rates to be used leading to faster separations. The optimal linear velocity for SFC is approximately three times greater than for HPLC [126]. With SFC, the consumption of organic solvent can be reduced to 88–98% compared to normal-phase HPLC [5]. Also, using carbon dioxide provides high diffusivity and highly efficient separations [101].

Recently, SFC popularity has increased because of its greener character and wider availability of commercial instrumentation, including accessories that can convert a conventional HPLC system to one with SFC capability. SFC is regarded as a separation technique for non-polar substances and also can be applied to polar and chiral compounds, as well as to drugs and proteins. The application of SFC for separation of pharmaceuticals is also reported [127,128]. SFC is used increasingly for analytical, semi-preparative and preparative scale purification of chiral compounds, including production of enantiomers [24,129]. SFC can be used as an alternative to LC for many drug substances, so it is gaining popularity in the pharmaceutical industry. Because of its high speed, short analysis time, limited environmental impact, low organic solvent consumption, SFC fulfills all the requirements of green analytical chemistry approaches [128]. The use of SFC in the environmental analysis of organic contaminants is reported [130–132].

In addition to using carbon dioxide as a supercritical fluid, it can also be used in the liquid state under appropriate pressure and temperature as a component of the mobile phase providing fast and efficient separations. The technique is known as enhanced fluidity chromatography [101].

Nowadays, the interest in hydrophilic interaction chromatography (HILIC) has been increasing and at present it is considered the preferred LC mode for the separation of polar and ionizable compounds such as pharmaceuticals. In HILIC, separation is achieved by partitioning between a water-enriched layer on the surface of a polar stationary phase and a mobile phase that contains a high percentage of an organic solvent such as acetonitrile. Using HILIC in the environmental analysis of pharmaceuticals is well documented in the literature [69,133–138]. Because using a high percentage of acetonitrile in HILIC is not a green approach, Pereira et al. proposed the use of enhanced-fluidity liquid (EFL) in HILIC by adding liquid carbon dioxide to the mobile phase composed of ethanol–water [139]. Using enhanced fluidity mode (water/ethanol/CO_2) allows HILIC separations to be performed in a greener fashion with the same performance as when using water/acetonitrile [139]. The application of EFL mobile phases in HILIC mode for the analysis of nucleosides and nucleotides is reported in the literature [140,141]. Nucleosides and nucleotides are compounds of interest for pharmaceutical chemistry. To the best of our knowledge, EFL mobile phases in HILIC mode have not been used in environmental analysis. In the near future, this trend is likely to receive more attention by researchers aiming at greening HILIC separations.

Ionic liquids are also considered as green solvents. Recently, ionic liquids have been used as additives in LC to improve the peak shape by pairing ion mechanism [142]. For green solvent selection, an ionic liquid could be a potential candidate for LC. The use of ionic liquids has attracted considerable interest because of their unique properties (e.g. electric conductivity, low volatility, thermostability) and an increasing number of publications focus on their use in preparing stationary phases of LC [143].

More recently, the use of micellar mobile phases containing nonionic surfactants has been explored as a green approach aiming at eluting compounds without the need of adding an organic solvent. The application of micellar mobile phase with LC for separation of pharmaceuticals is reported [144,145]. Also, the use of two-dimensional LC (2DLC) for the analysis of pharmaceuticals in

complex matrices has gained more interest such as [146]. Fast separations can be achieved in the second dimension by using high temperature LC, which is a green approach, and/or using short columns. On-line 2DLC may be considered a green technique because it allows reduction in solvent consumption and waste generation, prevention of sample contamination or sample loss, possibility of automation and shorter analysis time compared to off-line mode [24].

3. Green aspects of gas chromatography

GC is a separation technique that does not use solvents but relies on the separation of the analytes in the gas phase. It is used mainly for the analysis of semi-volatile and volatile compounds. GC is considered a green approach because its eluents are usually helium and hydrogen, which are gases harmless to the atmosphere. However helium is the most commonly used carrier gas in GC because of its high optimum linear velocity, non-toxicity, non-flammability and inertness, helium is a non-renewable resource [24]. With the awareness about the run out of this precious gas, hydrogen seems to be the best alternative as a carrier gas in GC. Its van Deemter curve is very flat which allows separations to be conducted at higher flow rates with little loss in efficiency leading to short analysis time. One approach to make GC greener is the reduction of the analysis time leading to increased sample throughput which is commonly referred as fast capillary GC. This may be achieved by using shorter columns with small internal diameter without sacrificing separation and resolution. Fast GC reduces overall analysis time leading to significant savings in time and energy [147]. Fast chromatography can be especially attractive for laboratories where many routine samples are analyzed every day. It can also be advantageous when quick results are needed. Increasing column temperature during GC analysis is referred to temperature-programmed GC (TPGC). The use of temperature programming in GC is an important parameter which provides many benefits such as better separation for solutes with a wide boiling points range, improved peak symmetry and improved detection limits [24]. The use of programmed temperature vaporizers for environmental analysis is well documented in the literature such as [148–154]. To achieve ultrafast temperature programming, low thermal mass technology (LTM) which introduced in 2001 [24]. LTMGC is considered a green technique aiming at greening GC separations because resistive heating of a GC column can reduce the power consumption by approximately a factor of 200, and increase the column heating speed (up to 1800 $^{\circ}$C min^{-1}; achievable rates depend on column mass, configuration and column void times), which can potentially reduce the analysis time [24]. Another technology introduced to make GC greener is the resistively heated nickel-clad fused silica columns [155]. This technology is considered green because it allows rapid heating and cooling with low power consumption making it suitable for fast GC analysis and for portable instruments [24]. However the main tool for the analysis of pharmaceuticals in most studies is LC due to the polarity of pharmaceuticals, many analytical methods based on GC–MS have been developed to determine various pharmaceuticals in different environmental samples such as [156–165].

4. Application of direct chromatographic techniques

The application of direct chromatographic techniques is a step forward in reducing the environmental impact of chromatographic analyses. Direct chromatographic analysis allows the determination of analytes in a sample without any pre-treatment or sample preparation which is the most polluting step in the entire chromatographic analysis [166]. The use of direct methodologies is limited only to samples with relatively clean matrices [24], otherwise the chromatographic columns might quickly deteriorate due to deposition of sample components that do not elute from the column. GC methods are usually more readily adaptable to the elimination of sample preparation step than LC. The early work on direct GC methods was focused on the development of on-column injection. The application of on-column GC for the environmental analysis in water is documented in the literature such as [167–173]. Another approach of using direct GC is to prevent the solvent from reaching the column by using a liner filled with sorbent [174]. The use of GC with sorbent-packed liner for the analysis of environmental pollutants is reported [175,176].

LC methods are less amenable to eliminating sample pre-treatment as it requires the injected sample to be absolutely clean, so there are hardly any absolutely direct LC methods. However, there are some successful applications of direct LC methods in environmental analysis such as [177–183]. Application of direct chromatographic methodologies is considered a green approach aiming at greening the analysis because it provides reduction of analysis time and elimination of sample preparation step which allows placing the chromatograph at-line or on-line, which may further reduce the analysis time. These benefits lead to minimizing environmental impact of chemical processes through real-time monitoring.

5. Placing the chromatograph with respect to the investigated medium

The traditional approach of chromatographic analysis involves collection of the sample, sample pre-treatment followed by final analysis. All of these activities generate negative environmental impact. Therefore, locating the chromatograph on-line or at-line may reduce the analysis time and minimize the consumption of reagents. The shorter time of analysis and the possibility of locating the chromatograph on-line or at-line is a step towards fulfilling the need for the real-time monitoring of chemical processes. On-line chromatography is achieved when the analytical device is located near the investigated medium. In this case, sample is collected and analyzed periodically and automatically and on-line sample preparation is usually applied [2]. The advantage of using on-line chromatography is minimal loss of sample representativity because sample is directly analyzed without being transported nor stored. Application of on-line chromatographic techniques in environmental analysis is documented in the literature [184–187]. In addition to on-line mode, at-line is also known where the analytical device is brought to the investigated medium by the analyst. In this case, sample is analyzed at the site of collection. Environmental analysis using at-line chromatographic techniques is also documented [188–191].

6. Green aspects of biological techniques

Biological methods are used for screening and diagnosis of organic compounds in environmental samples of water, sludge and sediments. The most relevant biological techniques or bio-detectors applied to environmental analysis can be classified according to their technical principles into (bioassays, immunoassays and biosensors) or the type of measurement (screening method and specific measurement) [192]. Immunoassays are based on the reversible binding of antibodies with antigens. The binding properties of an antibody to an antigen have been used for the development of a wide variety of analytical techniques applicable in environmental monitoring [193–196].

Immunoassays are considered as green techniques because they provide rapid analysis, simple sample pre-treatment, low volumes of sample required and low use of solvents, reduced energy consumption and possibility of in situ analysis [3]. The main drawbacks of these techniques are poor thermal and chemical stability of immune-reagents, cross reactivity between structurally-related compounds, and possible matrix effects. At present, most immunochemical advances in environmental analysis have been carried out using enzyme-linked immunosorbent assays (ELISAs). Several methods have been used for the environmental analysis of emerging pollutants using ELISAs [46,197–202]. Biosensors are also considered green because of its capabilities of automation, miniaturization, on-line and at-site analysis, with minimal waste production and energy cost. Biosensors are chemical sensors that use active, biologically derived components integrated with a suitable transducer [3]. It is capable of providing specific quantitative or semi-quantitative analytical information. Several reviews on biosensors and biological techniques for environmental analysis have been published in recent years [203,204].

7. Conclusions

Chromatographic techniques have the potential to be greener at all steps of the analysis. Greening LC separations becomes the main goal for many researchers aiming at reducing solvent usage and protecting the environment from hazardous effect of organic solvents. Traditional methods used for the analysis of pharmaceuticals require large volumes of organic solvents with large volumes of waste production. So developing green methods is highly demanded aiming at eliminating or reducing the amount of organic solvents consumed while maintaining the chromatographic performance. In this review, recent trends for greening LC analysis have been discussed. Many strategies have been developed to save solvent consumption such as shortening the analysis time or replacing the traditional organic modifiers used in RP–LC with safe alternatives. These options offer many benefits both environmentally and economically. Fast green separations can be achieved by using high mobile phase temperature, fully porous sub-2 μm with UPLC systems and superficially porous particles. GC is a relatively green separation method because its eluents are usually helium and hydrogen, which are gases harmless to the atmosphere. Faster GC separation can be achieved by reducing the inner diameter and the length of the capillary columns, working above optimal carrier gas velocities and using fast temperature programming. SFC is also considered as green technique because it fulfills all the requirements of green analytical chemistry approaches. Carbon dioxide is non-toxic and environmentally friendly with low viscosity allowing high flow rates to be used leading to faster separations. Miniaturization is also considered a promising approach in solvent savings. Another approach aiming at greening chromatographic analysis is locating the chromatograph on-line or at-line which is considered a step towards fulfilling the need for the real-time monitoring of chemical processes. Greening biological techniques is gained great interest. Immunoassays and biosensors are generally greener techniques because they provide rapid analysis, simple sample pre-treatment, low volumes of sample required and low use of solvents, reduced energy consumption and possibility of in situ analysis.

Acknowledgements

The authors gratefully acknowledge faculty of Clinical Pharmacy, University of Dammam. Financial support from the Natural Sciences and Engineering Research Council (NSERC) of Canada (Grant no. 108054) is acknowledged.

References

[1] S. Armenta, S. Garrigues, M. d. l. Guardia, Green Anal. Chem. Trends Anal. Chem 27 (2008) 497–511.
[2] M. Tobiszewski, J. Namies´nik, Trends Anal. Chem 35 (2012) 67–73.
[3] M. Farre´, S. Pe´rez, C. Gonçalves, M.F. Alpendurada, D. Barcelo, Trends Anal. Chem 29 (2010) 1347–1362.
[4] R.E. Majors, D. Raynie, LC–GC N. Am 29 (2011) 118–135.
[5] C.J. Welch, N.J. Wu, M. Biba, R. Hartman, T. Brkovic, X.Y. Gong, R. Helmy, W. Schafer, J. Cuff, Z. Pirzada, L.L. Zhou, Trac-Trend Anal. Chem. 29 (2010) 667–680.
[6] W.W. Buchberger, J. Chromatogr. A. 1218 (2011) 603–618.
[7] D.M. i. Pavlovic´, S. Babic´, A.J.M. Horvat, M. Kaštelan-Macan, Trends Anal. Chem 26 (2007) 1062–1075.
[8] J. Curyło, W. Wardencki, J. Namieśnik, Polish J. Environ. Stud 16 (2007) 5–16.
[9] P. Sandra, B. Tienpont, F. David, LC–GC Eur. 24 (2011) 120–133.
[10] M. Tobiszewski, A. Mechlin´ska, B. Zygmunt, J. Namies´nik, Trends Anal. Chem 28 (2009) 943–951.
[11] H. Shaaban, T. Gorecki, in: F. Ramos (Ed.), Liquid Chromatography: Principles, Technology and Applications, NOVA, New York, 2013, pp. 239–268.
[12] P.K. Zarzycki, M.M. Slaczka, M.B. Zarzycka, M.A. Bartoszuk, E. Wlodarczyk, M.J. Baran, J. Steroid Biochem. Mol. Biol. 127 (2011) 418–427.
[13] O. Nunez, H. Gallart-Ayala, C.P.B. Martins, P. Lucci, J. Chromatogr. A. 1228 (2012) 298–323.
[14] F. Gritti, G. Guiochon, J. Chromatogr. A 1228 (2012) 2–19.
[15] D. Guillarme, J. Ruta, S. Rudaz, J.L. Veuthey, Anal. Bioanal. Chem. 397 (2010) 1069–1082.
[16] N. Tanaka, H. Kobayashi, N. Ishizuka, H. Minakuchi, K. Nakanishi, K. Hosoya, T. Ikegami, J. Chromatogr. A. 965 (2002) 35–49.
[17] N.J. Wu, J. Dempsey, P.M. Yehl, A. Dovletoglou, D. Ellison, J. Wyvratt, Anal. Chim. Acta. 523 (2004) 149–156.
[18] A. Abrahim, M. Al-Sayah, P. Skrdla, Y. Bereznitski, Y.D. Chen, N.J. Wu, J. Pharm. Biomed 51 (2010) 131–137.
[19] F. Gritti, G. Guiochon, J. Chromatogr. A. 1221 (2012) 2–40.
[20] D.T.T. Nguyen, D. Guillarme, S. Rudaz, J.L. Veuthey, J. Sep. Sci. 29 (2006) 1836–1848.
[21] A. Pena, D. Chmielova, C.M. Lino, P. Solich, J. Sep. Sci. 30 (2007) 2924–2928.
[22] J. Bones, P. Nesterenko, K. Thomas, B. Paull, Intern. J. Environ. Anal. Chem 86 (2006) 487–504.
[23] J. Bones, K.V. Thomas, B. Paull, J. Chromatogr. A. 1132 (2006) 157–164.
[24] J. Plotka, M. Tobiszewski, A.M. Sulej, M. Kupska, T. Gorecki, J. Namiesnik J. Chromatogr. A. 1307 (2013) 1–20.
[25] J.H. Knox, J. Chromatogr. Sci 15 (1977) 352–364.
[26] H. Poppe, J. Chromatogr. A 778 (1997) 3–21.
[27] M. Farre, M. Petrovic, D. Barcelo, Anal. Bioanal. Chem. 387 (2007) 1203–1214.
[28] D.A. Skoog, F.J. Howler, T.A. Nieman, Principles of Instrumental Analysis, fifth ed., Brooks/Cole, Florence, USA, 1998.
[29] J.M. Cunliffe, S.B. Adams-Hall, T.D. Maloney, J. Sep. Sci. 30 (2007) 1214–1223.
[30] R. Russo, D. Guillarme, T.T.N.D,C. Bicchi, S. Rudaz, J.L. Veuthey, J. Chromatogr. Sci 46 (2008) 199–208.
[31] P. Sandra, LC–GC Eur 23 (2010) 240–259.
[32] H. Chang, J. Hu, M. Asami, S. Kunikane, J. Chromatogr. A. 1190 (2008) 390–393.
[33] K. Demeestere, M. Petrovic, M. Gros, J. Dewulf, H. Van Langenhove, D. Barcelo, Anal. Bioanal. Chem. 396 (2010) 825–837.
[34] R. Lopez-Serna, M. Petrovic, D. Barcelo, Chemosphere 85 (2011) 1390–1399.
[35] B. Kasprzyk-Hordern, R.M. Dinsdale, A.J. Guwy, J. Chromatogr. A. 1161 (2007) 132–145.
[36] J.C. Van De Steene, W.E. Lambert, J. Am. Soc. Mass Spectrom 19 (2008) 713–718.
[37] L. Sun, W. Yong, X. Chu, J.M. Lin, J. Chromatogr. A. 1216 (2009) 5416–5423.
[38] H. Zhou, C. Wu, X. Huang, M. Gao, X. Wen, H. Tsuno, H. Tanaka, Water Environ. Res. 82 (2010) 2239–2248.
[39] H.-X. Wang, Y. Zhou, Q.-W. Jiang, Microchem. J. 100 (2012) 83–94.
[40] L. Bijlsma, J.V. Sancho, E. Pitarch, M. Ibanez, F. Hernandez, J. Chromatogr. A. 1216 (2009) 3078–3089.
[41] D.R. Baker, B. Kasprzyk-Hordern, J. Chromatogr. A. 1218 (2011) 1620–1631.
[42] F. Hernandez, M. Ibanez, E. Gracia-Lor, J.V. Sancho, J. Sep. Sci. 34 (2011) 3517–3526.
[43] E. Gracia-Lor, J.V. Sancho, F. Hernandez, J. Chromatogr. A. 1218 (2011) 2264–2275.
[44] F. Hernandez, L. Bijlsma, J.V. Sancho, R. Diaz, M. Ibanez, Anal. Chim. Acta. 684 (2011) 87–97.
[45] E. Gracia-Lor, J.V. Sancho, F. Hernandez, J. Chromatogr. A. 1217 (2010) 622–632.
[46] M. Farre, M. Kuster, R. Brix, F. Rubio, M.J. Lopez de Alda, D. Barcelo J. Chromatogr. A. 1160 (2007) 166–175.
[47] H. Shaaban, T. Górecki, J. Sep. Sci. 35 (2012) 216–224.
[48] H. Shaaban, T. Gorecki, J. Sep. Sci. 36 (2013) 252–261.
[49] M. Gros, S. Rodriguez-Mozaz, D. Barcelo, J. Chromatogr. A. 1248 (2012) 104–121.

[50] N. Cimetiere, I. Soutrel, M. Lemasle, A. Laplanche, A. Crocq, Environ. Technol 34 (2013) 3031–3041.
[51] M. Petrovic, B. Skrbic, J. Zivancev, L. Ferrando-Climent, D. Barcelo, Sci. Total Environ 468 (2014) 415–428.
[52] L. Ferrando-Climent, S. Rodriguez-Mozaz, D. Barcelo, Anal. Bioanal. Chem. 405 (2013) 5937–5952.
[53] L. Vergeynst, H. Van Langenhove, P. Joos, K. Demeestere, Anal. Bioanal. Chem. 406 (2014) 2533–2547.
[54] M.B. Cerqueira, J.R. Guilherme, S.S. Caldas, M.L. Martins, R. Zanella, E.G. Primel, Chemosphere 107 (2014) 74–82.
[55] A.L. Batt, M.S. Kostich, J.M. Lazorchak, Anal. Chem 80 (2008) 5021–5030.
[56] B. Kasprzyk-Hordern, R.M. Dinsdale, A.J. Guwy, Talanta 74 (2008) 1299–1312.
[57] J.J. Kirkland, Anal. Chem (1992) 1239–1245.
[58] K.K. Unger, R. Skudas, M.M. Schulte, J. Chromatogr. A. 1184 (2008) 393–415.
[59] J.M. Cunliffe, T.D. Maloney, J. Sep. Sci. 30 (2007) 3104–3109.
[60] J.J. Salisbury, J. Chromatogr. Sci 46 (2008) 883–886.
[61] H. Shaaban, T. Gorecki, Anal. Methods 4 (2012) 2735–2743.
[62] A. Fanigliulo, D. Cabooter, G. Bellazzi, D. Tramarin, B. Allieri, A. Rottigni, G. Desmet, J. Sep. Sci. 33 (2010) 3655–3665.
[63] M.A. Rostagno, N. Manchon, M. D'Arrigo, E. Guillamon, A. Villares, A. Garcia-Lafuente, A. Ramos, J.A. Martinez, Anal. Chim. Acta. 685 (2011) 204–211.
[64] A. Tolgyesi, V.K. Sharma, J. Fekete, J. Chromatogr. B 879 (2011) 403–410.
[65] Y. Lu, Q. Shen, Z. Dai, H. Zhang, H. Wang, J. Chromatogr. A. 1218 (2011) 929–937.
[66] Y. Lu, Q. Shen, Z. Dai, H. Zhang, Anal. Bioanal. Chem. 398 (2010) 1819–1826.
[67] S. Wang, J. Wen, L. Cui, X. Zhang, H. Wei, R. Xie, B. Feng, Y. Wu, G. Fan J. Pharm. Biomed. Anal. 51 (2010) 889–893.
[68] Y. Hsieh, C.J. Duncan, J.M. Brisson, Anal. Chem 79 (2007) 5668–5673.
[69] I. Tarcomnicu, A.L. van Nuijs, W. Simons, L. Bervoets, R. Blust, P.G. Jorens, H. Neels, A. Covaci, Talanta 83 (2011) 795–803.
[70] M. Pedrouzo, F. Borrull, E. Pocurull, R.M. Marce, J. Sep. Sci. 34 (2011) 1091–1101.
[71] D. Bratkowska, N. Fontanals, P.A. Cormack, F. Borrull, R.M. Marce, J. Chromatogr. A. 1225 (2012) 1–7.
[72] H. Shaaban, T. Gorecki, Talanta 100 (2012) 80–89.
[73] N.M. Djordjevic, P.W.J. Fowler, F. Houdiere, J. Microcolumn. Sep 11 (1999) 403–413.
[74] S. Fekete, E. Olah, J. Fekete, J. Chromatogr. A. 1228 (2012) 57–71.
[75] C.V. McNeff, B. Yan, D.R. Stoll, R.A. Henry, J. Sep. Sci. 30 (2007) 1672–1685.
[76] D. Guillarme, S. Heinisch, J.L. Rocca, J. Chromatogr. A 1052 (2004) 39–51.
[77] F.D. Antia, C. Horváth, J. Chromatogr. A 435 (1988) 1–15.
[78] H. Chen, C. Horvath, J. Chromatogr. A. 705 (1995) 3–20.
[79] J. Li, P.W. Carr, Anal. Chem. 69 (1997) 2530–2536.
[80] G. Vanhoenacker, P. Sandra, J. Sep. Sci. 29 (2006) 1822–1835.
[81] B.J. Vanderford, R.A. Pearson, D.J. Rexing, S.A. Snyder, Anal. Chem 75 (2003) 6265–6274.
[82] M. Gros, M. Petrovic, D. Barcelo, Anal. Bioanal. Chem. 386 (2006) 941–952.
[83] H. Shaaban, T. Górecki, Chromatographia 74 (2011) 9–17.
[84] H. Shaaban, T. Gorecki, Anal. Chim. Acta. 702 (2011) 136–143.
[85] D. Thomas, LC–GC Eur (2009) 9–10.
[86] S. Chen, A. Kord, J. Chromatogr. A. 1216 (2009) 6204–6209.
[87] S. Yang, J. Cha, K. Carlson, Rapid Commun. Mass Spectrom. 18 (2004) 2131–2145.
[88] D. Richter, U. Dunnbier, G. Massmann, A. Pekdeger, J. Chromatogr. A. 1157 (2007) 115–121.
[89] M.S. Diaz-Cruz, M.J. Garcia-Galan, D. Barcelo, J. Chromatogr. A. 1193 (2008) 50–59.
[90] L. Tong, P. Li, Y. Wang, K. Zhu, Chemosphere 74 (2009) 1090–1097.
[91] Q.T. Dinh, F. Alliot, E. Moreau-Guigon, J. Eurin, M. Chevreuil, P. Labadie, Talanta 85 (2011) 1238–1245.
[92] T.V. Madureira, J.C. Barreiro, M.J. Rocha, Q.B. Cass, M.E. Tiritan, J. Chromatogr. A. 1216 (2009) 7033–7042.
[93] H.B. Lee, K. Sarafin, T.E. Peart, J. Chromatogr. A. 1148 (2007) 158–167.
[94] M. Letzel, K. Weiss, W. Schussler, M. Sengl, Chemosphere 81 (2010) 1416–1422.
[95] D. Perret, A. Gentili, S. Marchese, A. Greco, R. Curini, Chromatographia 63 (2006) 225–232.
[96] J. Magner, M. Filipovic, T. Alsberg, Chemosphere 80 (2010) 1255–1260.
[97] C. Boix, M. Ibanez, J.V. Sancho, N. Leon, V. Yusa, F. Hernandez, Food Chem 160 (2014) 313–320.
[98] C. Fanali, L. Dugo, P. Dugo, L. Mondello, Trends Anal. Chem 52 (2013) 226–238.
[99] P. Vinas, M. Pastor-Belda, N. Campillo, M. Bravo-Bravo, M. Hernandez-Cordoba, J. Pharm. Biomed. Anal. 94 (2014) 173–179.
[100] P. Vi~nas, M. Pastor-Belda, N. Campillo, M. Bravo-Bravo, M. Hernández-Córdoba, J. Pharm. Biomed 94 (2014) 173–179.
[101] M. Kaljurand, M. Koel, Crit. Rev. Anal. Chem. 41 (2011) 2–20.
[102] R.L.V. Ribeiro, C.B.G. Bottoli, K.E. Collins, C.H. Collins, J. Braz. Chem. Soc 15 (2004) 300–306.
[103] A. Salvador, A. Chisvert, Anal. Chim. Acta. 537 (2005) 15–24.
[104] D.D. Orsi, L. Gagliardi, R. Porr'a, S. Berri, P. Chimenti, A. Granese, I. Carpani, D. Tonelli, Anal. Chim. Acta. 555 (2006) 238–241.
[105] N. Haq, M. Iqbal, F.K. Alanazi, I.A. Alsarra, F. Shakeel, Arabian J. Chem (2012).
[106] P.D. Rainville, J.L. Simeone, S.M. McCarthy, N.W. Smith, D. Cowan, R.S. Plumb, Bioanal 4 (2012) 1287–1297.
[107] F. Sadeghi, L. Navidpour, S. Bayat, M. Afshar, J. Anal. Methods Chem 2013 (2013) 1–10.
[108] A. Balaguer, A. Chisvert, A. Salvador, J. Sep. Sci. 31 (2008) 229–236.
[109] F. Tache, S. Udrescu, F. Albu, F. Micale, A. Medvedovici, J. Pharm. Biomed. Anal. 75 (2013) 230–238.
[110] S. Heinisch, J.L. Rocca, J. Chromatogr. A. 1216 (2009) 642–658.
[111] R.M. Smith, R.J. Burgess, J. Chromatogr. A. 785 (1997) 49–55.
[112] T. Greibrokk, T. Andersen, J. Sep. Sci. 24 (2001) 899–909.
[113] T. Greibrokk, T. Andersen, J. Chromatogr A. 1000 (2003) 743–755.
[114] T. Teutenberg, O. Lerch, H.J. Gotze, P. Zinn, Anal. Chem. 73 (2001) 3896–3899.
[115] O. Chienthavorn, R.M. Smith, S. Saha, I.D. Wilson, B. Wright, S.D. Taylor, E.M. Lenz, J. Pharm. Biomed. Anal. 36 (2004) 477–482.
[116] A.M. Edge, S. Shillingford, C. Smith, R. Payne, I.D. Wilson, J. Chromatogr. A. 1132 (2006) 206–210.
[117] S.M. Fields, C.Q. Ye, D.D. Zhang, B.R. Branch, X.J. Zhang, N. Okafo J. Chromatogr. A. 913 (2001) 197–204.
[118] R.M. Smith, O. Chienthavorn, S. Saha, I.D. Wilson, B. Wright, S.D. Taylor J. Chromatogr. A. 886 (2000) 289–295.
[119] Y. Yang, A.D. Jones, C.D. Eaton, Anal. Chem 71 (1999) 3808–3813.
[120] R. Tajuddin, R.M. Smith, J. Chromatogr. A. 1084 (2005) 194–200.
[121] M.M. Sanagi, H.H. See, W.A. Ibrahim, A.A. Naim, J. Chromatogr. A. 1059 (2004) 95–101.
[122] T. Yarita, R. Nakajima, M. Shibukawa, Anal. Sci 19 (2003) 269–272.
[123] R.M. Smith, J. Chromatogr. A. 1184 (2008) 441–455.
[124] T.L. Chester, J.D. Pinkston, Anal. Chem 74 (2002) 2801–2811.
[125] P. Raveendran, Y. Ikushima, S.L. Wallen, Acc. Chem. Res. 38 (2005) 478–485.
[126] N. Wu, Q. Tang, Y. Shen, M.L. Lee, Anal. Chem. 71 (1999) 5084–5092.
[127] K. De Klerck, D. Mangelings, Y. Vander Heyden, J. Pharm. Biomed Anal. 69 (2012) 77–92.
[128] J.M. Płotka, M. Biziuk, C. Morrison, J. Namies´nik, Trends Anal. Chem 56 (2014) 74–89.
[129] A. Dispas, P. Lebrun, P. Sassiat, E. Ziemons, D. Thiebaut, J. Vial, P. Hubert J. Chromatogr. A. 1256 (2012) 253–260.
[130] L. Toribio, M.J. del Nozal, J.L. Bernal, J.J. Jimenez, M.L. Serna, J. Chromatogr. A. 823 (1998) 163–170.
[131] T. Yarita, Y. Horimoto, J. Yamada, A. Nomura, Anal. Sci. 8 (1992) 811–815.
[132] T. Yanta, A. Nomura, Y. Horlmoto, S. Gonda, J. Chromatogr. A. 750 (1996) 175 181.
[133] A.L. van Nuijs, I. Tarcomnicu, W. Simons, L. Bervoets, R. Blust, P.G. Jorens, H. Neels, A. Covaci, Anal. Bioanal. Chem. 398 (2010) 2211–2222.
[134] F. Qin, Y.Y. Zhao, M.B. Sawyer, X.F. Li, Anal. Chim. Acta. 627 (2008) 91–98.
[135] A.L. van Nuijs, I. Tarcomnicu, L. Bervoets, R. Blust, P.G. Jorens, H. Neels, A. Covaci, Anal. Bioanal. Chem. 395 (2009) 819–828.
[136] K.M. Peru, S.L. Kuchta, J.V. Headley, A.J. Cessna, J. Chromatogr. A. 1107 (2006) 152–158.
[137] A. Gheorghe, A. van Nuijs, B. Pecceu, L. Bervoets, P.G. Jorens, R. Blust, H. Neels, A. Covaci, Anal. Bioanal. Chem. 391 (2008) 1309–1319.
[138] A. Gheorghe, A. v. Nuijs, B. Pecceu, L. Bervoets, P.G. Jorens, R. Blust, H. Neels, A. Covaci, Anal. Bioanal. Chem. 391 (2008) 1309–1319.
[139] S. Pereira Ados, A.J. Giron, E. Admasu, P. Sandra, J. Sep Sci. 33 (2010) 834–837.
[140] G.S. Philibert, S.V. Olesik, J. Chromatogr. A. 1218 (2011) 8222–8230.
[141] J.W. Treadway, G.S. Philibert, S.V. Olesik, J. Chromatogr. A. 1218 (2011) 5897–5902.
[142] Y. Wang, M. Tian, W. Bi, K.H. Row, Int. J. Mol. Sci. 10 (2009) 2591–2610.
[143] M. Zhang, X. Liang, S. Jiang, H. Qiu, Trends Anal. Chem 53 (2014) 60–72.
[144] N. Youngvises, T. Chaida, S. Khonyoung, N. Kuppithayanant, W. Tiyapongpattana, A. Itharat, J. Jakmunee, Talanta 106 (2013) 350–359.
[145] J.J. Fernandez-Navarro, M.J. Ruiz-Angel, M.C. Garcia-Alvarez-Coque, J. Sep. Sci. 35 (2012) 1303–1309.
[146] Y. Zhang, L. Zeng, C. Pham, R. Xu, J. Chromatogr. A. 1324 (2014) 86–95.
[147] C.A. Cramers, H.G. Janssen, M.M. van Deursen, P.A. Leclercq, J. Chromatogr. A. 856 (1999) 315–329.
[148] A. Delgado, O. Posada-Ureta, M. Olivares, A. Vallejo, N. Etxebarria, Talanta 117 (2013) 471–482.
[149] A.M. Carro, S. Fernandez, I. Racamonde, D. Garcia-Rodriguez, P. Gonzalez, R.A. Lorenzo, J. Chromatogr. A. 1253 (2012) 134–143.
[150] E. Bizkarguenaga, O. Ros, A. Iparraguirre, P. Navarro, A. Vallejo, A. Usobiaga, O. Zuloaga, J. Chromatogr. A. 1247 (2012) 104–117.
[151] A. Iparraguirre, P. Navarro, A. Prieto, R. Rodil, M. Olivares, L.A. Fernandez, O. Zuloaga, Anal. Bioanal. Chem. 402 (2012) 2897–2907.
[152] C. Guitart, J.W. Readman, Anal. Chim. Acta. 658 (2010) 32–40.
[153] R. Hu, L. Zhang, Z. Yang, Anal. Bioanal. Chem. 390 (2008) 349–359.
[154] M. del Nogal Sanchez, C. Perez Sappo, J.L. Perez Pavon, B. Moreno Cordero, Anal. Bioanal. Chem. 404 (2012) 2007–2015.
[155] S.D. Stearns, H. Cai, J.A. Koehn, M. Brisbin, C. Cowles, C. Bishop, S. Puente, D. Ashworth, J. Chromatogr. A. 1217 (2010) 4629–4638.
[156] E. Terzopoulou, D. Voutsa, G. Kaklamanos, Environ. Sci. Pollut. Res. Int (2014).
[157] C.H. Lee, Y. Shin, M.W. Nam, K.M. Jeong, J. Lee, Talanta 129 (2014) 552–559.
[158] J. Manso, E. Larsson, J.A. Jonsson, Talanta 125 (2014) 87–93.
[159] M.H. Devier, K. Le Menach, L. Viglino, L. Di Gioia, P. Lachassagne, H. Budzinski, Sci. Total Environ 443 (2013) 621–632.
[160] N. Migowska, M. Caban, P. Stepnowski, J. Kumirska, Sci. Total Environ. 441 (2012) 77–88.
[161] M.G. Pintado-Herrera, E. Gonzalez-Mazo, P.A. Lara-Martin, Anal. Bioanal. Chem. 405 (2013) 401–411.
[162] L. Guo, H.K. Lee, J. Chromatogr. A. 1235 (2012) 26–33.

[163] J.T. Yu, K.J. Bisceglia, E.J. Bouwer, A.L. Roberts, M. Coelhan, Anal. Bioanal. Chem. 403 (2012) 583–591.
[164] G.G. Noche, M.E. Laespada, J.L. Pavon, B.M. Cordero, S.M. Lorenzo, J. Chromatogr. A. 1218 (2011) 9390–9396.
[165] A. Prieto, S. Schrader, M. Moeder, J. Chromatogr. A. 1217 (2010) 6002–6011.
[166] W. Wardencki, J. Curylo, J. Namiesnik, J. Biochem. Biophys. Method 70 (2007) 275–288.
[167] S.K. Golfinopoulos, T.D. Lekkas, A.D. Nikolaou, Chemosphere 45 (2001) 275–284.
[168] B. Yu, Y. Song, L. Han, H. Yu, Y. Liu, H. Liu, J. Chromatogr. A. 1356 (2014) 221–229.
[169] C. Aeppli, M. Berg, T.B. Hofstetter, R. Kipfer, R.P. Schwarzenbach, J. Chromatogr. A. 1181 (2008) 116–124.
[170] M. Wortberg, W. Ziemer, M. Kugel, H. Muller, H.J. Neu, Anal. Bioanal. Chem. 384 (2006) 1113–1122.
[171] Z. Polkowska, Chemosphere 57 (2004) 1265–1274.
[172] M. Tobiszewski, J. Namiesnik, Anal. Bioanal. Chem. 399 (2011) 3565–3572.
[173] L. Zwank, T.C. Schmidt, S.B. Haderlein, M. Berg, Environ. Sci. Technol 36 (2002) 2054–2059.
[174] E. Hoh, K. Mastovska, J Chromatogr. A. 1186 (2008) 2–15.
[175] R. Kubinec, J. Adamuscin, H. Jurdakova, M. Foltin, I. Ostrovsky, A. Kraus, L. Sojak, J. Chromatogr. A. 1084 (2005) 90–94.
[176] M. Moeder, S. Schrader, U. Winkler, R. Rodil, J. Chromatogr. A. 1217 (2010) 2925–2932.
[177] S.B. Huang, T.J. Mayer, R.A. Yokley, J. Agric. Food. Chem. 56 (2008) 2595–2602.
[178] S.B. Huang, T.J. Mayer, R.A. Yokley, R. Perez, J. Agric. Food. Chem. 54 (2006) 713–719.
[179] A. Latorre, A. Rigol, S. Lacorte, D. Barcelo, J. Chromatogr. A. 991 (2003) 205–215.
[180] R. Lopez-Serna, M. Petrovic, D. Barcelo, J. Chromatogr. A. 1252 (2012) 115–129.
[181] S. Bayen, X. Yi, E. Segovia, Z. Zhou, B.C. Kelly, J. Chromatogr. A. 1338 (2014) 38–43.
[182] J. Mathew, D.L. Schroeder, L.B. Zintek, C.R. Schupp, M.G. Kosempa, A.M. Zachary, G.C. Schupp, D.J. Wesolowski, J. Chromatogr. A. 1231 (2012) 46–51.
[183] K.J. Bisceglia, A.L. Roberts, M.M. Schantz, K.A. Lippa, Anal. Bioanal. Chem. 398 (2010) 2701–2712.
[184] T. Barri, S. Bergstrom, J. Norberg, J.A. Jonsson, Anal. Chem 76 (2004) 1928–1934.
[185] T.C. Chen, G.R. Her, J. Chromatogr. A. 927 (2001) 229–235.
[186] P.S. Simone Jr., G.T. Anderson, G.L. Emmert, Anal. Chim. Acta. 570 (2006) 259–266.
[187] C.C. Chang, G.R. Her, J. Chromatogr. A. 893 (2000) 169–175.
[188] I.K. Kiplagat, P. Kuban, P. Pelcova, V. Kuban, J. Chromatogr. A. 1217 (2010) 5116–5123.
[189] A.J. Bednar, A.L. Russell, C.A. Hayes, W.T. Jones, P. Tackett, D.E. Splichal, T. Georgian, L.V. Parker, R.A. Kirgan, D.K. MacMillan, Chemosphere 87 (2012) 894–901.
[190] J. Ji, C. Deng, W. Shen, X. Zhang, Talanta 69 (2006) 894–899.
[191] H.W. Liu, Y.T. Liu, B.Z. Wu, H.C. Nian, H.J. Chen, K.H. Chiu, J.G. Lo, Talanta 80 (2009) 903–908.
[192] M. Farre´, R. Brix, D. Barcelo, Trends Anal. Chem. 24 (2005) 532–545.
[193] C. Barzen, A. Brecht, G. Gauglitz, Biosens. Bioelectron. 17 (2002) 289–295.
[194] V. Pacakova, L. Loukotkova, Z. Bosakova, K. Stulik, J. Sep. Sci. 32 (2009) 867–882.
[195] P.B. Luppa, L.J. Sokoll, D.W. Chan, Clin. Chim. Acta. 314 (2001) 1–26.
[196] M. Farre´, L. Kantiani, D. Barcelo, Trends Anal. Chem 26 (2007) 1100–1112.
[197] M. Farre, R. Brix, M. Kuster, F. Rubio, Y. Goda, M.J. Lopez de Alda, D. Barcelo, Anal. Bioanal. Chem. 385 (2006) 1001–1011.
[198] A. Deng, M. Himmelsbach, Q.Z. Zhu, S. Frey, M. Sengl, W. Buchberger, R. Niessner, D. Knopp, Environ. Sci. Technol 37 (2003) 3422–3429.
[199] W.L. Shelver, L.M. Kamp, J.L. Church, F.M. Rubio, J. Agric. Food. Chem. 55 (2007) 3758–3763.
[200] M. Farre, J. Ramon, R. Galve, M.P. Marco, D. Barcelo, Environ. Sci. Technol 40 (2006) 5064–5070.
[201] J. Ramon-Azcon, R. Galve, F. Sanchez-Baeza, M.P. Marco, Anal. Chem 78 (2006) 71–81.
[202] S. Kurosawa, M. Nakamura, J.W. Park, H. Aizawa, K. Yamada, M. Hirata, Biosens. Bioelectron. 20 (2004) 1134–1139.
[203] S. Rodriguez-Mozaz, M.J. Alda, M.P. Marco, D. Barcelo, Talanta 65 (2005) 291–297.
[204] S.M. Borisov, O.S. Wolfbeis, Chem. Rev. 108 (2008) 423–461.

Talanta 132 (2015) 753–759

Contents lists available at ScienceDirect

Talanta

journal homepage: www.elsevier.com/locate/talanta

Development of magnetic graphene @hydrophilic polydopamine for the enrichment and analysis of phthalates in environmental water samples

Xianying Wang [a], Guoxin Song [b,*], Chunhui Deng [a,*]

[a] Department of Chemistry, Fudan University, Shanghai 200433, China
[b] Research Center of Analysis and Measurement, Fudan University, Shanghai 200433, China

ARTICLE INFO

Article history:
Received 22 July 2014
Received in revised form
1 October 2014
Accepted 2 October 2014
Available online 22 October 2014

Keywords:
Magnetic graphene@polydopamine
Phthalates
Magnetic solid-phase extraction
Gas chromatography–mass spectrometry
Ambient water

ABSTRACT

Magnetic graphene @hydrophilic polydopamine composites were successfully fabricated via a simple solvothermal reaction and self-polymerization of dopamine. Benefit from the excellent characteristics of strong magnetic responsivity, super-hydrophilicity and abundant π-electron system, the prepared material showed great potential as a magnetic solid phase extraction (MSPE) sorbent. In this work, six kinds of phthalates (PAEs) were selected as the target analytes to evaluate the extraction ability of the adsorbents combined with MSPE-GC–MS. And various extraction parameters were optimized by selecting the pH value of samples, the amount of sorbents, adsorption and desorption time, the type and volume of eluting solution. Meanwhile, the whole extraction process could be finished in 30 min. Under the optimized conditions, validations of the method were evaluated as well. And the results presented excellent linearity with a wide range of 50–20,000 μg/L ($R^2 > 0.9991$). The detection of limits were in the range from 0.05–5 μg/L ($S/N=3$). Therefore, the novel magnetic graphene@polydopamine composites were successfully used as the sorbents for the enrichment and analysis of PAEs in real water samples. This proposed method provided a simple, efficient and sensitive approach for the determination of aromatic compounds in real environmental samples.

© 2014 Elsevier B.V. All rights reserved.

1. Introduction

Recently, magnetic materials have been exploited in many fields, such as catalysis [1], biomedicine [2], cell imaging [3], and separation science [4]. These materials are superparamagnetic, and usually possess large surface area, high adsorption capacity [5]. In separation science, they are always combined with solid phase extraction (SPE) to help analyze small molecules in real samples and it has been developed as a new method called magnetic solid phase extraction (MSPE) [6–8]. In MSPE, the magnetic materials and sample solution could be easily separated with an external magnetic field without the need of centrifugation or filtration. Among the magnetic materials, iron oxides such as magnetite (Fe_3O_4) are widely used in MSPE [9–11]. Since the simple iron oxides have little selectivity and sometimes can form large aggregates, lots of functionalized materials have been developed.

Among the variety of functionalized magnetic materials, graphene-based materials have attracted great attention with its excellent characteristics of large surface area (2630 m^2/g), good thermal stability and easy modification on the surface [12,13]. Moreover, benefit from delocalized π-electron system from graphene sheets, the material could extract benzene series compounds via π–π interaction [14,15]. And in order to simplify the preconcentration procedure, it is widely used to combine graphene with Fe_3O_4 microspheres to separate sorbents from matrix via an external magnetic field [16,17]. However, with the hydrophobicity of graphene, the materials could not well disperse in aqueous samples, which would affect the extraction efficiency sometimes. So, it requires chemical modification to improve the property.

Dopamine, which is widely known as a neurotransmitter, has attracted much interest in different fields since 2007 [18], such as in drug delivery, biosensing and interfacing with cells [19]. It could spontaneous polymerize in weak alkaline solution at room temperature. Besides, the generated polydopamine was successfully coated on metal oxides [20,21], polymers [22], carbon nanotubes [23]. And polydopamine has good biocompatibility, great environmental stability and excellent dispersibility in water [24]. Moreover, it has π electrons that could help absorb aromatic compounds via π–π interaction [25]. Inspired by these wonderful characteristics, we designed and synthesized the hybrid magnetic material combined graphene with polydopamine.

In this work, we synthesized magnetic graphene coated with polydopamine (mag-graphene@PDA) via a solvothermal reaction

* Corresponding authors. Tel.: +86 21 65643983; Fax: +86 21 65641740
E-mail address: chdeng@fudan.edu.cn (C. Deng).

http://dx.doi.org/10.1016/j.talanta.2014.10.014
0039-9140/© 2014 Elsevier B.V. All rights reserved.

and self-polymerization of dopamine. The prepared material has super-hydrophilicity and strong magnetic responsivity. To evaluate the extraction performance of the materials as the MSPE sorbents, six kinds of phthalates were selected as the target analytes. It is well known that phthalates (PAEs) are hazardous to human health [26–28]. And some compounds may cause hormone disrupting effects and malformation [29,30]. But PAEs have been widely used as polymer additives in industries of plastics and they can migrate into environment. So, the analysis of PAEs from environmental matrix becomes a meaningful task. Herein, the prepared composites were successfully developed as the sorbents for the enrichment and analysis of PAEs in environmental water samples.

2. Experimental

2.1. Reagents and materials

A mixture of phthalate standards containing dimethyl phthalate (DMP), diethyl phthalate (DEP), butyl benzyl phthalate (BBP), di-n-butyl phthalate (DBP), bis-2-ethylhexyl phthalate (DEHP) and di-n-octyl phthalate (DNOP) was purchased from Sigma-Aldrich Chemical Company (Shanghai, China). Graphene was acquired from J&K Chemical Corporation (Beijing, China). Dopamine hydrochloride was bought from Alfa Aesar (Tianjin, China). All other chemical and reagents were of the highest grade commercially available. Distilled water was purified by a Milli-Q system (Milford, MA, USA).

The working standard solution of PAEs was prepared by dissolving PAEs in methanol at a concentration of 100 μg/mL and was stored at 4 °C for the following usage. Pond water samples were obtained from Xiyuan in Shanghai, China, and analyzed within one day.

2.2. Preparation of mag-graphene@PDA composites

The synthetic route of the mag-graphene@PDA composites was presented in Fig. 1. And the magnetic graphene was synthesized via a solvothermal reaction in our previous work [31]. Briefly, graphene (400 mg) was dispersed into 50 mL concentration nitric acid with magnetic stirring for 8 h. Then, the dispersion was centrifuged, washed with distilled water for several times until it turned neutral and dried in vacuum at 50 °C. And in the solvothermal reaction, the magnetic graphene was fabricated according to the previous study with a little modification [32]. $FeCl_3 \cdot 6H_2O$ (200 mg) was dispersed into 40 mL ethylene glycol solution and the dried acid-treated graphene (150 mg) was added under magnetic stirring for 1 h. Then 150 mg trisodium citrate, 1.8 g sodium acetate and 1.0 g poly (ethylene glycol) (PEG-20000) were added into the solution and stirred for 0.5 h. The mixture was transferred into the airtight steel container and heated in an oven at 200 °C for 12 h. The products were collected by magnetic separation, washed with ethanol and dried in vacuum at 50 °C.

For synthesis of the mag-graphene@PDA composites, 400 mg of dopamine hydrochloride was dissolved in 400 mL of Tris buffer (10 mM). Then 100 mg of mag-graphene was added and mechanically stirred for 16 h at room temperature. The prepared mag-graphene@PDA was collected by magnetic separation and washed with ethanol for several times. The mag-graphene@PDA composites were dried in vacuum at 50 °C before use.

2.3. Instrument and analytical conditions

Fourier transform infrared spectra (FT-IR) were collected on Nicolet Fourier spectrophotometer using KBr pellets (USA). Transmission electron microscopy (TEM) images were taken on a JEOL 2011 microscope (Japan) operated at 200 kV. Sample was dispersed in ethanol and dried on a holey carbon film copper grid for analysis. Scanning electronic microscopy (SEM) images were recorded on a Philips XL30 electron microscope (Netherland) operating at 20 kV. A thin gold film was sprayed on the sample before characterization. Powder X-ray diffraction (XRD) patterns were recorded on a Bruker D4 X-ray diffractometer with Ni-filtered Cu K_α radiation (40 kV, 40 mA).

The GC–MS instrument was Thermo Focus DSQ. The extracted compounds were separated using a HP-5MS capillary column (30 m × 0.25 mm, 0.25 μm). The injection temperature was set to 250 °C and the sample was injected at a splitless mode. Helium

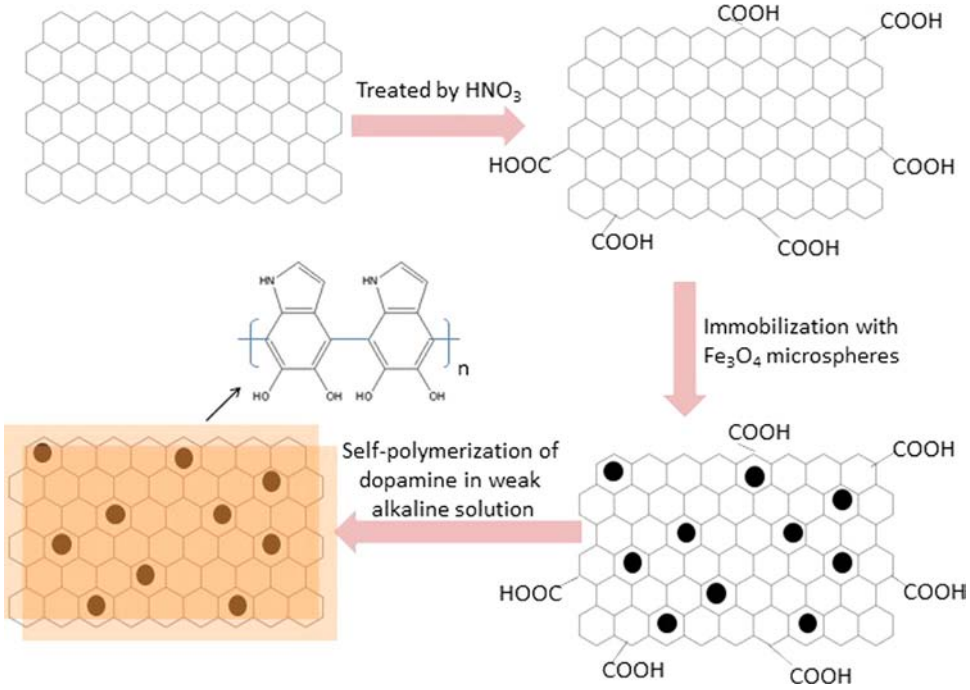


Fig. 1. Synthetic route of mag-graphene@PDA composites.

(99.999%) was used as carrier gas at a flow rate of 1.0 mL/min. The oven temperature program was held for 2 min at 100 °C, raised to 300 °C at a rate of 30 °C/min and held for 6 min. The quantitative analysis was performed in the selected ion monitoring (SIM) mode. And the ion source and transfer line temperature were both maintained at 250 °C. The ionization energy was 70 eV.

2.4. Procedure of MSPE

10 mL distilled water containing 500 μg/L phthalates standard was added in a vial with PTFE-silicone septum. And 15 mg mag-graphene@PDA composites were put into the vial to extract the analytes by vortex for 10 min. Then a magnet bar was used to isolate the materials and the sample solution was removed. 0.5 mL of dichloromethane was introduced to the vial to elute the analytes under vibration for 10 min. The magnet bar was placed beside the vial and the eluting solution was collected. 3, 4, 5-Tribromobiphenyl was selected as the internal standard (I. S.). The appropriate amount (20 μg/ml) of I.S. was added to water samples for the method validation. Finally, 1.0 μL of the obtained solution was injected into the GC–MS for analysis.

2.5. Method validation

The calibration curves were evaluated by analyzing a series of phthalates of the concentration range (50–20,000 μg/L). The limits of detection ($S/N=3$) were calculated by the analysis of the water sample with a low concentration, which ranged from 0.05–5 μg/L. And they were examined by three replicate analytes. The limits of quantification were estimated on the basis of $S/N=10$. The method precision was investigated by five replicate analytes of phthalates in water with the concentration (500 μg/L) under the optimized conditions, and was calculated with the relative standard deviations (RSD). In addition, accuracy was evaluated with the recovery rate of the target analytes. And it was investigated by preconcentrating the standard-spiked water samples (500 μg/L) with the optimized procedure, and determined by comparing real values with the calculated values.

2.6. Sample collection and analysis

In order to evaluate the extraction performance of the proposed method in real samples, pond water samples were analyzed as the environmental water samples. And pond water samples were collected from Xiyuan, Shanghai, China, which were stored at 4 °C until use. In contrast, 500 μg/L of phthalates standard was added in real water samples. The extraction procedure was performed under the optimal conditions.

3. Results and discussion

3.1. Characterization of mag-graphene@PDA composites

In this work, the mag-graphene composites were synthesized via a solvothermal reaction. Then dopamine was polymerized on the mag-graphene composites in alkaline buffer. The polymerization procedure was fast and simple.

The size and morphology of the mag-graphene@PDA composites were characterized by SEM and TEM. The SEM images (Fig. 2(a) and (b)) showed the magnetic particles were well dispersed on the surface of graphene sheets and the diameter of the Fe_3O_4 microsphere was about 200 nm. The TEM images (Figs. 2(c) and 2(d)) suggested that the polydopamine layer was successfully coated on the mag-graphene composites and the coating layer was about 70 nm. The characteristic diffraction peaks of Fe_3O_4 microspheres around 30°, 35°, 43°, 53°, 57° and 62° were obtained from the XRD pattern (Fig. 3). And the strong peak at 26° indicated the graphitic layers were observed

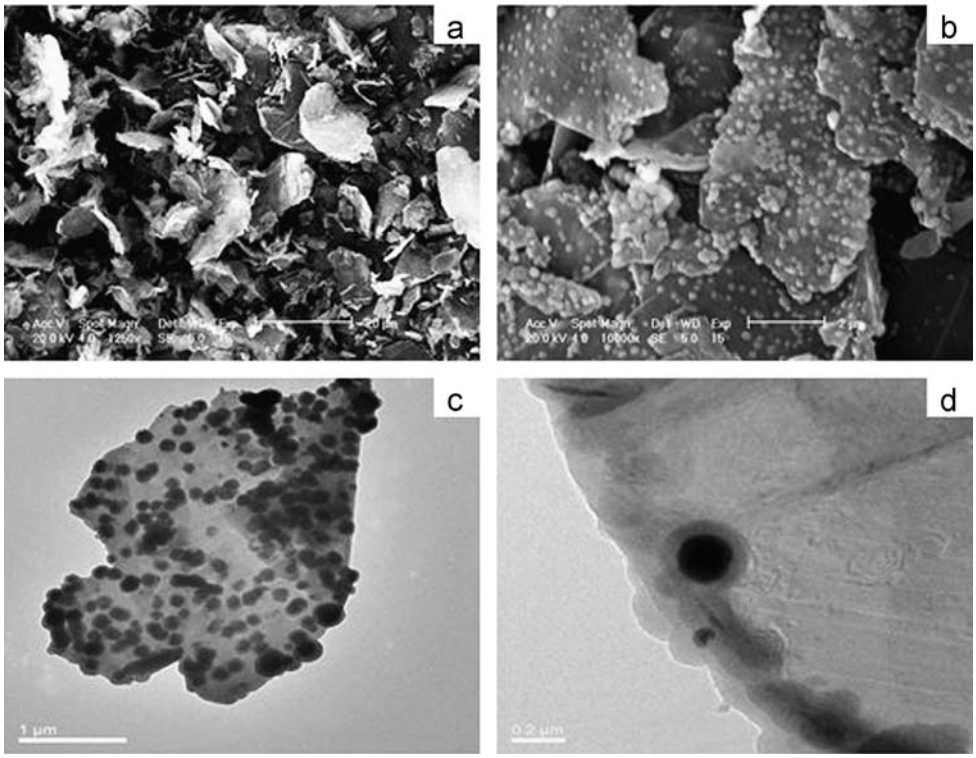


Fig. 2. SEM images (a) and (b) and TEM images (c) and (d) of mag-graphene@PDA.

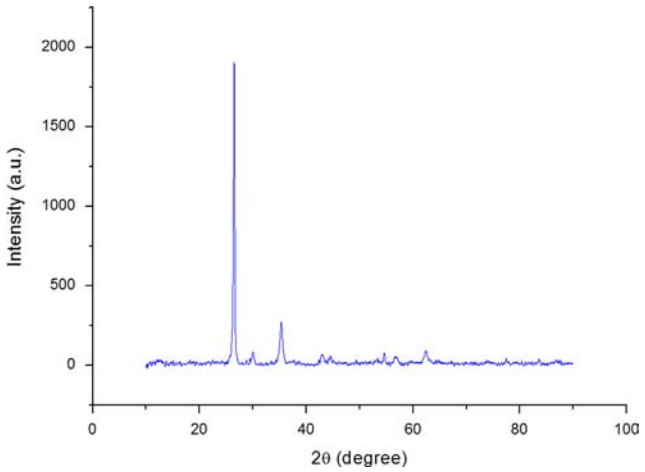


Fig. 3. XRD patterns of mag-graphene@PDA.

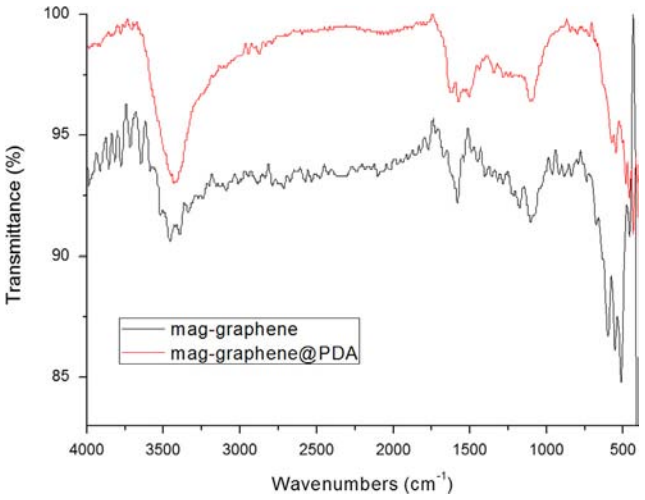


Fig. 4. The FT-IR spectra of mag-graphene and mag-graphene@PDA.

simultaneously. The result was in accordance with the previous reports [33,34].

FT-IR spectra (Fig. 4) demonstrated the successful polymerization of dopamine coated on the surface of mag-graphene. The signal at 548 cm^{-1} and 3429 cm^{-1} belonged to Fe–O–Fe stretching of Fe_3O_4 and O–H vibration of the hydroxyl groups on the surface. And the peak at 1109 cm^{-1} was assigned to C–N stretching vibration. The adsorption peak at 1616 cm^{-1} and 1344 cm^{-1} were ascribed to the C=O stretching carboxylic groups and C=C vibration of graphene framework. The adsorption band at 1574 cm^{-1} and 1508 cm^{-1} originated from the aromatic C=C vibration. All the results indicated that mag-graphene was successfully coated by polydopamine.

3.2. Optimization of the extraction process

The mag-garphene@PDA composites have benzene rings from dopamine, so it is easy to adsorb aromatic compounds via π–π interaction. Meanwhile, hydroxyl group contained on dopamine makes it shows excellent dispersibility in water, which can ensure an effective contact with the target anayltes in aqueous phase. In order to improve the extraction efficiency of this method, variety of extraction parameters were studied, including pH of the sample solution, amount of adsorbents, adsorption and desorption time, type and volume of eluting solution.

The pH value of the sample solution plays an important part for the adsorption process because it could affect the ionization form of the target analytes and the surface charge of the adsorbents. The pH values (5, 7, 9) of the sample solutions were adjusted by the addition of hydrochloric acid or sodium hydroxide solution. The results showed in Fig. 5(a) revealed that the extraction efficiency reduced obviously with the pH value of 9. And there was no clear difference between the pH value of 5 and 7. Therefore, it was not necessary to adjust the pH value before the analysis of general water samples. To ensure the maximum recovery of the analytes, the amount of sorbents was studied in the range from 0.5 mg/mL to 2.0 mg/mL. Based on the results (Fig. 5(b)), when the amount of mag-graphene@PDA reached 1.5 mg/mL, it was enough for most of the PAEs and there was no significant difference between 1.5 mg/mL and 2.0 mg/mL. Thus, 1.5 mg/mL was considered to be the optimized amount of sorbent. Next, adsorption time was an essential condition to assure the sufficient contact between the sorbents and the target analytes. Fig. 5(c) showed the influence of adsorption time in the range of 5–30 min. Due to the excellent hydrophilicity of dopamine, the sorbents could well disperse in water samples. And extend the time to 10 min, there was no significant difference. As a result, 10 min was selected as the best adsorption time.

During the desorption process, there were three parameters that should be optimized. Elution solvent was an important role for the desorption process. In this work, four different kinds of solvents were experimented, including methanol, acetone, isopropanol and dichloromethane. According to the results showed in Fig. 5(d), dichloromethane revealed the best eluting performance, while methanol, acetone and isopropanol had relative low desorption ability for the PAEs. Since the solvent of dichloromethane had a similar polarity with the target analytes and possessed the characteristic of hydrophobicity which could interact with PAEs, it was not difficult to explain the good eluting efficiency of dichloromethane. Thus, dichloromethane was used as the desorption solvent in the following work. And desorption time was also another important factor. Variety of desorption time (in range from 5–20 min) was studied in this work. As the results showed in Fig. 5(e), there was no obvious difference when the desorption time extended to 10 min. And it showed the system had reached the desorption balance after 10 min. So, 10 min was selected as the optimal condition. Another experimental parameter was the volume of desorption solvent. In order to obtain the maximum eluting performance, 0.3, 0.5 and 0.8 mL of dichloromethane were chosen in this work. Fig. 5(f) showed that when the volume was 0.5 mL, the eluting efficiency was best. Therefore, 0.5 ml of dichloromethane was chosen for further analysis.

3.3. Adsorption capacity

In order to investigate the adsorption capacity of mag-graphene@PDA, DBP was selected as a model analyte. And the adsorption capacity was evaluated with a series of standard solutions in the range of 2–14 mg/L under the optimized extraction procedure. After the preconcentration, mag-graphene@PDA was separated from the solvent, and the concentration of DBP in the elution solvent was analyzed. When the concentration of the standard solution was up to 10 mg/L, the extraction yield became stable and the adsorption capacity reached the maximum. Finally, the adsorption capacity of mag-graphene@PDA was investigated to be 4.9 mg/g.

3.4. Validation of the method

Under the optimized conditions, a series of method validation were studied, such as the limit of detection (LOD), recovery, precision and linearity. All the results were listed in Table 1. In this work, linearity of the calibration curves were obtained in a

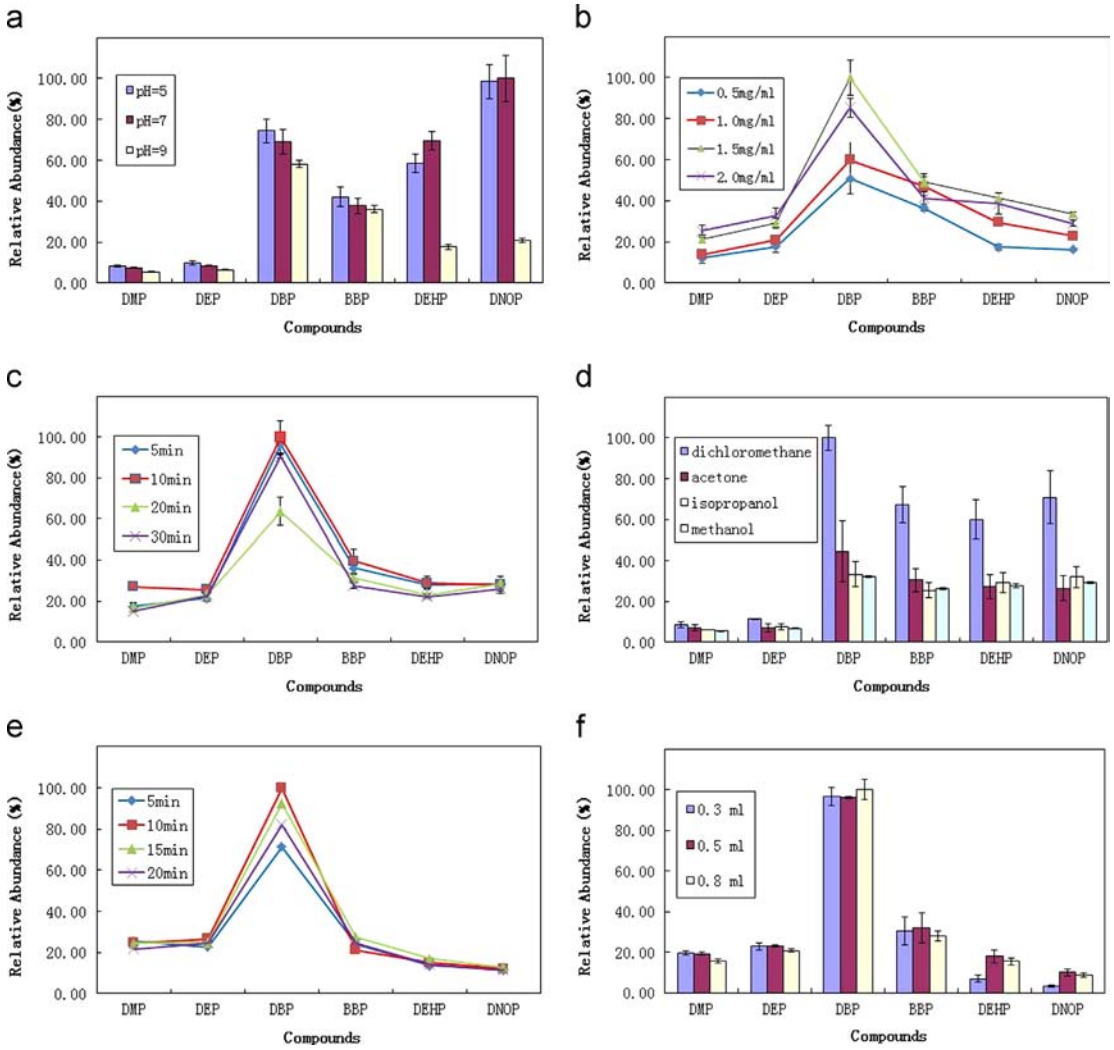


Fig. 5. Optimization of the extraction process (a) pH values (5, 7 and 9) of water samples; (b) the adsorbent amounts (0.5, 1.0, 1.5 and 2.0 mg/ml); (c) adsorption time (5, 10, 20 and 30 min); (d) species of desorption solutions (dichloromethane, acetone, isopropanol, methanol); (e) desorption time (5, 10, 15 and 20 min); and (f) volumes of desorption solutions (0.3, 0.5 and 0.8 mL) ($n=3$).

Table 1
Validation of mag-graphene@PDA based on SPE-GC–MS procedure.

Analytes	Confirmation ions (m/z)	Linear range (μg/L)	R^2	LOD (μg/L)	LOQ (μg/L)	Intra-day RSD (%)	Recovery (%)
DMP	163,194	50–20,000	0.9996	5	16.67	5.05	43.0
DEP	149,167,177	50–20,000	0.9991	5	16.67	3.80	47.3
DBP	149,223	50–20,000	0.9997	0.05	0.17	6.21	94.9
BBP	149,223	50–20,000	0.9996	5	16.67	6.87	96.5
DEHP	149,167	50–20,000	0.9998	0.5	1.67	6.88	79.6
DNOP	149,223	50–20,000	0.9995	5	16.67	8.31	84.7

wide range from 50–20,000 μg/L. And the corresponding values (R^2) were more than 0.9991. The LOD values varied from 0.05–5 μg/L on the basis of $S/N=3$. And on the basis of $S/N=10$, the LOQ values were evaluated ranging from 0.17–16.67 μg/L. Precision values of the method was investigated by the intra-day RSDs ($n=5$) and the values were less than 8.31%. The recovery of the analytes ranged from 79.6–96.5%, except the relative lower values of 43.0% for DMP and 47.3% for DEP. And it could be interpreted that the two targets had shorter ester chains, which resulted in a relatively weak hydrophobicity. As a result, it was not so favorable for the extraction from aqueous samples. But all these validation results have demonstrated that the method based on MSPE technique was reliable and the proposed method could be used to analyze environmental water samples.

3.5. Analysis of the environmental water sample

To investigate the applicability of the proposed method, mag-graphene@PDA was used to extract the target analytes in pond water samples. Under the optimized conditions, water samples were analyzed by the method in this work. Fig. 6(a) showed the GC–MS chromatogram, and the chromatogram of the PAEs spiked pond water was showed in Fig. 6(b), respectively. As a result, DMP, DBP and DEHP were detected in water samples and the concentration of DBP was 8.01 μg/L. The contents of DMP and DEHP were below LOQ, while DEP, BBP and DNOP were not observed. The extraction factor of PAEs was 20.

Compared with the previous work focused on analyzing phthalates in water samples (Table 2), the proposed method in this work had comparable LOD values and wider linear range. Benefit from the excellent magnetic responsivity of mag-graphene@PDA, the materials could be separated from the solvent in 20 s with a magnetic bar and the extraction time in this method was similar

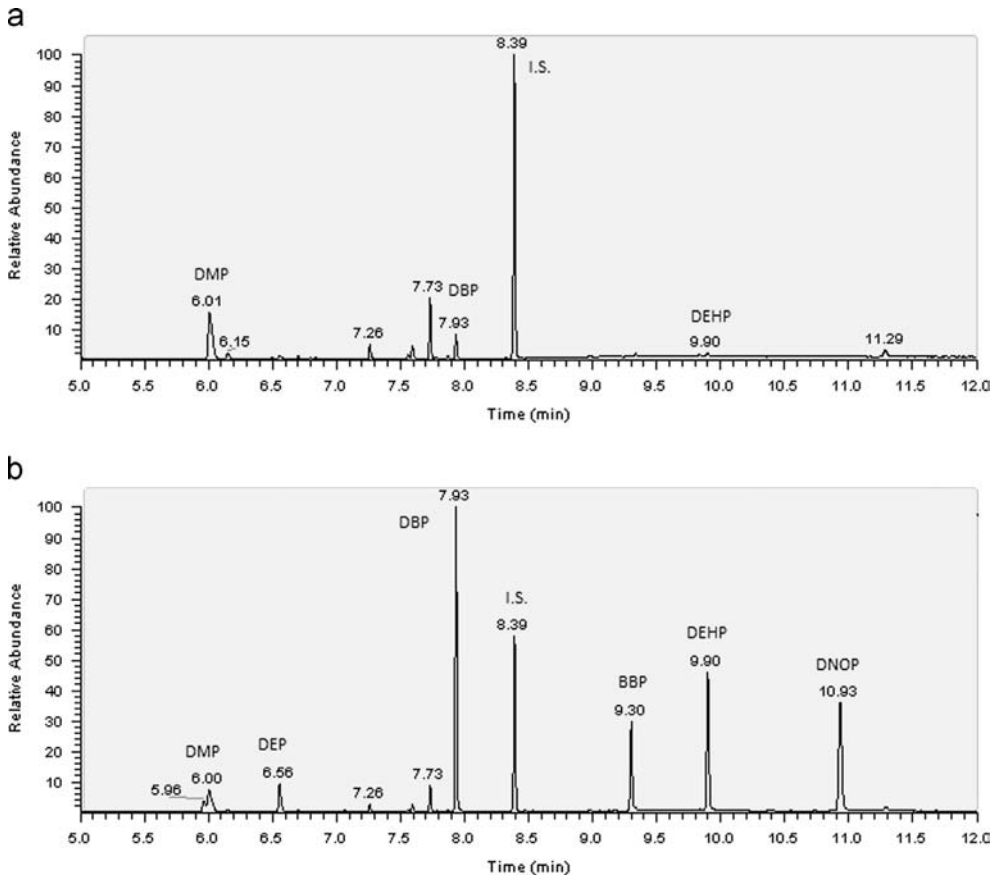


Fig. 6. The GC–MS chromatograms of (a) pond water samples and (b) 500 μg/L PAEs-spiked pond water samples by the proposed method.

Table 2
Comparison of mag-graphene@PDA-SPE with previous analytical methods for the determination of phthalates.

Methods	Matrix	Absorbent	Linear range (μg/L)	LOD (μg/L)	Adsorption time	Ref.
SPE-GC–MS	Saliva	Poly (EGDMA-MATrp)	100–2000	3–10	90	[35]
SPE-GC–MS	Serum	Water Oasis MAX SPE cartridge	2–1000	0.7–4.5	–	[36]
LPME-HPLC/UV	Landfill leachates	Carbon tetrachloride	5–50,000	1.2–2.2	40	[37]
SPE-GC–MS	Water	C18-Fe3O4@mSiO2	50–3000	25–77	10	[38]
SPE-GC–MS	Water	mag-MCNTs	50–10,000	0.08–0.47	10	[39]
SPE-GC–MS	Water	mag–graphene@polydopamine	50–20,000	0.05–5	10	This work

or even shorter than other works. All these results demonstrated that the method was applicable for analysis of PAEs in water samples.

4. Conclusions

In this work, a facile synthesis of mag-graphene@PDA composites was introduced via a simple polymerization of dopamine coating method. Due to the excellent characteristics of hydrophilicity and magnetic responsivity, the sorbents could easily disperse into aqueous samples and the whole extraction procedure required only 30 min. Meanwhile, the proposed method combined with GC–MS exhibited good linearity and high selectivity for the extraction of PAEs from water samples. Finally, the magnetic-graphene@PDA composites were successfully used as the sorbents for the enrichment of PAEs in real water samples. Based on the results, the MSPE method combined with GC–MS technique was established. And magnetic-graphene@PDA composites are recommendable as the promising sorbents for further environmental analysis.

Acknowledgments

This work was supported by the 973 Project ((2013CB911201), (2012CB910602)), the 863 Project (2012AA020202), and the National Natural Science Foundation of China (21075022), (20875017), and (21105016).

References

[1] R. Li, P. Zhang, Y.M. Huang, P. Zhang, H. Zhong, Q.W. Chen, J. Mater. Chem. 22 (2012) 22750.
[2] N. Kohler, C. Sun, A. Fichtenholtz, J. Gunn, C. Fang, M.Q. Zhang, Small 2 (2006) 785.
[3] X.L. Zhao, H.L. Zhao, H.H. Yuan, M.B. Lan, J. Biomed. Nanotechnol. 10 (2014) 262.
[4] B. Peng, J.H. Zhang, R.H. Lu, S.B. Zhang, W.F. Zhou, H.X. Gao, Analyst 138 (2013) 6834.
[5] L.G. Chen, T. Wang, J. Tong, Trends Anal. Chem. 30 (2011) 1095.
[6] L. Bai, B. Mei, Q.Z. Guo, Z.G. Shi, Y.Q. Feng, J. Chromatogr. A. 1217 (2010) 7331.
[7] Y.L. Hu, Z.L. Huang, J. Liao, G.K. Li, Anal. Chem. 85 (2013) 6885.
[8] Y.B. Luo, Q.W. Yu, B.F. Yuan, Y.Q. Feng, Talanta 90 (2012) 123.
[9] X.F. Chen, N. Ding, H. Zang, H. Yeung, R.S. Zhao, C.G. Cheng, J.H. Liu, T.-W.D. Chan, J. Chromatogr. A. 1304 (2013) 241.
[10] Z.Y. He, D.H. Liu, R.H. Li, Z.Q. Zhou, P. Wang, Anal. Chim. Acta 747 (2012) 29.

[11] H.M. Jiang, T. Yang, Y.H. Wang, H.Z. Lian, X. Hu, Talanta 116 (2013) 361.
[12] Q. Liu, J.B. Shi, G.B. Jiang, Trends Anal. Chem. 37 (2012) 1.
[13] M.J. Allen, V.C. Tung, R.B. Kaner, Chem. Rev. 110 (2010) 132.
[14] W.N. Wang, R.Y. Ma, Q.H. Wu, C. Wang, Z. Wang, Talanta 109 (2013) 133.
[15] S.L. Zeng, N. Gan, R. Weideman-Mera, Y.T. Cao, T.H. Li, W.G. Sang, Chem. Eng. J. 218 (2013) 108.
[16] X.J. Cao, J.Y. Chen, X.M. Ye, F.F. Zhang, L.X. Shen, W.M. Mo, J. Sep. Sci. 36 (2013) 3579.
[17] L. Wang, X.H. Zang, Q.Y. Chang, G.J. Zhang, C. Wang, Z. Wang, Food Anal. Methods 7 (2014) 318.
[18] H. Lee, S.M. Dellatore, W.M. Miller, P.B. Messersmith, Science 318 (2007) 426.
[19] J. Liebscher, R. Mrówczyński, H.A. Scheidt, C. Filip, N.D. Hădade, R. Turcu, A. Bende, S. Beck, Langmuir 29 (2013) 10539.
[20] Y.H. Yan, Z.F. Zheng, C.H. Deng, X.M. Zhang, P.Y. Yang, Chem. Commun. 49 (2013) 5055.
[21] Y.R. Ma, H.Y. Niu, X.L. Zhang, Y.Q. Cai, Chem. Commun. 47 (2011) 12643.
[22] L.P. Zhu, J.Z. Yu, Y.Y. Xu, Z.Y. Xi, B.K. Zhu, Colloids Surf. B 69 (2009) 152.
[23] C.Y. Shi, C.H. Deng, X.M. Zhang, P.Y. Yang, ACS Appl. Mater. Interfaces 5 (2013) 7770.
[24] Y.H. Yan, Z.F. Zheng, C.H. Deng, Y. Li, X.M. Zhang, P.Y. Yuan, Anal. Chem. 85 (2013) 8483.
[25] Y.R. Ma, X.L. Zhang, T. Zeng, D. Cao, Z. Zhou, W.H. Li, H.Y. Niu, Y.Q. Cai, ACS Appl. Mater. Interfaces 5 (2013) 1024.
[26] J.J. Rios, A. Morales, G. Márquez-Ruiz, Talanta 80 (2010) 2076.
[27] Q. Ye, L.H. Liu, Z.B. Chen, L.M. Hong, J. Chromatogr. A 1329 (2014) 24.
[28] M. Aragón, R.M. Marcé, F. Borrull, Talanta 101 (2012) 473.
[29] E. Diamanti-Kandarakis, J.P. Bourguignon, L.C. Giudice, R. Hauser, G.S. Prins, A.M. Soto, R.T. Zoeller, A.C. Gore, Endocr. Rev. 30 (2009) 293.
[30] T. Murahashi, S. Sasaki, T. Nakajima, J. Health Sci. 49 (2003) 72.
[31] C.Y. Shi, J.R. Meng, C.H. Deng, J. Mater. Chem. 22 (2012) 20778.
[32] H Deng, X.L. Li, Q Peng, X Wang, J.P. Chen, Y.D. Li, Angew. Chem. Int. Ed. 44 (2005) 2782.
[33] S.W. Li, Z.Y. Niu, X. Zhong, H.L. Yang, Y.J. Lei, F.W. Zhang, W.Q. Hu, Z.P. Dong, J. Jin, J.T. Ma, J. Hazard. Mater. 42 (2012) 229–230.
[34] M. Zhao, C.H. Deng, X.M. Zhang, ACS Appl. Mater. Interfaces 5 (2013) 13104.
[35] B. Osman, E.T. Özer, N. Besirli, S. Güçer, Polym. Test 32 (2013) 810.
[36] Z.Y. Guo, P.P. Gai, J. Duan, J.X. Zhai, S.S. Zhao, S. Wang, D.Y. Wei, Biomed. Chromatogr. 24 (2010) 1094.
[37] J.R. Yao, H. Xu, L.L. Lv, D.D. Song, Y.F. Cui, T.Z. Zhang, Y.Q. Feng, Anal. Chim. Acta. 616 (2008) 42.
[38] Z.B. Li, D.N. Huang, C.F. Fu, B.W. Wei, W.J. Yu, C.H. Deng, X.M. Zhang, J. Chromatogr. A 1218 (2011) 6232.
[39] S.L Fu, L. Ding, S.H. Zhu, Y.N. Jiao, Q. Gong, J.T. Chen, X.H. Wu, L.B. Wang, Chin. J. Chromatogr. 29 (2011) 737.

Talanta 132 (2015) 760–768

Contents lists available at ScienceDirect

Talanta

journal homepage: www.elsevier.com/locate/talanta

In-situ spectroelectrochemical characterization of the electrochemical growth and breakdown of a lead dodecanoate coating on a lead substrate

Michel De Keersmaecker [a], Mark Dowsett [b], Rosie Grayburn [a,b], Dipanjan Banerjee [c], Annemie Adriaens [a,*]

[a] Department of Analytical Chemistry, Ghent University, Krijgslaan 281-S12, 9000 Ghent, Belgium
[b] Department of Physics, University of Warwick, Coventry CV4 7AL, UK
[c] DUBBLE@ESRF (BM26), BP 220, 38043 Grenoble, France

ARTICLE INFO

Article history:
Received 23 June 2014
Received in revised form
6 October 2014
Accepted 12 October 2014
Available online 28 October 2014

Keywords:
SR-XRD
Lead
Voltammetry
Lead dodecanoate coating
Acetic acid
Spectroelectrochemistry

ABSTRACT

This paper concerns a time lapse spectroelectrochemical study of the growth of lead dodecanoate layers on a lead substrate in an aqueous solution using cyclic voltammetry. In-situ synchrotron radiation X-ray diffraction measurements were carried out on station BM26A (DUBBLE) at the European Synchrotron Radiation Facility (ESRF) in France. The diffraction pattern images were taken using a two-dimensional Mar CCD camera. After deposition of the coating, a spectroelectrochemical study of a linear sweep voltammetry experiment using an acetic acid electrolyte, simulating 'active' lead corrosion, was carried out on both a bare and lead dodecanoate coated sample. The results show that the coating inhibits the formation of new lead corrosion products.

© 2014 Elsevier B.V. All rights reserved.

1. Introduction

Many ancient lead based artifacts suffer severe corrosion in wooden (such as oak) display cases which are used for storage or exhibition purposes in museums worldwide [1]. The increase of relative humidity and temperature create an acidic microclimate in the wooden cases. The production of these organic acids is a consequence of hydrolysis of acetyl groups of hemicellulose in the wood [2]. Other sources for the formation of organic acids are the presence of plastics, glues, human bodies, varnishes, formaldehyde, etc. [3–5]. Corrosion studies, conducted in Europe, have demonstrated that the emission of formic and acetic acid are the primary responsible compounds for the irreversible damage of the artifacts [6–9].

Potential countermeasures against the corrosion of these historical lead, lead-tin and other lead alloy artifacts are commonly based on two strategies: either the change of the nearby environment and/or the development and application of a protective coating [10]. In this paper, we focus on the latter approach. A successful coating should have following characteristics: stable, reversible, cheap and aesthetically justified [11].

An interesting candidate for a protective coating on lead has been found in the deposition of saturated linear monocarboxylates of the type $CH_3(CH_2)_{n-2}COONa$ ($n=7$–11), hereafter called NaC_n. Initial studies by Rocca et al. [12–14] show that the immersion of lead and copper metal objects in NaC_n results in their protection due to the growth of a layer consisting of a crystalline metal monocarboxylate complex $(CH_3(CH_2)_{n-2}COO)_2M$, hereafter called $M(C_n)_2$. When a clean lead surface is immersed in a sodium carboxylate solution, a layer of the corresponding lead carboxylate is formed. A higher chain length of the saturated carbon chain of the monocarboxylate commonly provides a higher inhibition and protection efficiency [15,16]. The formed layers are hydrophobic, and practically invisible for thicknesses on the micron scale [17]. These coatings may provide long-term protection through the exclusion of water and/or air and therefore become a suitable candidate for the protection of the extensive amounts of lead in museum objects, pipe organs, and other heritage-related artifacts.

In this work, we perform an in-situ spectroelectrochemical study of the deposition process of a lead dodecanoate coating using cyclic voltammetry. The spectroelectrochemical insight allows us to study the growth of the lead dodecanoate layer as a function of time. Furthermore, we try to look at the influence of

Abbreviations: SR-XRD, Synchrotron Radiation X-ray Diffraction; ESRF, European Synchrotron Radiation Facility; ICDD, International Centre for Diffraction Data

* Corresponding author. Fax: +32 9 264 4960.
E-mail address: annemie.adriaens@ugent.be (A. Adriaens).

http://dx.doi.org/10.1016/j.talanta.2014.10.035
0039-9140/© 2014 Elsevier B.V. All rights reserved.

the cyclic voltammetry procedure on the growth of the coating. Using the Beer–Lambert law, hypothetical calculations are added to predict the thickness of the coating layer as a function of time. After the electrochemical growth, the air-dried coating has been tested in-situ for its corrosion inhibitive properties using a standard corrosion testing procedure in an aqueous acetic acid solution. The in-situ XRD data gives us information about the inhibition time, the corrosion products and the decomposition of the coating.

2. Experimental section

2.1. Materials

A 0.05 mol L^{-1} inhibitor solution was prepared by dissolving 1.252 g of dodecanoic acid (98%, Sigma-Aldrich, USA) in 250 mL deionized water and by subsequently neutralizing the obtained suspension with a standardized 0.25 mol L^{-1} NaOH solution. The addition of NaOH helps the dissolution of the dodecanoic acid, HC_{12}, which is only slightly soluble in water. NaOH is added up to reach a pH value of approximately 9 (just before the equivalence point) [25]. The initially turbid solution was heated to 25–30 °C and stirred during 1 h to neutralize all the acid and to obtain a clear and transparent sodium dodecanoate, NaC_{12}, solution.

Experiments were carried out on coupons made from 99.99% pure lead (Goodfellow, Cambridge, Ltd., UK). The coupons were pressed from a lead metal sheet and their edges machined so as to seal into the holder in the exposure cell (Fig. 1). These are 2 mm thick, and 12.6 mm in diameter (A_s = 1.2469 cm^2). All coupons were pre-treated by mechanical polishing. They were first roughly ground on a wetted silicon carbide paper of grit P600, subsequently grit P1200. Thereafter, the surface was fine-polished during 15 min using a polishing cloth (12″ micro cloth PSA 10/PK, Buehler, USA) with diamond polish dissolved in oil with a particle size of 6 μm and subsequently 1 μm (MetaDi Diamond Suspension, Buehler). To remove as much diamond as possible from the polished lead surface, the coupon was rinsed with isopropanol (99.5%, reagent grade) and cleaned in an ultrasonic bath for 30 s. Some of the polishing particles will, however, always remain stuck into the lead matrix because of its soft nature. The last step of the procedure consisted of polishing the cleaned coupons by pressing them firmly on a bare micro cloth. At the end, a shiny blue–white surface was obtained.

2.2. Deposition and corrosion testing procedure

The growth of the lead dodecanoate coating was carried out by immersing the lead coupons in the NaC_{12} solution described above, and performing 10 consecutive cyclic voltammetric scans between −1.3 and 1.5 V vs. SCE at a scan rate of 20 mV s^{-1} [16]. After the deposition and upon drying the coupons to air, the lead dodecanoate coated samples were corroded using linear sweep voltammetry (LSV) in a 5 μg L^{-1} acetic acid solution with a potential range from −1 V to 1.5 V and a scan rate of 1 mV s^{-1} ('corrosion test' procedure). The electrochemical measurements were done using a PalmSens handheld potenstiostat/galvanostat controlled by the PalmSensPC software package (PalmSens, The Netherlands).

2.3. Synchrotron measurements

Both the growth of the coating as well as its corrosion inhibition was studied using in-situ synchrotron radiation X-ray diffraction measurements (SR-XRD). All experiments were performed at DUBBLE (station BM26A) at the ESRF in France [18]. An X-ray beam with a wavelength of 1.5498 Å (8 keV) and with dimensions of 1 mm × 200 μm was used to bombard the sample surface. A Mar CCD 165 detector (Mar USA Inc., Evanston, IL, USA), consisting of 2048 × 2048 individual elements with a pixel size of 79 μm, was used to record the two-dimensional diffraction patterns of the deposited layers. X-rays were incident at 10°. The axis of the CCD camera was at 40.5° to the incident beam, and the face was 130 mm from the intersection between the beam axis and the surface. A fast shutter was used to shield the sample from X-ray damage between exposures.

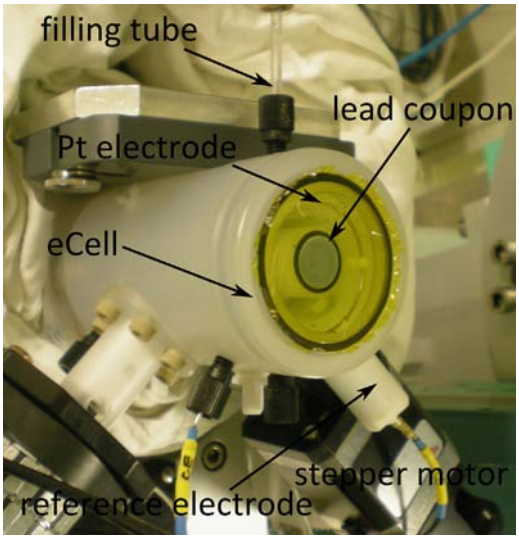


Fig. 1. The set-up on the DUBBLE beamline for time-lapse SR-XRD – the eCell Mk IV is shown here with a Kapton window. The lead coupon is fitted into a dedicated holder to be placed in the middle of the eCell (is used as a working electrode).

For the experiments the eCell Mk IV (see Fig. 1) was used, of which the prototype has been published by Dowsett and Adriaens [19]. The eCell is an electrochemical/environmental cell consisting of a 40 mL polychlorotrifluoroethylene (PCTFE) cup, with inner and outer diameters of 30 and 44 mm, respectively, configured to take electrodes or coupons with a diameter of 12.6 mm in a holder from which they can easily be demounted. The cell is used for a particular (electro)chemical treatment (in this case the electrochemical treatment of the lead sample in the NaC_{12} solution), while at the same time the metal surface is analyzed through a thin electrolyte layer using the XRD spectroscopic technique. The piston is driven by a variable-speed motor (type BLDC 58, McLennan Servo Supplies, Ltd., UK), using remote control from outside the X-ray hutch. A sequence of surface powder diffraction images was recorded through a 6 μm Kapton window and approximately 100 μm of the electrolyte solution. In Fig. 1, the Ag/AgCl reference and counter electrode are indicated. During the growth sequence (ca.1 h), the sample was automatically moved between the analysis position (close to the window) and deeper (1 cm down) in the solution by the eCell control system. Data collection was synchronized with this movement: actual collection time was 5 s per image, time in between images was 35 s. For the corrosion test experiment a collection time of 10 s per image and the time between the images was 50 s.

2.4. Spectral processing

All diffraction patterns were processed using the esaProject 2012 software [20–21]. It is analytical software, which handles both two dimensional XRD powder diffractograms from devices such as the Mar CCD 165, as well as a huge range of spectra, all in native format, and provides an acquisition to publishing capability for XRD, X-ray absorption spectroscopy (XAS), X-ray emitted optical luminescence (XEOL), and other spectroscopic data with a rapidly developing image

stack and spectrum data mining capability. For the growth of the lead dodecanoate layer and the corrosion test experiment a sequence of around 100 Mar CCD images was taken. The images were batch processed using esaProject through the reprojection algorithm. The one-dimensional diffraction patterns from DUBBLE are simply integrated out of the reprojected image, by summing image rows.

The peaks present in the diffraction pattern are a consequence of constructive interference following Bragg's law [22]:

$$n\lambda = 2d \sin\theta \quad (1)$$

where n is an integer, d is the interplanar distance, λ is the wavelength of the incident wave and θ is the angle between the incident ray and the scattering planes.

For the ease of comparison, the abscissae of all diffraction patterns are given as intensity vs. wave number q [23]:

$$q = \frac{2\pi}{d} = \frac{4\pi \sin\theta}{\lambda} \quad (2)$$

This formula ensures that the peaks are compared on a common scale. The growth process images were made by assembling a plot of all the extracted one-dimensional spectra as a function of time [24]. The colors in the pattern set image represent the intensities of the corresponding 2θ angle.

3. Results and discussion

3.1. Growth of a coating on lead using cyclic voltammetry with a scan rate of 20 mV s^{-1}

The lead coupons are immersed in a NaC_{12} solution (see Section 2.1). Afterwards, 10 consecutive cyclic voltammetric scans are carried out in-situ between −1.3 and 1.5 V vs. SCE at a scan rate of 20 mV s^{-1} to produce the coating. During the electrochemical treatment, XRD spectra are taken.

Fig. 2A shows a reprojected Mar diffractogram from a lead dodecanoate coated coupon acquired on DUBBLE. The acquisition time was 10 s. The two bottom rings in the images refer to $q = 1.5514$ Å^{-1} and 1.7262 Å^{-1} from the lead dodecanoate coating (pattern reference number 00-009-0712 for lead dodecanoate in the ICDD database). The coarse polycrystallinity of the lead substrate is demonstrated by the streaky nature of the lead rings. On the other hand, the evenly spaced rings which represent the lead dodecanoate are smooth and homogeneous. This tells us that the coating is formed from small and random poly crystals [21]. The lead dodecanoate rings demonstrate the c-axis alignment of the coating from the localization of the intensity to the center of the image. By integrating the different image rows as a function of the diffraction angle θ, a one-dimensional pattern is constructed as shown in Fig. 2B. The 1D diffraction pattern shows us clearly the diffraction peaks of the formed lead dodecanoate coating between 1.5 Å^{-1} and 2.0 Å^{-1}. The (111) and (200) lead diffraction peaks, however, form an intense narrow peak at higher q-space values around 2.1907 Å^{-1} and 2.5305 Å^{-1} (pattern reference number 03-065-2873 in the PDF-2 ICDD database (2012)). Due to atmospheric corrosion and electrochemical oxidation of the lead substrate, lead(II)oxide is detected. At 2.0435 Å^{-1}, a small (101) lead (II)oxide diffraction peak is detected (pattern reference number 03-065-1471 in the PDF-2 ICDD database (2012)). This is in agreement with previous findings in our research group [25–26]. The presence of small concentrations of OH^--ions in the aqueous solution ensures the formation of PbO (litharge) [27,28]:

$$Pb\,(s) + 2\,OH^-(aq) \rightleftharpoons PbO(s) + H_2O + 2\,e^- \quad E_0 = -0.002V \text{ vs. SCE} \quad (3)$$

In addition to the formation of lead(II)oxide, due the high oxidation potentials, lead(IV)oxide (PbO_2, plattnerite) is produced. The (110), (101) and (200) plattnerite diffraction peaks at 1.7952 Å^{-1}, 2.2234 Å^{-1} and 2.5398 Å^{-1} are clearly detected (pattern reference number 00-025-0447 in the PDF-2 ICDD database (2012)). The first oxidative scan to 1.5 V provides together with the presence of OH^--ions an ideal environment for the production of

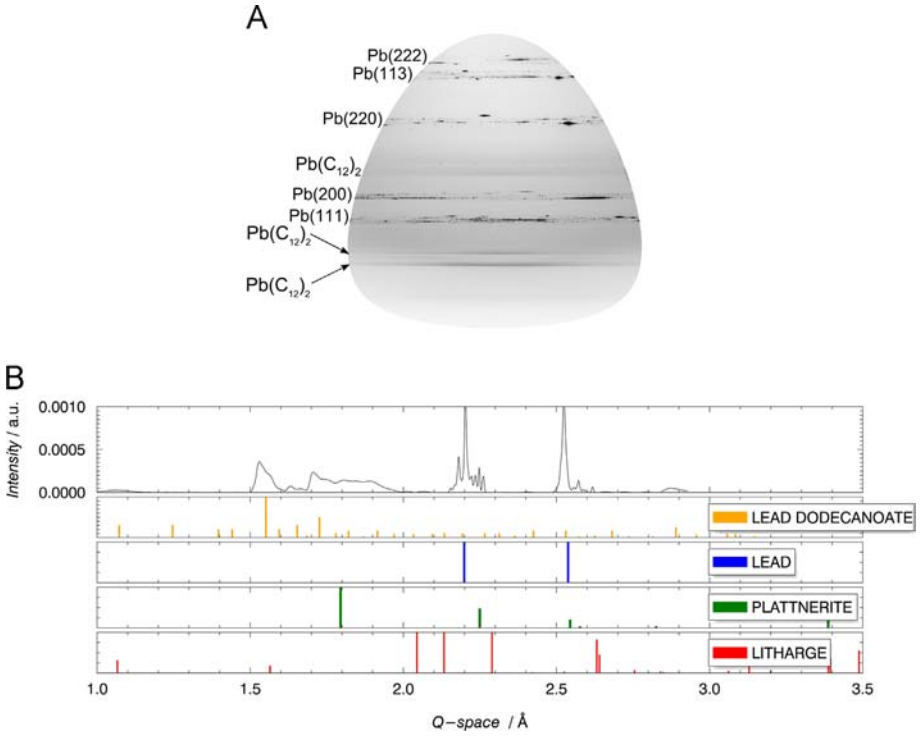


Fig. 2. (A) Reprojected image of a Mar SR-XRD diffraction pattern from a lead dodecanoate coated lead coupon acquired on the DUBBLE beamline at the ESRF. The acquisition time was 10 s. (B) The XRD pattern of the lead dodecanoate coated lead sample calculated using integration.

PbO_2 [28,29]:

$$PbO(s)+2\,OH^-(aq)\rightleftharpoons PbO_2(s)+H_2O+2\,e^-$$
$$E_0=+0.86\ \text{V vs. SCE} \quad (4)$$

Fig. 3 shows the first voltammetric scan of the deposition of the lead dodecanoate coating with a scan rate of 20 mV s^{-1} using the eCell system. This voltammetric scan explains the formation of all the products mentioned in Fig. 2B. The anodic peak (A_1) is characteristic for a passivation process, because the current drops to a low value corresponding to the passive state. This process can be explained using two consecutive steps. At the start, lead dissolves and forms a soluble lead salt with dodecanoate as anion explained by a series of adsorption reactions [16]:

$$Pb+C^-_{12(ads)}\rightleftharpoons PbC_{12(ads)}+e^- \quad (5)$$

$$PbC_{12(ads)}+C^-_{12}\rightleftharpoons Pb(C_{12})_{2(ads)}+e^- \quad (6)$$

$$Pb(C_{12})_{2(ads)}\rightleftharpoons Pb(C_{12})_{2(aq)} \quad (7)$$

After that, there is a precipitation of a crystalline salt film Pb $(C_{12})_2$ (s) on the electrode surface when the solubility product of the salt is exceeded. The formation is described by the dissolution-precipitation mechanism [16]. After precipitation the film, as a consequence of crystallization, stays on top of the surface without dissolving during the cathodic process. After the third scan, only lead dodecanoate compounds present in the solution are reduced and oxidized. This oxidation process ensures the lead dodecanoate coating is formed rapidly. Above 0.5 V, the current forms a peak (A_2) which represents the production of lead(IV) oxides. This initially formed oxidative layer is then partly reduced in two steps (R_2 and R_1) to form lead metal. Table 1 shows the calculation of the potential of the peaks measured in the cylic voltammogram based on the Pourbaix diagram of lead-water and the solubility product of lead dodecanoate.

Fig. 4 shows the pattern set image of all diffraction patterns recorded during the progressive growth process of the lead dodecanoate coating on a bare lead coupon using cyclic voltammetry with a scan rate of 20 mV s^{-1} in a 0.05 mol L^{-1} aqueous NaC_{12} solution as a function of time. The total length of the experiment is 46 min. In addition, the relevant diffraction lines are indicated, obtained from the reference spectra present in the ICCD database. All diffraction peaks of the lead dodecanoate coating clearly increase during the cyclic voltammetric measurement up to a maximum intensity due to complete coverage of the lead substrate surface. The reduction of the surface during the reverse scan in the cyclic voltammetric procedure stimulates the formation of metallic lead, which allows the intensity of the lead diffraction peaks to range around a stable value. All the q-values of the lead diffraction peaks seem to be shifted to a more positive value (+ 0.077 $Å^{-1}$). A possible explanation is the strain in the upper lead crystal structure due to the fast oxidation processes. The diffraction peaks of the lead(IV)oxide show an increase after the start of the time lapse measurement, but stabilize very quickly to a maximum value.

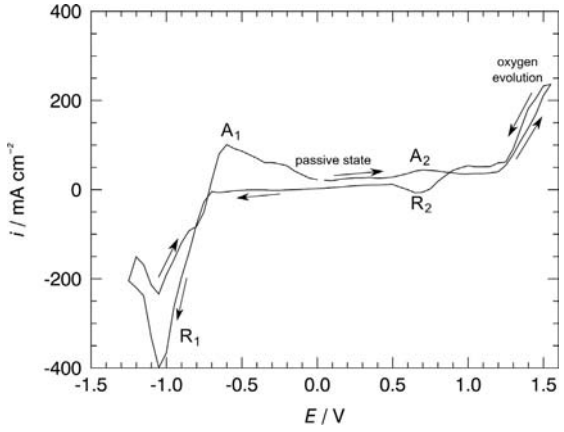


Fig. 3. The first voltammetric scan of the cyclic voltammetric deposition of the lead dodecanoate coating with a scan rate of 20 mV s^{-1}.

Fig. 5 shows the peak areas extracted from the diffraction patterns of the change in surface composition in real time using 10 consecutive cyclic voltammetric scans with a potential range from −1.3 V to 1.5 V and a scan rate of 20 mV s^{-1}. Fig. 5A shows the peak area of the lead dodecanoate peaks at 1.5514 $Å^{-1}$, 1.7262 $Å^{-1}$ and 2.8902 $Å^{-1}$ extracted from a stack of recorded two-dimensional SR-XRD patterns. The observed growth in peak area of all three curves is due to the progressive formation of the lead dodecanoate coating during the different voltammetric scans. The experimental graphs for all peak areas calculated at three different q-space values are fitted to an exponential growth curve based on the following equation:

$$I=I_m\left(1-e^{-\frac{t}{\tau}}\right) \quad (8)$$

with τ is the time constant and I_m is the intensity for $t\rightarrow\infty$.

The fitted values are presented in Table 2. The fitted time constant τ, in seconds, gives some idea as to the relative speed of the lead dodecanoate coating growth. The low time constant given by the exponential fit of the peak area of the diffraction peak at 1.5514 $Å^{-1}$, indicates a fast growth of this peak due the growth of the lead dodecanoate layer. After 10 consecutive cycles, a steady state value is measured, because of the saturation of all binding sites on the lead substrate.

Fig. 5B shows the small change of the (101) peak area of lead(II) oxide over time. The lead(II)oxide growth results from the direct contact of the lead surface with the NaC_{12} solution. For the fitting of the lead(II)oxide signal, however, the fact of a native oxide layer due to atmospheric corrosion should be taken into account using the following equation:

$$I=I_0+I_m(1-e^{-\frac{t}{\tau}}) \quad (9)$$

with I_0 the peak area of the diffraction peak at the start of the exponential growth.

The diffraction peak of lead(II)oxide keeps growing very slowly, which is due to the oxidative treatment and the presence of OH^--ions in the NaC_{12} inhibitor solution (Eq. 3). In Fig. 5B, the peak area of the diffraction peak of lead(II)oxide seems to change continuously, which

Table 1
Thermodynamic analysis of the cylic voltammogram based on the Pourbaix diagram of lead-water and the solubility product of lead dodecanoate.

Peak	Reaction	*E* calculation
A_1	$Pb(s)+2\,OH^-\rightleftharpoons PbO(s)+H_2O+2\,e^-$	$E_{A_1}=E_{0,A_1}-0.059\ \text{pH}$ $=-0.533\ \text{V vs SCE}$
R_1	$Pb(C_{12})_2(s)+2\,e^-\rightleftharpoons Pb(s)+2\,C^-_{12}(aq)$	$E_{R_1}=E_{0,A_1}-0.059\ \text{pH}+0.0295\log\frac{K_{sp}}{[C^-_{12}]^2}=-0.929\ \text{V vs SCE}$ $K_{sp}[Pb(C_{10})_2]=8.91.10^{-17}$ [30]
A_2 en R_2	$Pb^{2+}(s)+4\,OH^-(aq)\rightleftharpoons PbO_2(s)+2\,H_2O+2\,e^-$	$E_{A_2}=E_{R_2}=E_{0,A_2}-0.059\ \text{pH}-0.0295\log\frac{K_{sp}}{[C^-_{12}]^2}$ $=0.722\ \text{V vs SCE}$

Table 2
List of the values of the exponential fit of the growth process of the lead dodecanoate coating using cyclic voltammetry with a scan rate of 20 mV s^{-1}.

	$Q(Å^{-1})$	I_m(a.u.)	τ(s)	I_0(a.u.)
$Pb(CH_3(CH_2)_{10}COO)_2$	1.5514	$3.13 \times 10^{-5} \pm 0.5\%$	$630 \pm 2.5\%$	–
	1.7262	$6.9 \times 10^{-6} \pm 6\%$	$1700 \pm 15\%$	–
	2.8902	$2.83 \times 10^{-6} \pm 0.9\%$	$1110 \pm 2.9\%$	–
PbO	2.0435	$2.6 \times 10^{-7} \pm 13.9\%$	$1800 \pm 45\%$	$2.5 \times 10^{-7} \pm 4.9\%$
PbO_2	1.7926	$2.0 \times 10^{-6} \pm 12.9\%$	$390 \pm 21.7\%$	$8.9 \times 10^{-8} \pm 10.5\%$
	2.5398	$8.2 \times 10^{-6} \pm 2.0\%$	$780 \pm 4.7\%$	$9.5 \times 10^{-6} \pm 2.0\%$
Pb	2.2681	$1.93 \times 10^{-5} \pm 3.1\%$	$570 \pm 9.2\%$	$2.69 \times 10^{-5} \pm 1.0\%$
	2.6079	$8.7 \times 10^{-6} \pm 3.8\%$	$220 \pm 7.4\%$	$1.90 \times 10^{-6} \pm 2.8\%$

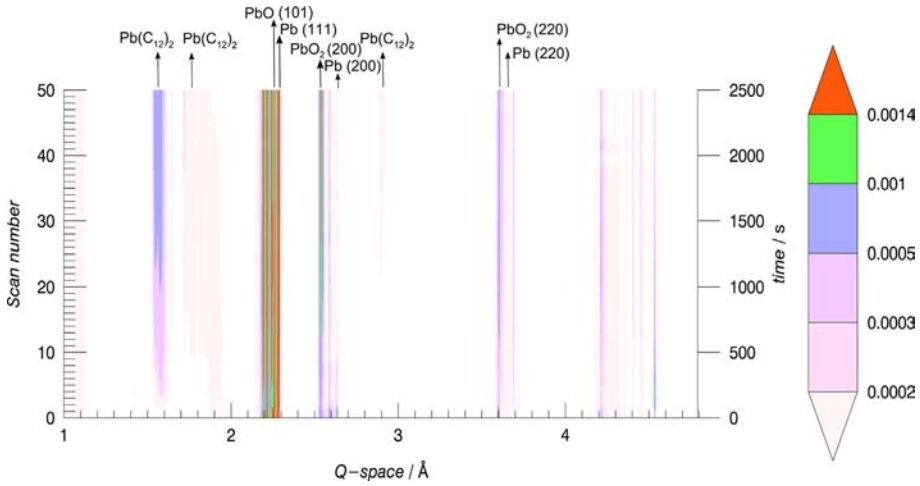


Fig. 4. A pattern set image of all diffraction patterns recorded during the growth process of the lead dodecanoate coating on a bare lead coupon using cyclic voltammetry with a scan rate of 20 mV s^{-1} in a 0.05 M aqueous sodium dodecanoate solution (as a function of time).

can be explained by the quick change of oxidation and reduction processes (due to the CV procedure) taking place at the lead surface.

Fig. 5C shows the area of the (110) and (200) plattnerite diffraction peaks at 1.7926 $Å^{-1}$ and 2.5398 $Å^{-1}$. The lead(IV)oxide growth results from the direct contact with OH^--ions in the inhibitor solution and the presence of a lead(II)oxide corrosion layer (Eq. 4). The most sensitive diffraction peak at 2.5398 $Å^{-1}$ shows small fluctuations in the calculated peak area, which are related to the alternating oxidation and reduction process due to the cyclic voltammetric deposition procedure (see second *x*-axis representing the number of CV cycles). At the start, lead(IV)oxide grows very fast due to the high vertex potential (1.5 V). The peak area reaches a maximum due to saturation of the surface.

Fig. 5D shows the peak area of the (111) and (200) lead peaks at 2.2681 $Å^{-1}$ and 2.6079 $Å^{-1}$ (taking into account the 0.077 shift of the peaks) extracted from the consecutive diffraction patterns. The observed decrease in peak area is due to surface coverage by the lead dodecanoate coating or by some corrosion products, which reduces the interaction of X-rays with the lead bulk metal. The formation of this coating layer reduces the peak area of the lead diffraction peaks. This information proves that a layer is continuously covering the lead surface of the substrate. The intensity of the lead characteristic peaks drops rapidly at the starting point and stagnates after the first two scans, which demonstrates the formation of a lead dodecanoate coating layer during the first voltammetric scan. An explanation of the changing of the peak shapes could be the reorientation of the lead crystals. The exponential fit of the lead peak is given by:

$$I = I_0 + I_m e^{-\frac{t}{\tau}} \tag{10}$$

The small oscillations in the calculated peak area of the peak at 2.2681 $Å^{-1}$ are related to the alternating oxidative and reductive process due to the cyclic voltammetric deposition procedure. All above-mentioned products have been identified using XPS, as reported in a previous communication of our group [31]. Furthermore, a hypothetical scheme is drafted for the lead dodecanoate growth on a lead sample (see Fig. S1).

Using the decay of the peak area of the most intense (111) lead peak, we can calculate the lead dodecanoate coating thickness. Consider we have a coating of thickness d on the surface of the lead substrate, the incoming X-ray beam will be attenuated on its way through the surface, and then the fraction scattered into the peak will be attenuated some more on the way out. The total attenuation of the lead peak will therefore depend on the total path length on the coating as a function of time following the Beer–Lambert law [32]:

$$\ln\left(\frac{A_k(t)}{A_0}\right) = -\left(\frac{\mu}{\rho}\right) d(t) \tag{11}$$

where A_k (t) is the peak area of the lead (111) peak at immersion time k (time dependent), A_0 is the peak area of the lead peak for no attenuation, d (t) is the mean mass thickness (mass per unit area or g cm^{-2}) of the lead dodecanoate layer and (μ/ρ) is the mean mass attenuation coefficient for the lead dodecanoate layer at 8 keV ($=122.3$ cm^2 g^{-1} (see NIST database)) [33]. This quantification gives us information on the thickness of the lead dodecanoate layer by simply dividing the mass thickness results by the density of lead acetate (comparable for lead dodecanoate), 3.25 g cm^{-3}.

This total path length is written as a function of the thickness of the coating. If we consider a X-ray beam incident at θ_i to the

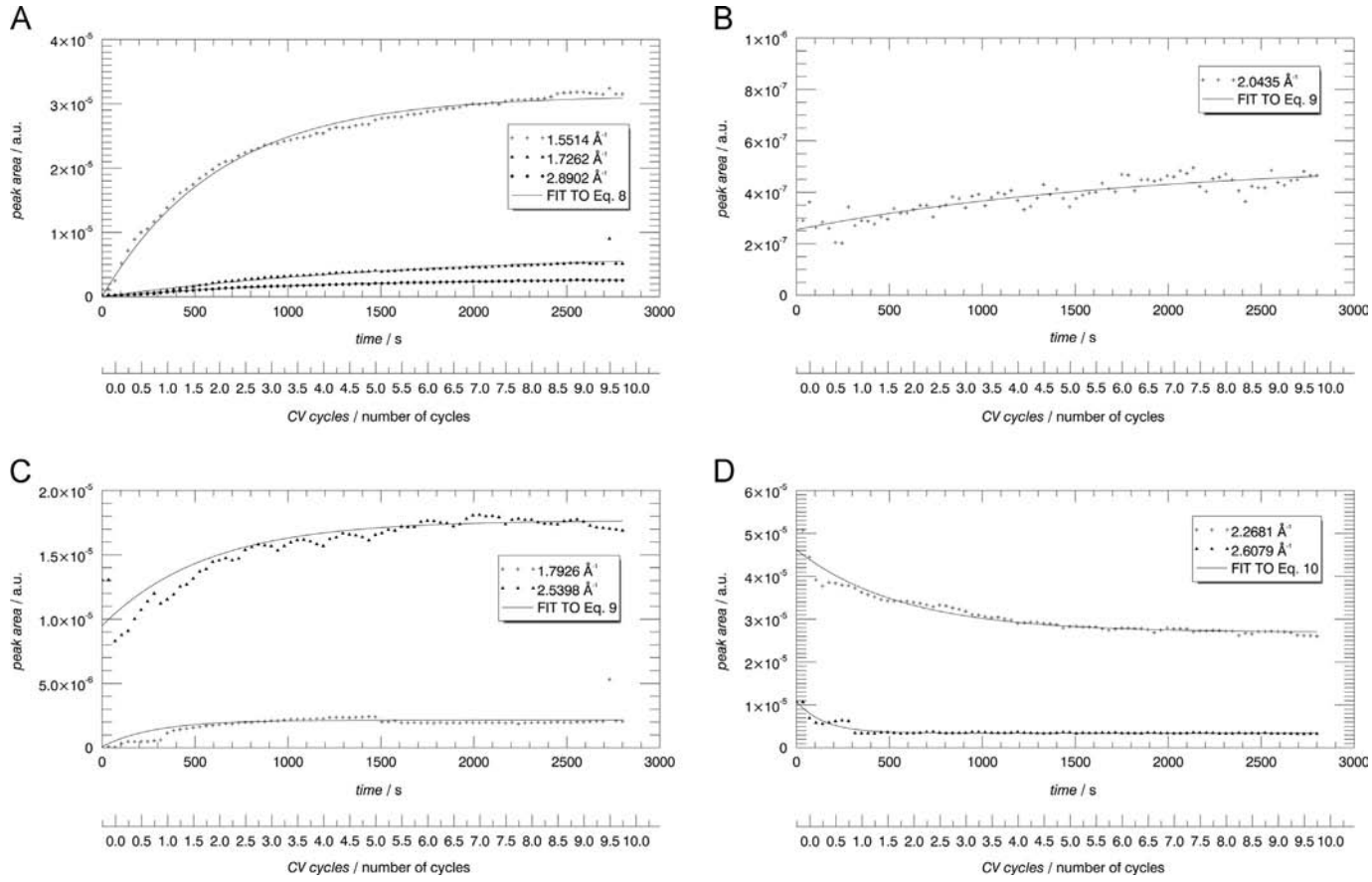


Fig. 5. The peak areas extracted from the diffraction patterns of the growth of the lead dodecanoate coating in real time using 10 consecutive cyclic voltammetric scans with a range from −1.3 V to 1.5 V and a scan rate of 20 mV s^{-1}. The peak areas were extracted from (A) lead dodecanoate at 1.5514 $Å^{-1}$, 1.7262 $Å^{-1}$ and 2.8902 $Å^{-1}$, (B) litharge at 2.0435 $Å^{-1}$, (C) plattnerite at 1.7926 $Å^{-1}$ and 2.5398 $Å^{-1}$ and (D) lead at 2.2681 $Å^{-1}$ and 2.6079 $Å^{-1}$ (taking into account the 0.077 shift of the peaks).

surface and scattered at $2\theta_s$ into the diffraction peak, the length of the inward path will be $d/\sin(\theta_i)$and the length of the outgoing path $d/\sin(2\theta_s-\theta_i)$. The total path length t will therefore be [32]:

$$t = d\left[\frac{1}{\sin(\theta_i)}+\frac{1}{\sin(2\theta_s-\theta_i)}\right] \quad (12)$$

To calculate the thickness d from the total path length, the equation is rewritten as follows:

$$d = t\left[\frac{\sin(\theta_i)\sin(2\theta_s-\theta_i)}{\sin(\theta_i)+\sin(2\theta_s-\theta_i)}\right] \quad (13)$$

where θ_i is the incident angle ($=10^\circ$) and $2\theta_s$ is the two-theta angle for the Pb(111) peak.

Fig. 6 shows the calculated thickness of the lead dodecanoate coating as a function of immersion time. The error lines are based on the fitting error on the measured peak areas of the lead (111) peak. After 1 h, the thickness of the lead dodecanoate layer is around 1.5 μm. The fast deposition is related to the fast oxidation of the lead metal in the solution due to the use of cyclic voltammetry. The reduction processes in the backward scan do not allow the lead dodecanoate film to form a thick layer. As predicted by the graph in Fig. 6, the thickness of the lead dodecanoate layer tends towards asymptotic behavior due to the passivation of the surface and adsorption of the incoming X-rays by the protective layer.

Table 2 shows statistically different time constants from the fitting implying different growth rates for the different compounds. The different τ values for the lead dodecanoate show that one peak grows faster than the other. This suggests an anisotropic growth of the lead dodecanoate crystal structure from a sodium dodecanoate aqueous solution. Probably due to the fact of the lamellar structure of the crystal, one layer is formed faster than another in the crystal [34]. Another explanation is the anisotropic formation of a lower temperature mesophase involving increased lateral disorder [35].

3.2. Corrosion test of the lead dodecanoate coated lead coupon

After the deposition, the coupons are dried in the air. Then, the coated samples are corroded using linear sweep voltammetry (LSV) in a 5 μg L^{-1} acetic acid solution with a potential range from −1 V to 1.5 V and a scan rate of 1 mV s^{-1}. During the electrochemical treatment again XRD spectra are taken.

Fig. 7 shows the peak areas extracted from the corrosion of the lead dodecanoate coated lead sample in real time using a LSV scan with a potential range from −1 V to 1.5 V and a scan rate of 1 mV s^{-1} in an acetic acid solution. The total length of the experiment is 41 min. The relevant q-space values of the most important corrosion products are shown (see also Fig. S2), obtained from the reference spectra present in the ICCD database. The initial coated sample shows diffraction lines between a q-value of 1 and 2 $Å^{-1}$. These peaks originate from the well-ordered lamellar lead dodecanoate crystals as described by Lacoutre et al. [36]. Drying the sample in air ensures that the formed complexes reorganize and form less distorted lamellar crystal structures. The most important corrosion product that could be identified in the first diffractogram is a lead carbonate compound (plumbonacrite), but still there is overlap with the lead dodecanoate diffraction peaks (see also Fig. S3). Due to presence of CO_2 in the ambient air during drying, hydrogen carbonate is formed in the aqueous solution, which reacts with the

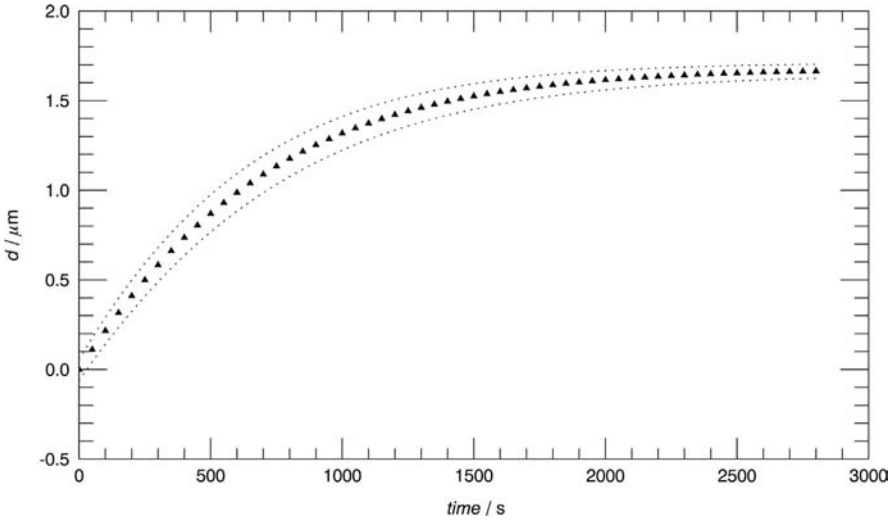


Fig. 6. The calculated thickness (d) of the lead dodecanoate coating as a function of immersion time.

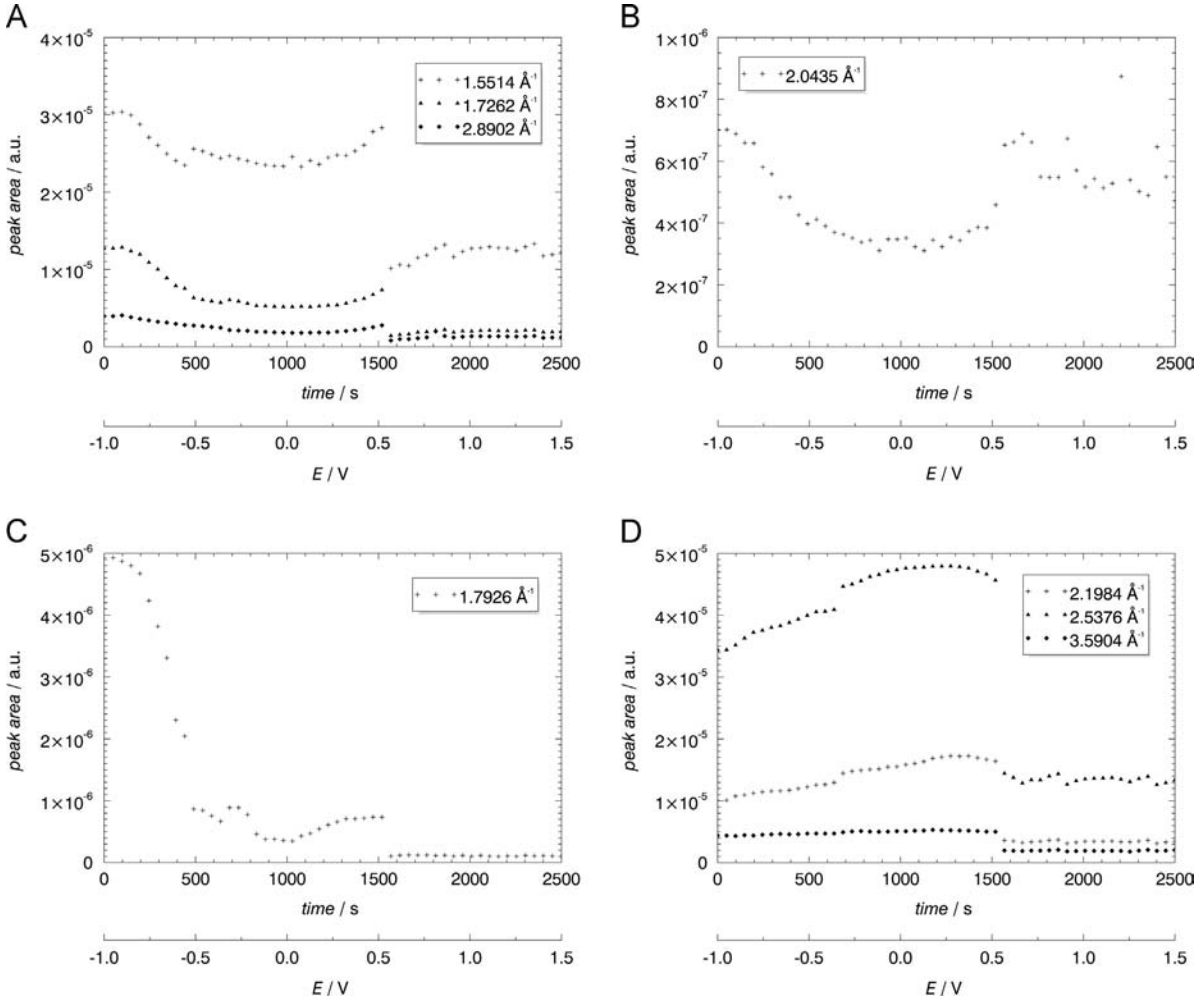


Fig. 7. The peak areas extracted from the diffraction patterns of the corrosion test of the lead dodecanoate coated lead sample in real time using a LSV scan with a range from −1 V to 1.5 V and a scan rate of 1 mV s^{-1}: (A) lead dodecanoate at 1.5514 $Å^{-1}$, 1.7262 $Å^{-1}$ and 2.8902 $Å^{-1}$, (B) litharge at 2.0435 $Å^{-1}$, (C) plattnerite at 1.7926 $Å^{-1}$ and (D) lead at 2.1984 $Å^{-1}$, 2.5376 $Å^{-1}$and 3.5904 $Å^{-1}$.

PbO at the surface to form carbonates [5]:

$$CO_2(g)+H_2O(aq)\rightleftharpoons HCO_3^-(aq)+H^+(aq) \quad (14)$$

$$6\,HCO_3^-(aq)+10\,PbO(s)+6\,H^+(aq)\rightleftharpoons Pb_{10}O(OH)_6(CO_3)_6(s)+3\,H_2O(aq) \quad (15)$$

Next to the lead dodecanoate coating and plumbonacrite, lead(II) oxide and lead(IV)oxide are present due to the high oxidation potential during deposition. During the cathodic polarization (up to −0.5 V), the lead dodecanoate complexes and lead(II)oxide corrosion products

seem to be reduced to form metallic lead (Fig. 7A and B). The lead(IV) oxide is clearly reduced at a higher rate (Fig. 7C). The cathodic current ensures a big loss of lead corrosion products, but does not destroy the deposited lead dodecanoate coating. Due to these reduction reactions, metallic lead is formed as seen in the first part of the peak area plot extracted from the (200) lead diffraction peak at 2.5376 $Å^{-1}$ (Fig. 7D).

After −0.5 V, the anodic polarization starts. It is noticeable that peak areas of all compounds shown in Fig. 7 stagnate from −0.5 V to 0.5 V. This is explained by supposing a protective region (and corrosion inhibition) for the lead dodecanoate coating present on the lead sample. In this region, no corrosion takes place due to the fact that no extra crystalline corrosion products are being formed. The SR-XRD patterns recorded at these potentials do not change as a function of time.

Around the potential of 0.5 V, major changes occur on top of the coated lead sample. A sudden drop in the peak area of the lead dodecanoate diffraction peaks explains the cracking and destruction of the lead dodecanoate coating so that the acetic acid starts to attack the lead sample (Fig. 7A). This implies that a small amount of acetic acid in the aqueous solution attacks and decomposes the hydrophobic lead dodecanoate crystal layer due to its acidic character. The presence of acetic acid ensures the start of a very fast 'active' corrosion process forming new lead acetate complexes starting with the acidification of the surface resulting in lead(II)oxide dissolution [37].

Fig. 7B shows that higher potentials induce the production of lead(II)oxide. Due to the reaction with acetic acid, these water soluble lead acetate complexes will associate with these formed lead(II)oxides present on the surface as follows [38]:

$$2\ PbO\ (s) + Pb^{2+}(aq) + 2\ CH_3COO^-(aq) + H_2O \rightleftharpoons Pb(CH_3COO)_2.2\ PbO \cdot H_2O(s) \quad (16)$$

The formed water insoluble lead acetate oxide hydrate cannot be identified due to the fact that the range of our measurements did not extend to 0–0.5 A^{-1}. The main lead acetate peak appears around 0.3 A^{-1}.

The formation of lead(IV) species, however, is unlikely at these lower oxidative potentials and without the presence of basic hydroxide species (see Fig. 7C). The peak area of the diffraction peak of lead drops suddenly together with the accumulation of corrosion products on the lead surface (see Fig. 7D). Next to the production of lead hydroxy carbonates and lead acetate oxide hydrate, the formation of dodecanoic acid on the surface explains the decrease of the lead peak area. Acids (Eq. 17) attack the hydrophobic lead dodecanoate coating re-converting the lead complexes into lead ions and dodecanoic acid [12]:

$$Pb(C_{12})_2 + 2\ H^+ \rightleftharpoons Pb^{2+} + 2\ HC_{12} \quad (17)$$

The formation of dodecanoic acid could not be confirmed using XRD, as it is no crystalline compound (could be verified using Raman spectroscopy) under these circumstances. In any case, the scattering from the hydrocarbon chain is very weak in comparison with that from the lead planes in the lead dodecanoate. One must keep in mind that this corrosion process is enormously accelerated due to the use of LSV. Real time corrosion processes would proceed much more slowly. Furthermore, a hypothetical scheme is drafted for the corrosion test measurement of a lead dodecanoate coated lead sample based on the SR-XRD patterns (see Fig. S4).

To be able to compare a reference on the acetic acid corrosion on lead, the same corrosion test procedure was applied on a bare lead coupon during 41 min. During the measurement, the only visible diffraction peaks are the ones of the bare lead substrate. Afterwards, the coupon was dried in air and a diffraction pattern was recorded (see Fig. S5). Most of the formed lead corrosion products are soluble in the acidic water making it impossible to detect them during the in-situ growth [39]. First of all, the (111) and (200) lead diffraction lines form intense narrow peaks. Close to the lead diffraction lines, the (110), (101) and (200) plattnerite diffraction peaks are detected. The low intensity peaks between q-space values of 1–1.5 $Å^{-1}$ evidence the presence of a lead carboxylate complex. The presence of acetic acid in the corrosive solution results in the formation of insoluble lead acetate oxide hydrate using reaction (Eq. (16)). The lead acetate complexes can be converted to lead hydroxy carbonates [9]. The formation of lead hydroxy carbonates is confirmed by the presence of the (115) plumbonacrite diffraction peak. Compared to the protected sample, the bare sample starts to corrode at lower potentials, which explains the higher relative intensities of these diffraction peaks associated with the active acetic acid corrosion. The lower relative intensities of the diffraction peaks predict a protective behavior of the lead dodecanoate coating on the lead samples.

4. Conclusions

In-situ spectroelectrochemical measurements have demonstrated that a crystalline lead dodecanoate coating immediately forms at the start of the experiment using cyclic voltammetry. Later on, during the drying process the formed complexes reorganize and lead hydroxy carbonates are formed. In addition to the lead dodecanoate coating, small quantities of other lead corrosion products are detected, which are explained by the oxidation of the surface and atmospheric corrosion. During the reductive scan, these lead corrosion products are reduced to form lead metal. The consecutive cyclic voltammetry scans ensure the formation of a lead dodecanoate coating up to the saturation of the surface. The fast and thin layer deposition, however, is related to the oxidation of the lead metal using cyclic voltammetry. The reduction processes do not allow the lead dodecanoate film to form a thick layer.

An accelerated 'active' corrosion test in acetic acid has been conducted on a bare and a lead dodecanoate coated lead coupon. In both cases, lead acetate oxide hydrate is formed due to the formation of lead oxides and lead acetates in the aqueous corrosive acetic acid solution. The bare sample formed much more corrosion products compared to the coated sample, which indicates the inhibitive properties of the coating.

Not only is the electrochemical coating method in an aqueous solvent quick and inexpensive (the materials are all cheap substances mass produced for industrial applications), but the deposited layers of lead dodecanoate are considerably hydrophobic and therefore potentially more protective. The method may be extended to using cotton drenched or a spray can filled with the inhibitor solution to apply the lead dodecanoate coating, increasing the range of possible applications in archeaometry and conservation.

Acknowledgments

The authors acknowledge the financial support from the Research Foundation – Flanders (FWO). esaProject and the eCell design are copyright 2013 Dowsett and Adriaens, and made available by EVA Surface Analysis.

Appendix A. Supporting information

Supplementary data associated with this article can be found in the online version at http://dx.doi.org/10.1016/j.talanta.2014.10.035.

References

[1] T. Clarke, Nature 427 (2004) 8–9.
[2] B. Tjeerdsma, H. Militz, Holz als Roh- und Werkstoff 63 (2) (2005) 102–111.
[3] L.T. Gibson, C.M. Watt, Corros. Sci. 52 (2010) 172–178.
[4] P.C. Arni, G.C. Cochrane, J.D. Gray, J. Appl. Chem. 15 (1965) 305–313.
[5] A. Niklasson, L. Johansson, J. Svensson, J. Electrochem. Soc. 152 (2005) B519–B525.
[6] D. Thicket, Relative effects of formaldehyde, formic and acetic acids on lead, copper and silver, Report 1997/12, The British Museum, 1997.
[7] S.G. Clark, E.E. Longhurst, J. Appl. Chem. 11 (1961) 435–443.
[8] C. Chiavari, C. Martini, D. Prandstaller, A. Niklasson, L.-G. Johansson, J.-E. Svensson, A. Åslund, C.J. Bergsten, Corros. Sci. 50 (9) (2008) 2444–2455.
[9] A. Niklasson, Atmospheric corrosion of historic lead organ pipes, Chalmers University of Technology, Göteborg, Sweden, 2007 (Ph.D. thesis).
[10] M. De Keersmaecker, K. De Wael, A. Adriaens, Prog. Org. Coat. 74 (2012) 1–7.
[11] J. Tétreault, E. Cano, M. van Bommel, D. Scott, M. Dennies, M.-G. Barthés-Labrousee, L. Minel, L. Robbiola, Studies Conserv. 48 (4) (2003) 237–250.
[12] E. Rocca, C. Rapin, F. Mirambet, Corros. Sci. 46 (2004) 653–665.
[13] E. Rocca, G. Bertrand, C. Rapin, J.C. Labrune, J. Electroanal. Chem. 503 (2001) 133–140.
[14] E. Rocca, J. Steinmetz, Corros. Sci. 43 (2001) 891–902.
[15] A. Frignani, V. Grassi, F. Zucchi, F. Zanotto, Mater. Corros. 61 (2010) 1–8.
[16] K. De Wael, M. De Keersmacker, M.G. Dowsett, D. Walker, P.A. Thomas, A. Adriaens, J. Solid State Electrochem. 14 (2010) 407–413.
[17] A. Adriaens, F. De Bisschop, M.G. Dowsett, B. Schotte, App. Surf. Sci. 254 (2008) 7531–7998.
[18] S. Nikitenko, A.M. Beale, A.M.J. van der Eerden, S.D.M. Jacques, O. Leynaud, M.G. O'Brien, D. Detollenaere, R. Kaptein, B.M. Weckhuysen, W. Bras, J. Synchrotron Radiat. 15 (2008) 632–640.
[19] M.G. Dowsett, A. Adriaens, Anal. Chem. 78 (2006) 3360–3365.
[20] A. Adriaens, M.G. Dowsett, K. Leyssens, B. Van Gasse, Anal. Bioanal. Chem. 387 (2007) 861–868.
[21] A. Adriaens, M.G. Dowsett, Surf. Eng. 24 (2) (2008) 84–89.
[22] W.L. Bragg, Proceedings of the Cambridge Philosophical Society 17 (1913) 43–57.
[23] D.B. Williams, C.B. Carter, in: D.B. Williams, C.B. Carter (Eds.), Transmission Electron Microscopy, 2nd Edition,Springer Science, New York, 1996, pp. 191–200.
[24] M.G. Dowsett, A. Adriaens, C. Martin, L. Bouchenoire, Anal. Chem. 84 (11) (2012) 4866–4872.
[25] M.G. Dowsett, A. Adriaens, B. Schotte, G. Jones, L. Bouchenoire, Surf. Interface Anal. 41 (2009) 565–572.
[26] M.G. Dowsett, A. Adriaens, B. Schotte, G. Jones, L. Bouchenoire, Metal 07 (3) (2007) 26–31.
[27] C. Leygraf, T.E. Graedel, Atmospheric Corrosion, 1st edition, Wiley Interscience, New York, 2000.
[28] P. Delahay, M. Pourbaix, P. Van Rysselberghe, J. Electrochem. Soc. 98 (2) (1951) 57–64.
[29] P. Rüetschi, B.D. Cahan, J. Electrochem. Soc. 105 (7) (1958) 369–377.
[30] S. Mauchauffée, E. Meux, Chemosphere 69 (5) (2007) 763–768.
[31] M. De Keersmaecker, D. Depla, K. Verbeken, A. Adriaens, J. Electrochem. Soc. 161 (3) (2014) C126–C137.
[32] R. Grayburn, M.G. Dowsett, M. De Keersmaecker, E. Westenbrink, J.A. Covington, J.B. Crawford, M. Hand, D. Walker, P.A. Thomas, D. Banerjee, A. Adriaens, Corros. Sci. 82 (2014) 280–289.
[33] C.T. Chantler, K. Olsen, R.A. Dragoset, J. Chang, A.R. Kishore, S.A. Kotochigova, D.S. Zucker, X-ray Form Factor, Attenuation and Scattering Tables, Detailed tabulation of atomic form factors, photoelectric absorption and scattering cross section, and mass attenuation coefficients for $Z=1$–92 from $E=1$–10 eV to $E=0.4$–1.0 MeV (2001).
[34] T. Hashimoto, N. Sakamoto, Macromolecules 28 (13) (1995) 4779–4781.
[35] A.M. Amorim Da Costa, H.D. Burrows, C.F.G.C. Geraldes, J.J.C. Teixeira-Dias, C.G. Bazuin, D. Guillon, A. Skoulois, E. Blackmore, G.J.T. Tiddy, D.L. Turner, Liq. Cryst. 1 (3) (1986) 215–226.
[36] F. Lacoutre, M. François, C. Didierjean, J.-P. Rivera, E. Rocca, J. Steinmetz, Acta Crystallogr. C57 (2001) 530–531.
[37] S. Gobom, On the complex formation of tin(II) and lead(II) with acetate ions (Ph.D. thesis), Inorganic Chemistry, Göteborg University, Götenborg, Sweden, 1977.
[38] A. Niklasson, L.-G. Johansson, J.-E. Svensson, Corros. Sci. 50 (11) (2008) 3031–3037.
[39] R.M.A. Lieth, Preparation and Crystal Growth of Materials with Layered Structures, 1st edition, Reidel Publishing Company, The Netherlands (1977) 263.

Talanta 132 (2015) 769–774

Contents lists available at ScienceDirect

Talanta

journal homepage: www.elsevier.com/locate/talanta

Vortex-assisted low density solvent liquid–liquid microextraction and salt-induced demulsification coupled to high performance liquid chromatography for the determination of five organophosphorus pesticide residues in fruits

Ketsarin Seebunrueng [a], Yanawath Santaladchaiyakit [b], Supalax Srijaranai [a,*]

[a] Materials Chemistry Research Center, Department of Chemistry, Faculty of Science, Khon Kaen University, Khon Kaen 40002, Thailand
[b] Department of Chemistry, Faculty of Engineering, Rajamangala University of Technology Isan, Khon Kaen Campus, Khon Kaen 40000, Thailand

ARTICLE INFO

Article history:
Received 3 July 2014
Received in revised form
10 October 2014
Accepted 11 October 2014
Available online 18 October 2014

Keywords:
Low density solvent
Vortex-assisted low density solvent liquid–liquid microextraction
Salt-induced demulsification
Organophosphorus pesticide
Fruit

ABSTRACT

A simple and rapid microextraction method, vortex-assisted low density solvent liquid–liquid microextraction and salt-induced demulsification (VLLME–SID) coupled to high performance liquid chromatography (HPLC) was developed for the determination of organophosphorus pesticide (OPP) residues in fruits. The studied OPPs were azinphos-methyl, parathion-methyl, fenitrothion, diazinon and chlorpyrifos. For VLLME–SID, a mixture of low density solvents (1-dodecanol and hexane) was used as the extraction solvent under vortex agitation for enhancing dispersion. After complete dispersion, the emulsion was formed and the OPPs were extracted into extraction solvent droplets. Then, the emulsion was quickly broken up into two clear phases after the addition of $AlCl_3$ as a demulsifier. Centrifugation was not required in this procedure. Under the optimal conditions, high enrichment factors (180–282), low limit of detections (LODs) (0.05–1 ng mL^{-1}) and good precision (RSD $\leq$ 7% for retention time and peak area) were obtained. The proposed method was successfully applied to the analysis of OPP residues in fruit samples (watermelon, grape, and cantaloupe). The LODs for samples were in the range 0.0006–0.0015 mg kg^{-1} which are below the established EU-MRLs (0.01–0.3 mg kg^{-1}). Good recoveries were also obtained (80–104%).

© 2014 Elsevier B.V. All rights reserved.

1. Introduction

Pesticides are extensively used to control pests and prevent diseases in various crops, such as fruits, vegetables and cereals. Organophosphorus pesticides (OPPs) are used instead of banned organochlorine compounds, because of their efficient control of pests and lower persistence in the environment. OPPs affect the enzyme acetyl-cholinesterase which controls nerve function not only in insects but also animals and humans [1]. Because of their persistence, water solubility, bioaccumulation and potential toxicity, OPPs may be present in a wide range of fruits, vegetables, foodstuff and agricultural runoff [2]. Therefore, it is necessary to develop analytical methods with high sensitivity, selectivity and simplicity for the determination of OPP residues in various samples to ensure health safety and international trade [3,4].

Chromatographic methods including gas chromatography (GC) and high-performance liquid chromatography (HPLC) have been widely used for the separation and quantification of OPP residues in various samples such as water [1], soil [5], fruit [6–8], tea [9], milk [10] and biological samples [11]. Since OPPs are mostly present in complex sample matrices, they cannot be injected directly into chromatographic systems. Therefore, an appropriate sample-preparation step is necessary before instrumental analysis. Good sample preparation can not only eliminate interferences but can also increase the concentration of the analytes, thus enhancing the apparent sensitivity of the analytical method.

Dispersive liquid–liquid microextraction (DLLME) has been recognized as an effective preconcentration method for various target compounds [12,13]. DLLME is based on a ternary solvent system including an aqueous solution, a water immiscible solvent (extraction solvent) and a water miscible solvent (dispersive solvent). The dispersion (cloudy solution) and very fine droplets occur immediately, just after the rapid injection of the mixture solution of extraction and dispersive solvents into aqueous solution. During this step, the analytes enter the extraction phase

* Corresponding author. Tel.: +66 43 009700x42175.
E-mail address: supalax@kku.ac.th (S. Srijaranai).

http://dx.doi.org/10.1016/j.talanta.2014.10.020
0039-9140/© 2014 Elsevier B.V. All rights reserved.

and are concentrated. Subsequently, the extraction solvents with higher density than water are separated from aqueous phase by centrifugation. DLLME provides many advantages such as simplicity, high enrichment factors, and rapid extraction times [14].

However, there are some limitations in DLLME mostly arising from the solvents used in this technique. These include (i) the use of hazardous chlorinated solvents having density higher than water [15], and (ii) the use of dispersive solvents, resulting in decreased partition coefficients of analytes into the extraction solvent [16]. Another limitation of DLLME is the extra time required for the centrifugation step.

Several strategies have been attempted to address these limitations and also to achieve high extraction efficiency using more "green" extraction methods. The first efforts use extraction solvents having densities lower than water and/or the solidification of floated organic solvents [17,18]. However, for this approach, special homemade narrow-necked devices are required. Other strategies involve the use of surfactants instead of water miscible dispersive solvents [19]. In addition, vortex agitation or application of ultrasound energy have been employed in dispersion process [16,20,21].

Recently, demulsified DLLME has been introduced with its advantages of simplicity and fast extraction [15,22–24]. In demulsified DLLME, the demulsifier is added to facilitate the phase separation of the aqueous phase and the organic extraction phase, thus the centrifugation step is omitted. The demulsifiers used are water miscible organic solvents which are mostly used as the dispersive solvent. This approach still suffers from the decreased partition coefficients of analytes into the extraction solvent [15,22–24].

Therefore, it is a challenge to develop demulsified DLLME with new demulsifiers. As an alternative demulsifiers, electrolytes, or salts, can reduce the zeta potential, hence decrease the stability of hydrophobic colloids (an emulsion solution) and increase the ionic strength of solution, leading to flocculation and coalescence of fine droplets of the extraction solvent [25–27]. Thus, the separation of two phases is expected from the addition of electrolyte into emulsion.

In the present work, vortex-assisted low density solvent liquid–liquid microextraction and salt-induced demulsification (VLLME–SID) preconcentration of OPPs residues prior to analysis by high performance liquid chromatography have been developed. For the VLLME–SID, the solvent having a density lower than water was used as extraction solvent. A vortex agitator was used for dispersion (without the addition of dispersive solvent). Salts were investigated as a new demulsifier to address the large volume problem of the conventional solvent-demulsified DLLME. In addition, the extraction can be performed using a 10-mL narrow-necked volumetric flask and common laboratory glassware. A modified QuEChERS (Quick, Easy, Cheap, Effective, Rugged, and Safe) method [28] was used for fruit samples preparation before VLLME–SID and analysis by HPLC.

2. Experimental

2.1. Chemicals and reagents

All chemicals were of at least analytical reagent grade. The analytical standards of organophosphorus pesticides (OPPs) were obtained from Dr. Ehrenstorfer GmbH (Germany), including azinphos-methyl, parathion-methyl, fenitrothion, diazinon and chlorpyrifos. The stock solutions of each pesticide were prepared at 1000 mg L^{-1} by dissolving an appropriate amount in methanol (MeOH). 1-undecanol, 1-dodecanol and 2-dodecanol were purchased from Sigma-Aldrich (USA). 1-Octanol was obtained from Panreac (Spain). n-Hexane was obtained from Lab-Scan Analytical Sciences (Ireland). Methanol (HPLC grade) was obtained from RCI Labscan Ltd. (Thailand) and acetonitrile (HPLC grade) was obtained from Merck (Germany). Sodium chloride (APS, Australia), magnesium sulfate anhydrous (Panreac, Spain), magnesium chloride (Carlo Erba, France), sodium acetate (Carlo Erba, France), acetic acid (Carlo Erba, France), aluminum chloride anhydrous (Ajax Finechem Pty Ltd, New Zealand) and aluminum sulfate hexahydrate (Fluka, Switzerland) were utilized. All solutions were prepared in deionized water with the resistivity of 18.2 MΩ cm from RiO_s™ Type I Simplicity 185 (Millipore Waters, USA).

2.2. Instruments

The HPLC system (Waters, Massachusetts, USA) consisted of an in-line degasser, a 600E quaternary pump, and a Waters 2996 photodiode array detector (DAD). Empower software was used to control the system and for the acquisition and analysis of data. The separation of the studied pesticides was carried out on a Chromolith RP-18e (2 mm × 50 mm, 1.5 μm) column (MERCK, Germany). A vortex mixer (50 Hz) from Scientific Industries, INC (USA) was used. Other equipments including a thermostatted water bath (ISOTEMP 228, Thermo Fisher Scientific, Massachusetts, USA), a Rotavapor R-200 (Buchi Labortechnik AG, Switzerland) and automatic shaker (SSeriker, Vision Scientific, Korea) were also used.

2.3. Sample preparation

Fruit samples including cantaloupe, watermelon (yellow pulp and red pulp) and grape were randomly purchased from local markets at Khon Kaen province in Northeast Thailand. Peels of the fruit samples (except grape) were removed. The edible parts of samples (500 g) were cut and blended using a commercial food mixer. A modified QuEChERS method [28] was applied for sample preparation of the studied fruit samples. Briefly, a precisely weighed representative sample portion (about 10 g) was placed in a 50 mL centrifugation tube and mixed with 20 mL of 1% (v/v) acetic acid in ACN. Then the mixture was shaken at 300 rpm for 5 min using automatic shaker. After that, anhydrous $MgSO_4$ (15 g) and sodium acetate (1 g) were added and the mixture was immediately shaken manually. The solution was then centrifuged at 3000 rpm for 5 min. The supernatant was subsequently evaporated to dryness using a rotary evaporator (40 °C water bath). The resulting residue was re-dissolved with 10.00 mL of water before extraction by VLLME–SID.

2.4. VLLME–SID procedure

A 10 mL aliquot of a standard solution of the OPP mixture or sample solution was placed in a 10 mL volumetric flask. A mixture of 15 μL hexane and 15 μL 1-dodecanol was added into the sample solution. The solution was then vortexed at 1800 rpm for 1 min, forming a cloudy solution. After the addition of 1% (w/v) of $AlCl_3$, the solution was clear and quickly separated into two phases and the extraction phase floated on the surface of the solution. The floated extraction phase was collected using a micro-syringe and then injected into the HPLC for analysis.

2.5. HPLC conditions

The separation of OPPs was performed on a Chromolith RP-18e (2 mm × 50 mm, 1.5 μm) column with gradient elution using ACN and water, at a flow rate of 1.0 mL min^{-1} and detection at 210 nm. The injection volume was 10 μL. The gradient elution profile of ACN and water (%v/v) was programmed as follows: 35% (v/v) ACN (0–1.5 min), followed by an increase to 70% (v/v) ACN (1.5–2 min) and then held at 70% (v/v) ACN until 8 min. After that, the composition of mobile phase was returned to the initial value of

35% (v/v) ACN in order to equilibrate the column for the next run. Using the above mentioned conditions, the separation of five OPPs was successfully obtained within 6 min with the resolution greater than 2.2.

3. Results and discussion

3.1. Type of the extraction solvent

A choice of extraction solvent is a key parameter for high extraction efficiency of DLLME. The extraction solvent is considered based on a high extraction capability for the target analytes and compatibility with HPLC chromatographic separation. In this study, the immiscible solvents having density lower than water were investigated, including hexane, 1-octanol, 1-undecanol, 1-dodecanol and 2-dodecanol. The extraction efficiency was evaluated by enrichment factor (EF). The EF was calculated based on the analyte concentration in the floated phase ($C_{floated}$) divided by the initial analyte concentration in the aqueous samples (C_0) [18]. Fig. 1 shows the effect of extraction on EF. It is clearly seen that types of extraction solvent affect the extraction efficiency for both a number of the analytes extracted and the EF. The differences in the extraction efficiencies of solvents may be discussed in terms of polarity (log K_{ow}) [29] and water solubility of solvents [30]. Among the solvents investigated, the most polar solvent, 1-octanol (log K_{ow}=3.15), could not extract any analytes studied. This may due to the high water solubility of 1-octanol (water solubility ~814 mg/L). Three OPPS (azinphos-methyl, parathion-methyl and fenitrothion) were extracted by 1-undecanol, while, four OPPS (azinphos-methyl, parathion-methyl, fenitrothion and diazinon), were extracted by both 1-dodecanol and 2-dodecanol. Although, 1-dodecanol and 2-dodecanol could extract four OPPs (the same OPPs), 1-dodecanol provided higher EF than 2-dodecanol. This may be explained by the lower polarity of 1-dodecanol compare to 2-dodecanol and 1-undecanol. The water solubilities of these alcoholic solvents are in the order: 6.9 mg/L (1-dodecanol), 16.2 mg/L (2-dodecanol), and 43.0 mg/L (1-undecanol) which also agree well with their log K_{ow} as follow: 1-dodecanol (5.13), 1-undecanol (4.72) and 2-dodecanol (4.70). The non-polar solvent, hexane, could extract four OPPS (azinphos-methyl, parathion-methyl, fenitrothion and chlorpyrifos). It was found that the least polar analyte, chlorpyrifos (log K_{ow}=4.66), was extracted only by hexane. As these results show, a single extraction solvent could not extract all targeted OPPs in this study.

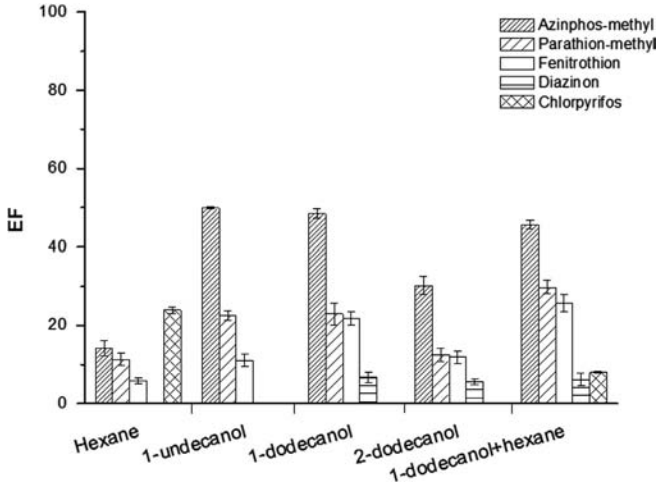


Fig. 1. The effect of extraction solvent on EF of OPPs. Extraction conditions: water sample volume (10.00 mL), extraction solvent volume (100 μL), vortex time (20 s at 1800 rpm), 0.5 g of $Al_2(SO_4)_3$ and 0.05 mg L^{-1}OPPs (each).

A combination of extraction solvents was then used to test the feasibility for extracting and preconcentrating OPPs. The mixture of 1-dodecanol and hexane (1:1, v/v) was investigated. As the result show, the mixture of extraction solvent of 1-dodecanol and hexane was effective for extraction of all target OPPs. Consequently, 1-dodecanol mixed with hexane at 1% (v/v) was chosen for further studies.

3.2. Effect of the extraction solvent volume

The extraction solvent volume influences directly the extraction efficiency. Enough extraction solvent is required for quantitative extraction. On the other hand, a large volume of extraction solvent results in dilution of the extraction phase [22]. As a compromise between high extraction efficiency and minimizing the dilution effect, the volume of 1-dodecanol and hexane (1:1 (v/v)) was investigated from 20 μL to 90 μL. The volume of extraction solvent lower than 30 μL was difficult to handle when collecting the extract phase. The highest EF was obtained at 30 μL and then decreased dramatically with increasing extraction solvent volume from 40 μL due to the dilution effect. Therefore, 30 μL of a mixture of 1-dodecanol and hexane was chosen (Fig. 2).

3.3. Effect of vortex extraction time

Without dispersive solvents, a vortex agitation is a simple alternative way to enhance extraction efficiency in a short time. A vortex mixer facilitates the dispersion of the extraction solvent into the aqueous solution resulting in enhancement of extraction efficiency [20]. In this study, a 10-mL narrow-necked volumetric flask was used as a simple and convenient extraction device. The vortex rotational speed was fixed at 1800 rpm and different vortex times were investigated, from 0.5 to 5 min. It is clearly seen that the extraction equilibrium could reach within a short time (1 min) and also providing high EF for all target analytes. After 1 min, the EF of all target analytes was constant. Based on these results, the use of vortex agitation for 1 min at 1800 rpm was chosen.

3.4. Effect of salt demulsifier

In general, the addition of salt decreases the solubility of analytes in aqueous solution, due to salting-out effect [16]. Thus, analytes transfer efficiently to the extraction (organic) phase. It has been reported that strong electrolyte salts can be used as demulsifier to break-up the emulsion [25,26,31]. After the water immiscible extraction solvent and aqueous solution were mixed using a

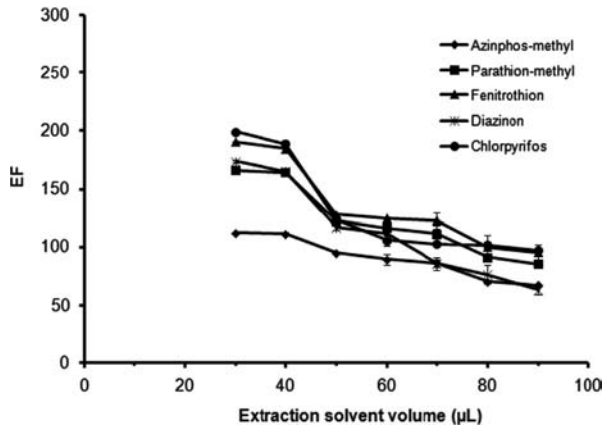


Fig. 2. The effect of extraction solvent volume on the EF. Extraction conditions: water sample volume (10.00 mL), 1-dodecanol: hexane (1:1, v/v) as extraction solvent, vortex time (20 s at 1800 rpm), 0.5 g of $AlCl_3$ and 0.05 mg L^{-1}OPPs (each).

vortex mixer, an emulsion was formed. The addition of electrolytes into solution may reduce zeta potential and the stability, particularly of hydrophobic colloids. Thus, the repulsion of the droplets of extraction solvent in the solution was decreased [27], resulting in agglomeration of fine droplets of extraction solvent and finally the phase separation was easily obtained. Various salts were studied at 1.0%, w/v, such as sodium chloride (NaCl), sodium sulfate (Na_2SO_4), magnesium sulfate ($MgSO_4$), magnesium chloride ($MgCl_2$), aluminum chloride ($AlCl_3$) and aluminum sulfate ($Al_2(SO_4)_3$). It is clearly seen (Fig. 3) that $AlCl_3$ provided the highest efficiency. This may due to the stronger interaction between the larger charge of the salt and the emulsion. $AlCl_3$ was chosen for further studies because it is the most effective demulsifier. Notice that increasing the % w/v of $Al_2(SO_4)_3$ to obtain the same amount (mole) as $AlCl_3$, the obtained EFs were not significantly different.

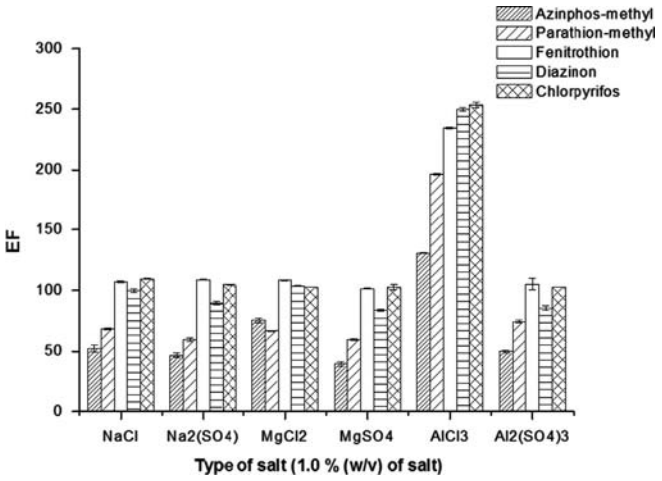


Fig. 3. The effect of type of salt as demulsifier on the EF. Extraction conditions: water sample volume (10.00 mL), 30 μL of 1-dodecanol: hexane (1:1, v/v) as extraction solvent, vortex time (1 min at 1800 rpm), 1.0% w/v of salt and 0.05 mg L^{-1}OPPs (each).

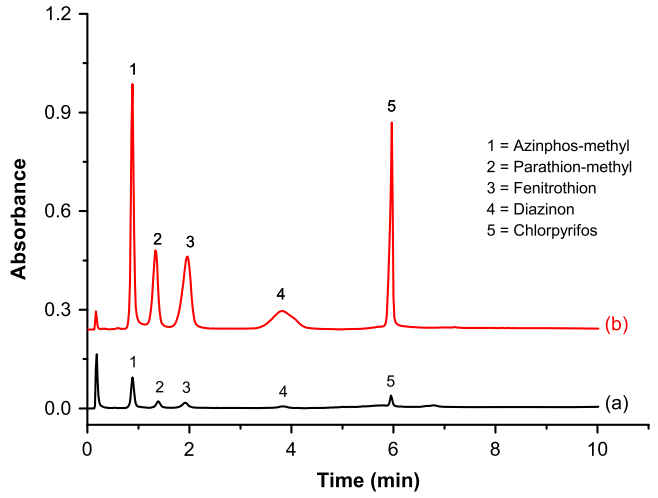


Fig. 4. Chromatograms of the studied OPPs obtained using on a Chromolith RP-18e (2 mm × 50 mm, 1.5 μm) column and injection volume as 10 μL, (a) direct analysis without preconcentration (5 mg L^{-1} of each OPP) and (b) using VLLME–SID conditions: 15 μL of 1-dodecanol mixed with 15 μL of hexane as extraction solvent, vortex 1 min at 1800 rpm, 1.0% (w/v) of $AlCl_3$ as demulsifier and 0.5 mg L^{-1} of each OPP.

The amount of $AlCl_3$ was then investigated from 0.5–10% (w/v). The results indicated that 1.0% (w/v) gave the highest EF, after that the EF was constant over the studied range. It was found that the amount of $AlCl_3$ affected directly on the phase separation. For lower amounts of $AlCl_3$ (less than 1.0% (w/v)), the extraction phase and the aqueous phase were not clearly separated. Thus, 1.0% (w/v) $AlCl_3$ was chosen as the optimum demulsifier concentration.

3.5. Quantitative analysis and method validation

A typical chromatogram obtained from the VLLME–SID method compared to direct injection analysis (before preconcentration) under the optimum conditions is shown in Fig. 4. The analytical performance and validation parameters, including linear ranges, limits of detection (LODs), precisions (intra-day and inter-day) and enrichment factors (EF), were evaluated. The results are listed in Table 1. Good linearity was observed in the range 0.5–500 ng mL^{-1} with a coefficient of determination (r^2) higher than 0.9998. The obtained LODs were from 0.05 to 1 ng mL^{-1}. The intra-day (repeatability) and inter-day (reproducibility) precisions of the developed method are expressed as the relative standard deviations (RSD) of several measurements ($n=5$) of the standard mixture (at 10 ng mL^{-1} each) in a day and three executive days, respectively. High precision was obtained with RSDs of retention time less than 2.7%, while RSDs of peak area were below 6.7%. High EF ranging from 180 to 282 were obtained.

3.6. Fruit analysis

The matrix-match calibration was constructed to eliminate matrix interference in samples. The solutions of fruit extracts after QuEChERS were spiked with the target OPPs at five concentration levels in the range of 0.001–0.5 mg kg^{-1} before VLLME–SID and analysis. Calibration curves show good linearity over the studied concentration ranges with the coefficient of determination (r^2) greater than 0.995. LODs of the target analytes in samples were also investigated using 3.3 × (SD *y*-Intercept/Average Slope) and limits of quantitation (LOQs) were statistically determined using 10 × (SD *y*-Intercept/Average Slope) [32]. The obtained LODs are in the range of 0.0006–0.0015 mg $kg^{-1}$for all the studied OPPs in the fruit samples. These are below the established EU-MRLs (0.01–0.3 mg kg^{-1}). LOQs were in the range of 0.0020–0.0055 mg kg^{-1}. The identification and

Table 1
Analytical performance of the proposed method for the studied OPPs standard solution.

Pesticide	Linear equation	Linearity (ng mL^{-1})	r^2	LOD (ng mL^{-1})	EF	Intra-day ($n=5$), %RSD		Inter-day ($n=5\times3$ days), %RSD	
						t_R	area	t_R	area
Azinphos-methyl	$Y=8{,}490{,}908X+9597$ ($Y=55{,}369X-8478$)[a]	0.5 – 500	0.9999	0.05 (50)	197	2.0	3.5	2.6	6.7
Parathion-methyl	$Y=5{,}296{,}248X-3996$ ($Y=26{,}518X-5834$)	1.0 – 500	0.9999	0.3 (100)	222	1.5	2.5	2.4	6.0
Fenitrothion	$Y=6{,}837{,}688X+2940$ ($Y=24{,}235X-7162$)	1.0 – 500	0.9998	0.3 (100)	282	1.5	4.2	2.4	5.6
Diazinon	$Y=4{,}212{,}274X-21{,}268$ ($Y=13{,}872X-6472$)	5.0 – 500	0.9999	1.0 (500)	180	2.2	2.9	2.7	3.5
Chlorpyrifos	$Y=6{,}261{,}339X-8403$ ($Y=25{,}417X-16{,}328$)	0.5 – 500	0.9999	0.05 (100)	232	0.6	1.4	0.6	3.7

[a] Values reported in parentheses are obtained from without preconcentration method (direct injection).

confirmation of peaks were performed using three criteria: (1) comparison of retention times to those of the standard, (2) addition of known amounts of the expected OPPs and observation of the increase in peak area, (3) comparison of absorption spectra with the standards using a photodiode array detector. For this analysis, no contamination by OPPs was detected in cantaloupe and watermelon, but azinphos-methyl and parathion-methyl were found in grape sample at concentration of 0.0054 ± 0.0010 mg kg^{-1} and 0.0087 ± 0.0013 mg kg^{-1}, respectively. To test the accuracy of the proposed method, recovery was investigated by spiking known concentrations (0.0075, 0.010 and 0.025 mg kg^{-1}) of mixed standard OPPs into samples before QuEChERS and VLLME–SID. All experiments were performed in triplicate. Fig. 5 shows the chromatograms of a grape sample (blank) and grape with mixed OPPs (0.025 mg kg^{-1} each). The results (Table 2) indicate good analytical performance of the proposed method with average recoveries of all the studied OPPs ranged from 80% to 104% and good precision with relative standard deviation (RSD) less than 12%.

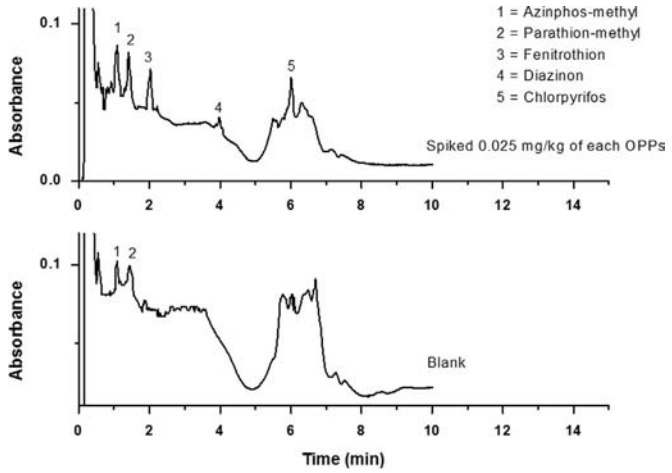


Fig. 5. Chromatograms of grape sample (blank) and grape sample spiked with 0.025 mg kg^{-1} of each OPP extracted using QuEChERS and VLLME–SID. The VLLME–SID conditions: 15 μL of 1-dodecanol mixed with 15 μL of hexane as extraction solvent, vortex 1 min at 1800 rpm and 1.0 (% w/v) of $AlCl_3$ as demulsifier.

3.7. Comparison to the other sample preconcentration methods for OPPs in fruit samples

The extraction efficiency of the proposed VLLME–SID method was compared to the other sample preconcentration techniques for the determination of OPP residues in fruits in terms of LOD, recovery, RSD, extraction time, EF and solvent volume (Table 3). The analytical features in terms of accuracy and precision obtained from the proposed method were comparable to those from the other methods. LODs of the proposed method are lower than the others. In addition, the proposed method is superior to the others in term of using small amounts of organic solvents, short extraction times and simple procedures. Therefore, it can be used as an alternative technique to the conventional DLLME and the other complicated extraction methods for analysis OPP residues in fruit samples.

4. Conclusions

A new demulsified DLLME method for the preconcentration of OPP residues including azinphos-methyl, parathion-methyl, fenitrothion, diazinon and chlorpyrifos in fruit samples using VLLME–SID method and analysis by HPLC–DAD has been successfully developed. The chromatographic analysis was performed on a short Chromolith RP-18e column (2 mm × 50 mm, 1.5 μm) with gradient elution using ACN and water, at a flow rate of 1.0 mL min^{-1}, and detection at 210 nm. The injection volume was 10 μL. The separation of five OPPs was successfully obtained within 6 min with the resolution greater than 2.2. The VLLME–SID used extraction solvent (1:1 (v/v) of 1-dodecanol and hexane) without dispersive solvent and in the presence of salt (as demulsifier) under vortex agitation. The method is easy, rapid, and uses less organic solvent; therefore it is environmental friendly and does not require any special

Table 2
The determination of OPPs and recovery in the studied fruit samples (n=3).

Pesticide	Spiked (mg kg^{-1})	Cantaloup			Watermelon (red)			Watermelon (yellow)			Grape		
		Found (mg kg^{-1})	Recovery (%)	RSD (%)	Found (mg kg^{-1})	Recovery (%)	RSD (%)	Found (mg kg^{-1})	Recovery (%)	RSD (%)	Found (mg kg^{-1})	Recovery (%)	RSD (%)
Azinphos-methyl	0	ND	–	–	ND	–	–	ND	–	–	0.0054	–	–
	0.0075	0.0067	89.2	4.15	0.0076	101.8	4.84	0.0065	86.3	5.06	0.0129	100.1	3.62
	0.010	0.0090	89.9	5.93	0.0097	97.0	4.69	0.0090	89.7	2.56	0.0141	87.5	1.91
	0.025	0.0249	99.8	4.54	0.0253	101.4	1.67	0.0244	97.4	8.32	0.0275	88.7	4.16
Parathion-methyl	0	ND	–	–	ND	–	–	ND	–	–	0.0087	–	–
	0.0075	0.0063	84.0	1.50	0.0074	98.5	4.04	0.0061	82.1	1.05	0.0156	92.3	9.02
	0.010	0.0082	81.7	1.74	0.0105	104.6	1.29	0.0080	80.1	1.86	0.0183	96.4	3.02
	0.025	0.0228	91.1	7.14	0.230	91.8	2.48	0.0206	82.6	5.40	0.0308	88.6	2.91
Fenitrothion	0	ND	–	–	ND	–	–	ND	–	–	ND	–	–
	0.0075	0.0062	82.9	3.06	0.0076	101.3	2.68	0.0074	98.6	1.50	0.0064	84.8	1.69
	0.010	0.0094	94.3	2.61	0.0099	98.6	1.41	0.0105	104.8	1.48	0.0101	101.1	2.24
	0.025	0.0257	103.0	0.84	0.2500	100.1	1.89	0.0215	86.1	4.12	0.0212	85.0	1.56
Diazinon	0	ND	–	–	ND	–	–	ND	–	–	ND	–	–
	0.0075	0.0072	96.9	3.58	0.0060	80.5	1.09	0.0069	91.8	6.22	0.0075	99.7	4.20
	0.010	0.0100	99.8	1.12	0.0102	102.0	2.94	0.0098	98.0	2.90	0.0097	97.4	11.66
	0.025	0.0248	98.7	2.92	0.0248	99.1	3.86	0.0227	91.0	5.15	0.0234	93.6	6.70
Chlorpyrifos	0	ND	–	–	ND	–	–	ND	–	–	ND	–	–
	0.0075	0.0070	93.6	5.91	0.0075	100.6	1.32	0.0060	80.3	6.61	0.0063	84.3	7.84
	0.010	0.0086	85.6	3.46	0.0096	95.8	1.89	0.0080	80.4	5.40	0.0096	95.9	4.11
	0.025	0.0236	94.5	9.57	0.0261	104.5	0.68	0.0256	102.5	4.60	0.0231	92.3	6.49

ND: Not detected.

Table 3
Comparison of VLLME–SID with other preconcentration techniques for the determination of the OPP residues by HPLC in fruits.

Method	Sample	No. of analytes /Separation time (min)	Injection volume (μL)	Solvent volume (μL)	Extraction time (min)[a]	LOD (μg kg^{-1})	Recovery (%)	RSD (%)	EF	Ref.
Mixed catanionic CPE–HPLC–DAD	Pomelo, apple and pineapple	6/15	20	300	20	3–10	77–104	0.4–11	18–27	33
UASE–DLLME–SFO–HPLC–UV	Watermelon, melon and ribbed melon	4/8	20	1150	12	1–4	88–107	≤9	NR	34
IL-VA-DLLME–HPLC–UV	Apple and pear	6/23	20	1050	6	0.061–0.73	69–110	2.3–5.7	<300	35
VLLME–SID–HPLC–DAD	Grape, watermelon and cantaloupe	5/6	10	15	1	0.6–1.5	80–104	≤7	180–282	This method

NR=not reported.
Abbreviation: Mixed catanionic CPE, mixed cationic-anionic surfactant cloud-point extraction; HPLC, high performance liquid chromatography; DAD, diode array detector; UASE, ultrasound-assisted solvent extraction; DLLME, dispersive liquid–liquid microextraction; SFO, solidification of floating organic drop; UV, ultra-violet detector; IL-VA-DLLME, ionic liquid-vortex assisted dispersive liquid–liquid microextraction.
[a] Extraction time (not include the time for sample preparation).

homemade devices. High enrichment factors (180–282), low LODs (0.05 to 1 ng mL^{-1}) and good repeatability (RSD ≤ 7%) were obtained. Overall, VLLME–SID is an excellent approach to the determination of studied OPPs in fruit samples (watermelon, grape and cantaloupe). Azinphos-methyl and parathion-methyl were found in grape at concentrations of 0.0054 ± 0.0010 mg kg^{-1} and 0.0087 ± 0.0013 mg kg^{-1}, respectively, however, they are lower than the regulatory limit for pesticides residues.

Acknowledgements

The Thailand Research Fund (TRF) through the Royal Golden Jubilee (RGJ) Ph.D. Program (Grant no. PHD/0203/2553) is gratefully acknowledged for financial support to K. Seebunrueng and S. Srijaranai. The valuable suggestions from Prof. Richard L. Deming (California State University of Fullerton, USA) are also acknowledged.

References

[1] L. Fu, X. Liu, J. Hu, X. Zhao, H. Wang, X. Wang, Anal. Chim. Acta 632 (2009) 289.
[2] C. Wang, Q. Wu, C. Wu, Z. Wang, J. Sep. Sci. 34 (2011) 3231.
[3] EU pesticide database, 2005, Pesticide EU-MRLs Database Regulation (EC) No 396/2005,⟨http://www.ec.europa.eu/food/plant/protection/pesticides/index_en.htm⟩.
[4] FAO/WHO Food standard; CODEX Alimentarius, Pesticide residues in food and feed, 2012 ⟨http://www.codexalimentarius.net/pestres/data/pesticides/ index.html?lang=en⟩.
[5] Z. Yang, Y. Liu, D. Liu, Z. Zhou, J. Chromatogr. Sci. 50 (2012) 15.
[6] Z. Wang, X. Zhao, X. Xu, L. Wu, R. Su, Y. Zhao, C. Jiang, H. Zhang, Q. Ma, C. Lu, D. Dong, Anal. Chim. Acta 760 (2013) 60.
[7] W-j. Zhao, X-k. Sun, X-n. Deng, L. Huang, M-m. Yang, Z-m. Zhou, Food Chem. 127 (2011) 683.
[8] D. Sharma, A. Nagpal, Y.B. Pakade, J.K. Katnoria, Talanta 82 (2010) 1077.
[9] S. Moinfar, M.R.M. Hosseini, J. Hazard. Mater. 169 (2009) 907.
[10] F.M. Rodrigues, P.P.R. Mesquita, L.S. Oliveira, F.S. Oliveira, A.M. Filho, P.A.P. Pereira, J.B. Andrade, Microchem. J. 98 (2011) 56.
[11] H. Tsoukali, G. Theodoridis, N. Raikos, I. Grigoratou, J. Chromatogr. B 822 (2005) 194.
[12] M. Rezaee, Y. Assadi, M.M. Hosseini, E. Aghaee, F. Ahmadi, S. Berijani, J. Chromatogr. A 1116 (2006) 1.
[13] M. Rezaee, Y. Yamini, M. Faraji, J. Chromatogr. A 1217 (2010) 2342.
[14] S. Boonchiangma, W. Ngeontae, S. Srijaranai, Talanta 88 (2012) 209.
[15] B. Majidi, F. Shemirani, Talanta 93 (2012) 245.
[16] J. Regueiro, M. Llompart, C. Garcia-Jares, J.C. Garcia-Monteagudo, R. Cela, J. Chromatogr. A 1190 (2008) 27.
[17] C. Wu, H. Liu, W. Liu, Q. Wu, C. Wang, Z. Wang, Anal. Bioanal. Chem. 397 (2010) 2543.
[18] M.I. Leong, S.D. Huang, J. Chromatogr. A 1216 (2009) 7645.
[19] X. You, S. Wang, F. Liu, K. Shi, J. Chromatogr. A 1300 (2013) 64.
[20] E. Yiantzi, E. Psillakis, K. Tyrovola, Talanta 80 (2010) 2057.
[21] M.D. Luque de Castro, F. Priego-Capote, J. Chromatogr. A 1190 (2008) 27.
[22] Y. Xia, M. Cheng, F. Guo, X. Wang, J. Cheng, Anal. Chim. Acta 724 (2012) 47.
[23] H. Chen, R. Chen, S. Li, J. Chromatogr. A 1217 (2010) 1244.
[24] T.T. Liang, Z.H. Lv, T.F. Jiang, Y.H. Wang, Electrophoresis 34 (2013) 345.
[25] P. Canizares, F. Martinez, C. Jimenez, C. Saez, M.A. Rodrigo, J. Hazard. Mater. 151 (2008) 44.
[26] C.W. Melton, S.J. Anderson, C.F. Dye, W.E. Chase, R.E. Heffelfinger, Development of a rapid analytical method for determing asbestos in water. Athens, Georgia: US Environmental Protection Agency, Environmental Research Laboratory (1978) 19.
[27] G.M. Fair, J.C. Geyer, D.A. Okun, Water and Wastewater Engineering, Vol. 2, John Wiley & Sons, Inc., New York, 1968.
[28] R. Romero-González, A.G. Frenich, J.L.M. Vidal, Talanta 76 (2008) 211.
[29] W. Karcher, J. Devillers, Practical Applications of Quantitative Structure-Activity Relationships (QSAR) in Environmental Chemistry and Toxicology, Kluwer the language of science, Italy, 1990.
[30] Estimation Programs Interface (EPI) Suite Download EPI Suite v4.11, U.S. Environmental Protection Agency, November, 2012.
[31] M.J. Chen, Y.T. Liu, C.W. Lin, V.K. Ponnusamy, J.F. Jen, Anal. Chim. Acta 767 (2013) 81.
[32] E. Jagerdeo, M.A. Montgomery, M. Sibum, T.A. Sasaki, M.A. LeBeau, J. Anal. Toxicol. 32 (2008) 571.
[33] K. Seebunrueng, Y. Santaladchaiyakit, S. Srijaranai, Anal. Bioanal. Chem. 404 (2012) 1539.
[34] M. Pirsaheb, N. Fattahi, M. Shamsipur, Food Control 34 (2013) 378.
[35] L. Zhang, F. Chen, S. Liu, B. Chen, C. Pan, J. Sep. Sci. 35 (2012) 2514.

Talanta 132 (2015) 775–784

Contents lists available at ScienceDirect

Talanta

journal homepage: www.elsevier.com/locate/talanta

Ultra-high performance liquid chromatography tandem mass spectrometric method for the determination of tamoxifen, *N*-desmethyltamoxifen, 4-hydroxytamoxifen and endoxifen in dried blood spots—Development, validation and clinical application during breast cancer adjuvant therapy

Marina Venzon Antunes [a,b,*], Suziane Raymundo [b], Vanessa de Oliveira [b], Dilana Elisabeth Staudt [b], Gustavo Gössling [c], Giovana Piva Peteffi [b], Jorge Villanova Biazús [c], José Antônio Cavalheiro [c], Marie Tre-Hardy [d], Arnaud Capron [d], Vincent Haufroid [d], Pierre Wallemacq [d], Gilberto Schwartsmann [a,c], Rafael Linden [b]

[a] *Pós-graduação em Ciências Médicas, Faculdade de Medicina, Universidade Federal do Rio Grande do Sul, Porto Alegre, RS, Brazil*
[b] *Instituto de Ciências da Saúde, Universidade Feevale, Novo Hamburgo, RS, Brazil*
[c] *Hospital de Clínicas de Porto Alegre, Porto Alegre, RS, Brazil*
[d] *Louvain Center for Toxicology and Applied Pharmacology, Université Catholique de Louvain, Brussels, Belgium*

ARTICLE INFO

Article history:
Received 22 September 2014
Received in revised form
17 October 2014
Accepted 19 October 2014
Available online 29 October 2014

Keywords:
Dried blood spot
Tamoxifen
Endoxifen
4-Hydroxytamoxifen
N-desmethyltamoxifen
LC–MS/MS

ABSTRACT

A LC–MSMS method for the simultaneous determination of tamoxifen, *N*-desmethyltamoxifen, 4-hydroxytamoxifen and endoxifen in dried blood spots samples was developed and validated. The method employs an ultrasound-assisted liquid extraction and a reversed phase separation in an Acquity® C18 column (150 × 2.1 mm, 1.7 μm). Mobile phase was a mixture of formic acid 0.1% (v/v) pH 2.7 and acetonitrile (gradient from 60:40 to 50:50, v/v). Total analytical run time was 8 min. Precision assays showed CV % lower than 10.75% and accuracy in the range 94.5 to 110.3%. Mean analytes recoveries from DBS ranged from 40% to 92%. The method was successfully applied to 91 paired clinical DBS and plasma samples. Dried blood spots concentrations were highly correlated to plasma, with $rs > 0.83$ ($P < 0.01$). Median estimated plasma concentrations after hematocrit and partition factor adjustment were: TAM 123.3 ng mL^{-1}; NDT 267.9 ng mL^{-1}, EDF 10.0 ng mL^{-1} and HTF 1.3 ng mL^{-1}, representing in average 98 to 104% of the actually measured concentrations. The DBS method was able to identify 96% of patients with plasma EDF concentrations below the clinical threshold related to better prognosis (5.9 ng mL^{-1}). The procedure has adequate analytical performance and can be an efficient tool to optimize adjuvant breast cancer treatment, especially in resource limited settings.

© 2014 Elsevier B.V. All rights reserved.

1. Introduction

Tamoxifen (TAM) [*trans*-1-(4-β-dimethylaminoethoxyphenyl)-1,2-diphenyl-1-butene] has been the mainstay hormonal treatment for breast cancer for more than 30 years, with significant impact on the survival rates of patients. However, besides the therapeutic benefits of TAM in the general population, 30 to 50% of patients under TAM pharmacotherapy have tumor recidives or present resistance to the treatment [1].

The usual presentation of TAM is TAM citrate tablets, containing 10 or 20 mg of the pure *trans* isomer, with the recommended posology of 20 mg per day. TAM pharmacologic activity is dependent of its bioativation by cytochrome P 450 enzymes [2,3]. CYP3A4 and 3A5 convert TAM to *N*-desmethyltamoxifen (NDT), this being the largest primary metabolic route. NDT undergoes 4-hydroxylation via CYP2D6, being biotransformed into 4-hydroxy-*N*-desmethyltamoxifen or (Z)-endoxifen (EDF). CYP2D6 also catalyzes the metabolism of TAM to 4-hydroxy-TAM (HTF) [4]. The antiestrogenic activity of TAM is mainly due to EDF, which, as HTF, is up to 100 times more potent to inhibit the proliferation of

* Correspondence to: Universidade Feevale, ERS 239, n° 2755, Zip Code 93352-000, Novo Hamburgo, RS, Brazil. Tel.: +55 51 358 8800 9039.
E-mail address: marinaantunes@feevale.br (M.V. Antunes).

http://dx.doi.org/10.1016/j.talanta.2014.10.040
0039-9140/© 2014 Elsevier B.V. All rights reserved.

estrogen-dependent cells, and usually have plasma concentrations up to 6 times higher than HTF [5].

EDF plasma concentrations were widely variable among patients, what could be explained by polymorphisms in the gene encoding CYP2D6 and by interactions with enzyme modulating agents, leading to insufficient plasma EDF levels in many individuals [6]. Along CYP2D6, CYP3A and CYP2C9 enzymes were related to EDF formation, but to a lesser extend [2]. Recently, Teft et al. [7] described reduced EDF plasma concentrations during the winter months, which was associated to low plasma 25-hydroxyvitamin D levels. These authors suggested that CYP3A4 activity together with sunlight exposure is an underscored factor in the evaluation of the therapeutic efficacy of TAM.

In a recent clinical study, Madlensky et al. [8] exploited the relation between the clinical outcome of hormonal therapy and serum concentrations of TAM and its metabolites, suggesting that adequate therapeutic outcome is dependent to the achievement of a threshold EDF concentration. Patients presenting trough EDF plasma levels above 5.9 ng mL^{-1} had a 26% reduction of recurrences comparing with patients with EDF concentrations below this threshold. These findings, along with the increasing knowledge about TAM metabolism modulating agents, encouraged studies with individualized dose adjustments, with increased doses for patients with impaired EDF formation (30 or 40 mg day^{-1}) [9–11]. Moreover, the metabolic ratio [NDF]/[EDF] has been described as an appropriate surrogate of CYP2D6 activity, rendering useful clinical information about TAM metabolism [5]. Considering the available evidence, therapeutic drug monitoring of TAM and its main metabolites during hormonal therapy of breast cancer could be an important tool to obtain optimal pharmacological response, recognizing patients eligible to higher TAM doses or alternative pharmacotherapy.

Several methods for the measurement of TAM and metabolites in serum or plasma samples were described [6,12–14]. To obtain these conventional samples, it is necessary to perform a phlebotomy in a proper facility, also considering pharmacokinetically appropriated collection times. A novel option for therapeutic drug monitoring that has been emerging recently is testing in dried blood spots on paper (DBS), collected by finger prick [15–17], mainly due to the stabilization of the analytes by drying and the possibility of postal transportation, once DBS samples are usually non-bio hazardous. Also, this novel matrix allows the possibility of training patients to take their own samples and flexible collection times, more adequate to their personal posology [18].

The use of DBS for TAM and metabolites measurements could be a very useful strategy to optimize the use of this drug in breast cancer, potentially allowing continuous monitoring of EDF levels during a long-time treatment, without requiring patients to come to a specialized center. However, considering the small blood volume present in a DBS obtained after a finger prick and the low concentrations of TAM and metabolites, especially EDF, this application requires highly sensitive analytical methods. In view of the above, the objective of this study was to develop and validate a method for determination of TAM and its metabolites NDT, EDF e HTF in DBS using ultra performance liquid chromatography-positive electrospray ionization tandem mass spectrometry and evaluate its performance in clinical samples of breast cancer patients.

2. Experimental

2.1. Reagents, materials and reference standard samples

Tamoxifen, 4-hydroxy tamoxifen e clomifen citrate (E/Z) were acquired from Sigma (Saint Louis, USA). *N*-desmethyl tamoxifen chloridrate and *N*-desmethyl-4-hidroxy tamoxifen (E/Z) were obtained from Toronto Research Chemicals (North York, Canada). Tris(hidroxymethyl)aminomethane was obtained from Nuclear (Diadema, Brazil). Formic acid, metanol, acetonitrile, *n*-propanol and hexane (60% *n*-hexane) were bought from Merck (Darmstadt, Germany). Purified water was obtained from an Elga Purelab Ultra® system from Veolia Labwater (High Wycombe, UK). Whatman 903 paper was obtained from GE Healthcare (Westborough, USA).Finger prick blood samples were collected using Medlance® Plus Special lancets (0.8 mm blade) from Medlance Plus Special (Marietta, USA).

2.2. Preparation of solutions and standards

TAM, NDT and EDF (E/Z) stock solutions were prepared in methanol to obtain a concentration of 1 mg mL^{-1}. The stock solution of HTF was prepared in methanol to obtain a concentration of 0.1 mg mL^{-1}. Stock was diluted with methanol to obtain intermediate solutions of EDF and HTF at 20 μg mL^{-1} and intermediate solutions of TAM, NDT e EDF at 40 μg mL^{-1} (20 μg mL^{-1} of the Z-fraction of EDF). Working solutions were prepared by dilution of the intermediate solution with methanol. Calibration samples were prepared in whole blood diluting working solutions at 1:20 with whole blood free from the analytes, as described in the *linearity* section. Clomifene citrate stock (internal standard, IS) solution was prepared in methanol at 1 mg mL^{-1} concentration. Intermediate clomifene solutions were prepared by dilution of the stock with methanol (10.0 μg mL^{-1}) and further diluted to 0.1 μg mL^{-1}. DBS extraction solution was prepared by dilution of the clomifene intermediate (0.1 μg mL^{-1}) with methanol to obtain a concentration of 0.1 ng mL^{-1}.

2.3. Sample preparation

Quality control and calibration samples were prepared by pipetting 60 μL aliquots of spiked blood onto Whatman 903 paper and leaving them to dry at room temperature for 3 h before processing. DBS discs were obtained by perforation, using a 10 mm punch cutter, and two discs were used for extraction. Discs were cut in half, transferred to polypropylene microtubes and 1000 μL of extraction solution was added (clomifene 0.1 ng mL^{-1} in methanol), followed by 1 min vortexing. After 45 min h in an ultrasonic bath, 850 μL of extract was transferred to a clean polypropylene microtube and dried at 55 °C under a gentle stream of air. The dried extract was recovered with 100 μL of mobile phase, transferred to an autosampler vial and a 25 μL aliquot was injected into the LC–MS/MS system.

2.4. UHPLC–MS–MS equipment and conditions

Samples were analyzed using a TSQ Quantum Access triple quadrupole mass spectrometer with an electrospray source, coupled to an Ultimate 3000 XRS UHPLC system, controlled by the Xcalibur software, all from Thermo Scientific (San Jose, USA). Separation was performed in an Acquity C18 column (150 × 2.6 mm, p.d. 1.7 μm) from Waters (Milford, USA), maintained at 50 °C and eluted at a mobile phase flow rate of 0.4 mL min^{-1}. The mobile phase consisted of formic acid 0.1% pH 2.7 (eluent A) and acetonitrile plus 0.1% formic acid (eluent B). Initial eluent composition was 60% A, maintained for 3 min, and followed by a linear 1 min ramp to 50%, which was maintained for until 5.5 min. The mobile composition returned to 60% A at 6 min. Equilibration time was 2 min. Injection volume was 25 μL. The MS conditions were as follows: electrospray ionization (ESI), positive mode, capillary voltage of 4 kV; sheath gas, nitrogen at a flow rate of 50 arbitrary units; auxiliary gas, nitrogen at flow rate of ten arbitrary units; collision

gas, argon; vaporizer temperature, 400 °C; and ion transfer capillary temperature, 220 °C. The scan time was set at 0.3 s per transition. The following transitions were used for MRM acquisition: TAM *m/z* 372→72 (quantitation) and *m/z* 372→70 and 372→129 (qualification); NDT *m/z* 358→58 (quantitation) and *m/z* 358→129 and 358→178 (qualification); EDF *m/z* 374→58 (quantitation), *m/z* 374→152 and 374→223 (qualification); HTF *m/z* 388→72 (quantitation) and *m/z* 388→129 and 388→223 (qualification); IS (clomifene) *m/z* 406→100 (quantitation) and *m/z* 406→72 and 406→58 (qualification). Collision energies were 23, 19, 19, 24 and 24 eV for TAM, NDT, EDF, HTF and IS, respectively.

2.5. Selectivity

Blank DBS samples obtained from 6 different human sources were prepared as described above to check for the presence of chromatographic peaks that might interfere with detection of analytes or IS.

2.6. Benchtop stability

For estimation of stability of processed samples under the conditions of analysis, control DBS samples were extracted as described above, in sextuplicate. Quality control low (QCL) samples had TAM, NDT, EDF e HTF at 21.0; 45.0; 3.0 and 1.8 ng mL^{-1}, respectively. Quality control high (QCL) samples had TAM, NDT, EDF and HTF at 210.0; 450.0; 30.0 and 10.8 ng mL^{-1}, respectively. The extracts obtained at each concentration were pooled. Aliquots of these pooled extracts at each concentration were transferred to autosampler vials and injected under the conditions of a regular analytical run at time intervals of 1 h, during 12 h. Stability of analytes was tested by regression analysis plotting absolute peak areas corresponding to each compound at each concentration *vs.* injection time. Using the obtained linear regression, the concentration after 12 h was calculated. A decrease or increase of up to 10% in the measured peak areas was considered as acceptable.

2.7. Stability of analytes in DBS at varying temperatures

For evaluation of thermal stability of TAM and metabolites in DBS samples, quality control DBS samples (QCL and QCH), previously described, were maintained at −20 °C, 25 °C e 45 °C and analyzed (triplicate) on days 2, 6, 8, 10, 13, 15, 17 e 20 after spotting in the paper. Stability was considered acceptable if all results were within the range of 85–115% of the concentrations measured at the beginning of the series.

2.8. Linearity

Aliquots of 950 μL blank blood (Hct 35%), were enriched with 50 μL of the corresponding stock solutions to obtain seven calibration levels of samples containing TAM (300, 225, 150, 75, 30, 15, 7.5 ng mL^{-1}), NDT (600, 450, 300, 150, 60, 30, 15 ng mL^{-1}), EDF (40, 30, 20, 10, 4, 2, 1 ng mL^{-1}) and HTF (50, 15, 10, 5, 2, 1, 0.5 ng mL^{-1}). Calibration samples were applied to Whatman 903 paper (12 × 60 μL for each level), dried at room temperature and analyzed within 24 h. Replicates ($n=6$) at each concentration were analyzed as described at item 2.5. Calibration curves were calculated relating the area ratios from TAM, NDT, EDF and HTF peaks to the IS peak and with the nominal concentrations of the calibration samples. Homoscedasticity of calibration data was evaluated with *F*-test at the confidence level of 95%. Curves were fitted using least-squares linear regression using several weighting factors ($1/x$, $1/x^2$, $1/y$, $1/y^2$). Calibration models were assessed using coefficients of correlation (r) and cumulative percentage relative error ($\sum$%RE) [19]. Daily calibration curves using the same concentrations (single measurement at each concentration level) were analyzed with each batch of validation and clinical samples.

2.9. Precision and accuracy

Aliquots of blank blood were enriched with methanolic solutions and applied to paper to obtain quality control DBS samples containing TAM, NDT, EDF and HTF at concentrations of 21.0; 45.0; 3.0 and 1.8 ng mL^{-1}, respectively (quality control low, QCL), 70.0; 150.0; 10.0 and 6.0 ng mL^{-1}, respectively (quality control medium, QCM) and 210.0; 450.0; 30.0 and 18.0 ng mL^{-1}, respectively (quality control high, QCH). Control samples were maintained at room temperature and analyzed within 24 h as item 2.5. The quality control samples were analyzed as described above in triplicate on each of 5 days. Within-assay precision and between-day precision were calculated by one-way ANOVA with the grouping variable "day" and were expressed as CV%. Accuracy was defined as the percentage of the nominal concentration represented by the concentration estimated with the calibration curve. The acceptance criteria for accuracy were mean values within ±15% of the theoretical value and for precision a maximum CV of 15% was accepted [20].

2.10. Lower limit of quantification

An independent DBS quality control sample at the lowest point of the calibration curve at concentrations of 7.5; 15.0; 1.0; 0.5 ng mL^{-1} for TAM, NDT, EDF and HTF, respectively, was included in the accuracy and precision experiments (quality control at the limit of quantitation, QCLOQ) and was tested in triplicate in three different days. The acceptance criteria established for the limit of quantification was accuracy within 100 ± 20% of the nominal value and an imprecision with of maximum 20% [20].

2.11. Influence of hematocrit on analytes concentrations assayed in DBS samples

Aliquots of blood containing different Hct% (25, 30, 35, 40, 45 and 50%) were prepared by centrifuging EDTA whole blood and then combined with appropriate volumes of cells and plasma. TAM and metabolites were added to these aliquots of blood to achieve concentrations of QCL: 21.0; 45.0; 3.0 and 1.8 ng mL^{-1} and QCH: 210.0; 450.0; 30.0 and 18.0 ng mL^{-1} for TAM, NDT, EDF and HTF, respectively, which were then pipetted onto Whatman 903 paper, followed by drying at room temperature for 3 h. The DBS obtained were analyzed in triplicate for each concentration and Hct% as described in item 2.5. The influence of the Hct% on TAM and metabolites measurements was determined as the percentages of nominal concentrations that were actually measured in the DBS.

2.12. Matrix effect and extraction yield

Matrix effect was evaluated by a post-extraction spike method. Three series of quality control samples (QCL, QCM and QCH) were prepared in order to assess extraction yield and matrix effect on ionization as follows: (A) solutions of TAM, metabolites and IS prepared in mobile phase solutions in order to obtain final concentrations equivalent to 100% extraction yield and directly injected onto column. (B) DBS extracts samples from 5 different sources (mixed before application on paper), post-extraction spiked with TAM, metabolites in mobile phase containing IS. (C) DBS extracts samples from 5 different sources (mixed before application on paper) enriched with TAM and metabolites before extraction. Each quality control sample was analyzed in quintuplicate. Matrix effect (ME) on ionization was estimated as the percentages of reduction or increase of TAM, NDT, EDF, HTF and IS areas on post-extraction spiked (B), comparing to directly injection of

solutions (B), calculated as ME=[100%−(B/A%)]. Extraction yields (EY) were calculated comparing the analyte/IS area ratio before extraction (C) and after extraction (B), using the formula EY=C/B%.

2.13. Application of the method

The study was conducted in accordance with the Declaration of Helsinki and was approved by the Research Ethics Committee at the Hospital de Clínicas de Porto Alegre. A total of 91 patients on adjuvant hormonal treatment with tamoxifen (20 mg day^{-1}) for at least 4 months were enrolled in the study with informed consent. Data on age, weight, body mass index (BMI), race, compliance (obtained from the number of TAM tablets taken monthly) and menopause status were recorded, in addition to the duration of TAM therapy and any concomitant therapies considered as CYP2D6 inhibitors. Blood samples were taken 18–24 h after the last TAM intake, patients being fasten for 4 h. Capillary blood was collected after finger prick using a 2.0 mm penetration, 0.8 mm blade contact-activating lancet (Medlance®). Blood spots were collected on 2 circles of the Whatman 903 DBS card and allowed to dry for at least 3 h at room temperature.

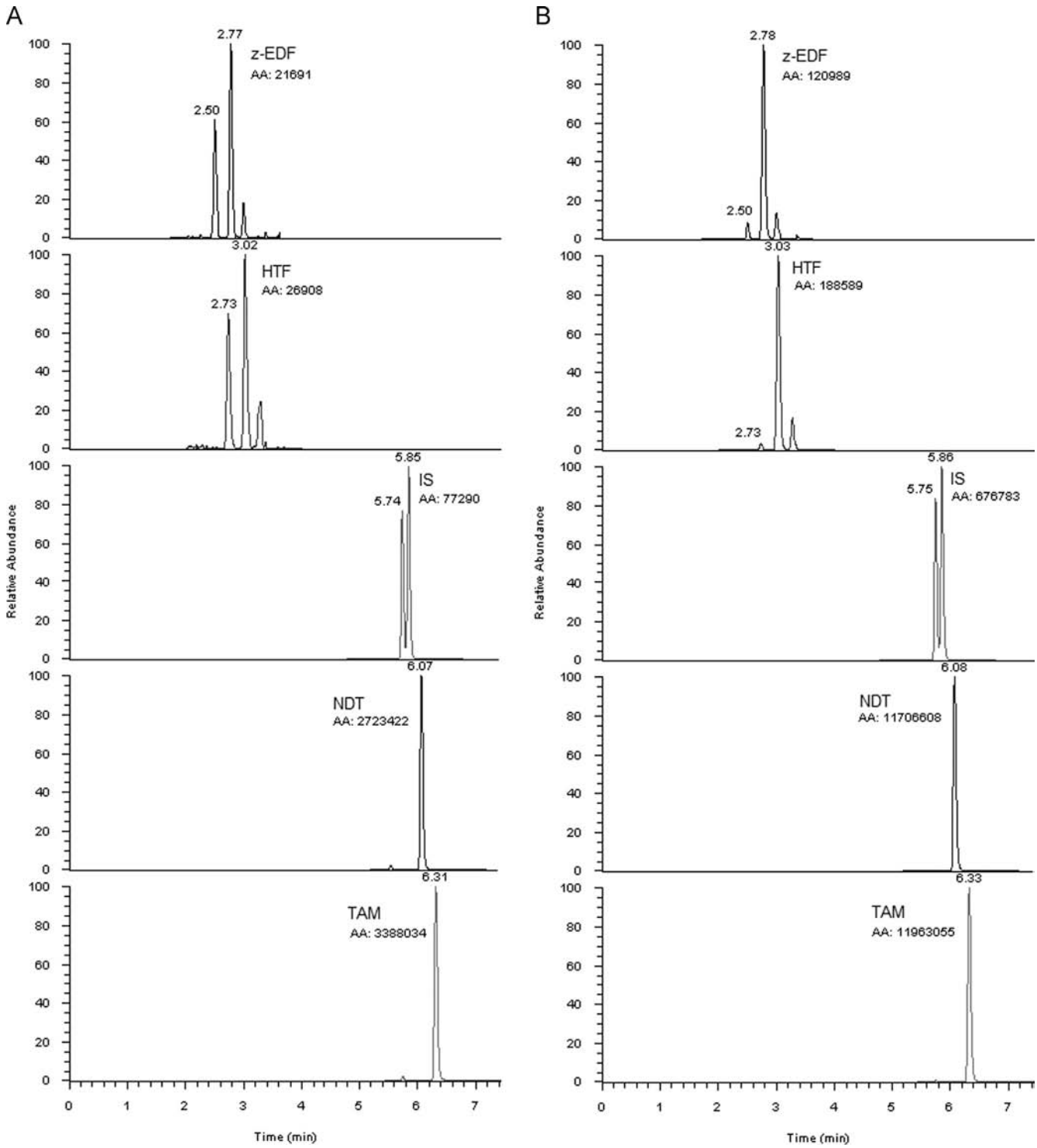


Fig. 1. Chromatograms obtained from DBS and plasma analyses. (A) Plasma EDF 9.9, HTF 1.5, NDT, 188.3, TAM 111.8 (ng mL^{-1}); (B) dried blood spot EDF 4.8, HTF 1.2, NDT, 166.0, TAM 100.0 (ng mL^{-1}). Transitions: EDF 374→58 (*m*/*z*), HTF 388→72 (*m*/*z*), IS 406→100 (*m*/*z*), NDT 358→58 (*m*/*z*) TAM 372→72 (*m*/*z*).

Analyses were performed within 3 days. Venous blood was simultaneously collected within an interval of ± 15 min by venipuncture into two EDTA tubes. One tube was used for Hct% determination, the other was immediately centrifuged and plasma was transferred to polypropylene tubes, stored at −70 °C until analysis within one month. Concentrations of TAM, NDT, EDF and HTF were measured through daily calibration curves and estimated plasma concentrations (EPC) were obtained after adjustment of DBS concentrations by patients Hct % and use of a correction factor, as follows:

$$EPC = [(\text{DBS concentration})/(1-\text{Hct})] \times \text{correction factor}$$

Correction factors were estimated so that the ratio of mean DBS to mean plasma levels would be equal to 1.

2.14. Determination of TAM and metabolites in plasma

A 0.2 mL aliquot of plasma was transferred to screw cap glass tube and 0.1 mL of the IS solution (clomiphene 0.01 μg mL^{-1}), 0.1 mL of Tris buffer pH 10 and 2 mL of extraction solvent (hexane: *n*-propanol 95:5, v/v). After homogenization for 30 min and centrifugation at 3000*g* for 10 min, a 1.6 mL aliquot of the supernatant was transferred to a polypropylene microtube and dried at 55 °C for 15 min under air stream. The extract was resuspended with 0.15 mL of mobile phase and a 25 μL aliquot was injected into the LC–M/MS system. The chromatographic conditions and mass detector parameters were the same as those used for the DBS samples. Concentrations were calculated with daily calibration curves. The method was linear from 0.5 to 600 ng mL^{-1} with LLOQ of 7.5 ng mL^{-1} for TAM, 15 ng mL^{-1} for NDT, 1 ng mL^{-1} for EDF and 0.5 ng mL^{-1} for HTF. Accuracy and imprecision were acceptable with accuracy of 90.7–107.5%, and percent coefficient of variation within and between assay in the range of 4.8–13.4.

2.15. Statistical analysis

Initially, a descriptive analysis of the study variables was conducted. The precision validation parameters were evaluated using ANOVA. Medians and 25% and 75% percentiles for TAM, NDT, EDF, HTF levels and metabolic ratio [NDT]/[EDF] were determined. Analytes in DBS (y) *vs* measured plasma concentrations (x), as well as estimated plasma (y) *vs* measured plasma concentrations (x) were assessed by Passing–Bablok regression [21] and Spearman correlation. The presence of outliers and tendencies were evaluated using Bland Altman plots [22] of estimated plasma concentrations *vs* measured plasma concentrations as well as DBS *vs* measured plasma concentrations. Acceptation criteria for the agreement between estimated and measured plasma concentrations were based on the guideline on Bioanalytical Method Validation of the EMA, the difference in concentration should be within ± 20% of their mean for at least 67% of the samples [23].

The effect of concomitant CYP2D6 inhibitors was tested for TAM, NDT, EDF, HTF and metabolic ratio [NDT]/[EDF] from measured and estimated plasma data obtained from patients stratified in 2 cohorts based on the use or not of CYP2D6 inhibitors by Mann–Whitney test. DBS levels of EDF and the DBS metabolic ratio [NDT]/[EDF] were further compared between these 2 cohorts with plasma EDF above or below the threshold of efficacy of 5.9 ng mL^{-1} by Mann–Whitney test. Analyses were conducted using SPSS version 17.0 and MedCalc version 12.3, $P < 0.05$ was considered statistically significant.

3. Results and discussion

3.1. Chromatography and preparation of samples

The LC–MS/MS system proved to be an appropriate system for determination of TAM and its main metabolites in DBS samples. TAM, NDT, HTF and EDF are structurally very similar, with demethylation and/or hydroxylation, resulting in slight differences of polarity. Reversed phase C18 columns appeared appropriate to separate TAM metabolites [24]. In this study an Acquity® C18 column (150 × 2.1 mm, 1.7 μm) was used, separating TAM and the 3 metabolites in a 8 min run, with reduced mobile phase consumption of 3.2 mL per analysis. Retention times were 2.77 min for EDF, 3.02 min for HTF, 5.85 min for IS, 6.07 min for NDT and

Table 1
Method validation parameters, linearity, precision, accuracy and extraction yield and benchtop stability.

Analyte	Linear regression weighting factor 1/x	Quality control	Nominal concentration (ng mL^{-1})	Precision (CV %)		Accuracy (%)	Extraction yield (%)	Ion suppression/ enhancement (%)	Concentration change after 12 h (%)
				Intra-assay	Inter-assay				
Tamoxifen	$y=0.613x-0.403$	LLOQ	7.5	9.09	7.01	93.9	–	–	
	$r=0.996$	QCL	21.0	8.95	6.31	100.2	89.8	−20.4	−3.9
		QCM	70.0	5.13	8.58	98.5	91.3	−24.2	–
		QCH	210.0	8.18	5.10	102.8	93.4	−24.0	−8.1
N-desmethyltamoxifen	$y=0.222x-0.1913$	LLOQ	15.0	7.93	10.04	92.0	–	–	
	$r=0.997$	QCL	45.0	6.73	7.61	99.5	81.5	−34.4	−0.8
		QCM	150.0	6.75	8.51	99.4	88.5	−34.5	–
		QCH	450.0	9.10	5.17	94.5	84.5	−35.3	−3.2
(Z)-Endoxifen	$y=0.117x-0.0701$	LLOQ	1.0	7.46	11.48	97.5	–	–	–
	$r=0.991$	QCL	3.0	6.59	7.68	96.7	47.9	−11.1	9.2
		QCM	10.0	8.72	10.77	105.2	48.5	−11.3	–
		QCH	30.0	12.30	6.53	98.0	46.1	−12.0	−2.7
4-Hydroxytamoxifen	$y=0.533x-0.0912$	LLOQ	0.5	12.07	7.93	90.6	–	–	–
	$r=0.991$	QCL	1.8	8.98	11.54	94.6	38.1	−5.9	5.2
		QCM	6.0	10.42	5.75	110.3	39.4	−6.6	–
		QCH	18.0	8.53	7.13	98.9	41.2	−2.7	−5.8
Clomiphene (IS)		LLOQ						–	
		QCL						+9.1	
		QCM						+6.7	
		QCH						+8.7	

LLOQ: lower limit of quantification, QCL: quality control low, QCM: quality control medium, QCH: quality control high. (linearity $n=42$, precision and accuracy $n=45$, extraction yield $n=30$, ion suppression $n=30$).

6.31 min for TAM. Fig. 1 illustrates chromatograms from DBS and plasma samples.

No interfering compounds were identified in the 6 DBS samples processed free from TAM and analytes. Additionally, the tandem mass spectrometry results in inherent specificity analysis, in which chromatograms are monitored through the transition of molecular ion to three products (1 quantifying and 2 confirmatory ions).

Sample preparation was simple, based on ultrasound-assisted liquid extraction of analytes from paper punches containing approximately 90 μL of blood. Extraction yield was higher for the least polar compounds, with average of 91.5% for TAM and 84.8% for NDT, comparing to 47.5% for (Z)–(Z)–EDF and 39.6% for HTF. Besides the lower extraction recoveries of EDF and HTF, the method presented satisfactory sensitivity considering the extent of concentrations found in clinical samples, with LLOQ of 1.0 ng mL^{-1} for EDF and 0.5 ng mL^{-1} for HTF [25,14,11,26].

3.2. Method validation

Extracts from DBS containing TAM and metabolites at QCL and QCH concentrations were stable during the 12 h bench stability test, with maximum variation in analytical response of 9.2%, indicating that large batches can be analyzed without taking special measures to preserve extracts. Calibration data exhibited significant heteroscedasticity, with F_{exp} ranging from 495.1 to 1237.0 ($F_{tab\ (6;\ 5;\ 0.95)}=4.95$). The regression using a weighting factor of $1/x$ offered the best ∑%RE of the models tested, with values below 1×10^{-9} and this weighting factor was used for all subsequent validation tests and for analysis of the clinical samples. The coefficients of correlation were above 0.99 for all weighting factors. The results of the precision and accuracy experiments, assessed by analyzing low, medium and high concentration quality control samples, were satisfactory, as shown in Table 1. Intra-assay imprecision were in the range of 5.13 to 12.30% and inter-assay imprecision was 5.10 to 11.54%, demonstrating that the method is adequately repeatable. Accuracy was estimated at 94.6 to 110.3%, which is also within the limits of acceptance for bioanalytical methods recommended by Shah et al. [20]. The quality control samples at the lower limit of quantification (LLOQ) of 7.5; 15; 1.0; 0.5 ng mL^{-1} for TAM, NDT, EDF and HTF presented acceptable imprecision (from 7.01 to 12.07%) and accuracy (90.6 to 97.5%).

Due to its high specificity and sensitivity LC–MS/MS is considered as the method of choice for quantitative analysis of compounds in biological matrices. However molecules originating from the sample matrix that coelute with the compounds of interest can interfere with the ionization process, causing ion suppression or enhancement [27]. Post-extraction spiked method analysis showed (Z)–EDF and HTF ionization suppression within 12% and IS ionization enhancement effect of 8%, indicating that co-eluting matrix components appear to have a minimal effect on the considered analytes. TAM and NDT demonstrated to be more affected by matrix effect with average suppression of 22.9 and 34.7% respectively. Similar observation was pointed out on a previously described LC–MS/MS method [28], where matrix ionization suppression (plasma samples) was larger for NDT (38% area reduction) comparing to other TAM metabolites.

As reported above, matrix components do influence to some extent TAM and NDT ionization and consequently the overall process efficiency, requiring therefore the preparation of calibration and control samples in a DBS matrix reflecting at best the composition of the samples to be analyzed. More important that the absolute matrix effect, no significant variability among concentrations and samples was observed in our method. Additionally, TAM and NDT presented high extraction yields (>81%), allowing analysis with satisfactory sensitivity and linearity range comprising clinical samples concentrations after a 20 mg/daily intake of TAM [25,11,26].

Thermal stability was also tested in DBS samples at the concentrations of QCL and QCH after storage at −20 °C, 25 °C and 45 °C up to 20 days. These temperatures were selected to simulate conditions that samples sent by regular mail could potentially be exposed. No changes were observed neither for TAM nor for NDT on DBS stored over a period of 20 days at the tested temperatures (maximum variance of 14%). However, (Z)–EDF and HTF were stable at −20 and 25 °C (maximum variance of 15%) but not at 45 °C, with an increase on concentrations, which ranged from 38% at day 2, to 47% after 20 days. In absence of any data in the literature regarding TAM and metabolites stability on DBS samples, we assumed that increase of metabolite concentrations at higher temperature could be the consequence of TAM and NDT degradation. Tested EDF and HTF levels were approximately 10 fold lower than TAM and NDT, therefore more likely affected by any minor changes in TAM and NDT concentrations. Another possible explanation for this finding could be the production of isobaric interfering compounds on DBS samples under high temperatures. Both hypotheses should be further tested.

Information about the thermal, light, and chemical stability of the analytes in DBS matrix must be available in order to explore its logistic advantages. When using transport by regular mail it is important to be aware that the inner temperature of mailboxes in full sun exposure can reach about 60 °C in summer months [29]. Up to now there is no data in the literature regarding the stability of EDF and HTF in DBS samples. Considering our findings on EDF and HTF stability and the high temperatures during summer time, it is reasonable to recommend that temperature during transport and storage of DBS cards for TAM and metabolites measurement should be controlled and not exceed 25 °C.

Table 2
Patients demographic characteristics ($N=91$).

Characteristic	($N=91$)
Age (years)	
Mean (±SD)	56.3 (10.1)
Range	28–78
Hematocrit (%)	
Mean (±SD)	36.0 (2.4)
Range	30.6–43.5
Race/ethnicity (n)	
Caucasian	75
Others	16
Menopause status (n)	
Pre menopause	41
Post menopause	50
Tamoxifen duration (months)	
Median (Percentiles 25–75)	15 (9–23)
Range	(4–45)
Marital status (n)	
Single	14
Married	45
Divorced	12
Widowed	20
CYP2D6 inhibitor drug (n)	
Weak/moderately	11
Strong	7
Adverse effects (n) no/yes	
Hot flashes	44/47
Vaginal bleeding	88/3
Vaginal discharge	60/31
Vulvar Itching	73/18
Nausea or vomiting	76/15
Dizzeness	75/16
Cutaneous rash	82/9
Alopecia	68/23
Thrombosis	87/4

3.3. Impact of hematocrit on determination of TAM and metabolites

The impact of different Hct% levels on calculated concentrations of TAM and metabolites during analysis of DBS samples was tested at concentrations of QCL and QCH prepared in blank blood with Hct% ranging from 25 to 50 and quantified by analytical curves prepared using blood with Hct% of 35. Variation from nominal concentrations found in control samples were within ± 13% for Hct 25%, ± 10% for Hct 30%, ± 10% for Hct 35%, ± 8% for Hct 40%, ± 16% for Hct 45% and ± 20% for Hct 50%. Highest variations from target were found at Hct 45% and 50% and were above 15% which was the cutoff for acceptability. This is probably due to increased viscosity of the blood and hence reduced dispersion through the paper. In contrast, DBS prepared with blood with Hct percentages ranging from 25 to 40 presented results within the range of acceptability (87–108%). On this basis, analytical curves prepared using blood with Hct% of 35 are applicable to samples from patients with Hct% within 25–40, covering most of patients Hct% range (30.6 to 43.6, mean 36). Seven patients had Hct% above 40, where calculated concentrations have to be corrected accordingly.

Besides DBS samples being obtained from capillary blood, venous blood was used to determine the patient Hct%, considering the absence of difference between capillary and venous Hct% [29]. Yang et al. [30] also found no difference between Hct% measured in venous and capillary blood.

3.4. Clinical application and method comparison

A total of 91 patients on adjuvant hormonal treatment with tamoxifen (20 mg day^{-1}) were enrolled in this study. Patient's demographic and clinical data are presented in Table 2. All patients were classified as adherent to TAM, with reported use of 30 tablets monthly. The patient population displayed a mean age of 56.3 years, mean BMI of 27.0 kg m^{-2} and mean Hct% of 36.0 (range 30.6–43.5), 75 patients were Caucasian and 16 were brown (*parda*-a Brazilian national census classification) or black. Hot flashes were the major adverse effect (51.6%). Eighteen patients (19.8%) reported concomitant use of CYP2D6 inhibitors drugs: 11 on weak inhibitors (*e.g.* venlafaxine, citalopram and haloperidol) and 7 on strong inhibitors (*e.g.* fluoxetine and bupropion).

The developed method was used to analyze DBS concentrations of TAM and its metabolites, paired with plasma analyses. Analytes concentrations were highly variable in both matrices, as presented in Table 3. Median DBS levels in the whole cohort were: TAM 100.0 ng mL^{-1}; NDT 202.0 ng mL^{-1}, (Z)–EDF 5.9 ng mL^{-1} and HTF 0.9 ng mL^{-1} and median plasma concentrations were: TAM 123.2 ng mL^{-1}; NDT 263.5 ng mL^{-1}, EDF 9.1 ng mL^{-1} and HTF 1.4 ng mL^{-1}. Plasma trough concentrations were consistent with those previously reported in the literature [25,11,26]. EDF levels were 6.5-fold higher than HTF concentrations, with the 5.7-fold [14] and 6.8-fold [31] previously reported, confirming the predominance of EDF over HTF.

Tamoxifen, NDT, EDF and HTF concentrations in DBS were in average 80%, 77%, 59% and 72% of those measured in plasma. EPC were calculated from DBS concentrations after adjustment by patients Hct% and using the correction factors of 0.84; 0.78; 1.12; 0.87 for TAM, NDT, EDF and HTF respectively. After Hct% and factor correction, median estimated plasma levels were: TAM 123.3 ng mL^{-1}; NDT 267.9 ng mL^{-1}, EDF 10.0 ng mL^{-1} and HTF 1.3 ng mL^{-1}, thus estimated levels represented in average 98 to 104% of the actually measured plasma concentrations. The differences between EPC and

Table 3
Patients median, percentiles, range and correlations of TAM, NDT, EDF, HTF, and metabolic ratio [NDT]/[EDF] concentrations in plasma, dried blood spot and estimated plasma ($N=91$).

Analyte	Sample	Median (P25–P75) (ng mL^{-1})	Range (ng mL^{-1})	Mean ± SD relation to measured plasma (%)	Passing Bablok regression to measured plasma	Spearman correlation to measured plasma (*rs*)
Tamoxifen	Measured plasma	123.2 (101.5–165.5)	52.6–307.8	–	–	–
	Dried blood spot	100.0 (82.58–123.0)	40.0–290.0	80 ± 11	$y=0.688x+0.872$ (P=0.65)	0.917**
	Estimated plasma	123.3 (101.4–154.1)	49.9–364.3	98 ± 14	$y=0.982x+0.804$ ($P=0.69$)	0.911**
***N*-desmethyltamoxifen**	Measured plasma	263.5 (188.3–353.0)	85.6–575.9	–	–	–
	Dried blood spot	202.0 (140.0–262.1)	76.3–504.0	77 ± 14	$y=0.739x+9.592$ ($P=0.20$)	0.883**
	Estimated plasma	267.9 (177.4–350.0)	104.4–664.3	102 ± 19	$y=1.018x+3.854$ ($P=0.39$)	0.877**
(Z)-Endoxifen	Measured plasma	9.1 (5.8–15.1)	2.4–40.3	–	–	–
	Dried blood spot	5.9 (3.1–9.0)	1.0–24.2	59 ± 17	$y=0.566x-0.041$ (P=0.31)	0.895**
	Estimated plasma	10.0 (5.2–15.4)	1.5–41.3	104 ± 30	$y=1.053x-0.4376$ ($P=0.35$)	0.897**
4-Hydroxytamoxifen	Measured plasma	1.4 (0.9–1.8)	0.7–3.9	–	–	–
	Dried blood spot	0.9 (0.6–1.3)	0.5–3.2	72 ± 18	$y=0.761x+0.008$ ($P=0.31$)	0.842**
	Estimated plasma	1.3 (0.8–1.8)	0.5–4.4	99 ± 25	$y=1.061x-0.012$ ($P=0.33$)	0.839**
Metabolic ratio [NDT]/[EDF]	Measured plasma	25.8 (16.3–45.9)	5.1–175.4	–	–	–
	Dried blood spot	37.5 (19.6–67.9)	7.4–230.7	139 ± 41	$y=1.508x-3.308$ ($P=0.63$)	0.895**
	Estimated plasma	28.1 (14.7–50.9)	5.5–173.0	105 ± 31	$y=1.120x-2.134$ ($P=0.71$)	0.897**

NDT: *N*-desmethyltamoxifen; EDF: endoxifen; P25: percentile 25; P75: percentile 75, *rs*: spearman correlation coefficient.
P value as Cusum test for linearity.

** $P<0.01$ Spearman correlation.

measured plasma concentrations were within ±20% for most samples, 87 (97%) TAM, 86 (95%) NDT, 73 (80%) EDF and 80 (88%) HTF, being in accordance with the EMA acceptation criteria for the agreement between methods [23].

DBS concentrations and EPC were highly correlated to measured plasma concentrations with $rs > 0.83$ ($P < 0.01$) for all associations. Passing–Bablok regressions were performed in order to evaluate the existence of constant and/or proportional errors. Comparison of DBS (y) and measured plasma (x) concentrations returned in intercept 95% confidence intervals of −0.6472 to 10.0400 for TAM, −9.1216 to 28.0722 for NDT, −0.5097 to 0.4635 for EDF, −0.09409 to 0.09373 for HTF and −5.9314 to 0.3608 for the ratio [NDT]/[EDF] indicating no constant error. However, slope 95% confidence intervals showed the presence of proportional difference between methods: 0.6086 to 0.7879 for TAM, 0.6577 to 0.8289 for NDT, 0.4979 to 0.6402 for EDF, 0.6598 to 0.8512 for HTF and 1.3389 to 1.6789 for the ratio [NDT]/[EDF]. When EPC (y) and measured plasma levels (x) were compared, intercept 95% confidence intervals were −11.8954 to 17.8583 for TAM, −30.1816 to 26.4940 for NDT, −1.0641 to 0.7439 for EDF and 0.1460 to 0.1349 for HTF, indicating no constant error. At this evaluation, slope 95% confidence intervals showed to have no proportional differences: 0.8343 to 1.1120 for TAM, 0.9113 to 1.1465 for NDT, 0.9205 to 1.1744 for EDF, and 0.9289 to 1.1778 for HTF, indicating that when the effect of Hct% and multiplication factor are taken into account, methods are comparable. Cusum test P values were all > 0.05, indicating no significant difference from linearity.

Estimated plasma concentrations (EPC) of TAM and metabolites were also compared to measured plasma concentrations (MPC) by Bland–Altman plots (Fig. 2). The mean difference of the concentrations in plasma and estimated plasma concentrations using individual Hct% were 4.0 ng mL^{-1} for TAM, −0.7 ng mL^{-1} for NDT, 0.0 for EDF and 0.06 ng mL^{-1} for HTF, with only 4, 5 and 3 values (out of 91) outside the ±1.96 standard deviation range for TAM and NDT, EDF and HTF, respectively. Moreover, differences were also distributed randomly around the mean, indicating the absence of systematic errors which were proportional to TAM and metabolites levels.

Our data showed a wide range of EDF plasma concentrations among patients, with a 16.8 fold difference between the lowest (2.4 ng mL^{-1}) and the highest (40.3 ng mL^{-1}) measurement. The amplitude of concentrations may be attributed to the interindividual pharmacokinetic variability, including polymorphisms of CYP2D6 and CYP3A4 and drugs interactions [1,2,4–7]. Thus, we evaluated the impact of CYP2D6 inhibitors on EDF levels and [NDT]/[EDF] metabolic ratio in both matrices and found reduced metabolites concentrations in patients under concomitant use of CYP2D6 inhibitors drug inhibitors (Table 4) as compared to the group without use of drug inhibitors, as follows: median DBS

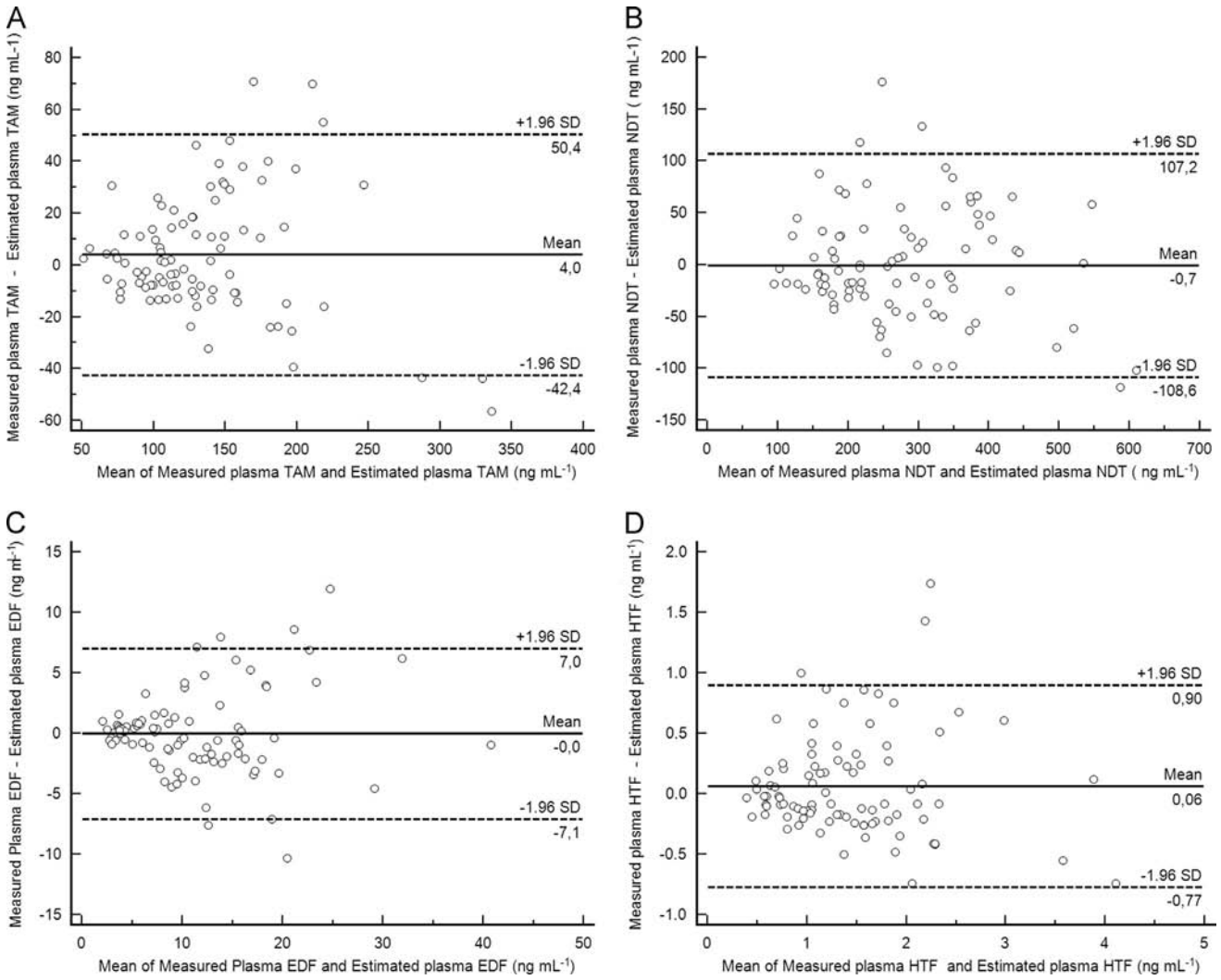


Fig. 2. Method comparison, Bland Altman plot of estimated plasma *vs* measured plasma concentrations of TAM (A), NDT (B), EDF (C) and HTF (D) in clinical samples ($N = 91$).

3.5 ng mL^{-1} *vs* 5.8 ng mL^{-1}, EPC 6.1 ng mL^{-1} *vs* 10.2 ng mL^{-1} and measured plasma 5.5 ng mL^{-1} *vs* 10.1 ng mL^{-1} ($P<0.05$ in DBS and EPC, and $P<0.01$ in measured plasma). Moreover, the frequency of patients with EDF levels below the threshold of optimal clinical activity (5.9 ng mL^{-1}) was higher in patients taking CYP2D6 inhibitor drug, 50% (9 of 18), compared to patients without CYP2D6 inhibitors, 20.5% (15 of 73) (Fisher Exact test, $P<0.05$).

The metabolic ratio [NDT]/[EDF], depending on CYP2D6 metabolism, was also affected by the use of drug inhibitors, as observed in both matrices: median DBS 40.5 *vs* 32.0, EPC 24.0 *vs* 40.5 and measured plasma 20.8 *vs* 53.3 for patients taking or not inhibitors respectively ($P<0.05$ in DBS and EPC, and $P<0.01$ in measured plasma). Thus, DBS based monitoring method showed to have equivalent capacity to identify differences on EDF levels and metabolic ratio between CYP2D6 metabolism affected or not by drug interactions as does the usual plasma measurement.

Based on these findings, it was interesting to evaluate if it was possible to identify, through DBS samples, patients with EDF plasma levels below 5.9 ng mL^{-1}. Overall, 24 patients (26.4%) had EDF measured plasma concentrations <5.9 ng mL^{-1}, of these 23 (96%) also presented estimated plasma concentrations below the threshold. Only 4 patients with estimated plasma concentrations <5.9 ng mL^{-1} had measured plasma concentrations above it (6.07 ng mL^{-1}, 6.18 ng mL^{-1}, 6.48 ng mL^{-1} and 7.94 ng mL^{-1}), but still close to the threshold. Thereafter, using Passing–Bablok regression equation, we extrapolated the plasma EDF threshold to DBS concentration and found a proposed DBS threshold of 3.3 ng mL^{-1} (Fig. 3). Using the DBS proposed threshold, as previously observed on estimated plasma results, we were able to identify 23 of 24 samples with measured plasma concentrations <5.9 ng mL^{-1}. The high prevalence of patients with low EDF levels could be related to the high frequency of use of inhibitor drugs (20%) and other factors such as genetic polymorphisms of CYP2D6 and/or other enzymes to be further evaluated.

Additionally we compared DBS and estimated plasma EDF concentrations between groups of measured EDF above or below 5.9 ng mL^{-1} and found reduced levels at the last group as well: median EDF DBS 2.0 ng mL^{-1} *vs* 7.0 ng mL^{-1} and 3.6 ng mL^{-1} *vs* 12.5 ng mL^{-1} ($P<0.01$), for DBS and estimated plasma respectively. Similarly DBS and estimated plasma [NDT]/[EDF] metabolic ratio were also significantly different between groups of EDF plasma levels

Table 4
Endoxifen levels and metabolic ratio of [NDT]/[EDF] in patients taking or not CYP2D6 inhibitor drugs and according to EDF plasma threshold 5.9 ng mL^{-1} ($N=91$).

Patients	*n*	Endoxifen DBS (ng mL^{-1})	Estimated plasma Endoxifen (ng mL^{-1})	Measured plasma Endoxifen (ng mL^{-1})	DBS [NDT]/[EDF]	Measured plasma [NDT]/[EDF]	Estimated plasma [NDT]/[EDF]
		Median (P25–P75)					
No CYP2D6 inhibitor drug	73	5.8 (3.3–9.2)	10.2 (5.9–16.2)	10.1 (6.2–15.5)	32.0 (12.9–42.8)	20.8 (14.6–41.7)	24.0 (13.0–42.8)
Taking CYP2D6 inhibitor drug	18	3.5 (2.1–6.7)	6.1 (3.7–11.6)	5.5 (4.0–8.4)	40.5 (27.8–73.8)	53.3 (34.1–69.5)	40.5 (27.8–73.8)
	P	<0.05	<0.05	<0.01	<0.05	<0.01	<0.05
Plasma EDF <5.9 ng mL^{-1}	24	2.0 (1.9–2.5)	3.6 (3.2–4.4)	–	90.2 (61.3–144.1)	67.5 (42.7–91.5)	67.3 (45.9–108.0)
Plasma EDF ≥ 5.9 ng mL^{-1}	67	7.0 (4.9–9.5)	12.5 (9.2–16.4)	–	28.6 (16.6–39.7)	19.7 (13.6–31.4)	21.4 (12.5–29.7)
	P	<0.01	<0.01	–	<0.01	<0.01	<0.01

P value as Mann–Whitney test.

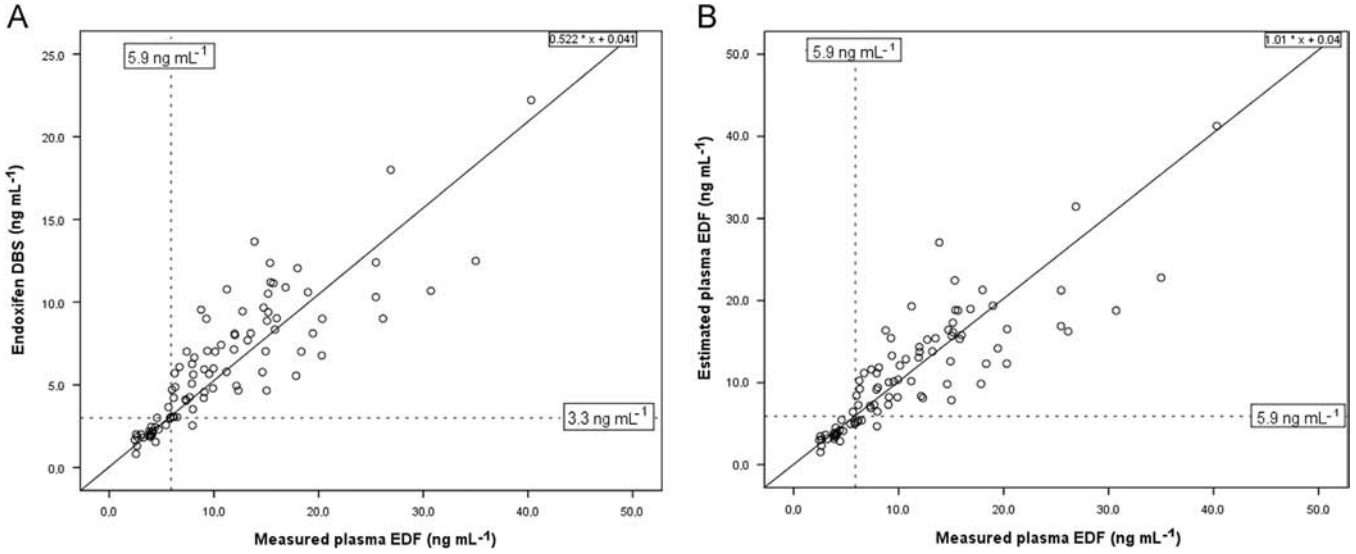


Fig. 3. Correlation of EDF concentrations in DBS and plasma (A); correlation of estimated plasma EDF concentration and EDF measured plasma concentration (B) ($N=91$). Dashed lines indicate EDF minimum therapeutic threshold concentration in plasma (5.9 ng mL^{-1}) [8] and proposed EDF concentration threshold in DBS, extrapolated from plasma concentrations (3.3 ng mL^{-1}).

(Table 4). In summary, the DBS method was able to identify with high accuracy (96%) patients with plasma EDF levels below the clinical threshold related to better prognosis as well as impaired CYP2D6 metabolism through [NDT]/[EDF] metabolic ratio.

4. Conclusions

A method for determination of TAM and its major metabolites in DBS using LC–MS/MS was developed and validated. Transport and storage of DBS samples require special attention, since EDF and HTF concentrations in control samples increased after storage at 45 °C. TAM, NDT, EDF, HTF concentrations in DBS and estimated plasma were highly correlated to measured plasma concentrations. We found a high prevalence of patients with EDF level below the clinical threshold of 5.9 ng mL^{-1} which were effectively identified through DBS samples. These findings suggest that DBS based therapeutic monitoring of TAM can be an efficient tool to optimize adjuvant breast cancer treatment, allowing patients to collect blood samples at their home within the appropriate time to obtain trough samples, facility transport conditions and handling safety. In addition, our results also offer insight into the effects of CYP2D6 inhibitors on TAM metabolism to EDF.

Acknowledgments

This work was supported by CNPq/FNRS (CNPq registry number 490408/2011-7) and FAPERGS (registry number 1255-2551/13-2) grants.

References

[1] W. Schroth, L. Antoniadou, P. Fritz, M. Schwab, T. Muerdter, U.M. Zanger, W. Simon, M. Eichelbaum, H. Brauch, J. Clin. Oncol. 33 (2007) 5187–5193.
[2] T.E. Mürdter, W. Schroth, L. Bacchus-Gerybadze, S. Winter, G. Heinkele, W. Simon, P.A. Fasching, T. Fehm, German Tamoxifen and A.I. Clinicians GroupM. Eichelbaum, M. Schwab, H. Brauch, Clin. Pharmacol. Ther. 89 (2011) 708–717.
[3] V.C. Jordan, Steroids 72 (2007) 829–842.
[4] M.E. Irarrázaval, Rev. Med. Chile 139 (2011) 89–99.
[5] M.V. Antunes, R. Linden, T.V. Santos, P. Wallemacq, V. Haufroid, J.F. Classen, H. Andreolla, N. Costa, T.O. Fontanive, D.D. Rosa, Ther. Drug Monit. 34 (2012) 422–431.
[6] S.F. Teunissen, H. Rosing, R.H.T. Koornstra, S.C. Linnb, J.H.M. Schellensc, A.H. Schinkel, J.H. Beijnen, J. Chromatgr. B: Anal. Technol. Biomed. Life Sci. 877 (2009) 2519–2529.
[7] W.A. Teft, I.Y. Gong, B. Dingle, K. Potvin, J. Younus, T.A. Vandenberg, M. Brackstone, F.E. Perera, Y.H. Choi, G. Zou, R.M. Legan, R.G. Tirona, R.B. Kim, Breast Cancer Res. Treat. 139 (2013) 95–105.
[8] L. Madlensky, L. Natarajan, T. Tchu, M. Pu, J. Mortimer, S.W. Flatt, D.M. Nikoloff, G. Hillman, M.R. Fontecha, H.J. Lawrence, B.A. Parker, A.H.B. Wu2, J.P. Pierce, Clin. Pharm. Ther. 89 (2011) 718–725.
[9] K. Kiyotani, T. Mushiroda, C.K. Imamura, Y. Tanigawara, N. Hosono, M. Kubo, M. Sasa, Y. Nakamura, H. Zembutsu, Breast Cancer Res. Treat. 131 (2012) 137–145.
[10] W.J. Irvin Jr, C.M. Walko, K.E. Weck, J.G. Ibrahim, W.K. Chiu, E.C. Dees, S.G. Moore, O.A. Olajide, M.L. Graham, S.T. Canale, R.E. Raab, S.W. Corso, J.M. Peppercorn, S.M. Anderson, K.J. Friedman, E.T. Ogburn, Z. Desta, D.A. Flockhart, H.L. McLeod, J.P. Evan, L.A. Carey, J. Clin. Oncol. 29 (2011) 3232–3239.
[11] N.G.L. Jager, H. Rosing, J.H.M. Schellens, S.C. Linn, J.H. Beijnen, Breast Cancer Res. Treat. 143 (2014) 477–483.
[12] K.H. Lee, B.A. Ward, Z. Desta, D.A. Flockhart, D.R. Jones, J. Chromatogr. B: Anal. Technol. Biomed. Life Sci. 791 (2003) 245–253.
[13] Y.B. Zhu, Z. Zhang, J.J. Zou, Z.X. Yu, D.W. Xiao, J. Pharm. Biom. Anal. 46 (2008) 349–355.
[14] M.V. Antunes, D.D. Rosa, T.S. Viana, H. Andreolla, T.O. Fontanive, R. Linden, J. Pharm. Biomed. Anal. 76 (2013) 13–20.
[15] J. Arpini, M.V. Antunes, L.S. Pacheco, D. Gnatta, M.F. Rodrigues, E. Keitel, R. Linden, Clin. Biochem. 46 (2013) 1905–1908.
[16] N.G.L. Jager, H. Rosing, J.H.M. Schellens, J.H. Beijnen, S.C. Linn, Breast Cancer Res. Treat. 146 (2014) 137–144.
[17] L. Rhoden, M.V. Antunes, P. Hidalgo, C.A. da Silva, R. Linden, J. Pharm. Biom. Anal. 96 (2014) 207–212.
[18] T.W. McDade, S. Williams, J. Snodgrass, Demography 4 (2007) 899–925.
[19] A.M. Almeida, M.M. Castel-Branco, A.C. Falcão, J. Chromatgr. B: Anal. Technol. Biomed. Life Sci. 774 (2002) 215–222.
[20] V.P. Shah, K.K. Midha, J.W.A. Findlay, H.M. Hil, J.D. Hulse, J. McGilveray, G. McKay, K.J. Miller, R.N. Patnaik, M.L. Powell, A. Tonelli, C.T. Viswanathan, A. Yacobi, Pharm. Res. 17 (2000) 1551–1557.
[21] H. Passing, W. Bablok, J. Clin. Chem. Clin. Biochem. 21 (1983) 709–720.
[22] J.M. Bland, D.G. Altman, Lancet, i (1986) 307–310.
[23] European Medicines Agency, Guideline on Bioanalytical Method Validation, European Medicines Agency (2011) 4–10.
[24] S.F. Teunissen, H. Rosing, A.H. Schinkel, J.H.M. Schellens, J.H. Beijnen, Anal. Chim. Acta 683 (2010) 21–37.
[25] J. Gjerde, M. Hauglid, H. Breilid, S. Lundgren, J.E. Varhaug, E.R. Kisanga, G. Mellgren, V.M. Steen, E.A. Lien, Ann. Oncol. 19 (2008) 56–61.
[26] D.D. Heath, S.W. Flat, A.H. Wu, M.A. Pruitt, C.L. Rock, Br. J. Biomed. Sci. 71 (2014) 33–39.
[27] A.V. Eeckhaut, K. Lanckmans, S. Sarre, I. Smolders, Y. Michott, J. Chromatgr. B: Anal. Technol. Biomed. Life Sci. 23 (2009) 2198–2207.
[28] E. Dahmane, T. Mercier, B. Zanolari, S. Cruchona, N. Guignarda, T. Buclina, S. Leyvrazc, K. Zamanc, C. Csajkaab, L.A. Decosterd, J. Chromatgr. B: Anal. Technol. Biomed. Life Sci. 878 (2010) 3402–3414.
[29] P. Timmerman, S. White, S. Globig, S. Lüdtke, L. Brunet, J. Smeraglia, Bioanalysis 14 (2011) 1567–1575.
[30] Z.W. Yang, S.H. Yang, L. Chen, J. Qu, J. Zhu, Z. Tang, Clin. Lab. Haem. 23 (2001) 155–159.
[31] Y. Jin, Z. Desta, V. Stearns, B. Ward, H. Ho, K.H. Lee, T. Skaar, A.M. Storniolo, L. Li, A. Araba, R. Blanchard, A. Nguyen, L. Ullmer, J. Hayden, Z. Lemler, R.M. Weinshilboum, J.M. Rae, D.F. Hayes, D.A. Flockhart, J. Natl. Cancer Inst. 97 (2005) 30–39.

Talanta 132 (2015) 785–789

Contents lists available at ScienceDirect

Talanta

journal homepage: www.elsevier.com/locate/talanta

Microchannel conductivity measurements in microchip for on line monitoring of dephosphorylation rates of organic phosphates using paramagnetic-beads linked alkaline phosphatase

Mohammed Kechadi [b], Bruno Sotta [c], Jean Gamby [a,b,*]

[a] CNRS, UMR 8235, LISE, F-75005 Paris, France
[b] Sorbonne Universités, UPMC Univ Paris 06, UMR 8235, Laboratoire Interfaces et Systèmes Electrochimiques, F-75005 Paris, France
[c] Sorbonne Universités, UPMC Univ Paris 06, UMR 7622, Laboratoire Biologie des Semences, 4 Place Jussieu, F-75005 Paris, France

ARTICLE INFO

Article history:
Received 8 July 2014
Accepted 8 October 2014
Available online 19 October 2014

Keywords:
Microchip
Admittance
Conductometry
Enzyme
Dephosphorylation

ABSTRACT

This paper presents the use of polymer coated microelectrodes for the realtime conductivity monitoring in a microchannel photoablated through the polymer without contact. Based on this strategy, a small conductometry sensor has been developed to record in time conductivity variation when an enzymatic reaction occurs through the channel. The rate constant determination, k_2, for the dephosphorylation of organic phosphate–alkaline phosphatase–superparamagnetic beads complex using chemically different substrates such as adenosine monoesterphosphate, adenosine diphosphate and adenosine triphosphate was taken as an example to demonstrate selectivity and sensivity of the detection scheme. The k_2 value measured for each adenosine phosphate decreases from 39 to 30 s^{-1} in proportion with the number (3, 2 and 1) of attached phosphate moiety, thus emphasizing the steric hindrance effect on kinetics.

© 2014 Elsevier B.V. All rights reserved.

1. Introduction

In the recent years, the growing development of microfluidic systems for ultrasensitive medical diagnostics on chip has been integrated as new module for smartphone application [1–3]. For this challenge, electrical transduction methods are more suitable for the detection of ionic species (oxidable or reducable) because of their high sensitivity and no need labelling step is required [4–6]. The relevance of electrochemical detection on microchips with improvement of micro nanoelectrode fabrication [7–12] has been widely proven, including the application of amperometric detection [13–16], and potentiometric [17–19]. However, contactless to the microelectrodes as electrical detection scheme with the electrolyte is the most promising [20–23]. Indeed, the non contact measurement scheme with two microelectrodes galvanically isolated has several advantages conversely to the contact mode. For instance, in the microelectrophoresis field [23–25], some drawbacks due to interference associated with the contacting electrode and the electrolyte, such as non specific adsorption, degradation or electrode corrosion, bubbles formation due to the water electrolysis, are suppressed by measuring the contactless conductivity of the electrolyte in the separation channel. Moreover, this configuration enables an electronic decoupling as the detector for measuring conductivity is effectively isolated from the high voltage applied in the same channel for the separation and ions migration. Another significant advantage is that the networking and alignment of the detector are simplified making it possible electrode positioning anywhere in the separation channel.

A new strategy for microelectrode without contact with the streaming electrolyte in the microchannel has been developed in the recent years [26–28]. It differs from the previous strategies by the use of microelectrodes that are embedded in an insulating dielectric polymer (PET) thanks to laser photoablation process. Indeed, the laser permits a close positioning of the microchannel with a near distance to the fluidic channel bottom equals to 2–5 μm. In this work the capacitive effect originates from coupling between the electronic charges (two planar microband electrodes) on one side of the dielectric PET layer and the ionic charges (streaming electrolyte in microchannel) in contact with the other side of the dielectric PET layer [26]. A detailed methodology for non contact impedance in dielectric microdevice was published and a procedure was proposed to eliminate the contribution of the surronding PET layer comprised between the two embedded microelectrodes [29,30]. This procedure enables a clear enhancement of the microchannel impedance contribution from the microchip global impedance. The non-contact geometry was previously tested for adsorption monitoring of BSA protein on photoablated PET [31] and for testing the biomolecular recognition

* Corresponding author at: CNRS, UMR 8235, LISE, F-75005 Paris, France. Tel.: +33144273640; fax: +33144274074.
E-mail address: jean.gamby@upmc.fr (J. Gamby).

http://dx.doi.org/10.1016/j.talanta.2014.10.011
0039-9140/© 2014 Elsevier B.V. All rights reserved.

between two proteic ligands i.e. BSA adsorbed on PET and the corresponding antibodies Ab-BSA [32].

However, in this paper the reaction takes place not on the PET substrate but on superparamagnetic beads immobilised in the detection zone [33]. Conversely to previous work [34] where microchannel impedance variation was monitored during enzymatic conversion of an enzymatic substrate, the present paper concerns the calibration of the detection scheme by using the microchannel conductivity which is determined through the cell constant accurately determined for this goal. The biological model proposed is the determination of dephosphorylation rate constant of the complexes enzyme-beads-organic phosphate measured using three adenosine phosphate biomolecules such as adenosine monoesterphosphate (AMP), adenosine diphosphate (ADP), adenosine triphosphate (ATP) that occurs on alkaline–phosphatase-linked superparamagnetic-beads in polymer microchannel. Indeed, the possibility to distinguish between the dephosphorylation rate constants for these enzyme phosphate complexes having close molecular structures is also evidenced.

2. Experimental

2.1. Chemicals

Adenosine monophosphate (AMP), adenosine diphosphate (ADP) and adenosine triphosphate (ATP) were purchased from Sigma Aldrich; 2-methylaminoethanol (MAE) was from Fluka Analytical. Magnesium chloride, sodium chloride, Tris(hydroxymethyl)aminomethane (Tris) were purchased from Sigma Aldrich. The washing buffer was made of 100 mM Tris supplemented with 500 mM NaCl. The substrate buffer was 100 mM 2-methylaminoethanol with 2 mM $MgCl_2$. Washing and substrate buffers were adjusted to pH 9 with HCl and NaOH. The organic phosphates were diluted in the substrate buffer: 16.1 mM AMP, 10.6 mM ADP, 11.7 mM ATP. Deionized water was used as regeneration solution. Alkaline Phosphatase at 3 mg mL^{-1} was from intestine of veal (Boehringer, Mannhein). Microbeads 1.8 μm (Dynabeads) were purchased from Invitrogen France. The microbeads concentration was equal to 10 mg mL^{-1} with 4×10^8 microbeads per milliliter in phosphate buffer saline (PBS), pH 7.4, containing 0.1% BSA and 0.02% NaN_3.

2.2. Microchannel networks

The non contact microchip device used in this work was described elsewhere [20,35]. Briefly, admittance measurements were carried out through a polyethylene terephthalate (PET) microchannel photoablated having a cross-section shape with a depth of 50 μm, a top width of 100 μm and a length of 1.4 cm. The distance separation between both microelectrodes is 120 μm edge to edge. The electrode fabrication is achieved using a carbon ink loaded with gold nanoparticles, thermally sealed by a polyethylene (10 μm)/polyethylene terephthalate (25 μm) (PE/PET) layer with a total thickness of 35 μm. The distance separation in the PET band between the two planar microelectrodes and the main microchannel is equal to 5 μm and the detection surface area per microelectrode is 8.8×10^{-4} cm^2.

2.3. Microchannel admittance measurement protocol

The current measured is related to the total admittance of the microdevice. Measurements were performed using a frequency response analyzer (FRA 1255B, Solartron U.K.) associated with a dielectric interface 1296 (Solartron, U.K.) which extends the frequency range from 1 Hz to 10 MHz. Experiments were performed using the company-made software SMaRT. Electric admittance spectroscopy measurements have been performed by applying a 3 V ac voltage amplitude through the microelectrodes at 1 MHz fixed frequency. To analyze these results, a physical model displayed on Fig. 1 is used as described previously [29].

3. Results and discussion

3.1. Microchannel conductivity without direct electrical contact

The characteristics of this kind of interface with an insulated layer sandwiched between two galvanic isolated microelectrodes can be represented as a dielectric system with, on the one part of the thin polymer layer, electronic charges on microelectrodes and, on the other part, ionic charges in the microchannel. An electrical equivalent circuit can be drafted, considering admittances for each part of the microdevice as displayed in Fig. 1. The global admittance, Y_G, through the microdevice using free contact microelectrodes configuration, is given by the sum:

$$Y_G(\omega)=Y_1(\omega)+Y_2(\omega) \quad (1)$$

wherein ω is the angular frequency (rad s^{-1}), defined by $\omega=2\pi f$, where f is the frequency (Hz).

The detailled admittances Y_1 and Y_2 in Eqs. (2) and (3) can be decomposed for each branch i.e. through the microchannel and through the direct coupling between the two embedded microelectrodes, respectively.

$$Y_1(\omega)=\frac{1}{\frac{2}{j\omega C_{PET,5\ \mu m}}+\frac{2}{(j\omega)^{a_{int}}Q_{int}}+\frac{R_S}{1+j\omega C_C R_S}} \quad (2)$$

and

$$Y_2(\omega)=j\omega C_{PET,120\ \mu m} \quad (3)$$

The 5 μm thickness of the PET layer isolated microelectrodes from the small channel makes it to behave as a capacitor $C_{PET,1}$ and was equal to 14×10^{-11} F. The 120 μm thickness of the PET layer separated the two microelectrodes also behaves as a capacitor $C_{PET,2}$ and was equal to 8×10^{-13} F. The PET/microchannel interface is represented by a non ideal capacitor which is defined by

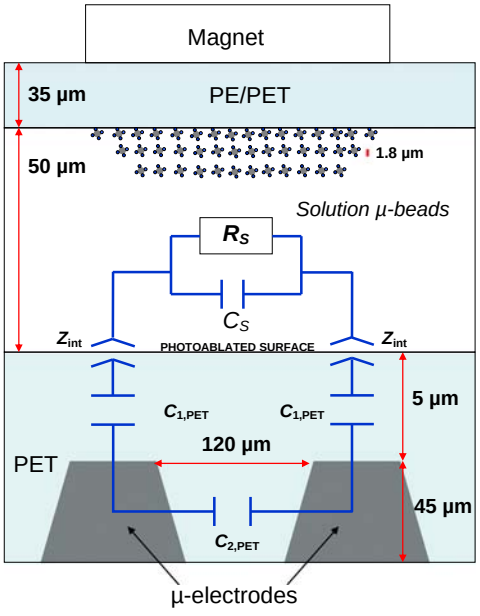


Fig. 1. Schematic description of the small conductometric sensor in PET microchip through the dielectric microelectodes/PET/microchannel interfaces with an superimposed equivalent electrical circuit.

a constant phase element CPE with Q_{int} and α_{int} being the CPE element and the CPE exponent, respectively. The CPE exponent α_{int} takes into account the role of the photoablated PET surface at the microchannel bottom. In previous work alpha α_{int} was found equal to 0.5 and $Q_{int}=4.7\times10^{-8}\,\Omega^{-1}\,s^{-\alpha}$ [29]. The change on the interfacial CPE parameter is neglected to the aim of this paper as the organic phosphate dephosphorylation occurs on Alcaline Phosphatase linked beads and not on the PET photoablated surface [31,32,36].

In the microchannel, the admittance Y_{CH} is represented by a parallel association $R_S//C_C$ circuit. The resistance, R_S, is characteristic to the electrolyte resistance while C_C is an intrinsic parameter linked to the cell geometry named the cell capacitance. This latter was estimated to $C_C=3\times10^{-13}$ F [29,32]. As mentioned previously, the target application is the real-time monitoring of the microchannel conductivity that is given through the relative variation of the conductance (Y_1 real admittance part, $\Delta\Re e\,(Y_1)$). Indeed, the derivative expression of Eq. (2) leads to Eq. (4), in which conductance is conversely proportional to the microchannel resistance at fixed frequency.

$$\Delta\Re e(Y_1)=\Delta\left[\frac{1}{R_S}\right] \tag{4}$$

This can finally lead to an analytical expression for determining the microchannel conductivity variation at fixed frequency taking into account the cell constant, K, as follows:

$$\Delta\sigma=K\Delta\Re e(Y_1) \tag{5}$$

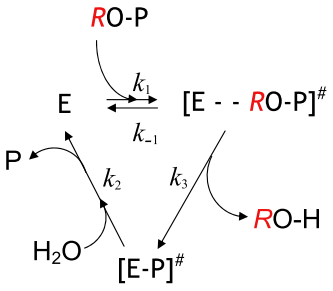
where K is the cell constant equals to $5\times10^{3}\,m^{-1}$ and $\Delta\sigma$ expressed in $S\,m^{-1}$.

3.2. Kinetics of enzymatic conversion of organic phosphate

Scheme 1 presents in brief the catalytic hydrolysis mechanism for organic phosphate involving intermediate phosphorylation of ALP enzyme, E, where $[E\text{-ROP}]^{\#}$ and $[E\text{-Pi}]^{\#}$ are the Michaelis complex and the phosphoryl enzyme, respectively. The reaction products RO-H and Pi are the corresponding alcohol (from substrates which are chemically different via R in RO-P) and the released inorganic phosphate, respectively. As displayed in Scheme 1, the ratio of two kinetic constants k_1/k_{-1} is an equilibrium constant because k_1 is known as a diffusion-controlled rate (10^9–$10^{10}\,M^{-1}\,s^{-1}$) [37]. The last step constitutes the rate-determining enzymatic step as expressed in the following Eq. (6) since hydrolysis of the phosphoryl enzyme is the rate determining step.

$$v=\frac{d[\mathrm{Pi}]}{dt}=\frac{k_2k_3}{k_2+k_3}[E-\mathrm{RO}-P]^{\neq} \tag{6}$$

where k_3 and k_2 are the constants of the phosphorylation and dephosphorylation rates, respectively.



Scheme 1. Simplified mechanism of alkaline phosphatase ALP (E) for catalytic hydrolysis of organic phosphate compounds (RO-P) involving intermediate phosphorylation of E, where $[E\text{-ROP}]^{\#}$ and $[E\text{-Pi}]^{\#}$ are the Michaelis complex and the phosphoryl enzyme, respectively.

In order to determine the dephosphorylation rate with the following organic phosphate biomolecules: AMP, ADP, ATP the procedure described below was followed for various concentrations of ALP. The experimental data consist, for each organic phosphate concentration, in a set of conductivity experimental curves that were recorded as a function of the measurement time, t. Samples were introduced by capillarity in the PET microchannel with a total volume of 80 nL. The detection procedure of the microchannel conductivity was preferred at 1 MHz fixed frequency (fast acquisition) with time until a baseline between each step. As displayed in Fig. 1, a permanent magnet located above the conductometry sensor was switched on the position ON [33]. The procedure for monitoring experiments of ALP catalyzing dephosphorylation was divided in three steps (see Fig. 2). The step one consisted in measuring the conductance for microchannel filled with substrate buffer (100 mM MAE and 0.2 mM $MgCl_2$). Then, in step two, the microchannel was filled with beads linked ALP enzyme. For instance, an ALP-μbeads sample (see Table S1 in Supplementary material) was introduced on the channel and the measurement protocol described above was followed until a baseline was reached. The step three consisted in loading the channel with organic phosphate sample as illustrated with ADP in Fig. 2. Magnification of step 3 as it appears on Fig. 3 highlights the net increase of the measured conductance with time. A normalization step was performed by subtracting the background conductivity σ_0 at t_0. For that purpose, $\Delta\sigma$ variation against time during catalytic dephosphorylation of ADP is plotted from typical $\Delta\sigma=f(t)$. At the end, the initial rate, ν_i-slope, of $\Delta\sigma$ variation in time (see Eq. (7) and Fig. 3) gives information about the conversion kinetics of phosphate biomolecule.

$$\nu_i=\frac{d\Delta\sigma}{dt} \tag{7}$$

where the unit is in $S\,m^{-1}\,s^{-1}$.

Obviously, the conductivity variation in presence of ALP-μbead is due to the ionic charge increase in microchannel solution when the catalytic hydrolysis starts. In fact, when the phosphoryl complex is hydrolysed, the substrate (ADP) level decays and product amounts (AMP and phosphate ion) increase (see Scheme 1 and Fig. 3). The experimental protocol described in Fig. 2 and Fig. 3 was performed for the three organic phosphate biomolecules in presence of various concentration for ALP-μbeads (see Table S1 in Supplementary material). All data rates obtained,

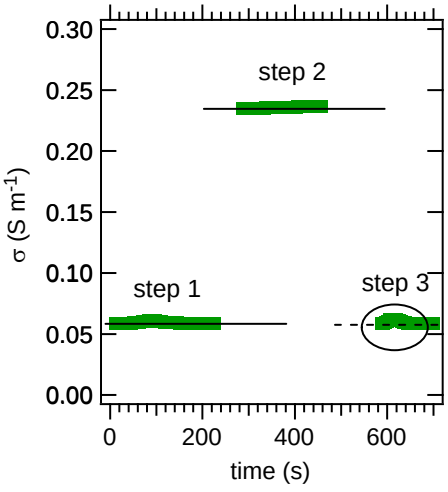


Fig. 2. Measurement protocol for catalytic ADP dephosphorylation. In step 1: Conductivity level for microchannel filled with substrate buffer. In step 2: Conductivity level for microchannel filled with ALP-linked beads (0.045 pM ALP-μbeads, see Table S1 in Supplementary material). In step 3: Conductivity level for microchannel filled with 16.1 mM ADP as organic phosphate.

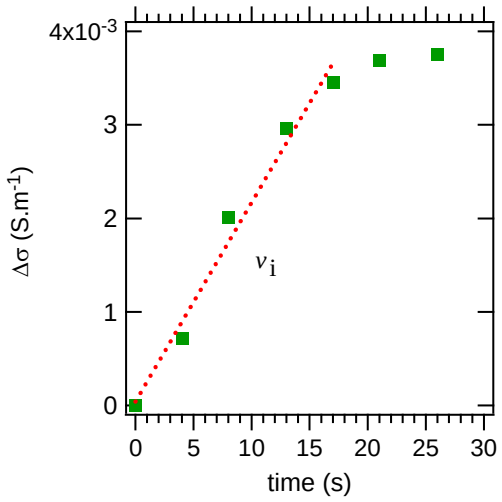


Fig. 3. Magnification of step 3 where the microchannel conductivity was normalized with σ_0 (background conductivity) at t_0 (reaction starts) when 16.1 mM ADP concentration was in presence of 0.045 pM ALP-μbeads.

including standard deviations, are listed in Table S1 in Supplementary material. The mean values of dephosphorylation kinetics rate for each used organic phosphate was obtained through the ν_i-slope listed in Table 1.

The dephosphorylation rate constant, k_2, is obtained by plotting the initial rate (ν_i-slope in Table 1) against the total enzyme concentration. As displayed in Fig. 4, a pseudo-first-order kinetic behaviour can be observed due to the low enzyme concentration that is negligible in comparison with the high organic phosphate concentration (see Table 1). The linear fits obtained using Eq. (8) have a slope which corresponds to the dephosphorylation rate constant, k_2, and k_0 without enzyme.

$$\nu = k_2[\mathrm{ALP}] + k_0 \tag{8}$$

with k_2 in S m^{-1} (pM s)$^{-1}$ and k_0 in S m^{-1} s^{-1}.

The obtained values for k_2 and k_0 listed in Table 2 have been converted using the method sensitivity (1 μS m^{-1} pM^{-1}) in order to compare these values with standard units i.e. in s^{-1} and pM^{-1} s^{-1}, respectively. The obtained values are in agreement with those published and obtained with optical methods [38,39]. Assuming that k_2 is negligible in comparison with k_3 (see Eq. (6)), k_2 becomes equivalent to the hydrolysis catalytic constant, k_{cat}. The means values of $k_{2,\ AMP}$ (39.4 s^{-1}) > $k_{2,\ ADP}$, > (32.8 s^{-1}) > $k_{2,\ ATP}$, (30.2 s^{-1}) are close in the adenosine series and show steric hindrance effect according to the number phosphate groups (1, 2 and 3), respectively.

4. Conclusions

Microchannel conductivity detection using electric admittance on polymer coated microelectrodes in microchip is a very sensitive method for monitoring chemical reaction such as dephosphorylation of organic phosphate in low volume reagent. This has been illustrated with a presented methodology for monitoring enzyme kinetics with ultralow (45 fM) concentration of ALP enzyme added in the microchannel. Detection through this microdevice permits small consumption of reagents in comparison with other assays. Measurement of kinetic rates can be measured after a few seconds for an assay in comparison with the traditional ELISA microtitration plates where the data processing is long. Furthermore, this detection scheme could be extended for any enzymatic substrates since the detected product does not need to be a chromophoric or electroactive species. The different dephosphorylation kinetics rate obtained with adenosine phosphate substrates on alcaline phosphatase-linked beads underline sensitivity and selectivity of the method. This opens a new way for fast medical diagnostics in low volume reagent or for biological screening of ligands of interest such as natural phosphoproteins having no chromogenic or electrochemical property [40].

Table 1
The obtained ν_i-slopes according to the fit using Eq. (7) (see Table S1 in Supplementary material for more details).

ν_i, initial rate $\times 10^{-5}$ (S m^{-1} s^{-1})			ALP enzyme concentration ($\times 10^{-12}$ M)			
			1.21	0.405	0.135	0.045
Organic phosphate ($\times 10^{-3}$ M)	16.1	AMP	4.58	3.24	2.96	2.28
	10.6	ADP	3.87	2.48	2.26	1.83
	11.7	ATP	3.65	2.36	2.07	1.86

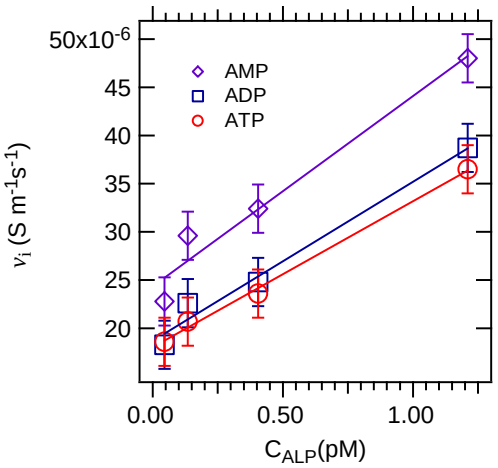


Fig. 4. Calibration curves of dephosphorylation rate of ALP-μbeads for AMP, ADP, ATP substrates. The maximum rate, ν_i-slope, is plotted against ALP concentration with a fixed organic phosphate concentration. Each point represents the mean of experiments with ALP concentrations (from 0.045 pM to 1.21 pM). The linear fits (solid lines) are performed using Eq. (8) (in the text).

Table 2
The obtained values for k_2 and k_0 according to the fit using Eq. (8).

Kinetic constants of enzymatic conversion	k_2 (s^{-1})	k_0 (M^{-1} s^{-1})
AMP	39.4	48.6
ADP	32.8	37.4
ATP	30.2	36.2

Acknowledgements

The authors thank Prof Hubert Girault and Dr Philippe Flückiger for allowing them access to experimental facilities at the EPFL center of MicroNano Technology, Lausanne.

Appendix A. Supporting information

Supplementary data associated with this article can be found in the online version at http://dx.doi.org/10.1016/j.talanta.2014.10.011.

References

[1] J.M. Ruano-Lopez, M. Agirregabiria, G. Olabarria, D. Verdoy, D.D. Bang, M. Bu, A. Wolff, A. Voigt, J.A. Dziuban, R. Walczak, J. Berganzo, Lab Chip 9 (2009) 1495–1499.
[2] V. Oncescu, D. O'Dell, D. Erickson, Lab Chip 13 (2013) 3232–3238.
[3] V. Oncescu, M. Mancuso, D. Erickson, Lab Chip (2014).
[4] J.S. Rossier, M.A. Roberts, R. Ferrigno, H.H. Girault, Anal. Chem. 71 (1999) 4294–4299.
[5] J.S. Rossier, R. Ferrigno, H.H. Girault, J. Electroanal. Chem. 492 (2000) 15–22.
[6] H. Wang, Y. Liu, C. Liu, J. Huang, P. Yang, B. Liu, Electrochem. Commun. 12 (2010) 258–261.
[7] D.W.M. Arrigan, Analyst 129 (2004) 1157–1165.
[8] M.E. Sandison, J.M. Cooper, Lab Chip 6 (2006) 1020–1025.
[9] S. Méance, K. Papin, J. Gamby, G. Aubry, Q. Kou, A.-M. Haghiri-Gosnet, Microelectron. Eng. 88 (2011) 1798–1800.
[10] A.J. Wain, Electrochemistry at nanoelectrodes, Electrochemistry, Volume 12, The Royal Society of Chemistry (2014) 44–86 (Chapter 2).
[11] M. Faure, A. Pallandre, S. Chebil, I. Le Potier, M. Taverna, B. Tribollet, C. Deslouis, A.-M. Haghiri-Gosnet, J. Gamby, Lab Chip 14 (2014) 2800–2805.
[12] S. Méance, J. Gamby, M. Faure, Q. Kou, A.-M. Haghiri-Gosnet, Talanta 129 (2014) 150–154.
[13] H. Hinkers, C. Sundermeier, R. Lürick, F. Walfort, K. Cammann, M. Knoll, Sens. Actuators, B 27 (1995) 398–400.
[14] Y. Liu, H. Wang, J. Huang, J. Yang, B. Liu, P. Yang, Anal. Chim. Acta 650 (2009) 77–82.
[15] A. Meunier, R. Fulcrand, F. Darchen, M. Guille Collignon, F. Lemaître, C. Amatore, Biophys. Chem. 162 (2012) 14–21.
[16] S.K. Jha, R. Chand, D. Han, Y.-C. Jang, G.-S. Ra, J.S. Kim, B.-H. Nahm, Y.-S. Kim, Lab Chip 12 (2012) 4455–4464.
[17] J. Janata, Chem. Rev. 90 (1990) 691–703.
[18] T.-Y. Chiang, C.-H. Lin, RSC Adv. 4 (2014) 379–385.
[19] N. Ibáñez-García, M. Baeza, M. Puyol, R. Gómez, M. Batlle, Electroanalysis 22 (2010) 2376–2382.
[20] J. Vacík, J. Zuska, I. Muselasová, J. Chromatogr. A 320 (1985) 233–240.
[21] A.J. Zemann, E. Schnell, D. Volgger, G.K. Bonn, Anal. Chem. 70 (1998) 563–567.
[22] J.A. Fracassi da Silva, N. Guzman, C.L. do Lago, J. Chromatogr. A 942 (2002) 249–258.
[23] J.G.A. Brito-Neto, J.A. Fracassi da Silva, L. Blanes, C.L. do Lago, Electroanalysis 17 (2005) 1198–1206.
[24] J. Lichtenberg, N.F. de Rooij, E. Verpoorte, Electrophoresis 23 (2002) 3769–3780.
[25] M. Vazquez, C. Frankenfeld, W.K.T. Coltro, E. Carrilho, D. Diamond, S.M. Lunte, Analyst 135 (2010) 96–103.
[26] J. Gamby, J.-P. Abid, H.H. Girault, J. Am. Chem. Soc. 127 (2005) 13300–13304.
[27] J. Gamby, M. Lazerges, C. Pernelle, H. Perrot, H.H. Girault, B. Tribollet, Lab Chip 7 (2007) 1607–1609.
[28] J. Gamby, J.P. Abid, M. Abid, J.P. Ansermet, H.H. Girault, Anal. Chem. 78 (2006) 5289–5295.
[29] M. Kechadi, J. Gamby, L. Chaal, H. Girault, B. Saidani, B. Tribollet, Electrochim. Acta 105 (2013) 7–14.
[30] M. Kechadi, J. Gamby, L. Chaal, B. Saidani, B. Tribollet, J. Flow Chem. 3 (2013) 81–86.
[31] M. Kechadi, L. Chaal, B. Tribollet, J. Gamby, Analyst (Cambridge, U. K.) 139 (2014) 1492–1497.
[32] M. Kechadi, B. Sotta, L. Chaal, B. Tribollet, J. Gamby, Analyst 139 (2014) 3115–3121.
[33] F. Sarreshtedari, H. Kokabi, J. Gamby, K.A. Ngo, H.-J. Krause, M. Fardmanesh, J. Electr. Eng. 63 (2012) 27–30.
[34] M. Faure, B. Sotta, J. Gamby, Biosens. Bioelectron. 58C (2014) 61–67.
[35] J. Gamby, A. Rudolf, M. Abid, H.H. Girault, C. Deslouis, B. Tribollet, Lab Chip 9 (2009) 1806–1808.
[36] M. Kechadi, M. Faure, B. Sotta, J. Gamby, J. Flow Chem. 4 (2014) 66–71.
[37] C.P. Andrieux, B. Limoges, D. Marchal, J.-M. Savéant, Anal. Chem. 78 (2006) 3138–3143.
[38] C. Lazdunski, M. Lazdunski, Eur. J. Biochem. 7 (1969) 294–300.
[39] M. Kulp, M. Kaljurand, J. Chromatogr. A 1032 (2004) 305–312.
[40] K.D. Green, M.K.H. Pflum, J. Am. Chem. Soc. 129 (2006) 10–11.

Talanta 132 (2015) 790–795

Contents lists available at ScienceDirect

Talanta

journal homepage: www.elsevier.com/locate/talanta

A label-free fluorescent assay for free chlorine in drinking water based on protein-stabilized gold nanoclusters

Xiaoli Xiong [a], Yan Tang [a], Liangliang Zhang [b], Shulin Zhao [b,*]

[a] College of Chemistry and Materials Science, Sichuan Normal University, Chengdu 610068, China
[b] Key Laboratory for the Chemistry and Molecular Engineering of Medicinal Resources (Ministry of Education), College of Chemistry and Pharmacy, Guangxi Normal University, Guilin 541004, China

ARTICLE INFO

Article history:
Received 24 July 2014
Received in revised form
6 October 2014
Accepted 10 October 2014
Available online 29 October 2014

Keywords:
Au nanoclusters
Fluorescence probe
Free chlorine
Label-free fluorescent assay

ABSTRACT

Bovine serum albumin stabilized Au nanoclusters (BSA–AuNCs) were demonstrated as a novel fluorescence probe for sensitive and selective detection of free chlorine in drinking water. The fluorescence of BSA–AuNCs was found to be quenched effectively by the free chlorine, and the decrease in fluorescence intensity of BSA–AuNCs allowed the sensitive detection of free chlorine in the range of 0.8–800 μM. The detection limit is 0.50 μM at a signal-to-noise ratio of 3. The present fluorescent assay for free chlorine possesses low detection limit, wide linear range and good selectivity. Real tap water samples were analyzed with satisfactory results, which suggested its potential for water quality analysis.
© 2014 Elsevier B.V. All rights reserved.

1. Introduction

Liquid chlorine, sodium hypochlorite and bleaching powder are adopted by more than 80% of waterworks as disinfectants in water treatment process to remove pathogenic bacteria, viruses, and microorganisms, as well as organic and inorganic chemicals. As a result, a certain amount of residual chlorine in municipal tap water is essential to prevent breeding of bacteria and germs. The residual free chlorine mainly includes dissolved chlorine (Cl_2), hypochlorous acid (HClO), and hypochlorite (ClO^-) [1], which are strictly regulated to ensure water quality. If the chlorine content exceeds the standard, it will pose a threat to life in many ways. Firstly the redundant free chlorine possesses a pungent odor, and is harmful to the respiratory system. Secondly it is very easily and rapidly absorbed into the human body by any pore, such as skin, nostril and oral cavity, causing a variety of bodily diseases [2]. Furthermore, immoderate chlorine reacts with organic matter existing in the water to generate various carcinogens, such as trihalomethanes (THMs) [3–5]. Therefore, it is necessary to monitor the concentration of residual free chlorine in water.

Currently, the determination of free chlorine has been conducted by several analytical methods including colorimetric methods, [6–8], fluorescence methods [9], chemiluminescence methods [10,11] and electrochemical methods [12,13]. Among these methods, N-N-diethyl-p-phenylenediamine (DPD) colorimetric method is the most commonly and widely one to be used [6]. The use of toxic reagents and complicated instrumentation limit the scope of their practical applications and necessitates an interest in the development of efficient measurement techniques with simplicity, high sensitivity, cost effectiveness and selectivity to determine free chlorine in water.

As an emerging fluorescent nanomaterial, bovine serum albumin (BSA) stabilized gold nanoclusters (BSA–AuNCs) have recently been paid intense attention because of their simple and green synthesis and red emission as well as photostability and biocompatibility [14]. BSA–AuNCs have been applied in the label-free determination of metal ions such as Hg^{2+} and Cu^{2+}, biological molecules like cysteine and dopamine, and nitrites [15–19]. Herein we found that the free chlorine could quench the fluorescence of BSA–AuNCs, and decrease in fluorescent intensities was correlated linearly to the concentration of free chlorine. Based on these phenomena, the use of the BSA–AuNCs as a selective fluorescence probe for detection of free chlorine was investigated.

2. Experimental

2.1. Materials

Bovine serum albumin (BSA) was purchased from Shanghai Sangon Biotechnology Co., Ltd. (Shanghai, China). Tetrachloroauric (III) acid trihydrate ($HAuCl_4 \cdot 3H_2O$) and sodium hypochlorite

* Corresponding author. Tel.: +86 773 5845973; fax: +86 773 5832294.
E-mail address: zhaoshulin001@163.com (S. Zhao).

http://dx.doi.org/10.1016/j.talanta.2014.10.022
0039-9140/© 2014 Elsevier B.V. All rights reserved.

(NaClO) were obtained from Sinopharm Chemical Reagent Co., Ltd (Shanghai, China). All other reagents used in this work were of analytical grade and were used without further purification. Water was purified with a Milli-Q plus 185 equipment from Millipore (Bedford, MA, USA) and used throughout the work.

2.2. Apparatus

Fluorescence spectra were measureed on an LS-55 fluorescence spectrometer (Perkin-Elmer, USA) equipped with a 10 mm quartz cuvette. The emission spectra were recorded in the wavelength range of 550–700 nm upon excitation at 365 nm. Slits for both the excitation and the emission were 15 nm. UV–vis absorption spectra were measured with a Cary UV–vis spectrophotometer (Agilent Technologies, United Kingdom).

2.3. Synthesis of fluorescent BSA–AuNCs

BSA–AuNCs using BSA as "biological templates" were synthesized in aqueous solution following a previous method with a slight modification [14]. All glasswares used in the experiment were cleaned with freshly prepared aqua regia, and rinsed with ethanol and superpure water thoroughly prior to use. 15.0 mL of 10.0 mM $HAuCl_4$ solution was added to 15.0 mL of 50.0 mg/mL BSA solution under vigorous stirring at 37 °C. After 2 min, 1.5 mL of 1.0 M NaOH solution was introduced to adjust the pH value and the mixture was incubated at 37 °C for 12 h. The color of the solution changed from light yellow to light brown, and then to deep brown. The obtained AuNCs were further purified by ultrafiltration and dialysis [20]. The first step was carried out on a 30,000 MW filter and centrifuged at 3000 rpm for 15 min at 4 °C to remove unreacted BSA. The obtained solution was then dialyzed in superpure water for 48 h to remove unreacted $HAuCl_4$ and NaOH, and the final solution was stored at 4 °C in a refrigerator for use. The concentration of the AuNCs in the following experiments was approximately evaluated based on the measured BSA concentration.

2.4. Detection procedure of free chlorine

For free chlorine determination 30 μL of prepared BSA–AuNCs solution was diluted with phosphate buffer solution (20 mM, pH 5.0), and 12 μL of different concentrations of sodium hypochlorite was added. Then, the solution of reaction volume 120 μL was mixed thoroughly on a vortex mixer. After 20 min reaction, the absorption spectra and fluorescence emission spectra of BSA–AuNCs in the presence of free chlorine were measured. All measurements were carried out at room temperature. To study the usefulness of this method for free chlorine detection in real samples, the relevant metal ions and non-metallic ion were used for the interference experiments.

2.5. Determination of free chlorine in tap water

For the analysis of the real samples, the tap waters collected freshly from various locations were not subjected to any pretreatment in this experiment. Water samples should be determined immediately after sampling, which should avoid light, stirring and heating. To validate the assay, a standard addition method was applied by spiking different concentrations of hypochlorite solutions to water. The procedure was the same as above, except that the standard hypochlorite solution was replaced by the sample.

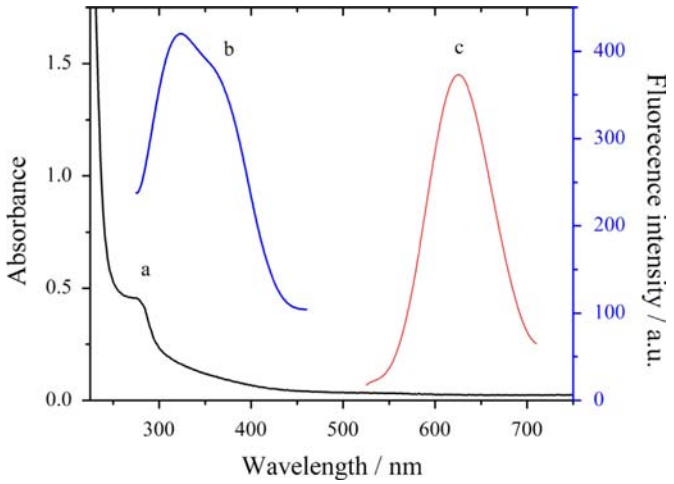


Fig. 1. The UV–vis absorption (a), the fluorescence excitation (b) and fluorescence emission (c) spectra of BSA–AuNCs solution.

3. Result and discussion

3.1. Characteristics of BSA–AuNCs

BSA–AuNCs were prepared according to a method described previously [14]. The optical properties of BSA–AuNCs were detected by UV–vis absorption and fluorescence spectra. As shown in Fig. 1, the absorption spectrum of BSA–AuNCs appeared as a strong absorption band at 278 nm [21]. On the basis of the previous studies, pure BSA exhibited an absorption maximum at 278 nm and this peak remained almost unchanged after the conjugation with AuNCs [22]. Moreover, the absorption spectrum misses the characteristic surface plasmon resonance peak of Au nanoparticles (NPs), indicating the formation of the nanoclusters rather than the nanoparticles [23]. The fluorescence excitation and emission spectra of prepared BSA–AuNCs are shown in Fig. 1. Upon being excited at 365 nm, the BSA–AuNCs showed an emission band centered at 630 nm. The character of the spectra was consistent with the literature [14,24,25], which suggested the successful preparation of BSA–AuNCs.

The aqueous solution of BSA–AuNCs was deep brown in color (Fig. 2a) and exhibited a red fluorescence (Fig. 2c) under UV light. After addition of free chlorine the original deep-brown color of BSA–AuNCs became yellow (Fig. 2b), and a very-weak blue fluorescence was observed under UV light (Fig. 2d).

3.2. Fluorescence response of BSA–AuNCs to free chlorine

The effect of free chlorine on the fluorescence emission was investigated. As indicated in Fig. 3, upon the addition of free chlorine to a solution of BSA–AuNCs, the red fluorescence of BSA–AuNCs became very-weak fluorescence (Fig. 3b), and the fluorescence intensity of BSA–AuNCs was effectively quenched by free chlorine. The fluorescence quenching effect may be attributable to oxidation of Au atoms in the AuNCs by free chlorine [26–29]. To prove this hypothesis, the effect of a commonly used oxidant on the fluorescence emission was investigated. Experimental results show that oxidants with stronger oxidation capability than that of free chlorine (such as $KMnO_4$) can also quench the fluorescence of BSA–AuNCs. In addition, because the fluorescence emission was originated from intra-band transitions of free electrons of the AuNCs, charge transfer behavior may cause the fluorescence quenching. As can be seen from Fig. 2 the original deep-brown color of the AuNCs became dark, and very-weak blue fluorescence was observed in 365 nm light. The very-weak blue fluorescence is a characteristic of the aromatic side groups

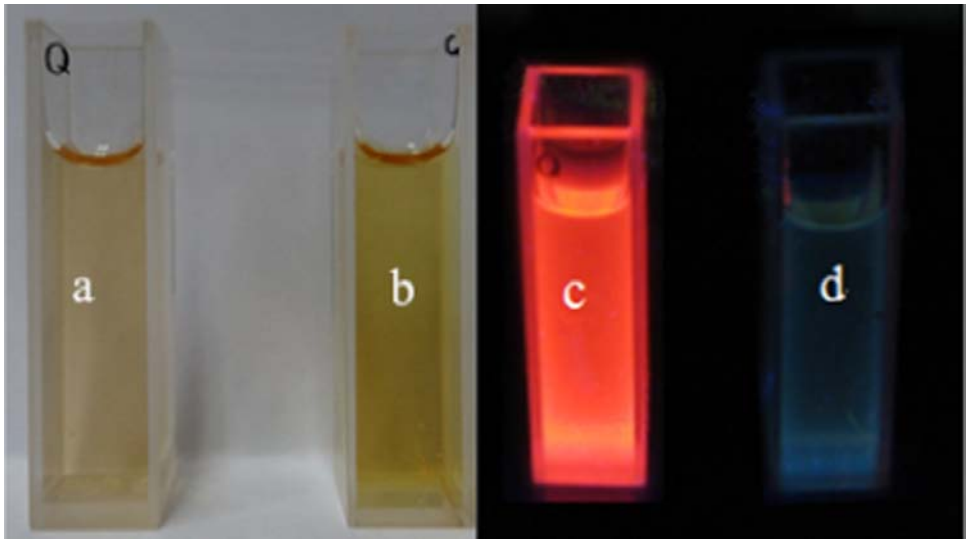


Fig. 2. Photographs of BSA–AuNCs solution in the absence (a, c) and presence (b, d) of free chlorine with natural light (left) and UV (right) irradiation. (For interpretation of the references to color in this figure, the reader is referred to the web version of this article.)

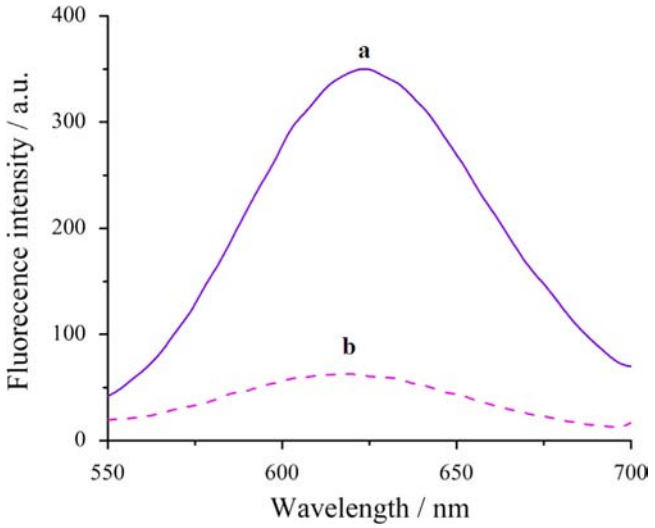


Fig. 3. Fluorescence response of BSA–AuNCs to free chlorine. (a) Fluorescence spectrum of BSA–AuNCs and (b) fluorescence spectrum of BSA–AuNCs in the presence of free chlorine. The pH of solution was 5.0. The concentration of BSA–AuNCs was 6 mg/mL. Reaction time was 20 min at room temperature.

in the amino acid residues of the BSA protein (tryptophan, tyrosine and phenylalanine) [14,22,27]. Based on these findings, we concluded that the mechanism for the fluorescence quenching behavior was more likely due to the oxidation state change of AuNCs during the course of the reaction period.

3.3. Optimization of the sensing system

Prior to the application of proposed fluorescent method for the detection of free chlorine in water some key factors, including the concentration of BSA–AuNCs, the pH value of reaction solution, reaction temperature and time, need to be further optimized.

3.3.1. Concentration of BSA–AuNCs

The concentration of BSA–AuNCs plays a key role in this sensing system. With the increase of BSA–AuNCs concentration from 2 mg/mL to 25 mg/mL, the fluorescence intensity also increased (Fig. 4A). Free chlorine can result in the fluorescence quenching of BSA–AuNCs solution. The fluorescence quenching efficiency increased with increasing of BSA–AuNCs concentration and reached the maximum when 6.0 mg/mL BSA–AuNCs was used, whereas it tended to decrease with further increase of BSA–AuNCs (Fig. 4B). In order to obtain the best signal-to-noise ratio, 6.0 mg/mL of BSA–AuNCs was chosen for this study.

3.3.2. Reaction temperature and time

The purpose of this method is to determine free chlorine in tap water; therefore room temperature was selected as the reaction temperature. To understand the response rate of the fluorescence signal of BSA–AuNCs to free chlorine, time-dependent fluorescence change upon addition of 400 μM free chlorine was monitored. As shown in Fig. 5 the fluorescence intensity of BSA–AuNCs solution decreased rapidly with reaction time up to 1 min, and changed slowly during 2 h reaction subsequently. Taking the reduced fluorescence of BSA–AuNCs with time into account, the experimental procedure was carried out at room temperature for 20 min.

3.3.3. The pH of reaction solution

In order to achieve sensitive detection of free chlorine, the effect of reaction solution pH on the fluorescence of BSA–AuNCs was investigated. Fig. 6 reveals that upon adding the material the fluorescence quenching efficiency changs apparently in weakly acidic, neutral and weakly alkaline solutions, while fluorescence intensity changes are relatively stable from pH 4.0 to 6.0. The largest signal–noise ratio can be obtained at pH 5.0. Free chlorine exists mainly as hypochloric acid (HClO) in acidic, neutral and weakly alkaline solutions, and as hypochlorite anion (ClO^-) in strongly alkaline solutions. The ClO^- exhibits weaker oxidation capability than the HClO [1,30]. Therefore, a comparatively weak acidic environment at pH 5.0 (phosphate buffer, 20 mM) was chosen for optimal sensing system.

3.4. Sensitivity of the sensing system

Under the optimal experimental conditions, the capability of this sensing system was evaluated for quantitative detection of free chlorine. Fig. 7 displays the fluorescence spectra of BSA–AuNCs solution in the presence of various concentrations free chlorine. As shown in Fig.7 the fluorescence intensity of BSA–

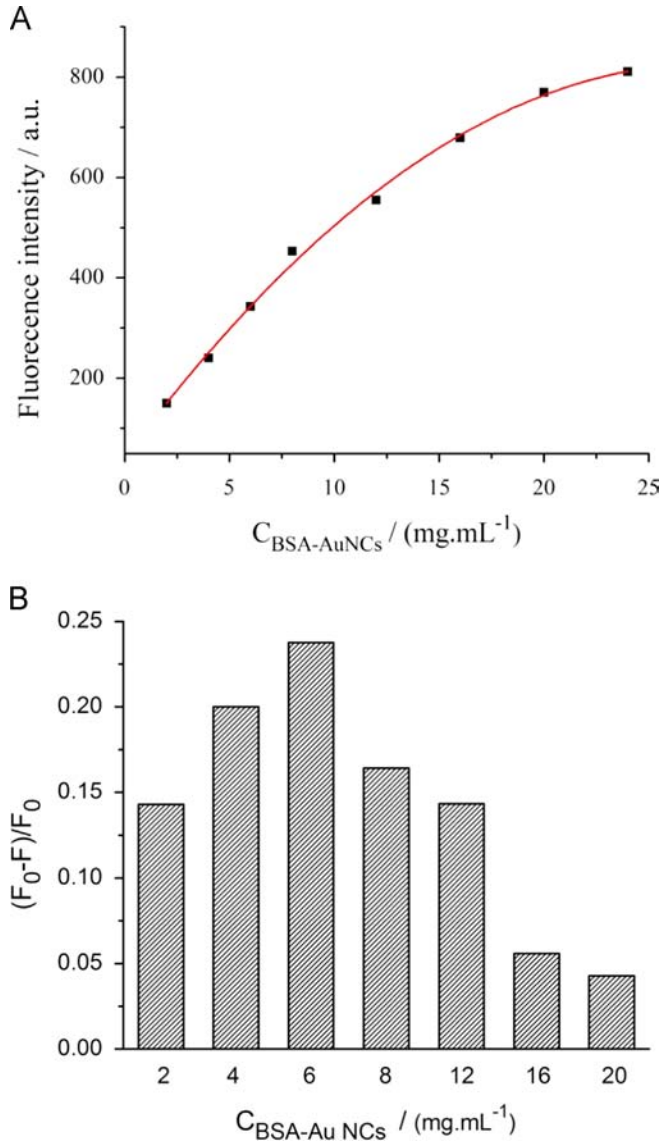


Fig. 4. Concentration-dependent fluorescence of BSA–AuNCs solution (A) and concentration-dependent fluorescence quenching efficiency of BSA–AuNCs to 200 μM free chlorine. Other experiment conditions were as in Fig. 3.

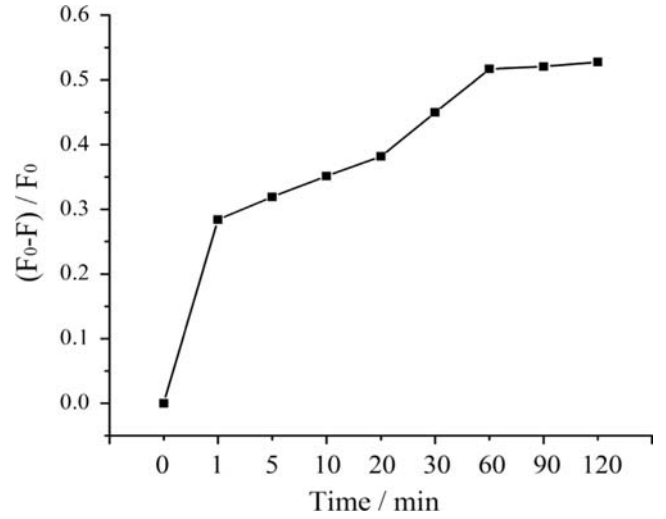


Fig. 5. Time-dependent fluorescence quenching efficiency of BSA–AuNCs to 400 μM free chlorine. Experimental conditions were as in Fig. 3.

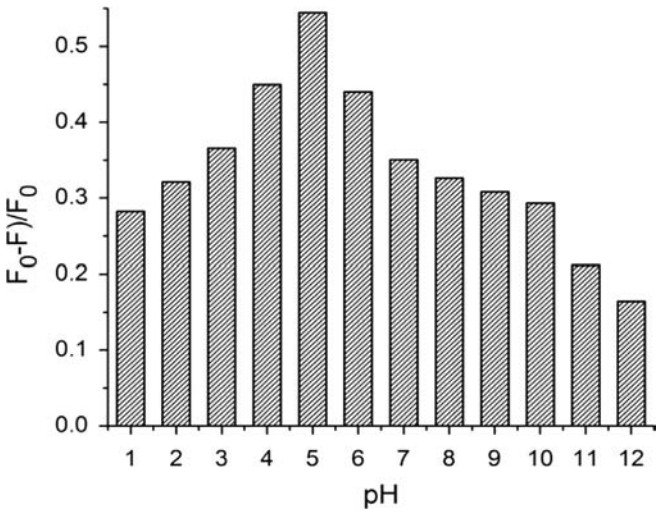


Fig. 6. The fluorescence quenching efficiency of BSA–AuNCs to 700 μM free chlorine at different pH values. Other experiment conditions were as in Fig. 3.

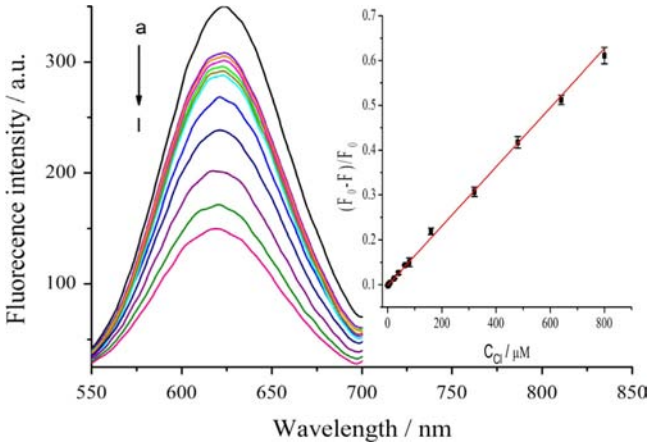


Fig. 7. The fluorescence response of BSA–AuNCs upon addition of various concentrations free chlorine (from a to l: 0, 0.8, 4.0, 8.0, 24, 40, 64, 80, 160, 320, 480, 640 and 800 μM). Inset: plot of the fluorescence quenching efficiency versus free chlorine concentration. Experiment conditions were as in Fig. 3.

Table 1
Comparison of analytical methods for the free chlorine quantification.

Method	Linear range (μM))	Limit of detection (μM))	References
Colorimetric (DPD)	0.67–56	0.67	[31]
Electrochemistry	1.0–932	1.0	[32]
Chemiluminescence	2.0–1000	2.0	[33]
Colorimetric	0–90	2.0	[34]
Fluorescence	0.5–5.0	0.5	[35]
Fluorescence	0.8–800	0.5	This work

AuNCs at 630 nm decreases gradually with increasing of concentration of free chlorine, indicating that the addition of analyte can effectively oxidize the BSA–AuNCs and lead to fluorescence quenching. The calibration curve for free chlorine was established according to the fluorescence quenching efficiency $(F_0-F)/F_0$ (Fig. 7 inset). The regression equation is $(F_0-F)/F_0=6.6034\times 10^{-4}C+0.0985$ with a linear range from 0.8 to 800 μM ($R^2=0.9975$) and the limit of detection (LOD) at 3σ ($\sigma=S_0/S$; S_0, standard deviation of blank sample; S, slope of the calibration curve) is 0.5 μM, which implies more sensitive than those of many of the free chlorine assays ever reported (Table 1). The reproducibility of the sensing system was investigated by

operating six repeated measurements of 30 μM free chlorine, and the relative standard deviation (RSD) was found to be 4.2%.

3.5. Specificity of the sensing system

To detect free chlorine in real samples such as tap water, the selectivity of proposed sensing system was evaluated. As mentioned above for the fluorescence quenching mechanism, only oxidants of oxidation capability more than that of free chlorine would quench the fluorescence of BSA–AuNCs. However, most of the natural water does not contain strong oxidizing agents. Therefore, the proposed sensing system was tested with a variety of environmentally relevant cations (Ca^{2+}, Mg^{2+}, Fe^{3+}, Cu^{2+}, Cd^{2+}, Ag^{+}, Pb^{2+}, Co^{2+}, NH_4^+) and anions (Br^-, F^-, NO_3^-, $CH_3CO_2^-$, SO_4^{2-}, SO_3^{2-}, PO_4^{2-}, CO_3^{2-}, HCO_3^-) (each 1 mM) to evaluate the selectivity under optimal conditions with 700 μM free chlorine. The results are shown in Fig. 8. As can be seen, the fluorescence intensity of BSA–AuNCs is almost same without and with ion target except Cu^{2+}, whereas a significant fluorescence decrease was observed in the presence of free chlorine. And the interference from Cu^{2+} can be eliminated by triethanolamine. These features contributed to the excellent selectivity toward free chlorine, rendering the BSA–AuNCs highly suitable for the analysis of environmental samples.

3.6. Application in tap water sample

From above described results, the applicability of proposed BSA–AuNCs fluorescence probe for detection of free chlorine in tap water was carried out. A standard addition method was used for evaluation of the accuracy and credibility of proposed method. Tap water samples are analyzed by the proposed procedures and the results are presented in Table 1. It can be seen that the concentrations of free chlorine in these tap water samples are found to be in the range of 15.95–26.45 μM, and the recoveries are found to be in the range of 94.8–105.3%. The assay precision was examined by repeatedly analyzing each tap water sample five times within a working day. The RSDs were between 1.8% and 5.6%. Table 2.

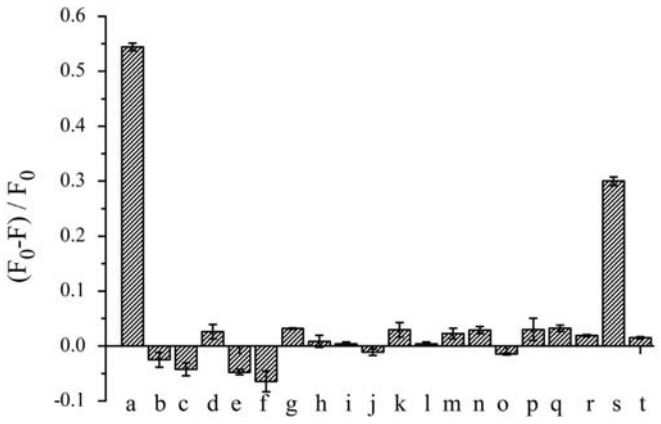


Fig. 8. Selectivity of fluorescence probe for free chlorine over other ions. The concentration of free chlorine was 700 μM; the concentrations of other common ions were all 1.0 mM (a: Cl, b: Ca^{2+}, c: Mg^{2+}, d: Fe^{3+}, e: Cd^{2+}, f: Ag^{+}, g: Pb^{2+}, h: Co^{2+}, i: NH^{4+}, j: Br^-, k: F^-, l: NO^{3-}, m: CH_3CO^{2-}, n: SO_4^{2-}, o- SO_3^{2-}, p: PO_4^{2-}, q: CO_3^{2-}, r: HCO_3^- s: Cu^{2+}, t: Cu^{2+} + triethanolamine. Experimental conditions were as in Fig. 3.

Table 2
Determination of free chlorine in drinking water.

Sample	Found (μM)	Added (μM)	Total found (μM)	Recovery (%)	RSD (%, $n=5$)
Tap water 1	15.95	10.00	26.08	101.3	4.2
		20.00	34.91	94.8	3.4
		30.00	44.98	96.8	2.2
Tap water 2	26.45	10.00	36.63	101.8	2.7
		20.00	46.93	102.4	3.7
		30.00	58.04	105.3	1.8
Tap water 3	21.73	10.00	31.36	96.3	4.1
		20.00	41.86	100.7	5.6
		30.00	52.77	103.5	3.7

4. Conclusion

A novel and facile fluorescent assay has been developed for sensitive detection of free chlorine in drinking water using BSA–AuNCs as the fluorescence probe. The detection mechanism was based on the oxidation of BSA–AuNCs by free chlorine, which resulted in the decrease of BSA–AuNCs fluorescence intensity. This method required no complicated preparation procedure and also exhibited an environmentally friendly feature with high sensitivity and good selectivity. The developed method has been applied for detection of free chlorine in tap water, which presages more opportunities for studying the environmental systems in future applications.

Acknowledgments

Financial support from National Natural Science Foundation of China (No. 21175030) is gratefully acknowledged.

References

[1] Y.Q. Dong, G.L. Li, N.N. Zhou, R.X. Wang, Y.W. Chi, G.N. Chen, Anal. Chem. 84 (2012) 8378–8382.
[2] J.R. Haag, R.G. Gieser, J. Am. Med. Assoc. 249 (1983) 2507–2508.
[3] E. Emmanuel, G. Keck, J.M. Blanchard, P. Vermande, Y. Perrodin, Environ. Int. 30 (2004) 891–900.
[4] A. Tofant, M. Ostovic, S. Wolf, A. Ekert Kabalin, Z. Pavicic, J. Grizelj, Vet. Med. 55 (2010) 394–398.
[5] A.F. Hinckley, A.M. Bachand, J.S. Reif, Environ. Health. Perspect. 113 (2005) 1808–1813.
[6] L. Moberg, B. Karlberg, Anal. Chim. Acta 407 (2000) 127–133.
[7] X.D. Lou, Y. Zhang, J.G. Qin, Sens. Actuators B 161 (2012) 229–234.
[8] U. Pinkernell, B. Nowack, H. Gallard, U.V. Gunten, Water Res. 34 (2000) 4343–4350.
[9] A.P. Singh, O.G. Tsay, D.P. Murale, T. Jun, H. Liew, Y.H. Suh, D.G. Churchill, Analyst 138 (2013) 2829–2832.
[10] D.F. Marino, J.D. Ingle, Anal. Chem. 53 (1981) 455–458.
[11] J.J. Claver, M.C.V. Miron, L.F.C. Vallvey, Anal. Chim. Acta 522 (2004) 267–273.
[12] M. Murata, T.A. Ivandini, M. Shibata, S. Nomura, A. Fujishima, Y. Einaga, J. Electroanal. Chem. 612 (612) (2008) 29–36.
[13] S.Y. Kishioka, T. Kosugi, A. Yamada, Electroanalysis 17 (2005) 724–726.
[14] J.P. Xie, Y.G. Zheng, J.Y. Ying, J. Am. Chem. Soc. 131 (2009) 888–889.
[15] J. Xie, Y. Zheng, J.Y. Ying, Chem. Commun. 46 (2010) 961–963.
[16] Z. Lin, F. Luo, T. Dong, L. Zheng, Y. Wang, Y. Chi, G. Chen, Analyst 137 (2012) 2394–2399.
[17] M.L. Cui, J.M. Liu, X.X. Wang, L.P. Lin, L. Jiao, L.H. Zhang, Z.Y. Zheng, S.Q. Lin, Analyst 137 (2012) 5346–5351.
[18] Y. Tao, Y. Lin, J. Ren, X. Qu, Biosens. Bioelectron. 42 (2013) 41–46.
[19] J. Zhang, C. Chen, X. Xu, X. Wang, X. Yang, Chem. Commun. 49 (2013) 2691–2693.
[20] Z. Zhelev, R. Bakalova, H. Ohba, R. Jose, Y. Imai, Y. Baba, Anal. Chem. 78 (2006) 321–330.
[21] T.T. Chen, Y.H. Hu, Y. Cen, X. Chu, Y. Lu, J. Am. Chem. Soc. 135 (2013) 11595–11602.
[22] L. Shang, Y.Z. Wang, J.G. Jiang, S.J. Dong, Langmuir 23 (2007) 2714–2721.
[23] C.Z. Zheng, H.P. Wang, X. Wei, C.Y. Xu, J.G. Liang, H.Y. Han, Spectrochim. Acta A 118 (2014) 897–902.
[24] D. Cao, J. Fan, J. Qiu, Y. Tu, J. Yan, Biosens. Bioelectron. 42 (2013) 47–50.
[25] P. Zhang, X.X. Yang, Y. Wang, N.W. Zhao, Z.H. Xiong, C.Z. Huang, Nanoscale 6 (2014) 2261–2269.
[26] F. Wen, Y.H. Dong, L. Feng, S. Wang, S.C. Zhang, X.R. Zhang, Anal. Chem. 83 (2011) 1193–1196.
[27] Y.L. Liu, K.L. Ai, X.L. Cheng, L.H. Huo, L.H. Lu, Adv. Func. Mater 20 (2010) 951–956.

[28] F. Samari, B. Hemmateenejad, Z. Rezaei, M. Shamsipur, Anal. Methods 4 (2012) 4155–4160.
[29] H. Li, Y. Guo, L. Xiao, B. Chen, Biosens. Bioelectron. 59 (2014) 289–292.
[30] T. Aoki, M. Munemorl, Anal. Chem. 55 (1983) 209–212.
[31] Standard Methods for the Examination of Water and Wastewater, 16th ed., APHA, AWWA, WPCF, Washington, 1985, pp. 309–314.
[32] T.H. Tsai, K.C. Lin, S.M. Chen, Int. J. Electrochem. Sci. 6 (2011) 2672–2687.
[33] T. Nakagama, M. Yamada, T. Hobo, Anal. Chim. Acta 231 (1990) 7–12.
[34] X.D. Lou, Y. Zhang, J.G. Qin, Z. Li, Sens.Actuators B 161 (2012) 229–234.
[35] Y. Yan, S.H. Wang, Z.W. Liu, H.Y. Wang, D.J. Huang, Anal. Chem. 82 (2010) 9775–9781.

Talanta 132 (2015) 796–802

Contents lists available at ScienceDirect

Talanta

journal homepage: www.elsevier.com/locate/talanta

MicroQuEChERS–nanoliquid chromatography–nanospray–tandem mass spectrometry for the detection and quantification of trace pharmaceuticals in benthic invertebrates

Alexandra Berlioz-Barbier [a], Robert Baudot [a], Laure Wiest [a], Marion Gust [b], Jeanne Garric [b], Cécile Cren-Olivé [a], Audrey Buleté [a,*]

[a] Université de Lyon—Institut des Sciences Analytiques, UMR 5280 CNRS-Equipe TRACES, Université Lyon1, ENS-Lyon—5 rue de la Doua, 69100 Villeurbanne, France
[b] IRSTEA, UR MAEP, Laboratoire d'écotoxicologie, 5 rue de la Doua, 69009 Lyon, France

ARTICLE INFO

Article history:
Received 22 July 2014
Received in revised form
9 October 2014
Accepted 14 October 2014
Available online 29 October 2014

Keywords:
Nano-liquid chromatography
MicroQuEChERS
Tandem mass spectrometry
Gastropods
Endocrine disruptors
Extraction
Validation

ABSTRACT

Due to industrialization and the use of chemical products in everyday life, various types of drugs and pesticides are present in our environment, which threaten and cause negative impacts on aquatic ecosystems. The consequences of these pollutants are gradually becoming visible. Recent evidence confirms that long term exposure to environmental pharmaceutical concentrations can induce adverse effects in aquatic vertebrates and invertebrates such as reproductive impairments and collapse wild populations. Consequently, one of the challenges of environmental science is to evaluate the associated risks.

In this context, a new methodology has been developed using nano-LC-nano-ESI MS/MS to quantify traces of two pharmaceuticals (a neuropharmaceutical drug, fluoxetine, and an anticonvulsant drug, carbamazepine) in two molluscs, *Potamopyrgus antipodarum* and *Valvata piscinalis*, which are both prosobranch gastropods. A simple and quick extraction method was developed based on a modified and miniaturized version of the QuEChERS method. The procedure involves the extraction of approximately 10 mg of wet mollusc tissue by 500 μL of a mixture of acetonitrile/water/hexane (50/20/30) and 100 mg of buffer salt. Thus, the extraction step was carried out on an individual scale.

The sensitivity of this method allowed for the detection of levels as low as 18 ng/g and 128 ng/g for carbamazepine and fluoxetine, respectively, with recoveries of greater than 85% for the two targeted compounds. This method was then applied to both gastropod species exposed to fluoxetine under laboratory conditions. The results provide evidence of bioaccumulation in both *P. antipodarum* and *V. piscinalis* and reveal the inter-species differences.

© 2014 Elsevier B.V. All rights reserved.

1. Introduction

In addition to the classical priority pollutants (pesticides, polychlorinated biphenyls, polycyclic aromatic hydrocarbons), the non-regulated so-called emerging contaminants have become an important topic of research interest, especially with regard to their environmental occurrence. These chemicals are produced on a large scale worldwide, are used in a wide range of applications and have become indispensable to our modern society. Among them, pharmaceuticals are a large and diverse group of compounds that are used in significant quantities worldwide to prevent, cure and treat diseases. These ubiquitous environmental pollutants can enter the aquatic ecosystem via wastewater treatment plant discharges or direct industrial waste, and tend to deposit and accumulate in sediments, soils and biota because of their physical and chemical properties [1]. The occurrence of pharmaceuticals in the aquatic environment has been reported over the past decade or so, with over 80 human drugs detected at low μg/L concentrations in wastewater treatment plant effluents, surface water, groundwater, soils, and aquatic organism tissues worldwide [2–5].

Molluscs are well known as filtering organisms which have been previously used in persistent organic pollutant (POP) monitoring programmes due to their high bioaccumulation capacity, their fixed location and their high population density [6–9]. Moreover, the analysis of these organisms may provide information about the fraction of environmental pollution that is bioavailable to aquatic organisms [8]. In any case, pollutants present in aquatic biota can affect all of the trophic levels by means of their

* Corresponding author.
E-mail address: audrey.bulete@isa-lyon.fr (A. Buleté).

http://dx.doi.org/10.1016/j.talanta.2014.10.030
0039-9140/© 2014 Elsevier B.V. All rights reserved.

bioaccumulation along the food chain [10,11]. For all of these reasons, the development of analytical tools for the quantification of traces of micropollutants in biotic environmental matrices such as benthic invertebrates is required.

In this study, two compounds of interest, namely fluoxetine and carbamazepine, have been chosen. Fluoxetine is a widely used antidepressant, frequently found in aquatic ecosystems and in the environment [12,13] at concentrations of up to μg/L. Carbamazepine is also ubiquitous in aquatic ecosystems [7,14]. Moreover, it has been highlighted that they both exhibit dissimilar effects on the reproduction of two gastropod species, *Potamopyrgus antipodarum* and *Valvata piscinalis* [15].

For the analysis of pharmaceuticals in biotic samples, extraction techniques such as soxhlet extraction, sonication [16], microwave assisted extraction (MAE) [17] and pressurized liquid extraction (PLE) [18,19] have been employed. However, the disadvantages of these sample preparation methods include the use of large amounts of organic solvent and the time required for the preparation of each sample. Furthermore, an efficient clean-up to remove interferences was mandatory to prevent the presence of interfering substances, particularly lipids, which can affect the sensitivity of the method and reduce the LC column life. Solid-phase extraction (SPE) [17,18,20] and gel permeation chromatography (GPC) [19,21] have been the most commonly used purification techniques.

In 2003, a new extraction procedure called QuEChERS (Quick, Easy, Cheap, Effective, Rugged and Safe) was developed by Anastassiade et al. [22] and was first used to extract pesticides from food matrices such as fruits and vegetables. This method is based on a salting out extraction with a solvent (mainly acetonitrile) followed by a dispersive solid-phase extraction (dSPE). Since 2003, the two steps of this method have been optimized and adjusted several times. Moreover, two different standards for the first step have been developed: the American standard (AOAC), which involves the use of acetate salts in order to buffer the liquid–liquid extraction and avoid the degradation of base-sensitive pesticide [23], and the European standard EN 15662, which involves the use of citrate buffer [24]. In 2008, Przbylski et al. optimised a previously developed method for high fat content matrices by adding a small fraction of hexane in acetonitrile to remove lipids from the extract [25]. Regarding the second step (clean-up), it initially consisted of dSPE based on primary and secondary amine bonded silica (PSA). However, in 2006, Leandro et al. used PSA and octadecyl bonded silica (PSA/C18) to eliminate apolar interferences [26]. One of the advantages of the QuEChERS method is that it requires low solvent consumption. Therefore, this technology is of great interest because of its favourable toxicological, environmental and economic aspects. It has recently been used for the extraction of various compounds (veterinary drugs, pesticides, pharmaceuticals) in different complex matrices such as animal tissues [27], soil [28,29] or honeybees [30].

The last step in the analytical process is the identification and the quantification of pharmaceuticals. This step is usually based on liquid chromatography (LC) [17,18,31] or gas chromatography (GC) [32] coupled with mass spectrometry (MS) detection because it provides the high selectivity, specificity and sensitivity required for these types of studies.

In the last decade, great attention has been paid to developing miniaturized analytical systems that can offer reliable separations and higher sensitivity with the use of smaller volumes of both the solvent and sample [33]. Nano-liquid chromatography (Nano-LC) introduced in 1988 by Karlsson and Novotny [34] is a chromatographic technique that uses capillary columns with an internal diameter (ID) of less than 100 μm. In fact, the sensitivity can be increased by reducing the ID of the column and keeping constant all other experimental parameters. Downscaling from conventional LC columns of 4.6 mm ID to 100 μm ID results in a sensitivity gain of nearly 2000 [35], which can be ascribed to both a reduction of analyte dilution [36] and an increase in efficiency [37]. Conversely, the injected volume sample is limited to < 10 nL because of the low column volumes (due to the small ID), which counterbalances the theoretical improvement in sensitivity to a large extent [38]. Consequently, large volume injection methods have been successfully investigated and applied. Both on-column focusing [39,40] and the use of trapping columns [41,42] have been described for the effective preconcentration of a wide range of analytes. The coupling of a nano-LC system with mass spectrometry can also be used to increase the sensitivity. For example, using an electrospray ionisation interface as a continuous flow ionisation technique enhances the ionisation process because the number of ions increases in the gas phase, thereby improving the sensitivity [43]. The largest application for nano-LC is proteomic analysis [44–46]; however, it has not been as widely applied in other important fields such as environmental analysis. Consequently, it is necessary to explore the potential of nano-LC in environmental field analysis.

To this end, the aim of this study was to establish an analytical strategy consisting of one single extraction for fluoxetine and carbamazepine based on a modified and miniaturized QuEChERS method, followed by analysis using nano-LC–MSMS. Indeed, nano-chromatography coupled with mass spectrometry (nano-LC-nano-ESI MS/MS) increases the detection sensitivity, reduces the amount of sample required and is shown to be a good tool to investigate the bioaccumulation potential of pharmaceuticals in gastropods.

2. Materials and method

2.1. Materials

Both target compound standards and isotopically labelled standards (carbamazepine-d10 and fluoxetine-d5) were obtained from Sigma-Aldrich (Saint-Quentin Fallavier, France) with purity higher than or equal to 97%. Individual stock solutions of each compound were prepared at concentrations of 1000 mg/L in acetonitrile (ACN) and stored at -20 °C. Working solutions were prepared by the adequate mixture and dilution of the stock solutions in ACN. For the *ex-situ* exposure experiments, fluoxetine (98%, purity) from Interchim (Montluçon, France) was used.

LC–MS grade ACN, hexane and formic acid were obtained from Fluka (Sigma-Aldrich, St-Quentin Fallavier, France). Pure water (18.2 MΩ cm) was obtained from our MilliQ device manufactured by Millipore (Saint Quentin en Yvelines, France). “Citrate QuEChERS kits” were obtained from Agilent Technologies (Massy, France), in which salts were packaged separately and consisted of 4 g of anhydrous $MgSO_4$, 1 g of sodium chloride, 1 g of sodium citrate dihydrate and 500 mg of disodium citrate sesquihydrate. 15 mL centrifuge tubes for PSA/Cl8 dispersive SPE were purchased from Carlo-Erba (Val de Reuil, France). The PSA/C18 tubes contain 900 mg of anhydrous $MgSO_4$, 150 mg of PSA bonded silica and 150 mg of C18 bonded silica.

2.2. Sample collection

P. antipodarum and *V. piscinalis* were obtained from long term cultures established in IRSTEA (National Research Institute of Science and Technology for Environment and Agriculture, Lyon, France). These cultures were initiated with snails that originated from natural populations collected in the Rhône River. The snails were kept 6 weeks at 21 ± 1 °C in 20 L stainless aquaria filled with reconstituted water (mixture of natural spring water and deionized water)and fed with Tetramin® fish food (Tetrawerke, Melle, Germany) as previously described by Gust et al. [15] before experiments. These snails were used as blank matrix or for the development step.

Fluoxetine exposures on both *P. antipodarum* and *V. piscinalis* were performed simultaneously according to a procedure which was previously published by Gust et al. [15]. Briefly, snails from each species were placed in the same test beakers filled with 0.5 L to avoid any differences in the exposure conditions. The beakers were set at 21 ± 1 °C with a 16:8 h light:dark photoperiod. A flow-through system was used which consisted of beakers filled with continuously renewed test water (four renewals a day) and a continuous pumping system. For each tested concentration, it consisted of clean water and a fluoxetine-spiked solution allowing the required exposure concentrations to be obtained after mixing. The fluoxetine-spiked stock solution was renewed every three days and kept at an ambient temperature (18 °C) and in darkness, based on its stability under these conditions [47]. The nominal exposure concentrations included 11.1, 33.3 μg/L and a control for both species. They were chosen in accordance with the biological effects previously observed in these species [15]. Adult snails, with a size of approximately 4.3 mm (±0.2) and 4.0 mm (±0.2) for *P. antipodarum* and *V. piscinalis,* respectively, were used at the start of the experiment.

Six replicates per concentration and three replicates of solvent control were prepared and exposed for 7 (*V. piscinalis*) and 14 days (*P. antipodarum*). Each replicate contained 25 organisms of *P. antipodarum* and 17 of *V. piscinalis*.The specific conductivity, temperature and pH of the water were monitored daily. The snails were fed with 1.5 mg/individual Tetramin® fish food (Tetrawerke, Melle, Germany) per working day, corresponding to the *ad libitum* conditions.

2.3. Sample preparation

One gastropod was weighed in a 1.5 mL centrifuge tube and ground with a pestle. A volume of 250 μL of ACN, 100 μL of water, 150 μL of hexane, 50 μL of ISTD working solution at 50 μg/L and 100 mg of "citrate QuEChERS" salts were then added to the centrifuge tube. The tube was then immediately shaken by hand, vortexed for 10 s and centrifuged for 2 min at 5000 rpm. Afterwards, an aliquot of 150 μL of supernatant was sampled in a 1.5 mL eppendorf tube. The extract was then diluted in ACN/H_2O (50:50) for nano-LC injection.

2.4. LC–MS/MS

The system used for LC–MS/MS was a nanoliquid chromatography Ultimate3000 (Thermo Fisher®, Villebon sur Yvette, France) coupled to a triple quadrupole mass spectrometer Qtrap3200 from ABSciex® (Darmstadt, Germany) equipped with a Nanospray® II interface (ESI) (AB Sciex®, Darmstadt, Germany). The data were processed using the Analyst 1.5 software package.

Chromatographic separation was performed in two steps: a preconcentration step on a C18 pre-column (5 μm, 300 Å, Thermo Fisher®, Villebon sur Yvette, France) followed by separation on a Pepmap C18 column (C18 3 μm × 75 μm × 100 Å, Thermo Fisher®, Villebon sur Yvette, France). The capillary column was directly connected to a ten-port valve to minimize the dead volume and dispersion of injected plug sample. Both ends of pre-column were also connected to the ten-port valve.

In the final optimised configuration, the column oven temperature was set at 30 °C and an injection volume of 1 μL (in μL pickup mode) of the sample was loaded for 4.5 min onto the pre-column at a flow rate of 20 μL/min using a loading solvent consisting of pure water and ACN (98/2) with 0.1% (v/v) formic acid. Once the compounds were trapped (loading step), the valve position was changed to connect the pre-column with the analytical column.

Next, the analytes were back flushed with the mobile phase delivered by the nano-pump into the reversed phase column at a flow rate of 0.3 μL/min. The targeted compounds were separated using (A) H20:ACN (98:2) with 0.1% of formic acid and (B) ACN: H20 (80:20) with 0.1% of formic acid. The following elution program was used: from 40% to 100% (B) in 5 min and 100% (B) for 15 min. The column was re-equilibrated for 20 min at the initial composition of the gradient between runs.

MS/MS detection was performed in multiple reaction monitoring (MRM) mode using the NanoSpray® II source in positive ion mode. For each compound, the declustering potential (DP), energy potential (EP), collision energies (CE) of two MRM transitions were optimised from a continuous flow of a standard injection (1 mg/L solution in 50/50 (A) and (B) at 10 μL/min) to obtain the maximum signal intensities. One MS/MS transition (MRM 1) was used for the quantification, and a second MS/MS transition (MRM 2) was selected for confirmation for each targeted compound. The selected parent and fragment ions, MS/MS conditions and retention times are listed in Table 1.

2.5. Method performance and validation

The development method combining the sample preparation and the LC–MS/MS analysis was validated following the International Conference on Harmonization (ICH) guidelines [48]. The limit of detection (LOD) was determined as the analyte concentration that produced a peak signal of three times larger than the background noise from the chromatogram using MRM 2. The limit of quantification (LOQ) was determined as the analyte concentration that produced a peak signal of ten times larger than the background noise from the chromatogram using MRM 1. Each value of the estimated detection and quantification limits was checked by extracting and analysing samples of blank matrix spiked before extraction at different concentrations. The validation strategy is outlined in Fig. 1. It was performed on three days with concentrations ranging between LOQ and 50LOQ. More precisely, on each day, six samples of blank matrix spiked with six levels of concentration (C1=5LOQ, C2=10LOQ, C3=20LQ, C4=30LOQ, C5=40LOQ and C6=50LOQ) were extracted to examine the linearity. Linearity was considered to be validated if the correlation coefficient measured in this concentration range was found to be greater than 0.99.

The repeatability and recoveries were evaluated for three levels of concentration: C2, C4 and C6. For each day, two additional samples of blank matrix spiked with a particular concentration level (first day C2, second day C4 and third day C6) were extracted to determine the repeatability. The repeatability is associated with the intra-day precision, which is expressed as the relative standard deviation (RSD) of a series of measurements carried out under the same conditions by the same manipulator and on the same day. Each day, three samples of blank matrix were spiked at the same concentration before the extraction. The signals of these samples ($S_{\text{spiked before extraction}}$) were compared with those of samples spiked at C2, C4 or C6 after extraction ($S_{\text{spiked after extraction}}$) in order to

Table 1
Retention time (*Rt*), MS/MS parameters: quantitation transitions, precursor product ions, desclustering potential (DP), energy potential (EP), collision energies (CE), and transition ratio.

Analytes	*Rt* (min)	Precursor ion (*m/z*)	Product ion (*m/z*)	DP (V)	EP (V)	CE (V)	Transition ratio
Carbamazepine	18.7	237.2	194.2	61	10	27	10
		237.2	179.2	61	10	47	
Carbamazepine-d10	18.6	247.2	204.3	46	4	29	–
Fluoxetine	16.9	310.2	148.3	41	5.5	13	30
		310.2	91.1	41	5.5	27	
Fluoxetine-d5	16.9	315.2	153.2	36	4	14	–

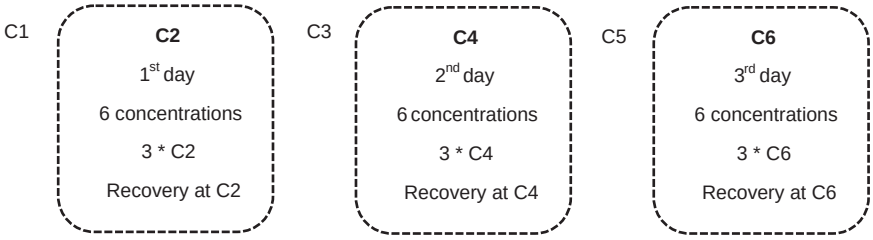


Fig. 1. Validation plan on three days.

determine recoveries. Consequently, three replicates per day of validation were used to evaluate recoveries and repeatability.

Intermediate precision, also named inter-day precision, was also evaluated at the same levels of concentration as those used for the repeatability measurements. The intermediate precision can be determined by introducing variations in the process, such as different conditions, different manipulators or different days. In our case, the procedures were performed over a period of three days and different bottles of solvents were used. For the LC–MS/MS analysis, due to a matrix effect the signals of samples spiked before extraction had to be corrected using the signals of the isotopically labelled compounds carbamazepine-d10 and fluoxetine-d5 (S_{IsoLab}). The intermediate precision was expressed as the RSD of the ratio $S_{spiked\ before\ extraction}/S_{IsoLab}$ as a percentage. For each validated concentration level, five replicates were used to determine the intermediate precision.

As recommended in ICH guidelines [48], with respect to the repeatability, all the RSDs should be less than or equal to 20%. Additionally, for the intermediate precision, the RSDs should be below 30%.

2.6. Quantification

Matrix-matched calibration was used for quantification. In each batch, 6 calibration points prepared as described in Section 2 with concentration ranges between LOQ and 50LOQ were injected. The quantification was carried out by two replicate injections. The instrumental performance was checked using the injection of Quality Control samples which corresponded to a standard solution of targeted compounds at 50 ng/mL. The extraction performance was checked using the signal peak areas of carbamazepine-d10 and fluoxetine-d5. Fluoxetine and carbamazepine were identified by their retention times, the two MRM transitions and the specific ratios of the responses of the transitions with deviations $<20\%$ with respect to the ratios of the analytical standards.

3. Results and discussion

3.1. Method development

3.1.1. Sample extraction

The QuEChERS extraction method consisted of two major steps: a liquid/liquid buffered extraction followed by a dispersive SPE clean up. In the first step, an organic phase allows the extraction of the analytes from the matrix. Several organic solvents such as acetone, ethyl acetate or acetonitrile can be used; however, the efficiency of extraction solvent depends on specific matrix and targeted compounds. Nevertheless, acetonitrile has already been used for the extraction of pharmaceuticals and various compounds in mollusc tissues [49,50]. Because water and acetonitrile are miscible, a buffered mixture of salts and $MgSO_4$ must also be added in order to induce phase separation. This procedure increases the passage of the target compounds into the organic phase and improves the pH-dependent stability of the substances, resulting in increased recovery of the analytes [51]. Due to a limited number of available biotic organisms, some of the extraction parameters were fixed: the quantity of added salts (100 mg), the quantity of water added (100 μL), the type of buffered salts (chosen according to the standard Method EN 15662 [24]) and the type extraction solvent (acetonitrile). The type of liquid/liquid extraction is chosen based on the affinity of the analytes for each phase. This affinity is dependent first on the compound, second on the nature of the solvents and finally on the volume of solvents used for extraction. Thus, the volume of acetonitrile was optimized first in order to carry out an efficient extraction.

To determine the influence of the volume of ACN used in the first step of the extraction, the signal of each molecule was compared after extraction with different quantities of acetonitrile in the range of 50 to 250 μL. The results obtained with three replicate measurements for each experiments were normalized with respect to the maximum response and are presented in Fig. 2. For both compounds the highest signal intensity was reached for 250 μL of ACN. Consequently, this volume was used for all subsequent extractions of target analytes from biotic organisms.

In the QuEChERS method, the clean-up step is performed using dispersive SPE [22]. The dSPE sorbent should retain the matrix co-extractants but not the target analytes. To selectively trap the matrix impurities, different dSPE sorbents such as PSA, PSA/C18, and graphite carbon black are available. PSA is used to eliminate polar organic acids, sugars and lipids, whereas PSA/C18 removes also non polar compounds. For our application we used PSA/C18 to evaluate the efficiency of the dSPE clean-up. The choice of this sorbent was justified by the high concentration of lipids contained in the extracts from the biotic matrices. PSA/C18 is also recommended by the European standard [24] for the clean-up of highly fatty matrices such as meats or cereals. In addition, one sample was extracted without the clean-up step.

Fig. 3 presents the recoveries of the two molecules in the presence and absence of the dSPE phase. Three replicate measurements were carried out for each experiment. The results show no significant difference in the case of carbamazepine, whereas the recoveries are better without dSPE in the case of fluoxetine. Indeed, the use of PSA/C18 decreased the recovery of fluoxetine by a factor of 6. These results can be explained by the relative hydrophobicity of fluoxetine, which has a logP value of 4.05, while logP of carbamazepine is approximately 2.45.

This test revealed that the PSA/C18 sorbent is not suitable for the dispersive SPE clean-up step proposed in the original QuEChERS method. Because the dSPE clean-up retains fluoxetine, this step was omitted and replaced by an addition of hexane. Indeed, it has been shown that this solvent allows for the elimination of non-polar and fatty compounds [25]. Thus, to investigate the impact of hexane on biotic matrix samples, 100 μL of this solvent were added during the extraction step. The benefit of adding hexane could be immediately observed during the experiment: the samples cleaned with hexane appeared clearer and less viscous. This solvent efficiently eliminated lipids and ensured the defatting of the sample. Moreover, when the volume of hexane was lower than 100 μL, the partition between ACN and hexane phases was not clearly visible. Consequently, the

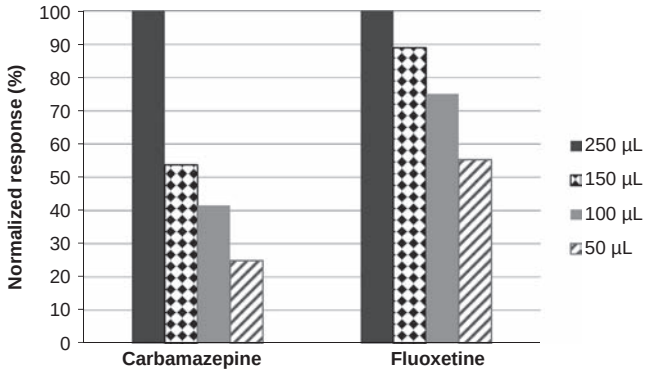


Fig. 2. Normalized responses of target compounds obtained (at 300 ng/g wet weight) using different quantities of acetonitrile (replicate measurements, $n=3$).

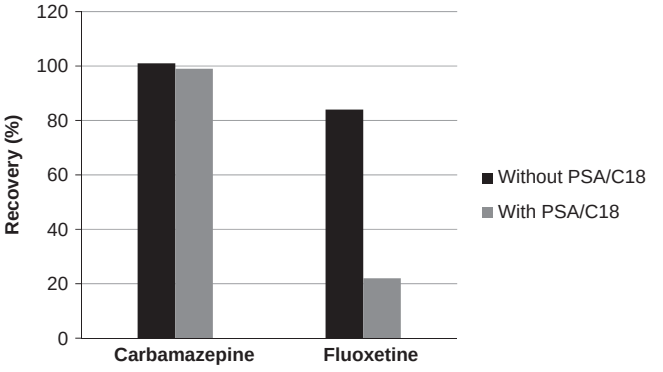


Fig. 3. Recoveries of target compounds obtained (at 300 ng/g wet weight) using PSA/C18 dSPE and without dSPE (replicate measurements, $n=3$).

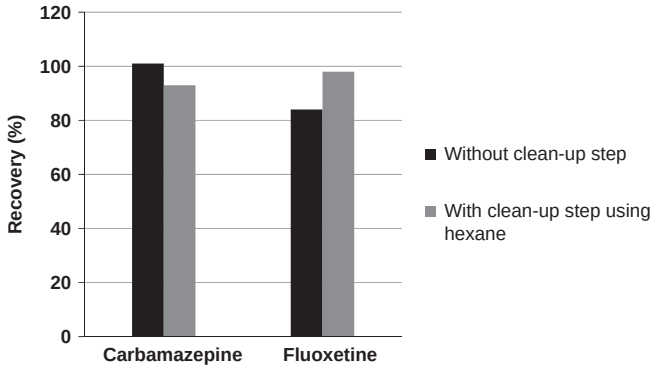


Fig. 4. Recoveries of target compounds (at 300 ng/g wet weight) obtained using hexane clean-up and without clean-up step (replicate measurements, $n=3$).

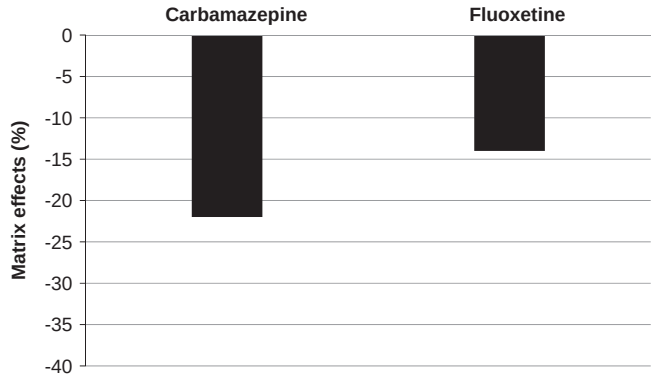


Fig. 5. Matrix effects of the target compounds (at 300 ng/g wet weight) obtained with optimized method (replicate measurements, $n=3$).

recovery of the cleaned extract was poorly repeatable. For these reasons, the addition of 100 µL of hexane was chosen for the clean-up step as a dSPE replacement. The recoveries of each target compound obtained with the optimized method including the extraction and purification steps are presented in Fig. 4 and are compared with those obtained without the purification step.

3.1.2. *Matrix effects*

Matrix effects that can cause the enhancement or suppression of the analytical signals are frequently observed in the chemical analysis field. This phenomenon is due to matrix compounds that are eluted with the same retention time as the target compounds [52]. Matrix effects depend on the nature of the matrix and the efficiency of the sample preparation step. Therefore, the sample preparation step should eliminate interfering compounds while retaining the target analytes. To thoroughly study this phenomenon, the biotic samples were spiked after the extraction, and the corresponding signals ($S_{\text{spiked matrix}}$) were compared with those of the standard (S_{solvent}) with the same concentration. The matrix effects for our application were determined with the following equation:

$$\text{Matrix effect}\ (\%) = \left(\frac{S_{\text{spiked matrix}}}{S_{\text{solvent}}} - 1\right) \times 100$$

and the results are presented in Fig. 5.

The results indicate that ion suppression was observed for both targeted compounds, with the maximum ion suppression of 22% found for carbamazepine. Applying an external calibration to complex matrices such as biotic matrices would certainly lead to errors in quantification. Therefore, three calibration strategies can be employed in this study: an internal standard, standard addition and matrix-matched calibrations. Internal standard calibration is an efficient method to correct matrix effects. For example, in order to correct for the ion suppression, deuterated internal standards of compounds can be used. The internal standard undergoes the same interferences as that of the analyte; thus, the phenomenon of ion suppression is similar for the analyte and the internal standard. Standard addition is also an interesting but very time-consuming method, especially when a large number of samples have to be analysed. Finally, matrix-matched calibration is a useful method to correct matrix effects, however only if a blank matrix is available and if the ion suppression/enhancement matrix effects used for the calibration are the same as those for the samples analysed. One of the objectives of this study was to apply the analytical method to a large number of samples to obtain an overview of environmental contamination, so standard addition calibration could not be used. Finally, because a blank matrix (see Section 2.2) was available, matrix-matched calibration was chosen. To make sure that the ion suppression/enhancement matrix effects were the same for the calibration and the analytes, the extraction performance was checked using the signal areas of fluoxetine-d5 and carbamazepine-d10.

3.2. *Nano-LC–MS/MS*

The optimization of the ESI–MS/MS parameters was performed by direct infusion into the electrospray source (Table 1). Two MRM transitions were monitored for each compound: the more sensitive ion was used for the quantification and the second for confirmation. Both positive and negative ionisation modes were tested. The better choice will provide the best selectivity of the transitions and the smallest noise for the product ions. For both target compounds, positive ionisation mode was selected. Another approach for increasing the MS/MS sensitivity is improvement in the ionisation

efficiency of the analyte undergoing quantification. The ionisation efficiency of a target compound can be increased by the use of mobile phase additives such as formic acid or ammonium acetate. These modifiers are often commonly used in bioanalysis [53]. Both of the selected analytes showed more efficient ionisation when using formic acid as an additive.

Optimising the nanochromatographic conditions of small molecule analysis is challenging because of the technology used: nanochromatography is a relatively recent development in chromatography driven by advances in proteomics. Nanochromatography columns are adapted for peptide separation, which means that they are designed for molecules with molecular weights of up to 3000 Da. In contrast, the two molecules of interest in this study weighed 237 g/mol (carbamazepine) and 310 g/mol (fluoxetine). Nevertheless, the advantage of using a nano-LC system, which is a miniaturization of a chromatographic system and electrospray source, is that it improves the analytical performance. Therefore, the system enables handling small volumes, working with a limited matrix quantity and increasing of the sensitivity. From a detailed examination of the current literature it is clear that the selected pharmaceuticals have never been analysed by nano-LC. To develop the nano-LC separation, a capillary column with 75 μm ID was used with a silica-based C18 stationary phase ;(3-μm particle size) with virtually zero silanophilic activity. The choice of this column was based on the results of several reports that used the C18 stationary phase for the separation of pharmaceuticals by HPLC [17–19]. To increase the sensitivity of the method, an on-line preconcentration procedure using a trapping μ-pre-column (C18 300 μm × 5 mm × 100 Å, Dionex®) was applied because it previously provided higher sensitivities in several nano-LC applications [41,42].

Regarding the pre-concentration step, the key factor for obtaining good sensitivity is the loading time (or switching time), which can be defined as the time that the mobile phase is pumped into the μ pre-column once the sample has been loaded. To obtain the best sensitivity, various loading times were compared. Fig. 6 presents the normalized response of the two target compounds for loading times of 4 min, 4.5 min and 5 min on the cartridge. The best loading time was determined to 4.5 min because a shorter time was not able to elute the pre-column to a sufficient extent and a longer loading time produced lower efficiency. Indeed, the most polar compound, carbamazepine in this case, was desorbed and directed into the waste.

With this column, different isocratic and gradient elution programs were tested. Complete separation with good efficiency was achieved using a mobile phase (A) of water and ACN (98/2) with 0.1% of formic acid and a mobile phase (B) of ACN and water (80/20) with 0.01% of formic acid. The separation of the two target compounds under these conditions was achieved in less than 20 min, and the column was re-equilibrated for 20 min between runs.

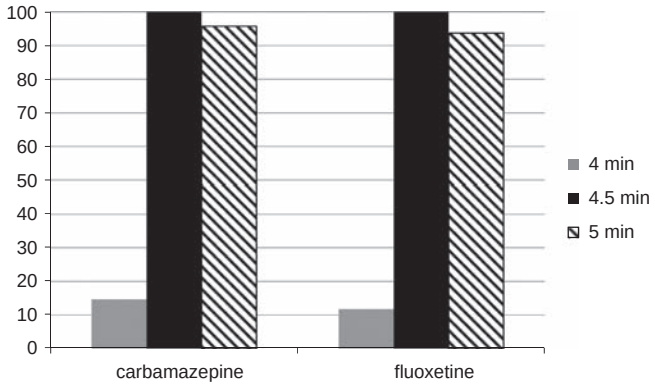


Fig. 6. Normalized responses of the target compounds with different loading times (replicate measurements, $n=3$).

3.3. Method validation and performance

Method validation is an important requirement in the practice of chemical analysis. This step is crucial in order to prove the repeatability of the developed QuEChERS-LC–MS/MS method with respect to the actual validation criteria [54]. The criteria used for the validation method were the limit of quantification, linearity, recovery, inter-day precision and intra-day precision.

Satisfactory recoveries (> 85%) were obtained for both compounds. The intra- and inter-day precisions were measured to be less than 15% and 20%, respectively, for the compounds of interest. The correlation coefficients of the performed regressions were greater than 0.99. The limits of detection were found to be in the range of environmental contaminant concentrations, which is between 16 and 127 ng/g for carbamazepine and fluoxetine, respectively. The limits of quantification were measured to be 48 and 343 ng/g for carbamazepine and fluoxetine, respectively.

If we compare the instrumental detection limits for the two studied compounds obtained with nano-LC-nano-ESI–MS/MS to those obtained with LC–ESI–MS/MS from a previous study with the same detector, we find a 50-fold and 125-fold increase in the sensitivities for carbamazepine and fluoxetine, respectively. Such sensitivities allow for the study of a unique gastropod.

3.4. Application to ex situ experiments

After a short exposure (7 and 14 days) at different concentrations (11 and 33 μg/L), the quantification of fluoxetine in both *P. antipodarum* and *V. piscinalis* was carried out (Table 2) using triplicate measurements. Fluoxetine was quantified for both sentinel species; however, no significant differences were noted between the fluoxetine concentrations in *P. antipodarum* after 7 or 14 days, suggesting that the bioconcentration steady state had already been achieved by 7 days of exposure in this species. A previous study reports that in the Japanese medaka, the bioconcentration steady state was achieved after only 3 days of exposure. Therefore, it was estimated that the fluoxetine steady state was also reached in *V. piscinalis*, even though measurements were only performed on day 7.

Concentrations of fluoxetine in *P. antipodarum* were significantly higher than in *V. piscinalis*, implying a higher bioconcentration of the parent compound in *P. antipodarum* after 7 days of exposure. These results reveal an inter-species difference in the accumulation of fluoxetine. As this method was carried out on one gastropod, a metabonomics approach could be possible to characterize biological responses.

4. Conclusion

Using a combination of a single and quick extraction and nanoliquid chromatography coupled to tandem mass spectrometry analysis, the developed nano-LC-nano-ESI–MS/MS method offers

Table 2
Concentrationof fluoxetine in *P. antipodarum* and *V. piscinalis* after a short exposure (7 and 14 days) at different doping concentrations (11 and 33 μg/L) (average of three replicates measurements per experiments).

Fluoxetine (μg/L)			Control	11 μg/L	33 μg/L
Fluoxetine (μg/g ww)	*P. antipodarum*	J0	< LD	–	–
		J7	< LD	1.2 ± 0.2	5.5 ± 0.2
		J14	< LD	1.8 ± 0.3	6.3 ± 0.5
	V. piscinalis	J0	< LD	–	–
		J7	< LD	< LD	2.8 ± 1.1

the sensitivity and selectivity necessary for the detection of the target analytes in the ng/g range.

Moreover, this analytical method combines extraction and purification of the extracts in a single step in order to comply with the principles of Green Chemistry, to simplify the experimental procedure and to better avoid sources of contamination. The method was successfully applied to the analysis of two gastropod species, *V. piscinalis* and *P. antipodarum*, exposed to various levels of fluoxetine concentration.

This study has investigated the accumulation of pharmaceuticals in gastropod molluscs for the first time. The results indicate an inter-species difference in the amount of bioaccumulation between the two molluscs. The success of this method allows us to foresee one possible outlook for future studies: as this study was carried out on one gastropod, a metabolomics approach may be possible to characterize the biological responses in order to better understand the diversity of responses between both molluscs. Additionally, as there is little quantification data for fluoxetine detected in the different mollusk species in the literature, the developed method can be used to extend knowledge about pharmaceutical bioaccumulation mechanisms, thus improving understanding of biological effects.

Acknowledgements

This work was funded by CNRS (PEPS-EDD 2009), which is gratefully acknowledged.

References

[1] W.C. Li, Environ. Pollut. 187 (2014) 193–201. http://dx.doi.org/10.1016/j.envpol.2014.01.015.
[2] G. McEneff, L. Barron, B. Kelleher, B. Paull, B. Quinn, Sci. Total Environ 476–477 (2014) 317–326. http://dx.doi.org/10.1016/j.scitotenv.2013.12.123.
[3] D.J. Lapworth, N. Baran, M.E. Stuart, R.S. Ward, Environ. Pollut. 163 (2012) 287–303. http://dx.doi.org/10.1016/j.envpol.2011.12.034.
[4] D. Fatta-Kassinos, S. Meric, A. Nikolaou, Anal. Bioanal. Chem. 399 (2011) 251–275. http://dx.doi.org/10.1007/s00216-010-4300-9.
[5] K. Wille, M. Claessens, K. Rappé, E. Monteyne, C.R. Janssen, H.F. De Brabander, et al., J. Chromatogr. A 1218 (2011) 9162–9173. http://dx.doi.org/10.1016/j.chroma.2011.10.039.
[6] G. Pojana, A. Gomiero, N. Jonkers, A. Marcomini, Environ. Int. 33 (2007) 929–936. http://dx.doi.org/10.1016/j.envint.2007.05.003.
[7] S.L. Klosterhaus, R. Grace, M.C. Hamilton, D. Yee, Environ. Int. 54 (2013) 92–99. http://dx.doi.org/10.1016/j.envint.2013.01.009.
[8] M. Gust, T. Buronfosse, O. Geffard, R. Mons, H. Queau, J. Mouthon, et al., Water Res. 44 (2010) 4517–4528. http://dx.doi.org/10.1016/j.watres.2010.06.019.
[9] C. Schmitt, C. Vogt, B. Van Ballaer, R. Brix, A. Suetens, M. Schmitt-Jansen, et al., Ecotoxicol. Environ. Saf 73 (2010) 1574–1579. http://dx.doi.org/10.1016/j.ecoenv.2010.07.014.
[10] D. Gui, R. Yu, X. He, Q. Tu, L. Chen, Y. Wu, Chemosphere 114 (2014) 106–113. http://dx.doi.org/10.1016/j.chemosphere.2014.04.028.
[11] A. Zenker, M.R. Cicero, F. Prestinaci, P. Bottoni, M. Carere, J. Environ. Manage. 133 (2014) 378–387. http://dx.doi.org/10.1016/j.jenvman.2013.12.017.
[12] M.M. Schultz, E.T. Furlong, D.W. Kolpin, S.L. Werner, H.L. Schoenfuss, L.B. Barber, et al., Environ. Sci. Technol. 44 (2010) 1918–1925. http://dx.doi.org/10.1021/es9022706.
[13] C.D. Metcalfe, X.-S. Miao, B.G. Koenig, J. Struger, Environ. Toxicol. Chem. SETAC 22 (2003) 2881–2889.
[14] N.G. Dodder, K.A. Maruya, P. Lee Ferguson, R. Grace, S. Klosterhaus, M.J. La Guardia, et al., Mar. Pollut. Bull. 81 (2014) 340–346. http://dx.doi.org/10.1016/j.marpolbul.2013.06.041.
[15] M. Gust, T. Buronfosse, L. Giamberini, M. Ramil, R. Mons, J. Garric, Environ. Pollut. 157 (2009) 423–429. http://dx.doi.org/10.1016/j.envpol.2008.09.040.
[16] R. Fernandez-Torres, M.A. Bello Lopez, M. Olias Consentino, M. Callejon Mochon, J.L. Perez-Bernal, Anal. Chim. Acta 675 (2010) 156–164. http://dx.doi.org/10.1016/j.aca.2010.07.026.
[17] R. Cueva-Mestanza, M.E. Torres-Padron, Z. Sosa-Ferrera, J.J. Santana-Rodriguez, Biomed. Chromatogr. 22 (2008) 1115–1122. http://dx.doi.org/10.1002/bmc.1033.
[18] J. Wang, P.R. Gardinali, Anal. Bioanal. Chem. 404 (2012) 2711–2720. http://dx.doi.org/10.1007/s00216-012-6139-8.
[19] B. Huerta, A. Jakimska, M. Gros, S. Rodriguez-Mozaz, D. Barcelo, J. Chromatogr. A 1288 (2013) 63–72. http://dx.doi.org/10.1016/j.chroma.2013.03.001.
[20] G.C. Nallani, P.M. Paulos, L.A. Constantine, B.J. Venables, D.B. Huggett, Chemosphere 84 (2011) 1371–1377. http://dx.doi.org/10.1016/j.chemosphere.2011.05.008.
[21] A.M. Al-Ansari, A. Saleem, L.E. Kimpe, V.L. Trudeau, J.M. Blais, J. Chromatogr. B—Anal. Technol. Biomed. Life Sci. 879 (2011) 3649–3652. http://dx.doi.org/10.1016/j.jchromb.2011.09.033.
[22] M. Anastassiades, S.J. Lehotay, D. Štajnbaher, F.J. Schenck, J. AOAC Int. 86 (2003) 412–431.
[23] S.J. Lehotay, J. AOAC Int. 90 (2007) 485–520.
[24] Norme NF EN 15662 Aliments d'origine végétale. Méthode polyvalente de détermination des résidus des pesticides par CG-SM et SL/SM/SM avec extraction/partition avec de l'acétonitrile et nettoyage par SPE dispersés—AFNOR, n.d. ⟨http://www.decitre.fr/livres/norme-nf-en-15662-aliments-d-origine-vegetale-5552120002693.html⟩ (accessed July 15, 2014).
[25] C. Przybylski, C. Segard, J. Sep. Sci. 32 (2009) 1858–1867. http://dx.doi.org/10.1002/jssc.200900016.
[26] C.C. Leandro, R.J. Fussell, B.J. Keely, J. Chromatogr. A 1085 (2005) 207–212. http://dx.doi.org/10.1016/j.chroma.2005.06.054.
[27] G. Stubbings, T. Bigwood, Anal. Chim. Acta 637 (2009) 68–78. http://dx.doi.org/10.1016/j.aca.2009.01.029.
[28] M.-V. Salvia, E. Vulliet, L. Wiest, R. Baudot, C. Cren-Olivé, J. Chromatogr. A 1245 (2012) 122–133. http://dx.doi.org/10.1016/j.chroma.2012.05.034.
[29] M. Asensio-Ramos, J. Hernandez-Borges, L.M. Ravelo-Perez, M.A. Rodriguez-Delgado, Anal. Bioanal. Chem. 396 (2010) 2307–2319. http://dx.doi.org/10.1007/s00216-009-3440-2.
[30] L. Wiest, A. Bulete, B. Giroud, C. Fratta, S. Amic, O. Lambert, et al., J. Chromatogr. A 1218 (2011) 5743–5756. http://dx.doi.org/10.1016/j.chroma.2011.06.079.
[31] S. Chu, C.D. Metcalfe, J. Chromatogr. A 1163 (2007) 112–118. http://dx.doi.org/10.1016/j.chroma.2007.06.014.
[32] A. Azzouz, B. Souhail, E. Ballesteros, Talanta 84 (2011) 820–828. http://dx.doi.org/10.1016/j.talanta.2011.02.016.
[33] A. Rios, A. Escarpa, B. Simonet, Analytical performance of miniaturized analytical systems, in: Miniaturization Anal. Syst., John Wiley & Sons, Ltd, 2009 pp. 357–363. ⟨http://onlinelibrary.wiley.com/doi/10.1002/9780470748091.ch10/summary⟩ (accessed July 15, 2014).
[34] K. Karlsson, M. Novotny, Anal. Chem. 60 (1988) 1662–1665. http://dx.doi.org/10.1021/ac00168a006.
[35] J.P. Chervet, M. Ursem, J.B. Salzmann, Anal. Chem. 68 (1996) 1507–1512. http://dx.doi.org/10.1021/ac9508964.
[36] J.P.C. Vissers, J. Chromatogr. A 856 (1999) 117–143. http://dx.doi.org/10.1016/S0021-9673(99)00692-5.
[37] S.C. Hsieh, J.W. Jorgenson, Anal. Chem. 68 (1996) 1212–1217. http://dx.doi.org/10.1021/ac950682m.
[38] J.N. Alexander, G.A. Schultz, J.B. Poli, Rapid Commun. Mass Spectrom. 12 (1998) 1187–1191 (doi:10.1002/(SICI)1097-0231(19980915)12:17 < 1187::AID-RCM300 > 3.0.CO;2-T).
[39] M.E. Leon-Gonzalez, N. Rosales-Conrado, L.V. Perez-Arribas, L.M. Polo-Diez, J. Chromatogr. A 1217 (2010) 7507–7513. http://dx.doi.org/10.1016/j.chroma.2010.09.076.
[40] G. D'Orazio, S. Fanali, J. Sep. Sci. 31 (2008) 2567–2571. http://dx.doi.org/10.1002/jssc.200800114.
[41] G. D'Orazio, A. Cifuentes, S. Fanali, Food Chem. 108 (2008) 1114–1121. http://dx.doi.org/10.1016/j.foodchem.2007.11.062.
[42] M. Asensio-Ramos, G. D'Orazio, J. Hernandez-Borges, A. Rocco, S. Fanali, Anal. Bioanal. Chem. 400 (2011) 1113–1123. http://dx.doi.org/10.1007/s00216-011-4885-7.
[43] C. Legido-Quigley, N.W. Smith, D. Mallet, J. Chromatogr. A 976 (2002) 11–18. http://dx.doi.org/10.1016/S0021-9673(02)01156-1.
[44] L. Hu, K.-S. Boos, M. Ye, R. Wu, H. Zou, J. Chromatogr. A 1216 (2009) 5377–5384. http://dx.doi.org/10.1016/j.chroma.2009.05.030.
[45] H. Kalay, M. Ambrosini, P.H.C. van Berkel, P.W.H.I. Parren, Y. van Kooyk, J.J.G. Vallejo, Anal. Biochem. 423 (2012) 153–162. http://dx.doi.org/10.1016/j.ab.2012.01.015.
[46] G.-C. Gil, J. Brennan, D.J. Throckmorton, S.S. Branda, G.S. Chirica, J. Chromatogr. B—Anal. Technol. Biomed. Life Sci. 879 (2011) 1112–1120. http://dx.doi.org/10.1016/j.jchromb.2011.03.028.
[47] J.-W. Kwon, K.L. Armbrust, J. Pharm. Biomed. Anal. 37 (2005) 643–648. http://dx.doi.org/10.1016/j.jpba.2004.09.057.
[48] ICH International Conference Harmonization of technical requirements for registration of pharmaceuticals for human use. Paper presented at the ICH harmonised tripartite duideline, validation of analytical procedures: text and methodology Q2 (R1) 2005.
[49] M. Picot Groz, M.J. Martinez Bueno, D. Rosain, H. Fenet, C. Casellas, C. Pereira, et al., Sci. Total Environ. 493 (2014) 162–169. http://dx.doi.org/10.1016/j.scitotenv.2014.05.062.
[50] M.J. Martínez Bueno, C. Boillot, H. Fenet, S. Chiron, C. Casellas, E. Gómez, J. Chromatogr. A 1305 (2013) 27–34. http://dx.doi.org/10.1016/j.chroma.2013.06.071.
[51] R.E. Majors,QuEChERS—A New Technique for Multiresidue Analysis of Pesticides in Foods and Agricultural Samples, Lc Gc Asia Pac 11 (2008) ⟨http://www.chromatographyonline.com/lcgc/article/articleDetail.jsp?id=490102&sk=&date=&pageID=2⟩ (accessed July 15, 2014).
[52] S. Souverain, S. Rudaz, J.-L. Veuthey, J. Chromatogr. A 1058 (2004) 61–66. http://dx.doi.org/10.1016/j.chroma.2004.08.118.
[53] P.D. Rainville, N.W. Smith, D. Cowan, R.S. Plumb, J. Pharm. Biomed. Anal. 59 (2012) 138–150. http://dx.doi.org/10.1016/j.jpba.2011.10.021.
[54] M. Rambla-Alegre, J. Esteve-Romero, S. Carda-Broch, J. Chromatogr. A 1232 (2012) 101–109. http://dx.doi.org/10.1016/j.chroma.2011.10.050.

Talanta 132 (2015) 803–808

Contents lists available at ScienceDirect

Talanta

journal homepage: www.elsevier.com/locate/talanta

Ultrasensitive electrochemical immunosensor for squamous cell carcinoma antigen detection using lamellar montmorillonite-gold nanostructures as signal amplification

Hongying Jia, Picheng Gao, Hongmin Ma, Yueyun Li, Jian Gao, Bin Du, Qin Wei *

Key Laboratory of Chemical Sensing & Analysis in Universities of Shandong, School of Chemistry and Chemical Engineering, University of Jinan, Jinan 250022, PR China

ARTICLE INFO

Article history:
Received 26 August 2014
Received in revised form
13 October 2014
Accepted 15 October 2014
Available online 23 October 2014

Keywords:
Electrochemical immunosensor
Lamellar montmorillonite-gold nanostructures
Nitrogen-doped graphene sheets
Squamous cell carcinoma antigen

ABSTRACT

Sodium montmorillonites (Na-Mont), which could be transformed from nano-montmorillonites, have large surface area, chemical stability, nontoxicity, high cation exchange property and superior adsorption ability. In this paper, Na-Mont were used as a support of polyaniline (PANI) and gold nanoparticles (AuNPs) via the interaction of aniline and $HAuCl_4$ solution. A sandwich-type electrochemical immunosensor was developed to detect squamous cell carcinoma antigen (SCC-Ag). It used nitrogen-doped graphene sheets (N-GS) for the immobilization of primary anti-SCC antibodies (Ab_1) and the combined Na-Mont-PANI-AuNPs nanocomposites as labels. Na-Mont-PANI-AuNPs have excellent catalytic ability towards the reduction of H_2O_2, thus enhance the sensitivity of the immunosensor. The immunosensor exhibits a wide linear range (1 pg/mL–5 ng/mL), a low detection limit (0.3 pg/mL), good reproducibility, selectivity and stability. This new type of immunosensor with Na-Mont-PANI-AuNPs as labels may provide potential application for the detection of SCC-Ag.

© 2014 Elsevier B.V. All rights reserved.

1. Introduction

Squamous cell carcinoma antigen (SCC-Ag), a glycoprotein with isoforms ranging from 45 to 55 kDa, is a subtype of TA-4 and belongs to the ovalbumin family of serine proteinase inhibitors [1–3]. There is a close relationship between high level of SCC-Ag in human serum and cervical cancer, squamous cell carcinoma of the lungs, esophageal cancer, and so on [4]. The serum level of SCC-Ag would increase in parallel to the growth of the tumor size or the recurrence of the disease [5]. Recently, radioimmunoassay [6], enzyme-linked immunosorbent assay [7] and chemiluminescence enzyme immunoassay [8] have been used to detect SCC-Ag in serum. Although these methods are widely used, there is still a highly demand for developing a sensitive, simple and low-cost method for the early detection of SCC-Ag. Electrochemical immunosensor is a miniaturized analytical device. Due to its many merits such as high sensitivity, precise current measurement and the cost-effectiveness, it has attracted much attention in analytical chemistry. To aim at this demand, herein, we had developed a convenient sandwich-type immunosensor based on Na-montmorillonite-polyaniline-gold nanoparticles (Na-Mont-PANI-AuNPs) and nitrogen doped graphene sheets (N-GS) for the sensitive detection of SCC-Ag. There are two basic issues for increasing the sensitivity of the immunosensor, one is the capture of primary antibody (Ab_1) onto electrode surface, and the other is the signal amplification strategy.

In recent years, many kinds of nanomaterials, such as silica nanoparticles, carbon nanotubes, titanium dioxide nanoparticles and nano-montmorillonites have been used as labels for signal amplification in electrochemical immunosensors [9–12]. Nano-montmorillonites belong to aluminosilicate clay minerals that could be converted to sodium montmorillonites (Na-Mont) by reacting with NaCl solution [13]. Na-Mont which consisted of layered structures have proved to be an ideal host due to their inherent advantages, such as large surface area, high cation exchange capacity, superior adsorption ability, nontoxicity and chemical stability and so on [14–18]. Based on the cation exchange ability of Na-Mont, many organic molecules with polar functional groups and ions can be intercalated into the interlayer space of montmorillonites [15]. Polyaniline (PANI) have aroused extensive attention in the application of electrochemical immunosensor due to their interesting conductivity, electronic and catalytic characteristics [19,20]. Gold nanoparticles (AuNPs) also have many advantages including its good catalytic performances, easy preparation, good biocompatibility and strong bonding ability [21–23]. Usually, aniline would exist in the form of cations in acidic solution, so it can insert into Na-Mont and react with the added $HAuCl_4$ solution. Due to the large surface and cation exchange ability of Na-Mont [24,25], AuNPs and PANI could form largely in the interlayer structures based on the

* Corresponding author. Tel.: +86 531 82765730; fax: +86 531 82765969.
E-mail address: sdjndxwq@163.com (Q. Wei).

http://dx.doi.org/10.1016/j.talanta.2014.10.033
0039-9140/© 2014 Elsevier B.V. All rights reserved.

reaction of $HAuCl_4$ and aniline. The secondary anti-SCC antibodies (Ab_2) can be adsorbed onto the Na-Mont surface based on its excellent adsorption ability and the Ab_1 could be immobilized by N-GS due to its excellent electronic conductivity, large surface areas and amounts of edge sites [26–28].

Hence, we proposed a new type electrochemical immunosensor for the sensitive detection of SCC-Ag by using Na-Mont-PANI-AuNPs nanostructures as labels. To the best of our knowledge, this is the first time that Na-Mont-PANI-AuNPs nanostructures have been prepared through intercalation strategy and used as labels for electrochemical immunosensor construction.

2. Materials and methods

2.1. Apparatus and reagents

The montmorillonites were purchased from the Fangzi Bentonite Plant (Weifang, Shandong Province, China). Bovine serum albumin (BSA, 96–99%) was purchased from Sigma. The SCC-Ag, Ab_1 and Ab_2 were purchased from Beijing Kwinbon Biotechnology Co., Ltd. (Beijing, China). Aniline, $HAuCl_4 \cdot 4H_2O$, chitosan and $K_3[Fe(CN)_6]$ were obtained from Sinopharm Chemical Reagent Shanghai Co., Ltd., China (Beijing, China). KH_2PO_4 and Na_2HPO_4 were of analytical reagents grade and used without further purification. Phosphate buffered solutions (PBS) were prepared using 0.067 mol/L Na_2HPO_4 and 0.067 mol/L KH_2PO_4 stock solution. All other chemicals and solvents were of analytical grade. Ultrapure water was used throughout the experiment.

All electrochemical measurements were performed on a CHI760D electrochemical workstation (Chenhua Instrument Shanghai Co., Ltd., China). Scanning electron microscope (SEM) images were recorded using field emission SEM (ZEISS, Germany). Transmission electron microscope (TEM) images were obtained from a Hitachi H-800 microscope (Japan). Conventional three-electrode system was used for all electrochemical measurements: a glassy carbon electrode (GCE, 4 mm in diameter) as working electrode, a platinum wire electrode as the counter electrode and a saturated calomel electrode (SCE) as the reference electrode.

2.2. Synthesis of nitrogen-doped graphene sheets (N-GS)

N-GS were synthesized through thermal annealing of graphite oxide in ammonia [29]. Graphite oxides (GO) were prepared from graphite powder by a modified Hummers' method [30]. In brief, a 9:1 (v:v) mixture of 36 mL H_2SO_4 and 4 mL H_3PO_4 solution were added

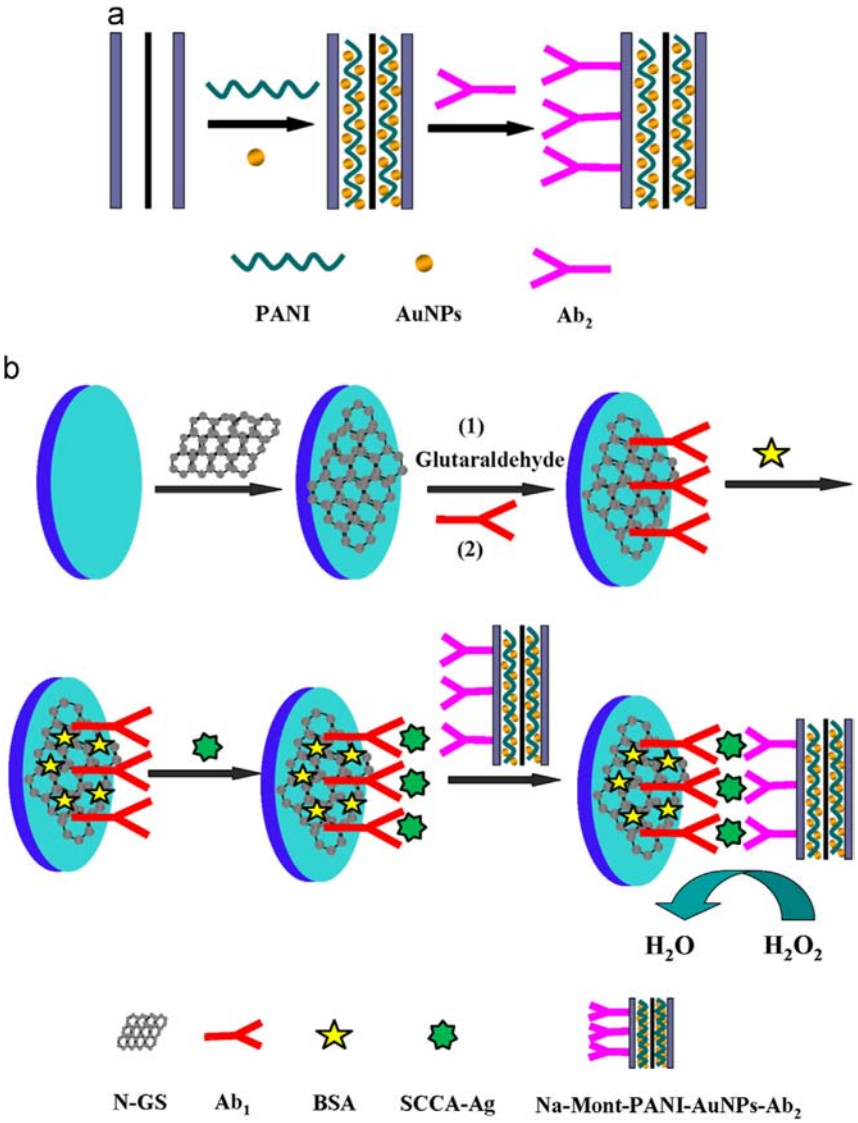


Fig. 1. Schematic representation of the preparation of the Na-Mont-PANI-AuNPs-Ab_2 (a) and the fabrication processes of the immunosensor (b).

into the mixture of 1.8 g $KMnO_4$ and 0.3 g graphite flakes and the reaction was under 50 °C for 12 h in a three flask. Then 30 μL H_2O_2 was added into the solution after stirring for 0.5 h and the products were washed by hydrochloric acid (0.2 M) and ethyl alcohol by drying after reaction. The synthesized GO (50 mg) were dispersed in 25 mL ultrapure water with a concentration of 2 mg/mL, then the pH of the solution was raised up to 10 by the addition of 30% $NH_3 \cdot H_2O$. After stirring for 10 min, 100 mL *N*,*N*-dimethyl formamide was added to the mixture and they were reacted at 153 °C for 1 h. Finally, the black sediment was filtered and washed with ultrapure water to neutral. The solids were dried to gain N-GS and the obtained N-GS were then dispersed in chitosan (0.5 wt%) until used.

2.3. Synthesis of sodium montmorillonites (Na-Mont)

According to Yan's report [31], 25.0 g natural montmorillonites with 29.3 g NaCl powder were dispersed in 0.5 L ultrapure water. The solution was shaken for 12 h. After that, the remaining solids were washed with ultrapure water repeatedly until no free of chloride ions were detected by $AgNO_3$ solution. The products were dried at 85 °C for 24 h. They were ground in an agate mortar and then kept in a sealed bottle.

2.4. Synthesis of Na-Mont-PANI-AuNPs

About 10.0 μL aniline were added into 50.0 mL ultrapure water to form 0.0022 M aniline solution, then they were added into 100 mL 0.2 M sulphuric acid solution for the protonation of aniline. Next, 1.06 g Na-Mont was dispersed in the acidic solution along with shaking uniformly for 3 h. In this process, the protonated aniline would insert into the interlayer of Na-Mont. 300 μL 1% $HAuCl_4$ solution was added into above mixture with gently stirring, it can be observed that the solution color changed from yellow to light green and then to dark green. After discarding the supernatant, the Na-Mont-PANI-AuNPs nanocomposites were obtained.

2.5. Preparation of Na-Mont-PANI-AuNPs-Ab_2 labels

Fig. 1a showed the schematic illustration for the preparation of Na-Mont-PANI-AuNPs-Ab_2 labels. Typically, 0.25 mL of 10 μg/mL Ab_2 was added into the Na-Mont-PANI-AuNPs solution and the mixture were placed at 4 °C under shaking for 12 h. Ab_2 could be loaded into channels of the Na-Mont-PANI-AuNPs. The obtained Na-Mont-PANI-AuNPs-Ab_2 was washed with PBS (pH 7.4). The resulting bioconjugates were redispersed in 1 mL of PBS at 4 °C until used.

2.6. Fabrication of the immunosensor

Fig. 1b showed the preparation process of the immunosensor. A GCE with 4 mm diameter was polished with 1.0, 0.3 and 0.05 μm alumina powder and thoroughly cleaned with ultrapure water before use. First, 6.0 μL of N-GS solution (2 mg/mL) which was dispersed in chitosan (0.5 wt%) was modified onto the electrode. After drying, the electrode was thoroughly cleaned with PBS to remove unbounded N-GS. Then 3 μL of glutaraldehyde (2.5%) was dropped onto the electrode surface to immobilize the Ab_1 and incubated for 1 h. Next, 6.0 μL of Ab_1 (10 μg/mL) solution was added onto electrode surface and incubated for another 1 h. The excess Ab_1 was washed by PBS. The modified electrode was then incubated with 1 wt% BSA solution to block nonspecific binding sites. Subsequently, different concentrations of SCC-Ag solution were added to the electrode surface and incubated for another 1 h.

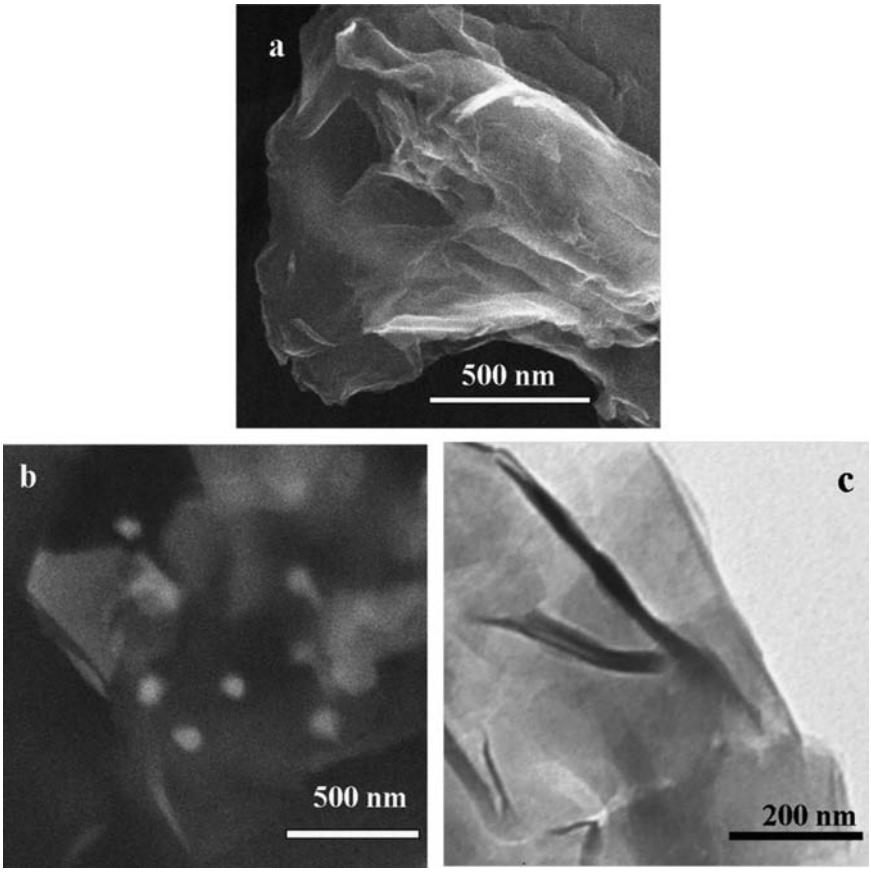


Fig. 2. SEM images of N-GS (a) Na-Mont-PANI-AuNPs (b) and TEM image of Na-Mont (c).

Finally, the prepared Na-Mont-PANI-AuNPs-Ab_2 solution was dropped onto electrode surface and incubated for another 1 h via specific antibody-antigen interaction. The modified electrode was washed three times to remove unbound Na-Mont-PANI-AuNPs-Ab_2. The well-prepared electrode was stored at 4 °C prior to use.

2.7. Detection of SCC-Ag

Electrochemical characteristics of modified electrode were measured by amperometric measurements in PBS (pH 6.4). A detection potential of −0.4 V was selected for amperometric measurement. After the background current was stabilized, 5 mM H_2O_2 was added into PBS and the changed current was recorded. All electrochemical measurements were conducted in a harmony electrochemical condition at 25 °C.

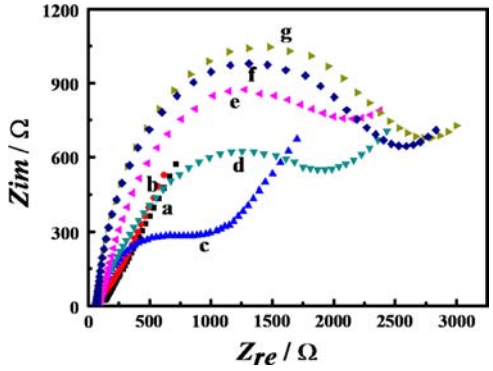


Fig. 3. Nyquist plots of the electrochemical impedance spectroscopy (EIS) for each immobilized step. The bare GCE (a), N-GS/GCE (b), glutaraldehyde/N-GS/GCE (c), Ab_1/glutaraldehyde/N-GS/GCE (d), BSA/Ab_1/glutaraldehyde/N-GS/GCE (e), SCC-Ag/BSA/Ab_1/glutaraldehyde/N-GS/GCE (f), Na-Mont-PANI-AuNPs-Ab_2/SCC-Ag/BSA/Ab_1/glutaraldehyde/N-GS/GCE (g).

3. Results and discussion

3.1. Characterization of N-GS and Na-Mont-PANI-AuNPs nanostructures

In this study, SEM and TEM were used to characterize N-GS and Na-Mont-PANI-AuNPs nanostructures. N-GS were used to increase Ab_1 loading because of its large surface area. Fig. 2a shows the SEM image of a wrinkle paper-like structure of N-GS. Na-Mont-PANI-AuNPs were used to incubate Ab_2 and Fig. 2b displays the SEM image of Na-Mont-PANI-AuNPs. It can be seen that the layered wrinkle structured Na-Mont and AuNPs were dispersed evenly in the interlamination of Na-Mont. From the TEM image of Na-Mont (Fig. 2c), it could be concluded that the layered structure with large specific surface area can immobilize more Ab_2 and improve the sensitivity of immunosensor.

3.2. Characterization of the immunosensor fabrication

Electrochemical impedance spectroscopy (EIS) has been employed to be a powerful tool to characterize the interface properties of surface-modified immunosensor during the process of fabrication and assembly. It is well known that the changes in electrochemical impedance show the chemical obstruction occurring in the electrochemical sensors [32]. The impedance spectra consist of a semicircle portion and a linear portion. The semicircle portion at higher frequencies indicates the electron-transfer limited process and the linear portion at low frequencies represents the diffusion-limited process. The semicircle diameter corresponds to the electron-transfer resistance (R_{et}). As shown in the Nyquist curves (Fig. 3), both GCE (curve *a*) and N-GS modified electrode (curve *b*) appear to be a very small semicircle domain nearly linear, which implies of a diffusion-limiting step in the electron-transfer process. Subsequently, for Ab_1 modified electrode (curve *c*), the larger semicircle indicated that Ab_1 was immobilized onto the electrode and the hydrophobic

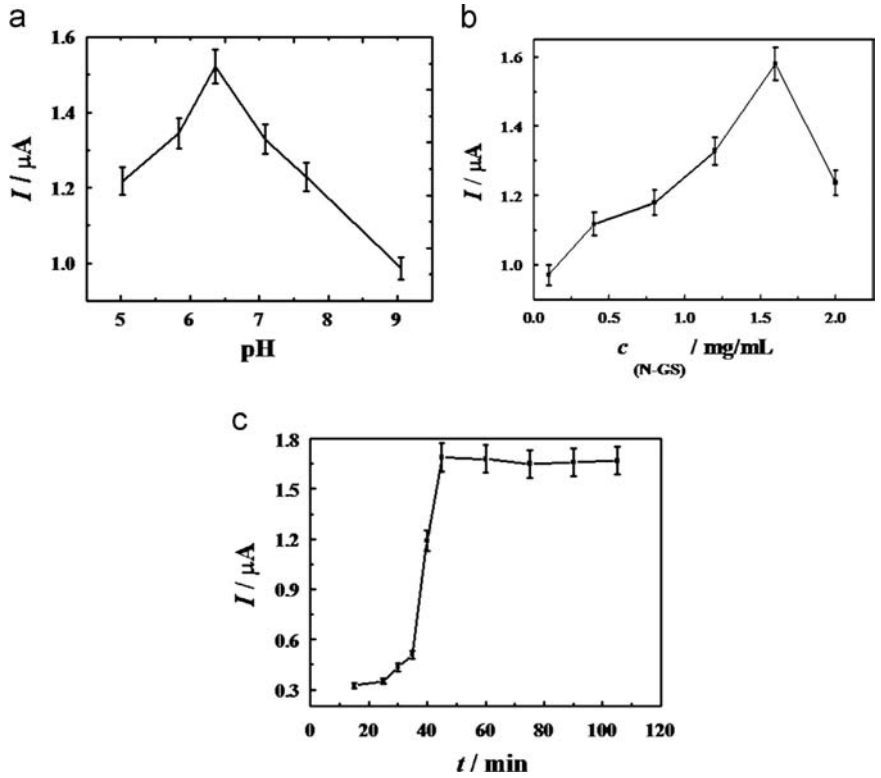


Fig. 4. Effect of pH (a), the concentration of N-GS (b), and incubation time (c) on the response of the immunosensor to 0.5 ng/mL SCC-Ag.

layer of protein was insulated the conductive support, thus hindering interfacial electron transfer. The R_{et} of the electrode further increased after modification of BSA, which indicated the successful immobilization of BSA. Additionally, after successful incubation of SCC-Ag and Na-Mont-PANI-AuNPs-Ab_2, the R_{et} elevated again (curves *e* and *f*). EIS Nyquist plots demonstrated that the immunosensor had been fabricated successfully and could be used for the detection of SCC-Ag.

3.3. Optimization of experimental conditions

The immunosensor was fabricated based on the chemical reaction of Na-Mont-PANI-AuNPs labels towards H_2O_2 reduction. The injected H_2O_2 solution in the electrolyte would result in saltation of current response, then SCC-Ag could be quantified based on specific recognized immunoreaction between antibody and antigen.

In order to obtain the best electrochemical signal responses, the experimental conditions were optimized. For the immunosensor with the same concentration of SCC-Ag (0.5 ng/mL), the pH value of working solution plays an important role in the current response. As shown in Fig. 4a, it could be found that the amperometric responses increased with the increase of pH values from 5.0 to 6.4 and then decreased from 6.4 to 9.0. These results indicated that Na-Mont-PANI-AuNPs displayed best catalytic performance towards H_2O_2 reduction at pH 6.4, then pH 6.4 PBS was used as the optimal electrolyte solution in the following experiments.

In addition, the amount of N-GS has a great effect on the electrochemical behavior of immunosensor. N-GS influenced the electrochemical signals of both the coated electrode and the loaded of Ab_1. As seen in Fig. 4b, with the increased concentration of N-GS, the current response increased and then decreased. Therefore, the optimal concentration of N-GS was 1.5 mg/mL.

Furthermore, incubation time has a great influence on the sensitivity of the immunosensor. In the fabricating process of the immunosensor, after adding SCC-Ag onto electrode surface, various incubation times were investigated for the detection of 0.5 ng/mL SCC-Ag. As shown in Fig. 4c, the current response increased with the incubation time increasing initially, but further increasing incubation time did not significantly change the signal. Hence, 45 min was selected for the optimal antigen-antibody interaction time.

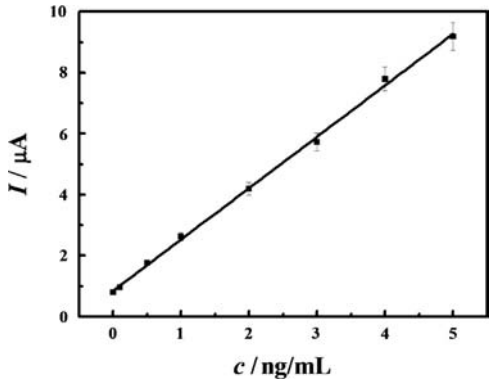


Fig. 5. Calibration curve of the immunosensor toward different concentrations of SCC-Ag, errorbar=RSD (n=5).

Under the optimal conditions, the immunosensor using Na-Mont-PANI-AuNPs as labels was used to detect different concentrations of SCC-Ag. The relationship between the current responses and different concentrations of SCC-Ag towards 5 mM H_2O_2 by reduction in pH 6.4 PBS at −0.4 V was shown in Fig. 5. The current responses increased linearly with the increasing of SCC-Ag concentrations in the range from 1 pg/mL to 5 ng/mL. The equation of the calibration curve was I (μA)=0.8432+1.686 $c_{\text{SCC-Ag}}$ (ng/mL) (r=0.998) with a detection limit of 0.3 pg/mL. The sensitivity of our immunosensor is favorable in detecting cancer marker compared with previous reports [33–37] in Table 1. The low detection limit may be attributed to three factors: (1) N-GS could greatly increase the loading number of Ab_1 and facilitate electron transfer due to its good biocompatibility and high conductivity; (2) as discussed above, Na-Mont-PANI-AuNPs with large surface area could immobilize amounts of Ab_2, which greatly increases the sensitivity of the immunosensor; (3) PANI and AuNPs with good electrochemical conductivity could accelerate electron transfer and possess good catalytic performance towards H_2O_2 reduction.

3.4. Reproducibility, stability and selectivity of the immunosensor

In order to evaluate the reproducibility of immunosensor, five immunosensors were prepared to detect 0.5 ng/mL SCC-Ag under the same conditions. The relative standard deviation (RSD) achieved from these five measurements was 3.18%. The result suggested the precision and reproducibility of the proposed immunosensor were both good.

The study on the stability of immunosensor was measured by periodically checking current response. When the immunosensor was not in use, it was stored in a refrigerator at 4 °C. The current response of the immunosensor still retained 94% and 85% of the initial value after one week and three weeks, respectively. The slow decrease in the current response may be due to the gradual denature of SCC-Ag and anti-SCC antibody.

The selectivity of the immunosensor was tested for its important role in analyzing biological samples. The effect of possible inhibitors that might interfere with the response of immunosensor had been investigated. SCC-Ag (0.5 ng/mL) solution containing 100 ng/mL of interfering substances (BSA, glucose, vitamin C and AFP) was measured by immunosensor. As a result, the current variation due to the interfering substances was less than 5% of that without interferences. These results indicated the selectivity of the immunosensor was acceptable.

3.5. Real sample analysis

In order to evaluate the feasibility of the electrochemical immunosensor for practical application, the detection of SCC-Ag in human serum samples was evaluated using standard addition methods. 1.00 ng/mL, 2.00 ng/mL and 4.00 ng/mL of SCC-Ag solutions were added into serum samples and analyzed by the proposed immunosensor. The results are shown in Table 2. It can be seen that the RSD

Table 1
A comparison of the performance of the described and referenced immunosensors for the detection of SCC-Ag.

Electrode materials	Linear range	Detection limit	*R*-square	References
Magnetic mesoporous nanogold/thionine/$NiCo_2O_4$ HPR-nanogold/graphene nanosheets	2.5 pg/mL–15 ng/mL	1.0 pg/mL	0.9867	[33]
Fluorescein isothiocyanate (FITC) and *N*-(aminobutyl)-*N*-(ethylisoluminol) (ABEI)	0.5–20 ng/mL	0.02 ng/mL	0.9964	[34]
Bimetallic gold-silver nanoclusters (AuAg NCs)	0.005–20 ng/mL	1.3 pg/mL	0.9899	[35]
Semiconductor carboxylated graphitic carbonnitride (g-C_3N_4)	0.025–10 ng/mL	8.53 pg/mL	0.9917	[36]
Carbon-supported Pd-Au (Pd-Au/C)	0.005–2 ng/mL	1.7 pg/mL	0.995	[37]
Lamellar montmorillonite-PANI-Gold	0.001–5 ng/mL	0.33 pg/mL	0.998	This work

Table 2
Results for determination of SCC-Ag in human serum samples.

Initial SCC-Ag concentration in sample (ng/mL)	Added SCC-Ag concentration (ng/mL)	The detection content (ng/mL)	RSD (%, $n=5$)	Recovery (%)
	1.00	1.77, 1.79, 1.82, 1.83, 1.76	1.70	99.7
0.800	2.00	2.83, 2.86, 2.84, 2.78, 2.79	1.20	101
	4.00	4.62, 4.71, 4.81, 4.89, 4.75	2.14	99.1
	1.00	1.48, 1.54, 1.53, 1.44, 1.47	2.82	99.5
0.500	2.00	2.54, 2.50, 2.56, 2.66, 2.59	3.30	102
	4.00	4.47, 4.42, 4.53, 4.59, 4.35	2.08	99.3

was from 1.20% to 3.30% and the recoveries were between 99.0% and 102%. Thus, the presented method could meet the demand for clinical determination of SCC-Ag in serum samples.

4. Conclusions

In this work, a novel sandwich-type immunosensor for the det ection of SCC-Ag had been developed. The immunosensor was fabricated by immobilizing Ab_1 onto N-GS and using Na-Mont-PANI-AuNPs as labels. N-GS with large surface area enhanced the amount of Ab_1 immobilized onto electrode surface and the Na-Mont-PANI-AuNPs showed excellent catalytic performance towards H_2O_2 reduction. Then the proposed immunosensor showed low detection limit for the detection of SCC-Ag. The simplicity, good sensitivity and reproducibility of the immunosensing platform may be quite promising in clinical application for the detection of SCC-Ag.

Acknowledgments

This study was supported by the Natural Science Foundation of China (No. 21175057, 21375047, 21377046) and the Science and Technology Plan Project of Jinan (No. 201307010), and QW thanks the Special Foundation for Taishan Scholar Professorship of Shandong Province and UJN (No. ts20130937).

References

[1] H. Zhang, S. Qi, Clin. Chim. Acta 412 (2011) 1572–1577.
[2] Y. Wang, Y. Zhang, Y. Su, F. Li, H. Ma, H. Li, B. Du, Q. Wei, Talanta 124 (2014) 60–66.
[3] W. Pongsapich, C. Samphaiboon, S. Sukpanichnant, Oral Oncol. 49 (2013) S93–S156.
[4] X. Li, X. Zhang, H. Ma, D. Wu, Y. Zhang, B. Du, Q. Wei, Biosens. Bioelectron. 55 (2014) 330–336.
[5] Q. Li, D. Tang, J. Tang, B. Su, G. Chen, M. Wei, Biosens. Bioelectron. 27 (2011) 153–159.
[6] W. Neunteufel, G. Tatra, Ch. Bieglmayer, Gynecol. Obstet. Invest 29 (1990) 154–157.
[7] S. Cataltepe, C. Schick, C.J Luke, S.C. Pak, D. Goldfarb, P. Chen, J Tanasiyevic, R. Marshall, G. Posner, Clin. Chim. Acta 295 (2000) 107–127.
[8] David shitrit, Boris Zingerman, Ariella Bar-gil shitrit, Dekel shlomi, Mordechai R. Kramer, Lung Cancer 10 (2005) 501–507.
[9] B. Qu, X. Chu, G. Shen, R. Yu, Talanta 76 (2008) 785–790.
[10] J. Li, G. Liu, W. Zhang, W. Cheng, H. Xu, S. Ding, J. Electroanal. Chem. 708 (2013) 95–100.
[11] W. Liang, R. Yuan, Y. Chai, Y. Li, Y. Zhuo, Electrochim. Acta 53 (2008) 2302–2308.
[12] R. Feng, Y. Zhang, H. Li, D. Wu, X. Xin, S. Zhang, H. Yu, Q. Wei, B. Du, Anal. Chim. Acta 758 (2013) 72–79.
[13] M.U. Alvi, S. Zulfiqar, C.T. Yavuz, H.-S. Kweon, M.I. Sarwar, Ind. Eng. Chem. Res. 52 (2013) 6908–6915.
[14] M. Harper, C J. Environ. Sci. Technol. 24 (1990) 55–62.
[15] L. Bromberg, C.M. Straut, A. Centrone, E. Wilusz, T.A. Hatton, ACS Appl Mater Inter 3 (2011) 1479–1484.
[16] T Polubesova, S Eldad, B Chefetz, Environ. Sci. Technol 44 (11) (2010) 4203–4209.
[17] K. Parida, G.B.B. Varadwaj, S. Sahu, P.C. Sahoo, Ind. Eng. Chem. Res. 50 (2011) 7849–7856.
[18] B. Wicklein, M. Darder, P. Aranda, E. Ruiz-Hitzky, Langmuir 26 (2010) 5217–5225.
[19] G. Lai, H. Zhang, T. Tamanna, A. Yu, Anal. Chem. 86 (2014) 1789–1793.
[20] Y. Cui, H. Chen, L. Hou, B. Zhang, B. Liu, G. Chen, D. Tang, Anal. Chim. Acta 738 (2012) 76–84.
[21] X. Liu, W. Li, L. Li, Y. Yang, L. Mao, Z. Peng, Sens. Actuators B 191 (2014) 408–414.
[22] H. Peng, Y. Hu, A. Liu, W. Chen, X. Lin, X. Yu, J. Electroanal. Chem. 712 (2014) 89–95.
[23] J. Tang, B. Su, D. Tang, G. Chen, Biosens. Bioelectron. 25 (2010) 2657–2662.
[24] M. Ilic, E. Koglin, A. Pohlmeier, H.D. Narres, M.J. Schwuger, Langmuir 16 (2000) 8946–8951.
[25] M.M. Nobrega, V.L. Martins, R.M. Torresi, M.L.A. Temperini, J. Phys. Chem. C 118 (2014) 4267–4274.
[26] R. Feng, Y. Zhang, H. Ma, D. Wu, H. Fan, H. Wang, H. Li, B. Du, Q. Wei, Electrochim. Acta 97 (2013) 105–111.
[27] L. Zhao, S. Li, J. He, G. Tian, Q. Wei, H. Li, Biosens. Bioelectron. 49 (2013) 222–225.
[28] D. Wu, H. Fan, Y. Li, Y. Zhang, H. Liang, Q. Wei, Biosens. Bioelectron. 46 (2013) 91–96.
[29] D. Long, W. Li, L. Ling, J. Miyawaki, I. Mochida, S. Yoon, Langmuir 26 (2010) 16096–16102.
[30] D.C. Marcano, D.V. Kosynkin, J.M. Berlin, A. Sinitskii, Z. Sun, A. Slesarev, L. B. Alemany, W. Lu, J.M. Tour, ACS Nano 4 (2010) 4806–4814.
[31] L. Yan, Y. Xu, H. Yu, X. Xin, Q. Wei, B. Du, J. Hazard. Mater. 179 (2010) 244–250.
[32] W. Pongsapich, C. Samphaiboon, S. Sukpanichnant, Oral Oncol. 49 (2013) S105.
[33] Q. Li, D. Tang, J. Tang, B Su, G Chen, M Wei, Biosens. Bioelectron. 27 (2011) 153–159.
[34] H. Zhang, S. Qi, Clin. Chim. Acta 412 (2011) 1572–1577.
[35] X. Zhang, F. Li, W. Qin, B. Bu, D. Wu, H Li, Sens. Actuators B 194 (2014) 64–70.
[36] X. Li, X. Zhang, H. Ma, D Wu, Y. Zhang, B. Du, Q. Wei, Biosens. Bioelectron. 55 (2014) 330–336.
[37] J. Gao, B. Du, X. Zhang, A. Guo, Y. Zhang, D. Wu, H. Ma, Q. Wei, Anal. Chim. Acta 833 (2014) 9–14.

Talanta 132 (2015) 809–813

Contents lists available at ScienceDirect

Talanta

journal homepage: www.elsevier.com/locate/talanta

Cleaved DNAzyme substrate induced enzymatic cascade for the exponential amplified analysis of L-histidine

Jing-Lin He [a,*], Ping Wu [a], Shuang-Li Zhu [a], Ting Li [a], Pan-Pan Li [a], Jian-Nan Xiang [b], Zhong Cao [a,**]

[a] Hunan Provincial Key Laboratory of Materials Protection for Electric Power and Transportation, School of Chemistry and Biological Engineering, Changsha University of Science and Technology, Changsha 410004, PR China

[b] State Key Laboratory for Chemo/Biosensing and Chemometrics, College of Chemistry and Chemical Engineering, Hunan University, Changsha 410082, PR China

ARTICLE INFO

Article history:
Received 21 July 2014
Received in revised form
13 October 2014
Accepted 16 October 2014
Available online 28 October 2014

Keywords:
Self-cleaved DNAzyme
Enzymatic cascade
L-Histidine
Exponential amplified analysis

ABSTRACT

A novel strategy of cleaved DNAzyme substrate induced enzymatic cascade has been devised for the exponential amplified detection of L-histidine. The enzyme strand carries out hydrolytic cleavage of the substrate strand in the presence of L-histidine. The cleaved DNAzyme substrates introduce the polymerase/endonuclease reaction cycles as primers. The L-histidine acts as the activator for enzymatic cascade amplification generating a distinguishable fluorescence enhancement. A good nonlinear correlation (R=0.9994) between fluorescence intensity and the logarithm of the L-histidine concentration is obtained over the range from 50 nM to 1.0 mM. The detection limit was estimated as 30 nM. This efficient amplification of the fluorescence signal is attributed to the L-histidine induced cooperation of Klenow Fragment polymerase (exo$^-$) and Nb.BbvCI endonuclease reaction. The activation of such enzymatic cascades through analyte-DNAzyme interactions has a substantial impact on the development of exponential amplified DNAzyme sensors.

© 2014 Elsevier B.V. All rights reserved.

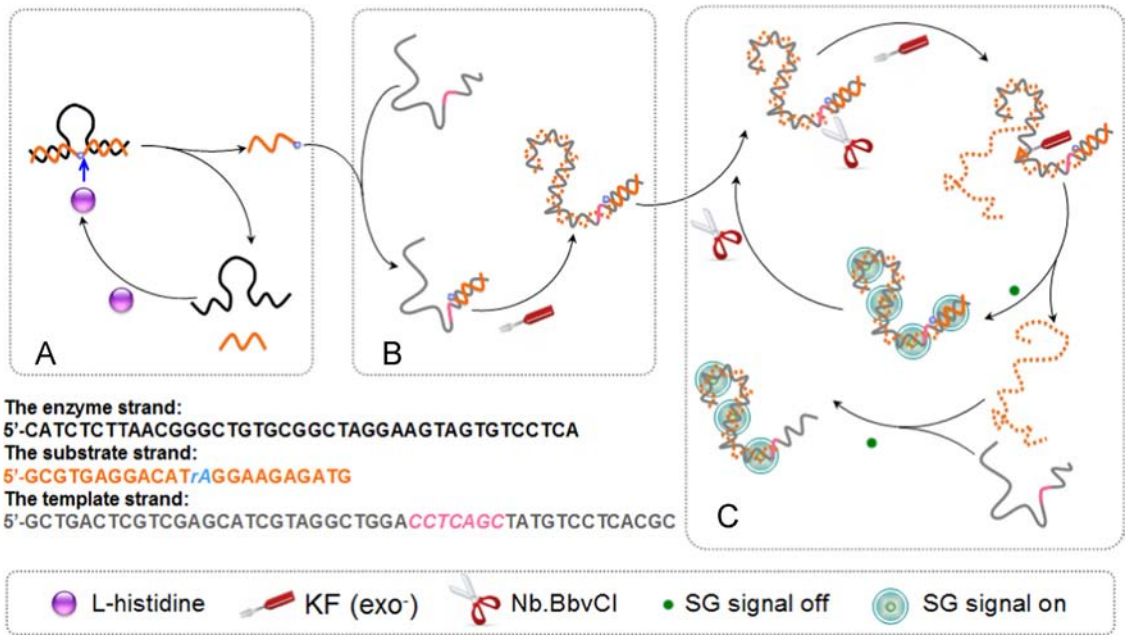
1. Introduction

The enzymatic cascade reaction induced by target recognition event has become a core technology in medical diagnostics [1–3]. In the nucleic acid–based enzymatic cascade assays, the exponential isothermal amplification of DNA often employs a strand displacement polymerase and a single-strand nicking enzyme to continuously replicate one strand of a DNA duplex under a constant temperature [4–8]. Since the target can activate circular polymerization reactions, enzymatic cascade mediated strategy offers a versatile method with high sensitivity and specificity. Liu et al. [9] presented a sensitive MicroRNA amplified detection based enzymatic cascade. Tian et al. [10] described a novel exponential isothermal amplification of telomere repeat assay for measuring telomerase activity in cell extracts. Li et al. [11] reported proximity-dependent isothermal cycle amplification strategy in aptamer–cocaine complexes coupled with surface enhanced Raman scattering. Among these sensing systems, the enzymatic cascade assay has distinct advantages of ultra-high amplification efficiency and great potential for target testing. So far as we know, enzymatic cascade has rarely been implemented for the development of DNAzyme sensor studies perhaps due to the difficult control of flexible joint in variable structure of cleavage responsible DNAzyme.

Elevated levels of serum histidine are characteristic of histidinemia [12], which is one of the inborn errors of amino acid metabolism that increases person's chances of developing intellectual disability, behavioral problems, or learning disorders [13]. The recognition and quantification of histidine for diagnosis of histidinemia has emerged as one of the fastest growing areas in clinical chemistry [14–16]. The L-histidine-dependent DNAzyme [17,18] possessing a specific catalytic activity has shown a great potential in diagnosis application [19–21]. Willner's group evaluated L-histidine-dependent DNAzymes to yield the horseradish peroxidase-mimicking catalytic nucleic acids, which enable a simple and effective detection of L-histidine [22]. Enzyme mediate signal amplification offers an efficient way to improve the sensitivity. Kong and co-workers employed an endonuclease based enzymatic recycling cleavage strategy in the design of DNAzyme-based sensors [23]. This assay is sensitive and specific, but the drawbacks of requirement of doubly-labeled molecular beacon are limited to a laboratory setting and a practice complexity. However, an even higher sensitivity is desired if these sensors are to be used in complex cellular or environmental samples to ensure large signal-to-noise ratios. We intend to devise a cleaved DNAzyme

* Corresponding author. Tel./fax: +86 731 89922951.
** Corresponding author. Tel.: +86 731 82618798.
E-mail addresses: jinglin_he@hotmail.com (J.-L. He), zhongcao2004@163.com (Z. Cao).

http://dx.doi.org/10.1016/j.talanta.2014.10.037
0039-9140/© 2014 Elsevier B.V. All rights reserved.



Scheme 1. Schematic representation of the cleaved DNAzyme substrate induced enzymatic cascade strategy for the amplified detection of L-histidine.

substrate induced enzymatic cascade strategy for isothermal amplified determination of L-histidine using cleaved substrate as the replication trigger. The combination of the DNAzyme and the polymerase/endonuclease reaction cycles leads to the direct activation of enzymatic cascade amplification. It would be of great interest to develop DNAzyme-based sensors with exponential amplification for the output signal.

2. Experimental section

2.1. Materials and reagents

L-histidine cofactor-dependent nucleic acid cleaving DNAzyme was applied for L-histidine determination. Oligonucleotides were customer-designed and supplied by Sangon Biotechnology Co. Ltd. (Shanghai, China), as shown in Scheme 1. The substrate strand contains a single, sessile ribo-adenine (rA) indicated as an italic nucleotide. The deoxynucleotide triphosphates (dNTPs) and exo$^-$-Klenow Fragment polymerase (KF (exo$^-$)) were obtained from Sangon Biotechnology Co. Ltd. Nicking endonuclease Nb.BbvCI (Nb.BbvCI), exo$^-$-vent DNA polymerase (Vent (exo$^-$)) and Taq DNA polymerase were purchased from New England Biolabs Ltd (USA). L-histidine was obtained from Sigma-Aldrich Inc. DNA stock solutions and L-histidine solution were prepared in NEBuffer 2 (1 × concentrate). SYBR Green I (SG, 20 × concentrate) was supplied by Generay Biotech. Co., Ltd (Shanghai, China). Ultrapure water was obtained through a laboratory ultrapure water system series (Kertone water treatment Co., Changsha, China) with an electrical resistance larger than 18.25 MΩ. All solutions were sterilized throughout the experiments.

2.2. Apparatus and fluorescence measurements

Fluorescence emission spectra were performed on Hitachi F-7000 fluorescence spectrometer (Japan) linked to a personal computer. Excitation and emission slits were all set for 10.0 nm band-pass. The SG fluorophore was excited at 495 nm, and the emission spectra were collected from 508 to 618 nm. The fluorescence intensity at 523 nm was used to evaluate the performance of the proposed assay. Fluorescence spectra were collected using 0.2 × 1 cm^2 quartz cuvettes containing 100 μL of solution. All measurements were carried out at room temperature unless stated otherwise.

2.3. Enzymatic cascade amplification and L-histidine detection

The working solution including 100 nM of the enzyme strand, 20 nM of the substrate strand was incubated with L-histidine at required concentration for 30 min. Then 300 nM of the template strand was added into the mixture and kept for 10 min. The result solution was subjected to an enzymatic cascade step. The replication solution containing 5 U KF (exo$^-$), 10 U Nb.BbvCI and 2.5 mM dNTPs was introduced into the system, and incubated at 37 °C for 30 min. After the injection of SG, the system solution were diluted to 100 μL, and then performed to estimate the fluorescence performances.

2.4. Agarose gel electrophoresis

Analysis by electrophoresis was carried out under nondenaturing conditions on 3% agarose gels with GoldView (Dingguo Biotechnology, Beijing, China) staining, cast and run in 0.5 × TBE buffer (pH 7.9). The enzymatic cascade amplification reaction was set in a volume of 12 μL containing 10 μM enzyme strand, 2 μM substrate strand, 5.0 mM L-histidine, 30 μM template strand, 2.5 mM dNTPs, 5 U KF (exo$^-$) and 10 U Nb.BbvCI. Electrophoresis was performed at a constant potential of 100 V for 60 min with loading of 10 μL of each samples into the centermost lanes. The resulting gel was excited and imaged using a Tanon MP device (Shanghai, China).

3. Results and discussion

3.1. Design strategy of cleaved DNAzyme substrate induced enzymatic cascade assay

Scheme 1 depicts schematically the assay protocol of the cleaved DNAzyme substrate induced enzymatic cascade for the amplified detection of L-histidine. The DNAzyme is composed of a 41-mer enzyme strand (in black) and a 23-mer substrate strand (in orange). The enzyme strand is designed to hybridize to the two

ends of the substrate strand. In the middle of the substrate strand, a ribo-adenosine (rA in blue) was introduced as the cleavage site. When the DNAzyme is incubated with solutions containing L-histidine, the enzyme strand carries out catalytic reactions to hydrolytic cleavage of the substrate strand at the scissile rA [18]. Then the substrate is broken into two pieces and dissociated from the enzyme strand. The released enzyme strand could then hybridize to another substrate strand and initiated another cycle of cleavage with the released L-histidine (Scheme 1A). The cleaved 13-mer strand with the rA designed to hybridize with 48-mer template strand (in grey) triggers the enzymatic cascade amplification cycles. With the KF (exo$^-$), the replication of template domain induces the primer extension to form a full-length double strand DNA (dsDNA) containing a recognition site (in pink) for the Nb.BbvCI (Scheme 1B). Nb.BbvCI recognizes the double-stranded 5′-CCTCAGC-3′/5′-GCTGAGG-3′ site and cuts the GCTGAGG strand at the second nucleotide downstream from the site [24]. The cleavage opens a new site for a new replication. The 3′ end of the nicked DNA fragments is extended by KF (exo$^-$) and displaces the previously synthesized strand, which is designed to hybridize to a new template strand. The enzymatic cascade based polymerization regenerates the completely dsDNA to initiate another cycle of nicking, polymerization and displacement (Scheme 1C). Finally the fluorescence dye, SYBR Green I (SG), inserts into the DNA double helix to generate a distinguishable fluorescence enhancement. Thus the amount of replicated products corresponds to the amount of the cleaved strand and indirectly reflects the amount of L-histidine. In the absence of L-histidine, the DNAzyme is so stable to assemble that the cleavage activity is dramatically reduced. Therefore, since L-histidine could displace the primer and trigger the enzymatic cascade polymerization circularly, exponential fluorescence enhancement could be observed even with a trace amount of the L-histidine. Hence the presented method not only shows the high sensitivity in comparison with the traditional methods, but also provides the great potential in the early clinic diagnosis.

3.2. Target induced enzymatic cascade amplification of the L-histidine detection

Our results, as shown in Fig. 1, demonstrated that the enzymatic cascade probes have excellent sensitivity. The DNAzyme only has a very low fluorescence intensity of intercalated SG (~160.0, curve *a*). After introducing L-histidine into DNAzyme solution, the SG emission is even feeble due to weak interaction between SG and single-strand hydrolytic fragments (curve *a*′). This result suggested that the substrate is cut into two overhangs and released from the DNAzyme under the experimental conditions. But a reversed trend is observed for the other three systems. The fluorescence intensity of SG for the DNAzyme/template solution after addition of L-histidine (curve *b*′) is more intense as compared to that from the DNAzyme/template solution (curve *b*), owning to the high-affinity hybridization between the template and released 13-mer strand. As a controlled experiment, the SG emission intensity of KF (exo$^-$) polymerization products of DNAzyme/template solution in the absence (curve *c*) or presence (curve *c*′) of L-histidine were studied to fully characterize the proposed system. The response of analytes was represented by relative fluorescence intensity (RFI), an initial ratio of fluorescence enhancement (F–F_0) to the fluorescence background (F_0). KF (exo$^-$) involved assay in L-histidine solution shows a clear increase signal (RFI=0.33) in causing KF (exo$^-$) replication triggered by the cleaved strand. A fluorescent background (curve *d*) is observed when delivered enzymatic cascade assay cooperating KF (exo$^-$) and Nb.BbvCI. This phenomenon is most likely the result of nonspecific hydrolytic reaction of the substrate strand and initiating partial replication. The enzymatic cascade assay shows an extraordinary increase (RFI=0.62) in fluorescence upon addition of 50 μM L-histidine (curve *d*′), indicating the enormous efficiency of enzymatic cascade amplification as compared with KF (exo$^-$)-amplified assay. As expected, the enzymatic cascade amplification was not limited to one round of cycling. In fact, the proposed strategy was regarded as a chain reaction since there were cross-replications between the sense and antisense structures. It can be seen that the fluorescence signal increases exponentially when the number of replication cycles is increased.

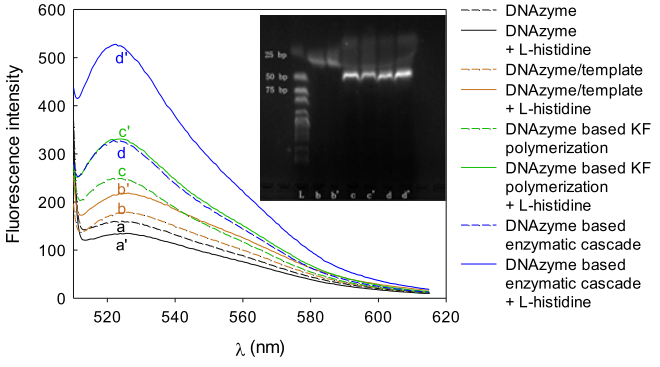


Fig. 1. Fluorescence spectra of the DNAzyme based assays for L-histidine determination. In fluorescence experiments: [enzyme strand]=10 nM; [substrate strand]=2.0 nM; [L-histidine]=50 μM; [template]=30 nM; [KF (exo$^-$)]=5.0 U; [Nb.BbvCI]=10 U; [dNTP]=250 μM; [SG]=1 × concentration. The inset shows the gold view stained agarose gel (3.0%) analysis of different assays. In electrophoresis experiments: [enzyme strand]=10 μM; [substrate strand]=2.0 μM; [L-histidine]=5.0 mM; [template]=30 μM; [KF (exo$^-$)]=5.0 U; [Nb.BbvCI]=10 U; [dNTP]=2.5 mM.

3.3. Electrophoresis characterization

As a further support for this novel DNAzyme based enzymatic cascade assay, the amplification products were characterized by 3.0% agarose gel electrophoresis (Fig. 1, inset). The mixture of DNAzyme and temperate strands in the absence (lane b) and presence (lane *b*′) of L-histidine produce fast migration bands due to small molecules and stem helix of DNAzyme. A slower migration band without L-histidine appears in the lane *c*. This band revealed a fraction of KF (exo$^-$) products triggered by nonspecific hydrolysis of the substrate. The replication is carried out when DNAzyme was added into the mixture containing template and L-histidine during the KF (exo$^-$) polymerization (lane *c*′). An observable fluorescent band is also at the same migration position in the lane d, indicating that the nonspecific hydrolyzed substrate could trigger the polymerase/endonuclease reaction. The enzymatic cascade assay with L-histidine provides a significant product band (lane *d*′), suggesting the existence of amounts of nicked strands produced by the polymerase/endonuclease replication cycles. These results were consistent with the fluorescence emission spectra in the main figure.

3.4. Optimization of experimental condition

Fig. 2 shows the time courses of incubating KF (exo$^-$) and Nb.BbvCI with different L-histidine concentrations. The target of 1.0 mM, which is barely detectible by the proposed assay, induces quick increase in fluorescence intensity in the enzymatic cascade amplification step. The increase in fluorescence intensity indicated continuous synthesis of the double strand DNA. The signal plateaus in about 30 min because the cleaved primers are used up. The increase in fluorescence intensity slows down with the dilution of the L-histidine. Taking the 50 μM time course as an example, the fluorescence intensity increases almost linearly with

time until it reaches a plateau over 60 min (data not shown). The signal trend is the same when the target concentration dropped to 500 nM. The background (0 nM sample) keeps at a low level before 30 min, indicating that the substrate strand without L-histidine is hard to initiate the replication in 30 min due to its binding affinity in DNAzyme structure. The false positive signal occurs after 30 min because of the nonspecific hydrolyzation of rA contained substrate. After repeating the time courses for three times each, 30 min was set as the optimized incubating time at the enzymatic cascade amplification step.

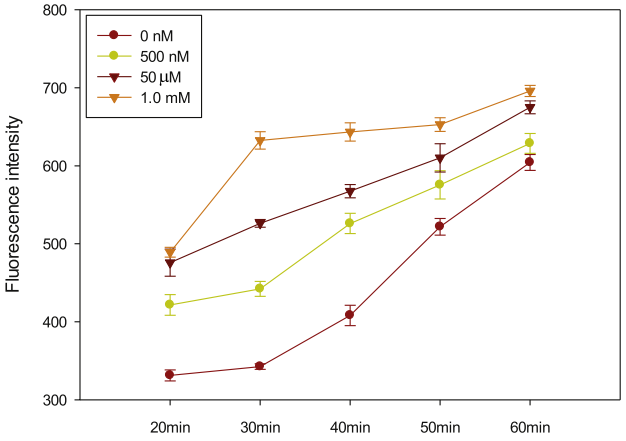


Fig. 2. Time course of incubating KF (exo$^-$) and Nb.BbvCI at various L-histidine concentrations (0 nM, 500 nM, 50 μM, 1 mM). The experimental conditions were the same as those for fluorescence experiments in Fig. 1. All experiments were prepared in NEBuffer 2, pH=7.5. The error bars represent to standard deviation with n=3.

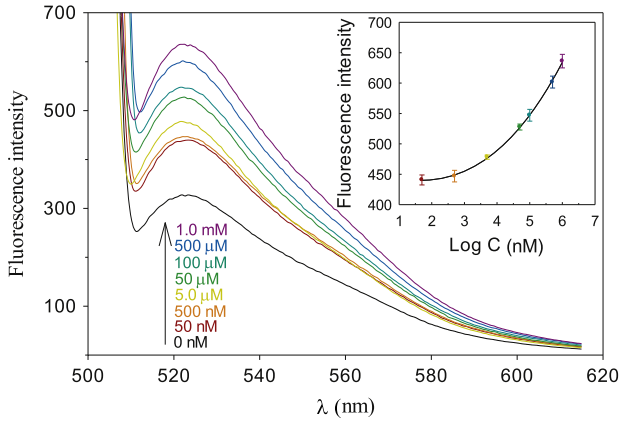


Fig. 3. Fluorescence spectra of the cleaved DNAzyme substrate induced enzymatic cascade assay upon incubation with different L-histidine concentrations (0 nM–1.0 mM). Inset: curve describing the exponential relationship between the fluorescence enhancement and the logarithm of the concentrations of L-histidine. The experimental conditions were the same as those for fluorescence experiments in Fig. 1. Each data point was performed in triplicate.

3.5. Quantification of L-histidine by cleaved DNAzyme substrate induced enzymatic cascade assay

Fig. 3 presents the fluorescence intensity as a function of the L-histidine concentration. In the absence of L-histidine, the DNAzyme keeps its stable stem-loop structure and results in the lowest fluorescence response (F=331.0). After the addition of 50 nM L-histidine, the intensity shift resulting from the replication products increases (F=443.3) because parts of DNAzyme react with L-histidine and release strands, which initiate the enzymatic cascade reaction. It demonstrated that an enzymatic cascade assay can recognize specifically its target to produce ordinary DNA duplex in the nanomole range. The 20,000-fold serial dilutions, in the range of 50 nM–1.0 mM, of L-histidine were used to generate a standard curve for enzymatic cascade assay. The inset demonstrates the cubic logarithm of the L-histidine concentration dependence of fluorescence intensity. The standard nonlinear curve is described using the equation (R=0.9994), $F=0.6800(\mathrm{LgC})^3+3.942(\mathrm{LogC})^2-18.65\mathrm{LogC}+457.1$, where F is the value of fluorescence intensity, Log$C$ is the logarithm of the L-histidine concentration. This nonlinear response phenomenon could be attributed to the release of cleaved strand from DNAzyme. These strands worked as primers, which induced the cooperation of enzyme network and thus resulted in an efficient increase of the effective fluorescence signal. The detection limit was estimated as 30 nM from three times the standard deviation corresponding to the blank sample detection. The detection results for analyzing the concentration of L-histidine were comparable with otheroptical DNAzyme probes [25] or even superior to the previously reported L-histidine assays listed in Table 1, indicating high sensitivity of the designed method for detection of its targets.

3.6. Selectivity of the enzymatic cascade assay and the application in serum samples

The selectivity of the sensing system is another important parameter for a biosensor. We chose four kinds of natural amino acids (L-alanine, L-arginine, L-cysteine, and L-leucine), which have a structure

Table 1
Comparison of analytical performance of various methods for determination of L-histidine.

Method/technique	Detection range	Detection limit	Detection time	Ref.
Label-free dsDNA-Cu NPs based probe. Fluorescence quenching	10 μM–250 μM	5 μM	50 min	[16]
Ferrocene-DNAzymes modified electrode. Square-wave voltammetry	0.1 pM–50 nM	0.1 pM	18 h	[19]
Ferrocene-DNAzymes/gold nanoparticle–graphene nanosheet composites modified electrode. Square wave voltammetry	10 pM–10 μM	0.1 pM	30 h	[20]
Texas red-DNAzymes based probe. Fluorescence polarization	0.6 μM–5 μM	0.6 μM	3 h	[21]
Horseradish peroxidase-mimicking DNAzyme based probe. Chemiluminescence	0.5 mM–100 mM	—	—	[22]
DNAzyme sensor involving nicking endonuclease cleavage. Fluorescence	2 μM–100 μM	200 nM	50 min	[23]
DNAzyme based sensor producing proximity-dependent surface hybridization. Differential pulse voltammetry	1 μM–1 mM	300 nM	17 h	[24]
Complex imprinted polymer-based pencil graphite electrode. Differential pulse anodic stripping voltammetry	64 nM–2.2 μM	13 nM	13 h	[26]
Cleaved DNAzyme substrate induced enzymatic cascade. Fluorescence	50 nM–1.0 mM	50 nM	70 min	This work

similar to that of L-histidine. As shown in Fig. 4, the enzymatic cascade assay displays a specific response to the L-histidine at 50 μM concentrations. But nearly negligible RFI change are observed after the enzymatic cascade assay reacting with 100 μM L-alanine, L-arginine, L-cysteine, and L-leucine. The specificity can be well addressed when the target L-histidine is present in low concentrations compared to nontarget amino acids. These results confirmed that the developed strategy has sufficient specificity and L-histidine can be identified with high selectivity. To investigate the application of the assay, 50-fold diluted serum samples were tested to obtain calibration curves at different L-histidine concentrations (Fig. 5). Since L-histidine concentration in normal human plasma ranges from 1.998 μM to 169.8 μM [26], the human serum samples were diluted 50 times with NEBuffer 2. The L-histidine -spiked serum samples were prepared by adding L-histidine in 50-fold diluted serum samples. Then blind tests were conducted using the calibration curves to evaluate the reliability of the method. An exponential plot ($R=0.9958$) of the RFI against the logarithm of concentration of L-histidine (50 nM–1.0 mM) is expressed as: $RFI=1.322\times10^{-3}(LogC)^3+2.213\times10^{-2}(LogC)^2-9.512\times10^{-2}LogC+0.4339$. On the basis of real sample test (solid circles), the results are in good agreement with those obtained in NEBuffer (open circles).

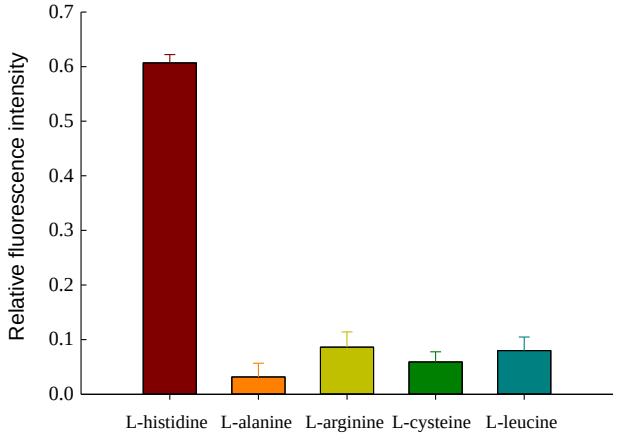


Fig. 4. Selectivity of enzymatic cascade reaction for L-histidine (50 μM) over other common natural amino acids (100 μM). The experimental conditions were the same as those for fluorescence experiments in Fig. 1. Each data point was performed in triplicate.

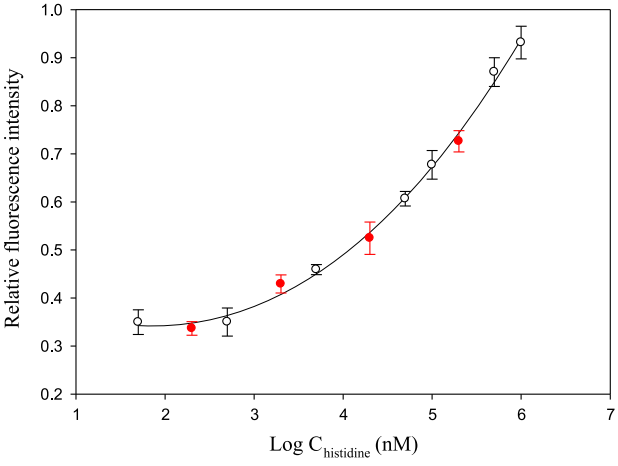


Fig. 5. Exponential response of the RFI of the assay after the standard addition of L-histidine into 50-fold diluted serum samples (solid plots) and the NEBuffer (open circles). The experimental conditions were the same as those for fluorescence experiments in Fig. 1. Error bars indicate standard error of triplicate tests.

These results revealed that the cleaved DNAzyme substrate induced enzymatic cascade assay has a promise in practical application with great accuracy and reliability for L-histidine detection.

4. Conclusion

In summary, the present study has combined an L-histidine cofactor-dependent DNAzyme and the polymerase/endonuclease reaction cycles for amplified fluorescent analysis. The L-histidine acted as the activator for enzymatic cascade amplification generating multiple duplex structures. The efficiency of the enzymatic cascade depended on the concentration of its analyte, which produced primers in closed replication system. Our novel method was able to quantify target levels as low as nanomolar sensitivity. This cleaved DNAzyme substrate induced enzymatic cascade strategy showed great potential for future use in clinical tests owing to its sensitive, isothermal, and cost-efficient features. The activation of such enzymatic cascades through analyte-DNAzyme interactions was not only valuable to activate the cooperation of muti-enzyme networks, but also had a substantial impact on the development of amplified DNAzyme sensors.

Acknowledgements

This work was financially supported by the National Science & Technology Support Program of China (no. 2012BAC17B01), National Natural Science Foundation of China (nos. 21105005, 21275022, and 21075011), the Science Foundation of Hunan Provincial Education Department (no. 12B002), Hunan Provincial Key Laboratory of Materials Protection for Electric Power and Transportation (nos. 2013CL01), and program for new century excellent talents in university (no. NCET-10-0138), Ministry of Education of the People's Republic of China.

References

[1] Y. Tan, Q. Guo, X. Zhao, X. Yang, K. Wang, J. Huang, Y. Zhou, Biosens. Bioelectron. 51 (2014) 255–260.
[2] X. Li, T. Ding, L. Sun, C. Mao, Biosens. Bioelectron. 30 (2011) 241–248.
[3] Y. Zhang, J. Hu, C. Zhang, Anal. Chem. 84 (2012) 9544–9549.
[4] G. Wang, C. Zhang, Anal. Chem. 84 (2012) 7037–7042.
[5] E. Tan, B. Erwin, S. Dames, T. Ferguson, M. Buechel, B. Irvine, K. Voelkerding, A. Niemz, Biochemistry 47 (2008) 9987–9999.
[6] X. Wang, B. Yin, P. Wang, B. Ye, Biosens. Bioelectron. 42 (2013) 131–135.
[7] Y. Zhao, L. Qi, F. Chen, Y. Zhao, C. Fan, Biosens. Bioelectron. 41 (2013) 764–770.
[8] A.R. Connolly, M. Trau, Angew. Chem. Int. Ed. 122 (2010) 2780–2783.
[9] Y. Liu, M. Zhang, B. Yin, B. Ye, Anal. Chem. 84 (2012) 5165–5169.
[10] L. Tian, Y. Weizmann, J. Am. Chem. Soc. 135 (2013) 1661–1664.
[11] Y. Li, Y. Zeng, Y. Mao, C. Lei, S. Zhan, Biosens. Bioelectron. 51 (2014) 304–309.
[12] M. Ishikawa, H. Saito, H. Morishita, T. Ito, T. Kato, Y. Wada, Acta Paediatr. Jpn. 29 (1987) 444–448.
[13] M. Ishikawa, Acta Paediatr. Jpn. 29 (1987) 224–228.
[14] A. Yamaguchi, Y. Mizushima, M. Fukushi, Y. Shimizu, Y. Kikuchi, N. Takasugi, Screening 1 (1992) 49–62.
[15] T. He, D. Quinn, E. Fu, Y. Wang, J. Chromatogr. B 727 (1999) 43–52.
[16] Y. Liu, R. Hu, T. Liu, X. Zhang, W. Tan, G. Shen, R. Yu, Talanta 107 (2013) 402–407.
[17] A. Roth, R.R. Breaker, Proc. Natl. Acad. Sci. U.S.A 95 (1998) 6027–6031.
[18] G.M. Emilsson, R.R. Breaker, Cell. Mol. Life Sci. 59 (2002) 596–607.
[19] L. Li, Z. Chen, H. Zhao, L. Guo, Biosens. Bioelectron. 26 (2011) 2781–2785.
[20] J. Liang, Z. Chen, L. Guo, L. Li, Chem. Commun. 47 (2011) 5476–5478.
[21] N.B. Amaral, S. Zuliani, V. Guieu, C. Ravelet, S. Perrier, E. Peyrin, Anal. Bioanal. Chem. 406 (2014) 1173–1179.
[22] J. Elbaz, B. Shlyahovsky, I. Willner, Chem. Commun. 13 (2008) 1569–1571.
[23] R. Kong, X. Zhang, Z. Chen, H. Meng, Z. Song, W. Tan, G. Shen, R. Yu, Anal. Chem. 83 (2011) 7603–7607.
[24] R. Hu, T. Fu, X. Zhang, R. Kong, L. Qiu, Y. Liu, X. Liang, W. Tan, G. Shen, R. Yu, Chem. Commun. 48 (2012) 9507–9509.
[25] B. Yin, B. Ye, W. Tan, H. Wang, C. Xie, J. Am. Chem. Soc. 131 (2009) 14624–14625.
[26] B.B. Prasad, D. Kumar, R. Madhuri, M.P. Tiwari, Biosens. Bioelectron. 28 (2011) 117–126.

Talanta 132 (2015) 814–828

Contents lists available at ScienceDirect

Talanta

journal homepage: www.elsevier.com/locate/talanta

Review

Chromium and its speciation in water samples by HPLC/ICP-MS – technique establishing metrological traceability: A review since 2000

Barbara Markiewicz, Izabela Komorowicz, Adam Sajnóg, Magdalena Belter, Danuta Barałkiewicz *

Department of Trace Element Analysis by Spectroscopy Method, Faculty of Chemistry, Adam Mickiewicz University in Poznań, 89b Umultowska Street, 61-614 Poznań, Poland

ARTICLE INFO

Article history:
Received 23 July 2014
Received in revised form
25 September 2014
Accepted 2 October 2014
Available online 14 October 2014

Keywords:
Speciation analysis
Chromium speciation
HPLC/ICP-MS
Water samples
Review

ABSTRACT

Chromium holds a special position among living organisms because depending on its species it can be either essential or toxic. Cr(VI) even at very low concentrations is harmful and carcinogenic, while Cr(III) is a necessary microelement for cellular metabolism. Therefore, a simple analysis of Cr concentration in collected samples will not be able to distinguish these differences effectively: for a proper chemical analysis we need to perform a reliable detection and quantification of Cr species. Separation and detection of chromium can be accomplished with high performance liquid chromatography hyphenated to inductively coupled plasma mass spectrometry (HPLC/ICP-MS) in a one-step. Our review assembles articles published since 2000 regarding chromium speciation in water samples with the use of HPLC/ICP-MS. It addresses the following issues: chromium chemistry, the possibilities of dealing with interferences, metrological aspects, analytical performance and speciated isotope dilution mass spectrometry (SIDMS) which is a definitive measurement method. The authors would like to advocate this hyphenated advanced technique as well as the metrological approach in speciation analysis of chromium.

© 2014 Elsevier B.V. All rights reserved.

Contents

1. Introduction . . . 815
   1.1. Cr(III) vs. Cr(VI): the good and the evil twin . . . 815
   1.2. Determination of chromium species . . . 815
   1.3. Legal norms concerning the concentration of chromium in drinking water . . . 815
2. Environmental occurrence of chromium . . . 816
   2.1. Chromium chemistry . . . 816
   2.1.1. pH value . . . 816
      2.1.2. Oxidation/reduction reactions . . . 816
      2.1.3. Precipitation/dissolution reactions . . . 816
      2.1.4. Adsorption/desorption reactions . . . 817
   2.2. Chromium in water systems . . . 817
3. Analytical problems in quantification by ICP-MS and their manners of reduction . . . 818
   3.1. Interferences . . . 818
      3.1.1. Spectral interferences . . . 818
      3.1.2. Non-spectral interferences . . . 819
   3.2. Reaction/collision cells . . . 819
   3.3. Other approaches to dealing with interferences . . . 819
4. Speciation analysis of chromium by HPLC/ICP-MS . . . 823
5. Metrological approach to measurement . . . 823

* Corresponding author. Tel.: +48 61 829 15 73; fax: +48 61 829 15 55.
E-mail address: danutaba@amu.edu.pl (D. Barałkiewicz).

http://dx.doi.org/10.1016/j.talanta.2014.10.002
0039-9140/© 2014 Elsevier B.V. All rights reserved.

5.1. Method validation . . . 824
5.1.1. Linearity . . . 824
5.1.2. LOD and LOQ . . . 824
5.1.3. Precision . . . 824
5.1.4. Trueness . . . 824
5.2. Traceability of measurement result . . . 824
5.3. Estimation of uncertainty budget . . . 825
6. Speciated isotope dilution ICP-MS as a definitive method for determining chromium species . . . 825
7. Conclusion . . . 826
Acknowledgment . . . 827
References . . . 827

1. Introduction

1.1. Cr(III) vs. Cr(VI): the good and the evil twin

Element toxicity, bioavailability and transport properties depend on the specific form in which element is present in the environment rather than its total amount. Along with an improvement of analytical methods, speciation analysis has attracted more attention [1]. A lot of research focus on chromium, as it is widely used in industrial processes, including: metallurgy (production of stainless steel, ferro- and nonferrous alloys), refractory industry (high temperature-resistant materials used as linings for furnaces) and chemical manufacturing (textile dyes, pigments, electroplating, leather tanning and wood preservatives). Large quantities of chromium compounds are released into the environment which has an adverse effect on the ecosystem [2–5]. Additionally, dissolved species of chromium in relatively high concentrations can occur naturally [6,7].

Chromium is an extraordinary example of an element which different species show opposite types of behavior. This phenomenon occurs in the case of some other metals but not to such an extent. The two most widespread oxidation states of chromium: Cr(III) and Cr(VI) differ with respect to their mobility and bioavailability. In general, Cr(III) compounds are relatively immobile and poorly soluble compared to highly mobile, soluble and, consequently, more bioavailable Cr(VI) compounds [8–10]. These differences extend to the chemical and biochemical reactivity of both species. Cr(III) in trace amounts is an essential nutrient for the human body: it is involved in carbohydrate, lipid and protein metabolism [11–13]. Nevertheless, it appears that the free ion of Cr(III) has no biological activity unless bound to a suitable organic ligand. Its properties are not unequivocally established. Additionally, it has also been reported that Cr(III) picolinate, which may be used as a micronutrient and dietary supplement, can cause harmful effects on human cells, although in very rare cases [5]. By contrast, Cr(VI) is explicitly toxic because of its high oxidation potential and ability to penetrate biological membranes. The ability of Cr(VI) (or actually the CrO_4^{2-} ion) to diffuse freely through cell membranes is possible due to its structural similarity to anions such as SO_4^{2-} or PO_4^{3-}, which are transported by suitable anion exchange channels. The reduced form of chromium is practically unable to enter the cell by the same ion channels, thus Cr(VI) compounds are recognized as 1000 times more cytotoxic. However, intracellular Cr(III), which is the terminal product of the Cr (VI)-reduction, can also exhibit toxic effects e.g., by suppressing the activity of some metallo-enzymes or reaction with macromolecules (including DNA) [14].

Since 1990, the International Agency on Research Cancer (IARC) has classified Cr(VI) compounds to Group 1, known as human carcinogens. The US Environmental Protection Agency (USEPA) has also considered this chromium species as a mutagenic and carcinogenic agent. Epidemiological studies have shown that exposure to Cr(VI) can induce a variety of clinical problems among which are an increased incidence of cancer and dermal disease [5].

1.2. Determination of chromium species

Due to significant differences in the biochemical properties of both Cr species there is an obvious need for their accurate quantification. In consequence, speciation analysis takes an important role in an environmental monitoring. Numerous papers concerning analytical methods for chromium speciation in water samples have been published during recent years. Among these approaches, HPLC/ICP-MS has proved to be a powerful analytical tool. The high diversity of chromatographic separation mechanisms determines various applications of the HPLC technique. The ICP-MS is a preferred detector in elemental speciation analysis owing to its unique analytical capabilities. Currently, as one of the most robust commercially available instruments, ICP-MS presents many advantages that include elemental specificity, multi-isotope detection and extremely low detection limits [15,16]. Furthermore, it offers high sensitivity of measurements along with a wide linear dynamic range. In addition, ICP-MS can be easily coupled online with HPLC [17].

1.3. Legal norms concerning the concentration of chromium in drinking water

The World Health Organization (WHO) has recommended that the concentration of Cr in drinking water should be 0.05 mg L^{-1} or less [18]; a similar value has also been published by the Council of the European Union [19]. However, according to the drinking water standards laid down by the Environmental Protection Agency (EPA), in the United States the permissible level of chromium is 0.10 mg L^{-1} [20]. However, the recommended values of Cr concentration in drinking water do not take into consideration particular species of this element. They provide just a temporary solution implemented because no routine or reliable method exists for the determination of low concentrations of chromium in water.

The number of articles concerning elemental speciation has increased appreciably over the last two decades, particularly since 1995 [21,22] and many different analytical strategies have been developed to deal with quantification of Cr forms existing in the nature. The papers (also overview articles) have covered various topics such as environmental occurrence [2,23,24], risk assessment, health effects [5,25–29] and analytical approaches (including offline and online methods) [3,21,30–41]. In a recently published comprehensive overview the application of the isotope dilution technique, which provides the highest quality of metrological traceability in chromium speciation analysis in different matrices, was widely described [41].

In this review we present a new perspective for the determination of chromium chemical forms in water. We focus on the problems connected with obtaining reliable and competent results,

which are basic requirements for any projected legislation concerning chromium species determination in water. Unlike other reviews, besides presenting several issues related to chromium occurrence in water environments, determination of chromium species by the HPLC/ICP-MS method and accompanying problems, this work raises an important issue regarding the quality assurance of obtained analytical results: method validation, the traceability and uncertainty of the measured results.

2. Environmental occurrence of chromium

2.1. Chromium chemistry

Cr can exist in several oxidation states from 0 to VI. The two forms of chromium commonly found in the environment are Cr (III) and Cr(VI). The intermediate states: Cr(II), Cr(IV), Cr(V) are unstable products in oxidation and reduction reactions of trivalent and hexavalent chromium, respectively [2,8,11]. The prevalent forms of chromium might undergo a series of transformations, changing from one into another under the influence of various physicochemical processes. In many cases, disruption of the chemical balance between particular species strongly depends on pH value. Additionally, redox reaction, precipitation/dissolution and adsorption/desorption can cause Cr conversions. Some of these aspects are discussed below [9,10,12,24].

2.1.1. pH value

In aqueous solution (assuming the absence of other complexing agents besides H_2O or OH^-), Cr(III) exists as a hexa-aqua complex $Cr(H_2O)_3^{3+}$ (abbreviated as Cr^{3+}) which has hydrolysis products as demonstrated by equations (Eqs. 1–3).

$$Cr(H_2O)_3^{3+} + H_2O \leftrightarrow Cr(OH)(H_2O)_5^{2+} + H_3O^+ \quad (1)$$

$$Cr(OH)(H_2O)_5^{2+} + H_2O \leftrightarrow Cr(OH)_2(H_2O)_4^{3+} + H_3O^+ \quad (2)$$

$$Cr(OH)_2(H_2O)_4^{+} + H_2O \leftrightarrow Cr(OH)_3^0 + H_3O^+ \quad (3)$$

The deprotonated forms of hexaaquachromium(3+) can be simply abbreviated to $Cr(OH)^{2+}$, $Cr(OH)_2{}^+$ and $Cr(OH)_3{}^0$. The presence of these hydroxo species in the environment is closely related to pH. In more acidic solutions ($pH \approx 4$), Cr^{3+} is the predominant species of Cr(III). Under slightly acidic conditions its hydrolysis generates $Cr(OH)^{2+}$ and $Cr(OH)_2{}^+$. Within a pH range from neutral up to alkaline Cr(III) tends to precipitate as a virtually insoluble $Cr(OH)_{3\,(s)}$, which is transformed into soluble $Cr(OH)_4^-$ in more basic solutions ($pH > 12$), because of its amphoteric properties. As a consequence, in a pH range typical for natural waters (approximately 4–9), $Cr(OH)^{2+}$ and $Cr(OH)_3{}^0$ are the prevalent aqueous forms of Cr(III).

In the case of Cr(VI), pH-value and its total concentration determine the relative fractions of these species occurring in a solution. H_2CrO_4 belongs to the strong acids and is only observed below pH 1. As a result of its dissociation the following products are formed: $HCrO_4^-$ at a pH from about 1–6.5 and at a Cr(VI) concentration below 0.01 mol L^{-1}, whereas $Cr_2O_7{}^{2-}$ is prevalent in more concentrated solutions ($c > 0.01$ mol L^{-1}) and $CrO_4{}^{2-}$ at pH-value higher than 6.5 over the entire concentration range. All of the above-mentioned Cr(VI) oxyanions are present in a pH range of natural waters [2,8,9].

2.1.2. Oxidation/reduction reactions

Redox potential (Eh) and pH play a crucial role in the interconversion of both stable states of chromium. To understand the behavior of Cr(III) and Cr(VI), please refer to the Eh–pH diagram for chromium species in aquatic environments presented in Fig. 1. Under acidic conditions, Cr(VI) exhibits a high positive Eh value, which means it is a strong oxidizing agent and is easily reduced by electron donors such as organic matter or appropriate inorganic compounds widespread in water systems. At neutral pH, the Cr(III)–Cr(VI) proportion is related to the oxygenation of solution. By contrast, in more alkaline media, the oxidizing character of hexavalent chromium is much less effective and thus it has a tendency to remain in this state rather than be reduced [2,9].

The concentration of reducers and oxidation mediators also regulates the redox behavior of chromium. Even though the Eh value of the Cr(VI)/Cr(III) couple is high there are several oxidants in the natural aquatic environment that can oxidize Cr(III) into Cr(VI) but only a few of them are found at sufficient levels. Dissolved oxygen does not affect the oxidation of Cr(III) if additional compounds are absent. Only in the presence of manganese oxides Cr(III) can be readily converted to Cr(VI). Although hexavalent Cr reduction is less privileged thermodynamically, this process can be carried out because the concentrations of reductants are high enough. Consequently, the major factors in the water body taking part in the transformation of Cr(VI) into Cr(III) are: Fe^{2+}, S^{2-}, dissolved organic matter (e.g., humic acid), as well as the activity of microorganisms [7,10,13,42,43].

Sunlight also plays an essential role in the regulation of chromium chemistry in surface water. It has been proven that photochemical generation of Cr(III) and Cr(VI) is possible. The sunlight contributes to the reduction of iron which affects the formation of hydrogen peroxide and both of these reducing agents favor the reduction of Cr(VI). Additionally, sunlight influences the oxidation of manganese (which determines Cr(III) formation), breaks organic bindings of chromium and thereby releases its inorganic species [7]. However, the problem of Cr(III) oxidation to more toxic Cr(VI) may be intensified owing to the anthropogenic contamination of water and an application of ozone in water treatment systems.

2.1.3. Precipitation/dissolution reactions

Precipitation and dissolution are other important aspects that influence the distribution of Cr species in the environment. They are ruled by the solubility of the chromium compounds, which varies between individual Cr species [7]. Under conditions prevalent in surface waters, Cr(III) solubility is limited by the formation of insoluble chromium hydroxides, including mixed ones (e.g., $(Cr, Fe)(OH)_3$). The amount of soluble Cr(III) is extensively regulated by the precipitation of these hydroxides, especially mixed iron–chromium that have even lower solubility than $Cr(OH)_3$ [24,42]. However, trivalent chromium exhibits a tendency to form various complexes with naturally

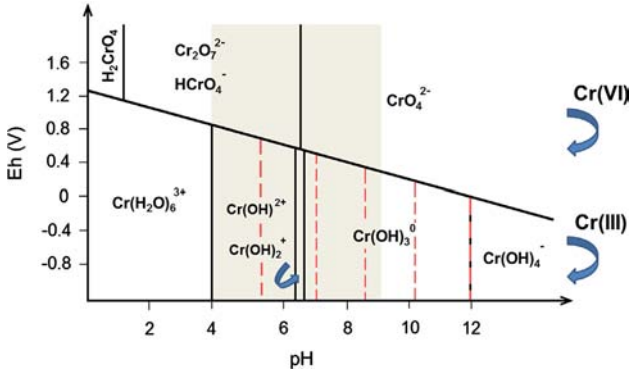


Fig. 1. Trivalent and hexavalent species of chromium in water environments as a function of Eh vs. pH; assuming the presence of H_2O, OH^- only and the concentration of total $Cr = 10^{-6}$ mol L^{-1}. The dotted lines demonstrate precipitated Cr(III) as $Cr(OH)_{3\,(s)}$, and the gray zone illustrates the typical range for pH in natural waters [2,9,10].

occurring macromolecular substances such as fulvic or humic acids. This complexation reduces the efficiency of Cr(III) precipitation and affects the mobility of organic ligands. If humic compounds are bound to sediment or soil, we observe the removal of Cr(III) from aquatic environments due to formation of its stationary complexes.

A large number of Cr(VI) compounds (chromates and dichromates) are water-soluble at wide range of pH. However, they can also exist as solid minerals containing different divalent cations (e.g., Ba^{2+}, Sr^{2+}, Pb^{2+}, Ca^{2+}). The solubilities of CrO_4^{2-}, $Cr_2O_7^{2-}$ and above mentioned cations are governed by pH, and it has been shown that the dichromates are, in principle, highly soluble as opposed to the chromates [7,8,44]. Therefore, the mobility of hexavalent anionic forms is relatively greater than trivalent chromium, which causes the first ones to be more available for living organisms in soil-water systems [9,42,45].

2.1.4. Adsorption/desorption reactions

The concentration of chromium in natural aquatic systems is also controlled by adsorption and desorption reactions. Sorption causes the migration of Cr from the aqueous phase to the surface of suspended and settled sediments. The equilibrium of this process depends on complex environmental conditions such as pH, surface area or density of active sites [43]. Hexavalent chromium can be adsorbed on particle surfaces (which have protruding –OH groups), including iron and aluminum oxides as well as kaolinite. Iron oxides are the dominant adsorbents in acidic to neutral oxidized soils and ground water. The sorption of dissolved Cr(VI) is higher at lower pH values. However, Cr(VI) anions are generally weakly adsorbed on minerals due to their being repelled by the negative charge of soil particles [13]. On the other hand, Cr(III) species are attracted to partially negatively charged surfaces such as silicates, and organically-bound Cr(III) can also adsorb on or desorb from the organic substances [2,7,8,45].

2.2. Chromium in water systems

Chromium and its compounds present in water come mostly from anthropogenic sources but natural Cr release cannot be neglected. In combination with other elements, Cr naturally occurs in the environment mainly as an ore mineral – chromite ($FeCr_2O_4$). The primary natural sources of this element, contributing to an increase of its concentration in aquatic systems, are: weathering of rocks, wet precipitation and dry fallout from the atmosphere (e.g., volcanic dust, forest wildfires), as well as run-off from terrestrial areas. As mentioned earlier, Cr contamination of water and soil is caused by intensive industrial activities to a much greater extent than natural release. However, elevated levels of naturally occurring Cr(VI) in ground and surface waters (exceeding the value of total Cr for drinking water recommended by the WHO) have been observed. This is a consequence of a release of Cr(III) to solution from rocks (e.g., ultramafic) and then its oxidation by commonly found MnO_2 [6]. The introduction of sewage, which is rich in chromium, into waters (mostly surface waters) has become a serious problem and may be a result of the discharge of industrial waste (e.g., from metallurgical and electroplating plants, tanneries or from dyeing and other chemical factories) as well as sanitary landfill leaching [45,46]. The industrial use of Cr is associated with chromite mining. In 2011 its total world mine output was approximately $24\,000 \times 10^3$ metric tons. Large reserves of this ore exist in Kazakhstan, South Africa, India and the United States [10]. The majority of chrome ore production (90%) is consumed by metallurgical industries, while chemical and refractory industries equally account for 5%. Chemical processes in which chromium is used influence the quantity and species of Cr later released in sewage outflows. The above mentioned activities employ an oxidized form of Cr [2,7,12,24].

Typically, lakes are characterized by high levels of biological activity and high ratios of sediment-to-water surface area that control transport of metals. Significant amounts of organic matter, which are responsible for establishing reductive and complexing conditions, favor reduction of Cr(VI). Subsequently, the fate of chromium depends on the various processes discussed above. Chromium enters the ocean in two ways: by rivers or atmospheric fallout. In the ocean waters an equilibrium exists between dissolved and precipitated Cr. The most prevalent form of chromium in seawater is found in chromates (besides estuaries), as a result of the oxidizing character of these waters and the low concentration of suspended solids.

When examining the distribution of chromium species in ground water, we should take into account their solubility and ability to be

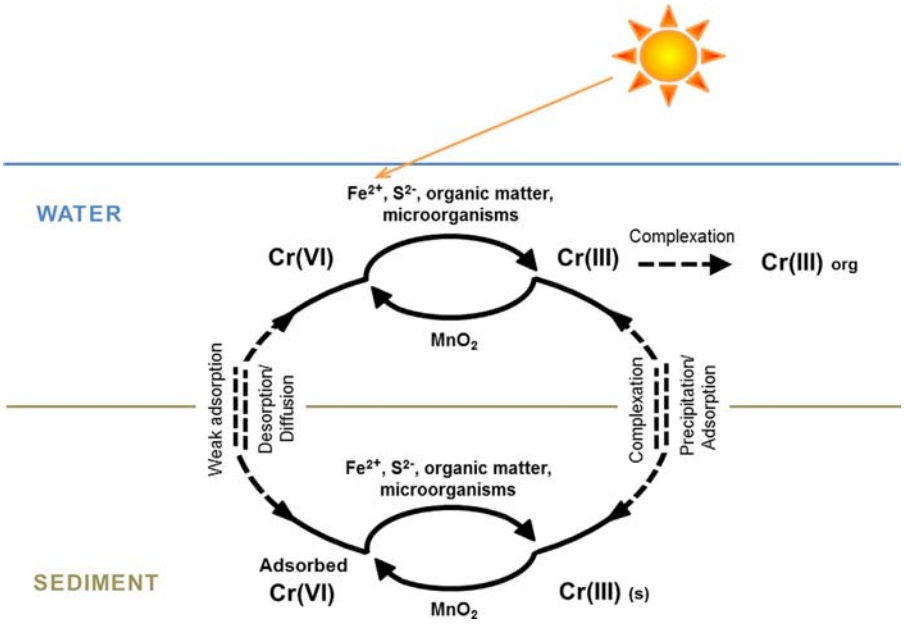


Fig. 2. The chromium cycle in the water-sediment system [2,9,23].

sorbed by soil or aquifer materials. These factors are governed by the chemistry of this type of water and the properties of soil or aquifer material. In general, Cr(III) is immobile in most ground waters due to the formation of poorly soluble compounds (in neutral to alkaline pH values). Hexavalent chromium, in turn, tends to be the most mobile form of Cr in shallow ground water. Chromium species behave similarly in surface waters [7]. The transformations and movement of chromium species in the environment are illustrated in Fig. 2.

Natural concentrations of total chromium in surface waters (except regions with substantial chromium deposits) are very low, normally between 1 and 10 $\mu g\,L^{-1}$, and in lake water do not exceed 5 $\mu g\,L^{-1}$ [47]. Total Cr concentration in surface waters in Europe ranges from $< 0.01\ \mu g\,L^{-1}$ to 43.3 $\mu g\,L^{-1}$, with a median value of 0.38 $\mu g\,L^{-1}$ [13]. Chromium concentration in sea water is one order of magnitude lower than in rivers and freshwater lakes, most of the samples contain 0.1 $\mu g\,L^{-1}$–0.5 $\mu g\,L^{-1}$ of Cr. In ground water the content of chromium is comparable to the typical amount of this element found in surface waters [45,48]. Total Cr level in drinking waters is predominantly less than 2 $\mu g\,L^{-1}$, however, a higher concentration of chromium (120 $\mu g\,L^{-1}$) has also been noted [18]. Concentrations of specific species of Cr in various water samples, which have been analyzed using HPLC/ICP-MS, are summarized in Table 1.

3. Analytical problems in quantification by ICP-MS and their manners of reduction

3.1. Interferences

Elemental speciation, as previously discussed, involves the coupling of two analytical tools: a highly selective separation technique with a sensitive detection. Among numerous methods described in the literature concerning the quantification of chromium species, most of the recent ones are based on the ICP-MS as a detector. The ICP-MS instrument provides many advantages, however, it also presents some pronounced difficulties such as spectral and non-spectral interferences, in particular quadruple ICP-MS (qICP-MS).

3.1.1. Spectral interferences

Spectral interferences occur mainly due to polyatomic and isobaric ions, which have the same mass-to-charge ratios (m/z^+) as the analyte of interest. For the determination of chromium by ICP-MS, four Cr isotopes with natural abundances between 2.4% and 83.8% are available. Nevertheless, all of these isotopes are affected by numerous polyatomic species, which are formed by interaction between constituents of gaseous plasma (Ar), reagents and sample matrix (O, H and less often C, N, Cl, S, P) [49]. The polyatomic interferences on $^{52}Cr^+$, including $^{40}Ar^{12}C^+$ and $^{35}Cl^{16}O^1H^+$ are the most frequent ones for ICP-MS detection of Cr. Despite the fact that determination of chromium has some difficulties, ^{52}Cr is preferred by researchers because it is the most abundant isotope (83.8%) [12,28,32,50,51]. Additionally, isobaric interferences are caused by isotopes of other elements that overlap ions at the masses of interest, but doubly charged ions derive only from elements with a low second ionization energy, therefore their formation depends on the ionization source [49]. Spectral interferences associated with the measurement of chromium ions using ICP-MS are listed in Table 2.

A variety of approaches can be applied to effectively overcome interferences caused by the limited resolving power of qICP-MS. In order to eliminate isobaric and doubly charged ions, the usage of alternative isotopes of the analyte is recommended. Moreover, mathematical correction (also as an option in the software of contemporary ICP-MS) can be used for isobaric interferences, while the optimization of operational conditions of the instrument is suitable for doubly charged forms [49,52]. In turn, the application of multipole collision (hexapole or octapole) or reaction cells (in upgraded qICP-MS), mathematical correction, cool plasma conditions, high resolution ICP mass spectrometer or optimization of the chromatographic separation reduces the level of polyatomic interferences to a great extent [17,37,44,53–55].

Table 1
The concentration of chromium in varied water samples.

Sample		Naturally occurring concentration [$\mu g\,L^{-1}$]		References
		$^{52}Cr(III)$	$^{52}Cr(VI)$	
Natural water	Surface water	$< 1.60 \pm 0.06$	$< 1.20 \pm 0.08$	[44]
	Lake water	0.116 ± 0.007	0.050 ± 0.012	[3]
		0.08	*< LOD*	[71]
	Pond water	0.272 ± 0.019	0.083 ± 0.010	[3]
	SLEW-3 (estuarine water)	0.205 ± 0.038	*< LOD*	[74]
	River water	1.08–1.27 or *< LOD*	0.96–1.70	[70]
	Ground water	0.17	0.87	[77]
		$< 1.60 \pm 0.08$	$< 1.20 \pm 0.08$	[44]
	Porewater	No data	0.73–1.17 or *< LOD*	[50]
	Tap water	0.066 ± 0.006	*< LOD*	[3]
		$< 1.60 \pm 0.02$	2.30 ± 0.03	[44]
		0.080 ± 0.024	0.135 ± 0.009	[69]
		< LOQ	0.297 ± 0.024–1.032 ± 0.082	[72]
	Municipal water	0.14–0.56	3.7 or *< LOD*	[71]
Beverage	Bottled water	0.12–0.31	*< LOD*	[71]
		0.005–0.05	0.055–0.24	[67]
		0.036 ± 0.006–0.060 ± 0.005	0.054 ± 0.003–0.409 ± 0.002	[68]
Industrial water	River water/stream (discharge of urban and industrial effluents)	No data	< 5.9[a]	[75]
		1.65 ± 0.09	*< LOD*	[4]
	Waste waters	22.2 ± 1.3	31.7 ± 1.8	[53]
		26.2 ± 1.6	48.0 ± 2.3	[32]
	Brines from industrial process	0.82 ± 0.10–5.10 ± 0.60	21.0 ± 1.5–233 ± 16[a]	[54]

[a] Monitored isotope – ^{53}Cr.

Table 2
Spectral interferences, including the most common (in bold) associated with chromium detection by ICP-MS [65,97–99].

Isotope	Interferences	
	Isobaric	Polyatomic
^{50}Cr (4.3%)[a]	$^{50}V^+$, $^{50}Ti^+$	$^{34}S^{16}O^+$, $^{36}Ar^{14}N^+$, $^{35}Cl^{15}N^+$, $^{36}S^{14}N^+$, $^{32}S^{18}O^+$, $^{33}S^{17}O^+$
^{52}Cr (83.8%)[a]	–	$\mathbf{^{40}Ar^{12}C^+}$, $^{35}Cl^{16}O^1H^+$, $^{36}Ar^{16}O^+$, $^{37}Cl^{15}N^+$, $^{34}S^{18}O^+$, $^{36}S^{16}O^+$, $^{38}Ar^{14}N^+$, $^{36}Ar^{15}N^1H^+$, $^{35}Cl^{17}O^+$
^{53}Cr (9.5%)[a]	–	$\mathbf{^{37}Cl^{16}O^+}$, $^{38}Ar^{15}N^+$, $^{38}Ar^{14}N^1H^+$, $^{36}Ar^{17}O^+$, $^{36}Ar^{16}O^1H^+$, $^{35}Cl^{17}O^1H^+$, $^{35}Cl^{18}O^+$, $^{36}S^{17}O^+$, $^{40}Ar^{13}C^+$
^{54}Cr (2.4%)[a]	$^{54}Fe^+$	$^{37}Cl^{16}O^1H^+$, $^{40}Ar^{14}N^+$, $^{38}Ar^{15}N^1H^+$, $^{36}Ar^{18}O^+$, $^{38}Ar^{16}O^+$, $^{36}Ar^{17}O^1H^+$, $^{37}Cl^{17}O^+$, $^{19}F_2{}^{16}O^+$

[a] Abundance of naturally occurring chromium isotope recommended by IUPAC.

3.1.2. Non-spectral interferences

Non-spectral interferences called matrix-effects are induced by the sample matrix or mobile phases when organic compounds as well as inorganic salts are contained. They contribute to clogging the nebulizer, the sampling and skimmer ICP-MS cones, they can also accumulate on the torch and the ion lens, causing distortions by increasing or decreasing signal intensities. Incorrect measurements stemming from non-spectral interferences are usually overcome with the use of appropriate calibration procedures e.g., standard addition method or internal standardization [49,52].

3.2. Reaction/collision cells

Among currently available approaches to cope with the problem of spectral interferences, dynamic reaction cells (DRC) as well as multipole collision cells (MCC) are one of the most effective. The DRC is a rf/DC quadrupole placed inside the enclosed reaction chamber which is positioned between the single lens ion optics and the mass filter. The DRC is pressurized with a reactive gas in order to carry out ion-molecule reactions intended to suppress plasma-based polyatomic interferences [56]. The bandpass of the DRC is selected in a manner so as to control the generation of new interfering species within the reaction cell. Removal or reduction of polyatomic interferences has been achieved by different processes including neutralization or exchange reaction between interference ions and gaseous molecules pressurizing the cell. Products of these reactions are swept from the chamber with a continuous fresh reaction gas stream [57–61]. As a consequence of these interactions, the obtained chemical forms are characterized by another m/z^+ than the analyzed ion or they are converted into neutral species which cannot be recognized by the detector. Preferred reaction gases as well as the mixtures (e.g., with argon) used in the DRC are: ammonia, methane, hydrogen or oxygen [62,63]. The selection of gas depends on its ability to undergo a gas phase chemical reaction with the polyatomic species and to remove them. An exemplary interaction between NH_3, as an extensively employed reaction gas, and argon plasma ion was demonstrated as follows [56]:

$$Ar^+ + NH_3 \rightarrow NH_3{}^+ + Ar \text{ (neutralization)}$$

According to scheme presented above, the major interference $^{40}Ar^{12}C^+$, which occurs at the same m/z^+ as $^{52}Cr^+$, can also be transformed into neutral species by ammonia [58]:

$$^{40}Ar^{12}C^+ + NH_3 \rightarrow NH_3{}^+ + {}^{40}Ar + {}^{12}C$$

Carbon-based interferences react much faster with NH_3 than chromium, and thus the interfering ions will be effectively reduced. As can be seen, the ionization energy of Cr (6.8 eV) is lower than NH_3 (10.2 eV), therefore, the electron transfer from ammonia to chromium ion is endothermic and the reaction is not observed to proceed [64].

MCC similar to the DRC employ rf to focus the ion beam instead of separating ions according to their m/z^+ like a typical mass analyzer. However, in the case of collision technology, non-reactive gases (e.g., He, H_2, Xe) are introduced into the cell and they can attenuate or even eliminate polyatomic interferences by an ion–molecule collision mechanism. In order to separate the collision product from the analyte, kinetic energy discrimination (KED) is used. Particular ions will be distinguished, while the analyte ions will have higher energy than the interfering ions [62,65,66].

In the reviewed articles the application of DRC/MCC technology was one of the most frequently adopted approaches used to overcome spectral interferences. Sakai et al. used H_2 as a collision cell gas for attenuating $^{40}Ar^{12}C^+$ and $^{35}Cl^{16}O^1H^+$, primary based-matrix interferences at m/z^+ 52 [67]. Chen et al. reported that an octopole reaction system can be used for determination of $^{52}Cr^+$ in the presence of chloride, using either an He or H_2 mode [53]. However, the authors also recommended H_2 cell gas to efficiently remove polyatomic spectral interferences. By contrast, Wang et al. suppressed polyatomic interferences from chlorine and carbon by application of a mixture of 7.28% H_2/He, while McSheehy et al. utilized a mixture of 8% H_2/He as the collision cell gas for preventing $^{40}Ar^{12}C^+$ [28,68]. An alternative approach to the above mentioned system was collision/reaction interface (CRI), where a collision/reaction gas had been introduced through the sampler or skimmer cones [69]. The use of H_2 CRI gas at 70 mL min^{-1} appreciably eliminated the problem of chlorine-based and carbon-based interferences and so enabled a reliable determination of $^{52}Cr^+$. Bednar et al. employed methane as a reaction gas in DRC for attenuating $^{40}Ar^{12}C^+$ interferences at m/z^+ 52 and 53 [44]. Tsoi and Leung applied DRC technology to overcome polyatomic ions in multi-elemental speciation analysis of seven forms of arsenic, chromium, and selenium altogether [70]. They tested the efficiency of the interference reduction by optimizing the following DRC conditions: gas flow rate and rejection parameter q (Rpq) using various reaction gases including NH_3, CH_4 and O_2. The experiments revealed that the preferable gas for determination of all seven analytes of interest is CH_4. Its capability of dealing with the problem of chloride interferences, under the optimal conditions of the reaction cell, was demonstrated by the analysis of 250 mg L^{-1} NaCl solution. However, Neubauer et al. suppressed interferences encountered during trace element speciation of arsenic and chromium, using O_2, which reduces the $^{40}Ar^{12}C^+$ ions on $^{52}Cr^+$ and forms a new species $^{75}As^{16}O^+$ free from interfering ions [71]. Other authors selected NH_3 as the DRC gas to remove a great part of the chlorine-based and carbon-based polyatomic interferences, predominantly occurring in chromium determination. [50,72,73]. They studied influential operating parameters for the DRC system (gas flow rate and Rpq) to achieve the optimal signal to noise (S/N) ratio. In particular Chang et al. and Wolf et al. effectively reduced the interfering background peaks at m/z^+ 52 as well as 53 (under the optimized DRC conditions) by three or even four orders of magnitude [3,12].

3.3. Other approaches to dealing with interferences

An alternative approach to resolve the problem of spectral interferences is the use of mathematical correction [49,52,55]. As previously mentioned (Section 3.1.1), corrections may be applied for evaluating the formation of $^{40}Ar^{12}C^+$ and $^{35}Cl^{16}O^1H^+$, being the

Table 3
Analytical and metrological aspects concerning chromium species determination in water matrices by HPL/ICP-MS based on the literature review since 2000.

No.	Sample	Sample storage and preservation conditions	Chromatographic separation	HPLC operating conditions	Validation characteristics[a]	References
	1. Species 2. Matrix	1. Type of container 2. Temperature (°C) 3. Acidification	1. Column 2. Elution type 3. Mobile phase 4. Complexing agent	1. Mobile phase flow rate (mL min^{-1}) 2. Column temperature (°C) 3. Injection volume (μL) 4. Retention time ($_{min}$) i. Cr(III) ii. Cr(VI) iii. Total analysis time	1. *LOD* (μg L^{-1}) i. Cr(III)[b] ii. Cr(VI) 2. Precision (%) i. Cr(III) ii. Cr(VI) 3. Recovery (%) i. Cr(III) ii. Cr(VI)	
1	1. Cr(III), Cr(VI) 2. Brines from industrial process	1. No data 2. No data 3. No data	1. Anion exchange: ANX3202 CETAC Tech. (2 mm × 200 mm), guard disc 2. Isocratic 3. 60 mM HNO_3 4. No data	1. No data 2. No data 3. 20 4. i. 1.30 ii. 3.30 iii. 5.00	1. i. ^{52}Cr, R[c]=300: 0.080 (HP)[c], 0.040 (CP)[c], ^{52}Cr, R=3000: 0.050 (HP), ^{53}Cr, R=300: 0.060 (HP), 0.140 (CP), ^{53}Cr, R=3000: 0.170 (HP), ii. ^{52}Cr, R=300: 0.190 (HP), 0.070 (CP), ^{52}Cr, R=3000: 0.120 (HP), ^{53}Cr, R=300: 0.150 (HP), 0.280 (CP), ^{53}Cr, R=3000: 0.360 (HP) 2. No data 3. No data	[54]
2	1. Cr(III), Cr(VI) 2. Reference Material (synthetic and estuarine water)	1. No data 2. No data 3. HNO_3	1. Anion exchange: IonPac AS7 Dionex (4 mm × 250 mm, 10 μm), guard column: IonPac AG7 Dionex (4 mm × 50 mm, 10μm) Isocratic 2. 50 mM NH_4NO_3, pH=8.0 3. EDTA	1. 1.5 2. No data 3. 1000 i. 4.30 ii. 10.80 iii. 11.50	1. i. ^{52}Cr: 0.005 ^{53}Cr: 0.007 ii. ^{52}Cr: 0.012 ^{53}Cr: 0.016 2. 4.8 for 0.05 μg L^{-1}, for Cr species i. 94–97 ii. 98–101	[74]
3	1. Cr(VI), As(III), As (V), MMA, DMA, Se(IV), Se(VI) 2. Surface water (located in an industrial area)	1. Polyethylene bottles 2. Cooling (4) 3. Without	1. Anion exchange: PRP-X100 Hamilton (4.1 mm × 250 mm, 10 μm) 2. Gradient 3. A: 20 mM NH_4NO_3 B: 60 mM NH_4NO_3, pH=8.7 for A and B 4. No data	1. 1.0 2. No data 3. 100 i. 9.40 ii. 14.00	1. ii. 0.2 2. ii. 2.6 (ST)[c] for 0.45 μg L^{-1} 1.6 (ST) for 10 μg L^{-1} 0.6 (ST) for 100 μg L^{-1} 3.6 (LT)[c] for 10 μg L^{-1} 3. ii. 80–100	[75]
4	1. Cr(III), Cr(VI) 2. Surface water (located in an industrial area)	1. No data 2. Freezing (−20) 3. No data	1. Ion exchange: IonPac CS5A Dionex (4 mm × 250 mm, 9 μm), guard column: IonPac CG5A Dionex (4 mm × 50 mm, 9 μm) 2. Gradient 3. A: 0.35 M HNO_3 B: 1 M HNO_3 4. No data	1. 1.0 2. No data 3. 100 i. 7.15 ii. 2.60 iii. 9.00	1. i. ^{52}Cr: 0.32; ^{53}Cr: 0.38 ii. ^{52}Cr: 0.19; ^{53}Cr: 0.20 2. for 10 μg L^{-1} i. ^{52}Cr: 3.8 (ST) ^{53}Cr: 4.0 (ST) ii. ^{52}Cr: 1.8 (ST) ^{53}Cr: 2.5 (ST) iii. 0–56 iv. 101–102	[4]
5	1. Cr(III), r(VI) 2. Ground water	1. No data 2. No data 3. No data	1. Anion exchange: ANX4605 CETAC Tech. 2. Isocratic 3. 0.06 M HNO_3 4. No data	1. 1.0 2. No data i. 200 ii. 0.90 iii. 2.00 iv. 2.90	1. No data 2. No data 3. No data	[77]

Table 3 (*continued*)

No.	Sample	Sample storage and preservation conditions	Chromatographic separation	HPLC operating conditions	Validation characteristics[a]	References
6	1. Cr(III), Cr(VI) 2. Mineral water	1. No data 2. No data 3. No data	1. Anion exchange: G3268A Agilent (4.6 mm × 30 mm) 2. Isocratic 3. 5 mM EDTA, pH=7.0 4. EDTA	1. 1.2 2. Ambient i. 500 ii. 1.00 iii. 2.40 iv. 3.00	1. i. 0.0132 ii. 0.0158 2. for 0.5 μg L^{-1} i. 0.80 (RT)[c] 1.87 (PA)[c] 2.28 (PH)[c] ii. 0.57 (RT); 1.79 (PA); 3.01 (PH) iii. 100–105 iv. 95–102	[67]
7	1. Cr(III), Cr(VI) 2. Waste water, lake water and seawater	1. No data 2. No data 3. No data	1. Anion exchange: G3154A/101 Agilent, guard column: G3154A/102 Agilent 2. Isocratic 3. 20 mM NH_4NO_3, pH=5.9 4. EDTA	1. 1.0 2. 30 3. 50 i. 4.50 ii. 8.59 iii. 10.00	1. i. 0.3 ii. 0.4 2. for 20 μg L^{-1} i. 1.9 ii. 2.8 iii. 92.3–98.5 iv. 91.1–94.5	[53]
8	1. Cr(III), Cr(VI) 2. Waste water	1. No data 2. No data 3. No data	1. Anion exchange: G3154A/101 Agilent, guard column: G3154A/102 Agilent 2. Isocratic 3. 20 mM NH_4NO_3, 10 mM $NH_4H_2PO_4$, pH=7.0 4. EDTA	1. 1.0 2. 30 i. 50 ii. 4.21 iii. 5.77 iv. 7.00	1. i. 0.2 ii. 0.1 2. for 10 μg L^{-1} i. 2.8 ii. 1.9 3. 91.5–104.3 for Cr species	[32]
9	1. Cr(III), Cr(VI), Se (IV), Se(VI) 2. Surface, ground and tap water, synthetic laboratory sample (high salted)	1. No data 2. Cooling (4), 10 (AT)[c] 3. No data	1. Anion exchange: IonPac AS-11 Dionex (4.1 mm × 250 mm), guard column: IonPac AG-11 Dionex (4.1 mm × 50 mm) 2. Isocratic 3. 20 mM NaOH 4. EDTA	1. 1.25 2. 25 3. 35 i. 0.40 ii. 2.80 iii. 4.00	1. i. ^{52}Cr: 0.8; ^{53}Cr: 1.5 ii. ^{52}Cr: 0.6; ^{53}Cr: 0.7 2. No data i. ^{52}Cr: 78–114; ^{53}Cr: 80–111 ii. ^{52}Cr: 85–114; ^{53}Cr: 85–113	[44]
10	1. Cr(III), Cr(VI) 2. Tap water	1. Polyethylene bottles 2. No data 3. Without	1. Ion exchange: IonPac AG7 Dionex (4 mm × 50 mm, 10 μm) 2. Gradient 3. A: 0.1 M NH_4NO_3 (pH=4.0) B: 0.8 M HNO_3 4. No data	1. 1.5 2. Ambient 3. 50 i. 3.40 ii. 1.30 iii. 7.50	1. i. 0.04 ii. 0.02 2. No data 3. 101.5 for Cr species	[69]
11	1. Cr(III), Cr(VI), As (III), As(VI), MMA, Se(IV), Se (VI) 2. River water	1. Polypropylene bottles 2. Cooling (4) 3. Without	1. Anion exchange: PRP-X100 Hamilton (4.6 mm × 150 mm, 5 μm), guard column: PRP-X100 Hamilton 2. Gradient 3. A: 0.5 mM $NH_4H_2PO_4$, 10 mM NH_4NO_3 B: 30 mM NH_4NO_3, pH=6.0 for A and B 4. EDTA	1. 2.0 2. No data 3. 200 i. 6.01 ii. 8.35 iii. 11.00	1. i. 0.24 ii. 0.29 2. No data 3. 92.7–108.2 for Cr species	[70]

Table 3 (*continued*)

No.	Sample	Sample storage and preservation conditions	Chromatographic separation	HPLC operating conditions	Validation characteristics[a]	References
12	1. Cr(III), Cr(VI) 2. River sediment pore water	1. No data 2. No data 3. No data	1. Anion exchange: IonPac AS7 Dionex (4 mm × 250 mm, 10μm) 2. Isocratic 3. 60 mM NH_4NO_3, pH=8.0 4. EDTA (in the 2nd option)[c]	1. 1.0 2. No data 3. 100 4. No data	1. i. 0.23, 0.10 (with ETDA) ii. 0.14, 0.11 (with ETDA) 2. i. 12, 9.2 (with ETDA) ii. 11, 5.7 (with ETDA) for 12–13 QC calibration check samples 3. i. 76–140, 1.3–180 (with ETDA) ii. 62–90 but in majority of samples Cr(VI) was not recovered, all spiked samples had zero (or virtually zero) percent recovery of Cr(VI) (with ETDA)	[78]
13	1. Cr(III), Cr(VI) 2. Lake, pond and tap water	1. No data 2. No data 3. No data	1. Reverse phase: CR C8 PerkinElmer (3 mm × 30 mm, 3 μm) 2. Isocratic 3. 0.6 mM EDTA, 2 mM TBAP, 2% (v/v) MeOH, pH=6.9 4. EDTA	1. 1.0 2. Ambient 3. 100 4. i. 1.90 ii. 3.10 iii. 4.00	1. i. ^{52}Cr: 0.063; ^{53}Cr: 0.117 ii. ^{52}Cr: 0.061; ^{53}Cr: 0.115 2. ^{52}Cr: <2 (ST) for 1 μg L^{-1}, for Cr species i. 90.9–95.3 ii. 89.6–109.8	[3]
14	1. Cr(III), Cr(VI) 2. Tap water	1. No data, glass HPLC vials 2. No data 3. No data	1. Reverse phase: 3CR C8 PerkinElmer (4.6 mm × 33 mm, 3 μm) 2. Isocratic 3. 1 mM TBAH, 0.6 mM EDTA, 2% MeOH, pH=6.9 4. EDTA	1. 1.5 2. Ambient 3. 50 i. 1.15 ii. 1.80 iii. 3.00	1. i. 0.050 μg L^{-1} ii. 0.050 μg L^{-1} 2. No data 3. No data	[73]
15	1. Cr(III), Cr(VI), As (III), As(V) 2. Lake, river, municipal and bottled water	1. Polyethylene/ polypropylene bottles 2. No data 3. Without	1. Reverse phase: Pecosphere C8 PerkinElmer (30 mm, 3 μm) 2. Isocratic 3. 1.0 mM TBAH, 0.5 mM EDTA, 5% MeOH, pH=7.2 4. EDTA	1. 1.5 2. No data 3. 50 i. 1.10 ii. 1.80 iii. 2.50	1. No data 2. No data 3. No data	[71]
16	1. Cr(III), Cr(VI) 2. Mineral and spring water	1. No data 2. No data 3. No data	1. Reverse phase: Hypersil GOLD™ Thermo (4.6 mm × 150 mm, 5 μm) 2. Isocratic 3. 0.25 mM TBAP, mM EDTA, pH=6.9 4. EDTA	1. 0.8 2. No data 3. 50 and 200 i. 3.58 ii. 4.33 iii. No data	1. i. 0.039 (I^c – 50 μL) 0.017 (I – 200 μL) ii. 0.017 (I – 50 μL) 0.009 (I – 200 μL) 2. No data i. 90–110 ii. 98–106	[68]
17	1. Cr(III), Cr(VI) 2. Natural water	1. No data, glass HPLC vials 2. Cooling (10), 10 (AT) 3. Without	1. Reverse phase: 3CR C8 PerkinElmer (4.6 mm × 33 mm, 3 μm) 2. Isocratic 3. 2.0 mM TBAH, 0.5 mM EDTA, 5% (v/v) MeOH, pH=7.6 4. EDTA	1. 1.5 2. 35 i. 50 ii. 1.10 iii. 1.70 iv. 2.00	1. i. 0.09 ii. 0.06 2. 3 for 2 μg L^{-1}, for Cr species i. 107.0–138.8 ii. 55.2–108.5	[12]

Table 3 (*continued*)

No.	Sample	Sample storage and preservation conditions	Chromatographic separation	HPLC operating conditions	Validation characteristics[a]	References
18	1. Cr(III), Cr(VI) 2. Sediment and porewater	1. Polyethylene bottles 2. Cooling (4) 3. Without	1. Reverse phase: 3CR C8 PerkinElmer (4.6 mm × 33 mm, 3 μm) 2. Isocratic 3. 2.0 mM TBAH, 0.6 mM EDTA, pH=6.9-7.0 4. EDTA	1. 1.5 2. No data 3. 50 i. 0.90 ii. 1.25 iii. No data	1. *LOQ*[c]: 0.30–0.50 for Cr species 2. No data 3. No data	[50]
19	1. Cr(III), Cr(VI) 2. Human urine	1. Polyethylene bottles 2. Freezing (-80) 3. Without	1. Reverse phase: PRP-1 Hamilton, (4.6 mm × 150 mm, 5μm) 2. Isocratic 3. 2.0 mM TEAH, pH=3.5 4. EDTA	1. 1.5 2. Ambient 3. 100 i. 1.09 ii. 2.02 iii. 4.00	1. 0.03 for Cr species 2. No data ii. 94.8–105	[28]
20	1. Cr(III), Cr(VI) 2. Tap water	1. Polyethylene bottles, glass HPLC vials 2. Freezing, Peltier-cooled autosampler tray 3. No data	1. Reverse phase: 3CR C8 PerkinElmer (4.6 mm × 33 mm, 3 μm) 2. Isocratic 3. 0.8 mM TBAH, 0.6 mM EDTA, pH=6.9 4. EDTA	1. 1.2 2. 25 3. 50 i. 1.42 ii. 1.92 iii. 3.00	1. i. 0.094 ii. 0.10 2. for 2 μg L^{-1} i. 1.5 (ST) 3.4 (LT) ii. 1.6 (ST) 3.5 (LT) iii. 100–115 iv. 93–106	[72]

[a] The parameters typically found in the reviewed articles.
[b] Determination of ^{52}Cr, unless otherwise stated.
[c] *R* – mass resolution; HP – hot plasma conditions; CP – cool plasma conditions; ST – short-term precision; LT – long-term precision; RT – retention time; PA – peak area; PH – peak height; AT – autosampler temperature; *LOQ* – limit of quantification; *I* – injection volume; in the 2nd option – two ways of chromium species determination were performed without and with EDTA, in the first and the second analysis, respectively.

most common interferences in total chromium determination at m/z^+ 52 by ICP-MS. Even though it is cost-effective, taking into consideration all the interfering ions is not an easy task, especially in complicated matrices [69]. This is probably the reason why mathematical equations were less popular as solutions in the reviewed papers.

Another way to avoid polyatomic interferences is the optimization of chromatographic separations, especially in the case of ion exchange chromatography because it enables interfering ions to be isolated from chromium species. Chlorides were not applied as components of mobile phases in order to reduce chlorine-based spectral interferences. Different solutions with high ionic strength such as NH_4NO_3, $NH_4H_2PO_4$ and EDTA were often used for the Cr(III) and Cr(VI) elution [53,74,75]. However, the presence of the above-mentioned reagents in mobile phases causes an instrumental instability of ICP-MS which can be decreased by using diluted HNO_3 [4]. Additionally, Gürleyük and Wallschläger as well as Séby et al. reported that a separation between the chromium species and carbon- or sulfur-based polyatomic interferences is achievable [4,74]. Effective elimination of $^{40}Ar^{12}C^+$, which co-elutes with Cr (VI), was also performed under cool plasma conditions. In contrast, the $^{35}Cl^{16}O^1H^+$, which interferes with the determination of Cr(III), was not reduced [54]. However, those spectral interferences generated by carbonate and chloride ions were separated with a high resolution ICP-MS instrument; unfortunately, its main disadvantage is a significant loss in sensitivity [54,52,76,77].

4. Speciation analysis of chromium by HPLC/ICP-MS

HPLC/ICP-MS technique enables speciation analysis of chromium at very low concentration levels. It may be achieved by involving the DRC mode, which significantly decreases the background signal. The quality of separation is provided by selection of the mobile and stationary phase. Using HPLC/ICP-MS online system chromium speciation analysis takes only several minutes. Additionally, the measurement consumes very little sample volume and usually requires minimal sample pretreatment. More detailed information about this online method applied for chromium speciation is given in Table 3, which contains data from papers concerning Cr speciation in water samples published since 2000. The data include: (i) type of sample, its storage and preservation conditions; (ii) parameters of the separation process; (iii) HPLC operation conditions and (iv) figures of merit.

5. Metrological approach to measurement

The authors would like to emphasize the importance of chemical metrology in the analytical process. The metrological approach has been introduced by international organizations such as the ISO or BIPM through numerous documents, standards and guidelines describing the analytical processes in detail and providing an opportunity to compare measurement results worldwide. Three main concepts need to be taken into consideration while discussing the metrological approach, namely: (i) analytical validation; (ii) metrological traceability and (iii) uncertainty of the measurement result. Unfortunately, the above mentioned aspects are not always presented in all of the papers. The last column in Table 3 contains the validation parameters from articles regarding Cr speciation, namely the limit of detection (*LOD*), precision and recovery. The validity of methods and procedures used for Cr speciation in water samples, industrial processes brines, waste waters and human urine has been tested by various authors.

A description and commentary of method validation (linearity, *LOD*, limit of quantification (*LOQ*), precision and trueness), traceability and uncertainty of measurement result is presented below.

5.1. Method validation

5.1.1. Linearity

Linear range is a range of concentrations in which the output signal from the detector is linearly correlated with the concentration of the analyte in standard solutions. The HPLC/ICP-MS technique allows a wide range of linearity to be achieved. The presented papers show the linear calibration range up to 4 or 5 orders of magnitude: 1 $\mu g\,L^{-1}$–1000 $\mu g\,L^{-1}$ and 0.1 $\mu g\,L^{-1}$–1000 $\mu g\,L^{-1}$, respectively [32,78]. The lowest concentrations were chosen by Sakai et al., (0.05 $\mu g\,L^{-1}$–1.0 $\mu g\,L^{-1}$), Chang and Jiang as well as Neubauer et al. (0.1 $\mu g\,L^{-1}$–10 $\mu g\,L^{-1}$) and Tsoi and Leung (0.1 $\mu g\,L^{-1}$–100 $\mu g\,L^{-1}$), in contrast, the highest were chosen by Gürleyük and Wallschläger (50 $\mu g\,L^{-1}$–5000 $\mu g\,L^{-1}$) and Chen et al., (1 $\mu g\,L^{-1}$–1000 $\mu g\,L^{-1}$) [3,32,67,70,71,74]. For the majority of calibration graphs the correlation coefficients were very good, usually up to 0.999 and higher.

5.1.2. LOD and LOQ

One of the most important parameters in the speciation analysis is *LOD*. It is defined as the concentration or amount of analyte which can be reliably determined with a given level of confidence. In general, the most popular method of *LOD* estimation is 3 times standard deviation (*SD*) of a certain analytical response, specifically: (i) 3 times *SD* of blank [68,78], (ii) 3 times *S/N* ratio [32,53,67,71,75], 3 times *SD* of the background signal [3,54,74] and 3 times *SD* of a low level analyte sample [70]. Barałkiewicz et al. presented three approaches to *LOD* estimation which are: the modified blank determination method, the graphical method and linear regression method [72]. The above methods; 3 times *SD*, 3 times *S/N* and 3 times of the background signal; do not take into consideration the influence of the parameters of the calibration curve, namely the slope, interception and their errors. Also, usually little is known about the number of replicates of samples or blank used for estimating *LOD*. A knowledge of these factors is important for the selection of an appropriate *LOD* estimation approach. Methods relying on 3 times *SD* of blank or *S/N* determine the ability of the apparatus or detector to recognize the analyte on the lowest possible level. Measurements are usually carried out using blank samples or calibration standards without matrix. The *LOD* estimated by such methods is called the instrumental detection limit. Another type of *LOD* is the method detection limit where the lowest analyte level is determined in real samples and includes the possible effects caused by matrix and interferences, besides instrumental noise. It is crucial to remember to always present the *LOD* value with a description of method and numbers of replicates used for its estimation in order to compare it with different research [79].

The *LOD* values presented in the reviewed papers vary to a great extent in the range 0.005 $\mu g\,L^{-1}$–1.5 $\mu g\,L^{-1}$ with the most common values being around 0.04 $\mu g\,L^{-1}$–0.4 $\mu g\,L^{-1}$. Vanhaecke et al. calculated *LOD* for different detector conditions [54]. The application of cool plasma conditions or increasing resolution to $R=3000$ cause the *LOD* at m/z^+ 52 to decrease slightly and at m/z^+ 53 cause a slight increase. The authors of the papers presented in Table 3 obtained higher *LOD* values at m/z^+ 53 than at m/z^+ 52 due to much lower ^{53}Cr isotope abundance [3,4,44,54,74]. A smaller volume of injected sample generates higher *LOD*, a similar effect is observed in precision values [68]. Application of DRC/MCC technology enables the background count rate to decrease significantly, which translates to the lower *LOD* values [12,70].

The *LOQ* is usually omitted in papers, however, several authors have presented it as either an *LOQ* or a practical quantification limit (*PQL*). McSheehy et al. and Burbridge et al. calculated *LOQ* as 10 times the *SD* of the blank while Barałkiewicz et al. used 3 times the *LOD* [68,72,78]. To calculate *PQL*, Wolf et al. measured several samples with low concentrations until the result was within the $\pm$ 20% of the true concentration value [12].

5.1.3. Precision

Precision is a parameter describing the spread of values obtained by performing repeated analysis of a sample. Depending on the time period that separates subsequent analysis, there is repeatability, an analysis performed during one day and intermediate precision, one over the course of several days or longer. Precision is usually presented as *SD* or relative standard deviation (*RSD*). The values of *RSD* for both Cr species ranged from 0.6% to 12% with the most frequent values lying between 1.5% and 3.6% in the papers presented in Table 3. Precision should be stated with the number of replicates, which was not always the case in the reviewed articles. Several authors have evaluated the intermediate precision by analyzing samples over three different days which resulted in a more than two-fold higher long-time precision value compared to short-time precision [72,75]. Chang and Jiang have shown that there is no significant difference in the precision between the standard and DRC mode [3]. It is also noticeable that higher concentrations of analyte contribute to better precision values [75].

5.1.4. Trueness

To confirm if the obtained result is in accordance with the true value the trueness is determined. In the reviewed papers this was achieved by calculating recoveries of real samples spiked with a known amount of analyte. The lowest and highest recoveries for all Cr species are 0% and 180%. Such extremely low and high values are considered unacceptable and are probably due to interconversions of Cr species in the presence of Mn, Fe, sulfides or organic carbon such as humic substances, plant exudates as well as heat treatment of the samples [12,78]. Most of the recoveries fall within the range of 90%–110% which is generally considered as very good, as presented in Table 3. The values that are usually acceptable are 75%–125% [72]. By assessing the recoveries one can determine whether the sample matrix, container material or eluent could cause conversions of Cr species in the sample. Seby et al. has noticed that low recoveries of Cr(III) can be explained by its precipitation as $Cr(OH)_3$ in an alkaline medium [4].

5.2. Traceability of measurement result

Traceability is a property of a measurement result whereby the result of the measurement can be related to a reference through a documented unbroken chain of calibrations, each contributing to the measurement uncertainty [80]. One of the best ways to establish traceability is to apply CRM. Unfortunately, there are no appropriate CRMs that possess the specified species concentration that would match the matrix of the samples. Usually CRMs are certified for total chromium concentration without distinguishing for Cr(III) and Cr(VI). BCR CRM 544 was one of the few CRMs with certified Cr(III) and Cr(VI) content available in the past and applied for Cr speciation in surface waters [4,68,81]. Currently no CRM with certified concentration values of Cr(III) and Cr(VI) forms is available due to difficulties with maintaining the stability of Cr species, which is the most important property of CRMs.

One way to overcome the lack of CRMs is to spike the real samples with a known amount of Cr species. This method is widely applied in speciation analysis [53,82–84]. The result is then compared to the unspiked sample value and presented as the recovery. One must keep in mind that standard spiking is not a fully metrologically accepted method of establishing traceability in measurements. SIDMS has been

Table 4
SIDMS for determination of Cr(III) and Cr(VI) in water.

No.	Sample 1. Species/ isotope ratio 2. Matrix	Preparation of isotopic spike solutions 1. Cr(III) 2. Cr(VI)	Technique separation, detection and interference elimination	Optimization of ICP-MS for ID measurements	Concentration	Figures of merit	References
1	1. ^{50}Cr(III), ^{53}Cr (VI); Four isotope ratios: ($^{50}Cr/^{52}Cr$) for Cr(III) and Cr (VI), ($^{53}Cr/^{52}Cr$) for Cr(III) and Cr (VI) 2. Drinking, river and deionized water	1. ^{50}Cr-enriched spike (Isotec Inc. Lot # 2691) for ^{50}Cr(III); ^{50}Cr metal dissolved in HCl 2. ^{53}Cr-enriched spike (Isotec Inc. Lot # 2692) for ^{53}Cr(VI); ^{53}Cr oxide dissolved in hot $HClO_4$, followed by adjusting pH to 12 with concentrated NH_4OH and oxidizing with H_2O_2	ANX4605Cr anion exchange column (CETAC Tech.) coupled to a VG PlasmaQuad system (Fisons) Interference elimination: $^{40}Ar^{12}C^+$ to ^{52}Cr by subtracting background from sample spectrum; no other isobaric interferences were observed	Dead time – daily optimization Mass discrimination – every 4 h Dead time and mass discrimination factors were optimized with use natural isotopic abundance Cr standard SRM 979	Cr(III): $<$ *LOD* in all matrices Cr(VI): (0.52–51.1) ng g^{-1} for river water (1.31–46.5) ng g^{-1} for drinking water ($<$ *LOD*–42.5) ng g^{-1} for deionized water	*LOD*: 0.21 ng g^{-1} for Cr(III) 0.37 ng g^{-1} for Cr(VI)	[91]
2	1. ^{50}Cr(III), ^{53}Cr (VI); Two isotope ratios: ($^{50}Cr/^{52}Cr$) for Cr(III), ($^{53}Cr/^{52}Cr$) for Cr(VI) 2. Ground and surface water	1. No data 2. No data	ANX4605Cr anion exchange column (CETAC Tech.) coupled to a VG PlasmaQuad 3 ICP-MS (ThermoElemental)	No data	Cr(III): ($<$ 0.01–5.8) mg L^{-1} for ground water (0.10–0.13) mg L^{-1} for surface water Cr (VI): ($<$ 0.01–95.2) mg L^{-1} for ground water (1.32–1.70) mg L^{-1} for surface water	*LOD*: 0.01 mg L^{-1} for each species Precision: $\pm$ 1% (for 50 mg L^{-1}) $<\pm$ 10% (for 5 mg L^{-1})	[94]
3	1. ^{50}Cr(III), ^{53}Cr (VI); Four isotope ratios: ($^{50}Cr/^{52}Cr$) for Cr(III) and Cr (VI), ($^{53}Cr/^{52}Cr$) for Cr(III) and Cr (VI) 2. Local nullah spiked water samples	1. ^{50}Cr-enriched spike (Lot# I1-8991B) for ^{50}Cr(III); ^{50}Cr metal dissolved in HCl, the solution was gently heated without boiling 2. ^{53}Cr-enriched spike (Lot# I1-8991A) for ^{53}Cr(VI); ^{53}Cr oxide dissolved in $HClO_4$, the solution was gently heated without boiling, then it was oxidizing by NH_4OH and H_2O_2; the excess of the last one was removed by boiling for 30 min.	Species separation: iron hydroxide co-precipitation Detection: Elan 6100 DRC-ICP-MS system (PerkinElmer SCIEX) Interference elimination:– DRC technology: *Rpq*=0.45; *Rpa*=0.0	Dead time – 50 ns Mass discrimination – correction factor K: ^{50}Cr – 1.08; ^{53}Cr – 0.96 Dead time and mass discrimination factors were optimized with use natural isotopic abundance Cr standard SRM 979	Cr(III): S[a]: (5.2–103.3) μg L^{-1}, M[a]: (5.2–97.8) μg L^{-1} Cr(VI): S[a]: (5.4–103.2) μg L^{-1}, M[a]: (6.2–106.6) μg L^{-1}	*LOD*: 0.4 μg L^{-1} for Cr(III) 0.04 μg L^{-1} for Cr(VI) Recovery: 90.7–97.9 for Cr(III) 101.4–107.3 for Cr(VI)	[64]

[a] *S* – spike concentration [μg L^{-1}] and *M* – measured concentration [μg L^{-1}].

effectively used for Cr speciation. As a definitive measurement method, the SIDMS provides the highest quality of metrological traceability. This issue is described more extensively in Section 6.

5.3. Estimation of uncertainty budget

Uncertainty is one of the most important parameters to prove the usefulness and reliability of the analytical method. It is defined by the limits around the obtained analytical result where the true value can be found with a given level of confidence. Depending on the method, uncertainty is calculated using numerous components of the analytical process, parameters connected with preparation of the sample and the measurement itself. There are several approaches to assess uncertainty, two of them are applied by Barałkiewicz et al. [72], namely, the modeling approach and the single-laboratory validation approach. The uncertainties presented in papers from Table 3 are based only on standard deviation of repeated measurements of sample, which is called instrumental uncertainty [3,4,12,32,53,67,74,75,78].

6. Speciated isotope dilution ICP-MS as a definitive method for determining chromium species

The combination of two analytical tools: HPLC with ICP-MS in recent years has played an important role in the characterization of element species. These techniques working as an online coupled system enable the isotope dilution technique to be applied. SIDMS allows a highly accurate and precise determination of numerous elemental forms including Cr species in various sample matrices [37,39,41,84,86]. For IDMS analysis, accurate and precise results can be obtained by using the isotope ratio of the isotope-diluted sample for determining the analyte concentration, rather than the absolute intensity measurement [87]. The principle of this method relies on the alteration of natural isotopic abundances of an endogenous form of an analyte by the addition of an accurately known amount of an enriched isotopic spike [76,88–90]. According to data from the literature, the optimum performance of the IDMS analysis is usually achieved by using the isotope ratio of the isotope-diluted sample in a range of 0.1–10 [85,89]. However, it is

recommended that the isotope ratio of added enriched spike to the reference isotope (analyte naturally occurring in the sample) should be 1:1 [88,91,92]. Considering that IDMS determinations are based on an isotope ratio measurement, at least two isotopes must remain free from spectral interferences. Therefore, particular care should be taken with regard to the ICP-IDMS analysis because, as mentioned previously, the problem of interferences is present and thus they might disturb the obtained results [85,90]. In order to obtain unbiased chromium isotope ratio measurements in water samples DRC technology was used (Table 4). Additionally, optimization of a detector dead time and mass discrimination factors have to be performed to get accurate and precise results.

The application of multiple spiking procedures enables detection of the species transformations that may occur at every step of the analytical process, during sampling, storage, sample preparation and measurement. This means that the original concentrations of different species in a sample can be accurately determined, which cannot be achieved by any other analytical method [64,91]. Species interconversions in environmental matrices commonly found during sample pretreatment are a large problem in trace and ultra-trace element speciation. For this reason, the isotope-dilution step should take place before Cr(III)–Cr(VI) transformations, so potential loss of part of an analyte of the isotope-diluted sample will not have any influence on the final result because the isotope ratio of the sample will remain constant [87,89,90].

The prerequisite for accurate results using IDMS is to achieve effective equilibrium between the added enriched isotopic spike and the natural abundant species in the sample [92]. In the case of total element analysis, fulfillment of the foregoing condition is easier as only the equilibration of the spike with all determined species of the analyte is necessary, whereas in element speciation performed by SIDMS it is required that no species interconversion occurs prior to their complete separation [85].

Comparing quantification strategies including the isotope dilution technique, external calibration or standard additions, it can be observed that only the first takes no account of instrumental sensitivity. Consequently, the isotope ratio measurement is largely unaffected by instrumental instabilities such as signal drift or matrix effects and therefore the instabilities will have no impact on the species concentration in a sample [87,88]. The basis of the isotope dilution technique and general equations for determination of the species concentration are detailed in overall reviews as well as in the US EPA method 6800 [85,90,93].

In world literature, there are relatively few articles concerning SIDMS of chromium in water samples [64,91,94]. The first work to consider SIDMS in application to chromium species determination was published in 1998 [91]. The authors described the first standard method for environmental measurements and outlined the general procedures for SIDMS application in an analysis of drinking water, river water and deionized water samples. Simultaneously, they indicated the potential that SIDMS could offer as a diagnostic tool for the validation of other methods of speciation analysis. The second group took on similar research determined chromium species in ground and surface waters in the vicinity of chromite ore processing residue disposal sites [94]. The results obtained by those authors showed that Cr was present predominantly ($>90\%$) in a hexavalent form as CrO_4^{2-}. In turn, Ma and Tanner developed an IDMS method for determining Cr(III) and Cr(VI) in natural waters (local nullah spiked water samples) [64]. They described an approach that, allowed chromium species to be determined without any need for a separation instrument connected to an ICP-MS spectrometer. In this work DRC, with ammonia as a reaction gas, was involved in the elimination of interferences. The applications of SIDMS for determining chromium species in water matrices are presented in Table 4 together with details concerning isotopic spikes, their preparation, analytical techniques used, optimization of ICP-MS parameters for ID measurements, determined concentration levels and figures of merit.

At this point the significance of the adequate preparation of Cr isotopic spike solutions must be emphasized. It should be remembered that a thorough preparation process is the most important step in the analytical procedure. Different approaches to isotopic spike solution preparation were widely commented by Novotnik et al. [95]. The authors pointed out the risk, which in the previously reported procedures may arise depending on the excess of H_2O_2 remains. The pe-pH relationships of $CrO_4^{2-}/Cr(OH)_3$ and O_2/H_2O_2 couples show that H_2O_2 is an oxidant of Cr(III) at $pH > 7.5$; while, at lower pH values, it becomes a reductant and in this condition its strength as a reductant strongly increases [96]. Hence, H_2O_2 is used as an oxidizing and/or reducing agent in the preparation process of chromium spike solutions. However, if H_2O_2 residues are still present in the solution it can cause artefacts in chromium speciation [95]. In order to be sure that no excess of the reducing oxidizing agents remain in the prepared solution, Novotnik et al. developed a new procedure involving alkaline melting of $^{50}Cr(III)$ enriched oxide for the preparation of pure $^{50}Cr(VI)$ spike solution. No other oxidizing agents except air oxygen were used for quantitative oxidation of Cr(III)–Cr(VI). Cr(III) was quantitatively oxidized to Cr(VI) with air oxygen without applying any other oxidizing agents. Furthermore, the authors suggested that a microwave assisted digestion procedure of ^{53}Cr enriched oxide could be used in order to prepare $^{53}Cr(III)$ spike solution without any need for reducing agents. FPLC coupled with ICP-MS was used to examine the purity of $^{50}Cr(VI)$ and $^{53}Cr(III)$ spike solutions [95].

Therefore, in spite of difficulties with spectral interferences affecting the measured Cr isotopes as well as those connected with the preparation of isotopic spike solutions, SIDMS offers the highest accuracy and precision, hence it can be considered as a reference or the highly qualified definitive method for element speciation analysis [86].

7. Conclusion

How is the issue of chromium speciation presented in the literature published since 2000?

Trace speciation of chromium is a topic of considerable importance due to great differences in the biochemical behavior of its single chemical forms. Chromium is an excellent example of an element whose species present opposite effects: Cr(III) is essential for living organisms, while Cr(VI) is considered toxic. To date researchers have described many analytical aspects concerning the speciation analysis of chromium in water matrices by HPLC/ICP-MS, especially in terms of the development of new procedures, improving existing ones as well as dealing with the problem of eliminating the interferences accompanying chromium species determination.

What are the outlooks?

Currently, we have to provide mathematically proven competent results of chromium species determination. Such results are essential in health protection and doping control, radiochemistry, trace analysis of toxic elements in the environment, food and materials, as well as in verification of the purity of products. We have no other alternative than to introduce metrology rules into chemical measurements, thus solving problems related to insufficient knowledge of the three basic metrological principles: validation of measurement procedure, establishing traceability and uncertainty of measurement results.

Nowadays the online HPLC/ICP-MS system has become commercially available and its purchase should be perceived as an investment. Additionally, using this hyphenated technique in combination with SIDMS offers a huge potential to establish the highest quality of metrological traceability. Such an attitude to scientific research on

speciation analysis, especially in chromium species determination in water, will broaden our knowledge, alter our points of view and show a new direction. Most of all, it will prove efficient in practice.

Acknowledgment

This work was financially supported by the Research Project of the Polish Ministry of Science and Higher Education, MNiSzW N N204 140439.

References

[1] I. Komorowicz, D. Barałkiewicz, Talanta 84 (2011) 247–261.
[2] J. Kotaś, Z. Stasicka, Environ. Pollut. 107 (2000) 263–283.
[3] Y.L. Chang, S.J. Jiang, J. Anal. At. Spectrom. 16 (2001) 858–862.
[4] F. Séby, S. Charles, M. Gagean, H. Garraud, O.F.X. Donard, J. Anal. At. Spectrom. 18 (2003) 1386–1390.
[5] P. Hoet, in: R. Cornelis, H. Crews, J. Caruso, K.G. Heumann (Eds.), Food, Medicine and Occupational Health, John Wiley & Sons Ltd., New York, 2005, pp. 136–154.
[6] C. Oze, D.K. Bird, S. Fendorf, PNAS 104 (2007) 6544–6549.
[7] F.T. Stanin, M. Pirnie, in: J. Guertin, J.A. Jacobs, C.P. Avakian (Eds.), Chromium (VI) Handbook, CRC Press, Florida, 2004, pp. 163–204.
[8] D. Metze, N. Jakubowski, D. Klockow, in: R. Cornelis, H. Crews, J. Caruso, K.G. Heumann (Eds.), Food, Medicine and Occupational Health, John Wiley & Sons Ltd., New York, 2005, pp. 120–134.
[9] N. Unceta, F. Séby, J. Malherbe, O.F.X. Donard, Anal. Bioanal. Chem. 397 (2010) 1097–1111.
[10] B. Dhal, H.N. Thatoi, N.N. Das, B.D. Pandey, J. Hazard. Mater. 250–251 (2013) 272–291.
[11] A.P. Vonderheide, J. Meija, K. Tepperman, A. Puga, A.R. Pinhas, J.C. States, J.A. Caruso, J. Chromatogr. A 1024 (2004) 129–137.
[12] R.E. Wolf, J.M. Morrison, M.B. Goldhaber, J. Anal. At. Spectrom. 22 (2007) 1051–1060.
[13] Inorganic chromium(III) compounds, Concise International Chemical Assessment Document 76, WHO, England, 2009.
[14] M. Sugiyama, Environ. Health Perspect. 92 (1991) 63–70.
[15] M.J. Tomlinson, L. Lin, J.A. Caruso, Analyst 120 (1995) 583–589.
[16] J.A. Caruso, M. Montes-Bayon, Ecotoxicol. Environ. Safe. 56 (2003) 148–163.
[17] C.A.P. de Leon, M. Montes-Bayon, J.A. Caruso, J. Chromatogr. A 974 (2002) 1–21.
[18] Guidelines for drinking water quality, third ed., vol. 1, Recommendations, WHO, Geneva, 2008.
[19] Council directive of 3 November 1998 on the quality of water intended for human consumption, Official Journal of European Communities, L 330/32,5.12/98.
[20] US EPA (United States Environmental Protection Agency), Edition of the Drinking Water Standards and Health Advisories, EPA 882-R-04-005, Office of Water U.S. Environmental Protection Agency, Washington, DC, Winter, 2004.
[21] A.K. Das, M. de la Guardia, M.L. Cervera, Talanta 55 (2001) 1–28.
[22] K.A. Francesconi, M. Sperling, Analyst 130 (2005) 998–1001.
[23] R.J. Bartlett, Environ. Health Perspect. 92 (1991) 17–24.
[24] A.M. Zayed, N. Terry, Plant Soil 249 (2003) 139–156.
[25] D.M. Stearns, J.P. Wise Sr, S.R. Patierno, K.E. Wetterhahn, FASEB. J. 9 (1995) 1643–1648.
[26] S. Ueno, N. Susa, Y. Furukawa, M. Sugiyama, Toxicol. Appl. Pharmacol. 135 (1995) 165–171.
[27] G. Kim, E.J. Yurkow, Cancer Res. 56 (1996) 2045–2051.
[28] H.J. Wang, X.M. Du, M. Wang, T.C. Wang, H. Ou-Yang, B. Wang, M.T. Zhu, Y. Wang, G. Jia, W.Y. Feng, Talanta 81 (2010) 1856–1860.
[29] M. Costa, Toxicol. Appl. Pharmacol. 188 (2003) 1–5.
[30] J. Ščančar, R. Milačič, F. Séby, O.F.X. Donard, J. Anal. At. Spectrom. 20 (2005) 871–875.
[31] A.M. Yusof, C.H. Chia, A.K.H. Wood, J. Radioanal. Nucl. Chem. 273 (2007) 533–538.
[32] Z.L. Chen, M. Megharaj, R. Naidu, Talanta 72 (2007) 394–400.
[33] V. Gómez, M.P. Callao, Trends Anal. Chem. 25 (2006) 1006–1015.
[34] C.H. Collins, S.H. Pezzin, J.F.L. Rivera, P.S. Bonato, C.C. Windmöller, C. Archundia, K.E. Collins, J. Chromatogr. A 789 (1997) 469–478.
[35] C. Sarzanini, E. Mentasti, J. Chromatogr. A 789 (1997) 301–321.
[36] K. Fytianos, J. AOAC Int. 84 (6) (2001) 1763–1769.
[37] M. Popp, S. Hann, G. Koellensperger, Anal. Chim. Acta 668 (2010) 114–129.
[38] M. Shoaib, H.M. Al-Swaidan, J. Chem. Soc. Pak. 34 (6) (2012) 1585–1593.
[39] R. Rakhunde, L. Deshpande, H.D. Juneja, Crit. Rev. Environ. Sci. Technol. 42 (2012) 776–810.
[40] M.J. Marqués, A. Salvador, A. Morales-Rubio, Fresenius J. Anal. Chem. 367 (2000) 601–613.
[41] J. Ščančar, R. Milačič, J. Anal. At. Spectrom. 29 (2014) 427–443.
[42] A.D. Apte, V. Tare, P. Bose, J. Hazard. Mater. B128 (2006) 164–174.
[43] D.E. Kimbrough, Y. Cohen, A.M. Winer, L. Creelman, C. Mabuni, Environ. Sci. Technol. 29 (1999) 1–46.
[44] A.J. Bednar, R.A. Kirgan, W.T. Jones, Anal. Chim. Acta 632 (2009) 27–34.
[45] A. Bielicka, I. Bojanowska, A. Wiśniewski, Pol. J. Environ. Stud. 14 (2005) 5–10.
[46] T. Zuliani, J. Ščančar, R. Milačič, Anal. Bioanal. Chem. 405 (2013) 7231–7240.
[47] Chromium in drinking water, Background document for development of WHO Guidelines for Drinking water Quality, WHO/SDE/WSH/03.04/4, WHO, Geneva, 2003.
[48] R. Świetlik, Pol. J. Environ. Stud. 7 (1998) 257–266.
[49] R.F.J. Dams, J. Goossens, L. Moens, Mikrochim. Acta 119 (1995) 277–286.
[50] A.M. Graham, A.R. Wadhawan, E.J. Bouwer, Environ. Toxicol. Chem. 28 (2009) 471–480.
[51] USEPA, Method 200.8, Rev. 5.4, US Environmental Protection Agency, 1994.
[52] Guidelines for sampling, transport, storage and chemical characterisation of environmental and human samples, vol. 2.1.0, German Environmental Specimen Bank, 2011.
[53] Z.L. Chen, M. Megharaj, R. Naidu, Talanta 73 (2007) 948–952.
[54] F. Vanhaecke, S. Saverwyns, G. De Wannemacker, L. Moens, R. Dams, Anal. Chim. Acta 419 (2000) 55–64.
[55] F. Laborda, M.P. Górriz, E. Bolea, J.R. Castillo, Spectrochim. Acta Part B 61 (2006) 433–437.
[56] S.D. Tanner, V.I. Baranov, At. Spectrosc. 20 (2) (1999) 45–52.
[57] E.R. Denoyer, S.D. Tanner, U. Völlkopf, Spectroscopy 14 (2) (1999) 43–54.
[58] K. Neubauer, U. Völlkopf, At. Spectrosc. 20 (2) (1999) 64–68.
[59] D.E. Nixon, K.R. Neubauer, S.J. Eckdahl, J.A. Butz, M.F. Burritt, Spectrochim. Acta Part B 57 (2002) 951–966.
[60] S.D. Tanner, V.I. Baranov, in: G. Holland, S.D. Tanner (Eds.), Plasma Source Mass Spectrometry: New Developments and Applications, Royal Society of Chemistry, Cambridge, 1997, pp. 46–62.
[61] U. Völlkopf, V. Baranov, S.D. Tanner, in: G. Holland, S.D. Tanner (Eds.), Plasma Source Mass Spectrometry: New Developments and Applications, Royal Society of Chemistry, Cambridge, 1997, pp. 63–79.
[62] S.D. Tanner, V.I. Baranov, J. Am. Soc. Mass Spectrom. 10 (1999) 1083–1094.
[63] S.D. Tanner, V.I. Baranov, U. Völlkopf, J. Anal. At. Spectrom. 15 (2000) 1261–1269.
[64] H.L. Ma, P.A. Tanner, Talanta 77 (2008) 189–194.
[65] R. Thomas, A beginner's guide for ICP-MS, Spectroscopy tutorial. Online available at: ⟨http://matematicas.udea.edu.co/~carlopez/beginer_guide_icpms.pdf⟩.
[66] Agilent brochure, Collision/Reaction Cells in ICP-MS, 2010. Online available at: ⟨https://www.chem.agilent.com/Library/articlereprints/Public/5990_5955EN%20HR.pdf⟩.
[67] T. Sakai, E. McCurdy, S. Wilbur, Agil. Appl. Note, 2005.
[68] S. McSheehy, F. Seby, M. Nash, Thermo Appl. Note 40837 (2006).
[69] L. Xing, D. Beauchemin, J. Anal. At. Spectrom. 25 (2010) 1046–1055.
[70] Y.K. Tsoi, K.S.Y. Leung, J. Anal. At. Spectrom. 25 (2010) 880–885.
[71] K.R. Neubauer, W.M. Reuter, P.A. Perrone, Z.A. Grosser, PerkinElmer Appl. Note, 2004.
[72] D. Barałkiewicz, B. Pikosz, M. Belter, M. Marcinkowska, Accredit. Qual. Assur. 18 (2013) 391–401.
[73] K. Neubauer, W. Reuter, P. Perrone, PerkinElmer Appl. Note, 2003.
[74] H. Gürleyük, D. Wallschläger, J. Anal. At. Spectrom. 16 (2001) 926–930.
[75] Y. Martínez-Bravo, A.F. Roig-Navarro, F.J. López, F. Hernández, J. Chromatogr. A 926 (2001) 265–274.
[76] L. Yang, E. Ciceri, Z. Mester, R.E. Sturgeon, Anal. Bioanal. Chem. 386 (2006) 1673–1680.
[77] S.-H. Nam, Y.-I. Park, J.-J. Kim, S.-H. Han, W.-H. Kim, Bull. Korean Chem. Soc. 25 (4) (2004) 447–451.
[78] D.J. Burbridge, I. Koch, J. Zhang, K.J. Reimer, Chemosphere 89 (2012) 838–843.
[79] M. Belter, A. Sajnóg, D. Barałkiewicz, Talanta 129 (2014) 606–616.
[80] JCGM 200:2012 International Vocabulary of Metrology – Basic and General Concepts and Associated Terms (VIM) 3rd edition. Online available at ⟨http://www.bipm.org/utils/common/documents/jcgm/JCGM_200_2012.pdf⟩.
[81] L. Ebdon, L. Pitts, R. Cornelis, H. Crews, O.F.X. Donard, P. Quevauviller, Trace Element Speciation for Environment, Food and Health, The Royal Society of Chemistry, Cambridge, 2001.
[82] I. Komorowicz, D. Barałkiewicz, Rapid Commun. Mass Spectrom. 28 (2014) 159–168.
[83] Q. Xie, R. Kerrich, E. Irving, K. Liber, F. Abou-Shakra, J. Anal. At. Spectrom. 17 (2002) 1037–1041.
[84] A. Castillo, A.F. Roig-Navarro, O.J. Pozo, J. Chromatogr. A 1202 (2008) 132–137.
[85] K.G. Heumann, Anal. Bioanal. Chem. 378 (2004) 318–329.
[86] P. Rodríguez-González, J.I. García Alonso, J. Anal. At. Spectrom. 25 (2010) 239–259.
[87] L. Yang, Z. Mester, R.E. Sturgeon, J. Anal. At. Spectrom. 17 (2002) 944–949.
[88] S.J. Hill, L.J. Pitts, A.S. Fisher, Trends Anal. Chem. 19 (2000) 120–126.
[89] A.G. Coedo, T. Dorado, I. Padilla, F.J. Alguacil, J. Anal. At. Spectrom. 15 (2000) 1564–1568.
[90] P. Rodríguez-González, J.M. Marchante-Gayón, J.I. García Alonso, A. Sanz-Medel, Spectrochim. Acta Part B 60 (2005) 151–207.
[91] H.M. Skip Kingston, D. Huo, Y. Lu, S. Chalk, Spectrochim. Acta Part B 53 (1998) 299–309.
[92] M. Monperrus, E. Krupp, D. Amouroux, O.F.X. Donard, R.C. Rodríguez Martín-Doimeadios, Trends Anal. Chem. 23 (2004) 261–272.
[93] USEPA, Method 6800, Elemental and speciated isotope dilution mass spectrometry, Test methods for evaluating solid waste, physical/chemical methods, SW 846, Update IVA, US Government Printing Office (GPO), Washington DC, 2007.

[94] J.G. Farmer, R.P. Thomas, M.C. Graham, J.S. Geelhoed, D.G. Lumdson, E. Paterson, J. Environ. Monit. 4 (2002) 235–243.
[95] B. Novotnik, T. Zuliani, A. Martinčič, J. Ščančar, R. Milačič, Talanta 99 (2012) 83–90.
[96] M. Pettine, L. Campanella, F.J. Millero, Environ. Sci. Technol. 36 (2002) 901–907.
[97] EN ISO 17294-2, Water quality – application of inductively coupled plasma mass spectrometry (ICP-MS). Part 2. Determination of 62 elements, 2004.
[98] T.W. May, R.H. Wiedmeyer, At. Spectrosc. 19 (5) (1998) 150–155.
[99] Isotopic compositions of the elements 1997, IUPAC (International Union of Pure and Applied Chemistry), Pure Appl. Chem. 70 (1) (1998) 217–235.

Talanta 132 (2015) 829–835

Contents lists available at ScienceDirect

Talanta

journal homepage: www.elsevier.com/locate/talanta

Short wavelength Raman spectroscopy applied to the discrimination and characterization of three cultivars of extra virgin olive oils in different maturation stages

Irene Gouvinhas [a,*,1], Nelson Machado [a,1], Teresa Carvalho [b], José M.M.M. de Almeida [c,d,1], Ana I.R.N.A. Barros [a,1]

[a] CITAB – CITAB, University of Trás-os-Montes and Alto Douro, 5001-801 Vila Real, Portugal
[b] Instituto Nacional de Investigação Agrária, (INIAL.P.), Elvas, Portugal
[c] Department of Physics, University of Trás-os-Montes and Alto Douro, 5000-801 Vila Real, Portugal
[d] INESC-TEC, Rua do Campo Alegre, 687, 4169-007 Porto, Portugal

ARTICLE INFO

Article history:
Received 11 June 2014
Received in revised form
14 October 2014
Accepted 18 October 2014
Available online 28 October 2014

Keywords:
Raman spectroscopy
Extra virgin olive oil
Maturation stages
Cultivars
Peroxide value
Acidity

ABSTRACT

Extra virgin olive oils produced from three cultivars on different maturation stages were characterized using Raman spectroscopy. Chemometric methods (principal component analysis, discriminant analysis, principal component regression and partial least squares regression) applied to Raman spectral data were utilized to evaluate and quantify the statistical differences between cultivars and their ripening process.

The models for predicting the peroxide value and free acidity of olive oils showed good calibration and prediction values and presented high coefficients of determination (>0.933). Both the R^2, and the correlation equations between the measured chemical parameters, and the values predicted by each approach are presented; these comprehend both PCR and PLS, used to assess SNV normalized Raman data, as well as first and second derivative of the spectra.

This study demonstrates that a combination of Raman spectroscopy with multivariate analysis methods can be useful to predict rapidly olive oil chemical characteristics during the maturation process.
© 2014 Elsevier B.V. All rights reserved.

1. Introduction

The quality of olive oil is influenced by a great number of factors, namely the nature of the cultivar and geographic origin [1], the fruit ripening degree [2,3], where important chemical changes occur, the irrigation regimes [2], the oil extraction technology and the storage of the oil [4] and agricultural practices [5]. Nutritional and sensory properties of extra virgin olive oils (EVOO) were also affected by these factors. Thus, the European Community (EC) Council of Regulation established standards on olive oil production regarding labeling giving the origin for virgin and extra virgin olive oils to avoid consumers being misled about their true characteristics and origin [6]. Some of the important quality parameters consist on peroxide value (PV) and free acidity (FA) determination [7]. However, these conventional measurements are time consuming and require large amounts of reagents and solvents, which are often toxic, besides being very expensive.

Infrared (IR), mainly Fourier Transform Infrared (FTIR), and Raman, are vibrational spectroscopic techniques widely used for food and feed analysis [8,9]. These optical spectroscopic methods provide information about the chemical composition of various food and biological materials, and molecular structure, without requiring large amount of samples or sample preparation and pre-treatments [10]. Furthermore, these techniques have a great potential due to their simplicity, rapidity, low-cost and reproducibility, besides being non-destructive [11].

Both techniques assess the same physical property – molecular vibrations – but present different selection rules. In one hand, the vibrational modes corresponding to a change in polarizability, such as the symmetrical vibrations of covalent bonds in the non-polar groups, (*e.g.* C=C bond stretching), give rise to intense Raman bands. While in the other hand, IR absorption is related to a change in the electrical dipole moment as the molecules vibrate, with the vibrational modes involving polar groups, such as C=O and O-H, showing intense infrared absorption bands [12]. Therefore, one of the major advantages of Raman spectroscopy is

* Corresponding author. Tel.: +351259350283; fax: +351259350480.
E-mail address: igouvinhas@utad.pt (I. Gouvinhas).
[1] www.utad.pt.

http://dx.doi.org/10.1016/j.talanta.2014.10.042
0039-9140/© 2014 Elsevier B.V. All rights reserved.

the almost negligible influence of water and carbon dioxide on Raman spectra, as opposed to IR absorption spectroscopy [13]. Additionally, as the infrared peaks are often broad, they tend to overlap, being rather difficult to found isolated or well-defined peaks, and these might be also influenced from the aforementioned atmospheric components, which display also broad peaks. This problem is overcome in Raman, where a spectrum is normally composed of isolated bands, besides the previously mentioned advantage of the insignificant contributions from atmospheric gases and water in the Raman spectra.

Furthermore, in Raman, if the excitation wavelength matches the electronic absorbance of a chemical system, its Raman signal will be enhanced by resonance, making this technique suitable for monitoring particular compounds, or properties related to specific constituents of a sample. Thus, Raman spectroscopy can provide useful qualitative and quantitative information on chemical composition of olive oils. For instance, El-Abassy et al. (2009) took advantage of the resonance phenomenon in carotenoids at 514.5 nm excitation, and their correlation with free fatty acid (FFA) content, to assess the FFA percent values in distinct EVOO´s using Raman spectroscopy. Actually, the concentrations of both FFA, and carotenoids, change during the ripening process, with an inversely proportional trend, therefore, the changes occurring in those bands corresponding to carotenoids, can be (indirectly) related to the variations in the FFA content [14].

In fact, in the last years, Raman spectroscopy combined with chemometric data analysis methods allowed researchers to determine the total unsaturation in oils [15], the FFA contents [14,16], to discriminate and classify oils [17], to detect oil adulteration [18], and to distinguish the ripening stages of olive fruit [19]. Additionally, the rapid spreading, and developments occurred, concerning portable Raman devices, which are nowadays available with a variety of excitation wavelengths (*e.g.* 1064, 785, 671 and 532 nm), widen the potential of this technique, that can be now used *In situ*, a major advantage regarding this kind of work.

However, to the best of our knowledge, no comprehensive study has been undertaken involving chemometric analyses of the Raman spectra, combined with analytical parameters (peroxide value and free acidity), to discriminate varietal origin of olive oil and different maturation stages of cultivars 'Cobrançosa', 'Galega' and 'Picual' growing in Alentejo region.

Moreover, the vast majority of the aforementioned works have been undertaken with resort to excitation wavelengths within the NIR range (mainly the 1064 radiation from the Nd:YAG), while some authors have more recently used excitation wavelengths within the visible range for the study of olive oils, with optimal performance [14,20]. Therefore, the aim of this study was to use short wavelength Raman spectroscopy (488 nm excitation) associated with chemometrics in order to differentiate EVOO's produced with olives from three cultivars on three different maturation stages. Discrimination was achieved using an unsupervised method, principal component analysis (PCA).

Furthermore, quantitative models for the rapid prediction of the peroxide value and acidity of EVOO's based on Raman spectral data and on its 1st and 2nd derivatives were developed using the principal component regression (PCR) and the partial least square regression (PLS-R) methods.

2. Material and methods

2.1. Sampling

The present work was carried on monovarietal extra virgin olive oils from three cultivars (cv. 'Cobrançosa', 'Galega' and 'Picual'). The olive fruits were obtained from a certified olive orchard, at the National Plant Breeding Station, at Elvas (Portugal) during the crop season 2012/2013.

Only healthy olive fruits, without any kind of infection or physical damage, were collected from ten different trees of comparable age and vigor and located in distinct points of the same growing area. Thus, differences in climate conditions, agricultural practices and geographical were excluded. Olives were handpicked at three ripening stages, except Picual cultivar olives that were picked during two harvesting periods. The harvesting dates are presented in Table 1. For the classification of the maturity index, the olives were evaluated according to their skin and pulp color [21]. The ripeness index (RI) values range from 0 (100% intense green skin) to 7 (100% purple flesh and black skin).

After harvesting, the olive fruits were immediately transported to the laboratory mill where they were processed within 24 h. For the production of each olive oil, three kilos of fresh olive fruits were used using an Abencor system (INIA I.P., Elvas, Portugal) where olives were crushed with a hammer crusher and the past mixed at 25 °C for 30 min, centrifuged without addition of warm water and then filtered and transferred into dark glass bottles without headspace and stored in the dark at 4 °C until analysis. All samples were classified as extra virgin olive oils according to the EU regulations [7].

2.2. Quality chemical indices determination

For all the samples, the determination of the physicochemical quality indexes, free acidity (expressed as % of oleic acid) and peroxide value (expressed as meq O_2/kg), were performed according to the official method described in the EEC Reg. No. 2568/91 and subsequent amendments, which focus on the characteristics of olive oil and olive-residue oil and on relevant methods of analysis [7].

2.3. Raman spectra measurement

The Raman spectra were collected in the 250–3050 cm^{-1} spectral range, at room temperature, with a T64000 Jobin-Yvon triple spectrometer, coupled to a liquid-nitrogen-cooled CCD detector. The excitation line was the 488 nm of an Ar laser, and the incident laser power was kept below 100 mW on the sample, to avoid self-heating. A confocal Olympus microscope equipped with a 100X objective (NA=0.95) was used to focus the laser radiation on the sample and for collecting the Raman scattered signal in a back-scattering geometry. Under these conditions, which were maintained for all experiments, the spectral slit width was about 2.0 cm^{-1}. A substrate of crystalline silicon was used under the same conditions as an external standard for calibration, by recording the position of its well-defined Raman band at 520.0 cm^{-1}.

For the measurement, a drop of olive oil was placed directly on a special microscope slide with a small concavity by pipetting a

Table 1
Description of olive fruits at each sampling date.

Cultivar	Maturity stage	Sample code	Harvest date	RI[a]
Cobrançosa	Green	Cob G	02/10/2012	0.4
	Semi-ripe	Cob SR	12/10/2012	2.1
	Ripe	Cob R	08/11/2012	5.5
Galega	Green	Gal G	02/10/2012	0.4
	Semi-ripe	Gal SR	12/10/2012	2.1
	Ripe	Gal R	08/11/2012	5.5
Picual	Green	Pic G	02/10/2012	0.4
	Ripe	Pic R	08/11/2012	5.5

[a] Ripening Index.

few drops. The integration time was set to 20 s and each recorded Raman spectrum is the average of five accumulations. The time necessary for acquire one spectrum was about 4 minutes. For each olive oil sample, four replicates were measured in identical conditions, for each one the microscope was focused on two different points and the corresponding Raman spectra recorded, therefore, retrieving eight spectra for each sample.

2.4. Mathematical treatment of data set

The Raman spectral data can be considered as a multidimensional set of variables where each spectrum consists of hundreds of variables, corresponding to the Raman intensities (counts) recorded at the different Raman shifts (cm^{-1}). These data sets were then analyzed by a multivariate analysis method as described below.

A principal component analysis (PCA) was applied to inspect differences between samples. The PCA transforms a large number of potentially correlated factors into a smaller number of uncorrelated factors (principal components, PCs), and thus reduces the size of the data set.

For qualitative analysis, principal components contributing to the variance of the data set were subjected to discriminant analysis (DA) in an attempt to predict the likelihood of a sample belonging to a previously defined group. Since the raw spectral data could not be used because of the strong correlation between the wavenumbers, uncorrelated PCs resulting from PCA were employed. DA is a statistical method used to find a linear combination of structures, which characterizes or separates classes of objects or observations. The resulting arrangement may be used as a linear classifier or dimensionality reduction priori to classification.

Both PCR and PLS regression methods are utilized to model a response variable when a biological system is analyzed through a large number of predictor variables that are highly correlated or even collinear [22]. Both methods give rise to new predictor variables, usually known as principal components (PC) or latent variables that are linear combinations of the original predictor variables. Those components are calculated in different ways, PCR creates PC's to explain the observed variability in the predictor variables, without considering the response variable. In PLS-R the response variable is taken into account and, consequently, leads to models that can fit the response variable with fewer factors [23]. Whether or not it ultimately translates into a useful model depends on the specific biological system.

2.5. Treatment of spectral data

Pre-treatment of the raw spectral data included several steps. To subtract the fluorescence background the baseline of each spectrum was approximated by a fourth-order polynomial. After smoothing the spectra were normalized using the standard normal variate (SNV) method [24,25]. First and 2^{nd} derivatives were determined by the Savitzky–Golay method [26].

The Raman spectra were collected in the 250–3050 cm^{-1} spectral range. However, it was found that well-defined Raman bands associated with free fatty acids and with changes due to oxidation could be observed in specific regions. The most relevant spectral region that can be linked to free acidity and to the peroxide value is the region between 950–1800 cm^{-1}, in accordance with El-Abassy et al. (2009) [14]. The inclusion of irrelevant spectral information in the Chemometrics procedures yields an over-fitting model.

2.6. Model selection

For quantitative analysis of chemical parameters of olive oil samples, factors considerably contributing to the variance of the data set were regressed using principal component regression (PCR) and partial least squares regression (PLS-R) onto the referred variables. This multivariate calibration technique, sometimes called factor analysis, transform the original variables (Raman spectra) into the new ones (known as factors), which are linear combination of original variable.

The method relied on two steps, so-called calibration and validation. In the calibration step, a mathematical model was built to establish a correlation between the matrix of Raman spectra (predictor variables) and the concentration of analytes of interest (response variables) used a set of observations usually named calibration set. In the validation step, the developed calibration model was used to calculate the concentration of samples not used to set-up the model [26].

The quality of the fitting was scrutinized by the root mean square error of calibration (RMSEC), multiple coefficient of determination or regression coefficient (R^2, where R is the correlation factor) and by the root mean square error of cross validation (RMSECV). The optimum number of factors either for PLS-R or PCR models was determined using Leave-One-Out (LOO) cross-validation method. The optimal number of factors is the one that minimizes the RMSECV.

PCA, DA, PCR and PLS-R calculations were performed using the XLSTAT-v2006.06 package (Addinsoft, Inc).

3. Results and discussion

3.1. Chemical analysis

The regulated quality indices studied in this work (free acidity and peroxide value) are displayed in Table 2. In all samples of cv Cobrançosa, Galega and Picual olive oils, analytical parameters were widely within the limits established in the European Legislation for EVOO [27].

The PV is useful once it's an indicator of the initial stage of oxidation, where the primary oxidation products are measured. As can be seen, PV decreased as the maturation stage increased and were significantly lower in Galega and Picual olive oils in the first and latest ripening stage than in Cobrançosa olive oils. This behavior can be explained by a decrease in the activity of lipoxygenase enzyme [28]. Furthermore, for each cultivar studied,

Table 2
Means and standard deviations for peroxide value and free acidity of olive oil samples from cv's Cobrançosa, Galega and Picual in three maturation stages, for four replicates ($n=4$).

Cultivar		Peroxide value (meq O_2/kg)	Free acidity (% oleic acid)
Cobrançosa	Green	$8.33^{aA} \pm 0.42$	$0.29^{aA} \pm 0.01$
	Semi-ripe	$6.69^{bA} \pm 0.42$	$0.24^{bA} \pm 0.01$
	Ripe	$4.97^{cA} \pm 0.25$	$0.31^{aA} \pm 0.02$
	p	< 0.001	< 0.001
Galega	Green	$6.66^{aB} \pm 0.33$	$0.21^{aB} \pm 0.01$
	Semi-ripe	$7.50^{bB} \pm 0.37$	$0.17^{bB} \pm 0.01$
	Ripe	$3.34^{cB} \pm 0.17$	$0.24^{cB} \pm 0.01$
	p	< 0.001	< 0.001
Picual	Green	$8.27^{aA} \pm 0.41$	$0.31^{aA} \pm 0.02$
	Ripe	$3.33^{bB} \pm 0.17$	$0.17^{bC} \pm 0.01$
	p	< 0.001	< 0.001

For each cultivar, means with different lower case letters differ significantly. For each maturation stage, means with different capital letters differ significantly.

significant differences of PV were evident during the maturation process.

Regarding free acidity, this percentage didn't show a trend during fruit ripening of cultivars studied. For Cobrançosa and Galega samples, free acidity decreased from the first to the second maturation stage and then increased in the ripe stage. However, olive oil samples from Picual cultivar presented free acidity values ranged between 0.31 ± 0.02 to $0.17 \pm 0.01\%$ in green and ripe stages, respectively. Usually, olives at a later stage of ripening originate oils with higher levels of acidity due to a progressive enzymatic activity, especially by lipolytic enzymes, and are more sensitive to pathogenic infections and mechanical damage [28]. This increase has been observed for Cobrançosa and Galega cultivars, but not for Picual olive oils that revealed a significant decrease of free fatty acids during maturation, in agreement with previously reported data by Garcia et al. (1996) [29].

3.2. Raman spectra of olive oil

Representative Raman spectral data in the range of 950 and 1800 cm^{-1} together with its 1st and 2nd derivatives are shown in Fig. 1 for EVOO from cv Cobrançosa in three maturation stages.

The Raman spectrum includes bands that can provide information on biochemical changes occurring during the maturation of olives used to produce the olive oils [19]. Some of these bands are displayed in the aforementioned region and correspond to the peaks: at 1749 cm^{-1}, associated to the ester stretching mode υ (C=O), at 1651 cm^{-1}, due to stretching mode υ (C=C) of the cis double bond, at 1439 cm^{-1} and 1303 cm^{-1}, assigned to the methylene (CH_2) scissoring and twisting deformations, respectively, and at around 1267 cm^{-1}, related to the scissoring deformation in the cis unsaturated moiety δ (=C-H) [30]. These bands are assigned to fatty acids, both free and in triacylglycerols, therefore, being directly related to the fatty acid content of each sample. It must be mentioned that the band at 1267 cm^{-1} is very week under 488 nm excitation. This band has been pointed out by Baeten [30], and more recently by Machado [31], which related its intensity loss to the degradation of the *cis*-unsaturated moiety, occurring during the peroxidation process, therefore, being proposed for monitoring the oxidation status.

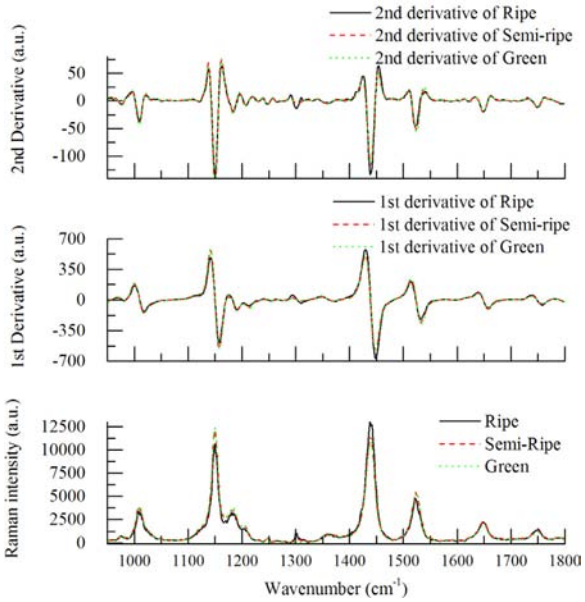


Fig. 1. Raman spectra between 950 and 1800 cm^{-1} of extra virgin olive oil from cv Cobrançosa in three maturation stages together with its 1st and 2nd derivatives.

Regarding the spectral changes due to compositional differences, there are three more bands to be pointed at around 1009 cm^{-1}, 1150 cm^{-1} and 1523 cm^{-1}, attributed to carotenoids, and assigned to the (C-CH_3) deformation, υ (C-C) and υ (C=C) mode, respectively [32]. These compounds are natural antioxidants, responsible for different characteristics of distinct EVOO's, and their quantity changes during the maturation process [19]. Their bands are not observed in investigations using laser excitation wavelengths within the Infrared range (*e.g.* 785, 1064 nm), however, they became visible under shorter excitation wavelengths, such as the 488 nm laser line presently used. Therefore, short wavelength excitation improves differentiation between olive oils produced using distinct cultivars, in different maturation stages. Similar results were reported in El-Abassy et al. (2009) using 514.5 nm excitation [14].

3.3. Supervised olive oil maturation monitoring using Raman spectral data

3.3.1. Preliminary analysis of the spectral data set

Standardized (SNV) Raman spectral data collected between 950 and 1800 cm^{-1} of the 64 spectra (8 spectra for each maturation stage, resulting in 24 spectra from Olive cv Cobrançosa and Galega, in three maturation stages, and 16 from Picual cv in two maturation stages) were subjected to PCA. It was found that the variance of the data set, based in 425 original variables (wavenumbers), is described by 47 principal components but 95% of the total variance is explained by the first 11 principal components.

In statistics, communality is defined as the sum of the squared factor loadings for all factors for a given original variable. It is the variance in that variable accounted for by all the factors. In other words, the communality measures the percentage of variance in a given variable explained by all the factors jointly and may be interpreted as the consistency of the indicator [33]. By definition, the initial value of the communality in PCA is 1. Small communalities values after extraction indicate variables that do not fit well the factor solution and should be dropped from the analysis [34]. According to Stevens (2002), a lower limit of 0.6 should be used [35].

Wavenumbers (variables) for which the communality value of each principal components out of the eleven was higher or equal to 0.6 were considered as meaningfully explaining the variance of the spectral data set and then were considered as prospective wavenumbers associated with the biochemical changes happening during maturation of olives used to produce the olive oil samples. These wavenumbers are in agreement with the above mentioned bands related to compositional differences, and belong to the following intervals: 997 to 1023 cm^{-1}, 1139 to 1161 cm^{-1}, 1295 to 1309 cm^{-1}, 1425 to 1455 cm^{-1}, 1511 to 1537 cm^{-1}, 1631 to 1665 cm^{-1} and 1737 to 1761 cm^{-1}. This new set of 86 variables, each one corresponding to a Raman intensity, collected from the above-mentioned intervals (one registered for each 2 cm^{-1}), was then selected for additional analyses. The band at 1267 cm^{-1}, used by other authors, has been left out after this selection procedure of intervals for DA. This is probably due to the low intensity of this band, under the presently used excitation of 488 nm, which led its variation to be insignificant for this analysis.

A new PCA performed on this reduced spectral data set showed that 89% of the variance could be explained by five principal components. These variables were then subjected to a discriminant analysis based on the known membership (maturation stage) of each sample analyzed, constituting the dependent variable.

The observation diagram represented in 2 is defined by discriminant factors F1 and F2, which explained the total variance. The cultivars of green ripening stage are in the lower left side of the plot, with exception of Picual, placed near the center. EVOO's

of Cobrançosa and Galega cultivars in semi-ripe stage are mostly located in positive part of F2 axis and negative part of F1 axis. EVOO' samples in ripe stage are located in the right side of the F1/F2 plane. The classification in Table 3, resulting from the discriminant analysis, provided 96.5% correct classification for the calibration set and 81.9% correct classification when cross-validated. A high degree of correct classification (91.7%) is achieved for ripe EVOO, as opposed to the semi-ripe group that has 25% probability of being classified as green. Thus, though not being suitable for the discrimination between green and semi-ripe EVOO's, discriminant analysis allows the possibility to distinguish EVOO samples obtained from ripe fruits.

3.3.2. PCR and PLS-R models for prediction of peroxide value and free acidity

PLS-R and PCR calibration models were carried out in order to determine a relationship between predictor variables (Raman scattering intensities) and the chemical characteristics of olive oils referred above. Specifically, the main goal was to develop a model able to predict the peroxide value and free acidity, considering the high relevance these parameters for consumers of EVOO.

Actually, as the olive oil Raman spectrum contains contributions from different species, each observable band might either correspond to a specific component, or to a sum of different contributions (bands) arising from distinct chemical systems. Thus, Raman is suitable for the assessment of these chemical parameters – peroxide value and free acidity – due to the different contributions of the samples' constituents, which vary, and also to the chemical modifications related to these parameters, which are reflected in the behavior of certain bands. For instance, some Raman signs are specifically related to the peroxide value, such as the vibrational modes due to the conjugated (C=C-C=C) system formed due to the peroxidation process (stretching ~1660 cm^{-1}),

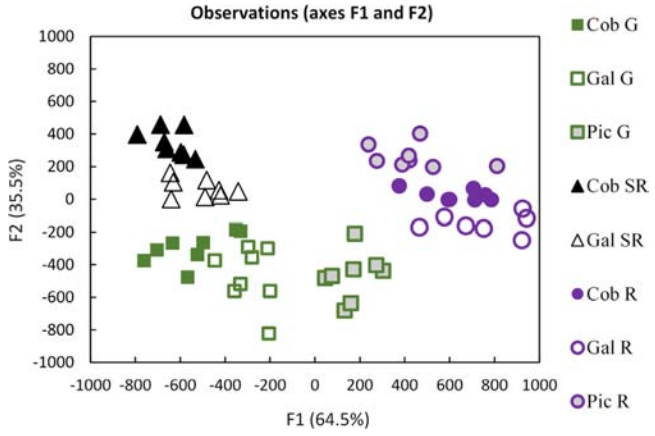


Fig. 2. Observations diagram from a principal component analysis of extra virgin olive oil samples from cv's Cobrançosa, Galega and Picual in three maturation stages, using the normalized (SNV) Raman spectral data.

or the loss of intensity in bands corresponding to the intact fatty acids, such as the band at 1267 cm^{-1} [30,31].

Furthermore, triacylglycerides represent different chemical systems, respecting free fatty acids or glycerol molecules. For example, the band at 1749 cm^{-1}, is raised by the carbonyl ν (C=O) mode, either from the free fatty acids (carboxylic group), or from the triglyceride bonded fatty acids (ester group), displaying slightly different frequencies. Thus, the shape of this band, and Raman features on the corresponding interval (1737–1761 cm^{-1}), retrieve information on the free acidity. Moreover, fatty acids might undergo structural changes when inserted in a triglyceride, these conformational changes are reflected in the frequency of the ν(C=C) mode [36]. Therefore, the band at 1651 cm^{-1}, corresponding to the ν(C=C) modes of the fatty acids, arises as meaningful for the assessment of free acidity. Additionally, in our case, the three bands of carotenoids (1009, 1150 and 1523 cm^{-1}), whose intensities are known to be inversely proportional to the FFA content [14], can be detected. Therefore, there is a rational relationship between Raman obtained data, and these chemical parameters, both free acidity and peroxide value, thus, this spectroscopic technique displays the potential for their assessment.

PLS regression method is able to collect information from large spectral intervals, correlating changes therein to the concentration of specific constituents, and concomitantly consider other possible contributions to these changes not related to the sample constitution [37]. On the other way, in PCR method the spectral and concentration information are incorporated into the model in one step [38].

The results achieved for the PLS-R and PCR calibrations of peroxide value and free acidity in terms of R^2, RMSEC and RMSECV, either for normal spectra, from 950 to 1800 cm^{-1}, and its 1st and 2nd derivatives are presented in Table 4. The high value of R^2 and the lowest of RMSEC and RMSECV indicate the good performance and precision of the models. Furthermore, to obtain a good calibration model, the number of regression factors used should be the lowest as possible [39]. The plot of the measured concentrations of the chemical parameters against the predicted values based on Raman scattering intensities reveals the quality of the models. To illustrate the quality of the models established in this work, PLS-R calibrations are presented in Fig. 3a) and b).

Moreover, though some authors undertook previous works resorting to spectral intervals bellow 1600 cm^{-1} [14], the usefulness of the bands in the 1600–1800 cm^{-1} interval, which reached a relative intensity high enough for its variations to be considered in the model, has been observed in the present study, also Korifi has previously considered these bands, in a study conducted with the 532 nm excitation [20] Therefore, it can be elated that, besides the enhanced intensity of these bands, the improved sensitivity due to the use of a lower excitation wavelength, allows the retrieval of useful information from the shape of these bands, which are raised by contributions from different chemical systems.

For both chemical parameters under analysis, the multivariate calibrations showed, in general, the highest value of R^2 and the lowest of RMSECV when using the 1st derivative of the spectral

Table 3
Confusion matrix for the training and for the cross-validation sets based on the maturation stage. Observed classifications in the rows. Predicted classifications in columns.

From/To	Calibration					Cross-validation				
	Green	Semi-ripe	Ripe	Total	% correct	Green	Semi-ripe	Ripe	Total	% correct
Green	23	1	0	24	95.8	19	5	0	24	79.2
Semi-ripe	1	15	0	16	93.8	4	12	0	16	75.0
Ripe	0	0	24	24	100	2	0	22	24	91.7
Total	24	16	24	64	96.5	25	17	22	64	81.9

Table 4
Partial least squares and principal component regressions based calibrations for quantification of peroxide value and acidity, using the Raman spectral data and its 1st and 2nd derivatives.

Chemical parameter	Regression method	Factor	Spectra	Equation		R^2		RMSE	
				Calibration	Validation	Calibration	Validation	Calibration	Validation
Peroxide value	PLS-R	4	Normal	y=0.83 x+1.23	y=0.82 x+1.27	0.979	0.966	0.80	0.85
		4	1st der	y=1.01 x−0.02	y=1.04 x+0.10	0.986	0.971	0.68	0.72
		5	2nd der	y=0.99 x+0.04	y=0.98 x+0.07	0.965	0.956	0.74	0.81
	PCR	5	Normal	y=1.01 x−0.08	y=1.04 x−0.17	0.975	0.968	0.84	0.89
		3	1st der	y=0.90 x+0.61	y=0.93 x+0.42	0.989	0.981	0.72	0.77
		5	2nd der	y=1.01 x−0.08	y=1.04 x−0.17	0.937	0.888	0.77	0.83
Free acidity	PLS-R	4	Normal	y=0.93 x+1.19	y=1.13 x−0.11	0.992	0.987	0.02	0.03
		3	1st der	y=1.01 x+0.04	y=1.04 x−0.01	0.994	0.988	0.01	0.02
		4	2nd der	y=0.98 x+0.59	y=1.11 x+0.31	0.981	0.952	0.02	0.03
	PCR	4	Normal	y=0.83 x+1.23	y=1.02 x−0.05	0.988	0.984	0.02	0.04
		4	1st der	y=0.97 x+0.03	y=1.05 x−0.32	0.991	0.990	0.02	0.02
		5	2nd der	y=0.88 x+0.61	y=0.97 x+0.24	0.969	0.933	0.03	0.04

RMSE of Peroxide value in meq O_2/kg; RMSE value of Acidity in %.

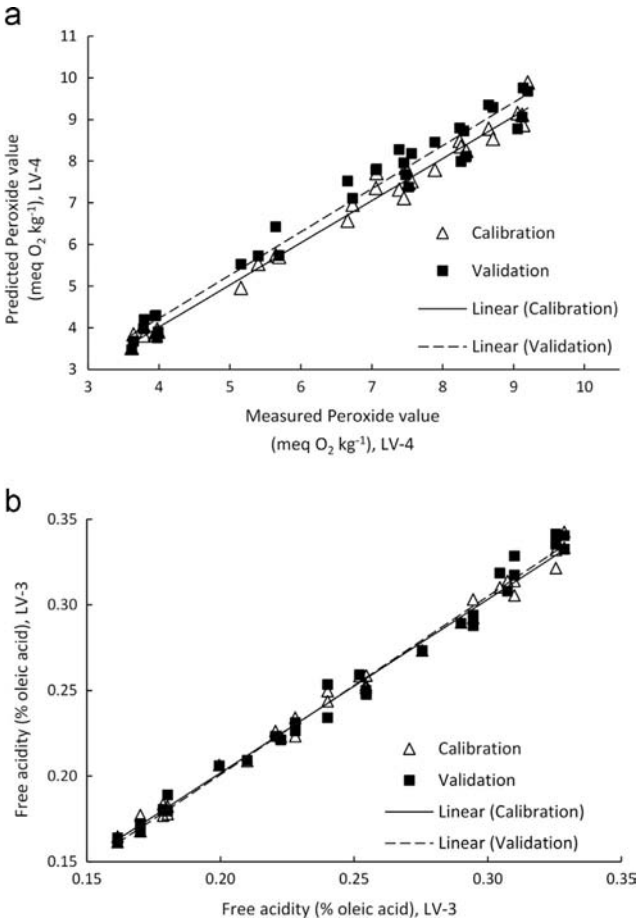


Fig. 3. PLS-R calibration models for the relationship between measured values and Raman predicted values of: a) peroxide values and of b) free acidity of olive oil.

data. In general, PLS-R offers enhanced results compared to others regression methods, such as PCR [40] or multiple linear regression (MLR) for quantitative analysis of chemical parameters [23]. In our study, despite both calibration models presented good prediction values, it was also PLS-R method that showed the best results, displaying good performances for both the prediction of peroxide value, and free acidity.

The relationship between measured values of the chemical parameters predicted values based on Raman scattering intensities showed R^2 values ranging from 0.937 to 0.994 using the calibration set and from 0.933 to 0.990 when cross validated. The RMSECV were as low as 0.72 meq O_2/kg for the peroxide value, when using the 1st derivative and a PLS model with 4 factors. However, a slightly higher value of 0.77 meq O_2/kg was attained for a simpler 3 factor PCR model. For the free acidity the lowest RMSECV value was 0.02% attained for both PCR and PLS-R models, the latter being simpler (3 factors) than the former.

4. Conclusion

In the present work, Raman spectroscopy, alongside with multivariate analysis methods, has been successfully used, in order to monitor free acidity and peroxide values in EVOO's, as well as to distinguish ripe from non-ripe oils. Since each Raman spectrum is constituted of several different contributions, arising from distinct constituents, these unique Raman features, corresponding to each species, render a possibility to the assessment of the samples' content through this methodology.

Furthermore, the use of a short wavelength excitation, 488 nm, allowed, not only, to observe bands due to carotenoids, which are important for these assessments, but also to register good quality spectra, so as to retrieve information from bands raised by distinct constituents.

In order to correlate the Raman spectra with the quality parameters assessed, as well as to evaluate the best approach to do so, the present work has been conducted with resort to two distinct approaches, PCR and PLS-R. Both have shown good results, and best performance when applied to the first derivative of the spectra, for the prediction of either peroxide value, or free acidity. In the latter case both approaches, PCR and PLS-R, retrieve similar results, presenting R^2 values of 0.990 and 0.988, respectively, and equal errors for cross-validation. In the case of peroxide value, PLS-R displays somewhat lower errors of validation in comparison to PCR (0.72 *vs* 0.77 meq O_2/kg) therefore, the former being proposed as the most suitable for these determinations.

Additionally, Raman shows some advantages over Infrared technique, which are exploited by the advent of the Raman portable devices, bringing the hot prospect of the *in situ* monitoring of these quality parameters. Therefore, this methodology represents an important trend, respecting the assessment of these quality parameters in field.

Acknowledgments

This work was supported by the Project 'PhD grant SFRH/BD/78013/2011 to IG from the Fundação para a Ciência e Tecnologia.

This work is financed by the ERDF – European Regional Development Fund through the COMPETE Programme (operational programme for competitiveness) and by National Funds through the FCT – Fundação para a Ciência e a Tecnologia (Portuguese Foundation for Science and Technology) within project «FCOMP-01-0124-FEDER-037281».

This work was also supported by the Project INNOFOOD - INNOvation in the FOOD sector through the valorization of food and agro-food by-products - NORTE-07-0124-FEDER-0000029, financed by the North Portugal Regional Operational Programme (ON.2 – O Novo Norte) under the National Strategic Reference Framework (QREN), through FEDER, as well as by PIDDAC through FCT/MEC, and by the project PEst-OE/AGR/UI4033/2014.

References

[1] A. Bakhouche, J. Sánchez, R. Beltrán-Debón, J. Joven, A. Segura-Carreter, A. Fernández-Gutiérrez, Food Res. Int. 50 (2013) 401–408.
[2] M. Machado, C. Felizardo, A.A. Fernandes-Silva, F.M. Nunes, A. Barros, Food Res. Int. 51 (2013) 412–421.
[3] C. Sousa, I. Gouvinhas, D. Barreira, M.T. Carvalho, A. Vilela, J. Lopes, P. Martins-Lopes, A.I. Barros, J. Am. Oil Chem. Soc. http://dx.doi.org/10.1007/s11746-013-2406-x.
[4] S. Dabbou, I. Gharbi, S. Dabbou, F. Brahmi, A. Nakbi, M. Hammami, Afr. J. Biotechnol. 10 (74) (2011) 16937–16947.
[5] J. Ayton, R.J. Mailer, A. Haigh, D. Tronson, D. Conlan, J. Food Lipids. 14 (2007) 138–156.
[6] European Commision. Commission Regulations (EC), Off. J. Eur. Comm., L155 (2002) 27–31.
[7] European Community Commission Regulation (EEC) Off. J. Eur. Comm., L248 (1991) 1–83.
[8] E.C.Y Li-Chan, P.R. Griffiths, J.M. Chalmers, Applications of Vibrational Spectroscopy in Food Science, Analysis of Food, Drink and Related Materials, Volume II, John Wiley and Sons, Chichester, UK, 2010.
[9] M. Holse, F.H. Larsen, A. Hansen, S.B. Engelsen, Food Res. Int. 44 (1) (2011) 373–384.
[10] B.J. Marquardt, J.P. Wold, Food Sci. Technol 37 (1) (2004) 1–8.
[11] L. Kyung-Min, J. Timothy, Y. Herrman, J. Cereal. Sci. 59 (2014) 70–78.
[12] A.M.A. Pistorius, Spectrosc. Eur 7 (1995) 8–15.
[13] A. Zaja, J. Hanuza, L. Dymin ska, Food Chem. 156 (2014) 333–338.
[14] R.M. El-Abassy, P. Donfack, A. Materny, J. Am. Oil. Chem. Soc. 86 (2009) 507–511.
[15] R.C. Barthus, R.J. Poppi, Vib. Spectr 26 (1) (2001) 99–105.
[16] B. Muik, B. Lendl, A. Molina-Díaz, M.J. Ayora-Cañada, Anal. Chim. Acta 487 (2003) 211–220.
[17] H. Yang, J. Irudayaraj, M.M. Paradkar, Food Chem. 93 (2005) 25–32.
[18] V. Baeten, J.A.F. Pierna, P. Dardenne, M. Meuren, D.L. García-González, R. Aparicio-Ruiz, J. Agr. Food Chem. 53 (2005) 6201–6206.
[19] M. López-Sanchez, M.J. Ayora-Cañada, A. Molina-Díaz, J. Agric. Food Chem. 58 (2010) 82–87.
[20] R. Korifi, Y. Le Dréau, J. Molinet, J.N. Artaud, Dupuy, J. Raman Spectrosc. 42 (2011) 1540–1547.
[21] M. Uceda, M. Hermoso, El Cultivo del Olivo, Junta de Andalucia Ediciones Mundi-Prensa (1998) 547–572.
[22] J.N. Miller, J.C. Miller (Eds.), Pearson Education Limited, Edinburgh Gate Harlow, 2005.
[23] P.D. Wentzell, L.V. Montoto, Chemometr. Intell. Lab. Syst. 65 (2003) 257–279.
[24] A. Nunes, J. Martins, A.S. Barros, A.C. Galvis-Sánchez, I. Delgadillo, Sens. Instrum. Food Qual 3 (2009) 187–191.
[25] A. Bendini, L. Cerretani, F. Virgilio, P. Belloni, G. Lercker, T.G. Toschi, Eur. J. Lipid Sci. Technol. 109 (2007) 498–504.
[26] M. De Luca, F. Oliverio, G. Loele, G. Ragno, Chem. Intel. Lab. Syst. 96 (2009) 14–21.
[27] European Community Commission Regulation (EEC), Off. J. Eur. Comm., L23 (2011) 1–13.
[28] F. Gutiérrez, B. Jiménez, A. Ruiz, M.A. Albi, J. Agric. Food Chem. 47 (1999) 121–127.
[29] J.M. Garcia, S. Seller, M.C. Pérez-Camino, J. Agr. Food Chem. 44 (1996) 3516–3520.
[30] V. Baeten, J. Agric. Food Chem. 46 (1998) 2638–2646.
[31] N.F.L. Machado, L.A.E. Batista de Carvalho, J.C. Otero, M.P.M. Marques, J. Raman Spectrosc. 43 (2012) 1991–2000.
[32] P.S. Bernstein, J. Pure Appl. Chem. 74 (2002) 1419–1425.
[33] H. Abdi, L.J. Williams, Comput. Stat. 2 (2010) 43–459.
[34] A.P. Field, Discovering Statistics using SPSS, 2nd Edition, Sage, London, 2005.
[35] J.P. Stevens, Applied Multivariate Statistics for the Social Sciences, 4th Edition, Erlbaum, Hillsdale, NJ, 2002.
[36] M. Motoyama, Bull. NARO Inst. Livest. Grassl. Sci. 12 (2012) 19–68.
[37] Y.B. Che Man, Z.A. Syahariza, M.E.S. Mirghani, S. Jinap, J. Bakar, Food Chem. 90 (2005) 815–819.
[38] B.C. Smith, Quantitative Spectroscopy: Theory and Practice, Academic Press, Amsterdam (2002) 125–179.
[39] L.U. Hui-Shan, X.U. Hui-Rong, Y. Yi-Bin, F.U. Xia-Ping, Y.U. Hai-Yan, T.J. Hai-qing, Zhejiang Uni. Sci 7 (2006) 794–799.
[40] Y. Liang, O.M.K. Valheim, Chemometr. Intell. Lab. Syst. 32 (1996) 1–10.

Talanta 132 (2015) 836–844

Contents lists available at ScienceDirect

Talanta

journal homepage: www.elsevier.com/locate/talanta

High resolution/accurate mass (HRMS) detection of anatoxin-a in lake water using LDTD–APCI coupled to a Q-Exactive mass spectrometer

Audrey Roy-Lachapelle [a], Morgan Solliec [a], Marc Sinotte [b], Christian Deblois [c], Sébastien Sauvé [a,*]

[a] Department of Chemistry, Université de Montréal, Montréal, QC, Canada
[b] Direction du Suivi de l'État de l'Environnement (DSEE), Ministère du développement durable, de l'environnement et de lutte aux changements climatiques (MDDELCC), Québec, QC, Canada
[c] Centre d'expertise en analyse environnementale (CEAEQ), Ministère du développement durable, de l'environnement et de lutte aux changements climatiques (MDDELCC), Québec, QC, Canada

ARTICLE INFO

Article history:
Received 14 July 2014
Received in revised form
6 October 2014
Accepted 10 October 2014
Available online 31 October 2014

Keywords:
High resolution mass spectrometry
LDTD–APCI
Anatoxin-a
Phenylalanine
Cyanobacteria

ABSTRACT

A new innovative analytical method combining ultra-fast analysis time with high resolution/accurate mass detection was developed to eliminate the misidentification of anatoxin-a (ANA-a), a cyanobacterial toxin, from the natural amino acid phenylalanine (PHE). This was achieved by using the laser diode thermal desorption–atmospheric pressure chemical ionization (LDTD–APCI) coupled to the Q-Exactive, a high resolution/accurate mass spectrometer (HRMS). This novel combination, the LDTD–APCI–HRMS, allowed for an ultra-fast analysis time (< 15 s/sample). A comparison of two different acquisition modes (full scan and targeted ion fragmentation) was made to determine the most rigorous analytical method using the LDTD–APCI interface. Method development focused toward selectivity and sensitivity improvement to reduce the possibility of false positives and to lower detection limits. The Q-Exactive mass spectrometer operates with resolving powers between 17 500 and 140 000 FWHM (m/z 200). Nevertheless, a resolution of 17 500 FWHM is enough to dissociate ANA-a and PHE signals. Mass accuracy was satisfactory with values below 1 ppm reaching precision to the fourth decimal. Internal calibration with standard addition was achieved with the isotopically-labeled (D_5) phenylalanine with good linearity ($R^2 > 0.999$). Enhancement of signal to noise ratios relative to a standard triple-quadrupole method was demonstrated with lower detection and quantification limit values of 0.2 and 0.6 μg/L using the Q-Exactive. Accuracy and interday/intraday relative standard deviations were below 15%. The new method was applied to 8 different lake water samples with signs of cyanobacterial blooms. This work demonstrates the possibility of using an ultra-fast LDTD–APCI sample introduction system with an HRMS hybrid instrument for quantitative purposes with high selectivity in complex environmental matrices.

© 2014 Elsevier B.V. All rights reserved.

1. Introduction

Cyanotoxins are produced by cyanobacteria, commonly known as blue–green algae. They are naturally encountered in natural waters after the proliferation of a cyanobacterial bloom favored in eutrophic and hypertrophic water [1,2]. The principal families, with their most studied toxins, are the hepatotoxins (microcystins, nodularins, cylindrospermopsin), the neurotoxins (anatoxin-a, anatoxin-a(s), homoanatoxin-a, saxitoxins, BMAA), the cytotoxins (aplysiatoxin, debromoaplysiatoxin, lyngbyatoxin, cylindrospermopsin) and the endotoxins (lipopolysaccharides) [3,4]. Among the neurotoxins, anatoxin-a (ANA-a) has a vast distribution with 10 cyanobacteria genera responsible for their production—*Anabaena*, *Aphanizomenon*, *Arthrospira*, *Cylindrospermum*, *Microcystis*, *Nostoc*, *Planktothrix* (*Oscillatoria*), *Phormidium* and *Raphidiopsis* [1]. Our main target cyanotoxin, ANA-a, is an alkaloid compound (p*K*a 9.4, M.W. = 165.24 g/mol), stable under acidic conditions (pH = 2) but degradable under natural conditions at high pH and in contact with sunlight. Degradation products include the non-toxic metabolites dihydroanatoxin-a and epoxyanatoxin-a [2,5]. ANA-a is a potent neuromuscular blocking agent with a high toxicity (LD_{50}) of 200–250 μg/kg for mouse, causing irreversible inhibition of the acetylcholinesterase activity and accumulation of acetylcholine in

* Correspondence to: Université de Montréal, Department of Chemistry, CP 6128 Centre-Ville, Montréal, QC, Canada H3C 3J7. Tel.: +1 514 343 6749; fax: +1 514 343 7586.
E-mail address: sebastien.sauve@umontreal.ca (S. Sauvé).

http://dx.doi.org/10.1016/j.talanta.2014.10.021
0039-9140/© 2014 Elsevier B.V. All rights reserved.

the neuromuscular junctions. High doses of ingested ANA-a can cause continuous stimulation of the respiratory muscles, leading to asphyxiation [6]. Several animal mortality have been regularly attributed to ANA-a for cattle, wildlife, and pets, and some documented confirmations have also been published [7,8]. Although the World Health Organisation (WHO) has not established guidelines for ANA-a concentrations in drinking and recreational waters, several jurisdictions have implemented such guidelines into their risk management of this neurotoxin. To date, Canada and New Zealand tolerate concentrations below 3.7 μg/L and 6 μg/L respectively in drinking water. In addition, three U.S. states, California, Oregon and Washington, tolerate concentrations from 1 μg/L for drinking water and as high as 100 μg/L for recreational waters [9]. Lower amount of ANA-a are produced in natural blooms compared to other cyanotoxins (e.g. microcystins), but due its non-negligible toxicity, it is important to assess the presence of the toxin in drinking and recreational waters for public and animal safety [4,10].

Most of the techniques developed for the detection of ANA-a are based on liquid chromatography coupled with tandem mass spectrometry (LC–MS/MS) [4,10–12]. Spectroscopic detection methods are avoided mainly for the lack of sensitivity due to the instability of ANA-a in contact with UV light and the impossibility to detect the degradation products [11–14]. Therefore, mass spectrometric detection following a chromatographic separation gives higher accuracy, sensitivity as well as selectivity. Unfortunately, phenylalanine (PHE), an essential amino acid present in natural waters, is an isobaric interference of ANA-a and they cannot be resolved by using a triple-quadrupole mass spectrometer [15]. Indeed, given their similar molecular masses and identical fragmentation prior to mass spectrometric detection, their similar liquid chromatography (LC) retention time can potentially lead to the misidentification of ANA-a. Different LC strategies have been proposed to achieve sufficient separation of ANA-a and PHE, but further work is needed since the required analyses are long and costly [13,16–18]. The use of high resolution mass spectrometry (HRMS) for cyanotoxins was presented for the first time by James et al. [19]. with the study of the fragmentation pathways of ANA-a, using a hybrid quadrupole time-of-flight mass spectrometer (QqTOF-MS) and a quadrupole ion-trap mass spectrometer (QIT-MS). According to the mass difference of ANA-a and PHE, a resolution of 4500 FWHM (full width at half maximum) is needed to achieve a mass separation to 10% valley. These instruments have sufficient resolving power to distinguish the signals compared to the minimal resolution needed [20]. Given the different MS instruments and hybrids, the use of HRMS becomes interesting to reduce the presence of false positives due to isobaric interferences and improve the selectivity of ANA-a detection.

Previously, a technique was proposed using laser diode thermal desorption–atmospheric pressure chemical ionization-tandem mass spectrometry (LDTD–APCI-MS/MS) for the analysis of ANA-a in natural waters [21]. The LDTD is a sample introduction apparatus using thermal desorption prior to atmospheric pressure ionization that significantly reduces the analysis time by eliminating the liquid chromatography step. The analytical approach requires a simple sample preparation method by eliminating the time consuming extraction procedures normally required for ANA-a and it is combined with the LDTD–APCI prior to MS detection allowing for an analysis time of 15 s/sample [1,22]. This analytical pathway gave a robust alternative for the high throughput analysis of ANA-a in water containing cyanobacterial blooms. However, the isobaric interference, PHE, was an issue since there is no chromatographic separation before ionization. The problem was solved by the use of a pseudo-separation of both compounds using the LDTD laser power, given that the desorption of ANA-a takes place at a temperature lower than PHE [21].

In order to resolve the PHE interference, a new approach is proposed, the LDTD–APCI–HRMS. It couples the LDTD interface with a high-resolution and accurate-mass (HR/AM) detection using a benchtop Orbitrap mass spectrometer, the Q-Exactive. The Orbitrap is combined to a high-performance quadrupole precursor selection and a higher energy collisional dissociation (HCD) cell, thereby giving a powerful tool for the screening of various compounds in environmental matrices. Moreover, the use of an S-lens increases the ion flux through the quadrupole, improving sensitivity and signal intensity [23]. Various HRMS mass spectrometers are known to be alternatives to triple quadrupole instruments with slightly higher instrument costs [20]. Time of flight (TOF) and QTOF have similar resolving power, up to 40 000 FWHM offering a mass accuracy lower than 5 ppm. On the other hand, Orbitrap and LTQ-Orbitrap instruments have better performances with resolving power up to 70 000 FWHM with mass accuracy lower than 2 ppm [20,24–26]. Compared to other Orbitrap mass spectrometers, the performances of the Q-Exactive are slightly better with resolving power up to 140 000 FWHM and mass accuracy <3 ppm with external mass calibration and <1 ppm with internal mass calibration (use of a lock mass) [27]. Furthermore, the main advantage of the Q-Exactive hybrid resides in the quadrupole mass filter combined with a HCD cell offering the possibility of precursor ion fragmentations analogous to an MS/MS mass spectrometer, thus giving a high specificity in ion selection [28]. The Q-Exactive was previously used for peptides sequencing, metabolomics and relatively few studies explored the possibility of quantifying small molecules in environmental matrices [28–30]. The aim of this study was to develop and validate a new analytical method for the ANA-a detection in lake water using a novel instrument combination, the LDTD–APCI–HRMS, in order to resolve the isobaric interference from phenylalanine. The possibility to couple the LDTD as a sample introduction prior to detection with the Q-Exactive instrument for higher sensitivity and selectivity is demonstrated. The sensitivity and selectivity of two different detection modes, full scan (FS) and targeted ion fragmentation (t-MS^2) are evaluated with the use of LDTD–APCI for an environmental water matrix. Several HRMS parameters were optimized to enhance mass resolution and accuracy, duty cycle and signal intensity. The method validation is done with the use of deuterated phenylalanine (PHE-D_5) as an internal standard. Under these conditions, the method detection limit and quantification limit (MDL and MQL), linear dynamic range, accuracy, precision and matrix effect were determined. The method was applied to real freshwater samples with cyanobacterial blooms and proved to be suitable for ANA-a detection in presence of PHE with a lower MDL relative to the previously developed analytical method using a triple-quadrupole MS instrument [21].

2. Materials and methods

2.1. Chemicals and reagents

(±)-Anatoxin-a/furamate salt standard, 99%, was purchased from Abcam Biochemicals (Cambridge, MA, USA). DL-Phenylalanine standard, 99%, was obtained from Sigma-Aldrich Chemical Co. (Oakville, ON, Canada). DL-Phenylalanine (Ring-D_5) standard, 98%, was obtained from Cambridge Isotope Laboratories, Inc. (Andover, MA, USA). Sodium hydroxide, 97%, and formic acid, 95%, were purchased from Sigma-Aldrich Chemical Co. (Oakville, ON, Canada). Methanol (MeOH) was of analytical grade purity from Fisher Scientific (Whitby, ON, Canada). Deionized/distilled water (dd-H_2O) was used for dilution. Compressed air (Ultra Zero Certified grade; ≤ 2 ppm water) used as carrier gas was purchased from MEGS Specialty Gases, Inc. (St-Laurent, QC, Canada).

2.2. Stock solution and cyanobacterial bloom samples

The solutions were prepared and stored according to previous protocol with modifications [21]. Stock standard solutions of ANA-a/furamate salt (100 mg/L) were prepared with acidified water (0.1 M formic acid, pH~2) and were stored at −20 °C for a maximum of 4 months. A 100 mg/L stock solution of DL-PHE was prepared daily in dd-H_2O. The DL-PHE-D_5 (100 mg/L) stock solution was prepared in dd-H_2O and was stored at −20 °C for a maximum of one month [17]. All working solutions were prepared daily in dd-H_2O with pH adjusted to 2 with formic acid and diluted in MeOH (50:50 v/v). Environmental samples were provided by the monitoring program realized by the *Ministère du Développement Durable, de l'Environnement, et de lutte aux changements climatiques,* (MDDELCC—The province of Quebec Ministry of the Environment) (Québec, Canada). All targeted lakes were chosen for their high occurrence of cyanobacterial blooms in different regions from the province of Québec, Canada. ANA-a was previously quantified by LC–MS/MS by the Centre d'Expertise en Analyse Environnementale du Québec (CEAEQ), the analytical services of the MDDELCC. The samples were acidified for preservation (0.1 M formic acid, pH~2) and then submitted to a freeze-thaw lysis three times to break the cells walls and leach the toxin, followed by a filtration using 0.45 μm nitrocellulose membrane obtained from Whatman (Florham Park, NJ, USA). The solutions were then prepared the same way as for the working solutions.

2.3. LDTD–APCI parameters

The desorption and ionisation of ANA-a, PHE and PHE-D_5 were performed using the T-960 LDTD–APCI ionization interface model and the instrument was controlled by LazSoft 4.0 software (Phytronix Technologies, Québec, QC, Canada) integrated with the Excalibur 2.2 Software (Thermo Fisher Scientific, Waltham, MA, USA). The LDTD apparatus was described in previous work [21,22,31,35]. Briefly, 2 μL of sample is spotted into a LazWell 96-well sample metal plate. After complete solvent drying at 40 °C (about 5 min), the back of the sample well is heated by an infrared laser (980 nm, 20 W, continuous) in the LDTD instrument. After the sample desorption, a carrier gas flow (2 L/min), set at 50 °C to avoid temperature variation, transfers the gas phase molecules to positive APCI ionisation followed by the MS detection. In previous work, we used lower laser power for a pseudo-separation of ANA-a and PHE since the amino acid desorption is substantially decreased with a lower temperature compared to the targeted toxin [21]. In this study, a higher temperature is needed to desorb both compounds since the internal standard is the amino acid PHE labeled with deuterium (PHE-D_5). In this manner, tests of different laser powers, from 10 to 60%, were performed by spiking 250 μg/L of ANA-a and 200 μg/L of PHE-D_5 in blank water matrix from a lake sample ($n=6$). The laser pattern was optimized to the following settings: 2 s at 0%, 1 s ramping from 0% to 45%, 2 s hold at 45%, 0.1 s from 45% to 0% and 2 s hold at 0%, with a total desorption time of 7 s/sample. APCI ionization in positive mode is within these parameters: ion sweep gas 0.3, sheath gas, auxiliary gas and skimmer offset are set to 0 (all arbitrary values), vaporizer temperature 0 °C and capillary temperature 350 °C.

3. HRMS parameters

Detection of compounds was performed using a Q-Exactive mass spectrometer controlled by the Excalibur 2.2 Software (Thermo Fisher Scientific, Waltham, MA, USA). Instrument calibration in positive mode was done within 24 h to avoid mass shifts in detection with a direct infusion of a LTQ Velos ESI Positive Ion Calibration Solution (Pierce Biotechnology Inc. Rockford, IL, USA.). All the Q-Exactive parameters were optimized toward mass resolution and accuracy for better quantification, sensitivity and selectivity. The different optimization tests were performed by spiking 250 μg/L of ANA-a and 200 μg/L of PHE-D_5 in blank water matrix from a lake sample ($n=6$). Full scan (FS) and targeted MS/MS (t-MS^2) modes were optimized and compared to determine which was best suited for LDTD analysis in environmental water matrices. A lock mass (m/z 155.1185—$C_8H_{14}N_2O$) was chosen from matrix background as internal standard for mass accuracy enhancement during spectral data acquisition. The mass range of FS mode was within m/z 100–200. The data were acquired at a resolving power of 35 000 FWHM at m/z 200. The automatic gain control (AGC) target for a maximum capacity in C-trap was set at 3×10^6 ions for a maximum injection time of 100 ms. As for t-MS^2, a mass inclusion list has to be used including the precursor ion masses and their expected retention time and a time of 0.2 min was set as the total analysis time. The precursor ions are filtered by the quadrupole which operates at an isolation width of 0.4 amu. A resolving power of 17 500 FWHM at m/z 200 was used. The AGC target was set at 10^5 ions for a maximum injection time of 50 ms. All optimized collision energies, precursor ions and fragment ions are shown in Table 1.

3.1. Data analysis and method validation

All data treatment was performed using the Excalibur 2.2 Software (Thermo Fisher Scientific, Waltham, MA, USA). The method validation was done according to the recommendation of validation protocol for environmental chemistry analysis from the Québec's MDDELCC guidelines [32]. The second most abundant observed ion was used as confirmation ion for each target compounds in both

Table 1
Parameters of HRMS detection.

Compound	Ion type	Chemical formula	Calculated exact mass (m/z)	Average experimental exact mass (m/z)	NCE[a] (%)	Mass accuracy[e] (ppm)	Confirmation Ion[b] (m/z)
ANA-a	Precursor Product[c]	$C_{10}H_{15}NO_2+H$	166.12319	166.1231	27	0.72	167.1253
	Product[d]	$M-NH_3+H$	149.09664	149.0965		0.67	150.0987
		$M-NH_3-H_2O+H$	131.08608	131.0859		0.68	132.0811
PHE-D_5	Precursor Product	$C_9H_6D_5NO_2+H$	171.11819	171.1181	32	0.65	171.1202
		$M-NH_3+H$	154.09164	154.0917		0.70	154.0939
PHE	Precursor Product	$C_9H_{11}NO_2+H$	166.08680	166.0867	31	0.72	167.0889
	Product	$M-NH_3+H$	149.06025	149.0601		0.77	150.0623
		$M-NH_3-H_2O+H$	131.04969	131.0496		0.76	132.0519

[a] Fragmentation energy for precursor ion in HCD cell.
[b] Second abundant ion in isotopic pattern.
[c] Quantification ion (most abundant MS/MS transition).
[d] Confirmation ion (second most abundant MS/MS transition).
[e] Second abundant ion in isotopic pattern.

detection modes (FS and t-MS^2) and the isotopic ratio was confirmed with $<10\%$ of intensity variations (Table 1). Two fragment ions, with the highest signal intensity, were selected as quantification and confirmation ions (Table 1) and the relative intensities of their ratios were used for confirmation of the targeted compounds and to avoid false positives. The quantification ion, with the highest signal intensity, was used to establish the limits of detection and quantification. Mass scale stability was assessed by measuring the mass measurement accuracy of each ion (precursors and fragments) for each concentration level of the linear dynamic range of the calibration. Mass accuracy stability of measurements over time was evaluated in FS mode for ANA-a (250 μg/L) over a month for a total of 120 acquisitions. Selectivity was improved with the optimization of the extracted masses from acquisition data, and the mass tolerance was set to 5 ppm ($\pm$2.5 ppm). The masses were selected at three points of a LDTD peak for a target compound, two at the extremities and one at the top. Each concentration level of the internal calibration was analyzed in triplicates using standard addition (ranging from 0.5 to 1000 μg/L). Seven-point calibration curves were prepared with blank bloom water matrices for validation. The concentration of internal standard PHE-D_5, (200 μg/L), was selected for its capacity to correct the signal variation of ANA-a with three different concentrations on the calibration curve, 1, 50 and 750 μg/L (data not shown). Method detection limit (MDL) and method quantification limit (MQL) were established by calculating 3 and 10 times respectively the standard deviation of the mean value of 6 spiked blank matrix samples ($n=6$) containing approximately 5 times the estimated concentration for detection limit (1 μg/L). Accuracy, interday/intraday variations, and matrix effects were determined with three different concentrations on the linearity range (1, 50 and 750 μg/L, $n=6$) in blank relevant matrix. Intraday repeatability was estimated over six weeks. Accuracy values were determined by the relative error (%) and precision values were defined as the relative standard deviation (%). The matrix effect was determined by comparing spiked blank relevant matrix with spiked pure solvent samples and the ratios gave the signal recovery and were expressed as percentage.

All validation parameters were determined for both scan modes (FS and t-MS^2) for performance comparison. Statistical comparison was used when needed with the Statistical Package for Social Science (SPSS 21.0, Chicago, IL) for Windows. ANOVA test and Tukey's post hoc tests were used with statistical significance defined as $P<0.05$.

4. Results and discussion

4.1. Solutions pH and LDTD laser pattern optimization

The pH of the working solutions was optimized to consider the presence of PHE-D_5 with ANA-a in the samples and therefore increase signal intensity. The p*K*a of ANA-a is 9.4 and the p*K*a's of PHE, are 2.18 and 9.09 [33,34]. The effect of the pH on signal intensity was studied between pH 2 and 13. As shown in Supplementary materials Fig. A-1, it is found that above neutral pH, signal intensities decrease. First, for ANA-a, it is known that it is unstable in alkaline conditions and degrades into its metabolites [2]. Also, with a pH lower than 9.4, the global charge state is positive, which improves ionization stability and reproducibility prior to MS detection. As for PHE-D_5, considering both p*K*a values, its global charge becomes negative in alkaline conditions with pH higher than 9.1. Finally, the pH in the working solutions was adjusted to 2, for higher stability and to improve the storage conditions of ANA-a.

The LDTD parameters were previously optimized and discussed for ANA-a, including deposition solvent, carrier gas flow and laser pattern including laser power [21,22,35]. However, the LDTD laser power was selected in order to have a minimum desorption of PHE without affecting ANA-a. In the proposed method, there is no need to separate the two compounds with laser desorption since the isobaric masses are distinguished through high resolution mass detection. Furthermore, the internal standard PHE-D_5, has to be desorbed with the same amount of energy as PHE. Fig. 1 presents the new condition results with the same correlation of signal intensity with the laser power (%) of ANA-a and PHE compared to the first optimization [21]. For optimal desorption of both compounds, laser power was set at 45% since PHE-D_5 signal does not significantly increase above a laser power of 40% ($P>0.05$), but ANA-a signal significantly decreases for a laser power above 45% ($P<0.05$). The parameters were optimized to the following settings: 2 s at 0%, 1s ramping from 0% to 45%, 2 s hold at 45%, 0.1 s from 45% to 0% and 2 s hold at 0%, for a total desorption time of 7 s.

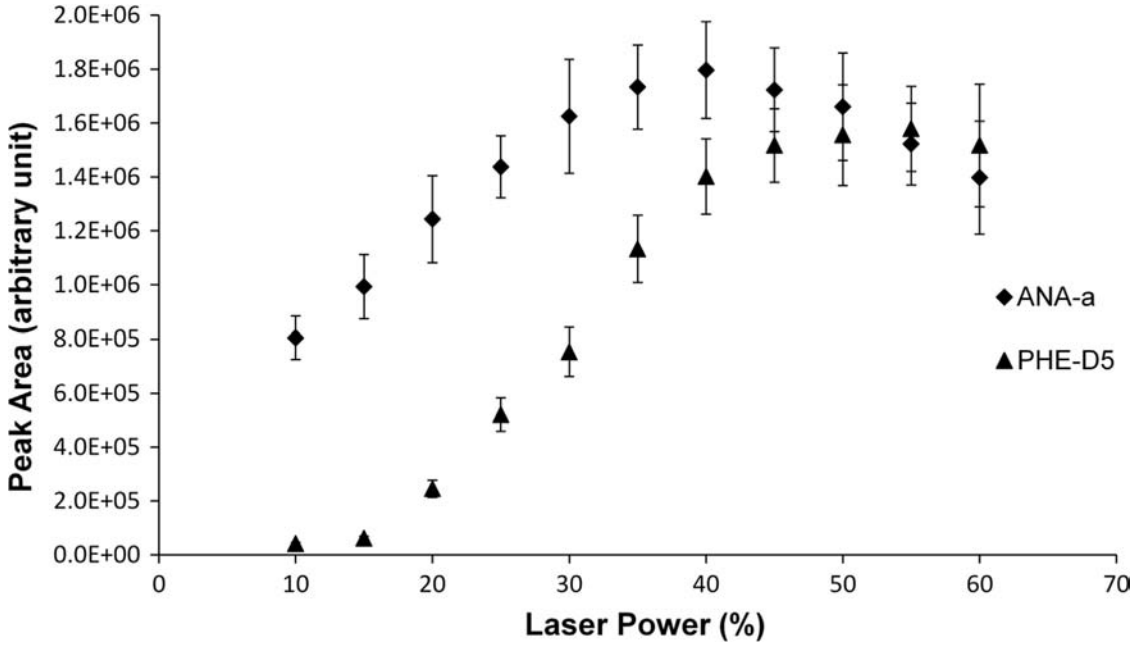


Fig. 1. Effect of LDTD laser power on average peak area of the target compound, ANA-a and PHE-D_5. Vertical error bars represent standard deviations from the mean ($n=6$).

A slightly shorter pattern was used for analysis without affecting the desorption step.

4.2. LDTD–APCI–HRMS parameters optimization

Signal intensity and selectivity are two major parameters when optimizing an analytical method in complex matrices with low concentrations of target analytes (μg/L to low ng/L). According to the European Commission, the confirmation criteria for MS/MS detection consists of using two different transitions for a precursor ion. For HRMS detection operated in full scan mode at a resolution higher than 10 000 FWHM, the second-most abundant ion in isotopic pattern must be distinctive with 10% of peak height [36]. The Q-Exactive is a two dimensional Orbitrap and it can thus enhance selectivity using both criteria, thereby reducing the possibility of false positives in complex analytical conditions [37]. The LDTD is a sample introduction technique which eliminates the separation step prior to detection in order to increase sample analysis time as well as sample throughput and there is no criteria given using this apparatus for analysis confirmation with a hybrid HRMS detector. Considering these, the following optimization of different HRMS parameters are presented in both FS and t-MS^2 scan modes to determine the optimal detection method using the LDTD–APCI coupled with the Q-Exactive mass spectrometer.

A lock mass is used in HRMS detection, for internal mass correction of the measured accurate mass. According to the manufacturer recommendations, external and internal mass calibrations (with and without lock mass) give mass accuracies of <1 ppm and <3 ppm, respectively, under defined conditions [27]. A lock mass is selected for its constant presence in samples and its signal must be stable throughout the analysis. Fig. A-2 presents the different lock masses used for mass correction and they were selected according to their detection in empty LDTD plate wells, pure solvent blanks and in the bloom water sample matrix background in FS mode (m/z 50–300), depending on their abundance and recurrence. The results show the distribution of mass shifts ($n=12$) of the precursor ion of ANA-a (m/z 166.1232) in FS mode including the maxima, minima, quartiles and median corrected with different lock mass target. Each exact masses used are presented with their corresponding molecular formula. Without the use of a lock mass in complex matrix, the mass shift of the target ion is higher than 3 ppm, however, m/z 131.1184, 155.1184 and 195.1487 make a significant correction to the accurate measured mass with mass shift lower than 3 ppm. The selected mass was m/z 155.1184 according to its capability to permit significant mass correction with mass shift lower than 1 ppm and with less mass variation (RSD $<15\%$) ($P<0.05$).

The Q-Exactive has the ability to temporarily trap the ions in the detector, unlike a triple quadrupole mass spectrometer which operates with a continuous path to the detection. For Orbitrap analyzers, the automatic gain control (AGC) is the total ion population injected and it has to be pre-defined as the AGC target. The injection time (IT) of the population to the detector will vary depending on the number of ions introduced to the mass analyzer. Therefore, the AGC target is selected to have a maximum of target ions travelling to the detector and which compete with the background molecules. Moreover, injection time will affect the duty cycle of the detection, which establishes the number of measurements essential for accurate quantification. A compromise between signal intensity and repeatability is made under specific conditions. For a FS scan, large amounts of background ions are analyzed with targeted compounds so the AGC target should be high enough to "trap" these ions and increase their signal intensity. As for the t-MS^2 scans, much fewer ions are transferred to the Orbitrap analyzer, since only targeted precursors are transferred to the C-trap and then fragmented [23,30]. Fig. A-3 presents the variation of signal intensity of ANA-a and PHE-D_5 for different AGC targets with different maximum ion time injections of both FS and t-MS^2 scan modes. The selected AGC targets were 3×10^6 ions for a maximum of 100 ms and 10^5 ions for a maximum of 50 ms, respectively. These results were selected in accordance with the previous explanations.

The main novelty of the Q-Exactive mass spectrometer compared to other Orbitrap analyzers is the use of a high-performance quadrupole precursor selection and a HCD cell which enables SIM and MS/MS experiments. The use of a precursor mass filter and fragmentation leads to great improvements of selectivity in complex matrices for a HRMS instrument. As for triple quadrupole mass analysis, two fragments were selected, one for quantification and one for confirmation. The optimized energies with their respective fragments are presented in Table 1.

The selectivity of HRMS analysis is principally determined by the resolving power (RP) and the mass tolerance (MT) [30,37]. First, using higher RP enables a better mass accuracy, thus a higher selectivity. Yet, increasing the RP decrease the number of acquisitions for an analysis due to duty cycles [37]. For quantitative measurements with acceptable RSDs, it is generally agreed that a LC peak must count at least seven acquisition points [23]. This notion is also considered for a LDTD acquisition peak. The LDTD desorption is faster than a usual elution time for a LC peak for a target compound. Therefore, the number of acquisition points in relation with RP was studied to yield the best compromise between selectivity and repeatability. The tested RP were between 17 500 and 140 000 FWHM (m/z 200) for both FS and t-MS^2 scan modes with results shown in Fig. 2. As previously explained, the number of acquisition points decreases with the increase of RP for both scan modes. Accordingly, due to a decrease of duty cycle for t-MS^2 analysis, less data is acquisitioned. With these criteria, the selected RP for FS scans was 35 000 FWHM (m/z 200) and 17 500 FWHM (m/z 200) for t-MS^2. Second, by narrowing the mass tolerance of a monitored ion in a mass extraction window, selectivity is greatly enhanced by reducing the presence of false positives. However, mass tolerance must consider the accuracy of a target mass given that minimizing a mass tolerance window can eliminate the presence of masses outside the established range. Fig. 3 presents the optimization of the mass tolerance for the mass extraction of the ANA-a quantification fragment in t-MS^2 mode. An adequate mass tolerance was chosen to be 5 ppm (±2.5 ppm), by comparing mass tolerances between 1 and 10 ppm. With mass windows smaller than 5 ppm, there is a mass distortion and there is no difference on the signal with a larger window. According to Kaufmann et al. [37], with FS scans using an Exactive mass spectrometer, the resolving power must be higher than 50 000 (m/z 200) with a MT of maximum 5 ppm for a comparable selectivity with conventional MS/MS experiments with SRM acquisitions. Unfortunately, the FS mode using the LDTD–APCI interface, in this case, does not permit quantitative analysis with resolving power higher than 35 000 FWHM (m/z 200) because of the limited amount of data points during the acquisition (the peak width is approximately 0.5 s). On the other hand, considering that the t-MS^2 scan mode can be compared to a traditional SRM experiment for its levels of ion selection, the use of a resolving power of 17 500 FWHM (m/z 200) with a MT of 5 ppm is more selective than FS acquisitions and should be more selective than a common SRM experiment considering the high mass discrimination.

4.3. Data analysis and method validation

To confirm the signal resolution of ANA-a and PHE, a FS data acquisition was recorded at 17 500 FWHM (m/z 200). The respective signal of ANA-a and PHE are presented at the left of the mass spectrum (Fig. 4) and they are complete separated. This is in accordance with the resolution needed (>4500 FWHM) to dissociate the two signals considering their difference in mass values.

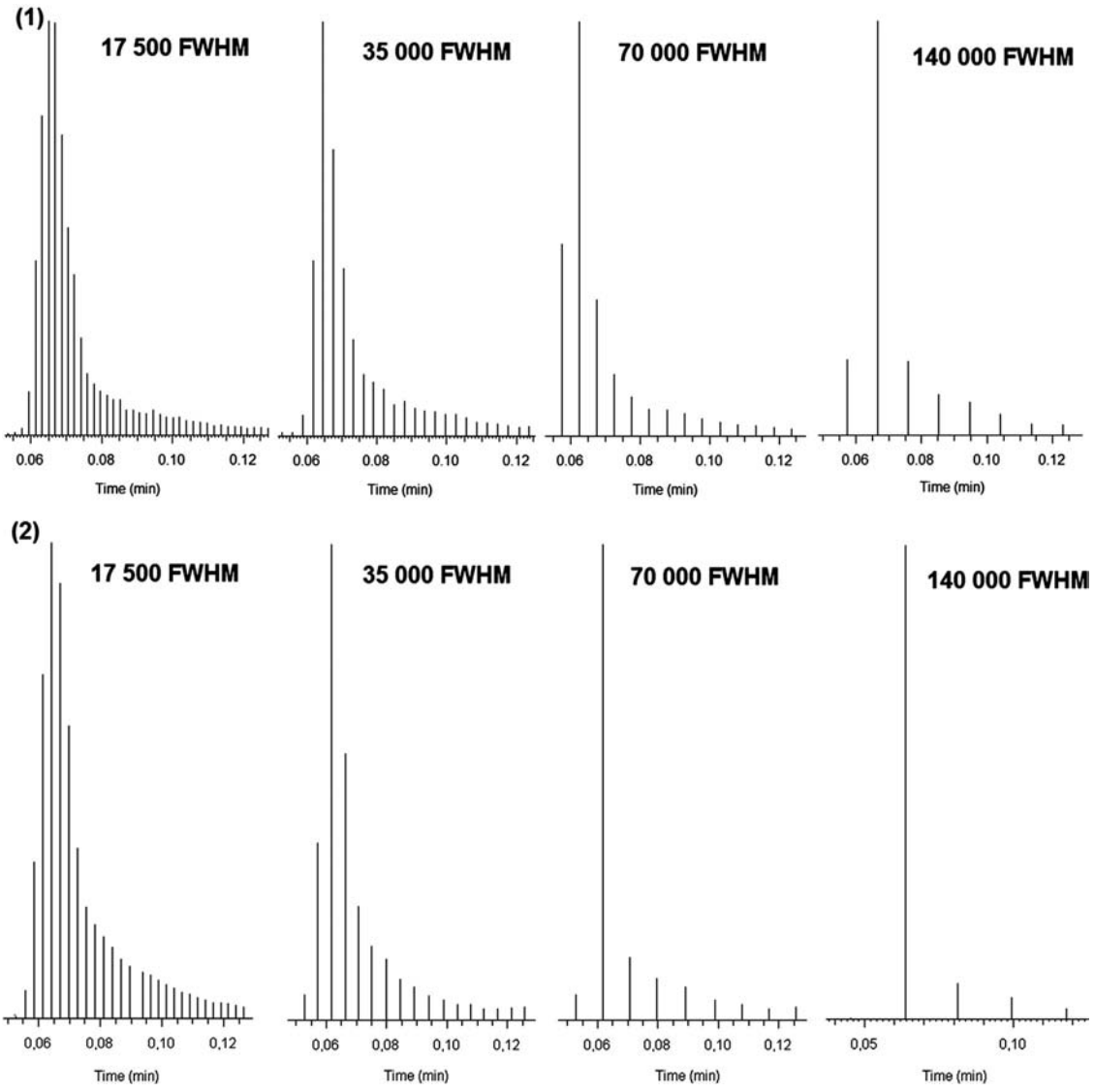


Fig. 2. Examples of the number of data acquisition for a LDTD peak of ANA-a with the different resolving powers scanned by (1) FS mode and (2) t-MS^2 mode.

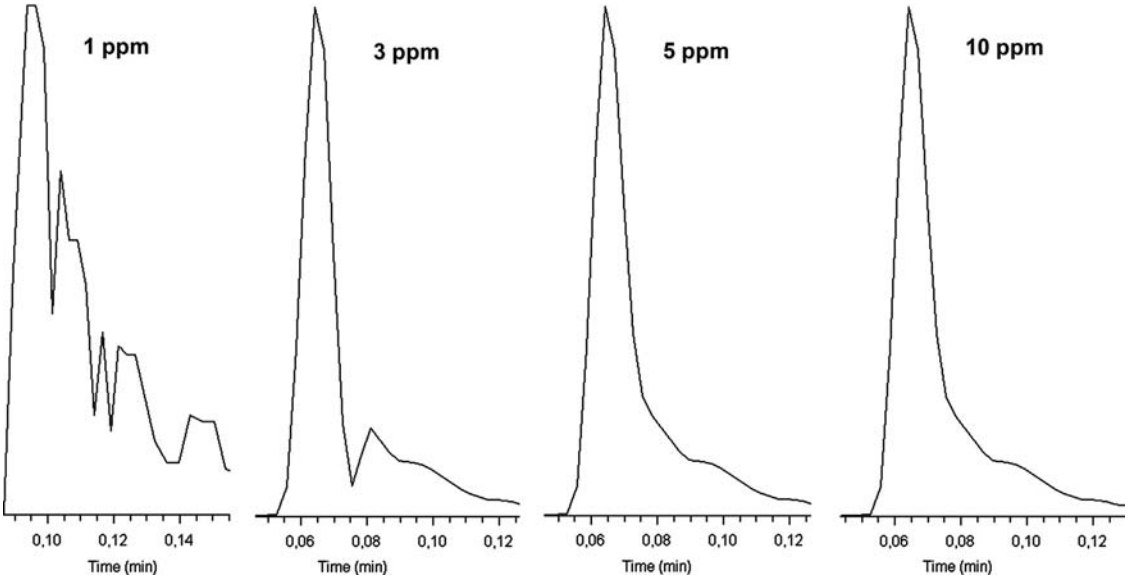


Fig. 3. Effect of different mass tolerances from the mass extraction of the ANA-a quantification fragment (m/z 149.0965) by t-MS^2 mode and impact on the LDTD peak shape distortion.

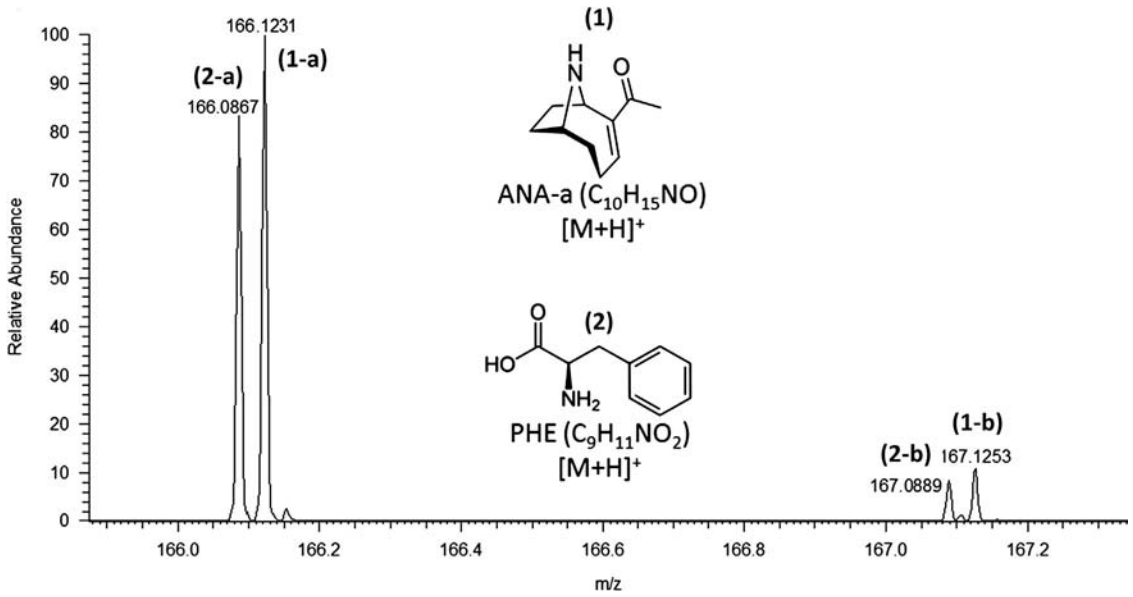


Fig. 4. Mass spectrum of (1) ANA-a and (2) PHE acquisitioned in FS scan mode with a resolving power of 17 500 FWHM (*m*/*z* 200). (1-a) and (2-a) are the resolved signals and (1-b) and (2-b) are the signals of the first characteristic isotopes of both compounds.

Table 2
Comparison of method validation parameters for experience modes (FS and t-MS^2).

Experience mode	R^2	Linearity range (μg/L)	MDL (μg/L)	MQL (μg/L)	Standard avg. RSD (%)
FS	0.998	1.5–1000	0.5	1.5	10
t-MS^2	0.999	0.5–1000	0.2	0.6	5

To the right, the characteristic isotopes of the two compounds appear with relative heights of approximately 10%. The use of isotopically-labeled phenylalanine (PHE-D_5) as internal standard was justified by the unavailability of isotopically-labeled ANA-a and by its structural analogy. Moreover, PHE-D_5 has also been successfully used as internal standard in previous work [17]. We used a seven-point internal calibration curve based on a standard addition by spiking ANA-a in blank relevant matrix with a linear dynamic range between 0.5 and 1000 μg/L analyzed in triplicates. The concentration of PHE-D_5 used in every measure is 200 μg/L and was optimised considering the lowest variability of signal ratio (ANA-a/ PHE-D_5) throughout the calibration curve (data not shown). Table 2 summarizes the validation parameters for the two experience modes. With the Q-Exactive operating in t-MS^2 (targeted ion fragmentation), the MDL and MQL (n=6) were lower than for the FS (full scan) mode with values of 0.2 and 0.6 μg/L compared to 0.5 and 1.5 μg/L. Overall, these results are an improvement compared to previous values obtained using a triple quadrupole mass spectrometer which ranged from 1 to 4 μg/L [21]. Accuracy, expressed as relative errors (RE—%), intraday/interday precisions, expressed as relative standard deviations (RSD—%) and matrix effect expressed as the percentage of signal recovery of replicate measurements (n=6), are summarized in Table 3 and were evaluated with three concentration levels from the calibration curve, 1, 50 and 750 μg/L in blank relevant matrix. Overall, the data showed similar accuracy for both scan modes at higher concentrations with ≤15% RE. However, at the lowest concentration, FS mode showed lower accuracy with >15% RE. The t-MS^2 experiment offered less measurement variability (≤10% RSD) compared to FS experiment (≤15% RSD). As for the signal recovery of ANA-a for FS mode at higher concentrations and for t-MS^2 mode for all concentrations, results showed no significant matrix effect in the analysis with values ranging from 96 to 108% with a precision <15%. However, at

Table 3
Parameters for FS and t-MS^2 detection by LDTD–APCI–HR/MS in positive ionization mode (PI)→$[M+H]^+$.

Experience mode	QC concentrations (μg/L)	Accuracy (RE %)	Intraday (RSD %)	Interday (RSD %)	Signal recovery from matrix effect (%)
FS	1	17	12	15	172
	50	13	10	12	108
	750	11	11	13	98
t-MS^2	1	9	9	8	102
	50	6	10	9	96
	750	8	8	7	98

the lowest concentration for FS mode, the signal recovery was 172% with a precision of 16% showing that significant signal enhancement due to matrix effect occurs at low concentrations with this scan mode. Two fragments ions of ANA-a were selected and their second most abundant isotope was monitored for ion confirmation to avoid false positives for HRMS analysis (Table 1). The mass accuracy for all ions monitored in HRMS is shown in Table 1 and the values were deemed acceptable (0.65–0.76 ppm) compared to instrument standard values for internal calibration with lock mass (<1 ppm). Mass scale stability is shown in Fig. A-4 and mass accuracy variation is stable with average mass accuracies of <0.8 ppm and RSD variation of <10%. The assessment of mass accuracy stability of measurements over time is shown on Fig. A-5 with 120 acquisitions. An average mass accuracy of <0.8 ppm with RSD variation of <15% over 4 weeks of analysis shows an acceptable stability of exact mass measurements. Finally, the developed method was tested on positive cyanobacterial bloom samples of 8 different lakes around the province of Québec, Canada, obtained during the proliferation season. The detection was done with the two optimized scan modes and the selectivity was evaluated by comparing the new quantification approaches with a parallel certified standard LC–MS/MS analysis performed by the CEAEQ (Table 4). Except for sample no 5, all concentrations were reported below our determined limits of detection (<0.1–0.01 μg/L). For the t-MS^2 analytical method, the only positive sample was no 5, with a concentration of 0.21 μg/L, which is similar to the value reported by the CEAEQ (<0.2 μg/L). Inversely, the FS method gives considerably higher concentration of ANA-a for samples no 1, 2,

Table 4
Anatoxin-a detection in lake samples using LDTD–APCI–HR/MS and LC–MS/MS.

No. sample	Location	Date	ANA-a detection FS (μg/L)	ANA-a detection t-MS^2 (μg/L)	ANA-a detection by LC–MS/MS (μg/L)
1	Estrie	2013-06-14	2.5 (11)	ND	< 0.1
2	Estrie	2013-06-14	1.1 (9)	ND	< 0.02
3	Saguenay	2013-06-20	ND	ND	< 0.01
4	Saguenay	2013-06-20	ND	ND	< 0.01
5	Abitibi-Témiscamingue	2013-06-24	1.9 (10)	0.21 (7)	< 0.2
6	Abitibi-Témiscamingue	2013-07-31	ND	ND	< 0.01
7	Abitibi-Témiscamingue	2013-07-31	1.6 (12)	ND	< 0.02
8	Montérégie	2013-08-01	ND	ND	< 0.01

ND—not detected.

5 and 7 with values ranging from 1.1 and 2.5 μg/L and these samples had the characteristic of being highly charged in green algae. The presented results clearly show the presence of false positives in the FS scan analysis and the lack of selectivity of the analytical method. Furthermore, the validation was done with only one sample from the lot. Normally, reported concentrations are very low, around the concentrations of our tested samples. This is in agreement with the low occurrence of ANA-a production in cyanobacterial blooms [1,4]. Nonetheless, the evaluated MDL and MQL of the present developed method are substantially lower than the pertinent guidelines in Canada (3.7 μg/L) making it a valid approach for the screening ANA-a for risk management purposes. Globally, an analytical pathway using precursor selection and fragmentation is the method of choice for a quantitative detection using the LDTD–APCI–HRMS with the Q-Exactive mass spectrometer instrument with confirmed selectivity and sensitivity. Moreover, high resolution mass spectrometry is a method of choice for the resolution of isobaric interferences as demonstrated with the signal separation of ANA-a and the amino acid phenylalanine.

5. Conclusion

A new analytical method was explored, the LDTD–APCI–HRMS, using a mass spectrometric hybrid, the Q-Exactive. This method was successfully used to resolve the misidentification of the cyanobacterial toxin, anatoxin-a, from the essential amino acid, phenylalanine. Two scan modes were explored (FS and t-MS^2) to determine the best detection method for selective, sensitive and quantitative analysis. FS mode did not show good results in terms of selectivity given an important presence of false positives in charged complex matrices. On the other hand, the use of t-MS^2 greatly increases the selectivity of compound detection. An internal calibration with standard addition was also validated with the isotopically-labeled phenylalanine (PHE-D_5) as internal standard. The method was validated and deemed linear with correlation coefficients (R^2) above 0.999. MDL and MQL ranged from 0.2 to 1.5 μg/L, and with better sensitivity compared to the previous study of ANA-a analysis using the LDTD–APCI-MS/MS. Accuracy and precision values were below 15% and the signal recovery showed no significant matrix effect with values ranging from 96 to 108% except for FS detection at the lowest concentration which showed a precision higher than 15% and a signal enhancement with a recovery of 172%. With the use of a lock mass, mass accuracy was below 1 ppm with low variation (< 15%). The LDTD–APCI–HRMS is a powerful tool for the screening of anatoxin-a at lower concentrations than established guidelines (3.7 μg/L) in natural and recreational water with simple sample preparation, fast quantification responses (< 15 s/samples), high-throughput analysis and high selectivity. Compared to traditional MS/MS and HRMS detection, the Q-Exactive has the advantage of combining high-performance precursor selection with a high resolution and accurate mass detection. It would be possible, for future work, to adapt this analytical technique for the detection of ANA-a in different matrices such as plant extract and animal tissues given that such performances are attractive for fast trace level detection of contaminants in complex environmental matrices.

Acknowledgments

The Fond de Recherche Québec Nature et technologies and the Natural Sciences and Engineering Research Council of Canada (NSERC) are acknowledged for financial support. We thank Thermo Fisher Scientific and Phytronix Technologies for their support. We also thank Paul Fayad and Sung Vo Duy for their technical help and scientific support.

Appendix A. Supporting information

Supplementary data associated with this article can be found in the online version at http://dx.doi.org/10.1016/j.talanta.2014.10.021.

References

[1] J. Osswald, S. Rellan, A. Gago, V. Vasconcelos, Environ. Int. 33 (2007) 1070–1089.
[2] B.A. Neilan, L.A. Pearson, J. Muenchhoff, M.C. Moffitt, E. Dittmann, Environ. Microbiol. 15 (2013) 1239–1253.
[3] D. Drobac, N. Tokodi, J. Simeunovic, V. Baltic, D. Stanic, Z. Svircev, Arh. Hig. Rada. Toksiko 64 (2013) 305–316.
[4] R. Kaushik, R. Balasubramanian, Crit. Rev. Environ. Sci. Technol. 43 (2013) 1349–1383.
[5] K.J. James, A. Furey, I.R. Sherlock, M.A. Stack, M. Twohig, F.B. Caudwell, O.M. Skulberg, J. Chromatogr. A. 798 (1998) 147–157.
[6] J.K. Fawell, R.E. Mitchell, R.E. Hill, D.J. Everett, Hum. Exp. Toxicol. 18 (1999) 168–173.
[7] E.J. Faassen, L. Harkema, L. Begeman, M. Lurling, Toxicon 60 (2012) 378–384.
[8] B. Puschner, B. Hoff, E.R. Tor, J. Vet. Diagn. Invest. 20 (2008) 89–92.
[9] I. Chorus, Federal Environment Agency, Germany, 2012, ch. January 2012, p. 151.
[10] F.A. Dorr, V. Rodriguez, R. Molica, P. Henriksen, B. Krock, E. Pinto, Toxicon 55 (2010) 92–99.
[11] S.H. Wong, E. Hindin, J. Am. Water Works Assoc. **74** (1982) 528–529.
[12] K. Harada, Y. Kimura, K. Ogawa, M. Suzuki, A.M. Dahlem, V.R. Beasley, W.W. Carmichael, Toxicon **27** (1989) 1289–1296.
[13] A. Furey, J. Crowley, B. Hamilton, M. Lehane, K.J. James, J. Chromatogr. A 1082 (2005) 91–97.
[14] A. Afzal, T. Oppenlander, J.R. Bolton, M.G. El-Din, Water Res. 44 (2010) 278–286.
[15] M. Gugger, S. Lenoir, C. Berger, A. Ledreux, J.C. Druart, J.F. Humbert, C. Guette, C. Bernard, Toxicon 45 (2005) 919–928.
[16] S. Bogialli, M. Bruno, R. Curini, A. Di Corcia, A. Lagana, J. Chromatogr. A 1122 (2006) 180–185.
[17] I.K. Dimitrakopoulos, T.S. Kaloudis, A.E. Hiskia, N.S. Thomaidis, M.A. Koupparis, Anal. Bioanal. Chem. 397 (2010) 2245–2252.
[18] S.A. Oehrle, B. Southwell, J. Westrick, Toxicon 55 (2010) 965–972.
[19] K.J. James, J. Crowley, B. Hamilton, M. Lehane, O. Skulberg, A. Furey, Rapid Commun. Mass Spectrom. 19 (2005) 1167–1175.
[20] M.P. Balogh, Spectroscopy 19 (2004) 34–40.
[21] P. Lemoine, A. Roy-Lachapelle, M. Prévost, P. Tremblay, M. Solliec, S. Sauvé, Toxicon **61** (2013) 165–174.
[22] P.B. Fayad, M. Prévost, S. Sauvé, Anal. Chem. 82 (2010) 639–645.
[23] Y. Zhang, Z. Hao, M. Kellmann, A. Huhmer, ed. C. Thermo Fisher Scientific, San Jose, 2012, ch. 12.
[24] A. Makarov, E. Denisov, A. Kholomeev, W. Baischun, O. Lange, K. Strupat, S. Horning, Anal. Chem. 78 (2006) 2113–2120.
[25] J.L.H. Jiwan, P. Wallemacq, M.F. Herent, Clin. Biochem. 44 (2011) 136–147.
[26] Y. Moulard, L. Bailly-Chouriberry, S. Boyer, P. Garcia, M.A. Popot, Y. Bonnaire, Anal. Chim. Acta 700 (2011) 126–136.
[27] T.F. Scientific, in: Q Exactive™, 2012, vol. Revision C—1288120.

[28] A. Michalski, E. Damoc, J.P. Hauschild, O. Lange, A. Wieghaus, A. Makarov, N. Nagaraj, J. Cox, M. Mann, S. Horning, Mol. Cell. Proteomics (2011) **10**.
[29] K.P. Bateman, M. Kellmann, H. Muenster, R. Papp, L. Taylor, J. Am. Soc. Mass Spectrom. 20 (2009) 1441–1450.
[30] G. Fedorova, T. Randak, R.H. Lindberg, R. Grabic, Rapid Commun. Mass Spectrom. 27 (2013) 1751–1762.
[31] A. Roy-Lachapelle, P.B. Fayad, M. Sinotte, C. Deblois, S. Sauvé, Anal. Chim. Acta 820 (2014) 76–83.
[32] Centre d'Expertise en Analyse Environnementale du Québec, DR-12-VMC, Québec, Canada, 2009.
[33] A.M.P. Koskinen, H. Rapoport, J. Med. Chem. **28** (1985) 1301–1309.
[34] W.M. Haynes, CRC Handbook of Chemistry and Physics, 94th ed., CRC Press, 2013–2014.
[35] M. Boisvert, P.B. Fayad, S. Sauvé, Anal. Chim. Acta 754 (2012) 75–82.
[36] The Comission of the European Communities, Off. J. Eur. Communities (2002) 8–36.
[37] A. Kaufmann, P. Butcher, K. Maden, S. Walker, M. Widmer, Anal. Chim. Acta 673 (2010) 60–72.

Talanta 132 (2015) 845–850

Contents lists available at ScienceDirect

Talanta

journal homepage: www.elsevier.com/locate/talanta

Microwave-assisted synthesis of carbon dots and its potential as analysis of four heterocyclic aromatic amines

C. López [a,b], M. Zougagh [b,c], M. Algarra [d,*], E. Rodríguez-Castellón [d], B.B. Campos [e], J.C.G. Esteves da Silva [e], J. Jiménez-Jiménez [d], A. Ríos [a,b]

[a] Department of Analytical Chemistry and Food Technology, University of Castilla-La Mancha, 13004 Ciudad Real, Spain
[b] Regional Institute for Applied Chemistry Research, IRICA, 13004 Ciudad Real, Spain
[c] Albacete Science and Technology Park, 2006 Albacete, Spain
[d] Department of Inorganic Chemistry, University of Málaga, Campus de Teatinos s/n, 29071 Málaga, Spain
[e] Centro de Investigação em Química, Departamento de Química e Bioquímica, Faculdade de Ciências da Universidade do Porto, Porto, Portugal

ARTICLE INFO

Article history:
Received 26 June 2014
Received in revised form
30 September 2014
Accepted 8 October 2014
Available online 31 October 2014

Keywords:
Carbon dots
Heterocyclic aromatic amines
Sensor
Fluorescence quenching

ABSTRACT

Fluorescent water soluble carbon nanoparticles, in short carbon dots (CDs), was synthesized from lactose by microwave assisted hydrochloric acid method. Characterized by TEM and DLS to obtain the morphology shape (average 10 nm in size), with a higher negative surface charge supported by the composition was obtained by XPS spectroscopy. The maximum of the emission was centered at 450 nm with a lifetime of 2.1 ns. Without further functionalization of the CDs a nanosensor was obtained that responded exponentially to HAAs in the 0.35–0.45 mg L^{-1} concentration range by fluorescence static quenching, demonstrated by the lifetime analysis of the CDs in presence of HAAs. Some amino compounds were selected as model for interferences to evaluate the selectivity of this method, showing a notorious added value, with recoveries around 98%. The accuracy of the method was in terms of RSD about 2.5%. The results suggest their promising applications in chemical sensing.

© 2014 Elsevier B.V. All rights reserved.

1. Introduction

The International Agency for Research on Cancer (IARC) regards some of the heterocyclic aromatic amines (HAAs) as possible human carcinogens such as (2-amino-3,4-dimethyl-imidazo [4,5-f]-quinoline, 2-amino-3,8-dimethyl-imidazo [4,5-f] quinoxaline and 2-amino-3,4,8-trimethylimidazo [4,5-f]-quinoxaline, 2-amino-3,7,8-trimethyl-imidazo [4,5-f]-quinoxaline (class 2B) and 2-amino-3-methylimidazo [4,5-f]-quinoline (class 2A) [1–3]. Therefore, an important issue in Analytical Chemistry as the main source is the cooked food when the proteins are converted at high temperatures due to the incomplete their combustion process.

Chromatographic methods are the most widely used when analyzed grilled, barbecued or fried meat and fish and urine samples, being HPLC–MS the main analytical technique used previous microextraction procedure [4–13]. HPLC with different detection systems such as UV [14–16] and fluorescence [17,18]; GC–MS [19–23] and by electrophoresis capillary (CE) [24–28], an extensive revision of all this techniques and compared can be found in literature [29]. Very few references to other techniques have been found in the literature for the analysis of these harmful metabolites, except for improvements in the processes of extraction prior to chromatographic analysis such as the used of supercritical fluids [27] and ionic liquids [30], making interesting the development of new alternatives as the sensitive luminescent techniques for their analysis is an important and interesting challenge in the analysis of HAAs [31].

Nanotechnology offers the best alternative, which combines the easiest design of nanoparticles with their cheap cost and luminescent properties, being the emerging system based in carbon dots (CDs) the best candidates to be applied as a detection system of any analyte to study due to its application in many other areas of analysis. These systems are the one of the lasts discover where heavily functionalized carbon networks are involved, which were firstly discovered by simple purification of carbon nanotubes and nowadays can be obtained by means a great variety of simple process [32–37].

This work shows the photoluminescent characteristics of CDs prepared from lactose using microwave process. The advantages of this treatment include faster preparation method, good fluorescence efficiency, reproducibility and stability of the obtained nanoparticles. Furthermore, the exploitation of the sensorial ability of these CDs gives rise to an excellent tool for the quantification, and without any further functionalization, of four different HAAs, by the quenching effect on the fluorescence of CDs.

* Corresponding author. Tel.: +34 952 131873; fax: +34 952 132000.
E-mail address: malgarra67@gmail.com (M. Algarra).

http://dx.doi.org/10.1016/j.talanta.2014.10.008
0039-9140/© 2014 Elsevier B.V. All rights reserved.

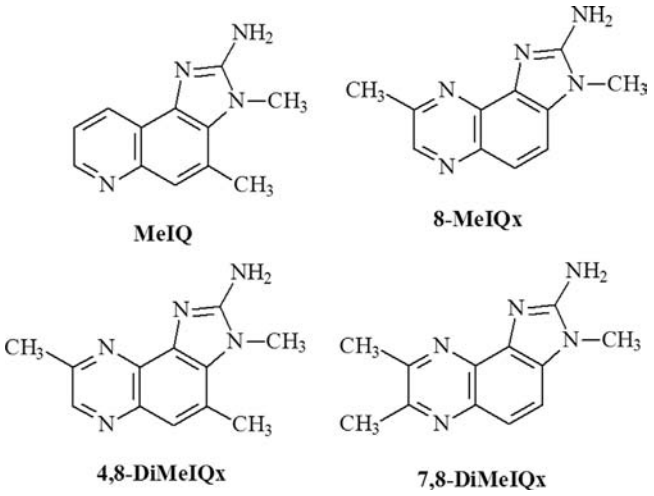


Fig. 1. Chemical structures of the heterocyclic aromatic amines: 2-amino-3,4-dimethyl-imidazo (MeIQ); 2-amino-3,8-dimethyl-imidazo [4,5-f]-quinoxaline (8-MeIQx); 2-amino-3,4,8-trimethylimidazo [4,5-f]-quinoxaline (4,8-DiMeIQx) and 2-amino-3,7,8-trimethyl-imidazo [4,5-f]-quinoxaline (7,8-DiMeIQx).

2. Experimental

2.1. Chemicals

Lactose monohydrate (99%) and hydrochloric (37%) were purchased from Panreac S.A.U. (Barcelona, Spain), 2-amino-3,4-dimethyl-imidazo [4,5-f]-quinoline (MeIQ), 2-amino-3,8-dimethyl-imidazo [4,5-f]-quinoxaline(8-MeIQx), 2-amino-3,4,8-trimethylimidazo [4,5-f]-quinoxaline (4,8-DiMeIQx), 2-amino-3,7,8-trimethyl-imidazo [4,5-f]-quinoxaline (7,8-DiMeIQx), 2-Amino-1-methyl-6-phenyilimidazo [4,5-b]-pyridine (PhIP) and 2-amino-1-methyl-imidazo [4,5-f]-quinoline (iso-IQ) (Fig. 1), were supplied from Toronto Research Chemicals Inc. (North York, ON, Canada). Ethylamine, trimethylamine, lysine, arginine and tyrosine were purchased from Sigma-Aldrich. Ultrapure water used throughout all experiments was purified through a Millipore system. All reagents were used as received without further purification.

2.2. Synthesis of CDs

With ultrasounds, CDs were prepared by mixing a solution of lactose 1 M (50 mL) with concentrated HCl (50 mL). The mixture

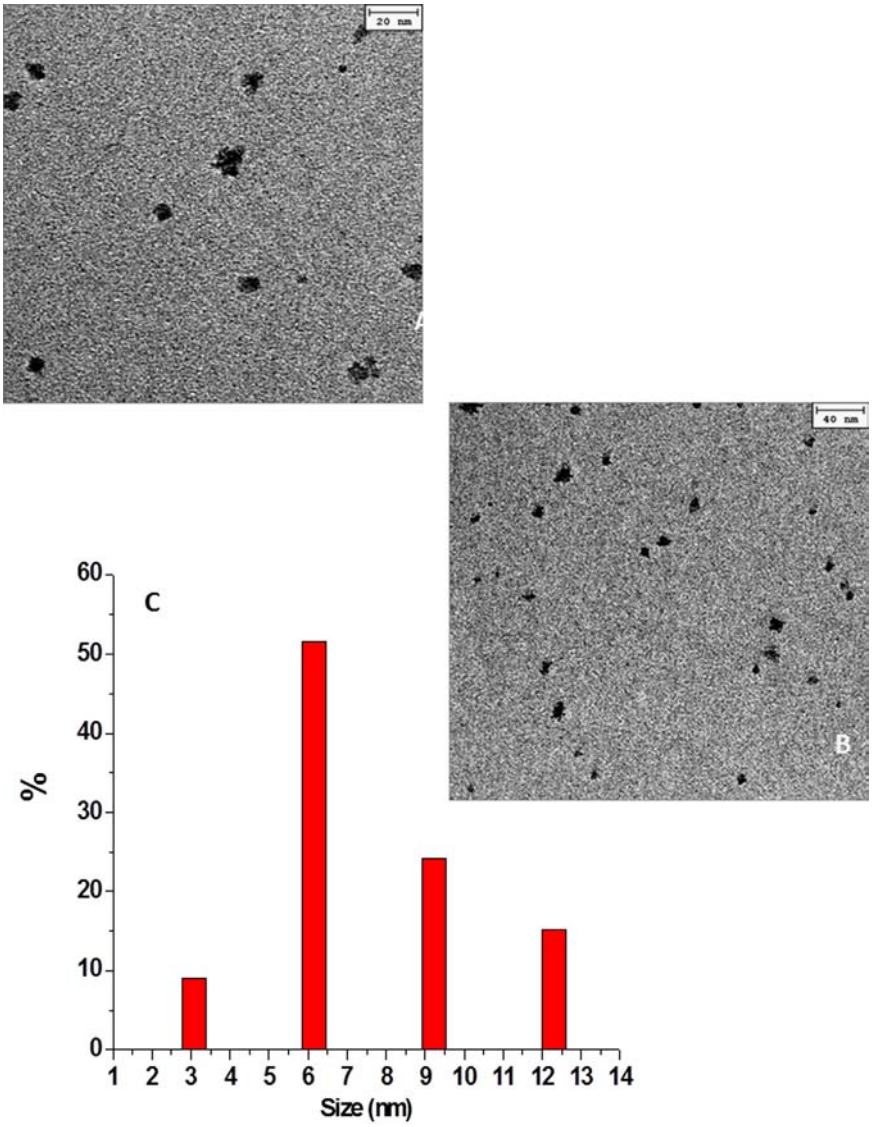


Fig. 2. (A and B) Typical TEM images of CDs thus synthesized at different magnification by assisted microwave procedure at 160 °C, and (C) The corresponding CDs size distribution histogram.

was transferred into a 100 mL Teflon vessel and submitted to a hydrothermal microwave treatment at 160 °C for 15 min (ANTON Microwave 3000 at 20 bar and 750 W), obtaining a brown colour product. The sample was cooled down naturally and the resulted solution was centrifuged, filtered, neutralized to pH 7, centrifuged again and lyophilized to afford the fluorescent CDs for further characterization and use.

2.3. Characterization of CDs and data analysis

PhotonTechnology International (PTI) Inc. Quanta Master 40 spectrofluorometer that was equipped with a 75 W continuous Xenon arc lamp. An ASOC-10 USB interface FeliX GX software was used for fluorescence data acquisition and also controlled the hardware for all system configurations. The slits width for excitation and emission widths were both 2 nm. All optical measurements were performed in 10 mm quartz cell at room temperature. Fluorescence lifetime analysis was done using an Edinburgh Instruments FLS920, equipped with a Xe lamp (450 W) as excitation source for steady state fluorescence measurements and monochromatic LEDs (PicoQuant PLS), controlled by a PDL 880-B system. Fluorescence decays were interpreted in terms of a multi-exponential: $I(t)=A+\Sigma B_i \exp^{-t/\tau i}$, where A and B_i are the pre-exponential factors and τ_i the decay times. Transmission Electron Microscopy (TEM) analysis was carried out with a Philips CM-200. The size and zeta potential (ζ) of CDs were determined using a Zetasizer Nano ZS (Malvern Instruments, U.K.) equipped with a 4 mW HeNe laser operating at $\lambda=633$ nm. Size measurements were recorded with dynamic light scattering (DLS), at 25 °C in a polystyrene cell (ZEN0040) at a scattering angle of 173° and were average of three tests. The ζ measurements were also performed at 25 °C in polycarbonate folded capillary cells, incorporated with gold plated electrodes (DTS1061) and deionized H_2O was the dispersion medium. Both, size and ζ were automatically obtained by the software, using the Stokes–Einstein and the Henry equation, with the Smoluchowski approximation. X-ray photoelectron spectroscopic (XPS) studies were performed on a Physical Electronic PHI 5700 spectrometer using non-monochromatic Mg-*K*a radiation (300 W, 15 kV, 1253.6 eV) for analyzing the core-level signals of the elements of interest with a hemispherical multichannel detector. The spectra of powdered samples were recorded with a constant pass energy value at 29.35 eV, using a 720 μm diameter circular analysis area. The X-ray photoelectron spectra obtained were analyzed using PHI ACESS ESCA-V6.0F software and processed using Multipak 8.2B package. The binding energy values were referenced to adventitious carbon C 1s signal (284.8 eV). Shirley-type background and Gauss–Lorentz curves were used to determine the binding energy.

2.4. Procedure

For the evaluation of HAAs as possible quenchers of the CDs fluorescence in solution, microliters of stock solutions (1000 mg L^{-1}) of chosen analytes were added to 50 μL of CDs keeping constant the final volume to 5 mL. The concentrations ranging upward from 0.5 to 10 mg L^{-1} were measured to obtain the Stern–Volmer plot.

3. Results and discussion

An easiest, rapid and hydrothermal procedure, assisted by microwave treatment, previous purification process, was chosen to obtain CDs from lactose which exhibited a strong emission. The most attractive feature of this method is that the surface passivation step is not necessary, since the starting material. Fig. 2A and B shows the TEM images of CDs at different magnifications revealing, that the synthesis procedure without any modification, could easily disperse in water with a narrow size distribution showing a mean diameter around 10.99 ± 3.97 nm (Fig. 2C). The zeta potential (ζ) of the CDs synthesized by this procedure afforded high negative charge (-29.1 ± 1.46 mV), in accordance with previous results when carbohydrates are used as CDs precursors, where a high density of susceptible functional groups to be in the surface [35], the XPS analysis supported this hypothesis due to synthesis procedure carried out.

The surface composition and elemental analysis for the resultant CDs were characterized by XPS technique. The XPS results indicate that these CDs are composed, in atomic concentration %, of C: 79.99%; O: 14.06%, Na: 3.59; Cl: 2.36%. The C 1s spectrum of CDs (Fig. 3A) is

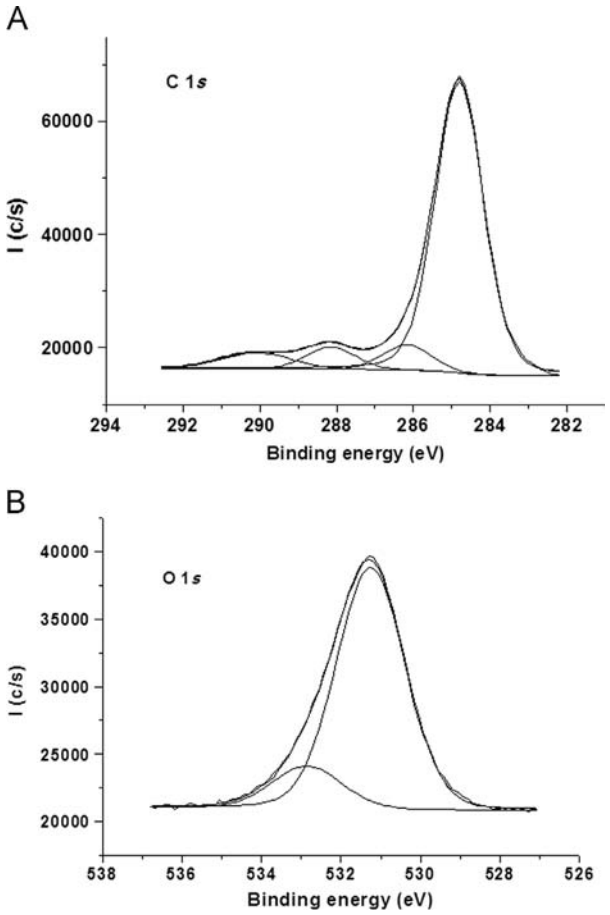


Fig. 3. (A) C 1s and (B) O 1s cores level spectra for CDs.

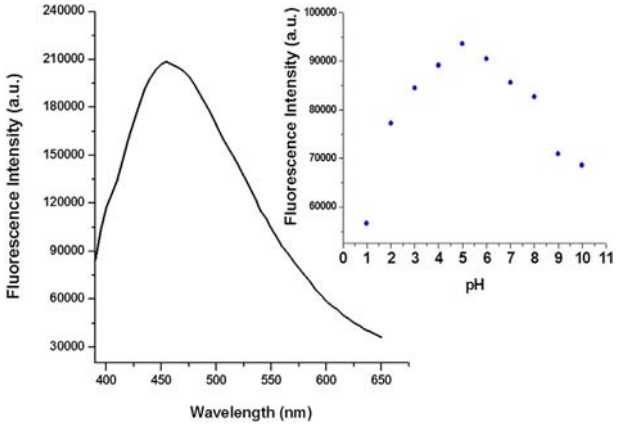


Fig. 4. Fluorescence spectra of CDs obtained from lactose after microwave treatment ($\lambda_{exc}=350$ nm; slit widths: 5.5 nm). Inset: the influence of pH on the intensity of CDs at 450 nm.

composed of four contributions at 284.8 (81%), 286.3 (7%), 288.2 (6%) and 290.1 eV (6%). The first and main contribution at 284.8 eV is assigned to graphitic carbon plus adventitious carbon. The second one at 286.3 eV to carbonyl groups and the contributions at higher binding energy (288.2 and 290.1 eV) to carboxylic and carbonate groups, respectively. The O 1s core level spectrum shows and asymmetric signal that can be decomposed in two contribution at 531.3 eV (85%) and 532.9 eV (15%) assigned to oxygen of carbonyl and carboxylate groups (Fig. 3B). The Cl $2p_{3/2}$ signal appears at 199.1 eV, typically of chlorine covalently bonded to carbon (Cl–C). Finally, the Na 1s signal is symmetric and centred at 1071.2 eV, being assigned to Na^+ as counter ion of the carboxylic group. To further elucidate the surface features of the CDs, various spectroscopic analyses were used, the ATR spectra two prominent bands are observed at 3240 and 1644 cm^{-1}, which correspond to the stretching of –OH and C=O bonds, respectively. The Raman spectrum of the as-prepared CDs was also measured which, in addition to the IR features, revealed distinct peaks: (i) at 1610 cm^{-1} due to the carbonyl groups attached to the CDs, which are bonded to donor groups (ii) a weak band at 1345 cm^{-1} typical of carbon nanostructures in this case due to the CDs core vibrations, i.e.: carbonaceous structure and (iii) at 1078 cm^{-1} likely arising from the C–C and C–O bending modes. Both together, the IR and Raman spectra provide spectroscopic evidences of the composition of the CD dots complementary to that of XPS in this study (Supplementary material).

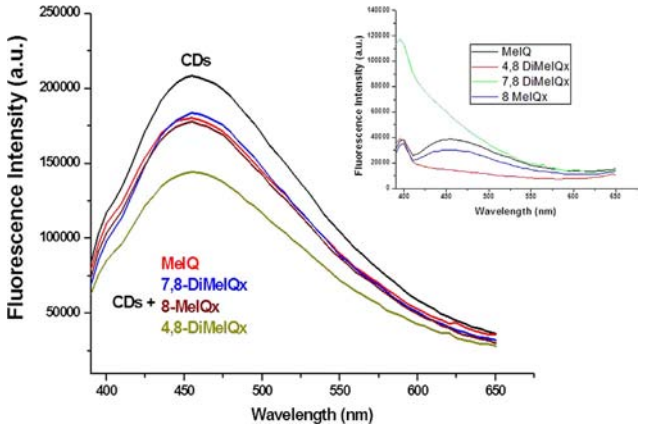


Fig. 5. Influence of HAAs on the fluorescence intensity of synthesized CDs when excited at 350 nm. (Inset the fluorescence of the four HAAs studied).

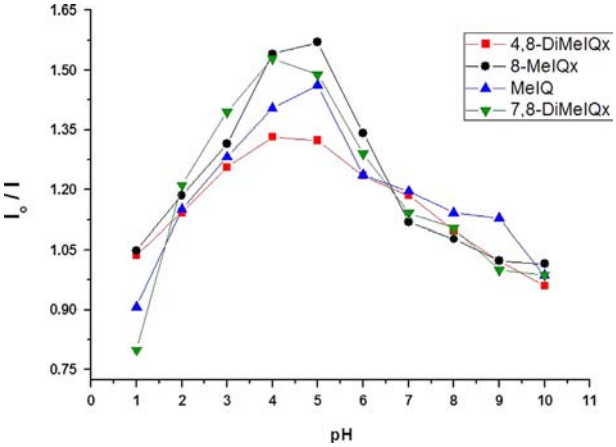


Fig. 6. Influence of the pH on the quenching effect of HAAs at 450 nm.

The influence of the thermal effect was studied over the CDs, and was observed that after the synthesis of CDs by the proposed method, when heated until 100 °C, only an increasing on the fluorescence intensity was observed, around 13% (Supplementary material).

Fig. 4 shows the fluorescence spectra of CDs with a maximum of emission at 450 nm (λ_{exc}=350 nm), showing a full width at half maximum (FWHM) of 152 nm, relative high value, indicating their great size distribution dependence. The stability of CDs was investigated under three different conditions sunlight exposure, ambient light and dark. For this purpose, aliquots of 100-fold dilutions of CDs were prepared and exposed under these conditions during several intervals of times. In all cases the fluorescence intensity at 450 nm were recorded. In general, CDs remain stable for long periods (three months). In addition, CDs are photo-stable when they remain under continuous irradiation. No abnormalities in their fluorescence because of sunlight exposition were observed either.

The influence of pH on the fluorescence activity of CDs was also studied. Inset Fig. 4 shows the pH-response of photoluminescence behavior of the different water-soluble CDs, in which the fluorescence generally tends to increase when increasing the pH of the medium in the range between 1 and 5, and decrease when the pH is high tan 5. It is noticeable than this synthesis procedure increases the fluorescence intensity when increases the pH until 5. No aggregation neither variation in the maximum emission wavelength was observed with the pH 5 for CDs. The analysis of the fluorescence decays shows that the lifetimes, calculated with a three component decay time model was:

$$\mathbf{I}(t) = 1.501 \times 10^2 + 1.057 \times 10^3 e^{(-t/\tau_1)} + 3.019 \times 10^2 e^{t/\tau_2} (\chi = 1.155)$$

with τ_1=2.41 and τ_2=7.84 ns, respectively, showing a higher goodness of the fitting (χ). Luminescence decays showed that CDs produced by assisted microwave HCl treatment method have the presence of different emissive sites, at 450 nm of emission (λ_{exc}=350 nm), as supported by the presence of different functional groups supported by XPS analysis [38].

The dilution of CDs effects on the fluorescence intensity. Five dilutions of CDs in proportions 1:10, 1:20, 1:50, 1:100 and 1:200 with ultra-pure water and PBS solution were investigated. In both cases, optimized dilutions of 100-fold for CDs were observed and considered as stock solutions for their higher fluorescence intensity. The study of the interaction of different chemical species with the surface of CDs is widely reported in the literature [33–35]. It has revealed that the luminescence properties of these nanomaterials strongly depend on their surface atoms and their environment [39,40]. This work is focused in the interaction established between the different surface functional groups of the synthesized CDs with four HAAs (MeIQ, 8-MeIQx, 4,8-DiMeIQx and 2,7,8-DiMeIQx), which affect on the fluorescence intensity of the CDs (Fig. 5). For understanding the possible influence of these HAAs on the luminescence intensity of

Table 1
Interferences of other related amines on the determination of the selected HAAs, expressed in recoveries (%).

Interferent	Tolerance ratio (m m^{-1})	MeIQ Recovery (%)	8-MeIQx Recovery (%)	4,8-DiMeIQx Recovery (%)	7,8-DiMeIQx Recovery (%)
Aliphatic amines: ethylamine and trimethylamine	1000	100	100	100	100
Aminoacids: lysine, arginine and tyrosine	900	95–99	98–101	97–99	95–97
Others heterocyclic amines: PhIP and Iso-IQ	250	100	99, 102	94, 97	96, 98

CDs, the fluorescence emission spectrum of each HAAs (λ_{ex}=350 nm) was observed. Any significant emission was observed at the 400–650 nm range (inset in Fig. 5). When each HAAs was added to the CDs aqueous solution, a quenching effect on the CDs emission band (λ_{em}=450 nm) was observed. Previously to the determination of the selected HAAs, were carried out the pH study, MeIQ, 8-MeIQx, 4,8-DiMeIQx and 7,8-DiMeIQx, with a p*K*a 5.95, 5.86, 5.56 and 5.65, respectively, have their N atom in the 3 position of imidazole ring as their most basic centre [41]. These analytes, protonated at pH < 5, interact with a negative charged surface of CDs by hydrogen bonded of amine groups of HAAs and carboxylic groups of CDs, causing maximum quenching of fluorescence at pH 5 (Fig. 6). At pH > 5 a quenching decrease since the negative charged amino groups of HAAs.

In order to assess the feasibility of the proposed analytical method, the effect of other group of amines on the fluorescence signal of CDs was also checked. This study included aliphatic amines (ethylamine and trimethylamine), aminoacids (lysine, arginine and tyrosine), and others HAAs such as (2-Amino-1-methyl-6-phenyilimidazo[4,5-b]-pyridine (PhIP) and 2-amino-1-methyl-imidazo [4,5-f]-quinoline (iso-IQ), that were added over the CDs ten levels of concentrations (10, 50, 100, 250, 400, 500, 600, 800, 900 and 1000 mg L^{-1}). The results obtained indicated that these amines did not produce any noticeable effect in the fluorescence signal of the CDs with 1 mg L^{-1} of HAAs.

The results of including significant levels of possible interferents are presented in Table 1. The results indicated that the aliphatic amines and amino acids did not quench CDs fluorescence emissions with each HAAs which in turn would give rise to erroneous HAAs levels being determined (tolerance ratio of 1000 m m^{-1}). In the case of others HAAs such as PhIP and iso-IQ, the tolerance ratio was 250. The dependence of the measured luminescence intensity signal with increasing concentrations of HAAs was observed to follow the well-known Stern–Volmer equation ($I_0/I=1+K_{sv}$ [Q]), where I_0 is the luminescence signal at 450 nm of CDs in absence of HAAs and I is the same signal in the presence of increasing concentration of HAAs. Hence, (I_0/I) were plotted versus each HAA concentration. It is interesting to remark that this plot did not fit a conventional linear equation. An upward curvature was observed, typical behavior of charged quenchers Fig. 7 shows the logarithmic known Stern–Volmer plots and calibration equations of MeIQ, 8-MeIQx, 4,8-DiMeIQx and 7,8-DiMeIQx. These molecules do not contact at all in the surface of the CDs, only a partial amount of molecules of HAAs, indicating that both dynamic and static quenching seem to act together, here suggesting a more complex quenching model [42,43]. However, when $\ln(I_0/I)$ was plotted versus the concentration of each HAAs a good linear relationship ($r^2 > 0.995$) was obtained, in other words the quenching of the fluorescence of CDs has an exponential relationship with the concentration of HAAs ($I_0/I=e^{\alpha[HAAs]}$), where α represents the constant associated to the quenching effect.

Therefore, this signal could be used to develop a HAAs determination method based on luminescence quenching of CDs by DiMeIQx at optimum conditions. The precision in terms of relative standard deviation (RSD) was 0.25, 0.35, 0.57 and 0.75% for MeIQ, 8-MeIQx, 4,8-DiMeIQx and 7,8-DiMeIQx, respectively; being the reproducibility (for 1 mg L^{-1} of each HAA, n=5) of RSD value less than of 2.5% in all cases. The limit of quantification, were 0.35, 0.41, 0.45 and 0.36 mg L^{-1} for MeIQ, 8-MeIQx, 4,8-DiMeIQx and 7,8-DiMeIQx, respectively. To check this effect, the analysis of the fluorescence decays shows that the lifetimes of the components (Table 2), calculated with a component decay time model for CDs, in the presence of increasing concentration of 4,8-DiMeIQx is not particularly sensitive to the presence of the quencher. They do not depend of the HAA concentration, demonstrating the static quenching effect over CDs linked to the formation of a stable complex between the fluorophore and 4,8-DiMeIQx in this case. Fig. 8 shows the lifetime decay curves of the fluorescence emission, which can be fitted to four components.

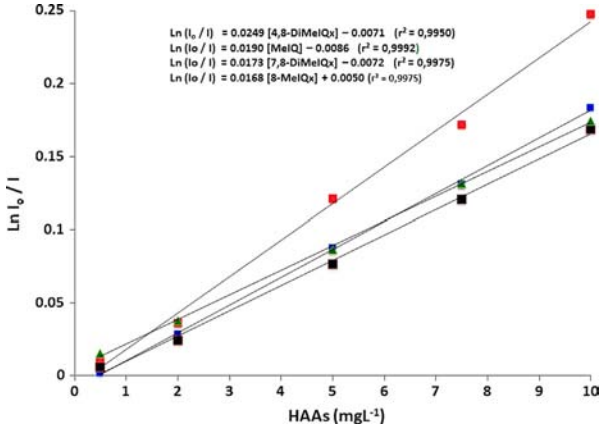


Fig. 7. Calibration graphs obtained for HAAs at 450 nm.

4. Conclusions

In summary, a fluorescent analytical method based on the quenching of the un-functionalized carbon fluorescent nanoparticles,

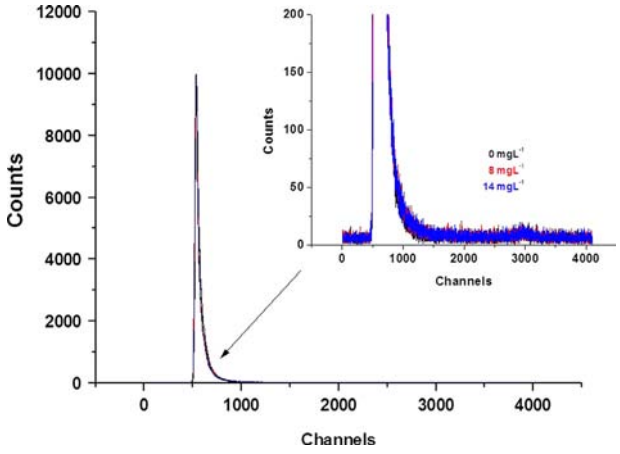


Fig. 8. Fluorescence lifetime curves of CDs obtained from lactose. A four component exponential-decay curve is fitted to the selected data after background subtraction. Inset is the magnification of the bottom of the decay curves at different concentrations.

Table 2
Lifetime intensity decays of CDs obtained from lactose treated with HCl.

Fluorescence Lifetime Parameters	**HAA=0 (mg L^{-1})**	**HAA=8 (mg L^{-1})**	**HAA=14 (mg L^{-1})**
τ_i(ns)/B_i (10^{-2})	0.28 ± 0.03/2.40 ± 0.05	0.21 ± 0.05/3.94 ± 0.07	0.25 ± 0.07/7.92 ± 0.13
τ_i(ns)/B_i (10^{-2})	1.10 ± 0.20/2.32 ± 0.02	0.76 ± 0.08/2.00 ± 0.02	0.93 ± 0.08/3.25 ± 0.06
τ_i(ns)/B_i (10^{-2})	2.93 ± 0.07/0.160 ± 0.003	2.69 ± 0.09/0.339 ± 0.004	2.75 ± 0.04/0.238 ± 0.003
τ_i(ns)/B_i (10^{-2})	7.90 ± 0.20/6.83 ± 0.11	6.40 ± 0.20/7.30 ± 0.18	7.30 ± 0.40/1.91 ± 0.02
χ	1.034	1.091	1.120
A	6.07 ± 0.30	13.49 ± 0.35	10.78 ± 0.31

obtained by the assisted microwave treatment of lactose by HCl, and was used as potential system to quantify heterocyclic aromatic amines at μM range of concentration static quenching effect was demonstrated, after analysis of the fluorescence lifetime decay curves, no effect was detected when used 4,8-DiMeIQx as heterocyclic aromatic amine probe at different concentration. CDs can selectively recognize certain homologues amines, and give a sensitive signal response, showing their promising use in the chemical sensing HAAs.

Acknowledgements

Authors are gratefully to Grant SFRH/BD/84318/2012 to FCT (Lisbon, Portugal) and Andalucía Tech Program from Univ Málaga (Spain). Financial support from the Spanish Ministry of Economy and Competitiveness (CTQ2013-48411-P) is gratefully acknowledged. The support given through an "INCRECYT" research contract to M. Zougagh is also acknowledged.

Appendix A. Supporting information

Supplementary data associated with this article can be found in the online version at http://dx.doi.org/10.1016/j.talanta.2014.10.008.

References

[1] IARC, Monographs on the Evaluation of Carcinogenic Risks to Humans. Some Naturally Occurring Substances: Food Items and Constituents, Heterocyclic Aromatic Amines and Mycotoxins, vol. 56, 1993.
[2] K. John, S. Beedanagari, Heterocyclic Aromatic Amines , Encyclopaedia of Toxicology (2014) 855–863 (third ed.).
[3] K. Puangsombat, P. Gadgil, T.A. Houser, M.C. Hunt, J.S. Smith, Meat Sci. 90 (2012) 739.
[4] P. Pais, E. Moyano, L. Puignou, M.T. Galceran., J. Chromatogr. A 778 (1997) 207.
[5] E. Barceló-Barrachina, E. Moyano, M.T. Galcerán, J. Chromatogr. A 1054 (2004) 409.
[6] M.R. Khan, R. Busquets, F.J. Santos, L.J. Puignou, J. Chromatogr. A 1194 (2008) 155.
[7] T. Polak, D. Došler, B. Žlender, L. Gašperlin, LWT Food Sci. Technol 42 (2009) 504.
[8] M. Iwasaki, H. Kataoka, J. Ishihara, R. Takachi, G.S. Hamada, S. Sharma, L. Le Marchand, S. Tsugane, J. Food Compos. Anal. 23 (2010) 61.
[9] H. Kataoka, T. Inoue, K. Saito, H. Kato, K. Masuda, Anal. Chim. Acta 786 (2013) 54–60.
[10] J.H. Shin, Y.C. Na, J.H. Chung, S. Gorinstein, Y.G. Ahn, Y. Gyong, Anal. Bioanal. Chem 447 (2014) 169.
[11] R. Busquets, J. Jönsson, A. Jan, H. Frandsen, L. Puignou, M.T. Galceran, K. Skog, Mol. Nutr. Food Res. 53 (2009) 1496.
[12] J.H. Shin, Y.C. Na, J.H. Chung, S. Gorinstein, Y.G. Ahn, Anal. Biochem 447 (2014) 169.
[13] H. Frederiksen, H. Frandsen, Drug Metab. Dispos 32 (2004) 661.
[14] B.H. Chen, D.J Yang, Chromatographia 48 (1998) 223.
[15] U. Gerbl, M. Cichna, M. Zsivkovits, S. Knasmüller, G. Sontag, J. Chromatogr. B 802 (2004) 107.
[16] B. Janoszka, Food Chem. 120 (2010) 463.
[17] M.G Knize, C.P Salmon, E.C Hopmans, J.S Felton, J. Chromatogr. A 763 (1997) 179.
[18] M. Gibis, J. AOAC Int. 92 (2009) 715.
[19] S. Vainiotalo, K. Matveinen, A. Reunanen, Fresenius J. Anal. Chem 345 (1993) 462.
[20] R. Reistad, O.J. Rossland, K.J. Latva-Kala, T. Rasmussen, R. Vikse, G. Becher, J. Alexander, Food Chem. Toxicol. 35 (1997) 945.
[21] E. Richling, M. Kleinschnitz, P. Schreier, Eur. Food Res. Technol. 210 (1999) 68.
[22] T.A. Sasaki, J.M. Wilkins, J.B. Forehand, S.C. Moldoveanu, Anal. Lett. 34 (2001) 1749.
[23] L. Warzecha, B. Janoszka, U. Blazczyk, M. Sróżyk, D. Bodzek, C. Dobosz, J. Chromatogr. B 802 (2004) 95.
[24] S. Sentellas, E. Moyano, L. Puignou, M.T. Galceran, J. Chromatogr. A 1032 (2004) 193.
[25] P. Viberg, K.G. Wahlund, K. Skog, J. Chromatogr. A 1133 (2006) 347.
[26] X.Q Fei, C. Li, X.D. Yu, H.Y. Chen, J. Chromatogr. B 854 (2007) 224.
[27] F. Andrés, M. Zougagh, G. Castañeda, A. Ríos, Electrophoresis 31 (2010) 2165.
[28] F. Andrés, M. Zougagh, J.L. Sánchez-Rojas, A. Rios, Talanta 83 (2011) 1562.
[29] S. Sanz Alaejos, J.H. Ayala, V. González, A.M. Afonso, J. Chromatogr. B 862 (2008) 15.
[30] A. Martin-Calero, J.H. Ayala, V. González, A.M. Afonso, Anal. Bioanal. Chem. 394 (2009) 937.
[31] A. Sahar, S. Portanguen, A. Kondjoyan, E. Dufour, Eur. Food Res. Technol 231 (2010) 803.
[32] J.C.G. Esteves da Silva, H. Gonçalves, Trends Anal. Chem 30 (2011) 1327.
[33] A. Cayuela, M.L. Soriano, M. Valcárcel, Anal. Chim. Acta 804 (2013) 246.
[34] M. Algarra, B.B. Campos, K. Radotić, D. Mutavdžić, T.J. Bandosz, J. Jiménez-Jiménez, E. Rodriguez-Castellon, J.C.G. Esteves da Silva, J. Mater. Chem. A 2 (2014) 8342.
[35] M. Algarra, M. Pérez-Martín, M. Cifuentes-Rueda, J. Jiménez-Jiménez, J.C.G. Esteves da Silva, T.J. Bandosz, E. Rodríguez-Castellón, J.T. López-Navarrete, J. Casado, Nanoscale 6 (2014) 9071.
[36] F. De Andrés, M. Zougagh, G. Castañeda, A. Ríos, Anal. Bioanal. Chem. 397 (2010) 223.
[37] Y. Dong, R. Wang, H. Li, J. Shao, J. Chi, X. Lin, G. Chen, Carbon 50 (2012) 2810.
[38] R.L. Liu, D.Q. Wu, S.H. Liu, H. Koynov, W. Knoll, Q. Li, Angew. Chem. Int. Ed. 48 (2009) 4598.
[39] A. Cayuela, M.L. Soriano, M.C. Carrión, M. Valcárcel, Anal. Chim. Acta 820 (2014) 133.
[40] Y. Liu, C.Y. Liu, Z.Y. Zhang, Appl. Surf. Sci. 263 (2012) 481.
[41] S.D. Mendonsa, R.J. Hurtubise, J. Chromatogr. A 841 (1999) 239.
[42] R.J. Hurtubise, A.H. Ackerman, B.W. Smith, Appl. Spectrosc. 62 (2008) 682.
[43] J.R. Lackowiz, Principles of Fluorescence Spectroscopy , second ed., Springer, New York, NY (1999) 243.

Talanta 132 (2015) 851–856

Contents lists available at ScienceDirect

Talanta

journal homepage: www.elsevier.com/locate/talanta

Second-order advantage maintenance with voltammetric data modeling for quantitation of ethiofencarb in the presence of interferences

Nielene Mora Diez [a,*], Agustina Guiberteau Cabanillas [a], Antonio Silva Rodríguez [a], Héctor C. Goicoechea [b,**]

[a] Department of Analytical Chemistry, Faculty of Sciences, University of Extremadura, 06006, Badajoz, Spain
[b] Laboratorio de Desarrollo Analítico y Quimiometría (LADAQ), Cátedra de Química Analítica I, Facultad de Bioquímica y Ciencias Biológicas, Universidad Nacional del Litoral-CONICET, Ciudad Universitaria, 3000, Santa Fe, Argentina

ARTICLE INFO

Article history:
Received 9 August 2014
Received in revised form
27 September 2014
Accepted 1 October 2014
Available online 15 October 2014

Keywords:
Ethiofencarb
Voltammetry
Multivariate curve resolution
Differential pulsed voltammetry
Unfolded partial least squares regression followed by residual bilinearization

ABSTRACT

This work presents the development of a method based on a voltammetric determination coupled to second-order data modeling with multivariate curve resolution-alternating least-square (MCR-ALS) and unfolded partial least squares regression followed by residual bilinearization (U-PLS/RBL) for the quantitation of the pesticide ethiofencarb in the presence of interferences in tap water.

The determination of ethiofencarb by voltammetry is possible on the basis that this pesticide is hydrolysed in alkaline media giving rise to a compound which shows an oxidation peak at Ep=0.80 V. But some other pesticides belonging to the same family can be considered as interferences due to the high overlapping in their signals. The two such interferences are fenobucarb and bendiocarb, which have not been included in the calibration step.

The possibility of second-order multivariate calibration was studied by using the hydrolysis time as the third variable, and MCR-ALS and U-PLS/RBL. Good results were obtained in this determination in spite of the high overlapping in voltammetric signals.

© 2014 Elsevier B.V. All rights reserved.

1. Introduction

Ethiofencarb [(2-ethylthiomethyl-phenyl)-N-methyl carbamate] is a systemic insecticide widely used in agriculture, which acts as a cholinesterase inhibitor. The World Health Organization lists ethiofencarb as “highly hazardous” and it is considered by the European Union's Nordic Council of Ministers as “dangerous for the environment” [1]. For these reasons, a wide range of analytical techniques has been developed for its identification and determination at trace levels.

A literature search reveals that the quantitation of the product or its residues is performed mainly by using separative techniques. Gas chromatography–mass spectrometric (GC–MS) methods with various derivatization reagents have been used [2]. High performance liquid chromatography (HPLC) is the most common technique used to analyze this pesticide [3] using reverse phase equipped with different detectors. Tandem mass spectrometry (MS/MS) has been used for sensitive quantitation. Although these methods have high selectivity and sensitivity, they inherently rely on expensive instruments. Consequently, it is attractive to develop simple and cheap methods for the quantitation of ethiofencarb.

As regards the use of voltammetric techniques for the latter analysis, only one paper has been reported [4]. Barroso et al. performed a basic study on the voltammetric behavior of ethiofencarb at a glassy carbon electrode and at a hanging mercury electrode by using cyclic voltammetry and square wave voltammetry. Finally, they applied the electrochemical study of the reaction product of alkaline ethiofencarb hydrolysis in the development of a FIA system with amperometric detection.

The determination of ethiofencarb by voltammetry is possible on the basis that this pesticide is hydrolysed in alkaline media giving rise to a compound which shows an oxidation peak at Ep=0.80 V at the glassy carbon electrode, which corresponds to the phenol derivative product. But some other pesticides belonging to the same family can be considered as interferences due to the high overlapping in their signals [5,6].

Usually, as voltammetry is not a separative technique, full selectivity cannot be obtained with it because by using any kind of working electrode (mercury, carbon etc.) different types of analytes can show overlapped signals. However, this problem can be overcome by using chemometric tools. When this occurs

* Corresponding author.
** Corresponding author. Tel.: +54 3424575206 × 190.
E-mail addresses: Nielene@unex.es (N.M. Diez), hgoico@fbcb.unl.edu.ar (H.C. Goicoechea).

http://dx.doi.org/10.1016/j.talanta.2014.10.006
0039-9140/© 2014 Elsevier B.V. All rights reserved.

generating second-order data and its proper modeling with multiway algorithms can guarantee selectivity by mathematical means, allowing resolution and quantitation of analytes with overlapped signals [7,8]. This is possible because the information provided by second-order data if adequately decomposed by suitable algorithms can be uniquely ascribed to the analyte of interest, even in the presence of unexpected components not considered in the calibration stage. This property has been called "the second-order advantage" and avoids the requirement of physically removing interferences [9]. There are three well-known second-order algorithms able to handle third-order data arrays deviating from trilinearity, as is expected to occur with second-order voltammetric data: multivariate curve resolution-alternating least-squares (MCR-ALS) [10], parallel factor analysis 2 (PARAFAC2) [11] and unfolded partial least squares followed by residual bilinearization [12]. They are able to take into account changes in signal shape of components from sample to sample. When MCR-ALS is performed in the so-called extended mode, the challenge is overcome by building an augmented data matrix by appending calibration and test data matrices in the time direction. In this way the rows represent in this case voltammograms and the columns time profiles, alleviating the problems associated with sample-to-sample differences in this dimension [13].

A large number of works have been published concerning the chemometric modeling of second-order data generated by different techniques. As an example, a search in Scopus using "HPLC" and "second-order data" as keys revealed that 132 papers were published since 1985 to date, MCR-ALS being the algorithm of choice to solve most of the analytical problems at hand [8,14]. However, to the best of our knowledge, a reduced number of papers have been published regarding the development of analytical methodologies based on second-order voltammetric data, most of them using MCR-ALS [15–17]. In the present work the development of a method for the determination of ethiofencarb in the presence of two other insecticides (fenobucarb and bendiocarb) of the same family, which have not been included in the calibration step, was attempted. The possibility of exploiting the second-order advantage by implementing three-way calibration was studied by using the hydrolysis time as the second mode and applying a well-established algorithm: MCR-ALS. In addition, unfolded partial least squares regression followed by residual bilinearization (U-PLS/RBL) [18] was implemented considering the possibility of a better performance owing to non-linearities usually present in electrochemical data [19,20]. To the best of our knowledge this latter algorithm was used for first time for modeling second-order voltammetric-hydrolisis time data, and as will be shown performs better than MCR-ALS for the kind of data analyzed in the present report.

2. Experimental

2.1. Apparatus and software

All experiments were performed using an Autolab AUT 12.v PSTAT10 (Ecochemie, The Netherlands) in combination with a Metrohm VA-663 stand, with a tree electrode system: working electrode of glassy carbon (GCE), an Ag/AgCl saturated KCl reference electrode and a Pt wire auxiliary electrode. The system is monitored by the general purpose electrochemical system version 4.0 (GPES4) software package (Ecochemie, Ultrecht, The Netherlands).

The GCE was polished at the start of the work, with aqueous slurry of 0.5 μm alumina powder. For electrode regeneration between measurements, it was polished for one minute in a cotton disk soaked in dimethylformamide and for another minute in a cotton disk soaked in water.

All the algorithms were implemented in MATLAB 7.10 [21]. Those for applying MCR-ALS are available in the internet at http://www.mcrals.info/. U-PLS/RBL was implemented with an integrated chemometric toolbox (MVC2) available in the literature [22]

2.2. Chemicals and reagents

Ehiofencarb (97.5%) was obtained from Dr. Ehrenstorfer (Augsburg, Germany); bendiocarb (99%) and fenobucarb (98%) were obtained from Riedel-de Haën (Seelze, Germany). They were used without further purification, and their solutions of them in ultrapure water (40 μg mL^{-1}) were prepared and stored in the dark at 4 °C.

HPLC-grade water was obtained from a Milli-Q system (Millipore, Bedford, MA., USA). All other chemicals were of analytical reagent grade.

2.3. Preparation of standard solutions and samples for the validation study

The calibration data sets were built by using only pure standard solutions of ethiofencarb under the above selected conditions. This was done in order to prove that the second-order advantage is exploited when analyzing validation mixture samples of three compounds. Solutions for calibration were randomly prepared, by convenient dilutions of stock solution in order to obtain the necessary concentrations. The range of concentration was between 2.5 and 10.0×10^{-6} mol L^{-1}.

The samples for the validation set were mixtures of ethiofencarb, endiocarb and fenobucarb prepared in tap water. The specific validation concentrations of the nine samples are provided in Table 1. An inter-day precision study was performed analyzing sample number 1 during three consecutive days in triplicate and then performing an ANOVA test.

2.4. Sample preparation

The calibration and validation samples were prepared as follows. In a 25.0 mL volumetric flask a suitable volume of the pesticide(s) was taken; 5 mL of $NaClO_4$ 0.5 mol L^{-1}, 1 mL of NaOH 0.2 mol L^{-1} and pure (standards) or tap (validation samples) water to a volume near 20 mL were added, after shaking for a few seconds, and allowed to stand for t min (hydrolysis time). Then, 0.2 mL of glacial acetic acid was added and the solution was diluted to the mark with pure/tap water. The obtained solution was transferred to the electrochemical cell and the differential pulse voltammogram (DPV) in the range +0.4–1.0 V was registered at the following instrumental conditions: scan rate 15 mV s^{-1} and pulse amplitude 50 mV.

Table 1
Composition of the nine samples validation set.

Sample	Ethiofencarb (μmol L^{-1})	Fenobucarb (μmol L^{-1})	Bendiocarb (μmol L^{-1})
1	9.50	7.50	9.00
2	6.25	9.50	6.00
3	8.55	6.09	6.00
4	3.00	7.50	9.00
5	8.55	8.91	3.00
6	3.95	8.91	6.00
7	3.95	6.09	9.00
8	6.25	5.50	3.00
9	6.25	7.50	3.00

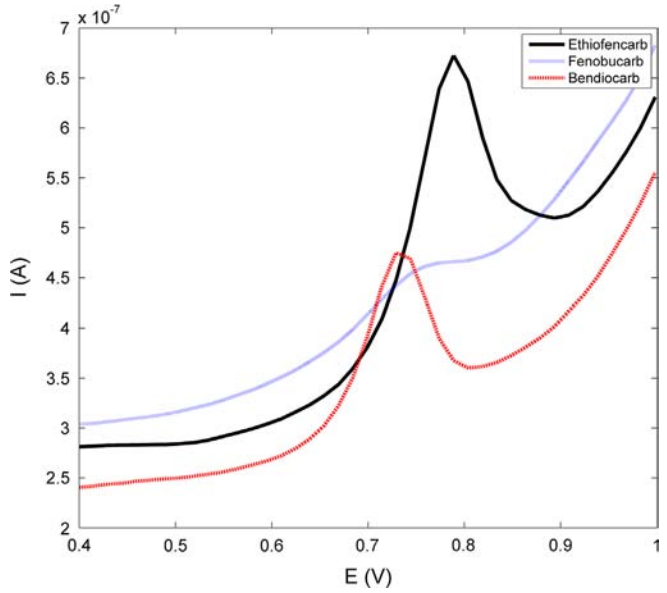


Fig. 1. Voltammograms at hydrolysis time =4 min, corresponding to pure standard solutions of ethiofencarb 6.25 μmol L^{-1}, fenobucarb 10.00 μmol L^{-1} and 6.00 μmol L^{-1} of bendiocarb.

3. Results and discussion

3.1. General considerations

The determination of ethiofencarb by voltammetry is possible on the basis that this pesticide is hydrolysed in alkaline media giving rise to a compound which shows an oxidation peak at around Ep=0.80 V. But some other pesticides belonging to the same family can be considered as interferences due to the high overlapping in their signals. The two interferences selected for this study are fenobucarb and bendiocarb. Voltammograms at hydrolysis time of 4 min corresponding to pure standard solutions of ethiofencarb 6.25×10^{-6} mol L^{-1}, fenobucarb 10.00×10^{-6} mol L^{-1} and 6.00×10^{-6} mol L^{-1} of bendiocarb are showed in Fig. 1.

In order to study the possibility of determining ethiofencarb in the presence of interferences, second-order data and chemometric algorithms were studied. The calibration data sets were built by using only pure standard solutions of ethiofencarb and the samples for the validation set were mixtures of ethiofencarb, bendiocarb and fenobucarb prepared in tap water.

Second-order data were obtained by recording the voltammograms of each sample at different hydrolysis times as the third variable. The hydrolysis time employed were 1, 2, 3 and 4 min. There were 41 points in each voltammogram obtained, taking into account the scan potential interval employed and the experimental conditions. Then for each sample a matrix of 41×4 was recorded.

3.2. Asymmetric least squares (ALS) background correction adapted to second-order data

A background matrix **F** ($J\times K$) is estimated from the data matrix **M** ($J\times K$), where J and K are the number of digitized potentials and the hydrolysis time, respectively. With this purpose, a $\mathbf{B}_1$ ($L\times J$) spline basis matrix along the rows of the **M** matrix and a $\mathbf{B}_2$ ($M\times K$) spline basis matrix along the columns of the **M** matrix are used along with a compromise of 3 basis functions [23], i.e., $L=M=3$. **F** can be represented as

$$f_{j,k}=\sum_{L,M} b1_{LJ}\, b2_{MK}\, a_{LM} \tag{1}$$

where a_{LM} is the (L,M) element of an **A** matrix containing the regression coefficients, which can be calculated by minimizing the following cost function:

$$Q=\sum_{L,M}\nu_{JK}(y_{JK}-f_{JK})^2+p. \tag{2}$$

In Eq. (2), y is the experimental signal, f is a smooth trend (the baseline approximation), and ν is the prior weights. The elements of ν should have large values in the parts of the signal where it is allowed to affect the estimation of the baseline. Considering the choice of the following asymmetric weights: $\nu_{JK}=p$ if $\nu_{JK}>f_{JK}$ and $\nu_{JK}=1-p$ if $\nu_{JK}\le f_{JK}$ with $0<p<1$, positive deviations from the trend will result in weights different from negative residuals. Experience shows that starting from $\nu\cong1$, and iterating between the two computations, quickly and reliably leads to a solution in about 10 iterations. The penalty term in Eq. (2) is defined as follows:

$$p=\left[\sum_{L}(\Delta_1^{d}\mathbf{a}_{\cdot L})^2+\sum_{L}(\Delta_2^{d}\mathbf{a}_{\cdot M})^2\right] \tag{3}$$

where Δ_1 and Δ_2 are differences of order d calculated for each column ($\mathbf{a}_{\cdot L}$) and row ($\mathbf{a}_{\cdot M}$) of **A**, respectively. If different values are used for the regularization parameter Δ, the penalty may have different influences for vertical and horizontal directions.

Fig. 2 depicts a plot of the four voltamograms recorded at different hydrolysis times (see above) for a water sample previously spiked with the three studied analytes. The four voltammograms correspond to a data matrix **M** (41×4). The background estimation **F** depicted as individual voltammograms (41×4) obtained via ALS is also shown in Fig. 2, and, as can be seen, the background contribution is significant within the entire range. The estimated matrix was obtained by setting L and M to a value of 3 and the asymmetry parameter (p) in Eq. (2) to 0.005. The subtraction of the **F** matrix from the **M** matrix provides the background corrected voltammograms shown in Fig. 2. All further experimental data were background subtracted, generating an ALS matrix within the ranges of interest. Fig. 3 shows the landscape obtained after background correction of data corresponding to Fig. 2.

3.3. MCR-ALS analysis

MCR-ALS is an algorithm capable of handling data sets deviating from trilinearity, i.e., data in which kinetic time shifts or signal

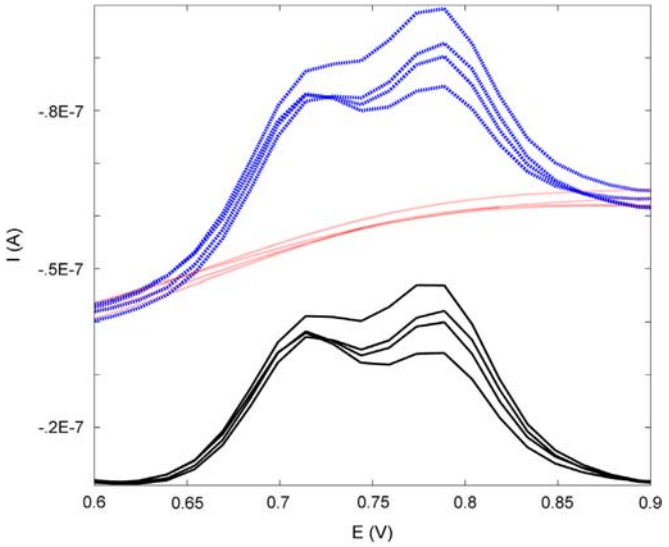


Fig. 2. Voltammograms corresponding to validation sample number 1, before and after background correction.

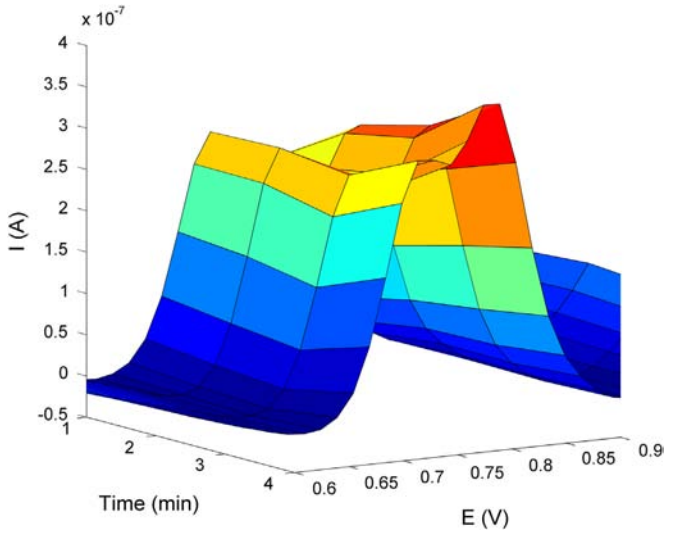


Fig. 3. Landscape plotted for validation sample number 1 after background correction.

shape changes occur for analytes from sample to sample [8]. With this purpose, the strategy of augmenting matrices along the mode which is suspected of breaking the trilinear structure is implemented. Thus, if matrix-to-matrix variation of profiles occurs along the column direction, a column-wise augmented matrix is created. The bilinear decomposition of the augmented matrix **D** is performed according to the expression

$$\mathbf{D}_{\text{aug}} = \mathbf{C}_{\text{aug}}\mathbf{S}^{\text{T}} + \mathbf{E}_{\text{aug}} \quad (4)$$

in which the rows of $\mathbf{D}_{\text{aug}}$ contain the voltammograms (K sensors) as a function of time of hydrolysis (J times), the columns of $\mathbf{C}_{\text{aug}}$ contain the time profiles of the N compounds involved in the process, the columns of **S** their related voltammograms, and $\mathbf{E}_{\text{aug}}$ is a matrix of residuals not fitted by the model. Decomposition of $\mathbf{D}_{\text{aug}}$ is achieved by iterative least-square minimization of $\|\mathbf{E}_{\text{aug}}\|$, under suitable constraining conditions. In this work the implemented constrains were non-negativity in the spectral profiles, unimodality and non-negativity in the time profiles, and correspondence among species and samples in the case of samples containing uncalibrated interferents. $\mathbf{D}_{\text{aug}}$ is built by placing one on top of another the calibration sub-matrices and each of the test data sub-matrices. Thus, while the pure voltammogram of each compound should be the same in all experiments and this mode must be selective, the temporal profiles in the different $\mathbf{C}_{\text{aug}}$ sub-matrices need not share a common shape.

The first modeling step consisted in building an augmented data matrix $\mathbf{D}_{\text{aug}}$ in the temporal mode of $\{[(I+1)\times 4]\times 41\}$ by stacking the data matrices corresponding to each test sample followed by those of the standard samples for the analyte ethiofencarb (I).

This algorithm needs initialization with system parameters as close as possible to the final results. Therefore, analyte and interference voltammograms are required as the resolution is based on the selectivity in the latter mode. In this work, the selection of the purest voltammogram for the interferents was made based using homemade routines based on SIMPLISMA (simple interactive self-modeling mixture analysis) [24]. The number of contributing species in the system under study when applying singular value decomposition (SVD) was always equal to the real number of components, i.e. three when analyzing test samples.

Fig. 4A shows the voltammograms retrieved for all the three mentioned components in validation sample number 1. As can be

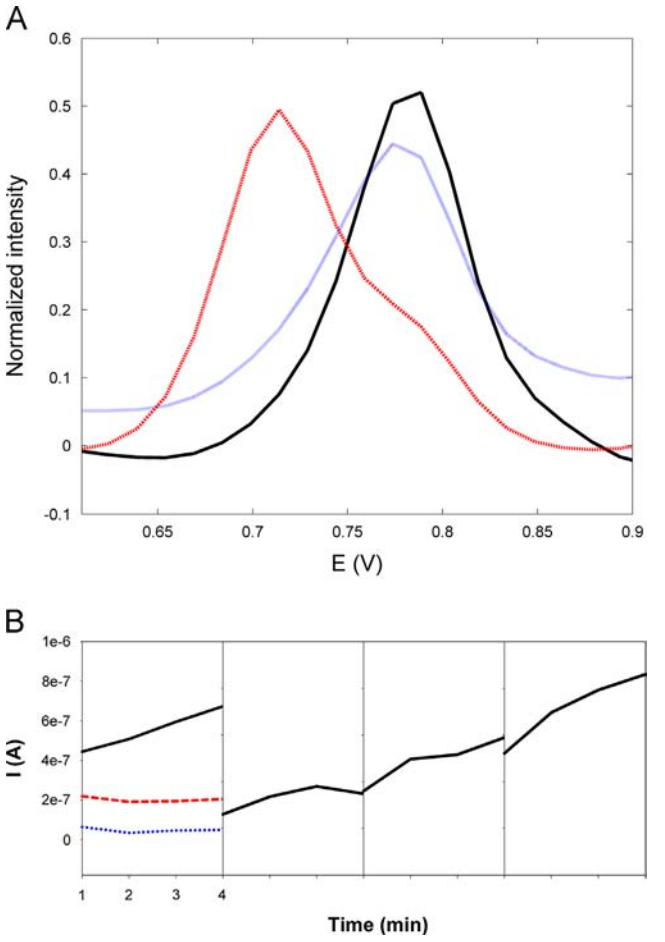


Fig. 4. (A) Voltammogram profiles retrieved with MCR-ALS for validation sample number 1 and (B) time profiles retrieved with MCR-ALS when analyzing validation sample number 1 and three pure standard solutions of ethiofencarb at 3.60, 6.25 and 10.00 μmol L^{-1}.

appreciated there exists a high degree of overlapping among analyte and interferents signals but the profile corresponding to the analyte (in black) has a peak at 0.79 V, which agrees well with the peak that presents this compounds (see Fig. 1). In addition, Fig. 4B shows the corresponding time evolution profiles in this particular sample and the ones retrieved for three ethiofencarb standard samples at 3.60×10^{-6}, 6.25×10^{-6} and 10.00×10^{-6} mol L^{-1}. As was mentioned before, the areas under the kinetic profiles were used to build a calibration curve that allowed us to obtain the concentration of ethiofencarb in the validation samples.

3.4. U-PLS/RBL modeling

The U-PLS method has already been described in detail [25], as well as the U-PLS/RBL combination [26]. The first step in the application of U-PLS/RBL was the assessment of the optimum number of calibration factors (A). This was done by resorting to the leave-one-out cross-validation procedure, which computes the ratios $F(A)=\text{PRESS}(A<A^*)/\text{PRESS}(A)$, where PRESS is the predicted error sum of squares, defined as $\text{PRESS}=\sum(\text{ci, act}-\text{ci, pred})^2$, A is a trial number of factors and A^* corresponds to the minimum PRESS. The number of optimum factors was selected as the one leading to a probability of less than 75% and $F>1$. Since the present study was carried out with pure standards of ethiofencarb, and because the blank signal was eliminated by the pre-treatment procedure, it was expected that the parameter A is equal to 1.

Table 2
Predictions on validation samples containing two interferents by MCR-ALS and UPLS/RBL.

Sample	Ethiofencarb (μmol L^{-1})				
	Nominal	MCR-ALS		U-PLS/RBL	
		Prediction	Recovery (%)	Prediction	Recovery (%)
1	9.50	9.30	97.9	9.35	98.4
2	6.25	6.40	102.4	6.30	100.8
3	8.55	7.80	91.2	8.65	101.2
4	3.00	3.50	116.7	3.28	109.3
5	8.55	8.70	101.8	8.69	101.6
6	3.95	4.30	108.9	4.15	105.1
7	3.95	4.30	108.9	4.12	104.3
8	6.25	6.00	96.0	6.10	97.6
9	6.25	6.30	100.8	6.30	100.8
REP (%)	–	5.86	–	2.54	–

However, two additional latent variables were necessary to model the variability of the data by U-PLS. This fact would allow inference about the presence of non-linearities, which are usually found in electrochemical data [19]. On the other hand, this would allow explaining the better performance of this algorithm compared with MCR-ALS (see below).

The next step was to estimate the number of unexpected components in validation samples via the post-calibration RBL procedure. This was done by considering the variation of the residual as a function of the trial number of unexpected components [26]. The stabilization of the residual around the instrumental noise ($\sim 5 \times 10^{-8}$ A) suggested two unexpected components. The good agreement that exists among the predicted and the nominal concentrations of ethiofencarb (see Table 2) demonstrates the success of RBL in extracting the spectral contributions of both unknown components from the sample. This ability, which refers to the second-order advantage with the U-PLS/RBL algorithm, makes prediction possible with no potential interference from the sample.

The predictive ability of both algorithms was compared through the elliptic joint confidence region (EJCR) test [27]. In this case, it should be remarked that both ellipses contain the theoretically predicted value of the slope (1) and the intercept (0) (Fig. 5B). On the other hand, a better performance in term of precision can be observed for the U-PLS/RBL algorithm. This fact could be explained based on a better ability to compensate the non-linearities which are usually present in electrochemical data, as was commented above. Nevertheless, it can be concluded that both methods reach accurate predictions.

In addition repeatability (or intra-assay) and intermediate variations (or inter-assay) were studied, performing analyte determinations with the U-PLS/RBL algorithm in validation sample number 1, during three consecutive days. The obtained values (average and standard deviation) are the following (in μmol L^{-1}): 9.33 (0.09_7), 9.28 (0.08_8) and 9.37 (0.09_5), respectively. On the other hand, in order to further evaluate the inter-assay precision, an analysis of variance was performed for the recoveries obtained for each concentration level during the three days, in such a way that both within-condition and between-condition variances were taken into account. The *p*-values obtained, which are greater than 0.05, allowed us to conclude that there are no significant differences between the mean recoveries for each level in the three different days studied with a confidence level of 0.05. From this study, it can be concluded that the developed method presents acceptable precision.

Finally it should be commented that PARAFAC was also implemented but, as was expected, worse results than those obtained with MCR-ALS were obtained. This fact can be due to the characteristics of the data under study in the present report: non-trilinearity of the three-way array and non-linearity between signal and concentration.

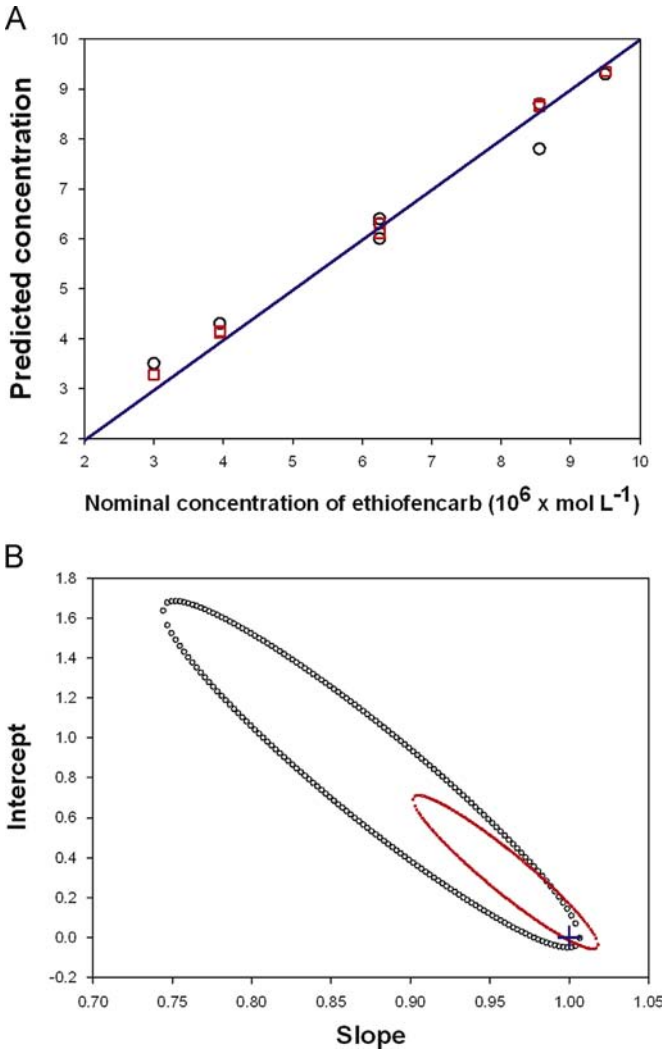


Fig. 5. (A) Predicted against nominal ethiofencarb concentrations in validation samples by MCR-ALS (black circles) and UPLS (red squares). (B) Elliptic joint confidence regions for predictions by MCR-ALS (black circles) and UPLS (red squares). (For interpretation of the references to color in this figure legend, the reader is referred to the web version of this article.)

4. Conclusions

The applicability of voltammogram evolution as a function of hydrolysis time in alkaline media accomplished through second-order multivariate calibration methodology has been demonstrated for the first time. The extreme overlap between the electroanalytical first-order signal shown by the target analyte and the interferences can be evaded by incorporation of the second-order signals using the kinetic hydrolysis time differences of the three components. Consequently, the feasibility of using second-order voltammetric data modeled with multivariate curve resolution-alternating least-square (MCR-ALS) and unfolded partial least squares regression followed by residual bilinearization (U-PLS/RBL) for the quantitation of the pesticide ethiofencarb was demonstrated in the presence of interferences in tap water. Considering the complexity of the data at hand, U-PLS/RBL (which was implemented for first time for voltammetric data) showed

a better performance than MCR-ALS in terms of predictive ability. Nevertheless, both algorithms reach reasonably good results.

It should be remarked that although more research and experimental work is necessary, this strategy show promise for quantitation of ethiofencarb at a lower cost than using more sophisticated techniques like HPLC–MS for example.

Acknowledgments

The authors are grateful to Ministerio de Economía y Competitividad of Spain (Project CTQ2011-25388) and Gobierno de Extremadura (Project GR1003-FQM003), both co-financed by European FEDER funds and Universidad Nacional del Litoral (Project CAI+D 2011 N 11-11), to CONICET (Consejo Nacional de Investigaciones Científicas y Técnicas, Project PIP 2012–14 N 455) and to ANPCyT (Agencia Nacional de Promoción Científica y Tecnológica, Project PICT 2011-0005) for financial support.

References

[1] ⟨http://www.toxipedia.org/display/toxipedia/Ethiofencarb⟩, Accessed May 30, 2014.
[2] E.Y. Yang, H.S. Shin, J. Chromatogr. A 1305 (2013) 328–332.
[3] B. Kmellar, P. Fodor, L. Pareja, C. Ferrer, M.A. Martinez-Uroz, A. Valverde, A.R. Fernandez-Alba, J. Chromatogr. A 1215 (2008) 37–50.
[4] M.F. Barroso, M. Carmo, V.F. Vaz, M. Goreti, F. Sales, P. Paiga, C. Delerue-Matos., Anal. Lett. 39 (2006) 2387–2403.
[5] A. Guiberteau, I. Durán-Merás, T. Galeano, T.J.F. Laranjinho, N. Mora, M.F. Suárez, F. Salinas, Mikrochim. Acta 137 (2001) 135–140.
[6] A. Guiberteau Cabanillas, T. Galeano Díaz, F. Salinas, J.M. Ortiz, J.M. Kauffmann, Electroanalysis 9 (1997) 952–955.
[7] G.M. Escandar, N.M. Faber, H.C. Goicoechea, A. Muñoz de la Peña, A.C. Olivieri, R.J. Poppi, Trends Anal. Chem. 26 (2007) 752–765.
[8] G.M. Escandar, H.C. Goicoechea, A. Muñoz de la Peña, A.C. Olivieri, Anal. Chim. Acta 806 (2014) 8–26.
[9] K.S. Booksh, B.R. Kowalski, Anal. Chem. 66 (1994) 782A–791A.
[10] R. Tauler, Chemom. Intell. Lab. Syst. 30 (1995) 133–146.
[11] R. Bro, Doctoral Thesis, University of Amsterdam, The Netherlands, 1998.
[12] A.C. Olivieri, G.M. Escandar, Practical Three-way Calibration, first ed., Elsevier, Amsterdam, 2014.
[13] R. Tauler, M. Maeder, A. de Juan, Multiset data analysis: extended multivariate curve resolution, in: S. Brown, R. Tauler, B. Walczak (Eds.), Comprehensive Chemometrics, Elsevier, Oxford, 2009, pp. 473–505.
[14] H.C. Goicoechea, M.J. Culzoni, M.D. Gil García, M. Martínez Galera, Talanta 83 (2011) 1098–1107.
[15] A. Koobi, S.M. Ghoreishi, S. Masoum, M. Behpour, Bioelectrochemistry 94 (2013) 100–107.
[16] M. Kooshki, H. Abdollahi, S. Bozorgzadeh, B. Haghighi, Electrochim. Acta 56 (2011) 8618–8624.
[17] Y. Ni, S. Kokot, Anal. Chim. Acta 626 (2008) 130–146.
[18] M.J. Culzoni, H.C. Goicoechea, M. Bearzoti, M. Cabezón, A.C. Olivieri, Analyst 131 (2006) 718–723.
[19] S.R. Hernandez, G.G. Ribero, H.C. Goicoechea, Talanta 61 (2003) 743–753.
[20] T. Galeano-Díaz, A. Guiberteau-Cabanillas, A. Espinosa-Mansilla, M.D. López-Soto., Anal. Chim. Acta 618 (2008) 131–139.
[21] MATLAB 7.10 (2010) The MathWorks Inc., Natick, Massachussets, USA.
[22] A.C. Olivieri, W. Hai-Long, Y. Ru-Qin, Chemom. Intell. Lab. Syst. 96 (2009) 246–251.
[23] K. Kaczmarek, B. Walczak, S. de Jong, B.G.M. Vandginste, Acta Chromatogr. 15 (2005) 82–96.
[24] W. Windig, J. Guilment, Anal. Chem. 63 (1991) 1425–1432.
[25] S. Wold, P. Geladi, K. Esbensen, J. Øhman, J. Chemom. 1 (1987) 41–56.
[26] A.C. Olivieri, J. Chemometr. 19 (2005) 253–265.
[27] R. Jordi, F.X. Rius, Trends Anal. Chem. 16 (1997) 211–216.

Talanta 132 (2015) 857–863

Contents lists available at ScienceDirect

Talanta

journal homepage: www.elsevier.com/locate/talanta

Polyethyleneimine–iron phosphate nanocomposite as a promising adsorbent for the isolation of DNA

Lin-Lin Hu, Bo Hu, Li-Ming Shen, Dan-Dan Zhang, Xu-Wei Chen *, Jian-Hua Wang *

Research Center for Analytical Sciences, College of Sciences, Northeastern University, Box 332, Shenyang 110819, China

ARTICLE INFO

Article history:
Received 20 August 2014
Received in revised form
20 October 2014
Accepted 21 October 2014
Available online 29 October 2014

Keywords:
Iron phosphate
Polyethyleneimine
Nanocomposite
Solid-phase extraction
DNA

ABSTRACT

A polyethyleneimine (PEI)–iron phosphate ($FePO_4$) nanocomposite is prepared by immobilization of PEI onto the surface of $FePO_4$ nanoparticles via electrostatic interaction. The obtained PEI–$FePO_4$ nanocomposites are spherical with a size centered in ca. 100 nm. They provide a novel adsorbent for the solid-phase extraction of DNA from complex sample matrices. At pH 4, 50 μg mL^{-1} of DNA (salmon sperm DNA sodium salt) in 1.0 mL aqueous solution are quantitatively adsorbed (100%) by 2 mg of the PEI–$FePO_4$ nanocomposites, and meanwhile the coexisting albumin at a same concentration level is not retained, demonstrating the favorable selectivity of the nanocomposites to DNA against proteins. The adsorption behaviors of DNA onto the PEI–$FePO_4$ nanocomposites fit *Langmuir* model, corresponding to an adsorption capacity of 61.88 mg g^{-1}. The adsorbed DNA could be readily recovered by using a 0.04 mol L^{-1} Britton–Robinson (BR) buffer at pH 10, resulting in a recovery of 85%. The nanocomposites have been further used for the isolation of DNA from a series of real sample matrices, including synthetic λ-DNA sample, human whole blood and *Escherichia coli* cell lysate. The extraction efficiency and the purity of the recovered DNA are at least comparable to those achieved by using the reported sorbent materials or commercial kits. In addition, the DNAs isolated from human whole blood and *E. coli* cell lysate are of high quality, which have been further demonstrated by using them as templates for successful PCR amplifications.

© 2014 Elsevier B.V. All rights reserved.

1. Introduction

DNA-based assays are fundamental tasks in molecular biology and life science studies. In biological samples, DNA concentration is generally very low in comparison with those of coexisting proteins, e.g., ng level of DNA versus mg level of proteins in μL volume of whole blood in addition to even high concentrations of other sample matrix components [1]. In this respect, the isolation and purification of DNA from complex biological sample matrices is a critical issue and it is mandatory in forensic, clinic analysis and molecular biochemistry applications, with the aim to obtain qualified templates for the subsequent downstream processes including polymerase chain reaction, cloning, sequencing and hybridization [2–4]. Among the various methodologies for DNA extraction/purification, solid-phase extraction (SPE) is the most popular approach which is able to provide rapid and efficient isolation/purification of DNA along with certain extent of preconcentration. Further, the use of volatile and harmful organic solvents is generally avoided. Conventionally, silica has been one of the most useful sorbent material for the adsorption/purification of DNA, due to its ease of surface modification and favorable biocompatibility [5,6]. DNA could be efficiently adsorbed onto positively charged surface of amino-modified silica nanoparticles without any extra binding agents and the adsorbed DNA is protected from enzymatic cleavage [7]. Aqueous media of high ionic strength are usually necessary to promote the adsorption of DNA on silica as a result of a series of interactions [8]. In aqueous medium, DNA exists as a large negatively charged polyanion with phosphate groups on the nucleic acid backbone, thus it could be readily captured on positively charged sorbent materials [9]. This offers an effective strategy for DNA extraction/purification based on ionic interactions with cationic moieties [10]. Immobilization of silane moieties on the surface of various solid supports has been demonstrated to be an effective way to introduce positive charge for facilitating ionic interaction with DNAs [11,12].

Some other sorbent materials have recently been reported for the adsorption of DNAs. The superparamagnetic iron oxide is found to be able to adsorb DNA [13]. In practical applications, magnetic particles with size of <30 nm are preferential which are well dispersed without aggregation [14]. DNA extraction has been performed by using 3-[2-(2-aminoethyl)-ethylamino]-propyltrimethoxysilane and hyper-branched polyamidoamine dendrimer modified bacterial magnetic particles as adsorbents [15], and an

* Corresponding authors. Tel.: +86 24 83688944; fax: +86 24 83676698.
E-mail addresses: chenxuwei@mail.neu.edu.cn (X.-W. Chen), jianhuajrz@mail.neu.edu.cn (J.-H. Wang).

http://dx.doi.org/10.1016/j.talanta.2014.10.047
0039-9140/© 2014 Elsevier B.V. All rights reserved.

improvement on DNA adsorption efficiency is observed with the presence of a large number of amino groups [16]. Polyethylenimine (PEI) is a multivalent cationic agent with abundant amino groups. PEI-modified magnetic Fe_3O_4 nanobeads have been used as a medium for the purification of plasmid DNA from bacterial cell lysates [17]. The obtained plasmid DNA is of good quality and free of other contaminant molecules in the culture medium.

Iron phosphate ($FePO_4$) nanoparticles provide a biocompatible medium and it has gained interest in various fields including gas storage and adsorption [18]. The potentials for the use of fluoridized iron phosphate in the selective adsorption of protein species of interest have been previously reported [19]. It is expected to provide special selectivity for DNA adsorption with iron phosphate by combining the features of amino groups in PEI. Therefore, in the present study $FePO_4$ nanoparticles are used as solid support for the immobilization of PEI, and the obtained PEI–$FePO_4$ nanocomposite is used as a powerful adsorbent for the selective extraction of DNA. DNA is selectively adsorbed on the PEI–$FePO_4$ nanocomposites at pH 4 via electrostatic interaction, and the adsorption equilibrium is reached within a very short time, i.e., 30 s. The adsorbed DNA could be recovered by using Britton–Robinson (BR) buffer at pH 10. The developed extraction protocol is applied to the extraction of DNAs from different matrices including synthetic λ-DNA samples, human whole blood and *Escherichia coli* cell lysate. The DNAs recovered are demonstrated to be high purity and suitable for downstream PCR amplification.

2. Experimental

2.1. Materials

Branched polyethyleneimine (Mw ≈ 25 kDa) was received from Aldrich (Milwaukee, MI, USA). Bovine serum albumin (BSA) and salmon sperm DNA sodium salt were purchased from Sigma (St. Louis, MO) and used as received. DL2000 DNA Marker and λ-DNA were from Takara Biotechnology (Dalian, China). 2 × Power Taq PCR MasterMix, Proteinase K and whole blood genomic DNA extraction kit (Spin-Column) were obtained from BioTeke Corporation (Beijing, China). AxyPrep plasmid Miniprep kit was the product of Axygen Biotechnology Co. Ltd. (Hangzhou, China). Primers for 500 bp fragment of λ-DNA, 580 bp fragment of human P53 gene and 700 bp fragment of GFP gene were provided by Sangon Biotech (Shanghai, China). Cetyltrimethyl Ammonium Bromide (CTAB), $(NH4)_2Fe(SO_4)_2 \cdot 6H_2O$, HCl, H_3PO_4, HAc, H_3BO_3, NaCl, urea, EDTA and Triton X-100 were purchased from Sinopharm Chemical Reagent Co. Ltd (Shanghai, China). Agarose was the product of Hispanagar Company (Spain).

All the reagents used were at least of analytical reagent grade unless specified. 18 MΩ cm deionized water was used throughout.

Human whole blood samples from healthy volunteers were provided by the Hospital of Northeastern University (China). After adding appropriate amount of anticoagulant, the blood samples were stored in a refrigerator at −20 °C for future use.

2.2. Preparation of $FePO_4$ nanoparticles

$FePO_4$ nanoparticles were prepared in a microwave system based on a literature protocol with minor modifications [20]. Shortly, 1.2 g of urea and 0.1 g of CTAB were dissolved in 40 mL of $(NH_4)_2Fe(SO_4)_2 \cdot 6H_2O$ solution (0.1 mmol). Then 0.1 mmol of H_3PO_4 was added. The mixture was vigorously stirred until a homogeneous solution was obtained. The homogeneous reaction mixture was afterwards transferred into a 300 mL round-bottom flask and placed in an UWave-1000 Microwave · Uv · Us Synthesis/Extraction Reactor (Sino Microwave Chemistry Technology Co. Ltd, Shanghai, China) for carrying out the reaction at 80 °C for 15 min. The product was eventually cooled down to room temperature.

2.3. Immobilization of PEI onto $FePO_4$ nanoparticles and characterizations of the PEI–$FePO_4$ nanocomposites

400 mL of the above mentioned $FePO_4$ solution and 10 mL of PEI solution (5 mg mL^{-1}) were mixed together, and the mixture was then sonicated for 2 h under ultrasound irradiation to facilitate the immobilization of PEI onto the surface of $FePO_4$ nanoparticles. After centrifugation at 10,000 rpm for 3 min, the supernatant was discarded and the residue was collected and washed with double-distilled water for three times. The final product was dried at 50 °C for 6 h for future use.

The morphologies of the obtained PEI–$FePO_4$ nanocomposites were monitored by a Superscan SSX-550 Scanning Electron Microscope (Shimadzu, Japan) at 200 kV. FT-IR spectra was recorded with a Nicolet 6700 spectrometer (Thermo Electron, USA) from 400 cm^{-1} to 4000 cm^{-1} with a resolution of 2.0 cm^{-1}. The surface charge properties of the PEI–$FePO_4$ nanocomposites were investigated by measuring the Zeta potential with a ZEN3600 Nano Zetasizer (Malvern, England). Absorption spectra were recorded on a U-3900 UV–vis spectrophotometer (Hitachi, Japan) with a 1.0 cm quartz cell.

2.4. DNA adsorption on PEI–$FePO_4$ nanocomposites

The dependence of DNA adsorption on the variation of pH value was investigated within a range of pH 2–12. 2 mg of the PEI–$FePO_4$ nanocomposites were added into 1.0 mL of DNA aqueous solution (50 μg mL^{-1}), and the mixture was then shaken vigorously for 30 s to facilitate the adsorption of DNA. After phase separation by centrifugation at 8000 rpm for 3 min, the supernatant was collected to quantify the DNA content remained in the original aqueous solution by monitoring the soret band of DNA at 260 nm.

For the recovery of the adsorbed DNA, the PEI–$FePO_4$ nanocomposites were prewashed with ethanol (70%, v/v) to remove the loosely retained matrix components via physical adsorption. 1.0 mL of Britton–Robinson (BR) buffer solution at pH 10 (0.04 mol L^{-1}) was then added as a stripping reagent. The mixture was oscillated for 5 min to facilitate the stripping of the retained DNA from the PEI–$FePO_4$ nanocomposites. After centrifugation at 8000 rpm for 3 min, the supernatant with the recovered DNA was collected for the ensuing investigations.

2.5. Sample preparation

A 200 μL aliquot of synthetic sample consisting of 3.5 mg L^{-1} λ-DNA, 0.1 g L^{-1} BSA and 0.3 mol L^{-1} $MgCl_2$ was diluted to 1000 μL by using a 0.01 mol L^{-1} BR buffer at pH 4.

A 250 μL aliquot of human whole blood sample was mixed with 20 μL of proteinase K (20 μg μL^{-1}). After incubating at room temperature for 15 min, the mixture was put into a water bath of 56 °C for further incubating for 10 min, and the lysate was then diluted to 1000 μL by using a 0.01 mol L^{-1} BR buffer at pH 4.

E. coli DH-5a cells containing PEGFP-C1 plasmid were cultured overnight in a shaker flask at 37 °C in 100 mL of LB medium containing 50 mg L^{-1} Kanamycin. 1.5 mL of *E. coli* cell cultures were pelleted at 8000 rpm for 3 min by centrifugation. The cells were then mixed with a 100 μL of 10% Triton-X solution containing 400 μg proteinase K. After incubating at room temperature for 15 min, the mixture was put into a water bath of 56 °C for 10 min, and the lysate was then diluted to 1000 μL by using a 0.01 mol L^{-1} BR buffer at pH 4.

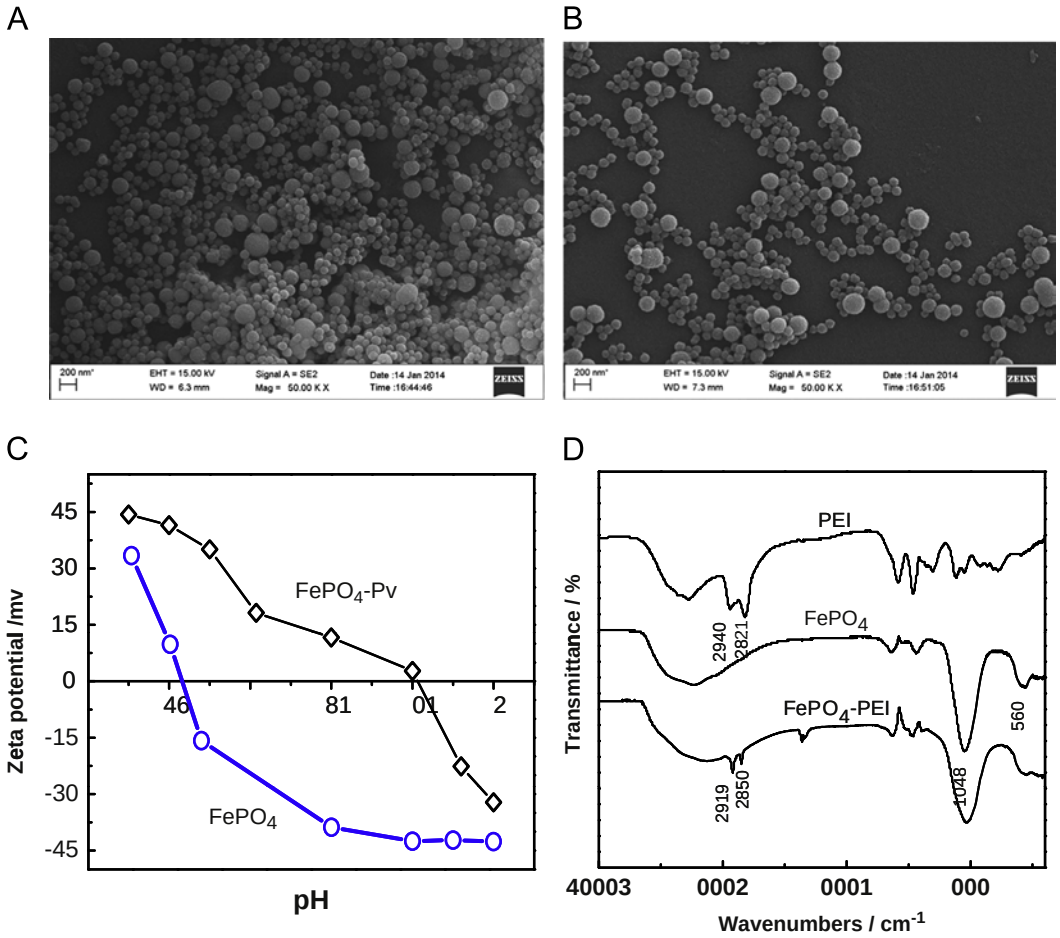


Fig. 1. SEM images of (A) bare $FePO_4$ and (B) PEI–$FePO_4$ nanocomposites. (C) Zeta potential of the bare $FePO_4$ and PEI–$FePO_4$ nanocomposites. (D) FT-IR spectra of PEI, bare $FePO_4$ and PEI–$FePO_4$ nanocomposites.

3. Results and discussion

3.1. Characterization of the PEI–$FePO_4$ nanocomposites

The SEM images of bare $FePO_4$ and the PEI–$FePO_4$ nanocomposites are illustrated in Fig. 1A and B, where microspheres with sizes of 90–200 nm (centered in ca. 100 nm) are observed for both $FePO_4$ and PEI–$FePO_4$ nanocomposites. It seems that the immobilization of PEI onto $FePO_4$ surface poses virtually no change on the morphology and size distribution of the nanoparticles. However, the obtained PEI–$FePO_4$ nanocomposites are well dispersed with much less aggregation with respect to that observed for the bare $FePO_4$ nanoparticles. The improvement on dispersion is favorable for DNA adsorption as more interaction sites should be provided in an aqueous medium.

This immobilization of PEI onto the surface of $FePO_4$ nanoparticles is most probably facilitated by the electrostatic interaction between them. As illustrated clearly that the surface of bare $FePO_4$ nanoparticles is negatively charged with a ζ potential of ca. -18 mV within a range of pH 4–12. After modification with PEI, a positively charged surface is achieved for the PEI–$FePO_4$ nanocomposites within pH 3–10. At a higher pH value, i.e., pH > 10, the surface of PEI–$FePO_4$ nanocomposites turns to negatively charged. These results might be ascribed to the abundant amino groups in the structure of PEI. The decrease of pH value, i.e., the increase of $[H^+]$, results in protonatation of the amino groups, which contributes to a higher ζ potential [21]. The surface charge property of the PEI–$FePO_4$ nanocomposites is obviously favorable for the adsorption of DNA within a neutral medium and followed by desorption of DNA in a medium at pH > 10.

FT-IR spectra of PEI, bare $FePO_4$ and PEI–$FePO_4$ nanocomposites are shown in Fig. 1D. The absorption bands at 560 cm^{-1} and 1048 cm^{-1} in the spectrum of $FePO_4$ nanoparticle are attributed to the asymmetric vibrations of O–P–O [22] and Fe–O–P bond [23]. These bands are also clearly identified in the spectrum of PEI–$FePO_4$ nanocomposites. After the modification of PEI, the absorption bands at 3300–3600 cm^{-1}, 2850 cm^{-1} and 2919 cm^{-1}, which are the characteristic stretching vibrations of N–H, vibration of $-CH_3$ and $-CH_2$ of PEI, are all observed in the spectrum of PEI–$FePO_4$ nanocomposites [24]. These observations well suggest the successful immobilization of PEI onto the $FePO_4$ nanoparticles.

3.2. Selective adsorption of DNA on PEI–$FePO_4$ nanocomposites

The pH-dependent adsorption behaviors of DNA onto the PEI–$FePO_4$ nanocomposites are investigated and the results are shown in Fig. 2A. It is obvious that favorable adsorption of DNA, i.e., ca. 100% adsorption efficiency, is achieved at pH 2–5. At pH > 5, a significant drop of the adsorption efficiency is encountered, and the adsorption of DNA becomes marginal at pH > 10. These observations could be well explained by the electrostatic interaction between DNA moiety and the PEI–$FePO_4$ nanocomposites. As illustrated in Fig. 1C that at pH 2–10, the surface of PEI–$FePO_4$ nanocomposites is positively charged with the ζ potential ranges from 45 mV to 3 mV, while the polyanionic DNA moiety is negatively charged within the same pH range. Therefore, at a lower pH value the strong electrostatic attraction between polyanionic DNA moiety and the PEI–$FePO_4$ nanocomposites facilities the adsorption of DNA and eventually results in a favorable adsorption efficiency.

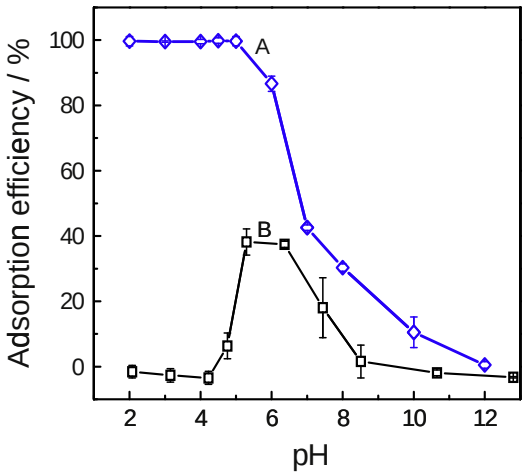


Fig. 2. pH-Dependent adsorption efficiency of (A) DNA and (B) BSA. The amount of PEI–$FePO_4$ nanocomposites: 2 mg; DNA concentration: 50 μg mL^{-1}; BSA concentration: 50 μg mL^{-1}; adsorption time: 30 s.

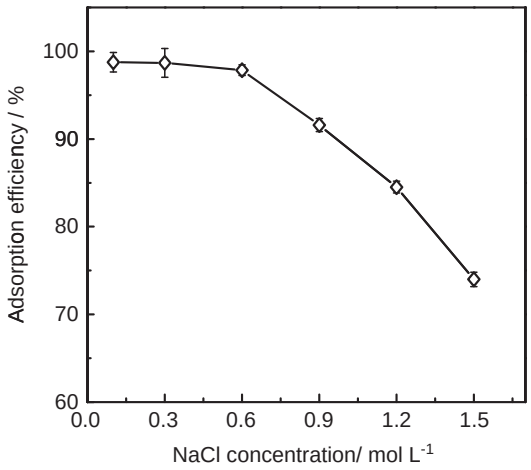


Fig. 3. The effect of ionic strength on the adsorption of DNA. The amount of PEI–$FePO_4$ nanocomposites: 2 mg; DNA concentration: 50 μg mL^{-1}; pH: 4; adsorption time: 30 s.

The increase of pH value gives rise to a decrease of positive surface charge of the PEI–$FePO_4$ nanocomposites, which leads to a decrement of electrostatic attraction between DNA and the PEI–$FePO_4$ nanocomposites. This causes a gradual drop of the adsorption efficiency. At pH > 10, the surface of the PEI–$FePO_4$ nanocomposites turns to negatively charged and thus the electrostatic repulsion deteriorates the adsorption of DNA.

In the adsorption of DNA from biological samples, the potential interference from coexisting proteins is a critical issue. In this respect, the adsorption of protein by the PEI–$FePO_4$ nanocomposites is investigated with BSA as a model. As shown in Fig. 2B a maximum adsorption of BSA is achieved at a pH value close to its isoelectric point, i.e., pI ~4.8, while virtually no adsorption on BSA is observed at pH < 4 or pH > 8. It is known that BSA is positively charged at a pH value of lower than its isoelectric point, i.e., pH < pI, thus its adsorption is prohibited at pH < 4 due to the electrostatic repulsion between the BSA and the positively charged PEI–$FePO_4$ nanocomposites. With the increase of pH value to exceed the isoelectric point, BSA turns to neutral and then to negatively charged, the electrostatic attraction with the positively charged PEI–$FePO_4$ nanocomposites facilitates its adsorption. By further increasing the pH value a decrease of BSA adsorption is encountered similar to that described for the case of DNA adsorption. In practical applications, the adsorption of DNA is conducted at pH 4, where the adsorption of protein is avoided at same experimental conditions. On the other hand, further experiments have indicated that at pH 4 the presence of protein, i.e., BSA at a same concentration level, causes no effect on the adsorption of 50 μg mL^{-1} DNA.

Generally, the ionic strength exhibits significant effect on the adsorption behaviors of biomacromolecules on solid materials in which electrostatic interaction plays a governing role on the adsorption process [25]. In the present case, the effect of ionic strength is investigated by introducing certain amount of NaCl (0–1.5 mol L^{-1}) into the DNA sample solution. The experimental results illustrated a substantial decrease on the adsorption efficiency of DNA with the increase of the ionic strength (Fig. 3). This observation further indicates that the adsorption of DNA onto the PEI–$FePO_4$ nanocomposites is mainly governed by electrostatic interaction [26].

As mentioned previously that selective adsorption of DNA onto the surface of the PEI–$FePO_4$ nanocomposites is achieved at pH 4 with coexisting proteins. It has been further demonstrated that the adsorption of DNA is a fast process and the adsorption equilibrium is reached within 30 s. The dynamic adsorption isotherm at room temperature within a DNA concentration range

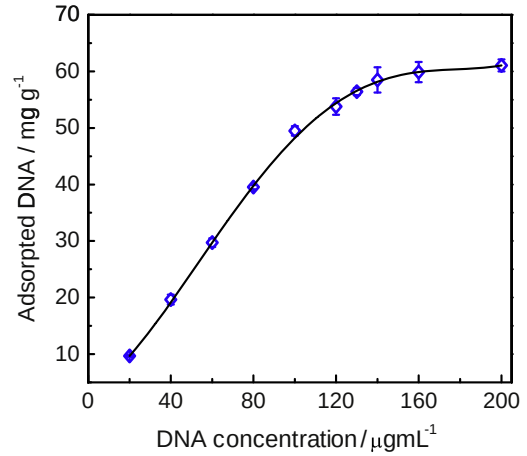


Fig. 4. Adsorption isotherm of DNA onto the PEI–$FePO_4$ nanocomposites recorded at pH 4 by using 2 mg of the PEI–$FePO_4$ nanocomposites with an adsorption time of 30 s.

of 20–200 mg L^{-1} is illustrated in Fig. 4. The experimental data fit *Langmuir* theoretical adsorption model as expressed in the following:

$$Q^* = \frac{Q_m \times C^*}{K_d + C^*}$$

C^* is the DNA concentration in aqueous solution, Q^* denotes the amount of DNA retained by the PEI–$FePO_4$ nanocomposites. Q_m represents the maximum adsorption capacity and K_d is the dissociation constant. An adsorption capacity of 61.88 mg g^{-1} is derived by fitting the experimental data. Table 1 compares the maximum DNA sorption capacity of the present nanocomposite with those of other materials reported in the literatures. It is obvious that the PEI–$FePO_4$ nanocomposite offers a relatively higher sorption capacity for DNA.

3.3. DNA recovery from the PEI–$FePO_4$ nanocomposites

As discussed in the previous section that electrostatic interaction is the major driving force for the adsorption of DNA onto the PEI–$FePO_4$ nanocomposites. The adsorption of DNA is strongly dependent on the variation of pH value and ionic strength of the sample solution. Therefore, the recovery of the adsorbed DNA from the surface of PEI–$FePO_4$ nanocomposites could be facilitated by

Table 1
The maximum adsorption capacities of DNA by various adsorbents.

Adsorbent	Sorption capacity ($mg\ g^{-1}$)
Ionic liquid-modified Fe_3O_4 nanoparticles [27]	19.8
Fe_3O_4@SiO_2-NH magnetic nanoparticles [28]	27.9
Aminosilane-modified bacterial magnetic particles [11]	60
PEI-modified Fe_3O_4 nanoparticles [14]	70
PEI–$FePO_4$ nanocomposites (this work)	61.88

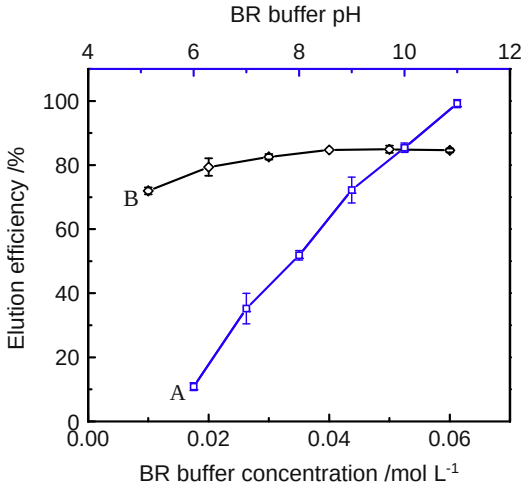


Fig. 5. (A) pH-Dependent recovery of DNA from the surface of PEI–$FePO_4$ nanocomposites. 2 mg PEI–$FePO_4$ nanocomposites; DNA concentration: 50 μg mL^{-1}; adsorption time: 30 s; stripping time: 5 min. (B) The variation of DNA recovery with ionic strength of the stripping reagent. 2 mg PEI–$FePO_4$ nanocomposites; DNA concentration: 50 μg mL^{-1}; pH 10; adsorption time: 30 s; stripping time: 5 min.

regulating either the pH value or the concentration of electrolyte in the stripping reagent or eluent. Taking into consideration that the collected DNA should fulfill the requirement for further biological investigations, e.g., PCR amplification, a BR buffer solution is preferential for this purpose. Fig. 5A illustrates the pH-dependent recovery of DNA within a range of pH 6–11. It is obvious that an increase of the pH value results in a significant improvement on the recovery of DNA, and at pH 11, ca. 100% recovery is achieved. Considering that a too strong alkali medium tends to cause conformational change on the DNA moiety, a BR buffer solution at pH 10 is adopted.

The ionic strength of the stripping reagent is controlled by regulating the concentration of the BR buffer solution, and the dependence of DNA recovery on the ionic strength is shown in Fig. 5B. An improvement of DNA recovery from ca. 70% to 85% is achieved by increasing the BR buffer concentration from 0.01 mol L^{-1} to 0.04 mol L^{-1}, and the recovery remains virtually unchanged by further increasing the BR buffer concentration up to 0.06 mol L^{-1}. The increase of BR buffer concentration, i.e., the ionic strength, shields the electrostatic interaction between DNAs and the PEI–$FePO_4$ nanocomposites. Therefore, for the ensuing experiments, a BR buffer concentration of 0.04 mol L^{-1} is adopted for DNA stripping, giving rise to a recovery of 85%.

3.4. DNA isolation from synthetic sample, human whole blood and E. coli cell lysate

The PEI–$FePO_4$ nanocomposites have been applied for the isolation of DNA from various real sample matrices, including synthetic λ-DNA sample, human whole blood and *E. coli* cell lysate. The DNAs recovered from these samples are then used as templates for PCR-amplification by a MyCycler™ thermal cycler (Bio-Rad Laboratories, USA).

For the synthetic λ-DNA sample, a 500 bp DNA fragment was amplified using the forward primer 5′-GATGAGTTCGTGTCCGTACAACTGG-3′ and the reverse primer 5′-GGTTATCGAAATCAGCCACAGCGCC-3′. The PCR cocktail consists of 4 μL of the recovered λ-DNA, 2 μL of forward/reverse primer (10 μmol L^{-1}) and 25 μL of 2 × Power Taq PCR Master Mix in a final volume of 50 μL. The PCR temperature program is 95 °C for 5 min, 35 cycles at 95 °C for 30 s, 68 °C for 1 min, and 72 °C for 1 min, with a final extension at 72 °C for 10 min.

For the human whole blood sample, a 543 bp P53 gene fragment was amplified using the forward primer 5′-CCACCATCCACTACAACTACAT-3′ and the reverse primer 5′-GCTTGCTTACCTCGCTTAG-3′. The PCR cocktail consists of 2 μL of the recovered λ-DNA, 1 μL of forward/reverse primer (10 μmol L^{-1}), 13 μL of 2 × Power Taq PCR Master Mix in a final volume of 25 μL. The PCR temperature program is 95 °C for 5 min, 35 cycles at 95 °C for 30 s, 57 °C for 30 s, and 72 °C for 1 min, with a final extension at 72 °C for 5 min.

For the *E. coli* cell lysate, 2 μL (10 mg mL^{-1}) RNase was added to eliminate the interference from RNA, and then a 700 bp EGFP gene fragment was amplified using the forward primer 5′-CCTG GATCCATGGTGAGCAAGGGCGAGGAG-3′ and the reverse primer 5′-GCGCTCGAGTTACTTGTACAGCTCGTCCATG-3′. The PCR cocktail consists of 2 μL of the recovered λ-DNA, 2 μL forward/reverse primer (10 μmol L^{-1}), 25 μL of 2 × Power Taq PCR Master Mix in a final volume of 50 μL. The PCR temperature program is 94 °C for 5 min, 35 cycles at 94 °C for 60 s, 56 °C for 30 s, and 72 °C for 1 min, with a final extension at 72 °C for 10 min.

The quantity and quality of the isolated DNAs from the above sample matrices are estimated by measuring the absorbance at 260 nm (A_{260}) and the absorbance ratio at 260 nm/280 nm (A_{260}/A_{280}), respectively. In the present study, the concentration of the isolated DNAs can be read directly from the Synergy H1 hybrid multi-mode microplate reader by measuring its UV absorbance at 260 nm. Consequently, the quantity of isolated DNAs is calculated according to its concentration and the eluent volume.

By using the PEI–$FePO_4$ nanocomposites as adsorbent for DNA extraction, 4.6 μg of human genomic DNA and 19.1 μg plasmid DNA are isolated from 200 μL of human whole blood and 1.5 mL of *E. coli* cell culture. The yields for DNA extraction by using the PEI–$FePO_4$ nanocomposites as adsorbent are comparable to those obtained by previously reported adsorbents as shown in Table 2. The A_{260}/A_{280} ratio for the recovered DNA from human whole blood and *E. coli* cell lysate are ca. 1.88 and 1.90, respectively, indicating that the extracted DNA templates are of high purity with negligible protein contamination. Especially, extraction of DNAs with PEI–$FePO_4$ nanocomposites exhibits a few distinct advantages, including (1) PEI–$FePO_4$ nanocomposites are readily available with low cost; (2) they entail a fast equilibrium within 30 s; (3) they avoid the use of chaotropic reagents and eliminate potential contamination of the recovered DNA sample which generally tends to inhibit PCR amplification; (4) a simple manipulation of the pH value facilitates flexible recovery of DNA with a favorable efficiency of 85%.

Fig. 6 illustrates the electrophoretograms for the PCR products. It can be seen that the 500 bp, 543 bp and 700 bp amplified products from λ-DNA, human whole blood gene and *E. coli* cell lysate are clearly identified (as illustrated in the lanes 2,3 in Fig. 6A–C). It is noticeable that comparable results are observed for the DNAs isolated from the corresponding sample matrices by using the PEI–$FePO_4$ nanocomposites as adsorbent with respect to those obtained by using the commercial DNA extraction kits. It is worthy to notice that no PCR amplified products are observed when directly using the synthetic λ-DNA sample, human blood and *E. coli*

Table 2
Yields of DNAs from human whole blood and *E. coli* cell culture with extraction by various adsorbents.

Adsorbent	DNA yields (human whole blood, μg/200 μL)	Adsorbent	DNA yields (*E. coli* cell culture, μg/1.5 mL)
Fe_3O_4/Au composite particles [29]	4–10	magnetite [13]	9.9
Amino (APTES or AEEA) silane-coated microchip [12]	0.4	PEI–Fe_3O_4 magnetic nanoparticles [14]	17.5
Bifunctional core–shell magnetic nanoparticles [30]	1.7	AEEA coated bacterial magnetic particles [15]	10.8
Whole blood genomic DNA extraction kit (Spin-Column)	3–6	Fe_3O_4@SiO_2-NH magnetic nanoparticles [28]	15.75
PEI–$FePO_4$ nanocomposites (this work)	4.6	PEI–$FePO_4$ nanocomposites (this work)	19.1

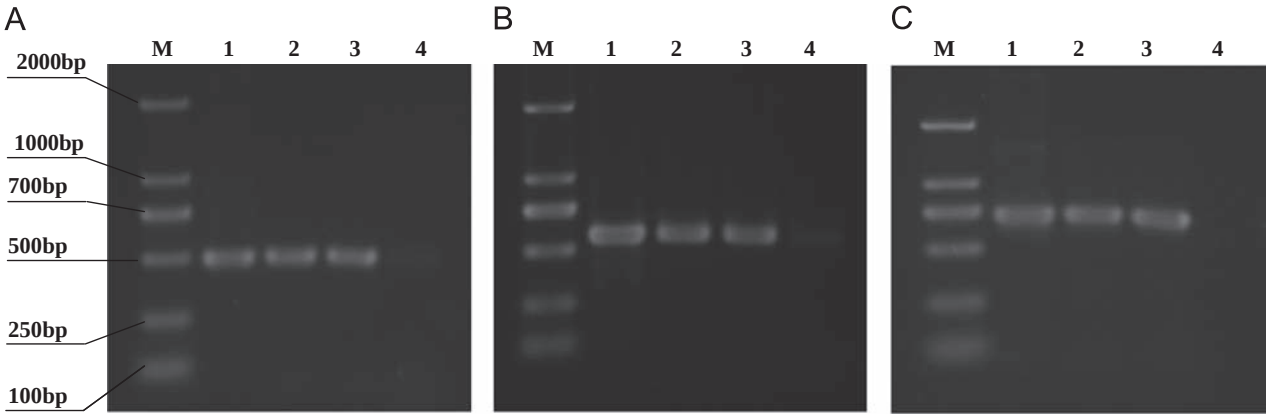


Fig. 6. The electrophotograms for the PCR products. (A) λ-DNA sample. M: DL-2000 DNA Marker; lane 1: PCR product from λ-DNA; lane 2 and 3: PCR products from λ-DNA isolated by the PEI–$FePO_4$ nanocomposites; lane 4: PCR product from the synthetic λ-DNA sample without extraction. (B) Human whole blood. M: DL-2000 DNA Marker; lane 1: PCR product from blood DNA, extracted with commercial kits (whole blood genomic DNA extraction kit (Spin-Column)); lane 2 and 3: PCR products from blood DNA isolated by the PEI–$FePO_4$ nanocomposites; lane 4: PCR product from blood without extraction. (C) *E. coli* cell lysate. M: DL-2000 DNA Marker; lane 1: PCR product from *E. coli* cell lysate extracted with commercial kits (AxyPrep plasmid Miniprep kit); lane 2 and 3: PCR products from *E. coli* cell lysate isolated by the PEI–$FePO_4$ nanocomposites; lane 4: PCR product from *E. coli* cell lysate without extraction.

cell lysate as templates. The successful PCR amplifications further demonstrate that the DNAs isolated from human whole blood and *E. coli* cell lysate are of high purity, indicating the favorable efficiency of PEI–$FePO_4$ nanocomposites for DNA adsorption.

4. Conclusions

Polyethyleneimine (PEI) is immobilized on the surface of $FePO_4$ nanoparticles via electrostatic interactions. The obtained PEI–$FePO_4$ nanocomposites exhibit favorable selectivity for the adsorption of DNAs with high efficiency in biological samples at pH 4 driven by the electrostatic interaction between the negatively charged poly-anionic DNA moiety and the positively charged amino groups on the surface of the PEI–$FePO_4$ nanocomposites. The retained DNAs can be readily recovered by simply manipulating the pH value. The PEI–$FePO_4$ nanocomposites have been demonstrated for the isolation of DNAs from a series of real sample matrices, including synthetic λ-DNA sample, human whole blood and *E. coli* cell lysate. The DNAs isolated by using the PEI–$FePO_4$ nanocomposites as adsorbent are well suitable for PCR amplifications.

Acknowledgement

The authors appreciate financial supports from the Natural Science Foundation of China (21275027, 21235001 and 21375013), the Program of New Century Excellent Talents in University (NCET-11-0071) and Fundamental Research Funds for the Central Universities (N110805001, N120405004 and N130105002) are highly appreciated.

References

[1] J. Wen, L.A. Legendre, J.M. Bienvenue, J.P. Landers, Anal. Chem. 80 (2008) 6472–6479.
[2] A. Ziegler, A. Koch, K. Krockenberger, A. Großhenning, Hum. Genet. 131 (2012) 1627–1638.
[3] A. Alonso, P. Martín, C. Albarrán, P. García, O. García, L.F.D. Simón, J.G. Hirschfeld, M. Sancho, C.d.l. Rúa, J.F. Piqueras, Forensic Sci. Int. 139 (2004) 141–149.
[4] R. Drmanac, S. Drmanac, Z. Strezoska, T. Paunesku, I. Labat, M. Zeremski, J. Snoddy, W.K. Funkhouser, B. Koop, L. Hood, R. Crkvenjakov, Science 260 (1993) 1649–1652.
[5] X.W. Chen, Z.R. Xu, B.Y. Qu, B.Y. Qu, Y.F. Wu, J. Zhou, H.D. Zhang, J. Fang, J.H. Wang, Anal. Bioanal. Chem. 388 (2007) 157–163.
[6] X.X. He, H.L. Huo, K.M. Wang, W.H. Tan, P. Gong, J. Ge, Talanta 73 (2007) 764–769.
[7] X.X. He, K.M. Wang, W.H. Tan, B. Liu, X. Lin, C. He, D. Li, S.S. Huang, J. Li, J. Am. Chem. Soc. 125 (2003) 7168–7169.
[8] H. Tian, A.F.R. Huhmer, J.P. Landers, Anal. Biochem. 283 (2000) 175–191.
[9] M.E. Park, J.H. Chang, Mater. Sci. Eng., C 27 (2007) 1232–1235.
[10] Y. Fang, J.H. Hoh, FEBS Lett. 459 (1999) 173–176.
[11] T. Nakagawa, R. Hashimoto, K. Maruyama, T. Tanaka, H. Takeyama, T. Matsunaga, Biotechnol. Bioeng. 94 (2006) 862–868.
[12] T. Nakagawa, T. Tanaka, D. Niwa, T. Osaka, H. Takeyama, T. Matsunaga, J. Biotechnol. 116 (2005) 105–111.
[13] M.J. Davies, J.I. Taylor, N. Sachsinger, I.L. Bruce, Anal. Biochem. 262 (1998) 92–94.
[14] C.L. Chiang, C.S. Sung, T.F. Wu, C.Y. Chen, C.Y. Hsu, J. Chromatogr. B 822 (2005) 54–60.
[15] B. Yoza, M. Matsumoto, T. Matsunaga, J. Biotechnol. 94 (2002) 217–224.
[16] B. Yoza, A. Arakaki, T. Matsunaga, J. Biotechnol. 101 (2003) 219–228.
[17] C.L. Chiang, S.S. Ching, J. Magn. Magn. Mater. 302 (2006) 7–13.
[18] T.B. Zhang, Y.C. Lu, G.S. Luo, Ind. Eng. Chem. Res. 52 (2013) 6962–6968.

[19] S.S. Tang, W.J. Wang, X.W. Chen, J.H. Wang, Anal. Bioanal. Chem. 401 (2011) 3283–3892.
[20] Y.J. Yin, H. Zhang, P. Wu, B. Zhou, C. Cai, Nanotechnology 21 (2010) 1–10.
[21] X.L. Wang, L.Z. Zhou, Y.J. Ma, X. Li, H. Gu, Nano Res. 2 (2009) 365–372.
[22] Z.C. Shi, A. Attia, W.L. Ye, Q. Wang, Y.X. Li, Y. Yang, Electrochim. Acta 53 (2008) 2665–2673.
[23] K.M. Nawal, B. Asim, M. Masahiko, F. Masahiro, Ind. Eng. Chem. Res. 45 (2006) 7748–7751.
[24] M.L. Chen, M.L. Shen, X.W. Chen, J.H. Wang, Macromol. Biosci. 10 (2010) 906–915.
[25] U.V. Dortmund, F. Chemie, O.H. Strass, O. Hollmann, C. Czeslik, Langmuir 22 (2006) 3300–3305.
[26] T. Ehtezazi, U. Rungsardthong, S. Stolnik, Langmuir 19 (2003) 9387–9394.
[27] M. Ghaemi, G. Absalan, Microchim. Acta 181 (2014) 45–53.
[28] X.W. Chen, Q.X. Mao, J.W. Liu, J.H. Wang, Talanta 100 (2012) 107–112.
[29] M. Zhao, X.Q. Zhang, S. Wang, C. Chen, Y. Cui, J. Med. Coll. PLA 24 (2009) 239–243.
[30] X. Xie, X.R. Nie, B.B. Yu, X. Zhang, J. Magn. Magn. Mater. 311 (2007) 416–420.

Talanta 132 (2015) 864–870

Contents lists available at ScienceDirect

Talanta

journal homepage: www.elsevier.com/locate/talanta

A highly selective and sensitive fluorescent probe for quantitative detection of Hg^{2+} based on aggregation-induced emission features

Aizhi Wang, Yunxu Yang*, Feifei Yu, Lingwei Xue, Biwei Hu, Weiping Fan, Yajun Dong

Department of Chemistry and Chemical Engineering, School of Chemistry and Biological Engineering, University of Science and Technology Beijing, Beijing 100083, China

ARTICLE INFO

Article history:
Received 31 July 2014
Received in revised form
19 October 2014
Accepted 22 October 2014
Available online 31 October 2014

Keywords:
Fluorescent probe
Quantitative detection
Mercury ion
Aggregation-induced emission

ABSTRACT

A π-conjugated cyanostilbene derivative of (Z)-2-(4-nitrophenyl)-3-(4-(vinyloxy)phenyl)acrylonitrile (**CN-vinyl**) had been designed, synthesized and confirmed by the standard spectroscopic analyses. **CN-vinyl** possesses an unusual high emissive aggregation-induced emission (AIE) feature in a tetrahydrofuran/water mixture (2:8, v/v). The fluorescence intensity of **CN-vinyl** can be quenched linearly with the addition of Hg^{2+} in a range of 0–50 μM with a correlation coefficient of $R^2=0.9957$. The detection limit of Hg^{2+} is 37 nM. The mechanism for Hg^{2+}-mediated optical properties of **CN-vinyl** is due to the selective cleavage of vinyl group by Hg^{2+}. Accuracy of the proposed methodology was evaluated by means of the recovery study in real samples and the analyzing certified reference material of the standard solution of Hg^{2+}. By this novel strategy, **CN-vinyl** can be used for quantitative detection of Hg^{2+} as well as the presence of other physiological relevant metal ions.

© 2014 Elsevier B.V. All rights reserved.

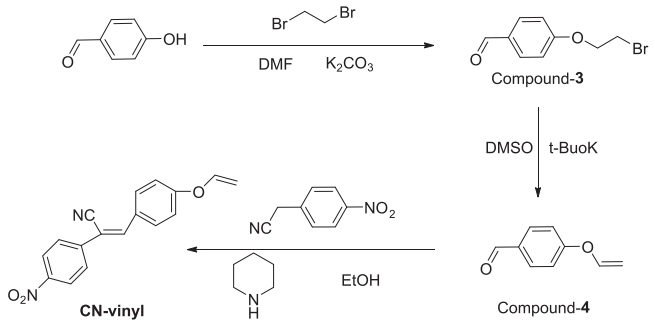
1. Introduction

Mercury, a class of heavy metal distributed throughout the environment by both natural processes and human activities, has long been identified as one of the most toxic heavy metals and a kind of persistent contaminant [1,2]. It can first be transformed into organic mercury after being absorbed from the environment by organisms, and then accumulated highly in trophic animals through the food chain [3,4]. According to recent reports, the toxicity of Hg^{2+} can induce a variety of syndromes and harmful effects [5], such as damage DNA, disable normal functions of liver and kidney, disrupt the immune system homeostasis [6–9] etc. Therefore, efficient monitoring the trace amount of Hg^{2+} with highly selective and sensitive is remarkably important for human health. Conventional analytical techniques include spectrophotometry, atomic absorption spectrometry, inductively coupled plasma–mass spectroscopy (ICP–MS), cold-vapor atomic fluorescence spectrometry (CV-AFS), ultraviolet–visible spectrometry, and X-ray absorption spectroscopy [10–15]. Whereas, these methods require expensive intricate instrumentation and complicated sample preparation processes. Moreover, the complexity makes them unsuitable for using in on-site Hg^{2+} analyses. Different from the traditional Hg^{2+} analyses, fluorescence probe offers several advantages for Hg^{2+} measurements because of its high sensitivity, lower detection limit, non-sample destructing and simple operation. In consequence, these unique characteristics make it favorable for both detection and imaging of Hg^{2+} in biological samples [16]. Many Hg^{2+} chemosensors with fluorescence response have been reported, such as, proteins conjugated polymer and diblock copolymer fluorescence sensors, biomolecules fluorescence sensors, foldamer-based fluorescence sensors, inorganic gold nanoparticles and CdS nanoparticles, and small organic molecule fluorescence probes [9,17–20]. However, luminescence of these conventional fluorophores often becomes weakened or quenched at high concentration or solid state due to the thermodynamically favorable process under the driving forces of intermolecular π–π stacking interaction of aggregation. The outcome of this effect is the sacrifice of the fluorescence emission efficiency and reduction of sensing performance.

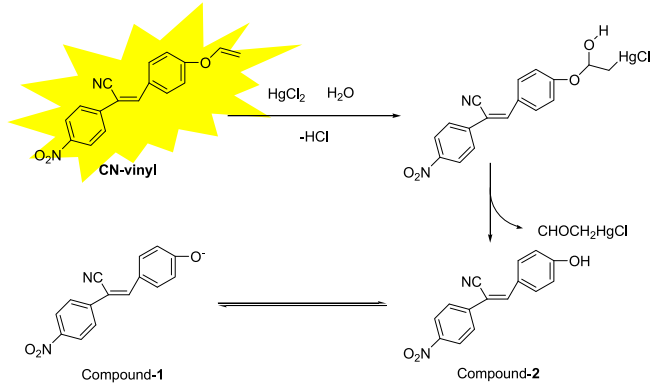
Fortunately, in 2001, Tang and co-workers first observed an intriguing phenomenon [21] that is the exact opposite of the aggregation-caused quenching (ACQ). Some practically non-luminescent in the solution state but become strongly emissive when aggregated or in the solid state due to suppression of nonradiative deactivation associated with restriction of intramolecular rotations (RIR). Then a large number of so called "aggregation-induced emission (AIE)" active molecules have since been developed, example of which including siloles, 1-cyano-trans-1, 2-bis-(4′-methylbiphenyl) ethylene (CN-MBE), 2, 5-diphenyl-1, 4-distyrylbenzene (DPDSB) derivatives, fluorenonearylamine derivatives, diphenyldibenzofulevne (DPDBF) derivatives, conjugated polymers, and so on [22–29]. Most of them can be employed as optical devices or bioprobes.

* Corresponding author. Tel.: +86-010-62333871
E-mail address: yxyang@ustb.edu.cn (Y. Yang).

http://dx.doi.org/10.1016/j.talanta.2014.10.048
0039-9140/© 2014 Elsevier B.V. All rights reserved.



Scheme 1. Synthesis of CN-vinyl.



Scheme 2. The reaction mechanism of CN-vinyl with Hg^{2+}.

Zhu et al. have demonstrated that the vinyl group is useful to design Hg^{2+} probe [30]. Inspired by their works, a novel fluorescence turn-off probe **CN-vinyl** ((*Z*)-2-(4-nitrophenyl)-3-(4-(vinyloxy)phenyl) acrylonitrile) toward Hg^{2+} was designed and synthesized (as shown in Scheme 1). **CN-vinyl** is a potential AIE cyanostilbene derivatives based on π-conjugated fluorophore, and the vinyl group as a recognition site with unique and high reactivity toward Hg^{2+}. We hypothesized that the reaction of CN-vinyl with Hg^{2+} would result in the cleavage of the vinyl group and the recognition mechanism is shown in Scheme 2. In addition, compound-**2** (*Z*)-3-(4-hydroxyphenyl)-2-(4-nitr-ophenyl)acrylonitrile was also synthesized as a contrast of CN-vinyl and the synthetic route is shown in Fig. S1.

2. Experimental section

2.1. Reagents and apparatus

All reagents and solvents were commercially available and were used without further purification unless otherwise stated. The water used for investigating was distilled prior to use. 4-nitrobenzylcyanide and p-hydroxybenzaldehyde were purchased from Alfa Aesar. MeHgCl was purchased from Dr. Ehrenstorfer Germany. The certified reference material of the standard solution of Hg^{2+} was purchased from General Research Institute for Nonferrous Metals, China and the certificate information is shown in Table S1. Stock solutions of metal ions (2.5 mM, Li^+, Na^+, K^+, Mg^{2+}, Ca^{2+}, Al^{3+}, Fe^{2+}, Fe^{3+}, Mn^{2+}, Cu^{2+}, Co^{2+}, Ni^{2+}, Pb^{2+}, Zn^{2+}, Sn^{2+}, Ag^+, Cd^{2+}, Ba^{2+}, Cr^{3+}, $MeHg^+$, Hg^{2+}) were prepared in deionized water. Stock solution of **CN-vinyl** (2.5 mM) was prepared by dissolving 18.2 mg **CN-vinyl** in 25 ml THF. Phosphate buffer solutions (PBS) were prepared by combining proper amounts of NaH_2PO_4 and NaOH and adjusted by a pH meter. Purification of reaction products was carried out by flash chromatography using silica gel (300–400 mesh, Branch of Qingdao Haiyang Chemical Co., Ltd.).

Infrared spectra were recorded on a Shimadzu IR-8400S spectrophotometer. ^1H NMR and ^{13}C NMR spectra were recorded at 400 MHz on a Varian Gemin-400 respectively. ESI-MS spectra were obtained on Bruker spectrometers. All absorption and fluorescence spectra in this work were recorded in Pgeneral TU-1901 and Hitachi F-4500 fluorescence spectrometers. All pH values were measured with a Model pHS-3C pH meter (Shanghai, China). Analytical TLC was carried out on silica gel plates (HSGF254, 0.2 mm, Yantai Chemical Industry Research Institute). Melting points were measured with RD-II melting point apparatus (uncorrected, Tainjin Xintianguang Instrument Company).

2.2. Synthesis

2.2.1. Synthesis of 4-(2-bromoethoxy)benzaldehyde (compound-**3**)

A similar method was adopted to synthesize the titled compound according to literature [31]. To a solution of p-hydroxybenzaldehyde (1.22 g, 0.01 mol) and anhydrous K_2CO_3 (4.14 g, 0.03 mol) in 20 ml DMF, requisite linear chain aliphatic dibromoethane (9.35 g, 0.05 mol) was added and then stirred at 80 °C for 1 h. After the reaction was finished (controlled by TLC), the reaction mixture was cooled to 0 °C and quenched with 1 M HCl. The mixture was then extracted with $CHCl_3$ and the organic layer was washed with water, dried over anhydrous Na_2SO_4, and then filtered out. Excess solvent was evaporated under reduced pressure and the resultant solid left was purified by column chromatography (EtOAc/petroleum ether=1:5 as eluent) to afford compound-**3** (1.63 g, 72% yield). mp 52–54 °C. IR (KBr) *ν*: 1685, 1602, 1577, 1506, 1253, 1163, 831 cm^{-1}. ^1H NMR (400 MHz, $CDCl_3$) *δ*: 9.88 (s, 1H), 7.83 (d, *J*=8.8 Hz, 2H), 7.00 (d, *J*=8.8 Hz, 2H), 4.36 (t, *J*=6.4 Hz, 2H), 3.65 (t, *J*=6.4 Hz, 2H).

2.2.2. Synthesis of 4-(vinyloxy)benzaldehyde (compound-**4**)

A similar method was adopted to synthesize the titled compound according to the literature [32]. To a solution of compound-**3** (0.227 g, 0.001 mol) in DMSO (10 mL), t-BuOK (0.224 g, 0.002 mol) was added. The reaction mixture was stirred at 25 °C for 4 h, after which it was diluted with EtOAc (20 mL), washed with H_2O (3 × 10 mL) and then brine (20 mL). The organic layer was dried, filtered, and concentrated. The crude product was purified by column chromatography (EtOAc/petroleum ether=1:5 as eluent) to afford compound-**4** as a colorless oil (0.082 g, 56% yield). IR (KBr) *ν*: 1697, 1645, 1598, 1504, 1299, 1249, 1161, 958, 833 cm^{-1}. ^1H NMR (400 MHz, $CDCl_3$) *δ* (ppm): 9.90 (s, 1H), 7.85 (d, *J*=8.8 Hz, 2H), 7.09 (d, *J*=8.8 Hz, 2H), 6.67 (dd, *J*=6.0 Hz, 13.6 Hz, 1H), 4.92 (dd, *J*=2.0 Hz, 13.6 Hz, 1H), 4.61 (dd, *J*=1.6 Hz, 6.0 Hz, 1H).

2.2.3. Synthesis of (*Z*)-2-(4-nitrophenyl)-3-(4-(vinyloxy)phenyl) acrylonitrile (***CN-vinyl***)

To a mixture of compound-**4** (0.148 g, 0.001 mol) and 4-nitrobenzylcyanide (0.162 g, 0.001 mol) in absolute EtOH (5 mL), piperidine (0.255 g, 0.003 mol) was added with dropwise. After the reaction mixture was stirred at room temperature for 3 h, the obtained precipitated was filtered, washed with EtOH, dried and purified by column chromatography (CH_2Cl_2/petroleum=1:2 as eluent), a yellow solid was obtained. (0.233 g, 79% yield). mp 175–177 °C. IR (KBr) *ν*: 2212, 1643, 1596, 1579, 1508, 1336, 1257, 1180, 848 cm^{-1}. ^1H NMR (400 MHz, DMSO-d) *δ* (ppm): 8.34 (d, *J*=8.8 Hz, 2H), 8.28 (s, 1H), 8.06–8.00 (m, 4H), 7.27 (d, *J*=8.8 Hz, 2H), 7.03 (dd, *J*=6.0 Hz, 13.6 Hz, 1H), 4.89 (dd, *J*=1.6 Hz, 13.6 Hz, 1H), 4.62 (dd, *J*=1.6 Hz, 6.0 Hz, 1H). ^{13}C NMR (DMSO) *δ* (ppm): 158.9, 147.6, 147.3, 146.06, 140.7, 132.5, 132.3, 130.6, 128.3, 127.2, 124.8, 118.0, 117.1, 116.7, 106.7, 97.4, 97.3. ESI-MS (*m/z*): calcd for: $C_{17}H_{12}N_2O_3$ $[M+Cl]^-$ 327.05, found 327.1. Anal. calcd for: $C_{17}H_{12}N_2O_3$, C, 69.86; H, 4.14; N, 9.58; found: C, 70.55; H, 4.07; N, 9.56.

2.3. Analytical procedure

To characterize the AIE property of **CN-vinyl**, 100 μL stock solution of **CN-vinyl** (25 mM) was added to 10 mL THF/water (10:0, 4:6, 3:7, 2:8, 1:9, v/v, containing 50 mM NaH_2PO_4–NaOH). As shown in Fig. S10, the effect of water volume fraction on the pH was measured in THF/water containing 50 mM PBS. When THF and PBS was mixed well, the acidity of the solution decreased slightly (pH=7.21–7.94) compared with PBS (pH=7.0). It is probably due to the restricting ionization of acid induced by THF. Then, the mixed solution was incubated at room temperature for 15 min and was transferred to a 1 cm quartz cell for absorption spectra and fluorescence spectra.

In a standard detection method of Hg^{2+}, the test solution was prepared by placing 100 μL stock solution of **CN-vinyl** and 1.9 ml THF into a test tube, diluted to 10 mL with 50 mM PBS at pH=7.0, added appropriate amount of Hg^{2+} ions, incubate at room temperature for 15 min, and then record the fluorescence spectra.

To evaluate any possible facts which may affect the response of the fluorescence intensity caused by interfering ions, three sequences of addition were attempted. (1) The interfering metal ions were added to the test solution, and then Hg^{2+} was added to explore whether the reaction of **CN-vinyl** with Hg^{2+} ions was affected by the interfering metal ions; (2) Hg^{2+} ions were added to the test tube ahead, and then other interfering metal ions were added to explore whether the fluorescence intensity of reaction product was effected by interfering metal ions; (3) Hg^{2+} ions and interfering metal ions were added to the test tubes at the same time to simulate the application in real sample analysis. All of them were allowed to incubate at room temperature for 15 min following to record the fluorescence spectra.

For application in real sample analysis, the concentration of Hg^{2+} in real samples was detected by the standard addition method. $HgCl_2$ (4.1 mg) was added to 500 ml volumetric flask and diluted to metered volume with three real water samples which contain 50 mM PBS at pH=7.0 respectively, and gave 30 μM real sample solutions of Hg^{2+}. Moreover, the certified standard solution of Hg^{2+} (2.5 ml) was transferred to a 500 ml volumetric flask and diluted with PBS (50 mM, pH=7.0) to the metered volume, and give a 25 μM standard solution of Hg^{2+}. Subsequently, 100 μL stock solutions of **CN-vinyl** and 1.9 ml THF were placed into test tubes and diluted to 10 mL with the three real samples and the standard solution of Hg^{2+} respectively, and gave the test solutions. Finally, the fluorescence emission spectra were recorded.

All fluorescence spectra were recorded in the range from 480 nm to 650 nm using a 456 nm excitation wavelength. The excitation and emission bandwidths were set to 5 nm and 10 nm respectively.

3. Results and discussion

3.1. Aggregation-induced emission characteristics of CN-vinyl

We first studied the optical properties of **CN-vinyl** and compound-**2**. As shown in Fig. S11, both the absorption spectra of **CN-vinyl** and compound-**2** in THF solution exhibited three absorption bands at 245.0, 291.5, 365.5 nm and 249, 293.5, 368 nm respectively. Although **CN-vinyl** has a longer π-conjugated unit, it showed a blue-shift spectrum due to a more twisted conformation caused by the cyano and vinyl group. This process had been supported by the theoretical calculations which was performed at B3LYP/6–31G (d) basis in the Gaussian 09 package. The optimized molecular structures and HOMO and LUMO energy levels of **CN-vinyl** and compound-**2** are shown in Fig. S12. Obviously, both of them have strong intramolecular charge transfer (ICT) effect from the electron cloud distribution. The calculated energy band gap for **CN-vinyl** is 3.456 eV, which is wider than that of compound-**2** (3.392 eV). Hence, the results of theoretical studies are consistent with the absorption spectra.

The characteristics of **CN-vinyl** were investigated in THF/water (from 10:0 to 1:9, v/v) phosphate buffer solution (PBS, 50 mM, pH=7.0) and the results are shown in Figs. 1 and 2. As expected, there was a structured absorption spectra and almost no fluorescence emission could be detected in dilute THF solution, suggesting that **CN-vinyl** is non-fluorescence when dispersed in its "solution" state. However, its fluorescence spectra in a THF/water mixture with a high water fraction (80%) had an intensive band at 537 nm, and showed a leveling-off in the ultraviolet region of the absorption spectra (commonly observed in nanoaggregates suspension). The fluorescence increased by 79 times compared with that in pure THF and a lower THF volume fraction was found to enhance the AIE fluorescence intensity. These results correlated well with the fact that more aggregates were formed in poorer solvents. On the other hand, the maximum peak in the absorption spectra of the nanoparticle suspension of **CN-vinyl** had a clearly red-shift (12 nm) compared with that of dilute solution (as shown in Fig. 2). This result implied that there is an extension of the effective conjugation length which was caused by the planarization of twist molecular in nanoparticles. The new shoulder band (the arrow) observed around 450 nm should be resulted from the

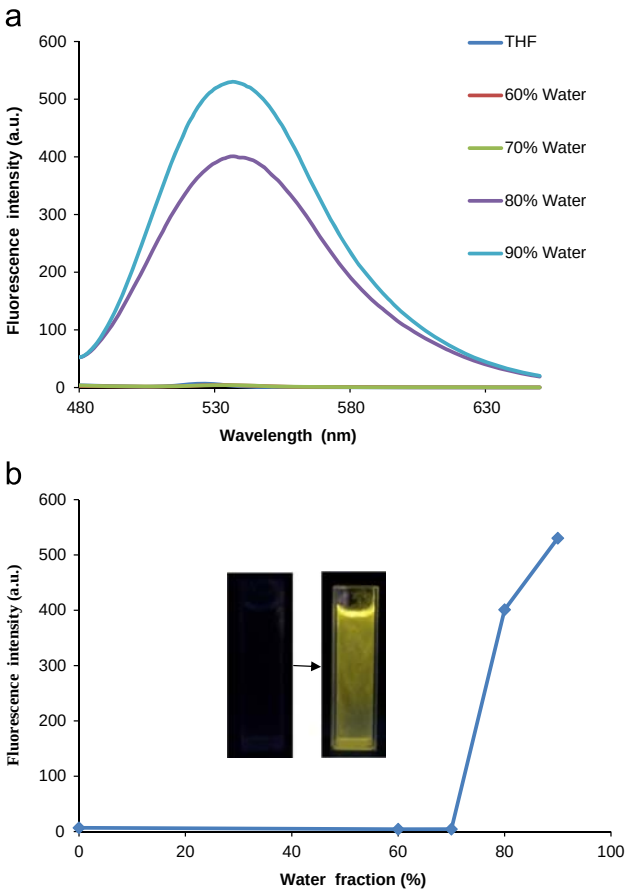


Fig. 1. (a) Fluorescent spectra of **CN-vinyl** (25 μM) in a THF/water mixture (excitation wavelength was 456 nm) (b) Effect of water volume fraction on the emission intensity of **CN-vinyl** (25 μM) in THF/water containing 50 mM PBS at pH 7.0. Inset show photographs of **CN-vinyl** (25 μM) in dilute THF solution and a THF/water mixture with a high water fraction under a UV lamp (365 nm). Excitation and emission was at 456 nm/537 nm respectively.

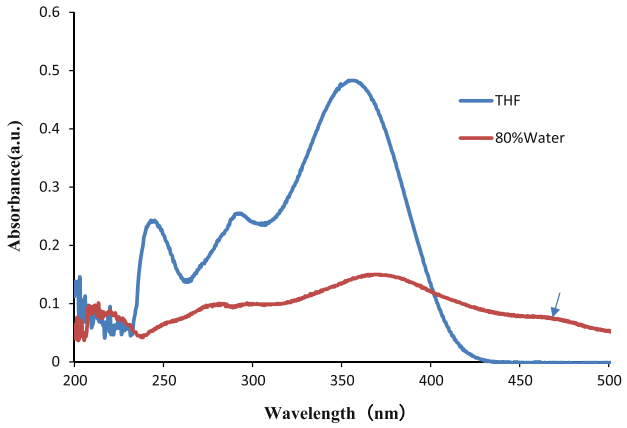


Fig. 2. Absorption spectra of **CN-vinyl** (25 μM) in a THF/water mixture.

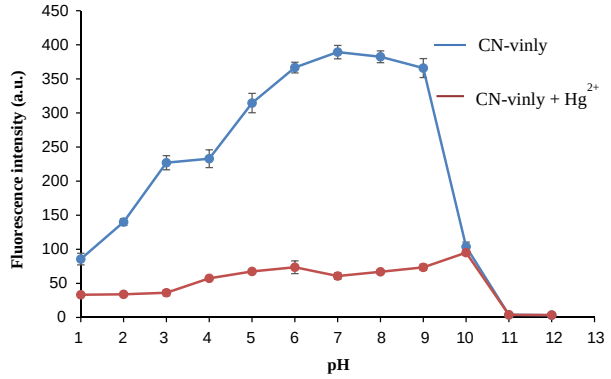


Fig. 3. Effect of pH on the emission intensity of probe **CN-vinly** (25 μM) at 537 nm in the absence and presence of 50 μM of Hg^{2+}. All measurements were taken in PBS (50 mM, pH=7.0) at25 °C. Excitation and emission were at 456 nm/537 nm respectively.

J-type aggregation. These date clearly indicated that **CN-vinyl** exhibits a significant feature of AIE.

3.2. Optimization of the analytical condition

The reaction conditions, such as pH, incubation time and buffer capacity of PBS, play an important role in the sensing process. The effects of pH value on the fluorescence intensity of **CN-vinyl** (25 μM), and the mixture of **CN-vinyl** (25 μM) with Hg^{2+} (50 μM) in THF/water (2:8, v/v) were investigated at first. As shown in Fig. 3, the fluorescence intensity of **CN-vinyl** decreased gradually with the rising of pH from 7.0 to 1.0 due to the formation of oxonium ion. However, when pH increased up to 10, there was almost no fluorescence because of the 1, 4-addition reaction of OH^- to α, β-unsaturated cyano compound, which lead to destruction of the conjugate structure. As **CN-vinyl** displayed a strong fluorescence changes in the pH range of 6–9 upon the addition of Hg^{2+}, and considering the application of samples in physiological or environmental, pH=7.0 was thus chosen as the experiment condition. In addition, the results of time-dependent fluorescence measurement of **CN-vinyl** (25 μM) and Hg^{2+} (50 μM) in THF/water (2:8, v/v, PBS, pH=7.0) is displayed in Fig. S13, of which would be quenched completely after 15 min. So, all the results of the assay were tested at the time of 15 min after the **CN-vinyl** was mixed with the Hg^{2+}. Finally, the buffer capacity of PBS (pH=7.0) was explored. As shown in Figs. S14 and 15, we could see that pH present a relatively stable value even if the concentration of Hg^{2+} ions or other interfering metal ions reach its maximum (50 μM) in 50 mM PBS.

3.3. Fluorescence detection of Hg^{2+} based on **CN-vinyl**

The fluorescence spectra of **CN-vinyl** upon titration with Hg^{2+} was recorded in THF/water (2:8, v/v) buffered by 50 mM PBS at pH=7.0 to investigated the quenching behavior of Hg^{2+} ion. As shown in Fig. 4, **CN-vinyl** itself showed a very strong emission. However, the fluorescence of **CN-vinyl** (25 μM) at 537 nm was dramatically decreased upon the addition of Hg^{2+} and followed a slight red-shift. Simultaneously, a perceived fluorescence color change of **CN-vinyl** was observed from yellow to colorless (Fig. 4, insert). It was plausible to suppose that a water-soluble species (should be compound-**2**) increased and the formation of aggregation of **CN-vinyl** decreased with the cleavage of the vinyl group upon the addition of Hg^{2+} to **CN-vinyl**. The quenching of photoluminescence is observed at a lower concentration of Hg^{2+}. The change of emission intensity became constant and caused 7-fold decrease when the addition of Hg^{2+} added to 2.0 equiv. (50 μM). There was an approximately linear relationship (R^2=0.9957) between fluorescence intensity at 537 nm and Hg^{2+} concentration in the range of 0 to 50 μM (Fig. 5). The detection limit was found to be 37 nM on the basis of the equation $L_{OD}=3\delta/m$ (δ was the standard deviation of the blank solution and m is the absolute value of the slope between fluorescence intensity and Hg^{2+} concentration) (Fig. S16). Above results demonstrated that our

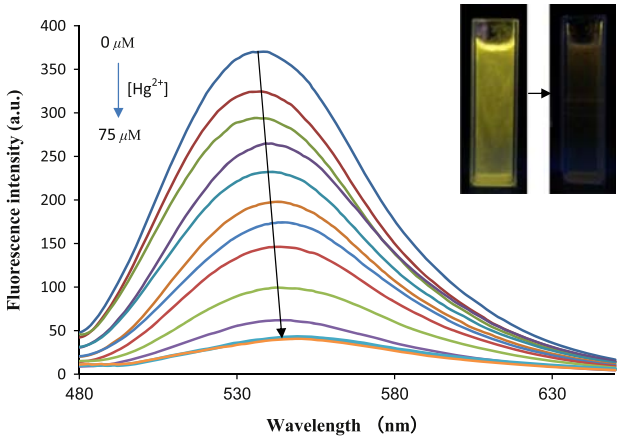


Fig. 4. Fluorescence spectra of **CN-vinyl** (25 μM) in the presence of different concentrations of Hg^{2+} ion at a THF/water mixture (2:8, v/v); Inset: fluorescence color change of **CN-vinyl** (25 μM) in the absence and presence of Hg^{2+} (2.0 equiv.). All measurements were taken in PBS (50 mM, pH 7.0) at 25 °C. Excitation wavelength was 456 nm.

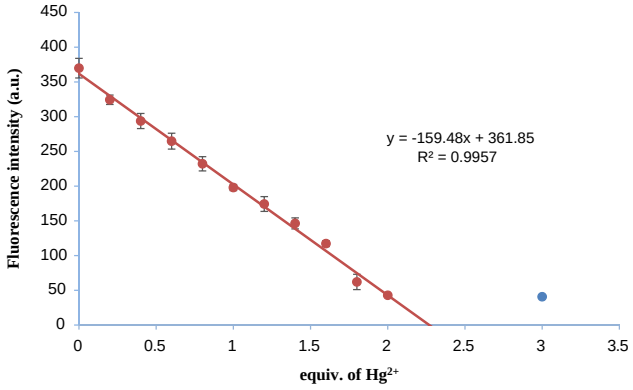


Fig. 5. The relationship between fluorescence intensity and Hg^{2+} concentration. Plots of the fluorescence intensity obtained from the reaction of **CN-vinyl** (25 μM) with Hg^{2+} (0–2.0 equiv.).All measurements were taken in PBS (50 mM, pH 7.0) at 25 °C. Excitation and emission were at 456 nm/537 nm respectively.

proposed **CN-vinyl** could detect Hg^{2+} in quantitative and with excellent sensitivity by the fluorescence spectrometry method.

3.4. Reaction mechanism

It has been reported that Hg^{2+} could selectively cleave the vinyl group by the oxymercuration reaction [33]. To verify our design principle of **CN-vinyl** for Hg^{2+}, the reaction mechanism was studied by ^1H NMR and mass spectra. Compound-**2** was isolated from the reacting system to confirm that the breakage action of **CN-vinyl** with Hg^{2+} had indeed produced after Hg^{2+} was added to **CN-vinyl**. ^1H NMR spectra of **CN-vinyl**, the isolated reaction product of compound-**2** and the synthesized compound-**2** were shown in Fig. 6A–C. Upon the addition of Hg^{2+}, three protons of **CN-vinyl** corresponding to the protons of vinyl group around 7.03, 4.94 and 4.62 ppm dramatically disappeared. Meanwhile, a new peak at 10.46 ppm which assigned to the released phenolic hydroxyl group emerged from the concomitant reaction. About the mass spectra, a same peak of $[M-H]^-$ (265.1*m/z*) for the isolated reaction product of compound-**2** and the synthesized compound-**2** were also found respectively. Especially, the isolated product of compound-**2** displayed a same absorption (Fig. S17) and fluorescence spectrum (Fig. S18) with the synthesized compound-**2.** All these experimental facts support the proposed oxymercuration reaction and the breakage reaction of **CN-vinyl** with Hg^{2+}.

3.5. Selectivity of *CN-vinyl* to Hg^{2+} over other metal ions

Selectivity is a very important parameter for evaluating the performance of a chemosensor. Twenty-one kinds of metal ions (2.0 equiv., 50 μM), such as Li^+, Na^+, K^+, Mg^{2+}, Ca^{2+}, Al^{3+}, Fe^{2+}, Fe^{3+}, Mn^{2+}, Cu^{2+}, Co^{2+}, Ni^{2+}, Pb^{2+}, Zn^{2+}, Sn^{2+}, Ag^+, Cd^{2+}, Ba^{2+}, Cr^{3+}, $MeHg^+$, Hg^{2+} (50 μM) were investigated by fluorescent spectra in THF/water (2:8, v/v, PBS, pH=7.0) solution at λ_{ex}=456 nm (Fig. 7). We can see that only Hg^{2+} (50 μM) could cause a significant fluorescent decrease emission of **CN-vinyl**. Especially, $MeHg^+$, a specific organic interferent, has no obvious fluorescence response change to **CN-vinyl** due to its more weak electrophilic to vinyl group compared to Hg^{2+}. Then, the interference of other metal ions was explored with three different sequences of addition of interfering ions and Hg^{2+}. The process was described in detail in analytical procedure and no remarkable

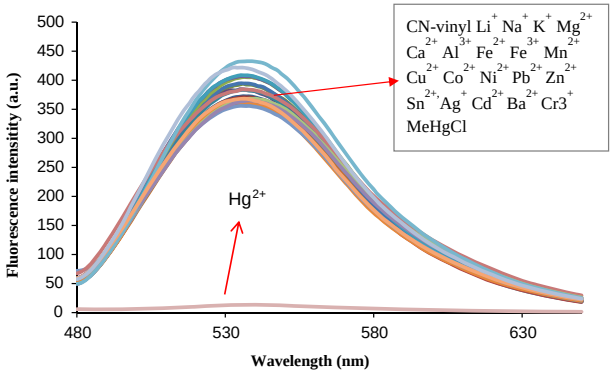


Fig. 7. Fluorescent spectra of **CN-vinyl** (25 μM) in the presence of various metal ions (50 μM) in THF/water (2:8, v/v); All measurements were taken in a pH 7.0 PBS (50 mM) at 25 °C, Excitation wavelength was 456 nm.

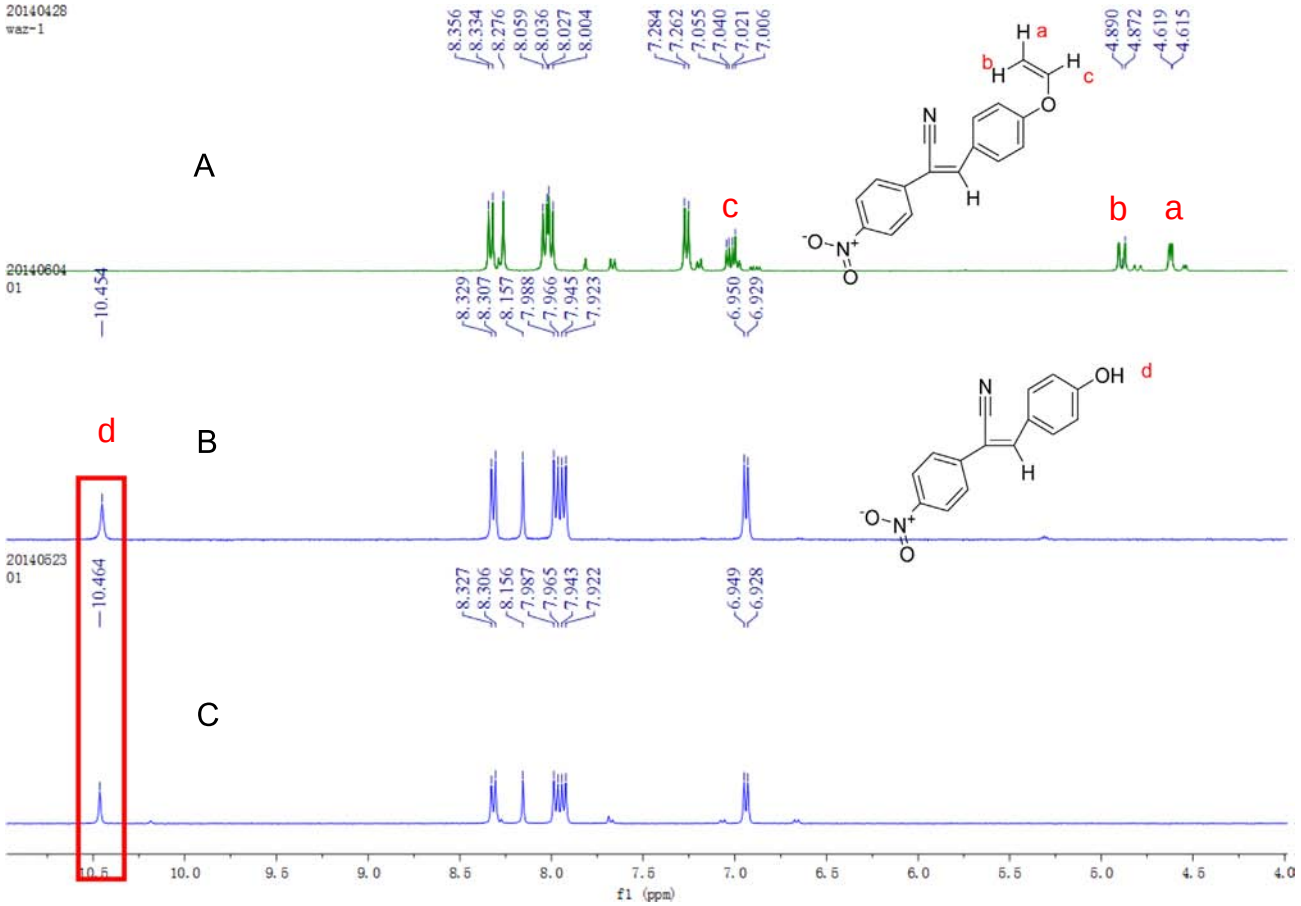


Fig. 6. Partial ^1H NMR spectra of **CN-vinyl** (25 mM) upon addition of Hg^{2+} (2.0 equiv.) in DMSO-d6. (A) only **CN-vinyl**, (B) the isolated aggregates of compound-**2** after **CN-vinyl** reacted with Hg^{2+} in DMSO for 15 min, (C) the synthesized compound-**2**.

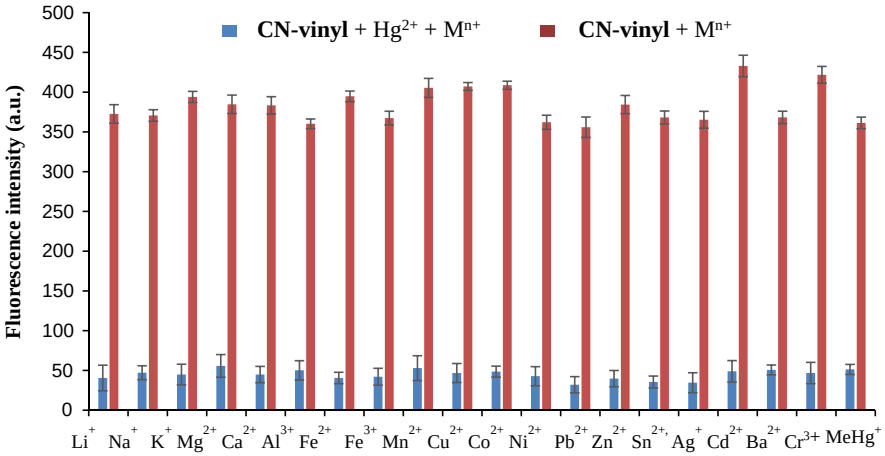


Fig. 8. Fluorescence intensity effects from the reaction of **CN-vinyl** (25 μM) with Hg^{2+} in the presence of other metal ions (50 μM) which was added after Hg^{2+}. All measurements were taken in a pH 7.0 PBS (50 mM) at 25 °C, Excitation and emission were at 456 nm/537 nm respectively.

Table 1
Detection of Hg^{2+} in real samples.

Sample	Added (μM)	Detected (μM)	Recovery (%)	RSD (%)
Tap water	0	Not detected	–	–
	30	30.82	102.73	2.91
Qinghe river	0	Not detected	–	–
	30	30.74	102.49	3.29
Weiming lake	0	Not detected	–	–
	30	30.38	101.27	1.91

Table 2
Detection in certified reference material of standard solution of Hg^{2+}.

Sample	Diluted concentration (μM)	Detected (μM)	Recovery (%)	RSD (%)
Standard solution of Hg^{2+}	25	25.32	101.28	2.80

changes were detected with the three assay ways in the presence of coexisting metal ions including organic mercury as shown in Fig. 8 and Figs. S19, S20. All these results showed that **CN-vinyl** has remarkable sensing selectivity to Hg^{2+}, which made it suitable for practical Hg^{2+} detection.

4. Analysis of Hg^{2+} in real sample

Three water samples were collected from Qinghe River in Beijing (sample 1), Weiming Lake in Beijing (sample 2) and tap water (sample 3). The results for the determination of Hg^{2+} were shown in Table 1 and no Hg^{2+} was detected in the three blank samples. When Hg^{2+} was added to them, the recovery was determined three times by the standard addition method and in range of 100–103%. These results demonstrate that the proposed assay strategy is successful in the detection of Hg^{2+} in real sample. In order to further demonstrate the accuracy of this method, the detection in certified reference material of standard solution of Hg^{2+} was carried out according to the analytical procedure. The results are summarized in Table 2 and it shows good agreement between the expected and found values. All these data above indicate the proposed method can be used to analyze Hg^{2+} accurately.

5. Conclusions

In summary, we have designed and synthesized a "turn off" quantitative fluorescence probe **CN-vinyl** and confirmed by the standard spectroscopic analyses. **CN-vinyl** possesses unusual AIE characteristic, and interestingly, has remarkable sensing selectivity to Hg^{2+}, which weaken with the increase of Hg^{2+} and showed a good linear relation (R^2=0.9957) with Hg^{2+} concentration in the range of 0 to 50 μM. There was no interference of coexist metal ions to Hg^{2+} with this assay and it could be used to detect Hg^{2+} with a low concentration limit of 37 nM. By means of NMR and MS analyses, the mechanism for Hg^{2+}-mediated optical properties of **CN-vinyl** is depicted. It has a potential to be used to detect Hg^{2+} ion in river, lake or tap water. The present study provides valuable information for designing fluorescent probes for Hg^{2+} by taking advantage of the selective cleavage of vinyl group by Hg^{2+}.

Acknowledgments

We thank the Science and Technology Innovation Foundation for the College Students of Beijing (No. 13220055), the National Natural Science Foundation of China (No. 20972015), and the Natural Science Foundation of Beijing (No. 2112026) for financial support.

Appendix A. Supporting information

Supplementary data associated with this article can be found in the online version at http://dx.doi.org/10.1016/j.talanta.2014.10.048.

References

[1] H.Y. Chang, T.M. Hsiung, Y.F. Huang, C.C. Huang, Environ. Sci. Technol. 45 (2011) 1534–1539.
[2] H.H. Harris, I.J. Pickering, G.N. George, Science 301 (2003) 1203.
[3] T. Agusa, T. Kunito, H. Iwata, I. Monirith, T.S. Tana, A. Subramanian, S. Tanabe, Environ. Pollut. 134 (2005) 79–86.
[4] J.P. Bourdineaud, R. Rossignol, D. Brethes, Int. J. Biochem. Cell Biol. 45 (2013) 16–22.
[5] C.B. Huang, H.R. Li, Y. Luo, L. Xu, Dalton Trans. 43 (2014) 8102–8108.
[6] E.M. Nolan, S.J. Lippard, Chem. Rev. 108 (2008) 3443–3480.
[7] I. Hoyle, R.D. Handy, Aquat. Toxicol. 72 (2005) 147–159.
[8] N. Zhou, H. Chen, J. Li, L. Chen, Microchim. Acta 180 (2013) 493–499.
[9] H.N. Kim, M.H. Lee, H.J. Kim, J.S. Kim, J. Yoon, Chem. Soc. Rev. 37 (2008) 1465–1472.
[10] K.E. Lorber, Waste Manag. Res. 4 (1986) 3–13.
[11] M.S. Hosseini, H. Hashemi-Moghaddam, Talanta 67 (2005) 555–559.
[12] N.W. Khun, E. Liu, Electrochim. Acta 54 (2009) 2890–2898.

[13] J. Manzoori, M. Sorouraddin, A.á.H Shabani, J. Anal. At. Spectrom. 13 (1998) 305–308.
[14] A. Bernaus, X. Gaona, J.M. Esbrí, P. Higueras, G. Falkenberg, M. Valiente, Environ. Sci. Technol. 40 (2006) 4090–4095.
[15] N.H. Bings, A. Bogaerts, J.A.C. Broekaert, Anal. Chem. 78 (2006) 3917–3946.
[16] X. Xue, F. Wang, X. Liu, J. Am. Chem. Soc. 130 (2008) 3244–3245.
[17] L.J. Fan, Y. Zhang, W.E. Jones, Macromolecules 38 (2005) 2844–2849.
[18] C.C. Huang, H.T. Chang, Anal. Chem. 78 (2006) 8332–8338.
[19] J.S. Lee, M.S. Han, C.A. Mirkin, Angew. Chem. 46 (2007) 4093–4096.
[20] P. Li, H. Liu, L. Yang, J. Liu, Talanta 106 (2013) 381–387.
[21] J. Luo, Z. Xie, J.W.Y. Lam, L. Cheng, B.Z. Tang, H. Chen, C. Qiu, H.S. Kwok, X. Zhan, Y. Liu, D. Zhu, Chem. Commun. (2001) 1740–1741.
[22] R. Deans, J. Kim, M.R. Machacek, T.M. Swager, J. Am. Chem. Soc. 122 (2000) 8565–8566.
[23] B.K. An, S.K. Kwon, S.-D. Jung, S.Y. Park, J. Am. Chem. Soc. 124 (2002) 14410–14415.
[24] Z. Xie, B. Yang, G. Cheng, L. Liu, F. He, F. Shen, Y. Ma, S. Liu, Chem. Mater. 17 (2005) 1287–1289.
[25] S. Kim, Q. Zheng, G.S. He, D.J. Bharali, H.E. Pudavar, A. Baev, P.N. Prasad, Adv. Funct. Mater. 16 (2006) 2317–2323.
[26] Y. Liu, X. Tao, F. Wang, J. Shi, J. Sun, W. Yu, Y. Ren, D. Zou, M. Jiang, J. Phys. Chem. C 111 (2007) 6544–6549.
[27] H. Tong, Y. Dong, Y. Hong, M. Häussler, J.W. Lam, H.H.-Y. Sung, X. Yu, J. Sun, I.D. Williams, H.S. Kwok, J. Phys. Chem. C 111 (2007) 2287–2294.
[28] Y. Liu, X. Tao, F. Wang, X. Dang, D. Zou, Y. Ren, M. Jiang, J. Phys. Chem. C 112 (2008) 3975–3981.
[29] M. Wang, D. Zhang, G. Zhang, D. Zhu, Chem. Commun. (2008) 4469–4471.
[30] B. Zhu, W. Wang, L. Liu, H. Jiang, B. Du, Q. Wei, Sens. Actuators B 191 (2014) 605–611.
[31] S. Manohar, S.I. Khan, S.K. Kandi, K. Raj, G. Sun, X. Yang, A.D. Calderon Molina, N. Ni, B. Wang, D.S. Rawat, Bioorg. Med. Chem. Lett. 23 (2013) 112–116.
[32] U.G. Lalloo, R. Naidoo, A. Ambaram, Curr. Opin. Pulm. Med. 12 (2006) 179–185.
[33] J. Jiang, W. Liu, J. Cheng, L. Yang, H. Jiang, D. Bai, W. Liu, Chem. Commun. 48 (2012) 8371–8373.

Talanta 132 (2015) 871–876

Contents lists available at ScienceDirect

Talanta

journal homepage: www.elsevier.com/locate/talanta

Synthesis of graphene supported graphene-like C_3N_4 metal-free layered nanosheets for enhanced electrochemical performance and their biosensing for biomolecules

Hui Gu [a], Tianshu Zhou [b], Guoyue Shi [a,*]

[a] Department of Chemistry, East China Normal University, 500 Dongchuan Road, Shanghai 200241, PR China
[b] School of Ecological and Environmental Sciences, East China Normal University, 500 Dongchuan Road, Shanghai 200241, PR China

ARTICLE INFO

Article history:
Received 27 July 2014
Received in revised form
15 September 2014
Accepted 18 September 2014
Available online 31 October 2014

Keywords:
C_3N_4
Graphene
Electrochemical performance
Metal-free catalyst
Biosensing

ABSTRACT

A new strategy for the assembly of graphene-like C_3N_4 on graphene is reported. Transmission electron microscopy (TEM), thermogravimetric analysis (TGA), Raman spectroscopy, Fourier transform infrared spectroscopy (FTIR), X-ray diffraction (XRD), and X-ray photoelectron spectroscopy (XPS) clearly demonstrated that g-C_3N_4 was successful in the reduction of GO and the immobilization of g-C_3N_4 on the graphene surface. Investigation of their electrochemical behaviour for several redox systems was conducted, which indicated the unique electron structure endows the G–g-C_3N_4 with faster transfer and proper amount of g-C_3N_4 could make G–g-C_3N_4 advantageous in terms of improving the redox current and promoting electron transfer. Finally, several electroactive biomolecules, such as uric acid (UA), norepinephrine (NE), tyrosine (Tyr), tryptophan (Trp), acetaminophen (APAP) and rutin, were used to probe the biosensing capacity of G–g-C_3N_4 films by using the cyclic voltammetric method.

© 2014 Elsevier B.V. All rights reserved.

1. Introduction

The development of nanoscience and nanotechnology has inspired scientists to continuously explore new electrode materials for constructing an enhanced electrochemical platform. Exploring materials combining good characteristics of electrochemistry (e.g., high sensitivity, low cost, and good compatibility) with unique properties of nanomaterials (e.g., electronic, optical, magnetic, mechanical, and catalytic) has become one of the most exciting topics [1]. Recently, metal-free graphene-like carbon nitride polymer, referred to as g-C_3N_4, is a rising star in the areas of photocatalytic hydrogen production [2,3], metal-free heterogeneous catalysis in various organic systems [4], and oxygen reduction for fuel cells [5], due to its peculiar thermal stability, appropriate electronic structure and low cost of preparation [6,7]. However, reports of study on its electrochemical performance are rare. Based on previous theory [8,9] a relatively high nitrogen doping can enhance the electron-donor property of the carbon matrix, which greatly improves the interaction between carbon and guest molecules, thus resulting in high and stable catalytic activity. g-C_3N_4, because of its high nitrogen content and facile synthesis procedure, may provide relatively significant catalytic activity.

Nevertheless, the poor conductivity of g-C_3N_4 is a serious problem strongly restricting the electron transportation and limiting the electrocatalytic activity [10]. Graphene, a two dimensional JI carbon structure material with unique electronic properties, large theoretical specific surface area and environmental benignity, has been recognized as a superior candidate for the construction of catalysts [11,12]. Therefore, we incorporated the g-C_3N_4 onto the surface of graphene as G–g-C_3N_4 to promote the electron transfer ability of g-C_3N_4 and increase the active sites of graphene [13]. Here, we took a facile step-by-step metal-free casting method. In brief, after impregnating graphene oxide with the liquid precursor (cyanamide, $CN–NH_2$) 1–3 times, the resulting composites were calcined at 823 K in an inert Ar atmosphere for 4 h to synthesize g-C_3N_4 in situ on the surface of graphene oxide. Consequently, the obtained G–g-C_3N_4@1#, G–g-C_3N_4@2#, and G–g-C_3N_4@3# showed good electrochemical performance as expected. The synthesis route for the development of promising electrocatalysts proposed here is facile, of low cost and environment friendly.

2. Materials and methods

2.1. Chemicals

Dopamine (DA), uric acid (UA), norepinephrine (NE), Hexaammineruthenium (III) chloride ($Ru(NH_3)_6Cl_3$) and cyanamide solution (50 wt%) were all purchased from Sigma Co. L-tryptophan (Trp), L-tyrosine (Tyr), rutin trihydrate (RT), and acetaminophen (APAP) were all purchased from Sinopharm Chemical Reagent Co. Ltd. $(NH_4)_2FeSO_4$,

* Corresponding author. Tel.: +86 21 54340043.
E-mail address: gyshi@chem.ecnu.edu.cn (G. Shi).

http://dx.doi.org/10.1016/j.talanta.2014.09.042
0039-9140/© 2014 Elsevier B.V. All rights reserved.

and $K_3Fe(CN)_6$ were purchased from Shanghai Chemical Reagent Company (Shanghai, China). H_2O_2 (30 wt%) was from Beijing Chemical Co. (Beijing, China). The supporting electrolyte was 0.1 M phosphate buffer solution (PBS) prepared with 0.1 M Na_2HPO_4 and 0.1 M KH_2PO_4 and the pH value was adjusted to 7.4 with NaOH. Double-distilled water was used for preparation of all solutions and for washing.

2.2. Synthesis of G–g-C_3N_4 and TGO

Graphene oxide was synthesized from graphite by a modified Hummers method [14,15]. 0.25 mL cyanamide solution (50 wt%) and 0.25 mL H_2O were added into 50 mg fresh graphene oxide. After ultrasonicating for 30 min, the mixture was stirred overnight and dried statically at 40 °C in air for 12 h. The same impregnation procedure was repeated once, twice, and three times in order to increase the loading of precursors on the graphene oxide. The dried powder was calcined at 550 °C for 4 h in Ar atmosphere and a heating rate of 2.3 °C/min to get the final G–g-C_3N_4 product. Additionally, the preparation of the thermal treatment graphene oxide (TGO) was similar to that of G–g-C_3N_4 nanosheets except that there was no addition of cyanamide solution.

2.3. Synthesis of g-C_3N_4

g-C_3N_4 was synthesized according to a procedure described in a previous literature [16]. In detail, dicyandiamide was heated at 550 °C for 4 h in static air at a ramp rate of 2.3 °C/min; the cooling rate was kept at around 1 °C/min. The resultant yellow agglomerates were milled into powder in a mortar. The nanosheets were prepared by thermal oxidation etching of the bulk g-C_3N_4 obtained as above in static air as follows: 400 mg of the bulk g-C_3N_4 was placed in an open ceramic container and was heated at 550 °C for 2 h at a ramp rate of 5 °C/min. A light yellow powder of g-C_3N_4 nanosheets was finally obtained with a yield of about 5.6%.

2.4. Preparation of G–g-C_3N_4@1#, G–g-C_3N_4@2#, G–g-C_3N_4@3#, TGO, g-C_3N_4 and TGO+g-C_3N_4 electrodes

Prior to modification, the glassy carbon (GC) electrode (2 × 1.5 cm^2) used in the electrochemical experiments was polished with alumina paste (0.05 μm) on a micro-cloth and subsequently ultrasonically cleaned thoroughly with acetone, NaOH (1:1), HNO_3 (1:1) and doubly distilled water and then dried at room temperature. The G–g-C_3N_4@1#, G–g-C_3N_4@2#, G–g-C_3N_4@3#, TGO, g-C_3N_4 and TGO+g-C_3N_4 electrodes were obtained by casting 3 μL of 1 mg/mL G–g-C_3N_4@1#, G–g-C_3N_4@2#, G–g-C_3N_4@3#, TGO, g-C_3N_4 and TGO+g-C_3N_4 suspension, respectively, on the surface of a well-polished GC electrode and dried in air. Finally, the modified electrodes were activated by 20 successive scans at a scan rate of 50 mV/s in phosphate buffer solution (pH 7.4) until a steady voltammogram was obtained.

3. Results and discussion

3.1. Characteristics of G–g-C_3N_4, g-C_3N_4

The weight contents of g-C_3N_4 in G–g-C_3N_4@1#, G–g-C_3N_4@2#, and G–g-C_3N_4@3# composites were tested to be about 37.4, 53.7, and 74.7 wt%, respectively, by thermogravimetric analysis (TGA) under flowing N_2 atmosphere (see Fig. 1a). Here we selected

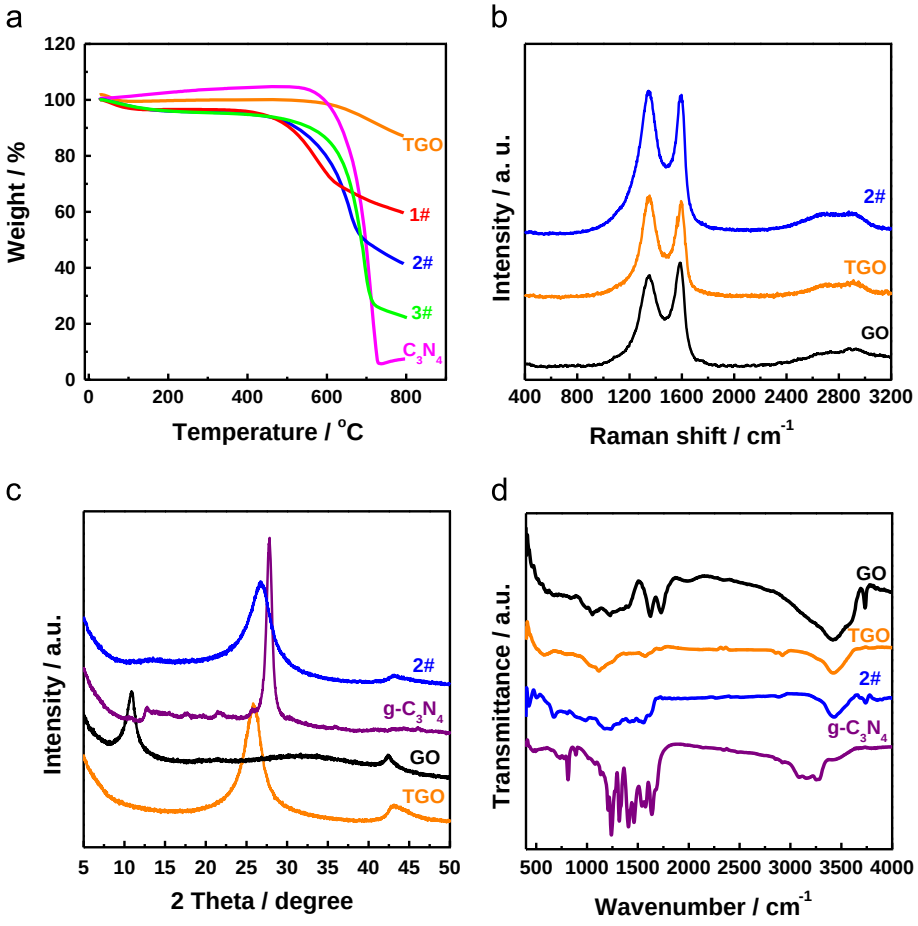


Fig. 1. (a) TGA curves of TGO, G–g-C_3N_4@1#, G–g-C_3N_4@2#, G–g-C_3N_4@3# and g-C_3N_4; (b) representative Raman spectra of GO, TGO and G–g-C_3N_4@2#; (c) typical XRD patterns of GO, TGO, G–g-C_3N_4@2# and g-C_3N_4 and (d) FTIR spectra of GO, TGO, G–g-C_3N_4@2# and g-C_3N_4.

G–g-C_3N_4@2# obtained by two times precursor impregnation as an example. For better understanding of the structure and properties of the as-prepared G–g-C_3N_4, TGO and g-C_3N_4 were taken as references. From the Raman spectra (see Fig. 1b) the D band (1351 cm^{-1}) corresponding to defects in the curved graphene sheets, the staging disorder, and the G band (1597 cm^{-1}) related to the sp^2 hybridized carbon of graphene were observed for both samples. In agreement with previous reports for chemically reduced GO [17,18] the *D*/*G* intensity ratio increased from 0.92 (GO) to 1.07 (TGO) and 1.02 (G–g-C_3N_4@2#), which illustrated the good reduction of TGO and G–g-C_3N_4 from GO. The results also indicate more disorder of the TGO than G–g-C_3N_4@2#, which may be due to the CN–NH_2 creates a layered g-C_3N_4 template for better reduction of GO [19]. From the X-ray diffraction (XRD) patterns (see Fig. 1c) the interplanar distance of G–g-C_3N_4@2#, based on the diffraction peak, is between those of TGO and g-C_3N_4, indicating that crystalline g-C_3N_4 layers were separated by graphene sheets [20]. The typical Fourier transform infrared spectroscopy (FTIR) spectrum (see Fig. 1d) also implied the successful immobilization of g-C_3N_4 on the graphene surface [21] and XPS examinations confirmed this result as well (see ESI, Fig. S1†).

Fig. 2 gives representative transmission electron microscopy (TEM) overviews of these samples. TGO displays crumpled multilayer sheets and the g-C_3N_4 on graphene obtains a layered film G–g-C_3N_4 which is relatively flat. From G–g-C_3N_4@1#, we can also clearly identify the crumpled curve from graphene. To clearly confirm the layer structure, high magnification TEM of TGO, G–g-C_3N_4@1#, G–g-C_3N_4@2#, and G–g-C_3N_4@3# was further examined (see ESI, Fig. S2†). With another one or two more casting procedures, the transparency decreases obviously because of the g-C_3N_4 films covered on graphene.

3.2. Electrochemical behaviour for different redox species of G–g-C_3N_4

Several redox systems with different electrode kinetics were selected to firstly study the electrochemical properties of G–g-C_3N_4. The cyclic voltammograms (CVs) of various redox species of $Fe(CN)_6^{3-/4-}$, $Ru(NH_3)_6^{3+/2+}$, $Fe^{2+/3+}$, and dopamine at diverse modified electrodes are illustrated in Fig. 3 and their cyclic voltammetric data and electroactive surface areas are summarized in Table S1. All the CVs data were obtained out and recorded for 5 scans and the reported CVs here are for the third scan, which is rather stable and more or less of the same CVs pattern as that of the later scans. $Ru(NH_3)_6^{3+/2+}$, involving simple electron transfer on most electrodes including diamond and sp^2 carbon, is relatively insensitive to surface microstructure, surface oxides and adsorbed monolayers on sp^2 carbon electrodes [22]. Therefore, we took this redox system as an example. G–g-C_3N_4 composites, showing enhanced peak currents and relatively lower ΔE_p values, displayed faster and more reversible behaviour of the $Ru(NH_3)_6^{3+/2+}$ couple. Moreover, we found that the CVs were rather stable, and the repeatability and long-term cyclic voltammograms (CVs) of the above six compounds at G–g-C_3N_4@1#, G–g-C_3N_4@2#, G–g-C_3N_4@3#, TGO, and mixed TGO stability were also quite good (data not shown) even 1 or 2 years later. Considering the reversible redox reaction of $Ru(NH_3)_6^{3+/2+}$ on the G–g-C_3N_4 electrodes, the density of the electronic states should be sufficient to support the rapid electron transfer of $Ru(NH_3)_6^{3+/2+}$. This redox system also selected for further investigation on the effect of scan rate on the peak current (see ESI, Fig. S3†). For scan rates in the range from 0.02 to 0.35 mV/s, the oxidative and reduction peak currents of the G–g-C_3N_4@1# electrode increase linearly with the

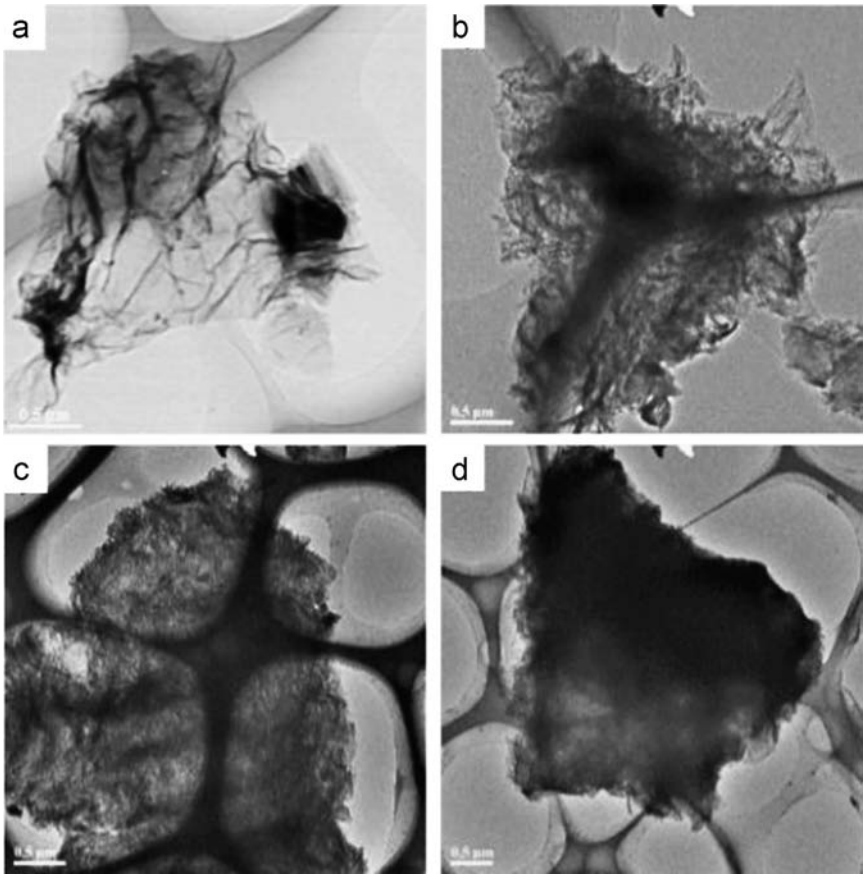


Fig. 2. Typical TEM images of (a) TGO, (b) G–g-C_3N_4@1#, (c) G–g-C_3N_4@2#, and (d) G–g-C_3N_4@3#.

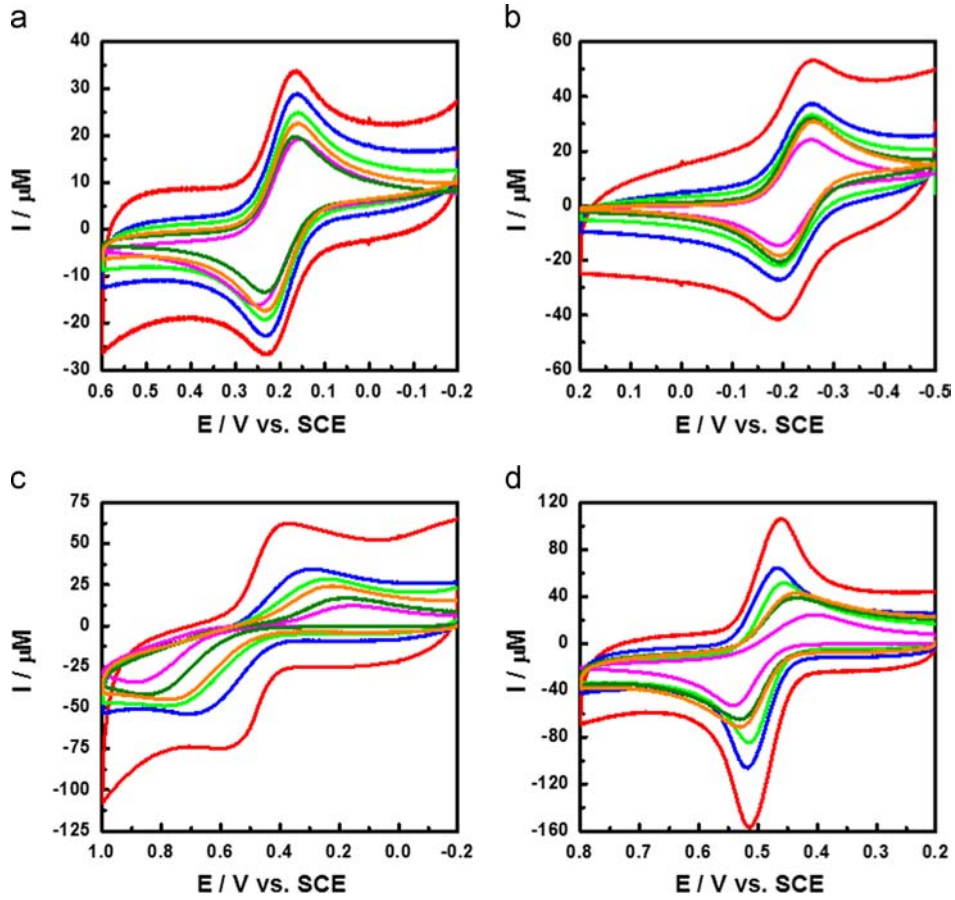


Fig. 3. Cyclic voltammograms for four kinds of redox systems at G–g-C_3N_4@1#, G–g-C_3N_4@2#, G–g-C_3N_4@3#, TGO, mixed TGO+g-C_3N_4, and g-C_3N_4 (up to down) electrodes deoxygenated with N_2: (a) 1.0 mM $Fe(CN)_6^{3-/4-}$ in 0.2 mM KCl, (b) 1.0 mM $Ru(NH_3)_6^{3+/2+}$ in 0.2 mM KCl, (c) 1.0 mM $Fe^{2+/3+}$ in 0.1 M $HClO_4$ and (d) 1.0 mM dopamine in 0.1 M $HClO_4$. Data shown are for the third scan. Scan rate 100 mV s^{-1}.

square root of the scan rate, implying that the reaction is controlled by semi-infinite linear diffusion. Furthermore, the specific electroactive surface areas for these electrodes are calculated in the ESI according to the Randless–Sevcik equation [23,24] and summarized in Table S1. Compared with other materials, the G–g-C_3N_4 composites displayed remarkably higher electroactive surface areas. In the four different redox systems the results shown in Table S1 are in keeping with each other, which suggests that the unique electron structure endows the G–g-C_3N_4 with faster transfer. Especially G–g-C_3N_4@1# shows the highest peak current and largest electroactive surface area, indicating that too much g-C_3N_4 on graphene could make them disadvantageous in terms of improving the redox current and promoting electron transfer. Nevertheless, impregnating graphene oxide with less CN–NH_2 cannot produce g-C_3N_4, thus restricting obtaining of good composites.

3.3. *Electrochemical behaviour for different electroactive biomolecules of G–g-C_3N_4*

The important characteristics described above enable G–g-C_3N_4 to be a good material for electrochemical sensing and biosensing. Here the electrochemical behaviours of two biomolecules [uric acid (UA) and norepinephrine (NE)], two amino acids [tyrosine (Tyr), tryptophan (Trp)] and two drugs [acetaminophen (APAP), rutin], which are all electroactive, were investigated. Fig. 4 shows cyclic voltammograms (CVs) of the above six compounds at G–g-C_3N_4@1#, G–g-C_3N_4@2#, G–g-C_3N_4@3#, TGO, mixed TGO+g-C_3N_4, and g-C_3N_4 electrodes. We used bare GC electrode to compare the electrochemical performance here. All the oxidation peak currents of these six compounds are increased at G–g-C_3N_4 electrodes relative to the currents at TGO, mixed TGO+g-C_3N_4, and g-C_3N_4 electrodes, indicating a favourable catalytic activity of G–g-C_3N_4 toward the oxidation of the compounds. At the G–g-C_3N_4@1# electrode, all show a remarkable increase in the peak currents relative to that at the other five electrodes. This illustrates that appropriate amount of g-C_3N_4 on graphene not only can optimize the structure of the graphene but can also have a synergic effect on each other, which can further enhance electrochemical reactivity of G–g-C_3N_4@1# electrode. The great electrochemical performance of the G–g-C_3N_4@1# electrode toward H_2O_2 and O_2 serves as a further verification of the above results (see Fig. 5). As the G–g-C_3N_4@1#, G–g-C_3N_4@2#, G–g-C_3N_4@3#, TGO, mixed TGO+g-C_3N_4, g-C_3N_4 and GC electrodes can produce different background currents in blank solution, the background current is deducted from the linear sweep voltammetry (LSV). Upon G–g-C_3N_4@1#, G–g-C_3N_4@2#, and G–g-C_3N_4@3# electrodes, both on-set potential and peak potential of the reduction reaction shift to more positive positions with a concomitant increase in the peak currents density than those of mixed TGO+g-C_3N_4, TGO, and g-C_3N_4 electrodes (Table 1). However, because of the poor conductivity of g-C_3N_4, the on-set potential and peak potential of the reduction reaction were just slightly negative to g-C_3N_4 electrode. Such results clearly indicate a significant improvement in the catalytic activity when g-C_3N_4 is incorporated onto the graphene due to the enhanced electron transfer efficiency. Much higher current and lower overpotential are found on G–g-C_3N_4@1# electrode in comparison with other electrodes, which further reveals that G–g-C_3N_4@1# is an excellent material for

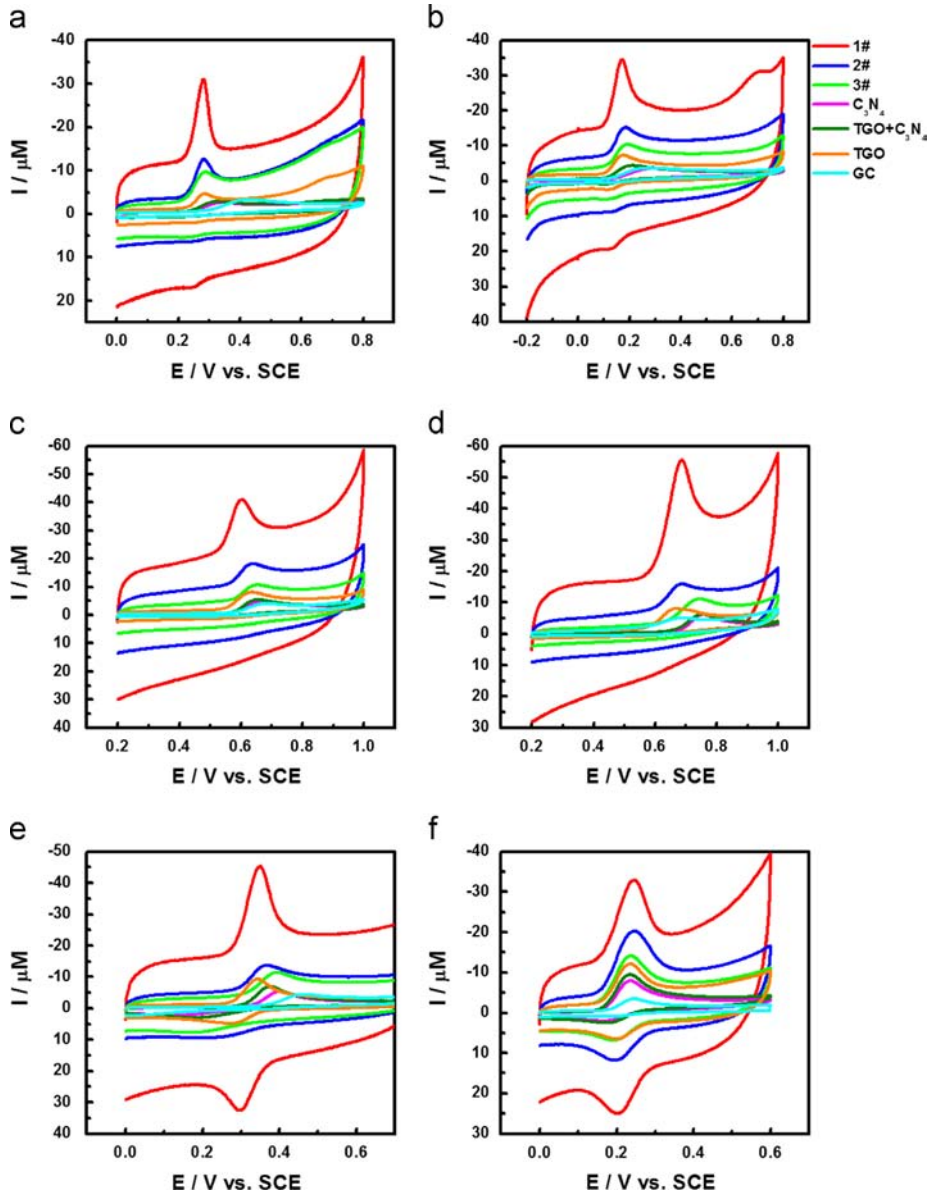


Fig. 4. CVs of 50 μM (a) UA, (b) NE, (c) Tyr, (d) Trp, (e) APAP, and (f) rutin at G–g-C_3N_4@1#, G–g-C_3N_4@2#, G–g-C_3N_4@3#, TGO, mixed TGO + g-C_3N_4, g-C_3N_4 and GC electrodes in 0.2 M phosphate buffer (pH 7.4). Scan rate 100 mV s^{-1}.

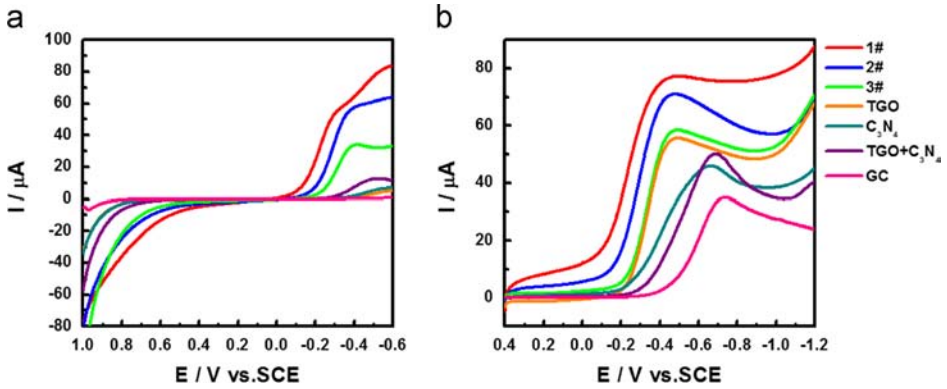


Fig. 5. Background deducted LSV responses of G–g-C_3N_4@1#, G–g-C_3N_4@2#, G–g-C_3N_4@3#, mixed TGO + g-C_3N_4, TGO, g-C_3N_4 and GC electrodes in 0.2 M phosphate buffer (pH 7.4) (a) containing 5 mM H_2O_2 and (b) saturated with O_2.

Table 1
Summary of reduction performances on G–g-C_3N_4@1#, G–g-C_3N_4@2#, G–g-C_3N_4@3#, TGO, mixed TGO+g-C_3N_4, g-C_3N_4 and GC electrodes in 0.2 M phosphate buffer (pH 7.4) containing 5 mM H_2O_2 or saturated with O_2.

		On-set potential (V)	Peak potential (V)	Peak current response (μA)
H_2O_2	G–g-C_3N_4-1#	0	−0.30	82.98
	G–g-C_3N_4-2#	−0.05	−0.39	63.38
	G–g-C_3N_4-3#	−0.10	−0.40	32.78
	TGO	−0.22	−0.54	6.904
	TGO+g-C_3N_4	−0.21	−0.50	11.22
	g-C_3N_4	−0.25	−0.57	4.168
	GC	−0.39	−0.58	0.89
O_2	G–g-C_3N_4-1#	−0.05	−0.40	74.44
	G–g-C_3N_4-2#	−0.11	−0.42	68.35
	G–g-C_3N_4-3#	−0.18	−0.45	56.80
	TGO	−0.22	−0.65	45.91
	TGO+g-C_3N_4	−0.27	−0.68	50.04
	g-C_3N_4	−0.30	−0.70	44.89
	GC	−0.36	−0.74	35.03

electrochemical sensing. Additionally, excellent reproducibility and its great long-term stability was also tested using G–g-C_3N_4@1# electrode for these compounds after 1 or 2 years resulting in a relative standard deviation of 2.5% (data not shown here).

4. Conclusion

In conclusion, layered G–g-C_3N_4 composites were synthesized through a facile step-by-step casting route and electrocatalytically investigated. Compared with the TGO, mixed TGO+g-C_3N_4 and g-C_3N_4, G–g-C_3N_4 exhibited much higher electrochemical performance. Furthermore, we found a proper amount of g-C_3N_4 on graphene which could improve the electrocatalytic activities for redox reaction. We believe that the results could bring important applications in sensors.

Acknowledgements

This work was funded by National Natural Science Foundation of China (21175044, 21277048).

Appendix A. Supporting information

Supplementary data associated with this article can be found in the online version at http://dx.doi.org/10.1016/j.talanta.2014.09.042.

References

[1] S.J. Guo, D. Wen, Y.M. Zhai, S.J. Dong, E.K. Wang, Acs Nano 4 (2010) 3959.
[2] P. Niu, L. Zhang, G. Liu, H.-M. Cheng, Adv. Funct. Mater. 22 (2012) 4763.
[3] J. Liu, Y. Zhang, L. Lu, G. Wu, W. Chen, Chem. Commun. (Camb.) 48 (2012) 8826.
[4] X.H. Li, J.S. Chen, X. Wang, J. Sun, M. Antonietti, J. Am. Chem. Soc. 133 (2011) 8074.
[5] Y. Zheng, Y. Jiao, J. Chen, J. Liu, J. Liang, A. Du, W. Zhang, Z. Zhu, S.C. Smith, M. Jaroniec, G.Q. Lu, S.Z. Qiao, J. Am. Chem. Soc. 133 (2011) 20116.
[6] A. Du, S. Sanvito, Z. Li, D. Wang, Y. Jiao, T. Liao, Q. Sun, Y.H. Ng, Z. Zhu, R. Amal, S.C. Smith, J. Am. Chem. Soc. 134 (2012) 4393.
[7] Y.-S. Jun, W.H. Hong, M. Antonietti, A. Thomas, Adv. Mater. 21 (2009) 4270.
[8] Y. Wang, Y.Y. Shao, D.W. Matson, J.H. Li, Y.H. Lin, Acs Nano 4 (2010) 1790.
[9] Z.H. Sheng, L. Shao, J.J. Chen, W.J. Bao, F.B. Wang, X.H. Xia, Acs Nano 5 (2011) 4350.
[10] F. Zhao, H.H. Cheng, Y. Hu, L. Song, Z.P. Zhang, L. Jiang, L.T. Qu, Sci. Rep. 4 (2014).
[11] H. Gu, Y. Yang, J.X. Tian, G.Y. Shi, Acs Appl. Mater. Interfaces 5 (2013) 6762.
[12] S. Yasuda, L. Yu, J. Kim, K. Murakoshi, Chem. Commun. 49 (2013) 9627.
[13] Q. Liu, J. Zhang, Langmuir 29 (2013) 3821.
[14] H. Gu, Y. Yu, X. Liu, B. Ni, T. Zhou, G. Shi, Biosens. Bioelectron. 32 (2012) 118.
[15] W.S. Hummers, R.E. Offeman, J. Am. Chem. Soc. 80 (1958) 1339.
[16] P. Niu, L.L. Zhang, G. Liu, H.M. Cheng, Adv. Funct. Mater. 22 (2012) 4763.
[17] K. Krishnamoorthy, M. Veerapandian, R. Mohan, S.-J. Kim, Appl. Phys. A 106 (2011) 501.
[18] A.L. Higginbotham, D.V. Kosynkin, A. Sinitskii, Z.Z. Sun, J.M. Tour, Acs Nano 4 (2010) 2059.
[19] X.H. Li, S. Kurasch, U. Kaiser, M. Antonietti, Angew. Chem. Int. Ed. Engl. 51 (2012) 9689.
[20] Y. Sun, C. Li, Y. Xu, H. Bai, Z. Yao, G. Shi, Chem. Commun. (Camb.) 46 (2010) 4740.
[21] R.C. Dante, P. Martin-Ramos, L.M. Navas-Gracia, F.M. Sanchez-Arevalo, J. Martin-Gil, J. Macromol. Sci. Part B-Phys. 52 (2013) 623.
[22] A.E. Fischer, Y. Show, G.M. Swain, Anal. Chem. 76 (2004) 2553.
[23] Y. Sanguansak, P. Srimuk, A. Krittayavathananon, S. Luanwuthi, N. Chinvipas, P. Chiochan, J. Khuntilo, P. Klunbud, T. Mungcharoen, M. Sawangphruk, Carbon (2013).
[24] Y. Yu, Q. Sun, X. Liu, H. Wu, T. Zhou, G. Shi, Chemistry 17 (2011) 11314.

Talanta 132 (2015) 877–883

Contents lists available at ScienceDirect

Talanta

journal homepage: www.elsevier.com/locate/talanta

Short communication

Direct analysis of ethylenediaminetetraacetic acid (EDTA) on concrete by reactive-desorption electrospray ionization mass spectrometry

D. Lebeau *, P.E. Reiller, C. Lamouroux

CEA, DEN, DPC, F-91191 Gif-sur-Yvette, France

ARTICLE INFO

Article history:
Received 30 July 2014
Received in revised form
10 October 2014
Accepted 14 October 2014
Available online 31 October 2014

Keywords:
EDTA
Concrete
DESI
Imaging

ABSTRACT

Analysis of organic ligands such as ethylenediaminetetraacetic acid (EDTA) is today an important challenge due to their ability to increase the mobility of radionuclides and metals. Reactive desorption electrospray ionization mass spectrometry (reactive-DESI-MS) was used for direct analysis of EDTA on concrete samples. EDTA forms complexes and those with Fe^{III} ions are among the most thermodynamically favored. This complexing capacity was used to improve the specific detection of EDTA directly on a concrete matrix by doping the solvent spray of DESI with a solution of $FeCl_3$ to selectively create the complex between EDTA and Fe^{III}. Thus, EDTA sensitivity was largely improved by two orders of magnitude with reactive-DESI-MS experiments thanks to the specific detection of EDTA as a $[EDTA\text{-}4H+Fe^{III}]^-$ complex. The proof of principle that reactive DESI can be applied to concrete samples to detect EDTA has been demonstrated. Its capacity for semi-quantitative determination and localization of EDTA under ambient conditions and with very little sample preparation, minimizing sample manipulations and solvent volumes, two important conditions for the development of new methodologies in the field of analytical chemistry, has been shown.

© 2014 Elsevier B.V. All rights reserved.

1. Introduction

Organic complexing molecules are widespread both in the environment and in industrial processes. In the nuclear industry, these molecules can be used at different stages of the fuel cycle as radionuclide-chelating agents. In decontamination processes, various ligands are used, and in particular aminopolycarboxylic acids, due to their ability to form strong complexes with radionuclides in solution [1,2].

One of the most used aminopolycarboxylic agents is ethylenediaminetetraacetic acid (EDTA). The control of its presence in nuclear waste is important in the management of intermediate and low-level waste (ILLW) and its maximum concentration is now restricted. EDTA is able to chelate not only actinides but also most alkaline earth and heavy metals ions, which can increase the mobility of radionuclides and heavy metals after leaching processes [3].

Several analytical tools have already been developed for the detection and/or quantification of aminopolycarboxylic acids. These include gas chromatography [4–6], liquid or gas chromatography coupled with mass spectrometry [1,7–12], capillary electrophoresis [13,14], or direct analysis by mass spectrometry [15]. However, all these techniques are time-consuming and require the analytes to be in solution. Several steps are also usually required prior to analysis such as extraction, desalting, derivatization, pretreatment or clean-up protocols. Thus, the development of an analytical method for EDTA detection and quantification directly in a concrete, matrix used for ILLW, without any solubilization step or extraction of the molecule constitutes a great advantage.

With the recent development of ambient mass spectrometry (AMS) and the introduction of desorption electrospray ionization (DESI) [16] and direct analysis in real time (DART) [17], the acquisition of mass spectra under atmospheric conditions is now available directly at the surface of samples with little or no sample preparation [18]. DESI-MS enables the analysis of a large range of compounds, including volatile or semi-volatile molecules [19,20], non-polar [21], or polar compounds [22], inorganic ions or proteins [23]. Moreover, a wide variety of surfaces can be used, including conductive or non-conductive surfaces (e.g., glass, paper, metal, plastic, thin-layer chromatography, porous silicon, nano-porous aluminium).

Many applications over large areas can be explored [23–32], permitting high-throughput analysis [33,34], and qualitative or

Abbreviations: EDTA, ethylenediaminetetraacetic acid; ILLW, intermediate and low-level waste; AMS, ambient mass spectrometry; DESI, desorption electrospray ionization; DART, direct analysis in real time; MSI, mass spectrometry imaging; MALDI, matrix-assisted laser desorption ionization; SIMS, secondary ion mass spectrometry; MeOH, methanol; ACN, acetonitrile; *m/z*, mass-to-charge ratio; LOD, limit of detection; LOQ, limit of quantification; *S/N*, signal-to-noise ratio

* Corresponding author. Tel.: +33 1 69 08 80 34; fax: +33 1 69 08 54 11.
E-mail address: diane.lebeau@cea.fr (D. Lebeau).

http://dx.doi.org/10.1016/j.talanta.2014.10.031
0039-9140/© 2014 Elsevier B.V. All rights reserved.

quantitative detection [21,34,35]. Finally, chemical imaging is also possible under ambient pressure and without surface pretreatment, which is an important advantage over usual mass spectrometry imaging (MSI) techniques such as matrix-assisted laser desorption ionization (MALDI) [36] and secondary ion mass spectrometry (SIMS) [37].

Even though the mechanism of the DESI process is not yet completely elucidated, it is suggested that the solubility of the analyte in the spray solution is an important factor in the desorption/ionization process [38,39]. Moreover, it has been shown that ion/molecule reactions can occur at the interface between the charged microdroplets of the solvent and the solid sample [40]. Thus, if the spray solvent is correctly doped with a suitable compound, the analyte of interest forms a specific characteristic adduct [25]. This method known as reactive DESI enables to improve the selectivity and sensitivity of the produced complex [41].

The choice of the solvent is not the only critical parameter. The surface is also an important parameter. The chemical composition, porosity, texture, and electrical conductivity have been reported to affect desorption/ionization and analyte detection. It has been shown that surfaces of high conductivity reduce responses whereas inert and hydrophobic surfaces increase them [30,42]. Hence the surface properties play a significant role in the charge transfer process [42].

Concrete analysis by ambient mass spectrometry has already been performed by DART [17]. In this work, we have chosen DESI-MS to take advantage of reactive-DESI experiments and thereby increase the chemical selectivity of EDTA in DESI ionization. This article presents a feasibility study of reactive-DESI-MS experiments for semi-quantitative analysis and imaging of EDTA on concrete under ambient conditions without sample preparation.

2. Material and methods

2.1. Chemicals and reagent

All used chemicals used were analytical grade reagents. Ethylenediaminetetraacetic acid disodium salt dihydrate (EDTA.$Na_2 \cdot 2H_2O$) and iron (III) chloride hexahydrate ($FeCl_3 \cdot 6H_2O$) were purchased from Sigma-Aldrich (Saint-Quentin Fallavier, France). Methanol and acetonitrile were of HPLC reagent grade (J.T. Baker). Deionized water at 18.2 MΩ was prepared by a Milli-Q purification system (Millipore).

2.2. Instrumentation

DESI-MS experiments were carried out using an LCT XE Premier (Waters, Manchester, UK) equipped with the DESI ion source Omnispray from Prosolia (Indianapolis, IN). The DESI spectra were recorded in negative mode. The distance between the mass spectrometer inlet orifice and the cone entrance was 8 cm (due to the Z-spray design), connected by a stainless steel line. The spray needle voltage was initially set to 3.5 kV and nitrogen operating at 100 psi was employed as both the drying and the nebulizing gas. The infusion syringe pump delivered the solvent at 5 μL/min. The source temperature was initially set to 150 °C and the sample cone voltage was tuned at 30 V.

Due to the low mass-to-charge ratio of the studied molecules, the desorption angle was 55° and the sample distance was around 2 mm. Others source geometries were optimized for each sample in order to obtain the best ionization efficiency. Different spray solvents such as methanol and acetonitrile were tested. This optimization of the DESI conditions is presented in Section 3. For the reactive-DESI experiments, a solution at 40 μM of $FeCl_3 \cdot 6H_2O$ in methanol was utilized as the spray solvent. Spectra were acquired at 1 scan/s over a mass range of m/z 50 to 1000 with an acquisition time of 2 min.

2.3. Sample preparation

Several surfaces were considered: Omni Slides™ Hydrophobic Arrays (Prosolia Inc.) and concrete samples. For analysis on hydrophobic spots 1 μL of EDTA solutions diluted in methanol at the appropriate concentration was spotted at the surface and allowed to dry as possible before analysis. The spread of solution on each spot was estimated by dividing the number of moles deposited by the area over which the sample was distributed (r=1 mm). For the analyses on concrete, concrete samples that were 1 cm high and a few centimeters wide were cut with a mineral saw to obtain flat surfaces. The aim was to maintain the same capillary-to-surface distance during all DESI analyses. 10 μL of EDTA solution with an appropriate concentration in methanol were directly deposited at the concrete without further treatment. The spots were allowed to dry as possible before analysis.

2.4. Semi-quantitative analysis on concrete

Several concrete samples were prepared with approximately the same surface. A stock solution of EDTA in methanol at 10 mM was prepared. 10 μL of diluted solution of EDTA in methanol at known concentrations (0.1, 0.5, 1, and 5 mM) were then spotted onto the concrete surface. Due to the spread of the solution on the surface, absolute concentrations of EDTA were estimated by dividing the number of deposited moles by the area over which the sample was distributed (r=1.5 cm). The resultant concentration ranged from 5.65 to 565 pmol/mm². All samples were dried several hours at room temperature before analysis to be sure that concrete samples are as dried as possible.

To control for the possible uneven distribution of the compound on the concrete slice, several spectra were collected at different points of the concrete sample. The final intensity of the characteristic EDTA ion was taken as the average of all intensities of this ion on the various sample surface points. Mass spectra were acquired at 1 s/scan over a mass range of m/z 50 to 1000 for 2 min. Concentrations were then plotted as a function of the intensity of the targeted ion. Each data point of the calibration curve represented an average of the data obtained from three different concrete samples spotted with the same concentration of EDTA.

2.5. Image acquisition

1 mL of EDTA solution in methanol was spotted at the center of a concrete sample and allowed to dry as possible at room temperature before analysis. The final concentration on the concrete after the drying step was 650 pmol/mm². A step of 500 μm in the y-direction and a velocity of 500 μm/s in the x-direction were employed. One mass spectrum was collected every second over a mass range m/z 100–1000. The time to record an image depended on the sample size and ranged from 1 to 2 h. The data was then converted using the Firefly™ conversion software (Prosolia Inc., Indianapolis, IN, USA) and ionic images were generated with the BioMap software (www.maldi-msi.org).

3. Results and discussion

3.1. Optimization of DESI conditions

The aim of this work was to demonstrate the feasibility of EDTA detection directly in its environment. In a first step, the DESI conditions (ionization mode and solvents choice) were optimized to enable the EDTA detection.

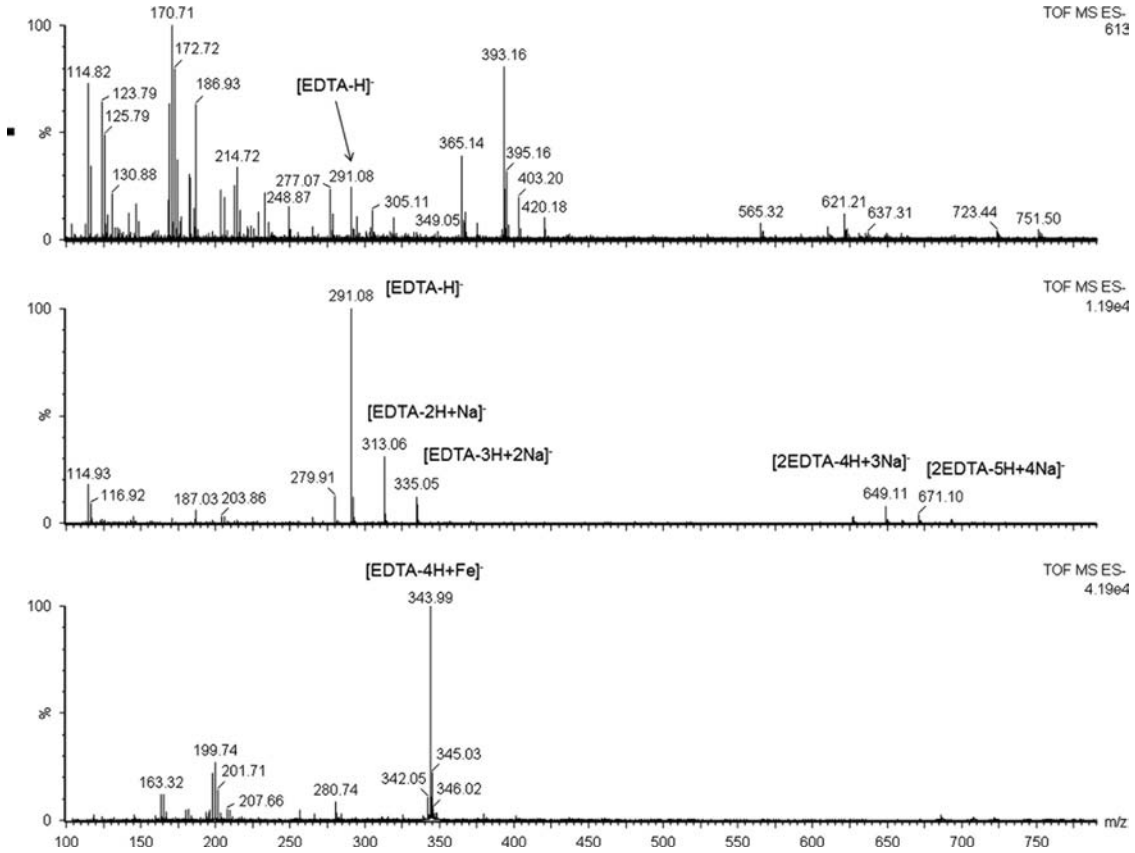


Fig. 1. Solvent comparison for EDTA analysis on Omni Slides Hydrophobic Arrays by DESI. Spray solvents used are (a) ACN, (b) MeOH and (c) 40 μM of FeCl3 in MeOH. EDTA concentration was 3 nmol/mm² for all DESI spectra.

3.1.1. Ionization conditions

EDTA is an organic complexant with four acidic functions. Thus, this molecule possesses four mobile hydrogens, and is therefore easily detected in negative mode after deprotonation of acidic functions. To reach the best sensitivity, experimental conditions were first optimized on a model surface, the Omni Slides™ Hydrophobic Arrays from Prosolia Inc. To obtain the best sensitivity in all cases, the choice of the solvent is an important parameter in the method development [43]. As with electrospray, two widely used solvents, methanol (MeOH) and acetonitrile (ACN) were tested in DESI.

Fig. 1a and Fig. 1b show DESI spectra of 3 nmol/mm² of EDTA detected with respectively ACN and MeOH. Changing the organic solvent from ACN to MeOH had a significant effect on the sensitivity. When ACN was used as the spray solvent (Fig. 1a), a large number of peaks were observed but only one EDTA ion corresponding to the deprotonated molecule $[EDTA\text{-}H]^-$ at *m/z* 291 was detected. This peak presented a low signal-to-noise ratio and was not the most intense peak. All other peaks were believed to come from the surface or solvent contamination.

When MeOH was used as the spray solvent (Fig. 1b), and with the same EDTA concentration, the molecular ion $[EDTA\text{-}H]^-$ (*m/z* 291) was the major peak. Adducts and aggregates of the molecule were also detected: $[EDTA\text{-}2H+Na]^-$ at *m/z* 313, $[EDTA\text{-}3H+2Na]^-$ at *m/z* 335, $[2EDTA\text{-}3H+2Na]^-$ at *m/z* 627, $[2EDTA\text{-}4H+3Na]^-$ at *m/z* 649 and $[2EDTA\text{-}5H+4Na]^-$ at *m/z* 671. Peaks coming from the environment, as those observed with ACN, could here be suppressed due to the better signal-to noise ratio of the EDTA peak.

The intensity of the molecular ion $[EDTA\text{-}H]^-$ was also improved by two orders of magnitude by using methanol as the spray solvent. The choice of the solvent is known to be an important parameter in the DESI process, and Badu-Tawiah et al. have shown that the solubility of the analyte in the solvent is crucial for the desorption process [38]. Since the analyte is solubilized in the spray solvent, highly hydrophobic compounds are better ionized with hydrophobic solvents, whereas hydrophilic molecules are better ionized with polar solvent. Since EDTA is a hydrophilic molecule, it seemed reasonable that it was better detected with a protic solvent such as methanol.

3.1.2. Limit of detection and reactive-DESI

In the next step, the limit of detection (LOD) was investigated. Dilutions of the EDTA stock solution from 10 to 0.001 mM were prepared. If we consider the spread of the solution on the spot, the concentrations ranged from 3 nmol/mm² to 0.3 pmol/mm². These concentrations were chosen according to the estimated EDTA concentration in disposal areas. Under the optimized experimental conditions described previously, the LOD of EDTA (a threshold cut-off of 3:1 signal-to-noise ratio (*S/N*) was chosen for the $[EDTA\text{-}H]^-$ ion at *m/z* 291) was determined to be 300 pmol/mm².

To improve this LOD, the reactive-DESI method was investigated and an appropriate reagent was added to the spray solvent. EDTA is known to create particularly stable 1:1 complexes with many metals. Among the possible metal ions, the Fe^{III} ion was chosen for two reasons. First, this transition metal presents one of the highest stability constants ($\log_{10}K = 25.1$) [44] with EDTA. Second, the use of ferric ions to increase the limit of detection of EDTA in solution has already been demonstrated in the literature, with several analytical methods, such as HPLC [45] or LC-ESI–MS [46], thanks to the formation of a negative charged complex $[EDTA\text{-}4H+Fe^{III}]^-$ in aqueous solution. The spray solvent was doped with a solution of $FeCl_3$. Bergers et al. have shown that a large excess of ferric ions enables to obtain an enhanced limit of detection [45].

Fig. 1c presents a DESI spectrum of 3 nmol/mm² of EDTA detected by reactive-DESI using a spray solvent of 40 μM of $FeCl_3$ in MeOH. EDTA was detected at *m*/*z* 344 as $[EDTA\text{-}4H+Fe^{III}]^-$. This ion was the only form of EDTA observed in this DESI spectrum. No free form of EDTA or different adducts or aggregates of EDTA were detected. Only two forms of iron chloride ions $[Fe^{II}Cl_3]^-$ and $[Fe^{III}Cl_4]^-$, respectively, at *m*/*z* 161 and 196, were observed. It was deduced that the total amount of EDTA has been converted into an $[EDTA\text{-}4H+Fe^{III}]^-$ complex. This result confirms that the Fe^{3+} ion reacts rapidly and selectively with EDTA.

The limit of detection using the reactive-DESI method was then studied. The same range of concentration as when determining the LOD by DESI was used (from 3 nmol/mm² to 0.3 pmol/mm²). By reactive-DESI, the LOD ($S/N=3$ for $[EDTA\text{-}4H+Fe^{III}]^-$ ion at *m*/*z* 344) was determined at 3 pmol/mm², i.e., two orders of magnitude lower than the LOD obtained under classic DESI conditions. The reactive-DESI experiment enabled to attain an LOD lower than the estimated concentration of EDTA in concrete disposal. In the next step, this method of detection of EDTA by reactive-DESI directly on concrete was now investigated.

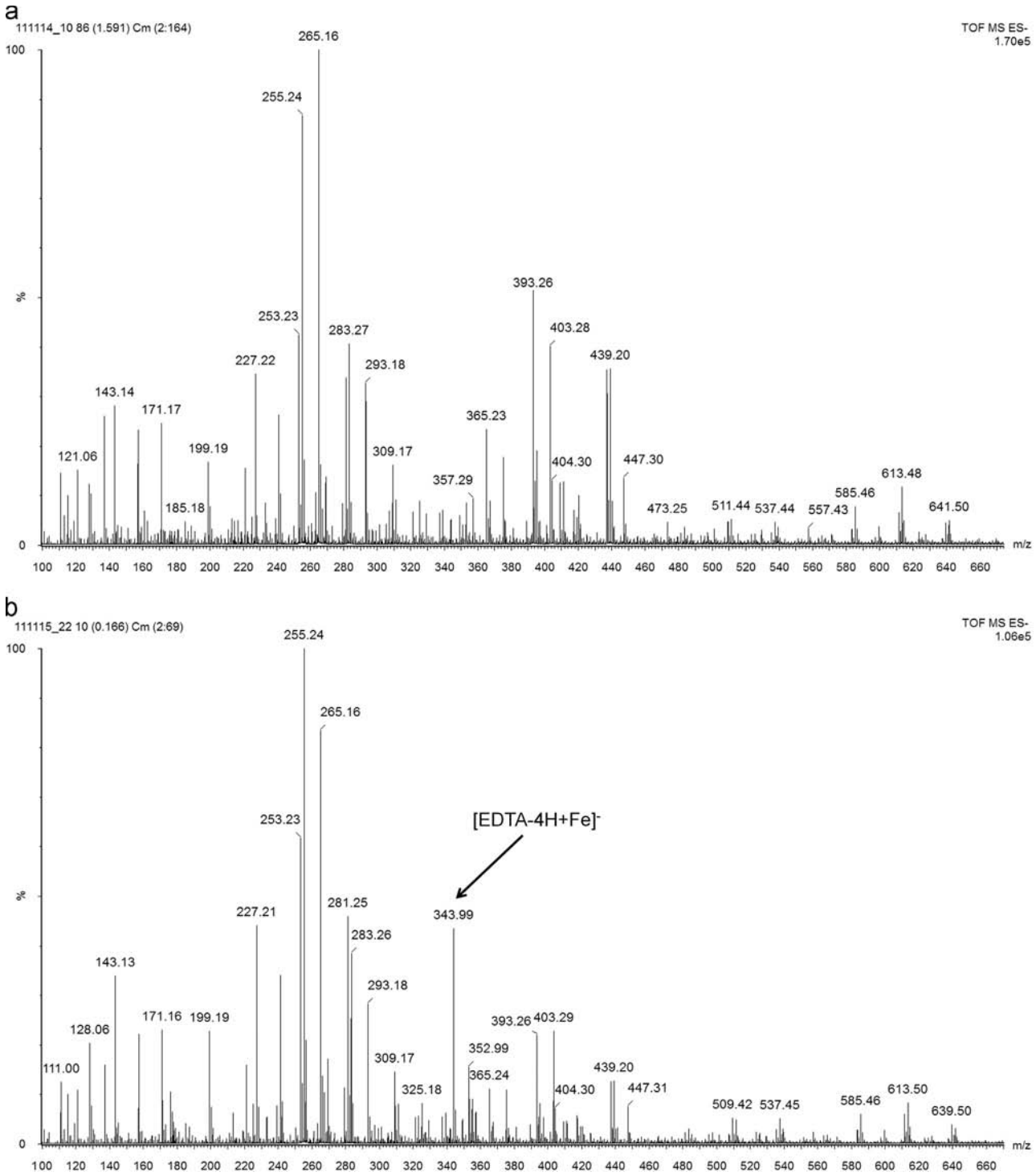


Fig. 2. DESI spectra of EDTA on concrete sample obtained with (a) MeOH as the spray solvent and (b) $FeCl_3$ solution in MeOH as the spray solvent.

3.2. EDTA detection on concrete surface

3.2.1. EDTA detection on concrete by reactive-DESI

First, the DESI spectrum of a concrete sample surface was studied. Fig. 2a presents the DESI spectrum obtained with MeOH as the spray solvent. A large number of peaks was detected since concrete is a very complex matrix containing both organic and inorganic compounds such as oxides, polyols, carboxylic acids, polymers, etc …. However, none of the observed peaks from the matrix was detected in the mass range of any expected EDTA ions, i.e., deprotonated EDTA (*m*/*z* 291) or the EDTA complex with iron (*m*/*z* 344). In a case where EDTA is present at a surface, it is important that its attribution be unambiguous.

The detection of EDTA at the concrete surface with only MeOH as the spray solvent was not possible. This can be explained by the significant porosity of the concrete matrix. The spray solvent was found to be rapidly absorbed by the matrix and the charged microdroplets of the solvent had no time to interact with the solid sample. To allow the spray solvent time to react with the analyte, different optimizations were realized by increasing or decreasing the solvent flow rate. Takats et al. have shown that increasing the nebulizing gas flow rate yielded smaller sizes of the spray droplets and increased their velocity [32]. In these conditions, the desolvation efficiency and the production of secondary droplets under impact were enhanced. However, no signal corresponding to EDTA ions could be observed, regardless of whether the nebulizing gas flow rate was increased or decreased. This result can be explained both by the diffusion capacity into the concrete surface and by the DESI mechanism. At a low gas flow rate, the droplets velocity was too low and did not produce secondary droplets because of the concrete absorbing the solvent. At a high gas flow rate, the initial droplet size was too small and the droplets evaporated before reaching the sample surface.

Reactive-DESI experiment was thus tested with the aim to selectively extract the targeted molecule of the complex matrix thanks to the fast reaction between iron and EDTA. As in the previous experiment on hydrophobic spots, the spray solvent used was doped with a solution of $FeCl_3$ at 40 μM in methanol. Fig. 2b shows a DESI spectrum of EDTA at 200 pmol/mm² on the concrete surface obtained by reactive DESI. The identified ions of EDTA were the same as those observed after deposit on hydrophobic spots. The peak of the complex $[EDTA\text{-}4H+Fe^{III}]^-$ at *m*/*z* 344 was consistently detected as the more intense peak of the EDTA ions, and no other EDTA ions, such as free EDTA ions or adducts or aggregates, were identified. This result also indicates that the chelation of iron by EDTA was fast enough and that the 'droplet pick up' DESI mechanism has time to occur before that concrete absorb the solvent. Fe(III) ions had time to interact with the EDTA at the surface, demonstrating the possibility to directly detect EDTA at a concrete surface by reactive-DESI.

In concrete matrices, various metal species are present, e.g., Ca (II), Mg(II), K^+, Na^+, Al(III). However, all these cations have a lower $\log_{10}K$ value than the Fe(III) ion, which is also present in cement pastes but to a lesser extent. This explains why it is not possible to observe chelating EDTA with these other ions. Moreover, Bradbury and Sarott have demonstrated that the complexing power of an organic ligand can be significantly reduced on cement because of the competition between chelating molecules and inorganic complexing ions like hydoxy ions, which can be found in very high concentration in concrete interstitial water [47]. This explains why only Fe(III) was chelated by the targeted molecule independently of the other cations present in the matrix.

The speciation of EDTA with Fe^{III} also depends on the pH. Serne et al. have shown that with the exception of divalent transition metals complexes, EDTA-metal complexes appear to be readily dissociated at alkaline pH [48]. Moreover, EDTA is weakly sorbed onto cement pastes, i.e., at high pH value [49,50]. Thus, the EDTA present at the surface is prone to react with Fe(III) ions from the spray solvent. Reactive-DESI is thus a fast enough reaction, since ferric ions can react with EDTA, and the DESI process takes place before diffusion of the spray solvent into concrete. The concrete matrix with all its significant chemical or physical features, e.g., highly alkaline pH or high concentrations of salts, thus does not seem to hinder the detection of $[EDTA\text{-}4H+Fe^{III}]^-$ complex. We have demonstrated the feasibility to selectively detect EDTA, in its chelated form with Fe(III), at the surface of a concrete sample without any surface pretreatment thanks to reactive-DESI.

3.2.2. Semi-quantitative analysis of EDTA on concrete samples

Each concrete samples was spotted with EDTA solution at different concentrations (from 565 to 5.65 pmol/mm²). The relationship between the EDTA concentrations on the concrete surface and the MS response (absolute peak height for the corresponding ion) were verified and each point of the calibration curve was the result of an average of 3 replicates. After reactive-DESI analysis, the intensity of the $[EDTA\text{-}4H+Fe^{III}]^-$ ion at *m*/*z* 344 was plotted against the concentration in pmol/mm². The points obtained were satisfactorily represented by a linear regression with a determination coefficient of 0.9985 as shown in Fig. 3. The linearity was assessed by the method of least squares. The relative standard deviation between each measured peak height was better than 25%. It is worth noting that at a concentration higher than 1000 pmol/mm^2 the linearity of the relationship was no longer assured. This loss of linearity was believed to be due to an effect of ion suppression as shown by Takats et al. [32] or to the too high EDTA concentration compared with that of iron. There was no free iron available to induce more [EDTA/Fe] complexes.

Under these experimental conditions, the LOD was determined to be 5.65 pmol/mm² (*S*/*N*=3 for $[EDTA\text{-}4H+Fe^{III}]^-$ ion at *m*/*z* 344) and the limit of quantification was 14 pmol/mm² (*S*/*N*=10 for $[EDTA\text{-}4H+Fe^{III}]^-$ ion at *m*/*z* 344). The limit of detection of EDTA on concrete was close to the limit of detection of the EDTA deposited on the hydrophobic spots and analyzed by reactive-DESI. This confirms, as discussed in the previous section, that the matrix, i.e., concrete, did not seem to interfere with the detection of the $[(EDTA\text{-}4H+Fe^{III}]^-$ complex in MeOH spray. These limits of detection and quantification were estimated by dividing the number of deposited moles by the area over which the solution had spread in the *x*- and *y*-directions. Nevertheless, a solution on concrete sample also diffuses in the *z*-direction. The amount of EDTA that diffused into the concrete matrix when the MeOH solution was spotted was difficult to evaluate. In this case, the

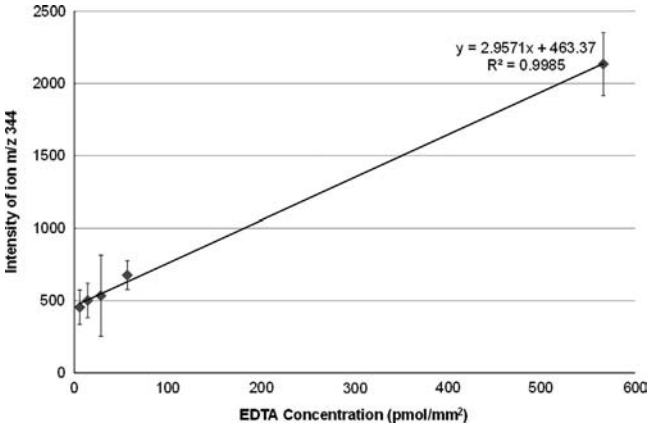


Fig. 3. Calibration curve obtained from 5 samples with different EDTA concentrations (in pmol/mm²) on a concrete surface obtained by plotting the peak height of ion *m*/*z* 344 against the EDTA concentration.

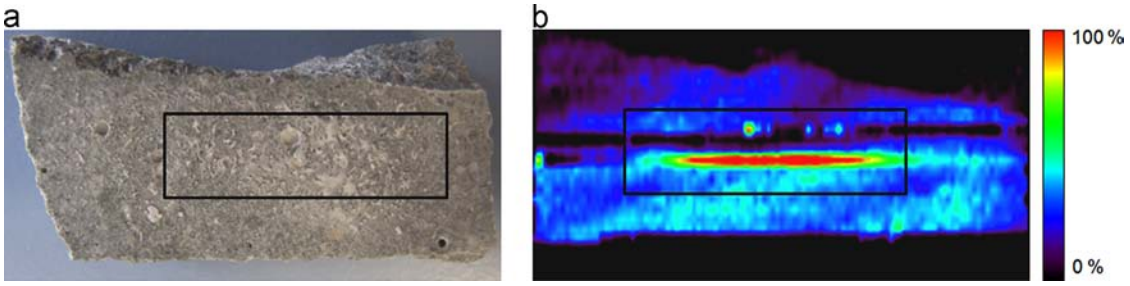


Fig. 4. (a) Optical image of a concrete sample and (b) ionic image of the complex [EDTA-4H+Fe] (m/z 343.9).

limits of detection and quantification that have been determined may be even better than those given above. We conclude that the reactive-DESI can be favorably used to analyze and quantify EDTA on samples coming from a concrete canister.

3.2.3. DESI imaging

This analytical method for detection of EDTA on concrete surfaces by reactive-DESI was developed to control the presence of the substance on a concrete canister, for example before its disposal. In this context, a representative sample can be scanned to evaluate the distribution of EDTA at its surface. To realize this work, imaging analysis using mass spectrometry has been developed and is now presented to show the spatial distribution of EDTA at the sample's surface. Fig. 4a displays the optical image of a concrete sample doped with EDTA, and the ion image of the peak at m/z 344 identified as the complex $[EDTA\text{-}4H+Fe^{III}]^-$ is shown in Fig. 4b. Thus, there was a good correlation between the EDTA distribution at the surface and the ion image of the EDTA complex.

It is concluded here that using reactive-DESI for imaging analysis of a sample of concrete doped with EDTA is possible under ambient conditions and without sample preparation. It has to be noted that the ionic image of the complex ion presented an elongated distribution and not the expected circular one. This could be explained by the strong diffusing power of concrete. The EDTA is mainly diffusing on the y-direction.

Albeit imperfect, this method brings some advantages in comparison with other imaging techniques using mass spectrometry such as SIMS or MALDI, and can even be complementary to these two methods. MALDI and SIMS techniques require a sample preparation with matrix or metal deposition [51] which can produce a high background signal below m/z values of 300 and may thus limit the ability to detect low-mass signals such as EDTA. Moreover, the DESI ionization is soft enough to keep all non-covalent complexes and allow the formation of specific ions.

4. Conclusions

This study has demonstrated the feasibility of EDTA detection on concrete surfaces without sample preparation using reactive DESI. An MSI analysis has also shown that a distribution of the complexing agent on the concrete is possible. The selective and strong chelation of iron by EDTA allows the selective detection, localization and quantification of this molecule in a complex matrix. Thus, a complete analysis of a specific organic compound in conventional and imaging mode proved to be possible using the methodology described in this article. The huge advantage in these reactive-DESI experiments is the very limited sample preparation, reducing sample manipulations and quantities of used solvent used - two important conditions in the development of methodologies in the context of nuclear facilities.

Nevertheless, several limitations of this method should also be reported. First, the time for the analysis of this surface of approximately 7 cm² was quite long (approximately 50 min). To reduce this analysis time the large-area DESI-MS technique may be an option [52]. This modified DESI source is able to scan larger surfaces than the conventional DESI sources, thanks to its 200-times larger desorption/ionization area. With this source, the total scanning time is reduced, however the spatial resolution may also be lowered.

The second limitation of our analytical method is that the analyzed sample should be as flat as possible to keep the same capillary-to-surface distance during all DESI analyses. When quantification or imaging experiments are required, this limitation cannot be solved.

One of the important challenges that needs to be solved in DESI analysis is the low spatial resolution. In this experiment the spatial resolution was estimated to approximately 500 μm because of the strong absorbing power of the concrete and its high capacity of diffusion. It is thus not yet possible to precisely observe EDTA molecules which are localized in the pores of the concrete matrix (from 0.5 nm to 5 μm) [53] or outside the pores. Moreover, due to the inherent diffusion tacking place at the surface of the porous concrete examined by DESI, it is unlikely that this resolution will ever be attained. However, the aim of this method was the demonstration that chelating molecules as EDTA can be detected via DESI-MS analysis, and this was proven here. This analytical approach can now be applied to other aminopolycarboxylic agents.

References

[1] M. Unger, E. Mainka, W. König, Fresenius J. Anal. Chem. 329 (1987) 50–54.
[2] L. du Bois, de Maquille, L. Renaudin, F. Goutelard, A. Jardy, J. Vial, D. Thiebaut, J. Chromatogr. A 1276 (2013) 20–25.
[3] V. Jedináková-Křižová, J. Radioanal. Nucl. Chem. 229 (1998) 13–18.
[4] B. Nowack, Environ. Sci. Technol. 36 (2002) 4009–4016.
[5] C. Randt, R. Wittlinger, W. Merz, Fresenius J. Anal. Chem. 346 (1993) 728–731.
[6] M. Sillanpää, J. Sorvari, M. Sihvonen, Chromatographia 42 (1996) 578–582.
[7] L. Zheng, D.G. Watson, J.N. Tettey, C.A. Clements, Talanta 76 (2008) 1165–1169.
[8] Z. Chen, Q. Sun, Y. Xi, G. Owens, J. Sep. Sci. 31 (2008) 3796–3802.
[9] T. Kemmei, S. Kodama, A. Yamamoto, Y. Inoue, K. Hayakawa, J. Chromatogr. A 1171 (2007) 63–68.
[10] T.P. Knepper, A. Werner, G. Bogenschutz, J. Chromatogr. A 1085 (2005) 240–246.
[11] S. Loyaux-Lawniczak, J. Douch, P. Behra, Fresenius J. Anal. Chem. 364 (1999) 727–731.
[12] J.B. Quintana, T. Reemtsma, J. Chromatogr. A 1145 (2007) 110–117.
[13] G. Owens, V. Ferguson, M. McLaughlin, I. Singleton, R. Reid, F. Smith, Environ. Sci. Technol. 34 (2000) 885–891.
[14] A. Padarauskasa, G. Schwedt, J. Chromatogr. A 773 (1997) 351–360.
[15] K. Grant, G. Mong, R. Lucke, J. Campbell, J. Radioanal. Nucl. Chem. 211 (1996) 383–402.
[16] Z. Takats, J.M. Wiseman, B. Gologan, R.G. Cooks, Science 306 (2004) 471–473.
[17] R.B. Cody, J.A. Laramee, H.D. Durst, Anal. Chem. 77 (2005) 2297–2302.
[18] R.G. Cooks, Z. Ouyang, Z. Takats, J.M. Wiseman, Science 311 (2006) 1566–1570.
[19] H. Chen, M. Li, Y.P. Zhang, X. Yang, J.J. Lian, J.M. Chen, J. Am. Soc. Mass Spectrom. 19 (2008) 450–454.
[20] M. Li, H. Chen, B. Wang, X. Yang, J. Lian, J. Chen, Int. J. Mass Spectrom. 281 (2009) 31–36.
[21] N.E. Manicke, J.M. Wiseman, D.R. Ifa, R.G. Cooks, J. Am. Soc. Mass Spectrom. 19 (2008) 531–543.
[22] G. Corso, G. Paglia, D. Garofalo, O. D'Apolito, Rapid Commun. Mass Spectrom. 21 (2007) 3777–3784.
[23] Y.S. Shin, B. Drolet, R. Mayer, K. Dolence, F. Basile, Anal. Chem. 79 (2007) 3514–3518.

[24] H. Chen, N.N. Talaty, Z. Takats, R.G. Cooks, Anal. Chem. 77 (2005) 6915–6927.
[25] I. Cotte-Rodriguez, Z. Takats, N. Talaty, H. Chen, R.G. Cooks, Anal. Chem. 77 (2005) 6755–6764.
[26] P.A. D'Agostino, J.R. Hancock, C.L. Chenier, C.R. Lepage, J. Chromatogr. A 1110 (2006) 86–94.
[27] D. Ifa, J. Wiseman, Q. Song, R. Cooks, Int. J. Mass Spectrom. 259 (2007) 8–15.
[28] D.R. Ifa, L.M. Gumaelius, L.S. Eberlin, N.E. Manicke, R.G. Cooks, Analyst 132 (2007) 461–467.
[29] A.T. Jackson, J.P. Williams, J.H. Scrivens, Rapid Commun. Mass Spectrom. 20 (2006) 2717–2727.
[30] T.J. Kauppila, N. Talaty, P.K. Salo, T. Kotiaho, R. Kostiainen, R.G. Cooks, Rapid Commun. Mass Spectrom. 20 (2006) 2143–2150.
[31] M. Nefliu, A. Venter, R.G. Cooks, Chem. Commun. (Cambridge) (2006) 888–890.
[32] Z. Takats, J.M. Wiseman, R.G. Cooks, J. Mass Spectrom. 40 (2005) 1261–1275.
[33] X. Ma, M. Zhao, Z. Lin, S. Zhang, C. Yang, X. Zhang, Anal. Chem. 80 (2008) 6131–6136.
[34] N.E. Manicke, T. Kistler, D.R. Ifa, R.G. Cooks, Z. Ouyang, J. Am. Soc. Mass Spectrom. 20 (2009) 321–325.
[35] J.H. Kennedy, J.M. Wiseman, Rapid Commun. Mass Spectrom. 24 (2010) 309–314.
[36] P. Chaurand, S.A. Schwartz, R.M. Caprioli, J. Proteome Res. 3 (2004) 245–252.
[37] R. Castaing, G.J. Slodzian, Microscopie 1 (1962) 395–399.
[38] A. Badu-Tawiah, C. Bland, D.I. Campbell, R.G. Cooks, J. Am. Soc. Mass Spectrom. 21 (2010) 572–579.
[39] G.J. Van Berkel, B.A. Tomkins, V. Kertesz, Anal. Chem. 79 (2007) 2778–2789.
[40] H. Chen, I. Cotte-Rodriguez, R.G. Cooks, Chem. Commun. (Cambridge) (2006) 597–599.
[41] M. Girod, E. Moyano, D.I. Campbell, R.G. Cooks, Chem. Sci. 2 (2011) 501–510.
[42] M. Volny, A. Venter, S.A. Smith, M. Pazzi, R.G. Cooks, Analyst 133 (2008) 525–531.
[43] F.M. Green, T.L. Salter, I.S. Gilmore, P. Stokes, G. O'Connor, Analyst 135 (2010) 731–737.
[44] D.C. Harris, Quantitative Chemical Analysis, eighth ed., 2011.
[45] P. Bergers, A. de Groot, Water Res. 28 (1994) 639–642.
[46] A. Dodi, V. Monnier, J. Chromatogr. A 1032 (2004) 87–92.
[47] M.H. Bradbury, F.A. Sarott, Nagra Technical Report 93-08, 1994.
[48] R.J. Serne, K.J. Cantrell, C.W. Lindenmeier, A.T. Owen, I.V. Kutnyakov, R.D. Orr, A.R. Felmy, Report NUREG/CR-6758, PNNL-13774, 2002.
[49] M. Dario, M. Molera, B. Allard, in: Report TR-04-04. SKB, Stockholm, Sweden, 2004.
[50] I. Pointeau, N. Coreau, P.E. Reiller, Radiochim. Acta 96 (2008) 367–374.
[51] K. Chughtai, R.M. Heeren, Chem. Rev. 110 (2010) 3237–3277.
[52] S. Soparawalla, G.A. Salazar, E. Sokol, R.H. Perry, R.G. Cooks, Analyst 135 (2010) 1953–1960.
[53] R. Kumar, B. Bhattacharjee, Cem. Concr. Res. 33 (2003) 155–164.

Talanta 132 (2015) 884–888

Contents lists available at ScienceDirect

Talanta

journal homepage: www.elsevier.com/locate/talanta

Conductometric determination of ammonium ion with a mobile drop

Pheeraya Jaikang [a,b], Kate Grudpan [a,b], Tinakorn Kanyanee [a,b,*]

[a] Department of Chemistry, Faculty of Science, Chiang Mai University, Chiang Mai 50200, Thailand
[b] Center of Excellence for Innovation in Analytical Science and Technology, Chiang Mai University, Chiang Mai 50200, Thailand

ARTICLE INFO

Article history:
Received 2 September 2014
Received in revised form
19 October 2014
Accepted 20 October 2014
Available online 29 October 2014

Keywords:
Mobile drop
Conductometry
Ammonium determination

ABSTRACT

A mobile drop based approach was utilized for the conductometric determination of aqueous ammonium ion. A liquid drop was manipulated by gravity to remain or move out of a conductivity measurement zone located on a hydrophobic path. A dilute sulfuric acid drop functioned as a micro gas absorber. Gaseous NH_3 was liberated from a sample containing NH_4^+ by adding NaOH and purged to flow over the absorber drop. As H^+ in the absorber drop was converted to NH_4^+, the conductivity decreased. The rate of the conductivity decrease thus ultimately depended on the NH_4^+ concentration in the sample. While the sample could be complex, the liberation of NH_3 gas essentially freed the analyte of interest from the matrix and allowed the use of an otherwise nonselective detector. The system was applied to the determination of NH_4^+ in some natural waters without prior filtration; the results agreed well with those from a manual indophenol blue method. The approach exhibited a limit of detection (LOD) of 5 μM and a relative standard deviation (RSD) of < 5%. The mobile drop gave a constant volume of the gas absorbing solution and provided a cost-effective and simple analytical platform.

© 2014 Elsevier B.V. All rights reserved.

1. Introduction

Ammonium (NH_4^+) is a globally important micronutrient. High NH_4^+ levels in natural waters indicate deteriorated water quality, generally from anthropogenic sources. Analyses for NH_4^+ are routine in agriculture, soil science and environmental studies. The most widely used method for NH_3/NH_4^+ determination is the spectrophotometric indophenol blue method [1], based on the Berthelot reaction.

One successful approach to NH_4^+ determination has been to convert aqueous NH_4^+ to gaseous NH_3 by adding base and collecting the produced gas for quantitation; this has the further virtue of removing matrix interferences. In flow analysis systems, NH_4^+ has been commonly converted inline to unionized NH_3 in the donor stream and letting the NH_3 thus formed diffuse through a gas diffusion unit (GDU) into an acceptor stream for measurement. The GDU may be fabricated with or without a membrane. Different detectors have been used with a GDU in a flow system for NH_4^+ determination. Frenzel et al. used flow injection (FI) with a GDU prior to potentiometric measurement of NH_4^+ [2–4]. Conductometry, normally a nonselective technique, has been used with a FI-GDU system for measuring Kjeldahl Nitrogen in milk and chicken digests [5]. Contactless conductometry works particularly well with small bore tubing; this has also been used for NH_4^+ determination with a FI-GDU system [6]. Other automated flow methods, e.g., sequential injection [7], multi syringe FI [8,9], and multi-commutation FI [10,11] have all been used with a GDU and spectrophotometric NH_4^+ determination. Fluorometric detection, a more sensitive technique has also been similarly used, for both sea water [12] and fresh water [13].

The conversion of an aqueous analyte species of interest to the gaseous state (and thus liberating it from a matrix potentially containing interferents) is not unique to the NH_4^+/NH_3 system, the same principle is used in hydride generation atomic spectroscopy. Hydride generation coupled with chemiluminescence detection (HG-CL) permitted a portable sensitive system for measuring arsenic in drinking water [14]. Generation of H_2S from an aqueous sample and measurement with a micro gas analysis system was used for the determination of sulfide in natural waters [15]. Cyanide in a blood sample was converted to gaseous HCN and collected in a porous membrane containing a chromogenic reagent to permit measurement using disposable platforms [16]. A membraneless setup avoids membrane fouling problems [17,18]. The flow analysis coupled with membraneless format has been developed [17–19]. Air segmentation in such systems can have advantages [20]; this has been applied to ethanol determination [21].

A liquid drop represents a small volume that has no membranes and a large surface/volume ratio, well suited for gas sampling without involving any membranes. A soluble gas can be scavenged by a drop and the product concentration can accumulate rapidly. The product can then be measured in-situ, often with a short overall analytical

* Corresponding author at: Department of Chemistry, Faculty of Science, Chiang Mai University, Chiang Mai 50200, Thailand. Tel./fax: +66 53 941910.
E-mail address: tinakorn.kanyanee@cmu.ac.th (T. Kanyanee).

http://dx.doi.org/10.1016/j.talanta.2014.10.046
0039-9140/© 2014 Elsevier B.V. All rights reserved.

cycle. Liquid drops are easily manipulated, represent very low reagent consumption and waste generation and provide for low-cost methods [22]. Liquid drops/films have been extensively used for gas collection and analysis, e.g., for many different gases at a time with a capillary electrophoresis (CE) system [23–25], or by simple LED-based photometry for NO_2 [26], NH_3 [27], H_2S [28], SO_2 [29], etc. Although conductometry is non-selective, it can provide highly sensitive measurements with simple instrumentation. Toda et al. [30] used a renewable hemispherical drop of dilute acid atop the tip of an annular tubular electrode assembly that monitored the conductivity of the drop. As breath ammonia flowed over the drop it reduced the conductance by neutralizing the acid; the rate of conductivity decrease was a direct measure of the breath ammonia concentration. Although a liquid film/bubble [31] can provide an even greater surface/volume ratio than a drop, a liquid drop based system is simpler to set up.

Drops moving by gravity have the added advantage of incorporating both flow and transient examination capabilities. An inclined platform on which a drop falls and moves is particularly conducive to this; Liu and Dasgupta [32] introduced transient electrokinetic injection in CE based on this principle. Recently, we have refined the ability to control drop movement by using a hydrophobic inclined path for drop movement and a suspended probe with a hydrophilic exterior in the transit path to stop the drop by adhesion, and then allow it to move down again by allowing additional drop(*s*) to merge whence the gravitational force overcomes adhesion forces [33]. The use of this system was then demonstrated for microcoulometric titrations of analytes in the drop.

In this paper we demonstrate another application of this inexpensive versatile platform using the moving drop for (NH_3) gas collection, quantitating the collected gas conductometrically by momentarily stopping the drop at a measurement probe and then transmitting all to waste by sending a merging wash drop. Ammonia gas was liberated from a NH_4^+-containing solution by alkalinization and purging and directed to the drop. Results from real samples are compared with spectrophotometric determination by the indophenol blue method, which often requires sample pretreatment [34].

2. Experimental

2.1. Reagents and solution

All reagents were of analytical reagent grade. Sulfuric acid (0.1 M) was used as the gas absorbing liquid drop; this was prepared by dilution from 98% H_2SO_4. The NH_4^+ stock standard solution (10 mM) was freshly prepared by dissolving 0.1593 g of NH_4Cl (www.merck-millipore.com) in 0.1 M H_2SO_4 and adjusting the volume to 100.00 mL with 0.1 M H_2SO_4. Diluted standards were prepared daily using 0.1 M H_2SO_4. Because the H_2SO_4 may itself contain traces of NH_4^+, the exact concentration of NH_4^+ in the standards were determined by the Indophenol Blue method [34], the requisite reagents were prepared as instructed therein. For liberating gaseous NH_3 from NH_4^+ bearing samples, 4 M NaOH was prepared by dissolved 24 g NaOH in 150 mL deionized water.

Water samples for analysis consisted of surface water from the Ping River and local ponds in the Chiang Mai area, Thailand. Sulfuric acid (2 mL 98% acid per 500 mL Sample) was added to the samples before storage at 4 °C in the dark in polyethylene bottles [2].

2.2. Experimental setup

The system is schematically depicted in Fig. 1. A polymethylmethacrylate (PMMA) tube (2.0 cm i.d., 2.4 cm o.d., 20.0 cm length), equipped with end-caps, is used as the incline; normal inclination angle was ~23° from the horizontal plane. The bottom cap was connected by a drain tube to a waste container. A length of Polytetrafluoroethylene (PTFE) tape (plumber's tape) was placed lengthwise inside the PMMA tube to provide a hydrophobic path. A PEEK tube segment (0.5 × 1.6 × 10.0 mm i.d. × o.d. × length, www.upchurch.com) was affixed through a hole in the PMMA tube as shown and functioned as the drop head. A second drop head was similarly located, ~2 cm behind the first one. Disposable syringes were employed for manually dispensing H_2SO_4 and deionized water through the first and second drop heads, respectively. The drop size largely depends on both the i.d. and o.d. of the drop head terminus and the material. For the present case, drop volume was ~25 μL [33]. The liquid drop moves by gravity and is stopped through adhesion at the conductivity probe. In this position the drop is exposed to the gas generated from the sample. After the gas exposure and conductivity measurement step, a drop of DI water is dispensed on the path, merges with the extant drop and together flows down to waste. Relatively little residual liquid adheres to the conductivity probe. Because this becomes part of the measurement and calibration process and there is no residual free NH_3 in this liquid and the measurement is based on the rate of conductivity decrease and not absolute values, the residual adherence causes no perceptible error.

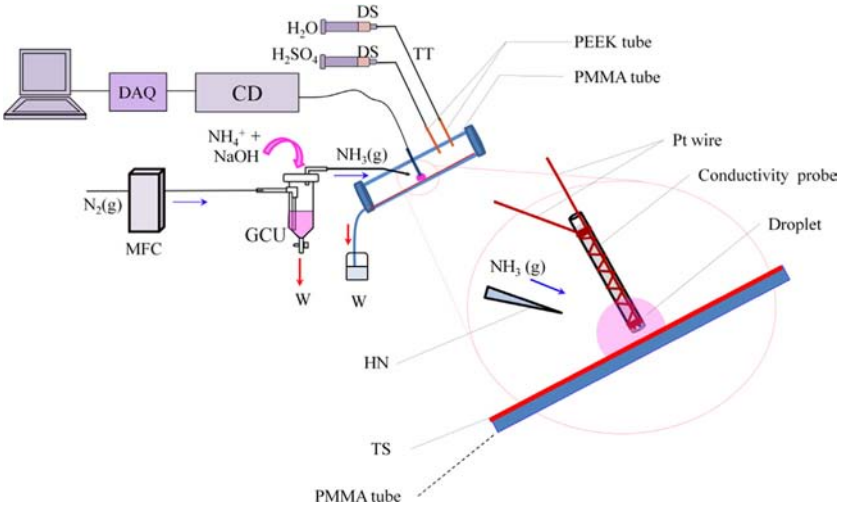


Fig. 1. The experimental setup: the mobile drop on the hydrophobic path with conductivity measurement for NH_4^+/NH_3 determination, MFC=Mass flow controller, GCU=Gas Conversion Unit, HN=hypodermic needle, CD=conductivity detector, DAQ=Data acquisition, TS=Teflon sheet, DS=Disposable syringe, TT=Teflon tube, *W*=waste.

The conductivity probe was made from a glass tube (1 × 1.5 × 65 mm i.d. × o.d. × length). One platinum wire (0.3 mm dia.) was inserted through the tube and affixed centrally at the mouth of the tube and the other was wrapped around the tube and fixed in place with epoxy adhesive. Only a small length at the end was left uncoated at the terminus for liquid contact. The wire termini were ~1 mm apart. The cell constant was ~33.0 cm^{-1}. The conductivity cell entered the PMMA tube wall in a perpendicular fashion and affixed thereto with hot-melt adhesive such that the tip was ~1.0 mm above the PTFE path. The conductance was measured by a commercial instrument (model 712 conductometer, www.metrohm.com). The instrument analog output was acquired at 5 Hz by a 22-bit A/D card (Emant300, www.emant.com). Custom software was written in-house in Visual Basic for data acquisition.

The gas conversion unit (GCU) was fabricated from a 50 mL polypropylene centrifuge tube (www.corning.com) as depicted in Fig. 1. A rubber cap was placed on top to seal the unit and also to function as a septum for reagent injection. The bottom of the chamber was connected with an on/off valve to drain out the solution to waste after the experiment. Nitrogen gas, flow controlled by a digital mass flow controller (0–2.0 L/min, Model MQ0002B/C, www.azbil.com) at 200 mL/min (ambient temperature) was used to bubble through the solution in the GCU: the gas entered through an elbow connector and used a 0.2 mm i.d. tube for bubbling.

The effluent gas traveled through a polycarbonate tube and terminated in a 21 ga. hypodermic needle that was affixed through the PMMA tube at an angle, the needle tip being ~1 cm from the liquid drop and directed at it. The gas flow creates circulating mixing, at least in the outer layer of the drop [27].

2.3. Experimental procedure

Ammonium bearing standards or samples in 0.1 M H_2SO_4 (5.00 mL) were transferred into the GCU by a transfer pipette. The H_2SO_4 absorber drop was manually dispensed and allowed to stop at the conductivity probe. The 4 M NaOH solution (5 mL) was then manually delivered to the GCU. The solution needs to be strongly alkaline for ammonia to be fully released and this is accomplished by the significant amount of NaOH added. Next the MFC was activated to begin purging of the GCU; this led to both mixing of the solution and transport of the evolved NH_3 out of the GCU. As NH_3 reacted with H^+ in the drop, the conductivity decreased; this was recorded for 200 s. The rate of decrease of the conductivity (RDC) was calculated. The RDC for a blank was similarly measured. The net RDC for various NH_4^+ samples were plotted against the known concentrations. The indophenol blue method was used for comparative measurements [28]; the absorbance due to the blue product was measured at 630 nm spectrophotometrically (CE1010, www.cecilinstruments.com).

3. Result and discussion

3.1. Fraction of ammonium volatilized

It is difficult to estimate how long it will require a solution of to be a purged of a volatile dissolved gas as this depends on many factors such as bubble size, gas flow rate and the operative Henry's law constant (K_H). For gases with a high K_H, such as NH_3, quantitative purging (> 99%) requires a time too long to be practical for analysis. Measurement of residual NH_3/NH_4^+ in the GCU solution after 200 s of bubbling under the stated conditions suggested that ~15% at room temperature (28 °C) on average is removed and this provides satisfactory results under the proposed procedure.

3.2. Analytical signal profile

As high mobility H^+ (λ_{H+} 349.8 S cm^{-2} $equiv^{-1}$) is converted to much lower mobility NH_4^+ (λ_{NH4+} 73.5 S cm^{-2} $equiv^{-1}$), the conductivity will decreases. The initial signal decrease is linear with time (Fig. 2a) and the slope (RDC) was linearly related to the NH_4^+ concentration (Fig. 2b). The relationship between the RDC and the ammonium concentration in the range 5–100 μM is linear and described by an equation

$$\mathrm{RDC}\ (\mu S/\mathrm{cm\ s}) = 0.0913\left[\mathrm{NH_4^+}\ (\mu M)\right] + 0.2725, \quad r^2 = 0.9957 \qquad (1)$$

The temporal profile of the conductance also reaches a minimum at the point the free acid is completely neutralized (hereinafter called time for lowest conductivity, TLC). Following the minimum, the excess ammonia leads to the formation of NH_4^+ and OH^- and increases the conductivity again [30]. The TLC, predictably, changes with varying sample [NH_4^+] concentration as shown in Fig. 2. Regardless of the concentration TLC has a finite

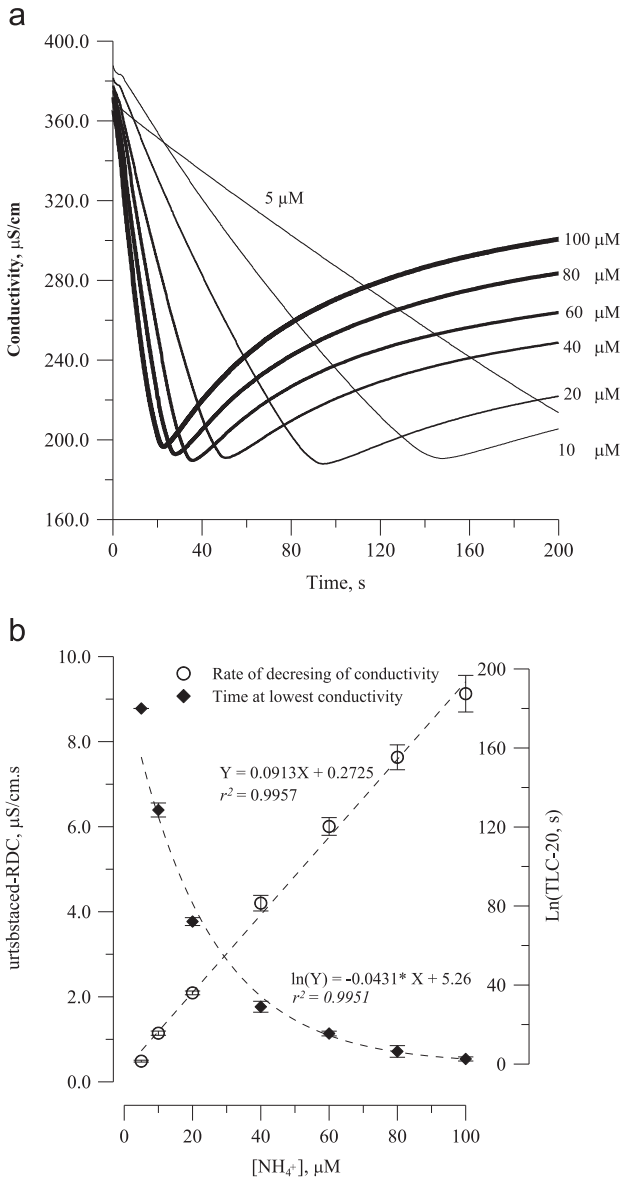


Fig. 2. (a) Typical temporal profile of conductivity signals (50 μM H_2SO_4) which decrease due to 5–100 μM NH_4^+. 4 M NaOH and N_2 flow rate 200 ml/min were employed to convert NH_4^+ /NH_3. (b) Relationship of subtracted rate of decreasing of conductivity and ln(TLC-20) vs NH_4^+ concentration.

minimum value (~20 s) as a finite time is required for the gas to be liberated, transported, absorbed, and the droplet sufficiently mixed for the conductance minimum to be registered. Once this finite value is subtracted from the apparent TLC value, the logarithm of this value also bears a relationship with the analyte concentration, at least up to 100 μM:

$$\ln(\mathrm{TLC, s} - 20) = -0.431 \times \left[NH_4^+, \mu M\right] + 5.26, r^2 = 0.9951$$

Using 50 μM H_2SO_4, the interday operations (4 day study) were observed to give slopes of calibrations (RDC vs $[NH_4^+]$) (5–100 μM NH_4^+) which differed by no more than 10%.

3.2.1. Parametric effects

Parameters that affect the performance of this analytical system include drop volume, gas flow rate, added NaOH amount, sample volume, as well as electrode alignment and liquid drop delivery and removal.

3.2.2. Drop volume

The PEEK drop head as listed provided a drop volume of 25 ± 1 μL ($n = 10$) as determined gravimetrically. Deliberately changing the volume of the liquid drop (by 3 drops, ~75 μL) required that the incline be changed to ensure drop adherence. Increasing the drop volume makes a little change of slope of calibration graph (RDC vs $[NH_4^+]$). From the base case of a single drop taken as unity, the slope decreases to 0.9 and 0.8, respectively, for 2 and 3 delivered drops. As the delivery of drops significantly less than 25 μL in volume was difficult to achieve reproducibly, this was not pursued. A single 25 μL drop also centers itself well on the present probe.

3.2.3. Gas flow rate

The N_2 purge gas not only carries the liberated NH_3 to the measurement drop absorber, but also helps the mixing of the GCU content. The gas flow rate affects the exit humidity (very slow flow rates can lead to moisture supersaturation of the exit humidity, potential condensation on exit tube walls and wall losses) and collection efficiency by the drop [35] (at very high gas flow rates, not only the collection efficiency will be poor, the drop shape is distorted and in an extreme case can be dislodged from the electrode. We studied gas flow rates in the 50–600 mL/min range; at 50 mL/min, the observed signals from samples were barely discernible from that of a blank. At the other extreme, at 600 mL/min, the drop became so skewed and unstable, no meaningful measurement was possible. Fig. 3 shows results for 100, 200 and 500 mL/min gas flow rates: although 500 mL/min provided the highest sensitivity, at high flow rates, the GCU solution was nebulized and contamination of the drop by the aerosol made for a high and poorly reproducible blank. In contrast, at 200 mL/min, the RDC of a blank was indistinguishable from that obtained after adding 1 M NaCl, indicating nebulization did not occur.

3.2.4. NaOH concentration

In principle, an NaOH concentration just over 0.2 M is sufficient to neutralize an equal volume of a sample containing 0.1 M H_2SO_4. But the pH needs to be high enough (≥ 11) where the concentration of NH_4^+ is negligible compared to that of NH_3. We investigated 0.2–6 M NaOH for this purpose and 4 M NaOH provided the highest calibration slope (RDC). This concentration is high enough to deal with highly acidic samples such as those encountered with Kjeldahl digests [5].

3.2.5. Sample volume

We studied sample volume effects only over a small range (4.80–5.20 mL), over this range, the RDC signal was not perceptibly affected. Note that it is the concentration of NH_3 in the solution in the GCU rather than its amount that will be the primary determinant of the gas concentration. The tolerance to a modest amount of volume uncertainty suggests that a 5 mL disposable syringe, rather than a volumetric pipette, should be sufficient for sample transfer.

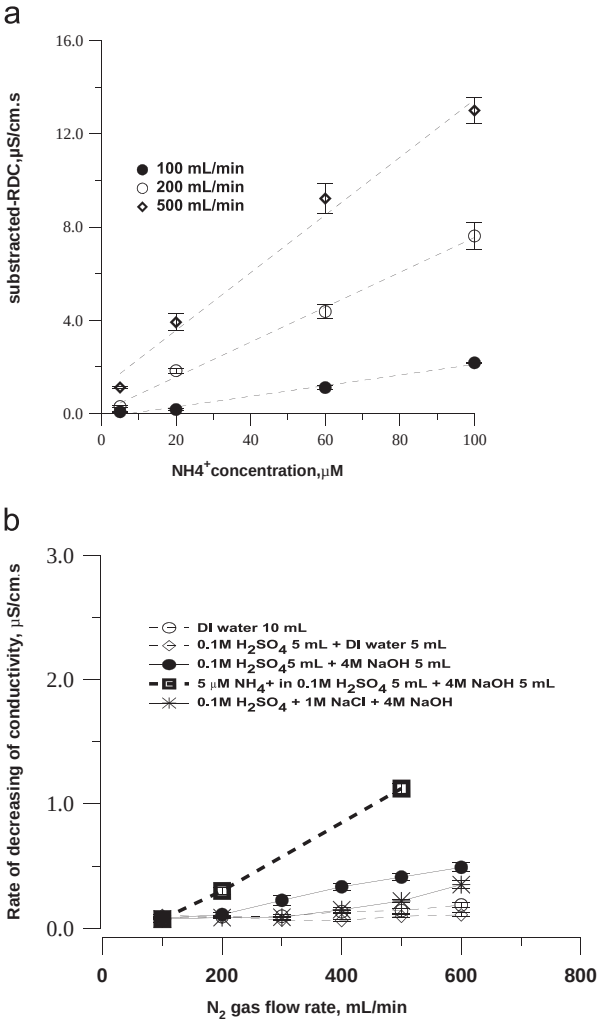


Fig. 3. Effect of N_2 gas flow rate to the subtracted rate of decreasing of conductivity of 50 μM H_2SO_4 at Pt electrode: (a) RDC vs NH_4^+ 5–100 μM with using N_2 flow rate 100, 200 and 500 mL/min, (b) RDC vs N_2 Flow rate of various sets of solution in GCU (DI water, 0.1 M H_2SO_4+DI water, 0.1 M H_2SO_4+4 M NaOH, 5 μM NH_4^+ in 0.1 M $H_2SO_4^+$ 4 M NaOH, 0.1 M H_2SO_4+1 M NaCl+4 M NaOH).

3.3. Extending the operational range to desired analyte concentrations through choice of absorber acid concentration

The absorber acid concentration can influence the linear range of calibration graph. We investigated various H_2SO_4 concentrations (5, 50, 200, 500, and 1000 μM) for this purpose. It was found that using a lower acid concentration will obviously be better to improve the lower working range of this method. Data from a sulfuric acid concentration of 5 μM was difficult to reproduce. Regarding, possibility on that a lower concentration of H_2SO_4 could be interfered by CO_2 in air as in the studies on breath NH_3 by Toda et al. that 5%v/v of CO_2 can affect measurements with a 50 μM H_2SO_4 absorber [30]. In the present application, as long as the stock absorber is protected from CO_2 absorption, the drop is really exposed primarily to a water and ammonium bearing N_2 atmosphere during measurement. We conservatively judge, for example with 50 μM H_2SO_4, the limit of detection (LOD), was ~5 μM NH_4^+ as the lowest concentration in linear calibration curve of RDC vs $[NH_4^+]$. The absorber acid concentration should be

Table 1
Determination of NH_4^+ in water by using proposed method (50 μM H_2SO_4 with Cu-electrode, 4 M NaOH, and N_2 flow rate 200 mL/min) and indophenols blue method.

Water sample	Ammonium concentration (μM)	
	Proposed method	Indophenols method
A-Pond	5.9 ± 0.2	7.0 ± 0.0
B-River (#1)	5.1 ± 0.3	5.0 ± 0.0
C-River (#2)	6.1 ± 0.2	6.0 ± 0.0
D-River (#3)	24.6 ± 0.4	24.5 ± 0.1
E-River (#4)	13.4 ± 0.3	13.9 ± 0.0
F-River (#5)	13.3 ± 0.5	13.8 ± 0.0
G-River (#6)	13.1 ± 0.5	13.0 ± 0.0
H-River (#7)	11.7 ± 0.4	12.1 ± 0.0

Triplicate results: mean ± SD.

chosen based on the anticipated analyte concentration; for a high concentration sample such as those in Kjeldahl digests [5], a high acid concentration needs to be chosen.

3.4. Choice of electrode materials

Low cost materials, such as copper wire that can easily be taken from normal electrical cable, were employed as an alternative to platinum [5].

3.5. Interferences

As demonstrated by the lack of any response to the incorporation of 1 M NaCl in the GCU solution, nonvolatile materials do not interfere. Heavy metals that cause problems in the indophenol blue method by forming precipitates are automatically separated by matrix isolation. Only possible interferents in this approach would be low molecular weight volatile amines. It is well known that the volatile amine concentrations in natural waters are far lower compared to that of NH_4^+ [10]. We nevertheless tested the response of the system to ethylamine and diethylamine; at the 5 μM level (this would be unacceptable based on odor) these changed the RDC of 50 μM NH_4^+ by ~5%.

3.6. Natural samples

Results for several natural water samples are reported in Table 1. The results agree well with that of the indolphenol blue method, $y=0.9809+0.462$, $r=0.9987$. We did observe some carry-over; for best results repeat runs were made and data from the first run for each sample was discarded. In replicate measurements ($n=3$), the typical variance was ~ < 5%.

4. Conclusion

This work aims to develop a cost-effective procedure for the determination of ammonia/ammonium ion, by employing a mobile drop system that is simple and requires no conventional pumps and injection valves. The components used are inexpensive. The mobile drop platform serves for facile manipulation of solutions.

Here, a drop defines a measured volume of solutions and moving of the drops offer enables handling of solutions without using conventional tools such as pipette, beakers, etc. It is cost effective and down scaling chemical analysis. This would be useful for some places where budget is limited. The designed GCU can handle a solid sample without extraction. Application for the determination of soil NH_3-N is in progress. Application to other analytes such as carbonate or sulfite will further be developed as an extension of some previous works [36,37].

Acknowledgement

The authors would like to thank Professor Purnendu K. Dasgupta, the University of Texas at Arlington, Arlington, Texas, USA for his help during manuscript preparation. We acknowledge the Thailand Research Fund (TRF), International Foundation for Science (W-5094-1), University and Human Resource Development in Science Project (Science Achievement Scholarship of Thailand, SAST), and the Center of Excellence for Innovation in Analytical Science and Technology (I-ANALY-S-T), Chiang Mai University.

Appendix A. Supporting information

Supplementary data associated with this article can be found in the online version at http://dx.doi.org/10.1016/j.talanta.2014.10.046.

References

[1] B. Haghighi, S. Farrokhi Kurd, Talanta 64 (2004) 688–694.
[2] W. Frenzel, Fresenius J. Anal. Chem. 336 (1990) 21–28.
[3] W. Frenzel, C. Liu, Fresenius J. Anal. Chem. 342 (1992) 276–280.
[4] H. Shen, T.J. Cardwell, R.W. Cattrall, Anal. Chim. Acta 367 (1998) 193–199.
[5] J. Junsomboon, J. Jakmunee, Anal. Chim. Acta 627 (2008) 232–238.
[6] H.L. Braz, D.T. Ito, J.A.F. Silva, C.L. Lago, J.J. Pedrotti, Electroanalysis 23 (2011) 2594–2600.
[7] R.A. Segundo, R.B.R. Mesquita, M.T.S.O.B. Ferreira, C.F.C.P. Teixeira, A.A. Bordalo, A.O.S.S. Rangel, Anal. Methods 3 (2011) 2049–2055.
[8] J. Klimundova, R. Forteza, V. Cerda, Int. J. Environ. Anal. Chem. 83 (2002) 233–246.
[9] M.I.G.S. Almeida, J.M. Estela, M.A. Segundo, V. Cerdà, Talanta 84 (2011) 1244–1252.
[10] S.M. Oliveira, T.I.M.S. Lopes, I.V. Toth, A.O.S.S. Rangel, Anal. Chim. Acta 600 (2007) 29–34.
[11] S.M. Oliveira, T.I.M.S. Lopes, I.V. Toth, A.O.S.S. Rangel, J. Environ. Monit. 11 (2009) 228–234.
[12] R.J. Watson, E.C.V. Butler, L.A. Clementson, K.M. Berry, J. Environ. Monit. 7 (2005) 37–42.
[13] M.J. Almendral-Parra, A. Alonso-Mateos, M.S.Fuentes Prieto, J. Fluorescence 20 (2010) 55–65.
[14] M.K. Sengupta, Z.A. Hossain, S.-I. Ohira, P.K. Dasgupta, P. K, Environ. Pollut. 158 (2010) 252–257.
[15] K. Toda, H. Kuwahara, S. Ohira, Environ. Sci. Technol. 45 (2011) 5622 (–562).
[16] Y. Tian, P.K. Dasgupta, S.B. Mahon, J. Ma, M. Brenner, J.H. Wang, G.R. Boss, Anal. Chim. Acta 768 (2013) 129–135.
[17] N. Choengchan, P. Wilairat, P.K. Dasgupta, S. Motomizu, D. Nacapricha, Anal. Chim. Acta 579 (2006) 33–37.
[18] P. Mornane, J. Haaka, T.J. Cardwell, R.W. Cattrall, P.K. Dasgupta, S.D. Kolev, Talanta 72 (2007) 741–746.
[19] K. Sereenonchai, P. Saetear, N. Amornthammarong, K. Uraisin, P. Wilairat a, S. Motomizu, D. Nacapricha, Anal. Chim. Acta 597 (2007) 157–162.
[20] S. Teerasong, S. Chan-Eam, K. Sereenonchai, N. Amornthammarong, N. Ratanawimarnwong, D. Nacapricha, Anal. Chim. Acta 668 (2010) 47–53.
[21] N. Ratanawimarnwong, T. Pluangklang, T. Chysiri, D. Nacapricha, Anal. Chim. Acta 796 (2013) 61–67.
[22] H. Liu, P.K. Dasgupta, Trends Anal. Chem. 15 (1996) 468–475.
[23] P.K. Dasgupta, S. Kar, Anal. Chem. 67 (1995) 3853–3860.
[24] S. Kar, P.K. Dasgupta, J. Chromatogr. 739 (1996) 379–387.
[25] S. Kar, P.K. Dasgupta, Am. Lab. 29 (1997) 17C (–17M).
[26] A. Cardoso, P.K. Dasgupta, Anal. Chem. 67 (1995) 2562–2566.
[27] S. Liu, P.K. Dasgupta, Anal. Chem. 67 (1995) 2042–2049.
[28] A. Cardoso, H. Liu, P.K. Dasgupta, Talanta 44 (1997) 1099–1106.
[29] M.R. Milani, A.A. Cardoso, Microchem. J. 74 (2003) 75–82.
[30] K. Toda, J. Li, P.K. Dasgupta, Anal. Chem. 78 (2006) 7284–7291.
[31] T. Kanyanee, W.L. Borst, J. Jakmunee, K. Grudpan, J. Li, P.K. Dasgupta, Anal. Chem. 78 (2006) 2786–2793.
[32] H. Liu, P.K. Dasgupta, Anal. Chem. 69 (1997) 1211–1216.
[33] T. Kanyanee, P. Fuekhad, K. Grudpan, Talanta 115 (2013) 258–262.
[34] Determination of ammonia in the atmosphere (indophenols method), in: J.P. Lodge Jr. (Ed.), Method of Air Sampling and Analysis, third ed.,CRC Press, USA, 1988, p. 379.
[35] T. Kanyanee, J. Jakmunee, K. Grudpan, P.K. Dasgupta, J. Am. Chem. Soc. 132 (2010) 18045–18047.
[36] M. Oshima, Y. Wei, M. Yamamoto, H. Tanaka, T. Takayanagi, S. Motomizu, Anal. Sci. 17 (2001) 1285–1290.
[37] C. Chinvongamorn, K. Pinwattana, N. Praphairaksit, T. Imato, O. Chailapakul, Sensors 8 (2008) 1846–1857.

Talanta 132 (2015) 889–893

Contents lists available at ScienceDirect

Talanta

journal homepage: www.elsevier.com/locate/talanta

Short communication

Separation of isomeric amines with ion mobility spectrometry

Jaakko Laakia [a,b,*], Tiina J. Kauppila [c], Alexey Adamov [b,c], Alexey A. Sysoev [d,e], Tapio Kotiaho [b,c]

[a] Federal University of Rio de Janeiro, Department of Chemistry, LAGOA-LADETEC, Ilha do Fundão, Rio de Janeiro, RJ 21941-909, Brazil
[b] Laboratory of Analytical Chemistry, Department of Chemistry, University of Helsinki, P.O. Box 55, FI-00014, Finland
[c] Division of Pharmaceutical Chemistry and Technology, Faculty of Pharmacy, University of Helsinki, P.O. Box 56, FI-00014, Finland
[d] National Research Nuclear University MEPhI, Kashirskoe shosse 31, 115409 Moscow, Russia
[e] Linantec Ltd., Kashirskoe shosse 31, 115409 Moscow, Russia

ARTICLE INFO

Article history:
Received 14 August 2014
Received in revised form
21 October 2014
Accepted 24 October 2014
Available online 31 October 2014

Keywords:
Ion mobility spectrometry (IMS)
Atmospheric pressure chemical ionization (APCI)
Atmospheric pressure photoionization (APPI)
Isomeric amines

ABSTRACT

Eight selected isomeric amines were ionized using atmospheric pressure chemical ionization and atmospheric pressure photoionization producing a protonated molecule $[M+H]^+$ for each amine. The mobility of these ions was measured by ion mobility spectrometry. The amine compound class was shown to have an important role in mobility separation of the amines. 2,4,6-collidine, *N*,*N*-dimethylaniline and *N*-methyl-*o*-toluidine with highest observed mobilities have a *N*-heterocyclic aromatic ring, or are tertiary or secondary amines, respectively, whereas the rest of the compounds with lower mobilities were primary amines. It is suggested that the protonated $-NH_2$ group ($-NH_3^+$) interacts more with the drift gas, and therefore the primary amines have lower mobilities. The effect of the drift gas was tested by mixing argon or helium with the nitrogen drift gas. The presence of argon shifted the mobilities towards lower values, while with helium the mobility shifted towards higher values. However, in neither case did this result in better separation of the unresolved compounds.

© 2014 Elsevier B.V. All rights reserved.

1. Introduction

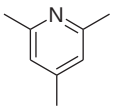
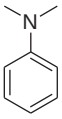
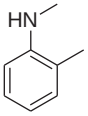
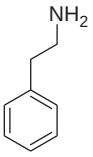
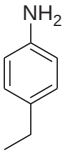
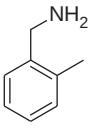
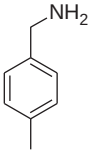
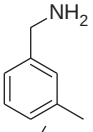
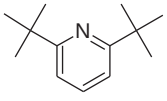
In ion mobility spectrometry (IMS) the analyte ions travel through a counter-flow drift gas in an electric field. The ions interact with the drift gas, which results in specific drift times for different ions. The analysis is commonly conducted at ambient pressure, which allows the construction of small portable IMS devices, which are widely used in field applications, for example, to detect explosives and warfare agents [1,2]. In the laboratory the IMS drift tube can be attached to a mass spectrometer (MS) [3,4]. This combination allows simultaneous access to mass and mobility data, for example to study different ionic structures of the same molecule [5,6], separating isomers of di-*tert*-butylphenol [7] or ovalbumin *N*-linked glycans [8] or distinguishing between different conformations of peptides [9].

Here, the main aim was to study the separation of isomeric amines ($M_r = 121$, $C_8H_{11}N$, Table 1) with IMS in order to understand better how compound structure affects separation. In addition, it was investigated how the addition of helium and argon to the nitrogen drift gas affects the separation of these amines. This report completes the preliminary presentation of the results [10]. Some of the amines in our study, namely 4-ethylaniline [11], *N*,*N*-dimethylaniline [12,13] and 2,4,6-collidine [13–15], have been studied before with IMS, but the whole set of isomeric amines used in this study was not included to the compounds studied. The drift gas has a significant role in separating ions, and changes in drift gas polarizability and radius will result in different interaction with analyte ions, and can thus produce different drift times [14,16–18]. For the compounds studied here, the effect of the drift gas on the mobility has been studied earlier for 2,4,6-collidine by using nitrogen, air, helium, argon, carbon dioxide and sulfur hexafluoride as drift gases [14]. The drift gas studies include also for example the use of drift gases, such as nitrogen, helium, argon, and carbon dioxide for amines other than those studied here [14,17], as well as peptides [17], and cocaine and its metabolites, amphetamines and benzodiazepines [18]. Here, our aim was to investigate how the addition of different proportions of helium and argon to the nitrogen drift gas affects the separation of the model amines.

* Corresponding author at: Federal University of Rio de Janeiro, Department of Chemistry, LAGOA-LADETEC, Avenida Athos da Silveira Ramos, 149 - Centro de Tecnologia - Bloco A, Sala 603, Cidade Universitária, Ilha do Fundão, Rio de Janeiro, RJ 21941-909, Brazil. Tel.: +55 21 3938 7130/3938 7134; fax: +55 21 2260 3967/3938 7489.
E-mail addresses: laakia@iq.ufrj.br (J. Laakia), tapio.kotiaho@helsinki.fi (T. Kotiaho).

http://dx.doi.org/10.1016/j.talanta.2014.10.052
0039-9140/© 2014 Elsevier B.V. All rights reserved.

Table 1
Summary of the reduced mobility K_0 ($cm^2\ V^{-1}\ s^{-1}$) values for the isomeric amines ($M_r = 121$) and 2,6-di-tert-butylpyridine ($M_r = 191$) measured with an IMS-FP instrument using nitrogen as the drift gas. Mobility values are not normalized with the mobility of 2,6-DtBPyr (average of eight measurements). The mobility values of amines are the average of four measurements; two within one day, which were then repeated on the second day.

Compound	Abbreviation	Structure	K_0 ($cm^2\ V^{-1}\ s^{-1}$) APCI	K_0 ($cm^2\ V^{-1}\ s^{-1}$) APPI
2,4,6-collidine[a]	2,4,6-Col		1.80	1.81
N,*N*-dimethylaniline[a]	*N*,*N*-DMA		1.75	1.75
N-methyl-*o*-toluidine[a]	*n*-M-*o*-T		1.70	1.69
2-phenethylamine[b]	PEA		1.62	1.62
4-ethylaniline[b]	4-EA		1.58	1.58
2-methylbenzylamine[c]	2-MBA		1.61	1.61
4-methylbenzylamine[c]	4-MBA		1.60	1.57
3-methylbenzylamine[c]	3-MBA		1.60	1.58
2,6-di-*tert*-butylpyridine[d]	2,6-DtBPyr		1.47	

[a] Measured from Mix A.
[b] Measured from Mix B.
[c] Measured individually.
[d] Measured from Mix B and Mix C.

2. Experimental section

2.1. Chemicals

The amines *N*-methyl-*o*-toluidine (> 95%), 2-methylbenzylamine (> 96%), 4-methylbenzylamine (> 97%), 3-methylbenzylamine and 4-ethylaniline (> 98%), 2-phenethylamine (> 99%), *N*,*N*-dimethylaniline (> 99.5%) and 2,6-di-*tert*-butylpyridine (> 97%) were purchased from Sigma-Aldrich (Steinheim, Germany) and 2,4,6-collidine (> 99%) from Merck (Darmstadt, Germany). Stock solutions (5 mM) were prepared in methanol (HPLC, Lab-scan, Dublin, Ireland) and diluted further with methanol:toluene (95:5%) (HPLC, Baker, Deventer, Holland) to give 50 and 100 μM solutions.

2.2. Instrumentation

The mobility distributions were recorded using a custom-made drift tube ion mobility spectrometer equipped by a Faraday plate detector (IMS-FP) [19] and the mass spectrometric data were recorded using an ion mobility spectrometer-mass spectrometer (IMS-MS) [3]. In the IMS-FP the length of the drift region was 13.85 cm. The instrument was operated using a Bradbury–Nielsen (B–N) type ion gate with a 200 μs gate opening time. The drift gas flow was set to 1.9–2.5 L min^{-1} and measurements were conducted at room temperature (294–297 K). Nitrogen, and mixtures of nitrogen and argon or helium were used as drift gases. The desolvation and drift fields were both set to 316 V cm^{-1}.

A custom-made program was used to operate the instrument. During the total measurement time of 25 s 500 drift time transients were summed up to achieve drift time distribution. The obtained data were processed by a ChemStation 10.02 program code (Agilent Technologies, Inc., PaloAlto, CA, USA), with custom-made macros to calculate reduced mobilities of the ions detected. The IMS-MS was operated in continuous ion flow mode (both B–N gates open) to record the mass spectra [3]. The desolvation and drift fields were set to 304 and 316 V cm^{-1}, respectively. The nitrogen drift gas flow was ~2.4 L min^{-1}. The mass spectrometer was a triple–quadrupole mass spectrometer API-300 (SCIEX Applied Biosystems, Toronto, ON, Canada) operated in positive ion mode with a declustering potential of 5 V, and a mass range of m/z 30–300. The data were collected by Analyst 1.4.1 program code (Applied Biosystems/MDS SCIEX, Concord, ON, Canada).

2.3. Gases

Nitrogen for the drift and nebulizer gases was produced from compressed air with a heatless dryer Dominic Hunter Pneudri MiDAS 4 (Parker Hannifin Ltd., Gateshead, England) and a NGLCMS20 (Labgas Instrument Co., Espoo, Finland) or N2-MISTRAL-0 (LNI Schmidlin AG, Neuheim, Switzerland) nitrogen generator. The N_2 gas was further purified using a hydrocarbon and moisture trap. The level of humidity was measured using a humidity gauge (Vaisala DMT242; Helsinki, Finland) downstream from the drift tube. The bottled gases were purchased from AGA (Espoo, Finland) with a 99.999% purity for argon and 99.996% for helium. The drift gas mixtures were produced using two EL-Flow mass flow controllers (Bronkhorst, Ruurlo, the Netherlands).

2.4. Ionization

The samples were delivered to the ionization region using a custom-made heated nebulizer [19], which was heated up to 423 K. The samples were delivered with a PHD 2000 Advanced Syringe Pump (Harvard Apparatus GmbH, Hugstetten, Germany) into a nebulizer (the injection speed was 180 μL h^{-1}), where the nitrogen gas flow at 1.6-1.8 L min^{-1} carried the sample vapor to the ionization region. Two different ionization methods were used in this study: (1) atmospheric pressure chemical ionization (APCI) was conducted using an acupuncture needle (the corona needle potential was 2.0–2.2 kV), and (2) atmospheric pressure photoionization (APPI), using a krypton discharge lamp (PKS-100, Cathodeon, Ltd., Cambridge, England) with 10 and 10.6 eV photons.

3. Results and discussion

3.1. Ionization

Most of the experiments were conducted with an IMS-FP instrument operated in positive ion APCI or APPI mode. Mass spectra measured with the IMS-MS instrument confirmed that all the amines produced protonated molecules $[M+H]^+$ with positive APCI and APPI. Furthermore, both ionization methods resulted in a reaction ion peak (RIP).

3.2. Mobilities

All the reduced mobilities for isomeric amines were recorded with IMS-FP using APCI or APPI, and are summarized in Table 1. The mobility measurements were mainly done using three different mixtures of the analytes: Mix A (2,4,6-Col, *N*,*N*-DMA, *n*-M-*o*-T and 2-MBA), Mix B (PEA, 4-EA and 2,6-DtBPyr) and Mix C (2-, 3- and 4-MBA, and 2,6-DtBPyr). The mobility order was confirmed by measuring the amines individually. As an example of the reproducibility of the measurements the reduced mobility of 2,6-DtBPyr $K_0 = 1.47$ cm^2 V^{-1} s^{-1} with the relative standard deviation of 0.3% ($n=8$, on two different days) measured using APCI is reported. 2,6-DtBPyr is nowadays a commonly used IMS standard [19–22]. However, in this study reduced mobility values were not normalized with the reduced mobility of 2,6-DtBPyr.

Due to the different experimental conditions it is difficult to compare the reduced mobility values obtained in this study to the ones previously published [11–15]. However, the reduced mobility values in Ref [13] for 2,4,6-Col (1.83 cm^2 V^{-1} s^{-1}) and N,N-DMA (1.81 cm^2 V^{-1} s^{-1}) measured at 150 °C and using air as the drift gas are close to the values reported in Table 1, showing the same mobility order, but smaller differences in mobilities. Interestingly, Karpas et al. have reported that anilines typically form two mobility peaks, one for nitrogen-protonated, and one for ring-protonated species [12,13]. Later, this has been proven by mobility separation of different forms of protonated aniline molecules formed by electrospray ionization, and interpreting the subsequently measured collision induced dissociation (CID) mass spectra of the mobility separated protonated molecules [6]. It was observed that the nitrogen-protonated ions had longer drift time than the ring-protonated ions due to stronger interaction with the drift gas. However, in our study photoionization and corona discharge ionization produced only one mobility peak for each amine meaning that only one protonation site (most likely nitrogen) was preferable.

Based on the reduced mobility values presented in Table 1 and Fig. 1, two different amine groups can be separated. The first group contains the amines 2,4,6-Col, *N*,*N*-DMA and *n*-M-*o*-T, which contain a *N*-heterocyclic aromatic ring, or a tertiary or secondary amino group, respectively. These amines have clearly faster mobilities than the second group containing primary NH_2-groups (PEA, 4-EA, and 2-, 3- and 4-MBA). From Fig. 1A and Table 1 it can be seen that the amines in the first group can be separated from each other, and they have clearly different mobility values. Fig. 1A shows also that the first group of amines can be easily separated from a second group amine 2-MBA. Reduced mobilities of the amines in the second group are very close to each other. PEA and 4-EA could be separated from each other (Fig. 1B), but the mixture of 2-, 3- and 4-MBA produced a single mobility peak (Fig. 1C).

The clear separation of isomeric amines 2,4,6-Col, *N*,*N*-DMA and *n*-M-*o*-T could be explained by the varying number of carbon containing groups attached to the nitrogen atom, or by the aromatic nitrogen being surrounded by two methyl groups in *ortho* position, i.e. the charge in the *N*-protonated molecule is shielded by the alkyl groups, resulting in decreased interaction of the protonated molecule with the drift gas, and therefore higher mobility. Because of a similar shielding effect of the charged site, some molecules, such as 2,6-DtBPyr [20,21] and tetraalkylammonium halides [23], have been found suitable as IMS instrumental standards, and their reduced mobilities have been observed to be minimally affected by e.g. impurities of the drift gas. Interestingly, PEA was separated from 4-EA, even though both compounds have $-NH_2$ groups (Fig. 1B). The reason for this might be that the protonated PEA forms a "loop" via $-NH_3^+$ interaction with the benzene ring, resulting in a more closely-packed shape. Therefore protonated PEA is likely to interact less with the drift gas than the protonated 4-EA, which cannot form a similar "loop". This is also supported by the slightly higher mobility of PEA (Table 1, Fig. 1B). Similar loop formation has been reported in an IMS study for protonated diamines and polyamines [24]. In addition, very recently it has been shown by infrared multiple-photon dissociation spectroscopy that for the protonated phenylalkylamines, $C_6H_5(CH_2)_nNH_3^+$ ($n=2$–4), the most stable ion geometry has

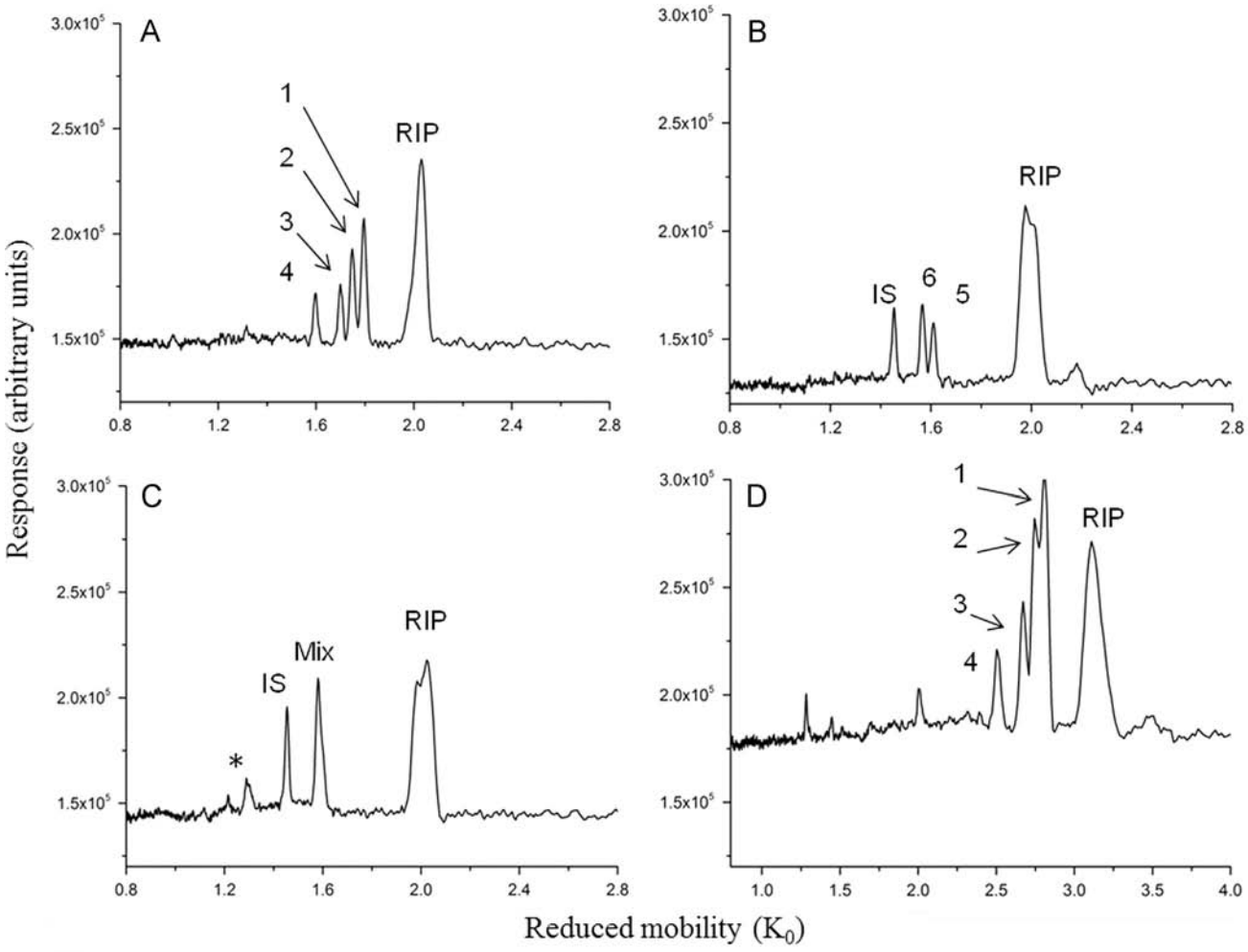


Fig. 1. Positive APCI ion mobility spectra of mixtures of isomeric amines measured with IMS-FP instrument (A and D) 1=2,4,6-Col, 2=*N*,*N*-DMA, 3=*n*-M-*o*-T and 4=2-MBA, (B) 5=PEA and 6=4-EA, and (C) Mix=2-, 3-, and 4-MBA. In Fig. (A)–(C) the drift gas was nitrogen and in Fig. (D) the drift gas mixture was 33% helium and 67% nitrogen. RIP=reaction ion peak, IS=2,6-DtBPyr and the asterisk indicates possible amine cluster ions.

interactions between the aromatic ring and the $-NH_3^+$ group causing folding of the side chain [25].

The effect of drift gas composition was studied using positive APCI–IMS–FP, sample mixture A, and a varying amount of helium or argon in the nitrogen drift gas. The addition of helium shifted all the peaks towards higher mobility (Fig. 2A), and separation of the amines was deteriorated at higher helium concentrations (Fig. 1D vs. 1A). On the contrary, the addition of argon to the nitrogen drift gas shifted all the peaks towards lower mobility (Fig. 2B), but the reduced mobility of the reaction ion peak (RIP) stayed more or less constant after the first argon addition. In addition, it was observed that peak heights of the analytes increased as the amount of helium in the drift gas increased, but with increasing amount of argon in the drift gas the peak heights were observed to decrease. These results are in good agreement with literature, where it has been reported for many compounds that reduced mobilities increase, when helium is used as the drift gas instead of nitrogen, and decrease, when argon is used as the drift gas [14,18]. Of the compounds used here, for 2,4,6-collidine clearly higher mobility in helium than in argon has been reported [14]. The observed changes in the peak height, and the effect of helium on resolution are also in good agreement with literature. It has been reported that helium provides clearly better sensitivity and argon lower, when compared to the use of nitrogen as drift gas [17]. In the same study it was hypothesized that the sensitivity changes are due to increased amount of reactions in the drift tube, since longer drift times allow more reactions, and the presence of different gases may cause differences in ionization efficiency in the electrospray process. In the same study it was also reported that shorter drift times in helium drift gas provide lower resolving power. Comparison of Fig. 1A and D confirms this observation.

4. Conclusions

The selected isomeric amines produced $[M+H]^+$ ions with APCI and APPI. Both ionization methods produced a single mobility peak for each amine. Two subgroups from the model compounds could be identified based on reduced mobility. Compounds with *N*-heterocyclic aromatic ring, tertiary or secondary amino groups (2,4,6-collidine, *N*,*N*-dimethylaniline and *N*-methyl-*o*-toluidine, respectively) had clearly higher reduced mobilities than the rest of the amines, which had a primary $-NH_2$ group (2-phenethylamine, 4-ethylaniline, and 2-,3- and 4-methylbenzylamine). 2,4,6-Col, *N*,*N*-DMA and *n*-M-*o*-T could also be separated from each other, while the primary amines had mobility values very close to each other. However, PEA could be separated from 4-EA. The extent of how much the adjacent groups are shielding the protonated nitrogen is expected to be the major explanation for the different reduced mobilities. In other words: the more protected the charge, the less the ionized analyte can interact with the drift gas, and therefore it can move faster through the drift tube.

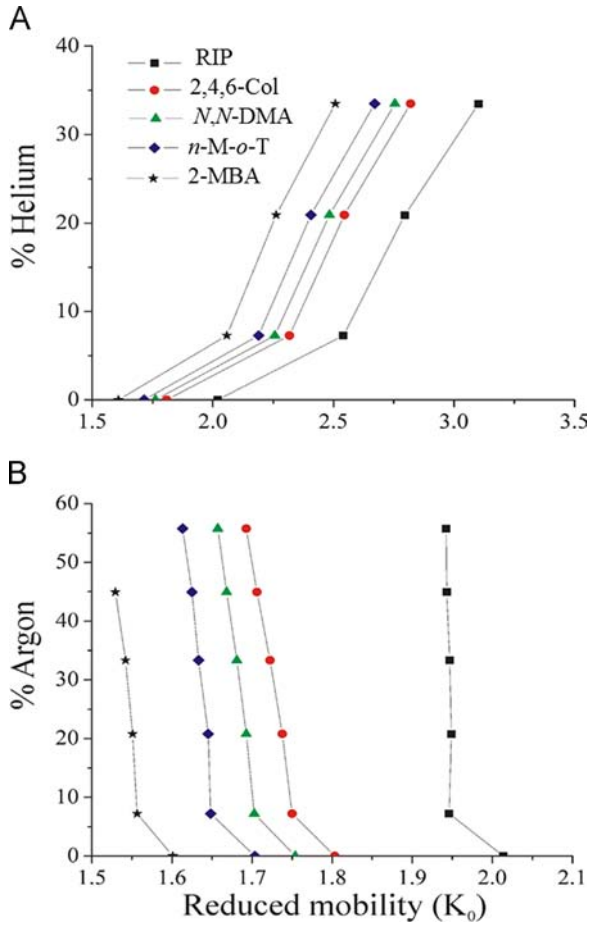


Fig. 2. Reduced mobility values of isomeric amines measured with a positive APCI–IMS–FP instrument. Helium (A) or argon (B) mixed in the nitrogen drift gas.

When argon was mixed with nitrogen drift gas all the peaks shifted towards lower reduced mobility, and a reduction in the peak height was observed, whereas the opposite behavior was observed with helium, which shifted all the peaks towards higher reduced mobility and increased peak height.

Acknowledgments

The project was supported by the Academy of Finland (Project nos.: 114132, 122018, 125758 and 255559). Docent Elina Kalenius and Jyrki Viidanoja are thanked for stimulating conversations. Prof. Herbert H. Hill, Jr. is acknowledged for a conversation regarding the structures of protonated amines.

References

[1] G.A. Eiceman, Z. Karpas, Ion Mobility Spectrometry, second ed., CRC Press Taylor & Francis, Boca Raton, 2005.
[2] G.A. Eiceman, J.A. Stone, Anal. Chem. 76 (2004) 390 A–397 A.
[3] A. Sysoev, A. Adamov, J. Viidanoja, R.A. Ketola, R. Kostiainen, T. Kotiaho, Rapid Commun. Mass Spectrom. 18 (2004) 3131–3139.
[4] A.B. Kanu, P. Dwivedi, M. Tam, L. Matz, H.H. Hill, J. Mass Spectrom. 43 (2008) 1–22.
[5] J. Laakia, A. Adamov, M. Jussila, C.S. Pedersen, A.A. Sysoev, T. Kotiaho, J. Am. Soc. Mass Spectrom. 21 (2010) 1565–1572.
[6] P.M. Lalli, B.A. Iglesias, H.E. Toma, G.F. de Sa, R.J. Daroda, J.C. Silva Filho, J.E. Szulejko, K. Araki, M.N. Eberlin, J. Mass Spectrom. 47 (2012) 712–719.
[7] J. Laakia, C.S. Pedersen, A. Adamov, J. Viidanoja, A. Sysoev, T. Kotiaho, Rapid Commun. Mass Spectrom. 23 (2009) 3069–3076.
[8] M.D. Plasencia, D. Isailovic, S.I. Merenbloom, Y. Mechref, D.E. Clemmer, J. Am. Soc. Mass Spectrom. 19 (2008) 1706–1715.
[9] A.E. Counterman, D.E. Clemmer, Anal. Chem. 74 (2002) 1946–1951.
[10] J. Laakia, A. Adamov, A. Sysoev, T. Kotiaho, Separation of isomeric amines with ion mobility spectrometry, in: Proceedings of the 19th Annual Conference on Ion Mobility Spectrometry (ISIMS 2010), Albuquerque, USA, 2010.
[11] H. Borsdorf, K. Neitsch, G.A. Eiceman, J.A. Stone, Talanta 78 (2009) 1464–1475.
[12] Z. Karpas, Z. Berant, R. Stimac, Struct. Chem. 1 (1990) 201–204.
[13] Z. Karpas, Anal. Chem. 61 (1989) 684–689.
[14] Z. Karpas, Z. Berant, J. Phys. Chem. 93 (1989) 3021–3025.
[15] F.W. Karasek, S.H. Kim, S. Rokushika, Anal. Chem. 50 (1978) 2013–2016.
[16] A.B. Kanu, H.H. Hill Jr., Talanta 73 (2007) 692–699.
[17] G.R. Asbury, H.H. Hill, Anal. Chem. 72 (2000) 580–584.
[18] L.M. Matz, H.H. Hill Jr, L.W. Beegle, I. Kanik, J. Am. Soc. Mass Spectrom. 13 (2002) 300–307.
[19] A. Adamov, T. Mauriala, V. Teplov, J. Laakia, C.S. Pedersen, T. Kotiaho, A.A. Sysoev, Int. J. Mass Spectrom. 298 (2010) 24–29.
[20] G.A. Eiceman, E.G. Nazarov, J.A. Stone, Anal. Chim. Acta 493 (2003) 185–194.
[21] R. Fernandez-Maestre, C.S. Harden, R.G. Ewing, C.L. Crawford, H.H. Hill, Analyst 135 (2010) 1433–1442.
[22] A.K. Viitanen, T. Mauriala, T. Mattila, A. Adamov, C.S. Pedersen, J.M. Mäkelä, M. Marjamäki, A. Sysoev, J. Keskinen, T. Kotiaho, Talanta 76 (2008) 1218–1223.
[23] J. Viidanoja, A. Sysoev, A. Adamov, T. Kotiaho, Rapid Commun. Mass Spectrom. 19 (2005) 3051–3055.
[24] Z. Karpas, S.E. Bell, Y.F. Wang, M. Walsh, G.A. Eiceman, Struct. Chem. 5 (1994) 135–140.
[25] B. Chiavarino, M.E. Crestoni, M. Schütz, A. Bouchet, S. Piccirillo, V. Steinmetz, O. Dopfer, S. Fornarini, J. Phys. Chem. A 118 (2014) 7130–7138.

Talanta 132 (2015) 894–901

Contents lists available at ScienceDirect

Talanta

journal homepage: www.elsevier.com/locate/talanta

A novel method for the study of molecular interaction by using microscale thermophoresis

Yexuan Mao [a], Lanlan Yu [a,*], Ran Yang [a], Ling-bo Qu [a,b,**], Perter de B. Harrington [c]

[a] College of Chemistry and Molecular Engineering, Zhengzhou University, Kexue Road, Zhengzhou 450001, PR China
[b] School of Chemistry & Chemical Engineering, Henan University of Technology, Zhengzhou 450001, PR China
[c] Center for Intelligent Chemical Instrumentation, Department of Chemistry and Biochemistry, Clippinger Laboratories, OHIO University, Athens, OH 45701-2979, USA

ARTICLE INFO

Article history:
Received 7 May 2014
Received in revised form
21 September 2014
Accepted 28 September 2014
Available online 31 October 2014

Keywords:
Microscale thermophoresis
Molecular interaction
Bovine serum albumin
Fluorescein isothiocyanate
Competitive binding study

ABSTRACT

The fundamental studies for the binding events of protein and its partner are crucial in drug development. In this study, a novel technology named microscale thermophoresis (MST) was applied in the investigation of molecular interaction between an organic dye fluorescein isothiocyanate (FITC) and bovine serum albumin (BSA), and the results were compared with those obtained from conventional fluorescence spectroscopy. The MST data demonstrated that with a short interaction time, FITC showed a high binding affinity for BSA by weak interaction instead of labeling the protein. By using competitive strategies in which warfarin and ibuprofen acted as the site markers of BSA, FITC was proven to mainly bind to the hydrophobic pocket of site II of BSA compared to site I of BSA. Except for the binding affinity, MST also provided additional information with respect to the aggregation of BSA and the binding of FITC to BSA aggregates, which is unobtainable by fluorescence spectroscopy. This work proves that MST as a new approach is powerful and reliable for investigation of protein–small molecule interaction.

© 2014 Elsevier B.V. All rights reserved.

1. Introduction

In vivo, cellular signaling involves a series of recognition events, leading from an external stimulus to a cellular response. Each recognition event is the binding between a protein and a partner that ranges from a small-molecule ligand to a macromolecular compound, which is the center of biological and biochemical processes in living organisms [1–3]. Notably, the interactions between biomolecules such as protein-protein and protein–small molecule with a wide range of affinities, have generated great interests for fundamental investigations in vivo and the development of targets for drugs [4–6]. Moreover investigation on these recognition events helps elucidate the structural nature of bioaffinity of drugs and their binding sites. Equilibrium binding experiments are extensively applied in the investigation of binding and competitive binding events in biological systems [7]. Recently, competitive binding behaviors have aroused more concerns to investigate the interactions between proteins and their ligands.

Up to present, a variety of powerful tools have been developed to study biomolecular interactions, such as absorption spectroscopy, circulardichroism [8], fluorescence spectroscopy [9], isothermal titration calorimetry (ITC) [10,11], fluorescence polarization (FP) [12,13], surface plasmon resonance (SPR) [14,15], dynamic light scattering (DLS) [16] and so on. These approaches are useful and convenient for investigating biomolecular interaction, but also have some disadvantages. For instance, fluorescence quenching or fluorescence correlation spectroscopy can be applied to analyze equilibrium constants of the interactions. However, these methods are only suited for a few interactions, as they crucially rely on molecular size and size-change upon binding parameters, the relative position of fluorophores to each other [17], and consumption larger quantities of sample or require extensive data analysis [18].

Although ITC is the most common nonfluorescent method that can monitor and record a biological binding process by microcalorimetry, obtaining the complete thermodynamic data requires long acquisition times and a relatively large amount of sample to obtain an adequately heat signal [19,20]. FP is a fully automated high-throughput analysis, but the limited lifetimes of the fluorescent dyes and the molecular weight change on binding hinder its applicability and sensitivity.

Although SPR is based on the changes of the physical optics of bound molecules and has relatively high sensitivity, it is not applicable in free solution because it relies on immobilizing one of the binding partners onto a thin noble metal film. Nonspecific binding of sample components onto the metal film may also interfere with the measurement. DLS is a label-free analytical

* Corresponding author. Tel.: +86 37167756886; fax: +86 37167756886.
** Corresponding author at: The College of Chemistry and Molecular Engineering, Zhengzhou University, Kexue Road, Zhengzhou 450001, PR China. Tel: +86 13525561266.
E-mail addresses: yulanlan@zzu.edu.cn (L. Yu), qulingbo@zzu.edu.cn (L.-b. Qu).

http://dx.doi.org/10.1016/j.talanta.2014.09.038
0039-9140/© 2014 Elsevier B.V. All rights reserved.

technology, using the relationship of time-dependent fluctuations of light scattered by molecules in solution, applied in free solution binding investigations. However, this approach requires an obvious difference in the dynamic radius (r_H) of the unbound partners relative to the complex. Considering r_H scales with the cube root of the molecular volume, the sensitivity of large particles is higher than that of smaller particles [21,22].

Recently, a new method microscale thermophoresis (MST) technology has emerged, monitoring the directed movement of fluorescently labeled molecules through temperature gradients. Distinguished from the other binding measurements, MST is a highly sensitive probe for many kinds of binding-induced interactions such as molecular size, charge, hydration shell or conformation [37]. Typically, the size, charge, and hydration entropy obtained by the thermophoresis of the fluorescently labeled molecules do not differ from those obtained from the unlabeled complexes. Furthemore, MST possesses several advantages including easy implementation, faster speeds (about 1 min), and lower sample requirements (e.g., microliter volumes). In addition, a wide variety of buffer solutions can be used and there is no practical limitation on molecular size or weight for the binding partners.

In this study, the interaction between fluorescein isothiocyanate (FITC) and albumin bovine serum (BSA) was investigated by using MST, which provides a new method for biomolecular interaction and proves the feasibility of MST for biomolecular interaction studies. FITC is currently the most widely used fluorescein dye for protein labeling, imaging and so forth. In the biological pharmacology field, serum albumin (SA) protein is the most abundant soluble protein found in blood plasma [23], which can combine with many kinds of endogenous or exogenous compounds such as amino acids, fatty acids, drugs, and many other small molecules [24,25]. BSA is an SA protein often used in biological investigations because it has a 76% sequence homology with human serum albumin.

The binding regions of BSA have been previously indentified by crystallography [26,27], which contain three structurally similar domains (I, II, and III) with each domain including two sub-domains. Sudlow's sites I and II are known as the common high affinity regions. The two tryptophan residues Trp-134 and Try-212 of BSA are located in sites I and II, respectively [28,29]. An anticoagulant drug warfarin and an anti-inflammatory drug ibuprofen have been demonstrated as stereotypical marker ligands for sites I and II, respectively [30]. Therefore by using binding studies, it is possible to identify the location of BSA that binds FITC. In this study, MST is demonstrated as a new approach for biomolecular interaction and the results are compared with those from conventional fluorescence spectroscopy.

2. Experimental

2.1. Apparatus

Fluorescence spectra were recorded on 970CRT spectrofluorometer (Shanghai, China). The width of the excitation and emission slits were 5.0 nm and 10.0 nm, respectively. The sensitivity was 3.

The binding affinity study was investigated on the microscale thermophoresis instrument (NanoTemper Tchnologies GmbH, Munich, Germany). The value of K_d was calculated by NT ANALYSIS SOFTWARE provided by NanoTemper Technologies GmbH. All the pH values were measured with a PHS-3C precision pH meter (Leici Devices Factory of Shanghai, China), which was calibrated with standard buffer solutions each day.

2.2. Materials and reagents

BSA was purchased from Roche Pharmaceuticals, Ltd. (Shanghai). Warfarin and ibuprofen were purchased from the National Institute for the Control of Pharmaceutical and Logical Products (China). FITC was purchased from Aladdin Reagent (Shanghai). Phosphate buffer solution (PBS) was prepared at a pH of 7.4 and a concentration of 10 mmol L^{-1} and was used in all experiments. All chemicals and reagents were of analytical grade and used without further purification.

2.3. Labeling procedure

BSA was dissolved in PBS (pH 7.4, 0.01 mol L^{-1}) with a concentration of 20 mg mL^{-1}, and FITC was dissolved in dimethyl sulfoxide (DMSO) with a concentration of 1 mg mL^{-1}. BSA was titrated by FITC slowly with a final mass ratio of 1:0.15 (BSA: FITC). The mixture of BSA and FITC was incubated at 277 K for 8 h in darkness. Subsequently, 30 μL of NH_4Cl (5.0 mol L^{-1}) was added to the mixture with a final concentration of 50 mmol L^{-1} to quench the reaction. Unreacted FITC and the FITC-labeled BSA were separated on a G-50 Sephadex column with 0.01 mol L^{-1} PBS eluent. Finally, the concentration of FITC-labeled BSA was determined as 0.9 μmol L^{-1} with a UV–vis spectrophotometer.

2.4. Theoretical background of MST

MST is a method based on micro-thermal effect of mobility. The directional movements of molecules on a microscopic scale are highly sensitive to many kinds of binding-induced interaction such as molecular size, charge, hydration shell or conformation (The details were reported by Seidel et al. [31]). When the liquid is heated locally, the molecules begin to move along the temperature gradient from high temperature to low temperature. As the movement reaches an equilibrium state, the spatial concentration distribution of the liquid can be expressed by the equation:

$$\frac{c_{hot}}{c_{cold}} = \exp[-S_T(T-T_0)] = \exp(-S_T\Delta T) \approx 1 - S_T\Delta T \quad (1)$$

for which c_{hot} is molecular concentration in the hot area; c_{cold} is molecular concentration in the cold area; S_T is the Soret coefficient; T_0 is the initial temperature; T is the elevated temperature. Although the theory of thermophoresis is nascent, most theories consider that various parameters may influence S_T, such as size, charge, hydration layer and solvation entropy. The Soret coefficient may be expressed by the following equation:

$$S_T = \frac{A}{kT}\left(-\Delta s_{hyd}(T) + \frac{\beta\sigma_{eff}^2}{4\varepsilon\varepsilon_0 T} \times \lambda_{DH}\right) \quad (2)$$

for which A represents the molecule's surface area, σ_{eff} is the effective charge, Δs_{hyd} is the hydration entropy of the molecule-solution interface, λ_{DH} is the Debye-Hüeckel screening length, ε is the dielectric constant, and β is temperature derivative of ε.

Fig. 1 is a schematic of the MST instrument for signal acquisition for a single capillary that contains the fluorescent species and its binding partner. An infrared (IR) laser is coupled into the light path of fluorescence excitation and emission, is focused on the sample to the exact spot where fluorescence emission is detected. The fluorescence within the capillary is excited and measured through the same optical elements. Initially, the infrared laser is off and there is no temperature gradient in the solution. Therefore the fluorescent species is homogenously distributed and a steady fluorescence signal is acquired. Once the infrared (IR) laser is switched on, the focused spot is heated immediately. The increase of temperature leads to a strong decrease in fluorescence due to the sensitivity of fluorescence quantum yield with respect to temperature, which creates an observable temperature jump. Due to thermophoretic molecular motion, the fluorescence decreases slowly until reaching a steady state when the thermophoretic motion is counterbalanced by the mass diffusion. Because of the short timescale of the temperature

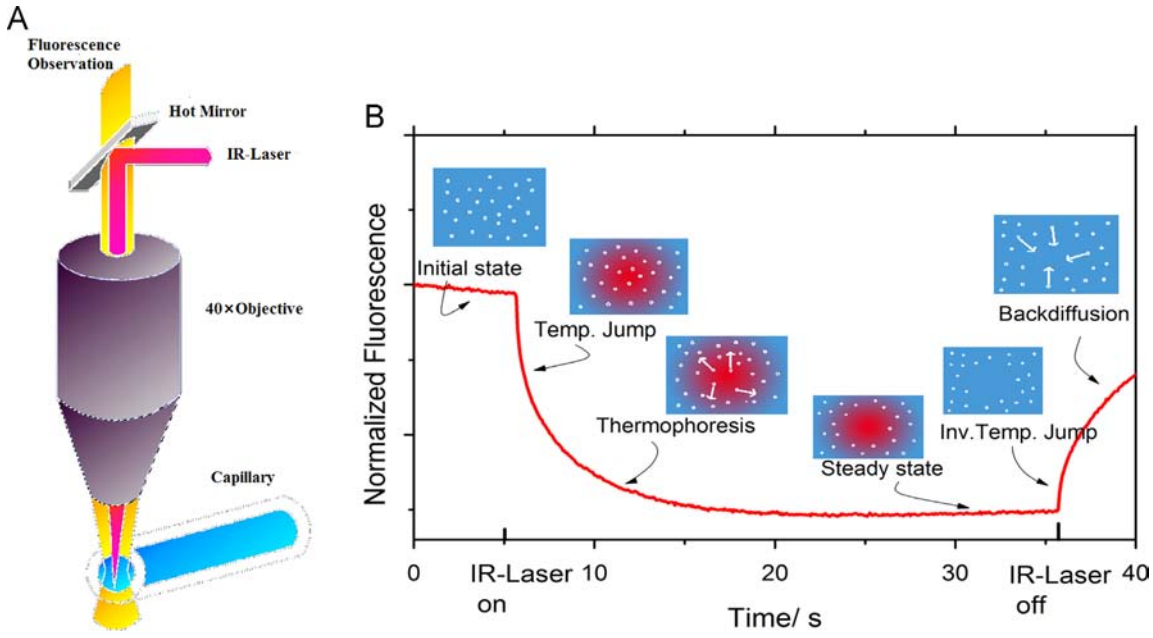


Fig. 1. A displays the experimental instrument of MST. The measurements are investigated in capillary. An infrared laser coupled into the light path of fluorescence excitation and emission is focused on the sample to exact spot where fluorescence intensity is measured. B is a typical MST signal for a given capillary. [36].

jump process (about 100 ms), it can be consequently distinguished from the following slower thermophoretic process. When the IR-laser is switched off, the fluorescence increases suddenly because of the decrease in local temperature, which results in a reversed temperature jump. After a short time of fluorescence recovery, the fluorescence increases gradually until achieving a steady state due to back-diffusion.

The dissociation constant K_d quantifies the binding affinity by analyzing the change in F_{norm}, which is the relative fluorescence (normalized fluorescence). F_{norm} is used for quantifying the concentration of fluorescent molecules and is defined by the following equation, including both the temperature jump process and the thermophoresis process.

$$F_{norm} = \frac{F_{hot}}{F_{cold}} = 1 + \left(\frac{\delta F}{\delta T} - S_T\right)\Delta T = \frac{c_{hot}}{c_{cold}} + \frac{\delta F}{\delta T}\Delta T \tag{3}$$

In the above equation, F_{hot} is the fluorescence in the hot area and the F_{cold} is the fluorescence in the cold area, both of which are the results from all fluorescent species in solution. When a fluorescent species binds to a non-fluorescent ligand and forms a fluorescent complex, the thermonphoretic signals of the bound species and unbound species are linearly superposed and described by the following equation

$$F_{norm} = (1-x)F_{norm,unbound} + xF_{norm,bound} \tag{4}$$

for which the F_{norm} is the total normalized fluorescence, $F_{\mathrm{norm,\ unbound}}$ is the normalized fluorescence of the unbound fluorescent species, $F_{\mathrm{norm,\ bound}}$ is the normalized fluorescence of the bound fluorescent complex and x is the fraction of the bound fluorescent species. By titrating a fluorescent species with a fixed concentration of a non-fluorescent ligand with varying concentrations and recording, F_{norm} is recorded versus different concentrations of the non-fluorescent ligand and the data are fitted according to different mathematical models.

Applying the law of mass action, the binding behavior of molecules can be described by a variety of models. The simplest binding model is the partner bound with its ligand at ratio of 1:1, which can be expressed as

$$AL \Leftrightarrow A + L \tag{5}$$

for which A is the binding partner; L is the titrating ligand; AL is the bound complex of A and L. Subsequently, the dissociation constant K_d can be defined as

$$K_d = \frac{[A][L]}{[AL]} \tag{6}$$

for which [A] is the equilibrium concentration of the free partner; [L] is the concentration of the free titrating ligand; [AL] is the concentration of bound complex of A and L. As the free equilibrium concentrations of A and L are not easily known, the analytical concentrations of A and L are used instead, which are expressed as:

$$c_A = [A] + [AL] \tag{7}$$

$$c_L = [L] + [AL] \tag{8}$$

for which c_A is the analytical concentration of A and c_L is the analytical concentration of L. Combining the above Eqs. (6)–(8), the dissociation constant K_d may be expressed as

$$K_d = \frac{(c_A - [AL])(c_L - [AL])}{[AL]} \tag{9}$$

Typically, the binding behavior of A and L is investigated by titration in microscale thermophoretic experiments. A is a fluorescent substance with a fixed concentration and L is the titrating ligand which is increased in concentration. Hence, the fraction bound of A can be described as:

$$x = \frac{[AL]}{c_A} = \frac{c_A + c_L + K_d - \sqrt{(c_A + c_L + K_d)^2 - 4c_A c_L}}{2c_A} \tag{10}$$

Combining the Eqs. (4) and (10), the value of K_d can be calculated by NT ANALYSIS SOFTWARE provided by NanoTemper Tchnologies GmbH.

2.5. MST experiments

The concentration of FITC stock solution was 0.4 μmol L^{-1} prepared in PBS (0.01 mol L^{-1}, pH of 7.4) and FITC also acted as a means of monitoring thermophoretic movement due to its fluorescence. A serial dilution of BSA (0.02 μmol L^{-1} to 2.0 mmol L^{-1}) in the same buffer (PBS pH 7.4) was prepared and mixed with the

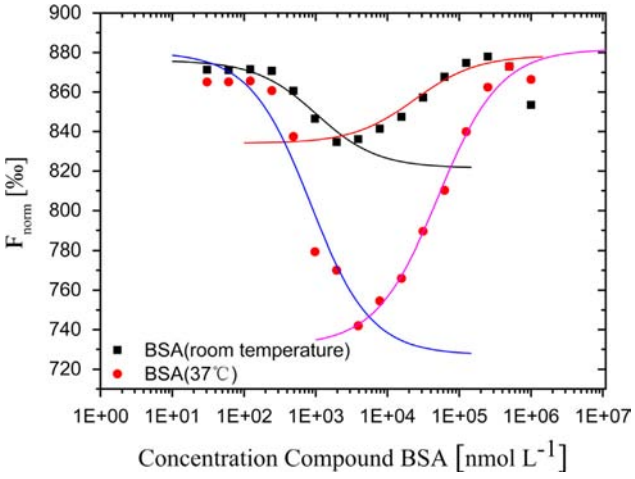


Fig. 2. The binding curves of FITC with BSA obtained from MST. FITC was titrated by BSA at room temperature (black dots) and 37 °C (red dots). The signal indicated the binding behavior between BSA and FITC is a biphasic event. The FITC concentration was kept constant at 0.2 μmol L^{-1}. The BSA concentration was ranging from 1.0 mmol L^{-1}. (For interpretation of the references to color in this figure legend, the reader is referred to the web version of this article.)

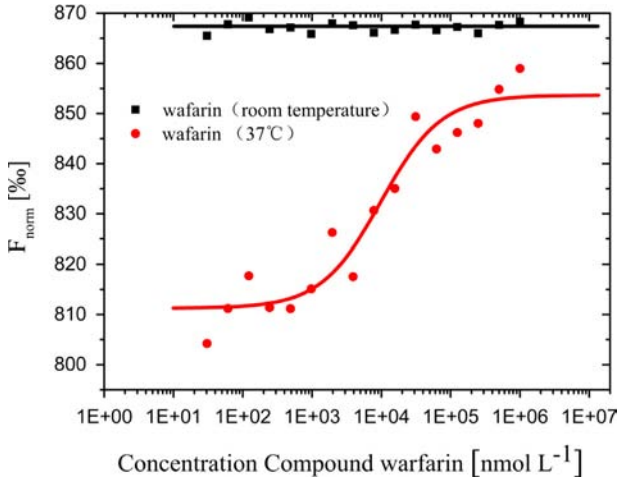


Fig. 3. Competitive experiments by MST. The binding of warfarin to a constant amount of FITC-BSA was quantified at room temperature (black dots) and 37 °C (red dots). Because of the binding in a competitive experiment with two ligands present, the fitting curves are just a guide to the eyes. The amplitude of F_{norm} signal indicates the degree of competition. The final concentration of FITC and BSA were fixed as 0.2 μmol L^{-1} and 0.6 μmol L^{-1}, respectively, and warfarin with varying concentrations was added. (For interpretation of the references to color in this figure legend, the reader is referred to the web version of this article.)

above FITC stock solution with the volume ratio of 1:1. In the first competitive binding study, the concentrations of FITC and BSA were fixed as 0.4 μmol L^{-1} and 1.2 μmol L^{-1}, respectively. After FITC was fully mixed with BSA (regarded as FITC-BSA), a serial dilution of warfarin (or ibuprofen) was added starting at 1 mmol L^{-1}. In the second competitive binding study, the BSA was pre-saturated with warfarin (or ibuprofen), and then the FITC with a fixed concentration of 0.4 μmol L^{-1} was mixed with a series of warfarin (or ibuprofen) saturated BSA. For the BSA aggregation investigation, the FITC labeled-BSA at the fixed concentration of 0.9 μmol L^{-1} were mixed with a series of unlabeled BSA at varying concentrations. All the solutions were filled in the standard glass capillaries after the sample mixing and immediately measured by MST. Data analyses and curve fitting were carried out using the Nanotemper Analysis software. All the experimental parameters used by the MST instrument were fixed with a LED power of 20% and a laser power of 80%.

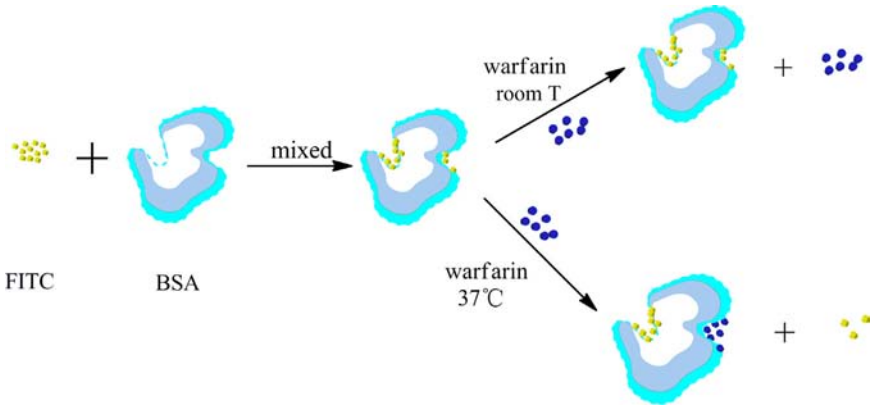
2.6. Fluorescence spectroscopy experiments

In fluorescence measurements, BSA was introduced in an amount such that its concentration was always constant at 0.02 mmol L^{-1} for each sample. FITC solution was pipetted into these samples so as to obtain a series of quenching curves from 0–0.14 mmol L^{-1}, yielding 12 samples. The second series of solutions with the mixture of BSA and warfarin or ibuprofen (their concentration ratio was fixed as 1:1) was prepared as above and FITC was added to give different concentrations that ranged from 0–0.036 mmol L^{-1}, yielding 8 samples for the mixture of BSA and warfarin. The third series FITC was added to yield a range of concentrations from 0–0.028 mmol L^{-1} and 7 samples for the mixture of BSA and ibuprofen. All of these solutions were scanned on the fluorophotometer in the range of 300–450 nm with the excitation wavelength of 280 nm at 298 K.

3. Results and discussion

3.1. Interaction between FITC and BSA by MST

The interaction between FITC and BSA was investigated at room temperature and 37 °C with MST. During the experiment, the final FITC concentration was fixed at 0.2 μmol L^{-1}. By titrating FITC with an increasing concentration of BSA, the binding curves were obtained, which are given in Fig. 2. At the initial three points, due to the low concentration of BSA compared to FITC, only a small amount of FITC was bound to BSA, which resulted that the F_{norm}, an indicator of thermophoretic property of binding partners, was



Scheme 1. Depiction of the competitive interaction between FITC-BSA and warfarin at room T or 37 °C.

dominated by free FITC with its value about 860–870 units. As the BSA concentration increased, the F_{norm} decreased first, indicating a binding process between FITC and BSA, and then recovered to almost the same level at both room temperature and 37 °C, which suggests a biphasic binding pattern. At room temperature, FITC had a higher binding affinity for BSA with a K_d of 0.963 μmol L^{-1} (black) and a lower binding affinity with K_d of 23.8 μmol L^{-1} (red). At 37 °C, similar results were obtained with K_d of 0.783 μmol L^{-1} (blue) and 50.1 μmol L^{-1} (pink) for high and low binding affinities, respectively.

3.2. Competitive interaction study by MST

Sudlow's sites I and II are high affinity regions of BSA for a variety of molecules, such as dyes, drugs and small molecules. To locate the binding region of BSA upon binding with FITC, warfarin and ibuprofen were used as marker ligands for site I and II, respectively. A competitive strategy was applied to locate the FITC when binding to BSA. The final concentrations of FITC and BSA were fixed at 0.2 μmol L^{-1} and 0.6 μmol L^{-1}, respectively. After FITC was fully mixed with BSA (regarded as FITC-BSA), a serial dilution of warfarin was added starting at 1 mmol L^{-1}. These samples were measured by MST at both room temperature and 37 °C, and the results are given in Fig. 3. At room temperature, the value of F_{norm} was constant at 860 units with the increasing concentration of warfarin (0.01 μmol L^{-1} to 1 mmol L^{-1}), which value was consistent with that of FITC-BSA's at the same concentration in Fig. 2. This result implies that warfarin is not the competitor for the binding site between FITC and BSA, and FITC does not locate at site I. However, at 37 °C, the F_{norm} value changed from about 800 units to 860 with the increasing concentration of warfarin. In Fig. 2, when the concentration of FITC and BSA were 0.2 μmol L^{-1} and 0.6 μmol L^{-1}, respectively, the F_{norm} value was 800 units at 37 °C. Therefore the F_{norm} recovery from 800 to 860 units in Fig. 3 was probably due to the replacement of FITC with warfarin and the release of free FITC. This result suggests that FITC might interact with BSA at site I to some extent at elevated temperatures. At the higher temperatures site I may open up to permit some FITC binding. This interaction process is depicted in Scheme 1.

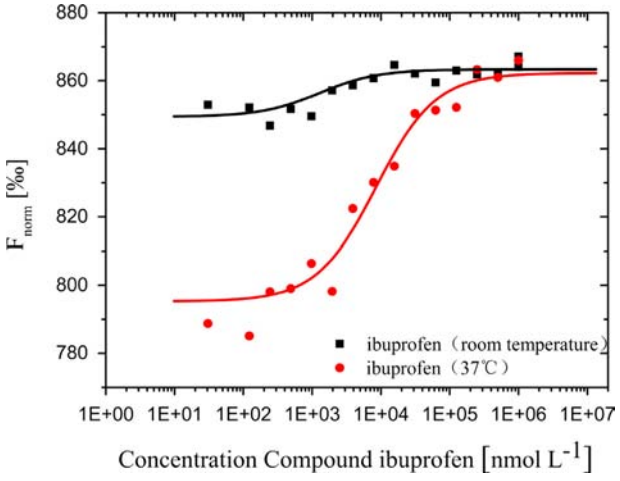
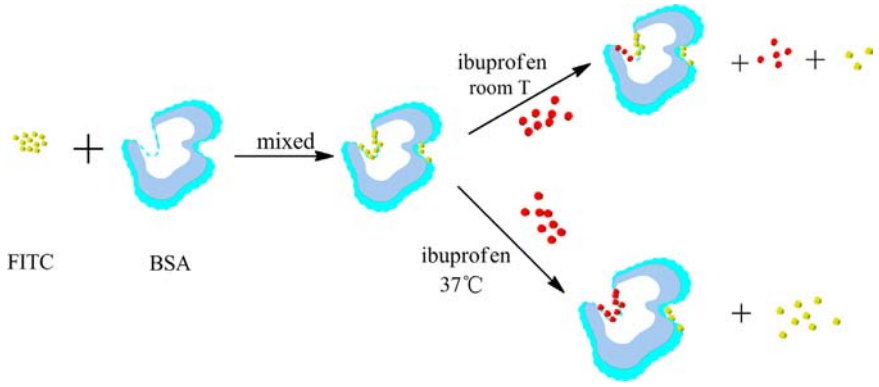


Fig. 4. Competitive experiments by MST. The binding of ibuprofen to a constant amount of FITC-BSA was quantified at room temperature (black dots) and 37 °C (red dots). Due to the presence of two ligands, the fitting curves are just a guide to the eyes. The final concentration of FITC and BSA were fixed as 0.2 μmol L^{-1} and 0.6 μmol L^{-1}, respectively, and ibuprofen with varying concentrations was added. (For interpretation of the references to color in this figure legend, the reader is referred to the web version of this article.)

Subsequently, ibuprofen which has high affinity for the site II of BSA was chosen as the competitor and added to the mixture of FITC-BSA. The final concentration of FITC and BSA were still fixed as 0.2 μmol L^{-1} and 0.6 μmol L^{-1}, respectively, and mixed thoroughly. With the increasing addition of ibuprofen (0.01 μmol L^{-1} to 1.0 mmol L^{-1}), the F_{norm} signal increased slightly from about 840 to 860 units at room temperature, which is indicative of substitution of ibuprofen for FITC (Fig. 4). The released free FITC led to a recovery of F_{norm} to 860 units. When the temperature was increased to 37 °C, similar results were obtained. The F_{norm} value started at 800 units, which is exactly the signal level for FITC-BSA thermophoresis, and finished at with about 860 units, in accordance with the signal level of free FITC. From these results, it is deduced that ibuprofen has partly displaced FITC by binding at site II. The competitive process is described in Scheme 2. Because the replacement of FITC by ibuprofen happened at both room temperature and 37 °C, FITC is most likely more inclined to bind at site II of BSA.

FITC is a frequently used organic dye to label proteins by forming covalent bonds with lysine or arginine in most common labeling method [32]. Usually in the most protocols, the labeling process requires several hours, but in this study, FITC only mixed with BSA for several minutes. Whether this short incubation time will lead to labeling process is unknown. Therefore it is necessary to distinguish whether the interaction between FITC and BSA in this study is a labeling process or weak interaction due to electrostatic interaction, hydrophobic interaction, etc. Another competitive strategy was used to make a distinction between these two possible processes. Because warfarin and ibuprofen specifically bind to sites I and II of BSA, respectively, the BSA which was saturated beforehand by warfarin or ibuprofen was subjected to the FITC-BSA interaction study. When BSA is saturated with warfarin or ibuprofen, either site I or site II are completely



Scheme 2. Depiction of the competitive interaction between FITC-BSA and ibuprofen at room T or 37 °C.

occupied, which might lead to a weaker or unchanged interactions with FITC depending on the different processes of binding.

A fluorescence quenching experiment was performed to determine the minimum amount of warfarin and ibuprofen at which BSA is saturated by achieving the maximum fluorescence quenching. According to the results, the fluorescence quenching effect was maximized when the concentrations of warfarin and ibuprofen were 50 and 300 times as much as that of BSA, respectively.

Subsequently, the final FITC concentration was fixed at 0.2 μmol L^{-1} and mixed with a serial dilution of the mixture of BSA and warfarin or ibuprofen (the concentration ratio was fixed as 1:50 for BSA and warfarin, and the ratio was fixed as 1:300 for BSA and ibuprofen) starting at BSA concentration of 8.0 μmol L^{-1} at room temperature (Fig. 5). After data fitting, the K_d of FITC binding to warfarin-saturated BSA was 1.24 μmol L^{-1} and the K_d of FITC binding to ibuprofen-saturated BSA could not be calculated accurately because the signals never reached a stable value. The difference between these two curves excluded the possibility of the FITC labeling process, because if FITC had formed covalent interactions with BSA, the dissociation constant would remain constant regardless of the presence of warfarin or ibuprofen. However, the K_d of FITC binding to ibuprofen-saturated BSA could not be obtained and differed from the K_d of FITC binding to BSA, and thus FITC interacts with BSA by a weak interaction instead of a labeling process. The K_d of FITC binding to warfarin-saturated BSA is approximately equal to that of FITC binding to free BSA, which demonstrates that thermophoretic movement is not affected by excess amount of warfarin. This result indicates that FITC is more inclined to have a higher affinity for site II of BSA, which is displayed in Scheme 3. When FITC added to the ibuprofen-saturated BSA, because site II was occupied by ibuprofen, a lower binding affinity was achieved, confirming that FITC binds biphasically, FITC tends to interact with site II of BSA to a large extent, and with site I to a lesser degree.

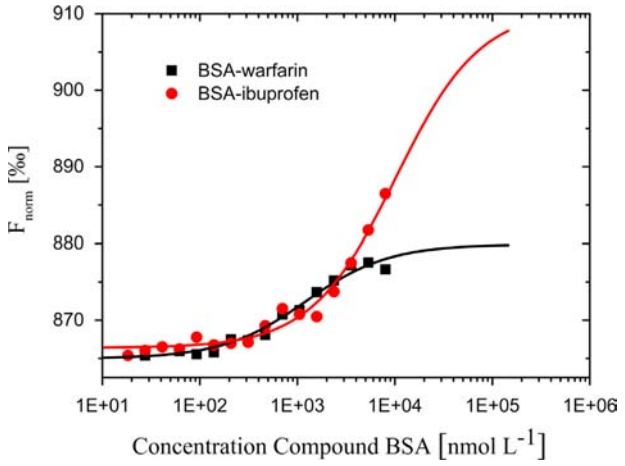


Fig. 5. The binding curves of FITC with warfarin-saturated BSA or ibuprofen-saturated BSA. The signal of black dots showed a constant amount of FITC (0.2 μmol L^{-1}) was titrated by warfarin-saturated BSA (the concentration ratio of BSA and warfarin was 1:50). The signal of red dots showed a constant amount of FITC (0.2 μmol L^{-1}) was titrated by ibuprofen-saturated BSA (the concentration ratio of BSA and ibuprofen is 1:300). (For interpretation of the references to color in this figure legend, the reader is referred to the web version of this article.)

3.3. Property of BSA in solution

In Fig. 2, a biphasic binding pattern was observed, which indicates two forms of BSA binding to FITC. To elucidate the reason for the increase of F_{norm} with respect to BSA concentration, a serial dilution of BSA was added into FITC-labeled BSA. The FITC-labeled BSA was fixed at 0.9 μmol L^{-1}. With the increasing addition of free BSA, a binding curve was obtained with the K_d of 2.01 μmol L^{-1}, which indicates that BSA tends to aggregate at this concentration (Fig. 6). The value of K_d is almost in line with the concentration (about 2.0–4.0 μmol L^{-1}) corresponding to the

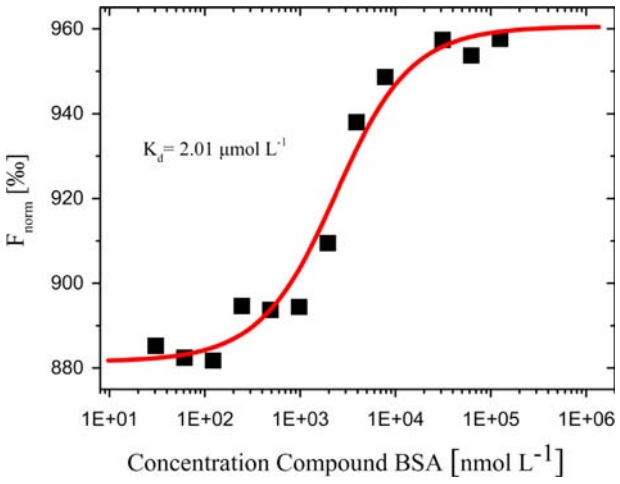
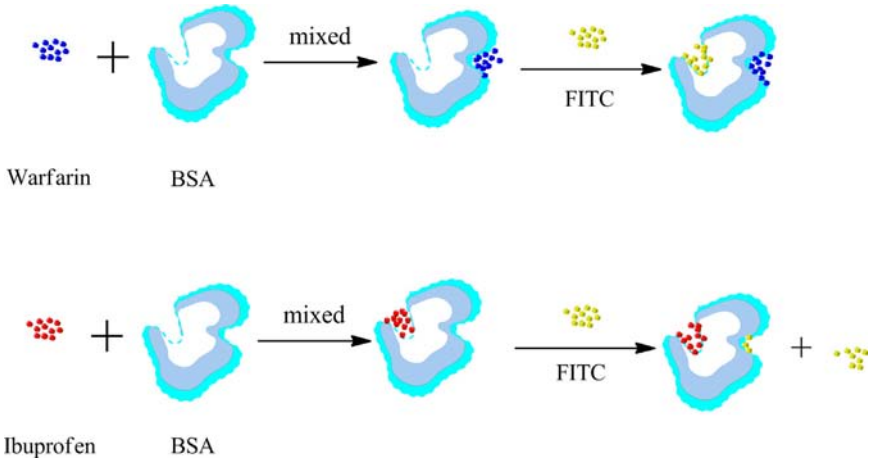


Fig. 6. MST quantified aggregation of BSA. A constant amount of labeled BSA–FITC (9.0 μmol L^{-1}) was titrated by unlabeled BSA. The value of K_d was corresponding to the lowest value of F_{norm} from the interaction between FITC and BSA.



Scheme 3. Depiction of FITC interacting with BSA in the presence of site markers-saturated.

lowest value of F_{norm} in Fig. 2, confirming that FITC binds to the aggregate of BSA which results in a second binding process.

3.4. Fluorescence measurements

MST is a new method for biomolecular interaction investigation, and thus conventional fluorescence spectroscopy method was applied to verify the results obtained from MST. Warfarin and ibuprofen were still selected respectively as the marker of site I or site II for the competitive study.

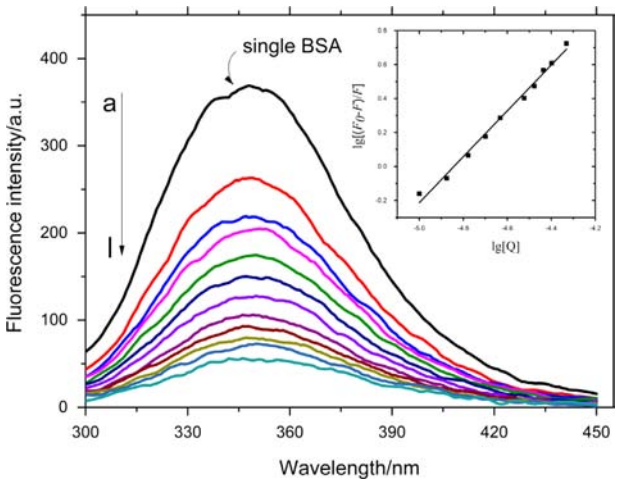


Fig. 7. Fluorescence emission spectra of BSA (0.02 mmol L^{-1}) in the presence of FITC with different concentrations (0–0.14 mmol L^{-1}). λ_{ex}=280 nm. Inset: the linear relationship for quenching BSA by FITC.

BSA shows intrinsic fluorescence mainly due to the two tryptophan residues [33], which are strongly affected by the interaction between BSA and molecules. When the increasing amounts of FITC were added to a BSA solution of constant concentration, the fluorescence of tryptophan at 340 nm decreased gradually without obvious shift in emission wavelength (As can be seen in Fig. 7). The fluorescence intensity decrease is probably attributed to dynamic quenching, static quenching or both of the two. To clarify the mechanism, the quenching process was first assessed by the Stern-Volmer equation [34] assuming a dynamic quenching:

$$F_0/F = 1 + K_q\tau_0[Q] = 1 + K_{SV}[Q]$$

In the above equation, F_0 and F are the fluorescence intensities of the protein before and after the addition of quencher (in this case, FITC), respectively; K_q is the quenching rate constant of the biomolecule; τ_0 is the average lifetime of the protein without the quencher, and generally taken as 10^{-8} s; [Q] is the concentration of the quencher, and K_{SV} is the dynamic quenching constant. The Stern–Volmer plots for the interaction of FITC and BSA were calculated to be in accordance with linear model. The value of K_{SV} was 3.1×10^5 L mol^{-1} (with a correlation coefficient r of 0.9987) and the corresponding K_q was calculated as about 3.1×10^{13} L mol^{-1} s^{-1}, which was much larger than the maximum scatter collision quenching constant (2.0×10^{10} L mol^{-1} s^{-1}) for biomolecules. Therefore, the interaction between FITC and BSA is possibly a process of static quenching rather than dynamic quenching.

Due to the deduction that the binding of FITC to BSA is a static fluorescence quenching process, which results in the formation of non-fluorescent compound, the fluorescence intensity could be described by the Scatchard equation [35]

$$\lg[(F_0 - F)/F] = \lg K_a + n \lg[Q]$$

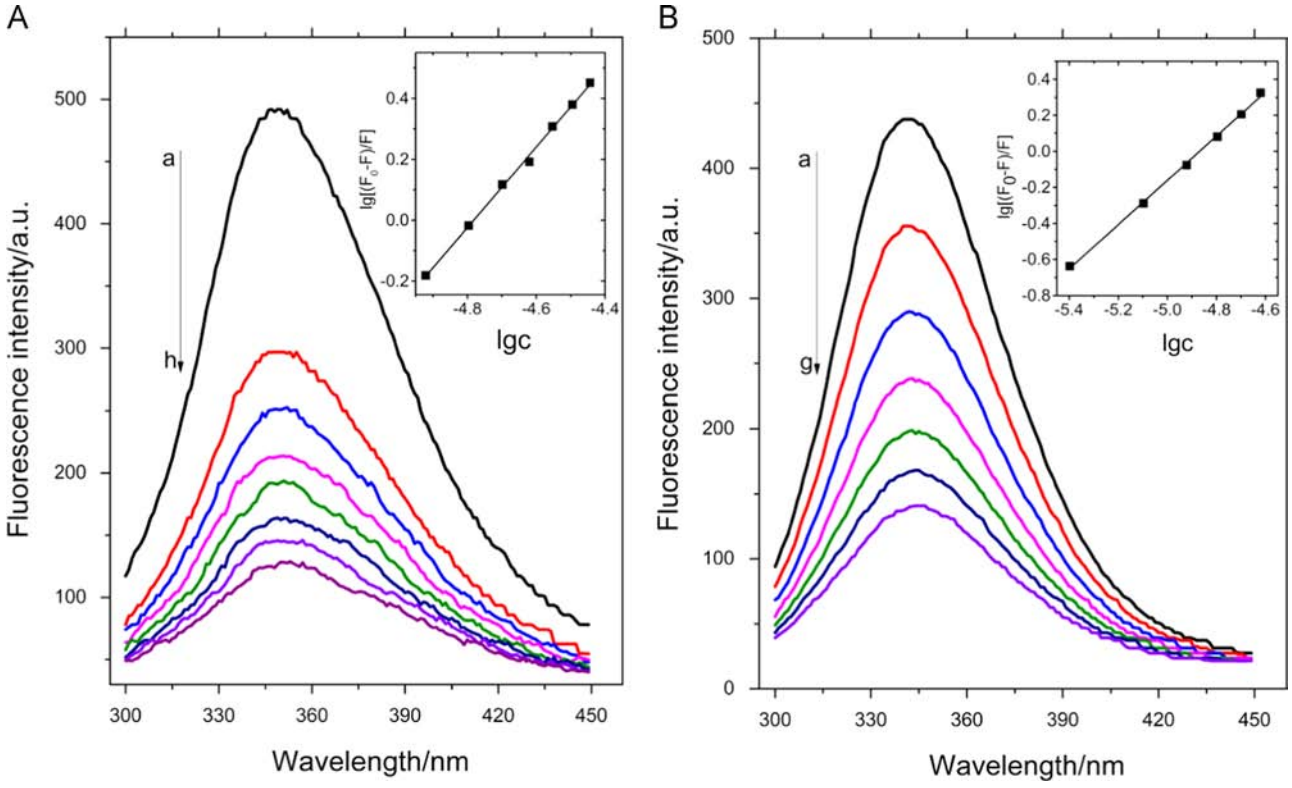


Fig. 8. (A) Fluorescence emission spectra of BSA-warfarin (0.02 mmol L^{-1}) (their concentration ratio was fixed as 1:1) in the presence of FITC with different concentrations (from a to h: 0.000, 0.012, 0.016, 0.020, 0.024, 0.028, 0.032 and 0.036 mmol L^{-1}). (B) Fluorescence emission spectra of BSA-ibuprofen (0.02 mmol L^{-1}) (their concentration ratio was fixed as 1:1) in the presence of FITC with different concentrations (from a to h: 0.000, 0.004, 0.008, 0.012, 0.016, 0.020 and 0.024 mmol L^{-1}).λ_{ex}=280 nm. Inset: the linear relationship for quenching.

Table 1
Binding constants of FITC-BSA system in the absence and presence of site markers at 298 K.

Site marker	Scatchard equation	r	$K_a/10^6$ L mol^{-1}
Without markers	$Y=(1.36)X+6.55$	0.9957	3.47
Warfarin	$Y=1.32X+6.32$	0.9993	2.09
Ibuprofen	$Y=1.23X+5.97$	0.9990	0.93

for which K_a is the binding constant, implicating the degree of interaction between BSA and FITC, and n is the number of binding sites. Depending on the linear relationship between $\lg[(F_0-F)/F]$ and lg[Q], K_a was calculated to be 3.47×10^6 L mol^{-1}. The reciprocal of this K_a value (2.88×10^{-7} mol L^{-1}) is on the same order of magnitude as the dissociation constant K_d obtained by MST, which suggests that MST provides reliable results. For comparison, the influence of warfarin or ibuprofen on the binding of FITC to BSA was investigated by titrating the pre-mixed 1:1 BSA-warfarin (or ibuprofen) solution with a series concentration of FITC (as given in Fig. 8A and B). The increasing amount of FITC produced a gradual decrease in fluorescence intensity of BSA-warfarin (or BSA-ibuprofen) mixture and the corresponding K_a was calculated, which are listed in Table 1. The binding constants changed from 3.47×10^6 L mol^{-1} to 2.09×10^6 L mol^{-1} and 0.93×10^6 L mol^{-1} in the presence of warfarin and ibuprofen, respectively. Accordingly, the decrease of K_a in the presence of ibuprofen was much larger than that in the presence of warfarin, which also indicates that FITC mainly tends to bind with the site II of BSA, and with the site I of BSA to a smaller extent. These results are consistent with those from MST.

4. Conclusions

In this study, a novel approach microscale thermophoresis was applied to investigate the interaction between BSA and a small organic dye FITC. FITC exhibits a strong binding affinity for BSA. FITC is mainly prone to interacting with the hydrophobic pocket of site II of BSA, while it also binds to site I of BSA to a lesser degree. These results from MST were in accordance with those from fluorescence spectroscopy, indicating the feasibility and reliability of MST in the application of protein–small molecule interaction. In addition, MST also demonstrated that FITC not only binds to BSA, but also binds to BSA aggregates, providing some detailed information about the BSA aggregation which was not obtained by fluorescence spectroscopy. Therefore MST is a powerful and reliable approach for protein–small molecule interaction. Combined with other advantages of MST, such as the low sample consumption which only needs several microlitres and nano molarity level, the simplicity of mixing, the fast measurement, the diversity of analytical solution especially in native environment and so on, MST is notably suitable in the application involved precious and expensive sample analysis.

Acknowledgments

This work was financially supported by the National Natural Science Foundation of China (21002093) and the national science and technology support program project funds (No. 2012BAD37B04).

References

[1] T. Pawson, P. Nash, Genes Dev. 14 (2000) 1027–1047.
[2] P. Legrain, J. Wojcik, J.M. Gauthier, Trends Genet. 17 (2001) 346–352.
[3] P. Uetz, Curr. Opin. Chem. Biol. 6 (2002) 57–62.
[4] S.J. Boulton, A. Gartner, J. Reboul, P. Vaglio, N. Dyson, D.E. Hill, M. Vidal, Science 295 (2002) 127–131.
[5] S. Jones, J.M. Thornton, Proc. Natl. Acad. Sci 93 (1996) 13–20.
[6] A.G. Cochran, Chem. Biol. 7 (2000) R85–R94.
[7] M.H.A. Roehrl, J.Y. Wang, G. Wagner, Biochemistry 43 (2004) 16056–16066.
[8] S.A. Jayasinghe, R. Langen, Biochemistry 44 (2005) 12113–12119.
[9] Y. Ni, R. Zhu, S. Kokot, Analyst 136 (2011) 4794–4801.
[10] X. Du, Z. Wang, Y. Zheng, H. Li, J. Ni, Q. Liu, Inorg. Chem. 53 (2014) 1672–1678.
[11] F.R. Alves, F.A.O. Carvalho, J.W.P. Carvalho, M. Tabak, Biopolymers 101 (2014) 1065–1076.
[12] Y. Huang, M. Shi, L. Zhao, S. Zhao, K. Hu, Z. Chen, J. Chen, H. Liang, Biosens. Bioelectron. 54 (2014) 285–291.
[13] Q. Yue, T. Shen, L. Wang, S. Xu, H. Li, Q. Xue, Y. Zhang, X. Gu, S. Zhang, J. Liu, Biosens. Bioelectron. 56 (2014) 231–236.
[14] S.G. Patching, BBA-Biomembranes 2014 (1838) 43–55.
[15] T. Xue, X. Cui, W. Guan, Q. Wang, H. Wang, K. Qi, D.J. Singh, W. Zheng, Biosens. Bioelectron. 58 (2014) 374–379.
[16] E. Härtl, N. Dixit, A. Besheer, D. Kalonia, G. Winter, Eur. J. Pharm. Biopharm. 85 (2013) 781–789.
[17] A. Masi, R. Cicchi, A. Carloni, F.S. Pavone, A. Arcangeli, Adv. Exp. Med. Biol. 674 (2010) 33–42.
[18] V.I. Razinkov, M.J. Treuheit, G.W. Becker, Curr. Drug Discov. Technol. 10 (2013) 59–70.
[19] Thomas Wiseman, Samuel Williston, John F. Brandts, Lung-Nan Lin, Anal. Biochem.. 179 (1989) 131–137.
[20] J.E. Ladbury, B.Z. Chowdhry, Chem. Biol. 3 (1996) 791–801.
[21] S. Fujime, S. Ishiwata, J. Mol. Biol. 62 (1971) 251–265.
[22] A.D. Hanlon, M.I. Larkin, R.M. Reddick, Biophys. J. 98 (2010) 297–304.
[23] B.K. Paul, A. Samanta, N. Guchhait, J. Phys. Chem. B 114 (2010) 6183–6196.
[24] G. Zhang, B. Keita, J.C. Brochon, P. Oliveira, L. Nadjo, C.T. Craescu, S. Miron, J. Phys. Chem. B 111 (2007) 1809–1814.
[25] K. Adachi, H. Watarai, Anal. Chem. 78 (2006) 6840–6846.
[26] A. Papadopoulou, R.J. Green, R.A. Frazier, J. Agr. Food Chem. 53 (2005) 158–163.
[27] H. Bian, M. Li, Q. Yu, Z. Chen, J. Tian, H. Liang, Int. J. Biol. Macromol. 39 (2006) 291–297.
[28] R. Perez-Ruiz, C.J. Bueno, M.C. Jimenez, M.A. Miranda, J. Phys. Chem. Lett. 1 (2010) 829–833.
[29] J. Li, P. Yao, Langmuir 25 (2009) 6385–6391.
[30] G. Sudlow, D.J. Birekett, D.N. Wade, Mol. Pharmacol. 12 (1976) 1052–1061.
[31] S.A.I. Seidel, P.M. Dijkman, W.A. Lea, G. Bogaart, M. Jerabek-Willemsen, A. Lazic, J.S. Joseph, et al., Methods 59 (2013) 301–315.
[32] S. Tang, H. Lin, H. Gong, Energy Procedia 17 (2012) 1798–1804.
[33] J.R. Lakowicz, Principles of Fluorescence Spectroscopy, 3rd ed., Springer, Heidelberg, 2006.
[34] P.D. Ross, S. Subramanian, Biochemistry 20 (1981) 3096–3102.
[35] T.K. Maiti, K.S. Ghosh, S. Dasgupta, Bioinformatics 64 (2006) 355–362.
[36] M. Jerabek-Willemsen, C.J. Wienken, D. Braun, P. Baaske, S. Duhr, ASSAY and Drug Development Technologies 9 (2011) 342–353.

Talanta 132 (2015) 902–908

Contents lists available at ScienceDirect

Talanta

journal homepage: www.elsevier.com/locate/talanta

In situ measurement of solution concentrations and fluxes of sulfonamides and trimethoprim antibiotics in soils using o-DGT

Chang-Er Chen [a], Wei Chen [a], Guang-Guo Ying [b], Kevin C. Jones [a,b], Hao Zhang [a,*]

[a] Lancaster Environment Centre, Lancaster University, Lancaster LA1 4YQ, United Kingdom
[b] State Key Laboratory of Organic Geochemistry, Guangzhou Institute of Geochemistry, Chinese Academy of Science, Guangzhou 510640, China

ARTICLE INFO

Article history:
Received 2 May 2014
Received in revised form
13 August 2014
Accepted 18 August 2014
Available online 30 October 2014

Keywords:
DGT
Antibiotics
Soils
Bioavailability
Flux
In situ

ABSTRACT

Techniques, such as Diffusive Gradients in Thin-films (DGT), which either minimally disturb the soil or perturb it in a controlled way are most likely to provide information relevant to toxicity. Herein, we report the first use of DGT for organics (o-DGT) in soil systems to gain insight into the mobility and lability of four antibiotics—sulfamethoxazole (SMX), sulfamethazine (SMZ), and sulfadimethoxine (SDM), trimethoprim (TMP) in soil. In experiments where the same known amount of antibiotics were spiked into the soil, which was then further modified with NaOH, NaCl or dissolved organic matter, directly measured soil solution concentrations (C_{soln}) of these antibiotics were in the order: SMX > SMZ ≈ SDM > TMP. The *R* values (ratio of concentrations measured by o-DGT and directly in solution) were 0.56, 0.41, 0.40 and 0.28, respectively, indicating that the removal of these antibiotics from the solution can be to some extent resupplied by release from the solid phase. The nonlinearity of the relationship between o-DGT fluxes and the reciprocal of diffusive layer thickness (Δg) also suggested that soil solution concentrations were only partially sustained by the solid phase. The potential fluxes of these antibiotics in this soil were 5.4, 3.6, 2.4, and 1.2 pg/cm^2/s for SMX, SMZ, SDM, and TMP, respectively. o-DGT is a promising tool for understanding the fate and behaviour of polar organic chemicals in soil, and it potentially provides an *in situ* approach for assessing their bioavailability.

© 2014 Elsevier B.V. All rights reserved.

1. Introduction

Antibiotics are one of the most important classes of pharmaceuticals, widely used in our daily life, for human and veterinary purposes to cure or prevent some bacteria associated diseases. As some of the dose of antibiotics administered to animals or humans is not metabolized, it is excreted and enters effluent streams and reaches the environment [1]. Antibiotics are incompletely removed by wastewater treatment plants (WWTPs) [2], and discharged as parent compounds or easily re-transferable metabolites. Their adverse effects, particularly promotion of antibiotic resistance [3], has raised their profile within environmental science and ecology as a problem contaminant [4]. Antibiotics could enter the soil system through sludge/manure application or effluent irrigation. However, although these rather polar organic compounds have been in use for over half a century, knowledge of their fate and behaviour in soil systems is still not fully understood [5,6].

Understanding the interactions between contaminants and soils is essential for their risk assessment. Currently, there is a lack of understanding of both chemical speciation in soil solution and the kinetics of exchange between solution and solid phase. Most of the current knowledge on the environmental behaviour of antibiotics in soils has been gained by batch [6–13] or dynamic column [14,15] studies. While the information provided by such procedures is useful, information it does not relate directly to the *in situ* transfer of antibiotics between solids and solution, even though it is this *in situ* information which is essential for understanding their bioavailability/mobility and developing predictive models. Traditional approaches such as chemical extraction disrupt chemical equilibria, which may affect the distribution of species in solution, while dynamic column techniques also change soil conditions from the natural *in situ* situation. *In situ* chemical measurements which either minimize disturbance or perturb the solution in a controlled way [16] offer an alternative approach.

Recently we developed a novel passive kinetic sampler—Diffusive Gradients in Thin-films for organics (o-DGT) to measure antibiotics in solutions *in situ* [17]. It has been successfully employed to measure the concentrations of antibiotics in WWTP [18]. The DGT technique has been successfully and widely used to assess the availability, toxicity and lability of inorganic chemicals in soils and sediments [19,20]. In the present study, availability

* Corresponding author. Tel.: +44 1524 593899.
E-mail address: h.zhang@lancaster.ac.uk (H. Zhang).

http://dx.doi.org/10.1016/j.talanta.2014.08.048
0039-9140/© 2014 Elsevier B.V. All rights reserved.

refers to all the fraction of chemicals that can be accumulated by o-DGT, while lability particularly is used in reference to the susceptibility of a compound to desorption from soil particles. Most studies using passive equilibrium samplers to investigate availability/toxicity [21,22] in soil/sediment have been focused on persistent organic pollutants (POPs), with little work on polar organic chemicals (POCs). To start to fill this knowledge gap, we applied the o-DGT technique to soils and present the first measurements by o-DGT of antibiotics in a soil system. This study was performed on soils in which sodium azide (NaN_3) was added to inhibit the microbial activity [23], to facilitate investigation of physico-chemical processes.

2. Theory of o-DGT

The DGT technique is based on Fick's first law of diffusion [24]. A resin layer is separated from bulk solution (with a concentration C) by an analyte-permeable diffusion layer of thickness Δg, comprising an agarose or polyacrylamide hydrogel, known as the diffusive gel, plus a filter membrane (Fig. 1). Analyte diffuses through the diffusion layer (with a diffusion coefficient D) and is rapidly bound by the resin in the binding gel. For well stirred solutions or a hypothetical fully sustained sediment/soil (see fully supplied case (i) later), C is constant outside the o-DGT unit and a constant concentration gradient is maintained in the diffusion layer during the deployment time (t) (case (i) in Fig. 1). The flux (F) of analyte diffusing through the diffusion layer is determined by Eq. (1):

$$F = \frac{DC}{\Delta g} \quad (1)$$

In practice, the flux of an analyte from soil to an o-DGT device can be calculated from the measured mass (M) accumulated during the deployment time through a well-defined exposure area (A) (Eq. (2)). This assumption of a steady state flux requires that capacity of the binding layer is not approached. A high capacity that fulfils this condition has been established [17]:

$$F = \frac{M}{At} \quad (2)$$

In soil systems, the flux from the solid phase to solution, F_{ss}, induced by o-DGT may not be the same as the potential maximum flux from the solid phase to solution, F_m. Depending on the characteristics of the o-DGT device and the soil properties, F_{ss} will be a fraction of F_m and is therefore regarded as a partial flux. The directly measured o-DGT flux (F_{DGT}) of analyte from the solid phase to solution and its relationship to F_{ss} and F_m can be considered for three possible conditions [16] (Fig. 1).

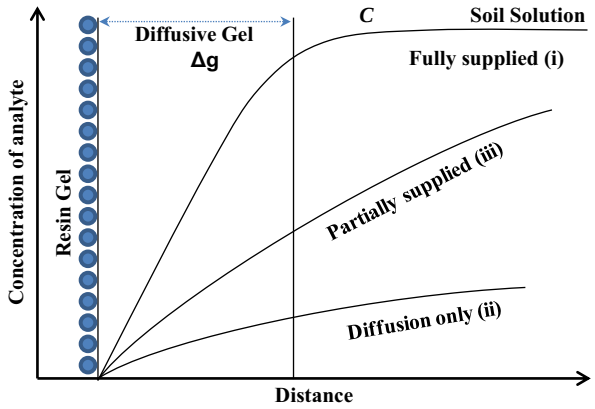


Fig. 1. Schematic of concentration gradients in o-DGT and soil.

2.1. Fully supplied

This is typically the case in well stirred solutions where C is independent of the distance from the membrane. In soils or sediments, analyte taken up from the pore water by the o-DGT is rapidly resupplied from the solid phase provided there is a labile pool size, which results in an effective buffer to maintain a constant concentration in the pore water. In this case, the concentration in soil solution or pore water can be calculated by Eq. (3):

$$C = \frac{M\Delta g}{DAt} \quad (3)$$

The F_{DGT} can be calculated by Eq. (2). It is likely to be less than F_m as the flux could be higher if an o-DGT device with a different geometry and higher demand for the analyte was used.

2.2. Diffusion only

There is no resupply from the solid phase to the soil solution *i.e.* $F_{ss} \approx 0$. The only supply of analyte to a DGT device is diffusion. The concentration in the soil solution at the surface of the device will gradually decline, with this depletion in concentration progressively extending further into the soil away from the surface of the o-DGT device, resulting in a concentration gradient in the soil. Consequently F_{DGT} declines with deployment time.

2.3. Partially supplied

There is some re-supply of analyte from the solid phase to solution, but it is insufficient to sustain the initial concentration in the soil solution and to satisfy the DGT demand. In this case, $F_{ss} \approx F_{DGT} \approx F_m$.

In general, case (iii) is the most likely and expected phenomena, particularly for organic chemicals, which may be supplied from the solid phase to solution by breaking the forces of various interactions, including electrostatic, surface complexation and hydrogen bonding [25]. Case (i) and (ii) are two extremes for soils and sediments, but they may be approached.

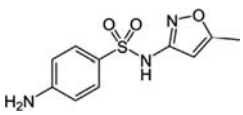
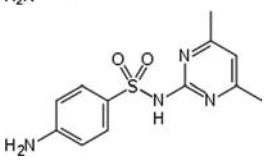
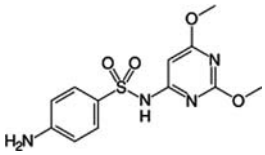
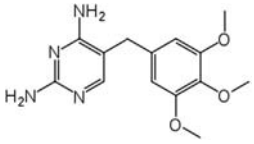
The ratio (R) of o-DGT measured concentration (C_{DGT}) to the independently measured soil solution concentration (C_{soln}) is an indicator of the extent of depletion of solution concentrations at the DGT interface (Eq. (4)) [26]:

$$R = \frac{C_{DGT}}{C_{soln}} \quad (4)$$

R can help identify the different cases mentioned above. If $R=1$ (in practice, $R \geq 0.95$), then the analyte in the soil solution is fully supplied by the solid phase. If $0.1 < R < 0.95$, then it is partially supplied. If $R < 0.1$, it would be seen as diffusion only case, with no resupply from the solid phase to the solution. Generally higher R values indicate that the labile pool size of the analyte is large and/or a fast resupply rate.

The above mentioned cases can also be identified using approaches that do not rely on the measurement of R. Deployment of o-DGT devices with various thicknesses of diffusive layers (different Δg) for the same time can provide plots of fluxes against $1/\Delta g$, while deployments with a constant Δg for different times provide plots of fluxes versus time. In both cases the lines increase linearly with $1/\Delta g$ or time for the fully supplied case, but are curved for the partially supplied or diffusion only cases (Fig. S1).

Table 1
Physiochemical properties and chemical structures of antibiotics in this study

Compound	Structure	CAS	MW	S_W (mg/L)[a]	p$Ka_{1,2}$	logK_{ow}[b]
SMX		723-46-6	253.3	610	1.9, 5.6	0.89
SMZ		57-68-1	278.3	1500	2.1, 7.5	0.89
SDM		122-11-2	310.3	343	2.5, 5.9	1.63
TMP		738-70-5	290.3	400	3.2, 6.8	0.91

[a] Water solubility from Ref. [28].
[b] Obtained from EPI suite 4.0, USEPA.

3. Methods and materials

3.1. Chemicals

Four antibiotics—sulfamethoxazole (SMX, purity > 98%), sulfamethazine (SMZ, purity > 99%), sulfadimethoxine (SDM, purity > 98.5%), trimethoprim (TMP, purity > 99%) and ^{13}C-Caffeine (^{13}C-CAF as the internal standard [27], purity > 99%) were supplied by Sigma-Aldrich (Poole, UK). Their physiochemical properties are given in Table 1.

Antibiotic stock solutions were dissolved in pure methanol. Acetonitrile (ACN) and methanol (MeOH) were purchased from Fisher (Poole, UK). Humic acid (used as the dissolved organic matter—DOM) was obtained from the International Humic Substances Society.

3.2. Soil sample and treatments

The soil was collected from near Preston, Lancashire, U.K. The physico-chemical properties of this soil are: texture clay loam, maximum water holding capacity (MWHC) 46%, pH 6.5 (dH_2O), sand 56%, silt 25%, clay 19% and soil organic matter (SOM) 4.8% [29]. The soil was air dried and passed through a 2 mm sieve to remove roots and stones prior to experiments.

The soil was spiked with antibiotic solutions. Spiking solutions were prepared in methanol and added to soils, to deliver individual antibiotic concentration of 2.5 mg/kg in order to be detected in the solution. NaN_3 (10 mM) was added to inhibit the microbial activity [23]. To minimise solvent effects, the antibiotic solutions were first added to 25% of the soil and allowed to vent totally (to avoid potential effect of MeOH) before mixing well with the remaining soil (*i.e.* 75% of the soil) following the procedure in previous study [30]. Blank soil that was not augmented with antibiotics, but treated with the same amount of pure MeOH, was also prepared following the same procedure. The soils were then wetted to 50% MWHC by adding appropriate amounts of MQ water (high purity water, Milli-Q water system, UK), mixed well and left to equilibrate at room temperature. After 1, 2, 4, 7, 10, 15, and 19 days, soil was wetted to 100% MWHC 24 h before o-DGT deployment, and mixed well to obtain a soil slurry [16]. This pre-test established the time for reaching equilibrium and further experiments were conducted after 15 days equilibration. Soils were also modified using NaOH, NaCl and DOM to produce soils with different pH, ionic strength and organic matter for investigating their effects on fluxes from the solid phase to solution. In summary, six treatments were carried out. A, soil spiked with antibiotics; B, soil A mixed with blank soil (1:1) to produce soils with different antibiotic concentration; C, soil A further spiked with 0.01 M NaOH; D, soil A further spiked with 0.1 M NaOH; E, soil A further spiked with 0.1 M NaCl; F soil A further spiked 1.1% DOM. The resulting pH and SOM are given in Table 2.

3.3. o-DGT preparation and deployment

Standard o-DGT devices with 0.5 mm XAD18 resin gels, 0.8 mm agarose diffusive gels and polyethersulfone (PES) filter membranes were prepared as in our previous study [17]. o-DGT units were also made with different thicknesses of diffusive gels. The diffusive layer thickness including the PES filter ranged from 0.14 to 2.14 mm.

Deployment in the soil followed the standard procedures for using DGT in soils [16]. Briefly, a small amount of soil paste was applied gently onto the filter surface of the o-DGT devices and then pushed gently onto the soil surface with a slight twisting movement, enabling good contact between the soil and the device. All o-DGT devices were deployed for 24 h at room temperature (18 ± 3 °C). Photographs of laboratory deployment are provided in Fig. S2.

3.4. o-DGT retrieval and soil sampling

After deployment, o-DGT devices were retrieved. Soil particles were jet washed away with MQ water, the binding gel was removed (Fig. S2) and put into amber glass vials. An appropriate amount of internal standard was added. To extract the target chemicals 5 mL of MeOH was added into the vial followed by 20 min ultrasonication and the process repeated with a further 5 mL of MeOH. As recovery of all analytes was > 95%, 100% recovery was assumed in calculations [17].

Table 2
Concentrations (mean (SD)) of 4 antibiotics in soil solution and o-DGT measured fluxes in soils with various modifications ($n=3$).

Treatments[a]	BK	A	B	C	D	E	F
pH (dH_2O)	6.6	6.6	6.6	6.9	7.6	6.5	6.3
SOM	4.8%	4.8%	4.8%	4.8%	4.8%	4.8%	5.9%
Solution concentrations (ng/mL)							
TMP	0	24.5 (3.5)	9.93 (1.6)	23.5 (2.3)	26.3 (7.4)	28.9 (4.3)	28.4 (2. 6)
SMZ	0	196 (16.1)	106 (9.7)	189 (10.8)	196 (20.9)	182 (49.1)	219 (18.9)
SMX	0	519 (41.2)	267 (27.3)	506 (23.9)	655 (65.9)	456 (137)	587 (67.1)
SDM	0	203 (12.1)	94.1 (14.0)	212 (11.2)	410 (29.5)	175 (42.1)	222 (21.2)
Acetonitrile extract—C_s (ng/g, dw[b])							
TMP	0	839 (47)	348 (29)	806 (25)	884 (35)	936 (47)	840 (62)
SMZ	0	696 (14)	185 (40)	686 (62)	668 (41)	630 (19)	693 (95)
SMX	0	1754 (57)	649 (32)	1664 (103)	1608 (132)	1616 (75)	1815 (181)
SDM	0	2042 (45)	1067 (159)	1975 (63)	1852 (128)	1940 (30)	2143 (42)
Fluxes (pg/cm^2/s)							
TMP	0	0.44 (0.01)	0.22 (0.04)	0.48 (0.02)	0.54 (0.04)	0.55 (0.01)	0.51 (0.01)
SMZ	0	2.76 (0.15)	1.12 (0.19)	2.68 (0.13)	2.97 (0.03)	2.58 (0.08)	2.59 (0.07)
SMX	0	5.40 (0.17)	2.29 (0.36)	5.60 (0.36)	7.36 (0.34)	4.91 (0.12)	5.01 (0.32)
SDM	0	2.60 (0.14)	0.87 (0.13)	2.78 (0.19)	5.92 (0.06)	2.31 (0.05)	2.58 (0.08)

[a] BK, blank soil—no antibiotics added; A, spiked antibiotics, B, BK+A (1/1 w/w); C, A+0.01 M NaOH; D, A+0.1 M NaOH; E, A+0.1 M NaCl; F, A+1.1% DOM.
[b] Dry weight based.

The pooled extract was blown down to dryness with a gentle N_2 flow, reconstructed in 1 mL of MeOH, and filtered through 0.2 μm PP syringe filters (Pall, UK) into a 2 mL GC vial.

About 5 g of the soil slurry was sampled and centrifuged at 3000 rpm for 30 min to obtain soil solution. The solution was filtered (with 0.2 μm PP syringe filters, Pall, UK) into 1 mL glass vials. The rest of the soil was extracted twice with 10 mL acetonitrile (ACN) [10]. All the samples were reconstructed in initial mobile phases before being injected into the HPLC.

3.5. Chemical analysis

A Thermo Finnigan HPLC coupled with a photodiode array detector was employed to analyze the antibiotics by UV absorbance at 265 nm. A Varian Pursuit C18 LC column (150 × 2.1 mm, 3 μm) was used to separate antibiotics. The mobile phase used was: 0.2% formic acid in MQ water (A) and acetonitrile (B). The gradient procedure was optimised at: 0–1 min, 10% B, then increase to 70% B within 11 min, followed by increasing to 100% B in 1 min, hold for 5 min, after that decrease to the initial condition within 1 min. Finally, 10 min of post run ensured re-equilibration of the column before the next injection. The injection volume was 10 μL and the column temperature was set at 30 °C. The quantification of antibiotics was based on an internal standard method following a previous study [27], and the instrument detection limits were 1–5 ng/mL.

3.6. Quality assurance/control (QA/QC)

Blank soils without spiking antibiotics were analyzed and no target compounds were detected (Table 2). The caffeine (which might interfere with the internal standard analysis) was not detectable. Every batch of samples was analyzed in parallel with a standard solution and blank (initial mobile phase) to check the instrument performance. Values within 5% of the previous measurements were considered acceptable.

4. Results and discussion

4.1. Concentrations in soil solution

In a pilot experiment with sterile soils, soil solution concentrations (C_{soln}) decreased over the first 7 days after spiking, but changed insignificantly (ANOVA, $p > 0.05$, SPSS, IBM Statistics 20) after 7 days (Table S1). This indicates the added chemicals have reached equilibrium with the soils. Subsequent studies were conducted with soils allowed to equilibrate for 15 days.

Although the 4 antibiotics were spiked to the same concentration (*i.e.* 2.5 mg/kg), the C_{soln} varied between compounds (Table 2), with SMX the highest, followed by SDM, SMZ and TMP. C_{soln} for TMP was much lower than that for the three sulphonamides. Different from traditional soil-solution partition coefficient (K_d) which refers to the total solid phase concentration, this study uses labile soild phase-solution phase partition coefficient (K_{dl}) since the labile fraction in the soil particles was refered here, estimated by the ACN extraction. TMP has a higher K_{dl} than SMX, SMZ and SDM, and SMX has the lowest value, which is consistent with previous studies of K_d [10,31]. C_{soln} for SMZ was comparable to or slightly higher than for SDM, even though they have different logK_{ow} values of 0.89 and 1.63, respectively. These results suggested that chemical structure is an important factor affecting the fate of antibiotics in soil, different chemical structure results in different steric hindrance, p*K*a, etc. K_{ow} is not the only key parameter to contol the fate of these polar organic chemicals [25]. Mass balance estimates showed that nonextractable (ACN) fractions are (69 ± 8)%, (76 ± 8)%, (67 ± 9)%, and (60 ± 8)% for TMP, SMZ, SMX, and SDM, respectively.

4.2. Concentrations measured by o-DGT

The *D* values for these antibiotics, taken from a previous study [18], are 4.19E−06, 3.29E−06, 3.15E−06, and 3.11E−06 cm^2/s at 18 °C for SMX, SMZ, SDM, and TMP, respectively. The appropriate values were used in Eq. (3) in calculating concentrations measured by o-DGT (C_{DGT}). Like directly measured pore water concentrations they declined with aging time. *R* values for each antibiotic were obtained using Eq. (4).

For the aged soils, concentrations calculated from o-DGT correlated well with independently measured C_{soln} (Fig. 2). This results in averaged *R* values of 0.56, 0.41, 0.40, and 0.28 for TMP, SMZ, SDM, and SMX, respectively. The higher *R* value of TMP than the other three antibiotics at a given time indicates that it can be resupplied more quickly by the solid phase than SDM, SMZ and SMX and/or it has a larger labile reservoir.

A lower o-DGT concentration than that measured directly in soil solution indicates that the solution concentrations of these

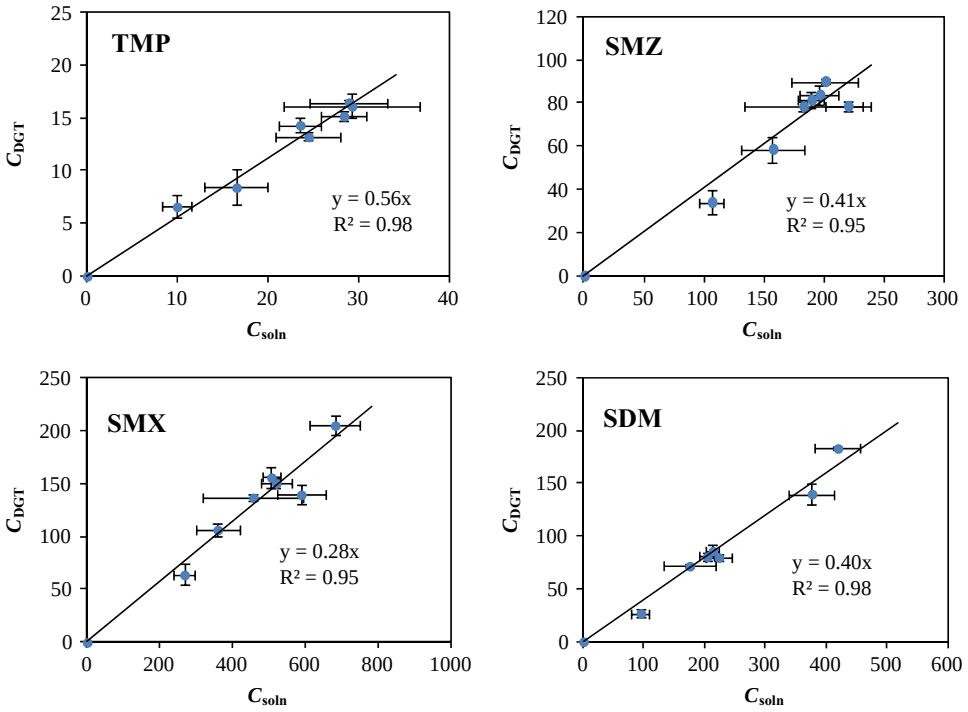


Fig. 2. Relationships between o-DGT measurement (C_{DGT}, ng/mL) and directly measured soil solution concentrations (C_{soln}, ng/mL) of 4 antibiotics in soils (error bars: SD for triplicate measurements).

antibiotics were only partially sustained by the solid phase [16]. The lower C_{DGT} than C_{soln} could be due to: (1) some species in the solution being unavailable to the o-DGT and/or (2) kinetic limitation of the resupply from the solid phase to soil solution. During deployment, the antibiotics at the surface of o-DGT devices were consumed, resulting in a decrease in the soil solution concentration at the interface. The removal of antibiotics in the solution at this interface could not be sufficiently rapidly resupplied by desorption from the solid phase. Consequently the concentration was depleted and the flux to the o-DGT device was less than the maximum possible flux, and the mean concentration measured by o-DGT, C_{DGT}, was lower than the initial solution concentrations, C_{soln}.

The acetonitrile extractable fraction was used here to estimate the labile solid phase concentrations in soil, and then K_{dl} could be derived. They were constant for each of the 4 antibiotics in the variously modified soil except for SDM in the soil at pH 7.6, for which the obtained K_{dl} (5.0) was only about half of the value obtained (10.6) for lower pH soils. As R was the same (0.40) for this higher pH soil, the desorption rate, k, must be larger. It appears that the desorption rate constant (and K_{dl}) is only sensitive to pH for SDM, whereas for TMP, SMZ and SMX it is independent of pH.

4.3. Fluxes from solid phase to solution

As discussed above, in most cases, these antibiotics in this soil solution are partially sustained by resupply from the solid phase. Therefore, the o-DGT results should be interpreted as fluxes rather than concentrations. The calculated, time-averaged, fluxes to o-DGT (F_{DGT}) are approximately equal to the average fluxes from solid phase to solution induced by o-DGT (F_{ss}) (given in Table 2).

Environmental changes (such as irrigation and application of manure or sludge) in the soil system will change soil properties (*e.g.* pH, cation exchange capacity—CEC and soil organic matter—SOM) which will consequently lead to different flux responses of these antibiotics from soil particles to soil solution. Fig. 3 shows the effect of soil pH on the fluxes of these 4 antibiotics from solid phase to solution. Good correlations were observed between the fluxes and soil pH (6.3–7.6). Less sensitivity of the fluxes for TMP and SMZ to pH might be due to the pH values studied being within (nearly all for SMZ and partly for TMP) the range of pKa_1 to pKa_2 (Table 1), where there are no big changes in the speciation. Increasing pH appears to facilitate the fluxes from solid phase to solution, which is consistent with previous studies [6,7,25]. At higher pH there is a greater proportion of anionic species, resulting in higher electrostatic repulsion between anionic sulphonamides and the negatively charged soil surface. Increasing soil pH leads to remobilizing the antibiotics, raising the risks of these antibiotics in terms of exposure to microorganisms or contamination of ground water.

Ionic strength and SOM affect sulphonamides and TMP differently. Both increasing of the ionic strength and SOM enhanced ($p < 0.05$) fluxes of TMP from the solid phase to the solution (Table 2). This could be due to the decreasing thickness of the electrical double layer of the charged surface [6] and competition between SOM and TMP [32]. However, it seems that both ionic strength and SOM suppressed slightly the fluxes of sulphonamides (SMZ, SMX and SDM) from soil particles, although not significantly for the SOM effect. The ionic strength effect in this study for SAs is inconsistent with a study by Białk-Bielińska and co-workers [6], where they found increasing ionic strength decreased the K_d of SAs. This might be attributed to the different composition of the exchangeable cations [7,32].

Deployment of o-DGT with different thicknesses of diffusive gel layers can help to characterize the transport of antibiotics from soil solids to solutions. For example, o-DGT with 0.8 mm and 0.5 mm diffusive gels were deployed in the soils for the same time. If concentration measured by o-DGT with 0.8 mm gel was higher than that by o-DGT with the 0.5 mm gel, it indicates the antibiotic in the soil solution was partially supplied by the solid phase. Obtaining lower C_{DGT} with thinner gels (0.5 mm) than thicker ones (0.8 mm) implies resupply from the solid phase cannot satisfy the demand of the uptake of o-DGT with a 0.5 mm gel, hence the solution is only partially resupplied due to limited labile pool or/and kinetic limitation. This is consistent with the observations made by comparing C_{DGT} with C_{soln} (R values).

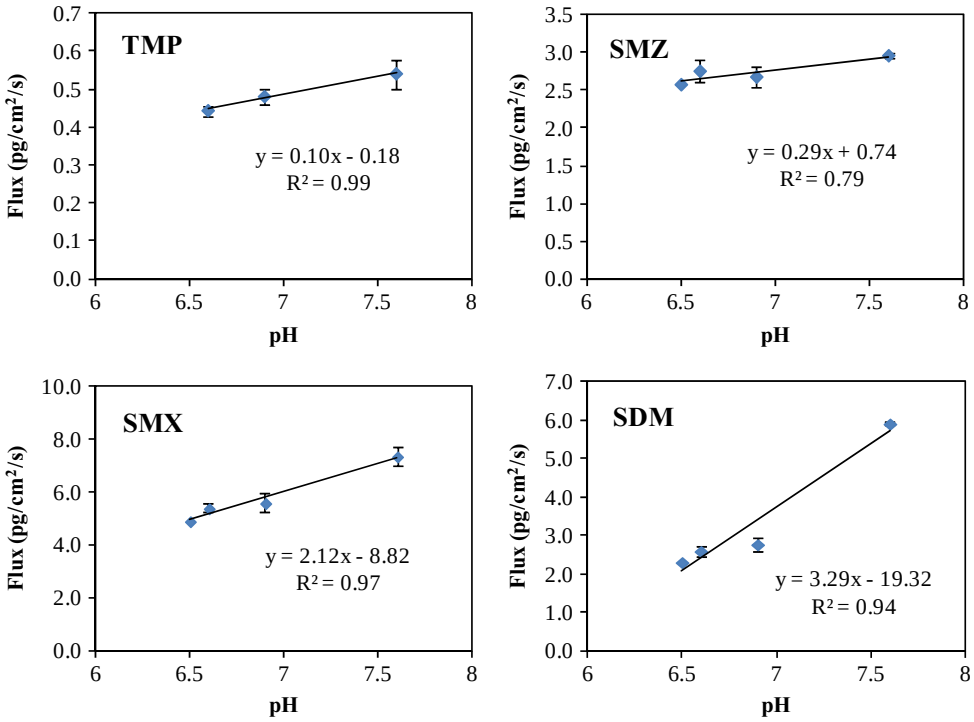


Fig. 3. Relationships between fluxes of antibiotics from solid phase to solution and soil pH (error bars: SD for triplicate measurements).

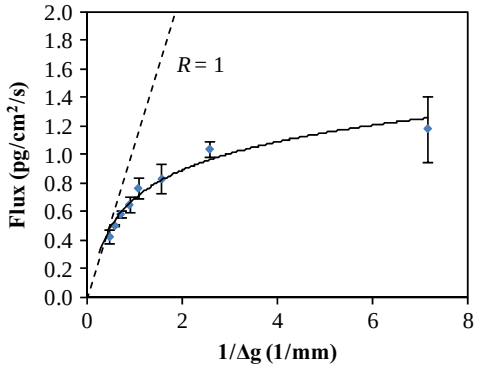


Fig. 4. o-DGT Fluxes of TMP *vs* reciprocal of diffusive layer thickness in the clay loam soil (dash line represents theoretical line according to Eq. (1) where $R=1$; error bars: SD for duplicate measurements).

Deployment of o-DGT with various thicknesses of diffusive gel layers can offer further information (Fig. 4). A nonlinearity of the plot of flux against the $1/\Delta g$ again suggests the concentrations of these antibiotics in the soil solution were partially supplied by desorption from the soil particles. A straight line interpretable with a slope of *DC* would only be expected if there was full supply from the solid phase (no kinetic limitation), where *R* should be 1 (shown in Fig. 4, TMP as an example). Although the demand for the o-DGT with thicker diffusion layers was smaller, it could not be satisfied by the resupply from the solid phase, as shown by the data points being lower than the $R=1$ line. Lower values than the theoretical slope and the apparent approach to a plateau suggest a kinetic limitation on the supply from solid phase to solution.

Deployments of o-DGT with thicker diffusion layers than those used here might enable accurate measurement of slope, *DC*, and derivation of the solution concentration, facilitating quantitative comparison with *R*. Fluxes of o-DGT with the thinnest diffusive layer are limited by the supply from soil to solution and so give potential fluxes of these antibiotics from this soil. The values were 5.4, 3.6, 2.4, and 1.2 pg/cm^2/s for SMX, SMZ, SDM and TMP, respectively. The fluxes measured using the standard o-DGT (0.8 mm diffusion gel) are about 60% for TMP and 80% for sulphonamides of the potential fluxes.

5. Conclusions and environmental implications

An important finding of this work is that when antibiotics are removed from solution, as they might be by biota, they are to an extent rapidly supplied by the solid phase. This resupply is most significant for SMX and least for TMP. Values obtained for the potential maximum supply fluxes of each antibiotic from soil to solution have the potential to be used in models of biological uptake. They could be used to estimate maximum possible uptake, as limited by transport form the soil.

This work has demonstrated that o-DGT is an *in situ* technique, which can provide quantitative measurements of antibiotic remobilization fluxes from soil to soil solution, and this might be linked to their bioavailability. DGT measured fluxes of metals have proved to be a good surrogate for plant uptake [19]. There is an urgent need to establish whether the bioavailability of antibiotics in soil/sediment can be predicted by o-DGT measurements. o-DGT opens up the possibilities of both directly obtaining kinetic information of polar organic chemicals such as antibiotics in natural or contaminated soil/sediment systems and providing an *in situ* measurement of bioavailability. In doing so it is likely in the future to enhance our understanding of the behaviour of these organic chemicals in the environment and improve risk assessment and associated models.

Acknowledgment

The authors thank Dr. Vassil Karloukovski, Kirk Semple, Olusoji Igunnugbemi and Ihuoma Anyanwu for their support or kind help in the soil pretreatment. We are grateful to the Chinese Scholarship Council (CSC) for sponsorship of Chang-Er Chen. Kevin Jones is grateful to the Chinese Academy of Sciences (CAS) for a Senior

Visiting International Scientist Professorship position. This study was also supported by the UK–China Bridge Project.

Appendix A. Supporting information

Supplementary data associated with this article can be found in the online version at http://dx.doi.org/10.1016/j.talanta.2014.08.048.

References

[1] Y.F. Xie, X.W. Li, J.F. Wang, G. Christakos, M.G. Hu, L.H. An, F.S. Li, Sci. Total Environ. 430 (2012) 126–131.
[2] N. Ratola, A. Cincinelli, A. Alves, A. Katsoyiannis, J. Hazard. Mater. 239 (2012) 1–18.
[3] C.W. Knapp, J. Dolfing, P.A.I. Ehlert, D.W. Graham, Environ. Sci. Technol. 44 (2010) 580–587.
[4] K. Kummerer, Chemosphere 75 (2009) 435–441.
[5] Z.S. Fan, F.X.M. Casey, H. Hakk, G.L. Larsen, E. Khan, Water Air Soil Pollut. 218 (2011) 49–61.
[6] A. Białk-Bielińska, J. Maszkowska, W. Mrozik, A. Bielawska, M. Kołodziejska, R. Palavinskas, P. Stepnowski, J. Kumirska, Chemosphere 86 (2012) 1059–1065.
[7] J.A. Gao, J.A. Pedersen, Environ. Sci. Technol. 39 (2005) 9509–9516.
[8] C. Accinelli, W.C. Koskinen, J.M. Becker, M.J. Sadowsky, J. Agric. Food Chem. 55 (2007) 2677–2682.
[9] M. Teixido, J.J. Pignatello, J.L. Beltran, M. Granados, J. Peccia, Environ. Sci. Technol. 45 (2011) 10020–10027.
[10] F. Liu, G.G. Ying, J.F. Yang, L.J. Zhou, R. Tao, L. Wang, L.J. Zhang, P.A. Peng, Environ. Chem. 7 (2010) 370–376.
[11] W. Lertpaitoonpan, S.K. Ong, T.B. Moorman, Chemosphere 76 (2009) 558–564.
[12] A. Wehrhan, T. Streck, J. Groeneweg, H. Vereecken, R. Kasteel, J. Environ. Qual. 39 (2010) 654–666.
[13] R. Kasteel, C.M. Mboh, M. Unold, J. Groeneweg, J. Vanderborght, H. Vereecken, Environ. Sci. Technol. 44 (2010) 4651–4657.
[14] S.T. Kurwadkar, C.D. Adams, M.T. Meyer, D.W. Kolpin, J. Environ. Manage. 92 (2011) 1874–1881.
[15] C. Strauss, T. Harter, M. Radke, J. Environ. Qual. 40 (2011) 1652–1660.
[16] H. Zhang, W. Davison, B. Knight, S. McGrath, Environ. Sci. Technol. 32 (1998) 704–710.
[17] C.-E. Chen, H. Zhang, K.C. Jones, J. Environ. Monit. 14 (2012) 1523–1530.
[18] C.-E. Chen, H. Zhang, G.-G. Ying, K.C. Jones, Environ. Sci. Technol. 47 (2013) 13587–13593.
[19] H. Zhang, F.J. Zhao, B. Sun, W. Davison, S.P. McGrath, Environ. Sci. Technol. 35 (2001) 2602–2607.
[20] P.N. Williams, H. Zhang, W. Davison, S.Z. Zhao, Y. Lu, F. Dong, L. Zhang, Q. Pan, Environ. Sci. Technol. 46 (2012) 8009–8016.
[21] P. Mayer, J. Tolls, L. Hermens, D. Mackay, Environ. Sci. Technol 37 (2003) 184a–191a.
[22] A. Jahnke, P. Mayer, M.S. McLachlan, Environ. Sci. Technol. 46 (2012) 10114–10122.
[23] A.B.A. Boxall, P. Blackwell, R. Cavallo, P. Kay, J. Tolls, Toxicol. Lett. 131 (2002) 19–28.
[24] H. Zhang, W. Davison, Anal. Chem. 67 (1995) 3391–3400.
[25] J. Tolls, Environ. Sci. Technol. 35 (2001) 3397–3406.
[26] H. Ernstberger, W. Davison, H. Zhang, A. Tye, S. Young, Environ. Sci. Technol. 36 (2002) 349–354.
[27] W.H. Xu, G. Zhang, S.C. Zou, X.D. Li, Y.C. Liu, Environ. Pollut. 145 (2007) 672–679.
[28] L.J. Zhou, G.G. Ying, S. Liu, J.L. Zhao, F. Chen, R.Q. Zhang, F.Q. Peng, Q.Q. Zhang, J. Chromatogr. A 1244 (2012) 123–138.
[29] A.H. Rhodes, A. Carlin, K.T. Semple, Environ. Sci. Technol. 42 (2008) 740–745.
[30] A.H. Rhodes, L.E. McAllister, K.T. Semple, Environ. Pollut. 158 (2010) 1348–1353.
[31] L.J. Zhou, G.G. Ying, S. Liu, J.L. Zhao, B. Yang, Z.F. Chen, H.J. Lai, Sci. Total Environ. 452 (2013) 365–376.
[32] H. Haham, A. Oren, B. Chefetz, Environ. Sci. Technol. 46 (2012) 11870–11877.

Talanta 132 (2015) 909–914

Contents lists available at ScienceDirect

Talanta

journal homepage: www.elsevier.com/locate/talanta

Short communication

A new direct laser photo-induced fluorescence method coupled on-line with liquid chromatographic separation for the simultaneous determination of anilides pesticides

O.M.A. Mbaye [a], A. Maroto [b], M.D. Gaye-Seye [a], L. Stephan [b], L Deschamps [b], J.J. Aaron [c], P. Giamarchi [b,*]

[a] Laboratoire de Photochimie et d'Analyse, Faculté des Sciences et Techniques, Université C.A. Diop, Dakar, Sénégal
[b] Université de Brest, UMR CNRS 6521, Faculté des Sciences, Université de Brest, 6 Avenue Victor Le Gorgeu, 29285 Brest Cedex, France
[c] Université Paris-Est, Laboratoire Géomatériaux et Environnement (EA 4508), UPEMLV, 77454 Marne-la-Vallée Cedex 2, France

ARTICLE INFO

Article history:
Received 15 July 2014
Received in revised form
16 August 2014
Accepted 18 August 2014
Available online 16 September 2014

Keywords:
Photo-induced fluorescence (PIF)
Anilide pesticides
Photoproducts
Laser fluorescence
HPLC

ABSTRACT

A new direct laser photo-induced fluorescence high performance liquid chromatography (DL-PIF–HPLC) method is developed for the simultaneous determination of three anilide pesticides, namely carboxin, monalide and propanil. DL-PIF–HPLC uses a tunable Nd:YAG-OPO laser to obtain fluorescent photoproduct(s) and to simultaneously analyze their fluorescence in a short acquisition time with an intensified CCD camera, which improves the selectivity (by choosing the suitable excitation wavelength), increases the sensitivity (due to the high energy of the laser beam) and reduces the time of analysis, relative to the classical PIF methods. However, one of the main drawbacks of PIF methods is the presence of interferences with other compounds, such as other pesticides from the same group yielding similar fluorescent photoproducts, which reduces their selectivity. The analytical interest of DL-PIF–HPLC to avoid these interferences is demonstrated. The DL-PIF spectra, chromatographic conditions and analytical performances of DL-PIF–HPLC are presented for the simultaneous determination of three anilide pesticides. The calibration curves are linear over one order of magnitude and the limits of detection are in the ng mL^{-1} range. The new DL-PIF–HPLC system has the advantage to combine the performances of both techniques, DL-PIF and liquid chromatography, and to improve the analysis selectivity.

© 2014 Elsevier B.V. All rights reserved.

1. Introduction

Pesticides are widely used in agriculture to improve productivity and, consequently, they can produce residues in crops, soils and surface water. Their persistence is an important matter of concern due to their toxicity and possible carcinogenicity. The presence of pesticides could affect the ground water quality, and/or disrupt water treatment plants. Therefore, it is important to develop sensitive and selective analytical methods for determining pesticides in surface water or seawater. Monitoring pesticides at low concentrations is usually performed by chromatographic techniques preceded by a preconcentration step, such as solid-phase extraction (SPE) or solid-phase micro-extraction (SPME). Many pesticides thermally unstable or non-volatile are difficult or impossible to analyze using gas chromatography. Therefore, high performance liquid chromatography (HPLC) is usually preferred. HPLC coupled to tandem mass spectrometry (MS/MS) offers a powerful tool for multiresidue pesticide determination [1,2]. Nonetheless, fluorimetric detection has the advantage of being more sensitive than classical UV absorption and less expensive than MS detection.

Many pesticides are naturally non-fluorescent, but they can be photolysed into rapidly-formed strongly fluorescent photoproducts upon UV irradiation. PIF conversion has been widely applied to the determination of pesticides for stationary media [3,4] as well as in flow injection analysis [5,6]. As an alternative to classical PIF, we have recently developed a different method based on direct laser photo-induced fluorescence (DL-PIF) [7,8]. This method uses a tunable Nd:YAG-OPO laser to obtain fluorescent photoproduct(s) and to simultaneously analyze their fluorescence in a short acquisition time with an intensified CCD camera. Compared to classical PIF, the use of a tunable laser improves the sensitivity (due to the high energy of the laser beam) and also the selectivity because the suitable wavelength can be chosen to excite and form only the PIF compounds of a given pesticide. However, as in classical PIF, several pesticides from the same

* Corresponding author.
E-mail address: philippe.giamarchi@univ-brest.fr (P. Giamarchi).

http://dx.doi.org/10.1016/j.talanta.2014.08.052
0039-9140/© 2014 Elsevier B.V. All rights reserved.

family cannot be analysed simultaneously if they have similar photoreactivity and form the same PIF compounds. PIF methods are then considered as broad specific routine methods useful to monitor the total amount of pesticides of a given family [3,5]. To overcome this problem, and to improve the selectivity of the method, it is necessary to couple chromatography to PIF.

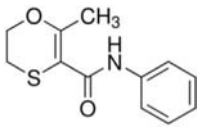
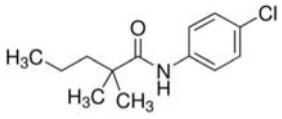
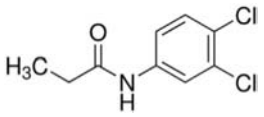
Chromatography has been already coupled to classical PIF for the determination of pesticides. A post-column photoreactor is used to irradiate the non-fluorescent pesticides with an UV lamp and to transform them into strongly fluorescent photo-products that are subsequently detected with a fluorimetric detector [9–11]. In this way, the problem of selectivity of classical PIF is improved thanks to the chromatography separation. Following this strategy, we have coupled for the first time chromatography to DL-PIF in order to improve the sensitivity of the chromatographic method. The aim of this paper is to develop and optimize a new DL-PIF method, based on the on-line coupling between high performance liquid chromatography (HPLC) and DL-PIF detection. As an example, we investigated the application of the DL-PIF–HPLC method to three anilide pesticides namely carboxin, monalide and propanil (Table 1), and we reported the analytical performances of this method.

2. Material and methods

2.1. HPLC–DL-PIF system

Liquid chromatography was performed with a C18 column ($150 \times 3.9\ mm^2$, 5 µm particle size). The system was equipped with a "Milton Roy" pump and a manual injector valve with a 200 µL sample loop. The post-column photochemical derivatization of the pesticides was carried out in a 450 µL flow cell (quartz Suprasil, Hellma) that was irradiated with a Nd:YAG tunable laser in order to simultaneously form the photoinduced compounds and measure their fluorescence [18]. The laser source was a Powerlite Precision 9010 (Continuum, Santa Clara, USA) pulsed Nd:YAG pump laser beam at a 10 Hz repetition rate, with a Sunlite EX Optical Parametric Oscillator (OPO) and FX-1 UV frequency extension system from Continuum, which permits continuous

Table 1
Chemical properties of monalide, carboxin and propanil.

Carboxin	Formula	$C_{12}H_{13}NO_2S$	
	Molecular weight	235.30 g/mol	
	Water solubility (20 °C)	134.0 mg/L	
Monalide	Formula	$C_{13}H_{18}ClNO$	
	Molecular weight	239.70 g/mol	
	Water solubility (20 °C)	22.8 mg/L	
Propanil	Formula	$C_9H_9Cl_2NO$	
	Molecular weight	218.08 g/mol	
	Water solubility (20 °C)	95.0 mg/L	

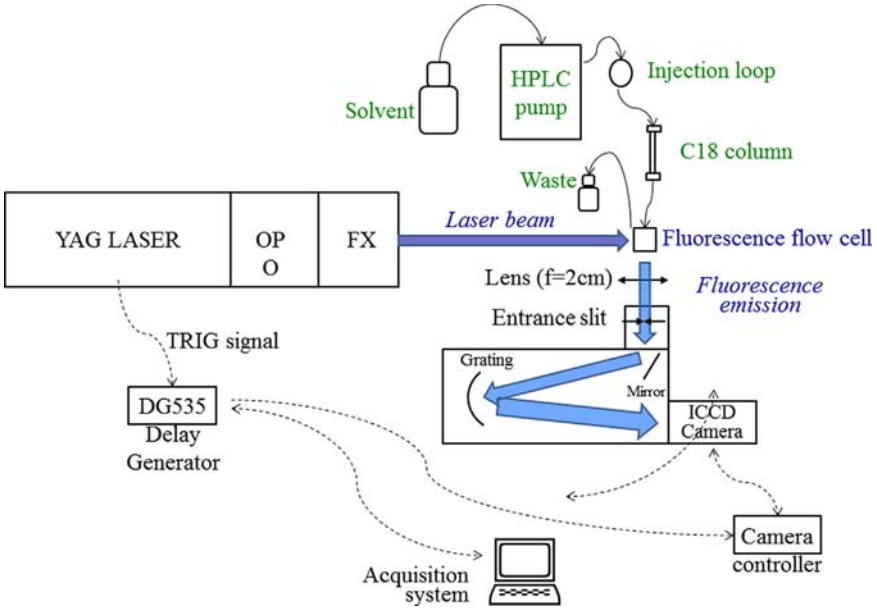


Fig. 1. Description of the experimental system (OPO=optical parametric oscillator, FX frequency extension system). Electronic connections are in dotted lines.

wavelength scanning from 225 to 1750 nm (LYOPO program). The available energy in the UV domain ranges from 2 mJ at 225 nm to 10 mJ per pulse at 275 nm [12,13]. The PIF fluorescence was collected at 90° angle from the excitation beam and focussed with a *f*/8 cm lens to the spectrometer entrance slit. The SpectraPro-550i spectrometer (Acton Research Corporation, Acton, MA, USA) has a 550 mm focal length and is equipped with a triple grating turret. The fluorescence was measured with an ICCD-MAX intensified CCD Camera (Princeton instruments, Trenton, NJ, USA) with a 512 × 512 pixel array optimized for the UV–visible domain. The camera is operated with a ST-133 controller (RS Princeton Instruments, Trenton, NJ, USA) for data acquisition. Timing control is achieved with a DG 535 digital delay/pulse generator (Stanford Research System Inc, Sunnywale, CA, USA). The WINSPEC 32-bit Windows software package (Roper Scientific Inc, Trenton, NJ, USA) provides acquisition, display and processing functions. Fig. 1 shows a schema of the whole system.

2.2. Absorption and fluorescence spectrophotometer

UV–visible absorption spectra were recorded on an Eclipse UV–visible spectrophotometer (Varian) and excitation fluorescence spectra with a Cary Eclipse fluorescence spectrophotometer (Varian).

2.3. Reagents

Carboxin, monalide and propanil were purchased from Sigma-Aldrich. Methanol was obtained from Sigma. All the reagents were of analytical reagent grade. Ultrapure water (Millipore Mro-MQ System) was used for the experimental work.

Stock standard solutions of the pesticides (200 mg/mL) were prepared by dissolving the compounds in methanol. An ultrasonic bath was used to obtain complete dissolution; then, solutions were stored in the dark. Serial dilutions were performed to obtain the working standard solutions. The working solutions were prepared in 60:40 (v/v) methanol–water mixture.

2.4. Sample preparation and chromatographic conditions

The water samples analysed were from the Senegal River, from the Atlantic Ocean of the Dakar seaside (Senegal) and from Penmarc'h seaside (France). The samples were filtered through a filter disk (45 μm) in order to eliminate the suspended organic matter and collected in 0.5 L amber glass bottles samples. The filtered samples were spiked with the anilide pesticides at two concentration levels (0.05 and 0.20 μg mL^{-1}).

A SPE C18 cartridge (LiChrolut RP-18E 200 mg 40–63 μm) was preconditioned with 2 mL of methanol followed by 5 mL of ultrapure water. 50 mL of the spiked water samples were passed through the cartridge. After elution of the polar compounds by 5 mL of pure water, the pesticides were eluted, leading to a 10-times pre-concentration factor. The samples were analysed in isocratic conditions with a methanol–water mixture (60:40 v/v). The flow rate was of 0.8 mL min^{-1}.

2.5. Statistical calculations

Statgraphics software (Statpoint Technologies), was used for statistical computation.

3. Results and discussion

3.1. Photo-induced fluorescence properties

Carboxin, monalide and propanil exhibited no native fluorescence, while UV irradiation yielded the formation of strongly fluorescent photoproducts. Fig. 2 compares the absorbance spectra of each pesticide with the excitation and emission fluorescence spectra of their photo-induced compounds (PIF) formed after 1 min of laser irradiation in a 3 mL fluorescence cell. The main absorption bands for carboxin, monalide and propanil were respectively 251, 247 and 251 nm (Table 2). One can see that carboxin formed two PIF compounds whereas monalide and propanil formed only one. For carboxin, the excitation emission couple (EEC) of its PIF compounds was of 230/370 nm (PIF 1) and 242/430 nm (PIF 2). The EEC of the photo-induced compoundsof monalide and propanil were,

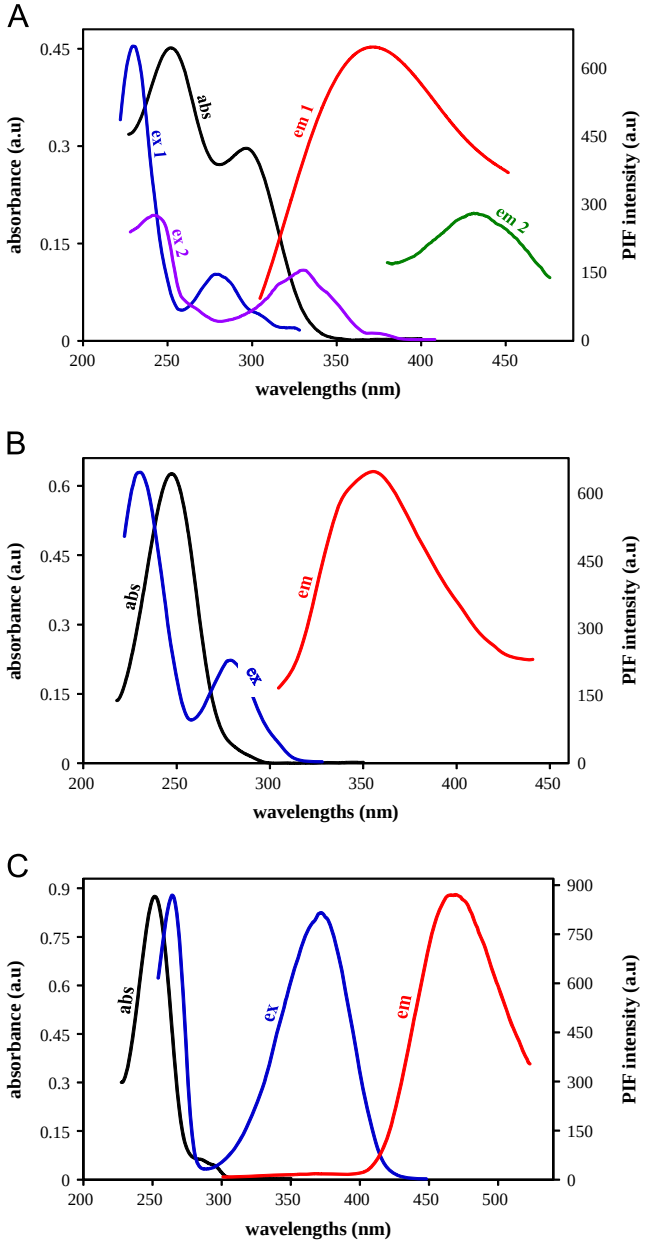


Fig. 2. Comparison of the UV–absorption spectra of the pesticides under study with the fluorescence excitation and emission spectra of the photo-induced compounds formed after 1 min of laser irradiation of the pesticides at 1 μg mL^{-1} in methanol–water mixture (60:40 v/v). (A) Carboxin; (B) monalide; and (C) propalil.

Table 2
UV absorption of monalide, carboxin and propanil and fluorescence properties of their photoproducts in methanol–water mixture 60:40 (v/v).

Pesticide		Absorbance λ_{max} (nm)	Fluorescence	
			λ_{EX} (nm)	λ_{EM} (nm)
Carboxin		251/296		
	PIF 1		230/280	370
	PIF 2		242/330	430
Monalide		247		
	PIF 1		230/280	354
Propanil		251		
	PIF 1		264/370	464

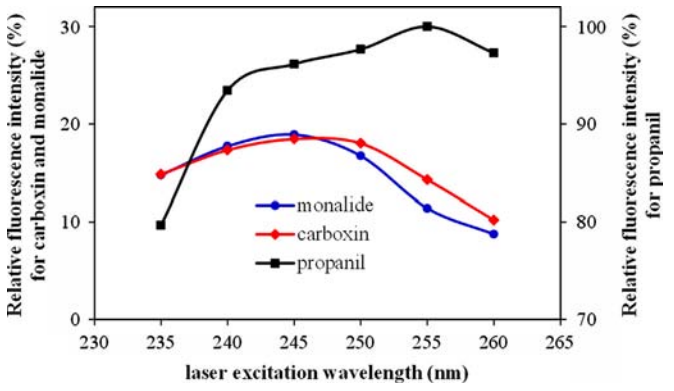


Fig. 3. Optimization of the laser excitation wavelength for carboxin, monalide and propanil. The fluorescence emission of carboxin, monalide (left axis) and propanil (right axis) are measured at 370, 354 and 464 respectively.

respectively, 230/354 nm and 264/464 nm (Table 2). Fig. 2 shows that the photo-induced compounds of carboxin and monalide have very similar fluorescence properties, while the photo-induced fluorescence of propanil is significantly red shifted.

3.2. HPLC–direct laser photo-induced fluorescence analysis

One of the limitations of classical PIF methods is the matrix effects due to the presence of interfering fluorescent compounds such as humic and fulvic acids. Even if the photo-induced fluorescence can be corrected by the fluorescence background of the interfering compounds, the measurement of a small change of fluorescence due to the target pesticide (with a very low concentration) on top of high native background fluorescence can reduce the sensitivity of the method and lead to systematic errors. Moreover the presence of other organic compounds, intrinsically fluorescent or not, can induce fluorescence quenching and reduce the fluorescent quantum yield of the PIF compounds leading to an error in the pesticide determination.

More problematic are the interferences with other compounds producing under UV irradiation PIF photoproduct(s). This is the case of pesticides from several chemical families, i.e. pyrethroids [5], chlorophenoxyacids [6], phenylureas [9], benzoylureas [10], sulfonylureas [14], etc. The worst interference problem is occurring when the pesticides under study belong to the same chemical class, and forms photo-products with very similar fluorescent behaviour. This is the case for monalide and carboxine. These pesticides cannot be individually analysed by classical PIF or DL-PIF methods when the samples contain simultaneously both pesticides. To overcome the limitations of classical PIF and DL-PIF, we have coupled HPLC to DL-PIF (Fig. 1). In this way, the problem of selectivity and matrix effects is improved thanks to the chromatographic separation.

To maximize the sensitivity of the HPLC–DL-PIF method, the formation of the photo-products has to be maximized (i.e. the wavelength should be set at the maximum UV absorption of the pesticide) but, at the same time, the photo-products have to be excited at their maximum excitation wavelength in order to maximize their fluorescence. However, the maximum absorption of the pesticide has seldom the same wavelength as the maximum excitation wavelength of its photo-induced compounds. Ideally, two wavelengths should then be used: one to form the photo-products and another to measure their fluorescence. Since the Nd:YAG laser can be tuned only at one wavelength at a time, we had to find a compromise between both wavelengths. For this purpose, we have compared for each pesticide the absorption spectrum and the emission spectrum of its PIF compounds (Fig. 2). In this way, we can see that the laser wavelength should be set approximately at 260 nm for propanil and at 240 nm for monalide and carboxin. Nonetheless, the energy of the laser is maximum at 275 nm and diminishes for lower wavelengths. Since the formation of the photo-products diminishes when the laser energy diminishes; we have studied the laser induced photo-induced fluorescence as a function of the laser wavelength. Fig. 3 shows that the maximum florescence intensity is obtained at 255 nm for propanil, and at 245 nm for monalide and carboxin.

We have obtained a good chromatographic separation of the three pesticides (Fig. 4). To maximize sensitivity, the laser was tuned during the chromatographic analysis. As carboxin is the first pesticide eluted at 5.4 min, the laser is set at 245 nm from the start to 7.0 min. To analyse propanil the second pesticide eluted at 10.2 min the laser then is tune to 255 nm (at the speed of

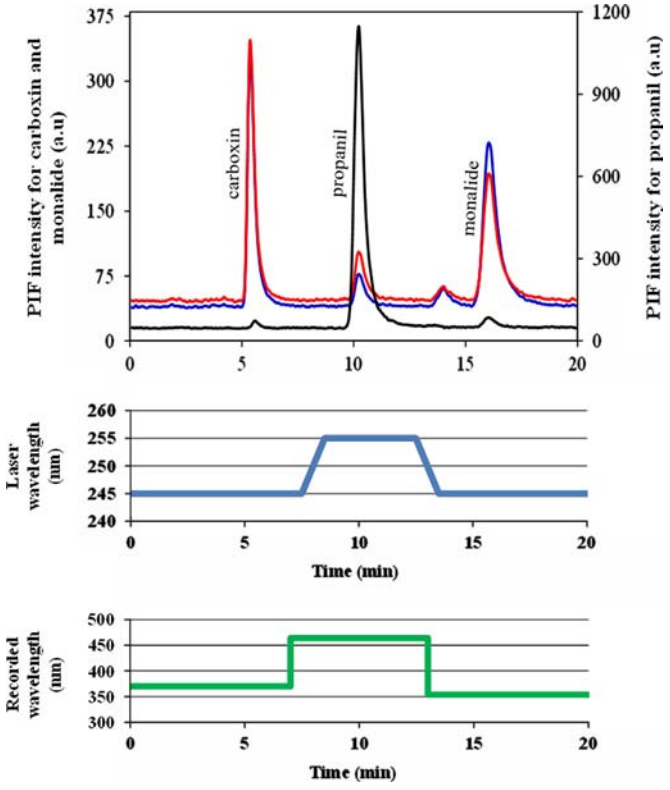


Fig. 4. Upper panel: chromatographic separation of carboxin, monalide and propanil. Laser irradiation is set at 245 nm for carboxin and monalide and 255 nm for propanil, PIF fluorescence detection is set at 370 nm for carboxin, 354 nm for monalide, and 464 nm for propanil. Middle panel: evolution of the laser excitation wavelength versus the time. Lower panel: evolution detected wavelength versus the time.

10 mn min^{-1}). At the end, to detect monalide eluted at 16.1 min the laser is tuned again to 245 nm. At this last wavelength the laser is ready for the next analysis. The "time line" of the laser wavelength is shown in Fig. 4 below the chromatogram.

At the same time the chromatograms are recorded at three emission wavelengths, firstly at 354 nm to detect monalide, then 464 nm for propanil and at last at 370 nm for carboxin. The time line of the recorded wavelength is shown at the bottom of the Fig. 4.

We have then validated the method following the standard ISO 8466-2 [15]. We have first conduct the statistical evaluation of the linear calibration function, followed by the evaluations of the detection and quantification limits.

The calibrations have been calculated with 7 different pesticides concentration from 0.01 to 5 μg mL^{-1} and 2 or 3 duplication per value. The results obtained are presented in Fig. 5 and Table 3 shows the performance parameters of the HPLC–DL-PIF methods. The propanil give the most sensitive result with a slope of 133.87 au mL μg^{-1}, while monalide and carboxin are less sensitive with a slope of 28.97 and 30.47 au mL μg^{-1} respectively. For the three pesticides the intercept are not significantly different from zero with p value for carboxin, monalide and propanil of 0.36, 0.12 and 0.08 respectively.

The linear function has been tested by variance analysis (Table 4), for each pesticide, at 5% confidence level. In all cases the regression variance of the linear model is found significantly greater than the residual variance (p value < 0.01 in all cases). Moreover, the lack of fit variance is not significantly greater than the pure error variance (p value for carboxin, monalide and propanil of 0.30, 0.09 and 0.91 respectively). Consequently the linear range could be validated from 0.01 to 5 μg mL^{-1}.

The instrumental detection limits (without pre-concentration) obtained for carboxin, monalide and propanil are respectively 3.2, 3.6 and 0.5 ng mL^{-1}. We can notice a great improvement of the analytical performance of our method compared to other results obtained by classical HPLC PIF. For example, the detection limits were 70 ng mL^{-1} for propanil, about 200 ng mL^{-1} for phenylureas pesticides [16] and about 15 ng mL^{-1} for pyrethroids [17] and benzoylureas [10].

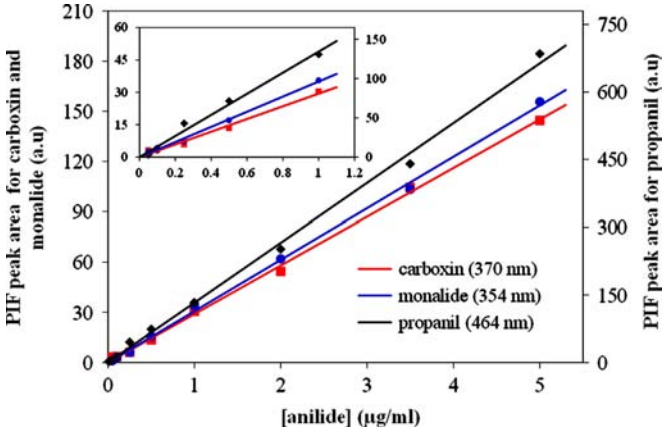


Fig. 5. Calibration curves of carboxin, monalide and propanil. Laser irradiation is set at 245 nm for carboxin and monalide and 255 nm for propanil, PIF fluorescence detection is set at 370 nm for carboxin, 354 nm for monalide, and 464 nm for propanil.

Table 3
Analytical figures of merit for the determination of monalide, carboxin and monalide by HPLC–DL-PIF.

	Carboxin	Monalide	Propanil
$\lambda_{EX}/\lambda_{EM}$ (nm)	245/370	245/354	255/464
Linear range (μg mL^{-1})	0.05–5	0.05–5	0.01–5
R^2	0.992	0.991	0.996
b	28.97	30.47	133.87
s_b	0.79	0.61	2.30
a	1.46	2.26	7.57
s_a	1.57	1.38	4.1
p_a	0.36	0.12	0.08
s_{res}	5.79	4.56	17.77
Detection limit (ng mL^{-1})[a]	3.18	3.64	0.53
Quantification limit (ng mL^{-1})[b]	10.61	12.14	1.77
RSD (%) (for 1 μg mL^{-1})[c]	5.03	5.96	2.15

a, intercept; s_a, standard deviation of the intercept; p_a, intercept p value; b, slope; s_b, standard deviation of the slope; R^2, determination coefficient; s_{res}, residual standard deviation.

[a] Calculated as the concentration of analyte giving a signal-to-noise (S/N) ratio of 3.

[b] Calculated as the concentration of analyte giving a signal-to-noise (S/N) ratio of 10.

[c] Relative standard deviation ($n=10$).

3.3. HPLC DL PIF analytical applications

The usefulness of the method was tested with recovery studies carried out in samples from Senegal River water which irrigates one of the most important agricultural areas of Senegal and can be submitted to some pesticide pollution. As river effluents can transfer the pesticide residue to seawater and induce fish contamination studies have been also carried out on sea water samples from Dakar seaside and Penmarc'h seaside.

The water samples were spiked with 0.05 and 0.2 μg mL^{-1}, extracted by SPE, and analysed by HPLC–DL-PIF as described in Section 2.4. The recoveries obtained can be observed in Table 5. The recovery values were very close to 100%, ranging from 89.5% to 115.9%. The relative standard deviation of the concentration found ranged from 1.2% to 7.2%. The HPLC–DL-PIF method is then suitable to determine anilide pesticides in river and sea water samples. Since the anilide pesticides were 10-fold pre-concentrated, the instrumental detection and quantification limits (Table 2) diminished also 10 times when the water samples are analysed by HPLC–DL-PIF. Thanks to SPE and also to the high sensitivity of the DL-PIF detection, it was then possible to detect and quantify the anilide pesticides of water samples in the order of ppb (ng mL^{-1}).

Table 4
Evaluation of the linear functions by variance analysis.

Pesticide	Source	Sum of squares	d.o.f.	Mean square	F	p value
Carboxin	Regression	45077.80	1	45077.80	1344.40	0.00
	Residual	704.13	21	33.53		
	Lack of fit	245.12	6	40.85	1.34	0.30
	Pure error	459.01	15	30.60		
	Total	45781.90	22			
Monalide	Regression	51256.20	1	51256.20	2456.73	0.00
	Residual	375.54	18	20.86		
	Lack of fit	206.31	6	34.38	2.44	0.09
	Pure error	169.24	12	14.10		
	Total	51631.80	19			
Propanyl	Regression	1065.83×10^3	1	1065.83×10^3	3374.88	0.00
	Residual	8.53×10^3	27	0.32×10^3		
	Lack of fit	0.96×10^3	7	0.14×10^3	0.36	0.91
	Pure error	7.57×10^3	20	0.38×10^3		
	Total	1074.36×10^3				

d.o.f, degree of freedom; F; calculated Fischer value.

Table 5
Mean recoveries obtained for river water and sea water samples spiked at 0.05 and 0.20 μg mL^{-1}. The samples are purified and preconcentrated 10 times by solid-phase-extraction.

Sample	Pesticide	Added (μg mL^{-1})	Found (μg mL^{-1})	Recovery [a] (%)	R.S.D [b] (%)
River water	Propanil	0.05	0.046	91.9	6.3
		0.20	0.190	95.6	4.6
	Monalide	0.05	0.049	98.9	7.1
		0.20	0.200	100.2	7.2
	Carboxin	0.05	0.054	108.8	5.4
		0.20	0.232	115.9	5.5
Sea water (Dakar, Senegal)	Propanil	0.05	0.049	98.3	2.1
		0.20	0.187	93.5	4.6
	Monalide	0.05	0.054	107.0	2.2
		0.20	0.185	92.3	6.2
	Carboxin	0.05	0.049	98.4	1.2
		0.20	0.207	103.5	3.6
Sea water (Brittany, France)	Propanil	0.05	0.046	92.9	4.2
		0.20	0.200	99.7	4.0
	Monalide	0.05	0.045	89.5	3.5
		0.20	0.189	94.5	5.2
	Carboxin	0.05	0.050	100.1	4.8
		0.20	0.209	104.7	5.6

[a] Triplicate measurements for each concentration.
[b] RSD=relative standard deviation.

4. Conclusion

We have shown in former papers that the DL-PIF method has better analytical performances and shorter times of analysis than classical PIF. However, the main drawbacks of classical and DL-PIF methods are the matrix effects due to fluorescent compounds or to other pesticides that form also under UV irradiation photo-products with very similar fluorescence behaviour. To solve these problems, the coupling of HPLC with DL-PIF detection allows one to combine the advantages of both techniques. The chromatographic separation significantly improves the selectivity of the DL-PIF method, and pesticides belonging to the same family, such as carboxin and monalide, yielding similar photoproducts, can be simultaneously analysed. At the same time, the DL-PIF determination of the compounds at the specific excitation wavelength can improve the selectivity of the method in case of insufficient chromatographic resolution.

Acknowledgements

O.M.A Mbaye thanks the University of Brest for its mobility scholarship.

References

[1] D. Ortelli, P. Edder, C. Corvi, Anal. Chim. Acta 520 (2004) 33–45.
[2] I. Ferrer, E.M. Thurman, J. Chromatogr. A 1175 (2007) 24–37.
[3] J.J. Aaron, A. Coly, Analusis 28 (2000) 699–709.
[4] O.M.A. Mbaye, M.D. Gaye Seye, A. Coly, A. Tine, M.A. Oturan, N. Oturan, J.J. Aaron, Microchem. J. 110 (2013) 579–586.
[5] M. Mbaye, M.D. Gaye Seye, J.J. Aaron, A. Coly, A. Tine, Anal. Bioanal. Chem. 400 (2011) 403–410.
[6] A.M. García-Campaña, J.J. Aaron, J.M. Bosque-Sendra, Talanta 55 (2001) 531–539.
[7] A. Maroto, P. Kissingou, A. Diascorn, B. Benmansour, L. Deschamps, L. Stephan, J.Y. Cabon, P. Giamarchi, Anal. Bioanal. Chem. 401 (2011) 3011–3015.
[8] P. Diaw, A. Maroto, O. Mbaye, M.D. Gaye-Seye, L. Stephan, A. Coly, L. Deschamps, A. Tine, J.J. Aaron, P. Giamarchi, Talanta 116 (2013) 569–574.
[9] A. Muñoz de la Peña, M.C. Mahedero, A. Bautista-Sánchez, J. Chromatogr. 950 (2002) 287–291.
[10] M. Martinez-Galera, T. López-López, M.D. Gil-Garcia, J.L. Martinez-Vidal, P. Parrilla Vazquez, J. Chromatogr. A 918 (2001) 79–85.
[11] A.R. Mughari, P. Parrilla Vásquez, M. Martínez Galera, Anal. Chim. Acta 593 (2007) 157–163.
[12] L. Burel, P. Giamarchi, L. Stephan, Y. Lijour, A. Le Bihan, Talanta 60 (2003) 295–302.
[13] P. Giamarchi, L. Burel, L. Stephan, Y. Lijour, A. Le Bihan, Anal. Bioanal. Chem. 374 (2002) 490–497.
[14] A. Coly, J.J. Aaron, Talanta 49 (1999) 107–117.
[15] Standard ISO 8466-2:2001,Water quality – Calibration and evaluation of analytical methods and estimation of performance characteristics, reviewed in 2012.
[16] A. Muñoz de la Peña, M.C. Mahedero, A. Bautista-Sánchez, Talanta 60 (2003) 279–285.
[17] T. López-López, M.D. Gil-Garcia, J.L. Martinez-Vidal, M. Martinez-Galera, Anal. Chim. Acta 447 (2001) 101–111.
[18] L. Burel, P. Giamarchi, L. Stephan, Y. Lijour, A. Le-Bihan, J. Fluoresc. 16 (2006) 177–183.

Talanta 132 (2015) 915–921

Contents lists available at ScienceDirect

Talanta

journal homepage: www.elsevier.com/locate/talanta

Simultaneous determination of blockers and agonists by on-fiber derivatization in self-made solid-phase microextraction coating fiber

Wei Liu [a,b], Zhiming Yan [a], Xiayang Huang [a], Jinfeng Chen [a,c], Minghua Lu [a,b], Lan Zhang [a,b,*], Guonan Chen [a]

[a] Ministry of Education Key Laboratory of Analysis and Detection for Food Safety (Fuzhou University), China
[b] Test Center of Fuzhou University, Fuzhou University, Fuzhou, Fujian 350002, China
[c] Longyan Entry-Exit Inspection and Quarantine Bureau, Longyan, Fujian 364000, China

ARTICLE INFO

Article history:
Received 10 April 2014
Received in revised form
19 July 2014
Accepted 21 July 2014
Available online 30 July 2014

Keywords:
Blockers
Agonists
On-fiber derivatization
Solid-phase microextraction
Gas chromatography–mass spectrometry

ABSTRACT

An environmentally friendly and sensitive method for determination of blockers and agonists was described in this paper. The method is based on a homemade sol–gel solid-phase microextraction (SPME) coating with simultaneous on-fiber derivatization and subsequent gas chromatography mass spectrometry (GC/MS) analysis. The influences of the main factors on the type and thickness of the homemade fiber coatings, conditions of the derivatization, extraction and desorption of SPME were investigated in detail. The proposed procedure showed limits of detection lower than 0.2 ng mL^{-1}. The linearity was in the 0.5–150 ng mL^{-1} for clenbuterol and 1.0–100 ng mL^{-1} for metoprolol and propranolol. The variation in measurements (repeatability) was below 8.7% ($n=6$) and the degree of difference between (reproducibility) was below 11.4% ($n=3$). In the application, spiked human saliva samples and real human saliva samples were analyzed, it was found that saliva would affect the detection of propranolol when it was a very low content. The established method can be feasible in practical application and helpful for agonists and blockers preliminary screening during the competition.

© 2014 Elsevier B.V. All rights reserved.

1. Introduction

Clenbuterol is one of the most widely used β2-adrenoceptor agonists, while metoprolol and propranolol are the most common β-antagonists (β-blockers). They both work on the body's β-adrenergic receptors with contrary effects and they are structural related amino alcohols. So they can be manipulated and analyzed together with similar detection procedures. The mainstream methods for determination of blockers and agonists include GC–MS [1,2], liquid chromatography [3,4], Capillary electrophoresis mass spectrometry (CE-MS) [5,6] and liquid chromatography–tandem mass spectrometry (LC–MS/MS) [7–9]. The involved biological samples include hair [10], whole blood [11], serum [12], plasma [13,14] and urine [5]. In the Medical Commission of the International Olympic Committee, the β2-agonists and β-blockers have been forbidden, and the official detection requirement is concentration of 0.5 μg mL^{-1} in urine by GC–MS after derivatization.

In fact, no matter what kind of biological sample analysis, the pretreatment and concentration is essential. And the new sample preparation method solid-phase microextraction (SPME) integrated sampling, extraction, concentration and sample introduction into one step, it has been considered as a very powerful sample preparation tool [15]. While introducing derivatization in SPME-GC/MS can further expand the application areas of SPME-GC/MS and bring lower limits of detection (LODs), there have been some researches and several reviews on this topic [16–20]. In brief, achieve derivatization operation during SPME-GC/MS process have three modes: in the gas chromatography injector port [21], in the sample matrix [22–24] and on the fiber coating after SPME sampling [25,26]. The injection-derivatization method is the inchoate derivatization approach of SPME-GC/MS which might lead to incomplete derivatization reaction and possible damage to the capillary column because of the excessive derivative agent. Derivatization reaction in the sample matrix with SPME sampling simultaneously is the simplest mode but with some limitations. While the derivatization occurs on the SPME fiber coating, the fiber is not only a separation/extraction device but also being turned into a reaction vessel. It makes the whole process simple and fast.

Until now, GC–MS is the major detection technique for beta2-agonists and beta-antagonists, and analysis of β2-agonists and

* Correspondence to: Department of Chemistry, Fuzhou University, Fuzhou 350002, Fujian, China. Tel.: +86 591 87892448; fax: +86 591 87893207.
E-mail address: zlan@fzu.edu.cn (L. Zhang).

http://dx.doi.org/10.1016/j.talanta.2014.07.064
0039-9140/© 2014 Elsevier B.V. All rights reserved.

β-blockers in saliva is a great choice because of its noninvasive, easy to collect and less confidential in comparison with blood and urine. In this paper, homemade sol–gel SPME coatings were prepared and contrasted for on-fiber derivatization and SPME operation; an entire GC–MS determination method for blockers and agonists was trying to establish and the application in positive saliva samples were realized so as to the unlimited and sensitive preliminary screening of clenbuterol, metoprolol and propranolol in competitions.

2. Experimental procedures

2.1. Chemicals and reagents

Silylating reagents of N-methy-N-(trimethylsilyl) trifluoroacetamide (MSTFA) was obtained from Sigma (SIGMA, St. Louis, MO, USA). Clenbuterol, metoprolol and propranolol (Fig. 1) were from national institute for the control of pharmaceutical and biological products (Beijing, China). Methyl methacrylate (MMA), benzoyl peroxide (BPO), tetramethyl orthosilicate (TMOS), trifluoroacetic acid (TFA) and polyethylene glycol 20 000 (PEG 20 000) were from Sinopharm Chemical Reagent Co. Ltd. (Shanghai, China). Hydroxy-terminated silicone oil (OH-TSO) and poly methyl hydrogen siloxane (PMHS) were purchased from Santai Organic Silica Material Factory (Zhejiang, China). Divinylbenzene (DVB) was obtained from Shengzhong Fine Chemical Co. Ltd. (Shanghai, China).

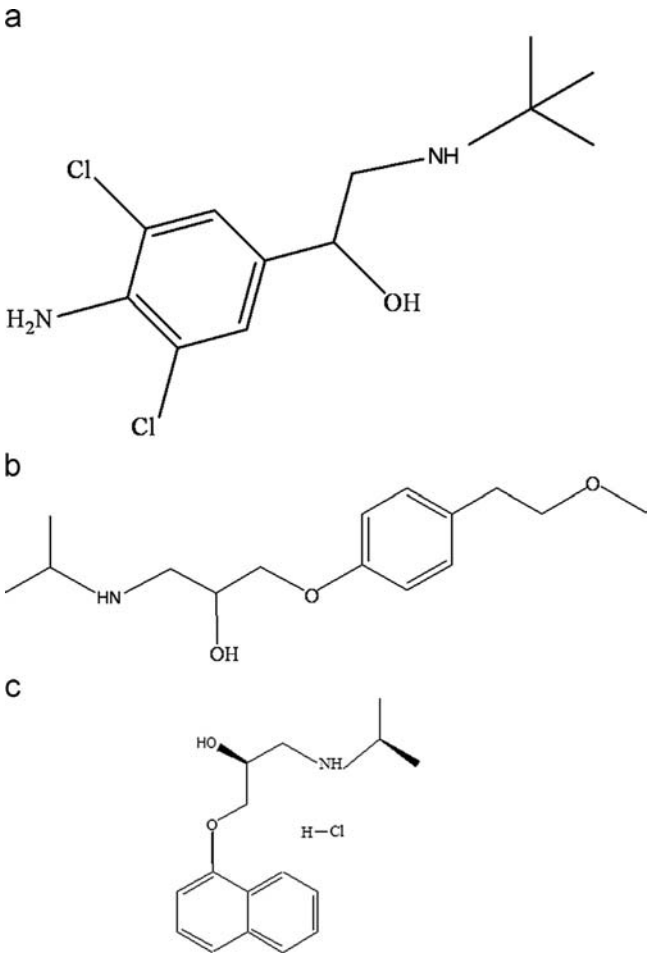


Fig. 1. Structures of the studied molecules.

A stock standard mixture containing clenbuterol, metoprolol and propranolol (1.00 mg mL^{-1}, respectively) was prepared in methanol and stored at 4 °C.

Working standard solutions were prepared by diluting with methanol and renewed every week. Spiked water samples were prepared weekly by adding the appropriate volume of the working standards solution to the 20 mL water sample. Milli-Q ultrapure water (Millipore, Bedford, USA) was used throughout the experiments and the resistivity was about 18 MΩ cm (25 °C).

2.2. Instrumentation and operating conditions

All the gas chromatographic experiments were performed on an Agilent 6890N-5973I GC-MSD (Hewlett-Packard, Palo Alto, CA, USA). A HP-5MS GC column (0.25 μm film thickness, 0.25 mm × 30 m, Agilent Technologies) was used for separation.

The SPME device for manual extraction was consisted in a homemade holder assembly and several replaceable homemade fiber assemblies, which were prepared as described in reference [27]. The thickness of the homemade SPME fiber coating was monitored by environmental scanning electron microscope (XL30 ESEM, Philips).

The injector temperature was maintained at 270 °C. Splitless injection was employed and the injection volume was 1.0 μL. The oven temperature was set at 80 °C for 1 min, and then increased to 260 °C at 25 °C min^{-1} and held for 1 min, and then heated at 15 °C min^{-1} to 300 °C. Carrier gas was helium (Purity > 99.999%) and the flow rate was set at 1.2 mL min^{-1}. The electron impact (EI) ion source, quadrupole mass analyzer, and the interface temperature were maintained at 230, 150 and 300 °C, respectively. Electron impact ionization (70 eV) was utilized. *m*/*z* range was 50–550, and solvent delay was 7 min. Positive mode was used for detection. Selected ion monitoring (SIM) was employed for quantitative measurement. For clenbuterol, the qualitative ions were 57, 73, 86 and 262 (*m*/*z*), and the quantitative ion was 86 (*m*/*z*); for metoprolol, the qualitative ions were 72, 101, 223 and 324 (*m*/*z*), and the quantitative ion was 72 (*m*/*z*); for propranolol, the qualitative ions were 72, 115, 144 and 215 (*m*/*z*), and the quantitative ion was 72 (*m*/*z*).

2.3. Preparation of the homemade SPME fiber coatings

Before sol–gel coating, commercial silica fiber (Yongnian Optical Fiber Factory, Yongnian, Heibei Province, China) was immersed in acetone for 15 min to remove the polyimide on its surface, then rinsed with water and dried. After that, a rehydroxylation process was performed to maximize the number of silanol groups on the silica surface before the preparation of fiber coatings. At first, the fiber was immersed in 1.00 mol L^{-1} sodium hydroxide solution for 60 min to increase the number of silanol groups on fiber wall, then rinsed with water and dried. Finally, the fiber was immersed in 0.10 mol L^{-1} hydrochloric acid for 20 min to reestablishment of equilibrium, then rinsed with water again and dried. The procedure was repeated for 3 times.

Then, four different fibers coatings with different polarities – carbowax–divinylbenzene (CW–DVB), carbowax (CW), hydroxyl silicone oil–polymethylhydrosiloxane (OH-TSO–PMHS) and polyacrylate (PA) – were prepared according to the procedures in our previous work [27]. Briefly, for the preparation of OH/TSO–PMHS fiber coating, a volume of 600 μL of TMOS (precursor), 440 μL of OH-TSO (coating polymer), 60 μL of PMHS (deactivation reagent), and 400 μL of TFA (acid catalyst) were thoroughly shaken and degasification for 5 min by supersonic purifier. The mixture was then centrifuged at 4000 r min^{-1} for 5 min. The precipitate was removed and the top clear sol solution was used for fiber coating. For the preparation of CW fiber coating, 400 μL of TMOS, 200 μL of

OH-TSO, 50 μL of PMHS, 300 μL of 99% TFA, 200 mg of PEG-20,000 and 300 μL of acetone were mixed in a 2 mL tube. For CW/DVB fiber coating, 400 μL of TMOS, 200 μL of OH-TSO, 50 μL of PMHS, 300 μL of TFA, 200 μL of DVB, 200 mg of PEG-20,000 were mixed, and for PA fiber coating, 300 μL of TMOS, 220 μL of OH-TSO, 30 μL of PMHS and 200 μL of 99% TFA were mixed. When fibers were dipped vertically into a freshly prepared sol solution, it was held inside the sol solution for 20 min with sol–gel coating forming on the bare outer surface of the fiber end. For each fiber, this coating process was repeated for 3 times. Then it was placed in a desiccator at room temperature for 12 h.

2.4. SPME and derivatization procedure

The SPME fibers were conditioned on GC injection port at 250 °C for 2 h before use. A 20 mL of measured solution was placed in a 25 mL glass vial with a silicon-septum cap and spiked with analytes, and mixed with 4.5 g of NaCl adjusted pH to 11.00 with 1.0 mol L^{-1} NaOH. The vial was capped, and placed on a stirrer and heated to 30 °C with 650 r min^{-1} for 30 min. After extraction, the fiber was exposed in the headspace of a 2.0 mL sample vial containing 3.0 μL MSTFA at 40 °C for 10 min. Finally, the fiber was pulled out from the vial and immediately inserted into the GC injection port for thermal desorption with 270 °C and 4 min.

2.5. Sample preparation

Saliva samples were collected from three healthy male volunteers. All saliva samples were collected before or 2 h after eating 50.00 mg metoprolol. To obtain the mixed saliva samples, each volunteer was told not to swallow the saliva but to store it 6 min in their mouths when sampling. Then, saliva was collected in Eppendorf tubes and stored at −20 °C immediately. Every saliva sample was taken out of 200 μL in serum bottle, added 4.50 g NaCl for SPME extraction and diluted to 20.00 mL by deionized water then adjusted to pH 11.00 with 1.00 mol L^{-1} NaOH solution.

3. Results and discussion

Because clenbuterol, metoprolol and propranolol are polar materials and cannot respond in GC/MS without derivatization, they need to be derivatized to achieve good recoveries and precision. In this paper, based on the merits of on-fiber derivatization method introduced above, the typical derivatizing reagent for hydroxyl compounds (the silylating reagent of MSTFA with β-agonists and β-blockers) was chosen to be loaded on the fiber after analytes extraction [28,29]. In optimization experiments, every measuring datum was repeated three times, and an average was applied.

3.1. Selection of SPME fiber

Fiber coating is one of the key factors in the extraction efficiency to analytes. One objective of this study was to select the suitable SPME fiber coating for the extraction and derivatization of blockers and agonists from aqueous samples.

In this experiment, three types of homemade fiber coating were selected for investigation as strong polar coatings CW and CW–DVB, moderate polar coating PA and weak polar coating OH-TSO/PMHS. As the rule of "like dissolves like", it could be seen from Fig. 2 that CW–DVB fiber exhibited the best effect to all three analytes.

Fiber thickness, one of critical factors in the determination of the adsorption capacity of SPME fiber coating, is related to the number of coating times. Coating fiber of the CW–DVB column was executed from 2 to 5 layers, and the thickness of them were about 10, 21, 32 and 39 μm, mesured by ESEM. It was found that the adsorption amount of analytes reached maximum when 32 μm fiber coating was used.

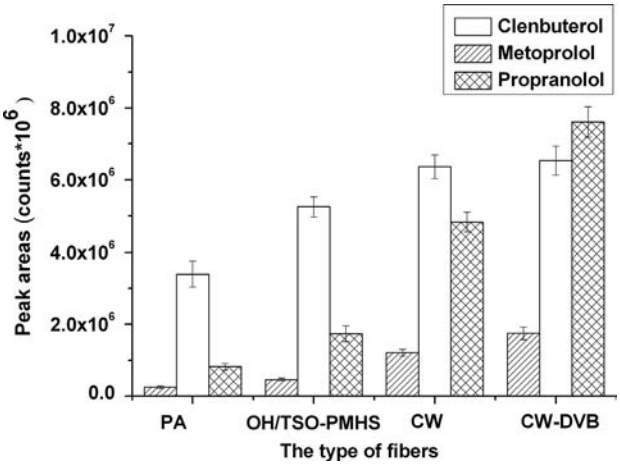


Fig. 2. Selection of SPME fiber coatings. SPME conditions: extraction temperature, 30 °C; extraction time, 30 min; stirring rate, 650 r min^{-1}; pH, 11.00; NaCl concentration, 0.225 g mL^{-1}; MSTFA, 3 μL; derivatization temperature, 40 °C; derivatization time, 10 min; desorption temperature, 270 °C; desorption time, 4 min. The concentrations of clenbuterol, metoprolol and propranolol were 2.0 ng mL^{-1}, respectively.

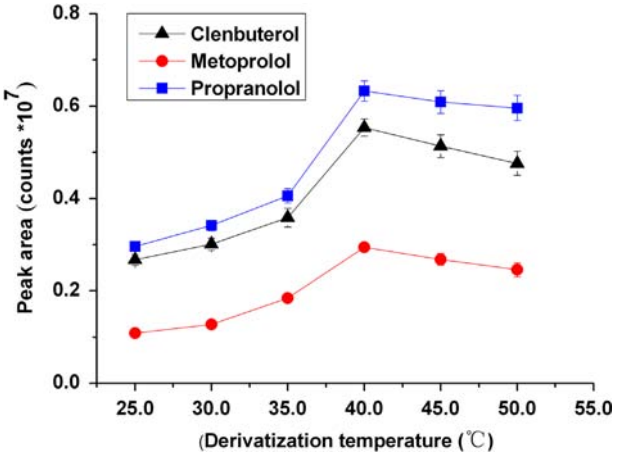


Fig. 3. Selection of derivatization temperature. CW–DVB fiber coating, other SPME conditions are as Fig. 2. The concentrations of clenbuterol, metoprolol and propranolol were 2.0 ng mL^{-1}, respectively.

3.2. Optimization of derivatization reactions

The derivatization reaction was affected by various parameters, including the reaction temperature, the derivatization time and the volume of the reagent. The derivatization conditions were optimized to achieve both high derivatization yield and high extraction efficiency.

First of all, the effect of the reaction temperatures was tested at 25 °C, 30 °C, 35 °C, 40 °C, 45 °C and 50 °C with 3 μL MSTFA to the analytes, respectively. When the temperature was lower than 40 °C, the extraction yields was positively correlated with the temperature; but when the temperature was higher than 40 °C, the correlation was reversed because of the side reactions of derivatization (Fig. 3). So, the derivatization temperature was chosen at 40 °C.

In order to examine the effect of the reaction time on the derivatization efficiency, experiments were performed at 5, 8, 10,

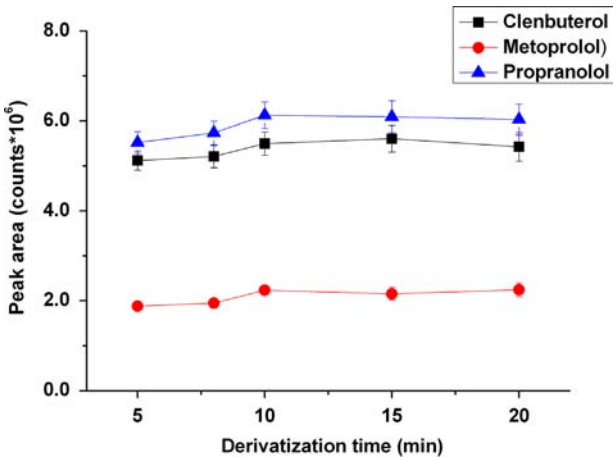


Fig. 4. Selection of derivatization time. CW–DVB fiber coating, other SPME conditions are as Fig. 2. The concentrations of clenbuterol, metoprolol and propranolol were 2.0 ng mL^{-1}, respectively.

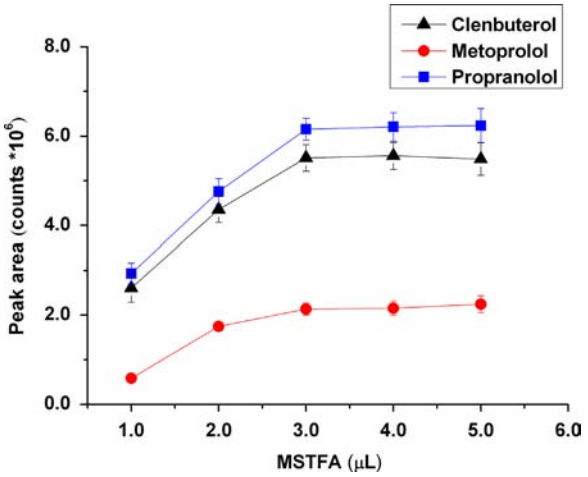


Fig. 5. The volume of MSTFA. CW–DVB fiber coating, other SPME conditions are as Fig. 2. The concentrations of clenbuterol, metoprolol and propranolol were 2.0 ng mL^{-1}, respectively.

15 and 20 min by using MSTFA at 40 °C. As shown in Fig. 4, the highest peak area for the derivatives of compounds was at 10 min and with no significant change until 20 min. As a result, subsequent experiments were carried out using a 10 min derivatization time.

Although the amount of derivatization reagents should be enough for the derivative reaction, immoderate excess of derivatization reagents is actually disadvantageous to the fiber coating lifetime. In this experiment, the effect of 1–5 μL of derivatization reagent MSTFA was compared with the same amount of analytes at 40 °C for 10 min. It can be seen from Fig. 5 that the peak areas of three TMS derivatives increased as the volume of MSTFA increased to a maximum of 3 μL. As a consequence, 3 μL of reagent was used to ensure that enough derivatizing reagent was present during the extraction process.

3.3. Optimization of SPME extraction conditions

Many factors, including extraction temperature, extraction time, stirring speed, pH of the solution and concentration of NaCl, can influence SPME extraction efficiency. These parameters were carefully optimized in this SPME study.

The effect of extraction temperature to the target compounds was examined from 20 to 60 °C and the results were illustrated in

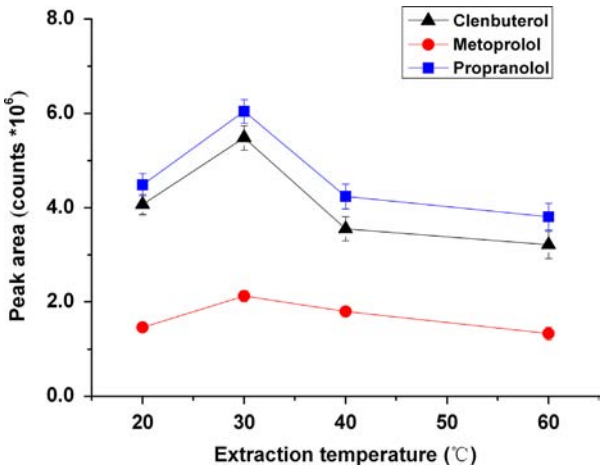


Fig. 6. Selection of extraction temperature. CW–DVB fiber coating, other SPME conditions are as Fig. 2. The concentrations of clenbuterol, metoprolol and propranolol were 2.0 ng mL^{-1}, respectively.

Fig. 6. Temperature affects both the kinetics and the thermodynamics of the extraction process of analytes. Higher temperature can accelerate the mass transference; at the same time, partition coefficients of the analytes between the fiber and the solution decrease with the increase of temperature. In conclusion, the effect of various temperatures on the response of metoprolol was insignificant, whereas the effects on propranolol and clenbuterol reached maximum at 30 °C; thus 30 °C was selected as the optimum value.

The duration of SPME extraction was also studied. SPME is an equilibrium-based technique, and the best extraction efficiency usually reached after equilibrium. To find the optimum extraction time, the samples were stirred at 30 °C with 650 r min^{-1} for 5–60 min. It was found that the responses of metoprolol and clenbuterol increased with increasing extraction time until 30 min and propranolol reached maximum at 45 min. Taking into account of the effect of extraction time to all three analytes, 30 min was selected as the extraction time.

The optimization of stirring speed was performed from 500 to 1100 r min^{-1}. The results indicated that increasing stirring speed to 650 r min^{-1} could markedly enhance the extraction amounts of compounds, especially propranolol. High stirring speed can accelerate the diffusion from the bulk of the sample solution to the coating surface and reduce the equilibrium time, while the frangible silicon dioxide fiber could be damaged with excessively high stirring speed. So, 650 r min^{-1} was selected.

One of the most important parameters in the extraction process is the pH. pH values influenced not only the dissociation of functional groups in analytes, but also the surface properties of the fiber. Generally, in order to increase the extraction efficiency of the target compounds in sample solution, appropriate pH should be chosen to keep these compounds as molecular form and prevent them from dissociating during the SPME process. The effect of the pH of the sample solution was examined by varying pH from 8.00 to 12.00 (adjusted by 1.0 mol/L HCl and 1.0 mol/L NaOH). At pH 11.00, all three analytes achieved maximum responses.

Increasing the ionic strength of the sample solution can reduce the solubility of analytes in water due to the formation of hydration spheres around the ionic salt molecules. However, the additional ions brought competitive adsorption with analytes and changed the surface properties of the fiber, which were unfavorable for the extraction. For investigating the effect of salt addition, various concentrations of NaCl in sample solutions (0, 0.075, 0.150, 0.225, 0.300 and 0.350 g mL^{-1}) were tested. Results showed that

0.225 g mL^{-1} NaCl yielded the most extracted amounts to all three target compounds; hence NaCl concentration of 0.225 g mL^{-1} was chosen for next experiments.

3.4. Optimization of desorption conditions

After SPME extraction and derivatization, the target compounds were desorpted using the GC injection port. With respect to the desorption conditions, both the desorption temperature and the desorption time were optimized.

For removing the extracted analytes from the fiber coating to the vaporizing chamber, the temperature of injection port, namely the desorption temperature, was optimized from 240 to 290 °C (Fig. 7). Optimal desorption temperatures were decided by the capabilities of the instrument, the properties of analytes and the specifications of the SPME fiber. The SPME fiber used in this method could endure 290 °C with gradually degradation and the inappropriate temperature would result in the coating bleed of the fiber and could be disadvantageous to the chromatographic column. Considering precision and recovery, 270 °C was chosen as suitable desorption temperature.

Then, for achieving the total desorption of analytes with no memory effects, desorption time was optimized and the optimal time for extracting maximal amounts of all compounds was 4 min.

To sum up, the optimal conditions of extraction, derivatization and desorption were as follows: in 20 mL spiked water solution, adjusting pH to 11.0, including 0.225 g mL^{-1} NaCl, using 32 μm homemade CW–DVB fiber coating extracted analytes for 30 min with 650 r min^{-1} stirring rate at 30 °C; then derivatization for 40 °C and 10 min with 3.0 μL MSTFA; desorption was performed in 270 °C for 4 min.

After choosing related influence factors, the typical total ion current (TIC) chromatograms and the extracted ion current (EIC) chromatograms of three analytes in blank water solution and spiked water solutions (2.0 ng mL^{-1} and 100 ng mL^{-1}) were given as Fig. 8a and b. It could be seen from Fig. 8a that, derivatization introduced some impurities to the SPME fiber in the TIC mode; but it did not affect the detection of extracted ions of clenbuterol (ion 86), metoprolol (ion 72) and propranolol (ion 72) (see Fig. 8b). It demonstrated that the water matrix and SPME fiber did not affect the detection of clenbuterol, metoprolol and propranolol.

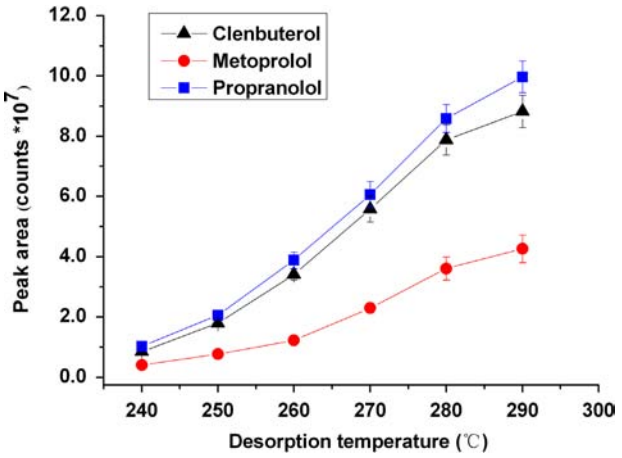


Fig. 7. Selection of the desorption temperature. CW–DVB fiber coating, other SPME conditions are as Fig. 2. The concentrations of clenbuterol, metoprolol and propranolol were 2.0 ng mL^{-1}, respectively.

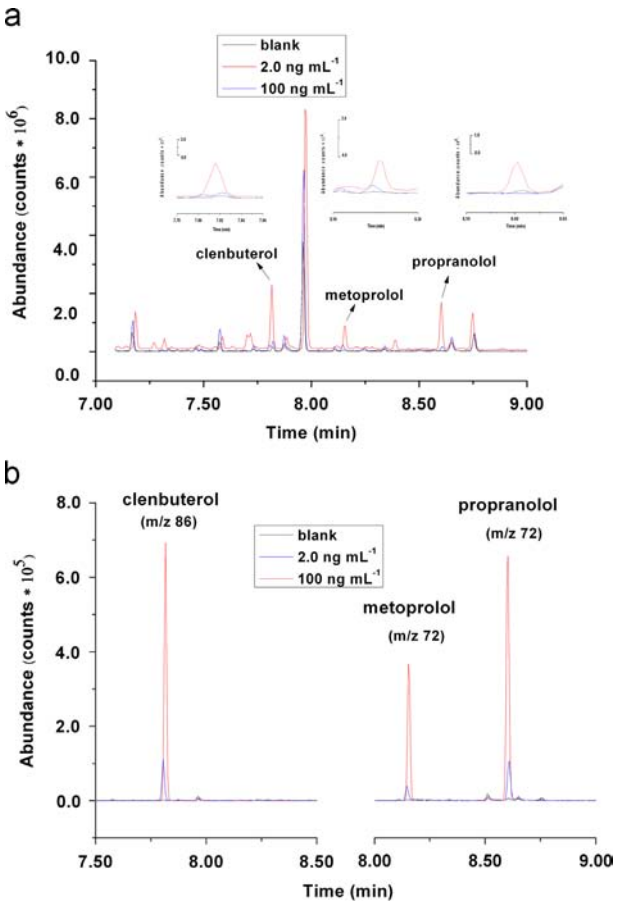


Fig. 8. The chromatograms of analystes with on-fiber derivatization after SPME. (a) TIC chromatogram, and (b) EIC chromatogram. CW–DVB fiber coating, SPME conditions are as Fig. 2.

3.5. Method performance

Calibration solutions with spiked deionized water samples were adsorbed, derivatizated, desorpted, analyzed with the optimized conditions and detected with GC–MS. The regression curves, correlation coefficients (R^2), linear ranges and limits of detection (LODs) of three targets were shown in Table 1. The linearity of this method was investigated over a concentration range of 0.5–150 ng mL^{-1} for clenbuterol and 1.0–100 ng mL^{-1} for metoprolol and propranolol. The linear relationship between peak areas and concentrations were observed with R^2 greater than 0.9933. This allowed the quantification of the compounds by the method of external standardization. The LODs for the analytes were estimated at S/N=3 under GC/MS conditions (SIM mode) by considering the lowest concentration of each of the analytes. The LODs were lower than 0.2 ng mL^{-1}.

Repeatability, expressed as the relative standard deviation of the analysis of seven samples spiked at 100 ng mL^{-1}, was below 8.7% (n=6). Reproducibility between days, expressed as the relative standard deviation of three samples spiked at 100 ng mL^{-1} and analyzed on three different days, was below 11.4% (n=3).

3.6. Method application

3.6.1. Spiked and real human saliva sample analysis

Each of the 200 μL blank saliva sample obtained from healthy people was added 4.50 g NaCl and diluted with deionized water to 20.00 mL. Then they were adjusted by 1.00 mol L^{-1} NaOH to pH

Table 1
The regression equations, linearity, correlation coefficients, LODs, repeatability and reproducibility of the method[a].

Analytes	Equation[b]	R^2	Linear range (ng mL^{-1})	LOD[c] (ng mL^{-1})	Repeatability[d] (%RSD, n=6)	Reproducibility[e] (%RSD, n=3)
Clenbuterol	y=298100x+10555	0.9977	0.5–150	0.2	7.2	10.6
Metoprolol	y=117237x+16144	0.9933	1.0–100	0.5	8.7	11.4
Propranolol	y=334490x+39156	0.9985	1.0–100	0.5	8.3	10.9

[a] Conditions as in Fig. 8.
[b] S/N=3.
[c] The parameters, x and y, refer to the concentration of the target compound (ng mL^{-1}) and the corresponding peak area.
[d] 100 ng mL^{-1}.
[e] 100 ng mL^{-1}.

Table 2
Extraction recoveries of spiked saliva samples by SPME with on-fiber derivatization[a].

Analytes	Recoveries (%RSD, n=3)		
	1.0 (ng mL^{-1})	5.0 (ng mL^{-1})	50 (ng mL^{-1})
Clenbuterol	109.7 (7.9)	112.7 (7.3)	106.1 (8.6)
Metoprolol	111.4 (9.0)	105.5 (8.2)	107.7 (7.4)
Propranolol	120.3 (13.1)	116.8 (11.7)	114.5 (12.0)

[a] Conditions as in Fig. 8.

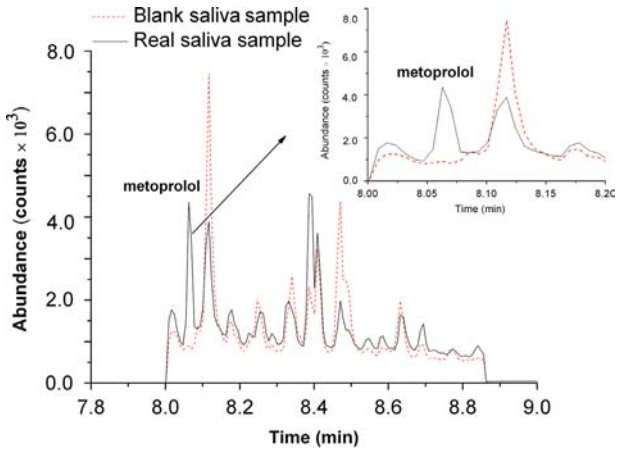


Fig. 9. The EIC chromatograms of blank and positive metoprolol saliva samples. SPME conditions are as Fig. 8.

11.00. After that, the diluted saliva solutions were spiked with analytes to 1.0, 5.0 and 50 ng mL^{-1}, respectively. Under the optimized conditions, the blank and spiked target compound solutions were detected three times, and the recoveries and precisions were given in Table 2.

As shown in the table, the recoveries of the target compounds were between 105.5% and 120.3%,, and the precisions were lower than 13.1%; so this method could be used for lightly determination of trace clenbuterol, metoprolol and propranolol in real saliva positive samples without more tedious additional disposals such as deproteinization.

3.6.2. Application to positive human saliva sample analysis

A male volunteer was treated with one pill of metoprolol tablet (~50 mg metoprolol) and the saliva was collected after 2 h. After pre-treatment with description in 2.3.6, the proposed method was applied to the detection of metoprolol in collected positive saliva samples under the optimal conditions. The EIC chromatograms (ion 72) of metoprolol positive saliva samples and blank saliva samples using optimized parameters were shown in Fig. 9.

It could be seen that there was an obvious chromatographic peak in positive saliva sample chromatogram at metoprolol's peak time which was significantly different from the blank sample chromatogram, and unfortunately, a small peak of blank saliva sample was found appearing at the position of propranolol in the EIC chromatogram for ion 72. It would affect the detection of extracted ion of propranolol when propranolol was a very low content.

4. Conclusion

A selective analytical method based on SPME followed by on-fiber derivatization with MSTFA coupled to GC–MS was used to determine clenbuterol, metoprolol and propranolol. The important parameters involved in the method such as appropriate polarity and thickness of fiber coating material with consistent extraction, derivatization and desorption parameters were evaluated. This method is timesaving and easy to perform as the total analytical time is less than 1 h; it is environmental friendly and avoids using toxic organic solvents and excess derivatization reagents. This method is fully validated and shown to be suitable for the simultaneous confirmation and quantitation of blockers and agonists with good LODs lower than 0.2 ng mL^{-1}. The repeatability was below 8.7% (n=6) and the reproducibility was lower than 11.4% (n=3). This simple and sensitive method has been applied to the measurement of clenbuterol, metoprolol and propranolol in human saliva. It showed that in saliva samples the performance of the method is still descent in presence of enzymes and proteins. The established method can offer a preliminary screening means for clenbuterol, metoprololand and propranolol. Since on the one side, large competitions have huge amount of samples need to screening and on the other side, confirmation of abuse drugs still using urine samples. This method was feasible in practical application and helpful for agonists and blockers control during the competition. It can provide an alternative option to extend the scope of doping monitoring and biological monitoring of blockers and agonists.

Acknowledgments

This work was supported by the National Natural Science Foundation of China (21275029 and 21405018), National Basic Research Program of China (No. 2010CB732403), the Program for Changjiang Scholars and Innovative Research Team in University (No. IRT1116) and the Nature Sciences Funding of Fujian Province (2010J05021).

References

[1] S. Yang, X. Liu, Y. Xing, D. Zhang, S. Wang, X. Wang, Y. Xu, M. Wu, Z. He, J. Zhao, J. Chromatogr. Sci. 51 (2013) 436–445.
[2] A. Gonzalez-Antuna, P. Rodriguez-Gonzalez, I. Lavandera, G. Centineo, V. Gotor, J.I. Garcia Alonso, Anal. Bioanal. Chem. 402 (2012) 1879–1888.
[3] M.D. Gil Garcia, B. Penas Pedrosa, M. Martinez Galera, Talanta 83 (2011) 1665–1672.
[4] W. Liu, Z. Wei, Q. Zhang, F. Wu, Z. Lin, Q. Lu, F. Lin, G. Chen, L. Zhang, Talanta 88 (2012) 43–49.
[5] Y. He, X. Li, P. Tong, M. Lu, L. Zhang, G. Chen, Talanta 104 (2013) 97–102.
[6] Y. Jin, C. Chen, L. Meng, J. Chen, M. Li, Z. Zhu, Talanta 89 (2012) 149–154.
[7] C. Li, Y.-L. Wu, T. Yang, Y. Zhang, W.-G. Huang-Fu, J. Chromatogr. A 1217 (2010) 7873–7877.
[8] X.-B. Chen, Y.-L. Wu, T. Yang, J. Chromatogr. B 879 (2011) 799–803.
[9] Y. Wu, H. Miao, S. Fan, Y. Zhao, Sci. China-Chem. 53 (2010) 832–840.
[10] P. Kintz, V. Dumestre-Toulet, C. Jamey, V. Cirimele, B. Ludes, J. Forensic Sci. 45 (2000) 170–174.
[11] M. Josefsson, A. Sabanovic, J. Chromatogr. A 1120 (2006) 1–12.
[12] A. Aresta, C.D. Calvano, F. Palmisano, C.G. Zambonin, J. Pharm. Biomed. 47 (2008) 641–645.
[13] B. Yilmaz, A. Asci, S. Arslan, J. Sep. Sci. 33 (2010) 1904–1908.
[14] X. Hu, J. Pan, Y. Hu, G. Li, J. Chromatogr. A 1216 (2009) 190–197.
[15] J. Deng, Y. Yang, X. Wang, T. Luan, TrAC Trends Anal. Chem. 55 (2014) 55–67.
[16] M.A. Farajzadeh, N. Nouri, P. Khorram, TrAC Trends Anal. Chem. 55 (2014) 14–23.
[17] A.M. Casas Ferreira, M.E. Fernandez Laespada, J.L. Perez Pavon, B. Moreno Cordero, J. Chromatogr. A 1296 (2013) 70–83.
[18] S.N. Atapattu, J.M. Rosenfeld, J. Chromatogr. A 1296 (2013) 204–213.
[19] N.H. Snow, Adv. Chromatogr. 48 (2010) 373–388.
[20] E.E. Stashenko, J.R. Martínez, TrAC Trends Anal. Chem. 23 (2004) 553–561.
[21] L. Pan, J. Pawliszyn, Anal. Chem. 69 (1997) 196–205.
[22] A. Valenzuela, G. Lespes, W. Quiroz, L.F. Aguilar, M. Bravo, Talanta 125 (2014) 196–203.
[23] C. Coscollà, S. Navarro-Olivares, P. Martí, V. Yusà, Talanta 119 (2014) 544–552.
[24] Z. Cui, K. Zhang, Q. Zhou, J. Liu, G. Jiang, Talanta 85 (2011) 1028–1033.
[25] D.R. Parkinson, J.M. Warren, J. Pawliszyn, Anal. Chim. Acta 661 (2010) 181–187.
[26] R. Peñalver, N. Campillo, M. Hernández-Córdoba, Talanta 87 (2011) 268–275.
[27] W. Liu, L. Zhang, S. Chen, H. Duan, X. Chen, Z. Wei, G. Chen, Anal. Chim. Acta 631 (2009) 47–53.
[28] W. Liu, L. Zhang, Z. Wei, S. Chen, G. Chen, J. Chromatogr. A 1216 (2009) 5340–5346.
[29] C. Brunelli, C. Bicchi, A. Di Stilo, A. Salomone, M. Vincenti, J. Sep. Sci. 29 (2006) 2765–2771.

Talanta 132 (2015) 922–928

Contents lists available at ScienceDirect

Talanta

journal homepage: www.elsevier.com/locate/talanta

Synthesis of g-C_3N_4/Fe_3O_4 nanocomposites and application as a new sorbent for solid phase extraction of polycyclic aromatic hydrocarbons in water samples

Man Wang, Shihai Cui, Xiaodi Yang**, Wentao Bi*

Jiangsu Collaborative Innovation Center of Biomedical Functional Materials, Jiangsu Key Laboratory of Biomedical Materials, College of Chemistry and Materials Science, Nanjing Normal University, Nanjing 210023, China

ARTICLE INFO

Article history:
Received 8 June 2014
Received in revised form
25 August 2014
Accepted 31 August 2014
Available online 6 September 2014

Keywords:
g-C_3N_4
Fe_3O_4
Magnetic solid phase extraction
Polycyclic aromatic hydrocarbons

ABSTRACT

An easy preparation of g-C_3N_4/Fe_3O_4 nanocomposites by chemical co-precipitation has been demonstrated. The as-prepared materials were characterized by X-ray diffraction, transmission electron microscopy, Fourier transform infrared spectroscopy and thermogravimetric analysis. The high affinity of g-C_3N_4 toward polycyclic aromatic hydrocarbons and the magnetic behavior of Fe_3O_4 were combined to provide an efficient and simple magnetic solid phase extraction (MSPE). The adsorption and desorption of polycyclic aromatic hydrocarbons on g-C_3N_4/Fe_3O_4 were examined. Different factors affecting the magnetic solid phase extraction of polycyclic aromatic hydrocarbons were assessed in terms of adsorption, desorption, and recovery. Under the optimized conditions, the proposed method showed good limits of detection (LOD, S/N=3) in the range of 0.05–0.1 ng mL^{-1} and precision in the range of 1.8–5.3% (RSDs, n=3). This method was also successfully applied to the analysis of real water samples; good spiked recoveries over the range of 80.0–99.8% were obtained.

© 2014 Elsevier B.V. All rights reserved.

1. Introduction

Polycyclic aromatic hydrocarbons (PAHs) are a widely distributed group of environmental persistent pollutants, which are ubiquitous in aquatic environments and suspected to be endocrine disrupters. They have aroused great attention to their influences on environment, especially aquatic environment. The Environmental Protection Agency (EPA) (e.g. maximum contaminant levels for benzo(a)pyrene and benz(a)anthracene in ambient water were 0.2 and 0.1 μg mL^{-1}, respectively) and European Union (EU) have taken some PAHs as priority pollutants for monitoring purposes [1,2]. Most PAHs do not dissolve easily in water (supplementary file). Due to their trace concentration and wide distribution in water environments, it is required and vital to develop efficient analytical techniques [3]. However, the direct determination of extremely low concentrations of analytes can be difficult, owing to matrix interferences or insufficient sensitivity of analytical techniques. Therefore, preliminary separation and preconcentration of trace analytes from matrices is usually required. Solid-phase extraction (SPE) and liquid-liquid extraction (LLE) are the most commonly used techniques for sample preconcentration. Of these methods, SPE has become a powerful tool in trace analysis [4], because of its high recoveries, enrichment factors, low consumption of organic solvents, and the possibility of combining with chromatography and spectroscopic techniques. On the other hand, a high recovery and enrichment factor can be obtained only if a suitable sorbent is used. In recent years, we have seen an intense growth of interest in materials with graphite-like structures, such as graphene (G) and graphene oxide (GO), owing to their large surface area and hexagonal array of carbon atoms in graphite sheets which are ideal for strong interactions with other molecules [5,6]. They were used as sorbent for the preconcentration of small molecules [7,8], and both sides of the planar sheets are available for molecule adsorption. As a novel two-dimensional graphite analogue, graphitic carbon nitride (g-C_3N_4) is emerging recently and may be a viable alternative to separation and preconcentration of organic compounds in solutions.

g-C_3N_4 has a stacked two-dimensional structure (2D sheets of tri-s-triazine connected via tertiary amines) and is made from simple precursors under ambient conditions at a low cost. Moreover, it is the most stable allotrope of carbon nitride [9,10]. Compared with other inorganic semiconductor counterparts, g-C_3N_4 is an eco-friendly organic material and exhibit great potential for energy conversion, storage, and environmental applications including direct methanol fuel cells, catalysis, photocatalysis, and CO_2 capture [11]. Above all, the dispersity of g-C_3N_4 in water is much better than that of G with strong affinity (π–π stacking and

* Corresponding author. Tel.: +86 25 85891705; fax: +86 25 85891707.
** Corresponding author. Tel.: +86 25 83598648.
E-mail addresses: yangxiaodi@njnu.edu.cn (X. Yang), biwentao@njnu.edu.cn (W. Bi).

http://dx.doi.org/10.1016/j.talanta.2014.08.071
0039-9140/© 2014 Elsevier B.V. All rights reserved.

hydrophobic interactions) for nonpolar carbon-based ring compounds [12]. These properties suggest the possibility of g-C_3N_4 as a novel sorbent for SPE and as a new material for the adsorption and preconcentration of organic analytes.

On the other hand, sufficient dispersity of nanomaterials usually creates difficulties in separating and recycling. As one of the most widely used magnetic materials, Fe_3O_4 nanoparticles, has good stability, easy synthesis, high surface area and good solubility in water. On the other hand, they aggregate easily and cannot adsorb analytes effectively because of the simplicity of its surface [13]. Therefore, immobilizing Fe_3O_4 particles on the surface of nanomaterials is an effective solution, as it can easily be separated from solution with an external magnet [14]. This approach can efficiently increase the recovery of nanoparticles and recycle time, and it is therefore our goal to design and prepare g-C_3N_4/Fe_3O_4 composite materials. Moreover, the application of this kind of magnetic material for SPE was defined as magnetic solid phase extraction (MSPE). MSPE technology exhibits significant advantages in separation science. The sorbent is dispersed in a sample solution instead of being packed into an SPE cartridge providing a sufficiently large contact area between sorbents and analytes, and can be rapidly separated from the matrix by an external magnetic field [15,16].

To examine the feasibility of this g-C_3N_4/Fe_3O_4 nanocomposite for MSPE, seven PAHs were selected as model compounds. Key factors, including concentration of PAHs, ionic strength, pH, eluent, amount of sorbent, time, etc., were systematically optimized to achieve excellent MSPE efficiency. Moreover, a quick, selective and sensitive method was established by combining MSPE with high performance liquid chromatography (HPLC) to analyze seven PAHs in real water samples.

2. Experimental

2.1. Chemicals

Melamine (>99.0%), naphthalene (Naph) (>99.5%), acenaphthylene (Acy) (>98.0%), phenanthrene (Ph) (>99.0%), anthracene (An) (>99.5%), fluoranthene (Flt) (>98.0%), pyrene (Pyr) (>98.0%) and benz[a]anthracene (BaA) (>98.0%) were purchased from Aladdin Industrial Inc. (Shanghai, China). Ferric chloride hexahydrate (>97.0%), ferrous chloride tetrahydrate (>98.0%), and ammonia water (25.0%) were obtained from Sinopharm Chemical Reagent CO., Ltd (Shanghai, China). Distilled water was filtered using a vacuum pump (Division of Millipore, USA) and filter (HA-0.45, Division of Millipore, USA) prior to use. All other solvents were of HPLC or analytical grade.

2.2. HPLC analysis and characterization

The HPLC system consisted of a Waters 1525 Binary HPLC Pump, a Waters 2707 Autosampler (20.0 μL sample loop) and a variable wavelength 2489 UV dual channel detector. Data processing was carried out using a Millennium 3.2 consisting of a HP Vectra 500PC. HPLC was performed by using a commercial C_{18} column (4.6 × 150 mm, 5.0 μm) purchased from Thermo Fisher Scientific Inc. The mobile phase was methanol/water (80/20, *v*/*v*) at a flow rate of 1.0 mL min^{-1}, and detection was performed at a UV wavelength of 254 nm.

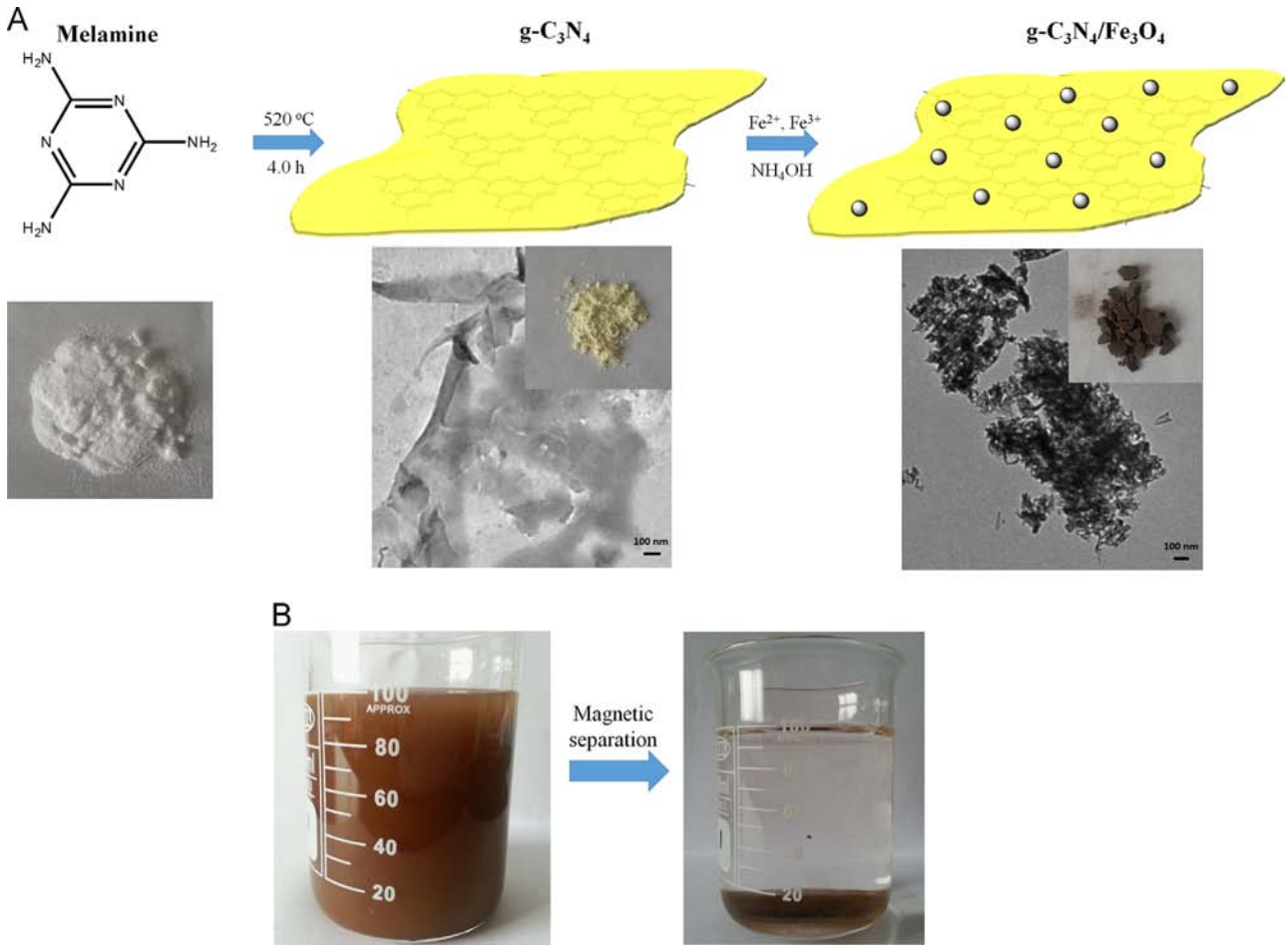


Fig. 1. Schematic representation of depositing Fe_3O_4 nanoparticles on a g-C_3N_4 with morphology exhibitions.

X-ray diffraction (XRD) studies were carried out on a Rigaku D/max 2500/PC instrument. Transmission electron microscopy (TEM) was executed on a Hitachi H-7650. Fourier transform infrared (FT-IR, Bruker Tensor 27) spectra were obtained between 400 and 4000 cm^{-1} at a scan rate of 20 scans min^{-1} using KBr pellets. Thermogravimetric measurements were performed on a NETZSCH STA 449 F3 Jupiter simultaneous thermal analyzer at a heating rate of 10 °C min^{-1} in air.

2.3. Preparation of g-C_3N_4/Fe_3O_4 nanoparticles

g-C_3N_4 was prepared by directly heating melamine to 520 °C for 4 h in a N_2 atmosphere [17]. The g-C_3N_4/Fe_3O_4 nanocomposites were obtained by chemical co-precipitation [18,19]. According to a typical procedure, g-C_3N_4 (70.0 mg) was dispersed in 250.0 mL of ethanol/water (1:2) and ultrasonicated for 6 h at room temperature. $FeCl_3 \cdot 6\,H_2O$ (0.92 g) and $FeCl_2 \cdot 4\,H_2O$ (0.45 g) at a molecular ratio of 2:3 were added to the suspension of g-C_3N_4 at 65 °C. Next, the ammonia solution was injected into the reaction mixture until the pH reached 10.0. The resulting mixture was stirred at 80 °C for another 30 min, after which the reaction mixture was cooled and washed several times with ethanol and double-distilled water. The as-prepared nanocomposite was named g-C_3N_4/Fe_3O_4-1 and was dried in air at 80 °C (Fig. 1).

Alternatively, another synthetic method was proposed and used to synthesize the g-C_3N_4/Fe_3O_4 composite. Fe_3O_4 nanoparticles were first synthesized using the same procedure without the addition of g-C_3N_4. The obtained nanoparticles were mixed with melamine in ethanol and dried in air. The mixture was then heated to 520 °C for 4 h. The obtained nanocomposite was named g-C_3N_4/Fe_3O_4-2.

2.4. Preparation of the standard stock solution

PAHs, including Naph, Acy, Ph, An, Flt, Pyr, and BaA were dissolved in methanol to obtain standard stock solutions at a concentration of 0.1 mg mL^{-1}. The stock solutions were stored at 4.0 °C. Working solutions were prepared daily by diluting the standard stock solutions with deionized (DI) water.

2.5. Multicomponent adsorption of PAHs on g-C_3N_4/Fe_3O_4

The sorbents (1.0 mg) were sonicated and vibrated with 1.0 mL of aqueous standard PAH solution (0.3 μg mL^{-1} PAHs mixture with adding a small amount of methanol) in vials at room temperature until the concentration of target compounds ceased decreasing and the equilibrium adsorption was obtained. The amounts of PAHs adsorbed on the sorbents were calculated by subtraction, and the adsorption percentage (%) was calculated by adsorbed amount/maximum theoretical adsorbed amount. The reproducibility was assessed over five tests.

2.6. Procedure of MSPE

g-C_3N_4/Fe_3O_4 (10.0 mg) was used to extract the analytes from 100.0 mL real water samples. The extraction was carried out for 10.0 min to ensure that most of the analytes were adsorbed on the solid phase. The magnetic adsorbents were separated from water by a magnetic field. To elute the adsorbed analytes, 1.0 mL (0.5 mL × 2 times) of a 1:1 mixture of methanol/acetonitrile was added and the vial was subsequently subjected to ultrasonic irradiation for 5 min. After elution, the solutions were collected and analyzed by HPLC.

3. Results and discussion

3.1. Characterization of g-C_3N_4/Fe_3O_4

First, the as-prepared g-C_3N_4/Fe_3O_4 samples were characterized by XRD [20]. As shown in Fig. 2, the XRD peaks of the pure Fe_3O_4 sample were in good agreement with the standard magnetite Fe_3O_4. For g-C_3N_4, a strong peak at 27.41 corresponded to the (0 0 2) crystal plane of g-C_3N_4. The diffraction peaks of g-C_3N_4 and Fe_3O_4 were observed in the XRD pattern of g-C_3N_4/Fe_3O_4-1, and were weaker than that of pure g-C_3N_4, indicating that g-C_3N_4/Fe_3O_4-1 was a two-phase composite composed of g-C_3N_4 and Fe_3O_4. In contrast, the characteristic diffraction peak of g-C_3N_4 disappeared in g-C_3N_4/Fe_3O_4-2, and the structure of Fe_3O_4 was different. These phenomena can be explained by the evaporation of melamine and oxidation of Fe_3O_4 at high temperatures under air.

In addition, FT-IR spectra of g-C_3N_4/Fe_3O_4-1 (Fig. 3) showed the successful formation of g-C_3N_4/Fe_3O_4 [21]. The most intense signal at 570 cm^{-1} was assigned to the Fe–O stretch of Fe_3O_4 [22]. The strong absorption band in the range of 1200–1650 cm^{-1} was assigned to the typical skeletal stretching vibrations of the s-triazine or tri-striazine and the sharp peak centered at 808 cm^{-1} was a characteristic breathing mode of the triazine unit. The broad adsorption band at 3100–3300 cm^{-1} corresponded to the stretching vibration modes of residual N–H components or O–H bands, associated with uncondensed amino groups and absorbed H_2O

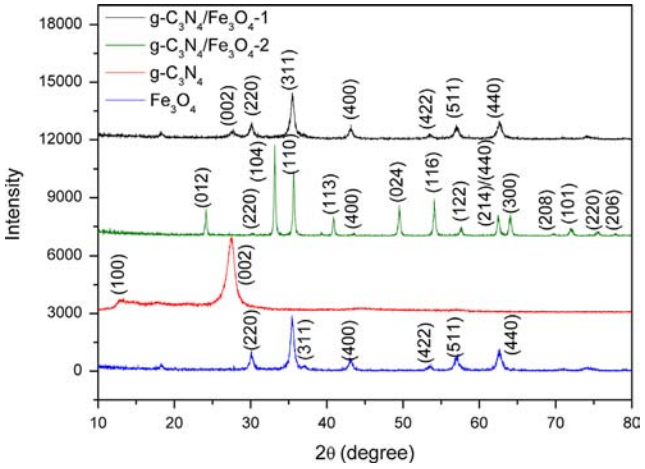


Fig. 2. XRD patterns of g-C_3N_4, Fe_3O_4 and g-C_3N_4/Fe_3O_4.

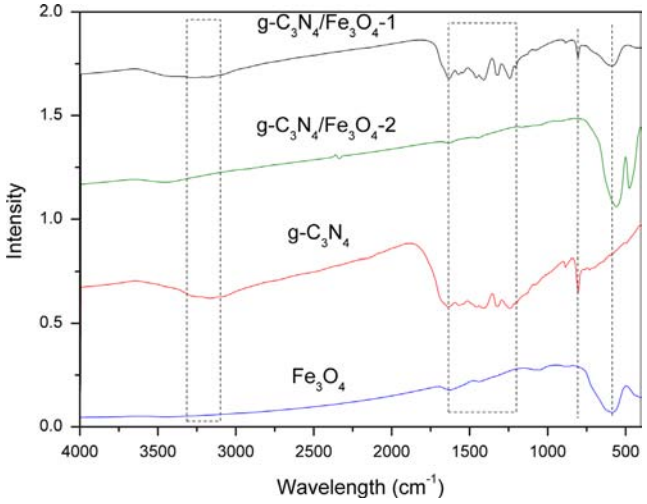


Fig. 3. FT-IR spectra of g-C_3N_4, Fe_3O_4 and g-C_3N_4/Fe_3O_4.

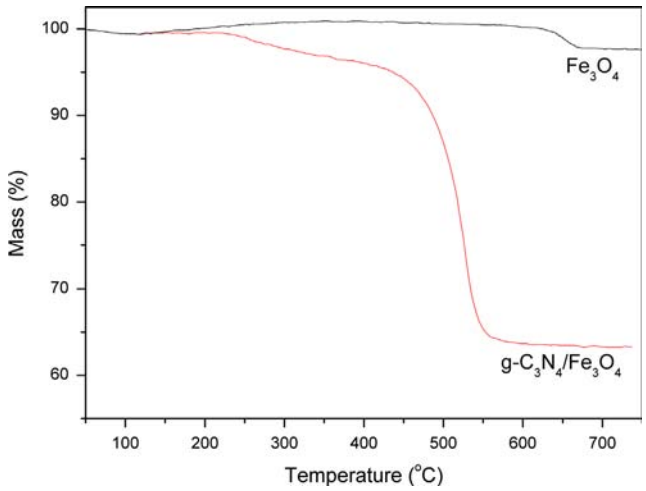


Fig. 4. TGA curves of Fe_3O_4 and g-C_3N_4/Fe_3O_4.

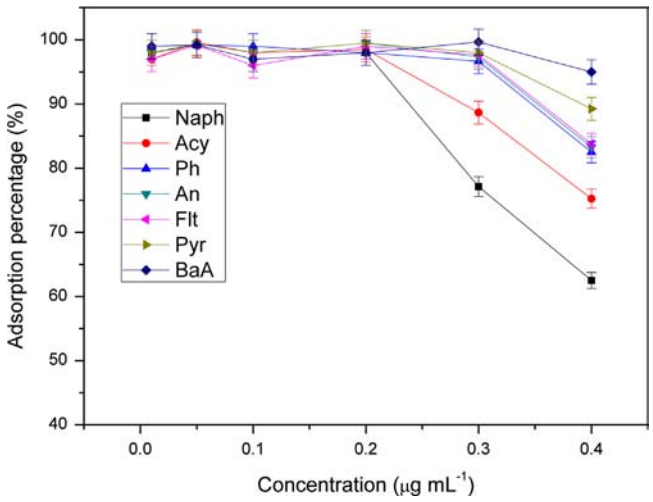


Fig. 5. Effect of initial concentration of PAHs on adsorbed amount of PAHs on g-C_3N_4/Fe_3O_4.

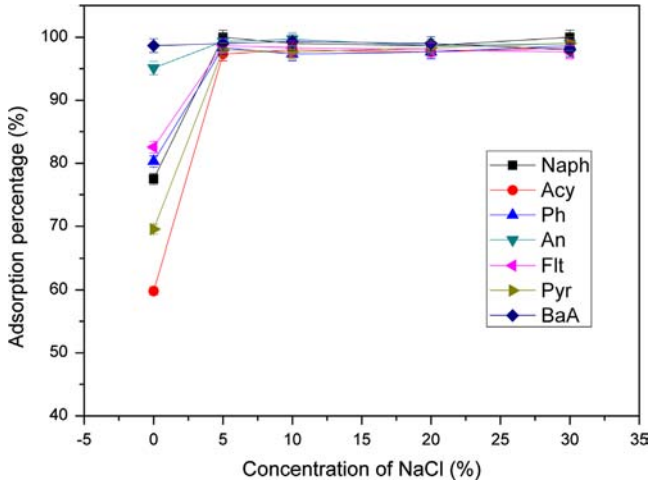


Fig. 6. Effect of NaCl% on adsorbed amount of PAHs on g-C_3N_4/Fe_3O_4.

molecules, respectively. Similarly, these peaks were not observed in the spectrogram of g-C_3N_4/Fe_3O_4-2.

Thermogravimetric analysis was used to determine the thermal stability of the g-C_3N_4/Fe_3O_4 nanocomposite, as the weight loss observed between 500 °C and 550 °C was associated with the loss of the g-C_3N_4. Fig. 4 shows the TGA curves for Fe_3O_4 and g-C_3N_4/Fe_3O_4-1. From 500 °C to 550 °C, approximately 2.61% and 36.26% mass loss was observed for Fe_3O_4 and g-C_3N_4/Fe_3O_4-1, respectively.

Fig. 1 shows the TEM images of pure g-C_3N_4 and g-C_3N_4/Fe_3O_4-1. Pure g-C_3N_4 consisted of a transparent sheet structure, whereas in g-C_3N_4/Fe_3O_4-1, dark Fe_3O_4 nanoparticles were deposited on the surface of g-C_3N_4. Overall, g-C_3N_4/Fe_3O_4-1 was successfully synthesized and could be used for further experiments of the MSPE of PAHs in this study.

3.2. Optimization of the MSPE procedure

Before applying the magnetic sorbent g-C_3N_4/Fe_3O_4 in the MSPE of real samples, factors that influence the adsorption and desorption of target analytes on g-C_3N_4/Fe_3O_4 nanocomposites should be investigated and optimized. Because MSPE was achieved by the adsorption and subsequent desorption of PAHs on the sorbents, the amounts adsorbed and desorbed indicate the performance of g-C_3N_4/Fe_3O_4. Meanwhile, ultrasonication was used to suspend the g-C_3N_4/Fe_3O_4 nanocomposite in water. The aggregated nanocomposite is disrupted by ultrasonic vibrations leading to an increase in the total solid surface which contacts water or target compounds.

3.2.1. Adsorption

The initial concentration of PAHs in water samples dictates the maximum amount that can be adsorbed theoretically, and can affect the actual adsorbed amount on the g-C_3N_4/Fe_3O_4 nanocomposite. High adsorption efficiencies of PAH compounds were observed at low concentrations such as 0.01–0.2 μg mL^{-1} (Fig. 5). The adsorption of seven PAHs nearly reached the maximum theoretical adsorption when the concentrations were below 0.2 μg mL^{-1}. The efficiencies decreased with further increase of the concentration, which was attributed to the limited adsorption capacity of g-C_3N_4/Fe_3O_4. To investigate other effects on the adsorption behavior and avoid errors in MSPE process, 0.3 μg mL^{-1} PAHs was selected.

The effect of the ionic strength was evaluated using sodium chloride as a model electrolyte within the concentration range of 0–30.0% (*w*/*v*) (Fig. 6). The adsorption of PAHs increased with increasing NaCl concentrations up to 5.0% due to a salting-out effect [23], and remained almost constant in this interval. The results indicated that the addition of NaCl had a negligible effect on the extraction recovery of the analytes when the concentration was higher than 5.0% (*w*/*v*). Hence, 5.0% NaCl was added to the all samples in subsequent experiments.

Generally, the pH of the solution is a crucial factor in the adsorption process, because pH not only changes the formation of the analytes but also alters the interaction between the sorbents and the analytes. Thus, it was necessary to investigate the effect of pH on adsorption efficiency by adding appropriate volumes of 1M NaOH or 1M HCl. As shown in Fig. 7, the adsorption efficiency of PAHs increased upon increasing the pH from 3.44 to 6.86. However, upon further increase of the pH value, the adsorption efficiency of BaA decreased. Although PAHs exist as neutral molecules under ordinary conditions and are unlikely to be influenced by a change in the solution pH, the pH of the solution may affect the g-C_3N_4/Fe_3O_4 formation and dispersity in water. Acidic conditions may cause some leaching of Fe_3O_4, thereby decreasing the adsorption of PAHs on the g-C_3N_4/Fe_3O_4 nanocomposite. Relatively basic conditions are conductive to g-C_3N_4/Fe_3O_4, but slightly decrease the dispersity of the sorbent in water by affecting the remaining amino groups and negative charge on

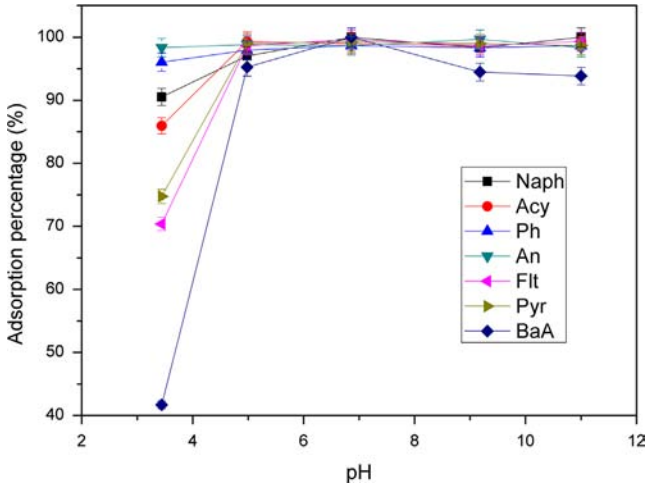


Fig. 7. Effect of pH values on adsorbed amount of PAHs on g-C_3N_4/Fe_3O_4.

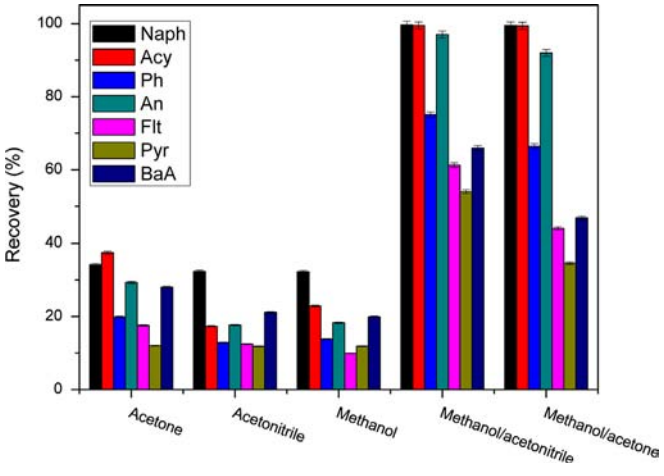


Fig. 8. Effect of type of solvents on recovery of PAHs.

g-C_3N_4. Therefore, the adsorption of BaA, the PAH with the largest molecular size, was decreased.

3.2.2. Desorption

The organic solvent is one of the most important factors that affect the MSPE procedure directly, and the extraction efficiency strongly relies on the properties of the eluent. Therefore, 10.0 mg of g-C_3N_4/Fe_3O_4 was used to extract the analytes from 10.0 mL of spiked water samples (concentration: 0.3 μg mL^{-1}). Considering that HPLC was used for the analysis of the PAHs and the remaining water on the surface of g-C_3N_4/Fe_3O_4 due to previous dispersion in water for adsorption, five organic solvents and mixtures (1.0 mL) including methanol, acetonitrile, acetone, methanol/acetone (1/1, *v*/*v*) and methanol/acetonitrile (1/1, *v*/*v*) were compared for their eluting efficiency. As shown in Fig. 8, the desorption efficiency was significantly affected by the eluent. Single solvent systems were not efficient for the elution of the condensed ring PAHs with good dispersity because of the relative hydrophilicity of g-C_3N_4/Fe_3O_4 and hydrophobicity of PAHs. Methanol/acetonitrile (1/1, *v*/*v*) provided the highest elution efficiency and was chosen as the eluent for MSPE.

3.2.3. Optimization of MSPE

Although a very small amount of sorbent was required in the adsorption of trace PAHs in water samples according to the theoretical adsorption capacity of g-C_3N_4/Fe_3O_4, a larger amount

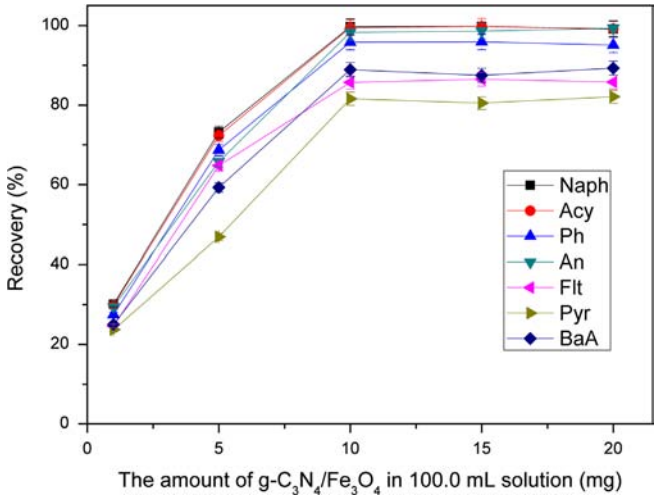


Fig. 9. Effect of g-C_3N_4/Fe_3O_4 amount on recovery of PAHs.

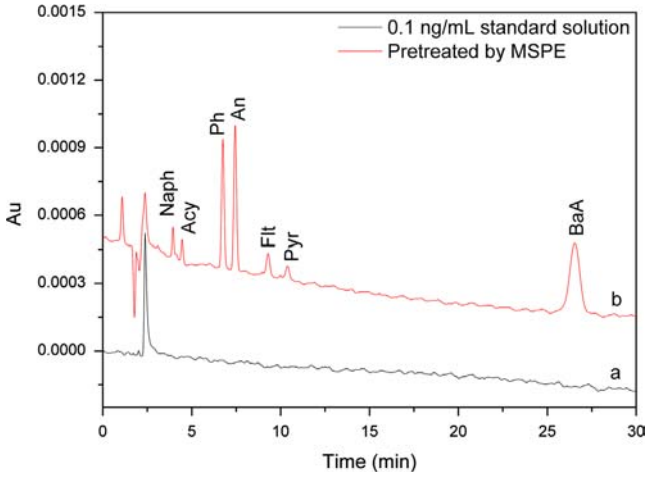


Fig. 10. Chromatogram of water samples with 0.1 ng mL^{-1} PAHs: (a) water sample without MSPE, (b) water sample after MSPE using g-C_3N_4/Fe_3O_4.

was needed to achieve facile phase separation and to obtain a higher recovery. To choose the optimum dosage of the sorbent (g-C_3N_4/Fe_3O_4) for the MSPE of PAHs from spiked aqueous samples (0.1 ng mL^{-1}), different amounts of sorbent were investigated in the range of 1.0 to 20.0 mg (Fig. 9). The recoveries increased with increasing sorbent from 1.0 to10.0 mg, and then stabilized with a further increase. This result indicated that 10.0 mg of the sorbent was sufficient to extract PAHs from 100.0 mL of aqueous sample.

The extraction time profiles were studied by varying the absorption time between 5 and 30 min. The recoveries reached a maximum at 10 min. Therefore, it can be concluded that extraction equilibrium between the aqueous phases and the sorbent was reached after 10 min.

The eluent volume was optimized because the amount of methanol/acetonitrile (1/1, *v*/*v*) can affect the elution efficiency. When the volume of the elution solvent was in the range of 0.5–1.0 mL, the recoveries increased with increasing eluent volume. On the other hand, the recoveries remained almost unchanged when the eluent volume was further increased. The highest recoveries were achieved when the volume of the eluent was 1.0 mL. Therefore, 1.0 mL (0.5 mL each time and washed two times) methanol/acetonitrile (1/1, *v*/*v*) was selected for elution. Under optimal conditions, 100.0 mL of spiked water samples (0.1 ng mL^{-1}) were

pretreated and analyzed by HPLC (Fig. 10). In comparison with the chromatogram of standard solution without MSPE (Fig. 10a), clear chromatographic peaks of PAHs were observed in Fig. 10b after preconcentration.

Table 1
Linear ranges, correlation coefficients, calibration equations, limit of detection and limit of quantitation of MSPE.

Analyte	Linear range (ng mL^{-1})	Calibration equation	r^2	LOD (ng mL^{-1})	LOQ (ng mL^{-1})
Naph	0.1–20.0	A=629.3C+31.3	0.9978	0.08	0.27
Acy	0.1–20.0	A=317.3C+6.2	0.9971	0.10	0.33
Ph	0.1–20.0	A=2313.8C+20.7	0.9989	0.06	0.21
An	0.1–20.0	A=10726.1C+24.3	0.9996	0.05	0.17
Flt	0.1–20.0	A=533.1C+6.3	0.9985	0.08	0.27
Pyr	0.1–20.0	A=385.5C+13.6	0.9975	0.09	0.31
BaA	0.1–20.0	A=15104.6C+548.6	0.9997	0.05	0.17

A:peak area C:concentration

3.3. Reusability of g-C_3N_4/Fe_3O_4

To investigate the recyclability of the sorbent, g-C_3N_4/Fe_3O_4 was reused in MSPE. After five times of recycling, there was no obvious decrease or increase in the analyte recoveries. The recoveries of PAHs were 97.8–99.6% for Naph, 98.2–99.4% for Acy, 93.4–95.1% for Ph, 97.1–98.6% for An, 84.9–86.5% for Flt, 80.0–81.8% for Pyr and 86.7–88.9% for BaA. The results indicate that g-C_3N_4/Fe_3O_4 is stable and no carryover of analytes occurred during MSPE procedure, indicating good reusability.

3.4. Analytical performance and application

A series of experiments were conducted to determine the linearity, reproducibility, and limit of detection (LOD) of the method. All parallel experiments were repeated three times and the results are listed in Table 1. The calibration plots were drawn by analyzing 100.0 mL of distilled water spiked with different analytes

Table 2
Recoveries obtained in the determination of PAHs in spiked environmental water samples (n=3).

PAHs	C_s	Standard solution			Tap water			Qixia Lake			Xuanwu Lake		
		C	R	RSD	C	R	RSD	C	R	RSD	C	R	RSD
Naph	0	1.00			ND			ND			ND		
	1.00	1.99	99.5	5.3	0.97	97.3	5.2	0.99	98.5	5.1	0.98	98.1	5.5
	5.00	5.98	99.7	4.6	4.87	97.4	4.2	4.99	99.8	3.8	4.86	97.2	4.6
Acy	0	1.00			ND			1.37			ND		
	1.00	1.98	99.0	4.9	0.97	97.1	4.6	2.35	99.2	4.2	0.98	98.4	3.7
	5.00	5.96	99.3	4.4	4.95	99.0	4.1	6.33	99.4	3.1	4.94	98.8	2.1
Ph	0	1.00			ND			ND			ND		
	1.00	1.91	95.5	5.1	0.95	94.7	4.9	0.95	94.5	4.5	0.96	95.8	4.2
	5.00	5.72	95.3	4.3	4.68	93.6	4.5	4.77	95.4	3.3	4.81	96.2	2.7
An	0	1.00			ND			ND			ND		
	1.00	1.97	98.5	3.5	0.98	97.5	3.6	0.99	99.0	3.7	0.99	99.2	3.6
	5.00	5.91	98.5	2.7	4.88	97.6	2.8	4.79	95.8	3.7	4.89	97.8	3.1
Flt	0	1.00			ND			ND			ND		
	1.00	1.72	86.0	2.4	0.86	85.5	2.7	0.85	85.2	2.8	0.86	85.5	2.4
	5.00	5.17	86.2	1.8	4.38	87.6	2.3	4.41	88.2	2.5	4.40	88.0	1.7
Pyr	0	1.00			ND			ND			ND		
	1.00	1.63	81.5	3.9	0.81	81.0	4.0	0.81	81.3	3.6	0.80	80.1	3.9
	5.00	4.90	81.7	3.3	4.07	81.4	2.8	4.02	80.4	2.6	4.00	80.0	2.5
BaA	0	1.00			ND			2.81			ND		
	1.00	1.76	88.0	3.7	0.87	86.5	3.9	3.45	90.5	2.9	0.85	85.4	3.0
	5.00	5.35	89.2	2.9	4.43	88.6	2.2	6.69	85.7	1.8	4.39	87.8	1.6

ND: not detected C: concentration of found phenolic compounds (ng mL^{-1}) C_s: concentration of spiked phenolic compounds (ng mL^{-1})
R: recovery (%) RSD: relative standard deviation (%)

Table 3
Comparison of different methods for PAHs extraction.

Method	Particle size	Surface area (m^2 g^{-1})	Chemical composition (weight %)	Detection	Amount of sorbent (mg)	Sample volume (mL)	LODs (ng mL^{-1})	RSD (%)	Recovery (%)	Refs.
Multi-walled carbon nanotubes (MCNT) based SPE	60–100 nm i.d., 5–15 μm length	40–300	100% CNT	GC–MS	150	500	0.002–0.0085	1.2–12.1	70.0–127.0	24
Fe_3O_4/GO-based MSPE	5 μm	N.A.	16.7% GO, 83.8% Fe_3O_4	HPLC-UV	40	50	0.09–0.19	1.7–11.7	76.8–103.2	25
Carbon-ferromagnetic nanocomposites-based MSPE	7.3 nm	16	55.2% Carbon, 44.8% Fe_2O_3	GC–MS	10	20	0.015–0.335	3.6–9.3	N.A.	26
C_{18}/Fe_3O_4-based MSPE	200–260 nm	N.A.	5.11% C_{18}, 94.89% Fe_3O_4	GC–MS	50	20	0.8–36	2.0–10.0	N.A.	27
Liquid-liquid extraction	N.A.	N.A.	N.A.	HPLC-UV	N.A.	1000	0.002–3.3	4.5–12.3	71.4–103.0	28
g-C_3N_4/Fe_3O_4-based MSPE	70–160 nm	89.2	36.26% g-C_3N_4, 63.74% Fe_3O_4	HPLC-UV	10	100	0.05–0.1	1.8–5.3	80.0–99.8	This work

*N.A.: not available

in the range from 0.1 ng mL^{-1} to 20.0 ng mL^{-1}. The correlation (r^2) of these curves was above 0.997. The reproducibility of a spiked water sample (1.0 ng mL^{-1}) was evaluated, and the RSD values were 1.8–5.3%. The detection and quantification limits were calculated based on S/N=3 and S/N=10, with values from 0.05–0.1 ng mL^{-1} and 0.17–0.33 ng mL^{-1}. Overall, the method had a good linear range, low detection limit and high reproducibility. The method was then compared with other previous extraction methods that were used for the determination of PAHs in water samples [24–28], the results are summarized in Table 2. The present method required smaller amounts of the sorbent, or conveniently manipulation, but exhibited better or similar performance.

Finally, real water samples from a tap, Qixia Lake and Xuanwu Lake were collected and analyzed. None of the seven types of PAHs were detected in the non-spiked water samples except for the sample from Qixia Lake (1.37 ng mL^{-1} of Acy and 2.81 ng mL^{-1} of BaA). The results were proved by using Method 550, U.S. EPA., and 1.12 ng mL^{-1} of Acy and 3.05 ng mL^{-1} of BaA from water sample of Qixia Lake were detected. Spiked samples were analyzed to calculate the recoveries of the seven PAHs. Table 3 lists the concentrations of the detected analytes and their recoveries. All the recoveries were in the range of 80.0–99.8% with relative standard deviations (RSDs) of 1.6–5.5%. Therefore, g-C_3N_4/Fe_3O_4 has potential application in the analysis of nonpolar carbon-based ring compounds in water samples.

4. Conclusions

g-C_3N_4/Fe_3O_4 was synthesized by chemical co-precipitation and was evaluated in terms of the adsorption and desorption of seven PAHs. The MSPE conditions using magnetic nanocomposites were optimized and applied to the pre-treatment of PAHs from water samples prior to HPLC with UV detection. Low limits of detection, good linearity and recovery were obtained indicating that g-C_3N_4/Fe_3O_4 has potential application in the pretreatment of water samples and other environmental nonpolar pollutants containing carbon-based ring structures and in the removal of PAHs from water samples.

Acknowledgments

This research was supported by Program of Natural Science Research of Jiangsu Higher Education Institutions of China (Grant No. 2013103TSJ0089), the National Natural Science Foundation of China (Grant No. 21177061) and the Priority Academic Program Development of Jiangsu Higher Education Institutions, Jiangsu Collaborative Innovation Center of Biomedical Functional Materials.

Appendix A. Supporting information

Supplementary data associated with this article can be found in the online version at http://dx.doi.org/10.1016/j.talanta.2014.08.071.

References

[1] A.E. McGowin, in: L.M.L. Nollet (Ed.), Chromatographic Analysis of the Environment, CRC Press, Boca Raton, FL, 2006, pp. 555–616.
[2] H.D. Liang, D.M. Han, X.P. Yan, J. Chromatogr. A 1103 (2006) 9–14.
[3] Y. Huang, Q. Zhou, G. Xie, J. Hazard. Mater. 193 (2011) 82–89.
[4] Y. Picó, M. Fernández, M.J. Ruiz, G. Font, J. Biochem. Biophys. Meth. 70 (2007) 117–131.
[5] F. Augusto, L.W. Hantao, N.G.S. Mogollón, S.C.G.N. Braga, Trac-Trends Anal. Chem 43 (2013) 14–23.
[6] M. Valcarcel, S. Cardenas, B.M. Simonet, M.Y. Moliner, R. Lucena, Trac-Trends Anal. Chem 27 (2008) 34–43.
[7] R. Sitko, B. Zawisza, E. Malicka, Trac-Trends Anal. Chem 51 (2013) 33–43.
[8] H. He, J. Klinowski, M. Forster, Chem. Phys. Lett. 287 (1998) 53–56.
[9] X. Wang, K. Maeda, A. Thomas, K. Takanabe, G. Xin, J.M. Carlsson, K. Domen, M. Antonietti, Nat. Mater. 8 (2009) 76–80.
[10] P. Niu, L. Zhang, G. Liu, H. Cheng, Adv. Funct. Mater. 22 (2012) 4763–4770.
[11] Y. Zheng, J. Liu, J. Liang, M. Jaroniec, S.Z. Qiao, Energ. Environ. Sci 5 (2012) 6717–6731.
[12] X. Zhang, X. Xie, H. Wang, J. Zhang, B. Pan, Y. Xie, J. Am. Chem. Soc. 135 (2013) 18–21.
[13] H.H. Yang, S.Q. Zhang, X.L. Chen, Z.X. Zhuang, J.G. Xu, X.R. Wang, Anal. Chem. 76 (2004) 1316–1321.
[14] X. Li, G.T. Zhu, Y.B. Luo, B.F. Yuan, Y.Q. Feng, Trac-Trends Anal. Chem 45 (2013) 233–247.
[15] A. Ballesteros-Gomez, S. Rubio, Anal. Chem. 81 (2009) 9012–9020.
[16] S. Zhang, H. Niu, Z. Hu, Y. Cai, Y. Shi, J. Chromatogr. A 1217 (2010) 4757–4764.
[17] X. Wang, S. Wang, W. Hu, J. Cai, L. Zhang, L. Dong, L. Zhao, Y. He, Mater. Lett. 115 (2014) 53–56.
[18] S. Kumar, T. Surendar, B. Kumar, A. Baruah, V. Shanker, J. Phys. Chem. C 117 (2013) 26135–26143.
[19] X. Xia, C. Zhou, D. Tong, M. Liu, D. Zhang, M. Fang, W. Yu, Mater. Lett. 64 (2010) 2620–2623.
[20] X. Zhou, B. Jin, R. Chen, F. Peng, Y. Fang, Mater. Res. Bull. 48 (2013) 1447–1452.
[21] F. Chang, Y. Xie, C. Li, J. Chen, J. Luo, X. Hu, J. Shen, Appl. Surf. Sci. 280 (2013) 967–974.
[22] Z. Zhang, J. Kong, J. Hazard. Mater. 193 (2011) 325–329.
[23] F. Galán-Cano, M.C. Alcudia-León, R. Lucena, S. Cárdenas, M. Valcárcel, J. Chromatogr. A 1300 (2013) 134–140.
[24] J. Ma, R. Xiao, J. Li, J. Yu, Y. Zhang, L. Chen, J. Chromatogr. A 1217 (2010) 5462–5469.
[25] Q. Han, Z. Wang, J. Xia, S. Chen, X. Zhang, M. Ding, Talanta 101 (2012) 388–395.
[26] L. Bai, B. Mei, Q.Z. Guo, Z.G. Shi, Y.Q. Feng, J. Chromatogr. A 1217 (2010) 7331–7336.
[27] Y. Liu, H.F. Li, J.M. Lin, Talanta 77 (2009) 1037–1042.
[28] Determination of polycyclic aromatic hydrocarbons in drinking water by liquid-liquid extraction and hplc with coupled ultraviolet and fluorescence detection, Method 550, U.S. EPA.

Talanta 132 (2015) 929–938

Contents lists available at ScienceDirect

Talanta

journal homepage: www.elsevier.com/locate/talanta

Nano-liquid chromatography coupled to time-of-flight mass spectrometry for phenolic profiling: A case study in cranberry syrups

María del Mar Contreras [a,b], David Arráez-Román [a,b,*], Alberto Fernández-Gutiérrez [a,b], Antonio Segura-Carretero [a,b]

[a] Department of Analytical Chemistry, Faculty of Sciences, University of Granada, Avenida Fuentenueva s/n, 18071 Granada, Spain
[b] Research and Development Functional Food Centre (CIDAF), Bioregión Building, Health Science Technological Park, Avda. Del Conocimiento s/n, 18016 Granada, Spain

ARTICLE INFO

Article history:
Received 15 September 2014
Received in revised form
15 October 2014
Accepted 24 October 2014
Available online 31 October 2014

Keywords:
Cranberry
Lock-mass calibration
Miniaturization
Nano-liquid chromatography
Phenolic compounds

ABSTRACT

A new method based on nano-liquid chromatography coupled to time-of-flight mass spectrometry (nano-LC–TOF–MS) using lock-mass calibration was developed to facilitate the accurate and routine characterization and quantification of phenolic compounds. Thus, it was applied to study cranberry syrups, in which, using negative ionization mode, a total of nine phenolic compounds were unequivocally identified using standards and 38 tentatively taking into account their retention time, accurate mass (errors < 5 ppm) data and isotope pattern, as well as literature. Among them, 13 compounds, belonging to flavonols and iridoids conjugated with phenolic acids, were reported for first time in cranberry or cranberry based-products. The analytical method was also validated using chlorogenic acid, *p*-coumaric acid, (+)-catechin, (−)-epicatechin, procyanidin A2, quercetin 3-*O*-glucoside, quercetin 3-*O*-rhamnoside, quercetin, and myricetin standards. In this way, the analytical method showed adequate linearity, with R^2 above 0.99, and acceptable values of intra- and inter-day repeatability of the retention time and peak area. The detection limits and quantification were between 1.0–15.6 ng mL^{-1} and 2.0–62.5 ng mL^{-1}, respectively. The method can be extended to characterize phenolic compounds in other food and plant matrices, and as well biological samples.

© 2014 Elsevier B.V. All rights reserved.

1. Introduction

The characterization of beneficial food constituents to formulate novel functional ingredients or pharmaceutical preparations continues to attract scientific and industrial attention, because these compounds may contribute in prevention and mitigation of diseases, promote health and wellbeing with a reduction of health care costs. As example, American cranberry (*Vaccinium macrocarpon*) (Ericaceae fam.) is a rich source of bioactive phenolic compounds with antiproliferative, antioxidant [1] anti-inflammatory and anticarcinogenic activities [2], as well as antimicrobial activity related to reduction of urinary-tract infections [3,4]. In fact, different sorts of pharmaceutical products containing cranberry have been launched in the market. Thus, robust, fast, and low-cost quantification methods, are required as quality control of phenolic compounds. In this sense, novel analytical methods to determine cranberry phenolics are based on the use of ultra-high-pressure-liquid chromatography (UHPLC), using sub-2 μm particles, coupled to UV, diode-array and fluorescence detectors and/or mass spectrometry (MS) [5–7].

Currently, other trends in modern analytical chemistry include the miniaturization of liquid chromatography (LC). Advances in this separation technology have enabled the development of nano-LC, which employs capillary columns with internal diameters (i.d.) ranging between 10 and 100 μm [8]. This column i.d. provides a good compromise between sensitivity, loadability, and robustness [9]. In the case of sensitivity, it is especially improved when nano-LC is coupled with MS. In this context, nano-LC has been recently coupled to UV and MS to analyze phenolic compounds in olive oil and other phytochemicals such as gibberellins, phytosterols and methylxantines in different food matrices [10–13]. However, this technique also presents several drawbacks often subjected to far more methodological problems than a conventional HPLC, such as presence of void volumes or easily generation of mixing chambers [14]. However, owing to the advantages that offer nano-LC, including sensitivity, lower cost effectiveness and to be an eco-friendly technique with low solvent demand, developing new methods to characterize phenolic compounds in both plant extracts/products and biological samples is imperative. In contrast, the applicability of

* Corresponding author at: Department of Analytical Chemistry, Faculty of Sciences, University of Granada, Avenida Fuentenueva s/n, 18071 Granada, Spain. Tel.: +34 958 248409; fax: +34 958 249510.
E-mail address: darraez@ugr.es (D. Arráez-Román).

http://dx.doi.org/10.1016/j.talanta.2014.10.049
0039-9140/© 2014 Elsevier B.V. All rights reserved.

nano-LC in the proteomics field has grown faster than for the analysis of phytochemicals.

In the case of coupling nano-LC with high-resolution MS, calibration of the MS spectra is one of the most critical parameters to consider in the achievement of the accuracy that allows performing characterization studies with high reliability. In this sense, several strategies based on internal and external calibration could be found in literature. Our research group has previously employed both calibration modes [10,15]. However, in the first approach it required to use well-known phenols found in the studied matrix, that is not always possible, and in the second study a solution of sodium formate cluster was introduced externally using a pump before each run, but it could not be automated. Thus, in this study lock-mass calibration and nano-LC coupled to time-of-flight-MS were applied to assure the mass accuracy and the routine analysis of phenolic compounds in both negative and positive ionization modes. For this purpose, the method was applied to characterize cranberry syrups as example of plant product matrix and also validated for quantification. This study allows assuring the application of the method to characterize unknown phenolic compounds in other food and plant matrices as well as biological samples.

2. Material and methods

2.1. Chemicals

All chemicals were analytical MS reagent grade. Formic acid and acetonitrile used for preparing mobile phases were obtained from Fluka (Sigma-Aldrich, Steinheim, Germany) and Fisher Scientific (Loughborough, Leics, UK), respectively. A G560E Vortex-Genie 2 (Scientific Industries, Bohemia, NY, USA) was used for mixing and water was deionized by using a Milli-Q system (Millipore, Bedford, MA, USA).

2.2. Cranberry syrup

Commercial cranberry syrup (Urell®, Pharmatoka Lab., France) was purchased from a local pharmacy (syrup 1) and an experimental gamma-irradiated syrup, prepared with the same commercial extract of American cranberry, was also procured. The preparation was according to Iswaldi et al. [5]: 200 μL of cranberry syrup was dissolved at final volume of 4 mL in methanol, vortexed for 2 min and filtered with a polytetrafluoroethylene (PTFE) syringe filter (0.2 μm pore size). Afterwards, for the analysis by nano-LC–TOF–MS, samples were additionally diluted 1/40 in mobile phase A containing 10% of methanol (dilution solvent).

2.3. Preparation of standards

Standards of 7-hydroxycoumarin, *p*-coumaric acid, chlorogenic acid, (+)-catechin, (−)-epicatechin, myricetin, quercetin, and quercetin-3-*O*-glucoside were purchased from Sigma–Aldrich, whereas quercetin-3-*O*-rhamnoside (quercitrin) and procyanidin A2 were from Extrasynthese (Genay, France). Purity was at least higher than 96%. Stock solutions of each compound were prepared at 1 mg mL^{-1} in methanol and stored at −20 °C. Then, stock solutions were diluted to appropriate working concentrations with dilution solvent, ranging from 5 μg mL^{-1} to the detection limit.

2.4. Chromatographic and MS conditions

Analyses were made with a commercially available EASY-nLC™ (Bruker Corporation, Bremen, Germany), equipped with three pumps, three pressure sensors, four valves, two flow sensors, an autosampler, and a touchscreen (see schematic diagram in Supporting information, Fig. S1). Chromatographic separation was performed with a commercial C18 capillary column (360 μm o.d., 75 μm i.d., length 10.1 cm, 3 μm of particle size; NanoSeparations, Nieuwkoop, The Netherlands). An on-line short capillary pre-column (360 μm o.d., 100 μm i.d., length 20 mm, 5 μm of particle size, NanoSeparations) was used before the analytical column with the intention of trapping of the compounds and working with volumes in the order of μL (see "loading position" Fig. S1). Mobile phases consisted of 1% formic acid in water (phase A) and acetonitrile (phase B) at a constant flow rate of 0.3 μL min^{-1} using the following multi-step linear gradient: 0–2 min, from 5% B to 26% B; 2–14.5 min, from 26% B to 31% B; 14.5–21 min, from 31% B to 36% B; 21–23 min, from 36% B to 60% B; 23 to 25 min, from 60% B to 80% B; 25 to 26 min, 80% B; from 26 to 28 min, 80% B to 5% B. Finally, the initial conditions were maintained for 12 min (total run 40 min).

Before starting the analysis, the pre-column and column were re-equilibrated with phase A at 2.5 μL min^{-1} for 2 min and 0.3 μL min^{-1} for 8.3 min, respectively. The sample (1 μL) was loaded into the pre-column at 2.5 μL min^{-1} for 0.6 min. The flow rate used to elute the compounds in the analytical column was 0.3 μL min^{-1}. Samples were maintained at 15 °C in the autosampler.

The nano-LC instrument was coupled to a micrOTOF™ (Bruker Corporation). The C18-column was connected with a nano-spray interface presenting a tapered fused silica sprayer needle (outer tip, 300 μm) by a peek union. The spraying conditions were adjusted for the abovementioned flow rate (0.3 μL min^{-1}) to achieve stable spray across the entire gradient: nebuilizing gas pressure, 0.5 bar, drying gas temperature and flow 150 °C and 5.0 L min^{-1}, respectively. The selected parameters of MS analysis in negative ion mode were as follows: capillary voltage, 3.7 kV; end-plate offset, −500 V; capillary exit, −80 V; skimmer 1, −50 V; skimmer 2, −23 V; hexapole 1, −22 V; hexapole RF, 70 V; lens transfer time 50 μs; lens pre-pulse storage time, 3 μs; and spectra rate 2 Hz. In positive ion mode, the parameters were set at the same values as in the negative ion mode, but with the opposite polarity. All operations were controlled by HyStar software (Bruker Corporation) and data processing was performed with DataAnalysis 4.0 software (Bruker Corporation), which provided a list of possible elemental formulas by using the SmartFormula™ editor based on a CHNO algorithm. For the generated molecular formulas, it provides the deviation between the measured mass and theoretical mass (error) (Da and ppm) and the comparison of the theoretical with the measured isotope patterns (msigma value or $m\sigma$) for increasing the confidence in the suggested molecular formula. TargetAnalysis™ 1.2 (Bruker Corporation) was used for targeted screening.

2.5. Calibration of the spectra

All the spectra were calibrated prior to the compound identification by external calibration and/or lock-mass calibration function available in the software DataAnalysis 4.0. For external calibration, the calibrant was a sodium formate cluster containing 5 mM sodium hydroxide and 0.2% formic acid in water:isopropanol (1:1, v/v), injected at the end of each run with a 74900-00-05 Cole Palmer syringe pump (Vernon Hills, IL, USA). For this purpose, it was connected manually to the nano-spray interface, owing to, with the instrumentation used in this work, external calibration could not be performed automatically. For lock-mass calibration, hexakis (2,2-difluoroethoxy)phosphazine was dissolved at 2 mg mL^{-1} in 2-propanol. This calibrant solution was applied to an adsorber material, which was placed inside a reservoir from Bruker and then

mounted on top of the spray shield of the TOF (Fig. S1). The intensity was at least 2000 counts for each ion.

2.6. Validation of the analytical method

2.6.1. Limit of detection (LOD) and quantification (LOQ)

The limit of detection (LOD) was determined through successive dilutions of the standard mixture until peaks with a signal-to-noise ratio near three ($S/N \geq 3$) were reached [16,17]. The limit of quantification (LOQ) was also determined through successive dilutions, being defined as the concentration that resulted in peaks with a signal-to-noise ratio above 8 ($S/N \geq 8$) [16]. For this, to extract ion chromatograms and estimate the S/N ratio using DataAnalysis software, the mass window selected was 100 mDa.

2.6.2. Linearity

The calibration curves were plotted by determining the linear relationship between the concentration of 9 selected phenolic compounds standards vs. their peak area in the extracted ion chromatogram of the molecular ions ($[M-H]^-$). Three replicates and at least six different concentrations were used to build the curves. The estimation of the regression parameters was done by the ordinary least squares method. The assumption of linear regression was checked by ANOVA and lack-of-fit test using Statgraphics Centurion 16.2.04 software (StatPoint Technologies, Inc., Warrenton, VA, USA; www.statgraphics.com).

2.6.3. Intra- and inter-day repeatability

Intra-day repeatability was estimated by the relative standard deviation (RSD) of the peak areas and the retention time for six consecutive analyses of the cranberry syrup (syrup 1), and inter-day repeatability was estimated by the RSD of the areas and the retention time for 10 consecutive analyses of the syrup performed on two different days (separated by 1 week) [18].

2.6.4. Accuracy

Accuracy was evaluated accordingly [18,19] and calculated over the linear range. For this purpose, pure standard were prepared to reach a final concentration of 50 and 100 ng mL^{-1} in dilution solvent and a selected syrup (syrup 1) was prepared as for analysis, but spiked at the latter levels. The analyte concentrations were estimated and the accuracy was calculated by the ratio of this calculated concentration versus the theoretical (spiked) concentration. All samples were analyzed in triplicate.

3. Results and discussion

3.1. Selection of the analytical conditions

The mobile phases selected were according with Iswaldi et al. [5], but mobile phase A was 1% formic acid in water and without organic solvent to avoid the loss of more polar compounds during the load step in the trapping column. Preliminary studies (data not

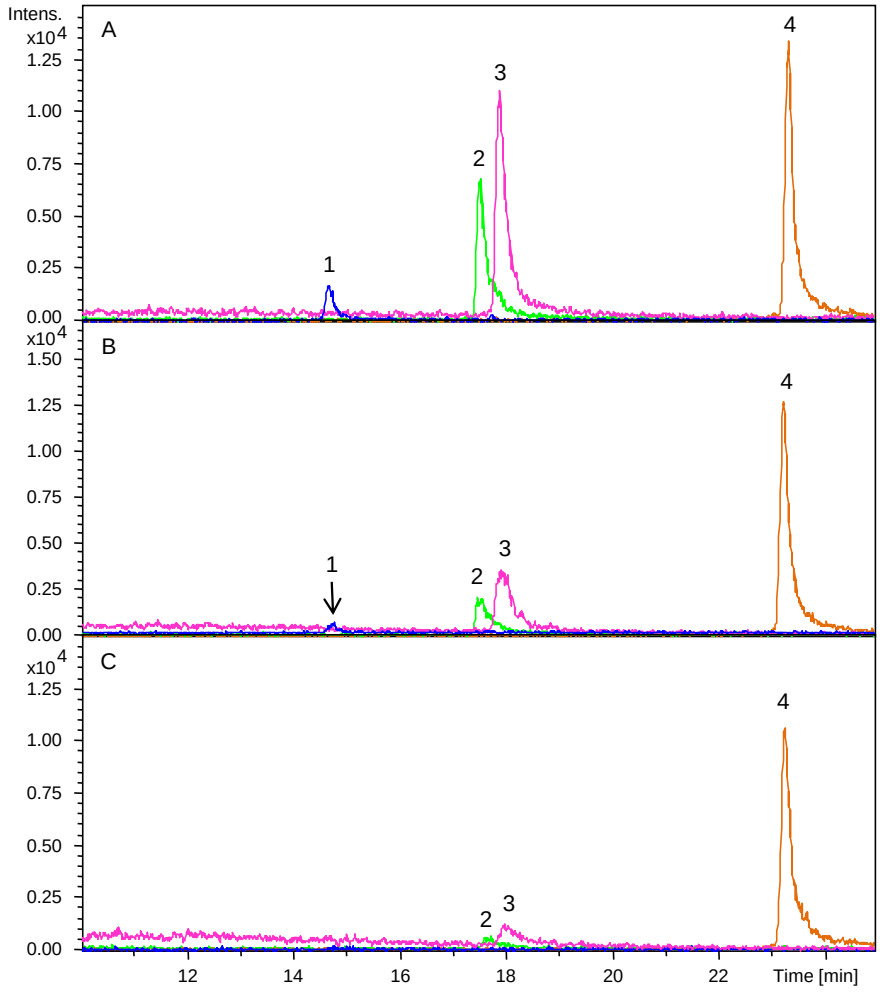


Fig. 1. Effect of the loading volume on the trapping of several phenolic compounds at 500 ng mL^{-1} using a C18 pre-column, an injection volume of 1 μL, and a load flow rate of 2.5 μL min^{-1}: (A) 1.5 μL, (B) 3.0 μL, and (C) 15.0 μL. Extracted ion chromatograms in negative ionization mode of compound 1: (+)-catechin; 2: *p*-coumaric acid; 3: 7-hydroxycoumarin; 4: quercetin.

shown) were made to assess the best way to equilibrate the pre-column and column. It implied the time for equilibration using an adequate flow to avoid higher system pressures and disturbing nebulization; for example, the maximum recommended flow in the used nano-ESI source is up to 0.5 μL min^{-1}. Thus, pre-column and column were equilibrated with the mobile phase A at 2.5 μL min^{-1} for 2 min and 0.3 μL min^{-1} for 8.3 min, respectively, the system pressure being lower than 120 bar.

Another important step using this instrument was to optimize the on-column trapping of the analytes of interest in the pre-column [10]. Therefore, using mobile phase A at 95% (gradient initial conditions), the appropriate sample-loading volume and speed during the loading/washing step (see Fig. S1) of the analysis were established using phenolic standards with different polarities and retention properties in C18 stationary phase. As an example, Fig. 1 shows the effect of different loading volumes; when the volume was too large, the most hydrophilic compounds, especially (+)-catechin (compound **1**), were displaced from the pre-column. Thus, for a injection volume of 1 μL, the best loading conditions were a load volume of 1.5 μL at 2.5 μL min^{-1}. This injection volume is also appropriate for future works with biological samples, where the sample volume/amounts could be limited. Moreover, the gradient was also modified to allow the better separation of the compounds. Fig. 2 shows the retention properties of phenolic compounds from commercial cranberry syrup by the optimized nano-LC–TOF–MS method in negative ionization mode.

3.2. Selection MS parameters

To optimize MS transfer, a methanolic solution composed by *p*-coumaric acid, 7-hydroxycoumarin, (+)-catechin and quercetin (500 ng mL^{-1}) was injected off-line in negative and positive ion modes. All ions were detected under the conditions tested, the MS signal being in general higher with the parameters set as indicated in Section 2 (for an example, see Fig. S2A of Supporting information). These results were also confirmed by on-line injection with the nano-LC instrument and the mobile phases selected (as example, see Fig. S2B, using negative ionization mode).

3.3. Lock-mass calibration

For high accuracy, the mass analyzer must be calibrated using known masses along the *m/z* range, and then applying a correction. In this work, the lock-mass calibration function was tested using hexakis(2,2-difluoroethoxy)phosphazine ($C_{12}H_{18}F_{12}N_3O_6P_3$), which is a common component of tuning mix (see Agilent brochure of G2431A/G2431-60001). This compound was selected because it is an artificial compound, presents an intermediate mass-to-charge ratio in the selected mass-range analysis, and it was detected in both negative (theorical monoisotopic *m/z* value of 601.9790) and positive (theorical monoisotopic *m/z* 622.0290) ion

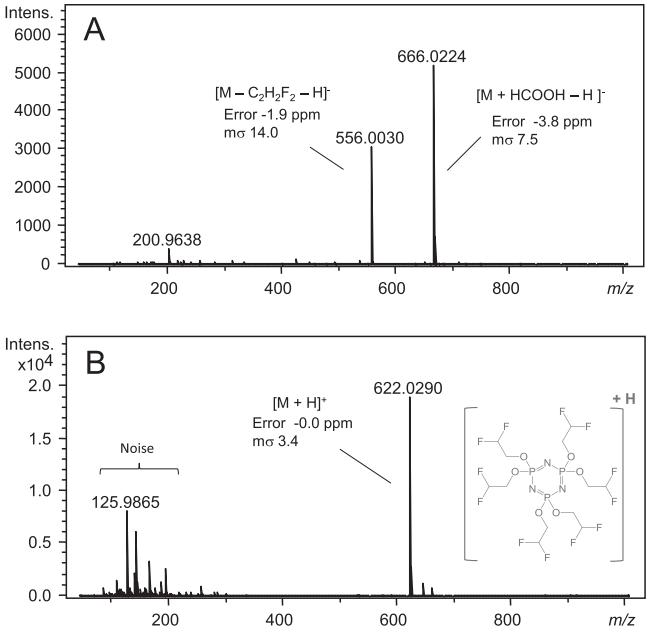


Fig. 3. MS spectra of hexakis(2,2-difluoroethoxy)phosphazine, which was used as lock-mass calibrant, in (A) negative and (B) positive ionization modes.

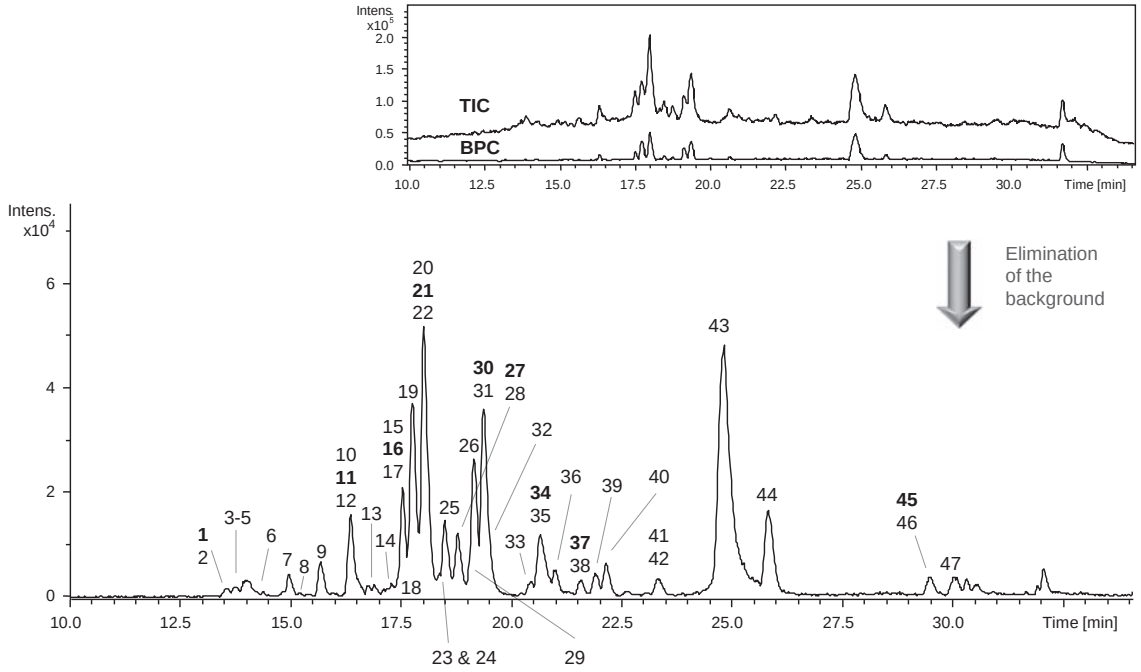


Fig. 2. Base peak chromatogram (BPC) in negative ionization mode after the elimination of the spectral background of a commercial cranberry syrup. Compounds are numbered according to Table 1 and the most abundant ones in each peak are given in bold. Superior panels show raw total ion chromatogram (TIC) and BPC.

Table 1
Phenolic compounds characterized in cranberry syrup by nano-LC–TOF–MS in negative and positive ionization modes and using external and lock-mass calibrations: class, retention time, molecular formula, theoretical *m/z*, msigma value, measured *m/z* and error.

No	Phenolic compounds	TR (min)	Molecular formula (M)	Negative ionization mode $[M-H]^-$						Positive ionization mode $[M+H]^+$					
				Theoretical (*m/z*)	msigma	Lock-mass calibration		External calibration		Theoretical (*m/z*)	msigma	Lock-mass calibration		External calibration	
						Measured (*m/z*)	Error (ppm)	Measured (*m/z*)	Error (ppm)			Measured (*m/z*)	Error (ppm)	Measured (*m/z*)	Error (ppm)
Phenolic acids															
1	Coumaroyl-hexoside I[a]	13.5	$C_{15}H_{18}O_8$	325.0929	29.3	325.0919	3.0	325.0927	0.6			ND			
3	Chlorogenic acid*[a]	13.7	$C_{16}H_{18}O_9$	353.0878	39.0	353.0885	−2.1	353.0878	−5.3	355.1024	12.7	355.1017	1.8	355.1037	−3.9
4	Sinapoyl-hexoside[a]	13.8	$C_{17}H_{22}O_{10}$	385.1140	525.3	385.1137	0.9	385.1145	−1.2			ND			
5	Coumaroyl-hexoside II[a]	13.8	$C_{15}H_{18}O_8$	325.0929	17.3	325.0918	3.3	325.0914	4.5			ND			
9	Dihydroferulic acid 4-*O*-D-glucuronide[a]	15.7	$C_{16}H_{20}O_{10}$	371.0984	5.3	371.0986	−0.7	371.0997	−3.5	373.1129	54.8	373.1117	3.4	373.1138	−2.3
12	*p*-Coumaric acid	16.6	$C_9H_8O_3$	163.0401	30.0	163.0398	1.8	163.0409	−5.3	165.0546	33.9	165.0556	−5.9	165.0566	−12.1
Flavonoid—Simple flavanols and oligomers															
2	(+)-Catechin*[a]	13.6	$C_{15}H_{14}O_6$	289.0718	94.7	289.0689	10.0	289.0708	3.4	291.0863	17.7	291.0833	10.5	291.0854	3.2
6	Procyanidin B type isomer I[a]	14.2	$C_{30}H_{26}O_{12}$	577.1351	64.7	577.1356	−5.5	577.1378	−4.6	579.1497	34.2	579.1478	3.3	579.1506	−1.5
7	(−)-Epicatechin*	15.0	$C_{15}H_{14}O_6$	289.0718	15.5	289.0704	4.7	289.072	−0.8	291.0863	5.7	291.0859	1.5	291.0872	−2.9
8	Procyanidin trimer A type I	15.2	$C_{45}H_{36}O_{18}$	863.1829	234.1	863.1778	6.1	863.1887	−6.7	865.1974	72.8	865.1994	−2.2	865.2042	−7.8
15	Procyanidin B type isomer II[a]	17.4	$C_{30}H_{26}O_{12}$	577.1351	67.2	577.1408	−9.9	577.1351	−8.8	579.1497	34.3	579.1534	−6.4	579.1573	−13.1
20	Procyanidin A2*[a]	17.9	$C_{30}H_{24}O_{12}$	575.1195	5.1	575.1217	−3.8	575.1205	−1.7	577.1341	17.9	577.1333	1.4	577.1345	−0.7
23	Procyanidin trimer A type II	18.3	$C_{45}H_{36}O_{18}$	863.1829	95.6	863.1783	5.3	863.1764	−3.3	865.1974	72.8	865.1962	1.4	865.2006	−3.7
Flavonoid–flavonols															
11	Myricetin 3-*O*-galactoside[a]	16.3	$C_{21}H_{20}O_{13}$	479.0831	3.1	479.0823	1.7	479.0828	0.7	481.0977	5.5	481.0984	−1.4	481.1001	−5.2
13	Myricetin pentoside I[ab]	16.8	$C_{20}H_{18}O_{12}$	449.0725	35.9	449.0730	−1.1	449.0735	−2	451.0871	37.3	451.0897	−5.7	451.0915	−9.8
14	Myricetin pentoside II[b]	17.3	$C_{20}H_{18}O_{12}$	449.0725	26.8	449.0755	−6.7	449.0761	−8	451.0871	15.5	451.0861	2.2	451.0877	−1.2
17	Myricetin pentoside III[b]	17.5	$C_{20}H_{18}O_{12}$	449.0725	9.5	449.0737	−2.6	449.074	−3.3	451.0871	9.5	451.0881	−2.2	451.0890	−4.1
19	Quercetin 3-*O*-glucoside*[a]	17.7	$C_{21}H_{20}O_{12}$	463.0882	6.2	463.0895	−2.8	463.0891	−2	465.1028	3.8	465.1019	1.8	465.1045	−3.8
25	Quercetin 3-*O*-xylopyranoside[a]	18.5	$C_{20}H_{18}O_{11}$	433.0776	19.0	433.0778	−0.3	433.0793	−4	435.0922	4.5	435.0923	−0.2	435.0936	−3.3
26	Quercetin 3-*O*-arabinopyranoside[a]	18.8	$C_{20}H_{18}O_{11}$	433.0776	10.9	433.0786	−2.3	433.0792	−3.6	435.0922	2.8	435.092	0.4	435.0942	−4.7
27	Kaempferol 3-*O*-glucoside	18.8	$C_{21}H_{20}O_{11}$	447.0933	26.8	447.0929	0.8	447.0951	−4.1	449.1078	5.6	449.1080	−0.5	449.1084	−1.3
28	Quercetin 3-*O*-arabinofuranoside[a]	19.1	$C_{20}H_{18}O_{11}$	433.0776	15.3	433.0794	−4.0	433.0797	−4.7	435.0922	4.8	435.0929	0.9	435.0939	−3.9
29	Isorhamnetin 3-*O*-galactoside	19.3	$C_{22}H_{22}O_{12}$	477.1038	84.7	477.1053	−3.0	477.1045	−1.4	479.1184	19.4	479.1195	−2.3	479.1201	−3.6
30	Quercetin 3-*O*-rhamnoside*[a]	19.4	$C_{21}H_{20}O_{11}$	447.0933	12.5	447.0941	−1.9	447.0942	−2	449.1078	5.6	449.1080	−0.5	449.1084	−1.3
31	Syringetin-3-*O*-glucoside/galactoside	19.4	$C_{23}H_{24}O_{13}$	507.1144	15.7	507.1145	−0.2	507.1151	−1.4	509.1290	4.7	509.1304	−2.7	509.1307	−3.4
32	Quercetin hexoside	19.6	$C_{21}H_{20}O_{12}$	463.0882	22.0	463.0905	−4.9	463.0903	−4.6	465.1028	25.2	465.1028	−0.1	465.1030	−0.5
34	Myricetin*[a]	20.6	$C_{15}H_{10}O_8$	317.0303	8.8	317.0296	2.2	317.0307	−1.3	319.0448	2.1	319.0441	2.3	319.0457	−2.6
35	Methoxyquercetin pentoside I[c]	20.6	$C_{21}H_{20}O_{11}$	447.0933	24.6	447.0937	−0.9	447.096	−6.1	449.1078	2.2	449.1082	−0.8	449.1086	−1.6
36	Methoxyquercetin pentoside II[c]	21.0	$C_{21}H_{20}O_{11}$	447.0933	9.5	447.0940	−1.6	447.0945	−2.6	449.1078	7.5	449.1073	1.3	449.1072	1.4
37	Methoxyquercetin pentoside III[c]	21.6	$C_{21}H_{20}O_{11}$	447.0933	6.0	447.0946	−2.9	447.0951	−4.1	449.1078	27.1	449.1073	1.3	449.1064	3.2
38	Methoxyquercetin rhamnoside	21.6	$C_{22}H_{22}O_{11}$	461.1089	48.4	461.1110	−4.4	461.1096	−1.4	463.1235	32.1	463.1260	−2.5	463.1250	−3.3
39	Syringetin pentoside	21.9	$C_{22}H_{22}O_{12}$	477.1038	16.9	477.1045	−1.4	477.1039	−0.1	479.1184	15.7	479.1172	2.6	479.1160	5.1
41	Myricetin 3-*O*-(2″-*O*-*p*-hydroxybenzoyl)-α-rhamnopyranoside	23.2	$C_{28}H_{24}O_{14}$	583.1093	37.9	583.1098	−0.7	583.1085	1.4	585.1239	40.2	585.1212	4.6	585.1186	9.1
42	Quercetin-3-(6″-coumaroyl)-β-galactoside	23.3	$C_{30}H_{26}O_{14}$	609.1250	12.8	609.1270	−3.4	609.1257	−1.2	611.1395	2.3	611.1381	1.4	611.1388	1.1
43	Quercetin*[a]	24.8	$C_{15}H_{10}O_7$	301.0354	16.1	301.0347	2.3	301.0366	−4	303.0499	1.3	303.0494	1.8	303.0502	−0.9
44	Kaempferol 3-*O*-β-D-(6″-*p*-hydroxybenzoyl)-galactopyranoside[a]	25.8	$C_{28}H_{24}O_{13}$	567.1144	−3.4	567.1163	−1.9	567.1163	−3.4	569.1290	11.1	569.1286	0.7	569.1290	−0.1
46	Kaempferol	29.5	$C_{15}H_{10}O_6$	285.0405	94.7	285.0392	4.5	285.041	−1.8	287.0550	109.1	287.0555	−1.7	287.0559	−3.0
47	Isorhamnetin	30.0	$C_{16}H_{12}O_7$	315.0498	12.1	315.0510	3.9	315.0504	2	317.0656	6.7	317.0649	2	317.0654	0.6
Flavonoid–flavanonols															
10	Dihydromyricetin	16.3	$C_{15}H_{12}O_8$	319.0459	37.2	319.0458	0.3	319.0452	2.3			ND			
Flavonoid–isoflavones															
40	Biochanin A-7-*O*-glucoside[a]	22.1	$C_{22}H_{22}O_{10}$	445.1140	42.0	445.1149	−1.9	445.1146	−1.2	447.1286	123.3	447.1265	4.5	447.1271	3.3

Table 1 (*continued*)

No	Phenolic compounds	TR (min)	Molecular formula (M)	Negative ionization mode $[M-H]^-$						Positive ionization mode $[M+H]^+$					
				Theoretical (*m/z*)	msigma	Lock-mass calibration		External calibration		Theoretical (*m/z*)	msigma	Lock-mass calibration		External calibration	
						Measured (*m/z*)	Error (ppm)	Measured (*m/z*)	Error (ppm)			Measured (*m/z*)	Error (ppm)	Measured (*m/z*)	Error (ppm)
Flavonoid–dihydrochalcones															
33	Phloridzin	20.4	$C_{21}H_{24}O_{10}$	435.1297	14.4	435.1305	−2.0	435.1304	−1.6			ND			
Iridoids conjugated with phenolic acids															
16	10-*p-trans/cis*-coumaroyl-1S-monotropein	17.5	$C_{25}H_{28}O_{13}$	535.1457	6.0	535.1470	−2.4	535.1474	−3.2	537.1544	26.1	537.1587	2.9	537.1603	0
18	10-*p-trans/cis*-coumaroyl-1S-dihydromonotropein	17.6	$C_{25}H_{30}O_{13}$	537.1614	17.1	537.1612	0.2	537.1602	1.3			ND			
21	10-*p-trans/cis*-coumaroyl-1S-dihydromonotropein	18.0	$C_{25}H_{30}O_{13}$	537.1614	8.0	537.1626	−2.2	537.1626	−2.4	539.1759	8	539.1759	0.1	539.1772	−2.4
22	10-*p-trans/cis*-coumaroyl-1S-monotropein	18.1	$C_{25}H_{28}O_{13}$	535.1457	221.1	535.1479	−4.2	535.1456	0.1			ND			
24	10-*p-trans/cis*-coumaroyl-1S-monotropein isomer	18.4	$C_{25}H_{28}O_{13}$	535.1457	132.2	535.1473	−3.1	535.1472	−2.9			ND			
45	Besperuloside	29.5	$C_{23}H_{24}O_{11}$	475.1246	12.1	475.1240	1.3	475.1241	1.1			ND			

* Phenolic compounds verified with commercial standards.
[a] Compounds previously characterized by HPLC–DAD–TOF–MS, using C18 column (150 × 4.6 mm, 1.8 μm particle size) [5].
[b] Myricetin 3-*O*-arabinoside, myricetin 3-*O*-xyloside and quercetin 3-*O*-galactoside have been described in cranberry.
[c] Isorhamnetin 3-*O*-xyloside has only been described in *Vaccinium* L. spp.

modes with high relative abundance, when the tuning mix was injected off line (data not shown). With the analytical conditions, the formic adduct (theorical monoisotopic *m/z* value of 666.0199, $[C_{12}H_{18}F_{12}N_3O_6P_3+HCOOH-H]^-$) and the latter positive ion (*m/z* 622.0290) were detected in negative (Fig. 3A) and positive (Fig. 3B) ion modes, respectively, and so selected to apply the lock-mass calibration function. Afterwards, the recalibration of the MS spectra was successful, with *m/z* errors being lower than 5 ppm in both negative and positive ionization modes, which were similar to those measured using external calibration and a sodium formate cluster introduced with a pump at the end of the analysis (see Table 1).

For high-mass resolution, the calibrant can be included either within the sample itself (internal calibration) [10] or, alternatively, can be introduced externally (external calibration) [11,15]. However, in the first case, for example, it requires the application of a quality control (with several known compound standards) every two or three analyses to use their calibration parameters in the following samples. On the other hand, our system does not present a valve to select automatically the introduction of the flow from the nano-LC, the tuning solution for the primary daily calibration of the TOF or for recalibration of MS data. Thus, with the present instrumentation, external calibration is tedious since the analyst has to connect the calibrant pump to the nano-ESI source manually, and injections during night are limited. Remarkably, the applied mass corrections by lock-mass calibration enabled to maintain the mass error below 5 ppm even up to three weeks, without the requirement of that daily external calibration of the mass analyzer. This also implies to reduce the number of insertions and removals of the fingertight fitting, which connect the column with the interface, and could result in its damage, leading to wrong adjustments of the column tubing and so generating leaks which are difficult to detect or huge chambers of dead volumes where the separated compounds are mixed (see "the practical guide to nano-LC troubleshooting" by [14] and some of the difficulties that the analyst could find when working with this miniaturized technique instead an HPLC).

3.4. Identification of phenolic compounds in cranberry syrup

In general, phenolic compounds were tentatively identified based on the generated molecular formula using exact mass and isotope pattern data, retention time, fragmentation via in-source collision-induced dissociation (ISCID) together with literature concerning cranberry and Ericaceae family. When possible, phenolic compounds were studied in depth by matching with standards.

3.4.1. Negative ionization mode

Fig. 2 shows the base peak chromatogram (BPC) in negative ionization mode of commercial syrup sample after noise/background elimination and 47 compounds characterized by nano-LC–TOF–MS, whereas Table 1 shows their retention times, theoretical *m/z*, msigma values, and experimental *m/z* and error by both lock-mass and external calibration.

Thus, it was possible to characterize five phenolic acid derivatives, four flavanols (simple and low-mass oligomers), 10 flavonols, and an isoflavone, in common with our previous analysis by HPLC–DAD–TOF–MS [5]. Furthermore, the phenolic acid *p*-coumaric acid, the flavanol (−)-epicatechin, several isomers of flavonols, i.e. isorhamnetin (3′-methoxyquercetin) and isorhamnetin 3-*O*-galactoside, quercetin-3-(6″-coumaroyl)-β-galactoside, myricetin pentoside, kaempferol 3-*O*-glucoside, and methoxyquercetin derivatives were also detected. These compounds were previously described by several authors in cranberry fruit or cranberry-based products

Table 2
Analytical parameters for the nano-LC–TOF–MS method: linear range, regression coefficients for calibration curves ($y=a+bx$), R^2, limits of detection (LOD) and quantification (LOQ), relative standard deviation (%) obtained for intra- and inter-day repeatability of peak area and retention time, accuracy and lack-of-fit significance (p-value).

Selected phenolic compounds	Range (ng mL^{-1})	a	b	R^2	LOD (ng mL^{-1})	LOQ (ng mL^{-1})	Repeatability (peak area)		Repeatability (retention time)		Accuracy (%)	Lack-of-fit (p)
							Intra-day (%)	Inter-day (%)	Intra-day (%)	Inter-day (%)		
Chlorogenic acid	LOQ-1000		46.71	0.990	15.6	31.3	14.3	14.7	0.6	0.8	100.6	0.83
p-Coumaric acid	LOQ-5000		119.18	0.998	15.6	31.3	8.7	13.6	0.8	0.8	96.1	0.23
(+)-Catechin	LOQ-2500	−4309.29	54.40	0.987	15.6	62.5	9.5	12.2	0.8	0.9	81.3	0.10
(−)-Epicatechin	LOQ-1000		92.23	0.993	3.9	15.6	5.8	9.9	0.8	1.0	93.3	0.53
Procyanidin A2	LOQ-1000	2058.72	89.48	0.992	7.8	15.6	8.1	7.5	0.8	0.9	105.1	0.22
Quercetin 3-*O*-glucoside	LOQ-2500	9837.13	270.16	0.989	1.0	2.0	7.1	5.8	0.8	0.9	97.0	0.74
Quercetin 3-*O*-rhamnoside	LOQ-1000	8712.79	565.66	0.994	1.0	2.0	4.0	4.8	0.8	1.0	107.4	0.06
Quercetin	LOQ-1000		1030.33	0.998	3.9	7.8	4.6	6.0	0.8	1.0	102.6	0.07
Myricetin	LOQ-2500		480.72	0.995	15.6	31.3	7.5	11.4	0.8	0.9	99.7	0.80

All regression coefficients (a, b) presented are significantly different from zero ($p<0.05$).

[1,6,7,20–23]. Quercetin hexoside (**32**) could be quercetin 3-*O*-galactoside, which was previously characterized in cranberry [1,21].

Notably, in our study, other phenolic compounds which were previously described in other *Vaccinium* spp. or the family Ericaceae were characterized for first time in cranberry, e.g. flavonols dihydromyricetin (ampelopsin) (**10**) [24], syringetin (3′,5′-*O*-dimethylmyricetin) 3-*O*-hexoside (**31**) and pentoside (**39**) [20,25,26], methoxyquercetin rhamnoside (**38**) [26], and three pentosides (**35**–**37**) [20,22], as well as kaempferol (**46**) [20,27], and the dihydrochalcone phloridzin (phlorizin) (**33**) [28,29]. The compound myricetin 3-*O*-(2″-*O*-*p*-hydroxybenzoyl)-α-rhamnopyranoside (**41**) was previously found in *Limonium sinense* (Plumbaginaceae fam.) [30].

Moreover, five iridoids conjugated with phenolic acids (**16**, **18**, **21**, **22** and **24**), also described in *Vaccinium* spp., were tentatively identified as 10-*p*-*trans*- and 10-*p*-*cis*-coumaroyl-1*S*-monotropein (vaccinoside/andromedoside) or 10-*p*-*trans*- and 10-*p*-*cis*-coumaroyl-1*S*-dihydromonotropein isomers [27,31]. The benzoyl iridoid derivative besperuloside (**45**) was also characterized for first time in cranberry and previously described in *Globularia* (Plantaginaceae fam.) [32].

3.4.2. Positive ionization mode

In positive ionization mode the background was higher than in negative ionization mode and, after the elimination of the spectral background, the chromatographic peaks could be clearly visualized in the BPC. Thus, the major part of the latter compounds (a total of 38), using either lock-mass calibration or external calibration, were also characterized in this mode (Table 1). In general, in positive ion mode and under our MS conditions, several of the *O*-glycosides compounds showed lower stability than in the negative ion mode and were partially fragmented. It bears noting that the characterization of these fragments enabled the confirmation of the structure of compounds with the same molecular formula, reaffirming the characterization in negative mode. For example, compounds **29** and **39** (Fig. S3, supporting information) with molecular formula $C_{22}H_{22}O_{12}$ were assigned to isorhamnetin 3-*O*-galactoside and syringetin pentoside, respectively.

However, the analytical conditions were not adequate to detect anthocyanins, which require more acidic conditions to improve their MS signal [5] even in positive ionization mode. On the other hand, more acid mobile phase A may also improve peak shape, resolution and analysis time of anthocyanins [33,34], but it requires further works.

3.5. Validation of the quantification by nano-LC–TOF–MS

Nano-LC–TOF–MS in negative ionization mode was selected for the simultaneous quantification of phenolic compounds in this syrup matrix, since a major number of compounds were characterized comparing with positive ionization mode. The validation parameters of sensibility, linearity, repeatability and accuracy are shown in Table 2. The LOD values ranged between 1.0 and 15.6 ng mL^{-1} and the LOQ values between 2.0 and 62.5 ng mL^{-1}. These data are lower than those reached by previous analytical methods used for the analysis of cranberry products using HPLC or UHPLC methods [5,7,16], and/or comparable to other nano-LC methods [10,12,33]. Therefore, this underscores the potential of the nano-LC–TOF–MS for future works studying phenolic compounds in biological matrices. On the other hand, the LOD and LOQ values were also examined in positive mode, being as low as in the negative ionization mode (Table S1, supporting information). The values for the coefficient of determination (R^2) were above 0.99, indicating that the fits were adequate. In all cases, the regression was significant ($p<0.05$) and lack-of-fit was not observed ($p>0.05$), confirming linearity in the studied concentration ranges.

Regarding the intra- and inter-day repeatability of the retention time, the RSD values were lower than 1% for all the compounds studied. The intra- and inter-day repeatability of the peak area depended on the compound considered, with values ranging between 4.0 and 14.7%, and being acceptable in comparison with other previously reported methods using nano-LC coupled to MS analyzing phytochemicals [10,11,33]. The accuracy of the method was also verified spiking craberry syrup 1 with standards at two levels (50 ng mL^{-1} and 150 ng mL^{-1}) under the linear range. In overall, the mean value for each compound ranged between 81.3 and 107.4% (Table 2). The worst value was observed for (+)-catechin (81.3%) when was analyzed in the first syrup matrix. In any case, the values met acceptance criteria [35].

As commented above, our system allows to perform on-column trapping step to introduce relative high volumes of sample (in this case 1 μL) and trap the analytes of interest. Although in this study concentration was not a critical problem, the objective was to optimize the method for further characterization works. In this sense, samples were highly diluted previously to perform the analysis (see Section 2), but residual sugars where detected along the MS spectrogram (Fig. S4), which could indicate that these highly polar components may remain into the system. Therefore,

Table 3
Concentration ($\mu g\ mL^{-1}$) of phenolic compounds determined in the selected syrups.

	Commercial syrup	Experimental syrup
Phenolic acids		
Coumaroyl-hexose I[a]	32.8 ± 5.2	22.0 ± 5.3
Chlorogenic acid[b]	145.3 ± 13.4	81.9 ± 9.5
Sinapoyl-hexose	< LOQ	< LOQ
Coumaroyl-hexose II[a]	35.7 ± 1.7	12.1 ± 2.3
Dihydroferulic acid 4-*O*-D-glucuronide[a]	122.8 ± 15.1	54.6 ± 7.6
p-coumaric acid[a]	44.7 ± 1.7	ND
Flavonoid—simple flavanols and oligomers		
(+)-Catechin[c]	49.2 ± 3.6	ND
Procyanidin B type isomer I[d]	20.6 ± 3.4	16.5 ± 3.4
(−)-Epicatechin[e]	93.2 ± 5.3	37.5 ± 6.1
Procyanidin trimer A type I	< LOQ	< LOQ
Procyanidin B type isomer II[d]	7.5 ± 0.7	1.2 ± 0.7
Procyanidin A2[d]	329.4 ± 4.8	125.6 ± 9.06
Procyanidin trimer A type II	< LOQ	ND
Flavonoid–flavonols		
Myricetin 3-*O*-galactoside[f]	93.5 ± 4.3	76.7 ± 5.0
Myricetin pentose I	< LOQ	< LOQ
Myricetin pentose II[f]	3.6 ± 0.8	< LOQ
Myricetin pentose III[f]	76.2 ± 7.6	42.5 ± 4.5
Quercetin 3-*O*-glucoside[f]	340.4 ± 25.0	325.5 ± 26.7
Quercetin 3-*O*-xylopyranoside[f]	81.2 ± 0.9	41.8 ± 0.6
Quercetin 3-*O*-arabinopyranoside[f]	71.6 ± 4.7	40.9 ± 2.2
Kaempferol 3-*O*-glucoside	< LOQ	< LOQ
Quercetin 3-*O*-arabinofuranoside[f]	169.7 ± 6.7	90.7 ± 5.2
Isorhamnetin 3-*O*-galactoside[f]	9.3 ± 1.7	37.2 ± 2.8
Quercetin 3-*O*-rhamnoside[g]	133.4 ± 9.6	35.9 ± 1.2
Syringetin-3-*O*-glucoside/galactoside[f]	67.6 ± 7.0	61.5 ± 2.6
Quercetin 3-*O*-galactoside[f]	10.7 ± 1.9	1.2 ± 1.1
Myricetin[h]	110.4 ± 5.9	38.3 ± 3.6
Methoxyquercetin pentose I[f]	1.4 ± 0.3	< LOQ
Methoxyquercetin pentose II[f]	26.8 ± 1.9	19.1 ± 0.7
Methoxyquercetin pentose III[f]	17.5 ± 2.8	9.7 ± 1.8
Methoxyquercetin rhamnoside	< LOQ	< LOQ
Syringetin pentose[f]	26.8 ± 4.2	9.7 ± 1.4
Myricetin 3-*O*-(2″-*O*-*p*-hydroxybenzoyl)-α-rhamnopyranoside [g]	1.1 ± 0.5	< LOQ
Quercetin-3-(6″-coumaroyl)-β-galactoside[f]	21.0 ± 1.7	3.2 ± 1.2
Quercetin[i]	233.9 ± 10.8	69.9 ± 6.4
Kaempferol 3-*O*-β-D-(6″-*p*-hydroxybenzoyl)-galactopyranoside[f]	132.9 ± 12.2	28.8 ± 1.8
Kaempferol	< LOQ	< LOQ
Isorhamnetin[i]	14.0 ± 1.2	4.9 ± 0.5
Flavonoid–flavanonols		
Dihydromyricetin[h]	13.7 ± 0.6	13.9 ± 0.2
Flavonoid–isoflavones	NQ	NQ
Biochanin A-7-*O*-glucoside	NQ	NQ
Flavonoid–dihydrochalcones	NQ	NQ
Phloridzin	NQ	NQ
Iridoid conjugated with phenolic acid		
10-*p*-*trans*/*cis*-coumaroyl-1*S*-monotropein[a]	282.7 ± 22.2	2.4 ± 1.3
10-*p*-*trans*/*cis*-coumaroyl-1*S*-dihydromonotropein[a]	71.5 ± 7.7	52.8 ± 5.0
10-*p*-*trans*/*cis*-coumaroyl-1*S*-dihydromonotropein[a]	663.0 ± 43.9	138.6 ± 9.9
10-*p*-*rans*/cis-coumaroyl-1*S*-monotropein[a]	77.4 ± 9.0	22.3 ± 2.1
10-*p*-*trans*/*cis*-coumaroyl-1*S*-monotropein isomer[a]	43.8 ± 5.4	3.6 ± 1.5
Besperuloside	NQ	NQ

Concentration data representing mean value ± standard deviation ($n=3$); LOQ, limit of quantification; NQ, not quantified. That is concentration estimated using curve of:

[a] *p*-Coumaric acid.
[b] (+)-Catechin.
[c] Chlorogenic acid.
[d] Procyanidin A2.
[e] (−)-Epicatechin.
[f] Quercetin 3-*O*-glucoside.
[g] Quercetin 3-*O*-rhamnoside.
[h] Myricetin.
[i] Quercetin.

our loading conditions were not enough to perform a large clean-up of the samples by washing these highly polar compounds from the pre-column with mobile phase A (at 95%), but with the compromise to retain more polar phenolic compounds (e.g. Fig. 1). Amongst the polar fraction, sugars are commonly present in phenolic extracts of plants [36] and so of interest as possible MS

interferents upon our analytical conditions due to their aforementioned behaviour. This a critical disadvantage compared when working in proteomics field, where the application of the nano-LC has spread widely. In these works a common strategy is to introduce a mix of peptides (protein hydrolysate) in the nano-LC system and the possible loss of amino acids or several polar peptides during the loading (normally, higher washing volumes are used) is not so relevant, whenever the characterized peptides may define the precursor protein (e.g. see applications in [37]). Although matrix compounds such as sugars might influence reproducibility and accuracy [38], remarkably, the estimated values for these parameters are acceptable as commented above.

3.6. Quantification and semi-quantification of phenolic compounds in cranberry syrups

The validated nano-LC–TOF–MS method was applied to estimate the quantities of phenolic compounds in both cranberry syrups with the use of the aforementioned calibration curves (Table 3). Thus, the MS response of the other phenolic compounds, which were not available as commercial standards, were calculated assuming similar responses for compounds of the same class/subclass and taking into account if they were glycosilated or aglycones when possible. For this purpose, a targeted analysis was performed using the software TargetAnalysis™ 1.2 [39], enabling the MS spectra to be automatically calibrated using lock-mass calibration, matching the phenolic compounds with previously characterized ones while taking into account retention time (error narrow range 0.2 min), accurate *m/z* (error narrow range < 5 ppm) and isotope pattern (msigma threshold 150), and determine the peak area. Successfully, the method enabled to detect the compounds in the samples in a faster way with high level of confidence taking into account the later parameters. Afterwards, the amounts of the detected phenolic compounds were estimated (Table 3). Among the phenolic families determined, the contents of flavonols and phenolic acid conjugated with iridoids were the highest in both syrups. In general, the individual values for each phenolic compound from commercial syrup were within the range of those previously determined in our previous works using HPLC–UV based-curves [5]. Other methods based on nano-LC characterized between 1 and 18 phenolic compounds in pollen, juice, olive oil, tea or honeysuckle, whereas quantified a lower number of them, ranging from **1** to **7** compounds [10,12,33,40,41]. Thus, our results remark that the application of our methodology to explore other vegetable matrices or biological samples is suitable.

4. Conclusion

In the present study, a nano-LC–TOF–MS using lock-mass calibration strategy with a single *m/z* ion, was successfully applied to make accurate mass measurements lower or close to 5 ppm, allowing the characterization of 47 (*m/z* ranging from 163.0398 to 863.1783) and 39 (*m/z* ranging from 165.0556 to 865.1994) phenolic compounds in negative and positive ionization mode, respectively. Several of these compounds were reported here for first time in cranberry. The method was also validated in negative ionization mode and showed adequate inter- and intra-day repeatability of retention time and peak area, and linearity. Thus, these results demonstrate that this miniaturized technique could be implemented for the characterization and simultaneous quantification of phenolic compounds in new plant matrices as well as biological matrices, with the advantage of using minimum volumes of mobile phases and sample, as well as achieving high sensitivity.

Conflict of interest

The authors declare no competing financial interest.

Acknowledgements

The authors are grateful to the Spanish Ministry of Economy and Competitiveness for the Juan de la Cierva contract and to the Andalusian Regional Government Council of Innovation and Science for the Excellence Projects P11-CTS-7625.

Appendix A. Supporting information

Supplementary data associated with this article can be found in the online version at http://dx.doi.org/10.1016/j.talanta.2014.10.049.

References

[1] X. He, R.H. Liu, J. Agric. Food Chem. 54 (2006) 7069–7074.
[2] C.C. Neto, J.W. Amoroso, A.M. Liberty, Mol. Nutr. Food Res. 52 (2008) S18–S27.
[3] L.Y. Foo, Y. Lu, A.B. Howell, N. Vorsa, Phytochemistry 54 (2000) 173–181.
[4] J. Uberos, M. Nogueras-Ocana, V. Fernandez-Puentes, R. Rodriguez-Belmonte, E. Narbona-López, A. Molina-carballo, et al., Open Access J. Clin. Trials 4 (2012) 31–38.
[5] I. Iswaldi, A.M. Gómez-Caravaca, D. Arráez-Román, J. Uberos, M. Lardón, A. Segura-Carretero, et al., J. Pharm. Biomed. Anal. 58 (2012) 34–41.
[6] M.C. Díaz-García, J.M. Obón, M.R. Castellar, J. Collado, M. Alacid, Food Chem. 138 (2013) 938–949.
[7] F. Sánchez-Patán, B. Bartolomé, P.J. Martín-Alvarez, M. Anderson, A. Howell, M. Monagas, J. Agric. Food Chem. 60 (2012) 3396–3408.
[8] M. Asensio-Ramos, J. Hernández-Borges, A. Rocco, S. Fanali, J. Sep. Sci. 32 (2009) 3764–3800.
[9] M.R. Gama, C.H. Collins, C.B.G. Bottoli, J. Chromatogr. Sci. 51 (2013) 694–703.
[10] R. García-Villalba, A. Carrasco-Pancorbo, G. Zurek, M. Behrens, C. Bässmann, A. Segura-Carretero, et al., J. Sep. Sci. 33 (2010) 2069–2078.
[11] M.-L. Chen, X.-M. Fu, J.-Q. Liu, T.-T. Ye, S.-Y. Hou, Y.-Q. Huang, et al., J. Chromatogr. B 905 (2012) 67–74.
[12] C. Fanali, A. Rocco, Z. Aturki, L. Mondello, S. Fanali, J. Chromatogr. A 1234 (2012) 38–44.
[13] A. Rocco, S. Fanali, J. Chromatogr. A 1216 (2009) 7173–7178.
[14] M. Noga, F. Sucharski, P. Suder, J. Silberring, J. Sep. Sci. 30 (2007) 2179–2189.
[15] R. Quirantes-Piné, V. Verardo, D. Arráez-Román, S. Fernández-Arroyo, V. Micol, M.F. Caboni, et al., Anal. Bioanal. Chem. 404 (2012) 3081–3090.
[16] F. Sánchez-Patán, M. Monagas, M.V. Moreno-Arribas, B. Bartolomé, J. Agric. Food Chem. 59 (2011) 2241–2247.
[17] S. Grimalt, O.J. Pozo, J.V. Sancho, F. Hernández, Anal. Chem. 79 (2007) 2833–2843.
[18] M. del M. Contreras, B. Gómez-sala, P.J. Martín-Alvarez, L. Amigo, M. Ramos, I. Recio, Anal. Bioanal. Chem. 397 (2010) 2825–2832.
[19] E. Hurtado-Fernández, T. Pacchiarotta, M. Gómez-Romero, B. Schoenmaker, R. Derks, A.M. Deelder, et al., J. Chromatogr. A 1218 (2011) 7723–7738.
[20] Z. Su, Pharm. Crop 3 (2012) 7–37.
[21] G. Borges, A. Degeneve, W. Mullen, A. Crozier, J. Agric. Food Chem. 58 (2010) 3901–3909.
[22] I.O. Vvedenskaya, R.T. Rosen, J.E. Guido, D.J. Russell, K.A. Mills, N. Vorsa, J. Agric. Food Chem. 52 (2004) 188–195.
[23] L.-Z. Lin, J.M. Harnly, J. Agric. Food Chem. 55 (2007) 1084–1096.
[24] J.B. Harborne, C.A. Williams, Phytochemistry 10 (1971) 2727–2744.
[25] C. Ma, K. Dastmalchi, G. Flores, S. Wu, P. Pedraza-Peñalosa, C. Long, et al., J. Agric. Food Chem. 61 (2013) 3548–3559.
[26] U. Vrhovsek, D. Masuero, L. Palmieri, F. Mattivi, J. Food Compos. Anal. 25 (2012) 9–16.
[27] J. Hokkanen, Liquid Chromatography/Mass Spectrometry of Bioactive Secondary Metabolites—In vivo and In vitro Studies, University of Oulu, 2013.
[28] E.I. Mejía-Meza, J.A. Yáñez, C.M. Remsberg, N.M. Davies, B. Rasco, F. Younce, et al., Int. J. Food Eng. 4 (2008) 1–6 (art10).
[29] B. Łata, M. Wińska-krysiak, Folia Hortic. 22/1 (2010) 31–35.
[30] L.C. Lin, C.J. Chou, Planta Med. 66 (2000) 382–383.
[31] A. Turner, S.-N. Chen, D. Nikolic, R. van Breemen, N.R. Farnsworth, G.F. Pauli, J. Nat. Prod. 70 (2007) 253–258.
[32] R.M. Taskova, C.H. Gotfredsen, S.R. Jensen, Phytochemistry 67 (2006) 286–301.
[33] C. Fanali, L. Dugo, G. D'Orazio, M. Lirangi, M. Dachà, P. Dugo, et al., J. Sep. Sci. 34 (2011) 150–159.
[34] A.M. Gómez-Caravaca, V. Verardo, M. Toselli, A. Segura-carretero, A. Fernández-Gutiérrez, M.F. Caboni, J. Agric. Food Chem. 61 (2013) 5328–5337.
[35] U.S. Department of Health and Human Services – Food and Drug Administration, Guidance for Industry – Bioanalytical Method Validation, 2013.

[36] I.M. Abu-Reidah, D. Arráez-Román, R. Quirantes-Piné, S. Fernández-Arroyo, A. Segura-Carretero, A. Fernández-Gutiérrez, Food Res. Int. 46 (2012) 108–117.
[37] C. Esteve, C. Montealegre, M.L. Marina, M.C. García, Talanta 92 (2012) 1–14.
[38] J.C. Van De Steene, W.E. Lambert, J. Am. Soc. Mass Spectrom. 19 (2008) 713–718.
[39] I. Iswaldi, D. Arráez-Román, A.M. Gómez-Caravaca, M. del M. Contreras, J. Uberos, A. Segura-Carretero, et al., Food Chem. Toxicol. 55 (2013) 484–492.
[40] C. Fanali, L. Dugo, A. Rocco, J. Chromatogr. A 1313 (2013) 270–274.
[41] F. Hu, C. Deng, Y. Liu, X. Zhang, Talanta 77 (2009) 1299–1303.

Talanta 132 (2015) 939–944

Contents lists available at ScienceDirect

Talanta

journal homepage: www.elsevier.com/locate/talanta

Study on aggregation behavior of Cytochrome C–conjugated silver nanoparticles using asymmetrical flow field-flow fractionation

Sun Tae Kim [a], Yong-Ju Lee [b], Yu-Sik Hwang [b], Seungho Lee [a,*]

[a] Department of Chemistry, Hannam University, Daejeon 305-811, South Korea
[b] Gyungnam Department of Environmental Toxicology, Korea Institute of Toxicology, Jinju 660-844, South Korea

ARTICLE INFO

Article history:
Received 22 April 2014
Received in revised form
16 May 2014
Accepted 20 May 2014
Available online 10 June 2014

Keywords:
Asymmetrical flow field-flow fractionation (AsFlFFF)
Cytochrome C–conjugated AgNPs
Aggregation
ζ-potential
UV–vis spectroscopy

ABSTRACT

In this study, 40 nm silver nanoparticles (AgNPs) were synthesized using the citrate reduction method and then the surface of AgNPs was modified by conjugating Cytochrome C (Cyto C) to improve stability and to enhance bioactivity and biocompatibility of AgNPs. It is known that Cyto C may undergo conformational changes under various conditions of pH, temperature, ionic strength, etc., resulting in aggregation of the particles. These parameters also affect the size and size distribution of Cyto C–conjugated AgNPs (Cyto C–AgNP). ζ-potential measurement revealed that the adsorption of Cyto C on the surface of AgNPs is saturated at the molar ratio [Cyto C]/[AgNPs] above about 300. Asymmetrical flow field-flow fractionation (AsFlFFF) analysis showed that hydrodynamic diameter of AgNPs increases by about 4 nm when the particle is saturated by Cyto C. The aggregation behavior of Cyto C–AgNP at various conditions of pH, temperature and ionic strength were investigated using AsFlFFF and UV–vis spectroscopy. It was found that the aggregation of Cyto C–AgNP increases with decreasing pH, increasing temperature and ionic strength due to denaturation of Cyto C on AgNPs and reduction in the thickness of electrostatic double layer on the surface of Cyto C–AgNP.

© 2014 Elsevier B.V. All rights reserved.

1. Introduction

Metallic nanoparticles are of interest in the field of life science due to their unique chemical, physical and biological properties [1]. Surface modification of metallic nanoparticles with polymer or protein is an approach to stabilize the nanoparticles. Surface modifications with a suitable agent such as organic molecules, surfactant, protein or polymer prevent aggregation, and improve biocompatibility and stability of the metallic nanoparticles in suspensions [2–4].

Among metallic nanoparticle, silver nanoparticles (AgNPs) are of particular interest because of their unique characteristics including antimicrobial activities, which often depend on their size and shape. They can be used as biosensor materials, fibers, superconducting materials, cosmetic products, and electronic components [5–8].

AgNPs are often coated with various types of anions, polymers or proteins to improve their biocompatibility and stability and also to control toxicity [9,10]. Cytochrome C (Cyto C) is a highly water soluble protein which is often used to coat nanoparticles to improve their biocompatibility. Sometimes Cyto C undergoes conformational changes as it becomes partially unfolded upon adsorption onto the surface of nanoparticles. The unfolded Cyto C adsorbed on a nanoparticle interacts with other Cyto C in suspension causing protein aggregation on nanoparticle surface, which results in nanoparticle aggregation [11,12]. The unfolding of Cyto C induced by presence of denatures or change in pH, temperature or ionic strength has been studied using light scattering [13]. It has been reported that aggregation of Cyto C–AgNP induces a coupling of the localized surface plasmon resonance of AgNPs, and may cause color change at various pH [12].

The effects of pH and ionic strength on aggregation behavior of nanoparticles in aqueous suspensions have been studied in terms of the change in the hydrodynamic diameter of particles [14,15]. It has been reported that the combined effect of pH, ionic strength, capping agent, ionic composition and other characteristics of the suspending liquid play a significant role in formation of aggregates or stability of the nanoparticles [16]. Appropriate analytical tool is thus required to detect and quantify aggregates.

Various analytical techniques such as light scattering, separation, spectroscopy and microscopy are employed to monitor aggregation of bioconjugated nanoparticles including dynamic light scattering (DLS) [17,18], size-exclusion chromatography (SEC) [19,20], UV-vis spectroscopy [21,22], electron microscopy (EM) [23,24]. Each technique has its own merits and limitations for characterization of bioconjugated nanoparticles. DLS provides hydrodynamic diameter and its distribution using the Stokes–Einstein equation, and is fast and simple to operate. However its

* Corresponding author. Tel.: +82 42 629 8822; fax: +82 42 629 8811.
E-mail address: slee@hannam.kr (S. Lee).

http://dx.doi.org/10.1016/j.talanta.2014.05.060
0039-9140/© 2014 Elsevier B.V. All rights reserved.

application to polydisperse samples or quantification of aggregates is often limited [25]. SEC provides size-based separation of particles, and yields useful information on size distribution of particles. However the resolution of SEC may be hampered by nonspecific interaction of the sample with stationary phase, and its application to larger particles is rather limited due to lower resolution. UV–vis spectroscopy provides information on aggregation in suspension, but requires fairly concentrated sample for measurement. EM allows one to view the size and shape of individual nanoparticles. During EM measurement, however, the sample suspension is dried and put on a high-vacuum, which may cause shrinkage and agglomeration of particles.

Field-flow fractionation (FFF) is a family of size-based separation techniques capable of providing separation and characterization of macromolecules or particles ranging in size from 1 nm up to about 100 μm [26]. Among the members of FFF family, asymmetrical flow field-flow fractionation (AsFlFFF) is particularly useful for separation and characterization of bioconjugated nanoparticle [27,28] and protein aggregates [28–31].

In this study, 40 nm AgNPs were synthesized using the citrate reduction method [32]. Then the surface of the nanoparticles were modified by conjugating Cyto C at various molar ratios of Cyto C to AgNPs, [Cyto C]/[AgNPs]. AsFlFFF was then used for separation and quantification of Cyto C–conjugated AgNPs (Cyto C–AgNP) obtained at various pH, temperature and ionic strengths. Also, the aggregation behavior of Cyto C–AgNP was studied using AsFlFFF and UV–vis spectroscopy. Aim of this study is to determine the size and size distribution of Cyto C–AgNP and to study stability of Cyto C–AgNP in suspension at various conditions.

2. Theory

In AsFlFFF, the hydrodynamic diameter (d_H) of a particle is related with its retention time (t_r) by [33]

$$d_H = \frac{2V^o kTt_r}{\pi\eta w^2 F_c t^o} \quad (1)$$

where V^o is the void volume of the AsFlFFF channel, k is the Boltzmann constant, T is the absolute temperature (k), η is the viscosity of the carrier liquid, w is the channel thickness, F_c is the volumetric cross-flow rate, and t^o is the void time (the elution time of the species that are not retained). Using Eq. (1), an AsFlFFF fractogram of the particles can be converted directly to a size distribution.

3. Experimental

3.1. Chemicals

Silver nitrate ($AgNO_3$), trisodium citrate, sodium azide and Cyto C were purchased from Sigma-Aldrich (St. Louis, MO, USA). Sodium phosphate buffer solution (PBS) was prepared by adjusting the concentrations of sodium dihydrogen phosphate and disodium hydrogen phosphate to achieve desired pH and ionic strength. Cyto C was prepared in 20 mM PBS at pH 7.2.

3.2. Synthesis of citrate–silver nanoparticles and preparation of Cyto C–AgNP

Silver nanoparticles were prepared by the citrate reduction of silver nitrate, first reported by Lee and Meisel with some modifications [32]. A 200 mL of 0.0001 M $AgNO_3$ solution was heated to boil at 100 °C. 7.5 mL of 1% (w/v) sodium citrate solution was then added and the solution was refluxed for 35 min. The temperature, stirring rates were held constant during preparation. In other to obtain the Cyto C–AgNP, pH of AgNPs suspension was adjusted to 11 by adding 0.1 M NaOH. The isoelectric point of Cyto C is near 10, and Cyto C is stable and no aggregation occurs at pH 11 [11]. At pH above the isoelectric point, Cyto C molecules become negatively charged, and produce Cyto C–AgNP via electrostatic interaction. Then, 0.01 mg/mL or 0.1 mg/mL solutions of Cyto C in PBS buffer was added at desired molar ratio of [Cyto C]/[AgNPs]. The suspension was kept at 4 °C for 1 day.

3.3. Determination of concentration of silver nanoparticles

The concentration of silver nanoparticles was determined by the method which has been previously reported by Liu et al. for gold nanoparticle analysis [34]. The average number of atoms per nanoparticle is defined as

$$N = \frac{\pi\rho d^3}{6M} N_A \quad (2)$$

where N is the number of atoms per nanoparticle, ρ is the density of silver (10.5 g/cm^3), d is the average diameter of nanoparticles, M is the atomic mass of silver (107.868 g), and N_A is the number of atoms per mole (Avogadro's number).

The molar concentration C of the nanoparticles in suspension was determined by

$$C = \frac{N_T}{NVN_A} \quad (3)$$

where N_T is the total number of silver atoms added as $AgNO_3$, N is the number of atoms per nanoparticle in Eq. (2), and V is the volume of the reaction solution. The concentration of silver nanoparticles synthesized in this study was calculated to be 4.55×10^{-11} mol/L from Eqs. (2) and (3).

3.4. Asymmetrical flow field-flow fractionation (AsFlFFF)

The AsFlFFF system used in this study was the Eclipse AF4 (Wyatt Tech., Europe GmbH, Dernbach, Germany) assembled with a 350 μm-thick Mylar spacer and a regenerated cellulose membrane (Millipore, Bedford, MA, USA) having the cut-off molecular weight of 10 kDa. The channel geometry was trapezoidal with the tip-to-tip length of 26.5 cm and breadths at the inlet and the outlet of 2.2 and 0.6 cm, respectively. To measure the channel thickness, 52 ± 2 nm polystyrene beads having a narrow size distribution were injected with the carrier solution of water containing 0.02% FL-70 and 0.02% NaN_3. The channel thickness determined from the retention time of 52 ± 2 nm polystyrene beads was 238 μm.

A HPLC pump (Futecs P-6000, Daejeon, Korea) was used to deliver the carrier liquid into the AsFlFFF channel. The channel and the cross-flow rates were measured using liquid flow meters (Optiflow 1000, Agilent Technologies, Palo Alto, CA, USA). Eluted particles were monitored using a Model-500 UV detector (Chrom tech Inc., MN, USA) with the wavelength set at 410 nm. The detector signal was collected by using FFF analyzer software supplied by Quantum Soft. (Daejeon, Korea). The 20 μL particle suspension was injected into the AsFlFFF channel using a 20 μL loop injector (Rheodyne, Cotati, CA, USA). A syringe pump (Model 100, KD Scientific, USA) was used to inject the sample suspension into the AsFlFFF channel at the flow rate of 0.2 mL/min for 60 s.

3.5. Other instruments

DLS and ζ-potential measurements were made at the scattering angle of 90° (for DLS measurement) and 17° (for ζ-potential measurement), respectively, with a Zetasizer Nano ZS90 (Malvern

instrument, Worcestershire, UK) equipped with a He–Ne laser (633 nm) as the light source. All measurements were repeated three times for a DLS analysis and ten times for a ζ-potential measurement, respectively. The results were presented as the mean size or ζ-potential ± one standard deviation. UV-3101-PC spectrophotometer (Shimadzu, Kyoto, Japan) was used for UV–vis spectroscopic analysis of AgNPs.

4. Results and discussion

4.1. Formation of Cyto C–AgNP

The ζ-potential measurement of nanomaterial provides not only information on the electrical potential on the surface ('surface charge'), yielding an insight into stability of nanometerials in suspension, but also the thickness of the electrical double layer on the surface of bioconjugated nanometerials [11,35]. As the amount of protein adsorbed on the nanoparticle increases, the surface charge varies, and eventually reaches a stable value, indicating the nanoparticle surface is saturated with the protein.

In order to obtain saturated Cyto C–AgNP, ζ-potential was measured by varying the molar ratio, [Cyto C]/[AgNPs], at pH 11. Fig. 1 shows ζ-potential measured for Cyto C–AgNP prepared at various molar ratios of [Cyto C]/[AgNPs] ranging from 0 up to 500. As shown in Fig. 1, ζ-potential of AgNPs increases as [Cyto C]/[AgNPs] increases at the beginning, which suggests that the surface charge of AgNPs is neutralized upon adsorption of Cyto C. ζ-potential of the bare AgNPs was -61 ± 4.5 mV and increases rather quickly with increasing [Cyto C]/[AgNPs] until the molar ratio reaches about 100. At [Cyto C]/[AgNPs] higher than about 100, ζ-potential still increases with [Cyto C]/[AgNPs], but at much slower rate. Further increase in [Cyto C]/[AgNPs] above about 300 did not lead to significant changes in ζ-potential. It seems that Cyto C–AgNP is formed by electrostatic attraction of the negatively charged carboxylate groups on AgNPs and the positively charged Cyto C.

4.2. Characterization of Cyto C–AgNP

In order to determine the size of Cyto C adsorbed on AgNPs, hydrodynamic diameter was determined using AsFlFFF and DLS. Fig. 2 shows AsFlFFF fractograms (Fig. 2(a)) and size distributions (Fig. 2(b)) of three types of AgNPs (bare AgNPs and Cyto C–AgNP obtained at [Cyto C]/[AgNPs] of 300 and 20,000). Both Cyto C–AgNP were prepared at pH 11. The AsFlFFF channel flow rate

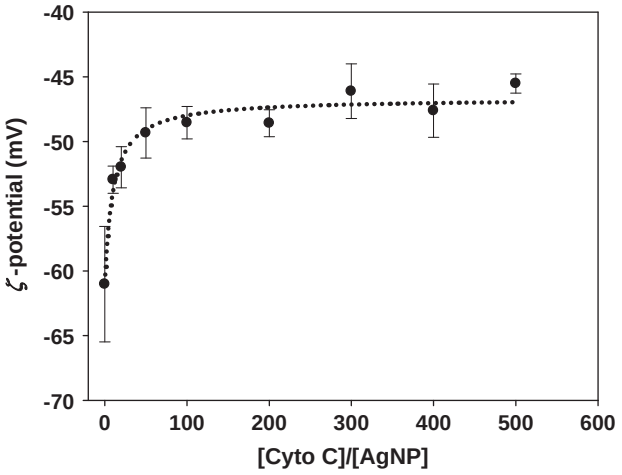


Fig. 1. Variation of ζ-potential of Cyto C–AgNPs with molar ratio of [Cyto C]/[AgNPs].

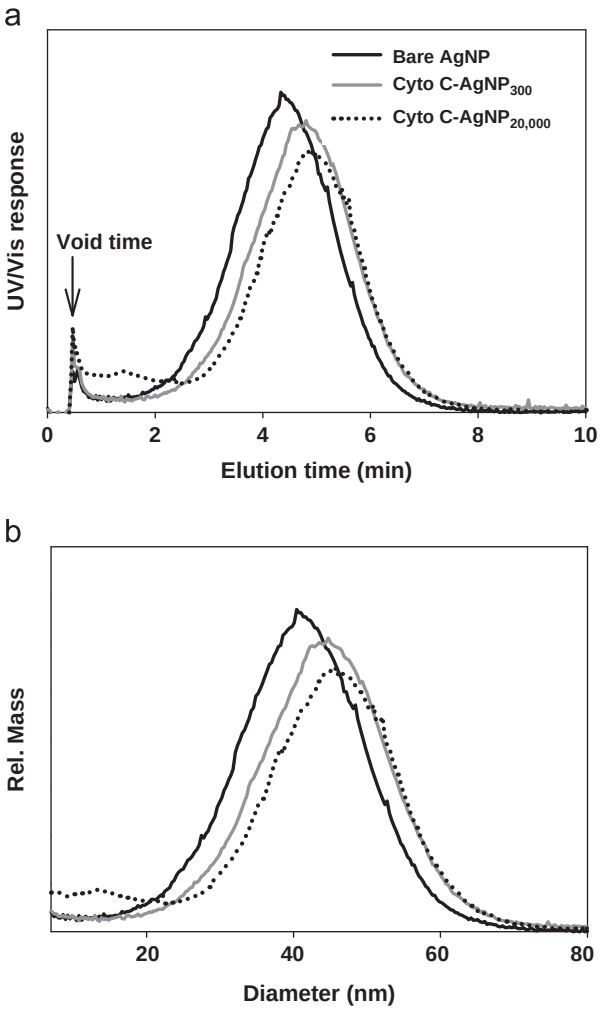


Fig. 2. AsFlFFF fractograms (a) and size distributions (b) of bare AgNPs and Cyto C–AgNP obtained at [Cyto C]/[AgNPs] of 300 and 20,000. The channel and cross-flow rate were 0.49 and 1.05 mL/min, respectively.

and the cross-flow rate were 0.49 and 1.05 mL/min, respectively. As shown in Fig. 2(a), the elution time of AgNPs at peak was increased by about 0.5 min when the particles were treated with Cyto C at [Cyto C]/[AgNPs] of 300 due to an increase in hydrodynamic diameter of the particles. This increase in the elution time of about 0.5 min is translated to an increase in the hydrodynamic diameter of about 4 nm (from 40.4 ± 0.4 to 44.5 ± 0.2 nm) as shown in Fig. 2(b). Each run was repeated 2 or more times.

The size increase of the Cyto C–AgNP was clearly supported by UV-vis spectroscopy, as shown in Fig. 3(a). The maximum absorbance of bare AgNPs appeared at 410 nm, and the full width at half maximum (FWHM) was 77 nm, indicating the particles have a narrow size distribution [36]. When AgNPs was conjugated with the Cyto C at [Cyto C]/[AgNPs] of 300, the UV-vis absorption band was red-shifted to 416 nm, and FWHM increases to 79 nm. It has been reported that the red shift is caused by alteration of the refractive index of AgNPs by the Cyto C layer, resulting particle size increase [11].

Fig. 3(b) shows size distributions of the same two AgNPs obtained from DLS. It can be seen that the hydrodynamic diameter of AgNPs was increased from 47 ± 0.5 to 55 ± 1.1 nm due to adsorption of Cyto C molecules on the AgNPs surface. It is seen that the hydrodynamic diameters from DLS (Fig. 3(b)) are somewhat larger than those from AsFlFFF (Fig. 2(b)) for the same

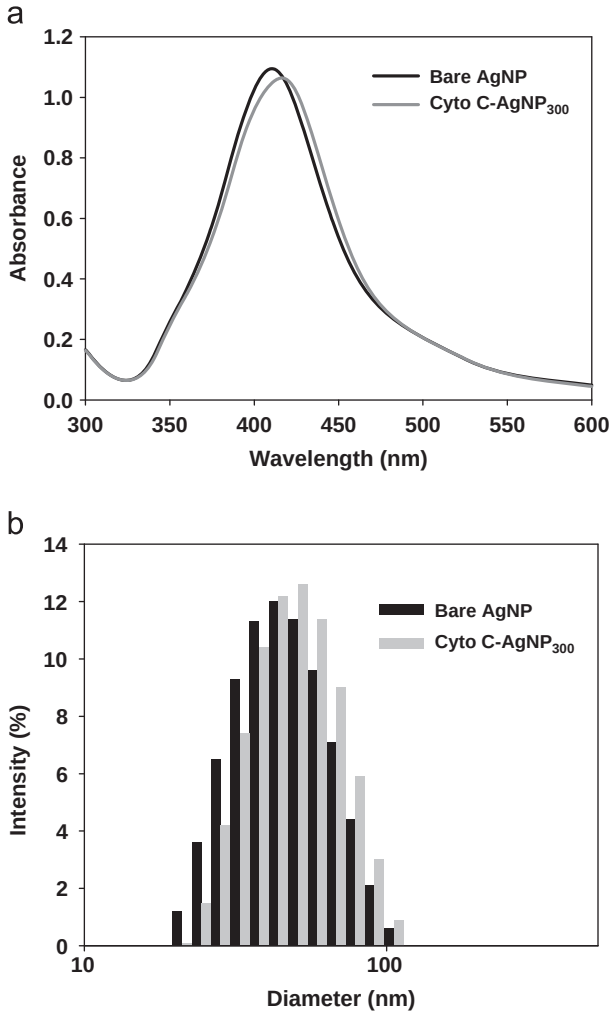


Fig. 3. UV-vis spectra (a) and DLS data (b) of bare AgNPs and Cyto C–AgNP obtained at [Cyto C]/[AgNPs] of 300.

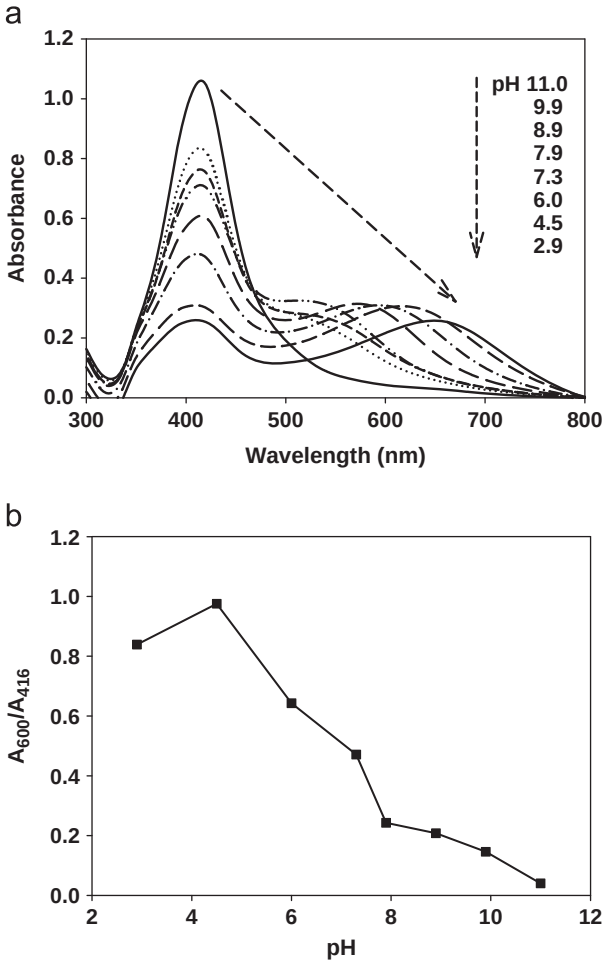


Fig. 4. Variation of UV-vis absorption spectra (a) and absorption ratio (b) of Cyto C–AgNP with pH.

sample. DLS measurements may have been overestimated due to bias toward large particles [37].

As shown in Fig. 2(b), addition of an excess of Cyto C ([Cyto C]/[AgNPs] of 20,000) did not change the particle size significantly as compared to that of Cyto C–AgNP obtained at the molar ratio of 300. This indicates the AgNPs particle surface is already saturated by Cyto C at the molar ratio of 300, and there will exist a large amount of free Cyto C in solution. The earlier eluting band that appears between the void time and about 2 min in Fig. 2(a) corresponds to those free Cyto C and their aggregates. When Cyto C was injected alone at the same condition, it was eluted together with the void peak as expected. At the molar ratio of 300, all (or most) of Cyto C molecules are adsorbed on AgNPs forming a uniform layer on the surface of the particles. On the other hand, at the molar ratio of 20,000, many of free Cyto C molecules are present between particles, resulting in reduction in repulsive force between particles. This may explain why the ζ-potential measured at the molar ratio of 20,000 (-23.6 ± 1.6 mV) was much lower than that measured at 300.

4.3. *Quantification of aggregates in Cyto C–AgNP suspension determined by UV–vis spectroscopy and AsFlFFF*

UV–vis spectroscopy can be employed to characterize bioconjugated nanoparticles in terms of the size, aggregation behavior and the change in refractive index [38]. Fig. 4(a) shows variation of UV–vis spectra of Cyto C–AgNP with pH. As pH decreases from 11.0 to 2.9, the absorbance of the first band (at 416 nm) gradually decreases, and the second band is red shifted from around 520–670 nm. The red shift was observed by the change in color of the suspension from yellow to red and then finally to a grey-blue as aggregation of Cyto C–AgNP proceeds as reported previously [12].

The ratio of the absorbance at 600 nm to that at 416 nm (A_{600}/A_{416}) can be used as a measure of particle aggregation as it will increase proportionally as aggregation increases [11,12]. Fig. 4(b) shows variation of A_{600}/A_{416} with pH, which shows gradual decrease of A_{600}/A_{416} with increasing pH. This indicates aggregation of AgNPs decreases as pH increases.

Fig. 5 shows variation of UV–vis spectra and AsFlFFF fractogram of Cyto C–AgNP with storage time at pH 10. As shown in Fig. 5(a), UV–vis absorbance of Cyto C–AgNP at 416 nm gradually decreases with storage time, while a new band at around 600 grows. This indicates aggregation of Cyto C–AgNP increases with increasing storage time. In order to quantify the aggregation behavior, the particles were analyzed by AsFlFFF as shown in Fig. 6(b). Experimental conditions were same as those in Fig. 2(a), except that the cross-flow was turned off after 10 min to allow complete elution of the aggregates. It can be seen that the area of first peak gradually decreases, while that of the second peak (which corresponds to aggregates) gradually increases with increasing storage time. It seems the Cyto C molecules adsorbed on AgNPs become increasingly unfolded and interact with Cyto C molecules on other

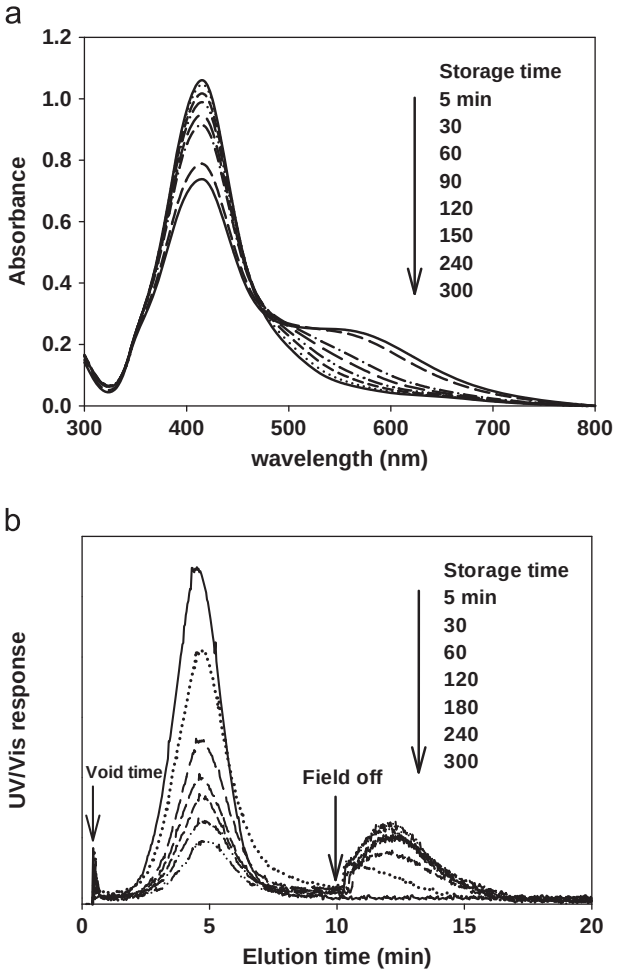


Fig. 5. Variation of UV-vis spectra (a) and AsFlFFF fractogram of Cyto C–AgNP with storage time at pH 10.

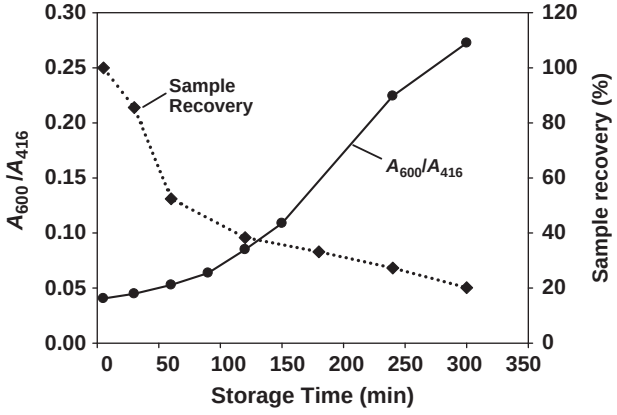


Fig. 6. Variation of UV-vis absorption ratio and sample recovery of Cyto C–AgNP with storage time.

particles that are protonated in the solution with increasing storage time [12,13,39].

Sample recovery R of Cyto C–AgNP in AsFlFFF can be determined by

$$R = \left(\frac{A}{A_o}\right) \times 100\% \quad (4)$$

where A and A_o are the AsFlFFF peak area of unaggregated Cyto C–AgNP in the elution time range of 0–10 min with and without the cross-flow, respectively. The peak area A decreases with increasing storage time, and thus R decreases.

Fig. 6 shows plots of A_{600}/A_{416} of Cyto C–AgNP and the sample recovery, R, in AsFlFFF as a function of storage time. It can be seen that the sample recovery in AsFlFFF decreases rapidly by about 50% after 60 min of storage, and then decreases slowly down by about 20% after 300 min. On the other hand, the absorption ratio slowly increases from about 0.04 to 0.085 after 120 min of storage, and then rapidly increases up to 0.27 after 300 min. It is noted that, while UV/vis spectroscopy provides qualitative information on the existence of aggregation of Cyto C–AgNP in suspension, AsFlFFF provides quantitative information from the sample recovery data.

4.4. Effect of temperature and ionic strength on stability of Cyto C–AgNP in solution

Fig. 7 shows variation of AsFlFFF fractogram of Cyto C–AgNP with storage temperature (Fig. 7(a)) and with the ionic strength of the suspending liquid (Fig. 7(b)) at pH 11. In both Fig. 7(a) and (b), the external field (cross-flow) was turned off after 10 min.

In Fig. 7(a), Cyto C–AgNP suspensions were stored at seven different temperatures of 25, 50, 55, 60, 65, 70, and 80 °C in preheated water bath for 1 h on a horizontal shaker (shaken at 200 cycles/min). At 25 °C, no elution was observed after the external field was turned off as shown in Fig. 7(a), and the sample recovery, R, was determined to be 100% from Eq. (4). As the storage

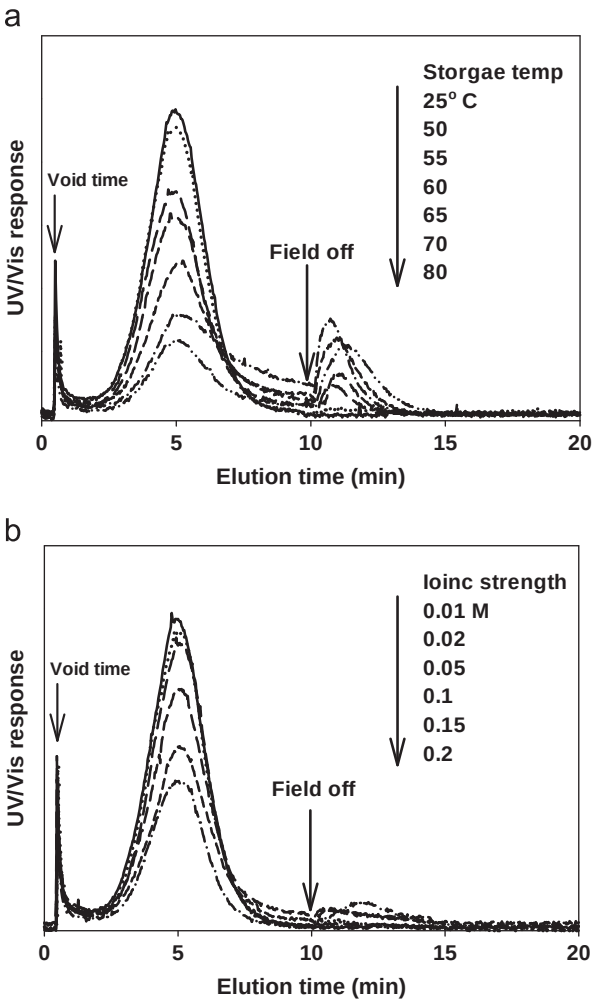


Fig. 7. Variation of AsFlFFF fractogram of Cyto C–AgNP with storage temperature (a) and ionic strength at pH 11.

temperature increases, the peak area decreases gradually, and, at the same time, the elution band area observed after 10 min gradually increases. As mentioned earlier, partially unfolded Cyto C molecules adsorbed on an AgNPs interacts with Cyto C on other AgNPs, and results in aggregation of the AgNPs. Results shown in Fig. 7(a) indicate that higher storage temperature promotes unfolding of Cyto C's, and causes more aggregation of Cyto C–AgNP.

In Fig. 7(b), Cyto C–AgNPs were stored at 25 °C for 1 h in suspension liquids of six different ionic strengths. The ionic strength was adjusted by adding appropriate amount of sodium chloride. It can be seen that, as the ionic strength of the suspension liquid increases, the peak area decreases gradually, and, at the same time, the elution band area observed after 10 min gradually increases. This suggests aggregation of Cyto C–AgNP increases with increasing ionic strength of the suspension liquid. It seems that, as the ionic strength increases, the thickness of the electrical double layer on the surface of the AgNPs decreases, and the electrostatic repulsion between particles decreases, promoting aggregation of the particles.

5. Conclusion

In this study, AsFlFFF was employed to determine the average size and size distribution of AgNPs, and to study the aggregation behavior of Cyto C–AgNP at various conditions of pH, temperature, ionic strength and storage time. Results showed that adsorption of Cyto C on the surface of AgNPs is saturated at the molar ratio ([Cyto C]/[AgNPs]) above about 300, and, from AsFlFFF analysis, the hydrodynamic diameter of the particles increases by about 4 nm.

Results suggest that AsFlFFF is a useful tool not only for the analysis of the size distribution of nanoparticles, but also for quantitative monitoring of aggregation behavior of bioconjugated nanoparticles.

Acknowledgment

This study was supported by the research project for Environmental Risk Assessment of Manufactured Nanomaterials (KK-1403-02) funded by the Korea Institute of Toxicology (KIT, Korea). The authors acknowledge the support provided by the National Research Foundation (NRF) of Korea.

Reference

[1] P.K. Jain, X. Huang, I.H. El-Sayed, M.A. El-Sayed, Acc. Chem. Res. 41 (2008) 1578–1586.
[2] D. Long, G. Wu, S. Chen, Radiat. Phys. Chem. 76 (2007) 1126–1131.
[3] M.J. Meziani, Y.P. Sun, J. Am. Chem. Soc. 125 (2003) 8015–8018.
[4] D.G. Yu, W.C. Lin, M.C. Yang, Bioconjug. Chem. 18 (2007) 1521–1529.
[5] S.W.P. Wijnhoven, W.J.G.M. Peijnenburg, C.A. Herberts, W.I. Hagens, A.G. Oomen, E.H.W. Heugens, B. Roszek, J. Bisschops, I. Gosens, D. Van De Meent, S. Dekkers, W.H. De Jong, M. Van Zijverden, A.J.A.M. Sips, R.E. Geertsma, Nanotoxicology 3 (2009) 109–138.
[6] R. Vaidyanathan, K. Kalishwaralal, S. Gopalram, S. Gurunathan, Biotechnol. Adv. 27 (2009) 924–937.
[7] G.A. Sotiriou, S.E. Pratsinis, Curr. Opin. Chem. Eng. 1 (2011) 3–10.
[8] M.S. Sumitha, K.T. Shalumon, V.N. Sreeja, R. Jayakumar, S.V. Nair, D. Menon, Part A: Pure Appl. Chem. 49 (2012) 131–138.
[9] A. Ravindran, A. Singh, A.M. Raichur, N. Chandrasekaran, A. Mukherjee, Colloids Surf. B: Biointerfaces 76 (2010) 32–37.
[10] Y. Cheng, L. Yin, S. Lin, M. Wiesner, E. Bernhardt, J. Liu, J. Phys. Chem. C 115 (2011) 4425–4432.
[11] I. Gomes, N.C. Santos, L.M.A. Oliveira, A. Quintas, P. Eaton, E. Pereira, R. Franco, J. Phys. Chem. C 112 (2008) 16340–16347.
[12] J. Park, I. Choi, Y. Kim, J. Yi, Bull. Korean Chem. Soc. 32 (2011) 3433–3436.
[13] Y.J. Shiu, U.S. Jeng, Y.S. Huang, Y.H. Lai, H.F. Lu, C.T. Liang, I.J. Hsu, C.H. Su, C. Su, I. Chao, A.C. Su, S.H. Lin, Biophys. J. 94 (2008) 4828–4836.
[14] R.F. Domingos, N. Tufenkji, K.J. Wilkinson, Environ. Sci. Technol. 43 (2009) 1282–1286.
[15] R.A. French, A.R. Jacobson, B. Kim, S.L. Isley, L. Penn, P.C. Baveye, Environ. Sci. Technol. 43 (2009) 1354–1359.
[16] A.A. Keller, H. Wang, D. Zhou, H.S. Lenihan, G. Cherr, B.J. Cardinale, R. Miller, J.I. Zhaoxia, Environ. Sci. Technol. 44 (2010) 1962–1967.
[17] T. Pons, H.T. Uyeda, I.L. Medintz, H. Mattoussi, J. Phys. Chem. B 110 (2006) 20308–20316.
[18] H. Jans, X. Liu, L. Austin, G. Maes, Q. Huo, Anal. Chem. 81 (2009) 9425–9432.
[19] D.G. Mullen, M. Fang, A. Desai, J.R. Baker Jr., B.G. Orr, M.M. Banaszak Holl, ACS Nano 4 (2010) 657–670.
[20] D.G. Mullen, A.M. Desai, J.N. Waddell, X.M. Cheng, C.V. Kelly, D.Q. McNerny, I.J. Majoras, J.R. Baker Jr, L.M. Sander, B.G. Orr, M.M. Banaszak Holl, Bioconj. Chem. 19 (2008) 1748–1752.
[21] K.C. Grabar, R. Griffith Freeman, M.B. Hommer, M.J. Natan, Anal. Chem. 67 (1995) 735–743.
[22] R.T. Tom, A.K. Samal, T.S. Sreeprasad, T. Pradeep, Langmuir 23 (2007) 1320–1325.
[23] X. Qian, X. Zhou, S. Nie, J. Am. Chem. Soc. 130 (2008) 14934–14935.
[24] Y. Wang, Y. Shen, A. Xie, S. Li, X. Wang, Y. Cai, J. Phys. Chem. C 114 (2010) 4297–4301.
[25] G.D.J. Phillies, Anal. Chem. 62 (1990) 1049a–1057A.
[26] J.C. Giddings, Science 260 (1993) 1456–1465.
[27] D.H. Tsai, F.W. Delrio, A.M. Keene, K.M. Tyner, R.I. MacCuspie, T.J. Cho, M.R. Zachariah, V.A. Hackley, Langmuir 27 (2011) 2464–2477.
[28] A. Zattoni, D.C. Rambaldi, P. Reschiglian, M. Melucci, S. Krol, A.M.C. Garcia, A. Sanz-Medel, D. Roessner, C. Johann, J. Chromatogr. A 1216 (2009) 9106–9112.
[29] W. Fraunhofer, G. Winter, Eur. J. Pharm. Biopharm. 58 (2004) 369–383.
[30] D.C. Rambaldi, P. Reschiglian, A. Zattoni, Anal. Bioanal. Chem. 399 (2011) 1439–1447.
[31] S. Cao, J. Pollastrini, Y. Jiang, Curr. Pharm. Biotechnol. 10 (2009) 382–390.
[32] P.C. Lee, D. Meisel, J. Phys. Chem. 86 (1982) 3391–3395.
[33] B. Wittgren, K.G. Wahlund, H. Dérand, B. Wesslén, Macromolecules 29 (1996) 268–276.
[34] X. Liu, M. Atwater, J. Wang, Q. Huo, Colloids Surf. B: Biointerfaces 58 (2007) 3–7.
[35] K. Rezwan, A.R. Studart, J. Vörös, L.J. Gauckler, J. Phys. Chem. B 109 (2005) 14469–14474.
[36] M.W. Meyer, E.A. Smith, Analyst 136 (2011) 3542–3549.
[37] R.F. Domingos, M.A. Baalousha, Y. Ju-Nam, M.M. Reid, N. Tufenkji, J.R. Lead, G.G. Leppard, K.J. Wilkinson, Environ. Sci. Technol. 43 (2009) 7277–7284.
[38] K.E. Sapsford, K.M. Tyner, B.J. Dair, J.R. Deschamps, I.L. Medintz, Anal. Chem. 83 (2011) 4453–4488.
[39] D. Zhang, O. Neumann, H. Wang, V.M. Yuwono, A. Barhoumi, M. Perham, J.D. Hartgerink, P. Wittung-Stafshede, N.J. Halas, Nano Lett. 9 (2009) 666–671.

Talanta 132 (2015) 945–953

Contents lists available at ScienceDirect

Talanta

journal homepage: www.elsevier.com/locate/talanta

Retention behavior of microparticles in gravitational field-flow fractionation (GrFFF): Effect of ionic strength

In Suk Woo [a], Euo Chang Jung [b], Seungho Lee [a,*]

[a] Department of Chemistry, Hannam University, Daejeon 305-811, Korea Republic
[b] Nuclear Chemistry Research Center, Korea Atomic Energy Research Institute, Daejeon 305-353, Korea Republic

ARTICLE INFO

Article history:
Received 27 April 2014
Received in revised form
28 May 2014
Accepted 29 May 2014
Available online 10 June 2014

Keywords:
Gravitational field-flow fractionation (GrFFF)
Microparticles
Ionic strength
Viscosity
Resolution

ABSTRACT

Retention behavior of micron-sized particles in gravitational field-flow fractionation (GrFFF) was studied in this study. Effects of ionic strength and flow rate as well as the viscosity of the GrFFF carrier liquid was investigated on the size-based selectivity (S_d), retention ratio (R), and plate height (H) of micron-sized particles using polystyrene latex beads as model particles. It was found that the retention ratio of microparticles increases with increasing flow rate or the viscosity of the carrier liquid as the particles are forced away from the accumulation wall by increased hydrodynamic lift forces (HLF). On the other hand, the retention time increases (retention ratio decreases) with increasing ionic strength of the carrier liquid at the same flow rate, due to decreased repulsive interaction between the particles and the channel accumulation wall (glass in this study) allowing the particles approach closer to the wall. Results suggest the ionic strength of the carrier liquid plays a critical role in determining retention of microparticles in GrFFF as well as the viscosity or the flow rate of the carrier liquid. It was found that the resolution and the separation time could be improved by increasing the carrier viscosity and by carefully adjusting the ionic strength of the carrier liquid.

© 2014 Elsevier B.V. All rights reserved.

1. Introduction

Field-flow fractionation (FFF) is a family of elution-based separation techniques that utilize a thin flow channel, where an external field is applied vertically to the direction of the carrier flow [1–3]. The external field forces the particles move across the channel, impelling them to approach the channel accumulation wall [4]. Particles of different sizes are separated as they migrate down the channel at different rates by the channel flow having a parabolic profile [5–7]. FFF is capable of providing separation and characterization of macromolecules and particles which are in sizes from a few nanometers to a few tens of microns [8–10] including blood cells [11–13].

Gravitational field-flow fractionation (GrFFF) is a member of FFF family, and employs the Earth's gravity as the external field. GrFFF is usually applied for separation of micron-sized particles where larger particles are eluted earlier than smaller ones.

In GrFFF, particles are eluted by the "lift-hyperlayer" mode [13–21], where the particles are lifted up from the accumulation wall by the HLF, and, as a result, the particles are focused into a narrow zone ('hyperlayer') at a distance away from the accumulation wall. The hyperlayer is located at the position where the effective particle weight F_G equals HLF. The 'lift-hyperlayer' mode is also called 'focusing' mode.

Various ways of changing the external field force in GrFFF have been suggested [5], which includes changing of the channel angle [10,22], the density of the carrier liquid [6,23], and the carrier viscosity [4,22,23]. In our previous report [22], effect of the carrier viscosity and the channel angle on the retention behavior of microparticles in GrFFF was investigated. It has been reported that the retention in FFF may be affected by the particle-wall and particle-particle interactions (electrostatic repulsion and van der Waals attraction) depending upon the carrier composition (mainly the ionic strength) and experimental conditions (e.g., flow rate, field strength, and channel dimension) [24,25]. This work focuses on the effect of the ionic strength and the flow rate of the carrier liquid. Effect of the ionic strength and flow rate as well as the viscosity of the carrier liquid on various retention (and thus the resolution-related) parameters such as the retention ratio (R), plate height (H), distance of particles from the accumulation wall (δ), size-based selectivity (S_d), and resolution (R_s) was investigated using micron-sized polystyrene (PS) latex beads as model particles. Hydroxypropyl methyl cellulose (HPMC) was added to the carrier liquid to change the viscosity of the carrier liquid without affecting density as in our previous report [22].

* Corresponding author. Tel.: +82 42 629 8822; fax: +82 42 629 8811.
E-mail address: slee@hannam.kr (S. Lee).

http://dx.doi.org/10.1016/j.talanta.2014.05.061
0039-9140/© 2014 Elsevier B.V. All rights reserved.

2. Theory

2.1. Retention in GrFFF

In GrFFF theory, the retention ratio (R) is given by [7]

$$R = 3\gamma\frac{d}{w} \tag{1}$$

where d is the particle diameter and w is the channel thickness. The γ is the 'steric correction factor' that is known to vary with experimental conditions such as the field strength, carrier flow rate and the particle size [26–28]. As the carrier flow rate increases or the field strength decrease, γ increases [18,29]. Experimentally, R can be measured from

$$R = \frac{t^o}{t_r} \tag{2}$$

where t^o is the channel void time and t_r is the sample retention time. γ can thus be determined from Eq. (1) by measuring R of particles of known diameter using Eq. (2). As suggested by Eqs. (1) and (2), t_r increases as the particle size decreases in GrFFF, providing a size-based separation.

The size-based selectivity (S_d) is the absolute value of the slope of a GrFFF calibration plot ($\log t_r$ *vs.* $\log d$) and is given by [27,30,31]

$$S_d = \left|\frac{d\log t_r}{d\log d}\right| \tag{3}$$

2.2. Near-wall lift force (F_{NW})

The near-wall lift force F_{Nw} is the force exerted on particles in the region near the wall, and is given by [18,26,32]

$$F_{Nw} = 6C\eta u\frac{a^3}{w\delta} \tag{4}$$

where C is an empirical dimensionless coefficient, η is the viscosity of the carrier liquid, u is the average linear flow velocity of the carrier liquid, a is the particle radius, and δ is the closest distance between the particle surface and the channel bottom (accumulation wall). The F_{NW} plays an important role in determining the equilibrium position of a particle in a FFF channel [21]. It can be seen from Eq. (4) that F_{Nw} increases with particle size, flow rate, viscosity of carrier liquid, and with decreasing channel thickness [4,6,20].

At some point, the lift force in Eq. (4) becomes sufficient to counter the gravitational force and result in a particle equilibrium position established above the wall ($\delta > 0$). If the inertial contribution to lift force is negligible, then the net force F_{net} on a particle in the direction away from the wall is given by [22]

$$F_{net} = \frac{6Ca^3\eta\langle\nu\rangle}{w\delta} - F_G \tag{5}$$

where F_G is the force on the particle due to gravity (equal to (4/3) $a^3\Delta\rho G$, where $\Delta\rho$ is the difference between the particle density and fluid density and G is the acceleration due to gravity or 9.81 m/s^2). The particle equilibrium position is given when the net force becomes zero. Rearranging Eq. (5) with $F_{net}=0$ gives:

$$\delta_{eq} = \frac{9}{2}\frac{C\langle\nu\rangle\eta}{\pi w\Delta\rho G} \tag{6}$$

It is noted that that δ_{eq} is independent of the particle size.

Electrostatic repulsion between the negatively charged accumulation wall (glass) and negatively charged particles may also contribute to elevation of the particle zone [33]. Thus the difference between the retention behaviors of the particles in different carrier liquid compositions could be explained by a combination of the hydrodynamic lift forces (HLF) and the electrostatic force [6].

2.3. Plate height (H)

Plate height H is a measure of band broadening, and is usually consisted of several contributing factors including the non-equilibrium effect (H_n), instrumental effect (H_i), sample polydispersity (H_p) and the diffusion of particles (H_D). The total plate height H is thus given by $H = H_n + H_i + H_p + H_D$ [34]. In GrFFF, particles are eluted either by the steric or the lift-hyperlayer mode, and thus it can be assumed that H_n and H_i are similar for particles of different sizes. If the particle polydispersity (and thus H_p) remains same for all samples, the band broadening would be mainly caused by H_D, the diffusion of particles [34,35]. Diffusion increases with decreasing particle size, and thus H is expected to increases as the particle size decreases.

H can be measured from the well-known relationship, $H = L/N$, where L is the GrFFF channel length and N is the number of the theoretical plate that can be obtained from the half peak width ($w_{1/2}$) and the elution volume of the peak (A) by $N = 5.54(A/w_{1/2})^2$ [35].

2.4. Resolution

As a measure of resolution (R_s), a resolution factor R_s* was defined as [34]

$$R_s^* = \frac{S_d}{\sum H} \tag{7}$$

where $\sum H$ is sum of plate height of each particle sample.

3. Experimental

3.1. Materials

Polystyrene (PS) latex beads having nominal diameters of 6, 12, and 20 μm were obtained from Fluka AG (Steinheim, Germany), and 40 μm beads from Duke Scientific (Palo Alto, CA, USA). All PS beads have density of 1.05 g/mL. Two HPMC products (HPMC H-7509 and HPMC H-8384) were obtained from Sigma Aldrich (St. Louis, MO, USA). HPMC-7509 provides higher viscosity than HPMC-8384 at the same concentration. All chemicals were used without further purification. FL-70, a mixture of anionic and non-ionic compounds, was purchased from Fisher Scientific (Fair Lawn, NJ, USA), and sodium azide (NaN_3) were purchased from Sigma-Aldrich (St. Louis, MO, USA).

The PS latex bead samples were diluted with the GrFFF carrier liquid before being injected into the channel. The GrFFF carrier liquid was de-ionized and distilled water having various concentrations of FL-70, sodium azide, and hydroxyl propyl methyl cellulose (HPMC). HPMC was added to adjust the viscosity of the carrier liquid without affecting density of the liquid. Carrier liquids of seventeen different compositions (denoted 'A-1', 'A-2', 'A-3', 'A-4', 'B-1', etc.) were prepared in this study, and are listed in Table 1. The ionic strength is also shown for each carrier liquid. It can be seen that the ionic strengths of the carrier liquids with HPMC added (Carrier liquid-C's and D's) are in a relatively narrow range between 4.28 and 4.32. The viscosity of the carrier liquid was measured with a VIBRO SV-10 viscometer (A&D Company, Tokyo, Japan).

Table 1
GrFFF carrier liquids used in this study.

Carrier liquid	Composition	Viscosity[a] η (cP)	Ionic strength I (mM)
W	Water	1.000	0.0001
A-1	0.05% FL-70	1.023	0.600
A-2	0.1% FL-70	1.033	1.200
A-3	0.2% FL-70	1.027	2.400
A-4	0.3% FL-70	1.033	3.600
B-1	0.1% FL-70+0.01% NaN_3	1.047	2.738
B-2	0.1% FL-70+0.02% NaN_3	1.057	4.277
B-3	0.1% FL-70+0.03% NaN_3	1.070	5.815
B-4	0.1% FL-70+0.04% NaN_3	1.077	7.353
C-1	0.1% FL-70+0.02% NaN_3+0.02% HPMC-7509	1.207	4.282
C-2	0.1% FL-70+0.02% NaN_3+0.05% HPMC-7509	1.417	4.286
C-3	0.1% FL-70+0.02% NaN_3+0.07% HPMC-7509	1.700	4.288
C-4	0.1% FL-70+0.02% NaN_3+0.09% HPMC-7509	1.897	4.289
D-1	0.1% FL-70+0.02% NaN_3+0.02% HPMC-8384	1.160	4.289
D-2	0.1% FL-70+0.02% NaN_3+0.05% HPMC-8384	1.273	4.303
D-3	0.1% FL-70+0.02% NaN_3+0.07% HPMC-8384	1.300	4.312
D-4	0.1% FL-70+0.02% NaN_3+0.09% HPMC-8384	1.343	4.321

[a] Viscosities of carrier liquids are averages of three measurements.

3.2. Gravitational field-flow fractionation (GrFFF)

The GrFFF channel was cut in a 200 μm-thick spacer. The dimensions of the channel were 2 and 50 cm in width and length, respectively. Particle suspensions were injected directly into the channel using a 50 μL syringe (Hamilton Co., Reno, NV, USA) through a rubber septum. After the injection, the particles were allowed to settle by stopping the channel flow for 3 minutes [4,36]. The sample would be eluted on resumption of the flow. The carrier liquid was pumped by a Young-Lin SP930D HPLC pump (Seoul, Korea). The elution of the particles was monitored by Young-Lin M720 UV detector at the operating wavelength of 254 nm.

4. Result and discussion

4.1. Effect of flow rate

As mentioned earlier, flow rate affects the hydrodynamic lift forces (HLF). GrFFF retention ratios of 40, 20, 12, and 6 μm PS latex beads obtained at various flow rates in carrier liquids of seventeen different compositions are shown in Fig. 1(a), (b), (c), and (d), respectively. As expected, for all samples, R generally increases with increasing flow rate. And R is always higher for larger particles at the same flow rate, showing GrFFF provides size-based separation of particles. Dotted lines in (Fig. 1) represent R values calculated from Eq. (1) with $\gamma = 1$. It can be seen that, as the

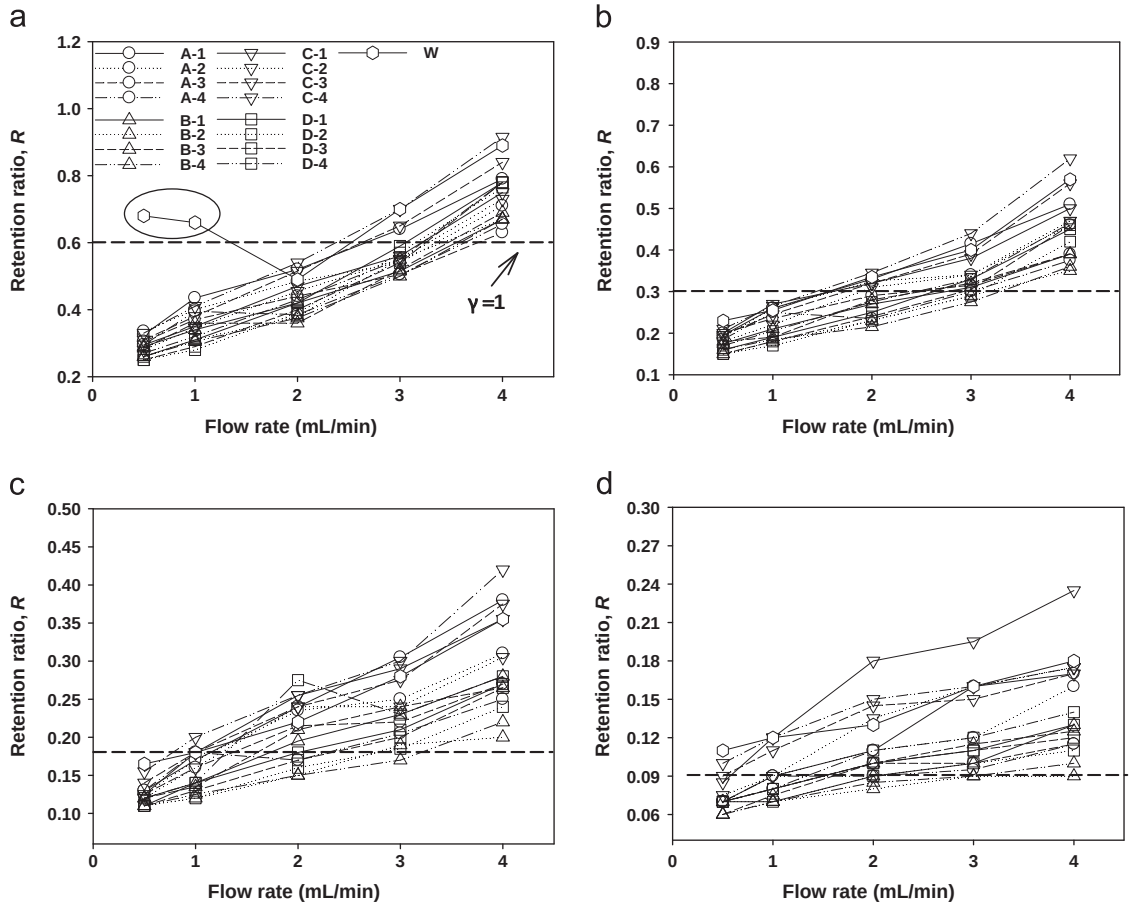


Fig. 1. Effect of flow rate on R of 40 (a), 20 (b), 12 (c) and 6 μm (d) PS beads in GrFFF with various carrier liquid compositions. Dotted lines are for cases of $\gamma = 1$.

Table 2
Effects of channel flow rate on size-based selectivity, S_d, in GrFFF.

Carrier liquid	S_d at flow rate (mL/min) of				
	0.5	1.0	2.0	3.0	4.0
C-1	0.703	0.678	0.629	0.655	0.771
C-2	0.685	0.568	0.505	0.553	0.615
C-3	0.660	0.630	0.670	0.764	0.824
C-4	0.645	0.632	0.685	0.773	0.863
D-1	0.689	0.695	0.739	0.869	0.960
D-2	0.697	0.704	0.772	0.936	1.021
D-3	0.697	0.707	0.758	0.858	0.982
D-4	0.698	0.718	0.682	0.811	0.926

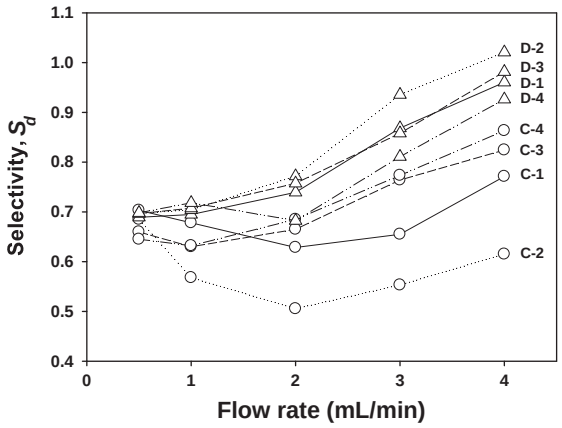


Fig. 2. Effect of flow rate on S_d in GrFFF with various carrier liquid compositions.

flow rate increases, the particles are forced away from the accumulation wall by increased HLF, resulting in a gradual increase in R with the flow rate.

It is noted that, for 40 μm particles with the carrier liquid of pure water (Fig. 1(a)), R does not follow the general trend at the flow rate lower than 2 mL/min (those in circled area), where the R values are much higher than those in other carrier compositions, and decreases as the flow rate increases. At the flow rate higher than 2 mL/min, R follows the general trend (increases with increasing flow rate) again. Those high R's are probably due to electrostatic repulsion between particles and the glass wall (used as the channel accumulation wall) at low ionic strengths. As the flow rate increases, particles are lifted up by stronger HLF, and effect of the electrostatic interaction becomes insignificant. This phenomenon was not observed for smaller particles, suggesting the electrostatic repulsion is insignificant for smaller particles at the same conditions.

The size-based selectivity S_d was determined at various channel flow rates using Eq. (3), and the results obtained with carrier liquids containing HPMC (carrier liquid C's and D's) are listed in Table 2 and Fig. 2. It can be seen that no general trend in S_d with flow rate was observed at the flow rate below about 2 mL/min. At the flow rate above about 2 mL/min, S_d tends to increase as the flow rate increases. It is seen that all S_d's in the carrier liquids with HPMC-7509 (Carrier C's) are lower than those in the carrier liquids with HPMC-8384 (Carrier D's). However no general trends in S_d with the carrier viscosity nor the ionic strength were observed, suggesting that S_d may be determined by a combination of some other factors as well as the carrier viscosity and ionic strength. It is interesting that the highest S_d was obtained with the carrier liquid 'B-2' (water with 0.1% FL-70 and 0.02% NaN_3), which is the carrier composition generally used in FFF.

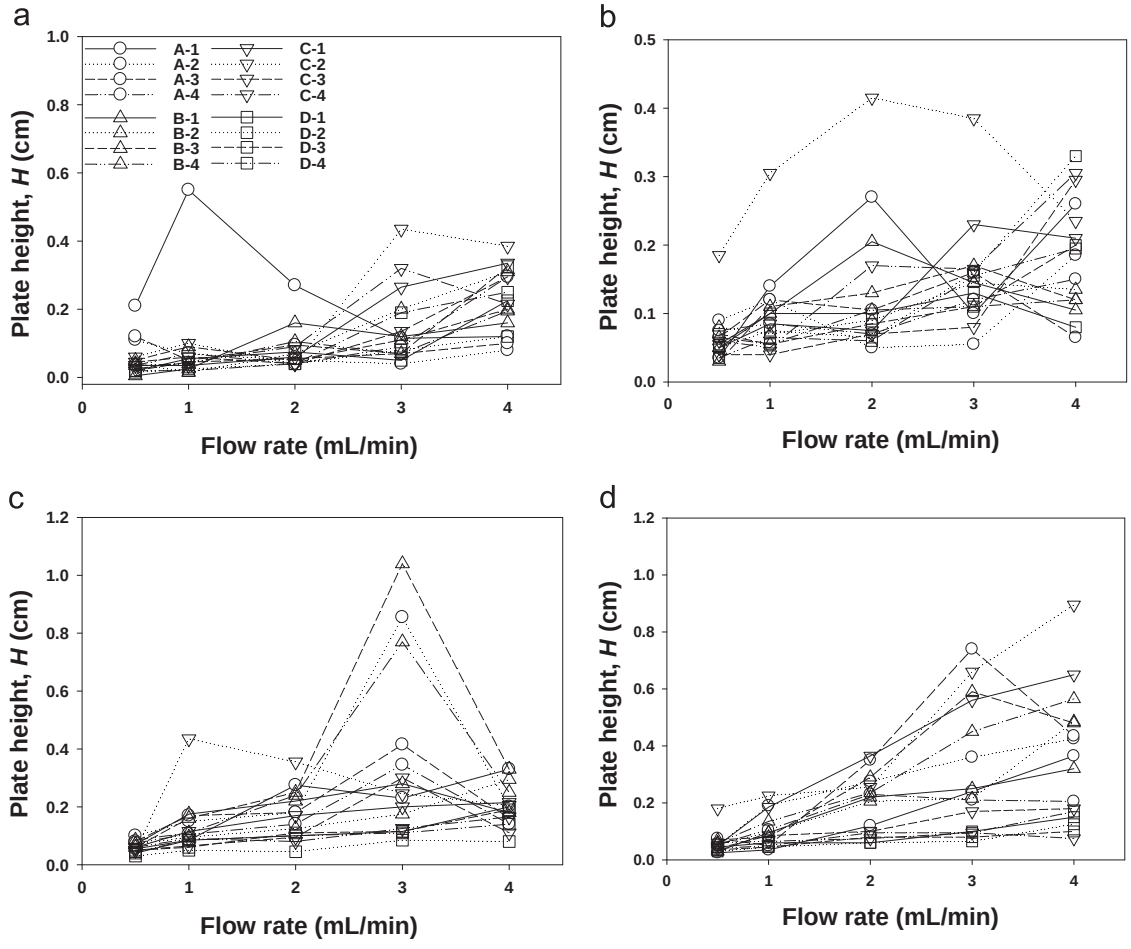


Fig. 3. Effect of flow rate on H for 40 (a), 20 (b), 12 (c) and 6 μm (d) PS beads in GrFFF with various carrier liquid compositions.

Table 3
Effects of ionic strength on retention time of PS latex beads in GrFFF.

Carrier liquid	t_r[a] (min) measured for PS beads having nominal diameter (μm) of			
	6	12	20	40
W	16.00	10.28	7.32	2.83
A-1	21.60	10.90	7.26	4.53
A-2	20.80	11.03	7.36	4.72
A-3	23.18	11.96	8.05	5.08
A-4	25.33	13.33	9.23	5.90
B-1	25.68	13.31	9.00	5.60
B-2	26.50	15.33	10.20	6.06
B-3	25.10	14.12	9.85	5.25
B-4	25.28	14.75	10.10	6.20

[a] Retention time t_r is average of two measurements made at flow rate of 1 mL/min.

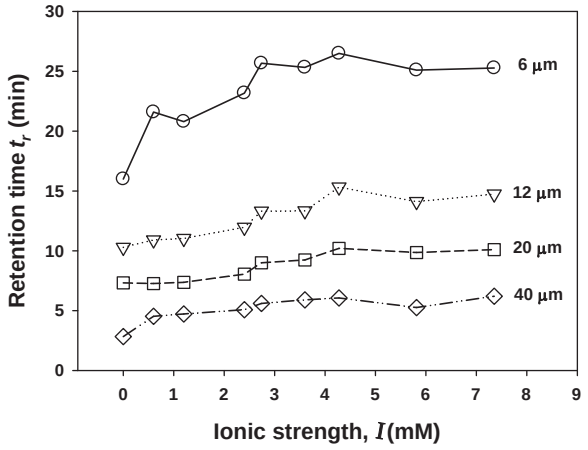


Fig. 4. Effect of ionic strength of carrier liquid on GrFFF retention of 6, 12, 20, and 40 μm latex beads in various carrier liquid compositions. Flow rate was fixed at 1 mL/min.

As shown in Eq. (3), only the retention time difference ($d \log t_r$) is taken into account in S_d calculation. If the degree of band broadening remains constant, higher S_d will result in higher resolution (R_s). Usually the band broadening is measured by the plate height H. Fig. 3 shows plate heights measured at various flow rates for 40, 20, 12 and 6 μm PS beads, respectively, in various carrier compositions. It can be seen that, for the same size particles, H tends to slowly increase as the flow rate increases, which agrees with the results reported previously [12,37].

4.2. Effect of ionic strength

Table 3 shows retention time t_r of PS latex beads measured at the flow rate of 1 mL/min with various carrier liquid compositions. t_r's in Table 3 are averages of two measurements. As shown in Table 3, at all conditions, t_r decreases with increasing diameter as expected (size-based separation). The data shown in Table 3 are plotted in Fig. 4. It can be seen in Fig. 4 that, for each PS bead sample, t_r increases with increasing ionic strength. As mentioned earlier, the retention behaviors of particles in various carrier liquid compositions could be explained by a combination of the lift force and the electrostatic force [6]. At a constant flow rate, the lift forces will be the same for particles for particles of the same size, and the difference in retention time shown in Fig. 4 can only be explained by the difference in the electrostatic interaction.

Effects of ionic strength in FFF have been extensively studied in previous reports [21,25,38]. Usually the repulsive interaction between particles and between particles and the channel wall is

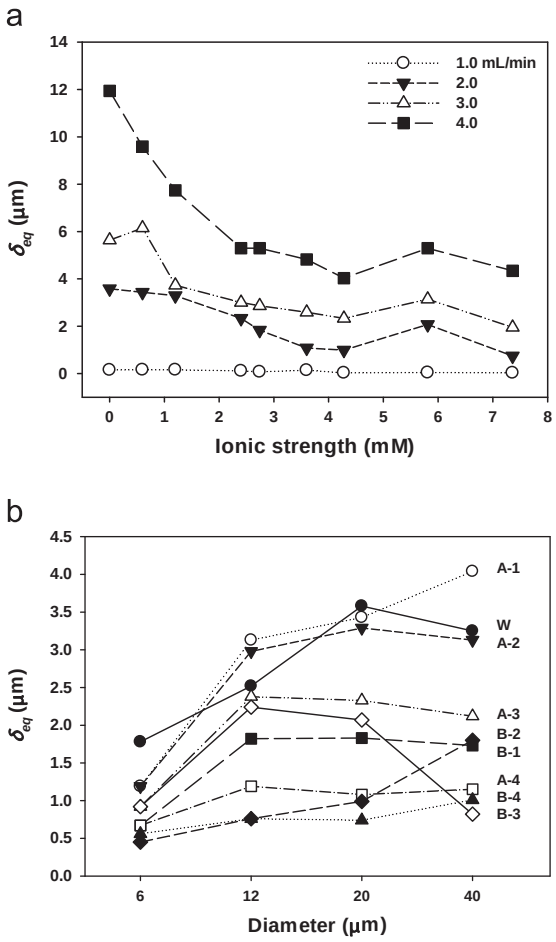


Fig. 5. Effect of ionic strength on δ_{eq} in GrFFF observed at various flow rates for 20 μm PS latex beads (a) and for PS beads of various sizes at 2 mL/min (b).

stronger in pure water than in a solution, and decreases as the ionic strength increases [38] allowing particles approach closer to the channel bottom, which results in increasing retention with increasing ionic strength as shown in Fig. 4. The retention time tends to level off after the ionic strength reaches about 4 mM, and the retention times obtained with the carrier liquids of B-2, 3, and 4 (last three data points for each particle size) are similar. This suggests water with 0.1% FL-70 and 0.02% NaN_3 (Carrier B-2) is appropriate as the carrier liquid for GrFFF separation of PS latex beads (or may be for many other types of particles).

The δ in Eq. (4) is the closest distance between the particle surface and the channel bottom (accumulation wall), and is zero

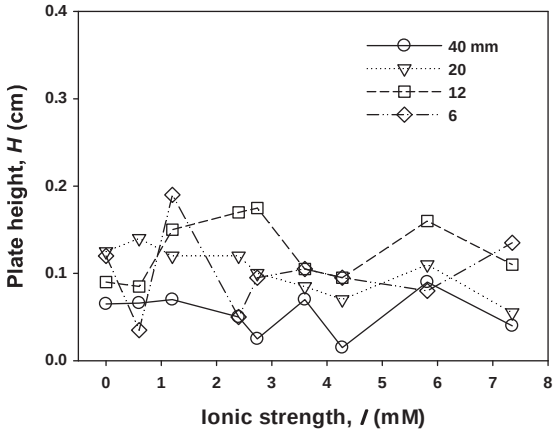


Fig. 6. Effect of ionic strength on plate height for PS latex beads in GrFFF at flow rate of 1 mL/min.

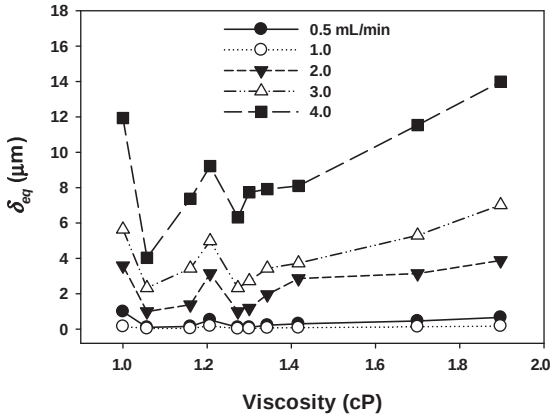


Fig. 8. Effect of viscosity on δ_{eq} of 20 μm PS latex beads in GrFFF at various flow rates.

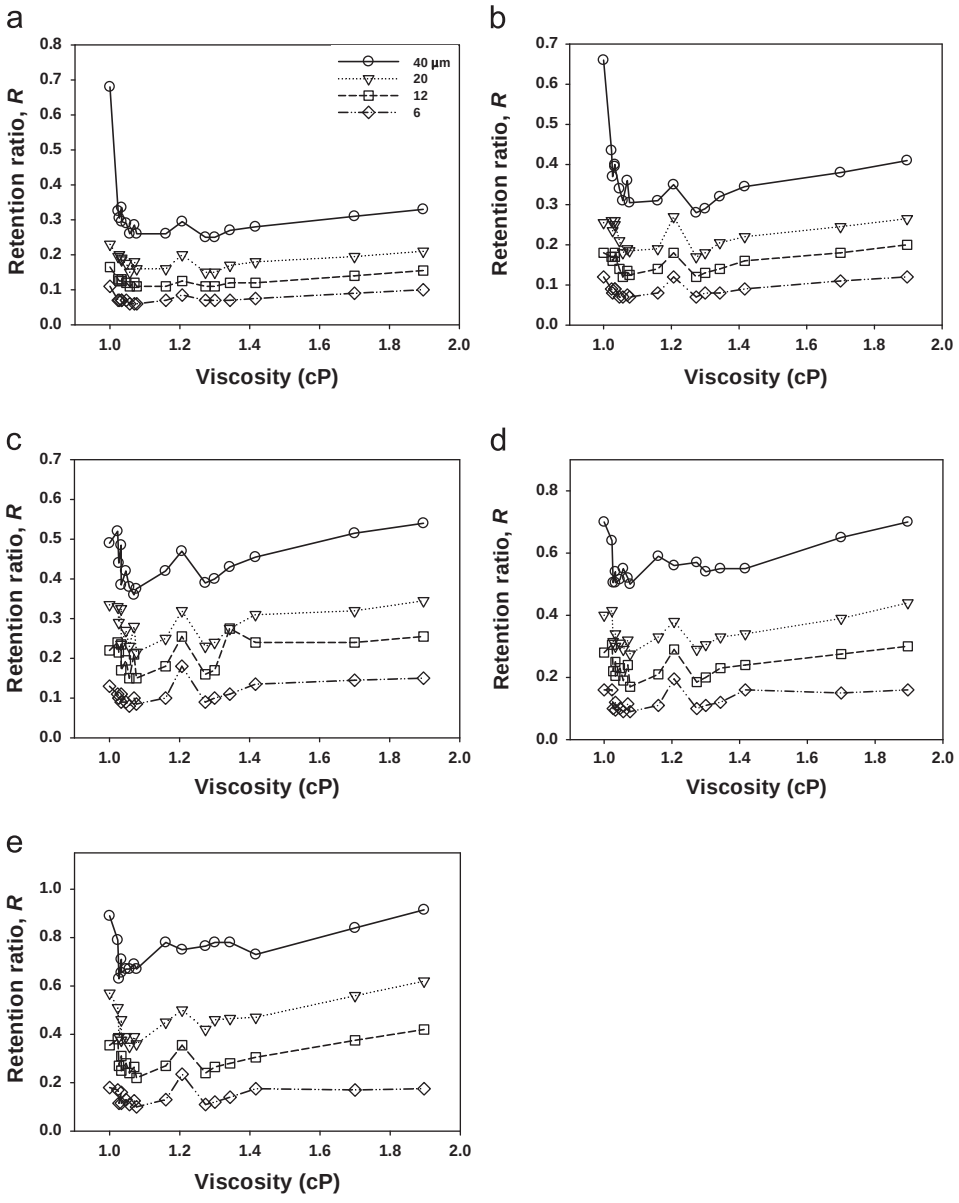


Fig. 7. Effect of viscosity of carrier liquid on retention ratio (R) of PS beads in GrFFF at flow rate of 0.5 (a), 1 (b), 2 (c), 3 (d) and 4 mL/min (e), respectively.

when the particle is on the channel bottom, and will increases as the particle is lifted away from the channel bottom. The δ_{eq} can be determined experimentally for each particle from its retention ratio R. The effect of the ionic strength on δ_{eq} is expected to be the same as that on R (shown in Fig. 4) as R is proportional to δ_{eq}. Fig. 5 (a) and (b) are plots of δ_{eq} vs. ionic strength obtained at various flow rates for 20 μm PS latex beads and for PS beads of various sizes at a fixed flow rate of 2 mL/min, respectively. In Fig. 5(a), at the same flow rate, δ_{eq} decreases as the ionic strength increases due to reduced repulsive interaction between particles and the channel bottom, and then levels off. It can be seen that, unlike at higher flow rates, the changes in δ_{eq} with ionic strength at lower flow rates (0.5 and 1 mL/min) are insignificant, and δ_{eq} stays close to 0, suggesting particles stay close to the channel bottom due to relatively lower (or insignificant) lift force. The lift force increases with increasing flow rate, and it seems higher lift force multiply the influence of the ionic strength on δ_{eq}. It can also be seen in Fig. 5(a) that, at the same ionic strength, δ_{eq} increases as the flow rate increases due to increased lift forces. In Fig. 5(b), δ_{eq} is plotted against particle diameter, and no general trend in δ_{eq} with particle diameter was observed as expected from Eq. (6).

Fig. 6 shows effect of ionic strength on plate height, H, for PS latex beads of various sizes. No general trend in H with ionic strength was observed. It seems there is no correlation between H and the ionic strength of the carrier liquid in the tested range.

4.3. Effect of viscosity

In accordance with Eq. (4), lift force increases with increasing viscosity of the carrier liquid, and thus the retention ratio is also expected to increases. Fig. 7 shows the effect of the carrier viscosity on retention ratio of PS latex beads at various flow rates. It can be seen that, at all flow rates, the retention ratio generally increases with increasing carrier viscosity, as expected. At the carrier viscosity near 1, retention ratios are high due to repulsive interaction between particles and the channel bottom as mentioned earlier. Fig. 8 shows δ_{eq} determined for 20 μm PS latex beads from the data in Fig. 7. As expected, δ_{eq} tends to increase with the carrier viscosity at relatively higher range of the carrier viscosity. Fig. 9 shows again that there is no general trend in H with the carrier viscosity.

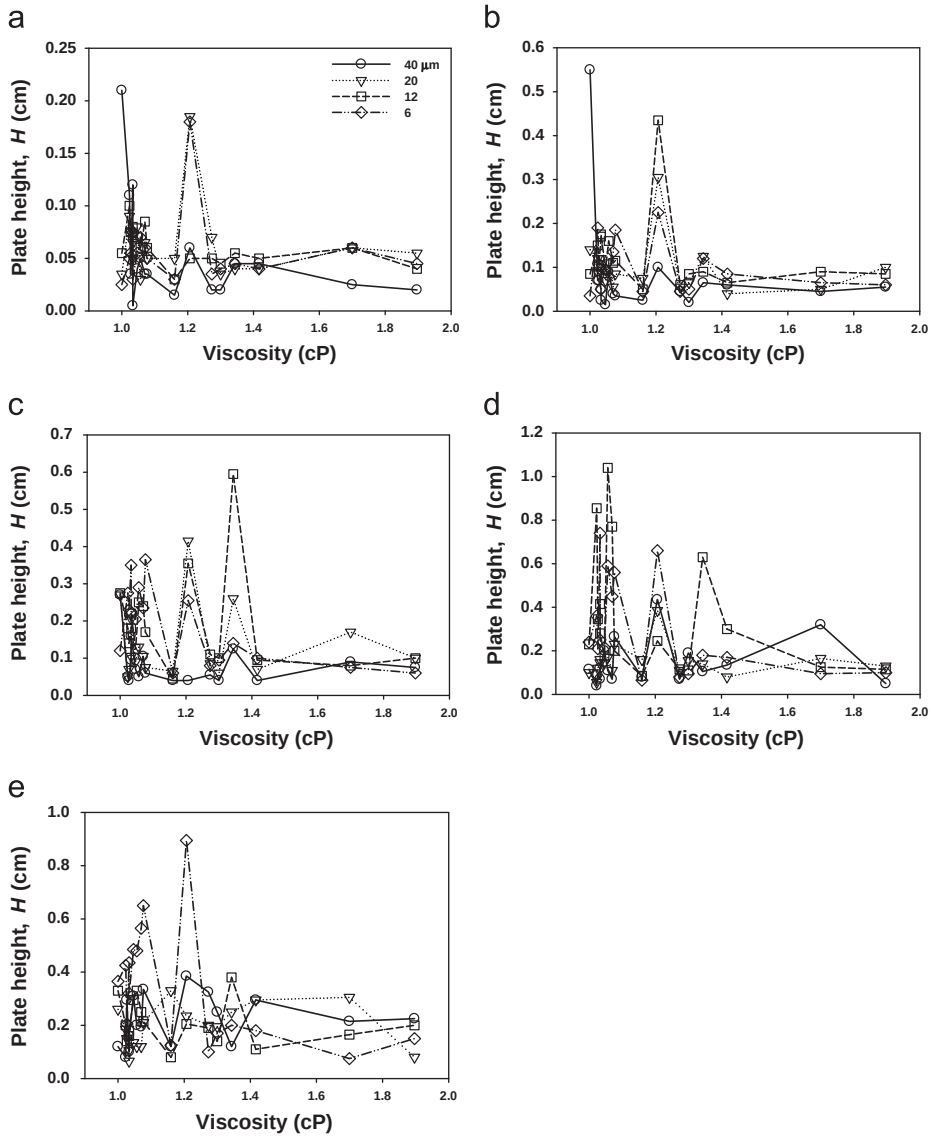


Fig. 9. Effect of viscosity of carrier liquid on plate height (H) of PS beads in GrFFF at flow rate of 0.5 (a), 1 (b), 2 (c), 3 (d) and 4 mL/min (e), respectively.

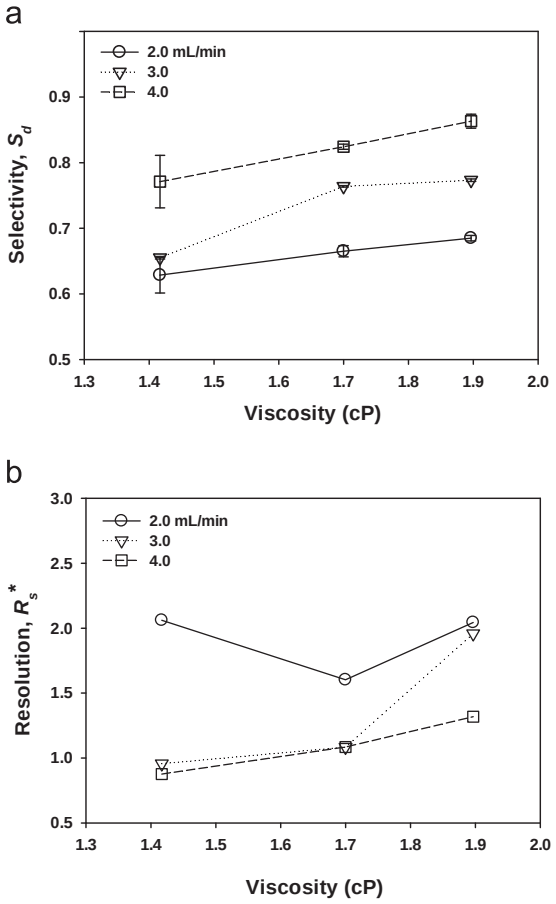


Fig. 10. Effect of viscosity on selectivity (S_d) and resolution (R_s^*) of PS latex beads in GrFFF observed at various flow rates.

Fig. 10(a) and (b) show effects of the carrier viscosity on selectivity (S_d) and resolution (R_s^*), respectively. As shown in Fig. 10(a), the selectivity increases with increasing viscosity of the carrier liquid in the flow rate range of 2–4 mL/min. At flow rates lower than 2 mL/min, the trend was not clear (data are not shown). In Fig. 10(b), the resolution (calculated from Eq. (7)) also increases with increasing carrier viscosity at relatively higher range of the carrier viscosity. From Figs. 9 and 10, it can be concluded that improved resolution with increasing viscosity observed in this study is caused mainly by the improvement in selectivity with the carrier viscosity (not by the plate height).

5. Conclusion

Retention behavior of microparticles in gravitational field-flow fractionation (GrFFF) was studied in this study. It seems the ionic strength of the carrier liquid plays a critical role in determining the size-based selectivity, retention ratio, and plate height, thus the resolution of microparticles in GrFFF as well as the viscosity or the flow rate of the carrier liquid. The repulsive interaction between particles and between particles and the channel wall decreases as the ionic strength increases, allowing particles approach closer to the channel bottom, which results in increasing retention with increasing ionic strength. Results suggest that the resolution and the separation time could be improved in GrFFF by increasing the viscosity and by carefully adjusting the ionic strength of the carrier liquid.

Acknowledgments

The authors acknowledge the support provided by the National Research Foundation (NRF) of Korea (NRF-2014M2A8A5021929).

References

[1] M.N. Myers, Overview of field-flow fractionation, J. Microcolumn Sep. 9 (1997) 151–162.
[2] J. Janča, Field-flow fractionation: analytical and micropreparative methodology, Mikrochim. Acta 111 (1993) 135–162.
[3] R. Chantiwas, R. Beckett, K. Grudpan, Size-based speciation of iron in clay mineral particles by gravitational field-flow fractionation with electrothermal atomic absorption spectrometry, Spectrochim. Acta—Part B Atom. Spectrosc. 60 (2005) 109–116.
[4] J. Plocková, J. Chmelík, Different elution modes and field programming in gravitational field-flow fractionation: field programming using density and viscosity gradients, J. Chromatogr. A 1118 (2006) 253–260.
[5] J. Chmelík, Different elution modes and field programming in gravitational field-flow fractionationl. A theoretical approach, J. Chromatogr. A 845 (1999) 285–291.
[6] J. Plocková, J. Chmelík, Different elution modes and field programming in gravitational field-flow fractionation. 2. Experimental verification of the range of conditions for flow-rate and carrier liquid density programming, J. Chromatogr. A 868 (2000) 217–227.
[7] K.D. Caldwell, T.T. Nguyen, M.N. Myers, J.C. Giddings, Observations on anomalous retention in steric field-flow fractionation, Sep. Sci. Technol. 14 (1979) 935–946.
[8] P. Reschiglian, A. Zattoni, B. Roda, E. Michelini, A. Roda, Field-flow fractionation and biotechnology, Trends Biotechnol. 23 (2005) 475–483.
[9] J.C. Giddings, Field-flow fractionation: analysis of macromolecular, colloidal, and particulate materials, Science 260 (1993) 1456–1465.
[10] M.R. Park, D.Y. Kang, J. Chmelik, N. Kang, J.S. Kim, S. Lee, Different elution modes and field programming in gravitational field-flow fractionation. Effect of channel angle, J. Chromatogr. A 1209 (2008) 206–211.
[11] S. Rasouli, E. Assidjo, T. Chianéa, P.J.P. Cardot, Experimental design methodology applied to the study of channel dimensions on the elution of red blood cells in gravitational field flow fractionation, J. Chromatogr. B: Biomed. Sci. Appl. 754 (2001) 11–21.
[12] A. Bernard, B. Paulet, V. Colin, P.J.P. Cardot, Red blood cell separations by gravitational field-flow fractionation: instrumentation and applications, Trends Anal. Chem. 14 (1995) 266–273.
[13] A. Bernard, C. Bories, P.M. Loiseau, P.J.P. Cardot, Selective elution and purification of living *Trichomonas vaginalis* using gravitational field-flow fractionation, J. Chromatogr. B: Biomed. Appl. 664 (1995) 444–448.
[14] C. Contado, P. Reschiglian, S. Faccini, A. Zattoni, F. Dondi, Continuous split-flow thin cell and gravitational field-flow fractionation of wheat starch particles, J. Chromatogr. A 871 (2000) 449–460.
[15] J. Janoušková, M. Budinská, J. Plocková, J. Chmelík, Optimization of experimental conditions for the separation of small and large starch granules by gravitational field-flow fractionation, J. Chromatogr. A 914 (2001) 183–187.
[16] R. Chantiwas, R. Beckett, J. Jakmunee, I.D. McKelvie, K. Grudpan, Gravitational field-flow fractionation in combination with flow injection analysis or electrothermal AAS for size based iron speciation of particles, Talanta 58 (2002) 1375–1383.
[17] J.C. Giddings, M.N. Myers, K.D. Caldwell, J.W. Pav, Steric field-flow fractionation as a tool for the size characterization of chromatographic supports, J. Chromatogr. A 185 (1979) 261–271.
[18] P.S. Williams, M.H. Moon, Y. Xu, J.C. Giddings, Effect of viscosity on retention time and hydrodynamic lift forces in sedimentation/steric field-flow fractionation, Chem. Eng. Sci. 51 (1996) 4477–4488.
[19] J. Pazourek, J. Chmelik, Experimental study on the separation of silica gel supports by gravitational field-flow fractionation. II. Sample preparation, stop-flow procedure and overloading effect, J. Chromatogr. A 715 (1995) 259–265.
[20] J. Plocková, F. Matulík, J. Chmelík, Different elution modes and field programming in gravitational field-flow fractionation: IV. Field programming achieved with channels of non-constant cross-sections, J. Chromatogr. A 955 (2002) 95–103.
[21] J. Pazourek, J. Chmelik, Optimization of the separation of micron-sized latex particles by gravitational field-flow fractionation, Chromatographia 35 (1993) 591–596.
[22] S. Lee, D.Y. Kang, M. Park, P.S. Williams, Effect of carrier fluid viscosity on retention time and resolution in gravitational field-flow fractionation, Anal. Chem. 83 (2011) 3343–3351.
[23] R. Sanz, L. Puignou, P. Reschiglian, M.T. Galceran, Gravitational field-flow fractionation for the characterisation of active dry wine yeast, J. Chromatogr. A 919 (2001) 339–347.
[24] M.H. Moon, Effect of carrier solutions on particle retention in flow field-flow fractionation, Bull. Korean Chem. Soc. 16 (1995) 613–619.
[25] Y. Mori, K. Kimura, M. Tanigaki, Influence of particle-wall and particle-particle interactions on retention behavior in sedimentation field-flow fractionation, Anal. Chem. 62 (1990) 2668–2672.

[26] P.S. Williams, T. Koch, J.C. Giddings, Characterization of near-wall hydrodynamic lift forces using sedimentation field-flow fractionation, Chem. Eng. Commun. 111 (1992) 121–147.
[27] S. Lee, M.N. Myers, R. Beckett, J.C. Giddings, Particle separation and characterization by sedimentation/cyclical-field field-flow fractionation, Anal. Chem. 60 (1988) 1129–1135.
[28] M.H. Moon, J.C. Giddings, Extension of sedimentation/steric field-flow fractionation into the submicrometer range: size analysis of 0.2–15-μm metal particles, Anal. Chem. 64 (1992) 3029–3037.
[29] P. Reschiglian, G. Torsi, Determination of particle size distribution by gravitational field-flow fractionation: dimensional characterization of silica particles, Chromatographia 40 (1995) 467–473.
[30] S. Lee, J. Calvin Giddings, Experimental observation of steric transition phenomena in sedimentation field-flow fractionation, Anal. Chem. 60 (1988) 2328–2333.
[31] M.N. Myers, J.C. Giddings, Properties of the transition from normal to steric field-flow fractionation, Anal. Chem.® 54 (1982) 2284–2289.
[32] P.S. Williams, L. Seungho, J.C. Giddings, Characterization of hydrodynamic lift forces by field-flow fractionation. Inertial and near-wall lift forces, Chem. Eng. Commun. 130 (1994) 143–166.
[33] P.S. Williams, M.H. Moon, J.C. Giddings, Influence of accumulation wall and carrier solution composition on lift force in sedimentation/steric field-flow fractionation, Colloids Surf. Physicochem. Eng. Asp. 113 (1996) 215–228.
[34] J. Pazourek, K.G. Wahlund, J. Chmelík, Effect of flowrate and ionic strength on retention of nonporous micron-sized silica gel particles in gravitational field-flow fractionation, J. Microcolumn Sep. 8 (1996) 331–338.
[35] H.J. Sant, B.K. Gale, Geometric scaling effects on instrumental plate height in field flow fractionation, J. Chromatogr. A 1104 (2006) 282–290.
[36] H.J. Sant, W.K. Jung, B.K. Gale, Reduction of end effect-induced zone broadening in field-flow fractionation channels, Anal. Chem. 78 (2006) 7978–7985.
[37] J. Pazourek, E. Urbankova, J. Chmelik, Experimental study on the separation of silica gel supports by gravitational field-flow fractionation, J. Chromatogr. A 660 (1994) 113–118.
[38] S. Lee, P.O. Nilsson, G.S. Nilsson, K.G. Wahlund, Development of asymmetrical flow field-flow fractionation-multi angle laser light scattering analysis for molecular mass characterization of cationic potato amylopectin, J. Chromatogr. A 1011 (2003) 111–123.

Talanta

The International Journal of Pure and Applied Analytical Chemistry

Aims & Scope

Talanta provides a forum for the publication of original research papers, preliminary communications, and critical reviews in all branches of pure and applied analytical chemistry. Papers are evaluated based on established guidelines, including the fundamental nature of the study, scientific novelty, substantial improvement or advantage over existing technology or methods, and demonstrated analytical applicability. Original research papers on fundamental studies, and novel sensor and instrumentation development, are especially encouraged. Novel or improved applications in areas such as clinical and biological chemistry, environmental analysis, geochemistry, and materials science and engineering are welcome.

Analytical performance of methods should be determined, including interference and matrix effects, and methods should be validated by comparison with a standard method, or analysis of a certified reference material. The developed method should especially comprise information on selectivity, sensitivity, detection limits, accuracy, and reliability. However, applying official validation or robustness studies to a routine method or technique does not necessarily constitute novelty. Proper statistical treatment of the data should be provided. Relevant literature should be cited, including related publications by the authors, and authors should discuss how their proposed methodology compares with previously reported methods.

Since classical spectrophotometric measurements and applications (including derivative spectrophometry), fluorimetry, solvent extraction, titrimetry, chemometrics, etc. are well established and are considered routine analytical methods, studies in such areas should demonstrate a unique and substantial advantage over presently known systems. New reagents or systems should demonstrate clear advantage, and their presentation should be comprehensive rather than generating a series of similar papers for several analytes or similar reagents. Modifications of reagents should demonstrate significant improvements. Obvious application of known chemistries or methods to established instrumental techniques are discouraged.

Application of established analytical approaches to relatively simple matrices having no major interferences, such as pharmaceutical preparations, are discouraged unless considerable improvements over other methods in the literature are demonstrated. Papers dealing with analytical data such as stability constants, pK_a values, etc. should be submitted to more specific journals, unless novel analytical methodology is demonstrated, or important analytical data are provided which could be useful in the development of analytical procedures.

Editors-in-Chief

Professor G.D. Christian, University of Washington, Department of Chemistry, 36 Bagely Hall, P.O. Box 351700, Seattle,WA 98195-1700, U.S.A.

Professor J.-M. Kauffmann, Université Libre de Bruxelles (ULB), Faculty of Pharmacy, Campus Plaine CP 205/6, Boulevard du Triomphe, B-1050 Brussels, Belgium, Fax: +32 2 650 5225, Tel: +32 2 650 5215, Email: talanta@ulb.ac.be

Associate Editors

Professor J.-H. Wang, Research Center for Analytical Sciences, Northeastern University, Box 332, Shenyang 110004, China

Professor J.L. Burguera, Los Andes University, IVAIQUIM, Faculty of Sciences, P.O. Box 542, 5101-A Mérida, Venezuela.

Dr Ian McKelvie, School of Chemistry, The University of Melbourne, Victoria 3010, Australia, Phone: +61 3 8344 6567, Email: ian.mckelvie@gmx.com.

Assistant Editors

Dr R.E. Synovec, Department of Chemistry, University of Washington, Box 351700, Seattle, WA 98195-1700, U.S.A.

Ms. Dominique (D.) Mertens, Université Libre de Bruxelles, Faculty of Pharmacy, Service de Chimie Analytique Instrumentale et, Bioélectrochimie, Campus Plaine CP 205/6, Boulevard du Triomphe - B-1050 Brussels, Belgium, Email: dmertens@ulb.ac.be, Tél : +32 (0)2 650 52 47, Fax : +32 (0)2 650 52 25

Talanta

R. Apak (Istanbul, Turkey)
E. Bakker (Auburn, AL, U.S.A.)
D. Barceló (Barcelona, Spain)
B. Birch (Luton, UK)
J.-L. Capelo-Martinez (Caparica, Portugal)
O. Chailapakul (Thailand)
D.S. Chung (Seoul, Korea)
S. Cosnier (Grenoble, France)
M. del Valle (Barcelona, Spain)
A.A. Galal (Giza, Egypt)
A.G. Gonzales (Seville, Spain)
M. Hernandez-Cordoba (Spain)
P. Hubert (Liège, Belgium)
J. Kalivas (Pocatella, ID, U.S.A.)
A.A. Karyakin (Moscow, Russia)
S. Kolev (Melbourne, Australia)
J.-M. Lin (Beijing, China)
S. Motomizu (Okayama, Japan)
R. Niessner (München, Germany)
J.A. Nobrega (São Carlos, SP, Brazil)
A.C. Olivieri (Rosario, Argentina)
S. Ozkan (Ankara, Turkey)
J.-M. Pingarron (Madrid, Spain)
M.D. Porter (Salt Lake City, UT, U.S.A.)
V. Remcho (Corvallis, OR, U.S.A.)
M. Shamsipur (Kermanshah, Iran)
Y.-H. Shao (Beijing, China)
P. Solich (Hradec Králové, Czech Republic)
D.G. Themelis (Thessaloniki, Greece)
K. Thurbide (Calgary, AB, Canada)
T. Toyo'oka (Shizuoka, Japan)
D.L. Tsalev (Sofia, Bulgaria)
B. Walczak (Katowice, Poland)
J. Wang (Tempe, AZ, U.S.A.)
J.D. Winefordner (Gainesville, FL, U.S.A.)
X.-H. Xia (Nanjing, China)
X.-P. Yan (Tianjin, China)
E.A.G. Zagatto (Piracicaba, SP, Brazil)
X. Zhang (Beijing, China)

Copyright © 2014 Elsevier B.V. All rights reserved

Talanta

The International Journal of Pure and Applied Analytical Chemistry

Editors-in-Chief

Professor G.D. Christian, University of Washington, Department of Chemistry, 36 Bagely Hall, P.O. Box 351700, Seattle, WA 98195-1700, U.S.A.

Professor J.-M. Kauffmann, Université Libre de Bruxelles (ULB), Faculty of Pharmacy, Campus Plaine CP 205/6, Boulevard du Triomphe, B-1050 Brussels, Belgium, Fax: +32 2 650 5225, Tel: +32 2 650 5215, Email: talanta@ulb.ac.be

Associate Editors

Professor J.-H. Wang, Research Center for Analytical Sciences, Northeastern University, Box 332, Shenyang 110004, China
Professor J.L. Burguera, Los Andes University, IVAIQUIM, Faculty of Sciences, P.O. Box 542, 5101-A Mérida, Venezuela
Dr Ian McKelvie, School of Chemistry, The University of Melbourne, Victoria 3010, Australia, Phone: +61 3 8344 6567, Email: ian.mckelvie@gmx.com

Assistant Editors

Dr R.E. Synovec, Department of Chemistry, University of Washington, Box 351700, Seattle, WA 98195-1700, U.S.A.
Ms. Dominique (D.) Mertens, Université Libre de Bruxelles, Faculty of Pharmacy, Service de Chimie Analytique Instrumentale et, Bioélectrochimie, Campus Plaine CP 205/6, Boulevard du Triomphe - B-1050 Brussels, Belgium, Email: dmertens@ulb.ac.be, Tél : +32 (0)2 650 52 47, Fax : +32 (0)2 650 52 25

Advisory Board

Chairman: Professor J.D. Winefordner, Gainesville, FL, U.S.A.

Talanta

R. Apak (Istanbul, Turkey)
E. Bakker (Auburn, AL, U.S.A.)
D. Barceló (Barcelona, Spain)
B. Birch (Luton, UK)
J.-L. Capelo-Martinez (Caparica, Portugal)
O. Chailapakul (Thailand)
D.S. Chung (Seoul, Korea)
S. Cosnier (Grenoble, France)
M. del Valle (Barcelona, Spain)
A.A. Galal (Giza, Egypt)
A.G. Gonzales (Seville, Spain)
M. Hernandez-Cordoba (Spain)
P. Hubert (Liège, Belgium)
J. Kalivas (Pocatella, ID, U.S.A.)
A.A. Karyakin (Moscow, Russia)
S. Kolev (Melbourne, Australia)
J.-M. Lin (Beijing, China)
S. Motomizu (Okayama, Japan)
R. Niessner (München, Germany)
J.A. Nobrega (São Carlos, SP, Brazil)
A.C. Olivieri (Rosario, Argentina)
S. Ozkan (Ankara, Turkey)
J.-M. Pingarron (Madrid, Spain)
M.D. Porter (Salt Lake City, UT, U.S.A.)
V. Remcho (Corvallis, OR, U.S.A.)
M. Shamsipur (Kermanshah, Iran)
Y.-H. Shao (Beijing, China)
P. Solich (Hradec Králové, Czech Republic)
D.G. Themelis (Thessaloniki, Greece)
K. Thurbide (Calgary, AB, Canada)
T. Toyo'oka (Shizuoka, Japan)
D.L. Tsalev (Sofia, Bulgaria)
B. Walczak (Katowice, Poland)
J. Wang (Tempe, AZ, U.S.A.)
J.D. Winefordner (Gainesville, FL, U.S.A.)
X.-H. Xia (Nanjing, China)
X.-P. Yan (Tianjin, China)
E.A.G. Zagatto (Piracicaba, SP, Brazil)
X. Zhang (Beijing, China)

Volume 132(2015)



ELSEVIER Amsterdam – Boston – London – New York – Oxford – Paris – Philadelphia – San Diego – St. Louis